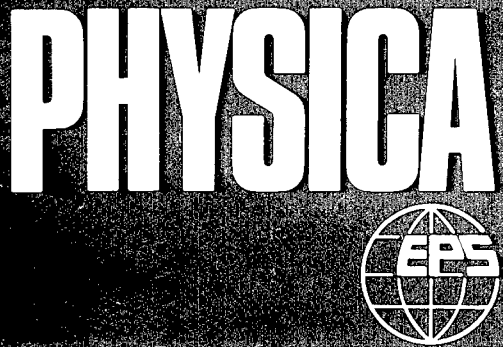


VOLUMES 308–310
DECEMBER III 2001

ISSN 0921–4526



B

CONDENSED MATTER



Proceedings of the 21st International
Conference on Defects in
Semiconductors

ICDS–21

held in Giessen, Germany
16–20 July 2001

Guest Editor:
D.M. Hofmann

20020531 090

NORTH-HOLLAND

<http://www.elsevier.com/locate/physb>

PHYSICA B

An interdisciplinary journal of research on condensed matter

Editors:

F.R. de Boer, Van der Waals Zeeman Laboratory, Valckenierstraat 65, 1018 XE Amsterdam, The Netherlands

Telefax: + 31-20-699 4800; e-mail: frb@phys.uva.nl

L. Degiorgi, Solid State Physics Laboratory, HPF-F3/F1 ETH-Zürich, CH-8093 Zürich, Switzerland

Telefax: + 41-1-633-1072; e-mail: degiorgi@solid.phys.ethz.ch

Z. Fisk, National Magnetic Field Laboratory, 1800 E. Paul Dirac Street, Tallahassee, FL 32306-4005, USA

Telefax: + 1-505-665 2992. Editorial office e-mail: phys.let@tdo-serv.lanl.gov

R. Jochemsen, Kamerlingh Onnes Laboratorium, Rijksuniversiteit Leiden, P.O. Box 9504, 2300 RA Leiden, The Netherlands

Telefax: + 31-71-527-5404; e-mail: reyer@phys.leidenuniv.nl

Advisory editorial board:

A.O.E. Animalu, Lagos

R. Blinc, Ljubljana

R. de Bruyn Ouboter, Leiden

R. Coehoorn, Eindhoven

J. Flouquet, Grenoble

A.J. Freeman, Evanston, IL

H. Fujii, Hiroshima

P. Fulde, Stuttgart

T. Goto, Tokyo

T. Hicks, Monash

C. Janot, Grenoble

G. Kido, Tsukuba

M. Krusius, Helsinki

G.H. Lander, Karlsruhe

J.J. van Loef, Delft

J.C. Maan, Nijmegen

Y. Onuki, Osaka

F.M. Peeters, Antwerp

A. Polman, Amsterdam

C. Rudowicz, Hong Kong Sar

T. Satoh, Sendai

V. Sechovsky, Prague

G. Solt, Villigen

F. Steglich, Darmstadt

M.A. Strzhemechny, Kharkov

G. van Tendeloo, Antwerp

M. Tosi, Pisa

R. Tournier, Grenoble

P. Wachter, Zürich

P.R. Wyder, Grenoble

Aims and scope

Physica B (Condensed Matter) contains papers and review articles in the realm of physics of condensed matter. Both experimental and theoretical contributions are invited, although theoretical papers should preferably be related to experimental results.

Abstracted/indexed in:

Current Contents: Physical, Chemical and Earth Sciences; *Aluminium Industry Abstracts*, *EI Compendex Plus*, *Engineered Materials Abstracts*, *Engineering Index*, *INSPEC*, *Metals Abstracts*, *Physics Briefs*.

Subscription information

Physica B (ISSN 0921-4526) is published monthly. For 2001, volumes 291–306 are scheduled for publication. Subscription prices are available upon request from the Publisher. A combined subscription with *Physica A*, *Physica C*, *Physica D* and *Physica E* is available at a reduced rate.

Subscriptions are accepted on a prepaid basis only and are entered on a calendar year basis. Issues are sent by surface mail except to the following countries where air delivery via SAL is ensured: Argentina, Australia, Brazil, Canada, China, Hong Kong, India, Israel, Japan, Malaysia, Mexico, New Zealand, Pakistan, Singapore, South Africa, South Korea, Taiwan, Thailand, USA. For all other countries air mail rates

are available upon request. Please address all enquiries regarding orders and subscriptions to:

Elsevier Science B.V.

Customer Support Department

P.O. Box 211, 1000 AE Amsterdam

The Netherlands

Telephone: + 31-20-485 3757; Telefax: + 31-20-485 3432

Claims for issues not received should be made within six months of our publication (mailing) date.

Author enquiries

For enquiries relating to the submission of articles (including electronic submission), the status of the accepted articles through our Online Article Status Information System (OASIS), author Frequently Asked Questions and any other enquiries relating to Elsevier Science, please consult <http://www.elsevier.com/locate/authors/>

For specific enquiries on the preparation of electronic artwork, consult <http://www.elsevier.com/locate/authorartwork/>

Contact details for questions arising after acceptance of an article, especially those relating to proofs, are provided when an article is accepted for publication.

US Mailing Notice

Physica B (ISSN 0921-4526) is published monthly by Elsevier Science, Molenwerf 1, P.O. Box 211, 1000 AE Amsterdam, The Netherlands. The annual subscription price in the USA is US\$ 4961 (valid in North, Central and South America only), including air speed delivery. Periodicals postage paid at Jamaica, NY 11431.

USA postmasters: Send address changes to *Physica B*, Publications Expediting Inc., 200 Meacham Avenue, Elmont, NY 11003.

Airfreight and mailing in the USA by Publications Expediting Inc., 200 Meacham Avenue, Elmont, NY 11003.

© The paper used in this publication meets the requirements of ANSI/NISO Z39.48-1992 (Permanence of Paper).



North-Holland, an imprint of Elsevier Science

Printed in The Netherlands

REPORT DOCUMENTATION PAGE				Form Approved OMB No. 0704-0188	
<small>Public reporting burden for this collection of information is estimated to average 1 hour per response, including the time for reviewing instructions, searching existing data sources, gathering and maintaining the data needed, and completing and reviewing the collection of information. Send comments regarding this burden estimate or any other aspect of this collection of information, including suggestions for reducing the burden, to Department of Defense, Washington Headquarters Services, Directorate for Information Operations and Reports (0704-0188), 1215 Jefferson Davis Highway, Suite 1204, Arlington, VA 22202-4302. Respondents should be aware that notwithstanding any other provision of law, no person shall be subject to any penalty for failing to comply with a collection of information if it does not display a currently valid OMB control number.</small> PLEASE DO NOT RETURN YOUR FORM TO THE ABOVE ADDRESS.					
1. REPORT DATE (DD-MM-YYYY) 29-03-2002		2. REPORT TYPE Conference Proceedings		3. DATES COVERED (From - To) 16 July 2001 - 21 July 2001	
4. TITLE AND SUBTITLE 21st International Conference on Defects in Semiconductors Physica B Condensed Matter, Vol. 308-310, December 2001				5a. CONTRACT NUMBER F61775-01-WF066	
				5b. GRANT NUMBER	
				5c. PROGRAM ELEMENT NUMBER	
				5d. PROJECT NUMBER	
6. AUTHOR(S) Conference Committee				5d. TASK NUMBER	
				5e. WORK UNIT NUMBER	
7. PERFORMING ORGANIZATION NAME(S) AND ADDRESS(ES) University of Paderborn Warburger Str. 100A Paderborn D-33098 Germany				8. PERFORMING ORGANIZATION REPORT NUMBER N/A	
9. SPONSORING/MONITORING AGENCY NAME(S) AND ADDRESS(ES) EOARD PSC 802 BOX 14 FPO 09499-0014				10. SPONSOR/MONITOR'S ACRONYM(S)	
				11. SPONSOR/MONITOR'S REPORT NUMBER(S) CSP 01-5066	
12. DISTRIBUTION/AVAILABILITY STATEMENT Approved for public release; distribution is unlimited.					
13. SUPPLEMENTARY NOTES					
14. ABSTRACT The Final Proceedings for 21st International Conference on Defects in Semiconductors, 16 July 2001 - 21 July 2001 This is an interdisciplinary conference. Topics include defects in important semiconductor and crystalline materials such as silicon, SiC, and diamond, as well as the theory of impurity centers, and diagnostic and fabrication techniques.					
15. SUBJECT TERMS EOARD, Electronic Devices, Materials, Solid state lasers					
16. SECURITY CLASSIFICATION OF:			17. LIMITATION OF ABSTRACT UL	18. NUMBER OF PAGES 1242	19a. NAME OF RESPONSIBLE PERSON Alexander J. Glass, Ph. D.
a. REPORT UNCLAS	b. ABSTRACT UNCLAS	c. THIS PAGE UNCLAS			19b. TELEPHONE NUMBER (Include area code) +44 (0)20 7514 4950

PHYSICA B

ADVISORY EDITORIAL BOARD:

A.O.E. Animalu, Lagos
R. Blinc, Ljubljana
R. de Bruyn Ouboter, Leiden
R. Coehoorn, Eindhoven
J. Flouquet, Grenoble
A.J. Freeman, Evanston, IL
H. Fujii, Hiroshima
P. Fulde, Stuttgart
T. Goto, Tokyo
T. Hicks, Monash

C. Janot, Grenoble
G. Kido, Tsukuba
M. Krusius, Helsinki
G.H. Lander, Karlsruhe
J.J. van Loef, Delft
J.C. Maan, Nijmegen
Y. Onuki, Osaka
F.M. Peeters, Antwerp
A. Polman, Amsterdam
C. Rudowicz, Hong Kong Sar

T. Satoh, Sendai
V. Sechovsky, Prague
G. Solt, Villigen
F. Steglich, Darmstadt
M.A. Strzhemechny, Kharkov
G. van Tendeloo, Antwerp
M. Tosi, Pisa
R. Tournier, Grenoble
P. Wachter, Zürich
P.R. Wyder, Grenoble

VOLUME 308-310, 2001

PHYSICA B

CONDENSED MATTER

Editors:

F.R. DE BOER
L. DEGIORGI
Z. FISK
R. JOCHEMSEN

NORTH-HOLLAND

© 2001 Elsevier Science B.V. All rights reserved.

This journal and the individual contributions contained in it are protected by the copyright of Elsevier Science B.V., and the following terms and conditions apply to their use:

Photocopying

Single photocopies of single articles may be made for personal use as allowed by national copyright laws. Permission of the Publisher and payment of a fee is required for all other photocopying, including multiple or systematic copying, copying for advertising or promotional purposes, resale, and all forms of document delivery. Special rates are available for educational institutions that wish to make photocopies for non-profit educational classroom use.

Permissions may be sought directly from Elsevier Science Global Rights Department, PO Box 800, Oxford OX5 1DX, UK; phone: (+44) 1865 843830, fax: (+44) 1865 853333, e-mail: permissions@elsevier.co.uk. You may also contact Global Rights directly through Elsevier's home page (<http://www.elsevier.com>), selecting first 'Customer Support', then 'General Information', then 'Permissions Query Form'.

In the USA, users may clear permissions and make payment through the Copyright Clearance Center Inc., 222 Rosewood Drive, Danvers, MA 01923, USA; phone: (978) 7508400; fax: (978) 7504744, and in the UK through the Copyright Licensing Agency Rapid Clearance Service (CLARCS), 90 Tottenham Court Road, London W1P 0LP, UK; phone (+44) 20 7631 5555, fax: (+44) 20 7631 5500. Other countries may have a local reprographic rights agency for payments.

Derivative works

Subscribers may reproduce tables of contents or prepare lists of articles including abstracts for internal circulation within their institutions.

Permission of the Publisher is required for resale or distribution outside the institution.

Permission of the Publisher is required for all other derivative works, including compilations and translations.

Electronic storage or usage

Permission of the Publisher is required to store electronically any material contained in this journal, including any article or part of an article. Contact the Publisher at the address indicated.

Except as outlined above, no part of this publication may be reproduced, stored in a retrieval system or transmitted in any form or by any means, electronic, mechanical, photocopying, recording or otherwise, without prior written permission of the Publisher.

Address permissions request to: Elsevier Science Global Rights Department, at the mail, fax and e-mail addresses noted above.

Notice

No responsibility is assumed by the Publisher for any injury and/or damage to persons or property as a matter of products liability, negligence or otherwise, or from any use or operation of any methods, products, instructions or ideas contained in the material herein. Although all advertising material is expected to conform to ethical (medical) standards, inclusion in this publication does not constitute a guarantee or endorsement of the quality or value of such product or of the claims made of it by its manufacturer.

☺ The paper used in this publication meets the requirements of ANSI/NISO Z39.48-1992 (Permanence of Paper).

Proceedings of the 21st International Conference on Defects in Semiconductors



ICDS-21

held in Giessen, Germany
16-20 July 2001

Guest Editor:

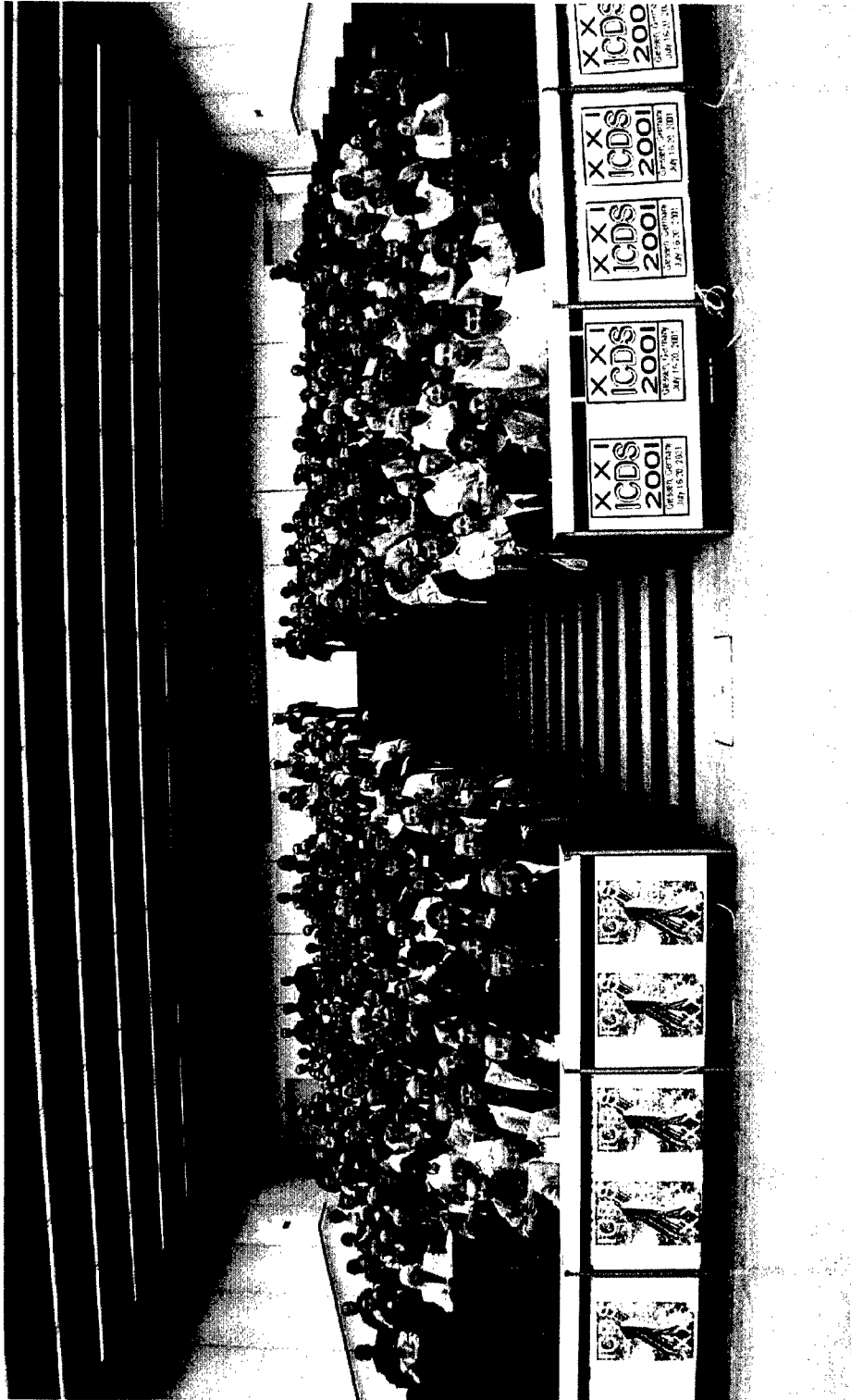
Detlev M. Hofmann

*I. Physikalisches Institut
Justus-Liebig-Universität
Heinrich-Buff-Ring 16
D-35392 Giessen
Germany*



ELSEVIER

AQ F02-08-1612



Preface and Acknowledgements

These are the proceedings of the 21st International Conference on Defects in Semiconductors, ICDS-21, which was held at the Justus-Liebig University of Giessen, Germany, between July 16–20, 2001. The ICDS had not been held in Germany since 1974, when it took place in Freiburg under the chairmanship of Prof. A. Seeger (ICDS-8). Since then the ICDS has been held every two years in the USA, Japan or Europe. Compared to the two preceding conferences in Aveiro, Portugal (1997) and in Berkeley, USA (1999), the conference in Giessen expanded considerably as to the number of participants as well as contributions, demonstrating that the field is timely, active and striving.

In Giessen there were 350 registered participants from 40 countries with strong representations from Germany (88), Japan (51), USA (36), Russia (27), Great Britain (20), Ukraine (17) and Poland (11). The rather large number of participants from Eastern European countries was made possible by special support given to the ICDS by the Deutsche Forschungsgemeinschaft, the University of Paderborn, the University Society of Giessen, the USA (Air Force, Navy) and many other institutions and industrial firms. Without that support, which is gratefully acknowledged, the participation of so many Eastern Europeans and also of many young scientists would not have been possible.

At the conference four plenary talks were delivered on the first day, followed by 86 oral contributions in two parallel sessions and 272 posters in two poster sessions as well as 8 “late news” posters, bringing the total number of accepted contributions to 384.

The poster sessions were held after the oral afternoon session later in the afternoon and into the evening with plenty of space also for small discussion groups at tables in the large hall between the lecture theatres. There was ample food and drink available during the poster sessions so that most delegates stayed much longer than the official time, having and enjoying intense and lively discussions.

The scientific scope was wider than before in that, apart from more traditional silicon problems and a strong representation of group III-nitrides, ZnO appeared as a new focus and the silicon carbide community concerned with defects found its way to the ICDS for the first time in larger numbers. Two of the plenary talks were on theory of defects reflecting the trend that theory has made much progress during the last years to provide almost an “instrumental” arm to defect studies. The other two were on applications of the knowledge on impurity diffusion in SiGe to produce world-record-fast devices and on a historical view into ZnO, which all of a sudden is experiencing an enormous revival.

The proceedings will again be published in an archival journal, *Physica B*, following the preceding ICDS. All papers were refereed during the conference, an enormous task, for which the organizers would like to thank the many referees, but also the vast majority of delegates who delivered their papers at the beginning of the conference. Special thanks to Dr. D. Hofmann who took care of the Proceedings.

It gives us great pleasure to thank the members of the International Advisory and Programme committees for their active advice and input into the programme. We thank in particular those members of the Programme Committee (Profs. Emtsev, Jantsch, Nielsen and Stutzmann) who came to Giessen for two days to help to shape the final programme. We also thank the session chairs for their help to keep the sessions on time and to ensure good discussions.

We owe the smooth running and the harmonious atmosphere at the conference to the many members of the Giessen physics department who worked with so much enthusiasm in the local conference team under

the guidance of the conference secretary, Dr. A. Hofstätter, and the supervision of the treasurer, Dr. E. Pitt. A big thankyou to all of you.

Last but not least we would like to thank all the attendees for making this another exciting conference and for conveying us the optimistic feeling that the next conference in this series will be as lively and interesting as this one was.

Bruno K. Meyer, *Chair*
Johann-Martin Spaeth, *Chair*

Conference Information

International Steering Committee

Gordon Davis, UK
Eugene E. Haller, USA
Bruno K. Meyer, Germany
M. Helena Nazare, Portugal
J. Martin Spaeth, Germany
Michael Stavola, USA

International Advisory Committee

F. Danie Aurret, South Africa
Brian Bech Nielsen, Denmark
Maria J. Caldas, Brazil
Jim Chadi, USA
Vadim V. Emtsev, Russia
Wolfgang Jantsch, Austria
Hiroshi Katayama-Yoshida, Japan
Lionel C. Kimerling, USA
Jerzy Langer, Poland
Masashi Mizuta, Japan
Ron Newman, UK
Martin Stutzmann, Germany
Chris Van de Walle, USA
George Watkins, USA
Jörg Weber, Germany

Programme Committee

Brian Bech Nielsen, Denmark
Marilia J. Caldas, Brazil
Leszek Dobaczewski, Poland
Vadin V. Emtsev, Russia
Stewart Goodman, South Africa
Eugene E. Haller, USA
Wolfgang Jantsch, Austria
Alexander Kaplyanskii, Russia
Thomas A. Kennedy, USA
Bruno K. Meyer, Germany
Masashi Mizuta, Japan
Yasunori Mochizuki, Japan
Bo Monemar, Sweden
Anthony R. Peaker, United Kingdom
Johann-Martin Spaeth, Germany
Martin Stutzmann, Germany
Wladyslaw Walukiewicz, USA

Corbett Prize Winners

S. Goennenwein (Munich)
B. Hourahine (Exeter)
Y.-S. Kim (Taejon)

Local Organizers

Secretary

Albrecht Hofstaetter, Univ. Giessen

Treasurer

Eberhard Pitt

Local Arrangements, Public Relation and Sponsoring

Arthur Scharmann, Univ. Giessen
Dietrich Schwabe, Univ. Giessen
Willi Kriegseis, Univ. Giessen

Transportation

Helge E. Höchsmann, Univ. Giessen

Secretaries at the registration

Anja Denhardt, Univ. Giessen
Daniela Musaeus, Univ. Giessen

Arrangements for accompanying persons

Gundel Hofstaetter, Giessen
Marion Meyer, Giessen
Anne Spaeth, Paderborn

Session Chairs

C. Ammerlaan
F.D. Aurret
B. Bech Nielson
M.J. Caldas
J. Chadi
B. Clerjeaud
G. Davis
V.V. Emtsev
S. Goodman
E.E. Haller
R. Helbig
R. Jones
H. Katayama-Yoshida
V. Kisielowski
R. Newman
O. Pankratov
G. Pensl
M. Stavola
M. Stutzman
C. Van de Walle
K. Wada
W. Walukiewicz
E. Weber
J. Weber

Supporters of ICDS-21

The following supporters of ICDS-21 are gratefully acknowledged:

European Office of Aerospace Research & Development (EOARD)
Airforce Office of Scientific Research
Unites States Air Force Research Laboratory
US Office of Naval Research
International Field Office London
Deutsche Forschungsgemeinschaft
Deutsche Physikalische Gesellschaft
Wilhelm und Else Heraeus Stiftung
Universität Paderborn
Gießener Hochschulgesellschaft
Lambda Physik
Semikron
Schunk
Pfeiffer Vacuum
AIXTRON
Unaxis
Freiberger Compound Materials
Infineon
Messer
Karstadt
Xerox
Leica Microsystems

Contents

Conference Photograph	vi
Preface and Acknowledgements	vii
Conference Information	ix
Supporters of ICDS-21	x
1. Plenary papers	
The fascinating dynamics of defects in silicon S.K. Estreicher, P.A. Fedders and P. Ordejón	1
Thermal double donors in Si and Ge R. Jones, J. Coutinho, S. Öberg and P.R. Briddon	8
Misfortune, challenge, and success: defects in processed semiconductor devices H. Cerva, M. Engelhardt, M. Hierlemann, M. Pölzl and T. Thenikl	13
2. Gallium nitride	
<i>2.1. Doping</i>	
Optical study of GaN:Mn co-doped with Mg grown by metal organic vapor phase epitaxy R.Y. Korotkov, J.M. Gregie, B. Han and B.W. Wessels	18
Photoluminescence and lattice location of Eu and Pr implanted GaN samples T. Monteiro, C. Boemare, M.J. Soares, R.A. Sá Ferreira, L.D. Carlos, K. Lorenz, R. Vianden and E. Alves	22
Investigation of the defect structure of GaN heavily doped with oxygen R.Y. Korotkov, F. Niu, J.M. Gregie and B.W. Wessels	26
Mn-related absorption and PL bands in GaN grown by metal organic vapor phase epitaxy R.Y. Korotkov, J.M. Gregie and B.W. Wessels	30
Photoluminescence properties of Er doped GaN H. Przybylińska, A. Kozanecki, V. Glukhanyuk, W. Jantsch, D.J. As and K. Lischka	34
Compensation mechanism in MOCVD and MBE grown GaN:Mg H. Alves, M. Böhm, A. Hofstaetter, H. Amano, S. Einfeldt, D. Hommel, D.M. Hofmann and B.K. Meyer	38
Green and red emission in Ca implanted GaN samples T. Monteiro, C. Boemare, M.J. Soares, E. Alves and C. Liu	42
Study of dopant activation in bulk GaN:Mg R. Piotrkowski, E. Litwin-Staszewska, T. Suski and I. Grzegory	47

2.2. Point and extended defects

Magnetic resonance studies of defects in GaN with reduced dislocation densities E.R. Glaser, J.A. Freitas Jr., G.C. Braga, W.E. Carlos, M.E. Twigg, A.E. Wickenden, D.D. Koleske, R.L. Henry, M. Leszczynski, I. Grzegory, T. Suski, S. Porowski, S.S. Park, K.Y. Lee and R.J. Molnar	51
Radiation-induced defects in n-type GaN and InN V.V. Emtsev, V.Yu. Davydov, E.E. Haller, A.A. Klochikhin, V.V. Kozlovskii, G.A. Oganessian, D.S. Poloskin, N.M. Schmidt, V.A. Vekshin and A.S. Usikov	58
A radiation-produced defect in GaN displaying hyperfine structure with three Ga atoms G.D. Watkins, L.S. Vlasenko and C. Bozdog	62
Electron paramagnetic resonance of GaN detected by recombination afterglow U. Rogulis, S. Schweizer and J.-M. Spaeth	66
Defect-related noise in AlN and AlGaIn alloys S.T.B. Goennenwein, R. Zeisel, S. Baldovino, O. Ambacher, M.S. Brandt and M. Stutzmann	69
Positively charged muonium centers in aluminum and gallium nitrides R.L. Lichti, S.F.J. Cox, E.A. Davis, B. Hitti and S.K.L. Sjuue	73
Ga vacancies in electron irradiated GaN: introduction, stability and temperature dependence of positron trapping K. Saarinen, T. Suski, I. Grzegory and D.C. Look	77
Influence of defects in low-energy nitrogen ion beam assisted gallium nitride thin film deposition J.W. Gerlach, S. Sienz, W. Attenberger and B. Rauschenbach	81
ODEPR and yellow luminescence intensity in GaN under high pressure K. Michael, U. Rogulis, F.K. Koschnick, Th. Tröster, J.-M. Spaeth, B. Beaumont and P. Gibart	85
Investigation of structural defects of thick GaN grown by flow-modulated hydride vapor-phase epitaxy W. Zhang, H.R. Alves, T. Riemann, M. Heuken, P. Veit, D. Meister, W. Kriegseis, D.M. Hofmann, J. Christen and B.K. Meyer	89
Characterization of $\text{Al}_x\text{Ga}_{1-x}\text{N}$ layers grown by molecular beam epitaxy H. Kim and T.G. Andersson	93
AFM study of lattice matched and strained InGaAsN layers on GaAs Y. Park, M.J. Cich, R. Zhao, P. Specht, H. Feick and E.R. Weber	98
In-plane and in-depth nonuniformities in defect distribution in GaN and InGaIn epilayers M. Godlewski, E.M. Goldys, G. Pozina, B. Monemar, K. Pakula, J.M. Baranowski, P. Prystawko and M. Leszczynski	102
Strain relaxation in $\text{GaN}_x\text{P}_{1-x}$ alloy: effect on optical properties I.A. Buyanova, W.M. Chen, E.M. Goldys, M.R. Phillips, H.P. Xin and C.W. Tu	106
Positron annihilation in AlN and GaN N.Yu. Arutyunov, V.V. Emtsev, A.V. Mikhailin and V.Yu. Davidov	110
Distribution of the lateral correlation length in GaN epitaxial layers J. Kozłowski, R. Paszkiewicz, R. Korbutowicz and M. Tlaczala	114

2.3. Impurities

The role of oxygen and hydrogen in GaN

- B. Clerjaud, D. Côte, C. Naud, R. Bouanani-Rahbi, D. Wasik, K. Pakula, J.M. Baranowski, T. Suski, E. Litwin-Staszewska, M. Bockowski and I. Grzegory 117

Hydrogen vibrational lines in HVPE GaN

- M.G. Weinstein, F. Jiang, M. Stavola, B.B. Nielsen, A. Usui and M. Mizuta 122

Properties of carbon as an acceptor in cubic GaN

- U. Köhler, M. Lübbbers, J. Mimkes and D.J. As 126

Electrically active defects in AlGaN alloys grown by metalorganic chemical vapor deposition

- D. Seghier and H.P. Gislason 130

3. Silicon

3.1. Hydrogen

Electronic levels of isolated and oxygen-perturbed hydrogen in silicon and migration of hydrogen

- K.B. Nielsen, L. Dobaczewski, S. Søgård and B.B. Nielsen 134

Piezospectroscopic analysis of the hydrogen-carbon complexes in silicon

- O. Andersen, L. Dobaczewski, A.R. Peaker, K.B. Nielsen, B. Hourahine, R. Jones, P.R. Briddon and S. Öberg 139

Formation mechanism of hydrogen-induced (1 1 1) platelets in silicon

- Y.-S. Kim and K.J. Chang 143

Vibrational properties of H-related defects in silicon

- J.M. Pruneda, J. Junquera, J. Ferrer, P. Ordejón and S.K. Estreicher 147

Structural properties of hydrogen-induced platelets in silicon: a Raman scattering study

- E.V. Lavrov and J. Weber 151

Quadruplevoids in amorphous Si:H

- T. Krüger and A.F. Sax 155

New hydrogen-related radiation-induced deep-level center in boron-doped silicon

- N. Yarykin, O. Feklisova and J. Weber 159

Fermi-level dependence of formation of hydrogen molecules in crystalline silicon

- K. Ishioka, N. Umehara, T. Mori, K. Ohtsuka, M. Kitajima, K. Murakami and S. Hishita 163

Defects agglomeration in the vicinity of hydrogen-related vacancy-type complexes in proton-implanted silicon

- S.Zh. Tokmoldin and B.N. Mukashev 167

Multivacancies trapping hydrogen molecules

- T. Mori, K. Otsuka, N. Umehara, K. Ishioka, M. Kitajima, S. Hishita and K. Murakami 171

Defect-related photoinduced absorption in amorphous silicon

- E. Morgado 174

Hydrogen-induced formation of defects nanoclusters in crystalline silicon

- Kh.A. Abdullin, Yu.V. Gorelinskii and B.N. Mukashev 178

Low-temperature photoluminescence characterization of defects formation in hydrogen and helium implanted silicon at post-implantation annealing A.V. Mudryi, F.P. Korshunov, A.I. Patuk, I.A. Shakin, T.P. Larionova, A.G. Ulyashin, R. Job, W.R. Fahrner, V.V. Emtsev, V.Yu. Davydov and G. Oganessian	181
Hydrogen enhanced thermal donor formation in p-type Czochralski silicon: application to low temperature active defect-engineering A.G. Ulyashin, R. Job, I.A. Khorunzhii and W.R. Fahrner	185
On defects created in 45 keV H ⁺ -implanted n-type Cz Si: a fluence dependence and isochronal annealing study P.N.K. Deenapanray	190
DLTS study of defects in hydrogen plasma treated p-type silicon L. Wu and A.W.R. Leitch	193
Evidence for H ₂ ⁺ trapped by carbon impurities in silicon B. Hourahine, R. Jones, S. Öberg, P.R. Briddon, V.P. Markevich, R.C. Newman, J. Hermansson, M. Kleverman, J.L. Lindström, L.I. Murin, N. Fukata and M. Suezawa	197
The strange behavior of interstitial H ₂ molecules Si and GaAs S.K. Estreicher, J.L. McAfee, P.A. Fedders, J.M. Pruneda and P. Ordejón	202
Raman scattering study of vacancy-hydrogen related defects in silicon E.V. Lavrov, J. Weber, L. Huang and B.B. Nielsen	206
On the nature of hydrogen-related centers in p-type irradiated silicon O. Feklisova, N. Yarykin, E.B. Yakimov and J. Weber	210
Simulation of hydrogen penetration in silicon under wet chemical etching O. Feklisova, S. Knack, E.B. Yakimov, N. Yarykin and J. Weber	213
Complexes of point defects and impurities in electron-irradiated CZ-Si doped with hydrogen A. Nakanishi, N. Fukata and M. Suezawa	216
Temperature dependences of line widths and peak positions of optical absorption peaks due to localized vibration of hydrogen Si M. Suezawa, N. Fukata, M. Saito and H. Yamada-Kaneta	220
Complexes of point defects and hydrogen generated by electron-irradiation of hydrogenated Si at low temperatures M. Suezawa, Y. Takada, T. Tamano, R. Taniguchi, F. Hori and R. Oshima	224
Observation of two coupled defect levels on the hydrogen-passivated Si (1 0 0) surface A.J. Reddy, J. Michel and L.C. Kimerling	228
<i>3.2. Doping and impurities</i>	
Terahertz emission from silicon doped by shallow impurities H.-W. Hübers, S.G. Pavlov, M.H. Rummeli, R.Kh. Zhukavin, E.E. Orlova, H. Riemann and V.N. Shastin	232
Mobility of interstitial B in Si analyzed by a stochastic reorientation model B. Ittermann, D. Peters, M. Füllgrabe, F. Kroll, H. Ackermann and H.-J. Stöckmann	236
Stress-induced splitting of the electronic level related to a platinum-hydrogen complex in silicon K. Fukuda, Y. Iwagami, Y. Kamiura, Y. Yamashita and T. Ishiyama	240

Valence force field analysis on nitrogen in silicon H. Harada, I. Ohkubo, T. Mikayama, Y. Yamanaka and N. Inoue	244
Spectroscopic characterization of implanted boron in microcrystalline silicon by β -NMR F. Mai, B. Ittermann, M. Füllgrabe, M. Heemeier, F. Kroll, K. Marbach, P. Meier, H. Mell, D. Peters, H. Thieß, H. Ackermann and H.-J. Stöckmann	248
Magnetic resonance and FTIR studies of shallow donor centers in hydrogenated Cz-silicon B. Langhanki, S. Greulich-Weber, J.-M. Spaeth, V.P. Markevich, B. Clerjaud and C. Naud	253
P-type doping of hydrogenated amorphous silicon films with boron by reactive radio-frequency co-sputtering Y. Ohmura, M. Takahashi, M. Suzuki, N. Sakamoto and T. Meguro	257
Dopant boron concentration dependence on electron irradiation enhanced defects in Czochralski silicon T. Tamano, F. Hori, R. Taniguchi, R. Oshima and K. Hoshikawa	261
Interstitial carbon reactions in n-Si induced by high-energy proton irradiation K. Kono, H. Amekura and N. Kishimoto	265
On the correlation character between the structure perfection and electroluminescent properties of terbium doped silicon monoxide films V.S. Khomchenko, L.I. Berejinskij and M.V. Sopinskyy	268
The control mechanism of the impurity agglomeration triggered by ion impacts S.T. Nakagawa	272
Optical absorption peaks observed in electron-irradiated n-type Si M. Suezawa, N. Fukata and A. Kasuya	276
Essential difference in concentration profile of Au in Si after annealing above or below 850°C M. Morooka	280
3.3. Oxygen	
Interaction between self-interstitials and the oxygen dimer in silicon J.L. Lindström, T. Hallberg, J. Hermansson, L.I. Murin, B.A. Komarov, V.P. Markevich, M. Kleverman and B.G. Svensson	284
Isotopic effects on vibrational modes of thermal double donors in Si and Ge L.I. Murin, J.L. Lindström, V.P. Markevich, T. Hallberg, V.V. Litvinov, J. Coutinho, R. Jones, P.R. Briddon and S. Öberg	290
Chemical and structural characterization of oxygen precipitates in silicon by infrared spectroscopy and TEM O. De Gryse, P. Clauws, O. Lebedev, J. Van Landuyt, J. Vanhellemont, C. Claeys and E. Simoen	294
Effect of oxygen on exciton transitions in silicon A.N. Safonov and G. Davies	298
Disturbance of oxygen by isovalent impurity atoms in silicon L.I. Khirunenko, V.A. Zasuha, Yu.V. Pomozov and M.G. Sosnin	301
Over-coordinated oxygen in the interstitial carbon-oxygen complex J. Coutinho, R. Jones, P.R. Briddon, S. Öberg, L.I. Murin, V.P. Markevich and J.L. Lindström	305
Expanded model for anharmonic vibrational excitation of oxygen in silicon H. Yamada-Kaneta	309

The effect of high temperature–high pressure treatment on the annealing behavior of VO center in neutron-irradiated Czochralski silicon C.A. Londos, M. Potsidou, A. Misiuk, V.V. Emtsev and J.Bak-Misiuk	313
Effect of stress on accumulation of oxygen in silicon implanted with helium and hydrogen A. Misiuk, A. Barcz, V. Raineri, J. Ratajczak, J. Bak-Misiuk, I.V. Antonova, W. Wierzchowski and K. Wieteska	317
Incorporation of oxygen or di-hydrogen in silicon monovacancy: spin-resonance study of defect excited state T. Mchedlidze, N. Fukata and M. Suezawa	321
Thermal donors and radiation-induced defect states in transmutation doped gamma-irradiated silicon S.I. Budzulyak, Yu.P. Dotsenko, V.M. Ermakov, V.V. Kolomoets and E.F. Venger	325
Ab initio study of atomic oxygen adsorption on the Si(1 1 1)7 × 7 surface M.J. Caldas, R.J. Baierle, R.B. Capaz and E. Artacho	329
<i>3.4. Erbium</i>	
Defects and their influence on the luminescence of rare-earth ions implanted in single crystal Si N.A. Sobolev	333
Time-resolved investigation of the mid-infrared-induced enhancement of Er ³⁺ emission in Si M. Forcales, I.V. Bradley, J.-P.R. Wells and T. Gregorkiewicz	337
Observation of Zeeman effect in photoluminescence of Er ³⁺ ion imbedded in crystalline silicon N.Q. Vinh, H. Przybylińska, Z.F. Krasil'nik, B.A. Andreev and T. Gregorkiewicz	340
Erbium in SiO _x environment: ways to improve the 1.54 μm emission G. Kocher, H. Przybylinska, M. Stepikhova, L. Palmetshofer and W. Jantsch	344
Excitation of Si:Er with sub-band-gap energies M.A.J. Klik and T. Gregorkiewicz	348
Shallow donors in silicon coimplanted with rare-earth ions and oxygen V.V. Emtsev Jr., C.A.J. Ammerlaan, B.A. Andreev, G.A. Oganessian, D.S. Poloskin and N.A. Sobolev	350
Site-selective excitation of Er ³⁺ ions in oxygen-rich silicon A. Kozanecki, D. Kuritsyn, H. Przybylińska and W. Jantsch	354
Erbium excitation across the bulk of silicon wafer: an effect of p–n junction at Si/Si:Er interface N.Q. Vinh, I.N. Yassievich and T. Gregorkiewicz	357
Electrically active centers in light emitting Si:Er/Si structures grown by the sublimation MBE method V.B. Shmagin, B.A. Andreev, E.N. Morozova, Z.F. Krasil'nik, D.I. Kryzhkov, V.P. Kuznetsov, E.A. Uskova, C.A.J. Ammerlaan and G. Pensl	361
Light emission from erbium doped nanostructures embedded in silicon microcavities N.T. Bagraev, A.D. Bouravleuv, W. Gehlhoff, L.E. Klyachkin, A.M. Malyarenko, M.M. Mezdrogina, V.V. Romanov and A.P. Skvortsov	365
Erbium in Si and GaN: extended versus point defects P.H. Citrin, D.R. Hamann and P.A. Northrup	369
Spectroscopic ellipsometry study of the layer structure and impurity content in Er-doped nanocrystalline silicon thin films M. Losurdo, M.F. Cerqueira, M.V. Stepikhova, E. Alves, M.M. Giangregorio, P. Pinto and J.A. Ferreira	374

Determination of the atomic configuration of Er–O complexes in silicon by the super-cell FLAPW method M. Hashimoto, A. Yanase, H. Harima and H. Katayama-Yoshida	378
Study of Er-related defects in a-Si:H(Er)/c-n-Si heterostructures by thermally activated current spectroscopy J. Vovk, A. Nazarov, V. Lysenko, O. Kon'kov and E. Terukov	382
Spectroscopic characterisation of the erbium impurity in crystalline semiconductors C.A.J. Ammerlaan	387
<i>3.5. Metallic impurities</i>	
Ultra-fast diffusion mechanism of the late 3d transition metal impurities in silicon Y. Kamon, H. Harima, A. Yanase and H. Katayama-Yoshida	391
Nitrogen effect on gold diffusion in Cz Si A.L. Parakhonsky, E.B. Yakimov and D. Yang	396
New electron spin resonance spectra from iron–vacancy pair in silicon: II. Hyperfine interactions and isotopic effect T. Mchedlidze and M. Suezawa	400
Evolution of copper–hydrogen-related defects in silicon S. Knack, J. Weber, H. Lemke and H. Riemann	404
Electronic and atomic structure of transition-metal–hydrogen complexes in silicon P.T. Huy and C.A.J. Ammerlaan	408
Time-resolved photoluminescence study of Si:Ag N.Q. Vinh, M.A.J. Klik and T. Gregorkiewicz	414
Detection of diffusional jumps of interstitial Fe in silicon by Mössbauer spectroscopy H.P. Gunnlaugsson, M. Dietrich, M. Fanciulli, K. Bharuth-Ram, R. Sielemann, G. Weyer and ISOLDE Collaboration	418
New electron spin resonance spectra from iron–vacancy pair in silicon: I. Defect with two values for the spin T. Mchedlidze and M. Suezawa	421
Theoretical study of pressure-induced negative effective U of a tungsten atom in crystalline silicon I. Kitagawa and T. Maruizumi	424
Precipitation-enhanced diffusion of nickel in dislocation-free silicon studied by in-diffusion and annealing processes S. Tanaka, H. Kitagawa and T. Ikari	427
Diffusion of ^{195}Au in amorphous Si_3N_4 and Si_4N_3 T. Voss, S. Matics, A. Strohm, W. Frank, G. Bilger and ISODLE Collaboration	431
Properties of Cr in hydrogenated Si Y. Sato, T. Takahashi and M. Suezawa	434
Optical absorption spectra of platinum-related defects in silicon N. Fukata, K. Saito and M. Suezawa	438
<i>3.6. Point and extended defects</i>	
Identification of getter defects in high-energy self-implanted silicon at $R_p/2$ R. Krause-Rehberg, F. Börner, F. Redmann, J. Gebauer, R. Kögler, R. Kliemann, W. Skorupa, W. Egger, G. Kögel and W. Triftshäuser	442
Nanoindentation pop-in effect in semiconductors H.S. Leipner, D. Lorenz, A. Zeckzer, H. Lei and P. Grau	446

Mechanical strength of nitrogen-doped silicon single crystal investigated by three-point bending method G. Wang, D. Yang, D. Li, Q. Shui, J. Yang and D. Que	450
Self-interstitial clusters in silicon T.A.G. Eberlein, N. Pinho, R. Jones, B.J. Coomer, J.P. Goss, P.R. Briddon and S. Öberg	454
Self-interstitial-oxygen related defects in low-temperature irradiated Si L.I. Khirunenko, L.I. Murin, J.L. Lindström, M.G. Sosnin and Yu.V. Pomozov	458
Divacancies in proton irradiated silicon: characterization and annealing mechanisms R. Poirier, S. Roorda, F. Schiettekatte, M. Lalancette and J. Zikovsky	462
Do we know the energy levels of radiation defects in silicon? L.F. Makarenko	465
Dopant interaction with a dislocation in silicon: local and non-local effects A. Antonelli, J.F. Justo and A. Fazzio	470
Modeling the subsurface region of Cz-Si wafers with properly fabricated bulk FZ-Si samples T. Mchedlidze, N. Fukata and M. Suezawa	474
High-energy proton radiation induced defects in tin-doped n-type silicon E. Simoen, C. Claeys, V. Privitera, S. Coffa, A.N. Larsen and P. Clauws	477
Interface strain in thermal Si/SiO ₂ analysed by frequency-dependent electron spin resonance D. Pierreux and A. Stesmans	481
C–V and G–V characterization of defects in ultrathin SiO ₂ thermally grown on RF plasma-hydrogenated silicon S. Alexandrova, A. Szekeres and E. Halova	485
Electrically active centers in partial dislocations in semiconductors J.F. Justo and L.V.C. Assali	489
Kinetic Monte Carlo study of dislocation motion in silicon: soliton model and hydrogen enhanced glide S. Scarle, N. Martsinovich, C.P. Ewels and M.I. Heggie	493
Do we really need configuration interaction theory to understand the negative vacancy in silicon? U. Gerstmann, E. Rauls, H. Overhof and Th. Frauenheim	497
Equilibrium concentration of vacancies under the anisotropic stress field around an impurity K. Tanahashi, N. Inoue and Y. Mizokawa	502
<i>3.7. Defect reactions</i>	
Mechanisms of capture- and recombination-enhanced defect reactions in semiconductors Y. Shinozuka	506
Dynamics of Si self-interstitial clustering using the fast-diffusing I ₃ cluster M. Gharaibeh, S.K. Estreicher and P.A. Fedders	510
Defect reactions associated with the dissociation of the phosphorus–vacancy pair in silicon V.P. Markevich, O. Andersen, I.F. Medvedeva, J.H. Evans-Freeman, I.D. Hawkins, L.I. Murin, L. Dobaczewski and A.R. Peaker	513

4. Germanium

- Enhanced oxygen dimer and thermal donor formation in irradiated germanium studied by local vibrational mode spectroscopy
P. Vanmeerbeek, P. Clauws and W. Mondelaers 517
- Correlated to random transition of ionized impurity distribution in n-type Ge:(As, Ga)
J. Kato, K.M. Itoh and E.E. Haller 521
- Ion-implantation and diffusion behaviour of boron in germanium
S. Uppal, A.F.W. Willoughby, J.M. Bonar, A.G.R. Evans, N.E.B. Cower, R. Morris and M.G. Dowsett 525
- Vacancies and self-interstitials in germanium: a picture derived from radioactive probes
R. Sielemann, H. Hässlein, Ch. Zistl, M. Müller, L. Stadler and V.V. Emtsev 529

5. SiGe alloys

- The interstitial boron and the boron-germanium complex in silicon-germanium crystals
J. Hattendorf, W.-D. Zeitz, N.V. Abrosimov and W. Schröder 535
- Interstitial oxygen in GeSi alloys
I. Yonenaga, M. Nonaka and N. Fukata 539
- Self-diffusion of ^{71}Ge in Si-Ge
A. Strohm, T. Voss, W. Frank, J. Räisänen and M. Dietrich 542
- Low temperature muonium behaviour in Cz-Si and Cz-Si_{0.91}Ge_{0.09}
P.J.C. King and I. Yonenaga 546
- Interaction of divacancies with Ge atoms in Si_{1-x}Ge_x
L. Khirunenko, Yu. Pomozov, M. Sosnin, N. Abrosimov and W. Schröder 550
- High resolution minority carrier transient spectroscopy of defects in Si and Si/SiGe quantum wells
J.H. Evans-Freeman and M.A. Gad 554
- Alloy fluctuations in Si_{1-x}Ge_x crystals
G. Kocher, W. Jantsch, N. Abrosimov, S. Egorov, A. Zabrodskii, B. Andreev and H.G. Grimmeiss 558

6. Diamond

- The new assignment of hyperfine parameters for deep defects in diamond
U. Gerstmann and H. Overhof 561
- Transition metals in diamond: Do chemical trends arise from ab initio calculations?
K. Johnston and A. Mainwood 565
- Annealing of monovacancies in electron and γ -irradiated diamonds
S. Dannefaer, A. Pu, V. Avalos and D. Kerr 569
- Defect-induced graphitisation in diamond implanted with light ions
A.A. Gippius, R.A. Khmel'nitsky, V.A. Dravin and A.V. Khomich 573

Modelling electron energy-loss spectra of dislocations in silicon and diamond C.J. Fall, J.P.G. Goss, R. Jones, P.R. Briddon, A.T. Blumenau and T. Frauenheim	577
The variation of optical absorption of CVD diamond as a function of temperature C. Piccirillo, G. Davies, A. Mainwood and C.M. Penchina	581
Photoelectrical properties of the 1.682-eV and 3 H centres in diamond K. Iakoubovskii and A. Stesmans	585
Photo-EPR studies on the AB ₃ and AB ₄ nickel-related defects in diamond R.N. Pereira, W. Gehlhoff, N.A. Sobolev, A.J. Neves and D. Bimberg	589
Electrically detected magnetic resonance studies of phosphorus doped diamond T. Graf, M.S. Brandt, C.E. Nebel, M. Stutzmann and S. Koizumi	593
High-temperature high-pressure annealing of diamond Small-angle X-ray scattering and optical study A.A. Shiryayev, M.T. Hutchison, K.A. Dembo, A.T. Dembo, K. Iakoubovskii, Yu.A. Klyuev and A.M. Naletov	598
Volume expansion and stress tensors for self-interstitial aggregates in diamond J.P. Goss, R. Jones and P.R. Briddon	604
Modeling fluorescence of single nitrogen-vacancy defect centers in diamond A.P. Nizovtsev, S.Ya. Kilin, C. Tietz, F. Jelezko and J. Wrachtrup	608
Irradiation effects in semiconducting diamonds N. Kristianpoller, D. Weiss and R. Chen	612
Nickel related defects in diamond: the 2.51 eV band M.H. Nazaré, J.C. Lopes and A.J. Neves	616
7. Silicon carbide	
<i>7.1. Intrinsic and extended defects</i>	
Positively charged carbon vacancy in 6H-SiC: EPR study V.Ya. Bratus, I.N. Makeeva, S.M. Okulov, T.L. Petrenko, T.T. Petrenko and H.J. von Bardeleben	621
The annealing product of the silicon vacancy in 6H-SiC Th. Lingner, S. Greulich-Weber, J.M. Spaeth, U. Gerstmann, E. Rauls and H. Overhof	625
Illumination effects in irradiated 6H n-type SiC observed by positron annihilation spectroscopy F. Redmann, A. Kawasuso, K. Petters, H. Itoh and R. Krause-Rehberg	629
Formation and annihilation of intrinsic-related defect centers in high energy electron-irradiated or ion-implanted 4H- and 6H-silicon carbide M. Weidner, T. Frank, G. Pensl, A. Kawasuso, H. Itoh and R. Krause-Rehberg	633
Calculation of hyperfine parameters of positively charged carbon vacancy in SiC T.T. Petrenko, T.L. Petrenko, V.Ya. Bratus and J.L. Monge	637
DLTS study of defects in 6H- and 4H-SiC created by proton irradiation D.V. Davydov, A.A. Lebedev, V.V. Kozlovski, N.S. Savkina and A.M. Strel'chuk	641

Interstitial-based vacancy annealing in 4H-SiC E. Rauls, T.E.M. Staab, Z. Hajnal and Th. Frauenheim	645
The ground state of silicon vacancies in 6H-SiC and 15R-SiC Th. Lingner, S. Greulich-Weber and J.-M. Spaeth	649
Positron annihilation study of vacancy-type defects in silicon carbide co-implanted with aluminum and carbon ions T. Ohshima, A. Uedono, H. Abe, Z.Q. Chen, H. Itoh, M. Yoshikawa, K. Abe, O. Eryu and K. Nakashima	652
Interstitials in SiC: a model for the D _{II} center A. Mattausch, M. Bockstedte and O. Pankratov	656
Vacancies in He-implanted 4H and 6H SiC epilayers studied by positron annihilation A. Kawasuso, M. Weidner, F. Redmann, T. Frank, P. Sperr, R. Krause-Rehberg, W. Triftshäuser and G. Pensl	660
Vacancy type defects in Al implanted 4H-SiC studied by positron annihilation spectroscopy J. Slotte, K. Saarinen, A.Yu. Kuznetsov and A. Hallén	664
Negatively charged vacancy defects in 6H-SiC after low-energy proton implantation and annealing M.-F. Barthe, D.T. Britton, C. Corbel, A. Hempel, L. Henry, P. Desgardin, W. Bauer-Kugelmann, G. Kögel, P. Sperr and W. Triftshäuser	668
Electron paramagnetic resonance studies of a carbon vacancy-related defect in as-grown 4H-SiC V.V. Kononov, M.E. Zvanut, V.F. Tsvetkov, J.R. Jenny, St.G. Müller and H.McD. Hobgood	671
Defects in 4H silicon carbide J.P. Bergman, L. Storasta, F.H.C. Carlsson, S. Sridhara, B. Magnusson and E. Janze'n	675
Neutral and negatively charged silicon vacancies in neutron irradiated SiC: a high-field electron paramagnetic resonance study P.G. Baranov, E.N. Mokhov, S.B. Orlinskii and J. Schmidt	680
Detection of defects in SiC crystalline films by Raman scattering S. Nakashima, Y. Nakatake, Y. Ishida, T. Talkahashi and H. Okumura	684
<i>7.2. Impurities</i>	
Electrical and optical properties of erbium-related centers in 6H silicon carbide O. Klettke, S.A. Reshanov, G. Pensl, Y. Shishkin, R.P. Devaty and W.J. Choyke	687
Contactless studies of semi-insulating 4H-SiC W.E. Carlos, W.J. Moore, G.C.B. Braga, J.A. Freitas Jr., E.R. Glaser and B.V. Shanabrook	691
Influence of annealing temperature upon deep levels in 6 H SiC F. Perjeru, R.L. Woodin and M.E. Kordesch	695
EPR and photoluminescence studies of semi-insulating 4H-SiC samples E.N. Kalabukhova, S.N. Lukin, W.C. Mitchel, A. Saxler and R.L. Jones	698
Defect correlated emission and electrical properties of 4H- and 6H-SiC epitaxial layers doped by nuclear transmutation doping (NTD) H. Heissenstein, H. Sadowski and R. Helbig	702

Characterization of deep centers in bulk n-type 4H-SiC Z.-Q. Fang, D.C. Look, A. Saxler and W.C. Mitchel	706
Photoluminescence study of beryllium implantation induced intrinsic defects in 6H-silicon carbide S. Fung, X.D. Chen, C.D. Beling, Y. Huang, Q. Li, S.J. Xu, M. Gong, T. Henkel, H. Tanoue and N. Kobayashi	710
Luminescence characterization of titanium related defects in 6H-SiC Yu.M. Suleimanov, I. Zaharchenko and S. Ostapenko	714
Beryllium implantation induced deep levels in 6H-silicon carbide X.D. Chen, S. Fung, C.D. Beling, M. Gong, T. Henkel, H. Tanoue and N. Kobayashi	718
Passivation of p-type dopants in 4H-SiC by hydrogen B. Aradi, A. Gali, P. Deák, N.T. Son and E. Janzén	722
First-principles studies of Ti impurities in SiC K.O. Barbosa, V.V.M. Machado and L.V.C. Assali	726
Deep level defects in sublimation-grown 6H silicon carbide investigated by DLTS and EPR K. Irmischer, I. Pintilie, L. Pintilie and D. Schulz	730
Diffusion of boron in silicon carbide K. Rüschemschmidt, H. Bracht, M. Laube, N.A. Stolwijk and G. Pensl	734
 8. GaAs and AlGaAs	
<i>8.1. Point and extended defects</i>	
Identification of arsenic antisite defects with EL2 by nanospectroscopic studies of individual centers A. Hida, Y. Mera and K. Maeda	738
Study of As self-diffusion in GaAs using sulfur as a tracer N. Engler, H.S. Leipner, R.F. Scholz, P. Werner and U. Gösele	742
On the microscopic structure of the EL6 defect in GaAs Th. Steinegger, B. Gründig-Wendrock, M. Jurisch and J.R. Niklas	745
Magneto-optical and ODEPR investigations of native defects in substrate-free LT-MBE grown GaAs I. Tkach, K. Krambrock, C. Steen, P. Kiesel and J.-M. Spaeth	749
On the problem of the EL2 structure in semi-insulating GaAs: high-frequency ODEPR/ODENDOR measurements in W-band I. Tkach, K. Krambrock and J.-M. Spaeth	753
Capture kinetics at deep-level defects in lattice-mismatched GaAs-based heterostructures O. Yastrubchak, T. Wosiński, A. Mąkosa, T. Figielski and A.L. Tóth	757
Passivation of growth defects in GaAs/AlGaAs multiple quantum well structures by CF ₄ plasma T.S. Shamirzaev, K.S. Zhuravlev, A.Yu. Kobitski, H.P. Wagner and D.R.T. Zahn	761
Exciton localization dynamics due to intrinsic interface defects within growth island terraces of all-binary GaAs/AlAs quantum wells K. Fujiwara and K.H. Ploog	765

Metastable irradiation induced defects in Be doped $\text{Al}_{0.5}\text{Ga}_{0.5}\text{As}$ MBE layers J. Szatkowski, E. Placzek-Popko, A. Hajdusianek, A. Johansen and C. Soerensen	769
Raman probing of the wave function of collective excitations in the presence of disorder Yu.A. Pusep, S.S. Sokolov, W. Fortunato, J.C. Galzerani and J.R. Leite	772
Deep-level transient spectroscopy study of electron traps in rapid thermally annealed SiO_2 -capped n-type GaAs layers grown by metalorganic chemical vapour deposition P.N.K. Deenapanray, M. Lay, D. Åberg, H.H. Tan, B.G. Svensson, F.D. Auret and C. Jagadish	776
<i>8.2. Impurities</i>	
Acceptor-hydrogen complexes in semiconductors under pressure M.D. McCluskey, K.K. Zhuravlev, B.R. Davidson and R.C. Newman	780
Donor-acceptor recombination in δ -doped type II GaAs/AlAs superlattices D.V. Gulyaev, A.M. Gilinsky, A.I. Toropov, A.K. Bakarov and K.S. Zhuravlev	784
The DX^- -centre formation at high electric fields in planar-doped GaAs:Si M. Asche and O.G. Sarbey	788
Study of vacancy-type defects after Cu diffusion in GaAs V. Bondarenko, K. Petters, R. Krause-Rehberg, J. Gebauer and H.S. Leipner	792
Luminescence properties of Dy-doped GaAs grown by organometallic vapor phase epitaxy Y. Fujiwara, T. Koide, S. Jinno, Y. Isogai and Y. Takeda	796
Investigation of Cu-related deep levels in semi-insulating GaAs by PICTS G. Zychowitz, W. Siegel, T. Steinegger, G. Kühnel and J.-R. Niklas	800
The effect of Si site-switching in GaAs on electrical properties and potential fluctuation H.G. Svavarsson, J.T. Gudmundsson, G.I. Gudjonsson and H.P. Gislason	804
Incorporation and thermal stability of defects in highly p-conductive non-stoichiometric GaAs:Be P. Specht, M.J. Cich, R. Zhao, J. Gebauer, M. Luysberg and E.R. Weber	808
Native point defects in non-stoichiometric GaAs doped with beryllium J. Gebauer, R. Zhao, P. Specht, F. Börner, F. Redmann, R. Krause-Rehberg and E.R. Weber	812
Rhodium-related deep levels in n-type MOCVD GaAs M. Zafar Iqbal, A. Majid, S. Haidar Khan, A. Ali, N. Zafar, A. Dadgar and D. Bimberg	816
Stress-induced transformation of defects in homoepitaxial beryllium-doped GaAs thin films J. Bak-Misiuk, A. Misiuk, K.S. Zhuravlev, J.Z. Domagala, J. Adamczewska and V.V. Preobrazhenskii	820
Carbon incorporation during growth of GaAs at low temperatures J. Herfort, W. Ulrici, M. Moreno, M. Luysberg and K.H. Ploog	823
Study of depth distribution of metastable hydrogen-related defects in n-type GaAs O.A. Soltanovich, E.B. Yakimov, V.A. Kagadei and L.M. Romas	827
Zinc diffusion enhanced Ga diffusion in GaAs isotope heterostructures H. Bracht, M.S. Norseng, E.E. Haller and K. Eberl	831
Vibrational modes of a hydrogen-impurity centre in LEC-GaAs W. Ulrici and M. Jurisch	835

Nitrogen solubility and N-induced defect complexes in epitaxial GaAs:N S.B. Zhang and S.-H. Wei	839
Plasmon-like oscillations of the electrons localized by the DX centers in doped $\text{Al}_x\text{Ga}_{1-x}\text{As}$ Yu.A. Pusep, A.J. Chiquito, W. Fortunato and J.C. Galzerani	843
9. Other III-V compounds	
Defect engineering in III-V ternary alloys: effects of strain and local charge on the formation of substitutional and interstitial native defects A.A. Bonapasta and P. Giannozzi	846
Interplay of nitrogen and hydrogen in $\text{In}_x\text{Ga}_{1-x}\text{As}_{1-y}\text{N}_y/\text{GaAs}$ heterostructures A. Polimeni, G.B.H. von Högersthal, M. Bissiri, V. Gaspari, F. Ranalli, M. Capizzi, A. Frova, A. Miriametro, M. Geddo, M. Fischer, M. Reinhardt and A. Forchel	850
Mechanism of zinc diffusion in gallium antimonide S.P. Nicols, H. Bracht, M. Benamara, Z. Liliental-Weber and E.E. Haller	854
Carbon-doped MOCVD InP is semi-insulating up to 700°C R.C. Newman, B.R. Davidson, J. Wagner, M.J.L. Sangster and R.S. Leigh	858
Motional properties of positive muonium in gallium III-V compounds R.L. Lichti, K.H. Chow, B. Hitti, E.A. Davis, S.K.L. Sjøe and S.F.J. Cox	862
Substitutional incorporation of arsenic from GaAs substrates into MOVPE grown InSbBi thin films M.C. Wagener, J.R. Botha and A.W.R. Leitch	866
Deep-level defects in MBE-grown Ga(As,N) layers P. Krispin, S.G. Spruytte, J.S. Harris and K.H. Ploog	870
Effects of structural defects on the activation of sulfur donors in $\text{GaN}_x\text{As}_{1-x}$ formed by N implantation J. Jasinski, K.M. Yu, W. Walukiewicz, Z. Liliental-Weber and J. Washburn	874
Incorporation of nitrogen in GaAsN and InGaAsN alloys investigated by FTIR and NRA H.Ch. Alt, A.Yu. Egorov, H. Riechert, J.D. Meyer and B. Wiedemann	877
Partly filled impurity band formation in compensated InP:Mn S.B. Mikhlin and K.F. Shtel'makh	881
Optically induced Auger recombination of Yb^{3+} in p-type InP M.A.J. Klik, I.V. Bradley, J.-P.R. Wells and T. Gregorkiewicz	884
Dopant interactions and Mg segregation in $(\text{Al}_x\text{Ga}_{1-x})_{0.5}\text{In}_{0.5}\text{P}$ heterostructures P.N. Grillot, S.A. Stockman, J.-W. Huang and Y.L. Chang	888
Luminescence properties of Er,O-codoped GaAs/GaInP double heterostructures grown by organometallic vapor phase epitaxy A. Koizumi, N. Watanabe, K. Inoue, Y. Fujiwara and Y. Takeda	891
Diffusion of zinc in gallium phosphide under defect-free phosphorus-rich conditions J. Pöpping, N.A. Stolwijk, U. Södervall, Ch. Jäger and W. Jäger	895

10. II–VI compounds

Defect analysis and engineering in ZnO C.G. Van de Walle	899
Electronic structure and ferromagnetism of transition-metal-impurity-doped zinc oxide K. Sato and H. Katayama-Yoshida	904
Magnetic resonance experiments on the green emission in undoped ZnO crystals F. Leiter, H. Zhou, F. Henecker, A. Hofstaetter, D.M. Hofmann and B.K. Meyer	908
First-principles study of the compensation mechanism in N-doped ZnO E.-C. Lee, Y.-S. Kim, Y.-G. Jin and K.J. Chang	912
Control of valence states for ZnS by triple-codoping method T. Yamamoto, S. Kishimoto and S. Iida	916
Probing the shallow-donor muonium wave function in ZnO and CdS via transferred hyperfine interactions J.S. Lord, S.P. Cottrell, P.J.C. King, H.V. Alberto, N.A. de Campos, J.M. Gil, J.P. Duarte, R.C. Vilão, R.L. Lichti, S.K.L. Sjøe, B.A. Bailey, A. Weidinger, E.A. Davis and S.F.J. Cox	920
Investigation of the defect structure in $\text{Cd}_{1-x}\text{Zn}_x\text{Te}$ by positron lifetime spectroscopy M. Martyniuk and P. Mascher	924
Influence of the molecular spin–orbit interaction on the orbital triplet levels $^4\text{T}_1$ and $^4\text{T}_2$ of Mn^{2+} in ZnS R. Parrot and D. Boulanger	928
High temperature electrical conductivity of undoped ZnS K. Lott, L. Törn, O. Volobujeva and M. Leskelä	932
Mechanism of laser damage of transparent semiconductors V.A. Gnatyuk	935
Stability of chlorine-based complex defects in group II–VI semiconductors V. Valdna	939
Excitation mechanism of blue anti-Stokes and 2.4 μm infrared emission in ZnSe:Cr V.Yu. Ivanov, A.A. Shagov, A. Szczerbakow and M. Godlewski	942
Donor–acceptor pair transitions in ZnO substrate material K. Thonke, Th. Gruber, N. Teofilov, R. Schönfelder, A. Waag and R. Sauer	945
Optical properties and surface morphology of Li-doped ZnO thin films deposited on different substrates by DC magnetron sputtering method G.A. Mohamed, E. Mohamed and A.A. El-Fadl	949
Metastable defect characterization in $\text{Cd}_{0.9}\text{Mn}_{0.1}\text{Te}:\text{In}$ E. Placzek-Popko and P. Becla	954
Vacancies in CdTe: experiment and theory S. Lany, V. Ostheimer, H. Wolf and Th. Wichert	958
The strange diffusivity of Ag atoms in CdTe H. Wolf, M. Deicher, V. Ostheimer, A.R. Schachtrup, N.A. Stolwijk, Th. Wichert and ISODLE Collaboration	963

Investigation of lattice defects by means of their drift under electric field N.E. Korsunskaya, I.V. Markevich, L.V. Borkovskaya, L.Yu. Khomenkova, M.K. Sheinkman and O. Yastrubchak	967
Laser shock wave stimulated defects in p-CdTe crystals A. Baidullaeva, A.I. Vlasenko, A.V. Lomovtsev and P.E. Mozol'	971
Magnetic resonance studies of ZnO W.E. Carlos, E.R. Glaser and D.C. Look	976
Defect identification by means of electric field gradient calculation S. Lany, V. Ostheimer, H. Wolf, Th. Wichert and ISODLE Collaboration	980
Photoluminescence studies in ZnO samples C. Boemare, T. Monteiro, M.J. Soares, J.G. Guilherme and E. Alves	985
Defect reactions of implanted Li in ZnSe observed by β -NMR F. Kroll, B. Ittermann, M. Füllgrabe, F. Mai, K. Marbach, D. Peters, W. Geithner, S. Kappertz, M. Keim, S. Kloos, S. Wilbert, R. Neugart, P. Lievens, U. Georg and ISODLE Collaboration	989
Control of the electric and magnetic properties of ZnO films H. Tabata, M. Saeki, S.L. Guo, J.H. Choi and T. Kawai	993
11. Other semiconductors	
Modulation of deep level structures in SiO ₂ upon nitrogen incorporation S. Jeong and A. Oshiyama	999
Non-linear 2-mm waveband EPR spectroscopy of spin/charge excitations in organic semiconductors V.I. Krinichnyi	1003
Effects of codoping using Na and O on Cu-S divacancy in p-type CuInS ₂ T. Yamamoto, T. Watanabe and Y. Hamashoji	1007
Coordination defects in chalcogenide amorphous semiconductors studied by positron annihilation lifetime O.I. Shpotyuk, J. Filipecki, M. Hyla, A.P. Kovalskiy and R.Ya. Golovchak	1011
Energy levels of native defects in zinc germanium diphosphide W. Gehlhoff, R.N. Pereira, D. Azamat, A. Hoffmann and N. Dietz	1015
NMR investigation of CdF ₂ :Ga D. Hilger, S.A. Kazanskii, A.I. Ryskin and W.W. Warren Jr.	1020
Scattering of charge carriers in semiconductors: models and their criteria V.V. Mikhnovich Jr.	1023
Mg-H and Be-H complexes in c-BN N.M.C. Pinho, V.B. Torres, R. Jones, S. Öberg and P.R. Briddon	1027
Influence of substitution of P by As on exciton and biexciton states in Zn(P _{1-x} As _x) ₂ crystals O.A. Yeshchenko, M.M. Biliy and Z.Z. Yanchuk	1031
DX center gratings in real-time holography S.A. Kazanskii, A.I. Ryskin, A.S. Scheulin, R.A. Linke and A.E. Angervaks	1035

Dielectric response of semiconducting and photochromic CdF_2 on microwaves S.A. Kazanskii, D.S. Rumyantsev and A.I. Ryskin	1038
Stacking faults and excitons in AgI S. Mochizuki	1042
Valence-change- and defect-induced white luminescence of Eu_2O_3 S. Mochizuki, Y. Suzuki, T. Nakanishi and K. Ishi	1046
Defects in heteroepitaxial $\text{CeO}_2/\text{YSZ}/\text{Si}(001)$ films by precise X-ray rocking curve distribution fitness C.-H. Chen, N. Wakiya, A. Saiki, T. Kiguchi, K. Shinozaki and N. Mizutani	1050
Influence of semiconductor film structural imperfection on the physicochemical interaction rate in As_2S_3 -Cu system M.V. Sopinskyy	1054
Native defects and rare-earth impurities interaction in IV-VI crystals D. Zayachuk, Ye. Polyhach, E. Slynko, O. Khandozhko, V. Kempnyk and D. Baltrunas	1057
Quantum chemical modeling of chlorine-doped defects in a-Se A.S. Zyubin, O.A. Kondakova and S.A. Dembovsky	1061
Photoluminescence of vacuum-deposited CuGaS_2 thin films J.R. Botha, M.S. Branch, A.G. Chowles, A.W.R. Leitch and J. Weber	1065
Hall effect and surface characterization of Cu_2S and CuS films deposited by RF reactive sputtering Y.B. He, A. Polity, I. Österreicher, D. Pfisterer, R. Gregor, B.K. Meyer and M. Hardt	1069
Characterization of RF reactively sputtered Cu-In-S thin films Y.B. He, A. Polity, R. Gregor, D. Pfisterer, I. Österreicher, D. Hasselkamp and B.K. Meyer	1074
EDMR of MEH-PPV LEDs G.B. Silva, L.F. Santos, R.M. Faria and C.F.O. Graeff	1078
The role of structural properties and defects for the performance of Cu-chalcopyrite-based thin-film solar cells H.W. Schock and U. Rau	1081
Positive and negative magnetoresistance in the system silver-selenium G. Beck and J. Janek	1086
12. Low-dimensional studies	
Benefits of microscopy with super resolution C. Kisielowski, E. Principe, B. Freitag and D. Hubert	1090
Role of metal impurities in the growth of chains of crystalline-silicon nanospheres H. Kohno, T. Iwasaki, Y. Mita, M. Kobayashi, S. Endo and S. Takeda	1097
An electron spin resonance study of $\text{Si}_{1-x}\text{Ge}_x$ alloy nanocrystals embedded in SiO_2 matrices—effects of P doping K. Toshiyuki, M. Tokunaga, S. Takeoka, M. Fujii and S. Hayashi	1100
Single impurity centers embedded in self-assembled silicon microcavities N.T. Bagraev, A.D. Bouravleuv, L.E. Klyachkin and A.M. Malyarenko	1104

Defect related photoluminescence in Si wires T. Torchynska, J. Aguilar-Hernandez, A.I.D. Cano, G. Contreras-Puente, F.G.B. Espinoza, Yu.V. Vorobiev, Y. Goldstein, A. Many, J. Jedrzejewski, B.M. Bulakh and L.V. Scherbina	1108
The influence of Coulomb effects on the electron emission and capture in InGaAs/GaAs self-assembled quantum dots M.M. Sobolev and V.M. Lantratov	1113
Electronic transport through N quantum dots under DC bias W.Z. Shangguan, T.C. Au Yeung and Y.B. Yu	1117
Excitation of Tm^{3+} by the energy transfer from Si nanocrystals K. Watanabe, H. Tamaoka, M. Fujii, K. Moriwaki and S. Hayashi	1121
13. Novel theoretical and experimental approaches	
Formation energy of vacancy in silicon determined by a new quenching method N. Fukata, A. Kasuya and M. Suezawa	1125
Configuration interaction applied to resonant states in semiconductors and semiconductor nanostructures I.N. Yassievich, A. Blom, A.A. Prokofiev, M.A. Odnoblyudov and K.-A. Chao	1129
Defect diagnostics in multicrystalline silicon using scanning techniques I. Tarasov, S. Ostapenko, W. Seifert, M. Kittler and J.P. Kaleis	1133
Resonance ultrasonic diagnostics of defects in full-size silicon wafers A. Belyaev and S. Ostapenko	1137
A new approach to analysis of mosaic structure peculiarities of gallium nitride epilayers A.G. Kolmakov, V.V. Emtsev, W.V. Lundin, V.V. Ratnikov, N.M. Shmidt, A.N. Titkov and A.S. Usikov	1141
The strain field around a single point defect in semiconductors spatially resolved by electric field modulation scanning tunneling spectro-microscopy A. Hida, Y. Mera and K. Maeda	1145
Thermo-mechanical stability of wide-bandgap semiconductors: high temperature hardness of SiC, AlN, GaN, ZnO and ZnSe I. Yonenaga	1150
Capacitance X-ray absorption fine structure measurement using scanning probe A new method for local structure analysis of surface defects M. Ishii	1153
Positron lifetime beam for defect studies in thin epitaxial semiconductor structures A. Laakso, K. Saarinen and P. Hautojärvi	1157
Measurement of diffusion lengths in quaternary semiconducting thin layers by spectrum imaging T. Walther	1161
Trapped carrier electroluminescence (TraCE)—A novel method for correlating electrical and optical measurements F.H.C. Carlsson, L. Storasta, J.P. Bergman and E. Janzén	1165

14. Defects in devices

Defects related to DRAM leakage current studied by electrically detected magnetic resonance T. Umeda, Y. Mochizuki, K. Okonogi and K. Hamada	1169
Process-induced defects in nitrogen doped Czochralski silicon in diode processes J. Lu, D. Yang, J. Yang, D. Tian, Y. Shen, X. Ma, L. Li and D. Que	1173
n-Channel conductance spectroscopy of deep defects in low temperature grown GaAs C. Steen, P. Kiesel, S. Tautz, S. Krämer, S. Soubatch, S. Malzer and G.H. Döhler	1177
Deep-level transient spectroscopy analysis of proton-irradiated n^+/p InGaP solar cells N. Dharmarasu, M. Yamaguchi, A. Khan, T. Takamoto, T. Ohshima, H. Itoh, M. Imaizumi and S. Matsuda	1181
Induced lattice defects in InGaAsP laser diodes by high-temperature gamma ray irradiation H. Ohyama, T. Hirao, E. Simoen, C. Claeys and S. Onoda	1185
Defect characterization by DLTS of AlGaIn UV Schottky photodetectors M.J. Legodi, S.S. Hullavarad, S.A. Goodman, M. Hayes and F.D. Auret	1189
Anomalous temperature dependence of electroluminescence intensity in InGaIn single quantum well diodes A. Hori, D. Yasunaga, A. Satake and K. Fujiwara	1193
Production and properties of p-n junctions in reactively sputtered ZnO S. Tüzemen, G. Xiong, J. Wilkinson, B. Mischuck, K.B. Ucer and R.T. Williams	1197
Defects in scintillators based on ZnS–ZnSe solid solutions O.A. Christich, E.I. Gorohova, S.B. Mikhrin, P.A. Rodnyi and A.S. Potapov	1201
Interface defects in integrated hybrid semiconductors by wafer bonding P. Kopperschmidt, St. Senz and R. Scholz	1205
Effect of proton irradiation on the characteristics of GaAs Schottky barrier diodes R.R. Sumathi, M. Udhayasankar, J. Kumar, P. Magudapathy and K.G.M. Nair	1209
Studies on the application of CVD diamonds as active detectors of ionising radiation B. Marczevska, T. Nowak, P. Olko, M. Nesladek and M.P.R. Waligórski	1213
Radiation defects in STI silicon diodes and their effects on device performance K. Hayama, H. Ohyama, E. Simoen, C. Claeys, A. Poyai, T. Miura and K. Kobayashi	1217
Fabrication of periodic nanohole multilayer structure on silicon surface toward photonic crystal Y. Ohno, N. Ozaki and S. Takeda	1222
Impact of lattice defects on the performance degradation of Si photodiodes by high-temperature gamma and electron irradiation H. Ohyama, T. Hirao, E. Simoen, C. Claeys, S. Onoda, Y. Takami and H. Itoh	1226
List of Contributors	1230
Subject Index	1237



ELSEVIER

Physica B 308–310 (2001) 1–7

PHYSICA B

www.elsevier.com/locate/physb

The fascinating dynamics of defects in silicon

S.K. Estreicher^{a,*}, P.A. Fedders^b, P. Ordejón^c^a *Physics Department, Texas Tech University, Lubbock, TX 79409-1051, USA*^b *Physics Department, Washington University, St. Louis, MO 63130, USA*^c *Institut de Ciència de Materials, CSIC, U.A.B., E-08193 Bellaterra, Barcelona, Spain*

Abstract

Ab initio molecular-dynamics (MD) simulations are increasingly being used to study defects in silicon. Simulated quenching and/or conjugate gradient calculations are now common tools to explore the minima of complicated potential energy surfaces. However, the real dynamics are in the constant-temperature runs. These highly computer-intensive simulations are still limited to real times of the order of picoseconds. However, they provide a fantastic window into processes that are beyond the reach of static ($T = 0$ K) calculations. In this paper, the challenges of constant-temperature ab initio MD simulations are discussed and examples given: the formation of H_2^* , the diffusion of small self-interstitial clusters, the restless interstitial H_2 molecule, and the dynamic calculation of vibrational frequencies from the velocity–velocity autocorrelation function. The results are obtained using methods based on Sankey's 'ab initio tight-binding' approach, with atomic-like basis sets rather than plane waves. © 2001 Elsevier Science B.V. All rights reserved.

Keywords: Molecular-dynamics; Silicon; Hydrogen; Self-interstitials

1. Introduction

This paper discusses the use of ab initio molecular-dynamic (MD) simulations in constant-temperature mode to study the dynamic behavior of point defects in crystalline silicon. 'Ab initio' refers to the way in which the electronic problem is solved, and implies that the method contains no parameters fitted to experimental data. This avoids the transferability problems that are often associated with the use of semiempirical parameters. However, these calculations do involve approximations and user inputs. Density-functional theory is used to solve the electronic problem within the local-density or generalized-gradient approximations. The theorist chooses the basis set type (plane waves or local basis) and size. The core electrons are hidden by ab initio pseudopotentials. Periodic supercells of finite size approximate the host crystal: 64 host atoms cells have been the norm, but 128 or 216 cells are

becoming common. The k -point sampling is often reduced to just one point, although larger samplings are needed and are increasingly used. On a more fundamental level, the electronic excited states are ignored as are the nuclear quantum effects such as zero-point energies, tunneling, quantum rotational states, or nuclear spins.

Yet, the predictive power of ab initio theory has dramatically improved over the past decade. Quantities such as defect geometries, energetics (binding and formation energies, activation energies for diffusion, etc.) and vibrational properties are now predicted quite reliably in many cases. Typical accuracies for local vibrational modes (LVMS) are of the order of 5–8%, which still means 100 cm^{-1} or more for H-related complexes. Other quantities notoriously difficult to calculate include DLTS levels and photoluminescence bands. Processes that involve more than one charge state are also very tricky. These include recombination-enhanced and Bourgoin–Corbett diffusion processes.

Beyond the calculation of observable properties, an important purpose of theory is to provide information on defects and processes that are not observable. The

*Corresponding author. Tel.: +1-806-742-3723; fax: +1-806-742-1182.

E-mail address: stefan.estreicher@ttu.edu (S.K. Estreicher).

properties of the isolated self-interstitial are only known through theory. There are numerous examples of 'simple' initial situations which result in complex final structures following an anneal or implant, and precious little experimental information can be obtained about the occurrences during the energetic treatment. Examples include the formation of oxygen-related thermal donors (with or without H enhancement) or of {311} self-interstitial platelets.

One step beyond *ab initio* static methods is the inclusion of nuclear (or rather, ionic: nucleus+core electrons), kinetic energy. The simplest way to achieve this is to remain within the Born–Oppenheimer approximation and treat the ions as classical point masses that obey Newton's laws of motion and are decoupled from the electronic problem. In semiconductors such as Si that have band gaps of the order of thousands of degrees, the electrons are left in their ground state (zero electronic temperature) and the temperature of the sample is determined by the ionic kinetic energy. The explicit inclusion of nuclear quantum mechanics within a dynamic scheme is still some years in the future as concerning point defects in semiconductors. Extensive quantum treatments will ultimately be required to understand some features of impurities such as H and its light isotope muonium. The quantum effects associated with heavier ions, say O or Si, are less important.

The inclusion of classical dynamics in constant-temperature mode opens up a whole new world in the study of point defects in semiconductors. This became obvious when the diffusion of a proton was first calculated [1] in 1989 using *ab initio* MD simulations. Since then, MD simulations have become a household name, even though most authors use such simulations in *static* mode, using conjugate gradients to explore complicated energy surfaces and discuss the properties of a system at a local minimum of the potential energy. There have been far fewer *dynamic* (constant-temperature) studies of defects. This paper deals with dynamic studies, the problems associated with them, and with examples of results that cannot be extracted from static calculations. The examples are (1) *defect reactions*, the formation of the H_2^+ complex, (2) *defect diffusion*, the diffusion of small self-interstitial clusters, (3) *the restless H_2* , an interstitial molecule which bounces within its tetrahedral cage even at low temperatures, and (4) *the dynamic calculation of LVMs* from the velocity–velocity autocorrelation function. This paper is not a review of the field. Numerous authors are developing or using *ab initio* (and semiempirical) MD codes in order to discover the dynamics of defects, in the bulk and on surfaces. A review of MD simulations has been recently published (for a recent review, see Ref. [2]) and several excellent monographs are available (See, e.g. Refs. [3,4]).

2. Classical MD simulations

As mentioned above, the idea behind classical MD simulations is simple. Assuming the Born–Oppenheimer approximation, one separates the electronic from the ionic problem. The ions are classical objects and the temperature of the system is related to their kinetic energy. The electrons are treated quantum-mechanically in their ground state. The total energy is calculated at a time t . Its gradient gives the force on each ion and Newton's laws of motion are solved to obtain their positions and velocities at the time $t + \Delta t$. Each ion is moved to its new position, assigned its new velocity and the electronic problem is solved again. One can simulate annealing or quenching by adding or removing a fraction of the kinetic energy every few time steps, or force the convergence towards a minimum of the potential energy (at 0 K) using conjugate gradients. In this case, it is desirable to use a large cell, a converged basis set, and more than one k point in order to describe the equilibrium properties as accurately as possible.

The time step Δt must be chosen carefully. In the case of the interstitial H_2 molecule in Si, the H–H stretch mode is around 3600 cm^{-1} , which is about 10^{14} Hz . A complete oscillation takes place every 10 fs or so. In order to describe the motion of the proton, 30–50 time steps are needed per oscillation, which implies that Δt is of the order of 0.2 fs. For heavier (and therefore slower) ions such as Si, 2.0 fs can be used. A rapid quench or a conjugate gradient calculation typically involves a few hundred time steps in order to reduce the largest force component below 0.03 eV/\AA or so.

Constant-temperature simulations imply substantial computer effort. With $\Delta t = 1.0\text{ fs}$, one thousand time steps is only one ps real time! Many thousands of time steps are required in order to do meaningful dynamics and even then, there is no certainty that anything at all will happen. The dynamics of interest include defect reactions or diffusion which are basically chemical reactions. Once a reaction begins, it occurs in a very short time. The killers are the attempt frequency and activation energy. In order for an Si–H bond to break or for O_i to jump for one bond-centered (BC) site to another, one must wait for all the neighboring host atoms to be at the precisely 'right' place and move with the 'right' velocity. Then, everything happens very quickly. The trick is in looking exactly at the right time. This may be tricky to set up, since the dynamics are rarely what one expects them to be.

In order to maximize the probability of success, one begins with the smallest realistic cell, basis set, and number of k points, assigns some high temperature, runs as many time steps as possible, and prays a lot. A healthy amount of experience and luck do help. However, if some interesting dynamics does happen, one knows better what to expect and how to prepare runs at

lower temperatures with larger cells and/or basis sets. In many cases, however, nothing happens and one has wasted a lot of CPU time. We can dream of a novel computer that would be 1000 times faster. Then, one could simulate a few nanoseconds, and/or increase the cell size to a few thousand atoms, and/or sample more k points, but probably not all these parameters can be varied simultaneously. For the foreseeable future, the art of constant-temperature dynamics will remain the art of compromise.

The computer outputs include the position and velocity of every ion in the system at every time step. This can be turned into movies which are comparable to an incredible ‘theoretical microscope’ with atomic resolution in space and femtosecond resolution in time [5]. Movies are very visual and therefore very convincing. One must constantly remind oneself that only the tiniest window in time is seen. Indeed, the longest *ab initio* simulations done to date span a few tens of picoseconds, hardly enough to reach equilibrium or steady state. Further, this is theory, *ab initio* yes, but theory nonetheless, which includes all the approximations listed above.

We use the SIESTA [6,7] code in our calculations. It is a first-principles self-consistent density-functional method with all the usual features of first-principles density-functional codes. The basis sets for the electronic states consist of numerical linear combinations of atomic orbitals of the Sankey type [8,9] rather than plane waves. These basis sets are flexible, ranging here from minimal (single-zeta, SZ) to double-zeta with polarization functions (DZP).

3. Examples

The four examples below, all in Si, illustrate situations, which would be either very difficult or outright impossible to describe using static methods. The first deals with the radiation-induced transition of interstitial H_2 into the H_2^* complex. This result involves the interactions between native defects and an interstitial impurity. The second is the surprisingly fast diffusion of small self-interstitial clusters. This counter-intuitive result shows that small aggregates may diffuse through a crystal much faster than the dissociated species. The third example involves the interstitial H_2 molecule, which moves rapidly within its tetrahedral interstitial cage and bounces off its ‘walls’, thus exchanging energy with the host crystal. The fourth and the last example deals with the calculation of LVMs at finite temperature using the velocity–velocity autocorrelation function.

3.1. A mechanism for H_2^* formation

The two simplest hydrogen dimers in Si are the interstitial H_2 molecule and the H_2^* complex. The

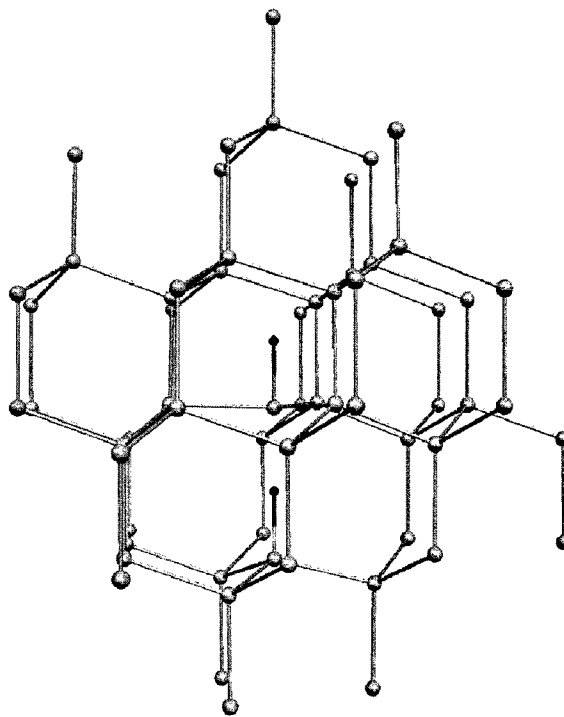


Fig. 1. The H_2^* complex forms when a vacancy and a self-interstitial recombine near interstitial H_2 .

molecule is common in samples grown in a hydrogen ambient or exposed to such an ambient near the melting point then quenched, as well as in plasma-etched samples. Interstitial H_2 gives rise to a tiny Raman [10] and infra-red [11] line. However, irradiation renders this ‘hidden’ hydrogen very visible indeed [12]. In particular, the H_2^* complex always appears in irradiated samples. This dimer, shown in Fig. 1, has one Si–Si bond replaced by two Si–H bonds along the same trigonal axis, one H near the BC site and the second in an antibonding (AB) configuration. This complex has been predicted some years ago by Deak et al. [13] and Chang et al. [14], then identified by IR spectroscopy by Holbech et al. [15]. It anneals above 200°C.

We studied the interactions between interstitial H_2 molecules and a nearby vacancy or self-interstitial [16]. MD simulations at 1000 K show that the molecules dissociate very quickly and the result is either the partially saturated vacancy {V,H,H} or a self-interstitial complex with two Hs {I,H,H}. Similarly, H_2 melts when placed inside a larger void, the ring-hexavacancy [17]. Molecular H_2 cannot survive inside an unpassivated internal void in Si.

Ron Newman suggested that the {V,H,H} or {I,H,H} complexes might further react with I or V, respectively, effectively resulting in vacancy-interstitial recombination at H_2 . We were successful with the reaction {I,H,H} + V → H_2^* , which is the more energetic of the

two possible reactions [18]. Starting with a vacancy and the {I,H,H} complex in the same 64-Si atoms cell (quenched to make sure that the simulation begins at a local minimum of the potential energy), we raised the temperature to 1000 K and let go for 8000 time steps. The calculation was not performed using SIESTA, but a Harris-functional version of the Sankey code. The reaction occurred with the Hs first forming two Si–H bonds along different trigonal axes. A single H jump resulted in H_2^* at the very end of the simulation [5].

3.2. The diffusion of small self-interstitial clusters

Large concentrations of self-interstitials (Is) are generated during energetic processes such as ion implantation. The isolated I has never been detected experimentally. However, Is precipitate and form large platelets in {3 1 1} planes which become reservoirs of Is later involved in the transient-enhanced diffusion of the B acceptor [19]. A number of theorists have studied the stable structures of small I_n clusters and various precipitation mechanisms (See Ref. [20] and references therein) involving $I + I + I + \dots \rightarrow I_n$. From the systematic geometry optimizations, we obtained a series of stable and metastable configurations of self-interstitial clusters I_n , with $n = 1, 2, 3$, and 4. Our most stable geometry [21] for the tri-interstitial, I_3^a , is an equilateral triangle centered at a BC site. It involves the substantial relaxation of only two host atoms, the two nearest-neighbors (NNs) on either side of the I_3^a triangle (Fig. 2, top). An alternative configuration, which we label I_3^b (Fig. 2, bottom), was proposed by Coomer et al. [22] as the complex responsible for the W photoluminescence band. It consists of an identical equilateral triangle in the {1 1 1} plane. However, it shifts and involves three adjacent BC sites and thus requires six host atoms to relax substantially. Although there is now an agreement [23] that I_3^a is more stable than I_3^b , constant-temperature MD simulations [24] show that both complexes exhibit unexpected dynamic behavior, even at low temperatures.

In the case of I_3^b , the three self-interstitials easily exchange sites, thus continuously turning around the trigonal axis. The stable I_3^a complex diffuses extremely fast as its center of mass (CM) shifts from BC to BC site at the picosecond time scale. This occurs at 1000 K in the 64-host atoms cell with an SZ basis set as well as in the 128-host atoms cell with a DZP set. It also occurs, albeit more slowly, with simulation temperatures as low as 77 K. It is unusual to see dynamics at 77 K at the ps time scale. Although no reliable diffusivity should be extracted from a handful of diffusion jumps, it is tempting to derive an order of magnitude. From our longest simulation (1000 K, 64-cell, SZ basis), we get a huge number, just under $10^4 \text{ cm}^2/\text{s}$. There are two other I_n clusters which diffuse at the picoseconds time scale at 1000 K. Both of them also involve a single BC site in

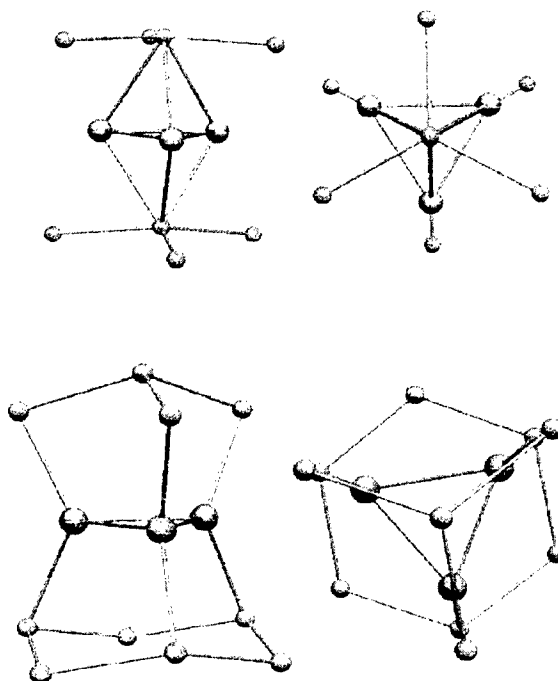


Fig. 2. Side and top (along $\langle 111 \rangle$, top) views of the tri-interstitial clusters. The stable configuration (I_3^a , top), an equilateral triangle centered at a single BC site diffuses very fast even at low temperatures. The metastable configuration (I_3^b , bottom) involves three adjacent BC sites. At $T > 0 \text{ K}$, the three Is exchange positions around the trigonal axis, but the center of mass remains in place.

their stable configuration. They are I_2 and one (of twelve) configurations of I_4 .

In all cases, the diffusion mechanism is the same. The Is in these complexes all aim at exchanging site with one of the two host atoms nearest to the BC site. These two atoms are already displaced from their ideal substitutional sites and are being pushed by two, three, or even four Is. Thus, several Is join forces in expelling one host atom. As soon as this occurs, the other members of the complex only need to rearrange the entire complex to become centered at a BC site adjacent to the original one.

We also looked at the possibility that the fast-diffusing I_3 clusters interact with each other and precipitate. Such a precipitation takes place at a substantial gain in energy when two (or more) I_3^a 's diffuse toward each other along specific lattice directions [20], suggesting that the building blocks of extended structures could be the fast-diffusing I_n complexes described above rather than an isolated I.

3.3. The restless interstitial H_2

The third example involves the interstitial H_2 molecule in Si. This impurity exhibits unexpected features

(for a discussion and references, see Refs. [25,26]). The observed stretch mode is some 550 cm^{-1} lower than the free molecule. The mode is Raman and IR active, and shows no hint of ortho/para splitting. A single HD line is seen, and its frequency is much higher and its amplitude much smaller than expected. Further, uniaxial stress experiments imply that H_2 and D_2 have C_1 symmetry, and that the piezospectroscopic tensors of H_2 and D_2 are identical. Static calculations fail to explain most of these data.

Constant-temperature MD simulations of interstitial H_2 in Si at 77 K show that the molecule continuously moves around the tetrahedral site and bounces off the walls of its cage, thus exchanging energy with its host. The average position of the CM of H_2 moves away from the T site along the $\langle 100 \rangle$ direction as the temperature increases and H_2 visits anharmonic regions of the potential. Further, the CM moves slightly off the $\langle 100 \rangle$ axis under uniaxial stress. The rapid motion of the molecule may also have something to do with the absence of ortho/para splitting [25,26].

3.4. Dynamic calculations of vibrational frequencies

The last example deals with the calculation of vibrational frequencies. The prediction of LVMs for light impurities such as H provides an important link between theory and experiment. The simplest way to estimate frequencies is to calculate total energies at 0 K for a cell relaxed close enough to equilibrium so that a maximum force component in the entire system is of the order of 0.01 eV/\AA . Then, an atom is physically displaced by small amounts $\pm d$ along a specific direction and the frequency of this atom along this direction is extracted from the curvature of the potential energy. In the case of an Si–H stretch mode for example, this would involve displacing H along the Si–H direction. One can either keep the rest of the cell (or cluster) fixed following the displacement of one atom (which underestimates the reaction of the host crystal) or allow the atoms to relax (which overestimates this reaction).

There is no accepted standard for how large the displacement d should be. Quantum chemists typically use 0.01 \AA but in the ‘defect community’, displacements of the order of 0.05 \AA have been used. This issue can be overcome by calculating the total energy for several displacements $\pm d_1, \pm d_2, \dots$ then fitting the potential energy to a polynomial of degree higher than 2. Given a sufficient computer time, this process can be repeated along the three Cartesian directions for all the atoms in the cell, thus allowing the calculation of the entire dynamical matrix. Such methods have been used by a number of authors (for references, see [27]) to calculate LVMs with typical accuracies of the order of 5–8% relative to experimental values.

A recently developed alternative is to use density-functional perturbation theory. The idea is to calculate the dynamical matrix elements analytically from the derivative of the density matrix of the relaxed cell relative to the nuclear displacements, thus setting $d = \delta R_\alpha$, an infinitesimal displacement of nucleus α . This allows the calculation of the entire dynamical matrix, including all the phonons and LVMs, within a purely harmonic approach [27]. Typical frequencies are within 1–5% of the experimental data.

However, actual measurements are done at non-zero temperatures and include the dynamics of the system, such as the coupling of LVMs to phonons, for example. One can extract vibrational frequencies dynamically within constant-temperature MD simulations from the Fourier transform of the velocity–velocity autocorrelation function [3,4,26]. This involves evaluating the integral of the scalar product of velocities at times t and $t + \tau$. In order to obtain good statistics, long simulation times are required. Since the simulations can be done at any desired temperature, LVMs can be obtained as a function of T . In principle, one could extract the entire dynamical matrix from autocorrelation functions but in practice, this requires considerable amount of computer time.

At present, we can only share preliminary results. The full testing of how the frequencies vary with cell-size, basis set and other parameters is under way. We calculated the stretch frequencies of H_2 , HD, and D_2 both in the gas phase and in Si. The calculations involved 12,000 time steps at $T = 30\text{ K}$, with a DZP basis set for H or D and an SZ basis set for the Si atoms. Fig. 3 shows the calculated frequencies for H_2 , HD, and D_2 in Si and in free space. The experimental data are shown as small lines for comparison.

For the free molecules, the measured values in the gas phase are 4161 , 3632 , and 2994 cm^{-1} , respectively. The calculated H_2 line is too low by 0.6% (25 cm^{-1}), HD by 0.1% (5 cm^{-1}) and D_2 by 1.2% (37 cm^{-1}). The agreement is extremely good.

For the molecules in Si, the D_2 , HD, and H_2 lines calculated at 30 K differ from the IR data at 10 K by $+6$, -4 , and 138 cm^{-1} (!), respectively. The first two frequencies are surprisingly similar to the measured values, but the third one is totally out of line. Preliminary results with different basis sets show that the lines do shift, but the errors relative to experiment for D_2 and HD are similar, while that for H_2 is different. At this point, we cannot rule out that some theoretical factor is to be blamed. Maybe the time step is too long or the basis set not converged. However, these parameters work well for free H_2 . There is another possibility. Maybe the classical H_2 molecule in Si should have a frequency higher than the one observed (more in line with the free H_2 value) and some quantum behavior is to be blamed for the lower observed frequency? The

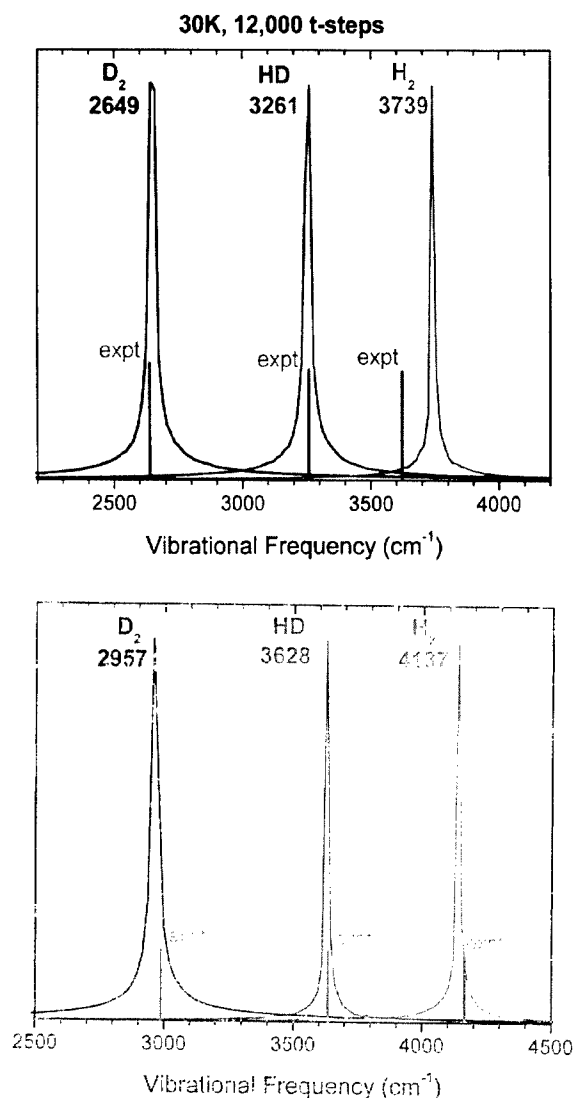


Fig. 3. Stretch frequencies of interstitial D_2 , HD, and H_2 in Si (2649, 3261, and 3739 cm^{-1} , respectively) calculated from the Fourier transform of the velocity-velocity autocorrelation function at 30 K (12,000 time steps) in the 64-Si cell with an SZ basis on Si and a DZP basis on H (or D). Compared to IR measurements at 10 K, D_2 is 6 cm^{-1} too high, HD 4 cm^{-1} too low, and H_2 138 cm^{-1} (!) too high. In contrast, the calculated frequencies of the free molecules are all close to the gas-phase Raman data.

heavier D_2 and HD might not exhibit this quantum behavior. This would imply that it is not the HD line that is too high but the H_2 line that is too low. Indeed, the calculated (classical) frequencies have HD with an anharmonicity much closer to the expected one, about 60 cm^{-1} [28]. A quantum behavior for H_2 could also have something to do with the piezospectroscopic tensors of H_2 and D_2 [29,30].

4. Discussion

Theory as a tool in the study of defects in semiconductors has evolved from methods capable of performing geometry optimizations using semiempirical techniques in small clusters, to ab initio Hartree-Fock and density-functional theory in larger cluster or periodic supercells, to the inclusion of classical dynamics within an ab initio scheme. Despite the fact that numerous approximations remain, the predictive power of theory for geometries, energetics, vibrational frequencies, and a few other measurable quantities has improved dramatically. The examples discussed in this paper illustrate how constant-temperature MD simulations provide new and unexpected insights into the behavior of defects. If such a simulation is successful, one often sees processes occurring in a way more elegant or complicated than intuition suggests. Constant-temperature MD simulations are highly computer-intensive, but this is one problem that technological progress will likely alleviate with time. We have little doubt that much more remains to be acquired from this window into the fascinating dynamics of impurities and defects in semiconductors.

Acknowledgements

The work of SKE is supported in part by a grant from the R.A. Welch Foundation, a contract from the National Renewable Energy Laboratory, and a research award from the Humboldt Foundation. PO acknowledges the support of the Fundación Ramón Areces (Spain). The authors thank the High Performance Computing Center at Texas Tech's Institute for Environmental and Human Health for the generous amount of computer time.

References

- [1] F. Buda, G.L. Chiarotti, R. Car, M. Parrinello, *Phys. Rev. Lett.* 63 (1989) 294.
- [2] S.K. Estreicher, P.A. Fedders, in: D.A. Jelski, T.F. George (Eds.), *Computational Studies of New Materials*, World Scientific, Singapore, 1999.
- [3] J.M. Haile, *Molecular-Dynamics Simulations*, Wiley, New York, 1992.
- [4] M.P. Allen, D.J. Tildesley, *Computer Simulations of Liquids*, Oxford, Clarendon, 2000.
- [5] The reader is invited to view mpeg movie segments at <http://jupiter.phys.ttu.edu/stefanke>.
- [6] E. Artacho, D. Sánchez-Portal, P. Ordejón, A. García, J.M. Soler, *Phys. Stat. Sol. B* 215 (1999) 809.
- [7] D. Sánchez-Portal, P. Ordejón, E. Artacho, J.M. Soler, *Int. J. Quant. Chem.* 65 (1997) 453.
- [8] O.F. Sankey, D.J. Niklewski, *Phys. Rev. B* 40 (1989) 3979.

- [9] O.F. Sankey, D.J. Niklewski, D.A. Drabold, J.D. Dow, *Phys. Rev. B* 41 (1990) 12750.
- [10] A.W.R. Leitch, V. Alex, J. Weber, *Phys. Rev. Lett.* 81 (1998) 421.
- [11] R.E. Pritchard, M.J. Ashwin, J.H. Tucker, R.C. Newman, *Phys. Rev. B* 57 (1998) R15048.
- [12] T.S. Shi, G.R. Bai, M.W. Qi, J.K. Zhou, *Mater. Sci. Forum* 10–12 (1988) 597.
- [13] P. Deak, L.C. Snyder, J.W. Corbett, *Phys. Rev. B* 37 (1988) 6887.
- [14] K.J. Chang, D.J. Chadi, *Phys. Rev. Lett.* 62 (1989) 937.
- [15] J.D. Holbech, B. Bech Nielsen, R. Jones, P. Stich, S. Öberg, *Phys. Rev. Lett.* 71 (1993) 875.
- [16] S.K. Estreicher, J.L. Hastings, P.A. Fedders, *Phys. Rev. B* 57 (1998) R12663.
- [17] S.K. Estreicher, J.L. Hastings, P.A. Fedders, *Appl. Phys. Lett.* 70 (1997) 432.
- [18] S.K. Estreicher, J.L. Hastings, P.A. Fedders, *Phys. Rev. Lett.* 82 (1999) 815.
- [19] For a recent review, see *MRS Bull.* 25 (2000), pp. 14, 22, 28, 39, and 45.
- [20] M. Gharaibeh, S.K. Estreicher, P.A. Fedders, in these Proceedings (ICDS-21), *Physica B* 308–310 (2001).
- [21] M. Gharaibeh, S.K. Estreicher, P.A. Fedders, *Physica B* 273–274 (1999) 532.
- [22] B.J. Coomer, J.P. Goss, R. Jones, S. Öberg, P.R. Briddon, *Physica B* 273–274 (1999) 505.
- [23] R. Jones, private communication.
- [24] S.K. Estreicher, M. Gharaibeh, P.A. Fedders, P. Ordejón, *Phys. Rev. Lett.* 86 (2001) 1247.
- [25] S.K. Estreicher, K. Wells, P.A. Fedders, P. Ordejón, *J. Phys. Cond. Mat.* 13 (2001) 6271.
- [26] S.K. Estreicher, J.L. McAfee, P.A. Fedders, J.M. Pruneda, P. Ordejón, in these Proceedings (ICDS-21), *Physica B* 308–310 (2001).
- [27] J.M. Pruneda, J. Junquera, J. Ferrer, P. Ordejón, S.K. Estreicher, in these Proceedings (ICDS-21), *Physica B* 308–310 (2001).
- [28] J.A. Zhou, M.J. Stavola, *Phys. Rev. Lett.* 83 (1999) 1351.
- [29] A.M. Stoneham, *Phys. Rev. Lett.* 84 (2000) 4777.
- [30] J.A. Zhou, E. Chen, M.J. Stavola, *Phys. Rev. Lett.* 84 (2000) 4778.



ELSEVIER

Physica B 308–310 (2001) 8–12

PHYSICA B

www.elsevier.com/locate/physb

Thermal double donors in Si and Ge

R. Jones^{a,1}, J. Coutinho^{a,*,1}, S. Öberg^{b,2}, P.R. Briddon^c^a*School of Physics, The University of Exeter, Exeter EX4 4QL, UK*^b*Department of Mathematics, Luleå University of Technology, S-97187 Luleå, Sweden*^c*Department of Physics, The University of Newcastle upon Tyne, Newcastle upon Tyne NE1 7RU, UK*

Abstract

Three experiments appear to cast doubt on self-interstitial-free models of the family of thermal donors, based on oxygen defects of increasing size. These are (a) the rapid transformation of TDD(N) into TDD($N + 1$) with activation energies considerably lower than that of oxygen diffusion, (b) the lack of any appreciable spin-density on oxygen in TDD(N)⁺, and (c) the observation of only *two* oxygen related vibrational modes associated with each donor. However, we show that the oxygen-only model of the donors is compatible with experiment for a structure involving an insulating core with normal oxygen coordination, surrounded by over-coordinated oxygen atoms which are responsible for the donor activity. It is also shown that the calculated stress-energy tensors for the early donors are in good agreement with the measurements. © 2001 Elsevier Science B.V. All rights reserved.

PACS: 61.72.Bb; 61.72.Cc; 61.72.Ji; 61.72.Lk; 66.30.Jt; 71.15.Mb

Keywords: Silicon; Germanium; Oxygen; Thermal donors

1. Introduction

Thermal double donors (TDD) are formed by annealing oxygen rich Si or Ge at temperatures between 300°C and 500°C. They comprise a family of at least 16 double donors which form sequentially and are distinguished by their increasingly shallow levels [1]. In spite of extensive studies, they remain a mystery. There are in essence two current models. The first, much favoured in theoretical studies [2–6], suggests that they consist of an increasing number of O atoms surrounding a core containing at least one over-coordinated oxygen defect. The second considers them to be a silicon self-interstitial-oxygen complex I_nO_m [7,8]. It must be admitted that the bulk of experimental evidence favours the latter. Three examples reveal the difficulties of the oxygen-only model. Firstly, the activation energy for the transformation of TDD(N) into TDD($N + 1$) varies

from 1.2 eV for $N = 1$, to 1.7 eV for larger N in Si. This leads to an anomalously fast transformation when compared with the 2.5 eV migration barrier for oxygen [9]. Secondly, EPR and ENDOR studies on the NL8 family, assigned to TDD(N)⁺, reveal two shells of O atoms, apparently bridging neighbouring Si atoms, possessing almost infinitesimally small spin-densities [10,11]. The isotropic ¹⁷O hyperfine interaction is less than 0.5 MHz in NL8 and much less than 3 MHz found on oxygen in VO⁺, in spite of the fact that oxygen in VO⁺ is located in a nodal plane of the spin-density [12]. How, one wonders, can the source for the donor activity be oxygen when there is so little spin-density associated with it? Thirdly, the oxygen-only model requires an increasing number of oxygen related local vibrational modes (LVMs) to be associated with the later donors, but only at most two such modes have been assigned to any donor [13,14].

Despite the obvious difficulties of the oxygen-only model, it has not been possible, in spite of many attempts, to produce convincing models of self-interstitial-oxygen clusters with the properties of the donors: we found, for example, the well-known IO₂ model from

*Corresponding author.

E-mail address: coutinho@exce.ex.ac.uk (J. Coutinho).

¹ Acknowledges support from EPSRC and INTAS.² Acknowledges support from TFR and INTAS.

Ref. [8] to be unstable. Thus, any credible proposal based on an oxygen-only model must also address the three fundamental questions listed above.

We show that this model, perhaps surprisingly, can account for the above difficulties. Further, it also *quantitatively* explains the variation of the piezospectroscopic tensor and the local vibrational modes [15].

The calculations reported here use the first-principles AIMPRO density functional code on cells of up to 160 Si atoms. The details of the method have been given before in an extensive treatment of oxygen defects in Si and Ge [16], and will not be repeated.

2. Formation and diffusion of oxygen chains

We find, in agreement with previous work, that oxygen atoms cluster preferentially along $[110]$ directions with decreasing Si–O–Si angles with increasing chain length (see Fig. 1a). The chains have energies relative to quartz, ranging from 1.81 eV, for the single interstitial, to about 0.36 eV per oxygen atom for the infinite chain. Thus, they are metastable with respect to an SiO_2 precipitate and presumably will break up after sufficiently long anneals.

Consider, now the migration of such chains. As the chain moves through the lattice along the $[110]$ valley in which it lies, a single or group of O atoms moves to the symmetric Y-lid configuration as illustrated in Fig. 1b. An upper limit for the diffusion barrier is found by relaxation with a constraint that forces atoms to approach this configuration [16]. In Si, this energy drops from 2.2 eV for the single oxygen species to 1.4, 1.3 and 1.2 eV for O_n , $n = 2, 3$ and 4. For Ge, there are similar reductions. The observed migration barriers for oxygen in Si is 2.5 eV and hence the theory, in common with other similar calculations underestimates

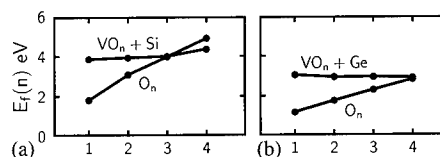


Fig. 2. Formation energies of VO_n defects and staggered O_n chains, (a) Si, (b) Ge. Formation of each VO_n defect implies the creation of a bulk Si/Ge atom.

the diffusion barriers by about 12–15% [17,18]. Nevertheless a rapid diffusion of oxygen chains is to be expected with a barrier around 1.2 and 1.0 eV in Si and Ge, respectively. The marked reduction of the migration barriers comes from two effects. Firstly, the decreasing Si–O–Si angles which bring the staggered form closer to the Y-lid form, and secondly, the absence of Si dangling bonds at the saddle point for all clusters *except* O_1 . With isolated oxygen concentrations of $\sim 10^{18} \text{ cm}^{-3}$ and maximum donor concentrations of $\sim 10^{16} \text{ cm}^{-3}$ the diffusing chain will most likely encounter a single oxygen interstitial, either lying in the same or a nearby $\langle 110 \rangle$ valley. In the latter case, there will have to be single oxygen jump before a longer chain is formed. It is this rapid chain diffusion which enables long chains to grow rapidly [19], but raises the question as to whether the increasing stress leads to a kick-out of a Si interstitial.

The formation energies of VO_n defects, depicted in Fig. 2, show that the interstitial ejection is exothermic when about four O atoms are clustered. However, at this stage, the barrier to the process will be limited by the formation energy of an I_{Si} or I_{Ge} atom, which we estimate to be around 3.3 eV in both Si and Ge. This implies that at the temperatures where thermal donors are formed, self-interstitials are not produced but rather long chains of oxygen atoms are formed.

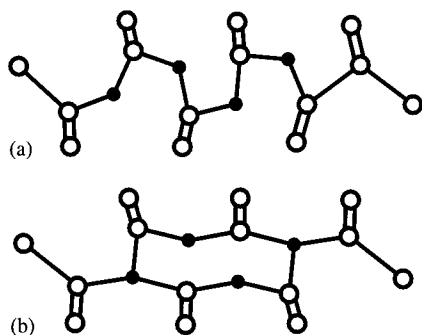


Fig. 1. (a) The staggered O_4 chain aligned along $[110]$. (b) Structure close to saddle-point for migration of the chain. This structure could be displaced to 'fall' either into (a) or the structure in (a) displaced along $[110]$. White and black spheres are Si and O atoms, respectively.

3. The O-2NN model

The energies per O-atom of several *periodic infinite* chains were investigated (see Fig. 3). The most stable is the O-2NN model, shown in Fig. 3a, where oxygen atoms are bonded to second neighbour Si atoms in two parallel chains along $[110]$. We found these chains to be bonded ionically together, with each oxygen atom divalent, and each Si atom tetravalent.

It is tempting to identify the O-2NN chains with the donors. Although they have the same C_{2v} symmetry for odd n , this cannot be correct. The band structures for bulk Si and the infinite O-2NN chain, in same supercell, are shown in Fig. 4a and b, respectively. These demonstrate that the chain is insulating with a highest

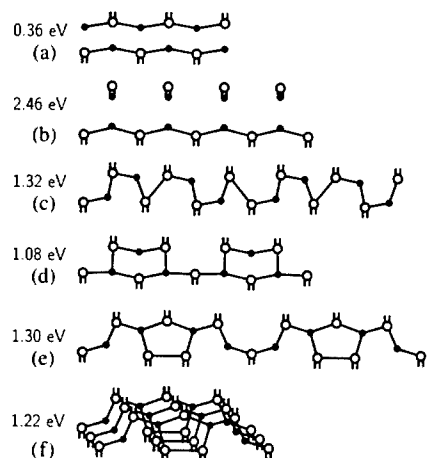


Fig. 3. Periodic infinite sub-oxide chains. (a) O-2NN. (b) VO₂. (c) O₂-1NN. (d) Ring. (e) D-Ylid. (f) parallel D-Ylid. Formation energies per O-atom are shown on the left-hand side of each structure.

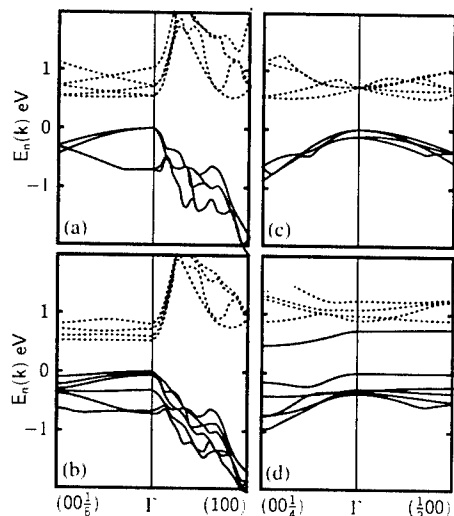


Fig. 4. Band structure for (a) defect-free Si in 48 Si atom supercell, and (b) the same supercell containing the infinite O-2NN chain from Fig. 3a. Solid and dashed lines represent filled and empty states. Band gap of 0.54 eV in (a) is a consequence of density functional theory. Reciprocal-space points are in units of $2\pi/a_0$, where a_0 is the Si lattice constant. Note degenerate valleys along (00 1) and (1 0 0) in (a) are split in (b). (c) and (d) show band structures for 112 Si atom defect-free supercell and same cell containing O₉-2NN as in Fig. 6. Note that (d) exhibits double donor behaviour.

occupied band close to that of bulk Si. They also reveal that the six degenerate lowest empty bands associated with the $\langle 100 \rangle$ valleys in bulk Si are split in O-2NN, with the lowest pushed downwards by ~ 0.2 eV from their centre of mass by the [00 1] stress arising from

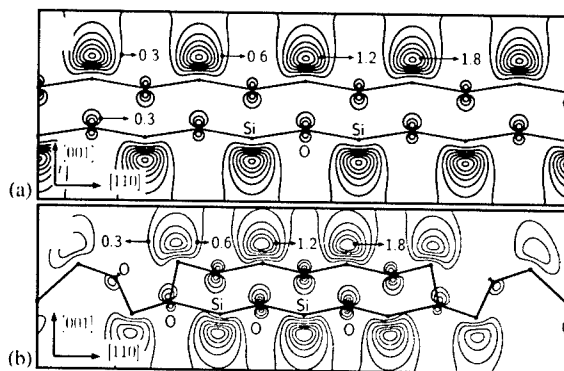


Fig. 5. Contour plot of $|\psi_{nk}(\mathbf{r})|^2 \times 1000$ for (a) the lowest unoccupied band in the infinite O-2NN chain, and (b) the highest occupied band in the O₉-2NN chain. For both, \mathbf{k} -points in the middle of the zone along (00 1) were taken. Contour levels are the same in both plots.

oxygen. The ionic character of the sub-oxide is supported by Fig. 5a, which shows that the wavefunction of the stress induced gap level is localized on the Si cations and avoids the oxygen anions as expected for conduction band states in ionic materials.

4. Thermal double donors

Finite O_n-2NN chains are terminated by O-atoms bridging Si nearest neighbours as shown in Fig. 6. Consequently, a topological defect involving an over-coordinated O-atom or an under-coordinated Si-atom, must be present at the interface between the two types of oxygen atoms. The calculations indicate that the former occurs. While short O_n-1NN chains (Fig. 1a), are more stable than short O_n-2NN chains, the reverse is true for long ones and the cross-over occurs around $N = 6$ and 8 oxygen atoms.

Whereas the infinite chain is insulating, the finite chain is not. The highest occupied state in O₉-2NN shown in Fig. 4d now edges the conduction band. It might then be expected that the wavefunction of this shallow double donor level must be localized on the over-coordinated oxygen atoms but, as Fig. 5b shows, this is not the case. The donor state is the *same* stress-induced gap state found for the infinite O-2NN chain. We understand this as follows. The interface region leads to an energy level lying *above* the strain induced gap level due to the O-2NN core. Consequently, electrons drop into the stress induced gap state with minimal overlap with oxygen. This explains the EN-DOR/EPR results for a lack of spin-density on oxygen even though oxygen is the source of the donor activity. The strain induced level is also consistent with the effect of uniaxial stress on electronic IR absorption [20].

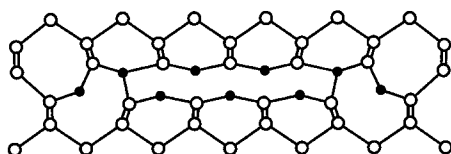


Fig. 6. O_9 -2NN identified with TDD(4) or TDD(5). This grows along $[1\ 1\ 0]$, and is orthogonal to $[0\ 0\ 1]$. Note over-coordinated oxygen occurs at interface of two types of oxygen.

We can now identify the donors with different oxygen chains. The chains with odd number of oxygen atoms have C_{2v} symmetry but ones with even numbers have C_{2h} symmetry. The vibrational modes of O_2 and O_3 have been identified and these species are not thermal donors [21]. TDD(0) may be identified with a chain of perhaps four or five O atoms suggesting TDD(N) is O_n with $n = N + 4$ or $N + 5$. This agrees with observations that a loss of around 9–10 oxygen atoms per TDD from solution accompanies the formation of the average donor, taken to be TDD(5) or TDD(6) [22,7]. We have also mentioned above that O_n -2NN chains are more stable than O_n -1NN chains for more than 6–8 O-atoms. We are not convinced by the recent suggestion that different donors are alternative conformations with the same number of O-atoms. This is because the barriers between these conformations are too low—around 0.3 eV [19], and stress-alignment experiments show that the donors can be aligned with barriers comparable with single oxygen diffusion. Thus, during stress alignment, the cluster appears to dissociate and subsequently reforms with a different alignment.

Recent high field EPR experiments indicate that the symmetry of all the donors, except the second, is not strictly C_{2v} although the difference appears small [23]. Furthermore, ENDOR studies [10,11] indicate the presence of two shells of ^{17}O hyperfine tensors with axes around 62° with $[0\ 0\ 1]$ and close to that expected from oxygen lying between neighbouring Si atoms. These considerations could be accommodated for example, if the left over-coordinated O-atom in Fig. 6 were shifted one step to the right resulting in a strict loss of symmetry and creating three shells of normal oxygen atoms lying near the ends of the chain.

The compressive stresses exerted by the O-2NN core and O-1NN ends are different. The former lies along $[0\ 0\ 1]$ and the latter along $[1\ 1\ 1]$ and $[\bar{1}\ \bar{1}\ 1]$. Thus the $[0\ 0\ 1]$ displacement of Si along the chains is different for the two regions. Table 1 shows that the central Si atoms exert a very large compressive strain which decreases with the length of the chain. This has implications for the stress-energy or piezospectroscopic tensors for the donors. We have evaluated these tensors in a way described earlier [16]. Table 1 shows that the calculated tensors for the smaller C_{2v} chains possess principal

Table 1

Calculated $[0\ 0\ 1]$ displacements (\AA), $\delta_c(0\ 0\ 1)$ and $\delta_c(0\ 0\ 1)$, of central and end Si-atoms, and stress-energy tensor elements B along $[0\ 0\ 1]$ and $[1\ 1\ 0]$ (eV), for O_n -2NN chains. Observed tensors for the early TDD members were measured by FTIR spectroscopy and EPR (starred values) [24,25]. Note TDD(N) is identified with O_{N+4} -2NN or O_{N+5} -2NN

Calc.	O_5 -2NN C_{2v}	O_6 -2NN C_{2h}	O_7 -2NN C_{2v}	O_∞ -2NN
$\delta_c(0\ 0\ 1)$	0.43	0.42	0.41	0.34
$\delta_c(0\ 0\ 1)$	0.22	0.22	0.22	—
$B_{0\ 0\ 1}$	−13.8	−13.2	−12.1	—
$B_{1\ 1\ 0}$	10.5	9.9	8.3	—
Obs.	TDD(2)	TDD(3)	TDD(4)	
$B_{0\ 0\ 1}$	−12.2	−11.9	−11.4	
$B_{1\ 1\ 0}$		10.3*	8.5*	

values very close to those observed by electronic infrared and EPR experiments. Note that O_6 -NN has C_{2h} symmetry, and hence two principal directions of the tensor are rotated by $\theta = 9^\circ$ from the $[0\ 0\ 1]$ and $[1\ 1\ 0]$ crystallographic axes. It is unclear whether this angle lies inside the experimental error for the tensors of those donors displaying lower symmetry than C_{2v} [23]. However, the calculations correctly reproduce the principal values of the stress tensor and their variation with donor species. We note the decreasing $[0\ 0\ 1]$ strain with increasing N would result in shallower strain induced states consistent with the decreasing donor level.

5. Conclusions

In conclusion, we have shown that oxygen atoms lying in chains diffuse quickly and form extended chains lying along $[1\ 1\ 0]$. The most stable long chains involve O-atoms linking second neighbouring Si atoms (O-2NN). The chains are less stable than an SiO_2 precipitate but form through their rapid kinetics. The activation energy for the kick-out of a single Si interstitial appears to be considerable and will not occur during the early-stages at 450°C . The chains give rise to a compressive stress along the $[0\ 0\ 1]$, leading to a stress induced empty gap level lying below the conduction-band, whose effective-mass wave-function is localised on ~ 1000 surrounding Si atoms. The ends of the finite chain are terminated by O-1NN atoms. The donor activity arises from a pair of over-coordinated O-atoms at the interfaces between two species of oxygen in the chain. The energy levels of these regions lie above the stress induced gap level and electrons preferentially occupy the latter.

The two types of oxygen lead to different stress distributions. The core region is highly compressive along [001] while the end region leads to stress along the chain. The magnitudes of the calculated stress-energy tensor are consistent with experimental values. The same model also accounts for the vibrational modes of the donors [15].

It is to be noted that the model suggests that single donors can be formed by substitution of O or Si by group-III or group-V impurities. Other possibilities include substitution of O by a tri-valent complex as a C–H unit. The former probably leads to the NL10(Al) family [26,27] and the later to the H-related shallow thermal donors [28].

References

- [1] R. Jones (Ed.), Early stages of oxygen precipitation in Silicon, NATO ASI series, Vol. 17, Kluwer Academic Publishers, Dordrecht, 1996.
- [2] L.C. Snyder, J.W. Corbett, in: J.C. Mikkelsen, S.J. Pearton, J.W. Corbett, S.J. Pennycook (Eds.), Oxygen, Carbon, Hydrogen and Nitrogen in Silicon, Vol. 59, p. 207, MRS Symposia Proceedings, Materials Research Society, Pittsburgh, 1985.
- [3] R. Jones, *Semicond. Sci. Technol.* 5 (1990) 255.
- [4] D.J. Chadi, *Phys. Rev. Lett.* 77 (1996) 861.
- [5] M. Pesola, Young Joo Lee, J. von Boehm, M. Kaukonen, R.M. Nieminen, *Phys. Rev. Lett.* 82 (2000) 4022.
- [6] M. Ramamoorthy, S.T. Pantelides, *Appl. Phys. Lett.* 75 (1999) 115.
- [7] R.C. Newman, *J. Phys. C: Solid State Phys.* 18 (1985) L967.
- [8] P. Deák, L.C. Snyder, J.W. Corbett, *Phys. Rev. B* 45 (1992) 11612.
- [9] R.C. Newman, *J. Phys.: Condens. Matter* 12 (2000) R335.
- [10] J. Michel, J.R. Nicklas, J.-M. Spaeth, *Phys. Rev. B* 40 (1989) 255.
- [11] J.-M. Spaeth, in: R. Jones (Ed.), Early stages of oxygen precipitation in Silicon, NATO ASI series, Vol. 17, Kluwer Academic Publishers, Dordrecht, 1996, p. 83.
- [12] R. van Kemp, M. Sprenger, E.G. Sieverts, C.A.J. Ammerlaan, *Phys. Rev. B* 40 (1989) 4054.
- [13] J.L. Lindström, T. Hallberg, *Phys. Rev. Lett.* 72 (1994) 2729.
- [14] J.L. Lindström, T. Hallberg, in: R. Jones (Ed.), Early stages of oxygen precipitation in Silicon, NATO ASI series, Vol. 17, Kluwer Academic Publishers, Dordrecht, 1996, p. 41.
- [15] L.I. Murin, J.L. Lindström, V.P. Markevich, T. Hallberg, V.V. Litvinov, J. Coutinho, R. Jones, P.R. Briddon, S. Öberg, *Nucl. Instr. and Meth., in these Proceedings (ICDS-21)*, *Physica B* 308–310 (2001).
- [16] J. Coutinho, R. Jones, P.R. Briddon, S. Öberg, *Phys. Rev. B* 62 (2000) 10824.
- [17] M. Ramamoorthy, S.T. Pantelides, *Phys. Rev. Lett.* 76 (1996) 267.
- [18] H.B. Capaz, L.V.C. Assali, L.C. Kimerling, K. Cho, J.D. Joannopoulos, *Phys. Rev. B* 59 (1999) 4898.
- [19] Young Joo Lee, J. von Boehm, M. Pesola, R.M. Nieminen, *Phys. Rev. Lett.* 86 (2001) 3060.
- [20] M. Stavola, K.M. Lee, J.C. Nability, P.E. Freeland, L.C. Kimerling, *Phys. Rev. Lett.* 54 (1985) 2639.
- [21] L.I. Murin, V.P. Markevich, in: R. Jones (Ed.), Early stages of oxygen precipitation in Silicon, NATO ASI series, Vol. 17, Kluwer Academic Publishers, Dordrecht, 1996, p. 329.
- [22] D.K. Schroder, C.S. Chen, J.S. Kang, X.D. Song, *J. Appl. Phys.* 63 (1988) 136.
- [23] R. Dirksen, T. Gregorkiewicz, C.A.J. Ammerlaan, *Phys. Stat. Sol. (B)* 210 (1998) 539.
- [24] J.M. Trombetta, G.D. Watkins, J. Hage, P. Wagner, *J. Appl. Phys.* 81 (1997) 1109.
- [25] G.D. Watkins, in: R. Jones (Ed.), Early stages of oxygen precipitation in Silicon, NATO ASI series, Vol. 17, Kluwer Academic Publishers, Dordrecht, 1996, p. 1.
- [26] T. Gregorkiewicz, D.A. van Wezep, H.H.P.Th. Bekman, C.A.J. Ammerlaan, *Phys. Rev. Lett.* 59 (1987) 1702.
- [27] C.A.J. Ammerlaan, I.S. Zevenbergen, Yu.V. Martynov, T. Gregorkiewicz, in: R. Jones (Ed.), Early stages of oxygen precipitation in Silicon, NATO ASI series, Vol. 17, Kluwer Academic Publishers, Dordrecht, 1996, p. 61.
- [28] C.P. Ewels, R. Jones, S. Öberg, J. Miro, P. Deák, *Phys. Rev. Lett.* 77 (1996) 865.



ELSEVIER

Physica B 308–310 (2001) 13–17

PHYSICA B

www.elsevier.com/locate/physb

Misfortune, challenge, and success: defects in processed semiconductor devices

H. Cerva^{a,*}, M. Engelhardt^b, M. Hierlemann^c, M. Pölzl^d, T. Thenikl^a

^aSiemens AG, Corporate Technology, Otto Hahn Ring 6, D-81730 München, Germany

^bInfineon Technologies, Corporate Research, Otto Hahn Ring 6, D-81730 München, Germany

^cInfineon Technologies, Corporate Frontend, Otto Hahn Ring 6, D-81730 München, Germany

^dInfineon Technologies, Technology and Process Development, A-9500 Villach, Austria

Abstract

Process-induced defects are still a key issue in semiconductor device production. The increasing miniaturization and number of process steps as well as the introduction of new materials and processes make the understanding of defect generation more complex. In this paper, we describe small defects in silicon, such as dry etching damage, implantation mask defects, and silicidation defects, which may be considered as nuclei for secondary defect formation. In two examples, transmission electron microscopy and stress simulation are applied to study source-drain transistor leakage and dislocation formation at trench corners in silicon. © 2001 Elsevier Science B.V. All rights reserved.

Keywords: Dislocation; Stress; Device; Transmission electron microscopy

1. Introduction

Every introduction of a new process or material in semiconductor device manufacturing has entailed defect formation. This has always required elucidating the mechanisms of defect generation in order to optimize device fabrication. The application of continuously improved diagnostic techniques for defect analysis and the correlation to the electrical device performance in a mass production environment was described as a “Gear of Challenge” [1]. Considering today’s economic impact of the microelectronics industry, the “Wheel of Misfortune”—as the control of process-induced defects was described almost 25 years ago [2]—has transformed into a “Disc of Success” [3]. Lately, Bergholz and Gilles [4] reviewed the success story of research on defects in silicon wafer material by emphasizing the continuous input from both academic and industrial research over 40 years! A recent collection of references on the progress of process-induced defects can be found in Ref. [3]. In this paper, we focus first on a selection of

small “harmless” process-induced defects that serve as nuclei for the generation of electrically detrimental defects later in the process. Secondly, we show, by way of example, how stress simulation and analysis may help to eliminate or even avoid defects.

2. Nuclei and primary defects

Failure analysis of single devices in finished integrated circuits by transmission electron microscopy (TEM) reveals, very often, relatively large defects, i.e. having the size of the device feature. To find the root cause, either a detailed TEM analysis of the failure has to be carried out or the possible defect formation mechanism occurring during individual process steps has to be explored by various analytical techniques. Here, we present a few processes where TEM has revealed small lattice imperfections (nuclei) or small dislocations (primary defects) which may incubate electrical malicious secondary defects in a later stage of processing.

Plasma etching, with, e.g. chlorine- and bromine-based chemistry, is used for etching trenches into the silicon substrate which serve as capacitors in memory

*Corresponding author. Fax: +49-89-636-42256.

E-mail address: hans.cerva@mchp.siemens.de (H. Cerva).

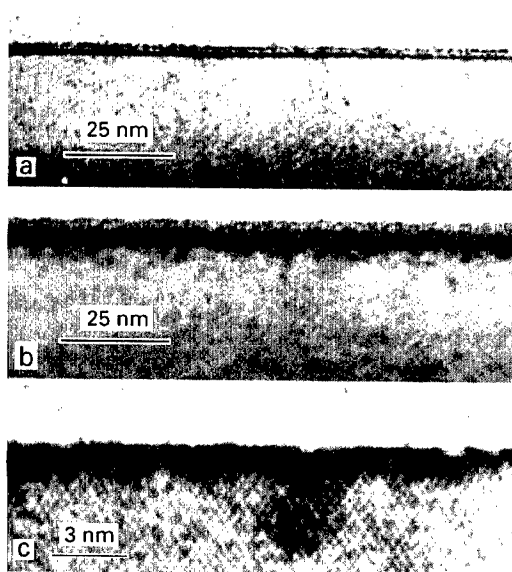


Fig. 1. TEM cross sections of chlorine-plasma-etched (100) Si surfaces: with (a) low, (b,c) high power, (c) $\langle 110 \rangle$ high-resolution lattice image.

chips, or as device isolation, or for vertical transistors. High and uniform etch rates, high selectivity to the etch mask, and others are required for an optimum trench profile. When using a magnetically confined tri-electrode etch reactor, the generation of the reactive species and their extraction towards the substrate may be controlled independently via two separate RF power supplies. Engelhardt [5] showed that the substrate degradation increased with higher bias voltages leading to higher kinetic energies of the species impinging on the surface. Figs. 1a–c are TEM cross sections displaying the silicon (100) surfaces processed with chlorine at low and high RF power level. At low power, only the native oxide layer (Fig. 1a) and an adsorbate of chlorine were detected in Auger spectroscopy profiles, whereas at high power, a larger amorphous zone comprising oxide and amorphous Si (Fig. 1b) as well as chlorine implanted to a depth of about 10 nm were found. The dark spots below the amorphous zone represent point defect clusters and surface roughness, which is more clearly visible in the lattice image of Fig. 1c. These irregularities are potential sites for secondary defect generation: Fig. 2a displays a plate-like NiSi_2 precipitate at a trench sidewall. It was formed after rapid thermal annealing (1200 °C/30 s, N_2) from the inadvertent metal contamination during the etch process. Though it was not directly confirmed, it may be speculated that a strongly degraded surface offers more precipitation sites. Fig. 2b shows a dislocation half-loop nucleated at a 1 μm deep and approximately 0.4 μm wide trench after a 800 °C/450 min wet oxidation. It is interesting that such

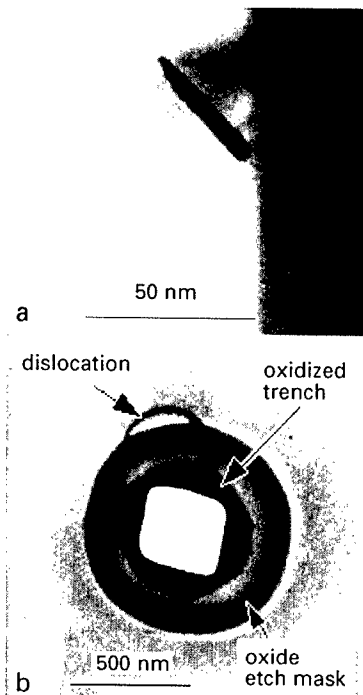


Fig. 2. (a) TEM cross section of an NiSi_2 precipitate in silicon at a trench sidewall; (b) TEM plainview of a dislocation generated at an oxidized trench in Si.

dislocations formed only after a particular trench etch condition and chemistry. Geometrical differences in the trench shape or oxide thickness could be ruled out. Thus, the dislocation may have nucleated at the defective amorphous/crystalline trench interface formed after etching and cleaning (such as in Fig. 1c). It was demonstrated in the past that dry etching of contact holes with CHF_3 produces lattice damage [6,7], which gives rise to oxidation-induced stacking faults when no appropriate post-treatment was carried out to remove the damage [8].

Another type of primary defect, generating secondary dislocations, which are, e.g. subject to glide into the substrate due to a stress field, are implantation mask-edge defects. High-dose amorphizing implants give rise to these vacancy-type defects in the silicon substrate below the mask edge. These defects have been observed regularly in various technologies for the last 15 years and are described in detail in Ref. [9]. Fig. 3 is a TEM plainview image showing a long dislocation pinned to a mask-edge defect.

Contact holes, filled with tungsten, use thin barrier layers of Ti/TiN to avoid a reaction with silicon. Due to annealing, finally, a thin TiSi_2 film is created below the TiN. The formation of TiSi_2 from Ti and the substrate causes, first, a compressive stress at elevated temperature whereas this stress becomes strongly tensile when

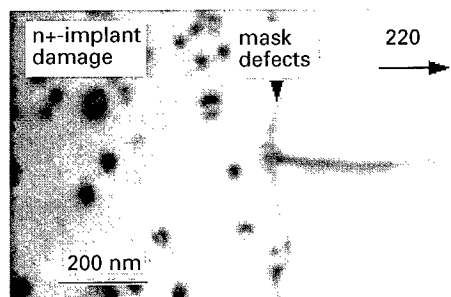


Fig. 3. TEM planview image of a dislocation pinned at implantation mask edge defects.

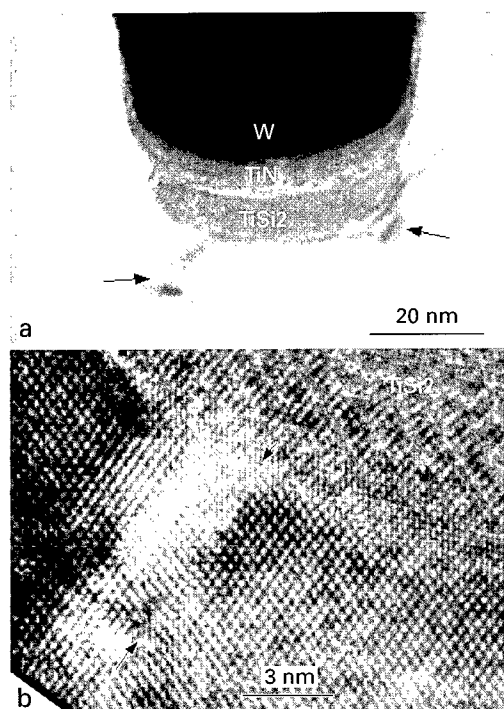


Fig. 4. TEM cross sections: (a) Defects (arrows) in Si at the bottom of a W-filled contact hole; (b) high-resolution lattice image showing a missing $\{111\}$.

cooling down to RT. When a critical layer thickness is surpassed, the stresses may exceed the critical shear stress on the active slip system (usually $\{111\}\langle 110 \rangle$) [10]. This becomes even worse with decreasing feature size. Moreover, the titanium silicide reaction goes along with volume shrinkage of about 15% and an emission of vacancies into the silicon [11]. Fig. 4a shows a contact hole with about 60 nm in diameter and a relatively thick TiSi_2 layer of about 12 nm. Below both sides of this film, for each contact in the array, defects, 10 nm in size, were generated. A high-resolution image (Fig. 4b) reveals a

half-loop dislocation with a missing $\{111\}$ plane. The dislocations were, thus, produced by the silicidation. They might lower the nucleation barrier for secondary dislocations when a high stress source should become active later in the process.

3. Stress-induced (secondary) defects

The following two examples demonstrate technology processes where secondary defects are released at nuclei due to high mechanical stress fields.

Fig. 5a is a schematic cross section of a power MOS transistor, which showed I_{DSS} leakage, i.e. a

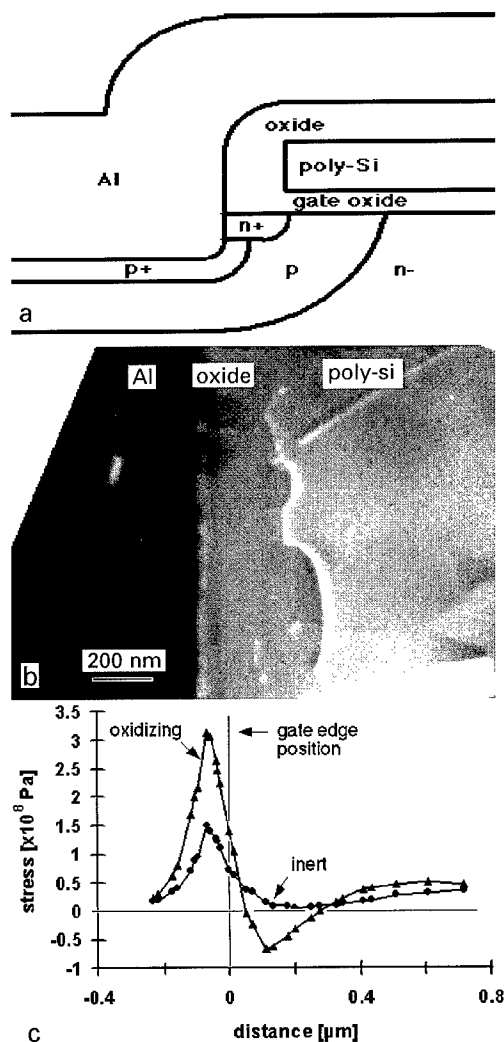


Fig. 5. (a) Schematic cross section of a power MOS transistor; (b) darkfield TEM planview image of a dislocation below the gate oxide; (c) shear stress along a (100) plane 50 nm below the gate oxide after an oxidizing and an inert anneal.

drain-source leakage current at zero gate voltage. TEM planview inspection of such affected transistors identified Lomer-type dislocations lying shallow (ca. 50 nm) below the gate oxide on $\{100\}$ planes (Fig. 5b). They extended from beneath the poly-Si gate edge up to 250 nm into the transistor channel. It was evident that their origins were the mask edge defects at the poly-Si gate edge from the source n^+ -implantation regarding the dislocation lines bowing back to the edge. Their movement on the $\{100\}$ planes must have been released by the injection of silicon interstitials under high lateral stress. Such a phenomenon was described previously by Mader [12] assuming a critical resolved shear stress (RSS) of 1.7×10^7 Pa for glide on $\{100\}$ at 900°C . The critical process step, which led to this failure, was found by 2D-device process stress simulation with TSUPREM-4 [13]. The n^+ -implantation anneal had been carried out in an oxidizing ambient at 900°C for 30 min. Fig. 5c compares the shear stress on a $\{100\}$ plane, 50 nm below the gate oxide and in the direction perpendicular to the gate edge, for an oxidative and an inert anneal. The shear stress could be reduced by 50% for nitrogen anneals. This sufficed to avoid the defect formation and leakage. We note that the calculated stress at the dislocation nucleation point exceeded the critical RSS reported in Ref. [12] in both cases by factors of 10 and 20. Transistors with similar leakage behavior were also observed by other authors [14,15].

Trenches in the silicon substrate are usually filled with poly-Si or oxides, which have high intrinsic stress

leading to strong compressive or tensile stress at the trench corners [16]. During the development of a novel read-only memory with trench technology [17], dislocations gliding on $\{111\}$ planes were generated in an early version of the device at the bottom corners (TEM cross section in Fig. 6a, planview image in Fig. 6b). The device consisted of long trenches with several vertical transistors on both trench sidewalls. The stored information differed whether the gate was accomplished with poly-Si, or filled with tetraethylorthosilicate (TEOS) oxide. TEOS also isolated the transistors in the long trenches. First, the trenches were completely filled with TEOS. During a successive anneal, the TEOS became densified and shrunk by approximately 7%. The TEOS was then etched and substituted by poly-Si according to the programming. The final process, which did not use TEOS, did not generate dislocations. For both cases, 2D stress simulations with TSUPREM-4 were carried out. The shear stresses on $\{111\}$ planes are tensile at the bottom corners. The linescans of the shear stresses on $\{111\}$ planes ("A" and "B" in Fig. 6a) are plotted in Fig. 6c. For the plane "A", the stress is compressive in the corner (-4×10^7 Pa) whereas for plane "B", it is tensile (7×10^7 Pa). The stresses at the bottom corners are about 50% higher for the process with TEOS. For the $\{111\}$ plane "A", a 60° dislocation would come to rest at about 400 nm from the trench corner when considering a critical RSS of $0.1\text{--}0.6 \times 10^7$ Pa for glide on $\{111\}$ [16]. In case of the $\{111\}$ plane "B", the resting distance would be 150 nm. This fits for the closest

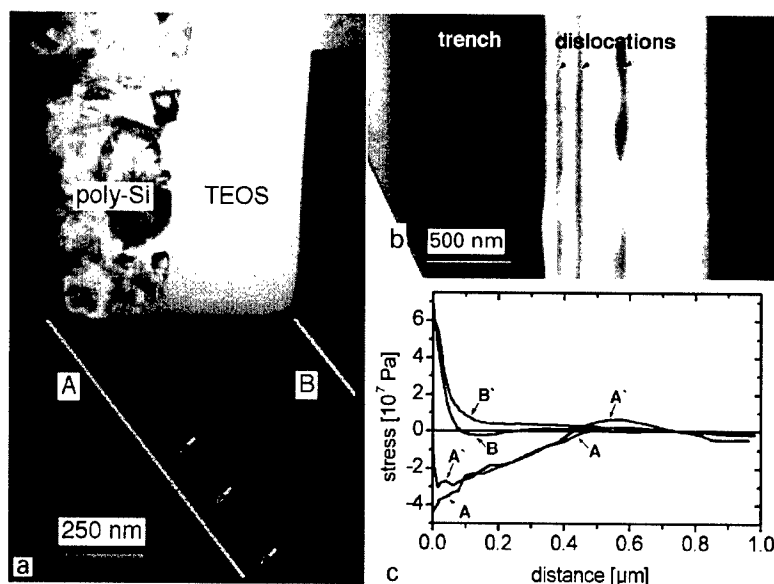


Fig. 6. (a) TEM cross section of a trench in Si filled with poly Si and TEOS. Dislocations (arrows) lie on common $\{111\}$ planes A and B; (b) TEM planview image of a trench with the generated dislocations parallel to the bottom corner; (c) shear stress along $\{111\}$ for process with (A, B) and without (A', B') TEOS.

dislocations observed in Figs. 6a and b only. In this situation, the nucleation stress exceeded the critical RSS by a factor of 10.

In future, a quantification of the local mechanical stresses becomes desirable. This requires one to predict the stresses necessary for dislocation nucleation correctly and to estimate the influence of the nuclei. Presently, efforts are being undertaken to measure the local strains with high spatial resolution by convergent beam electron diffraction in the TEM and comparing these values with stress simulations [18,19].

4. Conclusion

The mechanisms for defect generation have, in principle, stayed the same over the years, but it becomes a more complex and delicate matter to trace the root cause in today's technology. More than ever, it is important to recognize and eliminate the defects in the development or early phase of production to ensure economic yield and device reliability. Therefore, a kind of premonition system for defect generation could be envisaged. It should comprise a better understanding of the various nuclei for defect generation, and of the stresses occurring during processes, as well as local stress measurement techniques with high spatial resolution.

References

- [1] L. Fabry, Y. Matsushita, *Electrochem. Soc. Proc.* 98–1 (1998) 1459.
- [2] G.A. Rozgonyi, *Electrochem. Soc. Proc.* 77–2 (1977) 504.
- [3] B.O. Kolbesen, H. Cerva, *Electrochem. Soc. Proc.* 99–1 (1999) 19.
- [4] W. Bergholz, D. Gilles, *Phys. Stat. Sol. (B)* 222 (2000) 5.
- [5] M. Engelhardt, *Mater. Sci. Forum* 140–142 (1993) 541.
- [6] H. Cerva, E.G. Mohr, H. Oppolzer, *J. Vac. Sci. Technol. B* 5 (1987) 590.
- [7] M. Engelhardt, *Electrochem. Soc. Proc.* 96–12 (1996) 457.
- [8] G. Nallapati, K.V. Liko, Fifth International Symposium on Plasma Process-Induced Damage, American Vacuum Society, 2000, pp. 61–64.
- [9] H. Cerva, *Defect Diffusion Forum* 148–149 (1997) 103.
- [10] A. Steegen, I. De Wolf, K. Maex, *J. Appl. Phys.* 86 (1999) 4290.
- [11] D.-S. Wen, P. Smith, C.M. Osburn, G.A. Rozgonyi, *J. Electrochem. Soc.* 136 (1989) 466.
- [12] S. Mader, in: J.F. Ziegler (Ed.), *Ion Implantation: Science and Technology*, Academic Press, New York, 1984, p. 63.
- [13] TSUPREM-4 Users Manual, Release 2000.4, Avant! Corp., Fremont, CA, USA, 2000.
- [14] C.-F. Ni, S.-J. Wu, H.-H. Chang, C.-Y. Lan, Y.-S. Ho, Y.-C. Harn, S.-L. Shu, Second International Symposium on Plasma Process-Induced Damage, American Vacuum Society, 1997, pp. 85–88.
- [15] G. Chang, R. Ai, H.-D. Chiou, *Electrochem. Soc. Proc.* 97–12 (1997) 123.
- [16] S.M. Hu, *J. Appl. Phys.* 70 (1991) R53.
- [17] E. Bertagnolli, F. Hofmann, J. Willer, R. Mary, F. Lau, P.W. von Basse, M. Bollu, R. Thewes, U. Kollmer, U. Zimmermann, M. Hain, W.H. Krautschneider, A. Rusch, B. Hasler, A. Kohlhasse, H. Klose, 1996 Symposium on VLSI Technology, IEEE, Piscataway, NJ, 1996, pp. 58–59.
- [18] A. Armigliato, in: A.G. Cullis, J.L. Hutchison (Eds.), *Microscopy of Semiconducting Materials XII*, IoP Publishing, Bristol, 2001, in preparation.
- [19] A. Kenda, H. Cerva, P. Pongratz, in: A.G. Cullis, J.L. Hutchison (Eds.), *Microscopy of Semiconducting Materials XII*, IoP Publishing, Bristol, 2001, in preparation.



ELSEVIER

Physica B 308–310 (2001) 18–21

PHYSICA B

www.elsevier.com/locate/physb

Optical study of GaN:Mn co-doped with Mg grown by metal organic vapor phase epitaxy

R.Y. Korotkov, J.M. Gregie, B. Han, B.W. Wessels*

Department of Materials Science and Engineering, Northwestern University, Materials and Life Science Building, 2225 N. Campus Drive, Evanston, IL 60208-3108, USA

Abstract

Optical properties of a series of semi-insulating Mn-doped GaN co-doped with Mg were studied using photoluminescence (PL). A strong PL emission band at 1.0 eV was observed upon co-doping. The new band exhibited a rich fine structure with peaks at 1.057, 1.048, 1.035, 1.032, 1.020, 1.014, 1.008, 1.000 and 0.988 ± 0.001 eV. The integrated and relative intensities of these lines varied as a function of the Mn concentration and excitation source. The measured luminescence decay time was 20–95 μ s and depended on emission energy. © 2001 Elsevier Science B.V. All rights reserved.

Keywords: GaN; Photoluminescence; Mn doping

1. Introduction

The luminescence properties of the transition metal element Mn have been widely studied in III–V semiconductor compounds [1–3]. Manganese preferentially incorporates on the metal site forming an acceptor. Photoluminescence (PL) studies have shown that Mn can form donor–acceptor pairs (DAP) in these compounds. Furthermore, manganese has been shown to have intra-atomic transitions involving the d-shell electrons. The identification of the specific transition involved in optical spectra is often complicated by the presence of the two types of transitions [3,4]. Substitutional Mn will form the Mn^{2+} (d^5) and Mn^{3+} (d^4) states if placed on the cation site in III–V compounds [1–4]. It has been shown that three defect centers are formed in III–V semiconductors. They are a neutral acceptor, A^0 (d^4), an ionized acceptor (when an electron is captured by the A^0 from the valence band (VB)), A^- (d^5) and a neutral acceptor formed by a complex with a hole, A^0 (d^5+h) [5]. A negative acceptor (A^-) and complex (d^5+h) were observed for the GaAs:Mn, whereas the A^0 and A^- states were detected in GaP [5]. In GaN, the d^5 ion configuration was observed in EPR studies of

unintentionally doped [6] and intentionally Mn-doped GaN [7,8].

Little is known about the Mn-related optical emission and absorption GaN. It is expected that the spin forbidden transition within Mn d^5 ion will have low intensity and long lifetime. We have recently investigated the absorption and PL spectra of Mn-doped epitaxial GaN [9]. A weak broad band was observed at 1.25 ± 0.02 eV in the PL spectra of Mn-doped samples with the full-width at half-maximum (FWHM) of 250–300 meV for above band gap excitation. The independence of the energy peak position of this band with temperature and a long ~ 8 ms decay times indicated that it was likely related to the spin forbidden transition, ${}^4T_1-{}^6A_1$ of Mn (d^5) ion [10]. The energy position for this band was similar to that (1.3 eV) for ${}^4T_1-{}^6A_1$ recombination observed for Fe^{3+} in GaN [11].

In this paper, PL properties of the GaN:Mn co-doped with Mg are investigated. A new strong PL band with a rich structure is observed on the low energy side of the 1.25 eV band previously reported in Mn-doped GaN samples [9].

2. Experimental

The MOVPE growth of the Mn-doped GaN layers has been previously described [9]. For the Mn, Mg co-

*Corresponding author. Tel.: +1-847491-3537; fax: +1-847-491-7820.

E-mail address: b-wessels@nwu.edu (B.W. Wessels).

doping experiments, the Mg source partial pressure was $0.18 \mu\text{mol}/\text{min}^1$ and Mn source partial pressure was varied in the broad range from 0.02 to $5 \mu\text{mol}/\text{min}$. The epitaxial layer consisted of a 20 nm GaN nucleation layer, a 500 nm Mg-doped ($0.03 \mu\text{mol}/\text{min}$) layer grown at 1060°C , and a 2–2.5 μm thick Mn, Mg co-doped layer grown at 1060°C . As-grown Mn–Mg epilayers had semi-insulating behavior. The Mg co-doped samples were annealed at 850°C to produce p-type material. Photoluminescence spectra were measured over the spectral range of 0.7–1.2 eV. Photoluminescence was excited with either the 325 nm line of a He–Cd laser or a semiconductor laser with excitation wavelength of 973.8 nm. The excitation densities of these lasers were 0.32 and $3 \text{ W}/\text{cm}^2$, respectively. The PL signal was dispersed by a Zeiss monochromator with a resolution of 2 meV at $1 \mu\text{m}$ and detected with a high sensitivity Ge-detector and a lock-in amplifier. The sample temperature was varied from 20 to 300 K using a closed cycle helium cryostat. The He–Cd laser intensity was varied using neutral density filters in the range of 2×10^{-3} – $10 \text{ W}/\text{cm}^2$. All PL spectra were normalized to account for the spectral responsivity of the Ge-detector as well as the monochromator. Transient PL decay curves were excited using 500 MHz pulsed 974 nm laser. The system resolution was limited by the Ge-detector rise time of 16 μs .

3. Results and discussion

A new strong band with a peak at approximately 1.0 eV was observed in the PL upon co-doping with Mg. It was composed of a series of sharp lines with FWHM of ~ 3 – 10 meV . A PL spectrum of this fine structure obtained with below band gap excitation (974 nm) is shown in Fig. 1. Note, however, that the 1.25 eV PL band observed in Mn-doped samples was not detectable above the excitation 974 nm laser noise suggesting that the new sharp emission was activated in GaN:Mn by co-doping with Mg.² The major energies of the sharp lines observed in the co-doped samples spectra are summarized in Table 1. They are at 1.057, 1.048, 1.035, 1.032, 1.020, 1.014, 1.008, 1.000 and $0.988 \pm 0.001 \text{ eV}$. A few weak transitions were also observed on the lower energy side of the main band as seen in Fig. 1. This fine structure was observed with both extrinsic and intrinsic

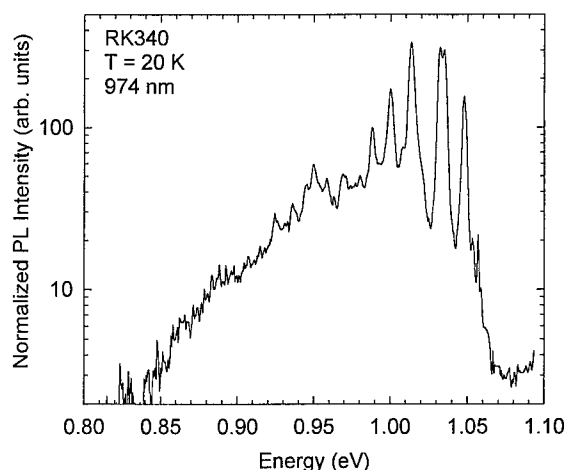


Fig. 1. PL spectrum for one of the co-doped samples (RK 340) obtained with 974 nm excitation at 20 K. The energies of the fine structure are listed in Table 1 for the strongest lines.

excitation sources [12]. It was observed with above band gap energies of 325 nm He–Cd laser as well as below band gap 632.8 and 974 nm lasers. The positions of the peaks were the same for these excitation sources. However, the integrated and relative intensities varied as a function of the excitation wavelength indicating that each major separate emission line is likely to have its own excitation spectra.

To study the effect of Mn concentration on the integrated intensity of the 1.0 eV band, a series of co-doped films were grown with different Mn concentrations. In this experiment, the Mg acceptor concentration was constant, whereas the Mn concentration varied. The normalized PL spectra for this series of samples are shown in Fig. 2. The integrated intensity of the 1.0 eV band increased at first with the increase of Mn-partial pressure and then decreased [12]. Note that the energy positions of the sharp emission lines were the same for these samples indicating that the optically active centers involved were of the same nature in all studied samples. However, relative intensities of these lines varied as a function of the Mn concentration indicating that the concentration of the optically active centers involved in the separate sharp lines changed with Mn concentration.

To detail the nature of the 1.0 eV band it was studied as a function of temperature and excitation intensity. Thermal quenching of the luminescence was studied under 974 nm excitation. All bands except one were thermally quenched above 100 K with activation energy of $\sim 70 \text{ meV}$ as shown in Fig. 3.³ The intensity of the

¹This Mg partial pressure was used to achieve $p = 2 \times 10^{17} \text{ cm}^{-3}$ in Mn-doped GaN [13].

²It is important to note that our undoped GaN samples did not exhibit emission bands in the near infra-red. Previously observed Co^{2+} , $(\text{Cr}^{4+}/\text{Ti}^{2+})$ and Fe^{3+} emission bands at 1.047, 1.19 and 1.3 eV [1,14] were not detected in our undoped GaN samples. Therefore, the observed fine structure is specifically related to the Mn–Mg co-doped samples.

³A slightly different activation energy of 0.1 eV was calculated for the experimental data obtained under 325 nm excitation.

Table 1

Energy positions and lifetimes of sharp peaks observed in Mg co-doped GaN:Mn samples and Mn-doped samples (1.25 eV band)

Energy (eV)	1.057	1.048	1.034	1.032	1.02	1.013	0.988	0.986	0.95	1.25
τ (μ s)	40	95	68	68	52	42	54	54	49	8000

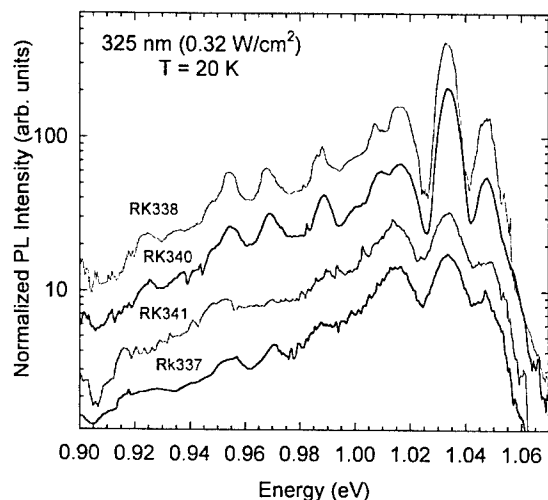


Fig. 2. Above band gap excited (325 nm) PL spectra of co-doped samples at 20 K grown with different Mn concentrations. The Mg partial pressure was constant (0.18 μ mol/min). The Mn partial pressures were 4.54, 1.36, 0.079 and 0.02 μ mol/min for samples RK 341, RK 340, RK 338 and RK 337, respectively.

highest energy transition observed at 1.057 eV first increased from 20 to 100 K and then decreased with the increase of the temperature, $T > 100$ K. The increase of 1.057 eV band was likely due to interactions with phonons. The PL intensity of the lines comprising the 1.0 eV band increased linearly with excitation power as shown in Fig. 4 for selected transitions under 325 nm excitation. In addition, for below band gap excitation the intensity of the sharp structure linearly increased with excitation power [12].

To determine whether these emission lines were associated with intra-d shell transitions, the luminescent recombination lifetime was measured on the co-doped samples. A PL decay curve for transitions at 1.032 eV is shown in Fig. 5. The PL intensity decayed exponentially at low temperature (20 K). The decay time was 66 μ s. The lifetime of the sharp lines (40–90 μ s) in the co-doped samples was two orders of magnitude smaller than that observed for the characteristic 1.25 eV Mn band for the Mn-doped GaN samples [10]. In this case, the lifetime was of the order of ~ 8 ms. Furthermore, each emission line had slightly different recombination lifetime, as shown in Table 1, suggesting that emission lines in the

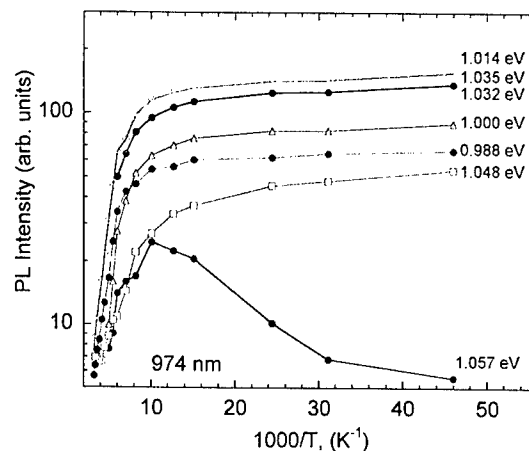


Fig. 3. Thermal quenching of the individual transitions of the 1.0 eV band excited with 974 nm excitation.

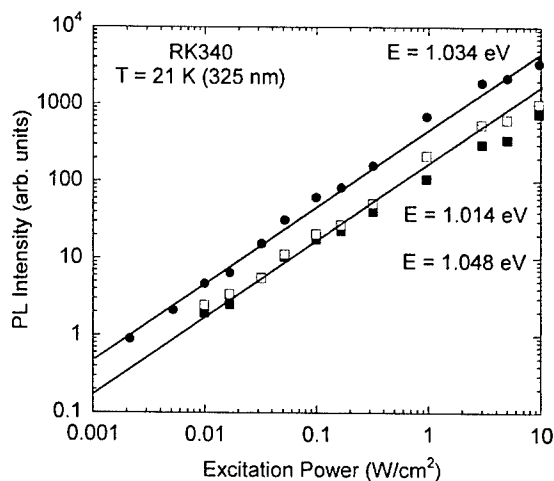


Fig. 4. Excitation intensity dependence of the PL intensity for three sharp lines obtained with above band gap excitation (325 nm) at 20 K.

fine structure are associated with different recombination centers.

The dramatic change in the luminescence spectra of Mn doped GaN upon co-doping with Mg was unexpected. Its origin is not understood. Co-doping with Mg acceptors may potentially lead to several changes in

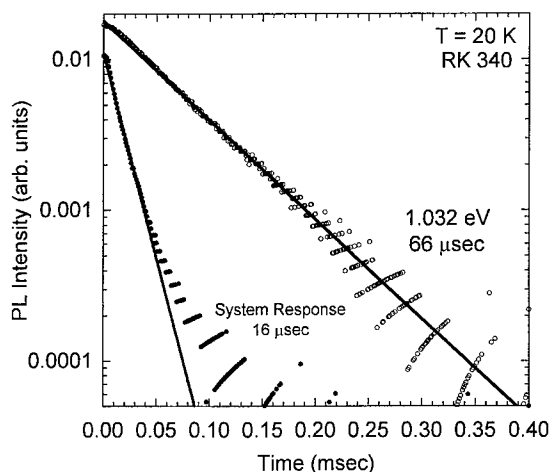


Fig. 5. Transient PL spectra of one of the co-doped samples obtained at 1.032 eV, 20 K. The calculated exponential decay (66 μ s) is shown with a solid line. System response of 16 μ s is shown for comparison.

the optical behavior of Mn. Addition of Mg could lead to complex formation. Furthermore, interactions with Mg may distort the Mn-ion surroundings. The alteration of the Mn-ion (d^5) surroundings changes the environmental symmetry of Mn ion leading to the breakdown of the selection rules by the appreciable sextet–quartet mixing [2,3]; consequently, the forbidden $^4T_1-^6A_1$ transition becomes allowed. The decrease of the lifetime for the 1.0 eV PL band by two orders of magnitude from 8 ms observed in Mn-doped GaN seems to support changes in local symmetry in co-doped samples.⁴

While co-doping with Mg could lead to changes in local symmetry, addition of Mg acceptors will also lower the Fermi energy, potentially leading to a change in the charge state of Mn. In addition, lowering of the Fermi level will result in increased compensation of the p-doped GaN with donors, D. An alternative explanation is that the observed fine structure could involve $Mn^{3+}-D$ and $Mn^{2+}-D$ centers. The alteration of the Fermi energy upon co-doping could potentially stabilize one of these complexes. Indeed a model involving transitions from $Cr^{3+}-D$ to $Cr^{2+}-D$ was proposed to explain the fine structure consisting of 19 lines observed in absorption spectrum of Cr in GaAs [4].

⁴The fact that the observed fine structure in co-doped GaN is formed on the low energy side of the 1.25 eV band in GaN:Mn can be explained by the fact that in the moderately doped GaN:Mn, two exponential decays were observed with the lifetime of 200 μ s centered at 1.38 ± 0.02 eV and 8 ms centered at 1.1 ± 0.05 eV [9,14]. The last transition was assigned to $^4T_1-^4A_1$ recombination of Mn in GaN.

4. Conclusions

In conclusion, the luminescent properties of semi-insulating Mn-doped GaN co-doped with Mg were studied. Upon co-doping, a strong PL band at 1.0 eV was observed. The PL band displayed a rich fine structure at low temperature. It is comprised of at least 10 emission lines separated by 2–10 meV. The FWHM of these lines varied from 3 to 10 meV and was limited by the resolution of the monochromator. Transient spectroscopy measurements indicated the 1.0 eV PL band decayed exponentially with a lifetime of 20–90 μ s. The measured lifetimes were at least two orders of magnitude shorter than that observed for the $^4T_1-^6A_1$ transition at 1.25 eV in Mn-doped GaN.

Acknowledgements

This work was supported by the Office of Naval Research under grant N00014-01-0012.

References

- [1] L. Eaves, A.W. Smith, M.S. Skolnick, B. Cockayne, J. Appl. Phys. 53 (1982) 4955.
- [2] L. Samuelson, M.-E. Pistol, S. Nilsson, Phys. Rev. B 33 (1986) 8776.
- [3] F. Bantien, J. Weber, Phys. Rev. B 37 (1988) 10111.
- [4] M. Jaros, Deep Levels in Semiconductors, Adam Hilger Ltd., Bristol, 1982.
- [5] J. Szczytko, A. Twardowski, K. Swiatek, M. Palczewska, M. Tanaka, T. Hayashi, K. Anado, Phys. Rev. B 60 (1999) 8304.
- [6] P.G. Baranov, I.V. Ilyin, E.N. Mokov, A.D. Roenkov, Semicond. Sci. Technol. 11 (1996) 1843.
- [7] W. Gebicki, J. Strzeszewski, G. Kalmer, T. Szyszko, S. Podsiadlo, Appl. Phys. Lett. 76 (2000) 3870.
- [8] M. Zajac, R. Doradzinski, J. Gorski, J. Szczytko, M. Lefeld-Sosnowska, M. Kaminska, A. Twardowski, M. Palczewska, E. Grzanka, W. Gebicki, Appl. Phys. Lett. 78 (2001) 1276.
- [9] R.Y. Korotkov, J.M. Gregie, B.W. Wessels, in: U. Mishra, M. Shur, C. Wetzel, B. Gil, K. Katsumi (Eds.), GaN and Related Alloys 2000, Proc. Mat. Res. Soc. Symp. G3(7) 2000.
- [10] R.Y. Korotkov, J.M. Gregie, B.W. Wessels, in these Proceedings (ICDS-21), Physica B 308–310 (2001).
- [11] R. Heitz, A. Hoffman, I. Broser, Phys. Rev. B 55 (1997) 4382.
- [12] R.Y. Korotkov, J.M. Gregie, B.W. Wessels, to be published.
- [13] R.Y. Korotkov, J.M. Gregie, B.W. Wessels, Appl. Phys. Lett. 78 (2001) 222.
- [14] K. Pressel, S. Nilsson, R. Heitz, A. Hoffmann, B.K. Meyer, J. Appl. Phys. 79 (1996) 3214.



ELSEVIER

Physica B 308–310 (2001) 22–25

PHYSICA B

www.elsevier.com/locate/physb

Photoluminescence and lattice location of Eu and Pr implanted GaN samples

T. Monteiro^{a,*}, C. Boemare^a, M.J. Soares^a, R.A. Sá Ferreira^a, L.D. Carlos^a,
K. Lorenz^b, R. Vianden^b, E. Alves^b

^aDepartamento de Física, Universidade de Aveiro, 3810-193 Aveiro, Portugal

^bInstituto Tecnológico e Nuclear, Sacavém, Portugal

Abstract

Rare earth (RE) ions implanted GaN films were studied by optical spectroscopy and RBS techniques. Sharp emission lines due to intra-4fⁿ shell transitions can be observed even at room temperature for the Eu³⁺ and Pr³⁺. The photoluminescence spectra recorded by the above band gap excitation reveal dominant transitions due to the ⁵D₀→⁷F_{1,2,3} lines at 6004, 6211 and 6632 Å for the Eu³⁺ and ³P_{0,1}→³F_{2,3} at 6450 and 6518 Å, respectively, for the Pr³⁺. We report on the temperature dependence of the intra-ionic emissions as well as on the lattice site location of the RE detailed angular scans through the <0001> and <10 $\bar{1}$ 1> axial directions; which indicates that for Pr, complete substitutionality on the Ga sites was achieved while for Eu a Ga displaced site was found. © 2001 Elsevier Science B.V. All rights reserved.

Keywords: GaN; Implantation; PL; RBS

1. Introduction

Eu³⁺ and Pr³⁺ are known to be efficient activators in several hosts giving rise to strong red luminescence from the ⁵D_J→⁷F_J and ³P_J→³F_J multiplets, respectively [1–11].

It is known that these rare earth (RE) ions can be incorporated into the GaN samples either by the in-grown process [12–16] or the ion implantation technique [17–22]. Its narrow emission lines associated with the weak dependence of intensity on temperature put into evidence the possibility of achieving full color display devices based on the GaN using the intra-4fⁿ transitions from the RE ions, where Eu³⁺ or Pr³⁺ stands for the red emission, Er³⁺ for the green and Tm³⁺ or Ce³⁺ for the blue [13–16,23]. Actually, yellow and orange emissions were achieved from the ELDs fabricated on the GaN films codoped with Er and Eu [16]. Despite the

progress made in the GaN devices doped with the RE ions, the fundamental properties of intra-ionic luminescence are far to be exploited.

In this work, we focus on the photoluminescence (PL) and RBS studies of the Eu and Pr implanted GaN samples. From the experimental data, the site symmetry of the RE ions in the GaN is discussed and a tentative assignment of the emission levels is made.

2. Experimental

The wurtzite undoped ($n < 5 \times 10^{16} \text{ cm}^{-3}$) GaN layers were epitaxially grown by Metal Organic Chemical Vapor Deposition on c-plane sapphire substrates with a thickness of 1.3 μm. The Eu³⁺ and Pr³⁺ were implanted at room temperature with an energy of 160 keV and at doses of $D = 5 \times 10^{14} \text{ cm}^{-2}$. The measured implantation ranges were determined to be 40 nm. The samples were annealed in a rapid thermal annealing apparatus between graphite strips under flowing N₂ gas at 1000°C for 120 s. The RBS/channelling studies were

*Corresponding author. Tel.: +351-34-370-824; fax: +351-34-424-965.

E-mail address: tita@fis.ua.pt (T. Monteiro).

performed with a 1 mm diameter collimated beam of 2 MeV He^+ ions. The backscattered particles were detected at 140° and close to 180° with respect to the incoming beam direction using silicon surface barrier detectors with the resolutions 13 and 16 keV, respectively. Full angular scans were carried out across the $\langle 0001 \rangle$ and the $\langle 10\bar{1}1 \rangle$ axial directions using a two-axis goniometer.

The PL measurements were carried out with a 325 nm CW He–Cd laser and the excitation power density was typically less than 0.6 W cm^{-2} . A 325 nm band pass filter was used to attenuate lines other than the 325 nm laser line and a low pass sharp cutoff filter was used to stop the laser light. The PL was measured at temperatures between 14 and 300 K using a closed cycle helium cryostat. The luminescence was dispersed by a Spex 1704 monochromator (1 m , 1200 mm^{-1}) and detected by a cooled Hamamatsu R928 photomultiplier.

The Raman spectra were obtained at room temperature in a Jobin Yvon—Spex T64000 using the 514.5 nm line of an Ar ion laser as excitation source.

3. Results and discussion

In Fig. 1, a comparison between the visible intra- $4f^6$ luminescence observed in the Eu^{3+} implanted GaN and in-grown doped samples is shown. The PL spectra were obtained by the above band gap excitation at 14 K. The $^5\text{D}_0 \rightarrow ^7\text{F}_2$ transition produces the strongest emission lines, either at 14 K or at room temperature, for both samples. Minor lines are observed in the studied spectral range. The lines were tentatively assigned to different $^5\text{D}_{0,1} \rightarrow ^7\text{F}_{0,1,2,3,4}$ transitions in accordance with the previous results for the Eu^{3+} in several hosts [3–12, 14–16]. One of the main features concerning the two emission spectra is the appearance of the forbidden $^5\text{D}_0 \rightarrow ^7\text{F}_0$ transition in the in-grown sample, due to admixture with other J levels, being undetected in the implanted sample.

It has been pointed out that the trivalent RE ions in the GaN assume a substitutional Ga site being in a relaxed C_{3v} symmetry [9,17]. In accordance with this site symmetry, the state with $J = 2$ splits into a nondegenerate A level and a two-fold degenerated E level. Even in this site symmetry, three lines for the $^5\text{D}_0 \rightarrow ^7\text{F}_2$ transition have been reported [11] due to further splitting of the E level. The PL spectra put in evidence that in both samples, the ion must be in a lower site symmetry than the referred trigonal symmetry [9,17] as observed by a closer view of the $^5\text{D}_0 \rightarrow ^7\text{F}_2$ emission in the implanted sample (inset (b) of Fig. 1) and in the in-grown sample, where a total lift of the J -degeneracy of the multiplets can be seen. The likely candidates for the lower site symmetry of the RE ions are C_2 , C_i , C_1 , C_{2v} , D_2 , D_{2h} , C_{2h} and C_{1h} site

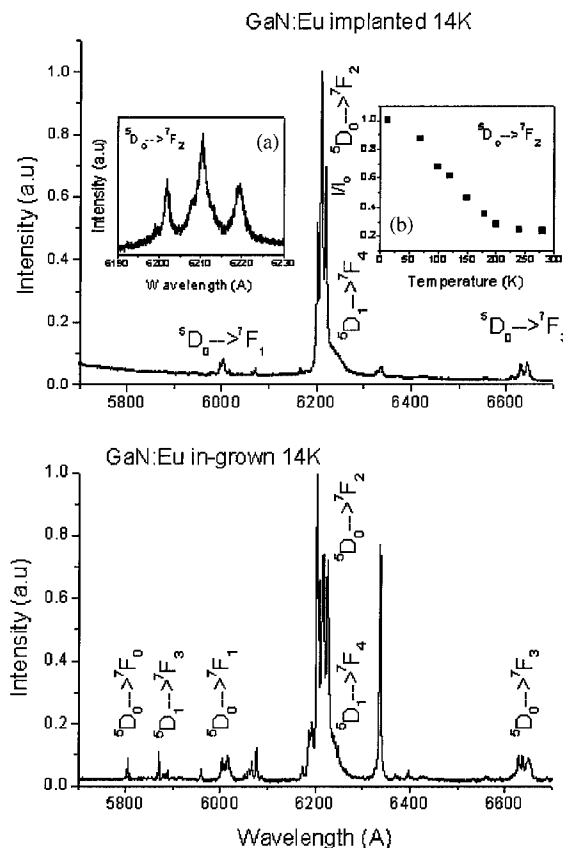


Fig. 1. The PL spectra of the implanted and in-grown GaN samples obtained by the He–Cd excitation at 14 K. In the inset (a) of the upper picture, a high resolution of the $^5\text{D}_0 \rightarrow ^7\text{F}_2$ transition for the implanted sample is present. The inset (b) shows the dependence of the integrated intensity on the temperature for this transition, obtained under constant illumination.

symmetries. However, from the fact that the $^5\text{D}_0 \rightarrow ^7\text{F}_2$ transition is the strongest one, we can exclude the hypothesis that the ion is located in sites with inversion symmetry in both samples. This fact associated with the missing of the $^5\text{D}_0 \rightarrow ^7\text{F}_0$ transition in the implanted sample allows one to tentatively assign the ion site symmetry to the D_2 point group. Some of the observed lines in the PL spectra cannot be directly assigned to the intra- $4f^6$ transitions. They are probably either due to the anti-Stokes luminescence or cooperative vibronic transitions as being currently observed for the triply ionized RE ions in several hosts, even at low temperatures [24–31].

The Raman spectra performed in a $z(x\bar{x})\bar{z}$ configuration at room temperature for both implanted samples (Eu and Pr) presents, besides the characteristics E_2 and $\text{A}_1(\text{LO})$ of the GaN lattice, two local modes at 362 and 380 cm^{-1} as previously observed in the implanted samples [32]. In order to test if they are related to

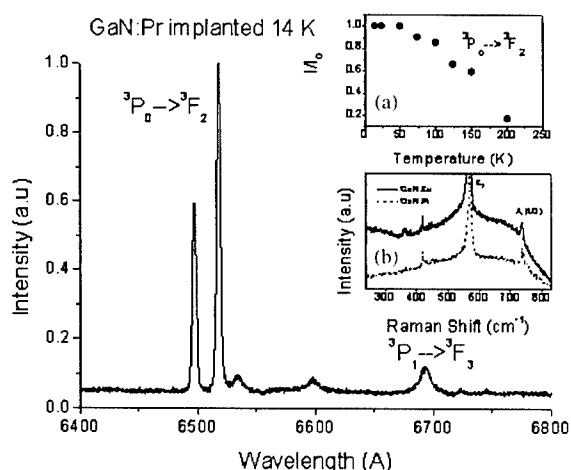


Fig. 2. The PL spectra of the Pr implanted GaN sample obtained by the He–Cd excitation at 14 K. In the inset (a), the dependence of the integrated intensity on temperature, obtained under constant illumination, for the $^3P_0 \rightarrow ^3F_2$ transition is shown. The inset (b) shows the Raman spectra of the Eu and Pr implanted samples.

vibronic transitions. excitation luminescence (PLE) studies will be done.

In the inset (b) of Fig. 1, the dependence of the PL integrated intensity with the temperature for the $^5D_0 \rightarrow ^7F_2$ transition is shown. The intensity decreases near one order of magnitude in the studied temperature range.

Similar spectroscopic studies were performed for the Pr implanted GaN samples. The PL spectra obtained by the above band gap excitation at 14 K are shown in Fig. 2. The dependence of the PL integrated intensity

with the temperature of the $^3P_0 \rightarrow ^3F_2$ transition, as well as the previously mentioned Raman spectra of both implanted samples, are added.

The strongest emission lines are identical to those previously observed by several authors for the $^3P_0 \rightarrow ^3F_2$ transition [18,19,21] indicating that the Pr^{3+} ion is in C_{3v} symmetry. The lines are slightly displaced in energy and they are sharper than those previously reported [21]. Similar to the Eu^{3+} luminescence, the dependence of the integrated intensity on the temperature for the $^3P_0 \rightarrow ^3F_2$ transition decreases near one order of magnitude in the studied temperature range (inset (a) of Fig. 2).

The lattice site location of the Pr and Eu was done performing detailed angular scans through the $\langle 0001 \rangle$ and $\langle 10\bar{1}1 \rangle$ axes. For the $\langle 0001 \rangle$ axis, both the Pr and Eu curves coincide with the Ga one (not shown) indicating that the RE are located along this direction [33]. However, for the $\langle 10\bar{1}1 \rangle$ axis, while the Pr and Ga curves nearly overlap, the Eu curve is narrower, as shown in Fig. 3. This fact indicates that the Eu ions are displaced towards the middle of the $\langle 10\bar{1}1 \rangle$ axis. According to the simulations [33], the curve can be well reproduced by a displacement of 0.2Å along the $\langle 0001 \rangle$ axis. The RBS/C data put in evidence that the Eu^{3+} is in a Ga displaced site. This is in accordance with a lower site symmetry for the RE ion.

4. Conclusions

The PL and RBS analyses were made in the Eu and Pr implanted GaN samples. The results indicate that the Eu^{3+} is in lower site symmetry than trigonal C_{3v} symmetry both in the implanted and in-grown samples. In the last one, more than one environment for

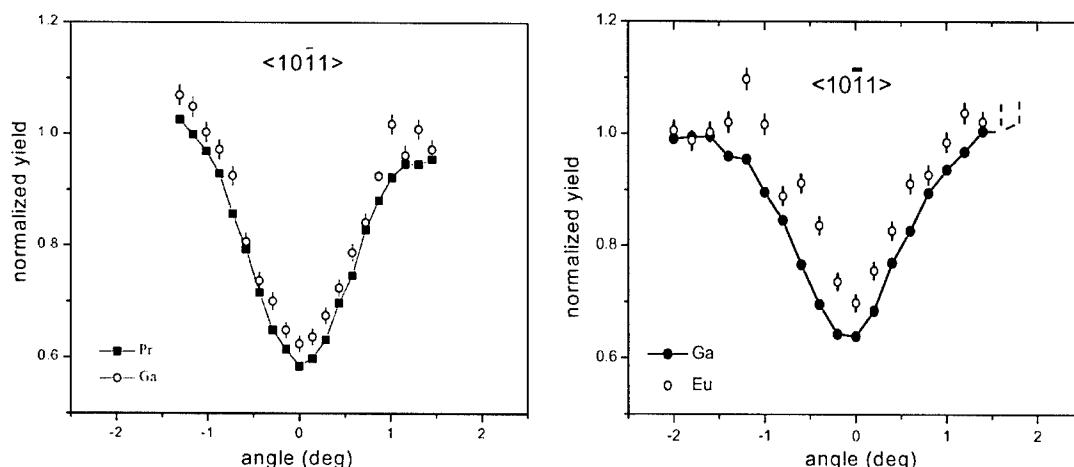


Fig. 3. The angular scans along the $\langle 10\bar{1}1 \rangle$ direction for the GaN films implanted with the Pr (left) and Eu (right) after annealing at 1000°C for 120 s. Both samples were implanted with a nominal dose of $5 \times 10^{14} \text{ cm}^{-2}$.

the Eu^{3+} may coexist. For the Pr implanted samples, the data pointed to a substitutionality of the ion in the Ga sites. For both implanted ions, a decrease close to one order of magnitude for the integrated intensity dependence on temperature is observed. Some of the observed PL lines are probably due to cooperative vibronic transition. In order to get further information on the nature of these emission lines, the PLE measurements are under way.

References

- [1] R. Balda, J. Fernández, I. Saéz de Ocáriz, M. Voda, A.J. García, N. Khaidukov, *Phys. Rev. B* 59 (1999) 9972.
- [2] W.M. Yen, W.C. Scott, A.L. Schawlow, *Phys. Rev.* 136 (1964) A271.
- [3] J.D. Kingsley, J.S. Prener, *Phys. Rev.* 126 (1962) 458.
- [4] L.G. DeShazer, G.H. Dieke, *J. Chem. Phys.* 38 (1963) 2190.
- [5] J.A. Koningstein, *Phys. Rev.* 136 (1964) A717.
- [6] N.C. Chang, J.B. Gruber, *J. Chem. Phys.* 41 (1964) 3227.
- [7] C. Brecher, H. Samelsin, A. Lempicki, R. Riley, T. Peters, *Phys. Rev.* 155 (1967) 178.
- [8] W.T. Carnall, P.R. Fields, K. Rajnak, *J. Chem. Phys.* 49 (1968) 4450.
- [9] L. Arizmendi, J.M. Cabrera, *Phys. Rev. B* 31 (1985) 7138.
- [10] L.D. Carlos, R.A. Sá Ferreira, V. De Zea Bermudez, Celso Molina, Luciano A. Bueno, Sidney J. L. Ribeiro, *Phys. Rev. B* 60 (1999) 10042.
- [11] M. Yin, J.-C. Krupa, E. Antic-Fidancev, A. Lorriaux-Rubens, *Phys. Rev. B* 61 (2000) 8073.
- [12] W.M. Jadwisieniczak, H. Lozykowski, I. Berishev, A. Bensaoula, I.G. Brown, *J. Appl. Phys.* 89 (2001) 4384.
- [13] R. Birkhahn, M. Garter, A.J. Steckl, *Appl. Phys. Lett.* 74 (1999) 2161.
- [14] S. Morishima, T. Maruyama, M. Tanaka, Y. Masumoto, K. Akimoto, *Phys. Stat. Sol.* 176 (1999) 113.
- [15] J. Heikenfeld, M. Gartner, D.S. Lee, R. Birkhahn, A.J. Steckl, *Appl. Phys. Lett.* 75 (1999) 1189.
- [16] D.S. Lee, J. Heikenfeld, R. Birkhahn, M. Garter, B.K. Lee, A.J. Steckl, *Appl. Phys. Lett.* 76 (2000) 1525.
- [17] H.J. Lozykowski, W.M. Jadwisieniczak, J. Han, I.G. Brown, *Appl. Phys. Lett.* 77 (2000) 767.
- [18] L.C. Chao, A.J. Steckl, *Appl. Phys. Lett.* 74 (1999) 2364.
- [19] J.M. Zavada, R.A. Mair, C.J. Ellis, J.Y. Lin, H.X. Jiang, R.G. Wilson, P.A. Grudowski, R.D. Dupuis, *Appl. Phys. Lett.* 75 (1999) 790.
- [20] U. Wahl, J.P. Araújo, L. Peralta, J.G. Correia, ISOLDE Collaboration, *J. Appl. Phys.* 88 (2000) 1319.
- [21] H.J. Lozykowski, W.M. Jadwisieniczak, I. Brown, *J. Appl. Phys.* 88 (2000) 210.
- [22] J.B. Gruber, B. Zandi, H.J. Lozykowski, W.M. Jadwisieniczak, I. Brown, *J. Appl. Phys.* 89 (2001) 7973.
- [23] A.J. Steckl, M. Gartner, D.S. Lee, J. Heikenfeld, R. Birkhahn, *Appl. Phys. Lett.* 75 (1999) 2184.
- [24] F. Auzel, *Phys. Rev. B* 13 (1976) 2809.
- [25] E.Ya. Arapova, N.Z. Zamkovets, N.N. Sibeldin, Yu.P. Timofeev, S.A. Fridman, V.A. Tsvetkov, *Opt. Spectros.* 41 (1976) 524.
- [26] A. Meijerink, C. De Mello Donegá, A. Ellens, J. Sytsma, G. Blasse, *J. Lum.* 58 (1994) 26.
- [27] N. Yamada, S. Shionoya, *J. Phys. Soc. Japan* 31 (1971) 841.
- [28] K. Soga, H. Inoue, A. Makishima, *J. Lum.* 55 (1993) 17.
- [29] E. Cohen, H.W. Moos, *Phys. Rev.* 161 (1967) 258.
- [30] M. Tanaka, G. Nishimura, T. Kushida, *Phys. Rev. B* 49 (1994) 16917.
- [31] M. Tanaka, T. Kushida, *Phys. Rev. B* 60 (1999) 14732.
- [32] W. Limmer, W. Ritter, R. Sauer, B. Mensching, C. Liu, B. Rauschenback, *Appl. Phys. Lett.* 72 (1998) 2589.
- [33] E. Alves, K. Lorenz, R. Vianden, C. Boemare, M.J. Soares, T. Monteiro, *Mod. Phys. Lett. B* (2001), to be published.



ELSEVIER

Physica B 308–310 (2001) 26–29

PHYSICA B

www.elsevier.com/locate/physb

Investigation of the defect structure of GaN heavily doped with oxygen

R.Y. Korotkov, F. Niu, J.M. Gregie, B.W. Wessels*

Department of Materials Science and Engineering and Materials Research Center, Northwestern University, 2225 N. Campus Drive, Evanston, IL 60208-3108, USA

Abstract

The defect structure of oxygen-doped GaN grown by MOVPE was investigated. At high oxygen pressures, a super-linear increase of electron concentration as a function of partial pressure was observed. Electron concentrations as high as $7 \times 10^{19} \text{ cm}^{-3}$ were measured. Formation of micropits was observed by scanning electron microscopy in heavily doped samples. Cross-sectional transmission electron microscopy studies indicated the presence of epitaxial precipitates located on the cavity surface. The precipitates are believed to be related to gallium oxide. Using spatially resolved photoluminescence (PL), a broad PL band at 3.56 eV was observed near the micropit regions. The band was attributed to free-electron recombination from the highly degenerate areas associated with oxygen. © 2001 Elsevier Science B.V. All rights reserved.

Keywords: O-doped GaN; Microcavities; Photoluminescence

1. Introduction

Oxygen is known as a potential source of residual donors in GaN, although its doping behavior is not well understood [1–4]. The electrical properties of oxygen donors in GaN are somewhat controversial. Ionization energy values have ranged from 4 to 75 meV as determined by Hall-effect and optical measurements [1,5–8]. This large variation can be partially attributed to difficulties in their determination from Hall effect, presumably due to sample dopant inhomogeneities. A low temperature-conductivity tail is observed even in moderately doped GaN:O [8,9], which complicates calculations. Two possible explanations that account for this effect are the presence of a high conductivity layer at the layer substrate interface [10] or the formation of an impurity band [7]. SIMS studies corroborate the former model, since large concentrations of oxygen were observed within the first micron of the GaN film [11].

While it is now generally believed that oxygen is the shallow donor often responsible for the high residual background n-type conductivity in GaN, there are still unanswered questions regarding its incorporation. For example, we previously demonstrated that the electron concentration, n , increased with increasing partial pressure of oxygen as the square root from 1×10^{17} to $8 \times 10^{18} \text{ cm}^{-3}$ [8]. However, it was also observed that the electron concentration increased super-linearly at higher oxygen partial pressures. In this paper, we present structural, optical, and electrical characterization of heavily oxygen-doped epilayers. Hexagonal surface microcavities (micropits) are formed on the surface of heavily oxygen-doped samples with $n > 10^{19} \text{ cm}^{-3}$. Spatially resolved photoluminescence (PL) data provide evidence that the observed emission band at 3.56 eV is associated with oxygen doping and the presence of micropits.

2. Experimental

Oxygen-doped GaN epilayers were grown by MOVPE, as described elsewhere [8]. In brief, after deposition of the GaN buffer layer at 600°C, the

*Corresponding author. Tel.: +1-847-491-3537; fax: 1-847-491-7820.

E-mail address: b-wessels@northwestern.edu (B.W. Wessels).

temperature was ramped to 1060°C and 50 nm of undoped GaN was deposited. This step was followed by the deposition of 2 μm of oxygen-doped GaN. Scanning electron microscopy (SEM) images were taken using a Hitachi S-4500 microscope. Typical operating conditions were 5–20 kV, with a magnification of 50–30,000 \times . High-resolution TEM was carried out with a Hitachi HF-2000 cold field emission microscope operating at 200 kV. The PL measurement setup was previously described [12]. He–Cd laser excitation was used. For spatially resolved measurements, the laser was focussed to a spot size of 20 μm .

3. Results and discussion

The surface morphology of deliberately oxygen-doped GaN was investigated. The surface of as-grown, undoped GaN films as seen in Fig. 1(a) is featureless when grown at high temperatures (1000–1070°C). As the partial pressure of oxygen is increased, the surface morphology remains unchanged for carrier concentration $<10^{19}\text{cm}^{-3}$. At this concentration, hexagonal-shaped microcavities are formed on the surface, as seen in Figs. 1(b) and (c). The concentration of the pits increased with free electron concentration, as seen by comparing Figs. 1(b) and (c), indicating that the formation of these surface microcavities was oxygen-related. The surface of the oxygen-doped sample with a RT electron concentration of $7 \times 10^{19}\text{cm}^{-3}$ was rough and completely covered with pits. A high-magnification SEM image of one of the microcavities is shown in Fig. 1(d).

Table 1

Electrical properties of GaN:O films

Sample	$P(\text{O}_2)$ (Pa)	T (K)	NH_3 (sccm)	$n \times 10^{18}$ (cm^{-3})
RK120	0	1333	1400	0.1
RK216	0.4	1333	1400	1.8
RK213	6.2	1333	1400	16
RK217	12.1	1333	1400	29
RK234	10.3	1333	940	20
RK232	10.3	1273	1400	61
JG125 (GaN:Si)	0	1333	1400	30

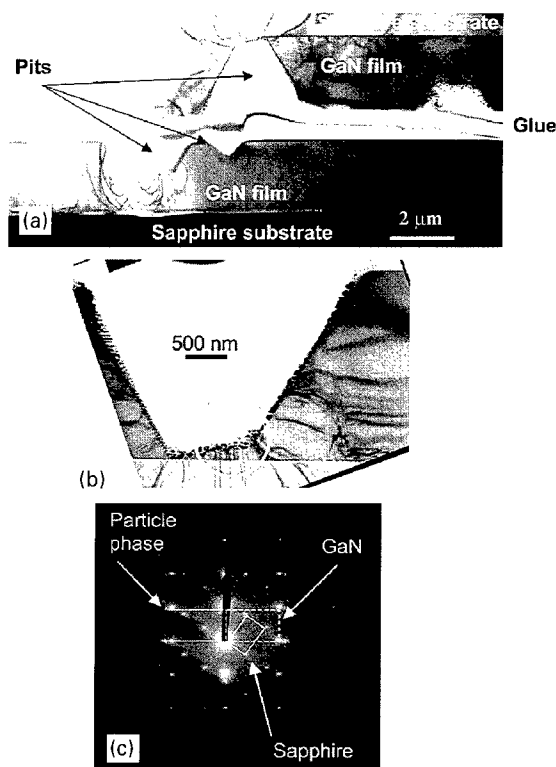


Fig. 2. (a) XTEM micrograph of GaN films grown on sapphire showing O-doping induced pits, (sample RK234, $n = 2 \times 10^{19}\text{cm}^{-3}$); (b) high-resolution XTEM image of a deep pit, with visible precipitate formation on the sidewalls; (c) SAD pattern of circled region of (b) that includes the $\text{Al}_2\text{O}_3/\text{GaN}/$ particle interface.

To determine the structure of the microcavities, TEM studies of highly oxygen-doped layers were conducted. A cross-sectional micrograph of a highly oxygen-doped sample RK234 (see Table 1) is shown in Fig. 2(a). It shows two pieces of a GaN sample grown on sapphire attached to each other by glue introduced during TEM sample preparation. Several pits are evident at the

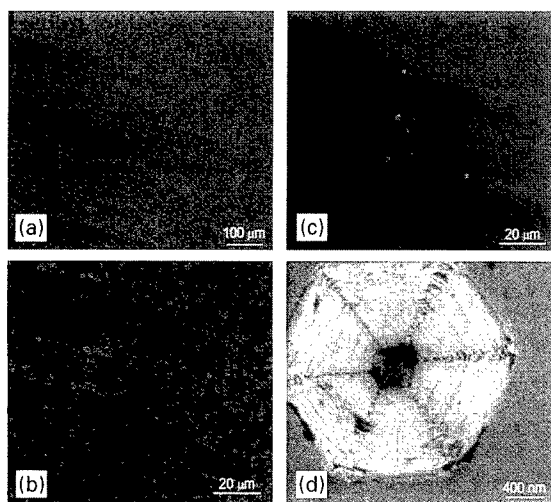


Fig. 1. SEM planar view image of oxygen-doped samples with (a) $n = 8 \times 10^{18}$, (b) 2.1×10^{19} , (c) $1.1 \times 10^{19}\text{cm}^{-3}$ and (d) high-resolution image of the pit.

surface of the GaN films. The depth of the pits varied, with some pits originating at the buffer layer surface. At the same time, several pits that nucleated during later stages of the GaN growth were also observed. Interestingly, a new epitaxial compound in the form of grains was observed on the pit surface (Fig. 2(b)). The structure of these grains was analyzed and compared to bulk GaN using selective area diffraction (SAD) patterns as shown in Fig. 2(c). Based on the fact that the SAD pattern of the grain regions was aligned in the same crystallographic direction as the GaN, it was concluded that these grains formed a textured epitaxial arrangement with GaN. The detailed work will be published elsewhere [13,14]. However, as to the identification of this second phase, we propose that it is likely a gallium oxide phase such as Ga_2O_3 or $\text{GaN}_x\text{O}_{1-x}$. The formation of a second phase of oxide at high partial pressures of oxygen is predicted from thermodynamic calculations [3]. The present study indicates that the solubility limit of oxygen in epitaxial GaN is of the order of $1 \times 10^{19} \text{ cm}^{-3}$.

PL measurements at 20 K were conducted on heavily oxygen-doped GaN layers to determine whether or not oxygen introduces radiative centers. The samples studied are summarized in Table 1. A PL spectrum of a moderately O-doped sample (RK216) is shown in Fig. 3 for comparison. It consists of a strong donor-bound exciton (DBE) (FWHM = 5 meV) PL band located at 3.482 eV with a smaller shoulder of the free exciton (FE) at 3.49 eV, and so-called two-electron transitions at 3.458 and 3.463 eV, respectively. The exciton transitions are assigned by comparing their temperature-quenching behavior, and are in line with earlier results [5]. In heavily oxygen-doped samples, two DBEs were observed as shown in Fig. 3. The most intense exciton transition was at 3.482 eV for O-doped

samples with $n < 1 \times 10^{19} \text{ cm}^{-3}$, and at 3.472 eV for the samples with higher electron concentrations. Since the intensity ratio of the DBE transition at 3.482 eV to the FE transition was independent of partial pressure of oxygen, it was concluded that it did not involve an oxygen-bound exciton. In contrast, the relative PL intensity of the 3.472 eV DBE to the FE peak increased with partial pressure of oxygen as seen in Fig. 3. Therefore, we attribute the PL peak at 3.472 eV to an oxygen-related bound exciton.

The PL spectrum of a highly oxygen-doped ($2 \times 10^{19} \text{ cm}^{-3}$) sample also exhibited a broad band extending to energies above the band gap in addition to the FE, DBE and ABE transitions. The band was observed above band gap as a shoulder to the FE and DBE transitions at 3.56 eV, as seen in Figs. 3 and 4. The intensity of this band increased with increasing partial pressure of oxygen, indicating that it was sensitive to the incorporation of oxygen in the film. As seen from this figure, the 3.56 eV band broadened when the electron concentration was increased (Table 1). However, no separate peak was observed, even at the highest electron concentration (RK232). The 3.56 eV band was only observed in heavily O-doped samples with electron concentrations higher than 10^{19} cm^{-3} . We propose that the 3.56 eV band observed in highly oxygen-doped samples is due to free electron recombination.

To identify the origin of this band in highly oxygen-doped samples, spatially resolved PL experiments were conducted.¹ It can be seen in Fig. 4 that the intensity of the 3.56 eV band is higher in the pit regions than in nearly pit-free areas. Therefore, the 3.56 eV band PL is associated with the regions covered by hexagonal pits. The degenerate regions are formed in the vicinity of the hexagonal pits in agreement with spatially resolved PL, SEM, TEM and SIMS data. A similar broad, asymmetric band was previously observed in HVPE-grown, undoped GaN. In that case, it was related to localized degenerate regions using spatially resolved cathodoluminescence [15].

4. Conclusions

In this work, we have presented a study of heavily oxygen-doped GaN films grown by MOVPE. For higher electron donor concentrations, $n > 10^{19} \text{ cm}^{-3}$, the formation of surface microcavities or micropits was observed. The pits were associated with oxide micro-precipitates. These studies indicate that the solubility of oxygen in GaN is limited by the formation of Ga_2O_3 -

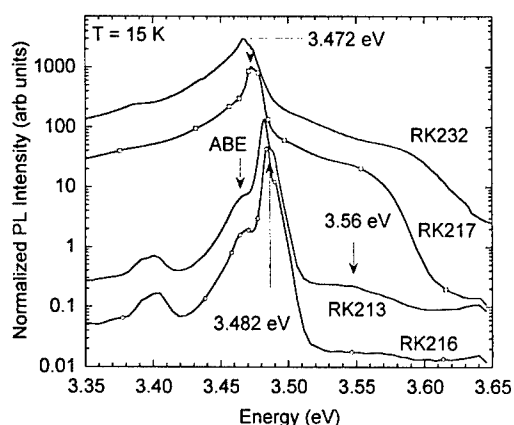


Fig. 3. PL spectra of oxygen-doped and undoped samples at 20 K. Two DBEs transitions are shown with arrows for the sample grown with different oxygen partial pressures (see Table 1).

¹ Hexagonal shaped pits and clusters can be observed with the help of optical microscopy. The He–Cd laser beam was focused ($d \sim 20 \mu\text{m}$) both on the nearly pit-free regions (b in Fig. 4) and pit-clusters (a in Fig. 4).

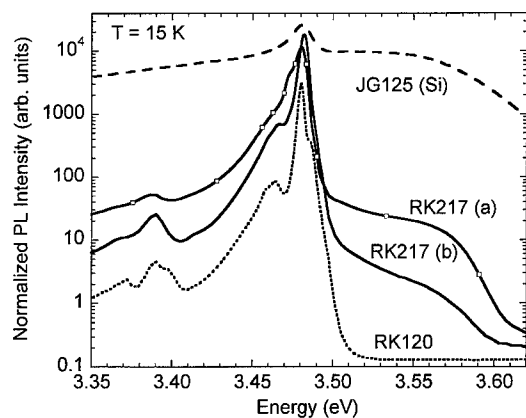


Fig. 4. LT PL spectra of nearly pit-free (RK217a) and pit-covered (RK217b) surface of highly oxygen-doped ($2.9 \times 10^{19} \text{ cm}^{-3}$) sample. The spectra of an undoped sample (RK120) and a highly Si-doped sample (JG125) are shown for comparison.

related precipitates. Using spatially resolved PL measurements, these micropit regions were correlated with the 3.56 eV band due to free electron recombination in degenerate regions. These structural defects are likely responsible for the low mobility of the highly oxygen-doped layers.

Acknowledgements

This work is supported by the Office of Naval Research under grant N00014-01-0012.

References

- [1] M. Illegems, H.C. Montgomery, *J. Phys. Chem. Solids* 34 (1973) 885.
- [2] B.-C. Chung, M. Gershenson, *J. Appl. Phys.* 72 (1992) 651.
- [3] C.G. van de Walle, C. Stampfl, J. Neugebauer, *J. Crystal Growth* 195 (1998) 314.
- [4] C. Wetzel, T. Suski, J.W. Ager III, E.R. Weber, E.E. Haller, S. Fischer, B.K. Meyer, R.J. Molnar, P. Perlin, *Phys. Rev. Lett.* 78 (1997) 3923.
- [5] R. Niebuhr, K.H. Bachem, U. Kaufmann, M. Maier, C. Mertz, et al., *J. Electron. Mat.* 26 (1997) 1127.
- [6] J.C. Zolper, R.G. Wilson, S.J. Pearton, R.A. Stall, *Appl. Phys. Lett.* 68 (1996) 1945.
- [7] M.A. di Forte-Poisson, F. Huet, A. Roman, M. Tordjman, et al., *J. Crystal Growth* 195 (1998) 314.
- [8] R.Y. Korotkov, B. Wessels, *MRS Internet J. Nitride Semicond. Res.* 5S1 (2000) W380.
- [9] W. Gotz, R.S. Kern, C.H. Chen, H. Liu, D.A. Steigerwald, *Mat. Sci. Eng. B59* (1999) 211.
- [10] D.C. Look, R.J. Molnar, *Appl. Phys. Lett.* 70 (1997) 3377.
- [11] G. Popovici, W. Kim, A. Botchkarev, H.P. Tang, H. Morkoc, J. Solomon, *Appl. Phys. Lett.* 71 (1997) 3885.
- [12] M.A. Reshchikov, F. Shahdipour, R.Y. Korotkov, M.P. Ulmer, B.W. Wessels, *Physica B* 273–274 (1999) 105.
- [13] R.Y. Korotkov, F. Niu, B.W. Wessels, in preparation.
- [14] P.J. Dean, J.D. Cuthbert, D.G. Thomas, R.T. Lynch, *Phys. Rev. Lett.* 18 (1967) 122.
- [15] B. Arnaudov, T. Paskova, E.M. Goldys, R. Yakimova, S. Evtimova, I.G. Ivanov, A. Henry, B. Monemar, *J. Appl. Phys.* 85 (1999) 7888.



ELSEVIER

Physica B 308–310 (2001) 30–33

PHYSICA B

www.elsevier.com/locate/physb

Mn-related absorption and PL bands in GaN grown by metal organic vapor phase epitaxy

R.Y. Korotkov, J.M. Gregie, B.W. Wessels*

Department of Materials Science and Engineering and Materials Research Center, Northwestern University, Materials and Life Science Building, 2225 N. Campus Drive, Evanston, IL 60208-3108, USA

Abstract

In this paper, the optical absorption and photoluminescence spectra of semi-insulating Mn-doped GaN films were studied. Two characteristic bands were observed in the absorption spectra of Mn-doped epilayers at 300 K. The integrated intensities of these bands increased with increasing Mn concentration indicating that they were Mn-related. An analysis of the temperature behavior of the absorption band with a maximum at 1.5 eV indicated that it involved a free to bound transition from the valence band to the deep Mn-acceptor level. Photoluminescence measurements of Mn-doped films indicated the presence of an intra 3d-shell transition of the Mn ion. The luminescence band at 1.25 ± 0.02 eV is tentatively attributed to the ${}^4T_1(G) \rightarrow {}^6A_1(S)$ transition. © 2001 Elsevier Science B.V. All rights reserved.

Keywords: Gallium nitride; Transition metals; Manganese; Absorption

1. Introduction

Manganese has extensively been studied as a dopant in II–VI [1] and III–V [2,3] materials for optical applications [3]. The features of the optical spectra of Mn-doped films have usually been assigned to internal 3d-shell transitions within the Mn ion. The free Mn^{2+} ion with d^5 electron configuration has a 6S ground and a 4G first excited state [2]. A crystal field of trigonal symmetry in the wurtzite structure leads to the splitting of the 4G excited state into three states, 4T_1 , 4T_2 and 4A_1 , (from the lowest to the highest energy) [4–7]. The ground state of the Mn ion, 6A_1 , is unaffected by the crystal field. Therefore, a series of transitions including ${}^6A_1 \rightarrow {}^4T_1$, ${}^6A_1 \rightarrow {}^4T_2$ and ${}^6A_1 \rightarrow {}^4A_1$ are often observed in absorption for Mn in wide gap hosts.

Manganese has been shown to form an acceptor level when it substitutes in the group-III metal site [2]. The binding energy of the Mn acceptor varies from 113 meV in GaAs to 400 meV in GaP and InP [2,3,8]. The binding

energies of Mn were found to follow a universal trend [9]. Caldas et al. indicated that the transition metal binding energies are referenced to the vacuum level and independent of the band edges of the host crystal [9].

The behavior of Mn in GaN has received limited attention [10]. However, electron paramagnetic resonance (EPR) studies of residual Mn impurities in GaN grown by the sublimation ‘sandwich method’ [11] and GaMnN grown by the ammonothermal method [12] unambiguously identified the presence of the $Mn^{2+} d^5$ ion. Furthermore, Raman scattering studies of GaMnN observed new bands around 300 and 667 cm^{-1} [12]. We previously reported our preliminary data on the absorption and PL spectra of deliberately Mn-doped GaN grown by metal organic vapor phase epitaxy (MOVPE) [13,14]. It was shown that Mn introduced two well-resolved characteristic absorption bands in the GaN thin films. In this paper, the optical properties of a series of GaN samples deliberately doped with Mn are reported.

2. Experimental

The MOVPE growth of Mn-doped GaN layers has been previously described [13]. Optical absorption–

*Corresponding author. Tel.: +1-847-491-3537; fax: +1-847-491-7820.

E-mail address: b-wessels@northwestern.edu (B.W. Wessels).

reflection measurements at room temperature and in the 300–1200 nm range were performed using a Cary-500 spectrometer. Absorption spectra at 20–300 K were measured in the range 0.8–1.63 eV using a quartz halogen lamp and Zeiss monochromator with a resolution of 1.5 nm at 1 μ m. A Ge-detector was used to measure transmittance of the sample. All absorption spectra were normalized to account for the spectral responsivity of the lamp and Ge-detector as well as the monochromator. Transient PL decay curves were excited using 20 Hz, 4 ns pulses of N₂ laser with an excitation energy of 3.68 eV. The signal was detected using a Hamamatsu photomultiplier tube (R632) with a rise time of 9 ns.

3. Results and discussion

The normalized reflectance spectra of a series of undoped and Mn-doped samples at room temperature are shown in Fig. 1. The studied samples are reported in Table 1. It can be seen from Fig. 1 that in addition to the characteristic band gap absorption at 3.4 eV, observed in the undoped sample, two new well-resolved bands have been observed for the Mn-doped samples. The first band has a minimum at 1.5 ± 0.02 eV with a full width half maximum (FWHM) of 370 meV. The second band has an onset at 2.0 eV and a minimum at 2.8 ± 0.05 eV. Its asymmetrical shape indicates that it may be comprised of two separate bands. The absolute intensities of these two bands increase systematically with an increase of the Mn dopant, indicating that they are Mn-related.

Table 1

Absorption coefficients and resistivities of undoped and Mn-doped films at $T = 296$ K

Sample #	Mn (μ mol/min)	Resistivity (Ω cm)	α (2.9 eV) (cm^{-1})	α (1.5 eV) (cm^{-1})
JG38	12.7	> 100	3688	1405
JG40	7.6	> 100	3232	1221
RK342	4.5	> 100	1076	330
RK326	Undoped	0.1	—	—

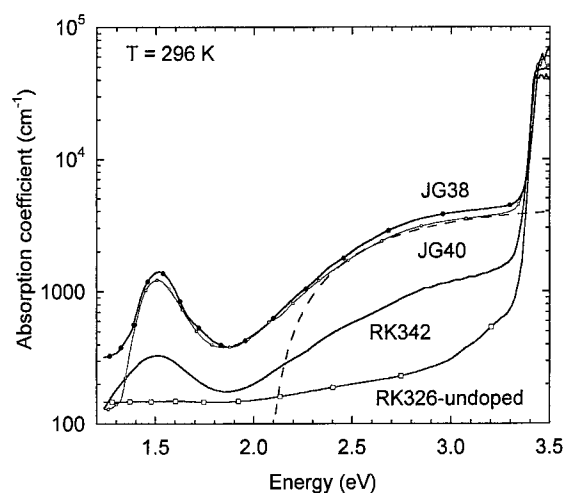


Fig. 2. Absorption coefficient as a function of energy for a series of undoped and Mn-doped samples listed in Table 1. The dashed line is a calculated fit using an ionization energy of 2.1 eV.

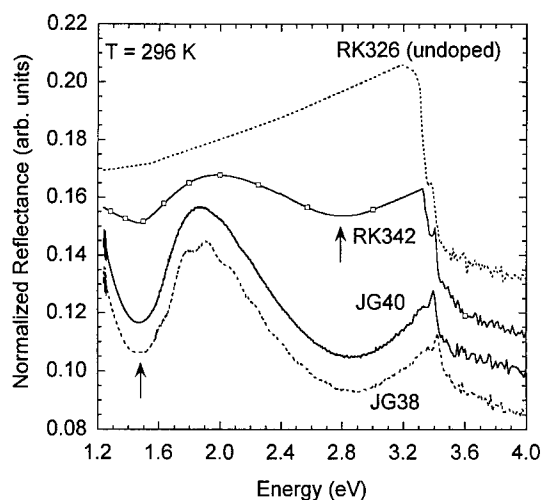


Fig. 1. Room temperature reflectance spectra of undoped, and a series of Mn-doped samples (Table 1). Two new transitions at 1.5 and 2.9 eV observed in Mn-doped samples are labeled with arrows.

To determine the absorption coefficient of Mn-doped GaN films, polarized ($E \perp c$) transmission and reflection spectra were measured at 295 K. The absorption coefficient was calculated based on these measurements [13]. The dependence of the absorption coefficient as a function of energy for undoped and a series of Mn-doped epilayers is shown in Fig. 2. The maximum values of the absorption coefficient for the observed bands are also presented in Table 1. The nominally undoped GaN film is transparent in the visible region with the band edge absorption onset at $E_g \sim 3.42 \pm 0.02$ eV at room temperature. However, two absorption bands are formed in Mn-doped GaN. The first band has an onset at 1.4 eV and a maximum at 1.5 ± 0.01 meV. This band has an asymmetrical shape with an FWHM of 245 ± 10 meV. The second band is seen as a broad shoulder with an onset at 2.1 eV. This absorption occurs over a wide energy range (2.1–2.9 eV). The intensity of both bands systematically increased with Mn dopant as shown in Table 1.

The low temperature absorption spectrum of GaN:Mn was measured. The variation of the absorption band shape with temperature for the 1.5 eV band is shown in Fig. 3. At 20 K, a fine structure was resolved. We attributed the first sharp peak at 1.418 ± 0.001 eV to the zero-phonon line (ZPL) of the Mn free to bound acceptor transition, E_0 [14]. The fine structure at higher energies of the low temperature spectrum was attributed to coupling with two local vibration modes with energies of 20 and 73 meV. The observed fine structure is a characteristic feature of an absorption band involving a deep defect level and its phonon replicas [7,15].

With increasing temperature, however, the sharp peaks involved in the Mn-absorption band become less resolved, as seen in Fig. 3. Although the line shape changes, the total absorption intensity is approximately independent of temperature, such that as the intensity of the ZPL decreases the intensities of the side bands increase [7,15]. Therefore, the 'area conservation law', that is a characteristic feature of absorption involving a deep level, governs the behavior of the absorption spectrum at higher temperatures, as seen in Fig. 3. At room temperature a broad band (FWHM = 340 meV) is observed.

Based on the configuration coordinate analysis of the temperature-dependent behavior of the 1.5 eV band, it is concluded that this band involves a deep Mn-acceptor level, and not an internal 3d-shell transition. The position of this level is placed at 1.42 eV based on the ZPL. The level position with respect to the valence band is at $E_A = E_V + 1.42$ eV based on deep level optical spectroscopy measurements [14]. The threshold of the 2.1 eV band was independent of temperature (22 and 300 K), as seen in Fig. 4. Weak shoulders were also observed in the absorbance curve at 2.3 ± 0.05 and 2.7 ± 0.05 eV at $T = 22$ K.

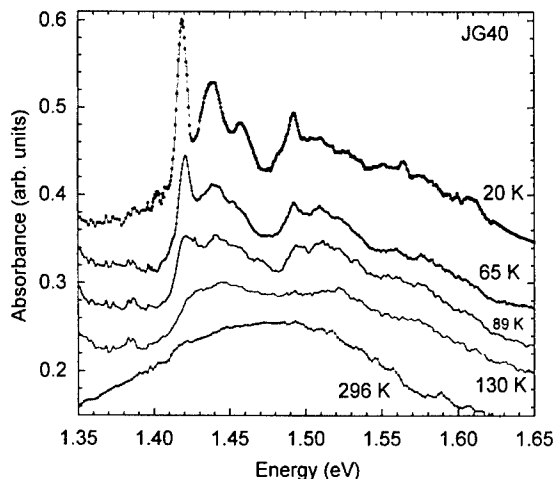


Fig. 3. Absorbance spectra of the heavily Mn-doped film at different temperatures.

A broad PL band at 1.25 ± 0.02 eV was observed in Mn-doped samples [13]. The peak position of this band was independent of temperature. The transient decay curves obtained for the 1.25 eV band at different temperatures for one of the samples are shown in Fig. 5. The decay was exponential at low temperature. The calculated decay curve ($\tau = 7.8$ ms) is shown with a solid line in Fig. 5. A long decay time is a characteristic feature of forbidden transitions, such as $^4T_1 \rightarrow ^6A_1$ [2,6]. At high temperature, the decay time decreases and the decay curves become non-exponential. Similar behavior was observed for the Mn internal transitions in ZnS, where long decay times of 1.6 ms were measured [16]. In that case, the decay curve was non-exponential due to non-radiative recombination processes that become important at high temperatures for the Mn ion.

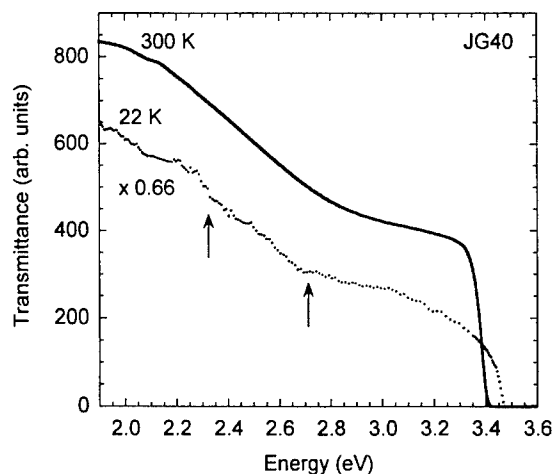


Fig. 4. Absorption spectra of the heavily Mn-doped films at 22 and 300 K.

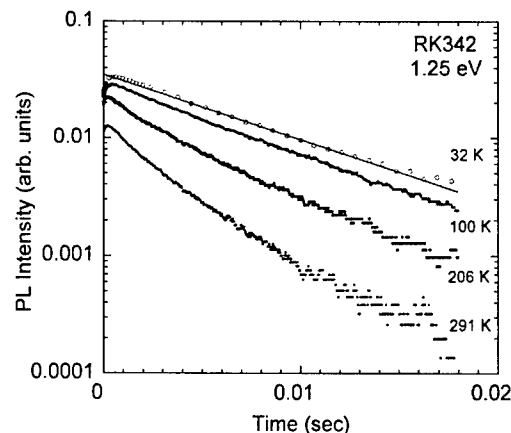


Fig. 5. PL decay curves at 1.25 eV measured at different temperatures (RK342). The calculated exponential decay with a lifetime of 7.8 ms is shown with a solid line.

A proposed energy level scheme for Mn in GaN is as follows: the Mn-acceptor level is located at $E_v + 1.42$ eV. The observed higher lying absorption bands at 2.1 and 2.8 eV are tentatively associated with electron excitation from this level to the conduction band¹ and electron excitation from the VB to the first excited state (4T_1).^{2,3} The observed photoluminescence band at 1.25 eV is attributed to an intra d-shell transition from the first excited state to the ground state given as $^4T_1 \rightarrow ^6A_1$. Higher lying 3d excited states are believed to be degenerate with the conduction band and thus, are not observed in photoluminescence measurements.

4. Conclusions

The optical absorption and photoluminescence properties of semi-insulating Mn-doped GaN films were studied. Two characteristic absorption bands were observed in the spectrum of Mn-doped epilayers at 300 K. The integrated intensities of these bands increased with increasing Mn concentration, indicating that they were Mn related. An analysis of the temperature behavior of the absorption band with a maximum at 1.5 eV indicated that it involved a free to bound transition from the valence band to the deep Mn-acceptor level. Photoluminescence measurements of Mn-doped films indicated the presence of an intra 3d-shell transition of the Mn ion. The luminescence band at 1.25 ± 0.02 eV is tentatively attributed to the $^4T_1(G) \rightarrow ^6A_1(S)$ transition.

Acknowledgements

This work is supported by the NSF GOALI program under grant DMR-9705134 and ONR grant # N00014-01-0012.

References

- [1] W. Park, T.C. Jones, W. Tong, S. Schon, M. Chaichimansour, B.K. Wagner, *J. Appl. Phys.* 84 (1998) 6852.
- [2] F. Bantien, J. Weber, *Phys. Rev. B* 37 (1988) 10111.
- [3] V.F. Masterov, B.E. Samorukov, *Sov. Phys. Semicond.* 12 (1977) 363.
- [4] R. Heitz, A. Hoffmann, I. Broser, *Phys. Rev. B* 45 (1992) 8977.
- [5] R. Heitz, A. Hoffmann, I. Broser, *Phys. Rev. B* 55 (1997) 4382.
- [6] D.S. McClure, *Solid State Phys.* 9 (1954) 488.
- [7] B. Henderson, G.F. Imbusch, *Optical Spectroscopy of Inorganic Solids*, OUP, Oxford, 1989.
- [8] S.A. Abagyan, G.A. Ivanov, G.A. Koroleva, Y.N. Kuznetsov, Y.A. Okunev, *Sov. Phys. Semicond.* 9 (1975) 243.
- [9] M.J. Caldas, A. Fazzio, A. Zunger, *Appl. Phys. Lett.* 45 (1984) 671.
- [10] P.G. Baranov, I.V. Ilyin, E.N. Mokov, A.D. Roenkov, *Semicond. Sci. Technol.* 11 (1996) 1843.
- [11] M. Zajac, R. Doradzinski, J. Gorski, J. Szczytko, M. Lefeld-Sosnowska, M. Kaminska, A. Twardowski, M. Palczewska, E. Grzanka, W. Gebicki, *Appl. Phys. Lett.* 78 (2001) 1276.
- [12] W. Gebicki, J. Strzeszewski, G. Kamer, T. Szyszko, S. Podsiadlo, *Appl. Phys. Lett.* 76 (2000) 3870.
- [13] R.Y. Korotkov, J.M. Gregie, B.W. Wessels, in: U. Mishra, M. Shur, C. Wetzel, B. Gil, K. Katsumi (Eds.), *GaN and Related Alloys 2000*, Proc. Mat. Res. Soc. Symp. G3.7 (2000).
- [14] R.Y. Korotkov, J.M. Gregie, B.W. Wessels, unpublished.
- [15] K.K. Rebane, *Impurity Spectra of Solids*, Plenum, New York, 1970.
- [16] W. Park, T.C. Jones, S. Schon, W. Tong, M. Chaichimansour, B.K. Wagner, C.J. Summers, *J. Cryst. Growth* 184–185 (1998) 1123.

¹ This assignment assumes a large degree of compensation of the GaN, which is usually the case.

² The higher lying intra-ion transitions, $^6A_1 \rightarrow ^4T_2$ and $^6A_1 \rightarrow ^4A_1$ are likely to occur at 2.1 and 2.7 eV based on the observed transition in GaN:Fe³⁺ [5] absorption spectra, however, the intensity of these forbidden transitions has to be small. In contrast, large absorption coefficients were measured for the 2.1 eV band (Table 1), which were higher than that of the 1.5 eV band.

³ It is important to note, however, that several different states of Mn, such as Mn²⁺, Mn³⁺, Mn⁴⁺ can potentially introduce several deep levels in the band gap giving rise to several free to bound transitions as in Ref. [7].



ELSEVIER

Physica B 308–310 (2001) 34–37

PHYSICA B

www.elsevier.com/locate/physb

Photoluminescence properties of Er doped GaN

H. Przybylińska^{a,*}, A. Kozanecki^a, V. Glukhanyuk^a, W. Jantsch^b,
D.J. As^c, K. Lischka^c

^a*Institute of Physics, Polish Academy of Sciences, Al. Lotników 32/46, 02-668 Warsaw, Poland*

^b*Institute of Semiconductor and Solid State Physics, Johannes Kepler University, Linz, Austria*

^c*Department of Physics, University of Paderborn, Paderborn, Germany*

Abstract

The Er³⁺ photoluminescence (PL) near 1.54 μm and PL excitation in Er-implanted GaN was investigated. We have found three different classes of optically active Er centers, with different excitation mechanisms. The majority of the incorporated Er ions can be excited only resonantly and the emission intensity decreases quite strongly with the temperature for high Er concentrations, due to excitation energy migration. The PL of centers dominating under above-band-gap illumination is mediated primarily by donor–acceptor pair recombination and has the same temperature dependence as the near-band-edge PL. We also find centers excited by broad, below-gap absorption bands, associated with deep traps, whose PL intensity is temperature independent. © 2001 Elsevier Science B.V. All rights reserved.

Keywords: Erbium; Gallium nitride; Photoluminescence

1. Introduction

Erbium doped semiconductors have been extensively studied over the last decade as a potential light source emitting at 1.54 μm , which is of great interest for optical fiber communication systems. As the emission is due to intra-4f-shell transitions, the lines are sharp and the wavelength is temperature insensitive, which makes the system particularly attractive. The drawback, however, is the strong temperature quenching of the emission intensity with decreasing band gap of the semiconductor host [1]. This has stimulated a wide interest in Er doping of GaN [2–4]. Visible and infrared electroluminescence of in situ Er doped GaN employing the impact excitation mechanism has been already achieved [5]. However, devices employing the much more efficient excitation channel involving electron hole pairs have not been reported yet. Such applications might be possibly realized on Er implanted GaN, as in this case the electron-hole mediated luminescence seems to be very

efficient. In this paper, we investigate Er-implanted GaN by means of photoluminescence (PL) and PL excitation spectroscopy and compare the efficiency and quenching behavior of different centers under direct and interband excitation.

2. Experiment

The samples used in this study were (i) nominally undoped and (ii) Mg doped GaN layers grown by MOCVD on Al₂O₃ substrates, as well as (iii) cubic, Mg doped GaN grown by MBE on GaAs substrates. All layers had a similar width of about 500 nm. The Mg doped samples had a room temperature hole concentration of 10^{17} cm^{-3} prior to implantation. Er was implanted at 800 keV into the undoped GaN/Al₂O₃ and at 300 keV into Mg doped GaN. The TRIM code estimated mean projected and straggling ranges were about 52 and 15 nm for 300 keV, 122 and 32 nm for the 800 keV implants, respectively. The estimated Er peak concentrations were about $2.5 \times 10^{18} \text{ cm}^{-3}$ in both GaN/Al₂O₃ samples and an order of magnitude lower in GaN/GaAs. The samples were subsequently annealed in

*Corresponding author. Tel.: +48-22-843-68-61; fax: +48-22-843-09-26.

E-mail address: przyby@ifpan.edu.pl (H. Przybylińska).

the temperature range of 900°C–1000°C in nitrogen gas flow for up to 30 min. Photoluminescence and PLE experiments were carried out in the temperature range of 5–300 K. The PL was excited with argon ion and tunable Ti:sapphire lasers, dispersed through a SPEX monochromator, and detected by a liquid nitrogen cooled Ge detector through a long pass filter with a cut-off at 1.2 μm . The spectra shown in the paper were typically taken at a power level of about 130 mW and at a spectral resolution of less than 0.1 nm. The data are not corrected for the detector and monochromator response.

3. Results and discussion

Low temperature Er^{3+} PL spectra measured for the GaN/ Al_2O_3 sample implanted with 800 keV Er ions are shown in Fig. 1. The spectra were obtained at three different excitation regimes: above band gap (351 nm), below band gap (514 nm), and resonant $^4\text{I}_{15/2} \rightarrow ^4\text{I}_{11/2}$ excitation (984.6 nm). In each case, the dominant emission comes from different Er centers. The broad PL line in the middle trace of Fig. 1 shows no structure even at a spectral resolution of 0.03 nm. Its shape does not change when varying the pump wavelength in the whole visible range of the Ar laser, indicating that the excitation does not proceed via intra shell transitions of Er but rather by a broad, trap-related absorption band. The dependence of the integrated PL intensity on pump

wavelength is shown in the inset. The emission under resonant Er excitation was found to be an order of magnitude less intense than that excited with above- and below-gap light, which is not surprising as the intra-4f transitions have very low absorption cross sections. The fact that none of the centers active under visible or UV can be excited resonantly indicates that the concentration of such centers is rather low.

Fig. 2 shows the PLE spectra taken at the detection wavelength of 1537.4 nm. At low temperatures (upper trace) the spectrum consists of many narrow lines which clearly belong to more than one center of different site symmetry. Though the relative intensities of the individual lines change with the detection wavelength no single Er center can be resolved. At elevated temperatures (>100 K), moreover, the PLE spectra for each detection wavelength become identical and additional PLE lines appear at lower wavelengths. At 300 K, they dominate in the excitation spectrum as shown in the middle trace of Fig. 2. This suggests that there is significant energy migration among different Er centers. In the lower trace of Fig. 2, the resonant transitions to the $^4\text{I}_{9/2}$ manifold can be seen, superimposed on a broad band showing a contribution from another type of Er center which is not excited resonantly but via a deep defect.

In the Mg doped sample grown on sapphire under above-gap excitation (see Fig. 3a), we observe the same

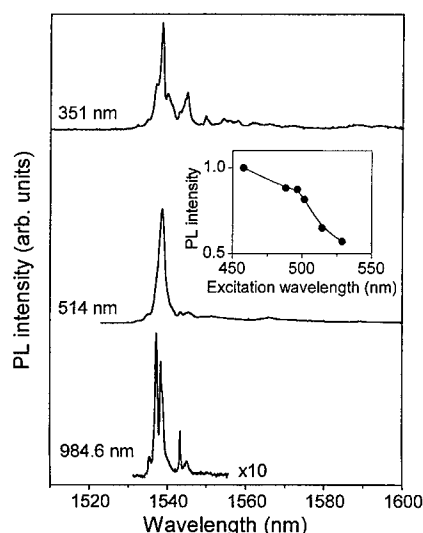


Fig. 1. PL spectra of 800 keV Er-implanted GaN recorded at 7 K for three different excitation regimes: above-band-gap (top), below-band-gap (middle), and intra-4f-shell (bottom). Excitation wavelengths are indicated. The inset shows integrated PL intensity as a function of the pump wavelength. The solid line is a guide for the eye.

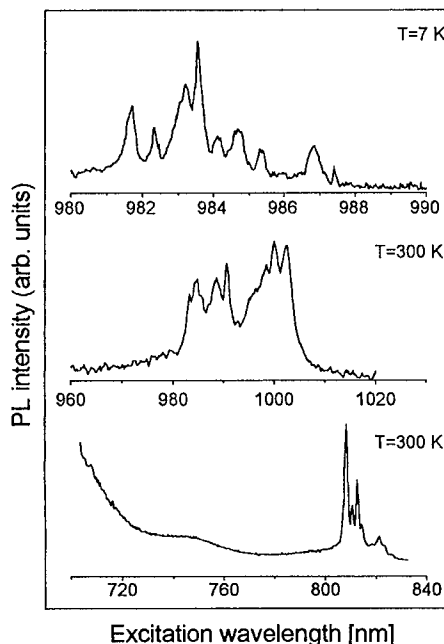


Fig. 2. PL $^4\text{I}_{15/2} \rightarrow ^4\text{I}_{11/2}$ excitation spectra recorded at 7 and 300 K, and $^4\text{I}_{15/2} \rightarrow ^4\text{I}_{9/2}$ excitation spectra at 300 K in 800 keV Er-implanted GaN. The detection wavelength is 1537.4 nm.

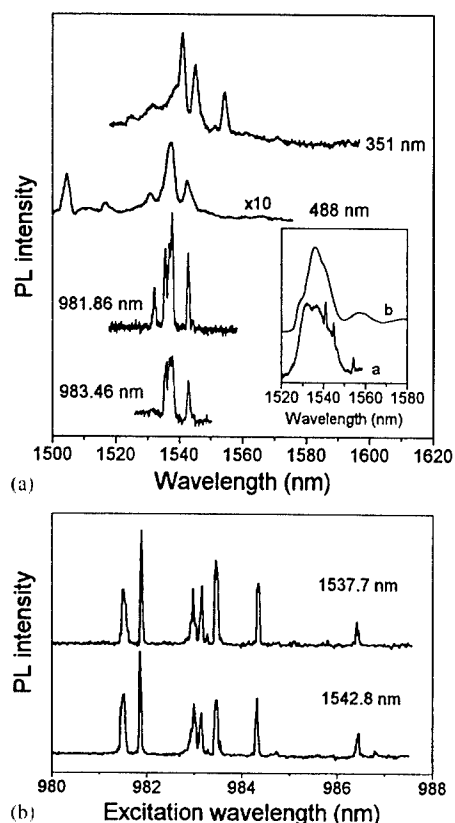


Fig. 3. PL (a) and PLE (b) spectra of 300 keV Er-implanted GaN:Mg/Al₂O₃ at various pump and detection wavelengths, at 6 K. The inset shows the PL spectrum excited at 351 nm with the beam focussed on a different spot (trace a) as compared to the PL of ErO_x precipitates in the bulk GaN:Er.

kind of luminescence as reported by Kim et al. [4], superimposed on a very broad background extending from a PL band peaked at about 700 nm. This band stems from implantation induced defects and appears also after Si implantation. Under excitation in the range of about 980 nm the defect related PL is no longer seen. The resonantly excited Er PL as well as the PL excitation spectra shown in Fig. 3(b) have extremely narrow line widths, indicating that the involved Er centers reside at sites with very little fluctuation of the crystal field potential. A similar, very weak PL spectrum (with some extra lines related to other centers) is also seen under the 488 nm pump wavelength. The Er distribution, however, is not uniform and if the exciting beam hits a different spot a very intense broad band appears, as shown in the inset of Fig. 3a. This band is identical to the one observed in bulk Er doped GaN grown at Unipress, which contained precipitates of a phase resembling Er oxide. In the Mg doped GaN/GaAs, we can also distinguish the PL of different Er centers under resonant and visible to UV pump wavelengths, with the most intense emission occurring for below-band-gap excitation.

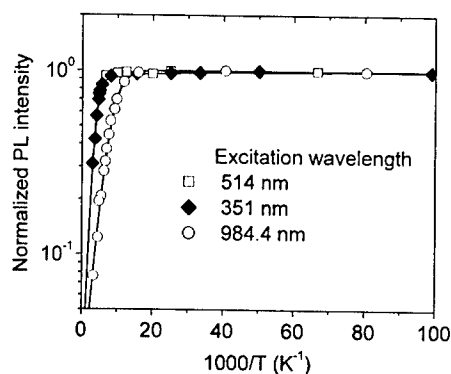


Fig. 4. Temperature dependencies of the integrated PL intensity under excitation at 351 nm (diamonds), 514 nm (squares), and 984.4 nm (circles).

The temperature dependence of the luminescence intensity in the three excitation regimes is entirely different, as shown in Fig. 4 for the undoped GaN/Al₂O₃ sample. The PL intensity of Er centers excited with above gap illumination decreases with a deactivation energy of 95 ± 10 meV, which is responsible for the loss of intensity by almost half an order of magnitude at 300 K. The dominant excitation mechanism seems to be energy transfer from recombining donor–acceptor pairs and the deactivation energy is most probably related to the ionization energy of the shallower of the impurities involved. The other impurities must be deeper as we see no visible Er-related luminescence in any of the implanted samples. The PL intensity of Er centers excited via a broad, below-band-gap absorption band, in contrast, is thermally stable up to room temperature indicating that the traps mediating in the excitation process are much deeper. Surprisingly, centers excited directly into the 4f-shell show the strongest temperature quenching, with a smaller deactivation energy. This temperature quenching might be related to excitation energy migration at high Er concentrations as it is greatly reduced in the GaN/GaAs sample with an order of magnitude lower Er peak concentration.

4. Conclusions

The luminescence and luminescence excitation of Er-implanted GaN was studied. We found that Er excitation under above-band-gap illumination is mediated primarily by donor–acceptor pair recombination. This PL has a similar temperature dependence as that near the band edge. It was also found that direct excitation into the 4f-shell leads to a much more pronounced PL temperature quenching than any other excitation mechanism, which suggests that at the Er doping levels employed there might be considerable energy migration among the luminescent centers likely

to be excited by direct absorption. The most efficient excitation channel seems to be mediated via deep trap centers, introduced most probably by implantation. The extra advantage of such an excitation mechanism for possible applications in IR emitting LEDs is that the visible, competing Er luminescence is suppressed.

Acknowledgements

Work supported by the FWF, BM:BWK and GMe, Vienna.

References

- [1] P.N. Favennec, H. L'Haridon, M. Salvi, D. Moutonnet, Y. LeGuillou, *Electron. Lett.* 25 (1989) 718.
- [2] R.G. Wilson, R.N. Schwartz, C.R. Abernathy, S.J. Pearton, N. Newman, M. Rubin, T. Fu, J.M. Zavada, *Appl. Phys. Lett.* 65 (1994) 992.
- [3] J.T. Torvik, C.H. Qiu, R.J. Feuerstein, J.I. Pankove, F. Namavar, J. *Appl. Phys.* 81 (1997) 6343.
- [4] S. Kim, S.J. Rhee, X. Li, J.J. Coleman, S.G. Bishop, *Appl. Phys. Lett.* 76 (2000) 2403.
- [5] M. Garter, J. Scofield, R. Birkhahn, A.J. Steckl, *Appl. Phys. Lett.* 74 (1999) 182.



ELSEVIER

Physica B 308–310 (2001) 38–41

PHYSICA B

www.elsevier.com/locate/physb

Compensation mechanism in MOCVD and MBE grown GaN:Mg

H. Alves^{a,*}, M. Böhm^a, A. Hofstaetter^a, H. Amano^b, S. Einfeldt^c, D. Hommel^c,
D.M. Hofmann^a, B.K. Meyer^a

^a*Physics Institute, University of Giessen, Heinrich-Buff-Ring 16, 35392 Giessen, Germany*

^b*Department of Electrical and Electronic Engineering, Nagoya, Japan*

^c*Institute of Solid State Physics, University of Bremen, University Germany*

Abstract

We studied GaN grown by metal organic chemical vapour deposition (MOCVD) and molecular beam epitaxy doped with different Mg concentrations by photoluminescence, Hall and SIMS measurements. For the MOCVD samples, due to compensating deep donors a saturation of the hole density versus the Mg concentration is observed. These donors are also related to a 2.9 eV recombination observed in photoluminescence. Assuming that the compensating donors formed during growth processes involve nitrogen vacancies, hydrogen and a complex of both species, we are able to calculate the free hole concentration as a function of the Mg concentration for both growth methods. © 2001 Elsevier Science B.V. All rights reserved.

Keywords: GaN; Mg-acceptor; Compensating donors

1. Introduction

P-type conduction of GaN is typically obtained by doping with Mg, which acts as an acceptor. Typical values of the free hole concentration at room temperature (RT) are in the 10^{17} – 10^{18} cm⁻³ range. These values are sufficient for applications like light emitting diodes, but for others such as lasers, higher hole concentrations are desirable.

The high Mg acceptor binding energy and compensation effects, observed in the highly doped films, are the main reasons why higher values for the free hole concentration cannot be achieved. In GaN:Mg grown by MOCVD the additional effect of hydrogen has to be considered. In the as-grown state of the samples it passivates the incorporated Mg, and post growth treatments are needed for its activation [1,2]. The

molecular beam epitaxy (MBE) growth of GaN is hydrogen free, and the Mg acceptors are electrical active already in the as-grown state of the samples. Further, the compensation effects in MBE material are lower than in MOCVD material.

Theoretical calculations predicted that nitrogen vacancies (V_N) are the dominant compensating defects [3,4] in p-type GaN. Also experimentally this defect or complexes of it with Mg seem to be the most probable compensation centres [5,6].

We performed photoluminescence (PL), Hall and SIMS measurements on MOCVD and MBE grown GaN:Mg doped with different Mg concentrations. With the help of these experiments we were able to obtain information on the compensation and the presence of defects in the material. These informations are used to guide our calculations for the free hole concentration as a function of the Mg concentration. It turned out that the presence of hydrogen which mediates the V_N formation in MOCVD grown GaN:Mg is the important feature to explain the higher degree of compensation in these samples.

*Corresponding author. Tel.: +1-49-641-9933106; fax: +1-49-641-9933119.

E-mail address: hroldao@yahoo.com (H. Alves).

2. Experimental details

The experiments were performed on Mg-doped GaN epitaxial layers grown by MOCVD and MBE. A AlN buffer layer was used for the MOCVD samples, and a typical growth temperature is 1040°C [1]. The MBE samples were grown in an EPI 930 MBE system equipped with a radio frequency nitrogen plasma source. The growth temperature was 750°C [7]. The typical GaN layer thickness is 1 μm . For each sample the Mg doping concentration is determined by secondary ion mass spectroscopy (SIMS).

For the luminescence experiments, we used the 325 nm line of a HeCd (30 mW) laser as excitation source, and a grating monochromator in connection with a photomultiplier for detection. All the PL measurements were performed at 4.2 K in an Oxford bath cryostat.

Ohmic contacts in van der Pauw geometry were used for Hall-effect measurements.

3. Experimental results

The symbols in Fig. 1 show the experimental data of the free hole concentration as a function of the Mg concentration, for the MOCVD (full circles) and the MBE samples (full triangles).

For Mg concentrations up to $1 \times 10^{19} \text{ cm}^{-3}$, the free carrier concentration increases for both MOCVD and MBE samples. It roughly follows the linear increase expected from Fermi statistics. The scattering in data in this Mg concentration range is most likely caused by different concentrations of residual shallow donors such as O and Si. The typical concentrations of such species in MOCVD GaN are about $1 \times 10^{17} \text{ cm}^{-3}$.

For the MOCVD samples we observe for Mg concentrations above $1 \times 10^{19} \text{ cm}^{-3}$, first a saturation

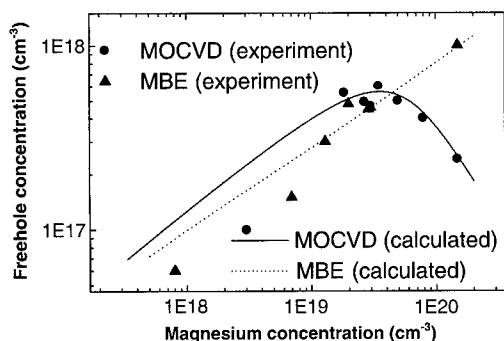


Fig. 1. Triangles and circles corresponds to the free hole concentration versus the magnesium concentration, for MBE and MOCVD, respectively. Solid line shows the calculated data for MOCVD and the dotted line the calculated data for MBE.

and then a decrease of the free hole concentration. This is different to the MBE case where the hole concentration continuously increases. Obviously compensation effects are stronger in the MOCVD samples.

The PL spectrum (Fig. 2a) of low doped MOCVD films is dominated by the shallow donor to Mg acceptor recombination (violet band) with zero phonon line positioned at 3.27 eV. One can also see a band positioned at 2.9 eV (blue band). Increasing the Mg content, this blue band develops, and dominates the spectrum for high Mg doped films. For the highest doping concentrations the LO-phonon structure of this band is less pronounced and it red shifts to 2.8 eV. Investigating the excitation power dependence of this PL band we find that the emission maximum depends strongly on the excitation powers. Such behaviour is typical for compensated material with potential fluctuations arising from charged impurities.

For the MBE samples (Fig. 2b) the PL spectra show independent of doping a dominating shallow to Mg acceptor recombination at 3.27 eV. The 2.9 eV recombination is always of low intensity.

From the experiments it is likely that the defects participating in the blue recombination are also responsible for the saturation of the free hole concentration in MOCVD material, i.e. they are compensating donors. Based on temperature dependent PL measurements we ascribe the blue band to a recombination between compensating deep donors and shallow Mg acceptors. Similar conclusions were obtained by other authors [5,6,8].

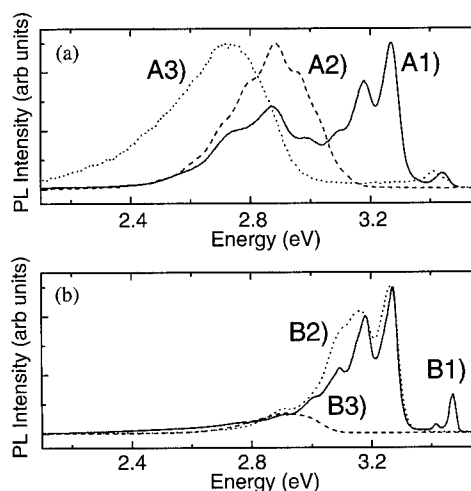


Fig. 2. (a) PL of MOCVD grown GaN:Mg: (A1) low doped sample, (A2) medium/high doped sample and (A3) high doped sample. (b) PL of MBE grown GaN:Mg: (B1) low doped sample, (B2) high doped sample and (B3) line shape of the 2.9 eV recombination.

4. Calculations and discussion

The above described observations show that in highly Mg doped GaN grown by MOCVD, deep donors are needed to explain the compensation behaviour, as well as the appearance of the 2.9 eV recombination. Van der Walle proposed that nitrogen vacancies (V_N), hydrogen (H) and complexes of both (V_NH) are the relevant defects to be formed in p-type GaN. We have used his results on the Fermi level position dependent formation energies, to calculate free hole concentration as a function of the Mg concentration [3]. The formation of the Mg–H complex was not considered here. Neugebauer et al. [4] showed that the formation of this complex during growth is of minor relevance.

The density of compensating defects is calculated by the following equation:

$$N_D = N_S \exp\left[\frac{-E_{For}}{k_B T}\right], \quad (1)$$

where N_S is the number lattice sites for a defect ($4.4 \times 10^{22} \text{ cm}^{-3}$ for substitutional defects in GaN), T the growth temperature, k_B the Boltzmann constant and E_{For} the donor formation energy according to Fig. 3. Although these formation energies were basically extracted from [3], we have slightly fitted them ($\sim 100 \text{ meV}$) to obtain the best agreement with our experimental results. Entropy contributions were shown to be small and are not considered here [4].

The Fermi level (E_F) during growth is calculated by [9]

$$E_F = -k_B T \ln \frac{2\beta^{-1}(N_A - N_D)}{\beta^{-1}N_V\alpha + N_D + \sqrt{(\beta^{-1}N_V + N_D\alpha)^2 + 4\beta^{-1}N_V(N_A - N_D)\alpha}}, \quad (2)$$

where α is $\exp(E_A/K_B T)$ with E_A the acceptor binding energy (160 meV), β the valence band degeneracy factor, N_V the density of states for the valence band and N_A the acceptor concentration. By an iteration process one is able to find the values for N_D and E_F which satisfy both equations. For the calculations we assumed that residual

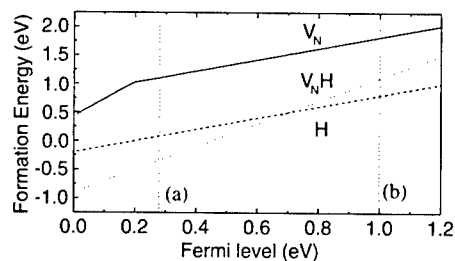


Fig. 3. Fitted formation energies for the three considered compensating donors. Lines a and b show the Fermi level position during growth (Mg concentration of $5 \times 10^{19} \text{ cm}^{-3}$) for MBE and MOCVD, respectively.

shallow donors are not present. By ignoring their existence we overestimate the free hole concentrations for low Mg concentrations. We further assume that the concentration of compensating donors stays constant during the cool down of the sample from growth temperature to RT. Finally, we are able to calculate free hole concentration as a function of the Mg incorporation by [9]

$$p = -\frac{N_D + \beta^{-1}N_V\alpha^{-1}}{2} + \sqrt{\beta^{-1}N_V\alpha^{-1}(N_A - N_D) + \left(\frac{N_D + \beta^{-1}N_V\alpha^{-1}}{2}\right)^2}. \quad (3)$$

Typical values for β and N_V are 3.6 and $3.2 \times 10^{19} \text{ cm}^{-3}$ at RT, 4.6 and $1.95 \times 10^{20} \text{ cm}^{-3}$ at 1000 K which is the growth temperature for MBE samples and 5.1 and $2.1 \times 10^{20} \text{ cm}^{-3}$ at 1300 K, the growth temperature for MOCVD.

In our calculations the information of growth technique enters in two different ways. The first one is the growth temperature, the second one is the hydrogen presence. For MBE we assume that hydrogen is not present thus only the formation of the nitrogen vacancy is considered. For MOCVD and in the presence of hydrogen the three defects, V_N , H and V_NH are of relevance. The low formation energy of the hydrogen centre (Fig. 3) plays here a central rule. In our calculations we find identical amounts of Mg and H centres to be present in as-grown MOCVD GaN:Mg.

P-type conductivity can be only reached when the hydrogen is removed which is done experimentally by a post-growth annealing treatment. For the calculations we assumed that all the H^+ centres are removed and that the V_NH^{2-} centres are transformed to the simple nitrogen vacancy defect. From the lines in Fig. 1 we can see a good agreement between the calculation and our experimental results for both MBE and MOCVD samples. As mentioned before, the deviation of the calculation to the experimental data for low doped samples is a result of ignoring residual shallow donor.

An important point that we can state from these calculations is that the main compensating centre for both growth techniques should be the nitrogen vacancy. This is supported by our PL results. The blue band is observed in MBE and MOCVD material at 2.9 eV. The red shift of the blue band, observed on some highly doped MOCVD grown samples, is related to band fluctuations which modify the peak position of the emission but do not change the structure of the involved

defects. Our calculations yield that the compensation ratio, i.e. the ratio between the concentrations of compensating donors and magnesium acceptors, is almost constant for the MBE samples ($\sim 3\%$). For the highly doped MOCVD samples the compensation can reach up to 20% which is also sufficient to account for the band fluctuations.

For the two growth methods the formation process of the V_N defect is different. In MBE it is directly formed, and in MOCVD it forms in addition by the intermediate V_NH complex. In fact the H incorporation and V_NH formation are essential to reproduce the strong compensation effect for the highly doped MOCVD samples. This effect could not be reproduced by assuming simply a higher growth temperature.

Some authors [10,11] reported that more than one compensating centre exists in MOCVD grown GaN:Mg. These centres could be related with remaining V_NH complexes or also, and especially at very high doping levels, with the V_NMg complex suggested by Kaufmann [5,6].

In summary our investigations show that the compensation effects observed in GaN:Mg grown by MBE and MOCVD can consistently be explained by the formation of V_N . The presence or absence of hydrogen

and the differences in growth temperature are sufficient to explain our experimental data.

References

- [1] H. Amano, M. Kito, K. Hiramatsu, I. Akasaki, *Jpn. J. Appl. Phys.* 28 (1989) L2112.
- [2] S. Nakamura, *Jpn. J. Appl. Phys.* 30 (1991) L1708.
- [3] C.G. Van de Walle, *Phys. Rev. B* 56 (16) (1997) 10020.
- [4] J. Neugebauer, C.G. Van de Walle, *Mater. Res. Soc.* 395 (1996) 645.
- [5] U. Kaufmann, M. Kunzer, H. Obloh, *Phys. Rev. B* 59 (1999) 5561.
- [6] U. Kaufmann, P. Scholtter, H. Obloh, K. Kohler, *Phys. Rev. B* 62 (2000) 10867.
- [7] S. Strauf, P. Michler, S. Einfeldt, D. Hommel, *Phys. Stat. Sol.* 216 (1999) 557.
- [8] H. Obloh, K.H. Bachem, D. Behr, in: B. Kramer (Ed.), *Advances in Solid State Physics*, Vol. 38, Vieweg Verlag, Braunschweig, 1999, p. 15.
- [9] J.S. Blackmore, *Semiconductor Statistics*, Pergamon Press, Oxford, 1962.
- [10] L. Eckey, J. Holst, *J. Cryst. Growth* 189/190 (1998) 523.
- [11] M.A. Reschikov, B. Wessels, *Phys. Rev. B* 59 (1999) 13176.



ELSEVIER

Physica B 308–310 (2001) 42–46

PHYSICA B

www.elsevier.com/locate/physb

Green and red emission in Ca implanted GaN samples

T. Monteiro^{a,*}, C. Boemare^a, M.J. Soares^a, E. Alves^b, C. Liu^b

^a Departamento de Física, Universidade de Aveiro, 3810 Aveiro, Portugal

^b Instituto Tecnológico e Nuclear, Sacavém, Portugal

Abstract

A comparison between unimplanted and annealed Ca implanted GaN samples was performed using PL and RBS techniques. Deep DAP recombination at 2.36 and 1.8 eV was found in both samples. New PL lines observed at 3.46, 3.368 and 2.59 eV in the implanted samples are discussed. Rutherford backscattering/channelling measurements reveal that 35% of Ca is located in substitutional Ga sites surrounded by complex defects. © 2001 Elsevier Science B.V. All rights reserved.

Keywords: GaN; Implantation; PL; RBS/C

1. Introduction

One of the major drawbacks of GaN based devices is the lack of suitable acceptors with lower ionisation energy than the 220 meV currently obtained with Mg doping [1]. In order to obtain controllable p-type conductivity, several workers studied the behaviour of potential acceptor species, for instance, Zn, Cd, Ca and Be, by in-grown doping or ion implantation [2–10]. While theoretical calculations predict for Ca_{Ga} an acceptor binding energy of 250–302 meV [11–13], temperature dependent Hall measurements showed that the ionisation level of Ca was 169 ± 12 meV [5]. Moreover, besides the previous work of Pankove [2], no other reports on photoluminescence (PL) studies were performed for Ca implanted samples.

In this work, we report PL studies in a set of Ca implanted samples with doses from 10^{13} to 10^{15} cm^{-2} . All the samples show, at room temperature, a similar green emission to the one previously observed by Pankove [2] and a broad red emission. Besides these two PL bands, both the emission band in blue and a structured near band edge (NBE) emission are observed at a low temperature. The PL bands were studied as a function of excitation density, time and temperature and

from these results, combined with X-ray emission (PIXE) and Rutherford backscattering/channelling analysis, the influence of Ca on luminescence as well as the contribution from optical active centres produced by annealing treatments is discussed.

2. Experimental

The wurtzite GaN layers were epitaxially grown on (0001)-plane sapphire substrates by MBE with a thickness of 1.5 μm . The Ca^+ ions were implanted either at room temperature or at 550°C with 180 keV and a fluence in the range from 5×10^{13} to $5 \times 10^{15} \text{ cm}^{-2}$. After implantation, the Ca samples were annealed at 1050°C for 15 min in flowing N_2 with a proximity cap. RBS/C analysis was carried out to determine the damage profiles and the lattice site location. The samples were mounted on a two-axis goniometer and channelling angular scans were performed along the [0001] and $[10\bar{1}1]$ directions [14]. The PL measurements were carried out with a 325 nm CW He–Cd laser and the excitation power density was typically less than 0.6 W cm^{-2} . A 325 nm band pass filter was used to attenuate laser lines other than the 325 nm line. PL was measured at temperatures between 14 and 300 K using a closed cycle helium cryostat. The luminescence was dispersed by a Spex 1704

*Corresponding author. Tel.: +351-34-370-824; fax: +351-34-24965.

E-mail address: tita@fis.ua.pt (T. Monteiro).

monochromator (1 m, 1200/mm) and detected by a Hamamatsu R928 photomultiplier. Excitation density was varied using a set of neutral density (ND) filters.

3. Results

In Fig. 1, a comparison between PL spectra of a 550°C implanted Ca^+ sample with $1 \times 10^{14} \text{ cm}^{-2}$ and annealed at 1050°C during 15 min and a virgin sample annealed under the same conditions is shown. The results reveal the excitonic lines at 3.485 and 3.453 eV in the virgin sample with full widths at half maximum (FWHM) of 26 and 6 meV, respectively. At lower energies, the PL of the unimplanted sample is dominated by broad emission bands in the blue (2.95 eV), green (2.36 eV) and red (1.8 eV). For the Ca implanted sample, a new emission line is observed at 3.46 eV as indicated by the arrow in the inset of Fig. 1. At lower energies, a strong narrow line with an FWHM of 4 meV is observed at 3.368 eV. Broad emission bands dominate the spectrum for lower energies, and as previously reported by Pankove [2] a strong green emission with a maximum at 2.5 eV is observed. Besides this emission band, the same broad bands were also observed in the unimplanted sample at 2.95 eV, 2.36 eV and 1.8 eV. The relative intensity of the emission bands is dependent on the laser spot position revealing that the luminescent defects are not uniformly distributed in the samples. The temperature dependence of PL is shown in Fig. 2. In the inset, the quenching of the 3.368 eV line is also

presented. Increasing temperature favours an inversion of the intensity of the 2.36 and 2.59 eV bands being consistent with a faster quenching for the 2.36 eV DAP. At room temperature, the green emission is peaked at 2.59 eV. The red 1.8 eV DAP presents a shift of 28 meV to higher energies with increasing temperatures.

In order to obtain information on the lattice site location of Ca, we performed detailed angular scans along the c -axis using the X-ray signal of Ca and Ga after annealing (Fig. 3). The curves show a minimum yield of 25% for Ga, while for Ca we have a value of 74%. Moreover, the Ca curve is now narrower than the Ga curve indicating that the Ca ions are displaced from the ideal Ga sites of the GaN lattice. This displacement is associated with the interaction of the Ca ions with defects present in its neighbourhood. According to the estimation [14]

$$f_{\text{sub}} = \frac{1 - \chi_{\text{min}}(\text{Ca})}{1 - \chi_{\text{min}}(\text{Ga})},$$

where f_{sub} is the fraction of impurity in substitutional sites, and $\chi_{\text{min}}(\text{Ca})$ and $\chi_{\text{min}}(\text{Ga})$ are the minimum yields at the channelling dips, we found a fraction of 35% of Ca in regular sites along the $[0001]$ direction.

4. Discussion

The high energy spectrum of both samples are characterised by an NBE emission peaked at 3.485 eV due to the overlap of DX, FXA and FXB emissions

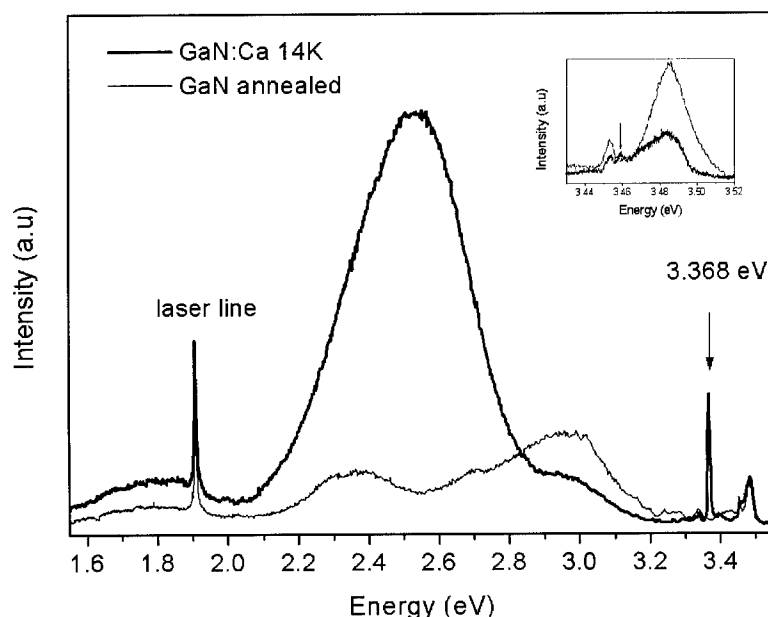


Fig. 1. Low temperature PL spectra of unimplanted and Ca implanted samples under He–Cd excitation. Inset: Enlarged spectra of NBE region;

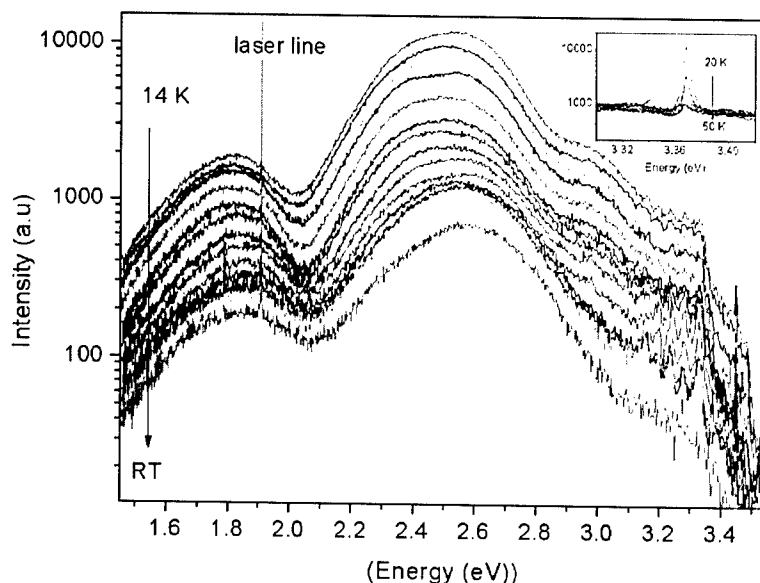


Fig. 2. Temperature dependence of PL spectra of Ca implanted samples under He Cd excitation for a fixed laser position.

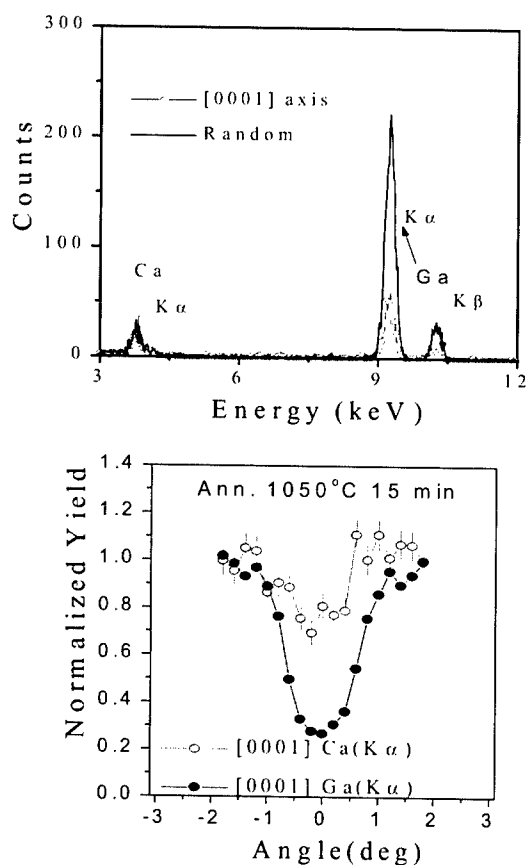


Fig. 3. Particle induced X-ray emission (PIXE) spectra for the GaN film implanted with Ca after annealing at 1050 C for 15 min (top) and angular scan along the c -axis (bottom).

currently assigned in MBE samples near 3.475, 3.483 and 3.489 eV, respectively [15,16]. For the implanted samples, two new PL lines at 3.46 and 3.368 eV are observed at 14 K after Ca implantation. According to theoretical calculations, Ca in Ga sites is expected to introduce a deep acceptor level. If the 3.46 eV line could be assigned to an exciton bound to neutral Ca, then an acceptor level 230 meV above the VB is expected. Concerning the 3.368 eV line, it must be mentioned that it is quite similar in energy to the previously observed I_3 line currently assigned to strongly localised excitons associated with excitons bound to stacking faults [17-19]. As for the I_3 line, the 3.368 eV emission observed in the implanted samples shows an excitonic nature with the quenching processes being dominated by an activation energy of 17 meV. However, it is also known that the I_3 line is usually accompanied by an emission at lower energies (3.309 eV), the I_4 line [17-19]. In our samples this is not the case, no I_4 line is observed. Theoretical studies of the electronic structure of stacking faults in GaN have been recently reported [20,21] and they reveal the presence of an electronic level 0.13 eV above the VB. On the other hand, the authors of Ref. [21] pointed out that stacking faults can bound a quantum-well-like region of zinc-blende (ZB) material surrounded by wurtzite (WZ) host. The ZB/WZ interface exhibits a type-II line up with $\Delta E_v \approx 0.07$ eV and $\Delta E_c \approx 0.27$ eV. In order to clarify the nature of the 3.368 eV emission line in Ca implanted samples more work is under way.

Deep emission levels are currently observed in undoped and intentionally doped GaN samples giving rise to blue [22,23], yellow [24] and red [25,26] PL bands.

It is also known that annealing treatments considerably alter deep emission levels. Namely, two emission bands at 2.3 and 2.6 eV have been shown to be enhanced by annealing effects [27]. In our unimplanted sample, the recombination is dominated by two DAP emissions at 2.36 and 1.8 eV, consistent with previous observations in MBE annealed samples [27]. The 2.36 and 1.8 eV emissions are also observed in Ca implanted samples. The main features in the Ca implanted samples are these new lines at 3.46 and 3.368 eV as well as the broad emission band at 2.59 eV. While the 2.36 and 1.8 eV bands show a DAP character, the 2.59 eV band shows a supralinear dependence on excitation density and no shifts of the band maximum are observed with increasing delay times, temperature and excitation density. The band has no DAP character. Similar observations were found in MBE annealed samples [27] and by CL studies [22] where the emission was found to be homogeneously distributed with single columns and attributed to a complex defect involving point defects. If the 2.59 eV band is due to the same defects responsible for the emission observed in unimplanted samples [22,27] then the 29.5 meV found for the activation energy could be ascribed to the activation energy for non-radiative processes of the centre rather than the ionisation energy. However, at the moment it cannot be excluded that Ca would be involved in the defect that gives rise to the 2.59 eV band. It is known that Ca implantation into GaN samples causes lattice expansion and only a part of the implanted species occupies Ga sites [6–9] being electrically compensated due to the formation of complex defects with donor-like point defects, such as $\text{Ca}_{\text{Ga}}\text{-VN}$ and/or $\text{Ca}_{\text{Ga}}\text{-Ga}_\text{N}$ [8]. Assuming that the acceptor is compensated by the presence of a deep donor located ~ 600 meV below the CB, the emission at 2.59 eV could be explained by a defect–defect recombination between the deep donor and the 300 meV acceptor. A schematic model showing this hypothesis for the emission bands is depicted in Fig. 4.

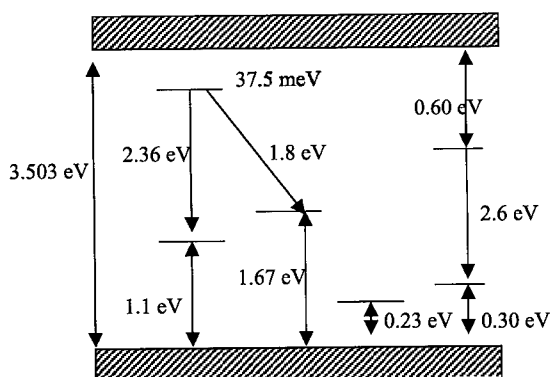


Fig. 4. Schematic model for the recombination processes.

5. Conclusions

New excitonic lines, as well as a broad emission at 2.59 eV without DAP characteristics were found in Ca implanted GaN samples. One of the excitonic lines at 3.46 eV is tentatively assigned to Ca on Ga sites, because 33% of the Ca can be found in nearly substitutional Ga sites by RBS. If so, the acceptor level is located at 230 meV above VB. As the samples do not show a p-type conductivity, deep donors probably compensate the acceptors. In order to determine the nature of the 3.368 eV emission more work is under way. We mentioned that this line occurs similar to the energy in the I_3 line; however, the line is not accompanied by the I_4 line currently assigned to excitons bound to stacking faults.

References

- [1] D.J. Dewsnap, J.W. Orton, D.E. Lacklison, L. Flannery, A.V. Andrianov, I. Harrison, S.E. Hopper, T.S. Cheng, C.T. Foxon, S.N. Novikov, B.Ya. Ber, Yu.A. Kudriavtsev, *Semicond. Sci. Technol.* 13 (1998) 927.
- [2] J.I. Pankove, J.A. Hutchby, *J. Appl. Phys.* 47 (1976) 5387.
- [3] M. Illegems, R. Dingle, R.A. Logan, *J. Appl. Phys.* 43 (1972) 3797.
- [4] C. Ronning, E.P. Carlons, D.B. Thomson, R.F. Davis, *Appl. Phys. Lett.* 73 (1998) 1622.
- [5] J.W. Lee, S.J. Pearton, J.C. Zolper, R.A. Stall, *Appl. Phys. Lett.* 68 (1996) 2102.
- [6] C. Liu, B. Mensching, K. Volz, B. Rauschenbach, *Appl. Phys. Lett.* 71 (1997) 2313.
- [7] C. Liu, B. Mensching, M. Zeitler, K. Volz, B. Rauschenbach, *Phys. Rev. B* 57 (1998) 2530.
- [8] H. Kobayashi, W.M. Gibson, *Appl. Phys. Lett.* 74 (1999) 2355.
- [9] E. Alves, C. Liu, M.F. da Silva, J.C. Soares, R. Correia, T. Monteiro, *MRS Proceedings* 647 (2001) O13.41.
- [10] W. Limmer, W. Ritter, R. Sauer, B. Mensching, C. Liu, B. Rauschenbach, *Appl. Phys. Lett.* 72 (1998) 2589.
- [11] F. Mireles, S.E. Ulloa, *Phys. Rev. B* 58 (1998) 3876.
- [12] J. Neugebauer, C.G. Van de Walle, *J. Appl. Phys.* 85 (1999) 3003.
- [13] H. Wang, A.B. Chen, *Phys. Rev. B* 63 (2001) 125212.
- [14] C. Liu, E. Alves, A.D. Sequeira, N. Franco, M.F. da Silva, J.C. Soares, *J. Appl. Phys.* 90 (2001) 1.
- [15] A.K. Viswanath, J.I. Lee, S. Yu, D. Kim, Y. Choi, C. Hong, *J. Appl. Phys.* 84 (1998) 3848.
- [16] M. Smith, G.D. Chen, J.Z. Li, J.Y. Lin, H.X. Jiang, A. Salvador, W.K. Kim, O. Aktas, A. Botchkarev, H. Morkoç, *Appl. Phys. Lett.* 67 (1995) 3387.
- [17] C. Wetzel, S. Fischer, J. Kruger, E.E. Haller, R.J. Molnar, T.D. Moustakas, E.N. Mokhov, P.G. Baranov, *Appl. Phys. Lett.* 68 (1996) 2556.
- [18] M. Cazzanelli, D. Cole, J.F. Donegan, J.G. Lunney, P.G. Middleton, K.P. O'Donnell, C. Vinegoni, L. Pavesi, *Appl. Phys. Lett.* 73 (1998) 3390.

- [19] G. Martínez-Criado, A. Cross, A. Cantarero, R. Dimitrov, O. Ambacher, M. Stutzmann, *J. Appl. Phys.* 88 (2000) 3470.
- [20] Z.Z. Bandić, T.C. McGill, Z. Ikonić, *Phys. Rev. B* 56 (1997) 3564.
- [21] C. Stampfl, C.G. Van de Walle, *Phys. Rev. B* 57 (1998) R15052.
- [22] G. Salviati, M. Albrecht, C. Zanolli-Fregonara, N. Armani, M. Mayer, Y. Shreter, M. Guzzi, Yu.V. Melnik, K. Vassilevski, V.A. Dmitriev, H.P. Strunk, *Phys. Stat. Sol. A* 171 (1999) 325.
- [23] A. Salvador, W. Kim, O. Aktas, A. Botchkarev, Z. Fan, H. Morkoç, *Appl. Phys. Lett.* 69 (1996) 2692.
- [24] T. Ogino, M. Aoki, *Jap. J. Appl. Phys.* 19 (1980) 2395.
- [25] U. Kaufmann, M. Kunzer, H. Obloh, M. Maier, Ch. Manz, A. Ramakrishnan, B. Santic, *Phys. Rev. B* 59 (1999) 5561.
- [26] D.M. Hofmann, B.K. Meyer, H. Alves, F. Leiter, W. Burkhard, N. Romanov, Y. Kim, J. Kruger, E.R. Weber, *Phys. Stat. Sol. A* 180 (2000) 261.
- [27] A. Bell, I. Harrison, D. Korakakis, E.C. Larkins, J.M. Hayes, M. Kuball, N. Grandjean, J. Massies, *J. Appl. Phys.* 89 (2001) 1070.



ELSEVIER

Physica B 308–310 (2001) 47–50

PHYSICA B

www.elsevier.com/locate/physb

Study of dopant activation in bulk GaN:Mg

R. Piotrkowski*, E. Litwin-Staszewska, T. Suski, I. Grzegory

High Pressure Research Center, Polish Academy of Sciences, Sokolowska 29/37, 01-142 Warsaw, Poland

Abstract

We have studied the time-dependent processes leading to the irreversible increase of conductivity in pressure-grown GaN:Mg. The analysis is based on a two-level model with a shallow ($E_v + 0.1$ eV) Mg-related acceptor level and a deep level at $E_v + 0.9$ eV. Our data indicate that the deep defect is present in all as-grown GaN:Mg samples and is generated in a large quantity by annealing above 600°C. The other process, which leads to the appearance of shallow Mg acceptors, is observed at temperatures as low as $\sim 300^\circ\text{C}$ and terminates below 600°C. From an analysis of the time dependences for both processes we found that the respective activation energies differ by a factor of 2. © 2001 Elsevier Science B.V. All rights reserved.

Keywords: GaN; Impurity and defect levels; Annealing; P-doping

Magnesium is practically the only acceptor impurity in Group-III nitrides. In most cases, however, it is electrically inactive in as-grown material and special annealing steps are required for obtaining efficient p-type conductivity [1]. Such Mg acceptor activation in MOCVD grown samples, which is achieved by annealing at temperatures 700–800°C, is attributed to the dissociation of Mg–N–H complexes. It was, however, pointed out that this temperature is much higher than that expected from the calculated energy of complex dissociation [2]. This means that additional information is needed to fully understand the mechanism of Mg activation processes.

With such motivation, we have studied thermally activated, time-dependent processes that lead to an increase of the p-type conductivity in bulk GaN:Mg. The crystals were grown under high N_2 pressure from Mg-rich Ga melt. The as-grown material has high resistivity due to the high background concentration of O donors which compensate the Mg acceptors. As we reported earlier [3], in this material an increase of Mg acceptor concentration is observed even at 300°C. Moreover, we indicated that in order to describe the

properties of the materials studied, a two-level scheme should be used. In addition to the shallow Mg acceptor, the deep level at $E_v + 0.9$ eV should be introduced. An important increase of deep state concentration was observed in the second annealing process between 600°C and 750°C.

In the present work, we concentrate on the kinetics of both annealing processes by analyzing the time dependences of resistivity measured during isothermal annealing. The details concerning crystal growth and sample preparation can be found in the previous paper [3].

In our experiment, we measured the sample resistivity, ρ , as a function of annealing time, at fixed temperature T_{ann} . The process of annealing was interrupted at certain moments and the dependence ρ vs. temperature was measured. The temperature in such measuring cycles was lower than T_{ann} , and the dependences $\rho(T)$ were reversible. Fig. 1 presents the results of such experiments for two GaN:Mg samples. The points on the left-hand side (Fig. 1a) show the sample resistivity decreasing with time during isothermal annealing. Those on the right-hand side (Fig. 1b) give the Arrhenius plots ρ vs. $(1/T)$ found in different points of annealing process. The evolution of the Arrhenius characteristics ρ vs. $(1/T)$ which is seen in Fig. 1b is typical for all samples studied by us. Initially, their slope (activation energy) is high and does not vary when the resistivity decreases during

*Corresponding author. Tel.: +48-22-632-3628; fax: +48-3912-0331.

E-mail address: rp@unipress.waw.pl (R. Piotrkowski).

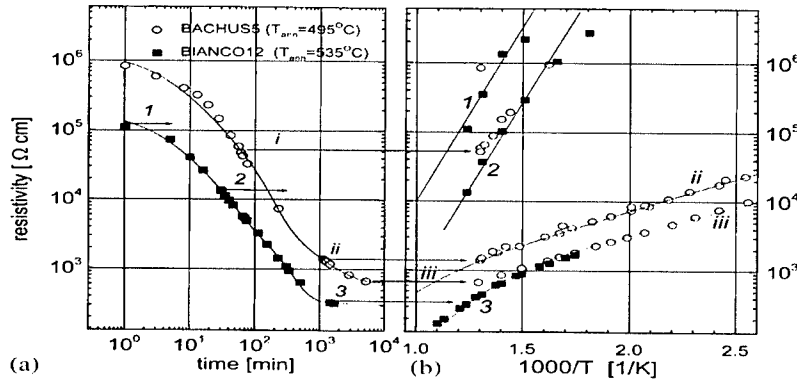


Fig. 1. (a) Time dependence of resistivity measured for two GaN:Mg samples during isothermal annealing and (b) resistivity ρ vs. $1/T$ measured at different stages of annealing process. Arrows mark the interruption in annealing processes (a) during which the measurements shown in (b) were performed. Continuous lines in (b) are calculated using Eq. (1) (see Fig. 2). The lines in (a) are calculated using the fitting from Fig. 3.

annealing. At some point it changes to the low value characteristic for Mg acceptors, and then remains constant up to the end of the process. Such a surprising behavior is explained by the model analysis that follows.

As we have remarked in the preceding work [3], the electrical properties of samples in which the saturation of ρ was achieved by annealing at $\sim 500^\circ\text{C}$, are stable only below 600°C . Above 600°C , a decrease of sample resistivity with time is observed again. Also in this case, we have carried out the experiments identical to that in Fig. 1. The feature which now characterizes the evolution of the Arrhenius dependences ρ vs. $(1/T)$ is the downward shift of their high-temperature part. The activation slope remains unchanged being equal to about 0.5eV .

The analysis of the results is based on the solution of the neutrality equation for p-type conduction with two acceptor levels that are strongly compensated:

$$p + N_D = \frac{N_A}{1 + 1/g \exp((E_A - E_F)/kT)} + \frac{N_{A1}}{1 + 1/g \exp((E_{A1} - E_F)/kT)}, \quad (1)$$

where p is the hole concentration given by $p = N_v \exp(-E_F/kT)$. We denote by N_A and E_A the concentration and energy of shallow acceptors, N_{A1} and E_{A1} apply to deep centers and g denotes the degeneracy factor. N_D is the concentration of compensating donors assumed equal to $5 \times 10^{19} \text{cm}^{-3}$, i.e. the concentration of oxygen atoms found by SIMS measurements.

In order to compare the results given by the solution of Eq. (1) with experiment, we calculated the resistivity

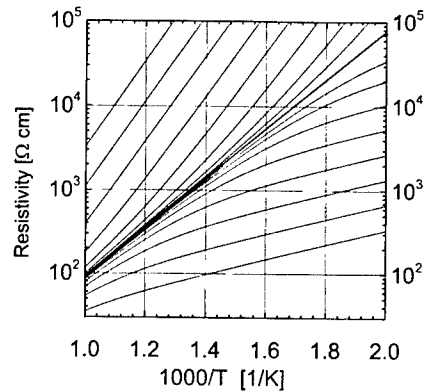


Fig. 2. Resistivity vs. inverse temperature $\rho(1/T)$ calculated in the model of two acceptor levels, heavily compensated by shallow donors ($N_D = 5 \times 10^{19} \text{cm}^{-3}$). Curves are calculated for constant concentration of deep ($E_A + 900 \text{meV}$) states $N_{A1} = 5.5 \times 10^{17} \text{cm}^{-3}$ varying shallow acceptor concentration N_A which increases from the top to the bottom of the figure. (The energy E_A assumed equal to 110meV .) The thick line corresponds to $N_A = N_D$.

as $\rho = 1/\sigma = 1/e\mu_h p$ with the single value of hole mobility $\mu_h = 5 \text{cm}^2/\text{Vs}$ [3].

An example of the results given by such model calculations is shown in Fig. 2. The shown set of curves ρ vs. $(1/T)$ illustrates the evolution of the Arrhenius dependences when only the shallow acceptor concentration N_A is varied. In the upper part of Fig. 2, N_A is assumed to be lower than the shallow donor concentration N_D , while in the lower part $N_A > N_D$.

Comparing Fig. 2 with the experimental results in Fig. 1b clearly indicates that the low-temperature annealing process can be explained as increasing the

concentration of shallow acceptors when the concentration of deep centers does not change. For the case when only one level determines the hole concentration (i.e. far from line $N_A = N_D$ in Fig. 2), Eq. (1) reduces to a simpler form. As a result, in the lower part of Fig. 2, the approximate solution of Eq. (1) gives $E_F = E_A - kT \ln(g(N_A/N_D - 1))$. The hole density is then proportional to the quantity $\Delta N_A = N_A - N_D$ and becomes $p = N_v(T)g\Delta N_A/N_D$. This means that $\Delta N_A(t)$ can be determined from the measured dependence $\rho(t)$, once E_A is known. Similarly, in the upper part of Fig. 2 (above apparent diagonal) we have $E_F = E_{A1} - kT \ln(g(N_{A1}/N_{D\text{eff}} - 1))$. In this case, the effective concentration of donors $N_{D\text{eff}}$ which compensate deep centers is given by the difference $N_D - N_A$, i.e., ΔN_A has an opposite sign. Also, in this case, ΔN_A can be calculated from the measured resistivity. The (constant) magnitude of deep center concentration, N_{A1} , can be determined directly from the experimental dependences, ρ vs. $(1/T)$, if they have the form of two-slope curves similar to that shown for sample BIANCO12 (3 in Fig. 1b) or determined from best fitting.

The time variation of ΔN_A , calculated in the described manner from experimental $\rho(t)$ data, is shown in Fig. 3. Two curves correspond to the data from Fig. 2. The third relates to sample LINDA6 where annealing at 550°C does not change the slope of the Arrhenius plots. All the dependences in Fig. 3 are fitted to a function which is the sum of two exponentials

$$\Delta N_A(t) = A_0 + A_1(1 - \exp(-t/\tau_1)) + A_2(1 - \exp(-t/\tau_2)) \quad (2)$$

with two amplitudes A_1, A_2 of the same order of magnitude and a ratio $\tau_1/\tau_2 \approx 10$. The total amplitude

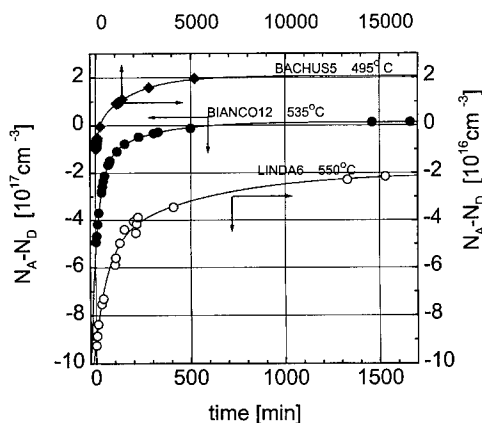


Fig. 3. Time variation of shallow acceptor concentration during low-temperature isothermal annealing, deduced from the measured R vs. time dependence. The continuous lines are fitted according to formula (2).

$A_1 + A_2$ corresponds to the increase of the effective concentration of Mg acceptors. As can be determined from Fig. 3, the greatest increase equals to $5.5 \times 10^{17} \text{ cm}^{-3}$. The hydrogen concentration found by the SIMS method for our samples is of the same order of magnitude. This makes plausible the hypothesis that the low-temperature annealing process is connected with the dissociation of complexes involving Mg–H pairs. Some additional experimental facts seem to indicate that the two exponential components that describe the kinetics really correspond to two processes, possibly involving Mg–H in different configurations (e.g. as described in Ref. [2]).

In the case of annealing at $T > 600^\circ\text{C}$, the resistivity decreases due to an increase in the concentration of deep centers, N_{A1} [3]. To determine the kinetics of this process, annealing data in two samples were analyzed.

This time the approximation used was $p = (N_v N_{A1}/g)^{1/2} \exp(-E_{A1}/2kT)$ derived from (Eq. (1)), when $N_{A1} \gg N_{D\text{eff}}$. In this manner we found that the final deep center concentration generated in the high-temperature process in the two samples measured at $T = 730^\circ\text{C}$ was equal to 6×10^{18} and $3.5 \times 10^{19} \text{ cm}^{-3}$ (the initial values of N_{A1} were about 10^{16} cm^{-3} – $5.5 \times 10^{17} \text{ cm}^{-3}$). The time dependences $N_{A1}(t)$ are exponential functions with the time constants reported in Fig. 4.

Fig. 4 is illustrated with the aim to get some idea as to how the presented results relate to Nakamura's process of Mg activation in MOCVD layers [1]. At first, we look for a simple model capable of reproducing the results of the isochronal annealing given in Ref. [1]. We found that such process should be characterized by a barrier of 2.85 eV. In Fig. 4, it is represented by the line 'N'. The points below this line represent the time constants for

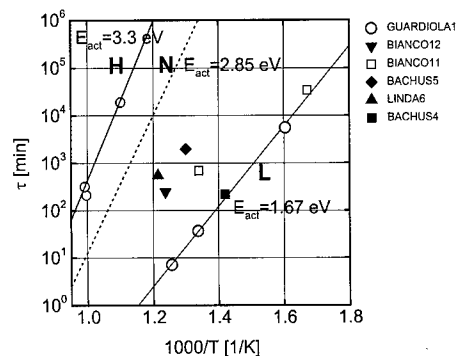


Fig. 4. Time constants of annealing kinetics as a function of inverse temperature. The line N corresponds to the annealing process in MOCVD samples (Experimental data from Ref. [1] reinterpreted to obtain activation times—see text). H relates to high-temperature annealing. The points below N correspond to low temperature process. The line L passes through the data measured on sample Guardiola1.

isothermal *low-temperature annealing*, found for six GaN:Mg samples. (The longer times, which determine the duration of annealing, are shown). Although the speed of this process differs from sample to sample, the thermally activated character is clearly seen for the sample GUARDIOLA1 (open circles). This sample was annealed at several temperatures starting from 305°C which enabled us to determine the dependence of the time constant on temperature. As can be seen, it corresponds to the process activated with energy 1.67 eV (see the straight line 'L'). As concerns the *high temperature process*, the corresponding time constants lie above the line N. The activation energy for this process can be estimated to be 3.3 eV which corresponds to line 'H'.

In summary, we have studied the evolution of the electrical properties in the bulk GaN:Mg, caused by annealing at temperatures 300–750°C. The presence of two defect levels, compensated by shallow oxygen

donors, are confirmed in all samples. In particular, the deep $E_v + 0.9$ eV center is responsible for initial Fermi level pinning in untreated samples and at the beginning of low temperature annealing. The shallow acceptor levels of Mg are created (in relatively low quantity) during annealing at low temperature and can become dominant. The high-temperature annealing process has an activation barrier 2 times greater than that of the low-temperature one. It causes, however, the generation of an important number of deep centers.

References

- [1] S. Nakamura, T. Mukai, M. Senoh, N. Iwasa, Jpn. J. Appl. Phys. 31 (Part 2) (1992) L139.
- [2] F.A. Reboredo, S.T. Pantelides, MRS Internet J. Nitride Semicond. Res. 4S1 (1999).
- [3] E. Litwin-Staszewska, et al., J. Appl. Phys. 89 (2001) 7960.



ELSEVIER

Physica B 308–310 (2001) 51–57

PHYSICA B

www.elsevier.com/locate/physb

Magnetic resonance studies of defects in GaN with reduced dislocation densities

E.R. Glaser^{a,*}, J.A. Freitas Jr.^a, G.C. Braga^{a,1}, W.E. Carlos^a, M.E. Twigg^a,
A.E. Wickenden^{a,2}, D.D. Koleske^{a,3}, R.L. Henry^a, M. Leszczynski^b, I. Grzegory^b,
T. Suski^b, S. Porowski^b, S.S. Park^c, K.Y. Lee^c, R.J. Molnar^d

^aNaval Research Laboratory, Washington, DC 20375-5347, USA

^bUNIPRESS, Polish Academy of Sciences, Sokolowska 29, 01-142 Warsaw, Poland

^cSamsung-SAIT, Suwon 440-600, South Korea

^dLincoln Laboratory, MIT, Lexington, MA 02173, USA

Abstract

Magnetic resonance experiments, including optically detected magnetic resonance (ODMR) and electron paramagnetic resonance (EPR), have been performed on Si-doped homoepitaxial GaN layers grown by MOCVD and on high quality, free-standing ($\sim 200\text{ }\mu\text{m}$ -thick) GaN grown by HVPE. This allowed us to obtain information on the properties of native defects and dopants in GaN with a significantly reduced density of dislocations ($<10^7\text{ cm}^{-2}$) compared to that typically observed ($\sim\text{mid } 10^8\text{--}10^{10}\text{ cm}^{-2}$) in conventional heteroepitaxial GaN layers. The high structural and optical quality of the layers was revealed by cross-sectional TEM and detailed low-temperature photoluminescence (PL) studies, respectively. ODMR at 24 GHz on strong shallow donor–shallow acceptor recombination from the Si-doped homoepitaxial layer reveals evidence for Si or C shallow acceptors on the N sites. EPR of the new free-standing HVPE GaN confirms the low concentration of residual donors ($\sim 10^{16}\text{ cm}^{-3}$) as determined by Hall effect measurements. In addition, new deep centers are found from ODMR on the 2.4 eV “green” PL band and on the broad emission less than 1.8 eV from the HVPE GaN template. However, contrary to expectations, the reduction of random strain fields (associated with dislocations) has not led to significant changes in the character of the magnetic resonance (such as resolved electron-nuclear hyperfine structure) compared to that typically found for heteroepitaxial GaN layers. © 2001 Elsevier Science B.V. All rights reserved.

Keywords: GaN; Homoepitaxial; Photoluminescence; Magnetic resonance; HVPE

1. Introduction

Dislocations are commonly thought to have a significant impact on the incorporation of impurities

and other point defects in GaN. Their influence on the electrical and optical properties of GaN and related alloys has been a subject of high interest. This includes their role as charged scattering centers and source of leakage paths in carrier transport in GaN materials and device structures [1,2]. Also, it has been suggested that radiative recombination processes such as the ubiquitous 2.2 eV “yellow” emission band occurs at or near dislocations [3].

The high levels of dislocations ($\sim\text{mid-}10^8\text{--}10^{10}\text{ cm}^{-2}$) typically found in conventional GaN heteroepitaxial layers are often thought to compromise the identification of residual defects and to influence the spin properties of dopants as investigated through magnetic

*Corresponding author. Tel.: +1-202-404-4521; fax: +1-202-767-1165.

E-mail address: glaser@bloch.nrl.navy.mil (E.R. Glaser).

¹Permanent Address: Physics Institute, Universidade de Brasilia, Brasilia, Brazil.

²Current Address: Army Research Laboratory, Adelphi, MD 20783-1197 USA.

³Current Address: Sandia National Laboratory, Albuquerque, NM 87185 USA.

resonance techniques. For example, random strain fields associated with the dislocations can strongly influence the spin properties of shallow acceptors derived from degenerate or nearly degenerate valence band states. Also, as a source of additional broadening, these strain fields can render electron-nuclear hyperfine structure unobservable.

In order to explore these issues, low-temperature photoluminescence (PL), electron paramagnetic resonance (EPR), and optically detected magnetic resonance (ODMR) have been performed on homoepitaxial GaN layers grown by MOCVD and on high-quality, free-standing (thick) GaN grown by HVPE. This allowed us to obtain information on the properties of native defects and dopants in GaN with dislocation densities at least 2–3 orders of magnitude smaller than usually observed for GaN deposited on Al_2O_3 or 6H-SiC substrates. Several new defects are revealed from these studies, including evidence for either shallow Si or C acceptors on the N sites in the GaN homoepitaxial layers and for new deep centers in the HVPE-grown GaN. However, contrary to expectations, the reduction of random strain fields (associated with the dislocations) has not led to significant changes in the character of the magnetic resonance compared to that typically found for conventional heteroepitaxial GaN [4–7].

2. Experimental background

PL and ODMR experiments were performed on GaN homoepitaxial layers grown by MOCVD on the (0001) Ga face of (unintentionally doped) GaN bulk crystals. More details on the high pressure–high temperature synthesis of these crystals and the particular treatment of the surfaces prior to deposition of the CVD layers are provided elsewhere [8–9]. In this work the PL and ODMR from a 1 μm -thick Si-doped ($\sim 1\text{--}2 \times 10^{17} \text{ cm}^{-3}$) GaN homoepitaxial layer are highlighted. This film was deposited on top of 5 μm of undoped MOCVD-grown GaN. Cross-sectional TEM measurements revealed the high structural quality of these undoped and Si-doped homoepitaxial layers with dislocation densities $< 10^7 \text{ cm}^{-2}$. However, it is possible that the dislocation densities are significantly lower as observed from defect selective etching experiments [10] of similar homoepitaxial layers grown on these GaN bulk crystals.

PL, EPR, and ODMR were also performed on thick ($\sim 200 \mu\text{m}$) free-standing (n-type) GaN grown by HVPE after laser-assisted liftoff from the parent 2 in dia. Al_2O_3 substrate [11]. We note that the ODMR was obtained on PL from the top (growth-surface) side of this material which was mechanically polished and reactive ion etched. Recent X-ray, AFM, TEM, and Raman scattering measurements [11–14] all indicate the high crystalline quality of this HVPE GaN. In particular, similar to that

found for the GaN homoepitaxial layers, dislocation densities $< 10^7 \text{ cm}^{-2}$ were revealed by TEM images [11]. Furthermore, variable-temperature Hall effect measurements [12,15] on samples from the same wafer or ones similar to those investigated in this work revealed remarkably low levels of residual shallow donors ($\sim 7 \times 10^{15}\text{--}1.2 \times 10^{16} \text{ cm}^{-3}$) and compensating acceptors ($\sim 2\text{--}3 \times 10^{15} \text{ cm}^{-3}$) and, in addition, the highest low-temperature electron Hall mobilities ($\sim 8000 \text{ cm}^2/\text{Vs}$) attained to date in bulk GaN.

High-resolution PL was obtained at 5 K with the 325 nm line from a He–Cd laser. This emission was analyzed by a 0.85-m double-grating spectrometer and detected by a GaAs PMT. The PL between 1.3 and 3.3 eV was also obtained at 1.6 K under the same photoexcitation conditions as employed in the ODMR experiments. This PL was generated by the 351 nm line from an Ar^+ -ion laser ($\sim 1 \text{ W/cm}^2$), analyzed by a 0.22-m double-grating spectrometer, and detected by a Si photodiode. The 9.5 GHz EPR and 24 GHz ODMR spectrometers used in this work are described elsewhere [5].

3. Results and discussion

3.1. GaN homoepitaxial layers

As observed by other groups [16–18], high-resolution PL studies confirmed the high-crystalline quality of our undoped and Si-doped GaN homoepitaxial layers [19]. In particular, the Si-doped homoepitaxial sample exhibits sharper excitonic PL (linewidths $\leq 1 \text{ meV}$) compared to that reported previously for GaN grown on Al_2O_3 with similar Si doping levels [20]. The PL below 3.4 eV from the Si-doped homoepitaxial layer is shown in Fig. 1. Strong recombination at 3.26 eV and a series of LO phonon replicas ($E_{\text{LO}} \sim 92 \text{ meV}$) at lower energies are observed. This emission shifts monotonically to lower energies with decreasing excitation power densities ($\sim 11 \text{ meV}$ with P_{exc} reduced from 1 to 0.001 W/cm^2). Based on these characteristics and previous work [21], this PL is attributed to a recombination between shallow Si donors ($E_{\text{d}} \sim 30 \text{ meV}$) and shallow acceptors ($E_{\text{a}} \sim 220 \text{ meV}$). Likely candidates for the shallow acceptors will be discussed shortly. In addition, as invariably observed to some degree of strength in most n-type (as-grown or Si-doped) CVD GaN [5], a broad “yellow” PL band at 2.2 eV is also found. No additional emission was observed from this layer between 1.3 and 1.8 eV.

The ODMR obtained on the 2.2 eV PL band from the Si-doped GaN homoepitaxial layer with $\mathbf{B} \perp c$ is shown in Fig. 2. For comparison, ODMR on similar emission from (n-type) heteroepitaxial GaN reference layers grown on Al_2O_3 [5] and 6H-SiC [22] is also provided.

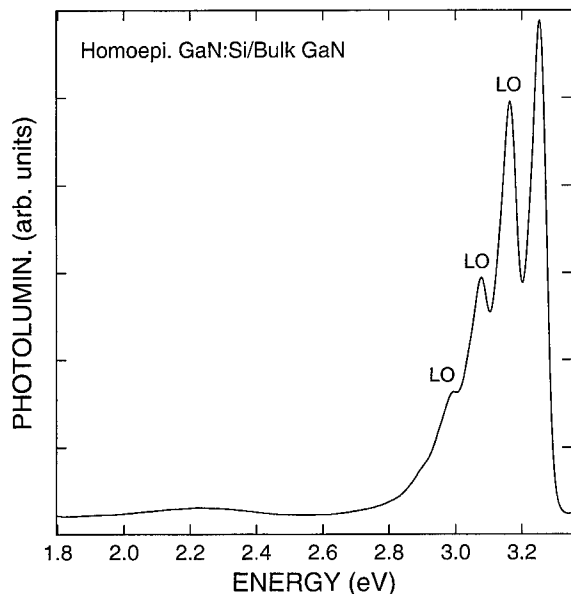


Fig. 1. PL obtained below 3.4 eV at 1.6 K from the Si-doped GaN homoepitaxial layer with $\sim 1 \text{ W/cm}^2$ of 351 nm radiation.

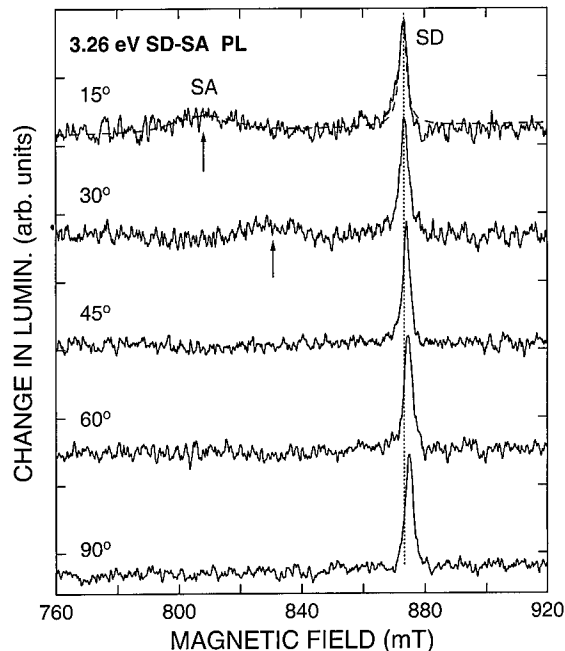


Fig. 3. ODMR obtained on the 3.26 eV SD-SA PL from the homoepitaxial GaN:Si film. The dashed curve is a two-component fit of the spectrum with \mathbf{B} 15° from the c -axis. The dotted line indicates the position of the SD resonance with \mathbf{B} near the c -axis.

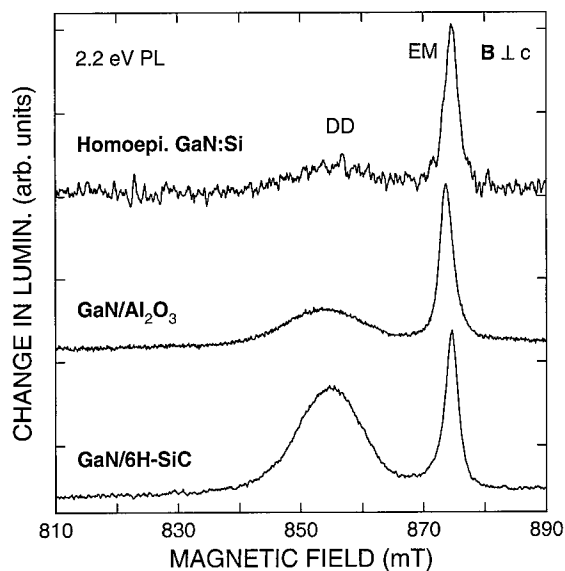


Fig. 2. ODMR spectra found at 24 GHz on the 2.2 eV "yellow" PL bands from the Si-doped homoepitaxial GaN layer and heteroepitaxial GaN layers grown on Al_2O_3 and 6H-SiC (EM=effective-mass donor, DD=deep defect).

The lower signal-to-noise ratio of the ODMR from the homoepitaxial layer (as also seen in Fig. 3) relative to that found for the reference samples mainly reflects the degradation of the microwave cavity mode due to the high conductivity of the bulk GaN substrate. However, it is clear that the character of the ODMR observed on

this emission in the three cases is quite similar. Unfortunately, in spite of the reduced level of dislocations, no resolved hyperfine structure could be observed in the magnetic resonance of the homoepitaxial layer. The sharp feature (FWHM $\sim 2\text{--}3 \text{ mT}$) with $g_{\parallel} = 1.952$ and $g_{\perp} = 1.949$ is assigned to (effective-mass) shallow donors based on the previous work [4,5]. The shallow donors are likely Si on the Ga sites although residual O on the N sites may also contribute to part of this signal based on recent evidence for the shallow nature of O impurities in GaN [23]. Most groups agree that the broad resonance (FWHM $\sim 15 \text{ mT}$) with $g_{\parallel} = 1.989$ and $g_{\perp} = 1.992$ is associated with a deep defect (DD). We first ascribed this feature to deep donors based, in part, on the small negative g -shift with respect to the free electron g -value of 2.0023 [5]. However, from a magnetic resonance standpoint, the donor or acceptor character of this center is an open question based on the observation of similar g -shifts for one of the extremal g -values (i.e., g_{\perp}) associated with shallow Mg acceptors in GaN [24,25].

Representative ODMR found on the strong 3.26 eV SD-SA PL from the Si-doped GaN homoepitaxial film is shown in Fig. 3. Two luminescence-increasing signals are observed. The first feature (labeled SD) is again attributed to shallow donors based on the resonance

parameters (i.e., $g_{\parallel}, g_{\perp} \sim 1.95$). The second line (labeled SA) is only observed above the background for $\mathbf{B} < 45^\circ$ from the c -axis. However, if we take this limited data set and the usual expression for the g -values in the case of axial symmetry that describes most of the magnetic resonance observed to date in GaN (i.e., $g(\theta) = (g_{\parallel}^2 \cos^2 \theta + g_{\perp}^2 \sin^2 \theta)^{1/2}$, where θ denotes the angle between \mathbf{B} and the c -axis), the extremal g -values for this resonance are $g_{\parallel} \sim 2.1$ and $g_{\perp} \sim 1.99$.⁴ Most notably, this g -tensor is quite similar to that found from EPR and ODMR of shallow Mg acceptors in heteroepitaxial Mg-doped GaN [23,24]. For example, a comparison of the ODMR found on the SD-SA emission from the homoepitaxial layer with that observed on equivalent emission from a Mg-doped GaN/Al₂O₃ heteroepitaxial layer with $[\text{Mg}] \sim 2.5 \times 10^{18} \text{ cm}^{-3}$ (grown in a separate CVD reactor) is shown in Fig. 4. Thus, based on the similar character of the PL bands and the magnetic resonance, the broad ODMR feature on the 3.26 eV PL from the Si-doped homoepitaxial layer is assigned to shallow acceptors.

We note that Mg had never been introduced as a dopant source in the reactor employed for the growth of these homoepitaxial layers. Thus, we propose that likely candidates for the residual shallow acceptors are C or Si on the N lattice sites. The amphoteric nature of Si and C has been established for other III-V semiconductors such as GaAs [26]. In addition, recent PL work suggests that Si also introduces an acceptor level in GaN with E_a

of $\sim 220 \text{ meV}$ [27]. Thus, this feature (SA) is tentatively assigned to Si_N shallow acceptors, but we can not rule out C_N being responsible for all or part of this signal. Additional work is underway to identify this defect [19].

The apparent loss of the shallow acceptor resonance in the homoepitaxial layer for $\theta \geq 45^\circ$, perhaps due to severe broadening, is not understood at this time. We note, however, that similar intensity behavior and broadening (though not to the same degree) are often observed from magnetic resonance of (effective-mass) shallow acceptors and holes with highly anisotropic g -tensors (i.e., $g(\theta) = g_{\parallel} \cos(\theta)$, $g_{\parallel} \sim 2-4$, $g_{\perp} \sim 0$) associated with the $m_j = \pm 3/2$ (heavy-hole) valence band in other semiconductors such as bulk 6H-SiC [28] and CdS [29] and SiGe quantum wells under tensile strain [30]. For such states, any inhomogeneity in g_{\parallel} will lead to a pronounced broadening of the resonance when $g(\theta)$ is rapidly changing as is the case with $\theta \geq 45^\circ$.

Finally, we note that the nearly isotropic g -tensor associated with the shallow acceptors in the Si-doped homoepitaxial GaN layer is quite different than the highly anisotropic g -tensor expected (given above) for such centers in WZ GaN from effective-mass theory [31]. This likely reflects a symmetry-lowering local distortion of the shallow acceptors. Overall, the present results suggest that (a) the non-effective mass like character is not specific to Mg_{Ga} shallow acceptors and (b) random strain fields associated with high dislocation densities do not appear to be the major source of perturbation responsible for the nearly isotropic g -tensors observed for shallow acceptors in conventional heteroepitaxial GaN.

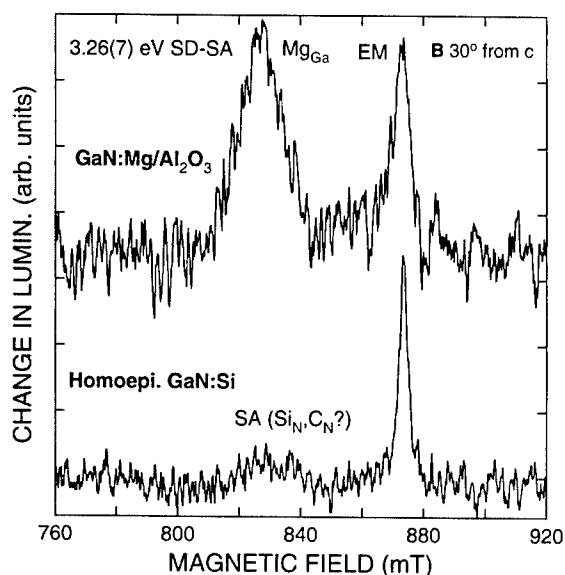


Fig. 4. Comparison of the ODMR observed on the SD-SA PL bands from a Mg-doped GaN/Al₂O₃ sample (from Ref. [24]) and the Si-doped GaN homoepitaxial layer. The emission from the Mg-doped GaN layer was analyzed through a 0.22 m double-grating spectrometer.

3.2. Free-standing (thick) HVPE GaN

Though not nearly as sharp as the excitonic PL observed from undoped GaN homoepitaxial layers with linewidths of $\sim 0.1 \text{ meV}$ [16-19], the bandedge emission from these free-standing (thick) HVPE GaN templates is characterized by linewidths less than 1 meV [14]. An example of a high-resolution PL spectrum obtained at 5 K that demonstrates the high crystallinity of this material is shown in the inset of Fig. 5. Both impurity-bound and free exciton lines are observed between 3.46 and 3.52 eV [14]. The PL below 3.3 eV from this sample is also shown in Fig. 5. Most notably, instead of the 2.2 eV "yellow" PL band, a broad "green" emission band at 2.4 eV is found. Recent lapping studies [13] of these templates with $\sim 15 \mu\text{m}$ removed from the

⁴We note that the highly anisotropic expression expected for the g -tensor (i.e., $g(\theta) = g_{\parallel} \cos(\theta)$, $g_{\perp} \sim 0$) of effective-mass shallow acceptors in WZ GaN (as found for shallow acceptors in other semiconductors with similar hexagonal crystal symmetry such as 6H-SiC and CdS) does not describe the g -values of this resonance.

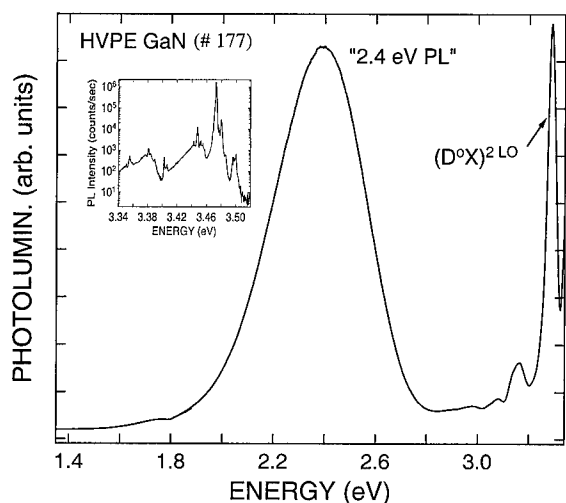


Fig. 5. PL spectrum obtained below 3.3 eV at 1.6 K from the free-standing HVPE GaN template. The small dip near 1.8 eV is a grating response. Inset: high resolution PL found at 5 K in the near-bandgap spectral regime (from Ref. [14]).

damaged back surface indicate that this emission is intrinsic to the bulk material (i.e., not a result of the post-growth treatment). One group has proposed that isolated Ga vacancies (V_{Ga}) or V_{Ga} -related complexes are involved in this “green” PL [32]. In addition, as typically observed from HVPE-grown GaN [33,34], this sample exhibits weak, broad emission between 1.4 and 1.8 eV (referred to as the “red” PL band).

A representative EPR spectrum obtained for the 170 μm -thick GaN template with $\mathbf{B} \perp c$ is shown in Fig. 6. The EPR for a 10 μm -thick HVPE-grown GaN/ Al_2O_3 reference sample with $n_{300\text{ K}} \sim 1 \times 10^{17} \text{ cm}^{-3}$ is also shown for comparison. Single lines with g_{\parallel} , $g_{\perp} \sim 1.95$ are found and ascribed to shallow donors as discussed earlier. Most notably, the density of spins associated with the signal from the Samsung sample is estimated to be $\sim 6 \times 10^{15} \text{ cm}^{-3}$ ($\pm 50\%$) from a comparison with the EPR of a P-doped Si standard. This density is in good agreement with the concentration of uncompensated shallow donors ($N_{\text{D}} - N_{\text{A}}$) determined from variable-temperature Hall effect measurements of samples from the same 2 in.-dia. wafer.

Unfortunately, additional structure was not revealed in the EPR of the Samsung HVPE GaN. In fact, due to a lower concentration of donors, this sample exhibits a broader EPR linewidth (FWHM ~ 27 G) compared to that found for the more highly conducting GaN/ Al_2O_3 layer (FWHM ~ 12 G) due to unresolved hyperfine structure between the spin of the (isolated) donors and the host lattice nuclei. This interaction is “averaged” out for GaN with larger concentrations of interacting

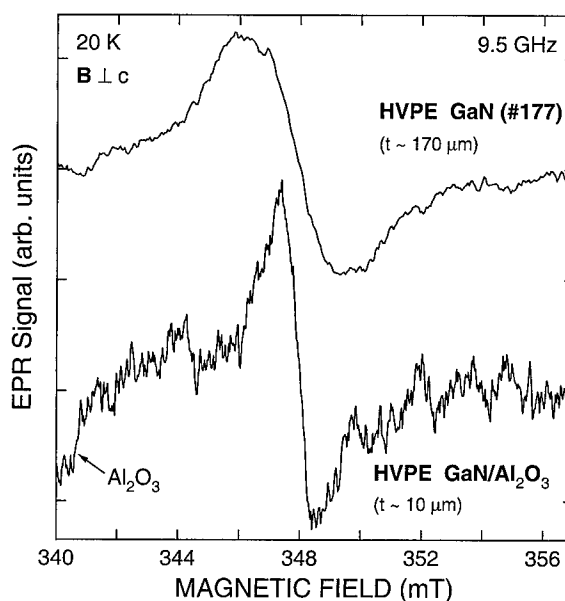


Fig. 6. EPR spectra obtained at 9.5 GHz for two HVPE-grown GaN samples. Top: free-standing GaN template ($n_{300\text{ K}} \sim 1 \times 10^{16} \text{ cm}^{-3}$). Bottom: GaN/ Al_2O_3 reference; $n_{300\text{ K}} \sim 1 \times 10^{17} \text{ cm}^{-3}$.

donors [35] as found in the 10 μm -thick HVPE GaN/ Al_2O_3 sample.

ODMR obtained on the 2.4 eV “green” PL band is shown in the top half of Fig. 7. As also found on the 2.2 eV “yellow” PL emission, the resonance labeled EM is assigned to effective-mass (shallow) donors. The second resonance, labeled A_1 , is new. It exhibits a strong intensity anisotropy with $g_{\parallel} = 1.975$ and $g_{\perp} = 1.969$. The g -values suggest a donor-like defect but the (axial) intensity anisotropy is more often found for acceptor-like defects associated with degenerate or nearly degenerate valence band states. Thus, though more work is clearly needed, we tentatively assign this feature to a deep acceptor of unknown origin. In addition, the g -tensor and intensity behavior of this center are quite different compared to that found for the deep defects (i.e., $g_{\parallel} = 1.989$ and $g_{\perp} = 1.992$) involved in the 2.2 eV “yellow” PL [5–7,22]. This indicates that these centers are of different origin.

ODMR found on the PL less than 1.8 eV is shown in the bottom half of Fig. 7. Two luminescence-increasing signals are observed. The first line at ~ 870 mT is again attributed to shallow donors. The second feature (labeled A_2) is also new. It is isotropic with $g = 2.019$ and a FWHM of ~ 25 mT. This signal is assigned to deep acceptors based on these magnetic resonance parameters and the near-midgap PL. We note that this defect is different than the deep center with $g_{\parallel} = 2.008$

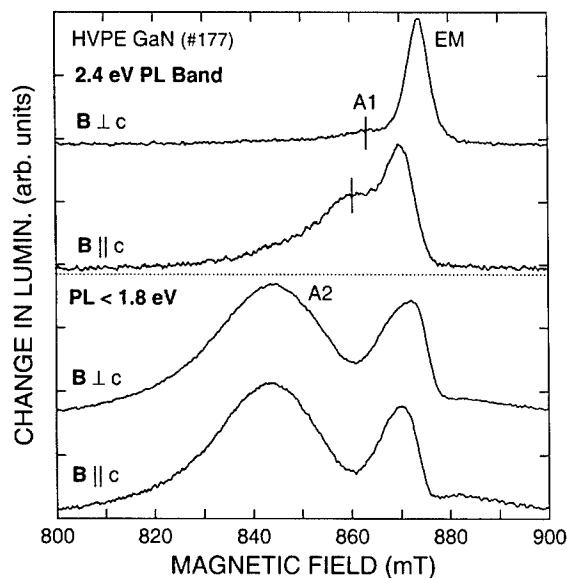


Fig. 7. ODMR found on the 2.4 eV “green” PL band and near-IR emission from the free-standing HVPE GaN sample. The features labeled A_1 and A_2 are tentatively assigned to acceptor-like defects.

and $g_{\perp} = 2.004$ revealed by ODMR on similar near-IR emission from other HVPE-grown GaN [25,36].

4. Summary

ODMR and EPR experiments have been performed on Si-doped homoepitaxial GaN layers grown by MOCVD and on free-standing (thick) GaN grown by HVPE. The high structural and optical quality of these materials was revealed by cross-sectional TEM and low-temperature PL studies, respectively. ODMR reveals several new defects, including evidence for either Si or C shallow acceptors on the N lattice sites in a Si-doped GaN homoepitaxial layer and for two new deep centers in the HVPE-grown GaN templates. In addition, EPR confirmed the low concentration of residual donors in these free-standing layers. The reduced dislocation densities, however, has not led to significant changes in the character of the magnetic resonance (such as resolved electron-nuclear hyperfine structure) compared to that found previously for conventional heteroepitaxial GaN. However, we suggest that the application of more sophisticated magnetic resonance techniques such as electron-nuclear double resonance (ENDOR) or optically detected—ENDOR should be pursued for identification of defects in these more pure GaN materials.

Acknowledgements

This work was supported by the Office of Naval Research. We thank B.V. Shanabrook (NRL) for helpful discussions.

References

- [1] H.M. Ng, D. Doppalapudi, T.D. Moustakas, N.G. Weimann, L.F. Eastman, *Appl. Phys. Lett.* 73 (1998) 821.
- [2] P. Kozodoy, J.P. Ibbetson, H. Marchand, P.T. Fini, S. Keller, J.S. Speck, S.P. DenBaars, UK Mishra, *Appl. Phys. Lett.* 73 (1998) 975.
- [3] F.A. Ponce, D.P. Bour, W. Götz, P.J. Wright, *Appl. Phys. Lett.* 68 (1996) 57.
- [4] W.E. Carlos, J.A. Freitas Jr., M. Asif Khan, D.T. Olson, J.N. Kuznia, *Phys. Rev. B* 48 (1993) 17878, and references therein.
- [5] E.R. Glaser, T.A. Kennedy, K. Doverspike, L.B. Rowland, D.K. Gaskill, J.A. Freitas Jr., M. Asif Khan, D.T. Olson, J.N. Kuznia, D.K. Wickenden, *Phys. Rev. B* 51 (1995) 13326.
- [6] T.A. Kennedy, E.R. Glaser, in: M. Stavola (Ed.), *Identification of Defects in Semiconductors, Semiconductors and Semimetals Vol. 51A*, Academic Press, San Diego, 1998, pp. 93–136.
- [7] B.K. Meyer, *Magnetic resonance investigations of group-III nitrides*, in: R.K. Willardson, E.R. Weber (Eds.), *Semiconductors and Semimetals, Vol. 57*, Academic Press, New York, 1999, pp. 371–406.
- [8] S. Porowski, *J. Cryst. Growth* 189/190 (1998) 153.
- [9] P. Prystawko, M. Leszczynski, B. Beaumont, P. Gibart, E. Frayssinet, W. Knap, P. Wisniewski, M. Bockowski, T. Suski, S. Porowski, *Phys. Stat. Sol. B* 210 (1998) 437.
- [10] I. Grzegory, S. Porowski, *Thin Solid Films* 367 (2000) 281.
- [11] S.S. Park, H.-W. Park, S.H. Choh, *Jap. J. Appl. Phys.* 39 (2000) L1141.
- [12] P. Visconti, K.M. Jones, M.A. Reshchikov, F. Yun, R. Cingolani, H. Morkoç, S. Park, K.Y. Lee, *Appl. Phys. Lett.* 77 (2000) 3743.
- [13] D. Huang, F. Yun, M.A. Reshchikov, D. Wang, H.H. Morkoç, D.L. Rode, L.A. Farina, Ç. Kurdak, H.T. Tsen, S.S. Park, K.Y. Lee, *Solid-State Electron.* 45 (2001) 711.
- [14] J.A. Freitas Jr., G.C.B. Braga, W.J. Moore, J.G. Tischler, J.C. Culbertson, M. Fatemi, S.S. Park, S.K. Lee, Y. Park, *J. Cryst. Growth* 231 (2001) 322.
- [15] A. Saxler, D.C. Look, S. Elhamri, J. Sizelove, W.C. Mitchell, C.M. Sung, S.S. Park, K.Y. Lee, *Appl. Phys. Lett.* 78 (2001) 1873.
- [16] C. Kirchner, V. Schwegler, F. Eberhard, M. Kamp, K.J. Ebeling, K. Kornitzer, T. Ebner, K. Thonke, R. Sauer, P. Prystawko, M. Leszczynski, I. Grzegory, S. Porowski, *Appl. Phys. Lett.* 75 (1999) 1098.
- [17] M. Leszczynski, B. Beaumont, E. Frayssinet, W. Knap, P. Prystawko, T. Suski, I. Grzegory, S. Porowski, *Appl. Phys. Lett.* 75 (1999) 1276.
- [18] K. Kornitzer, T. Ebner, K. Thonke, R. Sauer, C. Kirchner, V. Schwegler, M. Kamp, M. Leszczynski, I. Grzegory, S. Porowski, *Phys. Rev. B* 60 (1999) 1471.

- [19] J.A. Freitas, Jr., G.C. Braga, W.J. Moore, A.E. Wickenden, M. Leszczynski, I. Grzegory, S. Porowski, unpublished.
- [20] J.A. Freitas Jr., K. Doverspike, A.E. Wickenden, *Mat. Res. Soc. Symp. Proc.* 395 (1996) 485.
- [21] R. Dingle, M. Ilegems, *Solid State Commun.* 9 (1971) 175.
- [22] E.R. Glaser, T.A. Kennedy, S.W. Brown, J.A. Freitas Jr., W.G. Perry, M.D. Bremser, T.W. Weeks, R.F. Davis, *Mat. Res. Soc. Symp. Proc.* 395 (1996) 667.
- [23] W.J. Moore, J.A. Freitas, Jr., G.C.B. Braga, R.J. Molnar, S.K. Lee, K.Y. Lee, I.J. Song, *Appl. Phys. Lett.*, in press.
- [24] E.R. Glaser, T.A. Kennedy, J.A. Freitas Jr., B.V. Shanabrook, A.E. Wickenden, D.D. Koleske, R.L. Henry, H. Obloh, *Physica B* 273–274 (1999) 58.
- [25] E.R. Glaser, et al., *Mater. Sci. Eng. B*, in press.
- [26] L. Pavesi, M. Guzzi, *J. Appl. Phys.* 75 (1994) 4779.
- [27] J. Jayapalan, B.J. Skromme, R.P. Vaudo, V.M. Phanse, *Appl. Phys. Lett.* 73 (1998) 1188.
- [28] Le Si Dang, K.M. Lee, G.D. Watkins, W.J. Choyke, *Phys. Rev. Lett.* 45 (1980) 390.
- [29] J.L. Patel, J.E. Nicholls, J.J. Davies, *J. Phys. C* 14 (1981) 139.
- [30] E.R. Glaser, T.A. Kennedy, D.J. Godbey, P.E. Thompson, K.L. Wang, C.H. Chern, *Phys. Rev. B* 47 (1993) 1305.
- [31] A.V. Malyshev, I.A. Merkulov, A.V. Rodina, *Phys. Solid State* 40 (1998) 917.
- [32] M.A. Reshchikov, H. Morkoç, S.S. Park, K.Y. Lee, *Appl. Phys. Lett.* 78 (2001) 3041.
- [33] W. Götz, L.T. Romano, B.S. Krusor, N.M. Johnson, R.J. Molnar, *Appl. Phys. Lett.* 69 (1996) 242.
- [34] S.J. Rhee, S. Kim, E.E. Reuter, S.G. Bishop, R.J. Molnar, *Appl. Phys. Lett.* 73 (1998) 2636.
- [35] G. Denniger, R. Beerhalter, D. Reiser, K. Maier, J. Schneider, T. Detchprohm, K. Hiramatsu, *Solid State Commun.* 347 (1996) 347.
- [36] C. Bozdog, H. Przybylinska, G.D. Watkins, V. Härle, F. Scholz, M. Mayer, M. Kamp, R.J. Molnar, A.E. Wickenden, D.D. Koleske, R.L. Henry, *Phys. Rev. B* 59 (1999) 12479.



ELSEVIER

Physica B 308–310 (2001) 58–61

PHYSICA B

www.elsevier.com/locate/physb

Radiation-induced defects in n-type GaN and InN

V.V. Emtsev^{a,*}, V.Yu. Davydov^a, E.E. Haller^b, A.A. Klochikhin^a,
V.V. Kozlovskii^c, G.A. Oganessian^a, D.S. Poloskin^a, N.M. Shmidt^a,
V.A. Vekshin^a, A.S. Usikov^a

^a Division of Solid State Electronics, Ioffe Physicotechnical Institute, Russian Academy of Sciences, 194021 St. Petersburg, Russia

^b Department of Materials Science and Engineering, University of California at Berkeley, Berkeley, CA 94720, USA

^c Technical State University, 195251 St. Petersburg, Russia

Abstract

The electrical properties of the n-GaN and n-InN, subjected to proton irradiation, are studied. The irradiation of the n-InN results in an increasing concentration of charge carriers, whereas strong compensation effects take place in the proton-irradiated n-GaN. The annealing behavior of the radiation-induced defects in both materials is discussed briefly. © 2001 Elsevier Science B.V. All rights reserved.

PACS: 61.72.Ji; 61.80.Lj; 61.82.Fk

Keywords: Gallium nitride; Indium nitride; Irradiation

1. Introduction

Interest in experimental studies of the point defects in the GaN produced by irradiation with fast electrons and protons is steadily growing in the hope to obtain an understanding of the complex nature of native and impurity-related defects in this material; see for instance Refs. [1–6]. The situation for the irradiated InN layers is even worse, since the properties of the point defects in the InN are so far unknown.

The purpose of the present work is to investigate the production and annealing processes of the proton irradiation-induced defects in the n-GaN and n-InN.

2. Experimental

Layers of hexagonal n-GaN and n-InN on (0001) sapphire substrates were grown by the MOCVD and plasma-assisted MBE techniques, respectively. The

crystal structure of the layers were well characterized by X-ray diffraction and Raman spectroscopy. The layer thickness ranges from 1.0 to 1.5 μm . The as-grown n-InN layers were nominally undoped, with electron concentrations in the low 10^{20} cm^{-3} . In some cases, Mg or Dy impurities were added during growth for reducing the free electron concentration. Auger spectroscopy did not reveal any significant content of oxygen in the n-InN layers.

Samples were irradiated with protons of 150 keV. After irradiation, the samples were subjected to isochronal annealing in steps of 50°C or 100°C for 20 min in nitrogen.

Hall effect and conductivity measurements were carried out using the Van der Pauw technique. The Raman scattering measurements were taken at room temperature.

3. Results and discussion

In Figs. 1 and 2, several typical dependencies of the electron concentration and mobility, $n(T)$ and $\mu(T)$, in one of the n-InN layers are shown. As can be seen from

*Corresponding author. Tel.: 7-812-247-9952; fax: 7-812-247-1017.

E-mail address: emtsev@pop.ioffe.rssi.ru (V.V. Emtsev).

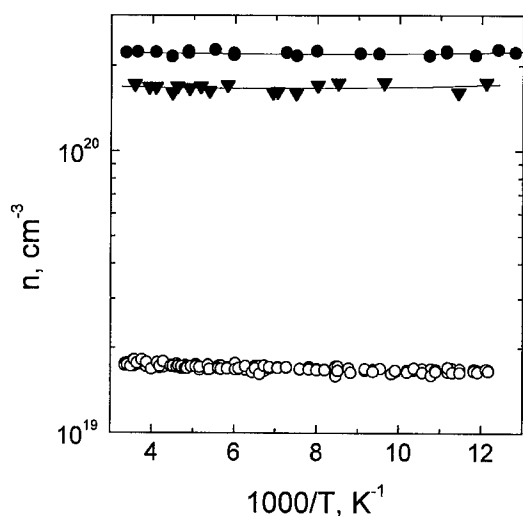


Fig. 1. Electron concentration versus reciprocal temperature in the n-InN counterdoped with Mg before the irradiation (open circles), after the proton irradiation (solid circles), and after annealing at $T = 300^\circ\text{C}$ (solid triangles). The irradiation dose, $\Phi = 1 \times 10^{16} \text{ cm}^{-2}$.

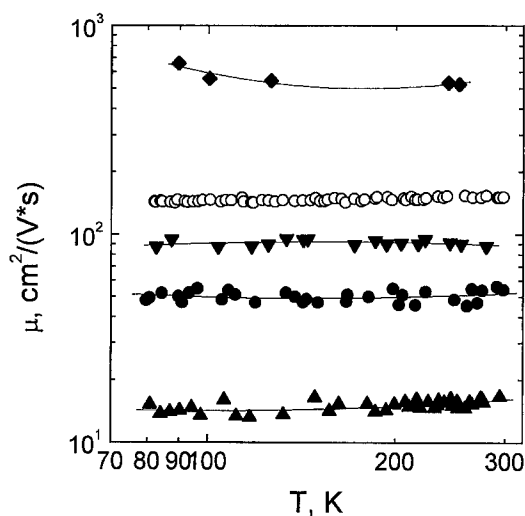


Fig. 2. Electron mobility versus temperature in the n-InN counterdoped with Mg before the irradiation (open circles), after the proton irradiation (solid circles), after annealing to $T = 300^\circ\text{C}$ (solid triangles down), $T = 450^\circ\text{C}$ (solid triangles up), and $T = 500^\circ\text{C}$ (solid diamonds). The irradiation dose, $\Phi = 1 \times 10^{16} \text{ cm}^{-2}$.

Fig. 1, proton irradiation results in a substantial increase in the concentration of the charge carriers. This effect was observed for all the samples, independent of the counterdoping. Evidently, the increase in the electron concentration in the n-InN after the irradiation is due to

the production of radiation-induced defects with shallow donor states. The production rate is the same, about $2 \times 10^4 \text{ cm}^{-1}$, over a wide dose range from 1×10^{15} to $1 \times 10^{16} \text{ cm}^{-2}$. All these experimental facts suggest that these defects are native. We believe that the native defects responsible for the net effect in the irradiated n-InN can be attributed to immobile nitrogen vacancies.

Up to $T = 100^\circ\text{C}$, there is no change in the $n(T)$ and $\mu(T)$ curves. A pronounced decrease in $n(T)$ by 30% was observed over a temperature interval of $T = 250\text{--}300^\circ\text{C}$; see Fig. 1. At this annealing stage, the annealed fraction of the electron mobility reached nearly 50%, as can be estimated from Fig. 2. At elevated temperatures, the annealing behavior of defects becomes rather complicated. First, a reverse annealing stage of the electron concentration and mobility takes place in the temperature interval from $T = 400^\circ\text{C}$ to 450°C . As a result, the concentration of charge carriers returns practically to the value measured in the irradiated n-InN and the mobility drops by an order-of-magnitude; see Fig. 2. After annealing to $T = 500^\circ\text{C}$, the $n(T)$ curves were found to be little affected but the electron mobility became much higher than that in the non-irradiated layers.

In accordance with the earlier observations [7], in Raman spectra of as-grown n-InN layers we also revealed the presence of a band at $\nu = 590 \text{ cm}^{-1}$; see Fig. 3. This band has been attributed to the L^- -LO mode of Raman scattering. Our study of the proton-irradiated n-InN clearly showed that the intensity of this band is dose dependent; see Fig. 3. Theoretical calculations of the cross-sections for three different models made it possible to conclude that the Raman scattering in the region of interest is associated with the short-range potential scattering process due to the presence of defects; see Fig. 4. As is seen in Fig. 3, the proposed model gives a satisfactory explanation to the experimental data. Details of calculations will be discussed in a separate paper.

Contrary to the n-InN, the proton irradiation of the doped n-GaN:Si leads to a substantial decrease in the concentration of the charge carriers; see Figs. 1 and 5. The electron removal rate estimated from the $n(T)$ curves given in Fig. 5 is about $1 \times 10^4 \text{ cm}^{-1}$. Surprisingly, the electron removal rate in the n-GaN:Si with a lower doping level is evidently smaller, at least by a factor of 3; see Fig. 5. It has been reported [1,6] that in the doped n-GaN:Si subjected to fast electron irradiation, the defect production rate is dependent on the doping level, too.

There are no significant changes in the $n(T)$ dependencies after the annealing of the proton-irradiated n-GaN to $T = 200^\circ\text{C}$, whereas the electron mobility decreases noticeably. The first annealing stage of defects takes place over a temperature interval of $T = 300\text{--}400^\circ\text{C}$. As is seen from Fig. 6, the mobility of the charge

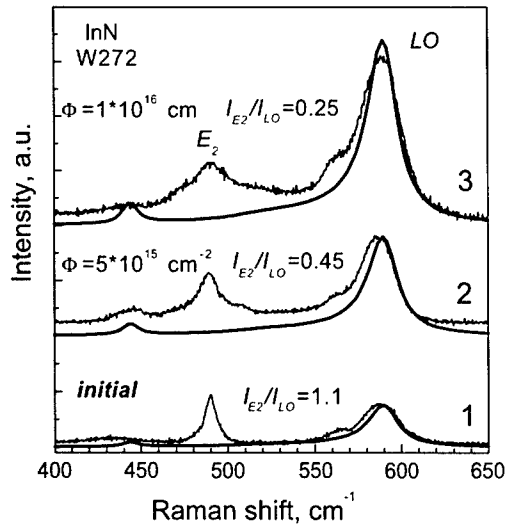


Fig. 3. The experimental and calculated Raman spectra in the n-InN before the irradiation (curve 1), after the proton irradiation at $\Phi = 5 \times 10^{15} \text{ cm}^{-2}$ (curve 2), and $\Phi = 1 \times 10^{16} \text{ cm}^{-2}$ (curve 3). Calculated spectra are shown by the broken line. The probability of the short-potential scattering process due to the defects is assumed to vary proportionally with the defect concentration. The ratios of the intensities of the E_2 and LO bands are given. The E_2 band is used as a reference, since its intensity is not sensitive to the presence of the defects.

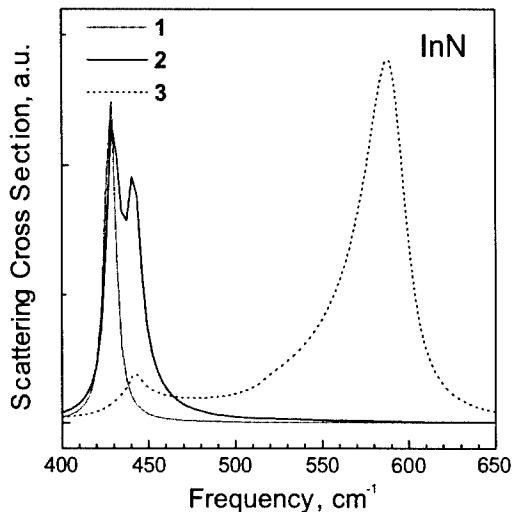


Fig. 4. Raman cross-section versus frequency in the range of L^- -LO modes calculated for three different scattering mechanisms in the InN. Perfect crystal, curve 1; defects with screened long-range potential and curve 2; defects with short-range potential, curve 3.

carriers continues to drop strongly. With the temperature increasing to $T = 600^\circ\text{C}$, the electron concentration and mobility in the irradiated n-GaN recover substan-

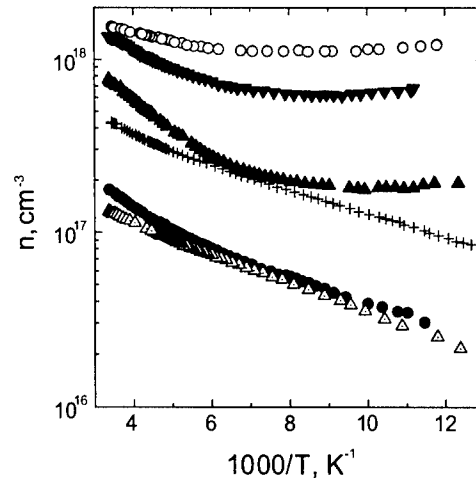


Fig. 5. Electron concentration versus reciprocal temperature in the heavily doped n-GaN:Si before the irradiation (open circles), after the proton irradiation (solid circles), and after annealing at $T = 400^\circ\text{C}$ (solid triangles up) and $T = 600^\circ\text{C}$ (solid triangles down). The irradiation dose, $\Phi = 1 \times 10^{14} \text{ cm}^{-2}$. For comparison purposes, two $n(T)$ curves for the moderately doped n-GaN:Si before the irradiation (crosses) and after the proton irradiation at the same dose (open triangles up) are also shown.

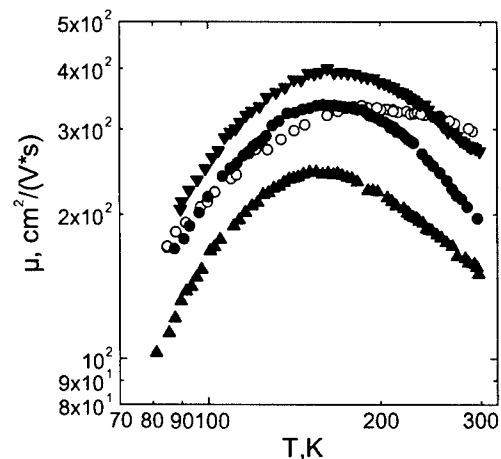


Fig. 6. Electron mobility versus temperature in the n-GaN:Si before the irradiation (open circles), after the proton irradiation (solid circles), after annealing at $T = 400^\circ\text{C}$ (solid triangles up) and $T = 600^\circ\text{C}$ (solid triangles down). The irradiation dose, $\Phi = 1 \times 10^{14} \text{ cm}^{-2}$.

tially. The mobility of the charge carriers becomes even larger than that in the initial n-GaN. After annealing at $T = 700^\circ\text{C}$, the fraction of unannealed defects turned out to be between 20% and 30%.

4. Conclusions

The behavior of defects in the n-GaN and n-InN produced by proton irradiation and subsequent annealing has been studied. From the data obtained on the n-InN it can be concluded that most likely the nitrogen vacancies with shallow donor states are responsible for the increasing concentration of free electrons in the irradiated n-InN. It has been demonstrated that in the Raman spectra, the intensity of a band at $\nu = 590\text{ cm}^{-1}$ in the proton-irradiated n-InN layers is dose-dependent. Theoretical calculations showed that the model of defects with short-range potential gives a satisfactory explanation for this band in Raman scattering. The first stage of defect annealing in the irradiated n-InN takes place at $T = 300^\circ\text{C}$.

The production rate of native defects in the irradiated n-GaN appears to be Fermi-level dependent. Two main recovery stages of the electron concentration over two intervals from $T = 300^\circ\text{C}$ to 400°C and from $T = 500^\circ\text{C}$ to 600°C have been found.

Acknowledgements

The work was supported by CRDF (grant # RP1-2258) and partly by The Russian Foundation for Basic Research (grant 99-02-18318).

References

- [1] V.V. Emtsev, V.Yu. Davydov, I.N. Goncharuk, E.V. Kalinina, V.V. Kozlovskii, D.S. Poloskin, A.V. Sakharov, N.M. Shmidt, A.N. Smirnov, A.S. Usikov, in: G. Davies, M.H. Nazare (Eds.), *Proceedings of the Materials Science Forum*, Vols. 258–263, Trans Tech Publications, Switzerland, 1997, pp. 1143–1148.
- [2] D.C. Look, D.C. Reynolds, J.W. Hemsky, J.R. Sizelove, R.L. Jones, R.J. Molnar, *Phys. Rev. Lett.* 79 (1997) 2273.
- [3] C. Bozdog, H. Przybylinska, G.D. Watkins, V. Härle, F. Scholz, M. Mayer, M. Kamp, R.J. Molnar, A.E. Wickenden, D.D. Koleske, R.L. Henry, *Phys. Rev. B* 59 (1999) 12479.
- [4] F.D. Auret, S.A. Goodman, F.K. Koschnick, J.-M. Spaeth, B. Beaumont, P. Gibart, *Appl. Phys. Lett.* 74 (1999) 407.
- [5] K.H. Chow, G.D. Watkins, A. Usui, M. Mizuta, *Phys. Rev. Lett.* 85 (2000) 2761.
- [6] V.V. Emtsev, V.Yu. Davydov, V.V. Kozlovskii, V.V. Lundin, D.S. Poloskin, A.N. Smirnov, N.M. Shmidt, A.S. Usikov, J. Aderhold, H. Klausling, D. Mistele, T. Rotter, J. Stemmer, O. Semchinova, J. Graul, *Semicond. Sci. Technol.* 15 (2000) 73.
- [7] V.Yu. Davydov, V.V. Emtsev, I.N. Goncharuk, A.N. Smirnov, V.D. Petrikov, V.V. Mamutin, V.A. Vekshin, S.V. Ivanov, M.B. Smirnov, T. Inushima, *Appl. Phys. Lett.* 75 (1999) 3297.



ELSEVIER

Physica B 308–310 (2001) 62–65

PHYSICA B

www.elsevier.com/locate/physb

A radiation-produced defect in GaN displaying hyperfine structure with three Ga atoms

G.D. Watkins*, L.S. Vlasenko¹, C. Bozdog

Department of Physics, Lehigh University, 16 Memorial Drive East, Bethlehem, PA 18015-3182, USA

Abstract

Electron-irradiation of undoped n-type GaN with 2.5 MeV electrons at room temperature produces a broad PL band at ~ 0.95 eV, and an $S = 1/2$ ODEPR center, labeled L1, is observed in it. The L1 signal reveals partially resolved structure, which can be matched accurately as arising from hyperfine interaction with three equivalent Ga atoms. Irradiation in situ at 4.2 K produces the 0.95 eV band but the L1 ODEPR signal emerges only upon subsequent annealing at room temperature, as another ODEPR signal identified as interstitial Ga disappears. The possibility that both L1 and the 0.95 eV PL arise from the Ga vacancy is discussed. © 2001 Elsevier Science B.V. All rights reserved.

Keywords: GaN; ODEPR; Ga interstitial; Ga vacancy

1. Introduction

Vital to successful device application of any semiconductor material is the understanding of its intrinsic defects, because they provide various diffusion mechanisms involved in processing and device degradation, as well as in often controlling background doping and compensation. In GaN, little is presently known concerning the properties of its isolated vacancies and interstitials.

The only direct and unambiguous method of introducing vacancies and interstitials for experimental study is by high-energy electron irradiation, where host atoms can be displaced from their lattice sites by Rutherford scattering. In addition, the only truly successful experimental technique for identifying and studying the defects has proven to be electron paramagnetic resonance, detected either directly (EPR) or optically (ODEPR). Studies combining electron irradiation and ODEPR have recently begun in GaN [1,2], and already the isolated interstitial Ga atom has been identified [3].

Here, we describe such further studies, in which a second defect produced by the irradiation, labeled L1, is described. The possibility that it is the isolated Ga vacancy is discussed.

2. Room-temperature electron irradiation

The results reported [1] for room-temperature irradiation of undoped (n-type) GaN by 2.5 MeV electrons can be summarized as follows: In all the samples studied (MOCVD, MBE, and HVPE), the irradiation was observed to cause a substantial decrease in the visible and band-edge luminescence, while two new bands were produced in the near infrared—a sharp zero phonon line at 0.88 eV with associated phonon structure, and a broader overlapping band centered at ~ 0.95 eV. An $S = 1$ ODEPR signal, labeled L2, was seen only in the 0.88 eV system, while in the 0.95 eV band, three new ODEPR signals, labeled L1, L3 and L4 were observed. Of particular interest in these studies were L3 and L4 because each displayed well-resolved hyperfine interaction (hf) from a single Ga nucleus, suggesting an involvement of some kind for an interstitial Ga atom.

In the present paper, we turn our attention to L1. We find that it also carries important hf information, as

*Corresponding author. Tel.: +1-610-758-3961; fax: +1-610-758-4561.

E-mail address: gdw0@lehigh.edu (G.D. Watkins).

¹Permanent address: A.F. Ioffe Physico-Technical Institute, St. Petersburg, Russia.

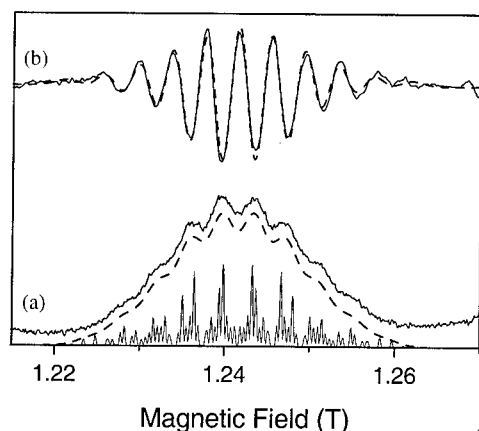


Fig. 1. (a) ODEPR spectrum of L1, and (b) its second derivative, for $\mathbf{B} \perp \mathbf{c}$, compared to predictions for hf interaction with three equivalent Ga atoms.

revealed by partially resolved structure, as shown in Fig. 1. A simulation of the structure assuming hf interaction with *three equivalent Ga nuclei* is also shown. In this simulation, the sticks represent the relative intensities and predicted positions for each of the lines that would arise from three identical $I=3/2$ Ga nuclei (60% ^{69}Ga , 40% ^{71}Ga , with $^{71}\mu/^{69}\mu = 1.2706$) and with a 100 MHz hf interaction for the ^{69}Ga $I=3/2$ nucleus. These sticks were convoluted with a single Gaussian of appropriate width in order to give the dashed curves, which match, remarkably with the structure and overall line shape, both of the spectrum and of its second derivative. The hf splitting appears isotropic, with no distinguishable difference (± 10 MHz) vs. the orientation of \mathbf{B} . Comparison of the measured 100 ± 10 MHz hf value with estimated values for the free ^{69}Ga atom [4], indicates that somewhere between 1.4% and 5% of the wavefunction is accounted for on each of the Ga atoms. (1.4% 4s character accounts for the isotropic part. The additional 3.6% allows for a maximum 4p contribution, reflecting an upper estimate for possible hf anisotropy of < 16 MHz.)

3. Electron irradiation at cryogenic temperatures

Before we consider possible defect models that might account for the three-Ga structure, let us first consider what we have learned concerning its formation. For this, we consider our more recent results for irradiation in situ at 4.2 K. As we have previously briefly reported [3], immediately after a low-temperature irradiation, the broad 0.95 eV PL band is present, but the 0.88 eV system is absent. However, none of the ODEPR signals present after room temperature irradiation (L1, L2, L3, L4) are observed. Instead, a new ODEPR signal is observed in

the 0.95 eV band, labeled L5, which we have identified as arising from the isolated interstitial Ga atom, as evidenced from its strong, well-resolved, Ga hf structure. Both this, and an accompanying ODEPR signal from the residual shallow donor, are negative, revealing a spin-dependent transfer process of an electron from the donor to paramagnetic Ga_i^{2+} , which competes with the 0.95 eV PL process. L5 is stable up to room temperature, at which point it decreases with an apparent time constant of several hours. Over this same time period, the 0.88 eV system emerges with its associated L2 ODEPR, as does L1, which is detected in the remaining 0.95 eV band. (Substantial loss of the 0.95 eV band also occurs during the room temperature annealing, but approximately $\sim 10\%$ of its original intensity immediately after the 4.2 K irradiation remains, and is stable, along with the L1 signal up to $\sim 600^\circ\text{C}$.)

From the disappearance of the interstitial Ga signal at room temperature, we conclude that it is mobile at this temperature. The simultaneous emergence at this temperature of the L1 spectrum, as well as the 0.88 eV PL band and its associated L2 ODEPR spectrum, strongly suggests that each may result directly or indirectly from the migration and trapping of the Ga interstitial.

Another important observation that must be factored into our modeling is that the broad 0.95 eV PL band is present immediately after the 4.2 K irradiation. It, therefore, must arise from an intrinsic defect itself. Although 90% of it is lost after room temperature annealing, the remaining component is stable to $\sim 600^\circ\text{C}$. L1 continues to be detected in it, disappearing with it at 600°C .

4. Models

The three equivalent Ga-atom hyperfine structure of L1 suggests three possibilities, which are illustrated in Fig. 2.

4.1. Trapped N vacancy

In Fig. 2(a), we show a nitrogen vacancy, which is missing one of its Ga nearest neighbors. This could result, as shown, from trapping of the vacancy by an impurity (X) on the Ga sublattice. Since the nitrogen vacancy is believed to be a shallow donor, a logical impurity might be a Group-II atom such as Mg, or Zn, each of which is an acceptor. With only a low-abundance nuclear spin isotope in either case, only the three remaining Ga atom neighbors would contribute to the structure.

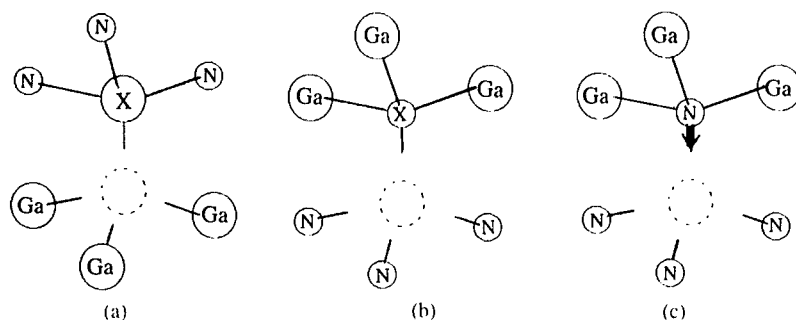


Fig. 2. Structural models for L1: (a) trapped N vacancy, (b) trapped Ga vacancy, (c) Jahn-Teller-distorted isolated Ga vacancy.

4.2. Trapped Ga vacancy

In Fig. 2(b), we show a Ga vacancy trapped next to an impurity (X) on the nitrogen sublattice. A logical trap might be a substitutional group-VI atom donor, such as the common impurity oxygen, which experiences a Coulomb attraction to the negative Ga-vacancy deep acceptor. In this case, the three Ga neighbors could be the three near neighbors back-bonded to the impurity atom, as shown. In such a model, the dominance of the Ga hf interactions over those of the three nitrogen near neighbors to the vacancy is helped by ~ 5 times greater Ga atomic hf values over those for N. The total concentration of the wavefunction required on the three Ga's, only between 4% and 15%, is reasonable. At the same time, the nitrogen hf contributions could provide the major remaining broadening. As in the case for a group-II atom above, group-VI atoms also have low-abundance magnetic nuclei, and would not contribute to the hf structure.

4.3. Isolated Ga vacancy

In Fig. 2(c), we show a distorted Ga vacancy in its paramagnetic V_{Ga}^{2-} charge state. Here, the inward distortion of the on-axis nearest neighbor nitrogen serves to shift some of the spin wavefunction onto its back-bonded three Ga neighbors, which could supply the observed hf interactions. We can expect such a Jahn-Teller distortion for the paramagnetic V_{Ga}^{2-} charge state because in cubic GaN, it would be degenerate with one hole in its t_2 vacancy orbital [5]. (It is isoelectronic to the V_{Zn} defect in cubic ZnSe, also with the configuration t_2^5 , and for it, direct EPR and ODEPR studies have confirmed strong inward relaxation of one of its Se neighbors [6].) Again, as in the trapped Ga vacancy model above, the four nearest nitrogen neighbor hyperfine interactions would have to be weak enough to serve only to broaden the lines.

5. Discussion

The model in Fig. 2(a) requires the motion at room temperature of the N vacancy, for the model in Fig. 2(b), the Ga vacancy. Although possible, the onset of long-range motion for either almost simultaneously with that of the Ga interstitial would be a coincidence. On the other hand, the emergence of the isolated Ga vacancy ODEPR could follow naturally as its perturbing nearby the Ga interstitial migrates away. In addition, the model in Fig. 2(c) suggests a natural explanation for the 0.95 eV luminescence, which we have argued above must arise from an intrinsic defect, as directly resulting from the vacancy itself. This can be seen in Fig. 3. Here, we have taken advantage of the calculations of Neugebauer and Van de Walle [7], who estimated the triple acceptor level ($3-/2-$) of the vacancy to be at $\sim E_V + 1.1$ eV. With this, it is possible to identify, as shown, the Stokes-shifted and broadened 0.95 eV luminescence as arising from hole capture by the non-paramagnetic V_{Ga}^{3-} , which Jahn-Teller distorts in moving from $V_{Ga}^{3-}(t_2^6)$ to $V_{Ga}^{2-}(t_2^5)$.

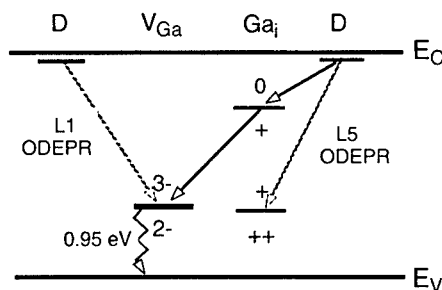


Fig. 3. Model for the 0.95 eV PL and its various feeding and competing processes, assuming that L1 arises from the Ga vacancy.

Immediately after the low-temperature irradiation, each vacancy has a Ga interstitial frozen-in nearby, which supplies a highly effective feeding mechanism for the luminescence, as shown. It allows a Coulomb-attractive transfer of electrons to the interstitials, which are in the non-paramagnetic Ga_i^+ charge state. The electrons can then be transferred to the nearby $\text{V}_{\text{Ga}}^{2-}$, followed by hole capture, to produce the 0.95 eV PL. At the same time, electron transfer to those interstitials in the paramagnetic Ga_i^{2+} charge state provides the competing spin-dependent process leading to the L5 PLODMR.

Also shown is the less-efficient spin-dependent feeding process seen in the L1 ODEPR, which involves Coulomb-repulsive direct electron transfer to the paramagnetic $\text{V}_{\text{Ga}}^{2-}$, followed by hole capture, which becomes an important feeding process only after the Ga interstitial migrates away.

If this model turns out to be correct, then we would have observed both partners of the Frenkel pairs on the Ga sublattice, and we would have learned that the isolated Ga vacancy is stable to $\sim 600^\circ\text{C}$, at which temperature, it can migrate and disappear. At present, this is a working model. Determining whether it is correct or not will require more critical tests in future studies.

Acknowledgements

This work has been supported jointly by the National Science Foundation, Grant Nos. DMR-97-04386 and DMR-00-93784, and the Office of Naval Research, Grant No. N00014-94-10017.

References

- [1] C. Bozdog, H. Przybylinska, G.D. Watkins, V. Härle, F. Scholz, M. Mayer, M. Kamp, R.J. Molnar, A.E. Wickenden, D.D. Koleske, R.L. Henry, *Phys. Rev. B* 59 (1999) 12479.
- [2] Mt. Wagner, I.A. Buyanova, N.Q. Thinh, W.M. Chen, B. Monemar, J.L. Lindström, H. Amano, I. Akasaki, *Phys. Rev. B* 62 (2000) 16572.
- [3] K.H. Chow, G.D. Watkins, A. Usui, M. Mizuta, *Phys. Rev. Lett.* 85 (2000) 2761.
- [4] K. Koh, D.J. Miller, *Atom. Data Nucl. Data Tables* 33 (1985) 235.
- [5] G.D. Watkins, in: K.A. Jackson, W. Schröter (Eds.), *Handbook of Semiconductor Technology*, (vol. 1), Wiley-VCH, Weinheim, 2000, p. 99 (Chapter 3).
- [6] G.D. Watkins, *J. Crystal Growth* 159 (1996) 338.
- [7] J. Neugebauer, C.G. Van de Walle, *Appl. Phys. Lett.* 69 (1996) 503.



ELSEVIER

Physica B 308–310 (2001) 66–68

PHYSICA B

www.elsevier.com/locate/physb

Electron paramagnetic resonance of GaN detected by recombination afterglow

U. Rogulis^{1,*}, S. Schweizer, J.-M. Spaeth*Department of Physics, University of Paderborn, Warburger Str. 100, 33095 Paderborn, Germany*

Abstract

X-irradiation at 4.2 K of GaN produces a long lasting recombination afterglow (RL). This afterglow quenches in high magnetic fields, but it can be increased by applying microwave radiation (93 GHz) yielding resonance lines (RL-EPR) for appropriate magnetic fields. For a free standing GaN 'lift-off' layer, two overlapping RL-EPR lines with different half-widths and almost isotropic g -values were observed. The spin-lattice relaxation times were in the range of several minutes. The two resonances are detected in the red spectral range of the RL; one of these resonances is observed in the photoluminescence-detected EPR (PL-EPR) as well. A different RL-EPR spectrum was recorded in a Mg-doped GaN layer: The RL-EPR showed the line of the shallow donor. The features of the RL-EPR spectra of the two different GaN samples shows that RL in GaN involves additional electron and hole traps and thus provides additional information unattainable in PL-EPR. © 2001 Elsevier Science B.V. All rights reserved.

Keywords: GaN; EPR; X-irradiation; Recombination afterglow

1. Introduction

GaN is a widely used material for blue laser diodes and other opto-electronic applications (see, for example, [1]). For AlN ceramics, doped with oxygen, magnetic resonance measurements yielded resonances which were attributed to the tunnelling recombination luminescence (RL) between well separated, oxygen related, donors and acceptors [2]. The method of recombination luminescence detected EPR (RL-EPR) was previously applied to the tunnelling RL in ionic crystals [3].

The motivation for the present work was to observe tunnelling recombination between the separated donor-acceptor pairs in GaN and to detect RL-EPR in comparison with that observed by the conventional photoluminescence detected EPR (PL-EPR) technique. We show that RL-EPR can provide additional information for the understanding of the recombination

processes in GaN and, in general, semiconductor materials.

2. Experimental

Two different GaN samples have been investigated: (i) a 250 μm thick free standing GaN 'lift-off' layer and (ii) Mg-doped MOVPE GaN layer on sapphire.

Luminescence-detected electron paramagnetic resonance spectra were recorded with a custom-built computer controlled spectrometer working at 93 GHz (W-band) with magnetic fields up to 4.5 T. All spectra were measured at 1.5 K using a cooled photomultiplier operating in the spectral range of 200–800 nm. In the case of PL-EPR measurements, the samples were excited in the UV spectral range with a deuterium lamp in combination with a 280 nm interference filter at 1.5 K. The PL-EPR was detected either in the integral luminescence for wavelengths larger than 380 nm or in different spectral ranges using edge filters.

The RL-EPR measurements, where the EPR is measured in the afterglow luminescence, were performed

*Corresponding author. Fax: +49-5251-603247.

E-mail address: sp_ur@physik.uni-paderborn.de (U. Rogulis).

¹Permanent address: Institute of Solid State Physics, University of Latvia, Riga, Latvia.

either after excitation at 4.2 K with an X-ray tube (tungsten anode, 60 kV, 15 mA, irradiation time 20 min) or a deuterium lamp (280 nm in combination with an interference filter, irradiation time 1–2 h). The RL-EPR was detected either in the integral RL or in different spectral ranges using edge filters. In all the RL-EPR spectra, the magnetic field dependent background was subtracted.

3. Results

The UV-excited photoluminescence spectrum of the 250 μm thick free standing 'lift-off' GaN layer consists of bands between the yellow and blue spectral ranges (Fig. 1(a)). PL-EPR of a GaN layer, recorded at 1.5 K in W-band (Fig. 2(c)), shows two resonance lines with g -values of 2.005 and 1.95, respectively, in good agreement with results obtained by Bayerl [4].

After X-irradiation of the GaN 'lift-off' layer at 4.2 K, a recombination afterglow was observed for several hours. Fig. 1(b) shows a Gaussian approximation of the RL spectral dependence, measured with a set of edge filters in the integral RL. The RL occurs in the red spectral range with a band maximum at approximately 1.8 eV (690 nm).

The afterglow quenches in high magnetic fields (up to 3.6 T) at 1.5 K. It increases by a factor of 3 when applying a microwave radiation of 93 GHz at appropriate field values showing intense RL-EPR signals (Figs. 2(a) and (b)). RL-EPR is strongly influenced by very long spin-lattice relaxation times of several minutes. Therefore, we tried to measure the spectra with different integration times. Fig. 2 shows RL-EPR spectra of the GaN 'lift-off' layer recorded with a longer integration

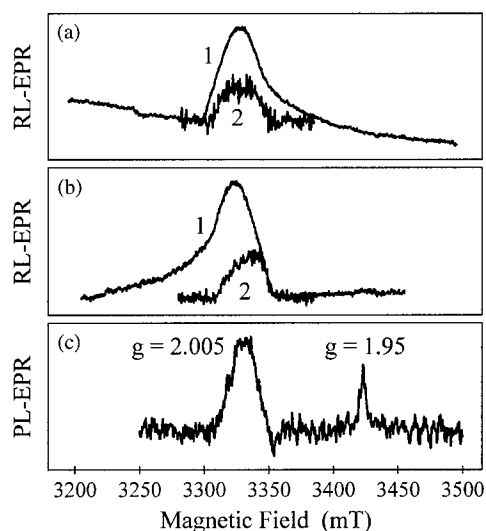


Fig. 2. RL-EPR and PL-EPR spectra of GaN 'lift-off' layer, recorded at 1.5 K in W-band, in the integral luminescence: (a) RL-EPR spectra measured by increasing the magnetic field: curve (1) recorded with an integration time of 6 mT/min, the magnetic field and time dependent background are not subtracted, curve (2) measured as an RL difference by switching 'on' and 'off' the microwave power with a period of 8 s; (b) the same as (a) but measured by decreasing the magnetic field and (c) PL-EPR spectrum of the GaN 'lift-off' layer, recorded at 1.5 K in W-band. The PL was excited at 280 nm and measured with a 380 nm edge filter.

time in the direction of increasing (left to right) field (Fig. 2(a), curve 1) and decreasing (right to left) field (Fig. 2(b), curve 1). Tagged RL-EPR spectra are depicted as curves 2 in Figs. 2(a) and (b) and have been measured with 'on-off' modulation, that is, the difference between the RL intensity, when the microwave power is switched on and that when it is switched off with a period of 8 s. Under these conditions, we can resolve in the RL-EPR two overlapping resonance lines with different half-widths and g -values closer to $g = 2.00$.

We observed RL and RL-EPR spectra also in a Mg-doped GaN layer. The RL-EPR of the Mg-doped GaN layer shows one structureless resonance line of the shallow donor with $g = 1.96$ (not shown) at 1.5 K.

4. Discussion

The long lasting (for several hours) afterglow-RL in GaN samples after switching off the X-ray excitation or prolonged above-band-gap UV excitation is weak compared to the PL intensity. It can be quenched in high magnetic fields and partially restored by applying a microwave power at resonance magnetic fields.

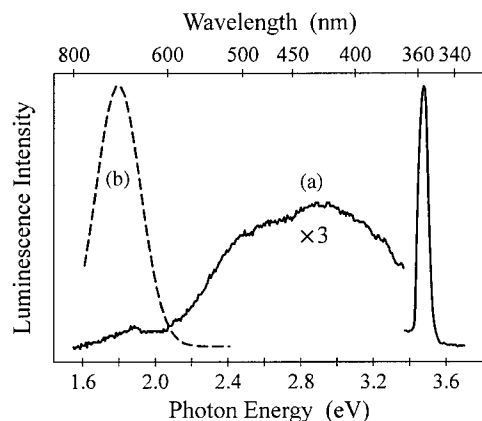


Fig. 1. Spectra of GaN 'lift-off' layer, recorded at 4.2 K: (a) UV-excited PL spectrum and (b) a Gaussian approximation of the RL spectral dependence, measured with a set of edge filters in the integral RL at 4.2 K.

Therefore, the recombination process occurs between spatially well-separated paramagnetic donors and acceptors and is spin-forbidden in a high field, where they are almost parallel at low temperature unless the spins are flipped to be anti-parallel by magnetic dipole transitions in which state they can recombine into the singlet ground state and emit the recombination luminescence.

The effect of X-irradiation is probably due to recharge donors and acceptors which are in the tunnelling distances from each other to a paramagnetic state. The two resonances of the GaN 'lift-off' layer are seen in the red spectral range of the RL; one of them seems to be the resonance observed at $g = 2.005$ even in PL-EPR.

The RL-EPR spectrum, observed in the Mg-doped GaN layer, shows different RL-EPR lines compared to those observed in the GaN 'lift-off' layer. The RL-EPR of the Mg-doped GaN layer shows only one resonance line in contrast to the PL-EPR where resonance lines of Mg-related acceptors have also been observed [5].

These features of the RL-EPR spectra in different GaN samples show that RL can involve different electron and hole traps from those observed in PL-EPR. It makes additional traps visible, particularly those with very long spin-relaxation times, which are not seen in PL-EPR. Additional investigations are necessary to further analyse the mechanism of the recombination afterglow in GaN.

5. Conclusion

A tunnelling recombination afterglow and RL-EPR in GaN have been observed. The RL spectral shape

differs from the PL spectral shape. The RL-EPR may show a part of the PL-EPR lines as well as new resonance lines, particularly those with very long spin-lattice relaxation times. Probably, the effect of X-irradiation is to recharge donors and acceptors which are in a tunnelling distance from each other to paramagnetic charge states. RL-EPR can provide additional information on the recombination processes and luminescences in GaN and other semiconductor materials.

Acknowledgements

The authors thank Prof. M. Stutzmann, W. Schottky Institut, TU München, for providing the 'lift-off' GaN sample and Prof. P. Gibart, CREA, Valbonne, for providing the Mg-doped MOVPE GaN layer.

References

- [1] S. Nakamura, G. Fasol, *The Blue Laser Diode*, Springer, Berlin, 1997.
- [2] S. Schweizer, et al., *Phys. Stat. Sol. B* 219 (2000) 171.
- [3] N.G. Romanov, et al., *Phys. Stat. Sol. B* 107 (1981) K119.
- [4] M.W. Bayerl, *Selected Topics of Semiconductor Physics and Technology*, Vol. 32, W. Schottky Institut, TU München, 2000, p. 155.
- [5] F.K. Koschnick, et al., *J. Cryst. Growth* 189–190 (1998) 561.



ELSEVIER

Physica B 308–310 (2001) 69–72

PHYSICA B

www.elsevier.com/locate/physb

Defect-related noise in AlN and AlGaN alloys

S.T.B. Goennenwein^{a,*}, R. Zeisel^a, S. Baldovino^{a,b}, O. Ambacher^a,
M.S. Brandt^a, M. Stutzmann^a

^aWalter Schottky Institut, Technische Universität München, Am Coulombwall, D-85748 Garching, Germany

^bLaboratorio MDM-INFM, Via C. Olivetti 2, I-20041 Agrate Brianza (MI), Italy

Abstract

The electronic noise properties of Si-doped AlN and Al_{0.3}Ga_{0.7}N are investigated. In AlN:Si, generation–recombination (g–r) noise is observed and shown to be linked to DX-centers. The potential energy barriers for capture into and emission from the DX[−] ground state are quantitatively determined from the noise measurements. In Al_{0.3}Ga_{0.7}N:Si, in addition to 1/*f* noise, we find two g–r noise processes. However, an unambiguous identification of their origin proves to be difficult. © 2001 Elsevier Science B.V. All rights reserved.

PACS: 72.70.+m; 71.55.-i; 81.05.Ea

Keywords: Electronic noise; DX-center; AlN; Group-III nitrides

1. Introduction

Recently, DX-like behavior of Si in AlN [1] and AlGaN alloys with high Al content [2] has been reported. Thus, in these materials, Si does not simply act as a shallow donor. Instead, it can form a complex, metastable deep defect. In AlGaAs alloys, such a behavior of Si and other dopants has been extensively studied [3]. It is of particular relevance for device applications, as it can seriously affect e.g. carrier densities. DX[−]-centers are formed because the donor atom can minimize its energy by undergoing a large lattice relaxation away from the substitutional position in combination with the capture of an extra electron. This is shown more quantitatively in the simplified configuration-coordinate diagram of Fig. 1. The lower parabola to the right corresponds to the lattice relaxed DX[−] ground state. The parabola above it symbolizes the thermodynamically metastable DX⁰ state, whereas the shallow substitutional donor level is depicted by the parabola to the left. The net energy difference between

the substitutional donor and the DX[−]-state (E_R in Fig. 1) governs the occupation of the two levels in thermal equilibrium. Thus, in AlN, the conductivity is not activated with ≈ 60 meV, as one would expect for a shallow effective mass donor in this material, but with $E_R = 345 \pm 3$ meV, a first experimental hint to the more complex DX-behavior of Si in AlN [1]. For the construction of a quantitative configuration coordinate diagram, especially for the determination of the potential energy barriers between DX[−] and d^0 states, electronic noise measurements have proven to be a valuable tool in AlGaAs alloys [4,5]. In this contribution, we show that from noise measurements the transition energies E_{up} and E_{down} (cf. Fig. 1) can be determined quantitatively for AlN:Si. We further compare the generation–recombination (g–r) noise observed in AlN:Si and in Al_{0.3}Ga_{0.7}N:Si.

2. Experimental

The samples investigated are epitaxial Al-face AlN and Al_{0.3}Ga_{0.7}N thin films grown by plasma-induced molecular beam epitaxy on (0001)-oriented sapphire substrates with a nominal Si doping density of $N_{Si} =$

*Corresponding author. Fax: +49-89-289-12737.

E-mail address: goennenwein@wsi.tum.de (S.T.B. Goennenwein).

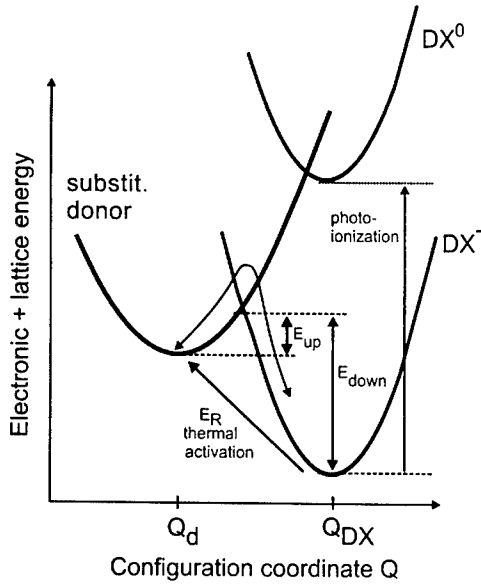


Fig. 1. Simplified configuration coordinate diagram of the Si DX-center in AlN showing the levels relevant to the investigations presented here. A complete configuration coordinate diagram is given in Ref. [1].

$3 \times 10^{19} \text{ cm}^{-3}$ in the AlN and $N_{\text{Si}} = 4 \times 10^{17} \text{ cm}^{-3}$ in the $\text{Al}_{0.3}\text{Ga}_{0.7}\text{N}$ samples. For $\text{Al}_{0.3}\text{Ga}_{0.7}\text{N} : \text{Si}$, a $\approx 10 \text{ nm}$ thick, nominally undoped AlN nucleation layer was grown before depositing the $\text{Al}_{0.3}\text{Ga}_{0.7}\text{N}$ layer. Alloyed-in Ti/Al/Pt/Au layers yielded good ohmic contacts. For the noise measurements, voltage fluctuations across the sample were amplified with a Stanford Research SR560 low-noise preamplifier and analyzed with a Stanford Research SR760 Fast-Fourier Transform spectrometer. A dry battery together with a series resistor of at least 20 times the sample resistance supplied the constant current necessary for the non-thermal noise measurements.

Typical non-thermal noise spectra from the AlN:Si and $\text{Al}_{0.3}\text{Ga}_{0.7}\text{N} : \text{Si}$ samples are shown in Fig. 2. Due to the strong non-thermal noise, corrections for thermal noise and amplifier noise have not been necessary. As expected for resistance noise, the noise power density S_U scales quadratically with the voltage drop U across the sample. As especially the $\text{Al}_{0.3}\text{Ga}_{0.7}\text{N} : \text{Si}$ samples show strong $1/f$ -noise in addition to g-r noise, it is more convenient to plot S_U/U^2 multiplied by frequency f . Then, the $1/f$ -noise appears as a constant background. In contrast, the Lorentzian characteristic of g-r noise

$$S_{U, \text{g-r}}(f) = \frac{S(f=0)}{1 + (2\pi f)^2 \tau^2}, \quad (1)$$

with the g-r noise power density $S(f=0)$ and the characteristic g-r time constant τ , becomes clearly discernible as a peak upon multiplication with f . The frequency where $f \times S_{U, \text{g-r}}/U^2$ peaks directly yields τ .

The second value characterizing g-r noise, $S(f=0)$, can be obtained using the identity $S(f=0) = 2S_{U, \text{g-r}}(f = (2\pi\tau)^{-1})$. This determination of $S(f=0)$ is not influenced by the low frequency $1/f$ -noise often observed. As evident from Fig. 2, both τ and $S(f=0)$ are strongly temperature dependent in AlN and $\text{Al}_{0.3}\text{Ga}_{0.7}\text{N}$.

3. Discussion

We now analyze the experimental results for AlN:Si in more detail. As discussed in Ref. [1], the DX-nature of Si in AlN is evident from the following experimental observations: At low temperatures and in the dark, the samples are observed to be highly resistive and no electron paramagnetic resonance (EPR) signal can be detected. Upon illumination with light of more than 1.5 eV, an increase of the conductivity by more than 7 orders of magnitude is observed. In addition, an EPR signal characteristic of shallow donors appears. Both the conductivity and the EPR signal persist after the light is switched off, and are quenched only at temperatures above 80 K. From persistent photoconductivity decay measurements, the transition energy (the potential barrier) impeding the transition from d^0 to DX^- (E_{up} in Fig. 1) can be estimated to $E_{\text{up}} \approx 100 \text{ meV}$. Because electronic noise, due e.g. to fluctuations of the number of mobile charge carriers, is governed by carrier dynamics, noise measurements can give valuable information about transition energies (E_{up} , E_{down} in Fig. 1). The most simple source of g-r noise is a two level system (TLS). In a very schematic picture, d^0 and DX^- can be considered as such a TLS, with charge carriers mobile only in d^0 . Machlup [6] showed that the g-r noise stemming from one single TLS is given by Eq. (1) with $S(f=0) = \pi^{-1} \tau_{\text{up}}^2 \tau_{\text{down}}^2 / (\tau_{\text{up}} + \tau_{\text{down}})^3$ and $\tau^{-1} = \tau_{\text{up}}^{-1} + \tau_{\text{down}}^{-1}$, where τ_{up} and τ_{down} are the carrier lifetimes in the two levels, respectively. Commonly, the electronic noise from DX-centers in AlGaAs alloys is interpreted following this idea [4]. The potential barriers E_{up} and E_{down} are assumed to govern the thermal activation of the lifetimes $\tau_{\text{up}} = \tau_{\text{up},0} \exp(E_{\text{up}}/kT)$ and $\tau_{\text{down}} = \tau_{\text{down},0} \exp(E_{\text{down}}/kT)$. $\tau_{\text{up},0}$ and $\tau_{\text{down},0}$ are considered to be independent of temperature, as the exponential factor by far dominates in the temperature range of interest here. Assuming $\tau_{\text{down}} \ll \tau_{\text{up}}$, the above expressions can be simplified to

$$S(f=0) \approx \pi^{-1} \tau_{\text{down}}^2 \tau_{\text{up}}^{-1}, \quad (2)$$

$$\tau^{-1} \approx \tau_{\text{down}}^{-1}. \quad (3)$$

Thus, because of Eq. (3), the thermal activation of τ directly yields $E_{\text{down}} = E_{\tau} = 391 \pm 8 \text{ meV}$. From Eq. (2), $E_{\text{up}} = 2E_{\text{down}} - E_{\text{Si}} = 48 \pm 27 \text{ meV}$. This value is in agreement with the one obtained from the relation evident from Fig. 1 $E_{\text{up}} = E_{\text{down}} - E_{\text{R}} = 46 \pm 9 \text{ meV}$,

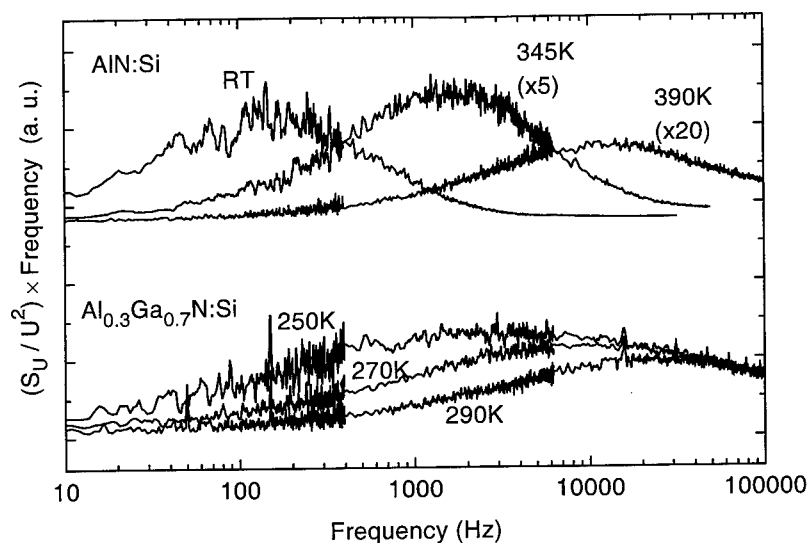


Fig. 2. Typical non-thermal noise spectra of an AlN:Si sample (upper part) and an $\text{Al}_{0.3}\text{Ga}_{0.7}\text{N}:\text{Si}$ sample at different temperatures. To discriminate the g-r noise against a $1/f$ -noise background, the noise power density was multiplied by frequency.

and with the values estimated from persistent photo-conductivity measurements [2]. The assumption $\tau_{\text{down}} \ll \tau_{\text{up}}$ can be justified by considering the other limiting case: $\tau_{\text{down}} = \tau_{\text{up}} = \tau_0$. Then, $\tau \propto \tau_0$ and $S(f=0) \propto \tau_0$, in contrast to experiment.

We proceed to analyze the findings in $\text{Al}_{0.3}\text{Ga}_{0.7}\text{N}:\text{Si}$. The conductivity is activated with 20 ± 1 meV, in good agreement with the value of ≈ 22 meV predicted for an effective mass donor. An EPR signal typical for shallow donors ($g = 1.97$) in AlGaN alloys of this composition [7] is observed at low temperatures and in the dark. Upon illumination, the EPR signal intensity is persistently increased, as well as the conductivity, however only by about 20%. Above room temperature, the non-thermal noise is dominated by $1/f$ -noise. Below 300 K, a comparatively weak g-r noise component is observed (cf. Fig. 2). As in the case of AlN, both the characteristic g-r frequency τ as well as the g-r noise power density $S(f=0)$ are found to be thermally activated. We obtain $E_{\tau,1} = (309 \pm 10)$ meV and $E_{S_0,1} = (366 \pm 8)$ meV. For $T < 210$ K, a second g-r contribution appears, again thermally activated, with $E_{\tau,2} = (192 \pm 12)$ meV and $E_{S_0,2} = (180 \pm 10)$ meV.

Thus, in the $\text{Al}_{0.3}\text{Ga}_{0.7}\text{N}$ samples, there is no unambiguous evidence for the DX-behavior of Si. This is not surprising, as DX^- is the stable ground state for Si in AlGaN alloys only for an Al content higher than 60% according to the calculations of Boguslawski and Bernholc [8]. However, Kirtley et al. [4] have shown that the noise properties of AlGaAs:Si are still dominated by noise related to DX-centers even for alloy compositions where the DX-center is resonant with the conduction band. Fig. 3 gives a simplified sketch of the model proposed by Kirtley

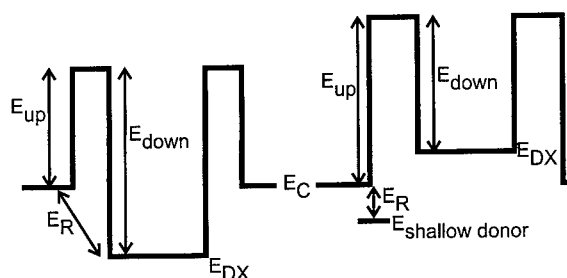


Fig. 3. Two-level system related to DX-centers for different alloy composition after Kirtley et al. [4]. The left part of the figure shows the energy levels for a deep DX-center, as it is encountered e.g. in AlN:Si. The right part suggests a possible situation for alloys in which the DX-center is not the energetically most favorable level at low temperatures (e.g. for DX resonant with the conduction band).

et al. In particular, the figure shows that while there is a sum rule connecting E_{up} , E_{down} and E_R for deep DX-centers (as e.g. in AlN:Si), there is no comparable relation between the activation of the conductivity and the characteristic g-r noise entities for DX-centers resonant with the conduction band. This makes an unambiguous identification of DX-centers as the noise source rather difficult. Thus, in the case of $\text{Al}_{0.3}\text{Ga}_{0.7}\text{N}:\text{Si}$, an attribution of the g-r noise observed to DX-centers is at best speculative. The data available so far, especially the observation of two separate g-r components, could just as well be explained in terms of conventional deep defects. Obviously, only further investigations with samples of varying alloy composition and Si doping density could help clarify the possible existence and

importance of DX-centers for low Al contents in AlGaIn alloys. On the other hand it is important to note that in $\text{Al}_{0.3}\text{Ga}_{0.7}\text{N} : \text{Si}$, g-r noise is observed, while in GaN only $1/f$ -noise is typically reported.

4. Conclusions

In summary, we have observed DX-behavior of Si in AlN. Noise spectroscopy has proven to be a valuable tool to quantitatively determine transition energies between DX^- and d^0 . In $\text{Al}_{0.3}\text{Ga}_{0.7}\text{N} : \text{Si}$, however, a weak persistent photoconductivity and persistent EPR signal as well as two independent g-r noise contributions are observed at low temperatures indicating the possible DX-behavior of Si in these alloys too.

Acknowledgements

The authors acknowledge financial support by the Deutsche Forschungsgemeinschaft (SFB 348).

References

- [1] R. Zeisel, M.W. Bayerl, S.T.B. Goennenwein, R. Dimitrov, O. Ambacher, M.S. Brandt, M. Stutzmann, *Phys. Rev. B* 61 (2000) R16283.
- [2] S.T.B. Goennenwein, R. Zeisel, U. Karrer, M.W. Bayerl, O. Ambacher, M.S. Brandt, M. Stutzmann, in: N. Miura, T. Ando (Eds.), *Proceedings of the 25th International Conference on Physics of Semiconductors* (2001) pp. 1597–1598.
- [3] D.V. Lang, in: S.T. Pantelides (Ed.), *Deep Centers in Semiconductors*, 2nd edition, Gordon and Breach Science Publishers, Yverdon, 1992.
- [4] J.R. Kirtley, T.N. Theis, P.M. Mooney, S.L. Wright, *J. Appl. Phys.* 63 (1988) 1541.
- [5] D.D. Carey, S.T. Stoddart, S.J. Bending, J.J. Harris, C.T. Foxon, *Phys. Rev. B* 54 (1996) 2813.
- [6] S. Machlup, *J. Appl. Phys.* 25 (1954) 341.
- [7] M.W. Bayerl, M.S. Brandt, T. Graf, O. Ambacher, J.A. Majewski, M. Stutzmann, D.J. As, K. Lischka, *Phys. Rev. B* 63 (2001) 165204.
- [8] P. Boguslawski, J. Bernholc, *Phys. Rev. B* 56 (1997) 9596.



ELSEVIER

Physica B 308–310 (2001) 73–76

PHYSICA B

www.elsevier.com/locate/physb

Positively charged muonium centers in aluminum and gallium nitrides

R.L. Lichti^{a,*}, S.F.J. Cox^{b,c}, E.A. Davis^d, B. Hitti^e, S.K.L. Sjøe^a

^a Physics Department, Texas Tech University, Lubbock, TX 79409-1051, USA

^b ISIS Facility, Rutherford Appleton Laboratory, Chilton OX11 0QX, UK

^c Department of Physics and Astronomy, University College London, London WCE 6BT, UK

^d Department of Physics and Astronomy, University of Leicester, Leicester LE1 7RH, UK

^e TRIUMF, 4004 Wesbrook Mall, Vancouver, B.C. V6T 2A3, Canada

Abstract

The Mu^+ defect centers in AlN and GaN are studied using muon nuclear-quadrupole level-crossing resonance (QLCR) and zero-field muon spin depolarization measurements. The dominant Mu^+ center is highly mobile, but QLCR spectra identify a second static Mu^+ state at $\text{AB}_{\parallel}(\text{N})$ sites in both nitrides. This state becomes mobile above 800 K in AlN, but converts to a Mu^- above 200 K in GaN. Zero-field data characterize local fields and motional properties for this state in AlN. Above 1100 K the mobile Mu^+ in AlN shows strong interactions and traps at another defect. © 2001 Elsevier Science B.V. All rights reserved.

PACS: 66.30.JT; 71.55.Eq; 76.75.+i

Keywords: Muonium; Hydrogen; GaN; AlN; Defect mobility

1. Introduction

The group-III nitrides, especially their alloys, are important materials for short wavelength optical devices. Hydrogen interacts with dopants and other defects to modify the electrical activity of the nitrides, see [1], as in other semiconductors. This activity makes hydrogen an important impurity, but also makes *isolated* hydrogen defects difficult to study. Muonium (Mu) is effectively a very light, short-lived pseudo-isotope of hydrogen formed by implanting positive muons. Muonium forms states very similar to those expected for hydrogen and, because of its short lifetime ($\tau = 2.197 \mu\text{s}$), Mu primarily occurs as an isolated impurity. Much of the experimental data associated with isolated H defects in many semiconductors comes from investigations of the muonium analog.

The wurtzite structure of GaN or AlN has two inequivalent bonds, thus there are two different bond-center (BC) sites, and two anti-bonding (AB) sites for each atom. AB_{\parallel} sites lie in a confined region formed by the stacking sequence and have Mu-Ga(Al) or Mu-N directions parallel to c . Each atom has three AB_{\perp} sites, directed at $\sim 70^\circ$ to c into unblocked channels providing a path for diffusion, or for local motion among three closely spaced sites. Based on theoretical studies [2–5] one can expect either BC or $\text{AB}(\text{N})$ sites for Mu^+ ; BC, $\text{AB}(\text{III})$, or more likely a symmetric central channel site for Mu^0 ; and either $\text{AB}(\text{III})$ or a more centralized channel location for Mu^- .

We previously investigated the sites and dynamics of Mu^- in n-type GaN [6–8], finding that Mu^- resides at the two Ga antibonding locations, and that the mobile Mu^- channel state completely dominates at high temperatures. In the present contribution, we report on the locations and dynamics found for Mu^+ centers in GaN and AlN. One of these states is quite mobile in both nitrides and represents the majority of charged

*Corresponding author. Tel.: +1-806-742-3697; fax: +1-806-742-1182.

E-mail address: xbrll@ttacs.ttu.edu (R.L. Lichti).

centers in higher quality AlN. This state is associated with a slowly relaxing component in zero-field muon spin depolarization measurements, where static centers have a distinctive signature characteristic of nuclear dipolar fields at their respective locations. Assignment of the weakly relaxing component to a mobile Mu^+ in the wurtzite channels is based on theoretical expectations and a process of elimination in GaN, where all other anticipated isolated states are separately identified. The lone remaining site, $\text{AB}_\perp(\text{N})$, gives a low energy state for Mu^+ [2,4] and should be relatively mobile. Unfortunately, extracting site details or accurate dynamics for this state is not possible, so the information remains qualitative for the primary Mu^+ centers. In the following we describe signals assigned to the less mobile (theoretically metastable) Mu^+ centers and summarize site assignments and dynamics.

2. Results and discussion

QLCR spectra are due to resonant cross relaxation between muon Zeeman levels and quadrupolar levels of a neighboring nucleus. These transitions are driven by dipole–dipole interactions between the muon and its neighbor which mix the muon spin states thereby reducing the muon polarization. Resonances occur for magnetic fields at which energies of non-interacting states of the combined muon and nuclear spins would cross. The locations and strengths of QLCR resonances carry information on the dipolar and nuclear quadrupolar interactions induced by the muon, thus contain details of the local defect structure. If the muon-induced electric field gradient (EFG) dominates the intrinsic one, as appears to be the case, its principle axis lies along the muon–nucleus bond. Each host atom has a quadrupole moment: $I = 3/2$ for both ^{69}Ga and ^{71}Ga ; $I = 5/2$ for ^{27}Al ; and $I = 1$ for ^{14}N . The two isotopes give a definitive identification of any Ga resonances. Strong Ga resonances imply Ga nearest neighbors and are assigned to Mu^- states or to Mu^+ in a BC site.

Fig. 1a shows a QLCR spectrum for GaN having both Mu^+ and Mu^- features. The Ga related lines are from the two $\text{AB}(\text{Ga})$ sites for Mu^- as previously reported [6,7]. To extract the N related line which overlaps the lower-field ^{71}Ga resonances, at each temperature the higher field ^{69}Ga lines were fit with all parameters free and the ^{71}Ga lines were then scaled according to theoretical expectations. The remaining feature just below 10 mT is a single line and results in smooth temperature dependences for the related fit parameters, giving considerable confidence in the spectral separation. No other lines are present below 150 K with comparable intensity, thus this line was assigned to an N atom with its EFG tensor aligned along the applied field direction, i.e. the c -axis.

The most reasonable option for a static isolated Mu center to associate with this N-related QLCR signal is a Mu^+ at the $\text{AB}_\parallel(\text{N})$ site. A BC_\parallel location could work except that no Ga resonances with a similar temperature dependence were observed. Any other muon position close enough to a nitrogen to give the correct intensity would result in an EFG tensor oriented well away from the c -axis. This state can therefore reasonably be assigned to a Mu^+ trapped in the confined cage region of the wurtzite structure. Since the signal is strongest at the lowest temperatures, it is most likely formed during implantation, when a bare muon enters the cage at the end of its thermalization path.

Fig. 2 displays the temperature dependence of the QLCR amplitudes for Mu^+ at $\text{AB}_\parallel(\text{N})$ and Mu^- at $\text{AB}_\parallel(\text{Ga})$, showing a transformation from Mu^+ to Mu^- near 200 K. Similarly, combined QLCR and depolarization data imply partial conversion of the mobile Mu^+ to Mu^- at $\text{AB}_\perp(\text{Ga})$ in this region and complete transformation above 600 K [8].

Results shown here suggest multiple transitions in the 200 K region, as do the depolarization data [6,8]. Obviously, a change from Mu^+ to Mu^- must go through a neutral, although perhaps unstable, Mu^0 state. Fits to the decrease in $\text{AB}_\parallel(\text{N})$ amplitude as two activated processes give $E_1 = 0.16(\pm 0.03)$ eV and $E_2 = 0.26(\pm 0.05)$ eV for transitions out of Mu^+ . A two step decrease in the mobile Mu^+ zero-field component for heavily doped n-type GaN is also consistent with these values [6].

For AlN, a strong resonance is seen at 4.2 mT in Fig. 1b with a weaker line centered near 6 mT. The strong resonance has the same characteristics as the N-related line in GaN, and is assigned to the same state, a Mu^+ at $\text{AB}_\parallel(\text{N})$. The second resonance has no visible partner, although a similar line at lower field could be obscured by the larger features. The width suggests slow dynamics for this second state and its temperature dependence does not match the dominant one. At present we cannot assign a site or symmetry to the weaker feature; although, a Mu^+ state at $\text{AB}_\perp(\text{N})$ would give two lines, the higher field one roughly in this position if the EFGs are similar for the two $\text{AB}(\text{N})$ locations, as seen (Fig. 1a) for Mu^- at $\text{AB}(\text{Ga})$ sites in GaN.

Motional dynamics could be extracted from the QLCR data; however, a more sensitive technique is zero-field depolarization, for details see [9]. For a static state in a system with numerous nearby nuclear moments, the depolarization follows a Gaussian Kubo–Toyabe (KT) function. In our analysis of AlN zero-field data, a KT component represents Mu^+ at $\text{AB}_\parallel(\text{N})$ and a slowly relaxing component is assigned to the mobile Mu^+ channel state. The primary parameter for a static state is the KT linewidth, Δ_{KT} , which characterizes the mean strength of randomly oriented

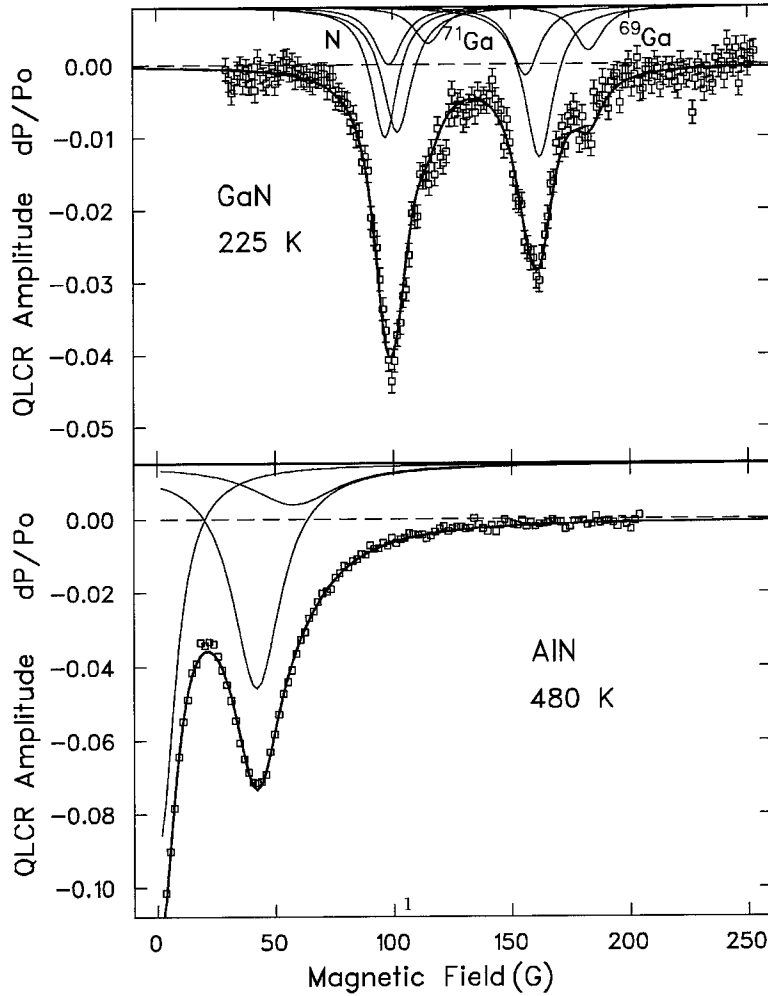


Fig. 1. Typical QLCR spectra; specifically shown for Mu^+ and Mu^- in partially compensated GaN (a) and Mu^+ in bulk polycrystalline AlN (b).

nuclear dipolar fields at equivalent sites. We obtain $\Delta_{\text{KT}} = 326(\pm 3)$ kHz for Mu^+ at $\text{AB}_{\parallel}(\text{N})$. When the Mu^+ state is mobile, the shape of this function changes with the hop rate, eventually becoming nearly exponential for rapid motion. Hop rates for two AlN samples shown in Fig. 3 were obtained from zero-field data analyzed with Δ_{KT} fixed to the static value. The activation energies found from these data sets are $1.04(\pm 0.07)$ eV and $0.96(\pm 0.06)$ eV. In our model of these states, this 1.0 eV barrier represents the energy required to escape from the cage into the channels, which would likely occur through BC_{\perp} sites with Mu^+ remaining attached to a single N atom.

The slowly relaxing component was treated as a Gaussian in the zero-field fits. The fraction of muons forming the low- T mobile state increased with visual quality of the samples from lowest (25%) in bulk polycrystalline AlN to highest (70%) in sublimation

grown single-crystal thick films, with a corresponding decrease in static Mu^+ (40% to 20%) and atomic-like Mu^0 (35% to 10%) fractions. Below 900 K the slow relaxation rate was nearly constant at $\sigma = 21(\pm 2)$ kHz in several samples. General characteristics suggest tunneling motion for this Mu^+ state; a very rough estimate of the hop rate gives $\nu_0 \approx 10$ MHz. For the largest cross-section film (deposited by CVD), the relaxation rate increased slowly above 950 K to 38 kHz at 1140 K implying stronger interactions with nuclear moments. At the highest temperature some fraction of the mobile Mu^+ species becomes trapped at another defect, yielding a static component with $\Delta_{\text{KT}} \geq 400$ kHz, significantly larger than for the static Mu^+ below 750 K.

In conclusion, we have investigated the sites and dynamics of Mu^+ defect centers in GaN and AlN. We find a QLCR signature of a static Mu^+ located at

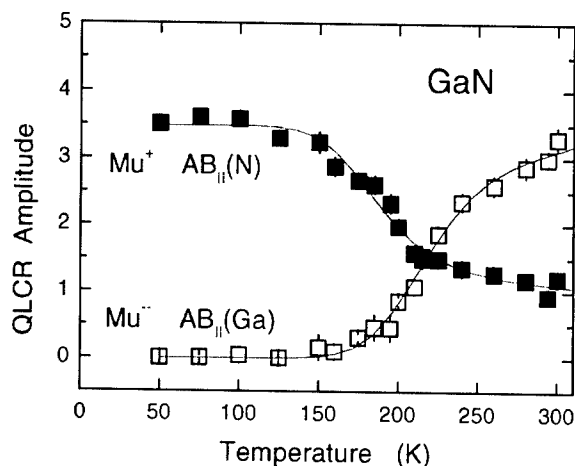


Fig. 2. Temperature dependent QLCR amplitudes showing a conversion from Mu^+ to Mu^- for AB cage sites in GaN.

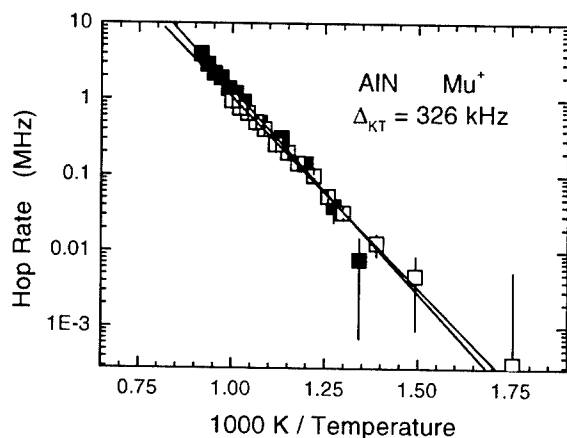


Fig. 3. Hop rates associated with the $\text{AB}_{\text{II}}(\text{N})$ site for Mu^+ in two AlN samples. The barriers for motion are about 1.0 eV.

$\text{AB}_{\text{II}}(\text{N})$ sites in both nitrides. This state converts to Mu^- in a complicated set of transitions near 200 K in (n-type) GaN and is extremely stable in AlN, where it shows

motion or site change dynamics only above 750 K with a characteristic energy very close to 1.0 eV. We infer the presence of a mobile Mu^- state in both nitrides from a slowly relaxing diamagnetic Mu component in zero-field depolarization measurements. In GaN, most of the mobile Mu^+ species also converts to a by-then-mobile Mu^- state at elevated temperatures. The mobile Mu^- state has nearly constant dynamics up to 900 K in AlN, but at higher temperatures shows increasing interactions and traps at an unknown impurity by 1150 K. Since the investigated AlN samples all have significant oxygen content, we suggest an oxygen related trap site, but have no direct evidence of the specific trapped state.

Acknowledgements

This work was supported by the Robert A. Welch Foundation (D-1321 [rll]) and by the UK EPSRC (GR/R25361 [sfjc, ead]). We wish to especially thank our sample suppliers, R. Molnar for the compensated GaN and J. Edgar for the sublimation-grown AlN. The CVD AlN film is from TDI, Inc.

References

- [1] S.J. Pearton, J.W. Lee, in: N.H. Nickel (Ed.), *Hydrogen in Semiconductors*, Academic Press, San Diego, 1999, p. 441.
- [2] S.M. Myers, et al., *J. Appl. Phys.* 88 (2000) 4676.
- [3] A.F. Wright, *Phys. Rev. B* 60 (1999) R5101.
- [4] J. Neugebauer, C. Van de Walle, *Phys. Rev. Lett.* 75 (1995) 4452.
- [5] S.K. Estreicher, D.E. Boucher, in: S.J. Pearton (Ed.), *GaN and Related Materials*, Gordon and Breach, New York, 1997, p. 171.
- [6] R.L. Lichti, et al., *Physica B* 273–274 (1999) 116.
- [7] R.L. Lichti, et al., *Physica B* 289–290 (2000) 342.
- [8] M.R. Dawdy, et al., *Physica B* 289–290 (2000) 346.
- [9] K.H. Chow, B. Hitti, R.F. Kiefl, in: M. Stavola (Ed.), *Identification of Defects in Semiconductors*, Academic Press, New York, 1997, p. 137.



ELSEVIER

Physica B 308–310 (2001) 77–80

PHYSICA B

www.elsevier.com/locate/physb

Ga vacancies in electron irradiated GaN: introduction, stability and temperature dependence of positron trapping

K. Saarinen^{a,*}, T. Suski^b, I. Grzegory^b, D.C. Look^c

^a *Laboratory of Physics, Helsinki University of Technology, P.O. Box 1100, 02150 HUT, Finland*

^b *UNIPRESS, High Pressure Research Center, Polish Academy of Sciences, 01-142 Warsaw, Poland*

^c *Semiconductor Research Center, Wright State University, Dayton, OH, USA*

Abstract

We have applied positron annihilation spectroscopy to show that 2 MeV electron irradiation at 300 K creates Ga vacancies in GaN with an introduction rate of 1 cm^{-1} . The Ga vacancies recover in long-range migration processes at 500–600 K with an estimated migration energy of $1.5(2) \text{ eV}$. Since the native Ga vacancies in as-grown GaN are stable up to 1300–1500 K, we conclude that they are complexes with oxygen impurities. The estimated binding energy of $2.2(4) \text{ eV}$ of such complexes is in good agreement with the results of theoretical calculations. © 2001 Elsevier Science B.V. All rights reserved.

Keywords: GaN; Ga vacancy; Irradiation; Positron annihilation

1. Introduction

Gallium nitride and its alloys form a class of important semiconductor materials for applications in optoelectronics at blue wavelength and electronic devices operating at high temperature and high voltage. Ga vacancies have been observed as important native defects in n-type GaN by positron annihilation spectroscopy [1,2]. However, the experiments so far have given only limited information on their formation mechanism during the crystal growth. Electron irradiation is a very valuable technique to introduce basic point defects in a controlled way. The annealing treatments of the irradiated material yield important information on the thermal stability of isolated intrinsic point defects. Such knowledge is helpful for understanding how native defects are formed during the growth.

Positrons get trapped at neutral and negative vacancies because of the missing positive charge of the ion

cores. The reduced electron density at vacancies increases the positron lifetime. In this paper, we apply positron annihilation spectroscopy to identify the Ga vacancies formed in 2 MeV electron irradiation of GaN bulk crystals. We study the annealing behavior of Ga vacancies and compare the thermal stabilities of native and irradiation-induced V_{Ga} . We further extend our earlier work [3] to discuss in greater detail the temperature dependence of positron lifetime in irradiated GaN.

2. Experimental details

The bulk GaN crystals were grown at a nitrogen pressure of 1.5 GPa and temperature of 1500°C [4]. Semi-insulating Mg-doped samples were chosen for the experiment, since these are free of native Ga vacancies as shown earlier [5]. The Mg and O concentrations of the samples were $[\text{O}] \approx [\text{Mg}] \approx 10^{20} \text{ cm}^{-3}$ according to secondary ion mass spectrometry [5]. The samples were irradiated with 2 MeV electrons at 300 K to two fluences of $\Phi = 3 \times 10^{17}$ and $1 \times 10^{18} \text{ cm}^{-2}$. The positron lifetime experiments were performed using conventional instrumentation with the time resolution 230 ps [2].

*Corresponding author. Laboratory of Physics, Helsinki University of Technology, P.O. Box 1100, 02150 Espoo, Finland. Tel.: +358-9-451-3111/3101; fax: +358-9-451-3116.

E-mail address: ksa@fyslab.hut.fi (K. Saarinen).

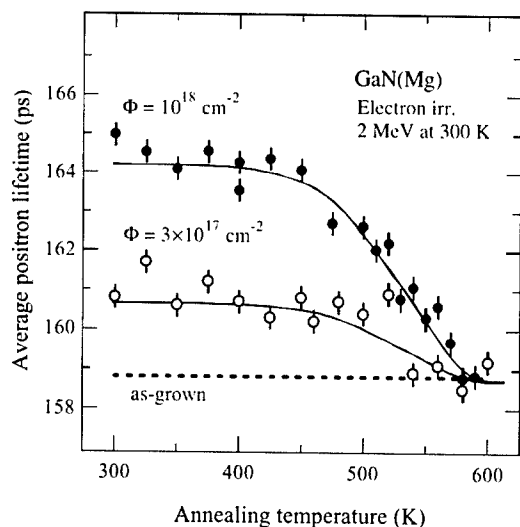


Fig. 1. Average positron lifetime as a function of annealing temperature T_{ann} in two GaN samples irradiated to fluences Φ . The measurement temperature was $T_{\text{meas}} = 300 \text{ K}$. The dashed line shows the level of the average positron lifetime in as-grown samples before irradiation [3].

To study simultaneously, the recovery of irradiation-induced defects and the temperature dependence of the positron lifetime spectrum, we annealed the samples in 10^{-3} mbar vacuum at temperatures T_{ann} and measured thereafter positron lifetimes as a function of measurement temperature T_{meas} from 80 K up to $T_{\text{ann}} - 50 \text{ K}$. The measurement time of positron lifetime spectrum (typically 3–4 h) is longer than the annealing time (30 min), which was observed to induce small recovery effects when measurements were performed close to T_{ann} . However, the final annealing curve (Fig. 1) was constructed of systematical data measured immediately after cooling the sample to room temperature from the annealing temperature T_{ann} .

3. Positron lifetime results

In unirradiated Mg-doped GaN samples only a single exponential decay component with a lifetime $\tau = 160 \text{ ps}$ is observed. As explained earlier [5], heavily Mg-doped GaN is free of Ga vacancies trapping positrons, and the lifetime $\tau = \tau_B = 160 \text{ ps}$ corresponds to positrons annihilating as delocalized particles in the defect-free GaN lattice. The 2 MeV electron irradiations with fluences $\Phi = 3 \times 10^{17}$ and $1 \times 10^{18} \text{ cm}^{-2}$, increase the average positron lifetime by 2 and 5 ps, respectively. This increase is a direct evidence of vacancy defects introduced in the samples in the electron irradiation. Fig. 1 shows the average positron lifetime τ_{av} at $T_{\text{meas}} = 300 \text{ K}$ as a function of the annealing temperature T_{ann} . Almost

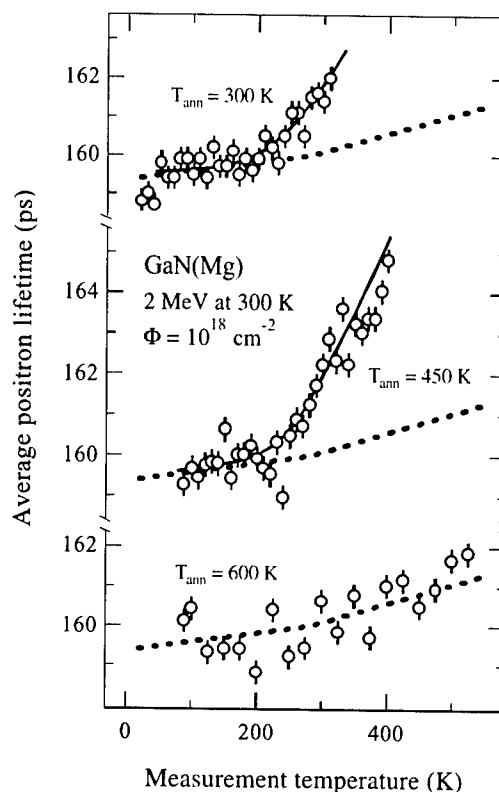


Fig. 2. Average positron lifetime as a function of measurement temperature T_{meas} . The temperature dependence was measured after annealing the sample at different temperatures T_{ann} . The dashed line shows the level of the average positron lifetime in as-grown samples before irradiation.

no recovery of τ_{av} is observed up to $T_{\text{ann}} = 450 \text{ K}$. At 500–600 K, the average lifetime decreases and finally coincides with the positron lifetime of about $\tau_B = 160 \text{ ps}$ in defect-free GaN. This indicates the recovery of the irradiation-induced vacancy defect at 500–600 K.

A careful experiment with high statistical accuracy [3] shows that the lifetime spectrum in irradiated GaN has two exponential components. The longer lifetime component, $\tau_2 = 235 \pm 5 \text{ ps}$ corresponds to positrons trapped at the irradiation-induced vacancy defect. This lifetime is the same as we have earlier found for native defects formed during the growth of n-type GaN [1,5]. The native vacancy is thus the same defect as that introduced by electron irradiation at 300 K, i.e. the open volume in both of them corresponds to a single missing atom from the lattice site. As explained earlier in detail [6], the defect with the lifetime $\tau_V = \tau_2 = 235 \pm 5 \text{ ps}$ can be identified as the Ga vacancy or a complex involving V_{Ga} .

The temperature dependencies $\tau_{\text{av}}(T_{\text{meas}})$ of the average positron lifetime after various annealing treatments are plotted in Fig. 2. After annealings at $T_{\text{ann}} = 300$ –450 K, the average lifetime decreases at low temperatures, indicating that fewer positrons

annihilate while trapped at vacancies. The same behavior has been observed earlier in as-grown Mg-doped GaN [5] as well as in many other semiconductors [7]. The decrease of τ_{av} is due to negative Mg_{Ga}^- ions capturing positrons at hydrogenic states at low temperatures [5]. This trapping prevents positrons from getting into the vacancy defects, thus decreasing the average lifetime towards the bulk value τ_B at low temperatures. After annealing at $T_{ann}=600$ K the average positron lifetime increases only slightly with temperature (Fig. 2). The slope of τ_{av} vs. T is similar to that found earlier in GaN(Mg) samples without vacancies and can be associated with the thermal expansion of the lattice. This confirms further that vacancies introduced in the electron irradiation recover after annealing at 500–600 K.

Fig. 1 shows that the concentration of Ga vacancies in 2 MeV electron irradiation increases with the fluence. The quantitative analysis of the V_{Ga} concentrations and the introduction rate can be done with the positron trapping model [7]. We proceed as earlier [5] and take into account both vacancies and negative ions as positron traps. When the concentration of negative ions is fixed to the Mg concentration $c_{ion}=10^{20} \text{ cm}^{-3}$ determined in these crystals using secondary-ion mass spectrometry [5], we can deduce the Ga vacancy concentrations from the measured average positron lifetime. Notice that the possible irradiation-induced negative ions do not play any role in this analysis because the concentration of negative Mg_{Ga}^- in the samples is 10–100 times larger than that of any defect formed in the irradiation.

Fig. 3 shows that the concentration of Ga vacancies increases linearly with the electron irradiation fluence in the range $\Phi = (0-10) \times 10^{17} \text{ cm}^{-2}$. The introduction rate is roughly $\Sigma_v = c_v/\Phi = 1 \text{ cm}^{-1}$. This is a typical value for primary defects formed in the irradiation. Furthermore, the same introduction rate has been determined for Frenkel pairs in the nitrogen sublattice using 0.7–1 MeV irradiation [8]. For 2 MeV electrons, the electrical experiments show a total acceptor introduction rate of $1-2 \text{ cm}^{-1}$ [9]. This value is close to that determined here for Ga vacancies, but other acceptors, such as the N interstitials [8], most likely also contribute in the electrical experiments.

Chow et al. [10] have recently applied optical detection of electron paramagnetic resonance (ODEPR) to observe the interstitial Ga and related defects in irradiated GaN. According to their results, the Ga interstitial is mobile at room temperature and subsequently gets trapped, perhaps by oxygen impurities in the sample. It is clear that this trapped Ga interstitial must have left a Ga vacancy behind in the irradiation. In perfect agreement with the results of Chow et al. [10] we thus detect the irradiation-induced Ga vacancy after similar 2 MeV irradiation at 300 K.

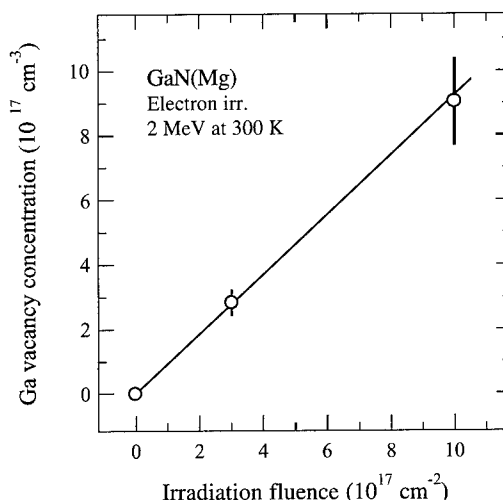


Fig. 3. The concentration of Ga vacancies as a function of 2 MeV electron irradiation fluence at 300 K. The solid line corresponds to the introduction rate of $\Sigma_v = 1 \text{ cm}^{-1}$ [3].

Fig. 1 shows that the Ga vacancies recover in 30 min isochronal heat treatments at 500–600 K. The defects associated with trapped Ga interstitials are stable at 500–600 K and anneal at clearly higher temperatures of 700–900 K according to Bozdog et al. [11,12]. This suggests that Ga vacancies recover by becoming mobile defects at 500–600 K. Assuming that the vacancy takes roughly 10^3-10^5 jumps with an attempt frequency 10^{13} s^{-1} in the 30 min annealing time, we can convert the recovery temperature of 600 K to an activation energy of $1.5(2) \text{ eV}$. This value can be taken as an estimate for the migration energy of Ga vacancies in GaN.

The native Ga vacancies observed in as-grown n-type GaN are stable up to much higher temperatures than 600 K, where the irradiation-induced Ga vacancies recover. This points out directly that the Ga vacancies formed during the growth are not isolated but belong to stable defect complexes, most likely with O impurities as suggested earlier [13]. At growth temperatures (typically >1300 K) negatively charged Ga vacancies are mobile and migrate in the lattice until they are trapped at positive oxygen donors. In fact, our preliminary results show that native Ga vacancy complexes recover in heat treatments at 1300–1500 K in samples grown by metal-organic chemical vapor deposition at about 1300 K. The recovery temperature of 1400 K corresponds to an activation energy of $3.7(2) \text{ eV}$, which can be interpreted as the sum $E_M + E_B$ of the migration energy of V_{Ga} and the binding energy of the $V_{Ga}-O_N$ complex. Taking the migration energy $E_M = 1.5(2) \text{ eV}$ determined above, we get a binding energy of $E_B = 2.2(4)$ for the $V_{Ga}-O_N$ pair. This value is in excellent

agreement with the theoretical estimates of 1.8–2.1 eV [14,15].

4. Conclusions

We have identified Ga vacancies formed with the introduction rate of 1 cm^{-1} in 2 MeV electron-irradiation of GaN bulk crystals at 300 K. The Ga vacancies recover in heat treatments at 500–600 K. According to previous ODEPR experiments [10–12] Ga interstitials are trapped by other defects at this temperature range and anneal only above 700 K. We thus conclude that Ga vacancies become mobile defects at 500–600 K and recover in long-range migration processes, with an estimated migration energy of 1.5(2) eV. These results indicate that the native Ga vacancies formed during the crystal growth are associated with defect complexes, probably with the oxygen donors. We estimate a binding energy of 2.2(4) eV for these complexes, indicating that they are stable at the elevated growth temperature of GaN. Our results show further that Mg impurities are negatively charged in highly resistive Mg-doped GaN bulk crystals.

References

- [1] K. Saarinen, et al., *Phys. Rev. Lett.* 79 (1997) 3030.
- [2] K. Saarinen, in: M.O. Manasreh (Ed.), *III-Nitride Semiconductors: Electrical, Structural and Defects Properties*, Elsevier, Amsterdam, 2000, p. 109.
- [3] K. Saarinen, et al., *Phys. Rev. B*, submitted for publication.
- [4] S. Porowski, et al., in: S.J. Pearton (Ed.), *GaN and Related Materials*, Vol. 2, Gordon and Breach, Amsterdam, 1997, p. 295.
- [5] K. Saarinen, et al., *Appl. Phys. Lett.* 75 (1999) 2441.
- [6] K. Saarinen, et al., *Physica B* 273–274 (1999) 33.
- [7] K. Saarinen, et al., in: M. Stavola (Ed.), *Identification of Defects in Semiconductors*, Academic Press, New York, 1998, p. 209.
- [8] D.C. Look, et al., *Phys. Rev. Lett.* 79 (1997) 2273.
- [9] D.C. Look, unpublished.
- [10] K.H. Chow, et al., *Phys. Rev. Lett.* 85 (2000) 2761.
- [11] C. Bozdog, et al., *Phys. Rev. B* 59 (1999) 12479.
- [12] M. Linde, et al., *Phys. Rev. B* 55 (1997) R10177.
- [13] J. Oila, et al., *Phys. Rev. B* 63 (2001) 045205.
- [14] J. Neugebauer, et al., *Appl. Phys. Lett.* 69 (1996) 503.
- [15] T. Mattila, et al., *Phys. Rev. B* 55 (1997) 9571.



ELSEVIER

Physica B 308–310 (2001) 81–84

PHYSICA B

www.elsevier.com/locate/physb

Influence of defects in low-energy nitrogen ion beam assisted gallium nitride thin film deposition

J.W. Gerlach^{a,*}, S. Sienz^a, W. Attenberger^b, B. Rauschenbach^a

^a *Institut für Oberflächenmodifizierung, Permoserstrasse 15, 04318 Leipzig, Germany*

^b *Institut für Physik, Universität Augsburg, Augsburg, Germany*

Abstract

Epitaxial GaN thin films were grown by low-energy nitrogen ion beam assisted deposition of gallium on *c*-plane sapphire. By applying X-ray diffraction and transmission electron microscopy, the influence of the ion irradiation induced defects on the formation of the undesired cubic GaN polytype in the hexagonal films is investigated. The results show that in all films containing the cubic polytype it appears in twinned form. An increase of the ion energy as well as the ratio of nitrogen ion flux and gallium atom flux (*I/A*-ratio) leads to an increase in the amount of cubic polytype in the films. The observations are discussed considering the ion beam induced defect creation. © 2001 Elsevier Science B.V. All rights reserved.

Keywords: Ion beam assisted deposition; GaN polytypes; XRD pole figures; Ion beam induced defects

1. Introduction

As the binding energy difference between the Ga–N bond in the stable hexagonal (wurtzitic) and metastable cubic (zincblende) polytype of GaN is only about 20 meV [1], the probability of stacking faults is high, i.e. zincblende GaN (*z*-GaN, *c*-GaN) often found in films intended to be purely wurtzitic GaN (*w*-GaN, *h*-GaN) and vice versa [2,3]. The necessary deposition conditions to obtain pure hexagonal films are published for GaN films grown by molecular beam epitaxy (MBE) or metal-organic vapour phase epitaxy (MOVPE) to be grown in the nitrogen-rich regime and at high temperatures [3,4]. The deposition of GaN films using energetic nitrogen ions is expected to influence these necessary growth conditions due to the large energy input into the surface region and the ion beam induced defect creation. The displacement energy of GaN, i.e. the energy that must be at least transferred in an elastic atomic collision in order to create a permanent point defect in GaN, is about 24 eV [5].

In this paper, the ion energy was chosen that high defects are created by ion impingement, but only within the first few nanometres of the growing GaN film. The appearance of the cubic polytype and the effect of the ion beam parameters on the cubic fraction of GaN films grown on *c*-plane sapphire, that is usually used for growth of *h*-GaN, is investigated.

2. Experimental

The GaN thin films were grown in a high vacuum chamber with a base pressure of 5×10^{-6} Pa by evaporating gallium with an effusion cell onto a *c*-plane sapphire substrate and simultaneously irradiating the growing film with hyperthermal nitrogen ions delivered by a Kaufman-type ion source. The gallium atom flux and the nitrogen ion flux was measured by a quartz crystal and a Faraday cup array, respectively. The process temperature, monitored by thermocouples, was held constant at 750°C. The arrival ratio of nitrogen ions to gallium atoms (*I/A*-ratio) was varied between 0.35 and 1.0 by alteration of the gallium flux at a constant nitrogen ion current density of 20 $\mu\text{A}/\text{cm}^2$. The ion energy *E* was

*Corresponding author. Tel.: +49-341-235-2682; fax: +49-341-235-2595.

E-mail address: jwgerlach@uni-leipzig.de (J.W. Gerlach).

in the range of 50–150 eV. The total film thickness of GaN was about 300 nm.

X-ray diffraction (XRD) measurements were performed with Cu-K α radiation using a four-circle goniometre with Eulerian cradle and a secondary graphite monochromator. To measure a pole figure the sample was rotated (azimuthal angle φ) at increasing sample tilts (polar angle χ) in a fixed θ - 2θ -geometry with a step width of 1° in φ and χ . The diffracted intensity distribution is illustrated in stereographic projection.

Cross-section TEM micrographs were obtained by an electron microscope with an acceleration voltage of 300 kV and an electronic image acquisition system.

3. Results and discussion

To distinguish between the *h*-GaN and *c*-GaN, texture measurements were performed. In Fig. 1 the hexagonal $\{10\bar{1}1\}$ and the cubic $\{111\}$ XRD pole figure of a typical GaN film containing both polytypes prepared by IBAD is shown. From the fact that distinct, separated and narrow pole density maxima are visible it can be concluded that the film is of high crystalline order. Further, the number of pole density maxima in the cubic pole figure reveals that the cubic polytype appears in a two-fold form in the film. If there were only one cubic crystallite orientation in the thin film, arranged by stacking (111) planes in the order ABCABCA..., then only three-pole density maxima at a polar angle of 70.5° with an equal azimuthal distance of 120° would be present in the pole figure. The existence of a second set of three-pole density maxima, rotated against the first set by 180° , proves the existence of the cubic rotational twin, arranged by stacking (111) planes in the order ACBACBA..., in the film. Consequently, the two cubic twins have the epitaxial relationship

$$c\text{-GaN}(111)\parallel c\text{-GaN}(\bar{1}\bar{1}\bar{1}),$$

and

$$c\text{-GaN}[1\bar{1}0]\parallel c\text{-GaN}[\bar{1}10].$$

In all samples grown for this study it was found that the ratio of diffracted intensity originating from the two twins is about unity. This is understandable, as the stacking orders given above have equal probabilities. The epitaxial relationship between hexagonal and cubic polytypes as derived from the pole figures is

$$h\text{-GaN}(0001)\parallel c\text{-GaN}(111),$$

and

$$h\text{-GaN}[2\bar{1}\bar{1}0]\parallel c\text{-GaN}[\bar{1}10] \text{ or } c\text{-GaN}[1\bar{1}0].$$

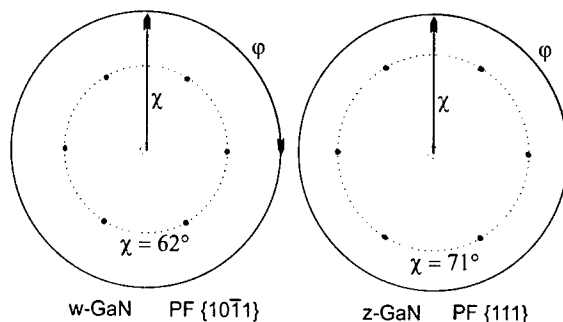


Fig. 1. Hexagonal $\{10\bar{1}1\}$ and cubic $\{111\}$ XRD pole figures of a thin GaN film containing a mixture of both polytypes. The dotted circles indicate the φ -scans that were measured to obtain the phase index.

These relationships arise from the $[0001]$ growth direction of the hexagonal GaN. Stacking faults in the hexagonal stacking sequence ABABA... can lead to the cubic polytype, as the (0001) plane of *h*-GaN and the (111) -plane of *c*-GaN are almost identical.

Together with the known epitaxial relationship between hexagonal GaN and sapphire [6] the epitaxial relationships between the cubic twins and sapphire are given by

$$\text{Al}_2\text{O}_3(0001)\parallel c\text{-GaN}(111),$$

and

$$\text{Al}_2\text{O}_3[1\bar{1}00]\parallel c\text{-GaN}[\bar{1}10] \text{ or } c\text{-GaN}[1\bar{1}0].$$

A semi-quantitative measure of the fraction of the cubic phase in the GaN film can be obtained by measuring φ -scans as indicated by the dotted circles in the pole figures in Fig. 1 and calculating the phase index (PIX), defined by

$$\text{PIX} = \frac{\int_0^{2\pi} I_{(111)} d\varphi}{\int_0^{2\pi} I_{(111)} d\varphi + \int_0^{2\pi} I_{(1\bar{1}\bar{1})} d\varphi} \quad (1)$$

with $I_{(hkl)}$ being the diffracted intensity. Obviously, the PIX does not give the real concentration of the *c*-GaN in the sample. For this purpose pure and mixed hexagonal and cubic GaN samples with known film thickness and with comparable crystalline quality would be necessary for obtaining calibration factors. However, in order to compare films with different cubic content the PIX is a simple and reliable measure.

As can be derived from Fig. 2a and b, showing the PIX as a function of the ion beam parameters I/A and E , the variation of both parameters influences the cubic amount in the GaN films. The first observation is the increase of the cubic amount with increasing I/A -ratio, i.e. increasing nitrogen to gallium arrival ratio. This is contrary to the results known from MBE and MOVPE, where the cubic amount drops with increasing nitrogen-rich growth and rises with increasing gallium-rich

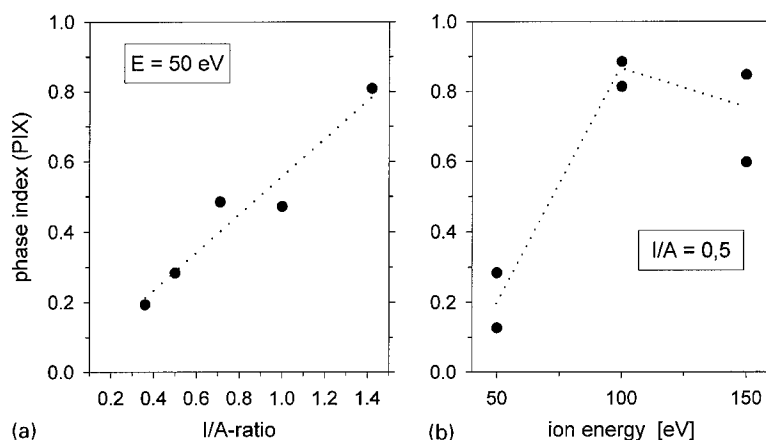


Fig. 2. Phase index PIX, i.e. cubic intensity fraction as a function of I/A -ratio (a) and ion energy (b).

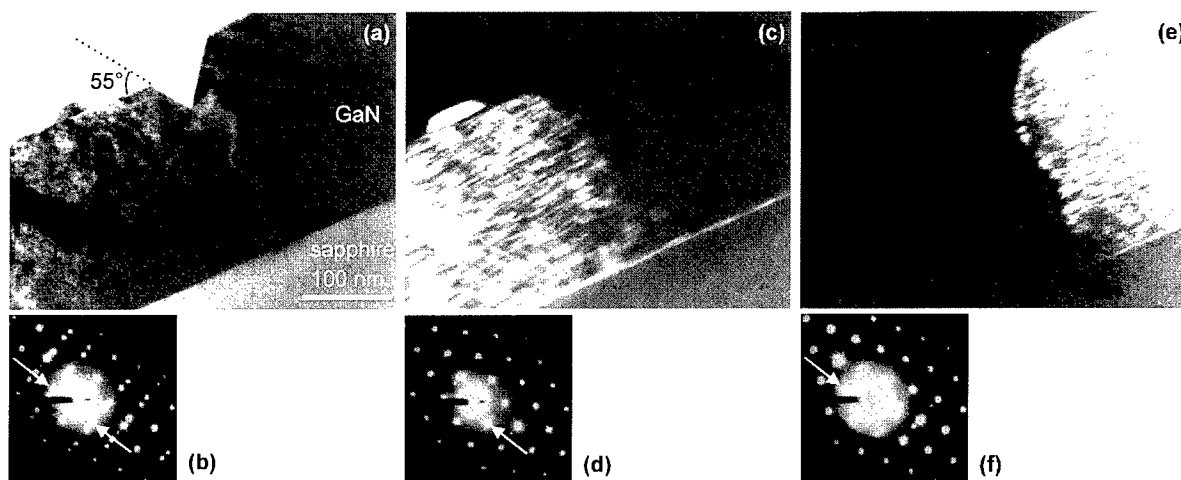


Fig. 3. TEM micrographs (zone axis: sapphire $[1\bar{1}00]$) of a GaN film deposited with $I/A = 0.7$ and $E = 50$ eV: bright field image (a) with corresponding diffraction pattern (b), dark field images excited with $(1\bar{1}1)$ of first cubic twin (c) and second cubic twin (e) with corresponding selected area diffraction patterns (d, f). The white arrows indicate the spots used for the dark field images.

growth [3,4]. A proof for this unfamiliar behaviour of the cubic phase content in GaN films grown by IBAD is that the density of gallium droplets observed on films prepared with I/A -ratios of 0.35 to 0.7 diminishes with increasing I/A -ratio and vanishes for $I/A = 1.0$ (not shown here). This marks the transition from gallium-rich to nitrogen-rich growth which would lead to a decrease in the cubic amount of MBE and MOVPE GaN films in contrast to the results obtained for IBAD GaN films. The second observation is the trend of the cubic fraction to increase with higher ion energies.

As XRD measurements deliver integral information due to the high penetration depth of X-rays, electron microscopical investigations were conducted to obtain

local information on the nature of the cubic polytype detected by XRD. Because both extended cubic domains as well as a high density of stacking faults could result in the obtained diffracted intensity ratios. The TEM cross-section bright-field micrograph of a GaN film deposited with $I/A = 0.7$ and $E = 50$ eV in Fig. 3a shows two regions divided by a v-shaped insertion at the film surface. The side walls of this insertion and the film surface build an angle of about 55°. This matches the angle between the (111) and (001) planes in cubic crystals and therefore it can be concluded that the insertion walls are (001) facets of coalesced cubic domains. The corresponding overall diffraction pattern (Fig. 3b) shows a variety of relatively sharp diffraction

spots. By choosing only one of these spots (marked with a white arrow) and creating a dark-field image with this single spot, in fact two domains (see bright image parts) can be distinguished in Fig. 3c and e which extend over the whole film thickness. The selected area diffraction patterns of the left and the right domain (Fig. 3d and f) are characteristic of cubic systems and can be assigned to two different cubic twins as already observed by XRD. It has to be noted that this selected sample region does not contain any hexagonal GaN at all, but that hexagonal GaN was found in other regions of the film.

The results presented above allow the following conclusions:

(i) The increase of the cubic fraction with both increase of I/A and E is definitely correlated with the ion beam irradiation during growth. The increase in the two parameters results in a higher defect production and, due to the larger penetration depth of nitrogen ions with higher ion energy, in a broader region where defects are created. However, it still has to be kept in mind that the mean projected range of nitrogen ions in GaN as calculated by the Monte-Carlo code TRIM [7] is only two to three monolayers for the chosen ion energies and the created defects are not annealed out at the deposition temperature (see Ref. [8]).

(ii) The formation of the cubic phase during ion beam assisted growth of GaN is a nucleation phenomenon at the substrate surface, as the domains extend over the whole film thickness and no growth of hexagonal GaN or the complementary cubic twin occurred in these domains.

(iii) The ion beam irradiation during deposition stabilizes the growth of the metastable cubic polytype. However, the mechanism of stabilization of the cubic phase due to ion beam induced defects in the surface region, that was also assumed by Lee et al. [9], is not clear up to now. Furthermore, it was found that the compressive stress in films of the present study was up to 600 MPa [10]. Therefore, an additional influence of mechanical stress on the polytype stabilization may be taken into account.

4. Summary

The influence of the ion irradiation during low-energy nitrogen ion beam assisted deposition of gallium on *c*-plane sapphire substrates was investigated with respect to the formation of the cubic polytype. The results show that *c*-GaN appears in large twinned domains and that an increase of the nitrogen ion to gallium atom flux ratio, as well as an increase of the ion energy favours the formation and stabilization of *c*-GaN.

Acknowledgements

The authors would like to thank the Deutsche Forschungsgemeinschaft for financial support, as well as H. Neumann and M. Zeuner of IOM Leipzig for operational support. The samples were prepared and measured at the University of Augsburg, Germany.

References

- [1] B.J. Min, C.T. Chan, K.M. Ho, *Phys. Rev. B* 45 (1992) 1159.
- [2] T. Kurobe, Y. Sekiguchi, J. Suda, M. Yoshimoto, H. Matsunami, *Appl. Phys. Lett.* 73 (1998) 2305.
- [3] D.J. As, K. Lischka, *Phys. Stat. Sol. A* 176 (1999) 475.
- [4] S. Oktyabrsky, K. Dovidenko, A.K. Sharma, J. Narayan, *Appl. Phys. Lett.* 74 (1999) 2465.
- [5] K.W. Böer, *Survey of Semiconductor Physics*, Vol. 1, Van Nostrand-Reinhold, New York, 1990, p. 629.
- [6] T.D. Moustakas, T. Lei, R.J. Molnar, *Physica B* 185 (1993) 36.
- [7] J.F. Ziegler, J.P. Biersack, U. Littmark, *The Stopping and Range of Ions in Solids*, Pergamon Press, New York, 1985.
- [8] J.W. Gerlach, D. Schrupp, R. Schwertberger, H. Neumann, M. Zeuner, B. Rauschenbach, *Surf. Coat Technol.* 128/129 (2000) 286.
- [9] N.-E. Lee, R.C. Powell, Y.-W. Kim, J.E. Greene, *J. Vac. Sci. Technol. A* 13 (1995) 2293.
- [10] J. Keckes, J.W. Gerlach, B. Rauschenbach, *J. Crystal Growth* 219 (2000) 1.



ELSEVIER

Physica B 308–310 (2001) 85–88

PHYSICA B

www.elsevier.com/locate/physb

ODEPR and yellow luminescence intensity in GaN under high pressure

K. Michael^a, U. Rogulis^{a,1,*}, F.K. Koschnick^a, Th. Tröster^a, J.-M. Spaeth^a,
B. Beaumont^b, P. Gibart^b

^aDepartment of Physics, University of Paderborn, Warburger Str. 100, 33095 Paderborn, Germany

^bCHREA-CNRS, Parc de Sophie Antipolis, Rue Bernard Gregory, F-06560 Valbonne, France

Abstract

Optically detected electron paramagnetic resonance (ODEPR) measurements in the yellow luminescence (YL) under pressures up to 7 GPa have been performed. A non-magnetic diamond anvil cell was designed, into which microwaves in the 4 mm band (72 GHz) could be coupled. One of the main limiting factors for the ODEPR measurements in the YL at high pressures is the strongly decreased the YL intensity at low temperatures. At normal pressure, when cooling the sample, the YL intensity increases. Under pressures of 5–10.8 GPa, the YL intensity decreases significantly upon cooling. ODEPR spectra of the undoped MOVPE GaN layer on sapphire measured in YL at 1.5 K at normal pressure showed resonance lines at $g_{\parallel} = 1.989$, and $g_{\parallel} = 1.952$ and a shoulder with $g_{\parallel} = 1.958$, respectively. At low temperatures under pressures of 5–10.8 GPa, a part of the YL intensity remains, but only the ODEPR line at $g_{\parallel} = 1.989$ is measured while that at $g_{\parallel} = 1.952$ disappears. The disappearing part of the YL is due to a donor–acceptor recombination from a DX-like donor, which is attributed to the oxygen on nitrogen sites (O_N) in agreement with theory and other experiments. © 2001 Elsevier Science B.V. All rights reserved.

Keywords: GaN; ODEPR; Yellow luminescence intensity; Pressure and temperature dependence

1. Introduction

GaN is an important material for opto-electronic applications in the visible and near UV spectral range [1]. In most nominally undoped metal organic vapor phase epitaxy (MOVPE)-grown GaN samples, an unwanted broad luminescence band centered around 2.2 eV, the so-called yellow luminescence (YL) is observed. The origin of this yellow luminescence has been actively debated [2–10].

The YL in n-type GaN was investigated under high hydrostatic pressure at room temperature by Suski et al.

[4]. A shift of the peak position of the YL with the shift of the conduction band up to a pressure of 20 GPa was found.

The aim of the present work was to investigate the optically detected electron paramagnetic resonance (ODEPR) and yellow luminescence intensity in wurtzite GaN under high hydrostatic pressures at low temperatures in order to obtain more information on the nature of the three ODEPR lines measured previously in the YL at ambient pressure and tentatively associated with shallow donors [10].

2. Experimental

Optically detected electron paramagnetic resonance measurements in the YL under pressures up to 7 GPa have been performed. A non-magnetic diamond anvil

*Corresponding author. Fax: +49-5251-603247.

E-mail address: sp.ur@physik.uni-paderborn.de (U. Rogulis).

¹Permanent address: Institute of Solid State Physics, University of Latvia, Riga, Latvia.

cell was designed, into which microwaves in the 4 mm band (72 GHz) could be coupled.

All its parts were made of a CuBe alloy with 2% Be. The type IIa diamonds having a low luminescence were supported by B_4C disks to provide a maximum aperture for the microwaves, which reached the sample without significant attenuation. The gasket material was Inconel X 600 which distorted the magnetic field only slightly. The sample chamber had typically 250–300 μm diameter and 70 μm thickness. The pressure was measured using the ruby fluorescence method [11,12]. The use of liquid Ar as transmission media implied that a minimum pressure of few GPa had to be applied as the lowest pressure to completely seal the sample chamber. The pressure cell was placed into a He bath cryostat (1.5 K) and in a magnetic field up to 4 T. The optical excitation was done with a halogen or deuterium lamp followed by filters. The PL, which was corrected for the above band gap excitation intensity and for the contribution of the diamonds, was recorded through appropriate filters with a photomultiplier. The above band gap excitation intensity decreased with increasing pressure. The EPR was detected as a microwave-induced increase of the YL intensity.

The GaN layers, approx. 3 μm thick, were nominally undoped and grown with MOVPE on sapphire, the thickness of which was reduced to about 20 μm with mechanical polishing. The sample diameter was 200–250 μm .

The limitation to 7 GPa, of the ODEPR measurements, is due to the strongly decreasing YL intensity only. The high-pressure cell itself allows for ODEPR experiments up to pressures of 30 GPa [13].

3. Results

The YL measured at 295 K under pressure shows a blue shift and decreases in intensity, it is hardly measurable at 18 GPa [13]. This result is in agreement with the observations of Suski et al. [4].

The intensity of the YL increases when cooling to low temperature under ambient pressure. However, as seen in Fig. 1, it strongly *decreases* when cooling under pressure. Its spectral shape remains almost unchanged when changing the temperature. As the quenching effect increases, the higher the pressure becomes (see Fig. 2 for various pressures), while the spectral shape always remains unchanged (see Fig. 1).

Fig. 3 shows the ODEPR spectra measured at 72 GHz at ambient pressure using a large sample of an undoped MOVPE GaN layer on sapphire ($5 \times 10 \text{ mm}^2$) and optimal excitation conditions. The sample was not in a cavity but directly irradiated with the 4 mm microwaves. A very good signal-to-noise ratio could be achieved. The three resonances resolved, already measured previously

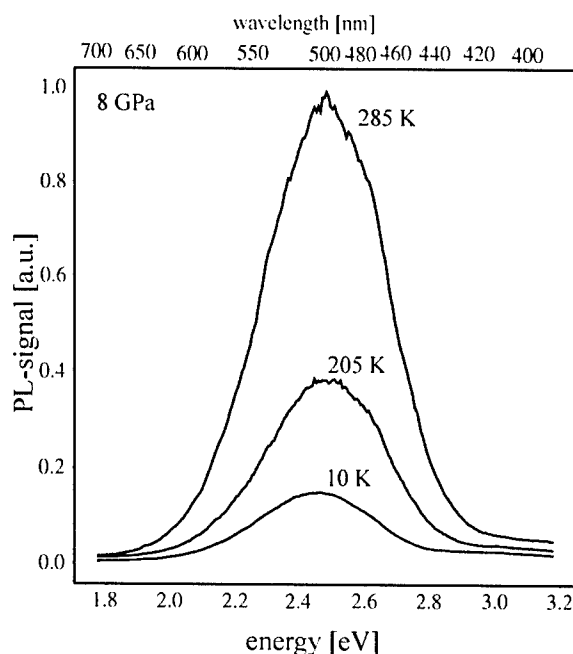


Fig. 1. PL signal of the YL at a pressure of 8 GPa for temperatures of 285, 205 and 10 K.

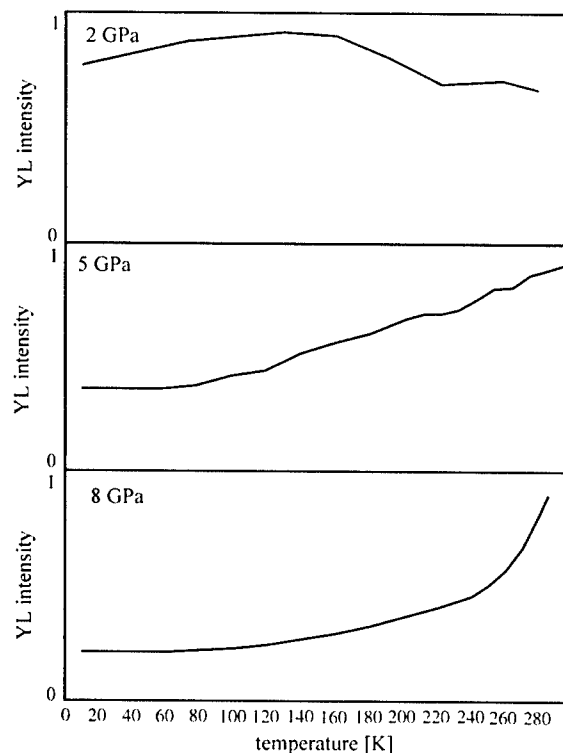


Fig. 2. Temperature dependence of the YL at different pressures.

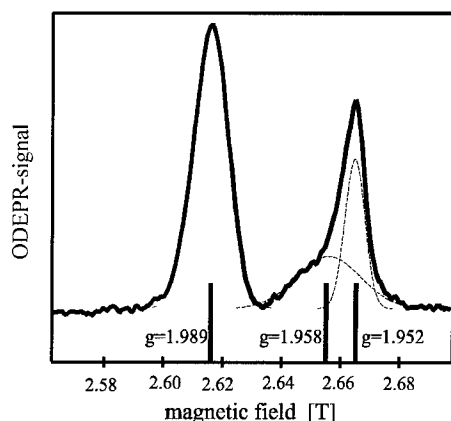


Fig. 3. ODEPR spectrum for $B||c$ measured in the YL at 72 GHz. The g -values of three resonance lines are shown.

[10], have been assigned to three shallow donors in Ref. [9] on the basis of a mapping investigation. The relative signal intensities of the line at $g_{||} = 1.989$ to that at $g_{||} = 1.952$ depend on the illuminated spot of the sample and can vary by as much a factor of 2. In Fig. 3, an average of the large sample is measured. The line at $g_{||} = 1.952$ was assigned to the residual donor ([3] and references therein).

Fig. 4 shows the results of the high-pressure ODEPR experiments. At ambient pressure, the two known resonances at $g_{||} = 1.989$ and $g_{||} = 1.952$ are clearly seen. The signal-to-noise ratio is much worse when measuring the ODEPR in the diamond anvil cell compared to Fig. 3, where a further resonance in the low-field shoulder of the line at $g_{||} = 1.952$ was detected at $g_{||} = 1.958$. Note that the magnetic field was corrected for the field shift by the pressure cell ($\sim 1\%$) and that the measurement time for each pressure was about 50 h. The relative signal intensity of the line at $g_{||} = 1.989$ to that of $g_{||} = 1.952$ is different from that of Fig. 3, since only a small piece of the sample with $\sim 250 \mu\text{m}$ diameter is used for the experiment with the diamond anvil cell, where the signal at $g_{||} = 1.952$ happens to be rather low compared to that at $g_{||} = 1.989$ [9]. The most important result is that the line at $g_{||} = 1.952$ previously ascribed to the residual donor disappears when pressure is applied, i.e. this donor belongs to that part of the YL which has a thermal barrier. The line at $g_{||} = 1.989$ does not disappear and it seems that the signal around $g_{||} = 1.958$ does not disappear either. However, due to the low signal-to-noise ratio, this cannot be stated with certainty. The line at $g_{||} = 1.989$ broadens somewhat under pressure.

One of the main limiting factors for the ODEPR measurements in the YL at high pressures is the significantly decreasing YL intensity at low temperatures.

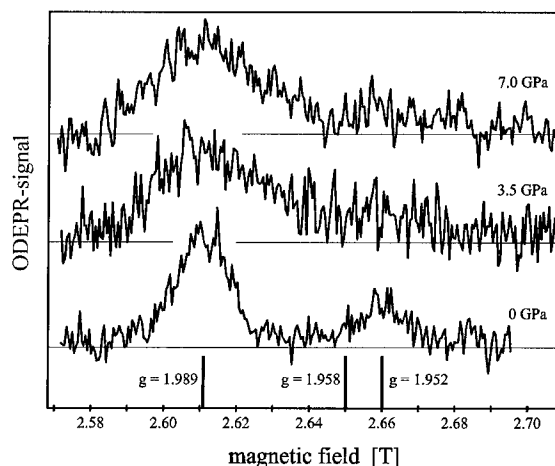


Fig. 4. ODEPR signal in the YL at different hydrostatic pressures. The sample size is about $200 \mu\text{m}$ in diameter.

4. Discussion

At low temperatures, the relative signal intensity of the line at $g_{||} = 1.952$ to that at $g_{||} = 1.989$ changes under high pressures such that the line at width $g_{||} = 1.952$ disappears which happens already at rather moderate pressures. This result shows that both ODEPR lines must belong to different recombination paths, in agreement with the result of the ODEPR mapping experiments [9].

The disappearance of the ODEPR line at $g_{||} = 1.952$ coincides with the disappearance of part of the YL by cooling to low temperatures under pressures of 5–10.8 GPa. Only part of the YL intensity remains. However, since the spectral shape of the YL remains almost unchanged at different temperatures and at pressures at least up to 8 GPa, both recombination paths of the YL must have very similar energy differences between donor and acceptor.

We propose that the disappearing recombination path of the YL involves a defect, which becomes a barrier at low temperatures and high pressures such as the DX-like donors [14] have. The disappearing part of the YL is due to a donor–acceptor recombination from a DX-like donor, which is attributed to O_N in agreement with theory [15] and other experiments [16].

Thus, we assign the residual donor to oxygen on nitrogen sites (O_N). It is well possible that Si_{Ga} is responsible for the shoulder at $g = 1.958$. An EPR study of Si-doped wurtzite GaN yielded $g_{||} = 1.9510$ in X-band [17]. It remains, however, unclear as to the nature of the other shallow donor with $g_{||} = 1.989$. It is only clear that this line cannot be the acceptor involved in the YL. Assuming recombination to the same acceptor, it will be a shallow donor with a very similar ionisation energy as O_N , perhaps within $\pm 50 \text{ meV}$.

Acknowledgements

Support by the ESPRIT project LAQUANI is gratefully acknowledged.

References

- [1] S. Nakamura, G. Fasol, in: *The Blue Laser Diode*, Springer, Berlin, 1997.
- [2] T. Ogino, M. Aoki, *Jpn. J. Appl. Phys.* 19 (1980) 2395.
- [3] E.R. Glaser, et al., *Phys. Rev. B* 51 (1995) 13326.
- [4] T. Suski, et al., *Appl. Phys. Lett.* 67 (1995) 2188.
- [5] P. Perlin, et al., *Phys. Rev. Lett.* 75 (1995) 296.
- [6] E. Calleja, et al., *Phys. Rev. B* 55 (1997) 4689.
- [7] K. Saarinen, et al., *Phys. Rev. Lett.* 79 (1997) 3030.
- [8] C.G. van de Walle, J. Neugebauer, in: F.A. Ponce, et al. (Eds.), *III–V Nitrides*, MRS Symposia Proceedings, MRS Meeting, Pittsburgh, PA, 1997, p. 861.
- [9] F.K. Koschnick, et al., *Appl. Phys. Lett.* 76 (2000) 1828.
- [10] F.K. Koschnick, et al., *J. Crystal Growth* 189–190 (1998) 561.
- [11] G.J. Piermarini, et al., *J. Appl. Phys.* 46 (1975) 2774.
- [12] R.A. Noack, W.B. Holzapfel, in: K.D. Timmerhaus, M.S. Barber (Eds.), *High Pressure Science and Technology*, Vol. 1, Plenum, New York, 1979, p. 748.
- [13] K. Michael, Doctoral Thesis, Paderborn, 1999.
- [14] H. Overhof, in: M. Merino (Ed.), *DX Centers—Donors in AlGaAs and Related Compounds*, Scitec, Zug, 1994, Defects Diffusion Forum 108, 1994, p. 11.
- [15] C.G. Van de Walle, et al., *Phys. Rev. B* 57 (1998) R2033.
- [16] C. Wetzel, et al., *Phys. Rev. B* 61 (2000) 8202.
- [17] M.W. Bayerl, in: *Selected Topics of Semiconductor Physics and Technology*, Vol. 32, W. Schottky Institut, TU München, 2000, p. 155.



ELSEVIER

Physica B 308–310 (2001) 89–92

PHYSICA B

www.elsevier.com/locate/physb

Investigation of structural defects of thick GaN grown by flow-modulated hydride vapor-phase epitaxy

Wei Zhang^{a,*}, Helder R. Alves^a, Till Riemann^b, M. Heuken^c, Peter Veit^b,
Dirk Meister^a, Wilhelm Kriegseis^a, Detlev M. Hofmann^a, Juergen Christen^b,
Bruno K. Meyer^a

^a *I. Physics Institute, University of Giessen, Heinrich-Buff-Ring 16, 35392 Giessen, Germany*

^b *Institute of Experimental Physics, Otto-von-Guericke-University Magdeburg, University Plaza 16, 39016 Magdeburg, Germany*

^c *Aixtron AG, Kackertstrasse 15-17, 52072 Aachen, Germany*

Abstract

We investigated the structural defects in GaN grown by hydride vapor-phase epitaxy via flow-modulation growth technique. It is found that the structural defects decrease greatly from the initial layer ($10^{10-12} \text{ cm}^{-2}$) above substrate to the top layer (10^7 cm^{-2}). Optical differential interference contrast microscopy and atomic force microscopy observations show that the semiconductor layers have also good homogeneity and morphology. © 2001 Elsevier Science B.V. All rights reserved.

Keywords: GaN; Morphology; Structural defects; Flow-modulation growth

1. Introduction

Structural quality of GaN films is of importance for the applications of this promising semiconductor. Significant progress in improving crystal quality has resulted in the development of blue LEDs, based on GaN, of high brightness [1,2]. However, the fabrication of high quality devices still demands high quality GaN. Hydride vapor-phase epitaxy (HVPE) has, therefore, attracted great interest, for it allows rapid growth of high-quality thick GaN epilayers. Recently, we developed flow modulation growth (FMG) techniques, in order to improve further, the crystalline quality of GaN films grown by HVPE [3,4]. In this study, the structure of the FMG-GaN films is investigated using transmission electron microscopy (TEM), cathodoluminescence (CL), optical differential interference contrast microscopy, atomic force microscopy (AFM), and X-ray diffraction (XRD).

2. Experimental procedure

The flow modulation growth is carried out at atmospheric pressure in a home-built vertical HVPE system [5]. The Ga source is GaCl in situ, formed upstream in the reactor by reacting the HCl gas with metallic gallium at 900°C and the N source is from NH₃. The growth of GaN is performed at 1050°C on a rotating substrate holder. More details of the growth parameters can be found elsewhere [4,5]. During growth, we periodically interrupt either NH₃ or HCl flow (flow of Ga source) but keep other parameters constant to modulate the GaN growth process periodically. When NH₃ flow is modulated, we call the growth process, NH₃ flow modulation and when HCl is modulated, it is called HCl flow modulation. For HCl flow modulation, the interruption of HCl flow is controlled for 30 min and the growth cycle of each sublayer is carried out for a time of 5–30 min. The NH₃ flow modulation is realized by switching off NH₃ for 20 s while keeping the growth cycle fixed at 15 s. All samples are grown on sapphire. Fig. 1 shows a schematic representation of the FMG process.

*Corresponding author.

E-mail address: wei.zhang@physik.uni-giessen.de (W. Zhang).

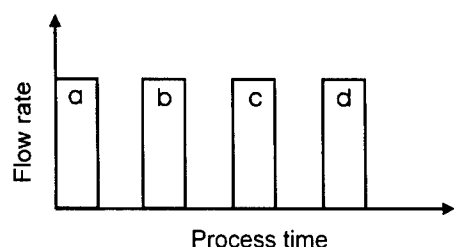


Fig. 1. The schematic representation of the FMG process.

The equipment used for TEM observations is a Philips CM 200. Low-temperature CL measurements were performed in a modified scanning electron microscope. A specific feature is the compilation of CL images, which map the local information at each sampling point. More details can be found elsewhere [6,7]. The surface morphology was investigated by optical differential interference contrast microscopy (ODICM) and AFM. These measurements were performed on a Nikon Eclipse E600 system for ODICM and on a Rastroscope 4000 for AFM. Crystallographic properties were evaluated by (0002) XRD measurements using a triple axis Siemens D5000 diffractometer system with a $\text{Cu K}\alpha_1$ ($\lambda = 1.54 \text{ \AA}$) radiation source operated at 45 kV and 20 mA.

3. Results and discussion

Fig. 2 shows the cross-sectional structure of GaN layers grown via FMG of HCl. There are four sublayers in the sample after three times of HCl interruptions. An abrupt reduction of structural defects can be found between two neighboring sublayers. Also, the defects are observed to decrease greatly from $10^{10-12} \text{ cm}^{-2}$ in the initial layer (a) above the substrate to 10^8 cm^{-2} in the upper sublayer (c) of the sample. A top view taken by CL shows that the pits at the top layer (d) are about 10^{7-8} cm^{-2} . We attribute the reduction of the defects to the “interruption” of the threading dislocation due to the interruption of the growth. During the interruption, defects such as dislocations may have time to move in the sublayers at such high temperature. Some may move to the edge of the films instead of threading into the subsequently grown sublayer. In addition, strain can relax completely for the interruption in an annealing process. Therefore, the abrupt decrease of defects can be observed and a top layer with much less defects can be obtained. A cross-sectional CL wavelength image of the FMG–GaN sample also shows that the homogeneity in the upper layers is improved [8]. This can also be explained by the interruption of threading defects and relaxation of strain. The improvements of both reduction of defects and homogeneity can also be observed in GaN layers grown via NH_3 flow modulation mode.

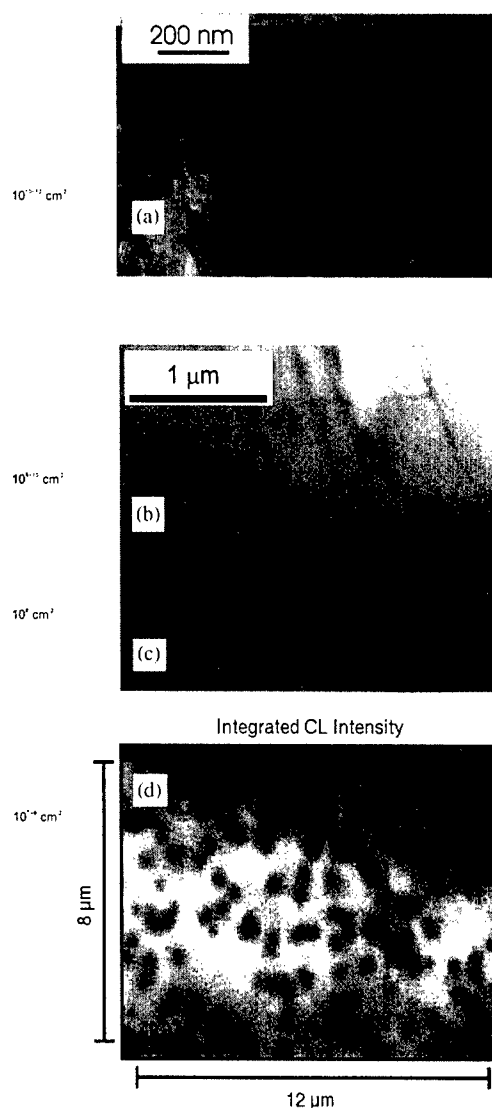


Fig. 2. TEM cross-sectional views of GaN grown via HCl flow modulation and a top view taken by CL: (a) is the initial layer, (b) the second sublayer, (c) the third sublayer layer, and (d) the top layer.

Fig. 3 shows the morphology of GaN layers taken by ODICM. There is a high density of cracks at the surface of GaN grown via HCl flow modulation while the GaN layers grown via NH_3 flow modulation exhibit almost crack-free surfaces. More microscopic views taken by AFM find that the former samples have large values of roughness ($\sim 4 \text{ nm}$) while the latter ones have smooth surfaces at atomic level ($0.5\text{--}0.9 \text{ nm}$). Considering the difference between the two FMG processes, we explain the different morphologies as follows: the interruption of HCl flow for 30 min at the growth temperature exposes the as-grown GaN to the corrosive ambient. This,

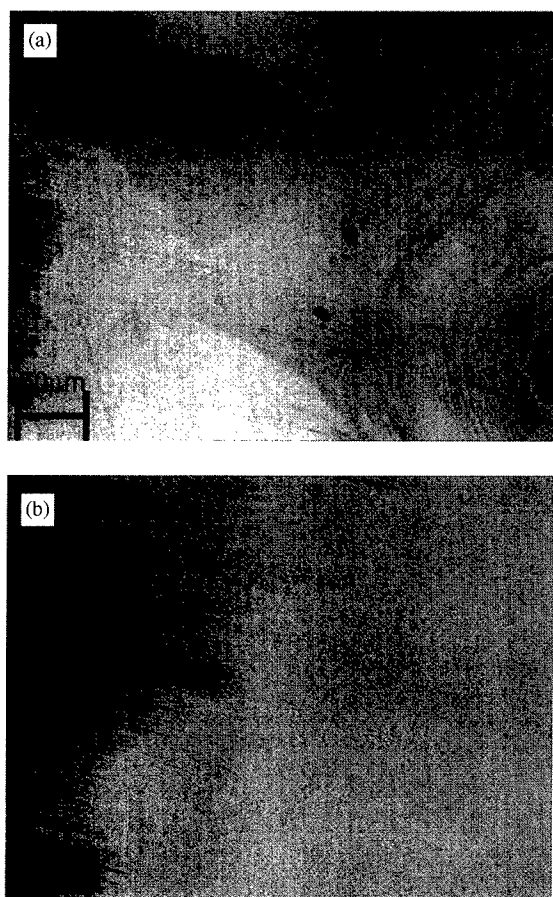


Fig. 3. The morphology of GaN grown via HCl flow modulation (a) and NH_3 flow modulation (b).

therefore, results in heavy etching of the surface of as-grown GaN so that it causes poor morphology in the subsequently overgrown layers and finally in the top layer. The smooth surface of GaN layers grown via NH_3 flow modulation is due to the Ga-rich growth conditions. The morphology of the lateral overgrown GaN is related to the local balance of III/V ratio in the gas phase and the density of Ga and N bonds [9]. Since the reduced N supply can greatly enhance the diffusion of Ga adatoms [10], the Ga diffusion on the as-grown plane will occur more easily. As a result, the lateral overgrowth will be greatly enhanced whereas the vertical growth could be suppressed, and a smooth surface is thus, obtained.

X-ray rocking curve measurements are performed. The full-width at half-maximum (FWHM) of the GaN (0002) X-ray rocking curves are 309 arcsec for GaN grown via HCl flow modulation and 335 arcsec for the sample via NH_3 flow modulation, respectively. As a reference sample, GaN grown directly on sapphire

without any flow modulation is also measured. The FWHM of its (0002) rocking curve is 423 arcsec. Since the FWHM is a measure of crystalline quality, it could be concluded that both the flow modulations cause improvements of the crystalline quality, which is in agreement with the above results taken by TEM and CL.

4. Summary

The structure of GaN layers grown by HVPE via HCl/NH_3 FMG is investigated with TEM, CL, ODICM, AFM, and XRD. It was found that defects decrease greatly from $10^{10-12} \text{ cm}^{-2}$ in the initial layer above substrate to 10^7 cm^{-2} in the top layer. Also, improved homogeneity is found in the upper layers of samples grown via both the flow modulations. We attribute the improvement of crystalline quality to the interruption of threading dislocations and the relaxation of strain. GaN layers grown via HCl flow modulation exhibit rough surfaces while the layers via NH_3 flow modulation have atomic smooth surface. The former is due to strong etching and the latter is attributed to enhanced Ga diffusion.

Acknowledgements

This work is financially supported by the “Schwerpunktsprogramm: III-V Nitrides” of the Deutsche Forschungsgemeinschaft (German Research Society). Wei Zhang is grateful to the Volkswagen Foundation and DAAD for scholarship.

References

- [1] S. Nakamura, M. Senoh, N. Iwase, S. Nagahama, *Jpn. J. Appl. Phys., Part 2* 34 (1995) L797.
- [2] S. Nakamura, M. Senoh, N. Iwase, S. Nagahama, T. Yamada, T. Mukai, *Jpn. J. Appl. Phys. Part 2* 34 (1995) L1332.
- [3] W. Zhang, S. Roesel, P. Veit, T. Riemann, H.R. Alves, D. Meister, W. Kriegseis, D.M. Hofmann, J. Christen, B.K. Meyer, *Proceedings of the International Workshop on Nitride Semiconductors, IPAP Conference Series*, Vol. 1, 2000, p. 27.
- [4] W. Zhang, S. Roesel, H.R. Alves, D. Meister, W. Kriegseis, D.M. Hofmann, B.K. Meyer, T. Riemann, P. Veit, J. Blaessing, A. Krost, J. Christen, *Appl. Phys. Lett.* 78 (2001) 772.
- [5] W. Zhang, T. Riemann, H.R. Alves, M. Heuken, D. Meister, D.M. Hofmann, J. Christen, A. Krost, B.K. Meyer, *J. Crystal Growth*, in press.
- [6] J. Christen, M. Grundmann, D. Bimberg, *J. Vac. Sci. Technol. B* 9 (1991) 2358.

- [7] F. Bertram, S. Srinivasan, F.A. Ponce, T. Riemann, J. Christen, R.J. Molnar, *Appl. Phys. Lett.* 78 (2001) 1222.
- [8] W. Zhang, T. Riemann, H.R. Alves, M. Heuken, P. Veit, D. Pfisterer, D.M. Hofmann, J. Blaesing, A. Krost, J. Christen, B.K. Meyer, *Phys. Stat. Sol.*, in press.
- [9] H. Marchand, X. Wu, J. Ibbetson, P. Fini, P. Kozodoy, S. Keller, J. Speck, S. DenBaars, U.K. Mishra, *Appl. Phys. Lett.* 73 (1998) 747.
- [10] T.K. Zywietz, J. Neugebauer, M. Cheffler, *Appl. Phys. Lett.* 73 (1998) 487.



ELSEVIER

Physica B 308–310 (2001) 93–97

PHYSICA B

www.elsevier.com/locate/physb

Characterization of $\text{Al}_x\text{Ga}_{1-x}\text{N}$ layers grown by molecular beam epitaxy

Hyonju Kim*, T.G. Andersson

Applied Semiconductor Physics, Department of Microelectronics and Nanoscience, Chalmers University of Technology and Göteborg University, S-412 96 Göteborg, Sweden

Abstract

Epitaxial $\text{Al}_x\text{Ga}_{1-x}\text{N}$ layers were grown by RF-plasma assisted molecular beam epitaxy. The Al mole fraction were derived from X-ray diffraction $\omega/2\theta$ symmetric reflections as $x = 0.11, 0.23$, and 0.29 , respectively. During the secondary ion mass sputtering analysis we found an interesting feature, expressed as *preferential sputtering in local areas*. A detailed atomic force microscope study revealed that this preferential sputtering caused a long tunnel penetrating the layer down to the sapphire substrate, and consequently gave rise to the abnormal increase of the O and Al content in the SIMS profile of the grown sample. The character of the long tunnel formed along the growth direction and the estimated density of the tunnels ($2 \sim 3 \times 10^6 \text{ cm}^{-2}$) suggest that the origin of the preferential sputtering can be the nanopipes centered at the screw dislocations. © 2001 Elsevier Science B.V. All rights reserved.

Keywords: AlGaN/GaN; MBE; SIMS

1. Introduction

Due to their direct wide band gap spanning from 3.4 to 6.2 eV, $\text{Al}_x\text{Ga}_{1-x}\text{N}$ alloys have been a growing research topic towards the applications in optoelectronic devices such as photodiodes, light emitting and laser diodes in the visible to ultraviolet wavelength region. For the realization of such devices with good performance, it is essential to grow thick $\text{Al}_x\text{Ga}_{1-x}\text{N}$ layer with a high AlN mole fraction x along with good crystalline quality. The crystalline quality of $\text{Al}_x\text{Ga}_{1-x}\text{N}$ layers has been improved significantly by growing them on high-temperature grown thick GaN layer. In addition, low temperature grown interlayers (ILs) in $\text{Al}_x\text{Ga}_{1-x}\text{N}$ layer have been found to decrease the density of threading dislocations, resulting in considerably improved crystalline quality [1–6]. However, with increased AlN mole fraction, the layer suffers the increasing in-plane tensile strain between the layer and

substrates and/or buffer layers, which increases the dislocation density and could ultimately cause cracks to spread through the layer. To overcome these problems it is indispensable to develop optimized buffer layer structures, which can mitigate the strain in $\text{Al}_x\text{Ga}_{1-x}\text{N}$ layers.

On the other hand, aluminum is known to react preferably with oxygen, resulting in high O contamination in $\text{Al}_x\text{Ga}_{1-x}\text{N}$ alloys [7,8]. The incorporation of O in $\text{Al}_x\text{Ga}_{1-x}\text{N}$ should be carefully kept in mind due to the induced deep levels (DX-center) in the band gap with increasing Al content [9]. In the previous report [10], we found that the presence of a small amount of Al (0.03 ~ 1%) in GaN is responsible for the additional O incorporation in the layer. However, the mechanism of how Al facilitates the O incorporation in the layer is still unknown and need to be studied more carefully.

In this study, we fabricated $\text{Al}_x\text{Ga}_{1-x}\text{N}$ layers with high Al content, i.e. above 10%. To obtain the concentration-depth profile of Al and O in $\text{Al}_x\text{Ga}_{1-x}\text{N}$ layers, we carried out secondary ion mass spectrometer (SIMS) analysis using Cs^+ ion as a primary beam. Since we, in an earlier investigation, found a quite high oxygen

*Corresponding author. Tel: +46-31-771-3327; fax: +46-31-772-3385.

E-mail address: hyonju@fy.chalmers.se (H. Kim).

concentration in the $\text{Al}_x\text{Ga}_{1-x}\text{N}$ layers with $x \leq 1\%$, a new set of samples was made with higher Al content and also with changed etching procedures for the substrate preparation. This new series of samples exhibited much reduced oxygen concentrations compared to the previous samples. Although it was not feasible to extend the obtained relationship between O and Al at the lower Al content ($\leq 1\%$) to higher Al mole fraction in this report, we found several interesting features during characterization of the grown structures.

2. Experiments

Epitaxial $\text{Al}_x\text{Ga}_{1-x}\text{N}$ layers were grown on (0001) sapphire substrates using RF-plasma assisted molecular beam epitaxy (MBE) technique. The substrates were ultrasonically degreased in trimethylethylene, acetone and methanol for 5 min in each step. With the purpose to remove oxides, the substrates were etched in two steps, $\text{HNO}_3:\text{H}_2\text{SO}_4$ (1:1) for 10 min, and then $\text{HCl}:\text{H}_2\text{O}_2:\text{H}_2\text{O}$ (5:3:3) for 3 min. Before growth, the substrates were outgassed at 700°C for 40 min in the growth chamber. Then the temperature was lowered to 600°C for a Ga-cleaning process to remove surface contaminants such as O- and C-compounds [11]. The process was repeated three times by evaporating the deposited Ga metals at elevated temperatures ($\sim 750^\circ\text{C}$). Subsequently, nitridation was carried out at 700°C for 40 min, and followed by the growth of thin ($\sim 10\text{ nm}$) AlN buffer layer at 650°C . To improve the crystalline quality, a thick GaN layer ($0.6\text{ }\mu\text{m}$) was grown at 760°C before the growth of $\text{Al}_x\text{Ga}_{1-x}\text{N}$ layer. Finally $0.6\text{ }\mu\text{m}$ thick $\text{Al}_x\text{Ga}_{1-x}\text{N}$ layers with different Al mole fraction were grown at the substrate temperature of 760°C . The RF-plasma power and N_2 gas flow rate were kept at 500 W and 2.3 sccm, respectively, during the growth of GaN and $\text{Al}_x\text{Ga}_{1-x}\text{N}$ layers.

To investigate the crystalline quality and derive Al mole fraction, X-ray diffraction (XRD) measurements were performed in a multi-crystal high resolution Philips Extended X-pert Material Research Diffractometer. To improve the resolution we used an analyzer crystal for all the measurements presented in this study. An atomic force microscopy (AFM) (Dimension 3000, Digital instruments) was also used for surface characterization of the grown samples.

In order to determine the distribution and concentration of oxygen impurities and aluminum in the layer, a Cameca IMS-6F SIMS instrument operating at a pressure of 1×10^{-9} mbar was used. In order to analyze the O concentration, we selected a Cs^+ primary beam, which was focused to a $25\text{ }\mu\text{m}$ diameter with an impact energy of 14.5 keV and a current of 80 nA. The primary beam was rastered over an area of $250 \times 250\text{ }\mu\text{m}^2$ and the secondary negative ions (O^- , Al^- , GaN^- , etc.) were

collected from the central area (approximately $50\text{ }\mu\text{m}$ in diameter) to avoid the effect from crater edges. The details for a standard sample of O implantation used for quantification were described elsewhere [10].

3. Results and discussion

Fig. 1 displays the XRD $\omega/2\theta$ symmetric (00.2) reflections for the three heterostructures of $\text{Al}_x\text{Ga}_{1-x}\text{N}/\text{GaN}$ grown at different Al-source temperatures while keeping the same Ga/N flux ratio. Using an analyzer crystal instead of a single slit, we could observe a well-separated $\text{Al}_x\text{Ga}_{1-x}\text{N}$ alloy peak from that of GaN as represented in the figure. In the assumption that the $0.6\text{ }\mu\text{m}$ thick $\text{Al}_x\text{Ga}_{1-x}\text{N}$ layers grown on GaN are fully relaxed and that the Vegard's law is valid, the Al mole fraction was derived from the symmetric reflections as 11%, 23%, and 29%, respectively. It is clear that the diffraction peak from alloy is shifted towards higher angle with increasing Al content, denoting a decrease in lattice constant c . It should be noted that the Al mole fraction of the sample with the highest concentration, #924, was determined by an average from the two alloy peaks as can be clearly seen in the Fig. 1.

A possible origin for the splitting of the alloy peak (#924) can be explained as a phase separation into two different compositions of $\text{Al}_x\text{Ga}_{1-x}\text{N}$ layer, as also observed by Görgens et al. for InGaN alloys [12]. They found two wurtzite phases of different indium composition in the layer. One was a pseudomorphically grown part with In mole fraction of 17%, the other a fully relaxed part with a higher In concentration of 28%. However, they could only observe the separation in asymmetric reflections because both phases had the same lattice constant c within the given resolution. In

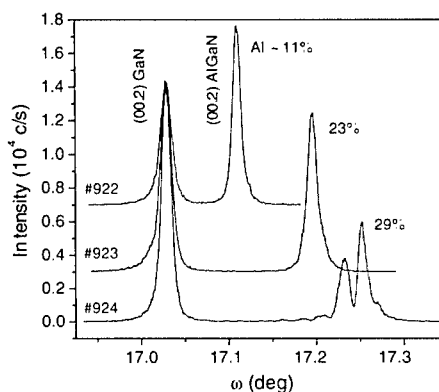


Fig. 1. HRXRD $\omega/2\theta$ symmetric (00.2) reflections for $\text{Al}_x\text{Ga}_{1-x}\text{N}/\text{GaN}$ heterolayers with different Al mole fraction grown on (0001) sapphire substrates. The XRD patterns of #922 and 923 were shifted along the y-axis for clarity.

our case, although we observed a clear separation in symmetric reflection, it is not possible to clarify the strain state, i.e., whether the layer is fully, or partially relaxed, or if it is pseudomorphically grown, etc. In order to fully understand these features, it will be necessary to proceed the investigation by performing the reciprocal space mapping for the asymmetric reflections.

The oxygen impurity concentrations in the $\text{Al}_x\text{Ga}_{1-x}\text{N}$ layers were determined from SIMS analysis and compared with the previous results obtained for lower Al concentrations ($x \leq 1\%$) as represented in Fig. 2. For the low Al-content we determined the empirical relation between the Al and O impurity concentrations as $C_{\text{O}}^i/C_{\text{O}}^b = 3.8 \times (C_{\text{Al}}/C_{\text{Al}}^i)^{0.27}$. In the formula, C_{O}^i (cm^{-3}) and C_{Al} (%) represent total O concentration and Al mole fraction, respectively, and the constants were given as $C_{\text{O}}^b \sim 10^{19} \text{ cm}^{-3}$ and $C_{\text{Al}}^i \sim 1\%$. As described in the previous report [10], we expect this empirical relationship can be used for the future work to elucidate the role of Al in the additional incorporation of O in the layer. On the other hand, the new set of samples with higher Al content exhibited much reduced oxygen concentrations compared to the previous samples. This reduced O level could arise from the changed etching procedures used for the substrate preparation. However, a further investigation will be needed before we discuss the effect of this chemical etching process here.

During the SIMS analysis we found an interesting feature, which we express as *preferential sputtering in local areas*. Fig. 3 shows a typical SIMS depth profile of the $\text{Al}_x\text{Ga}_{1-x}\text{N}/\text{GaN}$ heterostructure of the sample #923. As seen in the figure, O and Al concentrations exhibited abnormal increase from the middle of the $\text{Al}_x\text{Ga}_{1-x}\text{N}$ layer for oxygen and from the interface of

$\text{Al}_x\text{Ga}_{1-x}\text{N}/\text{GaN}$ for aluminum, respectively. A similar feature was observed for all three samples investigated in this work. After the examination of the surface inside the crater using optical microscopy and AFM, the origin of the sudden increase of the signal was found to be due to a preferential sputtering in local areas, which gave rise to a long ‘tunnel’ reaching the sapphire (Al_2O_3) substrate already in the middle of the SIMS sputtering process. Thus, these ‘tunnels’ are considered to be responsible for the observed abnormal increase of O and Al levels in the profile as given in Fig. 3. It also should be noted that due to the high Al content in $\text{Al}_x\text{Ga}_{1-x}\text{N}$ layer, the effect on Al concentration from the holes penetrating the layer are invisible in the $\text{Al}_x\text{Ga}_{1-x}\text{N}$ layer, while the O level already started to increase. An AFM image for one (#924) of the samples is given in Fig. 4, which clearly demonstrates holes of micron size threading the layer. The image was scanned on the surface where the ion sputtering was stopped in the middle of the GaN layer. A more-detailed study shows that the density of holes was slightly higher at the substrate surface ($3 \times 10^6 \text{ cm}^{-2}$) compared to the middle of $\text{Al}_x\text{Ga}_{1-x}\text{N}$ layer ($2.1 \times 10^6 \text{ cm}^{-2}$). The hole-size was found to grow gradually as the ion sputtering proceeded towards the substrate. The diameter of the holes was estimated to be in the range $0.5 \sim 0.8 \mu\text{m}$ in the middle of $\text{Al}_x\text{Ga}_{1-x}\text{N}$ layer, but with a larger size variation at the near substrate interface ranging $0.5 \sim 3 \mu\text{m}$.

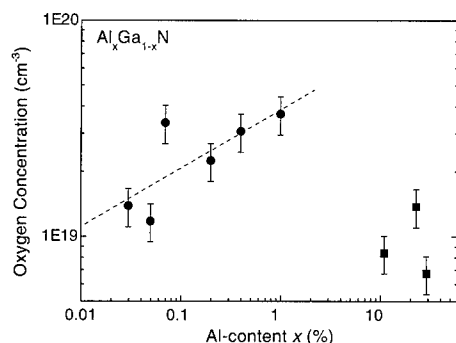


Fig. 2. Oxygen impurity concentration as a function of Al mole fraction in a logarithmic scale, determined from SIMS analysis. Samples with low Al content ($\leq 1\%$) are represented with closed circles, and high Al content ($\geq 10\%$) with squares. For details of the fitting (dashed line) at low Al content the reader is referred to Ref. [10].

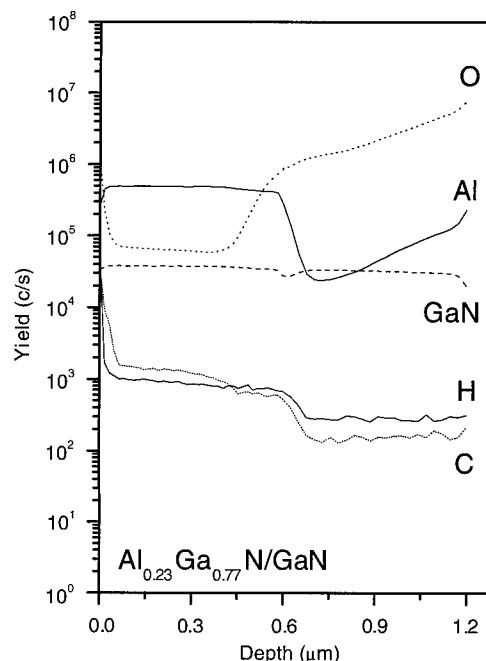


Fig. 3. Typical SIMS depth profile for the $\text{Al}_x\text{Ga}_{1-x}\text{N}/\text{GaN}$ (0.6/0.6 μm) grown by the MBE technique.

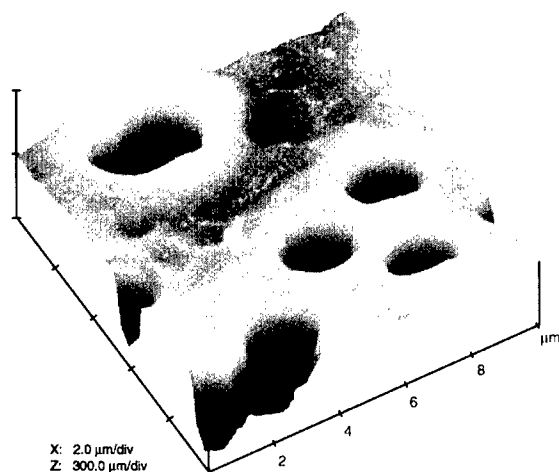


Fig. 4. AFM images of the surface after the SIMS sputtering was stopped in the middle of the GaN layer (#924). The image area is $10 \times 10 \mu\text{m}^2$.

The GaN and related alloys grown on sapphire substrates typically exhibit dislocation densities of $10^9 \sim 10^{10} \text{cm}^{-2}$, due to the large difference in lattice parameters and thermal expansion coefficient. While most of these dislocations are of pure edge type, some groups observed another type of defect, referred to as *nanopipes* or *micropipes* found at the cores of screw dislocations. Qian et al. [13–15] found tunnel-like defects, termed as open-core screw dislocations, aligned along the growth direction (*c*-axis) of the crystal and penetrating the entire GaN epilayer [14]. Their microscopic observations revealed the density of such nanopipes to $10^5 \sim 10^7 \text{cm}^{-2}$. If the origin of the preferential sputtering occurred during the SIMS analysis is associated with these nanopipes centered at the screw dislocations, the estimated hole-density ($\sim 10^6 \text{cm}^{-2}$) in this study is in a good agreement with their observations. In addition, the character of open-holes of nanopipes renders larger area exposed to the primary ion beams during the SIMS analysis. Therefore, the holes can be etched faster than other areas which explains the micron size of holes observed in our samples.

4. Conclusions

We have grown $\text{Al}_x\text{Ga}_{1-x}\text{N}/\text{GaN}$ heterostructures on sapphire (0001) substrates using the RF-plasma assisted MBE technique. The Al mole fraction was determined from HRXRD $\omega/2\theta$ symmetric reflections under the assumption that the alloy layer was fully relaxed and that the Vegard's law is valid. We found a splitting in the diffraction peak from $\text{Al}_x\text{Ga}_{1-x}\text{N}$ layer

with the highest Al content ($x = 0.29$), which can be ascribed to the phase separation into two different compositions, mostly with different Al contents.

The SIMS analysis revealed that after the change of the chemical etching process for the substrate preparation the oxygen impurity level was reduced compared to the previous samples. However a detailed investigation has yet to be performed to clarify the effect of the changed chemical etching process.

We found an interesting feature, expressed as 'preferential sputtering in local areas', during the SIMS analysis. The AFM investigation along with the optical microscope revealed that this preferential sputtering caused a long 'tunnel' (from submicron to several micron in diameter) penetrating the layer down to the substrate, which consequently gave rise to the abnormal increase of O and Al content in SIMS profile for the grown layers. The character of the long tunnel formed along the growth direction and the observed similar density of the tunnels ($2 \sim 3 \times 10^6 \text{cm}^{-2}$) suggest that the origin of the preferential sputtering or of the tunnels can be the nanopipes centered at the screw dislocations.

Acknowledgements

The authors wish to acknowledge the technical support regarding SIMS measurements and useful comments from Dr. U. Södervall.

References

- [1] C. Pernot, A. Hirano, M. Iwaya, T. Detchprohm, H. Amano, I. Akasaki, *Jpn. J. Appl. Phys. Part 2* (38) (1999) L487.
- [2] T. Kashima, R. Nakamura, M. Iwaya, H. Katoh, S. Yamaguchi, H. Amano, I. Akasaki, *Jpn. J. Appl. Phys. Part 2* (38) (1999) L151.
- [3] S.J. Hearne, J. Han, S.R. Lee, J.A. Floro, D.M. Follstaedt, E. Chason, I.S.T. Tsong, *Appl. Phys. Lett.* 76 (2000) 1534.
- [4] J. Han, K.E. Waldrup, S.R. Lee, J.J. Figiel, S.J. Hearne, G.A. Petersen, S.M. Myers, *Appl. Phys. Lett.* 78 (2001) 67.
- [5] H.K. Cho, J.Y. Lee, S.C. Choi, G.M. Yang, *J. Crystal Growth* 222 (2001) 104.
- [6] S. Kamiyama, M. Iwaya, N. Hayashi, T. Takeuchi, H. Amano, I. Akasaki, S. Watanabe, Y. Kaneko, N. Yamada, *J. Crystal Growth* 223 (2001) 83.
- [7] R.A. Youngman, J.H. Harris, *J. Am. Ceram. Soc.* 73 (1990) 3238.
- [8] C.R. Elsass, T. Mates, B. Heying, C. Poblentz, P. Fini, P.M. Petroff, S.P. DenBaars, J.S. Speck, *Appl. Phys. Lett.* 77 (2000) 3167.
- [9] M.D. McCluskey, N.M. Johnson, C.G. Van de Walle, D.P. Bour, M. Kneissl, W. Walukiewicz, *Phys. Rev. Lett.* 80 (1998) 4008.

- [10] Hyonju Kim, F. Falth, T.G. Andersson, JEM, 2001, in press.
- [11] T.G.G. Maffei, S.A. Clark, P.R. Dunstan, S.P. Wilks, D.A. Evans, F. Peiro, H. Riechert, P.J. Parbrook, Phys. Stat. Sol 176 (1999) 751.
- [12] L. Gorgens, O. Ambacher, M. Stutzmann, C. Miskys, F. Scholz, J. Off, Appl. Phys. Lett. 76 (2000) 577.
- [13] W. Qian, M. Skowronski, K. Doverspike, L.B. Rowland, D.K. Gaskill, J. Crystal Growth 151 (1995) 396.
- [14] W. Qian, G.S. Rohrer, M. Skowronski, K. Doverspike, L.B. Rowland, D.K. Gaskill, Appl. Phys. Lett. 67 (1995) 2284.
- [15] C. Kruse, S. Einfeldt, T. Bottcher, D. Hommel, D. Rudloff, J. Christen, Appl. Phys. Lett. 78 (2001) 3827.



ELSEVIER

Physica B 308–310 (2001) 98–101

PHYSICA B

www.elsevier.com/locate/physb

AFM study of lattice matched and strained InGaAsN layers on GaAs

Yeonjoon Park*, Michael J. Cich, Rian Zhao, Petra Specht,
Henning Feick, Eicke R. Weber

Department of Materials Science & Engineering, U.C. Berkeley, Berkeley, CA 94720, USA

Abstract

We studied strained & lattice matched InGaAsN, InGaAs, and GaAsN layers, grown on GaAs substrate with gas source molecular beam epitaxy. Nitrogen concentration and lattice-matched condition have been established from Vegard's law with X-ray diffraction. Atomic force microscope measurement, at 22-monolayer thickness, shows different growth mechanism for each composition. Especially, a mesh-like surface morphology of lattice matched InGaAsN has been revealed in this study. © 2001 Published by Elsevier Science B.V.

Keywords: InGaAsN; GS-MBE; AFM; Laser diode

1. Introduction

Since the first proposal by Kondow et al., [1], GaAsN and InGaAsN layers on GaAs substrate have attracted a lot of research interest due to its application for the long wave laser diode with an excellent high temperature performance. Shan et al. [2], explained the reduction of band-gap of GaAsN alloys with the strong perturbation of N atoms to the conduction band, which causes the splitting of the conduction band into two sub-bands. Laser diode operation at 1.3 μm wavelength for the optical fiber communication, has been demonstrated by several groups, including Kondow et al. [1,3], Steinle et al. [4], Livshits et al. [5] and Mars et al. [6]. Especially, Kitatani, Kondow et al. [7] fabricated 1.3 μm GaInNAs/GaAs single quantum well laser diode with a high characteristic temperature over 200 K. There have been only a few studies about the growth mode and the surface morphology of (In)GaAsN alloys. R.M. Feenstra et al. studied the local electric properties of GaAsN alloy with scanning tunneling microscope (STM) on the planar surface [8] and in cross-section [9]. Auvray et al. studied the growth mode of GaAsN on a 2° miscut

GaAs surface with different nitrogen concentration, using atomic force microscope (AFM) [10]. They found that the growth mode of GaAsN layer on vicinal GaAs substrate changes from a bunched step/terrace structure to indistinct 2D-nucleation structure when increasing the N content.

In our study, we tried to compare the growth mode differences of important layers, GaAs_{0.98}N_{0.02}, In_{0.4}Ga_{0.6}As, and In_{0.06}Ga_{0.94}As_{0.98}N_{0.02} layers on GaAs, which are used for 1.3 μm laser diode applications, with AFM and high resolution X-ray diffraction (HRXRD).

2. Experimental procedure

Gas source molecular beam epitaxy (GS-MBE) with DC nitrogen plasma source has been used to grow nitrogen-containing layers [11,12]. Since the kinetic energy of nitrogen plasma of our DC plasma source is determined by the gas-flow itself, it causes very low plasma damage to GaAs surface. A solid arsenic source (As₄) was used to give a beam equivalent pressure (BEP) of 2×10^{-5} Torr. The Ga vs. As BEP ratio was set to 1:20. Si doped n-GaAs substrates were used and the temperature of the substrates were monitored with

*Corresponding author.

E-mail address: ypark@argon.berkeley.edu (Y. Park).

diffuse reflective spectroscopy (DRS), whose long-term measurement error is $\pm 1^\circ$. All of the GaAs substrates were outgassed at 200°C and oxide removal was performed at 570°C in the MBE chamber. After the oxide removal, a rather spotty RHEED pattern was observed. A GaAs buffer layer of 200 nm-thickness was grown to achieve a higher-quality starting plane with a very sharp, clear, streaky (2×4) RHEED pattern. After the growth of the GaAs buffer layer, the substrate was cooled down to 500°C to incorporate indium, since the InAs desorption temperature is around 515°C . After all the buffer layers were prepared with the same condition, 22 mono-layers of a bare GaAs, $\text{In}_{0.4}\text{Ga}_{0.6}\text{As}$, $\text{GaAs}_{0.98}\text{N}_{0.02}$, or $\text{In}_{0.06}\text{Ga}_{0.94}\text{As}_{0.98}\text{N}_{0.02}$ were grown with specific control parameters, respectively. The growth rate of $0.75 \mu\text{m/h}$ was used. Capping layers were not grown in order to reveal the top surface for AFM studies. Direct after the growth of the thin layers, the substrate was cooled down for 10 min. in As over-pressure and then transferred to the atmosphere for AFM measurement. Park Scientific Instruments AutoProbe VP system was used for AFM studies. Since AFM measurements were directly performed within 10 min. after the growth, the effect of gallium-oxide formation was minimized. As a reference, the bare GaAs surface did not show any effect from the oxide in AFM images. $10 \mu\text{m} \times 10 \mu\text{m}$, $4 \mu\text{m} \times 4 \mu\text{m}$, and $2 \mu\text{m} \times 2 \mu\text{m}$ scan area

were used for AFM studies. We will write $10 \mu\text{m} \times 10 \mu\text{m}$ area scan as $10 \mu\text{m}$ scan for convenience.

To incorporate the right amount of indium and nitrogen, $0.5 \mu\text{m}$ thick layers were grown on GaAs to fabricate fully relaxed layers for symmetric (004) X-ray diffraction scan. Nitrogen concentration and lattice-matched condition were obtained from these preliminary experiments (Fig. 1(a)).

The symmetric (004) scan, and asymmetric (224) and (113) normal scans did not show any peak from the thin 22-monolayer-thick epi-layer. However, (113) Ω^+ , (224) Ω^+ normal scans with the detector at a glancing angle of 1.6° and 6.6° from the surface, have very strong sensitivities for the surface layers and they show clear epi-layer peaks (Fig. 1(b) and (c)).

3. Results and discussion

Fig. 1(a) shows the (004) symmetric diffraction peak of a $0.5 \mu\text{m}$ thick InGaAsN layer with 1.5% nitrogen concentration on a GaAs substrate. 1.25 sccm of nitrogen flow and 20 mA of plasma current were applied and the indium source temperature was controlled between 715°C and 735°C . The FWHM of the substrate peak was 0.015° and that of lattice matched InGaAsN was 0.025° . The layer with the least lattice mismatch of

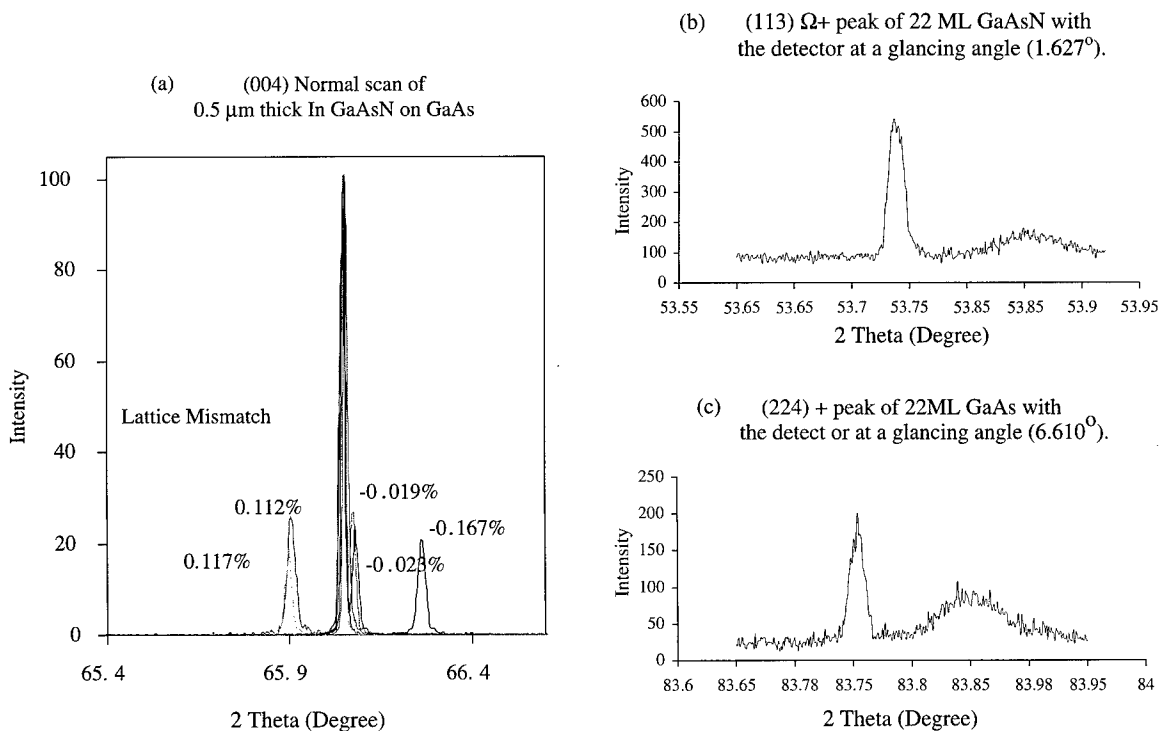


Fig. 1. High resolution X-ray diffraction scan.

–0.019% has a critical thickness far above 1 μm according to the Matthews–Blakeslee model. After lattice matched conditions were established with the different nitrogen concentration, these conditions were applied to the growth of the thin layer of 22-monolayer thickness. Assuming the coherently grown layer model, in-plane and out-of-plane lattice constants were obtained from (1 1 3) Ω^+ , (2 2 4) Ω^+ scans (Fig. 1(b) and (c)). An iterative method was used to include plane tilt angle $\Delta\tau$. Nitrogen concentration was obtained from Vegard's law.

AFM measurements of 10, 4, and 2 μm scans, show various growth modes (Fig. 2). AFM images of bare GaAs show a couple of bunched steps and its root-mean-square (RMS) roughness of 4 μm scan was 5.3 \AA . The measured step height was less than 15 \AA . The contrast is maximized to reveal detailed structures. Oxidation of GaAs is not observed. The white area with higher height at the left and right edges of the 10 μm image is the effect of the AFM tube scanner curvature correction. This effect is not observed in other images of smaller scan area.

$\text{In}_{0.4}\text{Ga}_{0.6}\text{As}$ shows the self-organized circular island growth mode, which is typically used as quantum dots.

The RMS roughness of the 4 μm scan is 80 \AA . The average island size is 75 nm and the average island height is 130 \AA . However, some of the islands were higher than 200 \AA , exceeding the intended layer thickness. The general island shape is like an isolated circular hemisphere.

GaAsN with 2% of nitrogen shows μm -size strained hills and small-island-growth on top of the hills (Fig. 2, 10 and 4 μm images). We believe the modulated hill structure corresponds to the bunched step-terrace structures on 2° miscut GaAs substrate, which is observed by Auvray et al. [10]. The size of the modulated hill structure is of the order of a few μm in lateral direction and 50 \AA in height. The RMS roughness of the 4 μm scan was 21 \AA . The existence of small islands with an average height of 20 \AA on the hills indicates that the growth mode may change from the layer-by-layer to the island growth. The black holes in the 10 μm AFM image were confirmed to be AFM tip indents formed in the initial approach. GaAsN is under tensile stress on a GaAs substrate and becomes softer than other layers. We confirmed that the AFM tip in the initial approach could generate crack-like indents on a GaAsN layer in different areas.

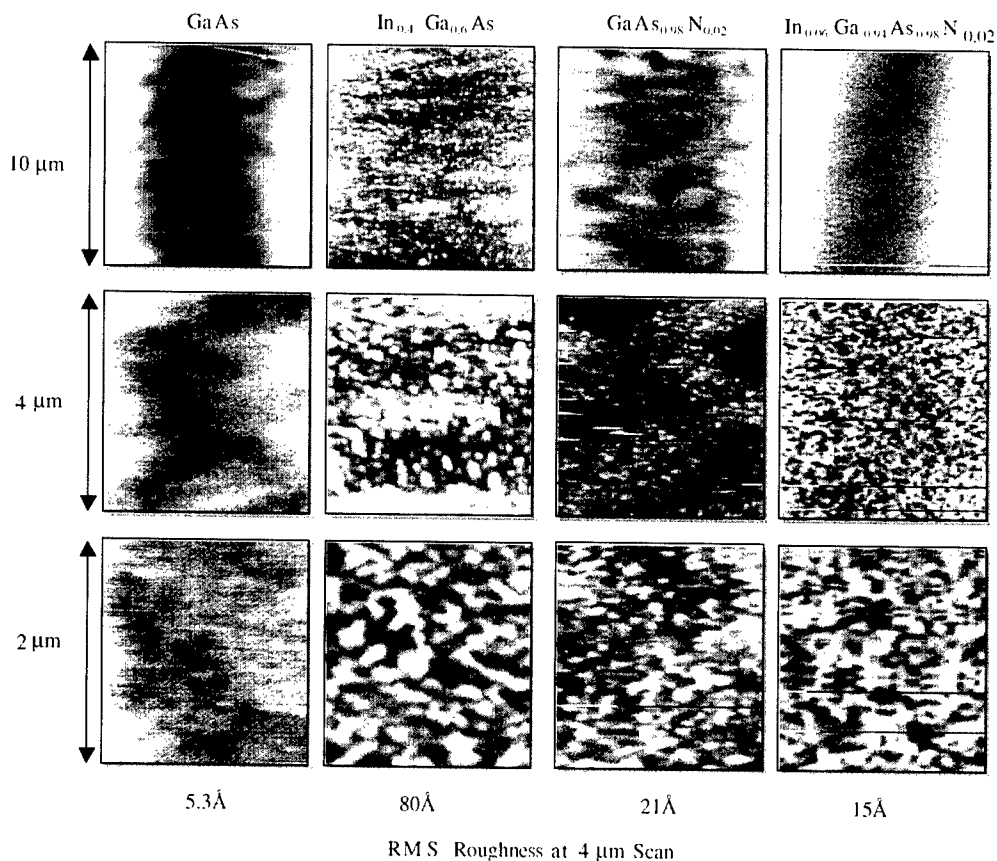


Fig. 2. AFM images of epi-layers (22 monolayer thickness) on GaAs.

The most interesting AFM data were obtained from the lattice matched $\text{In}_{0.06}\text{Ga}_{0.94}\text{As}_{0.98}\text{N}_{0.02}$ layer grown at $0.75\text{ }\mu\text{m/h}$ growth rate. 10 and $4\text{ }\mu\text{m}$ scans show flat mesh-like networked structures. The RMS roughness of $4\text{ }\mu\text{m}$ scan is $15\text{ }\text{\AA}$. This small number indicates the lattice-matched surface is flatter than other lattice mismatched layers even though there are a lot of meshed structures inside. However the growth mode is not a layer-by-layer growth. The measured average height of the mesh was $25\text{ }\text{\AA}$. We propose the following possibilities. (1) Local islands are formed first and these islands are connected together to create meshed structures. Since the surface adatom diffusion length determines the morphology, this indicates that the diffusion length of InGaAsN is smaller than that of GaAs or GaAsN. (2) Composition variation occurred during the growth and/or spinodal-decomposition-like composition-modulation-mechanism generated the meshed structure during the growth and cooling down process lasting 10 min. If this is a result of voluntary evolution into a composition modulation, such a meshed structure could be understood by a total energy argument. By adopting a large indium atom in the tensile convexed hill top region of the meshed structure and smaller nitrogen atom in the compressive concave bottom of the valley, the total strain energy of the epi-layer could be reduced. In this case, a faster growth rate and the reduction of the growth interruption should remove the meshed structure and bring back the layer-by-layer growth.

On the other hand, such a meshed structure can be utilized to confine carriers into small regions like quantum dots, so that we may raise the characteristic temperature of laser diodes even higher for a better performance at the high temperature. As a reference, Mars et al. [6] found the faster growth rate above $2\text{ }\mu\text{m/h}$ gives better crystal quality of thick InGaAsN layers.

In summary, we studied the growth modes of thin epi-layers of GaAs, $\text{In}_{0.4}\text{Ga}_{0.6}\text{As}$, $\text{GaAs}_{0.98}\text{N}_{0.02}$, and $\text{In}_{0.06}\text{Ga}_{0.94}\text{As}_{0.98}\text{N}_{0.02}$, which were grown on GaAs

substrates. Layer by layer growth of GaAs, circular island growth of InGaAs, modulated hill and small island formation of GaAsN, and the meshed network formation of InGaAsN were observed with AFM.

Acknowledgements

This research was performed in the Integrated Material Laboratory (<http://iml.berkeley.edu>) at U.C. Berkeley. The authors appreciate Robert Prohaska and James Parrish for the technical assistance.

This research was partly supported by AFOSR program under contract number F49620-01-1-0151.

References

- [1] M. Kondow, et al., *Jpn. J. Appl. Phys. Part 1*, 2B 35 (1996) 1273.
- [2] W. Shan, W. Walukiewicz, J. Ager III, E.E. Haller, et al., *Phys. Rev. Lett.* 82 (19) 1221.
- [3] M. Knowlton, T. Kitatani, K. Nakahara, T. Tanaka, *Jpn. J. Appl. Phys.* 38 (1999) L1355.
- [4] G. Steinle, F. Mederer, M. Kicherer, et al., *Electron. Lett.* 37 (10) (2001) 632.
- [5] D.A. Livshits, A.Y. Egorov, H. Riechert, *Electron. Lett.* 36 (16) (2000) 381.
- [6] D.E. Mars, S. Subramanya, J. Kruger, E.R. Weber, et al., *J. Vac. Sci. Technol. B* 17 (3) (1999) 272.
- [7] T. Kitatani, K. Nakahara, M. Kondow, et al., *Jpn. J. Appl. Phys.* 39 (2000) L86.
- [8] R.S. Goldman, R.M. Feenstra, et al., *Appl. Phys. Lett.* 69 (24) (1996) 3698.
- [9] H.A. McKay, R.M. Feenstra, et al., *Appl. Phys. Lett.* 78 (1) (2001) 82.
- [10] L. Auvray, et al., *J. Crystal Growth* 221 (2000) 475.
- [11] A. Anders, M. Kühn, *Rev. Sci. Instr.* 69 (3) (1998) 1340.
- [12] A.E. Zhukov, R. Zhao, P. Specht, E.R. Weber, et al., *Semicond. Sci. Technol.* 16 (5) (2001) 413.



ELSEVIER

Physica B 308–310 (2001) 102–105

PHYSICA B

www.elsevier.com/locate/physb

In-plane and in-depth nonuniformities in defect distribution in GaN and InGaN epilayers

M. Godlewski^{a,*}, E.M. Goldys^b, G. Pozina^c, B. Monemar^c, K. Pakula^d,
J.M. Baranowski^d, P. Prystawko^e, M. Leszczynski^c

^a*Institute of Physics, Polish Academy of Sciences, Al. Lotnikow 32/46, 02-668 Warsaw, Poland*

^b*Semiconductor Science and Technology Laboratory, Macquarie University, Sydney, Australia*

^c*Department of Physics & Measurement Technology, Linköping University, Linköping, Sweden*

^d*Institute of Experimental Physics, Warsaw University, Warsaw, Poland*

^e*High Pressure Research Center (Unipress), Polish Academy of Sciences, Warsaw, Poland*

Abstract

The in-plane and in-depth characteristics of the GaN and InGaN epilayers grown by the metalorganic chemical vapour deposition (MOCVD) on three different substrates (sapphire, SiC and bulk GaN) are evaluated. Relatively large intensity fluctuations of “edge” GaN and InGaN emissions are observed and are related to the details of the micro-structure of the GaN and InGaN films studied. The experiments indicate a nonuniform defect distribution in all types of the MOCVD films studied. In particular, the decoration of structural defects with impurities, an increased defect accumulation at the interfaces and a surprisingly small influence of the micro-structure on the in-plane homogeneity of the yellow band cathodoluminescence emission are observed. © 2001 Elsevier Science B.V. All rights reserved.

PACS: 61.72.F; 78.60.H; 73.20.H

Keywords: GaN; InGaN; Defects; Defect distribution

1. Introduction

The range of GaN-based optoelectronic devices emitting amber–violet light was commercialised. Despite wide range applications, their operation is not understood yet. Relatively high efficiency of light emission is observed for heavily defected structures, with dislocation densities typically in the range of 10^8 cm^{-2} . A surprisingly low efficiency of nonradiative recombination at the dislocations is related to the strong localisation effects present in the InGaN-based light emitting devices [1]. Strong localisation effects are commonly related to either details of the micro-structure of the GaN, InGaN and AlGaIn layers [2], or to the In fraction fluctuations in the InGaN [1]. Our recent

experimental results indicate that strong compensation effects are also present in the GaN samples, which results in the appearance of strong local electric fields and thus can also contribute to the localisation effects observed in the samples studied [3,4]. The role of the latter effect is evaluated in the present study.

2. Experimental

The (0001)-oriented n-type GaN films were grown by metalorganic chemical vapour deposition (MOCVD) on three different substrates—sapphire, SiC and bulk GaN. The latter layers are called the homoepitaxial films. Two InGaIn (3% of In)-on-GaN on sapphire samples, also grown by the MOCVD, were studied for comparison.

The photoluminescence (PL) experiments were performed at 2 K. The 351 nm UV line of an Ar⁺ laser was used for the PL excitation. The micro-PL spectra were

*Corresponding author. Tel.: +48-22-843-6861; fax: +48-22-843-0926.

E-mail address: godlew@ipfan.edu.pl (M. Godlewski).

measured in a Renishaw micro-Raman system with a resolution of 1.6 meV using a polarised 325 nm excitation at an excitation power density of 120 kW/cm². The PL emission spectra at single locations and emission maps, that is spatial distributions of emission from the sample, were taken at a spatial resolution typically of the order of $2 \times 2 \mu\text{m}$ and were measured at room temperature.

The cathodoluminescence (CL) and scanning electron microscopy (SEM) measurements were performed at 4 K on LEO 1550 computer controlled field emission scanning electron microscope, equipped with monoCL2 set-up for the CL studies of Oxford Instruments and helium temperature gas flow stage. In addition to a conventional CL, spot-mode CL, scanning CL and depth-profiling CL measurements were also performed. The latter experiment was carried out to estimate in-depth characteristics of the MOCVD structures. In this experiment, we varied an accelerating voltage, thus varying the penetration range of primary electrons [5].

3. Results and discussion

Four PL emission bands were observed in all the GaN samples studied; showing very different relative intensities and also different spectral widths. These are the excitonic edge PL, a structured shallow donor–acceptor pair (DAP) PL at about 3.2 eV, the blue band DAP PL at about 3.0 eV and the yellow DAP PL at 2.2–2.3 eV. The origin of these PL bands is described elsewhere [6] and will not be discussed here. Only for the homoepitaxial films, a well-resolved edge PL was observed. This PL was dominated by the recombination of excitons bound at neutral donors (DBE PL) at 3.472 eV and free excitonic (FE_A) PL at 3.478 eV. With increasing temperature, additional FE PL at 3.484 eV (FE_B PL) was also resolved.

We performed detailed micro-PL, CL, scanning CL and depth-profiling CL investigations to evaluate in-plane and in-depth characteristics of the PL emissions. In Fig. 1, we show depth-profiling CL spectra observed for the GaN films grown on sapphire. Similar results were obtained for all the samples studied. The excitonic edge PL emission is not observed from heavily defected interface-close regions of the structures and also is fairly weak when excited from surface-close regions of the films. Three defect-related PL emission bands also show depth-dependent properties. Whereas, the yellow DAP PL and the shallow DAP PL are the strongest when excited from interface-close regions of the films, the blue DAP PL is the strongest from the surface-close regions of the samples.

In our previous scanning CL investigations, we have shown the direct link between the micro-structures of the GaN epilayers and the in-plane fluctuations of the edge

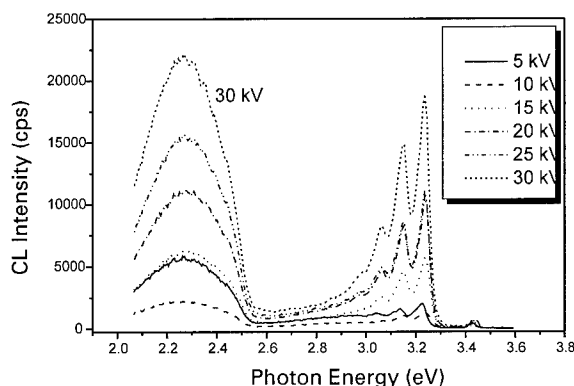


Fig. 1. The in-depth variations of the CL in the GaN/sapphire MOCVD-grown structure, measured at a temperature of 4 K at different accelerating voltages.

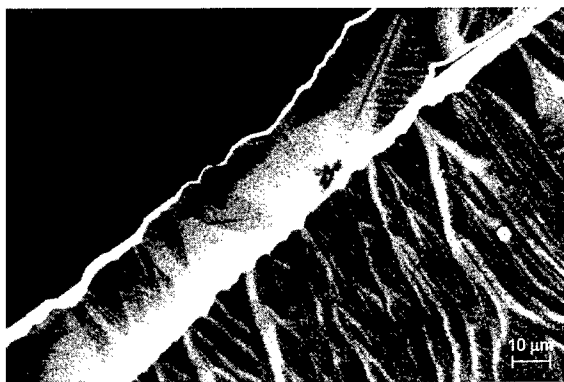


Fig. 2. The in-plane variations of the intensity of the edge CL emission in the GaN/GaN sample, measured at 4 K, 10 kV accelerating voltage and at 2000 \times magnification.

PL intensity [7]. From the SEM investigations, we could correlate the observed changes of the intensity of the excitonic edge PL with a granular micro-structure of the MOCVD epilayers. A very improved micro-structure, observed for the homoepitaxial GaN layers, results in different in-plane variation of the PL. Large areas of atomically flat surfaces are observed in the SEM study. These areas are interrupted by growth steps, often of the monolayer size. We found relatively few micro-defects, such as dislocations or hexagonal pits, commonly observed in other MOCVD-grown samples [8,9]. Fig. 2 shows a decoration of these steps with donor impurities. We observed a very enhanced DBE PL from the growth step regions of the layers, shown as bright regions in Fig. 2. A relatively weak FE PL is observed from these areas, which indicates that the FE excitons can diffuse to the growth step regions and be trapped there.

Fig. 3 shows another type of defect-related inhomogeneity, which we observed in homoepitaxial films. A very enhanced DBE excitonic PL is observed from the region of a large hexagonal pit. Also, the shallow DAP

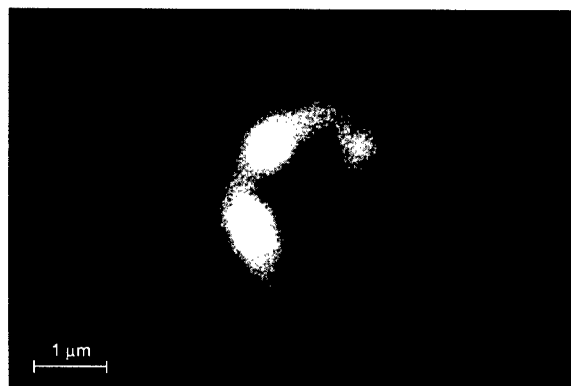


Fig. 3. The in-plane fluctuations of the DBE PL intensity in the GaN/GaN sample, measured at 4 K, 10 kV accelerating voltage, at $40\,000\times$ magnification and from the region close to a large hexagonal pit.

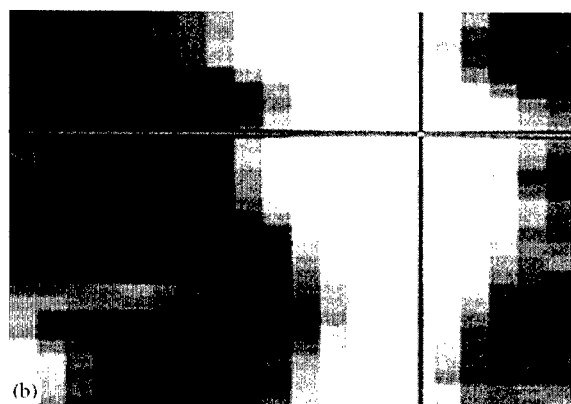
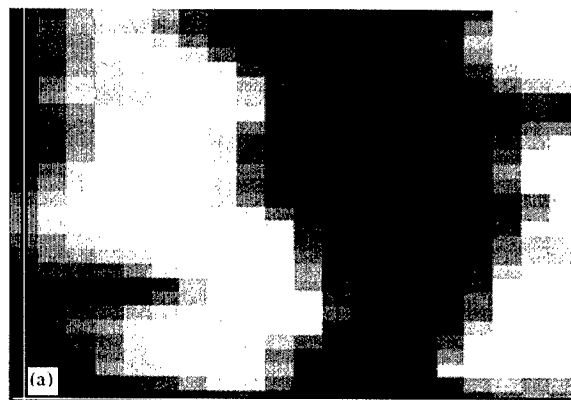


Fig. 4. The micro-PL maps of the excitonic edge PL (a) and the shallow DAP PL (b) observed for the InGaN-on-GaN/sapphire structure.

PL is enhanced (not shown) but two “deep” DAP PL emissions are weak. The enhanced edge PL at the hexagons were also observed for the HVPE-grown GaN samples and explained by doping nonuniformities [9].

In the case of the InGaN epilayers, the main mechanism of the PL intensity inhomogeneities was related to variations of the In fraction in the film plane [1]. If so, we should observe enhanced variations of the intensity of the edge PL and also of the other PL emissions and corresponding shifts of their spectral positions. Such enhanced PL intensity variations are not observed in the InGaN layers with small In fraction studied by us. In Fig. 4, we show maps of the PL intensity changes observed in the micro-PL study with the detection set at the excitonic and shallow DAP PL emissions. The data indicate that there is anti-correlation between the total intensity of the “edge” excitonic PL and the intensity of the shallow DAP PL emission. We explain such anti-correlation by inhomogeneities in defect distribution.

We also observed that the yellow PL is surprisingly in-plane homogeneous in the GaN layers. In the case of the GaN samples, the yellow PL is coming mostly from the regions close to the interface with substrates. We observed a different situation in the InGaN-on-GaN samples. The depth-profiling experiments for the InGaN samples indicate that this PL also comes from the upper layer of the structure, close to the InGaN-to-GaN interface. This is likely due to the fact that this layer is strained and thus is of a lower structural quality. Such anti-correlation, between the strength of the yellow PL and the sample quality, was observed by us in several cases [10].

4. Conclusions

The present studies demonstrate very complicated in-plane and in-depth variations of the defect-related PL emissions. These variations can only be partly explained by the micro-structure of the samples. They also relate to large inhomogeneities in the defect distribution. Our studies indicate that these nonuniformities in doping can also result in enhanced carrier/exciton trapping/localisation and can explain some of the observed in-plane and in-depth characteristics of the PL emissions.

Acknowledgements

This work was partly supported by grant no. 5 P03B 007 20 of KBN for the years 2001–2003.

References

- [1] S. Nakamura, M. Senoh, S. Nagahama, N. Iwasa, T. Matushita, T. Mukai, *MRS Internet J. Nitride Semicond. Res.* 4S1 (1999) G11.

- [2] M. Godlewski, E.M. Goldys, in: S.P. Asmontas, J. Gradauskas (Eds.), *Smart Optical Inorganic Structures and Devices*, Proc. SPIE 4318 (2001) 99.
- [3] E.M. Goldys, M. Godlewski, *Appl. Phys. A* 70 (2000) 329.
- [4] M. Godlewski, T. Suski, I. Grzegory, S. Porowski, J.P. Bergman, W.M. Chen, B. Monemar, *Physica B* 273–274 (1999) 39.
- [5] M. Godlewski, E.M. Goldys, M.R. Phillips, R. Langer, A. Barski, *J. Mater. Res.* 15 (2000) 495.
- [6] T.L. Tansley, E.M. Goldys, M. Godlewski, B. Zhou, H.Y. Zuo, In: S. Pearton (Ed.), *GaN and Related Materials*, Gordon and Breach, London, 1997, p. 233.
- [7] E.M. Goldys, M. Godlewski, R. Langer, A. Barski, *Appl. Surf. Sci.* 153 (2000) 143.
- [8] E.M. Goldys, T. Paskova, I.G. Ivanov, B. Arnaudov, B. Monemar, *Appl. Phys. Lett.* 73 (1998) 3583.
- [9] E.M. Goldys, M. Godlewski, T. Paskova, G. Pozina, B. Monemar, *MRS Internet J. Nitride Semicond. Res.* 6 (2001) Article 1.
- [10] M. Godlewski, E.M. Goldys, M.R. Phillips, R. Langer, A. Barski, *Appl. Phys. Lett.* 73 (1998) 3686.



ELSEVIER

Physica B 308–310 (2001) 106–109

PHYSICA B

www.elsevier.com/locate/physb

Strain relaxation in $\text{GaN}_x\text{P}_{1-x}$ alloy: effect on optical properties

I.A. Buyanova^{a,*}, W.M. Chen^a, E.M. Goldys^b, M.R. Phillips^c,
H.P. Xin^d, C.W. Tu^d

^aDepartment of Physics and Measurement Technology, Linköping University, 581 83 Linköping, Sweden

^bDivision of Information and Communication Sciences, Macquarie University, Sydney, Australia

^cMicrostructural Analysis Unit, University of Technology, Sydney, Australia

^dDepartment of Electrical and Computer Engineering, University of California, La Jolla, USA

Abstract

By using scanning electron microscopy and cathodoluminescence (CL), a decrease in radiative efficiency of GaNP alloy with increasing N content is seen due to the formation of structural defects. The defect formation is attributed to relaxation of tensile strain in the GaNP layer, which is lattice mismatched to GaP substrate. Several types of extended defects including dislocations, microcracks and pits are revealed in partly relaxed $\text{GaN}_x\text{P}_{1-x}$ epilayers with $x \geq 1.9\%$, whereas coherently strained layers exhibit high crystalline quality for x up to 4%. According to the CL measurements, all extended defects act as competing, non-radiative channels leading to the observed strong decrease in the radiative efficiency. From CL mapping experiments, non-uniformity of strain distribution around the extended defects is partly responsible for the broadening of the photoluminescence (PL) spectra recorded in the macro-PL experiments. © 2001 Elsevier Science B.V. All rights reserved.

Keywords: GANP; Extended defects; Luminescence; Strain

1. Introduction

Incorporation of a small amount of N in GaP is expected to cause a transition from an indirect band-gap in GaP to a direct band-gap in GaNP alloy [1,2], leading to much increased efficiency of light emission desirable for optoelectronic applications. Indeed, an increase in photomodulation signal associated with absorption edge of the alloy [2] and an enhancement in photoluminescence (PL) intensity [3] has been reported for $\text{GaN}_x\text{P}_{1-x}$ with $x < 1.3\%$. On the contrary, a further increase in N content causes rapid degradation of the optical quality evident from a strong PL quenching accompanied by a broadening in PL line width. Even though the exact mechanism of this degradation is not known so far, the effect has been naturally attributed to the formation of

some non-radiative (NR) defects in the alloy with high N content. The formation of NR defect can be partly caused by relaxation of tensile strain in the GaNP layer, which is lattice mismatched to GaP substrate [4]. In this paper, by using Raman scattering (RS), scanning electron microscopy (SEM), and cathodoluminescence (CL) measurements, we attempt to establish a link between the optical quality and the strain relaxation in the GaNP epilayers and GaNP/GaP multiple quantum wells (MQW) structures.

2. Samples and methods

All investigated structures were grown by gas-source molecular-beam epitaxy (GS MBE) on (100) GaP substrates. Both thick GaNP epilayers (with a thickness of 0.25–0.75 μm) and 7-period GaNP/GaP (70/200 Å) MQW structures were studied. N composition in the

*Corresponding author. Tel.: +46-13-281-745; fax: +46-13-142-337.

E-mail address: irb@ifm.liu.se (I.A. Buyanova).

alloy was determined from a simulation of a high-resolution X-ray rocking curve (XRC) data. The PL was excited by the 514 nm line of an Ar^+ ion laser. The resulting PL emissions were dispersed using a double-grating monochromator and detected by a photomultiplier tube. The Raman scattering spectra were obtained in the backscattering geometry using the 325 nm line of a He–Cd laser in a Renishaw micro-Raman system. A Gemini Leo microscope equipped with a MONOCL Oxford Instrument attachment was used for SEM and CL measurements. The CL spectra and images were taken at 7 K with an accelerating voltage of 15 kV.

3. Experimental results and discussion

Fig. 1 shows transformation of PL spectra as a function of N content x in the $\text{GaN}_x\text{P}_{1-x}$ alloy. A strong red shift of the PL emission with increasing x , which is clearly seen in both GaNP epilayers and GaNP/GaP MQW structures, represents a giant bowing effect in the alloy band-gap energy, consistent with previous findings [1–3]. In addition, a severe decrease in the PL intensity is observed for the GaNP epilayers with $x > 1\%$ —Fig. 1b. Since a similar increase in N content does not affect the PL intensity in the coherently strained MQW structures (Fig. 1a), this effect can be attributed to strain relaxation in the thick GaNP epilayers, degrading their structural quality.

To evaluate the biaxial strain in the thick GaNP epilayers, RS measurements were performed—see

Fig. 2a. The RS peaks related to the GaP-like longitudinal-optical (LO) phonon (labeled as LO_1) and a weak transverse-optic (TO) mode (labeled as TO_1) dominate the $350\text{--}420\text{ cm}^{-1}$ spectral range. The addition of nitrogen leads to the emergence of a new RS peak, LO_2 , at around 500 cm^{-1} . The LO_2 frequency is very close to that of the local mode of nitrogen in GaP at 488 cm^{-1} [5], suggesting that it represents the Ga–N bond vibrations in the GaP matrix. The frequency of the LO_1 mode decreases almost linearly with a slope of $\approx -1.1x\text{ cm}^{-1}$ for $x < 1.5\%$ (Fig. 2b), whereas a somewhat weaker compositional dependence is observed for the higher nitrogen compositions. On the other hand, the LO_2 frequency increases at a much higher rate of approximately $+2.6\text{ cm}^{-1}/x(\%)$.

The observed shift of the phonon frequencies can be caused by the alloying and/or residual biaxial strain in the GaNP. Assuming Vegard's law, the strain-induced shift in the phonon frequency can be estimated using the standard method given in Ref. [6]. The obtained shift of the LO_1 frequency is $-1.13x\text{ cm}^{-1}$ and is shown in Fig. 2b by the dotted line. The close match with the data shows that the strain is the dominant cause for the observed shift of the phonon frequencies. The weaker compositional dependence of the LO_1 frequency observed for $x > 1.5\%$ indicates partial relaxation of the

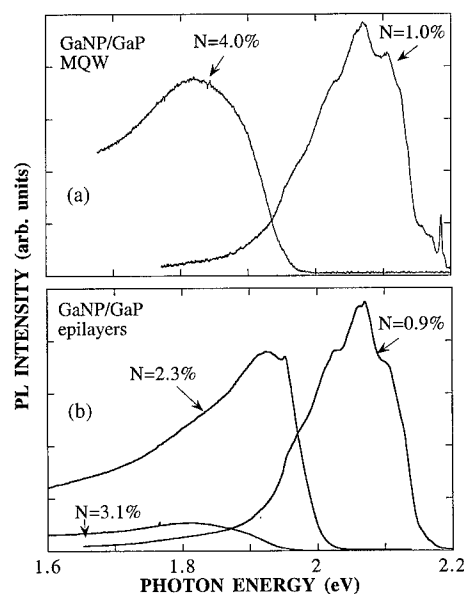


Fig. 1. PL spectra of the GaNP/GaP MQW structures (a) and GaNP epilayers (b) as a function of nitrogen content, taken at 4 K.

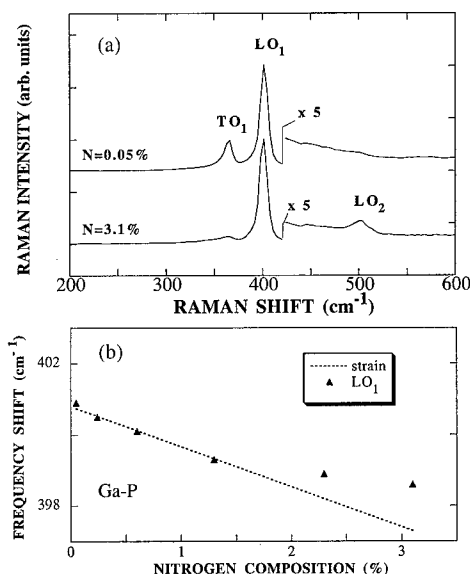


Fig. 2. (a) Room-temperature RS spectra of the GaNP epilayers with the lowest (0.05%) and highest (3.1%) N compositions studied. The spectra are normalized to the intensity of the LO_1 mode and shifted in the vertical direction, for clarity. (b) Frequency shift of the GaP-like (LO_1) phonon as a function of N content. The estimated shift of the LO_1 frequency due to the biaxial strain in the GaNP epilayer is shown by the dotted line.

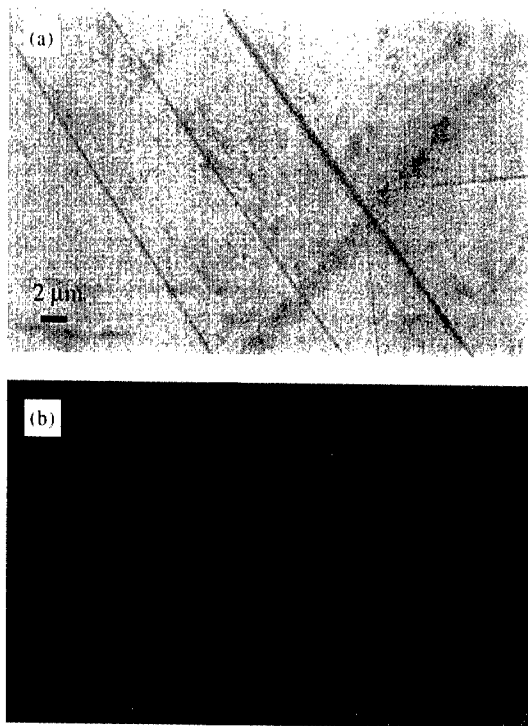


Fig. 3. Typical plan-view SEM (a) and corresponding panchromatic CL (b) images measured at 7 K from the partially relaxed $\text{GaN}_{0.03}\text{P}_{0.97}$ epilayer.

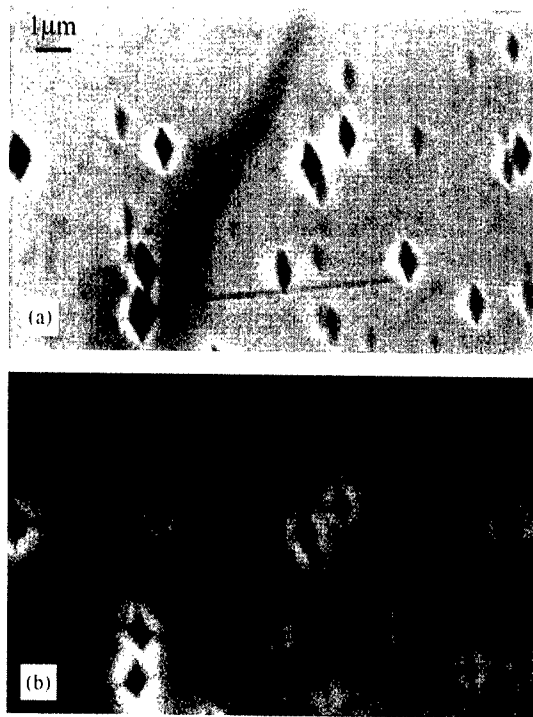


Fig. 4. The SEM (a) and corresponding panchromatic CL (b) images, taken at 7 K, showing the formation of pits in the partially relaxed $\text{GaN}_{0.03}\text{P}_{0.97}$ epilayer.

residual strain in the epilayers, also confirmed by the XRC measurements.

Effect of strain relaxation on the structural quality of the GaNP alloy can be determined by using SEM and CL measurements. The pseudomorphic GaNP epilayers with low N content ($< 1\%$) and strained $\text{GaN}_x\text{P}_{1-x}/\text{GaP}$ MQW structures with x up to 4% exhibit superior crystalline quality with very low density of extended defects. On the other hand, several types of structural defects such as dislocations and/or microcracks (Fig. 3a) are observed in the partially relaxed $\text{GaN}_x\text{P}_{1-x}$ epilayers with $x \geq 1.5\%$. The strain relaxation seems to be rather inhomogeneous, since defect density varies over the sample area. Moreover, formation of pits rather than misfit dislocations is observed within certain areas of the GaNP epilayers with $x \geq 3\%$ —Fig. 4a. The overall defect density strongly increases with increasing N composition.

All the defects appear as dark areas in the CL images (Figs. 3b and 4b), indicating that the surrounding regions have a higher concentration of NR recombination centers. Some of the dislocations and pits exhibit a bright halo around the dark image. This is typical for impurity segregation at the defect core leading to a zone around defect with a reduced concentration of the NR centers and, thus, bright halo in the CL images. The CL spectra measured from the dark area around the

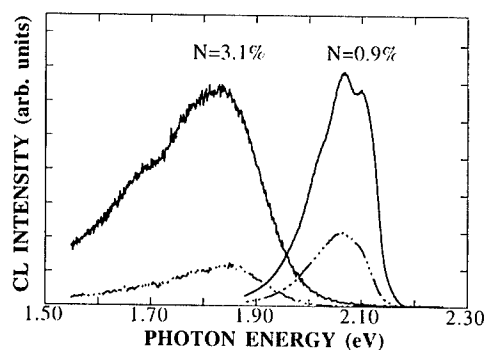


Fig. 5. CL spectra measured at 7 K from defect-free (solid lines) and dark line (dashed lines) areas from the GaNP epilayers with N composition of 0.9% and 3.1%.

dislocation/microcrack and defect-free area are shown in Fig. 5 by the dashed and solid lines, respectively. In addition to a severe decrease in the CL intensity, spectral position of the CL spectra, measured near the dislocation, is shifted towards higher energies. The observed shift indicates higher degree of strain relaxation around the extended defects. Thus, the non-uniformity in the biaxial strain is largely responsible for the severe broadening of the macro-PL spectra, observed in the partially relaxed structures.

4. Conclusions

We have studied the effect of strain relaxation on the optical quality of the GaNP alloy. By using the SEM and CL measurements, the decrease in radiative efficiency of the GaNP alloy with increasing N content is shown to be related to the formation of the extended structural defects. The defect formation is a result of strain relaxation in the GaNP layers, which are lattice mismatched to GaP substrate. According to the CL measurements, all extended defects act as competing, non-radiative channels, leading to the strong decrease in the radiative efficiency. From the CL mapping experiments, the non-uniformity in strain distribution around the extended defects is partly responsible for the broadening of the luminescence spectra recorded in the macro-PL experiments.

Acknowledgements

The authors would like to thank the Swedish Natural Science Research Council (NFR) for financial support.

The work at UCSD is partially supported by the National Renewable Energy Laboratory (#AAD-9-18668-07).

References

- [1] L. Bellaiche, S.H. Wei, A. Zunger, *Appl. Phys. Lett.* 70 (1997) 3558.
- [2] W. Shan, W. Walukiewicz, K.M. Yu, J. Wu, J.W. Ager III, E.E. Haller, H.P. Xin, C.W. Tu, *Appl. Phys. Lett.* 76 (2000) 3251.
- [3] X. Liu, S.G. Bishop, J.N. Baillargeon, K.Y. Cheng, *Appl. Phys. Lett.* 63 (1993) 208.
- [4] N.Y. Li, W.S. Wong, D.H. Tomich, K.L. Kavanagh, C.W. Tu, *J. Vac. Sci. Technol. B* 14 (1996) 2952.
- [5] D.G. Thomas, J.J. Hopfield, *Phys. Rev.* 150 (1966) 680.
- [6] F.H. Pollak, in: R.K. Willardson, A.C. Beer (Eds.), *Semiconductor and Semimetals*, Vol. 32, Academic Press, San Diego, 1990, p. 17.



ELSEVIER

Physica B 308–310 (2001) 110–113

PHYSICA B

www.elsevier.com/locate/physb

Positron annihilation in AlN and GaN

N.Yu. Arutyunov^{a,*}, V.V. Emtsev^b, A.V. Mikhailin^a, V.Yu. Davidov^b

^a *Institute of Electronics, UAS, 700170 Tashkent, Uzbekistan*

^b *Ioffe Physicotechnical Institute, RAS, 194021 St. Petersburg, Russia*

Abstract

The measurements of one-dimensional angular correlation of the annihilation radiation (1D-ACAR) have been carried out for AlN and GaN as well as for some related materials (Al, Ga, GaP, GaAs, GaSb) which have been used as samples of references the analysis of results. The numeral values of characteristic length of radius of spherical volume to be occupied by annihilating electron (r'_s) have differed significantly from the corresponding values (r_s) calculated by the conventional independent-particle-model (IPM) for ideal Fermi-gas: r'_s (AlN) $\simeq 1.28 r_s$, where r_s (AlN) $\simeq 1.61$ a.u., and r'_s (GaN) $\simeq 1.66 r_s$, where r_s (GaN) $\simeq 1.64$ a.u. The electron–positron “ion radii” reconstructed by the high-momentum components (HMC) of 1D-ACAR for Al^{3+} , Ga^{3+} cores as well as numeral r'_s values provide some reasons to believe that Ga- and Al-vacancies and their impurity complexes are effective centers of the positron localization in AlN and GaN; it is assumed that these complexes include V_{Ga} , V_{Al} , and N atom ($V_{\text{Ga}} - N_{\text{Ga}}$ in GaN and $V_{\text{Al}} - N_{\text{Al}}$ in AlN) where the nitrogen atom is likely to be in the configuration of substitution (anti-site), N_{Ga}^+ and N_{Al}^+ , respectively. © 2001 Elsevier Science B.V. All rights reserved.

Keywords: Positron; Annihilation; Nitrides; Defects

1. Introduction

In this work, an attempt aimed at “probing” the point defects has been undertaken by the thermalized positrons for AlN and GaN nitrides. Preliminary experiments have shown that the positron is partially localized in the area of vacancy-type point defects in these materials (roughly estimated concentration of the positron-sensitive centers has been over the range from 10^{17} to 10^{18} cm^{-3}). The annihilation radiation to be emitted out of the sample bears the information concerning the microstructure of defects; in our experiments the annihilation gamma-quanta have been detected by the measurements of the angular correlation. On the basis of the data obtained, the average electron density as well as the electron–positron “ion radius” which characterizes the ion radius of cores surrounding the positron have been estimated. The results indicate the presence of the vacancy complexes consisting of V_{Ga} ,

V_{Al} , and the atom of N in the anti-site configuration ($V_{\text{Ga}} - N_{\text{Ga}}$ in GaN and $V_{\text{Al}} - N_{\text{Al}}$ in AlN, respectively).

2. Experimental

The measurements have been conducted by the spectrometer of the angular correlations possessing the angular resolution $\sim 0.9 \text{ mrad}$ [1]; for more details about the experimental procedure see Ref. [2]. All measurements were performed at 18°C .

As AlN sample, the film (thickness $\sim 120 \mu\text{m}$) of p-type, $p \sim 10^{18} \text{ cm}^{-3}$, and as GaN sample the thick ($\sim 100 \mu\text{m}$) epitaxial film on the sapphire substrate, also of p-type, $p \sim 10^{17} \text{ cm}^{-3}$ have been used (for more details about samples, see Ref. [3]).

For a comparative analysis, experiments have been performed for metals Al and Ga as well as for a homologous pair of “perfect” single crystals GaP and GaAs related to GaN. These materials have served as the reference materials (more detailed information concerning the investigated materials of references is given in Ref. [3]).

*Corresponding author. Tel.: +998-71-133-0310; fax: +998-71-133-5330.

E-mail address: tassphy@sit.amsmail.com, n.arutyunov@yahoo.com (N.Yu. Arutyunov).

3. The positron annihilation in AlN and GaN: the 1D-ACAR data

The 1D-ACAR spectral curves recorded for AlN and GaN are characteristic of the ion-covalent bonding in the crystal lattice (the curves are not presented here; see Fig. 1 in Ref. [3]). The estimation of the average electron density obtained on the basis of the independent particle model (IPM) for ideal electron Fermi-gas (for more details see, for instance, Ref. [4]) leads to the magnitude of the electron radius (r_s) of the sphere occupied by one electron for AlN r_s (AlN) ≈ 1.61 a.u. and r_s (GaN) ≈ 1.64 a.u., respectively. The evaluation of half-width-on-half-maximum (HWHM, or $\theta_{1/2}$) of 1D-ACAR by the simplified expression $\theta_{1/2} \approx 9.923 r_s^{-1}$ (see Ref. [4] as well as Ref. [6,10]) has given the value $\theta_{1/2}$ (AlN) ≈ 6.16 mrad for AlN, and $\theta_{1/2}$ (GaN) ≈ 6.03 mrad for GaN; on the whole, the obtained experimental data are in agreement with these magnitudes though they both proved to be less in value, $\theta_{1/2}$ (AlN, exper.) ≈ 5.85 mrad and $\theta_{1/2}$ (GaN, exper.) ≈ 4.9 mrad. This correlation between the experimental and calculated data is qualitatively different from the picture to be observed for the whole range of the materials of references (see Fig. 1).

Directly related to the electron density, the value of Fermi-momentum θ_F has been found by the value of HWHM of the momentum density distribution (see Ref. [3]): $\text{HWHM} = (6.7\text{--}6.9) \times 10^{-3} m_0 c$ and $\text{HWHM} = (4.8\text{--}5.1) \times 10^{-3} m_0 c$ for AlN and GaN. Having assumed that the enhancement of the electron density around the positron does not distort significantly its average value in AlN and GaN (as it takes place for all

wide-gap semiconductors (Ref. [5])), one may estimate the r'_s parameter for the investigated materials within the framework of the ideal Fermi-gas model. It has proven to be that for both AlN and GaN, the electron density to be obtained by means of the experimental θ_F values is markedly lower in comparison with the magnitude to be predicted on the basis of the IPM approach for ideal electron Fermi-gas, r'_s (AlN) $\approx 1.28 r_s$ and r'_s (GaN) $\approx 1.66 r_s$. These numeral values indicate the process of the annihilation of positron in the regions of defects of a vacancy-type, where the distortions of the crystal lattice result in the decrease of the average electron density. In this connection, let us now consider these regions in the light of the results obtained for the high-momentum range ($\theta > \theta_F$) of 1D-ACAR.

4. Ion cores of AlN and GaN and high-momentum component of 1D-ACAR

It is well known that the 1D-ACAR within the region $\theta > \theta_F$ bears the information concerning the chemical nature of cores as the outer shell core electron wave functions 'retain' to a great extent their atomic character (for more details see, for instance Refs. [1,4,6–10]). Within the range $0 \leq r < \kappa_F^{-1}$ (κ_F is the absolute value of the electron wave vector) the dominant contribution to the detected momentum distribution is due to the exponentially subsiding part of the outer shell core electron wave functions. The overlapping of the positron and core electron wave functions reaches a maximum at length r_m and in itself is a parameter of HMC 1D-ACAR curve (some systematic data on the parameter r_m for various materials one may find, for instance, in Refs. [7–10]). A number of studies on the ion crystal and metals [4], high- T_c superconductors [7,8], and diamond-like semiconductors [9,10] have always evidenced that $r_m \approx r_i$, where r_i is the ion radius of that core which possesses the largest volume and least positive effective charge. Below, the results obtained for GaN and AlN are compared to the data available for metals Al and Ga as well as for GaP, GaAs, and GaSb which may serve as a certain standard for determination of a chemical nature of cores whose electrons give a contribution to the electron-positron annihilation in GaN and AlN.

The HMC of 1D-ACAR curves for metals mentioned above is characterized by the values of r_m (Al^{3+}) $\approx 0.519 \pm 0.011 \text{ \AA}$ and r_m (Ga^{3+}) $\approx 0.584 \pm 0.015 \text{ \AA}$, Ref. [3], which correlate well with the conventional magnitudes of ion radii: r_i (Al^{3+}) $\approx 0.53 \text{ \AA}$ and r_i (Ga^{3+}) $\approx 0.62 \text{ \AA}$, Ref. [12]. A similar picture for HMC of 1D-ACAR has been observed for homologous consequence of GaP, GaAs, and GaSb, where the relation $r_m(\text{Ga} \langle \text{B}^5 \rangle) / r_m(\text{Ga}^{3+})$ was found to be equal to 1,0086, 1,054, and 1,11 for $\langle \text{B}^5 \rangle = \text{P, As, and Sb}$, respectively (see also Refs. [6,10]).

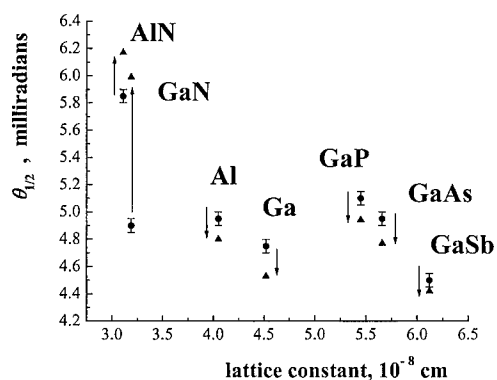


Fig. 1. The HWHM of 1D-ACAR ($\theta_{1/2}$) for AlN, GaN and materials of references vs. lattice constant: dots are experimental data, triangles are the results of calculations made on the basis of the model of ideal Fermi-gas of electrons [4,11]. The arrows shown here for clarity are directed from the experimental data to the calculated ones; the results for the nitrides are qualitatively different from those obtained for the materials of references (see text).

The estimated r_s values characterizing the average electron density in metals Al and Ga are r_s (Al) ≈ 2.07 a.u. and r_s (Ga) ≈ 2.19 a.u.; corresponding magnitudes of HWHM of 1D-ACAR curves are $\theta_{1/2}$ (Al) ≈ 4.8 mrad and $\theta_{1/2}$ (Ga) ≈ 4.53 mrad. These values and the experimental ones are in reasonably good agreement: $\theta_{1/2}$ (Al, exper.) ≈ 4.95 mrad and $\theta_{1/2}$ (Ga, exper.) ≈ 4.75 mrad (see Fig. 1). Let us now to apply these data on r_s and r_m values as a certain standard for a qualitative analysis of the results obtained for nitrides.

5. HMC of 1D-ACAR for AlN, GaN, and materials of references

The presence of four Ga^{3+} (or Al^{3+}) cores in the first coordination sphere of the negatively (effectively) charged nitrogen atom in the perfect crystal lattice of GaN (or AlN) creates conditions in which the outer shell core electrons of Ga^{3+} (or Al^{3+}) give a predominating contribution to the positron annihilation process in cores. If the value of r_m (Ga^{3+}) $\approx 0.584 \pm 0.015$ Å is supposed to be a standard length, then the deviation from this magnitude is less than 1% for GaP and 5% for GaAs. Indeed, as it has been established for most perfect GaP and GaAs—structurally closest materials to GaN nitride—the relations r_m (GaP)/ r_m (Ga^{3+}) and r_m (GaAs)/ r_m (Ga^{3+}) are close to unity, 1.0086 and 1.054, respectively, Ref. [10], i.e. within the accuracy of measurements the magnitude of the electron positron ‘ion radius’ r_m is determined by the 3d Ga^{3+} shell.

For the investigated nitrides, nevertheless, a somewhat different picture has been observed (see Fig. 2). Here, marked deviations of the r_m value from its standard magnitude have been revealed: the relation r_m (AlN)/ r_m (Al^{3+}) is, approximately, 1.249, and a somewhat less value 1.108 has been obtained for r_m (GaN)/ r_m (Ga^{3+}). It is important to emphasize that for GaN a similar magnitude of this relation was found when the tetrahedral structures served as standards: $\{r_m$ (GaN)/ r_m (GaP) $\} \approx 1.0986$ and $\{r_m$ (GaN)/ r_m (GaAs) $\} \approx 1.051$, i.e. again we have obtained for GaN the increase of r_m values within the interval from $\sim 5\%$ to $\sim 10\%$. Such an increase of r_m values in the investigated AlN and GaN, probably, reflects the availability of the increased distances between the cores of the nearest surroundings of positron resulting in a considerable decrease of the electron density around the positron as compared to the predicted values obtained by the IPM approach for the ideal electron Fermi-gas (see above). These two circumstances—the increase of the electron–positron ‘ion radius’ r_m in comparison with the chosen standard value and the decrease of the electron density around the positron in the crystal lattice indicate the process of annihilation of positrons trapped by vacancy-type defects, where the positron may

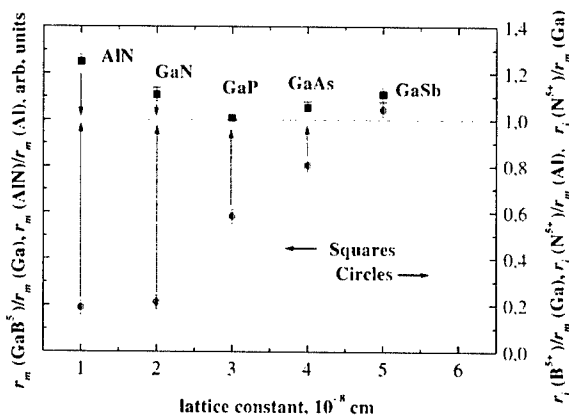


Fig. 2. Electron positron ‘ion radii’ (r_m) in nitrides and materials of references vs. the lattice constant: the squares indicate the deviations in magnitude of r_m from their standard values obtained for cores Al^{3+} and Ga^{3+} in corresponding metals; the circles are the same deviation of value obtained for the conventional ion radius (r_i) of B^{5-} , N^{5-} , P^{5-} , As^{5-} , and Sb^{5-} respectively (solid and dashed lines of different lengths are shown for clarity indicating the prevailing process of the annihilation of positrons in the outer shell of Al^{3+} and Ga^{3+} ion cores; the values of r_i were taken from Ref. [12]).

annihilate in the outer shells of Ga^{3+} in GaN and Al^{3+} in AlN.

Meanwhile, as is generally known, the N^{5+} -vacancies must have a repulsive potential for positron (see Ref. [5]). So, for self-consistent interpretation of the whole set of the obtained results it is required to put forward a supposition about the annihilation of positron in the region of complex, which includes Ga-vacancy in GaN and Al-vacancy in AlN. The defects of substitution N_{Ga}^+ and N_{Al}^+ (which are similar to anti-sites As_{Ga}^+ in GaAs) may be involved in the microstructure of such complexes. There are some reasons to believe that these defects, N_{Ga}^+ and N_{Al}^+ , compensate for the negative charge of Ga-vacancy or Al-vacancy. The centers consisting of the vacancies V_{Ga} or V_{Al} in which the electron density decreased and where the process of the positron annihilation occurred with outer shell core electrons of Ga^{3+} and Al^{3+} ,—such defects, may have the configuration $\text{V}_{\text{Ga}} - \text{N}_{\text{Ga}}^+$ in GaN and $\text{V}_{\text{Al}} - \text{N}_{\text{Al}}^+$ in AlN.

6. Conclusion

In this work, the results of measurements of 1D-ACAR for GaN and AlN are discussed. The radius per one electron r_s' estimated by 1D-ACAR data is higher by a factor of 1.28 and 1.66 for AlN and GaN, respectively, in comparison with the numeral values predicted within the framework of the IPM approach for ideal Fermi-gas of electrons.

The comparative analysis of systematic 1D-ACAR data for Al, Ga, GaP, GaAs, AlN, and GaN shows that the high-momentum component of 1D-ACAR is due to the annihilation of positrons in the outer shell of Ga^{3+} cores in GaN and Al^{3+} cores in AlN. Non-contradictory interpretation of the results is given on the basis of the positron annihilation in the regions of the vacancy complexes, $\text{V}_{\text{Ga}} - \text{N}_{\text{Ga}}$ in GaN and $\text{V}_{\text{Al}} - \text{N}_{\text{Al}}$ in AlN; for such defects, the nitrogen atom is likely to be in the configuration of substitution (anti-site), N_{Ga}^+ in GaN and N_{Al}^+ in AlN.

References

- [1] N.Yu. Arutyunov, A.S. Baltenkov, V.B. Gilerson, V.Yu. Trashchakov, *Sov. Phys. Semicond.* 20 (1986) 1099.
- [2] V. Goldanskii, *Physical Chemistry of Positrons and Positronium*, Nauka, Moscow, 1968.
- [3] N.Yu. Arutyunov, V.V. Emtsev, A.V. Mikhailin, V.Yu. Davidov, *Sov. Phys. Semicond.* 35 (2001), in press.
- [4] R.A. Ferrell, *Rev. Mod. Phys.* 28 (1956) 308.
- [5] M.J. Puska, S. Makinen, M. Manninen, R.M. Nieminen, *Phys. Rev. B* 39 (1989) 7666.
- [6] N.Yu. Arutyunov, *Mater. Sci. Forum* 105-110 (1992) 583.
- [7] N.Yu. Arutyunov, in: Y.C. Jean (Ed.), *Positron and Positronium Chemistry*, World Science Publication, Singapore, 1990, pp. 518–525.
- [8] V.F. Masterov, V.A. Kharchenko, N.Yu. Arutyunov, *Supercond.: Phys. Chem. Tech.* 5 (1992) 1211.
- [9] N.Yu. Arutyunov, *Solid State Phenom.* 57/58 (1997) 489.
- [10] N.Yu. Arutyunov, in: G. Kogel, P. Sperr (Eds.), *Positron Studies of Condensed Matter*, University of Bundeswehr, Munich, 1989, pp. 146–166.
- [11] A.T. Stewart, *Can. J. Phys.* 35 (1957) 168.
- [12] J. Suchet, *Chemical Physics of Semiconductors*, Van Nostrand, NY, 1965.



ELSEVIER

Physica B 308–310 (2001) 114–116

PHYSICA B

www.elsevier.com/locate/physb

Distribution of the lateral correlation length in GaN epitaxial layers

J. Kozłowski*, R. Paszkiewicz, R. Korbutowicz, M. Tlaczala

Institute of Microsystem Technology, Wrocław University of Technology, Janiszewskiego 11/17, 50 372 Wrocław, Poland

Abstract

GaN structures belong to the most popular wide-bandgap semiconductors. Large lattice mismatch existing between the layer and substrates (3.5% for SiC and even 16% in the case of sapphire substrate) results in structures with a large number of defects. The typical GaN epitaxial layer consists of dislocation-free regions with lateral dimensions equal to a few hundred nanometers. The dislocation density changes from 10^8 cm^{-2} inside the grains to 10^{10} cm^{-2} in the grain boundaries. The average value of the lateral correlation lengths (coherence wavelength) seems to be not quite satisfactory. Particularly, it is connected with lateral direction, because the vertical length is approximately equal to the thickness of the epitaxial layer. This paper presents the new approach for the determination of GaN crystallites dislocation-free block size distributions. This method is based on the X-ray peak profile analysis and solution of the Fredholm integral equation. The necessary peaks are obtained from the high-resolution X-ray diffractometry measurements. The obtained results have been shown for the various samples: GaN layers grown on low temperature buffer layer (GaN or AlN). Very interesting results were obtained in the first case, where two different sizes of the blocks appear. © 2001 Elsevier Science B.V. All rights reserved.

Keywords: X-ray diffraction; Lateral correlation length; GaN

1. Introduction

The GaN epitaxial layers exhibit a high density of structural defects. Dislocation densities may be up to 10^{10} cm^{-2} [1]. It is known that the columnar structure is typical for these epitaxial layers deposited on sapphire, or SiC substrate. Twist, tilt and sizes of the blocks as well as lattice strains should be controlled during the technological process. Metzger et al. [2] have been proposed some methods based on the X-ray measurements, which could be used in order to estimate some structural parameters of the GaN layers grown on *c*-plane sapphire. Especially, lateral correlation length and vertical correlation length of the GaN blocks inside the layer could be calculated.

In this paper, a new approach which allows to determine the distribution of the block sizes is proposed.

Our calculations are based on the X-ray peak profile analysis and solution of the Fredholm integral equation [3,4].

2. The model of X-ray diffraction by real crystal

The experimental X-ray diffraction line profile $h(s)$ may be treated as a convolution of the pure line profile $f(t)$ with a standard (instrumental) line profile $g(s - t)$:

$$\int_{-\sigma}^{\sigma} g(s - t) f(t) dt = h(s), \quad (1)$$

where σ is the limit of the diffraction angle for a single line.

If the layer consists of blocks of the same shape and different sizes distributed according to size distribution p , then the pure line profile is the sum of the pure line

*Corresponding author. Fax: +48-71-328-3504.

E-mail address: janx@wtm.ite.pwr.wroc.pl (J. Kozłowski).

profiles from crystallites:

$$\int_0^N \Phi(n, s) p(n) dn = f(s), \quad (2)$$

where $\Phi(n, s)$ is the inverse Fourier transform of function autocorrelation describing the crystalline block shape of the size characterised by number n and N is a sufficiently large number (N must be so large, that $p(n) = 0$ for $n > N$).

In the small area surrounding the Bragg angle, the angular profile of X-ray from a parallel beam diffracted by the layer consists of monocrystal blocks that can be interpreted after Kojdecki [4,5], Kojdecki, Mielcarek [6,7] and Wilson [8] as

$$\int_{-\sigma}^{+\sigma} \left[\int_0^N \Phi(n, s-t) p(n) dn \right] r(t) dt = f(s) \quad (3)$$

or as

$$\int_{-\sigma}^{+\sigma} \left[\int_0^N \Psi(n, s-t) v(n) dn \right] r(t) dt = f(s), \quad (4)$$

where $p(n)$ is the number-weighted size distribution, $v(n)$ the volume-weighted size distribution ($v(n) = p(n)n^3$) and $r(s)$ the lattice strain distribution, $\Psi(n, s) = \Phi(n, s)/n^3$.

The crystallite size distribution $p(n)$ (number-weighted) or $v(n)$ (volume-weighted) can be interpreted as a density of probability of finding a crystallite of an assumed size characterised by a number n in the analysed layer. The lattice strain distribution $r(t)$ can be interpreted as a density of probability of finding the crystallite, with interplanar distance (in analysed direction) differing $-td \cot(\Theta_0)$ from the averaged one ($t = \Theta - \Theta_0$, Θ —the Bragg angle).

Formula (4), evaluated from (3) can be treated as an equation, the solution of which is a pair of functions v and r characterising the investigated sample. Both Eqs. (1) and (4) are called ill-posed problems and they can be approximately solved only by special methods, e.g. based on Tikhonov's regularisation idea [3], presented by Kojdecki [4,6].

3. Results

The proposed method of the block size and lattice strain distribution determination was applied for the GaN/GaN/sapphire and GaN/AlN/sapphire epitaxial layers. The necessary measurements of the experimental as well as instrumental line profiles have been done using a MRD-Philips X-ray diffractometer. Triple-axis optics and $\Theta/2\Theta$ scan mode was provided. The calculations have been done for three pairs of instrumental and experimental line profiles. GaAs substrate was used as a reference crystal and the peaks presented in Table 1 were chosen, because they have quite similar angles of the

Table 1

X-ray peaks chosen for the profile measurements

GaAs		GaN	
<i>hkl</i>	$\omega/2\Theta$	<i>hkl</i>	$\omega/2\Theta$
002	15.8/31.6	002	17.3/34.6
115	29.27/90.14	015	31.99/105.17
244	6.6/109.67	144	10.96/100.12

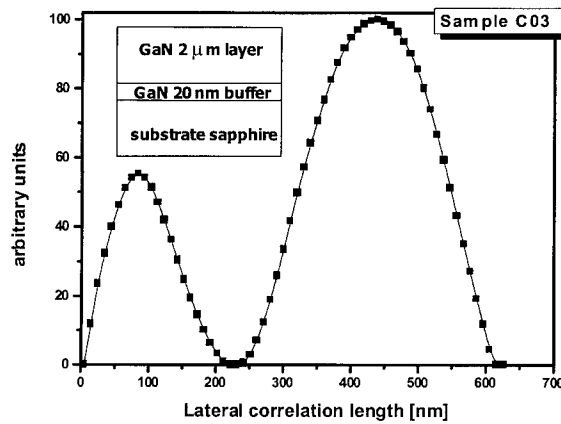


Fig. 1. Density of the lateral correlation length volume-weighted distribution in GaN/GaN_{buffer}/sapphire. Strain $\varepsilon = 2 \times 10^{-4}$.

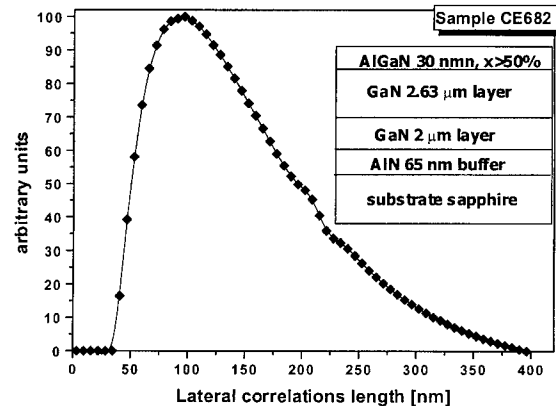


Fig. 2. Density of the lateral correlation length volume-weighted distribution in AlGaIn/GaN/GaN/AlN_{buffer}/sapphire. Strain $\varepsilon = 7 \times 10^{-5}$.

incident and diffracted beam (similar diffraction geometry).

The samples were prepared in an atmospheric pressure, single wafer vertical flow MOVPE system. Figs. 1–3 present the results (especially, density distribution of the lateral correlation lengths) obtained for the

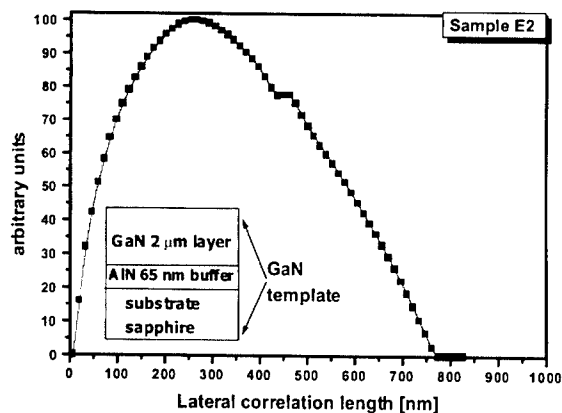


Fig. 3. Density of the lateral correlation length volume-weighted distribution in GaN/AlN_{buffer}/sapphire. Strain $\varepsilon = 7 \times 10^{-5}$.

three selected example layers. Sample C03 (Fig. 1) is the GaN layer deposited on the low temperature ($T \approx 800$ K) GaN buffer layer grown on the *c*-plane sapphire substrate.

Sample CE682 (Fig. 2) was grown as following: on *c*-plane sapphire substrate was deposited on a low temperature AlN buffer layer, then 2 μ m GaN layer was deposited in high temperature ($T = 1313$ K). Next, the temperature was decreased to room temperature, then it was raised to the growth value for the next deposition's step: there were two other layers deposited: GaN layer (2.63 μ m) and 30 nm of Al_{*x*}Ga_{1-*x*}N (*x* > 50%). This treatment was made for electrical measurements. The last sample E2 (Fig. 3) was GaN template on a sapphire substrate.

The lattice strain distribution $r(t)$ is obtained from formula (4), using the method described above. This is the second-order lattice strain (relative change of lattice parameter with respect to the average value). The value ε is the mean of the absolute second-order lattice strain.

In the first case (Fig. 1), two fractions of GaN grains are visible with the average lateral correlation lengths equal to 93.9 and 434.2 nm. It can be strictly connected with the double layer grown on the substrate. Sample C03 has strain $\varepsilon = 2 \times 10^{-4}$.

Sample CE682 (Fig. 2) has the small lateral correlation length of only 95.6 nm.

The sample E2 (Fig. 3) has the larger lateral correlation length of 258.8 nm.

In spite of the small correlation length sizes in sample CE682 the strain is equal to strain in sample E2

($\varepsilon = 7 \times 10^{-5}$). The grains of CE682 are very small, but temperature treatment in consequence gave a small value of strain.

4. Summary

The method, which can be used in order to obtain the structural information, is connected with the lateral correlation length distribution and additionally a lattice strain distribution in GaN layers. This is the first method of this kind. The average values of lateral correlation lengths of typical GaN structures published are in the same range as that presented in this paper. The obtained results confirm the differences between tested samples.

The proposed method seems to be very useful in the structural analysis of the non-perfect epitaxial layer.

Acknowledgements

This work was supported partially by the Scientific Research Committee (KBN) through Grant Nos. 8 T11B 057 18, 8 T11B 006 18 and 7 T08A 003 18.

References

- [1] S.D. Lester, F.A. Ponce, M.G. Craford, D.A. Steigerwald, *Appl. Phys. Lett.* 66 (1995) 1249.
- [2] T. Metzger, R. Hoepfer, E. Born, O. Ambacher, M. Schuster, H. Goebel, S. Christiansen, M. Albrecht, H.P. Strunk, *Philos. Mag. A* 77 (1998) 1013.
- [3] C.W. Groetsch, *The Theory of Tikhonov Regularization for Fredholm Equations of the First Kind*, Pitman Publishing Limited, London, 1984.
- [4] M.A. Kojdecki, *Int. J. Appl. Electromagn. Mater.* 2 (1991) 147.
- [5] M.A. Kojdecki, New criterion of regularisation parameter choice in Tikhonov method, Doctoral Dissertation, Institute of Mathematics of Polish Academy of Science, Warsaw, 1996 (in Polish).
- [6] M.A. Kojdecki, W. Mielcarek, *Mater. Sci. Forum* 321–324 (2000) 1040.
- [7] M.A. Kojdecki, W. Mielcarek, Materials from the Sixth European Powder Diffraction Conference, Budapest, 22–25 August, 1998.
- [8] A.J.C. Wilson, *Mathematical Theory of X-ray Powder Diffractometry*, Philips Technical Library, Eindhoven, 1963.



ELSEVIER

Physica B 308–310 (2001) 117–121

PHYSICA B

www.elsevier.com/locate/physb

The role of oxygen and hydrogen in GaN

B. Clerjaud^{a,*}, D. Côte^a, C. Naud^a, R. Bouanani-Rahbi^a, D. Wasik^b, K. Pakula^b,
J.M. Baranowski^b, T. Suski^c, E. Litwin-Staszewska^c, M. Bockowski^c, I. Grzegory^c

^a *Laboratoire d'Optique des Solides (UMR CNRS 7601), Université Pierre et Marie Curie, Case 80, 4 Place Jussieu,
F-75252 Paris cedex 05, France*

^b *Institute of Experimental Physics, Warsaw University, Hoza 69, 00-668 Warszawa, Poland*

^c *UNIPRESS, Polish Academy of Sciences, Sokolowska 29, 01-142 Warszawa, Poland*

Abstract

Several local vibrational modes (LVMs), observed in magnesium-doped high-pressure grown bulk samples, are attributed to two types of magnesium–oxygen complexes. The equivalent high-energy modes for beryllium–oxygen complexes are also observed in GaN:Be samples. Therefore, oxygen plays two roles for p-type doping of GaN: it compensates the acceptors and makes complexes with them. In addition to the well known LVM at 3125 cm^{-1} resulting from the passivation of the magnesium acceptor by hydrogen, two new modes at 4090 and 4110 cm^{-1} (at 6 K) are observed in as-grown OMVPE layers. We interpret them as originating from rotating hydrogen molecules in interstitial sites of the GaN lattice. Therefore, hydrogen passivates the acceptors and is also present in molecular form. © 2001 Elsevier Science B.V. All rights reserved.

Keywords: GaN; Acceptors; Hydrogen; Oxygen

1. Introduction

Some of the techniques of growth of gallium nitride introduce large amounts of unintentional impurities. On the one hand, undoped bulk materials grown under high pressure of nitrogen have a large electron concentration which is attributed to unintentional oxygen incorporation [1]. The same material doped with magnesium acceptors becomes either semi-insulating or slightly p-type [2,3]. The reason for this change of behaviour with magnesium doping can be (i) compensation between oxygen donors and magnesium acceptors; (ii) formation of Mg–O complexes; (iii) chemical gettering (formation of MgO precipitates). Among these possibilities, two received experimental support: UV reflectivity measurements suggested the formation of MgO precipitates [4] whereas positron annihilation experiments suggested the existence of negatively charged magnesium acceptors [5]. It must also be noted that the co-doping of GaN by both oxygen and acceptors has been suggested both experi-

mentally [6,7] and theoretically [8,9] to give rise to efficient p-type doping with high-hole mobility. In order to get further insights on these phenomena, we have investigated by local vibrational spectroscopy bulk material grown under high pressure and doped intentionally with magnesium and/or beryllium acceptors and unintentionally with oxygen.

On the other hand, as-grown magnesium-doped layers grown by organometallic vapour phase epitaxy (OMVPE) are known to contain large hydrogen concentrations coming out from the precursors. Hydrogen makes complexes with magnesium, which can be evidenced by local vibrational mode (LVM) spectroscopy [10–12]. An open question is whether it is the only role played by hydrogen in this material. In order to answer this question, we have also investigated as-grown OMVPE layers on sapphire substrates.

2. Samples and experiments

Bulk samples are grown by high-pressure synthesis method without seed. They are grown from the solution

*Corresponding author. Fax: +33-1-44-27-44-47.

E-mail address: bec@ccr.jussieu.fr (B. Clerjaud).

of nitrogen in liquid gallium under high pressures (≈ 1.5 GPa) at temperatures around 1500°C . Doping is achieved by adding 0.1–0.5% of magnesium or beryllium to the liquid gallium. The crystals we have investigated have a typical thickness around $300\ \mu\text{m}$ and lateral dimensions about 2 mm. They are of wurtzite structure with the c -axis perpendicular to the platelet.

Magnesium-doped epitaxial layers are grown by OMVPE at about 1000°C on sapphire substrates. They are of wurtzite structure with the c -axis perpendicular to the layer. Mg acceptor concentration exceeds 10^{19} cm^{-3} . As-grown samples are insulating at room temperature.

Infrared experiments have been performed with Bomem DA3+ or DA8 interferometers equipped with CaF_2 , KBr or mylar beam-splitters and cooled InSb, HgCdTe detectors or silicon bolometer. The samples can be cooled down to liquid helium temperature using Oxford Instruments CF 204 or CF 1204 cryostats.

Epitaxial layers have been investigated using the multitransmission set-up described in Ref. [12]. Bulk materials have been investigated with the wave vector of the light parallel to the c -axis.

3. Magnesium-doped bulk samples

In magnesium-doped bulk samples, in addition to the lattice absorption, two intense absorptions at 395.6 and 781.8 cm^{-1} , shown in Figs. 1 and 2, exist. They are observable at elevated temperature and, therefore, can be assigned to LVMs. The full widths at half maxima are 2 cm^{-1} for the 396 cm^{-1} mode and 2.5 cm^{-1} for the 782 cm^{-1} mode. The wave number of the high-energy mode being slightly lower than twice the low-energy mode, one can suspect the high-energy mode to be an

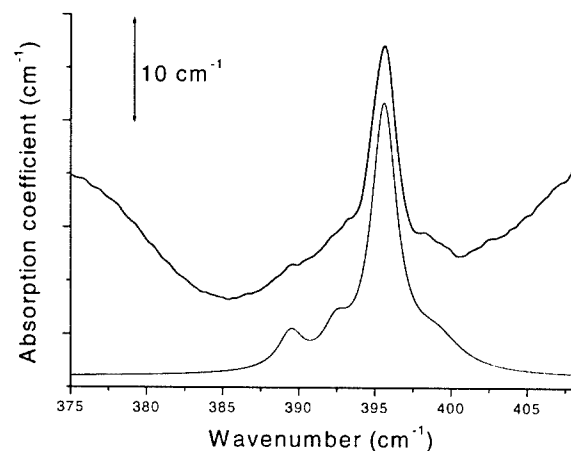


Fig. 1. Absorption spectrum of the magnesium-oxygen complex in the 400 cm^{-1} range at $T = 6\text{ K}$. The upper trace is the experimental spectrum while the lower one is a simulation.

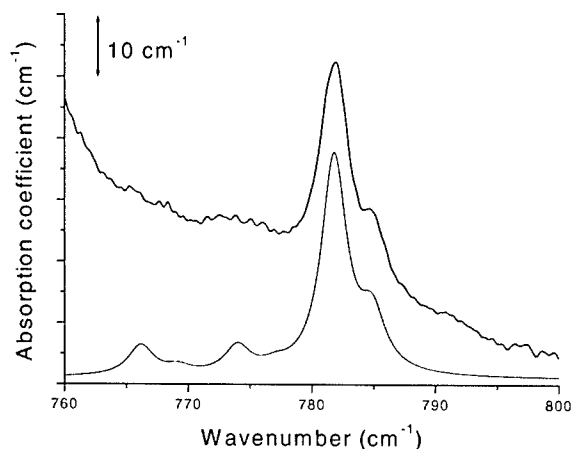


Fig. 2. Absorption spectrum of the magnesium-oxygen complex in the 800 cm^{-1} range at $T = 6\text{ K}$. The upper trace is the experimental spectrum while the lower one is a simulation.

overtone of the low-energy one. However, this possibility seems to be very unlikely as the intensity of the 782 cm^{-1} mode is twice larger than the 396 cm^{-1} mode. We believe that these modes are magnesium related. One of the reasons for this assignment is that they are not observed in beryllium-doped samples. Another one is that at energies lower than that of each main peak, two smaller ones are observed with intensities about 13% of the main peaks; they can be due to the ^{25}Mg and ^{26}Mg isotopes whose natural abundances are 10% and 11%, respectively, as it can be seen on the simulations shown in the lower traces of Figs. 1 and 2. In order to simulate the true absorption spectra, one needs to introduce a second set of lines consisting of ^{24}Mg related lines at 399 and 784.9 cm^{-1} and their ^{25}Mg and ^{26}Mg partners. In both spectra, the integrated intensity of the second set of lines is $1/4$ of the main set one. We assign these two sets of lines to two types of centres.

These LVMs are not due to "isolated" magnesium in substitution to gallium as they are already known from Raman spectroscopy [13–15] and do not fit to the observed wave numbers. Therefore, these LVMS are due to complexes involving magnesium. The most likely partner of magnesium is oxygen for the following reasons: (i) oxygen is the most important unintentional impurity in the samples we have investigated; (ii) the affinity of oxygen for magnesium is well known; (iii) the wave-number of the high-energy mode is in the range of the LO phonon in MgO (725 cm^{-1}). Therefore, we assign the two groups of LVMs to magnesium-oxygen complexes. It has to be emphasised that we do not have any direct proof of the involvement of oxygen in the complex; in particular, we could not find any evidence of LVMs related with ^{18}O as the natural abundance of ^{18}O is too low (0.2%) for allowing their observation in our experiments.

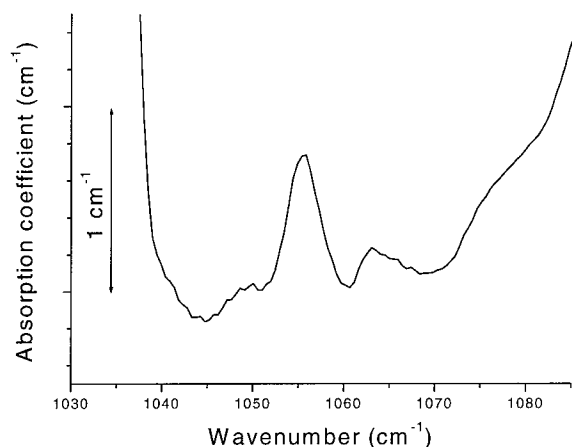


Fig. 3. Absorption spectrum of the beryllium–oxygen complex at $T = 6$ K.

4. Beryllium-doped bulk samples

The beryllium-doped bulk materials we have investigated are insulating at room temperature. In addition to the lattice absorption and to LVMs due to beryllium in substitution to gallium, one observes two modes at 1055 and 1063 cm^{-1} , which are shown in Fig. 3. For the same reasons as those developed in the previous section, we assign them to complexes involving beryllium and oxygen.

Bulk samples co-doped with magnesium and beryllium have also been investigated. One observes in them both the magnesium–oxygen complexes discussed in the previous section and beryllium–oxygen ones discussed in this section. This suggests that the acceptor–oxygen complexes contain only one acceptor atom.

5. Discussion on the acceptor–oxygen complexes

The main factor for determining the wave-number of a complex is the mass effect as the force constants do not depend so much of the bonds and occur at the power $1/2$. In this respect, if one considers an acceptor–oxygen bond, it is pertinent to compare its stretching LVM wave number with $f(m_A) = (1/m_A + 1/m_O)^{1/2}$ where m_A and m_O are the acceptor and oxygen masses, respectively. One can notice that the ratio of the high-energy modes wave numbers of the magnesium–oxygen and beryllium–oxygen complexes matches the $f(m_{\text{Be}})/f(m_{\text{Mg}})$ ratio.

We shall now discuss the structure of the acceptor–oxygen complexes. The simplest one can think of consists of oxygen in substitution to a nitrogen atom nearest neighbour to the acceptor in substitution to gallium (Fig. 4a). Such a complex ($\text{O}_\text{N}-\text{Mg}_{\text{Ga}}$ or $\text{O}_\text{N}-$

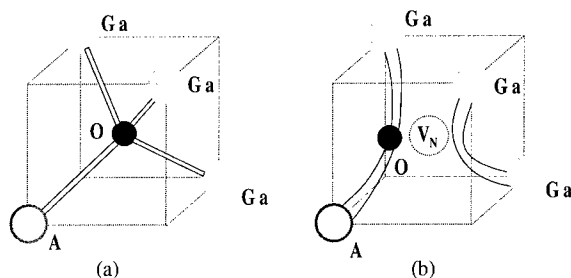


Fig. 4. Schematic representation of: (a) the $\text{A}-\text{O}$ complex; (b) the $(\text{A}_{\text{Ga}}-\text{O}-\text{Ga}, \text{V}_\text{N})$ defect. The “cubes” are there only for helping the perspective vision.

Be_{Ga}) has been considered by *ab-initio* calculations in the cubic phase of GaN [16] and it comes out that this defect is energetically favourable and has no level within the band gap. It seems quite likely that in wurtzite type GaN and in the case of replacement of magnesium by beryllium, one should reach the same conclusions. In the framework of this model, the modes at high energy would be assigned to the stretching modes and the modes around 396 cm^{-1} observed in Mg-doped samples to the transverse modes of the $\text{Mg}-\text{O}$ complexes. It is not clear why two types of complexes could be observed in the framework of such a model. One could think of two different geometries of the complexes: one with the acceptor–oxygen bond aligned along the c -axis and the other one in which this bond would be aligned along the other possible directions. However, this would not be compatible with our measurements as our experimental arrangement does not allow for the observation of the stretching vibrations of bonds aligned along the c -axis.

We believe that another type of complex is worth being considered: the $(\text{A}_{\text{Ga}}-\text{O}-\text{Ga}, \text{V}_\text{N})$ defect where A_{Ga} stands for the acceptor in substitution for gallium and V_N for the nitrogen vacancy. This defect, which is shown schematically in Fig. 4b, is an extension of the $(\text{Ga}-\text{O}-\text{Ga}, \text{V}_{\text{As}})$ complex observed in GaAs [17,18]; in fact, it can be considered as the same type of defect as the one discussed in the previous paragraph in which oxygen has relaxed in an off-centre position. Such a defect should be electrically active. In the framework of such a model, stretching vibrations of this complex should give rise to two modes corresponding to the modes at 782 cm^{-1} and to the one at 396 cm^{-1} in the case of magnesium doping. A splitting due to the two different gallium isotopes should exist. However, it should be small ($\leq 1 \text{ cm}^{-1}$) and not observable with the experimental line widths measured. In the framework of such a defect, several possibilities exist for explaining the occurrence of two types of complexes: (i) different charge states of the same complex; (ii) same charge state of non-equivalent complexes due to the wurtzite structure.

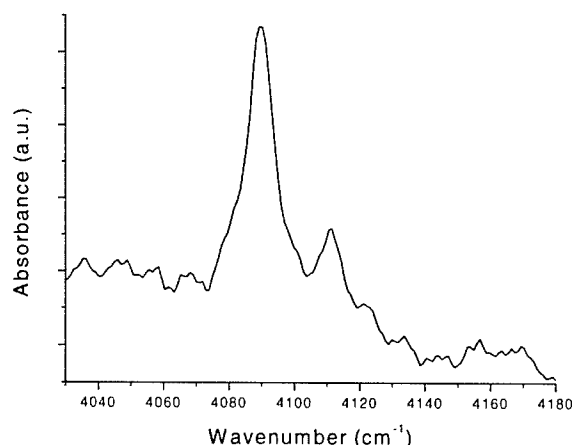


Fig. 5. Absorption spectrum of the H_2 molecule in GaN at $T = 6\text{ K}$.

6. Magnesium-doped OMVPE layers

As-grown samples are insulating at room temperature. In addition to the LVM at 3125 cm^{-1} due to magnesium–hydrogen complexes, two lines, shown in Fig. 5, at 4090 and 4110 cm^{-1} are observed at 6 K ; their line widths are about 10 cm^{-1} . They are due to local modes of vibration as they are still observed at room temperature slightly shifted (4087 and 4107 cm^{-1}). It has to be noted that no modes are observed around 2100 cm^{-1} , which means that these modes are not overtones. As hydrogen is known to be present in large quantities in these samples, the most likely candidate for such high-wave number modes is the hydrogen molecule. The wave number of the hydrogen molecule vibration in the lowest energy interstitial site of cubic GaN has been calculated to be 3847 cm^{-1} in the harmonic approximation and 3548 cm^{-1} taking into account anharmonic corrections [19]. It has to be noted that these calculations systematically underestimate the wave numbers even for the free hydrogen molecule. In the case of wurtzite type GaN, it has been calculated that the H_2 formation energy is lower than in cubic GaN [20], but, to our knowledge, no values for the LVM of the molecule has been published. Nevertheless, it seems that the modes we are observing are in the range expected for hydrogen molecules in GaN. Therefore, we assign these two modes to hydrogen molecules.

7. Discussion on the hydrogen molecule

The samples investigated are insulating. As it has been calculated that in insulating wurtzite type GaN, the most stable state of hydrogen is H_2 molecule at the centre of a trigonal channel [20], the experimental

observation of H_2 in insulating GaN is consistent with theory. The free hydrogen molecule is infrared inactive; in a noncentro-symmetric crystal field, the infrared transition becomes allowed. It has been pointed out that in wurtzite type GaN, a polarisation of the molecule occurs [20], which reinforces its “effective charge”.

In a free H_2 molecule, the Raman spectrum consists of two lines split by 5.9 cm^{-1} (ortho-para splitting). This is due to the coupling of the vibrational and the rotational motions of the free molecule via the anharmonicity of the molecule potential [21]. In the case of the H_2 molecule in GaAs, this splitting is 8.2 cm^{-1} [22]. When the molecule is in a crystal, it suffers the crystal potential in addition to the molecule potential; this will increase anharmonicity. For an interstitial molecule, the smaller the “cage” in which the molecule is enclosed, the larger the anharmonicity. Because of the smaller values of the GaN lattice parameters, the size of the “cage” in which the molecule is enclosed will be smaller than in GaAs and therefore, the ortho-para splitting will be larger in GaN than in GaAs. We attribute the two modes observed to rotating H_2 molecules, the low-energy mode being due to ortho-hydrogen and the high-energy mode to para-hydrogen. The 20 cm^{-1} ortho-para splitting observed reflects the small size of the channel in which the molecule is rotating. In the framework of this model, the intensity ratio between the ortho- and para-hydrogen transitions should be equal to the ratio of the degeneracies of the ground states of ortho- and para-hydrogen, i.e. 3 [22]; this is fully compatible with the experimental spectra.

It is to be noted that hydrogen-dependent lattice dilatation in epitaxial GaN films has been reported [23]. The interstitial H_2 molecules evidenced here might be responsible for this effect.

8. Conclusion

We have shown that in addition to its donor role, oxygen also makes complexes with the magnesium and beryllium acceptors. It is not yet clear whether these complexes are electrically active or not. In this respect, it is of importance to work out whether the two types of modes reported here could be due to two different charge states of the complex; experiments under illumination of the samples should be performed in order to give insight on the answer to this question.

It is now well known that hydrogen makes complexes with magnesium acceptors and passivates them. We have tried to diffuse hydrogen in beryllium-doped bulk materials in order to evidence complexes of beryllium with hydrogen; up to now we failed in observing these complexes.

We have evidenced H_2 molecules rotating in interstitial sites of the GaN lattice; the large ortho-para

splitting reflects the smallness of the “cage” in which the molecule is enclosed. The next step should be to investigate samples containing both hydrogen and deuterium in order to investigate H–D and D₂ molecules.

Note added in proof

The stretching mode wave number of the hydrogen molecule in wurtzite type GaN, calculated in the harmonic approximation, is 4235 cm^{-1} [24]; the inclusion of anharmonic corrections should lower this value.

Acknowledgements

We are very grateful to Michelle Jacquet and Nicole Lenain for the preparation of the samples for multi-transmission experiments and Christopher Latham for helpful discussions on the acceptor–oxygen complexes. T.S., E.L.-S., M.B. and I.G. acknowledge partial support from the Grant of the European Commission “Centre of Excellence”.

References

- [1] C. Wetzel, T. Suski, J.W. Ager III, E.R. Weber, E.E. Haller, S. Fischer, B.K. Meyer, R.J. Molnar, P. Perlin, *Phys. Rev. Lett.* 78 (1997) 3923.
- [2] E. Litwin-Staszewska, T. Suski, I. Grzegory, S. Porowski, P. Perlin, J.-L. Robert, S. Contreras, D. Wasik, A. Witowski, D. Côte, B. Clerjaud, *Phys. Stat. Sol. B* 216 (1999) 567.
- [3] E. Litwin-Staszewska, T. Suski, R. Pietrkowski, I. Grzegory, M. Bockowski, J.-L. Robert, L. Konczewicz, D. Wasik, E. Kaminska, D. Côte, B. Clerjaud, *J. Appl. Phys.* 89 (2001) 7960.
- [4] J.I. Pankove, J.T. Torvik, C.-H. Qiu, I. Grzegory, S. Porowski, P. Quigley, B. Martin, *Appl. Phys. Lett.* 74 (1999) 416.
- [5] K. Saarinen, J. Nissilä, P. Hautojärvi, J. Likonen, T. Suski, I. Grzegory, B. Lucznik, S. Porowski, *Appl. Phys. Lett.* 75 (1999) 2441.
- [6] O. Brandt, H. Yang, H. Kostial, K.H. Ploog, *Appl. Phys. Lett.* 69 (1996) 2707.
- [7] R.Y. Koroikov, J.M. Gregie, B.W. Wessels, *Appl. Phys. Lett.* 78 (2001) 222.
- [8] F. Bernardini, V. Fiorentini, A. Bosin, *Appl. Phys. Lett.* 70 (1997) 2990.
- [9] T. Yamamoto, H. Katayama-Yoshida, *Jpn. J. Appl. Phys.* 36 (1997) L180.
- [10] W. Götz, N.M. Johnson, D.P. Bour, M.D. McCluskey, E. Haller, *Appl. Phys. Lett.* 69 (1996) 3725.
- [11] B. Clerjaud, D. Côte, A. Lebkiri, *Phys. Stat. Sol. B* 210 (1998) 497.
- [12] B. Clerjaud, D. Côte, A. Lebkiri, C. Naud, J.M. Baranowski, K. Pakula, D. Wasik, T. Suski, *Phys. Rev. B* 61 (2000) 8238.
- [13] A. Kaschner, H. Siegle, G. Kaczmarczyk, M. Straßburg, A. Hoffmann, C. Thomsen, U. Birkle, S. Einfeldt, D. Hommel, *Appl. Phys. Lett.* 74 (1999) 3281.
- [14] H. Harima, T. Inoue, S. Nakashima, M. Ishida, M. Taneya, *Appl. Phys. Lett.* 75 (1999) 1383.
- [15] H. Harima, T. Inoue, Y. Sone, S. Nakashima, M. Ishida, M. Taneya, *Phys. Stat. Sol. B* 216 (1999) 789.
- [16] I. Gorczyca, A. Svane, N.E. Christensen, *Phys. Rev. B* 61 (2000) 7494.
- [17] C. Song, B. Pajot, F. Gendron, *J. Appl. Phys.* 67 (1990) 7307.
- [18] H.C. Alt, *Phys. Rev. Lett.* 65 (1990) 3421.
- [19] C.G. Van de Walle, J.P. Goss, *Mater. Sci. Eng. B* 58 (1999) 17.
- [20] A.F. Wright, *Phys. Rev. B* 60 (1999) R5101.
- [21] C. Cohen-Tannoudji, B. Diu, F. Laloë, in: *Mécanique Quantique*, Hermann, Paris, 1973.
- [22] J. Vetterhöffer, J. Wagner, J. Weber, *Phys. Rev. Lett.* 77 (1996) 5409.
- [23] J.-P. Zhang, X.-L. Wang, D.-Z. Sun, M.-Y. Kong, *Semicond. Sci. Technol.* 15 (2000) 619.
- [24] A.F. Wright, *J. Appl. Phys.* 90 (2001) 1164.



ELSEVIER

Physica B 308–310 (2001) 122–125

PHYSICA B

www.elsevier.com/locate/physb

Hydrogen vibrational lines in HVPE GaN

M.G. Weinstein^a, Fan Jiang^a, Michael Stavola^{a,*}, B. Bech Nielsen^b,
A. Usui^c, M. Mizuta^c

^aDepartment of Physics, Lehigh University, 16 Memorial Drive East, Bethlehem, PA 18015, USA

^bDepartment of Physics and Astronomy, University of Aarhus, Aarhus C, DK-8000, Denmark

^cPhotonic and Wireless Devices Research Labs, NEC Corporation, 2-9-1 Seiran, Ohtsu, Shiga 520-0833, Japan

Abstract

Several H-vibrational lines with frequencies between 3050 and 3250 cm⁻¹ have been observed in as-grown layers of GaN grown by hydride vapor phase epitaxy. H⁺ and D⁺ were also implanted into GaN samples with a range of energies up to 11 MeV. The implants gave rise to the same lines seen in the as-grown samples and a number of new lines in addition to those seen previously. A vibrational line at 2208 cm⁻¹ was produced by both H⁺ and D⁺ implantation and is assigned to a strongly bonded molecular complex. © 2001 Elsevier Science B.V. All rights reserved.

Keywords: GaN; H; Vibrational modes; Implantation

Hydrogen is well known to interact with the dangling bonds of native vacancy and interstitial defects in semiconductors. While hydrogenated native defects are sometimes found in as-grown crystals [1–4], a convenient method to produce these defects for study is by the implantation of H⁺ (or D⁺) [1,2,5,6]. In this paper, we report the observation of several H-vibrational lines in thick, as-grown crystals of GaN grown by hydride vapor phase epitaxy (HVPE). H⁺ and D⁺ were also implanted into HVPE GaN to produce hydrogenated lattice defects for our studies. These data provide insight into the origin and properties of the vibrational lines found in the HVPE GaN crystals.

Van de Walle proposed that H will interact with the N and Ga vacancies, V_N and V_{Ga}, in GaN and calculated the properties of the vacancy-H complexes [7]. For V_{Ga}, it was predicted that from one to four H atoms can terminate the N-dangling bonds of the defect. The H- and D-vibrational lines produced by the implantation of H⁺ and D⁺ into GaN have also been studied. Weinstein et al. discovered five H-vibrational lines between 3000 and 3150 cm⁻¹ in thin (≈4 μm) GaN epilayers that had been implanted with H⁺ and annealed near 450 °C [8].

Seager et al. discovered two lines at 3183 and 3219 cm⁻¹ in thin GaN layers that had been implanted with high doses of H⁺ (1–5 × 10¹⁷ cm⁻²) and annealed at T ≥ 600 °C [9].

Here we take advantage of the availability of thick GaN samples grown by HVPE for new studies of the hydrogenated lattice defects. H-containing defects present in the as-grown crystals can be sensitively detected. Further, the thick GaN samples can be implanted with a smaller local concentration of H or D compared to the thin layers studied previously, but with a greater total dose distributed over the thickness of the sample, giving stronger absorption lines with narrower widths.

The GaN samples used for our experiments were high quality, ≈400 μm thick, GaN single-crystal platelets grown at NEC by HVPE using a facet-initiated epitaxial overgrowth technique on GaN-nucleated sapphire substrates which were subsequently removed [10]. The dislocation density was typically 10⁷ cm⁻² and the unintentional n-type doping density was N_D ≈ 10¹⁷ cm⁻³. H⁺ and D⁺ were implanted at multiple energies through a 0.2 mm thick Al foil into the GaN. For H⁺, for example, 27 different energies between 5 and 7.6 MeV were used with a total dose of 4 × 10¹⁶ cm⁻², to produce a nearly uniform concentration of [H] = 3.6 × 10¹⁸ cm⁻³ in a layer 110 μm thick. For

*Corresponding author. Fax: +1-610-758-5730.

E-mail address: michael.stavola@lehigh.edu (M. Stavola).

one sample, H^+ and D^+ implantation energies and doses were selected to produce overlapping profiles of H and D, each with a concentration of $3.6 \times 10^{18} \text{ cm}^{-3}$ throughout a layer $110 \mu\text{m}$ thick. Samples were annealed in flowing N_2 . IR absorption spectra were measured at near 4 K, with resolution 0.5 cm^{-1} , with a Bomem DA.3 Fourier transform spectrometer. The spectra typically had oscillating baselines with a period of a few hundred wavenumbers that were subtracted.

An IR absorption spectrum, measured for a GaN sample grown by HVPE, is shown in Fig. 1, spectrum (a), and reveals five vibrational lines in the H-stretching range for the as-grown crystal. Other GaN crystals grown by HVPE showed similar H-vibrational lines. To explore the origin of these vibrational lines, HVPE GaN samples were implanted with H^+ or D^+ and then annealed at successively higher temperatures. Figs. 1 and 2 show spectra measured for the H- and D-stretching ranges, respectively. The frequencies of the vibrational lines are listed in Table 1. For annealing temperatures from 100°C to 550°C the lines seen previously in H^+ - or D^+ -implanted GaN by Weinstein et al. [8] emerged and sharpened, dominating the spectra. These H- and D-stretching lines are marked with a '*' in Figs. 1 and 2 and in Table 1.

For annealing temperatures of 600°C and above, the lines seen previously by Weinstein et al. decreased in intensity while a number of other vibrational lines with higher frequencies grew in strength. Several of these lines remained stable for annealing temperatures up to 900°C . The two H-stretching lines at 3188 and 3221 cm^{-1} (4 K)

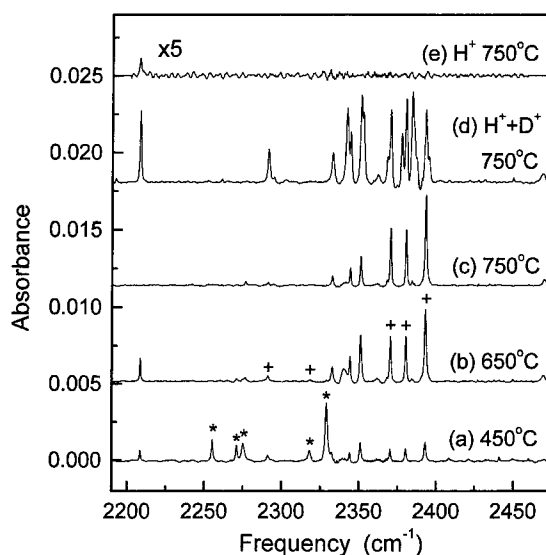


Fig. 2. Vibrational spectra (4 K) of HVPE GaN. Spectra (a)–(c) were measured for a sample that was implanted with D^+ and annealed isochronally (30 min) in $\approx 50^\circ\text{C}$ steps. Spectrum (d) was measured for a sample that had been implanted with overlapping profiles of H^+ and D^+ and isochronally annealed up to 750°C . Spectrum (e) was measured for the same H^+ -implanted sample whose spectra are shown in Fig. 1.

have frequencies similar to the lines at 3183 and 3219 cm^{-1} (300 K) that were reported previously by Seager et al. [9]. A comparison of the spectra measured for an as-grown sample [Fig. 1, spectrum (a)] with a sample that was implanted with H^+ and annealed at 750°C [Fig. 1, spectrum (d)] shows that H^+ implantation produces the same vibrational lines that were seen in the as-grown samples. The H-stretching lines that were seen in the as-grown samples and the corresponding D lines are marked with a '+' in Figs. 1 and 2 and in Table 1.

Several additional lines are also present and are most apparent in Fig. 2 that shows the D-stretching range. The frequencies of the three sharp lines between 2332 and 2351 cm^{-1} seen in spectra (b) and (c), and the frequencies of the corresponding H-stretching lines, are given in Table 1. In spectra (a) and (b), a line at 2208 cm^{-1} is seen that has no corresponding, isotopically shifted line in the H-stretching region of the spectrum.

Weinstein et al. assigned the H-stretching lines they found in GaN that had been implanted with H^+ and annealed at $\approx 450^\circ\text{C}$ to N–H bonds and suggested that these lines were due to V_{Ga} defects, created by the implantation, whose N-dangling bonds were terminated by different numbers of H atoms [8]. This assignment was based upon the calculations of the vibrational frequencies of $V_{Ga}H_n$ defects made by Van de Walle [7]

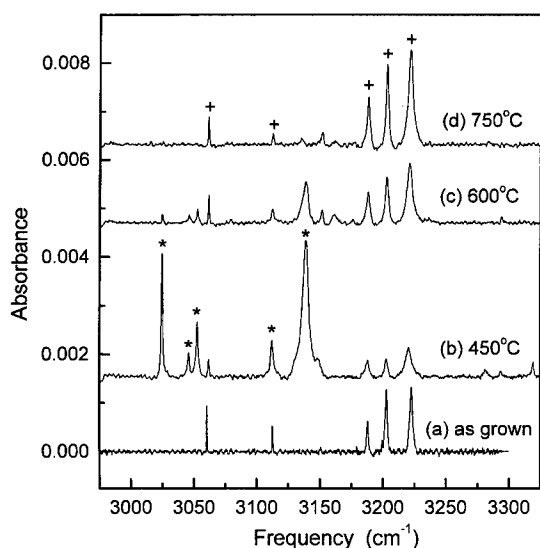


Fig. 1. Vibrational spectra (4 K) of HVPE GaN. Spectrum (a) is for an as-grown sample. Spectra (b)–(d) were measured following anneals at the temperatures shown for a sample that was implanted with H^+ and annealed isochronally (30 min) in $\approx 50^\circ\text{C}$ steps.

Table 1

Frequencies of vibrational lines seen in HVPE GaN that was implanted with H⁺ or D⁺, the frequency ratio, $\omega_{\text{H}}/\omega_{\text{D}}$, is also given.

ω_{H} (cm ⁻¹)	ω_{D} (cm ⁻¹)	$\omega_{\text{H}}/\omega_{\text{D}}$
3025*	2255*	1.341
3045*	2271*	1.341
3052*	2275*	1.342
3061 [†]	2291 [†]	1.337
3112* [†]	2318* [†]	1.343
3139*	2329*	1.348
3151	2332	1.351
3161	2344	1.349
3176	2351	1.351
3188 [†]	2370 [†]	1.345
3203 [†]	2380 [†]	1.346
3221 [†]	2393 [†]	1.346

*Frequencies for lines observed previously by Weinstein et al. for GaN epilayers that had been implanted with H⁺ or D⁺ (Ref. [8]).

[†]Frequencies for H-vibrational lines observed in the as-grown, HVPE-GaN samples and for the corresponding D lines observed in a D⁺-implanted sample.

(3100 cm⁻¹ for V_{Ga}H and 3470 cm⁻¹ for V_{Ga}H₄) and also upon the ratio $\omega_{\text{H}}/\omega_{\text{D}}$ for the corresponding H and D modes which was found to be typical of N–H bonds (≈ 1.34). Seager et al. also assigned the lines at 3183 and 3219 cm⁻¹, seen for GaN that had been implanted with H⁺ and annealed with $T \geq 600^\circ\text{C}$, to N–H bonds, but in this case, it was suggested that the H was bonded to the walls of cavities created by the implant and annealing cycle [9]. The ratio $\omega_{\text{H}}/\omega_{\text{D}}$ is given in Table 1 for the H- and D-stretching lines reported here and is close to 1.34, suggesting that all the H-vibrational lines are due to the stretching vibrations of N–H bonds, in agreement with the previous conclusions [8,9]. (We note that it is not possible to differentiate between H bonded to N or to another light atom, for example O, because both the vibrational frequency and value of $\omega_{\text{H}}/\omega_{\text{D}}$ would be similar.)

To further probe the rich spectrum of lines produced in GaN by H⁺ implantation, a sample was implanted with overlapping profiles of H⁺ and D⁺, and annealed at successively higher temperatures. A comparison of the vibrational spectra produced by the implantation of D⁺ alone and by overlapping profiles of H⁺ and D⁺, followed by an anneal at 750°C, is shown in Fig. 2, spectra (c) and (d), respectively. The presence of H and D in the GaN sample gives rise to a number of additional new D-stretching lines. (Corresponding new H lines were also seen in this sample.) This result shows that the vibrational lines that appear following an anneal with $T \geq 600^\circ\text{C}$ are due to multihydrogen complexes because these complexes give rise to new

lines when they contain combinations of both H and D. Other lines seen in the spectra did not show resolvable splittings.

Our results suggest that H⁺ implantation followed by annealing at temperatures with $T < 600^\circ\text{C}$ favors the formation of complexes that contain single (or at least fewer) H atoms. Annealing at higher temperatures favors the formation of complexes with multiple H atoms and higher vibrational frequencies. The presence of the vibrational lines shown in Fig. 1 in as-grown GaN samples, and for the reduced local H concentrations examined here, supports their assignment to H trapped at point defects rather than at the walls of cavities as was suggested by Seager et al. [9]. Therefore, we suggest that the defects responsible for the H- and D-vibrational lines seen in H⁺- and D⁺-implanted GaN are V_{Ga} or multi-V_{Ga} complexes, possibly trapped at impurity sites in some cases, whose N-dangling bonds are terminated by different numbers of H atoms. The vibrational lines seen in the as-grown GaN crystals have the same frequencies as the vibrational lines of the multihydrogen complexes seen for the later stages of isochronal annealing of the H⁺-implanted samples, consistent with their presence following crystal growth.

The vibrational line at 2208 cm⁻¹ is produced by the implantation of D⁺ into GaN [spectra (a) and (b) in Fig. 2] and was previously assigned to a D-stretching mode [8]. For the H⁺- and D⁺-implanted GaN samples studied here, it is clear that there is no isotopically shifted partner that corresponds to the 2208 cm⁻¹ line. Further, the 2208 cm⁻¹ line is also produced by the implantation of H⁺ into the samples [spectrum (e) in Fig. 2]. Therefore, the 2208 cm⁻¹ line cannot be due to a D-stretching mode! A recent example of another defect with a high vibrational frequency is a C–C pair that has been seen near 1800 cm⁻¹ in GaAs by Raman spectroscopy [11]. Here, we suggest that the 2208 cm⁻¹ line is also due to a complex of light, strongly bonded atoms, with the obvious possibilities being N, O, and C. (An N₂ molecule with sufficiently low symmetry in the wurtzite lattice to be IR active is an interesting possibility.) The presence of a strong 2208 cm⁻¹ line in the sample implanted with H⁺ and D⁺ [Fig. 2, spectrum (d)] is consistent with both implantations contributing to its intensity.

Clerjaud et al. have discussed the possibility that there can be defects in GaN with their transition moments along the *c*-axis of the sample [12]. In our measurements, a sample was turned to a 60° angle with respect to the viewing direction to produce a component of the polarization of the exciting light along the *c*-direction. Three new lines at frequencies of 2362, 2368, and 2403 cm⁻¹ were observed in the sample implanted with D⁺ when it was rotated away from normal incidence and, therefore, must be due to defects with their transition moments along the *c* direction.

We thank G.D. Watkins and B. Clerjaud for helpful discussions. The work at L.U. was supported by ONR Award No. N00014-94-1-0117 and NSF Grant No. DMR-9801843.

References

- [1] S.J. Pearton, J.W. Corbett, M. Stavola, *Hydrogen in Crystalline Semiconductors*, Springer, Heidelberg, 1992.
- [2] J. Chevallier, B. Clerjaud, B. Pajot, in: J.I. Pankove, N.M. Johnson (Eds.), *Hydrogen in Semiconductors*, Academic, Boston, 1991, p. 447.
- [3] G.R. Bai, M.W. Qi, L.M. Xie, T.S. Shi, *Solid State Commun.* 56 (1985) 277.
- [4] R. Darwich, B. Pajot, B. Rose, D. Robein, B. Theys, R. Rahbi, C. Porte, F. Gendron, *Phys. Rev. B* 48 (1993) 17776.
- [5] B. Bech Nielsen, L. Hoffman, M. Budde, *Mater. Sci. Eng. B* 36 (1996) 259.
- [6] M. Budde, B. Bech Nielsen, P. Leary, J. Goss, R. Jones, P.R. Briddon, S. Öberg, S.J. Breuer, *Phys. Rev. B* 57 (1998) 4397.
- [7] C.G. Van de Walle, *Phys. Rev. B* 56 (1997) R10020.
- [8] M.G. Weinstein, C.Y. Song, M. Stavola, S.J. Pearton, R.G. Wilson, R.J. Shul, K.P. Killeen, M.J. Ludowise, *Appl. Phys. Lett.* 72 (1998) 1703.
- [9] C.H. Seager, S.M. Meyers, G.A. Petersen, J. Han, T. Headley, *J. Appl. Phys.* 85 (1999) 2568.
- [10] A. Usui, H. Sunakawa, A. Sakai, A.A. Yamaguchi, *Jpn. J. Appl. Phys.* 36 (1997) L899.
- [11] J. Wagner, R.C. Newman, B.R. Davidson, S.P. Westwater, T.J. Bullough, T.B. Joyce, C.D. Latham, R. Jones, S. Öberg, *Phys. Rev. Lett.* 78 (1997) 74.
- [12] B. Clerjaud, D. Côte, A. Lebdiri, C. Naud, J.M. Baranowski, K. Pakula, D. Wasik, T. Suski, *Phys. Rev. B* 61 (2000) 8238.



ELSEVIER

Physica B 308 310 (2001) 126–129

PHYSICA B

www.elsevier.com/locate/physb

Properties of carbon as an acceptor in cubic GaN

U. Köhler*, M. Lübbbers, J. Mimkes, D.J. As

Universität Paderborn, FB6 — Physik, Warburger Str. 100, 33098 Paderborn, Germany

Abstract

Cubic gallium nitride epilayers were successfully doped with carbon using an e-beam evaporation source. Room temperature Hall measurements revealed hole concentrations up to $6 \times 10^{17} \text{ cm}^{-3}$ and hole mobilities of $200 \text{ cm}^2/\text{Vs}$. Low temperature (2 K) photoluminescence showed a donor–acceptor transition at 3.08 eV, which could clearly be assigned to the incorporation of a carbon acceptor. Thermal activation measurements were performed. They exhibited an activation energy of $E_A = 215 \text{ meV}$ both in photoluminescence and electrical measurements, respectively. © 2001 Elsevier Science B.V. All rights reserved.

Keywords: GaN; Carbon; Acceptor; Doping

1. Introduction

Gallium nitride (GaN) and GaN-based ternaries are semiconductors currently in the focus of both scientific and industrial research. Due to their large band gap they are well-suited for a wide range of applications, e.g. as light emitters in the green to ultraviolet range or as photodetectors, especially so for solar-blind sensors. The perspective of the use as sensors is even more attractive considering the mechanical hardness and chemical stability that make GaN appear extremely attractive for potential devices operating at high temperatures or under adverse conditions [1,2].

GaN possesses two known crystal phases, wurtzite and cubic. The latter is the metastable phase, so most of the progress that has been made has been reported for hexagonal phase material [3]. However, cubic GaN (c-GaN) is predicted to have many advantages due to its higher crystal symmetry, for example higher carrier mobility because of a smaller scattering coefficient and lower effective mass [4]. Readily available, high-quality cubic material such as GaAs—which may be doped and sport a backside contact—can be used as substrate.

Cleavage facets may easily be used as laser cavity mirrors.

For optoelectronic devices, controlled doping is essential. P-type doping of GaN poses, in contrast to n-type, a serious challenge. Up to now magnesium is the p-type dopant of choice for both hexagonal and cubic GaN. However, several disadvantages of Mg present a challenge, so the usually reported room temperature free hole concentration is in the upper range of 10^{17} cm^{-3} . In metalorganic vapor phase epitaxy (MOVPE) grown GaN, the Magnesium acceptor needs an extra thermal activation. Mg is rather volatile and substitutes Ga. Therefore, doping with Mg necessitates a low growth temperature and N rich conditions, which are disadvantageous for the growth of high-quality epitaxial layers [5,6]. Due to a large acceptor ionization energy, only about 5% of the incorporated Mg atoms are electrically active at room temperature. This problem is exacerbated by its tendency for self-compensation [7,8].

Carbon presents a viable alternative to magnesium as acceptor, when substituting nitrogen [9,10]. Due to its similar atomic radius, it is easily incorporated onto an N lattice site. In previous reports, carbon doping of hexagonal gallium nitride (h-GaN) led to semi-insulating properties or to a reduction of background electron concentration [11,12]. Cubic GaN with $p = 3 \times 10^{17} \text{ cm}^{-3}$ was reported, albeit with an extremely

*Corresponding author. Tel.: +49-5251-602698; fax: +49-5251-603490.

E-mail address: koehler@physik.uni-paderborn.de (U. Köhler).

reduced growth rate due to chlorine-induced back-etching from CCl_4 used for doping [13].

2. Experimental

Cubic gallium nitride was grown by means of rf plasma-assisted molecular beam epitaxy (MBE). Growth details are published elsewhere [6]. Molecular nitrogen was used for N supply. The substrates were semi-insulating GaAs(001). Carbon doping was accomplished by electron beam evaporation of a graphite rod and adjusting the applied power. The carbon flux was calibrated by growing C-doped gallium arsenide, assuming a similar sticking coefficient of C on GaAs and GaN. Comparison of the Hall values of hole concentration and mobility of the GaAs:C samples with literature allowed an estimate of carbon concentration and compensation in our GaAs:C layers [15]. As a result of this calculation, a carbon incorporation of $2 \times 10^{20} \text{ cm}^{-3}$ should possibly be achieved in GaN. This was confirmed with secondary ion mass spectroscopy (SIMS), where indeed a carbon concentration of $2 \times 10^{20} \text{ cm}^{-3}$ was measured.

Photoluminescence measurements were conducted between 2 K and room temperature in a He bath cryostat. A cw HeCd laser (325 nm) was used for excitation. Neutral density filters allowed a variation of the excitation power over four orders of magnitude. Spectra were recorded with a resolution of 0.2 nm. Hall effect measurements were performed in van der Pauw geometry between 77 and 420 K. The magnetic field measured 0.8 T, the samples were not illuminated during the experiment.

3. Results and discussion

The variation of the carbon influx has a profound influence on the photoluminescence spectra, as can readily be seen in Fig. 1. For moderate carbon concentrations, a PL band at $E = 3.08 \text{ eV}$ appears in spectra recorded at $T = 2 \text{ K}$. This transition is distinctly different from the well-known lines (D, X) that can also be seen at 3.27 eV and (D^0, A^0) at 3.16 eV [14]. As a more detailed analysis of this peak shows, this actually is a convolution of two separate luminescence lines separated by 25 meV at low temperatures. When increasing the temperature, the low-energy contribution thermalizes so that only the high-energy PL transition can be observed for temperatures exceeding 100 K . Therefore, it seems appropriate to attribute the lower line to a donor–acceptor recombination $(\text{D}^0, \text{A}^0)_\text{C}$, while the other is caused by a C-related band–acceptor transition, $(\text{e}, \text{A}^0)_\text{C}$. These two transition lines were fitted with Gaussians. The respective energetic positions

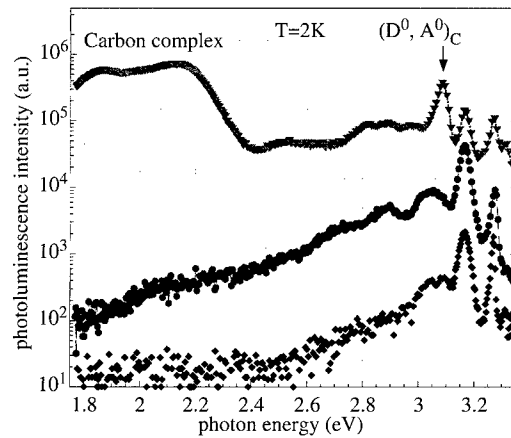


Fig. 1. Photoluminescence spectra of differently carbon doped GaN layers, bottom to top: nominally undoped, 5×10^{18} and $8 \times 10^{10} \text{ cm}^{-2} \text{ s}^{-1}$.

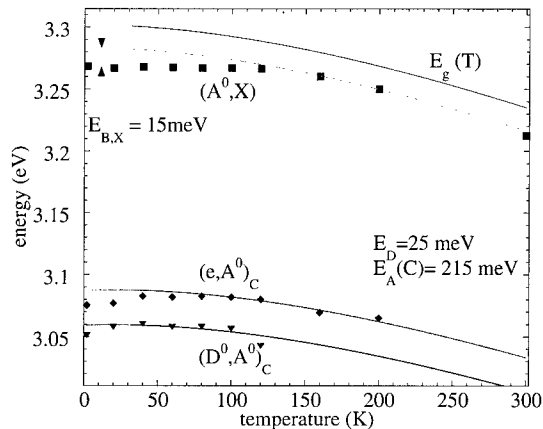


Fig. 2. Observed temperature shift of near-band edge PL transitions (squares: excitonic transition; diamonds: C-related band-acceptor transition, $(\text{e}, \text{A}^0)_\text{C}$; triangles: C-related donor-acceptor transition, $(\text{D}^0, \text{A}^0)_\text{C}$). The top curve denotes the gap energy as function of temperature, the lower curves are calculated for $(\text{e}, \text{A}^0)_\text{C}$ and $(\text{D}^0, \text{A}^0)_\text{C}$ transitions, respectively, using donor and acceptor energies of $E_\text{D} = 25 \text{ meV}$ and $E_\text{A} = 215 \text{ meV}$.

as a function of temperature are shown in Fig. 2. The analysis yielded an acceptor activation energy of $E_\text{A} = 215 \text{ meV}$, 15 meV below that of the Mg acceptor in c-GaN [16]. It is also below the known values for hexagonal GaN:C [7]. The full curves denote the calculated transitions as detailed, including a donor energy of 25 meV . This is the same ubiquitous donor which is also observed in undoped samples [14]. The variation of the gap energy, as lined out in the topmost curve, follows Ref. [17].

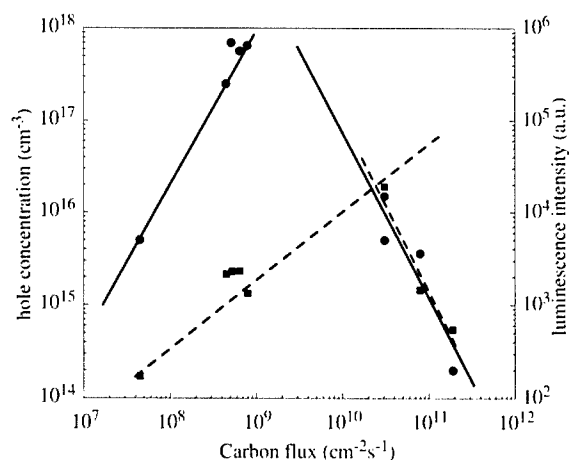


Fig. 3. Room temperature Hall effect hole concentration (dots) and low temperature PL intensity of C-related donor-acceptor transition (squares) as function of carbon flux. The lines (solid line: hole concentrations, dashed line: PL intensity) are guides to the eye.

The carbon-related transition increases steadily with carbon incorporation. As is visible in Fig. 3, the same is true for hole concentrations up to a certain saturation value, $6 \times 10^{17} \text{ cm}^{-3}$. At the same time, the room temperature Hall mobility of the holes is as high as $200 \text{ cm}^2/\text{Vs}$. Variable-temperature Hall effect measurements (not shown here) gave a thermal activation energy $E_A = 215 \text{ meV}$ of the carbon acceptor, which is in excellent agreement with the optical values. At higher carbon fluxes, however, Fig. 3 shows a drastic reduction in free hole concentration, indicative of the formation of additional compensating centers. The nature of this compensating mechanism remains unknown. Kaufmann et al. reported a similar phenomenon for magnesium doped MOVPE GaN layers with a maximum hole concentration of $6 \times 10^{17} \text{ cm}^{-3}$, albeit with mobilities $< 20 \text{ cm}^2/\text{Vs}$ [8]. They developed a model which involves self-compensation via the formation of MgV_N pairs. For GaN:C, it is tempting to assume an analogy from GaAs:C. In this system, it has been found that at high doping concentrations a compensating dicarbon complex forms [18]. This complex involves a split interstitial, i.e., one carbon atom on an As lattice site and another atom shifted along the [100] direction [19], and acts as a double donor in GaAs. An explanation along these lines might also account for a second interesting observation in Fig. 3: while the Hall effect free hole concentration decreases, there is still an increase in photoluminescence intensity of the carbon-related DAP transition, up to a tenfold higher carbon flux. Even this apparent decrease has to be looked upon with caution. For high carbon concentrations, a broad luminescence band evolves around 2.1 eV , and near-gap luminescence is quenched. Therefore, it is more helpful to consider the ratio of the

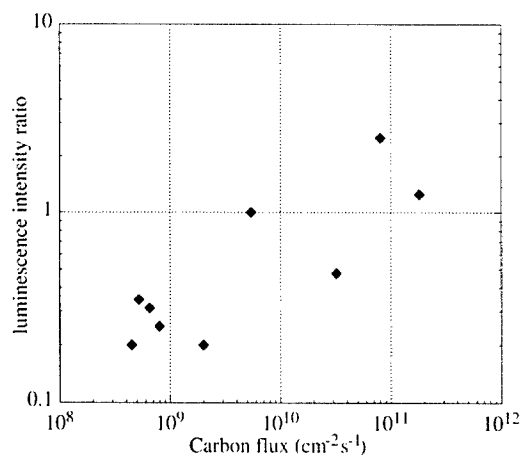


Fig. 4. Ratio of C-related donor-acceptor transition (3.08 eV) and prominent DAP transition (3.15 eV) observed in photoluminescence at $T = 2 \text{ K}$ as function of carbon incorporation.

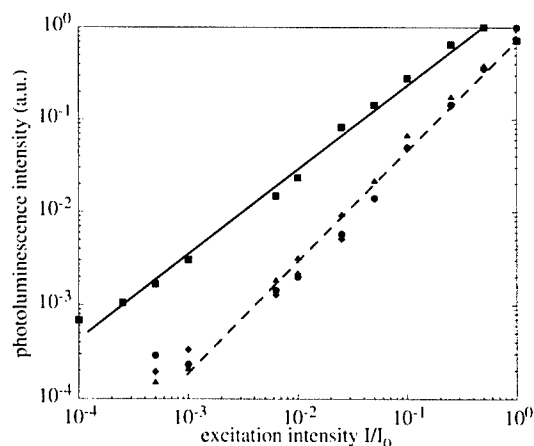


Fig. 5. Photoluminescence intensity of GaN:C with an estimated carbon density of 10^{19} cm^{-3} as function of excitation intensity. Diamonds, dots and triangles denote the near-band edge luminescence, the squares mark the deep luminescence.

$(\text{D}^0, \text{A}^0)_\text{C}$ emission to the other near-gap lines. The result is depicted in Fig. 4. It can be clearly seen as to how carbon acceptors are incorporated up to the highest experimentally available fluxes. More detailed calculations with respect of formation rate, activation energies and net doping effect need to be performed. Raman measurements will be employed in order to clarify the nature of this complex.

The existence of such a deep donor carbon complex may well be the cause of the deep luminescence observable in highly doped GaN layers (cf. Fig. 1). This donor would lie in the gap ca. 1.15 eV below the conduction band. Photoluminescence measurements carried out with varying excitation intensity at

$T = 2$ K clearly show the localized character of this red luminescence, as can be seen in the different exponent k in Fig. 5. The near-gap luminescence (denoted by diamonds, triangles and dots, respectively) can be described with a power law $I \sim L^{1.2}$, in agreement with the literature [20]. In contrast, the deep luminescence, marked by squares, follows $I \sim L^{0.95}$, as would be expected from a localized defect.

4. Conclusions

Successful p-type doping of MBE grown cubic gallium nitride epilayers has been demonstrated. Room temperature Hall effect measurements show hole concentrations up to $6 \times 10^{17} \text{ cm}^{-3}$ and hole mobilities of $200 \text{ cm}^2/\text{Vs}$. Photoluminescence showed a carbon-related transition at $E = 3.08 \text{ eV}$. With the help of temperature-dependent analysis, this line could be ascribed to a donor–acceptor transition with an activation energy $E_A = 215 \text{ meV}$. This is less than the previously reported magnesium activation energy and in excellent agreement with variable-temperature Hall measurements. At high carbon concentrations, near-edge luminescence quenching due to the formation of a deep level is observed. This deep defect lies 1.15 eV below the conduction band.

Acknowledgements

The authors gratefully acknowledge SIMS measurements by W. Kriegseis, W. Burkhart and B.K. Meyer. The work was supported by Deutsche Forschungsgemeinschaft (DFG) under project number As 107/1-3.

References

[1] H. Morkoc, S. Strite, G.B. Gao, M.F. Lin, B. Sverdlov, M. Burns, *J. Appl. Phys.* 76 (1994) 1363.

- [2] S.C. Jain, M. Willander, J. Narayan, R. van Overstraeten, *J. Appl. Phys.* 87 (2000) 965.
- [3] S. Nakamura, G. Fasol, *The Blue Laser Diode*, Springer, Berlin, 1997.
- [4] H. Okumura, H. Hamaguchi, K. Ohta, G. Feuillet, K. Balakrishnan, Y. Ishida, S. Chichibu, H. Nakanishi, T. Nagatomo, S. Yoshida, *Mater. Sci. Forum* 264–268 (1998) 1167.
- [5] S. Guha, N.A. Bojarczuk, F. Cardone, *Appl. Phys. Lett.* 71 (1997) 1685.
- [6] D. Schikora, M. Hankeln, D.J. As, K. Lischka, T. Litz, A. Waag, T. Buhrow, F. Henneberger, *Phys. Rev. B* 54 (1996) R8381.
- [7] S. Fischer, C. Wetzel, E.E. Haller, B.K. Meyer, *Appl. Phys. Lett.* 67 (1995) 1298.
- [8] U. Kaufmann, P. Schlotter, H. Obloh, K. Köhler, M. Maier, *Phys. Rev. B* 62 (2000) 10867.
- [9] F. Mireles, S.E. Ulloa, *Phys. Rev. B* 58 (1998) 3879.
- [10] P. Boguslawski, J. Bernholc, *Phys. Rev. B* 56 (1997) 9496.
- [11] S. Shimizu, S. Sonoda, *Proceedings of the International Workshop on Nitride Semic, IPAP Conference Series*, Vol. 1, 1999, p. 740.
- [12] U. Birkle, M. Fehrer, V. Kirchner, S. Einfeldt, D. Hommel, S. Strauf, P. Michler, J. Gutowski, *MRS Internet J. Nitride Semicond. Res.* 4S1 (1999) G5.6.
- [13] C.R. Abernathy, J.D. MacKenzie, S.J. Pearton, W.S. Hobson, *Appl. Phys. Lett.* 66 (1995) 1969.
- [14] D.J. As, F. Schmilgus, C. Wang, B. Schöttker, D. Schikora, K. Lischka, *Appl. Phys. Lett.* 70 (1997) 1311.
- [15] D.C. Look, *Electrical Characterization of GaAs Materials and Devices*, Wiley, New York, 1988.
- [16] D.J. As, T. Simonsmeier, B. Schöttker, T. Frey, D. Schikora, W. Kriegseis, W. Burkhart, B.K. Meyer, *Appl. Phys. Lett.* 73 (1998) 1835.
- [17] G. Ramírez-Flores, H. Navarro-Contreras, A. Lastras-Martínez, R.C. Powell, J.E. Greene, *Phys. Rev. B* 50 (1994) 8433.
- [18] B. Cheong, K.J. Chang, *Phys. Rev. B* 49 (1994) 17436.
- [19] B.R. Davidson, R.C. Newman, C.D. Latham, R. Jones, J. Wagner, C.C. Button, P.R. Briddon, *Phys. Rev. B* 60 (1999) 5447.
- [20] T. Schmidt, L.W. Zulehner, *Phys. Rev. B* 45 (1992) 8989.



ELSEVIER

Physica B 308–310 (2001) 130–133

PHYSICA B

www.elsevier.com/locate/physb

Electrically active defects in AlGa_xN alloys grown by metalorganic chemical vapor deposition

D. Seghier*, H.P. Gislason

Science Institute, University of Iceland, Dunhagi 3, IS-107 Reykjavik, Iceland

Abstract

We investigated two series of metalorganic chemical-vapor-deposition-grown Al_xGa_{1-x}N samples with Al compositions $x = 0.1$ and 0.3 and free electron concentrations 2.4×10^{17} and $5.2 \times 10^{17} \text{ cm}^{-3}$, respectively. Shallow and deep centers were investigated using electrical characterization methods. Capacitance vs. temperature measurements show the presence of a dominant donor level with a binding energy of about 118 meV in the sample with $x = 0.1$ and 90 meV in the sample with $x = 0.3$. Moreover, we observe a hysteresis in the capacitance–voltage measurements from the sample with higher x . Deep-level transient spectroscopy measurements show that this long time relaxation phenomenon is caused by the presence of interface defects between Au and the AlGa_xN layer, which become more significant with increase in x . The high Al mole fraction creates potential fluctuations at the surface of the sample and makes the surface behave as an interfacial layer. © 2001 Elsevier Science B.V. All rights reserved.

Keywords: AlGa_xN; Defects; Conductivity; Metalorganic chemical-vapor-deposition-grown

1. Introduction

GaN and its ternary solution with AlN are of great interest for applications in optoelectronics and high-temperature/high-power/high-frequency electronics [1,2]. When undoped, AlGa_xN layers tended to be n-type, and it was the high concentration of these unintentional donor defects that prevented AlGa_xN from being used to manufacture practical devices for many years. Recent advances in growth techniques of AlGa_xN films have dramatically reduced the concentration of the unintentional donors [3]. Yet, residual defects remain very much an issue, and their origin is unclear. They have often been attributed to nitrogen vacancies [4]. So far, few investigations of localized centers in AlGa_xN have been reported. A comprehensive study using optical measurements of electrically and optically active defects in AlGa_xN layers in a wide range of compositions was reported in Ref. [5]. However, much work must still be

done in order to understand the influence of point defects on the electrical properties of AlGa_xN.

In this work, we report results from electrical measurements on metalorganic chemical vapor deposition (MOCVD)-grown Al_xGa_{1-x}N samples with Al content $x = 0.1$ and 0.3 . We observe a dominant donor level and show that its activation energy depends on the Al mole fraction. In samples with $x = 0.3$, we argue that the surface is rough due to the rather high Al mole fraction and therefore, they behave as interfacial layers with defects which induce a long-time relaxation in the samples.

2. Experimental

Epitaxial layers of Al_xGa_{1-x}N were grown on GaN substrates by the EMCORE Corporation using MOCVD. The thickness of the layers was about 1.6 μm. Two samples labeled sample 1 and sample 2 with Al molar fraction $x = 0.1$ and 0.3 , respectively, were investigated. The free electron concentrations obtained by Hall measurements were 2.4×10^{17} and

*Corresponding author. Tel.: +354-525-4800/4708; fax: +354-552-8911.

E-mail address: seghier@hi.is (D. Seghier).

$5.2 \times 10^{17} \text{ cm}^{-3}$ in the two samples, respectively. The samples were cleaned with organic solvents before evaporating the metal contacts in a vacuum chamber. For Ohmic contacts, Al was evaporated on the AlGaN layer, which was subsequently annealed at 750°C for 1 min. Au was evaporated on the AlGaN layer as a Schottky contact. Conventional current–voltage ($I-V$) and capacitance–voltage ($C-V$) measurements were used to investigate the Schottky diodes and a standard deep-level transient spectroscopy (DLTS) setup, to characterize deep defects. The capacitance of the diodes was also measured as a function of the temperature at various frequencies.

3. Results and discussion

We measured the capacitance variation as a function of temperature at different AC frequencies in the samples. Fig. 1 shows the capacitance vs. temperature spectra measured at 100 kHz with a bias of 0 V for samples 1 and 2. After a smooth decrease between room temperature and approximately 160 K, the capacitance drops abruptly to a level at which it remains at lower temperatures. A corresponding drop of capacitance occurs at a lower temperature in sample 2. The $C-V$ measurements indicate that the samples are not completely depleted at 80 K since the capacitance still changes with reverse bias. Hence, we deduce that the abrupt decrease in capacitance is not due to a complete freeze-out of free carriers. From conductance vs. temperature measurements (not shown), we observe a peak at low temperature in both the samples. The

position of this peak is shifted to a lower temperature in sample 2. The temperature at which the conductance peak is observed corresponds to the inflection point in the capacitance vs. temperature spectra. The activation energies deduced from the plots of $\log(\omega/T^2)$ vs. $1/T$, where ω is the angular frequency of the AC signal and T the temperature, are 90 and 110 meV for the two samples, respectively.

From the $I-V$ measurements, we calculated the Schottky barrier height $\Phi_b = 0.9$ for sample 1 and 1.5 eV for sample 2, respectively, as described in Ref. [6]. For sample 1, the value of the barrier height agrees with Schottky's rule: $\Phi_b = \Phi_m - \chi$, while for sample 2, the value is lower than that predicted by this rule.

In Fig. 2, we show a $C-V$ plot for sample 2. The reverse voltage was scanned from 0 to 4.5 V (curve a) and after waiting for 30 min, the voltage was scanned back from 4.5 to 0 V (curve b). The capacitance decreases with increasing reverse bias as expected for a Schottky diode. However, it is important to notice that there is a hysteresis between the two curves. If one keeps the reverse bias applied to the diode constant, then the capacitance increases slowly until it reaches a saturation value. The relaxation time is longer at lower temperatures. The $C-V$ curves measured in sample 1 did not exhibit a significant hysteresis.

Fig. 3 shows the DLTS spectra measured from samples 1 and 2. For these measurements, a reverse bias of 2 V and a filling pulse of 1 V were used. Under these conditions, the investigated area is far from the interface which, however, may slightly contribute to the signal. It is clear that the DLTS signal is larger in sample 2 than in sample 1. In addition, the signal is broad and does not shift in temperature when the rate window is

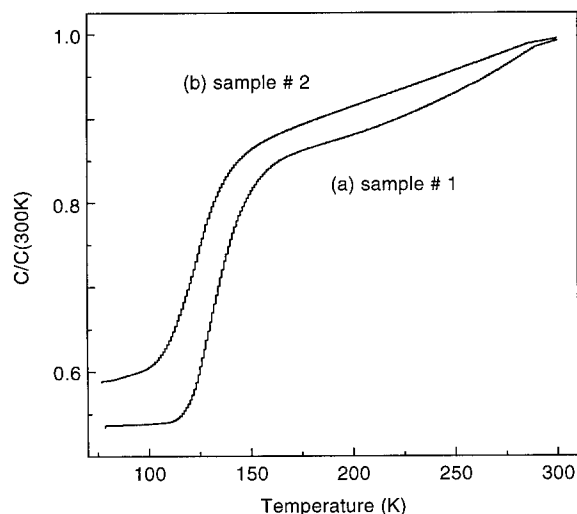


Fig. 1. Capacitance vs. temperature measured at 100 kHz (a) from sample 1 and (b) from sample 2. The capacitance has been normalized to its value at room temperature.

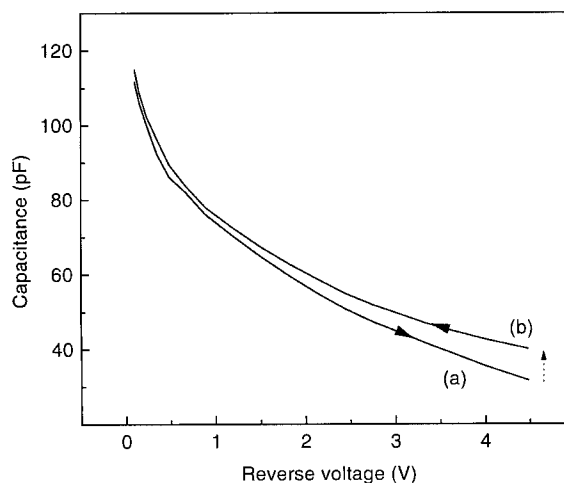


Fig. 2. $C-V$ plots from sample 2: (a) from 0 to 4.5 V; (b) from 4.5 to 0 V. The dotted arrow corresponds to a waiting time of 30 min.

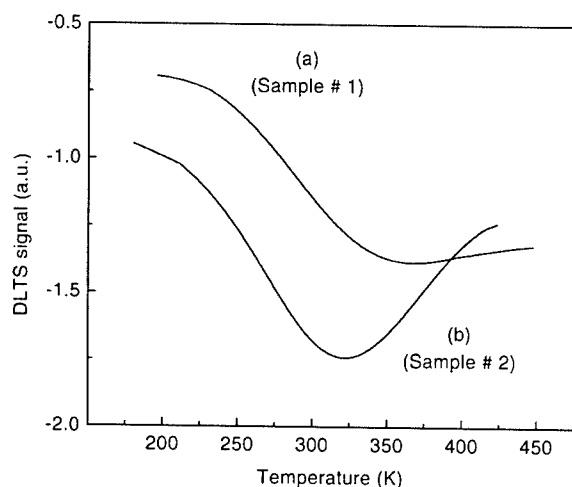


Fig. 3. DLTS spectra for (a) sample 1 and (b) sample 2. Reverse bias was 2 V and filling pulse 1 V.

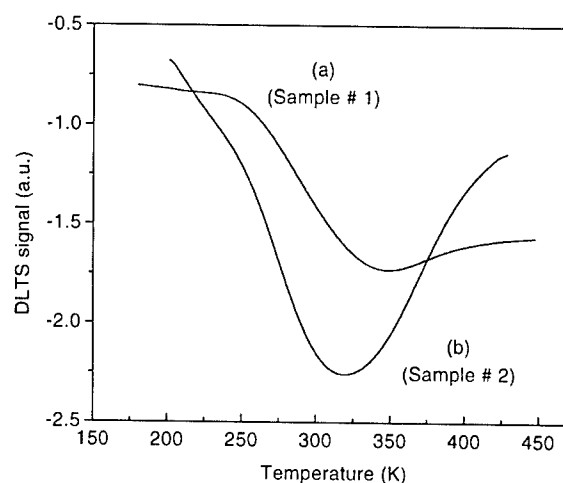


Fig. 4. DLTS spectra from (a) sample 1 and (b) sample 2. Reverse bias was 2 V and filling pulse 2 V.

changed as a signal related to a single energy level should do. Rather, it behaves as a signal arising from a continuum of energy levels in the band gap, for instance, interface states. In Figs. 4 (a) and (b) we show the DLTS spectra from samples 1 and 2, respectively, measured using a reverse bias of 2 V and a filling pulse of 2 V. The larger filling pulse ensures that the investigated area includes the interface between the metal and the semiconductor. While the amplitude of the DLTS signal of sample 1 is similar to the case of Fig. 3, it increases significantly for sample 2. Since the interface is included in the investigated area, we deduce that the defects responsible for the observed signal have a higher density at the interface for sample 2. Therefore, we assign the observed signal to a continuum of interface defects.

The admittance spectroscopy measurements clearly show the presence of a dominant donor level. The magnitude of the decrease in capacitance suggests that this is a dominating donor level. According to the $C-V$ measurements performed at low temperature, the samples are still conductive after this donor level becomes neutral. Hence, we deduce that this is not the shallowest donor in the samples. Alternatively, it might be the shallowest donor level in which case, there must be hopping conductivity at low temperatures in the samples. From the present data, it is difficult to conclude about the origin of the electrical conductivity of AlGaIn at low temperatures. The activation energy of the dominating donor level is lower in the sample with higher Al content (sample 2). This may explain why the electron concentration is higher in this sample at room temperature.

The DLTS measurements strongly suggest the presence of a continuum of energy levels at the interface with higher density in sample 2. We believe that the high

Al content results in a perturbed and rough surface causing these states. The potential fluctuation model proposed by Werner and Guttler [7] in a study of PtSi/Si diodes predicts that a deformation of spatial barrier distribution on inhomogeneous Schottky contacts may cause the difference in the values of Φ_b determined by $I-V$ measurements. Their model seems to be appropriate for the interpretation of the difference of the Φ_b values of AlGaIn in our study. The surface, thus, acts as an interfacial layer, which lowers the barrier, as pointed out in the model of Bardeen [8]. This would explain why we measure a lower value of Φ_b than that predicted by Schottky's rule in sample 2. The situation is different for sample 1 since it has a lower Al content. The continuum of energy levels in the band gap within this interfacial layer, which to some extent is similar to a MIS structure, is also responsible for the long-time relaxation observed in the $C-V$ plots. We do not believe that the reason for a low value of Φ_b in our samples with high Al content is a usual interfacial layer, that is an oxide layer or a damaged surface. If this were the case, samples with low x should also exhibit the same behavior.

4. Conclusion

Au/AlGaIn Schottky diodes were characterized using electrical methods for $x = 0.1$ and 0.3 . We observed a dominating donor level with activation energy dependent on the Al mole fraction. It is deeper in the sample with less Al content, which may explain the lower free electron concentration at low temperature in this sample. A barrier height lower than that predicted by Schottky's rule was measured in the sample with $x = 0.3$, and the $C-V$ characteristics exhibit a hysteresis

due to a long time relaxation process. The DLTS measurements reveal the presence of a continuum of energy levels in the band gap at the interface. The density of these states is higher in the sample with higher Al content. We attribute the lowering of the barrier in the sample with higher Al content to spatial fluctuations of Φ_b at the surface caused by the high Al content. The surface is, therefore, rough and behaves as an interfacial layer, which pins the Fermi level. Charging of this layer has a long time constant and, therefore, it is responsible for the hysteresis observed in the $C - V$ characteristics.

Acknowledgements

This research was supported by the Icelandic Research Council and the University of Iceland Research Fund. We are grateful to EMCORE for providing the samples used in this study.

References

- [1] M. Asif Khan, M.S. Shur, Q. Chen, *Appl. Phys. Lett.* 68 (1996) 3022.
- [2] J.F. Wu, B.P. Keller, S. Keller, D. Kapolnek, P. Kozodoy, S.P. Denbaars, U.K. Mishra, *Solid State Electron.* 41 (1997) 1569.
- [3] S.C. Strite, H. Mokoc, *J. Vac. Sci. Technol. B* 10 (1992) 1237.
- [4] S.C. Strite, in: J.H. Edgar (Ed.), *Properties of Group III Nitride*, INSPEC, London, 1994, pp. 268–271.
- [5] H.G. Lee, M. Gershenson, B.L. Goldenberg, *J. Electron. Mater.* 20 (1991) 621.
- [6] E.H. Rhoderick, R.W. Williams, *Metal-Semiconductor Contacts*, 2nd Edition, Clarendon, Oxford, p. 113.
- [7] J.H. Werner, H.H. Gutler, *J. Appl. Phys.* 69 (1991) 1522.
- [8] S.M. Sze, *Physics of Semiconductors*, Wiley, New York, 1981, p. 271.



ELSEVIER

Physica B 308–310 (2001) 134–138

PHYSICA B

www.elsevier.com/locate/physb

Electronic levels of isolated and oxygen-perturbed hydrogen in silicon and migration of hydrogen

K. Bonde Nielsen^{a,*}, L. Dobaczewski^b, S. Søgård^a, B. Bech Nielsen^a

^a*Institute of Physics and Astronomy, University of Århus, DK-8000 Århus, Denmark*

^b*Institute of Physics, Polish Academy of Sciences, al. Lotnikow 32/46, 02-668 Warsaw, Poland*

Abstract

The migration of monatomic hydrogen in crystalline silicon is governed by three potential energy surfaces corresponding to the three possible charge states of hydrogen. The H^0 and H^+ surfaces have minima at the bond-centre site (BC) and give rise to a donor state, whereas the H^- surface has minimum at the interstitial tetrahedral site (T) giving rise to an acceptor state. We review the current experimental status regarding these surfaces. The BC-donor and the T-site acceptor are found to exist in two closely related forms, which we explain by a distortion of the energy surfaces when hydrogen is trapped in the silicon lattice at the nearby interstitial oxygen. We show how this oxygen distortion acts as a catalyst for the conversion from H^- at T sites to H^+ at BC sites and retards the migration of H^+ through BC sites. © 2001 Elsevier Science B.V. All rights reserved.

Keywords: Deep levels; Silicon; Hydrogen; Oxygen

1. Introduction

The structure of isolated monatomic hydrogen embedded in crystalline silicon has been examined theoretically by several groups [1]. The consensus has emerged that the embedded hydrogen may exist in three charge states: H^- , H^0 , and H^+ . The total energy surface of the negative charge state has minima at tetrahedral interstitial sites (T) of the silicon crystal, whereas the neutral and positive charge states have minima at bond-centre sites (BC). The migration of hydrogen is governed by these surfaces. Experimentally, we may visualise this in terms of potential energy curves connecting the neighbouring BC and T sites in configuration space. In the present contribution, we collect the available experimental data regarding the monatomic hydrogen structures in silicon. We show that the configuration potentials of all three charge states become distorted in the vicinity of an interstitial oxygen impurity in the silicon crystal and discuss the consequences of this for hydrogen migration at low temperature.

2. The configuration potentials

The Fermi-level position determines the energetically most favourable charge state of monatomic hydrogen in silicon. According to theory [1] this implies that negatively charged hydrogen at or near the interstitial tetrahedral site is the most stable configuration in n-type material. We denote this configuration $H^-(T)$. Similarly, the configurations with neutral or ionised hydrogen at the bond-centre site are denoted by $H^0(BC)$ and $H^+(BC)$. The total energy of $H^0(BC)$ exceeds that of $H^-(T)$ in n-type silicon. However, $H^0(BC)$ may still coexist with $H^-(T)$ as a metastable configuration at low temperature. This metastable hydrogen defect gives rise to a donor level defined by the emission process $H^0(BC) \rightarrow H^+(BC) + e^-$. All the features mentioned are well established theoretically and experimentally. The donor emission signal is known from capacitance spectroscopy, and the barrier for the conversion $H^0(BC) \rightarrow H^-(T)$ has been established from the annealing of this signal. Fig. 1 depicts the complete configuration scheme of monatomic hydrogen as it emerges when all the available experimental data are used for its construction. It contains the basic features outlined

*Corresponding author. Fax: +45-8612-0740.

E-mail address: kbn@ifa.au.dk (K.B. Nielsen).

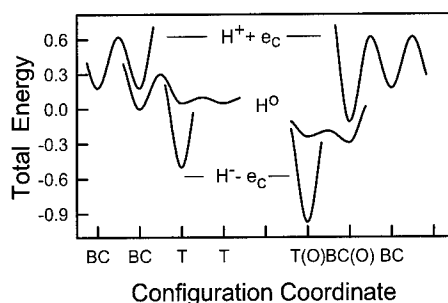


Fig. 1. Configuration diagram for the three charge states of isolated and oxygen-perturbed monatomic hydrogen in the silicon lattice. The zero of the energy scale has been chosen to be equal to the total energy of neutral hydrogen at the bond-centre position.

above and includes a set of potential curves indicating how these curves may be affected for hydrogen in the strain field of interstitial oxygen. A configuration scheme similar to that of Fig. 1 has been introduced earlier [2]. In this scheme, the H^- curves were tentative. With new data available regarding the acceptor states we review the main points in the construction of the configuration potentials and quantify the scheme further. We shall anticipate the conclusions and denote the oxygen perturbed minimum-energy configurations $H^-(T)-O_i$, $H^0(BC)-O_i$, and $H^+(BC)-O_i$.

In the previous work [2] the dynamic properties of the $H(BC)$ and $H(BC)-O_i$ donor centres were examined by the application of deep level transient spectroscopy (DLTS). The characteristics related to the formation of $H(BC)$ and $H(BC)-O_i$ are particularly relevant and may be summarised as follows. Both centres are abundant after low-temperature proton implantation giving rise to two signals, denoted by $E3'$ and $E3''$, observed when DLTS is applied in situ to as-implanted samples. The $H(BC)$ and $H(BC)-O_i$ centres are always present after implantation into the depletion layer of a reverse-biased diode. However, they are almost indistinguishable as far as their electronic properties (i.e. their DLTS signals) are concerned but can be discerned on the basis of characteristic differences in their formation and annealing properties. A key point for the assignment of oxygen to the perturbed centre is that $H^+(BC)-O_i$ converts to $H^+(BC)$ in oxygen-poor material, whereas in oxygen-rich material the reverse process occurs. A quantitative analysis of these thermal processes fixes the barrier for jumps between adjacent $H^+(BC)$ configurations to about 0.44 eV and shows that $H^+(BC)-O_i$ is stabilised by an additional energy of about 0.29 eV relative to the $H^+(BC)$ as indicated in the diagram. As a consequence of the perturbation the $H(BC)-O_i$ centre should have a lower symmetry than the $H(BC)$ centre. We have confirmed this by the application of

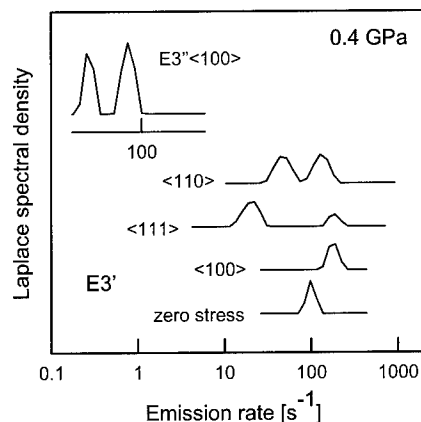


Fig. 2. Laplace DLTS spectra revealing the trigonal symmetry of the centre associated with the $E3'$ signal, and lower symmetry of the centre associated with the $E3''$ signal (inset).

uniaxial-stress DLTS. Fig. 2 depicts the preliminary stress data. The split pattern of the $E3'$ emission signal reveals the expected trigonal symmetry of $H(BC)$, whereas the splitting under $\langle 100 \rangle$ stress of the $E3''$ signal into two components indicates a lower (monoclinic-I) symmetry as expected for $H(BC)-O_i$. In the diagram (Fig. 1) the $H^+ + e_c$ total energy curves are fixed relative to the $H^0(BC)$ point. The almost equal activation energies of $E3'$ and $E3''$ (0.175 eV) are reflected by an equal separation at BC and BC(O) of the H^0 and H^+ curves.

To place the H^- curves, we note [2] that when the bias is removed at low temperature (< 70 K) the $E3''$ signal disappears instantaneously while the $E3'$ is unaffected. If the temperature is raised to 120 K then also $E3'$ disappears swiftly. However, the total strength of the original $E3' + E3''$ signal can be recovered. The tracking of charge accumulated in the depletion layer shows that both centres prior to the recovery have been converted temporarily into negative singly charged centres which anneals at ~ 250 K. If we assume that these hidden centres can be identified with the occupied acceptor states of near T-site hydrogen, $H^-(T)$ and $H^-(T)-O_i$, we may expect the annealing to be triggered by thermal electron emission from these states. The emission may then be observed as a capacitance transient at temperatures slightly below 250 K. Since $E3' + E3''$ completely dominates the DLTS spectra and can be recovered fully from the hidden centres, we may expect a substantial signal, large enough to be detected as a single-shot capacitance transient. As depicted in Fig. 3, such capacitance-transient measurement allowing for long decay times does indeed reveal the emission. The transient shown has been recorded with an oxygen-rich hydrogen-implanted diode with about 55% of the implants initially present as $H(BC)$ and the rest as

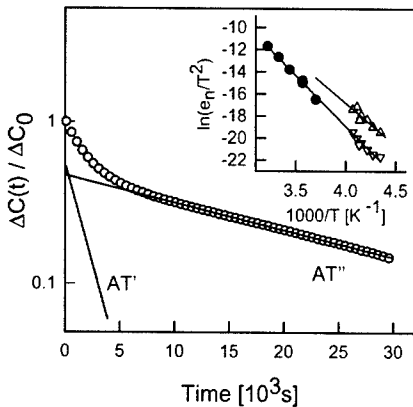


Fig. 3. Single-shot capacitance transient at 242 K revealing two components AT' and AT''. As inset, the Arrhenius analysis of AT''(▽) and AT'(Δ). The data (●) of Refs. [3,4] have been included.

H(BC)–O_i. Both centres were first converted into the negative hidden centres by bias-removal at 110 K. The capacitance transient was then recorded after reapplication of the bias at 242 K. As can be seen the transient consists of two exponential components of about 55% and 45% intensity. We ascribe the fast decay (55%) to electron emission from H[–](T) and label it AT'. The slow decay (45%) is analogously ascribed to emission from H[–](T)–O_i and labelled AT''. These assignments are based on the following observations: (1) The negative centres can be (partially) recovered after the application of a filling pulse and a second-shot transient recorded. This second-shot transient is still composed of AT' and AT''. However, now AT'' dominates. (2) For samples prepared so that essentially only H[–](BC)–O_i is present initially, the fast component AT' is absent in the first-shot transient.

From the transients AT' and AT'' measured at different temperatures we derive the Arrhenius plots depicted as an inset in Fig. 2. We note the agreement over many decades between our AT'' data and those obtained by Johnson et al. [3,4]. The linear-regression analysis yields the activation $\Delta H'' = 0.79 \pm 0.03$ eV for the emission from H[–](T)–O_i, and $\Delta H' = 0.65 \pm 0.10$ eV for the emission from H[–](T). The electron emission enthalpies found for H[–](T)–O_i and H[–](T) exceed those of the corresponding BC donor states in accordance with the expected negative-U property.

The negative-U property implies that H⁰(BC)–O_i and subsequently H[–](BC)–O_i, are swiftly formed after thermal electron emission from H[–](T)–O_i. In accordance with this the AT'' transient should have twice the amplitude of the E3'' transient. We find that the AT'' amplitude is larger than that of E3'' but only by a factor of about 1.5. We note that the barrier (0.79 eV) for the

emission from H[–](T)–O_i is larger than the barrier (0.73 eV) for release of hydrogen from H[–](BC)–O_i, as indicated by the H⁺ potential shown in Fig. 1 and discussed above. As a result the two-step emission H[–] → H⁰ + e[–] → H⁺ + 2e[–] from the T(O) site is followed by leakage of hydrogen away from the BC(O) site which accounts at least partly for the amplitude loss.

According to the diagram the energy of H⁰(BC)–O_i is lowered to about 0.3 eV with respect to the regular sites. This supports our anticipation that the emission from H(T)–O_i is followed by a swift transformation to H⁰(BC)–O_i so the first emission step may define an acceptor level as the energy difference between H⁰(BC)–O_i + e_c and H[–](T)–O_i in the usual sense. For this, we obtained the barrier for capture into H[–](T)–O_i from H⁰(BC)–O_i + e_c. This barrier (about 0.11 eV) is included in the H⁰ potential (Fig. 1) and subtracted from the AT'' activation energy to fix the H[–](T)–O_i point in the diagram corresponding to an acceptor level at 0.68 ± 0.08 eV below the conduction band.

For the solution-site H[–](T) the situation is more complicated. We obtained an activation enthalpy ΔH of about 0.65 eV but must use indirect arguments to estimate the level position. As mentioned earlier, we found that repeating the transient causes the H[–](T)–O_i signal dominate. This indicates that the solution-site activation enthalpy is actually the barrier against the release of hydrogen from H[–](T) to migrate as H⁰ through T sites. This migration may proceed swiftly as has been shown [2], and is indicated in the diagram by the small barrier between adjacent T sites. Most of the released hydrogen eventually traps at the oxygen-perturbed BC sites as H[–](BC)–O_i in the depletion layer of a reverse-biased diode at low temperature. The consequence of the analysis is that the concept of an acceptor level defined as the energy difference between H⁰(BC) + e_c and H[–](T) loses its meaning in practical terms, since it cannot be realised experimentally. Nevertheless, we may obtain an estimate for the total energy of H[–](T). The activation enthalpy for H⁰(BC) → H⁰(T) is known (0.295 eV), and the barrier has been estimated for the reverse process H⁰(T) → H⁰(BC) to be ~0.2 eV. Both are included in the H⁰ potential [2]. Furthermore, the swift diffusion observed under carrier injection [2] indicates a very small barrier of <0.1 eV for migration of H⁰ through T sites. In combination with the measured activation enthalpy these figures show that the total energy of H[–](T) is 0.40–0.60 eV lower than that of H⁰(BC) + e_c. This concludes the construction of the configuration diagram.

3. Low-temperature migration

With the configuration scheme at hand we may now quantify the properties of low-temperature hydrogen

migration. There are four essential points to make. (i) The barrier for migration of the neutral species H^0 in the open areas of the lattice through T sites is extremely low. This is confirmed theoretically by several authors [1], and, in particular, by recent molecular dynamics simulations [5,6], (ii) the barrier for jumps of H^0 from a T sites to a BC site is considerable. This point is still debated [3,4,7] and is crucial for the path of low-temperature migration, (iii) the strain field around defects (here oxygen impurities) influences the stability of hydrogen at BC and T sites, and (iv) the inversion of the donor and acceptor levels of monatomic hydrogen combined the effective negative-U behaviour of hydrogen at the perturbed site.

The characteristic migration cycle involving the trapping and mobilisation of hydrogen at low temperature is revealed clearly by the in situ DLTS data. Typically, after implantation at 60 K into the depletion layer of a reverse biased diode build on n-type silicon, the original signal $E3' + E3''$ associated with $H^+(BC)$ and $H^+(BC)-O_i$ accounts for $>80\%$ of the implanted protons. After low-temperature zero-bias annealing of these signals total recovery can be achieved by illumination of the annealed sample while under reverse-bias. In this case, the restored signal is practically all $E3''$ which accounts for all of the original signal or even more. Also, the original $E3'$ signal can be recovered. This happens when the forward-bias injection of holes is applied to p^+n -samples. In this case, $E3''$ is not recovered. However, the remaining strength of the original signal can be recovered as $E3''$ when subsequently the reverse-bias illumination is applied. The $E3'$ recovery is accompanied with long-range diffusion even at 65 K, whereas long-range diffusion (i) is not observed in connection with the $E3''$ recovery. With reference to the configuration scheme we explain the long-range diffusion during injection as a result of the continuous generation of $H^0(T)$ resulting in a steady-state population of swiftly moving H^0 species that eventually convert to metastable $H^0(BC)$. Also, the illumination generates highly mobile H^0 at T sites. However, because of the reverse bias these species convert to $H^+(BC)-O_i$ as soon as the oxygen strain-field is encountered. Due to the barrier (ii) this happens effectively without forming $H^+(BC)$ via $H^0(BC)$. The $H^+(BC)-O_i$ is bound by 0.73 eV (iii). As a consequence, H^+ will be released to diffuse and drift via BC sites (and oxygen perturbed BC sites) at around 245 K, and will eventually be swept out by the electrical field of the junction, in accordance with previous studies of hydrogen mobility [8]. When hydrogen is kept as $H^-(T)-O_i$ the migration sets in at a slightly higher temperature. This indicates that the annealing is initiated and essentially controlled by the electron emission $H^- \rightarrow H^0 + e^-$. The negative-U property (iv) then ensures a rapid conversion to the H^+ diffusion stage.

The present studies apply to low temperature and high oxygen content. The experimental evidence presented in Fig. 3 indicates that the deeper of the two hydrogen centres found may correspond to the acceptor state observed by Johnson et al. [3,4]. The two experiments have much in common. In both cases monatomic hydrogen is released from traps by illumination under bias and converted to H^- by the application of a flooding pulse. In our case, the hydrogen source is oxygen-trapped hydrogen, whereas the source in the experiment [3,4] is the compensated shallow donor. The main differences are that the temperatures of illumination and signal recording are lower in our case. Considering this similarity, and the consistency of the combined Arrhenius analysis (Fig. 3) we suggest that the two sets of data may have the same origin and conclude that the oxygen-perturbed sites may play a significant role in the migration scenario even at room temperature. The crucial point is the height of the barrier opposing the transformation $H^0(T) \rightarrow H^0(BC)$ as compared to the barrier for jump between adjacent T sites. With $\sim 10^{18} O_i \text{ cm}^{-3}$ we find that a barrier difference as low as 0.15 eV would be sufficient to produce primarily $H^-(T)-O_i$ by the illumination-flooding cycle at room-temperature designed [3,4] to release hydrogen from the compensated donors. For this to be true also for oxygen-poor material ($10^{16} O_i \text{ cm}^{-3}$) the barrier difference must be larger (0.25–0.3 eV). Such large barrier difference would comply with the barrier for the process $\mu^0(T) \rightarrow \mu^0(BC)$ (0.38 eV) reported in a recent muonium study [9] and with the small barrier (0.5–0.15 eV) for H^0 migration obtained by molecular dynamics simulations [5,6]. The simulations also foresee the trapping near

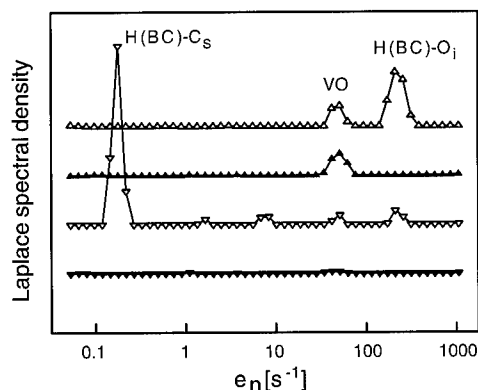


Fig. 4. The formation of a carbon-hydrogen centre in carbon-rich Si (V). Compared to the formation of the $H(BC)-O_i$ centre in oxygen-rich Si (Δ). Laplace spectra obtained after zero-bias annealing (110 K) of as-implanted samples and after subsequent illumination (75 K) are shown. The carbon centre is analogous to the oxygen centre and denoted by $H(BC)-C_s$ accordingly. See Ref. [11] for details.

interstitial oxygen at strained BC sites forming weakly bound hydrogen–oxygen structures. The existence of such weakly bound structures has been revealed by the identification of local vibration modes [10].

Finally, we mention that the presence of substitutional carbon in the samples may overrule the effect of oxygen. Fig. 4 depicts recent data obtained by *in situ* Laplace DLTS for float-zone samples with $1 \times 10^{17} \text{ C}_5\text{cm}^{-3}$ after implantation of hydrogen at low temperature. The data show that the $\text{H}(\text{BC})-\text{O}_i$ donor is heavily suppressed in favour of a dominating analogous carbon-perturbed hydrogen donor. This donor transforms during zero-bias annealing to a carbon–hydrogen acceptor [11], which is stable at room temperature. The $\text{H}(\text{T})-\text{O}_i$ acceptor is suppressed correspondingly and the migration properties of hydrogen may be affected.

4. Concluding remarks

We have shown that T sites in the proximity of interstitial oxygen act as trapping centres for H^- in the same way as the BC sites with oxygen nearby act as trapping centres for H^0 and H^+ . We concluded that the thermal electron emission initiates the escape of hydrogen from the T-site traps. We obtained the acceptor level of oxygen-perturbed monatomic hydrogen and demonstrated its negative-U property. We concluded that the presence of oxygen-perturbed centres plays a crucial role for migration of hydrogen at or below room temperature. The interstitial oxygen retards the migration of H^+ and acts as a catalyst for the conversion of hydrogen from T sites to BC sites.

Acknowledgements

This work has been supported by the Danish National Research Foundation through the Aarhus Centre for Atomic Physics (ACAP) and the KBN Grant No. 8T11B00315 in Poland.

References

- [1] S.K. Estreicher, *Mater. Sci. Eng. R14* (1995) 314, and references therein.
- [2] K. Bonde Nielsen, B. Bech Nielsen, J. Hansen, E. Andersen, J.U. Andersen, *Phys. Rev. B* 60 (1999) 1716.
- [3] N.M. Johnson, C. Herring, C.G. Van de Walle, *Phys. Rev. Lett.* 73 (1994) 130.
- [4] N.M. Johnson, C. Herring, C.G. Van de Walle, *Phys. Rev. Lett.* 74 (1995) 1889.
- [5] S.K. Estreicher, private communication.
- [6] S.K. Estreicher, Y.K. Park, P.A. Fedders, in: R. Jones (Ed.), *Early Stages of Oxygen Precipitation in Silicon*, NATO ASI Ser. 3 17 (1996) 179.
- [7] C.H. Seager, R.A. Anderson, S.K. Estreicher, *Phys. Rev. Lett.* 74 (1995) 4562.
- [8] C.H. Seager, R.A. Anderson, *Appl. Phys. Lett.* 53 (1988) 1181.
- [9] B. Hitti, S.R. Kreitzman, T.L. Estle, E.S. Bates, M.R. Dawdy, L.T. Head, R.L. Lichti, *Phys. Rev. B* 59 (1999) 4918.
- [10] B. Bech Nielsen, K. Tanderup, M. Budde, K. Bonde Nielsen, J.L. Lindström, R. Jones, S. Öberg, B. Hourahine, P. Briddon, *Mater. Sci. Forum* 258–263 (1997) 391.
- [11] O. Andersen, L. Dobaczewski, A.R. Peaker, K. Bonde Nielsen, B. Hourahine, R. Jones, P.R. Briddon, S. Öberg, *Mater. Sci. Forum* 258–263 (1997) 391.



ELSEVIER

Physica B 308–310 (2001) 139–142

PHYSICA B

www.elsevier.com/locate/physb

Piezospectroscopic analysis of the hydrogen–carbon complexes in silicon

O. Andersen^{a,*}, L. Dobaczewski^{a,b}, A.R. Peaker^a, K. Bonde Nielsen^c,
B. Hourahine^d, R. Jones^d, P.R. Briddon^e, S. Öberg^f

^a Centre for Electronic Materials, University of Manchester Institute of Science and Technology, P.O. Box 88, Manchester M60 1QD, UK

^b Institute of Physics, Polish Academy of Sciences, Warsaw, Poland

^c Institute of Physics and Astronomy, University of Aarhus, Aarhus, Denmark

^d Department of Physics, The University of Exeter, Exeter, UK

^e Department of Physics, The University of Newcastle upon Tyne, Newcastle upon Tyne, UK

^f Department of Mathematics, University of Luleå, Luleå, Sweden

Abstract

We have observed the donor ($E_c - 0.22$ eV) and acceptor ($E_c - 0.16$ eV) levels related to hydrogen–carbon complexes in silicon. The donor level is only detected at low temperatures after proton implantation. This hydrogen–carbon complex irreversibly reconfigures at temperatures above 225 K to a configuration characterized by the acceptor level, which is stable up to room temperature. The same acceptor level is also observed after atomic hydrogen diffusion. We have used Laplace transform deep level transient spectroscopy (DLTS) to show the influence of uniaxial stress on the electron emission process and the effect of the stress-induced alignment for the acceptor state. The pattern of the Laplace DLTS peak splittings indicate a trigonal symmetry of the defect. First principles calculations were carried out on the hydrogen–carbon defects with a view of determining their electrical levels and stress response for comparison with the experimental results. © 2001 Elsevier Science B.V. All rights reserved.

PACS: 61.72.B; 71.55.C; 71.70.F

Keywords: Hydrogen–carbon pair; Silicon; Uniaxial stress; Laplace DLTS

Hydrogen and carbon atoms are two of the most common unintentional impurities in silicon. Usually, carbon is incorporated into the crystals during growth, while hydrogen is introduced during subsequent technological processes. Hydrogen atoms form complexes with structural defects and impurities, which for shallow donors and acceptors can result in their passivation, i.e., a disabling of their electrical activity in the crystal. In the case of the initial electrically inactive iso-valent substitutional carbon impurity, the hydrogen–carbon pair formation results in the appearance of electronic energy levels in the silicon band gap [1].

There is some controversy about the donor/acceptor properties of the energy levels related to hydrogen bound to substitutional carbon in silicon [2]. In deep level transient spectroscopic (DLTS) measurements, the charge state of the defect is not determined directly. However, in most cases, the value of the directly measured carrier capture cross-section can indicate the charge of the defect. Henry and Lang [3] showed that for Coulombically attractive centres the carrier capture cross-section is expected to be $\geq 10^{-14}$ cm², while one can expect this value to be between 10^{-16} and 10^{-15} cm² for a neutral defect and $< 10^{-17}$ cm² for a repulsive centre. Alternatively, the observation of the Poole–Frenkel effect (barrier lowering in the depletion field and consequent enhancement of the emission rate) is indicative of a charged defect. However, an

*Corresponding author. Fax: +44-161-200-4770.

E-mail address: andersen@fs4.ee.umist.ac.uk (O. Andersen).

enhancement of the emission rate as a function of field must be interpreted with care as other mechanisms (tunnelling and impact ionization) can produce qualitatively similar effects from neutral as well as charged centres [4,5]. In this study, two different energy levels related to hydrogen–carbon pairs in n-type silicon are reported and according to the above criteria they have been assigned to the donor and acceptor levels. For the acceptor level, a complete piezospectroscopic analysis has been performed and the results compared with theoretical modelling.

The samples used for this study were prepared from 20 Ω -cm float zone n-type silicon doped with $\sim 10^{17}$ carbon atoms cm^{-3} . All the samples were cut from the same wafer with a (110) surface orientation in the shape of $1 \times 2 \times 7$ mm blocks with the longest sample edge along one of the major crystallographic directions ($\langle 100 \rangle$, $\langle 110 \rangle$ and $\langle 111 \rangle$). Hydrogen–carbon complexes were produced by either proton implantation at 70 K under a reverse bias with the energy of ~ 525 keV and a dose of $\sim 5 \times 10^{19} \text{ cm}^{-2}$ or by wet chemical etching at room temperature (HNO_3 and HF in the ratio 10:1). Czochralski grown 20 Ω -cm n-type silicon samples were implanted with protons under the same conditions as the carbon-rich samples for direct comparison. Gold Schottky diodes were formed for DLTS measurements.

We have applied the technique of high resolution Laplace DLTS [6] in combination with uniaxial stress to carry out a piezospectroscopic analysis of the observed hydrogen–carbon complexes. The stress partially lifts the spatial degeneracy of the defect which results in a splitting of the defect energy level. Assuming a random distribution of defects in non-equivalent orientations, the number of split lines and their intensity ratios reflect the symmetry class of the initial charge state of the given defect. The relative shifts of the total energies of the non-equivalent orientations with respect to the applied stress have been determined by applying the stress at sufficiently high temperature to reach thermodynamic equilibrium, and then quickly cooling the sample to the measured temperature. Subsequently, the occupancies of the non-equivalent orientations have been evaluated, and the relative energy shifts have been obtained from Boltzmann statistics. The charge state of the complex during the alignment process is controlled by the bias applied to the sample.

Zero stress Laplace DLTS spectra obtained below 103 K after proton implantation reveal two peaks of comparable concentration in the carbon-rich samples. One of these peaks is also seen in the oxygen-rich samples and can be assigned to overlapping donor levels of isolated bond centred hydrogen ($\text{E3}'$) and bond centred hydrogen perturbed by interstitial oxygen ($\text{E3}''$) as previously discussed [7]. The other peak only appears in the carbon-rich samples. We label it CH_1 . Fig. 1

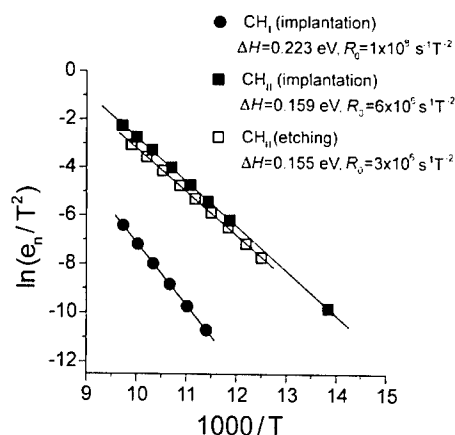


Fig. 1. Arrhenius plots for the electron emission from CH_1 (circles) and CH_{11} (squares) measured by Laplace DLTS. Activation enthalpies ΔH and pre-exponential factors R_0 are given.

shows the Arrhenius plot for the electron emission from CH_1 yielding the activation enthalpy $\Delta H \approx 0.22 \text{ eV}$ and the apparent (intercept) electron capture cross-section $\sigma_{n,a} \approx 2 \times 10^{-14} \text{ cm}^2$ obtained from the pre-exponential factor. The pre-exponential factor is similar to the values obtained for the well-established donor levels $\text{E3}'$ and $\text{E3}''$. The ionization process for CH_1 is influenced by the electric field in the space charge region, and the observed field dependence complies with the three-dimensional Poole–Frenkel effect expected for an electron trapped by a positively charged centre [4]. We conclude that CH_1 is a singly charged donor.

Several properties concerning the microscopic structure of CH_1 have been established. A direct comparison with the oxygen-rich samples shows that CH_1 behaves dynamically like $\text{E3}''$, i.e., bond centred hydrogen perturbed by interstitial oxygen [7]. Uniaxial stress measurements did not allow us to establish the exact symmetry class of CH_1 , but we can conclude that the centre has lower than trigonal symmetry. Finally, the CH_1 complex irreversibly converts to another hydrogen–carbon complex after zero bias annealing at 225 K (see below). These observations are all consistent with an atomic configuration $\text{SiH}_{\text{BC}}\text{SiC}_s$ in which hydrogen is bond centred between two silicon atoms located as the first and second nearest neighbour to the substitutional carbon atom.

The disappearance of CH_1 in the Laplace spectrum after zero bias annealing at 225 K is accompanied by the appearance of another hydrogen–carbon related peak labelled CH_{11} . The conversion ratio between CH_1 and CH_{11} is practically 1:1, indicating that CH_1 reconfigures to CH_{11} by local, thermally activated jumps of hydrogen around carbon. CH_{11} is stable at room temperature and is also observed in the etched samples. The Arrhenius

plots for the electron emission from CH_{II} (Fig. 1) confirm that the levels observed after implantation followed by annealing and after atomic diffusion of hydrogen are identical. In both cases the activation enthalpy is $\Delta H \approx 0.16 \text{ eV}$. The electric field dependence of the emission process for CH_{II} was studied under exactly the same experimental conditions as for CH_{I} . No field dependence was observed. Direct capture measurements using the filling-pulse method yielded an electron capture cross-section for CH_{II} of $\sigma_{\text{II}} \approx 2 \times 10^{-16} \text{ cm}^2$ with no measurable energy barrier for the capture process. From the lack of field dependence and the value of the electron capture cross-section, we conclude that CH_{II} is a deep acceptor. This is supported by the pre-exponential factor of the Arrhenius plots for the emission process (Fig. 1), which is almost two orders of magnitude smaller for CH_{II} than for CH_{I} .

We have carried out a detailed piezospectroscopic analysis of the CH_{II} complex. Fig. 2 shows Laplace DLTS spectra of CH_{II} measured at 85 K under uniaxial stress along the $\langle 111 \rangle$ direction. The spectra have been obtained with stress increments of 0.025 GPa from zero stress up to 0.5 GPa. It can be seen that CH_{II} splits into two components, which move linearly with the applied stress. The amplitude ratio for the split lines is approximately 3:1, and their amplitudes sum up to the value for the unstressed sample. In a similar way, the Laplace DLTS peak splits into two components with amplitude ratio 1:1 for stress along the $\langle 110 \rangle$ direction, while no line splitting is observed for the $\langle 100 \rangle$ stress direction. This splitting pattern establishes the trigonal symmetry of the CH_{II} complex in agreement with the results reported by Kamiura et al. [8,9].

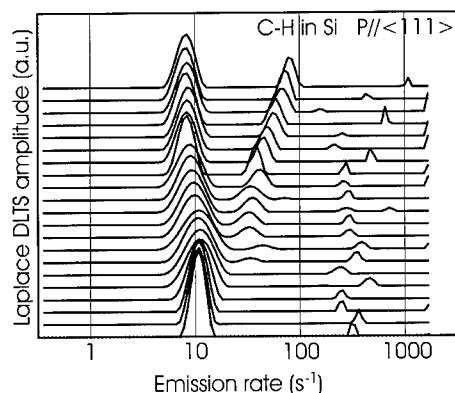


Fig. 2. Laplace DLTS spectra of the electron emission at 85 K from the CH_{II} complex under uniaxial stress along the $\langle 111 \rangle$ direction. The spectra have been obtained from zero stress (nearest to the front) up to 0.5 GPa with stress increments of 0.025 GPa. The two peaks originating from non-equivalent orientations of the CH_{II} complex are reliably resolved for stresses above 0.3 GPa.

The effect of stress on the defect total energy for a given charge state can be found from the relation $\Delta E = \sum B_{ij} \epsilon_{ij}$, where ϵ_{ij} are the components of the strain tensor and B_{ij} are the components of the corresponding piezospectroscopic tensor. For a trigonal defect stressed along the $\langle 111 \rangle$ direction, the difference in the total energy between the two non-equivalent orientations of degeneracy 1 and 3 is given by $\Delta E(1) - \Delta E(3) = 4B_{22}S_{44}P/3$, where S_{44} is a component for the silicon elastic compliance tensor ($S_{44} = 12.56 \times 10^{-3} \text{ GPa}^{-1}$), P is the stress ($P < 0$ for compressive stress), and B_{22} is the trigonal component of the piezospectroscopic tensor. The trigonal component B_{22} describes how the total energy of the defect changes when the defect is subjected to a stress along the trigonal axis, i.e., the $\langle 111 \rangle$ direction. The value of $\Delta E(1) - \Delta E(3)$ for the two charge states of the CH_{II} complex has been obtained by evaluating the relative occupancies of the two non-equivalent orientations after applying stress at $\sim 330 \text{ K}$ for sufficient time to reach the steady-state condition. From this analysis, we obtain $B_{22} = -5.3 \text{ eV}$ for the negatively charged centre (no bias applied during the alignment) and $B_{22} = -1.9 \text{ eV}$ for the neutral centre (reverse bias applied during the alignment). The negative value of B_{22} shows that the total energy of the CH_{II} complex is increased by compressive stress applied along the trigonal axis of the defect. We conclude that the relaxation of the CH_{II} complex along the trigonal axis is outward.

Theoretical modelling has been performed to investigate our hypothesis that the $E_{\text{c}} - 0.22 \text{ eV}$ donor level (CH_{I}) relates to the $\text{SiH}_{\text{BC}}\text{SiC}_{\text{s}}$ configuration of the hydrogen-carbon pair. Local density functional theory using both cluster and supercell geometries with a Gaussian basis set [10,11] has been applied. It has been found that the calculated donor level of $\text{SiH}_{\text{BC}}\text{SiC}_{\text{s}}$ lies at $E_{\text{c}} - 0.21 \text{ eV}$, i.e. very close to the observed value for the CH_{I} level. Further indirect evidence also exists for the assignment of CH_{I} with $\text{SiH}_{\text{BC}}\text{SiC}_{\text{s}}$, as this structure has previously been observed in proton-implanted material by Hoffmann et al. [12] by infrared absorption. As in the present work, it was observed by Hoffmann et al. that the $\text{SiH}_{\text{BC}}\text{SiC}_{\text{s}}$ configuration (responsible in our case for the donor level CH_{I}) disappears after annealing at $\sim 225 \text{ K}$.

The microscopic picture of the configuration responsible for the acceptor state CH_{II} is somewhat ambiguous. Both $\text{SiH}_{\text{BC}}\text{C}_{\text{s}}$ (bond centred hydrogen adjacent to the carbon) and $\text{SiC}_{\text{s}}\text{H}_{\text{AB}}$ (hydrogen anti-bonded to the carbon) have a trigonal symmetry and are predicted by our calculations to possess acceptor levels close to that observed for CH_{II} as shown in Table 1. However, the calculated piezospectroscopic parameters of $\text{SiC}_{\text{s}}\text{H}_{\text{AB}}$ in the neutral and negative charge states are in closer agreement with those observed by defect alignment (Table 1). The calculated formation energies for the

Table 1

Theoretical values of the acceptor levels and the piezospectroscopic parameters related to two different trigonal configurations of the hydrogen-carbon pair compared to the experimental values. The electrical levels are calculated with an error of ± 0.2 eV, while the theoretical stress behaviour is accurate to $\sim 20\%$

	Theory (eV)		Experiment (eV)
	SiH _{BC} C _s	SiC _s H _{AB}	CH _{II}
($-/0$) Level	0.15	0.33	0.16 ± 0.01
B_{22} (negative)	-6.0	-4.8	-5.3 ± 0.2
B_{22} (neutral)	-4.5	-2.8	-1.9 ± 0.2

SiH_{BC}C_s and SiC_sH_{AB} configurations in the negative charge state were found to be similar (within the calculation error). As a result, despite the fact that the measured piezospectroscopic parameters, when compared to the theoretical values for both configurations, might favour the SiC_sH_{AB} assignment this is far from conclusive. However, the convergence of the experimental and theoretical results strongly support the assignment of the acceptor level to either SiH_{BC}C_s or SiC_sH_{AB} and due to the similarities of the formation energies it seems likely that the trigonal centre observed by us is a mixture of both configurations.

In summary, two hydrogen-carbon related electrical levels have been observed in proton implanted n-type silicon. The first of these, the low symmetry donor CH_I, we assign to hydrogen trapped between two silicon atoms perturbed by a nearby substitutional carbon atom. The second centre, the trigonal acceptor CH_{II}, we

assign to hydrogen bonded directly to substitutional carbon.

Discussions with V.P. Markevich and R.C. Newman are acknowledged. This work has been supported in part in the UK by the Royal Academy of Engineering and the Engineering and Physical Science Research Council and by the Danish National Research Foundation through the Aarhus Center for Atomic Physics (ACAP).

References

- [1] A. Endrös, Phys. Rev. Lett. 63 (1989) 70.
- [2] P. Leary, R. Jones, S. Öberg, Phys. Rev. B 57 (1998) 3887.
- [3] C.H. Henry, D.V. Lang, Phys. Rev. B 15 (1977) 989.
- [4] S.D. Ganichev, E. Ziemann, W. Prettl, I.N. Yassievich, A.A. Istratov, E.R. Weber, Phys. Rev. B 61 (2000) 10361.
- [5] I. Izpura, E. Muñoz, F. Garcia, E. Calleja, A.L. Powell, P.I. Rockett, C.C. Button, J.S. Roberts, Appl. Phys. Lett. 58 (1991) 735.
- [6] L. Dobaczewski, P. Kaczor, I.D. Hawkins, A.R. Peaker, J. Appl. Phys. 76 (1994) 194.
- [7] K. Bonde Nielsen, B. Bech Nielsen, J. Hansen, E. Andersen, J.U. Andersen, Phys. Rev. B 60 (1999) 1716.
- [8] Y. Kamiura, N. Ishiga, Y. Yamashita, Jpn. J. Appl. Phys. 36 (1997) L1419.
- [9] Y. Kamiura, K. Fukuda, Y. Yamashita, J. Crystal Growth 210 (2000) 122.
- [10] R. Jones, P.R. Briddon, in: Semiconductors and Semimetals, Vol. 51, Academic Press, Boston, 1998 (Chapter 6).
- [11] J. Coutinho, R. Jones, P.R. Briddon, S. Öberg, Phys. Rev. B. 62 (2000) 10824.
- [12] L. Hoffmann, E.V. Lavrov, B. Bech Nielsen, B. Hourahine, R. Jones, S. Öberg, P.R. Briddon, Phys. Rev. B 61 (2000) 16659.



ELSEVIER

Physica B 308–310 (2001) 143–146

PHYSICA B

www.elsevier.com/locate/physb

Formation mechanism of hydrogen-induced (1 1 1) platelets in silicon

Yong-Sung Kim, K.J. Chang*

Department of Physics, Korea Advanced Institute of Science and Technology, 373-1 Kusung-dong Yusung-ku,
Taejeon 305-701, South Korea

Abstract

We suggest a structural model for the formation of hydrogen-induced (1 1 1) platelets in Si. We calculate the formation energies of various platelet structures using the first-principles pseudopotential method within the local-density-functional approximation. The formation mechanism involves a structural transformation from a double-layer- H_2^* structure into an H-saturated Si(1 1 1) internal surface structure with H_2 molecules generated in the platelet void. We also examine the energetics of the H-saturated Si(1 1 1) internal surface structures with various densities of H_2 molecules, and find an abrupt increase of the internal pressure built up in the void. © 2001 Elsevier Science B.V. All rights reserved.

PACS: 61.72.Bb; 61.72.Cc; 61.72.Nn

Keywords: Silicon; Hydrogen; Platelets

Hydrogen-induced platelets of a few tens of nanometers have been observed in heavily hydrogenated silicon crystals [1]. These platelets are basically extended planar defects with orientations along the crystalline planes of (1 0 0) and (1 1 1) [1–3]. Experiments have confirmed that the platelets consist of Si–H bonds, but their atomic structure is still a subject of interest.

To explain the structure and formation mechanism of the (1 1 1) platelets, several experimental and theoretical studies have been done. Recent theoretical calculations suggested that in the (1 1 1) platelets, an (1 1 1) monolayer of Si vacancies is decorated by H atoms, forming the so-called V platelets [4]. High-resolution transmission electron microscopy (HRTEM) images showed that H atoms saturate the broken bonds between adjacent (1 1 1) planes, suggesting an H-saturated internal (1 1 1)-surface structure $([2Si-H]_n)$ [5]. Based on H_2^* aggregates, Zhang and Jackson examined various structural models

such as single-layer- H_2^* ($[H_2]_n^S$), staggered- $[H_2]_n^S$, and double-layer- H_2^* ($[H_2]_n^D$) structures, and suggested that the $[H_2]_n^D$ structure is favorable for the (1 1 1) platelets [6].

In this work, we study various (1 1 1) platelet structures in Si, and propose a structural model for the formation of the (1 1 1) platelets, where the $[H_2]_n^D$ structure [see Fig. 1(a)] is initially formed and eventually transformed into the $[2Si-H]_n$ structure, with H_2 molecules accumulated in the interstitial region of the platelet [see Figs. 1(b)–(d)]. We also investigate the dependence of lattice dilation along the [111] direction on the density of H_2 molecules in the platelet void.

The total energies are calculated using the first-principles pseudopotential method within the local-density-functional approximation (LDA) [7]. The wave functions are expanded in a plane-wave basis set with a kinetic energy cutoff of 25 Ry. Details of the method have been given elsewhere [8].

We calculate the formation energies for various (1 1 1) platelet structures as a function of lattice dilation along the [111] direction (see Fig. 2). Among the three H_2^*

*Corresponding author. Tel.: +82-42-869-2531; fax +82-42-869-2510.

E-mail address: kchang@mail.kaist.ac.kr (K.J. Chang).

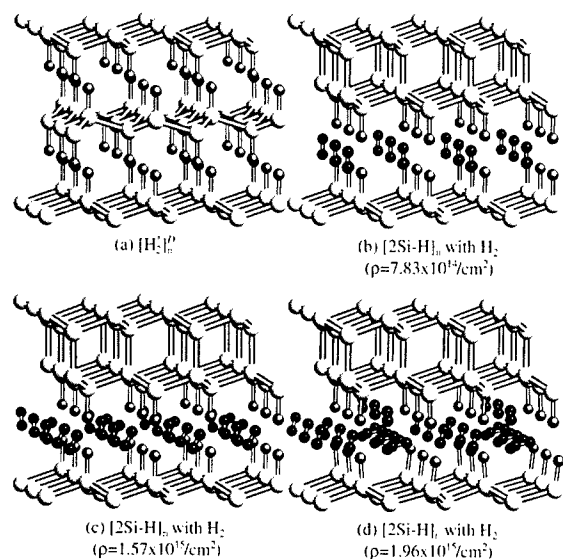


Fig. 1. The atomic geometries of the (a) $[H_2]_n^D$ and $[2Si-H]_n$ structures with (b) one, (c) two, and (d) three H_2 molecules per two Si-H bonds.

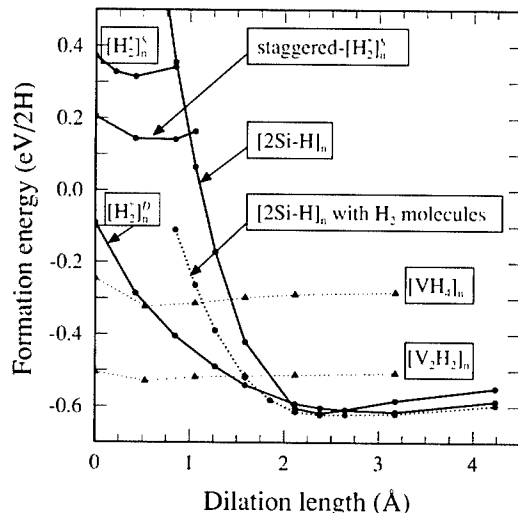


Fig. 2. The formation energies of various platelet structures plotted as a function of dilation length.

aggregates, the $[H_2]_n^D$ structure is lowest in energy. With zero dilation, vacancy-related $[VH_4]_n$ and $[V_2H_2]_n$ structures [4], where vacancy layers are decorated by H atoms, are found to be more stable than the $[H_2]_n^S$, staggered- $[H_2]_n^S$, $[H_2]_n^D$, and $[2Si-H]_n$ structures. The energy of the $[V_2H_2]_n$ structure is lower by about 0.4 eV than for the $[H_2]_n^D$ structure, and this energy is nearly independent of dilation length. However, as the dilation length increases, the vacancy-related structures become less stable, because the energies of the $[H_2]_n^D$

and $[2Si-H]_n$ structures decrease very rapidly. In addition, since it requires very high activation energies of 2.5–5 eV [4], the $[H_2]_n^D$ structure is considered to be energetically more favorable than the $[V_2H_2]_n$ structure for small dilation lengths. In fact, the (111) platelets have been observed predominantly in H-plasma treated samples, where the concentrations of vacancies and interstitials are extremely low [1]. At a dilation length of 2.2 Å, the $[2Si-H]_n$ structure is stabilized against the $[H_2]_n^D$ structure, with almost no interactions between the two facing H planes. As the lattice is expanded further above 2.7 Å, the $[2Si-H]_n$ structure becomes less stable than the $[H_2]_n^D$ structure.

The $[2Si-H]_n$ structure is extremely unstable for small lattice dilations because of the repulsive interactions between the two facing Si-H bond layers. When H_2 molecules are accumulated in the void region of the $[2Si-H]_n$ structure, the formation energy is slightly reduced. When the $[2Si-H]_n$ structure contains an H_2 molecule per two Si-H bonds, it has the same number of H atoms as the $[H_2]_n^D$ structure, with the molecule concentration of $7.83 \times 10^{14} \text{ cm}^{-2}$. This $[2Si-H]_n$ structure with H_2 molecules in the void is found to be lowest in energy for lattice dilations above 1.7 Å, as shown in Fig. 2. In this case, our LDA calculations show that the energy difference between the $[2Si-H]_n$ structure with H_2 molecules and the $[H_2]_n^D$ structure is just a few tens of meV for dilation lengths around 2 Å. With increasing the kinetic energy cutoff to 64 Ry, we find that the GGA calculations give the energy difference of about 0.1 eV at a dilation length of 2.3 Å, which is slightly increased, as compared to the LDA results. In the GGA calculations, we calculate the dilation length of 1.6 Å, where the $[2Si-H]_n$ structure with H_2 molecules becomes more stable than the $[H_2]_n^D$ structure, similar to the LDA estimate. Thus, we conclude that the LDA calculations describe correctly the energetics of various H-induced (111) platelet structures considered here.

Based on our calculations, we address that the formation of the (111) platelets is accompanied with the structural transformation from the $[H_2]_n^D$ structure into the $[2Si-H]_n$ structure with H_2 molecules, which is derived by increasing the lattice dilation. In this process, the activation energy is calculated to be about 1.8 eV [8]. The $[2Si-H]_n$ structure with H_2 molecules in the platelet void is consistent with recent HRTEM measurements, which exhibited the structure of atomic ledges on the (111) plane with broken bonds [5]. The HRTEM images also revealed a step structure in the (111) platelets [5]. When the $[H_2]_n^D$ structure is transformed into the $[2Si-H]_n$ structure with H_2 molecules, one of the two broken layers in the $[H_2]_n^D$ structure is recrystallized. If this recrystallization occurs in different broken layers in different regions, a step structure will be naturally formed.

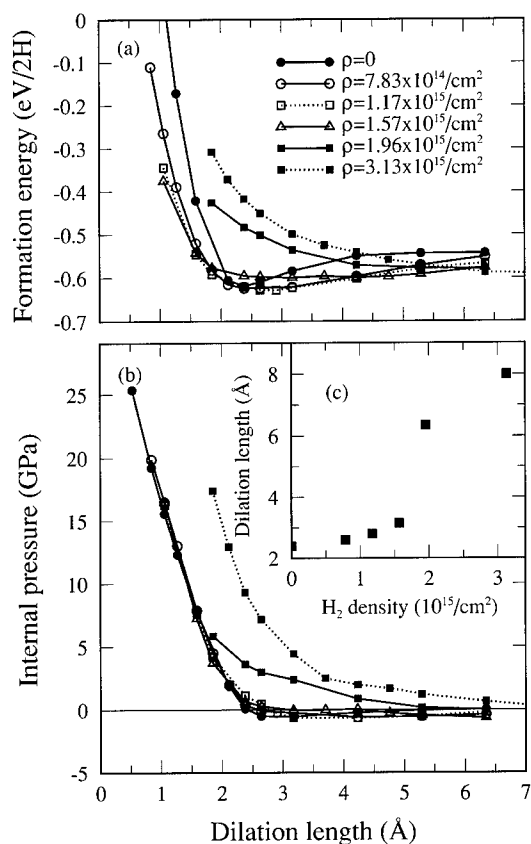


Fig. 3. The (a) formation energies and (b) internal pressures of the $[2\text{Si-H}]_n$ structures with various densities of H_2 molecules in the platelet void plotted as a function of dilation length. (c) The equilibrium dilation lengths at zero pressure drawn for various densities of H_2 molecules.

From the derivative of the total energy with respect to dilation length, we can estimate the pressure built up in platelets. At zero dilation length, the $[\text{H}_2^*]_n^D$ structure experiences an internal pressure of about 14 GPa along the $[111]$ direction. For the $[2\text{Si-H}]_n$ structure without H_2 molecules, the calculated internal pressure is zero at a dilation length of about 2.3 Å. When the $[\text{H}_2^*]_n^D$ structure has one H_2 molecule per two Si-H bonds, zero internal pressure occurs at 2.6 Å.

We also examine the energetics and pressures of the $[2\text{Si-H}]_n$ structures with various densities (ρ) of H_2 molecules in the platelet void. The calculated formation energies and internal pressures are plotted as a function of dilation length in Figs. 3(a) and (b). For molecule densities up to $\rho = 1.57 \times 10^{15} \text{ cm}^{-2}$, H_2 molecules are arranged in a single layer in the void of the $[2\text{Si-H}]_n$ structure, as shown in Figs. 1(b) and (c); each molecule is positioned near a tetrahedral site in the $[2\text{Si-H}]_n$ structure. In this case, the calculated formation energies are found to be similar, almost independent of ρ , and the

equilibrium dilation lengths, where internal pressures are zero, are close to 2.5 Å [see Fig. 3(c)]. For $\rho = 1.57 \times 10^{15} \text{ cm}^{-2}$, the $[2\text{Si-H}]_n$ structure has one H_2 molecule per Si-H bond, and H_2 molecules occupy all the tetrahedral sites in a single layer. Here, the shortest distance between two neighboring tetrahedral sites is calculated to be 2.35 Å, while the average inter-molecular distance is about 2.37 Å. This small difference between the two cases is due to the slight shift of the molecular positions from the tetrahedral sites. As H_2 molecules are further inserted in a single layer of the void, the inter-molecular distance is shortened, and the single layer configuration is no longer stable.

For $\rho = 1.96 \times 10^{15} \text{ cm}^{-2}$ with three H_2 molecules per two Si-H bonds, we find that H_2 molecules are arranged in multi-layers [see Fig. 1(d)], not in a single layer, although the molecule layers cannot be defined clearly in this configuration. The dilation length, where the formation energy has a minimum value, is increased abruptly to about 6.3 Å, as shown in Fig. 3(c). Such an abrupt increase is originated from the single-layer to multi-layer transition of the H_2 molecules in the platelet void. This result indicates that as the number of H_2 molecules increases in the void, the two facing hydrogenated layers in the $[2\text{Si-H}]_n$ structure repel each other due to the increase of internal pressure. Then, the formation energy tends to increase, as illustrated in Fig. 3(a).

Electron microscopy studies combined with continuum elasticity theory showed that applied stress is 1.05 GPa for dilation lengths of 3 ± 1 Å [5]. In our calculations, when the internal pressure is 1 GPa, the calculated dilation lengths lie in the range of 2.2–2.4 Å for the densities of H_2 molecules up to $\rho = 1.57 \times 10^{15} \text{ cm}^{-2}$. For $\rho = 1.96 \times 10^{15} \text{ cm}^{-2}$, where H_2 molecules are arranged in multi-layers, the dilation length at a pressure of 1 GPa is calculated to be 4.2 Å. Thus, we suggest that the densities of H_2 molecules lie in the range of 1.57 – $1.96 \times 10^{15} \text{ cm}^{-2}$ for experimentally measured internal pressures [5]. We point out that the $[111]$ platelets contain not only the H_2 molecules generated by the structural transformation from the $[\text{H}_2^*]_n^D$ structure into the $[2\text{Si-H}]_n$ structure but also extra molecules diffused from the Si bulk region.

In HRTEM measurements [1,5], the dilation length was shown to be smaller than 1 Å, while our calculated value is 2.4 Å at zero pressure for the $[2\text{Si-H}]_n$ structure without H_2 molecules. When samples are cut for HRTEM measurements, since H_2 molecules can be extracted from the void, the dilation length may be reduced. In this case, cutting the platelets may remove the H atoms in the $[2\text{Si-H}]_n$ structure, recovering the Si-Si bonds. Thus, HRTEM images may measure just the elongated Si-Si bonds along the $[111]$ direction. However, behind the cross-sectional surface, the $[2\text{Si-H}]_n$

structure still exists, with the elongated Si–Si bonds at the surface.

In conclusion, we find that the H-induced (111) platelets are formed by a structural transformation from the $[\text{H}_2^*]_n^{\text{D}}$ structure to the $[\text{2Si-H}]_n$ structure, accompanied with the generation of H_2 molecules in the void region. The $[\text{H}_2^*]_n^{\text{D}}$ structure, which is energetically most favorable in perfect Si, is more stabilized as the lattice is expanded, which reduces the internal pressure. Since the $[\text{2Si-H}]_n$ structure with H_2 molecules is stabilized against the $[\text{H}_2^*]_n^{\text{D}}$ structure for dilation lengths larger than 1.7 Å, the $[\text{H}_2^*]_n^{\text{D}}$ structure is eventually transformed into the $[\text{2Si-H}]_n$ structure with H_2 molecules generated in the void.

This work is supported by the supercomputing center in KISTI.

References

- [1] N.M. Johnson, et al., *Phys. Rev. B* 35 (1987) 4166.
- [2] G.F. Cerofolini, et al., *Phys. Rev. B* 46 (1992) 2061.
- [3] M.K. Weldon, et al., *J. Vac. Sci. Technol. B* 15 (1997) 1065.
- [4] F.A. Reboredo, et al., *Phys. Rev. Lett.* 82 (1999) 4870.
- [5] S. Muto, et al., *Philos. Mag. A* 72 (1995) 1057.
- [6] S.B. Zhang, et al., *Phys. Rev. B* 43 (1991) 12142.
- [7] M.L. Cohen, *Phys. Scripta*, T1 (1982) 5.
- [8] Y.-S. Kim, et al., *Phys. Rev. Lett.* 86 (2001) 1773.



ELSEVIER

Physica B 308–310 (2001) 147–150

PHYSICA B

www.elsevier.com/locate/physb

Vibrational properties of H-related defects in silicon

J.M. Pruneda^{a,*}, J. Junquera^b, J. Ferrer^a, P. Ordejón^c, S.K. Estreicher^d

^a *Departamento de Física, Facultad de Ciencias, Universidad de Oviedo, c./Calvo Sotelo s/n, 33007 Oviedo, Spain*

^b *Departamento de Física de la Materia Condensada C-III, Universidad Autónoma, E-28049 Madrid, Spain*

^c *Institut de Ciència de Materials de Barcelona, CSIC, Campus de la U.A.B., E-08193 Bellaterra, Barcelona, Spain*

^d *Department of Physics, Texas Tech University, Lubbock, TX 79409-1051, USA*

Abstract

We apply a new development of density functional perturbation theory to study the vibrational properties of hydrogen-containing complexes in silicon. A conjugate gradient algorithm within the SIESTA package is used to relax the atomic structure of the complexes. Then, the dynamical matrix of the entire supercell is computed analytically and diagonalized, leading to a complete vibrational spectrum. Results for hydrogen dimers, IH_2 , VH_n ($n = 1, 2, 3, 4$) and V_2H_6 defects are presented. © 2001 Elsevier Science B.V. All rights reserved.

PACS: 71.15.-m; 71.55.Gn; 63.20.Pw

Keywords: Local vibrational modes; Silicon; Hydrogen

1. Introduction

Hydrogen binds covalently in the immediate vicinity of many impurities and defects and this gives rise to a number of local vibrational modes (LVMs) well separated from the bulk phonon spectra [1]. The calculation of accurate LVMs at the ab initio level is a challenge, as it provides a critical link between theory and experiment. Typical accuracies in the calculated vibrational modes are within 3–10% of experimental data, which means in some cases a deviation of over 100 cm^{-1} .

Most authors calculate frequencies within the *frozen phonon* approximation. Conventional first-principles codes are used to compute the total energy of the system in the equilibrium configuration and for small displacements of selected atoms [2–6]. We propose here a different approach, based on the density functional perturbation theory (DFPT) [7,8]. In most cases, the comparison of the calculated and measured vibrational

frequencies is very favorable, improving on the results obtained by other techniques.

2. Methodology

We use the fully self-consistent ab initio SIESTA code [9,10]. The electronic energy is obtained from density-functional theory (DFT) [11,12] within the local density approximation. The exchange-correlation potential is that of Ceperley–Alder [13]. The electronic wave function is expressed in terms of a linear combination of pseudoatomic orbitals. In the present work, a double zeta basis is used to describe the valence electrons: two sets of s and p 's on Si, two s 's and one set of p 's on H. The host crystal is represented by a periodic supercell of 64 Si atoms with \vec{k} -point sampling reduced to Γ point.

In order to determine the equilibrium structure of the defects studied, we relax all the atomic coordinates with a conjugate gradient algorithm, reaching a tolerance in the forces of 0.01 eV/\AA . The dynamical matrix for the whole cell is computed from this ground state.

A new implementation of DFPT has been developed to compute the electronic response to infinitesimal

*Corresponding author.

E-mail address: pruneda@condmat.uniovi.es (J.M. Pruneda).

atomic displacements. Thanks to the ' $2n + 1$ ' theorem in DFPT, we can obtain analytically the dynamical matrix from the gradient of the density relative to *atomic coordinates*, without physically moving any atom. Note that merely linear effects are obtained in this method. Thus, one expects to obtain high-quality frequencies for the vibrational modes that are harmonic, but the frequencies of modes involving large anharmonic terms will be less accurate.

3. Results

LVMs have been studied for the H dimers (H_2 and H_2^*), the hydrogenated self-interstitial IH_2 complex, hydrogenated vacancy (VH_n , $n = 1, 2, 3, 4$) and V_2H_6 .

We focus here only on the stretching, and some bending modes of H.

3.1. Hydrogenated vacancies

In our calculations (Table 1), VH has monoclinic symmetry, and the H oscillates almost parallel to the $\langle 111 \rangle$ direction. In the orthorhombic VH_2 , the two equivalent hydrogens have stretching modes along the $\langle 100 \rangle$ and $\langle 001 \rangle$ directions. The calculated frequencies for these modes are 2121 and 2144 cm^{-1} respectively. VH_3 has C_{3v} symmetry. The A singlet involves the movement of the three H atoms towards the vacancy, while in the twofold degenerate E mode one of the atoms moves in opposition. VH_4 has T_d symmetry. In addition to the threefold degenerate mode T_2 mode at 2205, we

Table 1

Calculated and experimental frequencies for stretching modes in VH_n ($n = 1, 2, 3, 4$) and V_2H_6 ^a

	This work	Ref. [14]	Expt. (b)		This work	Ref. [14]	Expt. (b)
VH				VH₄			
A	2064(+1%)	2248(+10%)	2038	A ₁	2397	2404	No-IR
VD				T ₂	2265(+2%)	2319(+4%)	2222
A	1485(−1%)	1613(+7%)	1507	VH₃D			
VH₂				A ₁	2368(+5%)	2384(+6%)	2250
A ₁	2239(+4%)	2316(+7%)	2144	E	2266(+2%)	2319(+4%)	2224
B ₁	2199(+4%)	2267(+7%)	2121	A ₁	1645(+2%)	1677(+3%)	1620
VHD				VH₂D₂			
A	2221(+4%)	2292(+7%)	2134	A ₁	2336(+4%)	2364(+5%)	2244
A	1592(+2%)	1641(+5%)	1555	B ₁	2266(+2%)	2319(+4%)	2225
VD₂				A ₁	1666(+2%)	1690(+4%)	1628
A ₁	1607(+3%)	1658(+6%)	1564	B ₂	1627(+1%)	1663(+3%)	1615
B ₁	1581(+2%)	1625(+5%)	1547	VHD₃			
VH₃				A ₁	2303(+3%)	2342(+5%)	2236
A ₁	2224(+2%)	2318(+6%)	2185	A ₁	1689(+3%)	1705(+4%)	1636
E	2100(−2%)	2256(+5%)	2155	E	1627(+1%)	1664(+4%)	1616
VH₂D				VD₄			
A	2187(+0%)	2298(+5%)	2185	A ₁	1715	1721	No-IR
A	2099(−3%)	2256(+4%)	2167	T ₂	1627(+1%)	1664(+3%)	1617
A	1534(−3%)	1632(+3%)	1580	V₂H₆			
VHD₂				A _{1g}	2248(+3%)	—	2190 [16]
A	2144(−1%)	2277(+5%)	2177	A _{2u}	2237(+2%)	—	2191 [15]
A	1562(−2%)	1646(+4%)	1588	E _u	2180(+1%)	—	2166 [15]
A	1510(−4%)	1619(+3%)	1575	E _g	2170(+0%)	—	2165 [16]
VD₃							
A ₁	1594(+0%)	1661(+4%)	1594				
E	1510(−4%)	1619(+3%)	1576				

^aThe % in parentheses gives the error relative to experiment.

obtain an infra-red (IR) inactive singlet A_1 mode at 2265 cm^{-1} . V_2H_6 behaves as two weakly coupled VH_3 complexes. The vibrational modes of V_2H_6 are almost identical to those of VH_3 . The A_2 singlet at 2176 cm^{-1} induces a dipole along the $\langle 111 \rangle$ direction. In addition to this mode, and the IR-active E doublet, we obtain two IR-inactive modes at 2186 and 2134 cm^{-1} .

3.2. H_2 , H_2^* and IH_2

The trigonal H_2^* defect [17,19] consists of one hydrogen atom close to the antibonding (AB) site, and the other near the bond-centered (BC) site, forming an $Si-H\cdots Si-H$ structure. The $Si-H_{AB}$ bond length is slightly longer than the $Si-H_{BC}$ one

(1.580 \AA vs. 1.510 \AA in our calculations). This give rise to different stretch frequencies for the two atoms: 2135 cm^{-1} for H_{BC} and 1750 cm^{-1} for H_{AB} . We also obtain two nondegenerate wagging modes, both related to H_{AB} . The calculated modes with D substitutions are given in Table 2.

IR and Raman measurements of H_2 in silicon [22,25] reveal a considerable softening of the stretching mode with respect to the frequency of H_2 in the gas phase. The electron affinity of the Si atoms surrounding H_2 results in a weakening of the H–H bond and this reduces the vibrational frequencies. Even though the H–H stretch mode is not expected to be fully harmonic, our calculated frequency is close to the experimental one (Table 2) and lower than that for free H_2 (4194 cm^{-1}).

Table 2
LVMs for H_2 in the $\langle 100 \rangle$ alignment, $H_2^* = H_{AB}H_{BC}$ and IH_2^a

	This work	Other authors	Expt. (a)		This work	Other authors	Expt.
H_2^*				H_2 in Si			
(BC)	2135(+3%)	2164 ^b (+5%) 2100 ^c (+2%) 2070 ^d (+0%)	2062	(H_2)	3549(−2%)	3607 ^e (+0%) 3396 ^f (−6%)	3618 ^g
(AB)	1750(−5%)	1844 ^b (+0%)	1838	(DH)	3081(−6%)	3129 ^e (−4%)	3265 ^g
				(D_2)	2511(−5%)	2559 ^e (−3%)	2643 ^g
		1500 ^c (−18%) 1480 ^d (−19%)		IH_2			
(AB)	843, 839(+3%)	1002 ^b (+22%) 690 ^d (−16%)	817	A	2007(+1%)	2145 ^h (+8%) 1915 ⁱ (+3%)	1989 ^h
				B	2004(+1%)	2143 ^h (+8%)	1986 ^h
D_2^*				B	737(−1%)	(A) 775 ^h (+3%)	748 ^h
(BC)	1528(+2%)	1548 ^b (+3%)	1500	A	733(−1%)	(B) 768 ^h (+3%)	743 ^h
(AB)	1255(−6%)	1321 ^b (+1%)	1340	A	716	(B) 736 ^h	
(AB)	602(+2%)	712 ^b (+21%)	588	B	711	(A) 717 ^h	
(AB)	599	586 ^b	—				
$H_{BC}D_{AB}^*$				IHD/IDH			
(BC)	2132(+3%)	2159 ^b (+5%)	2058		2005/2007(+1%)	2144 ^h (+8%)	1988 ^h
(AB)	1257(−6%)	1324 ^b (+1%)	1342		1440/1438(−1%)	1540 ^h (+6%)	1447 ^h
(AB)	602(+2%)	712 ^b (+20%)	588		733/736(−2%)	771 ^h (+3%)	746 ^h
(AB)	599	612 ^b	—		714/714	727 ^h	
$D_{BC}H_{AB}^*$				ID ₂			
(AB)	1761(−5%)	1856 ^b (+0%)	1851	A	1440(−1%)	1540 ^h (+6%)	1448 ^h
(BC)	1519(+2%)	1538 ^b (+3%)	1488	B	1438(−1%)	1539 ^h (+6%)	1446 ^h
(AB)	843(+3%)	1002 ^b (+21%)	817	B	609	590 ^h	
(AB)	830	586 ^b	—	A	601	583 ^h	
				A	566	564 ^h	
				B	562	555 ^h	

^aThe % in parentheses gives the error relative to experiment.

^bRef. [17]

^cRef. [18]

^dRef. [19]

^eRef. [20]

^fRef. [21]

^gRef. [22]

^hRef. [23]

ⁱRef. [24].

Note that D substitutions fail to show the observed anharmonic shift [22].

Finally, IH_2 has two almost equivalent weakly coupled hydrogen atoms, with very similar stretching frequencies. Our relaxed structure has almost C_{2v} symmetry, with the A mode higher than the B mode, confirming early calculations [23]. We also reproduce the correct ordering for the bending modes at 737 and 732 cm^{-1} . Note that we predict that the two H's in this defect are slightly inequivalent. Thus, we obtain two different frequencies when one of the H's is substituted by D (IHD and IDH). Experimentally, only one IHD complex is observed. However, the spectrum obtained with an H/D mix shows three H lines at 1989 cm^{-1} (IH_2), 1988 cm^{-1} (IHD), and 1986 cm^{-1} (IH_2). If the HD line belonging to IDH were at $1988 + 1 = 1989 \text{ cm}^{-1}$, it would only affect the relative amplitudes of the two IH_2 lines. Even though our predicted frequencies for this defect are remarkably good, they are not accurate to a few cm^{-1} and the slight difference between IHD and IDH which we obtain could easily be an artifact of the calculation.

4. Conclusions

We propose a new development of DFPT, using localized atomic wavefunctions as a basis set, and apply it to the study of LVMs of H-related defects in silicon. In contrast to other methods, the dynamical matrix is computed analytically without actually displacing any atom. The calculations are based on the ground state density matrix as computed with the SIESTA package.

The defects included here involve a range of Si–H bonding configurations. In situations where larger anharmonic contributions are present, the accuracy of the method decreases somewhat ($\sim 5\%$). We note that this occurs, for example, when H is close to a BC position. However, in most cases the calculated frequencies are in remarkable agreement ($\leq 3\%$) with experimental data, implying not only that this perturbative approach is totally justified, but also that the ground state density matrix calculated with SIESTA is very reliable.

Acknowledgements

This work was supported by the Spanish DGESIC (Project PB96-0080-C02). SKE's research is supported

in part by a grant from the Welch Foundation, a contract from NREL, and a research award from the Humboldt Foundation.

References

- [1] S.J. Pearton, J.W. Corbett, M. Stavola, *Hydrogen in Crystalline Semiconductors*, Springer, New York, 1992.
- [2] R. Jones, P.R. Briddon, in: M. Stavola (Ed.), *The Identification of Defects in Semiconductors*, Semicond. Semimetals 51A (1998) 287.
- [3] B. Tuttle, C.G. Van de Walle, *Phys. Rev. B* 59 (1999) 12,884.
- [4] M. Saito, Y. Okamoto, A. Oshiyama, T. Akiyama, *Physica B* 273–274 (1999) 196.
- [5] K.G. Nakamura, K. Ishioka, M. Kitajima, K. Murakami, *Solid State Commun.* 101 (1997) 735.
- [6] K.G. Nakamura, K. Ishioka, M. Kitajima, E. Endou, M. Kubo, K. Miyamoto, *J. Chem. Phys.* 108 (1997) 3222.
- [7] S. Baroni, P. Giannozzi, A. Testa, *Phys. Rev. Lett.* 58 (1987) 1861.
- [8] X. Gonze, *Phys. Rev. A* 52 (1995) 1096.
- [9] E. Artacho, D. Sánchez-Portal, P. Ordejón, A. García, J.M. Soler, *Phys. Stat. Sol. b* 215 (1999) 809.
- [10] D. Sánchez-Portal, P. Ordejón, E. Artacho, J.M. Soler, *Int. J. Quantum. Chem.* 65 (1997) 453.
- [11] P. Hohenberg, W. Kohn, *Phys. Rev.* 136 (1964) B864.
- [12] W. Kohn, L.J. Sham, *Phys. Rev.* 140 (1965) A1133.
- [13] D.M. Ceperley, B.J. Alder, *Phys. Rev. Lett.* 45 (1980) 566.
- [14] B. Bech Nielsen, L. Hoffman, M. Budde, R. Jones, J. Goss, S. Öberg, *Mater. Sci. Forum* 196–201 (1995) 933.
- [15] B. Bech Nielsen, L. Hoffmann, M. Budde, *Mater. Sci. Eng. B* 36 (1996) 259.
- [16] E.V. Lavrov, J. Weber, L. Huang, B. Bech Nielsen, *Phys. Rev. B* 64 (2001) 035,204.
- [17] J.D. Holbeck, B. Bech Nielsen, R. Jones, P. Sitch, S. Öberg, *Phys. Rev. Lett.* 71 (1993) 875.
- [18] C.G. Van de Walle, *Phys. Rev. B* 49 (1994) 4579.
- [19] K.J. Chang, D.J. Chadi, *Phys. Rev. B* 42 (1990) 7651.
- [20] B. Hourahine, R. Jones, S. Öberg, R.C. Newman, P.R. Briddon, E. Roduner, *Phys. Rev. B* 57 (1998) 12,666.
- [21] C.G. Van de Walle, *Phys. Rev. Lett.* 80 (1998) 2177.
- [22] R.E. Pritchard, M.J. Ashwin, J.H. Tucker, R.C. Newman, E.C. Lightowers, M.J. Binns, S.A. McQuaid, R. Falster, *Phys. Rev. B* 56 (1997) 13,118.
- [23] M. Budde, B. Bech Nielsen, P. Leary, J. Goss, R. Jones, P.R. Briddon, S. Öberg, S.J. Breuer, *Phys. Rev. B* 57 (1998) 4397.
- [24] C.G. Van de Walle, J. Neugebauer, *Phys. Rev. B* 52 (1995) R14,320.
- [25] A.W.R. Leitch, V. Alex, J. Weber, *Phys. Rev. Lett.* 81 (1998) 421.



ELSEVIER

Physica B 308–310 (2001) 151–154

PHYSICA B

www.elsevier.com/locate/physb

Structural properties of hydrogen-induced platelets in silicon: a Raman scattering study

E.V. Lavrov^{a,b,*}, J. Weber^a^a *University of Technology, 01062 Dresden, Germany*^b *IRE RAS, 103907 Moscow, Russia*

Abstract

Different treatments of hydrogenation induce hydrogen containing plate-like defects on {111} crystallographic planes in silicon. Several structural models of the platelets were proposed of which the most prominent are: (a) A double layer of interstitial hydrogen H_2^* pairs and (b) hydrogen saturation of the Si–Si bonds at a {111} plane with H_2 molecules trapped within the platelet. Raman scattering studies reported that local vibrational modes related to the platelets appear around 2100 cm^{-1} , whereas a local mode at 4160 cm^{-1} was associated with H_2 trapped within the platelet. From an analysis of the polarized Raman scattering spectra of the 2100- and 4160-cm^{-1} bands we identify two different types of {111}-platelets described above, which exist simultaneously with concentrations depending on plasma conditions. © 2001 Elsevier Science B.V. All rights reserved.

PACS: 61.72.Ji; 61.72.Nn; 78.30.Am

Keywords: Silicon; Hydrogen; Platelet; Raman scattering

1. Introduction

High concentrations of hydrogen introduced into Si by plasma treatment create extended planar defects along the {111} crystalline planes, which are called platelets [1]. Electron microscopy [2], Raman scattering [3], as well as infrared absorption results [3] have shown that the fundamental blocks comprising these defects are Si–H bonds. A number of different structural models of the platelets have been suggested [2,4,5]. The most prominent of these are: a double layer of H_2^* , $[H_2^*]_n^D$, and hydrogen-saturated {111} planes, $[2Si-H]_n$, i.e., the configuration in which each Si–Si bond on an {111} plane is replaced by two Si–H bonds.

Here we present an analysis of the polarized Raman scattering spectra measured on the {111}-hydrogen-

induced platelets in Si. A first Raman scattering study by Heyman et al. showed that Raman active modes of the {111}-platelets are observed at approximately 2100 cm^{-1} [3]. Recent results by Leitch et al. showed that H_2 in the platelet has a local vibrational mode at 4160 cm^{-1} [6]. Our analysis of the 2100- and 4160-cm^{-1} bands identifies the two different types of platelets described above, which exist simultaneously with concentrations depending on the plasma conditions.

2. Experimental

Silicon samples used in this study were n-type, phosphorus-doped, Cz (100)-wafers with resistivity of $0.75\ \Omega\text{ cm}$. Hydrogen was introduced into the Si samples by means of a remote Dc-plasma system with sample temperature varied between room temperature to 300°C for a duration of 30 min–6 h.

The details of the Raman setup are described elsewhere [6]. Polarized Raman spectra were collected in a pseudobackscattering geometry. The polarization

*Corresponding author. ITTP, TU Dresden, Mommsenstr. 13, 01069 Dresden, Germany. Tel.: +49-351-463-3637; fax: +49-351-463-7060.

E-mail address: edward.lavrov@physik.phy.tu-dresden.de (E.V. Lavrov).

geometry is defined with respect to the sample surface (1 0 0): the x -, y -, and z -axis are parallel to [1 0 0], [0 1 0], and [0 0 1], while y' - and z' -axis are parallel to [0 1 1], and [0 $\bar{1}$ 1]. In the notation $\{a[b, c]d\}$, $a(d)$ refers to the propagation vector of the incident (scattered) light, while $b(c)$ refers to the polarization vector of the incident (scattered) light. As usual, the depolarization ratio, Δ , is defined as the ratio of the scattered light intensity polarized perpendicular to the excitation light, E^{in} , to the intensity parallel to E^{in} . In the notation $\Delta_{[xyz]}$, the subscript implies that the excitation light is polarized along the $[xyz]$ -axis.

3. Results

Fig. 1 shows room temperature polarized-sensitive spectra of a Si sample after exposure to hydrogen plasma at 150°C for 6 h. The broad band at 2100 cm^{-1} was previously assigned to the {111}-platelets [3], whereas the band lying at 4160 cm^{-1} was associated with H_2 trapped within platelets [6]. The polarized spectra of the 2100- cm^{-1} band shown in the figure are in qualitative agreement with previous data reported by Heyman et al. [3], i.e., $\Delta_{[110]} = 0$, which suggests the fully symmetric mode of a trigonal defect [7]. In the following discussion we want to consider only the value of $\Delta_{[110]}$ because both the 2100- and 4160- cm^{-1} bands, regardless of the conditions of the samples preparation, display $\Delta_{[110]} = 0$.

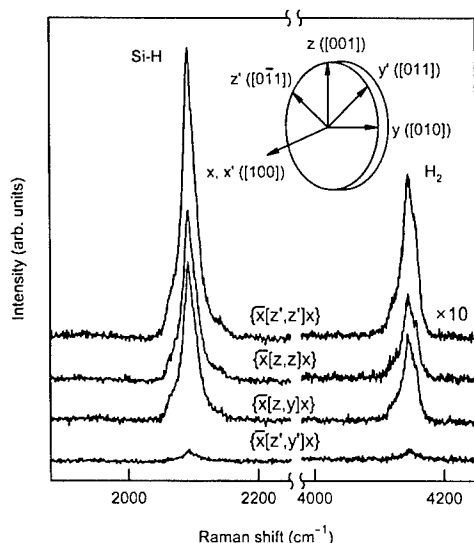


Fig. 1. Room temperature polarized Raman spectra after exposure to hydrogen plasma at 150°C for 6 h. Polarization geometry is defined with respect to the sample normal [1 0 0]. Spectra are offset vertically for clarity. Note that the intensity in the spectral range 1900–4300 cm^{-1} was scaled up by factor of 10.

As follows from the figure, $\Delta_{[110]}$ of the 2100- cm^{-1} band is close to one, whereas Heyman et al. reported $\Delta_{[110]} \cong 0.3$ [3]. Another striking feature is that the polarization properties of the 4160- cm^{-1} band are precisely the same as that of the 2100- cm^{-1} one. This may lead to the conclusion that H_2 is aligned along the [1 1 1] axis and, therefore, the 4160- cm^{-1} band displays the properties of the fully symmetric mode of a trigonal defect.

However, this assignment meets serious difficulties. According to calculations, H_2 positioned at the tetrahedral site of the perfect Si lattice has extremely small barriers for rotation [8]. As compared to the T_d site, H_2 in platelets is well isolated from the surrounding lattice and thus should rotate freely. The less obvious problem with the suggestion of aligned H_2 comes from the value of $\Delta_{[110]}$. With the known Raman tensor of free H_2 [9], $\Delta_{[110]}$ should be equal to 0.021, well below the experimental value.

All these problems can be solved if we model the platelet as a flat infinitely thin dielectric layer described by an isotropic, frequency-independent, real dielectric constant ϵ . This model takes into account deviation of the local electric field within the platelet from that of the incident electric field in the bulk of the sample.

According to the formalism proposed by Reed et al. [10], the local electric field in the platelet, E^{loc} may be written as

$$E^{\text{loc}} = A(\theta_{\text{in}}, \omega_{\text{in}}) E^{\text{in}}. \quad (1)$$

Matrix A is a function of the polar angle θ_{in} , measured with respect to the platelet normal, frequency of the excitation light, ω_{in} , and ϵ . The induced polarization \mathcal{P}^i of the oscillating Raman dipole is related to the local macroscopic electric field through the Raman tensor of the scatterer α^i , $\mathcal{P}^i = \alpha^i E^{\text{loc}}$, where i is either Si-H, or H_2 . If z is the bond axis, then α^i is diagonal and $\alpha_{xx}^i = \alpha_{yy}^i = \delta^i$, $\alpha_{zz}^i = 1$, where δ^i is bond anisotropy defined as the ratio of the dynamic molecular polarizabilities perpendicular and parallel to the bond axis. Thus, the electric field in the bulk of the sample E^{out} radiated by polarization \mathcal{P}^i with frequency ω_{out} in the direction making polar angle θ_{out} with the platelet normal, is given by

$$E^{\text{out}} = \frac{\omega_{\text{r}}^2}{c^2} A^T(\theta_{\text{out}}, \omega_{\text{out}}) \mathcal{P}^i, \quad (2)$$

where A^T is the transpose of A . Finally, we obtain that the intensity of the appropriate Raman band, I_i , is given by

$$I_i \propto \sum_{k \in \{111\}} |e^{\text{out}} A^T(\theta_{\text{out}}^k, \omega_{\text{out}}) \alpha^i A(\theta_{\text{in}}^k, \omega_{\text{in}}) e^{\text{in}}|^2, \quad (3)$$

where the summation is taken over four different possible orientations of the {111}-platelets in the lattice. Here, e^{in} and e^{out} are polarization vectors of

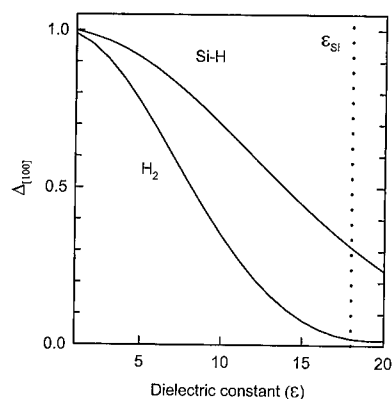


Fig. 2. Calculated depolarization ratio, $\Delta_{[1 0 0]}$, of the Si-H (2100 cm^{-1}) and H_2 (4160 cm^{-1}) Raman signals. Dotted line shows the dielectric constant of Si at 488 nm.

the incident and scattered light, respectively. In case of H_2 , Eq. (3) is averaged over all possible orientations of the principal axes of α^{H_2} with respect to the labor frame, whereas for the 2100-cm^{-1} band we assume that the Si-H bonds are aligned along the platelet normal.

$\Delta_{[1 0 0]}$ calculated from Eq. (3) for the 2100- and 4160-cm^{-1} bands as a function of ϵ is shown in Fig. 2. In our calculations we assumed that the Raman tensor of H_2 is the same as that of the free molecule [9], $\delta^{\text{H}_2} = 0.66$, whereas for the 2100-cm^{-1} band we used the value of the Si-H bond anisotropy $\delta^{\text{Si-H}} = 0.35$, obtained from the Raman study of vacancy-hydrogen complexes in Si [11].

It follows from Fig. 2 that the polarization properties of the 2100- and 4160-cm^{-1} bands derived from Fig. 1 ($\Delta_{[1 0 0]} \cong 1$) are explained very well by the model of the platelet with ϵ well below than that of Si. This is what one should expect for the $[\text{2Si-H}]_n$ platelets. Indeed, this model assumes that $[\text{2Si-H}]_n$ is an open structure comprising two hydrogenated Si(111) layers with H_2 trapped in between.

We also studied the dependency of $\Delta_{[1 0 0]}$ on the sample temperature during the plasma treatment. Fig. 3 shows the integrated intensities and $\Delta_{[1 0 0]}$ of the 2100- and 4160-cm^{-1} bands as a function of the sample temperature. As one can see, $\Delta_{[1 0 0]}$ of the H_2 signal remains constant, whereas at 50°C $\Delta_{[1 0 0]}$ of the 2100-cm^{-1} band is ≈ 0.5 . As the temperature rises, the 4160-cm^{-1} band grows up and when it reaches the maximal intensity, the 2100-cm^{-1} band becomes nearly depolarized. We interpret this transition as a change of the platelet from the optical dense structure without H_2 ($[\text{H}_2^*]_n^{\text{D}}$) to the $[\text{2Si-H}]_n$ structure accompanied by the formation of H_2 molecules in the interstitial region of the platelet. Indeed, according to Fig. 2, $\Delta_{[1 0 0]} = 0.5$ for the 2100-cm^{-1} band corresponds to $\epsilon = 14$, which is rather close to the dielectric constant of Si.

We believe that a double layer of $[\text{H}_2^*]_n^{\text{D}}$ is the most plausible candidate for the structure with $\epsilon = 14$.

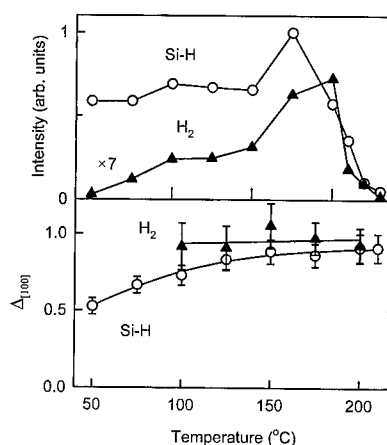


Fig. 3. Dependence of sample temperature during hydrogen plasma treatment on the integrated intensities (top figure) and on the depolarization ratio, $\Delta_{[1 0 0]}$, (bottom figure) of the Si-H (2100 cm^{-1}) and H_2 (4160 cm^{-1}) Raman signals. Note that the intensity of the Raman signal of H_2 was scaled up by factor of 7.

Apparently, of all proposed models for the {111}-platelets only this one is expected to have the highest value of ϵ due to the layer of Si atoms located it between the Si(111) surfaces [4]. This picture is in agreement with calculations of Kim and Chang [5], who found that $[\text{H}_2^*]_n^{\text{D}}$ has the lowest formation energy at small lattice dilations. When the lattice dilates the $[\text{H}_2^*]_n^{\text{D}}$ structure recrystallizes to $[\text{2Si-H}]_n$ accompanied by the formation of H_2 in the two Si(111) planes. This transformation occurs at 100°C , as seen from Fig. 3.

4. Summary

In summary, we presented a detailed analysis of the polarized Raman scattering spectra from the {111} hydrogen-induced platelets in silicon, which were hydrogenated by remote plasma exposure. Our analysis identifies two different structures, which exist simultaneously with concentrations depending on the plasma conditions.

Acknowledgements

E.V.L. acknowledges the Alexander von-Humboldt Foundation for financial support and the Russian Foundation for Basic Research (Grant No. 99-02-16652).

References

- [1] N.M. Johnson, F.A. Ponce, R.A. Street, R.J. Nemanich, Phys. Rev. B 35 (1987) 4166.

- [2] S. Muto, S. Takeda, M. Hirata, *Philos. Mag. A* 72 (1995) 1057.
- [3] J.N. Heyman, J.W. Ager III, E.E. Haller, N.M. Johnson, J. Walker, C.M. Doland, *Phys. Rev. B* 45 (1992) 13 363.
- [4] S.B. Zhang, W.B. Jackson, *Phys. Rev. B* 43 (1991) 12 142.
- [5] Y.-S. Kim, K.J. Chang, *Phys. Rev. Lett.* 86 (2001) 1773.
- [6] A.W.R. Leitch, V. Alex, J. Weber, *Phys. Rev. Lett.* 81 (1998) 421.
- [7] M. Cardona, in: M. Cardona, G. Güntherodt (Eds.), *Light Scattering in Solids II*, Springer, Berlin, 1982, pp. 19–172.
- [8] B. Hourahine, R. Jones, S. Öberg, R.C. Newman, P.R. Briddon, E. Roduner, *Phys. Rev. B* 57 (1998) 12 666.
- [9] C.M. Hartwig, J. Vitko Jr., *Phys. Rev. B* 18 (1978) 3006.
- [10] C.E. Reed, J. Giergiel, J.C. Hemminger, S. Ushioda, *Phys. Rev. B* 36 (1987) 4990.
- [11] E.V. Lavrov, J. Weber, L. Huang, B. Bech Nielsen, *Phys. Rev. B* 64 (2001) 035 204.

Quadruplevoids in amorphous Si:H

Thomas Krüger*, Alexander F. Sax

Institut für Chemie, Karl-Franzens-Universität Graz, Strassoldogasse 10, A-8010 Graz, Austria

Abstract

The mechanism of the Staebler–Wronski effect is still in question. We assume that a defect precursor A is transformed into the actual, metastable defect B by excitation and subsequent electron trapping. Calculations on two large, distorted silicon clusters are presented which contain a bent and a pyramidal void, respectively, created by removal of four adjacent silicon atoms. A QM/QM embedding procedure is employed using a density functional (BP86) and a semiempirical method (AM1). Full geometry optimization results in novel and unprecedented structure information. Excitation energies and electron attachment energies are presented. These findings substantiate the new ideas regarding the nature of A and B. © 2001 Elsevier Science B.V. All rights reserved.

Keywords: Staebler–Wronski effect; Amorphous Si:H; Microvoids; Embedding calculations

1. Introduction

In various applications amorphous hydrogenated silicon (a-Si:H) could serve as a cheap and technically more versatile replacement for crystalline silicon (c-Si). Unfortunately, however, the practical use of a-Si:H is limited by the well-known Staebler–Wronski effect (SWE) [1,2].

Despite a vast amount of experimental information its mechanism is still discussed controversially (see Ref. [3]). It is known that a-Si:H is interspersed with an enormous amount of microvoids. Assuming a spherical structure the mean void radius amounts to 3.3–4.3 Å [4–6]. It is plausible that certain sites of the inner void surfaces act as the (neutral) precursors (A) of the light-induced dangling bonds B.

We assume that the exposure of neutral A to sunlight enables A to trap an electron from the conduction band. By relaxation of this intermediate the metastable dangling bond B is formed. This assumption is corroborated by recent work indicating that the majority of light-induced defects is *negatively* charged [7]. The thermal reformation of A (the annealing

process) may be considered the reverse of the photo-electronic formation of B and will finally lead to electron-hole-recombination.

In order to substantiate the mechanistic concept mentioned above we have to obtain knowledge about the geometric and electronic structure of the voids' localized states as well as about the corresponding excitation and electron attachment energies. Results regarding voids from one to three adjacent Si atoms missing are given in a previous paper [3]. In the present article we will show the results of calculations on *quadruplevoids* (tetravoids).

2. Strategy and methods

The methods of theoretical chemistry result in *local* information about a system, and this is what we need to have. We use the following approach explained in detail in Ref. [3]: the system of interest is partitioned into two parts, where the more interesting part (the core) is treated at a higher level of theory, and the rest of the system (the bulk) is described by an approximate and computationally less demanding method. During the calculations the outer sphere of the core is saturated by H atoms (the link atoms). The embedding of the core into the bulk, i.e. the *coupling* of the two parts, is

*Corresponding author. Fax: +43-316-380-9893.

E-mail address: thomas.krueger@kfunigraz.ac.at (T. Krüger).

performed using the ONIOM scheme [8] which is implemented in the Gaussian98 program package [9]. To calculate the core we employ the combination of Becke's 1988 exchange [10] and Perdew's 1986 correlation functional [11] (BP86) together with the 6-31G* standard basis set. The bulk is treated by means of the semiempirical method AM1 [12,13]. The vertical excitation energies are calculated by use of the single-excitation CI method [14] based on the corresponding Hartree–Fock orbitals. All energy values given refer to the core plus link atoms only.

The material is modeled by the cluster $\text{Si}_{139}\text{H}_{116}$, an approximately spherical entity of T_d symmetry with a diameter of about 17 Å which is derived from a clipping of c-Si where the outer surfaces are hydrogenated. Four adjacent silicon atoms are removed from the center of the cluster, and the neighboring atoms are regarded as the core of the system. Then we allow for *total* geometry relaxation.

One could object that an investigation of voids in this cluster does not allow for statements regarding *amorphous* silicon, because its structure is derived from *crystalline* Si. However, during relaxation more or less severe distortions of the ideal lattice occur. The distance matrices of the *final* structures have been evaluated statistically to obtain distance histograms. These histograms show the typical features of the radial distribution function of an amorphous material.

The work of other authors regarding vacancies in silicon is appreciated in Ref. [3].

3. Results

If four adjacent Si atoms have to be removed, three arrangements are possible: either a *linear* (zigzag) or a *bent* or a *pyramidal* quadruplevoid will emerge. Since the linear arrangement is similar to the triplevoid already treated in the previous paper, we will concentrate on the bent and on the pyramidal quadruplevoid.

3.1. The bent quadruplevoid

Locally the bent quadruplevoid shows up C_2 symmetry. The overall symmetry of the whole system, however, is C_1 only. The core consists of the 10 atoms surrounding the void and two additional atoms belonging to the next sphere. This is necessary because we have to avoid situations where one bulk atom is bound to two core atoms so that linking the inner and outer part would become difficult (see Ref. [15]).

At the beginning of the geometry optimization (relaxation) 10 unpaired electrons (dangling bonds) are present. Eight of the corresponding Si atoms have a next-neighbor distance of 3.82 Å, whereas the remaining two are connected already by a Si–Si single bond. It is to

be expected that the system will try to overcome this situation by rearranging its atoms so that new bonds are formed. Fig. 1 shows the result of the process where the gray circles denote the original positions of the four atoms removed. The core atoms have moved towards one another in pairs, preserving the bent structure of the void. Five new bonds are created: four single bonds and one double bond connecting the two Si atoms which have already been bound. Note that the newly formed bonds are stretched by not more than 8% vs. the typical bond lengths in the unperturbed cluster. Considerably strained bonds (+30% vs. standard) which are sometimes discussed in the context of the SWE are not found at all.

The lowest excited singlet state of the core is located 1.43 eV above the ground state which fits very well into the band gap of a-Si:H. The transition is of HOMO→LUMO type where both orbitals are localized at the double bond. However, the oscillator strength of this transition amounts to $f = 0.024$ only, thereby indicating that the transition is very improbable to occur. There is no other excited state within the energy range relevant for the SWE.

This can be explained as follows: the most simple molecule possessing a Si–Si double bond is disilene (Si_2H_4). The HOMO→LUMO excitation requires a quite high energy of 4.25 eV, but this transition is allowed because of the high oscillator strength ($f = 0.656$). If, however, the four H atoms are positioned so that the surrounding of this double bond is equivalent to the highly distorted surrounding of the double bond in the bent void, then the excitation energy drops to 1.65 eV but also the oscillator strength decreases significantly ($f = 0.062$). This can be attributed to the fact that HOMO and LUMO partly lose their explicit bonding and antibonding character, respectively, because of the increased mixing with other orbitals.

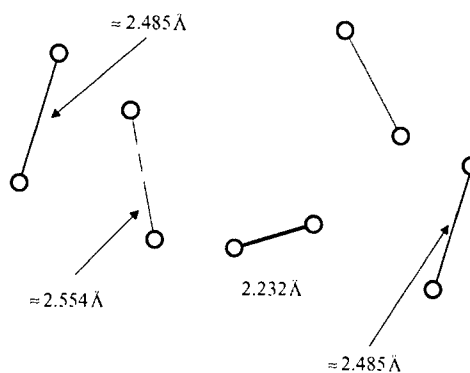


Fig. 1. Optimized structure of the bent quadruplevoid in $\text{Si}_{139}\text{H}_{116}$.

We assume that the primary step of the SWE is the trapping of a conduction band electron by an excited state of A. So B must be an anion (more precisely: the anionic part of a zwitterion [3]) if A is a neutral closed-shell system, i.e., A must be able to stabilize a negative charge. In case of the bent quadruplevoid the vertical electron attachment energy $E_{A,v}$ amounts to 2.77 eV. The excess electron is trapped at the double bond yielding $^{-}\text{Si-Si}^{\bullet}$.

3.2. The pyramidal quadruplevoid

As with the bent void 10 unpaired electrons are present at the beginning of the geometry optimization. The corresponding atoms belong to three different layers of the silicon lattice. The atom above the top of the pyramid, labeled “1” in Fig. 2, which is the only atom belonging to layer 1, is quite isolated from the next six radical centers in layer 2 (distance = 4.48 Å). The three atoms below the base of the pyramid belong to layer 3. The core consists of said 10 atoms in local C_3 symmetry and nine further Si atoms which had to be included due to the reason explained in the last section. The overall symmetry of the cluster is C_s .

The shape of the pyramidal void is much more spherical than the shape of the bent void. In consequence, to form five new bonds would require a much larger distortion of the bulk. So it seems possible that some of the unpaired electrons will stay unpaired. Fig. 2 shows the result of the optimization. Three new single bonds have been generated in layer 2 giving rise to a nine-membered ring. However, atom 1 remains isolated. In layer 3 the Si-Si distances become shorter by about 0.06 Å, but no double bonds are formed. Instead the originally three radical centers retain their character so that the electronic ground state of the pyramidal quadruplevoid is that of a fourfold singlet radical. Note that also this system does not possess any significantly elongated bonds.

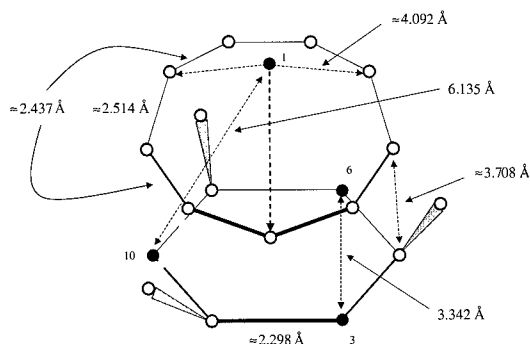


Fig. 2. Optimized structure of the pyramidal quadruplevoid in $\text{Si}_{139}\text{H}_{116}$. The void atoms occupy the corners of the polygons.

It is easy to reconstruct that atom 1 has not been incorporated into the system of the other atoms due to the strain exerted by the bulk. But what is about the three atoms belonging to layer 3? At the beginning of the optimization they are arranged in C_{3v} symmetry. So the three unpaired electrons occupy one totally symmetric orbital (a_1) and a pair of energetically higher but degenerate orbitals of e type. This situation gives rise to a Jahn-Teller distortion. Two of the three radical centers, labeled “3” and “6”, respectively, in Fig. 2, get closer to each other as far as it is admitted by the strain of the other atoms, and the two electrons occupy an energetically lower bonding orbital. The remaining center (“10”) is pushed to the left. The two unpaired electrons of 1 and 10 couple weakly yielding the core’s HOMO as the *antibonding* combination of the respective atom orbitals, whereas the *bonding* analogue (LUMO) is shifted to higher energies.

The HOMO \rightarrow LUMO transition needs an energy of 1.46 eV, but, in contrast to the situation with the bent quadruplevoid, it is highly probable due to an oscillator strength of $f = 0.622$.

The stabilization energy of an excess electron amounts to the remarkable value of 3.32 eV. Negative charge and spin density are delocalized over atoms 1 and 10.

4. Summary and outlook

In continuation of previous work [3] we have investigated quadruplevoids which could play a role in the mechanistic description of the SWE. They are generated by removing four adjacent Si atoms in the center of a hydrogenated Si-cluster. Then the total systems are allowed to relax energetically. In this process they try to repair the unfavorable starting configuration, but the tendency of the core to form new bonds is hindered partially by the bulk’s strain exerted on the core. *If* slightly stretched bonds can be generated, it will happen. *If*, however, the necessary rearrangement of bulk atoms would be too extensive, *then* the system reconciles itself to the existence of weakly coupled radical centers. Significantly stretched bonds have not been observed.

In contrast to its bent analogue the *pyramidal* quadruplevoid shows up a $S_0 \rightarrow S_1$ -transition which is both energetically favorable and electric dipole allowed. Moreover, this void is able to stabilize an excess electron by an energy as high as 3.32 eV. So it represents a structural entity in a-Si:H which meets the expectations regarding the metastable defect B and its precursor A.

Acknowledgements

The present work was supported by a grant (no. S7910-CHE) from the Austrian FWF.

References

- [1] D.L. Staebler, C.R. Wronski, *Appl. Phys. Lett.* 31 (1977) 292.
- [2] D.L. Staebler, C.R. Wronski, *J. Appl. Phys.* 51 (1979) 3262.
- [3] T. Krüger, A.F. Sax, *Phys. Rev. B*, 2001, in press.
- [4] D.L. Williamson, A.H. Mahan, B.P. Nelson, R.S. Crandall, *Appl. Phys. Lett.* 55 (1989) 783.
- [5] H. Mahan, D.L. Williamson, B.P. Nelson, R.S. Crandall, *Phys. Rev. B* 40 (1989) 12024.
- [6] Z. Remes, M. Vanecek, A.H. Mahan, R.S. Crandall, *Phys. Rev. B* 56 (1997) R12710.
- [7] J.A. Schmidt, R.D. Arce, R.R. Koropecski, R.H. Buitrago, *Phys. Rev. B* 59 (1999) 4568.
- [8] S. Dapprich, I. Komáromi, K.S. Byun, K. Morokuma, M.J. Frisch, *J. Mol. Struct. (Theochem)* 461–462 (1999) 1.
- [9] M.J. Frisch, et al., *Gaussian 98 (Revision A.7)*, Gaussian, Inc., Pittsburgh PA, 1998.
- [10] D. Becke, *Phys. Rev. A* 38 (1988) 3098.
- [11] J.P. Perdew, *Phys. Rev. B* 33 (1986) 8822.
- [12] M.J.S. Dewar, E.G. Zoebisch, E.F. Healy, *J. Am. Chem. Soc.* 107 (1985) 3902.
- [13] M.J.S. Dewar, C.H. Reynolds, *J. Comput. Chem.* 2 (1986) 140.
- [14] J.B. Foresman, M. Head-Gordon, J.A. Pople, M.J. Frisch, *J. Phys. Chem.* 96 (1992) 135.
- [15] T. Krüger, A.F. Sax, *J. Comput. Chem.*, 2001, in press.



ELSEVIER

Physica B 308–310 (2001) 159–162

PHYSICA B

www.elsevier.com/locate/physb

New hydrogen-related radiation-induced deep-level center in boron-doped silicon

N. Yarykin^{a,b,*}, O. Feklisova^a, J. Weber^b

^a*Institute of Microelectronics Technology RAS, Moscow region, 142432 Chernogolovka, Russia*

^b*University of Technology, D-01062 Dresden, Germany*

Abstract

The interaction of hydrogen impurity with radiation defects in silicon is studied by DLTS. Prior to the electron irradiation at room temperature, hydrogen was introduced into the p-type samples by wet chemical etching. Two new deep-level centers are detected only in float-zone crystals. The depth profiles of the new centers resemble those of the boron–hydrogen pairs. One center reveals a charge-driven bistability; the deep levels corresponding to both of its configurations as well as transformation kinetics are determined. Our results indicate that the bistable defect is interstitial in nature and includes boron and hydrogen. © 2001 Elsevier Science B.V. All rights reserved.

Keywords: Silicon; Hydrogen; Radiation defects; Bistability

1. Introduction

The dominant defects, which are created by room temperature electron irradiation, are mostly complexes of primary radiation defects with impurities like oxygen, carbon or shallow level dopants. Recently, hydrogen was also discussed as a common and, under certain conditions, an abundant impurity in silicon. The interaction of hydrogen with radiation defects in silicon has been studied for many years. Usually, hydrogen is introduced into the samples by chemical etching or plasma treatment *after* the irradiation with high energetic particles [1–4], when formation of the radiation-induced defect spectrum has already been completed. The hydrogen treatment after the irradiation process excludes the interaction of hydrogen with mobile radiation-induced species, such as vacancies and self-interstitials, which are not stable at room temperature. Another approach to investigate the hydrogen/radiation defect interaction is proton implantation, which simultaneously generates the intrinsic point defects and introduces the hydrogen atoms. Indeed, new hydrogen-related complexes [5,6], which are not observed using the

post-hydrogenation, have been revealed in this way. However, due to the simultaneous migration of hydrogen, vacancies, and interstitials, the formation process of stable defects is complicated and difficult to follow in detail. The situation can be simplified if silicon crystals are hydrogenated *before* irradiation. Several IR absorption and DLTS studies already showed that hydrogen-related complexes are formed by room temperature electron irradiation following pre-hydrogenation during growth or high-temperature treatment in hydrogen-containing atmosphere [7,8]. However, interpretation of the results is not straightforward because the state of hydrogen after high-temperature saturation is not fully understood. The purpose of the present work is to study the formation of radiation-induced defects in hydrogenated samples, where virtually all hydrogen atoms are bound in boron–hydrogen pairs before the electron irradiation.

2. Experimental

Boron-doped ($[B] = (0.8\text{--}2.5) \times 10^{15} \text{ cm}^{-3}$, Cz or FZ) silicon wafers were hydrogenated by chemical etching in HF:HNO₃ acid mixtures at ambient temperature. After Schottky diode preparation, the reverse-bias annealing

*Corresponding author. Fax: +7-095-962-8047.

E-mail address: nay@ipmt-hpm.ac.ru (N. Yarykin).

(RBA) procedure was applied to move hydrogen deeper in the crystals and to form well-defined profile of boron–hydrogen pairs [9]. A few samples were hydrogenated by H-plasma treatment at 100°C. The final hydrogen distribution was monitored by CV measurements. Hydrogenation did not introduce any deep-level centers in measurable concentration. The hydrogenated diodes were subjected to 1.5 or 6 MeV electron irradiation with a fluence of $(0.3\text{--}1.0) \times 10^{15} \text{ cm}^{-2}$ at nominal room temperature.

The measurements were performed on a computerized DLTS system with lock-in sine-wave correlation; the rate window was set in the range between 0.5 and 120 s^{-1} . The curves were taken during heating with rates of $3\text{--}9 \text{ K s}^{-1}$. Spatial distribution of the deep-level centers was calculated by digital differentiation of the DLTS signal dependence on the filling pulse amplitude at a fixed reverse bias. The inhomogeneous profile of shallow dopants, which was determined from the CV measurements, was properly included in the evaluation of the deep-level defect concentrations. The MCTS curves were measured using minority-carrier injection from an LED through the semitransparent Schottky contact.

3. Results

The DLTS spectrum after high-energy electron irradiation of the hydrogenated FZ sample is shown in Fig. 1. The DLTS parameters were set to monitor only the defects in the hydrogenated region. The dominant features of the majority-carrier trap spectrum (Fig. 1b) are the donor levels of the divacancy (V_2), interstitial carbon (C_i), and two overlapping peaks labeled MH3-B and H3, respectively. The MH3-B level appears in the spectrum only after cooling the sample from room temperature under reverse bias, indicating a charge-driven bistability of the center. However, no new deep level emerges in the lower half of the gap instead of MH3-B after zero-bias cooling. Therefore, the MCTS technique has been applied to monitor the defect levels in the upper half of the gap. The MCTS spectrum shown in Fig. 1(a) exhibits an electron trap (labeled MH3-A) with a metastable behavior complementary to that of MH3-B. Detailed measurements verify that the kinetics of the MH3-A center formation during zero-bias annealing in the temperature range from 195 to 215 K, is the same as the kinetics of the MH3-B center disappearance. Both levels disappear in our samples after several hours at 360 K. Thus, we conclude that the MH3-A and MH3-B levels belong to two different configurations of the MH3 bistable center. The MH3 and H3 defects are not detected after electron irradiation of pre-hydrogenated Cz-Si samples.

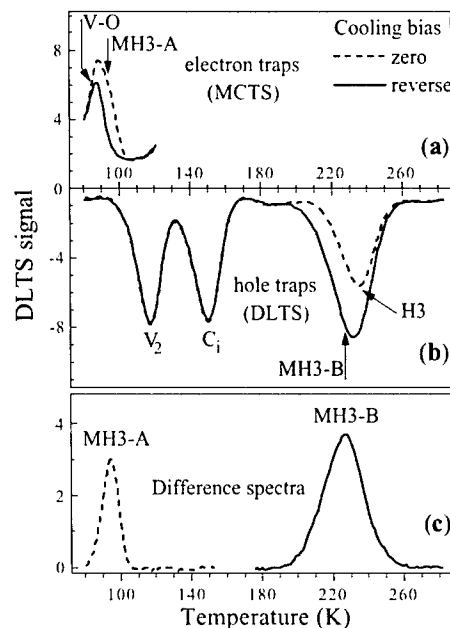


Fig. 1. MCTS (a) and DLTS (b) curves measured after cooling under different conditions for the pre-hydrogenated p-type FZ-Si irradiated with $7 \times 10^{14} \text{ cm}^{-2}$ of 6 MeV electrons, and the difference spectra (c) calculated by subtracting the curves in panels (a, b). The rate window is 52 s^{-1} for both DLTS and MCTS curves.

The energy of the observed levels was determined by measurements of the peak temperature positions at different correlator rate windows. Both MH3-A and MH3-B peaks strongly overlap with signals from other defects, and their correct positions can be determined only from the difference spectrum calculated by subtraction of the curves measured after zero- and reverse-bias cooling, see Fig. 1(c). The H3 peak maximum was determined after zero-bias cooling, when there was no perturbation from the MH3-B peak contribution. The energies for hole emission for the MH3-B and H3 levels were determined to be 0.44 and 0.51 eV, respectively. Only a rough estimate of $E_c - 0.22 \pm 0.04 \text{ eV}$ can be given for the MH3-A energy position, due to the liquid nitrogen cooling of the MCTS setup.

The depth distributions of the deep-level centers observed in FZ-Si are shown in Fig. 2 along with the net boron profile. The MH3 and H3 centers are strongly localized in the region around $1.8 \mu\text{m}$ from the surface, where 50% of boron is passivated during RBA before irradiation. The divacancies exhibit a rather flat profile. We have varied the concentration and depth distribution of boron–hydrogen pairs by performing the RBA treatment at different temperatures and voltages. In some samples, hydrogen has also been redistributed after chemical etching by furnace annealing without

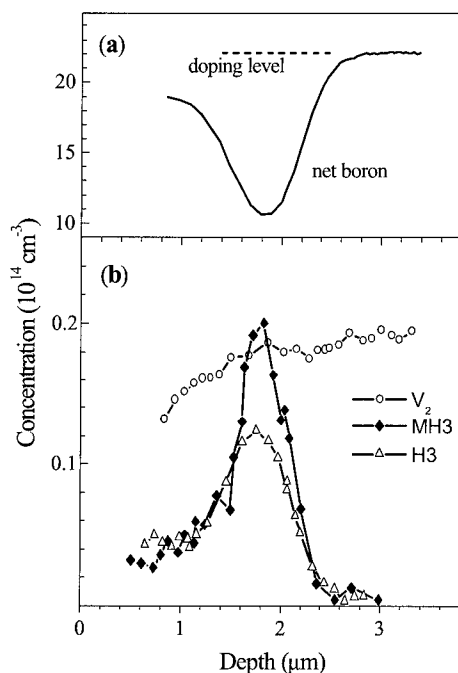


Fig. 2. The depth profiles of the boron acceptors (a) and the deep-level centers (b) formed in p-type FZ-Si after RBA hydrogenation and subsequent irradiation with the $5 \times 10^{14} \text{ cm}^{-2}$ fluence of 1.5 MeV electrons. The MH3 center concentration was measured in the B-configuration.

Schottky diodes. In all studied cases, the shape of the depth profiles of the MH3 and H3 centers resembles those of boron–hydrogen pairs. Thus, we conclude that the MH3 and H3 centers are hydrogen-related radiation defects.

4. Discussion

DLTS levels very similar to MH3-B and H3 have recently been found in epitaxially grown silicon after irradiation with α -particles [10]. The energies for hole emission for the $\text{H}\alpha_1$ and $\text{H}\alpha_2$ levels [10] as well as the transformation kinetics of the bistable $\text{H}\alpha_2$ match closely our values for H3 and MH3-B, respectively. The very similar energies give strong evidence to the identical nature of the defects observed in different crystals. Apparently, the samples used in Ref. [10] were contaminated with hydrogen during growth or diode preparation.

The MH3 and H3 centers have a number of similar features, but the MH3 centers have only been detected in pre-hydrogenated samples, while the H3 defects can also be formed by hydrogenation *after* irradiation (for more data on H3, see Ref. [11]). Taking also into account that

the MH3 center concentration follows the distribution of boron–hydrogen pairs, we conclude that the MH3 center forms by the capture of a mobile radiation-induced defect to the boron–hydrogen complex. The mobile defects formed at the highest concentrations in p-type silicon are known to be vacancies, self-interstitials, and their products, boron and carbon interstitials. The latter can be excluded from the following consideration because (i) C_i is immobile during electron irradiation at room temperature and (ii) C_i migration at 340 K results in no changes in the MH3 center concentration. Vacancies are also not likely to be involved in the MH3 formation since the divacancy depth profile (being comparable in concentration) remains essentially flat around the pile-up of the MH3 defects (Fig. 2). On the other hand, self- and boron-interstitials may be trapped by the $\text{B}_s\text{-H}$ pairs forming $\text{B}_i\text{-H}$ and $\text{B}_i\text{-B}_s\text{-H}$ complexes, respectively. Of the two possibilities, the latter gives a simple explanation for the absence of the MH3 centers in oxygen-rich Cz-Si. Indeed, the creation of the $\text{B}_i\text{-B}_s\text{-H}$ complex should be strongly suppressed in Cz material as most of boron interstitials are consumed by oxygen forming the B_iO_i complexes [12].

5. Conclusion

We have investigated the DLTS spectrum of stable radiation defects formed in p-type silicon which was hydrogenated by wet chemical etching and annealed at 340–430 K before the irradiation. The pre-hydrogenation of FZ-Si results in the appearance of two additional MH3 and H3 centers immediately after irradiation at room temperature. The defect depth profiles correspond to the distribution of boron–hydrogen pairs and, in the case when approximately 50% of boron have been converted to the $\text{B}_s\text{-H}$ pairs, the defect concentration is comparable with that of divacancies. The MH3 defect exhibits a charge-driven bistability with characteristic transformation temperatures about 200 and 260 K for the bias-off and bias-on conditions, respectively. The bistable center anneals out at 360–380 K, while the concentration of the H3 center increases during such annealing. The MH3 and H3 defects are not detected in Cz-Si. Analysis of the results allows us to tentatively ascribe the MH3 and H3 centers to interstitial complexes including hydrogen and boron.

Acknowledgements

The authors thank R. Sielemann for the help with electron irradiation. Fruitful discussions with R. Jones, A. Mesli, and E. Yakimov are greatly appreciated. The expert help of J. Bollmann and S. Knack in DLTS measurements and the technical assistance of B. Koehler

are acknowledged. The work is supported by Deutsche Forschungsgemeinschaft (436 RUS 113/166/0) and Russian Foundation for Basic Research (RFBR-DFG 00-02-04002).

References

- [1] S.J. Pearton, *Phys. Stat. Sol. A* 72 (1982) K73.
- [2] O.V. Feklisova, N. Yarykin, *Semicond. Sci. Technol.* 12 (1997) 742.
- [3] Y. Tokuda, H. Shimada, A. Ito, *J. Appl. Phys.* 86 (1999) 5630.
- [4] J. Hartung, J. Weber, *Phys. Rev. B* 48 (1993) 14161.
- [5] B. Bech Nielsen, P. Johannesen, P. Stallings, K. Bonde Nielsen, J.R. Byberg, *Phys. Rev. Lett.* 79 (1997) 1507.
- [6] M. Budde et al., *Phys. Rev. B* 57 (1998) 4397.
- [7] T.S. Shi, G.R. Bai, M.W. Qi, J.K. Zhou, *Mater. Sci. Forum* 10–12 (1986) 597.
- [8] V.P. Markevich, L.I. Murin, J.L. Lindström, M. Suezawa, *Solid State Phenom.* 69–70 (1999) 403.
- [9] T. Zundel, J. Weber, *Phys. Rev. B* 39 (1989) 13549.
- [10] M. Mamor, F.D. Auret, S.A. Goodman, W.E. Meyer, G. Myburg, *Appl. Phys. Lett.* 72 (1998) 3178.
- [11] O.V. Feklisova, N. Yarykin, E.B. Yakimov, J. Weber, *Physica B*, in these Proceedings (ICDS-21), *Physica B* 308–310 (2001).
- [12] P.J. Drevinsky, C.E. Caefer, S.P. Tobin, J.C. Mikkelsen, L.C. Kimerling, *Mater. Res. Soc. Symp. Proc.* 104 (1988) 167.



ELSEVIER

Physica B 308–310 (2001) 163–166

PHYSICA B

www.elsevier.com/locate/physb

Fermi-level dependence of formation of hydrogen molecules in crystalline silicon

K. Ishioka^{a,*}, N. Umehara^b, T. Mori^b, K. Ohtsuka^b, M. Kitajima^a,
K. Murakami^b, S. Hishita^c

^a Materials Engineering Laboratory, National Institute for Materials Science, Tsukuba, 305-0047 Japan

^b Institute of Material Science, University of Tsukuba, Tsukuba, 305-8573 Japan

^c Advanced Materials Laboratory, National Institute for Materials Science, Tsukuba, 305-0044 Japan

Abstract

We report a systematic investigation on the Fermi-level dependence of the formation of two different types of hydrogen molecules in silicon. Hydrogen molecule at the tetrahedral (T) site ($H_2(T)$) is formed only in heavily doped n-type below 200°C, but is observed both in the n- and p-type above 200°C. The temperature dependence is due to the increase of the thermally activated carrier concentration. The possible precursors of the $H_2(T)$ are $H^+(BC)$ and $H^0(BC)$ in the p-type, and $H^-(T)$ and H^0 in the n-type. The Fermi level dependence of the formation of the hydrogen molecule trapped in platelets ($H_2(p)$) above 250°C is very different from that below 250°C. The result suggests that platelets are formed from hydrogen-complexes other than the H_2^* above 250°C. © 2001 Elsevier Science B.V. All rights reserved.

PACS: 61.72.Tt; 63.20.Pw

Keywords: Hydrogen molecule; Crystalline silicon; Fermi level

Among a number of different configurations of hydrogen in semiconductor, molecular hydrogen (H_2) has been attracting an increasing attention especially since the first experimental confirmation of its existence in silicon (Si), in 1996 [1,2]. The H_2 in the Si is chemically inactive and predicted by many theoretical calculations to be very low in energy [3–5]. Recent vibrational spectroscopic studies revealed at least two types of the H_2 in crystalline Si after exposure to hydrogen plasma. The two H_2 have different vibrational frequencies corresponding to the different sizes of their trapping sites and accordingly the different strengths of interaction with their surroundings. The vibrational line at 4158 cm^{-1} has been attributed to the H_2 trapped in platelets [6], i.e., planar defects of diameters up to 100 nm, while that at 3605 cm^{-1} to the H_2 at the tetrahedral (T) interstitial site [7–9]. The intensities of the two H_2 depended strongly upon the substrate type

and the temperature during hydrogenation [10]. In the present study, we report a systematic study on the Fermi-level dependences of the formation of the H_2 in the Si. The Fermi-level position is controlled by doping P or B atoms in the Si over a wide range. Changing the Fermi-level position with respect to the band gap is expected to cast light upon the formation mechanisms of hydrogen molecules, since it would affect the stable configuration of atomic hydrogen in the Si [3–5].

Float zone (FZ) p-type Si wafers with a resistivity of $> 50\ \Omega\text{ cm}$ were used as silicon substrate. In order to obtain n- and p-type Si samples, 50 keV P^+ and 30 keV B^+ ions were implanted in the FZ Si wafers at various fluences ranging from 1×10^{12} to $1 \times 10^{15}\text{ P}^+/\text{cm}^2$ and from 1×10^{12} to $1 \times 10^{15}\text{ B}^+/\text{cm}^2$, respectively. The ion energies were selected to cover the optical penetration depth of the visible light used in the Raman scattering measurements. The implanted samples were annealed at 900°C for 30 min in an atmosphere of flowing N_2 gas to activate the implanted dopants and annihilate other defects. The resulting dopant

*Corresponding author. Fax: +81-208-592801.

E-mail address: ishioka.kunie@nims.go.jp (K. Ishioka).

concentrations ranged from 1.6×10^{17} to 1.6×10^{20} P/cm³ and 1.0×10^{17} to 1.0×10^{20} B/cm³. The Fermi level E_{Fermi} of each Si sample was estimated from the concentration and the hydrogenation temperature [11], neglecting passivation of dopants by atomic hydrogen. All the Si samples were hydrogenated with atomic hydrogen in a remote downstream of hydrogen plasma for 30 min. The samples were placed in the quartz tube 60 cm apart from the plasma to suppress the damage by the activated species. The error bar in the substrate temperature during hydrogenation was $\pm 10^\circ\text{C}$ for different positions in the furnace. The details of the method and hydrogenation conditions have been reported elsewhere [12,13]. Raman scattering measurements were performed at room temperature using a 514.5 nm light as an excitation source. In the present study, all the Raman intensities were normalized by the intensity of the optical phonon of Si of the same sample measured under the same condition.

Fig. 1 shows the Raman spectra of the Si samples after hydrogenation for 30 min at a substrate temperature of 165°C . The weak, relatively narrow Raman line around 3600 cm^{-1} was assigned to the H_2 at the T sites ($\text{H}_2(\text{T})$) in the preceding infrared [7,8] and Raman [9] studies. At this hydrogenation temperature, $\text{H}_2(\text{T})$ was observed only for the n-type Si samples. The small peak around 3650 cm^{-1} is the O–H stretching of water in the air and decreases under N_2 purge. The broader Raman line around 4150 cm^{-1} , which was attributed to the H_2 trapped in the platelets ($\text{H}_2(\text{p})$) [6], was observed for all the samples except very heavily doped n-type Si. We also

observed Raman band due to the Si–H bonds terminating platelets (Si–H(p)) around 2100 cm^{-1} , whose intensity showed a good correlation with that of the $\text{H}_2(\text{p})$.

The formation of the hydrogen molecules is not determined solely by the Fermi-level position, but is also affected by the hydrogenation temperature. Fig. 2 shows the Raman spectra of the Si samples after hydrogenation at 305°C . The formation of the $\text{H}_2(\text{T})$ was maximum in n-type, but was also observed in the p-type. The $\text{H}_2(\text{p})$ intensity exhibited a maximum for a moderately doped p-type Si. It is noted that the intensities of the $\text{H}_2(\text{T})$ and $\text{H}_2(\text{p})$ exhibited an anti-correlation to each other after hydrogenation at 305°C . Fig. 3 summarizes their Raman intensities after hydrogenation at different temperatures as a function of the Fermi-level position.

In the present study, hydrogen is introduced as neutral H atoms into the Si samples. The energetically favorable position and charge state in the Si are determined by the position of the Fermi level. In many calculations, there is an agreement that H is stable at a bond-center (BC) site with a positive charge in the p-type and at a T site with a negative charge in the n-type [3–5,14–16]. However, the global minimum for neutral H (H^0) is still controversial. We interpret the suppression of the $\text{H}_2(\text{T})$ formation in p-type below 200°C to be due to the Coulomb repulsion between two H^+ (BC) and the lack of electrons to form interatomic bonds [5]. Above 200°C on the other hand, the intrinsic carrier concentration exceeds the acceptor concentration. The H^+ (BC) acts as a donor with an electronic state slightly below the conduction band minimum [4,16–18], then captures an electron and forms $\text{H}^0(\text{BC})$. The reaction

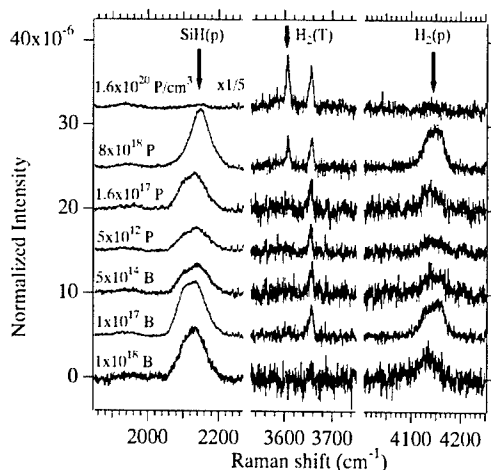


Fig. 1. The Raman spectra of the Si samples at different P and B doping concentrations after hydrogenation at 165°C for 30 min. The Raman lines around 2000 , 3600 and 4150 cm^{-1} are attributed to the SiH(p), $\text{H}_2(\text{T})$, and $\text{H}_2(\text{p})$, respectively. The vertical axis is normalized by the integrated Raman intensity of the optical phonon line of silicon.

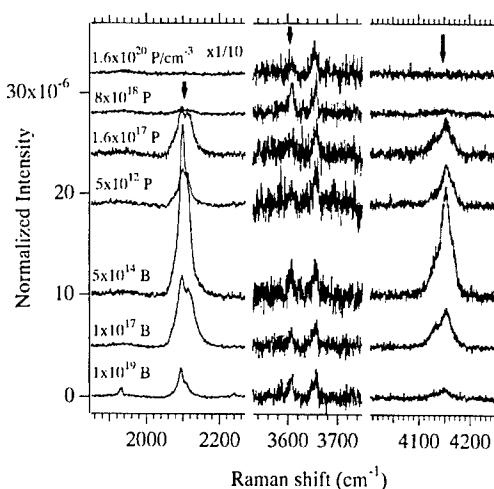


Fig. 2. The Raman spectra of the Si samples at different P and B doping concentrations after hydrogenation at 305°C for 30 min. The vertical axis is normalized by the integrated Raman intensity of the optical phonon line of silicon.

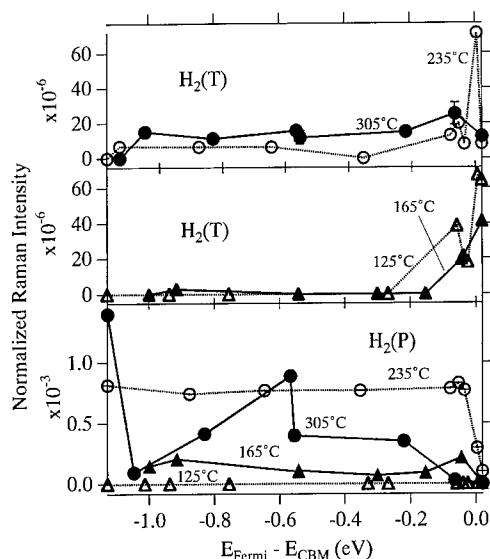


Fig. 3. The integrated Raman intensities of the $H_2(T)$ and $H_2(p)$ in the Si samples after hydrogenation as a function of the Fermi-level position E_{Fermi} . The intensities are normalized by that of the optical phonon of silicon. E_{CBM} denotes the conduction band minimum.

$H^0(BC) + H^+(BC) \rightarrow H_2(T)$ is thus promoted thermally in p-type at high temperatures. The effective formation of the $H_2(T)$ in heavily doped n-type below 200°C suggests the absence of Coulomb repulsion, i.e., the coexistence of the $H^-(T)$ and H^0 . Since $H(T)$ has on a deep level in the middle of the band gap [16] or closer to the valence band maximum [4], the maximum of $H_2(T)$ formation near the conduction band minimum may be explained better by assuming that H^0 is at the BC than at T.

Our results on the Fermi-level dependence of the $H_2(p)$ formation was very different from that of the platelet concentration studied by transmission electron microscopy (TEM) [17,18], which was increased monotonically as the Fermi level approached the conduction band minimum. A possible reason for the large discrepancy is the different methods of the sample preparation. In the previous TEM work, the samples were hydrogenated sequentially at two different temperatures (150°C and 275°C) to nucleate platelets and extend them up to 100 nm size, respectively. We have confirmed that, for the hydrogenation temperature above 250°C, the formation of the $H_2(p)$ is remarkably enhanced when the sample is exposed to the H atoms at a lower temperature in advance [10]. The resemblance of the Fermi-level dependences of the $H_2(T)$ in the present study and the platelet concentration in the previous TEM work suggests a possibility that the $H_2(T)$ is transformed into platelets when the sample is hydrogenated again at a higher temperature. We have

confirmed the possibility by performing thermal annealing on an n-type sample in which considerable amount of $H_2(T)$ and very little $H_2(p)$ were observed. After furnace anneal at 55°C for 30 min, the Raman peak of $H_2(p)$ was increased significantly. With increasing annealing temperature, the intensities $H_2(T)$ and $H_2(p)$ were decreased and increased, respectively. The result may also explain the anti-correlation between the intensities of the $H_2(T)$ and that of the $H_2(p)$ at 305°C.

The $H_2(p)$ formation below 235°C was not significantly dependent on the Fermi level except for very heavily doped n-type, whereas it exhibited a rather complicated dependence on the Fermi level at 305°C. Since the $H_2(p)$ is stable up to 400°C, the temperature dependence may be due to the thermal stability of the precursors of platelets [19]. Theoretical calculations suggest that the diatomic complex H_2^* is a precursor of the $\{111\}$ platelets [20,21]. An infrared absorption study reported that H_2^* was annealed out below 250°C [22], being consistent with our observation on the temperature dependence of $H_2(p)$. On the other hand, the insensitiveness of $H_2(p)$ intensity to the Fermi level is very different from the theoretically predicted Fermi-level dependence of H_2^* , and leaves room for other precursors. The Fermi-level dependence for 305°C hydrogenation, which has a maximum when the Fermi level is in the mid-gap, suggests that $H^+(BC)$ and $H^0(T)$ are involved in the formation of platelets.

In conclusion, we observed a significant Fermi level and temperature dependences of the formation of the two different types of H_2 in hydrogenated crystalline Si. The $H_2(T)$ is formed mainly from H^0 and $H^-(T)$ in the n-type and from $H^0(BC)$ and $H^+(BC)$ in the p-type. The latter mechanism is activated thermally above 200°C. The temperature dependence of the $H_2(p)$ formation is consistent with the model in which the H_2^* is the precursor, whereas the Fermi-level dependence suggests the existence of other configurations of hydrogen as the precursors.

References

- [1] K. Murakami, N. Fukata, S. Sasaki, K. Ishioka, M. Kitajima, S. Fujimura, J. Kikuchi, H. Haneda, Phys. Rev. Lett. 77 (1996) 3161.
- [2] N. Fukata, S. Sasaki, K. Murakami, K. Ishioka, K.G. Nakamura, M. Kitajima, S. Fujimura, J. Kikuchi, H. Haneda, Phys. Rev. B 56 (1997) 6642.
- [3] P. Deák, L.S. Snyder, J. Corbett, Phys. Rev. B 37 (1988) 6887.
- [4] C.G. van de Walle, Y. Bar-Yam, S.T. Pantelides, Phys. Rev. B 39 (1989) 10791.
- [5] S.K. Estreicher, M.A. Roberson, Phys. Rev. B 50 (1994) 17018.

- [6] A.W.R. Leitch, V. Alex, J. Weber, *Solid State Commun.* 105 (1997) 215.
- [7] R.E. Pritchard, M.J. Ashwin, J.H. Tucker, R.C. Newman, E.C. Lightowlers, M.J. Binns, S.A. McQuaid, R. Falster, *Phys. Rev. B* 56 (1997) 13118.
- [8] R.E. Pritchard, M.J. Ashwin, J.H. Tucker, R.C. Newman, *Phys. Rev. B* 57 (1998) R15048.
- [9] A.W.R. Leitch, V. Alex, J. Weber, *Phys. Rev. Lett.* 81 (1998) 421.
- [10] M. Kitajima, K. Ishioka, K. Murakami, K. Nakanoya, T. Mori, *Physica B* 273–274 (1999) 192.
- [11] A.S. Grove, *Physics and Technology of Semiconductor Devices*, Wiley, New York, 1967, pp. 100–106.
- [12] N. Fukata, S. Fujimura, K. Murakami, *Mater. Sci. Forum* 196–201 (1995) 873.
- [13] N. Fukata, S. Sasaki, S. Fujimura, H. Haneda, K. Murakami, *Jpn. J. Appl. Phys.* 35 (1996) 3937.
- [14] K.J. Chang, D.J. Chadi, *Phys. Rev. Lett.* 62 (1989) 937.
- [15] K.J. Chang, D.J. Chadi, *Phys. Rev. B* 40 (1989) 11644.
- [16] D.J. Chadi, C.H. Park, *Phys. Rev. B* 52 (1995) 8877.
- [17] B. Holm, K. Bonde Nielsen, B. Bech Nielsen, *Phys. Rev. Lett.* 66 (1991) 2360.
- [18] N.H. Nickel, G.B. Anderson, N.M. Johnson, J. Walker, *Phys. Rev. B* 62 (2000) 8012.
- [19] N. Fukata, K. Murakami, K. Ishioka, K.G. Nakamura, M. Kitajima, S. Fujimura, J. Kikuchi, H. Haneda, *Mater. Sci. Forum* 258–263 (1997) 211.
- [20] S.B. Zhang, W.B. Jackson, *Phys. Rev. B* 43 (1991) 12142.
- [21] Y.-S. Kim, K.J. Chang, *Phys. Rev. Lett.* 86 (2001) 1773.
- [22] M.K. Weldon, V.E. Marsico, Y.J. Chabal, A. Agarwal, D.J. Eaglesham, J. Sapjeta, W.L. Brown, D.C. Jacobson, Y. Caudano, S.B. Christman, E.E. Chaban, *J. Vac. Sci. Technol. B* 15 (1997) 1065.



ELSEVIER

Physica B 308–310 (2001) 167–170

PHYSICA B

www.elsevier.com/locate/physb

Defects agglomeration in the vicinity of hydrogen-related vacancy-type complexes in proton-implanted silicon

S.Zh. Tokmoldin*, B.N. Mukashev

Institute of Physics and Technology, Almaty 480082, Kazakhstan

Abstract

The results of IR studies of H interactions with radiation-induced defects in crystalline Si implanted with protons (Si:H) are presented. Wide doublets at ~ 1980 , 2060 and ~ 720 , 620 cm^{-1} with relatively low thermal stability (the doublets are fully annealed at 550 K) appear in IR absorption spectra of Si:H when implantation dose is increased. It is shown that the doublets may be assigned to nuclei of two hydrogenated amorphous phases with different densities. The Si:H stretching spectra of as-implanted samples are greatly simplified with the increasing implantation dose. Four groups of IR bands predominate at high implantation doses: 2222 cm^{-1} — VH_4 ; 2072 cm^{-1} — V_2H_2 ; the doublet at 2166 , 2191 cm^{-1} — V_2H_6 ; 1967 cm^{-1} —an interstitial-type complex and the doublet at 2107 , 2122 cm^{-1} —a vacancy-type complex. It is shown that the doublet at 2107 , 2122 cm^{-1} may be tentatively assigned to V_6H_{12} which can serve as nuclei or precursors of the $\{111\}$ platelets. © 2001 Elsevier Science B.V. All rights reserved.

Keywords: Silicon; Hydrogen; Vacancies; Platelets

1. Introduction

A lot of IR-active H-related defects were discovered in crystalline Si:H hydrogenated in different ways [1]. Intensive investigations using co-doping with H and D, uniaxial stress and impurity effect were not successful in unambiguously discriminating between hydrogenated vacancy- and interstitial-type complexes [2–5].

Earlier [6] we discovered correlated step function behavior of temperature dependence of anharmonicity between Si–H stretching lines lying above and below 2000 cm^{-1} . Detailed investigations [7–11] revealed that anharmonicity representing the Si–H dipole coupling to a defect host is sensitive to hybridization character and coordination of Si atom bonded to H that enables to make two most important conclusions:

1. Si–H stretching and bending lines may be separated into two different groups. Lines in the 2000 – 2250 and 550 – 700 cm^{-1} ranges are characteristic of vacancy-type complexes while lines in the 1900 – 2000 and 700 –

800 cm^{-1} ranges are connected with interstitial-type complexes.

2. The analysis of various molecular configurations of H-related complexes allows us to conclude that local Si–H modes of large complexes are mainly determined by simple structural units such as hydrogenated vacancies (VH , VH_2 , VH_3) and $\langle 100 \rangle$ split Si-interstitialcies (IH , IH_2).

Using these findings we have identified Si–H lines related to vacancy- and interstitial-type defects [7–11]: 2223 and 634 cm^{-1} — VH_4 ; 2166 , 2191 and 610 , 668 cm^{-1} — V_2H_6 ; 2072 and 610 cm^{-1} — V_2H_2 consisting of two VH structural units in $\text{VH} \oplus \text{VH}$ configuration; 2107 , 2122 and 588 , 610 , 694 cm^{-1} —a complex consisting of several VH_2 units in $\text{VH}_2 \oplus \text{VH}_2 \oplus \dots \oplus \text{VH}_2$ configuration; 1957 , 1967 and 718 , 750 cm^{-1} — $\{110\}$ interstitial chains consisting of two (or more) $\langle 100 \rangle$ -oriented IH and IH_2 structural units. All these assignments were confirmed in other works both theoretically [12–14] and experimentally [4,5,15].

In this paper, we study dose dependence of IR spectra of Si:H implanted with high-energy protons. We use the above-mentioned findings to consider an “amorphous”

*Corresponding author. Fax: +7-327-2-545224.
E-mail address: serik@sci.kz (S.Z. Tokmoldin).

background IR spectrum of Si:H and the behavior of local IR lines associated with vacancy-type complexes as well as of the 1.8μ band [16] related to V_2 .

2. Experimental details

High-purity Si crystals ($N_B < 10^{14} \text{ cm}^{-3}$, $N_{0,C} < 10^{15} \text{ cm}^{-3}$) were implanted near 300 K with 7 and 30 MeV protons up to doses of 10^{18} ion/cm^2 . The samples were heat treated for 15 min in the range of 125–650°C with the step 25°C. IR spectra of Si:H were measured at 80 and 300 K with the resolution of $0.5\text{--}4 \text{ cm}^{-1}$ in the $400\text{--}10000 \text{ cm}^{-1}$ spectral range.

3. “Amorphous” background in the Si:H spectra

Wide doublets at ~ 1980 , 2060 cm^{-1} and ~ 720 , 620 cm^{-1} (shown by dashed line in Fig. 1) appear in IR spectra of Si:H with the implantation dose. The doublets may be considered as an “amorphous” background of Si–H local vibrational spectra. They have relatively low thermal stability and are fully annealed at about 550 K. No direct correlation of the “amorphous” background annealing with changes in Si–H spectrum was found.

It is known [17] that H atoms in plasma-deposited a-Si:H may be bonded in SiH_1 , SiH_2 and SiH_3 configurations. The ratio between SiH_1 , SiH_2 and SiH_3 strongly depends on the growth conditions, the most qualitative a-Si:H consists of mainly SiH_1 -radicals with stretching and bending modes at $\sim 1990 \text{ cm}^{-1}$ and $\sim 630\text{--}640 \text{ cm}^{-1}$. It was found [18] that the Si–H

stretching band is monotonously displaced to $\sim 2060 \text{ cm}^{-1}$ with decreasing a-Si:H deposition temperature. This effect was explained by the SiH_1 bonds coordination which becomes close to tetrahedral.

The Si:H “amorphous” background is close to the SiH_1 stretching bands in a-Si:H spectrum while in bending range it includes the second component at 720 cm^{-1} and differs from a-Si:H spectrum. Taking into account the low thermal stability, the Si:H “amorphous” background may be associated with intermediate phases precursor to a-Si:H: groups at ~ 1980 , 720 cm^{-1} and ~ 2060 , 620 cm^{-1} may be assigned to SiH_1 -radicals in the vicinity of “amorphous” agglomerations of intrinsic interstitials and vacancies, respectively.

The “amorphous” agglomerations of H with intrinsic interstitials and vacancies may be considered as two different α_i - and α_v -phases. Since the $\sim 720 \text{ cm}^{-1}$ component is not observed in a-Si:H spectrum the α_i -phase differs from a-Si:H. Indeed, the density of agglomerations of intrinsic interstitial atoms in Si should be higher than the density of a matrix, while the density of a-Si:H prepared by H implantation [19] is lower than the density of Si. At the same time, IR spectrum of the α_v -phase is close to SiH_1 modes in a-Si:H obtained at low deposition temperatures [18] when the coordination of bonds is close to tetrahedral.

4. Dose behavior of point vacancy-type defects in Si:H

At low implantation doses the Si:H IR spectra contain a lot of Si–H lines as well as broad absorption bands due to electronic transitions of V_2 . Si–H spectrum is considerably simplified with implantation dose increasing and lines related to vacancy-type complexes such as VH_4 , V_2H_6 , etc. predominate.

Fig. 2 shows dose dependence of vacancy-type complexes and V_2 . The defects concentrations are saturated at a dose of $8 \times 10^{17} \text{ H}^+/\text{cm}^2$ and then begin to decrease, the V_2 removal is very abrupt. The “amorphous” background absorption related to α_i - and α_v -phases simultaneously grows. At the same time a group of relatively low-intensity Si–H lines in the $2100\text{--}2150 \text{ cm}^{-1}$ range is simplified and doublet lines at 2107 , 2122 cm^{-1} (at 77 K, 2104 , 2120 cm^{-1} at 300 K) appear and grow, this process correlates with the V_2 abrupt removal.

The data show that point H-related complexes are formed at initial implantation stage when concentrations of the α_i - and α_v -nuclei are low. These complexes effectively trap H atoms up to the saturation of all dangling bonds and are stabilized outside the α_i - and α_v -nuclei. At the following implantation stage point defects migrate to “amorphous” nuclei and are trapped there. At large implantation doses the α_i - and α_v -nuclei capture point complexes and join with the formation of a-Si:H.

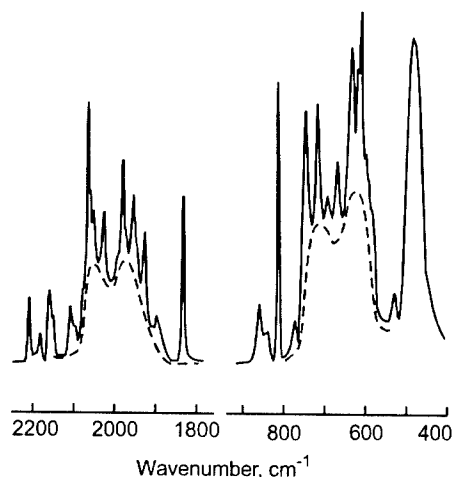


Fig. 1. An “amorphous” background in Si:H spectra. The background appears after 30 MeV proton implantation through aluminum foils at doses above $10^{17} \text{ H}^+/\text{cm}^2$.

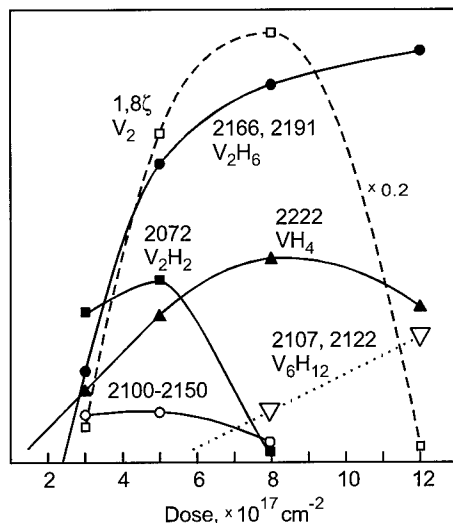


Fig. 2. Dose dependence of main IR lines in the spectra of crystalline Si implanted with 7 MeV protons at near room temperature.

These conclusions are in a good agreement with the data of experiments on hydrogenated a-Si:H prepared by ion implantation [19], in which it was shown that the dose of Si amorphization considerably decreases if a sample was previously implanted by H.

At low implantation doses the 2072 cm^{-1} line related to V_2H_2 consisting of two VH structural units in $\text{VH} \oplus \text{VH}$ configuration is most intense in Si-H spectrum (Fig. 2). At higher doses the 2072 cm^{-1} line is removed and this may be explained by trapping of additional H with the transformation of V_2H_2 to V_2H_6 . Indeed, annealing of the 2072 cm^{-1} line at a temperature of $\sim 570\text{ K}$ directly correlates with growth of the $2166, 2191\text{ cm}^{-1}$ doublet lines associated with V_2H_6 .

It is seen from dose dependences (see Fig. 2) that VH_4 forms before V_2H_6 and has different behavior. Annealing characteristics of these two centers do not also correlate with each other. The 2222 cm^{-1} line and the $2166, 2191\text{ cm}^{-1}$ doublet lines related to VH_4 and V_2H_6 , respectively, as well as the $2107, 2122\text{ cm}^{-1}$ doublet lines associated with a complex consisting of VH_2 units in $\text{VH}_2 \oplus \text{VH}_2 \oplus \dots \oplus \text{VH}_2$ configuration [7–11] are the most intensive local Si-H lines at high doses and after annealing above 600 K . So dose dependencies and annealing characteristics of Si-H lines related to vacancy-type defects reveal [8] that predominating complexes in Si:H are complexes containing even number of H atoms such as $\text{VH}_4, \text{V}_2\text{H}_2, \text{V}_2\text{H}_6$, etc. Intermediate complexes containing odd number of H atoms have unpaired electron on dangling Si-bonds and are acceptors, therefore, the complexes effectively traps H atoms which are in the $\dot{\text{I}}^+$ state. In [10], we found that these acceptor-like complexes serve as compensating

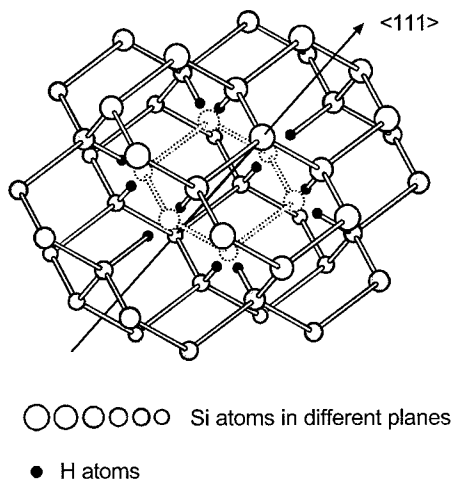


Fig. 3. Hydrogenated hexavacancy in Si. This complex can serve as nuclei or precursors of the $\{111\}$ platelets observed in [22].

centers for shallow donors. Weak lines in the $2000\text{--}2200\text{ cm}^{-1}$ range related to VH, VH_2 and VH_3 structural units may be assigned to these complexes.

The V_2 dose dependence does not correlate with dependencies for VH_4 and V_2H_6 (Fig. 2). Very abrupt V_2 removal at high doses correlates only with growth of the $2107, 2122\text{ cm}^{-1}$ doublet lines and its mechanism may be connected either with the V_2 capture in the vicinity of the α_i - and α_v -nuclei or with H-enhanced agglomeration of V_2 into multivacancy complexes. In the first case, it is expected that the α_i -nuclei will be removed while the α_v -nuclei will grow. However, we did not observe a noticeable change of the Si-H “amorphous” background. In the second case, one can expect the formation of multivacancy complexes such as $\{110\}$ planar tetravacancy chain and non-planar pentavacancy [20] as well as ring hexavacancy [21], which has to be most stable vacancy-type defect in Si.

Hydrogenated tetravacancy consisting of two end VH_3 units and two central VH_2 units should have doublet Si-H stretching modes near $2166, 2191\text{ cm}^{-1}$ and $2107, 2122\text{ cm}^{-1}$ with about equal intensity of related IR lines. In case of pentavacancy one should observe doublet lines near $2166, 2191\text{ cm}^{-1}$ and $2107, 2122\text{ cm}^{-1}$ related to three VH_3 and one VH_2 units, respectively, as well as a single line near 2072 cm^{-1} connected with VH unit; the intensities ratio for doublets and single line should be $3:1:1$. However, we did not observe any group of Si-H IR lines correlating with vibrations of hydrogenated tetravacancy and pentavacancy.

The V_2 removal may be caused by H-enhanced V_2 agglomeration with the formation of V_6H_{12} consisting of six VH_2 units (Fig. 3) which may be identified with the

2107, 2122 cm⁻¹ doublet as we proposed in [10]. Annealing temperature of the 2107 and 2122 cm⁻¹ doublets (> 600°C) is high in comparison with most other IR bands. This correlates with thermal stability of hexavacancy [21].

References

- [1] S.M. Mayers, et al., *Rev. Mod. Phys.* 64 (1992) 559.
- [2] G.R. Bai, et al., *Solid State Commun.* 56 (1985) 277.
- [3] B.B. Nielsen, et al., *Mater. Sci. Forum* 143–147 (1994) 845.
- [4] B.B. Nielsen, et al., *Mater. Sci. Eng. B* 36 (1996) 259.
- [5] M. Budde, et al., *Phys. Rev. B* 57 (1998) 4397.
- [6] B.N. Mukashev, et al., 38–41 (1989) 1039.
- [7] B.N. Mukashev, et al., in: K. Sumino (Ed.), *Defect Control in Semiconductors*, Elsevier Science Publishers, North-Holland, Amsterdam, 1990, pp. 429–434.
- [8] B.N. Mukashev, et al., *Physica B* 170 (1991) 545.
- [9] B.N. Mukashev, S.Zh. Tokmoldin, *Mater. Sci. Forum* 258–263 (1997) 223.
- [10] S.Zh. Tokmoldin, B.N. Mukashev, *Phys. Stat. Sol. B* 210 (1998) 307.
- [11] S.Zh. Tokmoldin, et al., *Physica B* 273–274 (1999) 204.
- [12] V.V. Frolov, B.N. Mukashev, *Phys. Stat. Sol. B* 148 (1988) K105.
- [13] P. Deak, et al., *Mater. Sci. Eng. B* 4 (1989) 57.
- [14] P. Deak, et al., *Physica B* 170 (1991) 253.
- [15] M. Suezawa, *Phys. Rev. B* 63 (2001) 035201.
- [16] L.J. Cheng, et al., *Phys. Rev.* 152 (1966) 761.
- [17] G. Lucovsky, et al., *Phys. Rev. B* 19 (1979) 2064.
- [18] D.E. Soule, et al., *Tetrahedrally Bonded Amorphous Semiconductors*, Carefree, Arizona, Proceedings of the AIP Conference No. 73, 1981, pp. 89–94.
- [19] P.S. Peercy, *Nucl. Instrum. Meth.* 182/183 (1981) 337.
- [20] Y.-H. Lee, J.W. Corbett, *Phys. Rev. B* 9 (1974) 4351.
- [21] J.L. Hastings, et al., *Mater. Sci. Forum* 258–263 (1997) 509.
- [22] J.N. Heyman, et al., *Phys. Rev. B* 45 (1992) 13363.



ELSEVIER

Physica B 308–310 (2001) 171–173

PHYSICA B

www.elsevier.com/locate/physb

Multivacancies trapping hydrogen molecules

T. Mori^a, K. Otsuka^a, N. Umehara^a, K. Ishioka^b, M. Kitajima^b,
S. Hishita^c, K. Murakami^{a,*}

^a*Institute of Applied Physics, University of Tsukuba, 1-1-1 Tennodai, Tsukuba, Ibaraki, Japan*

^b*Material Engineering Laboratory, National Institute for Materials Science, Tsukuba, Ibaraki, Japan*

^c*Advanced Materials Laboratory, National Institute for Materials Science, Tsukuba, Ibaraki, Japan*

Abstract

Hydrogen molecule has been observed in ion-implanted silicon and attributed to be trapped in a multi-vacancy ($H_2(MV)$). In order to clarify the structure of the multi-vacancy trap of $H_2(MV)$, we investigated correlation between thermal annealing of multi-vacancies and $H_2(MV)$. The results indicated that the main multi-vacancy trap is an H-terminated di-vacancy (V_2H_6) and that it is formed not only by ion-implantation, but also by transformation from larger multi-vacancy such as V_6 and V_{10} during hydrogenation. A broad Raman line observed at 2030 cm^{-1} may be attributed to the Si–H in the multi-vacancy trap. © 2001 Elsevier Science B.V. All rights reserved.

Keywords: Hydrogen molecule; Multi-vacancy; Annealing; Si–H

Hydrogen is an important impurity in semiconductors. It changes electrical properties by passivating dopants and terminating dangling bonds around defects [1]. Hydrogen molecule is chemically inactive, and has been observed by vibrational spectroscopies in silicon [2–4] and GaAs [5]. In silicon, three types of hydrogen molecules with different vibrational frequencies have been reported. The hydrogen molecules whose sharp Raman line appears at 3605 cm^{-1} was attributed to hydrogen molecule that is located at the tetrahedral (T) interstitial site of silicon lattice ($H_2(T)$) [6]. The broad Raman line at 4158 cm^{-1} is considered to be the hydrogen molecule trapped in a planar defect called platelet ($H_2(p)$) [4]. These two hydrogen molecules were observed in crystalline silicon after hydrogenation. On the other hand, the Raman line at 3822 cm^{-1} was observed in ion-implanted silicon and assigned as the hydrogen molecule trapped by multi-vacancies ($H_2(MV)$), because it was observed only in ion-implanted silicon [7,8]. A theoretical simulation indi-

cates that the vibration frequency of hydrogen molecule is affected significantly by the size of multi-vacancy, and is 3834 cm^{-1} for the hydrogen molecule trapped by a H-terminated di-vacancy (V_2H_6) [9]. According to the calculation, hydrogen molecule is not stable in V_2H_6 but at the nearest T site to it.

In ion-implanted silicon, single vacancies are unstable at room temperature and form various sizes of multi-vacancies such as di-vacancy (V_2) and four-vacancy (V_4) [10,11]. In our previous study, we performed detailed annealing experiments to study the stability of $H_2(MV)$ [12]. The observed annihilation of $H_2(MV)$ under thermal annealing was attributed to the diffusion of $H_2(MV)$ out of the multi-vacancy trap rather than the annihilation of the multi-vacancy itself, because $H_2(MV)$ was observed again when we re-hydrogenated the sample after thermal annealing. The activation energy of the thermal annihilation of $H_2(MV)$ was estimated to be 0.8 eV, and is interpreted to be the potential barrier for the hydrogen molecule to go out of the trap site to the neighboring T site. However, the structure of multi-vacancies has not been clear. In the present study, we investigated the thermal stability of the multi-vacancy trap itself, without H-termination.

*Corresponding author. Tel./fax: +81-298-53-5272.

E-mail address: murakami@ims.tsukuba.ac.jp (K. Murakami).

For this purpose, we carry out thermal annealing on freshly ion-implanted silicon and then hydrogenate each sample in order to investigate the structure.

Floating zone (FZ) p-type silicon wafers with a resistivity of $> 50 \Omega\text{cm}$ were used as silicon substrates. To obtain silicon samples with multi-vacancies, 200 keV Si^{+} were implanted in the FZ silicon wafer at a fluence of $2 \times 10^{14} \text{Si}^{+}/\text{cm}^2$. This fluence leads to an effective formation of $\text{H}_2(\text{MV})$ [7]. The ion energies were selected to cover the optical penetration depth of visible light used in the Raman-scattering measurements. The implanted samples were annealed at different temperatures between 50°C and 655°C for 30 min in an atmosphere of flowing N_2 gas to determine the thermal stability of multi-vacancies. The samples were then hydrogenated in a remote downstream of hydrogen plasma at 180°C for 30 min. The hydrogenation temperature corresponds to a very effective formation of $\text{H}_2(\text{MV})$ with no Raman line of $\text{H}_2(\text{p})$. Details of the method and hydrogenation conditions have been reported elsewhere [13]. Raman-scattering measurements were performed at room temperature using a 514.5 nm light as an excitation source. In the present study, all the Raman intensities were normalized by the intensity of the optical phonon of silicon measured for the same sample.

Fig. 1 shows the Raman spectra of ion-implanted silicon after thermal annealing at different temperatures followed by hydrogenation at 180°C . Only the Raman line of $\text{H}_2(\text{MV})$ around 3820 cm^{-1} was observed among the three hydrogen molecules for the samples hydrogenated without preceding thermal annealing (bottom in Fig. 1(a)). The Raman intensity of $\text{H}_2(\text{MV})$ was

decreased monotonically, with increasing annealing temperature before hydrogenation, and the Raman lines of $\text{H}_2(\text{p})$ around 4160 cm^{-1} were increased. It is noted that $\text{H}_2(\text{MV})$ was still observed after annealing at temperatures higher than 550°C . The line shape of $\text{H}_2(\text{MV})$ was hardly affected by annealing temperature. The Raman line of $\text{H}_2(\text{T})$ was not observed for any sample studied here. This may indicate that in silicon with high density of defects, there are other hidden $\text{H}_2(\text{T})$ which cannot be observed by Raman measurement.

The Raman spectra in the Si–H vibration region, shown in Fig. 1(b), consists of many peaks corresponding to Si–H bonds, since there are many kinds of H-terminated multi-vacancies in the ion-implanted sample. Most of the Si–H peaks were annealed below 400°C . After annealing at 550°C , no Raman lines were observed except for a small broad band at 2030 cm^{-1} and a prominent peak around 2130 cm^{-1} . The latter is the Si–H bonds of H-terminated platelets. The small peak at 2030 cm^{-1} is not observed in crystalline silicon without ion-implantation. It may be attributed to the Si–H bond that terminates the multi-vacancy trap of $\text{H}_2(\text{MV})$.

Fig. 2 summarizes the Raman intensity of $\text{H}_2(\text{MV})$ as a function of annealing temperature. The Raman intensity decreased gradually with increasing annealing temperature. No clear annealing stages were observed. This result suggests that several multi-vacancies with different annealing stages are involved in the trap of $\text{H}_2(\text{MV})$.

A theoretical simulation showed that hydrogen molecule is not stable in a H-terminated di-vacancy (V_2H_6) but at the nearest T site to V_2H_6 [9]. The

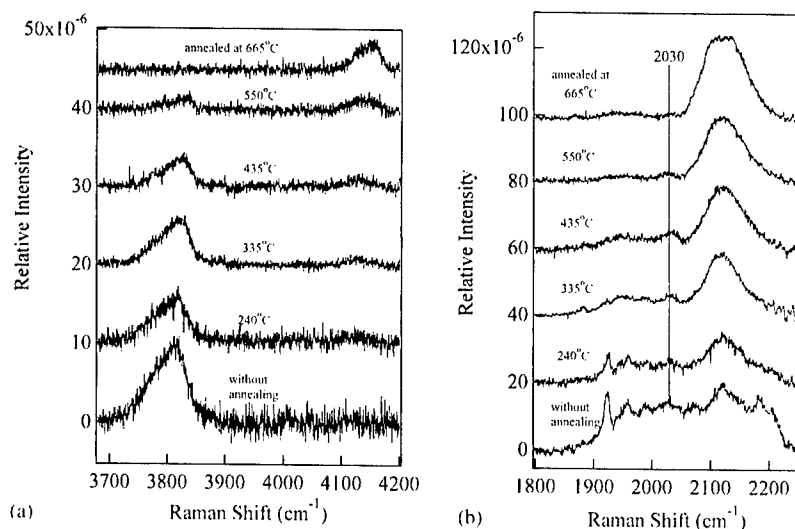


Fig. 1. Raman spectra of $\text{H}_2(\text{MV})$, $\text{H}_2(\text{p})$ (a), and Si–H stretching (b) for ion-implanted silicon annealed at different temperatures for 30 min followed by hydrogenation at 180°C . The samples were not sequentially annealed. Anneal performed at 240°C , 335°C , 435°C , 550°C and 665°C for each ion-implanted sample.

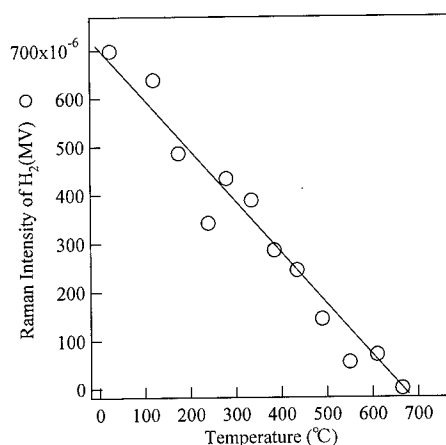


Fig. 2. The Raman intensity of H₂(MV) as a function of the annealing temperature.

vibrational frequency was calculated to be 3834 cm^{-1} for hydrogen molecule near V₂H₆. The vibrational frequency of hydrogen molecule trapped in tri-vacancy (V₃) and larger multi-vacancies was around 4000 cm^{-1} , comparable to that of H₂(p) and gaseous H₂. Thus, we propose that V₂H₆ is the main trap of H₂(MV). On the other hand, H₂(MV) was observed after annealing up to 600°C. This temperature is much higher than the experimentally determined annealing stage of negative di-vacancy (V₂⁻), 350°C and four-vacancy (V₄⁻), 400°C. Theoretical calculations predicted that multi-vacancies in silicon have magic numbers for their stabilities, i.e. six-vacancy (V₆) [9,14] and ten-vacancy (V₁₀) [9] are much more energetically favorable. However, the frequency of hydrogen molecule in such larger multi-vacancies should become higher. Taking into account that the observed vibrational frequency of H₂(MV) is almost independent of annealing temperature, we tentatively explain the H₂(MV) observed after high-temperature annealing as a result of transformation from V₆ and V₁₀ into V₂H₆ during hydrogenation. The transformation is plausible, since atomic hydrogen in silicon is very aggressive in breaking Si–Si bonds and forming H-related defects. Another possible explanation is that H₂(MV) is trapped in the nearest T site to multi-vacancies of various sizes, e.g. V₂, V₄, V₆ and V₁₀, assuming that the vibrational frequency is not significantly affected by the multi-vacancy size.

In conclusion, we have investigated the thermal stability of multi-vacancy to determine the structure which traps H₂(MV). The results indicated that the main

multi-vacancy trap is H-terminated di-vacancy (V₂H₆), and that it is formed not only by ion-implantation, but also by transformation from larger multivacancies such as V₆ and V₁₀ during hydrogenation. Another possibility is that multi-vacancies of various sizes trap hydrogen molecule at the nearest T site. The Raman line at 2030 cm^{-1} is attributed to the Si–H-terminating multi-vacancy trap of H₂(MV).

Acknowledgements

This work is in part supported by Grant-in Aid (Contract No. 11555001) for Scientific Researchers from the Ministry of Education, Science, Sports and Culture.

References

- [1] J.I. Pankov, N.M. Johnson (Eds.), *Hydrogen in Semiconductors, Semiconductor and Semimetals*, Vol. 34, Academic Press, New York, 1991.
- [2] R.E. Pritchard, M.J. Ashwin, J.H. Tucker, R.C. Newman, E.C. Lightowers, M.J. Binns, R. Falster, S.A. McQuaid, *Phys. Rev. B* 56 (1997) 13118.
- [3] A.W.R. Leitch, V. Alex, J. Weber, *Phys. Rev. Lett.* 81 (1998) 421.
- [4] K. Murakami, N. Fukata, S. Sasaki, K. Ishioka, M. Kitajima, S. Fujimura, J. Kikuchi, H. Haneda, *Phys. Rev. Lett.* 77 (1996) 3161.
- [5] J. Vetterhöffer, J. Wagner, J. Weber, *Phys. Rev. Lett.* 77 (1997) 5409.
- [6] R.E. Pritchard, M.J. Ashwin, J.H. Tucker, R.C. Newman, *Phys. Rev. B* 57 (1998) R15048.
- [7] K. Ishioka, M. Kitajima, S. Tateishi, K. Nakanoya, N. Fukata, T. Mori, K. Murakami, S. Hishita, *Phys. Rev. B* 60 (1999) 10852.
- [8] M. Kitajima, K. Ishioka, K. Nakanoya, S. Tateishi, T. Mori, N. Fukata, K. Murakami, S. Hishita, *Jpn. J. Appl. Phys.* 38 (1999) L691.
- [9] T. Akiyama, A. Oshiyama, *Jpn. J. Appl. Phys.* 38 (1999) L1363; private communication.
- [10] K.L. Brower, W. Beezhold, *J. Appl. Phys.* 43 (1972) 3499.
- [11] K. Murakami, K. Masuda, K. Gamo, S. Namba, *Jpn. J. Appl. Phys.* 12 (1973) 1307.
- [12] T. Mori, K. Otsuka, N. Umehara, K. Ishioka, M. Kitajima, S. Hishita, K. Murakami, *Physica B* 302–303 (2001) 239.
- [13] N. Fukata, S. Sasaki, S. Fujimura, H. Haneda, K. Murakami, *Jpn. J. Appl. Phys.* 35 (1996) 3937.
- [14] S.K. Estreicher, J.L. Hastings, P.A. Fedders, *Appl. Phys. Lett.* 70 (1997) 432.



ELSEVIER

Physica B 308–310 (2001) 174–177

PHYSICA B

www.elsevier.com/locate/physb

Defect-related photoinduced absorption in amorphous silicon

E. Morgado*

Centro de Física Molecular, Instituto Superior Técnico, Technical University of Lisbon, Av. Rovisco Pais, 1049-001 Lisboa, Portugal

Abstract

Photoinduced optical absorption in thin films of hydrogenated amorphous silicon (a-Si:H) is studied over the energy range related to electronic transitions involving the silicon dangling-bond defects, by using the dual-beam Constant Photocurrent Method (CPM). The subgap absorption in the range 0.8–1.4 eV is observed to increase with bias light intensity. Since CPM measures only transitions contributing to the photocurrent, the subgap absorption spectrum in undoped a-Si:H is dominated by transitions between singly occupied D^0 or doubly occupied D^- defect states and conduction band extended states. The photoinduced changes in the subgap absorption are consistent with numerical calculations with a recombination model for a-Si:H which yield dangling bond electronic occupations as a function of photogeneration rate. The results suggest that the observed changes in the optical absorption spectra are mainly determined by changes in the occupation of defects induced by the bias-light. © 2001 Elsevier Science B.V. All rights reserved.

Keywords: Amorphous silicon; Photoinduced effects; Photoconductivity; Recombination

1. Introduction

Electronic transport and recombination properties of hydrogenated amorphous silicon (a-Si:H) are strongly dependent on localised defect states in the semiconductor mobility gap. The Constant Photocurrent Method (CPM) [1] has been widely used to obtain information on the sub bandgap structure of a-Si:H alloys. Assuming uniform illumination through the thickness d of the sample ($\alpha d \ll 1$) the secondary photocurrent, I_{ph} , measured with coplanar electrodes, is proportional to the optical absorption coefficient and given by $I_{ph} \approx Ae\Phi\alpha d\eta[(\mu\tau)_e + (\mu\tau)_h]$, where A accounts for multiple reflections at film surfaces, e is the electron charge, Φ is the photon flux, α is the optical absorption coefficient, η is the quantum efficiency and $(\mu\tau)_e$, $(\mu\tau)_h$, are the mobility-lifetime products of electrons and holes,

respectively. In the CPM the secondary photocurrent, I_{ph} , is kept constant over the whole spectral range by adjusting the photon flux, $\Phi(h\nu)$, thus ensuring that the occupation of the electronic states and, therefore, the $\mu\tau$ products remain constant. The optical absorption spectrum, $\alpha(h\nu)$, can then be obtained from the measurement of the photon flux, $\alpha(h\nu) \approx \text{constant}/\Phi(h\nu)$. CPM measures only transitions contributing to the photocurrent, i.e., leading to the excitation of carriers to the extended states, and is dominated by the carrier with the higher mobility-lifetime product. It detects only transport paths with low defect densities, being practically insensitive to surface states in micrometer thick a-Si:H samples. By illuminating the sample with a second light beam the occupation of the gap states can be changed and additional information can be extracted from the corresponding absorption profiles. Those measurements with the so called light-bias CPM, or dual-beam CPM, generally yield an increase in the subgap absorption with bias light. The effect has received different interpretations like quasi-fermi level splitting [2–4],

*Corresponding author. Fax: 351-21-846-44-55.

E-mail address: emorgado@alfa.ist.utl.pt (E. Morgado).

defect relaxation [5], change in the electron recombination lifetime [6,7], and has been observed in undoped [2–4,6] as well as in n-type doped [7] a-Si:H thin films.

Quantitative analysis have been made by fitting the photoconductivity data with numerical models based on Simmons–Taylor statistics and a distribution of gap states consisting of band tails and different pictures for the defects, including two Gaussian bands of midgap donor-like and acceptor-like states [3,4], three Gaussian bands of midgap positively charged defect states above and negatively charged states below midgap as well as paramagnetic states close to midgap [8], a model later expanded with two more Gaussian defect distributions close to the valence and conduction bands [9].

In the present work we report dual-beam CPM measurements on undoped a-Si:H and discuss the results on the basis of a numerical recombination model involving band-tail states and correlated dangling bonds in their three states of charge D^+ , D^0 , D^- .

2. Experimental details

The sample used in this study is an undoped a-Si:H thin film produced by Plasma Enhanced Chemical Vapor Deposition from silane gas. The dual-beam CPM setup uses a tungsten-halogen lamp and a monochromator to produce the monochromatic probe beam. The AC photocurrent signal is detected by the lockin-technique with a chopper frequency of 10 Hz. Control of the probe beam light flux, in order to ensure a constant photocurrent, is obtained by varying the voltage applied to the lamp in combination with a set of neutral density filters. The probe beam light intensity is measured by a pyroelectric detector with a beam-splitter. The light bias beam is from a 2 mW He–Ne laser (633 nm) with appropriate attenuation. In order to minimise photodegradation effects during the CPM measurements, the sample was previously exposed to the laser beam over 2 h. All measurements were performed at room temperature.

3. Results and discussion

3.1. Light-bias CPM data

In Fig. 1 it is shown the CPM deduced optical absorption spectra for different values of the intensity of the laser bias beam in terms of the corresponding photogeneration rate in the sample. The CPM measurements have been made for a constant value of the photocurrent in the sample which corresponds to an

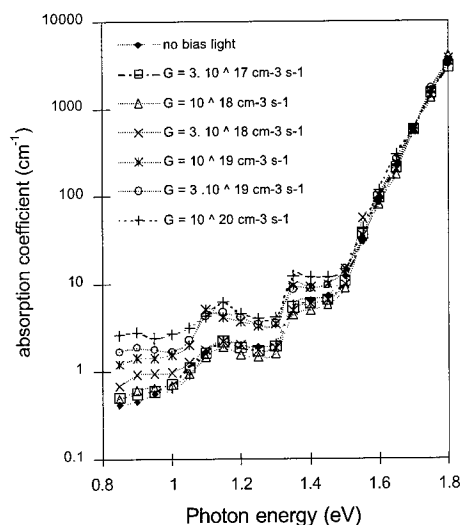


Fig. 1. CPM-derived optical absorption spectra of the a-Si:H sample for several bias beam intensities.

estimated photogeneration rate of $10^{14} \text{ cm}^{-3} \text{ s}^{-1}$ much lower than those produced by the bias beam in the experiments. This means that the electronic states occupation imposed by the laser beam is practically unperturbed by the photoconductivity measurements. The CPM-derived spectra were calibrated by matching to the optical absorption coefficient obtained from Optical Transmission Spectroscopy for the gap energy of a-Si:H around 1.7 eV. In the absorption in Fig. 1 one can distinguish the exponential absorption region related to transitions between band tail states for $1.5 \text{ eV} < E < 1.7 \text{ eV}$, and the sub gap region for $E < 1.5 \text{ eV}$ which is related to transitions involving the deep midgap states. Interference fringes due to multiple reflections at film surfaces are apparent in the low absorption region. A clear increase in the subgap absorption with bias light intensity can be observed in the spectra of Fig. 1. The dependence of the optical absorption coefficient on the bias photogeneration rate for several photon energy values is shown in Fig. 2. These results are in qualitative agreement with reported trends [2–9]. In the exponential absorption region, the spectra show a common Urbach slope of 50 meV. The deep defect density is currently estimated by the CPM technique, either from the integrated excess absorption up to the Urbach tail, or from the absorption coefficient at a single energy. Taking into account the different proposed calibration factors for the absorption coefficient at 1.2 eV [10] an estimate of the defect density is obtained in the range $3\text{--}7 \times 10^{16} \text{ cm}^{-3}$.

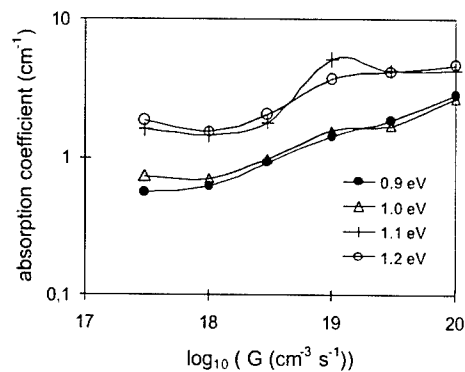


Fig. 2. Subgap absorption coefficient as a function of bias beam intensity for several energies.

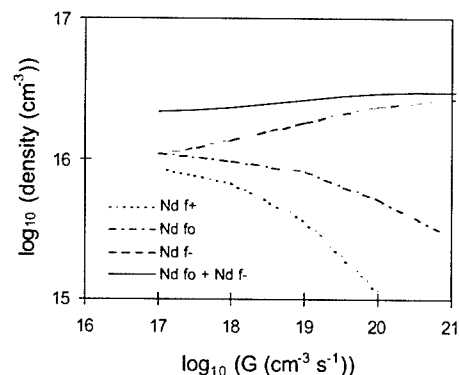


Fig. 3. Simulated dependence of dangling bond charge state densities on the bias beam intensity.

3.2. Numerical recombination model

In the following we compare the dual-beam CPM data with results from a numerical recombination model for a-Si:H which yields dangling bond occupations as a function of photogeneration rate [11]. The silicon dangling bond defect is represented by correlated discrete levels for the states of charge D^+ , D^0 , D^- , with respective occupation functions f^+ , f^0 , f^- and total density N_D . Conduction and valence band-tails of localised states have exponential distributions with characteristic energies E_{oc} and E_{ov} , respectively, and have electronic occupations determined by Simmons and Taylor statistics. In the dual-beam CPM the strong bias beam determines the electronic occupation of the gap states which is then sensed by the low intensity probe beam. In Fig. 3 one can see the calculated dependences of the densities of the different dangling

bond charge states on the photogeneration rate from the bias beam. The parameter values are: $N_D = 3 \times 10^{16} \text{ cm}^{-3}$, $E_{oc} = 30 \text{ meV}$, $E_{ov} = 50 \text{ meV}$, $E_c - E_{D^0} = 1 \text{ eV}$, $E_c - E_D = 0.6 \text{ eV}$, where E_c refers to the conduction band mobility edge, and capture cross sections of 10^{-17} cm^2 . In undoped a-Si:H the photocurrent is dominated by electrons; therefore, the CPM deduced optical absorption spectra in the low energy range reflect transitions between electron occupied gap states, the D^0 and D^- states, and the conduction band of extended states. According to Fig. 3, the quantity $N_D f^0 + N_D f^-$ increases with the photogeneration rate, consistently with the sub gap optical absorption enhancement observed in Figs. 1 and 2. A more detailed analysis that might separate the individual contributions of the D^0 and D^- states in the experimental data would require elaborate filtering procedures and extension to lower spectral energy ranges.

4. Conclusions

Photoinduced changes in the subgap optical absorption spectra of a-Si:H derived from the dual-beam CPM technique are reported. The effect is investigated over three orders of magnitude in the bias beam intensity. The observed optical absorption enhancement is qualitatively consistent with results from a recombination model, suggesting that the effect is associated with the increase in the combined density of singly and doubly occupied dangling bond defect states for increasing bias light intensity.

Acknowledgements

The author thanks Prof. Reinhard Schwarz for providing the a-Si:H sample produced at Technical University of Munich, Physics Department, Garching. The present work is supported by Fundação para a Ciência e Tecnologia.

References

- [1] M. Vanecek, J. Kocka, J. Stuchlik, A. Triska, Solid State Commun. 39 (1981) 1199.
- [2] S. Lee, S. Kumar, C.R. Wronsky, J. Non-Cryst. Solids 316 (1989).
- [3] S. Lee, M. Gunes, C.R. Wronsky, N. Maley, M. Bennet, Appl. Phys. Lett. 59 (1991) 1578.
- [4] M. Gunes, C.R. Wronsky, Appl. Phys. Lett. 61 (1992) 678.
- [5] D. Han, Y. Xiao, Mater. Res. Soc. Symp. Proc. 297 (1993) 327.

- [6] J. Liu, G. Lewen, J.P. Conde, P. Roca i Cabarrocas, J. Non-Cryst. Solids 164–166 (1993) 383.
- [7] T. Unold, H.M. Branz, M. Vanecek, Mater. Res. Soc. Symp. Proc. 420 (1996) 703.
- [8] M. Gunes, C.R. Wronsky, T.J. McMahon, J. Appl. Phys. 76 (1994) 2260.
- [9] L. Jiao, S. Semoushikina, Y. Lee, C.R. Wronsky, Mater. Res. Soc. Symp. Proc. 467 (1997) 233.
- [10] N. Wyrsh, F. Finger, T.J. McMahon, M. Vanecek, J. Non-Cryst. Solids 137&138 (1991) 347.
- [11] E. Morgado, Defect Diffusion Forum 134/135 (1996) 39.



ELSEVIER

Physica B 308–310 (2001) 178–180

PHYSICA B

www.elsevier.com/locate/physb

Hydrogen-induced formation of defects nanoclusters in crystalline silicon

Kh.A. Abdullin*, Yu.V. Gorelkinskii, B.N. Mukashev

Institute of Physics and Technology, 480082 Almaty, Kazakhstan

Abstract

Low-temperature hydrogen-assisted clusterization of aluminum impurity in silicon has been studied. It was found that hydrogen can decrease the diffusion barrier of the Al atom and initiate the migration of Al atoms at 180–200 K. As a result, an interstitial aluminum pair formation takes place in H-implanted silicon. The implantation with a dose $\geq 1 \times 10^{16}/\text{cm}^2$ causes formation of the clusters containing more than two aluminum atoms. © 2001 Elsevier Science B.V. All rights reserved.

Keywords: Silicon; Hydrogen; Enhanced diffusion; Nanoclusters

1. Introduction

Interstitial aluminum atom appears as a result of high-energy particle (e^- , p^+ , α^{++}) irradiation and the interaction of mobile self-interstitials Si_i and substitutional Al_s through the replacement mechanism [1,2]: $\text{Si}_i + \text{Al}_s \rightarrow \text{Si}_s + \text{Al}_i$. The Al_i is placed in the T_d interstitial site and the EPR spectrum Si-G18 [1–3] corresponds to a $(2+)$ charge state of the defect. A DLTS level $E_v + 0.18 \text{ eV}$ has been identified as arising from the second donor state $(+/2+)$ [4,5]. The Al_i is stable up to 20°C, when it begins to migrate with an activation energy of 1.2 eV and is replaced by G19–G21 defects. The G19 and G20 defects were identified as $\text{Al}_i\text{--Al}_i$ pairs, the G21 as unknown defect associated with one aluminum atom. The activation energy of the Al_i atom diffusion is reduced from 1.2 to 0.3 eV under injection condition [5] and the Al_i defect is annealed at room temperature under an injection current of 1 A/cm^2 in a time of $\sim 10^3 \text{ s}$.

In this paper, we discuss the phenomenon of hydrogen-enhanced diffusion of aluminum atom in silicon at $T \sim 180\text{--}200 \text{ K}$ [6,7]. Low-temperature hydrogen-enhanced diffusion of Al atoms is a unique

phenomenon, which may be caused by a tunnel mechanism.

2. Experimental procedure

Samples were fabricated from floating-zone-grown silicon (FZ-Si), doped with 5×10^{16} aluminum/ cm^3 . Hydrogen was incorporated either by proton implantation at 880 K or by thermal annealing in the presence of hydrogen species. In the latter case, the samples and hydrogen-free control ones were irradiated at 80 K with 30 MeV protons. Since the proton range ($\sim 4 \text{ mm}$) is far beyond the thickness of sample ($\sim 0.5 \text{ mm}$), hydrogen implantation in the bulk of the sample was completely avoided in this case.

3. Experimental results

EPR spectra Si-AA15 and Si-AA16 grow upon thermal annealing at $\sim 180\text{--}200 \text{ K}$ in the hydrogen-implanted samples as well as in the samples which were heat-treated in the presence of water vapor, and are not observed in control samples [6–8]. The Si-AA15 spectrum is the most dominating in comparison with the other spectra and consists of 11 groups of lines at any

*Corresponding author. Tel.: +7-3272-546-812; fax: +7-3272-545-244.

E-mail address: abdullin@sci.kz (K.A. Abdullin).

orientation of magnetic field in the $(0\bar{1}1)$ plane. A splitting between the lines does not pass through zero, therefore, the cause of the splitting is hyperfine interaction. The EPR spectrum consisting of 11 groups of lines (Fig. 1) can be formed only due to two nuclei (α and β) with a 100% abundant isotope of $I = 5/2$ involved in the structure of the center. These nuclei in our samples can be only nuclei of aluminum atoms involved in the defect. The Si-AA15 spectrum was stable up to room temperature and disappeared at 300 K for 10 min. The second spectrum, Si-AA16 ($S = 1/2$), has nearly isotropic g -tensor and consists of six groups of lines. Therefore, one nucleus with a 100% abundant isotope of $I = 5/2$ (^{27}Al) is involved in the structure of the AA16 defect. Its ^{27}Al hyperfine interaction is also nearly isotropic with weak trigonal distortion: $A_{||} = 823$ MHz, $A_{\perp} = 836$ MHz. The width of individual lines of the AA16 spectrum depends slightly on the direction of the magnetic field. The Si-AA16 spectrum is stable in the narrow temperature interval from 180 to 200 K. The known isolated aluminum interstitial Al_i (EPR spectrum G18 [1,2]) is not observed in both implanted and control samples immediately after 80 K implantation of hydrogen but appears in all samples annealed at ~ 260 – 280 K and there is no clear correlation of the AA15 and G18 spectra behavior.

Hyperfine interaction may be analyzed in terms of a one-electron wave function for the unpaired electron [9]. The observed hyperfine structure of the AA15 defect indicates that $\sim 18\%$ ($\sim 10\%$) of the unpaired spin wave function is located on the $\alpha(\beta)$ Al atoms and has $\sim 45\%$ 3s and $\sim 55\%$ 3p character. The resolved ^{29}Si hyperfine

structure can also be seen, its intensity corresponds to ~ 4 – 6 neighboring sites accounting for only $\sim 5\%$ of the wave function. The same analysis for the AA16 center indicates that about 30% of the wave function is localized on the single aluminum atom, with mostly 3s-like character ($\sim 80\%$).

The concentration of the Al–Al pairs (AA15 defects) varies proportionally with the hydrogen content and is increased in the range of the implantation doses from 1×10^{15} to $\sim 5 \times 10^{15}$ H/cm². But the implantation with a dose of $\sim 1 \times 10^{16}$ H/cm² (this dose corresponds to the hydrogen concentration of $\sim 2 \times 10^{18}$ H/cm³) results in the low AA15 defect concentration or does not introduce the AA15 pairs at all. A new complex EPR spectrum emerges instead (Fig. 2). The spectrum is observed only when the magnetic field direction coincides with the $\langle 100 \rangle$ axis of the sample. The complex spectrum disappeared upon annealing at room temperature, but a second new spectrum, very similar to the first one, emerged at 100°C annealing (Fig. 2). Permanent changes of the EPR spectra are observed up to 160–185°C annealing, then the complex spectrum and the Si-G18 spectrum are substituted by a spectrum similar with the Si-G19 spectrum (Al_i – Al_s pair). We suppose that the observed complicated spectrum belong to Al-containing defects, which are formed as a result of prolonged hydrogen-enhanced diffusion and precipitation of Al atoms. Thus, the defects consist of more than two Al atoms and are Al-containing nanoclusters.

4. Discussion

Hyperfine structure of the EPR spectrum Si-AA15 establishes, unambiguously, that two aluminum atoms are incorporated into the AA15 defect. The density of

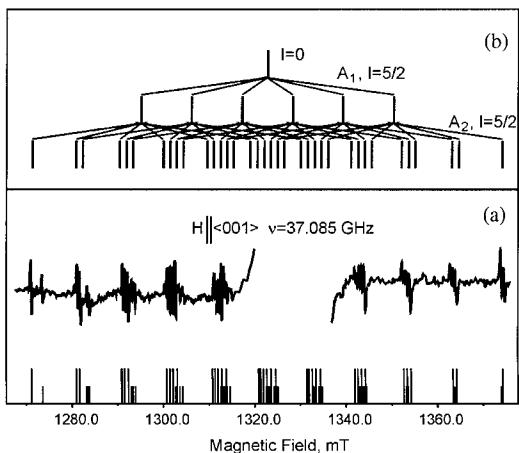


Fig. 1. (a) The EPR spectrum Si-AA15 at 77 K in FZ-Si:Al sample implanted with protons at 80 K to a dose of 3×10^{15} /cm² and annealed at ~ 200 K. Calculated positions of lines are also shown. (b) The formation of 11 groups of EPR lines due to hyperfine interaction of two nearly equivalent nuclei with a 100% abundant isotope of $I = 5/2$.

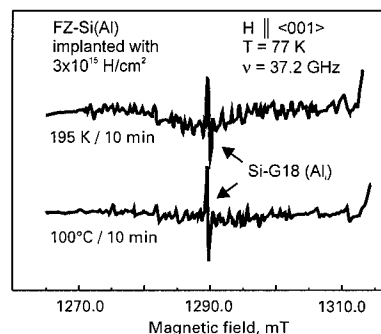


Fig. 2. EPR spectra of a FZ-Si:Al sample in which Si-AA15 and Si-AA16 spectra were observed and which, after room temperature annealing was again implanted by protons at 80 K to a dose of 3×10^{15} /cm² and then annealed at 195 K (1) and 100°C (2). One of the six Si-G18 spectrum lines is shown, which corresponds to a transition with $m_I = 1/2$.

defect AA15 is rather high and it is a dominant one after annealing at 200 K. In accordance with our estimation, the majority of aluminum atoms participate in the formation of the pairs. To reach other Al atoms and to form the Al–Al pairs, Al atoms should migrate at least by a distance of ~ 100 lattice constants. The Al atoms have to migrate as defect complexes. The unusual feature of such a migration is that low temperature is required (180–200 K).

The observed migration of Al atom cannot be an injection-assisted one. Indeed, if we propose that the annealing rate of Al_i under the conditions of irradiation is the same as in the case of the injection [5], the typical time of annealing will be about 10^9 h at the temperature of implantation (80 K), that allows us to eliminate the injection as a cause of enhanced migration of the Al atoms. Our results demonstrate that the presence of hydrogen atoms and radiation defects at low (180–200 K) temperature is necessary (and may be sufficient) to create the AA15 pairs. Hydrogen-enhanced migration of Al atom takes place due to the formation of some (Al–H) defect capable to migrate at 200 K. But $\text{Al}_i + \text{H}$ and $\text{Al}_i + \text{V}$ (Si–G9 [10]) defects are stable up to 400 K, so the (Al–H) mobile defects have to have an interstitial character. The estimation of the activation energy for diffusion of (Al–H)_i center gives the value as 0.22 eV.

The AA16 center is a suitable candidate for the $(\text{Al}_i + \text{H})$ defect. Indeed, the defect has a very narrow range of thermal stability (180–200 K) that coincides with the temperature of AA15 spectrum appearance. About 30% of the wave function appears to be accounted for on the Al atom. It is comparable to the case of the Al_i tetrahedral interstitial ($\sim 38\%$) [3]. The atomic orbitals are of 20% p character. This fact implies that the Al atom incorporated in the structure of the AA16 defect is slightly displaced from T_d site by some disturbance. It can be speculated that two atoms—an Al_i^{2+} and an $\text{H}_{T_d}^-$ —situated close to the two nearest tetrahedral interstitials, T_d , form the AA16 defect (Fig. 3). The atoms Al and H have to be displaced towards each other due to Coulomb attraction that can result in a decrease of the energy barrier between these two atoms. The migration barrier of (Al–H) defect would thus be expected to be reduced essentially. The low temperature of Al atom migration may be a consequence of a tunnel mechanism for the $(\text{Al}_i\text{--H})$ defect diffusion. Certainly, theoretical calculations have to be conducted in order to explain low-temperature hydrogen-enhanced migration of Al atom in silicon.

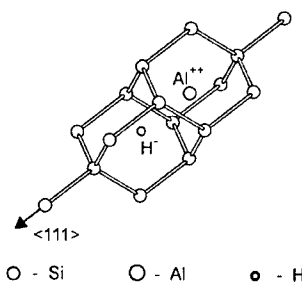


Fig. 3. Model of a $(\text{Al}_i^{2+} - \text{H}_{T_d}^-)$ center which can be responsible for Si-AA16 spectrum appearance and enhanced diffusion of Al atom.

Note that at low- and room-temperature, a solid solution of the Al impurity in silicon is in supersaturated state, but its decay is prevented by the low value of diffusion coefficient. The enhanced diffusion opens possibilities for the formation of a phase enriched with impurity atoms. The Al–Al pair (the A15 center) can be considered as the nucleus of a new phase, and the association of additional Al atoms with the AA15 defect can occur.

Thus, radiation-induced and hydrogen-enhanced diffusion may lead to formation of micro- and nanoclusters of a new, aluminum-enriched phase in the silicon matrix. It is of interest to check the existence of hydrogen-accelerated migration of the impurity boron and gallium, whose chemical properties are similar to aluminum in many respects.

References

- [1] G.D. Watkins, in: P. Baruch (Ed.), *Radiation Damage in Semiconductors*, Dunod, Paris, 1964, p. 97.
- [2] G.D. Watkins, *Mater. Sci. Forum* 143–147 (1994) 9.
- [3] K.L. Brower, *Phys. Rev. B* 1 (1970) 1908.
- [4] L.C. Kimerling, *Inst. Phys. Conf. Ser.* 31 (1977) 221.
- [5] J.R. Troxell, A.P. Chatterjee, G.D. Watkins, L.C. Kimerling, *Phys. Rev. B* 19 (1979) 5336.
- [6] Kh.A. Abdullin, B.N. Mukashev, Yu.V. Gorelkinskii, *Appl. Phys. Lett.* 71 (1997) 1703.
- [7] B.N. Mukashev, Kh.A. Abdullin, Yu.V. Gorelkinskii, *Phys.—Usp.* 43 (2000) 139.
- [8] Yu.V. Gorelkinskii, B.N. Mukashev, Kh.A. Abdullin, *Mater. Sci. Forum* 258–263 (1997) 1777.
- [9] G.D. Watkins, J.W. Corbett, *Phys. Rev.* 134 (1964) A1359.
- [10] G.D. Watkins, *Phys. Rev.* 155 (1967) 802.



ELSEVIER

Physica B 308–310 (2001) 181–184

PHYSICA B

www.elsevier.com/locate/physb

Low-temperature photoluminescence characterization of defects formation in hydrogen and helium implanted silicon at post-implantation annealing

A.V. Mudryi^a, F.P. Korshunov^a, A.I. Patuk^a, I.A. Shakin^a,
T.P. Larionova^a, A.G. Ulyashin^{b,*}, R. Job^b, W.R. Fahrner^b,
V.V. Emtsev^c, V.Yu. Davydov^c, G. Oganessian^c

^a*Institute of Solid State and Semiconductor Physics, National Academy of Sciences of Belarus, 220072 Minsk, Belarus*

^b*Department of Electrical Engineering, University of Hagen, Haldener Str. 182, D-58084 Hagen, Germany*

^c*Ioffe Physico-Technical Institute, Russian Academy of Sciences, 194021 St. Petersburg, Russia*

Abstract

The systematical low-temperature (4.2 K) photoluminescence (PL) study of the formation kinetics of optically active centers in H and He implanted CZ Si, annealed in the temperature range of 200–1000°C is presented. The samples were implanted with H (energy $E = 80$ keV, dose $D = 10^{15}/10^{16}$ cm⁻²) and He ($E = 150$ keV, $D = 5 \times 10^{14}$ cm⁻²) ions. It was found that the annealing of H or He implanted samples leads to the appearance and evolution of a number of zero-phonon lines as well as of broad bands. The origin of the observed lines and bands is discussed. It is assumed that the strong stresses around hydrogen-related structural defects (voids, bubbles) during the annealing at 500–700°C of H implanted Si lead to the formation of a specific optical center M' (~ 1.012 eV PL line). © 2001 Elsevier Science B.V. All rights reserved.

PACS: 61.72.T; 78.55

Keywords: Silicon; Implantation; Hydrogen; Helium; Photoluminescence

1. Introduction

H- and He-implanted Si has been studied extensively because of considerable technological importance of these atoms for the modification of the material properties [1–5]. It was shown that hydrogen in Si can passivate the shallow acceptor and donor impurities [6,7], oxygen-related thermal donors and other deep-level defects [1,8,9], dislocations [1,10], grain boundaries and dangling bonds [1,11]. On the other hand, hydrogen can form complexes with different impurities (C, O, transition-metals, etc.) in Si, which introduce new levels

in the band gap [12,13]. It was also found that the He atoms can be involved in the defect formation process of ion-implanted Si [14]. This work extends previous PL spectroscopy investigations of the H(He) implanted Si at post-implantation annealing, which were done earlier [13–16]. Emphasis is put on complex formation at high-temperature ($> 600^\circ\text{C}$) annealing. Evidence for a number of hydrogen- and helium-induced optical active complexes in ion-implanted Si is presented. The possible structure of these complexes is discussed.

2. Experimental

The material employed in these PL measurements was (100)-oriented Czochralski (CZ) silicon doped with

*Corresponding author. Fax: +49-2331-987-321.

E-mail address: alexander.ulyashin@fernuni-hagen.de (A.G. Ulyashin).

either phosphorus (n-type, 10 Ω cm) or boron (p-type, 12 Ω cm). The concentration of oxygen in all samples was specified as of about $\sim 8 \times 10^{18} \text{ cm}^{-3}$, and the carbon concentration was between 10^{16} and 10^{17} cm^{-3} . The samples were implanted with H ($E = 80 \text{ keV}$, $D = 10^{15}/10^{16} \text{ cm}^{-2}$) and He ($E = 150 \text{ keV}$, $D = 5 \times 10^{14} \text{ cm}^{-2}$) ions. An isochronal annealing of 20 min was carried out between 200 °C and 1000 °C in vacuum. PL measurements were performed at 4.2 K with the samples immersed in liquid helium. PL was excited by the Ar 488 nm laser line. The incident laser intensity was typically between 10 and 60 mW. The emission light was dispersed using a 0.6 m single grating monochromator and detected with a liquid-nitrogen-cooled Ge diode. Conventional lock-in detection was employed with the chopper ($\sim 20 \text{ Hz}$) placed in the exciting laser beam.

3. Results and discussion

Fig. 1 shows typical PL spectra of p-type CZ Si after 80 keV H⁺ implantation with dose 10^{16} cm^{-2} and following annealing at various temperatures. The spectra exhibit several intense luminescence lines labeled as $B_{\text{NP}}^{\text{BE}}$, $B_{\text{TA}}^{\text{BE}}$, $B_{\text{TO}}^{\text{BE}}$, and $B_{\text{TO+O}}^{\text{BE}}$ in the near-band-gap region. These lines arise from bound exciton (BE) recombination at boron as a shallow doping impurity. The luminescence in this spectral range includes the no-phonon (NP) line (optical transitions without the creation of phonons) and TA, TO, TO + O lines (optical transitions with the participation of momentum-conserving phonons, where TA, TO and O denote the transverse acoustical, transverse optical and zone center phonon, respectively). The assignments of these PL lines have been well established earlier [17]. The dominating PL line is the TO-phonon replica of the bound excitons $B_{\text{TO}}^{\text{BE}}$ at 1.093 eV. Besides these lines, three broad bands with energies of 1.029 (H1), 0.972 (H2) and 0.933 (H3) eV were observed in as-implanted and at 200 °C annealed samples. The H1 and H2 peaks can be interpreted as the NP line and TO-phonon replica, respectively, which originate from the radiative recombination at hydrogen-related defects. The H3 band can be attributed to another but also hydrogen-related defect. Such identification of the H1–H3 bands with hydrogen-related defects is based on the fact that these bands are absent in the spectra of Si after helium implantation with following annealing (see below). It is necessary to note that the H1–H3 bands were detected in the PL spectra of Si after hydrogenation [7]. Jonson et al. [7] suggested that hydrogen-containing extended defects ($\langle 111 \rangle$ platelets) are responsible for the H1–H3 bands. One can see (Fig. 1) that annealing at 200 °C results in a significant increase (up to ~ 10 times) of the intensity of the 1.0186 eV (W-line) PL NP line. The annealing at 300 °C and 400 °C produces a broad band and (at 400 °C)

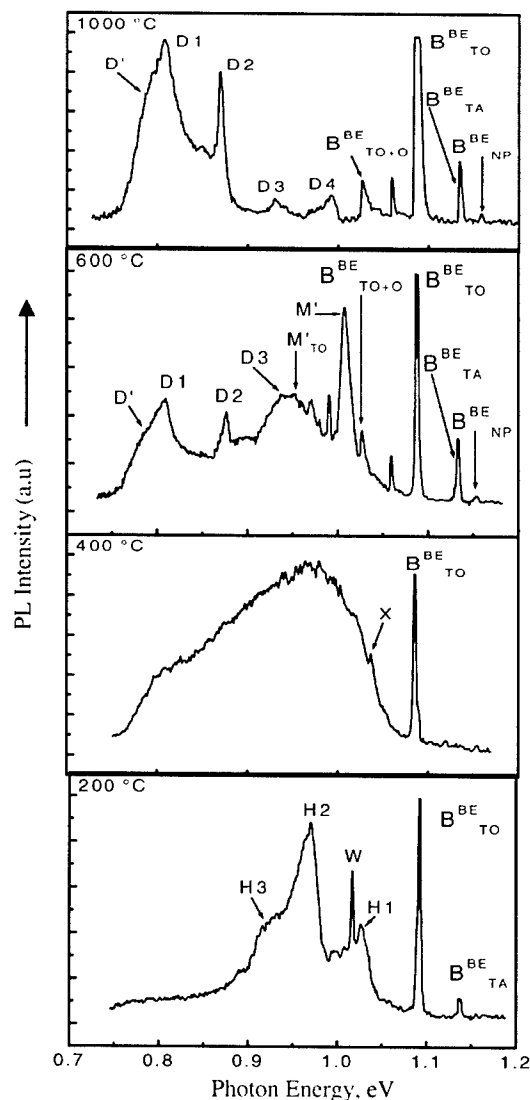


Fig. 1. PL 4.2 K spectra of H implanted ($E = 80 \text{ keV}$, $D = 10^{16} \text{ cm}^{-2}$) 12 Ω cm p-type Cz Si annealed in vacuum at different temperatures for 20 min.

an additional low-intensity NP line at 1.0399 eV (X-line). The luminescence centers responsible for the W- and X-lines are observed usually in Si after irradiation with high-energy particles such as neutrons and different kind of ions [18,19]. The microscopic structure of the W defects is identified as a trigonal center which involves Si interstitial or/and hydrogen atoms [14,20,21]. The X center possibly can be attributed to a vacancy-type defect [19–22]. Annealing of H-implanted Si layers at and above 500 °C causes a rapid growth of the intensity of D1–D4 bands. These bands might be related to dislocations [23]. At this stage of the thermal treatment, new NP PL lines at 1.012 eV (M') and its TO-phonon

replica at 0.954 eV (M'_{TO}) also occur in the PL spectra. Annealing at higher temperatures (600–1000°C) of 80 keV H^+ implanted with dose of 10^{16} cm^{-2} p-type CZ Si leads to the appearance of dislocation-related PL bands D1–D4 and to the D' band which is somewhat wider than D1 and has a peak at about 0.78 eV (Fig. 1). Fig. 2 shows the PL spectrum for n-type H implanted Si (with dose of 10^{15} cm^{-2}) after the 700°C annealing. One can see that in this case, the only M' (M'_{TO}) and D' bands are present but not D1–D4 ones. Moreover, the spectral shape of M' (M'_{TO}) and D' bands can be observed better in this case. It was also found that for n-type Si, the main peculiarities of PL spectra after the annealing at temperature range 200–1000°C are similar to those for p-type Si shown in Fig. 1. An analysis of the spectra for different Si samples allows us to assign the D' band to the recombination on defects which are different from those responsible for the D1 band. Fig. 3 shows the dependence of M' and D' intensities versus annealing temperature for n-type H implanted Si. It is necessary to note that the D' band was detected earlier in the PL spectra of Si implanted by H^+ and He^+ after annealing at 1000°C [16]. This band was recently also observed in PL spectra of Si samples implanted with H^+ and O^+ ions after the high-pressure–high-temperature annealing [24], in multicrystalline Si [25] and in Si–Ge structures with Ge quantum dots [26]. All these facts show that D' band appears in strained Si structures. This allows us to assume that the gettering and precipitation (near dislocations) of residual impurities such as carbon, oxygen or Si self-interstitials during high-temperature annealing might be responsible for the appearance of this band. Some assumptions about the nature of the M' and M'_{TO} bands also can be made. It is necessary to note that in Ref. [23], the PL spectra stacking-faults-related band D6 at 4.2 K ($\sim 1.0126 \text{ eV}$, similar to the energy of the M' line) was detected in plastically deformed silicon samples. It was observed that the D6 line disappeared after heat treatments at 390°C. In our case, the structure

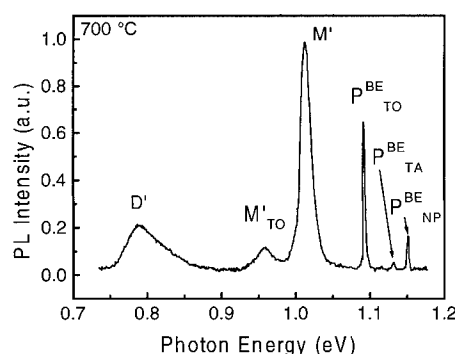


Fig. 2. PL 4.2 K spectrum of H implanted ($E = 80 \text{ keV}$, $D = 10^{15} \text{ cm}^{-2}$) $10 \Omega \text{ cm}$ n-type Cz Si annealed in vacuum at 700°C for 20 min.

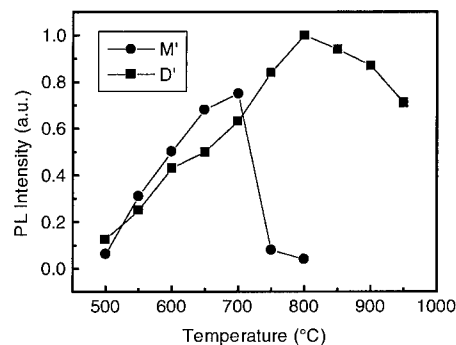


Fig. 3. PL (4.2 K) intensity dependencies of the D' and M' bands versus annealing (20 min) temperatures.

of the defects which are responsible for the M' band is different from stacking-faults because of the different temperature stability of the M' luminescence centers (Fig. 3). It can be assumed that during the annealing of H-implanted Si samples at 500–700°C, the formation of hydrogen-related nanovoids or nanobubbles occurs. We suggest that this process is responsible for the appearance and growth of M' (M'_{TO}) bands. Internal stresses can lead to the formation of the optically active structural defects. Similar to the M' band, the WL (NP) and WL(TO) bands were detected also in Si–Si/Ge and Si–Ge structures with Ge quantum dots [26,27], which are heavily stressed structures. Such stressed structures can be formed in H implanted Si due to hydrogen and oxygen gettering and precipitation at the buried implantation damage layers at high-temperature annealing [28]. Fig. 4 shows the PL spectra of He implanted (150 keV , $5 \times 10^{14} \text{ cm}^{-2}$ dose) n-type CZ Si annealed isochronal at different temperatures. The well-known NP lines with energies 0.9697 eV (A), 0.7894 eV (C), 0.9500 eV (G), 0.9353 eV (T), 0.9652 eV (I) and 0.7610 eV (Q) as well as D1–D4 bands can be observed in these spectra. The A, C, G, T, I and Q lines are related to the point defects, which include in their structures the residual impurities such as carbon, oxygen and hydrogen [12,14,18,19]. Annealing of the He-implanted samples at 200°C and 300°C produces also a high intensive line Z2 (1.012 eV) which is connected with the He-containing PL centers [14,19,20].

4. Conclusions

Our experimental results of 4.2 K PL measurements of the H and He implanted and annealed CZ Si can be summarized as follows:

1. Broad bands with energies of 1.029 (H1), 0.972 (H2) and 0.933 (H3) eV were observed in as hydrogen implanted and in annealed at 200°C after the

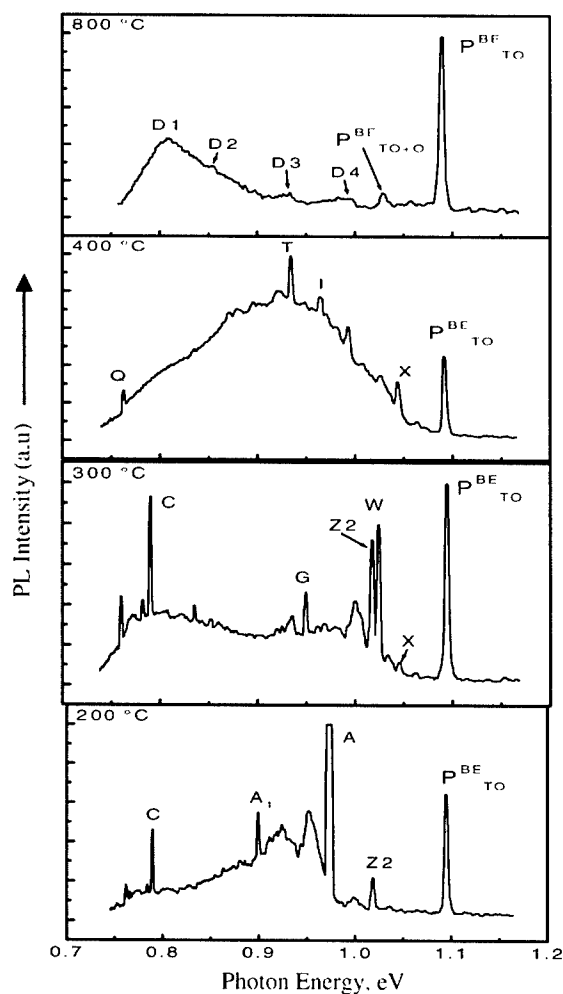


Fig. 4. PL 4.2 K spectra of He implanted ($E = 150$ keV, $D = 5 \times 10^{14} \text{ cm}^{-2}$) $10 \Omega \text{ cm}$ n-type Cz Si annealed in vacuum at different temperatures for 20 min.

implantation samples. The H1 and H2 peaks can be interpreted as the NP line and TO-phonon replica, respectively, which originate from the radiative recombination at hydrogen-related defects.

2. Annealing of the H implanted samples at 500–700 °C results in the appearance of the PL line at 1.012 eV (M') and its TO-phonon replica at 0.954 eV (M'_{TO}). These lines can be attributed to the specific defects induced by the internal stresses around hydrogen-related defects (nanovoids or nanobubbles).
3. Annealing of the H implanted samples at 600–1000 °C results in the appearance of D' band with the energy of 0.78 eV. This band can be attributed to the residual impurities near the dislocation region.
4. Annealing of the H or He implanted samples at 500–1000 °C results in the appearance of the D1–D4 bands, which can be attributed to the radiative recombination at dislocation-related centers.

References

- [1] S.J. Pearton, J.W. Corbett, M. Stavola, Hydrogen in Crystalline Semiconductors, Springer, Berlin, Germany, 1992.
- [2] V.V. Kozlovski, V.A. Kozlov, V.N. Lomasov, Fiz. Tekh. Poluprovodn. 34 (2000) 129.
- [3] R. Lüdemann, Mater. Sci. Eng. B 58 (1999) 86.
- [4] M. Bruel, Nucl. Instr. and Meth. B 108 (1996) 313.
- [5] M. Bruel, Electron. Lett. 31 (1995) 1201.
- [6] S.J. Pearton, J.W. Corbett, T.S. Shi, Appl. Phys. A 43 (1987) 153.
- [7] N.M. Johnson, C. Herring, D.J. Chadi, Phys. Rev. Lett. 56 (1986) 769.
- [8] R.C. Newmann, J.H. Tucker, A.R. Brown, S.A. McQuaid, J. Appl. Phys. 70 (1991) 3061.
- [9] H.J. Stein, S.K. Hahn, J. Appl. Phys. 75 (1994) 3477.
- [10] O.V. Feklisova, E.B. Yakimov, N.A. Yarykin, J. Weber, Mater. Sci. Eng. B 58 (1999) 60.
- [11] V.V. Afanas'ev, A. Stesmans, Mater. Sci. Eng. B 58 (1999) 56.
- [12] A.N. Safonov, E.C. Lightowers, Mater. Sci. Eng. B 58 (1999) 39.
- [13] H. Weman, J.L. Lindström, G.S. Oehrlein, B.G. Svensson, J. Appl. Phys. 67 (1990) 1013.
- [14] V.D. Tkachev, A.V. Mudryi, N.S. Minaev, Phys. Status Solidi A 81 (1984) 313.
- [15] L.T. Canham, M.R. Dyball, W.Y. Leong, M.R. Houlton, A.G. Cullis, P.W. Smith, Mater. Sci. Eng. B 4 (1989) 41.
- [16] A.G. Ulyashin, R. Job, W.R. Fahrner, A.V. Mudryi, A.I. Patuk, I.A. Shakin, Mater. Sci. Semicond. Process. 4 (2000) 297.
- [17] P.J. Dean, J.R. Haynes, W.F. Flood, Phys. Rev. B 161 (1967) 161.
- [18] V.D. Tkachev, A.V. Mudryi, Radiation Effects in Semiconductors, Conference Ser. N 31, Inst. of Phys., London, Bristol, 1977, p. 231.
- [19] G. Davies, Phys. Rep. 176 (1989) 83.
- [20] A.V. Mudryi, A.I. Patuk, I.A. Shakin, F.P. Korshunov, V.A. Zuev, Mater. Chem. Phys. 45 (1996) 185.
- [21] A.V. Mudryi, F.P. Korshunov, T.P. Larionova, A.I. Patuk, I.A. Shakin, in: Conference Proceedings of the International Symposium on Ion Implantation of Science and Technology, Naleczov, Poland, 1997, p. 139.
- [22] Z. Chechanowska, G. Davies, E.C. Lightowers, Solid State Commun. 49 (1984) 427.
- [23] R. Sauer, J. Weber, J. Stolz, E.R. Weber, K.H. Kusters, H. Alexander, Appl. Phys. A 36 (1985) 1.
- [24] A. Misiuk, H.B. Surma, I.V. Antonova, V.P. Popov, J. Bak-Misiuk, M. Lopez, A. Romano-Rodriguez, A. Barcz, J. Jun, Solid State Phenomena. 69–70 (1999) 345.
- [25] Y. Koshka, S. Ostapenko, I. Tarasov, S. McHago, J.P. Kalejs, Appl. Phys. Lett. 74 (1999) 1555.
- [26] O.G. Schmidt, U. Denker, K. Eberl, O. Kienrie, F. Ernst, Appl. Phys. Lett. 77 (2000) 2509.
- [27] H. Sunamura, N. Usami, Y. Shiraki, S. Fukatsu, Appl. Phys. Lett. 66 (1995) 3024.
- [28] R. Job, A.G. Ulyashin, W.R. Fahrner, A.I. Ivanov, L. Palmetshofer, Appl. Phys. A 72 (2001) 325.



ELSEVIER

Physica B 308–310 (2001) 185–189

PHYSICA B

www.elsevier.com/locate/physb

Hydrogen enhanced thermal donor formation in p-type Czochralski silicon: application to low temperature active defect-engineering

A.G. Ulyashin*, R. Job, I.A. Khorunzhii, W.R. Fahrner

Department of Electrical Engineering, University of Hagen, Haldener Street 182, D-58084 Hagen, Germany

Abstract

The incorporation of hydrogen into the p-type Czochralski (Cz) silicon by a plasma results in an enhanced thermal donor (TD) formation at temperatures around 400°C. Counter doping by the TDs and a rapid p–n junction formation occur in the p-type Cz Si. It is shown that the controlled TDs formation can be used for the low-temperature production of device structures: p–n junctions, p–n–p structures and structures with gradient doping. The characterization of the samples was done by the depth resolved spreading resistance probe (SRP) analysis. A kinetic model for the analysis of the hydrogen-enhanced TDs formation in the as-grown as well as in the Cz Si samples with denuded zone is developed. It can be concluded, that the controlled hydrogen enhanced TDs formation can be used as an alternative low-cost, low-temperature doping method, which might be favorable for active defect-engineering in the Cz Si. © 2001 Elsevier Science B.V. All rights reserved.

PACS: 61.72

Keywords: Silicon; Hydrogen; Thermal donors; Denuded zone

1. Introduction

The incorporation of hydrogen into the Czochralski (Cz) silicon by a plasma results in an enhanced thermal donor (TD) formation [1–5]. As a consequence, the n-type doping of the Cz Si can be provided at low (350–450°C) temperatures. Recently, it was shown [6–15] that the n-type counter doping of the initial p-type Cz Si material can be observed. TD concentrations up to $2\text{--}3 \times 10^{16} \text{ cm}^{-3}$ can occur, depending on the process temperatures, plasma power and treatment times and on the concentration of the interstitial oxygen in the Cz Si substrate. Therefore, a counter doping by the TDs and a rapid p–n junction formation can be observed in the p-type Cz Si if the acceptor concentration is not higher than about 10^{16} cm^{-3} . Moreover, it was shown that

when the interstitial oxygen concentration was changed by the three-step high temperature oxygen out-diffusion [11], which leads to the formation of the so-called denuded zone (DZ), a transistor type device structure (p–n–p) due to the hydrogen enhanced TDs formation was formed. The goal of the present paper is (i) the experimental investigations of the carrier profiles modified by the hydrogen enhanced TDs formation in the Cz Si samples with different thermal prehistory and (ii) the development of a kinetic model for the analysis of the hydrogen enhanced TDs formation in the as-grown as well as in the Cz Si with the DZ.

2. Experimental

The investigations were done on standard p-type (100) $10 \Omega \text{ cm}$ Cz Si wafers with thickness of about 370–380 μm . The carbon concentration was specified by $[C] \leq 5 \times 10^{16} \text{ cm}^{-3}$. The oxygen concentration was

*Corresponding author. Fax: +49-2331-987-321.

E-mail address: alexander.ulyashin@fernuni-hagen.de (A.G. Ulyashin).

$\approx 7\text{--}8 \times 10^{17} \text{ cm}^{-3}$ (specified). The one-step process, which involves the out diffusion of oxygen at high temperature (1100°C for 5 h in flowing nitrogen) was applied for the generation of the DZ. For the two-step hydrogen enhanced TDs formation process, the as-grown samples and samples with the DZ were exposed by a RF hydrogen plasma for 1 h at $T \approx 260^\circ\text{C}$ (first step) in a standard PECVD setup at 110 MHz, applying a hydrogen flux of 200 sccm (standard cubic centimeters per minute) and a power of 50 W. For comparison, another version of the first step process for the as-grown samples was done using a DC plasma reactor, where a plate voltage of 500 V and a current density of $400 \mu\text{A cm}^{-2}$ was applied for 10 min at 400°C . As the second step of the hydrogen enhanced TDs formation process, the post-hydrogenation annealing was done at 400°C and 450°C in air. After annealing, the samples were rapidly cooled down to room temperature. The samples were analyzed by the SRP measurements. The SRP measurements were done on a 4-point probe instrument with tungsten carbide tips. For the SRP measurements, the samples were beveled on a rotating quartz plate.

3. SRP analysis of hydrogen enhanced TDs formation in p-type Cz Si

Fig. 1 exhibits the resistance profiles of a $10 \Omega\text{cm}$ p-type Cz Si treated for 10 min by a DC plasma at 400°C and then annealed at 400°C and 450°C in air. One can see that at the initial stages of the hydrogen enhanced TDs formation (annealing time < 5 min), a strong compensation of the acceptors occurs which leads to the gradient carrier profiles in the sub-surface region of the Cz Si sample. After about 8 min annealing, the SRP profiles exhibit p–n junctions moving rapidly into the sample bulk with longer annealing times. For the case of the post-hydrogenation annealing at 450°C , the moving of the p–n junctions into the bulk is faster than at 400°C annealing. Almost the same behavior was observed in the case of the hydrogenation at 250°C for 1 h by a HF plasma with subsequent annealing at 400°C (Fig. 2). One can conclude that during the hydrogenation (first process step), the saturation of the sub-surface layer by hydrogen occurs without any essential (250°C hydrogenation) or slight (400°C hydrogenation) modification of the carrier profiles. At this stage, hydrogen can be involved in the structure of different complexes (molecular species) [16,17]. The total hydrogen concentration in the sub-surface layer is $\sim 10^{19} \text{ cm}^{-3}$ [18]. During the second stage (400°C , 450°C annealing), a release of the atomic hydrogen from these species occurs which provides the hydrogen enhanced TDs formation in the Cz Si. This formation leads to the gradient doping, due to the compensation, or to the p–n junction appearance

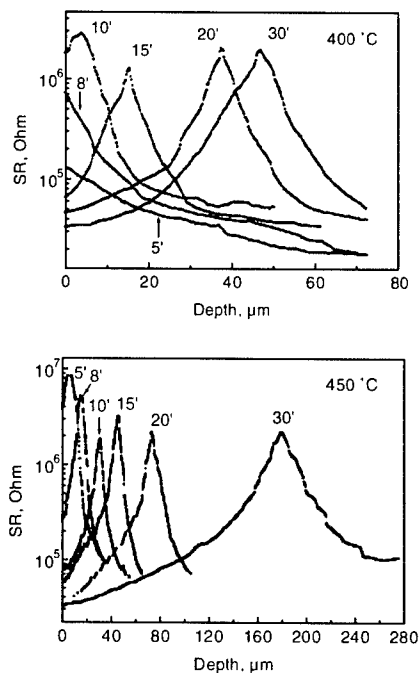


Fig. 1. The SRP profiles for the as-grown p-type Cz Si treated for 10 min by a DC hydrogen plasma at 400°C with subsequent annealing at 400°C and 450°C . The peaks of the resistance curves correspond to the p–n junction location.

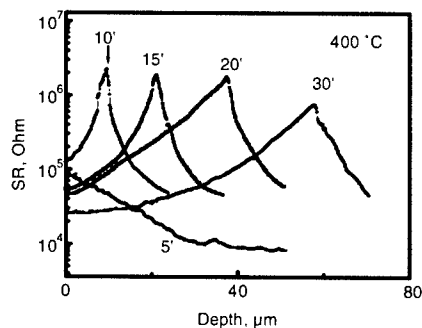


Fig. 2. The SRP profiles for the as-grown p-type Cz Si treated for 1 h by a HF hydrogen plasma at 250°C with subsequent annealing at 400°C . The peaks of the resistance curves correspond to the p–n junction location.

due to the counter doping in the initial p-type Cz Si. The p–n junctions exhibit the characteristics of linear graded junctions [7,9,12,13]. The diodes prepared by the hydrogen enhanced TDs counter doping of the p-type Cz Si were analyzed in [12,13]. It can be concluded that for a given Cz Si material (the oxygen concentration was the same in all cases), the rate of the hydrogen enhanced TDs formation depends mainly on the temperature and time of the post-hydrogenation annealing but not on the

method of the hydrogenation. Fig. 3 exhibits the resistance profiles of a 10 Ωcm p-type Cz Si with the DZ treated for 1 h at 250°C by a HF hydrogen plasma and then annealed at 400°C in air. One can see that in this case, the formation of the buried n-type region after 0.5 h of post-hydrogenation annealing occurs. This region originates as a result of the suppressed TDs formation in the DZ [11]. Thus, the formation of a transistor type (p–n–p) structure is possible.

4. Kinetic analysis of hydrogen enhanced TDs formation

We can describe the time dependence of the concentrations of atomic [H] and molecular [H₂] hydrogen as well as the TDs concentration [TD] by [15]

$$\frac{\partial[H]}{\partial t} = D_H \frac{\partial^2[H]}{\partial x^2} - K_1[H]^2 + 2K_2[H_2], \quad (1)$$

$$\frac{\partial[H_2]}{\partial t} = \frac{1}{2}K_1[H]^2 - K_2[H_2], \quad (2)$$

$$\frac{\partial[TD]}{\partial t} = C[O]^3[H] \left(1 - \frac{[TD]}{[TD]_{\max}}\right), \quad (3)$$

where D_H is the diffusion coefficient of the atomic hydrogen in the Si which is given by [19]

$$D_H = D_0 \exp\left(-\frac{E_a}{kT}\right), \quad (4)$$

where E_a is the activation energy of the diffusion ($E_a = 0.48$ eV) and $D_0 = 9.4 \times 10^{-3} \text{ cm}^2 \text{ s}^{-1}$; K_1 is the coefficient of the H₂ molecules formation, $K_1 = 8\pi R_0 D_H$ (where $R_0 = 5 \text{ Å}$ [20]); K_2 is the dissociation constant of the H₂-molecules, $K_2 = \nu \exp(-E_b/kT)$, where ν is the vibrational frequency for the dissociation of H₂ molecules ($\nu = 10^{13} \text{ s}^{-1}$ [21]) and E_b is the binding energy of H₂ ($E_b = 1.6$ eV [20]); $[TD]_{\max} = 10^{16} \text{ cm}^{-3}$ is the maximal thermal donors concentration; and C is a free

parameter. In our calculations, we used $C \approx 2.2 \times 10^{-60}$ and $1.1 \times 10^{-60} \text{ cm}^{-3}$ at 450°C and 400°C, respectively, to fit the experimental data.

In case of the DZ formation, the time dependence of the interstitial oxygen concentration [O] at the depth x from the surface for an annealing temperature T_a at a time t is given by the error function [22]

$$[O] = [O]_s + ([O]_0 - [O]_s) \operatorname{erf}\left(\frac{x}{2\sqrt{D_{OX} T t}}\right), \quad (5)$$

where [O] is the initial oxygen concentration for the as-grown sample; $[O]_s$ is the solubility of oxygen in the Si at a temperature T ; $D_{OX} T$ is the diffusion coefficient of oxygen in silicon at a temperature T_a . $[O]_s$ and $D_{OX} T$ are given by [22]

$$D_{OX} T = 0.13 \exp\left(-\frac{2.53 \text{ eV}}{kT}\right) \text{ cm}^2 \text{ s}^{-1},$$

$$[O]_s = 9 \times 10^{22} \exp\left(-\frac{1.52 \text{ eV}}{kT}\right).$$

The boundary conditions are the following:

At the front side ($x = 0$):

$$[H] = [H]_0 = 10^{18} \text{ cm}^{-3} \quad \text{when } t < t_H, \quad (6)$$

$$\left.\frac{d[H]}{dx}\right|_{x=0} = 0 \quad \text{when } t > t_H. \quad (7)$$

where t_H is the time of the hydrogenation, $[H]_0$ was taken as $[H]_0 = 10^{18} \text{ cm}^{-3}$ to fit the experimental data $[H]_{\text{total}} = [H] + [H_2] = \sim 10^{19} \text{ cm}^{-3}$ for $t = t_H$.

At the backside ($x = x_{\max}$):

$$\left.\frac{d[H]}{dx}\right|_{x=x_{\max}} = 0. \quad (8)$$

Initial conditions:

$$[H(x)] = 0; \quad [H_2(x)] = 0; \quad [TD(x)] = 0. \quad (9)$$

The system of Eqs. (1)–(3) with boundary conditions (6), (7), (8) and initial conditions (9) has been solved numerically.

Figs. 4 and 5 show the calculated electron concentrations originating from the TDs (double donors) during the annealing of the as-grown Cz Si at 400°C after the hydrogenation at 250°C for 1 h and during the annealing at 400°C and 450°C after the hydrogenation at 400°C for 10 min, respectively. One can see (Figs. 1, 2 and 4) that the calculations give a rather correct description for the p–n junctions' location. In case of the Cz Si with the DZ, calculations (Fig. 6) give also rather correct description for the location of the first p–n junction and a somewhat deeper location than in the experiment (Figs. 3 and 6) for the second p–n junction. This fact shows that not only the out diffusion of oxygen is important for the TDs formation in this case but also the

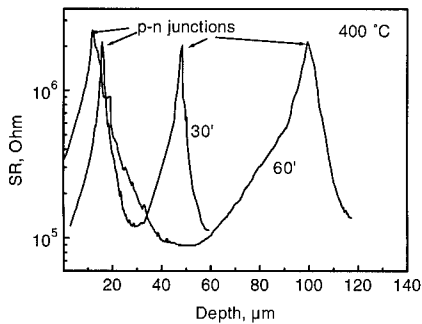


Fig. 3. The SRP profiles for the p-type Cz Si with the DZ (formed by 1100°C thermal heating for 5 h in flowing nitrogen) treated for 1 h by a HF hydrogen plasma at 250°C with subsequent annealing at 400°C. The peaks of the resistance curves correspond to the p–n junction location.

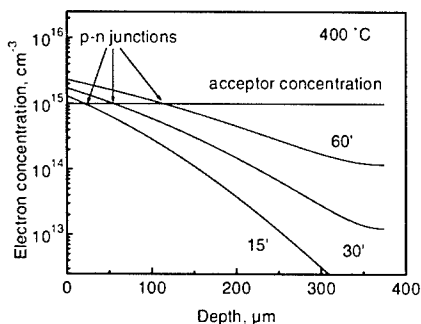


Fig. 4. The electron concentration due to the hydrogen enhanced TDs formation calculated according to Eqs. (1)–(4), (6)–(9) for the as-grown p-type Cz Si treated for 1 h by a hydrogen plasma at 250 °C with subsequent annealing at 400 °C.

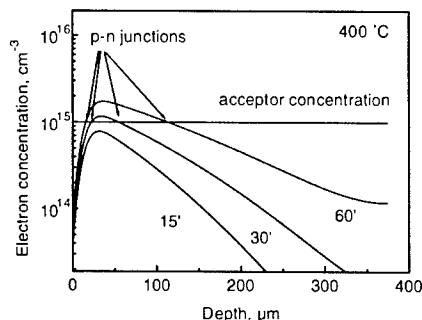


Fig. 6. The electron concentration due to the hydrogen enhanced TDs formation calculated according to Eqs. (1)–(9) for the p-type Cz Si with the DZ (formed by 1100 °C thermal heating for 5 h) treated for 1 h by a hydrogen plasma at 250 °C with subsequent annealing at 400 °C.

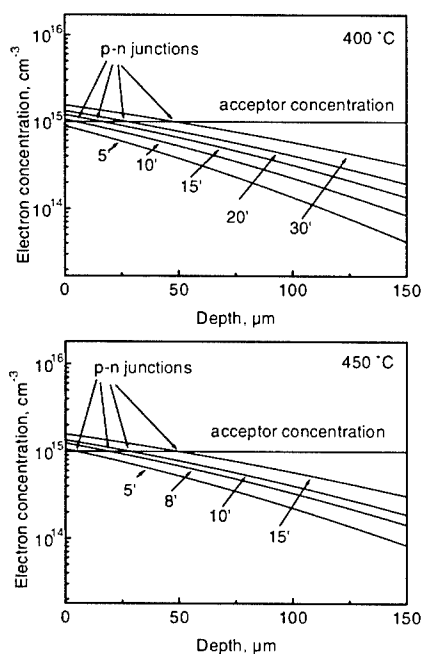


Fig. 5. The electron concentration due to the hydrogen enhanced TDs formation calculated according to Eqs. (1)–(4), (6)–(9) for the as-grown p-type Cz Si treated for 10 min by a hydrogen plasma at 400 °C with subsequent annealing at 400 °C and 450 °C.

oxygen precipitation during the DZ formation has to be taken into account.

5. Conclusions

The hydrogen enhanced TDs formation in the p-type Cz Si can be used for the low-temperature production of device structures: p–n junctions, p–n–p structures and

structures with gradient doping. This method of doping can be described numerically and can be used as an alternative low-cost, low-temperature one. A kinetic model for the analysis of the hydrogen enhanced TDs formation in the as-grown p-type Cz Si is developed and can be used for the simulation of the p–n junction location originated due to counter doping by the TDs. For the case of Cz Si with the DZ, this model has to be corrected. The oxygen precipitation during the DZ formation process has to be taken into account.

References

- [1] A.R. Brown, M. Clayborn, R. Murray, P.S. Nandra, R.C. Newman, J.H. Tucker, *Semicond. Sci. Technol.* 3 (1988) 591.
- [2] R. Murray, A.R. Brown, R.C. Newman, *Mater. Sci. Eng. B* 4 (1990) 299.
- [3] R.C. Newman, J.H. Tucker, A.R. Brown, S.A. McQuaid, *J. Appl. Phys.* 70 (1991) 3061.
- [4] H.J. Stein, S.K. Hahn, *Appl. Phys. Lett.* 56 (1990) 63.
- [5] H.J. Stein, S.K. Hahn, *J. Appl. Phys.* 75 (1994) 3477.
- [6] H.J. Stein, S.K. Hahn, *J. Electrochem. Soc.* 142 (1995) 1242.
- [7] A.G. Ulyashin, Y.A. Bumay, R. Job, G. Grabosh, D. Borchert, W.R. Fahrner, A.Y. Diduk, *Solid State Phenom.* 57–58 (1997) 189.
- [8] R. Job, D. Borchert, Y.A. Bumay, W.R. Fahrner, G. Grabosh, I.A. Khorunzhii, A.G. Ulyashin, *MRS Symp. Proc. Ser.* 469 (1997) 101.
- [9] A.G. Ulyashin, Y.A. Bumay, R. Job, W.R. Fahrner, *Appl. Phys. A* 66 (1998) 399.
- [10] R. Job, W.R. Fahrner, N.M. Kazuchits, A.G. Ulyashin, *MRS Symp. Proc. Ser.* 513 (1998) 337.
- [11] A.G. Ulyashin, A.N. Petlitskii, R. Job, W.R. Fahrner, *Electrochem. Soc. Proc.* 98–13 (1998) 211.
- [12] R. Job, J.A. Weima, G. Grabosh, D. Borchert, W.R. Fahrner, V. Raiko, A.G. Ulyashin, *Solid State Phenom.* 69–70 (1999) 551.

- [13] R. Job, W.R. Fahrner, A.G. Ulyashin, *Mater. Sci. Eng. B* 73 (2000) 197.
- [14] A.G. Ulyashin, A.I. Ivanov, I.A. Khorunzhii, R. Job, W.R. Fahrner, F.F. Komarov, A.C. Kamyshan, *Mater. Sci. Eng. B* 58 (1999) 91.
- [15] A.G. Ulyashin, I.A. Khorunzhii, R. Job, W.R. Fahrner, *Mater. Sci. Eng. B* 73 (2000) 124.
- [16] R. Job, A.G. Ulyashin, W.R. Fahrner, *Mat. Sci. Semicond. Proc.* 4 (2001) 257.
- [17] A.W.R. Leitch, V. Alex, J. Weber, *Phys. Rev. Lett.* 81 (1998) 421.
- [18] A. Ulyashin, R. Job, W.R. Fahrner, D. Grambole, F. Herrmann, *Solid State Phenom.* (2001), in preparation.
- [19] A. Van Wieringen, N. Warmoltz, *Physica* 22 (1956) 849.
- [20] J.T. Borenstein, J.W. Corbett, S.J. Pearton, *J. Appl. Phys.* 73 (1993) 2751.
- [21] D. Mathiot, *Phys. Rev. B* 40 (1989) 5867.
- [22] H.J. Ruitz, G.P. Pollack, *J. Electrochem. Soc.* 125 (1978) 128.



ELSEVIER

Physica B 308–310 (2001) 190–192

PHYSICA B

www.elsevier.com/locate/physb

On defects created in 45 keV H⁻-implanted n-type Cz Si: a fluence dependence and isochronal annealing study

Prakash N.K. Deenapanray*

Department of Electronic Materials Engineering, Research School of Physical Sciences and Engineering, Australian National University, Canberra ACT 0200, Australia

Abstract

Five electron traps E1 ($E_C = 0.17$ eV), E2 ($E_C = 0.22$ eV), E3 ($E_C = 0.29$ eV), E4 ($E_C = 0.43$ eV), and E5 ($E_C = 0.50$ eV) were created in n-Si by 45 keV H⁻ implantation. E1 (VO-centre) and E2 (V_2^{2-}) increased linearly with fluence in the range 5×10^{10} – 1×10^{12} cm⁻², while the hydrogen-related defects E3 (VO–H) and E5 showed a quadratic fluence dependence. E4 also exhibited a quadratic fluence dependence, which could be characteristic of overlapping traps, including VP, V_2^0 , VH, and V_2H . The ratio E3:E1 showed sign of saturation at the higher fluences, whereas E5:E2 increased monotonically with the increasing fluence. E3 and E5 increased with the annealing temperature at the expense of E1 and E2, respectively, up to 200°C, but without a one-to-one correlation. Two secondary defects E6 ($E_C = 0.20$ eV) and E7 ($E_C = 0.49$ eV), which we propose to be higher-order vacancy clusters, were observed above 350°C. © 2001 Elsevier Science B.V. All rights reserved.

Keywords: DLTS; Defects; Hydrogen; Isochronal annealing

1. Introduction

The interaction of H with deep levels in Si is a subject of both technological and scientific interest. Hydrogen can be introduced into the semiconductor material both intentionally and unintentionally through a host of ways, including growth, ion implantation, chemical cleaning, or exposure to a hydrogen plasma [1]. It is very mobile and exhibits a wide range of interactions with impurities and defects in crystalline semiconductors [2]. Over the past decade, much has been learned about the structure of hydrogen-related electron traps in Si. A deep level at $\sim E_C = 0.16$ eV has been identified as the H–C complex [3]. Due to the isoelectronic behaviour of substitutional C in crystalline Si, this level mainly reflects the electronic properties of the isolated hydrogen [4]. Defects E3 ($\sim E_C = 0.32$ eV) and E5 ($\sim E_C = 0.45$ eV) have also been related to hydrogen

complexes [5]. More recently, Laplace deep-level transient spectroscopy (DLTS) has been used in conjunction with EPR annealing data to identify E3 as the VO–H complex, as well as the acceptor levels of VH and V_2H in Si [6]. In general, no deep levels associated with the implanted species are observed by DLTS in room-temperature-bombarded Si, except for hydrogen. In this study, we report on the fluence dependence and isochronal annealing behaviour of defects, especially the H-related traps, introduced in n-Si by 45 keV H⁻ implantation.

2. Experimental procedure

n-type Czochralski (Cz) Si(100) wafers with resistivity of 0.7–1.1 Ω cm were implanted at RT by 45 keV H⁻ ions to fluences ranging from 5×10^{10} to 1×10^{12} cm⁻². The fluence rate was fixed at 1×10^{10} cm⁻² s⁻¹ for all implants. Isochronal annealing in the 150–600°C range was performed on samples implanted to 1×10^{11} cm⁻² for 15 min under Ar flow. Following chemical cleaning, including a final dip in 5% HF, Au Schottky contacts

*Corresponding author. Tel.: +61-2-6125-4434; fax: +61-2-6125-0511.

E-mail address: pnk109@rsphysse.anu.edu.au (P.N.K. Deenapanray).

were fabricated on samples by resistive evaporation. DLTS was used to study the fluence dependence and isochronal annealing behaviour of hydrogen-induced defects. Reverse bias and filling pulse conditions were chosen such that the region extending between 0.35 and 0.6 μm of each sample was probed by DLTS.

3. Results and discussion

DLTS spectrum (a) in Fig. 1 was taken from a sample implanted with 45 keV H^- ions to a fluence of $1 \times 10^{11} \text{ cm}^{-2}$. Spectra (b–d) are from samples annealed at 150°C, 200°C, and 500°C, respectively. Hydrogen implantation created five electron traps E1 ($E_C = 0.17 \text{ eV}$), E2 ($E_C = 0.22 \text{ eV}$), E3 ($E_C = 0.29 \text{ eV}$), E4 ($E_C = 0.43 \text{ eV}$), and E5 ($E_C = 0.50 \text{ eV}$). In the n-type Si, single vacancies created by H interact with each other, dopant atoms (e.g. P) and interstitial oxygen (O_i) to form the divacancy (V_2), VP- and VO-centres. Defects E1, E2, and E4 correspond to the well-known VO-centres, $\text{V}_2^{2-/}$, and the superposition of the VP-centres and $\text{V}_2^{1/0}$, respectively [7]. We will establish, in what follows, that E4 may also contain contributions from H-related defects. Since P and O_i are more efficient trapping centres for the single vacancies, they are produced in larger concentrations than V_2 [spectrum (a) in Fig. 1]. Interaction between implanted H and other defects produces E3 and E5 [5], with the former being the VO–H complex [6]. L  v  que et al. have recently proposed that E5 resulted from the interaction of H with V_2 [8]. The virtual nondetection of E4 in spectrum (c) and given that the VP-centre is thermally unstable above $\sim 180^\circ\text{C}$, reveals that defect E4 consisted mostly of VP-centres. More will be said about DLTS spectra (b–d) later.

Fig. 2(a) illustrates the fluence dependence for the introduction of electron traps in n-Si by 45 keV H-implantation. The VO-centre (E1) and $\text{V}_2^{2-/}$ (E2) are introduced linearly with ion fluence, albeit the latter is introduced in much lower concentrations. The linear fluence dependence of E2 shows that it is created as a primary event, and its lower concentration than E1 reveals that it has a higher energy formation threshold. Our results are consistent with a previous study using 200 keV H-implantation of Si in the fluence range from 3×10^9 to $1 \times 10^{11} \text{ cm}^{-2}$ [9]. On the other hand, E3 (VO–H) and E5 exhibit a quadratic dependence on hydrogen fluence. A near-quadratic dependence of the VO–H centre was also reported in Ref. [9] for fluences $< 5 \times 10^{10} \text{ cm}^{-2}$. The quadratic dependence clearly shows that the introduction rates of E3 and E5 become increasingly more favourable at the higher fluences when both H and other primary defects, such as VO, become more abundant. In contrast to the linear fluence dependence of the level at $E_C = 0.41 \text{ eV}$ reported in

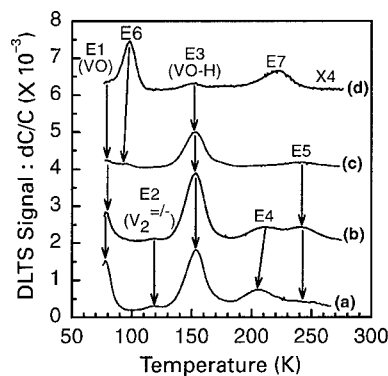


Fig. 1. DLTS spectra from (a) as-implanted n-Si, and samples annealed for 15 min at: (b) 150°C, (c) 200°C, and (d) 500°C. All samples were implanted with 45 keV H^- ions to a fluence of $1 \times 10^{11} \text{ cm}^{-2}$ at room temperature.

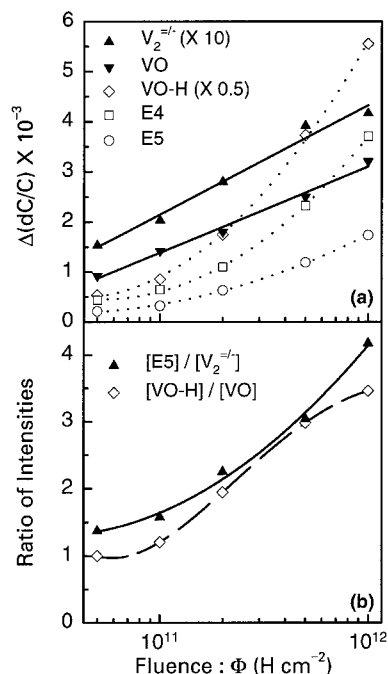


Fig. 2. Fluence dependence of (a) creation of E1 (VO), E2 ($\text{V}_2^{2-/}$), E3 (VO–H), E4, and E5, and (b) ratio E3:E1 and E5:E2.

Ref. [9], results shown in Fig. 2(a) reveal a quadratic dependence of E4 on fluence similar to E3 and E5. Assuming that E4 was the superposition of the primary defects VP and $\text{V}_2^{1/0}$, one would indeed expect a linear fluence dependence of E4. Bonde Nielsen et al. have recently shown that the activation enthalpies of $\text{VH}^{0/-}$ and $\text{V}_2\text{H}^{0/-}$ were 0.443 and $\sim 0.43 \text{ eV}$, respectively, which are practically indistinguishable from those for VP and $\text{V}_2^{1/0}$ [6]. We, therefore, propose that the

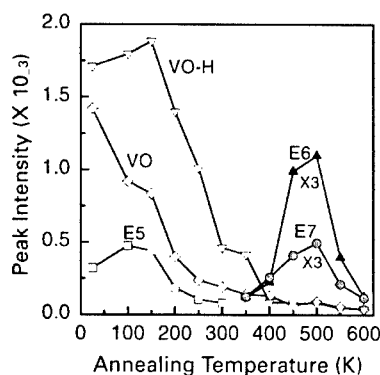


Fig. 3. Isochronal annealing behaviour of implantation-induced defects E1 (VO), E3 (VO-H), and E5, and secondary defects E6 and E7.

quadratic dependence of E4 on fluence could be due to the presence of the overlapping defect VH. It is pointed out here that annealing at 200°C [spectrum (c) in Fig. 1] should remove almost all of VH [6]. Furthermore, the larger fluences used in this study may account for the discrepancy between the results presented here and in Ref. [9].

Further insight is obtained on the introduction of E3 (VO-H) and E5 by comparing their intensities with respect to those of E1 (VO) and E2 (V_2^+), respectively, as shown in Fig. 2(b). The ratio $[VO-H]/[VO]$ increases initially but tends towards saturation at the higher fluences. Such a behaviour may be characteristic of the VO-H complex because of both the limited supply of O in samples and the formation of VO-H₂, which is electrically inactive [6], at the higher fluences. In contrast, the ratio $[E5]/[E2]$ increases monotonically with the increasing hydrogen fluence. Assuming the proposed relationship between E5 and V_2 [8], we speculate that the hydrogenation of V_2 is enhanced at the higher fluences when more V_2 are created in both direct events and combination of single vacancies (O trapping sites having been consumed).

We now turn to the isochronal annealing of defects as shown in Fig. 3. We have not measured the annealing of E2 because of the large uncertainty in measuring its peak intensity. The initial increase in E3 below 200°C does not correlate linearly with the decrease in E1. The relatively larger decrease in E1 could be attributed to the removal of an overlapping bistable C_iC_k pair [10], together with the further passivation of VO by H released from complexes with low thermal stability, such as H-C and VH. Both VO and VO-H are removed above 200°C. A comparison of spectra (a-c) in Fig. 1 clearly shows the annealing of V_2^+ . The removal of E2 is accompanied by the simultaneous increase in E5,

which establishes a relationship between E2 and E5 [8]. The removal of vacancy-related defects E1-E5 above 350°C is accompanied by the formation of secondary defects E6 ($E_C = 0.20$ eV) and E7 ($E_C = 0.49$ eV). The similar annealing behaviour of E6 and E7 suggests that they may be two charge states of the same defect. We have previously correlated the creation of similar defects in both MeV alpha-particle irradiated and Si-implanted n-type Si samples annealed above 300°C with the disappearance of V_2 [11,12], and concluded that they were higher-order vacancy complexes.

4. Conclusions

In summary, we have investigated the fluence dependence and isochronal annealing behaviour of defects created in 45 keV H-implanted n-Si. VO and V_2^+ exhibited linear fluence dependencies, whereas each of VO-H, E4, and E5 showed a quadratic dependence on fluence. In addition to the VP-centre and V_2^0 , the VH complex could also be a component of E4. The ratio $[E3]/[E1]$ showed saturation at the higher fluences typical of the limited supply of O and the further passivation of VO-H into electrically neutral VO-H₂. The initial increase of VO-H below 200°C could be due to the hydrogenation of VO upon release of H from less-thermally stable defects, such as H-C and VH. Annealing experiments have shown the close correlation between E5 and V_2 , as well as the creation of two higher-order vacancy complexes, E6 and E7, above 350°C. E6 and E7 could be the same defect but with different charge states.

References

- [1] S.J. Pearton, J. Electron. Mater. A 14 (1985) 737.
- [2] S.J. Pearton, J.W. Corbett, T.S. Shi, Appl. Phys. A 43 (1987) 153.
- [3] A.L. Endröss, Phys. Rev. Lett. 63 (1989) 70.
- [4] P.J.H. Denteneer, C.G. Van de Walle, S.T. Pantelides, Phys. Rev. Lett. 62 (1989) 1884.
- [5] B.G. Svensson, A. Hallén, B.U.R. Sundqvist, Mater. Sci. Eng. B 4 (1989) 285.
- [6] K. Bonde Nielsen, et al., Physica B 273–274 (1999) 167.
- [7] L.C. Kimberling, P. Blood, W.M. Gibson, Inst. Phys. Conf. Ser. 46 (1979) 273.
- [8] P. Lévêque, et al., Nucl. Instrum. Methods B 174 (2001) 297.
- [9] L. Palmetshofer, J. Reisinger, J. Appl. Phys. 72 (1992) 2167.
- [10] L.W. Song, X.D. Zhan, B.W. Benson, G.D. Watkins, Phys. Rev. B 42 (1990) 5765.
- [11] P.N.K. Deenapanray, et al., J. Appl. Phys. 84 (1998) 2565.
- [12] F.D. Auret, et al., J. Appl. Phys. 83 (1998) 5576.



ELSEVIER

Physica B 308–310 (2001) 193–196

PHYSICA B

www.elsevier.com/locate/physb

DLTS study of defects in hydrogen plasma treated p-type silicon

L. Wu*, A.W.R. Leitch

Department of Physics, University of Port Elizabeth, PO Box 1600, Port Elizabeth 6000, South Africa

Abstract

A deep level transient spectroscopy (DLTS) study of defects found in float-zone p-type silicon exposed to a DC hydrogen plasma is reported. DLTS measurements of these samples revealed three deep levels. Two of the levels are broad, with $E_T - E_V$ in the range 0.34–0.39 eV (H2) and 0.40–0.44 eV (H3); these appear as bands in the Arrhenius plot. The third level has an activation energy of 0.09 eV (H1). The variations in the capture cross-sections of H2 and H3 are believed to be strain-related. The concentration of H3 exceeds the other two levels and decreases rapidly into the samples with $\sim 10^{15} \text{ cm}^{-3}$ at a depth of 0.20 μm . H3 is tentatively ascribed to an extended defect. © 2001 Elsevier Science B.V. All rights reserved.

Keywords: Deep level transient spectroscopy; Silicon; Defects; Hydrogen

1. Introduction

Hydrogen is one of the most important impurities in silicon and is often used in the passivation of defect and other impurity states. It is commonly introduced into silicon via exposure to a hydrogen plasma. However, exposure to this plasma environment also creates defects in the material such as hydrogen platelets, H_2 molecules, point defects, etc. [1]. The damage caused by plasma is well known to be electrically active, which can be detrimental to the devices fabricated from the material.

There have been a few reports in the literature [2–6] on the electrical characteristics of defects induced through various plasma techniques, the majority of which were on n-type material. Hwang et al. [3] were amongst the first to detect deep levels in oxygen-precipitated p-type Cz–Si after hydrogen plasma processing; the deep levels were believed to be caused by the energetic ions in the plasma. Both Nam et al. [5] and Henry et al. [6] assigned the deep levels they found in their Cz material to some type of extended defect or possibly platelets.

There is considerable variation in the deep levels reported since the experiments were performed exclusively on Czochralski silicon (with the exception of Ref. [4], where the material type was not mentioned). In this material, the contribution of oxygen, such as thermal donors and oxygen precipitates, towards the formation of the defects cannot be excluded. For this reason, float-zone silicon was employed in this work and deep level transient spectroscopy (DLTS) was used to detect its electrical characteristics.

2. Experimental details

Boron-doped 0.1–0.6 Ωcm float-zone silicon wafers have been used in this study. Hydrogen was introduced into the samples in a remote DC hydrogen plasma with a voltage of 600 V applied across the plates. The samples were held at a temperature of 150°C, and a reverse bias was applied which accelerated the ions into the sample. These conditions were found to cause the passivation of the B-acceptors by the hydrogen through the formation of electrically neutral B–H complexes [7].

The samples were subsequently annealed at 300°C in an inert atmosphere after plasma exposure to restore the

*Corresponding author. Fax: +27-41-504-2573.

E-mail address: phblw@upe.ac.za (L. Wu).

dopant profile to its original state. Schottky barrier diodes (SBDs) were fabricated with Al Schottky contacts and Ga–In eutectic ohmic contacts. DLTS spectra were collected in the temperature range 40–320 K and the rate window was set using a lock-in amplifier. The activation energies ($E_T - E_V$) and apparent hole capture cross-sections σ_p were determined from the Arrhenius plot using the lock-in frequencies between 1 and 460 Hz. Reference samples underwent similar treatments with a zero plate voltage in the plasma system (i.e. no plasma exposure).

3. Results

DLTS spectra from different SBDs passivated under identical conditions are shown in Fig. 1. It was not possible to scan samples A and B to higher temperatures since leakage current became dominant at higher temperatures. It is evident from Fig. 1 that the plasma introduced a significant concentration of defects into silicon, which were all found to be within 0.3 μm of the semiconductor surface. Not all the DLTS peaks were present in the spectrum of each SBD. These irregular occurrences are ascribed to the non-uniform plasma conditions resulting in an inhomogeneous defect distribution. These peaks could not have originated from surface-related defects since we did not find any peaks in the reference sample. Three deep level traps could be identified; they are labelled H1, H2 and H3, with the latter being the dominant peak.

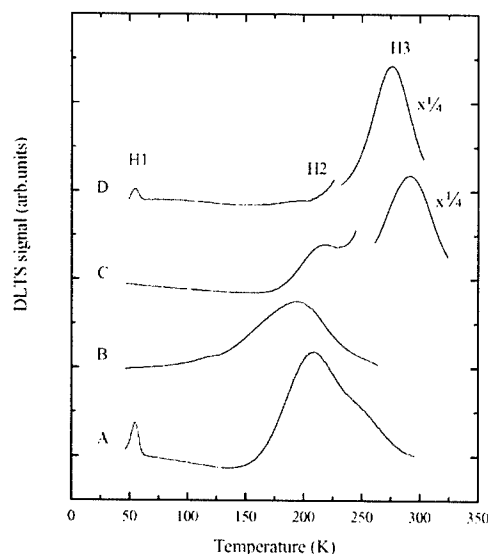


Fig. 1. DLTS spectra of selected SBDs taken at a frequency of 46 Hz ($\tau = 9.35$ ms) under a reverse bias of -1 V, filling pulse of $+1.3$ V and pulse width of 0.5 ms.

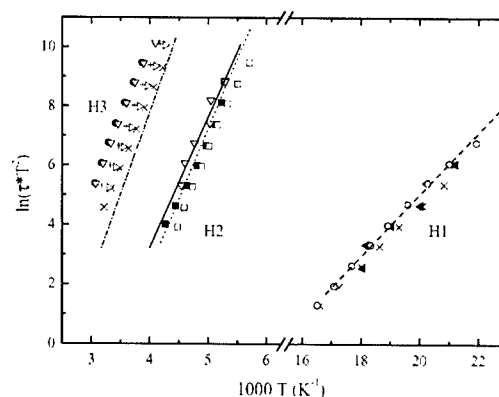


Fig. 2. Arrhenius plot of all deep levels found in plasma-exposed samples (markers). Included are data from Ref. [9] (dashed line), Ref. [11] (dotted line), Ref. [10] (solid line) and Ref. [6] (dot-dash line).

Table 1

Range of defect energy levels and effective capture cross-sections obtained for the defects found in Fig. 1

	$E_T - E_V$ (eV)	σ_p (cm^{-2})
H1	0.09	$2\text{E-}15$ – $7\text{E-}15$
H2	0.34–0.39	$2\text{E-}16$ – $6\text{E-}15$
H3	0.40–0.44	$1\text{E-}17$ – $5\text{E-}17$

Fig. 2 shows the Arrhenius plots of all the defects found in the plasma exposed material. Defects found in literature with similar trap signatures are also plotted in Fig. 2. It is seen that the Arrhenius data of the deep levels lie in three distinct bands. Each band is attributed to a single defect since the slopes, i.e. activation energy, are nearly identical. These defects are thought to exist in a varying strain field, thus affecting the hole capture rate and subsequently σ_p . Table 1 lists the ranges in which the defect energy levels and apparent capture cross-sections lie.

The average concentration of H1 was determined as $2 \times 10^{13} \text{ cm}^{-3}$ and typical concentration profiles of H2 and H3 are plotted in Fig. 3. It should be noted that the effect of the Debye free carrier tail was not taken into consideration during the calculation of the defect depth profiles. There is an extremely high concentration of defects near the surface (H3) that decreases with a near-exponential behaviour into the plasma-exposed material. A reasonable correlation exists between the profiles of H2 and H3 in the range 0.21–0.24 μm ; their creation likely arose from the same source, i.e. plasma damage and/or is hydrogen related. Experimental constraints due to the lower capacitance (and thus larger depletion width) at the temperature of the H2 peak maximum limited the start of the defect profiling to a depth of

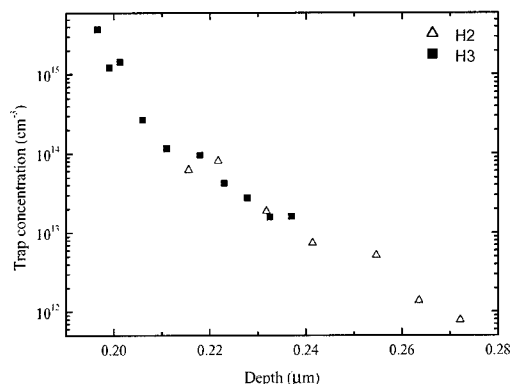


Fig. 3. Concentration profiles of the H2 and H3 deep levels.

0.21 μm . It is quite possible that the profile of H2 has the same trend as H3 before 0.21 μm .

The defect H3 exhibited anomalous behaviour during reverse bias annealing (RBA) at temperatures higher than 320 K. Upon RBA, the peak intensity decreased during the first 30 min after which it increased slightly in intensity. A zero bias anneal (ZBA) at 347 K restored the peak height to its original value. No new DLTS peak was detected during the annealing. Furthermore, there was no measurable change in the trap profile before and after RBA. It is believed that a complex reaction takes place during the RBA with at least two competing processes. Further investigations are continuing in this area.

4. Discussion

The likelihood of H1 (0.09 eV) being the FeB complex (known to occur at 0.10 eV [12]) was discounted given that no peak was seen in the reference sample, implying that there was no Fe contamination during the processing. A bistable $C_i - C_s$ defect, in which one of the configurations has the same activation energy as H1, was detected in electron-irradiated material [8]. Since H1 did not exhibit the described bistable behaviour, it therefore could not be identified with the carbon-related defect. However, excellent correspondence was found with an unidentified defect formed in dislocation-induced silicon [9], which is seen in Fig. 2. H1 is therefore ascribed to an intrinsic defect.

The trap signatures of both H2 and H3 varied from diode to diode. Although the activation energies change slightly, the more noteworthy feature is the considerable variation in the capture cross-sections. It is believed that the defects exist in a strain field, where the efficient capture of holes could be affected by the surrounding matrix.

The trap signature of H2 agrees relatively well with a defect ($E_T = 0.38$ eV, $\sigma_p = 1 \times 10^{-15}$ cm²) formed during electron-beam deposition [10], while Ref. [11] also detected a defect with similar energy and capture cross-section ($E_T = 0.41$ eV, $\sigma_p = 8 \times 10^{-15}$ cm²) in thermally quenched silicon (see Fig. 2). However, they did not observe any significant variation in the capture cross-section.

We now consider the H3 level. An additional factor contributing to the variation of its capture cross-section is the shifting of the peak maximum towards higher temperature during annealing. This shifting occurred for both zero bias and reverse bias anneals. For a lock-in frequency of 46 Hz, the temperature shifted from 286 to 301 K, where it then stabilised. The peak intensity also increased after ZBA. The broad nature of the H3 peak, coupled with its temperature behaviour, leads us to suggest that it may contain multiple peaks arising from a band of defects with closely spaced energy levels; during annealing the relative population of the various states could change, thereby shifting the position of the effective peak maximum. This might further imply that it is an extended defect. Henry et al. [6] detected a similar trap level at $E_V + 0.48$ eV (plotted in Fig. 2) after exposing Cz-Si to a D₂ plasma during reactive ion etching. However, they did not report any metastability or shifting of σ_p .

5. Conclusions

Three deep levels were detected in p-type float-zone silicon after exposure to hydrogen plasma, with a high concentration of defects near the surface. Two of the levels have variable capture cross-sections which could be attributed to the strained matrix around the defects and possibly extended defects. Trap signs similar to these three levels were found in either plasma-exposed electron irradiation or dislocation-induced Si.

Acknowledgements

The authors acknowledge the financial support of the National Research Foundation.

References

- [1] S.J. Pearton, et al., *Hydrogen in Crystalline Semiconductors*, Springer, Berlin, 1992.
- [2] A. Szekeres, et al., *Semicond. Sci. Technol.* 9 (1994) 1795.
- [3] J.M. Hwang, et al., *J. Appl. Phys.* 57 (1985) 5275.
- [4] N.M. Johnson, et al., *Phys. Rev. B* 35 (1987) 4166.

- [5] C.W. Nam, et al., *Mater. Sci. Eng. B* 36 (1996) 255.
- [6] A. Henry, et al., *J. Electrochem. Soc.* 138 (1991) 1456.
- [7] T. Zundel, J. Weber, *Phys. Rev. B* 39 (1989) 13549.
- [8] L.W. Song, et al., *Phys. Rev. B* 42 (1990) 5765.
- [9] L.C. Kimerling, J.R. Patel, *Appl. Phys. Lett.* 34 (1979) 73.
- [10] F.D. Auret, P.M. Mooney, *J. Appl. Phys.* 55 (1984) 984.
- [11] K. Nakashima, *Jap. J. Appl. Phys.* 24 (1985) 1018.
- [12] J.L. Benton, L.C. Kimerling, *J. Electrochem. Soc.* 129 (1982) 2098.



ELSEVIER

Physica B 308–310 (2001) 197–201

PHYSICA B

www.elsevier.com/locate/physb

Evidence for H_2^* trapped by carbon impurities in silicon

B. Hourahine^{a,1,*}, R. Jones^{a,1}, S. Öberg^{b,2}, P.R. Briddon^{c,1}, V.P. Markevich^{d,e,1},
R.C. Newman^{f,1}, J. Hermansson^{g,2}, M. Kleverman^{g,2}, J.L. Lindström^{e,2},
L.I. Murin^{e,3}, N. Fukata^h, M. Suezawa^h

^a School of Physics, The University of Exeter, Stocker Road, Exeter EX4 4QL, UK

^b Department of Mathematics, Luleå University of Technology, S-97187 Luleå, Sweden

^c Department of Physics, The University of Newcastle upon Tyne, Newcastle upon Tyne NE1 7RU, UK

^d Centre for Electronic Materials, UMIST, Manchester M60 1QD, UK

^e Institute of Solid State and Semiconductor Physics, Minsk 220072, Belarus

^f The Blackett Laboratory, Department of Physics, Imperial College, Centre For Electronic Materials Devices, London SW7 2BZ, UK

^g Department of Physics, University of Lund, S-22100 Lund, Sweden

^h Institute of Materials Research, Tohoku University, Sendai 980-8577, Japan

Abstract

Local mode spectroscopy and ab initio modelling are used to investigate two trigonal defects found in carbon-rich Si into which H had been in-diffused. Isotopic shifts with D and ^{13}C are reported along with the effect of uniaxial stress. Ab initio modelling studies suggest that the two defects are two forms of the CH_2^* complex where one of the two hydrogen atoms lies at an anti-bonding site attached to C or Si, respectively. The two structures are nearly degenerate and possess vibrational modes in good agreement with those observed. © 2001 Elsevier Science B.V. All rights reserved.

PACS: 61.72.-y; 61.72.Bb; 63.20.Pw

Keywords: Silicon; Hydrogen; Carbon; Impurity complexes; Absorption bands

1. Introduction

Hydrogen and carbon are common interstitial and substitutional impurities, respectively, in silicon [1,2]. The single hydrogen defect is highly mobile and is easily trapped by impurities and lattice defects. One prominent defect found in proton implanted Si, or Si containing H which has been e-irradiated, is the trigonal H_2^* centre

which contains two inequivalent H atoms. One H atom lies at a bond centred site and the other at a neighbouring anti-bonding site [3]. It might be expected that dilated Si–Si bonds due to the strain field surrounding substitutional carbon atoms will be trapping sites for H. However, the greater binding energy of H with C rather than Si [4] suggests that H will attach directly to C. Examples of defects where H bonds to Si rather than C are given in Ref. [5], while Ref. [6] exemplifies the second defect type. In other cases, it is not clear which type is present [7,8].

Recently, several local vibrational modes (LVMs) were observed in carbon-rich Si samples treated in a hydrogen ambient at high temperatures [9–12]. Some arise from a trigonal complex containing one carbon and two hydrogen atoms [9]. The LVMs of this defect, labelled $(\text{C}-H_2^*)_2$, are given in Table 1. Following previous theoretical results [13], it was suggested that

*Corresponding author. Tel.: +44-1392-264-198; fax: +44-1392-264-111.

E-mail address: bh@excc.ex.ac.uk (B. Hourahine).

¹The Engineering and Physical Science Research Council, EPSRC, UK are thanked for their financial support.

²Acknowledges financial support from TFR and KVA in Sweden.

³Thanks the Fund for Fundamental Research of the Republic of Belarus.

Table 1

Observed and calculated LVMs (cm^{-1}), for two forms of the C-H_2^* trigonal defect

$(\text{C-H}_2^*)_1$						
Suggested LVM assignment	$^{12}\text{C, H}$	$^{12}\text{CH, D}$	$^{12}\text{C, D}$	$^{13}\text{C, H}$	$^{13}\text{CH, D}$	$^{13}\text{C, D}$
A_1 (Si-H stretch)	2210.4	1606.05, 1607.3, 2210.4, 2214.5	1607.3	2210.4		1607.3
(Si-C)	665.3	649, 665.4	648.8	645.85		634.6
<i>Calculated $\text{H}_{ab}\text{CH}_b\text{Si}$</i>						
A_1 (C-H stretch)	2664.5	2177.8, 2662.9	1950.7	2657.4	2177.8, 2655.7	1940.5
A_1 (Si-H stretch)	2172.3	1560.5, 1946.2	1559.9	2172.2	1560.4, 1936.0	1559.9
E (C-H wag)	1018.4	750.7, 1018.4	750.7	1017.0	743.4, 1017.0	743.4
E (Si-C)	665.0	646.9, 665.0	646.9	645.6	633.4, 645.6	633.4
E (Si-H wag)	581.7	581.7, 536.3	536.3	581.7	536.2, 581.7	536.2
$(\text{C-H}_2^*)_2$						
Suggested LVM assignment	$^{12}\text{C, H}$	$^{12}\text{CH, D}$	$^{12}\text{C, D}$	$^{13}\text{C, H}$	$^{13}\text{CH, D}$	$^{13}\text{C, D}$
A_1 (C-H stretch)	2752.3			2745.1		
A_1 (Si-H stretch)	1921.8	1400.3, 1401.2, 1921.8, 1922.7	1401.2	1921.8		1401.2
E (Si-H wag)	792.0	571.8, 792.0, 793.2	571.6	792.0		571.4
Si-H wag overtone	1550.2					
<i>Calculated $\text{H}_{ab}\text{SiH}_b\text{C}$</i>						
A_1 (C-H stretch)	2736.3	2007.2, 2736.3	2006.3	2728.7	1996.4, 2728.6	1995.3
A_1 (Si-H stretch)	1923.3	1383.0, 1922.5	1383.0	1923.3	1383.0, 1922.4	1383.0
E (C-H wag)	896.5	813.3, 895.9	709.1	892.7	813.3, 892.1	694.6
E (Si-H wag)	812.3	634.9, 708.6	634.9	812.2	634.9, 694.1	634.8
E (Si-C stretch)	628.6	581.3, 628.6	581.3	612.7	576.1, 612.7	576.1

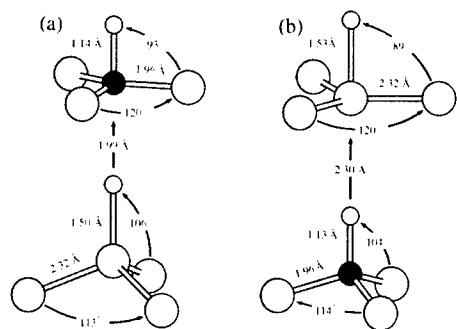


Fig. 1. The two degenerate C_{3v} structures for CH_2^* : (a) $\text{H}_{ab}\text{CH}_b\text{Si}$ and (b) $\text{H}_{ab}\text{SiH}_b\text{C}$. Relevant bond lengths and angles are shown where appropriate.

this complex is a H_2^* defect trapped near C. There are two possible trigonal forms of the centre where the anti-bonding sited H is bonded to Si or C (Fig. 1). The observed modes are somewhat more stable than H_2^* , which anneals at $\sim 200^\circ\text{C}$ [3], as they survive until $\sim 400^\circ\text{C}$ [9]. We show in the present work that there is another set of LVM absorption lines, which is related to the other form of C-H_2^* centre, labelled $(\text{C-H}_2^*)_1$. These

assignments are based on the analysis of positions, shifts, and splitting of LVM bands with different isotopic combinations (H, D, ^{12}C , ^{13}C). Application of uniaxial stress and comparison with ab initio modelling further strengthen the assignments.

2. Experimental and theoretical details

Samples for this study were prepared from lightly doped n-type and p-type float-zone-grown Si crystals with different carbon concentrations in the range $(1.5\text{--}3.0) \times 10^{17} \text{ cm}^{-3}$. A few samples were prepared from a crystal enriched with ^{13}C isotopes to about $8 \times 10^{17} \text{ cm}^{-3}$. Hydrogen and/or deuterium was introduced by a heat treatment at $1250\text{--}1350^\circ\text{C}$ for 30 min or 1 h in a H_2 (D_2) gas ambient at a gas pressure of about 1.0 or 1.5 atm, followed by a quench. The isochronal annealing was carried out in an argon atmosphere in temperature steps of 25°C in the range of $100\text{--}450^\circ\text{C}$, for 30 min at each temperature. The thickness of the samples was in most cases about 6 mm. The samples used for the uniaxial stress measurements had dimensions $10 \times 3 \times 2 \text{ mm}^3$. Optical absorption spectra were measured by Fourier transform infrared (FT-IR) spectrometers at

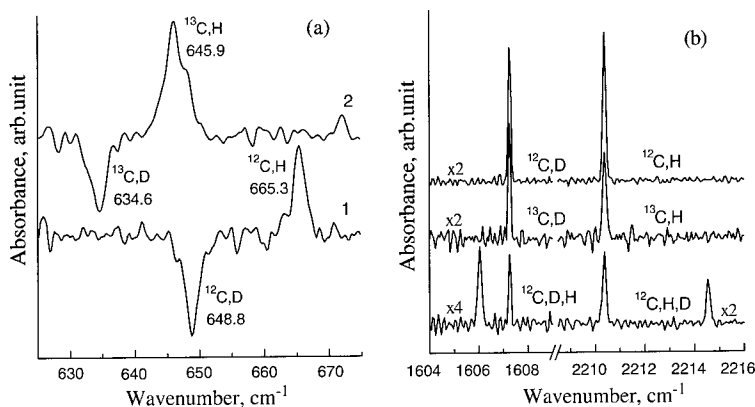


Fig. 2. (a) Difference absorption spectra measured at 10 K with a resolution 0.5 cm^{-1} for (1) Si: ^{12}C samples doped with hydrogen and deuterium and (2) Si: ^{13}C samples doped with hydrogen and deuterium (spectra of D-doped sample were subtracted from those of H-doped ones); (b) details of infrared absorption spectra, measured at 10 K with a resolution 0.1 cm^{-1} , on ^{12}C - and ^{13}C -rich Fz-Si samples, which were doped with hydrogen, deuterium and H + D mixture (50% + 50%). Multiplication factors for different parts of the spectra are indicated. All the samples were treated in H(D) gas ambient at 1350°C for 30 min with a gas pressure of about 1.5 atm.

$\sim 10\text{ K}$. The spectral resolution varied from 0.1 to 0.5 cm^{-1} .

The properties of C-H_2^* defects in silicon, were investigated by a local density-functional technique as implemented in the AIMPRO code [14]. The defects were inserted into 64 atom supercells and a 2^3 Monkhorst-Pack k-point sampling scheme used to integrate over the band structure [15]. The basis consisted of independent s- and p-Gaussian orbitals, with four different exponents, sited at each Si atom, four at the carbon atom, and three at the H atom. In addition, a single set of s- and p-Gaussian functions was placed between every neighbouring pair of atoms. The Hartree and Perdew-Zunger [16] exchange-correlation energies were calculated using a plane-wave intermediate fit with an energy cut-off of 200 Ry. All atoms were allowed to relax by a conjugate gradient method. The second derivatives of the energy were found for the atoms of the defects and their immediate neighbours, allowing vibrational modes to be calculated from the dynamical matrix, with additional entries in the matrix constructed from a Musgrave-Pople potential (further details are given in Ref. [17]).

3. Results

Among the many sharp absorption lines observed in the frequency ranges 660–690, 790–820, 1920–1960, 2120–2230, and 2680–2950 cm^{-1} [9–12], lines at 2210.4 cm^{-1} and 665.3 cm^{-1} are of particular interest in the present work (Fig. 2). A clear linear correlation was found between the intensities of these lines in

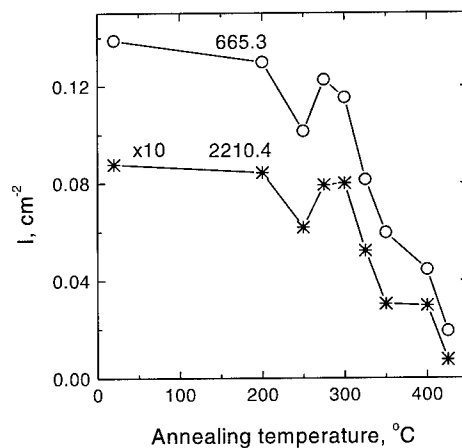


Fig. 3. Isochronal annealing temperature dependence of the integrated absorption intensity of the bands at 665.3 and 2210.4 cm^{-1} in a ^{12}C -rich Fz-Si sample which was treated in H_2 gas at 1350°C for 30 min. IR absorption measurements were carried out at 10 K with a resolution 0.5 cm^{-1} .

different samples and the lines were found to have an identical annealing behaviour as illustrated in Fig. 3. This suggests that they originate from the same defect. The positions of the lines of this complex, labelled $(\text{C-H}_2^*)_1$, in ^{12}C , ^{13}C , H and D material, as well as material containing a mixture of H and D, are given in Table 1.

The shift of the 665.3 cm^{-1} line with ^{13}C and D, as well as its splitting in the mixed H, D case, demonstrates that the defect contains one C and two H atoms. Similar conclusions arise from inspection of the shifts of the

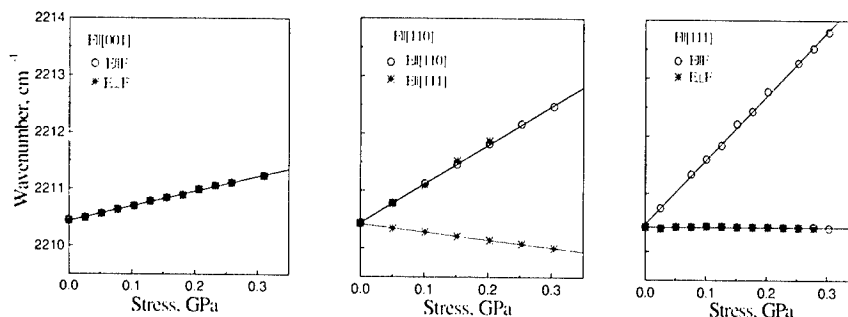


Fig. 4. The effect of uniaxial stress on the 2210.4 cm^{-1} mode. F denotes stress axis and E the electric-field direction of the incident light.

2210.4 cm^{-1} line except that its shift with ^{13}C is negligible. This implies that the H involved in the mode is not bonded directly to C and the 2210.4 cm^{-1} line is due to a stretch mode of Si–H. The 665.3 cm^{-1} mode is assigned to a perturbed mode of substitutional carbon at 607 cm^{-1} .

Fig. 4 shows the effect of uniaxial stress on the 2210.4 cm^{-1} mode. The splitting pattern is found to be consistent with the assignment to an A_1 mode of a defect possessing trigonal symmetry.

All combinations of pairs of hydrogen atoms at bond-centre and anti-bonding sites within one and two neighbouring sites of substitutional carbon were structurally relaxed. Two degenerate structures with C_{3v} symmetry were found to possess the lowest energy by at least $\sim 0.4 \text{ eV}$. These structures are similar to the H_2^* defect [3] and are shown in Fig. 1. The calculated LVMS are given in Table 1. The calculated Si–H stretch mode in $\text{H}_{ab}\text{CH}_b\text{Si}$ (Fig. 1a) at 2172 cm^{-1} is close to the observed mode at 2210.4 cm^{-1} . There are undetected C–H stretch and bend modes at 2664.5 and 1018.4 cm^{-1} , respectively. We assign the observed mode at 665.3 cm^{-1} to the E (C–Si) mode at the same frequency. The isotopic shifts are in good agreement with the experimental ones. Accordingly, we assign the $(\text{C–H}_2^*)_1$ defect to $\text{H}_{ab}\text{CH}_b\text{Si}$.

We now turn to the previously reported modes of $(\text{C–H}_2^*)_2$ [9]. These are in good agreement with the calculated modes of $\text{H}_{ab}\text{SiH}_b\text{C}$ shown in Fig. 1b. In particular, the C–H and Si–H stretch modes observed at 2752 and 1922 cm^{-1} are close to the calculated ones at 2736 and 1923 cm^{-1} . The Si–H wag mode at 792 is close to the calculated one at 812 cm^{-1} . Similarly, there is good agreement with the isotopic shifts. Accordingly, we assign the $(\text{C–H}_2^*)_2$ defect to $\text{H}_{ab}\text{SiH}_b\text{C}$.

Finally, for completeness, the stress-energy B -tensor for both forms of H_2^* were calculated. These tensors have not yet been experimentally measured. The tensors are evaluated directly by first relaxing the volume of the cubic cell and then calculating $\partial E / \partial \epsilon_{ij}$ with Cartesian

axes, where ϵ_{ij} is the strain [14]. For trigonal defects, the tensor has principal values $\frac{1}{3}B_{11} = -B_{22} = -B_{33}$ with the principle directions $\langle 111 \rangle$ (along the C_3 axis), $\langle 1\bar{1}0 \rangle$ and $\langle 11\bar{2} \rangle$. The values of B_{11} for $\text{H}_{ab}\text{CH}_b\text{Si}$ and $\text{H}_{ab}\text{SiH}_b\text{C}$ were found to be 7.69 and 11.15 eV per unit strain. The fractional volume changes for the defects in a 64 atom cubic cell were found to be 0.2% and 0.3% , respectively, i.e., $\Delta V / V_0 = 64 \times 0.2\%$. So the volume change caused by the defect is just $0.1 \times V_0$ where V_0 is the volume of Si atom (defined as $a_0^3/8$).

4. Conclusions

Local mode spectroscopy and ab initio modelling has identified two LVM bands observed at 2210.4 and 2752.3 with H stretch modes of two forms of C–H_2^* defects where H lies anti-bonded to C and Si, respectively. Several other modes are observed in each defect and related to particular atomic displacements.

References

- [1] S. Pearton, M. Stavola, J.W. Corbett, *Acta Metall.* 4 (1992) 332.
- [2] G. Davies, R.C. Newman, in: S. Mahajan (Ed.), *Handbook on Semiconductors*, Vol. 3, Elsevier, Amsterdam, 1994, p. 1557.
- [3] J.D. Holbeck, et al., *Phys. Rev. Lett.* 71 (1993) 875.
- [4] A.G. Gaydon, *Dissociation Energies and Spectra of Diatomic Molecules*, 3rd Edition, Chapman & Hall, London, 1968.
- [5] L. Hoffmann, et al., *Phys. Rev. B* 61 (2000) 16,659.
- [6] E.V. Lavrov, et al., *Phys. Rev. B* 62 (2000) 12,859.
- [7] A. Endrös, *Phys. Rev. Lett.* 63 (1989) 70.
- [8] Y. Kamiura, K. Fukuda, Y. Yamashita, T. Ishiyama, *Defect Diffusion Forum* 183 (2000) 25.
- [9] V.P. Markevich, et al., *Physica B* 302–303 (2001) 220.
- [10] N. Fukata, M. Suezawa, *J. Appl. Phys.* 86 (1999) 1848.
- [11] N. Fukata, M. Suezawa, *J. Appl. Phys.* 87 (2000) 8361.

- [12] N. Fukata, M. Suezawa, J. Appl. Phys. 88 (2000) 4525.
- [13] P. Leary, R. Jones, S. Öberg, Phys. Rev. B 57 (1998) 3887.
- [14] J. Coutinho, R. Jones, P.R. Briddon, S. Öberg, Phys. Rev. B 62 (2000) 10,824.
- [15] H.J. Monkhorst, J.D. Pack, Phys. Rev. B 13 (1976) 5188.
- [16] J.P. Perdew, A. Zunger, Phys. Rev. B 23 (1981) 5048.
- [17] R. Jones, P.R. Briddon, in: M. Stavola (Ed.), Identification of Defects in Semiconductors, Semiconductors and Semimetals, Vol. 51A, Academic Press, Boston, 1998 (Chapter 6).



ELSEVIER

Physica B 308–310 (2001) 202–205

PHYSICA B

www.elsevier.com/locate/physb

The strange behavior of interstitial H_2 molecules Si and GaAs

S.K. Estreicher^{a,*}, J.L. McAfee^a, P.A. Fedders^b, J.M. Pruneda^c, P. Ordejón^d^a Physics Department, Texas Tech University, Lubbock, TX 79409-1051, USA^b Physics Department, Washington University, St. Louis, MO 63130, USA^c Departamento de Física, Universidad de Oviedo, E-33007 Oviedo, Spain^d Institut de Ciència de Materials, CSIC, UAB, E-08193 Bellaterra, Barcelona, Spain

Abstract

Interstitial H_2 molecules have been observed in GaAs and in Si and behave very differently in the two hosts. In GaAs, H_2 has rotational symmetry, a stretch frequency close to the free-molecule value, and the Raman spectrum exhibits the expected ortho/para splitting. In Si, the symmetry is C_1 , the stretch frequency is about 550 cm^{-1} lower than that of free H_2 , and no ortho/para splitting is seen. In this paper, we use ab-initio molecular-dynamics simulations (SIESTA) to calculate the vibrational frequencies of H_2 using linear response theory as well as the velocity–velocity autocorrelation function. We also study the interactions between H_2 and O_i as well as paramagnetic H in Si. Based on these calculations and arguments about the formation process of H_2 , we argue that rapid $H_2 \rightleftharpoons H_T^0$ interactions are a possible candidate to explain the absence of ortho- H_2 in Si. © 2001 Elsevier Science B.V. All rights reserved.

Keywords: Molecular dynamics; Hydrogen; Silicon; Gallium arsenide

1. Introduction

The interstitial H_2 molecule in GaAs has been observed by Raman spectroscopy [1] and behaves like a near-free molecule. At 77 K, the Raman lines at 3926 and 3934 cm^{-1} are close to the free H_2 line (4160 cm^{-1}) and show an 8 cm^{-1} ortho/para splitting with 3:1 ratio. This implies that only the $j=0$ and 1 quantum rotational states are occupied and, therefore, that the molecule is spherically symmetric. This is confirmed by uniaxial stress experiments [2] which show no line splitting under [001], [110], or [111] stress. At room temperature, the H_2 , HD, and D_2 lines are at 3911, 3429, and 2827 cm^{-1} , respectively. The molecule has not been seen by infrared (IR) absorption spectroscopy. The isotope shifts and relative amplitudes are about as one would expect. First-principles calculations [3–7] predict that the center of mass (CM) of H_2 is at the tetrahedral interstitial site with four Ga nearest neighbors (NNs), T_{Ga} , and that the molecule is a nearly free rotator. The

calculated frequencies of H_2 are close to the measured ones, 3704 cm^{-1} in Ref. [6] and 3824 cm^{-1} in Ref. [7].

The behavior of H_2 in Si is different. The molecule is not just Raman [8] but also IR [9] active, the local vibrational mode (LVM) is much lower, just above 3600 cm^{-1} , and no ortho–para splitting is seen. Uniaxial stress experiments [10] imply C_1 symmetry. A single HD line is seen, but shifted relative to its expected position [10] and with a very low amplitude [11]. The IR lines are extremely sharp. Some fifteen theoretical papers (see Ref. [12] for details and references) have been published on H_2 in Si. Most authors find that the stretch frequency is substantially reduced relative to that of the free molecule, as observed. However, the CM is almost always found to be at the T site where the molecule should be a nearly free rotator. These predictions conflict with several key experimental data, notably the low symmetry, IR activity, and absence of ortho/para splitting.

Recent ab-initio molecular-dynamics (MD) simulations [12] of H_2 have shown that at $T > 0\text{ K}$ in Si, the average position of the CM moves off the T site along $\langle 100 \rangle$ and shifts off that axis under uniaxial stress. Further, the molecule moves within its tetrahedral cage

*Corresponding author. Tel.: +1-806-742-3723; fax: +1-806-742-1182.

E-mail address: stefan.estreicher@ttu.edu (S.K. Estreicher).

extremely fast. The amplitude of its oscillation changes abruptly as the oscillator exchanges energy with the host crystal. Similar MD simulations in GaAs show no such motion of the CM. This host is partly ionic and, at the T_{Ga} site, H_2 is surrounded by four positively charged Ga NNs and six negatively charged As NNs. The resulting electrostatic potential prevents the rapid motion of the molecule.

Our calculations are done using the SIESTA code [13,14] as described in Ref. [12]. These are classical MD simulations in which the electronic problem is solved at the ab-initio level within density-functional theory. The electronic basis sets consist of numerical linear combinations of atomic orbitals and vary from single zeta (SZ: one s and three p per Si for example) to double zeta (DZ) with polarization (P) functions (two sets of s and p and one set of d per Si for example). For the purpose of calculating vibrational frequencies, the host crystal is represented by periodic supercells of 64 Si atoms and the k -point sampling is reduced to the Γ -point.

2. Vibrational frequencies

They are obtained from two techniques. A *static* ($T = 0\text{ K}$) perturbative approach, based on linear response theory and discussed in Ref. [15], extracts the dynamical matrix analytically from the derivatives of the density matrix relative to atomic displacements. Specific LVMs are also calculated *dynamically* from the Fourier transform of the velocity–velocity autocorrelation function [16,17]. Here, the components of the velocities of each H atom along the H–H bond are saved at every time-step as the molecule moves around its cage and interacts with the Si host crystal. In the present work, we allow the system to evolve for 12,000 time-steps at $T = 30\text{ K}$.

The measured (gas phase) frequencies of *free* H_2 , HD, and D_2 are 4161, 3632, and 2994 cm^{-1} , respectively. The calculated values are 4185, 3625, and 2960 cm^{-1} with linear response theory and 4137, 3628, and 2957 cm^{-1} with the $v-v$ autocorrelation function and a DZP basis set. Note that the dynamically calculated frequencies are within 1% of the experimental values.

In GaAs, we calculated the frequencies so far only with the linear response theory. For interstitial H_2 , HD, and D_2 at the T_{Ga} site, the calculated (measured [1]) numbers are 3757 (3911), 3259 (3429), and $2657 (2957)\text{ cm}^{-1}$, respectively. For H_2 at the T_{As} site, the numbers are 3770, 3272, and 2667 cm^{-1} , respectively (H_2 has yet to be observed at the T_{As} site in GaAs). We find the energy difference between these two sites to be small, 0.08 eV.

In Si, the measured [9] frequencies of H_2 , HD, and D_2 are 3618, 3265, and 2643 cm^{-1} , respectively. Our static calculations predict 3550, 3082, and 2511 cm^{-1} , respec-

tively. The dynamic frequencies vary with the basis set used, most likely because of the rapid interactions between H_2 and the Si–Si bonds around its cage. A number of calculations are still under way and the results presented here are preliminary. With 12,000 time-steps at 30 K, a SZ basis set on the Si atoms, and a DZP basis set on the H atoms, we get for H_2 , HD, and D_2 3745, 3261, and 2649 cm^{-1} , respectively. While the D_2 and HD frequencies are very close to the IR values measured at 10 K (only +6 and -4 cm^{-1} off experiment, respectively), the H_2 number is off by 138 cm^{-1} ! Partial results with other basis sets also show shifts of the H_2 mode relative to experiment mode quite different from the shifts of D_2 and HD. This could be caused by the size of the time-step (0.2 fs), insufficient basis sets or total simulation times, or some quantum effect experienced by H_2 but not by the heavier HD or D_2 .

The substantial reduction ($\sim 550\text{ cm}^{-1}$) of the H_2 line in Si relative to free H_2 is predicted in most static calculations. It is in large part caused by the electron affinity of the four Si NNs and six second-NNs of H_2 at the T site. The calculated Mulliken charges [12] at 0 K show that each of these 10 Si atoms grabs a little electron density from H_2 which ends up slightly positively charged. This weakens the H–H bond, stretches the molecule, and causes a sharp drop in the frequency. No comparable delocalization of the molecular wavefunction occurs for H_2 in GaAs, which is surrounded by four positively charged Ga NNs and six negatively charged As NNs.

3. Interactions with impurities

H_2 molecules in Si have been observed [11] to trap in the vicinity of interstitial oxygen (O_i) with a binding energy of $0.26 \pm 0.02\text{ eV}$. Two distinct $\{\text{H}_2, \text{O}_i\}$ centers are formed. We performed geometry optimizations for numerous a priori possible configurations of H_2 near O_i in the 64 host-atoms cell, with a DZP basis set and a $2 \times 2 \times 2\ k$ points mesh, and found two configurations (Figs 1 and 2). The first, with binding energy 0.36 eV, has H_2 near a T site NN to O_i and the second, with binding energy 0.19 eV, has the molecule near a T site along the Si– O_i –Si bond.

We also calculated the binding energy of H_T^0 , neutral tetrahedral interstitial hydrogen, near H_2 . The energy gain for H_T^0 and H_2 at adjacent T sites relative to infinitely far apart is 0.16 eV (0.12 eV with H_T^0 and H_2 at second NN T sites).

4. Formation of H_2 in Si and ortho-to-para transition

The absence of distinct ortho- and para- H_2 lines in Si is very puzzling. At or below room temperature, free or

nearly free H_2 molecules have well-separated rotational states and only $j = 0$ and $j = 1$ are occupied. The latter is odd and three even combinations of spins are allowed: $\uparrow\uparrow$, $\uparrow\downarrow + \downarrow\uparrow$, or $\downarrow\downarrow$. The former is even, implying that an odd combination of nuclear spins is realized: $\uparrow\downarrow - \downarrow\uparrow$. This results in the well-known *o*- H_2 and *p*- H_2 lines with 3:1 intensity ratio. These lines are clearly visible in the case of H_2 in GaAs but not in Si. This can be explained in one of the two ways: (1) a hindering potential mixes the rotational j -states, a possibility suggested by Stoneham [18], and (2) the molecule is nearly free and some efficient mechanism flips the proton spins. Ortho-to-para transitions are typically induced by magnetic field gradients. Our MD simulations and the calculations of other authors suggest that H_2 in Si is a nearly free rotator, and dynamic runs show that the

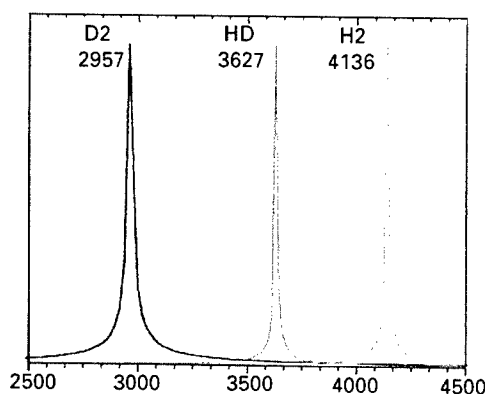


Fig. 1. Calculated vibrational frequencies of free H_2 , HD, and D_2 from the $r-r$ autocorrelation function. This is a 12,000 time-steps run at 30 K. The gas phase measured values are 4161, 3632, and 2994 cm^{-1} , respectively. Note that the calculated values are within 0.2–1.2% of the measured ones and that the isotope substitutions show the observed anharmonic shifts.

molecule moves extremely fast within its tetrahedral cage. Thus, we consider the latter possibility. The rapid motion of H_2 implies that it will experience a magnetic field gradient provided that a magnetic moment is nearby.

We reject ^{29}Si , the only Si isotope with a nuclear spin, as it is less than 5% abundant and has a very small magnetic moment: the ortho-to-para transition would require very long times. Raman spectra of samples kept at room temperature for two years after the plasma exposure still show the H_2 line with no ortho/para splitting [19]. Months of interactions of H_2 with ^{29}Si have failed to establish a Boltzman distribution of *o*- H_2 and *p*- H_2 . We also reject interactions between nearby *o*- H_2 molecules during the quench. Such interactions result [20] in ortho-to-para transitions in a-Si:H, but the measured rate constant 0.01 h^{-1} is far too low to explain the c-Si data. Further, no magnetic impurity is present in sufficient concentration in all the Si samples in which H_2 has been observed, except hydrogen itself. We are thus led to propose that *paramagnetic* hydrogen, with a magnetic moment arising from an electronic spin (~ 2000 times larger than a nuclear moment), is the culprit.

Hydrogen penetrates into Si in atomic form. This is obvious in plasma-exposed samples [8]. In samples hydrogenated in a gas at high temperatures, the concentration of hydrogen varies roughly as the square root of the gas partial pressure [21]. Thus, H_2 dissociates at the surface, H penetrates into the crystal in atomic form, and interstitial H_2 molecules form during the quench starting with atomic hydrogen, that is any combination of H_{BC}^+ , H_{BC}^0 , H_T^0 , and/or H_T^- .

We rule out the interactions between identically charged species since they involve a long-range repulsion. In p-type material, H_{BC}^+ is most likely to trap at B^- and form $\{H, B\}$ pairs, which are observed. H_{BC}^0 is a very

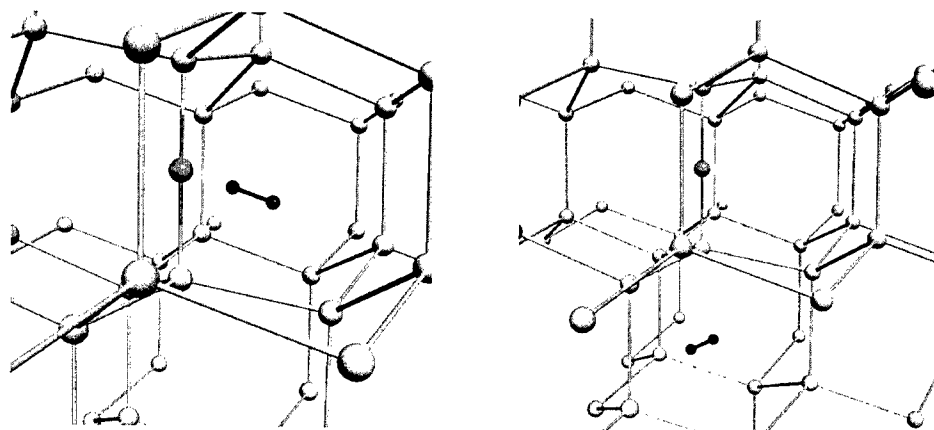


Fig. 2. The two configurations of H_2 near O, in Si. The most stable one is at left, with 0.36 eV binding energy, and a metastable one at right, with 0.19 eV.

strong IR center which is never seen in the samples containing H_2 . We also rule out the process $H_{BC}^+ + H_T^- \rightarrow H_2$ because this would *necessarily* lead to the formation of some H_2^* , the IR intensity of which is very much larger than that of H_2 . Even tiny amounts of H_2^* would be clearly visible in the spectra. For this reason, any H_2 formation process involving H_{BC} can be ruled out. Thus, we are left with $H_T^0 + H_T^0 \rightarrow H_2$. The metastable H_T^0 species is not present in any meaningful concentration in equilibrium. However, its contribution during the *dynamic* process while H_2 molecules form, cannot be ruled out. There is indirect evidence [22,23] that H_T^0 diffuses extremely fast. Our calculations of its activation energy for diffusion, 0.06–0.15 eV (to be corrected downward by the zero-point energy) makes it an extremely mobile species.

As H_T^0 s precipitate during the quench, most form H_2 molecules, but some fail to find a partner. They diffuse very rapidly in the crystal, trapping momentarily at H_2 s (see the binding energies above), thus generating large magnetic field gradients at H_2 (because of the rapid motion of both H_2 and H_T^0) or even forcing exchanges $H_T^0 + H_2 \rightarrow H_2 + H_T^0$. This would not lead to stable tri-hydrogen complexes but would induce ortho-to-para transitions very efficiently. Estimating a rate for such interactions is tricky. The rate is proportional to the concentrations of o - H_2 and H_T^0 , the diffusivity of H_T^0 , and some capture radius. In the Raman studies, concentrations are of the order of 10^{19} cm^{-3} , 1000 higher than in the IR studies. The diffusivity of H_T^0 is unknown, but the estimated [22,23] 25 orders of magnitudes (!) above that of H_{BC} at low temperatures suggest that any number is possible.

Acknowledgements

The work of SKE is supported in part by a grant from the R.A. Welch Foundation, a contract from the National Renewable Energy Laboratory, and a research award from the Humboldt Foundation. PO acknowledges the support of the Fundación Ramón Areces (Spain). Many thanks to the High Performance Com-

puting Center at Texas Tech's Institute for Environmental and Human Health for generous amounts of computer time.

References

- [1] J. Vetterhöfer, J. Wagner, J. Weber, Phys. Rev. Lett. 77 (1996) 5409.
- [2] A.W.R. Leitch, J. Weber, Phys. Rev. B 60 (1999) 13265.
- [3] L. Pavesi, P. Giannozzi, Phys. Rev. B 43 (1991) 2446.
- [4] L. Pavesi, P. Giannozzi, Phys. Rev. B 46 (1992) 4621.
- [5] S.J. Breuer, R. Jones, P.R. Briddon, S. Öberg, Phys. Rev. B 53 (1996) 16289.
- [6] Y. Omamoto, M. Saito, A. Oshiyama, Phys. Rev. B 56 (1997) R10016.
- [7] C.G. Van de Walle, Phys. Rev. Lett. 80 (1998) 2177.
- [8] A.W.R. Leitch, V. Alex, J. Weber, Phys. Rev. Lett. 81 (1998) 421.
- [9] R.E. Pritchard, M.J. Ashwin, J.H. Tucker, R.C. Newman, Phys. Rev. B 57 (1998) R15048.
- [10] J.A. Zhou, M. Stavola, Phys. Rev. Lett. 83 (1999) 1351.
- [11] R.C. Newman, R.E. Pritchard, J.H. Tucker, E.C. Light-owlers, Phys. Rev. B 60 (1999) 12775.
- [12] S.K. Estreicher, K. Wells, P.A. Fedders, P. Ordejón, J. Phys.: Condens. Matter 13 (2001) 6271.
- [13] E. Artacho, D. Sánchez-Portal, P. Ordejón, A. García, J.M. Soler, Phys. Status Solidi B 215 (1999) 809.
- [14] D. Sánchez-Portal, P. Ordejón, E. Artacho, J.M. Soler, Int. J. Quant. Chem. 65 (1997) 453.
- [15] J.M. Pruneda, J. Junquera, J. Ferrer, P. Ordejón, S.K. Estreicher, in these Proceedings (ICDS-21), Physica B 308–310 (2001).
- [16] J.M. Haile, Molecular-Dynamics Simulations, Wiley, New York, 1992.
- [17] M.P. Allen, D.J. Tildesley, Computer Simulations of Liquids, Oxford, Clarendon, 2000.
- [18] A. M.Stoneham, Phys. Rev. Lett. 84 (2000) 4777.
- [19] J. Weber, private communication.
- [20] W.E. Carlos, P.C. Taylor, Phys. Rev. B 25 (1982) 1435.
- [21] R.C. Newman, R.E. Pritchard, J.H. Tucker, E.C. Light-owlers, Physica B 273–274 (1999) 164.
- [22] K. Bonde Nielsen, B. Bech Nielsen, Mater. Sci. Eng. B 58 (1999) 163.
- [23] K. Bonde Nielsen, private communication.



ELSEVIER

Physica B 308–310 (2001) 206–209

PHYSICA B

www.elsevier.com/locate/physb

Raman scattering study of vacancy-hydrogen related defects in silicon

E.V. Lavrov^{a,b,*}, J. Weber^a, L. Huang^c, B. Bech Nielsen^d^a *University of Technology, 01062 Dresden, Germany*^b *IRE RAS, 103907 Moscow, Russia*^c *Duke University, Durham, NC 27708, USA*^d *University of Århus, DK-8000, Århus, Denmark*

Abstract

A Raman study of hydrogen stretching modes in vacancy-hydrogen defects (VH_n , $n = 1, 2, 3, 4$) is presented. The positions of the vibrational modes are compared to recent IR absorption results. The Raman lines exhibit pronounced polarization due to the $\langle 111 \rangle$ orientation of the silicon-hydrogen bond. Based on the defect symmetry derived from the polarization dependent Raman signals we assign the Raman lines measured at room temperature to the following defects: VH_4 : 2234 cm^{-1} (A_1 mode), 2205 cm^{-1} (T_2 mode); V_2H_6 : 2180 cm^{-1} (A_{1g} mode), 2155 cm^{-1} (E_g mode). We tentatively attribute the 2120 - and 2099-cm^{-1} lines to VH_2 and the 2022-cm^{-1} line to VH . © 2001 Elsevier Science B.V. All rights reserved.

Keywords: Silicon; Hydrogen; Vacancy; Raman scattering

1. Introduction

Hydrogen-related defects in silicon have been investigated extensively for the last two decades [1,2]. A model for the vacancy-hydrogen defects consisting of a single vacancy and up to four hydrogen atoms (VH_n with $n = 1, 2, 3, 4$) was developed, based on EPR, infrared absorption, and DLTS measurements, as well as on theoretical studies [3–14].

First Raman measurements on hydrogen-related defects in silicon were made on remote plasma hydrogenated samples [15]. A few Raman bands in the region 2000 – 2200 cm^{-1} were found and interpreted as hydrogen-related stretching modes of an extended defect called platelet. In this work we report on a Raman spectroscopy study of proton-implanted silicon. In our study, we are able to identify local vibrational modes

(LVMs) of different VH_n defects. Due to the selection rules, Raman spectroscopy gives a possibility to probe LVMs, which are not active in infrared absorption, and, which in combination with IR absorption and EPR studies allow us to better model the properties of the hydrogen-related defects in silicon.

2. Experimental

Silicon samples used in this study were n-type, phosphorus-doped, Cz (100)-wafers with resistivity of either 2 or $0.75 \Omega \text{ cm}$. Implantation doses varied from 1×10^{16} to $2.5 \times 10^{16} \text{ cm}^{-2}$. In order to study the thermal stability of the Raman lines a few samples were then annealed at 400°C in air. The annealing time varied from 2 min to 11 h.

The details of the Raman setup are described elsewhere [16]. Polarized Raman spectra were collected in a pseudobackscattering geometry. The polarization geometry is defined with respect to the sample surface (100): the x , y , and z axes are parallel to [100], [010], and [001], while y' and z' axes are parallel to [011], and

*Corresponding author. ITP, TU Dresden, Mommsenstr. 13, 01069 Dresden, Germany. Tel.: +49-351-463-3637; fax: +49-351-463-7060.

E-mail address: edward.lavrov@physik.phy.tu-dresden.de (E.V. Lavrov).

$[0\bar{1}1]$. In the notation $\{a[b,c]d\}$, $a(d)$ refers to the propagation vector of the incident (scattered) light, while $b(c)$ refers to the polarization vector of the incident (scattered) light.

3. Results and discussion

Fig. 1 shows typical room temperature Raman spectra measured on the hydrogen-implanted silicon: Label (a) refers to the as-implanted sample and (b) to the sample annealed at 400°C. The implantation gives rise to a number of Raman lines in the range of 1900–2250 cm^{-1} , which are characteristic of Si–H stretch LVMs. Indeed, in the deuterium-implanted sample, all these lines shift downwards in frequency by approximately a factor of $\sqrt{2}$, which proves that these are LVMs of hydrogen-related defects. The most prominent lines in the spectrum of the as-implanted sample are those at 1923, 1980, 2022, 2060, 2120, 2180, and 2234 cm^{-1} as well as a broad band centered at $\sim 2000 \text{ cm}^{-1}$. As can be seen from Fig. 1(b), annealing at 400°C removes the lines at 1923, 1980, 2022, and 2060 cm^{-1} from the spectrum and makes those at 2180 and 2234 cm^{-1} much stronger.

Careful investigation of the spectra shows that the lines at 2234, 2180, and 2120 have weak satellites located at 2205, 2155, and 2099 cm^{-1} , respectively (see the inset in Fig. 1). Relative intensities within each pair of these lines do not depend on the sample, implantation dose, as well as annealing temperature. Based on these findings we identify each pair of the lines as LVMs originating from the same defect.

Polarized Raman spectra measured on the sample annealed at 400°C and the as-implanted sample are presented in Figs. 2 and 3, respectively. As one can see, all Raman lines have maximum intensity in the $\{\bar{x}[z',z']x\}$ geometry, whereas in the $\{\bar{x}[z',y']x\}$ geometry they are very weak or nearly absent. This result may be

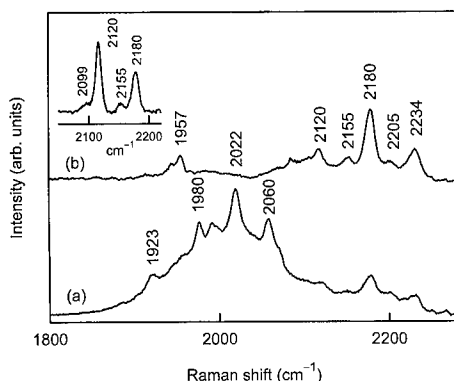


Fig. 1. Raman spectra measured at room temperature on the H_2^+ -implanted sample: (a) as-implanted sample and (b) after annealing at 400°C for 2 min. Spectra are offset vertically for clarity.

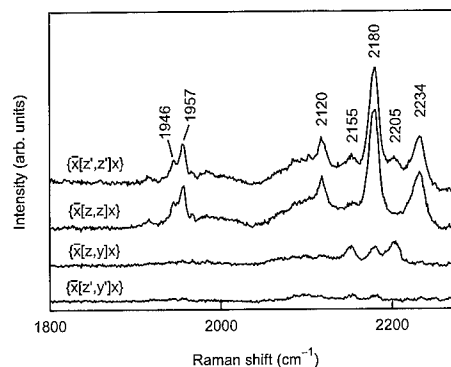


Fig. 2. Polarization Raman spectra measured at room temperature on the H_2^+ -implanted sample after annealing at 400°C for 2 min. Polarization geometry is defined with respect to the sample normal $[1\ 0\ 0]$. Spectra are offset vertically for clarity.

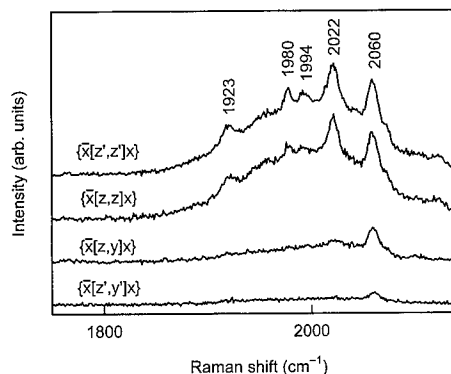


Fig. 3. Polarization Raman spectra measured at room temperature on the H_2^+ -as-implanted sample. Polarization geometry is defined with respect to the sample normal $[1\ 0\ 0]$. Spectra are offset vertically for clarity.

understood if we assume that the majority of the defects responsible for these Raman lines are vacancy-hydrogen complexes. Si–H bonds comprising these defects point almost in the $\langle 111 \rangle$ direction. Because LVMs spectroscopy probes the local trigonal symmetry of the Si–H bonds, this implies, according to the selection rules, maximal intensity in the $\{\bar{x}[z',z']x\}$ and zero intensity in the $\{\bar{x}[z',y']x\}$ geometry [17]. Let us now discuss the individual properties of the Raman lines.

3.1. 2205- and 2234- cm^{-1} lines

The two lines have the highest frequencies of all hydrogen-related Raman modes in our samples. The defect responsible for them is stable up to 400°C. At 10 K, the position of the 2205- cm^{-1} line (2223 cm^{-1}) coincides with that of the T_2 mode of VH_4 , whereas the frequency of the 2234- cm^{-1} line coincides with that

predicted for the infrared inactive A_1 mode of VH_4 [12]. It follows from the polarized spectra (see Fig. 2) that the intensity of the 2234-cm^{-1} line is maximum in the $\{\bar{x}[z', z']x\}$ and $\{\bar{x}[z, z]x\}$ geometries and equals zero in the $\{\bar{x}[z', y']x\}$ and $\{\bar{x}[z, y]x\}$ geometries, whereas intensity of the 2205-cm^{-1} line is maximum in the $\{\bar{x}[z', z']x\}$ and $\{\bar{x}[z, y]x\}$ geometries and equals zero in the $\{\bar{x}[z', y']x\}$ and $\{\bar{x}[z, z]x\}$ geometries. According to the selection rules for polarized Raman scattering, these properties are characteristic for the A_1 and T_2 modes of a cubic defect [17]. Based on this we assign the 2205- and 2234-cm^{-1} lines to the T_2 and A_1 modes of VH_4 .

3.2. 2155 and 2180-cm^{-1} lines

The defect responsible for the two lines is stable up to 400°C . At 10 K the 2155- and 2180-cm^{-1} lines shift upwards in frequency to 2165 and 2190 cm^{-1} , respectively, which is very close to the infrared absorption lines previously assigned to the E and A modes of V_2H_6 [18]. Polarization properties of the 2155- and 2180-cm^{-1} lines give support for the identification of the two lines as LVMs of V_2H_6 (see Fig. 2): Intensity of the 2180-cm^{-1} line is maximum in the $\{\bar{x}[z', z']x\}$ geometry and is reduced by more than 95% in the $\{\bar{x}[z', y']x\}$ geometry, whereas the 2155-cm^{-1} line is most intense in the $\{\bar{x}[z', z']x\}$ and $\{\bar{x}[z, y]x\}$ geometries and is much weaker in the $\{\bar{x}[z', y']x\}$ and $\{\bar{x}[z, z]x\}$ geometries. This is what is expected for the A and E modes of a trigonal defect.

The point group of V_2H_6 is D_{3d} , which implies that such a defect should possess four LVMs, labeled A_{1g} , E_g , A_{2u} , and E_u . The ungerade modes A_{2u} and E_u are active in infrared absorption, whereas the gerade modes A_{1g} and E_g are active in Raman scattering. The fact that the frequencies of the modes detected in Raman spectroscopy and infrared absorption are very close is consistent with our expectations. The repulsion between hydrogen atoms residing in the same vacancy is substantial and gives the dominant contribution to the $\sim 25\text{ cm}^{-1}$ splitting between the E and A modes (gerade and ungerade). However, the repulsion between two hydrogen atoms in two different vacancies will be much less due to the substantial large separation distance between the hydrogen atoms. The splitting between the gerade and the ungerade modes originates from the interaction between hydrogen atoms in different vacancies. Hence, a small splitting is expected in accordance with our observations.

3.3. 2099 and 2120-cm^{-1} lines

The defect responsible for the two lines is stable up to 400°C . At 10 K the 2099- and 2120-cm^{-1} lines shift upwards in frequency to 2121 and 2144 cm^{-1} , respectively, which coincide, within the accuracy of our setup, with the infrared absorption lines previously assigned to

the B_1 and A_1 modes of VH_2 [8,12]. Unfortunately, rather weak intensities of the two lines in our polarized Raman spectra did not allow to determine the symmetry of the defect. However, our data (see Fig. 2) do not contradict the C_{2v} (orthorhombic I) point group expected for VH_2 . Therefore, it would be quite tempting to identify the 2099- and 2120-cm^{-1} lines as LVMs of VH_2 . However, thermal stability of the defect is not in favor of this assignment: According to the FTIR absorption data [8,12], VH_2 decays at temperatures above 250°C , while the 2099- and 2120-cm^{-1} lines are present in the spectra after annealing at 400°C . Nevertheless, direct comparison with the FTIR data should be made with some care, because the doses employed in FTIR absorption studies were at least one order of magnitude less compared to ours, which may give a difference in thermal stability of the defect. Another explanation of the discrepancy in thermal stability of the 2099- and 2120-cm^{-1} lines and that of VH_2 could be that the defect responsible for these lines is VH_2 perturbed by VH_n ($n = 1, 2, 3$) [19]. Thus, both FTIR absorption and Raman scattering measurements made on the same sample are needed to investigate whether the two lines originate from VH_2 . Therefore, at this stage, we can only tentatively assign the 2099- and 2120-cm^{-1} lines to the LVMs of VH_2 .

3.4. 2022-cm^{-1} line

The defect responsible for this line decays at 400°C . Position of the 2022-cm^{-1} line in the spectra measured at 10 K (2038 cm^{-1}) coincides with the infrared absorption line tentatively assigned to a LVM of VH^0 [20]. Our polarization Raman measurements give support to this assignment (see Fig. 3): The 2022-cm^{-1} line is most intense in the $\{\bar{x}[z', z']x\}$ geometry and is reduced by more than 95% in the $\{\bar{x}[z', y']x\}$ geometry, which suggests the A mode of a trigonal defect.

4. Summary

Hydrogen-implanted silicon was studied by Raman scattering spectroscopy. From polarization of Raman lines in correlation with previous IR absorption studies and isotope substitution experiments the pairs of Raman lines at 2234 , 2205 and 2180 , 2155 cm^{-1} were assigned to the LVMs of VH_4 and V_2H_6 , respectively. We give a tentative assignment for the 2120- and 2099-cm^{-1} lines as LVMs of VH_2 and the 2022-cm^{-1} line as LVM of VH .

Acknowledgements

U. Goesele (MPI Halle) and B. Köhler (TU Dresden) are acknowledged for the help with organizing the

experiment. E.V.L. acknowledges the Alexander von-Humboldt Foundation for financial support and the Russian Foundation for Basic Research (Grant No. 99-02-16652).

References

- [1] J.I. Pankove, N.M. Johnson (Eds.), *Hydrogen in Semiconductors*, *Semiconductors and Semimetals*, Vol. 34, Academic Press, San Diego, 1991.
- [2] S.J. Pearton, J.W. Corbett, M. Stavola, *Hydrogen in Crystalline Semiconductors*, Springer, Berlin, 1992.
- [3] V.A. Singh, C. Weigel, J.W. Corbett, L.M. Roth, *Phys. Stat. Sol. B* 81 (1977) 637.
- [4] P. Deák, M. Heinrich, L.C. Snyder, J.W. Corbett, *Mater. Sci. Eng. B* 4 (1989) 57.
- [5] H. Xu, *Phys. Rev. B* 46 (1992) 1403.
- [6] C.G. Van de Walle, *Phys. Rev. B* 49 (1994) 4579.
- [7] M.A. Roberson, S.K. Estreicher, *Phys. Rev. B* 49 (1994) 17,040.
- [8] B. Bech Nielsen, L. Hoffmann, M. Budde, R. Jones, J. Goss, S. Öberg, *Mater. Sci. Forum* 196–201 (1995) 933.
- [9] Y.K. Park, S.K. Estreicher, C.W. Myles, P.A. Fedders, *Phys. Rev. B* 52 (1995) 1718.
- [10] B. Bech Nielsen, H.G. Grimmeiss, *Phys. Rev. B* 40 (1989) 12,403.
- [11] W.M. Chen, O.O. Awadelkarim, B. Monemar, J.L. Lindstöm, G.S. Oehrlein, *Phys. Rev. Lett.* 64 (1990) 3042.
- [12] B. Bech Nielsen, L. Hoffmann, M. Budde, *Mater. Sci. Eng. B* 36 (1996) 259.
- [13] B. Bech Nielsen, P. Johannesen, P. Stallinga, K. Bonde Nielsen, J.R. Byberg, *Phys. Rev. Lett.* 79 (1997) 1507.
- [14] P. Johannesen, J.R. Byberg, B. Bech Nielsen, P. Stallinga, K. Bonde Nielsen, *Mater. Sci. Forum* 258–263 (1997) 515.
- [15] J.N. Heyman, J.W. Ager III, E.E. Haller, N.M. Johnson, J. Walker, C.M. Doland, *Phys. Rev. B* 45 (1992) 13,363.
- [16] A.W.R. Leitch, V. Alex, J. Weber, *Phys. Rev. Lett.* 81 (1998) 421.
- [17] M. Cardona, in: M. Cardona, G. Güntherodt (Eds.), *Light Scattering in Solids II*, Springer, Berlin, 1982, pp. 19–172.
- [18] M. Budde, Ph.D. Thesis, University of Århus, Denmark, 1998.
- [19] B. Bech Nielsen, et al., unpublished.
- [20] P. Stallinga, P. Johannesen, S. Herstrøm, K. Bonde Nielsen, B. Bech Nielsen, *Phys. Rev.* 58 (1998) 3842.



ELSEVIER

Physica B 308–310 (2001) 210–212

PHYSICA B

www.elsevier.com/locate/physb

On the nature of hydrogen-related centers in p-type irradiated silicon

O. Feklisova^{a,b}, N. Yarykin^{a,b,*}, E.B. Yakimov^a, J. Weber^b

^a *Institute of Microelectronics Technology RAS, 142432 Chernogolovka, Moscow region, Russia*

^b *University of Technology, D-01062 Dresden, Germany*

Abstract

Hydrogen interaction with the radiation defects is studied by the DLTS and MCTS techniques. Hydrogenation was carried out during wet chemical etching in acid solutions and following reverse bias annealing at 380 K. The levels $H4 = E_v + 0.28$ eV and $E4 = E_c - 0.31$ eV are formed as a result of the hydrogenation in all samples irradiated with electrons at room temperature. The levels are not found in irradiated samples which were annealed at 620–650 K before the hydrogenation. Another prominent level $H3 = E_v + 0.51$ eV is introduced by hydrogenation of as-irradiated float-zone silicon. Czochralski samples have to be annealed at 450 K before hydrogenation to form the H3 level. The H3 center is not formed in the samples annealed at ~ 650 K before hydrogenation. The nature of the hydrogen-related centers is discussed. © 2001 Elsevier Science B.V. All rights reserved.

Keywords: Silicon; Hydrogen; Radiation defects

1. Introduction

In spite of many years of investigations, little is known about the complexes formed due to room-temperature hydrogenation of radiation-induced defects in silicon. In fact, only the VOH complex with the acceptor level at $E4 = E_c - 0.31$ eV has been studied in detail [1–3], including the tentative microscopic identification by the EPR technique [4]. Another prominent level $H4 = E_v + 0.28$ eV resulted from hydrogenation of irradiated Czochralski-grown silicon, has been ascribed to the COH complex based on a one-to-one correlation between the formation of this level and the C_iO_i complex passivation during reverse-bias annealing (RBA) at 380 K [5]. However, this assignment is not favored by the level structure of COH predicted by recent calculations [6]. Therefore, to gain further insight in the nature of the centers formed by hydrogenation of

irradiated silicon, we have studied silicon crystals with different content of the background impurities (O, C), paying special attention to the annealing kinetics of precursors of the hydrogen-related centers.

2. Experimental

Experiments were carried out on p-type silicon crystals grown by the Czochralski (Cz) and floating zone (FZ) method with boron concentrations $(0.6 \text{ to } 15) \times 10^{15} \text{ cm}^{-3}$. The samples were irradiated with 6 MeV electrons at room temperature. Hydrogen was incorporated into crystals during wet chemical etching (WCE) in acid solution ($\text{HF} : \text{HNO}_3 = 1 : 7$). The reverse-bias annealing (RBA) at 380 K was used to move hydrogen deeper into the crystals [7].

The semitransparent aluminum Schottky contacts were evaporated to allow standard DLTS and minority carrier transient spectroscopy (MCTS) measurements. However, the amplitudes of the MCTS peaks did not reflect the minority carrier trap concentration due to the front-side excitation.

*Corresponding author. Institute of Microelectronics Technology RAS, 142432 Chernogolovka, Moscow region, Russia. Fax: +7-095-962-8047.

E-mail address: nay@ipmt-hpm.ac.ru (N. Yarykin).

3. Results and discussion

The effect of hydrogenation on the deep-level spectrum of irradiated p-type FZ silicon is demonstrated in Fig. 1. The DLTS peaks of the major radiation defects, C_sC_i , divacancy (V_2), and C_iO_i , decrease, while two novel peaks, H4 and H3 = $E_v + 0.51$ eV, arise in the hydrogenated region. It is seen in Fig. 1 and is confirmed by detailed depth profile measurements in FZ crystals that the concentration of the H4 centers can exceed the initial (before hydrogenation) concentration of the C_iO_i complexes. This result rules out C_iO_i as a precursor of the H4 level. In addition, the H3 level, which was not detected after a similar treatment in Cz-Si [5], is prominent in the FZ crystals.

To learn more about the precursors of the H4 and H3 centers, the irradiated samples were subjected to thermal annealing in the temperature range 400–650 K. Two examples of the DLTS and MCTS spectra measured on the annealed samples before and after hydrogenation are displayed in Fig. 2. Annealing at 570 K (Figs. 2a and b) produces significant changes in the deep-level spectrum. The peaks related to the C_sC_i complex (not shown) and divacancy disappear, while the center identified earlier as the B_iC_s pair [8] is formed in significant concentrations. Nevertheless, the H4 and H3 centers are still formed after hydrogenation. The signature of the VO center is seen in the MCTS spectrum, and the E4 level also appears after hydrogenation. Annealing at higher temperatures (Fig. 2c and d) destroys the VO complex too. Neither H4 nor E4 levels are detected in such samples after hydrogenation, while H3 remains to be the dominant feature in the hydrogenated region.

A similar picture is observed in Cz-Si. Pre-annealing of the VO centers prevents both E4 and H4 level

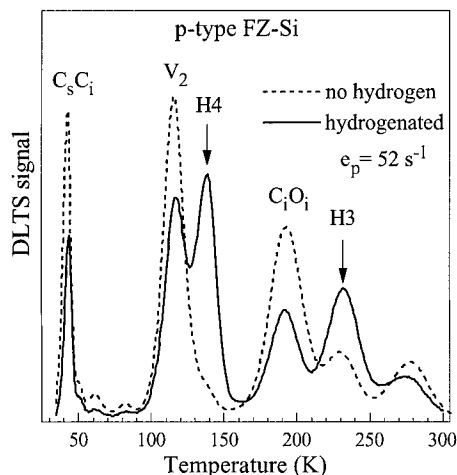


Fig. 1. DLTS spectra in p-type irradiated FZ-Si ($[B] = 2 \times 10^{15} \text{ cm}^{-3}$) before (dashed curve) and after (solid curve) hydrogenation. Rate window $e_p = 52 \text{ s}^{-1}$.

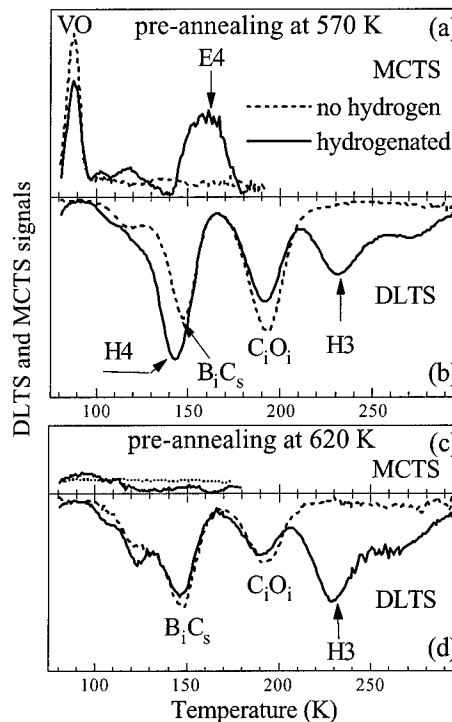


Fig. 2. MCTS (a,c) and DLTS (b,d) spectra measured in the FZ-Si pre-annealed at (a,b) 570 K and (c,d) 620 K before (dash curves) and after (solid curves) hydrogenation.

formation. The H3 level, which is not formed in as-irradiated Cz-Si, arises like in FZ-Si if the samples are annealed before the hydrogenation at ~ 450 K. The precursor of H3 is less stable in Cz-Si, and the H3 centers are not formed in Cz-Si after pre-annealing at ~ 600 K.

The H4 center is formed both in Cz and FZ irradiated crystals due to subsequent hydrogenation, as well as during proton implantation. On the other hand, the H4 concentration is very low after irradiation of pre-hydrogenated silicon. This indicates that the most probable mechanism of its formation is an addition of the hydrogen atom to a stable radiation defect. This precursor apparently does not contain shallow dopants, because H4 is created both in n- and p-type silicon in similar concentrations. The H4 center forms at higher concentrations than the V_2 , C_sC_i , and C_iO_i complexes. Only one electrically active stable radiation defect, VO, could be considered as the H4 precursor, which is consistent with the annealing data in Fig. 2. Taking into account that the H4 formation kinetics indicate that the center contains only one hydrogen atom [9], one can assume that H4 is a second level of the VOH complex. This assignment is supported by a similar annealing kinetics of the VOH and H4 levels [10]. Another

possibility, which should be discussed, is the formation of H4 by hydrogenation of an electrically inactive radiation-induced defect with the annealing temperature close to that of the VO centers.

The H3 center was reported in room-temperature proton implanted p-type silicon with different contents of background impurities (Cz, FZ, and epitaxial crystals) [11]. Our measurements show that the center can also be formed due to hydrogenation of the samples contained only stable radiation defects. We find that the H3 concentration is relatively high in the crystals with higher boron doping, but the centers are not detected in hydrogenated Al-doped samples, evidencing the boron-related nature of the H3 complex. This conclusion is supported by formation of the H3 precursor in irradiated Cz-Si after annealing at 450 K, which destroys the abundant B_iO_i complexes in Cz-Si. The boron-related precursor still escapes detection with electrical methods. However, the existence of a latent source of interstitial boron atoms in irradiated silicon is confirmed by the annealing-induced formation of the B_iC_i pairs in FZ-Si (Fig. 2), where the B_iO_i complexes are not detected.

4. Conclusion

Using the DLTS and MCTS technique, we have studied precursors of the prominent hydrogen-related $H4 = E_v + 0.28$ eV and $H3 = E_v + 0.51$ eV centers in irradiated p-type silicon. Comparison of the defect concentrations shows that among the stable electrically active complexes, only the VO center could be the precursor of the H4 level. This assumption is consistent with the annealing temperature of the H4 precursor. The

H3 center is a boron- and hydrogen-related complex with the precursor which anneals out at 600–650 K.

Acknowledgements

The authors thank J. Coutinho and R. Jones for communicating the results before publication and A. Mesli for supplying the Al-doped samples. This work is supported in part by the Deutsche Forschungsgemeinschaft (436 RUS 113/166/0) and Russian Foundation for Basic Research (00-02-04002).

References

- [1] O.V. Feklisova, N. Yarykin, *Semicond. Sci. Technol.* 12 (1997) 742.
- [2] Y. Tokuda, H. Shimada, A. Ito, *J. Appl. Phys.* 86 (1999) 5630.
- [3] K. Bonde Nielsen et al., *Physica B* 273–274 (1999) 167.
- [4] P. Johannesen, B. Bech Nielsen, J.R. Byberg, *Phys. Rev. B* 61 (2000) 4659.
- [5] O.V. Feklisova, N. Yarykin, E.B. Yakimov, J. Weber, *Physica B* 273–274 (1999) 235.
- [6] J. Coutinho, R. Jones, private communication.
- [7] T. Zundel, J. Weber, *Phys. Rev. B* 39 (1989) 13549.
- [8] P.J. Drevinsky, C.E. Caefer, S.P. Tobin, J.C. Mikkelsen, L.C. Kimerling, *Mater. Res. Soc. Symp. Proc.* 104 (1988) 167.
- [9] O.V. Feklisova, E.B. Yakimov, N. Yarykin, J. Weber, unpublished.
- [10] K. Irmscher, H. Klose, K. Maass, *J. Phys. C* 17 (1984) 6317.
- [11] S. Fatima, C. Jagadish, J. Lalita, B.G. Svensson, A. Hallén, *J. Appl. Phys.* 85 (1999) 2562.



ELSEVIER

Physica B 308–310 (2001) 213–215

PHYSICA B

www.elsevier.com/locate/physb

Simulation of hydrogen penetration in silicon under wet chemical etching

O. Feklisova^a, S. Knack^b, E.B. Yakimov^{a,*}, N. Yarykin^a, J. Weber^b

^a *Institute of Microelectronics Technology, Russian Academy of Sciences, 142432 Chernogolovka Moscow region, Russia*

^b *University of Technology, 01062 Dresden, Germany*

Abstract

The depth profiles of boron–hydrogen pairs formed in Si crystals by wet chemical etching (WCE) are calculated. The evolution of boron–hydrogen pair distribution after WCE is observed. The fits to the experimental profiles allow to estimate the hydrogen diffusivity at room temperature as $D_H = 2.4 \times 10^{-10} \text{ cm}^2/\text{s}$. © 2001 Elsevier Science B.V. All rights reserved.

Keywords: Silicon; Hydrogen; Diffusion; Shallow acceptor passivation

1. Introduction

Wet chemical etching (WCE) is used for hydrogen introduction into silicon to study the interaction of hydrogen with shallow and deep level defects [1–5]. The hydrogen diffusivity D_H at room temperature extracted from the WCE experiments [1,3] was found to be much higher than that extrapolated from the high-temperature (1000–1200°C) permeation study [6]. In these experiments, D_H was estimated under the assumption that the measured profiles of hydrogen-related defects were formed directly during WCE. Calculations of the boron–hydrogen profiles after WCE [7] showed that under this assumption a proper fit of measured profiles was possible for high hydrogen diffusivity ($D_H > 2 \times 10^{-9} \text{ cm}^2/\text{s}$). However, reasonable fits were also reported [7] for $D_H = 8 \times 10^{-11} \text{ cm}^2/\text{s}$ (the expected room temperature value from the literature [6]), with the additional assumption of a high enough free hydrogen concentration during WCE. The decay of the free hydrogen concentration after WCE leads to an apparent transient diffusion. Therefore, the problem of D_H evaluation from WCE experiments is closely associated with the question about the hydrogen concentration

near the surface during WCE and about the effect of hydrogen transient diffusion. To overcome this problem some additional information about the hydrogen concentration in the near-surface layer is necessary, which can be obtained from the evolution of the hydrogen–boron pair profile.

In the present work, the transient diffusion of hydrogen is experimentally detected in low doped p-Si crystals, and the hydrogen diffusivity at WCE temperature is estimated.

2. Experimental

The experiments were carried out on floating zone (FZ) grown p-type Si wafers doped with boron to a concentration of $4 \times 10^{13} \text{ cm}^{-3}$. To introduce hydrogen, the samples were etched in an acid mixture ($\text{HF}:\text{HNO}_3=1:7$), the etching rate was $2\text{--}4 \times 10^{-6} \text{ cm/s}$. The Schottky diodes of 3 mm in diameter were formed by thermal evaporation of Al on the freshly etched surface. The ohmic contacts were made by scratching an Al–Ga alloy onto the back surface of the samples. The profiles of the neutral hydrogen–boron pairs formed due to hydrogen–boron interaction were determined as a deficiency of electrically active boron concentration measured by the capacitance–voltage

*Corresponding author. Tel.: +7-095-9628074; fax: +7-095-9628047.

E-mail address: yakimov@ipmt-hpm.ac.ru (E.B. Yakimov).

($C-V$) method. To observe the hydrogen transient diffusion, the time between WCE and measurements was decreased to be as small as possible. The minimum time necessary to prepare the Schottky barriers and ohmic contacts and to start the $C-V$ measurements was about 18 min.

3. Simulation of hydrogen penetration

The calculations of the distribution of hydrogen and hydrogen-related centers are carried out under the assumption that boron is the most efficient hydrogen trap. The electric field effect due to boron passivation is included in the calculations. The following system describing the hydrogen transport is solved numerically:

$$\frac{\partial H}{\partial t} = D_{H1} \frac{\partial^2 H}{\partial z^2} + \frac{eD_{H1}}{kT} \frac{\partial}{\partial z} \left(H \frac{\partial \varphi}{\partial z} \right) + V \frac{\partial H}{\partial z} - \frac{H}{\tau} \frac{N_B}{N_{B_0}},$$

$$e\varphi = kT \ln \left(\frac{N_B}{N_{B_0}} \right),$$

$$\frac{\partial N_B}{\partial t} = V \frac{\partial N_B}{\partial z} - \frac{H}{\tau} \frac{N_B}{N_{B_0}}, \quad (1)$$

with the boundary condition

$$F_0 = \left. \frac{\partial H}{\partial z} \right|_{z=0} = \text{const}, \quad (1a)$$

where H is the hydrogen concentration, z the depth from the etched surface, V the etching rate, φ the electrostatic potential determined by the non-uniform boron passivation, N_{B_0} and N_B the boron concentrations before and after WCE, respectively, $\tau = (4\pi D_{H1} r_B N_{B_0})^{-1}$, r_B the radius for hydrogen capture by boron atoms and F_0 the hydrogen flow through the surface. The term including V describes the effect of moving crystal surface during WCE. Hydrogen transport after etching is simulated by the same equations with $V = 0$ and $F_0 = 0$.

In accordance with Ref. [7], the simulation shows that the final hydrogen-related defect profiles formed during WCE and subsequent hydrogen transient diffusion are controlled both by D_{H1} and F_0 and it is practically impossible to obtain these values separately by fitting one experimental profile only. However, taking into account that the evolution of the profiles is determined by the amount of free hydrogen available after etching, a fit to several profiles measured at different times after WCE allows one to get a more reliable D_{H1} estimation. The simulations show a more pronounced relaxation of the hydrogen distribution with longer duration in low doped crystals. In accordance with this prediction, we measure the hydrogen transient diffusion after WCE on low doped p-type Si wafers.

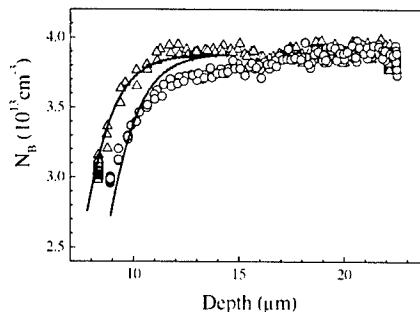


Fig. 1. Carrier concentration profiles measured 18 (triangles) and 30 min (circles) after WCE. The corresponding profiles calculated with $D_{H1} = 2.4 \times 10^{-10} \text{ cm}^2/\text{s}$ are shown by solid lines.

4. Experimental results and discussion

The typical charge carrier concentration profiles in p-type Si measured 18 and 30 min after WCE are presented in Fig. 1. Boron is passivated near the surface, and in the bulk the charge carrier concentration approaches the initial boron concentration. A longer storage time after WCE leads to boron passivation at larger depth, and in 30–40 min after WCE the boron profile is found to reach its final form. The change of the charge carrier profile with the storage time indicates the existence of free hydrogen (or some unstable hydrogen-related complexes) in the near-surface layers after WCE. In the simulation, we assume that hydrogen does not out-diffuse and that the effect of the Schottky barrier on hydrogen transport can be neglected. The fits to the experimental profiles are also presented in Fig. 1. The profiles were calculated with $D_{H1} = 2.4 \times 10^{-10} \text{ cm}^2/\text{s}$, which correlates well with the value extrapolated from high-temperature diffusion studies [6]. A decrease of D_{H1} leads to an increased difference between the two simulated profiles and to an increase of time necessary to reach the stable position. On contrary, an increase of D_{H1} leads to a decrease of the difference between the profiles.

5. Conclusion

Hydrogen penetration into p-type Si under WCE and subsequent transient diffusion was measured and the profiles were analysed. It is found that the measured final hydrogen–boron pair profiles can be well fitted with D_{H1} varying in a wide range under the assumption of a rather high free hydrogen concentration during WCE. The measurement of profile evolution allows one to determine the diffusivity D_{H1} at room temperature.

Acknowledgements

This work is supported in part by the Deutsche Forschungsgemeinschaft (Contract No. 436 RUS 113/166/0) and Russian Foundation for Basic Research (Grant 00-02-04002).

References

- [1] A.J. Tavendale, A.A. Williams, D. Alexiev, S.J. Pearton, *Mater. Res. Soc. Symp. Proc.* 104 (1988) 285.
- [2] E.Ö. Sveinbjörnsson, G.I. Andersson, O. Engström, *Phys. Rev. B* 49 (1994) 7801.
- [3] O.V. Feklisova, N. Yarykin, *Semicond. Sci. Technol.* 12 (1997) 742.
- [4] N. Yarykin, J.-U. Sachse, H. Lemke, J. Weber, *Phys. Rev. B* 59 (1999) 5551.
- [5] J.-U. Sachse, J. Weber, E.Ö. Sveinbjörnsson, *Phys. Rev. B* 60 (1999) 1474.
- [6] A. Van Wieringen, N. Warmoltz, *Physica (Utrecht)* 22 (1956) 849.
- [7] O.V. Feklisova, E.B. Yakimov, N.A. Yarykin, in: O. Bonnaud, T. Mohammed-Brahim, H.P. Strunk, J.H. Werner (Eds.), *Polycrystalline Semiconductors VI*, Scitec Publisher, Uetikon, Switzerland, 2001, pp. 121–126.



ELSEVIER

Physica B 308–310 (2001) 216–219

PHYSICA B

www.elsevier.com/locate/physb

Complexes of point defects and impurities in electron-irradiated CZ-Si doped with hydrogen

A. Nakanishi, N. Fukata, M. Suezawa*

Institute for Materials Research, Tohoku University, 2-1-1 Katahira, Aoba, Sendai 980-8577, Japan

Abstract

We studied complexes generated by electron-irradiation of CZ-Si crystals pre-doped with hydrogen (H) from the measurements of optical absorption spectra. Specimens were prepared from a non-doped CZ-Si crystal. They were doped with H by heating at 1300°C in H₂ gas. They were then irradiated with 3-MeV electrons at room temperature. We measured their optical absorption spectra by an FT-IR spectrometer at about 7 K. An 836-cm⁻¹ peak which is due to a V–O pair was very strong. Optical absorption peaks due to complexes of H and self-interstitial (I) such as IH₂ (1987-cm⁻¹ peak), I₂H₂ (1870-cm⁻¹ peak) and I₃H₂ (1959-cm⁻¹ peak) were stronger than those of FZ-Si. Due to isochronal annealing, the intensity of V–O pair decreases at above 100°C. Simultaneously with this decrease, two new peaks appeared at about 2126 and 2151 cm⁻¹. This is due to a formation of VOH₂ complex by a reaction between a V–O pair and a H₂. © 2001 Elsevier Science B.V. All rights reserved.

Keywords: Si; Oxygen; Hydrogen; Electron irradiation

1. Introduction

As shown in previous papers [1,2], we succeeded to detect vacancies (abbreviated as V hereafter), self-interstitials (I) and Frenkel-pairs (FP) generated by electron-irradiation of floating-zone grown Si (FZ-Si) crystals. They were detected not directly but indirectly: we detected them in the form of complexes of those point defects and hydrogen molecules (H₂) which were doped before irradiation. It is interesting to perform similar studies for the Czochralski-grown Si (CZ-Si) crystals since oxygen (O) concentration is very high in those crystals. We expect following two effects in the case of CZ-Si. First, it is expected that vacancies mainly form pairs with oxygen atoms and hence complexes of V and H₂ will not be formed since concentrations of O and H are around 1 × 10¹⁸ and 1 × 10¹⁶ cm⁻³, respectively. Second, the concentration of IH₂ is expected to be larger than that in FZ-Si since

recombination of V and I will be much reduced in CZ-Si compared with the case of FZ-Si if the formation of V–O pair occurs efficiently.

2. Experimental

Specimens were prepared from a high-purity (carrier density at RT was lower than about 4 × 10¹³ cm⁻³) CZ-Si crystal. Oxygen concentration determined from optical absorption at about 9 μm at RT with a conversion factor of 3.03 × 10¹⁷ atoms cm⁻² was 1.6 × 10¹⁸ cm⁻³. After cutting, mechanical shaping and chemical etching, specimens were doped with H by heating in H₂ gas at 1300°C for 1 h followed by quenching in water. Most hydrogen atoms are in a molecular state [3], H₂, and some form H₂O complexes [4]. They were then irradiated with 3-MeV electrons at RT. To determine thermal stability of defects, isochronal and isothermal annealing experiments were performed with the use of an oil-bath. Optical absorption spectra were measured with an FT-IR spectrometer at 7 K with a resolution of 0.25 cm⁻¹.

*Corresponding author. Tel.: +81-22-215-2040; fax: +81-22-215-2041.

E-mail address: suezawa@imr.edu (M. Suezawa).

3. Results and discussion

Fig. 1 shows an optical absorption spectrum at around 1900 cm^{-1} . Defects responsible for the 1987-cm^{-1} and 1990-cm^{-1} peaks and 1870-cm^{-1} peak were proposed to be due to an IH_2 and I_2H_2 complexes, respectively [1,2], where an IH_2 denotes a complex of one I and two H atoms. The 1959-cm^{-1} peak was proposed to be due to I_3H_2 based on the dependence of its intensity on the electron dose [5].

Fig. 2 shows the dependences of peak intensities of those complexes on the electron dose of FZ-Si and CZ-Si. The data points were omitted for simplicity. As clearly seen, the concentrations of I-related complexes in CZ-Si are larger than those in FZ-Si. As described in Section 1, this is probably due to low probability of mutual annihilation of V and I because V's easily form pairs with oxygen atoms (V–O pairs). The peak intensity due to VH_2 in CZ-Si was much weaker than that of IH_2 , being smaller than $1/10$ at the irradiation dose of $4 \times 10^{17}\text{ cm}^{-2}$, whereas about $2/3$ in the case of FZ-Si. This is also due to high efficiency of V–O pair formation.

Fig. 3 shows the isochronal annealing behaviors of V–O pair (836-cm^{-1} peak) and newly appeared 2126-cm^{-1} peak. Annealing duration was 30 min at each temperature. Two new peaks at 2126.4 (abbreviated as 2126 hereafter) and 2151.5 (2152 cm^{-1}) appeared due to annealing. The isochronal annealing behavior of the 2152-cm^{-1} peak was similar to that of the 2126-cm^{-1} peak, suggesting that the same defect is responsible for those peaks. Fig. 4 shows spectra of FZ-Si at as-irradiated state and that of CZ-Si annealed at 145°C . Two peaks which are almost of maximum intensity at as-irradiated state in FZ-Si were due to VH_2 complexes

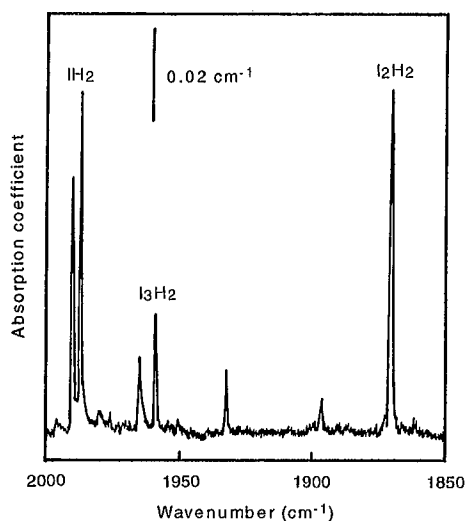


Fig. 1. Optical absorption spectrum around 1900 cm^{-1} . The complexes responsible for peaks are shown.

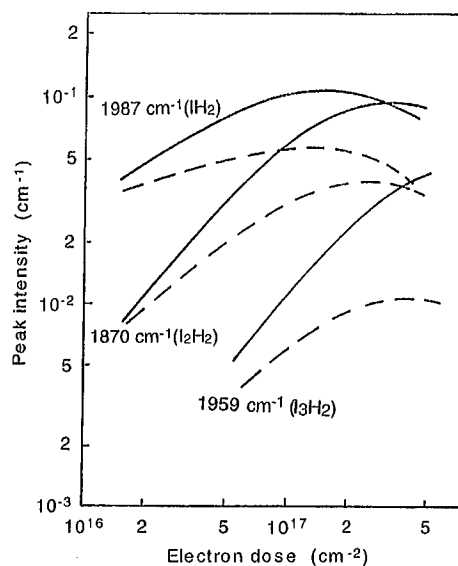


Fig. 2. The dependences of peak intensities of IH_2 , I_2H_2 and I_3H_2 on electron dose in CZ-Si (solid lines) and in high-purity FZ-Si (dashed lines).

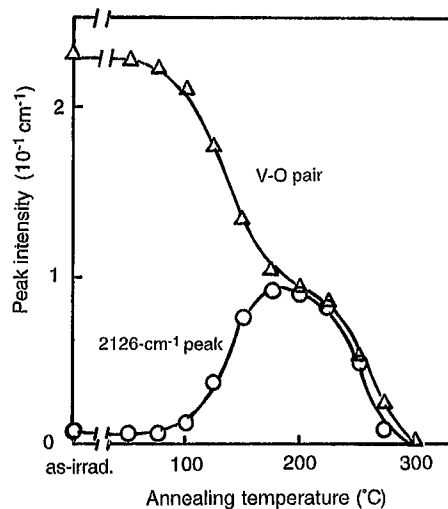


Fig. 3. Isochronal annealing curves of V–O pairs and the 2126-cm^{-1} peak. Annealing duration was 30 min at each temperature.

of different vibrational modes [6]. Similarity of two spectra and the isochronal annealing behaviors of V–O pair and the 2126-cm^{-1} peak below 200°C in Fig. 3 suggest that they are due to VOH_2 , supporting the model of Markevich et al. [7]. Markevich et al. found those peaks due to isochronal annealing of electron-irradiated n-type CZ-Si pre-doped with H and proposed that they are due to VOH_2 complexes based on theoretical calculations of vibrational frequencies of VOH_2 complexes.

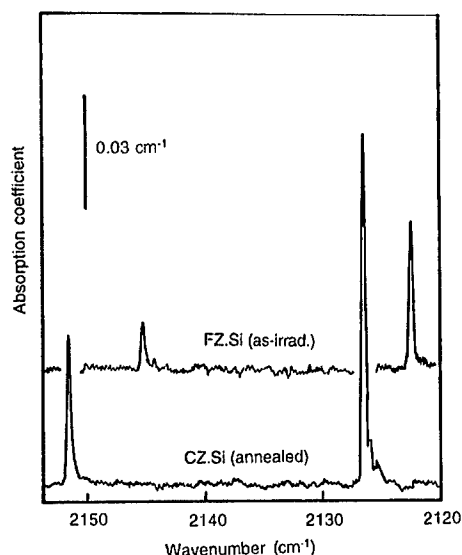


Fig. 4. Comparison of optical absorption spectra of FZ-Si at as-irradiated state and CZ-Si after annealing at 145°C for 260 min. The electron doses of the former and the latter specimens were 1.6×10^{17} and $8 \times 10^{16} \text{ cm}^{-2}$, respectively.

To determine the activation energies of two stages of the decrease of V–O pair in Fig. 3, we performed isothermal annealing experiments. Fig. 5 shows the increase of the intensity of the 2126-cm^{-1} peak due to annealing at 100°C. The solid line is the fitting curve to determine the time constant. This curve was deduced under the assumption that the reaction was of the second order, namely, reaction occurred between two kinds of defects with similar concentrations. The fitting is good, which supports the assumption of second order reaction. The activation energy determined from the dependence of time constant on the isothermal annealing temperature was $0.86 \pm 0.04 \text{ eV}$, which is in good agreement with that ($0.78 \pm 0.05 \text{ eV}$) of H_2 diffusion [8]. Hence, this result and above isochronal annealing behaviors clearly show that an H_2 diffuses to a V–O pair and forms a VOH_2 complex.

The activation energy around 230°C in Fig. 3 was determined to be about $1.68 \pm 0.19 \text{ eV}$. As shown in Fig. 3, concentrations of V–O pairs and VOH_2 complexes decrease simultaneously. This suggests reaction between V–O pairs and VOH_2 complexes. According to literatures, the activation energy of V–O pair migration was reported to be 1.3 eV [9,10], 1.8 and 2.27 eV [11]. Our data is in the range of reported values. VOH_2 complexes are thought to be more difficult to do diffusion motion than V–O pairs since they are larger in size than V–O pairs. We therefore propose that the higher temperature stage in Fig. 3 corresponds to the diffusion of a V–O pair to a VOH_2 complex, resulting in the formation of a $(\text{VOH})_2$ complex.

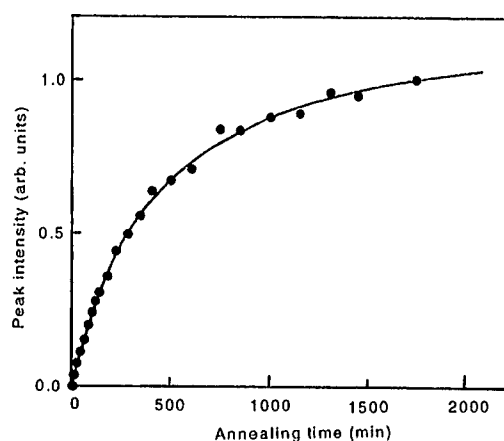


Fig. 5. Isothermal annealing curve of the 2126-cm^{-1} peak due to annealing at 100°C.

4. Conclusion

We studied point defects in electron-irradiated CZ-Si pre-doped with hydrogen by means of optical absorption method. The concentrations of complexes of self-interstitials and hydrogen atoms in CZ-Si were larger than those in FZ-Si. Two new peaks at 2126 and 2152-cm^{-1} appeared due to annealing at around 150°C. They are due to VOH_2 complexes which are formed by a reaction between a moving H_2 and an immobile V–O pair. Both V–O pairs and VOH_2 complexes disappeared at around 250°C probably due to the formation of $(\text{VOH})_2$ complexes by a reaction between moving V–O pairs and immobile VOH_2 complexes.

Acknowledgements

The authors would like to thank H. Yamada-Kaneta of Fujitsu Laboratories, Ltd. for supplying crystals used in this study. They also thank the Laboratory for Advanced Materials, for allowing us to use their FT-IR spectrometer and H. Takizawa of the JAERI Takasaki Institute for his help in electron irradiation. This work was partly supported by the JSPS Research for the Future Program under the project “Ultimate Characterization Technique of SOI Wafers for Nano-scale LSI Devices” and a Grant-in-Aid for Scientific Research on Priority Area (B) “Manipulation of Atoms and Molecules by Electron Excitation” from the Ministry of Education, Culture, Sports, Science and Technology of Japan.

References

- [1] M. Suezawa, Phys. Rev. B 63 (2001) 035201.
- [2] M. Suezawa, Phys. Rev. B 63 (2001) 035203.

- [3] R.E. Pritchard, et al., *Phys. Rev. B* 56 (1997) 13118.
- [4] V.P. Markevich, et al., *Mater. Sci. Forum* 196–201 (1995) 915.
- [5] A. Nakanishi, et al., unpublished.
- [6] B. Bech Nielsen, et al., *Mater. Sci. Forum* 196–201 (1995) 933.
- [7] V.P. Markevich, et al., *Phys. Rev. B* 61 (2000) 12964.
- [8] V.P. Markevich, M. Suezawa, *J. Appl. Phys.* 83 (1998) 2988.
- [9] G. Bemski, W.M. Augustyniak, *Phys. Rev.* 108 (1957) 645.
- [10] J.W. Corbett, et al., *Phys. Rev.* 121 (1961) 1015.
- [11] B.S. Svensson, G.L. Lindstroem, *Phys. Rev. B* 34 (1986) 8709.



ELSEVIER

Physica B 308–310 (2001) 220–223

PHYSICA B

www.elsevier.com/locate/physb

Temperature dependences of line widths and peak positions of optical absorption peaks due to localized vibration of hydrogen Si

M. Suezawa^{a,*}, N. Fukata^a, M. Saito^{a,b}, H. Yamada-Kaneta^c

^a*Institute for Materials Research, Tohoku University, 2-1-1 Katahira, Aoba, Sendai 980-8577, Japan*

^b*NEC Informatec System, Ltd., 34 Miyukigaoka, Tsukuba 305-8501, Japan*

^c*Fujitsu Lab., Morinosato-Wakamiya, Atsugi 243-0197, Japan*

Abstract

We studied the temperature dependences of line widths and peak positions of optical absorptions due to the hydrogen bound to point defects and acceptors in Si. Specimens were prepared from floating-zone-grown Si crystals of high-purity and of p-type, doped with group III acceptors. They were doped with H by heating at 1300°C in H₂ gas followed by quenching. The former specimen was then irradiated with 3 MeV electrons at RT to form complexes of H and point defects and the latter specimens were annealed at 150°C to form H–acceptor pairs. We measured their optical absorption spectra by an FT-IR spectrometer in the temperature range of 6 K and RT. Peaks due to localized vibrational modes of H bound to acceptors and point defects were well fitted with Lorentzian line shapes. The temperature dependences of those line widths and peak positions were analyzed with the dephasing model proposed by Persson and Ryberg. © 2001 Elsevier Science B.V. All rights reserved.

Keywords: Hydrogen; Silicon; Acceptor; Point defect; Line shape

1. Introduction

Hydrogen (H) in semiconductors is chemically active and easily forms pairs and complexes with other impurities and defects. Because of light mass, its vibrational frequencies of stretching modes are much higher than the bulk phonon frequencies. Moreover, the frequencies are sensitive to local atomic structure around H and are used to identify defects included in the complex (as a review article, see Refs. [1–3]).

One interesting feature of such localized vibrational modes is the temperature dependence of line widths and peak positions. The line width is known to be dominated by two dynamical processes, i.e., energy relaxation (relaxation time: T_1) and pure dephasing (T_2) [4]. Many studies have been done on the temperature dependences

of line widths and peak positions of H–dopant pairs in compound semiconductors [5]. There has been, however, no study on dephasing of H–impurity complexes and H–point defect complexes in Si.

2. Experimental

Specimens were prepared from various Si crystals grown by a floating-zone method (FZ-Si). After mechanical shaping and chemical polishing, they were doped with H by heating at 1300°C in H₂ gas followed by quenching in water. Hydrogen is in a state of H₂ molecule at RT [6]. A high-purity specimen was irradiated with 3-MeV electrons at RT to form H–point defect complexes. The total dose was $1.2 \times 10^{17} \text{ cm}^{-2}$. Specimens doped with group III acceptors with the concentrations of around $3 \times 10^{15} \text{ cm}^{-3}$ during crystal growth were annealed at 150°C to form H–acceptor pairs. Optical absorption spectra of these specimens

*Corresponding author. Tel.: +81-22-215-2040; fax: +81-22-215-2041.

E-mail address: suezawa@imr.edu (M. Suezawa).

were measured at various temperatures between 5 K and RT with an FT-IR spectrometer equipped with a continuous-flow-type liquid-helium cryostat. The resolution was 0.5 cm^{-1} in the case of H-acceptor pairs and 0.25 cm^{-1} in the case of H-point defect complexes.

3. Results, analysis and discussion

3.1. Atomic geometry

Prior to the description of experimental results, we describe the geometrical configurations studied in this paper. We roughly classify them into two groups. In the first group, H has one bond with one Si atom which is similar to H on the (111) surface, i.e., there are three Si atoms near the Si atom bonded to H, $[\text{Si}_3(\text{Si})\text{H}]$. The following complexes are thought to belong to this group; $\text{H}_2^*(\text{AB})$ (1838 cm^{-1} peak), $\text{VH}_2(1)$ and $\text{VH}_2(2)$ (2122 and 2145), V_2H_2 (2073), $\text{IH}_2(1)$ and $\text{IH}_2(2)$ (1987 and 1990) and I_2H_2 (1870), where $\text{H}_2^*(\text{AB})$ and VH_2 , for example, denote H at anti-bonding site in H_2^* and a complex of one V and two H atoms, respectively. Peak positions of optical absorption are shown in parentheses. In the second group, a H atom occupies the bond-centered site. Hence, H-acceptor pairs and $\text{H}_2^*(\text{BC})$ (2062) belong to this group, where BC denotes the bond-centered site. One characteristic feature of this group is that a H atom is squeezed between two large atoms, i.e., two Si atoms or Si atom and an acceptor atom.

3.2. Line width at very low temperature

At very low temperature, the line width of localized vibration is known to be dominated by energy relaxation process, i.e., the excited vibrational state is relaxed to the lowest vibrational state by emission of lattice phonons. Budde et al. [7] determined the vibrational lifetime (T_1) of bond-centered H in Si at very low temperatures by means of time-resolved, transient bleaching spectroscopy. The observed line width (Γ_0) at very low temperature was close to $1/2\pi cT_1$, where c represents the light velocity.

From the fittings of Lorentzians to the observed peaks cited in Section 3.1, we determined the peak positions and the line widths at half-maximum (FWHM: Γ) at various temperatures. Table 1 shows a summary of T_1 estimated from the line widths (Γ_0) at around 5 K. As can be clearly seen, T_1 of H-acceptor pairs and $\text{H}_2^*(\text{BC})$ are much shorter than those of H-point defect complexes. Hence, pairs of short relaxation time belong to the second group in Section 3.1. H atoms in those pairs occupy the bond-centered site and are squeezed much by the nearest two atoms (two Si or one Si and one acceptor) as described in Section 3.1. Hence, the coupling of the observed mode with surrounding lattice

Table 1

Relaxation time T_1 of H-acceptor pairs and H-point defect complexes in Si^a

Species	T_1 (ps)	Species	T_1 (ps)
B–H	1.5	$\text{H}_2^*(\text{AB})$	3.1
Al–H	0.70	$\text{H}_2^*(\text{BC})$	1.8
Ga–H	1.2	I_2H_2	6.3
In–H	0.46	$\text{IH}_2(1)$	7.3
		$\text{IH}_2(2)$	7.2
		$\text{V}_2\text{H}_2(2)$	15
		$\text{VH}_2(1)$	17
		$\text{VH}_2(2)$	16

^aI and V indicate a self-interstitial and a vacancy, respectively. VH_2 , for example, denotes a complex of one V and two H atoms.

modes is thought to be large, which is the reason for short relaxation time.

3.3. Temperature-dependent line width

At high temperatures, the line width is thought to be dominated by dephasing processes, i.e., the vibrating excited system elastically collides with low-frequency phonon modes without emitting energy [4]. Since the thermal excitation of low-frequency phonons is required in the dephasing mechanism, this process is negligible at the low-temperature limit but becomes dominant as the temperature rises. Hence, we introduce the normalized line width $(\Gamma - \Gamma_0)/\Gamma_0$ to analyze the dephasing process.

Persson and Ryberg [8] proposed a dephasing model to explain the temperature dependences of the line width and peak position of vibrational mode of molecules adsorbed on a metal surface under the assumption that the local vibrational mode interacts with one phonon mode of low frequency. It is not possible to obtain analytical expressions of peak shift ($\Delta\omega$) and the change of FWHM ($\Delta\Gamma$) for the general case. The analytical expressions of these temperature dependences, however, are given as follows for the limiting case. We show, here, only the case of weak coupling limit.

$$\Delta\omega = \delta\omega/\beta, \quad (1)$$

$$\Delta\Gamma = (2\delta\omega^2/\eta)(\beta + 1), \quad (2)$$

where $\beta = \exp(\hbar\omega_0/2\pi kT) - 1$, $\delta\omega$ is the coupling constant of two modes, ω_0 is the vibrational frequency of coupling low-frequency mode with line width η and h , the Planck constant.

Figs. 1 and 2 show the dependences of the normalized line widths, $(\Gamma - \Gamma_0)/\Gamma_0$, of H-acceptor pairs and complexes of H and point defects on temperature. Figs. 3 and 4 show the dependences of peak positions of those defects on temperature. Solid lines are fitting curves due to the dephasing model proposed by Persson and Ryberg [8]. In the above fittings, we used analytical

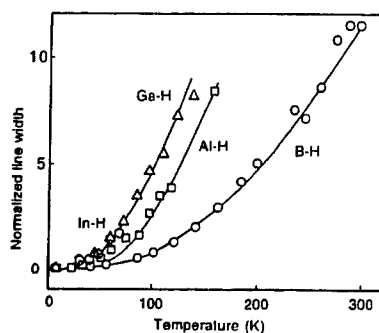


Fig. 1. Dependences of the line widths of optical absorption peaks due to H-acceptors on temperature. Solid lines are fitting curves due to Eq. (2).

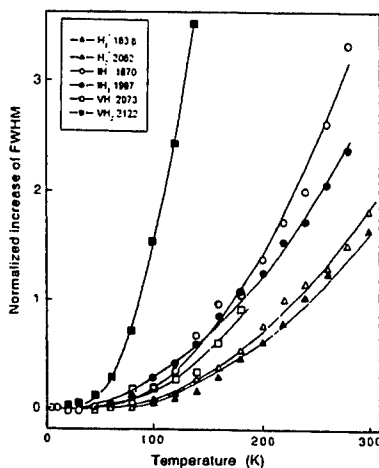


Fig. 2. Dependences of the line widths of optical absorption peaks due to complexes of H and point defects on temperature. Solid lines are fitting curves due to Eq. (2).

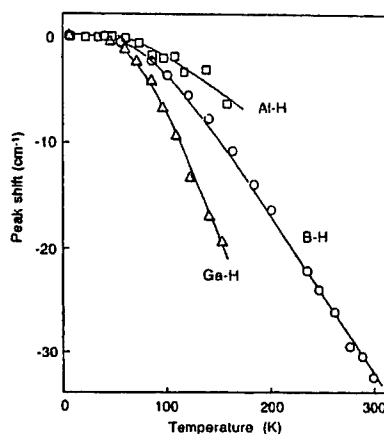


Fig. 3. Dependences of the peak shifts of optical absorption peaks due to H-acceptors on temperature. Solid lines are fitting curves due to Eq. (1).

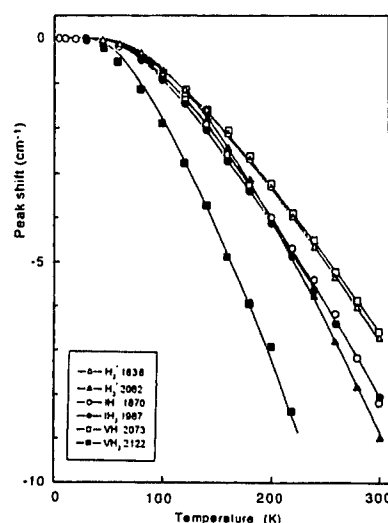


Fig. 4. Dependences of the peak shifts of optical absorption peaks due to complexes of H and point defects on temperature. Solid lines are fitting curves due to Eq. (1).

expressions, i.e., Eqs. (1) and (2), at the weak coupling limit: the line width of low-frequency mode is larger than the coupling constant.

In Figs. 1–4, the fittings themselves seem to be good. In the case of H–point defect complexes and $H_2^*(AB)$, the vibrational frequency (ω_0) of low-frequency mode determined from the fitting of line width agreed well to that determined from peak position and the condition of weak coupling limit was also satisfied. On the other hand, the vibrational frequency of low-frequency mode determined from the line width did not agree with that determined from the peak shift in the case of H–acceptor pairs, $H_2^*(BC)$ and IH_2 . Hence, Persson and Ryberg's model at the weak coupling limit is applicable to the former and not applicable to the latter.

4. Summary

We studied the temperature dependences of line widths and peak positions of optical absorption peaks due to H-acceptor pairs, H–point defect complexes and H_2^* in Si. We analyzed them with the dephasing model at the weak coupling limit proposed by Persson and Ryberg. This model explained well the behaviors of H–point defect complexes (except IH_2) and $H_2^*(AB)$ but not those of H-acceptor pairs, $H_2^*(BC)$ and IH_2 .

Acknowledgements

The authors thank the Laboratory for Advanced Materials for allowing to use their FT-IR spectrometer. This work was partly supported by the JSPS research for the Future Program under the project "Ultimate

Characterization Technique of SOI Wafers for Nano-scale LSI devices” and a Grant-in-Aid for Scientific Research on Priority Area (B) “Manipulation of Atoms and Molecules by Electron excitation” from the Ministry of Education, Culture, Sports, Science and Technology of Japan.

References

- [1] J.I. Pankove, N.M. Johnson (Eds.), *Hydrogen in Semiconductors*, Academic Press, Boston, 1991.
- [2] S.J. Pearton, J.W. Corbett, M. Stavola, *Hydrogen in Crystalline Semiconductors*, Springer, Berlin, 1992.
- [3] S.K. Estreicher, *Mater. Sci. Eng. R* 14 (1995) 319.
- [4] C.B. Harris, et al., *Phys. Rev. Lett.* 38 (1977) 1415.
- [5] M.D. McCluskey, E.E. Haller, in: N.H. Nickel (Ed.), *Hydrogen in Semiconductors II*, Academic Press, New York, 1999, p. 373.
- [6] R.E. Pritchard, et al., *Phys. Rev. B* 56 (1997) 13118.
- [7] M. Budde, et al., *Phys. Rev. Lett.* 85 (2000) 1452.
- [8] B.N.J. Persson, R. Ryberg, *Phys. Rev. B* 40 (1989) 10273.



ELSEVIER

Physica B 308–310 (2001) 224–227

PHYSICA B

www.elsevier.com/locate/physb

Complexes of point defects and hydrogen generated by electron-irradiation of hydrogenated Si at low temperatures

M. Suezawa^{a,*}, Y. Takada^b, T. Tamano^b, R. Taniguchi^b, F. Hori^b, R. Oshima^b

^a Institute of Materials Research, Tohoku University, 2-1-1 Katahira, Aoba, Sendai 980-8577, Japan

^b RIAST, Osaka Prefecture University, Sakai, Osaka 599-8570, Japan

Abstract

We studied point defects generated by electron-irradiation of hydrogenated Si crystals at low temperatures from the measurement of optical absorption due to hydrogen bound to point defects. Specimens of high-purity, n- and p-type floating-zone grown Si crystals were doped with H by heating in H₂ gas at 1300 °C followed by quenching. Then, they were irradiated with 6 MeV electrons at 270, 200 and 130 K. We measured their optical absorption spectra at 7 K with the use of an FT-IR spectrometer. The relative mobilities of various point defects were discussed from the relative intensities of 1838, 1987 and 2122 cm⁻¹ peaks which are due to H₂⁺, IH₂ and VH₂, respectively, where V, I and H₂⁺ denote a vacancy, a self-interstitial and H₂ in metastable state formed by a reaction between an H₂ and a Frenkel pair, respectively. © 2001 Elsevier Science B.V. All rights reserved.

Keywords: Si; Electron irradiation; Vacancy; Self-interstitial; Frenkel pair

1. Introduction

As shown in previous papers [1,2], we have succeeded in detecting self-interstitials (abbreviated as I hereafter) and Frenkel pairs (FP) as well as vacancies (V) from the measurements of optical absorption of hydrogenated silicon crystals after electron-irradiation at RT. They are detected not directly but indirectly, i.e., via the complexes of those point defects and hydrogen molecules (H₂). The formation of these complexes were interpreted to be due their diffusion to H₂, which is effectively immobile [3] at around RT. According to this interpretation, it seems possible to measure the relative diffusion rates of these point defects from the measurement of optical absorption intensities which are proportional to their concentrations. To obtain some bits of information on the mobilities of V, I and FP, we performed electron-irradiation of hydrogenated Si at

various temperatures and measured their optical absorption spectra.

2. Experimental

Specimens were prepared from floating-zone grown Si (FZ-Si) crystals of n-type (phosphorus concentration: $1.5 \times 10^{16} \text{ cm}^{-3}$), high-purity (p-type carrier concentration at RT was $4.5 \times 10^{12} \text{ cm}^{-3}$) and p-type (boron concentration: $1.5 \times 10^{16} \text{ cm}^{-3}$). After cutting out specimens from above crystals, they were mechanically shaped and chemically etched to the size of $4 \times 6 \times 11 \text{ mm}^3$. To dope hydrogen, they were sealed in quartz capsules together with H₂ gas and heated at 1300 °C for 50 min followed by quenching in water. Hydrogen in Si at RT is in a state of H₂ [4]. They were then irradiated at 270, 200 and 130 K with 6 MeV electrons using a linear accelerator with an irradiation dose of $5 \times 10^{16} \text{ cm}^{-2}$. Specimens were placed in a cooled nitrogen-gas flow during irradiation. The specimen temperature was monitored with a

*Corresponding author. Tel.: +81-22-215-2040; Fax: +81-22-215-2041.

E-mail address: suezawa@imr.edu (M. Suezawa).

thermocouple. We measured their optical absorption spectra with an FT-IR spectrometer installed with a continuous-flow-type liquid He cryostat. Measurement temperature was about 7 K and the resolution was 0.25 cm^{-1} .

3. Results and discussion

Prior to showing the experimental results, we should consider the formation process of various complexes of point defects and H_2 . Due to electron-irradiation of specimens, FPs are first formed. Some of them diffuse to H_2 and form complexes, H_2^* , and some dissociate into V and I. We assume the dissociation rate is temperature-independent. Since the migration energies of V and I are small [5], they diffuse to various sinks and traps during irradiation. There are many paths to form complexes. Some form complexes with H_2 such as VH_2 , V_2H_2 , IH_2 and I_2H_2 , where an IH_2 , for example, is a complex of one self-interstitial and two H atoms. Some form complexes by themselves, for example, V_2 . Hence, it is not easy to obtain accurate information about the mobilities of V, I and FP from the measurement of the concentrations of complexes. We should fully analyze the formation processes of all complexes to determine the mobilities of above point defects. In the following, however, we simply assume that the relative intensities of IH_2 , VH_2 and H_2^* correspond to relative mobilities of I, V and FP, respectively. Hence, the deduced results may be insufficient in accuracy.

Fig. 1 shows optical absorption spectra of high-purity Si crystals irradiated at 270 K (upper spectrum) and 130 K (lower one). As seen, the absorption due to IH_2 at 1987 and 1990 cm^{-1} was the strongest after the irradiation at 270 K. On the other hand, after irradiation at 130 K, it was much weaker than that irradiated at 270 K and those of VH_2 and H_2^* were similar to those irradiated at 270 K. These results clearly show two features that the mobility of I has larger temperature dependence than those of V and FP and the mobilities of V and FP are larger than that of I at 130 K. Fig. 1 is thought to support above assumption that the dissociation rate of FP is temperature-independent since the intensities of VH_2 and H_2^* are similar after irradiation at 270 and 130 K.

Fig. 2 shows optical absorption spectra of n-type Si crystals irradiated at 270 K (upper spectrum) and 130 K (lower one). As seen, the absorption due to IH_2 was the strongest after 270 K irradiation, similar to Fig. 1. On the other hand, after irradiation at 130 K, it decreased much and those of VH_2 and H_2^* became larger than those irradiated at 270 K. These results show that the mobility of I has different temperature dependence from those of V and FP. The intensity of VH_2 was weak after 270 K irradiation. This is due to preferential formation

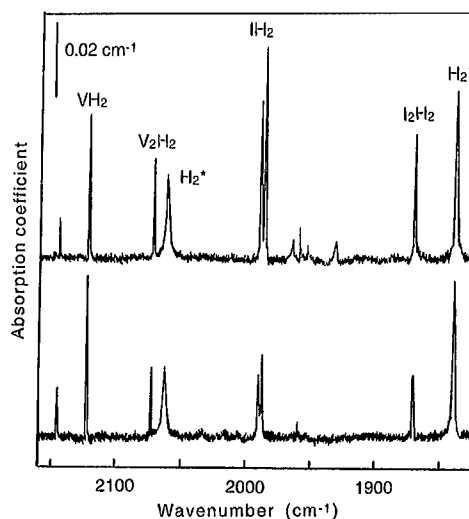


Fig. 1. Optical absorption spectra of high-purity specimens irradiated at 270 K (upper curve) and 130 K (lower curve). Complexes responsible for peaks were determined in previous studies [1,2].

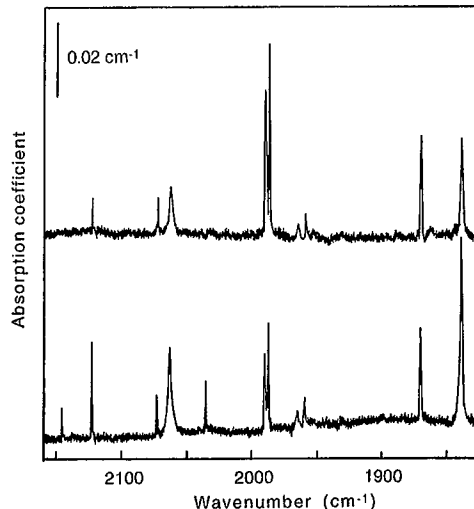


Fig. 2. Optical absorption spectra of n-type specimens irradiated at 270 K (upper curve) and 130 K (lower curve).

of V–P pair as shown in the previous study [2]. The intensity of VH_2 in Fig. 2 after 6 MeV electron-irradiation at 270 K is about a 2.5 factor larger than that after 3 MeV electron-irradiation at RT. Hence, there may be an effect of irradiation energy on the formation of V–P pair.

Fig. 3 shows optical absorption spectra of p-type Si crystals irradiated at 270 K (upper spectrum) and 130 K (lower one). As seen, the absorption due to VH_2 was the strongest after 270 K irradiation. On the other hand,

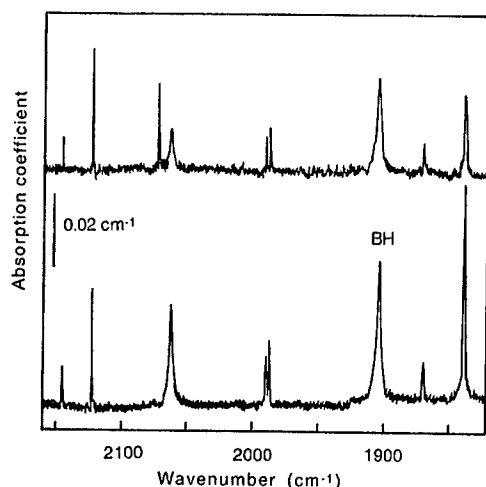


Fig. 3. Optical absorption spectra of p-type specimens irradiated at 270 K (upper curve) and 130 K (lower curve). BH denotes a pair of a boron atom and an H.

after irradiation at 130 K, the intensity of H_2^+ became the largest, much larger than that at 270 K irradiation. The intensity of VH_2 after 130 K irradiation was similar to that after 270 K irradiation. These results show that the mobility of FP has a different temperature dependence from that of V. The intensity of IH_2 was weak after 270 K irradiation. This is due to replacement of occupation sites between an I and a substitutional B [5]: $\text{I} + \text{B}(\text{s}) \rightarrow \text{B}(\text{i}) + \text{Si}(\text{s})$, where (i) and (s) denote the interstitial and substitutional sites, respectively. The intensity of IH_2 in Fig. 3 after 270 K irradiation is about factor 3.4 times larger than that after 3 MeV irradiation at RT. Hence, there may be an effect from irradiation energy on the replacement. According to Fig. 3, the probability for the replacement of occupation sites seems to decrease due to irradiation at 130 K.

Properties of irradiation-induced vacancies in Si have been extensively studied and clarified well [5]. Hence, we estimate the relative intensities, IH_2/VH_2 and H_2^+/VH_2 , to determine the relative migration energies of I and FP to that of V. Such a procedure is necessary to correct possible change of irradiation conditions, such as the focusing of the electron-beam, depending on the irradiation temperature. Fig. 4 shows the dependence of relative intensities on the temperature in high-purity specimens. From the slope, we obtained energies of 7.4 and 21 MeV for H_2^+ and IH_2 , respectively. These energies are thought to be the differences of migration energies of FP and V and of I and V, i.e., their migration energies are the sum of above values and the migration energy of vacancy. Hence, these results show that the migration energies of V, I and FP are similar during electron-irradiation. Within our knowledge, no one has shown the diffusion of FP. The migration of FP suggests long lifetime of FP, i.e., the annihilation of FP is not easy and

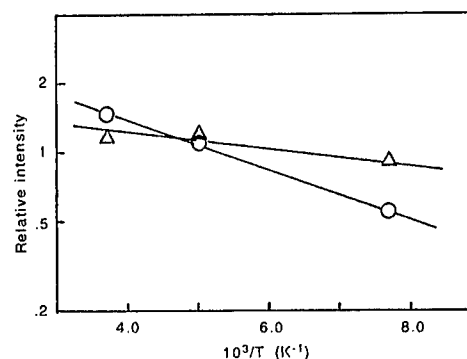


Fig. 4. The dependences of the relative intensities of IH_2/VH_2 (circles) and H_2^+/VH_2 (triangles) in high-purity specimens on the irradiation temperature.

there may be energy barrier for recombination of V and I.

It is well known that an I in p-type Si crystals diffuses athermally even at 4.2 K. This athermal motion is explained by the Bougoïn-Cobett mechanism [6]. According to this model, the position where an I in one charge state is at a potential minimum corresponds to a potential maximum for an I in another charge state. Thus, an I will move toward its new minimum-potential position each time its charge state changes. According to our experiment, however, there is a migration energy of I even in p-type Si crystals. The lifetime of the charge state at the maximum potential of I for athermal diffusion may be shorter than the time for one atomic jump for diffusion motion, probably because of thermal excitation of the charge at high temperatures.

4. Conclusion

We studied the effect of irradiation temperature on the formation of complexes of point defects and H_2 in hydrogenated Si crystals. Relative intensities of optical absorption peaks due to complexes of point defects and H_2 strongly depended on the irradiation temperature. We interpreted these results under a simplified assumption that the relative intensities correspond to the relative mobilities of relevant point defects. According to above assumption, we determined the migration energies of an I and a FP relative to that of V during electron-irradiation.

Acknowledgements

The authors thank the Laboratory for Advanced Materials for allowing us to use their FT-IR spectrometer. This work was partly supported by the JSPS research for the Future Program under the project

“Ultimate Characterization Technique of SOI Wafers for Nano-scale LSI devices” and a Grant-in-Aid for Scientific Research on Priority Area (B) “Manipulation of Atoms and Molecules by Electron excitation” from the Ministry of Education, Culture, Sports, Science and Technology of Japan.

- [3] V.P. Markevich, M. Suezawa, J. Appl. Phys. 83 (1998) 2998.
- [4] R.E. Pritchard, et al., Phys. Rev. B 56 (1997) 13118.
- [5] G.D. Watkins, in: R.W. Cahn, P. Haasen, E.J. Kramer (Eds.), Materials Science and Technology, Vol. 4, VCH, Weinheim, 1991, p. 105.
- [6] J. Bourgoin, J.W. Corbett, Phys. Lett. 38A (1972) 135.

References

- [1] M. Suezawa, Phys. Rev. B 63 (2001) 035201.
- [2] M. Suezawa, Phys. Rev. B 63 (2001) 035203.



ELSEVIER

Physica B 308–310 (2001) 228–231

PHYSICA B

www.elsevier.com/locate/physb

Observation of two coupled defect levels on the hydrogen-passivated Si (100) surface

A.J. Reddy*, J. Michel, L.C. Kimerling

Department of Materials Science and Engineering, Massachusetts Institute of Technology, Room 13-4110, 77 Massachusetts Ave., Cambridge MA 02139, USA

Abstract

We present the first electronic characterization of intrinsic defects on the hydrogen-passivated silicon surface. Surface recombination velocities, measured with radio-frequency photoconductance decay, show that lifetimes of both n- and p-type wafers change significantly with small changes in the background carrier concentration ($\eta \equiv \Delta n/p_0 \approx 0.05$). These effects are not explained by the Shockley-Read-Hall model for single-level defect recombination but can be understood by modeling the defect as a coupled, two-level (three charge state) system. By analogy with the P_b -center, these defects may be thought of as dangling bonds populated with zero, one, or two electrons. © 2001 Elsevier Science B.V. All rights reserved.

Keywords: Dangling bond; Minority carrier lifetime; Passivation; Surface defect

1. Introduction

Hydrogen passivation of the silicon surface is widely used to retard native oxide growth. Scanning tunneling microscopy (STM) studies of hydrogen-passivated silicon surfaces [1,2] show that dangling bonds arise at the ends of dimerized rows of the 2×1 surface reconstruction. Others have also shown that dangling bonds are formed when O_2 molecules dissolved in solution abstract hydrogen radicals from Si-H surface bonds [3].

We have previously used surface sensitive minority carrier lifetime measurements to study native oxide growth [4], metal deposition [5], and surface passivation [6]. We have further proposed the use of minority carrier lifetime as an in situ monitor for metal contamination in hydrofluoric (HF) acid baths [7]. More precise use of this technique requires a detailed understanding of the electronic nature of intrinsic surface defects.

2. Lifetime measurements

Lifetime measurements have been made using radio-frequency photoconductance decay (RF-PCD) [8]. Fig. 1 shows RF-PCD measurements for both n-type and p-type silicon samples immersed in 100:1 (0.5 wt%) HF solutions. The sample preparation procedure is described elsewhere [8]. A quartz halogen lamp with a maximum illumination of 1.5×10^{16} photons/(cm²s) has been used to change the background carrier concentration up to 5% for p-type wafers and 10% for n-type.

The Shockley-Read-Hall lifetime [9,10] for a single-level defect is given by

$$\tau_{SRH} = \frac{\tau_{LL} + \eta\tau_{HL}}{1 + \eta},$$

where τ_{LL} and τ_{HL} are the asymptotic low-level and high-level injection lifetimes, respectively, and η is the relative injection level ($= \Delta n/p_0$). This theory alone could explain the observed lifetime increase for the n-type data, if $\tau_{HL} \gg \tau_{LL}$, but is not consistent with the decrease in τ of over 50% for $\eta \approx 0.05$ observed for the p-type wafer.

*Corresponding author. Fax: +1-617-253-6782.

E-mail address: ajreddy@alum.mit.edu (A.J. Reddy).

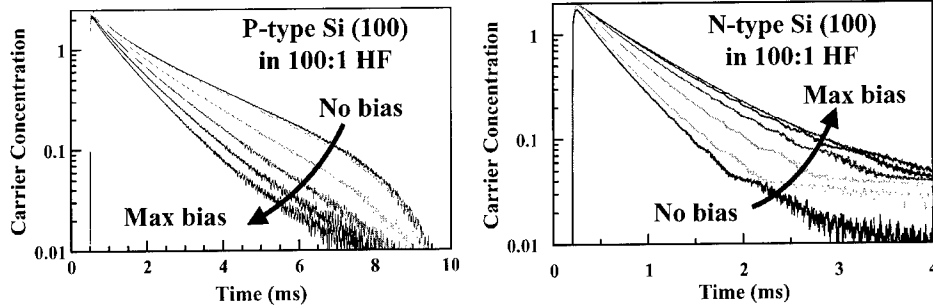


Fig. 1. Minority carrier lifetime data, taken with RF-PCD, for n- and p-type silicon wafers immersed in solutions of dilute HF (0.5 wt%).

There are many known models for non-exponential decays: surface diffusion transients, trapping sites, and surface band-bending. Attempts have been made to apply each of these to our data, but all have flaws. Surface transients apply only to lifetimes below the transit time ($\approx 16 \mu\text{s}$ for p-type Si). Trapping sites need to be present in a very large concentration and should slow the initial carrier decay rate for biased data, but no such decrease is observed. A band-bending explanation would require that excess electrons somehow generate a surface potential that is further attractive to electrons. Failure of these models has led to the development of the two-level defect model.

3. The two-level defect model

A two-level defect has three charge states, D^+ , D^0 , and D^- , as shown in Fig. 2. The two mid-gap states of the defect correspond to transitions between these states. The two levels are coupled, as the second level can be occupied only when the first is already filled. At equilibrium, the change in the Gibbs free energy must be zero for adding an electron to either level. The enthalpy change for populating each of these levels is simply the defect energy level minus the Fermi energy: $\Delta H_1 = E_{T1} - E_F$ and $\Delta H_2 = E_{T2} - E_F$. The total entropy for a two-level defect is defined by the number of microstates that correspond to a given macrostate, i.e., defect level occupations f_1 and f_2 . A microstate for coupled levels requires partitioning the N_D defects into (1) $(1 - f_1) \times N_D$ D^+ states, (2) $(f_1 - f_2) \times N_D$ D^0 states, and (3) $f_2 \times N_D$ D^- states. The total number of microstates is then:

$$\Omega = \frac{N_T!}{((1 - f_1)N_T)!(f_1 - f_2)N_T!(f_2 N_T)!}; \quad S_{\text{tot}} = k_B \ln \Omega.$$

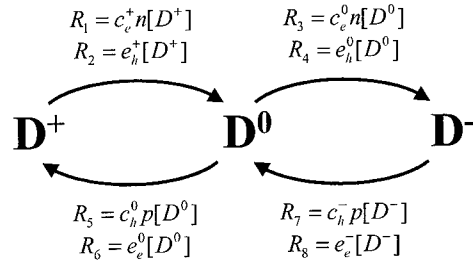


Fig. 2. Carrier-defect interactions in the two-level defect model. Each transition between states can occur either through capture of one carrier or emission of the opposite type of carrier.

The change in entropy involved in adding one electron to each defect level is then

$$\Delta S_1 = \Delta f_1 \times \left. \frac{\partial S_{\text{tot}}}{\partial f_1} \right|_{f_2} = k_B \ln \left(\frac{1 - f_1}{f_1 - f_2} \right),$$

$$\Delta S_2 = \Delta f_2 \times \left. \frac{\partial S_{\text{tot}}}{\partial f_2} \right|_{f_1} = k_B \ln \left(\frac{f_1 - f_2}{f_2} \right).$$

At equilibrium, $\Delta H = T\Delta S$, and the equilibrium defect occupations are determined to be

$$f_1 = \frac{1 + \beta}{1 + \beta + \alpha\beta}, \quad f_2 = \frac{1}{1 + \beta + \alpha\beta},$$

where $\alpha = \exp((E_{T1} - E_F)/k_B T)$ and $\beta = \exp((E_{T2} - E_F)/k_B T)$. From these equations, it is evident that $f_1 > f_2$ even when $E_{T1} > E_{T2}$, and there is no need to impose constraints that guarantee a physically meaningful value for $[D^0] = (f_1 - f_2)N_D$.

Assumptions about recombination kinetics are the same as the SRH model:

- capture is a first-order reaction between a defect site and a carrier,
- emission rates vary exponentially with the energy required, and
- defects are in quasi-equilibrium with both bands.

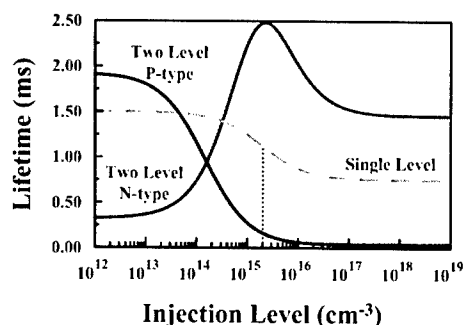


Fig. 3. Calculated recombination lifetimes for a typical single-level defect and for a two-level system that approximates the behavior of intrinsic defects on n- and p-type hydrogen-passivated Si (100) surface.

The four emission coefficients may be written in terms of capture coefficients and equilibrium defect occupations. The lifetime then varies with injection level as [11]

$$\tau(\Delta n) \equiv -\frac{\Delta n}{dn/dt} = \tau_0 \left(\frac{1 + \tau_{n1}\Delta n + \tau_{n2}\Delta n^2}{(1 + \tau_d\Delta n)(1 + \Delta n/(p_0 + n_0))} \right),$$

where τ_0 , τ_{n1} , τ_{n2} , and τ_d all can be written as functions of the four capture coefficients, the two energy levels, and the total concentration of defects.

Fig. 3 illustrates how the injection level dependence of a two-level defect can be much more complicated than the familiar SRH behavior of a single level. Defect levels for the two-level system have been chosen to roughly mimic the behavior we have observed for H-passivated silicon (100) surfaces. The parameter values are: $\sigma_c^1 = 10^{-16} \text{ cm}^2$, $\sigma_c^2 = 10^{-15} \text{ cm}^2$, $\sigma_h^1 = 10^{-16} \text{ cm}^2$, $\sigma_h^2 = 2 \times 10^{-15} \text{ cm}^2$, $E_{T1} = E_V + 0.95 \text{ eV}$, $E_{T2} = E_V + 0.63 \text{ eV}$. Different values for N_T have been used: $4 \times 10^{10} \text{ cm}^{-2}$ for p-type and 10^9 cm^{-2} for n-type. The doping level for all wafers was fixed at $2 \times 10^{15} \text{ cm}^{-3}$.

While the SRH lifetime changes only near the doping level, the two-level defect shows a much stronger dependence on Δn . The rapid lifetime drop observed for the p-type wafer is due to the speed of the D^0/D^- transition. At equilibrium, most defects are in the D^+ state, so this fast pathway is inaccessible. As the injection level increases, $[D^0]$ also increases and rapid recombination becomes possible. The lifetime continues to drop until the recombination rate is determined entirely by this D^0/D^- transition. For the n-type wafer near equilibrium, most defect sites are occupied and the fast D^0/D^- transition causes the lifetime to be low. The addition of excess carriers, combined with the high rate of electron emission from the shallow level E_{T1} , serves to decrease $[D^0]$ for moderate injection levels. The lifetime

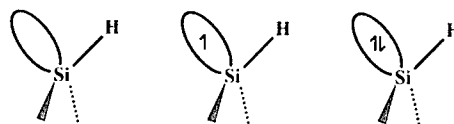


Fig. 4. Possible physical states corresponding to the three electronic states of the surface defect. Each may play important roles in common silicon surface reactions.

thus rises in the intermediate regime (near the wafer doping level), before dropping off in the intrinsic (high-level injection) regime.

4. Physical significance

The precise nature of the defects on the H-passivated surface are not known. In analogy with P_b -centers observed at the Si-SiO₂ interface, it is likely that these defects are dangling bonds. Fig. 4 represents the three physical states for this defect. As was stated in establishing the model, the unoccupied defect state would have a net charge of $+q$. Simply on electrostatic grounds, this site should be very attractive for dissociated F^- ions in solution. The doubly occupied state will serve similarly as a source for electrons. In the process of native oxidation, electrons are transferred from the silicon surface to an adsorbed O₂ molecule. The density of doubly occupied sites may therefore be the limiting species in the degradation of the Si-H passivation. Metal contamination of silicon wafers also occurs by electron transfer from the surface. The doubly occupied dangling bond may prove to be a rate-limiting factor in the rate of metal deposition.

5. Conclusions

A model had been developed for carrier recombination in a two-level defect system. Equilibrium defect occupations are not determined by the Fermi level alone and a more complete approach, based on the total defect entropy, is required. The recombination kinetics are also more complicated and can produce rapid changes in the lifetime even for injection levels well below the doping level. Experimental measurements suggest that silicon (100) wafers immersed in dilute HF solutions are an example of a two-level defect system. The lifetime changes observed on p- and n-type wafers are both explained by a rapid D^0/D^- transition and a slow D^-/D^0 transition. The three defect species identified by this model are likely states of a dangling bond and may play important roles in charge transfer at the silicon surface.

Acknowledgements

We would like to thank Patrick Taylor of Mitsubishi Silicon America for providing silicon wafers. Laurie Johnston of Kanto Chemical Corporation assisted by donating ultrapure chemicals. The RF-PCD measurement system was provided by Cambridge Metrology. This research was funded by the NSF-SRC Center for Environmentally Benign Semiconductor Manufacturing.

References

- [1] R.-P. Chem, D.-S. Lin, *Surf. Sci.* 454–456 (2000) 196–200.
- [2] M. McEllstrem, M. Allegier, J.J. Boland, *Science*. 279 (1998) 545–548.
- [3] C.P. Wade, C.E.D. Chidsey, *Appl. Phys. Lett.* 71 (1997) 1679–1681.
- [4] A.J. Reddy, T.A. Burr, J.K. Chan, G.J. Norga, J. Michel, L.C. Kimerling, *Mater. Sci. Forum* 258–2 (1997) 1719–1724.
- [5] G.J. Norga, M. Platero, K.A. Black, A.J. Reddy, J. Michel, L.C. Kimerling, *J. Electrochem. Soc.* 144 (1997) 2801–2810.
- [6] A.J. Reddy, J.V. Chan, T.A. Burr, R. Mo, C.P. Wade, C.E.D. Chidsey, J. Michel, L.C. Kimerling, *Physica B* 273–274 (1999) 468–472.
- [7] A.J. Reddy, J. Michel, B. Parekh, J.-H. Shyu, L.C. Kimerling, *J. Electrochem. Soc.* 147 (2000) 2337–2339.
- [8] G.J. Norga, M. Platero, K.A. Black, A.J. Reddy, J. Michel, L.C. Kimerling, *J. Electrochem. Soc.* 145 (1998) 2602–2607.
- [9] W. Shockley, W.T. Read, *Phys. Rev.* 87 (1952) 835.
- [10] R.N. Hall, *Phys. Rev.* 87 (1952) 387.
- [11] A.J. Reddy, Design principles for high performance, low environmental impact silicon cleans, Ph.D. Thesis, Department of Materials Science and Engineering, Massachusetts Institute of Technology, Cambridge, MA, 2001.



ELSEVIER

Physica B 308–310 (2001) 232–235

PHYSICA B

www.elsevier.com/locate/physb

Terahertz emission from silicon doped by shallow impurities

H.-W. Hübers^{a,*}, S.G. Pavlov^a, M.H. Rummeli^a, R.Kh. Zhukavin^b, E.E. Orlova^b,
H. Riemann^c, V.N. Shastin^b

^aDLR Institute of Space Sensor Technology and Planetary Exploration, Rutherfordstrasse 2, D-12489 Berlin, Germany

^bInstitute for Physics of Microstructures, Russian Academy of Sciences, GSP-105, 603600 Nizhny Novgorod, Russia

^cInstitute for Crystal Growth, Max-Born-Strasse 2, 12489 Berlin, Germany

Abstract

A new approach to generate stimulated emission in the terahertz (THz) range of the electromagnetic spectrum is presented. At low temperatures, population inversion between excited states of shallow impurity centers in silicon can occur due to peculiarities of electron–phonon interaction. The terahertz stimulated emission from impurity transitions was observed from bulk monocrystalline silicon doped by group V elements (P, Bi), excited by CO₂ laser radiation. © 2001 Elsevier Science B.V. All rights reserved.

PACS: 78.45.+h; 42.55.Px; 78.30.Am; 71.55.Cn

Keywords: THz; Stimulated emission; Shallow impurity; Silicon

1. Introduction

At present, semiconductor lasers which are based on intracenter transitions of optically excited highly non-equilibrium charge carriers are intensively studied. Silicon is one of the most promising materials for such lasers. Erbium-doped silicon [1,2] can operate at a wavelength of around 1.55 μm on intracenter 4f-shell optical transitions of Er atoms. Recently, it has been demonstrated that optically excited hydrogen-like impurity centers in silicon are an efficient source for far-infrared stimulated emission [3–7]. In the case of hydrogen-like centers, the strong influence of electron–phonon interaction on the charge carrier distribution tends to form an equilibrium distribution of charge carriers. However, the specific nature of the phonon-assisted relaxation at low temperatures allows to obtain population inversion due to the suppression of acoustical phonon emission [5] or resonant interaction with

optical phonons [7] for particular excited impurity states.

Non-equilibrium free charge carriers in silicon are created by optical excitation of shallow impurity centers with CO₂ laser radiation. The carriers, optically excited from the ground state into the conduction band, lose their energy by emitting acoustical or optical phonons. The following intracenter relaxation of free charge carriers is a fast cascade process [8]. In n-type Si doped by shallow donor centers, the 2p₀ excited state is comparatively far spaced from the lower s-type states. Relaxation from the 2p₀ state by an acoustical phonon is suppressed, because the wave vector for relaxation by acoustical phonons through the relatively large energy gap is beyond the localization of the impurity states.

As a result, for most of n-Si media, e.g. for silicon doped by phosphor (Si:P), the 2p₀ state is relatively long living (ca. 15 ns [5]). The lower 1s(E,T) states have lifetimes of the order of 0.1 ns [5]. The accumulation of photoexcited carriers in the 2p₀ state in Si:P enables a population inversion between the 2p₀ and 1s(E,T) excited states [4]. This can be used to form a 4-level laser scheme with the 2p₀ state as the long-living upper

*Corresponding author. Tel.: +49-30-67055596; fax: +49-30-67055507.

E-mail address: heinz-wilhelm.huebers@dlr.de (H.-W. Hübers).

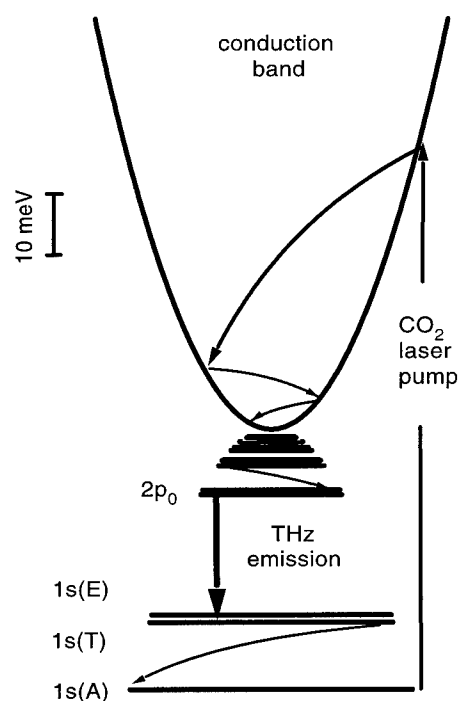


Fig. 1. The scheme of optical and non-radiative transitions in the Si:P when pumped by the CO₂ laser radiation: straight arrow down—far-infrared laser emission from the $2p_0 \rightarrow 1s(T)$ transition; arrow up—the CO₂ laser pump; and solid curved arrows down—relaxation of the photoexcited electrons due to emission of acoustical and optical phonons.

level (Fig. 1). Lasing from the $2p_0 \rightarrow 1s(E)$ transition in optically pumped Si:P was reported in [5,6]. For silicon doped by bismuth (Si:Bi), the $2p_0$ excited state has a very short lifetime (ca. 1 ps) because of resonant interaction with an optical phonon [9]. This results in a relatively small population of the split $1s(E, T)$ states, since the excited electrons relax from the $2p_0$ state directly to the $1s(A)$ ground state. This can be used to form a 4-level laser scheme with less populated lower levels, the $1s(E, T)$ states (Fig. 2). Lasing from the $2p_{\pm} \rightarrow 1s(E)$ transitions in optically pumped Si:Bi is reported in [7].

2. Sample preparation

Low compensated (<1%) Si:P samples were grown by Czochralski (Cz) and float zone procedure with simultaneous incorporation of phosphor from the melt. The size of the samples is $7 \times 7 \times 5 \text{ mm}^3$. The dominant phosphor concentrations in these samples are in the range $(0.08\text{--}9) \times 10^{15} \text{ cm}^{-3}$. A set of Si samples with phosphor concentration $N_P \approx 3 \times 10^{15} \text{ cm}^{-3}$ and a boron compensation in the range 0.2–35% was prepared from

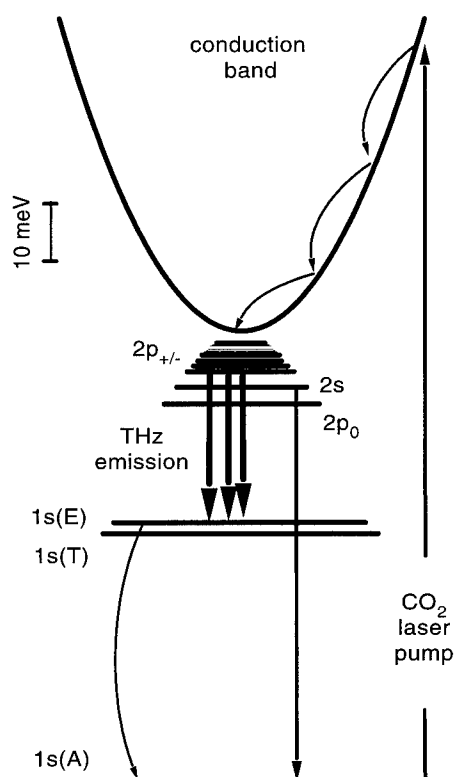


Fig. 2. The scheme of the optical and non-radiative transitions in the Si:Bi when pumped by the CO₂ laser radiation: straight arrow down—far-infrared laser emission from the $2p_{\pm} \rightarrow 1s(E)$ transition; arrow up—the CO₂ laser pump; and solid curved arrows down—relaxation of the photoexcited electrons due to the emission of acoustical and optical phonons.

float zone grown p-Si:B by neutron ($^{30}\text{Si}(n, \gamma) \rightarrow ^{31}\text{Si}(\beta^- / 2.6 \text{ h}) \rightarrow ^{31}\text{P}$). Si:Bi samples with donor concentrations $(0.05\text{--}2) \times 10^{15} \text{ cm}^{-3}$ were grown using the float zone technique. Samples with different doping concentrations were cut in the form of rectangular parallelepipeds ($7 \times 7 \times 5 \text{ mm}^3$) from the Si crystal and then polished to provide a high- Q resonator. The crystals with low doping concentration (ca. $5 \times 10^{13} \text{ cm}^{-3}$) were used to identify the dominant dopant as well as the concentration of the incorporated electrically active centers by means of the Fourier transform absorption spectroscopy.

3. Experimental setup

The samples were mounted in a holder which was immersed in a liquid helium (LHe) vessel (Fig. 3). A grating tunable TEA CO₂ laser with a peak output power up to 2.5 MW in the wavelength range 9.2–10.7 μm was used as the pump source. The losses of the

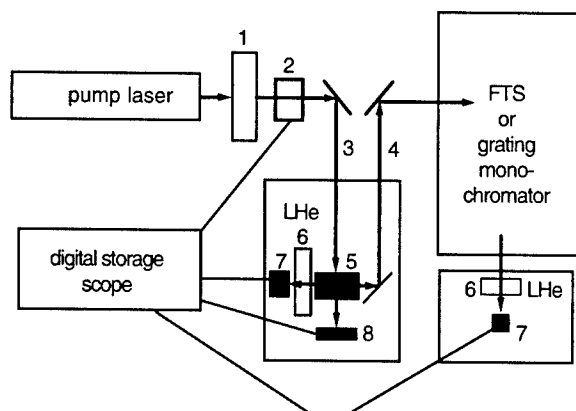


Fig. 3. The experimental setup for observation of the emission from Si: (1) pump laser attenuator; (2) photon drag monitor; (3) pump beam; (4) far-infrared laser beam; (5) Si sample; (6) far-infrared filters; (7) far-infrared detectors; and (8) detector for pump beam alignment.

incident pump power were estimated to be about 7 dB. The FIR emission from the optically pumped Si samples was registered by a LHe cooled Ge:Ga photodetector, mounted in the same holder. For measurements of the emission spectra, the FIR radiation from the Si sample was guided out of the vessel by a stainless steel light pipe into a Fourier transform spectrometer or a grating spectrometer. An external Ge:Ga detector was used to detect the signal.

4. Results

All Si:P samples doped higher than $5 \times 10^{14} \text{ cm}^{-3}$ showed spontaneous emission when pumped by a CO_2 laser. The spontaneous emission increases with increasing doping concentration. For these samples, stimulated emission was observed for doping concentration in the range $N_P = (0.8\text{--}3) \times 10^{15} \text{ cm}^{-3}$. The neutron transmutation doped samples, which are heavily compensated, have a reduced laser threshold. The CO_2 laser pump intensity, necessary to exceed the Si:P laser threshold, was about 30 kW cm^{-2} at the pump wavelength $10.6 \mu\text{m}$ (Fig. 4a). The terahertz emission pulse from the Si:P laser started together with the pump pulse and had a duration of 70–100 ns, comparable with the full-width of half-maximum of the pump laser pulse (Fig. 5a). The spectrum of the stimulated emission from the Si:P sample was measured by a grating spectrometer with a resolution of 0.2 cm^{-1} (Fig. 6). A line at $54.1 \mu\text{m}$ was recorded, which corresponds to the $2p_0 \rightarrow 1s(\text{T})$ intracenter P transition.

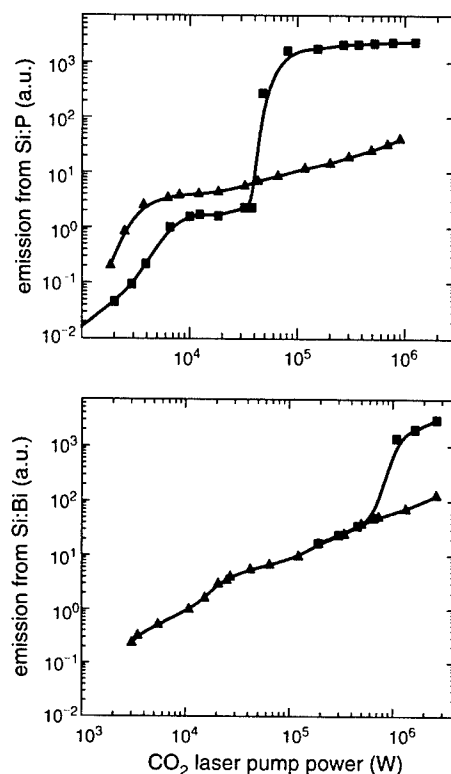


Fig. 4. The dependency of far-infrared emission from the Si:P (a) and the Si:Bi (b) on the incident peak power from a CO_2 laser at $10.6 \mu\text{m}$. The readings of the CO_2 laser power are from the photon drag monitor: (a) triangles are for spontaneous emission from the Si:P samples with a phosphor concentration $N_P = 9 \times 10^{15} \text{ cm}^{-3}$ and squares are for stimulated emission from the Si:P samples with a phosphor concentration $N_P = 3 \times 10^{15} \text{ cm}^{-3}$ and (b) triangles are for spontaneous emission from the Si:Bi sample as cut with a bismuth concentration $N_{\text{Bi}} = 2 \times 10^{15} \text{ cm}^{-3}$ and squares are for stimulated emission from the same sample after polishing in order to get a high-Q resonator.

Stimulated emission was observed from the Si:Bi sample with a doping concentration of $2 \times 10^{15} \text{ cm}^{-3}$ after the sample was polished in order to provide a high-Q resonator (Fig. 4b). The CO_2 laser pump intensity, necessary to exceed the Si:Bi laser threshold, was about 500 kW cm^{-2} at the pump wavelength $10.6 \mu\text{m}$ (Fig. 4b). A delay of the stimulated emission pulse (50–200 ns) with respect to the pump pulse was observed and the duration of the laser pulse was not shorter than that of the pump pulse (about $1 \mu\text{s}$) (Fig. 5b). The spectrum of the stimulated emission from the Si:Bi sample was measured by a FTS with a resolution of 0.4 cm^{-1} (Fig. 7). A line at 191.6 cm^{-1} ($52.2 \mu\text{m}$) was recorded. This corresponds to the $2p_{\pm} \rightarrow 1s(\text{E})$ intracenter Bi transition.

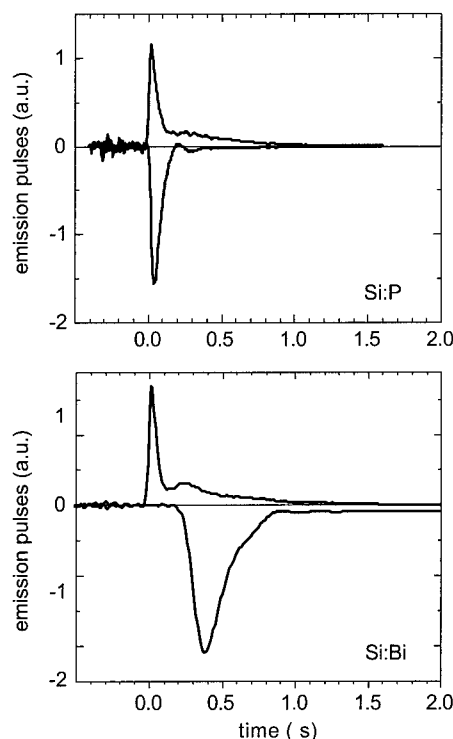


Fig. 5. Traces of pump pulses (up) from the CO₂ laser and terahertz emission pulses from the Si:P (a) and the Si:Bi (b), when pumped by radiation at 10.6 μm.

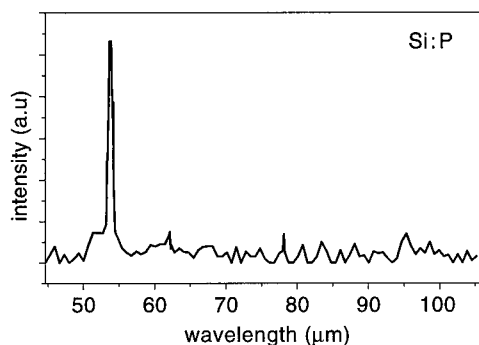


Fig. 6. The stimulated emission spectrum from the Si:P sample recorded by a grating spectrometer.

5. Summary

The experiments yield an optimum doping concentration for the Si:P laser of $N_D - N_A = (3-4) \times 10^{15} \text{ cm}^{-3}$ with a compensation $N_A/N_D \geq 0.3$. Similar values are expected for the Si:Bi laser. Compensation of the samples reduces the concentration of D^- centers. This reduces the internal optical losses due to absorption of

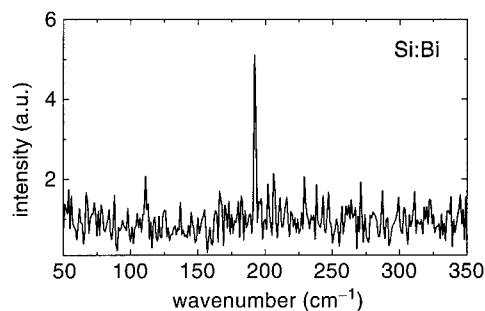


Fig. 7. The stimulated emission spectrum from the Si:Bi sample recorded by a Fourier transform spectrometer.

the FIR laser emission by the D^- centers and, as a result, the laser threshold. The measured emission spectra reveal that the transitions taking part in the laser schemes are $2p_0 \rightarrow 1s(T)$ for the Si:P and $2p_{\pm} \rightarrow 1s(E)$ for the Si:Bi. The latter yields a value of the binding energy for the $1s(E)$ state in the Si:Bi of 30.14 meV. The temporal behavior of stimulated emission pulse from the Si:Bi suggests that multi-valley phonon processes are involved. This requires further investigation. We conclude that far and mid-infrared emission from intracenter optical transitions can be obtained in a number of elemental semiconductors and compounds doped by shallow impurities.

Acknowledgements

This work was partly supported by the Deutsche Forschungsgemeinschaft and the Russian Foundation for Basic Research (joint grant #436 RUS 113/206/0 and #00-02-04010), RFBR grant #99-02-17958 as well as the European Union TMR program "INTERACT". The authors thank M.F. Kimmitt. S.G. Pavlov gratefully acknowledges support through the Alexander von Humboldt Stiftung.

References

- [1] H.A. Lopez, P.M. Fauchet, *Mater. Sci. Eng. B* 81 (2001) 91.
- [2] M.S. Bresler, et al., *Mater. Sci. Eng. B* 81 (2000) 52.
- [3] E.E. Orlova, R.Kh. Zhukavin, S.G. Pavlov, V.N. Shastin, *Phys. Status Solidi B* 210 (1998) 859.
- [4] H.-W. Hübers, et al., *Appl. Phys. Lett.* 74 (1999) 2655.
- [5] S.G. Pavlov, et al., *Phys. Rev. Lett.* 84 (2000) 5220.
- [6] E.E. Orlova, et al., *Physica B* 302–303 (2001) 342.
- [7] S.G. Pavlov, et al., *Phys. Rev. Lett.* (2001), submitted for publication.
- [8] M. Lax, *Phys. Rev.* 119 (1960) 1502.
- [9] N.R. Butler, P. Fisher, A.K. Ramdas, *Phys. Rev. B* 12 (1975) 3200.



ELSEVIER

Physica B 308–310 (2001) 236–239

PHYSICA B

www.elsevier.com/locate/physb

Mobility of interstitial B in Si analyzed by a stochastic reorientation model

B. Ittermann*, D. Peters, M. Füllgrabe, F. Kroll, H. Ackermann, H.-J. Stöckmann

Fachbereich Physik und Zentrum für Materialwissenschaften der Philipps Universität Marburg, D-35032 Marburg, Germany

Abstract

A density-matrix-based formalism is presented to extract activation parameters for the reorientational motion of an interstitial B defect in Si, a center created by ion implantation. β -radiation detected nuclear magnetic resonance (β -NMR) data show beginning mobility at $T \approx 240$ K. At $T = 410$ K the signal is lost even though the center is still present. The activation energy for its reorientation in p-type Si is determined to be $E_A = 0.53(2)$ eV. © 2001 Elsevier Science B.V. All rights reserved.

PACS: 61.72.Tt; 66.30.Jt; 82.56.Lz

Keywords: Si; Boron; Ion implantation; Diffusion; β -NMR

1. Introduction

Doping by ion implantation is state of the art in Si device technology. In order to model the final dopant distributions during and after the subsequent annealing step, precise diffusion data of the involved impurities and defects are needed. Conventionally, this information is obtained by various types of tracer experiments, where diffusion profiles are measured and analyzed. However, this access has limitations. First, these experiments are often restricted to high temperatures. Second, the information represented by a diffusion profile is a somewhat “integral” one, in the sense that the individual diffusing atom cannot be monitored directly in its jump process, but only the combined result of the motion of all involved species. It is very desirable, therefore, to supplement the profiling data by *spectroscopic* information on the details of the diffusion process.

In this paper we want to describe a stochastic model developed to extract quantitative activation parameters for the reorientational motion of an interstitial B center

in Si. This defect is created by ion implantation and observed for $T = 30$ –410 K. Although the model was developed specifically for the interpretation of β -radiation detected nuclear magnetic resonance (β -NMR) spectra, it should be easily adaptable to any other magnetic resonance technique.

The first β -NMR observation of the interstitial B defect in question, labeled B_i in the following, was reported in Refs. [1,2] after implantation of ^{12}B in Si. It is diamagnetic and observed in p-type, intrinsic, and weakly n-type, but not in n^+ Si. Its symmetry is not higher than C_{3v} and it is characterized by an axially symmetric electric field gradient (EFG) with a quadrupolar coupling constant of $e^2qQ/h = -360(15)$ kHz. Later on, the marked temperature dependence of the B_i -signal intensity in differently doped samples was investigated by Frank et al. [3] and qualitatively explained as a reorientational motion of the center, i.e., a change of the defect axis from one $\langle 111 \rangle$ direction to another. There is experimental evidence, but no final proof, that this reorientation is the elementary step of a true migration through the lattice. The B_i diffusion parameters provide important clues, therefore, to the understanding of the so-called “transient enhanced diffusion” of implanted B in Si, a technologically important effect known to involve B_i migration [4].

*Corresponding author. Tel.: +49-6421-282-2559; fax: +49-6421-282-6535.

E-mail address: bernd.ittermann@physik.uni-marburg.de (B. Ittermann).

Several common properties suggest that the described β -NMR center is identical to the one discovered and described much earlier by Watkins and coworkers [5–8]. There, it was created by low-temperature electron irradiation of Si:B and characterized by EPR and DLTS. The assumption is that β -NMR and EPR measure the same defect in different charge states (positive and neutral, respectively). The question is not finally settled, however, and in the following we will not be concerned with the structure but only with the diffusion properties of the center.

2. Theory

Our goal is to calculate the nuclear polarization $P = \langle I_z \rangle / I\hbar$ via

$$\langle I_z \rangle = \text{Tr}(\rho I_z), \quad (1)$$

where ρ is the density matrix of our system which has to be determined. Its evolution in time is described by the Liouville equation

$$\dot{\rho} = \frac{1}{\hbar} [\rho, \mathcal{H}]. \quad (2)$$

The Hamiltonian under consideration can be written as

$$\mathcal{H} = \mathcal{H}_Z + \mathcal{H}_Q + \mathcal{H}_{\text{RF}}, \quad (3)$$

where the first two terms denote the nuclear Zeeman and quadrupole interaction and the last one the interaction of the spins with the RF field. We now turn to averages over the β lifetime, which are actually observed in our experiments

$$\bar{\rho} = \lambda \int_0^\infty \rho(t) \exp(-\lambda t) dt, \quad (4)$$

with $\lambda = 1/\tau_\beta$. Writing Eq. (4) for $\bar{\rho}$ instead of ρ we can partially integrate the right-hand side and obtain

$$\bar{\rho} = \lambda [\bar{\rho} - \rho(0)] = \frac{1}{\hbar} [\bar{\rho}, \mathcal{H}], \quad (5)$$

where $\rho(0)$ represents the known spin polarization at $t = 0$. If \mathcal{H} does not explicitly depend on time this can be rewritten as

$$\lambda [\bar{\rho} - \rho(0)] = \frac{1}{\hbar} [\bar{\rho}, \mathcal{H}] \equiv -iL\bar{\rho}. \quad (6)$$

The Liouville operator L , defined on the right-hand side of Eq. (6), is a matrix of rank $(2I + 1)^2$. Finally, we can rearrange Eq. (6) as

$$\bar{\rho} = (\lambda + iL)^{-1} \lambda \rho(0). \quad (7)$$

For a single Hamiltonian, i.e., one specific orientation of our defect center, Eq. (7) is the solution of our problem. It represents a simple linear equation system, which can be solved numerically. The main advantage of this special formulation is, however, that it can easily be

extended to include stochastic jumps between different configurations, i.e., Hamiltonians.

In case of N possible defect states we can write

$$\rho = \sum_{k=1}^N \rho_k. \quad (8)$$

The equation of motion including jump processes then reads

$$\dot{\rho}_j = -iL\rho_j - \sum_{k \neq j} (w_{jk}\rho_j - w_{kj}\rho_k), \quad (9)$$

where w_{jk} is the jump frequency from site j to site k . In our specific C_{3v} case we have $N = 4$ and all exchange jumps are equivalent. Therefore, we can replace the w_{jk} by one common rate w , which we assume to be thermally activated according to $w(T) = w_0 \exp(-E_A/k_B T)$.

Using the abbreviation $\tilde{L}_k = 3w + \lambda + iL_k$ we arrive at the final master equation

$$\begin{pmatrix} \tilde{L}_1 & -w & -w & -w \\ -w & \tilde{L}_2 & -w & -w \\ -w & -w & \tilde{L}_3 & -w \\ -w & -w & -w & \tilde{L}_4 \end{pmatrix} \begin{pmatrix} \bar{\rho}_1 \\ \bar{\rho}_2 \\ \bar{\rho}_3 \\ \bar{\rho}_4 \end{pmatrix} = \lambda \begin{pmatrix} \rho_1(0) \\ \rho_2(0) \\ \rho_3(0) \\ \rho_4(0) \end{pmatrix}. \quad (10)$$

Substituting Eq. (10) into Eq. (1) and implementing a linear-equation solver into a standard least-squares algorithm, we can fit the calculated $P(T)$ values directly to our data. Since all Hamiltonians are determined by experiment, we have only three free fit parameters: w_0 , E_A , and a common amplitude factor.

So far, we have assumed a stationary Hamiltonian which is inappropriate, of course, for the RF term of Eq. (3). The time dependence of \mathcal{H}_{RF} is usually eliminated by going to a rotating coordinate system. This requires a first-order treatment of \mathcal{H}_Q , however, and therefore neglects all spin-lattice relaxation effects due to the reorientational fluctuations of its off-diagonal elements. Since this can be a very effective relaxation mechanism, such a limitation is not always acceptable. To overcome this problem we stick to an exact treatment of \mathcal{H}_Q in laboratory coordinates and use the fact that \mathcal{H}_{RF} contains only one single frequency ω .

We extend our former equation of motion to

$$\lambda[\rho - \rho(0)] = (-iL_0 + W)\rho + L_1(e^{i\omega t} + e^{-i\omega t})\rho, \quad (11)$$

where the first and second terms on the right-hand side represent the stationary and the time-dependent contribution to \mathcal{H} , respectively. ρ is the lifetime-averaged (the bar has been dropped for better readability) density matrix representing all different lattice sites and W is the jump matrix containing all w terms of Eq. (10). ρ is expanded in a Fourier series

$$\rho = \sum e^{in\omega t} \rho^n(t) \quad (12)$$

and by collecting coefficients we obtain

$$\lambda[\rho^n - \rho^n(0)] = [-i(L_0 - n\omega) + W]\rho^n + L_1(\rho^{n-1} + \rho^{n+1}), \quad (13)$$

where $\rho^n(0) = \delta_{n,0}\rho(0)$. Now we discard all higher orders of \mathcal{H}_{RF} and keep only $n = -1, 0, 1$. Physically, this means that multi-quantum transitions, the simultaneous absorption of two or more RF quanta, are neglected. This way, we obtain our final expression

$$\begin{aligned} \lambda\rho^1 &= [-i(L_0 - \omega) + W]\rho^1 + L_1\rho^0, \\ \lambda\rho^0 &= [-iL_0 + W]\rho^0 + L_1(\rho^{-1} + \rho^1) + \lambda\rho(0), \\ \lambda\rho^{-1} &= [-i(L_0 + \omega) + W]\rho^{-1} + L_1\rho^0, \end{aligned} \quad (14)$$

an equation system with additional couplings by the L_1 terms, three times larger than Eq. (10) but still quite manageable on modern workstations.

3. Experimental

A 1.5-MeV deuteron beam is used to produce radioactive ^{12}B probe nuclei (lifetime $\tau_\beta = 29.4$ ms, spin $I = 1$). A spin-polarized sub-ensemble is collected by recoil-angle selection and continuously implanted in the samples. The wide-spread recoil energies of ~ 0 –500 keV result in a flat implantation profile with $d_{\text{max}} \approx 1.2$ μm . In radioactive equilibrium we have about 2×10^4 ^{12}B nuclei simultaneously in the sample, which is kept in a magnetic field B_0 and can be exposed to a depolarizing (RF) field B_1 . The lifetime-averaged ^{12}B polarization is detected from the north/south asymmetry of the β -ray angular distribution (“ β asymmetry”). More experimental details of implantation β -NMR can be found, e.g., in Ref. [9].

The m substates of the ^{12}B spins are populated like $p_1 : p_0 : p_{-1} \approx 0.4 : 0.3 : 0.3$ under our experimental conditions, a rather accidental result of recoil polarization. In consequence, we cannot detect any ($m = 0 \leftrightarrow -1$) transitions in our RF scans.

4. Measurements and results

In Fig. 1 we plotted the amplitude of one B_i resonance in p-Si (10^{18} B/cm 3) vs. temperature. The data were measured in a slow temperature sweep (1 K/min) by irradiating the resonance of the low-frequency doublet of quadrupole satellites (see the inset of Fig. 1). The RF was on/off modulated at a rate of 0.25 s $^{-1}$ and the rf-induced polarization change was recorded. The crystal orientation was $\langle 110 \rangle \parallel B_0$, where the defect orientations are pairwise equivalent. A frequency modulation of ± 20 kHz was applied to ensure complete depolariza-

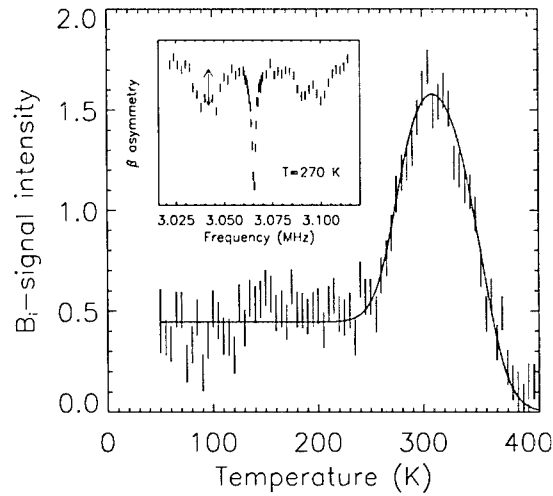


Fig. 1. Temperature dependence of the B_i -resonance intensity in p-type Si. $B_0 = 0.4$ T, $\langle 110 \rangle \parallel B_0$. $B_{1,\text{rot}} = 0.22$ mT, ± 20 kHz FM. The inset shows a spectrum of the center (for B_0 close to $\langle 100 \rangle$), the central line is due to substitutional B. The detected resonance is indicated by the double arrow. The solid line is a fit of the stochastic reorientation model. See text for more details.

tion even in the presence of an inhomogeneous broadening or a slight misalignment of the crystal.

Qualitatively, the figure shows three temperature regimes. At low temperatures, B_i is immobile and the detected signal is small since only two out of four defect orientations are detected. At $T \approx 240$ K, we have one reorientational jump per τ_β . The signal increases in the following since now *all* interstitial ^{12}B becomes (sooner or later) resonant at the irradiated frequency. The subsequent decrease for $T > 310$ K has two reasons: (i) the reorientation is so fast now, that the RF can no longer saturate the resonance, and (ii) the aforementioned spin–lattice relaxation which unavoidably accompanies the reorientation process.

The solid line in Fig. 1 is a fit of the formalism described in Section 2. It assumes the B_i fraction to be constant over the whole temperature range and describes the data well. Especially the signal loss for $T \gtrsim 400$ K has nothing to do with a disappearance of the defect, we are simply no longer able to detect it. For the B_i reorientation we obtain the following parameters:

$$w_0 = 10^{11.7(3)} \text{ s}^{-1}, \quad E_A = 0.53(2) \text{ eV}.$$

We would like to point out that an Arrhenius ansatz for B_i reorientation is justified only in p $^+$ -Si. It was shown in Ref. [3] that in intrinsic or n-type material the reorientation rates are enhanced by charge-state cycling. An implementation of Shockley–Read–Hall recombination rates into our formalism is straightforward and currently underway.

Acknowledgements

We gratefully acknowledge the hospitality of the Strahlencentrum der Universität Giessen, where all measurements were performed. This work was sponsored by the BMBF under contract No. AC5-MAR.

References

- [1] B. Fischer, W. Seelinger, E. Diehl, K.-H. Ergezinger, H.-P. Frank, B. Ittermann, F. Mai, G. Welker, H. Ackermann, H.-J. Stöckmann, *Mater. Sci. Forum* 83–87 (1992) 269.
- [2] W. Seelinger, B. Fischer, E. Diehl, K.-H. Ergezinger, H.-P. Frank, B. Ittermann, F. Mai, G. Welker, H. Ackermann, H.-J. Stöckmann, *Nucl. Instrum. Methods B* 63 (1992) 173.
- [3] H.-P. Frank, E. Diehl, K.-H. Ergezinger, B. Fischer, B. Ittermann, F. Mai, K. Marbach, S. Weißenmayer, G. Welker, H. Ackermann, H.-J. Stöckmann, *Mater. Sci. Forum* 143–147 (1994) 135.
- [4] H.S. Chao, S.W. Crowder, P.B. Griffin, J.D. Plummer, *J. Appl. Phys.* 79 (1996) 2352.
- [5] G.D. Watkins, *Phys. Rev. B* 12 (1975) 5824.
- [6] J.R. Troxell, G.D. Watkins, *Phys. Rev. B* 22 (1980) 921.
- [7] R.D. Harris, J.L. Newton, G.D. Watkins, *Phys. Rev. Lett.* 48 (1982) 1271.
- [8] R.D. Harris, J.L. Newton, G.D. Watkins, *Phys. Rev. B* 36 (1987) 1094.
- [9] B. Ittermann, G. Welker, F. Kroll, F. Mai, K. Marbach, D. Peters, *Phys. Rev. B* 59 (1999) 2700.



ELSEVIER

Physica B 308–310 (2001) 240–243

PHYSICA B

www.elsevier.com/locate/physb

Stress-induced splitting of the electronic level related to a platinum–hydrogen complex in silicon

K. Fukuda*, Y. Iwagami, Y. Kamiura, Y. Yamashita, T. Ishiyama

Faculty of Engineering, Okayama University, Tsushima-naka 3-1-1, Okayama 700-8530, Japan

Abstract

We have applied deep-level transient spectroscopy (DLTS) under uniaxial compressive stress to study the structure of a platinum- and hydrogen-related defect, which has a gap state at 0.14 eV below the conduction band minima in Si. The application of $\langle 100 \rangle$ and $\langle 111 \rangle$ stresses split the DLTS peak of the defect into two components with intensity ratios of 2.7:1 and 1.4:1, respectively, which were the ratios of the low-temperature peak to the high-temperature peak. Under $\langle 110 \rangle$ stress, this peak split into three components as an intensity ratio of two lower-temperature peaks to the high-temperature peak was 1.4:5:1. In addition, we observed the stress-induced alignment of the defect to the configuration corresponding to the low-temperature DLTS peak during the DLTS scan in the temperature range of 65–100 K, for all stress directions. Our results provide the first evidence to connect the electronic level at $E_c - 0.14$ eV to the atomic configuration of the Pt–H₂ complex with the C_{2v} symmetry previously identified by EPR. © 2001 Elsevier Science B.V. All rights reserved.

PACS: 61.72.Hh; 61.72.Yx; 71.55.Cn; 71.70.Fk

Keywords: DLTS; Platinum–hydrogen complex; Silicon; Stress-induced splitting

1. Introduction

Hydrogen is widely known to interact with transition-metal (TM) impurities in silicon and form various TM–hydrogen complexes. As a result, hydrogen causes the passivation of TM impurities or gives rise to new electronic states in the bandgap. In most cases, these complexes have been detected by deep-level transient spectroscopy (DLTS) since their formation often results in the appearance of new electronic levels [1–4], or the disappearance of the deep levels related to TM impurities. DLTS is useful to investigate the properties of electronic levels related to TM–hydrogen complexes, but provides no information about their structures. On the other hand, electron paramagnetic resonance (EPR) is a powerful technique to study the electronic states and

atomic configurations of complexes. However, EPR cannot make the exact determination of their electronic levels. Thus, there have often been some missing rings of a chain to connect the electronic states of defect complexes to their structural information.

Using DLTS under uniaxial stress, termed as stress DLTS, we can obtain more detailed microscopic information, which is not given by standard DLTS. If the electronic state of a defect whose symmetry is lower than that of the host crystal is orbitally singlet, the stress may lift its orientational degeneracy. In stress DLTS, this is observed as the splitting of a DLTS peak, and the relative intensities of the split peak components reflect the symmetry of the defects [5].

One of typical TM impurities, platinum, in Si has been known to form various hydrogen-involved complexes to produce deep levels in the bandgap. Among such complexes, one complex (Pt–H₂) involving two hydrogen atoms was identified by EPR combined with infrared (IR) absorption spectroscopy under uniaxial stress [6]. A recent DLTS study using depth profiling

*Corresponding author. Tel.: +81-86-251-8230; fax: +81-86-251-8237.

E-mail address: fukuda@ms.elec.okayama-u.ac.jp (K. Fukuda).

technique has proposed the determination of the number of hydrogen atoms involved in various platinum–hydrogen complexes [4], and has concluded that the complex having the electronic level at $E_c - 0.18$ eV is Pt–H₂ identified by EPR. Direct evidence is, however, still lacking.

In the present paper, we report on the first attempt to apply stress DLTS technique to study the structure of a platinum- and hydrogen-related complex, which has an electronic level at $E_c - 0.14$ eV. Considering the intensity ratios of split peaks under $\langle 100 \rangle$, $\langle 111 \rangle$ and $\langle 110 \rangle$ stresses and the stress-induced alignment of the complex observed during the DLTS scan, we determine the symmetry of the complex as C_{2v} and provide the first evidence to connect the electronic level at $E_c - 0.14$ eV to the atomic configuration of the Pt–H₂ complex previously identified by EPR.

2. Experimental procedure

We used n-type FZ silicon crystal ingots, which had a phosphorus density of $5.9 \times 10^{14} \text{ cm}^{-3}$. For stress experiments, many samples were cut from the ingots into square pillars with dimensions of $1 \times 1 \times 6 \text{ mm}^3$, the longest of which was parallel to the $\langle 111 \rangle$, $\langle 110 \rangle$ or $\langle 100 \rangle$ direction. Platinum was evaporated on one side of the samples, which were subsequently annealed at 850°C for 2 h in an argon atmosphere for the indiffusion of platinum. After the diffusion, the platinum-evaporated face of the samples was mechanochemically polished to remove the platinum remaining on the surface. Hydrogen was injected into the platinum-diffused samples by chemical etching (HF:HNO₃:CH₃COOH = 1:2:1) before the fabrication of Schottky contacts, which were formed by vacuum evaporation of gold on the polished and etched surface. Capacitance DLTS measurements were performed with a reverse bias of 5 V and a filling pulse of 5 V at rate windows of $116\text{--}928 \text{ s}^{-1}$ under uniaxial compressive stress of 0.6–1.0 GPa applied to the samples along their longest dimension. The stress was applied to the samples at the minimum temperature (typically 63 K) at which the DLTS scan started, and was held during the DLTS run up to 100 K and above.

3. Results

A typical DLTS spectrum taken at an emission rate $e_t = 116 \text{ s}^{-1}$ is shown in Fig. 1. Two dominant peaks, labeled E1 and Pt, appears at 85 and 125 K, respectively, and two small peaks, labeled E2 and E3, are seen at 160 and 270 K, respectively. The electronic levels and the electron-capture cross sections of these peaks are listed in Table 1. The activation energy and the

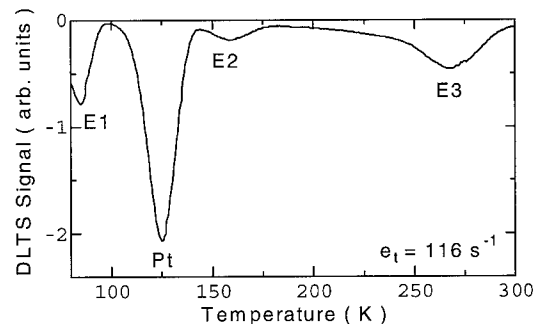


Fig. 1. DLTS spectrum recorded at an emission rate $e_t = 116 \text{ s}^{-1}$ of platinum-doped n-type silicon. No stress was applied during the DLTS scan. The energy levels and electron capture cross sections of the peaks are listed in Table 1.

electron-capture cross section of the Pt peak agree with those reported to be assigned to the acceptor level (Pt⁻⁰) of substitutional platinum [3]. The activation energies of E1 and E3 peaks are comparable with those of two Pt- and H-related levels reported in the literature [3,4], where they are labeled E(90) and E(250), respectively. We therefore tentatively assign these three peaks as indicated in Table 1. The E2 was detected in all of our samples, while it has not been reported so far. So, we conclude that the E2 peak is due to an unidentified defect unique to our Si crystal and experimental procedure. In the present work, we concentrate our attentions on the stress-induced peak splitting of the E1 peak.

Fig. 2 shows the DLTS spectra of the E1 peak recorded under uniaxial stresses along with $\langle 111 \rangle$ (a), $\langle 100 \rangle$ (b), and $\langle 110 \rangle$ (c) directions, shown by solid curves. In Fig. 2(b) and (c), dashed curves represent the fitting using the usual DLTS function and dotted curves represent spectra recorded under no stress, while these curves are not shown in Fig. 2(a) for legibility. Under compressive stresses along the $\langle 111 \rangle$ and $\langle 100 \rangle$ directions, we observed clear splitting of the E1 peak into two components, as shown in Fig. 2(a) and (b). In Fig. 2(b), the emission rate is increased to 1856 s^{-1} to shift the split peaks toward high temperatures, which are higher than the lowest attainable temperature (63 K) in our DLTS system. From the fitting, we have determined that the intensity ratios of low- to high-temperature split peaks is 1.4:1 for $\langle 111 \rangle$ stress, and 2.7:1 for $\langle 100 \rangle$ stress. Under a $\langle 110 \rangle$ stress, we obtained that the E1 peak split into three components as shown in Fig. 2(c) by increasing the emission rate to 4332 s^{-1} . From the fitting, we have determined that the intensity ratio of lower- to high-temperature split peaks is 1.4:5:1 for $\langle 110 \rangle$ stress. In addition, we observed an interesting feature that the second DLTS scan produced a quite different spectrum

Table 1

Energy levels and capture cross sections of the deep levels shown in Fig. 1

Label	Activation energy (eV)	Capture cross section (cm^2)	Assignment
E1	$E_c - 0.14$	9×10^{-16}	Pt–H related
Pt	$E_c - 0.22$	1×10^{-15}	Pt ⁰
E2	$E_c - 0.27$	5×10^{-16}	Unidentified
E3	$E_c - 0.55$	5×10^{-15}	Pt–H related

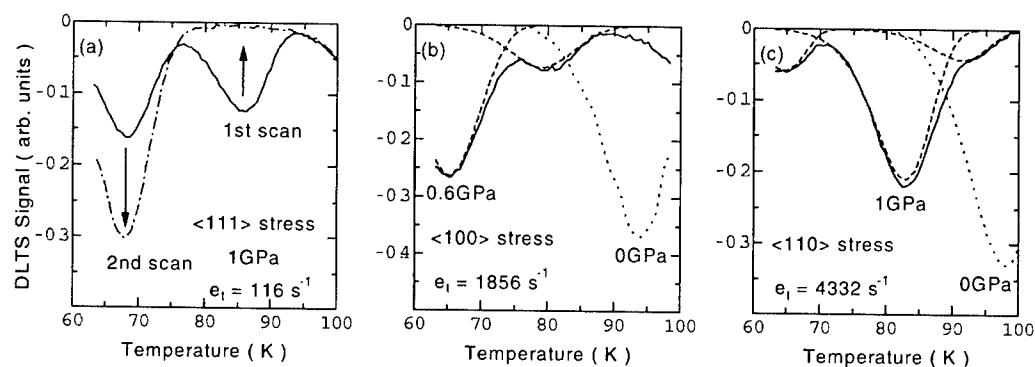


Fig. 2. DLTS spectra of the E1 peak due to a Pt- and H-related complex in Si under uniaxial compressive stresses. Solid curves indicate the spectra recorded at $e_1 = 116 \text{ s}^{-1}$ under a stress of 1 GPa along with the $\langle 111 \rangle$ direction (a), at $e_1 = 1856 \text{ s}^{-1}$ under a stress of 0.6 GPa along the $\langle 100 \rangle$ direction (b), and at $e_1 = 4332 \text{ s}^{-1}$ under a stress of 1 GPa along the $\langle 110 \rangle$ direction (c). In (b) and (c), dashed curves represent the fitting using the usual DLTS function and dotted curves represent spectra recorded under no stress, while these curves are not shown in (a) for legibility. In (a), a solid curve was recorded by the first DLTS scan, and a dashed-dotted curve was recorded by the second scan.

(the dashed-dotted curve in Fig. 2(a)), where the low-temperature peak increases with correlated decreasing of the high-temperature peak. This strongly suggests that the stress-induced alignment of the defect to the configuration corresponding to the low-temperature DLTS peak occurred during the two DLTS scans in the temperature range of 65–100 K. We also observed similar signature in the spectra taken by the second DLTS scan under both $\langle 100 \rangle$ and $\langle 110 \rangle$ stresses.

4. Discussion

Uniaxial stress generally splits not only a defect level but also the conduction band. Since DLTS detects the thermal emission of an electron from the defect level to the conduction band, we substantially observe the energy difference between all of the split defect levels and the lowest-energy component of the split conduction band. Therefore, DLTS-peak splitting is due to the splitting of the defect level. If the ground state of the defect is a singlet with a symmetry lower than that of the host lattice, the peak splitting results from the lift of orientational degeneracy of the defect and reflects the symmetry of the defect. From theoretical consideration, Kaplyanskii summarized the multiplicity of orienta-

tional degeneracy for all the possible defect symmetries in a cubic lattice, together with the number of components of the splitting and the residual multiplicity of orientational degeneracy under $\langle 100 \rangle$, $\langle 110 \rangle$ and $\langle 111 \rangle$ stresses [7]. Only the rhombic-I symmetry is consistent with our results in view of the number of components of the splitting, though the residual multiplicity of orientational degeneracy does not completely agree with the intensity ratios of split DLTS peaks. However, if we consider that the stress-induced alignment of the defect to the configuration corresponding to the low-temperature DLTS peak occurs during the DLTS scan, the intensity ratios of split DLTS peaks before the alignment should be 3:3, 1:4:1 and 4:2 for $\langle 111 \rangle$, $\langle 110 \rangle$ and $\langle 100 \rangle$ stress directions, respectively. Among all rhombic-I centers, only those with C_{2v} symmetry are possible in the lattice with T_d symmetry. Therefore, we conclude that the defect responsible for the E1 peak has C_{2v} symmetry and is identified as the Pt–H₂ complex previously observed by EPR.

5. Conclusions

We have applied DLTS under uniaxial compressive stress up to 1 GPa to study the structure of a

platinum- and hydrogen-related defect, which has an energy level at $E_c - 0.14\text{eV}$ in Si. The application of $\langle 100 \rangle$ and $\langle 111 \rangle$ stresses split the DLTS peak into two components with intensity ratios of 2.7:1 and 1.4:1, respectively, which were the ratios of the low-temperature peak to the high-temperature peak. Under $\langle 110 \rangle$ stress, this peak splits into three components as the intensity ratio of two lower-temperature peaks to the high-temperature peak is 1.4:5:1. In addition, we observed that repeated DLTS scans at 63–150 K under uniaxial stresses induced the low-temperature peak to grow with decaying high-temperature peak. This observation implies that the defect was aligned under applied stresses to the configuration corresponding to the low-temperature DLTS peak. Considering the influence of stress-induced alignment on the intensity ratios of split DLTS peaks, we have determined that the defect has the C_{2v} symmetry, which should have such ratios of orientational degeneracy as 4:2 under $\langle 100 \rangle$ stress, 1:4:1 under $\langle 110 \rangle$ stress and 3:3 under $\langle 111 \rangle$ stress. Therefore, we have identified our DLTS peak as arising from the Pt-H₂ complex previously identified by EPR. Thus, our results provide the first experimental evidence to connect the atomic configuration of the Pt-H₂ complex to its electronic state and also evidence for its stress-induced alignment.

Acknowledgements

This work was supported in part by a Grant-in-Aid for Scientific Research on Priority Areas (B) on 'Manipulation of Atoms and Molecules by Electronic Excitation' from the Ministry of Education, Culture, Sports, Science and Technology.

References

- [1] T. Sadoh, K. Tsukamoto, A. Baba, D. Bai, A. Kenjo, T. Tsurushima, *J. Appl. Phys.* 82 (1997) 1295.
- [2] N. Yalkin, J.-U. Sachse, H. Lemke, J. Weber, *Phys. Rev. B* 59 (1999) 5551.
- [3] J.-U. Sachse, E.O. Sveinbjornsson, W. Jost, J. Weber, H. Lemke, *Phys. Rev. B* 55 (1997) 16176.
- [4] J.-U. Sachse, J. Weber, E.O. Sveinbjornsson, *Phys. Rev. B* 60 (1999) 1474.
- [5] J.M. Meese, J.W. Farmer, C.D. Lamp, *Phys. Rev. Lett.* 51 (1983) 1286.
- [6] S.J. Uffring, M. Stavola, P.M. Williams, G.D. Watkins, *Phys. Rev. B* 51 (1995) 9612.
- [7] A.A. Kaplyanskii, *Opt. Spectrosc.* 16 (1964) 329.



ELSEVIER

Physica B 308–310 (2001) 244–247

PHYSICA B

www.elsevier.com/locate/physb

Valence force field analysis on nitrogen in silicon

H. Harada*, I. Ohkubo, T. Mikayama, Y. Yamanaka, N. Inoue

RIAST, Osaka Prefecture University, 1-2 Gakuencho, Sakai, Osaka 599-8570, Japan

Abstract

Nitrogen doping attracts attention because it reduces void defects drastically. But the mechanism has not been clarified yet. Various configurations of nitrogen have been proposed by using the first principles calculation but there is no description how the stress plays a role in determining these nitrogen configurations. We reveal normal vibration modes corresponding to well-known infrared absorption peaks at 766 and 963 cm^{-1} of nitrogen split interstitial (N–N) and derive force constants for bond stretching and bond bending. Local strain energy near nitrogen is calculated for the optimized structures of N–N, nitrogen–vacancy complex, substitutional N and interstitial N. As a result, it is found that in structures of N–N and $\text{N}_2\text{--V}_2$ with filled electron orbitals, strain energy plays an important role in the determination of the stable structure. © 2001 Published by Elsevier Science B.V.

Keywords: Nitrogen; Silicon; Molecular orbital; Valence force; Infrared absorption

1. Introduction

Nitrogen doping has attracted much attention because it reduces void defects drastically. But the mechanism has not been clarified yet. There are two important nitrogen configurations, split interstitial N pair (N–N complex) [1] and $\text{N}_2\text{--V}_x$ complexes at high temperature [2]. The N–N complex is considered to be related to the infrared absorption peaks at 766 and 963 cm^{-1} and $\text{N}_2\text{--V}_x$ complexes are related to void defect formation. Stress within these configurations plays an important role in determining detailed atomic configuration and defect formation. We have studied the role of stress in the defect formation and point defect kinetics in silicon crystals by the continuum elasticity treatment [3]. For the case of nitrogen which mainly locates in interstitial site, the valence force treatment seems to be a better way to reveal the atomic level behavior related to stress. However, in the cases of substitutional nitrogen it was reported to be unsuccessful [4]. We have made a preliminary study on nitrogen configuration determination using the force constants of

silicon, because there have been no reliable data for Si–N [5]. Valence force analysis on interstitial oxygen has succeeded in explaining the infrared absorption spectrum. In this study, we clarify the normal vibration modes of N–N complex by the semi-empirical molecular orbital (MO) method. As a result, it is found that the well-known 766 and 963 cm^{-1} peaks correspond to the antisymmetric stretching modes of H_2O -type nonlinear three-atom molecule and BF_3 -type planar four-atom molecule. By using the relationship between force constants and frequencies of these normal vibrations, force constants of nitrogen–silicon bonds related to stretch component and bending component are determined. The strain energies of unrelaxed and optimized structures of N–N complex and $\text{N}_2\text{--V}_2$ complex are calculated by using these force constants. It is found that the strain energy plays an important role in the determination of optimized structure. The strain energy for substitutional nitrogen and interstitial nitrogen is also calculated and discussed.

2. Analysis

The semi-empirical MO method is employed for the calculation of stable structure, normal vibration mode

*Corresponding author. Tel.: +81-722-52-1161/3550; fax: +81-722-54-9935.

E-mail address: harada@riast.osakafu-u.ac.jp (H. Harada).

and vibration frequency of N–N complex. For this purpose, $\text{Si}_2\text{N}_2(\text{Si}_2\text{H}_5)_2(\text{SiH}_3)_4$ cluster including Si_2N_2 rectangle terminated by hydrogen was used as shown in Fig. 1. We used the program “MOPAC2000” and MNDO-d (modified neglect of diatomic overlap with d-orbital) Hamiltonian is adopted under a precise convergent condition.

Using the valence force field model [6] we can estimate the atomic-level strain energy for the present cases. Keating defined the quantity λ_{mn} satisfying the translational invariance and the rotational invariance of strain energy as follows:

$$\lambda_{mn} = \frac{\mathbf{x}_m \cdot \mathbf{x}_n - \mathbf{X}_m \cdot \mathbf{X}_n}{2a}, \quad (1)$$

where \mathbf{X} and \mathbf{x} indicate displacements before and after deformation and a is lattice constant as shown in Fig. 2. Stretch component E_α and bending component E_β of strain energy are given by the following equations:

$$E_\alpha = \frac{1}{2} \alpha \sum_{m,n=1} \lambda_{mn}^2, \quad (2)$$

$$E_\beta = \beta \sum_{m=1, n>m} \lambda_{mn}^2. \quad (3)$$

α and β denote force constants related to stretch and bending, respectively. These are found as 194.1 and 55.28 N/m in crystalline silicon. Infrared absorption normal modes of molecules are generally analyzed using the valence force, and this is applicable to local vibrational mode of impurities as confirmed in the case of oxygen, in which the above force constants are obtained by solving the equation between the frequencies of normal mode of molecule and the force constants. In the case of H_2O , the equation between the vibrational frequencies of the antisymmetric stretch

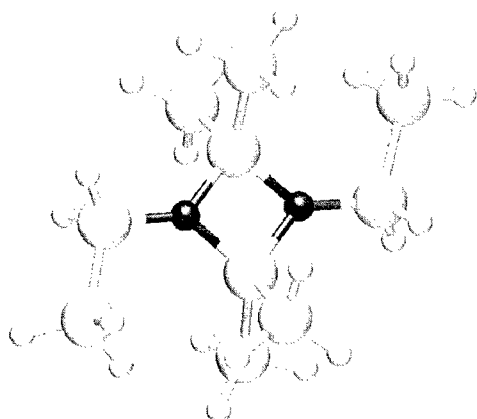


Fig. 1. $\text{Si}_2\text{N}_2(\text{Si}_2\text{H}_5)_2(\text{SiH}_3)_4$ cluster which includes Si_2N_2 rectangle structure. Black, large gray and small gray spheres represent nitrogen, silicon and hydrogen, respectively.

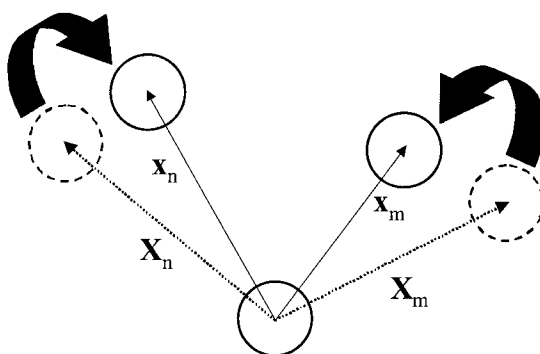


Fig. 2. Schematic of valence force treatment. Introduced quantity satisfies translation invariance and rotational invariance. \mathbf{X} and \mathbf{x} denote displacements before and after deformation.

mode and the stretch force constant is

$$4\pi^2 v^2 = \left(1 + \frac{2m_H}{m_O} \sin^2 \theta\right) \frac{\alpha}{m_H}, \quad (4)$$

where v is frequency, m and θ denote mass of species and half of the bond angle, respectively. In contrast, in the case of BF_3 ,

$$4\pi^2 (v_{AS}^2 + v_{AB}^2) = \left(1 + \frac{3m_F}{2m_B}\right) \left(\frac{\alpha}{m_F} + \frac{3\beta}{m_F}\right), \quad (5)$$

$$16\pi^4 v_{AS}^2 v_{AB}^2 = 3 \left(1 + \frac{3m_F}{m_B}\right) \frac{\alpha\beta}{m_F^2}. \quad (6)$$

Suffix AS and AB mean antisymmetric stretch vibration and antisymmetric bending vibration.

By using these force constants, we estimate strain energies within the third nearest silicon from nitrogen, in N–N complex, $\text{N}_2\text{--V}_2$ complex, substitutional nitrogen and interstitial nitrogen for optimized structures and initial structures as shown in Figs. 3 and 4. Small and large spheres represent nitrogen and silicon, respectively. In the initial structures, all silicon atoms are located at the lattice points as shown in Fig. 4. The role of stress in determining the optimized structures by the amount of change of strain energy from the initial structures to the optimized structures is discussed. The change of strain energy due to optimization is traced by rotating the line between Si atoms in the case of N–N complex and by changing Si–N–Si bond angle in the case of $\text{N}_2\text{--V}_2$ complex as shown in Fig. 4. For simplicity, the shape of Si_2N_2 is fixed and it is rotated to the position proposed by Jones [1].

3. Result and discussion

The atomic vibrational displacements of Si_2N_2 structure corresponding to strong infrared absorption near 766 and 963 cm^{-1} are found by the force calculation of

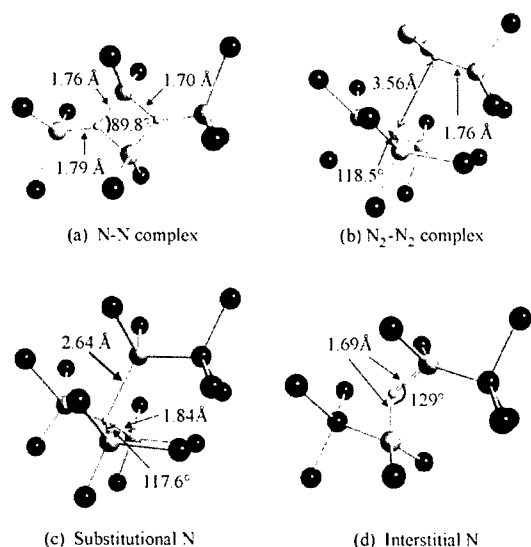


Fig. 3. Optimized structures of (a) N–N complex, (b) N_2 – V_2 complex, (c) interstitial nitrogen and (d) substitutional nitrogen. Small white, gray and black spheres represent nitrogen, relaxed silicon and silicon on sites, respectively.

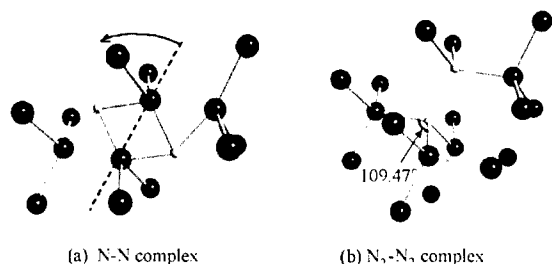


Fig. 4. Initial structures of (a) N–N complex (b) N_2 – V_2 complex. All silicon atoms are located at the lattice sites. Structure optimization is performed by rotating the broken line connecting Si–Si in N–N complex and by changing Si–N–Si bond angle in N_2 – V_2 complex.

$Si_2N_2(Si_2H_5)_2(SiH_3)_4$ cluster as shown in Fig. 5. Each displacement consists of antisymmetric stretch vibration of an H_2O -type nonlinear three-atom molecule and a BF_3 -type planar four-atom molecule, as expected. These wavenumbers are 750 and 943 cm^{-1} , close to the well-known 766 and 963 cm^{-1} related to N–N complex and transition dipoles of these vibrations are relatively higher than that of other modes. Thus, these vibration modes are considered to correspond to the observed 766 and 963 cm^{-1} peaks, respectively.

Thus, by solving Eq. (4) for the antisymmetric stretch vibration of the H_2O -type nonlinear three-atom molecule whose wavenumber is 766 cm^{-1} and (5) and (6) for the BF_3 -type planar four-atom molecule at 963 cm^{-1} , the force constants α and β are obtained to be 330 and

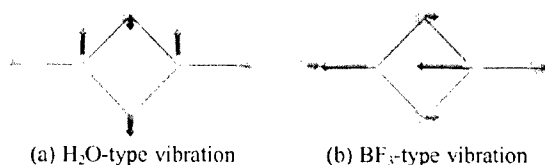


Fig. 5. Atomic displacements of N–N complex corresponding to normal vibration modes of (a) 750 and (b) 943 cm^{-1} .

29 N/m. There has been no successful report about force constants associated with nitrogen in crystalline silicon. In amorphous Si implanted with nitrogen and annealed, these values are reported as 227 and 9.2 N/m [7]. The present results are bigger than the reported ones, probably due to the stronger bonds in crystal than in amorphous structure.

Next, changes of strain energy accompanying structure deformation are calculated. As for N–N complex, the strain energy is plotted against the rotation angle as shown in Fig. 6. As for N_2 – V_2 complex, N atoms are located at the lattice points for the initial configuration (the unit shape is like that of nonplanar NH_3) while they are located where Kageshima proposed by the first principles calculation (the unit shape is like that of planar BF_3) [2]. It is found that in both cases, the optimized structure minimizes its strain energy. Thus, in both cases it is concluded that the strain energy plays an important role in determining the detailed atomic configuration. Table 1 summarizes strain energy for initial structures and optimized structures.

In cases of substitutional nitrogen and interstitial nitrogen, strain energy increases for optimization. It is to be noted that there is an odd electron in both cases, in contrast to the cases of N–N and N_2 – V_2 where no unbonded electron exists. Thus, it is considered that the charge effect rather than the stress effect determines these atomic configurations. Unsuccessful valence force treatment on substitutional nitrogen by Hjalmarsen was due to this charge effect.

4. Summary

Normal vibrational modes of nitrogen interstitial pair (N–N) are clarified by the MO calculation to be antisymmetric stretches of a BF_3 -type planar four-atom molecule and an H_2O -type nonlinear three-atom molecule, for observed peaks at 963 and 766 cm^{-1} , respectively. By solving the equation for the relation of vibrational frequencies and force constants, stretch and bending force constants of Si–N bonds are determined. By using these force constants, strain energy changes from the unrelaxed structures to the optimized structures are calculated for the N–N, N_2 – V_2 substitutional

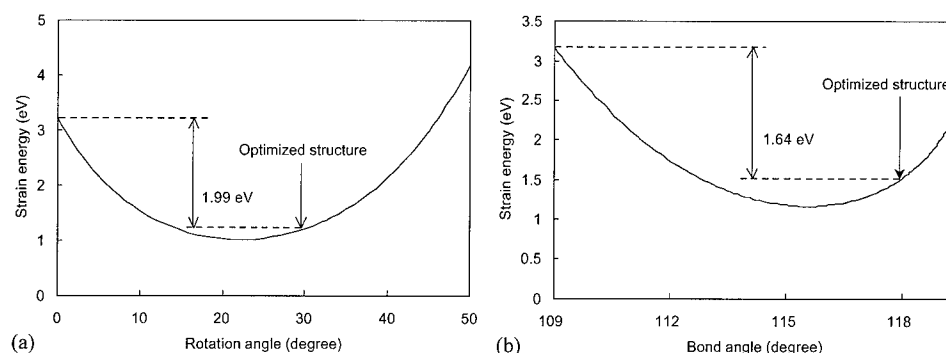


Fig. 6. Change of strain energy accompanying optimization for (a) N–N complex and (b) N₂–V₂ complex.

Table 1
Change of strain energy for initial structure and optimized structure

	Initial structure	Optimized structure (eV)
N–N	3.21	1.22
N ₂ –V ₂	3.17	1.53
Ns	2.10	3.39
Ni	0.537	0.561

nitrogen and interstitial nitrogen. In N–N and N₂–V₂ complexes, the optimized structure has the minimum strain energy, showing that the strain energy determines the detailed atomic configuration. In contrast, in interstitial and substitutional nitrogen, it is found that strain energy increases on optimizing the structure, suggesting that the charge effect is more important. It is concluded that in the case of closed structures strain energy plays an important role whereas in the case of structures with a lone electron, charge effect plays a more important role.

Acknowledgements

This work is partially supported by the JSPS for the future program. The authors are grateful to Y. Yokono for help in manuscript preparation.

References

- [1] R. Jones, S. Oberg, F.B. Rasmussen, B.B. Nielsen, *Phys. Rev. Lett.* 72 (1994) 1882.
- [2] H. Kageshima, A. Taguchi, *Appl. Phys. Lett.* 76 (2000) 3718.
- [3] K. Tanahashi, H. Harada, A. Koukitsu, N. Inoue, *J. Crystal Growth* 225 (2001) 294.
- [4] Harold P. Hjalmarson, Dwight R. Jennison, *Phys. Rev. B* 31 (1985) 1208.
- [5] H. Harada, Y. Matsuo, K. Tanahashi, A. Koukitsu, N. Inoue, K. Wada, *Physica B* 303 (2001) 386.
- [6] P.N. Keating, *Phys. Rev. B* 145 (1966) 637.
- [7] G. Lucovsky, J. Yang, S.S. Chao, J.E. Tyler, W. Czubytyj, *Phys. Rev. B* 28 (1983) 3234.



ELSEVIER

Physica B 308–310 (2001) 248–252

PHYSICA B

www.elsevier.com/locate/physb

Spectroscopic characterization of implanted boron in microcrystalline silicon by β -NMR

F. Mai, B. Ittermann*, M. Füllgrabe, M. Heemeier, F. Kroll, K. Marbach, P. Meier, H. Mell, D. Peters, H. Thieß, H. Ackermann, H.-J. Stöckmann

Fachbereich Physik und Zentrum für Materialwissenschaften der Philipps-Universität Marburg, D-35032 Marburg, Germany

Abstract

Spin-polarized, radioactive ^{12}B probe nuclei were implanted in microcrystalline Si with typical grain diameters of ~ 10 nm. Using β -radiation detected nuclear magnetic resonance (β -NMR) we observed broad, unstructured spectra at room temperature. This broadening is shown to be due to structural disorder. It is not caused by hydrogen or other contaminations of the samples. © 2001 Elsevier Science B.V. All rights reserved.

PACS: 61.72.Tt; 81.07.Bc; 61.46.+w

Keywords: $\mu\text{c-Si:H}$; Implantation; Doping; Boron; β -NMR

1. Introduction

Hydrogenated, microcrystalline Si ($\mu\text{c-Si:H}$) is used as a contact and substrate material in thin-film technology [1]. Its main advantage is the possibility of a cost-effective deposition in large areas. Considering applications, e.g., solar cells, $\mu\text{c-Si:H}$ is therefore a direct competitor to amorphous Si (a-Si:H). In this comparison it is hoped that the microcrystalline modification will show less degradation, better doping efficiency, higher carrier mobility, and, due to the lower band gap, better absorption in the near infrared.

Despite its historical name, $\mu\text{c-Si:H}$ is a material with nm-length scales. Compared to conventional polycrystalline solids its properties are influenced by a relatively high volume fraction of grain boundaries and open volumes. Additionally, the sample properties are affected by a hydrogen content of several at%, incorporated during deposition.

p-type doping of $\mu\text{c-Si:H}$ films is usually achieved in the deposition process by adding a certain amount of B_2H_6 to the process gas. We applied ion implantation, however, as an alternative approach to introduce B atoms into the samples after growth. In the present study we report a structural characterization of B in $\mu\text{c-Si:H}$ by means of β -radiation detected nuclear magnetic resonance (β -NMR).

2. Experimental

Radioactive ^{12}B (lifetime $\tau_{\beta} = 29.4$ ms, spin $I = 1$) is produced in the nuclear reaction $^{11}\text{B(d,p)}^{12}\text{B}$ using a primary beam of 1.5-MeV deuterons. Spin-polarized probe nuclei are collected by recoil-angle selection and continuously implanted in the samples with wide-spread recoil energies from ~ 0 to 500 keV. This results in a quite homogeneous implantation profile with a maximum depth of $d \approx 1.2$ μm . In radioactive equilibrium we have only about 2×10^4 ^{12}B nuclei simultaneously in the sample. The sample is kept in a magnetic field B_0 and can be exposed to a depolarizing radio-frequency (RF) field B_1 . The lifetime-averaged ^{12}B polarization is detected from the north/south asymmetry of the β -ray

*Corresponding author. Tel.: +49-6421-282-2459; fax: +49-6421-282-6535.

E-mail address: bernd.ittermann@physik.uni-marburg.de (B. Ittermann).

angular distribution. More experimental details are given in Ref. [2].

The nuclear polarization P in conventional NMR results from an almost linear variation of the m -substate population with m (Boltzmann polarization). This is markedly different in our case of recoil polarization. From previous studies we know our substate populations to be $p_1 : p_0 : p_{-1} \approx 0.4 : 0.3 : 0.3$. In consequence, we cannot detect any ($m = 0 \leftrightarrow -1$) transitions in our RF scans. A priori, there is no reason to expect the familiar symmetry of NMR spectra in our type of experiments.

Two-micrometer thick $\mu\text{-Si:H}$ films were deposited at $T = 280^\circ\text{C}$ by conventional plasma-enhanced chemical vapor deposition (PECVD) [1]. Structurally different samples were obtained by a variation of the SiH_4/H_2 ratio in the process gas. Raman spectroscopy was used to determine crystalline volume fractions of 76–87%. The difference to 100% is assumed to be due to grain boundaries [3]. The mean grain diameters, estimated from TEM and X-ray scattering data, were about 10 nm in films deposited with 1–5% SiH_4 in the process gas. The samples contained 2.5–5.5 at% H and were not intentionally doped.

3. Measurements and results

A β -NMR spectrum of ^{12}B in $\mu\text{-Si:H}$, measured at $T = 300\text{ K}$, is presented in Fig. 1. Almost identical data

were obtained in all samples investigated so far. Instead of one or more resolved resonances we find a broad frequency distribution with a full-width at half-maximum (FWHM) of $\sim 50\text{ kHz}$. This is in contrast to the situation in single crystalline Si, where, depending on the measuring conditions, linewidths below 1 kHz can be observed [4]. It is the main object of this paper to explore the nature of this broad spectrum.

In first-order perturbation theory, the energy of a given magnetic substate m of our ^{12}B spin $I = 1$ is given by

$$E_m = -h\nu_L m + \frac{e^2 q Q}{4I(2I-1)} \left(\frac{3}{2} \cos^2 \theta - \frac{1}{2} \right) (3m^2 - I(I+1)), \quad (1)$$

where $e^2 q Q$ is the so-called quadrupole coupling constant measuring the magnitude of the electric field gradient (EFG) at the ^{12}B position and θ is the angle between principal EFG axis and \mathbf{B}_0 (we assume an axially symmetric EFG tensor for simplicity).

The spectrum of Fig. 1 is centered at the Larmor frequency ν_L . It cannot be just the orientational averaging of Eq. (1) for one specific value of $e^2 q Q$, therefore. For ($\Delta m = 1$) transitions the peak of such a “powder pattern” would occur for $\theta = 90^\circ$ at $\nu = \nu_L + \frac{3}{8} e^2 q Q / h$. Due to our specific m substate population we would also observe a distinctly asymmetric spectrum. All this is clearly not the case in Fig. 1 and we can state

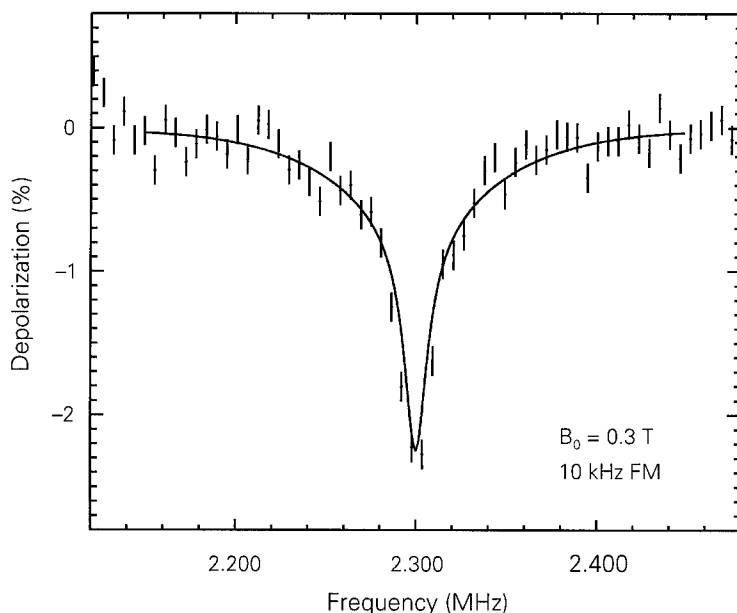


Fig. 1. Typical β -NMR spectrum of ^{12}B in $\mu\text{-Si:H}$ measured at $B_0 = 0.3\text{ T}$ and $T = 300\text{ K}$. The inhomogeneous frequency distribution has a full width at half maximum of $\sim 50\text{ kHz}$. In order to enhance the weak signals a frequency modulation of $\pm 10\text{ kHz}$ had been applied to measure this spectrum. The RF amplitude was $B_{1,\text{rot}} = 0.1\text{ mT}$. The solid lines are simulated spectra as explained in the text.

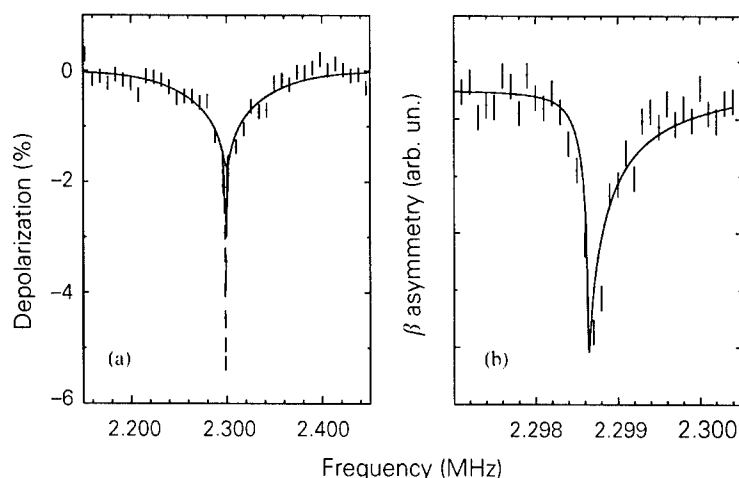


Fig. 2. (a) β -NMR spectrum of ^{12}B in $\mu\text{c-Si:H}$ measured with $B_{\text{L,rot}} = 0.29$ mT and without FM. $B_0 = 0.3$ T, $T = 360$ K. The sharp line in the center of the spectrum is due to a double-quantum (DQ) transition. All probe nuclei participate in this resonance, independent of their quadrupole shift. (b) A high resolution scan of the DQ line measured with reduced RF power ($B_{\text{L,rot}} = 0.12$ mT) at $T = 350$ K. The solid lines are simulated spectra as explained in the text.

that the observed distribution of NMR frequencies is not just the result of the polycrystallinity of the sample but reflects a corresponding distribution of ^{12}B defect states.

This is a surprising result, considering the high crystalline volume fractions in our samples. The β -NMR signatures of ^{12}B in crystalline Si (c-Si) are well known [4,5]: a Larmor resonance from substitutional B and a well-defined EFG [$e^2qQ/h = -360(15)$ kHz] from positively charged interstitial B. The data of Fig. 1 are distinctly different from what would have been obtained by just an orientational averaging of these c-Si features. The $\mu\text{c-Si:H}$ spectra are rather dominated by disorder which appears to be characteristic for this modification of Si.

Two possible sources could be responsible for the broadened β -NMR spectra: a distribution of local magnetic fields or of EFGs. The latter quantity measures the deviation of the local charge distribution from full cubic symmetry. Therefore, an EFG distribution reflects structural disorder. Magnetic disorder could be due to paramagnetic defects in the vicinity or due to the presence of H or other nearby impurities with non-vanishing magnetic moments. We can discriminate between these two possibilities with the help of Fig. 2. There we see another ^{12}B spectrum in $\mu\text{c-Si:H}$, this time recorded with higher RF power. The striking difference to Fig. 1 is the appearance of an additional, very sharp resonance just at ν_{L} , superimposed to the already known, broad spectrum. A higher-resolution scan of this new feature is depicted in Fig. 2(b). There we see that this line is only about 300 Hz wide and slightly asymmetric in shape.

From its unique dependence on RF power we can immediately identify the new signal as a so-called double quantum (DQ) resonance, where the ($m = \pm 1$) states are coupled directly by the simultaneous absorption of two RF quanta. The special properties of a DQ resonance compared to the normal ($\Delta m = 1$) ("single quantum", SQ) transition can be seen from Eq. (1). Both signals respond identically to magnetic disorder (a variation of ν_{L}) but the ($1 \leftrightarrow -1$) transition is (in first-order perturbation theory) not affected by the presence of an EFG.

Therefore, the sharpness of the experimentally observed DQ line excludes the presence of any magnetic broadening. This means, in turn, that only structural disorder is responsible for the wide distribution of SQ frequencies. From the residual DQ linewidth we can exclude the presence of H, N, or any other impurities carrying magnetic moments, in the vicinity of our ^{12}B probe nuclei.

Independent proof of an EFG is the observation of the ($\Delta m = 2$) resonance shown in Fig. 3. This transition from ($m = -1$) to ($m = +1$) by absorption of a single RF quantum is selection-rule forbidden and can only be observed in the presence of quadrupolar perturbation at rather low magnetic fields.

Both DQ and ($\Delta m = 2$) resonance had the familiar Lorentzian line shape if caused by a single, well-defined EFG. In our situation of an e^2qQ distribution we observe a corresponding broadening plus pronounced "distortions" of the experimental line shapes. These are second-order effects which are particularly important for the ($\Delta m = 2$) resonance of Fig. 3. In total, we can say that the ($\Delta m = 1$) spectrum (Figs. 1 and 2(a)), the DQ

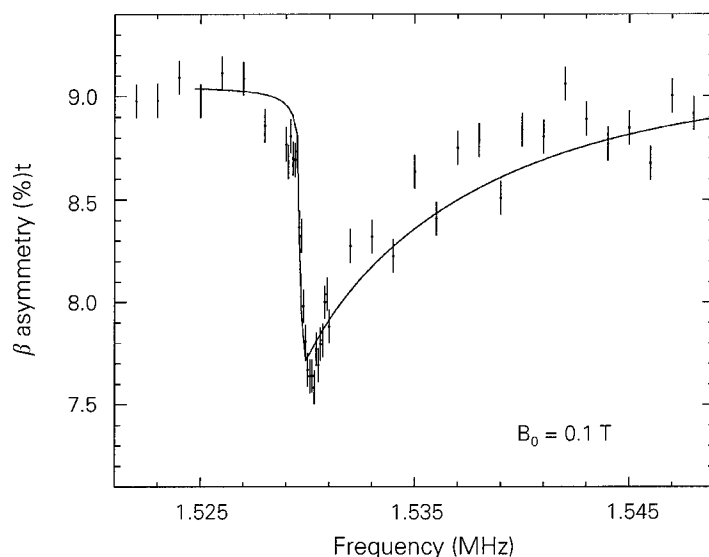


Fig. 3. ($\Delta m = 2$) spectrum of ^{12}B in $\mu\text{-Si:H}$ measured without FM at a lower magnetic field of $B_0 = 0.1$ T. $B_{1,\text{rot}} = 0.33$ mT, $T = 330$ K. The sharp onset of the spectrum occurs at twice the Larmor frequency. The pronounced asymmetry reflects the interplay between EFG distribution and (weakened) RF selection rules and is theoretically understood (solid line, see text for details).

resonance of Fig. 2(b) and the ($\Delta m = 2$) spectrum (Fig. 3) all reflect the same EFG distribution. The different matrix elements for each type of transition lead to the spectral distributions of characteristically different shape and width.

In order to reproduce the experimental spectra we calculated the homogeneous β -NMR-line shape for each magnitude and orientation of a given EFG (for simplicity assumed to be axially symmetric) by means of a density-matrix formalism to be described elsewhere. Then we averaged these data over all crystal orientations and an assumed distribution of EFG magnitudes.

The central result of this simulation is that only a *unimodal* distribution centered at $e^2qQ = 0$ can reproduce the experimental findings. This means that full tetrahedral symmetry is still the most likely configuration and that prolate and oblate charge distortions are equally probable. In our simulations we assumed a Gaussian distribution of e^2qQ/h with a standard deviation of $\sigma = 150$ kHz. All the solid lines in Figs. 1–3 were consistently calculated from this distribution taking the varying experimental parameters (B_0 and RF conditions) correctly into account. The so-obtained simulated spectra agree quite well with the experimental data; especially the peculiar line shapes of the higher-order transitions are almost perfectly reproduced.

We would like to emphasize that the necessity to reproduce three different types of transitions simultaneously is a quite rigorous test of the assumed EFG distribution. In the case of ^{12}B in amorphous Si, for instance, we observed SQ spectra quite similar to the one

of Fig. 1, but a much more rounded ($\Delta m = 2$) spectrum. Those spectra could only be described [6] by a completely different, bimodal e^2qQ distribution with a *minimum* at $e^2qQ = 0$.

4. Summary

After room-temperature implantation of ^{12}B at negligible concentrations in hydrogenated, microcrystalline Si we observe broad and unstructured β -NMR spectra. From a combined analysis of single quantum, double quantum, and ($\Delta m = 2$) spectra it is concluded that these frequency distributions reflect structural disorder, i.e., ^{12}B nuclei in randomly distorted surroundings. Pairing of the implanted B with H or other contaminants in the samples can be excluded on grounds of the very narrow DQ resonances observed. Despite a crystalline volume fraction of $\geq 75\%$ in our samples we could not detect any signals corresponding to the known substitutional or interstitial B in Si.

Acknowledgements

We would like to thank D. Ruff for his assistance in the preparation and characterization of the samples and W. Fuhs for various discussions. We gratefully acknowledge the hospitality of the Strahlenzentrum der Universität Giessen, where all β -NMR measurements were performed. This work was sponsored by the SFB 383 of the DFG and by the BMBF.

References

- [1] G. Willecke, in: J. Kanicki (Ed.), *Amorphous and Microcrystalline Semiconductor Devices*, Vol. 1, Artech House, Norwood, 1992, p. 55.
- [2] B. Ittermann, G. Welker, F. Kroll, F. Mai, K. Marbach, D. Peters, *Phys. Rev. B* 59 (1999) 2700.
- [3] D. Ruff, Ph.D. Thesis, University of Marburg, 1999.
- [4] H. Metzner, G. Sulzer, W. Seelinger, B. Ittermann, H.-P. Frank, B. Fischer, K.-H. Ergezinger, R. Dippel, E. Diehl, H.-J. Stöckmann, H. Ackermann, *Phys. Rev. B* 42 (1990) 11419.
- [5] W. Seelinger, B. Fischer, E. Diehl, K.-H. Ergezinger, H.-P. Frank, B. Ittermann, F. Mai, G. Welker, H. Ackermann, H.-J. Stöckmann, *Nucl. Instrum. and Meth. B* 63 (1992) 173.
- [6] F. Mai, B. Ittermann, M. Füllgrabe, M. Heemeier, F. Kroll, K. Marbach, P. Meier, H. Mell, D. Peters, H. Thieß, H. Ackermann, H.-J. Stöckmann, *Appl. Phys. Lett.* 79 (2001) 338.



ELSEVIER

Physica B 308–310 (2001) 253–256

PHYSICA B

www.elsevier.com/locate/physb

Magnetic resonance and FTIR studies of shallow donor centers in hydrogenated Cz-silicon

B. Langhanki^a, S. Greulich-Weber^{a,*}, J.-M. Spaeth^a, V.P. Markevich^b,
B. Clerjaud^c, C. Naud^c

^a Department of Physics, University of Paderborn, Warburger Strasse 100, 33098 Paderborn, Germany

^b Institute of Solid State and Semiconductor Physics, 220072 Minsk, Belarus

^c Laboratoire d'Optique des Solides, UPMC 4, Place Jussieu, F-75252 Paris cedex 05, France

Abstract

Three species of a shallow donor family (D1–D3) have been observed previously with infrared absorption (FTIR) and electron paramagnetic resonance (EPR) in hydrogenated Czochralski-grown Si crystals after irradiation with fast electrons and subsequent annealing in the temperature range of 300–550°C. In a further detailed EPR investigation, we resolved a hyperfine (hf) interaction with one ²⁹Si nucleus and revealed thus the incorporation of one silicon atom in the defect core. The incorporation of one hydrogen (deuterium) atom in the core of the D1 and D2 centers was observed in electron nuclear double resonance. High resolution FTIR on ¹³C enriched samples showed the incorporation of one C atom in the core. By comparison of the optical and magnetic resonance spectra with those obtained previously for Si-NL10(H) and shallow thermal donors (STD(H)) it is concluded that D1 is the first species of the STD(H) and that the STD(H) defects and the NL10(H) defects are identical. These shallow donor types incorporate one hydrogen atom and, as an other impurity, C in nominally undoped Si or Al (NL10(Al)). An atomic model of the STD(H)/NL10(H) defects is presented. © 2001 Elsevier Science B.V. All rights reserved.

Keywords: Silicon; Hydrogen; Shallow thermal donors; Magnetic resonance

1. Introduction

Upon heat treatment of oxygen-rich silicon at approximately 470°C two oxygen related defect centers show distinguishable absorption lines in Fourier transform infrared (FTIR) and photo thermal ionization spectroscopy. The centers were called thermal double donors (TDD) and shallow thermal donors (STD). They develop after annealing times of $t \approx 0.5$ and $t > 10$ h, respectively. The STDs appear with absorption bands in the range of 300–150 cm⁻¹ and corresponding ionization energies of 34–40 meV (e.g. Ref. [1]). After such heat treatments of Cz-Si, two paramagnetic centers are found

in (electron paramagnetic resonance) EPR as well. They were called NL8 for short annealing time of $t \approx 0.5$ h and NL10 for $t > 10$ h, respectively. The oxygen incorporation in the centers has been proven by electron nuclear double resonance (ENDOR) [2,3]. Several features (e.g. formation kinetics) suggest that the TDDs, found in FTIR, are identical with the NL8 defects, and that the STDs are identical with the NL10 centers [4].

The defects occurring after prolonged annealing ($t > 10$ h) can be divided into several families with a specific set of absorption lines for each of them in FTIR depending on the additional doping of the Si. Three families of STDs have been established so far: the STD(H) (incorporating hydrogen) [4], the STD(Al) (incorporating aluminum) [5], and the STD(X) (incorporation of nitrogen or lattice vacancies).

A new family of shallow thermal donors was found after hydrogenation and electron-irradiation of Cz-Si

*Corresponding author. Tel.: +49-5251-60-2740; fax: +49-5251-60-3216.

E-mail address: greulich-weber@physik.upb.de (S. Greulich-Weber).

and subsequent heat treatment in the range of 300–500°C [6,7]. The centers labeled D1–D3 show enhanced formation kinetics compared to the conventional STDs(H). In the irradiated Si:O:H samples, it is possible to choose the annealing conditions such that only one particular donor species dominates the spectra. This provides a better opportunity for structural studies of one particular species. We investigated the D1–D3 centers with FTIR and EPR spectroscopy and compared their properties with those of the STDs(H) and NL10(H) published previously. We show that the three types of shallow thermal donors (STD(H), NL10(H) and D1–D3) are “identical” and propose a structural model for them.

In FTIR investigations (resolution 0.5 cm^{-1}) it is found that the positions of some lines coincide in all the studied samples. Particularly, the lines due to D2 and D3 donors in irradiated samples are at the same positions as the corresponding lines in the spectrum of the non-irradiated sample (204.3 and 246.9 cm^{-1} for D2 and 198.3 and 241.2 cm^{-1} for D3) [6, 7]. These wave numbers are the same within experimental error as those cited in Ref. [4] for STD2(H) and STD3(H) centers confirming previous suggestions about the identity of the D2 and D3 donors and two centers of the STD(H) family [4,8].

Heat treatment at 350°C generates the D1 center with an isotropic EPR line at $g = 1.9987$. Heat treatment of the irradiated crystals at temperatures higher than 350°C results in a transformation of the D1–D2 centers. This leads to the transformation of the isotropic EPR signal to another one, the shape of which is characteristic for the defects with orthorhombic-I symmetry, C_{2v} point group. The orthorhombic-I symmetry of the D2 center was confirmed by detailed measurements in a K-band EPR spectrometer (25 GHz) and by electrical detection of EPR (EDEPR) at 72 GHz (V-band) with even better resolution. The principal values of the g -tensor are: $g_1||[001] = 1.99982(2)$, $g_2||[110] = 1.99722(2)$ and $g_3||[1\bar{1}0] = 1.99952(2)$. These values are close to those usually quoted for NL10 centers ($g_1 = 1.99959(2)$, $g_2 = 1.99747(2)$ and $g_3 = 1.99957(2)$) [2], but there is a small difference. The values of the D2 center indicate a slightly bigger anisotropy compared with the NL10 centers. The decrease in the concentration of the D2 centers and the appearance of the shallower D3 donors after annealing at 500°C leads to a more isotropic EPR with principal values of the g -tensor closer to those quoted for NL10 centers.

In the D1 EPR spectrum, when measured with increased integration time two satellite lines around the central line were detected. The ratio of the integrated area under the satellite lines to the total integrated area of all three lines is $4.7 \pm 0.2\%$. This value is in good agreement with the one expected for the hyperfine (hf) interaction with one ^{29}Si atom (natural abundance of ^{29}Si is 4.7%). From the angular dependence of the D1

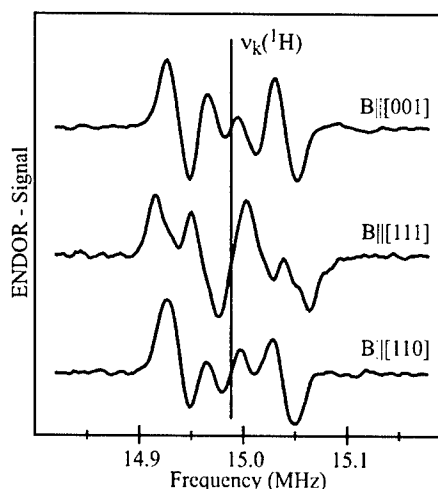


Fig. 1. X-band ENDOR spectra of an electron-irradiated Si:O:H sample annealed at 350°C , measured at 7K with illumination of the sample with white light. Indicated is the position of the frequency of the free hydrogen nucleus calculated for a static magnetic field of $B = 352\text{ mT}$. Three spectra for the main crystallographic orientations are given.

satellite lines an isotropic hf interaction with $a = 58 \pm 1\text{ MHz}$ is derived. Microwave power-dependent measurements of the D1 satellite lines confirmed the correlation of the central D1 resonance line and the satellite lines. Similar ^{29}Si satellite lines with an intensity of $5.6 \pm 0.2\%$ were observed for the D2 center ($a = 70 \pm 1\text{ MHz}$).

A further Cz-Si sample was hydrogenated and finally annealed for 50 h which resulted in intense NL10(H) EPR. Also, for this sample, a hf splitting with one ^{29}Si ($a = 71 \pm 1\text{ MHz}$) is observed for the first time, the intensity of the EPR satellite lines being again 5.3%. It is noted that the splitting constant a for the D2 and NL10(H) centers is larger than that obtained for D1.

In order to reveal further, the atomic structure of the D(1-3)-species and to find out whether they also contain hydrogen, as the NL10(H) centers do, ENDOR measurements have been carried out. Fig. 1 shows ENDOR spectra in the frequency range of 14.8–15.2 MHz for a sample which had a strong D1 EPR signal. The observed ENDOR lines are positioned symmetrically around the Larmor frequency of free hydrogen showing ^1H incorporation into the D1 donor. The spectra are anisotropic upon rotation of the sample. Because of the strongly overlapping ENDOR lines their angular dependence could not be analyzed unambiguously. A satisfactory simulation of the spectra for various orientations could, however, be achieved when assuming triclinic symmetry for the ^1H hf tensor with the z -axis pointing almost into a $\langle 110 \rangle$ direction (only 3° off). There is only one hydrogen atom interacting.

Table 1
 ^1H hf interaction constants from ENDOR^a

	a (kHz)	b (kHz)	b' (kHz)	δ (°)	ψ (°)	φ (°)	$Q_{[001]}$ (kHz)
D1 (^1H)	∓ 88	± 40	± 20	90	45	26	—
D2 (^1H)	∓ 75	± 25	± 5	90	45	26	—
D1 (^2H)	∓ 13	± 6	± 3	90	45	26	± 64
NL10 (H)	84.6	15.2	14.8	75	30	55	—
	80.6	15.0	11.4	70	35	50	—

^a For D1(^1H) the isotropic constant a has an error of $\pm 10\%$; an error for b, b' is difficult to estimate. The error for D2 constants are somewhat larger ($a: \pm 20\%$). The quadrupole constant for D1(^2H) is probably $\pm 20\%$. The data for NL10(H) were adopted for comparison from Martynov et al. [11].

When replacing ^1H by deuterium the much smaller hf interaction of ^2H due to the much smaller nuclear g factor of ^2H could not be resolved, however, a quadrupole interaction could be determined showing that at the H/D site there is an electrical field gradient. The hf interaction parameters in their usual form used in ENDOR [11] are listed in Table 1. The absolute signs of the hf constants cannot be determined experimentally, only their relative signs which are opposite. The choice of a negative isotropic part a is explained below.

In the ENDOR spectrum of a sample containing D2 centers the lines are again placed symmetrically around the Larmor frequency of ^1H but with a reduced width of the pattern compared to that of the D1 centers indicating a smaller ^1H hf interaction, assuming again triclinic symmetry (Table 1).

It had been speculated that carbon is involved in the formation of the shallow donors STD(H) and D1–D3, respectively [4,9,10]. Although a sample enriched with ^{13}C to about $1 \times 10^{17} \text{ cm}^{-3}$ was used and sufficient D1 centers were produced to see the ^1H ENDOR spectra, no trace of a ^{13}C ENDOR line was found. Probably, there is such a low spin density at ^{13}C that the hf interactions were too small to be seen in ENDOR.

In order to obtain further evidence, high resolution FTIR measurements (resolution 0.05 cm^{-1}) were performed at 6 K with the sample enriched in ^{13}C . Isotope shifts of $\Delta E = -0.18 \text{ cm}^{-1}$ for the exchange of H by D and $\Delta E = -0.05 \text{ cm}^{-1}$ for the exchange of ^{12}C by ^{13}C , respectively, have been observed. The data being very small and at the limit of resolution. Thus, the incorporation of C into the D1 center has been demonstrated and confirms earlier speculations [4,9].

Do the shallow thermal donors STD(H), NL10(H) and D1–D3 all have different structures or are they the same defects which have been observed with different experimental methods initially and have therefore received different names? The coincidence of FTIR lines of D2 and D3 with those of STD(H)2,3 confirms earlier suggestions [4] that the D centers are identical with the STD(H) centers. The detection of hydrogen in the D centers by ENDOR supports this further. On the other

hand, the EPR data of NL10 defects and those of D centers with respect to symmetry and g -values are so similar, that the identification of NL10 in nominally undoped Si with the D centers is strongly suggested. Comparison of the hydrogen ENDOR spectrum published by Martynov et al. [12] with that for D1 and D2 shows a practical identical spectral shape and frequency extent. Also, the hf data are very similar, if one allows for the rather poor signal-to-noise ratio in Ref. [11] and the fact that a superposition of several species may have been measured since it was not as easily possible as here to generate one species separately as described above for the D centers. The hydrogen hf data of Ref. [12] adopted to our representation with a, b, b' are given in Table 1 for comparison. Martynov et al. also assumed triclinic symmetry, but did not find the opposite signs of a and b, b' . In view of the uncertainty of the precise analysis of the ENDOR angular dependence due to line overlaps and/or low signal intensity we think that H in NL10 and D centers has the same hf interactions (with slight variations from species to species in the family). Thus, STD(H), D1–D3 and NL10(H) are members of the same defect family. The fact that we have observed a prominent ^{29}Si hf interaction in EPR for both D and NL10(H) and the isotope shift on the ^{13}C enriched sample in high resolution FTIR strongly supports the shallow defect model calculated by Ewels et al. [10] and shown in Fig. 2: the shallow donors have a $(\text{C}-\text{H})_i\text{-O}_{2i}$ structure as defect core. The C_i atom is placed slightly above the $(1\bar{1}0)$ plane in which next to the Si lattice atoms the two O_i are located. The H_i is bonded to the C_i in the $[110]$ direction, which was found to almost coincide with the ^1H hf tensor orientation. The Si atom bonded to C_i in the $\langle 001 \rangle$ direction lacks bonding of its fourth electron. All constituents of the core of the model C, Si and H have been identified. The negative sign of the isotropic hf constant of ^1H is consistent with this model since it can be explained by exchange polarization of spin density in C_i [13], which in turn is caused by polarization from unpaired spin density in the adjacent Si. Assuming that the experimentally found spin density of 1.3×10^{-2} at ^{29}Si induces 1.3×10^{-3} spin

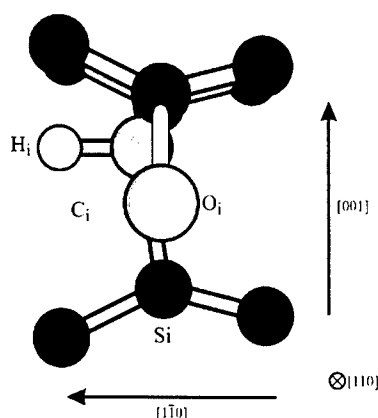


Fig. 2. Atomic model of the core structure of STD(H) on the basis of the calculations by Ewels et al. [10] and the results of this work.

density at the neighboring $^{13}\text{C}_i$, both the negative a value of ^1H and its b value can be quantitatively explained, using for a the known polarization effects of CH_3 radicals [13] (a full p_z orbital induces approximately -65 MHz at the proton) and for b the point dipole–dipole approximation using the CH-bond length of 1.2 \AA (for details see Ref. [14]).

The very low spin densities found are in qualitative agreement with the calculations of Ewels et al. [10] who due to a cluster calculation would overestimate the spin densities of these shallow and very extended defects. A direct comparison with their calculation is not possible since they give no explicit values in Ref. [10] (except for saying “very low”).

All the experimental results are consistent with the assignment of the D1, D2 and D3 centers to the STD(H)/NL10(H) family. The electronic properties of the D1 donor differ from those of the other STD(H) species (e.g. isotropic g factor versus, anisotropic ones of

NL10(H)), but it has the same core constituents and annealing behavior, in that D2 grows at the expense of D1. Thus, it appears that D1 is the first species of the STD(H) donor family and could be called STD(H)1.

References

- [1] H. Navarro, J. Griffin, J. Weber, L. Genzel, *Solid State Commun.* 58 (1986) 151.
- [2] T. Gregorkiewicz, D.A. van Wezep, H.H.P.Th. Bekman, C.A.J. Ammerlaan, *Phys. Rev. B* 35 (1987) 3870.
- [3] J. Michel, J.R. Niklas, J.-M. Spaeth, *Phys. Rev. B* 40 (1989) 1732.
- [4] R.C. Newman, J.H. Tucker, N.G. Semaltianos, E.C. Lightowers, T. Gregorkiewicz, I.S. Zevenbergen, C.J. Ammerlaan, *Phys. Rev. B* 54 (1996) R6803.
- [5] N. Meilwes, J.-M. Spaeth, V.V. Emtsev, G.A. Oganessian, *Semicond. Sci. Technol.* 9 (1994) 1346.
- [6] V.P. Markevich, M. Suezawa, K. Sumino, L.I. Murin, *J. Appl. Phys.* 76 (1994) 7347.
- [7] H. Hatakeyama, M. Suezawa, *J. Appl. Phys.* 82 (1997) 4945.
- [8] V.P. Markevich, T. Mchedlidze, M. Suezawa, L.I. Murin, *Phys. Stat. Sol. (b)* 210 (1998) 545.
- [9] R.C. Newman, M.J. Ashwin, R.E. Pritchard, J.H. Tucker, *Phys. Stat. Sol. (b)* 210 (1998) 519.
- [10] C.P. Ewels, R. Jones, S. Oberg, in: R. Jones (Ed.), *Early Stages of Oxygen Precipitation in Silicon*, Kluwer Academic Publishers, Dordrecht 1996, NATO ASI Series, Vol. 3, High Technology, Vol. 17, pp. 141–162.
- [11] J.-M. Spaeth, J.R. Niklas, B.H. Bartram, *Structural Analysis of Point Defects in Solids*, Springer Series in Solid State Sciences Vol. 43, Springer, Berlin, 1992.
- [12] Yu.V. Martynov, T. Gregorkiewicz, C.A.J. Ammerlaan, *Phys. Rev. Lett.* 74 (1995) 2030.
- [13] A. Carrington, A.D. McLachlan, *Introduction to Magnetic Resonance*, Harper & Row, New York, 1967.
- [14] B. Langhanki, Doctoral Thesis, University of Paderborn, 2001.



ELSEVIER

Physica B 308–310 (2001) 257–260

PHYSICA B

www.elsevier.com/locate/physb

P-type doping of hydrogenated amorphous silicon films with boron by reactive radio-frequency co-sputtering

Y. Ohmura^{a,*}, M. Takahashi^a, M. Suzuki^a, N. Sakamoto^a, T. Meguro^b

^aDepartment of Electronics and Computer Science, Iwaki Meisei University, 5-5-1, Iino Chuodai, Iwaki, Fukushima 970-8551, Japan

^bSemiconductors Laboratory, RIKEN, Wako, Japan

Abstract

B has been successfully doped into the hydrogenated amorphous Si films without using explosive and/or toxic gases SiH_4 or B_2H_6 by reactive radio-frequency co-sputtering. The target used for co-sputtering was a composite target composed of a B-doped Si wafer and B chips attached on the Si wafer with silver powder bond. The maximum area fraction of B chips used was 0.11. Argon and hydrogen pressures were 5×10^{-3} and 5×10^{-4} Torr, respectively. Substrates were kept at 200°C or 250°C during sputtering. The maximum B concentration in the film obtained was $2 \times 10^{19} \text{ cm}^{-3}$ from secondary ion mass spectroscopy measurement. Films with resistivity of 10^4 – $10^5 \Omega \text{ cm}$ were obtained, which was low for the above acceptor concentration, compared with other group III impurities doping, indicating the high doping efficiency of B. A heterostructure, which was prepared by co-sputtering these B-doped films on an n-type crystalline Si, shows a good rectification characteristic. A small photovoltaic effect is also observed.

© 2001 Elsevier Science B.V. All rights reserved.

Keywords: Hydrogenated amorphous silicon; Sputtering; Doping; Boron

1. Introduction

The reactive radio-frequency (RF) co-sputtering has been widely used as a safe and inexpensive method for fabrication of doped hydrogenated amorphous silicon (a-Si:H) or silicon-carbon alloy (a-SiC:H) films without using any toxic or explosive gases. For the dopant used, Al has been investigated most extensively [1–5]. Saito et al. prepared a-SiC:H films doped with Ga [6] and Ti [7] by the co-sputtering method. In these group III acceptor impurities used, however, the concentration in the film reached 10% or more to obtain films with a low resistivity, e.g. $10^5 \Omega \text{ cm}$, so long as the substrate was kept around 200°C during deposition, where the amorphous Si crystallizes rarely. In some cases, the resistivity has not decreased to $10^5 \Omega \text{ cm}$, even if the impurity concentration exceeds 10% by far. This may be due to the low doping efficiency of these impurities. Incidentally, little has been reported about B

doping by this method, although B is the most easily doped to high concentration in the crystalline Si counterpart. In this study, it has been demonstrated that B was successfully doped and low-resistivity a-Si:H films were obtained with relatively low concentration of B by the reactive co-sputtering method. In Section 2, experimental details on the film preparation and the evaluation method are described. Experimental results are shown and discussed in Section 3.

2. Experimental

The sputtering targets used in this experiment are undoped Si crystal of 80 mm in diameter, B-doped p-type Si wafers and Si-B composite targets, where several $5 \times 5 \times 1 \text{ mm}^3$ and/or $10 \times 10 \times 2 \text{ mm}^3$ B chips were attached to p-type Si wafers with silver powder cement. Substrates for sputtered films are optical glasses for UV-Vis optical measurement and electrical measurement, ITO glasses and heavily B-doped p-type Si wafers for electrical measurement and high-resistivity p-type Si

*Corresponding author. Fax: +81-246-29-0577.

E-mail address: ohmura@iwakimu.ac.jp (Y. Ohmura).

wafers for IR measurement. To investigate pn diode characteristics, films were sputtered on n-type Si wafers. The substrates were kept at 200°C or 250°C during deposition for 1 h. The film was prepared in a conventional RF sputtering system operating at 13.56 MHz. The base pressure of the system was of the order of 1×10^{-6} Torr. Argon and hydrogen partial pressures used were mostly 5×10^{-3} and 5×10^{-4} Torr, respectively. A RF power of 2 W/cm² was used. The deposition rate of about 2 Å/s was obtained. The film thickness was measured by a stylus monitor (Sloan DEKTAK IIA). The H concentration was obtained from IR absorption, which was measured by a Shimadzu FTIR 4100 spectrophotometer. The B concentration in the film was determined by secondary ion mass spectroscopy (SIMS) using a CAMECA DES II. For electrical measurement, aluminum was evaporated for the electrode. Through the stencil mask, Al dots of 2 mm in diameter were evaporated on films deposited on ITO glasses and p⁺ Si wafers. The co-planar electrodes were also formed with about 0.2 and 0.5 mm gaps for films on glasses. Electrical properties were determined by a Keithley 2400 SourceMeter.

3. Results and discussion

In most glow-discharge prepared, B-doped a-Si:H films, the B concentration is expressed in terms of partial pressure ratio B_2H_6/SiH_4 during deposition [8]. In this work, to know the net B concentration directly, SIMS measurement was performed. In Table 1, configurations and the B concentrations for four different targets A, B, C and D are shown. In target A, where the most B chips were attached on the Si wafer, the area fraction reaches about 0.11. It was found that the B concentrations were reasonably constant through the film and were reproducible for each target. Therefore, several data are hereafter shown as a function of B concentrations as in Table 1. Fig. 1 shows micro-Raman spectra determined using Jasco NRS-2000 Raman microspectrometer for films prepared from target A at 200°C and 250°C. No

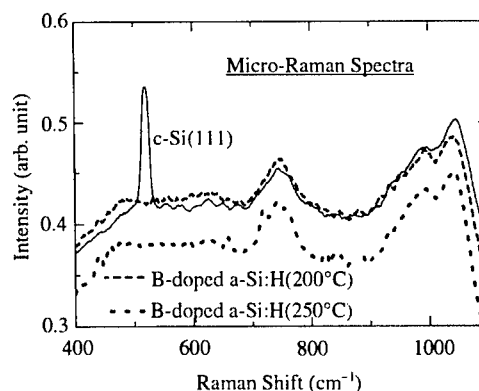


Fig. 1. Raman spectra for B-doped (2×10^{19} cm⁻³) a-Si:H films prepared at substrate temperatures 200°C and 250°C.

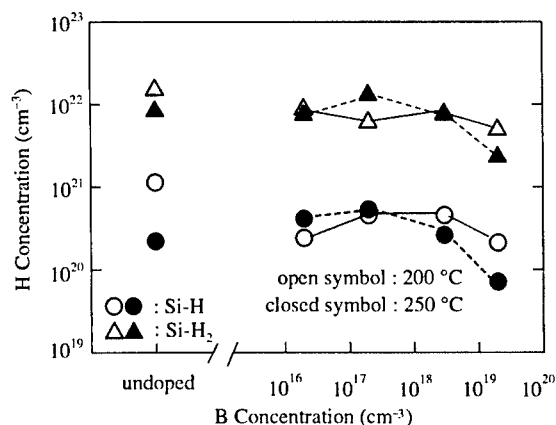


Fig. 2. Hydrogen concentrations of monohydride Si-H and dihydride Si-H₂ as a function of B concentration.

Table 1

Configurations of composite targets and B concentrations in the films determined by SIMS^a

Target	B chip area	Si target	B (SIMS) (cm ⁻³)
A	11%	p ⁺ Si	2×10^{19}
B	8%	p ⁺ Si	3×10^{18}
C		p ⁺ Si	2×10^{17}
D	p ⁺ Si 10%	p Si	2×10^{16}

^ap⁺ Si, B-doped 0.005–0.01 Ωcm Si wafer; p Si, B-doped 5 Ωcm Si wafer.

zone-center LO-TO phonon at 520 cm⁻¹, which is a sensitive signal for micro-crystalline Si formation, was observed even for the film prepared at 250°C, while the entire spectra are almost similar to those of the crystalline Si. Fig. 2 shows Si-H and Si-H₂ concentrations obtained from IR absorption bands at 2000 and 2100 cm⁻¹ for Si-monohydride and Si-dihydride stretching vibrations, respectively, using the method and the proportionality factors between the concentration and the optical densities determined by Langford et al. [9]. It is observed that, below 10^{19} cm⁻³ of B concentration, Si-H and Si-H₂ concentrations do not change significantly from those of undoped films, respectively, for both films prepared at 200°C and 250°C. Above 10^{19} cm⁻³, however, the hydrogen concentration decreases with B concentration, which is the same behavior as other impurities Al [5] or Ga [6].

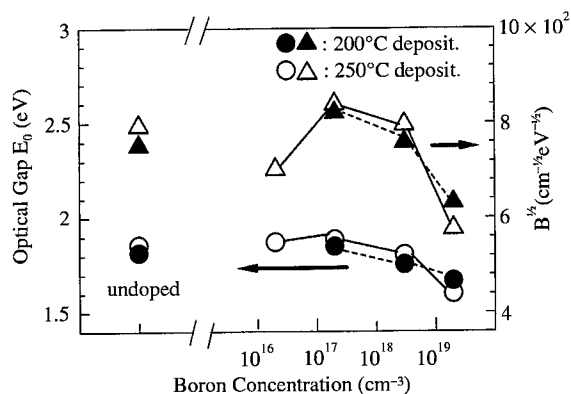


Fig. 3. Optical band gap E_0 and $B^{1/2}$ (see the text) obtained from the Tauc plot of the UV-Vis optical data as a function of B concentration.

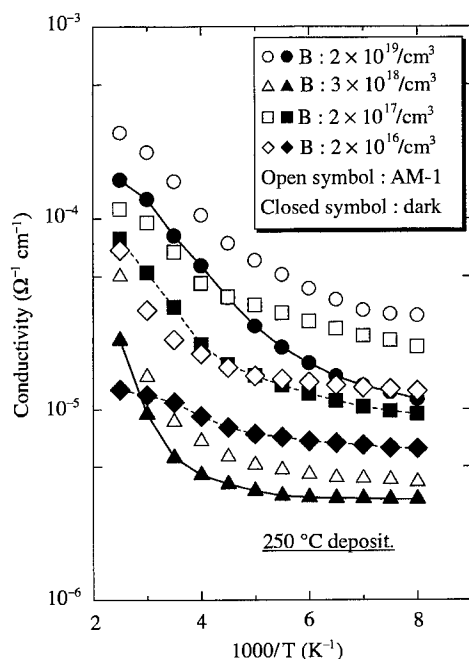


Fig. 4. Electrical conductivity as a function of temperature for B-doped a-Si:H films prepared at 250°C with and without AM-1 illumination.

although the transition concentration seems to depend on the impurity. In Fig. 3, the optical band gap E_0 and B factor are plotted against B concentration. Both quantities were obtained from Tauc plot of the optical data [10], $h\nu\alpha(v) = B(h\nu - E_0)^2$, where α is the absorption coefficient, with a simple assumption that two parabolic, conduction and valence bands are separated by the band gap E_0 [11]. Both E_0 and B have often been used as measures of disorder, decreasing with increasing

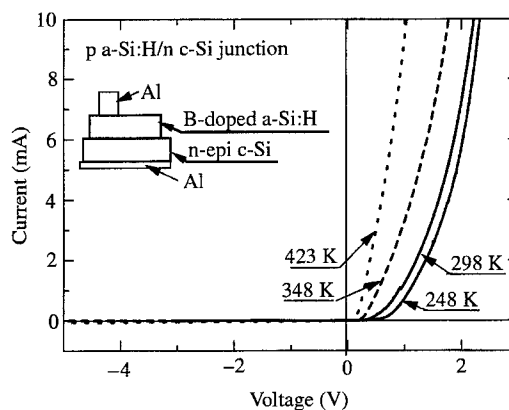


Fig. 5. $I-V$ characteristics for B-doped p-type a-Si:H/n-type epitaxial Si at different temperatures.

disorder. The optical data with the absorption coefficient above about 10^4 cm^{-1} have been used to avoid the interference effect. In Fig. 3, E_0 and $B^{1/2}$ obviously decrease, when B concentration exceeds 10^{18} cm^{-3} , which agrees with the data in a small B fraction region for hydrogenated Si-B alloy films prepared by the glow discharge deposition [8]. It is observed that, for films prepared both at 200°C and 250°C, both quantities at the middle B concentration are slightly higher than those of undoped films. In Fig. 4, the electrical conductivity is plotted as a function of temperature for B-doped a-Si:H films prepared at 250°C with and without AM-1 illumination. Although the order of the conductivity is not necessarily similar to that of B concentration for some films, the film for the target A has the maximum dark conductivity and the activation energy near room temperature is about 0.1 eV, which indicates that the Fermi level is close to the valence band edge. The photoconductivity, although small, is still observed for this film.

Finally, the diode data for B-doped a-Si:H/n-type crystalline Si junction will be presented. Fig. 5 shows an $I-V$ characteristic determined at several temperatures for a diode in which a-Si:H film was sputtered using the target A in the Table 1 on the n-type (100) Si epitaxial wafer through a hole of about 1 cm^2 of a stencil mask at 200°C. The electron concentration in the epilayer was $3 \times 10^{14} \text{ cm}^{-3}$. For forward bias $V_f \leq 0.4 \text{ V}$, the current I was expressed as $I \sim \exp(eV_f/nkT)$ with the n value near 2, indicating that the current is dominated by the recombination current in the space-charge region of the junction. For $V_f > 0.4 \text{ V}$, however, no diffusion current component with $n = 1$ is observed, but the current seems to be limited by the high series resistance of the film. It was found that the $I-V$ characteristics are particularly sensitive to the deposition temperature. The forward current is higher and the reverse current is

much smaller for the diode prepared at 250°C than that prepared at 200°C. The preliminary data showed that the short-circuit current of several tens $\mu\text{A}/\text{cm}^2$ was obtained for these diodes under AM-1 illumination.

4. Summary

It has been demonstrated that B-doped p-type a-Si:H films were prepared by the reactive RF co-sputtering using composite targets of B chips and Si wafers. No explosive and/or toxic gases, SiH_4 or B_2H_6 , were used. The B concentration in the film was directly measured by SIMS and could be controlled by the quantity of B chips and B concentration in the Si wafers in the composite target. The film of the maximum conductivity of about $5 \times 10^{-4} \text{Scm}^{-1}$ was obtained for the B concentration of $2 \times 10^{19} \text{cm}^{-3}$ and the Arrhenius plot near room temperature showed an activation energy of about 0.1 eV, indicating the Fermi level close to the valence band edge. The B-doped a-Si:H/n-type crystalline Si diode structure, which was prepared to confirm the p-type doping, showed a good rectification characteristic and a small photovoltaic effect was observed. These results show that B-doped a-Si:H films in this work contain high concentration of p-type carriers for relatively small B concentration, manifesting the high doping efficiency of sputtered B. Successful doping of B will pave the way for device fabrication by the sputtering

technique, although further optimization of, e.g., deposition condition is still necessary.

Acknowledgements

The authors are grateful to Dr. K. Sawada for the Raman scattering measurement.

References

- [1] M.G. Thompson, D.K. Reinhard, *J. Non-Cryst. Solids* 37 (1980) 325.
- [2] M. Dayan, N. Croitoru, Y. Lereah, *Phys. Lett.* 82 (1981) A306.
- [3] H. Niu, I. Yoshizawa, T. Shikama, T. Matsuda, M. Takai, *Jpn. J. Appl. Phys.* 23 (1984) L18.
- [4] H.S. Fortuna, J.M. Marshall, *Philos. Mag.* 53 (1986) B383.
- [5] N. Saito, Y. Tomioka, H. Senda, T. Yamaguchi, K. Kawamura, *Philos. Mag.* 62 (1990) B527.
- [6] N. Saito, Y. Inui, T. Yamaguchi, I. Nakaaki, *J. Appl. Phys.* 83 (1998) 2067.
- [7] N. Saito, Y. Inui, T. Yamaguchi, I. Nakaaki, *Thin Solid Films* 281–282 (1996) 302.
- [8] C.C. Tsai, *Phys. Rev.* 19 (1979) B2041.
- [9] A.A. Langford, M.L. Fleet, B.P. Nelson, W.A. Lanford, N. Maley, *Phys. Rev.* 45 (1992) B13367.
- [10] J. Tauc, in: J. Tauc (Ed.), *Amorphous and Liquid Semiconductors*, Plenum, New York, 1974, p. 159.
- [11] N.F. Mott, E.A. Davis, *Electronic Properties in Non-Crystalline Materials*, Clarendon, Oxford, 1979, p. 289.



ELSEVIER

Physica B 308–310 (2001) 261–264

PHYSICA B

www.elsevier.com/locate/physb

Dopant boron concentration dependence on electron irradiation enhanced defects in Czochralski silicon

T. Tamano^{a,*}, F. Hori^b, R. Taniguchi^b, R. Oshima^b, K. Hoshikawa^c

^a Department of Material Engineering, Osaka Prefecture University, 1-1, Gakuen-cho, Sakai, Osaka 599-8531, Japan

^b Research Institute for Advanced Science and Technology, Osaka Prefecture University, 1-2, Gakuen-cho, Sakai, Osaka 599-8570, Japan

^c Department of Education, Shinsyu University, 6-kuthi Nishi-Nagano, Nagano, Nagano 380-8544, Japan

Abstract

Positron annihilation lifetime experiments have been performed for CZ-Si with B concentration ranging over 8.3×10^{17} – $2.5 \times 10^{20}/\text{cm}^3$ irradiated with 6 MeV electrons at room temperature. The mean lifetimes were hardly changed in the specimens with B below $8.0 \times 10^{18}/\text{cm}^3$, and increased in the specimen above $8.6 \times 10^{19}/\text{cm}^3$ by irradiation. No remarkable lifetime change with B concentration was obtained with the increase of electron fluence up to $5 \times 10^{15} \text{ e}/\text{cm}^2$, and the mean lifetimes of the specimens with B more than $8.6 \times 10^{19}/\text{cm}^3$ increased with electron fluences higher than $1 \times 10^{16} \text{ e}/\text{cm}^2$. It is concluded that complex defect clusters of $\text{B}_x\text{O}_y\text{V}_z$ are formed by electron irradiation, which have shorter positron lifetimes than the bulk. © 2001 Elsevier Science B.V. All rights reserved.

Keywords: Positron lifetime; Czochralski-grown silicon; Electron irradiation; Dopant boron

1. Introduction

In our previous study for B-doped CZ-Si specimens ($[\text{B}]: 2 \times 10^{15}/\text{cm}^3$) irradiated at room temperature with 1 MeV electrons with fluences between 10^{14} and $10^{17} \text{ e}/\text{cm}^2$ [1], it was found that the mean positron lifetime of irradiated Si becomes shorter than that of as-grown Si, which is due to an irradiation induced short lifetime component (approximately 100 ps). We have concluded that the short-lifetime component is associated with a singular defect, because a vacancy should have a longer lifetime than that of the bulk. It has been suggested that such defects are formed by dopant B atoms, interstitial oxygen atoms, and electron irradiation induced vacancies. The components with longer lifetimes than that of the bulk were also observed, and they were accounted to relate with thermal donors and divacancies.

In this paper, we report the positron lifetime study on dopant B concentration dependence on the defect

complex with shorter lifetime in order to clarify the role of B atoms.

2. Experimental procedure

B-doped CZ-Si wafers with various B concentrations ($[\text{B}]: 8.3 \times 10^{17}, 8.0 \times 10^{18}, 8.6 \times 10^{19}, 2.5 \times 10^{20}/\text{cm}^3$) with [100] orientation and a thickness of about 1 mm were prepared. The B concentration was determined by converting the resistivities with ASTM F723-88. The concentration of oxygen atoms amounted to $1.0 \times 10^{18}/\text{cm}^3$, which was obtained by infrared absorption measurements using the conversion factor IOC-88 [2].

Each specimen was irradiated with 6 MeV electrons at room temperature using a linear accelerator. The fluences ranged from 3×10^{14} to $1 \times 10^{17} \text{ e}/\text{cm}^2$. The flux rate of electrons was $6.3 \times 10^{12} \text{ e}/\text{s cm}^2$.

Positron annihilation lifetimes were measured at room temperature. A radioactive ^{22}Na source with an activity of 346 kBq covered by thin Ni foils were used. The spectra were obtained by the fast-fast coincidence system. The full-width at half maximum (FWHM) of

*Corresponding author. Tel.: +81-722-54-9810; fax: +81-722-51-6439.

E-mail address: tamano@mtl.osakafu-u.ac.jp (T. Tamano).

the time resolution curves was 190 ps. Each lifetime spectrum was accumulated to 1×10^6 counts. The source components were calibrated using unirradiated FZ-Si specimens before and after each measurement. The lifetime spectra were analyzed and decomposed into two components with the RESOLUTION program [3].

3. Results and discussion

Fig. 1 shows the result of mean positron lifetime changes for the samples with different B concentrations as a function of electron irradiation doses. The lifetimes of the as-grown samples are roughly similar to each other; about 215 ps. The lifetime of the bulk Si has been reported to be 218 ps from experiments [4] and 215 ps from theoretical calculation [5]. The lifetimes of the samples below 8.0×10^{18} B-atoms/cm³ hardly change by irradiation. On the other hand, those above 8.6×10^{19} B-atoms/cm³ increase with irradiation. The amounts of Frenkel pairs formed by the electron irradiation are estimated to be 2.6×10^{17} /cm³ and 7.8×10^{14} /cm³ for the highest and the lowest fluence, respectively. Therefore, the positron lifetimes should be longer with the increasing irradiation dose. However, the irradiated samples with B below 8.0×10^{18} cm³ exhibit a somewhat different manner. It seems that a positron cannot be trapped by vacancies, in short, and the vacancies disappear by forming new types of defects. Boron concentration dependence of the electron irradiation is not observed below fluences of 1.0×10^{16} e/cm², while it is observed clearly above fluences of 1.0×10^{16} e/cm².

The positron lifetimes of two component analyses for the samples with different B concentrations are shown in Fig. 2 as a function of electron irradiation dose. The value of τ_1^{cal} is τ_1 calculated from τ_2 and I_2 of the two-state trapping model. The difference between τ_1^{cal} and τ_1 indicates that other types of defects coexist. The larger

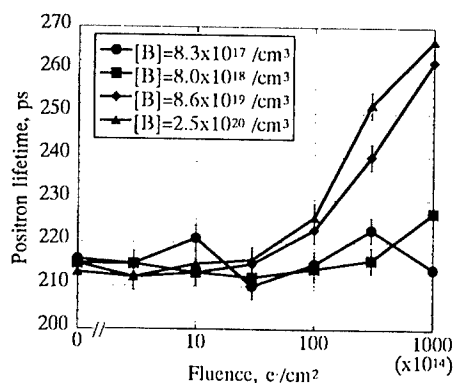


Fig. 1. Mean positron lifetime change for CZ-Si with different B concentrations as a function of electron irradiation dose.

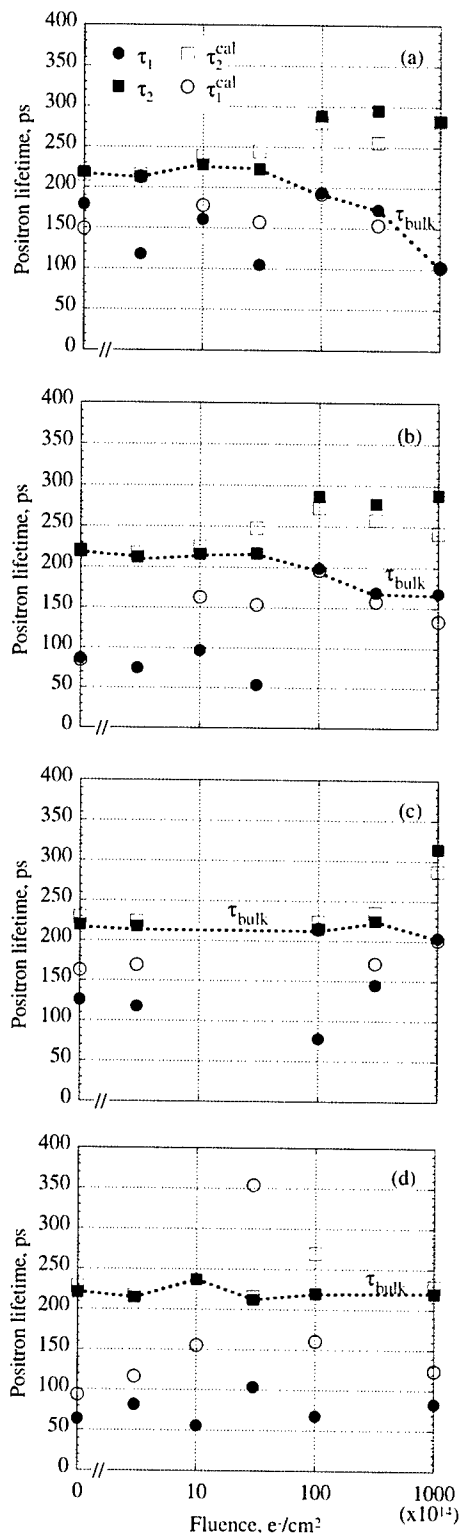


Fig. 2. Positron lifetimes for B-doped CZ-Si with different B concentration as a function of electron irradiation dose. (a) $[B] = 2.5 \times 10^{20}$ /cm³, (b) $[B] = 8.6 \times 10^{19}$ /cm³, (c) $[B] = 8.0 \times 10^{18}$ /cm³, and (d) $[B] = 8.3 \times 10^{17}$ /cm³.

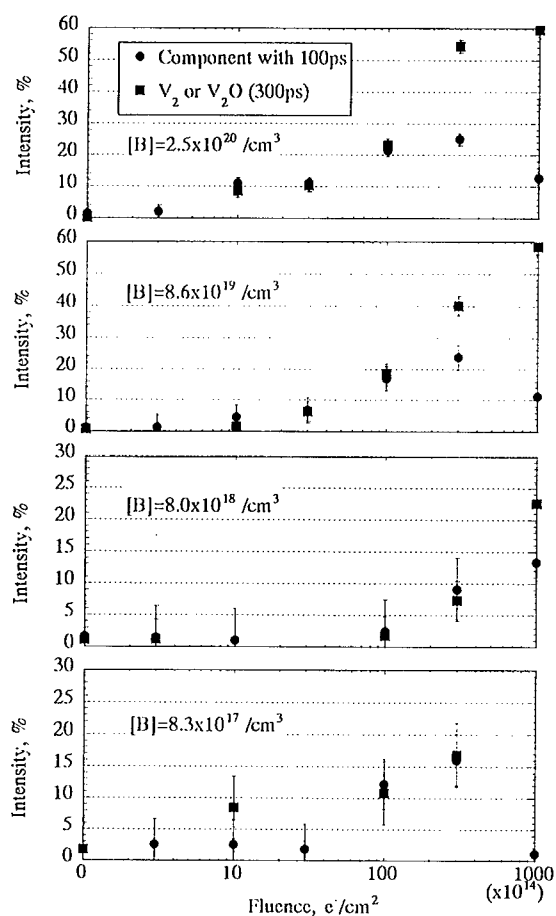


Fig. 3. Relative intensity change of each defect with electron irradiation dose.

the difference, the greater the other types of defects. A detailed discussion was already reported in a previous paper [6]. Fig. 2(d) shows the results for the positron lifetimes for the sample with $8.3 \times 10^{17}/\text{cm}^3$. Although the average lifetimes (τ_{av}) changes slightly at about 215 ps in a whole dose range, they could be decomposed into two components. In the ordinary two component analysis, τ_1 is usually thought to be the matrix. In the present case, however, we conclude that τ_2 is the matrix, and τ_1 is the defect, because τ_2^{cal} agrees with τ_2 , but not τ_1^{cal} with τ_1 . The average lifetime of the short-lifetime defects (τ_1) is about 80 ps. Dannefaer [5] suggested that the lifetime of positrons trapped by interstitial oxygen clusters (~ 100 ps) is shorter than that of positrons annihilated in the bulk (218 ps) in CZ-Si. Uedono et al. [8] have also reported that the lifetime of positrons trapped by the substitutional oxygen microclusters is 80 ps, and divacancies were also attributed to the formation of vacancy-oxygen microclusters in CZ-Si. The intensity of short-lifetime defect (I_1) is low, but the

short-lifetime defect appears in the whole irradiation range. The positron lifetime changes for the specimen with B of $8.0 \times 10^{18}/\text{cm}^3$ are presented in Fig. 2(c). The mean lifetime, τ_{av} does not change at about 215 ps, except for the lifetime at $1.0 \times 10^{17} \text{ e/cm}^2$. For each two-component analysis, it was checked whether τ_1 was the defect with shorter lifetime. As a result, we obtained both the bulk component and a short-lifetime component of about 100 ps with a defect intensity of about 10% with irradiation below $3.0 \times 10^{16} \text{ e/cm}^2$ as well as both the bulk and a long-lifetime component of 320 ps with an intensity of 18% with irradiation at $1.0 \times 10^{17} \text{ e/cm}^2$. The lifetime longer than that of the bulk agrees with that of a divacancy (V_2) or a complex with oxygen (V_2O) [5]. Fig. 2(b) shows the result for CZ-Si with 8.6×10^{19} B-atoms/ cm^3 . The analyses reveal that the short-lifetime defects are about 80 ps below $3.0 \times 10^{15} \text{ e/cm}^2$ and that the long-lifetime defects are about 290 ps above $1.0 \times 10^{16} \text{ e/cm}^2$. Fig. 2(a) for B-doped CZ-Si ($[B]: 2.5 \times 10^{20}/\text{cm}^3$) is similar to the specimen with B of $8.6 \times 10^{19}/\text{cm}^3$ in Fig. 2(b).

We obtained two types of defect lifetimes. One is a shorter lifetime defect about 100 ps, and the other is a longer lifetime defect about 300 ps like a V_2 type defect. Therefore, we try to fix these lifetimes, and compare each relative defect intensity as a function of electron dose as shown in Fig. 3. It should be noted that an ordinate scale of intensities becomes double between $8.0 \times 10^{18}/\text{cm}^3$ and $8.6 \times 10^{19}/\text{cm}^3$. It is found that for the samples with B above $8.6 \times 10^{19}/\text{cm}^3$, a fluence between 3×10^{15} and $1 \times 10^{16} \text{ e/cm}^2$ is a boundary range where the major defects change from the short-lifetime defects to the vacancy-type defects. The intensities of short-lifetime defects of all samples increase with fluence. Dependence of the short-lifetime defects on B concentrations was apparent. The intensity of short-lifetime defect becomes higher with increasing B concentration. It seems that B atoms accelerate the formation of short-lifetime defect and/or that B atoms are related to the short-lifetime defects.

The phenomena mentioned above can be explained as follows. Electron irradiation introduces a pair of vacancy (V) and a self-interstitial atom (Si_i) called a Frenkel pair. As for diffusion of B, Cowern et al. [9] proposed a kick-out mechanism that Si_i kicks substitutional B (B_s) out to the interstitial regions, and suggested that a B_s - Si_i pair is stable and interstitial B (B_i) is metastable. Therefore, it is thought that electron irradiation induces a kick-out mechanism, and then B_i diffuses and meets interstitial O (O_i). It is expected that B_i and O_i interact with each other and create a complex. The DLTS measurements by Khan et al. [10] have also suggested that the V-O-B or B_i - O_i appeared in CZ-Si. However, since B_i is metastable, a reverse kick-out mechanism may take place and a formation of B_s - O_i pair is certainly expected. We may consider excess B

atoms that are bound to the remaining V, but V_2B is known to be unstable at room temperature. Therefore, it is suggested that V remains independent. As the B concentration becomes high, the rate of kick-out mechanism will be large, resulting in the increase in concentration of the defect complex. A high dose of electron irradiation will create such a complex, but positron will not be trapped by it, because the defect complex with a shallow trapping site will be masked by vacancy type defects. The cause of disappearance of V-type defects for lower B concentration samples is considered by the supersaturated interstitial oxygen atoms that are residual without being perfectly relaxed by vacancies introduced by the present low electron fluences. It is accounted that an interstitial oxygen atom distorts the Si lattice and changes atomic spacings, because of a bigger covalent bonding radius than that of the Si bulk. Since interstitial oxygen atoms induce dilatational strains in the Si lattice, the formation of complex defects with vacancies is highly expected. On the other hand, the covalent bonding radius of B atoms is smaller than that of Si, because B atoms are located at substitutional lattice sites, and the lattice will be shrunk around B atoms. Hakala et al. have reported from ab-initio calculation [7] that the substitutional B atom relaxes the nearest-neighbor silicon atoms inwards by $\sim 12\%$ of the bulk bond length. Therefore, B atoms work partly the same as the vacancies. Since it is thought that interstitial O atoms are combined with B substitutional atoms, it is safely concluded that vacancies remain at free conditions like V_2 or V_2B in the samples above $8.6 \times 10^{19}/\text{cm}^3$. On the other hand, in the samples below $8.0 \times 10^{18}/\text{cm}^3$, the vacancies are trapped by the interstitial O atoms, because the number of B atoms is smaller. Accordingly, from the view of the short-lifetime defects, they were more relaxed by B atoms in the specimen with higher B concentrations and irradiation-induced vacancies than that with lower B concentration and the same number of vacancies.

The present study clearly indicates that the induced short-lifetime components are defect complexes with impure interstitial oxygen atoms, vacancies and doped B atoms. From a viewpoint of positron trapping, lifetimes shorter than that of the bulk result from both the smaller

Coulomb potential from the nucleus and the larger electron densities than those of the bulk. The proposed short-lifetime model is satisfied by the conditions, because both oxygen and B nuclei with smaller positive charges exhibit Coulomb repulsive forces smaller than that of the Si nucleus. Accordingly, positrons are easily trapped by such complexes, resulting in annihilation with electrons around oxygen and boron atoms at earlier times.

4. Conclusions

The short-lifetime component is responsible for a complex defect with impure interstitial oxygen atoms, doped B atoms and vacancies. It was concluded from the positron annihilation experiments that B-doped CZ-Si contains the complex $B_xO_yV_z$, which have a shorter positron lifetime than that of the bulk. It is found that B is related with the short-lifetime defects, and it accelerates the formation of short lifetime complexes.

References

- [1] T. Tamano, F. Hori, R. Oshima, T. Hisamatsu, *Jpn. J. Appl. Phys.* 39 (2000) 4693.
- [2] A. Baghdadi, W.M. Bullis, M.C. Croarkin, Yue-zhen Li, R.I. Scacc, R.W. Series, P. Stallhofer, M. Watanabe, *J. Electrochem. Soc.* 136 (1989) 2015.
- [3] P. Kirkegaard, M. Eldrup, O.E. Mogensen, N.J. Pedersen, *Comput. Phys. Commun.* 23 (1981) 307.
- [4] M. Saito, A. Oshiyama, *Phys. Rev. B* 53 (1996) 7810.
- [5] S. Dannefaer, G.W. Dean, D.P. Kerr, B.G. Hogg, *Phys. Rev. B* 14 (1976) 2709.
- [6] T. Tamano, F. Hori, R. Oshima, T. Hisamatsu, *Jpn. J. Appl. Phys.* 40 (2001) 452.
- [7] M. Hakala, M.J. Puska, R.M. Nieminen, *Phys. Rev. B* 61 (2000) 8155.
- [8] A. Uedono, Y. Ujihira, A. Ikari, O. Yoda, *Mater. Sci. Forum* 105 (1992) 1301.
- [9] N.E.B. Cowern, G.F.A. van de Walle, D.J. Gravesteijn, C.J. Vriezema, *Phys. Rev. Lett.* 67 (1991) 212.
- [10] A. Khan, M. Yamaguchi, S.J. Taylor, T. Hisamatsu, S. Matsuda, *Jpn. J. Appl. Phys.* 38 (1999) 2679.



ELSEVIER

Physica B 308–310 (2001) 265–267

PHYSICA B

www.elsevier.com/locate/physb

Interstitial carbon reactions in n-Si induced by high-energy proton irradiation

K. Kono*, H. Amekura, N. Kishimoto

National Institute for Materials Science, Nanomaterials Laboratory, 3-13 Sakura, Tsukuba, Ibaraki, 305-0003, Japan

Abstract

The effect of oxygen on the interstitial carbon reactions in n-Si created by high-energy proton irradiation was studied by an in situ DLTS measurement system. The suppression of Watkin's replacement reaction by trapping of interstitial silicon was studied. The release of the interstitial silicon from interstitial oxygen complex and the following interstitial carbon was studied by in situ DLTS measurement. Also, the effects of interstitial carbon reactions on CCD performance is discussed as an example of application. © 2001 Elsevier Science B.V. All rights reserved.

Keywords: Silicon; Defects; Interstitial; Oxygen

1. Introduction

Vacancies and self-interstitials in Si, induced by high-energy proton irradiation, react with impurities and form defect complexes, which produce undesirable deep levels and affect device operation. Most of the past studies on interstitial type defects focus on reactions after interstitial carbon (C_i) is created from substitutional carbon (C_s), replaced by self-interstitial (I) [1]. The reaction is called Watkin's replacement reaction and is known to take place as low as 4.2 K [2]. The C_i reacts with impurities and forms defect complexes. Since I is trapped by O at low temperature, the production of C_i and the defect complexes is suppressed by the presence of O [1,3]. In order to understand the whole damage processes, it is important to evaluate the dynamic reactions, including Watkin's replacement reaction. We studied the interstitial reactions using an in situ DLTS system integrated in the cyclotron.

We also briefly discuss the application of the study of the interstitial carbon reactions on actual device performance. The discussion is based on the cooled CCD onboard the NASA's Chandra X-ray observatory [4]. Its charge transfer channel was damaged by protons

during the passage of the radiation belts around the earth. We show the importance of understanding the whole process.

2. Experimental

The samples were cut from commercially available n-Si wafers. Either CZ wafers whose resistivity was $\sim 10 \Omega \text{cm}$ (phosphorus concentration: $7 \times 10^{14} \text{cm}^{-3}$) or FZ wafer whose resistivity was in the range $3\text{--}5 \Omega \text{cm}$ (phosphorus concentration: $3 \times 10^{15} \text{cm}^{-3}$) was used. The oxygen concentration of CZ samples was determined to be $2 \times 10^{18} \text{cm}^{-3}$ by atomic absorption analysis. By comparing the FT-IR signal with FZ and CZ sample the oxygen concentration of the FZ silicon was determined to be more than 10 times lower than that of CZ silicon. The carbon concentration in the wafer was determined by chemical analysis to be $3 \times 10^{17} \text{cm}^{-3}$ for CZ and $5 \times 10^{17} \text{cm}^{-3}$ for FZ sample. Samples were cut into rectangular shape and gold was vacuum evaporated on the front surface to form a Schottky diode. An ohmic contact was formed on the other surface.

Irradiation was conducted using the National Institute for Materials Science cyclotron. A proton beam of 17 MeV was used to irradiate the samples. A closed cycle

*Corresponding author. Tel.: +81-298-59-5057; fax: +81-298-59-5010.

E-mail address: kono.kenichiro@nims.go.jp (K. Kono).

refrigerator was used to cool the sample down to 50 K. In situ DLTS measurement was conducted right after irradiation or after annealing. The projectile range of the 17 MeV proton was calculated to be 1.7 mm according to the SRIM calculation, which insures the absence of hydrogen remains in the sample and the uniformity of the defects concentration over the depth range [5].

The beam current density of the proton was maintained at about 30 nA cm^{-2} and the total fluence was varied from 1.0×10^{13} to $7.2 \times 10^{13} \text{ ions cm}^{-2}$. The irradiation was conducted between 200 and 300 K.

In order to avoid the annealing during the temperature scan of DLTS, the upper limit of the scan was restricted to the irradiation temperature. In situ measurement was used to study the kinetic process of the defect reactions without annealing.

3. Experimental results

A typical DLTS result of the FZ silicon is shown in Fig. 1. The sample was irradiated at 200 K. Without annealing, the C_1 peak around 70 K (0.12 eV) can be clearly seen. At this temperature, the diffusion of C_1 and further reactions are impossible since the migration enthalpy is 0.84 eV [6]. Isochronal annealing of 30 min was conducted by increasing the temperature up to 400 K. An annealing at 350 K diffuses the C_1 and creates the C_1C_5 structure which overlaps VO at 98 K (0.18 eV).

Similarly the low temperature irradiation results of CZ silicon are shown in Fig. 2. After irradiation at 200 K, isothermal annealing was conducted since previous experiments showed that a lot of defect reactions can be observed at this temperature [7]. No C_1 -related signal is detected right after irradiation. This is due to the trapping of I by O [1,3]. The trapping was previously studied optically [3]. We have used in situ measurement

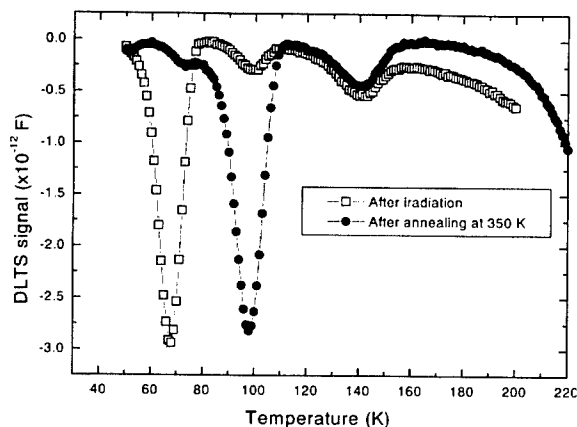


Fig. 1. n-type FZ silicon was irradiated at 200 K followed by isochronal annealing for 30 min. The peak at 70 K corresponds to C_1 . As the peak at 98 K increases, the peak at 70 K decreases.

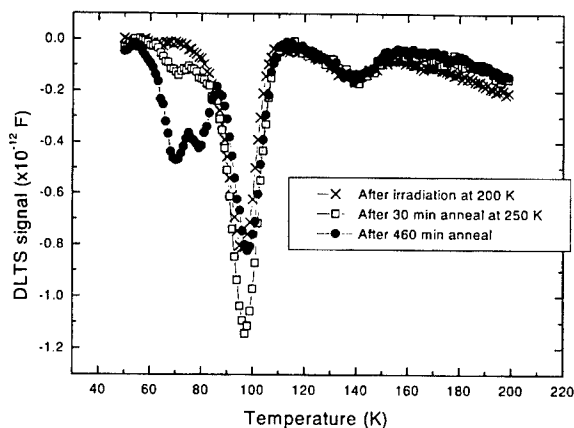


Fig. 2. n-type CZ silicon was irradiated at 200 K followed by isothermal annealing at 250 K. No interstitial carbon related peak is observed without annealing.

to prove the phenomena. The isothermal annealing was conducted to study the reaction with the slow dissociation of IO complex. The released I immediately replaces the C_5 and C_1 is created. The diffusion of C_1 at 250 K is still very limited. The C_1 reacts with C_5 and forms C_1C_5 which overlaps VO peak at 98 K (0.16 eV). However, during the isothermal annealing at 250 K, C_1 dissolves again and another level at 80 K (0.16 eV) is created [7].

4. Discussion

The result of isochronal annealing of the FZ silicon can be interpreted as follows. The diffusion of the C_1 becomes more active as temperature increases and C_1C_5 is formed which has a peak overlapping VO.

In the case of CZ silicon, I created during anneal is trapped by oxygen and no C_1 -related signal is detected. Only with annealing at 250 K C_1 is created. This is the clear indication of the trapping of the I by oxygen and the resulting suppression of the generation of the C_1 . After 30 min of annealing C_1C_5 at 98 K (0.18 eV) and C_1 at 70 K (0.12 eV) are observed. Continuous isothermal annealing dissolves C_1C_5 and increases C_1 (0.12 eV) and another structure at 80 K (0.16 eV). The difference in the reactions in FZ and CZ silicon is probably caused by the difference in phosphorus concentration which affects the charge states of the deep centers and the stability. The lower phosphorus concentration in CZ causes lower Fermi level and causes the states to remain neutral. The above charge state effect is considered to play an important role in the difference of the reactions. The detailed effects are still under investigation.

As an example to show the practical application of the knowledge of C_1 reactions, we analyze the case of the CCD. Similar analysis was done on radiation damage of

the NASA's Chandra X-ray observatory [4]. It has a CCD cooled around 150 K to detect X-rays. The radiation induced deep levels in the charge transfer channel caused the deterioration of the energy resolution by trapping of electrons. The maximum temperature its circuit could endure was 50°C.

In order to characterize the effect of the radiation defects on CCD performance, the value of CTI is found to be most important. The CTI stands for the charge transfer inefficiency and a larger value means more loss of charge during the transfer. Since the charge transfer is done repeatedly inside CCD, a slight increase in CTI can result in a great loss in electrons and can cause uncertainty in received light energy. The relationship between the capture by deep centers and CTI is [8]

$$\text{CTI} = \left(\frac{V_s}{N_s} N_t \right) \left(\exp \left(-\frac{T_t}{\tau_s} \right) \left(1 - \exp \left(-\frac{T_s}{\tau_s} \right) \right) \right),$$

where V_s is the volume of the signal charge packets, N_s is the number of electrons in the charge packets, N_t is the trap (deep centers) density, T_t is the transfer time in which carrier emission can occur, τ_t is the trap emission time constant, and T_s is the average time between charge packets. The emission time can be written as follows:

$$\tau_s = \frac{g}{\sigma_n v_t N_c} \exp \left(\frac{E_t}{kT} \right),$$

where g is the degeneracy of the trap level, σ_n is the capture cross section of the trap, v_t is the electron thermal velocity, N_c is the conduction band density of states and E_t is the energy level of the trap.

We have plotted the effects of radiation induced defects in Fig. 3. We analyze the effects of the change of structures in FZ and CZ silicon as an example.¹ Assume that FZ-Si is used for the manufacturing of the CCD. Since the CCD is maintained at 150 K, we only have C_1 and the vacancy type defects. The exact effect of CTI is not plotted in Fig. 3 since an accurate capture cross section was not available, but its energy level of 0.12 eV is too shallow to do any serious harm at 150 K. On the other hand C_1C_s produced by annealing is quite harmful as can be seen from Fig. 3. Therefore, in the case of FZ-Si annealing at room temperature will only damage the performance. Even if we assume that CZ-Si is used, the same conclusion is reached. At 150 K, no C_1 will be created because I created will be trapped by oxygen and the resulting IO does not capture the electrons. Also there is no decrease of vacancy related defects. This analysis shows why the annealing attempt of recovering the CCD performance failed and stresses the importance

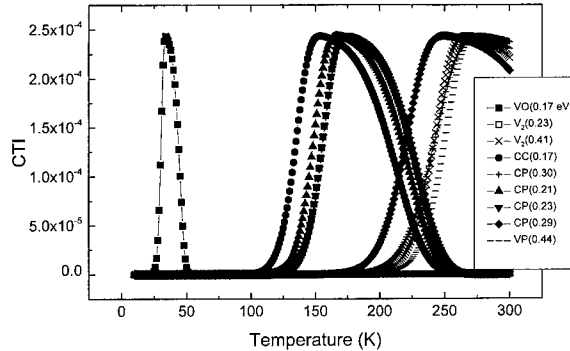


Fig. 3. The CTI of the maximum irradiation-induced electron capturing defects. To calculate CTI $v_t N_c = 1.6 \times 10^{21} \text{ T}^2 \text{ s}^{-1} \text{ cm}^{-2}$ is assumed. The capture cross sections used are as follows: VO(0.17 eV) $1 \times 10^{-14} \text{ cm}^{-2}$, $V_2(0.23)$ 4×10^{-16} , PV(0.44), $C_1C_s(0.17)$ 4×10^{-17} , CP(0.30) 1×10^{-17} , CP(0.29) 3×10^{-17} , CP(0.23) 4×10^{-16} , CP(0.21) 2×10^{-16} .

of the understanding the reactions of interstitial type defects.

5. Conclusion

The trapping of the silicon interstitial and the resulting suppression of Watkin's replacement mechanism was clearly shown by in situ DLTS measurement. The dynamic reactions of the interstitial carbon below room temperature were studied. The possibility of controlling the interstitial defects reactions by the oxygen concentration was clearly shown. The effect of the change of the C_1 -related defects on cooled CCD performance is discussed as an important example in studying the whole process of the interstitial defects.

References

- [1] L.C. Kimerling, M.T. Asom, J.L. Benton, P.J. Drevinsky, C.E. Cafer, *Mater. Sci. Forum* 38–41 (1989) 141.
- [2] G.D. Watkins, *Mater. Res. Soc. Symp. Proc.* 469 (1997) 139.
- [3] A. Brelot, J. Charlemagne, *Radiat. Effects* 9 (1971) 65.
- [4] K. Kono, J.G. Sandland, K. Wada, L.C. Kimerling, *Proceedings SPIE*, to be published.
- [5] J.F. Ziegler, J.P. Biersack, U. Littmark, *The Stopping and Range of Ions in Solids*, Pergamon Press, New York, 1985, Chapter 8, <http://www.research.ibm.com/ionbeams/>.
- [6] G.S. Oerlein, K. Krafcsik, J.L. Lindstrom, A.E. Jaworski, J.W. Corbett, *J. Appl. Phys.* 54 (1983) 179.
- [7] K. Kono, N. Kishimoto, H. Amekura, *Mater. Res. Soc. Symp. Proc.* 442 (1997) 287.
- [8] C. Dale, P. Marshal, B. Cummings, L. Shamey, A. Holland, *IEEE Trans. Nucl. Sci.* NS-40 (6) (1993) 1628.

¹Neither FZ or CZ silicon wafers we used are exactly identical to the one used for Chandra. But as an example to show the application of the knowledge it is sufficient.



ELSEVIER

Physica B 308–310 (2001) 268–271

PHYSICA B

www.elsevier.com/locate/physb

On the correlation character between the structure perfection and electroluminescent properties of terbium doped silicon monoxide films

V.S. Khomchenko, L.I. Berejinskij, M.V. Sopinsky*

Institute of Semiconductor Physics, National Academy of Sciences of Ukraine, 45, Prospect Nauky, 03028 Kyiv, Ukraine

Abstract

The present work is devoted to the investigation of structural changes accompanying the appearance of green and blue electroluminescence in thermally deposited $\text{SiO}_x:\text{Tb}$ ($x \sim 1$) films as a result of high-temperature processing. The non-destructive optical methods, specifically, measuring transmission spectra in ultraviolet, visible, near and far IR area, and multiangle ellipsometry have been used for such a research. Analysis of the obtained experimental results allows to conclude that the annealing-stimulated structural transformations in a matrix of terbium doped silicon monoxide films occur at both microstructural and macrostructural levels and have an essential and complex influence on the film radiative performances. © 2001 Elsevier Science B.V. All rights reserved.

Keywords: Microstructure; Macrostructure; Silicon monoxide; Electroluminescence

1. Introduction

Silicon monoxide films (SiO_x , $x \sim 1$) have attracted the attention of many researchers. Their physical properties are acceptable for the development of luminescent layers for the light-emitting structures. The ZnS films are widely used for this purpose. The SiO_x films, however, do not degrade in the presence of the atmospheric water vapour. Besides, unlike the ZnS films, they have a lower refraction index, allowing to substantially increase the radiation from thin-film electroluminescent structures (TFELS).

Recently [1], the new TFELS with terbium doped silicon monoxide emitting layer have been developed, in which for the first time the colour of the electroluminescence (EL) could be changed from green to blue. The EL colour change has been achieved by high-temperature processing. The present work is devoted to the

investigation of structural changes occurring in a matrix of thermally deposited $\text{SiO}_x:\text{Tb}$ ($x \sim 1$) films as a result of high-temperature processing.

2. Technique and samples

$\text{SiO}_x:\text{Tb}$ films with thickness of about 0.5 μm were obtained by simultaneous vacuum deposition of SiO_x and TbF_3 vapours volatilized from separate sources on pure silicon and sapphire substrates heated to the temperature of 200 °C. The residual pressure was 0.6 mPa and the deposition rate was ~ 1 nm/s. The film thickness was measured with an interferometer. The Tb concentration in films was 1.5 at%. The EL spectra were obtained using films deposited on the BaTiO_3 ceramic substrate.

The high-temperature treatment of films was done in air within 600–1000 °C range of annealing temperature (T_a) for 1 h with the subsequent slow cooling. Without this, $\text{SiO}_x:\text{Tb}$ films did not display any photo- or electro-luminescence. The IR- and the visible-transmission spectra were taken using Perkin–Elmer-599B and

*Corresponding author. Fax: +380-44-265-83-42.

E-mail address: sopinsk@class.semicond.kiev.ua (M.V. Sopinsky).

SPECORD UV VIS spectrophotometers. Ellipsometrical measurements were made with LEF-3M ellipsometer ($\lambda = 632.8$ nm).

3. Results and discussion

The EL spectra of $\text{SiO}_x:\text{Tb}$ films annealed at various T_a are shown in Fig. 1. It can be observed that annealing at 800°C results in the common EL of terbium with a maximum at $\lambda = 540$ nm. It corresponds to $^5\text{D}_4\text{--}^7\text{F}_5$ emissive transition [2]. Such an EL was earlier observed in $\text{SiO}_x:\text{Tb}$ films annealed at 600°C [3]. The rise of annealing temperature to 800°C considerably increases its intensity. However, annealing at higher T_a changes the EL spectrum a lot: the intensity of bands in blue area increases by about 2 orders of magnitude, and the dark blue EL becomes dominant. The intense band closer to $\lambda = 385$ nm ($^5\text{D}_3\text{--}^7\text{F}_6$) is observed in EL spectrum. The structure of Tb ion energy levels is well known [2], and the observed EL maxima matches it well. Therefore, the apparent changes in EL spectrum are tied to the violation of selection rules and probabilities of the relevant transitions of Tb^{3+} ion, which is the consequence of high-temperature annealing. This can be caused by the structural changes in an amorphous SiO_x network, or by the structural change of a cluster surrounding the impurity ion.

The optical constants (n : refraction index, κ : absorption index) and film thickness (d) were determined with

the help of the computer program described in [4,5]. The model of homogeneous and isotropic substrate and film was used. The following n values are obtained:

T_a ($^\circ\text{C}$)	200	600	800	1000
n	1.84	1.89	1.84	1.745

The $T(\lambda)$ transmission spectra of single-stage annealed $\text{SiO}_x:\text{Tb}$ films on sapphire substrates in the visible range of a spectrum are shown in Fig. 2. The behaviour of transmission spectra with an increase of annealing temperature is non-monotonous. In the interval of $T_a = 200\text{--}800^\circ\text{C}$, the long-wave shift of absorption edge increases with increase of T_a . However, further increase of T_a causes the short-wave shift of transmission spectrum of such films relative to the $T(\lambda)$ spectrum at $T_a = 800^\circ\text{C}$: the higher the T_a , the greater the shift. As a result, the film annealed at 1000°C becomes somewhat more transparent in the visible range of the spectrum than the initial as-deposited $\text{SiO}_x:\text{Tb}$ films.

Fig. 3 shows the $\text{SiO}_x:\text{Tb}$ IR-absorption spectra for the annealed film at varying temperatures. For the as-deposited film, the wide high-intensity absorption band with a maximum (ν_m) closer to 1000 cm^{-1} is observed. The shift of this band towards higher frequencies ($\nu_m = 1055\text{ cm}^{-1}$) occurring at just 600°C as well as some narrowing of it were observed. The annealing at 800°C

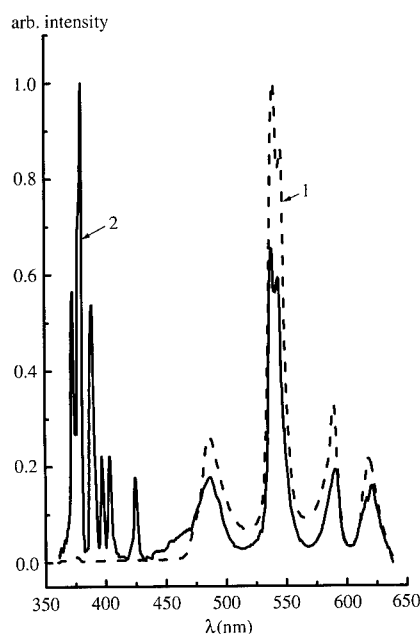


Fig. 1. The EL spectra of $\text{SiO}_x:\text{Tb}$ films annealed at 800°C (1) and 1000°C (2).

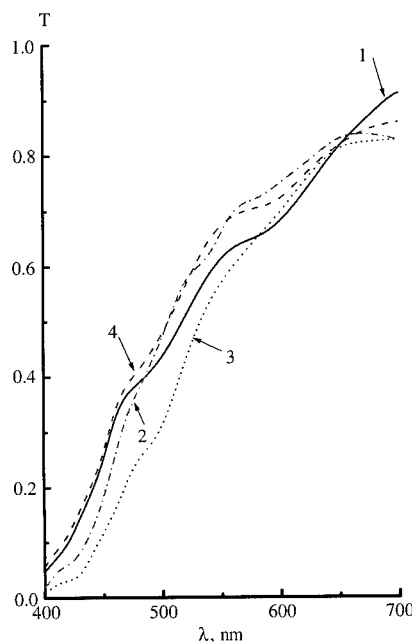


Fig. 2. Transmission spectra of $\text{SiO}_x:\text{Tb}$ films on sapphire substrate: as-deposited (1) and annealed at $T_a = 600^\circ\text{C}$ (2); 800°C (3); 1000°C (4).

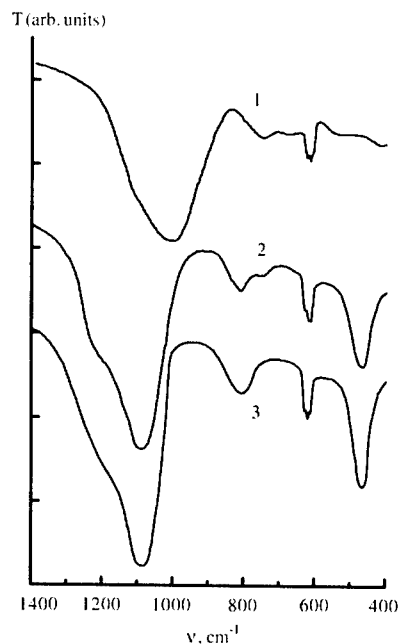


Fig. 3. IR-absorption spectra of as-deposited (1) and annealed in air (2,3) $\text{SiO}_x:\text{Tb}$ films. $T_a = 800^\circ\text{C}$ (2) and 1000°C (3).

causes further band shift towards higher frequencies ($\nu_m = 1085\text{ cm}^{-1}$), along with a further increase and narrowing. The extended shoulder appears on its high-frequency part. These are the typical features of the fused silica IR-spectrum. Also, besides this, there are absorption bands closer to 460 and 800 cm^{-1} , specific for the network of glassy SiO_2 . Annealing at 1000°C leads to an even more prominent display of SiO_2 spectra features in the absorption spectrum of annealed film.

The change of n at $\lambda = 632.8\text{ nm}$ located at the absorption edge (see Fig. 2) can be caused by the shift of the optical absorption edge, and accordingly, by a shift of dispersion curve $n(\lambda)$ [6]. In turn, the shift of optical absorption edge is caused by the change of microstructure of a film, i.e., in the case of amorphous films, change of statistical parameters describing the short- and middle-range order in them. On the other hand, the change in n can be caused as well by the film macrostructure change, such as its texture, degree of macroscopic compactness caused by occurrence or disappearance of pores, hollows, flaws (cracks), etc. [7].

The values of x in $\text{SiO}_x:\text{Tb}$ films were estimated using the obtained n values as well as using $n(x)$ dependences for thermally evaporated SiO_x films [8] and are given in Table 1. The x_E for as-deposited film is 1.17, and it decreases to $\sim 0.05\text{--}0.1$ at $T_a = 600\text{--}700^\circ\text{C}$. Apparently, the film structure changes are caused by secondary (after the deposition) redistribution of positions and bonds among the particles, and partial decomposition of random-bonding network which is accompanied by a

Table 1

Stoichiometry indexes for $\text{SiO}_x:\text{Tb}$ calculated from ellipsometrically measured refraction index (x_E) and from the IR-absorption peak position (x_{IR})

T_a	x_E	x_{IR}	x_{IR}/x_E
Deposition	1.17	1.18	0.01
600°C	1.12	1.63	0.51
800°C	1.17	1.96	0.79
1000°C	1.28	1.96	0.68

desorption of oxygen. At $T_a \sim 800^\circ\text{C}$, the rise of x becomes observable (caused, apparently, by further oxidation process). This oxidation intensifies at $T_a = 1000^\circ\text{C}$. However, there is no complete film oxidation for SiO_2 . This is also confirmed by the data on the optical absorption edge for these films (Fig. 2).

It has been shown in Refs. [9,10] that the microstructure of SiO_x films obtained by thermal evaporation of silicon monoxide corresponds to the random bonding model (RBM). Within the framework of the RBM model [11], the SiO_x film represents the single-phase statistical intermixture of $\text{Si}-(\text{Si}_i\text{O}_{4-i})$ ($0 < i < 4$) tetrahedra bound through bridging oxygen. In these works, the empirical $\nu_m(x)$ dependence for such films has also been determined. We have utilized these dependences to determine the oxygen content in our films. The values obtained are given in Table 1. For the as-deposited $\text{SiO}_x:\text{Tb}$ films, the value thus obtained is $x_{\text{IR}} = 1.18$. It conforms very well to $x_E = 1.17$. However, for the high-temperature annealed films, such conformity of x_E and x_{IR} values has not been observed. Thus, one can conclude that the microstructure of $\text{SiO}_x:\text{Tb}$ films annealed at high temperatures cannot be described by the RBM. Such films have an increased content of areas with SiO_2 -like stoichiometry (compared to the statistics of random bonding). However, at $T_a > 800^\circ\text{C}$ the improvement in the film homogeneity is observed. Apparently, such an ordering of film structure improves the carrier heating conditions in the electric field.

So, it has been shown that film structure changes and that light-emitting characteristics are non-monotonic when the annealing temperature rises. The occurrence of green EL ($T_a = 600\text{--}800^\circ\text{C}$) is accompanied by a structural reorganization of a matrix resulting in partial decomposition of deposited films. As a result, these films represent an intermixture of several phases— Si , SiO_x and SiO_2 . Films displaying blue EL ($T_a \sim 1000^\circ\text{C}$), have a comparatively higher content of oxygen, better compactness, and macroscopic homogeneity compared with both as-deposited and annealed at $600\text{--}800^\circ\text{C}$ films.

References

- [1] V.S. Khomchenko, et al. Proceedings of the VI International Symposium on Advanced Display Techniques, Partenit, Crimea, Ukraine, Vol. 126, October 1997.
- [2] I.H. Dieke, H.M. Crosswhite, *J. Appl. Opt.* 2 (1969) 675.
- [3] P.I. Didenko, et al., *Phys. Status Solidi A* 100 (1987) 501.
- [4] N.V. Sopinskii. *Optoelectron. Instrum. Data Process. (Avtometriya)* (1) (1997) 95 (English translation)
- [5] N.V. Sopinskii. *Russ. Microelectron.* 30 (1) (2001) 35 (English translation)
- [6] J.C. Phillips, *The fundamental Optical Spectra of Solids*, Academic Press, New York, London, 1966.
- [7] M. Popesku, H. Bradaczek, *J. Optoelectron. Adv. Mater.* 1 (1) (1999) 5.
- [8] H.K. Pulkov. Characterization of optical thin films. Balzers AG, FL-9496 Balzers, Liechtenstein.
- [9] M. Nakamura, et al., *Sol. State Commun.* 50 (1984) 1079.
- [10] A.L. Shabalov, M.S. Feldman, *Thin Solid Films* 151 (1987) 317.
- [11] H.R. Philipp, *J. Phys. Chem. Solids* 32 (1971) 1935.



ELSEVIER

Physica B 308–310 (2001) 272–275

PHYSICA B

www.elsevier.com/locate/physb

The control mechanism of the impurity agglomeration triggered by ion impacts

S.T. Nakagawa*

Simulation Science Center, Okayama University of Science, 1-1 Ridai-cho, Okayama 700-0005, Japan

Abstract

We have studied the agglomeration mechanism of impurity B ions due to a high-dose ion implantation into Si, making use of a defect analysis performed with a molecular dynamic simulation. Beyond a threshold level of impurity concentration, ion irradiation drastically changes the spatial distribution of crystal atoms, which promotes the agglomeration significantly. The lattice reaction for the ion impact was often synergistic and depended strongly on the temperature of the host target, even with the same condition of irradiation energy. At a temperature of 100 K, the agglomeration once increased then decreased, because dissociation took it over. Above 200 K, however, the agglomeration progressed with ion impact. Such an analysis was possible by means of *pixel mapping* that showed the long-range interactions between atoms in a crystal. © 2001 Elsevier Science B.V. All rights reserved.

PACS: 31.15.Qg; 61.80.Jh; 68.43.Jk

Keywords: Radiation annealing; Agglomeration; Molecular dynamics

1. Introduction

The impurity agglomeration is often observed due to high-dose (Φ) ion implantation, when the concentration exceeds a certain level. For example, the critical concentration is 1–2 at% for cases of Au, Ag, B, in Si [1]. We have looked at an experiment [2] of B implantation into Si(100) with an energy of 35 keV with $\Phi = 3 \times 10^{16} - 1 \times 10^{17} \text{ cm}^{-2}$ at RT, which confirmed the formation of B_{12} clusters. A qualitative explanation based on the formation enthalpy failed to explain the agglomeration of impurity ions with a few %, because impurity ions are separated from each other farther than 10 Å in average.

When a crystal is heavily irradiated, accumulated defects may cause a synergistic reaction of a phase transition or a new event [3]. It strongly depends on the temperature of the host crystal, T_h , and the irradiation energy, E , as well as amorphization of a crystal, the impurity agglomeration is a typical case of it. In this case

of B implantation into Si, the homogenous amorphization occurs at $T_h < 200\text{--}300 \text{ K}$ [4] and $\Phi > 10^{15} \text{ cm}^{-2}$ [5]. Since we are looking at a case of $T_h = \text{RT}$ and $\Phi \leq 10^{17} \text{ cm}^{-2}$ [2], the agglomeration mechanism should closely relate to amorphization.

Making use of molecular dynamics (MD) we proved that ion irradiation was indispensable for agglomeration. We reproduced the B agglomeration, up to B_{11} clusters, and also confirmed that the critical concentration for B clustering was 2% as was measured [1]. This concentration demanded us to solve the mechanism by considering long-range interactions between atoms. Therefore, we proposed a new analysis of pixel mapping (PM) that could reveal the cooperative behavior of atoms in a crystal [6], for studying the correlation between the lattice reaction and the agglomeration.

2. Method: parallel analyses during the course of MD simulation

In order to depict the lattice reaction for ion bombardment, we took T_h from 100 to 400 K. The

*Corresponding author. Tel./Fax: +81-86-25-69-458.

E-mail address: stnak@dap.ous.ac.jp (S.T. Nakagawa).

reason for the higher end of 400 K was being afraid of an irradiation heating, whereas the lower end was to suppress the thermal effect as much as possible. The elevated T_h was supposed to be less than 50°, while the nominal value was $T_h = \text{RT}$. The average energy of the projectiles entering the MD-box was 4.5 keV [1]. When we bombarded Si crystal whose initial concentration of impurity, C_0 , was a few % with energetic ions of $1 \text{ keV} \leq E \leq 5 \text{ keV}$, projectiles caused agglomeration but they themselves run through the MD-box [1]. Therefore, in the present calculation we analyze the intermediate processes resulting in the agglomeration, with the conditions $E_{\text{max}} = 5 \text{ keV}$ and $C_0 = 3\%$. The following quantities are calculated at each moment when the system is thermalized after each ion impact. The longest cooling time was 2 ps.

Three types of radial distribution functions, $g(r)$, were calculated, where r stands for the internuclear distance. The $g(r)$ for the Si–Si correlation shows the entire imperfection of the host crystal, that for the B–Si the stability of B atoms accommodated in a Si crystal, and that of B–B the progress of the agglomeration. We take the longest distance r for $g(r)$ 5 Å for all cases because of the cut-off lengths of the potentials adopted.

If agglomeration had started, the mesoscopic view of the intermediate process following ion irradiation is obtained from the size distribution of B_m clusters that is made of m B atoms. The index of agglomeration, $k(n)$, is the fraction of agglomerated B atoms in the MD-box after the n th impact:

$$k(n) = \frac{\sum_{m=2} m B_m(n)}{\sum_{m=1} m B_m(n)}. \quad (1)$$

We proposed a new method of PM, in order to analyze the cooperative change relating to defects in a crystal, which is parallelly done with the MD. It identifies atoms whether they are in the stable, metastable, or unstable sites. The detailed algebra is explained elsewhere [6]. The definition of $N_i(n)$ is the occupied fraction of the i th kind of pixel after the n th ion impact. When a Si crystal is perfect, a Si atom is placed in a stable pixel (1) or (2), which gives us $N_{(1)}(0) = N_{(2)}(0) = 0.5$. A metastable pixel {H} includes one “H-site” at its center, which is mathematically and physically paired with a (1) pixel. The similar relation stands between (2) and {T}. The ensemble of pixels (1) and (2) forms a real FCC structure, respectively, while that of the {H} or {T} forms a *virtual* one.

All the residual pixels offer unstable sites for the target atoms. The geometric relation of $\langle 1' \rangle$ with (1) is as follows. According to normal crystallography, an ensemble of the stable sites of a diamond crystal forms a honeycomb lattice on a (111) plane. Therefore, the centers of pixels (1) form such a honeycomb, whereas those of the unstable pixels $\langle 1' \rangle$ form a smaller honeycomb in the same plane, which is exactly half the

size. All other kinds of unstable pixels have the same relation to their own *parent lattice*. The superior difference of the PM to other analyses is to show the long-range information from an ensemble of atoms that locate at physically equivalent positions in a periodic crystal.

3. Results

The calculations were done with conditions of $E_{\text{max}} = 5 \text{ keV}$ and $C_0 = 3\%$. Before starting ion impact, we leave the system until the thermalization has been established for 2–3 ps, at longest. With this process, the initial state was $N_{(1)}(0) = N_{(2)}(0) = 0.5$ for Si atoms. The B atoms preferably occupied the metastable {T} or {H} sites, not substitutional ones. Here, the total number of the Si atoms is 4096 for $T_h = 400 \text{ K}$ and 1728 for other cases. The number of ion impacts is determined by a Monte-Carlo calculation. The experimental condition of $\Phi = 10^{17} \text{ cm}^{-2}$ corresponds to about 150 impacts onto an MD-box if it contains 1728 Si atoms. Then we took 200 projectiles at the maximum.

3.1. The lattice response described by $N_i(n)$ superior to $g(r)$

The three kinds of $g(r)$ were calculated during the course of the ion impacts at $T_h = 400 \text{ K}$. Each profile changed monotonously to its random one. Once a random state was achieved, the change looked irreversible. In the case of $T_h = 100 \text{ K}$, after a drastic disappearance of the Si atoms located at the stable states (1, 2), all the pixels were soon occupied with even probability, i.e., a random state was achieved [6]. On the other hand, no drastic change appeared in the case of $T_h = 400 \text{ K}$. Moreover, crystalline atoms react cooperatively in a more complicated way as is shown in Fig. 1. Fig. 1a shows the fraction of Si atoms accommodated at the stable (1, 2) and the metastable {T, H} pixels. Fig. 1b shows those of the unstable pixels $\langle 2', H' \rangle$ and $\langle 1', T' \rangle$. In Fig. 1c, the case of the B atoms is shown. The B atoms were accommodated at the {T, H} pixels, then (1, 2) pixels, as if they exchange the sites with the Si atoms.

The remarkable differences of the lattice reaction at T_h higher than 100 K are: (1) Pronounced peaks other than the stable ones appeared before the random state is achieved. That is, one kind of the unstable $\langle 2', H' \rangle$ sites dominated, then the metastable {T, H} sites appeared. (2) There appeared clear difference in the occupation rule between the $\langle 2', H' \rangle$ and $\langle 1', T' \rangle$ sites. Fig. 1 gives us the details of the synergistic reaction of a crystal according to the ion impacts. The first value of $N_{(1)}(0) = N_{(2)}(0) = 0.5$ implies that the crystal was almost perfect. When irradiation began, atoms were

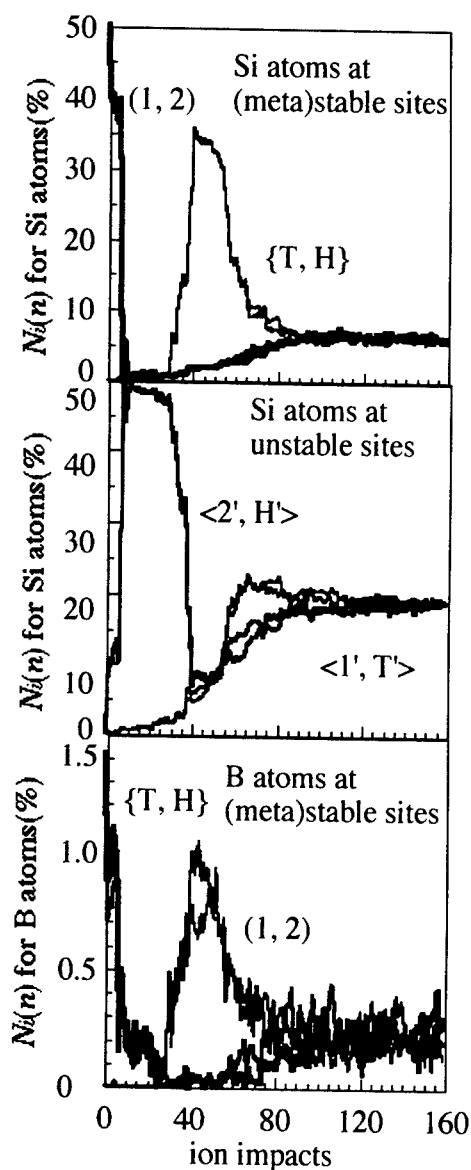


Fig. 1. The PM of Si atoms at 400 K, as the function of ion impact. The fraction of Si atoms accommodated at the stable (1,2) or the metastable {T,H} sites is shown in (a), while those of the unstable sites <1',2',T',H'> are shown in (b). The corresponding profile of the B atoms at the stable (1,2) or the metastable {T,H} sites is shown in (c).

synergistically moved to the unstable sites, then to the metastable sites. With further irradiation, such a cooperative movement is lost, where crystallinity existed no more.

3.2. The lattice reaction depending on T_h : $N_i(n)$

The rigidity of the target crystal depends on T_h , which is interestingly seen by the PM, as is shown by the

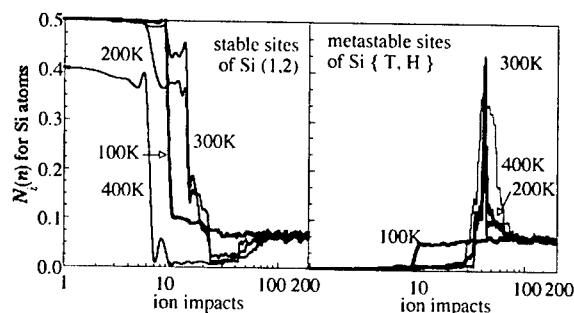


Fig. 2. The T_h dependence of the collapse of the Si crystal, by means of the PM for Si atoms. (a) Stable sites (1,2) and (b) metastable sites {T,H}.

abrupt decrease in Fig. 2a. At $T_h = 100$ K, the crystalline system was transferred almost straightforwardly to a random state, without dominant occupation of the unstable or metastable sites as was shown in Fig. 1. As is shown in Fig. 2b, metastable sites {T,H} grow as T_h increases. At $T_h = 200$ K, this peak was sharp but low; at $T_h = 300$ K, this peak became very sharp and high; then at $T_h = 400$ K it became distinguished. We knew that the reaction mechanism of the crystal definitely changed between 100 and 200 K.

3.3. The agglomeration promoted by the lattice deformation

At $T_h = 100$ K, the Si atoms had moved suddenly from the stable states. At the same time, agglomeration increase significantly progressed. The $k(n)$ defined by Eq. (1) once increased significantly across this critical moment, then decreased. The final decrease implies the dissociation by further ion impact.

Fig. 3 shows the T_h dependence of the $k(n)$. Lines are drawn to guide the eyes. The thick line indicates the case of $T_h = 100$ K, while thinner lines indicate $T_h \geq 200$ K. As a matter of course, both agglomeration and dissociation coexisted during the cluster-growth process and B_n clusters were positively produced at first. After this first stage, the competition between the agglomeration and dissociation became different depending on the T_h . At $T_h = 100$ K, the dissociation overcame the agglomeration finally. On the contrary, when the target was not extremely cold, i.e., $T_h \geq 200$ K, agglomeration looked continuously dominant although a tendency of saturation slightly appears finally. This behavior explained that the radiation annealing practically promoted the agglomeration.

4. Conclusions

We studied the correlation between impurity agglomeration and the crystal damage, by means of the parallel

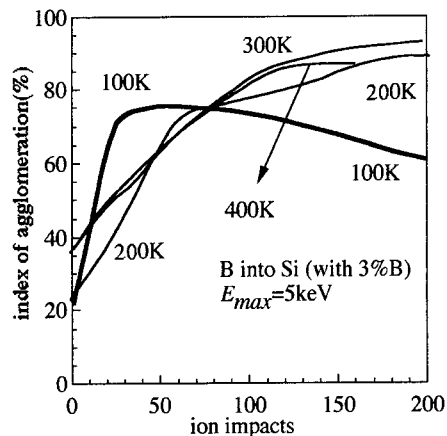


Fig. 3. The T_h dependence of the index of agglomeration as a function of the ion impacts. The thick line indicates the case of $T_h = 100$ K, the thinner ones from 200 to 400 K. Lines were drawn to guide the eyes.

analysis of a MD and PM [6], in the case of high-dose implantation of B ions into a Si crystal. We prepared a super-saturated B in Si, and examined how the lattice reaction progressed. The defect formation differed definitely between 100 and 200 K. At a low temperature of 100 K, the Si crystal collapsed abruptly at a moment during the ion impacts, then the spatial distribution of the Si atoms turned to be random immediately. Across the critical moment, agglomeration was drastically promoted. However, dissociation overcame the agglom-

eration finally. At temperatures higher than 200 K, such a cooperative response differed, where agglomeration always overcame the dissociation. Therefore, concluding remarks are: (1) The impurity agglomeration is due to the cooperative reaction of the crystal atoms performing long-range interactions. (2) The radiation annealing promoted the agglomeration.

Acknowledgements

The author is indebted to the financial support from the Frontier project of the Ministry of Education, Culture, Sports, Science and Technology of Japan.

References

- [1] S.T. Nakagawa, G. Betz, *Nucl. Instrum. Methods B* 180 (2001) 91–98.
- [2] I. Mizushima, et al., *Mater. Chem. Phys.* 54 (1998) 54–59.
- [3] H. Gnaser, *Low Energy Ion Irradiation of Solid Surfaces*, Springer Tracks in Modern Physics, vol. 146, Springer, Berlin, 1999, p. 190.
- [4] T. Motooka, S. Harada, M. Ishimaru, *Phys. Rev. Lett.* 78 (1997) 2980–2982.
- [5] M.A. Kumakhov, G. Shirmer, *Atomic Collisions in Crystal*, Gordon & Breach Sci. Pub, New York, 1989, p. 143.
- [6] S.T. Nakagawa, submitted to *Phys. Rev. B* (2001).



ELSEVIER

Physica B 308–310 (2001) 276–279

PHYSICA B

www.elsevier.com/locate/physb

Optical absorption peaks observed in electron-irradiated n-type Si

M. Suezawa^{a,*}, N. Fukata^a, A. Kasuya^b

^a*Institute of Materials Research, Tohoku University, 2-1-1 Katahira, Sendai 980-8577, Japan*

^b*Center for Interdisciplinary Research, Tohoku University, Sendai 980-8578, Japan*

Abstract

We found many optical absorption peaks in electron-irradiated n-type Si crystals. Specimens were prepared from various Si crystals. After chemical etching, they were irradiated with 3-MeV electrons at RT. Their optical absorption spectra were measured with an FT-IR spectrometer at temperatures in the range of 5 K and RT with a resolution of 0.25 cm^{-1} . Many optical absorption peaks were observed in the wavenumber range between 950 and 1600 cm^{-1} only in n-type (phosphorus-doped) floating-zone grown Si crystals. Hence, they are due to donors. They were not observed in Czochralski-grown Si (CZ-Si) crystals. This suggests that these peaks are due to complexes of phosphorus and vacancies since most vacancies in CZ-Si form pairs (A-center) with oxygen because of very high concentration of oxygen. They disappeared by annealing at above 200°C . © 2001 Elsevier Science B.V. All rights reserved.

Keywords: Si; Electron irradiation; Optical absorption; Donor

1. Introduction

Optical absorption measurements of electron-irradiated silicon crystals have been conducted since the 1950s (see, as a review, Ref. [1]). In these studies, many absorption peaks were observed. Some are due to electronic transitions associated with divacancy, and some are due to vibrational transitions associated with pairs of vacancies and oxygen atoms and so on. We found many optical absorption peaks in electron-irradiated floating-zone grown silicon crystals (FZ-Si). They are probably due to electronic transitions associated with vacancy–phosphorus pairs.

2. Experimental

Specimens used in this study were prepared from FZ-Si crystals of n-type and p-type (boron concentration: $1.5 \times 10^{16}\text{ cm}^{-3}$) and Czochralski-grown Si crystals

(CZ-Si) of n-type (phosphorus concentration: $5.2 \times 10^{15}\text{ cm}^{-3}$). The phosphorus (P) concentrations of the n-type FZ-Si specimens of F1, F2 and F3 were 1.5×10^{16} , 5.8×10^{15} and $2.4 \times 10^{15}\text{ atoms cm}^{-3}$, respectively. We irradiated specimens with 3-MeV electrons at RT and measured the optical absorption spectra of irradiated specimens with an FT-IR spectrometer equipped with a continuous-flow-type liquid helium cryostat in a temperature range between 5 K and RT. The spectral resolution was 0.25 cm^{-1} .

3. Results and discussion

Fig. 1 shows the optical absorption spectrum of electron-irradiated FZ-Si specimen, F1. Many peaks were observed. The spectrum of F2 was similar to Fig. 1. On the other hand, that of F3 showed only two peaks at about 1150.6 and 1156.5 cm^{-1} , which are the strongest peaks in Fig. 1. Other peaks were not observed probably because of small concentrations of defects in this specimen. The peak positions of Fig. 1 are at larger wavenumbers than those due to vibrational transitions except those of hydrogen, nitrogen and oxygen, the

*Corresponding author. Tel.: +81-22-215-2040; fax: +81-22-215-2041.

E-mail address: suezawa@imr.edu (M. Suezawa).

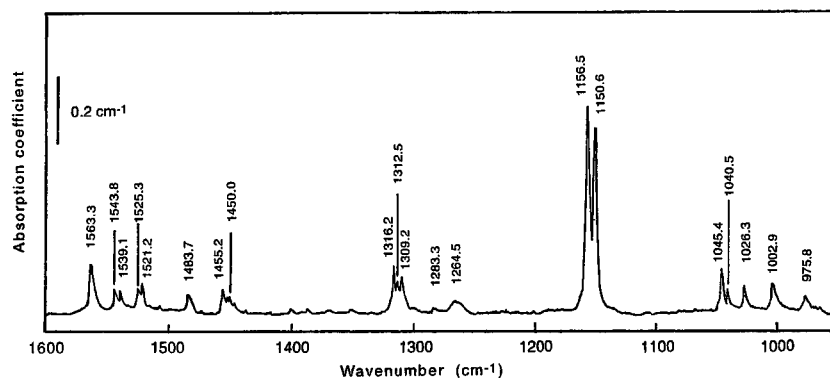


Fig. 1. Optical absorption spectrum of the specimen F1 after electron-irradiation of $4 \times 10^{16} \text{ cm}^{-2}$.

concentrations of which are very small in our specimens. Hence, these are due to electronic transitions associated with complexes, which include point defects generated by electron-irradiation of specimens. One evidence for electronic transitions is that these peaks were not observed in irradiated p-type FZ-Si. Complexes responsible for these peaks are thought to include vacancies (V) since these peaks were not observed in CZ-Si. Most vacancies generated by electron-irradiation of CZ-Si crystals are known to form pairs with oxygen atoms and some form divacancies, when the irradiation dose is below 10^{18} cm^{-2} [2]. We tried to classify these peaks assuming the effective-mass theory but were unsuccessful. Hence, we could not determine the number of species of complexes responsible for these peaks. This is discussed later in connection with temperature dependence of the peak intensities.

We propose that complexes responsible for these peaks include V and P according to following discussion. As is well-known, optical absorption peaks due to divacancies are observed at around 2700 cm^{-1} [3] and hence, divacancies are not responsible for these peaks. The probabilities to form complexes larger than divacancy are considered to be low, since the irradiation dose was not large. Hence, complexes composed of only vacancies are not the defects responsible for these peaks. Pairs of V and P, so-called the E-center, are known to be easily formed [4] due to irradiation of P-doped Si. According to a study by means of EPR method, the E-center has an acceptor level at about 0.44 eV below the bottom of the conduction band (E_c) [4]. It is EPR-inactive when the Fermi level is above that level. Kimerling et al. [5] found electron-trap levels at $E_c = 0.11, 0.20, 0.30$ and 0.44 eV in electron-irradiated n-type Si crystals. Some of them may be optically active. We tentatively propose that the V–P pairs in an appropriate charge state are responsible for these peaks. There may be high probability to form V_2P by reaction between an E-center and V. Lugakov and Luk'yanitsa [6] suggested

that the V_2P has acceptor levels at the lower half of the band gap. If this is the case, V_2P complexes are not responsible for our spectrum.

We should compare the above spectrum with that observed in neutron-irradiated Si. More than 40 optical absorption peaks, so-called the higher-order band (HOB), were found in neutron-irradiated Si crystals in the wavenumber range from 650 to 1300 cm^{-1} [7]. Their peak positions are different from those of Fig. 1. Moreover, as shown later, their thermal stability is also much different from those of Fig. 1. Hence, we conclude that the above peaks are different from the HOB.

Fig. 2 shows dependence of the intensity of the 1156.5 cm^{-1} peak in various specimens on the electron dose. In the case of specimens, F1, there is a peak at a dose of around $6 \times 10^{16} \text{ cm}^{-2}$. This peak seems to shift to lower doses as the phosphorus concentration becomes smaller as suggested from curves of F2 and F3. At low doses, the peak intensity of F1 increased as the dose increased probably due to the increase of V–P pairs. We should recollect our previous results in relation to this interpretation. As shown in a separate paper [8], we studied the formation of VH_2 complex due to electron-irradiation of hydrogen-doped Si crystals. The concentration of VH_2 complex increased as the irradiation dose increased in high-purity Si. On the other hand, it was very small in the specimen F1 doped with H. These results suggest that a V in the specimen F1 preferentially form a pair with a P and not with an H_2 . At doses higher than about $6 \times 10^{16} \text{ cm}^{-2}$, the intensity in the specimen F1 decreased as the dose increased. The dependences of the specimens F1, F2 and F3 on the electron dose are similar to each other at high doses: the slopes of curves in Fig. 2 was almost -1 . This is probably due to the saturation of V–P pair and the increase of acceptors formed by electron-irradiation. According to our experiment [9], the concentration of acceptors at the irradiation dose of $1 \times 10^{16} \text{ cm}^{-2}$ was about $9 \times 10^{14} \text{ cm}^{-3}$ and increased almost proportional to the

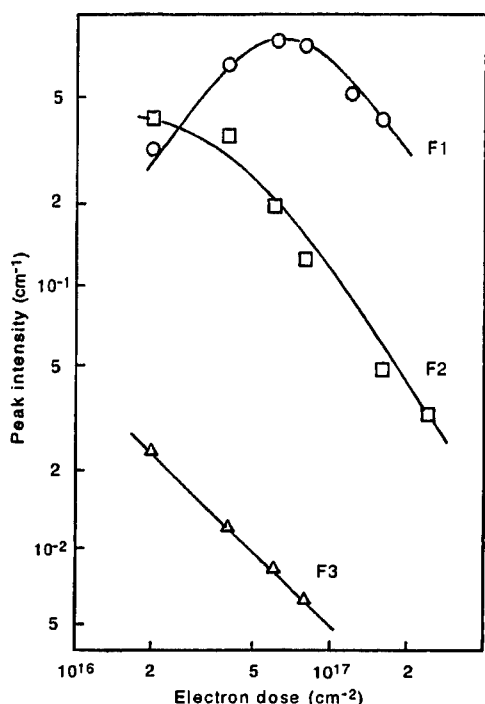


Fig. 2. Dependences of the intensity of the 1156.5 cm^{-1} peak in the specimens F1, F2 and F3 on the electron dose.

electron-dose. Hence, if the concentration of V–P pair is saturated at high doses, that of the appropriate charge state, which is responsible for the above optical absorption peaks decreases as the dose increases. Within our knowledge, the spectrum of Fig. 1 has not been reported even though a lot of studies have been performed for electron-irradiated Si crystals by means of optical absorption measurement method. This is probably due to the behavior shown in Fig. 2: Irradiation doses so far adopted were rather high, around 10^{18} cm^{-2} , and hence, the absorption intensities should have been very weak.

Fig. 3 shows the annealing behaviors of the 1156.9 cm^{-1} peak. The annealing duration was 30 min at each temperature. The peak intensity almost disappeared due to annealing at 225°C . This annealing stage agrees well with the second stage observed by Hirata et al. [10] in γ -irradiated n-type Si. According to them, this annealing stage is due to diffusion of V–P pairs to the sinks. In the case of the HOB, it is observed after annealing at $450\text{--}600^\circ\text{C}$ [7]. Hence, as indicated already, the HOB is different from our peaks.

We measured the dependence of peak intensities on the measurement temperature to determine the energy levels of the ground states of those peaks. The measured temperature range was too narrow to exactly determine those levels. It was clarified, however, that the dependences of intensities of the 1150.6 and 1156.5 cm^{-1}

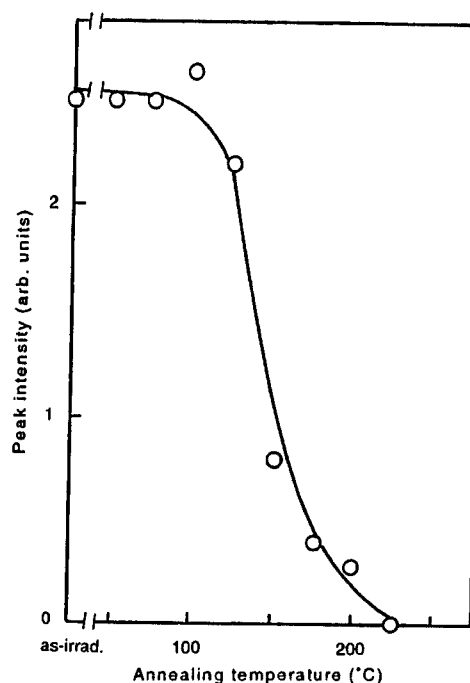


Fig. 3. Isochronal annealing behavior of the 1156.5 cm^{-1} peak due to annealing for 30 min at each temperature.

peaks, of the 1309.2 , 1312.5 and 1316.2 cm^{-1} peaks and of the 1563.3 cm^{-1} peak on temperature were similar. It means that the energy levels of these ground states are the same. Hence, we tentatively propose that the observed peaks are due to one kind of center, the V–P pair at an appropriate charge state. To clarify the properties of the ground state, further studies by means of EPR and DLTS methods are necessary.

4. Summary

We found many optical absorption peaks in electron-irradiated FZ-Si crystals of n-type only. They were not observed in electron-irradiated CZ-Si crystals. We proposed that these optical absorption peaks were due to electronic transitions of V–P pair in an appropriate charge state.

Acknowledgements

The authors thank the Laboratory for Advanced Materials for allowing using their FT-IR spectrometer. The authors also wish to thank H. Takizawa of the JAERI Takasaki Institute for his help in electron-irradiation. This work was partly supported by the JSPS research for the Future Program under the project

“Ultimate Characterization Technique of SOI Wafers for Nano-scale LSI Devices” and a Grant-in-Aid for Scientific Research on priority Area (B) “Manipulation of Atoms and Molecules by Electron Excitation” from the Ministry of Education, Culture, Sports, Science and Technology of Japan.

References

- [1] O.L.Curtis, in: J.H. Crawford Jr., L.M. Slifkin (Eds.), *Point Defects in Solids*, Vol. 2, Plenum Press, New York, London, 1975, p. 257.
- [2] A. Nakanishi, M. Suezawa, N. Fukata, unpublished.
- [3] E.J. Cheng, et al., *Phys. Rev.* 152 (1966) 761.
- [4] G.D. Watkins, J.W. Corbett, *Phys. Rev.* 134 (1964) A1359.
- [5] L.C. Kimerling, et al., *Solid State Commun.* 16 (1975) 171.
- [6] P.F. Lugakov, V.V. Luk'yanitsa, *Sov. Phys. Semicond.* 17 (1983) 106.
- [7] Y. Shi, et al. *Phys. Stat. Sol. (A)* 144 (1994) 139.
- [8] M. Suezawa, *Phys. Rev. B* 63 (2001) 035203.
- [9] M. Suezawa, unpublished.
- [10] M. Hirata, et al., *J. Phys. Soc. Japan* 27 (1969) 405.



ELSEVIER

Physica B 308–310 (2001) 280–283

PHYSICA B

www.elsevier.com/locate/physb

Essential difference in concentration profile of Au in Si after annealing above or below 850°C

Masami Morooka*

Fukuoka Institute of Technology, Wajirohigashi, Higashi-ku, Fukuoka 811-0295, Japan

Abstract

Indiffusion and out-diffusion profiles of Au in Si have been measured after a heat treatment at a higher or lower temperature than 850°C. The diffusion is slow and the profiles show a typical kick-out diffusion, in both heat treatments for the indiffusion above and below 850°C, and for the out-diffusion of Au supersaturated above 850°C. On the other hand, the out-diffusion of Au supersaturated below 850°C is very fast and the profile shows that it is flat. The essential difference in the concentration profiles are consistent with the change of the Au configuration supersaturated below 850°C from high-temperature substitutional Au to a low-temperature one. © 2001 Elsevier Science B.V. All rights reserved.

Keywords: Si: Au; Concentration profile of Au in Si; Impurity diffusion in Si; Gold state in silicon

1. Introduction

Au atoms in Si occupy interstitial and substitutional sites, and the substitutional Au exists in three states: low-temperature substitutional Au, high-temperature substitutional Au, and agglomerations of substitutional Au [1]. High-temperature substitutional Au diffuses slowly itself, and their atomic-flow is dominated by an interchange mechanism of Si atom with interstitial Au atom [2]. On the other hand, low-temperature substitutional Au diffuses rapidly by a ring mechanism [3] and their atomic-flow is limited by the diffusion itself [4]. The author et al. have reported that the annealing characteristics [5] resulting in the out-diffusion profile [6] of supersaturated substitutional Au in Si are affected dominantly by cooling down to room temperature or not before the heat-treatment for annealing, namely, they are fast and flat type or slow and inverse U-type corresponding to the diffusion of low-temperature substitutional Au or a high-temperature one, respectively.

In this paper, indiffusion and out-diffusion profiles of substitutional Au in Si have been measured after a heat

treatment at a higher or lower temperature than 850°C, which is the boundary temperature to change the gold configuration from high-temperature substitutional Au to a low-temperature one. The experimental results are consistent in that the excess over the thermal equilibrium concentration, namely, the amount of supersaturated Au atoms, change from high-temperature substitutional Au to a low-temperature one by cooling below 850°C after a pre-indiffusion.

2. Experimental details

Float-zoned (Fz) and extended-defect-free silicon crystals of about 1 mm thickness were used. About several tens nm of Au layers were evaporated on both surfaces of the specimen before heat treatment. In the experiment for the measurement of indiffusion profile, the specimens were heat-treated at 800°C or 900°C for 90 h. In one experiment for measurement of out-diffusion profile, specimens were heat-treated at 1150°C for 90 h for pre-indiffusion of Au, and one of them is used for the measurement of indiffusion profile, which is regarded as the initial profile for subsequent annealing. Au layers were evaporated again after removal of surface layers of the pre-indiffused specimen

*Corresponding author. Tel.: +81-92-606-3131; fax: +81-92-606-0751.

E-mail address: morooka@ce.fit.ac.jp (M. Morooka).

to transform the surface concentration into the thermal equilibrium value in the subsequent heat treatment [7], and the specimen was heat-treated at 800°C or 900°C for 90 h subsequent to re-heat-treatment at 1150°C for 30 min. In this case, specimen temperature decreases from 1150°C to the annealing temperature, and, substitutional Au supersaturated at the temperature are annealed out during the heat-treatment. In the other experiment for the measurement of out-diffusion profile, the specimen, on which Au layers were evaporated after the pre-indiffusion, was heat-treated directly at 800°C or 900°C for 90 h from room temperature without re-heat-treatment at 1150°C. In this case, the specimen is cooled to a room temperature before the annealing, and, substitutional Au supersaturated at the room temperature are annealed out during the heat treatment.

The concentration profile of substitutional Au is obtained by a capacitance measurement in lines with Au–Si Schottky diodes on an angle-lapped surface [8].

3. Experimental results

3.1. Indiffusion profiles at 800°C and 900°C

The concentration profiles of substitutional Au in Si after heat-treatment for indiffusion at 800°C for 90 h or at 900°C for 90 h are shown in Fig. 1. The indiffusion is very slow at the temperatures, and, at 800°C, the concentration is difficult to measure except near the specimen surface due to a concentration lower than the detection limit of our apparatus. Both indiffusion profiles seem to show a kick-out diffusion limited by the self-interstitial diffusion to the specimen surface, namely, a U-shaped profile.

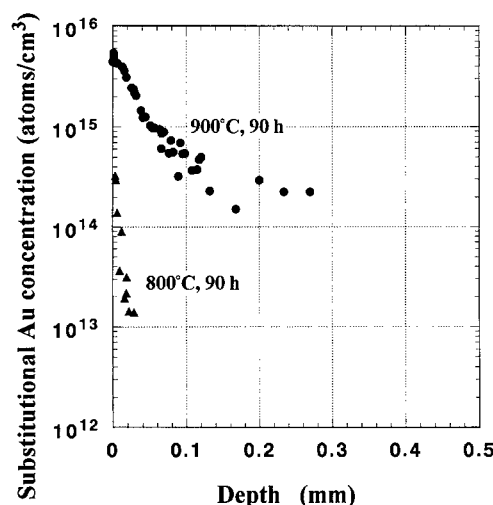


Fig. 1. Indiffusion profiles of substitutional Au in Si at 800°C and 900°C. The specimen thickness is about 1 mm.

3.2. Out-diffusion profiles at 800°C and 900°C

The concentration profiles of supersaturated substitutional Au in Si after heat-treatment at 800°C or 900°C for 90 h subsequently to re-heat-treatment at 1150°C for 30 min after the pre-indiffusion at 1150°C for 90 hours are shown in Fig. 2. The out-diffusion at 900°C is very slow and shows a typical kick-out diffusion, namely, an inverse U shape. On the other hand, at 800°C, the annealing is very fast in spite of the temperature lower than 900°C, and the profile shows a flat one due to homogeneous agglomeration of Au atoms [4]. The initial profile predicted from the profile of other specimens is shown in the figure.

3.3. Out-diffusion profiles at 800°C and 900°C without re-heat-treatment at 1150°C

The concentration profiles of supersaturated substitutional Au in Si after heat-treatment at 800°C or 900°C for 90 h after quenching to room temperature subsequent to the pre-indiffusion at 1150°C for 90 h are shown in Fig. 3. In this case, the out-diffusion even at 900°C is very fast additional to that at 800°C, and, both profiles below and above 850°C show a flat-type one due to the homogeneous agglomeration.

4. Discussion

To compare the indiffusion and out-diffusion characteristics, Figs. 1 and 2 are plotted together in Fig. 4.

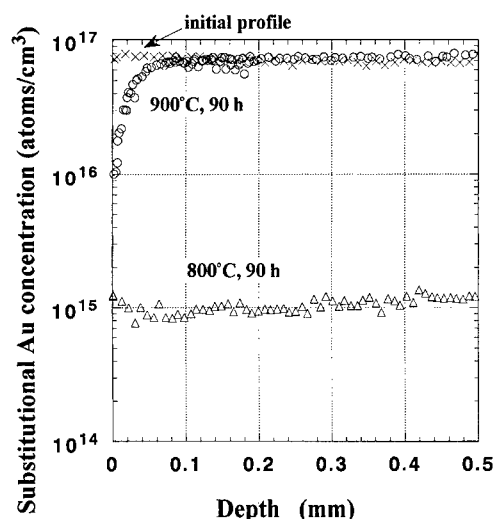


Fig. 2. Out-diffusion profiles of supersaturated substitutional Au in Si at 800°C and 900°C after re-heat-treatment at 1150°C for 30 min. The specimen thickness is about 1 mm.

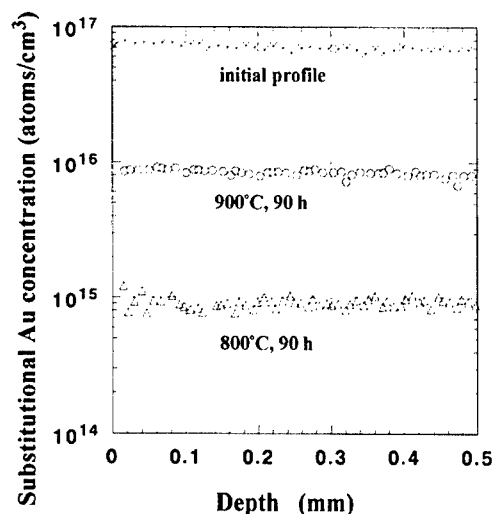


Fig. 3. Out-diffusion profiles of supersaturated substitutional Au in Si at 800°C and 900°C without re-heat-treatment at 1150°C. The specimen thickness is about 1 mm.

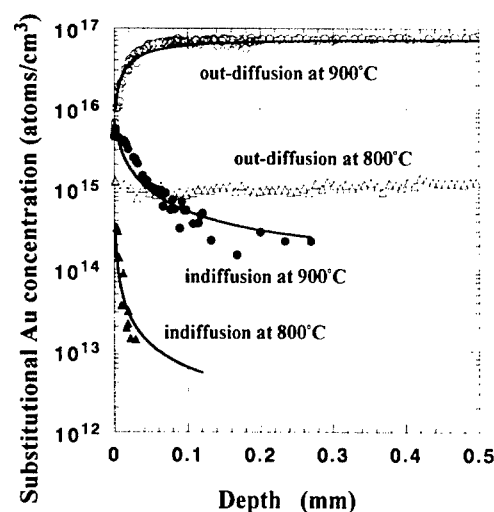


Fig. 4. Indiffusion and out-diffusion profiles of substitutional Au in Si. Data in Figs. 1 and 2 are re-plotted together in the figure for the comparison. The solid lines show the approximate equations for kick-out diffusion, Eqs. (1) or (2), using D^* as a fitting parameter.

The indiffusion profile at 900°C shows a U-shaped one, and even that at 800°C seems to show a U shape. Vacancy mechanism is dominant in the interstitial-substitutional impurity diffusion in Si below 950°C according to Frank et al. [9], nevertheless, self-interstitial seems to be dominant still at 800°C in our case. Therefore, the indiffusion of substitutional Au in Si below and above 850°C is limited by the diffusion of

self-interstitials to the specimen surface, and, Au indiffusion seems to occur via a kick-out mechanism independent of the indiffusion temperature. The out-diffusion profile at 900°C shows an inverse U shape, and the out-diffusion of substitutional Au supersaturated above 850°C is limited by the diffusion of self-interstitials from the surface, namely, also by the kick-out mechanism.

An approximate equation for the kick-out diffusion can be obtained for the indiffusion or for the out-diffusion as follows:

$$C = C_0(1 + L/\sqrt{tD^*})/(2 + L/\sqrt{tD^*})[1/(1 + x/\sqrt{tD^*}) + 1/\{1 + (L - x)/\sqrt{tD^*}\}] \quad (1)$$

or

$$C = C_0 - (C_i - C_0)(1 + L/\sqrt{tD^*})/(2 + L/\sqrt{tD^*}) \times [1/(1 + x/\sqrt{tD^*}) + 1/\{1 + (L - x)/\sqrt{tD^*}\}], \quad (2)$$

respectively, in the same way as for Eq. (43) in reference [10]. Here, the equations are multiplied by $(1 + L/\sqrt{tD^*})/(2 + L/\sqrt{tD^*})$ to fit the surface concentration, and the factor proposed by Morooka previously [7] is misprinted. C_0 , C_i , L , t , D^* and x show surface and initial concentrations, specimen thickness, time, a constant related to diffusion, and distance from the surface, respectively. D^* includes C_i and diffusion constant, furthermore, the equations are not so good in the case of a long diffusion time, therefore, the equations are not enough to discuss about a diffusion constant and are useful to distinguish the diffusion mechanism. The solid lines in Fig. 4 show Eqs. (1) or (2) for $C_0 = 10^{15} \text{ cm}^{-3}$ at 800°C and $C_0 = 9 \times 10^{15} \text{ cm}^{-3}$ at 900°C. C_i , L and t are used experimental values and D^* is used as a fitting parameter. The surface concentrations are a little larger than the solid solubility of Au in Si obtained by Stolwijk et al. [11].

On the other hand, the out-diffusion profile at 800°C shows a flat-type one in contrast to the out-diffusion at 900°C. The flat profile is a characteristic of the annealing of supersaturated low-temperature substitutional Au in Si due to the ring diffusion accompanied by a homogeneous agglomeration [4]. In this case, the annealing time of 90 h is long enough to recover the thermal equilibrium concentration at 800°C, and, the flat concentration is regarded as the solid solubility. The surface concentration in the indiffusion profile at 800°C is predicted to increase to the solubility.

The specimens used for the measurement shown in Fig. 3, were heat-treated at the annealing temperature directly from room temperature. In this case, substitutional Au supersaturated at room temperature, namely, below 850°C, are heat-treated at the annealing temperature. Therefore, the profile even at 900°C shows an out-diffusion profile for the low-temperature substitutional

Au, and shows a flat and fast one. The annealing time is also long enough to recover thermal equilibrium concentration at 900°C, and the flat concentration at 900°C is regarded as the solid solubility, which is the same as the surface concentration in the indiffusion profile at 900°C.

It is expected that, the total concentration of Au is nearly equal to the concentration of substitutional Au in the kick-out diffusion, namely, in the indiffusion below and above 850°C and in the out-diffusion supersaturated above 850°C, however, the total concentration is much larger than the substitutional Au in the flat and fast diffusion, namely, in the out-diffusion supersaturated below 850°C [7].

5. Conclusions

- (1) Substitutional Au in Si shows a concentration profile of slow and U or inverse U shape, in the case of indiffusion below and above 850°C, and in the case of out-diffusion supersaturated above 850°C.
- (2) Substitutional Au in Si shows a concentration profile of fast and flat shape, in the case of out-diffusion supersaturated below 850°C.
- (3) The above experimental results are consistent with the change of diffusion mechanism, namely, that the excess over the thermal equilibrium concentration of substitutional Au change the configuration from high-temperature substitutional Au to a low-temperature one by cooling below 850°C after a pre-indiffusion.

References

- [1] M. Morooka, et al., *Jpn. J. Appl. Phys.* 24 (1985) 133.
- [2] U. Gösele, et al., *Appl. Phys.* 23 (1980) 361.
- [3] M. Morooka, et al., *Jpn. J. Appl. Phys.* 25 (1986) 1161.
- [4] M. Morooka, *Mater. Sci. Forum* 258–263 (1997) 1789.
- [5] M. Morooka, et al., *Jpn. J. Appl. Phys.* 23 (1984) 124.
- [6] M. Morooka, *Physica B* 273–274 (1999) 408.
- [7] M. Morooka, et al., *Defect Diffusion Forum* 194–199 (2001) 623.
- [8] M. Morooka, *Res. Bull. Fukuoka Inst. Tech.* 31 (1998) 43.
- [9] W. Frank, et al., in: G.E. Murch, A.S. Norwick (Eds.), *Diffusion in Crystalline Solids*, Academic Press, New York, 1984, p. 134.
- [10] M. Takahashi, et al., *Jpn. J. Appl. Phys.* 31 (1992) 1134.
- [11] N.A. Stolwijk, et al., *Appl. Phys. A* 33 (1984) 133.



ELSEVIER

Physica B 308–310 (2001) 284–289

PHYSICA B

www.elsevier.com/locate/physb

Interaction between self-interstitials and the oxygen dimer in silicon

J.L. Lindström^{a,*}, T. Hallberg^b, J. Hermansson^a, L.I. Murin^c, B.A. Komarov^c,
V.P. Markevich^{c,d}, M. Kleverman^a, B.G. Svensson^c

^a Department of Physics—Solid State Physics, University of Lund, PO Box 118, SE-221 00 Lund, Sweden

^b Defence Research Establishment, PO Box 1165, SE-581 11, Linköping, Sweden

^c Institute of Solid State and Semiconductor Physics, 220072 Minsk, Belarus

^d Centre for Electronic Materials, UMIST, Manchester M60 1QP, UK

^e Solid State Electronics, Royal Institute of Technology, SE-164 40 Kista, Sweden

Abstract

Interactions between the oxygen dimer (O_{2i}) and silicon self-interstitials (I) and vacancies (V) have been studied in Czochralski-grown silicon (Cz-Si) crystals using infrared absorption and deep level transient spectroscopies. The focus in this report is on reactions of O_{2i} with I. The first step in this interaction is found to be the formation of a self-interstitial-dioxygen centre (IO_{2i}) with oxygen-related local vibrational mode (LVM) bands at 922 and 1037 cm^{-1} . During the second formation step, another centre, I_2O_{2i} , with LVM bands at 918 and 1034 cm^{-1} is suggested to appear. A Si-related band at about 545 cm^{-1} is also assigned to both the IO_{2i} and I_2O_{2i} centres. The IO_{2i} centre is found to be electrically active with an acceptor level at $E_c - 0.11$ eV. The both defects, IO_{2i} and I_2O_{2i} , are stable at room temperature and anneal out at about 400 and 550 K, respectively. © 2001 Elsevier Science B.V. All rights reserved.

Keywords: Silicon; Self-interstitials; Oxygen; Electron irradiation

1. Introduction

Silicon wafers used for integrated circuits require the presence of oxygen, due to its beneficial effects such as wafer hardening and intrinsic gettering [1,2]. The most common material, Czochralski-grown silicon, typically contains $\sim 10^{18} cm^{-3}$ of interstitial oxygen atoms (O_i) and is in a very large temperature range highly super-saturated. As a consequence clustering of oxygen atoms occurs, resulting in formation of different oxygen complexes from small clusters like dimers, trimers (O_{3i}) to oxygen-related thermal double donors (TDDs) and quartz precipitates.

It was found that oxygen atoms as well as oxygen-related complexes could interact with intrinsic defects of Si lattice, vacancies (V) and self-interstitials (I) [1,2]. V and I can be easily created upon irradiation of Si crystals with high energy particles (electrons, protons, ions, etc.). Electron-irradiated Cz-Si was a subject of many investigations [3–10]. Several oxygen-vacancy (V_nO_n) complexes have been identified, but very few complexes incorporating oxygen atoms and self-interstitials are known. Experimental studies of samples irradiated at around 80 K have showed that O_i can trap I and form IO_i complex [11–14], which is stable below 300 K. This defect has been found to trap an additional I and form I_2O_i [15,16].

Silicon self-interstitials were suggested to play an important role in the formation of oxygen-related TDDs [17,18]. The structure of these complexes, which were discovered almost 50 years ago is still a matter of debate.

*Corresponding author. Tel.: +46-46-2220929; fax: +46-46-2223637.

E-mail address: lennart.lindstrom@ftf.lth.se (J.L. Lindström).

According to one of the most popular models of TDDs, their core consists of a complex of two oxygen atoms and a silicon self-interstitial ($O_{2i}I$) [17]. The $O_{2i}I$ was suggested to be a double donor.

Recently, local vibrational mode bands due to oxygen dimers were identified in Si [19–21], and a method of enhanced formation of O_{2i} complexes was proposed [22,23]. In this work we present results of infrared (IR) absorption and deep level transient spectroscopy (DLTS) studies of interaction of oxygen dimers with V and I in electron- and gamma-rays-irradiated Cz–Si crystals.

2. Experimental

The samples used in this investigation were as-grown Cz–Si, doped with phosphorus to resistivities of about $60\ \Omega\text{cm}$. The concentrations of interstitial oxygen (O_i) and substitutional carbon (C_s) were monitored by measuring the well-known absorption bands at 1107 [24] and 605cm^{-1} [9], respectively. We also included samples doped with the isotope ^{18}O . The samples were polished to an optical surface on two sides and the dimensions were $10 \times 5 \times 3\text{mm}^3$. The electron irradiation was performed in a temperature regulated holder in air at temperatures in the range 320 – 650K to different doses from 5×10^{16} to $4 \times 10^{18}\text{cm}^{-2}$, using 2.5MeV electrons. The beam current was in the range 1 – 12mA/cm^2 . Some samples were irradiated with gamma-rays from a ^{60}Co source. Heat-treatments (HTs) were performed in a nitrogen ambient or in air.

IR absorption studies of LVMs were carried out using Fourier Transform IR (FT-IR) spectrometers. A spectral resolution of 0.5 – 1.0cm^{-1} was used and the samples were measured at 10K and at RT. DLTS measurements were carried out using a Semitrap DLS-83D system. Capture cross sections of electrons by deep traps (σ_n) were determined from the analysis of trap filling process upon applying pulses of different lengths. Gold Schottky diodes were prepared for the measurements.

3. Results and discussion

3.1. Formation of the oxygen dimer

Since the concentration of oxygen dimers in as-grown Cz–Si crystals is relatively low (around $1 \times 10^{15}\text{cm}^{-3}$) and IR studies of LVM bands typically require defect concentrations an order of magnitude higher for detailed investigations, a special technique has been developed [22,23], where the dimers are produced by electron irradiation (MeV) at about 650K in carbon-

lean material through the reaction



Using this technique we could prepare silicon samples with the dimer concentration up to $5 \times 10^{16}\text{cm}^{-3}$. It has been found that there is a considerable difference between carbon-lean and carbon-rich CZ-silicon in terms of possible reactions during irradiation [22,23]. The effective interaction of self-interstitials with substitutional carbon atoms according to the Watkins replacement mechanism,



is the main reason for that. One consequence of the self-interstitial-carbon interaction is that a high concentration of oxygen dimers according to (1) cannot be achieved in carbon-rich silicon. Another efficient trap for I is the vacancy-oxygen centre (VO) through the reaction



3.2. Irradiation of dimer-rich samples at 300K

In carbon-lean silicon samples irradiated at 650K the VO concentration after irradiation is much lower than the concentration of O_{2i} and the main traps for I at a repeated irradiation at 300K will therefore initially be according to



The IO_i complex is not stable above 300K , so reactions (4) and (5) are not effective during the irradiation at 300K and the main reactions should be (6), (7) and (1). The further irradiation at 300K will, however, lead to a rapidly increasing concentration of VO centres due to the dominating concentration of O_i and reaction (3) will very soon compete with reactions (6), (7) and (1). One can compare the concentration of O_{2i} (1012cm^{-1} band) in as-grown samples and after irradiation at 350°C ($F = 8 \times 10^{17}\text{e/cm}^2$) by an examination of spectra 1 and 2 in Fig. 1. The strong increase in $[O_{2i}]$ after the irradiation makes its concentration comparable to that of the VO_2 complex (889cm^{-1} band). The well-known VO-related band at 830cm^{-1} is not seen in the spectrum 2. Several new bands are appearing in absorption spectra after subsequent irradiation at room temperature (spectra 3–10 in Fig. 1). After irradiation with a fluence of $5 \times 10^{16}\text{e/cm}^2$, absorption bands at 911 and 1034cm^{-1} are seen (spectrum 4 in Fig. 1), further irradiation leads to the development of bands at 916

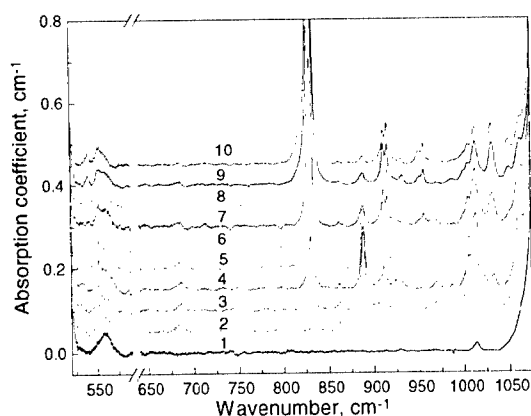


Fig. 1. Room temperature absorption spectra for C-lean n-Cz-Si ($\rho = 50 \Omega \text{ cm}$): (1) as-grown; (2) after electron irradiation at 350°C , $F = 8 \times 10^{17} \text{ cm}^{-2}$; (3–10) after RT irradiation, $F(\text{cm}^{-2})$: (3) 1×10^{16} , (4) 5×10^{16} , (5) 10^{17} , (6) 2×10^{17} , (7) 4×10^{17} , (8) 7×10^{17} , (9) 1.1×10^{18} , (10) 6×10^{18} .

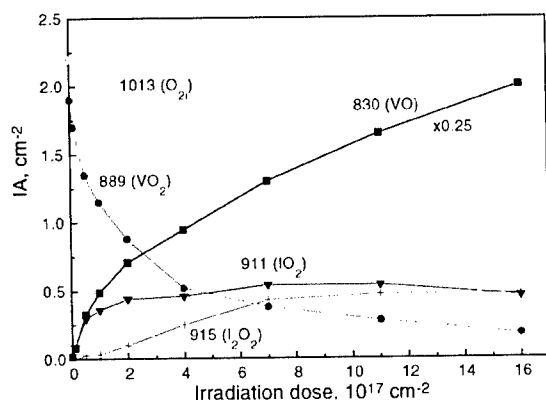


Fig. 2. Generation kinetics of some radiation-induced oxygen-related complexes upon electron irradiation at room temperature of a dimer-rich Cz-Si sample.

and 1031 cm^{-1} (spectra 6–10 in Fig. 1). It is suggested that the first pair of bands appears when IO_{2i} starts to form according to reaction (6) and after that reaction (7) can be activated resulting in the formation of I_2O_{2i} . There is also a weak band at 540 cm^{-1} , the development of which seems to correlate with that of the above mentioned pairs of bands. As the irradiation fluence increases the concentration of the vacancy-oxygen complex grows rapidly and the VO-related line at 830 cm^{-1} dominates in the spectra soon (spectra 6–10 in Fig. 1). This is also illustrated in Fig. 2, where the dose dependencies of the integrated intensities of the considered bands are shown. The observed dependencies can be described by reactions (1), (3), (6) and (7) taking

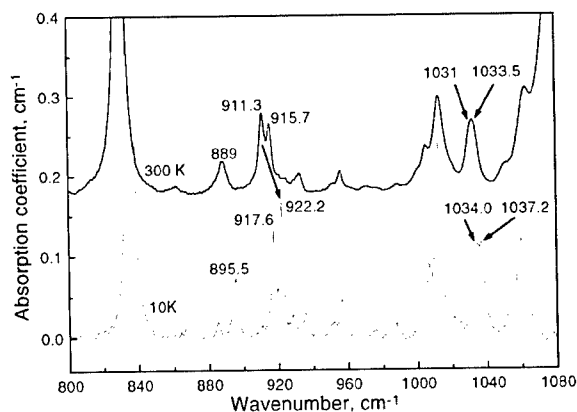


Fig. 3. Absorption spectra measured at 10 and 300 K for a C-lean Cz-Si sample after two-step electron irradiation: at 350°C with a fluence of 8×10^{17} and at RT with a fluence of $7 \times 10^{17} \text{ cm}^{-2}$.

into account differences in capture cross sections of self-interstitials by VO, VO_2 , O_{2i} , and IO_{2i} complexes.

An analysis of absorption spectra of irradiated oxygen-dimer-rich samples doped with ^{18}O reveals that the pairs of bands at 911 and 1034 cm^{-1} , and at 916 and 1031 cm^{-1} are oxygen-related LVMs, while the weak band at 540 cm^{-1} does not show any shift upon replacement of oxygen isotopes and therefore is suggested to be a Si-related LVM. In Fig. 3 one can see the temperature shifts of the bands upon the change of measurement temperature from 300 to 10 K. The band at 911 cm^{-1} shifts to 922 cm^{-1} , while the band at 916 cm^{-1} shifts to 918 cm^{-1} with the decrease of the measurement temperature. Typical shifts of oxygen-related LVMs in this wavenumber range is about 5–6 cm^{-1} . Exceptions are the LVMs at 1012 and 1060 cm^{-1} due to the oxygen dimer, the temperature shifts of which are extremely small (Fig. 3) [25].

3.3. Annealing studies

In order to investigate the thermal stability of the new defects (IO_{2i} and I_2O_{2i}), an isochronal annealing study has been done. Absorption spectra of an electron-irradiated sample after isochronal anneals are shown in Fig. 4. An examination of the spectra shows that the first appearing defect, IO_{2i} , has completely annealed out at 160°C and the second one, I_2O_{2i} , at 250°C . Disappearance of the IO_{2i} and I_2O_{2i} complexes is accompanied by an increase in intensities of the bands at 1012 and 1060 cm^{-1} due to the oxygen dimer, suggesting that reactions (6) and (7) have corresponding back-reactions. Self-interstitials released according to these back-reactions can take part in reactions like (1) and (3). Several other relatively weak bands have been observed upon

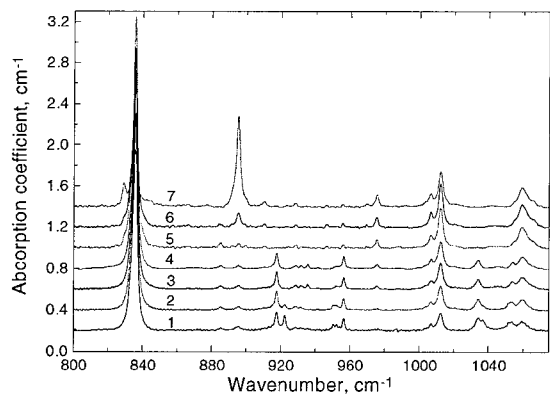


Fig. 4. Absorption spectra at 10 K for Cz-Si: (1) after two-step electron irradiation (350°C , $F = 8 \times 10^{17} + \text{RT}$, $F = 7 \times 10^{17} \text{ cm}^{-2}$) and at different stages of 20 min isochronal anneal, (2) 120°C , (3) 160°C , (4) 210°C , (5) 250°C , (6) 300°C , (7) 350°C .

annealing of the irradiated dimer-rich samples and an investigation of these bands is in progress. After anneals at higher temperatures the band at 895 cm^{-1} due to the VO_2 complex appears in the spectra (spectra 6 and 7 in Fig. 4).

3.4. Irradiation of as-grown materials

Simultaneously, with the irradiation of dimer-rich samples at 300 K, an as-grown sample with a high concentration of O_i ($1.3 \times 10^{18} \text{ cm}^{-3}$) and a very low carbon content ($< 10^{15} \text{ cm}^{-3}$) has been irradiated. Infrared absorption spectra for this sample are shown in Fig. 5. Weak bands have appeared after irradiation at the same positions as in dimer-rich samples. This result shows that in as-grown carbon-lean Cz-Si samples oxygen dimers are effective traps for self-interstitials at initial stages of electron irradiation.

3.5. DLTS results

It was found that DLTS spectra of electron- or gamma-rays-irradiated carbon-lean Cz-Si samples differ significantly from those of Cz-Si samples containing carbon. This difference is clearly seen in Fig. 6, where DLTS spectra in the temperature range 60–120 K for Cz-Si samples irradiated with gamma-rays from a ^{60}Co source are presented. The irradiation of a carbon-lean sample resulted in introduction of two dominant deep level centres with peak maxima at about 73 K (E_{73}) and 93 K (E_{93}) (spectrum 2 in Fig. 6), while for a sample with higher concentration of carbon only one dominant centre (E_{93}) is observed (spectrum 1 in Fig. 6). Fig. 7 shows Arrhenius plots of T^2 -corrected emission rates for both dominant centres induced by the irradiation.

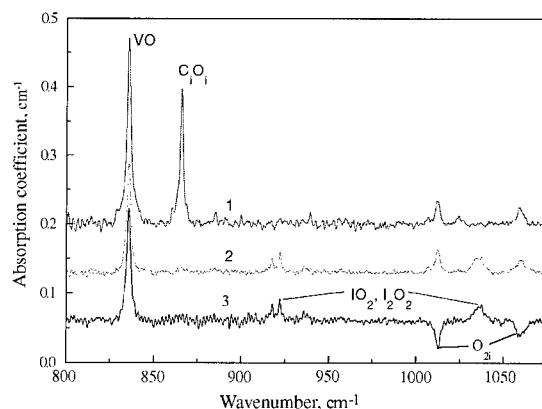


Fig. 5. Absorption spectra at 10 K for electron irradiated (RT, $F = 5 \times 10^{16} \text{ cm}^{-2}$) as-grown Cz-Si crystals with low ($< 10^{15} \text{ cm}^{-3}$, spectra 2 and 3) and intermediate carbon content ($5 \times 10^{16} \text{ cm}^{-3}$, spectrum 1). Spectrum 3 is a difference between the spectra of irradiated and as-grown samples.

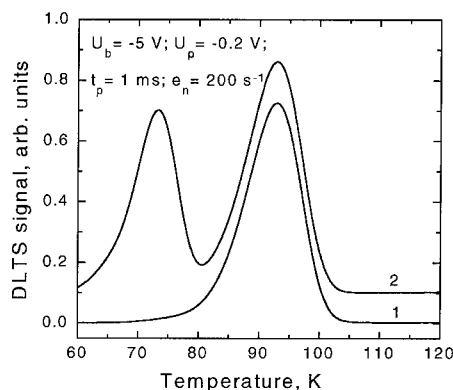


Fig. 6. DLTS spectra of Cz-Si samples with different carbon concentration after irradiation with gamma-rays from a ^{60}Co source. N_C : (1) $5 \times 10^{16} \text{ cm}^{-3}$, (2) $< 1 \times 10^{15} \text{ cm}^{-3}$. Fluence of irradiation was $5 \times 10^{16} \text{ cm}^{-2}$.

Activation energies for electron emission (E_n) were found to be 0.163 ± 0.001 and $0.128 \pm 0.001 \text{ eV}$ for E_{93} and E_{73} traps, respectively. Based on the comparison of the obtained trap parameters (E_n and σ_n) with those known from the literature on radiation-induced centres in Cz-Si [26,27], E_{93} peak was assigned to the oxygen-vacancy pair [3,4]. It was found that the electron capture cross section for the E_{73} trap is temperature dependent. The energy barrier for the electron capture was estimated to be about 0.02 eV. Taking this into account, the position of an energy level of the E_{73} trap was determined as $E_c - 0.11 \text{ eV}$. The obtained parameters of the E_{73} trap do not coincide with those of any known radiation-induced traps stable at room temperature

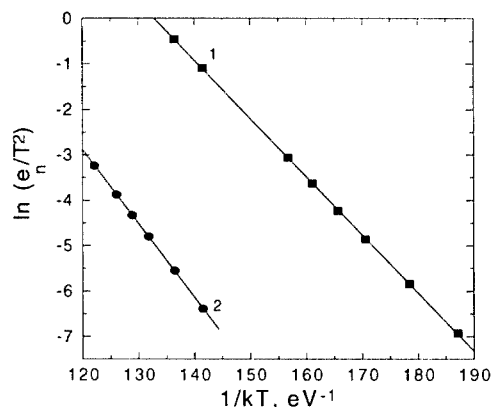


Fig. 7. Arrhenius plot of T^2 -corrected electron emission rates from (1) E_{73} and (2) E_{93} traps.

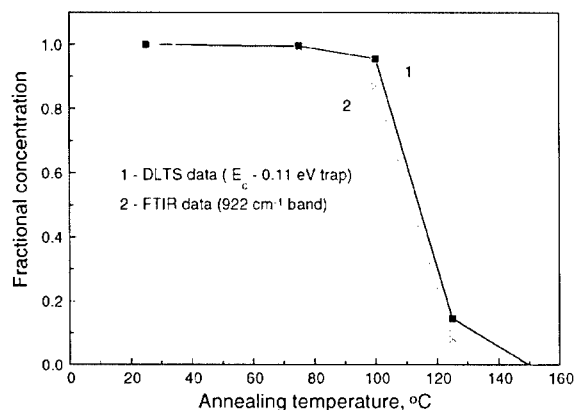


Fig. 8. Isochronal annealing behaviour (1) of the concentration of a centre with an acceptor level at $E_c - 0.11$ eV and (2) of the integrated intensity of the absorption band at 922 cm⁻¹.

[26,27]. The effect of electric field on the electron emission rate from the E_{73} trap is found to be negligible, indicating that the centre is of acceptor nature.

An isochronal annealing study shows that the E_{73} trap anneals out in the temperature range of 100–150°C and the elimination process is very similar to that of the defect responsible for the 922 and 1037 cm⁻¹ lines in the absorption spectra (Fig. 8). Based on the similarities in formation and annealing conditions it is suggested that the E_{73} trap is the same as a centre giving rise to the 922 and 1037 cm⁻¹ lines in IR absorption spectra of irradiated carbon-lean Cz-Si samples.

3.6. Uniaxial stress and an atomic model of IO_{2i} complex

It was found from uniaxial stress measurements that the 918 and 922 cm⁻¹ lines show the same splitting

behaviour. The polarisation of the components strongly indicates that the symmetry of centres is monoclinic I or lower. All the obtained experimental results are well in line with preliminary theoretical calculations for the IO_{2i} centre which points to a defect made up of a staggered oxygen dimer and a $\langle 110 \rangle$ -split self-interstitial [28].

3.7. Other self-interstitial-oxygen complexes

During irradiation at 650 K there is a band appearing at 1006 cm⁻¹ which has been suggested to be related to the oxygen trimer, O_{3i} [29]. This band can be observed in Fig. 4 as well as two bands at 956 and 1054 cm⁻¹, appearing together with the bands due to the IO_{2i} and I_2O_{2i} . An analysis of the spectra in Fig. 4 shows that the intensity of the 1006 cm⁻¹ band increases upon disappearance of the bands at 956 and 1054 cm⁻¹. It is suggested that the O_{3i} can also trap self-interstitials and the pair of lines at 956 and 1054 cm⁻¹ is tentatively assigned to an IO_{3i} complex.

4. Summary

During electron irradiation at 300 K of oxygen-rich carbon-lean samples a new group of defects has been revealed by IR spectroscopy. These defects are suggested to be formed by reactions between oxygen dimers and silicon self-interstitials. The first step in these reactions is the formation of the IO_{2i} centre with oxygen-related LVMs at 922 and 1037 cm⁻¹. The second step is the formation of the I_2O_{2i} centre with the corresponding LVMs at 918 and 1034 cm⁻¹. A Si-related band at 545 cm⁻¹ is common for both the complexes. Annealing studies of these centres show that the IO_{2i} anneals out below 450 K and the I_2O_{2i} below 550 K.

An acceptor level at $E_c - 0.11$ eV has been identified as related to the IO_{2i} complex on the basis of similarities in the formation and annealing behaviour of the level and the absorption bands at 922 and 1037 cm⁻¹. According to preliminary ab initio calculations [28], the obtained experimental characteristics of the IO_{2i} centre are consistent with those expected for a complex incorporating a staggered oxygen dimer and $\langle 110 \rangle$ -split silicon self-interstitial.

Acknowledgements

We thank TFR, KVA, SI. and FOA in Sweden for financial support. We also acknowledge financial support from the grant INTAS-Belarus 97-824. The authors would like to thank Prof. R. Jones and J. Coutinho for helpful discussions.

References

- [1] F. Shimura (Ed.), *Oxygen in Silicon, Semiconductors and Semimetals*, Vol. 42, Academic Press, London, 1994.
- [2] R. Jones (Ed.), *Early Stages of Oxygen Precipitation in Silicon*, High Technology, Vol. 17, NATO ASI Series, 3, Kluwer, Dordrecht, 1996.
- [3] G.D. Watkins, J.W. Corbett, *Phys. Rev.* 121 (1961) 1001.
- [4] J.W. Corbett, et al., *Phys. Rev.* 121 (1961) 1015.
- [5] Y.H. Lee, J.W. Corbett, *Phys. Rev. B* 13 (1976) 2653.
- [6] J.W. Corbett, G.D. Watkins, R.S. McDonald, *Phys. Rev.* 135 (1964) A1381.
- [7] J.L. Lindström, B.G. Svenson, *Mater. Res. Soc. Symp. Proc.* 59 (1986) 45.
- [8] B.G. Svenson, J.L. Lindström, *Phys. Rev. B* 34 (1986) 59.
- [9] G. Davies, R.C. Newman, in: T.S. Moss (Ed.), *Handbook on Semiconductors*, Vol. 3b, Elsevier Science, Amsterdam, 1994, p. 1557pp.
- [10] J.L. Lindström, et al., *Physica B* 273–274 (1999) 291.
- [11] R.E. Whan, F.L. Vook, *Phys. Rev.* 153 (1967) 814.
- [12] Brelot, J. Charmagne, in: J.W. Corbett, G.D. Watkins (Eds.), *Radiation Effects in Semiconductors*, Gordon and Breach, London, 1971, 125pp.
- [13] H.J. Stein, *Appl. Phys. Lett.* 55 (1989) 870.
- [14] Kh.A. Abdulin, B.N. Mukashev, Yu.V. Gorelkinskii, *Semicond. Sci. Technol.* 11 (1996) 1696.
- [15] L.I. Murin, et al., in: C.L. Claeys (Ed.), *Proceedings of the Second ENDEASD Workshop*, Kista-Stockholm, 2000, 248pp.
- [16] J. Hermansson, et al., *Physica B* 302–303 (2001) 188.
- [17] P. Deak, L.C. Snyder, J.W. Corbett, *Phys. Rev. B* 45 (1992) 11612.
- [18] R.C. Newman, *J. Phys.: Condens. Matter* 12 (2000) R335.
- [19] L.I. Murin, et al., *Phys. Rev. Lett.* 80 (1998) 93.
- [20] S. Oberg, et al., *Phys. Rev. Lett.* 81 (1998) 2930.
- [21] M. Pesola, et al., *Phys. Rev. Lett.* 82 (1999) 4022.
- [22] J.L. Lindström, et al., *Mater. Sci. Forum* 258–263 (1997) 367.
- [23] J.L. Lindström, et al., *Solid State Phenom.* 69–70 (1999) 297.
- [24] Baghdadi, et al., *J. Electrochem. Soc.* 136 (1989) 2015.
- [25] T. Hallber, et al., *Mater. Sci. Forum* 258–263 (1997) 361.
- [26] L.C. Kimerling, in: *Radiation Effects in Semiconductors*, Vol. 31 of IOP Series, London-Bristol, 1977, 221pp.
- [27] S.D. Brotherton, P. Bradley, *J. Appl. Phys.* 53 (1982) 5720.
- [28] J. Coutinho, R. Jones, private communication.
- [29] L.I. Murin, V.P. Markevich, in: R. Jones (Ed.), *Early Stages of Oxygen Precipitation in Silicon*, High Technology, Vol. 17, Kluwer, Dordrecht, NATO ASI Series, 3, 1996, 329pp.



ELSEVIER

Physica B 308–310 (2001) 290–293

PHYSICA B

www.elsevier.com/locate/physb

Isotopic effects on vibrational modes of thermal double donors in Si and Ge

L.I. Murin^{a,*}, J.L. Lindström^b, V.P. Markevich^c, T. Hallberg^d, V.V. Litvinov^e,
J. Coutinho^f, R. Jones^f, P.R. Briddon^g, S. Öberg^h

^a *Institute of Solid State and Semiconductor Physics, P. Brovki Street 17, Minsk 220072, Belarus*

^b *Department of Physics, Lund University, S-221 00 Lund, Sweden*

^c *Centre for Electronic Materials, UMIST, M60 1QD Manchester, UK*

^d *Defence Research Establishment, P.O. Box 1165, SE-58111 Linköping, Sweden*

^e *Belarusian State University, F. Scorina av. 4, 220050 Minsk, Belarus*

^f *School of Physics, University of Exeter, EX4 4QL Exeter, UK*

^g *Department of Physics, University of Newcastle, NE1 7RU Newcastle, UK*

^h *Department of Mathematics, Luleå University of Technology, S-97187 Luleå, Sweden*

Abstract

The local vibrational modes of thermal double donors in Si and Ge are investigated by FTIR and ab initio modelling. At most, two oxygen modes are detected from each donor, which exhibit regular shifts with increasing donor number. By using mixtures of ^{16}O and ^{18}O , it is found that in Si the upper band does not yield any new modes suggesting that any oxygen atom is decoupled from any other. However, the lower frequency bands exhibit unique mixed modes proving for the first time that oxygen atoms are coupled together and in close spatial proximity. Ab initio calculations demonstrate that the modes and their isotopic shifts are consistent with a model involving two parallel chains of oxygen atoms linking second neighbour Si atoms, terminated by O-atoms close to the normal position for interstitial O. © 2001 Elsevier Science B.V. All rights reserved.

PACS: 61.72.Bb; 61.72.Ji; 63.20.Pw; 71.15.Mb; 81.05.Cy; 81.40.Tv

Keywords: Silicon; Germanium; Thermal donors; Oxygen; Vibrational modes

1. Introduction

Heating oxygen rich silicon or germanium between 300°C and 500°C leads to the formation of a family of double donors called thermal double donors (TDD) [1–3]. They are believed to consist of oxygen atoms possibly linked with self-interstitials [4–9]. In this paper, we describe the results of infra-red absorption experiments and first principles modelling of the local vibrational modes (LVMS) of TDD(*N*) in both Si and Ge. Although thermal donors in Ge have received less

attention, the weaker background absorption and the high concentrations of TDD which can be introduced, makes it a particularly fruitful material to investigate.

Recently, two sets of vibrational bands have been assigned to the early members of the TDD family. These lie around 1000 and 750 cm^{-1} in Si [10,11], and 780 and 600 cm^{-1} in Ge [12–15]. The participation of oxygen in the modes is confirmed by isotopic shifts with ^{18}O . The observation of only two modes in each donor appears to be inconsistent with the model whose family members differ by the number of oxygen atoms [5,7,8,16], and offers indirect support to the self-interstitial model [6,4]. In this paper we report new infra-red data on the donors in Si and Ge. Further, we demonstrate that the observed modes, perhaps surprisingly, can be understood from

*Corresponding author. Tel.: +375-17-184-1290; fax: +375-17-284-0888.

E-mail address: murin@ifttp.bas-net.by (L.I. Murin).

an oxygen-only model, without the need for self-interstitials.

2. Experimental and theoretical details

In this study, three types of Si and Ge samples were used. The first (1) contained ^{16}O , while the second (2) mainly contained ^{18}O . The third (3) was co-doped with ^{16}O and ^{18}O . Concentrations of ^{16}O (^{18}O) were monitored by measuring the intensities of the absorption bands at 1107 (1058) and 856 (812) cm^{-1} in Si [17] and Ge [18], respectively. Thermal donors were generated by heating Ge and Si samples at 370°C and 420°C in air. The IR absorption measurements were carried out at 10 and 300 K using a Bruker 113v Fourier transform IR spectrometer. The spectral resolution was 0.5 or 1.0 cm^{-1} .

The vibrational modes of the model were found using 112 atom supercells and an ab initio total energy local density functional code (AIMPRO) [19]. The code evaluates the dynamical matrix of the defect from which the vibrational modes and their normal coordinates can be found. Previous studies indicate that the errors in the frequencies lie around 10%. A large complex involving a chain of Si–O–Si units possesses a great number of local modes, and only a few are detected. To ascertain the most intense modes we placed a charge Q on each O atom, and a charge $-mQ/2$ on each Si neighbour bonded to m O-atoms. The intensity of the mode is then related to the change in the dipole moment of the defect when the atoms are displaced according to their normal coordinates. Tests with other reasonable charge distributions did not lead to significant differences.

3. Results and discussion

Fig. 1 shows fragments of differential absorption spectra of Si:O samples heat-treated at 420°C for

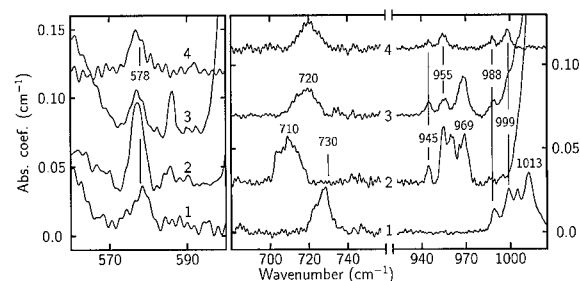


Fig. 1. Absorption spectra measured at 300 K for Si:O samples heat-treated at 420°C for 15 h: (1) $[\text{O}_i] = 1.3 \times 10^{18} \text{ cm}^{-3}$; (2) $[\text{O}_i] = 1.5 \times 10^{18} \text{ cm}^{-3}$; (3) and (4) $[\text{O}_i] = 8 \times 10^{17} \text{ cm}^{-3}$, $[\text{O}_i] = 7 \times 10^{18} \text{ cm}^{-3}$. The spectrum of a non-annealed sample was used as a reference in 4.

15 h. A signal recorded from a high-purity float-zone Si sample was subtracted from each spectrum. In all the samples (^{16}O , ^{18}O and $^{16}\text{O} + ^{18}\text{O}$), bands due to oxygen dimer, TDD(2) and TDD(3) (1013, 988 and 999 cm^{-1} , respectively), appear to be the dominant defects. The bands related to TDD are positioned in the wavenumber regions of 945–1000, 700–730 and 575–580 cm^{-1} . The TDD band at 580 cm^{-1} is reported for the first time. A clear linear correlation was found between the integrated intensity of this band and that of the bands at about 1000 and 750 cm^{-1} . All of these bands possess similar formation and annealing kinetics. The band at 580 cm^{-1} shows only a weak shift to higher frequencies with an increase in the TDD number, and is practically insensitive to an oxygen isotope substitution. In contrast, the 750 and 1000 cm^{-1} -bands undergo substantial shifts. It should be noted, however, that the ^{18}O isotope shift of the 750 cm^{-1} -bands is less than that of the 1000 cm^{-1} -bands ($^{16}\text{O}/^{18}\text{O} = 1.03$ and 1.045, respectively). By using mixtures of ^{16}O and ^{18}O , it is found that in Si the upper band does not yield any new modes suggesting that any oxygen atom is decoupled from any other. However, the lower frequency bands exhibit unique mixed modes proving for the first time that oxygen atoms are coupled together and in close spatial proximity.

Similar results have also been obtained for the 600 cm^{-1} -band in Ge co-doped with ^{16}O and ^{18}O (see Fig. 2), i.e., a unique mixed mode at about 595 cm^{-1} is observed after HT at 370°C for 15 h. However, unlike in Si, a mixed mode also appears in the upper band region at 755 cm^{-1} , along with ^{16}O and ^{18}O modes at 780 and 742 cm^{-1} .

Calculations of the vibrational spectra were based on a TDD model shown in Fig. 3(a), and discussed elsewhere at this conference [9]. Here, the core of TDD(N) consists of two parallel [110] chains of oxygen atoms bonded with second neighbour Si atoms (denoted

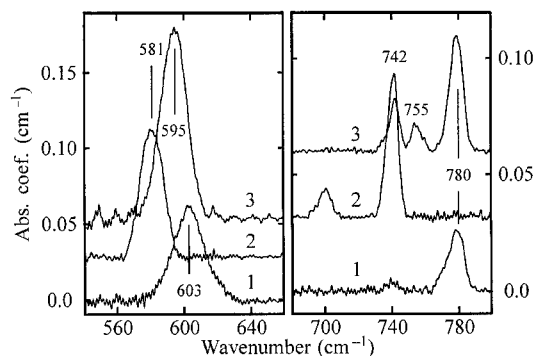


Fig. 2. Absorption spectra measured at 300 K for Ge:O samples heat-treated at 370°C for 20 h: (1) $[\text{O}_i] = 2.3 \times 10^{17} \text{ cm}^{-3}$; (2) $[\text{O}_i] = 3.2 \times 10^{17} \text{ cm}^{-3}$; (3) $[\text{O}_i] = 2.3 \times 10^{17} \text{ cm}^{-3}$, $[\text{O}_i] = 1.7 \times 10^{17} \text{ cm}^{-3}$.

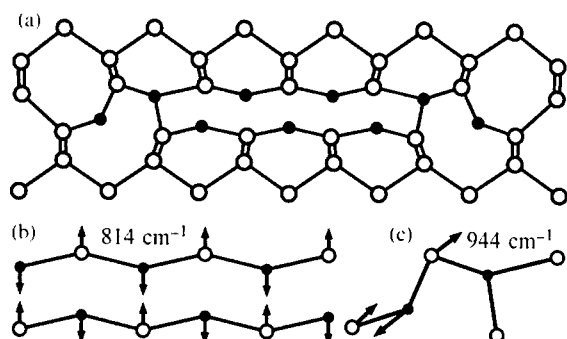


Fig. 3. (a) O_7 -2NN double donor. The white and black circles denote Si and O atoms, respectively. The two observed O-bands in TDD(N) at ~ 750 and ~ 1000 cm^{-1} in Si (~ 600 and ~ 780 cm^{-1} in Ge), are assigned to chain and end oxygen modes shown in (b) and (c) respectively.

by O -2NN). The ends consist of oxygen atoms bonded to neighbouring Si atoms denoted by O -1NN and their interface must necessarily contain over-coordinated O atoms. The O_n -2NN chain possesses C_{2v} (C_{2h}) symmetry for odd (even) n . We now discuss the vibrational properties of the chain.

To understand the LVMs of the donors, we first calculate the long wavelength modes of an infinite periodic O -2NN chain. The two IR-active modes lie at 564 and 814 cm^{-1} in Si and 323, 625 cm^{-1} in Ge. The 814 cm^{-1} is shown in Fig. 3(b) and clearly induces a dipole moment along $[001]$. The 564 cm^{-1} mode involves very little movement of oxygen atoms, and is localised to the Si atoms above and below the core whose bonds are compressed by the $[001]$ stress. This has a dipole moment along $[1\bar{1}0]$, and orthogonal to the chain. Thus, the simple periodic chain model explains why only a few oxygen modes can be detected in each donor, as only transverse long wavelength modes are IR-active.

We now consider the oxygen related modes arising from the ends of the chain [Fig. 3(c)]. The highest frequency modes, evaluated from the dynamical matrices of the end-O atoms, are given in Table 1. There is a 11 : 12 : 6 cm^{-1} increase with N in excellent agreement with the observed increases of 13 : 11 : 7 cm^{-1} for TDD(1), TDD(2), TDD(3) and TDD(4). For Ge, the calculated increments are 9 : 8 : 7 cm^{-1} compared with 5 : 4 : 3 cm^{-1} observed for TDD(1), TDD(2), TDD(3) and TDD(4). Thus, the model accounts for the shift in the high frequency mode with N .

We now turn to the effect of a 50–50 mixture of ^{16}O and ^{18}O . We consider O_7 -2NN and plot in Fig. 4 the calculated relative intensities of the local modes. We note that the end-mode at 944 cm^{-1} does not split in agreement with the data. This is because the displacement of the atoms shown in Fig. 3(c) is localised to the end O -1NN atom. However, in contrast with this, the

Table 1
Observed and calculated high frequency ^{16}O modes, cm^{-1} , of TDD(N) and O_{N+4} -2NN in Si^a

N	1	2	3	4
Calc.	940 (723)	951 (732)	963 (740)	969 (747)
Obs.	975 (769)	988 (774)	999 (778)	1006 (781)

^a Frequencies in Ge are given in brackets.

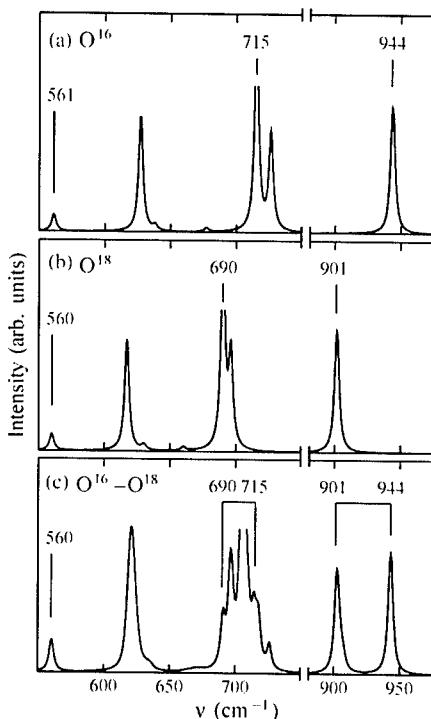


Fig. 4. Calculated IR-intensities of the modes for O_7 -2NN, broadened with Lorentzian functions by 4 cm^{-1} , and evaluated as described above. ^{16}O and ^{18}O spectra are shown in (a) and (b), respectively, whereas the 2⁷ combinations for a 50–50 ^{16}O – ^{18}O mixture are depicted in (c).

mode around 715 cm^{-1} due to the O -2NN core splits in the mixed case [Fig. 4(c)], again in agreement with the data. This reflects its chain origin illustrated in Fig. 3(b). The chain related 560 cm^{-1} Si mode is quite insensitive to O -substitution consistent with an assignment to the observed 580 cm^{-1} band. It is also important to note that the calculated $^{16}\text{O}/^{18}\text{O}$ ratios for the 715 and 944 cm^{-1} modes are 1.036 and 1.046, in good agreement with the observations. Fig. 4(a) also shows that other modes around 726 and 627 cm^{-1} in Si are expected to be IR-active but have not yet been detected.

In the case of Ge, both the end-mode at 748 cm^{-1} and the chain mode at 571 cm^{-1} (^{16}O) are, however, split in the mixed isotopic case, again in agreement with the data. The different behaviour of the end-mode from that

in Si is striking and originates from the closeness in the Ge–O–Ge angles at the ends and middle of the chain when compared with Si. This can be compared with the $\sim 140^\circ$ Ge–O–Ge and $\sim 160^\circ$ Si–O–Si angles for interstitial oxygen [19].

Acknowledgements

We thank TFR, KVA and SI in Sweden for financial support. We also acknowledge support from EPSRC and INTAS under Grant 97-0824.

References

- [1] F. Shimura (Ed.), *Oxygen in Silicon*, Vol. 42 of the series *Semiconductors and Semimetals*, Academic Press, San Diego, 1994.
- [2] R. Jones (Ed.), *Proceedings of the NATO Advanced Workshop on the Early Stages of Oxygen Precipitation in Silicon*, NATO ASI Series 3, Vol. 17, High Technology, Kluwer Academic Publishers, Dordrecht, 1996.
- [3] W. Gotz, G. Pensl, W. Zulehner, *Phys. Rev. B* 46 (1992) 4312.
- [4] R.C. Newman, *J. Phys. C* 18 (1985) L967.
- [5] L.C. Snyder, J.W. Corbett, in: J.C. Mikkelsen, S.J. Pearton, J.W. Corbett, S.J. Pennycook (Eds.), *Oxygen, Carbon, Hydrogen and Nitrogen in Silicon*, Vol. 59, MRS Symposia Proceedings, Materials Research Society, Pittsburgh, 1985, p. 207.
- [6] P. Deák, L.C. Snyder, J.W. Corbett, *Phys. Rev. B* 45 (1992) 11 612.
- [7] D.J. Chadi, *Phys. Rev. Lett.* 77 (1996) 861.
- [8] M. Pesola, Young Joo Lee, J. von Boehm, M. Kaukonen, R.M. Nieminen, *Phys. Rev. Lett.* 84 (2000) 5343.
- [9] R. Jones, J. Coutinho, S. Öberg, P.R. Briddon, in these *Proceedings (ICDS-21)*, *Physica B* 308–310 (2001).
- [10] J.L. Lindström, T. Hallberg, *Phys. Rev. Lett.* 72 (1994) 2729.
- [11] J.L. Lindström, T. Hallberg, in: R. Jones (Ed.), *Proceedings of the NATO Advanced Workshop on the Early Stages of Oxygen Precipitation in Silicon*, NATO ASI Series 3, Vol. 17, High Technology, Kluwer Academic Publishers, Dordrecht, 1996, pp. 41–60.
- [12] W. Kaiser, *J. Phys. Chem. Solids* 23 (1962) 255.
- [13] P. Clauws, *Mater. Sci. Eng. B* 36 (1996) 213.
- [14] V.P. Markevich, L.I. Murin, V.V. Litvinov, A.A. Kletchko, J.L. Lindström, *Physica B* 273–274 (1999) 570.
- [15] P. Clauws, P. Vanmeerbeek, *Physica B* 273–274 (1999) 557.
- [16] R. Jones, *Semicond. Sci. Technol.* 5 (1990) 255.
- [17] A. Baghdadi, W.M. Bullis, M.C. Croarkin, Y.-Z. Li, R.I. Scace, R.W. Series, P. Stallhofer, M. Watanabe, *J. Electrochem. Soc.* 136 (1989) 2015.
- [18] J. Millett, L.S. Wood, G. Bew, *Brit. J. Appl. Phys.* 16 (1965) 159.
- [19] J. Coutinho, R. Jones, P.R. Briddon, S. Öberg, *Phys. Rev. B* 62 (2000) 10 824.



ELSEVIER

Physica B 308–310 (2001) 294–297

PHYSICA B

www.elsevier.com/locate/physb

Chemical and structural characterization of oxygen precipitates in silicon by infrared spectroscopy and TEM

O. De Gryse^{a,*}, P. Clauws^a, O. Lebedev^b, J. Van Landuyt^b, J. Vanhellemont^c,
C. Claeys^d, E. Simoen^d

^a University of Gent, Krijgslaan 281 (S1), B-9000 Gent, Belgium

^b RUCA-EMAT, Groenenborgerlaan 171, B-2020 Antwerpen, Belgium

^c Ministry of Flanders, AWI, Boudewijnlaan 30, B-1000 Brussel, Belgium

^d IMEC, Kapeldreef 75, B-3001 Leuven, Belgium

Abstract

Infrared absorption spectra of polyhedral and platelet oxygen precipitates are analyzed using a modified Day–Thorpe approach (J. Phys.: Condens. Matter 11 (1999) 2551). The aspect ratio has been determined by TEM measurements. The reduced spectral function and the stoichiometry are extracted from the absorption spectra and the concentration of precipitated interstitial oxygen. One set of spectra reveal a Fröhlich frequency around 1100 cm^{-1} and another around $1110\text{--}1120\text{ cm}^{-1}$. It is shown that the shift in the Fröhlich frequency is not due to a different stoichiometry, but due to the detailed structure in the reduced spectral function. The oxygen precipitates consist of SiO_2 with $\gamma \approx 1.1\text{--}1.2 \pm 0.1$.
© 2001 Elsevier Science B.V. All rights reserved.

PACS: 61.72.Qq

Keywords: Silicon; Oxygen precipitation; Infrared spectroscopy; TEM

1. Introduction

Oxygen is one of the dominant impurities in Czochralski grown crystalline silicon (Cz). Depending on the thermal treatment oxygen precipitates (SiO_2) with different morphology are formed in Cz silicon [1]. In the literature different values of γ have been reported, ranging from 0.95 to 2 [2–4]. The precise phase, however, has an impact on the precipitate growth kinetics and thus on the interstitial oxygen depletion from the bulk [2]. Therefore, the identification of this phase is highly desirable.

The infrared absorption spectra can be reconstructed using an effective medium theory [3,5–7], only requiring the dielectric functions of the medium and the particles, the volume fractions and the aspect ratio. However, in the former approach [3,4] the analysis depends almost

entirely on the availability of dielectric functions of SiO_2 , which limits the certainty of the statements.

It is assumed that the SiO_2 precipitates consist of two phases [4]: amorphous silicon and amorphous SiO_2 . The effective dielectric function of a composite depends both on the geometry of the composite and on the dielectric functions of the components. The geometrical information can be summarized in the Bergman–Milton (BM) spectral density function [8,9], which is independent of the material parameters. If the spectral function can be extracted from experimental absorption spectra, the volume fractions of the components can be easily obtained, and thus the γ in SiO_2 . Day and Thorpe [10] showed that the spectral functions can be extracted from reflectance data if known properties of the spectral function are incorporated as constraints in the optimization problem. We will make use of their algorithm, but add more constraints, which will allow to obtain the spectral functions and volume fractions in the case of the SiO_2 precipitates in silicon.

*Corresponding author.

E-mail address: olivier.degryse@rug.ac.be (O. De Gryse).

2. Experimental

The investigated Si specimens contained an initial interstitial oxygen concentration between 7.5 and $10.2 \times 10^{17} \text{ cm}^{-3}$ (Table 1) and are divided into four groups of annealing schemes.

The first set of samples (i) received a nucleation step (800°C in N_2 for 24 h) followed by a high-temperature step (3 h, 1100°C in wet oxygen) (samples SD1 and SD2). The second group (ii) received a series of pretreatment followed by a high-temperature step at 1000°C for a duration ranging from 1 to 32 h (samples SD3 and SD4). The third group (iii) received nucleation step (16 h at 500°C), followed by a stabilization step (16 h at 800°C) and a growth step (8 h at 1050°C) (sample SD5) [11]. The last group (iv) received a very long treatment at 750°C in N_2 ambient for 265 h in order to produce a high density of stable oxide precipitate nuclei. This was followed by a treatment at 1050°C in Ar for 2 h (samples SD6, S1 and S2) [4]. The oxygen content before the annealing treatments was determined by measuring the height of the absorption peak at 1107 cm^{-1} at 300 K, using the IOC88 standard calibration conversion factor ($3.14 \times 10^{17} \text{ cm}^{-2}$) [12]. The interstitial oxygen remaining after annealing was determined at 6 K by measuring the height of the 1206 cm^{-1} peak [13]. In this way, the broad absorption peak at 300 K belonging to the remaining interstitial oxygen could be removed by subtracting a scaled 1107 cm^{-1} absorption peak from the experimental spectrum, leaving the spectrum of precipitated oxygen only [4]. Transmission electron microscopy (TEM) observations were performed at 200 keV along the $[001]$ direction (plan view) and along the $[011]$ direction (cross-section) on two samples (SD6 and S2).

3. Theory, model and simulations

The dielectric function can be obtained by assuming that the particles themselves are composites of inert

amorphous silicon (a-Si) ($\epsilon_m = 11.7$) and thermal oxidized SiO_2 [14] (t- SiO_2), and thus can be approximated with an effective medium theory. Because representation of the dielectric function of SiO_2 with damped harmonic oscillators is a rather crude approximation for amorphous solids [4,15] the dielectric function of t- SiO_2 was re-extracted using a Gaussian broadened harmonic oscillator model [15,16].

In the BM spectral representation the effective dielectric function of a two component material is given by [10]:

$$\epsilon_p = \epsilon_{pm} \left(1 - \frac{\sigma_{pp}}{s_{pm}} - \int_0^1 \frac{g(x)}{x(s_{pm} - x)} dx \right) \quad (1)$$

with ϵ_p , ϵ_{pm} , ϵ_{pp} the effective dielectric function of the composite, the dielectric function of the host (a-Si) and of the inclusion in the composite (t- SiO_2), σ_{pp} the weight of the delta function of the spectral function at the origin, $g(x)$ is the reduced spectral function [10], and $s_{pm} = [1 - \epsilon_{pp}/\epsilon_{pm}]^{-1}$. The reduced spectral function has some interesting properties [10]. $g(x)$ is zero at $x = 0$ and 1, and $g(x) \geq 0$ on the interval $[0,1]$. Furthermore the zeroth moment gives the volume fraction of the inclusion p_{pp} :

$$p_{pp} = \sigma_{pp} + \int_0^1 \frac{g(x)}{x} dx \quad (2)$$

and for an isotropic material the first moment satisfies: $\mu_1 = \int_0^1 g(x) dx = p_{pp}(1 - p_{pp})/3$.

The absorption spectrum for oxide particles in a silicon matrix is given by [3,6]: $\alpha = 2\pi\nu \text{Im}(\epsilon_{\text{eff}})/\text{Re}(\epsilon_{\text{eff}}^{1/2})$, with ν the wave number (in cm^{-1}), and $\epsilon_{\text{eff}}(\nu, f_s, f_d, \epsilon_m, \epsilon_p, y)$ the effective dielectric function [16] according to the continuum theory of Genzel and Martin [7] for spherical and oblate spheroidal [3,6] particles, where f_s and f_d are the volume fractions of polyhedral and platelet precipitates, ϵ_m and ϵ_p the dielectric function of the silicon matrix and the unknown effective dielectric function for the SiO_2 particles (see Eq. (1)), and y is the aspect ratio. The resonance wave number is given by the Fröhlich wave number (ν_s) for a sphere and by the longitudinal optical (LO) wave number (ν_{LO}) for a perfect disk, while for an oblate spheroid the resonance wave number (ν_d) lies between ν_s and ν_{LO} , depending on y . The absorption spectrum of the oxide precipitates is located in the reststrahlen region (the region between transverse optical wave number ν_{TO} and ν_{LO}) of t- SiO_2 . In the case of SiO_2 particles the medium consists of a rather inert medium (a-Si) and a medium with a strong resonance in the reststrahlen region. These two conditions should allow the extraction of the reduced spectral function.

The spectral functions are extracted by minimizing the following chi-squared function $\chi^2 = \chi_z^2 + \chi_c^2$, where $\chi_z^2 = \sum |\alpha(\nu_i) - \alpha(\nu_i, \sigma_{pp}, g(x), f_s, f_d, y)|^2$ and $g(x)$

Table 1
Oxygen concentration before and after heat treatments

Sample name	[O _i] (initial) (10^{17} cm^{-3})	[O _i] (final) (10^{17} cm^{-3})
SD1	10.3	1.5
SD2	10.5	4.9
SD3	10.2	6.1
SD4	9.81	2.7
SD5	8.09	6.23
SD6	10.17	2.13
S1	7.52	1.37
S2	7.94	0.94

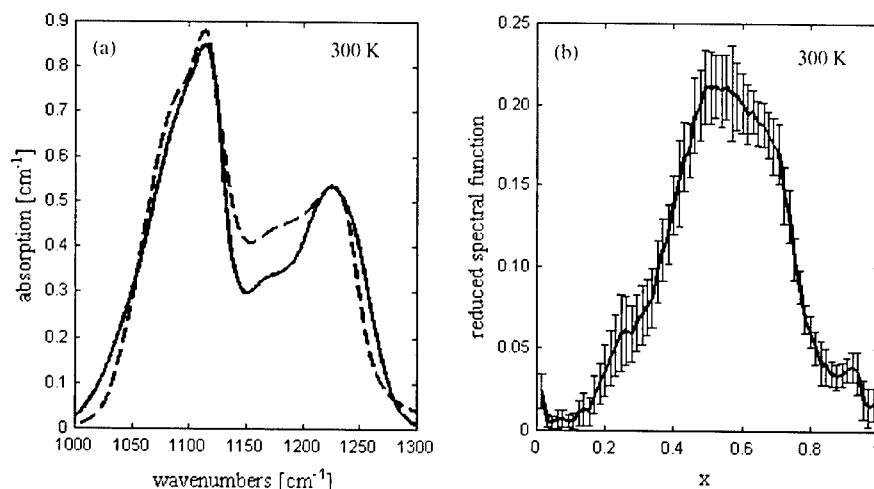


Fig. 1. Application of the optimization procedure to experimental absorption spectrum (set I). (a) Absorption spectrum of sample SD6 (solid line) and the best fit (dashed curve). (b) Average reduced spectral function for the samples of set I, with $\sigma_{pp} = 0.49 \pm 0.03$.

approximated as a histogram with 64 bins.¹ As the heart of the problem is an inhomogeneous Fredholm equation of the first kind (Eq. (1)), the problem will be ill-conditioned [10]. The standard strategy to tackle such a problem is to insert a priori knowledge into the chi-squared equations by means of a set of constraints (χ_c^2):

$$\chi_c^2 = \lambda_1 (\mu_1 - \frac{1}{2}p_{pp}(1 - p_{pp}))^2 + \lambda_4 (\nabla g(x))^2 + \lambda_2 (\Delta[O_i] - [O]_{pp})^2 + \lambda_3 [\Delta v_s^2 + v_d^2], \quad (3)$$

where $\Delta[O_i]$ is the disappeared interstitial oxygen, $[O]_{pp} = (f_s + f_d)p_{pp}C_{SiO_2}$ is the concentration of oxygen in the precipitates, and $C_{SiO_2} (= 4.6 \times 10^{22} \text{ cm}^{-3})$ is the oxygen in SiO_2 . The solution has to satisfy the first-moment relation (first term in Eq. (3)) [10]. The second term is a smoothing term, to prevent wild oscillations in $g(x)$ [10]. The third term states that all the disappeared interstitial oxygen ($\Delta[O_i]$) is in the precipitates ($[O]_{pp}$). The last term gives the differences between the experimental and the simulated v_s and v_d , as those are closely related with v_{TO} and v_{LO} , which in turn determine the dielectric function [5]. Tests on simulated spectra demonstrated that the algorithm is capable of extracting the volume fractions f_s, f_d, p_{pp} accurately and $g(x)$ with a modest accuracy, while the estimates on γ were somewhat underestimated [16]. The accurate determination of p_{pp} allows to determine the stoichiometry.

4. Results and discussion

The samples can be divided in two sets (Table 1). The first set of samples (set I, SD1–SD6) reveals two resonance wave numbers in the absorption spectra around 1115–1120 cm^{-1} and 1215–1225 cm^{-1} , traditionally assigned to polyhedral and platelet precipitates, respectively [1,6]. The second set (set II, S1–S2) consists of samples with only one resonance wave number around 1100 cm^{-1} , due to polyhedral precipitates [1]. As this resonance wave number is clearly shifted with regard to the samples of set I, one might expect that this is due to a different phase or to a different geometry of the medium.

One sample from set I (SD6) and one from set II (S2) were investigated with TEM. The first sample contained polyhedral and platelets, the latter having an aspect ratio around 0.04 ± 0.02 . No platelet precipitates were observed in the second (S2) sample, as expected.

The algorithm is applied on the two sets of samples. For set I a volume fraction (p_{pp}) of 0.71 ± 0.04 and for set II a slightly lower value of 0.66 ± 0.03 were obtained. This is equivalent with SiO_{γ} , with $\gamma = 1.20 \pm 0.10$ and 1.08 ± 0.07 , respectively. The difference in p_{pp} for the two sets is less than 7%, which is not significant, and their 95% confidence regions overlap. Hence, the shift of the Fröhlich wave number from 1110 to 1100 cm^{-1} is not related to a change in volume fraction but is rather due to the detailed picture of $g(x)$, and thus due to a slightly different geometrical structure of the composite. For the samples of set I $g(x)$ has a maximum around $x \approx 0.55$ (Fig. 1(b)), while for the samples of set II the maximum is located around $x \approx 0.3$ – 0.4 (Fig. 2(b)). The error bars

¹Contrary to Day and Thorpe [10], we do not use a symmetric effective dielectric function.

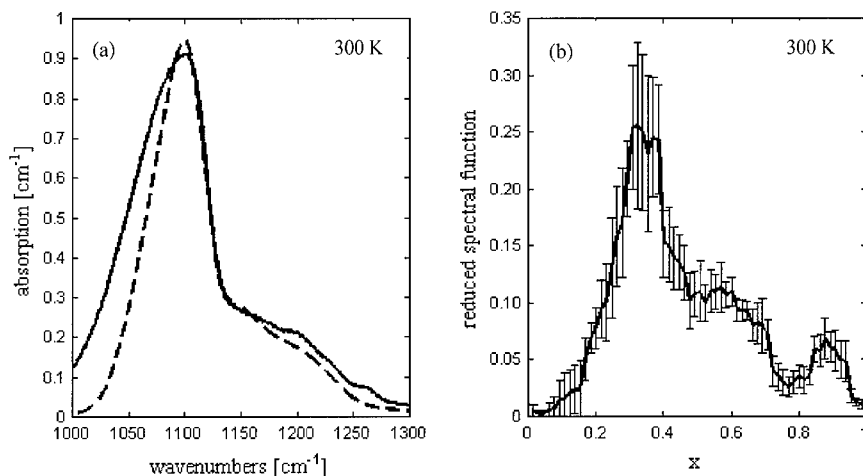


Fig. 2. Application of the optimization procedure to experimental absorption spectrum (set II). (a) Absorption spectrum of sample S2 (solid line), and the best fit (dashed curve). (b) Average reduced spectral function for the samples of set II., with $\sigma_{pp} = 0.43 \pm 0.02$.

of $g(x)$ for set II are somewhat larger, because the corresponding $g(x)$ has a rather narrow peak, which is much harder to resolve.

In Fig. 1(a) the absorption spectrum of sample SD6, together with the best fit is given. The obtained aspect ratio is 0.02, which is at the lower border of the error interval determined from the TEM measurements. In Fig. 2(a) an example of set II is given. In both cases the fits to the absorption spectra are good. Deviations can be due to the uncertainty on the dielectric function and to the use of an oscillator model to approximate the dielectric function. Generally, the constraints on the oxygen concentration (third term in Eq. (3)) agreed to within 15%, while the constraint on the first moment (first term in Eq. (3)) agreed to within 25%.

5. Conclusions

The modified Day–Thorpe algorithm has been adapted to the case of absorption spectra of SiO₂ precipitates in silicon and was more severely constrained. This permitted to determine the volume fraction of SiO₂ in the precipitates quite accurately. Also the reduced spectral functions for two sets of specimens with different Fröhlich wave number could be obtained with a moderate accuracy. The shift in the Fröhlich wave numbers is related to a different geometrical structure, of which the reduced spectral function is the emanation. The precipitates consist of SiO₂ with $\gamma = 1.1–1.2$. Regarding the wide range of experimental situations, the latter result seems to be quite general.

Acknowledgements

This work was performed with financial support from the National Science Foundation (FWO).

References

- [1] P. Gaworzewski, E. Hild, F.G. Kirscht, L. Vecsernyés, *Phys. Stat. Sol. A* 85 (1984) 133.
- [2] J. Vanhellemont, *J. Appl. Phys.* 78 (1995) 4297.
- [3] A. Borghesi, A. Piaggi, A. Sassella, A. Stella, B. Pivac, *Phys. Rev. B* 46 (1992) 4123.
- [4] O. De Gryse, P. Clauws, J. Vanhellemont, C. Claeys, *Mater. Sci. Forum* 257–263 (1997) 405.
- [5] C.F. Bohren, D.R. Huffman, *Absorption and Scattering of Light by Small Particles*, Wiley, New York, 1983.
- [6] S.M. Hu, *J. Appl. Phys.* 51 (1980) 5945.
- [7] L. Genzel, T.P. Martin, *Surf. Sci.* 34 (1973) 33.
- [8] D.J. Bergman, *Phys. Rep.* 43 (1978) 377.
- [9] G.W. Milton, *J. Appl. Phys.* 52 (1981) 5286.
- [10] A.R. Day, M.F. Thorpe, *J. Phys.: Condens. Matter* 11 (1999) 2551.
- [11] O. De Gryse, P. Clauws, L. Rossou, J. Van Landuyt, J. Vanhellemont, W. Mondelaers, *Electrochem. Soc. Proc.* 98–13 (1998) 398.
- [12] A. Baghdadi, W. Bullis, M. Croarkin, Y.-Z. Li, R. Scace, R. Series, P. Stallhofer, M. Watanabe, *J. Electrochem. Soc.* 136 (1989) 2015.
- [13] O. De Gryse, P. Clauws, *J. Appl. Phys.* 87 (2000) 3294.
- [14] P. Grosse, B. Harbeke, B. Heinz, R. Meyer, M. Offenber, *Appl. Phys. A* 39 (1986) 257.
- [15] T. Balz, R. Brendel, R. Hezel, *J. Appl. Phys.* 76 (8) (1994) 4811.
- [16] O. De Gryse, P. Clauws, O. Lebedev, J. Van Landuyt, C. Claeys, E. Simoen, J. Vanhellemont, *J. Appl. Phys.*, submitted for publication.



ELSEVIER

Physica B 308–310 (2001) 298–300

PHYSICA B

www.elsevier.com/locate/physb

Effect of oxygen on exciton transitions in silicon

A.N. Safonov, Gordon Davies*

Physics Department, King's College London, Strand, London WC2R 2LS, UK

Abstract

The spectral line shape of the α_1 no-phonon line of the exciton bound to phosphorus donors in silicon is asymmetric and it broadens rapidly with increasing oxygen concentration. We show that these effects can be accounted for by assuming that a neutral oxygen atom has a short-range potential, decreasing sufficiently rapidly with distance that the first-order effect on the exciton energy level is proportional to the exciton density on the oxygen atom. Different combinations of oxygen atoms around the phosphorous centers produce a variety of frequency shifts resulting in the inhomogeneous broadening of the α_1 line. Assuming that oxygen atoms are randomly distributed relative to the phosphorus donors, the profile of the α_1 line can be simulated and the strength of the short-range potential determined. © 2001 Elsevier Science B.V. All rights reserved.

PACS: 71.55.Cu; 78.55.Ap

Keywords: Silicon; Oxygen; Line widths

1. Introduction

Optical transitions in semiconductors are often inhomogeneously broadened by crystal imperfections. For example, point defects, dislocations and charge centers produce randomly distributed strain fields and electric fields that can affect the frequency of optical transitions. The line shapes of the transitions then depend on the statistical distributions of the fields at the optical centers. Consequently, line shapes can be used to monitor changes in the relative distributions of the defect and optical centers, for example during annealing treatments [1], and, as in this report, they reveal the nature of the perturbation produced by individual defects.

This paper is concerned with the effect of oxygen, one of the most common impurities in silicon, on localized exciton states bound to phosphorus donors. A substitutional phosphorus atom in silicon forms an effective-mass donor. The electron states are derived from the six equivalent conduction-band minima, which lie along

$\mathbf{k} \parallel \langle 001 \rangle$ directions. At the T_d site of the P atom, these six states transform as A_1 , E and T_2 states, with the orbital singlet state A_1 lowest [2]. An exciton may be captured by the center, with a small binding energy (4.7 meV; Ref. [3]). The two electrons now trapped at the P atom spin-pair in the A_1 state, and the hole orbits in a state derived from the Γ_8 valence-band maximum. Luminescence resulting from the recombination of the hole with one of the electrons has been well-studied, including its response to externally applied stresses [4]. We concentrate here on the sharpest spectral line, the so-called α_1 line, whose width can be less than 1 μeV in isotopically pure Si [5]. In pure natural-abundance Si the width is 5 μeV , increasing with oxygen content to 100 μeV at $[\text{O}] \sim 10^{18} \text{ cm}^{-3}$ [6]. At the same time, the line shape becomes highly asymmetric with a tail towards higher photon energies (Fig. 1). The broadening of the α_1 transition has been attributed to the spatial fluctuations of the band gap produced by the strain fields of the oxygen atoms. This effect can be calculated, since both the responses to strains of the α_1 line [4] and the strains produced by the oxygen are known [7]. We show below that the resulting line shape would be a symmetric doublet, very different from that observed (Fig. 2). Instead, we will show that the observed line

*Corresponding author. Tel.: +44-20-7848-2573; fax: +44-20-7848-2420.

E-mail address: gordon.davies@kcl.ac.uk (G. Davies).

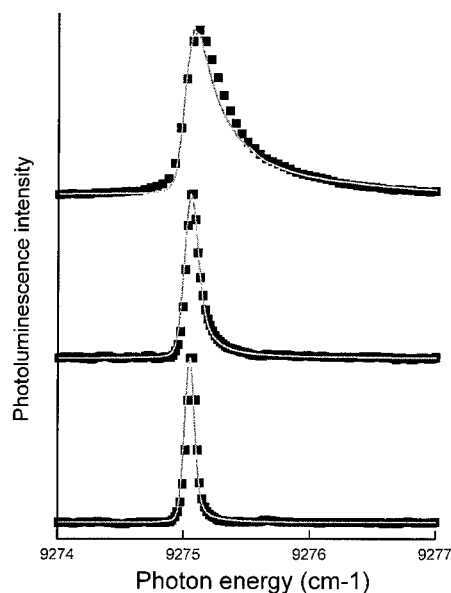


Fig. 1. Points show the measured spectrum of the α_1 transition in samples with an oxygen concentration of (a) $3 \times 10^{16} \text{ cm}^{-3}$, (b) $7 \times 10^{16} \text{ cm}^{-3}$, and (c) $3 \times 10^{17} \text{ cm}^{-3}$. The lines are the calculated spectra assuming a short-range potential at the oxygen atoms.

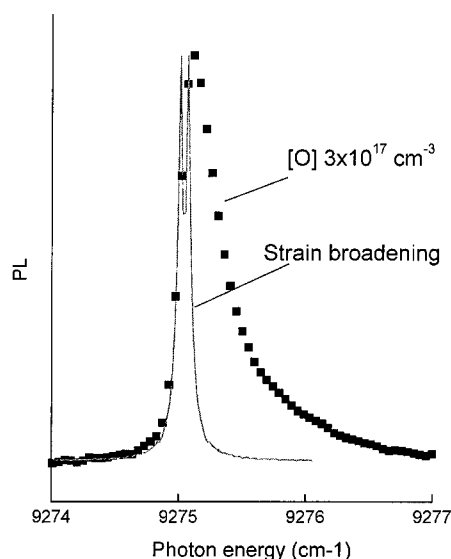


Fig. 2. Points show the measured spectrum of the α_1 transition in a sample with an oxygen concentration of $3 \times 10^{17} \text{ cm}^{-3}$. The line is calculated using strain broadening theory.

width and shape can be accounted for by assuming that the oxygen atoms are randomly distributed and that a neutral oxygen atom has a short-range potential, decreasing sufficiently rapidly with distance that its

first-order effect on the exciton energy level is proportional to the density of the exciton on the oxygen atom. Different combinations of oxygen atoms around the phosphorous centers produce a variety of frequency shifts, resulting in the inhomogeneous broadening of the α_1 line.

2. Experimental details

Silicon grown by the Czochralski process, using a crucible made of silica, contains a supersaturated concentration of oxygen. During a slow cool-down, or any post-growth heating, the oxygen atoms can become mobile and begin to precipitate. The samples used here had been specially processed for the experiments on isolated oxygen atoms and any small aggregates of oxygen had been thermally dissociated.

Photoluminescence spectra were measured using an Ar^+ laser, running at an output power of 100–200 mW, with the samples immersed in liquid helium at 4.2 K. The luminescence was measured at a resolution of $5 \mu\text{eV}$ using a Bomem DA8 Fourier transform spectrometer fitted with a North Coast Ge detector. To avoid experimentally-induced strain-broadening, the samples were tied to the sample holder using Teflon tape, and the spectra were measured at points remote from the tape.

3. Results and discussion

Interstitial oxygen is positioned between two silicon neighbors, with a Si–O–Si angle of 160° and Si–O bond length $\sim 0.16 \text{ nm}$ [8]. Since the Si–Si bond has length of 0.234 nm , an expansion of the silicon lattice is expected, and its volume increases at the rate of

$$\Delta V/V = 1.3 \times 10^{-23} [\text{O}], \quad (1)$$

where $[\text{O}]$ is the oxygen concentration in cm^{-3} [7]. The corresponding factor for substitutional carbon is $-1.95 \times 10^{-23} \text{ cm}^{-3}$ [9].

Within the elastic approximation the lattice displacement u at the distance r from a point defect in an infinite crystal would be $u = rA/r^3$, where A is a lattice mismatch parameter. The corresponding strain tensor e_{ij} at the point (r_1, r_2, r_3) a distance r from the oxygen atom is given by

$$e_{ij} = A/r^3 (\delta_{ij} - 3r_i r_j / r^2), \quad (2)$$

where $\delta_{ij} = 1$ if $i = j$ and is otherwise 0 [10]. It follows that the hydrostatic component of this field is equal to zero at any non-zero r . However, at $r = 0$ there is a local change of the volume occupied by the oxygen atom, with a magnitude $\Delta V_c = 4\pi A$ for each oxygen atom. In addition, there is a long-range contribution to the volume change associated with

the image forces at the surface of a finite crystal. This term gives a further dilatation for each oxygen atom of $\Delta V_s = 8\pi A(1 - 2\sigma)/(1 + \sigma)$, where σ is Poisson's ratio for an isotropic crystal; we take $\sigma = 0.22$ since $\langle 001 \rangle$ strains give the largest perturbation. The total volume change per oxygen atom is then

$$\Delta V = \Delta V_c + \Delta V_s = 12\pi A \frac{(1 - \sigma)}{(1 + \sigma)}, \quad (3)$$

allowing A to be found from Eq. (1) since the oxygen concentration is measurable [11]. Consequently, the strains e_{ij} are known from Eq. (1)

The effect of randomly distributed carbon impurities on the α_1 transition has been considered in Ref. [12]. It was shown that the presence of the inhomogeneous strain field produces not only a broadening but also a splitting of α_1 into two lines. Strain-broadening theory accurately fitted the data. Application of the same theory to the present samples, with oxygen as the strain source, gives the result in Fig. 2, substantially sharper than the experimental line shape, and a symmetric doublet rather than asymmetric singlet observed. It is clear that inhomogeneous strains cannot account for the oxygen broadening of the line.

To explain the effect of oxygen on the α_1 transition we shall consider a localized perturbation produced by each oxygen atom. We shall assume that the neutral O atom has a short-range potential located within a radius R_0 . Its effect on the exciton state is then proportional to the exciton density at the location of O atom. We assume that the exciton distribution can be described by a wavefunction of the form

$$\psi = \frac{1}{\sqrt{\pi R_b^3}} \exp\left(-\frac{r}{R_b}\right). \quad (4)$$

When R_0 is small in comparison with the 'Bohr radius' R_b , the energy shift of the exciton state is, in the first order,

$$\Delta h\nu = B \exp\left(-\frac{2r}{R_b}\right), \quad (5)$$

where B is an interaction parameter determined by the strength of the oxygen potential.

Using Eq. (5) and assuming that the oxygen atoms are randomly distributed in the silicon lattice, we can calculate the profile of the α_1 line. The solid lines on Fig. 1 show the simulated spectra obtained for oxygen concentrations (a) $3 \times 10^{16} \text{ cm}^{-3}$, (b) $7 \times 10^{16} \text{ cm}^{-3}$, and (c) $3 \times 10^{17} \text{ cm}^{-3}$, with $B = 0.8 \text{ meV}$ and $R_b = 2.2 \text{ nm}$. The calculated spectra have also been broadened by the random strain fields of the oxygen, as described above, and, to allow for broadening effects common to all the samples, the spectra have been broadened with the use of the line shape that corresponds to the experimental shape of α_1 at low [O] (0.2 part of Lorentzian and 0.8

part of Gaussian, both having half-width of $10 \mu\text{eV}$). The calculated spectra are in good agreement with the experimental results which are shown in Fig. 1 by dots.

In the model, the parameter R_b determines the extent of the volume sampled by the bound exciton, and so controls primarily the extent of the asymmetric tail. Its value is similar to the 'effective excitonic radius' quoted as $\sim 3.5 \text{ nm}$ [13]. The parameter B scales the width of the distribution. The value of B is consistent with the first-order perturbation of the excited state $\psi(r)$ by a perturbing potential $V(r)$ which is described by a constant potential V_0 located in the small volume R_0^3 occupied by the oxygen atom

$$\Delta E = \int d\mathbf{r} V(r) |\psi(r)|^2 = \frac{V_0 R_0^3}{\pi R_b^3} \exp(-2r/R_b).$$

Comparison with Eq. (5) gives $V_0 = B\pi R_b^3/R_0^3$, and hence a plausible value of $V_0 \sim 2.4 \text{ eV}$ if R_0 is an interatomic spacing.

We have shown that oxygen can increase the energy of the transition through the effect of its short-range (chemical) potential. The exciton bound to phosphorus is a simple case since its wave function will plausibly decrease slowly in space in the form of Eq. (4) and so its detailed structure is unimportant. The same mechanism could produce considerably larger upshifts at more tightly bound centres.

References

- [1] G. Davies, in: M. Stavola (Ed.), Identification of Defects in Semiconductors, Academic Press, San Diego, 1999, p. 2.
- [2] M.L.W. Thewalt, in: E.I. Rashba, M.D. Sturge (Eds.), Excitons, North-Holland, Amsterdam, 1982, p. 393.
- [3] M.A. Vouk, E.C. Lightowers, J. Phys. C 10 (1977) 3689.
- [4] M.L.W. Thewalt, J.A. Rostworowski, G. Kirczenow, Can. J. Phys. 57 (1979) 1898.
- [5] D. Karaiskaj, M.W.L. Thewalt, T. Ruf, M. Cardona, H.-J. Pohl, G. Deviatykh, P.G. Sennikov, H. Riemann, Phys. Rev. Lett. 86 (2001) 6010.
- [6] A.V. Lopatin, Ya.E. Pokrovskii, Zh. Eksp. Teor. Fiz. 87 (1984) 1381 [Sov. Phys. JETP 60, 793 (1984)].
- [7] D. Windisch, P. Bekker, Phys. Stat. Sol. A 118 (1990) 379.
- [8] D.R. Bosomworth, W. Hayes, A.R.L. Spray, G.D. Watkins, Proc. Roy. Soc. London Ser. A 317 (1970) 133.
- [9] J.A. Baker, T.N. Tucker, N.E. Moyer, R.C. Bichert, J. Appl. Phys. 39 (1968) 4365.
- [10] J.D. Eshelby, in: F. Seitz, D. Turnbull (Eds.), Solid State Physics, Advances in Research and Applications, Vol. 3, Academic press, New York, 1956, p. 79.
- [11] A. Baghadi, W.M. Bullis, M.C. Croarkin, Y.-Z. Li, R.I. Seace, R.W. Series, P. Stallhofer, M. Watanabe, J. Electrochem. Soc. 136 (1989) 2015.
- [12] A.N. Safonov, G. Davies, E.C. Lightowers, Phys. Rev. B 54 (1996) 4409.
- [13] V.G. Plekhanov, Opt. Spectrosc. 79 (1995) 715.



ELSEVIER

Physica B 308–310 (2001) 301–304

PHYSICA B

www.elsevier.com/locate/physb

Disturbance of oxygen by isovalent impurity atoms in silicon

L.I. Khirunenکو*, V.A. Zasuha, Yu.V. Pomozov, M.G. Sosnin

Institute of Physics, National Academy of Sciences of Ukraine, Prospect Nauki 46, 03028 Kyiv, Ukraine

Abstract

The diagram of electronic levels of A–Si–O–Si–A clusters (where A is carbon, germanium, tin or lead), has been obtained by group-theoretical analysis and molecular orbitals approaches. Three possible forms of Si substitution by isovalent impurity atoms are discussed. A linear A–Si–O–Si–A cluster and the clusters with A located in the second sphere relative to an oxygen atom with formation of a planar trans-configuration and a nonplanar cis-configuration were considered. It has been shown, that all these forms of Si substitution by isovalent impurity atoms lead to the decrease of the force constants and frequencies of local vibrations of Si–O–Si, respectively. © 2001 Elsevier Science B.V. All rights reserved.

Keywords: Silicon; Oxygen; Isovalent impurity; Disturbance

1. Introduction

Oxygen (O) is known to be the main and most intensively studied impurity in CZ-grown Si. It is one of the most active impurities in defect formation processes in Si. In recent years, the investigation of the properties of Si doped with isovalent impurities (IVI) has become a matter of considerable interest. It has been found that IVI in Si influence the diffusion of O and its precipitation at heat treatments, the formation processes of radiation defects. However, the mechanism of interaction between O and IVI atoms has not been adequately studied up to date.

The study of O properties in as-grown materials is interesting first of all. It is known that the doping of Si by IVI atoms leads to an appearance of the additional local modes in the frequency region corresponding to ν_3 vibrational mode of O [1–3] (Fig. 1). As it is seen from Fig. 1, for all IVI, additional bands appear on the low-frequency side relative to the band characteristic of Si, independent of the sign of the strain produced by IVI. In Refs. [1–3], additional bands observed were ascribed to the ν_3 vibrational mode of interstitial O disturbed

by IVI atom located in the second, third or fourth neighbouring site.

In this work, it is shown that an additional structure in the absorption spectrum of oxygen in IVI-doped silicon can appear due to the nonequivalent arrangement of IVI atom in the nearest Si–O–Si environment (in the second sphere relative to an oxygen atom).

2. Results and discussion

Oxygen is known to form in the Si lattice a Si–O–Si (Si_2O) quasimolecule oriented along the axis [1 1 1] [4–6]. Quasimolecule has D_{3d} symmetry and forms a $\text{Si}_3\text{--Si--O--Si--Si}_3$ cluster in Si. To explain the peculiarities observed in the absorption spectrum of O in IVI-doped Si, let us choose the following model. Si is known to have a tetrahedrally coordinated diamond structure, according to which the Si atoms are arranged pair-wise along the [1 1 1] axis with vacant lattice sites between them and form a $\bullet\text{--Si--Si--}\bullet$ chain (where the points denote the vacant lattice sites) [7,8]. These vacant lattice sites are possible places of the localization of IVI atoms. Consider the linear cluster A–Si–O–Si–A along the [1 1 1] axis, which is shown in Fig. 2a. First, consider the electronic structure of the Si_2O quasimolecule and then analyse the effect of C, Ge, Sn and Pb atoms on it.

*Corresponding author. Tel.: +380-44-265-98-21; fax: 380-44-265-55-88.

E-mail address: lukh@iop.kiev.ua (L.I. Khirunenکو).

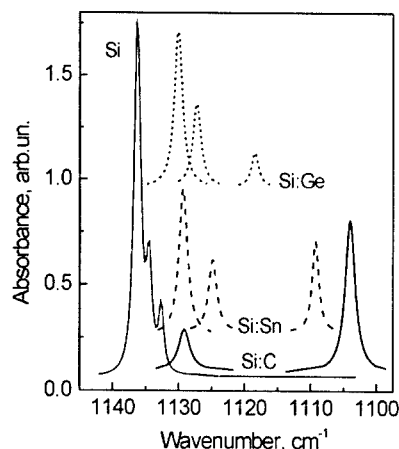


Fig. 1. Absorption bands of interstitial oxygen in Si and Si doped with Ge, Sn and C measured at 4.2 K with resolution 0.25 cm^{-1} . $N_{\text{Ge}} \approx 1.1 \times 10^{20} \text{ cm}^{-3}$; $N_{\text{Sn}} \approx 2 \times 10^{19} \text{ cm}^{-3}$; $N_{\text{C}} \approx 8 \times 10^{17} \text{ cm}^{-3}$.

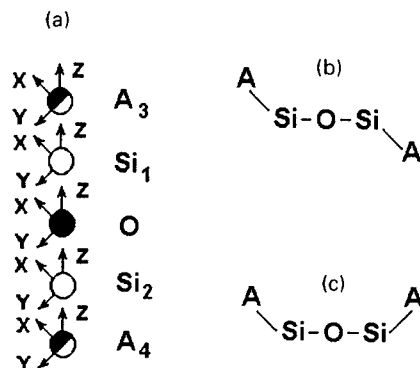


Fig. 2. Linear cluster A-Si-O-Si-A (a) and clusters with planar trans- (b) and nonplanar (c) cis-structures.

The energies of the 3s and 3p levels of the Si atom are $-14,965$ and -7755 eV [9] and the ones of the 2s and 2p levels of the O atom are $-34,078$ and $-17,238 \text{ eV}$ [10]. The energy values of the levels with opposite signs are known to correspond to ionization potentials. Thus, the 2s and 2p levels of the O atom lie below the 3s and 3p levels of the Si atom. The ionization energies and potentials of the *ns* and *np* levels of the Ge, Sn and Pb atoms are known to have lower values as compared with the Si atom and higher values for the C atom. This is accounted for by the fact that the position of the *ns* and *np* levels become higher when the principal quantum number increases in the order C, Si, Ge, Sn, Pb. Let us analyse the electronic structure of cluster A-Si-O-Si-A by the theoretical group analysis [11] and molecular orbital methods [12,13]. Table 1 gives a classification.

Table 1

Classification of AO's of oxygen atom and GO's of Si, C, Ge, Sn and Pb atoms in $\text{Si}_1\text{-O-Si}_2$ quasimolecule and $\text{A}_3\text{-Si}_1\text{-O-Si}_2\text{-A}_4$ cluster

$\text{H}\Pi_j$	O	$\Gamma\text{O}, \varphi_{\Pi_j}$	
		$\text{Si}_1\text{-Si}_2$	$\text{A}_3\text{-A}_4$
$\text{A}_{1g}(\text{E}_g^+)$	s	$(s_1 + s_2)/\sqrt{2}$ $(p_{z1} - p_{z2})/\sqrt{2}$	$(s_3 + s_4)/\sqrt{2}$ $(p_{z3} - p_{z4})/\sqrt{2}$
$\text{A}_{2u}(\Sigma_u^+)$	p_z	$(s_1 - s_2)/\sqrt{2}$ $(p_{z1} + p_{z2})/\sqrt{2}$	$(s_3 - s_4)/\sqrt{2}$ $(p_{z3} - p_{z4})/\sqrt{2}$
$\text{E}_g(\Pi_g)$		$(p_{x1} - p_{x2})/\sqrt{2}$ $(p_{y1} - p_{y2})/\sqrt{2}$	$(p_{x3} - p_{x4})/\sqrt{2}$ $(p_{y3} - p_{y4})/\sqrt{2}$
$\text{E}_u(\Pi_u)$	p_x p_y	$(p_{x1} + p_{x2})/\sqrt{2}$ $(p_{y1} + p_{y2})/\sqrt{2}$	$(p_{x3} + p_{x4})/\sqrt{2}$ $(p_{y3} + p_{y4})/\sqrt{2}$

obtained by the theoretical group analysis method, of the atomic orbitals (AO) of the O atom and group orbitals (GO) of Si and A atoms in the cluster $\text{A}_3\text{-Si}_1\text{-O-Si}_2\text{-A}_4$ with D_{3d} symmetry (in the case of the cluster in the crystal) and $\text{D}_{\infty h}$ symmetry (for isolated state) for a linear cluster. In this case, it was taken into account that in passing from group $\text{D}_{\infty h}$ to D_{3d} , the irreducible representations (IR) transform as follows [11]: $\Sigma_g^+ \rightarrow \text{A}_{1g}$, $\Sigma_g^- \rightarrow \text{A}_{2g}$, $\Sigma_u^+ \rightarrow \text{A}_{2u}$, $\Sigma_u^- \rightarrow \text{A}_{1u}$, $\Pi_g \rightarrow \text{E}_g$, $\Pi_u \rightarrow \text{E}_u$; The GO's are formed by the effects of the projection operator $\sum_R \chi^j(R) T_R$ on s and p AO, where T_R and $\chi^j(R)$ are the transformation operator and the character of IR *j* (A_{1g} , A_{2g} , E_u , A_{2u} , Π_g , etc.), respectively, to which the symmetry operation *R* corresponds. It is known [13] that symmetry operations transform the p_x , p_y , p_z AO equivalently to the *x*, *y* and *z* axes of the coordinate system.

According to the variational perturbation theory [14], the ϵ_{ij} energy levels and, corresponding to them, the molecular orbitals Ψ_{ij} of the quasimolecule and cluster are expressed as

$$\epsilon_{ij} = F_{ii,j} - \sum_{n \neq i} (F_{in,j} - F_{ii,j} S_{in,j})^2 / (F_{nn,j} - F_{ii,j}), \quad (1)$$

$$\Psi_{ij} = N_{ij} \left\{ \varphi_{ij} - \sum_{n \neq i} [(F_{in,j} - F_{ii,j} S_{in,j}) / (F_{nn,j} - F_{ii,j})] \varphi_{nj} \right\}, \quad (2)$$

$$N_{ij} = \left\{ 1 + \sum_{n \neq i} [(F_{in,j} - F_{ii,j} S_{in,j})^2 (F_{nn,j} - F_{ii,j})^{-2} - 2 S_{in,j} (F_{in,j} - F_{ii,j} S_{in,j}) (F_{nn,j} - F_{ii,j})^{-1}] \right\}^{-1/2}, \quad (3)$$

where *i* is the level number, *j* is the IR of the symmetry group, $F_{in,j}$ and $S_{in,j}$ are the matrix elements of the

Hartree-Fock operator \hat{F} and overlap integrals, and N_{ij} are normalization constants, which were obtained with the aid of the condition of normalization $\langle \Psi_{ij} | \Psi_{ij} \rangle = 1$. The energy of the two-fold degenerate level ε_{1E_g} to which the GO's of the Si₁ and Si₂ atoms (nonbonding MO's) correspond, is

$$\varepsilon_{1E_g} = \langle E_g | \hat{F} | E_g \rangle \approx \varepsilon_{3pSi} = -I_{3pSi}, \quad (4)$$

where ε_{3pSi} and I_{3pSi} are the ionization energy and potential of the 3p level of Si atom.

Fig. 3a shows the level diagrams obtained for the Si₂O quasimolecule. The electronic structure of complex systems, to which the A–Si–O–Si–A cluster belongs, can be constructed only by the method of linear combination of molecular orbitals (LCMO) [12,13] of interacting subsystems (fragments)—MO's of the Si₂O and GO's of A atoms (see Table 1 and Fig. 2a). A diagram of the A–Si–O–Si–A cluster obtained this way is shown in Fig. 3b. It follows from the diagram (Fig. 3a) and the formulae (1), (2) that the 1A_{2g}, 2A_{1g}, 3A_{1g} MO's of the Si₂O are nonbonding since the differences in the ionization potentials between the 2s level of the O atom and the 3s and 3p levels of the Si atom are large and are 19.113 and 26.323 eV. The 1A_{2g} MO is AO 2s of the O atom, and 2A_{1g}, 3A_{1g}, are linear combinations of GO's composed of AO 3s and 3p of Si atoms with opposite signs. The 1A_{2u}, 1E_u and 3A_{2u} MO's are of bonding and antibonding characters with the localization of electron

density inside and outside the Si–O–Si bond, respectively. The 2A_{2u} MO is weakly antibonding since the antibonding by the contribution of the AO 2p of the O atom is partially compensated by the contribution of the GO of Si atoms, which is composed of AO 3p_z. As it was already mentioned, the 1E_g MO's are nonbonding and are GO's composed of the AO 3p_x, 3p_y of Si atoms. The 1A_{1g}, 1A_{2u}, 1E_u MO's make a very small contribution to the formation of bonds between Si₂O and A atoms and Si atoms of the next environment spheres because their overlap integrals have the same GO symmetry, and hence, the matrix elements of the \hat{F} operator are negligible. The 2A_{1g}, 2A_{2u}, 1E_g, 3A_{1g}, 2E_u, 2A_{2u} MO's of the Si₂O contribute to the formation of their bonds since the electron densities of these MO's are concentrated on the Si atoms, which ensure their overlaps, and the matrix elements of the \hat{F} operator with the above GO's are nonzero. Thus, the 2A_{1g}, 2A_{2u}, 1E_g, 3A_{1g}, 2E_u, 3A_{2u} MO's are delocalized on the A and Si atoms of the next environment spheres of the Si₂O in crystal, and the 1A_{1g}, 1A_{2u}, 1E_u MO's are localized on the O atom and Si–O bonds, correspondingly. The latter MO's determine the locality (characteristicity) of the bonds of Si₂O and lead to the appearance of characteristic vibrational modes of the Si₂O in the absorption spectra. The LCMO method [12,13], which was employed by us in the study, showed that the bond between the Si₂O and the A atoms in the A–Si–O–Si–A cluster are formed by its 2A_{1g}, 2A_{2u}, 1E_g, 3A_{1g}, 2E_u, 3A_{2u} MO's and the GO's of the corresponding IR's of two atoms of A.

It follows from the level diagram of the A–Si–O–Si–A cluster shown in Fig. 3b that the bonds in the cluster are realized by the electrons of the 2A_{1g}, 2A_{2u}, 1E_g, 2E_u MO's, and that the 3A_{2u}, 3A_{1g} MO's are of a weak bonding or antibonding nature in accordance with formulae (1) and (2) since the bonding and antibonding contributions partially compensate each other. Since the 2A_{1g}, 2A_{2u} and 1E_g MO's of the Si₂O quasimolecule are nonbonding, their participation in the formation of bonds to the A atoms does not greatly affect the force constants and vibration frequencies of Si₂O. However, the participation of the antibonding 2E_u, 3A_{2u} MO's of Si₂O in the formation of bonds to A impurities weakens the intramolecular bonds of the quasimolecule, and, consequently, its force constants and hence, vibration frequencies decrease.

The possible nature of the shift of the vibrational absorption bands of the Si–O–Si quasimolecule (which are associated with the perturbation by A atoms), which was established for the linear A–Si–O–Si–A cluster, is also characteristic of cluster with planar trans-structure and nonplanar cis-structure, which are produced by the substitution of A atoms for Si atoms in the next environment sphere of quasimolecule as is shown in Figs. 2b and c. Here, as in the case of linear cluster, the force constants and vibration frequencies of the Si₂O

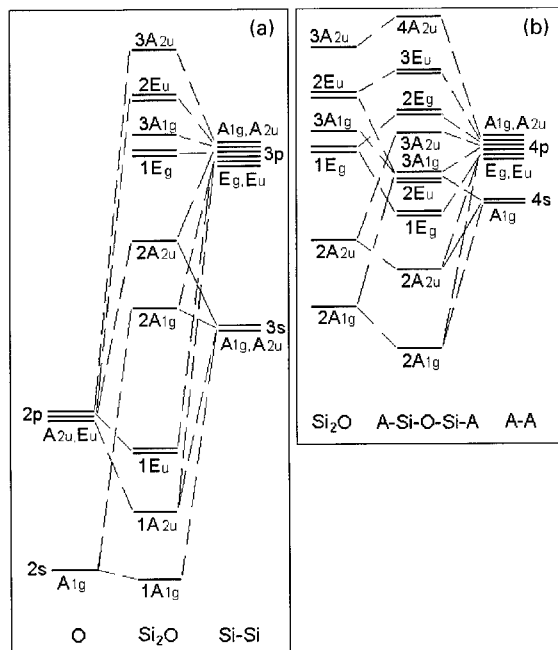


Fig. 3. Levels diagram Si–O–Si quasimolecule and A–Si–O–Si–A (A = C, Ge, Sn, Pb) cluster.

quasimolecule decrease due to the interaction of the antibonding $2E_u$ and $3A_{2u}$ MO's of Si_2O with A atoms. However, when the linear structure changes to the planar trans-structure or nonplanar cis-structure with an angle of 60° between Si–A bonds (Fig. 2c), the fully symmetric and antisymmetric states (Fig. 3b) transform according to the IR's of A_g and A_u of C_i symmetry group and A and B of C_2 symmetry group of the planar trans- and nonplanar cis-structures, respectively. This leads to the removal of the degeneracy of the states E_g and E_u , to the strengthening of the Si–A bonds, weakening of the bonds in the Si_2O and decreasing of the vibration frequencies since the number of the MO's of the Si_2O quasimolecule and GO's of the impurity atoms A, which refer to the same IR, increases. The above effects are more pronounced in the case of nonplanar cis-structure, for which GO's composed of s orbitals of A atoms contribute to interactions with both degenerate states E_g and E_u of the Si_2O quasimolecule and with only one state in the case of planar trans-structure.

Thus, the investigation carried out by the LCMO method show that additional bands can appear in absorption spectra of the Si_2O quasimolecule in silicon due to different forms of substitution of isovalent atoms for Si atoms in the second environment sphere of oxygen.

References

- [1] H. Yamada-Kaneta, C. Kaneta, T. Ogawa, *Phys. Rev. B* 47 (N15) (1993) 9338.
- [2] D. Wauters, P. Clauws, *Mater. Sci. Forum* 258–263 (1997) 103.
- [3] L.I. Khirunenko, Yu.V. Pomozov, M.G. Sosnin, *Physica B* 273–274 (1999) 317.
- [4] J. Hrostowski, B.J. Alder, *J. Chem. Phys.* 33 (1960) 980.
- [5] D.R. Bosomworth, N. Hayes, A.R.I. Spray, G.D. Watkins, *Proc. Roy. Soc. London Ser. A* 317 (1970) 133.
- [6] A.S. Oates, M. Stavola, *J. Appl. Phys.* 61 (1987) 3114.
- [7] C. Kittel, *Elementary Solid State Physics*, Wiley, New York, London, 1962, pp. 18–20.
- [8] Neil W. Ashcroft, N. David Mermin, *Solid State Physics*, Mir, Moscow, 1979, p. 21.
- [9] J.C. Slater, *Phys. Rev.* 98 (N4) (1955) 1039.
- [10] E. Clementi, A.D.A.D. McLean, *Phys. Rev.* 133 (2a) (1964) 419.
- [11] R. Hochstrasser, *Molecular Aspects of Symmetry*, Benjamin, New York, 1966.
- [12] V.A. Zasuha, *Theo. Exp. Chem.* 10 (1974) 155.
- [13] S.V. Volkov, V.A. Zasuha, *Quantum Chemistry of Coordinating Condensed Systems*, Naukova Dumka, Kiev, 1985, pp. 1085–1095.
- [14] P. McVeeny, B.T. Sutcliffe, *Methods of Molecular Quantum Mechanics*, Academic Press, London, New York, 1969.



ELSEVIER

Physica B 308–310 (2001) 305–308

PHYSICA B

www.elsevier.com/locate/physb

Over-coordinated oxygen in the interstitial carbon–oxygen complex

J. Coutinho^{a,*}, R. Jones^a, P.R. Briddon^b, S. Öberg^c, L.I. Murin^d, V.P. Markevich^e,
J.L. Lindström^f

^a School of Physics, University of Exeter, Exeter EX4 4QL, UK

^b Department of Physics, University of Newcastle, Newcastle NE1 7RU, UK

^c Department of Mathematics, Luleå University of Technology, S-97187 Luleå, Sweden

^d Institute of Solid State and Semiconductor Physics, Minsk 220072, Belarus

^e Centre for Electronic Materials, UMIST, Sackville Street, Manchester M60 1QD, UK

^f Department of Physics, University of Lund, S-221 00 Lund, Sweden

Abstract

The interstitial carbon–oxygen complex is one of the most prominent defects formed in e-irradiated Cz-Si containing carbon. Stress alignment investigations have shown that the oxygen atom only perturbs the carbon interstitial but the lack of a high frequency oxygen mode has been taken to imply that the oxygen atom is over-coordinated. Local vibrational mode spectroscopy and ab initio modeling are used to investigate the defect. We find new modes whose oxygen isotopic shifts, along with the piezospectroscopic stress-energy tensor support the trivalent model, thus providing evidence for oxygen over-coordination. © 2001 Elsevier Science B.V. All rights reserved.

PACS: 61.72.Bb; 61.72.Ji; 61.80.Az; 61.80.Fe; 63.20.Pw; 71.55.Cn; 81.05.Cy

Keywords: Silicon; Radiation defects; Oxygen; Carbon

1. Introduction

Low temperature e-irradiation of Si generates mobile Si interstitials which are readily trapped by substitutional carbon defects forming carbon interstitials (C_i). In turn, these are mobile at room temperature and subsequently complex with many impurities including oxygen. The interstitial carbon–oxygen center (C_iO_i) is a product of the latter interaction and is a stable defect with an annealing temperature around 350–450°C [1]. It has been detected by all four principal methods used to characterize defects. Electron paramagnetic resonance (EPR) relates the $C_iO_i^{(+)}$ defect to the G15 signal [2]. Its similarity with the magnetic properties of $C_i^{(+)}$ implies that the C-atom is only slightly affected by oxygen. The defect gives a prominent 0.7896 eV photoluminescent

(PL) signal (C-line) [3], associated with several local mode replicas [1]. Previous Fourier transform infra-red (FTIR) spectroscopic experiments have identified local vibrational modes (LVMs) at 1116, 865, 742, 550 and 529.8 cm^{-1} [4]. Finally, deep level transient spectroscopy (DLTS) has linked a donor level at $E_v + 0.38$ eV with the defect [5].

Based on stress alignment arguments, the structure shown in Fig. 1a was put forward [2]. On the other hand, as depicted in Fig. 1b, theoretical modeling proposed a strongly affected oxygen atom relative to its normal bond-centered placement. It was then argued that the greater electronegativity of carbon encouraged electron transfer from the dangling bond at the Si_2 atom, leading to an Si_2 –O oxidative bond at the expense of a lone pair orbital on oxygen [6].

Interest in the defect has recently arisen from two fronts: (i) the observation of its reduction by irradiating hydrogenated samples [7,8] and, (ii) the suggestion that

*Corresponding author.

E-mail address: coutinho@excc.ex.ac.uk (J. Coutinho).

the interaction between H and a prominent radiation-induced defect like VO or C_iO_i gives rise to the first member of a shallow donor family (labeled as DN with $N = 1, 2$ and 3) [9,10], with D2 and D3 identified as STD(H)2 and STD(H)3 members of the hydrogen-related shallow thermal donor family [STD(H) N] [11].

Oxygen over-coordination has been a matter of interest, as it is thought to be the origin for donor activity on thermal donors. A comprehensive study of the C_iO_i defect by FTIR and ab initio modeling is presented here, paying special attention to the coordination of the O-atom.

2. Experiments

The IR absorption analysis was carried out using a Bruker 113v Fourier transform IR spectrometer. The

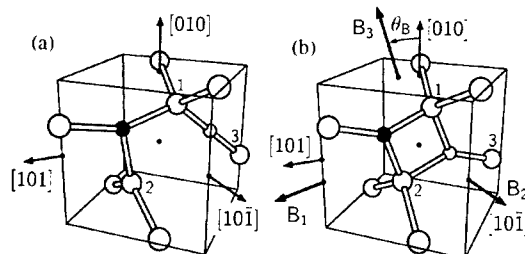


Fig. 1. Models for C_iO_i . (a) divalent oxygen model. (b) trivalent oxygen model. Gray, black and white atoms are Si, C and O. Crystallographic axes and principal directions of the B-tensor are also shown.

measurements were performed at 10 K and at room temperature (RT), with a spectral resolution of 0.5–1.0 cm^{-1} . Three types of Si:O,C samples were used. Sample (1) contained ^{16}O and ^{12}C , while sample (2) contained mainly ^{18}O and ^{12}C . Sample (3) was doped with ^{16}O and ^{13}C . Sample (1) was fabricated from ordinary phosphorus-doped Cz-Si with initial resistivity of 60 Ωcm , with oxygen and carbon concentrations of about 1×10^{18} and $3 \times 10^{17} \text{ cm}^{-3}$, respectively. Samples (2) and (3) consisted of float-zone Si material (Fz-Si) enriched with oxygen and carbon isotopes. In (2) the concentrations of $^{16}\text{O}_i$, $^{18}\text{O}_i$ and $^{12}\text{C}_s$ were 5×10^{16} , 1.5×10^{18} and $4 \times 10^{17} \text{ cm}^{-3}$, respectively, while (3) contained about $1 \times 10^{18} \text{ cm}^{-3}$ of $^{16}\text{O}_i$ and $1.5 \times 10^{18} \text{ cm}^{-3}$ of $^{13}\text{C}_s$. Irradiation with electrons (2.5 MeV) was performed at RT. Isochronal anneals of 30 min were carried out up to 600 °C in nitrogen ambient.

Fig. 2 shows fragments of differential absorption spectra of electron-irradiated Si samples doped with different O and C isotope combinations. Table 1 gives band frequencies for neutral C_iO_i and their ^{13}C and ^{18}O isotopic shifts. In descending frequency, they are labeled as the 1116, 865, 742, 585, 550, 540 and 529 cm^{-1} bands, respectively. Other than the 585 and 540 cm^{-1} modes, the bands are the same as those given earlier [1,4]. However, only carbon isotope effects had previously been studied by IR-absorption, and shifts were only found for the 1116 and 865 cm^{-1} lines.

The most important result is the observation of a significant 33.4 cm^{-1} oxygen isotopic shift *only* for the 742 cm^{-1} band, clearly indicating its oxygen character. This shift is in agreement with observations based on PL vibrational spectroscopy [1]. The present work then clearly shows that the highest oxygen related frequency

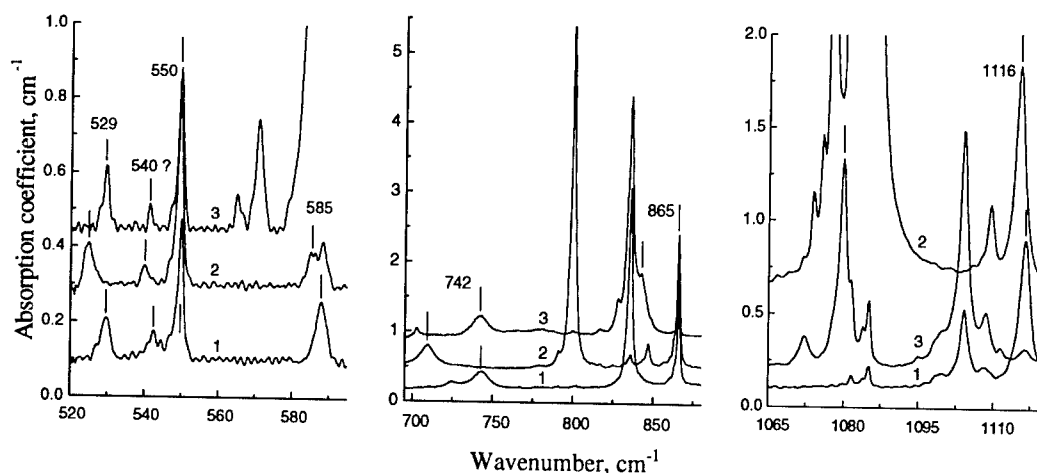


Fig. 2. Sections of the absorption spectra measured at 10 K for electron-irradiated Si samples: (1) $[^{16}\text{O}] = 1 \times 10^{18}$ and $[^{12}\text{C}] = 3 \times 10^{17} \text{ cm}^{-3}$, irradiation dose $F = 1 \times 10^{18} \text{ cm}^{-2}$; (2) $[^{18}\text{O}] = 1.5 \times 10^{18}$, $[^{16}\text{O}] = 5 \times 10^{16}$ and $[^{12}\text{C}] = 4 \times 10^{17} \text{ cm}^{-3}$, $F = 1.5 \times 10^{18} \text{ cm}^{-2}$; (3) $[^{16}\text{O}] = 1 \times 10^{18}$, $[^{13}\text{C}] = 1.5 \times 10^{18}$ and $[^{12}\text{C}] = 2^{17} \text{ cm}^{-3}$, $F = 1.5 \times 10^{18} \text{ cm}^{-2}$. The lines related to the C_iO_i complex are labeled.

Table 1

Observed and calculated LVMs (cm^{-1}), for $\text{C}_i\text{O}_i^{(0)}$. First two columns report absolute frequencies, whereas columns three onwards give their downward isotopic shifts

$^{16}\text{O}, ^{12}\text{C}$		$^{16}\text{O}, ^{13}\text{C}$		$^{18}\text{O}, ^{12}\text{C}$	
Obs.	Calc.	Obs.	Calc.	Obs.	Calc.
1116.3	1137.6	36.4	37.7	1.0	1.0
865.9	876.1	23.9	24.5	0.15	0.1
742.8	759.6	0.5	0.3	33.4	35.6
~588	593.4	—	0.1	~3	3.2
549.8	555.8	0.2	0.3	0.3	0.2
~542	544.7	~0.5	0.1	~1.5	0.5
529.6	544.2	0.1	0.0	5.2	5.4

lies at 742 cm^{-1} , compared with 1136 cm^{-1} for O_i , and possesses an ^{18}O shift considerably smaller than that of the asymmetric stretch mode in O_i (51.4 cm^{-1}) [12].

The low intensity and spectral location have probably prevented the detection of the 585 cm^{-1} band previously. In Si: $^{16}\text{O}, ^{12}\text{C}$, the 585 cm^{-1} band is masked by the X-line at 588.5 cm^{-1} due to the C_sO_i pair, as well as the fundamental mode at 589.1 cm^{-1} of $^{13}\text{C}_s$ which occurs with a natural abundance of 1.1%. However, its slight shift in ^{18}O -doped material is enough to distinguish it, allowing us to correlate this with other bands of the C_iO_i defect.

There are some hints that another weak band at $\sim 540\text{ cm}^{-1}$ is associated with the C_iO_i complex and labeled 540? in Fig. 2. In Si: $^{16}\text{O}, ^{12}\text{C}$ this band is superimposed on bands at 540.4 and 543.3 cm^{-1} due to C_iC_s [13]. However, it undergoes a $\sim 1.5\text{ cm}^{-1}$ shift in Si: $^{18}\text{O}, ^{12}\text{C}$ samples suggesting an oxygen defect. Moreover, since its isochronal annealing behavior is essentially the same as that of the other C_iO_i -related lines, we tentatively identify it with this defect.

3. Theory and modeling

We used an ab initio total energy density functional code (AIMPRO), with 64 Si-atom supercells. Details are described elsewhere [14]. LVMs were calculated by diagonalization of the dynamical matrix obtained from the ab initio code. Acceptor and donor levels are obtained by comparing energy differences $E(-) - E(0)$ and $E(0) - E(+)$ of a defect, with those of a standard defect with well-known acceptor and donor levels [15]. This was chosen to be the carbon-interstitial defect with acceptor and donor levels at $E_c - 0.10\text{ eV}$ and $E_v + 0.28\text{ eV}$, respectively. The stress-energy tensor B was calculated by deforming the defective supercell with a set of strain-tensors compatible with the symmetry of the defect, and solving $\Delta E = B \cdot \varepsilon$ [13].

In agreement with previous calculations [6], we find a ground state structure of C_iO_i , with both carbon and oxygen three-fold coordinated, forming two vertices of a ring as shown in Fig. 1b. Its 1.7 eV binding energy is consistent with its high thermal stability. Calculation of the energy levels shows that a deep donor level lies at $E_v + 0.36\text{ eV}$ in agreement with the observed DLTS level at $E_v + 0.38\text{ eV}$ [5]. No acceptor or second donor levels were found. A Mulliken bond population analysis of the highest occupied band gives 25.4% and 0.1% of spin density localized around the carbon and oxygen atoms respectively. The first is in agreement with the 28.6% spin localization on carbon measured for G15 [2]. Note that in spite the O-atom being over-coordinated, no gap level with overlap on oxygen occurs. Both the lone electron pair on O, and the donated electron pair in the $\text{Si}_2\text{-O}$ bonding state, resonate the valence band.

The principal directions of the calculated stress-energy tensor are shown in Fig. 1b. The C_{1h} symmetry of the defect implies that one principal direction (corresponding to the B_2 component) lies along $[1\ 0\ \bar{1}]$, but the other directions are rotated by an angle θ_B from the $[0\ 1\ 0]$ and $[1\ 0\ 1]$ axes. For the positively charged defect, the rotation angle is calculated to be $\theta_B = 22^\circ$, and the principal values of the tensor are 8.5, 2.3 and -11.8 eV for B_1 , B_2 and B_3 , respectively. Stress alignment experiments give 8.6, 0.2 and -8.8 eV for B_1 , B_2 and B_3 , and $\theta_B = 15^\circ$. Hence the model accounts well the observations.

The LVMs for the neutral defect are shown in Table 1. Of special interest is the unique oxygen-related mode lying at 760 cm^{-1} — well below the asymmetric stretch mode for interstitial oxygen at 1136 cm^{-1} . This is a characteristic of the weakened bonds of over-coordinated oxygen relative to those in Si-O-Si . The oxygen mode is very close to the observed band at 742.8 cm^{-1} . The observed and calculated ^{18}O -shifts are also very close, lying at 33.4 and 35.6 cm^{-1} respectively. Two carbon related modes are calculated to lie at 1138 and 876 cm^{-1} , close to the observed 1116 and 865 cm^{-1} bands. Their shifts with ^{13}C demonstrate that they are carbon related in agreement with the observations.

The four remaining low frequency modes at 593, 556, 545 and 544 cm^{-1} have not been assigned previously. They arise from vibrations of Si neighbors to the defect core, and are properly described only when energy second derivatives with these atoms are calculated directly from the ab initio program. These support the assignment of the 540 cm^{-1} band to C_iO_i (see Section 2).

4. Conclusions

Absorption bands produced by the C_iO_i defect have been studied in detail. FTIR data were obtained from Si samples doped with three combinations of dominant

oxygen and carbon isotopes, including for the first time the effect of ^{18}O . According to the calculations, we classify the LVMs as carbon-related 1116 and 865 cm^{-1} bands, the oxygen 742 cm^{-1} band, and the four low frequency 585 , 550 , 540 , 529 cm^{-1} bands, where the 585 and 540 cm^{-1} bands have not been reported previously. Of particular interest is the position and ^{18}O isotopic shift observed for the 742 cm^{-1} band (33.4 cm^{-1}), much less pronounced than that of O_i (51.4 cm^{-1}) [12]. These appear to be characteristic of oxygen over-coordination. The stress-energy tensor agrees well with the measurements, further supporting the ring structure found for the defect.

Acknowledgements

We thank TFR, KVA and SI in Sweden for financial support. We also acknowledge support from EPSRC and INTAS under grant 97-0824.

References

- [1] G. Davies, R.C. Newman, in: T.S. Moss, S. Mahajan (Eds.), *Handbook on Semiconductors*, Vol. 3b, Elsevier Science, Amsterdam, 1994, p. 1557.
- [2] J.M. Trombetta, G.D. Watkins, *Appl. Phys. Lett.* 51 (1987) 1103.
- [3] A.V. Yukhnovich, V.D. Tkachev, M.V. Bortnik, *Sov. Phys. Solid State* 8 (1966) 1044.
- [4] G. Davies, A.S. Oates, R.C. Newman, R. Wooley, E.C. Lightowlers, M.J. Binns, J.G. Wilkes, *J. Phys. C* 19 (1986) 841.
- [5] P.M. Mooney, L.J. Cheng, M. Suli, J.D. Gerson, J.W. Corbett, *Phys. Rev. B* 15 (1977) 3836.
- [6] R. Jones, S. Öberg, *Phys. Rev. Lett.* 68 (1992) 86.
- [7] O.V. Feklisova, N.A. Yarykin, *Semicond. Sci. Technol.* 12 (1997) 742.
- [8] O. Feklisova, N. Yarykin, Eu. Yakimov, J. Weber, *Physica B* 273–274 (1999) 235.
- [9] V. P. Markevich, M. Suezawa, K. Sumino, L.I. Murin, *J. Appl. Phys.* 76 (1994) 7347.
- [10] J. Coutinho, R. Jones, P.R. Briddon, S. Öberg, L.I. Murin, V.P. Markevich, J.L. Lindström, submitted for publication.
- [11] R.C. Newman, J.H. Tucker, N.G. Semaltianos, E.C. Lightowlers, T. Gregorkiewicz, I.S. Zevenbergen, C.A.J. Ammerlaan, *Phys. Rev. B* 54 (1996) R6803.
- [12] B. Pajot, E. Artacho, C.A.J. Ammerlaan, J.-M. Spaeth, *J. Phys.: Condens. Matter* 7 (1995) 7077.
- [13] E.V. Lavrov, L. Hoffman, B. Bech Nielsen, *Phys. Rev. B* 60 (1999) 8081.
- [14] J. Coutinho, R. Jones, P.R. Briddon, S. Öberg, *Phys. Rev. B* 62 (2000) 10824.
- [15] A. Resende, R. Jones, S. Öberg, P.R. Briddon, *Phys. Rev. Lett.* 82 (1999) 2111.



ELSEVIER

Physica B 308–310 (2001) 309–312

PHYSICA B

www.elsevier.com/locate/physb

Expanded model for anharmonic vibrational excitation of oxygen in silicon

H. Yamada-Kaneta*

Nano-electronic Materials Laboratories, Fujitsu Laboratories Limited, 10-1 Morinosato-Wakamiya, Atsugi 243-0197, Japan

Abstract

To consistently describe the infrared absorptions by the oxygen in silicon discovered previously (30-, 1100-, 1200-, and 1700-cm⁻¹ bands) and recently (600- and 1800-cm⁻¹ bands), our original model for the two-dimensional low-energy excitation of oxygen coupled to the A_{2u} local mode has been expanded so as to include the coupling to the A_{1g} local mode. In addition to the four unknown parameters contained in our original model, the expanded model contains two more parameters: the A_{1g} mode frequency and the A_{1g}-mode coupling constant. Employing the set of appropriate basis functions of sufficient size, we calculated the Hamiltonian matrix and then diagonalized it numerically. We have found the parameter values that well reproduce the energy levels we previously determined up to one-A_{2u}-phonon plus one-A_{1g}-phonon states. © 2001 Elsevier Science B.V. All rights reserved.

PACS: 62.72.Ji; 63.20.Pw; 78.30.Ly

Keywords: Oxygen; Oxygen impurities; Silicon; Infrared absorption

1. Introduction

In spite of the simple structure, the bond-interstitial oxygen in silicon (Si–O–Si center) causes the many infrared absorption lines that are classified into the 30-, 600-, 1100-, 1200-, 1700-, and 1800-cm⁻¹ bands, as summarized in Table 1 of Ref. [1]. Our earlier model for the impurity excitation of the Si–O–Si center took into account the two-dimensional (2D) low-energy anharmonic excitation (LEAE) of the oxygen and its coupling to the A_{2u} local mode [2]. Hereafter, we refer to this excitation as the *A_{2u}-mode-coupled 2D LEAE*. Our calculation described the energy levels (Fig. 4(a) in Ref. [2] and Fig. 2 in Ref. [3]¹) that well explain the

energies of the lines in the 30-, 1100-, and 1200-cm⁻¹ bands. We pointed out that the 1700-cm⁻¹ band could be a replica of the 1100-cm⁻¹ band caused by the interaction between the A_{2u}-mode-coupled 2D LEAE and the hypothetical A_{1g} local mode of an energy of about 613 cm⁻¹ [2]. Since then, existence of the A_{1g} local mode has been supported by many theoretical [4,5] and experimental [6,7] investigations.

Recent discoveries of the main lines in the 600- [6] and 1800-cm⁻¹ bands [7], together with our discovery and detailed investigation of the line-structure around them [1], were very important for us to uncover the overall energy-level scheme of the local-mode-coupled 2D LEAE: Combining the experimental findings for these new lines [1,6,7] with the previously determined energy-level scheme [2,3] of the A_{2u}-mode-coupled 2D LEAE, we determined the relevant part of the total energy levels (eigenenergies) up to nearly 1900 cm⁻¹. This is shown in Fig. 1. Hereafter we refer to these total energy levels (eigenenergies) as the *experimentally* determined ones. We suggested [1] that these total energy levels and thus, the observed infrared absorptions could be described by considering that the 2D LEAE is coupled not only to the

*Tel.: +81-462-50-8232; fax: +81-462-50-8162.

E-mail address: kaneta.hiroshi@jp.fujitsu.com
(H. Yamada-Kaneta).

¹It should be noted that there is a careless mistake in Fig. 2 of Ref. [3]. In the figure, the assignment of the 43.3-cm⁻¹ line and 49-cm⁻¹ line should be inverted: the former and the latter lines are assigned to the transitions $|0, \pm 2\rangle \rightarrow |0, \pm 3\rangle$ and $|0, \pm 1\rangle \rightarrow |1, 0\rangle$, respectively.

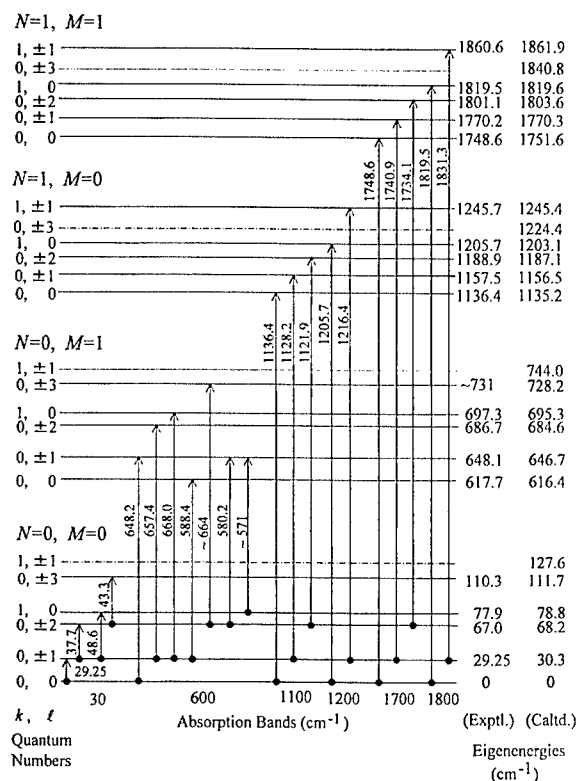


Fig. 1. Calculated eigenenergies of the two-dimensional low-energy anharmonic excitation of the oxygen coupled to the A_{2u} and A_{1g} local modes. These calculated (Cald.) eigenenergies given on the rightmost side are compared with the previously obtained [1] experimental (Exptl.) values of the eigenenergies which are given by each energy level. Here, the "experimental values of the eigenenergies" mean the eigenenergies determined by incorporating the values of the measured line-energies with the result of line assignment obtained theoretically and/or experimentally [1,2]. The previously obtained result for the line assignment is also shown. The lines observed in each absorption band are assigned to the transitions represented by the arrows. The values given by the arrows are the measured energies of the lines assigned to the indicated transitions. The calculated eigenenergies shown here are those obtained for the adjusted parameter values of the Set 1 given in Table 1.

A_{2u} local mode but also to the A_{1g} local modes. In other words, we determined the total energy levels up to the one- A_{2u} -phonon plus one- A_{1g} -phonon states ($M = N = 1$ states) [1]. Derivation of these total energy levels (Fig. 1) was based on our consideration that the 600-cm⁻¹ band is due to the transition dipole operators of the (x, y) -symmetry; namely, the (x, y) -displacement of the oxygen. Our recent experiment of the stress-induced dichroism of the main line at 648.2 cm⁻¹ has uncovered that this line is actually due to the transition dipoles of the (x, y) -symmetry [8], confirming our total energy-level scheme.

However, these total energy levels we obtained are not the result of theoretical treatment, but they are experimentally derived one's, in some sense. The purpose of this work is to demonstrate that the total energy levels we determined up to one- A_{2u} -phonon plus one- A_{1g} -phonon states (Fig. 1) can be described actually by adding the A_{1g} -mode coupling term to our original model Hamiltonian.

2. Hamiltonian and method of calculation

In the mathematical explanation below, we adopt the same notations and follow the same coordinate axes as introduced in our original paper [2]. Our original Hamiltonian for the A_{2u} -mode-coupled 2D LEAE is expressed by Eq. (5) in Ref. [2]:

$$\mathcal{H} = H^{(0)} + H^{(A_{2u})} + W^{(A_{2u})}, \quad (1)$$

where the three terms on the right-hand side represent, respectively, the 2D LEAE of the oxygen around the z -axis, the A_{2u} local mode, and the coupling between them. Due to the z -axial symmetry of the potential for the 2D LEAE, the angular momentum l is a good quantum number. Approximating $W^{(A_{2u})}$ by $W^{(A_{2u})}$ described by Eq. (7) in Ref. [2], we obtain another good quantum number N : the phonon number of the A_{2u} local mode. Accordingly, the eigenstates are represented as $|k, l, N\rangle$, where k distinguishes the eigenstates having the same (l, N) .

We next introduce the interaction between the A_{2u} -mode-coupled 2D LEAE and the A_{1g} local mode. We first examine qualitatively the following two candidates for the interaction terms that may describe the absorption lines in the 600-, 1700-, and the 1800-cm⁻¹ bands:

$$W^{(A_{1g})} = g_{A_{1g}} r^2 Q_{A_{1g}}, \quad (2)$$

$$\tilde{W}^{(A_{1g})} = \tilde{g}_{A_{1g}} Q_{A_{2u}}^2 Q_{A_{1g}}. \quad (3)$$

We proposed [2] that the interaction term (3) actually reproduces one- A_{1g} -phonon replica of the energy levels of one- A_{2u} -phonon states which are lying in the range 1136–1246 cm⁻¹. We speculated that this is how the 1700-cm⁻¹ band appears. However, we recently found that, if we apply the first order perturbation theory to the interaction (3), the oscillator strengths calculated by using the perturbed eigenfunctions vanish for the lines in the 600-cm⁻¹ band, contradicting the experiment. Thus, here we introduce the interaction term (2). As the first step of expanding our earlier model, we employ here the interaction term (2) only. We thus start with the following total Hamiltonian H :

$$H = H^{(0)} + H^{(A_{2u})} + W^{(A_{2u})} + H^{(A_{1g})} + W^{(A_{1g})}, \quad (4)$$

where $H^{(A_{1g})} \equiv \hbar \omega_{A_{1g}} b_{A_{1g}}^\dagger b_{A_{1g}}$ represents the A_{1g} local mode. The total Hamiltonian H is still axially

symmetric, and commutative with the A_{2u} phonon number operator $b_{A_{2u}}^\dagger b_{A_{2u}}$. Thus the eigenstates of H can still be specified by the good quantum numbers ℓ and N . However, the phonon number $M (= 0, 1, 2, \dots)$ of the A_{1g} local mode is no longer a good quantum number of H , because of the presence of the interaction term $W^{A_{1g}}$ that is not commutative with the A_{1g} phonon number operator. So far, we often adopted the A_{1g} phonon number M to specify the eigenstates of the total coupled system [1], namely, $|k, \ell, N, M\rangle$. Here we see that we can just regard M as an *approximate* good quantum number, only when the A_{1g} -mode interaction is weak enough. The present Hamiltonian (4) contains six unknown parameters: the coefficients α and β of the quartic potential for the 2D LEAE, the A_{2u} mode frequency $\omega_{A_{1g}}$, the A_{2u} mode coupling constant $g_{A_{2u}}$, the A_{1g} mode frequency $\omega_{A_{1g}}$, and the A_{1g} mode coupling constant $g_{A_{1g}}$.

We represent the total Hamiltonian in the matrix form by using the following basis functions:

$$|k, \ell, N, M\rangle \equiv [1/(2\pi)^{1/2}] e^{i\ell\varphi} \zeta_{k|\ell}(r, \varphi) |N\rangle |M\rangle, \quad (5)$$

where the part of the arguments (r, φ) on the right-hand side is the eigenfunction of a 2D harmonic oscillator of an appropriate excitation energy. The $|N\rangle$ and $|M\rangle$ are the N th and M th eigenfunctions of the A_{2u} and A_{1g} local modes, respectively. The analytical expressions for the matrix elements

$$\langle (k, \ell, N, M) | H | k', \ell', N', M' \rangle \quad (6)$$

can be easily derived by the similar method as in the original paper [2]. Since the matrix of H is sub-diagonal with respect to ℓ and N , we only have to diagonalize each submatrix specified by (ℓ, N) . We employed 40–50 basis functions for the harmonic oscillator part (i.e., the maximum number of k of the employed basis functions is 40–50), and 8–12 basis functions for the part of the A_{1g} local mode. Thus the size of the submatrix for each (ℓ, N) was nearly 320–600 dimensional. We numerically diagonalized these submatrices, and ascertained that the obtained relevant eigenvalues converged to their 6–7th significant figures.

3. Result of calculation

We adjusted the parameters ($\alpha, \beta, \omega_{A_{2u}}, g_{A_{2u}}, \omega_{A_{1g}}, g_{A_{1g}}$) so that the calculated eigenenergies would well fit with those obtained experimentally [1] which are given by each energy level in Fig. 1. The eigenenergies calculated for the adjusted parameter values of Set 1 (Table 1) are given on the rightmost side of Fig. 1. We see that the calculation has well reproduced the experimentally determined eigenenergies written by each energy level. As a quantity to indicate how the calculated eigenenergies are close to the experimentally

Table 1

Similar values of mean square deviation σ evaluated for different sets of the adjusted parameter values

Model parameters and mean square deviation σ	Set 1	Set 2	Set 3	Set 4
α (meV/Å ²)	−13.129	−13.563	−13.249	−13.118
β (meV/Å ⁴)	236.84	264.72	243.96	236.02
$\hbar\omega_{A_{2u}}$ (meV)	142.87	142.89	142.85	142.87
$\hbar g_{A_{2u}}/\omega_{A_{2u}}$ (meV/Å ²)	−26.770	−26.957	−26.626	−26.798
$\hbar\omega_{A_{1g}}$ (meV)	76.427	76.382	76.414	76.428
$g_{A_{1g}}(\hbar/2\omega_{A_{1g}})^{1/2}$ (meV/Å ²)	−12.028	−46.522	−26.325	−9.161
σ (cm ^{−1})	1.61	1.62	1.61	1.61

determined ones, we introduce the following mean square deviation σ :

$$\sigma \equiv \left[(1/n) \sum_{i=1}^n (E_i^{(\text{calc})} - E_i^{(\text{exptl})})^2 \right]^{1/2}, \quad (7)$$

where $E_i^{(\text{calc})}$ and $E_i^{(\text{exptl})}$ are the i th calculated and the experimentally determined eigenenergies, respectively. In Table 1, we also presented the values of σ . For the parameter values of the Set 1, we obtained $\sigma = 1.61 \text{ cm}^{-1}$, which means that the calculated eigenenergy deviates by 1.61 cm^{-1} on average, from the corresponding experimental value. In spite of our use of only the simplest (lowest order) interaction term (2) only, agreement between the calculated and the experimentally determined eigenenergies is fairly good. We have actually seen that the expanded model Hamiltonian (4) well reproduces the eigenenergies previously determined up to one- A_{2u} -phonon plus one- A_{1g} -phonon states, i.e., the states of $M = N = 1$.

4. Discussion

As seen from Table 1, for the other sets of the parameter values, Sets 2–4, the calculation reproduces the previously determined (experimentally determined) total energy levels, with similar small value of $\sigma (= 1.61 \text{ cm}^{-1})$. We see that, the obtained (adjusted) values of the parameters $\alpha, \omega_{A_{2u}}, g_{A_{2u}}$, and $\omega_{A_{1g}}$ are nearly the same for all sets. The value of β and $g_{A_{1g}}$ vary, with the value of σ kept unchanged. We further see that for the larger $g_{A_{1g}}$, we have the larger value of β . This suggests, that the strong A_{1g} -mode coupling reduces the effect of β . In other words, in the case of strong A_{1g} -mode coupling, the effective values of β is reduced from the obtained one shown in Table 1. This can be actually shown by the method of adiabatic approximation for the A_{1g} -mode coupling (2). The coupling is renormalized into the coefficient β of the fourth order term of the 2D

LEAE potential, to give an effective β that is smaller than the original one.

As pointed out above, the different parameter values equally well reproduce the experimentally determined total energy levels. The best way of obtaining (fixing) the true parameter values would be to examine whether or not the calculated intensity ratio of the main lines belonging to the different bands agrees with the corresponding experimental value: for example, the ratio of the intensity of the 648.2-cm^{-1} line to that of the 29.25-cm^{-1} line. The parameter values that reproduce the total energy levels and the line-intensity ratio at the same time would be the reliable ones. This kind of test calculation for the true parameter values is the next problem to be dealt with.

In conclusion, we have demonstrated theoretically that, by adding the A_{1g} -mode coupling to our original model Hamiltonian, we can reproduce the energy levels up to one- A_{2u} -phonon plus one- A_{1g} -phonon states. In order to uniquely determine the parameter values, we

have to examine the line-intensity ratio calculated for the parameter values that well describe the total energy levels.

References

- [1] H. Yamada-Kaneta, *Physica B* 302–303 (2001) 172.
- [2] H. Yamada-Kaneta, C. Kaneta, T. Ogawa, *Phys. Rev. B* 42 (1990) 9650.
- [3] H. Yamada-Kaneta, C. Kaneta, T. Ogawa, *Mater. Sci. Forum* 83–87 (1992) 419.
- [4] R. Jones, A. Umerski, S. Öberg, *Phys. Rev. B* 45 (1992) 11321.
- [5] E. Artacho, A. Lizón-Nortström, F. Ynduráin, *Phys. Rev. B* 51 (1995) 7862.
- [6] T. Hallberg, L.I. Murin, J.L. Lindström, V.P. Markevich, *J. Appl. Phys.* 84 (1998) 2466.
- [7] L.I. Murin, V.P. Markevich, T. Hallberg, J.L. Lindström, *Solid State Phenomena* 69–70 (1999) 309.
- [8] H. Takahashi, H. Yamada-Kaneta, S. Watanabe, M. Suezawa, to be presented elsewhere.



ELSEVIER

Physica B 308–310 (2001) 313–316

PHYSICA B

www.elsevier.com/locate/physb

The effect of high temperature–high pressure treatment on the annealing behavior of VO center in neutron-irradiated Czochralski silicon

C.A. Londos^{a,*}, M. Potsidou^a, A. Misiuk^b, V.V. Emtsev^c, J. Bak-Misiuk^d

^a Solid State Section, Physics Department, University of Athens, Panepistimiopolis, Zografos, Athens 157 84, Greece

^b Institute of Electron Technology, Al. Lotnikow 32/46, 02-668 Warszawa, Poland

^c Ioffe Physikotechnical Institute of the Russian Academy of Science, Polytechnicheskaya ul. 26, 194021 St. Petersburg, Russia

^d Institute of Physics, PAS, Al. Lotnikow 32/46, 02-668 Warszawa, Poland

Abstract

It is known that the application of high hydrostatic pressure on Si during heat treatment produces substantial changes in the properties of oxygen precipitates, which in turn, affect the behavior of various defects present in the crystal lattice. In this work, the annealing behavior of the VO complexes in Si samples subjected, before neutron irradiation, to different High Temperature–High Pressure (HT–HP) treatments at temperatures around 900°C and pressures up to 12 kbar, for $t = 5$ h, was investigated using Infrared spectroscopy. We found that (i) the samples pre-treated at $T_1 = 870^\circ\text{C}$ and $T_2 = 957^\circ\text{C}$, at atmospheric pressure and (ii) the samples pre-treated at $P_1 = 1$ bar and $P_2 = 12$ kbar, at $T_1 = 870^\circ\text{C}$, exhibit approximately the same difference in the annealing temperature of the VO complexes. The observed effect is explained by taking into account the impact of the HT–HP pre-treatment on the fraction of the self-interstitials bound at the SiO_x/Si interface of the oxygen precipitates and the Si matrix. We argue that the two regimes of pre-treatments (i) and (ii), see above, produce the similar effects upon self-interstitial aggregation processes in the presence of oxygen precipitates. © 2001 Elsevier Science B.V. All rights reserved.

Keywords: Silicon; Irradiation; High-pressure anneals

1. Introduction

High temperature (HT) treatment at $T > 400^\circ\text{C}$ of silicon crystals leads to the appearance [1] of structural defects such as various kinds of oxygen aggregates and precipitates, rod-like defects, dislocations, stacking faults and so on. These defects, in general, affect the properties and the behavior of the radiation-induced defects. It has been found [2], for instance, that the annealing temperature of the VO defects is considerably changed by variations in the duration of pre-heat treatment at $T = 600^\circ\text{C}$ and/or the initial oxygen concentration of the Czochralski silicon (Cz-Si). It was

suggested [2] that the annealing of the VO defects takes place through the capture of Si self-interstitials (Si_i 's) released from the SiO_x/Si interface of the Si matrix and the oxygen precipitates being formed after the 600°C pre-heat treatment. The Si_i 's generated [3,4] during the precipitation process tend to aggregate [5]. They generally form extended structural defects such as stacking faults. Reasonably, it is expected that the annealing process of the A-centers would be affected by the state and the ability of these Si_i 's to be released from the aggregates.

In order to understand the phenomenon, it is necessary to consider the effects on the Si_i 's due to the different kinds of oxygen aggregates and structural defects formed during pre-HT treatments at different temperatures. As a result of the HT treatment and the consequent formation of precipitates and structural

*Corresponding author. Tel.: +30-1-727-4726; fax: +30-1-725-7689.

E-mail address: hlontos@cc.uoa.gr (C.A. Londos).

defects, stress fields are locally created [6] around the precipitates and the extended defects. These elastic fields are anisotropic in general and attract the emitted Si_i 's. Concerning now, the annealing of the VO defects, the relation of the self-interstitial aggregates with the precipitates and the structural defects play a very important role, according to our opinion. The grade of binding of the self-interstitial aggregates is very significant, since it is expected to be different for different dominating precipitates and, therefore, for different temperatures of the HT treatments. Evidently, the Si_i 's, loosely bound at the interface are responsible for the dependence of the annealing behavior of the A-centers on the temperature of the pre-heat treatment. We assume that the binding force on the Si_i 's changes with increasing temperature, due to changes in the oxygen precipitates, i.e. their density, their shape and/or their size upon pre-heating. More specifically, we assume that pre-heating at two temperatures T_1 and T_2 with $T_2 > T_1$, results in a situation that the Si_i 's are more tightly bound at the interface in the latter temperature, T_2 . In other words, the Si_i 's are more effectively released during the course of the isochronal anneal in a material subjected to the lower temperature T_1 of pre-heat treatment.

On the other hand, the application of enhanced hydrostatic pressure during heat treatment has been found [7] to affect a lot of the features of the structural defects and the oxygen aggregates as, for example, the concentration of the dislocations, the density and the size of the precipitates and concentrations of the remaining oxygen interstitials, etc. Thus, pressure is another important parameter, which is expected to affect the behavior of the radiation defects, since every HT-HP pre-treatment establishes a different relation between the self-interstitial aggregates and the precipitates.

The purpose of this work was to investigate the annealing behavior of the VO defects and monitor the changes in the annealing temperature in dependence on the conditions of a HT-HP pre-treatment. We shall show that by considering that the binding of the Si_i 's at the SiO_x/Si interface depends on the HT-HP pre-treatment, we can explain the obtained experimental results of this study.

2. Experimental details

Five Cz-grown silicon samples with nearly the same initial oxygen concentrations ($O_i = 8.3 \times 10^{17} \text{ cm}^{-3}$), were subjected to different combinations of HT-HP pre-treatments, for the same time, $t = 5 \text{ h}$; see Table 1. Then, the samples were irradiated by fast neutrons at $T \approx 50^\circ\text{C}$. The fluence was about 10^{17} n/cm^2 . Afterwards, 15 min isochronal anneals were performed in steps of $\sim 10^\circ\text{C}$. After each annealing step, we employed IR measurements to monitor the annealing behavior of the 828 cm^{-1} LVM band of the VO defect.

3. Experimental results and discussion

In Table 1, the annealing temperature (T_{ann}) of the VO defects is indicated, for each sample. As seen, the beginning of the annealing process, i.e. T_{ann} , was found to be different for the different pre-HT-HP treatment regimes. It is well known that among a number [8] of available reaction paths, two reactions are the most important when the A-centers become mobile: $\text{VO} + \text{O}_i \rightarrow \text{VO}_2$, $\text{VO} + \text{Si}_i \rightarrow \text{O}_i$. These two reactions run in parallel, at least in the temperature range where the VO centers disappear and the VO_2 defects are formed. The emergence of the VO_2 defect in the IR spectra is related to the first reaction. An increase in the $[\text{O}_i]$ concentration observed during the VO decay verifies [9] that the second reaction takes place as well.

Let us now compare the behavior of the samples S_1 and S_2 , which were annealed at temperatures of $T_1 = 870^\circ\text{C}$ and $T_2 = 957^\circ\text{C}$, at atmospheric pressure. In these cases, the annealing temperatures of the VO defects are $T_{1\text{ann}} = 270^\circ\text{C}$ and $T_{2\text{ann}} = 292^\circ\text{C}$, respectively ($T_{2\text{ann}} > T_{1\text{ann}}$). First of all, we see that the annealing temperature is lower in both cases than the normal annealing temperature of the VO defects (about 300°C) [10] in silicon samples without any pre-heat treatment, a phenomenon being well known and discussed in the literature [2,6]. If the first reaction $\text{VO} + \text{O}_i \rightarrow \text{VO}_2$ is dominating in the annealing process,

Table 1
The annealing temperature T_{ann} of the VO defect for the various pre-HT-HP treated samples

Samples	T ($^\circ\text{C}$)	P (kbar)	t (h)	T_{ann} of the VO ($^\circ\text{C}$)	Comparison of T_{ann} ($^\circ\text{C}$)
S_1	870	10^{-3}	5	270 ± 4	$\Delta T_{12\text{ann}} = +22$
S_2	957	10^{-3}	5	292 ± 2	$\Delta T_{13\text{ann}} = +15$
S_3	870	12	5	285 ± 3	$\Delta T_{24\text{ann}} = +2$
S_4	957	12	5	290 ± 3	$\Delta T_{34\text{ann}} = +5$
S_5	900	12	5	284 ± 4	$\Delta T_{15\text{ann}} = +14$

then, one could expect that a larger increase in the oxygen diffusivity (and that of A-centers as well) in the case of pre-heat treatment at the higher temperature, would lead to a faster reaction between VO and O_i , resulting in a lower annealing temperature of the A-centers in the sample S_2 than in the sample S_1 . This expectation is opposite to what is observed (see Table 1). Therefore, the first reaction cannot provide a plausible explanation of the experimental data. Other factors should be taken into account, as well. If however, the second reaction $VO + Si_i \rightarrow O_i$ is the prevailing one, then one should consider the sources of the Si_i 's. These sources are oxygen aggregates and precipitates, which as we mentioned in the introduction, produce different strains in the lattice due to differences in their forms, as a result of the different pre-heat treatments.

Let us consider the sample S_1 subjected to a heat treatment at the lower temperature, $T_1 = 870^\circ\text{C}$. Si_i 's, if loosely bound to oxygen aggregates can be emitted and interacted with A-centers, (no matter whether A-centers are coming towards the precipitates or Si_i 's are emitted from the precipitates), as the temperature increases during the isochronal annealing sequence. This leads to a lower conversion temperature of the VO into the VO_2 , $T_{1\text{ ann}} = 270^\circ\text{C}$. However, in the case of the sample S_2 subjected to a higher temperature of heat treatment, $T_2 = 957^\circ\text{C}$, the dominating oxygen precipitates are different and, therefore, the binding of the Si_i 's is also different, compared to the sample S_1 . We assume that the Si_i 's are more tightly bound in this case. This means that it is more difficult to be emitted from the precipitates or in other words, the reaction $VO + Si_i \rightarrow O_i$, is now more difficult to realise. Alternatively, a higher temperature should be achieved in sample S_2 in order that the reaction $VO + Si_i \rightarrow O_i$ becomes significant. Notice now that this reaction results in the decay of A-centers, i.e. the concentration of A-centers is lowered and from reaction kinetics arguments, it is expected that the lower the concentration of A-centers, the higher the temperature of their conversion into the VO_2 complexes. Indeed, this was found experimentally ($T_{2\text{ ann}} = 292^\circ\text{C}$).

We shall now extend our model involving also the application of uniform stress during the pre-heat treatment process. Within the line of our argumentation, we suggest that an increase of stress (from 1 bar to 12 kbars) at a certain low temperature (870°C here) produces equivalent effect on the annealing temperature of the VO defects with an increase of the temperature (from 870°C to 957°C) at certain low stress (1 bar here). In other words, the increase of stress at low temperature ($T = 870^\circ\text{C}$) contributes to a change in the kind of the dominating precipitates (and the consequent binding of the Si_i 's at the interface), which is equivalent to the increase of temperature at low stress ($P = 1$ bar). Thus, comparing the samples S_1 and S_3 (see Table 1), we

actually see an increase of T_{ann} ($\Delta T_{13\text{ ann}} = 15^\circ\text{C}$) which is comparable to the increase of T_{ann} in the case of the samples S_1 and S_2 ($\Delta T_{12\text{ ann}} = 22^\circ\text{C}$).

Two additional observations should be reported:

(i) Annealing of the samples at high T (957°C here) should have practically no effect in the annealing temperature T_{ann} , irrespectively, of a low ($P = 1$ bar) or a high ($P = 12$ kbars) pressure applied during the anneal, since at high T (957°C), the precipitates have attained their final form and the application of pressure has no further effect on the binding of the Si_i 's at the interface. Actually, this is the case concerning the samples S_2 and S_4 , for which the annealing temperatures of the VO defects are practically the same; cf. $T_{2\text{ ann}} = 292^\circ\text{C}$ and $T_{4\text{ ann}} = 290^\circ\text{C}$ (Table 1).

(ii) On the other hand, if high stress (12 kbars here) is applied, the annealing temperature should not depend on the temperature of the pre-treatment (a low one $T_1 = 870^\circ\text{C}$ and a high one $T_2 = 957^\circ\text{C}$ here) since the oxygen precipitates have attained the final form due to the increase of pressure and that which is not affected by the increase of the temperature of the heat treatment. Actually, this is the case concerning the samples S_3 and S_4 which exhibit approximately equal annealing temperatures, i.e. $T_{3\text{ ann}} = 285^\circ\text{C}$, $T_{4\text{ ann}} = 290^\circ\text{C}$.

(iii) It is worth also noting that the sample S_5 , which has been subjected to a HT-HP treatment at $P = 12$ kbars but at an intermediate temperature $T_3 = 900^\circ\text{C}$ ($T_1 < T_3 < T_2$), shows an intermediate increase of $\Delta T_{\text{ann}} \approx 14^\circ\text{C}$, as one would expect from our model.

4. Conclusions

We have studied the annealing behavior of Cz-grown Si samples subjected to different HT-HP treatments prior to neutron irradiation. We have found that these treatments affect the annealing temperature of the VO center. More specifically, it has been found that (i) pre-treatments on two samples at temperatures $T_1 = 870^\circ\text{C}$ and $T_2 = 957^\circ\text{C}$, respectively, at $P = 1$ bar, cause the same change in the annealing temperature of the VO defects as (ii) pre-treatments on two samples at pressures $P_1 = 1$ bar and $P_2 = 12$ kbars, respectively, at the low temperature $T_1 = 870^\circ\text{C}$. We have explained the results by considering the effects of the HT-HP treatment on the grade of binding of the Si_i 's at the SiO_x /Si interface.

Acknowledgements

This work was supported by the NATO HTECH CRG974588 grant.

References

- [1] H. Bender, J. Vanhellemont, Oxygen in silicon, in: S. Mahajan (Ed.), *The Handbook of Semiconductors*, Vol. 3b, Elsevier, North-Holland, 1994, pp. 1637–1753.
- [2] K. Schmalz, K. Titterbach, V.V. Emtsev, Yu.N. Dalunda, *Mat. Sci. Forum* 38–41 (1989) 667.
- [3] A. Borgesi, B. Pivac, A. Sossella, A. Stella, *J. Appl. Phys.* 77 (1995) 4169.
- [4] U. Gösele, *Mat. Res. Soc. Symp. Proc.* 59 (1986) 419.
- [5] R.C. Newman, *Mat. Res. Soc. Symp. Proc.* 104 (1988) 25.
- [6] J. Jung, *Phil. Mag. A* 50 (1984) 257.
- [7] A. Misiuk, *Phys. Stat. Sol. (A)* 171 (1999) 191.
- [8] C.A. Londos, N.V. Sarlis, L.G. Fytros, *Phys. Stat. Sol. (A)* 163 (1997) 325.
- [9] C.A. Londos, N.V. Sarlis, L.G. Fytros, *J. Appl. Phys.* 84 (1998) 3659.
- [10] B. Svenson, J. Lindström, *Phys. Rev. B* 34 (1986) 8709.



ELSEVIER

Physica B 308–310 (2001) 317–320

PHYSICA B

www.elsevier.com/locate/physb

Effect of stress on accumulation of oxygen in silicon implanted with helium and hydrogen

A. Misiuk^{a,*}, A. Barcz^a, V. Raineri^b, J. Ratajczak^a, J. Bak-Misiuk^c,
I.V. Antonova^d, W. Wierzchowski^e, K. Wieteska^f

^a *Institute of Electron Technology, Al. Lotnikow 32/46, 02-668 Warsaw, Poland*

^b *CNR-IMETEM, Stradale Primosole 50, I-95121 Catania, Italy*

^c *Institute of Physics, PAS, Al. Lotnikow 32/46, 02-668 Warsaw, Poland*

^d *Institute of Semiconductor Physics, RAS, Novosibirsk, Russia*

^e *Institute of Electronic Materials Technology, Wolczynska 133, 01-919 Warsaw, Poland*

^f *Institute of Atomic Energy, 00-450 Swierk-Otwock, Poland*

Abstract

Pronounced oxygen segregation in helium-implanted Czochralski silicon, Cz-Si:He, treated at 1000–1400 K under atmospheric or enhanced, up to 1.2×10^9 Pa, hydrostatic pressure, HP, is observed. Annealing of hydrogen-implanted Cz-Si:H at 720–920 K- 10^5 Pa also results in the oxygen accumulation in the damaged volume while no accumulation is detected at ≥ 1 GPa and at ≥ 1230 K. The HP effect on transformation of post-implantation defects and on oxygen diffusivity can be responsible for oxygen accumulation in Cz-Si:(He, H). © 2001 Elsevier Science B.V. All rights reserved.

Keywords: Si:He; Si:H; Hydrostatic pressure; Oxygen accumulation

1. Introduction

Defect formation in silicon implanted with helium (inert dopant) or hydrogen (creating a weak H–Si bond) has become, in last years, a topic of considerable interest, both for practical reasons (gettering of contaminants and “smart cut” process) and for the extraordinary gas pressures attained in He/H-filled clusters and bubbles created upon annealing [1,2].

Enhanced hydrostatic pressure (HP) of inert gas (Ar) at annealing (HT-HP treatment) of He- and H-implanted silicon affects strongly its structure [3,4]. The effect of stress induced by enhanced Ar pressure on accumulation (gettering) of oxygen in He- and H-

implanted Czochralski silicon (Cz-Si) is the main subject of the present work.

2. Experimental

Cz-Si wafers (of 001 orientation), with concentration of interstitial oxygen, c_o , up to $1 \times 10^{18} \text{ cm}^{-3}$, were implanted with helium (Cz-Si:He, He^+ doses, $D = 5 \times 10^{15} - 3 \times 10^{17} \text{ cm}^{-2}$, energy $\leq 300 \text{ keV}$, He^+ projected range, $R_p \leq 1.35 \mu\text{m}$) or hydrogen (Cz-Si:H, H_2^+ dose $4 \times 10^{16} \text{ cm}^{-2}$, energy 130 keV, $R_p = 0.5 \mu\text{m}$).

Cz-Si:He and Cz-Si:H were treated under Ar pressure up to 1.2 GPa at temperature up to 1400 K for up to 10 h. The defect structure of the samples was investigated by transmission electron microscopy (TEM), X-ray reciprocal space mapping (XRRSM) and synchrotron topography done at HASYLAB, Hamburg. Oxygen and hydrogen depth profiles in the

*Corresponding author. Tel.: +48-22-548-7792; fax: +48-22-847-06-031.

E-mail address: misiu@ite.waw.pl (A. Misiuk).

annealed/treated samples were determined by secondary ion mass spectrometry (SIMS).

3. Results and discussion

The He implantation into Si results in creation of disturbed He-containing zone near R_p . The kind and concentration of defects (mostly He-filled clusters and bubbles) are dependent on He dose and energy, substrate temperature (in our case ≤ 350 K) as well as on the conditions of subsequent annealing/HT-HP treatment. During the annealing He atoms escape the Si matrix; this He removal is increasing with temperature [4].

TEM image of Cz-Si:He sample treated at 870 K is presented in Fig. 1. Annealing of such samples at 1270 K- 10^5 Pa for 1 h results in creation of bubbles while only dislocations were detected in Cz-Si:He ($c_0 = 1 \times 10^{18} \text{ cm}^{-3}$, $D = 5 \times 10^{16} \text{ cm}^{-2}$, 150 keV, $R_p = 0.88 \mu\text{m}$) treated at 1270 K-1.15 GPa for 1 h. As it follows from XRRSM, enhanced HP results in decreased intensity of X-ray diffuse scattering, an evidence of a better structural perfection of HT-HP treated Cz-Si:He as compared to that annealed at 10^5 Pa.

No oxygen accumulation at implantation-damaged zone was detected for Cz-Si:He ($D = 5 \times 10^{16} \text{ cm}^{-2}$)

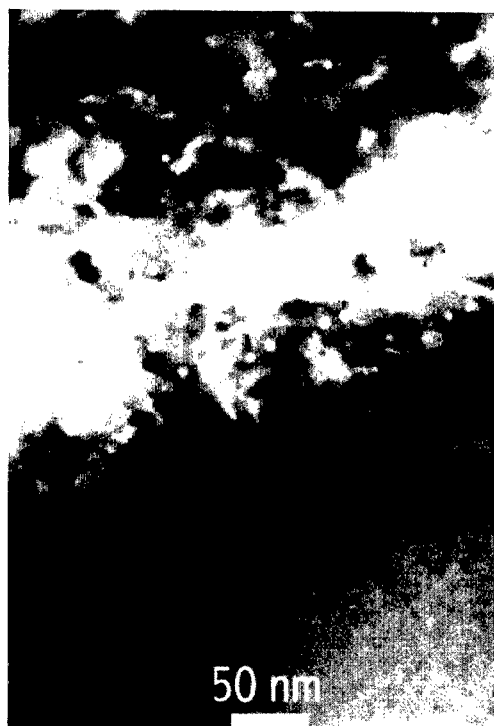


Fig. 1. TEM image of Cz-Si:He sample ($c_0 = 1 \times 10^{18} \text{ cm}^{-3}$, $D = 5 \times 10^{16} \text{ cm}^{-2}$, 300 keV, $R_p = 1.35 \mu\text{m}$) treated at 870 K-1.1 GPa for 10 h.

annealed below 1000 K at 10^5 Pa. The treatment under 1.1–1.2 GPa at 870–1000 K for 10 h results in the SIMS-detectable oxygen accumulation at damaged areas. Both the annealing and HT-HP treatment at 1270–1400 K results in the accumulation (Fig. 2).

Hydrogen implantation into Si also leads to creation of disturbed H-containing region. The generated H-filled clusters/bubbles are dependent on H dose and energy, temperature ($T \leq 470$ K) as well as on conditions of the annealing. During the annealing/HT-HP treatment H atoms outdiffuse from the Si matrix, the H loss being substantially suppressed under HP [3].

TEM image of the Cz-Si:H sample treated at 920 K-1.2 GPa is presented in Fig. 3. Two different disturbed areas were detected. The first one at a depth of 0.45–0.55 μm , corresponding to R_p of the main implanted species, H_2^+ , contains small bubbles and dislocations; the second one at the 0.8–1.0 μm depth originated from single H^+ ions present in the implanting beam and exhibits comparatively large bubbles. The prolonged annealing/treatment at temperatures up to 1400 K resulted in complete removal of hydrogen; however, numerous dislocations were still detected in Cz-Si treated at 1320 K-1.2 GPa for $t = 0.5$ h.

As it can be deduced from XRRSM [3,4] and synchrotron topographs, the intensity of X-ray diffuse scattering is lower and overall structural perfection is better in the case of the HT-HP treated Cz-Si:H samples, as compared to that annealed at 10^5 Pa.

The as-implanted Cz-Si:H sample ($c_0 = 8 \times 10^{17} \text{ cm}^{-3}$) indicated no oxygen accumulation near R_p ; annealing of that sample at 720 K- 10^5 for 0.5 h resulted

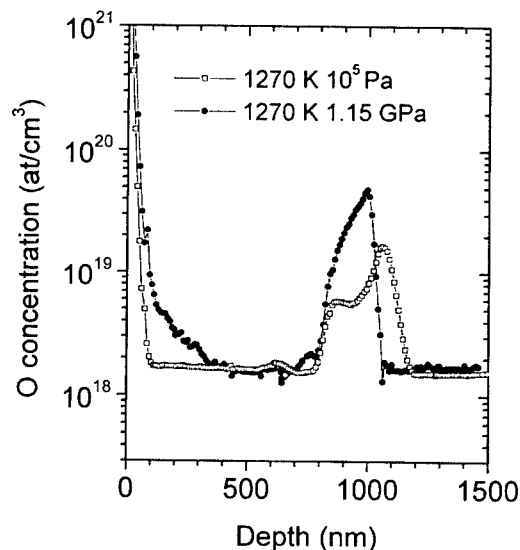


Fig. 2. SIMS depth profiles of oxygen in Cz-Si:He samples ($c_0 = 1 \times 10^{18} \text{ cm}^{-3}$, $D = 5 \times 10^{16} \text{ cm}^{-2}$, 150 keV, $R_p = 0.88 \mu\text{m}$) annealed/treated at 1270 K for 1 h.

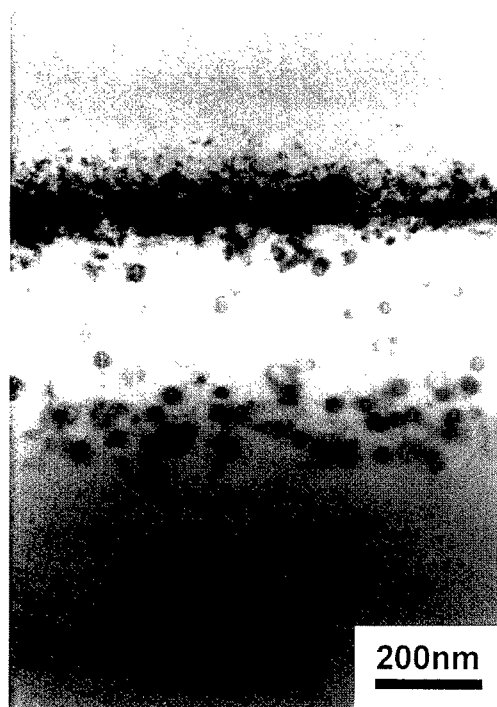


Fig. 3. TEM image of Cz-Si:H sample ($c_0 = 8 \times 10^{17} \text{ cm}^{-3}$, $D = 4 \times 10^{16} \text{ cm}^{-2}$, 130 keV, $R_p = 0.5 \mu\text{m}$) treated at 920 K-1.2 GPa for 0.5 h.

in a marked oxygen gettering by defects in the implantation-damaged layer (Fig. 4) and in hydrogen loss. The Cz-Si:H samples treated at (720–920) K-(1.1–1.2) GPa for up to 1 h do not indicate the oxygen accumulation (Fig. 5). Some traces of that accumulation were detected in Cz-Si:H treated at 920/1070 K-1.1 GPa for ≥ 1 h, while no accumulation was detected for the samples annealed at 1320 K- 10^5 Pa or treated at (1230–1370) K-(1–1.2) GPa.

The major differences, in respect of oxygen accumulation in Cz-Si:He vs. Cz-Si:H can be outlined as follows:

- Oxygen accumulation was detected only in Cz-Si:He annealed at $> 1000 \text{ K}-10^5 \text{ Pa}$; HP resulted in more pronounced gettering of oxygen. It is contrary to the case of Cz-Si:H where oxygen accumulation was detected upon annealing at 720–870 K- 10^5 Pa .
- High HP in Cz-Si:H treated at 720–870 K and at higher temperatures prohibited oxygen accumulation in damaged areas.

Effect of oxygen accumulation in implantation damaged and in the near-surface areas of Cz-Si:He, H is related to oxygen gettering on defects. Probably it

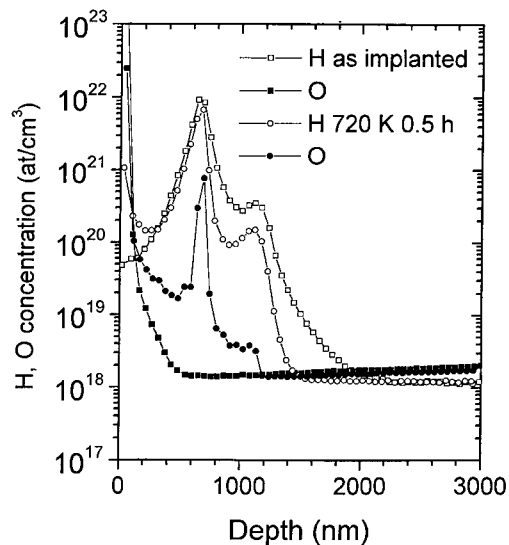


Fig. 4. Depth profiles of hydrogen and oxygen in Cz-Si:H samples, as-implanted and annealed at 720 K- 10^5 Pa for 0.5 h.

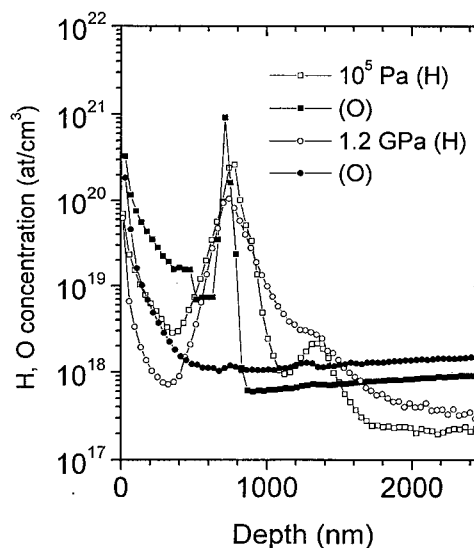


Fig. 5. Depth profiles of hydrogen and oxygen in Cz-Si:H samples, annealed/treated at 920 K- 10^5 Pa and 920 K-1.2 GPa for 0.5 h.

occurs mostly at the surface of initially He- or H-filled clusters and bubbles. Under HT-HP, more numerous but smaller size clusters are formed. The gettering activity is increasing with HP.

Most probably, the oxygen accumulation in the Cz-Si:H samples subjected to short-time anneals at 720–870 K- 10^5 Pa originates from increased diffusivity of oxygen in the presence of hydrogen [5]. The oxygen gettering was negligible in HP-HT treated Cz-Si:H. It

means that HP affects strongly oxygen diffusivity; oxygen mobility decreases dramatically with HP. From comparison of oxygen depth profiles for Cz-Si:He and Cz-Si:H, implanted with comparable He and H doses (hence, with similar extent of damage near R_p) and treated at >1000 K it follows also that the HP effect on the resultant defect structure of Cz-Si:He and Cz-Si:H is different. Both the annealed and HT-HP treated Cz-Si:He samples exhibit gettering activity at >1000 K, while the HT-HP processing of Cz-Si:H results in some specific structural changes in implantation-damaged areas. The implantation damaged area of HT-HP treated Cz-Si:H ceases to be active in respect of the oxygen accumulation.

In summary, this paper demonstrates an appearance of the enormous effect of oxygen segregation within the damaged volume. In order to realise the magnitude of this phenomenon, let us consider the integral of the oxygen peak formed as a result of the implantation and the HT-HP treatment of Cz-Si:He (Fig. 2, solid circles). Here oxygen content amounts to about 10^{16} cm $^{-2}$. This would correspond to the oxygen contained in the Cz-Si slab of about 100 μ m thickness. Taking the existing data for oxygen diffusion in Si, such extended transport within the semiconductor can be excluded. An alternative source of oxygen to be eventually gettered in the vicinity of R_p would be the oxygen contamination of the

ambient gas. However, even in such a case the transport from the surface would be enormous.

So further investigation is definitely needed to solve that question.

Acknowledgements

This work was supported in part by the Polish Committee for Scientific Research (grants no. 8T11B 072 19 and 2P 03B 14018).

References

- [1] G.F. Cerofolini, G. Calzolari, F. Corni, C. Nobili, G. Ottaviani, R. Tonini, *Mater. Sci. Eng. B* 71 (2000) 196.
- [2] V. Raineri, S. Coffa, E. Szilagy, J. Gyulai, E. Rimini, *Phys. Rev. B* 61 (2000) 937.
- [3] A. Misiuk, J. Bak-Misiuk, A. Barcz, A. Romano-Rodriguez, I.V. Antonova, V.P. Popov, C.A. Londos, *J. Jun. Int. J. Hydrogen Energy* 26 (2001) 483.
- [4] A. Misiuk, J. Bak-Misiuk, I.V. Antonova, V.P. Popov, V. Raineri, A. Romano-Rodriguez, A. Bachrouri, H.B. Surma, J. Ratajczak, J. Katcki, J. Adamczewska, E.P. Neustroev, *Comput. Mater. Sci.* 21 (2001) 515.
- [5] L. Zhong, F. Shimura, *J. Appl. Phys.* 73 (1993) 707.



ELSEVIER

Physica B 308–310 (2001) 321–324

PHYSICA B

www.elsevier.com/locate/physb

Incorporation of oxygen or di-hydrogen in silicon monovacancy: spin-resonance study of defect excited state

T. Mchedlidze*, N. Fukata, M. Suezawa

Institute for Materials Research, Tohoku University, 2-1-1 Katahira, Aoba-ku, Sendai 980-8577, Japan

Abstract

We attempted to detect changes in an ESR signal from the excited triplet state of a vacancy oxygen pair in FZ-Si samples caused by doping with hydrogen or deuterium prior to electron irradiation. The presence of vacancy-di-hydrogen (vacancy-di-deuterium) complexes in the doped samples was confirmed by the analysis of infrared absorption spectra. Complete similarity of the parameters and shape of the spectra in the doped samples to that in the reference FZ-Si and Cz-Si samples proves that the signal originates from the same defect for all the cases. Further investigations showed that carrier recombination conditions in the sample and numerous hardly controllable experimental settings affect the shape and intensity of the ESR signal, impeding the correct interpretation of the signal origin. © 2001 Elsevier Science B.V. All rights reserved.

Keywords: Si; O; H; Vacancy; ESR; SDR

1. Introduction

Various hydrogen-containing complexes in Si have long attracted considerable attention [1–3]. The structure and properties of some of these complexes have been established, while others still remain under investigation.

The attribution of the observed HVH optically detected magnetic resonance (ODMR) spectra [4,5], to an excited state of the vacancy-di-hydrogen (VH_2) complex in Si has been questioned [6] based on its similarity to the ESR SL1 spectra which is caused by an excited triplet state of vacancy–oxygen pair (VO^*) [7]. No final conclusion has been reached on the origin of the HVH spectra [8,9]. The main arguments supporting the possible VH_2 origin of the HVH spectra are the change in the shape of resonance peaks upon substitution of hydrogen (H) doping by deuterium (D) doping and the difference in the annealing properties between the vacancy–oxygen pair and the defect responsible for the HVH spectra.

The SL1 signal has several distinctive features. The presence of absorption and emission-related resonance peaks in the SL1 spectra, so-called double-signed spectra, signifies the involvement of a relevant defect in the carrier recombination process [7,10]. The SL1 signal can also be detected using spin dependent recombination (SDR) measurement methods [11,12]. The increase in the charge carrier recombination rate in the sample during the spin resonance on the recombination centers causes the appearance of SDR-related resonance peaks. All SDR peaks have similar sign. The overall recombination processes in the sample affect the ESR and SDR SL1 signals, i.e., the existence of other carrier recombination paths in the sample will suppress them. Thus, the SL1 signal can be termed “recombination controlled spin resonance”.

We attempted to determine the origin of spectra observed in Refs. [4–6] and to find the reasons for the contradictory observations.

2. Experimental

We used phosphorus doped FZ-Si ($\rho = 1000 \Omega \text{cm}$) and Cz-Si ($\rho = 10 \Omega \text{cm}$) samples. Sliced samples,

*Corresponding author. Fax: +81-22-215-2041.

E-mail address: teimuraz@imr.tohoku.ac.jp
(T. Mchedlidze).

mechanically and chemically polished, were annealed in quartz capsules filled with H_2 or D_2 or Ar gas at 1300°C for 1 h. After the annealing, samples were quenched by immersion in water. Annealed and as-grown samples were subjected to irradiation with 3-MeV electrons at room temperature with total doses from $d_e = 3 \times 10^{14}$ to $1 \times 10^{17} \text{ e/cm}^2$. The irradiated samples were stored at temperatures below -10°C .

We conducted FT-IR measurements to verify the presence of VH_2 (VD_2) and VO defects [3,13–17] and to estimate the concentration of interstitial oxygen (O_i) in the samples. Optical absorption spectra of the specimens were measured with an FT-IR spectrometer at 4.2 K. The resolution was 0.25 cm^{-1} .

Spin resonance measurements were conducted on a JEOL X-band ESR spectrometer using a TM_{011} mode MW resonator equipped with a continuous helium gas-flow cryostat. The samples were illuminated with interband light during measurements through the window in the resonator. The derivative of MW field absorption with respect to the magnetic field was measured using a lock-in amplifier and magnetic field modulation with an amplitude of 0.2–0.6 G and a frequency of 100 kHz. The measurements were conducted under constant illumination at 10–20 K.

3. Results and discussion

We carried out a careful ESR investigation of the SL1 spectra in as-grown, H or D doped or argon-annealed FZ-Si samples and Cz-Si samples after irradiation. In all cases the spectra can be characterized by Spin-Hamiltonian with the parameters presented in Refs. [6,7]. Moreover, no additional splitting or broadening of lines was detected in the samples doped with H or D. As seen in Fig. 1, the signal shapes for all samples were identical. These results prove that all the observed ESR spectra originate from the (VO^\bullet) . Differing from Stallinga and Nielsen [6], sample preparation procedures used in our investigation were close to those used by Chen et al. [4]. The presence of VH_2 (VD_2) defects in our H (D) doped and irradiated samples was verified by FT-IR measurements. Thus, our results contradict the conclusions made by Chen et al. [4,5] regarding the involvement of H (D) in the defect responsible for the HVH spectra. However, the above results do not answer the main arguments presented in Ref. [9] regarding the observed change in the resonance line shape and annealing kinetics of the relevant defect. We attempted to determine the possible origin of the contradiction.

First, we attempted to compare the concentration of recombination centers in the samples pre-annealed in the various ambient prior to irradiation. We compared the intensity of the SL1 signal, $I(\text{SL1})$ and the strength of IR absorption peak of the VO

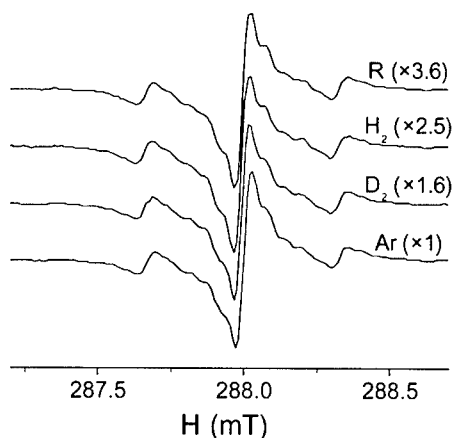


Fig. 1. The “0 \Rightarrow -1” ESR transition from the SL1 spectra in irradiated FZ-Si samples. Sample annealing ambient and amplification factors are indicated above the curves (“R” stands for the reference, as-grown sample). Measurement conditions: $B \parallel [110]$, $T_{\text{MEAS}} = 16 \text{ K}$. Inter-band light illumination, $f_{\text{RES}} = 9.06 \text{ GHz}$, $P_{\text{MW}} = 1 \text{ mW}$.

pair, $I(\text{VO})$ in the samples. The normalized ratios $I(\text{SL1})/I(\text{VO})$ for the samples vary in accordance with proportion $\text{Ar}:\text{D}_2:\text{H}_2 \approx 1:0.66:0.46$. This difference can be attributed only to the influence of recombination centers on the SL1 signal intensity. Namely, the overall concentration of recombination centers after irradiation is smaller in the samples pre-annealed in Ar and larger for the H-doped samples. Apparently, the overall concentrations of recombination centers in the H and D doped samples were also different. Our later investigation of defect creation in similar samples proved the above statements [18].

Next, a comparison of the ESR and SDR SL1 signals from the same Cz-Si sample was performed. By increasing the MW power during ESR measurements, it is possible to significantly increase the intensity of the MW electric field component in the volume of a sample. Thus, an effect related to SDR, i.e., change in the absorption of the MW electric field component during spin resonance [12], may be detected. We succeeded in the simultaneous detection of both ESR and SDR-related SL1 signals.

In Fig. 2, the observed spin resonance spectra are presented for a Cz-Si sample irradiated with $d_e = 3 \times 10^{14} \text{ e/cm}^2$ at three different levels of MW power. As seen, with the increase in the MW power, the intensity of the SL1 ESR spectrum with absorption and emission peaks is gradually decreasing, while the SDR SL1 spectrum, with single signed peaks, emerges and increases in intensity. Details of the transformation are presented in Fig. 3a. For the same MW power the width of the SDR related signal is noticeably larger than that of the ESR peak. As a result, a composite peak, much

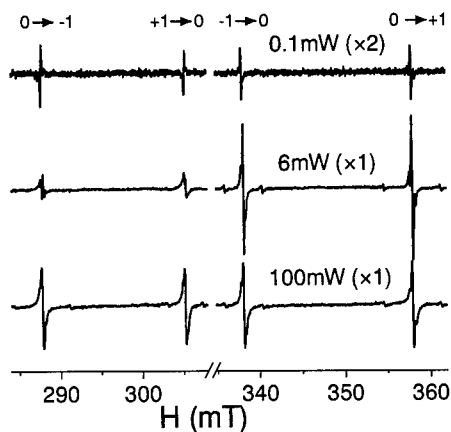


Fig. 2. The SL1 spectra from irradiated Cz-Si sample ($d_c = 3 \times 10^{14} \text{ e/cm}^2$). MW power and amplification factor are indicated above the curves. Other experimental conditions were same as those indicated in Fig. 1.

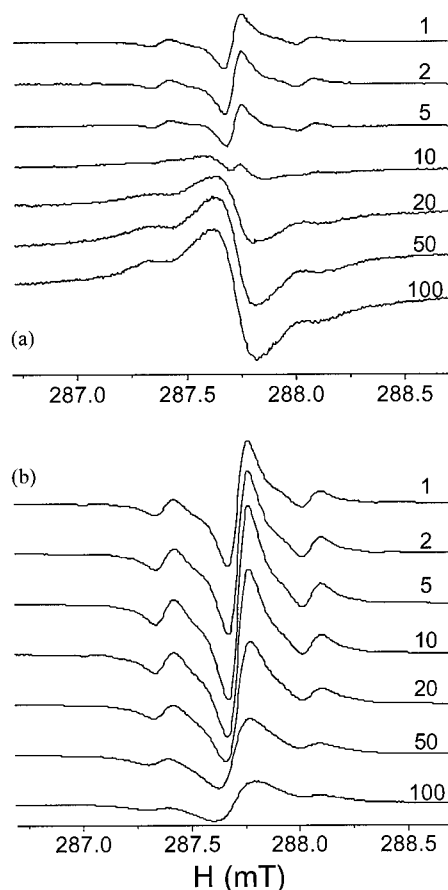


Fig. 3. The “0 \Rightarrow -1” ESR transition from the SL1 spectra in the Cz-Si sample. MW power (mW) is indicated above each curve. (a) $d_c = 3 \times 10^{14} \text{ e/cm}^2$, amplification factor = 10; (b) $d_c = 1 \times 10^{17} \text{ e/cm}^2$, amplification factor = 1. Other experimental conditions were the same as those indicated in Fig. 1.

different in shape from the ESR and SDR peaks, may resemble an additional HF splitting of a signal. It is interesting that ESR to SDR transformation does not occur in a similar sample with high d_c , even if it is placed in the same position in the resonator (see Fig. 3b). Measurements revealed that the “onset” MW power value for the transformation increases with the d_c , i.e. with the concentration of recombination centers in the sample. Irradiation dose dependence for the SL1 signal intensity in the Cz-Si samples also differed from that reported for the VO defect [16].

Although the properties of the SL1 signal presented herein deserve further investigation, this obviously exceeds the aims and limits of the present work. However, we can conclude that the observable shape and intensity of the SL1 signal depend on the recombination conditions in the sample, actual position of the sample inside the resonator, MW power, illumination conditions, etc.

Thus, we can explain contradictory observations with respect to the SL1 signal shape [4,6] as being due to the SL1 signal features. Namely, we suppose that the H and D doped samples after irradiation in Ref. [4] had different concentrations of recombination centers, as was the case in our samples. Such a difference, together with hardly controllable experimental conditions, could cause an observed change in the shape of the resonance peak by an admixture of ESR and SDR signal components in the detected ODMR signal [4]. Annealing strongly affects the recombination conditions inside an irradiated sample. Thus, it can be expected that a change in the recombination-controlled SL1 spectra intensity upon sample annealing will significantly differ from the change in VO concentration, as reported in Ref. [5].

In conclusion, a careful analysis of spectral parameters and the shape of the ESR spectra from H or D doped or Ar-annealed and subsequently electron irradiated samples revealed that the signal originates from the excited triplet state of the VO pair in all cases. The shape of the resonance peaks and the intensity of the signal depend on the VO pair concentration, on the carrier recombination conditions inside the sample and on numerous experimental settings. This complicated dependence is the result of the recombination-controlled nature of the SL1 spectra and can be applied to the investigation of recombination processes that take place in the sample.

References

- [1] J.I. Pankove, N.M. Johnson (Eds.), *Hydrogen in Semiconductors, Semiconductors and Semimetals*, Vol. 34, Academic Press, Boston, 1991.

- [2] N.H. Nickel (Ed). Hydrogen in Semiconductors II, Semiconductors and Semimetals, Vol. 61, Academic Press, San Diego, 1999.
- [3] R. Jones, et al., Solid State Phenom. 71 (2000) 173.
- [4] W.M. Chen, et al., Phys. Rev. Lett. 64 (1990) 3042.
- [5] W.M. Chen, et al., in: E.M. Anastassakis, J.D. Joannopoulos (Eds.), Proceedings of the 20th International Conference on the Physics of Semiconductors, World Scientific, Singapore, 1990, p. 2035.
- [6] P. Stallnga, B.B. Nielsen, Acta Phys. Pol. A92 (1997) 989.
- [7] K.L. Brower, Phys. Rev. B 4 (1971) 1968.
- [8] P. Stallnga, B.B. Nielsen, Phys. Rev. Lett. 80 (1998) 422.
- [9] W.M. Chen, et al., Phys. Rev. Lett. 80 (1998) 423.
- [10] G.D. Watkins, Phys. Rev. 155 (1967) 802.
- [11] B. Stich, S. Greulich-Weber, J.-M. Spaeth, J. Appl. Phys. 77 (1995) 1546.
- [12] L.S. Vlasenko, et al., Phys. Rev. B 52 (1995) 1144.
- [13] B.B. Nielsen, et al., Mater. Sci. Forum 196–201 (1995) 933.
- [14] M. Suezawa, Phys. Rev. 63 (2000) 035201.
- [15] M. Suezawa, Phys. Rev. 63 (2000) 035203.
- [16] G.D. Watkins, J.W. Corbett, Phys. Rev. 121 (1961) 1001.
- [17] J.W. Corbett, et al., Phys. Rev. 121 (1961) 1015.
- [18] T. Mchedlidze, N. Fukata, M. Suezawa, in these Proceedings (ICDS-21), Physica B 308–310 (2001).



ELSEVIER

Physica B 308–310 (2001) 325–328

PHYSICA B

www.elsevier.com/locate/physb

Thermal donors and radiation-induced defect states in transmutation doped gamma-irradiated silicon

S.I. Budzulyak, Yu.P. Dotsenko, V.M. Ermakov, V.V. Kolomoets*, E.F. Venger

Department of Galvanomagnetic Properties of Semiconductors, Institute of Semiconductor Physics, Prospect Nauki 45, 03028 Kyiv 28, Ukraine

Abstract

Transport phenomena are studied in uniaxially strained transmutation doped γ -irradiated n-Si(P) crystals. It is shown that thermal annealing of the transmutation doped Si results in the generation of different types of thermodonors. Tensorsensitivity mechanisms in highly strained transmutation doped silicon are identified as well. © 2001 Elsevier Science B.V. All rights reserved.

PACS: 61.80.-x; 62.82.Fk; 62.50.+p; 72.20.My

Keywords: Thermodonor; Uniaxial pressure; Defect states

1. Introduction

The neutron transmutation doping of semiconductors is known to provide a higher homogeneity of the impurity distribution within the crystal volume as compared to the method of doping from the melt. Homogeneous doping, in turn, results in a higher reliability of the devices operating on the principles of carrier heating. On the contrary, a heterogeneous current distribution for both crystal volume and p-n junction degrades the device performance because of microplasma appearance. The neutron transmutation doped (NTD) silicon is also characterized by a higher resistance to γ -irradiation. The technology of the neutron transmutation doping involves, as is well known, a high temperature annealing (at $\sim 800^\circ\text{C}$ for 2 h) in order to remove crystal damage induced by slow neutrons. Since the silicon crystals grown by floating zone (FZ) or Czochralski methods contain a substantial concentration of oxygen ($\approx 3 \times 10^{23}$ and $\approx 1 \times 10^{24} \text{ m}^{-3}$, respectively), the high temperature annealing is expected

to result in the generation of high temperature thermodonors.

Detection of the presence of high temperature thermodonors in NTD γ -irradiated silicon crystals is the aim of this work. Note that influence of thermodonors on NTD silicon properties should increase with a decrease of the phosphorus concentration. Therefore, for pure NTD crystals optimization of the technological regimes of neutron transmutation doping is very important.

2. Experimental

Irradiation of pure monocrystalline silicon crystals with slow neutrons was followed by a high temperature annealing $T \approx 800^\circ\text{C}$ for 2 h. A ^{60}Co source was used for γ -irradiation of transmutation doped silicon by relevant doses of γ -quanta at room temperature. γ -irradiation was performed on the samples with attached electrical contacts to prevent annealing of radiation-induced defects during the contact creation. Longitudinal tensorsensitive effect, Hall effect and their temperature dependencies were investigated using an installation for transport phenomena measurements under high uniaxial pressure. Pressure and temperature dependencies of the

*Corresponding author. Tel.: +380-44-265-6280; fax: +380-44-265-6391.

E-mail address: kolomoet@class.semicond.kiev.ua (V.V. Kolomoets).

Table 1
Parameters of investigated silicon crystals with phosphorus at the growth (samples #1, 4–6) and neutron transmutation doped (samples 2NTD, 3NTD, 7NTD, 8NTD). Letters a–d correspond to γ -irradiated NTD samples

Sample	ρ_{78} (Ωcm)	μ_{78} (cm^2/Vs)	$N_i = N_d + N_a$ (10^{14} cm^{-3})	$n_i = N_d - N_a$ (10^{14} cm^{-3})	N_d (10^{14} cm^{-3})	N_a (10^{14} cm^{-3})	$k = N_a/N_d$	Φ ($10^{17}\text{ quanta/cm}^2$)
1	15	20,800	0.396	0.202	0.3	0.096	0.32	0
2NTD	17	21,300	0.256	0.17	0.228	0.058	0.25	0
3NTD	5.3	20,500	1.84	0.58	1.2	0.62	0.52	0
4	4.55	19,100	1.3	0.72	1.0	0.28	0.28	0
5	15.5	14,500	5.13	0.28	2.7	2.4	0.9	0
6	3.2	17,600	1.7	1.12	1.4	0.28	0.2	0
7NTD	1.23	16,200	3.15	3.15	3.2	≈ 0.01	< 0.01	0
7a	1.43	14,600	3.35	3.0	3.2	0.15	0.05	1.36
7b	1.9	14,200	4.1	2.34	3.2	0.86	0.27	1.76
7c	7.75	12,900	5.7	0.63	3.2	2.53	0.8	2.1
7d	—	—	—	—	3.2	—	> 1	8.0
8NTD	0.63	14,470	7.2	7.2	7.2	≈ 0.01	0.01	0
8a	32.8	4750	14.0	0.4	7.2	6.8	0.94	8

—Parameter was not measured.

transport phenomena were used to reveal peculiarities of tensoeffects for the two types of crystals, NTD and doped with phosphorus from the melt. In order to obtain the ohmic electric contacts to the n-Si specimens the binary eutectic silicon–gold was used. The values of the main parameters of all measured specimens are listed in Table 1.

3. Results and discussion

In Fig. 1, the dependencies of resistivity vs. pressure for the case of longitudinal tensoresistivity (TR) measurements are compared for n-Si doped with phosphorus at the growth and NTD samples. For the former case (sample #1, Table 1), the TR effect is characterized by the saturation at pressure $X \approx 0.76$ GPa (curve 1, Fig. 1) and the following inessential ($\approx 1\%$) linear decrease of resistivity caused by an elastic change of the sample dimensions with pressure. For the NTD n-Si(P) (sample #7, Table 1), the presence of a maximum at pressure $X \approx 0.6$ GPa and the following exponential decrease of resistivity ($\approx 5\%$) in the pressure range 0.6–1.8 GPa is characteristic. These peculiarities of the TR effect in NTD silicon we associate with the strain-induced ionization of thermodonors which appear at high temperature annealing of crystals after neutron transmutation doping. In γ -irradiated NTD crystals (sample #7c, Table 1), the TR effect is characterized by the strain-induced ionization of A-centers (vacancy–oxygen atom [1,2]), which occurs in the pressure range 1.1–1.8 GPa (curve 3, Fig. 1). Note that the strain-induced ionization of the defect levels (P, TD, A-center) leading to a decrease of the crystals resistivity occurs on

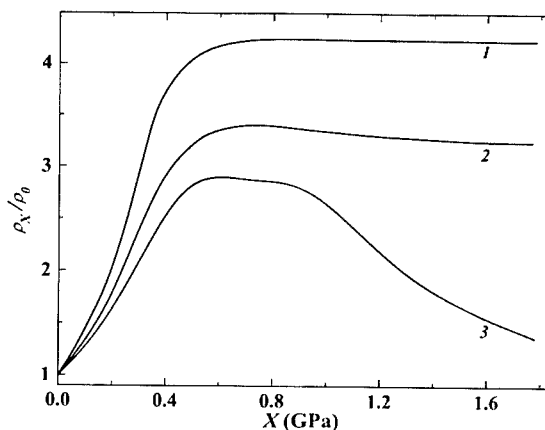


Fig. 1. The dependencies of $\rho_X/\rho_0 = f(X)$ longitudinal TRE for n-Si doped by phosphorus at the growth (1—sample 1) and by slow neutrons irradiation (2, 3—samples 7, 7c respectively). $X \parallel [001] \parallel J$; $T = 78$ K; Dose of γ -irradiation (quanta/cm^2): 1, 2—0; 3— 2.1×10^{17} .

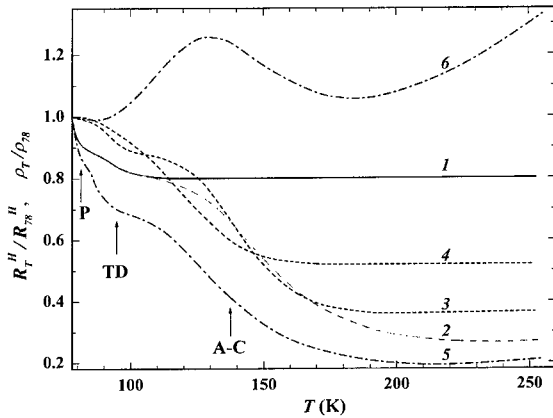


Fig. 2. Temperature dependencies of normalized Hall constant (R_T^H/R_{78}^H) for NTD n-Si(P) (1—sample 7NTD; 2–4—sample 7c) and normalized resistivity (ρ_T/ρ_{78}): 5—sample 8a; 6—sample 7c. Uniaxial pressure X (GPa): 0—1, 2, 5, 6; 0.4—3; 0.8—4.

the background of a resistivity increase which depends on the mechanism of intervalley redistribution of electrons. The presence of radiation-induced centers (P, A-centers) and high temperature thermodonors in NTD γ -irradiated silicon and dependence of their energy levels on the pressure is characterized by temperature dependencies of Hall effect (curves 2–4, Fig. 2) which was measured for sample #7cNTD. The presence of all defect levels (P, TD, A-center) is well detected in temperature dependencies of resistivity for the samples with a higher level of doping by electrically active phosphorus impurity (sample #8a, Table 1). At the same time, for crystals with dominant contribution of the acoustic scattering (sample #7c, Table 1) only presence of A-centers is clearly observable on the $\rho(T)$ dependence (curve 6, Fig. 2). Comparison of temperature dependencies of tenso-Hall effect (curves 2 and 3, Fig. 2) shows the full ionization of P impurity occurs at insignificant pressure (0.2–0.4 GPa). The obtained data prove the theoretical calculations of the uniaxial pressure influence the energy level position of shallow donors [3,4].

Even a more sensitive method to detect any deviation of the mechanism of TR effects from the classical mechanism of intervalley redistribution of electrons (Smith–Herring mechanism) is determination of the deformation potential constant (Ξ_u) in silicon [5]. In this case, the dependence of electron concentration ratio in the upper and lower valleys on pressure is determined via the TR effect data measured in a wide pressure region. For nondegenerated crystals, the ratio of electron concentration in the upper valley (n_2) to electron concentration in the lower one (n_1) is expressed as [6]

$$n_2/n_1 = \exp(-\Delta E/kT) \quad (1)$$

where ΔE is the energy splitting of valleys in uniaxially strained crystals.

Since $\Delta E \sim X$, there is a linear dependence of the logarithm of concentration ratio on the pressure for the tensoeffect mechanism caused only by the intervalley redistribution of electrons:

$$\lg(n_2/n_1) \sim X. \quad (2)$$

In accordance with this method, it was determined that only for sufficiently pure silicon crystals doped with phosphorus during growth can one obtain the linear dependence $\lg(n_2/n_1) = f(X)$ (curve 1, Fig. 3). It was also established that the linearity of the dependence $\lg(n_2/n_1) = f(X)$ occurs in such n-Si crystals only in a narrow temperature range (78–100 K) when pressure dependence of the f-scattering is not observed. The obtained data demonstrate that deviation from linearity of the dependence $\lg(n_2/n_1) = f(X)$ takes place for compensated n-Si(P) crystals (sample #5, Table 1) and NTD n-Si(P) (curves 4, and 2, 3, 5, respectively, Fig. 3).

According to comparison of curves 2, 3 and 5 in Fig. 3, the deviation from linearity in NTD silicon increases with the phosphorus concentration decrease that can be attributed in this case to the relative increase in contribution of strain-induced ionization of high temperature thermodonors. We assume that on conditions of approximately equal content of oxygen in

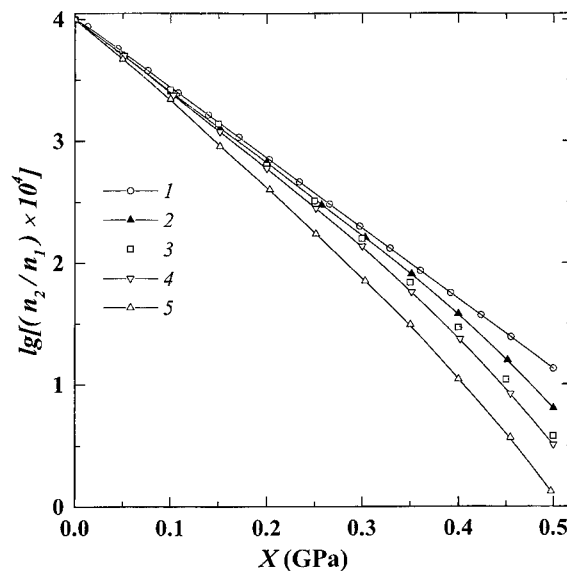


Fig. 3. The dependencies of $\lg(n_2/n_1)$ vs. uniaxial pressure X for silicon crystals doped with phosphorus at the growth (curves 1, 4—samples 1, 5 respectively) and neutron transmutation doped (curves 2, 3, 5—samples 7NTD, 3NTD, 2NTD respectively).

crystals and equal annealing temperature and time, concentration of thermodonors must be approximately equal in all NTD silicon crystals investigated in this work. Note that speed and anisotropy of energy levels shift of defects (P, TD, A-center) in silicon vs. uniaxial pressure are determined by defects structure and their energy levels in the forbidden band. This fact, as shown from analysis of the obtained data, determines the peculiarities of TR effects in highly strained γ -irradiated crystals of NTD silicon.

4. Conclusions

Analysis of TR effect data in NTD γ -irradiated silicon crystals allowed us to determine regularities of influence on the transport phenomena, additional strain-induced ionization of both radiation-induced energy levels (P, A-center) and levels of high temperature thermodonors which are generated in NTD silicon with high oxygen concentration during the annealing. Enhanced contribution of additional strain-induced ionization of thermodonor levels to tensoeffects with decreasing phosphorus concentration is explained by approximately constant concentration of thermodonors in crystals with equal content of oxygen and identical conditions of annealing.

The additional ionization of defect levels with increasing pressure results in a deviation from linearity of the dependence $\lg(n_2/n_1) = f(X)$. Whereas, linearity of this dependence is determined by intervalley redistribution mechanism (Smith–Herring mechanism), the analysis of dependencies $\lg(n_2/n_1) = f(X)$ in many-

valley semiconductors can be applied for TR mechanism identification in highly strained crystals. The most comprehensive information in terms of determination of tensorresistive effect mechanisms in the NTD γ -irradiated Si crystals as for the determination of dependencies of transport phenomena caused by the presence of various types of defects, was obtained by analysing both temperature and pressure dependencies of resistivity, Hall effect and the ratio of electron concentration in different valleys of the C-band shifted by deformation. It was demonstrated that the tensoeffects mechanism of intervalley redistribution is inherent only for pure n-Si crystals doped by hydrogen-like donors in a narrow temperature range (78–100 K). The analysis of the obtained data testifies that the slope change of the linear part of dependencies $\lg(n_2/n_1) = f(X)$ does not mean the change of magnitude of the deformation potential constant Ξ_u in n-Si crystals doped by various methods.

References

- [1] G.D. Watkins, J.W. Corbet, *Phys. Rev.* 121 (1961) 1001.
- [2] L.I. Panasyuk, et al., *Fiz. Tek. Poluprovodn.* 20 (1986) 545.
- [3] D. Wilson, G. Fecher, *Phys. Rev.* 124 (1961) 1068.
- [4] G.L. Bir, G.E. Pikus, *Symmetry and Strain-Induced Effects in Semiconductors*, Wiley, New York, 1974.
- [5] P.I. Baranskii, et al., *Fiz. Tek. Poluprovodn.* 10 (1976) 1387.
- [6] J.S. Blackmore, *Semiconductor Statistics*, Pergamon Press, New York, 1962.



ELSEVIER

Physica B 308–310 (2001) 329–332

PHYSICA B

www.elsevier.com/locate/physb

Ab initio study of atomic oxygen adsorption on the Si(1 1 1)7 × 7 surface

M.J. Caldas^{a,*}, R.J. Baierle^b, R.B. Capaz^c, E. Artacho^d

^a Instituto de Física, Universidade de São Paulo, R. do Matão tr R, 187, CP 66318, CEP 05508-900, São Paulo, SP, Brazil

^b Centro Universitário Franciscano, Santa Maria, RG, Brazil

^c Instituto de Física da Universidade Federal do Rio de Janeiro, CP 68528, CEP 21945-970 Rio de Janeiro, RJ, Brazil

^d Department of Earth Sciences, University of Cambridge, Downing Street, Cambridge CB2 3EQ, UK

Abstract

We study the initial steps of oxidation of the Si(1 1 1)-7 × 7 surface through modeling of different chemisorption sites for atomic O: adatom backbonds in faulted and unfaulted halves of the surface cell, and surface dimer bonds. We use ab initio calculations within local density approximation, and realistic simulation unit cells (4 × 2 and 6 × 3). Our results show the faulted adatom backbond to be favored over the unfaulted adatom backbond, and in-dimer insertion to be the stable adsorption site. We also use our results to interpret scanning tunneling microscopy results, and suggest that adatom adsorption is responsible for bright spots in unoccupied states images, while in-dimer adsorption could be related to dark sites. © 2001 Elsevier Science B.V. All rights reserved.

Keywords: Oxidation; Silicon surfaces; Oxygen adsorption

1. Introduction

Oxidation of silicon surfaces have been extensively studied recently due to the need to understand and control the Si/SiO₂ interface [1]. The initial stages of oxidation are very different for different surfaces, e.g., for the hydrogenated (1 1 1)Si-H or for the clean (1 1 1)Si-(7 × 7) reconstructed surface [2]. The differences may come not only from the presence of hydrogen but also from the different sites the 7 × 7 reconstruction [3,4] offers for oxygen incorporation. While in the (1 1 1)Si-H oxygen incorporation occurs almost exclusively in the surface Si atom backbonds [5], in the case of the Si-(7 × 7) surface incorporation is thought to occur mainly in adatom backbonds [2,6,7]. The basis for this consensus comes from the evidence provided by scanning tunneling microscopy (STM) images of the clean [8] and oxidized [9,10] surface, which clearly show the enhancement of the adatom features upon oxidation, in

the initial stages. The STM images taken with slow oxidation show [9] that the first two features to appear are: bright adatom spots, with a preference of 2:1 for the faulted half of the surface unit cell; and dark spots, which appear exclusively on faulted halves. With increasing oxidation times, and before the surface is fully oxidized, dark sites dominate and faulted halves are completely obscured.

The major controversy concerning the oxidation process concerns the existence [10,11] or not [12,13] of a molecular precursor, a metastable molecular O₂ species that would survive in the surface for a relatively long time, transforming to chemisorbed O in the adatom backbond. Several theoretical works were dedicated to the molecular precursor, focused on the adatom dangling-bond (DB) as the main “harpoon” to anchor an incoming O₂ molecule; the conclusions point always to the higher stability of any configuration that includes an O atom inserted in an adatom backbond [6,14]. It is important to emphasize, however, that all previous theoretical studies of oxidation of the Si-(7 × 7) surface were performed with simplifications of the surface unit cell, containing only the adatom and rest-atom surface

*Corresponding author. Tel.: +55-11-3818-6983; fax: +55-11-3818-6832.

E-mail address: mjcaldas@usp.br (M.J. Caldas).

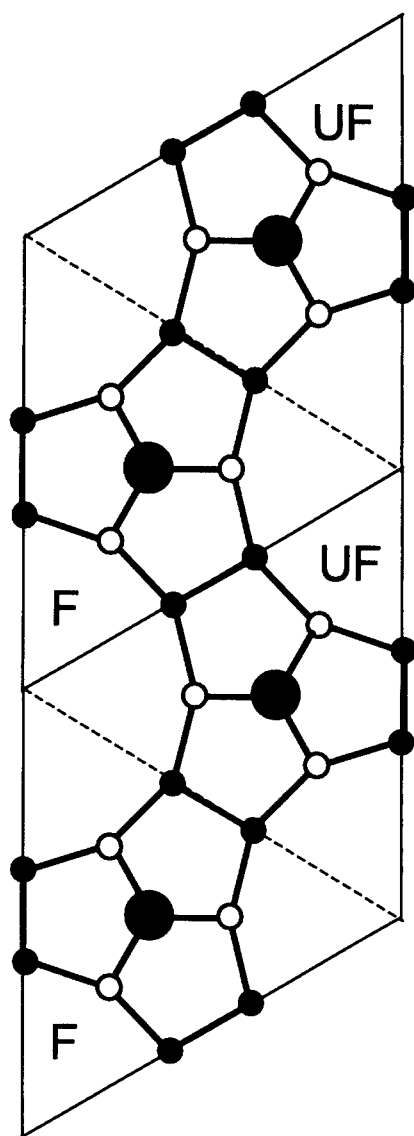


Fig. 1. Top view of the (6×3) cell used to simulate O adsorption on a Si (7×7) surface. For the sake of clarity, we show only the adatoms (larger dark circles), first layer atoms (white circles) and dimer atoms (smaller dark atoms). The corner holes are located on the vertices of the unit cells. The dashed lines separate the faulted (F) and unfaulted (UF) halves of the unit cell.

entities, in the unfaulted half of the unit cell. There was thus no possibility of comparing faulted and unfaulted halves, or to explore the other possible sites. From bulk defect studies, however, it is well known that the reaction of interstitial oxygen with vacancies is exothermic [15]. In the surface, although there are significant differences in environment, this could mean that insertion in the dimer site is energetically favored. On the other hand, simple geometric division of the unit cell

in regions tells us that “dimer regions” cover almost 40% of total area. We here present a theoretical study of atomic oxygen adsorption on the Si(111)- (7×7) surface, based on more realistic simulations which can take into account the differences between adatoms in the faulted and unfaulted surface, and include the surface dimers. Our results confirm that there is a small energy difference favoring backbond adsorption in the faulted half, and that backbond adsorption enhances the adatom feature in STM. We find, moreover, that insertion in the dimer bonds is indeed favored over backbond adsorption. However, this atomic configuration is not directly visible to STM, but could be related to the dark sites in the images.

2. Methodology

We simulate the Si(111)- (7×7) surface by repeated supercells in the slab model. Slabs are H-saturated on the back-surface, and contain six normal Si layers, plus surface layers, which depend on the surface unit cell. We use doubled (2×2) and (3×3) cells (4×2 and 6×3 , respectively, see Fig. 1) in order to isolate electrically and elastically the inserted O atoms. For the (3×3) cell there are two surface layers, with the stacking fault in one half, plus the adatoms, and we have then two adatoms (faulted and unfaulted), dimers and a corner hole. For the (2×2) cells, there are two surface layers plus the adatom, so we have in this case one adatom and one rest-atom; we use different (2×2) cells, one with normal Si coordination and the other with a stacking fault; calculations are also done for 4×2 -H cells, with one rest-atom DB saturated by hydrogen [14].

Calculations are done using ab initio density functional theory in the local density approximation, using the SIESTA code [16], norm-conserving pseudo-potentials [17] and Ceperley-Alder exchange correlation [18]. We use double-zeta local orbitals for the inner layers, and double-zeta plus polarization functions for the surface layers.¹ We relax all but the lowermost layer, starting from the initial theoretical lattice parameter for Si. We use the isosurfaces of $|\Psi|^2$ to interpret STM images [19]. To do that, we integrate $|\Psi|^2$ over the relevant energy region, in this case for the unoccupied states up to +0.5 eV from the Fermi energy.

3. Results and discussion

We study single atomic O insertion in the adatom backbonds, and in the surface dimer, comparing total energy differences in the stable configurations. We do

¹Orbital cutoff equivalent to a confinement energy shift of 0.3 eV; real-space grid equivalent to a cutoff energy of 130 Ry.

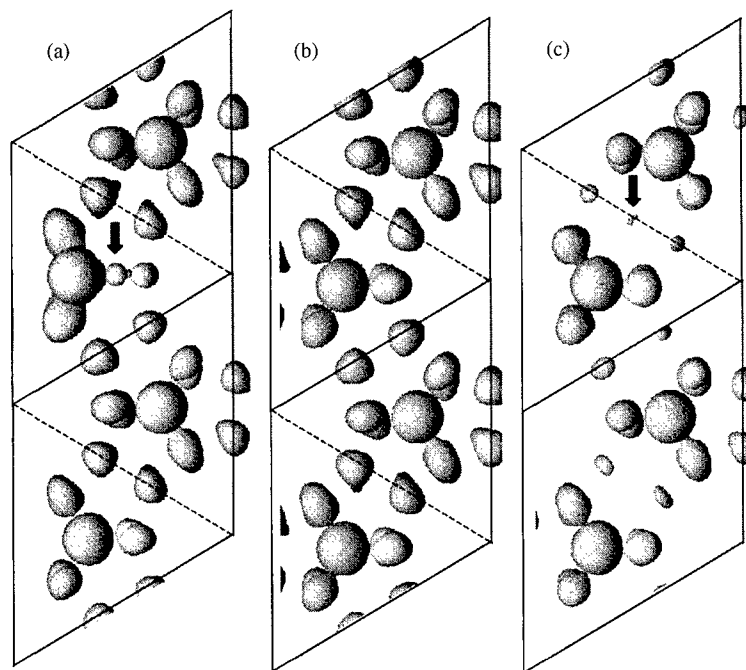


Fig. 2. Isosurfaces of $||\Psi||^2$ at equal densities for the clean Si (6×3) cell (b), for the same surface with an O atom in an adatom backbond (a) and with one O atom in a dimer bond (c). The arrows indicate the positions of O insertion in each case.

not study the silanone incorporation in dangling bonds [20], which is known to be less stable [6,21,22]. Incorporation in adatom backbonds is studied in two different environments: in the 6×3 cell, we compare directly faulted and unfaulted subsurface layers, and the environment mimics more closely corner adatoms, since it is flanked by dimers, and faces a corner hole. In the 4×2 cells, we compare energy differences for the clean and oxidized situations, and the environment includes rest-atoms, thus softening the surface layer. We note that the adatom DB occupation in these cells are never equal to the expected value in the 7×7 , but are similar, being $1/12$ higher or lower in the 6×3 and 4×2 -H, respectively.

Our results indicate that there are large lattice relaxations in all cases upon O insertion. Comparing adatom backbond insertion, relaxations are stronger in the 4×2 cells. The adatom actually moves laterally, as also found for regular surface atoms in the (111)Si-H surface [5], and this relaxation is easier in the softer environment of these cells. We find for adatom backbond adsorption that the faulted half is favored over the unfaulted half by ~ 0.05 eV. Insertion in the dimer bond is followed by even stronger relaxation, and releases surface strain energy. Accordingly, the energy gain is larger and dimer insertion is favored over the unfaulted adatom backbond by ~ 0.4 eV.

This result would seem to be in contradiction with STM experiments, insofar as dimer insertion was never

indicated as a possible candidate for STM image features. We show in Fig. 2 a comparison of isosurfaces of $||\Psi||^2$ for the clean 6×3 cell, and for O adsorption in the faulted adatom (results for the unfaulted adatom have similar character), and on the dimer bond. Comparing with Fig. 1, adatom DBs are seen in the first layer, and backbonds and dimer bonds are seen in the second layer from top; so, as expected, STM images of the clean surface would show mostly adatom DBs. What can be clearly seen is that adatom features are enhanced by backbond O insertion, supporting the association of the bright spots in STM images with this type of O adsorption. Furthermore, it is seen that dimer insertion bleaches all features, adatoms included. While O-related “unoccupied charge” distribution can be seen in this energy region for backbond insertion, O inserted in dimers are not visible at all. So, even if the STM tip could reach the second layer, in this bias there would be no states visible (in a previous study of the clean 7×7 surface by Qian and Chadi, it was shown that dimer states should be reached only at $\sim E_F - 2$ – 3 eV). We can thus speculate that the dark spots appearing immediately upon oxidation are related to O insertion in dimer bonds. We need further work to be able to distinguish the effects of dimer adsorption in faulted and unfaulted adatoms.

Summarizing, we find that O adsorption in faulted adatom backbonds are preferred over unfaulted adatom backbonds, and that features related to unoccupied

states of adatom dangling bonds are enhanced by backbond oxidation, supporting this assignment of bright spots in STM. Dimer insertion is favored by ~ 10 kT at room temperature, but seriously depletes all unoccupied states up to $\sim E_F + 0.5$ eV. It is possible that dark spots in STM images are related to dimer adsorption. In this case, our results support the view that oxidation of the (111)Si-(7×7) surface is dissociative, since both bright and dark spots are immediately seen on oxidation.

Acknowledgements

We thank Rosa Di Felice for fruitful discussions. This work is supported by CNPq and FAPESP. Calculations were performed at LCCA-USP.

References

- [1] A.M. Stoneham, M.A. Szymanski, A.L. Shluger, *Phys. Rev. B* (RC) 63 (2001) 1304.
- [2] K. Sato, et al., *Thin Solid Films* 369 (2000) 277.
- [3] K. Takayanagi, Y. Tanishiro, S. Takahashi, M. Takahashi, *Surf. Sci.* 164 (1985) 367.
- [4] G.-X. Qian, D.J. Chadi, *Phys. Rev. B* 35 (1987) 1288.
- [5] R.J. Baierle, M.J. Caldas, *Int. J. Mod. Phys. B* 13 (1999) 2733.
- [6] B. Schubert, P. Avouris, R. Hoffmann, *J. Chem. Phys.* 98 (1993) 7593.
- [7] K. Sakamoto, et al., *J. Electron Spectrosc. Relat. Phenom.* 114–116 (2001) 489.
- [8] R.J. Hamers, R.M. Tromp, J.E. Demuth, *Phys. Rev. Lett.* 56 (1986) 1972.
- [9] T. Hasegawa, M. Kohno, S. Hosoki, *Jpn. J. Appl. Phys.* 33 (1994) 3702.
- [10] I.-S. Hwang, R. Lo, T.T. Tsong, *Phys. Rev. Lett.* 78 (1997) 4797.
- [11] T. Jensen, et al., *Phys. Rev. B* 64 (2001) 5304.
- [12] K.Y. Kim, T.H. Shin, S.J. Han, H. Kang, *Phys. Rev. Lett.* 82 (1999) 1329.
- [13] F. Matsui, et al., *Phys. Rev. Lett.* 85 (2000) 630.
- [14] S.-H. Lee, M.-H. Kang, *Phys. Rev. B* 61 (2000) 8250.
- [15] R. Baierle, et al., *Physica B* 273,274 (1999) 260.
- [16] D. Sanchez-Portal, P. Ordejon, E. Artacho, J.M. Soler, *Int. J. Quantum Chem.* 65 (1997) 453.
- [17] N. Troullier, J.L. Martins, *Phys. Rev. B* 43 (1991) 1993.
- [18] D. Ceperley, B. Alder, *Science* 231 (1986) 555.
- [19] J. Tersoff, D.R. Hamann, *Phys. Rev. Lett.* 50 (1983) 1998.
- [20] K.D. Brommer, M. Galván, A. Dal Pino, J.D. Joannopoulos, *Surf. Sci.* 314 (1994) 57.
- [21] R.J. Baierle, M.J. Caldas, Optical properties of weakly oxidized Si : H nanoparticles, submitted for publication.
- [22] M.J. Caldas, *Phys. Stat. Sol. B* 217 (2000) 641.



ELSEVIER

Physica B 308–310 (2001) 333–336

PHYSICA B

www.elsevier.com/locate/physb

Defects and their influence on the luminescence of rare-earth ions implanted in single crystal Si

N.A. Sobolev*

Ioffe Physicotechnical Institute, Polytechnicheskaya 26, 194021 St. Petersburg, Russia

Abstract

With respect to the use of (111)-oriented silicon substrates, the modification of structural defects as well as electrically and optically active center spectra in solid-phase epitaxial recrystallized rare-earth doped Si layers has been investigated. TEM and X-ray diffraction revealed the presence of microtwins and dislocations in very high densities exceeding 10^{10} cm^{-2} in (111) Si: (Er,O). The formation of microtwins and dislocations in very high densities in (111) samples enabled us to observe some new effects and improve the characteristics of rare-earth doped Si-based light-emitting diodes (LEDs), in particular, to prepare avalanching and tunneling diodes characterized by uniform breakdown over the whole area of p–n junction and working at room temperature. Temperature enhancement of the rare-earth-related electroluminescence (EL) intensity in (111) LEDs is observed under avalanche and tunnel breakdown of p–n junctions. The enhancement is related to the formation of process-induced deep level centers. New centers emitting under reverse bias and characterized by the highest effective cross section for the excitation of Er^{3+} ions were first observed. The LEDs with EL of Ho^{3+} ions at room temperature have firstly been prepared. © 2001 Elsevier Science B.V. All rights reserved.

Keywords: Defects; Ion implantation; Rare-earth doped Si; Light-emitting structures

1. Introduction

Light-emitting structures based on Er-doped monocrystalline Si have attracted considerable interest for optoelectronic applications. To produce such structures, Polman with co-authors [1] suggested to use the solid phase epitaxial (SPE) technique. In the case of conventional dopant ions, the implantation is carried out in (100)-oriented substrates at room temperature. SPE recrystallization of layers amorphized by the Er-ion implantation under these conditions is followed by the formation of end-of-range defects and hairpin dislocations, which may be responsible for a relatively low intensity of Er-related luminescence. To prevent the structural defects formation, Franzo et al. [2] suggested implanting Er ions at 77 K. It allowed them to prepare light-emitting diodes (LEDs) which demonstrate a high intensity of Er-related electroluminescence (EL) under

tunneling breakdown of the p–n junction at room temperature. To prevent the hairpin dislocation formation, we suggested to implant Er ions into (111)-oriented substrates at room temperature some years ago [3]. The purpose of this paper is to review our recent results demonstrating the possibilities of the modification of the SPE technique for the engineering of structural defects and electrically and optically active centers as well as improvements of luminescence properties of rare-earth doped Si-based LEDs.

2. Experimental

Er was introduced into $5 \Omega \text{ cm}$ (111)- and (100)-oriented n-Cz–Si wafers with a double implant of 2.0 and 1.6 MeV ions at room temperature. The samples were implanted to a dose of 1×10^{14} , 3×10^{14} or $9 \times 10^{14} \text{ cm}^{-2}$, and the doses for each pair of implants were identical. To enhance the luminescence response,

*Tel.: +7-812-24-73885; fax: +7-812-24-71017.

E-mail address: nick@sobolev.ioffe.rssi.ru (N.A. Sobolev).

oxygen ions were coimplanted at 0.28 and 0.22 MeV energies, and implant doses were one order of magnitude larger than the erbium doses used. The oxygen implant energies were chosen such that their projected ranges matched those of the Er implants. To fabricate Si:(Ho,O) LEDs, the co-implantation of Ho ions into (111) n-Cz-Si at 2.0 and 1.6 MeV energies and $1 \times 10^{14} \text{ cm}^{-2}$ dose as well as of oxygen ions at 0.29 and 0.23 MeV energies and $1 \times 10^{15} \text{ cm}^{-2}$ dose was carried out at room temperature. The implantation produced a continuous amorphous layer extending from the surface to a depth of $\sim 0.7 \mu\text{m}$. Annealings were made in a chlorine-containing atmosphere at 620°C for 1 h to induce the SPE recrystallization of the amorphous layer and at 900°C for 0.5 h to produce optically active Er- and Ho-related centers and reduce the density of regrowth defects. The p^+-n^- junction was produced by 40 keV boron implantation at a dose of $5 \times 10^{15} \text{ cm}^{-2}$ into the front side of the wafer. The back side was implanted with phosphorus at 80 keV and a $1 \times 10^{15} \text{ cm}^{-2}$ dose. Titanium and gold sputtering, photolithography, as well as chemical etching, were performed to prepare LEDs with a mesa-like edge contour. SIMS, RBS, TEM, X-ray diffraction, transient-stimulated capacitance, capacitance-voltage, photoluminescence (PL) and EL techniques were used to study the properties of Si:(Er,O) structures. Structural, electrical and optical properties in Ho and O ion co-implanted Si were also studied to determine some details of defect formation and luminescence processes.

3. Results

TEM and X-ray diffraction techniques were used to study the microstructure of (111) Si:(Er,O) [4]. TEM showed that the SPE-regrown layer consists of at least two sublayers. The $0.2 \mu\text{m}$ -thick sublayer lies at the bottom of the regrown layer and contains small loop-like defects of high density (so-called end-of-range (EOR) defects). The $0.6 \mu\text{m}$ -thick sublayer spreads from the band of the EOR defects to the wafer surface. Its defect structure is more complex and consists of microtwins and dislocations. TEM and X-ray diffraction revealed that numerous microtwins formed on the (111) planes parallel and inclined to the surface are observed over the entire upper sublayer. The twins were found to be platelets with lateral dimensions of 15–30 nm and a thickness of about 2–9 nm, and their densities throughout the regrown layer were nonuniform. Dislocations form a dense spatial network propagating through the upper sublayer. The dislocation lines are rather highly curved than being linear. It does not allow us to identify them as hairpin (V-shaped) dislocations, which are observed in (100) Si layers recrystallized by SPE following amorphization using Si and Er ions. The

curvature of the dislocation lines can be due to the interaction between the dislocations and microtwins. The dislocation densities observed in the regrown layers were very high, with densities exceeding 10^{10} cm^{-2} . Within the implant fluence range studied, between 1×10^{14} and $9 \times 10^{14} \text{ Er/cm}^2$, the twin and dislocation densities were observed to increase with fluence, while the twin dimensions were found to decrease. The changes in the spectrum of structural defects in (111) samples, as compared with the (100) sample spectrum, allowed us to observe some new effects and improve the characteristics of LEDs. On the basis of (111) structures, we have prepared avalanching and tunneling diodes (ADs and TDs).

The first (111) ADs and TDs have been investigated in Refs. [3,5], respectively. The EL spectra of the reverse-biased samples contain a sharp luminescence line at a wavelength of $\lambda \sim 1.538 \mu\text{m}$ accounted by intra-4f shell transitions of Er^{3+} ions and a relatively weak radiation, practically independent of the wavelength. This radiation was observed in both avalanche and tunnel breakdown due to intraband transitions of hot carriers in Si. Fig. 1 shows the temperature dependence of the EL intensity at $\lambda \sim 1.538 \mu\text{m}$ (curve 2) in AD. An enhancement of the Er-related EL intensity takes place. On the contrary, a weak temperature quenching of the EL intensity takes place in (100) Si:(Er,O) diodes [2,6] (Fig. 1, curve 1). Capacitance spectroscopy measurements showed that the unusual temperature dependence of the EL intensity under fixed reverse current is related to the formation of deep level centers (hole traps) in the lower part of the forbidden gap [3]. The effective concentration of the traps are several times higher than the ionized center concentration in the space charge layer before the diode was switched into the breakdown regime. The non-exponential character of the measured capacitance decay may be related to the existence of several levels with different ionization energies or the zone of traps in the lower half. We suggest that the process-induced dislocations are responsible for the

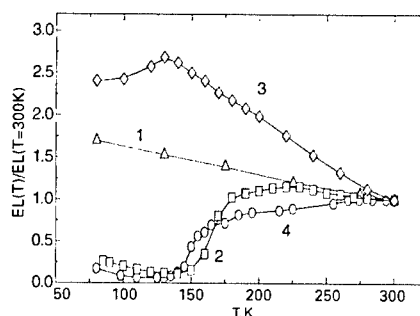


Fig. 1. Temperature dependence of rare-earth-related EL intensity in ADs and TDs at reverse bias in: 1—(100) Si:Er:O AD [6], 2—(111) Si:Er:O AD [3], 3—(111) Si:Er:O TD [7], and 4—(111) Si:Ho:O AD [10].

levels. The drop of Er^{3+} -related EL intensity, as the temperature decreases from 190 to 150 K (Fig. 1, curve 2), is associated with the smaller width of the space charge layer and the respective decrease in the concentration of Er-related centers which may be excited. The tunneling (111) LEDs have been investigated in Refs. [5,7]. Fig. 1 (curve 3) shows the temperature dependence of the EL intensity at $\lambda \sim 1.538 \mu\text{m}$ [7]. A temperature enhancement of the Er-related EL intensity also takes place.

The EL intensity as a function of the reverse current density passing through the diode can be described by solving the rate equation accounting for the excitation and deexcitation processes of Er^{3+} ions:

$$dN^*/dt = \sigma j(N - N^*)/q - N^*/\tau, \quad (1)$$

where N and N^* are the total and excited amount of Er ions, σ is the effective cross section for excitation, τ is the lifetime of the excited state $^4\text{I}_{13/2}$, j is the current density passing through the p-n structure, and q is the electron charge. The EL intensity is proportional to N^*/τ_{rad} , where τ_{rad} is the radiative lifetime of Er^{3+} ions. At steady state, solving Eq. (1) gives the dependence

$$\text{EL}(j)/\text{EL}_{\text{max}} = (\sigma j/q)/(\sigma j/q + 1), \quad (2)$$

where EL_{max} is the maximum EL intensity. From a fit to the data measured in Ref. [8], we have obtained $\sigma\tau = 8.7 \times 10^{-20} \text{ cm}^2 \text{ s}$ at 300 K. This value is one order of magnitude higher than that obtained by the authors in Ref. [9] for tunneling (100) diodes. Er-related EL intensity saturation achieved under the avalanche regime at current density is one order of magnitude lower than that under the tunnel regime. In order to separate the contribution of the excitation and deexcitation processes in the increase of $\sigma\tau$ values, it is possible to make independent measurements of the cross section σ and lifetime τ . The EL transient during the diode turn-on is described by solving Eq. (1) as

$$\text{EL}(t)/\text{EL}_{\text{max}} = [(\sigma j/q)/(\sigma j/q + 1)] \times \{1 - \exp[-(\sigma j/q + 1/\tau)t]\}. \quad (3)$$

The EL signal approaches the steady state with a characteristic time τ_{on} given by

$$1/\tau_{\text{on}} = \sigma j/q + 1/\tau. \quad (4)$$

According to Eq. (4), the dependence of $(1/\tau_{\text{on}})$ on the reverse current is linear. Its slope is proportional to the excitation cross section of Er^{3+} ions, σ , and its intersection with the ordinate axis is equal to the reciprocal of the lifetime of the Er^{3+} excited state $(1/\tau)$. Fig. 2 (curve 2) shows $1/\tau_{\text{on}}$ as a function of reverse current for AD [8]. A fitting of the experimental time dependencies of EL intensity rise at different current densities with Eq. (4) has given $\sigma = 2.3 \times 10^{-16} \text{ cm}^2$ and $\tau = 380 \mu\text{s}$ at 300 K [8]. An increase of σ and τ by ~ 3.8 times as compared with the

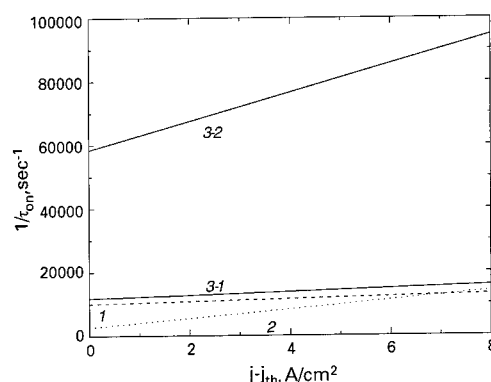


Fig. 2. Reciprocal time constant of EL intensity rise (τ_{on}) vs. the difference in the operating (j) and threshold (j_{th}) reverse current densities for centers studied in Si:Er:O ADs and TDs; 1—(100) TD [9], 2—(111) AD [8], 3-1 and 3-2—(111) TD [5].

corresponding data measured in tunneling diodes (Fig. 2, curve 1, $\sigma_{\text{tun}} = 6 \times 10^{-17} \text{ cm}^2$ and $\tau_{\text{tun}} = 100 \mu\text{s}$ [8]) takes place. The higher excitation efficiency under the avalanche regime than that under the tunnel breakdown may be due to a change of the energetic spectrum of hot carriers at the changes of the breakdown mechanisms.

The study of the kinetics of EL intensity when the reverse current is turned on in (111) TDs shows that the same kind of Er-related light-emitting centers is introduced in (100) TDs as well as in (111) ADs and TDs (Fig. 2, curves 1, 2 and 3-1). In (111) tunneling LEDs, we have also observed the formation of new kind of centers emitting under reverse bias (Fig. 2, curve 3-2). These centers are characterized by the highest $\sigma \sim 7 \times 10^{-16} \text{ cm}^2$. Such diodes exhibit the shortest characteristic rise time for Er-related EL in Si:(Er,O) LEDs.

The main physical relationships established in defect formation and luminescence in (111) Si:(Er,O) samples enabled us to prepare the first LEDs with EL of Ho^{3+} ions at room temperature [10]. The EL related to the internal 4f-shell transitions of Ho^{3+} ions from the first excited state ($^5\text{I}_7$) to the ground state ($^5\text{I}_8$) is observed at 300 K in the range from 1.9 to $2.2 \mu\text{m}$ [10]. The maximum intensity of the Ho-related EL in Si:(Ho,O) takes place at $\sim 1.96 \mu\text{m}$. Fig. 1 (curve 4) shows the temperature dependence of the EL intensity at $\lambda \sim 1.96 \mu\text{m}$ [10]. A temperature enhancement of the Ho-related EL intensity is also observed.

The comparison of the experimental data concerned with the structural defects and optical properties of (111) Si:(Er,O) and Si:(Ho,O) LEDs invites us to suppose that electrically and optically active centers belong to the complexes formed near the dislocations

and containing rare-earth ions and intrinsic point defects.

4. Summary

The use of the (1 1 1)-oriented substrates enabled us to modify spectra of structural defects, electrically and optically active centers. The effect of temperature enhancement of the Er- and Ho-related EL intensity is associated with the formation of deep level centers introduced in the lower part of the forbidden gap. The new Er-related light-emitting centers have been observed. They are responsible for the shortest-ever-recorded characteristic rise time for Er-related EL in LEDs under breakdown conditions.

Acknowledgements

This work was supported in part by the Russian Foundation for Basic Research (Grant No. 99-02-17750) and INTAS (Grant No. 99-01872).

References

- [1] A. Polman, J.S. Custer, E. Snoeks, G.N. van den Hoven, *Appl. Phys. Lett.* 62 (1993) 507.
- [2] G. Franzo, F. Priolo, S. Coffa, A. Polman, A. Carnera, *Appl. Phys. Lett.* 64 (1994) 2235.
- [3] A.M. Emel'yanov, N.A. Sobolev, A.N. Yakimenko, *Appl. Phys. Lett.* 72 (1998) 1223.
- [4] R.N. Kyutt, N.A. Sobolev, Yu.A. Nikolaev, V.I. Vdovin, *NIMS B173* (2001) 319.
- [5] A.M. Emel'yanov, N.A. Sobolev, M.A. Trishenkov, P.E. Khakushev, *Semiconductors* 34 (2000) 927.
- [6] N.A. Sobolev, A.M. Emel'yanov, K.F. Shtel'makh, *Appl. Phys. Lett.* 71 (1997) 1930.
- [7] N.A. Sobolev, A.M. Emel'yanov, Yu.A. Nikolaev, *Semiconductors* 34 (2000) 1027.
- [8] N.A. Sobolev, Yu.A. Nikolaev, A.M. Emel'yanov, K.F. Shtel'makh, P.E. Khakushev, M.A. Trishenkov, *J. Lumin.* 80 (1999) 315.
- [9] G. Franzo, S. Coffa, F. Priolo, *J. Appl. Phys.* 81 (1997) 2784.
- [10] N.A. Sobolev, A.M. Emel'yanov, R.N. Kyutt, Yu.A. Nikolaev, *Solid State Phenom.* 69–70 (1999) 371.



ELSEVIER

Physica B 308–310 (2001) 337–339

PHYSICA B

www.elsevier.com/locate/physb

Time-resolved investigation of the mid-infrared-induced enhancement of Er^{3+} emission in Si

M. Forcales^{a,*}, I.V. Bradley^{b,c}, J-P.R. Wells^{b,c}, T. Gregorkiewicz^a

^a Van der Waals–Zeeman Institute, University of Amsterdam, Valckenierstraat 65, NL-1018 XE Amsterdam, Netherlands

^b FOM Institute for Plasma Physics “Rijnhuizen”, P.O. Box 1207, NL-3430 BE Nieuwegein, Netherlands

^c Department of Physics, Heriot Watt University, Edinburgh EH14 4AS, UK

Abstract

Previously, we reported on the enhancement of Er photoluminescence (PL) in silicon upon mid-infrared (MIR) laser pulse fired at certain delay with respect to Nd:YAG pulsed primary excitation. This effect was explained as the ionization of traps by the MIR beam. The shallow nature of the traps was concluded from its temperature and wavelength dependence. In this contribution, we have studied temporal characteristics of the enhancement effect as a function of the delay time between the two pulses. Decay kinetics of erbium PL measured at 4 K was found to show two different time constants of 1 ms (fast) and 26 ms (slow). A correlation between the enhancement effect and the amplitude of the slow component of the Er PL has been observed. We also have noticed that the enhancement of Er emission is accompanied by subsequent quenching of the slow component, indicating redistribution of energy in the system. Based on the study, we conclude that MIR laser ionizes non-equilibrium traps whose thermalization is responsible for the slow component of the Er PL. © 2001 Elsevier Science B.V. All rights reserved.

Keywords: Erbium; Photoluminescence; Free electron laser

1. Introduction

Research on crystalline silicon doped with erbium has been performed in the last decade due to its importance for telecommunication. During the last years scientists tried to obtain efficient room temperature Er^{3+} luminescence by co-doping with oxygen in Si [1] or co-doping with Yb and Si nanocrystals in SiO_2 [2], but the excitation mechanism remains under dispute. Experimental data are usually based on experiments of amplitude and kinetics of Er PL under steady state conditions as a function of temperature. Unfortunately, many processes can be simultaneously activated while increasing temperature, so a new kind of approach has to be considered. A two-beam experiment performed at 4 K and done at the Dutch free electron laser facility (FELIX) offers such a possibility. In this case, we can

selectively induce individual transitions optically instead of thermally, making the system very attractive for spectroscopic studies. As a result of sample illumination by the first beam (pulsed frequency doubled Nd:YAG), the Er^{3+} characteristic transition at $1.54 \mu\text{m}$ is observed. The MIR pulse fired at certain delay can produce both enhancement and quenching of the Er PL. Temporal analysis of these effects is presented in this work. A set of rate equations to model our results will also be discussed.

2. Experimental

For details of the experimental set-up for two-beam experiments in the MIR, see for example Ref. [3]. In this study, several different crystalline silicon samples implanted with erbium and oxygen ions were investigated. While the amplitude and temporal characteristics of the MIR-induced enhancement effect showed some variation in different materials, the general features were

*Corresponding author. Tel.: +31-20-525-5644; fax: +31-20-525-5644.

E-mail address: manuef@science.uva.nl (M. Forcales).

common in all samples. The particular experimental data presented here for illustration of the results were obtained for a sample prepared from Czochralski-grown silicon implanted with Er at a dose of 10^{13} cm^{-2} and co-implanted with oxygen. The implantation was followed at 900°C annealing during 30 min.

3. Results and discussions

An illustration of the MIR-induced enhancement effect is shown in Fig. 1 for different delays. Extra PL identified uniquely as erbium emission initially grows, then reaches its maximum and finally decreases on a time scale of tens of milliseconds. Temporal characteristics of the MIR-induced enhancement effect are shown in the inset of Fig. 1. A time rise (τ_{rise}) of 1 ms is observed while a much longer component (τ_{decay}) around 26 ms is identified for the decay. Measurements done at low Nd:YAG pumping intensities [4] showed a maximum enhancement effect of Er PL for very short delays ($\tau_{\text{rise}} = 0$). If we consider saturation of the Er PL, it seems logical that additional excitation is only possible when Er^{3+} luminescence is outside saturation regime. Er kinetics at $1.54 \mu\text{m}$, as presented in Fig. 2, cannot be fitted with a single exponent that has a time constant of 1 ms (τ_{Er}). A double exponent is necessary to fit the signal in the whole range. It is interesting to notice that we can fit the slow component of Er PL kinetics (τ_{D}) using the value of τ_{decay} .

Although it is not clear from Fig. 1, enhancement is accompanied by a subsequent quench of the slow Er PL component. By scanning the MIR photon quanta energy for the enhancement and quenching amplitude, identical wavelength dependence are obtained. We therefore conclude that both effects are related to ionization of the same levels. In order to determine when the Er PL enhancement and quenching disappear, we performed

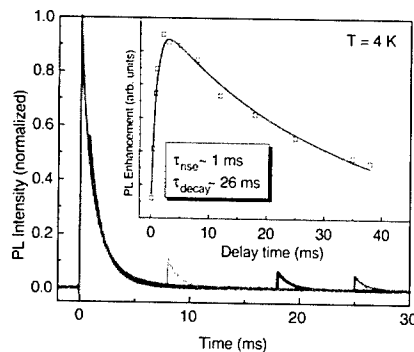


Fig. 1. Normalized Er PL kinetics at 4 K. MIR-induced Er PL enhancement effect for different delay times. As can be seen in the inset, the MIR-induced Er PL enhancement grows with τ_{rise} (1 ms) and disappears with τ_{decay} (26 ms).

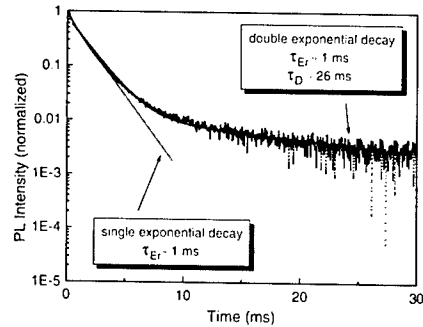


Fig. 2. Normalized Er PL kinetics at 4 K for high Nd:YAG pump intensities. The signal cannot be fitted with a single exponent τ_{Er} ($= \tau_{\text{rise}}$). A double exponent with τ_{Er} and τ_{D} is necessary to fit the complete kinetics.

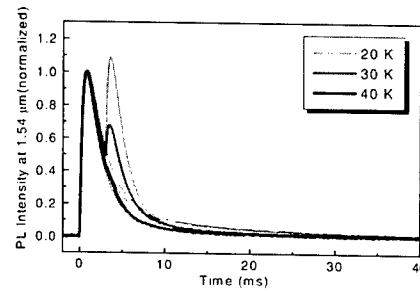


Fig. 3. Normalized Er PL kinetics for different temperatures. At $T = 20 \text{ K}$, the slow component is quenched after the enhancement, while at 40 K the slow component is no longer available so no enhancement is induced by the MIR pulse.

temperature dependence measurements. In Fig. 3, the normalized amplitude at $1.54 \mu\text{m}$ is plotted for different temperatures. Above 50 K both the effects disappear. A closer look at the low temperature kinetics revealed that the enhancement is only possible when the slow component is available.

Based on these results, the following model with a schematic illustration in Fig. 4 is proposed. We consider the dynamic population via a set of rate equations in which erbium (N_{Er}) and defect centers or traps (N_{D}) are excited by capturing excitons (N_{ex}) with a different absorption cross sections (σ_i) and with the possibility of saturation for both processes:

$$\frac{dN_{\text{ex}}}{dt} = G\delta(t) - \frac{N_{\text{ex}}}{t_0},$$

$$\frac{dN_{\text{Er}}}{dt} = \sigma_1 N_{\text{ex}} (N_{\text{total}}^{\text{Er}} - N_{\text{Er}}) - \frac{N_{\text{Er}}}{\tau_{\text{Er}}},$$

$$\frac{dN_{\text{D}}}{dt} = \sigma_2 N_{\text{ex}} (N_{\text{total}}^{\text{D}} - N_{\text{D}}) - \frac{N_{\text{D}}}{\tau_{\text{D}}},$$

where G is the exciton generation term and t_0 is the effective decay time of the excitons. Solving the rate

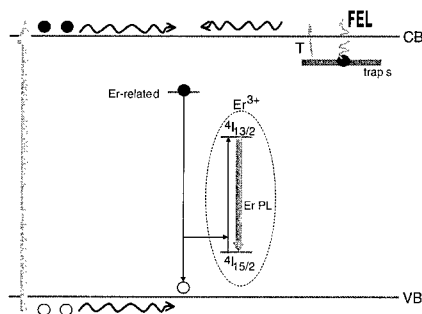


Fig. 4. A model to explain MIR-related enhancement and quenching of the Er PL. For explanation see text.

equations leads to an exponential decay of $N_{\text{Er}}(t)$ and $N_{\text{D}}(t)$. At the time when the FEL pulse is triggered (t_{FEL}) only ionization of traps occurs because they are shallow enough to be ionized by the MIR photon quanta energy (70–170 meV). The Er excited state population remains unaffected, basically because the Er-related center has already transferred its energy to Er^{3+} . From t_{FEL} , we can consider the same system of rate equations, but taking G_{FEL} as the new generation term, proportional to the concentration of traps at the time when the FEL is fired: $N_{\text{D}}(t_{\text{FEL}})$. In this way, a good description of the experimentally measured enhancement effect is obtained.

We will now address the microscopic nature of the slow $\tau_{\text{D}} \approx 26$ ms component appearing at $1.54 \mu\text{m}$ PL and spectroscopically proved to be Er emission. We identify it as being due to excitation of Er ions by thermal emission from the non-equilibrium traps. These traps are populated by the Nd:YAG pump pulse and while returning to equilibrium will thermally emit carriers, which can then recombine exciting Er ions. Since the time constant of thermal emission exceeds the

Er relaxation time (at 4 K), this slow excitation process will be directly reproduced in the kinetics of the Er-related PL signal [4]. Alternatively, carriers localized at these traps can be rapidly ionized by the FEL, resulting in an abrupt increase of the Er PL. A support of this model is obtained from the temperature dependence of the MIR-induced enhancement. As the temperature is increased, the thermal emission from traps becomes more efficient (and faster, for example at 50 K can be in the order of a nanosecond). The slow component of the Er PL vanishes and the enhancement effect is no longer possible.

4. Conclusions

Following all the results presented in this paper, we conclude that the MIR-induced enhancement effect is the result of excitation of erbium ions by free carriers released by the MIR from non-equilibrium traps available in the host silicon. Simultaneously, we can naturally explain the quenching effect induced optically by the MIR, as the ionized traps can no longer provide for a slow excitation mechanism of Er by their thermalization. From temperature dependence, we have found out that both effects disappear simultaneously above 50 K, so we conclude that the traps responsible for optical storage are shallow.

References

- [1] S. Coffa, et al., Phys. Rev. B 49 (1994) 16313.
- [2] A. Kozanecki, et al., Mater. Sci. Eng. B 81 (2001) 23.
- [3] I. Tsimperidis, et al., Phys. Rev. Lett. 81 (1998) 4748.
- [4] M. Forcales, et al., in preparation.



ELSEVIER

Physica B 308–310 (2001) 340–343

PHYSICA B

www.elsevier.com/locate/physb

Observation of Zeeman effect in photoluminescence of Er^{3+} ion imbedded in crystalline silicon

N.Q. Vinh^{a,*}, H. Przybylińska^b, Z.F. Krasil'nik^c, B.A. Andreev^c,
T. Gregorkiewicz^a

^a Van der Waals-Zeeman Institute, University of Amsterdam, Valckenierstraat 65, NL-1018 XE Amsterdam, Netherlands

^b Institute of Physics, Polish Academy of Sciences, Al. Lotników 32/46, PL-02 668 Warszawa, Poland

^c Institute for Physics of Microstructures, Russian Academy of Sciences, GSP-105, 603600 Nizhny Novgorod, Russia

Abstract

A successful observation of Zeeman effect on Er^{3+} -related photoluminescence in silicon is reported. In a sublimation MBE-grown Si/Si:Er superlattice, a clearly resolved splitting of major spectral components was observed in magnetic fields up to 5.5 T. The Zeeman effect was also investigated for the “hot line” appearing in the spectrum upon temperature increase. Based on the preliminary analysis of the data, the symmetry of the center responsible for the dominant emission line is identified as orthorhombic C_{2v} . Other spectral components originate from at least two more optically active, Er-related centers simultaneously present in the same sample. One of them most probably has cubic T_d symmetry. © 2001 Elsevier Science B.V. All rights reserved.

Keywords: Photoluminescence; Rare-earth ions; Zeeman effect

1. Introduction

Erbium in various host crystals gives rise to the characteristic emission at $\lambda \approx 1.54 \mu\text{m}$, due to the $^4I_{13/2} \rightarrow ^4I_{15/2}$ transition of the Er^{3+} ion. Since this particular wavelength is very nearly coincident with the absorption minimum of glass fibers used for telecommunication networks, erbium doping of semiconductors attracts considerable attention. The Si:Er system is of special interest in view of the highly successful and versatile silicon technology. As a result of a continued research effort, Si:Er-based devices, such as light emitting diodes and optical amplifiers, have been successfully developed. In contrast to that, many of the more fundamental aspects of the Si:Er system lack yet satisfactory understanding. In particular, the microstructure of the optically active Er center in silicon is not known.

For Er-doped GaAs, a combination of special growth techniques [1] and spectroscopic investigations [2–4] allowed the microscopic models of two different optically active centers to be proposed. In case of Si:Er, the situation is complicated due to a multiplicity of Er-related centers; more than 100 emission lines have been identified in a high-resolution infrared absorption study on Er-implanted Si [5]. These were assigned to emissions from several, simultaneously present Er-related centers. Moreover, again in contrast to GaAs:Er, but also to, e.g., GaN:Er, individual centers could not be separated by excitation spectroscopy, indicating an (equally) strong lattice coupling of all the species. Prominent formation of cubic center was shown by channeling experiments [6], which identified an isolated Er ion at a tetrahedral interstitial site as the main center generated in crystalline silicon by Er implantation. The channeling studies could not, however, conclude on optical activity of an isolated Er interstitial. Electron paramagnetic resonance has not been, so far, successful in identification of optically active Er-related centers in Si [7]. Also, attempts to observe the Zeeman effect in photolumines-

*Corresponding author. Tel.: +31-20-525-5644; fax: +31-20-525-5788.

E-mail address: nguyen@science.uva.nl (N.Q. Vinh).

cence (PL) of Si:Er were disappointing. Due to the earlier mentioned inhomogeneous character of the line width, application of magnetic field results in broadening and subsequent vanishing of emission lines.

2. Experimental

The recently developed sublimation MBE technique offers new possibilities to develop high quality Si:Er structures. The sample used in the current study has been prepared by this technique and features a quantum structure of 400 interchanged Si and Si:Er layers of a few nanometers thickness. Following the 30 min anneal at 800°C, PL emission from such a sample is at least an order of magnitude more intense than for usual materials prepared by ion implantation. Photoluminescence spectrum at $T = 4.2$ K, depicted in Fig. 1, contains only a few lines of a very small width: $\Delta E \approx 10 \mu\text{eV}$. Upon temperature increase, also shown in the figure, a higher energy “hot line” appears. It corresponds to a transition from a higher lying multiplet of the $^4I_{13/2}$ excited state. Based on the crystal field analysis, predominant formation of a single type of center, labeled Er-1, has been proposed [8,9]. In what follows we will present results of the magneto-optical spectroscopy on this material.

Experiments were performed at liquid-helium temperature using a cw Ar⁺-ion laser operating at 514.5 nm for sample excitation. The sample was placed in a split-coil superconducting magnet with optical access (Oxford Instruments Spectromag 4), providing magnetic fields up to 5.5 T. The emerging luminescence was dispersed by a high-resolution 1.5 m F/12 monochromator (Jobin Yvon THR-1500, equipped with a 600 grooves/mm grating blazed at 1.5 μm , and detected with a liquid-nitrogen cooled Ge detector (Edinburgh Instruments)). For

polarization measurements, a quarter-lambda plate and a linear polarization filter were used. The Zeeman effect was observed with magnetic field parallel to the $\langle 011 \rangle$ and $\langle 100 \rangle$ crystallographic directions of the sample, the latter one being also the stacking direction of the multilayer structure. The experimental configuration permitted the observation of the luminescence along and perpendicular to the field direction.

3. Results and discussion

In the crystal field of cubic symmetry, the $^4I_{15/2}$ ground and the $^4I_{13/2}$ lowest excited states split in two doublets (Γ_6 and Γ_7) and three quartets (Γ_8), and three doublets (Γ_6 and Γ_7) and two quartets (Γ_8), respectively. The lower symmetry crystal field splits the remaining quartets into doublets. Let us now consider transitions between two Kramers doublets (belonging to a particular configuration of a center of a not defined symmetry). In the magnetic field B , we should observe a splitting of the emission line into four components corresponding to two $\Delta M_J = 0$ (which are linearly polarized), and two $\Delta M_J = \pm 1$ circularly polarized transitions. These will appear at the field dependent energies:

$$h\nu_{1,2}(B) = h\nu(0) \pm \frac{1}{2}(G - g)\beta B$$

and

$$h\nu_{3,4}(B) = h\nu(0) \pm \frac{1}{2}(G + g)\beta B,$$

where G and g are the effective g -factors of the lower and upper doublet, respectively. In the experiment, we conclude that neither of the lines split off by the magnetic field shows any circular polarization. This indicates that we deal mostly with electric-dipole-type transitions, without spin flips. This is to be expected for Er, since the strong spin-orbit coupling, characteristic for the rare-earth ions, leads to the admixture of different excited configurations (with different L and S quantum numbers but the same J) to the 4I_J multiplets. In consequence, the linearly polarized $\Delta M_J = 0$ transitions are usually orders of magnitude stronger than the circularly polarized $\Delta M_J = \pm 1$ transitions. In the magnetic field, we should expect to see only transitions without a change of the effective spin.

The transition probabilities for the two lines are equal, since they involve Kramers conjugate states. Any difference in the PL intensities reflects the difference in the population of the magnetic field split states of the upper doublet. In principle, if the spin lattice relaxation time is much shorter than the radiative lifetime, one should be able to determine the g -factor of the upper doublet by comparing the line intensities as a function of B at constant temperature. Unfortunately, at 4.2 K, this is not the case. Studies of the temperature dependence at

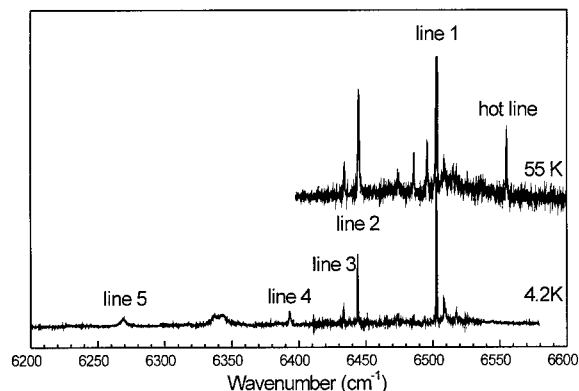


Fig. 1. PL spectrum of the multilayer Si/Si:Er structure used in the current study, as observed at two different temperatures. Individual lines are labeled as used in the text.

4.5 T show that the population of the upper split state decreases with increasing temperature at low temperatures—since the relaxation time is temperature dependent—and only above 30 K the thermalization is really fast enough to obtain any reliable g -factors.

Figs. 2(a) and (b) show the magnetic field-induced splitting of the strongest PL line (marked 1 in the spectrum depicted in Fig. 1) for $B \parallel \langle 100 \rangle$ and $B \parallel \langle 011 \rangle$ configurations. As can be seen, line 1 splits in the magnetic field into three components for $B \parallel \langle 100 \rangle$ and five components for $B \parallel \langle 011 \rangle$. The position of one of them, in both field orientations, almost does not move with the magnetic field strength—for this line, the effective g -factors of the upper and lower state must be almost equal. Assuming that all lines stem from one kind of center and there is no accidental overlap of two PL lines from centers of different symmetry at $B = 0$, we have to consider a low symmetry center with different orientations of the g -tensor axes of the possible configurations with respect to B direction. Naturally, each observed component would then involve transitions between two Kramers doublets.

Cubic T_d or trigonal C_{3v} symmetries cannot explain the observed splitting. It corresponds, however, very well to the orthorhombic $I(C_{2v})$ symmetry type. The number of lines and their relative intensities reflect the expected 2:1 for $\langle 100 \rangle$ and 4:1:1 for $\langle 011 \rangle$. Unfortunately, at this stage of research, due to the lack of experimental data at other field orientations (e.g., $\langle 111 \rangle$) individual g -factors of the upper and lower doublet cannot be uniquely determined.

The C_{2v} symmetry is also consistent with the magnetic field-induced splitting of the “hot line”. However, since also in this case we are dealing exclusively with $\Delta M_J = 0$

transitions, individual g -tensors of the involved states cannot be separated. Even assuming that the “hot line” belongs to the same center as line 1, which is a reasonable assumption, we can come up with different sets of g -factors giving an equally good fit. From numerical analysis, we can only conclude that one of the g -tensor values of the lower doublet must be close to zero.

The same C_{2v} symmetry type is also observed for line 4. We conclude, therefore, that lines 1, 4 and the “hot line” could correspond to the same center.

Lines 2 and 3 behave quite differently to lines 1, 4 and the hot line. For B along $\langle 100 \rangle$, line 2 splits into three symmetrical pairs. It cannot stem from transitions between two Kramers doublets of whatever symmetry, and there must be at least one quartet state involved. Since, for $B \parallel \langle 011 \rangle$ similar three pairs of lines are seen, the center seems to have a high symmetry, however, the number of lines is puzzling (for transitions between a cubic quartet and a doublet four lines are expected). At high magnetic fields (above 4 T), the line positions do not depend linearly on B any more and start to curve up to higher energies (especially the lower energy lines). Clearly, there appears to be some interaction between the involved states. One possible explanation is that we deal with a center of cubic symmetry which has a close lying doublet and quartet state in the excited state and a doublet in the ground state (or vice versa). There is no doubt that line 2 does not belong to the same center as line 1.

Line 3 splits into four pairs at $B \parallel \langle 100 \rangle$ and six pairs for $B \parallel \langle 011 \rangle$. It is clearly lower than the cubic site symmetry and must involve transitions between more than two doublets. The situation is clearer than for line

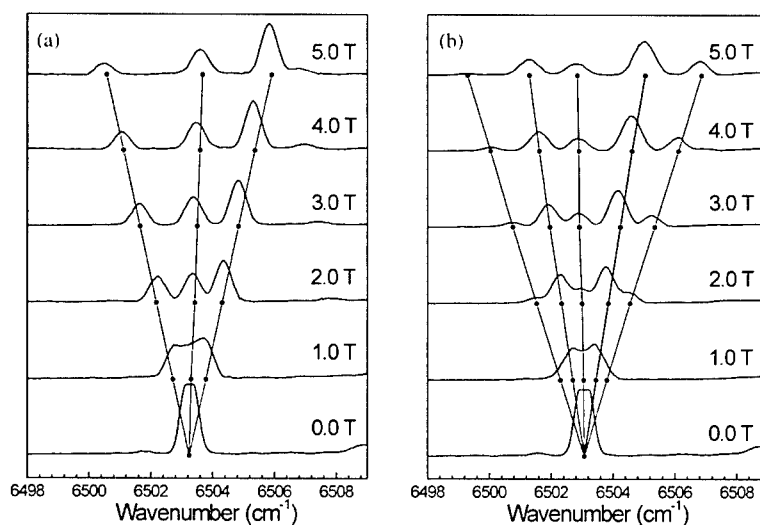


Fig. 2. Magnetic field-induced splitting of line 1 for (a) $B \parallel \langle 100 \rangle$ and (b) $B \parallel \langle 011 \rangle$ configuration.

2. From the analysis of the data, we conclude that there are two doublets in the excited state separated by about 3 cm^{-1} .

4. Conclusions

Based on the preliminary analysis of the Zeeman effect data, we conclude that the individual components of the Er-I PL spectrum originate from more than one (possibly three) different Er-related optically active centers. The symmetry of the most prominent one is tentatively identified as orthorhombic $I(C_{2v})$. At least one of the remaining spectral components corresponds to a cubic center (T_d). All the observed PL lines are due to electric dipole-induced transitions without spin flips. Therefore, precise determination of g -tensors at this moment is not possible.

In the continuation of the project, we will investigate Zeeman effect for an arbitrary field orientation, i.e., not along the main directions, where also circularly polarized $\Delta M_J = \pm 1$ transitions should appear. We will look carefully at the intensity changes of individual components at a higher temperature range $T > 30\text{ K}$, as induced both by temperature and field increase. In this

way, we hope to obtain independent information on Zeeman effect for the excited state, allowing for an unambiguous determination of g -tensors. Also, the polarization effects will be carefully investigated.

Acknowledgements

The authors express their gratitude to Dr V.P. Kuznetsov for growing the structure used in the study. This work was partially sponsored by NWO grant # 047.009.013, RFBR grant # 01-02-16439, and INTAS grant # 99-01872.

References

- [1] K. Takahei, et al., *J. Appl. Phys.* 76 (1994) 4332.
- [2] H. Ennen, et al., *J. Appl. Phys.* 61 (1987) 4877.
- [3] K. Takahei, A. Taguchi, *J. Appl. Phys.* 74 (1993) 1979.
- [4] D. Haase, et al., *Mat. Res. Symp. Proc.* 422 (1996) 179.
- [5] H. Przybylińska, et al., *Phys. Rev. B* 54 (1996) 2532.
- [6] U. Wahl, et al., *Phys. Rev. Lett.* 79 (1997) 2069.
- [7] J.D. Carey, et al., *Phys. Rev. B* 59 (1999) 2773.
- [8] B.A. Andreev, et al., *J. Cryst. Growth* 201/201 (1999) 534.
- [9] M.V. Stepikhova, et al., *Mater. Sci. Eng. B* 81 (2001) 67.



ELSEVIER

Physica B 308–310 (2001) 344–347

PHYSICA B

www.elsevier.com/locate/physb

Erbium in SiO_x environment: ways to improve the $1.54\text{ }\mu\text{m}$ emission

G. Kocher^{a,*}, H. Przybylinska^{a,b}, M. Stepikhova^{a,c}, L. Palmetshofer^a, W. Jantsch^a

^a *Institut für Halbleiter- und Festkörperphysik, Johannes Kepler Universität, Altenbergerstr. 69, A-4040 Linz, Austria*

^b *Institute of Physics, Polish Academy of Sciences, PL 02-668 Warsaw, Poland*

^c *Institute Physics of Microstructures RAS, 603600 Nizhny Novgorod, GSP 105, Russia*

Abstract

The only way to obtain room temperature electroluminescence at $1.54\text{ }\mu\text{m}$ from Si diodes due to intra-atomic transitions of erbium is the excitation of $\text{SiO}_2\text{:Er}$ clusters by hot electron injected in a reverse biased diode. Impact excitation of erbium and thus electroluminescence can be achieved in tunnelling diodes, although at very small excitation volume, which would cover only a small fraction of a wave guide. Making use of an avalanche process allows one to increase the excitation volume considerably. This requires accurate control of doping gradients and thus knowledge of the electrical activity and the distribution of the implanted dopants. We present data from SIMS and Hall effect investigations, which demonstrate significant deviations from TRIM simulations of the implantation profiles and the hitherto assumed electrical activity of Er in such environment. We present optimum parameters for design and realisation of diodes working at room temperature. © 2001 Elsevier Science B.V. All rights reserved.

Keywords: Erbium luminescence; Electroluminescence; Precipitates

1. Introduction

The search for Si based light sources for integration into Si technology is considered to be of utmost importance in semiconductor physics. One of the most promising approaches to reach this goal is the integration of erbium ions into Si host crystals. These ions emit near infrared light at a wavelength of $1.54\text{ }\mu\text{m}$ resulting from a radiative transition within the 4f shell.

Depending on doping, annealing conditions and co-doping with light elements—especially with oxygen—erbium produces a big variety of centres in silicon. These centres can be distinguished by their characteristic luminescence line patterns [1]. For these centres with their well-defined geometry, intra-shell excitation of Er can be achieved in a forward biased p–n junction via an energy transfer from recombining electron–hole pairs.

These devices show a high internal quantum efficiency at low temperatures [2] but also strong thermal quenching of their luminescence above 150 K.

Two different mechanisms are assumed to be responsible for this quenching: an Auger effect [3] and energy back transfer of the Er excitation energy to the host via a defect level, which seems also to be participating in the transfer of energy from the host to the Er 4f shell [4]. This defect level is characteristic for oxygen co-doped Si:Er.

One way to reduce Auger quenching is excitation in a reverse biased p–n junction. Here, Er is excited by highly inelastic impact with hot electrons (“impact excitation”) injected to the Er-doped region in the breakdown regime. In this case, the thermal quenching of luminescence is negligible and room temperature luminescence can be achieved [5–7]. The cross-section for the impact excitation, however, is small and therefore the efficiency is rather low. Furthermore, it turned out that the emission spectra of reverse biased diodes are modified. It changes from the characteristic sharp line spectra caused by crystal field splitting with line widths of less than

*Corresponding author. Tel.: +43-732-2468-9649; fax: +43-732-2468-9696.

E-mail address: gudrun.kocher@jk.uni-linz.ac.at (G. Kocher).

1 nm to a less structured band with a width of approximately 20 nm.

These broad features originate from Er in SiO_x precipitates [8]. The incorporation of Er in SiO_x clusters is achieved by Er and O implantation and subsequent annealing above 950°C, the threshold temperature for appreciable oxygen migration and formation of SiO_2 precipitates [9].

Impact excitation of erbium and thus electroluminescence can be achieved in tunnelling diodes, although at a very small excitation volume. Electrons participating in the impact excitation need an energy of more than 0.8 eV. The small mean free path of these electrons restricts the excitation volume to a layer of less than 40 nm thickness surrounding the p–n junction [5–7]. Making use of an avalanche process allows one to increase the excitation volume considerably. This requires accurate control of doping gradients and thus knowledge of the electrical activity and the distribution of the implanted dopants.

We find from SIMS measurements, that at the high temperatures required for the precipitate formation in our devices, the implanted Er profile remains practically constant, but the distribution of the light dopants changes significantly. We also find that the as-implanted profiles deviate substantially from those obtained in TRIM code simulations [10]. Another change appears in the electrical activity of our “optical dopant”: Hall measurements show that the electrical activity is rather low under the preparation conditions used.

We discuss here the optimum parameters for design and realisation of diodes working at room temperature according to our findings.

2. Design considerations

An important property entering design considerations is, of course, the electrical activity of the Er centres. We investigated our SiO_x :Er precipitates by means of Hall effect measurements. The measurements were performed on samples prepared by implanting Er and O into high resistivity Si substrates (Fig. 1). Whereas for isolated

centres a large portion can be electrically active, for our sample, we found that the sheet concentration of the free carriers is only a few percent of that of the incorporated Er ions after annealing.

The easiest way to achieve EL from reverse biased p–n junctions is to produce diodes with large doping gradients that show tunnelling breakdown [5–7]. But, as mentioned above, the participating electrons with sufficient energy for this kind of excitation have only a short ballistic penetration range. Therefore, only a small fraction of the incorporated Er is excited and the total efficiency of such a device is rather low. Laser operation of such a device, for example, would be impossible because population inversion would be excluded already by geometrical constraints.

A diode working in the avalanche breakdown regime would extend the excitation volume 10 times (see Table 1). In order to get avalanche breakdown, the electric field strength has to be adjusted accordingly. This can be done by adjusting the doping gradient. To achieve avalanche conditions in Si at room temperature, the doping gradient must not exceed a value of 10^{23} cm^{-4} [11]. The doping gradient in implanted structures is usually obtained by applying TRIM code simulation. In order to gain information on the actual structure of our diodes, we applied SIMS for two different structures at various annealing temperatures (Fig. 2).

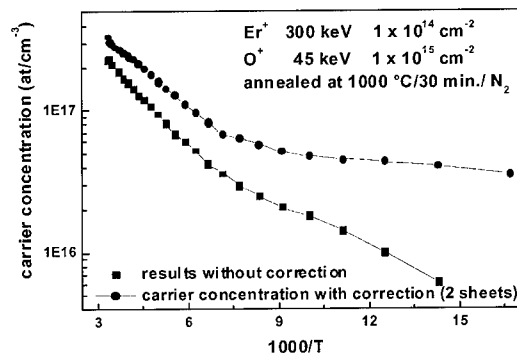


Fig. 1. Carrier concentration measured by Hall effect; substrate contribution was corrected by applying a two-sheet model.

Table 1
Parameters for tunnelling and avalanche diodes

	Tunnelling	Avalanche
Field strength, E (V/cm)	$> 10^6$	$< 6 \times 10^5$
Dopant gradient (lin. graded junct.) (cm^{-4})	$> 2 \times 10^{23}$	$< 10^{23}$
Voltage (V)	$< 4E_g/e$	$> 6E_g/e$
Er excitation cross-section (cm^2)	6×10^{-17} [7]	2.3×10^{-16} [12]
Excitation width (nm)	40	500

It turned out that the experimental values for the mean projected range R_p are about 20% larger than the values obtained by simulation [10]. The experimental values for the range straggling, R_p , are almost twice as large as TRIM table values. The same discrepancy was found for Er implanted into amorphous SiO_2 , so channelling effects appear unlikely as an explanation.

Due to the low electrical activity of Er under the preparation conditions used, this difference would not significantly change the electronic properties of a diode

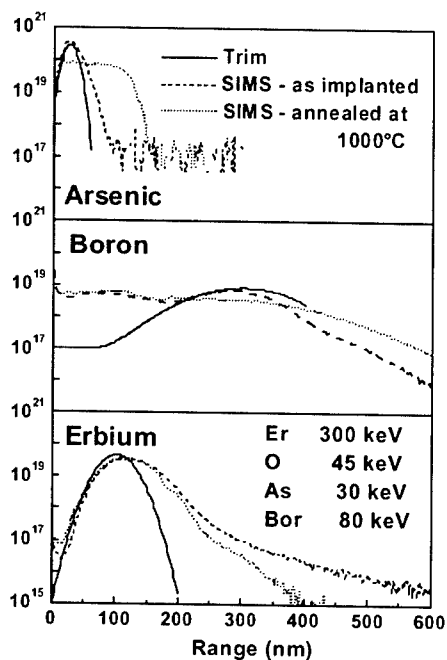


Fig. 2. Comparison of implantation profiles for Er and shallow dopants in p-Si substrate.

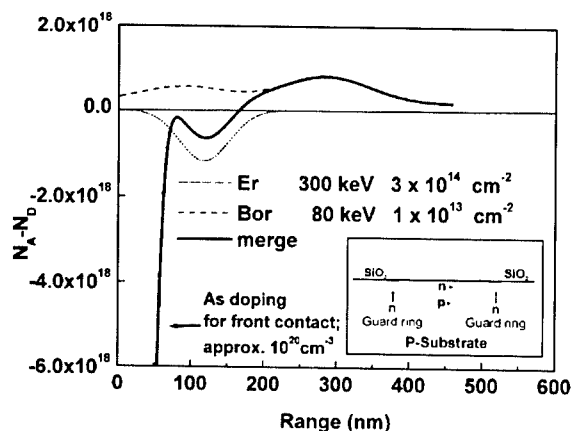


Fig. 3. Simulated doping profiles according to SIMS results. The inset shows a typical structure for an avalanche diode.

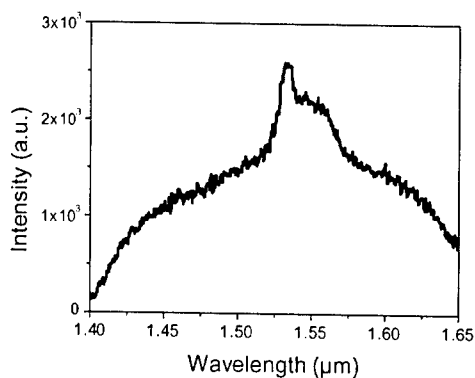


Fig. 4. Electroluminescence spectra of an avalanche diode taken at room temperature. The diode parameters are shown in Fig. 3.

but it may crucially impair the optimal spatial overlap of the Er profile with the avalanche excitation volume.

Although the Er profiles are substantially deeper than expected (Fig. 2), they do not diffuse at the high annealing temperatures necessary for the formation of $\text{SiO}_2:\text{Er}$ precipitates. The shallow dopants, however, do and this diffusion may alter the doping gradient significantly, and thus it has to be taken into account in designing an avalanche breakdown diode.

To adjust the doping gradient according to these results, we fitted the SIMS data with a Gaussian function containing exponential correction terms. A schematic diagram for our diode structure is shown as inset in Fig. 3. Although the implantation energies stayed the same, the implantation doses and annealing procedure had to be changed according to the SIMS results. In order to avoid excessive diffusion of shallow dopants, a two-step implantation and annealing procedure was adopted. After implanting Er and O and subsequent annealing at 1000°C for 30 min, an additional lithography and annealing step was inserted for arsenic and boron, which provide the contact and background doping, respectively. To keep the diffusion low, the annealing temperature was lowered to 400°C .

With the structure shown in Fig. 3, we were able to get room temperature luminescence of Er for excitation in reverse bias. The intensity of the luminescence increased at least one order of magnitude compared to a similar diode structure designed using TRIM code simulations only (Fig. 4).

3. Conclusions

Accurate control of doping gradients and thus knowledge of the electrical activity and the distribution of the implanted dopants are essential for the location and impurity gradient of the p-n junction. Careful

consideration has, thus, to be put into diode design in order to achieve avalanche rather than tunnelling breakdown in a diode. TRIM simulations turn out to be insufficient. After adjusting the diode design according to SIMS results, the intensity of the electroluminescence at room temperature increased by at least one order of magnitude.

Acknowledgements

This work was supported by the Gesellschaft für Mikroelektronik, and the Fonds zur Förderung der Wissenschaftlichen Forschung, Vienna, Austria.

References

- [1] H. Przybylinska, W. Jantsch, Yu. Suprun-Belevitch, M. Stepikhova, L. Palmetshofer, G. Hendorfer, A. Kozanecki, R.J. Wilson, B.J. Sealy, *Phys. Rev. B* 54 (4) (1996) 2532.
- [2] S. Coffa, G. Franzo, F. Priolo, *MRS Bull.* 23 (1998) 25.
- [3] J. Michel, J. Palm, F. Gan, F.Y.G. Ren, B. Zheng, S.T. Dunham, L.C. Kimerling, *Mater. Sci. Forum* 196–201 (1995) 585.
- [4] F. Priolo, G. Franzo, S. Coffa, A. Carnera, *Phys. Rev. B* 57 (1998) 4443.
- [5] G. Franzo, S. Coffa, A. Polman, A. Carnera, F. Priolo, *Appl. Phys. Lett.* 64 (1994) 17.
- [6] J. Stimmer, A. Reittinger, J.F. Nützel, H. Holzbrecher, Ch. Buchal, G. Abstreiter, *Appl. Phys. Lett.* 68 (1996) 23.
- [7] S. Coffa, G. Franzo, F. Priolo, *Appl. Phys. Lett.* 69 (1996) 2077.
- [8] W. Jantsch, G. Kocher, L. Palmetshofer, H. Przybylinska, M. Stepikhova, H. Preier, *Mater. Sci. Eng. B* 81 (2001) 86.
- [9] A. Bourret, L.C. Kimerling, J.M. Parsey, Jr. (Eds.), *Proceedings of the 13th International Conference on Defects in Semiconductors*, Metallurgical Society of AIME, NY, 1985, p. 129.
- [10] L. Palmetshofer, M. Gritsch, G. Hobler, *Mater. Sci. Eng. B* 81 (83) (2001) 83.
- [11] S.M. Sze, *Physics of Semiconductor Devices*, 2nd Edition, Wiley, NY, 1981, 96ff.
- [12] N.A. Sobolev, A.M. Emel'yanov, Yu.A. Nikolaev, *Semiconductors* 33 (1999) 926.

Excitation of Si:Er with sub-band-gap energies

M.A.J. Klik*, T. Gregorkiewicz

Van der Waals–Zeeman Institute, University of Amsterdam, Valckenierstraat 65, NL-1018 XE, Amsterdam, The Netherlands

Abstract

We have performed photoluminescence excitation spectroscopy on molecular beam epitaxy grown Si:Er with a high-power near-infrared laser pulse. It was found that luminescence from the Er^{3+} ion, originating from the intra-4f-shell transition $^4\text{I}_{13/2} \rightarrow ^4\text{I}_{15/2}$ could be induced by photon energies far below the band gap of the host material, but above energy of the 4f-shell transition. © 2001 Elsevier Science B.V. All rights reserved.

PACS: 32.80.Hd; 78.55.Ap

Keywords: Erbium; Silicon; Sub-band-gap excitation

The excitation mechanisms of rare-earth (RE) ions in semiconductors usually involve excitons or a RE-related energy level in the band gap of the host. The RE-ion can be photo-excited through the conduction band of the host material [1] or directly to the RE related level [2]. It is well known that the Er^{3+} ion can form a variety of complexes in the Si host material, most probably each with its own level within the band gap. Excitation spectroscopy is a powerful method to investigate these levels and their role in the excitation process. We have performed excitation experiments using a Nd:YAG (second harmonic) pumped optical parametric oscillator (OPO) crystal to produce a 5 ns pulsed laser beam with a wavelength range of 700–2200 nm and repetition rate of 20 Hz. The maximum pulse energy used in these experiments was 7 mJ at a wavelength of 700 nm. The sample under investigation was an oxygen-rich Si:Er layer of 1.8 μm , grown by molecular beam epitaxy (MBE) at a temperature of 560°C on top of a B-doped Si substrate. Luminescence from the sample was gathered using a single grating monochromator and a near-infrared photomultiplier tube with a flat response from 300 to 1600 nm. The sample was cooled to 10 K in an Oxford Instruments closed-cycle cryostat.

After excitation of the sample from the backside (substrate) with the OPO beam operating in the near infrared, a PL signal could be detected at 1.54 μm , originating from the intra-4f-shell transition $^4\text{I}_{13/2} \rightarrow ^4\text{I}_{15/2}$ of the RE ion Er^{3+} . Fig. 1 shows the normalized photo-luminescence excitation (PLE) spectrum measured at 1539 nm at a temperature of 10 K (gray). The photon flux of the OPO-beam is indicated in black. It is clear from the picture that luminescence can be observed for excitation photon energies between the band-gap energy E_g of the host material and the

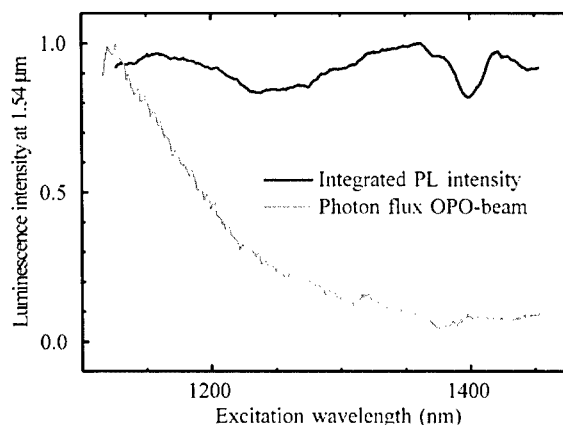


Fig. 1. PLE spectrum of Si:Er measured at a temperature of 10 K, using a high power pulsed excitation beam.

*Corresponding author. Tel.: +31-20-525-5644; fax: +31-20-525-5788.

E-mail address: mklik@science.uva.nl (M.A.J. Klik).

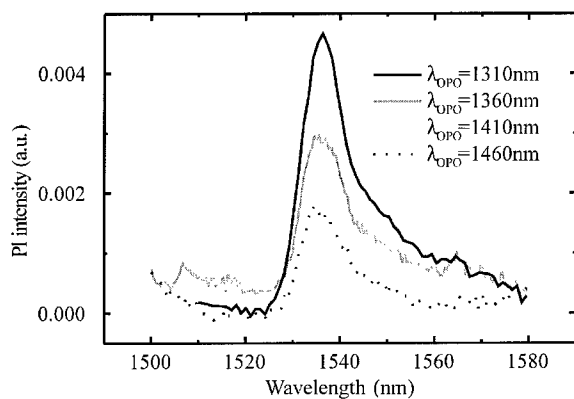


Fig. 2. Spectrum of Si:Er measured for four different excitation wavelengths. The PL intensity reduces for excitation energies close to that of the $^4I_{13/2} \rightarrow ^4I_{15/2}$ transition in the 4f-shell of Er^{3+} .

energy of the intra-4f-shell transition. The cross section for excitation decreases monotonically with smaller photon energy and vanishes for an energy below this transition. No resonant features are present in the range 1125–2200 nm. Although multi-photon absorption seems an obvious explanation for the observed excitation spectrum, the dependence of PL intensity on OPO-beam power shows a completely linear behavior, indicating other processes to be responsible for the excitation of the RE-ion with sub-band-gap photon energies. Fig. 2 shows the spectra of the Er intra-4f-shell luminescence for excitation wavelengths from 1310 to 1460 nm. It can be seen that the luminescence intensity decreases when the excitation energy approaches the energy of the intra-4f-shell transition.

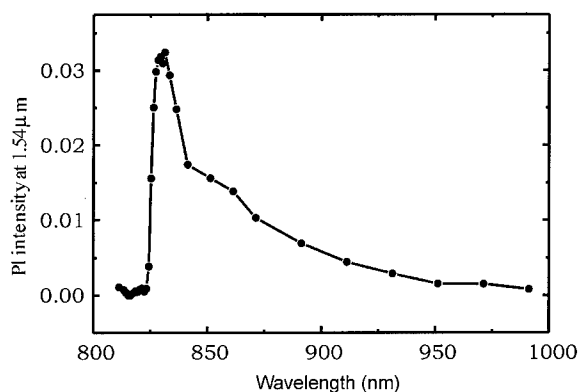


Fig. 3. PLE spectrum of GaAs:Er measured at 10 K.

At present, the observations cannot be explained by any of the (so far) considered models. For a better understanding of the processes responsible, more accurate measurements will be done on a variety of samples in the near future. For comparison, the PLE spectrum for MBE grown GaAs:Er was obtained using the same experimental setup (Fig. 3). Although both PLE spectra are very similar, the luminescence at 1.54 μm could only be observed for excitation wavelengths below 1000 nm.

References

- [1] K. Thonke, et al., *Semicond. Sci. Technol.* 5 (1990) 1124.
- [2] J. Palm, et al., *Phys. Rev. B* 54 (1996) 17603.



ELSEVIER

Physica B 308–310 (2001) 350–353

PHYSICA B

www.elsevier.com/locate/physb

Shallow donors in silicon coimplanted with rare-earth ions and oxygen

V.V. Emtsev Jr.^{a,*}, C.A.J. Ammerlaan^a, B.A. Andreev^b, G.A. Oganessian^c,
D.S. Poloskin^c, N.A. Sobolev^c

^a Van der Waals-Zeeman Institute, University of Amsterdam, Valckenierstraat 65, 1018 XE Amsterdam, The Netherlands

^b Institute for Physics of Microstructures, Russian Academy of Sciences, 603600 Nizhny Novgorod, GSP-105, Russia

^c Ioffe Physicotechnical Institute, Russian Academy of Sciences, 194021 St. Petersburg, Russia

Abstract

Formation processes of shallow donors in Czochralski-grown silicon coimplanted with rare-earth ions and oxygen are studied. There is no indication that rare-earth ions are components of the structures of shallow donors. However, intrinsic defects appear to be involved in the formation processes. These oxygen-related thermal donors survive even at $T = 900^\circ\text{C}$. They are responsible for the electrical conductivity in the implanted layers at cryogenic temperatures. © 2001 Elsevier Science B.V. All rights reserved.

Keywords: Silicon; Rare-earth ions; Implantation; Thermal donors

1. Introduction

Earlier [1–3] it has been established that in Czochralski-grown silicon (Cz-Si) implanted with rare-earth (RE) dopants (Dy, Ho, Er and Yb) and annealed to $T = 700^\circ\text{C}$ three main kinds of donor centers make their appearance: shallow donors at $\approx E_C - 40\text{ meV}$ and deeper donor centers at $\approx E_C - (60-80)\text{ meV}$ and $\approx E_C - (110-140)\text{ meV}$; see Fig. 1. All of them were found to be oxygen-related, since their formation takes place only in the presence of oxygen, no matter in Cz-Si implanted with RE ions [1] or float-zone silicon (FZ-Si) coimplanted with RE ions and oxygen [3]. Without oxygen coimplantation in FZ-Si only one kind of dominating donors at $\approx E_C - 200\text{ meV}$ can be detected; see Fig. 1 and Ref. [3]. Besides, a comparative study of various dopants in Cz-Si allowed to conclude that the position of donor centers at $\approx E_C - (60-80)\text{ meV}$ and $\approx E_C - (110-140)\text{ meV}$ are dependent on the chemical nature of RE impurities [1]. This is why these

centers have been identified as (RE-oxygen)-related complexes [1–3].

In the present paper, most attention has been paid to the formation of oxygen-related shallow donors responsible for the electrical conductivity of implanted layers at cryogenic temperatures.

2. Experimental

The initial materials were p-type Cz-Si wafers of $\rho \approx 20\ \Omega\text{cm}$. The oxygen concentration varied over a wide range, from $\approx 2 \times 10^{17}$ to $\approx 1 \times 10^{18}\text{ cm}^{-3}$. In some cases, n-type Si:P epilayers of $\rho \approx 20\ \Omega\text{cm}$ were grown on low-resistivity p-type Cz-Si substrates and then implanted with Er ions.

RE ions, mostly Er, were implanted at energies of 1.0–1.2 MeV. The RE implantation dose Φ varied in the range of 5×10^{11} – $1 \times 10^{13}\text{ cm}^{-2}$. In the case of oxygen coimplantation, the energy of oxygen ions was between 0.11 and 0.18 MeV. The implanted samples were annealed at $T = 700^\circ\text{C}$ for 30 min in a chlorine containing ambient. The radiation damage is mostly recovered at this annealing stage. At implantation doses $\Phi(\text{RE}) \geq 5 \times 10^{11}\text{ cm}^{-2}$, the implanted layers of

*Corresponding author. Tel.: +31-20-525-5642; fax: +31-20-525-5788.

E-mail address: emtsev@wins.uva.nl (V.V. Emtsev Jr.).

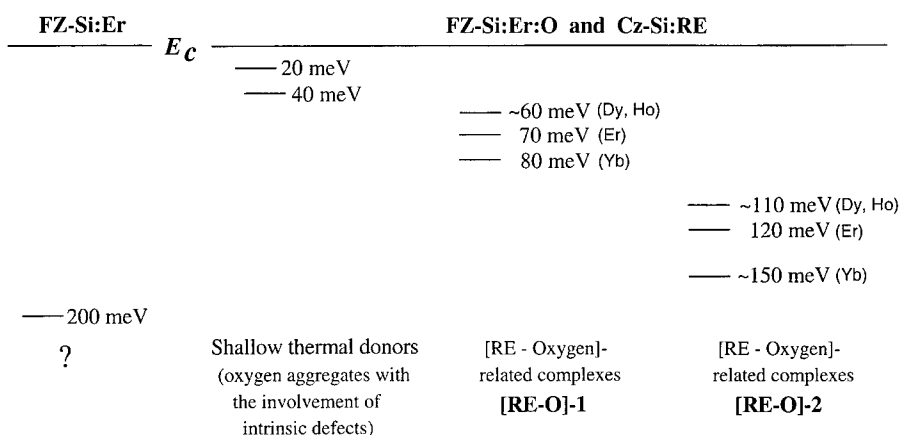


Fig. 1. Donor centers determining the electrical conductivity of FZ-Si and Cz-Si implanted with RE ions and annealed at $T = 700^\circ\text{C}$. The donor levels are shown with respect to the conduction band of silicon.

about $0.5\ \mu\text{m}$ in thickness became n-type, even in the initially p-type Cz-Si samples.

Electrical measurements of the electron concentration in implanted layers versus temperature, $n(T)$, were taken by means of the Van der Pauw technique over the temperature range from $T \approx 20$ – $300\ \text{K}$. Analysis of $n(T)$ curves was carried out on the basis of the corresponding equations of charge balance [4,5]. Photoconductivity spectra of several implanted layers at cryogenic temperatures were recorded in the range of 200 – $800\ \text{cm}^{-1}$ with the aid of an IFS-113 V Bruker spectrometer. The resolution was $1\ \text{cm}^{-1}$.

In some cases, implanted samples were subjected to $0.9\ \text{MeV}$ electron irradiation at room temperature to produce A-centers (oxygen-vacancy complexes) for partial compensation of shallow donor states.

3. Results and discussion

By way of example, in Fig. 2, three $n(T)$ curves are shown for the FZ-Si epilayers coimplanted with Er and O ions. The Er dose was fixed at a maximum, $\Phi(\text{Er}) = 1 \times 10^{13}\ \text{cm}^{-2}$, whereas the dose of oxygen coimplant varied between $\Phi(\text{O}) = 5 \times 10^{13}$ and $5 \times 10^{14}\ \text{cm}^{-2}$.

Analysis of all the $n(T)$ curves revealed some interesting features of the donor formation processes in Er implanted layers.

First, at $\Phi(\text{Er}) \leq 5 \times 10^{12}\ \text{cm}^{-2}$ the concentration of shallow thermal donors in Cz-Si:Er with high oxygen concentrations (about $1 \times 10^{18}\ \text{cm}^{-3}$) varies directly with the Er implantation dose. This observation is consistent with our earlier conclusion [3] that the intrinsic defects produced by Er ions play a key role as nucleation sites of oxygen aggregates (shallow thermal donors). In this way, the shallow thermal donors are substantially stabilized as compared to those usually formed during oxygen precipitation processes in conventional Cz-Si at

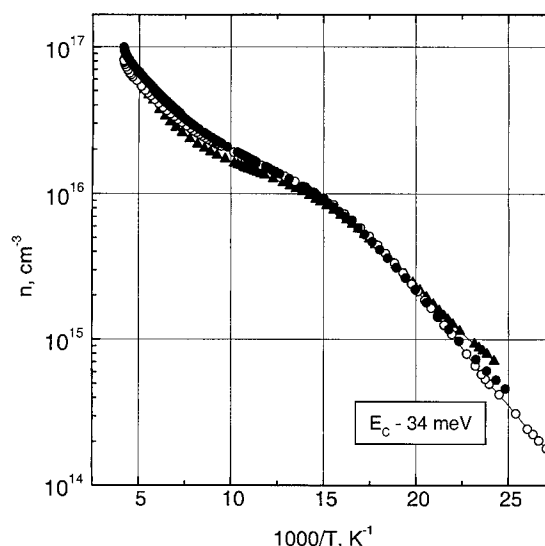


Fig. 2. Electron concentration against reverse temperature in the Fz-Si coimplanted with Er and O ions and annealed at $T = 700^\circ\text{C}$. Dose $\Phi(\text{Er}) = 1 \times 10^{13}\ \text{cm}^{-2}$. Dose $\Phi(\text{O}) = 5 \times 10^{13}\ \text{cm}^{-2}$ (open circles), 1×10^{14} (solid circles) and $5 \times 10^{14}\ \text{cm}^{-2}$ (solid triangles). Concentration of shallow donors (open circles), $2.8 \times 10^{16}\ \text{cm}^{-3}$.

$T = 700^\circ\text{C}$: cf. also [6–8]. The shallow thermal donors in Cz-Si:RE survive even after annealing to $T = 900^\circ\text{C}$ [1,2]. At $\Phi(\text{Er}) > 5 \times 10^{12}\ \text{cm}^{-2}$ there is a pronounced trend towards saturation of the concentration of shallow donors in Cz-Si:Er.

Second, as would be expected, the damage produced by oxygen ions turned out to be not so important for the formation of shallow thermal donors. Actually, the total concentration of shallow donors is close to $3 \times 10^{16}\ \text{cm}^{-3}$ at $\Phi(\text{O}) = 5 \times 10^{13}$ and $1 \times 10^{14}\ \text{cm}^{-2}$, whereas at $\Phi(\text{O}) = 5 \times 10^{14}\ \text{cm}^{-2}$ it even drops by 20%; see also Fig. 3. This

slight decrease may be due to increasing formation rate of electrically inactive oxygen precipitates in oxygen-rich samples.

In contrast to little importance of oxygen ions as a damaging factor, the contribution of heavy Er ions to the production of intrinsic defects being involved in the formation of shallow donor centers can be characterized in a quantitative way. Really, analysis of the curves $n(T)$ shown in Figs. 2 and 3 points to the fact that the production of oxygen-related shallow thermal donors in FZ-Si:Er:O versus FZ-Si:O is enhanced by three times. This observation agrees well with the conclusion concerning the involvement of intrinsic defects in the oxygen agglomeration processes. As seen from Fig. 3, only one kind of shallow thermal donors, similar to those formed in FZ-Si:Er:O, is also produced in FZ-Si:O, thus demonstrating the involvement of Er ions in the formation of deeper donor centers at $\approx E_C - 70$ and 120 meV.

Third, the shallow thermal donors considered, like similar donor species formed during heat treatment of conventional Cz-Si at $T < 700^\circ\text{C}$ [6], are distributed over their ionization energies from ≈ 40 to ≈ 25 meV, the gravity center being placed at ≈ 40 meV. This is evident from the analysis of the low-temperature portions of $n(T)$ curves whose slopes change over the interval given above with increasing Er dose. It is possible to prove this model in another way by partial compensation of the shallow donors due to deep acceptors, e.g. vacancy-oxygen complexes (so-called A-centers at $\approx E_C -$

170 meV [9]) produced in Cz-Si:Er layers subjected to fast-electron irradiation. A compensation effect of shallow thermal donors due to A-centers in electron irradiated Cz-Si:Er:O is shown in Fig. 4. What is more, the quantitative analysis showed that the distribution of these donors as well as the concentrations of Er-related deep donor centers do not change noticeably after irradiation, so the whole $n(T)$ curves for electron irradiated layers can be described in a satisfactory way by changing the concentration of A-centers only; see Fig. 4.

Fourth, our photoconductivity measurements on Dy-implanted layers revealed the presence of Thermal Double Donors (TDDs); see Fig. 5. Their concentration is roughly estimated to be about 10^{15} cm^{-3} . This family of thermal donor states at $\approx E_C - 70$ and $\approx E_C - 140$ meV usually makes its appearance in conventional Cz-Si during heat treatment at $T \leq 500^\circ\text{C}$; see for instance review paper [10]. They are known to be unstable above $T = 600^\circ\text{C}$. After annealing of the Dy implanted layers to $T = 700^\circ\text{C}$ one could expect to detect the presence of TDDs in trace concentrations only, about 10^{13} cm^{-3} .

4. Conclusions

The information gained in the present work provides additional strong support for our earlier identification of oxygen-related shallow thermal donors in Si implanted

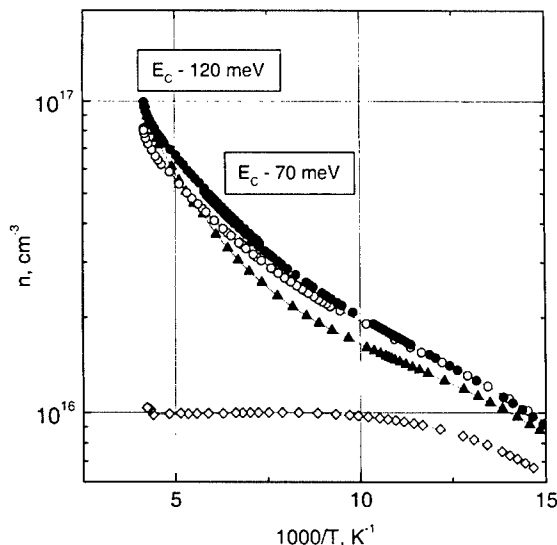


Fig. 3. Fragments of the $n(T)$ curves shown in the Fig. 2. For comparison purposes, the electron concentration against reverse temperature in the same FZ-Si implanted solely with O ions at $\Phi(\text{O}) = 5 \times 10^{14}\text{ cm}^{-2}$ and annealed at $T = 700^\circ\text{C}$ is also given (open diamonds). Concentration of [ErO]-1 centers (open circles), $2.5 \times 10^{16}\text{ cm}^{-3}$. Concentration of [ErO]-2 centers (open squares), $1.0 \times 10^{17}\text{ cm}^{-3}$.

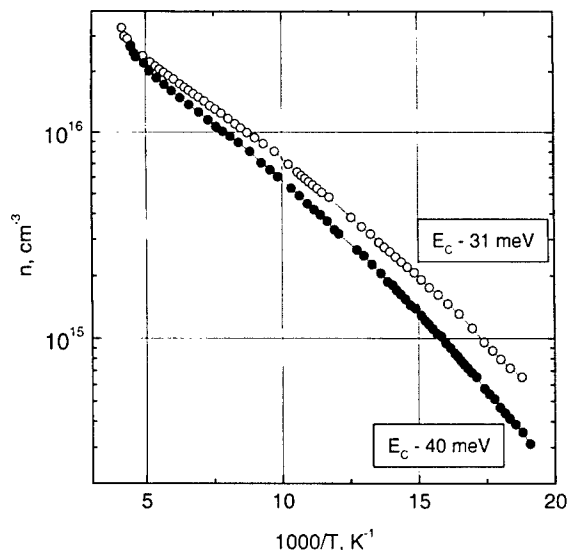


Fig. 4. Electron concentration against reverse temperature in the Cz-Si:Er before (open circles) and after fast electron irradiation (solid circles). Dose $\Phi(\text{Er}) = 1 \times 10^{13}\text{ cm}^{-2}$. Post-implantation annealing was performed at $T = 700^\circ\text{C}$. After the implantation and annealing the Er-doped layer was irradiated with 0.9 MeV electrons at a dose $1 \times 10^{17}\text{ cm}^{-2}$.

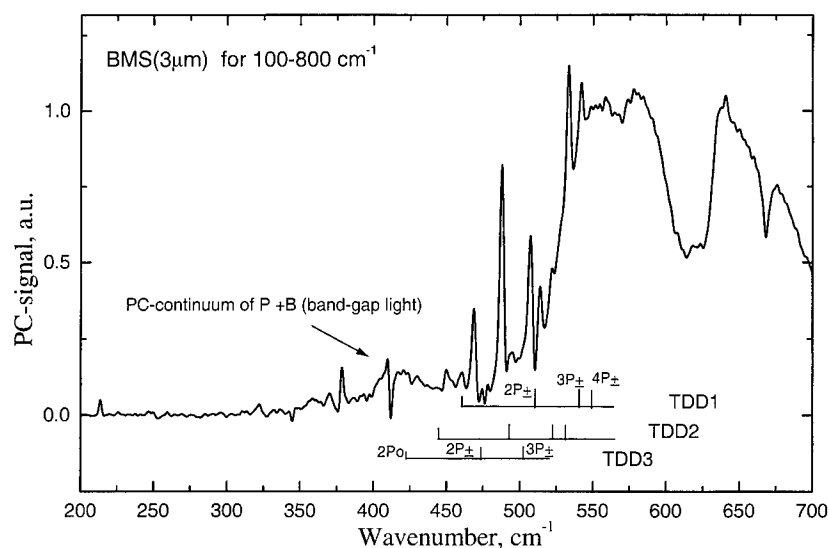


Fig. 5. Photoconductivity spectrum in the Cz-Si:Dy. Dose $\Phi(\text{Dy}) = 1 \times 10^{13} \text{ cm}^{-2}$. Postimplantation annealing was performed at $T = 700^\circ\text{C}$. The spectrum was recorded at $T \approx 30 \text{ K}$ under bandgap illumination. Three species of Thermal Double Donors are identified.

with RE impurities, first of all erbium. These shallow thermal donors are responsible for the electrical conductivity in implanted layers at cryogenic temperatures. The contribution of intrinsic defects produced by heavy RE ions to the formation of shallow donor centers has been studied in detail. The intrinsic defects serve as nucleation sites of growing oxygen aggregates.

Acknowledgements

The work was partly supported by INTAS (grant 99-018-72).

References

- [1] V.V. Emtsev, V.V. Emtsev Jr., D.S. Poloskin, E.I. Shek, N.A. Sobolev, *J. Lumin.* 80 (1999) 391.
- [2] V.V. Emtsev Jr., D.S. Poloskin, E.I. Shek, N.A. Sobolev, L.C. Kimerling, *Mater. Sci. Eng. B81* (2001) 74.
- [3] V.V. Emtsev, V.V. Emtsev Jr., D.S. Poloskin, E.I. Shek, N.A. Sobolev, J. Michel, L.C. Kimerling, *Solid State Phenom.* 69–70 (1999) 365.
- [4] J.S. Blakemore, *Semiconductor Statistics*, Pergamon Press, New York, 1962.
- [5] H.J. Hoffmann, H. Nakayama, T. Nishino, Y. Hamakawa, *Appl. Phys. A* 33 (1984) 47.
- [6] V.V. Emtsev, G.A. Oganessian, K. Schmalz, *Solid State Phenom.* 47–48 (1996) 259.
- [7] V.V. Emtsev, D.S. Poloskin, N.A. Sobolev, E.I. Shek, *Fiz. Tekh. Poluprovodn.* 28 (1994) 1084.
- [8] V.V. Emtsev, D.S. Poloskin, N.A. Sobolev, E.I. Shek, *Semiconductors (AIP)* 28 (1994) 624.
- [9] G.D. Watkins, J.W. Corbett, *Phys. Rev.* 121 (1961) 1001.
- [10] P. Wagner, J. Hage, *Appl. Phys. A49* (1989) 123.



ELSEVIER

Physica B 308–310 (2001) 354–356

PHYSICA B

www.elsevier.com/locate/physb

Site-selective excitation of Er^{3+} ions in oxygen-rich silicon

A. Kozanecki^{a,*}, D. Kuritsyn^a, H. Przybylińska^a, W. Jantsch^b

^a*Institute of Physics, Polish Academy of Sciences, Al. Lotników 32/46, 02-668 Warsaw, Poland*

^b*Institute für Halbleiterphysik, Johannes Kepler Universität, Linz A-4040, Austria*

Abstract

Photoluminescence excitation spectroscopy is used to study the location of Er^{3+} ions in oxygen-rich silicon and its excitation mechanisms. We find that Er luminescence excited within the range of the $^4\text{I}_{13/2}$ excited manifold of Er^{3+} consists of two features: a broad band independent of excitation wavelength, λ_{exc} , and a fluorescence narrowed line, dependent on λ_{exc} . These results show that Er^{3+} ions are excited via two energy transfer channels: the first one is due to non-radiative transfer of energy from excitons to the $^4\text{I}_{13/2}$ state, whereas the second one, leading to line narrowing, is typically resonant, site selective excitation of Er ions in silica glass. The results show that excitable Er ions are located most probably within nano-precipitates of SiO_2 . © 2001 Elsevier Science B.V. All rights reserved.

PACS: 61.72.Ww; 78.55.Hx

Keywords: Luminescence; Excitation mechanisms; Silicon oxide; Erbium

1. Introduction

Erbium-doped silicon is a promising material for light emitters operating at $1.54\mu\text{m}$, the most important wavelength for optical communication and prospective Si-based optoelectronics [1]. In spite of many efforts, however, the efficiency of the $1.54\mu\text{m}$ luminescence of Er^{3+} at room temperature (RT) is still too low for practical applications. The main reason for this appears to be an indirect excitation mechanism for the 4f shell of Er^{3+} , dominated by Auger-type interaction with charge carriers and excitons [2]. On the one hand, charge carrier mediated mechanisms of excitation ensure efficient energy transfer to Er centres at low temperatures. On the other they are also responsible for thermal quenching of the luminescence.

The quenching can be substantially reduced by codoping with oxygen [3] and also by employing wide band gap semiconductor hosts [4]. Efficient photoluminescence (PL) of Er^{3+} was obtained at RT in disordered Si-based materials with high oxygen contents, such as

porous silicon [5], semi-insulating polycrystalline silicon [6,7], or oxygen-rich silicon grown by laser ablation [8]. Moreover, the only Si:Er-based light emitters operating at RT were shown to employ silica nano-precipitates containing the Er [9,10].

The weak temperature quenching of the PL of Er^{3+} and lack of sharp emission lines, typical of oxygen-lean crystalline Si:Er [11], suggest that all the Er ions in oxygen-rich silicon layers are located within silica nano-precipitates. For such a location, direct optical excitation of Er^{3+} via absorption of photons should, in principle, be possible. It would result in fluorescence line narrowing (FLN), as different Er sites in silicon oxide precipitates would be selectively pumped [12].

In general, we should not expect direct optical excitation to be observed for pump wavelengths in the visible, because of the much higher absorption cross section of amorphous silicon (a-Si) than that of Er and, in effect, a dominant exciton mediated transfer of energy to the Er. On the other hand, resonant excitation of Er^{3+} ions should be easier to observe near $1\mu\text{m}$, where absorption in a-Si is relatively small.

In this work, we show using PLE spectroscopy and selectively excited PL that those Er^{3+} ions that can be

*Corresponding author. Tel.: +48-22-843-68-61; fax: +48-22-843-09-26.

E-mail address: kozana@ifpan.edu.pl (A. Kozanecki).

excited optically in Si(O):Er are indeed located within precipitates of SiO_x (or SiO₂) phase.

2. Experimental

The composition of the investigated layers was approximately SiO_x with an Er concentration of $\sim 10^{20} \text{ cm}^{-3}$. PL and PLE measurements were performed at helium temperatures. PL was excited using a Ti:sapphire laser chopped at 18 Hz and detected with liquid nitrogen cooled Ge detector. The spectra were normalised to a constant excitation power. A quartz sample implanted with 800 keV Er ions and annealed at 800°C served us as a reference.

3. Results and discussion

PLE spectra, measured at 5 K, of Er³⁺ in our samples of SiO:Er are presented in Fig. 1 for different detection wavelengths, λ_{det} . For an excitation wavelengths, λ_{exc} , within the range of ~ 975 – 986 nm the spectra depend on λ_{det} and for larger λ_{det} , the peak positions shift towards longer wavelengths. On an energy scale, the shift follows exactly a 1:1 correspondence. For λ_{exc} beyond the 975–986 nm range the PLE spectra are flat and do not depend on λ_{det} .

Fig. 2 shows selectively excited PL spectra of Er³⁺ near 1.5 μm . The spectra depend in a characteristic way on the pump energy. For $975 < \lambda_{\text{exc}} < 986$ nm in each spectrum, a narrow PL can be distinguished whose spectral position shifts reflecting the changes of the pump wavelength. This narrow PL is superimposed on a broad band which does not change in shape with λ_{exc} . For excitation at $\lambda_{\text{exc}} < 975$ nm and > 990 nm only a

broad emission is observed. Its intensity depends slightly on the pump wavelength.

For comparison, the PLE spectra in quartz implanted with Er ions at 800 keV and annealed at 800°C were measured (Fig. 3). Similarly as in Fig. 1, the peak positions in the spectra follow the changes in the detection energy. However, in contrast to Si(O):Er, a long wavelength cut-off, which for increasing λ_{det} shifts to shorter wavelengths, is clearly seen. The Er emission cannot be excited with pump wavelengths longer than 986 nm. As a result, it can be assumed that the low energy edge of the $^4I_{11/2}$ state is at ~ 1.2575 eV.

In quartz, excitation of the Er³⁺ is achieved by optical pumping—each laser wavelength can selectively excite some Er centres having an energy of the $^4I_{11/2}$ state at

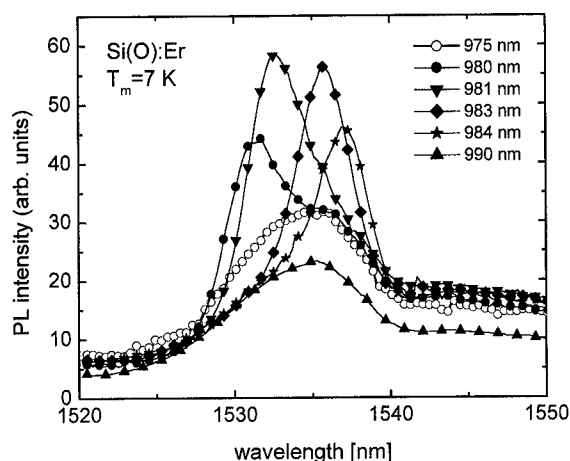


Fig. 2. Site-selective PL spectra of Er³⁺ in laser ablated silicon.

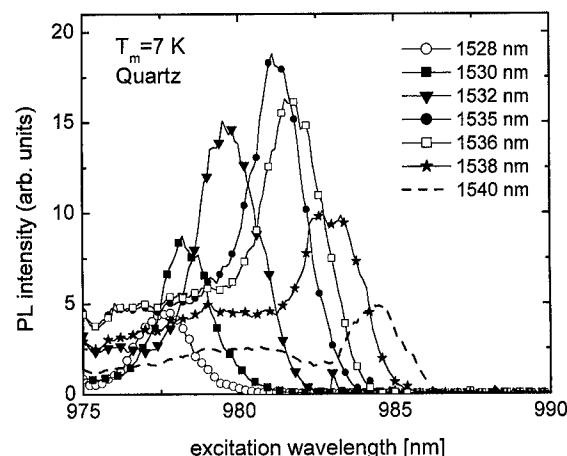


Fig. 3. PLE spectra of Er³⁺ ions in quartz implanted and annealed at 800°C.

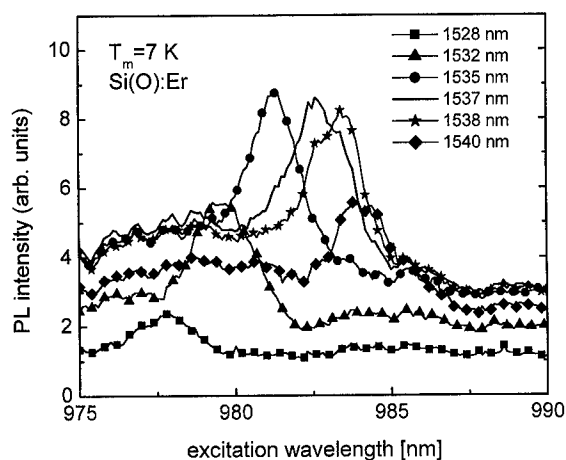


Fig. 1. PLE spectra of Er³⁺ in laser ablated silicon at 7 K.

resonance with the laser [12]. Then multi-phonon relaxation to the $^4I_{13/2}$ state of the originally excited ion takes place followed by emission near 1.5 μm . Since at low temperatures phonon-absorption-assisted excitation of Er ions is not possible, the centres having energies of their $^4I_{11/2}$ state higher than the pump light energy, by principle, cannot be excited. Therefore, a long-wavelength cut-off dependent on the λ_{det} is observed in the PLE spectra (Fig. 3).

The PLE spectra and selectively excited luminescence of erbium show that two excitation mechanisms of Er^{3+} are active. The first one is responsible for the dependence of the PL on λ_{exc} and λ_{det} . This is typical of site-selective excitation of Er ions in glasses and quartz [12,13]. The similarities in the PLE spectra in Figs. 1 and 3 indicate that the local atomic environment around Er ions in quartz and in Si(O):Er are similar. This finding supports our earlier suggestion that Er ions in Si(O):Er are located inside oxygen-rich clusters, presumably within micro- or nano-precipitates of SiO_x . Taking into account the composition of the layers ($\text{Si:O} \sim 1:1$) and the absence of sharp lines typical for the luminescence of Er^{3+} in crystalline Si at low temperatures [11], this conclusion appears to be justified. A larger inhomogeneous broadening of the PL bands in the oxygen-rich silicon implies a much larger variety of Er centres as compared to quartz. Such a location explains also the low temperature quenching of the Er PL [10].

The second excitation process is responsible for the constant background in the PLE spectra (Fig. 1) and the broad emission observed for selectively excited PL (Fig. 2). It can be attributed to the excitation via the band edge of silicon. As excitons are formed in a silicon rich phase or in Si micro-precipitates, which have a band gap E_g equal to that of bulk Si, only an excitation to the $^4I_{13/2}$ of Er^{3+} state is possible due to non-radiative energy transfer from excitons. The efficiency of such a process practically does not depend on the excitation wavelength in this relatively narrow range of 960–1000 nm, since the absorption cross-section of a-Si is almost constant there.

4. Summary

The results of PLE and selectively excited PL measurements prove that Er ions in oxygen-rich silicon are located inside silicon oxide clusters as they reveal, at

least in part, the behaviour typical of rare earth dopants in glasses. We also show that for such a location two excitation mechanisms of Er ions are possible: (i) resonant optical excitation to the $^4I_{11/2}$ state, which is responsible for fluorescence line narrowing, and (ii) excitation via the band edge of silicon to the $^4I_{13/2}$ state. The latter process is responsible for broad luminescence in selectively excited PL and a constant background in the PLE spectra.

Acknowledgements

This work is supported in Poland by the State Committee for Scientific Research (grant No. 7 T11B 007 21) and in Austria by the FWF, GMe, and ÖAD.

References

- [1] S. Coffa, G. Franzo, F. Priolo, *Mater. Res. Soc. Bull.* 23 (1998) 2325.
- [2] G. Franzo, F. Priolo, S. Coffa, A. Carnera, *Phys. Rev. B* 57 (1998) 4443.
- [3] J. Michel, J.L. Benton, R.F. Ferrante, D.C. Jacobson, D.J. Eaglesham, E.A. Fitzgerald, Y.-H. Xie, J.M. Poate, L.C. Kimerling, *J. Appl. Phys.* 70 (1991) 2672.
- [4] P.N. Favenec, H. l'Haridon, D. Moutonnet, M. Salvi, M. Gauneau, *Material Research Society Symposium Proceedings*, Vol. 301, 1993, p. 181.
- [5] T. Kimura, A. Yokoi, H. Horiguchi, R. Saito, T. Ikoma, A. Sato, *Appl. Phys. Lett.* 75 (1999) 3989.
- [6] G. van den Hoven, J.H. Shin, A. Polman, S. Lombardo, S.U. Campisano, *J. Appl. Phys.* 78 (1995) 2642.
- [7] S. Lombardo, S.U. Campisano, G.N. van den Hoven, A. Cacciato, A. Polman, *Appl. Phys. Lett.* 63 (1993) 1942.
- [8] Wai Lek Ng, M.P. Temple, P.A. Childs, F. Wellhofer, K.P. Homewood, *Appl. Phys. Lett.* 75 (1999) 97.
- [9] S. Lanzerstorfer, L. Palmetshofer, W. Jantsch, J. Stimmer, *Appl. Phys. Lett.* 72 (1998) 809.
- [10] W. Jantsch, S. Lanzerstorfer, L. Palmetshofer, M. Stephikova, H. Preier, *J. Lumin.* 80 (1999) 9.
- [11] H. Przybylińska, W. Jantsch, Yu. Suprun-Belevitch, M. Stephikova, L. Palmetshofer, G. Hendorfer, A. Kozanecki, R.J. Wilson, B.J. Sealy, *Phys. Rev. B* 54 (1996) 2532.
- [12] A.M. Jurdyc, B. Jacquier, J.C. Gâcon, J.F. Bayon, E. Delavaque, *J. Lumin.* 6061 (1994) 89.
- [13] A. Kozanecki, M. Stephikova, S. Lanzerstorfer, W. Jantsch, L. Palmetshofer, B.J. Sealy, C. Jeaynes, *Appl. Phys. Lett.* 66 (1995) 115.



ELSEVIER

Physica B 308–310 (2001) 357–360

PHYSICA B

www.elsevier.com/locate/physb

Erbium excitation across the bulk of silicon wafer: an effect of p–n junction at Si/Si:Er interface

N.Q. Vinh^{a,*}, I.N. Yassievich^b, T. Gregorkiewicz^a

^a Van der Waals—Zeeman Institute, University of Amsterdam, 65 Valckenierstraat, NL-1018 XE Amsterdam, Netherlands

^b A.F. Ioffe Physico-technical Institute, Russian Academy of Sciences, 194021 St. Petersburg, Russia

Abstract

It is known that emission from Er ions implanted into a silicon wafer can be excited by illumination of the non-implanted side of the sample. In such a configuration, energy has to be transferred across the entire thickness of the sample (300–500 μm), which exceeds by two orders of magnitude absorption depth of a 514.5 nm line of an Ar ion laser. We have shown that for the non-implanted side illumination configuration, the energy transfer process leads to a delay in the onset of Er photoluminescence signal, whose magnitude depends on the excitation power. In the present contribution, we investigate the microscopic mechanism responsible for this delay. We postulate that it can be related to exciton dissociation at a p–n junction created by Er doping at a Si/Si:Er interface. We confirm this hypothesis by showing that the actual value of the delay time can be tuned by a bias voltage applied to the junction. © 2001 Elsevier Science B.V. All rights reserved.

Keywords: Photoluminescence; Silicon; Erbium

1. Introduction

Erbium doping of silicon has recently become an extensively studied subject. The rare-earth erbium, when incorporated in silicon in the trivalent charge state, shows characteristic luminescence from an intra-4f transition at a wavelength of 1.54 μm . This emission can be observed both under optical or electrical excitation. This optical doping technique seems to be a promising way around the problem of the indirect band gap of silicon. If sufficiently high Er concentrations could be incorporated and activated, it would become possible to fabricate light emitting diodes, lasers, or optical amplifiers, based on silicon. This would enable the integration of optical and electronic technologies on the same chip. Therefore, a thorough understanding of the microscopic process responsible for the energy

transfer between the crystalline silicon matrix and the 4f-electron core of Er ions is of prime importance.

Some time ago it was reported that Er PL can be generated from the Er-implanted crystalline silicon wafer under conditions when the laser beam operating in the visible region is pointed at the non-implanted side of a wafer [1]. In such a configuration, excitation is absorbed at a distance of 350–500 μm from the Er-doped layer. Careful investigation [2] showed that PL spectra obtained under implanted and non-implanted side excitation were identical in their structure. Therefore, the same optically active centers are excited in both experimental configuration, i.e., excitation diffusion across the bulk of the material does not influence the “final” excitation mechanism responsible for the energy transfer to the rare-earth ion core. From the measurements of the kinetics of the process, it has been found out that for the non-implanted side excitation, the Er-related PL signal appears with a considerable delay of the order of a few milliseconds with respect to the excitation pulse. The actual magnitude of this delay was

*Corresponding author. Tel.: +31-20-525-5644; fax: +31-20-525-5788.

E-mail address: nguyen@science.uva.nl (N.Q. Vinh).

found to depend on the laser power. While the appearance of Er-related PL upon the backside illumination is normally attributed to long-range exciton diffusion, the observed long delay time was inconsistent with that model. Taking into account the appropriate material parameters, i.e., exciton life time and diffusion constant, a delay of a few microseconds can be expected, clearly at variance with the experiment.

In the current contribution, we explore the exciton dissociation at a p–n junction at Si/Si:Er interface as a possible mechanism responsible for the observed delay. We report that the actual value of the delay time can be changed by bias voltage applied to the junction.

2. Experimental

The experimental configuration used in this study is illustrated in Fig. 1. It allowed for an easy change between excitation of either the implanted side or the backside of the sample, while a DC voltage (–10 to +10 V) could be applied by electrical contacts on both surfaces. In both excitation modes, PL was collected from the Er-implanted side. The experiments were performed in a closed cycle cryostat in the temperature range between $T \approx 15$ and 150 K. An on–off modulated (25 Hz) argon laser operating at $\lambda = 514.5$ nm was used as an excitation source. The emerging PL signal was monitored with a high-sensitivity germanium detector (Edinburgh Instruments).

The investigation was conducted for a low-energy (300 keV, 3×10^{12} cm $^{-2}$ dose) Er-implanted oxygen-rich p-type (B-doped) Cz–Si wafer of approximately 350 μ m thickness. The sample was also co-implanted with oxygen (40 keV, 3×10^{13} cm $^{-2}$ dose) and annealed at 900°C in a nitrogen atmosphere for 30 min.

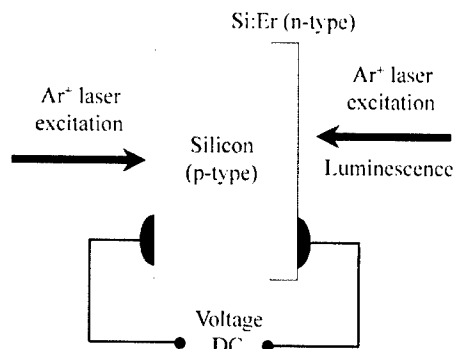


Fig. 1. Experiment allowing for excitation either of surface of the sample or electrical bias. Photoluminescence is detected from the Er-implanted side of the sample.

3. Results and discussion

For the sample used in the investigations, a strong PL spectrum was observed under different excitation conditions. Fig. 2 compares PL spectra obtained with and without electrical bias. As can be seen, spectral structure is not influenced by the bias and conclude that the same Er-related optical centers are activated under conditions of different electrical bias, as used in the present study.

We will first consider the case of excitation by a green laser pointed at the wafer side opposite to the Er-implanted layer. In this case, the relevant parameters are as follows: photon energy $h\nu = 2.4$ eV, absorption coefficient $\alpha = 10^4$ cm $^{-1}$, and pumping intensity $I = 3 \times 10^{16}$ cm $^{-2}$ s $^{-1}$. To analyze the exciton diffusion at distance s , we should solve the diffusion equation with a source of excitons near the surface ($x = 0$)

$$\frac{\partial N_{\text{ex}}}{\partial t} = D \frac{\partial^2 N_{\text{ex}}}{\partial x^2} - \frac{N_{\text{ex}}}{\tau_{\text{ex}}} + \alpha I g(t) \exp(-\alpha x) \quad (1)$$

for a continuous pumping

$$\frac{\partial N_{\text{ex}}}{\partial x} = 0 \quad \text{at } x = 0. \quad (2)$$

From this, we can get the exciton density flux $j_{\text{ex}}(x, t) = -D \partial N_{\text{ex}} / \partial x$ at $x = s \gg x^{-1}$ [3,4]:

$$j_{\text{ex}}(s, t) = \frac{I}{\sqrt{\pi}} \int_0^{t/\Delta t} dz \frac{1}{z^{3/2}} \exp \left[-\left(\frac{1}{z} + \frac{s^2}{4L^2} z \right) \right]. \quad (3)$$

Here N_{ex} , D , and τ_{ex} are the exciton concentration, diffusion coefficient, and the exciton lifetime, respectively. We introduce parameter $\Delta t = s^2/4D$ and the diffusion length of the excitons $L = \sqrt{D\tau_{\text{ex}}}$. The parameter Δt determines the diffusion-related time delay, i.e., the time necessary for an exciton to arrive at distance s due to diffusion. For a reasonable parameter value of $D = 90$ cm 2 s $^{-1}$ [5], the time delay $\Delta t = s^2/4D$ due to diffusion for the distance of

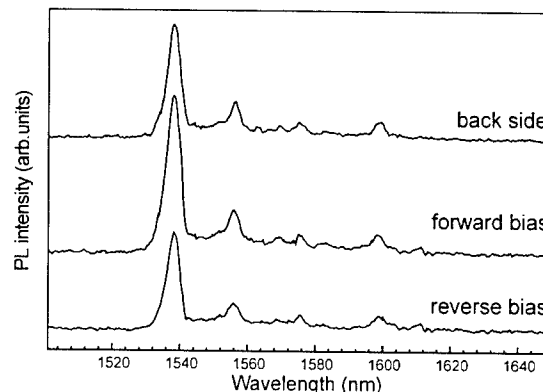


Fig. 2. PL spectra obtained for non-implanted side excitation with and without electrical bias.

$s \approx 350 \mu\text{m}$ is about $3.5 \mu\text{s}$, which is two order of magnitude faster than observed in the experiment.

Having excluded exciton diffusion across the silicon wafer as a possible reason for the long delay time observed in appearance of PL signal, we will now consider charge accumulation at Si/Si:Er interface as an alternative mechanism. Indeed, it is generally accepted [6] that erbium implantation into oxygen-rich silicon leads to the formation of donor centers with ionization energies in the $0.1\text{--}0.25 \text{ eV}$ range and concentration comparable to that of Er ions. Since the sample under investigation was prepared from p-type Si ($[B] = 10^{15} \text{ cm}^{-3}$) and the Er concentration in the implanted layer is $\sim 10^{18} \text{ cm}^{-3}$, a p-n junction should occur in equilibrium at the boundary with the Er-implanted layer. The excitons arriving at the p-n junction will therefore experience the electric field related to the depletion layer formation. In this field, whose value can reach 10^4 V/cm , the exciton will be divided into electrons and holes. These will gradually accumulate at a junction lowering the potential. Excitons will start to appear in the Er-doped layer and excite Er only after the depletion region has been removed due to charge compensation. We can expect that this effect can be influenced by biasing the junction. As illustrated in Fig. 3, the actual delay time can indeed be reduced under the forward bias condition, the effect being very similar to the earlier reported delay reduction upon increase of excitation density [2]. Fig. 4 shows in detail how the experimentally measured delay time can be turned by the electrical bias applied to the junction. For the purpose of this experiment, contacts were made with silver paste on the opposing faces of the sample, which was then placed in the low-temperature experimental set-up allowing for measurements in the two illumination configurations. In addition, DC voltage from a stabilized power supply could now be applied,

providing electric field across the thickness of the sample. Prior to the PL experiment, we measured the low-temperature I - V characteristics of the sample. The result, also depicted in Fig. 4, confirms that Er implantation into a p-type silicon substrate results in p-n junction formation. We then proceeded to investigate the PL signal delay time in the backside illumination configuration and under the applied bias. While the Er-related PL spectrum did not change (see Fig. 2), the kinetics of the signal were clearly influenced by the bias. As can be seen, under conditions of reverse bias the delay time can be increased as the depletion region increases; the delay time can be brought down to zero under forward bias. Following our interpretation, the applied forward bias reduces the depletion region to a level at which excitons diffusing towards the Er-implanted layer are no longer destroyed.

In order to evaluate quantitatively if the junction effect can account for the observed delay, we have to estimate the time necessary to compensate the change in the depleted region. The width of the depletion region is controlled by boron doping, and at low temperatures is given by

$$W \approx \sqrt{\frac{\epsilon(E_g - (E_D + E_B)/2)}{2\pi e^2 N_B}}, \quad (4)$$

where E_g is the energy gap, E_D and E_B are the binding energies of the Er-related donors and boron acceptors, respectively, e is the electron charge, and ϵ is the dielectric constant of silicon. The calculated depletion region of about $1 \mu\text{m}$ is situated predominantly in the p-type layer. The negative charge ($-N_B W$) is accumulated in the depletion region of the p-type layer, and the same positive charge ($+N_D W_D = N_B W$) is in the n-type layer.

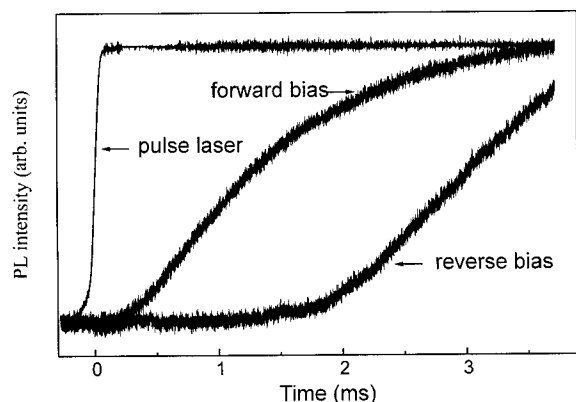


Fig. 3. Time development of the Er-related PL signal under non-implanted side excitation with electrical bias. The laser pulse is also shown.

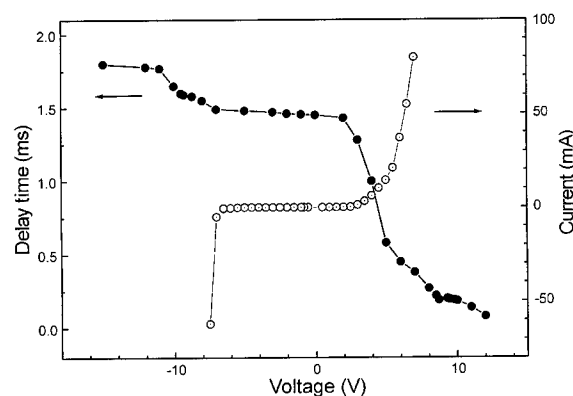


Fig. 4. Delay time of the Er PL observed for non-implanted side excitation as a function of electrical bias, and I - V characteristics of the (p-type) sample used in the experiment.

The time δt which is needed for the destruction of the p–n junction can be found from the equation

$$\int_0^{\delta t} dt j_{\text{ex}}(s, t) = N_B W, \quad (5)$$

where $j_{\text{ex}}(s, t)$ is given by Eq. (3). Assuming the fast diffusion process, we can use the equilibrium formula for finding the delay time δt

$$\delta t \frac{\sqrt{\pi}}{2\sqrt{2}} I \exp(-s/L) = N_B W. \quad (6)$$

From here the diffusion length L can be estimated. With the experimentally obtained value of the delay time δt in the millisecond range, we get $L \approx 60 \mu\text{m}$. Such a diffusion length corresponds to an exciton lifetime of $\tau_{\text{ex}} \approx 0.4 \mu\text{s}$. In our experiment, the lifetime of the free excitons is controlled by capture at neutral boron acceptors. This assumption is supported by the observation of bound exciton luminescence for non-implanted side excitation. In this case, we have

$$\frac{1}{\tau_{\text{ex}}} = N_B \sigma_{\text{ex}} \langle v \rangle, \quad (7)$$

where $\langle v \rangle$ and σ_{ex} are the thermal velocity and capture cross-section of free excitons, respectively. The calculated exciton lifetime corresponds to $\sigma_{\text{ex}} \approx 1.2 \times 10^{-15} \text{ cm}^2$, which is a reasonable value. Therefore, we conclude that the presence of the p–n junction can lead to the observed delay time.

4. Conclusions

The characteristic $\lambda = 1.54 \mu\text{m}$ emission of Er^{3+} ions implanted into a silicon wafer is excited by an Ar laser

pointed at the non-implanted side of the sample. In this experimental configuration, energy is transferred across the bulk of a Si wafer before reaching the Er-doped layer. It is found that the exciton diffusion across a p–n junction created by Er doping at the Si/Si : Er interface leads to a considerable delay between the excitation pulse and the appearance of Er-related PL. This is caused by the time necessary to accumulate charge to compensate the voltage at the junction and prevent dissociation of arriving excitons. It is shown that the particular value of this delay time can be changed by application of electric bias to the junction. Results of the research confirm that excitons are responsible for Er excitation in crystalline silicon at cryogenic temperatures.

Acknowledgements

This work was supported by grants from NATO (Linkage) and Nederlandse Organisatie voor Wetenschappelijk Onderzoek (NWO).

References

- [1] J. Michel, et al., J. Appl. Phys. 70 (1991) 2672.
- [2] B. Pawlak, et al., Mater. Sci. Eng. B 81 (2001) 59.
- [3] P.M. Chaikin, T.C. Lubensky, Principles of Condensed Matter Physics, Cambridge University Press, Cambridge, New York, Melbourne, 1995, p. 369.
- [4] B.J. Pawlak, et al., Phys. Rev. B 64 (2001) 132202.
- [5] M.A. Tamor, et al., Phys. Rev. Lett. 44 (1980) 1703.
- [6] G. Franzò, et al., Appl. Phys. Lett. 64 (1994) 2235.



ELSEVIER

Physica B 308–310 (2001) 361–364

PHYSICA B

www.elsevier.com/locate/physb

Electrically active centers in light emitting Si:Er/Si structures grown by the sublimation MBE method

V.B. Shmagin^{a,*}, B.A. Andreev^a, E.N. Morozova^a, Z.F. Krasil'nik^a,
D.I. Kryzhkov^a, V.P. Kuznetsov^b, E.A. Uskova^b, C.A.J. Ammerlaan^c, G. Pensl^d

^a *Institute for Physics of Microstructures, Russian Academy of Sciences, 603950 Nizhny Novgorod GSP-105, Russia*

^b *Nizhny Novgorod State University, Gagarin Avenue 23, 603600 Nizhny Novgorod GSP-105, Russia*

^c *Van der Waals-Zeeman Institute, University of Amsterdam, Valckenierstraat 65, 1018 XE Amsterdam, Netherlands*

^d *Institute of Applied Physics, University of Erlangen-Nurnberg, Staudtstrasse 7, Gebäude A3, D-91058 Erlangen, Germany*

Abstract

The electrically active centers in light-emitting Si:Er/Si structures grown by an original sublimation MBE (SMBE) method are investigated using admittance spectroscopy and deep level transient spectroscopy. It is shown that free carrier concentration in investigated structures is determined by shallow donors with ionization energies varying from 0.016 to 0.045 eV. The essential difference between deep level defects observed in SMBE Si:Er/Si structures and in Si:Er/Si structures produced by ion implantation is revealed. The causes of observed distinctions between electrical and optical properties of SMBE structures as well as distinctions between SMBE and ion implanted Si:Er/Si structures are discussed. © 2001 Elsevier Science B.V. All rights reserved.

Keywords: Sublimation MBE; Si:Er/Si structures; Electrically active centers

1. Introduction

Silicon doped with erbium has been attracting attention as promising material for producing effective light emitters radiating in the range of the maximal transparency of silica glass optical fibers ($\lambda \approx 1.5 \mu\text{m}$). Recently, there were demonstrated Si:Er/Si structures with rather high photo- (PL) and electroluminescence (EL) including PL and EL at room temperature produced with an original sublimation MBE method (SMBE)—MBE variant, in which molecular flows of Si and Er are formed using sublimation of Si crystal initially doped with Er and other necessary dopants [1–4].

We report here on electrically active centers detected in light-emitting SMBE Si:Er/Si structures and their transformation caused by post-growth heat treatment. The observed distinctions between electrical and optical

properties of SMBE structures as well as distinctions between SMBE and ion implanted Si:Er/Si structures are discussed.

2. Experimental

We investigated uniformly doped Si:Er/Si structures grown on n-Si and p-Si substrates with (100) orientation and specific resistivity of 20, 10 and $0.005 \Omega\text{cm}$. The sublimating sources were plates cut from Si:Er ingots with Er and O contents up to 5×10^{20} and $1 \times 10^{19} \text{cm}^{-3}$, respectively. The growth temperature varied from 400 K up to 600 K and the thickness of the layers from $0.2 \mu\text{m}$ up to $3 \mu\text{m}$. The post-growth annealing of the structures was carried out at $T = 900 \text{ K}$ in H_2 atmosphere.

Energy levels in the band gap of Si were investigated using DLTS and admittance spectroscopy at the temperature range from 10 to 350 K. Admittance measurements were conducted in a frequency range

*Corresponding author. Tel.: +7-831-267-5037; fax: +7-831-267-5553.

E-mail address: shm@ipm.sci-nnov.ru (V.B. Shmagin).

from 100 Hz to 1 MHz. The conductance and capacitance components of the current passing through the sample under investigation were taken by synchronous detection of the signal. DLTS measurements were performed at 400 kHz using double boxcar integrating technique [5]. Combining DLTS and admittance measurements has allowed us to identify both shallow and deep levels.

Schottky contacts were prepared by thermal evaporation of Pd onto the sample surface at 6×10^{-6} torr. The ohmic contact was prepared by rubbing an In–Ga alloy onto the back surface of the sample or evaporating a Schottky contact of large size (Si:Er layers on high-resistance p-Si substrates).

3. Results and discussion

All investigated SMBE Si:Er layers were n-type, irrespective of the growth temperature and annealing conditions. The free carrier concentration as it was shown by admittance measurements was 10^{16} – 10^{18} cm $^{-3}$ at $T = 300$ K and was determined by shallow centers with ionization energies of 0.016–0.045 eV. The background contamination introduced by the apparatus during SMBE process was near 2×10^{13} cm $^{-3}$ [4,6]. Note that this estimation does not take into account the residual impurities containing in Si:Er sources.

The admittance spectra $C(T)$ and $G(T)$ shown in Fig. 1 are taken at zero bias and test signal frequency of 80.6 kHz. Note that the peak in $G(T)$ and the step in $C(T)$ are caused by freezing out of the carriers in the neutral region of Schottky diode and the corresponding enhancement of its resistance which is inserted in turn with the capacitance of the space charge region. The change of test frequency results in a shift of the observed admittance spectra along the temperature axis. At the bottom of Fig. 1 an Arrhenius plot is given. The ionization energy obtained from the slope of the Arrhenius plot has the value of 0.016 eV. During data processing, we have considered the temperature dependence of the effective density of states in the conduction band $N_c(T) \sim T^{3/2}$ neglecting the temperature dependence of the carrier mobility.

The type of conductivity fixed by these shallow centers and their forming conditions encourage to relate them to thermal donors—oxygen-defect complexes formed in Si crystals under heat treatment. The role of Er in forming these centers is not clear up to now. Probably, the Er atoms because of their greater size in comparison with Si atoms introduce appreciable distortions to the Si lattice and accelerate thermal donor formation [7]. There are distinctions between the ionization energies of shallow levels observed in SMBE layers grown from various Si:Er sources. Probably, they are caused by distinctions in impurity contents of different Si:Er sources, espe-

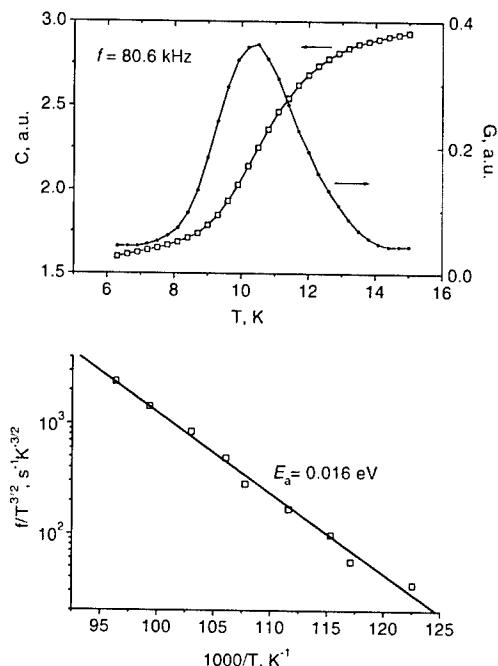


Fig. 1. Admittance spectra of shallow impurities in SMBE Si:Er/Si structure. The spectra are taken at frequency $f = 8 \times 10^2$ to 8×10^4 Hz and $U_{\text{bias}} = 0$.

cially it concerns such impurities as C, N, O which may be involved in the observed shallow defects.

A deep defect concentration is rather low in investigated SMBE structures. As-grown layers show usually a relative trap density $N_T/(N_D - N_A) < 0.1$. The ionization energies are in the range of 0.15–0.45 eV (Fig. 2). Their concentrations do not depend on the type of the used substrate and depend strongly on the growth and annealing conditions. Trap concentrations are maximal in layers grown at lower temperature ($T_{\text{growth}} < 500$ K) and decrease with increase of T_{growth} . The distinctive feature of these defects is that they are completely annealed by an additional post-growth heat treatment in particular by an annealing at 900 K during 30 min in H_2 atmosphere. In contrast, the post-growth annealing at the same conditions causes the transformation of light emitting centers but does not destroy the PL as a whole (Fig. 3). The PL connected with Er^{3+} passes through the minimum at $T_{\text{annealing}} = 750$ K and then strongly increases up to $T_{\text{annealing}} = 900$ K. It concludes that above mentioned deep electrically active centers do not participate in the energy transfer to Er^{3+} ions. Most likely, they are related to growth defects.

This is the most essential difference between the electrically active centers observed in SMBE and implanted Si:Er/Si layers. In implanted layers, one detects deep levels in the range of 0.1–0.3 eV including

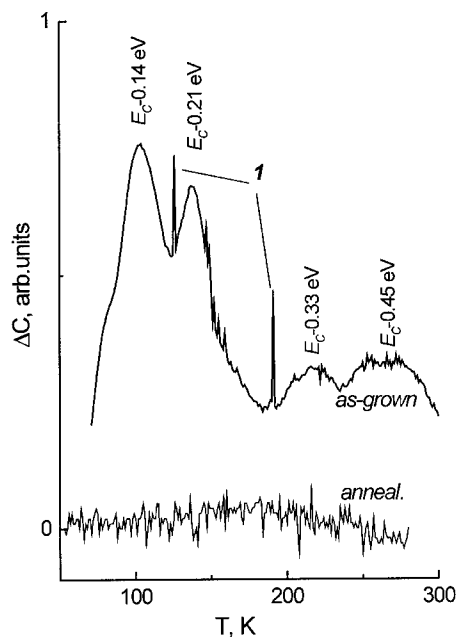


Fig. 2. DLTS spectra of a SMBE Si:Er/Si structure as-grown and after annealing ($T_{\text{growth}} = 430$ K, annealing conditions: 900 K, 30 min., H_2). The DLTS spectra are taken at $\tau_{\text{window}} = 0.6$ ms, $U_{\text{bias}} = -2$ V. 1—calibration pulses, the amplitude of calibration pulse is $\Delta C = 10^{-3} \times C$, where C is the diode capacitance at the temperature of calibration.

the level $E_c - 0.15$ eV which according to nowadays concepts is responsible for the transfer of energy to Er^{3+} [8]. In SMBE layers despite of the intensive PL connected with erbium we could not detect deep levels in the same energy range. We have summarized below some results obtained from capacitance and PL experiments with the Si:Er/Si structure uniformly doped with Er in SMBE process and revealing the intensive PL at liquid helium temperature. Its parameters are as follows: the substrate is Si:B, $20 \Omega \text{ cm}$; T_{growth} is 500°C ; the Si:Er layer width is $\sim 2.7 \mu\text{m}$; the structure was annealed at 800°C (30 min, H_2). Free carrier concentration slightly increases from 3×10^{16} on the surface to $2 \times 10^{17} \text{ cm}^{-3}$ in the interior of the Si:Er layer; Er and O concentrations determined from SIMS measurements are 1×10^{18} and $3 \times 10^{19} \text{ cm}^{-3}$ accordingly. The concentration of optically active centers related to erbium $N_{\text{Er}}^{\text{opt}}$ estimated from PL measurements is $2 \times 10^{16} \text{ cm}^{-3}$ [9]. On the other hand, the concentration of electrically active centers with the ionization energy in the range of 0.1–0.3 eV that could participate in the transfer of energy to Er^{3+} ions (via the mechanism of an exciton capture [8]) $N_{\text{Er}}^{\text{el}} < 1 \times 10^{13} \text{ cm}^{-3}$ (DLTS data). So, huge distinction between $N_{\text{Er}}^{\text{opt}}$ and $N_{\text{Er}}^{\text{el}}$ revealed in this experiment indicates that most probably the additional channels of energy transfer to Er^{3+} ions take place in

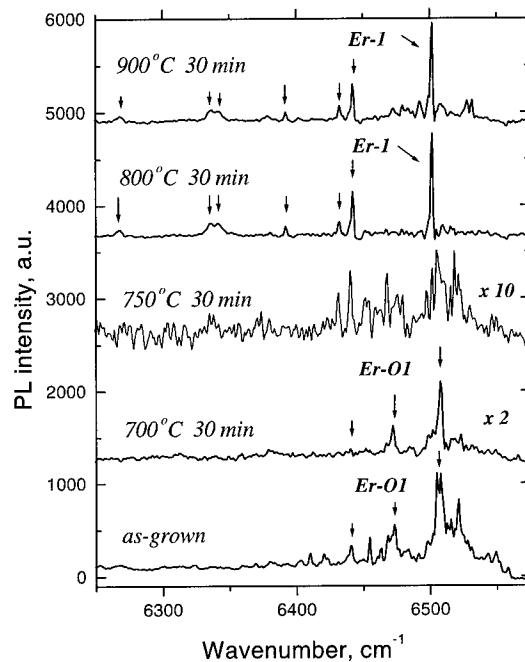


Fig. 3. PL spectra of uniformly doped Si:Er/Si structure depending on $T_{\text{annealing}}$. $T_{\text{growth}} = 430$ K [3].

SMBE Si:Er/Si structures in comparison with ion implanted ones.

4. Conclusions

In this contribution, we have presented the investigation of electrically active centers in Si:Er/Si structures produced by an original SMBE method. We have shown that the free carrier concentration is determined by shallow donors with ionization energy of 0.016–0.045 eV. The most unexpected result is that we have not yet detected any electrically active centers responsible for the energy transfer to Er^{3+} ions in investigated SMBE structures. So, we assume the presence of complementary channels in SMBE structures for the energy transfer to Er^{3+} ions in comparison with ion implanted structures.

Acknowledgements

The authors express their gratitude to Dr. O.A. Kuznetsov for carrying out of annealing procedures with Si:Er/Si structures. This work was supported in part by RFBR (grants # 99-03-32757, # 01-02-16439), INTAS (grant 99-01872) and NWO (grant 047.009.013).

References

- [1] B.A. Andreev, A.Yu. Andreev, H. Ellmer, et al., *J. Crystal Growth* 201/202 (1999) 534.
- [2] M.V. Stepikhova, B.A. Andreev, V.B. Shmagin, et al., *Thin Solid Films* 381 (2001) 164.
- [3] M. Stepikhova, B. Andreev, Z. Krasil'nik, et al., *Mater. Sci. Eng. B* 81/1–3 (2001) 67.
- [4] V.P. Kuznetsov, R.A. Rubtsova, *Semiconductors* 34 (2000) 519.
- [5] D.V. Lang, *J. Appl. Phys.* 45 (1974) 3023.
- [6] V.P. Kuznetsov, A.Yu. Andreev, O.A. Kuznetsov, et al., *Phys. Stat. Sol. A* 127 (1991) 371.
- [7] V.V. Emtsev, V.V. Emtsev Jr., D.S. Poloskin, et al., *Semiconductors* 33 (1999) 1192.
- [8] S. Libertino, S. Coffa, G. Franzo, F. Priolo, *J. Appl. Phys.* 78 (1995) 3867.
- [9] B.A. Andreev, M.S. Bresler, O.B. Gusev, et al., *Izvestiya Akademii Nauk. Ser. Phys.* 65 (2001) 272.



ELSEVIER

Physica B 308–310 (2001) 365–368

PHYSICA B

www.elsevier.com/locate/physb

Light emission from erbium doped nanostructures embedded in silicon microcavities

N.T. Bagraev^{a,*}, A.D. Bouravleuv^a, W. Gehlhoff^b, L.E. Klyachkin^a,
A.M. Malyarenko^a, M.M. Mezdrogina^a, V.V. Romanov^a, A.P. Skvortsov^a

^a A.F. Ioffe Physico-Technical Institute, Russian Academy of Sciences, 26 Polytechnicheskaya ul., 194021 St. Petersburg, Russia

^b Institut für Festkörperphysik, Technische Universität Berlin, D-10623 Berlin, Germany

Abstract

We present the findings of high efficient Er^{3+} -related $^4\text{I}_{13/2} \leftrightarrow ^4\text{I}_{15/2}$ absorption and emission from self-assembled quantum wells (SQW) embedded in silicon microcavities. The microcavities of this art are prepared by the short-time diffusion of boron into the Si(100) wafer doped with erbium. The intraband electron transitions accompanied by tunneling through strongly coupled SQW series are observed to excite the $^4\text{I}_{13/2} \rightarrow ^4\text{I}_{15/2}$ Er^{3+} -intracentre emission that is enhanced in the range of the Rabi splitting revealed by the transmission spectra. © 2001 Elsevier Science B.V. All rights reserved.

Keywords: Self-assembled silicon quantum wells; Erbium-related centres; Luminescence

1. Introduction

The preparation of erbium-doped semiconductor materials in the nanometer scale is recently in progress to yield both high efficiency and speed of light emitters based on the electroluminescence induced by the Er^{3+} -intra-4f-shell transition, $^4\text{I}_{13/2} \rightarrow ^4\text{I}_{15/2}$, near the wavelength equal to $1.54\mu\text{m}$ that corresponds to minimal losses in optical fibers. Porous Si [1] and quantum dots in self-assembled silicon quantum wells (SQW) [2] that are doped with erbium appear to provide a spatial confinement of non-equilibrium electrons and holes near the erbium-related centres to enhance the excitation of the Er^{3+} -ions. Besides, the Er^{3+} -related intracentre luminescence is enhanced from the ions incorporated into the microcavities tuned in the range of the $^4\text{I}_{13/2} \rightarrow ^4\text{I}_{15/2}$ transitions [3]. Here we report on high efficient electroluminescence from erbium doped SQW that are embedded in silicon microcavities revealed by

the transmission spectra, which is caused by strong coupling the Er^{3+} -ion f-electron states to the s-p electronic states of the host nanostructure.

2. Methods

The silicon (100) wafers of the n- and p-type were doped with erbium in the process of long-time diffusion accompanied by surface injection of vacancies. Erbium doping was done at the diffusion temperature of 1100°C on the working side of the wafers after covering the oxide overlayer with a mask and performing the subsequent photolithography. Then, short-time diffusion of boron and phosphorus was performed at the diffusion temperature of 800°C from gas phase under fine surface injection of primary defects, which leads to the ultra-shallow p^+-n and n^+-p junctions ($\cong 10\text{nm}$) controlled using the SIMS and STM techniques.

The cyclotron resonance (CR) angular dependencies show that the p^+ - and n^+ -diffusion profiles consist of SQW divided by heavily doped δ -barriers (Fig. 1). Besides, the self-assembled microdefects of the self-interstitials type that penetrate through the p^+ - and

*Corresponding author. Tel.: +007-812-247-9311; fax: +007-812-247-1017.

E-mail address: impurity.dipole@pop.ioffe.rssi.ru (N.T. Bagraev).

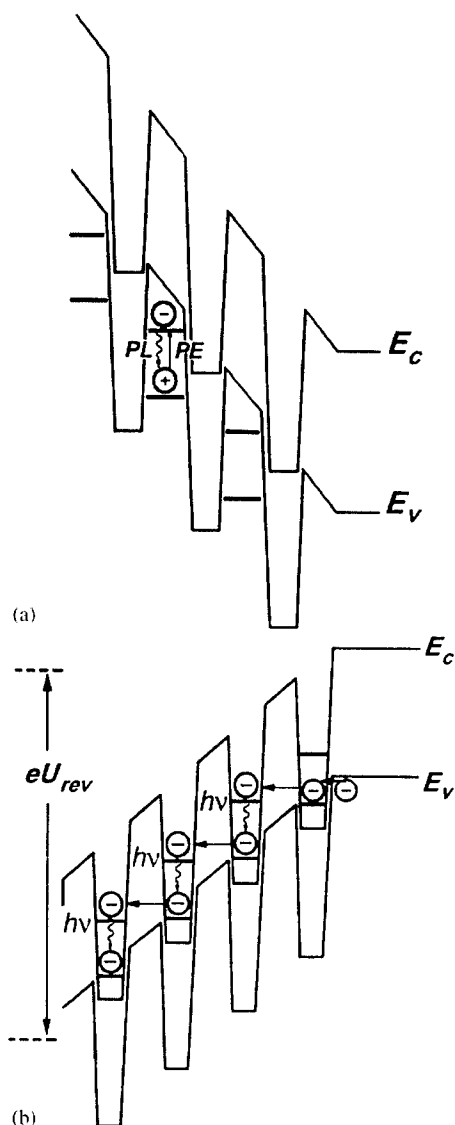


Fig. 1. The energy band diagram of ultra-shallow silicon p^+-n (a) and n^+-p (b) junctions that consist of quantum wells divided by heavily doped δ -barriers.

n^+ -diffusion profiles are found to be prepared by the oxidation and subsequent short time impurity diffusion (Fig. 2). The STM images obtained demonstrate the self-organization of these microdefects in the microcavity system that exhibits a distributed feedback identified by the FIR transmission spectra (Fig. 3).

3. Results

The erbium doped SQW embedded in microcavities obtained were studied using the magnetic susceptibility

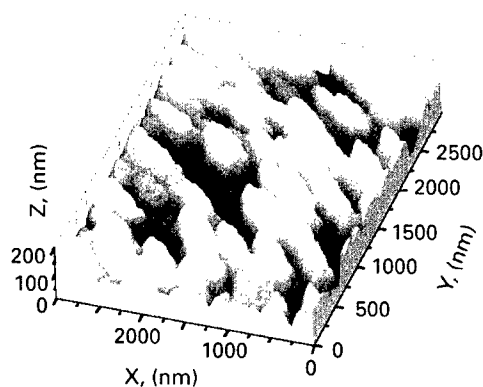


Fig. 2. STM images of the ultra-shallow boron diffusion profiles prepared at diffusion temperature of 800°C into the Si(100) wafer covered previously by thin oxide overlayer. $X \parallel [001]$, $Y \parallel [010]$, $Z \parallel [100]$.

and FIR transmission and electroluminescence techniques. The erbium-related centres inside the SQW have been found to represent the molecular defects, in which the antiferromagnetic erbium pairs bound by the exchange interaction through the action of valence electrons from three oxygen atoms [2]. The temperature and magnetic field dependencies of the magnetic susceptibility demonstrate that the antiferromagnetic erbium pairs being incorporated into SQW exhibit the Van-Fleck paramagnetism enhanced by the interplay between the spin correlations and the electron-vibration interaction [2].

The optically induced intraband transitions in the p^+ -type strongly coupled SQW (Fig. 1a) that are revealed by the angular dependencies of the Rabi splitting in the transmission spectra are observed to cause the Auger excitation of the $^4I_{13/2} \rightarrow ^4I_{15/2}$ Er^{3+} -intracentre absorption (Figs. 3 and 4). The SQW strong coupling seems to be due to the built-in electric field of the ultra-shallow p^+-n junctions which results in the Keldysh effect that is responsible for the spread of the resonance wavelengths up to 1.6 μm (Fig. 3d). Besides, built-in electric field gives rise to the Stark effect that perturbs p - f mixing caused by the 2D hole localisation on the Er-related centres incorporated into SQW [2]. This spatial confinement of the p -states and the localized f -electron states has to be enhanced by the SQW squeezing, which leads to high absorption efficiency at room temperature without any quenching that is a direct consequence of the enlarged range between quantum dimensional states (Figs. 3d and 4). Therefore, the utmost in effective energy transfer is observed owing to the SQW width equal to 2 nm, when the s - p -electron bandgap value is found as being equal to 2.6 eV, that allowed to record the high efficient $^4I_{13/2} \rightarrow ^4I_{15/2}$ electroluminescence from the n -type strongly coupled SQW (Fig. 1b) which is

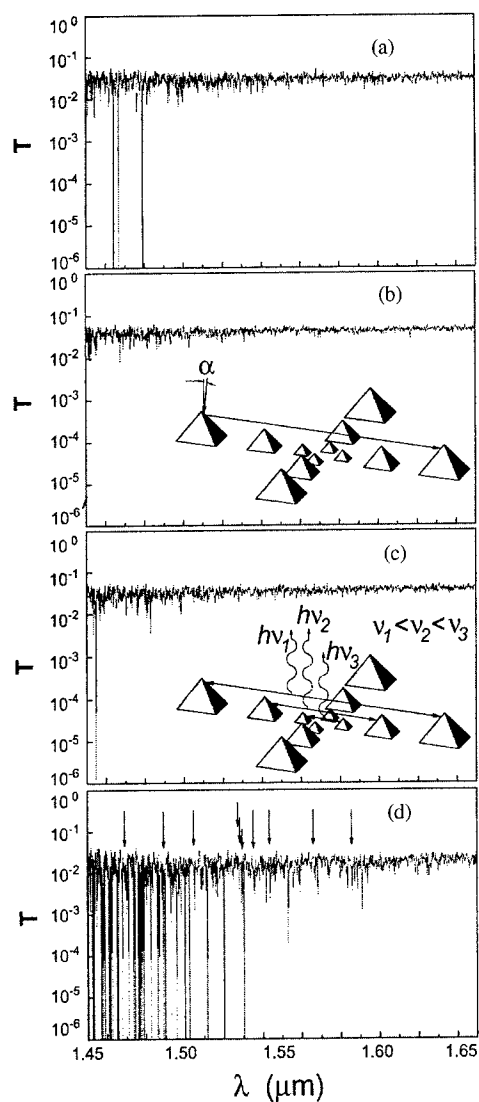


Fig. 3. The transmission spectra measured at different angles between the normal to the Si(100) surface and the light beam, α , that causes the $^4I_{13/2} \rightarrow ^4I_{15/2}$ Er^{3+} -intracenter absorption in the p-type erbium doped SQW embedded in the silicon microcavity. (a) $\alpha = -8^\circ$ (b) $\alpha = +2^\circ$ (c) $\alpha = +7^\circ$ (d) $\alpha = +17^\circ$. The inserts in (b) and (c) depict the model of self-assembled microcavity systems, respectively, in the regimes of the absorption and emission.

characterised by the Er^{3+} -multiplet structure (Fig. 5a). The number of observed EL lines corresponds to the trigonal symmetry of the Er-related centre (Fig. 5b) [2,4]. The $^4I_{13/2} \rightarrow ^4I_{15/2}$ electroluminescence is induced by the application of the reverse bias to the n^+-p junction that causes the electron tunneling from the valence band through the n-type SQW series (Fig. 1b).

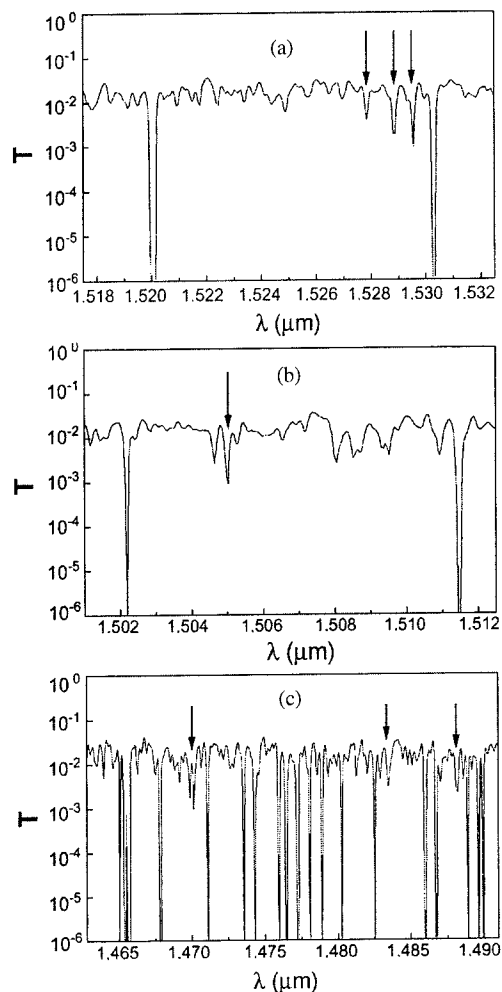


Fig. 4. Spectral dependence of the light transmission coefficient through the p-type erbium doped SQW embedded in the silicon microcavities tuned in the range of the $^4I_{13/2} \rightarrow ^4I_{15/2}$ transitions.

This resonant tunneling is accompanied by the cascade emission which is a basis of the EL excitation which is also enhanced by the Stark effect that appears to mix the Er^{3+} -f-states and the s-states of the SQW. Besides, the resonant electron tunneling through the SQW series results in an oscillating character as a function of the electric field value [2]. The EL oscillations are followed by the electron quantum confinement determined by the dimensions of the silicon nanostructures [2].

4. Conclusions

The high efficient absorption and emission found in the erbium doped silicon self-assembled quantum wells

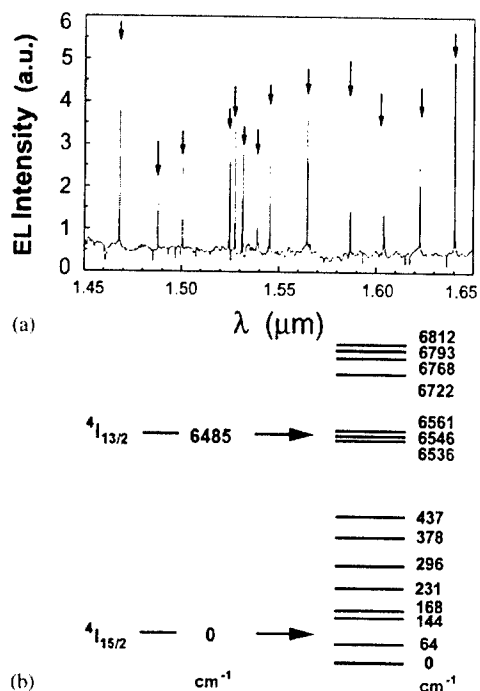


Fig. 5. The electroluminescence spectrum caused by the $4I_{13/2} \rightarrow 4I_{15/2}$ Er^{3+} -intracentre emission from n-type SQW doped with erbium, which are embedded in the silicon microcavity (a). Energy level diagram for the trigonal erbium-related centres that is obtained from the transmission and electroluminescence data (b).

embedded in the microcavity revealed by the transmission spectra has been shown to be due to a fast energy transfer into the 4f-shell transitions of the Er^{3+} -ions that is caused by strong sp-f mixing in built-in electric field.

References

- [1] M. Stepikhova, W. Jantsch, et al., Mater. Sci. Forum 258–263 (1997) 1533.
- [2] N.T. Bagraev, A.D. Bouravlev, W. Gehlhoff, et al., Physica B 273–274 (1999) 967.
- [3] L.C. Kimerling, in: H.G. Grimmeiss, et al., (Eds.), Proceedings of the 8th International Conference "GAD-EST", Scitec Publications, Zurich, 1999, pp. 131–143.
- [4] V.T. Gabrielyan, et al., Phys. Stat. Sol. A 3 (1970) K37.



ELSEVIER

Physica B 308–310 (2001) 369–373

PHYSICA B

www.elsevier.com/locate/physb

Erbium in Si and GaN: extended versus point defects

P.H. Citrin*, D.R. Hamann, P.A. Northrup

Bell Laboratories, Lucent Technologies, Room 3L-403, 600 Mountain Avenue, Murray Hill, NJ 07974, USA

Abstract

Extended X-ray absorption fine structure measurements show that Er defects in O-poor Si closely resemble bulk Er_3Si_5 with long Er–Si bonds, while in GaN, regardless of O content, Er substitutes for Ga sites as point defects with unusually short Er–N bonds. The structure and energetics of these two systems were examined in a series of density functional theory calculations. The detailed findings and excellent agreement with the data provide new insight into the origin of this very different Er-doping behavior. © 2001 Elsevier Science B.V. All rights reserved.

Keywords: Er-doped Si; GaN; EXAFS; Density functional theory

Erbium as a dopant in semiconductor hosts has been studied for more than 15 years [1–4], yet some of the most basic information about the Er structures remains controversial or unexplained. Does Er occupy interstitial or lattice sites in the form of point defects, or are the defects extended in the form of precipitates? How does the formation of Er defects depend on the specific semiconductor host and on the conditions of sample preparation, e.g., epitaxy versus ion implantation, Er concentration, or O impurities? Knowing the type of defect formed, what is its structure?

This paper addresses each of the above questions for the case of two Er-doped semiconductors, Si and GaN, and in the process reconciles a number of conflicting results reported for Er defect structures [5–11]. Our approach uses a combination of extended X-ray absorption fine structure (EXAFS) measurements, density functional theory (DFT) calculations, and simple chemical considerations. Where appropriate, we also make reference to scanning transmission electron microscopy (STEM) measurements discussed in a more extensive study [12]. We find that in O-poor Si, the formation of Er–Si point defects is energetically prohibitive and experimentally not observed.¹ Erbium

in Si forms, instead, extended defects of ErSi_{2-x} platelets, whose structure depends largely on Er concentration. By contrast, Er in GaN occupies Ga sites as point defects whose formation is insensitive to the abundantly present O. We argue that the difference in types of defects observed in Si:Er versus GaN:Er is traceable to the chemical/energetic differences between the metallic Er–Si and ionic Er–N bonds.

The samples measured here were grown by molecular beam epitaxy (MBE) and are the same ones used in previous studies [13,14]. Two Si:Er samples [13] consisted of 0.1- μm -thick films, deposited in a $<5 \times 10^{-11}$ Torr base pressure onto Si(100) substrates at 600°C, with total Er doses of $9 \times 10^{13} \text{ cm}^{-2}$ and $5 \times 10^{14} \text{ cm}^{-2}$. They are referred as high- (*H*) and low-dosed (*L*) samples. Meaningful volume concentrations cannot be established because strong Er surface segregation was observed, i.e., the Er density is non-uniform. The GaN:Er samples [14] consisted of 2.5- μm -thick films, grown on Si(111) substrates at 750°C, with effective volume concentrations ranging between $1\text{--}3 \times 10^{20} \text{ cm}^{-3}$ for Er and $5 \times 10^{18}\text{--}5 \times 10^{20} \text{ cm}^{-3}$ for O. Erbium L_3 -edge absorption measurements were performed at the NSLS using the Bell Laboratories X15B beamline [15]. Samples were cooled $<60 \text{ K}$ to minimize effects of thermal disorder, and data were obtained using Er $L_3\alpha$ fluorescence yield detection.

Theoretical calculations of the structure and energetics of Er in Si were carried out with the pseudopo-

*Corresponding author. Tel.: +1-908-582-5275; fax: +1-908-582-3620.

E-mail address: phc@bell-labs.com (P.H. Citrin).

¹ In O-rich Si, where Er getters O, point defects of ErO_6 -like structure are formed, cf., Ref. [6].

tential plane wave method implemented as Car-Parinello molecular dynamics [16]. The generalized gradient density functional of Perdew, Burke, and Ernzerhof (PBE) [17] was adopted because of its demonstrated ability to produce accurate structural energy differences. The Er pseudopotential was constructed using the electronic configuration $[\text{Xe}]4f^{11}5d^16s^2$ for the all-electron atom and treating the 4f electrons as part of the core using the generalized norm-conserving approach [18]. Non-linear core corrections [19] were included in the exchange-correlation energies. Brillouin zone samples were constructed following the Monkhorst and Pack [20] method, and convergence was tested for representative samples of the various structures considered. A cutoff of 18 Ry for the plane wave basis yielded excellent convergence of structural energy differences.

Fig. 1 shows Fourier transform (FT) regions of the Er L_3 -edge absorption data from the GaN:Er and Si:Er samples and the model compounds ErN and Er_3Si_5 . For clarity, only first nearest-neighbor shells are displayed. Qualitative comparison between the two Er-doped systems is striking, with the first-neighbor bond lengths differing by as much as $\sim 0.8 \text{ \AA}$. Using standard procedures [21] and relevant distances in model compounds, we find the average Er–Si distance in Si:Er is almost 3 \AA long while the Er–N distance in GaN:Er is the shortest measured bond length between Er and any other atom, including H.

Focusing first on Er-doped Si, the filtered, back-transformed EXAFS from the Er–Si shell in the *H* sample of Si:Er (*L* is very similar) is compared with that of Er_3Si_5 in Fig. 2. The Er–Si distance, R , is $\sim 0.04 \text{ \AA}$ longer in Si:Er, and the first-neighbor coordination, N , is $> 80\%^2$ of that in Er_3Si_5 .

A reliable local structure for Er_3Si_5 is needed to quantify R and N in Si:Er. Calculations for bulk Er_3Si_5 were carried out, which proved important beyond obtaining local structure. The results tested the overall accuracy of our methods by comparison with X-ray diffraction data [22], and provided an energy reference so that energies of Er defect structures could be presented relative to the phase-separated bulk materials. As shown in Fig. 3, Er_3Si_5 is a vacancy superlattice based on the AlB_2 structure with one of 6 Si missing from each graphitic-like Si layer [23]. This structure was optimized, yielding lattice parameters that are within 1% of experiment [22]. Internal relaxations relative to the hypothetical ErSi_2 structure in Fig. 3 were found to be substantial, with the 3 Si around the vacancy moving

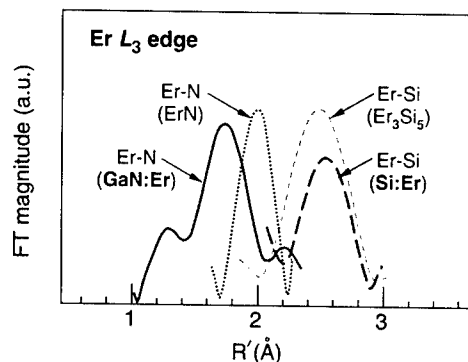


Fig. 1. Selected Fourier-transformed (FT) EXAFS data from Er doped in GaN and Si, along with model compound data. For clarity, only first-neighbor FT peaks are shown.

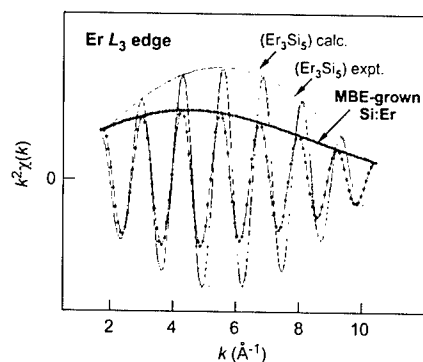


Fig. 2. Filtered EXAFS data from back-transforming the Er–Si FT peaks in Fig. 1. Also shown are simulated Er_3Si_5 data using Er–Si distances calculated here.

inward an average of 0.43 \AA . Such distortions result in a broad distribution of Er–Si bond lengths, $2.88\text{--}3.32 \text{ \AA}$. The individual bond lengths, unavailable from powder diffraction data [22], were used as input for the simulated EXAFS spectrum shown in Fig. 2, giving excellent agreement with experiment. For sample *H*, an average R of $2.97 \pm 0.04 \text{ \AA}$ and $N > 6.5$ are obtained (note that these values are not arithmetic means because nearer shells are preferentially weighted in EXAFS [21]).

Sample *H* was investigated with STEM [12] and found to contain (as originally suggested [13]) silicide precipitates within the film. Additionally, precipitates were found very near the surface where Er had segregated. Sample *L* showed similar signs of predominant silicide precipitates near the surface, but none were found within the film. These results explain why the EXAFS from *L* (not shown) closely resembles that from *H*, and why both *H* and *L* samples resemble Er_3Si_5 . If point defects are present in *L*, they are below experimental detection with STEM.

²This is a lower limit on N because a large fraction of the surface-segregated Er (Ref. [13]) is oxidized upon air exposure, so the total Er absorption used in normalizing N actually reflects coordination to both Si and O (the Er–O FT peak at $R' \approx 1.8 \text{ \AA}$ is not shown in Fig. 1).

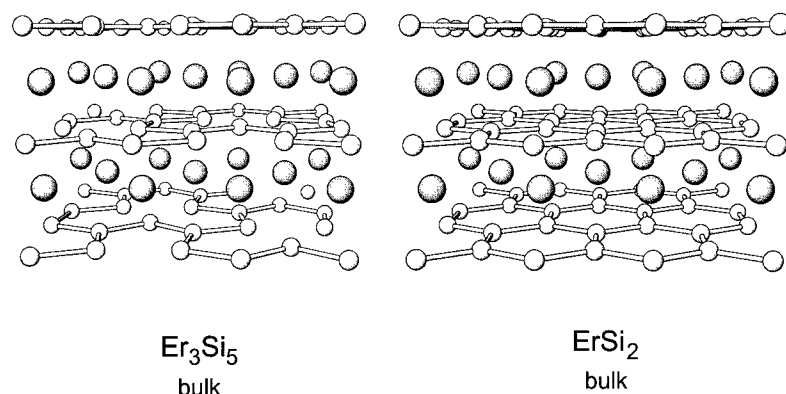


Fig. 3. Comparison between the most stable Er silicide structure containing Si vacancies, Er_3Si_5 , and the hypothetical ErSi_2 structure. For clarity, bonds between Er (dark balls) and Si are omitted.

Table 1

Energies and geometries of extended and point Er–Si structures in order of increasing energy. Δ is the energy per Er referenced to the separated phases of bulk Er_3Si_5 and Si, N is the Si coordination around Er, and R_{avg} is the average Er–Si distance

	Configuration	Δ (eV)	N	R_{avg} (Å)
Bulk	Er_3Si_5	0	10	3.03
	ErSi_2	0.3	12	3.06
Extended 2D Structures	Er–Si _{VAC} –Er bilayer (closed)	0.3	9	3.01
	Er–Si _{VAC} –Er bilayer (hollow)	0.6	8	3.01
	Er monolayer (closed)	0.7	8	3.01
	Er–Si–Er bilayer (hollow)	0.9	9	3.01
	Er monolayer (hollow)	1.2	6	3.01
Point Defects	Er–(vacancy) ₂	3.9	6	2.91
	Er–vacancy	4.3	10	2.96
	Er _{tetr.} interstitial	4.6	10	2.72
	Er _{substitutional}	4.6	4	2.70

Since point defects must exist in the dilute limit, it is natural to ask what the concentration limit is before Er silicide precipitates. Surface segregation for MBE-grown samples at 600°C limits this maximum concentration to $\leq 2 \times 10^{19} \text{ Er/cm}^3$ [13], while Er diffusion upon annealing ion-implanted samples at 900°C for 30 min limits this to $\leq 5 \times 10^{17} \text{ Er/cm}^3$ [12]. Significantly, previous structural work on Er-doped Si [5,6,8–11] all looked at samples with Er concentrations in excess of these limits, meaning that it is the structure of Er in silicide precipitates, not point defects (see footnote 2), which has been studied thus far.

In addition to kinetic processes, it is important to consider the energetics of forming Er point defects. A series of such defects was constructed using a cubic 64-atom Si supercell. For the tetrahedral interstitial, attempts to relax the Er site symmetry to C_{3v} failed, leading back to the T_d symmetry imposed in previous work [7]. This structure, substitutional Er, Er paired with a Si vacancy, and Er centered between a near-

neighbor pair of Si vacancies all yielded very large energy penalties, see Table 1.

We next studied the energetics of extended Er defect structures resembling silicides. Our model calculations used trigonal supercells containing 15–53 atoms, with the a lattice parameter constrained to that of bulk Si and the c lattice parameter and all internal coordinates free to relax. Silicide precipitates are observed to grow as (1 1 1)-oriented platelets [12,24], so our models contained Er sheets between Si (1 1 1) double layers. Results for the different structures are summarized in Table 1. Two models of Er monolayers are shown in Fig. 4, one centered over “hollow” sites and one over “closed” sites in the buckled Si bounding layers. These had 70–85% lower energies than any of the point defect models. The Er bilayer models had even lower energies. Centering Er over closed rather than hollow Si sites resulted in energy reductions of 0.5 and 0.3 eV for the Er monolayer and bilayers, respectively. Introducing vacancies in the quasi-graphitic Si layer between the Er bilayer gave an

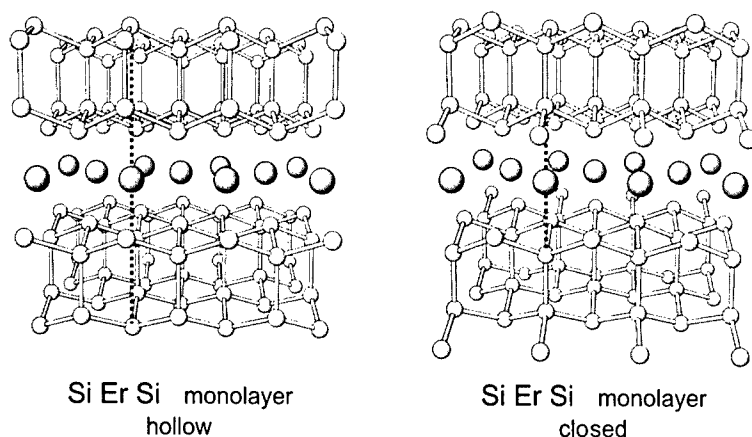


Fig. 4. Comparison between two extended defect structures resembling Er silicide. For clarity, bonds between Er (dark balls) and Si are omitted.

additional 0.3 eV reduction, paralleling the bulk Er_3Si_5 result.

Strong support exists for our calculated structures. STEM data from the MBE-grown sample *H* show Er monolayers in silicide-like precipitates with a noticeable absence of stacking faults in the Si network surrounding the platelets [12], while samples implanted with higher concentrations of Er show larger bilayer structures and clear evidence of stacking faults [12,24]. The only configuration satisfying these conditions for both the monolayer and bilayer structures is the one with Er centered over closed-sites, which we calculate for each to have the lowest energies.³

Looking at Er-doped GaN, we find that Er behaves completely differently than in Si. EXAFS data show [14] that Er occupies Ga sites as point defects up to concentrations $\geq 10^{21} \text{ Er/cm}^3$, that such defects are insensitive to similarly high O concentrations, and that the Er–N bond length of $2.17 \pm 0.02 \text{ \AA}$ is shorter than in bulk ErN by 0.25 Å.

Our theoretical methods required modifications to deal with the highly localized N valence electrons and the more localized Ga semi-core d electrons, which behave as valence electrons in the presence of N. Convergence required the use of adaptive curvilinear coordinates [26] and references therein, boosting average plane wave cutoffs of 50 Ry to a maximum value of 212 Ry where needed. A 48-atom rhombohedral supercell was constructed using the theoretically optimized GaN lattice parameters, with Er substitution on one Ga site. A relaxed Er–N bond length of 2.20 Å was obtained, 1.5% larger than the EXAFS result and consistent with the 1.6% PBE overestimate of the GaN lattice parameters. In strong contrast to the Er–Si point

defects, the energy penalty here relative to phase-separated bulk ErN and GaN was only 1.2 eV.

The high energies of the Er point defects in Si are relatively independent of coordination number and bond length (see Table 1). We suggest that the much lower energies of the extended defect structures (and of Er_3Si_5) arise from indirect metallic Er–Er bonding mediated by Si layers [12]. Because of the ionicity of the ErN and GaN:Er systems [14], this energy lowering mechanism is not available, reducing the possible energy that could be gained by segregating ErN platelets or clusters. Therefore, only direct, ionic Er–N bonds need be considered, and bond number versus bond strength (and length) arguments [14] are consistent with the short bonds and small energy penalty calculated here for the Er point defects in GaN.

Acknowledgements

We thank A. Polman and A.J. Steckl for the Er-doped Si and GaN samples, respectively, and M.J.A. de Dood for helpful discussions about the MBE-grown Si:Er. The X-ray absorption measurements were performed at the NSLS, Brookhaven National Laboratory, which is supported by the DOE, Division of Materials Science and Division of Chemical Sciences.

References

- [1] H. Ennen, J. Schneider, G. Pomrenke, A. Ousmane, Appl. Phys. Lett. 43 (1983) 943.
- [2] Mater. Res. Symp. 486 (1998).
- [3] Mater. Res. Symp. 422 (1996).
- [4] Mater. Res. Symp. 298 (1993).
- [5] Y.S. Yang, Z. Jingping, K.C. Heasman, B.J. Sealy, Solid State Commun. 72 (1989) 991.

³A study of early stage ErSi_2 growth on the Si(111) surface also reported closed sites, cf. Ref. [25].

- [6] D.L. Adler, D.C. Jacobson, D.J. Eaglesham, M.A. Marcus, J.L. Benton, J.M. Poate, P.H. Citrin, *Appl. Phys. Lett.* 61 (1992) 2181.
- [7] M. Needels, M. Schlüter, M. Lannoo, *Phys. Rev. B* 47 (1993) 15533.
- [8] J. Michel, F.Y.G. Ren, B. Zhang, D.C. Jacobson, J.M. Poate, L.C. Kimerling, *Mater. Sci. Forum* 143–147 (1994) 707.
- [9] A. Kozanecki, R.J. Wilson, B.J. Scaly, J. Kaczanowski, L. Nowicki, *Appl. Phys. Lett.* 67 (1995) 1847.
- [10] H. Przybylinska, W. Jantsch, Yu. Suprun-Belevitch, M. Stepikhova, L. Palmetshofer, G. Hendorfer, R.J. Wilson, B.J. Scaly, *Phys. Rev. B* 54 (1996) 2532.
- [11] U. Wall, A. Vantomme, J. De Watchtower, R. Moons, G. Langouche, J.G. Marques, J.G. Correia, ISOLDE Collaboration, *Phys. Rev. Lett.* 79 (1997) 2069.
- [12] P.H. Citrin, D.R. Hamann, P.A. Northrup, D.A. Muller, D.C. Jacobson, J. Michel, T. Chen, M. Platero, L.C. Kimerling, M.J.A. de Dood, A. Polman, to be published.
- [13] R. Serna, M. Lohmeier, P.M. Zagwijn, E. Vlieg, A. Polman, *Appl. Phys. Lett.* 66 (1995) 1385.
- [14] P.H. Citrin, P.A. Northrup, R. Birkhahn, A.J. Steckl, *Appl. Phys. Lett.* 76 (2000) 2865.
- [15] A.A. MacDowell, T. Hashizume, P.H. Citrin, *Rev. Sci. Instrum.* 60 (1989) 1901.
- [16] R. Car, M. Parrinello, *Phys. Rev. Lett.* 55 (1985) 2471.
- [17] J.P. Perdew, K. Burke, M. Ernzerhof, *Phys. Rev. Lett.* 77 (1996) 3865.
- [18] D.R. Hamann, *Phys. Rev. B* 40 (1989) 2980.
- [19] S.G. Louie, S. Froyen, M.L. Cohen, *Phys. Rev. B* 26 (1982) 1738.
- [20] H.J. Monkhorst, J.D. Pack, *Phys. Rev. B* 13 (1976) 5188.
- [21] P.A. Lee, P.H. Citrin, P. Eisenberger, B.M. Kincaid, *Rev. Mod. Phys.* 53 (1981) 769.
- [22] S. Auffret, J. Pierre, B. Lambert, J.L. Soubeyroux, J.A. Chroboczek, *Physica B* 162 (1990) 271.
- [23] H. Bender, M.F. Wu, A. Vantomme, H. Pattyn, B. Langouche, *Mater. Res. Soc. Symp. Proc.* 402 (1996) 499.
- [24] D.J. Eaglesham, J. Michel, E.A. Fitzgerald, D.C. Jacobson, J.M. Poate, J.L. Benton, A. Polman, Y.-H. Xie, L.C. Kimerling, *Appl. Phys. Lett.* 58 (1991) 2797.
- [25] M.H. Tuiller, P. Wetzel, C. Pirri, D. Bolmont, G. Gewinner, *Phys. Rev. B* 50 (1994) 2333.
- [26] D.R. Hamann, *Phys. Rev. B* 63 (2001) 75107.



ELSEVIER

Physica B 308–310 (2001) 374–377

PHYSICA B

www.elsevier.com/locate/physb

Spectroscopic ellipsometry study of the layer structure and impurity content in Er-doped nanocrystalline silicon thin films

M. Losurdo^{a,*}, M.F. Cerqueira^b, M.V. Stepikhova^c, E. Alves^d,
M.M. Giangregorio^a, P. Pinto^b, J.A. Ferreira^b

^a Centro di Studio per la Chimica dei Plasmi-CNR, Via Orabona no. 4, 70126 Bari, Italy

^b Departamento de Física, Universidade do Minho, Largo do Paço, 4700-320 Braga, Portugal

^c Institute for Physics of Microstructures RAS, 603590 Nizhny Novgorod GSP-105, Russia

^d Instituto Técnico Nuclear ITN, EN 10, 2686-953 Sacavém, Portugal

Abstract

Er doped nc-Si thin films have been investigated by spectroscopic ellipsometry (SE). The optical response of Er ions in a nc-Si/SiO matrix has been determined by SE, and it has been used to detect Er contents as low as ~ 0.2 at%. The complex layered nanostructure of nc-Si:Er:O has been resolved and it has been found that it is strongly influenced by the Er-doping and the oxygen in-depth distribution profile. SE results are discussed in comparison with data obtained by the standard methods of the X-ray diffraction, Rutherford backscattering and Raman spectroscopy. © 2001 Elsevier Science B.V. All rights reserved.

Keywords: Spectroscopic ellipsometry; Nanocrystalline silicon; Erbium

1. Introduction

Erbium doped nanocrystalline silicon, nc-Si:Er, thin films produced by RF magnetron sputtering have been reported to be effective emitters at the 1.54 μm wavelength (corresponding to the intra-4f transition of Er^{3+} ions) in a wide temperature range from 5 to 300 K [1]. Hence, they are attractive for applications in Si-based optoelectronic devices. However, the Er luminescence intensity in nc-Si thin films is strongly influenced by the complex nanostructure of films, i.e. the nanocrystalline volume fraction and crystallite size, and by the impurity content (mainly oxygen). Hence, it is important a detailed investigation of the “anatomy” of the nc-Si:Er,O films, i.e., the layered structure, the non-homogeneous distribution of the nc-Si and a-Si phases, and the in-depth distribution of the SiO phase, which are strongly dependent on the growth conditions.

In this contribution, the nanostructure of nc-Si:Er,O thin films deposited by the RF magnetron sputtering is analyzed by spectroscopic ellipsometry (SE). By the SE technique, the optical response of Er ions in a nc-Si/SiO matrix has been determined and used to evaluate Er contents as low as 0.2 at% in the layers. Additionally, SE analysis reveals the complex layered structure and impurity distribution in nc-Si:Er,O films, whose optical response is described by the Bruggeman effective medium approximation (BEMA). In contrast, data obtained by X-ray diffraction and Raman spectroscopy only provide the average value of the crystallinity over the whole film thickness. The effect of the Er content on the structure of nc-Si thin film is discussed.

2. Experimental

Erbium doped nanocrystalline silicon thin films were grown on glass substrates by the reactive magnetron sputtering in H_2/Ar atmospheres with various H_2 percentages. The target was a c-Si wafer where some pieces of high purity (99.99%) metallic erbium were

*Corresponding author. Tel.: +39-80-5443562; fax: +39-80-5442024.

E-mail address: cscpm18@area.ba.cnr.it (M. Losurdo).

added for the doping. Growth parameters, such as the temperature, T_{gr} , the RF power, and the type of atmosphere (hydrogen or argon rich) were varied to obtain films with different Er-, H- and O-content and different crystallinity and nanocrystal grain sizes, as shown in Table 1.

Spectroscopic ellipsometry measurements of the complex pseudodielectric function $\langle \epsilon \rangle = \langle \epsilon_1 \rangle + i\langle \epsilon_2 \rangle$ of the films were performed in the range 1.5–5.5 eV. SE measured the energy dependence of the ellipsometric angles Ψ and Δ , and, hence, of the ratio, ρ , between the complex reflectance coefficients of two components of

the polarized light, r_p , and r_s , respectively, parallel and perpendicular to the plane of incidence, according to the equation:

$$\rho = r_p/r_s = \tan \Psi \exp(i\Delta), \quad (1)$$

where Ψ is the amplitude ratio ($\tan \Psi = |r_p|/|r_s|$), and Δ is the phase difference ($\Delta = \delta_p - \delta_s$) between the p and s components. The pseudodielectric function, $\langle \epsilon \rangle$, was derived from the ρ parameter through the following equation [2]:

$$\langle \epsilon \rangle = \epsilon_0 \sin^2 \phi_0 [1 + \tan^2 \phi_0 (1 - \rho)^2 / (1 + \rho)^2], \quad (2)$$

Table 1
Growth conditions and sample parameters for undoped (Si#) and Er-doped (Er#) nc-Si films^a

Sample	T_{gr} (°C)	RH	RF (W)	d (nm)	Er (%)	O (%)	Si (%)	D_x (Å)	ϵ_x (%)	D_R (Å)	c_R (%)
Si13	250	0.63	80	581	0	7	72	96	0.12	71	53
Si12	350	0.63	80	511	0	5	80	64	0.2	71	66
Er13	250	0.63	80	742	0.2	12	88	48	0.02	73	75
Er12	350	0.63	80	901	0.2	5	95	48	0.13	78	67
Er3	100	0.17	40	786	4.7	16.3	78	Basically amorphous			

^a Here T_{gr} is the growth temperature; RH determines the hydrogen fraction in growth atmosphere derived from the ratio of partial pressures $RH = p_{H_2}/(p_{H_2} + p_{Ar})$; RF is the RF magnetron power; d is the thickness of the films, determined from the transmission spectra in UV-visible range; Er, O, and Si are elements content obtained by RBS method; D_x and ϵ_x are nc size and strain, determined by XRD method, D_R and c_R are the grain size and crystallinity of the films measured by Raman spectroscopy.

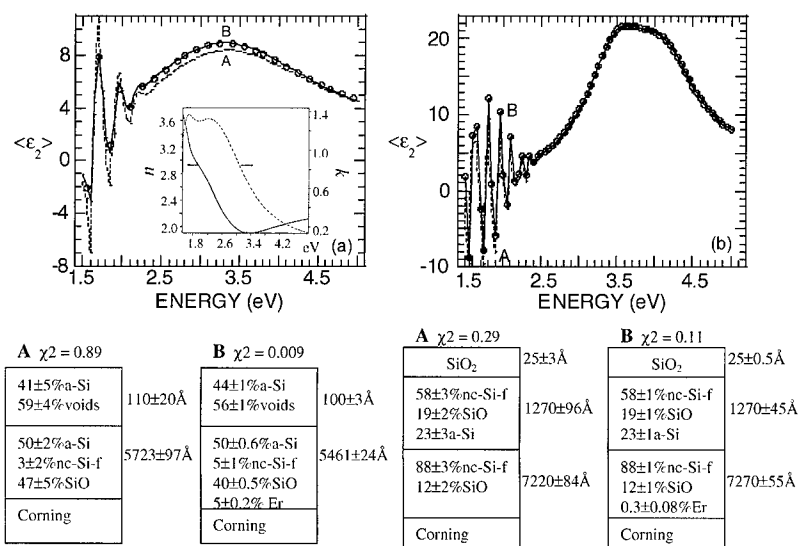


Fig. 1. SE spectra of the imaginary part, $\langle \epsilon_2 \rangle$, of the pseudodielectric function of samples with (a) high (sample Er3) and (b) low (sample Er12) Er-content. Fit results according to BEMA models with (continuous lines; models B) and without (dashed lines; models A) Erbium inclusion are also shown together with the corresponding BEMA models. The inset shows the optical response (in terms of the refractive index n and extinction coefficient k) of Er ions in the nc-Si/SiO matrix as determined by the least-squares regression analysis using a Lorentzian oscillators based dispersion equation in the high doped sample. The fit goodness, χ^2 , and 95% confidence limits of fit parameters are also shown.

where ϕ_0 is the angle of incident light and ϵ_0 is the ambient dielectric function.

SE spectra were analyzed in terms of optical models based on the Bruggeman effective medium approximation (BEMA) [3] applying the least-squares regression method for the fitting, where the fit goodness was estimated by the parameter χ^2 [4]. The 95% confidence limit of fit parameters was also evaluated. The dielectric function of a-Si, nc-Si-fine grains, nc-Si-large grains and silicon oxides (SiO_2 , SiO_x , SiO) reported in Ref. [5] were used in the BEMA analysis. SE studies were referred by measurements of transmission spectroscopy for the evaluation of the film thickness and accompanied by the measurements of RBS, XRD and Raman spectroscopy presented in Table 1.

3. Results and discussion

Fig. 1a shows the experimental SE spectrum of the imaginary part, $\langle \epsilon_2 \rangle$, of the pseudodielectric function of a nc-Si:ErO film whose RBS analysis gave an Er content of 4.7% (sample Er3). Different BEMA models have been tested in the fit analysis of this spectrum. It can be seen in Fig. 1a that a two-layer model (model A: dashed curve) which only considers the amorphous, crystalline silicon and SiO components does not provide a good fit, resulting in high values of the fit goodness parameter, $\chi^2 = 0.89$, and of 95% fit parameters confidence limits. Therefore, we concluded that the discrepancy in the calculated spectrum parameters could be related to the unaccounted response of Er impurity. Indeed, after introducing in the BEMA model a dispersion relation based on Lorentzian oscillators describing the dielectric response of erbium ions, a perfect fit, with lower $\chi^2 = 0.009$ and lower errors on fit parameter (layer thickness and constituent volume fractions), was obtained (model B: solid line), yielding a volume fraction of Er of about 5% (see model B), in excellent agreement with the RBS results. The determined dielectric response of erbium ions in a nc-Si/ SiO matrix used for the fitting models is shown in the inset of Fig. 1.

The sensitivity of SE to the Er content was also tested in samples with low Er-contents ($<1\%$). Fig. 1b shows the experimental and fit spectra for a sample with 0.2% of Er, as determined by RBS (sample Er12). By the inclusion of a 0.3% volume fraction of Er ions, the fit goodness parameter χ^2 decreases by a factor 3, and also errors on fit parameter decrease (see best fit BEMA models). In this case, the contribution of Er to the fit improvement is better seen in the low energy region (below 2.5 eV) where the optical response of Er reveals the strong absorption (see inset in Fig. 1a). It is worthy to note that the estimations of concentration performed by SE analysis are in good

accordance with the RBS values not only for Er but also for O atoms (compare the models and the values in Table 1).

A strong influence of the Er-doping on the nanostructure and optical properties of thin nc-Si films has been found. Fig. 2 contrasts the $\langle \epsilon_2 \rangle$ spectra of nc-Si films grown in identical conditions with (samples Er12 and Er13) and without (samples Si12 and Si13) Er-doping. The #12 and #13 samples only differ in the growth temperature of 350°C and 250°C, respectively. The comparison of SE spectra obtained for both sets shows that the inclusion of Er increases the amplitude of the pseudodielectric function, smoothes and nears the

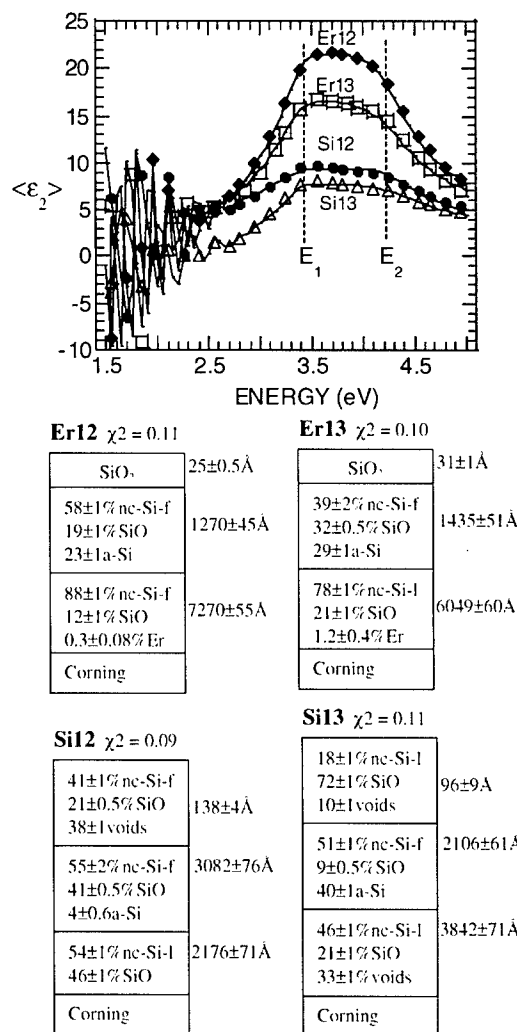


Fig. 2. SE spectra of the imaginary part, $\langle \epsilon_2 \rangle$, of the pseudodielectric function of samples with (Er12, Er13) and without (Si12, Si13) erbium inclusion. The best-fit results according to BEMA models are presented at the bottom. The fit goodness, χ^2 , and 95% confidence limits of fit parameters are also shown.

energetic position of the characteristic E_1 and E_2 peaks, which are indicative of the presence in films of the crystalline fraction [6]. The characteristic E_1 and E_2 peaks (at about 3.4 and 4.2 eV, respectively) become more pronounced in the spectra of undoped samples. Qualitatively, this spectral behavior provides indication on a larger grain size for undoped films, while smaller silicon grains are present in Er-doped films. In fact, the BEMA models of the undoped Si12 and Si13 samples include, in the inner and outer layers, the dielectric function of nc-Si-large grains, while the response of Er doped samples is mainly represented by the dielectric function of nc-Si-fine grains (the best-fit BEMA models obtained for these samples are presented at the bottom of Fig. 2.). This effect of the Er-content on the grain size has been confirmed by the X-ray diffraction measurements reported in Table 1, which reveal a strong (about 2 times) decrease of the grain size in samples doped with Er, so corroborating the SE results. In contrast, no variation of the grain size was detected by Raman. However, this apparent discrepancy is explained by the fact that the Raman method only probes the thin near-surface layer (within the second outer layer in the BEMA models) in the film, where the low-size crystal grain fraction dominates. Therefore, SE is sensitive to structural aspects, such as the different crystalline fraction and grain size in the different layers constituting the nc-Si:Er:O films, which otherwise cannot be resolved by XRD and Raman. In addition, SE data show that the larger grain size accompanies with a larger inclusion of the SiO component, since oxygen segregates at the grain boundaries (see Er12/Si12 samples in Fig. 2). It is thought that this Er effect on the grain size could be related to the preferential incorporation of Er ions into interstitial sites of the silicon network, so causing distortion of the lattice periodicity and

obstructing the crystal grain expansion during growth. However, further work is in progress to understand the mechanism of the evolution of nc-Si film structure with Er-doping.

4. Conclusions

Spectroscopic ellipsometry has been applied to the analysis of the nanostructure and chemical composition of Er-doped nc-Si thin films, produced by the RF magnetron sputtering. In contrast to the standard techniques of X-ray diffraction, Rutherford backscattering and Raman spectroscopy, which provide averaged structural and compositional data, ellipsometry reveals the complex layered structure and impurity distribution in nc-Si:Er:O films. It has been found that the inclusion of Er in nc-Si thin films lowers the Si crystallite sizes in nc-Si thin films. Additionally, SE shows a surprisingly high sensitivity to the Er content as low as 0.2 at%. The optical response of Er ions in a nc-Si/SiO matrix has also been determined.

References

- [1] M.F. Cerqueira, M.V. Stepikhova, J.A. Ferreira, *Mater. Sci. Eng. B* 81 (2001) 32.
- [2] E.A. Irene, *Thin Solid Films* 233 (1993) 96.
- [3] D.A.G. Bruggeman, *Ann. Phys. (Leipzig)* 24 (1965) 636.
- [4] G.E. Jellison, *Thin Solid Films* 313–314 (1998) 33.
- [5] M. Losurdo, R. Rizzoli, C. Summonte, G. Cicala, et al., *J. Appl. Phys.* 88 (2000) 2408.
- [6] D.E. Aspnes, A.A. Studna, *Phys. Rev. B* 27 (1983) 985.



ELSEVIER

Physica B 308–310 (2001) 378–381

PHYSICA B

www.elsevier.com/locate/physb

Determination of the atomic configuration of Er–O complexes in silicon by the super-cell FLAPW method

M. Hashimoto*, A. Yanase, H. Harima, H. Katayama-Yoshida

Department of Condensed Matter Physics, The Institute of Scientific and Industrial Research, Osaka University, Osaka 567-0047, Japan

Abstract

We determined the atomic configuration of Er–O complexes in silicon from the first principles using the super-cell FLAPW method within the local density approximation. We proposed two models of the atomic configuration of Er–O₆ complexes in silicon with C_2 symmetry, one is stable and the other is meta-stable in the thermal equilibrium conditions. Our proposed atomic configurations of Er–O₆ complexes are consistent with the experimental results of EPR and EXAFS measurements, which reported the existence of several stable and meta-stable low-symmetry centers and similarity to the C_2 -symmetry center of the Er₂O₃. © 2001 Elsevier Science B.V. All rights reserved.

Keywords: Ab initio calculation; Rare-earth impurity; Er–O complex; Silicon

1. Introduction

Erbium (Er) doped semiconductors attract much attention because of their sharp and temperature independent luminescence caused by intra-4f transition. These materials are expected to be applied to temperature-independent optoelectronic devices. One of the possible applications is optical fiber communication because of the sharp emission of intra-4f transition emitting 1.54 μm -wavelength-light which matches the minimum absorption rate of the light in silica-based optical fibers. Especially Er doped silicon (Si), which is the leading semiconductor in microelectronic applications, is a promising material to achieve fully Si-based optoelectronics.

Experiments performed until 1993 had shown that the low solubility of Er in Si prevents the incorporation of high Er concentrations. This difficulty was overcome by the co-doping method (co-doped with Er and oxygen (O)) in 1993 [1]. The improvement in the solubility of Er was due to the reduction of formation energy by forming Er–O complexes. However the structures of the com-

plexes are still not well understood. Extended X-ray absorption fine-structure (EXAFS) showed that the Er impurity is surrounded by a cage consisting of 4–6 O atoms [2]. Electron paramagnetic resonance (EPR) measurement revealed that the Er atom is surrounded by 6 O atoms and forms several low-symmetry impurity complexes; four Er–O complexes exist before annealing and two Er–O complexes do after annealing [3]. So far, precise atomic configurations of Er–O have not been reported in theory or experiment.

In this study, we performed ab initio calculations in order to determine the atomic configurations of Er–O complexes in Si. We propose two models of different atomic configurations of Er–O complexes in Si based upon the total energy calculation. one is stable and the other is meta-stable. As far as we know, this is the first clarification of concrete atomic configurations of Er–O complexes in Si based upon ab initio electronic structure calculations.

2. Models and calculation

Calculations of the electronic structure and total energy are performed by using the full-potential linearized augmented-plane-wave (FLAPW) method

*Corresponding author. Tel.: +81-6-6879-8539; fax: +81-6-6879-8535.

E-mail address: hashimoto@cmp.sanken.osaka-u.ac.jp (M. Hashimoto).

based on the local density approximation (LDA) [4]. For the exchange-correlation energy in the LDA, the analytical expression of Gunnarsson–Lundqvist is employed [5].

The angular momentum in the spherical wave expansion is truncated $l = 4$ and $l = 7$ for the potential and the wave functions, respectively. The cutoff energy of the plane wave is 19.42 Ry for the wave functions. We calculate the electronic structure and the total energy using only the point in the irreducible Brillouin zone, to achieve the self-consistency in the charge and the potential. The muffin-tin sphere radii for Er is chosen to be 1.116 and 0.576 for O and Si, respectively.

Rare Earth (RE) impurity in Si is taken into account by using super-cells containing 32 atoms. We use Lutetium (Lu) as RE impurity instead of Er since LDA does not estimate the exact states of open $4f^{11}$ shell in Er. The electron configuration of Lu is $4f^{14}5d^16s^2$ and it is ionized as Lu^{3+} with $4f^{14}$ closed-shell in a crystal. Since Er is ionized as Er^{3+} in the crystal and both $4f$ shell of Er and that of Lu are strongly localized around the nucleus, nucleus charge of Er and Lu are completely shielded by $4f$ electrons. Therefore the valence band of Lu is similar to that of Er.

3. Results and discussion

In order to determine the atomic configuration of the Er–O complexes in Si, first we investigated (1) the electronic structure and the most stable atomic configurations of isolated Er impurity in Si and next, (2) the most stable atomic configuration of isolated O impurity in Si. Finally, based on the above two atomic configurations, we investigated (3) the stable atomic configuration of Er–O complexes in Si.

We compared the total energy of the isolated Er impurity in Si located at the Tetrahedral (T_d) substitutional site and the T_d interstitial site. We found that the most stable atomic site of the isolated Er impurity in Si is at the T_d interstitial site (i.e. T_d interstitial site is 2.84 eV more stable than the T_d substitutional site). The stabilization of the Er impurity at the T_d interstitial site in Si is originated by the formation of the bond which are caused by the hybridization between Er-5d orbits and the Si sp^3 orbits [6].

We determined the atomic configuration of the isolated O impurity in Si. The most stable atomic site of O is at the off-bond-center site, where Si–Si bond length is 3.29 and O is located at the off-bond center site distorted 0.98 from the vertical line of the Si–Si bond.

In the calculation of (3), the models of the Er–O complexes were determined in the following way. We considered the Er impurity at the T_d interstitial site based on the stable atomic site of the calculated results of the isolated Er impurity. Next we considered the Er–

O complexes with 6 O atoms around the Er impurity at the T_d interstitial site, where O atoms are located at the Si–Si off-bond-center site based on the calculated results of the isolated O impurity. Twelve off-bond-center sites for O atoms are present around the Er impurity at the T_d interstitial site. We coordinated 6 O atoms at 6 of the twelve off-bond-center sites and picked up the low symmetry Er–O complexes from all possible atomic configurations because the EPR and EXAFS measurement indicate the low symmetry complexes in this system. These structures from our model have C_{2v} , C_2 and C_3 symmetry (the others have no symmetry). The structures are summarized in Fig. 1. We determined the stable atomic configuration of the Er–O complexes by comparing the total energy starting from these six Er–O complexes.

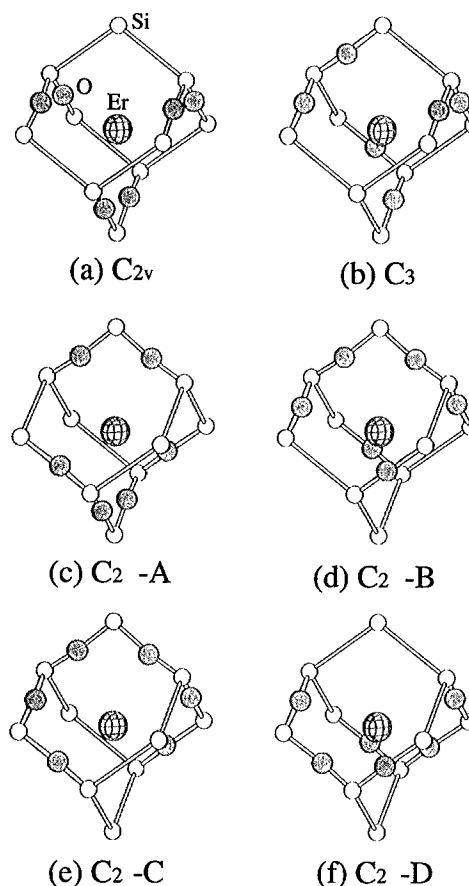


Fig. 1. Proposed models of atomic configuration of Er–O complexes in Si. The atom at the center of each figure is the Er atom. The white symbols indicate the Si atoms and the dark symbols indicate the O atoms. We show the symmetry and the atomic configuration of these complexes ((a) C_{2v} , (b) C_3 and (d)–(f) C_2). We label these complexes C_{2v} structure, C_3 structure, C_2 -A–D structures.

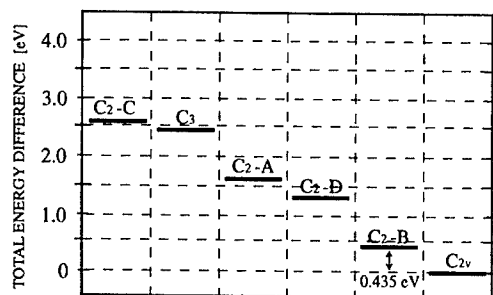


Fig. 2. The total energy difference between the possible candidates of six complexes (as defined in Fig. 1) measured from the most stable C_{2v} structure.

We show the calculated total energy differences in Fig. 2. From Fig. 2, we see that the most stable atomic configuration of the Er–O6 complex is the C_{2v} structure followed by the C_{2v} -B structure. The energy difference between them is 0.435 eV, therefore C_{2v} -B structure is meta-stable in thermal equilibrium. The order of the stability is C_{2v} (0 eV) < C_{2v} -B (0.435 eV) < C_{2v} -D (1.292 eV) < C_{2v} -A (1.577 eV) < C_3 (2.420 eV) < C_{2v} -C (2.502 eV), where we showed the total energy difference measured from the most stable C_{2v} structure.

To obtain more stable structures of Er–O complexes, we applied an additional lattice relaxation to the two lowest energy structures (C_{2v} structure and C_{2v} -B structure). The lattice relaxations were taken into account in the following procedures. First, we relaxed the 6 Si atoms around Er toward the Er atom while fixing the 6 O atoms. Next, we relaxed the 6 O atoms around Er while fixing the 6 Si atoms. As a result, we obtained more stable structures, Relaxed- C_{2v} (Fig. 3a) and Relaxed- C_{2v} -B (Fig. 3b). The local configuration is the same for Relaxed- C_{2v} and Relaxed- C_{2v} -B structure. We show the local structure of Er and O complex in Fig. 3c. This local structure and Er–O bond length is very similar to the structure of the Er_2O_3 . The Er–O bond length of the local C_2 symmetry center of the Er_2O_3 is 2.26. The bond length of Er–O complex in Si reported in EXAFS measurement is 2.27 [2].

We evaluated cohesive energy E_{coh} by the following expression:

$$E_{coh} = E_{(Er,6O,32Si)} - [E_{(Er,32Si)} + 6E_{(O,16Si)} - 48E_{(2Si; host)}], \quad (1)$$

where $E_{(Er,6O,32Si)}$, $E_{(Er,32Si)}$ and $E_{(O,16Si)}$ are the total energy for co-doping system, isolated Er impurity system and isolated O impurity system, respectively. $E_{(2Si; host)}$ is the total energy for pure Si crystal and is introduced to correct the difference in the number of Si atoms between the first and the second term. We obtained $E_{coh} = -1.449 \text{ Ry} = -19.713 \text{ eV}$ with using

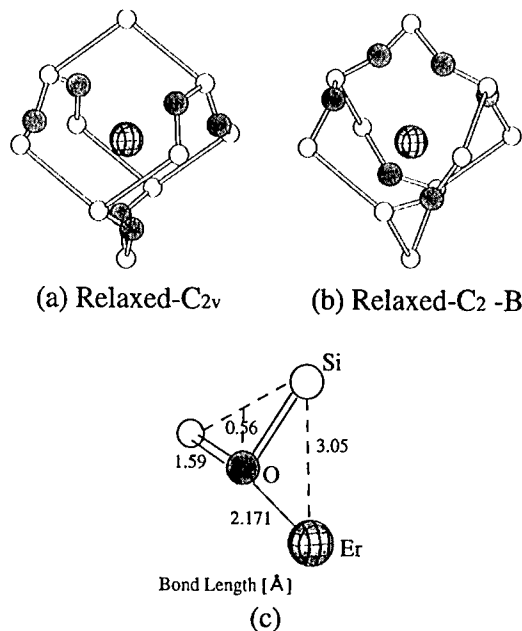


Fig. 3. The structures of the most stable two Er–O complexes (a) Relaxed- C_{2v} structure and (b) Relaxed- C_{2v} -B structure. (c) The local structure surrounding the Er atom is also shown.

the calculated value of $E_{(Er,6O,32Si)} = -48477.033 \text{ Ry}$ (for Relaxed- C_{2v}), $E_{(Er,32Si)} = -47595.990 \text{ Ry}$, $E_{(O,16Si)} = -9389.135 \text{ Ry}$ and $E_{(2Si; host)} = -1155.317 \text{ Ry}$, respectively. We obtained a negative value of the cohesive energy indicating that the formation of the complex with 1 Er and 6 O atoms is stable and that we can observe this complex in thermal equilibrium condition. This indicates that the experimental result, which reported Er impurities forming complexes with six O atoms, is consistent with our theoretical calculations in the thermal equilibrium condition.

As mentioned before, various kinds of Er–O complexes exist in Si in the thermal non-equilibrium doping method such as ion implantation; four Er–O complexes exist before annealing and two Er–O complexes do after annealing. From our calculated result, the variation of Er–O complexes could be attributed to the several meta-stable states due to the difference of coordination of 6 O atoms. Our interpretation of the experiments based upon the present calculation is that the four lowest energy Er–O complexes should exist before annealing in Si (such as C_{2v} , C_{2v} -B, C_{2v} -D and C_{2v} -A) and after annealing, four Er–O complexes convert to the two lowest energy Er–O complexes (C_{2v} and C_{2v} -B). EPR and EXAFS measurements, similarity between Er–O complex in Si and the local C_2 symmetry center of the Er_2O_3 was reported. From our study, Relaxed- C_{2v} structure should correspond to the local C_2 symmetry center of Er_2O_3 . Fig. 4 shows the O–Er–O angles of (a) the C_2

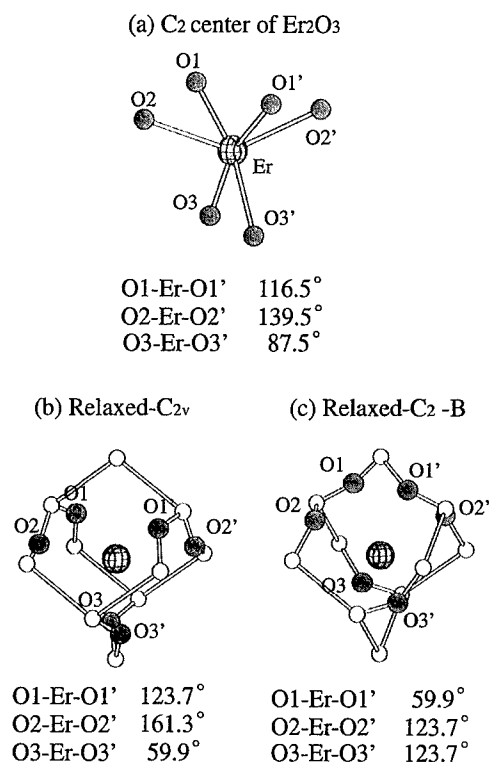


Fig. 4. The O–Er–O angles of (a) the C₂ symmetry center of the Er₂O₃, (b) Relaxed-C_{2v} structure and (c) Relaxed-C₂-B structure. Each angle is shown in the figures.

symmetry center of the Er₂O₃, (b) Relaxed-C_{2v} structure and (c) Relaxed-C₂-B structure. Since the trend of O–Er–O angles in the Relaxed-C_{2v} structure is similar to those of the C₂ symmetry center of the Er₂O₃, we conclude that these complexes have very similar atomic configurations. Determination of the local structure around Er impurity is essential for calculating the crystal field in the future by which we can predict the photoluminescence spectra of Er doped Si without using any adjustable parameters from experiments.

4. Summary

We studied the atomic configuration of Er–O complexes in Si by ab initio calculation using the FLAPW

method with super-cells based on LDA. We propose two possible candidates with different atomic configurations of Er–O₆ complexes in Si, one is stable and the other is meta-stable in the thermal equilibrium condition. Both of these complexes consist of one Er atom located at the T_d interstitial site and 6 O atoms at the Si–Si off-bond-center site. Both complexes have C₂ symmetry and one of these has similar atomic configuration to the local C₂ symmetry center of the existing Er₂O₃, which is consistent with the EXAFS and EPR measurements. Since the existence of several meta-stable Er–O complexes is proposed from the model, we conclude that the variation of these Er–O complexes come from the difference of the coordination of 6 O atoms around Er impurity, which agree very well with the result of the EPR measurement. We clarified the concrete atomic configuration of Er–O complexes in Si based on the ab initio calculation.

Acknowledgements

This work was partially supported by a Grant-In-Aid for Scientific Research on Priority Area (A) and (B), and Osaka University, SANKEN-COE from the Japanese Ministry of Education, Culture, Sports, Science and Technology.

References

- [1] A. Polman, J.S. Custer, E. Snoeks, G.N. van den Hoven, Appl. Phys. Lett. 62 (1993) 507.
- [2] A. Terrasi, G. Franzo, S. Coffa, F. Priolo, F. D'Acapito, S. Mobilio, Appl. Phys. Lett. 70 (1997) 1712.
- [3] J.D. Carey, R.C. Barklie, J.F. Donegan, Phys. Rev. B 59 (1999) 2773.
- [4] W. Kohn, L.J. Sham, Phys. Rev. A 140 (1965) 1133.
- [5] O. Gunnarsson, B.I. Lundqvist, Phys. Rev. B 13 (1976) 4274.
- [6] M. Hashimoto, A. Yanase, H. Harima, H. Katayama-Yoshida, in preparation.



ELSEVIER

Physica B 308 310 (2001) 382–386

PHYSICA B

www.elsevier.com/locate/physb

Study of Er-related defects in a-Si:H(Er)/c-n-Si heterostructures by thermally activated current spectroscopy

Ja. Vovk^{a,*}, A. Nazarov^a, V. Lysenko^a, O. Kon'kov^b, E. Terukov^b

^a *Institute of Semiconductor Physics, NASU, Prospekt Nauki 45, 03028 Kyiv, Ukraine*

^b *Joffe Physical and Technical Institute, RAS, Saint Petersburg, Russia*

Abstract

The paper is devoted to study of Er-related defects in electrical luminescence diode structures a-Si:H(Er)/c-n-Si, for which amorphous hydrogenated silicon film on crystalline Si substrate was fabricated both by plasma-enhanced chemical vapor deposition and magnetron-assisted silane-decomposition technique. Thermally activated current (TAC) spectroscopy by employing the thermally fractional cleaning method has been used. Observed TAC spectra have been shown to be weakly dependent on the film-deposited technique. It has been shown, that signal amplitude of the spectra increases, when Er concentration in a-Si:H increases. The traps with activation energies from 0.10 to 0.40 eV and from 0.5 to 0.6 eV have been charged both by light and thermal-bias stress, which allows to associate these with the deep levels in the band gap of the a-Si:H. The high-temperature current peaks with activation energies of 0.8–1.0 eV have been created only by thermal-bias stress and have been strongly dependent on the charging temperature. It has been suggested that these high-temperature thermally activated processes are related to polarization effects in the [Er–O] clusters, located in amorphous matrix of a-Si:H. The plausible origin of the observed deep levels and polarization processes is discussed. © 2001 Elsevier Science B.V. All rights reserved.

Keywords: Amorphous hydrogenated silicon; Erbium; Deep levels

1. Introduction

Intensive investigations of electrical and optical properties of Er-contained semiconductor matrixes are linked, first of all, with light emission by intra-f shell transition at wavelength of 1.54 μm , which does not depend on the semiconductor matrix and is situated in the region of minimum absorption for quartz fibers. Incorporation of Er into silicon could result in effective connection of silicon-based electronic devices to optical communication systems. However, the limited solubility of Er in crystalline Si and rapid thermal quenching of the Er emission at room temperature [1,2] lead to unsatisfactory results.

In Ref. [3–5] effective room photo- and electroluminescence of Er ions in amorphous hydrogenated silicon (a-Si:H(Er)) have been observed. However, up to

now, the careful study of deep levels in a-Si:H(Er) has not been performed. In this connection, the paper is devoted to a study of charge trapping by deep levels related to Er in a-Si:H matrix of a-Si:H(Er)/c-n-Si electroluminescence diode.

2. Samples and experimental details

The erbium-doped amorphous hydrogenated silicon with thickness near 1 μm has been deposited on crystalline n-type Si substrate both by using the magnetron-assisted silane-decomposition (MASD) technique [6] and the plasma-enhanced chemical vapor deposition (PECVD) in a gas atmosphere containing 25% SiH_4 and 75% Ar [7]. In the case of the MASD technique, Er concentration was varied from 1×10^{18} to $1 \times 10^{20} \text{ cm}^{-3}$ and was uniformly distributed through the a-Si:H(Er) film. Oxygen concentration was determined by SIMS method and was equaled to an average of $1 \times 10^{21} \text{ cm}^{-3}$.

*Corresponding author. Fax: 380-44-265-6177.

E-mail address: nazarov@lab15.kiev.ua (J. Vovk).

In the case of the PECVD technique, Er was inhomogeneously distributed in the a-Si:H film with maximum concentration of about $1 \times 10^{21} \text{ cm}^{-3}$ located near the a-Si:H/c-Si interface. The average oxygen concentration was $5 \times 10^{21} \text{ cm}^{-3}$. The measurement structure was an Al/a-Si:H(Er)/c-n-Si/Al diode with aluminium contact approximately 1 mm in diameter (see inset in Fig. 1).

The study of energetic spectrum of electrical active traps in the a-Si:H(Er) material has been performed by thermally activated current (TAC) spectroscopy in the temperature range from 80 to 350 K with linear sample heating of 0.4 K/s. The traps in the a-Si:H(Er) layer were charged either by visible light and bias applied to substrate contact (V_s in the inset in Fig. 1) at 77 K or by bias applied to substrate at 320 K. Activation energies of discharging processes were determined by fractional

thermal cleaning method of the TAC spectra, proposed in Ref. [8]. The charge built up in the a-Si:H(Er) film after charging of the traps has been estimated by high-frequency (1 MHz) capacitance–voltage ($C-V$) characteristics measured at 77 K.

3. Experimental results and discussion

The TAC spectra measured in the heterodiodes fabricated by MASD technique are presented in Fig. 1. The charging of the structures has been performed at 320 K by bias applied with both positive and negative polarity. In this case, the TAC spectra are sufficiently symmetrical with respect to the temperature axis (Fig. 1b) and show that the current peaks in the

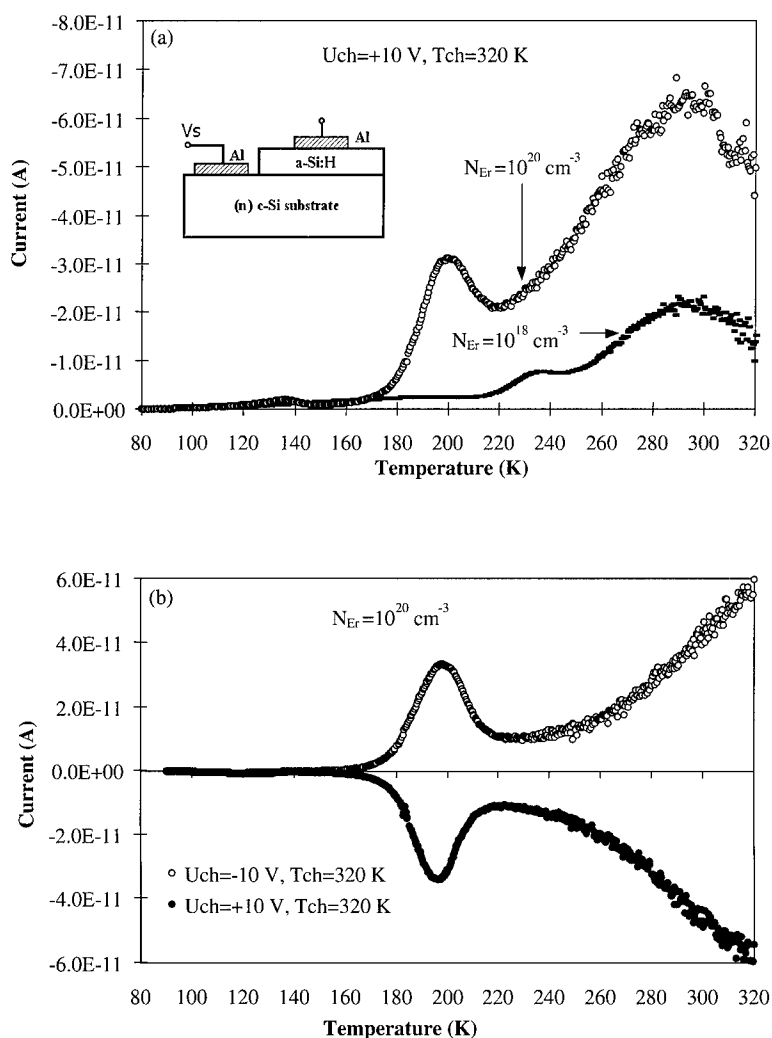


Fig. 1. Thermally activated current spectra of the Al/a-Si:H(Er)/c-n-Si heterodiode, fabricated by the MASD technique with different Er concentrations (a), and measured at different polarities of charging of the sample (b).

temperature range near 140, 190 and 230 K and from 290 to 340 K (Fig. 1a). Additionally, the increase of Er concentration results in the increase of TAC spectrum amplitude (Fig. 1a), that confirms a linkage of the observed current peaks with Er incorporation into the a-Si:H film. The structures containing Er and fabricated by PECVD method showed, principally, a TAC spectra similar to those obtained in the MASD samples (Fig. 2a). The initial structure, which contained no Er atoms in a-Si:H film, does not appear in any TAC peak in the temperature range from 140 to 340 K and current peaks of small amplitude have been observed in the temperature range from 80 to 140 K. Thus, we can conclude that all high-temperature TAC peaks in a-Si:H(Er)/c-n-Si structure are associated with Er incorporation into the a-Si:H matrix.

It should be noted that the effect of visible light and bias at liquid-nitrogen temperature leads to creation of

the TAC peaks only in the temperature range from 80 to 270 K both for the MASD and PECVD structures (see Fig. 2a). Thus, the TAC peaks, appearing in this temperature range, can be associated to the deep levels of charge traps located in the a-Si:H(Er) matrix.

The wide current peak observed in the temperature range from 270 to 340 K is created only in the case of charging the samples at temperatures above 260 K. The result observed is an evidence of the different nature of the high-temperature current peak from other low-temperature ones.

Measurement of $C-V$ characteristics before and after charging the structure by negative bias applied to substrate (forward bias) shows the net electron trapping in the a-Si:H(Er) film, whereas the charging by positive bias applied to the substrate (reverse bias) leads to the net hole trapping (Fig. 2b). Thus, a forward bias applied to the structure results in occupation of the deep levels

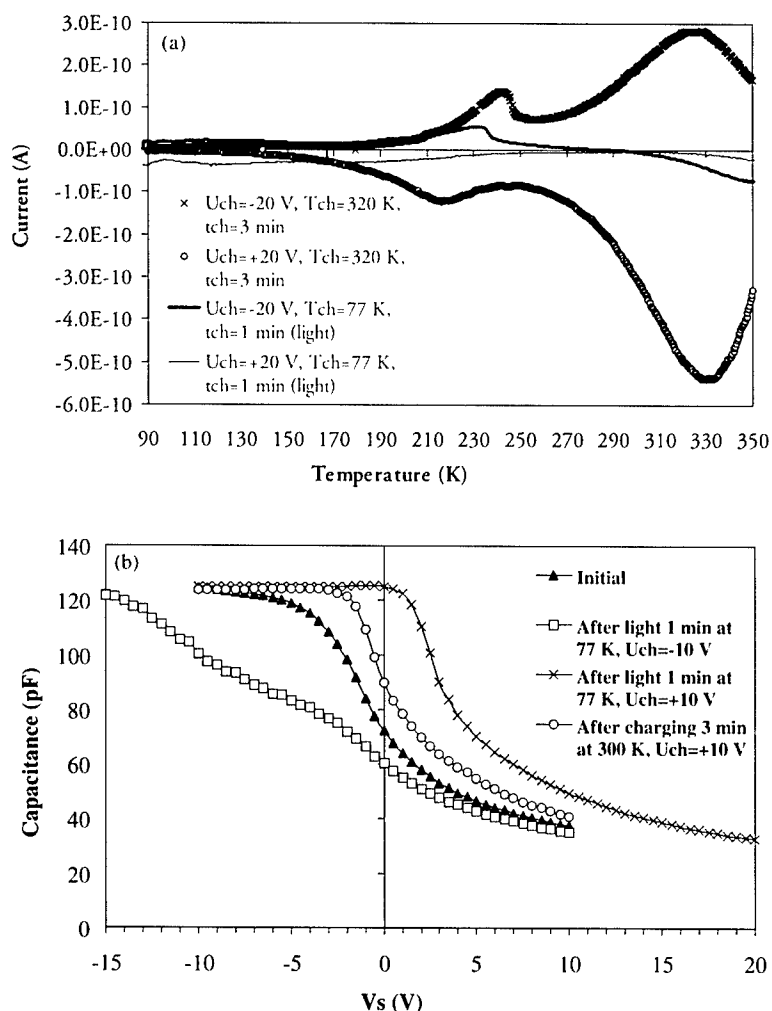


Fig. 2. Thermally activated current spectra (a) and capacitance voltage characteristics (b) measured on the PECVD heterodiode.

located in the upper half of the a-Si:H band gap, whereas the reverse bias applied leads to the charging of the deep levels located in the bottom half of the band gap.

Results of fractional thermal cleaning of the TAC spectra obtained for positive and negative bias, applied to the substrate during the charging of the MASD structures at high temperatures, are presented in Fig. 3. The energetic levels of the obtained electron traps are the following: $E_c - 0.10$, 0.40 , 0.55 , and 0.60 eV. The hole deep levels are $E_v + 0.20$, $E_v + 0.30$, $E_v + 0.50$ and $E_v + 0.60$ eV. The deep levels $E_v + 0.50$ and $E_c + 0.55$ eV possess the maximum amplitude of the TAC (that is maximum concentration in comparison with other deep levels).

The processes with activation energy near 0.85 – 1.00 eV corresponding to the high-temperature current peak are probably associated to polarization processes in erbium-oxide inclusions located in the a-Si:H matrix. Indeed, the Mössbauer spectroscopy method demonstrates that the a-Si:H(Er) films fabricated by the MASD technique contain [Er–O] clusters, in which the

Er^{3+} ions have the local surrounding similar to Er_2O_3 [9]. Additionally, it was shown in Ref. [10], that Er_2O_3 with excess of oxygen (that is similar to our case) has to contain the interstitial O^- ions and holes located at Er^{3+} ions. The hole and O^- ion represent a dipole, which can shift its position in the applied external electric field. Thus, we supposed that, in the [Er–O] clusters, the thermally polarized processes with activation energies from 0.85 to 1.00 eV can be connected to dipole polarization of the hole– O^- dipoles.

The hole trapping in the a-Si:H(Er) film at reverse bias of the a-Si:H(Er)/c-n-Si diode is in contradiction with the model of electroluminescence in such structure, which was suggested in Ref. [5]. In this regime of heterodiode operation, this model assumes that electrons are injected from Al electrode into the a-Si:H(Er) film followed by trapping at dangling bonds (D^0 -centers) and energy transfer (about 0.8 eV) to Er^{3+} ions, located near D^0 -centers. In this model, hole trapping was neglected. Our experiments demonstrate that in the considered devices, the applied reverse bias leads to effective hole trapping in the traps with deep levels

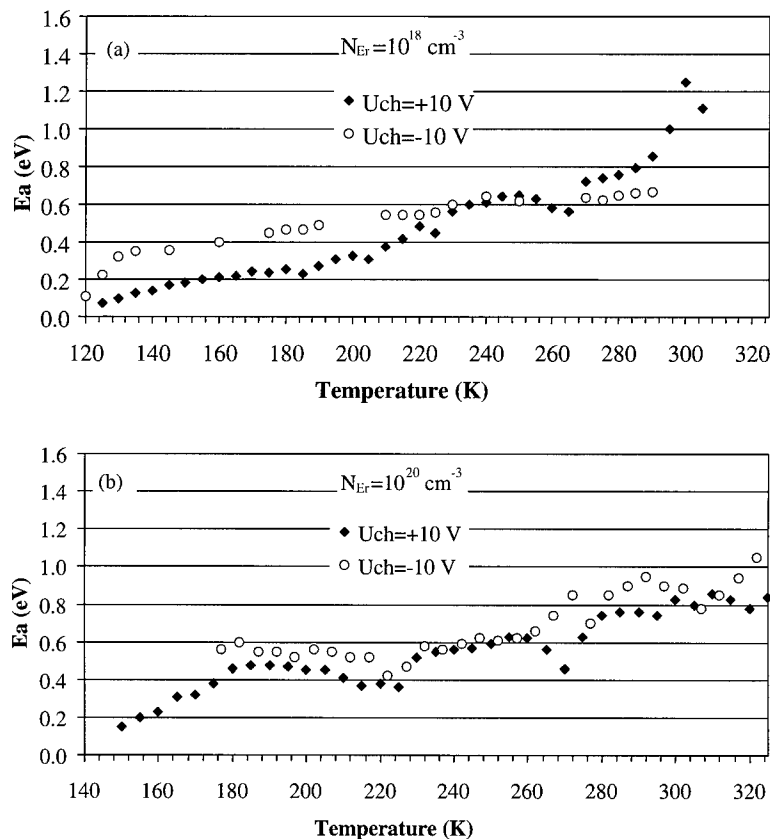


Fig. 3. Results of fractional thermal cleaning of the TAC spectra, measured on the MASD heterodiode with the a-Si:H(Er) film, doped by Er with concentrations of 1×10^{18} (a) and $1 \times 10^{20} \text{ cm}^{-3}$ (b).

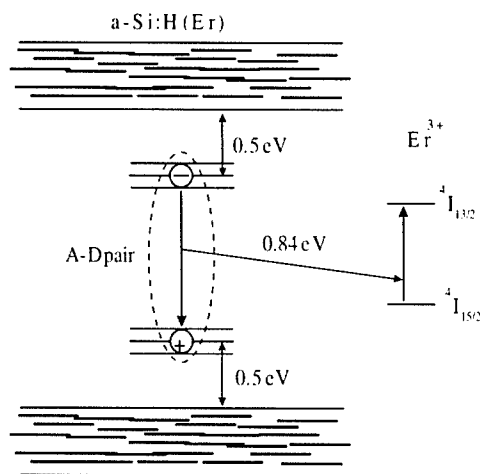


Fig. 4. Proposed model of resonance energy transfer from A–D pair, localized in $E_c - 0.50$ eV level and $E_v + 0.50$ eV level, to Er^{3+} in a-Si:H material.

$E_v + 0.50$ eV and, probably, has to be taken into account for the model of electroluminescence.

It should be noted that electron and hole traps are spatially correlated because of their location links with [Er–O] cluster location. Electron trapping at the levels $E_c - 0.55$ or 0.60 eV and hole trapping at the level $E_v + 0.50$ eV result in creation of donor–acceptor (D–A) pair located in vicinity of the [Er–O] cluster. The energy of the D–A annihilation is about 0.8 – 0.9 eV, which corresponds to the energy of resonance excitation (0.84 eV) of electron in Er^{3+} ion from the ground state $^4I_{15/2}$ to the $^4I_{13/2}$ state (Fig. 4). Since the Er–O bond

exhibits ionic properties, it can be considered as an $\text{Er}^{3+} - \text{O}^-$ dipole. Thus, the D–A pair created can interact with the Er–O bond by dipole–dipole interaction and during its annihilation to transfer the energy to Er by the dipole-mediated energy transfer [11], proposed by Förster for excitation transfer between molecules in gases or solutions and used in Ref. [12] for the a-Si:H(Er) material, in order to explain the energy transfer between dangling bonds and Er^{3+} ions located at sufficiently long distances (nearly 100 Å) from one another.

Acknowledgements

The work was partially supported by INCO-Copernicus project 977048-SIER.

References

- [1] P.B. Klein, et al., *Electron. Lett.* 24 (1988) 1503.
- [2] S. Lombardo, et al., *Appl. Phys. Lett.* 63 (1993) 1942.
- [3] M.S. Bresler, et al., *Appl. Phys. Lett.* 67 (1995) 3594.
- [4] J.H. Chin, et al., *Appl. Phys. Lett.* 68 (1996) 997.
- [5] O.B. Gusev, et al., *Appl. Phys. Lett.* 70 (1997) 240.
- [6] V. Marakhonov, et al., *J. Non-Cryst. Solids* 137&138 (1991) 817.
- [7] E.I. Terukov, et al., *Semiconductors* 32 (1998) 884.
- [8] Y. Gobrecht, et al., *J. Chem. Phys. Soc.* 27 (1966) 509.
- [9] V.F. Masterov, et al., *Semiconductors* 32 (1998) 659.
- [10] B.A. Kivtsov, et al., *Point Defects in Metal-VI Group Compounds (Rare Earth Metal Oxides and Lead Chalcogenides)*, Leningrad, FTI 1988, pp. 44 (in Russian).
- [11] T. Förster, *Discuss. Faraday Soc.* 27 (1959) 7.
- [12] H. Kühne, et al., *J. Appl. Phys.* 86 (1999) 896.



ELSEVIER

Physica B 308–310 (2001) 387–390

PHYSICA B

www.elsevier.com/locate/physb

Spectroscopic characterisation of the erbium impurity in crystalline semiconductors

C.A.J. Ammerlaan*

Van der Waals–Zeeman Institute, University of Amsterdam, Valckenierstraat 65, 1018 XE Amsterdam, Netherlands

Abstract

A scheme for the numerical calculation of energy levels of rare-earth ions in a crystalline solid is presented. Stark fields of cubic, trigonal, tetragonal, orthorhombic and monoclinic symmetry are considered. As examples, optical luminescence spectra of erbium in the semiconductors zinc selenide and silicon are analysed. Based on the optical characterisation, the g tensors for Zeeman splitting in an applied magnetic field are predicted for the crystal-field ground states of these centres. © 2001 Elsevier Science B.V. All rights reserved.

Keywords: Spectroscopy; Erbium; Zinc selenide; Silicon

1. Introduction

Spectroscopy is a general powerful tool for the investigation of electronic and atomic structure of matter, including solids and electronic centres in solids related to defects or impurities. By spectroscopy, transition energies and probabilities, parameters which are directly linked to the description of materials in fundamental terms of quantum mechanics are measured. Modern spectrometers, with high sensitivity and energy resolution, are capable of providing an abundance of very precise experimental data. In order to have the full profit of measured data, the interpretation in terms of solutions of the eigenvalue equations must be given. Unfortunately, often the system description is very complex due to, e.g., low symmetry or high spin. In general, an exact analytical solution of equations is only possible in specific cases of high symmetry. Applying perturbation theory, the range of analytical solutions can be extended, but perturbation methods suffer from limited applicability and unsatisfactory accuracy as well. To circumvent these strong limitations, the alternative method of numerical solution can be applied. This paper

describes a scheme for the calculation of energy levels, and at the same time wave functions, of rare-earth impurities in crystalline solids. The method is outlined and illustrated by the examples of the erbium ion in the semiconductor crystals zinc selenide and silicon, with the zincblende and diamond structures, respectively. The ground state of the Er^{3+} ion with electronic configuration $4f^{11}$ and, hence, orbital momentum $L = 6$ and spin $S = \frac{3}{2}$, is formed by spin–orbit interaction as a $^4I_{15/2}$ level. Calculations on this state are performed in the effective spin $J = \frac{15}{2}$ formalism. When included in a solid, the 16-fold degeneracy of the atomic state is partially lifted by crystal fields of ligand atoms of the host crystal with the formation of quartet and doublet levels. Application of a magnetic field, also considered in this paper, will result in 16 non-degenerate states.

2. Crystal-field Hamiltonian

In several cases, the erbium ion occupies a site of high symmetry, e.g. an undistorted substitutional site or interstitial T site. For rare-earth ions with $4f$ orbitals the only non-vanishing matrix elements are due to fourth- and sixth-order crystal-field operators. On the basis of a point-charge model, expressions for the potential are

*Corresponding author. Tel.: +31-20-5255614; fax: 31-20-5255788.

E-mail address: ammerlaan@science.uva.nl (C.A.J. Ammerlaan).

Table 1
Potentials representing the eight systems in the diamond crystal structure^a

System	Potential					
	x^2	y^2	z^2	xy	yz	zx
Cubic	—	—	—	—	—	—
Trigonal	—	—	—	δ	δ	δ
Tetragonal	—	—	γ	—	—	—
Orthorhombic-I	—	—	γ	δ	—	—
Monoclinic-I	—	—	γ	δ	ϵ	ϵ
Orthorhombic-II	—	β	γ	—	—	—
Monoclinic-II	—	β	γ	δ	—	—
Triclinic	—	β	γ	δ	ϵ	ζ

^a Normalised second-order operators are constructed in a way as demonstrated by Eq. (5).

derived as

$$V_4 = 35(x^4 + y^4 + z^4) - 21r^4 \quad (1)$$

and

$$V_6 = 231(x^6 + y^6 + z^6) - 315(x^4 + y^4 + z^4)r^2 + 90r^6. \quad (2)$$

Following the rules of quantum mechanics, the potentials are transformed into effective crystal-field operators. These are the familiar expressions $H_{cu4} = O_4^0 + 5O_4^4$ and $H_{cu6} = O_6^0 - 21O_6^4$. In case of lower

symmetry, additional operators are required. For the diamond and related crystal structures eight different systems can be distinguished, ranging from high-symmetry cubic, via axial trigonal and tetragonal, towards orthorhombic and monoclinic, to the lowest-symmetry case of the triclinic system. Associated crystal-field potentials represented by their leading second-order term are listed in Table 1. Again, the expressions for potential are transformed into operators by forming symmetrised forms of corresponding operators. From these operators, the matrix elements are formed in the basis set of the 16 spin states $|15/2, m_J\rangle$ of the erbium ion.

The more general expression as used in the analyses of cases to be presented is of the monoclinic-I form. It is given by

$$H_{cf} = V_{cf}(\cos \eta H_{cu} + \sin \eta H_{mo}) \quad (3)$$

with

$$H_{cu} = \sin \alpha H_{cu4} + \cos \alpha H_{cu6} \quad (4)$$

and

$$H_{mo} = \cos \gamma H_{zz} + \sin \gamma [\cos \delta H_{xy} + (1/2)\sqrt{2} \sin \delta (H_{yz} + H_{zx})]. \quad (5)$$

The usual scaling factors, $F(4) = 60$, $F(6) = 13860$, etc. are included in the operator expressions. Parameters η ,

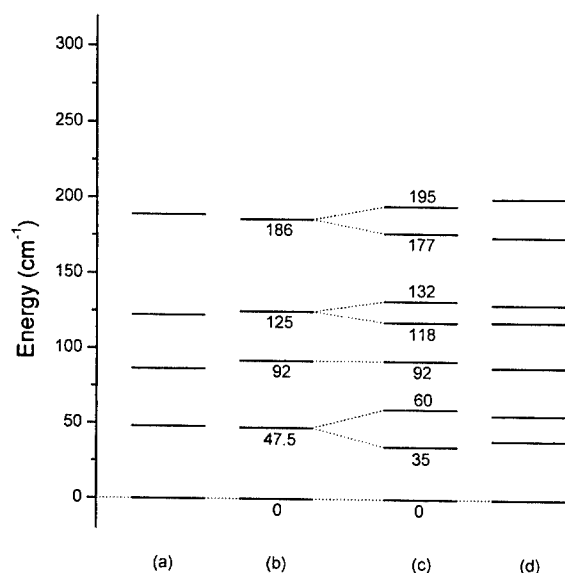


Fig. 1. Crystal-field energy levels in state $^4I_{15/2}$ of ZnSe:Er^{3+} . (c) Eight levels derived from the photoluminescence spectrum. (a) calculated levels in cubic symmetry with parameters $V_{cf} = 0.323$, $\alpha = -0.7^\circ$, (b) averaged to five-line spectrum, and (d) calculated levels in monoclinic-I symmetry, parameters $V_{cf} = 0.334$, $\eta = 26.3^\circ$, $\alpha = -2.7^\circ$, $\gamma = 37.0^\circ$, $\delta = 33.1^\circ$.

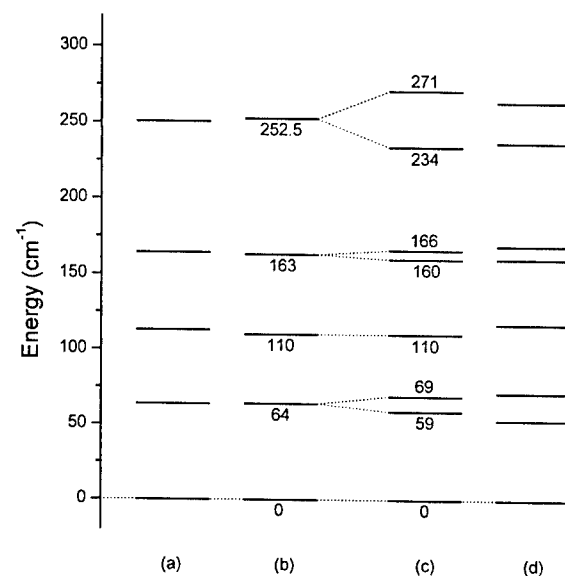


Fig. 2. Crystal-field energy levels in state $^4I_{15/2}$ of the Si-Er-I centre. (c) Eight levels derived from the photoluminescence spectrum. (a) calculated levels in cubic symmetry with parameters $V_{cf} = 0.430$, $\alpha = -1.7^\circ$, (b) averaged to five-line spectrum, and (d) calculated levels in orthorhombic-I symmetry, parameters $V_{cf} = 0.437$, $\eta = 19.3^\circ$, $\alpha = -2.0^\circ$, $\gamma = 24.8^\circ$, $\delta = 0^\circ$.

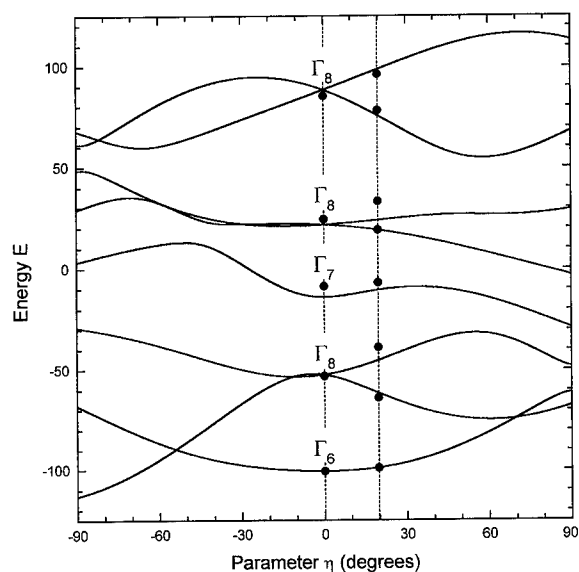


Fig. 3. Crystal-field energy levels E in state $^4I_{15/2}$ of the non-cubic ZnSe:Er^{3+} centre as a function of parameter η of tetragonal distortion, $V_{\text{cf}} = 0.323$, $\alpha = -0.7^\circ$. Data points in averaged cubic symmetry are shown at $\eta = 0^\circ$. Best match to potential with tetragonal symmetry is at $\eta = 19.7^\circ$.

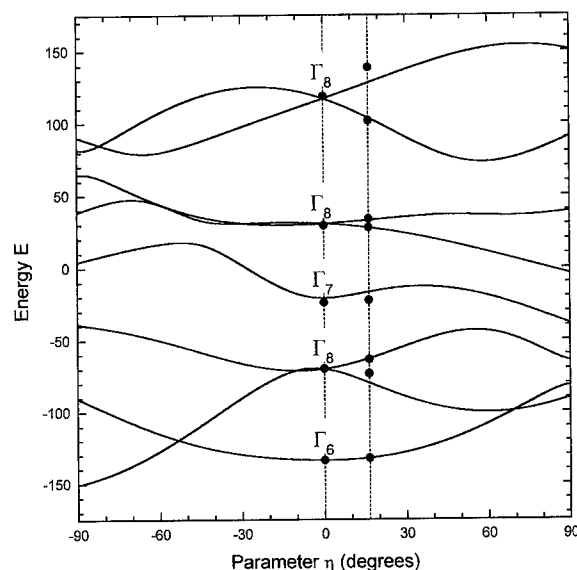


Fig. 4. Crystal-field energy levels E in state $^4I_{15/2}$ of the non-cubic centre Si-Er-1 as a function of parameter η of tetragonal distortion, $V_{\text{cf}} = 0.430$, $\alpha = -1.7^\circ$. Data points in averaged cubic symmetry are shown at $\eta = 0^\circ$. Best match to potential with tetragonal symmetry is at $\eta = 16.4^\circ$.

α , γ and δ , in the range $-90^\circ \leq \eta$, α , γ , $\delta \leq +90^\circ$, decide upon the form of the potential, the strength is given by factor V_{cf} . Energy eigenvalues, together with coefficients of wave functions, are obtained by diagonalisation of the 16×16 matrices.

3. Zeeman-effect Hamiltonian

By adding the energy of the Zeeman effect, the splitting of energy levels in a magnetic field $\mathbf{B}(B_x, B_y, B_z)$ can be calculated. The relevant Hamiltonian

$$H_{\text{mf}} = g_J \mu_B (B_x J_x + B_y J_y + B_z J_z) \quad (6)$$

does not introduce any new free adjustable parameters. For the ground state $^4I_{15/2}$ of erbium, the Landé factor $g_J = \frac{6}{5}$.

4. Luminescence spectra

Well-identified eight-line photoluminescence emission spectra are observed, among other substances, in zinc selenide and silicon [1,2]. From these spectra, the positions of the crystal-field states in the $^4I_{15/2}$ spin-orbit ground state are constructed. An inspection of the level diagrams, as given in Figs. 1(c) and 2(c), suggests

the presence of pairs of lines, which find their origin in a relatively small splitting of quartet levels in centres of near-cubic symmetry. On averaging the positions of line pairs, an analysis in cubic symmetry can be made [1]. The result is included in Figs. 1 and 2 in columns (a) and (b), and in Figs. 3 and 4 by the data points for $\eta = 0$. It can be concluded that satisfactory fits can be made. Also, with nearly equal values for the cubic field parameter α , the two spectra show a strong similarity.

Actually, the eight-line spectra belong to centres of lower-than-cubic symmetry. The splitting of quartet levels in an axial field of tetragonal symmetry is shown in Figs. 3 and 4, including experimental level positions at the best adjusted value of parameter η , governing the balance of cubic and tetragonal potentials. To obtain best match of the calculated level positions, least squares adjustments were made to the experimental data of both spectra. Parameter sets are summarised in Figs. 1 and 2. For the ZnSe centre a monoclinic-I potential was found to give best agreement. The Si-Er-1 centre was fitted with orthorhombic-I symmetry; adding any monoclinic-I component deteriorated the result. Typical root-mean-square errors are around 4 cm^{-1} , therefore larger than the estimated experimental errors of around 1 cm^{-1} .

5. Magnetic resonance spectra

With potential parameters determined from the optical spectra, the splitting of doublet levels in a magnetic field can be calculated in a straightforward manner with the Hamiltonian H_{mf} (Eq. (6)). Calculations were restricted to the regime of low magnetic field, in which the Zeeman effect is proportional to the magnetic field and, hence, the g tensors are constant. For centre ZnSe:Er^{3+} , the monoclinic-I symmetry is in agreement with the reported spectrum [1]. However, the calculated principal values $g_1 = 11.96$, $g_2 = 2.45$ and $g_3 = 4.86$ deviate substantially from values of the magnetic resonance spectrum labelled A. The identification of optical and EPR centres is thus not supported. For centre Si–Er-I, the calculated principal g values are $g_{[0,0,1]} = 3.33$, $g_{[1,1,0]} = 6.09$ and $g_{[1,-1,0]} = 10.27$. Evidently, the g tensor of an

orthorhombic Si–Er-I centre in silicon cannot be identified with the monoclinic-I EPR spectrum Si–OEr-I reported recently [3]. In view of different production conditions of the erbium optical centres the result is not surprising.

References

- [1] J. Dziesiaty, St. Müller, R. Boyn, Th. Buhrow, A. Klimakov, J. Kreissl, *J. Phys.: Condens. Matter* 7 (1995) 4271.
- [2] M.V. Stepikhova, B.A. Andreev, V.B. Shmagin, Z.F. Krasil'nik, V.P. Kuznetsov, V.G. Shengurov, S.P. Svetlov, W. Jantsch, L. Palmetshofer, H. Ellmer, *Thin Solid Films* 369 (2000) 426.
- [3] J.D. Carey, R.C. Barklie, J.F. Donegan, F. Priolo, G. Franzò, S. Coffa, *Phys. Rev. B* 59 (1999) 2773.



ELSEVIER

Physica B 308–310 (2001) 391–395

PHYSICA B

www.elsevier.com/locate/physb

Ultra-fast diffusion mechanism of the late 3d transition metal impurities in silicon

Y. Kamon, H. Harima, A. Yanase, H. Katayama-Yoshida*

Department of Condensed Matter Physics, The Institute of Scientific and Industrial Research, Osaka University, Osaka 567-0047, Japan

Abstract

Based upon *ab initio* electronic structure calculations with super-cells and an FLAPW method, we discuss the mechanism of the ultra-fast diffusion and the reduction of the migration barriers of the late 3d transition atom impurities of Co, Ni and Cu in silicon. The reduction mechanism of the migration barriers of the late 3d transition metal impurities is due to the pseudo-Jahn-Teller interaction, in which the six-fold-coordinated bonds are formed at the interstitial D_{3d} symmetry site and the energy gain by these bonds overcomes that of the four-fold-coordinated bonds at the tetrahedral T_d interstitial site. For Sc, Ti, V, Cr, Mn and Fe impurities in silicon, the T_d interstitial site is more stable than the D_{3d} site, however, for Co, Ni and Cu impurities, the D_{3d} interstitial site becomes more stable than the T_d interstitial site. Calculated migration barriers are in reasonably good agreement with the experimental data. We discuss the systematic variation of the chemical trend of the migration barrier of 3d transition metal impurities in silicon based upon the calculation. © 2001 Elsevier Science B.V. All rights reserved.

Keywords: Cu impurity; Cu-wire bonding; Diffusion; Migration barrier; Pseudo-Jahn-Teller interaction; Transition-metal impurity; Si; Diffusion coefficients

1. Introduction

The 3d transition metal impurities of Sc, Ti, V, Cr, Mn, Fe, Co, Ni and Cu (hereafter called 3d TM) in silicon show the large variation in the chemical trend of the diffusion coefficients up to 6 orders of magnitude in the difference within the 3d TM series [1]. Late 3d TM impurities in silicon, such as Co, Ni and Cu, diffuse ultra-fast and the measured diffusion coefficients are larger than that of Li or H. However, early 3d TM impurities, such as Sc, Ti, V and Cr, diffuse very slowly and the diffusion coefficient reduces almost 6 orders of magnitude compared with the late 3d TM impurities. For a long time, it has been believed that the large differences and chemical trend in the diffusion coefficient of 3d TM series in silicon is due to the difference of the

atomic size between the early 3d TM (large atomic size) and the late 3d TM (small atomic size). Diffusion coefficient (D) is given by $D = D_0 \exp(-\Delta E/k_B T)$, where ΔE is the migration barriers of the diffusion. Since the experimentally observed pre-factor D_0 of diffusion coefficient is approximately the same value for all the 3d TM impurities in silicon (see the data in Ref. [1]), the large chemical trend in the difference of D originates mainly from the difference of the diffusion barrier (ΔE) in the experiment. The experimental value ΔE changes one order from Sc (3.2 eV [1]), Ti (1.5–2.05 eV [1]), V (1.55–2.8 eV [1]), Cr (0.79–1.1 eV [1]), Mn (0.63–1.3 eV [1]), Fe (0.43–1.1 eV [1]), Co (0.37 eV [1]), Ni (0.13–0.76 eV [1]) to Cu (0.18–0.86 eV [1]) within the error bars depending on the various experimental methods. The mechanism of the large chemical trend in the observed ΔE should be ascribed to the electronic origin because the difference of the ΔE between the early 3d TM and the late 3d TM impurities in silicon is almost one order. So far, there is no *ab initio* electronic structure calculation to study the origin of the migration barriers

*Corresponding author. Tel.: +81-6-6879-8535; fax: +81-6-6879-8539.

E-mail address: hiroshi@sanken.osaka-u.ac.jp
(H. Katayama-Yoshida).

in the diffusion and the large chemical trend of the diffusion coefficients of 3d TM impurities in silicon.

Based upon the total energy calculation using *ab initio* electronic structure calculation by the FLAPW with super-cell method, we calculate the systematic variation of the migration barrier of the diffusion for 3d TM impurities of Sc, Ti, V, Cr, Mn, Fe, Co, Ni and Cu in silicon. We give the calculation method in Section 2. We discuss the principal mechanism of the reduction of the migration barrier of the late 3d TM impurities based upon the pseudo Jahn-Teller mechanism in Section 3. In Section 4, we give the calculated results and discussion. Summary is devoted in Section 5.

2. Calculation method

We used a full potential linearized augmented plane wave (FLAPW) method within the local density approximation (LDA) with the super-cells containing sixteen silicon atoms and one 3d TM. We assumed the non-magnetic state for the calculation of the migration barrier of 3d TM because most of the measurement of diffusion coefficient is done at high temperatures up to 1200°C. Here, solubility of Cu is about 10^{18} cm^{-3} at 1200°C and 10^{11} cm^{-3} at room temperature. It is well known from the EPR measurement that the isolated V, Cr, Mn and Fe impurities are located at the tetrahedral (T_d) interstitial site in silicon at low temperatures [2]. We have no available EPR data for Co, Ni and Cu impurities in silicon. Since these late 3d TM impurities diffuse very fast even at the low temperature, then it was very difficult to observe the EPR signals. We took into account the interstitial diffusion mechanism of 3d TM impurities in silicon and calculated the migration barrier through the interstitial diffusion mechanism. We did not take into account the kick-out mechanism or direct exchange mechanism of diffusion for 3d TM impurities in silicon. We have calculated migration barriers from the tetrahedral T_d interstitial site to the next nearest T_d site through the D_{3d} (the center of six-atom rings of the silicon, see Fig. 1). Total energy is calculated for seven positions of 3d TM on the straight lines between two T_d interstitial sites. The center of the nearest two T_d interstitial sites is the D_{3d} site. Since the large atomic radii of 3d TM at the interstitial site may bring a large lattice relaxation, we have taken into account the lattice relaxation in which we relaxed the first neighbor silicon with keeping its local symmetry. We used the Γ point for the total energy calculation in our super-cells. We expand the spherical harmonics up to $l = 7$ in each muffin-tin sphere ($r = 0.0991a$, where a is the lattice constant and $a = 10.86 \text{ \AA}$).

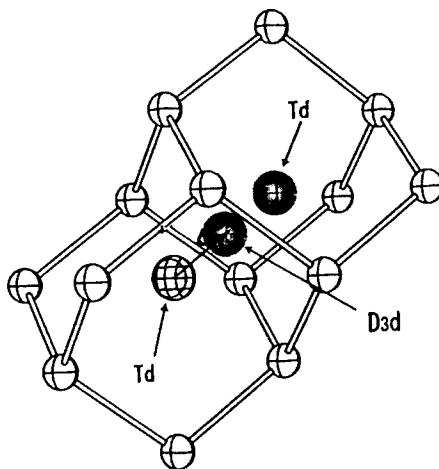


Fig. 1. Interstitial diffusion model through the path $T_d \rightarrow D_{3d} \rightarrow T_d$. For the total energy calculation, we take into account the lattice relaxation of first nearest neighbor silicon atoms.

3. Reduction mechanism of the migration barrier by pseudo-Jahn-Teller interaction

The general theory of the bi-stability of impurities in covalent semiconductors is given by a pseudo-Jahn-Teller interaction [3,4]. The ground state energy $E_0(Q)$ can be expanded by atomic displacement Q (see Fig. 2a),

$$E_0(Q) = E_0(0) + \frac{1}{2}(K_s + K_v)Q^2 + O(Q^4) + \dots \quad (1)$$

Here $K_s > 0$ is the static (s) elastic force constant, and $K_v < 0$ represent the charge relaxation due to the displacement-induced vibronic (v) coupling between the ground states $|0\rangle$ and excited states $|i\rangle$,

$$K_v = -2 \sum_{i \neq 0} \frac{|\langle 0 | \delta H / \delta Q | i \rangle|^2}{(E_i - E_0)}. \quad (2)$$

Pseudo-Jahn-Teller distortions ($K_s + K_v < 0$) are possible when the vibronic coupling competes favorably with static force constant (see Fig. 2b). Eqs. (1) and (2) suggest that one should search for structural instabilities in (i) intrinsically "soft" semiconductors (small K_s) such as amorphous semiconductors or semiconductor surface, and (ii) impurities with low-lying excited states that couple strongly to the ground state through displacement ($|K_v|$ large) such as the element with p-s coupling ($\langle 0 | = p$, $\langle i | = s$) in the second period of the periodic table or IIB–VI (IB–VII) semiconductors with d-s coupling ($\langle 0 | = d$, $\langle i | = s$) containing transition atoms [3].

Hydrogenated amorphous silicon (a-Si:H) is intrinsic soft (small K_s), therefore we have found a structural instability (bi-stability) $K_s + K_v < 0$ with p-s coupling between the states near the valence band maximum

(generally made up of atomic p-orbital) and the states near the conduction band minimum (generally s-orbitals) [5,6]. The impurity atoms of the second period of the periodic table, such as substitution nitrogen impurity in crystalline diamond (c-C:N), are also a candidate for the structural instabilities because p-s coupling between 2p- and 2s-orbital in nitrogen atom is very large (large $|K_v|$) with similar spatial distribution of 2p- and 2s-orbitals [7,8].

For the late 3d TM impurities such as Co, Ni and Cu in silicon, the impurity 3d states (e_g -states) in the band gap can couple strongly with the low-lying excited states of the conduction band ($4s$ -orbital) due to the strong d-s coupling in the pseudo-Jahn-Teller interaction. In the case of Cu impurity in silicon, the excitation energy from $3d^{10}4s^1$ to $3d^94s^2$ is very small compared with that of the early 3d TM such as Ti from $3d^34s^1$ to $3d^24s^2$. Then we can expect the structural instability for the late 3d TM impurities such as Co, Ni and Cu in silicon, in which T_d site becomes unstable due to the bi-stability and 3d TM impurity migrates from the T_d site to the more stable lower symmetry D_{3d} site by reducing the migration barrier. In this case we expect the reduction of the migration barrier with forming the bi-stability and the re-bonding from T_d site to D_{3d} site with forming another bond due to the strong d-s coupling in the pseudo-Jahn-Teller effect.

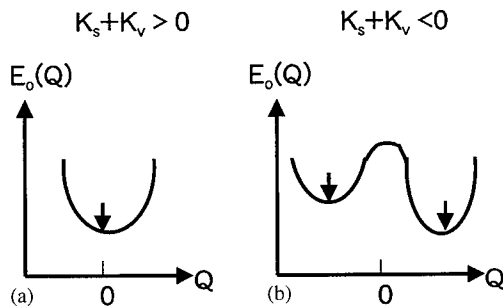


Fig. 2. Schematic explanation of the existence of bi-stability due to a pseudo-Jahn-Teller interaction. (a) Single local minimum, and (b) bi-stability of impurity site.

4. Calculated results and discussion

It is well known that the most of the 3d TM impurities in silicon are located at the tetrahedral interstitial site (T_d) by EPR experiments [2]. Very small Jahn-Teller distortions are observed due to the strong covalency relative to the ionicity in 3d TM impurities in silicon at the T_d site. Due to the p-d hybridization between the impurity 3d orbital and host p orbital at the T_d interstitial site, it forms a bonding state in the valence band and the anti-bonding counterpart is pushed up into the band gap. Since the p-d hybridization between the $3d\gamma$ [$3z^2-r^2$, x^2-y^2] orbitals and p orbitals [p_x, p_y, p_z] of the octahedrally coordinated second nearest neighbors is larger than the hybridization between the $3de$ [xy, yz, zx] orbitals and p orbitals [p_x, p_y, p_z] of the tetrahedrally coordinated first nearest neighbors, three degenerate t_{2g} -states are located below the two degenerate anti-bonding e_g -states [9,10]. The energy difference between the e_g - and t_{2g} -states is called the crystal field splitting (Δ_{CF}). If the exchange splitting (Δ_{EX}), the energy difference between the up spin and down spin states, is larger than the Δ_{CF} , high-spin state is realized [11]. Otherwise, the low-spin state is realized. Here, we did not take into account the spin-polarization because the diffusion experiment was done at high temperatures up to 1200°C.

Table 1 shows the stable atomic site and the calculated migration barriers with lattice relaxation and without lattice relaxation compared with the available experimental data. The large ionic radii of the early 3d TM impurities such as Sc, Ti, and V show the large lattice relaxation, however, the late 3d TM impurities such as Fe, Co, Ni and Cu show the small lattice relaxation (see Table 1). We found that the most stable atomic position of the Sc, Ti, V, Cr, Mn and Fe impurities in silicon is the T_d site, a maximum of the migration barrier is located at the D_{3d} site (the center site of the two connected T_d sites, and the center of six-fold-coordinated rings of silicon atoms in Fig. 1). On the other hand, the D_{3d} site becomes more stable for the late 3d TM impurities of Co, Ni and Cu in silicon. We show the adiabatic potential surface of Cu impurity in silicon through the migration path $T_d \rightarrow D_{3d} \rightarrow T_d$.

Table 1

Experimentally observed migration barriers [1], calculated migration barriers without lattice relaxation, calculated migration barriers with lattice relaxation of 3d transition metal impurities in silicon. The most stable atomic site of the impurity is indicated in the table

3d TM element	Sc	Ti	V	Cr	Mn	Fe	Co	Ni	Cu
Experiment (eV)	3.20	1.5–2.05	1.55–2.8	0.79–1.1	0.63–1.3	0.43–1.1	0.37	0.13–0.76	0.18–0.86
Calculation without lattice relaxation (eV)	5.48	4.97	3.96	2.78	1.74	0.95	0.49	0.75	0.35
Calculation with lattice relaxation (eV)	3.80	3.76	3.06	2.07	1.17	0.30	0.25	0.31	0.35
Most stable atomic site	T_d	T_d	T_d	T_d	T_d	T_d	D_{3d}	D_{3d}	D_{3d}

(see Fig. 3). The mechanism of the stability at the lower symmetry D_{3d} site of Co, Ni and Cu is due to the pseudo-Jahn-Teller interaction, as was discussed in Section 3, which is caused through the excitation from the $3d^n 4s^0$ to $3d^{n-1} 4s^1$. We compare the charge density of Cu impurity at the T_d site in $(1\bar{1}0)$ plane and the D_{3d} site in $(1\bar{1}0)$ plane (see Fig. 4). A weak

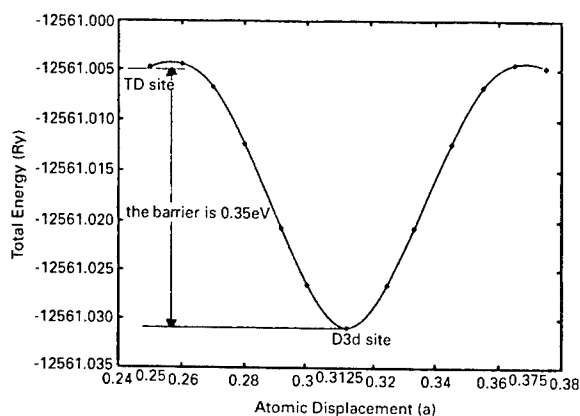


Fig. 3. Adiabatic potential surface of Cu impurities in silicon through the path $T_d \rightarrow D_{3d} \rightarrow T_d$. The position of Cu impurity's position is $(X, Y, Z) = (a, a, a)$ in the super-cell.

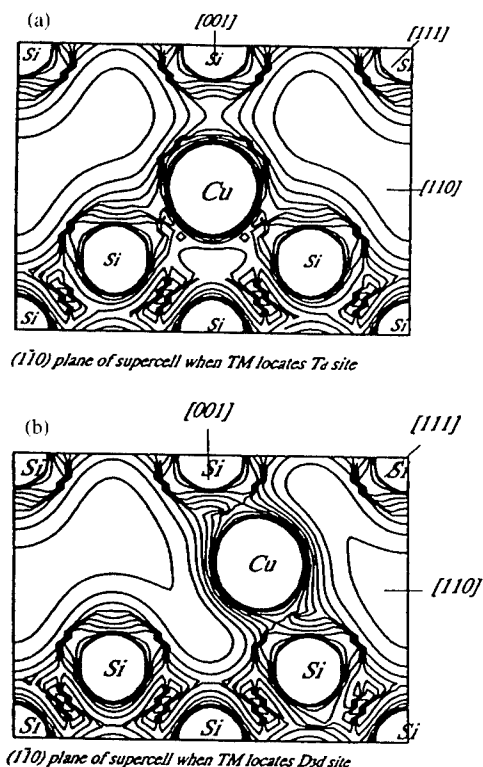


Fig. 4. Calculated the charge density of Cu impurity (a) at the T_d site in $(1\bar{1}0)$ plane and (b) the D_{3d} site in $(1\bar{1}0)$ plane.

bond between the anti-bonding state (conduction band) of silicon and Cu-4s state are formed at the D_{3d} site with stabilizing the bond. Since the coordination number of six at the D_{3d} site is larger than that of four at the T_d site, the energy gain at the D_{3d} site due to the pseudo-Jahn-Teller interaction overcomes that of at the T_d site. We can confirm this stability mechanism in the Cu-4s partial density of states in Fig. 5, in which the Cu-4s state are occupied below the Fermi level (E_F) with forming a bond between the Si anti-bonding state and the Cu 4s states (see Fig. 4). We calculate the diffusion

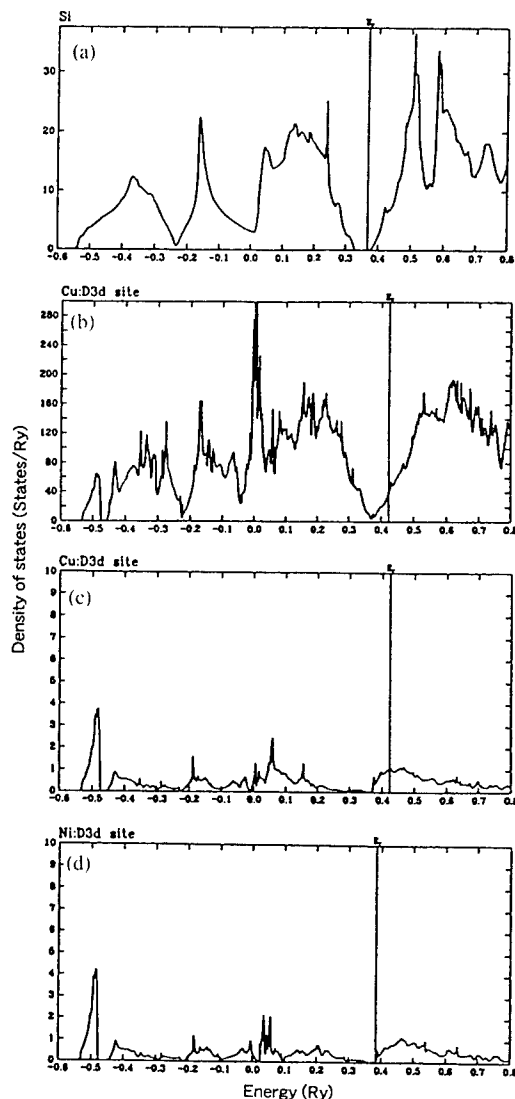


Fig. 5. Calculated (a) total density of states of host silicon in the super-cell, (b) total density of states of Cu at the D_{3d} site, (c) Cu-4s partial density of states at the D_{3d} site, where Cu-4s state are occupied below the Fermi level (E_F) with forming a bond between the Si anti-bonding state and the Cu-4s states, and (d) Ni-4s partial density of states at the D_{3d} site.

barriers using the adiabatic potential surfaces of the 3d TM impurities in silicon through the paths $T_d \rightarrow D_{3d} \rightarrow T_d$ and $D_{3d} \rightarrow T_d \rightarrow D_{3d}$ sites (see Fig. 2). Calculated diffusion barriers are in good agreement with the experimental data within the experimental error bars.

The development of the control method for the ultra-fast diffusion of Cu becomes very important from the technological point of view, because recently a Cu-wire bonding in silicon devices to reduce the contact resistivity has also become very important in silicon device technology where the migrated interstitial Cu impurity works deep in the impurity levels and acts as a carrier killer. In order to develop the impurity-gettering technology of Cu impurities in silicon, we should understand the mechanism of the ultra-fast diffusion of Cu. Then, we can speculate and design a new impurity-gettering technology of Cu impurity in silicon based upon the calculation.

5. Summary

We discuss the chemical trend of the migration barrier and the electronic structure of 3d transition metal impurities in silicon by *ab initio* electronic structure calculations with super-cells and FLAPW method. We calculate the electronic structure and migration barrier of diffusion of 3d TM impurities in silicon. We propose the mechanism of the ultra-fast diffusion and the reduction mechanism of the migration barriers of the late 3d transition atom impurities of Co, Ni and Cu in silicon. The reduction mechanism of the migration barriers of the late 3d transition metal impurities such as Co, Ni and Cu is due to the pseudo-Jahn-Teller interaction, in which the six-fold-coordinated bonds are formed at the lower D_{3d} symmetry at the interstitial site and the energy gain by these bonds overcomes that of the four-fold-coordinated bonds at the tetrahedral T_d interstitial site. For Sc, Ti, V, Cr, Mn and Fe, the T_d interstitial site is more stable than the D_{3d} site, however, for Co, Ni and Cu, the D_{3d} interstitial site becomes more

stable than the T_d interstitial site. Calculated migration barriers are in good agreement with the available experimental data.

Acknowledgements

This work was partially supported by a JSPS Research for the future Program in the area of Atomic Scale Surface and Interface Dynamics, a Grant-In-Aid for Scientific Research on the Priority Area (A), and (B), and Osaka University, SANKEN-COE from the Japanese Ministry of Education, Culture, Sports, Science and Technology.

References

- [1] E.R. Weber, Appl. Phys. A 30 (1983) 1.
- [2] G.W. Ludwig, H.H. Woodbury, Solid State Phys. 13 (1962) 223.
- [3] S-H. Wei, S.B. Zhang, A. Zunger, Phys. Rev. Lett. 70 (1993) 1639.
- [4] D.L. Becke (Ed.), Diffusion in Semiconductors, Springer, Berlin, 1998.
- [5] H. Katayama-Yoshida, N. Orita, in: K. Nasu (Ed.), Relaxations of Excited State and Photo-Induced Structural Phase Transitions, Springer Series in Solid-State Sciences, Vol. 124, Springer, Berlin, 1997, pp. 220–228.
- [6] T. Matsumura, H. Katayama-Yoshida, N. Orita, Proceedings of MRS Symposium (Amorphous Silicon Technology '95), Vol. 377, 1995, pp. 275.
- [7] T. Nishimatsu, H. Katayama-Yoshida, N. Orita, Proceedings of the 24th International Conference on the Physics of Semiconductors, D. Gershoni (Ed.), World Scientific, Singapore, 1999, pp. 201.
- [8] T. Nishimatsu, H. Katayama-Yoshida, N. Orita, Physica B 302/303 (2001) 149.
- [9] H. Katayama-Yoshida, A. Zunger, Phys. Rev. Lett. 53 (1984) 1256.
- [10] H. Katayama-Yoshida, A. Zunger, Phys. Rev. Lett. 55 (1985) 1618.
- [11] H. Katayama-Yoshida, Int. J. Mod. Phys. B1 (1987) 1207.



ELSEVIER

Physica B 308–310 (2001) 396–399

PHYSICA B

www.elsevier.com/locate/physb

Nitrogen effect on gold diffusion in Cz Si

A.L. Parakhonsky^a, E.B. Yakimov^{a,*}, D. Yang^b^a*Institute of Microelectronics Technology, Russian Academy of Sciences, 142432 Chernogolovka, Russia*^b*State Key Lab of Silicon Material, Zhejiang University, Hangzhou, China*

Abstract

Gold diffusion in Czochralski grown (Cz) Si with and without nitrogen, introduced during growth, has been studied. It is found that the Au concentration in substitutional positions after diffusion at 700°C, 750°C and 800°C in Cz Si doped with nitrogen is always less than that in usual Cz Si. A decrease of the substitutional Au concentration in nitrogen doped crystals can be explained under the assumptions that nitrogen or nitrogen-related centers stimulates oxygen precipitation and suppresses the grown-in defect formation. © 2001 Elsevier Science B.V. All rights reserved.

Keywords: Nitrogen; Silicon; Gold diffusion; Self-interstitials

1. Introduction

Gold and platinum diffusion is now widely used for studying the defect distribution in crystalline silicon [1–7]. These impurities are known to diffuse at high temperatures via the kick-out mechanism [8]. That means that gold can diffuse very quickly over interstitial sites Au_i and then Au_i are transformed into electrically active substitution sites Au_s via the kick-out reaction



This reaction is accompanied by self-interstitial *I* generation and the excess self-interstitials should be annihilated at sinks: the surface in defect-free silicon or additionally on bulk defects. Therefore, the *I* concentration and, in turn, the Au_s distribution is sensitive to the change of the self-interstitial generation or annihilation rates. So, the defects playing a role of effective sinks for self-interstitial atoms could lead to an essential increase in the Au_s concentration. Such an increase was observed in dislocated [1] or ion-implanted [4–6] silicon and in silicon containing

grown-in vacancy type defects [3]. On the other hand, a decrease in the Au_s concentration is usually associated with an enhanced self-interstitial generation that could lead to a reversion of the kick-out reaction. An essential decrease in the Au_s concentration was observed [2] after gold diffusion in Czochralski (Cz) grown silicon samples, in which the effective nucleation sites for oxygen precipitation were generated by preliminary annealing, and in Si with H- and He-implantation induced nanocavities [7].

Nitrogen is known to affect many of silicon properties [9]. Thus, it locks dislocations, increasing the Si wafer mechanical strength [10,11] and suppresses the creation of oxygen-related thermal donors [12,13]. Recently it was found that nitrogen can enhance the nucleation of oxygen precipitation [14] and suppress void defects aggregated by vacancies [15]. The nitrogen solubility limit in Si is rather small (about 10¹⁵ cm⁻³); usually it is present in silicon in an electrically inactive state, only a small part of the nitrogen interacting with oxygen produces shallow donors [16,17]. Therefore, only a limited number of characterization techniques can be used to reveal the nitrogen-related defects that study their effect on Si properties. One of such methods could be associated with a study of nitrogen effect on the generation and annihilation of intrinsic point defects by investigations of gold diffusion. The sensitivity of gold diffusion to grown-in defects increases with decreasing

*Corresponding author. Tel.: +7-095-9628074; fax: +7-095-9628047.

E-mail address: yakimov@ipmt-hpm.ac.ru (E.B. Yakimov).

diffusion temperature. Oxygen precipitation leading to self-interstitial generation also depends on the annealing temperature. Therefore, to separate the effect of both processes the gold diffusion should be carried out in a rather wide temperature range.

In the present paper a comparative study of the Au_s concentration in n-type Si grown by the Czochralski (Cz) method in an argon or nitrogen atmosphere after diffusion annealing in the temperature range from 700°C to 800°C, has been carried out. It is shown that in nitrogen containing crystals the Au_s concentration is lower than that in Si grown in an argon atmosphere. The results obtained are explained taking into account the nitrogen-related stimulation of oxygen precipitation and the suppression of vacancy type grown-in defect formation.

2. Experimental

Cz Si wafers of n-type conductivity with a thickness of 300 μm doped with phosphorus to a concentration of about 10^{14} cm^{-3} were used in our experiments. Nitrogen doped Si ingots (NCz) were grown in a nitrogen atmosphere while the Cz ingots without nitrogen were grown in similar conditions but in an argon atmosphere. Pairs of Cz and NCz Si wafers cut from almost the same tail or head parts of ingots, which contain very similar oxygen concentrations of about $1.0 \times 10^{18} \text{ cm}^{-3}$ and similar phosphorus concentrations, were compared. The oxygen and carbon concentrations in the samples were measured by IR absorption at room temperature using the calibration factors $3.14 \times 10^{17} \text{ cm}^{-2}$ for oxygen and $1.0 \times 10^{17} \text{ cm}^{-2}$ for carbon, respectively. The carbon concentration was less than $5 \times 10^{15} \text{ cm}^{-3}$. All samples studied were subjected to annealing at 650°C for 30 min after growth to anneal oxygen-related thermal donors. In the NCz samples nitrogen–oxygen shallow donors are formed under such annealing [16,17]. On one side of the samples, gold films with a thickness of about 30 nm were evaporated. Then gold diffusion annealing was carried out at 700°C, 750°C or 800°C for 1 h in air. After diffusion annealing a layer of about 50 μm thickness was removed by mechanical polishing from one side of all gold diffused samples. Then the samples were chemically etched for removing the damaged layer, and Schottky barriers were formed on the polished surface by thermal evaporation of Au. Ohmic contacts were produced by scratching the back side of the samples with the eutectic InGa alloy. The Au_s concentration and its depth profile were measured by deep level transient spectroscopy (DLTS). The total Au_s concentration was calculated as a sum of the concentrations of centers with the deep levels $E_c - 0.54 \text{ eV}$ and $E_c - 0.20 \text{ eV}$, associated with Au_s and gold–hydrogen complexes formed under chemical etching [18,19], respectively.

3. Results and discussion

First of all it should be mentioned that, as an extrapolation of high temperature data [1,20,21] shows (Fig. 1), after 1 h diffusion the Au_s concentration in the middle of the wafer at diffusion temperatures below 840°C should be lower than that of the Au_i solubility limit. Therefore the question arises if the resulting Au_s concentration is determined by the kick-out reaction at the diffusion temperatures used in the present study. To check this point the gold profile in Cz Si after 700°C diffusion was measured. It is seen (Fig. 2) that even in this samples, which demonstrates the deviation of Au_s concentration from that in defect-free Si (see below), the profile measured correlates well with that predicted by the kick-out mechanism. Besides, the measured Au_s concentrations correlate rather well with those predicted by the extrapolation of the high temperature data (Fig. 3). In this figure the results obtained on the

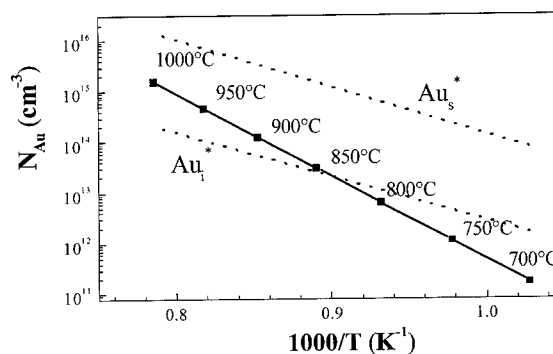


Fig. 1. Au_s concentration in the middle of the wafer after 1 h diffusion obtained by extrapolation from the high temperature experiments [1,20,21]. The solubility limits for Au_i and Au_s , calculated using the dependences presented in Ref. [21] are shown by dotted lines.

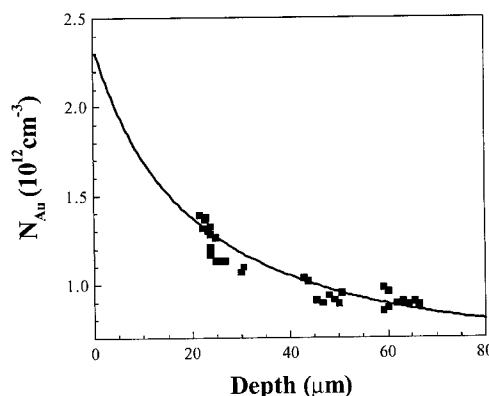


Fig. 2. Au_s profiles measured in Cz silicon after 700°C diffusion (points) and predicted by the kick-out mechanism (solid line).

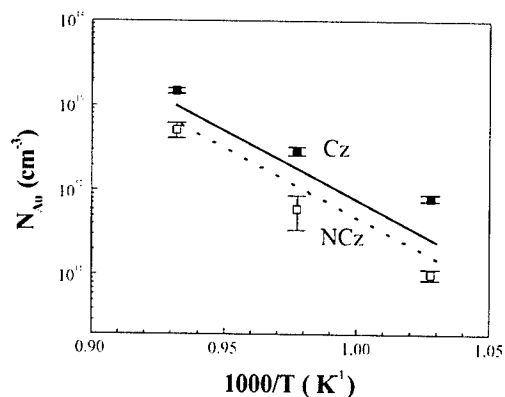


Fig. 3. Au_i concentrations measured by the DLTS in Cz and NCz silicon (head part of ingots) after diffusion annealing at 700°C, 750°C, and 800°C for 1 h. The predicted Au_i concentrations at the depth of 50 μm and in the middle of sample are shown by the solid and dotted lines, respectively.

samples cut from the head part of the ingots are presented. On the samples cut from the tail part of the ingots the results are practically the same.

It is seen that at all diffusion temperatures used, the Au_i concentration in NCz samples is lower than that in the corresponding Cz samples and the difference between the two types of crystals increases with decreasing diffusion temperature. The calculated Au_i concentrations in defect-free Si at a depth of 50 μm and in the middle of the wafer are also presented in Fig. 3. The first values are obtained by multiplying the last ones by 1.6 (the coefficient obtained from the kick-out profile). It is seen that the Au_i concentration in Cz samples after 750°C and 800°C diffusion is close to that in defect-free Si but after 700°C diffusion it is about three times larger. This could be explained assuming that some vacancy type grown-in defects are present in the Cz samples. At low diffusion temperatures these defects can play the role of sinks for self-interstitials that leads to the Au_i concentration increase. The increase of diffusion temperature leads to an increase of self-interstitial generation rate that can lead to the disappearance or reconstruction of these grown-in defects.

The Au_i concentration in NCz samples at all temperatures used is lower than that predicted for defect-free Si. This decrease can be explained as the result of an enhanced oxygen precipitation in such crystals that was already observed in Ref. [13]. Self-interstitials generated under oxygen precipitation can reverse the kick-out reaction and decrease the Au_i concentration. No effect of grown-in defects on the Au_i concentration was observed in NCz Si after 700°C diffusion. This could mean that the oxygen precipitation effect masks that of the grown-in defects or, more

probably, that nitrogen suppresses the formation of such defects.

4. Conclusion

Thus, the decrease of the Au_i concentration in NCz samples as compared with that in Cz samples after gold diffusion in the temperature range from 700°C to 800°C is observed. The difference is found to increase with decreasing of diffusion temperature. The results obtained can be explained by the effect of nitrogen on the grown-in defect formation and/or by the nitrogen-related enhancement of oxygen precipitation.

Acknowledgements

One of the authors, D. Yang, would like to thank the Natural Science Foundation of China for the financial supports (No. 59976035 and 50032010).

References

- [1] E. Yakimov, G. Mariani, B. Pichaud, *J. Appl. Phys.* 78 (1995) 1495.
- [2] E. Yakimov, I. Perichaud, *Appl. Phys. Lett.* 67 (14) (1995) 2054.
- [3] M. Jacob, P. Pichler, H. Russel, R. Falster, *J. Appl. Phys.* 82 (1997) 182.
- [4] C. Venezia, D.J. Eaglesham, T.E. Haynes, A. Agarwal, D.C. Jacobson, H.-J. Gossmann, F.H. Baumann, *Appl. Phys. Lett.* 73 (1998) 2980.
- [5] D.C. Schmidt, B.G. Svensson, N. Keskitalo, S. Godey, E. Ntsoenzok, J.F. Barbot, C. Blanchard, *J. Appl. Phys.* 84 (1998) 4214.
- [6] J.S. Williams, M.J. Conway, J. Wong-Leung, P.N.K. Deenapanray, M. Petravic, B.A. Brown, D.J. Eaglesham, D.C. Jacobson, *Appl. Phys. Lett.* 75 (1999) 2424.
- [7] I. Perichaud, E. Yakimov, S. Martinuzzi, *Electrochem. Soc. Proc.* 17 (2000) 341.
- [8] W. Frank, U. Gösele, H. Mehrer, A. Seeger, in: G.E. Murch, A.S. Nowick (Eds.), *Diffusion in Crystalline Solids*, Academic, Orlando, FL, 1984, p. 64 (Chapter 2).
- [9] H.J. Stein, in: J.C. Mikkelsen, S.J. Pearton, J.W. Corbett, S.J. Pennycook (Eds.), *Oxygen, Carbon, Hydrogen and Nitrogen in Crystalline Silicon*, Vol. 59, MRS, PA, 1985, p. 523.
- [10] K. Sumino, I. Yonenaga, M. Imai, T. Abe, *J. Appl. Phys.* 54 (1983) 5016.
- [11] D. Li, D. Yang, D. Que, *Physica B* 273–274 (1999) 553.
- [12] D. Yang, D. Que, K. Sumino, *J. Appl. Phys.* 77 (1995) 943.
- [13] D. Yang, R. Fan, L. Li, D. Que, K. Sumino, *J. Appl. Phys.* 80 (1996) 1493.
- [14] D. Yang, X. Ma, R. Fan, J. Zhang, L. Li, D. Que, *Physica B* 273–274 (1999) 308.
- [15] A. Ikari, K. Nakai, Y. Tachikawa, H. Deai, Y. Hideki, Y. Ohta, N. Masahashi, S. Hayashi, T. Hoshino, W. Ohashi, *Solid State Phenomena* 69 (1991) 161.

- [16] A. Hara, T. Fukuda, T. Miyabo, I. Hirai, *Appl. Phys. Lett.* 54 (1989) 626.
- [17] M. Suezawa, K. Sumino, H. Harada, T. Abe, *Jpn. J. Appl. Phys.* 25 (1986) L859.
- [18] E.O. Sveinbjornsson, O. Engstrom, *Appl. Phys. Lett.* 61 (1992) 2323.
- [19] A.L. Parakhonsky, O.V. Feklisova, S.S. Karelin, N.A. Yarykin, *Semiconductors* 30 (4) (1996) 362.
- [20] N.A. Stolwijk, B.J. Hölzl, W. Frank, E.R. Weber, H. Mehrer, *Appl. Phys. A* 39 (1986) 37.
- [21] H. Zimmermann, H. Ryssel, *Appl. Phys. A* 55 (1992) 121.



ELSEVIER

Physica B 308 310 (2001) 400–403

PHYSICA B

www.elsevier.com/locate/physb

New electron spin resonance spectra from iron–vacancy pair in silicon: II. Hyperfine interactions and isotopic effect

T. Mchedlidze*, M. Suezawa

Institute for Materials Research, Tohoku University, 2-1-1 Katahira, Aoba-ku, Sendai 980-8577, Japan

Abstract

We studied the TU2 and TU3 ESR spectra from an iron–vacancy pair in iron-doped and electron-irradiated float-zone grown silicon samples. Isotopic shifts in the fine structure term and hyperfine and superhyperfine interaction terms of the spin Hamiltonian are considered in detail. We obtained that the change in the spin value of the defect is accompanied by a modification of the iron atom position. The existing model fails to explain observed large anisotropy of the isotopic effect. © 2001 Elsevier Science B.V. All rights reserved.

Keywords: Si; Fe; Vacancy; ESR

1. Introduction

The presence of isotopic shifts in the ZFS (fine structure) term of the spin Hamiltonian of newly observed spectra from the iron–vacancy pair in Si requires simultaneous treatment of terms related to hyperfine (HF) and superhyperfine (SHF) splitting and the isotopic shift. A quantitative model of the isotopic shifts in the ESR spectra has not yet been developed. Qualitatively, the effect can be considered in terms of the theory for localized vibrational modes (see, for example, Ref. [1]).

Vibrations of atoms near equilibrium positions in a defect occur with local vibrational mode frequency $\omega_E \propto (M_0/M)^{1/2}$, where M_0 and M are the masses of lattice and defect atoms, respectively (Einstein's model). Hence, isotopes of the defect atom will affect ω_E . Lattice atom isotopes, which are neighbor to the defect, should affect “local” M_0 value, also causing variation in ω_E . Intensities of relevant vibrations will combine if several lattice atoms are situated in so-called neighbor shells, equivalent positions in relation to the defect (similar to

the SHF interactions in ESR). However, such effect should decrease sharply with the distance from the defect.

Change in the local vibration frequency may modify the interaction terms of the spin Hamiltonian if a local interatomic potential has significant anharmonic terms and/or if an interaction term nonlinearly depends on atom displacement amplitude. In one and/or both cases, the ESR signal splits up into a number of peaks defined by the total number of isotopes and the defect structure. The intensity of each peak is determined by the isotopic abundance and number of lattice sites in the relevant shell.

Isotopic shifts have been observed for hyperfine (HF) and superhyperfine (SHF) interaction terms [2–7] and for the ZFS term [8–12] of the spin Hamiltonian in various systems, including Si. However, the small magnitude of the effect prevented detailed investigation. Some theoretical aspects of the effect were also considered [13,14].

In the first part of our report [15], we presented results on unique properties of new TU2 and TU3 ESR spectra in Si and identified the composition of the related defect. Herein, we consider the microscopic structure of the defect, the HF and SHF terms and isotopic shifts in the ZFS term of the spin Hamiltonian.

*Corresponding author. Fax: +81-22-215-2041.

E-mail address: teimuraz@imr.tohoku.ac.jp
(T. Mchedlidze).

2. Experimental

Details of sample preparation and experimental procedures are given in the first part of the report [15]. Peaks related to the HF and SHF splitting in the TU2 and TU3 spectra were not well resolved. Moreover, peaks related to the isotopic shifts in the ZFS term complicated the spectra. To determine the positions and intensities of the individual resonance peaks, it was necessary to decompose the spectra.

Fitting of experimental spectra from samples doped with natural iron was carried out only after the isotopic shifts related to iron isotopes and HF splitting parameters were determined from analyses of Si samples enriched with ^{57}Fe and ^{54}Fe isotopes. All experimental spectra were fitted with the same, the least possible number of individual peaks having similar width and shape (a derivative of Gaussian function). Intensity of each peak was defined from the main peak, i.e. the $^{56}\text{Fe}^{28}\text{Si}$ isotope peak, using isotopic abundances and the supposed number of equivalent neighbor Si atoms in a shell. The width and intensity of the main peak were allowed to vary with a change in sample orientation.

3. Results and discussion

In Figs. 1a and b, the experimental and fitted spectra are presented together with “stick diagrams”. Similarly, precise fits were obtained for all sample orientations toward the static magnetic field except in the close vicinity of the “transient orientations” [15], where fitting was complicated by the small intensity and large width of the peaks.

The character of angular dependencies of the HF/SHF splitting and isotopic shifts was similar for all isotopes of iron and Si. In Figs. 2a and b, results obtained for the case of ^{57}Fe isotope are presented as a typical example. These data were obtained directly from experiments on ^{57}Fe -enriched samples. The fitted parameters for the HF interaction are presented in Table 1. The HF splitting anisotropy was not affected by the isotopic shifts of the ZFS term of the spin Hamiltonian.

From the fitting results for the TU2 and TU3 spectra, the SHF interaction with two shells of equivalent lattice atoms can be separated, one shell containing 3 Si atoms and the other containing 6 Si atoms in equivalent positions. Interestingly, the SHF interaction parameter of the shell with 3 Si atoms is larger than that of the shell with 6 Si atoms in the case of the TU3 spectra. On the contrary, for the TU2 spectra the interaction with atom shell containing 6 Si atoms is stronger. Considering the microscopic structure of the defect, two appropriate lattice sites along the defect axis to a neighboring vacancy can be proposed for the iron atom: a tetrahedral interstitial T_d site (3 Si atoms in the nearest shell and 6 in

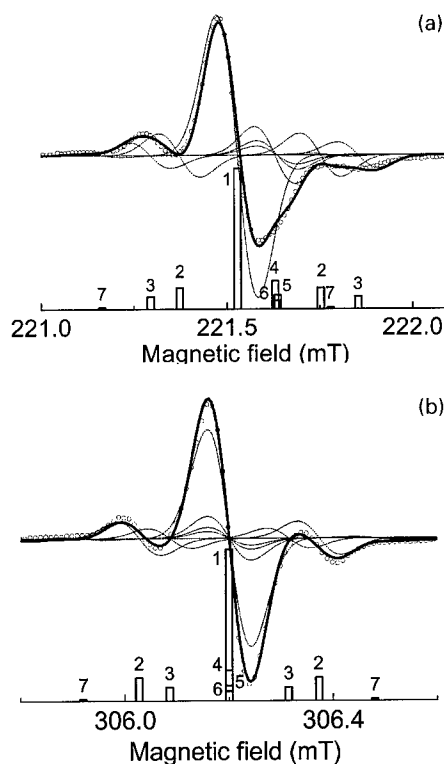


Fig. 1. Experimental (symbols) and fitted (thick line) TU3 spectra at $B \parallel [1\ 1\ 0]$ (a) and TU2 spectra at $B \parallel [1\ 1\ 1]$ (b). Thin dashed lines and numbered bars represent individual fitted peaks. Bar height corresponds to relative intensity. Numbers: (1) $^{56}\text{Fe}^{28}\text{Si}$; (2) $^{56}\text{Fe}^{29}\text{Si}$ (6 Si shell); (3) $^{56}\text{Fe}^{29}\text{Si}$ (3 Si shell); (4) $^{56}\text{Fe}^{30}\text{Si}$ (6 Si shell); (5) $^{56}\text{Fe}^{30}\text{Si}$ (3 Si shell); (6) $^{54}\text{Fe}^{28}\text{Si}$; (7) $^{57}\text{Fe}^{28}\text{Si}$. Experimental conditions: $f_{\text{RES}} = 9.064\text{ GHz}$, $T = 11\text{ K}$, B in the $(1\ \bar{1}\ 0)$ plane.

the second shell) and a position between the T_d and an antibonding (AB) site (6 Si atoms in the nearest and 3 in the second shell). Thus, we can suppose that the change in the magnitude of the defect spin in the magnetic field [15] is accompanied by modification of defect configuration: the iron atom positioned at the T_d site in the case of TU3 ($S = \frac{3}{2}$) is transferred closer to the AB site along the axis of the defect in the case of TU2 ($S = 1$). This microscopic model for the $(\text{Fe}_i\text{-V})^0$ pair in Si differs from that of substitutional iron $(\text{Fe}_s)^+$ proposed in [12] for the similar samples. However, we can suppose that the suppression of the TU2 and TU3 signal by the illumination, observed in our experiments, is caused by charging and transformation of the $(\text{Fe}_i\text{-V})^0$ pair to the $(\text{Fe}_s)^+$ configuration, responsible for the NL19 ESR spectra.

The magnitude of the isotopic shift of the TU3 spectra is constant in the limits of experimental error for rotation angles that are far from the transient orientations. The fractional change in the ZFS parameter

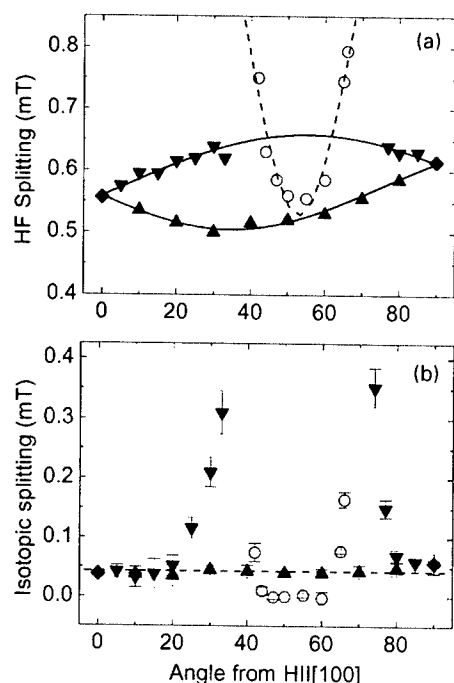


Fig. 2. Results of ^{57}Fe enriched Si sample measurements: HF splitting (a) and separation between the main $^{56}\text{Fe}^{28}\text{Si}$ peak and the center of $^{57}\text{Fe}^{28}\text{Si}$ HF doublet (b). Circles represent results for TU2; other symbols represent results for TU3 (∇) signal from defect axis parallel to $[1\ 1\ 1]$; (Δ) signal from $[1\ \bar{1}\ \bar{1}]$). Solid and dashed lines in (a) represent fitting results for the HF parameter. The dashed line in (b) represents averaged data for rotation angles far from the transient orientations. All experimental conditions are as indicated in Fig. 1.

Table 1

HF and SHF parameters of spin Hamiltonian. We used the factor $P(\text{mT}) = g \times 4.66855 \times P(10^{-4}\text{cm}^{-1})$ for conversion of energy units [16]

Parameter/shell ($\times 10^{-4}\text{cm}^{-1}$)	TU2	TU3
$A(^{57}\text{Fe})$	4.5 ± 0.2	6.48 ± 0.03
$A_-(^{57}\text{Fe})$	26.6 ± 1.4	5.07 ± 0.03
$A(^{29}\text{Si}/3\text{Si})$	2.2 ± 0.1	4.51 ± 0.06
$A_-(^{29}\text{Si}/3\text{Si})$	6 ± 2	6.86 ± 0.14
$A(^{29}\text{Si}/6\text{Si})$	3.2 ± 0.2	3.10 ± 0.04
$A_-(^{29}\text{Si}/6\text{Si})$	16 ± 2	4.52 ± 0.08

caused by the substitution of ^{56}Fe isotope with ^{57}Fe , calculated using the expression derived in Ref. [13], equals to $\delta D/D \approx -(1.4 \pm 0.2) \times 10^{-4}$. This value is close to that reported in Refs. [8,10,13], but much smaller than that reported for the NL19 spectra [12]. In the vicinity of the transient orientations, the magnitude of isotopic shift significantly increases for the TU3 spectra and emerges for the TU2 spectra.

Table 2

Isotopic splitting (ΔH) caused by iron and lattice atom isotopes in the TU3 spectra for the rotation angles far from the transient orientations

Isotope	Shell	ΔH (mT)
^{54}Fe		0.11 ± 0.02
^{57}Fe		-0.042 ± 0.005
^{29}Si	3 Si	0.046 ± 0.013
^{30}Si	3 Si	0.11 ± 0.02
^{29}Si	6 Si	0.035 ± 0.012
^{30}Si	6 Si	0.12 ± 0.02

In Table 2 experimental splitting magnitudes are presented for various isotopes and lattice atom shells in the case of the TU3 spectra. These data are calculated for rotation angles that are far from the transient orientations. It is clearly seen that isotopes of iron and those of the surrounding Si atoms modify the ZFS parameter in an opposite manner. A similar phenomenon was previously reported for the Sn–vacancy pair in Si [10] and agrees with Einstein's model. The shift magnitudes can also be fitted well with the $(M_0/M)^{1/2}$ dependence. In the limits of experimental errors we did not detect variation in the magnitude of the isotopic shifts with temperature in the range from 6 to 18 K.

Obtained results agree with the model for isotopic shifts [13] when sample rotation angle is far from the transient orientations. Observed anisotropy and large magnitude of the effect near the transient orientations requires further investigation and explanation. One possibility is to suppose that the amplitude of iron atom vibration close to the transient orientations becomes much larger due to the changes in defect structure, causing an increase in the isotopic shifts.

In conclusion, two different spin values for the ESR spectra of the iron–vacancy pair in silicon are related to the defect structure with different positions of iron atom along the axis to a neighboring vacancy. The TU3 spectra with $S = \frac{3}{2}$ originate from the configuration in which an iron atom is positioned at the T_d site, while the TU2 spectra with $S = 1$ originate from the defect with iron positioned between the T_d and AB sites. The cause of the observed transition remains to be established. The existing models for the isotopic shift cannot explain the anisotropy and large magnitudes of the shifts observed near the transition orientations.

References

- [1] M. Lanoo, J. Bourgoin, Point Defects in Semiconductors I, Theoretical Aspects, Springer, Berlin, Heidelberg, New York, 1981, p. 165.

- [2] Ch. Hoentzsch, J.M. Spaeth, *Phys. Stat. Sol. B* 94 (1979) 497, and references therein.
- [3] D. Purins, M. Karplus, *J. Chem. Phys.* 62 (1975) 320.
- [4] V.M. Orera, M.L. Sanjuan, M.M. Abraham, *J. Chem. Phys.* 88 (1988) 2976.
- [5] R.A. Zhitnikov, Yu.A. Dmitriev, *Sov. Phys. Tech. Phys.* 35 (1990) 92.
- [6] J.R. Morton, K.F. Preston, *J. Chem. Phys.* 75 (1981) 1126.
- [7] N. Bjerre, *J. Chem. Phys.* 76 (1982) 3347.
- [8] S.A. Marshall, *Phys. Rev.* 159 (1967) 191, and references therein.
- [9] K.M. Lee, et al., *Solid State Commun.* 37 (1981) 551.
- [10] G.D. Watkins, *Sol. State Commun* 17 (1975) 1205.
- [11] A.A. Bugai, et al., *Sov. Phys. Solid State* 23 (1981) 870.
- [12] S.H. Muller, et al., *Phys. Rev. B* 25 (1982) 25.
- [13] S.A. Marshall, J.A. Hodges, R.A. Serway, *Phys. Rev.* 136 (1964) A1024.
- [14] J.M. Spaeth, H. Seidel, *Phys. Stat. Sol. B* 46 (1971) 323.
- [15] T. Mchedlidze, M. Suezawa, in these Proceedings (ICDS-21), *Physica B* 308–310.
- [16] C. Rudowicz, *Magn. Res. Rev.* 13 (1987) 1.



ELSEVIER

Physica B 308–310 (2001) 404–407

PHYSICA B

www.elsevier.com/locate/physb

Evolution of copper–hydrogen-related defects in silicon

S. Knack^{a,*}, J. Weber^a, H. Lemke^b, H. Riemann^b^a*Dresden University of Technology, 01062 Dresden, Germany*^b*Institute for Crystal Growth (IKZ), Berlin, Germany*

Abstract

Copper-implanted silicon and floating-zone silicon doped with copper during crystal growth have been studied by means of capacitance spectroscopy (deep-level transient spectroscopy, DLTS) and photoluminescence (PL). The hydrogen was incorporated by either wet-chemical etching or hydrogen-plasma treatment. The evolution of defects after the incorporation of the impurities and further annealing steps was investigated. PL in combination with DLTS was used to unambiguously identify the copper–copper pair and clarify a recent controversy about the identification of the 1.014 eV luminescence line. Drift and diffusion experiments provide an insight into the structure of this center. © 2001 Elsevier Science B.V. All rights reserved.

Keywords: Copper; Hydrogen; Silicon; Defect reactions

1. Introduction

Copper impurities in silicon have been studied for a very long time. Recently, there has been a renewed interest in this field, which has been fueled by new applications of copper in semiconductor technology. Copper metalization for computer chips needs detailed knowledge about copper-diffusion [1,2] and suitable diffusion barriers in silicon. A defect which has been intensively studied recently was originally assigned to be a Cu-pair defect [3–5] and has now been re-interpreted in the light of a new PL-study as a defect containing a single Cu-atom [6,7]. The interstitial copper-species displays some similarities to the behavior of hydrogen in silicon: Both are fast diffusers, which is especially true for Cu; they can both form neutral complexes with shallow acceptors, where the hydrogen-complexes are thermally more stable; and both species can undergo reactions with many intrinsic or impurity defects [8]. In this paper we present data that confirm the original assignment of a Cu-pair defect and we also give details

of the interaction of copper-related defects with hydrogen.

2. Experimental

The defect reactions of copper and hydrogen were studied in two different sets of samples. (A) Copper was dissolved in the melt of silicon and incorporated into the crystal during the floating zone growth process. The boron concentration of the p-type crystals was about $2 \times 10^{15} \text{ cm}^{-3}$. A second p-type crystal was Cu-doped with the same technique but contained grown-in dislocations. The boron concentration for the dislocated crystal was about $1 \times 10^{14} \text{ cm}^{-3}$. (B) A set of p-type floating zone silicon with a boron concentration of $1 \times 10^{14} \text{ cm}^{-3}$ was copper implanted with various doses at room temperature and afterwards annealed at 700 °C for 30 min.

For copper indiffusion at room temperature, a piece of pure copper wire (99.999%) was dissolved in a mixture of HF : HNO₃ (1 : 6). Before photoluminescence (PL) or deep-level transient spectroscopy (DLTS) measurements samples were either etched in this copper saturated solution or in the same mix of acids without any copper.

*Corresponding author. Tel.: +49-351-463-5622; fax: +49-351-7060.

E-mail address: steffen.knack@physik.tu-dresden.de (S. Knack).

PL was excited with the 514.5 nm line of an argon-ion laser and measured at 4.2 K with a liquid nitrogen cooled germanium detector with a standard lock-in technique. The setup used for the DLTS measurements was a home-built system using analogue filtering of the transients and a liquid helium cryostat for measurements down to 40 K.

3. Results

Fig. 1 shows DLTS spectra of the dislocation-free silicon crystal and the PL-spectra from this sample is depicted in Fig. 2a. The zero phonon luminescence line at 1.014 eV is well known and has been extensively studied before [3–7]. In the following, we will call this luminescence center Cu_{PL} following the nomenclature of [6] and likewise denote the DLTS-center at $E_{\text{V}} + 0.1$ eV Cu_{DLTS} . In the as-grown dislocation-free samples these are the dominant centers in PL as well as in DLTS. In the dislocated material neither the PL- (Fig. 2b) nor the DLTS-signal (Fig. 3a) can be found. Instead, the levels for substitutional copper [9,10] and copper-hydrogen complexes [11] were measured with DLTS, while the photoluminescence showed a broad line at 0.807 eV which is related to dislocations [12].

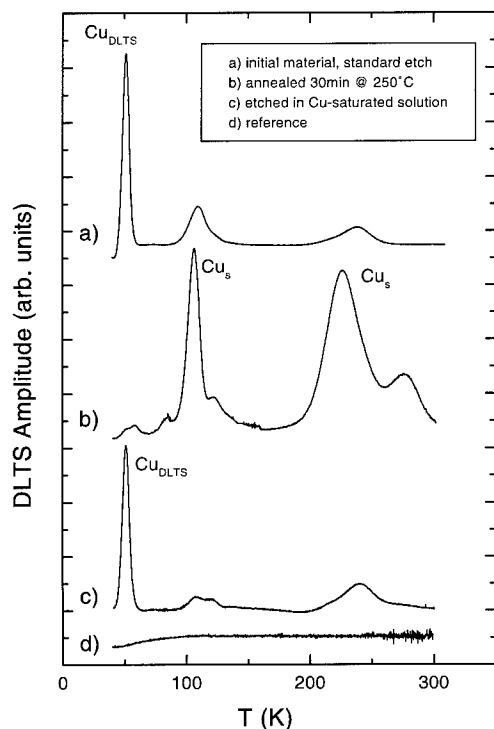


Fig. 1. DLTS-spectra of the melt-doped dislocation-free crystal (a) spectra taken after standard etch, (b) spectra taken after etching in copper solution, (c) spectra taken after an additional annealing step at 250°C for 30 min, and (d) reference sample.

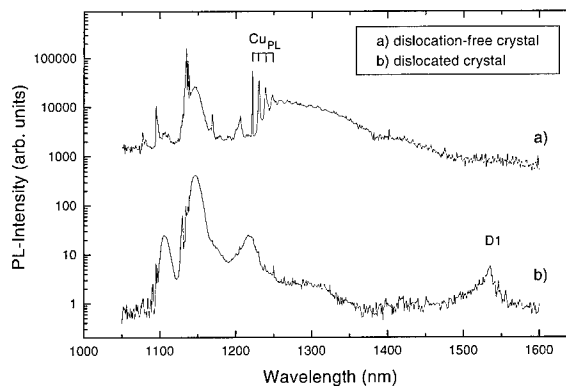


Fig. 2. Photoluminescence spectra of the dislocation-free crystal (a) and the dislocated crystal (b).

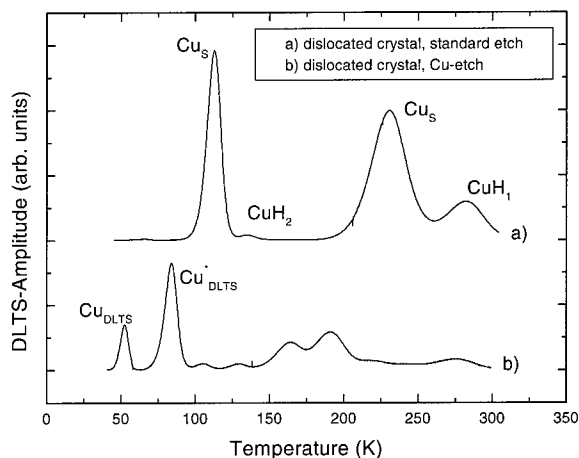


Fig. 3. DLTS-measurements of the melt-doped, dislocated crystal (a) spectra taken after standard etch and (b) spectra after etching in copper solution.

In the following, we describe some simple annealing and diffusion experiments performed with the dislocation-free samples: Annealing at 250°C for 30 min almost completely removes Cu_{DLTS} , instead the levels of substitutional copper and of the copper-hydrogen complexes are found (Fig. 1b). In the next step, the annealed sample is etched in a copper-containing solution, which again restores the signal Cu_{DLTS} (Fig. 1c). In a reference sample of FZ silicon with a similar boron-concentration but no Cu-doping, no defects could be detected after etching in the same Cu-containing solution (Fig. 1d).

In the dislocated sample the transformation from the substitutional Cu-defect to Cu_{DLTS} can be seen after etching with a Cu-containing solution (spectra 2b) but is not as efficient as in the dislocation-free material. The dominant DLTS peak comes from a level at $E_{\text{V}} + 0.185$ eV and is labeled $\text{Cu}_{\text{DLTS}}^*$. This level together

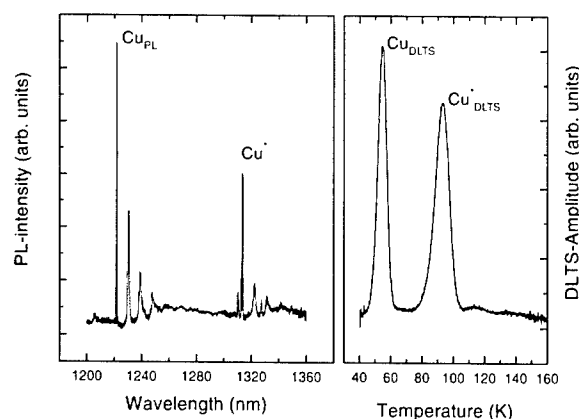


Fig. 4. PL and DLTS data of a Cu-implanted sample after annealing at 700 °C for 30 min and rapid quenching to room temperature.

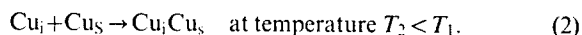
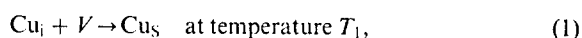
with Cu_{DLTS} is also found in the Cu-implanted samples that have been annealed at 700 °C for 30 min (Fig. 4). PL measurements on the implanted samples detected the features of both Cu_{PL} and a system of lines reported by Henry and coworkers in Refs. [13,14] and labeled as Cu' .

4. Discussion

The annealing and diffusion experiments show that the Cu_{DLTS} can be transformed into the defect attributed to substitutional Cu_{S} [9,10]. The PL measurements show an analogue behavior of the Cu_{PL} defect. Cu_{S} cannot be detected in luminescence, but the experiments are consistent with the former assignment of Cu_{DLTS} and Cu_{PL} to the same copper center [5]. The annealing experiments show that $\text{Cu}_{\text{DLTS,PL}}$ is thermally less stable than the substitutional copper. At room temperature, indiffusing interstitial copper is very efficiently bound to Cu_{S} and restores $\text{Cu}_{\text{DLTS,PL}}$. On the other hand, the defect cannot be formed at room temperature in samples where no Cu_{S} is present before the copper indiffusion. These results clearly suggest $\text{Cu}_{\text{DLTS,PL}}$ to be a copper-pair defect consisting of one substitutional and one interstitial copper atom.

In Ref. [6], Nakamura et al. observed a linear dependence of the Cu_{PL} signal on the total copper contamination. They annealed silicon samples containing varying Cu-concentrations below the solubility limit for 30 min at 700 °C. The intensity of Cu_{PL} then showed a linear dependence on the incorporated copper concentration, which led them to suggest that the defect consists of only one Cu-atom. However, also in terms of the pair-model, the linear concentration dependence of the $\text{Cu}_{\text{DLTS,PL}}$ defect can be understood. The law of mass action gives a quadratic dependence on the total copper concentration for the reaction: $\text{Cu} + \text{Cu} \rightarrow \text{Cu}_{\text{pair}}$.

However, this chemical equation does not describe the formation of the defect properly. The defect formation as evidenced by the above described experiments during annealing is rather a two-step process which can be described as



For very fast quenching after the annealing one can set $T_1 = 700^\circ\text{C}$ and T_2 as room temperature. At the elevated temperature, substitutional copper is formed. The concentration Cu_{S} is thus determined by Eq. (1). In the limit of low copper concentration one would therefore expect $[\text{Cu}_{\text{S}}] = k[\text{Cu}_{\text{tot}}]$, with $k < 1$.

When quenched to room temperature the remaining interstitial copper is still mobile and moves freely until trapped to some defect. The main sink for Cu_i is substitutional copper as copper–boron pairs are not stable at room temperature and the small fraction of Cu_i lost to the surface can be neglected. Thus, if $k > 0.5$ then $[\text{Cu}_i\text{Cu}_{\text{S}}] = [\text{Cu}_i] = (1 - k)[\text{Cu}_{\text{tot}}]$, otherwise $[\text{Cu}_i\text{Cu}_{\text{S}}] = [\text{Cu}_{\text{S}}] = k[\text{Cu}_{\text{tot}}]$. In both cases, the concentration dependence would be linear as observed in the experiment of Nakamura et al. [5].

In the limit of high copper concentration the solubility of substitutional copper at 700 °C would be reached and therefore $[\text{Cu}_{\text{S}}] = \text{const.} = [\text{Cu}_i\text{Cu}_{\text{S}}]$ as no additional $[\text{Cu}_{\text{S}}]$ can be formed at room temperature. Thus, for higher concentrations, a saturation of the copper-pair concentration would be expected as is also experimentally observed. The results from the melt-doped silicon samples support this analysis. In dislocation-free silicon, the copper-pair defect is found after crystal growth. This situation changes in dislocated material where the dislocations are a very efficient trap for the interstitial copper leaving no free interstitial copper at lower temperatures for the formation of the copper pair. From this discussion follows that the observed concentration dependence is consistent with the model of a $\text{Cu}_i\text{Cu}_{\text{S}}$ defect.

In an earlier study, a quadratic dependence of the PL-intensity on the Cu-concentration was found [4]. Here, Cu was incorporated in high concentrations and annealed so that the solubility for different temperatures ranging from 700 °C to 1200 °C was reached. In order to analyze this experiment within our model, the equilibrium concentrations for interstitial copper [15,16] and the vacancy [17,18] as well as the formation enthalpy for substitutional copper [8,19] have to be known. From the different sets of values that can be found in the literature we get $[\text{Cu}_{\text{PL}}] \propto [\text{Cu}_{\text{tot}}]^{2.2 \pm 0.2}$ which is very close to the experimental finding of $[\text{Cu}_{\text{PL}}] \propto [\text{Cu}_{\text{tot}}]^{2.0 \pm 0.2}$. Thus, together with previous experimental results on the symmetry of the center we confirm the original assignment of the $\text{Cu}_{\text{DLTS,PL}}$ signal to a $\text{Cu}_i\text{Cu}_{\text{S}}$ pair.

5. Conclusion

In the light of the annealing and diffusion experiments on copper-doped silicon samples, the concentration dependence of the 1.014 eV luminescence line and the $E_V + 0.1$ eV DLTS center is carefully analyzed and the originally proposed model of a Cu-pair defect revisited. No contradiction to the established model of the Cu_iCu_s defect can be found.

The microscopic origin of Cu^* and $\text{Cu}_{\text{DLTS}}^*$ is not clear. The luminescence feature with a zero-phonon line at 943.7 meV is found in samples with low Cu-contamination and has tetrahedral symmetry [13]. It is shifted in energy by -70 meV from the line at 1.014 eV. The fact that it shows up together with the DLTS-level at $E_V + 0.185$ eV, which is likewise shifted by approximately $+80$ meV from the Cu-pair at $E_V + 0.100$ eV suggests that the DLTS peak and the photoluminescence line are both due to the same defect which shows remarkable similarity to the Cu-pair defect.

Acknowledgements

The authors want to thank T. Heiser for helpful discussions. The technical assistance of B. Koehler is gratefully acknowledged. R. Botha is thanked for his help with photoluminescence measurements. This work was supported by Deutsche Forschungsgemeinschaft as project WE 1319/9-1.

References

- [1] A. Mesli, T. Heiser, *Phys. Rev. B* 45 (1992) 11632.
- [2] A.A. Istratov, C. Flink, H. Hieslmair, E.R. Weber, T. Heiser, *Phys. Rev. Lett.* 81 (1998) 1243.
- [3] N.S. Minaev, A.V. Mudryi, V.D. Tkachev, *Sov. Phys. Semicond.* 13 (1979) 233.
- [4] J. Weber, H. Bauch, R. Sauer, *Phys. Rev. B* 25 (1982) 7688.
- [5] H.B. Erzgraeber, K. Schmalz, *J. Appl. Phys.* 78 (1995) 4066.
- [6] M. Nakamura, S. Ishiwari, A. Tanaka, *Appl. Phys. Lett.* 73 (1998) 2325.
- [7] M. Nakamura, *Appl. Phys. Lett.* 73 (1998) 3896.
- [8] S.K. Estreicher, *Phys. Rev. B* 60 (1999) 5375.
- [9] H. Lemke, *phys. Stat. Sol. a* 95 (1986) 665.
- [10] S.D. Brotherton, et al., *J. Appl. Phys.* 62 (1987) 1826.
- [11] S. Knack, J. Weber, H. Lemke, *Physica B* 273–274 (1999) 387.
- [12] R. Sauer, J. Weber, J. Stolz, E.R. Weber, K.-H. Kuesters, H. Alexander, *Appl. Phys. A* 36 (1985) 1.
- [13] K.G. McGuigan, M.O. Henry, E.C. Lightowers, A.G. Steele, M.L.W. Thewalt, *Solid State Comm.* 68 (1988) 7.
- [14] K.G. McGuigan, M.O. Henry, M.C. Carmo, G. Davies, E.C. Lightowers, *Mat. Sci. Engr. B4* (1989) 269.
- [15] J.D. Struthers, *J. Appl. Phys.* 27 (1956) 1560.
- [16] R.N. Hall, J.H. Racette, *J. Appl. Phys.* 35 (1964) 379.
- [17] P.B. Rasband, P. Clancy, M.O. Thompson, *J. Appl. Phys.* 79 (1996) 8998.
- [18] R. Falster, V.V. Voronkov, F. Quast, *Phys. Stat. Sol. b* 222 (2000) 219.
- [19] U. Wahl, A. Vantomme, G. Langouche, J.P. Araujo, L. Peralta, J.G. Correia, *Appl. Phys. Lett.* 77 (2000) 2142.



ELSEVIER

Physica B 308–310 (2001) 408–413

PHYSICA B

www.elsevier.com/locate/physb

Electronic and atomic structure of transition-metal–hydrogen complexes in silicon

P.T. Huy^{a,b,*}, C.A.J. Ammerlaan^a

^a Van der Waals–Zeeman Institute, University of Amsterdam, Valckenierstraat 65–67, NL-1018 XE Amsterdam, Netherlands

^b International Training Institute for Materials Science, ITIMS Building, Dai Hoc Bach Khoa Hanoi, 1 Dai Co Viet Road, Hanoi, Viet Nam

Abstract

Electron paramagnetic resonance investigations on transition-metal-doped silicon, hydrogenated at high temperature in an environment of water vapor, have revealed three transition-metal–hydrogen related paramagnetic centers Si-NL65, Si-NL64, and Si-NL68, respectively, in the samples doped with platinum, gold, and palladium. The spectra, from the sample preparation conditions, and the experimentally observed hyperfine structures of 1:3:3:1–4:12:12:4–1:3:3:1 for the Si-NL65, 1:2:1–1:2:1–1:2:1–1:2:1 for the Si-NL64, and 1:1 for the Si-NL68 spectrum, were identified as complexes of one-platinum–three-hydrogen (Pt–H₃), one-gold–two-hydrogen (Au–H₂), and one-palladium–one-hydrogen (Pd–H₁), respectively. A detailed analysis of the spin-Hamiltonian parameters of the centers, the transition-metal and hydrogen hyperfine interactions, has been carried out providing adequate materials for establishing electronic and microscopic models of the newly observed centers. © 2001 Elsevier Science B.V. All rights reserved.

Keywords: Si: Defects; Transition-metal–hydrogen complexes; EPR

1. Introduction

The properties of transition-metal–hydrogen complexes (TM–H) in crystalline silicon have been studied intensively in the last 15 years. As a result of this effort, the electronic levels, the local vibrational modes, and the structure of a number of TM–H defects have been identified mostly by deep level transient spectroscopy (DLTS) [1,2], Fourier transform infrared and local vibrational mode (FTIR-LVM) spectroscopy [3,4]. These techniques have given valuable information about the position of the TM–H levels in the band-gap, their electron and hole capture cross sections, local vibrational modes associated with hydrogen, and the numbers of hydrogen atoms as well as their positions within the structure of the defects have been determined. However, little direct information has been obtained

about the microscopic structure and the chemical composition of TM–H related defects as the electron paramagnetic resonance (EPR) has failed to detect TM–H related centers so far. Up to now, the Pt–H₂ center was the only case in which both the structure of the defect, and its electronic properties were convincingly established using the combined results from EPR, IR-LVM, and theoretical calculations [1,2,5–7]. To overcome the handicap, in this paper, we report on the studies of TM-doped hydrogenated silicon by EPR. Three TM–H complexes have been observed and identified as containing one transition-metal atom and one, two and three hydrogen atoms, respectively, for the Pd–H₁, Au–H₂ and Pt–H₃ centers. Symmetries of the centers have been measured and determined as monoclinic-I for the Pd–H₁, triclinic for Au–H₂ and trigonal for Pt–H₃ centers. A detailed analysis of the experimental spectra has been carried out and enabled us to determine spin-Hamiltonian parameters of the centers. It was discovered that although the number of hydrogen atoms in each center is different, the hydrogen hyperfine

*Corresponding author. Tel.: +31-20-5255642; fax: +31-20-5255788.

E-mail address: pthuy@science.uva.nl (P.T. Huy).

interactions are very similar with their isotropic and anisotropic parts of about 10 and 1 MHz, respectively. This common character of observed hydrogen hyperfine interaction is reflected in the electronic and atomic models proposed for the centers in which the hydrogen atoms are concluded to favor the interstitial anti-bonding sites to the silicon nearest-neighbor atoms.

2. Experimental

Phosphorus-doped Czochralski-grown silicon with room-temperature resistivity in the range of 0.75–125 Ωcm was used in this study. The crystal was oriented and cut into bar-shaped samples with typical dimensions of $1.5 \times 1.5 \times 15 \text{ mm}^3$, and with the longest side parallel to the $[0\bar{1}1]$ crystal direction. Transition metals gold, platinum, and palladium were introduced by two different methods, either by evaporation or by rubbing TMs to one or all surfaces of the samples, and then heated at 1200–1300°C for several hours. The hydrogenation process was typically performed at 1250–1300°C for 30 min in the atmosphere of water vapor. After hydrogenation the samples were quenched in water at room temperature, then stored in liquid nitrogen till the first measurement. Magnetic resonance experiments were carried out using a superheterodyne spectrometer operating in the microwave *K*-band with the frequency near 23 GHz. The EPR spectra were measured at temperatures of 4.2–20 K.

3. Results

In the platinum-doped hydrogenated samples, after hydrogenation, depending on the cooling rate of the samples, two different Pt–H related spectra are observed. The first spectrum, which has quite high formation probability and is observable in all samples investigated, is characterized by a typical hyperfine structure of 1:2:1–4:8:4–1:2:1, identifying the well-known Pt–H₂ center [3–5]. The second spectrum, labeled Si-NL65, detectable only under visible-light illumination, has very low formation probability and is observable only in 2 of the 40 samples made with very fast cooling rate. The Si-NL65 spectrum, as depicted in Fig. 1, is characterized by a hyperfine structure with the relative intensity of the spectral lines typically of 1:3:3:1–4:12:12:4–1:3:3:1 as being due to the hyperfine interaction with a platinum atom ($I = 1/2$, 33.8% abundance), and three equivalent atoms with $I = 1/2$, 100% abundance. In Fig. 1 for comparison, the EPR spectrum of the Pt–H₂ center is also given and indicated by dashed arrows. The angular dependence of the Si-NL65 spectrum has been measured for the rotation of the magnetic field in the $(0\bar{1}1)$ plane from a $[100]$ to a

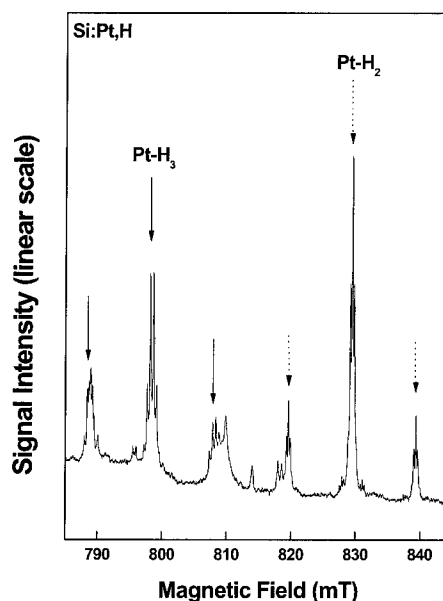


Fig. 1. EPR spectrum of the Si-NL65 center associated with the trigonal Pt–H₃ center observed in the platinum-doped hydrogenated sample under visible-light illumination for the magnetic field $B// [0\bar{1}1]$ direction, $T = 4.2 \text{ K}$, and microwave frequency $f = 22.71369 \text{ GHz}$. The spectrum is characterized by a 1:3:3:1–4:12:12:4–1:3:3:1 hyperfine structure. The Pt–H₂ spectrum with hyperfine structure of 1:2:1–4:8:4–1:2:1 is also observed and is indicated by dashed arrows.

$[0\bar{1}1]$ direction, as shown in Fig. 2, revealing the trigonal symmetry of the underlying defect.

In palladium-doped samples, the experimental results showed that after hydrogenation the EPR spectrum of the Pd_s^- center, which was observed strongly in the samples, has disappeared [8]. The EPR spectrum of Fe_i^0 , and in several samples the spectrum of the Pd–Fe pair, has emerged [9]. No immediate Pd–H spectrum was detected. Practically, the observed disappearance of the Pd_s^- center after hydrogen treatment suggests a possibility that all Pd_s^- centers have been converted to other Pd-related centers including the Pd–Fe pair. But as in the experiments only the Pd–Fe pair is observed with much lower intensity after hydrogenation (or not observed at all), the possibility of formation of Pd–H complexes, which are neutral or non-paramagnetic, has to be taken into account. It is known from DLTS experiments that by annealing the samples at temperatures of 400–550 K, one can promote the conversion processes in which the hydrogen-related centers capture or release one or more hydrogen atoms to form new complexes [10,11]. There is a possibility that the new-formed complexes are paramagnetic and observable by EPR. We therefore have carried out the isochronal thermal annealing of our samples. Results showed that after annealing at 450 K

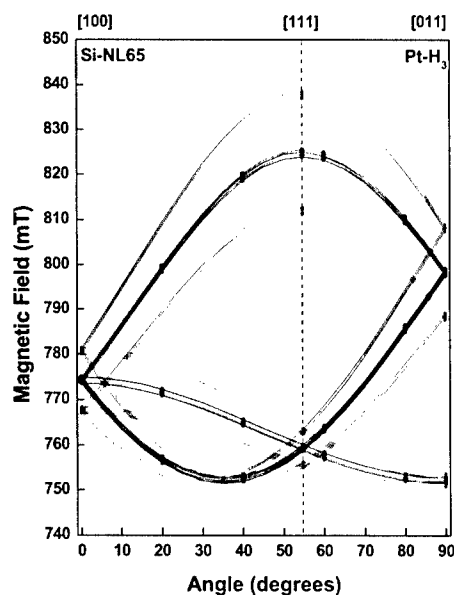


Fig. 2. Angular dependence pattern of the Si-NL65 spectrum as measured for rotation of the magnetic field in the $(0\bar{1}1)$ plane from the $[100]$ to $[011]$ directions. The experimental data recorded for temperature $T = 4.2$ K and microwave frequency $f = 22.731688$ GHz are presented as solid circles. The trigonal symmetry of the Pt-H_3 is clearly determined.

for 60 min. the EPR spectrum of the Pd_s^- center has weakly recovered. Further annealing revealed the gradual recovery of the Pd_s^- center. At the same time a new EPR spectrum is emerging. This spectrum, labeled Si-NL68 for further reference, achieves its highest intensity after annealing at 500 K for about 120 min, see Fig. 3. One of the difficult points in this experiment is, as can be seen in Fig. 3, the very low intensity of the Si-NL68 spectrum, even at its highest concentration. Also, the spectral lines are superimposed, in many parts, on the much stronger Pd_s^- and P_s^0 spectra. Fortunately, by careful measurements with slower scanning speed and highest resolution, we were still able to collect the positions of all the spectral lines versus the magnetic field when rotated in the $(0\bar{1}1)$ plane from the $[100]$ to $[011]$ directions. The corresponding pattern is shown in Fig. 4 presenting monoclinic-I symmetry for the Si-NL68 center. Especially, at the main directions $[100]$ and $[011]$, where the intensity of the spectrum is higher, we observed extra twofold splitting in each of the spectral lines. This splitting is in the order of 7–10 MHz and is anisotropic, providing evidence for the hyperfine interaction with a nucleus with spin $I = 1/2$ and 100% abundance.

In gold-doped samples, the EPR Si-NL64 spectrum of the Au-H_2 center is recorded directly after hydrogenation.

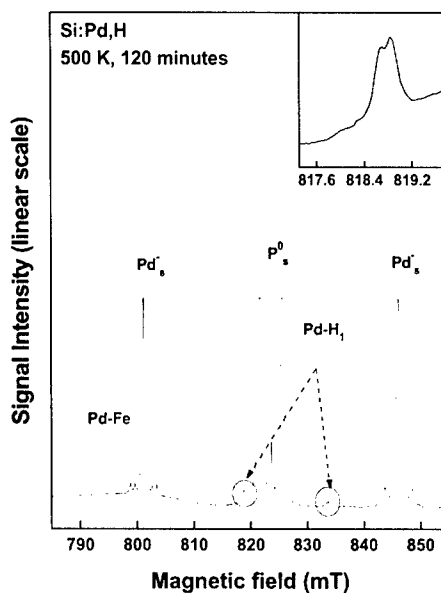


Fig. 3. EPR spectrum of the Si-NL68 center observed in the palladium-doped hydrogenated sample after an isochronal annealing at 500 K for 120 min. The Si-NL68 spectrum is characterized by a twofold splitting in each of the spectral lines as due to hyperfine interaction with one hydrogen atom ($I = 1/2$, 100%), as shown in the inset. Magnetic field $B \parallel [100]$.

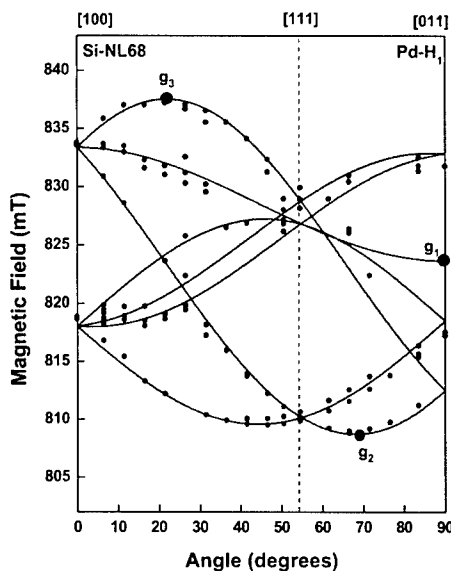


Fig. 4. Angular dependence pattern of the Si-NL68 spectrum observed for the rotation of the magnetic field in the $(0\bar{1}1)$ plane from the $[100]$ to $[011]$ directions, disclosing the monoclinic-I symmetry for the corresponding defect.

tion. The spectrum, as depicted in Fig. 5, as observed under visible-light illumination for the magnetic field about 10° away from the $[011]$ direction, shows a very complicated hyperfine structure with a large number of

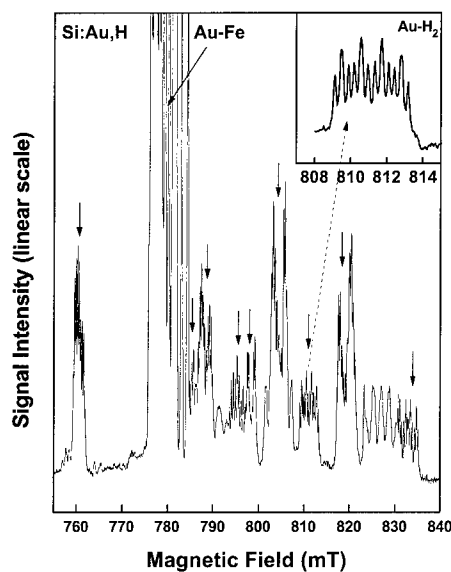


Fig. 5. Typical EPR spectrum of the Si-NL64 center observed in the gold-doped hydrogenated sample under visible-light illumination for the magnetic field about 10° away from the $[011]$ direction, with microwave frequency $f = 23.0217$ GHz, at temperature $T = 4.2$ K.

groups of spectral lines. This complexity of the spectrum makes the task of identification of the Si-NL64 center difficult. Fortunately, as shown in an extended view in the inset of Fig. 5, each group of spectral lines of the Si-NL64 spectrum is characterized by a very informative hyperfine structure with the relative intensity of 1:2:1-1:2:1-1:2:1-1:2:1 which can be attributed to the hyperfine interaction with one gold atom ($I = 3/2$, 100%) and two hydrogen atoms ($I = 1/2$, 100%). The spectrum has the rare low symmetry of triclinic, as given in Fig. 6.

4. TM-H identification

In all cases, from the experimental results as described above, the identification of the spectra as originating from TM-H complexes is directly established (except for ^{105}Pd in the Pd-H₁ center). Firstly, all spectra Si-NL64, Si-NL65, and Si-NL68 are observed after hydrogenation. They all exhibit extra splitting of twofold (1:1), threefold (1:2:1), and fourfold (1:3:3:1) revealing hyperfine interaction with one, two, and three hydrogen atoms, respectively, for the Si-NL68, Si-NL64 and Si-NL65 centers. The Si-NL65 spectrum is observed in the platinum-doped sample simultaneously with the Pt-H₂ spectrum. One can practically view the hyperfine structure of 1:3:3:1-4:12:12:4-1:3:3:1 as an extended picture of the hyperfine structure of 1:2:

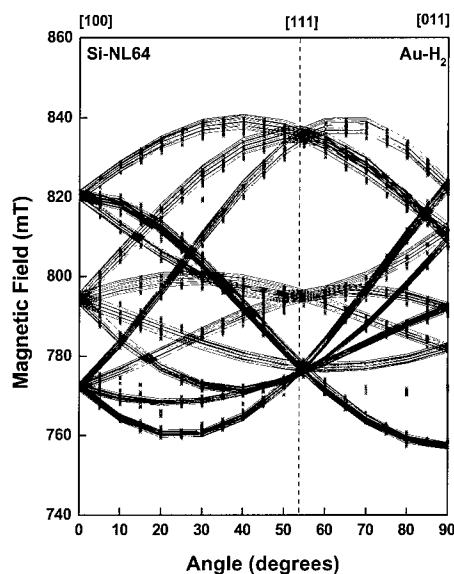


Fig. 6. Triclinic angular dependence pattern of the Si-NL64 spectrum observed for rotation of the magnetic field in the $(0\bar{1}1)$ plane from the $[100]$ to $[011]$ crystallographic directions. Experimental data recorded at $T = 4.2$ K, microwave frequency $f = 23.0217$ GHz.

1-4:8:4-1:2:1 of the Pt-H₂ center in which a third equivalent proton is added. As already concluded for the Pt-H₂ spectrum, the presence of one platinum atom is indicated by the resolved hyperfine splitting related to the ^{195}Pt isotope, nuclear spin $I = 1/2$ and natural abundance of 33.8%, resulting in the characteristic splitting of the resonance in three components with the intensity ratio of about 1:4:1. Presence of two equivalent hydrogen atoms is revealed by triplet structure with amplitudes scaling as 1:2:1 of all resonances due to the hyperfine fields created by two hydrogen atoms ($I = 1/2$, 100%). Combination of these interactions produces the hyperfine structure of 1:2:1-4:8:4-1:2:1 as observed in the experiments. Adding the third hydrogen atom, the hydrogen hyperfine structure becomes 1:3:3:1. Consequently, the 1:3:3:1-4:12:12:4-1:3:3:1 hyperfine structure is created when combined with hyperfine interaction due to a single platinum atom. This is the case for the Si-NL65 spectrum of the Pt-H₃ center. A similar interpretation is applied for the Si-NL64 spectrum of the Au-H₂ center. In this case, the observed structure of 1:2:1-1:2:1-1:2:1-1:2:1 can be explained as due to hyperfine interaction with one gold atom, nuclear spin $I = 3/2$ and 100% natural abundance (generating fourfold splitting) and two equivalent or nearly equivalent hydrogen atoms (generating 1:2:1 structure). For the Si-NL68 spectrum, due to low intensity of the spectrum, the hyperfine lines which represent the hyperfine

interaction with ^{105}Pd isotope ($I = 5/2$, 22.2%) are not strong enough for observation. The assignment to a Pd-H_1 complex, therefore, is tentative and based on the experimental observation of twofold splitting as due to interaction with one hydrogen atom and the appearance of only palladium-related centers in the investigated samples.

5. Electronic and atomic structure of TM-H complexes

From a summary of the spin-Hamiltonian parameters of the centers, as obtained from fittings of the angular dependencies (Figs. 2, 4 and 6) and results of the standard analysis based on linear-combination-of-atomic-orbitals (LCAO), given in Table 1, one can recognize that the g tensors of all centers largely deviate from $g_e = 2.0023$ of the free electron, implying the incorporation of a transition-metal impurity in the microscopic structures of the centers. The hydrogen hyperfine interaction tensors also show a striking similarity for all centers with isotropic part a of about 10 MHz, corresponding to a very low s -type spin density around 0.7% on the hydrogen positions. The small anisotropic component b^{H} of the hydrogen hyperfine interaction, may be

ascribed to the dipole-dipole interaction between the spins of proton and electron, considered as classical dipoles with separation R . From the observed values of b of around 1 MHz, a distance of $R = 0.4\text{--}0.5\text{ nm}$ is calculated. This value means a distance of $0.4\text{--}0.5\text{ nm}$ between the transition-metal atom and the proton, i.e., the hydrogen atom is anti-bonding to the silicon nearest neighbor. In all cases, the observed centers are stable at room temperature and have low symmetry, trigonal for the Pt-H_3 , monoclinic-I for the Pd-H_1 , and triclinic for the Au-H_2 centers, suggesting the substitutional position for the transition-metal atom. On this basis, the atomic model for each center is proposed, as sketched in Fig. 7, in which the transition-metal atom occupies the substitutional site, the hydrogen atom is interstitial and anti-bonding to a silicon nearest-neighbor atom. The position of the TM atom is depicted with respect to the symmetry of each center. As neutral gold is isoelectronic to negative platinum, quite likely spectrum Si-NL64 corresponds to the $[\text{Au}_i-(\text{H}_i)_2]^0$ center observed in the neutral charged state (the $(\text{Pt-H}_2)^-$ center is observed in negative charge state, see Refs. [3,5]). For the same reason, the Si-NL65 spectrum of the $(\text{Pt-H}_3)^0$ center is observed in the neutral charge state as well.

Table 1

Summary of spin-Hamiltonian parameters and some results of the analysis by the method of linear combination of atomic orbitals (LCAO) for transition-metal—hydrogen complexes

Center	Symmetry	Tensors	Parameters of spectra and centers		
(Pt-H_2)	Orthorhombic-I (C_{2v})	g	2.1299 ($[1\ 0\ 0]$)	1.9558 ($[0\ \bar{1}\ 1]$)	2.1683 ($[0\ 1\ \bar{1}]$)
		A^{Pt}	175.7 MHz	541.2 MHz	237.3 MHz
		A^{H}	9.8 MHz	7.9 MHz	8.2 MHz
		$\eta^2(H)$	$\sim 0.6\%$		
		b^{H}	$\sim 0.6\text{ MHz}$		
		R	$\sim 0.4\text{--}0.5\text{ nm}$		
$(\text{Pt-H}_3)^0$ (Si-NL65)	Trigonal (C_{3v})	g	1.9673 (g_{\parallel})	2.1569 (g_{\perp})	
		A^{Pt}	708.8 MHz	52.2 MHz	
		A^{H}	14.5 MHz	12.7 MHz	
		$\eta^2(H)$	$\sim 0.9\%$		
		b^{H}	$\sim 0.6\text{ MHz}$		
		R	$\sim 0.4\text{--}0.5\text{ nm}$		
Pd-H_1 (Si-NL68)	Monoclinic-I	g	1.998 ($[1\ 0\ 0]$)	2.0361	1.9651
		A^{H}	$\sim 7\text{--}10\text{ MHz}$	22° away from	22° away from
		b	$\sim 1\text{ MHz}$	$[0\ 1\ 1]$	$[1\ 0\ 0]$
$(\text{Au-H}_2)^0$ (Si-NL64)	Triclinic	g	2.1282 (g_{xx})	2.0689 (g_{yy})	2.0039 (g_{zz})
		A^{Au}	13.8 MHz	23.5 MHz	18 MHz
		A^{H}	8.67 MHz	11.39 MHz	8.54 MHz
		$\eta^2(H)$	~ 0.67		
		b^{H}	$\sim 0.9\text{ MHz}$		
		R	$\sim 0.4\text{--}0.5\text{ nm}$		

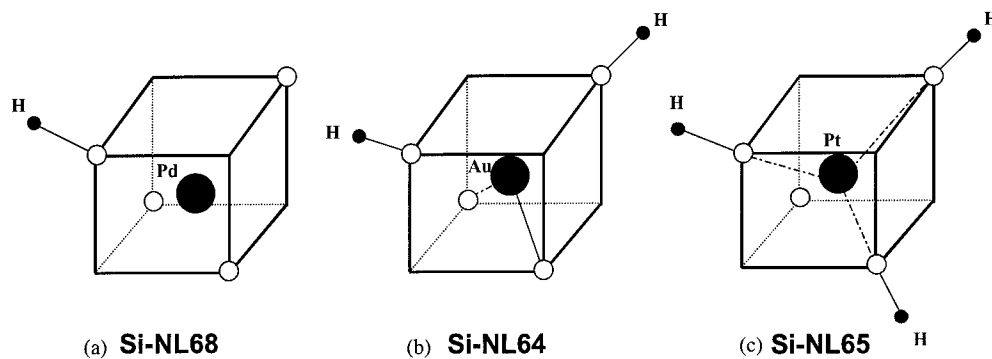


Fig. 7. Atomic models proposed for the monoclinic-I Pd-H₁ (a), the triclinic Au-H₂ (b), and the trigonal Pt-H₃ centers (c).

References

- [1] J. Weber, in: N.H. Nickel, W.B. Jackson, R.C. Bowman, R.G. Leisure (Eds.), *Hydrogen in Semiconductors and Metals*, Materials Research Society, Warrendale, 1998, p. 345.
- [2] J. Weber, W. Jost, H. Lemke, A. Mesli, J.-U. Sachse, E.Ö. Sveinbjörnsson, N. Yarykin, *Mat. Res. Soc. Symp. Proc.* 512 (1988) 345.
- [3] P.M. Williams, G.D. Watkins, S. Uftring, M. Stavola, *Phys. Rev. Lett.* 70 (1993) 3816.
- [4] M.J. Evans, M. Stavola, M.G. Weinstein, S.J. Uftring, *Mater. Sci. Eng. B* 58 (1999) 118.
- [5] M. Höhne, U. Juda, Yu.V. Martynov, T. Gregorkiewicz, C.A.J. Ammerlaan, L.S. Vlasenko, *Phys. Rev. B* 49 (1994) 13423.
- [6] S.J. Uftring, M. Stavola, P.M. Williams, G.D. Watkins, *Phys. Rev. B* 51 (1995) 9612.
- [7] A. Resende, R. Jones, S. Öberg, P.R. Briddon, *Phys. Rev. Lett.* 82 (1999) 2111.
- [8] H.H. Woodbury, G.W. Ludwig, *Phys. Rev.* 126 (1962) 466.
- [9] A.B. van Oosten, N.T. Son, L.S. Vlasenko, C.A.J. Ammerlaan, *Mater. Sci. Forum* 38–41 (1989) 355.
- [10] J.-U. Sachse, J. Weber, H. Lemke, *Mater. Sci. Forum* 258–263 (1997) 307.
- [11] E.Ö. Sveinbjörnsson, O. Engström, *Phys. Rev. B* 52 (1995) 4884.



ELSEVIER

Physica B 308–310 (2001) 414–417

PHYSICA B

www.elsevier.com/locate/physb

Time-resolved photoluminescence study of Si : Ag

N.Q. Vinh*, M.A.J. Klik, T. Gregorkiewicz

Van der Waals–Zeeman Institute, University of Amsterdam, 65 Valckenierstraat, NL-1018 XE Amsterdam, The Netherlands

Abstract

Photoluminescence band at 780 meV, previously assigned to silver-related centers in Si on basis of indirect arguments, is investigated in detail. For that purpose specially prepared samples doped with isotopically enriched silver are used. The photoluminescence spectrum exhibits characteristic structure consisting of narrow no-phonon lines and lower-energy phonon replicas. We observe isotope shift of the three main no-phonon lines which conclusively shows that silver is incorporated in the microscopic structure of the luminescent defect. From time-resolved photoluminescence lifetime of a few 100 μ s is determined. This is a characteristic fingerprint for recombination of excitons bound to isoelectronic centers. Further insight in the nature of the optically active Ag-related center is obtained from the temperature dependence of the lifetime. © 2001 Elsevier Science B.V. All rights reserved.

PACS: 78.55.Ap; 78.47.+p; 61.72.Ji

Keywords: Photoluminescence; Silicon; Silver

1. Introduction

Like other noble metals, silver is an important impurity in silicon. This is due to its interesting physical properties as well as possible applications for device manufacturing. When introduced into silicon, silver gives rise to two levels: an acceptor at $E_c - 0.54$ eV and a donor level at $E_v + 0.34$ eV [1]. The donor level has been observed in optical absorption [2]. Transition at the acceptor were not observed. Also low-temperature photoluminescence (PL) from Si : Ag has been reported. It has been found that silver-doped silicon exhibits a characteristic emission spectrum at 780 meV [3–5]. The photoluminescence spectrum consists of narrow no-phonon lines (termed A, B, C at energies 778.91, 779.85 and 784.31 meV, respectively) which are replicated at lower energies by local phonons. From replica of lines A and B, local phonon energies of approximately 6 and 15 meV were determined. At temperatures higher than 20 K phonon replicas of the C line were also

observed. The structure of the 780 meV band was identified as transitions from the effective-mass-theory electronic states near the conduction band to the ground state.

In the present work, we report on observation of the silver isotope shift of the no-phonon A, B, and C lines of the 780 meV band, providing direct microscopic evidence of silver involvement in the center responsible for this emission. Also, the decay time of these lines and its temperature dependence have been determined.

2. Experimental

The starting material for sample preparation was float-zone, p-type silicon, with resistivity of 75–125 Ω cm. Silver was introduced into the sample by evaporation, followed by diffusion at 1150°C for 4 h in a closed quartz ampoule containing 100 mbar of argon. After the diffusion step, samples were quenched to room temperature in water and chemically cleaned to remove the silver-rich surface layer. For diffusion both natural and isotopically enriched silver (99.5% of ^{107}Ag and 99.4% ^{109}Ag isotope) were used.

*Corresponding author. Tel.: +31-20-525-5644; fax: +31-20-525-5788.

E-mail address: nguyen@science.uva.nl (N.Q. Vinh).

The PL experiments were performed with a variable temperature continuous-flow cryostat accessing the 1.5–300 K range (Oxford Instruments Optistat CF). For excitation a cw argon-ion laser operating at 514.5 nm was used. All spectra were obtained with a 1.5 m F/12 monochromator (Jobin-Yvon THR-1500) and detected by a high-sensitivity germanium detector (Edinburgh Instruments).

Time-resolved measurements were carried out using a digital oscilloscope (Tektronic TDS 3000) in combination with an InP/InGaAs nitrogen-cooled photomultiplier tube (Hamamatsu R5509-72). For transient excitation a laser beam (at a 1 W continuous power) was passed through a pinhole and mechanical chopping (200 Hz). In this configuration, the experimentally measured system response time was 38 μ s.

3. Results and discussion

3.1. Isotope measurements

For all the investigated samples photoluminescence was measured for the energy range between the band gap energy of silicon and approximately 700 meV. Fig. 1 shows typical photoluminescence spectra obtained in this study from silver-doped silicon samples at 10 and 20 K. The band around 780 meV is similar to that observed earlier [3–5], and ascribed to silver on basis of sample preparation. In addition to that, two new and weaker PL bands at 806 and 811 meV, labeled D and E, respectively, were detected.

Fig. 2 presents high-resolution photoluminescence spectra of the 780 meV band recorded for samples doped with silver isotope ^{107}Ag , silver isotope ^{109}Ag and natural silver. The spectra of samples doped with isotopically enriched silver are similar to that in Fig. 1

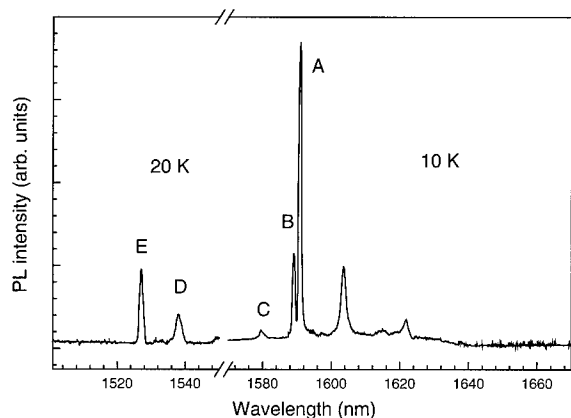


Fig. 1. 780 meV PL band observed in silver-doped silicon at $T = 10$ and 20 K.

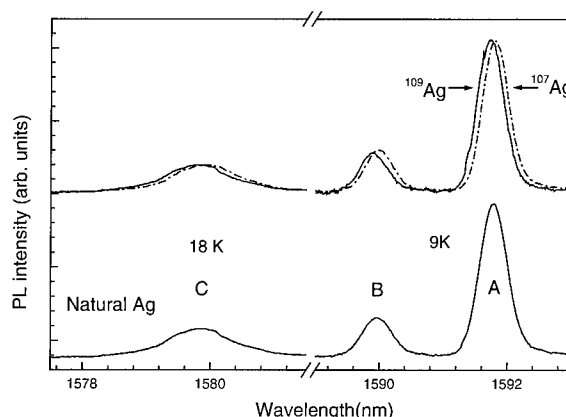


Fig. 2. A, B and C PL lines measured in silicon doped with isotopically enriched silver (upper curves) and natural silver (lower curve).

but with positions of ABC structure were shifted by ~ -0.017 meV for ^{107}Ag -doped silicon, and by $\sim +0.017$ meV for ^{109}Ag -doped silicon. We also note that PL lines in sample diffused with natural silver ($[^{107}\text{Ag}]:[^{109}\text{Ag}]$ as 52:48) are distinctly broader than those for ^{107}Ag or ^{109}Ag -doping. These results provide direct evidence that silver is involved in the microscopic structure of the center responsible for this emission.

The isotope shifts were observed also for the phonon satellites and are illustrated in Fig. 3 for the 773 and 765 meV replicas of lines A and B. Isotope shifts of luminescence lines are a convenient tool for the identification of the chemical nature of the optically active centers. The isotope effect for the bound exciton photoluminescence is related to the zero vibrations of the center and leads usually to an increase of the recombination energy for heavier nuclei [6,7]. For isoelectronic impurities in silicon such an effect has been experimentally observed for the copper–copper pair [8]. In this case, a 0.1 nm difference of the position of the PL line for the samples doped with ^{63}Cu and ^{65}Cu copper isotopes has been concluded.

In Fig. 4 high-resolution PL spectra of D and E bands at 25 K recorded in samples doped with monoisotopic silver are compared. In this case no isotope shift is observed and we can not conclude whether these lines are silver-related.

3.2. Luminescence decay time measurements

We have examined decay characteristics of A, B and C lines. The decay times are exponential over the entire temperature range and identical for all the components. Fig. 5 shows decay of A line experimentally measured at 4 and 20 K. The lifetimes measured for A line at 4 and 20 K are 248 ± 3 μ s, and 130 ± 5 μ s, respectively. The

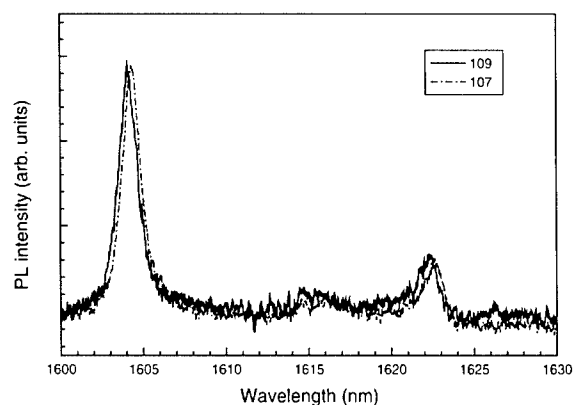


Fig. 3. Isotope effect for the phonon replicas of A and B lines.

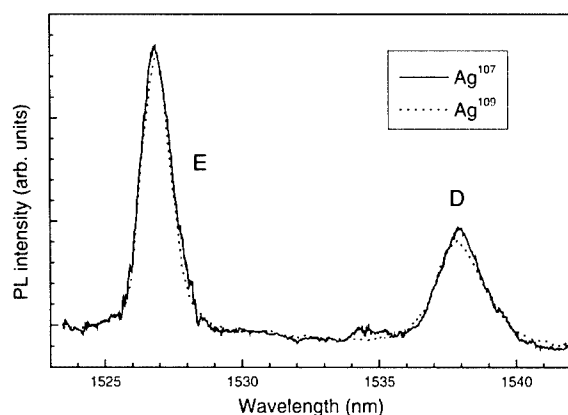


Fig. 4. Isotope effect for D and E PL lines.

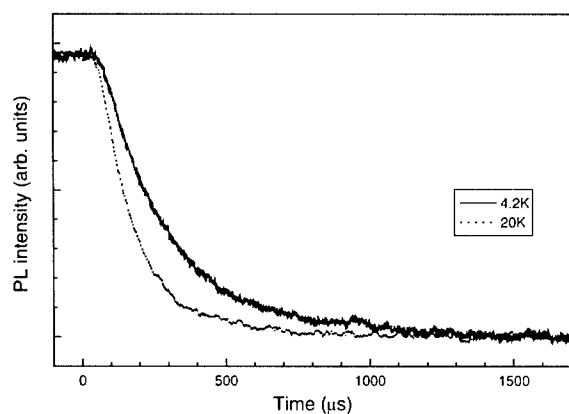


Fig. 5. Decay time for the A line of the 780 PL band measured at 4 and 20 K.

temperature dependence of the lifetime is depicted in Fig. 6. From the comparison with the temperature dependence of PL intensity [3], we assign the

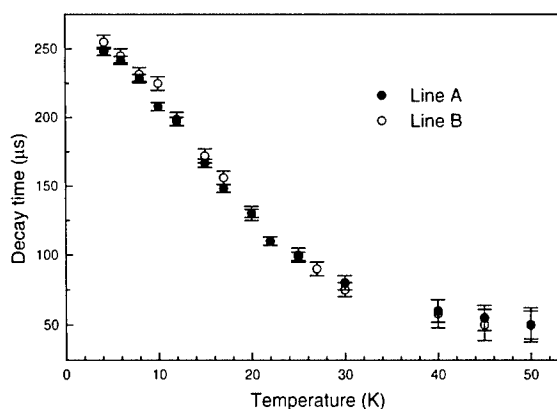


Fig. 6. The temperature dependence of decay times of A and B lines.

high-temperature decrease ($T \geq 30$ K) of the lifetime to dissociation of the exciton. The identical decay time of A, B and C lines is in agreement with the hypothesis that these lines originate from three thermalizing states of the same center [5]. At low temperatures, we obtain long decay times of about 250 μ s. This value is large when compared with the lifetimes of donor or acceptor bound excitons in silicon, which are in the ns range. For excitons bound to a donor or acceptor, the lifetimes strongly depend on the impurity binding energy E_i . Experimentally, approximate dependencies $\tau \propto E_i^{-4.6}$ for acceptor or $\tau \propto E_i^{-3.9}$ for donor were reported and the lifetime shortening was attributed to a localized phononless Auger recombination process [9]. For example, for excitons localized at In acceptors in silicon with $E_i = 154$ meV, the lifetime of $\tau = 2.7$ ns has been determined [9]. The lifetimes measured in this study are by a factor 10^5 longer and are consistent with a model that the A, B and C lines are due to recombinations of excitons bound at an isoelectronic trap [10,11].

5. Conclusion

The 780 meV luminescence lines observed in silver-doped silicon samples have been studied. For samples doped with isotopically enriched silver, we present conclusive microscopic evidence on participation of silver in the optically active center responsible for the 780 meV PL band. The experimentally measured long lifetimes of the three dominant no-phonon lines of the 780 meV band are in agreement with a model of radiative recombination of an exciton localized at an isoelectronic center.

References

- [1] N. Baber, et al., *J. Appl. Phys.* 62 (1987) 2553.
- [2] J. Olajos, et al., *Phys. Rev. B* 38 (1988) 10633.
- [3] M.H. Nazare, et al., *Mater. Sci. Eng. B* 4 (1989) 273.
- [4] N.T. Son, et al., *Phys. Rev. B* 49 (1994) 17428.
- [5] Meng-Xia Zhu, et al., *Mater. Sci. Forum* 258–263 (1997) 485.
- [6] V. Heine, et al., *Phys. Rev. B* 11 (1975) 3795.
- [7] N.Q. Vinh et al., *Phys. Rev. B.*, submitted for publication.
- [8] J. Weber, et al., *Phys. Rev. B* 25 (1982) 7688.
- [9] W. Schmid, *Phys. Status Solid. B* 84 (1977) 529.
- [10] G.S. Mitchard, et al., *Solid State Commun.* 29 (1979) 425.
- [11] S.P. Watkins, et al., *Solid State Commun.* 43 (1982) 687.



ELSEVIER

Physica B 308–310 (2001) 418–420

PHYSICA B

www.elsevier.com/locate/physb

Detection of diffusional jumps of interstitial Fe in silicon by Mössbauer spectroscopy

H.P. Gunnlaugsson^{a,*}, M. Dietrich^b, M. Fanciulli^c, K. Bharuth-Ram^d,
R. Sielemann^e, G. Weyer^a, the ISOLDE Collaboration^b

^a*Institute of Physics and Astronomy, University of Aarhus, Ny Munkegade, DK-8000 Aarhus C, Denmark*

^b*EP Division, CERN, CH-1211 Geneva 23, Switzerland*

^c*Laboratorio MDM-INFN, Via C. Olivetti 2, 20041 Agrate Brianza, Italy*

^d*Physics Department, University of Durban-Westville, Durban 4000, South Africa*

^e*Hahn-Meitner Institute, Glienickestr. 100, D-14109 Berlin, Germany*

Abstract

A technique to create radioactive, interstitial ^{57}Fe atoms in silicon at diffusion temperatures is reported, which allows for the detection of their diffusional jumps by the resulting line broadening in the Mössbauer spectra of the emitted 14 keV γ -radiation. Radioactive $^{57}\text{Mn}^+$ ($T_{1/2} = 1.5$ min) ions have been implanted into silicon crystals held at 400–700 K. As a result of the annealing of the radiation damage during the ^{57}Mn lifetime, the Mn atoms are found on substitutional lattice sites. In the subsequent decay of ^{57}Mn to the Mössbauer state of ^{57}Fe , an average recoil energy of 40 eV is imparted on the daughter atom. This leads to a replacement into interstitial sites for the majority of the Fe atoms, the remainder remains on substitutional sites. From the temperature dependent line broadening the diffusion coefficients for neutral and ionised interstitial Fe have been deduced. © 2001 Elsevier Science B.V. All rights reserved.

Keywords: Mössbauer spectroscopy; Iron; Silicon; Diffusion

1. Introduction

The controversial experimental results reported for the charge state dependence of the diffusivity of interstitial iron in silicon have been reviewed recently [1]. In particular, Heiser and Mesli [2] found positively charged interstitial Fe_i^+ to diffuse faster than neutral Fe_i^0 . The opposite behaviour was found by Koveshnikov and Rozgonyi [3]. Possible reasons for this discrepancy, related to the techniques and/or the materials applied, were discussed among the authors [4,5] as well as in Ref. [1].

In this contribution, an entirely different approach to solve this issue is reported. ^{57}Fe Mössbauer spectroscopy has been employed, utilising ion implantation of radioactive $^{57}\text{Mn}^+$ parent isotopes at elevated tempera-

tures, where the radiation damage from the implantation is basically annealed during the ^{57}Mn lifetime ($T_{1/2} = 1.5$ min) and the Mn atoms are found on substitutional lattice sites [6]. In the subsequent decay of ^{57}Mn to the Mössbauer state of ^{57}Fe , an average recoil energy of 40 eV is imparted on the daughter atom. This causes a replacement into interstitial sites for the majority of the Fe atoms. A fraction of less than 25% remains on the substitutional sites. Due to their athermal creation in a recoil process the interstitial Fe atoms can be considered as isolated and dilute. A few diffusional jumps of interstitial Fe during the lifetime of the Mössbauer state ($T_{1/2} = 100$ ns) lead to a broadening of their Mössbauer line at $T > 450$ K. This line broadening has been observed previously for interstitial ^{57}Fe in silicon [7] utilising recoil implantation of Coulomb-excited $^{57\text{m}}\text{Fe}$. Here, the implantation and measurement are performed within the lifetime of the Mössbauer state. It turned out that the radiation damage did not anneal out within that lifetime at

*Corresponding author. Tel.: +45-89423726; fax: +45-89420740.

E-mail address: hpg@ifa.au.dk (H.P. Gunnlaugsson).

diffusion temperatures and also it was questionable as to whether the interstitial Fe was in the neutral or ionised state [8].

2. Experimental

Radioactive ion beams of $^{57}\text{Mn}^+$ ($T_{1/2} = 1.5$ min) were produced at the ISOLDE facility at CERN using 1.4 GeV proton induced nuclear fission in a UC_2 target and the recently developed laser ion source [9]. Mn atoms were chemically selected via multiple-photon resonant laser ionisation and accelerated to 60 keV. Following mass separation, clean beams of $^{57}\text{Mn}^+$ were obtained. These were implanted into differently doped Si single crystals held at 300–800 K in an implantation chamber. Less than 10^{12} ions/cm² were implanted into each sample to avoid an overlap of the damage cascades during implantation. Mössbauer spectra were recorded with a resonance detector [10] at room temperature mounted on a velocity drive unit outside the implantation chamber. The detector was equipped with four 150 nm thick α - ^{57}Fe absorber layers. This detection method gives a rather complicated 6-fold emission spectrum due to the magnetic hyperfine interaction. However, benefits of this method are the narrow absorber line width and internally calibrated spectra. To allow easier visual inspection of the spectra, the 6-fold emission spectra have been transformed into a single emission feature.

3. Results and analysis

Fig. 1 shows the Mössbauer spectra recorded after implantation into n^+ - (P-doped $1.3 \times 10^{18} \text{ cm}^{-3}$) and p^+ -type (B-doped $3.3 \times 10^{18} \text{ cm}^{-3}$) Si at the temperatures indicated.

Several features can be seen directly in the figure. The general movement of the spectral components towards the right is as expected from the second order Doppler shift. At 475 K, virtually no line broadening is visible and the spectra are dominated by lines assigned to substitutional Fe [11] and interstitial Fe in the tetrahedral site [7,11]. The isomer shift of interstitial Fe is slightly different in n - and p -type material in accordance with the $\text{Fe}_i^{0/+}$ band-gap state [11]. As the temperature is increased to ~ 640 K, a clear broadening of the interstitial lines is observed in both cases. At temperatures above ~ 770 K, the interstitial line has practically disappeared from the spectra, which are now dominated by lines assigned to substitutional Fe and the recently reported new line, which was tentatively assigned to Fe_i -vacancy pairs [12]. Due to the occurrence of this line with increasing temperature, an accurate determination of the line broadening of the interstitial line is hampered.

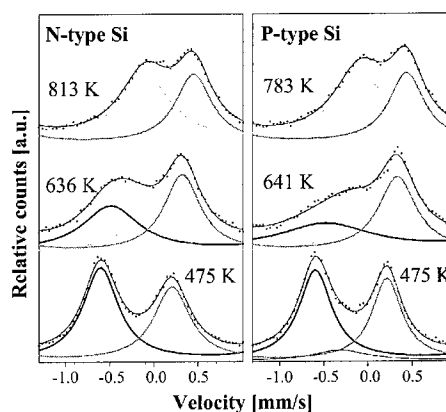


Fig. 1. Mössbauer spectra obtained after implantation of ^{57}Mn into n -type Si (left) and p -type Si (right) at the temperatures indicated. The thin solid line overlapping the experimental points shows the sum of the fitting components. The thicker lines show the individual components. The black line shows the interstitial line, the dark grey the substitutional line, and the light grey line the new line, which is tentatively attributed to Fe_i -vacancy pairs.

However, in a simultaneous fitting procedure including this line, reasonably accurate values could be determined in the temperature range 500–700 K. As can be seen in the spectra measured at ~ 640 K, the intensity of the new line is too small to affect the immediate conclusion that the line broadening of the interstitial line is larger in p - than in n -type material.

The relationship between the line width of the interstitial line in the Mössbauer spectra, Γ , and the macroscopic diffusion coefficient, D , is given by [13]

$$\Gamma = \Gamma_0 + \frac{12\hbar c D}{E_0 l^2}, \quad (1)$$

where Γ_0 is the experimental line width measured in units of Doppler velocity, \hbar Planck's constant, c the velocity of light, E_0 the energy of the Mössbauer transition ($= 14.4 \text{ keV}$) and l the elementary jump length, 2.35 \AA , assuming jumps between tetrahedral interstitial sites, i.e. a direct interstitial diffusion mechanism. From Eq. (1), it is observed that the line broadening $\Delta\Gamma = \Gamma - \Gamma_0$ is directly proportional to the diffusion coefficient. Fig. 2 shows the line broadening as a function of temperature in n^+ - and p^+ -type (B-doped, $2 \times 10^{19} \text{ cm}^{-3}$) samples.

4. Discussion and conclusions

The electronic consequences of the nuclear decay have been discussed in detail previously [8,11]. For the heavily doped p^{++} - and n^+ -type material employed here, the recoil-produced Fe_i can be safely assumed to be in the

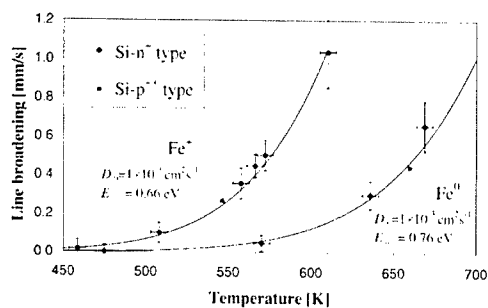


Fig. 2. Line broadening $\Delta\Gamma$ as a function of temperature for two of the samples used in this study. The solid lines represent the expected broadening for pure Fe_i^+ and pure Fe_i^0 charge states for the pre-factors and activation energies indicated.

ionised and neutral charge state, respectively. As seen from Fig. 2, the broadening in p^{++} -type material, i.e. the Fe_i^+ diffusivity is consistently larger than that of Fe_i^0 in the investigated temperature range. It is noteworthy that the broadening for Fe_i^+ is in agreement with the previously determined values [7], corroborating the argumentation [8] that the ionised state prevailed in that experiment. The temperature range, where a good accuracy for the line broadening of the interstitial lines is obtained, is rather narrow. Taking the error analysis into consideration, the pre-factor D_0 and the activation energy E_a of the diffusion coefficient $D = D_0 \exp(-E_a/kT)$ cannot be determined simultaneously with satisfactory accuracy. Using the values given by Heiser and Mesli [2] for D_0 as 10^{-2} and $1.4 \times 10^{-3} \text{ cm}^2/\text{s}$ for neutral and positively charged interstitial Fe, respectively, we obtain activation energies of 0.91(1) and 0.70(1) eV, respectively. While the latter value for Fe_i^+ is in reasonable agreement with the values obtained by Heiser and Mesli [2], 0.69, and Takahashi et al. [14], 0.68, the value for Fe_i^0 is considerably larger than their values of 0.84 and 0.80 eV, respectively. Obviously, the choice of the value for the pre-factor is critical. Taking this value to be $10^{-3} \text{ cm}^2/\text{s}$, common for both states, as suggested in Ref. [1] from an analysis comprising even high-temperature diffusion data, activation energies of 0.66(1) eV for Fe_i^+ and 0.76(1) eV for Fe_i^0 are obtained. The latter value, presumably a lower limit, is still hardly consistent with the value given by Koveshnikov and Rozgonyi [3], 0.56 eV. Irrespective of the difficulties in obtaining accurate values for D_0 and E_a presently, the

diffusivity of Fe_i^+ is found to be larger than that of Fe_i^0 in the temperature range investigated here.

Acknowledgements

This work has been supported by the Danish Natural Science Research Council within the ICE centre. Support from the EU HPRI programme (Contract No. HPRI-CT-1999-00018) is also acknowledged. U. Wahl is acknowledged for providing the p^{++} sample.

References

- [1] A.A. Istratov, H. Hieslmair, E.R. Weber, Appl. Phys. A 69 (1999) 13.
- [2] T. Heiser, A. Mesli, Phys. Rev. Lett. 68 (1992) 978.
- [3] S.V. Koveshnikov, G.A. Rozgonyi, Appl. Phys. Lett. 66 (1995) 860.
- [4] T. Heiser, A. Mesli, Appl. Phys. Lett. 68 (1996) 1868.
- [5] S. Koveshnikov, G. Rozgonyi, Appl. Phys. Lett. 68 (1996) 1870.
- [6] H.P. Gunnlaugsson, M. Fanciulli, M. Dietrich, K. Bharuth-Ram, R. Sielemann, G. Weyer, the ISOLDE Collaboration, Nucl. Instr. and Meth. B, 2001, in press.
- [7] P. Schwalbach, S. Laubach, M. Hartick, E. Kankeleit, B. Keck, M. Menningen, R. Sielemann, Phys. Rev. Lett. 64 (1990) 1274.
- [8] G. Weyer, S. Degroote, M. Fanciulli, V.N. Fedoseyev, G. Langouche, V.I. Mishin, A.-M. Van Bavel, A. Vantomme, the ISOLDE Collaboration, Mater. Sci. Forum 258–263 (1997) 437.
- [9] V.N. Fedoseyev, K. Bätzner, R. Catherall, A.H.M. Evens, D. Forkel-Wirth, O.C. Jonsson, E. Kugler, J. Lettry, V.I. Mishin, H.L. Ravn, G. Weyer, the ISOLDE Collaboration, Nucl. Instr. and Meth. B 126 (1997) 88.
- [10] G. Weyer, in: I.J. Gruverman, C.W. Seidel (Eds.), Mössbauer Effect Methodology, Vol. 10, Plenum Press, New York, 1976, p. 301.
- [11] G. Weyer, A. Burchard, M. Fanciulli, V.N. Fedoseyev, H.P. Gunnlaugsson, V.I. Mishin, R. Sielemann, The ISOLDE Collaboration, Physica B 273–274 (1999) 363.
- [12] H.P. Gunnlaugsson, M. Dietrich, M. Fanciulli, K. Bharuth-Ram, R. Sielemann, G. Weyer, the ISOLDE Collaboration, Phys. Scr., 2001, submitted for publication.
- [13] K.S. Singwi, A. Sjölander, Phys. Rev. 120 (1960) 1093.
- [14] H. Takahashi, M. Suezawa, K. Sumino, Phys. Rev. B 46 (1992) 1882.



ELSEVIER

Physica B 308–310 (2001) 421–423

PHYSICA B

www.elsevier.com/locate/physb

New electron spin resonance spectra from iron-vacancy pair in silicon: I. Defect with two values for the spin

T. Mchedlidze*, M. Suezawa

Institute for Materials Research, Tohoku University, 2-1-1 Katahira, Aoba-ku, Sendai 980-8577, Japan

Abstract

New ESR spectra from an iron-vacancy pair were detected in electron-irradiated float-zone grown silicon samples pre-doped with iron. The paramagnetic center reveals trigonal symmetry. The center is in a neutral state and has two spin values: $S = 1$ when the defect axis direction is close to that of the static magnetic field and $S = 3/2$ for other orientations. The obtained anisotropies of the ESR peak position and intensity suggest a transformation process for the spin magnitude. © 2001 Elsevier Science B.V. All rights reserved.

Keywords: Si; Fe; Vacancy; ESR

1. Introduction

Investigation of iron-related defects in silicon (Si) has remained a top priority research topic for more than four decades [1]. Detrimental for Si-based device operation but yet inevitable [2], iron-related defects reveal nontrivial and often unique properties. A large variety of iron complexes with dopant and other impurity atoms in Si have already been detected and studied [1,3]. Less attention, however, has been given to complexes of iron atoms with intrinsic Si defects (vacancies and self-interstitials). Several ESR spectra (named NL19-25) from iron-doped and subsequently electron-irradiated Si samples have been reported previously [4]. Among them, NL19 was interpreted to originate from a positively charged substitutional iron atom (Fe_S^+). If confirmed, this will be the first clear evidence of the existence of Fe_S in Si.

Recently, in similar samples, we detected new ESR spectra, which exhibit two values for the spin of the defect depending on the angle between the crystal axes and magnetic field. We herein present the results of our observations.

2. Experimental

We investigated float-zone grown n-type (phosphorus doped) and p-type (boron doped) Si samples of various resistivities. Mechanically and chemically polished Si samples, $3 \times 3 \times 12 \text{ mm}^3$ in size, were dipped in a 100 ppm FeCl_3 water solution, dried, and annealed at $1000\text{--}1200^\circ\text{C}$ in evacuated quartz capsules for iron doping. Natural iron or that enriched with ^{57}Fe or ^{54}Fe isotope was used for FeCl_3 preparation. Samples were quenched in iced water after doping. Iron-doped and reference samples were irradiated at room temperature with 3-MeV electrons (dose range $d = 0.1\text{--}1 \times 10^{17} \text{ e/cm}^2$) and were kept at temperatures below -10°C after irradiation.

We used a JEOL X-band ESR spectrometer with a TM_{011} mode microwave (MW) resonator and a continuous helium gas-flow cryostat. It was possible to illuminate the samples during measurements. The derivative of MW field absorption with respect to magnetic field ($\partial\chi''/\partial H_0$) was measured using a lock-in amplifier and magnetic field modulation with an amplitude of $0.1\text{--}0.6 \text{ G}$ and a frequency of 100 kHz . The spectra from the iron-related defect were observed in the temperature range from 6 to 18 K. We were not able to conduct measurements below 4.5 K for observation of the NL19 spectra in our samples.

*Corresponding author. Fax: +81-22-215-2041.

E-mail address: teimuraz@imr.tohoku.ac.jp
(T. Mchedlidze).

3. Results and discussion

In Fig. 1a, the anisotropy of the ESR peak positions is presented for the $[1\bar{1}0]$ rotation axis together with fitting curves. Expression for the spin Hamiltonian and the fitted parameters are presented in Table 1. (We used factor $P\{\text{mT}\} = g \times 4.66855 \times P\{10^{-4}/\text{cm}\}$ for conversion of energy units [5].) The paramagnetic center of trigonal symmetry (axis $C_3 \parallel \langle 111 \rangle$) was identified. Large zero-field splitting (ZFS) prevented detection of multiple ESR transition lines. We calculated ZFS parameters using the method described in [6]. The ESR signals could not be detected if the direction of the static magnetic field B was within the range of 12° – 18° from C_3 (“transient orientations”). In Table 1 and below, the spectra observed within the range $C_3 \pm 12^\circ$ are termed “TU2” and those observed outside of $C_3 \pm 18^\circ$ are designated as “TU3”. Close to the transient orientations, the amplitude of the ESR signal decreased and its width increased until the signal could not be separated from the experimental noise. Fig. 1b presents the anisotropy of the TU2 and TU3 signal intensity: $I = \int (\partial\chi''/\partial H_0) dH_0^2$.

The TU2 and TU3 spectra were detected in all iron-doped and e-irradiated samples except in a low

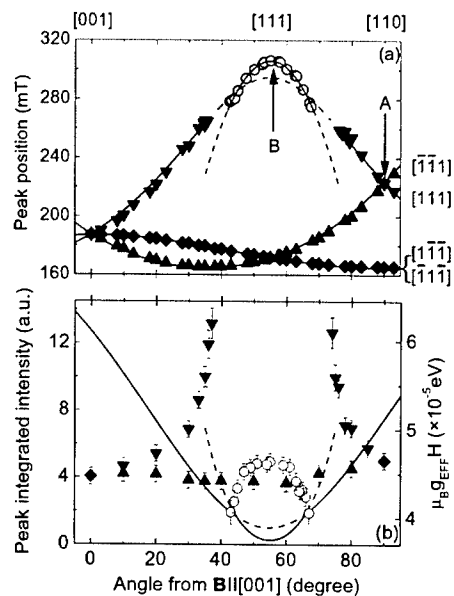


Fig. 1. (a) Measured (symbols) and calculated (lines) anisotropy of peak positions for TU2 (O) and TU3 (other symbols) spectra. Positions corresponding to dotted lines could not be observed. Axes of relevant defects are shown to the right of the graph. (b) Anisotropy of intensity (same meaning of symbols) for the TU2/TU3 signals, values for $[1\bar{1}\bar{1}]$ and $[\bar{1}11]$ axes are not shown. Lines represent anisotropy of spin-transition energy. Experimental conditions: $\nu_{\text{RES}} = 9.064 \text{ GHz}$, $T = 11 \text{ K}$. B in the $(1\bar{1}0)$ plane.

Table 1

Expression and parameters of spin Hamiltonian for the TU2 and TU3 ESR spectra. The HF and SHF terms of the spin Hamiltonian are treated separately in Ref. [9]

ESR spectra	TU2	TU3
Spin Hamiltonian	$H = \mu_B \vec{B} \cdot \vec{g} \cdot \vec{S} + \vec{S} \cdot \vec{D} \cdot \vec{S} + \dots$	
Symmetry	Trigonal	Trigonal
Spin	S	$3/2$
Principal g -values	g_{11}	2.114 ± 0.001
	g_{\perp}	2.47 ± 0.03
Effective g_{\perp}	5.11 ± 0.06	3.933 ± 0.007
ZFS (cm^{-1})	D	0.72 ± 0.01
		1.30 ± 0.03

resistivity ($1.1 \Omega \text{ cm}$) p-type sample. The intensity well correlated with interstitial iron concentration in the samples $I(\text{TU2, TU3}) \propto (C(\text{Fe}_i))^{0.2}$ and with the total irradiation dose $I(\text{TU2, TU3}) \propto d^{0.75}$. The $C(\text{Fe}_i)$ was estimated using the intensity of the relevant ESR signal with a g -factor of 2.069. $I(\text{TU2, TU3})$ was larger in samples with high starting resistivity. The ratio $I(\text{TU2})/I(\text{TU3})$ was the same in all measured samples for fixed experimental conditions such as directions, temperature and microwave power. Data illustrating the above statements are presented in Fig. 2. Both the TU2 and TU3 spectra were similarly suppressed by illumination of the sample with white light during the measurements. MW power saturation behavior, temperature dependence of signal intensity and relaxation times of the TU2 spectra differed from those of the TU3 spectra.

The shape of the ESR spectra at the positions indicated as “A” and “B” in Fig. 1a and various iron isotope compositions are presented in Fig. 3a–f. The shape of the TU3 signal (see Fig. 3a) remains

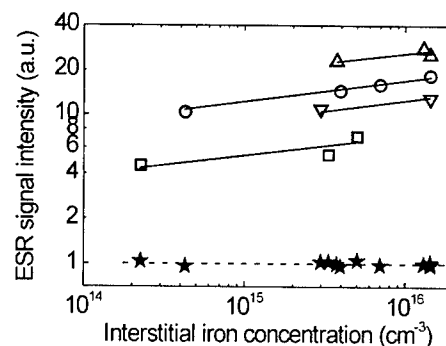


Fig. 2. $I(\text{TU2})$ (open symbols) and ratio $I(\text{TU2})/I(\text{TU3})$ (★) dependence on $C(\text{Fe}_i)$. Samples: p-type Si (\square) $1800 \Omega \text{ cm}$; (∇) $5 \Omega \text{ cm}$; n-type (\circ) $1000 \Omega \text{ cm}$; (Δ) $0.6 \Omega \text{ cm}$. The ratio was calculated for A (TU2) and B (TU3) positions shown in Fig. 1a. Irradiation dose = $5 \times 10^{16} \text{ e/cm}^2$. Lines are presented to guide the eye. All experimental conditions were as indicated in Fig. 1.

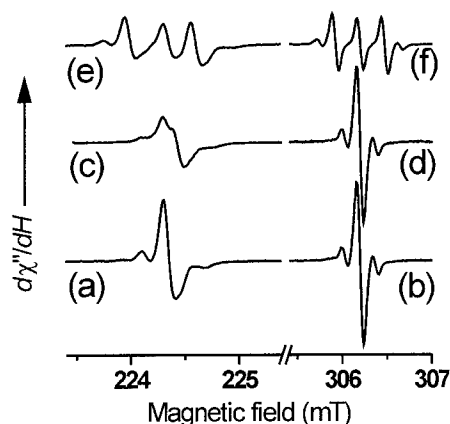


Fig. 3. Shapes of the signals corresponding to A (a, c, e) and B (b, d, f) positions in Fig. 1a. Iron isotope composition: (a, b) natural; (c, d) $\sim 50\%$ ^{54}Fe enriched and (e, f) $\sim 70\%$ ^{57}Fe enriched. All experimental conditions were as indicated in Fig. 1.

asymmetric for all directions where it can be detected. Small asymmetry for the TU2 spectra was detected close to the transient orientations. For the samples enriched with ^{57}Fe isotope, the center of gravity for the hyperfine (HF) $^{57}\text{Fe}^{28}\text{Si}$ satellite peaks of the TU3 spectra obviously differs from the position of the $^{56}\text{Fe}^{28}\text{Si}$ related peak (Fig. 3e), and for the samples enriched with ^{54}Fe isotope, isotope-related splitting is clearly observable (Fig. 3c). These observations unambiguously suggest the presence of an isotopic shift [7,8] in the ZFS term of the spin Hamiltonian. Due to the isotopic shifts, the HF/SHF terms in the spin Hamiltonian require special treatment and will be presented in the second part of our report together with a microscopic structure of the defect [9].

The above experimental results (see Figs. 2 and 3) suggest the presence of a single iron atom and a vacancy in the defect. The dependence of defect concentration on sample resistivity may be attributed to the capture of vacancies by phosphorus during irradiation in the n-type samples and to a smaller Fe_i concentration in p-type samples due to iron-boron pairing.

Let us now discuss the observed two spin values for the same defect. Different charge states can bring about different values of the spin for the Fe–V defect. Well-known Fe_i^0 and Fe_i^+ states of interstitial iron are the best example of such situation. However, the observed independence of the $I(\text{TU2})/I(\text{TU3})$ ratio (see Fig. 2a, solid star symbols) from sample conducti-

vity type, resistivity, irradiation dose and illumination conditions contradicts such an explanation. Besides, the observed anisotropy of the signal intensity suggests some transition process. To our knowledge, such a phenomenon has not been previously identified.

Based on our findings, we propose the following explanation. The effective spin $S = 1$ for the Fe–V defect can be explained if the iron atom forms strongly directed $4s4p^3$ hybridized orbitals with four Si atoms surrounding the vacancy. $S = 3/2$ can arise if one of the iron electrons is localized in a singlet configuration near a Si atom positioned along the defect axis. In both configurations, the defect remains electrically neutral. If both of these configurations have finite lifetimes, the defect may ‘choose’ a value for the spin that corresponds to a smaller energy of the defect in spin-excited state: $E = \mu_B g_{\text{eff}} H$. According to the experimental results (see Fig. 1b and Table 1), the $S = 1$ state results in lower energy for spin-transition if the direction of the magnetic field is within the $C_3 \pm 12^\circ$ range, while, on the contrary, $S = 3/2$ is “energetically favorable” outside this range. Thus, the spin of the defect will depend on inter-orientation of the defect axis and magnetic field. Another possibility is that the transverse-to-the-defect-axis magnetic field causes the described change in the electron configuration of the defect. Although we cannot exclude such a possibility, it seems to be less probable due to extremely small values of acting transverse magnetic fields for the transient orientations.

In conclusion, new ESR spectra were detected in the iron doped and subsequently electron irradiated FZ–Si crystals. An origin of the signal is an iron-vacancy pair in trigonal symmetry. The ESR center reveals unique property: the spin of the center changes in the magnetic field.

References

- [1] A.A. Istratov, et al., *Appl. Phys. A* 69 (1999) 13.
- [2] K. Graff, *Metal Impurities in Silicon-Device Fabrication*, Springer, Berlin, 1995.
- [3] C.A.J. Ammerlaan, *Solid State Phenom.* 6–7 (1989) 591.
- [4] S.H. Muller, et al., *Phys. Rev. B* 25 (1982) 25.
- [5] C. Rudowicz, *Magn. Res. Rev.* 13 (1987) 1.
- [6] W. Gehlhoff, et al., *Phys. Status Solidi B* 105 (1981) K91.
- [7] S.A. Marshall, et al., *Phys. Rev.* 133 (1964) A1427.
- [8] G.D. Watkins, *Solid State Commun.* 17 (1975) 1205.
- [9] T. Mchedlidze, M. Suezawa, in these Proceedings (ICDS-21), *Physica B* 308–310.



ELSEVIER

Physica B 308–310 (2001) 424–426

PHYSICA B

www.elsevier.com/locate/physb

Theoretical study of pressure-induced negative effective U of a tungsten atom in crystalline silicon

I. Kitagawa*, T. Maruizumi

Advanced Research Laboratory, Hitachi Ltd., 1-280 Higashi-Koigakubo, Kokubunji, Tokyo 185-8601, Japan

Abstract

The effects of local stress on the impurity level of tungsten metal in crystalline silicon were analyzed for the first time by using a first-principles computational method. We examined changes in the ionization energy associated with the tungsten impurity under hydrostatic or in-plane pressure of up to 1 GPa. A tungsten atom was located interstitially in the tetrahedral center position in crystalline silicon. It was found that as pressure increases, ionization energy (+/0) decreases, while ionization energy (+/+ +) increases. Moreover, negative effective U appears at around 600 MPa under hydrostatic pressure. This critical pressure is increased by the change of magneto-volume effect to 900 MPa under in-plane pressure. © 2001 Elsevier Science B.V. All rights reserved.

Keywords: Metal impurity; Pressure-induced negative effective U ; First-principles calculation

1. Introduction

Impurities and vacancies in semiconductors have localized electronic states. For example, a silicon vacancy has dangling bonds, which consist of sp^3 hybridization, and a transition-metal impurity has a localized d orbital. These localized states produce a deep level in the band gap, which seldom gives rise to the negative effective U phenomenon. The negative effective U of a silicon vacancy is caused by the change in effective electronic correlation with lattice relaxation [1]. In 3d transition metal impurities, an intrinsic electronic negative effective U appears without lattice relaxation [2]. However, the deep level of 5d transition metals in silicon has not been clarified by theoretically. With the dimensions of MOSFET (metal-oxide-silicon field-effect transistor) devices decreasing both horizontally and vertically, and with the use of noble metals as a gate electrode in these devices, it has become critical to understand how the local stress in a silicon substrate affects the ionization energy of metal impurity. Accordingly, we used a first-principles calculation to theoretically investigate tungsten impurities and we analyzed the

effect of various pressure conditions on the tungsten impurities.

2. Methods

The formation energy of defects in silicon in the charged state Q is given as

$$\Omega(Q, \mu_c) = E_D + Q(E_v + \mu_c) - \sum_s n_s \mu_s, \quad (1)$$

where E_D is the total energy of the supercell containing defects, μ_s is the energy per atom (denoted by “s”) in the perfect lattice, and n_s is the number of s atoms in the defect supercell. The electron chemical potential μ_c in Eq. (1) gives the position of the Fermi level in the band gap relative to E_v (the top of the valence band). Average potential correction [3] was used to calculate the position of E_v in the defect supercell. μ_{Si} tends to be saturated as the supercell size increase. The difference between values of μ_{Si} in supercell of 32 atoms and 64 atoms was within 0.001 eV. Moreover, μ_W was obtained from a perfect BCC structure of tungsten. We used a tetragonal supercell with lattice parameters $a = 10.78$, $b = 10.78$, and $c = 5.40$ Å. This supercell contains 32 silicon atoms. A tungsten atom was located in the tetragonal center

*Corresponding author. Fax: +81-42-327-7804.

E-mail address: i-kitaga@crl.hitachi.co.jp (I. Kitagawa).

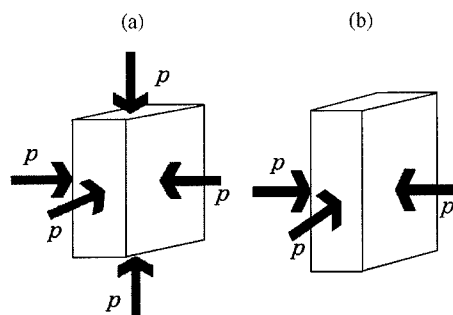


Fig. 1. Pressure conditions used in calculation: (a) hydrostatic, (b) in-plane.

interstitial position in the super cell. We applied two pressure conditions to the supercell: hydrostatic pressure of 1 GPa (Fig. 1(a)) and in-plane compression stress of 1 GPa (Fig. 1(b)). Under such pressure conditions, enthalpy was used instead of total energy of the defect supercell.

We performed the calculation of electronic structure by using the first-principles band-calculation package CASTEP [4]. This package solves the Kohn–Sham equations on a plane-wave basis via nonlocal pseudopotentials, that is, the Vanderbilt-type ultra-soft pseudopotential [5]. The electronic exchange–correlation was treated by the spin-polarized GGA (general gradient approximation), in which the exchange–correlation functional given by Perdew and Wang [6] was applied. The cut-off energy of the plane-wave basis set was 200 eV. The SCF convergence criterion per atom was 1×10^{-6} eV, and the tolerance for root-mean-square force was 0.05 eV/Å. To cancel the interaction between defect states in neighboring supercells, MP (Monkhorst and Pack) [7] $2 \times 2 \times 4$ mesh, which includes eight sampling points, was used. Then, prior to the evaluation of the ionization energy, full geometry optimization was done.

3. Results and discussion

To confirm the accuracy of the calculated formation energy, we first calculated the formation energies of a silicon vacancy (Fig. 2). It is important that the effect of k -point sampling on the total energy calculations, as discussed by Makov et al. [8]. In Fig. 2, the calculation result from the MP $2 \times 2 \times 4$ mesh is closer within 0.2 eV to the formation energy in 216 atoms (the gray line; calculated in [3]) than that of $\Gamma + L$ sampling.

Second, the pressure dependence of the ionization energy of the tungsten impurity is shown in Fig. 3. Ionization energy $(+/0)$ is 0.55 eV at zero pressure. Under hydrostatic pressure, ionization energy $(+/0)$ decreases to 0.51 eV at 1 GPa. Under in-plane pressure,

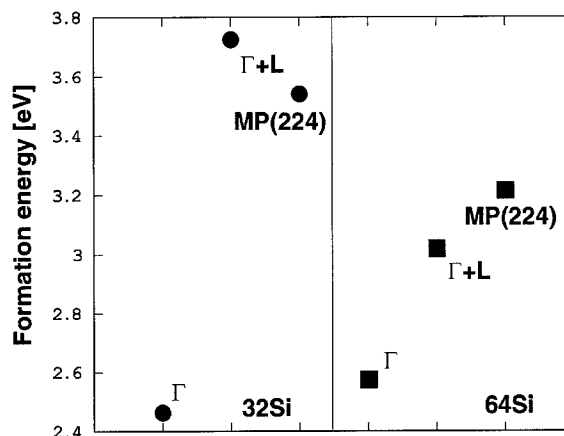


Fig. 2. Calculated formation energy of a neutral vacancy in silicon. The cell size is given on the bottom of each panel. The horizontal gray line indicates the calculation representing a 216-atoms cell by Puska et al. [3].

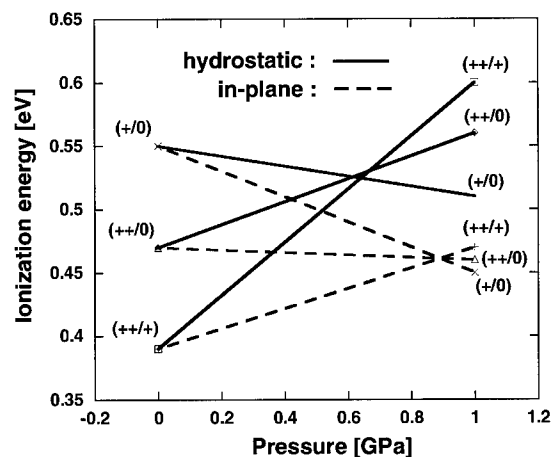


Fig. 3. Calculated ionization energy plot for W impurity.

ionization energy $(+/0)$ also decreases to 0.45 eV, which is shallower than that under hydrostatic pressure. Ionization energy $(++/0)$ is 0.39 eV at zero pressure. Under hydrostatic pressure, $(++/0)$ increases to 0.6 eV at 1 GPa. This abrupt increase of ionization energy $(++/0)$ causes the negative effective U . Ionization energy $(+/0)$ is 0.56 eV at hydrostatic pressure of 1 GPa. Under in-plane pressure, ionization energy $(++/0)$ also increases to 0.47 eV, and ionization energy $(+/0)$ decreases to 0.46 eV. The negative effective U does not appear under zero pressure. This theoretical result agrees with the experimental one in [9]. The ionization energies cross at around 600 MPa hydrostatic pressure, above, which the negative effective U appears. Under in-plane pressure, the crossing point increases to 950 MPa.

Table 1
Calculated spin moment of tungsten impurity (μ_B /unit cell)

Pressure (GPa)	$Q = 0$	$Q = +1$	$Q = +2$
0	1.00	1.60	0.00
1 (in-plane)	0.98	1.44	1.92
1 (hydro.)	1.00	1.60	0.10

Finally, we focus on the spin moment of tungsten impurity (Table 1). The spin moment is localized near the tungsten atoms under all pressure conditions. When the charge is neutral ($Q = 0$) and positive ($Q = +1$), high-spin states appear under all pressures. When the charge is double-positive ($Q = +2$), low-spin states appear under zero and hydrostatic pressure of 1 GPa, but the high-spin state appears under in-plane pressure of 1 GPa. It is thus concluded that the spin moment of the double-positive charge is influenced by the pressure condition.

From all the above results, we can investigate the mechanism of ionization energy of a 5d transition metal. It is known that a 5d transition metal, such as tungsten, has strong d-p hybridization between neighboring silicon and metal atoms and weaker exchange splitting than 3d transition metals [10]. These imply that the ionization energy, which is related with the spin-states of the metal, is affected under pressure condition. The volume of a tetrahedral cluster of nearest-neighbor silicon around tungsten is denoted by V and its spin moment is denoted by m_s . The change of volume-magnetic ratio is denoted by $|\Delta V/\Delta m_s|$, which is shown in Table 2. The magneto-volume interaction was changed under various pressures. Under zero pressure, $(|\Delta V/\Delta m_s|)^{0 \rightarrow 1}$ is larger than $(|\Delta V/\Delta m_s|)^{+1 \rightarrow +2}$, while $(|\Delta V/\Delta m_s|)^{0 \rightarrow 1}$ is less than $(|\Delta V/\Delta m_s|)^{-1 \rightarrow -2}$ under both 1 GPa pressure conditions (i.e. in-plane and hydrostatic). This difference between the zero pressure and the 1 GPa pressure conditions is therefore considered to be the origin of the negative effective U of tungsten in silicon. Under in-plane pressure, moreover, the high-spin-state and the large change of the volume-magnet ratio appear and the crossing point increases from 600 to 950 MPa. From our results, it is implied that the effect of

Table 2
Calculated $|\Delta V/\Delta m_s|$ of a tetrahedral cluster of nearest-neighbor silicon around tungsten

Pressure (GPa)	$Q(0 \rightarrow +1)$	$Q(+1 \rightarrow +2)$
0	0.075	0.056
1 (in-plane)	0.000	0.281
1 (hydro.)	0.075	0.150

magneto-volume on the ionization energy is larger than that in 3d transition metals.

4. Summary

We performed first-principles calculations of the electronic and geometrical structures of tungsten impurity in crystalline silicon. It was found that as pressure increases, the ionization energy ($+ / 0$) decreases, while ionization energy ($+ + / +$) increases. Negative effective U appears around a hydrostatic pressure of 600 MPa. It was also found that the change of magneto-volume effect increases this critical pressure to about 900 MPa under in-plane conditions.

References

- [1] P.W. Anderson, *Phys. Rev. Lett.* 34 (1975) 953.
- [2] H. Katayama-Yoshida, A. Zunger, *Phys. Rev. Lett.* 55 (1985) 1618.
- [3] M.J. Puska, S. Pökyö, M. Pesola, R.M. Nieminen, *Phys. Rev. B* 58 (1998) 1318.
- [4] CASTEP 4.0, Molecular Simulations Inc., San Diego, 1999.
- [5] D. Vanderbilt, *Phys. Rev. B* 41 (1990) 7892.
- [6] K. Burke, J.P. Perdew, Y. Wang, in: Dobson, et al. (Ed.), *Electronic Density Functional Theory: Recent Progress and New Directions*, Plenum Press, New York, 1998, p. 81.
- [7] H.J. Monkhorst, J.D. Pack, *Phys. Rev. B* 13 (1976) 5188.
- [8] G. Makov, R. Shah, M.C. Payne, *Phys. Rev. B* 53 (1996) 15513.
- [9] T. Ando, S. Isomae, C. Munakata, T. Abe, *J. Appl. Phys.* 70 (1991) 5401.
- [10] O. Gunnarsson, *J. Phys. F* 6 (1976) 587.



ELSEVIER

Physica B 308–310 (2001) 427–430

PHYSICA B

www.elsevier.com/locate/physb

Precipitation-enhanced diffusion of nickel in dislocation-free silicon studied by in-diffusion and annealing processes

Shuji Tanaka^a, Hajime Kitagawa^{a,*}, Tetsuo Ikari^b

^aDepartment of Electronics, Fukuoka Institute of Technology, 3-30-1 Wajiro-Higashi, Higashi-ku, Fukuoka 811-0295, Japan

^bDepartment of Electrical and Electronic Engineering, Miyazaki University, 1-1 Gakuen Kibanadai-nishi, Miyazaki 889-2192, Japan

Abstract

To examine the site-exchange mechanism of nickel atoms in dislocation-free silicon, the effect of nickel precipitates on the in-diffusion and annealing rates has been investigated. The variation of the concentration of substitutional nickel atoms with time in these processes follow well the theoretical prediction for the dissociative mechanism. It is suggested that nickel atoms in dislocation-free silicon exchange their sites via the dissociative mechanism, or the dominant point defects mediating the site exchange are vacancies. In-diffusion and annealing processes of nickel atoms are accelerated by the presence of the nickel precipitation, indicating that nickel precipitates, or precipitation-induced lattice defects play a role of sinks and sources of vacancies in the bulk. © 2001 Elsevier Science B.V. All rights reserved.

Keywords: Silicon; Nickel; Precipitation; Enhanced site-exchange rate

1. Introduction

Diffusion and electrical properties of 3d transition elements in silicon have been investigated by many researchers [1–4] from technological and scientific viewpoints. Among 3d transition-metal impurities in silicon, nickel is known to be a peculiar impurity because of the following reasons: First, nickel atoms occupy both substitutional and interstitial sites in silicon crystal. Second, while a large fraction of total atoms is interstitially dissolved, only substitutional atoms whose fraction are in the order of 10^{-3} to 10^{-4} of total dissolved atoms are electrically ionizable [5]. For this reason, nickel is a useful impurity for examining the site-exchange mechanism of impurity atoms in silicon by using an electrical measurement.

It has been proposed [5–7] that the site exchange of nickel atoms in dislocated silicon proceeds via a dissociative mechanism or a vacancy mechanism. In dislocated silicon, both the crystal surfaces and the dislocations act as sinks and sources (SS) of vacancies.

However, the site-exchange mechanism in dislocation-free silicon is an open question, since the experimental confirmation is still limited except for only a few studies [4,8–10]. We have recently proposed [8–10] that the site exchange of nickel atoms in dislocation-free silicon is due to the dissociative mechanism and that the crystal surfaces and a small fraction of nickel precipitates in the bulk can act as the SS of vacancies. The presence of inner SS may lead to an enhancement of site exchange rate.

The purpose of the present paper is to report the results of the in-diffusion and annealing processes of substitutional nickel atoms in dislocation-free silicon to examine the site-exchange mechanisms. It will be shown that the site exchange rates are enhanced by the precipitation of nickel.

2. Experimental

Starting silicon crystals used in the experiment were n-type, phosphorus-doped and dislocation-free wafers. Phosphorus content ranged from 1.3×10^{13} to $1.4 \times 10^{14} \text{ cm}^{-3}$. Nickel thin films were deposited by vacuum evaporation onto the surfaces of silicon slices.

*Corresponding author. Tel.: +81-92-606-3199; fax: +81-92-606-0726.

E-mail address: kitagawa@emat.fit.ac.jp (H. Kitagawa).

Nickel diffusion was carried out in flowing nitrogen gas ambient at diffusion temperatures. $T_D = 960^\circ\text{C}$. The concentration, C_s , of electrically active nickel atoms, namely substitutional nickel atoms was evaluated by measuring the electrical resistivity by means of the four-point probe method. For the in-diffusion process, C_s was measured as a function of diffusion time, t_D . For annealing process, C_s was measured as a function of annealing time, t_A , at an annealing temperature, $T_A = 960^\circ\text{C}$, after the sample was saturated with nickel at 1020°C . Nickel precipitates were observed using an infrared microscope (Olympus BHSM-IR) and a scanning electron microscopy (SEM, Elionix ERA-8800).

3. Results and discussion

It has been generally assumed that, in the in-diffusion and annealing processes, the distribution of C_s is uniform in the crystal. However, substitutional (or electrically active) nickel atoms are well known to manifest U-shaped distribution in silicon. Based on the observed distribution of C_s [10], we assumed here that the distribution is uniform after removing off a surface layer of thickness of around $0.2l$, where l is the thickness of the sample.

Experimental results are shown in Figs. 1 and 2 for in-diffusion and annealing processes, respectively. Note that Fig. 1 also includes the data for nickel in-diffusion in dislocated silicon. It is stressed here that one experimental point in Figs. 1 and 2 represent the averaged value over the values obtained from a few samples prepared independently. Curves show the theoretical values of Eqs. (1) and (2) predicted by the dissociative mechanism:

$$C_s/C_s^0 = 1 - \exp(-t_D/\tau) \quad (1)$$

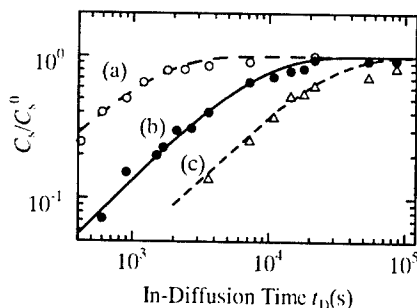


Fig. 1. In-diffusion process of nickel in dislocated and dislocation-free silicon crystals at $T_D = 960^\circ\text{C}$. \circ : Dislocated silicon with $l = 0.1\text{ cm}$, \bullet : dislocation-free silicon with $l = 0.1\text{ cm}$, and \triangle : dislocation-free silicon with $l = 0.4\text{ cm}$. Curves (a), (b) and (c) are calculated values of Eq. (1) with $\tau = 1.1 \times 10^3\text{ s}$, $6.8 \times 10^3\text{ s}$, and $2.2 \times 10^4\text{ s}$, respectively.

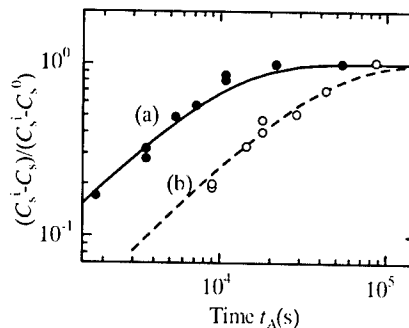


Fig. 2. Annealing process of nickel in dislocation-free silicon at $T_A = 960^\circ\text{C}$. The sample was first saturated with nickel at $T_D = 1020^\circ\text{C}$ ($C_s^i \approx 8.5 \times 10^{13}\text{ cm}^{-3}$). Curves (a) and (b) are the calculated values of Eq. (2) with (a) $\tau = 1.0 \times 10^4\text{ s}$ ($l = 0.05\text{ cm}$), and (b) $\tau = 4.3 \times 10^4\text{ s}$ ($l = 0.2\text{ cm}$).

for the in-diffusion process and

$$(C_s^i - C_s)/(C_s^i - C_s^0) = 1 - \exp(-t_A/\tau) \quad (2)$$

for annealing process. In Eqs. (1) and (2), superscripts 0 and i are the thermal equilibrium concentration and the concentration at $t_A = 0$, respectively. The experimental results agree well with the theory of the dissociative mechanism, suggesting that the dominant point defects mediating the site exchange of nickel atoms are vacancies as in the case of dislocated silicon [6,7]. However, in the annealing process, it has not yet been confirmed experimentally whether $(C_s^i - C_s)/(C_s^i - C_s^0)$ depends on C_s^i or not [6,7]. Furthermore, diffusion profile of C_s cannot exclusively determine the site-exchange mechanism [10]. We infer that these difficulties originate from the presence of nickel precipitates in the bulk, which will be discussed below.

Nickel precipitates in the crystal bulk of dislocation-free silicon. The nickel precipitates, which were identified by comparison between infrared microscope images of nickel-doped and undoped silicon crystals, are potential candidates for SS of vacancies. Nickel precipitates was confirmed by SEM observation. The radius of precipitates ranged typically from 1 to $3\text{ }\mu\text{m}$.

Fig. 3 shows the precipitation density, n_{pr} , as functions of t_D and T_D in the in-diffusion process at the center of the crystal. It can be seen that n_{pr} increases monotonically with the increase of t_D and T_D . This suggests that the precipitation process proceeds during the heat treatment as well as the quenching processes, and that heterogeneous nucleation sites of the precipitation are present in the bulk of dislocation-free silicon. Although the type of nucleation sites is unknown, spontaneous nucleation at the strain centers such as grown-in defects would be possible. Precipitates were observed only in the case of rapid quenching. Furthermore, any nickel precipitate in the bulk could not be

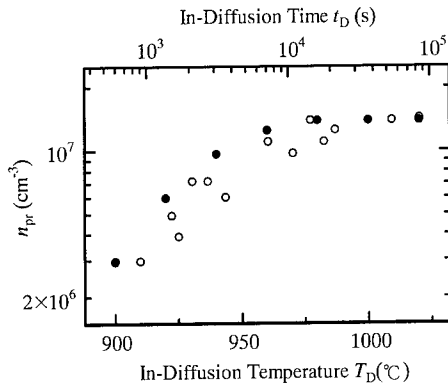


Fig. 3. The precipitation density, n_{pr} , as functions of T_D (°C) and t_D (s) in the in-diffusion process at the center of the crystal. Samples were prepared with the cooling rate of about 90°C s^{-1} .

observed after the heat treatment at temperatures lower than 860°C .

It has been reported [4,8–10] that the nickel precipitates accelerate significantly the site exchange rate, $1/\tau$, of nickel. Nickel precipitates formed at high temperatures or precipitate-induced lattice defects such as bound dislocations [12] possibly play a role as SS of vacancies. If the crystal surfaces and inner defects act as SS, $1/\tau$ in the in-diffusion and annealing processes may be described as [13,14]

$$\frac{1}{\tau} = \frac{C_v^0 D_v}{C_s^0 + C_v^0} \left[\left(\frac{\pi}{l} \right)^2 + G_{SS} \right], \quad (3)$$

where C_v^0 and D_v are the thermal equilibrium concentration and diffusion coefficient of vacancies, and $(\pi/l)^2$ describes the contribution from the surface SS to τ^{-1} and G_{SS} the contribution from the inner SS. If the spherical inner SS with radius r_0 is randomly distributed with the effective volume density, N_{SS} , in the bulk, G_{SS} can be given by [13]

$$G_{SS} = 4\pi r_0 N_{SS}. \quad (4)$$

Experimental data of τ in Figs. 1 and 2 are plotted as a function of l^2 in Fig. 4 in which the value of τ at $l^2 = 0.01 \text{ cm}^2$ is normalized to unity. Broken curves show the calculated value of Eqs. (3) and (4) with the N_{SS} values shown in the figure. The theoretical values of τ for $N_{SS} \approx (2-3) \times 10^5 \text{ cm}^{-3}$ in the in-diffusion process and for $N_{SS} \approx 3 \times 10^6 \text{ cm}^{-3}$ in the annealing process seem to fit qualitatively to the experimentally obtained values of τ . Thus precipitates or presumably precipitate-induced lattice defects may lead to the acceleration of the site-exchange rate of nickel in dislocation-free silicon. The site exchange of nickel atoms may be limited by the vacancy diffusion in the crystal from the SS since diffusion coefficient of vacancies is much lower than that of interstitial nickel atoms [6,7].

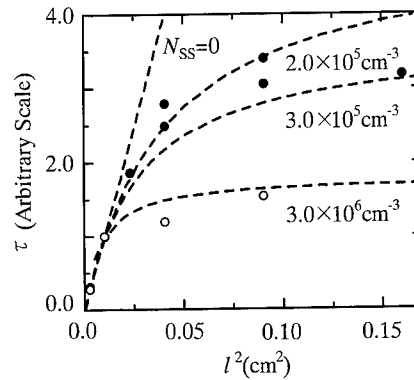


Fig. 4. Relationship between τ and l^2 in the in-diffusion process (●) and annealing process (○). The values of τ at $l^2 = 0.01 \text{ cm}^2$ are normalized to unity. Broken lines show the calculated values of Eqs. (3) and (4) with N_{SS} values indicated in the figure.

In dislocated silicon, on the other hand, it has been established [7] that both dislocations and crystal surfaces are the SS of vacancies. Hence the in-diffusion and annealing processes of substitutional impurity atoms are limited by the slower process, whether the generation and annihilation of vacancies at the SS or the diffusion of vacancies in the crystal. In order to compare the values of τ of the in-diffusion process between dislocated and dislocation-free silicon, we have re-examined the in-diffusion process for dislocated silicon crystals with dislocation densities, n_d , from 1.7×10^4 to $2.1 \times 10^4 \text{ cm}^{-2}$. It was found [10] that C_s varies with t_D in accordance with Eq. (1), and that $\tau n_d \approx 2 \times 10^7 \text{ s cm}^{-2}$ which is very consistent with the reported results [6,7] in which τn_d ranged from 2.1×10^7 to $3.5 \times 10^7 \text{ s cm}^{-2}$. This result indicates that the product τn_d is invariant for the dislocated silicon samples. The time constant, τ , of in-diffusion process (and also of annealing process, see Ref. [7]) is then inversely proportional to n_d . A reasonable explanation for this relation is that G_{SS} may be given by $G_{SS} = 2\pi n_d / \ln(r_d/r'_0)$ [6,7], where r_d and r'_0 are the half mean distance of dislocations and the effective radius of a dislocation for capturing a vacancy, respectively. Therefore, τn_d may be constant if dislocations are the dominant SS of vacancies.

Since the diffusion coefficient, of interstitial nickel atoms is high [5] and the solubility decays exponentially with the decrease of temperature [11], interstitial nickel atoms may diffuse out to the surface and/or form precipitates in the bulk. Seibt and Schröter [12] have revealed the morphology, structure and composition of nickel precipitates in the bulk. They [12] also proposed the model that the growth of the precipitates proceeds exclusively by the diffusion of interstitial nickel atoms to the dislocations bound to precipitates. Although we have not been successful to observe the bound dislocations, we consider that the bound dislocations play a

role of the SS of vacancies. To our knowledge, a series of our studies [4,8–10] is the first observation of the enhanced site-exchange diffusion in transition-metal impurity atoms in dislocation-free silicon due to the presence of precipitates or precipitation-induced lattice defects.

In summary, it was suggested that nickel atoms in dislocation-free silicon exchange their sites by the dissociative mechanism, i.e., the dominant point defects mediating the site exchange are vacancies. Nickel precipitates in dislocation-free silicon as well as in dislocated silicon. The crystal surfaces, and nickel precipitates or precipitate-induced lattice defects were found to play a role as the SS of vacancies, which increases significantly the site exchange rates.

References

- [1] E.R. Weber, *Appl. Phys. A* 30 (1983) 1.
- [2] A.A. Istratov, E.R. Weber, *Appl. Phys. A* 66 (1998) 123.
- [3] H. Nakashima, T. Sadoh, H. Kitagawa, K. Hashimoto, *Mater. Sci. Forum* 143–147 (1994) 761.
- [4] H. Kitagawa, *Solid State Phenom.* 71 (2000) 51.
- [5] M. Yoshida, K. Saito, *Jpn. J. Appl. Phys.* 6 (1967) 521.
- [6] H. Kitagawa, K. Hashimoto, M. Yoshida, *Jpn. J. Appl. Phys.* 21 (1982) 276.
- [7] H. Kitagawa, K. Hashimoto, M. Yoshida, *Physica B* 116 (1983) 323.
- [8] H. Kitagawa, S. Tanaka, *Physica B* 273–274 (1999) 391.
- [9] S. Tanaka, T. Ikari, H. Kitagawa, *Defect Diffusion Forum* 183–185 (2000) 171.
- [10] S. Tanaka, T. Ikari, H. Kitagawa, *Jpn. J. Appl. Phys.* 40 (2001) 1.
- [11] M. Yoshida, K. Furusho, *Jpn. J. Appl. Phys.* 3 (1964) 521.
- [12] M. Seibt, W. Schröter, *Philos. Mag.* 59 (1989) 337.
- [13] A.C. Damask, G.J. Dienes, *Point Defects in Metals*, Gordon and Breach, New York, 1963, p. 81.
- [14] H. Kitagawa, K. Hashimoto, M. Yoshida, *Jpn. J. Appl. Phys.* 21 (1982) 990.



ELSEVIER

Physica B 308–310 (2001) 431–433

PHYSICA B

www.elsevier.com/locate/physb

Diffusion of ^{195}Au in amorphous Si_3N_4 and Si_4N_3

T. Voss^a, S. Matics^a, A. Strohm^b, W. Frank^{a,b,*}, G. Bilger^c,
ISOLDE Collaboration^d

^a*Institut für Theoretische und Angewandte Physik, Universität Stuttgart, D-70550 Stuttgart, Germany*

^b*Max-Planck-Institut für Metallforschung, Heisenbergstr.1, D-70569 Stuttgart, Germany*

^c*Institut für Physikalische Elektronik, Universität Stuttgart, D-70550 Stuttgart, Germany*

^d*CERN, CH-1121 Geneva, Switzerland*

Abstract

The diffusion of implanted ^{195}Au in amorphous Si_3N_4 - and Si_4N_3 -layers has been investigated by means of a radiotracer technique. Except for as-produced a- Si_4N_3 , in which pronounced structural relaxation takes place during diffusion annealing, ^{195}Au was found to diffuse via interstitial-like mechanisms. A sudden freezing of the ^{195}Au -diffusivity in pre-annealed a- Si_4N_3 below about 880°C is attributed to a disorder–order phase transition. © 2001 Elsevier Science B.V. All rights reserved.

Keywords: ^{195}Au -diffusion in amorphous Si_3N_4 and Si_4N_3 ; Radiotracer technique; Interstitial-type diffusion mechanisms; Order–disorder phase transition

1. Introduction

The production of Si–(B)–C–N-type ceramics from polymeric precursors plays a significant rôle in the development of advanced materials [1]. In this production route, an intermediate amorphous state is passed from which the final polycrystalline ceramic produce evolves by diffusion-controlled crystallization.

Using polyvinylsilazane as precursor, the intermediate amorphous (a) state is a- $\text{Si}_{28}\text{C}_{36}\text{N}_{36}$. According to neutron- and X-ray-diffraction studies [2], this consists of a- Si_3N_4 and a-C domains. Previous investigations have shown that in a- $\text{Si}_{28}\text{C}_{36}\text{N}_{36}$ the diffusion of ^{71}Ge [3] and ^{195}Au [4] is controlled by the a- Si_3N_4 phase. More specifically, it has been proposed that ^{71}Ge is covalently incorporated and diffuses via smeared-out vacancies, whereas ^{195}Au squeezes through the meshes of the amorphous network in an interstitial-like manner.

Obviously, the preceding proposal how ^{71}Ge and ^{195}Au diffuse in a- Si_3N_4 are solely based on the investigations on a- $\text{Si}_{28}\text{C}_{36}\text{N}_{36}$. Hence, in this work

measurements of the diffusion of ^{195}Au in amorphous silicon nitride have been performed.

A problem in diffusion studies on amorphous solids is the metastability of these materials. This may lead to a structural relaxation during diffusion annealing. To determine the effect of such relaxations, ^{195}Au -diffusivities have been measured on both as-produced and pre-annealed a- Si_3N_4 .

It is not very likely that the amorphous silicon-nitride domains in a- $\text{Si}_{28}\text{C}_{36}\text{N}_{36}$ possess precisely the composition Si_3N_4 . Therefore, the influence of “chemical misfits” was tested by extending our ^{195}Au -diffusion studies on as-produced and pre-annealed amorphous silicon nitride of the composition Si_4N_3 .

2. Experiments

The specimens used in the present diffusion studies were 1 µm thick layers of a- Si_3N_4 or a- Si_4N_3 , which had been produced by sputter-deposition of Si onto Si-substrates in N_2 -atmosphere. Some of the specimens were pre-annealed for 2 h at 1050°C. The amorphousness of the layers was tested by electron diffraction.

*Corresponding author. Tel.: +49-711-689-1940; fax: +49-711-689-1922.

E-mail address: wfrank@mf.mpg.de (W. Frank).

The diffusion measurements were done by means of a radiotracer technique, in which 10^{16} radioactive ^{195}Au -atoms/ m^2 were implanted with a kinetic energy of 60 keV to depths of about 30 nm into $7 \times 7 \text{ mm}^2$ platelet-shaped specimens. The implantations were followed by isothermal diffusion anneals in the temperature regime of 835–1020 °C; the annealing durations were 20 min to 22.6 h. The diffusion profiles $C(x)$ were determined by serial sectioning with the aid of ion-beam sputtering and subsequent sectionwise measuring of the radioactivity ($C = ^{195}\text{Au}$ -concentration, x = depth coordinate). From these, the diffusion coefficients, D , were extracted by fitting an appropriate solution of the diffusion equation.

3. Results and discussion

3.1. Diffusion of ^{195}Au in $\text{a-Si}_3\text{N}_4$

Fig. 1 shows diffusion profiles of ^{195}Au in as-produced (○) and pre-annealed (●) $\text{a-Si}_3\text{N}_4$. Both profiles possess a hump α , where the peak of the implantation profile was located. This arises from ^{195}Au -atoms trapped by implantation-induced damage. The hump δ in the profile of the pre-annealed specimen is due to an accumulation of ^{195}Au -atoms at the $\text{a-Si}_3\text{N}_4$ -Si interface.

In the as-produced specimen, the regime β of the profile reflects the migration of the ^{195}Au -atoms during diffusion annealing. The diffusion coefficients of ^{195}Au in as-produced $\text{a-Si}_3\text{N}_4$ displayed in Fig. 2 (○) were determined from the regime β of such diffusion profiles. They obey an Arrhenius law

$$D = D_0 \exp(-H/kT) \quad (1)$$

with the pre-exponential factor $D_0 = 1.4 \times 10^{-8} \text{ m}^2 \text{ s}^{-1}$ and the diffusion enthalpy $H = 2.5 \text{ eV}$ (k is Boltzmann's constant, T is the temperature). As discussed by Matics and Frank [4] these values indicate that in as-produced $\text{a-Si}_3\text{N}_4$ ^{195}Au undergoes direct interstitial-like diffusion.

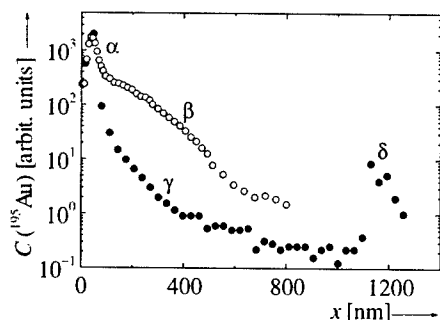


Fig. 1. Diffusion profiles of ^{195}Au in as-produced (○) and pre-annealed (●) amorphous Si_3N_4 after diffusion annealing at 933 °C for 16 h and at 932 °C for 16.6 h, respectively. For the discussion of the various parts of the profiles, α – δ , see text.

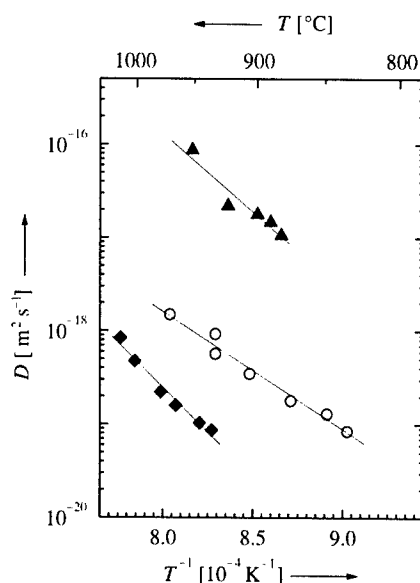


Fig. 2. Arrhenius plots of the diffusion coefficients of ^{195}Au in as-produced amorphous Si_3N_4 (○) and of ^{195}Au (▲) or ^{71}Ge (◆) in pre-annealed amorphous Si_3N_4 .

In the pre-annealed $\text{a-Si}_3\text{N}_4$ specimen (Fig. 1, ●), the major part γ of the diffusion profile has a shape that is characteristic of diffusion via the kick-out mechanism [5] and thus implies that ^{195}Au diffuses faster than in as-produced $\text{a-Si}_3\text{N}_4$.

A more detailed, admittedly speculative interpretation of the results on the diffusion of ^{195}Au in $\text{a-Si}_3\text{N}_4$ presented above is given in what follows. As in crystalline Si_3N_4 , important building blocks of the continuous random $\text{a-Si}_3\text{N}_4$ network are tetrahedra (in Fig. 3 represented by triangles) with 4 N-atoms at their corners and 1 Si-atom at their centres [6]. In as-produced $\text{a-Si}_3\text{N}_4$ these tetrahedra are damaged, distorted, and not well arranged. These imperfections hamper the direct diffusion of ^{195}Au in as-produced $\text{a-Si}_3\text{N}_4$.

Thermal annealing of $\text{a-Si}_3\text{N}_4$ perfects the tetrahedra and arranges them to establish a short-range order resembling the crystalline Si_3N_4 -structure. In this more perfect $\text{a-Si}_3\text{N}_4$, many neighbouring tetrahedra are grown together at their corners sharing an N-atom. In pre-annealed $\text{a-Si}_3\text{N}_4$, this network of grown-together tetrahedra constitutes paths for rapid diffusion of ^{195}Au . As shown in Fig. 3a, an Au-atom may either substitute an Si-atom (Au_s) or form a mixed dumbbell interstitial (Au_i) by sharing a central tetrahedron site with an Si-atom. The existence of these two configurations of gold atoms is a prerequisite for the operation of a kick-out mechanism [5] in which Au_i migrates by a jump of the Au-atom of the mixed dumbbell into the centre of a neighbouring tetrahedron. There either a new mixed dumbbell is formed or, by releasing a dumbbell Si self-interstitial (I), an immobile Au_s -atom is produced. The

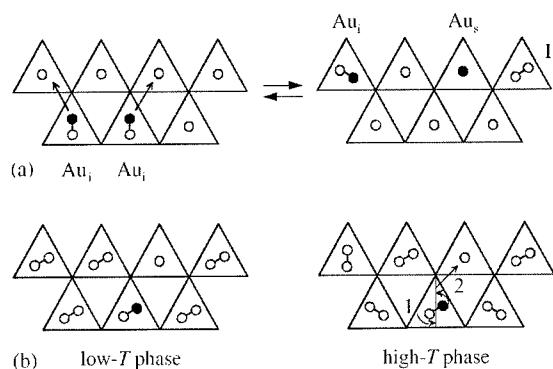


Fig. 3. Schematic illustration of diffusion mechanisms. The triangles stand for tetrahedra whose corners are formed by N-atoms. Empty and full circles represent Si-atoms and foreign atoms, respectively. (a) ^{195}Au -diffusion in pre-annealed amorphous Si_3N_4 (Au_i = mixed Si–Au dumbbell, Au_s = substitutional Au, I = dumbbell Si self-interstitial). (b) ^{195}Au - or ^{71}Ge -diffusion in pre-annealed amorphous Si_4N_3 (1 = reorientation of a mixed dumbbell, 2 = shift of a dumbbell configuration).

reversibility of these processes required for kick-out diffusion is indicated in Fig. 3a by the pair of arrows.

3.2. Diffusion of ^{195}Au in $\text{a-Si}_4\text{N}_3$

As a result of the “chemical misfit” of $\text{a-Si}_4\text{N}_3$, in its as-produced state ^{195}Au -diffusion is superimposed by pronounced concurrent structural relaxation. Hence, meaningful diffusion profiles cannot be measured on as-produced $\text{a-Si}_4\text{N}_3$.

An interesting phenomenon occurs in pre-annealed $\text{a-Si}_4\text{N}_3$. Within the small temperature interval 869–936°C, the diffusivities of both ^{195}Au and ^{71}Ge increase from unmeasurably small values to 10^{-17} and $10^{-19} \text{ m}^2 \text{ s}^{-1}$, respectively, and, at higher temperatures, obey Arrhenius laws (^{195}Au : $D_0 = 3.4 \times 10^{-3} \text{ m}^2 \text{ s}^{-1}$, $H = 3.4 \text{ eV}$; ^{71}Ge : $D_0 = 5 \times 10^{-4} \text{ m}^2 \text{ s}^{-1}$, $H = 3.8 \text{ eV}$) (Fig. 2). As will be shown below, these sudden diffusivity increases of both ^{195}Au and ^{71}Ge at similar temperatures may be ascribed to a structural phase transition.

In extension of the scenario (Fig. 3a) invoked to explain the diffusion mechanism of ^{195}Au in pre-annealed $\text{a-Si}_3\text{N}_4$ (Fig. 1, ●), we propose that pre-annealed $\text{a-Si}_4\text{N}_3$ may be constructed from pre-annealed $\text{a-Si}_3\text{N}_4$ by replacing 78% of the Si-atoms in the centres of the N-tetrahedra with Si-dumbbells (Fig. 3b). Si self-diffusion in pre-annealed $\text{a-Si}_4\text{N}_3$ is assumed to occur via an interstitialcy-like mechanism in which a Si-dumbbell configuration shifts into a dumbbell-free neighbouring tetrahedron (containing one Si-atom only). If the major axis of the dumbbell does not point to the N-corner shared with a dumbbell-free neighbouring tetrahedron, the dumbbell shift has to be preceded by a

reorientation of the dumbbell. This dumbbell reorientation is assumed to be the rate-controlling step in the Si self-diffusion in pre-annealed $\text{a-Si}_4\text{N}_3$. Conveying this model to foreign-atom diffusion (Fig. 3b), we suggest that ^{195}Au or ^{71}Ge diffuses in pre-annealed $\text{a-Si}_4\text{N}_3$ with the aid of mixed Si–Au or Si–Ge dumbbells in a corresponding manner.

The diffusion mechanisms in pre-annealed $\text{a-Si}_4\text{N}_3$ proposed above lead to a natural explanation of the sudden diffusivity rise of ^{195}Au and ^{71}Ge occurring when the diffusion temperature is raised through the interval 869–936°C. Below this temperature regime the dumbbells are aligned, at least domainwise, in a parallel direction (Fig. 3b, left). In this ferro-elastic state, the reorientation of the dumbbells is blocked and, as a result, diffusion is suppressed. Above this temperature regime (Fig. 3b, right), thermally activated reorientation of the dumbbells is possible. This results in a para-elastic state and enables dumbbell-mediated diffusion to occur.

The fact that the abrupt diffusivity changes of ^{195}Au and ^{71}Ge take place at similar temperatures is in accordance with their interpretation in terms of an order–disorder phase transition of pre-annealed $\text{a-Si}_4\text{N}_3$. Moreover, the similarity of both the diffusion enthalpies and the D_0 -values for ^{195}Au and ^{71}Ge (see above) is not surprising if one accepts that both elements diffuse via dumbbells. The preceding interpretation implies that in pre-annealed $\text{a-Si}_4\text{N}_3$ Si self-diffusion sets in at temperatures similar to the on-set temperatures of ^{195}Au - and ^{71}Ge -diffusion and that the activation enthalpy and the D_0 -value of Si self-diffusion are close to those of ^{195}Au and ^{71}Ge . These predictions permit one to test the preceding interpretation.

Acknowledgements

The authors would like to thank F. Aldinger and his collaborators for their interest in this work, D. Eversheim for his assistance during the ^{71}Ge -implantation at Bonn University, and M. Kelsch for the electron-diffraction studies. Financial support by the Deutsche Forschungsgemeinschaft within the framework of the research projects FR 999/8-2 and FR 999/8-3 as well as by the HPRI Programme of the European Community is appreciated.

References

- [1] J. Bill, F. Aldinger, Z. Metallkd. 87 (1996) 827.
- [2] J. Dürr, S. Schempp, P. Lamparter, J. Bill, S. Steeb, F. Aldinger, Sol. State Ionics 101–103 (1997) 1041.
- [3] S. Matics, W. Frank, J. Non-Cryst. Solids 266–269 (2000) 830.
- [4] S. Matics, W. Frank, Def. Diff. Forum 194–199 (2001) 947.
- [5] U. Gösele, W. Frank, A. Seeger, Appl. Phys. A23 (1980) 361.
- [6] T. Aiyama, T. Fukunaga, K. Nihars, T. Hirai, K. Suzuki, J. Non-Cryst. Solids 33 (1979) 131.



ELSEVIER

Physica B 308–310 (2001) 434–437

PHYSICA B

www.elsevier.com/locate/physb

Properties of Cr in hydrogenated Si

Y. Sato, T. Takahashi, M. Suezawa*

Institute of Materials Research, Tohoku University, 2-1-1 Katahira, Sendai 980-8577, Japan

Abstract

Properties of interstitial chromium (Cr_i) in hydrogenated p-type Si crystals were studied by means of an EPR method. Specimens were prepared from a floating-zone grown p-type Si crystal. They were doped with Cr by high temperature annealing in Cr vapor, followed by quenching. Then, they were doped with hydrogen (H) by annealing in H_2 gas followed by quenching. We measured their EPR spectra to determine the concentrations of Cr_i and CrB pair. The intensity of EPR spectrum due to Cr_i in hydrogenated Si was about one-tenth of that without H when they were doped at 1250°C. The heat of the solution of Cr in hydrogenated Si was determined to be about 1.9 eV which is much smaller than that (2.9 eV) without H doping. The migration energy of Cr_i in H-doped Si was determined to be 0.70 ± 0.09 eV, which is smaller than that (about 1 eV) without H. Site change from interstitial to substitutional was observed in the specimen co-doped with Cr and Cu. © 2001 Elsevier Science B.V. All rights reserved.

Keywords: Cr; Si; Hydrogen; EPR

1. Introduction

Hydrogen (H) in Si crystals is chemically active and easily forms pairs and complexes with other impurities and defects. Complexes of H and 5d transition metal impurities have been studied by means of EPR, FT-IR and DLTS methods. Their symmetries, number of H atoms included in the complexes as well as their energy levels have been clarified [1]. On the other hand, studies on complexes of H and 3d transition metal impurities have not been performed well. The 3d transition metals mainly occupy interstitial sites in contrast with 5d transition metals, which mainly occupy substitutional sites. They are harmful for silicon devices from practical viewpoint and have interesting properties from basic viewpoint. Their energy levels were determined by means of the DLTS method [2]. Takahashi and Suezawa studied Fe–H complexes by means of the EPR method [3]. They found that the solubility of Fe changes according to the co-doping of H and also found a new

EPR spectrum due to Fe–H pair. We performed a similar study on Cr. It has been clarified that Cr has properties much different from those of Fe.

2. Experiment

Specimens used in this experiment were cut out from a floating-zone grown silicon crystal of p-type (boron concentration: $2.5 \times 10^{15} \text{ cm}^{-3}$), since positively charged Cr , Cr_i^+ , is easily detected by EPR measurements. After mechanical shaping and chemical etching, Cr was doped by a vapor-pressure method, namely, specimens were sealed in evacuated quartz capsules together with a piece of Cr wire and were heated at appropriate temperature for duration longer than those estimated from the diffusion constant of Cr followed by quenching in water. Next, we doped specimens with H by heating specimens in H_2 gas (1 atm) followed by quenching. We measured their EPR spectra by an X-band spectrometer at 15 K to determine the concentrations of Cr_i^+ , CrB pair and Cr_s^0 , where the subscripts i and s denote interstitial and substitutional occupation sites, respectively, and superscripts 0 and + denote neutral charge state and positive charge state, respectively.

*Corresponding author. Tel.: +81-22-215-2040; fax: +81-22-215-2041.

E-mail address: suezawa@imr.edu (M. Suezawa).

3. Results and discussion

3.1. Solubility of Cr_i

Fig. 1 shows EPR spectra due to Cr_i^+ before (dashed line) and after (solid line) H-doping. The doping temperature was 1250°C. The EPR intensity due to Cr_i^+ was much reduced due to H-doping. To systematically study this reduction, we performed similar experiments after doping at various temperatures. Fig. 2 shows the results. As clearly seen, the apparent heat of solution, which corresponds to the slope of Fig. 2, decreases much due to H-doping. The apparent heat of solution determined from Fig. 2 were 2.9 ± 0.1 and 1.7 ± 0.1 eV for specimens without and with H-doping, respectively. The former agrees well to the reported data [4].

As for the origin of solubility reduction, we discuss three possibilities; out-diffusion of Cr during H-doping, formation of complexes of Cr and H during H-doping or during quenching and change of occupation sites from interstitial to substitutional sites during quenching. First, we estimated amount of out-diffusion with the use of diffusion data. It was too small to explain the observed results. Second, Sadoh et al. determined the energy levels due to CrH complexes by means of the

DLTS method [5]. We, however, did not observe any extra signal other than Cr_i^+ . We tentatively propose that the reduction of Cr_i solubility occurs due to change of occupation sites from interstitial to substitutional sites during quenching. For the site change to occur, vacancies are necessary. As shown in a separate paper [6], the concentration of vacancy in the form of complexes of vacancies and hydrogen atoms is high when hydrogen is doped. Hence, there is a high probability to change occupation sites during quenching.

3.2. Annealing experiments

In the case of Si co-doped with Fe and H, we observed the formation of Fe–H pairs due to annealing [3]. We studied the isochronal annealing behavior of Cr_i^+ . Fig. 3 shows the result. Circles and dashed line, which was drawn to guide the eye, show the annealing behaviors in the specimen without H-doping. Cr–B pairs were formed around 125°C corresponding to the decrease of Cr_i^+ . At above about 275°C, the intensity of Cr_i^+ decreased. On the other hand, decrease of Cr_i^+ occurred at $> 175^\circ\text{C}$ in the case of H-doped specimen, as shown by triangles and solid line, which was drawn to guide the eye. Hence, these results strongly suggest that diffusion rate of Cr_i^+ is faster in H-doped specimen.

To determine the migration energy of Cr_i^+ , we performed isothermal annealing experiments. Fig. 4 shows the formation of CrB pair due to isothermal annealings at various temperatures in specimens without H-doping. Solid lines are fitting curves due to the first order reaction. Fittings are good. The inset of Fig. 4 shows the dependence of time constant on the annealing temperature. From this inset, the activation energy

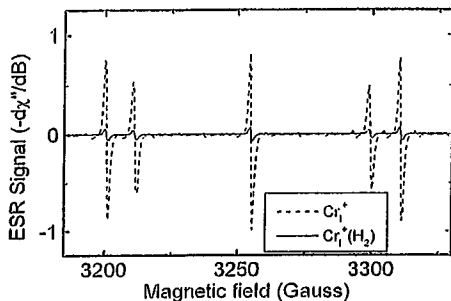


Fig. 1. EPR spectra of Cr_i^+ before (dashed line) and after (solid line) H-doping. Cr and H were doped at 1250°C.

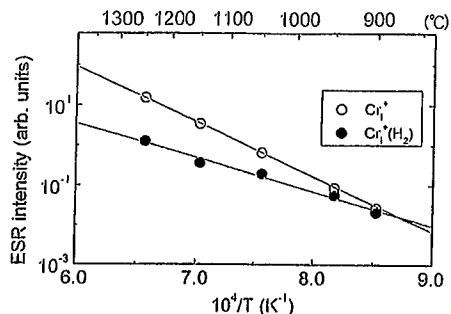


Fig. 2. The dependences of EPR intensity on the doping temperature. Cr and H were doped at the same temperatures.

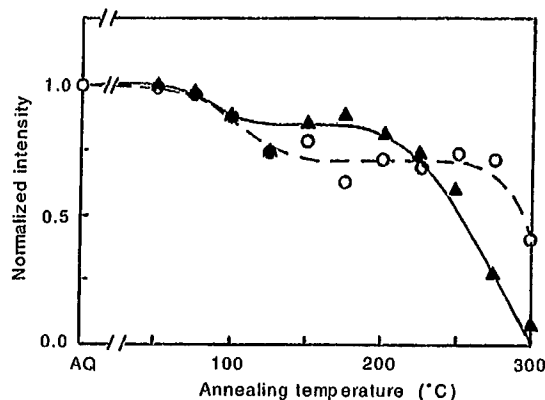


Fig. 3. Isochronal annealing curves of Cr_i^+ in Si without H-doping (circles and dashed line) and with H-doping (triangles and solid line). Annealing duration was 30 min at each temperature.

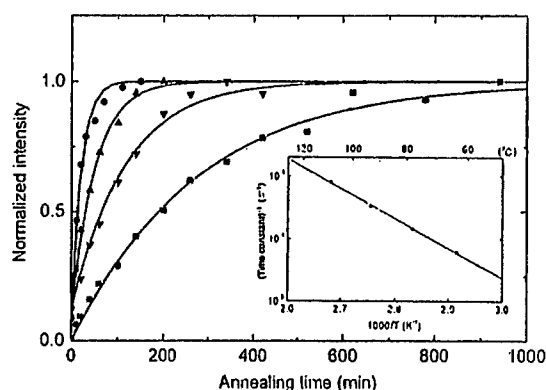


Fig. 4. Isothermal annealing curves for CrB formation in Si without H-doping. Solid lines were fitting curves due to the first-order reaction. Annealing temperatures of squares, inverse triangles, triangles and circles were 70°C, 80°C, 90°C and 100°C, respectively. The inset shows the dependence of the time constant on the annealing temperature.

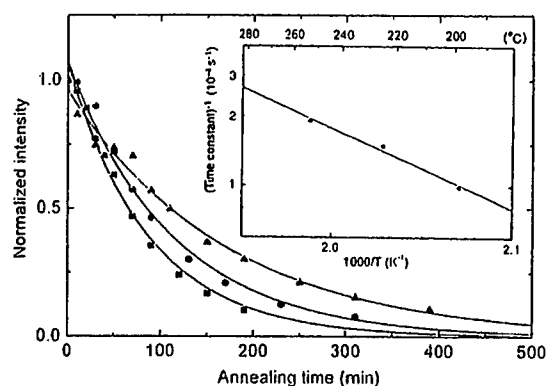


Fig. 5. Isothermal annealing curves of Cr_i in Si doped with H. Solid lines were fitting curves due to the first-order reaction. Annealing temperatures of triangles, circles and squares were 210°C, 220°C and 230°C, respectively. The inset shows the dependence of the time constant on the annealing temperature.

for the migration of Cr_i^+ was determined to be 0.95 ± 0.02 eV, which is in good agreement with the values reported so far (around 1.0 eV) [7]. We also performed isothermal annealing experiment of H-doped specimens. Fig. 5 shows the experimental results and fitting curves with the first order reaction. The inset shows the dependence of the time constant on the annealing temperature. The activation energy of Cr_i^+ diffusion was determined to be 0.70 ± 0.09 eV, which is smaller than the above value. Hence, there is a reduction of activation energy of Cr_i^+ diffusion due to H doping. Such reduction due to H-doping was first reported for the activation energy of oxygen diffusion in Si [8]. We do not have any explanation for the reduction in the case of Cr. It may be the same in the case of oxygen [9].

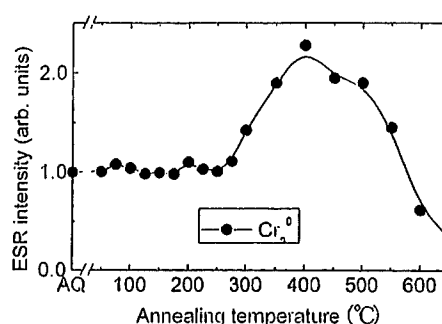


Fig. 6. Isochronal annealing curves of Cr_s in a specimen codoped with Cu and Cr. The concentration of Cu was about $1 \times 10^{18} \text{ cm}^{-3}$. AQ denotes the as-quenched state.

According to literatures on Cr_i diffusion [7], the activation energy determined at high temperature is about 1 eV and that determined at low temperature is about 0.8 eV [10,11]. Based on our results, we interpreted smaller activation energy at low temperature to be due to the effect of H since it was determined with the DLTS method. In this method, specimens should be etched to fabricate good Schottky contact. Hydrogen atoms probably come into Si crystals during etching and enhance the Cr_i diffusion.

In Section 3.1, we propose the site change of Cr during quenching. To confirm the site change, we performed annealing experiments of specimens codoped with Cu and Cr. Fig. 6 shows an isochronal annealing curve. The concentration of Cr_s increased at around 300°C and decreased at around 550°C. Hence, Cr_s is more stable than Cr_i . The activation energy for the increase of Cr_s was determined to be about 1.00 ± 0.07 eV, which is in good agreement with Cr_i diffusion. Hence, the site change is thought to occur due to Cr_i diffusion to vacancies, which are not in isolated state but in a state of complexes.

4. Summary

We studied the properties of Cr in Si doped with H by means of the EPR method. The heat of solution of Cr in H-doped specimens was determined to be 1.7 ± 0.1 eV, which is much smaller than that (2.9 ± 0.1 eV) without H-doping. The activation energy of Cr migration in H-doped specimens was determined to be 0.70 ± 0.09 eV, which is smaller than that (about 1.0 eV) without H-doping.

Acknowledgements

This work was partly supported by the JSPS Research for the Future Program under the project "Ultimate

Characterization Technique of SOI Wafers for Nano-scale LSI Devices” and a Grant-in-Aid for Scientific Research on Priority Area (B) “Manipulation of Atoms and Molecules by Electron Excitation” from the Ministry of Education, Culture, Sports, Science and Technology of Japan.

References

- [1] S.J. Uffring, et al., *Phys. Rev. B* 51 (1995) 9612.
- [2] J. Weber, *Material Research Society Symposium Proceedings*, Materials Research Society, Vol. 513, 1998, p. 345.
- [3] T. Takahashi, M. Suezawa, *Physica B* 273–274 (1999) 445.
- [4] E.R. Weber, *Appl. Phys. A* 30 (1983) 1.
- [5] T. Sadoh, et al., *J. Appl. Phys.* 75 (1994) 3978.
- [6] N. Fukata, M. Suezawa, *Proceedings of the Third International Symposium on Advanced Science and Technology in Silicon Materials*, The Japan Society for the Promotion of Science, 2000, p. 130.
- [7] N.T. Bendik, et al., *Sov. Phys. Solid State* 12 (1970) 150.
- [8] A.R. Brown, et al., *Semicond. Sci. Technol.* 3 (1988) 591.
- [9] S.K. Estreicher, *Phys. Rev. B* 41 (1990) 9886.
- [10] J. Zhe, et al., *Mater. Sci. Eng. B* 4 (1989) 185.
- [11] H. Nakashima, et al., *Mater. Sci. Forum* 143–147 (1994) 761.



ELSEVIER

Physica B 308–310 (2001) 438–441

PHYSICA B

www.elsevier.com/locate/physb

Optical absorption spectra of platinum-related defects in silicon

N. Fukata*, K. Saito, M. Suezawa

Institute for Materials Research, Tohoku University, Sendai 980-8577, Japan

Abstract

We studied optical absorption spectra of platinum (Pt)-doped Si and found new optical absorption peaks related to Pt. FZ-Si was separately doped with Pt and H by heating at 1300°C followed by quenching in water. Optical absorption spectra were measured at about 7 K with a Fourier transform infrared spectrometer. We observed a new peak at 1719.4 cm^{-1} in as-quenched specimens and also new peaks in the region from 1300 to 1500 cm^{-1} after annealing at above 500°C. From the isotope shift caused by deuterium doping, the dependence on excitation energy and the annealing behaviors, these peaks were found to be due to the electronic transition of Pt-related defects such as Pt clusters, rather than to the local vibrational modes of H. © 2001 Elsevier Science B.V. All rights reserved.

Keywords: Platinum; Hydrogen; Optical absorption; Silicon

1. Introduction

The characteristics of platinum (Pt) in Si have been extensively investigated to control the minority-carrier lifetime, which depends on its energy levels and thermal capture cross sections. There are several Pt-related defects which introduce deep levels in the band gap. The existence of isolated substitutional Pt [1–3], Pt pairs [4,5], 6-Pt clusters [6], Pt–hydrogen (H) complexes [7] and Pt–oxygen complexes [8,9] have so far been reported by studies using electron paramagnetic resonance (EPR) methods, deep level transient spectroscopy (DLTS), and optical absorption spectroscopy. To control the minority-carrier lifetime in fast-switching diodes, it is necessary to understand the properties of the above-mentioned defects, especially, defects introducing the midgap level. In this study, we investigated Pt-related defects in Si from the measurements of their optical absorption since optical absorption measurements have been shown in only a few reports. The formation of Pt-related defects was investigated in a wide temperature range and we found new optical absorption peaks due to

Pt-related defects. The characteristics and constituents of the Pt-related defects were investigated based on the annealing behaviors, isotope shift, and the dependence on excitation energy.

2. Experimental

We used high-purity n-type Si ($[P] = 4 \times 10^{12}\text{ cm}^{-3}$) with a size of about $6 \times 6 \times 12\text{ mm}^3$. To dope Si with Pt, specimens deposited with thin Pt films (40 nm in thickness on the opposite two wide surfaces) were sealed in quartz capsules together with Ar gas and heated at 1300°C for 8 h followed by quenching in water. The solubility of Pt is about 10^{17} cm^{-3} at 1300°C [10]. After Pt doping, the specimens were etched with a mixed acid to remove excess Pt from the surface since Pt tends to form silicide on the specimen surface. To dope Si with H (D), the specimens were then sealed in quartz capsules together with H_2 (D_2) gas and heated at 1300°C for 2 h followed by quenching in water. Detailed explanations of quenching conditions have been reported elsewhere [11,12].

Optical absorption spectra were measured at about 7 K with a Fourier transform infrared (FT-IR)

*Corresponding author. Tel.: +81-22-215-2043; fax: +81-22-215-2041.

E-mail address: fukata@imr.tohoku.ac.jp (N. Fukata).

spectrometer. The spectral resolution was 0.25 cm^{-1} . Low pass filters with cut-off energies of 0.328, 0.403, and 0.670 eV were used in FT-IR measurements to investigate the dependence of optical absorption peaks on excitation energy. Isochronal annealing was carried out for 30 min at each temperature in the range from 100°C to 800°C at 50°C intervals.

3. Results and discussion

In addition to the localized vibrational modes of H in a PtH_2 complex [5] at 1873.0 and 1891.8 cm^{-1} in an as-quenched specimen, we observed a new optical absorption peak at 1719.4 cm^{-1} as shown in Fig. 1. As for the strongest peak observed at 1880.8 cm^{-1} , based on their experiment on the isotope shift, Uftring et al. [7] have suggested that the number of H atoms included in the complex is one, although the detailed structure was not shown in their report. In our study, this peak was observed only in specimens doped with Pt and H. In a D-doped specimen, the 1880.8 cm^{-1} peak was shifted to 1358.5 cm^{-1} . In a specimen co-doped with H and D, no splitting of the 1880.8 (1358.5) cm^{-1} peak was observed. These results indicate that the 1880.8 cm^{-1} peak is due to the localized vibrational modes of H and that the number of H atoms included in the complex is one, the same conclusion as that of Uftring et al. [7]. The intensity of the 1880.8 cm^{-1} peak was higher than those of the 1873.0 and 1891.8 cm^{-1} peaks which are due to the PtH_2 complex. This result means that the complex responsible for the 1880.8 cm^{-1} peak is formed more easily than the PtH_2 complex during quenching. In the as-quenched specimen, almost all Pt atoms exist not in pairs or clusters but in isolated Pt or Pt–H complexes since the quenching speed is high enough to quench Pt

atoms [11]. Considering all these results, the 1880.8 cm^{-1} peak is probably due to the localized vibrational modes of H in the PtH complex.

Fig. 1 also shows the annealing behavior of optical absorption peaks observed in this study. With increasing annealing temperature, the intensity of the new 1719.4 cm^{-1} peak increases, in contrast with the decrease in intensity of the peaks due to the PtH_2 and PtH complexes. After annealing at above 500°C , we observed new peaks in the range of 1300 – 1500 cm^{-1} , which were not observed by Uftring et al. These peak positions changed with the annealing temperature. After annealing at 800°C , at least four peaks were observed at about 1301 , 1318 , 1452 and 1474 cm^{-1} as shown in Fig. 3. These five new peaks showed similar annealing behavior. These new peaks were also observed in a specimen doped with Pt only and did not shift as a result of D doping. Thus these new peaks are not due to the localized vibrational modes of H. Considering these results, these new peaks are probably due to electronic transitions associated with defect centers including Pt only.

Next, we investigated the dependence of these new peaks on the cut-off energy by placing a low pass filter between the specimen and the light source of FT-IR equipment. The intensities of these peaks changed depending on the cut-off energy of the low pass filters as shown in Fig. 2. This result suggests that these peaks are due to the electronic transition of Pt-related defects. Fig. 2 also shows another interesting result. There is an anticorrelation between the intensity of 1719.4 cm^{-1} peak and those of the other four peaks observed at about 1301 , 1318 , 1452 , and 1474 cm^{-1} . The intensity of the 1719.4 cm^{-1} peak increases with decreasing cut-off energy. In the case of the latter four peaks, the intensities decrease with decreasing cut-off energy. These latter four peaks showed the same dependence on excitation energy. Peak intensities increased monotonically with

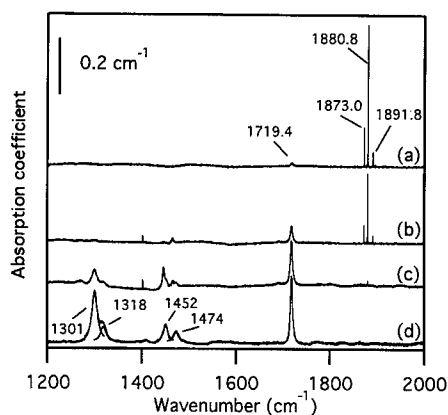


Fig. 1. Optical absorption spectra observed in Pt-doped Si (a) before and after annealing at (b) 500°C , (c) 600°C , and (d) 800°C . Deconvolutions of the optical absorption spectrum are added to the spectrum observed after annealing at 800°C .

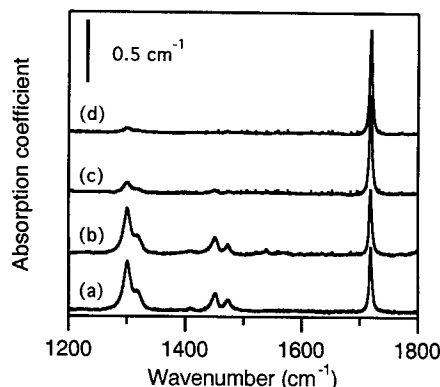


Fig. 2. Optical absorption spectra observed in Pt-doped Si (a) without and with low-pass filters of (b) 0.7 eV , (c) 0.403 eV , and (d) 0.328 eV .

excitation energy and were close to those without a low pass filter when a 0.670 eV-filter was used. It is thus indicated that the defect centers which give rise to the optical absorption at about 1301, 1318, 1452, and 1474 cm^{-1} become IR-active centers by illumination. This dependence on excitation energy, i.e., monotonic dependence without any peaks, suggests that excitation occurs between a localized state in the band gap and extended states.

Considering the annealing behaviors and the dependence on excitation energy of these new peaks, are probably due to the same Pt-related defect. The 1719.4 cm^{-1} peak intensity in p-type silicon was much greater than that in n-type silicon. Based on these results, these new peaks are probably due to hole transitions. Detailed explanations will be shown elsewhere. To determine the optical threshold energy of the excitation of these defect centers, we analyzed the data using Lucovsky's model, which gives the optical cross section for electronic transitions between a localized state and a band [13,14]. In this analysis, we assumed that the energy of illumination was the cut-off energy for each low pass filter since the highest energy had the strongest effect. Considering this, the optical cross section (σ) can be written as

$$\sigma = \sigma_0 \{ [4E_D(h\nu - E_D)] / (h\nu)^2 \}^{3/2}, \quad (1)$$

where E_D is the optical threshold energy and $h\nu$ is the photon energy. Eq. (2) is deduced from Eq. (1),

$$Y^{2/3} X^2 = 4E_D(X - E_D), \quad (2)$$

where $Y = \sigma/\sigma_0$, $X = h\nu$. In this experiment, σ/σ_0 is I/I_0 , where I and I_0 are the intensities of the optical absorption peak observed in experiments with and without a low-pass filter. Fig. 3 shows the relation between $Y^{2/3} X^2$ and X . They have a linear relation and

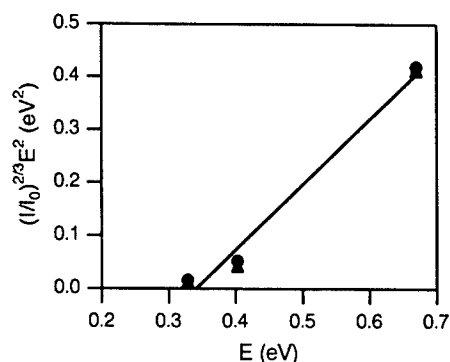


Fig. 3. Fitting of the excitation spectrum with Lucovsky's model. The closed circles (●) and the closed triangles (▲) are the data of the 1301 and 1318 cm^{-1} peaks and 1452 and 1474 cm^{-1} peaks, respectively.

we obtained an optical threshold energy of about 0.34 eV.

These new defects are formed by annealing. This fact shows that these new centers are probably not due to isolated Pt but rather to Pt clusters. According to Höhne et al. [6] 6-Pt clusters were formed by subsequent annealing at 540°C after indiffusion of Pt at 1200°C. The formation temperature of the new peaks observed in this study is close to that of 6-Pt clusters. In this study, Pt doping was performed at 1300°C where the solubility of Pt in Si is about 10^{17} cm^{-3} . Pt atoms introduced at 1300°C are supersaturated during annealing at below 1300°C and therefore probably form clusters by annealing at 800°C where the diffusion length of Pt atoms is on the order of 10^{-6} cm^{-3} [15]. After annealing at 800°C, we heated the specimen again at 1000°C for 1 h and annealed it at 800°C for 30 min. The intensities of the peaks observed in the region from 1300 to 1720 cm^{-1} decreased up to about 70% of those before. This decrease of the intensity is probably due to the precipitation of Pt atoms since heating at 1000°C precipitates Pt atoms introduced at 1300°C and therefore the new peaks do not come from the precipitates of Pt. Based on these considerations, the peaks observed in the region from 1300 to 1720 cm^{-1} are probably due to Pt clusters.

4. Conclusions

We observed a new optical absorption peak at 1719.4 cm^{-1} in as-quenched specimens in addition to the peaks due to the PtH_2 and the PtH , and new peaks in the range of 1300–1500 cm^{-1} after subsequent annealing at above 500°C. The optical threshold energy of the defects attributed to 1300–1450 cm^{-1} peaks was determined to be about 0.34 eV by applying Lucovsky's model. From the isotope shift by D-doping, the dependence on excitation energy, and the annealing behaviors, these peaks were found to be due to the electronic transition of Pt-related defects such as Pt clusters.

Acknowledgements

The authors wish to thank the Laboratory for Advanced Materials, Institute for Materials Research, Tohoku University for allowing them to use an FT-IR spectrometer.

References

- [1] G.W. Ludwig, H.H. Woodbury, *Solid State Phys.* 13 (1962) 223.

- [2] H. Lemke, *Phys. Stat. Sol. A* 86 (1984) K39.
- [3] H. Zimmermann, H. Ryssel, *Appl. Phys. Lett.* 58 (1990) 499.
- [4] H.J. von Bardeleben, D. Stiévenard, M. Brousseau, J. Barrau, *Phys. Rev. B* 38 (1988) 6308.
- [5] M. Höhne, *Phys. Rev. B* 45 (1999) 5883.
- [6] M. Höhne, U. Juda, *J. Appl. Phys.* 72 (1992) 3095.
- [7] S.J. Uftring, M. Stavola, P.M. Williams, G.D. Watkins, *Phys. Rev. B* 51 (1995) 9612.
- [8] U. Juda, O. Scheere, M. Höhne, H. Riemann, H.-J. Schilling, J. Donecker, A. Gerhardt, *J. Appl. Phys.* 80 (1996) 3435.
- [9] J.-U. Sachse, J. Weber, E.Ö. Sveinbjörnsson, *Phys. Rev. B* 60 (1999) 1474.
- [10] K.P. Lisiak, A.G. Milnes, *Solid State Electron.* 18 (1975) 533.
- [11] H. Takahashi, M. Suezawa, K. Sumino, *J. Appl. Phys.* 78 (1995) 3077.
- [12] N. Fukata, M. Suezawa, *J. Appl. Phys.* 87 (2000) 8361.
- [13] G. Lucovsky, *Solid State Commun.* 3 (1965) 299.
- [14] J.S. Blakemore, S. Rahimi, in: R.K. Willardson, A.C. Beer (Eds.), *Semiconductors and Semimetals* 20, Academic Press Inc., New York, 1984, p. 251.
- [15] D.J. Fisher (Ed.), *Defect and Diffusion Forum*, Scitec Publications, Switzerland, 1998, pp. 153–155.



ELSEVIER

Physica B 308–310 (2001) 442–445

PHYSICA B

www.elsevier.com/locate/physb

Identification of getter defects in high-energy self-implanted silicon at $R_p/2$

R. Krause-Rehberg^{a,*}, F. Börner^a, F. Redmann^a, J. Gebauer^a, R. Kögler^b,
R. Kliemann^b, W. Skorupa^b, W. Egger^c, G. Kögel^c, W. Triftshäuser^c

^a Martin-Luther-Universität Halle-Wittenberg, FB Physik, 06099 Halle, Germany

^b Forschungszentrum Rossendorf, PF 510119, 01314 Dresden, Germany

^c University der Bundeswehr München, Werner-Heisenberg-Weg 39, 85579 Neubiberg, Germany

Abstract

A strong gettering effect appears after high-energy Si self-implantation and subsequent annealing in two zones at the projected range of the silicon ions (R_p) and in a region at about $R_p/2$. The defects responsible for the impurity gettering at $R_p/2$ were studied by means of positron annihilation. It was found that diffusing Cu impurities were captured by small vacancy agglomerates. Monoenergetic positron beams with improved depth resolution were used to characterize the defects. Excellent depth resolution was obtained when samples were wedge-shaped polished and studied using the Munich Scanning Positron Microscope. © 2001 Elsevier Science B.V. All rights reserved.

Keywords: Silicon; Self-implantation; Gettering; $R_p/2$; Positron annihilation

1. Introduction

Impurity gettering in silicon is a major problem in semiconductor device fabrication particularly when the dimensions of the components shrink. After high-energy self-implantation and subsequent annealing, two getter zones were found by SIMS measurements after intentional impurity contamination [1,2]. The deeper zone is located at R_p (projected range of implanted Si ions). A network of interstitial-type dislocation loops are responsible for the gettering effect at R_p (found by TEM). A second pronounced getter zone is observed in the $R_p/2$ region (between surface and R_p). No extended defects were found in this zone by TEM. A controversial discussion about the nature of this defects have recently be overcome, and it is now widely accepted that open-volume defects are responsible for the gettering effect at $R_p/2$.

Positron annihilation spectroscopy is a unique tool to study open-volume defects in semiconductors [3]. Especially the technique variable energy positron annihilation spectroscopy (VEPAS) seems to be promising for the study of $R_p/2$. Here, the penetration depth of positrons and thus the information depth of the method can be controlled by the acceleration voltage of a monoenergetic positron beam. However, at higher positron energies (> 10 keV) the penetration profile becomes rather broad, so that buried defect layers in a depth of several microns can hardly be studied. Thus, an improvement of the depth resolution is necessary in order to treat the $R_p/2$ effect by positrons. In an earlier study [4], we removed the sample surface layer by layer by ion sputtering in order to obtain the optimum depth resolution for the VEPAS experiment. In this paper we present for the first time the use of a positron microscope for defect depth profiling.

2. Experimental details

Cz-silicon wafers were implanted by 3.5 MeV Si^+ (dose: $5 \times 10^{15} \text{ cm}^{-2}$). One sample was co-implanted

*Corresponding author. Fachbereich Physik, University Halle, Fr.-Bach-Platz 6, 06108 Halle (Saale) Germany.

Tel.: +49-345-552-5567; fax: +49-345-552-7160.

E-mail address: krause@physik.uni-halle.de (R. Krause-Rehberg).

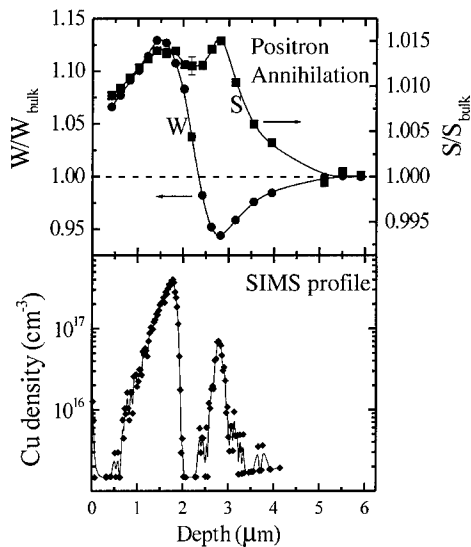


Fig. 1. VEPAS measurement of high-energy implanted and annealed Si after Cu contamination. Upper panel: results of doppler-broadening measurements at positron energy of 7.5 keV during stepwise sputtering of the sample. The depth (abscissa) was obtained by adding the mean implantation depth of the positrons (360 nm) to the etching depth. The S and W parameter were normalized to the bulk values. The lower panel shows the Cu depth profile obtained by SIMS.

with 4 MeV P^+ and a dose of $1 \times 10^{15} \text{ cm}^{-2}$ (sample in Fig. 1). For all samples, a rapid-thermal annealing (RTA) step (30 s at 900°C) was performed after implantation, followed by a Cu contamination of the sample (Cu^+ implantation into the backside of the sample, 20 keV, $1 \times 10^{13} \text{ Cu}^+ \text{ cm}^{-2}$). A further annealing step under Ar atmosphere (3 min at 700°C) was performed to realize the Cu diffusion. The VEPAS experiments presented in Figs. 1 and 2 were performed using a magnetically guided continuous positron beam system (for experimental details see Ref. [4]). The stepwise removal of the sample in Fig. 1 was realized by Ar^+ sputtering (2 kV, 10^{-6} mbar, 40 μA , 30 min, 60°, etching rate 3.4 nm/min). Special attention was paid to ensure that the defects created during sputtering in a thin surface layer are not affecting the defect detection in the sample region under observation. This was proved in a reference Si sample which did not show any positron traps after a removal of 200 nm by sputtering. The surface of the sample in Fig. 3 was polished in a wedge shape with a flat angle of 0.81°. This wedge was studied with the Munich Scanning Positron Microscope [5] with a constant positron incident energy of 8 keV, a lateral resolution of about 10 μm , and a time resolution of the positron lifetime measurement of about 250 ps. In order to obtain the defect depth scan, the positron lifetime spectrum was measured at 45 points each separated by

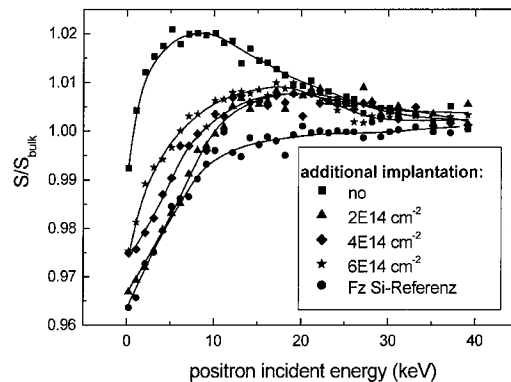


Fig. 2. Doppler broadening VEPAS measurement of self-implanted Si (3.5 MeV, $5 \times 10^{15} \text{ cm}^{-2}$, annealed 30 s at 900°C). A set of samples was additionally implanted by Si^+ ions into the $R_p/2$ region with increasing dose (indicated in the figure). Thereafter, the samples were chemically etched by 1.2 μm in order to obtain maximum sensitivity in the $R_p/2$ range with a conventional slow-positron beam.

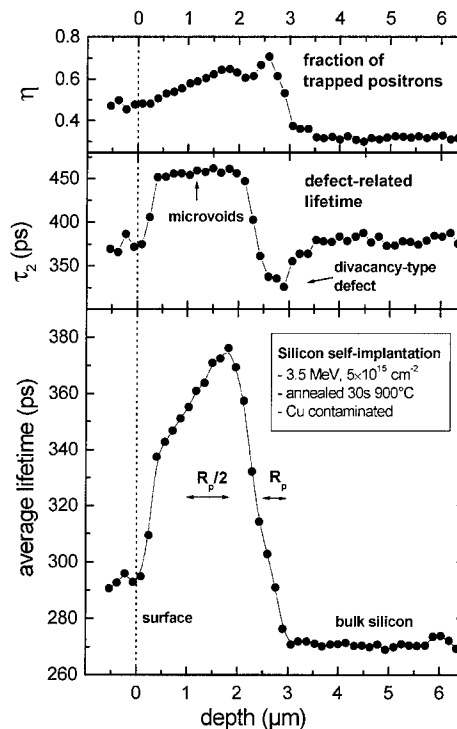


Fig. 3. Defect depth profile of a self-implanted Si sample (3.5 MeV, $5 \times 10^{15} \text{ cm}^{-2}$, annealed 30 s at 900°C, Cu contaminated) using the Munich Scanning Positron Microscope. The sample surface was wedge-shaped polished. The profile was then taken as a line scan along the wedge with constant positron energy of 8 keV. Each positron lifetime measurement is separated by 11 μm corresponding to a depth difference of 155 nm. The depth scale was calculated according to the wedge angle of 0.81°, and the mean positron implantation depth of 400 nm was added.

about 11 μm along the wedge. Thus, the depth difference between the individual measurements corresponds to about 155 nm which is distinctly smaller than the mean positron penetration depth at 8 keV. This is in silicon about 400 nm which gives therefore the depth resolution of the experiment. In contrast to conventional VEPAS, this resolution is constant for the whole depth range. The incident energy cannot be decreased in order to obtain a better depth resolution because the fraction of positrons which diffuse back to the surface would become too large.

3. Results and discussion

Fig. 1 shows the results of the defect depth scan after implantation, annealing, and Cu contamination [4]. The lower panel shows the Cu profile obtained by a SIMS depth scan. The gettering zones at $R_p/2$ and R_p are well visible. The upper panel presents the result of the VEPAS doppler-broadening measurement. The depth scan was obtained by successively sputtering the sample surface. The S parameter shows two pronounced peaks at $R_p/2$ and R_p , clearly indicating the presence of open-volume defects in both regions. In the R_p region, the W parameter is smaller than W_{bulk} . This is the expected behavior in case of positron trapping by vacancy-type defects. However, in the $R_p/2$ region, in addition to the S parameter, also the W parameter increases distinctly above the bulk value. This finding can only be understood when assuming that the open-volume defect is not entirely surrounded by silicon. Thus, it must be concluded that Cu atoms are built in the boundary of the vacancy-type defect in the $R_p/2$ region. On the other hand, this is not observed in the R_p region, where the gettering centers are obviously different from the positron trapping centers. From this results, additional Doppler-broadening coincidence measurements, and a study using the Munich Slow-positron Lifetime Beam it was concluded that small vacancy clusters capture the diffusing impurities at $R_p/2$ and divacancy-type defects probably bound to the interstitial-type dislocation loops are detected at R_p [4].

The first conclusion is supported by the following experiment: a set of high-energy self-implanted Si samples (3.5 MeV, $5 \times 10^{15} \text{ cm}^{-2}$, annealed 30 s at 900°C) was additionally implanted by Si^+ ions with increasing dose into the $R_p/2$ region (energy was chosen to have the projected range of the post-implanted Si^+ ions in the $R_p/2$ region of the high-energy implantation). The samples were then chemically etched by 1.2 μm in order to use a conventional slow-positron beam to study the $R_p/2$ region (Fig. 2). The upper curve (no post-implantation) exhibits a distinct increase compared to the defect-free reference sample due to positron trapping by vacancy agglomerates. The additional implantation

with a dose of $2 \times 10^{14} \text{ cm}^{-2}$ distinctly decreases the effect. Obviously, open-volume defects formed during high-energy self-implantation are partly filled by the implanted excess Si interstitials of the post-implantation. However, with increasing dose, the S parameter increases again due to the increasing number of open-volume defects created by the additional implantation.

The improvement of the depth resolution by stepwise ion sputtering of the sample makes it possible to show the defect profiles in a larger depth, e.g. at R_p . However, the experiment needs a long time (several days). Moreover, the sputtering is not completely homogeneous. Thus, after long-term etching the surface is not smooth any more. Another problem appears in a compound semiconductor due to selective sputtering. These drawbacks can be avoided by using a focused positron beam and a wedge-shaped sample. Fig. 3 shows the first result of this type of defect depth profiling. We used the Munich Scanning Positron Microscope to measure the defect profile in a high-energy self-implanted Si sample (3.5 MeV, $5 \times 10^{15} \text{ cm}^{-2}$, annealed 30 s at 900°C, Cu contaminated). A wedge of 0.81° was prepared by a polishing technique, which is used for spreading resistance measurements. In a reference experiment using a Si sample in as-grown state it was shown that the grinding defects only alter the surface annihilation parameters, but do not penetrate more than 100 nm into the sample.

The high quality of the obtained defect profile is obvious. Both defect zones which were found in Fig. 1 can also be seen. In the $R_p/2$ region, the defect-related lifetime is 450 ps thus indicating the existence of small vacancy clusters ($n \geq 10$). The cluster density increases to a depth of 1.8 μm . Around a depth of 2 μm , the cluster signal disappears, and a defect becomes detectable with an open volume comparable to a divacancy ($\tau_2 \approx 330$ ps). The fraction of trapped positrons is rather high. Since excess divacancies anneal below 370°C [6], the observed defects must be stabilized or being part of the dislocation loops present in this region. The positron lifetime of the bulk region ($> 3 \mu\text{m}$) is about 270 ps and thus distinctly larger than the lifetime of defect-free Si (218 ps). Due to the lack of defects, a distinct fraction of positrons (about 30%) diffuse back to the surface annihilating there at the surface or in the thin defect-rich surface layer remaining after mechanical polishing. However, in the R_p and $R_p/2$ region, the positron diffusion length is expected to be smaller than 100 nm, so that the influence of the surface can be neglected.

4. Conclusions

It can be concluded that the two methods of depth-resolution enhanced VEPAS enabled us to identify

different vacancy-type defects in high-energy self-implanted Si. In the $R_p/2$ region point defect clusters containing vacancy-type defects were undoubtedly found. Diffusing copper atoms are trapped there and are clearly detected by positrons to be in the direct surrounding of the annihilation site.

Acknowledgements

This work was supported by the Deutsche Forschungsgemeinschaft and the Bundesland Sachsen-Anhalt.

References

- [1] R. Kögler, et al., Nucl. Instrum. and Methods B 147 (1999) 96.
- [2] R.A. Brown, et al., J. Appl. Phys. 84 (1998) 2459.
- [3] R. Krause-Rehberg, H.S. Leipner, Positron Annihilation in Semiconductors, Springer, Berlin, 1999.
- [4] R. Krause-Rehberg, F. Börner, F. Redmann, Appl. Phys. Lett. 77 (2000) 3932.
- [5] A. David, et al., Mater. Sci. Forum 255–257 (1997) 741.
- [6] A. Polity, et al., Phys. Rev. B 58 (1998) 10363.



ELSEVIER

Physica B 308 310 (2001) 446–449

PHYSICA B

www.elsevier.com/locate/physb

Nanoindentation pop-in effect in semiconductors

H.S. Leipner^{a,*}, D. Lorenz^b, A. Zeckzer^b, H. Lei^a, P. Grau^b^a*Zentrum für Materialwissenschaften, Martin-Luther-Universität D-06099 Halle, Germany*^b*Fachbereich Physik, Martin-Luther-Universität D-06099 Halle, Germany*

Abstract

First direct evidence is given on the formation of dislocations in room-temperature nanoindentation experiments of gallium arsenide wafers. The formation of dislocation loops, which have been examined by transmission electron microscopy, can be related to the pop-in effect found in depth-sensitive hardness measurements. In the case of silicon, no dislocations are found. Instead, different high-pressure phases could be identified by Raman microscopy. © 2001 Elsevier Science B.V. All rights reserved.

Keywords: Deformation; Nanoindentation; Dislocation sources; Transmission electron microscopy

1. Introduction

The plastic deformation of semiconductors in the low temperature/high stress region is of particular interest due to the anticipated change in the dislocation motion. It is well accepted that dislocations are dissociated in the glide set and move via the thermal activation and migration of double kinks in a medium range of temperature and stress [1]. However, the calculation of Duesbery and Joós [2] demonstrated for silicon that the motion of perfect dislocations in the shuffle set has a lower activation energy at high stresses. The transition from the motion of dissociated glide set dislocations to the predominance of undissociated shuffle set dislocations is expected at a stress of about $0.01G$ (G shear modulus). It is difficult to extend the deformation experiments to the range of high stresses and low temperatures. One approach is the uniaxial compression under confining pressure. In the case of silicon, it has not been possible to go to deformation temperatures lower than 550 K, even with a confining pressure of 1.5 GPa [3]. The other difficulty is that existing glide set dislocations formed in a pre-deformation stage may

prevent the transition to a deformation mode which is fully controlled by shuffle set dislocations.

The second approach to high-stress deformation is the use of a diamond indenter. Because of its simplicity, nanoindentation is a very popular but still badly understood method for the study of local mechanical properties. In depth-sensitive hardness measurements, a sudden jump in the displacement may occur at a certain load. This finding is referred to as the pop-in effect. In this paper, we report on nanoindentation experiments and the investigation of the defect structure produced by the local deformation in GaAs and Si wafers.

2. Experimental details

The MTS Corp. Nanoindenter II was used for depth-sensitive hardness measurements. As measured by atomic force microscopy, the tip of the Vickers indenter used can be regarded as a sphere with a tip radius of about 1 μm . We investigated the force versus displacement curves during the penetration of the diamond tip in polished (001) and (111) surfaces of undoped liquid encapsulated Czochralski-grown GaAs wafers (supplied by Freiburger Compound Materials). Additionally, float zone (001) silicon wafers (Wacker) were studied. In order to investigate the defect structure at the indentations, the samples were indented at room temperature in

*Corresponding author. Martin-Luther-Universität, Zentrum für Materialwissenschaften, HoherWeg 8, D-06120 Halle, Germany. Tel.: +49-345-55-25-453; fax: +49-345-55-24-212.

E-mail address: leipner@physik.uni-halle.de (H.S. Leipner).

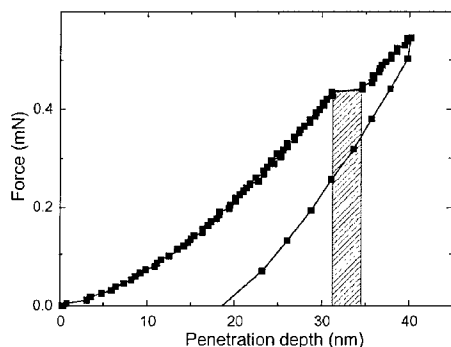


Fig. 1. Force versus penetration depth for a nanoindentation experiment on a polished (001)-oriented GaAs wafer. The discontinuity in the curve at the force of about 45 mN is referred to as the pop-in effect. The upper branch corresponds to the loading, the lower one to the unloading of the diamond tip. The lines are to guide the eye.

an array of 40×30 identical indents. The extension of the whole array was $780 \times 580 \mu\text{m}^2$. A maximum load of 0.550 mN has been chosen, because this value is close to the critical force of the pop-in effect occurring at 45 mN (Fig. 1). In this way, the state immediately after the pop-in could be examined microscopically for several indentations. The loading rate was 0.055 mN/s, the unloading rate 0.400 mN/s. After indentation, the samples were prepared by backside grinding, polishing, and argon ion milling for investigations by transmission electron microscopy (TEM). The TEM examination was carried out using bright-field diffraction contrast in a JEM 1000 microscope operating at 1 MV.

Raman measurements were carried out on impressions with an indenter load of up to 1 N using a Dilor LabRam Raman microscope. The 632.8 nm line of a He–Ne laser with a power of 25 mW was used for Raman scattering.

3. Results and discussion

3.1. Gallium arsenide

The examination of the indentations by TEM shows fourfold dislocation rosettes for (001) and threefold rosettes for (111) GaAs wafers. The dislocations have an extent of up to 200 nm from the indentation center (Fig. 2). Individual dislocation loops outside the tangled rosettes may appear up to a distance of 350 nm. The geometry of the dislocation slip corresponds to the $\{111\}\langle 1\bar{1}0 \rangle$ glide prism model derived for the dislocation patterns around Vickers microindentations produced with higher loads [4,5]. However, in contrast to the more extended rosettes at such indentations, no

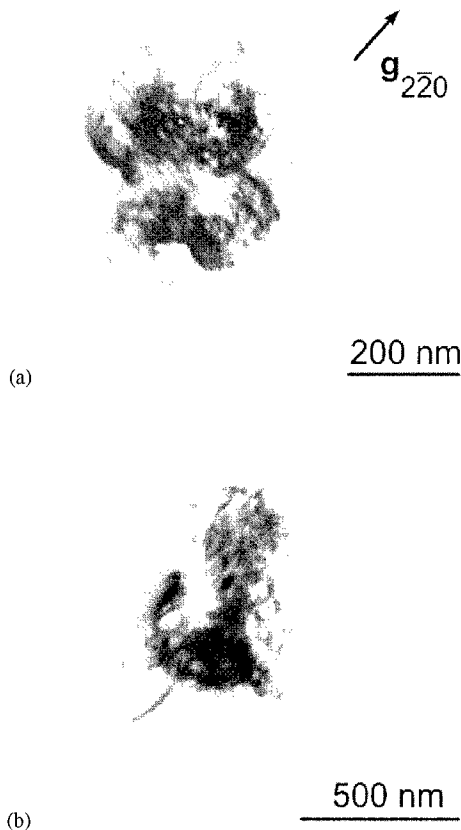


Fig. 2. Plan view TEM bright-field images of the dislocation rosettes at nanoindentations in (001) GaAs (a) and (111) GaAs (b). The diffraction vector \mathbf{g} is $2\bar{2}0$.

anisotropy due to different glide velocities of α and β dislocations appeared in our nanoindentation experiment. This may be due to the fact that the usual expression of thermally activated dislocation glide velocity [1],

$$v = B\tau^m \exp\left(-\frac{U}{k_{\text{BT}}}\right)$$

(B constant, τ resolved shear stress, m stress exponent, U activation energy, k_{B} Boltzmann constant, T temperature) cannot account for the extension of the loops in the high-stress regime.

Only perfect dislocation loops with Burgers vectors $\mathbf{b} = \frac{1}{2}\langle 110 \rangle$ could be identified in the TEM images according to the $\mathbf{g} \cdot \mathbf{b} = 0$ extinction rule (\mathbf{g} diffraction vector). No partial dislocations and stacking faults are recognized. TEM tilting experiments have shown that all loops have the Burgers vectors inclined to the surface. There is no indication of the formation of cracks or other phases, so the local deformation seems to proceed

exclusively by the formation and propagation of dislocations.

The dislocation rosettes at nanoindentations investigated by TEM represent the state after the following processes: (i) generation of embryonic dislocation loops giving rise to the pop-in effect, (ii) further plastic deformation via coalescence and expansion of these loops during or immediately after the pop-in, (iii) relaxation and stabilization of the dislocation structure upon unloading. The generation of loops can be understood as homogeneous dislocation nucleation. The elastic self-energy of a dislocation loop with the magnitude of the Burgers vector b and the radius r is given by [6]

$$E_c = \frac{Gb^2r}{4} \frac{2-\nu}{1-\nu} \left(\ln \frac{4r}{r_0} - 2 \right),$$

where ν is Poisson's ratio and r_0 the cutoff radius at the dislocation core. The strain energy released by the formation of the loop under the action of the resolved shear stress τ is

$$E_\tau = -\tau b \pi r^2.$$

Maximizing the total energy $E_c + E_\tau$ provides the critical radius r_c and the maximum free energy E_c of the loop formed. For 0 K ($E_c = 0$), the critical stress of dislocation nucleation is obtained as

$$\tau_c = \frac{Gb}{\pi e^3 r_0} \frac{2-\nu}{1-\nu}, \quad (1)$$

where e is the Euler number. With typical values of $r_0 = b/3$ and $\nu = 0.312$ for GaAs, we get $r_c \approx 0.7$ nm and $\tau_c \approx G/9 = 6$ GPa.

During depth-sensitive hardness measurements, the diamond indenter sphere is driven into the sample under continuous monitoring of load and penetration depth. In the indentation experiment, the maximum shear stress τ_T (Tresca stress) is directly proportional to the mean contact pressure p_m . It can be expressed with the effective Young's modulus E by the indenter radius and the penetration depth h , as it follows from the Hertzian contact theory of a hard sphere [7],

$$\tau_T = 0.465 p_m = 0.197 E \sqrt{\frac{h}{R}}.$$

Depending on the actual values of the penetration depth and the indenter radius R , the Tresca stress can be as high as 10 GPa. According to the calculations of dislocation theory given above, this amount of stress is sufficient for homogeneous dislocation nucleation in GaAs.

The number of loops formed can be estimated from the work done during the pop-in (critical force times the displacement). From the shaded area in Fig. 1, this work is obtained as 1.7×10^{-12} Nm. If this work is related to the energy of a critical-sized loop $E_c(r_c)$, we obtain that

5×10^4 loops must have been formed. A higher number of 1.3×10^6 loops is obtained when the total dissipation energy, as the area between the loading and the unloading curves (Fig. 1), is related to $E_c(r_c)$. Such an estimation provides the upper limit of the number of loops with a critical size in the nascent state, when it is assumed that the whole energy input by the indentation is transferred into the formation of dislocations. The number of extended loops found in the TEM images at one indentation site is not higher than 100. Eq. (1) represents the upper limit of the shear stress at 0 K. At higher temperatures, the thermal contribution lowers the shear stress and the critical radius becomes higher. After their formation, the embryonic loops grow further and coalesce under the action of the applied load. The unloading may give rise to a small relaxation of the dislocation structure, but the residual strain of the indent finally stabilizes the dislocation rosette pattern.

3.2. Silicon

The substructure around indentations in Si is completely different to that of GaAs. Despite the fact that a pop-in effect also occurs, no dislocations could be found. Only a high number of small cracks, which also appear at the surface (see the inset of Fig. 3), could be identified. The indentation stress is high enough to cause phase transitions in Si, which have been extensively studied by Kailer et al. [8]. In contrast to GaAs, the critical shear stress τ_c for the generation of dislocations in silicon is higher than that for the onset of phase transitions. The actual phases formed depend strongly on the indentation conditions, such as dwell time, loading, and unloading rate. Larger Vickers indentations produced

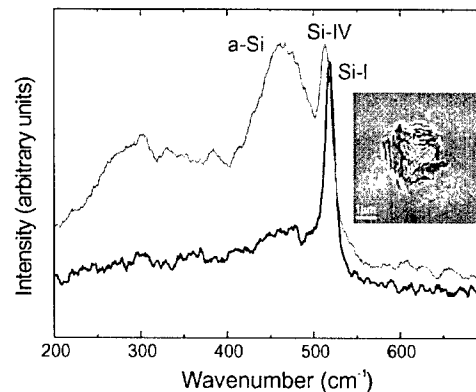


Fig. 3. Room temperature Raman spectra taken in the deformed region of a microindentation in silicon. The bands at 521 cm^{-1} are due to silicon with diamond structure (Si-I), hexagonal nanocrystalline Si (Si-IV), and amorphous Si (a-Si) [8]. The inset shows a secondary electron image of an indentation taken in a scanning electron microscope.

with higher loads extend to several micrometers. They have been examined by Raman microscopy. The result is shown in Fig. 3. The spectra taken in different positions of the indent distinctly differ. In the case of fast unloading (Fig. 3), bands due to amorphous and hexagonal Si could be identified in addition to the low pressure diamond structure.

4. Conclusions

In the case of silicon, different high-pressures phases could be identified by Raman microscopy. The occurrence of the different phases strongly depends on the indentation load and the loading/unloading rate. In contrast to Si, there are no indications of phase transitions in the case of GaAs. Instead, the pop-in effect in GaAs can be related to the formation of dislocation loops. First direct evidence by transmission electron microscopy is given on the formation of dislocations in room-temperature nanoindentation experiments of gallium arsenide. The number of loops generated have been estimated from energetical considerations and compared to the number found in TEM. Only perfect dislocation loops could be identified in the TEM images. These results are in agreement with the

motion of non-dissociated shuffle-set dislocations, which are supposed to occur in the low temperature/high stress deformation regime.

Acknowledgements

The work was supported by the Deutsche Forschungsgemeinschaft.

References

- [1] H. Alexander, H. Teichler, in: K.A. Jackson, W. Schröter (Eds.), *Handbook of Semiconductor Technology*, Vol. 1, Wiley-VCH, Weinheim, 2000, pp. 291–376.
- [2] M.S. Duesbery, B. Joós, *Philos. Mag. Lett.* 74 (1996) 253.
- [3] J. Rabier, J.L. Dermenet, *Phys. Stat. Sol. B* 222 (2000) 63.
- [4] P.B. Hirsch, P. Pirouz, S.G. Roberts, P.D. Warren, *Philos. Mag. B* 52 (1985) 759.
- [5] H.R. Höche, J. Schreiber, *Phys. Stat. Sol. A* 86 (1984) 229.
- [6] J.P. Hirth, J. Lothe, *Theory of Dislocations*, Wiley, New York, 1982.
- [7] B.R. Lawn, *J. Amer. Cer. Soc.* 81 (1998) 1977.
- [8] A. Kailer, Y.G. Gogotsi, K.G. Nickel, *J. Appl. Phys.* 81 (1997) 3057.



ELSEVIER

Physica B 308–310 (2001) 450–453

PHYSICA B

www.elsevier.com/locate/physb

Mechanical strength of nitrogen-doped silicon single crystal investigated by three-point bending method

G. Wang, D. Yang*, D. Li, Q. Shui, J. Yang, D. Que

State Key Lab of Silicon Materials, Zhejiang University, Hangzhou 310027, People's Republic of China

Abstract

The mechanical strength of nitrogen-doped Czochralski silicon (NCZ-Si) and conventional Czochralski silicon (CZ-Si) have been investigated by three-point bending method at room temperature. It was found that the mechanical strength of silicon had been increased markedly at room temperature due to the doping of nitrogen. The effects of the surface condition and the orientation of silicon crystal on mechanical strength were determined. The mechanism of the mechanical strength increased by nitrogen in silicon is also discussed. © 2001 Elsevier Science B.V. All rights reserved.

Keywords: Mechanical strength; Nitrogen; Silicon

1. Introduction

With the development of the large-scale integrated circuit (IC) and the increasing of the silicon wafer's diameter, it is important to improve the mechanical strength of silicon material and to diminish the warpage of silicon wafers. Moreover, the mechanical properties of silicon at room temperature often dictate fundamental limits on the fabrication and packaging of modern semiconductor devices, but less research was done [1–4].

However, the plasticity of silicon crystal has been extensively studied. Except for the intrinsic property, the surface condition of samples and the doped impurities were the important factors that influenced the strength of silicon. Sumino et al. [5] found that damage on the surface had great effect on silicon's mechanical strength at high temperatures. Impurities also have great effect on the mechanical strength of silicon at high temperature [6–11]. It was reported that the interstitial oxygen enhanced the tensile stress and pinned efficiently the movement of dislocations [6–8]. However, the pinning

effect of nitrogen on the mechanical property of silicon was much stronger than that of oxygen at high temperatures [9–11]. Moreover, the study of the mechanical property of silicon at room temperature is relatively scarcer. Chen et al. found by fracture that the different orientations of single crystal silicon had different mechanical strengths [1]. It was suggested that the fracture path depended not only on the level of resistance but also on the change of fracture energy with orientation [1,2]. Besides the intrinsic anisotropy mentioned above, the different extrinsic strength-limiting flaws and strength distributions would be operative depending on the manner in which a silicon component was stressed [2,3]. Also there is a theoretical computation that impurities would influence the fracture and ideal tensile strength of silicon crystal [12,13]. However, the influence of impurities on fracture process and fracture strength was seldom given attention.

In this paper, we measured the mechanical strength of CZ silicon and NCZ silicon by means of three-point bending at room temperature. The effects of surface condition and the orientation of samples on the mechanical strength were detected. The influence of nitrogen in silicon crystal was also discussed.

*Corresponding author. Tel.: +86-571-8795-1667; fax: +86-571-8795-2322.

E-mail address: mseyang@ dial.zju.edu.cn (D. Yang).

2. Experiment

Three inch, 40 Ω cm CZ silicon wafers with $\langle 111 \rangle$ orientation were used in our experiments. NCZ-Si and CZ-Si were grown under almost the same conditions, except for the protection atmosphere. The concentration of impurities was measured at room temperature by a Nicolet Impact410 Fourier transmission Infrared Spectroscope (FTIR) as shown in Table 1.

The wafers with the orientation of $\langle 111 \rangle$ and $\langle 110 \rangle$ were cut into bars with the dimension of $25 \times 5 \times 5 \text{ mm}^3$. Then the bars were divided into five groups. There were about four or five specimens in each group. In order to compare the influence of flaws on the surface of samples, two steps of pretreatment mechanical grinding were carried out. Groups 1 and 2 were only ground with Al_2O_3 . Groups 3–5 were mechanically polished by diamond grinding creams after Al_2O_3 grinding. All the groups after mechanical grinding and polishing were etched about 5 min in $\text{HF}:\text{HNO}_3=1:3$ (volume) etchant to remove surface damage. Finally, the mechanical strength of the samples was measured by three-point bending technique with a DKZ-5000 dynamoelectric bending machine at room temperature. The sample surface loaded forces were $\langle 111 \rangle$ and $\langle 110 \rangle$, respectively. According to the maximum compressive stress, the fracture strength is given by the following formula:

$$\sigma = \frac{3PL}{2BH^2},$$

where σ is the maximum compressive stress of bars, P is the loaded force, B , H and L ($L = 20 \text{ mm}$) are the width, height and length of pressing-groove, respectively.

3. Results and discussion

The fracture strength of CZ and NCZ silicon samples with different orientations are given in Table 2. It can be seen from Table 2 that for both CZ and NCZ silicon, the polishing pretreatment increased the fracture strength σ in comparison with only the grinding pretreatment. The fracture strength of NCZ silicon with $\langle 111 \rangle$ orientation was higher than that of CZ silicon after both grinding and polishing pretreatment. Furthermore, the fracture strength of the CZ silicon with $\langle 110 \rangle$ orientation was higher than that with $\langle 111 \rangle$ orientation.

It was found in our experiment that the initial crack appeared in the central position of the back surface of samples where the highest tensile stress was produced. Figs. 1(a) and (b) show the scanning electronic microscopy (SEM) photo of the fractal surface of a silicon sample with $\langle 111 \rangle$ orientation and its illustration. The SEM photo indicated that the fractal surface had three parts. The angles between each part were 120° and 70° , respectively. The part 1 was the initial crack part and was parallel to the $\{112\}$ plane. The parts 2 and 3 were considered as the $\{111\}$ planes.

It is well known that single crystal silicon is a brittle material. Its fracture process belongs to the cleavage fracture. The $\{111\}$ plane with the maximum atom density and the highest Young's modulus is the weakest one in which fracture is easy to generate. Tsai and Mecholsky [14] suggested that the fracture planes of $\{110\}$ with the $\{110\}$ and $\{100\}$ tensile surface both initiated on the $\{110\}$ plane and had the tendency to deviate to the $\{111\}$ plane. In one word, the crack generated on the original loading plane and then deviated from that plane to the $\{111\}$ plane. Hereafter, in our experiment, the initial crack plane was in the center of the backside surface where the highest tensile stress was produced. From Figs. 1(a) and (b), it is easy to get that the initial crack path was the $\{112\}$ plane. However, the weakest plane is the $\{111\}$ plane in silicon crystal. Therefore, with the crack path developing, the crack path kinked to the $\{111\}$ plane. Both NCZ-Si and CZ-Si showed the same fracture characteristics. It indicates that NCZ-Si has the same mechanism of fracture as CZ-Si.

Comparing the mechanical strength between the Groups 1 and 3, and Groups 2 and 4, respectively (Table 2), we found that the mechanical strength of smooth surface samples with little defects (polishing pretreatment) was higher than rough-surface ones (grinding pretreatment). It was the same for both CZ-Si and NCZ-Si. It is known that there are three parameters that have the relation to mechanical strength, according to the Griffith formula, as follows:

$$\sigma = \sqrt{\frac{4E\gamma}{\pi c}},$$

where E is the Young's modulus, γ the surface energy, and c the crack length. Generally speaking, Young's modulus is invariable for the same material in the same orientation. The surface energy is related to the

Table 1
Concentration of impurities in CZ and NCZ silicon samples

	C ($10^{15} \text{ atom/cm}^3$)	O ($10^{18} \text{ atom/cm}^3$)	N ($10^{15} \text{ atom/cm}^3$)
CZ-Si	2.6	1.6	—
NCZ-Si	1.0	1.8	1.0

Table 2
Data of fracture strength at room temperature

Group	Pre-treatment	Loading orientation	$\bar{\sigma}$ (N/mm ²)
1 (CZ)	Grinding	$\langle 111 \rangle$	186.5
2 (NCZ)	Grinding	$\langle 111 \rangle$	264.9
3 (CZ)	Polishing	$\langle 111 \rangle$	204.5
4 (NCZ)	Polishing	$\langle 111 \rangle$	286.9
5 (CZ)	Polishing	$\langle 1\bar{1}0 \rangle$	254.9

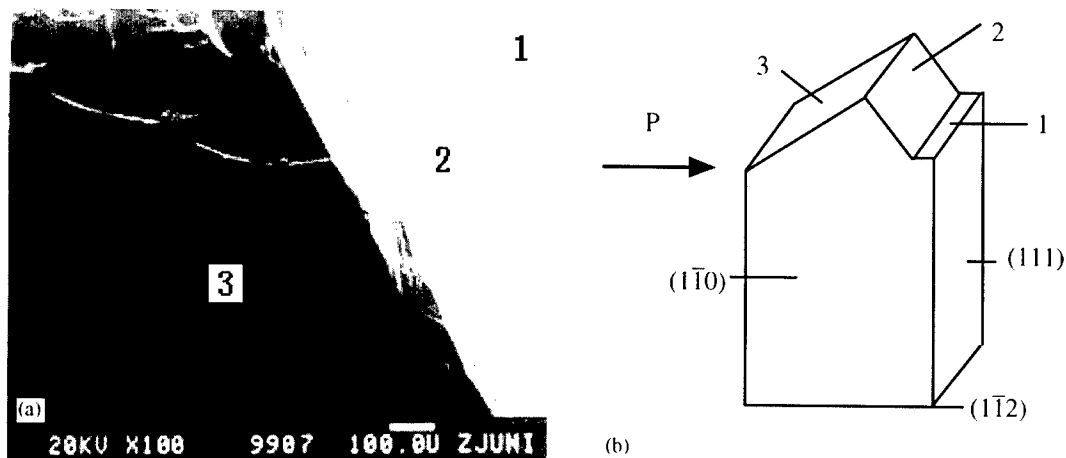


Fig. 1. The SEM photo (a) of the fractal surface of a silicon sample with $\langle 111 \rangle$ orientation and its illustration (b).

arrangement of atoms. For the same material and the same orientation, E and γ can be considered to be constant. Crack length c is the only factor to affect samples' mechanical strength. In general, grinding could induce a damage layer in the near surface of silicon samples, including a plastic deformation layer and an elastic deformation layer. By polishing, most of the damaged layer will be removed. In our samples, the ground silicon samples and the polished silicon samples were etched for the same time. Therefore, the residual stress in the ground silicon samples could exist while all of the damage in the polished silicon samples was removed by etching. The residual stress may have resulted in crack length which was longer in the ground silicon samples, so that the mechanical strength was lower. On the other hand, the surface roughness of polished samples was less than that of the grinding samples. After etching, the surface of both kinds of samples was still rough. The roughness can be taken as notches, which will lead to the concentration of stress when loaded. The rougher the surface, the deeper the notches were. Thus, the strength of bars would be lower when loaded for the samples with deeper notches. Therefore, from the viewpoint of both the residual

stress and surface roughness, the mechanical strength was surely lower for the grinding samples compared to the polishing samples.

Since single crystal silicon is an anisotropic material, the flexure strength should be different at different orientations. In our experiment, the flexure strength of Group 3 with $\langle 111 \rangle$ orientation and Group 5 with $\langle 110 \rangle$ orientation shows the difference. Although the initial crack appeared with the same $\{112\}$ plane in both groups, the crack path was different. The initial crack lay on the orientation of $\{11\bar{2}\}\langle 111 \rangle$ for the samples with $\langle 111 \rangle$ orientation and $\{11\bar{2}\}\langle 1\bar{1}0 \rangle$ for the samples with $\langle 110 \rangle$ orientation, respectively. As mentioned above, the crack path would develop to $\{111\}$ plane at last. But the initial crack orientation was not the same; the crack path would not be the same. From this viewpoint, the different crack path may be the reason for the different flexure strength for Groups 3 and 5.

However, our results also showed that the flexure strength of NCZ-Si was higher than that of CZ-Si. The reasons may be as below: (1) As nitrogen was doped in NCZ silicon, N–O, N–N and N–Si bonds were formed, which had the higher bond energy than Si–Si bond.

Consequently, more energy was needed in NCZ silicon than in CZ silicon when they were fractured. (2) During the cooling process of crystal growth, a large number of small-diameter and high-density oxygen precipitation cores were nucleated, which increased the dissipation of energy during the process of fracture. Also, the complex of impurities may cause the crack path variant and lead to the different flexure strength. (3) The doping impurities would shift the Fermi level and change the ideal tensile stress as reported [12,13]. Thus, the Shockley surface states produced during the crystal cleaving process (microscopically, double kink nucleation or migration) would influence the flexure strength greatly. The result indicates that nitrogen improves the mechanical strength of single crystal silicon at room temperature, whatever the surfaces of the samples are, rough or smooth if under the same fracture conditions.

4. Conclusions

We studied the flexure strength of single crystal silicon doped with nitrogen (NCZ) and the silicon without nitrogen (CZ) by three-point bending method at room temperature. The result indicates the doped nitrogen increase of the flexure strength of single crystal silicon. It is suggested that the nitrogen atom in silicon formed the bonds with silicon atom and oxygen atom, which improves the single crystal silicon's mechanical strength. Besides, nitrogen in silicon helped the formation of oxygen precipitation, which pins the dislocations in the process of fracture, leading to higher flexure strength. The surface condition of silicon has a great effect on its mechanical strength. The crack quantity and length on

the surface are the main factors. Different orientation plane is another factor to affect the mechanical strength, due to the different crack path.

Acknowledgements

The authors would like to thank the Natural Science Foundation of China for the financial supports (No. 59976035 and 50032010).

References

- [1] C.P. Chen, M.H. Leipold, *Ceram. Bull.* 59 (1980) 469.
- [2] A.A. Wereszczak, A.S. Barnes, K. Breder, S. Binapal, *J. Mater. Sci.* 11 (2000) 291.
- [3] K. McGuire, S. Danyluk, T.L. Baker, J.W. Rupnow, D. McLaughlin, *J. Mater. Sci.* 32 (1997) 1017.
- [4] F. Ebrahimi, S.I. Hussain, *Scr. Metall. Mater.* 32 (1995) 1507.
- [5] K. Sumino, I. Yonegaga, *Jpn. J. Appl. Phys.* 20 (1981) L685.
- [6] S.M. Hu, *Appl. Phys. Lett.* 31 (1977) 53.
- [7] K. Sumino, H. Harada, *Philos. Mag. A* 44 (1981) 1319.
- [8] T. Fukuda, A. Ohsawa, *J. Appl. Phys.* 73 (1993) 112.
- [9] I. Yonenaga, K. Sumino, *J. Appl. Phys.* 56 (1984) 2346.
- [10] L. Jastrzebski, G.W. Cullen, R. Soydon, et al., *J. Electrochem. Soc.* 134 (1987) 466.
- [11] D. Li, D. Yang, D. Que, *Phys. B* 273 (1999) 553.
- [12] K. Masuda-Jindo, V.K. Tewary, R. Thomson, *J. Mater. Res.* 6 (1991) 1553.
- [13] Y.M. Huang, J.C.H. Spence, O.F. Sankey, *Philos. Mag. A* 70 (1994) 53.
- [14] Y.L. Tsai, J.J. Mecholsky, *J. Mater. Res.* 6 (1991) 1248.



ELSEVIER

Physica B 308–310 (2001) 454–457

PHYSICA B

www.elsevier.com/locate/physb

Self-interstitial clusters in silicon

T.A.G. Eberlein^a, N. Pinho^{a,*}, R. Jones^{a,1}, B.J. Coomer^a, J.P. Goss^a,
P.R. Briddon^c, S. Öberg^{b,2}

^a School of Physics, The University of Exeter, Exeter EX4 4QL, UK

^b Department of Mathematics, Luleå University of Technology, S-97187 Luleå, Sweden

^c Department of Physics, The University of Newcastle upon Tyne, Newcastle upon Tyne NE1 7RU, UK

Abstract

Although there have been made many calculations for structures of the self-interstitial in Si and small aggregates of interstitials, I_n , there have been relatively few attempts to relate these defects with experimental data. Here, we discuss the assignments of the self-interstitial to the AA12 EPR centre and the di-interstitial to the P6 EPR centre. © 2001 Elsevier Science B.V. All rights reserved.

Keywords: Interstitials; AA12; P6; Ab initio theory

1. Introduction

Recently, the AA12 electron paramagnetic resonance (EPR) centre has been assigned to the self-interstitial in Si trapped at a tetrahedral site [1]. AA12 is an isotropic centre with a resolved 45 MHz hyperfine interaction with a single Si atom. Unresolved hyperfine interactions with shells of 4–6 Si atoms have also been detected. The small value of the hyperfine tensor suggests that only 1.5% of the spin density is localised in an s-orbital on the interstitial. The spectrum is found when p-Si is irradiated with 30 MeV protons (or 4.7 MeV α -particles) between 77 and 270 K, and subsequently the sample is illuminated with band gap light. The defect has been correlated with a minority carrier transient spectroscopy (MCTS) level at $E_c - 0.39$ eV and anneals at 350 K in the dark or at 77 K under minority carrier injection. The growth of other interstitial defects, such as C_i , Al_i and Si_i-O_i , is detected after the anneal. The implication is that the (+/+ +) level of I_1 lies at $E_c -$

0.39 eV and the defect is unstable when neutral. It seems strange that the defect is created in high energy proton irradiation as low energy irradiation results in an athermal movement of the interstitial even at 4.2 K. This is believed to be caused by an ionisation enhanced defect motion [2]. Similarly, rapid diffusion of interstitials occurs after 1.3 MeV proton implantation of n-Si. Hence, if the assignment is correct there must be some reason why the diffusion does not occur in the high energy proton irradiation experiments.

AA12 is not the only spectrum that has been assigned to a self-interstitial defect. The P6 EPR centre is formed in neutron, ion or MeV proton irradiated intrinsic Si [3,4]. Its g -tensor reveals a C_2 axis along [1 0 0] at 200 K, but at 300 K, the symmetry becomes D_2 or D_{2d} and anneals at 440 K. The activation energy for this change is only 0.2 eV and represents a thermally activated reorientation between equivalent sites. Uniaxial stress studies showed that the defect could reorientate at 100°C with an activation energy of 0.6 eV. This activation energy is similar to the anneal of the 0.4 eV DLTS level found in irradiated p-Si. The energy-stress tensor of P6 is consistent with a defect of D_{2d} symmetry with principal values and directions $B_1 = B_2 = 15.4$ eV along [1 0 0] and [0 1 0], and $B_3 = -30.8$ eV along [0 0 1]. Here, the C_2 axis in the low temperature form points along [0 1 0] through the unique Si atom.

*Corresponding author.

E-mail address: pinho@exce.ex.ac.uk (N. Pinho).

¹ EPSRC and the ENDEASD network are thanked for computer time and financial support respectively.

² Financial support by NFR and TFR, and computer support by PDC at KTH in Sweden are gratefully acknowledged.

Lee et al. [3] suggested that P6 is due to I_2^+ with three atoms sharing a lattice site resulting in a C_2 axis along [0 1 0]. Recent ab initio calculations [5] indicate that this structure is metastable and I_2 possesses C_{1h} symmetry at low temperatures, and C_{2v} when some distortion is allowed. In spite of this difference in symmetry, the defect was identified with P6. This cannot be correct and, therefore, the true nature of P6 is at present unresolved.

The results derived in this paper have been found using a first principles density functional method employing Gaussian orbitals (AIMPRO) [6]. The calculations for the energies have been carried out in supercells, but the electrical levels have been calculated from the ionisation energies of the defects, when embedded in large H-terminated clusters in a way described previously [7].

2. Single interstitial I_1

A number of possible locations for the interstitial were examined in 65 atom supercells. These were the T site with T_d symmetry, the H site with D_{3d} symmetry and the $\langle 110 \rangle$ -split interstitial with C_{2v} symmetry. In the neutral charge state the energies of the T interstitial and the $\langle 110 \rangle$ -split interstitial are equal to within the precision of the method (Table 1). The H interstitial is found to be about 0.16 eV higher in energy. The potential well in which the T interstitial is located is quite narrow and a small displacement of the interstitial can push it towards the H site lowering the symmetry to C_{3v} . This is probably due to a Jahn–Teller effect to be discussed below. In the negative charge state the [1 1 0] oriented interstitial has the lowest formation energy, while the T interstitial in the 1+ and 2+ charge states has the lowest energy. In the 2+ state, the T site is stable against small perturbations, i.e. when moved slightly from its equilibrium position, the atom returns during the relaxation. In general, the results for I_1 are in agreement with previous theory [8,9]. The formation energy for the interstitial at the T site in the neutral

charge state is found to be 3.36 eV, in good agreement with a previous calculation of 3.43 eV [9]. Increasing the supercell to 129 atoms or the MP scheme to 4^3 enhances the formation energy by only 0.05 and 0.01 eV. Therefore the calculations are converged with respect to the size of the supercell and the k -point sampling.

Electrical levels of the single interstitial were found by taking the relaxed structures from the supercell and embedding them in 297 atom clusters. Ionisation energies were then calculated and compared with standard defects such as hydrogen at a BC site, interstitial carbon, substitutional sulphur and the sulphur pair. The ionisation energy was then found using the difference in energy between the ionised and neutral defects [7]. The T interstitial possesses a t_2 level in the upper part of the gap which is occupied by two electrons when neutral. In this case a Jahn–Teller distortion splitting the t_2 manifold would be expected. This is probably the origin of the C_{3v} distortion. However, it seems that the distortion is small.

Table 2 gives the calculated ionisation energies and donor levels evaluated using the sulphur pair as a reference. We choose this as it has a (+/+ +) level very close to that of AA12. The error in the method is about 0.2 eV. The single donor level of I_1 at the T site is above the conduction band and thus the interstitial is always ionised at the T site. On the other hand, the [1 1 0] split interstitial has a donor level close to E_v and thus is only neutral in this site. Hole trapping of the neutral defect must then lead to a switch to the T site and subsequent

Table 1

Relative total energies for I_1 in eV. The values in square brackets are the results of Lee [3]

State	T	$\langle 110 \rangle$ -split	H
–1	0.15 [0.38]	0.00 [0.00]	0.40 [0.19]
0	0.00 [0.16]	0.05 [0.00]	0.16 [0.04]
+1	0.00 [0.00]	0.60 [0.59]	0.54 [0.47]
+2	0.00 [0.00]	1.19 [1.32]	1.02 [1.15]

Table 2

Calculated levels for some known defects and for I_1 and I_2 interstitial complexes

Defect	I_d	Calc. (0/+)	Expt. (0/+)	I_{dd}	Calc. (+/+ +)	Expt. (+/+ +)
S_2	4.54	M	0.19	6.04	M	0.37
S	4.66	0.32	0.3	6.40	0.73	0.6
C_i	5.12	0.78	0.89	—	—	—
H	4.51	0.16	0.15	—	—	—
I_1 T	4.04	—	—	5.75	0.08	0.39 ?
I_1 (1 1 0)	5.38	1.03	—	—	—	—
I_2 C	5.13	0.78	—	—	—	—
I_2 K	4.99	0.64	—	—	—	—

electron trapping would reverse this site change. In this way, rapid athermal diffusion could occur at low temperatures in the presence of irradiation. We find the second donor level of I_1 at the T site to lie at $E_c - 0.08$ eV and about 0.31 eV above the level attributed to AA12. This is at the very upper error limit expected in the method. This level should also exhibit a Poole-Frenkel effect. In the positive charge state, a Mulliken analysis shows that 7% of the spin density is localised on the interstitial in the three p-orbitals. The isotropic hyperfine interaction with the nucleus of the unique Si atom is then almost zero, consistent with low 1.5% value seen experimentally for AA12.

The diffusion barrier of the interstitial at the T site was then investigated. The H site is a saddle point on the diffusion path of I_1^{++} . The barrier in this charge state is found to be about 1 eV. If we use the Arrhenius diffusion equation $D = D_0 \exp(-Q/kT)$ with $D_0 = va^2$, where a is the distance between T sites ($a/\sqrt{2}$) and $v = 10^{13} \text{ s}^{-1}$, then the temperature at which the defect anneals is around 350 K, consistent with the anneal of the AA12 centre. In the metastable neutral charge state the diffusion barrier for T-H-T path is found to be below 0.2 eV, which is also consistent with the measured annealing of AA12 around 80 K under minority carrier injection.

3. Di-interstitial

Several structures with C_2 symmetry were first considered, being the most stable similar to the P6 model proposed by Lee et al. [3]. In this structure, shown in Fig. 1(L), two Si atoms are placed symmetrically around a substitutional atom roughly aligned along a cube axis. The original substitutional atom is displaced along $[010]$. We call this the L form. This is, however, not the lowest energy structure of I_2 . A lower energy structure for the neutral charge state has C_{1h} symmetry and is identical to that proposed by Kim et al. [5] and shown in Fig. 1(K). This structure can be found by placing an Si dimer, oriented along $[011]$, near to a substitutional atom. This atom is displaced away from the dimer so that the symmetry becomes C_{1h} with a (011) mirror plane. There is, however, another structure also having C_{1h} symmetry with comparable energy. This form, Fig. 1(C), is described in Ref. [10]. The C form is structurally very similar to the K form, but the $[011]$ dimer is added to a site near a bond centre, maintaining a (011) mirror plane. The formation energies of the neutral C, K, L forms of I_2 are 5.12, 5.19 and 6.17 eV. Table 3 shows the relative energies in each charge state. Clearly, the L form has an energy about 1 eV higher than the C_{1h} forms in all charge states. The K and C defects have competitive energies in all charge states.

Table 2 shows that the $(0/+)$ level of the stable C form of I_2 lies at $E_v + 0.3$ eV.

The diffusion energy of neutral I_2 was found by imposing constraints preventing the diffusing structure to relax to the equilibrium one [11]. The diffusion barrier along the path is quite complicated and is illustrated in Fig. 2. Step (i) shows the starting structure in the C form. The first step (ii) represents the transition to the saddle point between two symmetric versions of the C form. This costs 0.5 eV. Step (iv) involves a relaxation to the K form which is almost degenerate with the C form. Step (v) involves the movement of the single Si atom to a symmetric version of the K form (vi). The next step

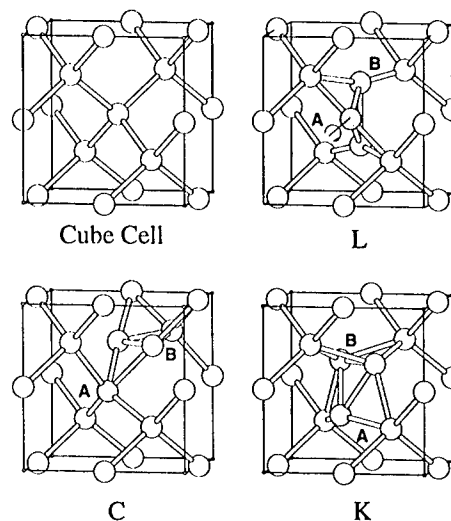


Fig. 1. Models of I_2 .

Table 3

Relative energies, eV, for the three forms of I_2 in various charge states

Charge	L	C	K
-1	1.07	0.00	0.04
0	1.05	0.00	0.07
+1	1.12	0.00	0.007

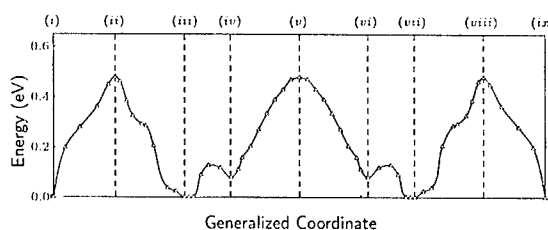


Fig. 2. Energetics of the diffusion path for I_2 .

takes us to the C form (vii). The steps (vii)–(x) complete the movement of the dimer through a lattice vector $a/\sqrt{2}$. Thus, the net migration barrier is about 0.5 eV. It is possible that another diffusion path exists with lower energy. Preliminary calculations also show that the migration barriers for the lowest energy I_3 is approximately 0.75 eV in the neutral charged state. These dramatic results show that both I_2 and I_3 are likely to diffuse *faster* than I_1^{++} .

We complete our investigation into I_2 by calculating the stress-tensor B for the L defect in a way described previously [11]. Relaxing the cell volume leads to an expansion of 0.8% and 0.3% for the neutral and positive defects, respectively. The B -tensor for the positive defect has principal values and directions $B_3 = -7.5$ eV along $[0.0, -0.3, 1.0]$, $B_2 = 6.1$ eV along $[0.0, 1.0, 0.3]$, and $B_1 = 1.5$ eV along $[1\ 0\ 0]$. Now, the observed values for P6 corresponding to the high temperature D_{2d} form are $B_1 = -30.4$ eV, along $[1\ 0\ 0]$, and $B_2 = B_3 = 15.4$ along $[0\ 1\ 0]$ and $[0\ 0\ 1]$, respectively. Clearly, the calculated values are very different from the experimental ones. This suggests that P6 is a distinct defect from I_2 .

4. Conclusions

We have shown that the single interstitial is stable at the T site in the positive and double positive charge state, and that it has symmetry and spin density consistent with the AA12 EPR centre. The calculated diffusion barrier of I_1^{++} is in agreement with the thermal annealing of AA12 in the dark at 350 K, and the lower diffusion barrier found for I_1^+ accounts for the loss of AA12 under electron injection. However, the $(+/+)$ calculated level is much more shallow than $E_c - 0.39$ eV reported for AA12. Therefore, we conclude that the AA12 defect is probably the long-sought self-interstitial, although there is uncertainty about the position of the second donor level. The calculations show that the defect does not possess a first $(0/+)$ level within the gap and the neutral defect would spontaneously ionise.

Turning to the di-interstitial we conclude that the lowest energy configuration found by Kim et al. is not the P6 EPR centre. Further, the Lee et al. model for I_2 is only metastable and has a B -tensor at variance with P6. The calculated diffusion barrier for I_2 is 0.5 eV, half that of I_1^{++} . The rapid mobility of I_2 at room temperature explains the absence of a dominant EPR centre that can be assigned to the defect. Other forms [12] are compact and highly mobile like I_2 . Thus, we expect I_4 defects to be formed at the same time as I_3 . I_4 has been linked with the B3 EPR centre which is known to be stable up to 500°C. This scenario of several coexisting self-interstitial aggregates is distinct from that assumed in sequential kinetic models of the growth of I_n clusters [13].

References

- [1] B.N. Mukashev, Kh.A. Abdullin, Yu.V. Gorelinskii, Phys. Stat. Sol. (A) 168 (1998) 73.
- [2] G.D. Watkins, Radiation Damage in Semiconductors, Dunod, Paris, 1964, p. 97.
- [3] Y.H. Lee, N.N. Gerasimenko, J.W. Corbett, Phys. Rev. B 14 (1976) 4506.
- [4] Y.H. Lee, Appl. Phys. Lett. 73 (1998) 1119.
- [5] J. Kim, F. Kirchoff, W.G. Aulbur, F.S. Khan, G. Kresse, Phys. Rev. Lett. 83 (1999) 1990.
- [6] R. Jones, P.R. Briddon, in: M. Stavola (Ed.), Identification of Defects in Semiconductors, Semiconductors and Semimetals, Academic Press, Boston, 1998, p. 287.
- [7] A. Resende, R. Jones, S. Öberg, P.R. Briddon, Phys. Rev. Lett. 82 (1999) 2111.
- [8] Won-Chang Lee, Sun-Ghil Lee, K.J. Chang, J. Phys.: Condens. Matter 10 (1998) 995.
- [9] R.J. Needs, J. Phys.: Condens. Matter 11 (1999) 10437.
- [10] B.J. Coomer, Ph.D. Thesis, University of Exeter, 2000.
- [11] J. Coutinho, R. Jones, P.R. Briddon, S. Öberg, Phys. Rev. B 62 (2000) 10824.
- [12] S.K. Estreicher, M. Gharaibeh, P.A. Fedders, P. Ordeján, Phys. Rev. Lett. 86 (2001) 1247.
- [13] N.E.B. Cowern, G. Mannino, P.A. Stolk, F. Roozeboom, H.G.S. Huizing, J.G.M. van Berkum, F. Cristiano, A. Claverie, M. Jaraíz, Phys. Rev. Lett. 82 (1999) 4460.



ELSEVIER

Physica B 308–310 (2001) 458–461

PHYSICA B

www.elsevier.com/locate/physb

Self-interstitial-oxygen related defects in low-temperature irradiated Si

L.I. Khirunenko^{a,*}, L.I. Murin^b, J.L. Lindström^c, M.G. Sosnin^a, Yu.V. Pomozev^a

^a *Institute of Physics, National Academy of Science of Ukraine, Prospect Nauki 46, 03028 Kiev 28, Ukraine*

^b *Institute of Solid State and Semiconductor Physics, Minsk 220072, Belarus*

^c *Department of Physics, Lund University, S-221 00 Lund, Sweden*

Abstract

The radiation-induced defects, which give rise to the absorption bands at 956, 944 and 936 cm⁻¹ in silicon and are suggested to be the self-interstitial–interstitial-oxygen-related complexes IO_i and I₂O_i, have been studied by FTIR. N-type C-rich Si crystals co-doped with ¹⁶O and ¹⁸O isotopes were irradiated at $T = 80$ K with 5 MeV electrons and then annealed isochronally up to 360 K. The oxygen isotopic shifts of the bands assigned to IO and I₂O are determined and a direct evidence of the oxygen incorporation in the defects is presented. Appearance of a number of new bands has been observed upon the interstitial carbon C_i annealing and they are attributed to precursors of the C_iO_i complex. © 2001 Elsevier Science B.V. All rights reserved.

Keywords: Silicon; Irradiation; Self-interstitials; Oxygen isotopes

1. Introduction

The silicon self-interstitial (I) is a fundamental intrinsic defect, which is always produced during Si crystal growth as well as in the course of high temperature processing and/or irradiation treatments. However, the isolated interstitial has not been properly identified, yet, which is probably due to its high migration ability [1]. It can interact efficiently with many other defects and impurities, resulting in the appearance of new centers. The best known process is the Watkins replacement mechanism when the group III impurities and substitutional carbon are ejected into interstitial sites [1,2]. Interaction of the Si self-interstitial with the interstitial oxygen (O_i) has also been proposed to play an important role in processes of radiation defect formation as well as in oxygen agglomeration at elevated temperatures [3,4]. In particular, enhanced oxygen diffusion was suggested to occur via a highly mobile IO_i complex [5–7]. Besides, such a complex was argued to be the core of the oxygen-related thermal double

donors [8]. However, experimental data available on the IO_i complex are controversial.

In 1966, Whan [9,10] revealed three vibrational IR absorption bands located at about 936, 944 and 956 cm⁻¹ at 80 K in irradiated Czochralski-grown silicon (Cz-Si). These bands were later assigned to arise from the IO_i complex. The bands appeared after irradiation by fast electrons at temperatures 80–150 K of oxygen-rich Si crystals, but not in oxygen-lean ones [9,11,12]. The presence of Ge or Sn (traps for vacancies) did not affect the formation of the 936, 944 and 956 cm⁻¹ bands while doping by carbon (a trap for I) reduced their formation substantially [12]. The bands at 944 and 956 cm⁻¹ are most likely associated with different configurations of the same center since their relative intensities could be changed reversibly at low temperatures upon the sample illumination and/or storage in darkness [9]. Both bands annealed out at about 200–250 K with a partial transformation into the 922 and 932 cm⁻¹ bands, related to interstitial carbon, and into the 936 cm⁻¹ band [11,12]. The 936 cm⁻¹ band anneals out already at about 350 K with a simultaneous increase in the intensity of the 9 μm band, i.e., in the concentration of interstitial oxygen atoms.

*Corresponding author.

E-mail address: lukh@iop.kiev.ua (L.I. Khirunenko).

These facts allowed all the three bands (at 944, 956 and 936 cm^{-1}) to be assigned to arise from the IO_i complex [12,13]. However, there are some observations that are not consistent with such an assignment for the 936 cm^{-1} band. Firstly, no IO_i complex that is stable at RT has hitherto been observed by any other technique. Secondly, there is a consensus that the IO_i complex is indeed formed during LT irradiation of the Cz-Si crystals, but it has also been established that the complex is only stable up to about 200–250 K. Dissociation of the IO_i complexes in this temperature region has been manifested in many experiments [11,12,14–17] via correlated appearance of interstitial carbon and/or aluminum atoms. Furthermore, similar thermal stability behavior of IO_i complexes was confirmed by the EPR technique [16]. Evidently, the 936 cm^{-1} band should arise from another, more stable defect. The Si interstitial pair and interstitial oxygen complex, I_2O_i , have been suggested recently [18,19] to be responsible for this band. Such a complex may be formed via the reaction $\text{I} + \text{IO}_i \rightarrow \text{I}_2\text{O}_i$.

Apparently, the local vibrational modes (LVMs) at 936 and $944(956)\text{ cm}^{-1}$ could be related to oxygen vibrations in the I_2O_i and IO_i complexes. To get a direct evidence of this, in the present paper, we have performed an IR absorption study of low-temperature radiation-induced defects in Si crystals co-doped with ^{16}O and ^{18}O isotopes.

2. Experimental

The relatively low resistivity ($0.2\text{--}0.3\ \Omega\text{ cm}$) n-type Si samples co-doped with oxygen isotopes ^{16}O and ^{18}O were used in this study. The ^{16}O , ^{18}O and carbon concentrations were determined from the intensity of the bands at 1107 , 1058 and 605 cm^{-1} at room temperature [2,20] and were about 1×10^{18} , 8×10^{17} and $4 \times 10^{17}\text{ cm}^{-3}$, respectively. Irradiation with electrons (5 MeV) was performed to doses $(3\text{--}5) \times 10^{17}\text{ cm}^{-2}$ using a microtron. The temperature of the samples during irradiation was about 80 K, after irradiation the samples were moved to a cryostat without heating. The isochronal annealing was carried out in temperature steps of 3–10 K in the range 80–363 K, for 15 min at each temperature. Absorption spectra were measured using a Bruker 113v Fourier Transform IR Spectrometer at 10 K with spectral resolution of 0.5 cm^{-1} .

3. Results and discussion

3.1. Si self-interstitial-oxygen related defects

Figs. 1a and b show typical infrared absorption spectra measured at 10 K in the region of 780–

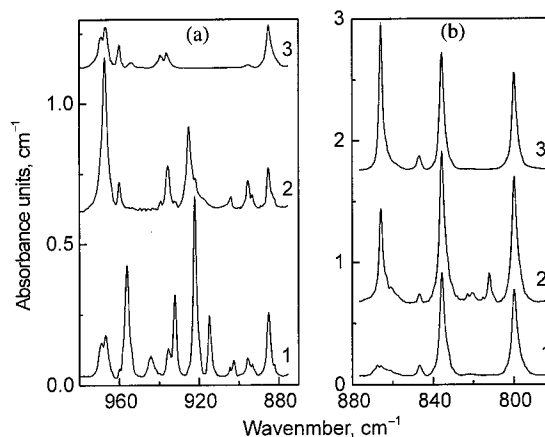


Fig. 1. Absorption spectra measured at 10 K for Si: ^{16}O , Si: ^{18}O and Si: C after irradiation at 80 K for a dose $5 \times 10^{17}\text{ cm}^{-2}$ (1) and subsequent annealing at 300 (2) and 363 K (3).

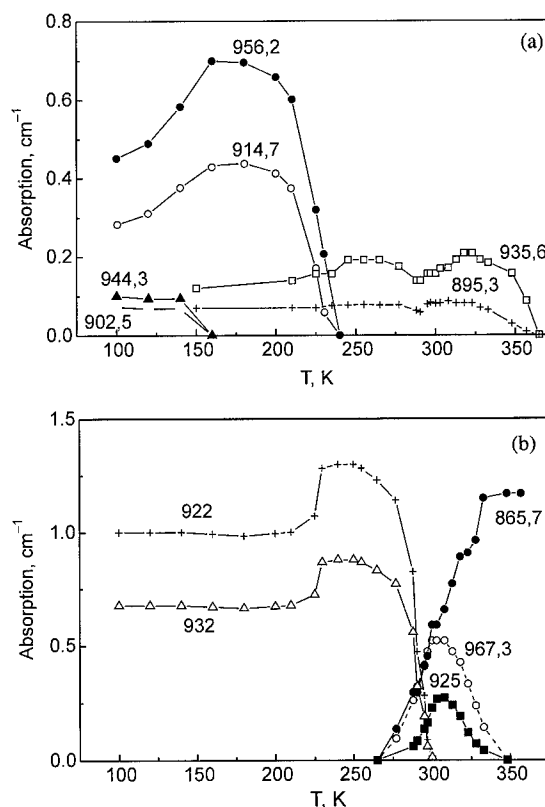


Fig. 2. The behavior of the absorption bands at annealing of irradiated Si: ^{16}O , ^{18}O , C.

980 cm^{-1} for investigated samples after irradiation at 80 K (1) and annealing at 300 (2) and 363 K (3). The annealing behaviors of some of the bands are shown in more detail in Figs. 2a and b, and their positions are

given in Table 1. In the as-irradiated sample, the most prominent bands at 836 and 800 cm^{-1} are due to oxygen (^{16}O and ^{18}O) vibrations in the neutral vacancy-oxygen (VO) center. The weaker bands at 885 and 847 cm^{-1} are related to the same center but in its negative charge state. The well-known bands at 922 and 932 cm^{-1} originate from C_i atoms. The bands at 944, 956 and 936 cm^{-1} appear to be the same as those observed previously [9–13,18,19] in Si: ^{16}O crystals, i.e., the former two arise from the IO_i complex, and the latter from the I_2O_i defect.

Of particular interest, here, are the bands at 903, 915 and 895 cm^{-1} . A linear correlation was found between the intensities of the former two bands and the bands at 944 and 956 cm^{-1} in samples irradiated with different doses, and the ratio of intensities was close to that of the ^{16}O and ^{18}O concentrations. Besides, all these bands have an identical annealing behavior, as illustrated in Fig. 2b. It should also be noted that the 903 and 915 cm^{-1} bands display reversible changes in intensity under illumination similar to those of the bands at 944 and 956 cm^{-1} . All these facts allow us to assign the 903 and 915 cm^{-1} bands as arising from an I^{18}O_i complex. In a similar way, the band at 895 cm^{-1} is found to be an ^{18}O isotope analog of the 936 cm^{-1} band, i.e., it is likely related to an I_2O_i defect. Both the bands (at 895 and 936 cm^{-1}) anneal out at about 350 K and their disappearance is accompanied by a decrease in intensity of the bands related to the A-center (see spectra (2) and (3) in Fig. 1b). Probably, the VO defect is the most efficient trap of I atoms released upon the I_2O_i dissociation.

It is worth mentioning that the observed oxygen isotopic shifts of the bands at 944, 956 and 936 cm^{-1} are typical for the asymmetrical stretching vibrations of divalent oxygen in Si. The data obtained may be useful when modeling the structure of IO and I_2O centers.

3.2. Interstitial carbon–oxygen related defects

One of the important findings of the present study is an observation of a number of new bands, appearing upon annealing of C_i (bands at 922 and 932 cm^{-1}) in the temperature range 270–300 K. The most intensive of them are located at about 925 and 967 cm^{-1} (see Fig. 2b). The newly observed defects are not very stable and start to anneal out at $T \geq 300$ K. Their disappearance results in a significant growth of the well-known band at 866 cm^{-1} related to the C_iO_i defect (e.g., see review [2] and references therein). It appears most likely that the new defects are precursors (some intermediate states) to a stable configuration of C_iO_i . Such a suggestion is in agreement with the results of previous DLTS studies [21], where a metastable configuration of this complex has been found. It should be noted that another well-known carbon-related defect, CsCi , is also formed via a metastable complex [2,22].

The bands at 925 and 967 cm^{-1} , according to their separation and relative intensities, are likely related to ^{18}O and ^{16}O vibrations in one of the C_iO_i metastable configurations. In such a configuration, the oxygen atom is probably two-coordinated (divalent) while in the most stable one, it is over-coordinated (trivalent) and gives rise to the band at 742 cm^{-1} [23]. The C_i -related bands are also expected for metastable C_iO_i states and there are some candidates. However, further studies are needed to identify them properly.

Acknowledgements

L.I.M. and L.J.L. thank TFR, KVA and SI in Sweden for financial support. The support from the Belarussian Republican Fund of Fundamental Research and from the grant INTAS-Belarus 97-0824 is also acknowledged.

References

- [1] G.D. Watkins, Mater. Sci. Forum 143–147 (1994) 9.
- [2] F. Shimura (Ed.), Oxygen in Silicon, Semiconductors and Semimetals, Vol. 42, Academic Press, London, 1994.
- [3] R. Jones (Ed.), Proceedings of the NATO Advanced Workshop on the Early Stages of Oxygen Precipitation in Silicon, Exeter, UK, 1996, NATO ASI Series 3, High Technology—Vol. 17, Kluwer, Dordrecht, 1996.
- [4] G. Davies, R.C. Newman, in: T.S. Moss (Ed.), Handbook on Semiconductors, Vol. 3b, Elsevier, Amsterdam, 1994, p. 1557.
- [5] B. Pajot, H. Compagnon, J. Lerouille, B. Clerjand, Physica B+C 117–118 (1983) 110.
- [6] A. Ourmazd, W. Schröter, A. Bourret, J. Appl. Phys. 56 (1984) 1670.
- [7] V.V. Voronkov, Semicond. Sci. Technol. 8 (1993) 2037.
- [8] P. Deak, L.C. Snyder, J.W. Corbett, Phys. Rev. B 45 (1992) 11612.

Table 1

Position and identification of the absorption bands observed in LT-irradiated Si: ^{16}O , ^{18}O , C

No.	Band position (cm^{-1})		Attribution
	^{16}O	^{18}O	
1	835.6	799.8	VO^0
2	885	846.7	VO
3	865.7		C_iO_i
4	1115.6		C_iO_i
5	956.2	914.7	IO_i
6	944.3	902.5	IO_i
7	935.6	895.3	I_2O_i
8	922.1		$^{12}\text{C}_i$
9	932.1		$^{12}\text{C}_i$
10	967.3	925.1	

- [9] R.E. Whan, *Appl. Phys. Lett.* 8 (1966) 131.
- [10] R.E. Whan, *J. Appl. Phys.* 37 (1966) 3378.
- [11] R.E. Whan, F.L. Vook, *Phys. Rev.* 153 (1967) 814.
- [12] A. Brelet, J. Charlemagne, in: J.W. Corbett, G.D. Watkins (Eds.), *Radiation Effects in Semiconductors*, Gordon and Breach, London, 1971, p. 161.
- [13] H.J. Stein, *Appl. Phys. Lett.* 55 (1989) 870.
- [14] H.J. Stein, in: J.W. Corbett, G.D. Watkins (Eds.), *Radiation Effects in Semiconductors*, Gordon and Breach, London, 1971, p. 125.
- [15] R.D. Harris, G.D. Watkins, in: L.C. Kimerling, J.M. Parsey Jr. (Eds.), *Proceedings of the 13th International Conference on Defects in Semiconductors*, Metallurgical Society of AIME, New York, 1985, p. 799.
- [16] Kh.A. Abdullin, B.N. Mukashev, Yu.V. Gorelkinskii, *Semicond. Sci. Technol.* 11 (1996) 1696.
- [17] B.N. Mukashev, Kh.A. Abdullin, Yu.V. Gorelkinskii, S.Z. Tokmoldin, *Mater. Sci. Eng. B* 58 (1999) 171.
- [18] L.I. Murin, V.P. Markevich, T. Hallberg, J.L. Lindstrom, M. Kleverman, J. Hermansson, B.G. Svensson, in: C.L. Claeys (Ed.), *Proceedings of the Second ENDEASD Workshop*, Kista-Stockholm, 2000, p. 248.
- [19] J. Hermansson, L.I. Murin, V.P. Markevich, T. Hallberg, J.L. Lindstrom, M. Kleverman, B.G. Svensson, *Physica B* 302–303 (2001) 188.
- [20] A. Baghdadi, et al., *J. Electrochem. Soc.* 136 (1989) 2015.
- [21] Kh.A. Abdullin, B.N. Mukashev, M.F. Tamendarov, T.B. Tashenov, *Phys. Lett. A* 144 (1990) 198.
- [22] S.P. Chappel, G. Davies, E.C. Lightowers, R.C. Newman, *Mater. Sci. Forum* 38–41 (1989) 613.
- [23] J. Coutinho, R. Jones, P.R. Briddon, S. Öberg, L.I. Murin, V.P. Markevich, J.L. Lindström, in: *Abstracts of the 21st International Conference on Defects in Semiconductors*, Giessen, 2001, p. 130.



ELSEVIER

Physica B 308–310 (2001) 462–464

PHYSICA B

www.elsevier.com/locate/physb

Divacancies in proton irradiated silicon: characterization and annealing mechanisms

R. Poirier*, S. Roorda, F. Schiettekatte, M. Lalancette, J. Zikovsky

Groupe de Recherche en Physique et Technologie des Couches Minces et Département de Physique, Université de Montréal, C.P. 6128 Succ. Centre-Ville, Montréal, Québec, Canada, H3C 3J7

Abstract

Annealing of divacancies produced by ion bombardment of crystalline silicon has been characterized using differential scanning calorimetry (DSC) and Fourier transform infrared absorption (FTIR). DSC at a rate of 40°C/min shows two clear peaks in the heat release, one at 140°C and the other at 240°C. The activation energies of these peaks were calculated assuming first order kinetics and found to be approximately 1.2 and 1.5 eV. The remaining fraction of divacancies with respect to annealing temperature was measured by FTIR and compared to the remaining fraction of defects calculated from the heat released in DSC. Annealing measurements are in agreement with previous work on electron and neutron irradiation of Si despite much higher defect concentrations. © 2001 Elsevier Science B.V. All rights reserved.

Keywords: Silicon; Divacancy; Ion implantation; Calorimetry; Annealing

1. Introduction

Despite more than three decades of work on vacancies and divacancies in crystalline silicon, some important aspects of these point defects are not completely known and understood. In particular, the formation energy of divacancies has yet to be measured experimentally. Our aim is to measure that formation energy. Several studies were conducted on electron irradiated Si [1]; however, defect concentrations were always much lower than in ion irradiated Si. In this paper we describe the preparation and characterization of Si samples with divacancy concentrations high enough to be used for such a measurement.

Divacancies are produced by bombardment with 8 MeV protons which have enough energy to completely go through the samples and produce defects without leaving residual hydrogen which would react very effectively with vacancy-type defects to produce unwanted point defects in our material [2,3]. The total amount of divacancies in an irradiated sample can be

measured using infrared absorption [1,4], electron spin resonance (ESR) [5], positron annihilation study (PAS) [6] and deep level transient spectroscopy (DLTS). However, a quantitative evaluation of the divacancy count in a sample is very difficult to achieve. We plan to eventually do this by establishing a correlation between these different methods. The heat released during a thermal anneal measured using differential scanning calorimetry (DSC) clearly indicates two annealing mechanisms of different activation energies. This raises questions about the annealing behaviour of divacancies that must be answered before we can evaluate their formation energy by simply taking the ratio of the heat released to the total number of divacancies in the sample.

2. Sample preparation and analysis techniques

The samples were cut from three types of $\langle 111 \rangle$ float-zone crystalline silicon manufactured by Wacker: nominally undoped Si which is in fact a high resistivity ($> 7000 \Omega \text{ cm}$) N-type crystal, N-type Si with a resistivity of about 60 cm and P-type Si with a resistivity of about

*Corresponding author. Fax: +1-514-343-6215.

E-mail address: poirier@lps.umontreal.ca (R. Poirier).

100 Ω cm. The dopant concentrations in the N-type and P-type samples are lower than $1 \times 10^{14} \text{ cm}^{-3}$ while oxygen and carbon impurities concentrations are lower than 1×10^{16} and $2 \times 10^{16} \text{ cm}^{-3}$, respectively. These are two orders of magnitude lower than the divacancy concentration in irradiated sample as measured by Fourier transform infrared absorption (FTIR).

High energy proton bombardment of silicon is used to create vacancies in the crystalline structure by displacing atoms. Vacancies have a high diffusivity at room temperature and can coalesce into divacancies [7]. To limit emitted radiation during and after the experiment, early bombardments were made with 3.5 MeV protons and the samples were thinned by mechanical polishing to 100 μm using SiC grinding disks to allow the protons to go through them. Reproducibility was difficult to obtain by this method and the thinning process was abandoned. We now rather use 8 MeV protons which have sufficient energy to go through 300 μm of Si while losing approximately 3.5 MeV in the sample. Samples are irradiated to a fluence of $5 \times 10^{16} \text{ ion/cm}^2$ with a beam current below 750 nA rastered over an area of 9 cm^2 , thus keeping the areal power density below 0.3 W/cm^2 . Furthermore, the samples are kept at liquid nitrogen temperature (77 K) during bombardment to avoid dynamical annealing of vacancies. After bombardment the samples are allowed to warm to room temperature and cut in pieces of approximately $5 \times 5 \text{ mm}^2$.

The irradiation damage was characterized with a Bomem DA3 Fourier transform infrared spectrometer with a CaF_2 beamsplitter and liquid-nitrogen-cooled MCT detector. A broad absorption peak around 1.8 μm associated with the divacancy [1,4] was observed in all irradiated samples. The absorbance (αd) of the 1.8 μm band, defined as the logarithm of the ratio of the sample intensity and of a reference intensity of an unirradiated sample measured under identical conditions, can be related to the areal density of divacancies (N_{vv}) in our sample using the criterion developed by Stein and co-workers [4] by the equation $N_{\text{vv}} = (\alpha d) 7.7 \times 10^{16} \text{ divacancies/cm}^2$.

The heat released during annealing of the radiation damage was monitored with a Perkin-Elmer DSC7 differential scanning calorimeter flushed with dry argon gas [8,9]. Two or three pieces of bombarded Si were stacked together in the sample pan of the DSC while the same number of unirradiated Si were loaded in the reference pan. Three identical scans from 20°C to 400°C at a rate of 40°C/min were made for each measurement, preceded and followed by an isotherm of several minutes to allow the calorimeter to stabilize. The difference between the first and second scan represents the heat released by defect annealing in the sample, while the third scan allowed us to ensure that the baseline remained constant between consecutive scans.

3. Results and discussion

Fig. 1 presents a DSC scan of two irradiated samples at a rate of 40°C/min. Two peaks are clearly observable, one at 140°C and the other at 240°C, thus identifying two distinct annealing mechanisms for divacancies in c-Si. Assuming first order kinetics and a constant prefactor of 15 THz, a typical phonon frequency in silicon, the activation energies of these processes are found to be approximately 1.2 and 1.5 eV. The positions of the peaks varies with scanning rate but the calculated activation energies remain constant. The values of these activation energies are bound to change depending on the validity of our assumptions which remain to be checked through isothermal annealing. Nevertheless, the activation energy of 1.2 eV agrees closely with values obtained from neutron and electron irradiation of silicon and is associated with the onset of divacancy migration [1,10]. The second mechanism remains to be identified, however it could be due to divacancy dissociation. The heat released may be integrated to yield the evolution of the divacancy concentration as shown in Fig. 2. Of course, by doing so we assume that the heat released is only due to divacancies, and that there is no contributions from simultaneously annealing interstitials, for example.

The divacancy concentration in ion irradiated samples, as measured by FTIR, is approximately 10^{18} cm^{-3} , while it was about 10^{15} cm^{-3} for electron irradiated Si with similar fluences [5]. Fig. 2 shows the fraction of remaining divacancies as measured by FTIR and calculated from the DSC curve from Fig. 1. The samples in the first set (open symbols) were thinned to 100 μm

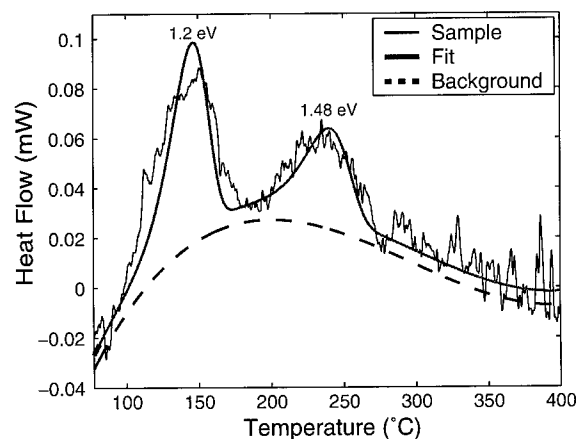


Fig. 1. DSC scan of two irradiated samples at a rate of 40°C/min. Two peaks are clearly observable, one at 140°C and the other at 240°C. Activation energies of 1.2 and 1.5 eV for the two processes respectively are obtained by fitting the peaks using first order kinetics and a constant prefactor of 15 THz.

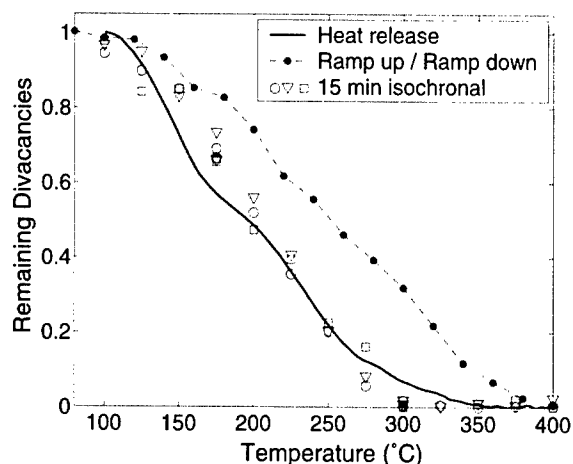


Fig. 2. Remaining fraction of divacancies as measured by FTIR and calculated from the DSC curve from Fig. 1. (A) Open symbols: 100 μm samples bombarded with 3.5 MeV protons annealed 15 min at the indicated temperature. (B) Solid circles: 300 μm samples bombarded with 8 MeV protons scanned from 20 °C to the temperature T and back at a rate of 80 °C/min. The dotted line is only a guide for the eye. (C) Solid line: remaining fraction of divacancies calculated by integrating the DSC curve in Fig. 1, assuming that the heat released is entirely due to divacancy annihilation.

and bombarded with 3.5 MeV protons before being annealed 15 min at the indicated temperature. No discernable difference between the three types of silicon can be observed. This either indicate that dopants concentration ($<10^{14} \text{ cm}^{-3}$) is too low to have an influence on the annealing mechanism or that they do not play a significant role in divacancy annihilation behaviour. This curve is comparable to the annihilation curve of neutron damage in silicon [10] even though defect concentrations were several orders of magnitudes higher in this study.

For the second set of data (filled circles), the samples were scanned in temperature from 20 °C to the temperature T and immediately cooled at a rate of 80 °C/min. The sample therefore received an equivalent thermal treatment and the results could then be directly compared to the third set of data (solid line) calculated by integrating the DSC curve in Fig. 1. If the heat released during annealing is entirely due to divacancies and if the 80 °C/min scan and DSC are equivalent, the second and third data set would coincide. Since they do not, either the kinetics are different or another process is emitting heat in the irradiated samples. This heat release

could be associated with the background shown by the dotted line in Fig. 1 and must be related to annihilation of defects not visible by FTIR.

4. Conclusions

DSC measurements clearly show two distinct peaks in the heat released during annealing of proton irradiated silicon. The activation energies of these peaks were calculated assuming first order kinetics and found to be approximately 1.2 and 1.5 eV. The remaining fraction of divacancies with respect to annealing temperature was measured by FTIR and compared to the remaining fraction of defects calculated from the heat released in DSC. This comparison appears to indicate that the heat released during annealing is in part due to defects other than the divacancy. Our annealing measurements are in agreement with previous work on electron and neutron irradiation of Si in spite of much higher defect concentrations.

Acknowledgements

Many thanks to Réal Gosselin and Louis Godbout for their help with the accelerator. This work was made possible by grants from the Natural Sciences and Engineering Research Council of Canada (NSERC) and Le Fond pour la Formation de Chercheurs et l'Aide à la Recherche du Québec (FCAR).

References

- [1] L.J. Cheng, J.C. Corelli, J.W. Corbett, G.D. Watkins, *Phys. Rev.* 152 (1966) 761.
- [2] S.T. Picraux, F.L. Vook, H.J. Stein, *Inst. Phys. Conf. Ser.* No 46 (1979) 31.
- [3] B.N. Mukashev, S.Z. Tokmoldin, M.F. Tamendarov, V.V. Frolov, *Physica B* 170 (1991) 545.
- [4] H.J. Stein, F.L. Vook, D.K. Brice, J.A. Borders, S.T. Picraux, *Radiat. Eff.* 6 (1970) 19.
- [5] G.D. Watkins, J.W. Corbett, *Phys. Rev.* 138 (1965) A543.
- [6] S. Szpala, P.J. Simpson, *J. Appl. Phys.* 89 (2001) 5991.
- [7] A. Bongiorno, L. Colombo, *Phys. Rev. B* 57 (1998) 8767.
- [8] S. Roorda, G. Kajrys, J. Graham, *Nucl. Inst. Phys. Res. B* 90 (1994) 412.
- [9] S. Roorda, *Mater. Res. Soc. Symp.* 316 (1994) 159.
- [10] L.J. Cheng, J. Lori, *Phys. Rev.* 171 (1968) 856.



ELSEVIER

Physica B 308–310 (2001) 465–469

PHYSICA B

www.elsevier.com/locate/physb

Do we know the energy levels of radiation defects in silicon?

L.F. Makarenko

*Department of Applied Mathematics and Computer Science, Belarus State University, F. Skaryna Avenue 4,
220050 Minsk, Belarus*

Abstract

The validity of a single-level model to interpret temperature dependences of charge carrier concentration in n-Si crystals irradiated by ^{60}Co gamma-rays is investigated. It is shown that the consideration of a vacancy–oxygen complex (A-center) in silicon as an isolated monovalent defect with energy level close to $E_c - 0.17\text{ eV}$ does not allow to describe adequately Hall effect data for crystals in which the A-center is dominant. From carbon related complexes the single-level model is adequate only for interstitial carbon C_i . The explanation of experimental data for a $C_i - C_s$ complex requires more complex models. The acceptable description of experimental dependences of $n(T)$ can be achieved only within the framework of various two-level models. However, the acceptance of any of them entails a conclusion that the investigated radiation defects are coupled in pairs even at very low irradiation fluences. © 2001 Elsevier Science B.V. All rights reserved.

Keywords: Silicon; Radiation defects; Energy levels

1. Introduction

For high-energy physics, particle detectors are required that keep their efficiency even when the concentration of radiation defects exceeds 100 times the concentration of doping impurity in weakly doped regions of the detector. It stimulated intensive investigations of radiation damage of detector-grade silicon (see review [1] and references therein). It would seem that the problem to develop prognostic models quantitatively predicting changes of performance characteristics of detectors under irradiation is quite easy. This opinion can be based on the knowledge accumulated over more than 40 years of development of radiation physics of silicon. Many efforts were spent for studies of detectors by deep level transient spectroscopy. Nevertheless, being based on the obtained data, it was not possible to establish a prognostic model which included as initial parameters, at first, defect concentration, entropy (ΔS_i) and enthalpy (ΔH_i) of ionization, capture cross-sections of charge carriers and, secondly, used known methods of

processes simulation in semiconductor devices. The models developed till now have a semi-empirical character [1]. This, in our opinion, can be related to incompleteness of radiation defect models. So, for example, for an oxygen–vacancy complex (A-center), two models have been suggested. The first model, which is generally accepted from the very beginning of radiation physics of silicon, describes the A-center as a defect with an acceptor level near to $E_c - 0.17\text{ eV}$ [2]. In Ref. [3] on the basis of magnetic spectroscopy data it was substantiated that the A-center is an amphoteric defect with an acceptor level near to $E_c - 0.17\text{ eV}$ and donor level near to $E_c - 0.76\text{ eV}$. Besides this it is necessary to take into account that the changes of characteristics of irradiated silicon detectors are due to the combined effect of several defects with close levels. For n-type silicon such defects are the oxygen–vacancy complex (V–O) and an interstitial carbon–substitutional carbon complex ($C_i - C_s$) which have their acceptor levels close to $E_c - 0.17\text{ eV}$ [4]. In this case it is difficult to establish what defect determines the kinetics of degradation processes in detectors and to optimize their radiation tolerance. Therefore, at present there is a problem of developing methods to test models of

E-mail address: makarenko@fpm.bsu.unibel.by
(L.F. Makarenko).

radiation defects in silicon and extract their parameters necessary for the following simulation of detector performance under irradiation.

2. Experimental results and discussion

Temperature dependences of the charge carrier concentration for silicon crystals irradiated with Co-60 gamma-rays are shown in Fig. 1. Czochralski-grown (oxygen-rich) and float-zone (oxygen-free) crystals were used (parameters of samples and details of experiment are described in Refs. [5,6]). For a preliminary estimation of occupancy levels for radiation defects under study it is possible to use differential curves (Fig. 2). One can see in the Czochralski-grown crystals a center with a level close to $F_{1\max} = E_c - 0.18\text{ eV}$ labeled here as $E \times (0.18)$. In the float-zone crystals a center with a level close to $F_{2\max} = E_c - 0.12\text{ eV}$ ($E(0.12)$) appeared immediately after irradiation at 200 K. After annealing at 375 K it disappeared and the appearance of a new defect $E(0.16)$ is observed.

The behavior of both types of crystals is familiar and well-known from the literature. In oxygen-rich silicon the oxygen-vacancy complex (the A-center) is formed. The concentration of other defects is negligibly small.

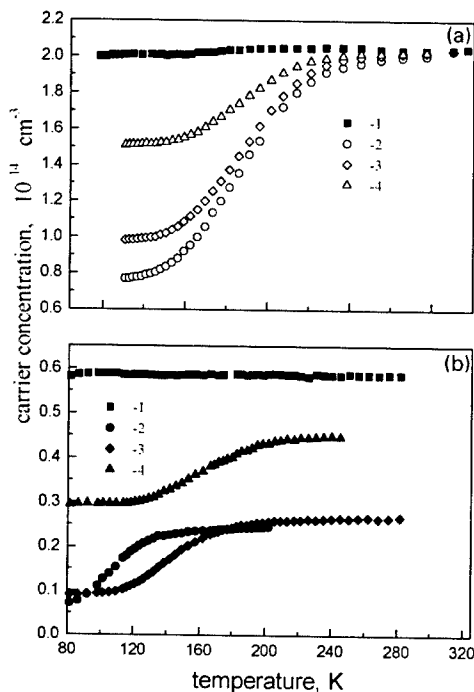


Fig. 1. Temperature dependences of the carrier concentration in n-Si with high (a) and low oxygen content (b): 1—as-grown crystals, 2—after gamma-irradiation, and 3,4—after subsequent annealing at different temperatures.

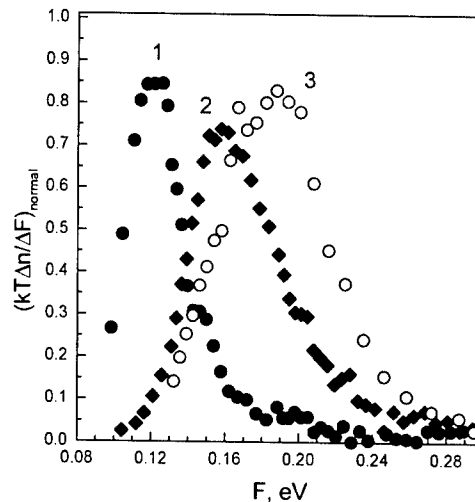


Fig. 2. Dependences of Δ_H on the distance (F) between the conduction band bottom (E_c) and the Fermi level (E_F) for interstitial C_i (1) and C_i-C_v (2) calculated from the 2nd and 3rd curves of Fig. 1(b), for O-V (3) complex calculated from curve 2 of Fig. 1(a).

The A-center is annealed at $T > 300^\circ\text{C}$. Formation of new electrically active defects is not observed with Hall-effect measurements. In oxygen-free crystals interstitial carbon (C_i) with occupancy level at $E_c - 0.12\text{ eV}$ ($E(0.12)$) and a phosphorus-vacancy complex (E-center) with an occupancy level at $E_c - 0.4\text{ eV}$ are observed after low temperature irradiation. At temperatures higher than 300 K, C_i becomes mobile. Migrating in the lattice it is trapped by a substitutional carbon atom (C_s). As the result a C_i-C_s complex with an energy level of $E_c - 0.16\text{ eV}$ is formed. As the annealing temperature is raised to 400 K, the E-center starts to anneal and the charge carrier concentration is increased. Simultaneously the concentration of $E(0.16)$ decreases, and the new defect with an energy level of $E_c - 0.20\text{ eV}$ ($E(0.20)$) appeared. The different amplitudes of the $\Delta_H(F)$ graphs in Fig. 2 are explained within the framework of a single-level model as due to different values of ionization entropy of the defects (ΔS_i). The less ΔS_i , the lower the maximum value of $\Delta_H(F)$.

It seems that the best way to estimate the adequacy of models used for interpretation of Hall effect data is the method of least squares with the subsequent analysis of residuals. Different suggestions on numbers of simultaneously ionized defects and of their charge states were used in this work. Concentration of charge carriers can be calculated from the neutrality equation. When in a semiconductor two simple centers (N_γ and N_β) and an amphoteric (N_i) center are available this equation reads

$$N_{\text{net}} = n + N_\gamma f_1(T, F, X_\gamma) + N_\beta f_1(T, F, X_\beta) + N_i f_2(T, F, X_i), \quad (1)$$

where f_1 and f_2 are occupation functions of single- and two-level centers, respectively, \mathbf{X} is a vector, whose components are ionization entropies and enthalpies of the centers (S_i, H_i , etc.).

The simplest of the used models is a single-level one when the change of carrier concentration with temperature is due to ionization of one simple monovalent defect ($N_\alpha \neq 0, N_\beta = 0, N_\gamma = 0$). The second model, utilized by us, is two-level I, in which ionization of two simple defects with close levels is considered ($N_\alpha \neq 0, N_\beta \neq 0, N_\gamma = 0$). The third model is two-level II when ionization of one divalent center takes place ($N_\alpha = 0, N_\beta = 0, N_\gamma \neq 0$).

The application of least squares method to Hall effect data consists in finding the minimum value of objective function

$$Q(\mathbf{X}) = \sum_i \left(\frac{n_{\text{fit}}(T_i, \mathbf{X}_N) - n_{\text{exp}}(T_i)}{n_{\text{fit}}(T_i, \mathbf{X}_N)} \right)^2 = \sum_i \delta_i^2, \quad (2)$$

where \mathbf{X}_N is the \mathbf{X} vector extended with concentrations of centers ($N_\alpha, N_\beta, N_\gamma$). The $n_{\text{exp}}(T_i)$ quantity is experimentally measured value of carrier concentration at the temperature of T_i , and $n_{\text{fit}}(T_i)$ is a value calculated from the appropriate neutrality equation setting temperature as T_i , and parameters of defects as \mathbf{X} . Secondly, after finding the minimum of the objective function the analysis of an error distribution of measurements is carried out.

Residuals included in Eq. (2) can be represented as $\delta_i = \delta_{i\text{random}} + \delta_{i\text{bias}}$. A random component $\delta_{i\text{random}}$ is connected to fluctuations of the current and Hall voltage during measurements. The biases determine the value of $\delta_{i\text{bias}}$ (for more extended discussion of errors see Ref. [5]). As measurements of n_{exp} at every temperature T_i are independent from each other, random component of residual is dominant and the graph $\delta_i(T)$ will look like a random variable with zero mean and approximately equal numbers of positive and negative values. If the model used to interpret experimental data is not true then a trend (nonrandom component) in $\delta_i(T)$ appears.

For the A-center first of all we estimate applicability of the single-level model with parameters determined by Wertheim in Ref. [7]: $\Delta H_i = 0.160$ eV and $\Delta S_i = -1.3$ k eV/K. As obvious from Fig. 3 (curve 2) this model results in too large values δ_i and a nonrandom course of the $\delta_i(T)$ dependence. The application of the single-level model with minimization of all parameters gives estimations of $\Delta H_i = 0.145$ eV and $\Delta S_i = -2.3$ k eV/K (the scattering of their experimental values is shown in Fig. 4) which agree with the results obtained in Ref. [8] for low irradiation doses. However, the estimated value of ionization enthalpy does not agree with the value $\Delta H_i = 0.17$ eV determined from measurements of strongly compensated crystals [8].

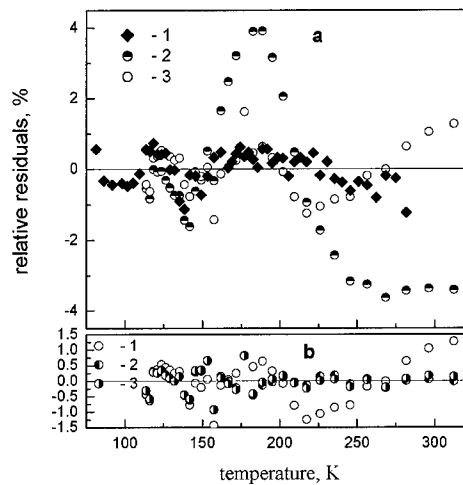


Fig. 3. Temperature dependences of relative residuals $\delta(T)$ for fitting by single-level (a) and two-level (b) models. Curve 1 (a) represents residuals for the C_1-C_8 . Other data are for the A-center. For additional explanations see the text.

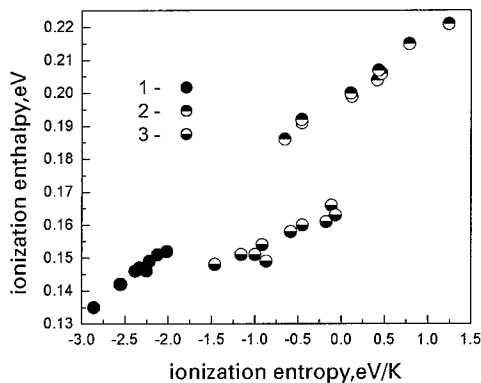


Fig. 4. Entropies and enthalpies of the A-center ionization estimated by the single- (1) and two-level II (2,3) models.

Distribution of residuals is not random (Fig. 3(a), curve 3) and their values are more than expected ones [5]. It allows us to draw a conclusion on inapplicability of the single-level model to describe occupancy function of the A-center.

Both two-level models result in much smaller values of residuals (Fig. 3(b), curves 2 and 3). The following parameters of defects are obtained. For two-level model I they are $\Delta S_i = (-0.3 \pm 0.7)$ k eV/K, $\Delta H_i = 0.159 \pm 0.009$ eV, $\Delta S_i = (+0.8 \pm 0.4)$ k eV/K, $\Delta H_i = (0.201 \pm 0.011)$ eV. For two-level model II: $\Delta S_{i42} = (-0.7 \pm 0.5)$ k eV/K, $\Delta H_i = (0.156 \pm 0.006)$ eV, $\Delta S_{i41} = (+0.2 \pm 0.6)$ k eV/K, $\Delta H_i = (0.202 \pm 0.011)$ eV. According to the values of residuals, both models are acceptable.

While analyzing data for interstitial carbon $E(0.12)$ it is necessary to take into account that in float-zone crystals along with carbon related centers the A-center can be also formed. Though in such crystals its concentration is small, its presence reveals in a high-temperature tail of $\Delta_i(F)$ dependence (Fig. 2, curve 1). Therefore, two-level model with fixed parameters of one defect (A-center) is to be used for data analysis. In following, this model is called a quasi-single-level model.

For C_i the values $\Delta H_i = 0.114$ eV and $\Delta S_i = -0.7$ kJ/K are obtained. The value of ionization entropy is equivalent to a degeneracy factor of $g = \frac{1}{2}$ as expected from the data of electron spin resonance experiments. The value of ionization enthalpy perfectly coincides with the activation energy of electron emission from $E(0.12)$ measured in Ref. [9]. So the occupancy function of C_i is well described by single-level model.

For the C_i-C_s complex the quasi-single-level model also results in small values of residuals (Fig. 3(a), curve 1). Estimated values for the defect parameters are $\Delta H_i = 0.125$ eV and $\Delta S_i = -3.2$ kJ/K. They do not agree however with the data obtained in other papers [4]. In our opinion such a small value of ionization entropy cannot be explained theoretically. More extended analysis of the Hall data for float-zone silicon will be published later [6].

Thus, it is possible to make a conclusion that from all the considered centers only interstitial carbon behaves as a simple monovalent defect. More studies are required to establish the actual models for the V–O and C_i-C_s complexes.

Till now all experimental data concerning the A-center in silicon were interpreted within the framework of a single-level model. A more or less consistent picture was developed to describe changes of electrical characteristics of the irradiated Czochralski-grown silicon. However, some experimental data are not satisfactorily explained within the framework of the single-level model. First of all those are the data on changes of ESR signal intensity of the A-center with irradiation fluence [5]. The application of the two-level models provides new capabilities to solve such problems.

It is necessary to select the most adequate model from the suggested ones. Both models suit to interpret the obtained Hall-effect data. But, as shown in Ref. [5] within the framework of the model of two independent defects it is difficult to achieve the agreement with data obtained by other methods. That is, the model of two coupled levels is preferable. However within the framework of this model two different assumptions on properties of the A-center are possible. The first one is the assumption of the amphoteric character of the A-center which was made in Ref. [5]. The second assumption is less obvious. As is known from studies of amorphous silicon [10], a pair of simple defects

behaves similarly as a divalent center and is characterized by just the same occupancy function. So one can interpret our data with an assumption that all the A-centers are coupled in pairs. Let us note that this assumption better agrees to the generally accepted mechanism of V–O complex annealing [11]. However, it requires a suggestion of a possible coupling mechanism.

However the acceptance of the second assumption needs finding a mechanism of pair correlation of these radiation defects. As shown above, one possible interpretation of the obtained data is the assumption that the A-centers are coupled in distant pairs. However it appears that the model of an amphoteric defect also entails the requirement about a pair correlation of radiation defects [5].

In general on the basis of all available data it is impossible to decide, which of the offered models is most adequate. To solve this problem more extensive studies with application of different experimental techniques are demanded.

3. Conclusion

In this paper radiation defects in silicon crystals irradiated with gamma-rays Co-60 are investigated using Hall effect measurements. The oxygen–vacancy complex prevails in the crystals with high oxygen content and carbon related centers (interstitial carbon C_i and pair C_i-C_s) are dominant in oxygen-free crystals.

With use of a least squares method, the validity of the single-level model to describe the occupation function of these defects is tested. It is established that this model can satisfactorily describe only the data for C_i . For the two other centers it is necessary to apply different two-level models. To come to an agreement of any of the two-level models with other data the assumption about a pair correlation of radiation defects in silicon is required.

However, the available data on the occupancy levels of the O–V and C_i-C_s complexes cannot be unambiguously interpreted.

Acknowledgements

This work was supported in part by Belarusian Republican Foundation for Fundamental Research Grant No. F00-226. The author thanks the Organizing Committee of the ICDS-21 for support of his participation in the Conference.

References

- [1] G. Lindstrom, et al., *Nucl. Instr. and Meth. A* 426 (1999) 1.

- [2] G.D. Watkins, J.W. Corbett, Phys. Rev. 121 (1961) 1001.
- [3] A.M. Frens, et al., Phys. Rev. Lett. 72 (1994) 2939.
- [4] L.W. Song, et al., Phys. Rev. B 42 (1990) 5765.
- [5] L.F. Makarenko, Semicond. Sci. Technol 16 (2001) 619.
- [6] L.F. Makarenko, Fiz. Tekhn. Poluprovodn, to be published.
- [7] G.K. Wertheim, Phys. Rev. 110 (1958) 1272.
- [8] E. Sonder, L.C. Templeton, J. Appl. Phys. 31 (1960) 1279.
- [9] J. Walker, C.T. Sah, Phys. Rev. B 7 (1973) 4587.
- [10] M.H. Brodsky (Ed.), Amorphous Semiconductors, Springer, Berlin, 1979.
- [11] J.W. Corbett, et al., Phys. Rev. A 135 (1964) 1381.



ELSEVIER

Physica B 308–310 (2001) 470–473

PHYSICA B

www.elsevier.com/locate/physb

Dopant interaction with a dislocation in silicon: local and non-local effects

Alex Antonelli^a, João F. Justo^{b,*}, A. Fazzio^c

^a Instituto de Física “Gleb Wataghin”, Universidade Estadual de Campinas, CP 6165, CEP 13083-970, Campinas, SP, Brazil

^b Departamento de Engenharia de Sistemas Eletrônicos, Escola Politécnica da Universidade de São Paulo, CP 61548, CEP 05424-970, São Paulo, SP, Brazil

^c Instituto de Física da Universidade de São Paulo, CP 66318, CEP 05315-970, São Paulo, SP, Brazil

Abstract

We performed a theoretical investigation on the interaction of arsenic impurities with a 30° glide partial dislocation in silicon. Our calculations were performed by ab initio total energy methods, based on the density functional theory and the local density approximation. We find that an arsenic atom, in a crystalline position, gives away one electron to the dislocation, becoming positively charged while the dislocation core is negatively charged. The interaction between arsenic and the core is essentially electrostatic, which leads to arsenic segregation. © 2001 Elsevier Science B.V. All rights reserved.

Keywords: Extended defects; Segregation; Dislocation

Dislocations are extended defects which are present in most crystalline solids. In semiconductors, they play an important role in the electronic properties of the material [1]. When dislocations are present in the active regions of the electronic devices, they give rise to leakage currents, as a result of dopant diffusion along the dislocation cores. On the other hand, dislocations are sometimes intentionally introduced far from the device active region to serve as sinks to undesirable impurities. In such context, the interaction of dislocations with point defects has received great attention recently [2,3].

In silicon, as well as in other zinc-blende semiconductors, dislocations generally belong to the {111} glide sets [4], lying along the $\langle 110 \rangle$ directions. It is energetically favorable for (screw and 60°) dislocations to dissociate into (30° and 90°) partial dislocations, with a stacking fault between the partials [5]. Dislocations move conservatively by thermally assisted formation and propagation of kinks [6], with the dislocation

velocity given by [4]:

$$v_d = v_0 \exp\left(-\frac{Q}{k_B T}\right), \quad (1)$$

where v_0 is a constant, Q is the activation energy, and k_B is the Boltzmann constant. Dopants can alter this dislocation activation energy. While $Q = 2.2$ eV in undoped silicon, it may decrease by as much as 0.5 eV [7,8] in n-type doped silicon. On the other hand, in p-type silicon, high concentrations of acceptor impurities increase the activation energy.

The interaction between dislocations and dopants could manifest itself as a non-local or as a local effect. The non-local effect results from the displacement of the Fermi level due to donor and acceptor doping. According to that model, the increase (decrease) in the dislocation mobility is a result of negatively (positively) charged dislocation cores, which decrease (increase) kink formation and migration energies [9]. The local effect would be the result of segregation of impurities in the dislocation core. For the dislocations to move, they should first break away from the impurity clouds which form in and around the dislocation cores. Therefore, dopant segregation towards the dislocation core controls

*Corresponding author. Tel.: +55-11-3818-5256; fax: +55-11-3818-5585.

E-mail address: jjusto@lme.usp.br (J.F. Justo).

the dislocation pinning. Measurements have shown that the binding energies of impurities in the dislocation core are as large as 0.5 eV [10].

Here, we have used *ab initio* total energy calculations [11,12] to investigate the arsenic interaction with the core of a 30° partial dislocation in silicon. We used a reference orthorhombic periodic simulation cell with 192 atoms, in which a 30° partial dislocation dipole was introduced by displacing the atoms according to the solution for the displacement field of a dislocation [4]. Fig. 1 shows the simulation cell from three different side views. The cell geometry is such that the dislocations of the dipole are four lattice parameters apart along a $\langle 112 \rangle$ direction (about 13.5 \AA) in the glide plane, which is enough to prevent core–core interactions. Arsenic atoms were introduced in different sites of the simulation cell. Of particular interest was the arsenic segregation energy, i.e., the total energy difference between a configuration with the arsenic impurity in a crystalline site (the farthest position away from the dislocation core) and one with the arsenic sitting inside the dislocation core [3].

Our calculations were performed by a two-step relaxation procedure, first using an empirical potential and later *ab initio* methods. For the configurations shown in Fig. 1, we initially relaxed the atomic positions using an empirical potential [13,14] combined with a conjugate gradient minimization method. The output configurations were used as input to the *ab initio* calculations, where the atomic relaxation was based on the Hellmann–Feynman forces. The initial relaxation, based on the empirical potential, saved considerable computational effort in the *ab initio* calculations, by releasing most of the stress generated by the disloca-

tions. The *ab initio* calculations were performed within the density functional theory in the local density approximation. The Kohn–Sham equations for the electrons of the system were solved using the Car–Parrinello method [12,15] with norm-conserving pseudopotentials [16,17]. The electronic wave functions were expanded in a plane-wave basis-set with kinetic energy up to 12 Ry. The sampling in the Brillouin zone was performed using the Γ -point. Atomic relaxations were performed until the Hellmann–Feynman forces were smaller than 0.02 eV/\AA in all atoms.

We first considered a configuration with the arsenic impurity in a crystalline-like position, the farthest position (inside the simulation cell) away from the dislocation core. This configuration is indicated by atomic position number 1 in Fig. 1a. For such configuration, we observed that the arsenic impurity gives away one electron becoming positively charged. This charge is captured by the dislocation core, occupying a dislocation-related level [18]. In a reconstructed core, the first unoccupied level has a spatial dispersion inside the dislocation line, with an antibonding character with relation to the reconstructed dimers. As a result, the dislocation core will become negatively charged. These results are in agreement with recent measurements which found that dislocation cores are negatively charged in doped semiconductors [19]. The arsenic segregation energy was computed by comparing the total energies between configurations with the arsenic in the crystalline environment (position 1) and in the dislocation core (position 2). We find a segregation energy of 0.18 eV. This result is consistent with other theoretical investigations on arsenic interaction with a 90° partial dislocation, in which segregation energy of about 0.15 eV was found [20].

The interaction leading to arsenic segregation in the dislocation core is typically electrostatic. This interaction may be interpreted within a donor–acceptor model, or an ionic model [21]. In that case, the acceptor level is the dislocation-related antibonding level and the donor is the arsenic level. The donor level inside the materials gap is shifted deeper in the gap, and therefore deactivated, by the interaction with the acceptor. The donor level (E_d) inside the materials gap is given by [21]

$$E_d = E_\infty + E_{el} + E_c, \quad (2)$$

where E_∞ is the donor level for the isolated arsenic, E_{el} is the elastic interaction of the arsenic with the host lattice, and E_c is the Coulomb interaction between the negatively charged dislocation core and the positively charged donor. The shift in the donor level (with relation to the isolated arsenic) is

$$\Delta E_d = \Delta E_{el} + \Delta E_c. \quad (3)$$

We found that the arsenic presence distorts only slightly the lattice in either a crystalline site or inside the

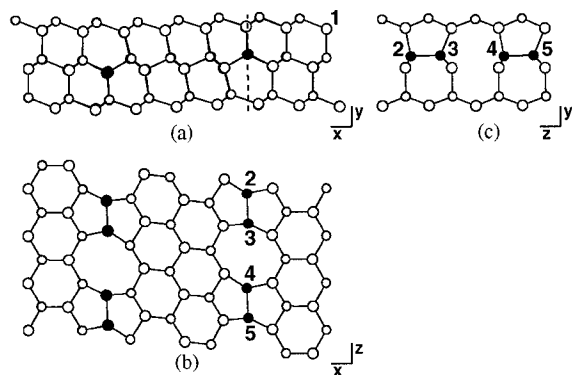


Fig. 1. Atomic configuration of a dislocation in the $\{111\}$ glide plane. x , y , and z axes are respectively parallel to the $[1\bar{1}2]$, $[111]$, and $[\bar{1}10]$ directions of the zinc-blende lattice. The figure shows three configuration side views: (a) a plane normal to the dislocation line (xy -plane), (b) the glide plane where the dislocation belongs to (xz -plane), and (c) the plane along the dashed line (zy -plane).

dislocation core, as compared to the respective atomic configurations without arsenic. Arsenic in position 1 (Fig. 1) does not break the local symmetry, only relaxing the first neighbors to 2.40 Å, compared to 2.35 Å for the crystalline interatomic distance in Si. Arsenic in position 2 also keeps the symmetry of the dislocation core dimer. Distance in the dimer (2, 3) changes from 2.45 Å in pure silicon to 2.50 Å with the arsenic impurity in position 2. Elastic interaction between arsenic and the lattice is negligible. Therefore, we can assume that $\Delta E_{\text{el}} \approx 0$, and the shift of the donor level essentially results from a Coulomb interaction [22]. In that sense, we speculate that the shift in the donor level is essentially determined by the arsenic segregation energy.

Table 1 presents the segregation energies for arsenic atoms and arsenic pairs. It is energetically favorable for an arsenic pair to segregate in the dislocation core, sitting in (2, 3) atomic positions. However, once the arsenic pair is in the dislocation core, it is energetically favorable that this pair dissociates, with the arsenic sitting in (2, 4) positions. Since the two arsenic atoms in the dislocation core are isoelectronic, they repel each other by a Coulomb interaction, lowering the total energy of the system. Fig. 2 shows the total electronic charge distribution for the dislocation containing one arsenic or one arsenic pair in the dislocation core. When arsenic atoms are paired in the dislocation core they keep a reconstruction-like configuration, although they are weakly bonded. This configuration is consistent

Table 1

Total energy change (E_{seg}) in the system for arsenic segregation in the dislocation core, and the distance between arsenic and its first neighbors. The first column shows the position of the arsenic atoms (according to Fig. 1). For a single arsenic, distances (d) are from its first neighbors, while for arsenic pairs distances are between the two arsenic. Energies are given in eV and distances in Å

	E_{seg}	d
(1)	0.00	2.40
(2)	−0.18	2.50
(1, 1*)	0.00	
(1, 2)	−0.67	
(2, 3)	−0.72	2.62
(2, 4)	−1.09	2.50

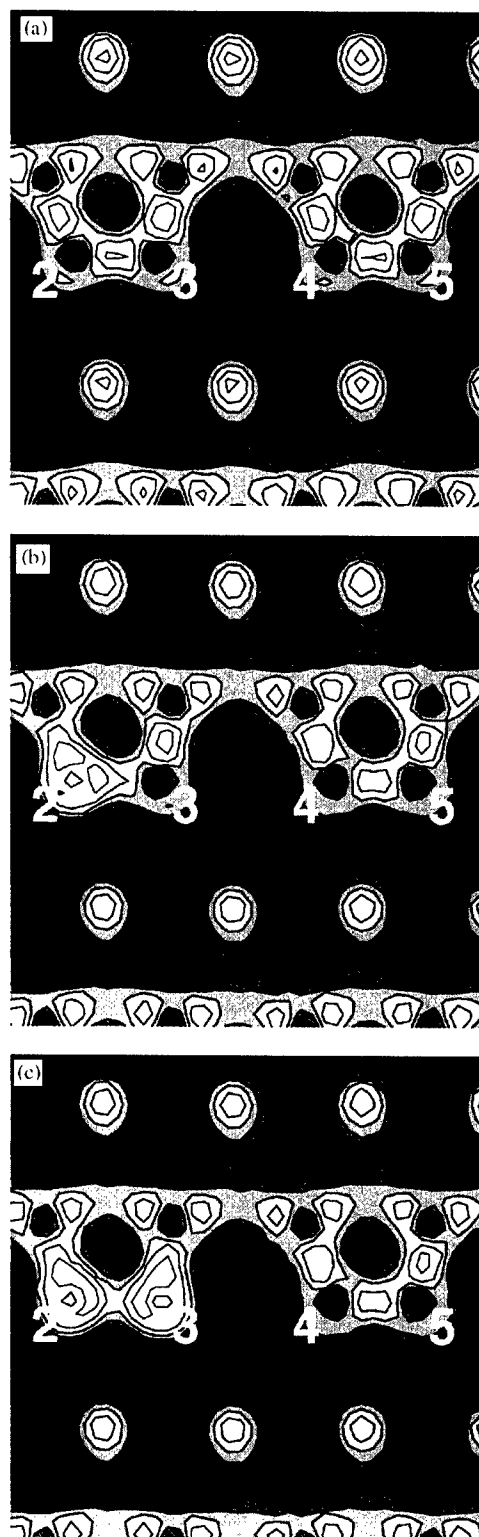


Fig. 2. Electronic charge distribution in the xy -plane (as shown in Fig. 1c): (a) total charge distribution for the pure silicon system with the reconstruction core bond (as represented by bonds between atoms 2 and 3 and between atoms 4 and 5); (b) total charge distribution of the system containing one arsenic atom in the dislocation core; and (c) total charge distribution of the system containing an arsenic pair in the dislocation core.

with arsenic pair segregation in grain boundaries in silicon [23].

In summary, we have investigated the electronic and structural properties of arsenic interaction with the core of a 30° partial dislocation. Our results on segregation towards the 30° partial dislocation is consistent with theoretical investigations on dopant segregation in other extended defects in silicon [3,23,24] and in gallium arsenide [25]. We also find that when an arsenic impurity is near the dislocation core, there is charge transfer from the arsenic to the dislocation, leaving the dislocation core negatively charged [19]. As a result, the dislocation Fermi level is raised by the arsenic presence. Although this is consistent with experimental findings, we still cannot elaborate on the role of this effect in the energetics of kink formation and migration [9].

Acknowledgements

This work was supported by Brazilian agencies CNPq and FAPESP. Calculations were performed using the computational facilities of the CENAPAD-São Paulo.

References

- [1] R. Labusch, W. Schröter, in: F.R.N. Nabarro (Ed.), *Dislocations in Solids*, Vol. 7, North-Holland, Amsterdam, 1980, p. 127.
- [2] J.F. Justo, M. de Koning, W. Cai, V.V. Bulatov, *Phys. Rev. Lett.* 84 (2000) 2172.
- [3] T. Kaplan, F. Liu, M. Mostoller, M.F. Chisholm, V. Milman, *Phys. Rev. B* 61 (2000) 1674.
- [4] J.P. Hirth, J. Lothe, *Theory of Dislocations*, Wiley, New York, 1982.
- [5] A. Olsen, J.C.H. Spence, *Philos. Mag. A* 43 (1981) 945.
- [6] V.V. Bulatov, J.F. Justo, W. Cai, S. Yip, A.S. Argon, T. Lenosky, M. de Koning, T. Diaz de la Rubia, *Philos. Mag. A* 81 (2001) 1257.
- [7] J.R. Patel, A.R. Chaudhuri, *Phys. Rev.* 143 (1966) 601.
- [8] J.R. Patel, L.R. Testardi, P.E. Freeland, *Phys. Rev. B* 13 (1976) 3548.
- [9] T. Suzuki, S. Takeuchi, H. Yoshinaga, *Dislocation Dynamics and Plasticity*, Springer, Berlin, 1991.
- [10] H. Alexander, in: F.R.N. Nabarro (Ed.), *Dislocations in Solids*, Vol. 7, North-Holland, Amsterdam, 1986, p. 115.
- [11] M.C. Payne, M.P. Teter, D.C. Allan, T.A. Arias, J.D. Joannopoulos, *Rev. Mod. Phys.* 64 (1992) 1045.
- [12] M. Bockstedte, A. Kley, J. Neugebauer, M. Scheffler, *Comput. Phys. Commun.* 107 (1997) 187.
- [13] M.Z. Bazant, E. Kaxiras, J.F. Justo, *Phys. Rev. B* 56 (1997) 8542.
- [14] J.F. Justo, M.Z. Bazant, E. Kaxiras, V.V. Bulatov, S. Yip, *Phys. Rev. B* 58 (1998) 2539.
- [15] R. Car, M. Parrinello, *Phys. Rev. Lett.* 55 (1995) 2471.
- [16] G.B. Bachelet, D.R. Hamann, M. Schluter, *Phys. Rev. B* 26 (1982) 4199.
- [17] L. Kleinman, D.M. Bylander, *Phys. Rev. Lett.* 48 (1982) 1425.
- [18] J.F. Justo, A. Antonelli, A. Fazzio, *Solid State Commun.* 118 (2001) 651.
- [19] P. Ebert, C. Domke, K. Urban, *Appl. Phys. Lett.* 78 (2001) 480.
- [20] A. Maiti, T. Kaplan, M. Mostoller, M.F. Chisholm, S.J. Pennycook, S.T. Pantelides, *Appl. Phys. Lett.* 70 (1997) 336.
- [21] G.W. Ludwig, H.H. Woodbury, *Solid State Phys.* 13 (1962) 223.
- [22] S. Pizzini, *Phys. Stat. Sol. A* 171 (1999) 123.
- [23] A. Maiti, M.F. Chisholm, S.J. Pennycook, S.T. Pantelides, *Phys. Rev. Lett.* 77 (1996) 1306.
- [24] J.F. Justo, A. Antonelli, T.M. Schmidt, A. Fazzio, *Physica B* 274 (1999) 473.
- [25] T.M. Schmidt, J.F. Justo, A. Fazzio, *Appl. Phys. Lett.* 78 (2001) 907.



ELSEVIER

Physica B 308–310 (2001) 474–476

PHYSICA B

www.elsevier.com/locate/physb

Modeling the subsurface region of Cz-Si wafers with properly fabricated bulk FZ-Si samples

T. Mchedlidze*, N. Fukata, M. Suezawa

Institute for Materials Research, Tohoku University, 2-1-1 Katahira, Aoba-ku, Sendai 980-8577, Japan

Abstract

Hydrogen and oxygen doped FZ-Si samples with a high concentration of intrinsic defects and contaminant atoms can be considered as a model bulk system for the subsurface device-active region of contemporary Cz-Si wafers. We investigated the creation of vacancy related complexes and the carrier recombination process in such samples using infrared absorption and spin resonance measurement methods. Both the defect creation and carrier recombination processes were found to be affected by the presence of hydrogen or deuterium in the samples. Moreover, we detected an isotopic effect, namely, a significant difference in the influence of hydrogen and deuterium. © 2001 Elsevier Science B.V. All rights reserved.

Keywords: Si; Vacancies; Hydrogen; Deuterium

1. Introduction

Technological progress has brought about changes in the fabrication of semiconductor devices: the active area of a device persistently ascends towards the surface of Cz-Si wafers. The environment of the wafer subsurface region differs drastically from the bulk: oxygen concentration is significantly reduced due to out-diffusion; concentrations of intrinsic defects (self-interstitials and vacancies) and contaminants are increased. Numerous technological processes, such as dry etching, irradiation, dopant in-diffusion, etc., cause an additional increase in the intrinsic defect concentration and “contamination” of the subsurface region by hydrogen [1,2]. Thus, in the subsurface region, defect formation mechanisms and defect structure may differ significantly from those in the wafer bulk. Investigation of the subsurface region with traditional “volume sensitive” methods (ESR, FT-IR, etc.) can only be done using simulative bulk samples. From the above, it follows that FZ-Si samples doped with oxygen, hydrogen and contaminants and subjected to irradiation can simulate the device-active region.

The effect of hydrogen on the defect creation, structure and properties in Si remains controversial [1–3]. Hydrogen in silicon passivates dopants, dangling bonds and deep level defects, creates various complexes with intrinsic defects, affects oxygen diffusion and thermal donor creation, actively interacts with transition metal atoms, and creates extended electrically active platelet defects. Strong isotope effects connected with hydrogen have also been observed [4–6]. The difference between the strength of Si–H bond and that of Si–D has been proposed as a source of hydrogen isotopic effects [6].

In the present work, we investigated the influence of hydrogen and deuterium doping on the formation of vacancy–oxygen pairs (VO) and divacancies (V_2) and on the carrier recombination processes in the systems modeling the subsurface layer of Cz-Si wafers.

2. Experimental

Starting materials for our investigation were n-type (P-doped, $\rho = 1000$ and $0.6 \Omega \text{cm}$) and p-type (B-doped, $\rho = 1800$ and $1.1 \Omega \text{cm}$) FZ-Si. Sliced samples, mechanically and chemically polished, were annealed at 1200°C

*Corresponding author. fax: +81-22-215-2041.

E-mail address: teimuraz@imr.tohoku.ac.jp (T. Mchedlidze).

for 1 h in quartz capsules filled with H_2 , D_2 or Ar. After the annealing, samples were quenched by immersion in water. Annealed samples were subjected to irradiation with 3-MeV electrons at room temperature (e-irradiation). Total irradiation doses were $d_e = 5 \times 10^{16}$ or $5 \times 10^{17} \text{ e/cm}^2$. After irradiation, the samples were kept at temperatures below -10°C in a refrigerator. Below, we will refer to the samples using three letters indicating conductivity type N or P, resistivity (high—H or low—L) and annealing ambient (argon—A, hydrogen—H, and deuterium—D).

We measured IR absorption in as-grown, annealed and irradiated samples. IR absorption spectra from the specimens $6 \times 6 \times 12 \text{ mm}^3$ in size were measured at 5 K using an FT-IR spectrometer and a continuous helium gas-flow cryostat. The resolution was 0.25 cm^{-1} . Several IR absorption peaks were monitored: that related to interstitial oxygen (O_i), observed at a wavenumber 1136 cm^{-1} , that related to a VO pair, at 835 cm^{-1} [7], that related to V_2 , at 2766 cm^{-1} [8], that related to H_2 , at 3618 cm^{-1} [9], and that related to the H_2^* complex, at 1838 cm^{-1} [10]. The relative intensities of FT-IR absorption peaks were calculated by fitting of the experimental absorption spectra with Lorentzian line-shape peaks. In low resistivity samples, FT-IR measurements were hampered due to a high level of noise from charge carriers.

In the irradiated samples, we measured the ESR signal from the excited triplet state of the VO defect, i.e., the SL1 spectra [11]. The ESR measurements were conducted at 16 K on a JEOL X-band ESR spectrometer using a TM_{011} mode microwave (MW) resonator equipped with a continuous helium gas-flow cryostat. Samples $3 \times 3 \times 12 \text{ mm}^3$ in size were illuminated during measurements through a window in the resonator. The derivative of the MW field absorption with respect to magnetic field was measured using a lock-in amplifier and magnetic field modulation with an amplitude of 0.2 G and a frequency of 100 kHz.

3. Results and discussion

In the present experiments, we did not dope FZ-Si samples with oxygen intentionally. However, unintentional doping of the samples with oxygen and hydrogen occurred from the material of the quartz capsules during high temperature annealing. As a result, O_i concentration in the samples after annealing increased 2–3 times and a H_2 related IR absorption peak appeared even for the samples annealed in argon or deuterium.

Intensities of the FT-IR absorption peaks in various samples after annealing and after subsequent irradiation are presented in Fig. 1. The fitted intensity of each peak was normalized to that of the strongest similar peak in the samples. Error bars in the figure represent the fitting

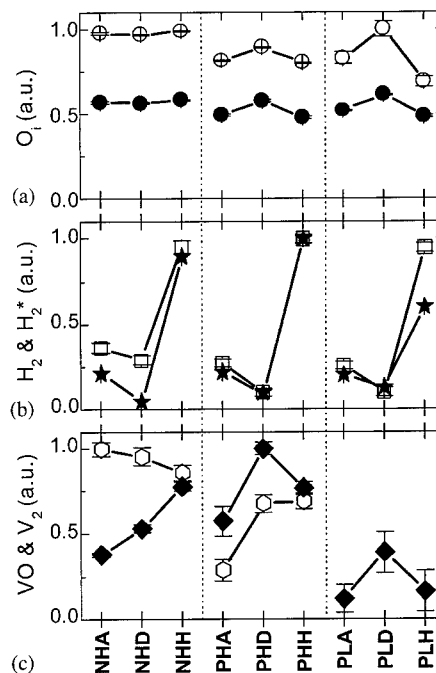


Fig. 1. Integrated IR absorption peak intensities normalized to that of the strongest similar peak in the samples. (a) O_i related peak before (\circ) and after (\bullet) irradiation; (b) H_2 (\square) and H_2^* (\star) related peaks; (c) VO (\circ) and V_2 (\diamond) related peaks. Lines are presented to guide the eye.

errors of the spectra. After annealing, we detected peaks related to O_i and H_2 (D_2). After irradiation of the samples, O_i , H_2^* , VO and V_2 related peaks were detected. We did not detect a VO related peak in the PL# samples after irradiation due to a high level of noise caused by charge carriers.

The most pronounced effects caused by hydrogen doping and isotopes were observed in the case of VO and V_2 defects. In the case of the NH# samples, hydrogen enhanced V_2 and suppressed VO creation. The effect of deuterium was similar, yet smaller. For the PH# samples, both VO and V_2 creation was enhanced by hydrogen and the effect of deuterium was even stronger in the case of V_2 . Similarly, enhancement caused by deuterium was detected for the V_2 related peak in the PL# samples.

For the samples annealed in hydrogen, the H_2^* related peak intensity was lower in the case of the PLH sample. This effect can be attributed to the lower concentration of the Frenkel pairs in the low resistivity sample during the irradiation [12]. Also, some variations were detected in O_i related peak intensity before irradiation. Interestingly, O_i concentration significantly decreased after irradiation (~ 40 – 50%). Furthermore, no correlation was observed between O_i decrease and VO pair creation. Thus, in addition to the VO pair creation, there would

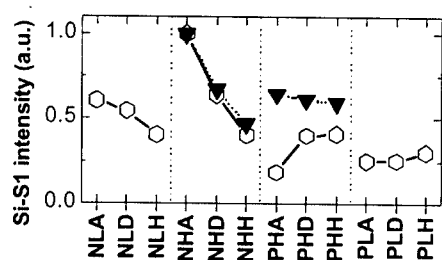


Fig. 2. Relative intensity of the SL1 signal in various samples after irradiation (○) and normalized ratio of the SL1 signal intensity to that of the VO related FR-IR peak (▼).

seem to be some irradiation or intrinsic defect assisted reaction path, which removes oxygen atoms from interstitial sites.

To avoid possible differences in the Q-factor of the resonator, the amplitude of the SL1 ESR spectra was normalized to the ESR signal from an external standard placed in the resonator. We compared intensity of the ESR and FT-IR signals from the VO complex in high resistivity samples. The results presented in Fig. 2 reveal that the SL1 signal intensity does not follow the VO concentration, but strongly depends on the annealing ambient of the NH# samples.

The SL1 signal arises during the recombination process of the illumination-excited charge carriers through the (VO)* excited triplet state [13]. Thus, the presence of other recombination paths in the sample causes a decrease in the SL1 signal intensity. Simple proof for such a supposition can be obtained from irradiation dose dependence for a normalized ratio of the SL1 signal intensity to that of the VO related FT-IR peak in Cz-Si samples (Fig. 3). The ratio monotonically decreases from unity, starting from the dose $d \cong 2-3 \times 10^{15} \text{ e cm}^{-2}$, showing strong correlation with the creation probability of V_2 . We can suppose that in the case of NH# samples, the increase in the concentration of divacancies for the D_2 and H_2 doped samples may be the reason for the observed decrease in the SL1 spectra intensity.

4. Summary

Significant effects connected with hydrogen doping and isotopes were detected in FZ-Si samples for the creation of VO and V_2 defects under irradiation. The effects depend on the type of conductivity even in the case of high resistivity samples. Enhancement of the

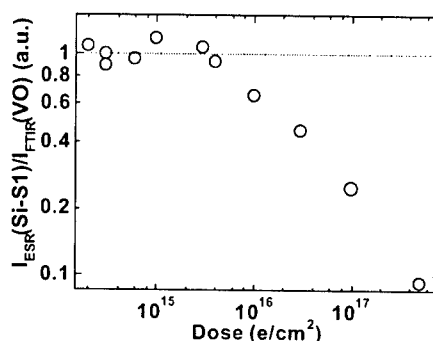


Fig. 3. Irradiation dose dependence for the normalized ratio of the SL1 signal intensity to that of the VO related FT-IR peak in Cz-Si samples. Irradiation was done with 3 MeV electrons at RT.

creation of divacancies and, probably, other recombination active defects causes a decrease in the intensity of the SL1 ESR spectra from the excited triplet state of the VO pair.

Experiments on the FZ-Si samples modeling the subsurface layer of modern materials for device fabrication revealed interesting results. At present, it is too early to speculate about the possible reasons for the observed effects. Further investigation is required to explain the origins of the observed phenomena. It would be interesting to include probable contaminant atoms, such as iron, copper, etc., in the investigation.

References

- [1] J.I. Pankove, N.M. Johnson (Eds.), *Hydrogen in Semiconductors*, in: *Semiconductors and Semimetals* 34, Academic Press, Boston, 1991.
- [2] N.H. Nickel (Ed.), *Hydrogen in Semiconductors II*, in: *Semiconductors and Semimetals*, Vol. 61, Academic Press, San Diego, 1999.
- [3] S.K. Estreicher, *Mater. Sci. Eng.* 14 (1995) 319.
- [4] J.W. Lyding, K. Hess, I.C. Kizilyalli, *Appl. Phys. Lett.* 68 (1996) 2526.
- [5] Ph. Avouris, et al., *Chem. Phys. Lett.* 257 (1996) 148.
- [6] C.G. Van de Walle, *J. Vac. Sci. Technol. A* 16 (1998) 1767.
- [7] J.W. Corbett, et al., *Phys. Rev.* 121 (1961) 1015.
- [8] L.J. Cheng, et al., *Phys. Rev.* 152 (1966) 761.
- [9] R.E. Pritchard, et al., *Phys. Rev. B* 57 (1998) R15048.
- [10] J.D. Holbeck, et al., *Phys. Rev. Lett.* 71 (1993) 875.
- [11] L. Brower, *Phys. Rev. B* 4 (1971) 1968.
- [12] M. Suzawa, *Phys. Rev. B* 63 (2000) 035203.
- [13] G.D. Watkins, *Phys. Rev.* 155 (1967) 802.



ELSEVIER

Physica B 308–310 (2001) 477–480

PHYSICA B

www.elsevier.com/locate/physb

High-energy proton radiation induced defects in tin-doped n-type silicon

E. Simoen^{a,*}, C. Claeys^{a,b}, V. Privitera^c, S. Coffa^c, A. Nylandsted Larsen^d,
P. Clauws^e

^aIMEC, Kapeldreef 75, B-3001 Leuven, Belgium

^bE.E. Dept., KU Leuven, Kasteelplein 10, B-3001 Leuven, Belgium

^cIMETEM—CNR, Stradale Primosole 50, I95121 Catania, Italy

^dInstitute of Physics and Astronomy, Ny Munkegade, University of Aarhus, DK-8000 Aarhus, Denmark

^eDepartment of Solid State Sciences, Ghent University, Krijgslaan 281 S1, B-9000 Gent, Belgium

Abstract

The formation of radiation defects in Sn-doped Float-Zone (FZ) and Czochralski (Cz) n-type silicon after a high-energy proton irradiation is studied by a combination of Deep Level Transient Spectroscopy (DLTS) and Photoluminescence (PL). Besides the Sn-V levels, evidence is found for at least three new Sn-related radiation defects, two electron traps close to the conduction band and one hole trap close to the valence band. No new PL lines have been identified so far in Sn-doped material. It is furthermore concluded that the Sn-related radiation defects do not show pronounced recombination activity, in the concentration range studied. © 2001 Elsevier Science B.V. All rights reserved.

Keywords: Tin vacancy; Proton irradiation; n-type silicon; Deep level transient spectroscopy; Photoluminescence

1. Introduction

It has only recently become clear that the Sn-V complex in irradiated silicon has 4 electronic levels in the band gap: next to the well-known donor levels at 0.066 and 0.317 eV above the valence band [1], two additional acceptor levels have been revealed in irradiated n-type silicon, 0.29 and 0.59 eV below the conduction band [2,3]. This implies that Sn-V is a unique five charge-state centre in silicon. The aim of this paper is to compare the formation of radiation defects in high energy (8 and 60 MeV) proton irradiated n-type Cz and FZ silicon, doped with Sn in the melt to concentrations in the range $\sim 10^{18} \text{ cm}^{-3}$. As reference material, tin-free n-type FZ and Cz silicon has been irradiated, in order to study the impact of Sn-doping on the formation

of cluster damage. DLTS and PL spectroscopy have been applied to investigate the created radiation defects. Beside the Sn-V related deep levels, evidence will be provided for the introduction of other Sn-related defects, at $E_c - 0.074 \text{ eV}$, $E_c - 0.083 \text{ eV}$ and at $E_v + 0.18 \text{ eV}$; their identity will be discussed. From PL at 12 K, further evidence is provided that the presence of Sn reduces the optical recombination activity of radiation defects and defect clusters, compared with tin-free material.

2. Experimental

Details about the samples studied are given in Table 1, indicating that the doping density of all silicon material is about $\sim 10^{14} \text{ cm}^{-3}$ n-type. The Sn-concentration has been measured by SIMS. Standard capacitance DLTS characterisation before and after proton exposure was

*Corresponding author. Tel.: +32-16-281-211; fax: +32-16-229-400.

E-mail address: simoen@imec.be (E. Simoen).

Table 1

Description of the samples used in the DLTS analysis of proton-radiation induced defects in n-type tin-doped or tin-free silicon

Substrate [Sn] (cm^{-3})	Device	ND ($\times 10^{14} \text{cm}^{-3}$)		Irradiation	
		Pre	Post	Energy (MeV)	Fluence ($\times 10^{11} \text{cm}^{-2}$)
n-FZ no	1 mm ² p-n	—	1.0	60	1.0
n-FZ no	1 mm ² p-n	—	1.2	61	5.0
n-FZ (10^{18})	3.14 mm ² Au	2.7	0.05	8	52.0
n-FZ (10^{18})	3.14 mm ² Au	2.6	1.9	60	1.0
n-Cz no	3.14 mm ² Au	1.9	1.6	60	1.0
n-Cz 1.7×10^{18}	3.14 mm ² Au	0.7	—	61	5.0
n-Cz 6.5×10^{18}	3.14 mm ² Au	1.2	—	61	5.0

performed either on 2 mm diameter Au Schottky barriers or on 1 mm² p-n junctions. The latter have been processed on the tin-free FZ references. In order to reveal the presence of hole traps in the Schottky diodes, an optical injection pulse, generated by a laser diode operating at a wavelength of 895 nm, was used.

Proton irradiations have been performed at different facilities. The 60–61 MeV exposures took place at the Cyclone cyclotron at Louvain-la-Neuve, while the 8 MeV irradiations were done at the TANDEM accelerator at Demokritos in Athens. No bias was applied to the diodes.

Photoluminescence characterisation was performed at 12 K, using carrier excitation by a 488 nm Ar laser, operated at 50 mW power. The Schottky barrier or p-n junction were removed by polishing and etching, in order to have acceptable surface recombination for PL.

3. Results

3.1. Pre-irradiation characterisation

Before irradiation, there are already some deep levels present in the starting material. An example is given in Fig. 1 for Sn-doped FZ and Cz (abbreviated FZ:Sn or Cz:Sn). The dominant peak at about 70 K in Cz:Sn corresponds with the second donor level of the oxygen thermal donors at $E_c - 0.139$ eV, as discussed elsewhere [2]. Typical concentrations are in the range of about 10%. It has been shown in addition that there is little interaction with the radiation defects [2]. The apparent activation energies of the other two levels are 0.142 and 0.165 eV; the latter peak could coincide with the V-O or A centre. It is not believed that the as-grown defects are Sn-related as a very similar spectrum has been found for the tin-free Cz reference material. As can be seen from Fig. 1, no deep levels are observed within the sensitivity limits of DLTS above 110 K.

The case is different for the FZ:Sn sample, where three peaks are observed before irradiation. They have apparent activation energy of 0.073, 0.143 and 0.563 eV

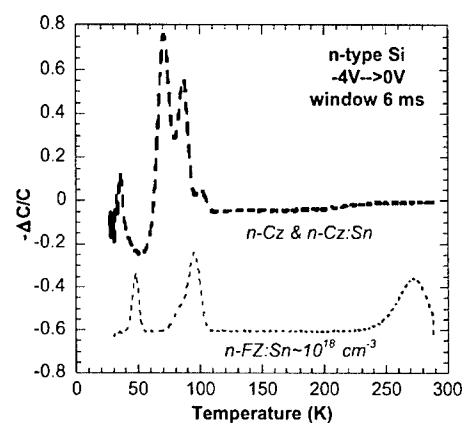


Fig. 1. DLT-spectrum of the FZ:Sn and Cz:Sn and the tin-free Cz n-type material. A 1 ms majority carrier pulse from -4 to 0 V was employed.

and appear to be typical for as-grown n-type high-purity FZ silicon [4,5]. Their origin has been discussed elsewhere [6]; briefly speaking, it is assumed that the 0.073 and 0.563 levels are different charge states of a self-interstitial-related defect. The origin of the 0.143 eV peak is unknown. Based on the K_T factor one can rule out the possibility that this level coincides with the $E_c - 0.142$ eV centre in Cz:Sn. The shoulder on the left of the 0.143 eV peak could be C-related [4,5]. In the reference FZ p-n junctions, no deep levels were revealed above the detection limit [7]. In addition, PL analysis before irradiation did not show up specific lines related to Sn. It is, therefore, concluded that Sn-doping by itself does not introduce optical recombination activity, in line with previous reports [8].

3.2. Post-irradiation characterisation

Fig. 2 summarises the 4 cases studied after 60–61 MeV proton irradiation. Beside the as-grown peaks, we can recognise additional deep levels, some of which are well-established from the past. The tin-free references are characterised by the presence of the A-centre and the

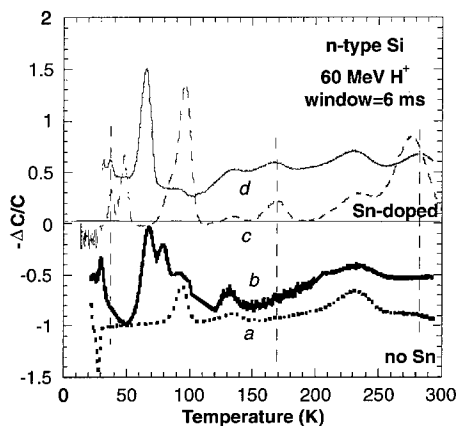


Fig. 2. DLT-spectra at 80 Hz after 60 MeV proton irradiation for a Sn-free n-type FZ (a) and Cz (b) sample and for a tin-doped FZ (c) and Cz (d) sample. The radiation fluence was 10^{11} cm^{-2} , except for case d, where the fluence was 5 times higher.

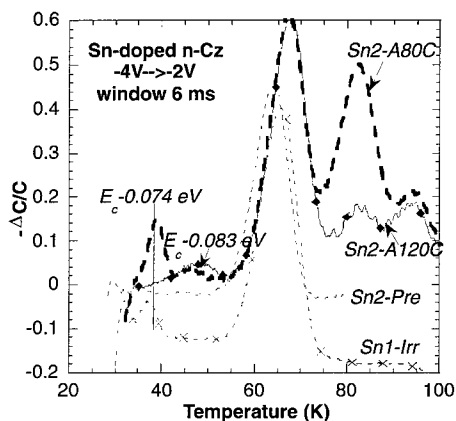


Fig. 3. DLT-spectrum of the n-type Cz:Sn samples before irradiation (Sn2-pre); after a $5 \times 10^{11} \text{ cm}^{-2}$ 61 MeV proton irradiation (Sn1-Irr); after the same irradiation and a 30 min anneal at 80°C under flowing Ar (Sn2-A80C); and for the same irradiation, after a 30 min anneal under Ar at 120°C (Sn2-A120C).

two acceptor states of the divacancy (V-V). The single acceptor has a higher magnitude and is broader than the double acceptor. In addition, the C_i-O_i hole trap at $E_v + 0.35 \text{ eV}$ is found under minority carrier injection conditions in the FZ and Cz material. The presence of carbon-related radiation defects is also confirmed by the observation of the 0.79 eV C- and the 0.97 eV G-line in PL [6,7,9].

In the Sn-doped samples, at least four additional electron traps can be observed in Fig. 2 or 3, two of which have been discussed in detail before [2,3]. They are ascribed to the single and double acceptor state of

the Sn-V. Furthermore, two shallow electron traps are found at $E_c - 0.074$ and 0.083 eV , which have only been observed in irradiated Sn-doped material (Fig. 3). As can be derived from Figs. 2 and 3, they occur both in Cz or FZ material, so that a correlation with oxygen is rather unlikely. They are, therefore, tentatively identified as Sn-related radiation defects. Similar shallow levels have been reported before in neutron-irradiated n-type FZ:Sn [10].

Fig. 3 shows spectra obtained after 60 MeV proton irradiation and annealing for 30 min at 80 or 120°C, for the Cz:Sn samples. No results are available for the FZ:Sn yet. It has been demonstrated that the Sn-V dissociates below 120°C for $\sim 10^{14} \text{ cm}^{-3}$ doped n-type material [2], which was lower than previously reported for p-type silicon [1] or for higher doped n-type Si [11,12]. According to Fig. 3, the shallowest level (0.074 eV) also disappears at or below 120°C, while the second peak (0.083 eV) is still observed—even seems to grow—after 120°C annealing. It is too early to come up with a definitive identification of these unknown centres, but at least the second peak is a candidate for one of the higher order Sn_mV_n defects, recently identified by EPR [13] and showing a higher thermal stability than Sn-V. A more systematic annealing study is required to further establish the nature of the peaks.

As reported elsewhere [6], in the 8 MeV proton-irradiated FZ:Sn sample, an unknown hole trap at $E_v + 0.18 \text{ eV}$ has been found as well. It is also tentatively assigned to a higher-order tin-vacancy complex. According to ab initio calculations, SnV_2 or Sn_2V_2 should have levels in both parts of the band gap [14], which could be well in line with the present observations.

Finally, Fig. 4 compares the PL spectrum before and after 60 MeV proton irradiation for a tin-doped FZ sample. On top of the phosphorus-related excitonic

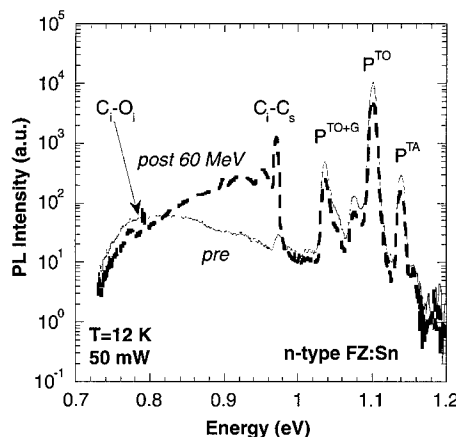


Fig. 4. PL spectra of a $\sim 10^{18} \text{ cm}^{-3}$ Sn-doped n-type FZ sample before (solid line) and after (dashed line) a 10^{11} cm^{-2} 60 MeV proton irradiation.

luminescence, additional lines are found, which have been identified as C-related radiation defects [7,9]. Qualitatively similar spectra are observed in the tin-free reference material [6]. This indicates that the Sn-V centres do not exhibit optical recombination activity.

4. Discussion

Summarising the above findings, it is clear that Sn-doped n-type silicon shows up a whole set of new radiation defects, which may affect the electrical properties, like the recombination or generation lifetime. The electronic characteristics of the Sn-V centre are now fairly well understood, both from an experimental and a theoretical viewpoint, but the search for the higher order tin-vacancy complexes is ongoing. It is also clear from comparing the FZ and Cz material that there seems to be little direct interaction between the formation of Sn-related radiation defects and interstitial oxygen.

It has been reported on several occasions that the trapping-ability of substitutional tin may help in controlling/suppressing the formation of detrimental radiation defects like the A- and E-centre or V-V [1,2,11,12]. A reduction of the trap introduction rate by a factor 3 for the $5 \times 10^{11} \text{ cm}^{-2}$ 60 MeV proton irradiations studied here (Cz:Sn), up to a factor 10 for 2 MeV electron irradiations have been reported [2,11,12]. However, this occurs at the cost of the creation of additional Sn_mV_n complexes, which in the end may result in a higher device degradation. However, for the conditions studied here, it is concluded that the optical recombination properties are better preserved in Sn-doped FZ silicon compared with the reference material [6]. In addition, preliminary recombination lifetime measurements of γ -irradiated Sn-doped Cz silicon confirm the better radiation resistance, for a Sn concentration in the range $\sim 10^{18} \text{ cm}^{-3}$ [15]. On the other hand, little or no improvement has been observed for $6.5 \times 10^{18} \text{ cm}^{-3}$ Sn-doping, suggesting that there

exists a delicate balance between the suppression of the harmful radiation defects on the one hand and the electrical activity of the additional Sn_mV_n centres on the other.

5. Conclusions

The formation of proton-irradiation defects in n-type Sn-doped Cz and FZ silicon has been compared. It was observed that the same types of defects are formed. Next to the Sn-V pairs, it is believed that two additional electron and one extra hole trap are created in Si:Sn. From the PL results, it is concluded that Sn or Sn-V do not introduce new lines. In spite of its four levels in the band gap, Sn-V is found to be not particularly recombination active compared with the standard radiation defects.

References

- [1] G.D. Watkins, J.R. Troxell, Phys. Rev. Lett. 44 (1980) 593.
- [2] E. Simoen, et al., Appl. Phys. Lett. 76 (2000) 2838.
- [3] A. Nylandsted Larsen, et al., Phys. Rev. B 62 (2000) 4535.
- [4] H. Lefèvre, Appl. Phys. A 22 (1980) 15.
- [5] H. Lefèvre, Appl. Phys. A 29 (1982) 105.
- [6] E. Simoen, et al., Proceedings of Symposium B of the E-MRS Spring Meeting, 5–8 June, 2001, to be published.
- [7] M.-A. Trauwert, et al., Mater. Sci. Eng. B 36 (1996) 196.
- [8] W. Wijarankula, J. Appl. Phys. (1991) 3018.
- [9] G. Davis, Phys. Rep. 176 (1989) 93.
- [10] R. Kozłowski, et al., In: C. Claeys (Ed.), Proceedings of 1st ENDEASD Workshop, 2000, p. 186.
- [11] B.G. Svensson, et al., Appl. Phys. Lett. 51 (1987) 2257.
- [12] B.G. Svensson, et al., J. Appl. Phys. (1992) 5616.
- [13] M. Fanciulli, J.R. Byberg, Phys. Rev. B 61 (2000) 2657.
- [14] M. Kaukonen, et al., Proceedings of Symposium B of the E-MRS Spring Meeting, 5–8 June, 2001, to be published.
- [15] E. Simoen, et al., Proceedings of GADEST 2001, Catania, Italy, 30 September–3 October, 2001, to be published.

Interface strain in thermal Si/SiO₂ analysed by frequency-dependent electron spin resonance

Dieter Pierreux*, André Stesmans

Departement Natuurkunde, Katholieke Universiteit Leuven, Celestijnenlaan 200D, 3001 Leuven, Belgium

Abstract

Thermal oxidation of Si gives intrinsically rise to the generation of Si dangling bond type defects at the Si/SiO₂ interface. In standard (1 1 1)Si/SiO₂ the dominant one observed by electron spin resonance (ESR) is the P_b (Si₃≡Si•) center. It is generally accepted that the driving agent for these defects is the occurrence of interfacial strain. A frequency dependent ESR study on these P_b defects has enabled the separation of the strain broadening component from other line broadening mechanisms, leading to a direct quantification of the associated interface stress. This resulted in the observation of thermal treatment induced variations in the strain broadening contribution indicating the existence of two different interfacial relaxation processes. © 2001 Elsevier Science B.V. All rights reserved.

Keywords: Si/SiO₂ interface; Defect; ESR; Strain

1. Introduction

Several studies have reported on the observation of an intrinsic SiO₂ film stress resulting from thermal oxidation of Si [1–4]. The origin of this stress has been attributed to the 120% molar volume expansion which results from the conversion of Si to SiO₂. As a result of this mismatch induced stress, dangling bond type defects are generated at the interface. In standard thermal (1 1 1)Si/SiO₂ the dominant paramagnetic interface defect observed by electron spin resonance (ESR) is the P_b center—interfacial (Si₃≡Si•) [5]. In the as-grown state, a P_b density of $\sim 4.9 \times 10^{12} \text{ cm}^{-2}$ is inherently incorporated for the oxidation range 300–950°C. This value appears strongly correlated with the constant interfacial intrinsic stress [6]. It is generally accepted that P_b defects occur at the interface to (partly) alleviate interfacial stress. Despite their generally malignant character, these defects, as sensed by ESR, may serve as sensitive probes for interface characterization. For one, the interface strain was formerly quantified in

terms of their *g*-factor distribution inferred from the magnetic field angle dependence of the ESR line width [6–8]. However, for larger areal defect densities, that method becomes unsuitable by interference of anisotropic two-dimensional dipolar broadening [9]; an extensive parameterised global fitting procedure is required to enable extraction of both anisotropic contributions.

In the present work this has been overcome by carrying out a detailed study of the P_b ESR properties as a function of the resonance frequency (X, K and Q band). This has enabled the separation of the strain broadening component from the dipolar one.

2. Experimental details

Sample slices (2 × 9 mm²), appropriate for ESR, were cut from 2-in diam. two-side polished (1 1 1) Si wafers (float zone; >100 Ω cm; p-type; thickness $\sim 70 \mu\text{m}$). After cleaning, the slices were thermally oxidised in a high-vacuum laboratory facility at $T_{\text{ox}} \sim 970^\circ\text{C}$ (1 atm, 99.9995% dry O₂) for $\sim 1 \text{ h}$ ($d_{\text{ox}} \sim 56 \text{ nm}$), terminated by cooling to room temperature in O₂ ambient (time constant $\sim 200 \text{ s}$). Subsequently, a first ESR sample

*Corresponding author. Tel.: +32-16-327-679; fax: +32-16-327-987.

E-mail address: dieter.pierreux@fys.kuleuven.ac.be (D. Pierreux).

was submitted to a post oxidation anneal (POA) in H_2 (1 atm, 99.9999%) for ~ 1 h at 780°C to enhance P_b density. Yet, as all P_b -defects are then automatically left passivated by H this was followed by a P_bH dissociation step in order to ESR-activate the defects, i.e., vacuum annealing ($<4 \times 10^{-7}$ Torr) at 605°C for ~ 1 h. A second sample received a POA in vacuum (POVA) at 1200°C for 37 min. A third sample, not submitted to any postoxidation thermal treatment, served as a reference. Conventional absorption-derivative X, K and Q band ESR-observations were made at 4.3 K.

3. Experimental results and discussion

3.1. As-oxidised (111)Si/SiO₂

Fig. 1 illustrates the influence of the resonance frequency ν on the P_b ESR signal, which will be analysed below.

The measured first derivative peak-to-peak linewidth ΔB_{pp}^T as a function of ν is shown in Fig. 2 for three values of φ_B , the angle between the applied magnetic field \mathbf{B} and the interface normal \mathbf{n} . A general increase in ΔB_{pp}^T with increasing ν and φ_B is clearly observed.

From φ_B -dependent observations, previous studies had concluded that the P_b ESR line width in standard (111)Si/SiO₂ consists of mainly two superimposed contributions [7,8]: In addition to an angle independent residual part, there is a considerable (supposedly) Gaussian type broadening monotonically growing for $\varphi_B \rightarrow 90^\circ$. The latter is attributed to strain-induced variations in the g tensor, predominantly in g_\perp . Underlying insight was provided by the work of Watkins and Corbett [7,10]. The supposedly Lorentzian residual linewidth contribution was mainly attributed to unresolved ^{29}Si superhyperfine broadening [7]. A later, more in-depth study of the residual line shape for $\mathbf{B} \parallel \mathbf{n}$

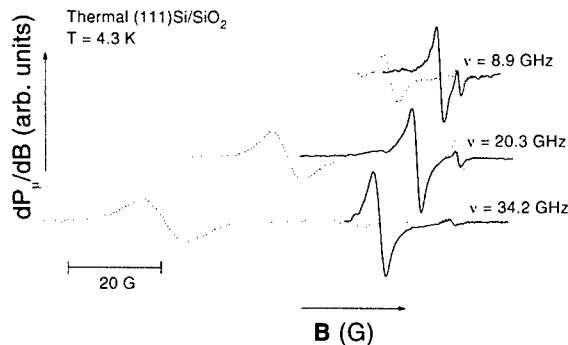


Fig. 1. Influence of resonance frequency ν on P_b ESR signal for the as-grown thermal Si/SiO₂ interface with $[P_b] \sim 5 \times 10^{12} \text{ cm}^{-2}$. For each ν , spectra for two directions of \mathbf{B} are shown: Solid lines: $\mathbf{B} \perp (111)$; Dotted lines: $\mathbf{B} \parallel (111)$.

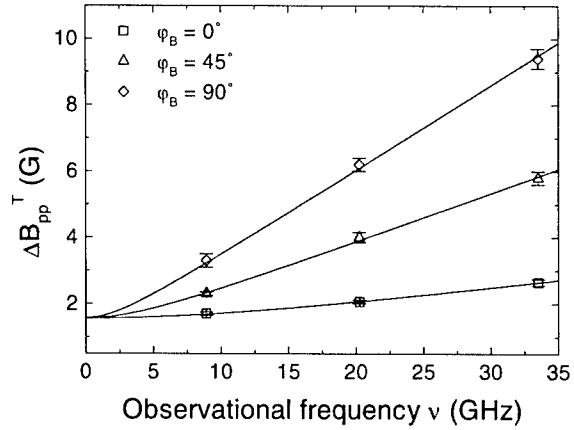


Fig. 2. Frequency dependence of the P_b ESR peak-to-peak line width of the as-grown reference sample for different orientations of \mathbf{B} : $\varphi_B = 0^\circ$ (\square), $\varphi_B = 45^\circ$ (\triangle), $\varphi_B = 90^\circ$ (\diamond).

interface revealed clearly the influence of a P_b -density dependent dipolar broadening [11].

As mentioned, it is our aim to quantify the interface strain in terms of the P_b g -factor distribution from frequency dependent measurements instead of the formerly φ_B dependence of ΔB_{pp}^T . Two approximations are made: first, it is assumed that the frequency independent part, mainly consisting of ^{29}Si superhyperfine and dipolar broadening is purely Lorentzian and void of strain; Second, the strain component ΔB_{pp}^{SB} can be related to Gaussian distributions in g and g_\perp with standard deviations σg and σg_\perp , respectively. To a first approximation, the frequency dependence of ΔB_{pp}^{SB} can then be expressed as

$$\Delta B_{pp}^{SB} = \frac{2h\nu}{\beta} \left(\frac{g \cos^2 \varphi_B}{g^3} \sigma g + \frac{g_\perp \sin^2 \varphi_B}{g^3} \sigma g_\perp \right). \quad (1)$$

This is a generalized approach of the one presented in Ref. [7] where $\sigma g = 0$ was assumed. The g map for rotation of \mathbf{B} from $\mathbf{B} \parallel \mathbf{n}$ ($\varphi_B = 0^\circ$) towards $\mathbf{B} \perp \mathbf{n}$ ($\varphi_B = 90^\circ$) contains one single branch, obeying

$$g = \sqrt{(g \cos \varphi_B)^2 + (g_\perp \sin \varphi_B)^2}, \quad (2)$$

with principal values inferred as $g = 2.00136 \pm 0.00003$ [6] and $g_\perp = 2.0088 \pm 0.0001$. The measured convolution of the frequency independent Lorentzian part and the Gaussian strain component is expected to be largely Voigt-like. The measured width ΔB_{pp}^T is then expected to be adequately described by

$$\Delta B_{pp}^T = \frac{1}{2} \Delta B_{pp}^L + \left((\Delta B_{pp}^G)^2 + \frac{1}{4} (\Delta B_{pp}^L)^2 \right)^{1/2}, \quad (3)$$

where ΔB_{pp}^L and ΔB_{pp}^G represent the Lorentzian and Gaussian linewidths of the Voigt shape. After inserting Eq. (2) for g in Eq. (1) and substituting Eq. (1) for ΔB_{pp}^{SB} ,

the curves in Fig. 2 are obtained as optimised least-squares-fits of Eq. (3) to the ΔB_{pp}^T -vs- ν data.

For $\mathbf{B} \perp (111)$, this resulted in $\Delta B_{pp}^L = 1.55 \pm 0.05$ and $\sigma g_{\parallel} = 0.00014 \pm 0.00001$, where the inferred value of σg_{\parallel} is found to be in good agreement with previously reported values [6,9] ($\sigma g_{\parallel} = 0.00015$). Here, it should be added that the reported value of $\sigma g_{\parallel} = 0.00032$ [6] was obtained by assuming a half Gaussian distribution to simulate the apparent asymmetry of the P_b -signal; when applying a full Gaussian distribution an extra factor ~ 2 needs to be taken into account. The obtained ΔB_{pp}^L can be read at the intercept of the ΔB_{pp}^T -axis as a direct result of the assumption that the Lorentzian part is frequency independent; Indeed, according to Eq. (3), $\Delta B_{pp}^T = \Delta B_{pp}^L$ for $\nu = 0$. This remaining component, void of strain, represents the residual line width composed of the intrinsic part $\Delta B_{pp}^{\text{int}}$ (mainly ascribed to unresolved ^{29}Si superhyperfine) and dipolar broadening $\Delta B_{pp}^{\text{dip}}$. The latter are separated using the Lorentzian addition rule $\Delta B_{pp}^L = \Delta B_{pp}^{\text{int}} + \Delta B_{pp}^{\text{dip}}$. From a former study [11], analysing the ESR line width (for $\mathbf{B} \parallel \mathbf{n}$) as a function of the $[P_b]$, the value $\Delta B_{pp}^{\text{int}} = 0.4 \text{ G}$ is inferred for $[P_b] \sim 5 \times 10^{12} \text{ cm}^{-2}$, from where $\Delta B_{pp}^{\text{int}} \sim 1.15 \text{ G}$. This emerging constant value may be compared with the reported value of $\Delta B_{pp}^R = 1.29 \pm 0.03 \text{ G}$ [11], deduced by extrapolation of the $\Delta B_{pp}^T(\mathbf{B} \parallel \mathbf{n}) - f$ relationship towards $f \rightarrow 0$, where f represents the defect concentration, to eliminate the dipolar contribution. The small deviation arises from the existence of a small σg_{\parallel} [6], not separated by extrapolation to $f \rightarrow 0$.

The σg_{\perp} value was derived for two field directions \mathbf{B} ($\varphi_B = 45^\circ, 90^\circ$; cf. Fig. 1) with σg_{\parallel} and ΔB_{pp}^L kept fixed at the values inferred from the fit for $\varphi_B = 0^\circ$, and varying only σg_{\perp} ; keeping ΔB_{pp}^L fixed is justified by the small anisotropic dipolar broadening for the present defect densities. The inferred value $\sigma g_{\perp} = 0.00076 \pm 0.00002$ is in good agreement with the previous values ($\sigma g_{\perp} = 0.00078; 0.00080$) [7,8]. The agreement of the obtained parameters substantiates the previous angle dependent method.

3.2. Thermal treatment

The measured P_b line widths for the samples subjected to postoxidation treatment are shown in Fig. 3. From optimised fitting along the lines outlined above two features become clear: While the σg_{\parallel} -value stays fixed at 0.00014, yet, there is an obvious decrease in the σg_{\perp} , i.e., 0.00046 ± 0.0002 for POVA and 0.00058 ± 0.0002 for POA (H_2). The unaltered value of σg_{\parallel} may be attributed to the inherently smaller sensitivity of g_{\parallel} to strain or, in a different point of view, might just indicate the residual spread on g_{\parallel} to be of a different nature. Yet, the remarkable drop in σg_{\perp} occurring after postoxidation treatment indicates the occurrence of stress relaxation at the Si/SiO₂ interface.

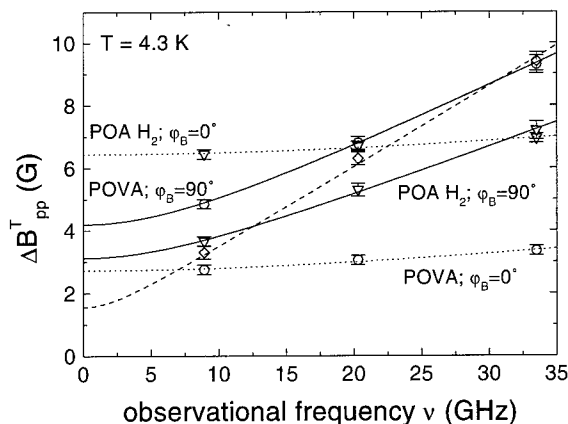


Fig. 3. Frequency dependence of the P_b ESR peak-to-peak line width of samples subjected to postoxidation thermal treatment: POVA (\circ), POA H_2 (∇). Solid and dotted lines represent least-squares fits using Eq. (3) for $\varphi_B = 90^\circ$ and $\varphi_B = 0^\circ$, respectively. For comparison, the data of the reference sample for $\varphi_B = 90^\circ$ (\diamond) (dashed curve fit) are also shown (see also Fig. 1).

A last item to be addressed in Fig. 3 is the larger $\Delta B_{pp}^T(\nu \rightarrow 0)$ value for the thermal treated samples as compared to the reference sample. This is ascribed to enhanced dipolar interactions due to strongly increased defect densities as a result of PO annealing of the Si/SiO₂ interface [12,13], determined as $\sim 2 \times 10^{13} \text{ cm}^{-2}$ and $\sim 3.4 \times 10^{13} \text{ cm}^{-2}$ for POVA and POA H_2 respectively. Indeed, a φ_B map of the ΔB_{pp}^T vs φ_B now clearly reveals anisotropic dipolar broadening.

4. Interpretation

According to the simple Maxwell viscoelastic model of a solid, stress relaxation occurs by viscous motion of a-SiO₂ material away from the growth interface. If assuming the rate of stress relief to be proportional to the stress (as is usually the case) then

$$\frac{d\sigma_i}{dt} = -\frac{\sigma_i}{\Gamma}, \quad (6)$$

where Γ is a constant, namely the viscoelastic relaxation time; σ_i is the intrinsic growth stress, i.e., the stress that is generated through the film growth process. From integrating Eq. (6), one obtains the expression $\sigma_i(t) = \sigma_i(0) \exp(-t/\Gamma)$ for the stress relief process where $\sigma_i(0)$ is the maximum intrinsic stress at the growth interface and t the oxidation or annealing time.

For the reference sample, the outer surface of the growing Si/SiO₂ film has been annealed at T_{ox} for the entire period of oxidation, whereas little so for oxide at the final interface. In consequence, virtually no stress relaxation via viscous flow has occurred for the interface region leading to a highly stressed interface. This is

mirrored in σg_{\perp} : the in-plane stress leads to variations in the defect's local environment over the interface resulting in slightly different g -tensors.

Within this model, the POVA results become clear, i.e. without further oxidising flux, the interface has the possibility to relieve stress during 37' at 1200°C. At this temperature the viscoelastic relaxation time Γ is small [14] and an efficient relaxation can occur. The less strained interface gives rise to smaller local defect environment variations leading to a lower σg_{\perp} . On the microscopic level, at the high anneal temperature, the interface may rearrange interfacial bonds and angles to attain a lower energetic state.

Former stress data show that almost no (viscoelastic) relaxation can occur during film growth or annealing for temperatures below 800°C [6,14]. The key point is that annealing at high temperature ($T_{\text{an}} > 950^{\circ}\text{C}$) represents a condition where Γ is comparable to, or shorter than, annealing time t_{an} , whereas for $T_{\text{an}} \leq 800^{\circ}\text{C}$, Γ is at least an order of magnitude larger than t_{an} . Consequently, the relaxation that occurs after POA in H_2 at 780°C is likely from another origin. The fit result for the latter sample can be consistently interpreted within the understanding of the defect-strain relationship: Defects are created to alleviate interfacial stress [6]. It was formerly observed that one effect of H_2 POA is an irreversible interfacial bond rupture, yielding additional defects indistinguishable from the pre-existing P_b defects [13]. Thus, the system may locally release stress associated energy through defect creation, thus locally relaxing the interface. At high defect densities, as in the present case, the local relaxation can become more global by percolation, leading to a generally lower intrinsic interface strain, reflected in the lower σg_{\perp} .

5. Conclusions

A frequency-dependent ESR study of the P_b defect has enabled to quantify the interface stress at the

(111)Si/SiO₂ interface. In contrast with field angle dependent results, which are complicated by the interference of anisotropic dipolar broadening at higher defect densities, this method is generally applicable.

For standard thermal (111)Si/SiO₂ the inferred values $\sigma g_{\parallel} = 0.00014$ and $\sigma g_{\perp} = 0.00076$ are in good agreement with previous field angle dependent results, confirming the previous insight in the constituent line broadening mechanisms.

In a study of the effect of postoxidation thermal treatments a marked influence on the strain broadening component is revealed, indicating the existence of two different interface relaxation processes: i.e., relaxation of interfacial stress through bond length and angles adjustment (in nonoxidising ambient) or interface defect creation.

References

- [1] E.P. EerNisse, *Appl. Phys. Lett.* 30 (1977) 290.
- [2] E.A. Irene, E. Tierney, J. Angillelo, *J. Electrochem. Soc.* 129 (1982) 2594.
- [3] E. Kobeda, E.A. Irene, *J. Vac. Sci. Technol. B* 4 (1986) 720.
- [4] E. Kobeda, E.A. Irene, *J. Vac. Sci. Technol. B* 5 (1987) 15.
- [5] P.J. Caplan, E.H. Pointdexter, B.E. Deal, R. R. Razouk, *J. Appl. Phys.* 50 (1979) 5847.
- [6] A. Stesmans, *Phys. Rev. B* 48 (1993) 2418.
- [7] K.L. Brower, *Phys. Rev. B* 33 (1986) 4471.
- [8] A. Stesmans, J. Braet, in: J.J. Simone, J. Buxo (Eds.), *Insulating Films on Semiconductors*, North-Holland, Amsterdam, 1986, p. 25.
- [9] A. Stesmans, B. Nouwen, *Phys. Rev. B* 61 (1999) 16068.
- [10] G.D. Watkins, J.W. Corbett, *Phys. Rev.* 134 (1964) 1359.
- [11] G. Van Gorp, A. Stesmans, *Phys. Rev. B* 45 (1992) 4344.
- [12] A. Stesmans, V.V. Afanas'ev, *Phys. Rev. B* 54 (1996) 11129.
- [13] A. Stesmans, V.V. Afanas'ev, *Appl. Phys. Lett.* 72 (1998) 2271.
- [14] J.T. Fitch, E. Kobeda, G. Lucovsky, E.A. Irene, *J. Vac. Sci. Technol. B* 7 (1989) 153.



ELSEVIER

Physica B 308–310 (2001) 485–488

PHYSICA B

www.elsevier.com/locate/physb

$C-V$ and $G-V$ characterization of defects in ultrathin SiO_2 thermally grown on RF plasma-hydrogenated silicon

S. Alexandrova^{a,*}, A. Szekeres^a, E. Halova^b^a *Institute of Solid State Physics, 72 Tzarigradsko Chaussee, Sofia 1784, Bulgaria*^b *Technical University, 8 Kl. Ohridski Blvd., Sofia 1797, Bulgaria*

Abstract

In the present study, results on the interface properties of ultrathin SiO_2 thermally grown on RF plasma-hydrogenated silicon structures are reported from a detailed study of the $C-V$ and $G-V$ characteristics taken at various frequencies. From frequency characterization, information is gained on the charged defects at the Si/SiO_2 interface. The frequency dispersion properties reveal the presence of either interface traps or laterally inhomogeneous distribution of defect centers within the oxide near the interface Si/SiO_2 . The amount and nature of the defects depend on the substrate temperature during plasma exposure. © 2001 Elsevier Science B.V. All rights reserved.

Keywords: Thermal SiO_2 ; Radiation-induced defects; Interface traps; Oxide charges

1. Introduction

Silicon surface cleaning before thermal oxidation is an essential step in the whole cycle of the fabrication of metal-oxide-Si (MOS)-based devices, especially in the deep submicron technological era. In recent years, this processing step has gained increased attention. Different techniques have been tested to obtain a stable and well-controlled surface, e.g. frozen gas bombardment [1] and organic contamination removal by UV/ozone [2]. Recently, we have suggested a RF hydrogen plasma treatment as a Si pre-oxidation cleaning procedure [3]. The fast initial oxide growth observed in this case would allow a better control of low-temperature oxidation at technologically reasonable times. The oxidation kinetics analysis has shown the formation of a defective surface overlayer, whose density is reduced by voids formation, left after the hydrogen plasma cleaning.

In the present study, results on the interface properties of the MOS structures with ultrathin SiO_2 grown thermally over hydrogenated silicon are reported from

a detailed study of the $C-V$ and $G-V$ characteristics at different frequencies between 10 kHz and 1 MHz. From the frequency characterization, information is gained on the charged defects at the Si/SiO_2 interface.

2. Experimental

In this study, the oxides were thermally grown to a thickness of about 13 nm in dry O_2 at a temperature of 850°C. The bare n-type (111)-oriented Si wafers of 5–10 Ωcm resistivity were initially treated by a typical wet RCA pre-gate oxide clean [4]. Shortly after cleaning, some of the wafers received dry cleaning by exposure to hydrogen plasma in a RF planar unit located on the lower grounded plate. The wafers were plasma treated with or without heating to 300°C. The gas pressure was 1 Torr; the input power at 13.56 MHz was 15 W. Some of the wafers were given an RCA clean only to serve as references.

For the electrical characterization, MOS capacitors were formed by vacuum evaporation of aluminum dots onto the thermally grown oxides followed by backside metallization.

*Corresponding author. Tel.: +359-2-7144513; fax: +359-2-9753632.

E-mail address: salex@issp.bas.bg (S. Alexandrova).

The $C-V$ and $G-V$ measurements were performed at room temperature in the frequency range 10 kHz–1 MHz. The measurement unit was a Precision Component Analyzer WAYNE KERR 6425.

3. Results and discussion

Fig. 1 gives the high frequency (10–200 kHz) $C-V$ characteristics of the MOS capacitors with oxides grown on RF plasma hydrogenated (111)Si. In this case, the silicon substrate was not heated during plasma hydrogenation. The $C-V$ characteristics show frequency dispersion. In the depletion region for a given gate voltage the capacitance increases with measurement frequency due to the time-dependent response of interface states. In accumulation no appreciable frequency dispersion is evident in this frequency range. At higher frequencies up to 1 MHz frequency dispersion related to the contribution of series resistance by the substrate was observed (not shown in Fig. 1) [5]. Because of this, the oxide capacitance was calculated from the MOS capacitance of the 10 kHz $C-V$ curve in strong accumulation, where the series resistance contribution is negligibly small. This value has been used further throughout the study for estimation of the defect concentrations.

The $G-V$ characteristics of the MOS capacitors are plotted in Fig. 2 for the same frequency interval. The conductance was found to increase with increasing measurement frequency.

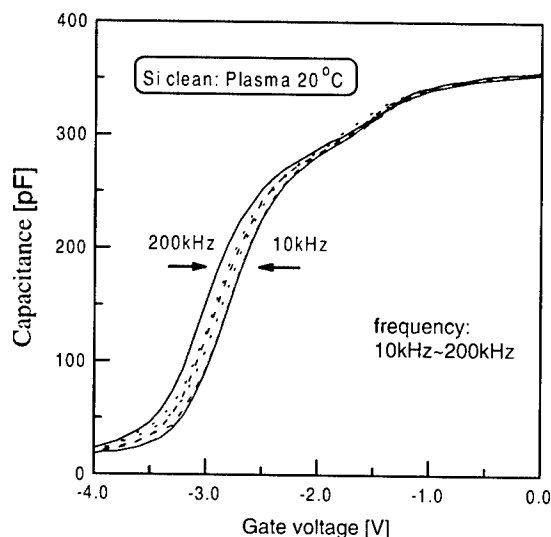


Fig. 1. Frequency dispersion of the $C-V$ curves of MOS capacitors with SiO_2 grown on (111)Si substrate hydrogenated in RF plasma without heating.

In Figs. 3 and 4 $C-V$ and $G-V$ characteristics of the MOS capacitors with Si substrates hydrogenated at a temperature of 300°C are displayed. Comparison with the results in Figs. 1 and 2 shows that silicon hydrogenation temperature plays an important role for the interface quality. At 300°C the $C-V$ curves shift to more positive voltages and shows much less frequency dispersion. The conductance peaks are substantially smaller. These results, indicating reduction in interface defect concentrations, can evidently be attributed to thermal annealing effect.

The specific shape of the $C-V$ curves as seen in Figs. 1 and 3 could also be indicative of nonhomogeneous distribution of the oxide charges [5].

The defect concentrations related to so-called fixed oxide charge and interface traps have been derived from the frequency dispersions of the $C-V$ and $G-V$ characteristics. The results are summarized in Table 1 where the concentrations of the reference oxides are also presented for comparative purposes.

The fixed oxide charge has been obtained from the difference between the experimental and theoretical flatband voltage and the values are given in Table 1. To obtain a more realistic estimation of the fixed oxide charge independent of the contribution of interface trap charge, an approximation approach has been applied based on simple high-frequency analysis of the $C-V$ frequency dispersion [6]. The approach requires examination of the linear dependence of the flatband voltages on logarithm of the measurement frequency. This linear relationship is displayed in Fig. 5 for two capacitors with silicon hydrogenated at two different temperatures. The

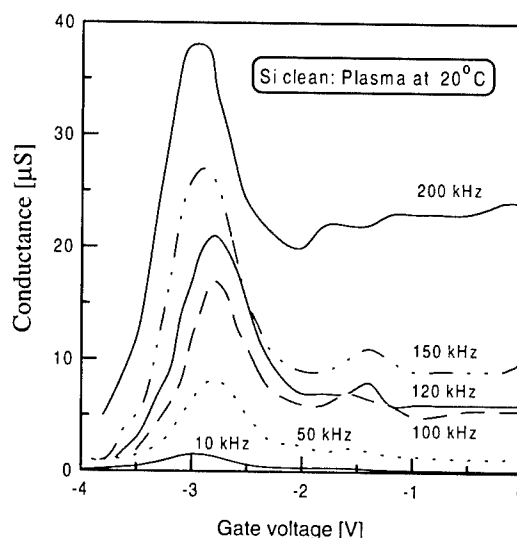


Fig. 2. Frequency dispersion of the $G-V$ curves of MOS capacitors with SiO_2 grown on (111)Si substrate hydrogenated in RF plasma without heating.

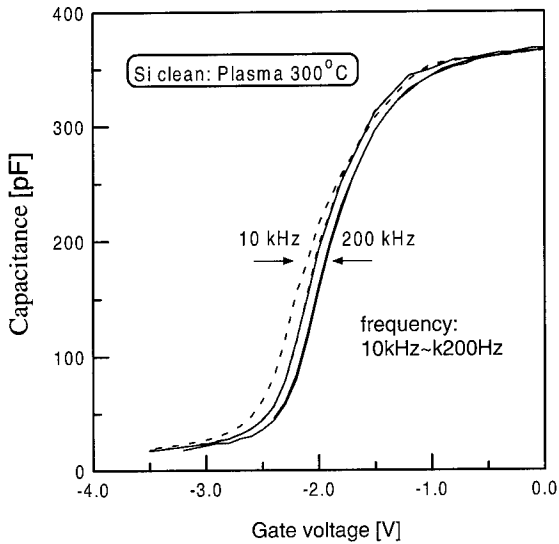


Fig. 3. Frequency dispersion of the $C-V$ characteristics of MOS capacitors with SiO_2 grown on (111)Si substrate hydrogenated in RF plasma at 300°C .

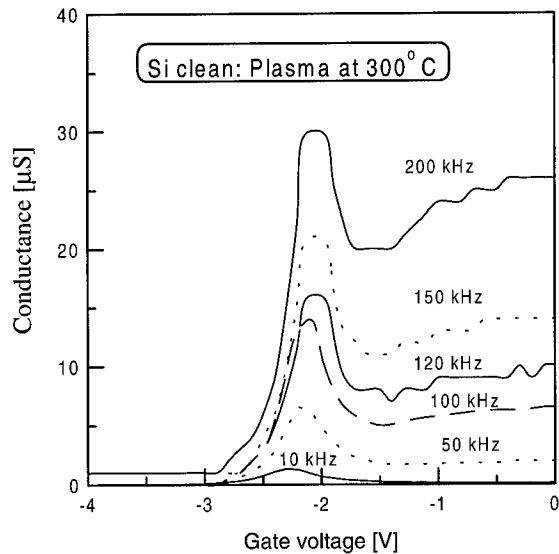


Fig. 4. Frequency dispersion of the $G-V$ characteristics of MOS capacitors with SiO_2 grown on (111)Si substrate hydrogenated in RF plasma at 300°C .

voltage V_f obtained from the interception of the two straight lines characterizes the intrinsic oxide charge $Q_f = C_{ox} V_f$ and amounts to $2.4 \times 10^{12} \text{ cm}^{-2}$. This charge can be regarded as inherent to the hydrogenated oxides. The variations observed in the fixed oxide concentration through the $C-V$ shifts are most probably related to charge located in interface traps.

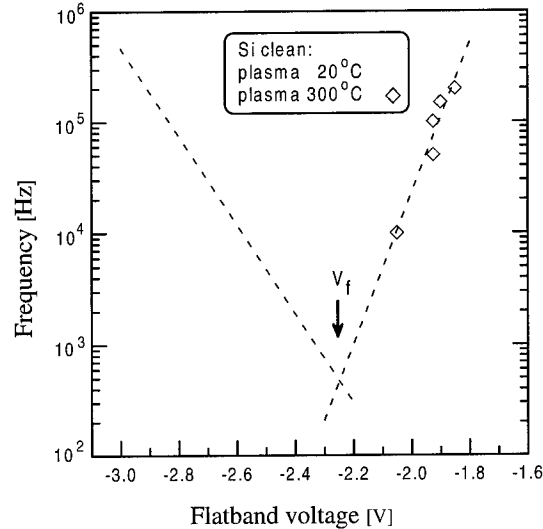


Fig. 5. High frequency approximation of flatband fixed oxide charge of SiO_2 grown on hydrogenated (111)Si substrate.

From Fig. 5 it can also be inferred that the frequency dispersion is more pronounced for lower hydrogenation temperature of the silicon, indicating higher overall density of defect centers.

Using the single-frequency approximation method developed in Ref. [7] the density of interface traps has been calculated. The results are presented in Table 1. It can be seen from the Table that the interface trap density, compared with the reference RCA silicon, is high for the silicon hydrogenated without heating and is reduced in silicon hydrogenated at elevated temperature (300°C). The higher density in the former case can be attributed to defects introduced by the plasma treatment during hydrogenation, which persist after oxidation. Formation of voids on silicon surfaces exposed to hydrogen plasma has been reported elsewhere [8]. The increase of the temperature up to 300°C seems to reduce the concentration of these surface defects. The concentration of the interface trap defect centers is consequently reduced to a level even below that of the reference MOS capacitor.

4. Conclusion

The electrical characterization of ultrathin (13 nm) SiO_2 , thermally grown on hydrogenated (111) silicon has revealed large interface defect densities (fixed oxide charge and interface traps) when hydrogenation has been performed without substrate heating. This is attributed to formation of defects on the Si surface. Increasing the temperature during hydrogenation results in lower defect densities ($1.7 \times 10^{11} \text{ eV}^{-1} \text{ cm}^{-2}$ and

Table 1

The interface defect densities of the Si/SiO₂ structures as obtained from *C–V* and *G–V* measurements

Si-substrate preparation	Fixed oxide charge (10^{12} cm^{-2})	Interface trap density ($10^{11} \text{ eV}^{-1} \text{ cm}^{-2}$)
Hydrogenated, without heating	4.8	20
Hydrogenated at 300°C	3.1	1.7
RCA	3.5	6.8

$3 \times 10^{12} \text{ cm}^{-2}$ for the interface traps and fixed oxide charge, respectively). The density of interface traps is decreased considerably in comparison to the standard RCA cleaned silicon. The reduction of the fixed oxide charge is apparently due to the contribution of charge trapped in interface states. An inherent fixed oxide charge value is evaluated ($\sim 2.4 \times 10^{12} \text{ cm}^{-2}$) from a high frequency *C–V* approximation.

Acknowledgements

This paper was presented at the 21st International Conference on Defects in Semiconductors thanks to the financial support of the Organizing Committee.

References

- [1] R. Sherman, D. Hirt, R. Vane, *J. Vac. Sci. Technol. A* 12 (1986) 1876.
- [2] G. Lippert, H.J. Osten, *J. Crystal Growth* 127 (1993) 476.
- [3] S. Alexandrova, A. Szekeres, *Thin Solid Films* 343/344 (1999) 385.
- [4] W. Kern, *RCA Rev.* 31 (1970) 871.
- [5] E.H. Nicollian, J.R. Brews, *MOS (Metal Oxide Semiconductor) Physics and Technology*, New York, Wiley, 1982.
- [6] S. Alexandrova, A. Szekeres, E. Halova, to be published.
- [7] W.A. Hill, C.C. Coleman, *Solid State Electron.* 23 (1980) 987.
- [8] P. Asoka-Kumar, H.J. Stein, K.G. Lin, *Appl. Phys. Lett.* 64 (1994) 1684.

Electrically active centers in partial dislocations in semiconductors

João F. Justo^{a,*}, Lucy V.C. Assali^b

^a Departamento de Engenharia de Sistemas Eletrônicos, Escola Politécnica da Universidade de São Paulo, CP 61548, CEP 05424-970, São Paulo, SP, Brazil

^b Instituto de Física da Universidade de São Paulo, CP 66318, CEP 05315-970, São Paulo, SP, Brazil

Abstract

We carried out a theoretical investigation on the properties of antiphase defects, or core reconstruction defects, in a 30° partial dislocation in Si and GaAs. The calculations were performed using ab initio total energy methods, based on the density functional theory. From the results on formation energies of these reconstruction defects, we predict that the concentration of dislocation-related electrically active centers should be considerably larger in GaAs than in Si. We also find that an antiphase defect in silicon may exist in positive, neutral, or negative charge states, with a Mott–Hubbard potential of 0.30 eV. © 2001 Elsevier Science B.V. All rights reserved.

Keywords: Extended defects; Point defects; Dislocations

1. Introduction

Dislocation motion is known to control the plasticity of materials. In semiconductors, they also affect the electronic properties by generating energy levels in the materials gap. As a result of the current requirements for device miniaturization, the physical properties of dislocations have attracted considerable interest over the last few years [1,2]. More recently, macroscopic properties of dislocations were found to be directly correlated to the atomistic events which occur inside the dislocation core [3–5]. In such a scenario, understanding the dislocation core properties became fundamental in order to develop better electronic devices. Here, we present a theoretical investigation on the structural and electronic properties of reconstruction defects which may form in the core of a 30° partial dislocation in silicon and in gallium arsenide.

In zinc-blende semiconductors, dislocations are generally confined to the {111} glide sets [6]. As a result of the strong covalent bonding, they are aligned along

$\langle 110 \rangle$ directions. It is energetically favorable for (screw and 60°) dislocations to dissociate into (30° and 90°) partial dislocations, with a stacking fault connecting the partials. In a III–V compound, such as gallium arsenide, dissociation may generate three types of dislocations: α , consisting of a 30° plus a 90° partial with the cores formed by type-V atoms; β , consisting of a 30° plus a 90° partial with the cores formed by type-III atoms; and a screw dislocation, consisting of two 30° partials, one of each type. In a type-IV semiconductor, α and β dislocations are identical. Here, we have focused our investigation on the 30° (α and β) partial dislocations because of their controlling role on the mobility of both 60° and screw dislocations [7].

Dislocations should generate a large number of electrically active centers, as a result of undercoordinated atoms in the dislocation core. Experimental data indicated otherwise, showing that semiconducting materials have low concentrations of dislocation-related active centers [8,9]. To overcome this apparent controversy, a model has been suggested in which atoms in the dislocation core recover their fourfold coordination by reconstruction, forming intra-core bonds [10]. Recent investigations have shown that core reconstruction of partial dislocations is, in fact, energetically favorable

*Corresponding author. Tel.: +55-11-3818-5256 (R. 217); fax: +55-11-3818-5585.

E-mail address: jjusto@lme.usp.br (J.F. Justo).

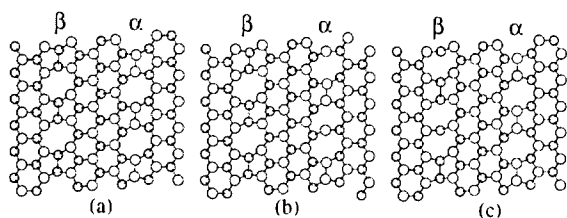


Fig. 1. Atomic configuration in a $\{111\}$ glide plane, with a 30° partial dislocation dipole lying along a $\langle 110 \rangle$ direction. The figure shows the α and β dislocations (a) with the reconstructed core, (b) with two α -APDs, and (c) with two β -APDs. Large and small circles represent atoms in the top (type V atoms) or in the bottom (type III atoms) of the glide plane, respectively. The figure only shows the intra-plane glide bonds.

[5,11]. Fig. 1a shows a $\{111\}$ glide plane containing the reconstructed cores of an α and a β 30° partial dislocation. Although core reconstruction is energetically favorable, it is still possible that a few of the core atoms remain unreconstructed at finite temperatures (Fig. 1b and c). These centers are called antiphase defects (APD), or reconstruction defects, and may generate electrically active centers in the gap of the material. Here, we have defined the α -APD and the β -APD as the reconstructed defects, respectively, in α and β dislocations in a III–V compound.

2. Theoretical model

Our calculations were performed using ab initio total energy methods. We considered a reference orthorhombic supercell with 288 atoms, in which a 30° partial dislocation dipole was introduced. The dislocation dipole contained an α and a β partial dislocation in GaAs, or two identical partials in Si. For the configurations presented in Fig. 1, an atomistic simulation based on ab initio methods is a formidable computational task. In order to perform such calculations, we initially relaxed the structures with a less expensive model, using an interatomic potential [12,13]. In such calculations, the shape of the super-cells was adjusted using the Parrinello–Rahman method [14], and therefore removing the internal stress generated by the dislocations. The output atomic configurations were used as input to the ab initio calculations, when full relaxation was finally performed. This two-step procedure can considerably reduce the computational cost in finding the equilibrium configurations, specially in the case of dislocations [15]. The ab initio [16] calculations were performed using the density functional theory in the local density approximation. The Kohn–Sham equations were solved by the Car–Parrinello scheme with norm-conserving pseudopotentials [17,18]. The electro-

nic wave functions were expanded in a plane-wave basis-set, with kinetic energy up to 10 Ry. The Brillouin zone was sampled by a set of two representative k -points [19]. These k -points were related to the dislocation line direction [5,20]. Geometric optimization of the atomic structures was performed by allowing atoms to relax until the Hellmann–Feynman forces were smaller than $0.02 \text{ eV}/\text{\AA}$.

3. Results and Discussions

Core reconstruction controls dislocation mobility, for example, activation energy for dislocation velocity scales with the core reconstruction energy [5,21]. From our calculations, we found that core reconstruction energy, or the energy required to break a core bond, is much larger for dislocations in Si than for α or β dislocations in GaAs. We found a reconstruction energy of 0.92 eV for a 30° partial dislocation in Si, while it is, respectively, 0.43 and 0.56 eV for $30^\circ\alpha$ and β partials in GaAs. Such a wide range of reconstructions energies is because reconstruction involves bonding between atoms of the same species. As a result, there is an additional electrostatic repulsion between the core atoms in GaAs as compared to Si, but still not strong enough to prevent core reconstruction. Bonds inside the dislocation core ranged from 2.27 to 2.49 \AA in Si, from 2.34 to 2.57 \AA in the α dislocation, and from 2.33 to 2.47 \AA in the β dislocation. For the bonds involved in the reconstructed core in silicon, angular distribution between bonds ranged from 92° to 124° , with an average of 108.8° . Several angles in the dislocation core were far away from the typical tetrahedral angle (109.47°). This may explain why even the reconstructed core generates energy levels in the materials gap [5].

We now consider the properties of the antiphase defects in Si and GaAs. In silicon, the APD formation energy is 0.82 eV . This value is in good agreement with another recent theoretical investigation [20], which found $(0.65 \pm 0.2) \text{ eV}$. It should be pointed out that the latter investigation [20] considered an artifact to use smaller simulations cells, which have compromised their result. From our results, the concentration of APDs in the dislocation core ($\rho = e^{-E_{\text{apd}}/k_B T}$) would be 10^{-5} of the atomic core sites at $T = 900 \text{ K}$. This value is consistent with experimental results on the concentration of electrically active centers in deformed silicon [8].

In the case of GaAs, formation energies are 0.36 and 0.44 eV for α -APD and β -APD, respectively. In both Si and GaAs, the APD energy scales with the respective core reconstruction energy, being around 80% of that energy. This provides a very good agreement with a recent model, in which it was suggested that dislocation activation energies scale with the dislocation core reconstruction energies [5]. With these low formation

energies of α and β -APDs, the concentration of electrically active centers should be considerably larger in deformed GaAs than in deformed Si. The bonds in an APD are considerably different from those in a reconstructed atom. In both Si and GaAs, we observed that the three respective neighboring atoms of an APD relax inward and form a near planar structure, with an average angle of 118° .

We additionally studied the electronic properties of the dislocation core in silicon, as shown in Fig. 2. As has been recently investigated, the unreconstructed core generates a half-filled one-dimensional band in the materials gap [5]. For the reconstructed core, this one-dimensional band splits up into a filled bonding and an empty antibonding state. On the other hand, an APD generates a bonding and an antibonding level inside the materials gap. The APD bonding level will be near the top of the dislocation-related bonding band, while the APD antibonding level would be at the bottom of the dislocation-related antibonding band.

The APD in silicon can stay in different charge states, depending on the position of the Fermi energy level. Here, the simulations were performed by removing (or inserting) two electrons in the system, and allowing all the atoms to relax. As shown in Figs. 1b or c, there were always two APDs in the simulation cells. Since these two APDs in each cell give degenerated energy levels in the materials gap, then by removing (or inserting) two electrons we could investigate the $+1$ (or -1) charge state of an individual APD. In order to understand the effects of an APD on the electronic conductivity of a deformed material, we searched for some electronic

charge trapping center resulting from the APD presence. For that, we computed the Mott–Hubbard potential (U) using the total energies of the system with the APD in neutral, positive and negative charge states. In the case of an APD in silicon, we found a positive $U = 0.30$ eV. This large Mott–Hubbard potential means that it is not energetically favorable for the APD in its neutral state to spontaneously capture an additional electron. Therefore, the APDs should be electrically active, being detectable by electron paramagnetic resonance (EPR) measurements.

In summary, we have investigated the structural and electronic properties of reconstruction defects in the core of a 30° partial dislocation in silicon and in gallium arsenide. We computed for the first time the formation energies of these antiphase defects. The concentration of APDs in the dislocation cores should be much larger in GaAs than in Si. We found that the formation energy of the antiphase defects scales with the respective reconstruction energy [5]. This suggests that all the energetics, and consequently the concentration of defects in the dislocation cores, should follow some universal scaling law. We additionally computed the Mott–Hubbard potential for an APD in silicon. The positive, and large, value of the potential indicates that the APDs in silicon are electrically active and detectable by EPR.

Acknowledgements

JFJ acknowledges the support of FAPESP (Fundação de Amparo à Pesquisa do Estado de São Paulo) under contract number 2000/11438-7. LVCA acknowledges the partial support of CNPq and FAPESP. The calculations were partially performed at the LCCA-CCE of the Universidade de São Paulo.

References

- [1] R. Labusch, W. Schröter, in: F.R.N. Nabarro (Ed.), *Dislocations in Solids*, Vol. 7, North-Holland, Amsterdam, 1980, p. 127.
- [2] H. Alexander, in: F.R.N. Nabarro (Ed.), *Dislocations in Solids*, Vol. 7, North-Holland, Amsterdam, 1986, p. 115.
- [3] V.V. Bulatov, J.F. Justo, W. Cai, S. Yip, A.S. Argon, T. Lenosky, M. de Koning, T. Diaz de la Rubia, *Philos. Mag. A* 81 (2001) 1257.
- [4] W. Cai, V.V. Bulatov, J.F. Justo, A.S. Argon, S. Yip, *Phys. Rev. Lett.* 84 (2000) 3346.
- [5] J.F. Justo, A. Antonelli, A. Fazzio, *Solid State Commun.* 118 (2001) 651.
- [6] J.P. Hirth, J. Lothe, *Theory of Dislocations*, Wiley, New York, 1982.
- [7] H. Alexander, H. Gottschalk, *Inst. Phys. Conf. Ser.* 104 (1989) 281.

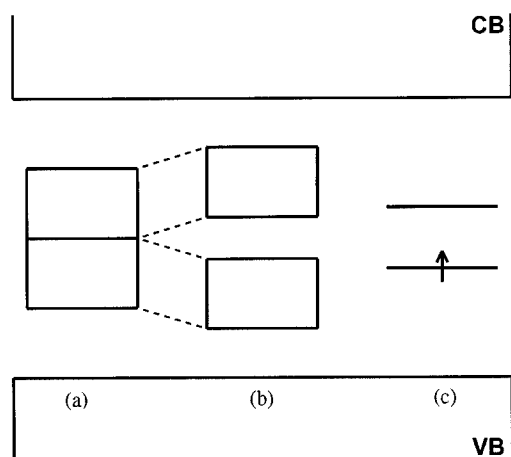


Fig. 2. Pictorial representation of the electronic band structure of a 30° partial dislocation in silicon. The figure shows the bands related to (a) the unreconstructed core, (b) the reconstructed core, and (c) the antiphase defect. Gray boxes represent filled electronic energy bands. VB and CB represent the valence and conduction bands, respectively.

- [8] E.R. Weber, H. Alexander, *J. Phys. (Paris) Colloq.* 44 (1983) C4–319.
- [9] H. Alexander, H. Teichler, in: R.W. Cahn, P. Haasen, E.J. Kramer (Eds.), *Materials Science and Technology*, Vol. 4, VCH, Weinheim, 1991, p. 249.
- [10] S. Marklund, *Phys. Stat. Sol. B* 100 (1980) 77.
- [11] J.R.K. Bigger, D.A. McInnes, A.P. Sutton, M.C. Payne, I. Stich, R.D. King-Smith, D.M. Bird, L.J. Clarke, *Phys. Rev. Lett.* 69 (1992) 2224.
- [12] M.Z. Bazant, E. Kaxiras, J.F. Justo, *Phys. Rev. B* 56 (1997) 8542.
- [13] J.F. Justo, M.Z. Bazant, E. Kaxiras, V.V. Bulatov, S. Yip, *Phys. Rev. B* 58 (1998) 2539.
- [14] M. Parrinello, A. Rahman, *J. Chem. Phys.* 76 (1982) 2662.
- [15] J.F. Justo, M. de Koning, W. Cai, V.V. Bulatov, *Phys. Rev. Lett.* 84 (2000) 2172.
- [16] M. Bockstedte, A. Kley, J. Neugebauer, M. Scheffler, *Comput. Phys. Commun.* 107 (1997) 187.
- [17] G.B. Bachelet, D.R. Hamann, M. Schluter, *Phys. Rev. B* 26 (1982) 4199.
- [18] L. Kleinman, D.M. Bylander, *Phys. Rev. Lett.* 48 (1982) 1425.
- [19] H.J. Monkhorst, J.D. Pack, *Phys. Rev. B* 13 (1976) 5188.
- [20] G. Csányi, S. Ismail-Beigi, T.A. Arias, *Phys. Rev. Lett.* 80 (1998) 3984.
- [21] J.F. Justo, V.V. Bulatov, S. Yip, *J. Appl. Phys.* 86 (1999) 4249.



ELSEVIER

Physica B 308–310 (2001) 493–496

PHYSICA B

www.elsevier.com/locate/physb

Kinetic Monte Carlo study of dislocation motion in silicon: soliton model and hydrogen enhanced glide

S. Scarle*, N. Martsinovich, C.P. Ewels, M.I. Heggie

CPES, University of Sussex, Falmer, Brighton, BN1 9QJ, UK

Abstract

The problems with dislocations in semiconductors are becoming tractable with modern computing by hybrid techniques. These apply static first principles calculations of energetics for important processes (e.g. kink formation and migration energies) and kinetic Monte Carlo techniques to follow the dynamic interaction of these processes over length and time scales inaccessible to, for example, molecular dynamic simulation. The simplest model system for covalent and ceramic solids is silicon, but there is debate over the structure and properties of dislocations there. The movement of the dislocation by the simple bond switching mechanism was studied from first principles, finding activation energies close to experiment, but lately the alternative mechanism invoking free radicals or solitons was found to give similar energies. We report results from an n-fold way kinetic Monte Carlo approach, applied to a simple system to verify the standard model for kink pair nucleation limited dislocation glide (the Hirth–Lothe model). We then apply an improved technique to the kinetics of the soliton model and to hydrogen enhanced dislocation glide. © 2001 Elsevier Science B.V. All rights reserved.

PACS: 61.72.Hh; 61.72.Bb; 61.72.Lk

Keywords: Monte Carlo simulation; Computer simulation; Dislocations; Silicon

1. Introduction

The strength of ductile materials is set by dislocation motion on the densest packed crystal glide planes. Dislocation motion comes about from the thermally activated process of generating kink pairs, which with the application of an external stress are forced apart. There is much evidence for the existence of kinks from pulse deformation, internal friction, weak-beam electron microscopy, and spectroscopy.

In this work we shall present two n-fold way kinetic Monte Carlo (nkMC) models of dislocation motion dynamics. From the first of which, general results from the model kink behaviour shall be shown and compared to the standard work in the field, Hirth–Lothe theory (HL) [1]. Following this, we shall use an improved description of the dislocation line in the nkMC to look

at soliton and hydrogen–soliton affected dislocation motion, at a 90° partial dislocation in silicon.

2. Description of models

Predictive calculation of mechanical properties is a fundamental problem in materials science. The only viable approach is using the idea of *multi-scale modelling*, where properties and energies of fundamental interactions are calculated using atomic scale techniques. The resulting data then being incorporated into larger scale simulations. We have taken previous density functional theory (DFT) calculations, carried out within the group using the AIMPRO code [2], and applied them to nkMC.

In both our models, dislocation segments are assumed to lie in Peierls minima. The lattice is infinite in the direction of motion and periodic in the direction perpendicular to the motion. The dislocation moves

*Corresponding author. Fax: +44-1273-677196.

E-mail address: s.scarle@sussex.ac.uk (S. Scarle).

under the influence of thermal fluctuations and an optional applied stresses. This is via the processes of double-kink nucleation and lateral kink motion in the basic point-wise model, whilst our more advanced model was run so as to include the motions of solitons and H-solitons, and hydrogen impacts on the dislocation line.

The initial state of the dislocation is taken to be perfectly straight, and it evolves via nkMC [3,4]. At each simulation step, all allowed *events* have a rate calculated for them. These can move the dislocation either with or against the stress, since thermal fluctuations can overcome the additional energy bias caused by the stress. Each event's rate is given by

$$R_i = \omega_0 \exp(-\Delta E_i/k_B T), \quad (1)$$

where i = event number, ΔE_i = energy barrier to event i and ω_0 = attempt frequency. The sum of all the rates is used to determine the time before the next event occurs, and the individual rates serve as probabilities for selecting each event.

Instead of attempting a random event and then accepting/rejecting it based on a criterion (the Metropolis Algorithm) [5]. We choose and execute an event from the entire list. So at each step, an event m is randomly chosen from the total M , such that

$$\frac{\sum_{i=0}^{m-1} R_i}{\sum_{i=1}^M R_i} < \xi_1 < \frac{\sum_{i=0}^m R_i}{\sum_{i=1}^M R_i}, \quad \Delta\tau = -\frac{\ln \xi_2}{\sum_{i=1}^M R_i}, \quad (2)$$

where $\Delta\tau$ = time increment, ξ_i = is a random number in the range 0–1. It is this variable time increment which makes nkMC more efficient than Metropolis when R_i 's differ greatly.

Our basic or point-wise model, is the standard manner of describing a dislocation line for Monte Carlo simulations [3,6,7]. The line is represented with a fixed number of sites. Each site i is characterized by its height H_i , being the distance travelled under the stress. For each site, movements up and down are possible which correspond to formation/annihilation or migration of kinks on the line. ΔE_i for these movements is calculated as follows: $\Delta E_i = 2F_k \pm s$ for backward and forward kink-pair nucleation, $\Delta E_i = -2F_k \pm s$ for backward and forward kink-pair annihilation $\Delta E_i = \pm s$ for backward and forward kink migration. With F_k = kink formation energy, $s = \sigma bhl$ the work done by the applied stress to move a kink, where σ = applied stress, b = Burger's vector, h = height of a kink and l = length of a site.

Our second and more flexible model uses what we call a *line-wise* description. The line is divided into a variable number of sections. Each section j is described by its length L_j sites, height H_j and what defect structure it ends with E_j (i.e. a positive or negative kink, soliton, etc.). Longer dislocation lines can be considered with this description, as nucleation events for entire sections of the line can be dealt with as a single event as opposed to many in point-wise. Also, it is far easier to introduce

further end structures to the simulation, and it is coded so that the properties of all ends required are fed in via a parameter file.

3. Investigation of HL model

It is known that dislocation motion is thermal activated with the following T dependence:

$$v = v_0 \exp\left(-\frac{E_A}{k_B T}\right) \quad (3)$$

and according to HL the activation energy $E_A = F_k + W_m$ = sum of kink formation energy F_k , and migration barrier W_m , for lines long enough to ensure that kink lifetime is limited by kink-kink annihilation (the length-independent regime). Whilst $E_A = 2F_k + W_m$ for lines shorter than the kink mean free path $\lambda \propto \exp(-F_k/k_B T)$ (the length-dependent regime).

Simulations were run using the point-wise model with $F_k = 0.2, 0.5$ and 0.8 , in the T range 400–1200 K with applied stress over $s = 0-0.8$ and $W_m = 0$. The dislocation line had 10,000 sites, but at low T in the length-dependent regime lines with 500–20,000 were considered. These parameters were chosen to test HL not to reproduce experimental data. The obtained results reflect basic theoretical predictions: velocity increases with increasing T , velocity faster at higher stress and small values of F_k , at very high $T > 5000$ K dependence of dislocation velocity is reversed and begins to decrease with T . As at high T thermal fluctuations become more influential than the applied stress and the dislocation motion stops being directed.

The T dependence of the dislocation velocity is of the right form; however, in the length regime $E_A \neq F_k$ as from HL, but $2F_k - 2s$. Whilst in the length-dependent regime it is $4F_k - 3s$; see Fig. 1. In order to find an explanation for these discrepancies kink-pair nucleation rate was obtained within the nkMC, and found to agree with HL:

$$J_N \sim \exp\left(-\frac{2F_k - s}{k_B T}\right). \quad (4)$$

The prefactor showing no F_k or s dependence. However, only kinks which survive can assist in the dislocation motion, so we consider fruitful kink-pair nucleation rate $J_F = J_N - J_A$ which is the difference between the rate of kink-pair nucleation J_N and annihilated J_A .

$$J_F \propto \exp\left(-\frac{4F_k - 3s}{k_B T}\right). \quad (5)$$

Using J_F in HL for dislocation velocity in the length-independent and length-dependent regimes gives the same T dependence of dislocation velocities as the nkMC.

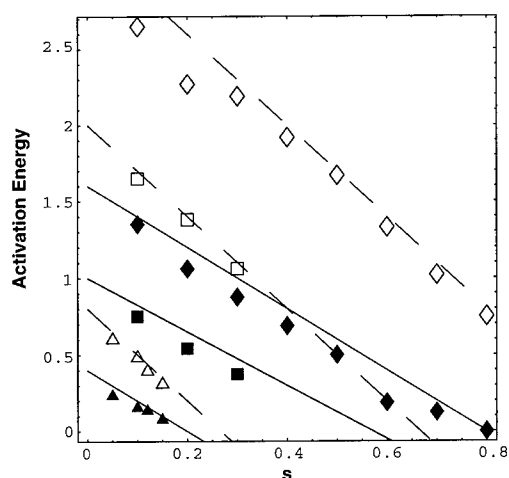


Fig. 1. Graph of E_A = activation energy vs. s . Points show nkMC calculations: triangles $F_k = 0.2$, boxes $F_k = 0.5$ and diamonds $F_k = 0.8$. Solid symbols for length independent and open ones for length dependent. Solid lines show $2F_k - 2s$ and dashed lines $4F_k - 3s$.

4. Soliton and HEDG results

There are two main atomistic models suggested for kink motion in Si, the Jones model or strained bond model, where kink formation and migration are by successive application of Stone–Wales transforms. AIMPRO calculations have given this an $E_A = 1.9$ eV [8]. The other model depends on solitons. The dislocation core of a 90° partial has a phase due to the left or right direction of its reconstruction bonds. At a phase boundary there exists anti-phase defects, or solitons, giving a dangling bond. In chemical terminology a ‘free radical’. It is highly reactive, so can migrate rapidly along the line nucleating kink pairs. These may occasionally be associated with kinks from time to time, but they have unequal lifetimes. AIMPRO calculations on this model give $E_A = 1.8$ eV. This means that both are in close agreement with other, and in broad agreement with experiment where $E_A = 2.2$ eV [9].

Dislocations in semiconductors can be strongly affected by a hydrogen plasma; core states may be passivated [10] and mobility changed. For Si, H reduces E_A from 2.2 to 1.2 eV, for hydrogen enhanced dislocation glide (HEDG) [9]. Assuming the soliton model, the steady state motion of the dislocation ought to be controlled by the migration and formation of solitons and hydrogenated or H-solitons, for which we use the previously published in-house results [11] produced using AIMPRO, for a soliton and a hydrogenated soliton on a 90° partial dislocation in Si, see Table 1. These results were used to form the simulation parameters for our nkMC. This work also appears to give $E_A \approx 1.2$ eV, as migration barriers for H-solitons

Table 1

Results from previous calculations [11]. Results from 231 atom clusters

Structure	Energy (eV)	
	without H	with H
Soliton migration barrier		
Along dislocation core	0.15	1.05 ^a
Initiating kink-pair	0.29	1.16
Formation energy compared to soliton		
Soliton: kink-pair	+0.11	−0.19

^aIndicates 186 atoms.

and kink H-soliton complexes ~ 1.1 – 1.2 eV. How the H is supplied to the dislocation is uncertain, since the effect depends on a pre-hydrogenation step (typically 1 h under H plasma between 470°C and 540°C). For our simulation, we shall take a population of H-atoms to be diffusing through the silicon and impacting the dislocation line. This H-flux may be expected to spontaneously nucleate soliton pairs and simultaneously, kink pairs, i.e., a complex of a H-soliton with a reconstructed kink pair will be formed in addition to a non-H-soliton. When two H-solitons meet they annihilate and we assume that the H_2 produced pipe diffuses out of the system.

Taking the kinetic theory result for atomic flux = $n\bar{v}/4$, where n = number density and \bar{v} = average particle velocity. With $\bar{v} = 3D/\lambda$, where λ = mean free path and D = diffusion coefficient = $9.1 \times 10^{-7} \exp(-0.48/k_B T) \text{ m}^2 \text{ s}^{-1}$, for c-Si [12]. Assuming that all H-atoms passing through the surface of a cylinder with radius λ centred on the dislocation line impact it, then the rate of impacts on section j will be $R_j = L_j D \pi n / 3$.

Fig. 2 shows our Arrhenius plot for the nkMC using the line-wise description with a shear stress of 70 MPa to match Yonenaga [9], analysis carried out on this plot gave this relation for dislocation velocity v_{dis}

$$v_{\text{dis}} = 6.8 \times 10^{-20} n^{0.98} \exp\left(-\frac{0.45}{k_B T}\right) \text{ m s}^{-1}, \quad (6)$$

where n = H concentration in cm^{-3} , v_{dis} increases with H-concentration in a basically linear fashion.

However, this $E_A = 0.45$ eV is far too low and seems to relate to our influx of H. We suspect that we are allowing our solitons too much freedom and their mean free path is too high, as we have no soliton H-soliton or soliton H interactions. We probably need to include a soliton capturing an H-atom event, and some form of mixed annihilation move whereby a soliton and a H-soliton annihilate to leave a bond centred H-atom (H_{BC}) in the dislocation core. This second move would require the inclusion of further H_{BC} interactions.

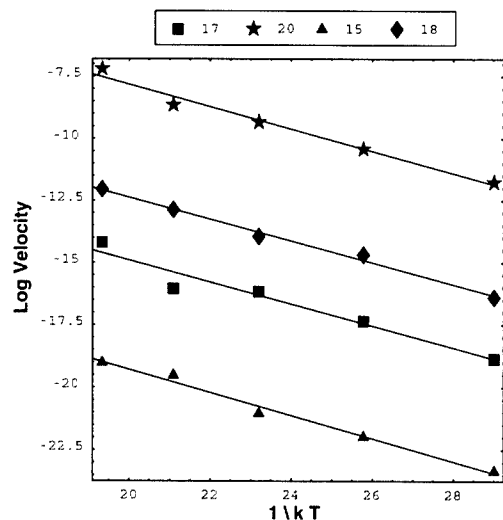


Fig. 2. Arrhenius plot of $\text{Log } v_{\text{dis}}$ versus $1/k_B T$ (eV). Legend gives x where $10^x \text{ cm}^{-3} = \text{H atom concentration}$.

5. Conclusions

Our starting work shows agreement to the standard HL theory once the annihilation rate of the kinks was correctly taken into account.

A new and highly adaptable approach to the Monte Carlo simulation of dislocations has been presented, through which the HEDG behaviour of 90° partial dislocations in Si has been investigated. This was in terms of solitons and H-solitons. This gave a $E_A = 0.45 \text{ eV}$, far too low, leading us to suspect further reactions need to be included.

However, the code used for this work is highly configurable meaning that these events can easily be

included. With the assistance of further AIMPRO calculations we will be able to look at the effect on dislocation motion from other dislocation defect structures, for example impurities and vacancies in the dislocation core.

Acknowledgements

We would like to thank the SHPCI for the use of the BFG.

References

- [1] J.P. Hirth, J. Lothe, Theory of Dislocations, Wiley, New York, 1982.
- [2] R. Jones, P.R. Briddon, Semicond. Semimet. 51A (1998) 287.
- [3] C.C. Battaile, et al., J. Appl. Phys. 82 (1997) 6293.
- [4] F.M. Bulnes, V.D. Pereyra, J.L. Riccardo, Phys. Rev. E 58 (1998) 86.
- [5] N. Metropolis, A.W. Rosenbluth, M.N. Rosenbluth, A.H. Teller, E. Teller, J. Phys. Chem. 21 (1953) 1087.
- [6] W. Cai, V.V. Bulatov, J.F. Justo, A.S. Argon, S. Yipp, Phys. Rev. Lett. 84 (2000) 33,463.
- [7] K. Lin, D.C. Chrzan, Phys. Rev. Lett. 60 (1999) 3799.
- [8] M.I. Heggie, R. Jones, Philos. Mag. B 48 (1983) 365, 48 (1983) 379.
- [9] Y. Yamashita, F. Jyobe, Y. Kamiura, K. Maeda, Phys. Status Solidi A 171 (1999) 27.
- [10] T. Sekiguchi, et al., J. Appl. Phys. 76 (1994) 7882.
- [11] C.P. Ewels, S. Leonì, M.I. Heggie, P. Jemmer, E. Hernández, R. Jones, P.R. Briddon, Phys. Rev. Lett. 84 (2000) 690.
- [12] H.M. Branz, Phys. Rev. B 60 (1999) 7725.



ELSEVIER

Physica B 308–310 (2001) 497–501

PHYSICA B

www.elsevier.com/locate/physb

Do we really need configuration interaction theory to understand the negative vacancy in silicon?

U. Gerstmann, E. Rauls, H. Overhof*, Th. Frauenheim

AG Theoretical Physics, Physics Department, University of Paderborn, D33095 Paderborn, Germany

Abstract

In its negative charge state, the lattice vacancy V^- in silicon experiences a C_{2v} Jahn–Teller distortion. In an LCAO picture, the unpaired electron of b_1 symmetry gives rise to a spin density that is concentrated in a $(1\bar{1}0)$ plane with a nodal (110) plane. Hence, the contact hyperfine (hf) interactions with all ligand nuclei in this plane should be zero. The order of magnitude of the nonzero albeit small contact interactions found experimentally was explained by configuration interaction (CI) theory. This raises the question whether the vacancy can be described without the incorporation of CI theory. We have performed an ab initio calculation using the standard local spin density approximation (LSDA) for the exchange–correlation interaction. We obtain the order of magnitude of the hf interaction with the nuclei in the (110) plane, if we just impose the C_{2v} symmetry on the unrelaxed V_{Si}^- defect state. When taking into account the properly relaxed ligand coordinates, we obtain quantitative agreement with experimental data. Thus for V_{Si}^- in silicon, correlation effects are important and are treated satisfactorily within the LSDA. © 2001 Elsevier Science B.V. All rights reserved.

PACS: 71.15.Mb; 71.55.Cn; 76.30.Da

Keywords: Configuration interaction; LSDA; Hyperfine interaction; Vacancies

1. Introduction

The first review [1] of the EPR spectra of the vacancy already showed that different charge states give rise to different symmetry-lowering Jahn–Teller distortions. In a simple LCAO picture the D_{2d} distortion of V_{Si}^+ and also the C_{2v} distortion of V_{Si}^- could be successfully explained [1,2].

A calculation of the electronic structure of the vacancy by ab initio methods proved to be a major challenge to theorists. Although the first total energy calculations were quite successful [3], it turned out that the calculation of the lattice relaxation was quite cumbersome (see e.g. Refs. [4–6]): the energy surface turned out to be extremely flat such that the position of

the minimum in the coordination space did depend on such details of the calculation like the supercell size and k-point sampling. It turns out that a supercell of at least 216 atoms is required to obtain the symmetry of the lattice relaxation predicted by the LCAO scheme [1] for the neutral vacancy.

For the vacancy in the paramagnetic V^- charge states extremely detailed experimental information is available from electron paramagnetic resonance (EPR) [1] and in particular from electron nuclear double resonance (ENDOR) experiment [7]. Yet, up to now most published theoretical papers dealt with V^0 and none did include spin polarization. The calculation of the hyperfine (hf) interactions with the ligand nuclei for V^- [8], based on the LDA ignoring spin polarization effects, simulates the magnetization density by the particle density of the unpaired gap state.

Since, this state transforms according to the b_1 irreducible representation of the point group C_{2v} , the

*Corresponding author. Tel.: +49-5251-60-2334; fax: +49-5251-60-3435.

E-mail address: h.overhof@phys.upb.de (H. Overhof).

particle density is concentrated in the $(1\bar{1}0)$ plane with a (110) nodal plane. Therefore, Sugino and Oshiyama [8] find the isotropic hf interaction to be zero by symmetry for all nuclei within this (110) plane. In contrast, experimental ENDOR data [7] exhibit small but nonzero contact hf interactions with several shells of nuclei within the (110) plane. Lannoo [9] has shown that the order of magnitude of these interactions can be accounted for in the LCAO picture if excited states are included in a configuration interaction (CI) scheme. This raises the question whether it is necessary to use CI in order to explain the small contact interactions with nuclei on the (110) plane.

In the local spin density approximation (LSDA), the spin density is represented by that of the Kohn–Sham orbitals. The paramagnetic state of V^- with spin $1/2$ is obtained by the occupation of the gap state which transforms according to b_1 with spin up, leaving the spin-down state of this orbital unoccupied. Since all the other orbitals are either unoccupied, or occupied both for spin-up and spin-down, the magnetization density reflects the b_1 symmetry. In a self-consistent calculation, however, the spin polarization of this b_1 orbital is transferred in part to all other Kohn–Sham orbitals. The resulting magnetization density, although still approximately reflecting the b_1 symmetry, may be nonzero even at the (110) nodal planes. Thus a LSDA treatment could in principle be sufficient to understand the hf interactions of V^- .

We investigate this question in the present paper. We start in the next section calculating the relaxed atomic geometry for the V^- state of the vacancy in a supercell calculation. With the atomic coordinates thus obtained we calculate the hf interactions. We show that while the larger interactions are found for nuclei in the $(1\bar{1}0)$ plane, much smaller interactions are found for nuclei in the (110) plane as observed experimentally. We obtain fair agreement of our calculated hf data with experimental ENDOR data [7]. Hence, there is no need to include CI into the calculation of the electronic state of V^- .

2. Total energy calculation of the relaxed geometry

For the calculation of the atomic geometry of the V^- defect we have used the self-consistent charge density-functional theory based tight-binding scheme (SCC-DFTB) [10]. In this calculation no spin polarization was taken into account. Our calculations were done for sc supercells containing 64, 216, and 512 atoms and for fcc supercells with 128 and 250 atoms, respectively. We relaxed all atoms in a conjugate-gradient calculation. Since the energy contour in the configuration space for V^0 is known to be extremely flat [6,5] we started with different point group symmetries (T_d , D_{2d} , C_{2v} , C_{3v} ,

and D_{3d}), keeping the symmetry constraint fixed during relaxation. We have also performed relaxations without symmetry constraints, obtaining similar results.

For the V^{2+} charge state the relaxation maintains the T_d symmetry corresponding to an energy gain of 1.1 eV. For the positive (neutral) charge states a D_{2d} Jahn–Teller distortion lead to an additional gain of 0.12 eV (0.29 eV).

For the negative charge state of the vacancy the 15% inwards relaxation of the nearest neighbors contributed 1.25 eV, while the D_{2d} and C_{2v} distortions accounted for 0.17 and 0.03 eV, respectively. Thus according to a spinless calculation we obtained for V^- a low-spin 2B_1 many-body ground state of C_{2v} symmetry. Since the alternative high-spin state could as well be the ground state, it is necessary to perform a spin-polarized calculation as well.

This has been done in a Green's function scheme using the relaxed coordinates of the SCC-DFTB calculation. Spin densities have been calculated using the linear muffin-tin orbitals method in the atomic-spheres approximation (LMTO-ASA) [11]. For the exchange-correlation potential we have used the LSDA results of Ceperley and Alder [12] in the Perdew–Zunger parametrization scheme [13], including the (small) spin polarization of the core states.

The energy of the 4A_2 high-spin state of V^- in T_d symmetry is by 0.09 eV larger than that of the 2B_1 state in C_{2v} symmetry. Although this difference of the total energies is quite small, we see that an ab initio calculation including the spin polarization predicts the 2B_1 ground state observed experimentally.

For V^- in silicon, the energy gain obtained by spin pairing with 0.11 eV is remarkably small, smaller by a factor of 3 (5) if compared with the respective value for the V_{Si}^- in SiC (V_C^- in diamond). In all cases the main contribution to the relaxation energy comes from the rather large tetrahedral inwards breathing relaxation (–1.25 eV for V^-), whereas the pairing contributes only –0.2 eV to the relaxation energy.

When relaxing the positions of the four nearest neighbors exclusively, we found the two neighbors (a and d in the notation of [1]) in the $(1\bar{1}0)$ plane to move somewhat closer than neighbors b and c . The same was observed by Sugino and Oshiyama [8] in their 64 atom supercell. However, when relaxing the next nearest neighbors as well, the orthorhombic relaxation is reversed, with an $a-d$ distance that is by 10% larger than the $b-c$ distance.

3. Hyperfine interactions

The hf interactions have been calculated using the LMTO-ASA Green's function scheme. For the vacancy in the singly positive charge state we obtain hf

interactions with the nearest neighbors which amount to $a = -99$ MHz and $b = -14.8$ MHz, values that compare well with the experimental data of 103.5 and 13.9 MHz ([1], the absolute signs have not been determined).

Our primary interest is focused on the negative charge state of the vacancy, because here experimental ENDOR data suggested the necessity of a CI calculation. We find minor changes only for the hf interactions with the nuclei in the $(1\bar{1}0)$ plane denoted by *Mad*, if we compare results obtained with spin polarization with those calculated ignoring spin polarization (as in Ref. [8]). But of course, for the nuclei in the (110) plane (denoted by *Mbc* and by *T*, respectively) the contact hf interactions are zero by symmetry in a calculation without spin polarization (as in Ref. [8]). The results listed in Table 1, obtained including spin polarization, compare hf interactions obtained for unrelaxed lattice positions, however assuming a C_{2v} symmetry of the defect, with those for fully relaxed coordinates, and with experimental ENDOR data [7]. Note that for the experimental contact interactions positive values have been assumed. As is evident from Table 1, the contact interactions for most *Mad* nuclei are negative. Since for ^{29}Si the nuclear gyromagnetic factor is negative, this means that the magnetization density at these nuclei is positive. Fig. 1 shows the spin density and the magnetization densities for V^- in the $(1\bar{1}0)$ and (110) planes, respectively. It is evident that most of the hf interaction with the *Mad* nuclei originates directly from the spin density of the gap state. The interactions with the *Mbc* nuclei are about two orders of magnitude

smaller in modulus than those with the *Mad* nuclei in the $(1\bar{1}0)$ plane. Yet the agreement with experimental data for the latter is comparable to the agreement observed for the former.

It is interesting to compare the magnetization densities in the (110) plane with the particle densities shown in Fig. 1. For the a_1' gap state (occupied both with spin-up and spin-down) the induced magnetization density is negative and closely resembles the (positive) particle density both in the (110) and the $(1\bar{1}0)$ plane, whereas for the a_1' resonance the induced magnetization is positive in both planes. In summary, the total magnetization density in the $(1\bar{1}0)$ plane is positive in rather large regions between the nuclear positions, however, with very small negative values at most of the *Mbc* nuclei. Among the excited configurations with 2B_1 symmetry the term denoted Ψ_4 in Ref. [9], for which the a_1' state is occupied as spin-up and the a_1' is occupied as spin-down, would lead to a magnetization density that matches that of the LSDA calculation for the (110) plane. The present LSDA predicts the magnetization density at the *Mad* nuclei to be negative (with the possible exception of *Mbc5*). Unfortunately, this prediction cannot be checked against experiment because the absolute signs of the experimental contact hf interactions are not known.

5. Conclusions

We have confirmed that the ligand hf interactions with the *Mad* nuclei can be obtained from the spin density of the unpaired gap state. However, the much

Table 1
Ligand hyperfine parameters for the V^- in silicon^a

Shell		Unrelaxed			Relaxed			Experimental		
		<i>a</i>	<i>b</i>	<i>b'</i>	<i>a</i>	<i>b</i>	<i>b'</i>	<i>a</i>	<i>b</i>	<i>b'</i>
<i>Mad1</i>	(1, 1, 1)	-230	-26.8	-0.1	-242.	-22.9	-0.59	355.8456	22.3034	1.2629
<i>Mad2</i>	(2, 2, 0)	-21.0	-3.4	-0.37	-35.1	-7.4	-0.08	50.2032	5.4894	0.6627
<i>Mad3</i>	(3, 3, 1)	-26.4	-0.10	-0.04	-14.6	-3.17	-0.14	30.5211	3.6690	0.2911
<i>Mad?</i>	(1, 1, $\bar{3}$)	0.12	-0.08	-0.05	-0.73	-0.26	-0.09			
<i>Mbc1</i>	(1, $\bar{1}$, 3)	2.24	0.08	0.08	1.81	0.14	0.10	2.1058	0.1763	0.0969
<i>Mbc2</i>	(2, $\bar{2}$, 0)	1.08	0.09	0.04	0.94	0.12	0.04	1.9976	0.2043	0.1757
<i>Mbc3</i>	(2, $\bar{2}$, 4)	1.02	0.04	0.03	0.82	0.05	0.03	0.8305	0.0674	0.0358
<i>Mbc4</i>	($\bar{2}$, 2, $\bar{4}$)	0.17	-0.002	0.003	0.25	-0.03	0.01	0.2096	-0.0319	0.0078
<i>Mbc5</i>	(1, $\bar{1}$, $\bar{1}$)	2.94	-0.28	0.204	-0.053	0.61	0.28	0.2038	0.6805	0.0744
<i>Mbc?</i>	(3, $\bar{3}$, $\bar{1}$)	0.21	-0.033	-0.005	0.022	-0.025	0.023			
<i>T1</i>	(0, 0, 4)	0.37	0.07	0.04	0.44	0.06	0.05	0.6662	-0.0741	-0.0323
<i>T2</i>	(0, 0, $\bar{4}$)	0.14	-0.027	-0.029	0.17	-0.12	0.03	0.2827	0.0327	0.0006

^aThe ligand hf interactions calculated for an unrelaxed V^- with a C_{2v} symmetry constraint and for the V^- with the relaxed coordinates from the SCC-DFTB calculation are compared with the experimental ENDOR data of Sprenger et al. [7].

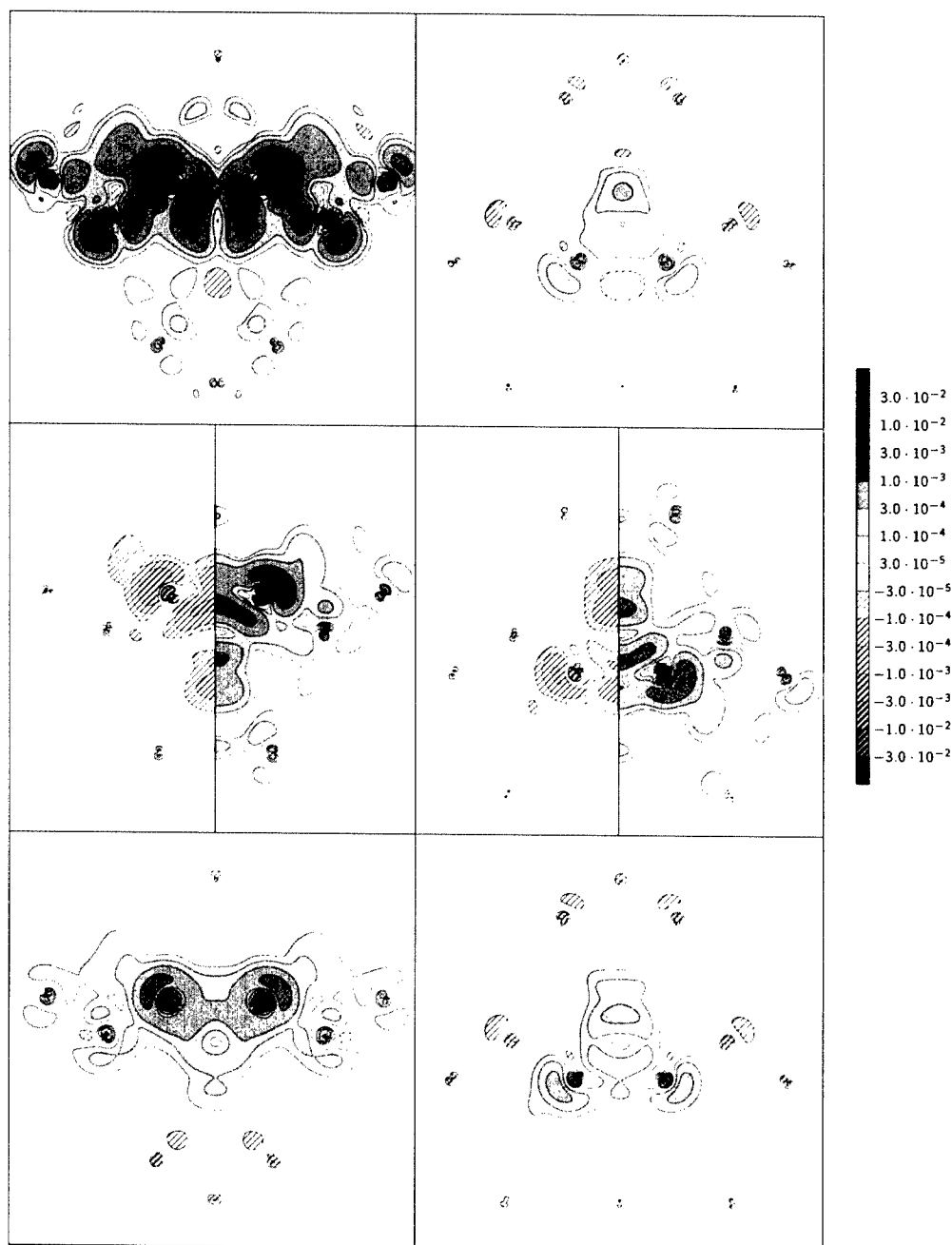


Fig. 1. Contour plots for the V^- vacancy. The top row shows the total magnetization density in the $(1\ 1\ 0)$ (left) and $(1\ \bar{1}\ 0)$ planes (right). In the center row the figures are split into magnetization density (left half) and particle density (right half) for the a' state in the $(1\ \bar{1}\ 0)$ (left figure) and $(1\ 1\ 0)$ planes (right figure). In the lower row the magnetization density induced in the valence band is shown in the $(1\ \bar{1}\ 0)$ plane (left) and in the $(1\ 1\ 0)$ plane (right).

smaller interactions with the Mbc and T nuclei cannot be obtained without a fair representation of the lattice relaxation and of the spin polarization that is caused by the unpaired spin of the gap state. The fair agreement with experimental data shown in this paper proves that

for V^- spin polarization effects are important and can be satisfactorily treated within the LSDA, without the need to include CI terms. This is quite fortunate, since presently quantitative CI calculation for V^- would be extremely ambitious.

Acknowledgements

We would like to thank the Deutsche Forschungsgemeinschaft for partial financial support for this work.

References

- [1] G.D. Watkins, in: P. Baruch (Ed.), *Radiation Damage in Semiconductors*, Dunod, Paris, 1965, pp. 97–113.
- [2] G.D. Watkins, in: S.T. Pantelides (Ed.), *Deep Centers in Semiconductors*, Gordon and Breach, New York, 1986, pp. 147–183.
- [3] G.A. Baraff, E.O. Kane, M. Schlüter, *Phys. Rev. B* 21 (1980) 5662.
- [4] M. Scheffler, J.P. Vigneron, G.B. Bachelet, *Phys. Rev. B* 31 (1985) 6541.
- [5] M.J. Puska, S. Pöykkö, M. Pesola, R.M. Nieminen, *Phys. Rev. B* 58 (1998) 1318.
- [6] J.L. Mercer, J.S. Nelson, A.F. Wright, E.B. Stechel, *Modelling Simul. Meter. Sci. Eng.* 6 (1998) 1.
- [7] M. Sprenger, S.H. Muller, E.G. Sieverts, C.A.J. Ammerlaan, *Phys. Rev. B* 35 (1987) 1566.
- [8] O. Sugino, A. Oshiyama, *Phys. Rev. Lett.* 68 (1992) 1858.
- [9] M. Lannoo, *Phys. Rev. B* 28 (1983) 2403.
- [10] Th. Frauenheim, G. Seifert, M. Elstner, Z. Hajnal, G. Jungnickel, D. Porezag, S. Suhai, R. Scholz, *Phys. Stat. Sol. B* 217 (2000) 41.
- [11] O. Gunnarson, O. Jepsen, O.K. Anderson, *Phys. Rev. B* 27 (1983) 7144.
- [12] D.M. Ceperley, B.J. Alder, *Phys. Rev. Lett.* 45 (1980) 566.
- [13] P. Perdew, A. Zunger, *Phys. Rev. B* 23 (1981) 5048.



ELSEVIER

Physica B 308–310 (2001) 502–505

PHYSICA B

www.elsevier.com/locate/physb

Equilibrium concentration of vacancies under the anisotropic stress field around and impurity

K. Tanahashi^{a,b,*}, N. Inoue^a, Y. Mizokawa^b

^aRIAST, Osaka Prefecture University, 1-2, Gakuencho, Sakai, Osaka 599-8570, Japan

^bCIAS, Osaka Prefecture University, 1-1, Gakuencho, Sakai, Osaka 599-8531, Japan

Abstract

Equilibrium concentration of vacancies under the anisotropic stress field around an impurity is investigated. The anisotropy of the work by anisotropic stress is considered. Threshold change of equilibrium concentration of vacancies corresponding to the reported change of void density by B and Sb doping is found. By using this, we can predict the void density change in doped Si. © 2001 Published by Elsevier Science B.V.

Keywords: Equilibrium concentration; Vacancies; Impurities; Stress

1. Introduction

Void defects (vacancy type defects) were found in as-grown Czochralski silicon (CZ) crystal. These cause the degradation of metal-oxide-semiconductor device performance [1]. Therefore, epitaxial wafer, which excludes void defects in device active region, has been used for hi-end devices. High concentration boron (B) doped CZ-Si is used as substrate of epitaxial film. It has been reported that the number of void defects decreases and the location of the oxidation induced stacking fault ring (OSF-ring) moves inward by high concentration B doping in CZ-Si [2]. Recently, there is a tendency that B concentration in epitaxial wafer decreases. This means that decrease of void defects due to B doping is suppressed. To control void defects, it is important to clarify the mechanism of the change of ones due to impurity doping. The change of defects is considered to be due to the change of point defect

concentration. Though various models such as Fermi level effect [3] and size effect [4] are proposed for the origin of point defect concentration change by doping, it is not clear yet.

We have been investigated the effects of stress on the behavior of point defects in a growing crystal [5]. We considered the change of equilibrium concentration of vacancies by the impurity doping is due to stress around impurity. On the basis of experimental data on increase of vacancy concentration due to Sn doping [6], we have successfully analyzed this by performing phenomenological treatment of equilibrium concentration change of vacancies as stress effect [7]. In this paper, we analyze this further by considering the anisotropic stress field around an impurity in detail. In Section 2, basic equations for the equilibrium point defect concentration under isotropic stress and the anisotropic stress field around an impurity are described. In Section 3, we consider the anisotropy of the work under the anisotropic stress field and formulate equilibrium concentration of vacancies in impurity doped Si. In Section 4, we calculate the change of equilibrium concentration of vacancies corresponding to the impurity species and concentration, which changes void density. We show that the change of void defects due to impurity doping is caused by stress by the impurity.

*Corresponding author. Tel: +81-722-51-5634; fax: +81-722-54-9935. Present address: Fujitsu Laboratories.

E-mail address: tanahashi@riast.osakafu-u.ac.jp (K. Tanahashi).

2. Basic equations

2.1. Equilibrium concentration of vacancies under isotropic stress

Previously, Cowern et al. [8] have formulated equilibrium concentration of vacancies under the homogeneous stress field [8]. It is determined by the work by stress, which is the product of stress σ and relaxation volume ΔV_F (<0) and given as

$$C_V^{\text{eq}} = C_0^{\text{eq}} \exp\left(\frac{\sigma \Delta V_F}{kT}\right). \quad (1)$$

Here, C_0^{eq} is equilibrium concentration in stress-free crystal. Equilibrium concentration increases under the compressive stress ($\sigma < 0$), because the work for formation of vacancy is positive ($\sigma \Delta V_F > 0$).

2.2. Anisotropic stress field around an impurity

Stress field around an impurity in Si matrix is not known yet. Rigid sphere insertion model has been used for the stress around an impurity whose size is different from the matrix atoms [9], i.e., silicon atom is removed from the matrix and impurity atom is put into the vacant site. Fig. 1 is the schematic illustration of displacement of silicon atoms around a large impurity. According to rigid sphere insertion model, around the large impurity compressive stress occurs along the radial (r) direction from the impurity and tensile stress does along its normal (θ and ϕ) directions. Displacement of silicon atom, u , is inversely proportional to the square of distance from impurity r and stress σ is inversely proportional to the cubic of one. They are described as follows:

$$u = \frac{c}{r^2}, \quad (2)$$

$$\sigma_{rr} = -4\mu \frac{c}{r^3}, \quad \sigma_{\theta\theta} = \sigma_{\phi\phi} = 2\mu \frac{c}{r^3}, \quad (3)$$

where $c = 4(r_i - r_0)r_0^2$ ($r \geq 2r_0$). Here r_i and r_0 are the atomic radius of impurity and silicon atom, respectively. μ is the shear modulus. It is to be noted that the stress field around impurity is highly anisotropic. Thus, we have to extend the theory by Cowern et al. to the case of anisotropic stress field.

3. Equilibrium concentration of vacancies under the anisotropic stress field around impurity

3.1. Anisotropy of the work under the anisotropic stress field around impurity

Equilibrium concentration of point defects under stress is determined by the work. The values of stress and relaxation volume are necessary to calculate the work. Stress is given in Section 2. Thus, we discuss another important factor, relaxation volume here.

As shown in Fig. 1, total work for formation of vacancies under the stress is sum of each component of the work along to r , θ and ϕ directions at the distance r from the impurity.

$$w_V = \sigma_{rr}\Delta V_r + \sigma_{\theta\theta}\Delta V_\theta + \sigma_{\phi\phi}\Delta V_\phi, \quad (4)$$

where ΔV_r , ΔV_θ and ΔV_ϕ are the relaxation volumes along r , θ and ϕ directions, respectively, as shown in Fig. 1. Fig. 2 is the schematic illustration of the change of relaxation volume under the anisotropic stress field around impurity. Fig. 2(a) shows the configuration of silicon atoms under the homogeneous stress field. Dotted line in Fig. 2(b) is the atomic volume corresponding to each atom in Fig. 2(a). Relaxation volume for formation of vacancies under homogeneous stress field is isotropic as shown by the broken line in Fig. 2(b). So far, there is no consideration of the change of relaxation volume under the anisotropic stress field. Here, we consider that the relaxation volume under the anisotropic stress field ΔV_F is changed anisotropically from that under the isotropic stress to relax anisotropic

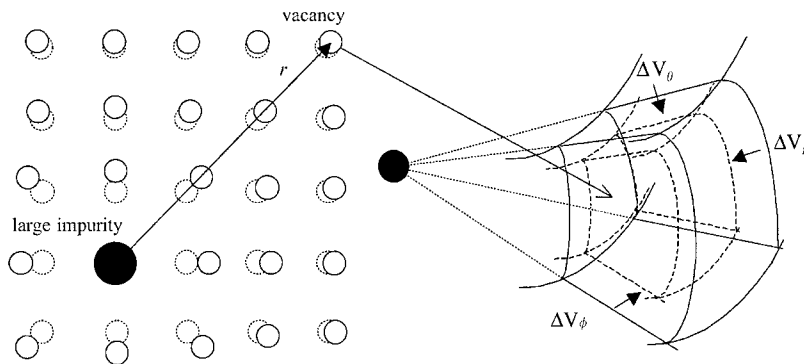


Fig. 1. Schematic illustration of displacement of silicon atom and volume change for formation of vacancy around a large impurity.

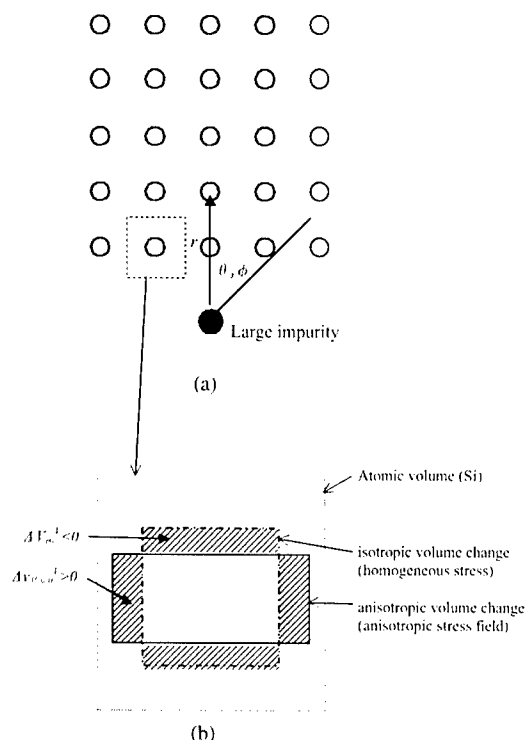


Fig. 2. Schematic illustration of the change of relaxation volume under the anisotropic stress field around an impurity.

stress. In case of large impurity doping as shown in Fig. 2(a), the inward relaxation around vacancy (displacement of surrounding atomic) is increased along the r direction (compressive), whereas decreased in the θ and ϕ directions (tensile) indicated by solid line in Fig. 2(b).

Next, we calculate w_V . Under the isotropic stress field, because of $\sigma_{rr} + \sigma_{\theta\theta} + \sigma_{\phi\phi} = 0$ as shown in Eq. (3), the sum of work by the homogeneous relaxation is zero. Under the anisotropic stress field, the relaxation volume changes to the hatched anisotropic region in Fig. 2(b). We call these anisotropic components of relaxation volume, Δv . In large impurity doped Si as shown in Fig. 2(b) it is clear that $\Delta v_r < 0$, $\Delta v_\theta > 0$, $\Delta v_\phi > 0$.

Because of $\sigma_{rr}\Delta v_r > 0$ ($\because \sigma_{rr} < 0$), $\sigma_{\theta\theta}\Delta v_\theta > 0$ ($\because \sigma_{\theta\theta} > 0$) and $\sigma_{\phi\phi}\Delta v_\phi > 0$ ($\because \sigma_{\phi\phi} > 0$) in large impurity doped Si, w_V is always positive and equilibrium concentration of vacancy increases. For the quantitative discussion, relaxation volume should be examined in more detail. Relaxation of stress is achieved by the removal of displacement u by impurity. Therefore, it is assumed that Δv has the same dependence on r with u . It is inversely proportional to the square of r and described as

$$\Delta v_{r,\theta,\phi} = \Delta v_{r_0,\theta_0,\phi_0} \frac{(2r_0)^2}{r^2}, \quad (5)$$

where Δv_0 is the relaxation volume for formation of vacancy at nearest-neighbor ($2r_0$) of impurity. Substituting Eqs. (3) and (5) into Eq. (4), w_V is described as a function of r ,

$$\begin{aligned} w_V &= -4\mu c \frac{1}{r^3} \times \Delta v_{r_0} \frac{(2r_0)^3}{r^2} + 2\mu c \frac{1}{r^3} \times \Delta v_{\theta_0} \frac{(2r_0)^3}{r^2} \\ &\quad + 2\mu c \frac{1}{r^3} \times \Delta v_{\phi_0} \frac{(2r_0)^3}{r^2} \\ &= -4\mu c \frac{(2r_0)^2}{r^5} \left(\Delta v_{r_0} - \frac{\Delta v_{\theta_0}}{2} - \frac{\Delta v_{\phi_0}}{2} \right) \\ &= -4\mu c \frac{(2r_0)^2}{r^5} \Delta V_R. \end{aligned} \quad (6)$$

Here $\Delta v_{r_0} - (\Delta v_{\theta_0}/2) - (\Delta v_{\phi_0}/2) = \Delta V_R$.

3.2. Formulation of equilibrium concentration of vacancies under the anisotropic stress by impurity

Using the work obtained in the above section, equilibrium concentration of vacancies under the anisotropic stress field is formulated. For simplicity, homogeneous distribution of impurities with constant distance d is considered. The work averaged from neighboring site of impurity, $2r_0$, to $d/2$ is given as

$$\begin{aligned} W &= \frac{\int_{2r_0}^{d/2} -4\mu c (2r_0)^2 / r^5 \Delta V_R 4\pi r^2 dr}{4\pi/3(d/2)^2 - 4\pi/3(2r_0)^2} \\ &= -48\mu c \Delta V_R \frac{1}{d^3}. \end{aligned} \quad (7)$$

The relationship of $1/d^3 = N$ (N is the concentration of impurity) is held for a homogeneous distribution. Therefore the work is given as a function of N ,

$$W = -48\mu c d^3 V_R N. \quad (8)$$

Using the work shown in Eq. (8), equilibrium concentration is given as

$$\begin{aligned} C_0^{\text{eq}} &= C_0^{\text{eq}} \exp(\sigma \Delta V_F / kT) \\ &= C_0^{\text{eq}} \exp(W / kT) \\ &= C_0^{\text{eq}} \exp(-48\mu c \Delta V_R N / kT) \\ &= C_0^{\text{eq}} \exp\{-192\mu(r_i - r_0)r_0^2 \Delta V_R N / kT\}, \end{aligned} \quad (9)$$

where C_0^{eq} is equilibrium concentration in undoped crystal. So far, the effect of stress due to impurity doping on the change of equilibrium concentration of vacancies is not known. In this paper, thus, it is found that the equilibrium concentration of vacancies has an exponential dependence on the product of $(r_i - r_0)$ and N . This is interpreted as follows; work per impurity is determined by the stress, i.e. difference of atomic radius between silicon and impurity. Also the work per unit volume is proportional to the number of impurity N .

4. Analysis of void density change by the stress due to impurity doping

Now, we calculate the equilibrium concentration of vacancies and discuss its role in the reported change of void densities by impurity doping. Recently, Ono et al. [10] reported that Sb doping increases COP (void) density in addition to the well known decrease of one by B doping [10]. In their report, B doping for $6 \times 10^{18}/\text{cm}^3$ and $1.5 \times 10^{19}/\text{cm}^3$ decreases void density, whereas Sb doping for $5 \times 10^{18}/\text{cm}^3$ increases one. On the other hand, B doping for $1 \times 10^{15}/\text{cm}^3$ does not change void density and the number of void defects in $1 \times 10^{18}/\text{cm}^3$ Sb doped Si is the same as that. Therefore, we consider that Sb doping for $1 \times 10^{18}/\text{cm}^3$ does not affect the void density.

The changes of equilibrium concentration of vacancies corresponding to impurity concentration corresponding to void density changes are calculated. Only unknown parameter for calculation is ΔV_R . It is assumed to be -6.67 \AA^3 ($\frac{1}{3}$ of atomic volume of silicon). Fig. 3 shows calculated results. Decreases of vacancy concentration by B doping for $1 \times 10^{15}/\text{cm}^3$, $6 \times 10^{18}/\text{cm}^3$ and $1.5 \times 10^{19}/\text{cm}^3$ are 0.0002% (cross mark), 0.96% (closed circle) and 2.39% (closed circle), respectively. On the other hand, increase of one by Sb doping for $1 \times 10^{18}/\text{cm}^3$ and $5 \times 10^{18}/\text{cm}^3$ are 0.011% (cross mark) and 0.53% (open circle), respectively. Though these values change by changing ΔV_R , relative amount keeps the same tendency. It is to be noted that the threshold changes of equilibrium concentration of vacancies required for void density change are nearly equal in the two cases (dotted lines in Fig. 3), irrespective of the dopant type, atomic size difference and impurity concentration. This supports that the change of void density is caused by the stress effect. As the threshold vacancy concentration corresponding to

void density change is found, we can predict void density change in any impurity doped Si.

5. Summary

We examine the stress effect due to impurity doping on the change of equilibrium concentration of vacancy. Considering the anisotropy of the work by the anisotropic stress due to impurity, equilibrium concentration of vacancies is formulated. The changes of equilibrium concentration of vacancies are calculated in B and Sb doped Si where void density change is reported. Threshold value corresponding to void density change is found, irrespective of the dopant type, atomic size difference and impurity concentration. This makes it possible to predict void density change in impurity doped Si.

Acknowledgements

We are grateful to Dr. H. Yamada-Kaneta for stimulating discussion and Y. Minamino for help in preparation of the manuscript. This work was partially supported by JSPS Research for the Future Program.

References

- [1] M. Itsumi, H. Akiya, T. Ueki, M. Tomita, M. Yamawaki, *J. Appl. Phys.* 78 (1995) 5984.
- [2] M. Suhren, D. Gräf, U. Lambert, P. Wagner, *J. Electrochem. Soc.* 144 (1997) 4041.
- [3] W. Wijaranakula, S. Archer, *Appl. Phys. Lett.* 65 (1994) 2069.
- [4] E. Dornberger, D. Graf, M. Suhren, U. Lambert, P. Wagner, F. Dupret, W. von Ammon, *J. Crystal Growth* 180 (1997) 343.
- [5] K. Tanahashi, N. Inoue, *J. Mater. Sci.* 10 (1999) 359.
- [6] N.S. Rytova, E.V. Solov'eva, *Sov. Phys. Semicond.* 20 (1986) 869.
- [7] K. Tanahashi, M. Kikuchi, T. Higashino, N. Inoue, Y. Mizokawa, *Physica B* 273 (1999) 493.
- [8] N.E.B. Cowern, W.J. Kersten, R.C.M. Dekruif, J.G.M. van Berkum, W.B. de Boer, D.J. Gravesteijn, C.W.T. Bulle-Liewma, in: G.R. Srinivasan, C.S. Murthy, S.T. Dunham (Eds.), *Proceedings of the 4th International Symposium on Process Physics and Modeling in Semiconductor Devices*, Electrochem. Soc. Proc., Vol. 96-4, Electrochem. Soc. Pennington, NJ, 1996, p. 95.
- [9] A.E.H. Love, *A Treatise on the Mathematical Theory of Elasticity*, Dover, New York, 1944.
- [10] T. Ono, H. Horie, M. Miyazaki, H. Tsuya, G.A. Rozgonyi, *Defects in Silicon III*, The Electrochemical Society, 1999, p. 300.

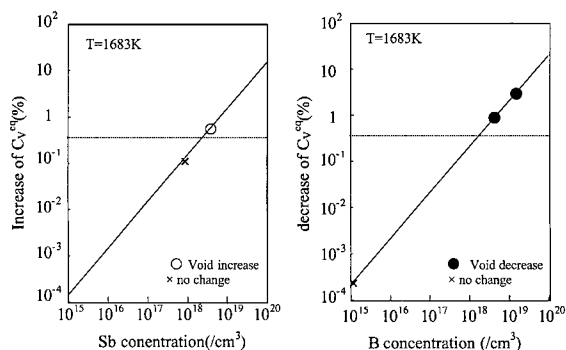


Fig. 3. Calculated change of equilibrium concentration of vacancies due to impurity doping.



ELSEVIER

Physica B 308–310 (2001) 506–509

PHYSICA B

www.elsevier.com/locate/physb

Mechanisms of capture- and recombination-enhanced defect reactions in semiconductors

Yuzo Shinozuka*

Faculty of Systems Engineering, Wakayama University, Skaedani 930, Wakayama, 640-8510, Japan

Abstract

Proposed mechanisms on defect reactions in semiconductors (defect creation, annihilation, multiplication, reconstruction, impurity diffusion, etc.) are reexamined with particular attention to the instability of the lattice and the transient lattice vibration induced by successive carrier captures. (1) Thermal activation process to overcome the potential barrier U_n : it depends on the electronic state n and the reaction rate is given by $p_0 \exp(-U_n/k_B T)$. (2) Instability mechanism: the lattice relaxation after an electronic transition at a defect promptly induces the reaction coordinate Q_R . (3) Phonon kick mechanism (single capture): if the relaxation mode Q_1 partially includes Q_R , an electronic transition to the state n enhances the defect reaction during the lattice relaxation time $\tau \sim 2\pi/\Delta\omega$ where $\Delta\omega$ is the width of the frequency distribution of related phonons. (4) Phonon kick mechanism (recombination): if N pairs of electron and hole are captured within a short period $\tau \sim 2\pi/\Delta\omega$ and the central frequency ω_R of Q_R is not so different from ω_0 of Q_1 , the band gap energy E_g is transformed by a series of coherent carrier captures into the lattice vibration energy. The defect reaction rate is given by $(\omega_0/2\pi)\exp(-E_i^{\text{act}}/k_B T)$ because only the first capture ($i = e, h$) is to be activated. On the other hand, if ω_R is much different from ω_0 , the rate is $(\omega_0/2\pi)\exp(-U_0^*/k_B T)$ with $U_0 = (E_i^{\text{act}} + E_i^{\text{th}})$ because the N phonon-kicks are out of phase. © 2001 Elsevier Science B.V. All rights reserved.

Keywords: Defect reaction; Instability; Phonon kick; Coherent capture

1. Introduction

Electronic transitions sometimes induce or enhance defect reactions in semiconductors, such as impurity diffusion, structural change of a defect (creation, annihilation and multiplication), and climb and glide motions of dislocation [1]. Several models have been proposed so far to explain mechanisms, which can be classified into two categories as schematically shown in Fig. 1 [2]. One is the structural instability mechanism (Fig. 1(a)) where an electronic excitation to a particular state of the defect induces a symmetry breaking atomic motion such as the off-center displacement. The other mechanism is the recombination enhanced (phonon kick) mechanism (Fig. 1(b))

[3–5], where the transient lattice vibration induced by carrier capture(s) enhances the defect reaction. In order to control defect reactions in semiconductors, detailed understanding of the mechanisms and their relations are necessary. The purpose of the present paper is to review the proposed mechanisms and classify them with particular attention to the lattice instability and the dynamics of the lattice relaxation after electronic excitations.

2. Instability

2.1. Thermal process

The stable lattice structure of a condensed material is different for different electronic states. Then electronic transitions (excitation, deexcitation, carrier capture, etc) affect the atomic movements around defects, sometimes

*Corresponding author. Tel.: +81-734-57-8236; fax: +81-734-57-8237.

E-mail address: yuzo@sys.wakayama-u.ac.jp (Y. Shinozuka).

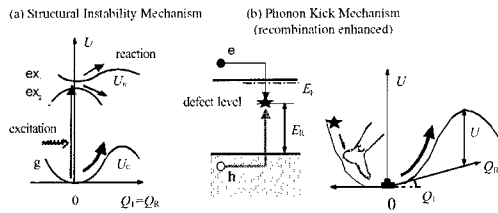


Fig. 1. Two categories of mechanisms for defect reactions enhanced by electronic excitations.

inducing defect reactions. Usually defect reactions are induced by a thermal activation of phonons to overcome the potential barrier U_n , which depends on the electronic state n . The reaction rate p is given by $p_0 \exp(-U_n/k_B T)$, with a prefactor $p_0 \sim 2\pi/\omega_0$, where ω_0 is the mean phonon frequency. In Fig. 1(a) an electronic excitation to ex_1 decreases the potential barrier height (from U to U_1) of the reaction. Then we can expect the Fermi energy dependence of the reaction rate. The reaction rate is increased as $p_0 \exp(-U_n/k_B T)$ during the life time τ of the excited state. Thus the enhancement of the reaction can be observed only in the case of $p\tau > 1$.

2.2. Instability

In Fig. 1(a) an excitation to ex_2 state promptly generates the instability of the lattice. If the lattice relaxation mode is symmetric such as A_{1g} mode, it unlikely generates the reaction. Thus the off-center distortion plays an important role in (the precursor stage of) the defect reaction.

Many substitutional impurities in tetrahedrally bonded covalent semiconductors have been found to show the off-center instability to C_{3v} , such as DX-center in AlGaAs, EL2 in GaAs and N in Si. It can be understood with the Jahn–Teller effect [6], which states that if the electronic state is degenerate the atomic structure automatically lowers the symmetry to reduce the degeneracy. In order to discuss the off-center instability of an impurity in semiconductors, the key point is whether the J–T displacements contain the displacement R_0 of the impurity atom located at the center [7]. It has been shown that an impurity atom at any position with the inversion symmetry, such as O_h does not show the instability caused by the J–T effect. This is because the irreducible representations for any system with the inversion symmetry are classified into gerade and ungerade. All the J–T distortion modes are gerade while the displacement of the central atom always belongs to ungerade modes. On the other hand, those positions without the inversion symmetry show the off-center instability for degenerate electronic states. For example, in T_d case, triply degenerate T_1 and T_2 states induce T_2 -type mode resulting in the off-center

instability. El-Maghraby and Shinozuka [8] have comprehensively studied the structural instability in the T_d symmetry system including the effect of spin and the electron–electron interaction. One of the most striking results is that due to the absence in electron–hole symmetry in the sp^3 bonded system, deep neutral acceptors A^0 always show the off-center instability. This presents a possibility of AX-center, which may explain the low efficiency of p-type doping in some semiconductors.

2.3. Impurity diffusion

Let us next discuss the impurity diffusion by the interstitial mechanism, where an impurity atom diffuses via interstitial positions. An interstitial impurity may occupy a larger vacant site in the host lattice, then they have high point symmetry and we can then apply the above result. If a localized electronic state which shows the off-center J–T instability at a position A continuously changes into a state which does not show at a position B and vice versa, the diffusion is enhanced by the electronic excitation and deexcitation. The self-interstitial in Si is shown to be of this type [9]. This mechanism is similar to the Bourgoin–Corbett mechanism [10,11], where the electronic transition is a carrier capture process.

3. Recombination enhanced defect reaction

3.1. Configuration diagram for deep-level defect

Some deep-level defects whose electronic state strongly couples with the lattice act as a nonradiative multiphonon recombination center [12,13]. Fig. 2 shows a typical example of the configuration coordinate

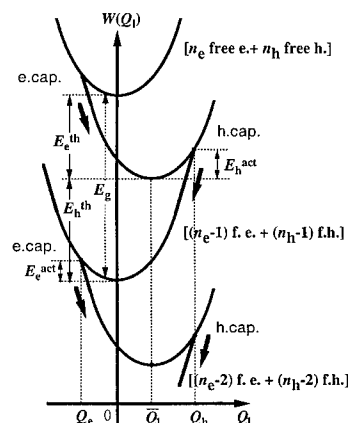


Fig. 2. The configuration coordinate diagram for non-radiative multiphonon recombination process at deep-level defects.

diagram of a deep-level defect. Since there are many carriers in real situation, the system cannot be treated as the ground state + a few excited states. In Fig. 2 [n_e free e + n_h free h] indicates that there are n_e free electrons and n_h free holes with neutral defect (D^0) in order to discuss the correlation between successive captures. Let q_k denote the k th normal mode of the lattice vibration coupled with a localized electronic state with an angular frequency ω_k . The suffix k stands for the wave numbers and the modes. Without loss of generality we assume that the equilibrium positions of lattice modes are $\{q_k = 0\}$ when the defect is neutral (D^0) and $\{q_k = \bar{q}_k\}$ when the defect is occupied by an electron (D^-). It is convenient to introduce the interaction mode $Q_1 = (1/\bar{Q}_1) \sum_k \omega_k^2 \bar{q}_k q_k$ where \bar{Q}_1 denotes its equilibrium position for D^- . The net effect of lattice distortions $\{q_k\}$ to the electron-hole system appears only through Q_1 in the adiabatic approximation. The lattice relaxation energy is given by $E_{LR} = \sum_k \omega_k^2 \bar{q}_k^2 / 2 \equiv \bar{Q}_1^2 / 2$. After an electron (hole) capture which needs an activation energy, $E_c^{\text{act}}(E_h^{\text{act}})$, transient lattice vibrations are induced, where $q_k \propto \cos \omega_k t$. The motion of Q_1 shows damping oscillation because it consists of many normal modes with different frequencies. During the relaxation an electronic energy equal to the thermal depth $E_c^{\text{th}}(E_h^{\text{th}} = E_g - E_c^{\text{th}})$ of an electron (hole) is converted to phonon energies. As a result of an e-h pair recombination, the electronic energy, $E_g = E_c^{\text{th}} + E_h^{\text{th}}$, is converted to the lattice vibration energy.

3.2. Enhanced reaction by single capture

When the defect is partially isolated and can be considered as a defect molecule, a carrier capture supplies the thermal energy ($\sim E_c^{\text{th}}$ or E_h^{th}) to the molecule. Then the reaction rate will be increased as $p \exp(-U_0^*/k_B T)$ with $U_0^* \sim U_0 - E_c^{\text{th}}$ (or E_h^{th}). This is the Week-Tully-Kimerling mechanism [3]. Another mechanism has been proposed by Sumi [4,5], who discussed the time evolution of the transient lattice vibration after a capture, neglecting the damping. He showed that the activation energy U_0 for a defect reaction is reduced to $U_0 - (E_i^{\text{act}} + E_i^{\text{th}})$

or

$$\left(\sqrt{U_0} - |\cos \theta| \sqrt{E_i^{\text{act}} + E_i^{\text{th}}} \right)^2 / (1 - \cos^2 \theta),$$

where $i = e$ or h , and θ is the angle between Q_1 and Q_R .

3.3. Correlation between successive captures

It has been suggested that the transient vibration induced by a carrier capture enhances the probability of a following capture of the opposite carrier [2,4,5,12,13].

Recently Shinozuka and Karatsu have simulated the transient lattice vibration induced by successive captures and its effect on the subsequent capture process [14–16]. If N pairs of electrons and holes are sequentially captured by the defect, each occurred at $t_{e1} < t_{h1} < t_{e2} < t_{h2} < \dots < t_{eN} < t_{hN}$, the time evolution of $Q_1(t)$ for $t_{hN} < t$ is given by

$$Q_1(t) = Q_1^{\text{before}}(t) + \bar{Q}_1 \left\{ - \sum_j^N \exp[-\Delta\omega^2(t - t_{ej})^2/4] \cos \omega_0(t - t_{ej}) + \sum_j^N \exp[-\Delta\omega^2(t - t_{hj})^2/4] \cos \omega_0(t - t_{hj}) \right\}, \quad (1)$$

for a system whose phonon frequency ω_k distribution is given by a Gaussian with the central frequency ω_0 and the width $\Delta\omega$. Here $Q_1^{\text{before}}(t)$ is the time dependence if the captures of N electron-hole pairs were absent. Thus, $Q_1(t)$ is shown to be a linear combination of damping oscillations, each starts at time t_{ej} or t_{hj} and lasts for the same duration $\tau \sim 2\pi/\Delta\omega$. It should be called here that the nonradiative capture time t_{ej} and t_{hj} cannot take an arbitrary value but should be obeyed by a probability process: the capture takes place only when $Q_1(t)$ crosses a critical point Q_c or Q_h , the intersection of two adiabatic potentials (Fig. 2).

3.4. Reaction enhanced by successive captures

Finally we discuss the effect of the transient vibration Eq. (1) on defect reactions. We will use the following assumptions:

- The first electron capture takes place by a thermal activation Q_1 to Q_c with the activation energy E_c^{act} .
- If $Q_1(t)$ crosses at the point $Q_c(Q_h)$ of the adiabatic potentials, there is a probability $p_e(p_h)$ per time to capture an electron (hole) nonradiatively. $p_e(p_h) \sim \omega_0/2\pi$ in the adiabatic limit [4,5].
- The motion of the reaction coordinate is given by $Q_R(t) = \sum_k f_k q_k(t)$, whose frequency distribution is given by a Gaussian with the central frequency ω_R and the width $\Delta\omega$.
- If $Q_R(t)$ overcomes the critical point Q_c , the defect reaction takes place.

Fig. 3 shows a typical example of the time evolutions of the interaction mode $Q_1(t)$ and the reaction mode $Q_R(t)$. The values of parameters used are indicated in the figure. As can be seen, every capture process enhances the vibration of $Q_1(t)$. On the other hand, it is not so for $Q_R(t)$ in $\omega_0 \neq \omega_R$ case, because the timing of push and pull for $Q_R(t)$ is out of phase.

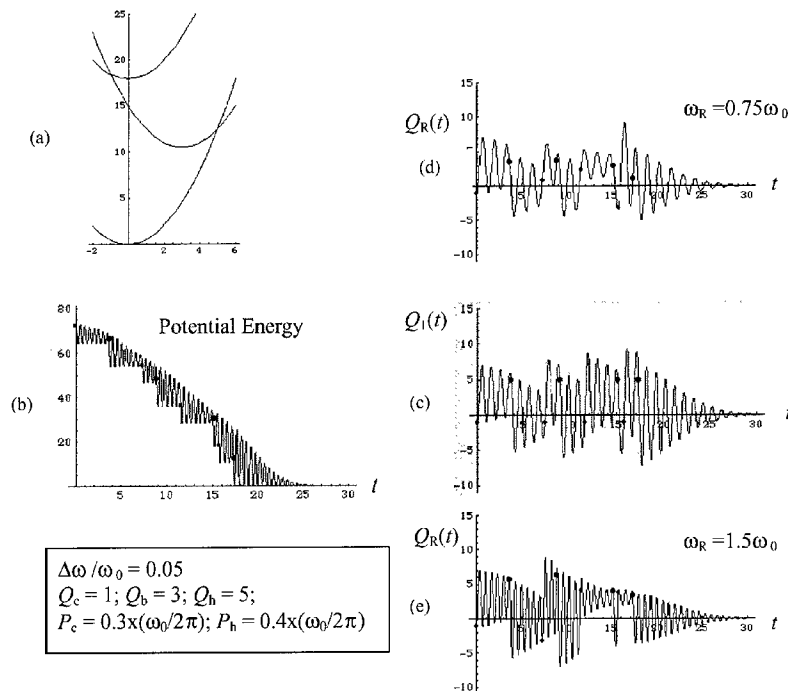


Fig. 3. The transient lattice vibrations induced by successive carrier captures for the interaction mode $Q_1(t)$ and the reaction coordinate $Q_R(t)$. Large (small) black circle in (b)–(e) indicates the capture time $t_{c/h}$ of an electron (hole).

4. Summary

Proposed mechanisms on defect reactions in semiconductors are reexamined with particular attention to the instability of the lattice and the transient lattice vibration induced by successive carrier captures. The possibility of defect reaction has been discussed in connection with the instability of the lattice and the transient induced lattice vibration. In the latter case, the condition for the coherent captures turns out to be $p_e\tau \sim p_h\tau \sim \omega_0/\Delta\omega > 1$. Then if N pairs of electrons and holes are captured within a short period $\sim 2\pi/\Delta\omega$, the amplitude of the interaction mode $Q_1(t)$ increases remarkably. If the central frequency ω_R of the reaction coordinate Q_R is not so different from ω_0 of the interaction mode Q_1 , the band gap energy $E_g = E_e^{\text{th}} + E_h^{\text{th}}$ can be transformed by a series of coherent carrier captures into the lattice vibration energy. The defect reaction rate is given by $(\omega_0/2\pi)\exp(-E_i^{\text{act}}/k_B T)$ because only the first capture ($i = e, h$) is to be activated. On the other hand, if ω_R is much different from ω_0 , the rate is $(\omega_0/2\pi)\exp(-U_0^*/k_B T)$ with $U_0 = (E_i^{\text{act}} + E_i^{\text{th}})$ because the N phonon-kicks are out of phase.

Acknowledgements

The work is supported by the Grant-in-Aid for Scientific Research on Priority Areas (B) "Manipulation

of Atoms and Molecules by Electronic Excitation" by the Japanese Ministry of Education, Culture, Sports, Science and Technology.

References

- [1] O. Ueda, Reliability and Degradation of III–V Optical Devices, Artech House, Boston, London, 1996.
- [2] Y. Shinozuka, Defect in Optoelectronic Materials, in: K. Wada, S.W. Pang (Eds.), Gordon and Breach, London, 1999 (Chapter 8).
- [3] J.D. Weeks, J.C. Tully, L.C. Kimerling, Phys. Rev. B 12 (1975) 3286.
- [4] H. Sumi, Phys. Rev. B 29 (1985) 4616.
- [5] H. Sumi, J. Phys. C 17 (1984) 6071.
- [6] H.A. Jahn, E. Teller, Proc. Roy. Soc. A 161 (1937) 220.
- [7] Y. Shinozuka, Mater. Sci. Forum 83–87 (1992) 527.
- [8] M. El-Maghraby, Y. Shinozuka, J. Phys. Soc. Japan 67 (1998) 3524.
- [9] M. Saito, A. Oshiyama, O. Sugino, Phys. Rev. B 47 (1993) 13205.
- [10] J.C. Bourgoin, J.M. Corbett, Phys. Lett. 38 A (1972) 135.
- [11] J.C. Bourgoin, J.M. Corbett, Radiat. Eff. 36 (1978) 157.
- [12] Y. Shinozuka, J. Phys. Soc. Japan 51 (1982) 2852.
- [13] Y. Shinozuka, Jpn. J. Appl. Phys. 32 (1993) 4560.
- [14] Y. Shinozuka, T. Karatsu, Mater. Sci. Forum 258–263 (1997) 659.
- [15] Y. Shinozuka, Proceedings of the MRS 1996 Fall Meeting 442, Defects in Electronic Materials II, p. 225.
- [16] Y. Shinozuka, T. Karatsu, Physica B 273–274 (1999) 999.



ELSEVIER

Physica B 308–310 (2001) 510–512

PHYSICA B

www.elsevier.com/locate/physb

Dynamics of Si self-interstitial clustering using the fast-diffusing I_3 cluster

M. Gharaibeh^a, S.K. Estreicher^{a,*}, P.A. Fedders^b

^a Physics Department, Texas Tech University, Lubbock, TX 79409-1051, USA

^b Physics Department, Washington University, St. Louis, MO 63130, USA

Abstract

Recent ab initio molecular-dynamics simulations have shown that the di-interstitial (I_2) and the stable tri-interstitial (I_3^a) clusters in Si are highly mobile. In these complexes, the two (or three) self-interstitials share a single bond-centered site, a feature which greatly facilitates exchange processes and is responsible for the rapid diffusion. In this contribution, we consider the possibility that the precipitation of self-interstitials results from the clustering of I_3 'units' rather than isolated Is. We study the interactions $I_3 + I_3 \rightarrow I_6$ and $I_6 + I_3 \rightarrow I_9$ by bringing an I_3 toward either another I_3 or I_6 along various crystalline directions in 216 host atoms supercells. The calculations show that these reactions occur at a substantial gain in energy and that the stacking along some directions is energetically preferred over others. The $I_6 + I_2 \rightarrow I_8$ reaction leads to a very stable cluster. The results suggest that precipitation mechanisms involving rapidly moving self-interstitial clusters could play an important role in the formation of extended defects. © 2001 Elsevier Science B.V. All rights reserved.

Keywords: Molecular dynamics; Self-interstitials; Silicon

1. Introduction

Large concentrations of self-interstitials (Is) in Si are generated during common processing steps, such as ion implantation. The self-interstitials rapidly form large precipitates, in particular $\{311\}$ platelets, which play critical role(s) in the transient-enhanced diffusion of the shallow B acceptor; recent reviews are in Ref. [1]. A number of theorists have been involved in the calculation of the structures and electronic properties of small I_n clusters [2–12] as well as precipitation mechanisms [13,14]. The clustering or precipitation is always assumed to result from interactions involving isolated and fast-diffusing Is. However, the energies gained in the reaction $I_{n-1} + I \rightarrow I_n$ are often found to be roughly constant for many values of n , with larger energy gains for specific small clusters such as I_3, I_4 or I_8 . No

conclusive precipitation mechanism has yet emerged from calculations.

Recent ab initio molecular-dynamics (MD) simulations [15] have shown that the I_2 cluster as well as the most stable configuration of the I_3 complex (originally labeled I_3^a) diffuse remarkably fast even at low temperatures. Both of these clusters are centered around a single bond-centered (BC) site and this feature facilitates the exchange processes involved in the diffusion. In this paper, we examine the possibility that the highly mobile I_3 is the building block of larger defect structures by studying the reactions $I_3 + I_3 \rightarrow I_6$ and $I_6 + I_3 \rightarrow I_9$.

2. Methodology

Our MD simulations are done using the SIESTA code [16,17] as described in Ref. [15]. In a nutshell, these are classical MD simulations in which the electronic problem solved at the ab initio level within density-functional theory. The electronic basis sets consist of numerical linear combinations of atomic orbitals. The

*Corresponding author. Tel.: +1-806-742-3723; fax: +1-806-742-1182.

E-mail address: stefan.estreicher@ttu.edu (S.K. Estreicher).

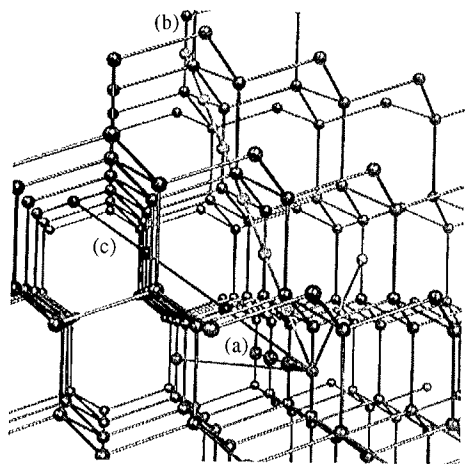


Fig. 1. The 216-atoms cell (or I_6) is around a centrally located BC site and the second I_3 is placed at other BC sites along various crystalline directions. The directions which lead to large energy gains as the two complexes get closer to each other are labeled: (a) $\langle 0\bar{1}1 \rangle$, (b) $\langle 0\bar{1}\bar{1} \rangle$ and (c) $\langle 2\bar{1}1 \rangle$.

crystal is represented by a periodic supercell of 216 host atoms and the k -point sampling is reduced to the Γ point. The basis set on those Si atoms that are at essentially undisturbed crystalline sites is single zeta, but a double-zeta polarized set is used on all the atoms that are away from perfect sites. For example, in the case of I_3 , only the three Is and their two Si nearest-neighbors have the larger basis set. Since the calculations scale as N^3 , where N is the total number of orbitals in the cell, this compromise allows systematic calculations to be performed.

Fig. 1 shows the 216-atoms cell. We place I_3 (or I_6) around a centrally located BC site then place another I_3 at BC sites along various crystalline directions. All the BC sites shown by dots on the figure are considered. For every I_3+I_3 or I_6+I_3 combination, all the structures are quenched and their energies recorded. These complexes are very similar to the isolated I_3 and I_3 or I_6 when at large distances, but they interact and form new complexes when closer to each other.

3. Results

The calculated gains in energy as I_3 approaches another I_3 as a function of their separation and for various approach directions are shown in Fig. 2. The distance between the two complexes is defined as the separation between their respective geometrical centers. In the nearest possible separation, the I_6 complex has formed. Only the easiest approach directions are shown. Note that the largest separation between the two complexes in this cell is slightly over 10 Å, a separation

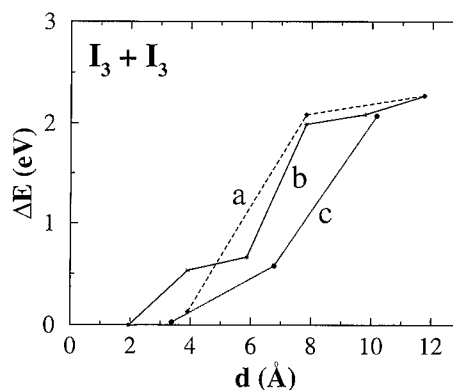


Fig. 2. Energy gained as the two I_3 complexes get closer to each other to form I_6 . One I_3 is at the origin, the second approaches from the right along the directions shown in Fig. 1.

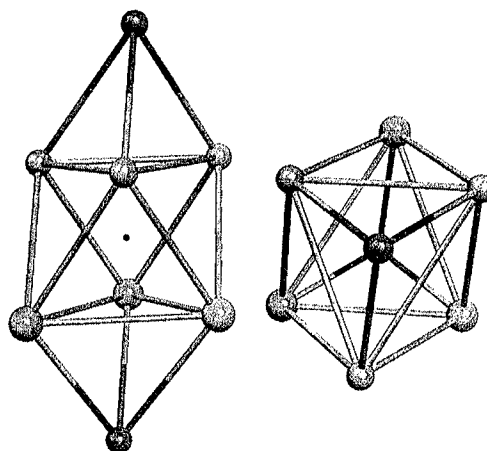


Fig. 3. The most stable configuration of the I_6 clusters consists of two identical triangles rotated by 60° relative to each other, centered at BC site (dot). The side and top views are shown.

at which some interaction already occurs. We estimate that the reaction $I_3+I_3 \rightarrow I_6$ releases at least 2.5 eV, which is a substantial gain.

We found more than a dozen possible configurations of I_6 . The most stable one is shown in Fig. 3. It is best described as two identical triangles in $\{111\}$ planes, separated by 2.0 Å and centered at a BC site. The triangles are not exactly equilateral (the sides are 2.51, 2.69, and 2.87 Å, respectively) but the entire complex is close to trigonal. It is remarkable that the most stable I_3 and I_6 complexes are both centered at a single BC site. In these two defects, only two host atoms need to be substantially displaced from the equilibrium sites (about 1.6 Å in the case of I_6) in order to accommodate the entire complex.

The calculated gain in energy as I_3 approaches I_6 as a function of their separation and for various approach

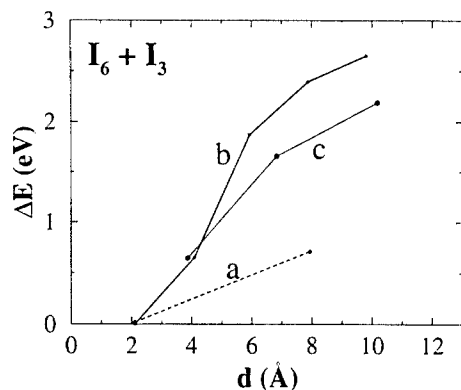


Fig. 4. Energy gained as I_3 gets closer to I_6 to form I_9 . The I_6 complex is at the origin and I_3 approaches from the right along the directions shown in Fig. 1.

directions is shown in Fig. 4. The distance between the two complexes is defined as the separation between their respective geometrical centers. In the nearest possible separation, the I_9 complex has formed. Only the easiest approach directions are shown. The reaction $I_6 + I_3 \rightarrow I_9$ releases about 3.0 eV, a gain even larger than that for $I_3 + I_3 \rightarrow I_6$.

We have not yet studied all the possible configuration of I_9 . But the most likely structure can be described as distorted I_6 and I_3 complexes at the second-nearest BC sites. Note that if an even more stable structure of I_9 emerges, the gain in energy that occurs during the clustering will be even larger than 3 eV mentioned above.

The I_8 cluster has been mentioned [12] as a likely precursor of I_n platelets and/or a particularly stable complex. For this reason, we have also considered the reaction $I_6 + I_2 \rightarrow I_8$, which could easily occur since I_2 is highly mobile as well [15]. Preliminary calculations give an energy gain of at least 3.2 eV, confirming that this cluster is particularly stable.

4. Discussion

The issue of self-interstitial precipitation is a challenge for ab initio theory. If one begins with a locally large concentration of Is, they will quickly form small clusters I_n , with $n = 2, 3, 4$, etc. but if I is the only fast-diffusing species, the process is likely to stop there unless a continuous supply of Is is provided. However, theory predicts that the I_2 and one I_3 clusters (as well as one configuration of I_4 [18]) are extremely mobile even at low temperatures. This opens the possibility that the precipitation of Is involves contributions from small clusters such as I_2 or I_3 attracting each other and forming larger precipitates. We have now shown that the

reactions $I_3 + I_3 \rightarrow I_6$ and $I_6 + I_3 \rightarrow I_9$ result in large energy gains of over 2.5 and 3.0 eV, respectively, strongly suggesting that the formation of large precipitates could well involve such clusters.

Acknowledgements

The work of SKE is supported in part by a grant from the R.A. Welch Foundation, a contract from the National Renewable Energy Laboratory, and a research award from the Humboldt Foundation. The authors thank the High Performance Computing Center at Texas Tech's Institute for Environmental and Human Health for the generous amount of computer time.

References

- [1] T.E. Haynes, MRS Bull. 25 (2000) 14; H. Bracht, MRS Bull. 25 (2000) 22; R. Falster, V.V. Voronkov, MRS Bull. 25 (2000) 28; N. Cowern, C. Rafferty, MRS Bull. 25 (2000) 39; M.E. Law, G.H. Gilmer, M. Javaiz, MRS Bull. 25 (2000) 45.
- [2] R. Rashband, P. Clancy, M.O. Thompson, J. Appl. Phys. 79 (1996) 8998.
- [3] Y.H. Lee, Appl. Phys. Lett. 73 (1998) 1119.
- [4] J. Kim, F. Kirchhoff, W.G. Aulbur, J.W. Wilkins, F.S. Khan, G. Kresse, Phys. Rev. Lett. 83 (1999) 1990.
- [5] L. Colombo, Physica B 273–274 (1999) 458.
- [6] B.J. Coomer, J.P. Goss, R. Jones, S. Öberg, P.R. Briddon, Physica B 273–274 (1999) 505.
- [7] B.J. Coomer, J.P. Goss, R. Jones, S. Öberg, P.R. Briddon, J. Phys. Cond. Matter 13 (2001) L1.
- [8] M. Gharaibeh, S.K. Estreicher, P.A. Fedders, Physica B 273–274 (1999) 532.
- [9] R. Humble, Proc. R. Soc. (London) A 381 (1982) 65.
- [10] N. Arai, S. Takeda, M. Kohyama, Phys. Rev. Lett. 78 (1997) 4265.
- [11] M. Kohyama, S. Takeda, Phys. Rev. B 60 (1999) 8075.
- [12] N.E.B. Cowern, G. Mannino, P.A. Stolk, F. Roozeboom, H.G.A. Huizing, J.G.M. van Berkum, F. Cristiano, A. Claverie, M. Jaraiz, Phys. Rev. Lett. 82 (1999) 4460.
- [13] J. Kim, F. Kirchhoff, J.W. Wilkins, F.S. Khan, Phys. Rev. Lett. 84 (2000) 503.
- [14] J. Kim, J.W. Wilkins, F.S. Khan, A. Canning, Phys. Rev. B 55 (1997) 16186.
- [15] S.K. Estreicher, M. Gharaibeh, P.A. Fedders, P. Ordejón, Phys. Rev. Lett. 86 (2001) 1247.
- [16] E. Artacho, D. Sánchez-Portal, P. Ordejón, A. García, J.M. Soler, Phys. Stat. Sol. (b) 215 (1999) 809.
- [17] D. Sánchez-Portal, P. Ordejón, E. Artacho, J.M. Soler, Int. J. Quant. Chem. 65 (1997) 453.
- [18] M. Gharaibeh, S.K. Estreicher, unpublished.



ELSEVIER

Physica B 308–310 (2001) 513–516

PHYSICA B

www.elsevier.com/locate/physb

Defect reactions associated with the dissociation of the phosphorus–vacancy pair in silicon

V.P. Markevich^{a,*}, O. Andersen^a, I.F. Medvedeva^b, J.H. Evans-Freeman^a,
I.D. Hawkins^a, L.I. Murin^b, L. Dobaczewski^{a,c}, A.R. Peaker^a

^aCentre for Electronic Materials, UMIST, Main Building, Room D30A, Sackville Street, P.O. Box 88, Manchester M60 1QD, UK

^bInstitute of Solid State and Semiconductor Physics, Minsk, Belarus

^cInstitute of Physics, Polish Academy of Sciences, Warsaw, Poland

Abstract

The generation and annihilation of defects upon electron irradiation and subsequent annealing has been studied by high-resolution deep level transient spectroscopy (Laplace DLTS) in phosphorus-doped silicon crystals which were grown by the vacuum float zone technique. It was found that the disappearance of phosphorus–vacancy pairs in the temperature range of 125–175°C is accompanied by a significant reduction in the concentration of C_i-C_s complexes and formation of a defect with an acceptor level at $E_c - 0.21$ eV. The level was assigned to a pair of substitutional carbon atoms (C_s-C_s), which is formed when the free vacancy released upon E-centre annealing is captured by the C_i-C_s complex. © 2001 Elsevier Science B.V. All rights reserved.

PACS: 81.40.W; 61.72.C; 78.30.A

Keywords: Silicon; Vacancy–phosphorus pair; Carbon–carbon pair; Laplace DLTS

1. Introduction

The E-centre (phosphorus–vacancy pair) is one of the dominant defects induced by electron irradiation in phosphorus-doped oxygen-lean float-zone-grown (FZ) Si crystals [1]. The defect introduces an acceptor level at about $E_c - 0.45$ eV into the gap [1,2]. Detailed information about electronic properties and structure of this defect in its neutral charge state was obtained by Watkins and Corbett from electron spin resonance data and electron–nuclear double resonance measurements [1].

The E-centre was found to anneal out at about 150°C with annealing well described by first order kinetics [3–6]. This suggests that the dissociation of the complex occurs or it diffuses to a trap species with a high

concentration. However, in spite of a large number of papers related to investigations of the E-centre annihilation process, the annealing mechanism(s) of the complex is uncertain. From the results on the recovery of stress-induced alignment, an activation energy of the defect re-orientation was found to be 0.93 ± 0.05 eV [1]. This value was considered to be the activation energy for the diffusion of the neutral phosphorus–vacancy pair in the lattice. Practically the same value of activation energy has been obtained from studies of the E-centre annealing process [3–6],¹ and the conclusion drawn that the annealing process is related to the migration of the E-centre through the lattice as an entity to some species of trap. The origin of these traps, however, has not been identified unambiguously, and products of the interaction have not been detected. On

*Corresponding author. Tel.: +44-161-2004746; fax: +44-161-2004770.

E-mail address: markev@fs4.ee.umist.ac.uk (V.P. Markevich).

¹It was found in Refs. [5,6] that the annealing process of the E-centre is charge-state dependent, being faster in the neutral state ($\Delta E \approx 0.95$ eV) and slower in the negative charge state ($\Delta E \approx 1.25$ eV).

the other hand, there are some indications that the dissociation of the E-centres with the release of free vacancies could occur upon annealing at about 150°C. Supporting evidence for this hypothesis is an increase in A-centre (oxygen–vacancy pair [7,8]) concentration upon disappearance of E-centres [1,9].

2. Experimental

In the present study we have applied the Laplace DLTS technique [10] in combination with low-temperature photoluminescence measurements to study defect reactions associated with the disappearance of the phosphorus–vacancy pair in silicon. Two types of phosphorus-doped Si crystals were used with initial resistivities of 1 and 60 Ωcm. The crystals were grown by the vacuum float zone technique that results in low oxygen content.² Oxygen was not detectable in the crystals by optical absorption measurements at room temperature and so has a concentration of $<10^{15} \text{ cm}^{-3}$, the concentration of substitutional carbon atoms was found to be about $5 \times 10^{15} \text{ cm}^{-3}$. The samples were irradiated with 6 MeV electrons at room temperature. 30 min isochronal annealing was carried out in a nitrogen ambient in the range of 75–350°C with temperature increments of 25°C or 50°C. Changes in defect concentrations upon isothermal annealing at 175°C were also investigated. Gold Schottky diodes were used for the DLTS and LDLS measurements.

3. Experimental results and discussion

Fig. 1 shows conventional DLTS spectra for electron-irradiated samples with initial resistivity of 60 Ωcm just after irradiation and at different stages of isochronal annealing. Several deep levels were introduced into the samples by the irradiation. From the analysis of electron emission and capture processes from/into the traps by means of the Laplace DLTS technique, the values of activation energies for emission and capture cross sections were determined. The results are summarised in Table 1, where the information about the origin of the traps is given as well. This information is based on the comparison of the obtained trap parameters with those known from the literature on radiation-induced traps in FZ-Si crystals [2,11]. The dominant traps induced by irradiation were found to be the interstitial–substitutional carbon pair (C_i-C_s) and the vacancy–phosphorus

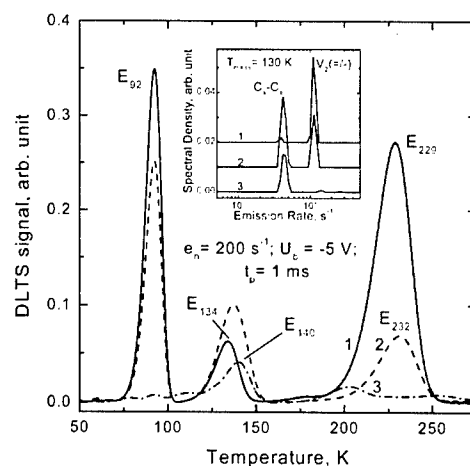


Fig. 1. DLTS spectra of FZ-Si samples with initial resistivity of 60 Ωcm after (1) electron irradiation with a fluence of $3 \times 10^{13} \text{ cm}^{-2}$ and subsequent annealing at (2) 200°C and (3) 350°C for 30 min. Inset shows Laplace DLTS spectra at 130 K for Fz-Si samples conventional DLTS spectra of which are shown in Fig. 1.

complex, concentrations of divacancies and A centers were about 25% and less than 5%, respectively, of that of the P–V centre.³

In photoluminescence (PL) spectra of irradiated samples a dominant PL line at 969.5 meV with its characteristic phonon-assisted sideband (“G” line [12]) was observed. This line is known to be related to the C_i-C_s complex [12].

Annealing of the samples in the temperature range 125–175°C resulted in a significant decrease in the magnitude of the DLTS peak at 229 K (E_{229}). It is believed that this process is related to the elimination of E-centres upon annealing. The peak with maximum at about 232 K (E_{232}) remaining after annealing at 200°C (spectrum 2 in Fig. 1) is related to the electron emission from the singly negatively charged state of divacancy. An examination of the spectra shows also significant changes in the magnitudes of peaks with maxima at about 92 K and 134 K (E_{92} and E_{134} , respectively), the former being decreased and the later being increased upon annealing. Application of the Laplace DLTS technique shows that the increase in the magnitude of the peak in the range of 120–150 K is related to the appearance of another electron trap (E_{140}) with emission rates close to those for the electron emission from the doubly negatively charged state of divacancy (E_{134}). The insert in Fig. 1 shows the Laplace DLTS spectra

²Our estimations, which are based on the comparison of introduction rates of V–O and V–P complexes in the crystals with carefully determined phosphorus concentration, give [O] values lower than 10^{14} cm^{-3} in some crystals.

³We used a method of variable filling pulse lengths, which was proposed in Ref. [11], to determine concentrations of A-centres and C_i-C_s complexes.

Table 1
Parameters of deep level traps, which were observed in electron-irradiated FZ-Si crystals

Trap label	Activation energy for electron emission (eV)	Capture cross-section (cm ²)	Identification
E_{92}	0.161	2.4×10^{-15a}	$C_i-C_s(-/0)$
E_{134}	0.240	$5.5 \times 10^{-16} \times \exp(-0.017 \text{ eV/kT})$	$V_2(=/-)$
E_{140}	0.228	$1.8 \times 10^{-16} \times \exp(-0.018 \text{ eV/kT})$	$C_s-C_s(-/0)$
E_{229}	0.453	3.5×10^{-15}	$V-P(-/0)$
E_{232}	0.428	2.2×10^{-15}	$V_2(-/0)$

^a Determined from the data on emission rates (other data are measured directly).

at 130 K for the samples, conventional DLTS spectra of which are shown in Fig. 1. Just after irradiation a peak related to the electron emission from the $V_2(2-)$ state dominates in the spectrum, while after annealing at 200°C two peaks with comparable concentrations are seen. Further annealing at 350°C resulted in disappearance of the $V_2(2-/-)$ -related peak, leaving only a peak which appears after annealing at 125–175°C.

Activation energies for electron emission from the E_{134} and E_{140} traps are given in Table 1. Expressions describing the capture cross sections are also given in Table 1. Our results on the emission and capture characteristics for the E_{134} are consistent with those reported in literature for the $V_2(2-/-)$ level [2]. On the basis of combined analysis of the emission and capture processes for the E_{140} trap, a conclusion was drawn that the trap is of acceptor nature with the energy level at about $E_c - 0.21$ eV.

Let us consider now the possible origin of the defects, which can be formed upon E-centre annealing at 125–175°C. Fig. 2 shows changes in trap concentrations upon isothermal annealing at 175°C of an electron-irradiated sample with initial resistivity of 1 Ω cm. As it was mentioned above, a significant decrease in E-centre concentration is accompanied by a decrease in concentration of C_i-C_s complexes and by the formation of a defect with an acceptor level at $E_c - 0.21$ eV (E_{140}). Practically a one-to-one anti-correlation in concentration of annealed C_i-C_s complexes and created E_{140} complexes was observed. This suggests that the E_{140} complex is formed at the expense of C_i-C_s complexes. PL measurements also showed a significant decrease in intensity of the G line upon annealing at 125–175°C. Similar results on annealing of the G line were obtained earlier for FZ-Si samples, which were irradiated with gamma-rays from a ^{60}Co source [13].

The C_i-C_s complex is known to be stable up to about 250°C [12]. So, two possible mechanisms of the decrease in its concentration in the temperature range 125–175°C can be considered. Firstly, if the main mechanism of the E-centre elimination at about 150°C is its migration as an entity before being trapped, the capture of mobile E-

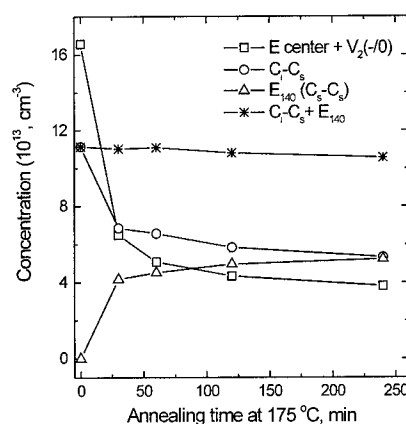


Fig. 2. Changes in concentrations of defects in an electron-irradiated FZ-Si sample with initial resistivity of 1 Ω cm upon isothermal annealing at 175°C. Fluence of irradiation was $1 \times 10^{15} \text{ cm}^{-2}$.

centres by the C_i-C_s complexes can occur, that can result in the formation of two-carbon-phosphorus complex. No information about existence of such a complex has been reported so far, so the structure and properties of 2C-P defect are uncertain. Secondly, the dissociation of the E-centres upon heat-treatments at 125–175°C can lead to the appearance of free mobile vacancies. The vacancies, upon their motion in the lattice, can interact with the C_i-C_s complexes transforming them into a pair of two substitutional carbon atoms (C_s-C_s). C_s-C_s complex was recently identified by combined EPR, optical absorption and ab initio modelling studies in electron-irradiated carbon-rich Si crystals [14,15]. The main mechanism of the C_s-C_s formation was supposed to be the capture of mobile vacancies by the C_i-C_s complexes [15]. According to the results of Refs. [14,15], the C_s-C_s complex introduces an acceptor level into the upper half of the gap, and there should be an energy barrier for the electron capture into the neutral C_s-C_s complex. All these properties of the C_s-C_s complex are consistent with those found in the present work for the E_{140} trap. In addition the high thermal stability of

the E_{140} trap is consistent with that found for the C_s-C_s [15]. So, it is suggested that the E_{140} trap, which was observed in the present work upon E-centre annealing is related to the C_s-C_s complex. An important consequence of such an identification is that the disappearance of E-centres upon annealing at about 150°C should be associated with their dissociation.

It should be noted that the magnitude of the decrease in the C_i-C_s concentration was only about a half of that for the E-centre practically in all the samples we have studied (Fig. 2). So, there should be another trap for mobile P–V or free vacancies, and this trap accounts for almost half of the annihilated E-centres. Except the E_{140} , we have not observed the appearance in significant concentration of any other defects with deep levels in the upper part of the gap upon E-centre annealing. Further studies are required to identify the second channel of the E-centre disappearance.

Summarising, we found that the disappearance of the vacancy-phosphorus complexes upon annealing of electron-irradiated FZ-Si crystals at 125–175°C is accompanied by a significant decrease in concentration of the C_i-C_s complexes, and by formation of a defect with an acceptor level at $E_c - 0.21$ eV. It is suggested that the level is related to a pair substitutional carbon atoms. The C_s-C_s complex is formed when a free vacancy released upon E-centre annealing is captured by the C_i-C_s complex.

Acknowledgements

The EPSRC in the UK is thanked for its financial support. We also acknowledge financial support from the Fund for Fundamental Research of the Republic of Belarus.

References

- [1] G.D. Watkins, J.W. Corbett, *Phys. Rev.* 134 (1964) A1359.
- [2] S.D. Brotherton, P. Bradley, *J. Appl. Phys.* 53 (1982) 5720.
- [3] E. Sonder, L.C. Templeton, *J. Appl. Phys.* 34 (1963) 3295.
- [4] M. Hirata, et al., *J. Appl. Phys.* 38 (1967) 2433.
- [5] L.C. Kimerling, H.M. DeAngelis, C.P. Carnes, *Phys. Rev. B* 3 (1971) 427.
- [6] L.C. Kimerling, H.M. DeAngelis, J.W. Diebold, *Solid State Commun.* 16 (1975) 171.
- [7] G.D. Watkins, J.W. Corbett, *Phys. Rev.* 121 (1961) 1001.
- [8] J.W. Corbett, et al., *Phys. Rev.* 121 (1961) 1015.
- [9] C.E. Barnes, G.A. Samara, In: *MRS Symposia Proceedings* No. 46, Materials Research Society, Pittsburgh, 1985, p. 471.
- [10] L. Dobaczewski, et al., *J. Appl. Phys.* 76 (1994) 194.
- [11] L.W. Song, et al., *Phys. Rev. B* 42 (1990) 5765.
- [12] G. Davies, R.C. Newman, in: T.S. Moss (Ed.), *Handbook on Semiconductors*, Vol. 3b, Elsevier, Amsterdam, 1994, p. 1557.
- [13] L.I. Murin, *Phys. Status Sol. (A)* 93 (1986) K147.
- [14] J.R. Byberg, et al., *Phys. Rev. B* 61 (2000) 12939.
- [15] E.V. Lavrov, et al., *Phys. Rev. B* 62 (2000) 158.



ELSEVIER

Physica B 308–310 (2001) 517–520

PHYSICA B

www.elsevier.com/locate/physb

Enhanced oxygen dimer and thermal donor formation in irradiated germanium studied by local vibrational mode spectroscopy

P. Vanmeerbeek^{a,*}, P. Clauws^a, W. Mondelaers^b

^a *Department of Solid State Sciences, Ghent University, Krijgslaan 281-S1, 9000 Gent, Belgium*

^b *Department of Subatomic and Radiation Physics, Ghent University, Belgium*

Abstract

Oxygen-doped Ge has been irradiated with 2 MeV electrons and isochronally annealed between 80°C and 440°C. Local vibrational mode absorption at 525.5, 780.9 and 817.9 cm⁻¹ is assigned to three modes of the oxygen dimer. The wave number positions are in excellent agreement with corresponding modes in Si and with published ab initio calculations. The enhanced formation of dimers and thermal donors (TD), due to irradiation and the sequential annealing of dimer and early TD bands, support the model of the dimer as the first agglomeration step preceding TD formation. Two absorption bands at 621.6 and 669.1 cm⁻¹ are assigned, respectively, to the neutral and negative charge state of the A-centre (VO) in Ge. © 2001 Elsevier Science B.V. All rights reserved.

Keywords: Germanium; Thermal donor; Irradiation; Oxygen dimer

1. Introduction

The oxygen dimer should be the first oxygen agglomeration step preceding thermal donor (TD) formation in Si and may represent the fast diffusing species explaining the kinetics of TD formation. The dimer in Si is experimentally accessible through the local vibrational mode (LVM) absorption spectrum and four modes seem to be well-established [1,2]. Several papers have been published on the calculation of stable dimer configurations as well [2–4]. In Ge, where oxygen related defects have been less extensively studied than in Si, striking similarities with Si are found for all oxygen related defects identified so far [5]. In our previous study of LVM absorption from TDs in Ge [6], the attention was drawn to weak absorption bands at 780 and 818 cm⁻¹ that always appear in oxygen-doped Ge submitted to a dispersion quench, together with small traces of TD1 and TD2 as detected in the far-infrared electronic absorption spectrum. This is indicative of the

formation of relatively simple oxygen clusters during rapid cooling from high temperature, so the peaks mentioned seemed good candidates for the oxygen dimer in Ge. This assignment seemed substantiated by the almost perfect scaling from the positions of dimer bands in Si [6]. Ab initio calculations by Coutinho et al. [2] predict four modes for the staggered dimer in Ge. The latter consists of two Ge–O–Ge units sharing one Ge and would be the stable dimer form [2].

Here, we report on the LVM absorption in oxygen-doped Ge after irradiation and subsequent isochronal annealing. The primary purpose of the treatments (irradiation, isochronal annealing) was to increase the assumed LVM absorption from the dimers and to follow the evolution into the temperature range of early TD formation. An increased dimer concentration would also favour the observation of other, possibly weaker dimer bands.

2. Experimental

Before irradiation, the oxygen-doped Ge was submitted to a 5 min dispersion at 900°C followed by a

*Corresponding author. Tel.: +32-9-264-4369.

E-mail address: piet.vanmeerbeek@rug.ac.be (P. Vanmeerbeek).

quench to room temperature (RT). The interstitial oxygen concentration measured after the quench was $[O_i] = 2.9 \times 10^{17} \text{ cm}^{-3}$ as determined from the amplitude of the 856 cm^{-1} band (RT), using the conversion factor $[O_i] = \alpha_{\text{max}} \times 10^{16} \text{ cm}^{-2}$ with α_{max} the amplitude in cm^{-1} [7]. The Ge was irradiated with 2 MeV electrons to a fluence of $5 \times 10^{17} \text{ cm}^{-2}$, the temperature during irradiation was kept close to RT. Isochronal anneals of 20 min in the temperature range 80–440°C (increments of 40°C) were performed in the flowing argon. The infrared spectra were recorded at RT, 80 K and 6 K using a nominal resolution of 1 and 0.25 cm^{-1} . The electron concentration was monitored by resistivity and Hall-effect measurements at RT.

3. Experimental results and discussion

The infrared absorption spectra measured after different treatments (quenched, irradiated and annealed) are summarised in Fig. 1. The wave number range corresponds to the LVM range below the O_i peak at 862.3 cm^{-1} . The results are in general agreement with the old data [8,9], however, the improved resolution and sensitivity allow to detect components or weak bands not reported before. In agreement with our earlier experiments [6], two small peaks at 780.3 and 817.9 cm^{-1} are seen in the quenched sample. After the irradiation, a large number of LVM peaks appear, the O_i peak having diminished to 89% of its original amplitude. The evolution of the spectrum during annealing shows that new defects are formed while others disappear. A Ge

reference sample without oxygen doping showed no LVM peaks after irradiation or subsequent annealing. These results indicate that all LVM bands observed should be oxygen related and are probably due to defects containing at least one oxygen atom. In the later annealing stages, the absorption evolves into the LVM bands due to TDs designated before as “600”, “740” and “780”, which refers to their average position at RT [6]. After the 440°C treatment, the amplitude of the O_i peak has decreased further to 74%. On the whole, we observed 64 LVM absorption peaks in the wave number range between 515 and 910 cm^{-1} , of which 23 belong to the TDs [6,10]. The other peaks may be cataloged in at least seven different groups according to their different annealing behaviour. In this paper, the discussion is limited to absorption bands related to the oxygen dimer, the TDs and the VO defect (A-centre).

3.1. Oxygen dimer

As shown in Figs. 1 and 2, the peaks at 780.3 and 817.9 cm^{-1} , that we tentatively attribute to the dimer, become stronger during electron irradiation, grow further during annealing towards 200°C and disappear after the 320°C treatment. It is clear from Fig. 2 that the annealing of the two peaks is identical. In Fig. 2, other bands have been included that show a similar annealing curve and may be considered candidates for other dimer modes. The correspondence with the two major bands is the best for the bands at 525.5 and 766.0 cm^{-1} , while the 572.9 and 801.2 cm^{-1} bands show a somewhat different curve or annealing temperature. We thus end up with

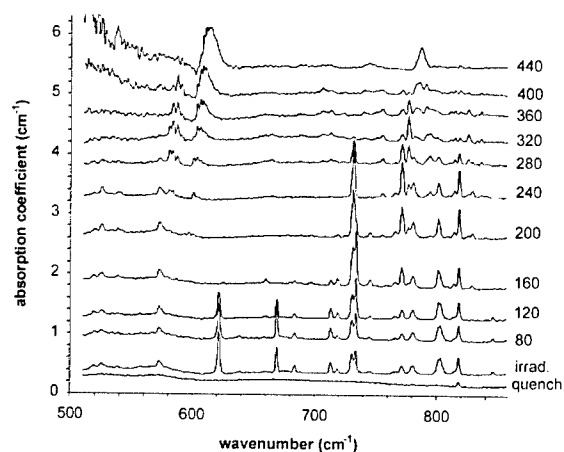


Fig. 1. Infrared absorption spectra of oxygen-doped Ge at 5 K and resolution 1.0 cm^{-1} , after different treatments. The isochronal annealing temperature in $^\circ\text{C}$ is indicated with the graphs. The spectra are vertically shifted, lattice absorption has been subtracted.

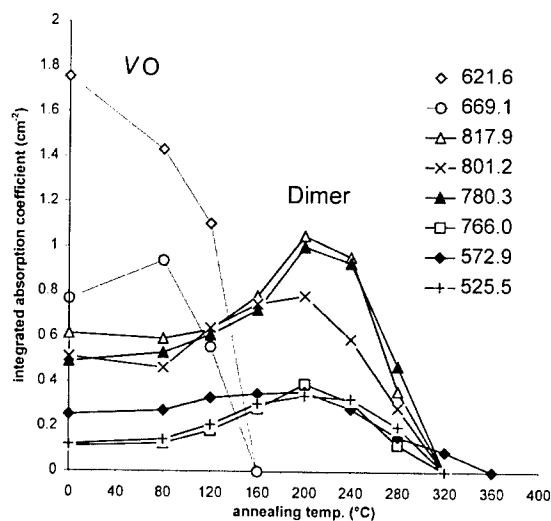


Fig. 2. Isochronal annealing curves of LVM bands attributed to VO and to the oxygen dimer; 0°C corresponds to the as-irradiated material.

Table 1
Comparison of experimental positions (cm^{-1}) of LVM bands due to oxygen defects in Ge and Si (low temperature values)^a

	Si	Ge	Factor
O_i	1136.0	862.5	1.32
	1059.8 [10]	817.9	1.30
	—	(801.2)	—
	1012.4 [10]	780.3	1.30
O_2	—	766.0	—
Dimer	—	(572.9)	—
	690.1 [10]	525.5	1.31
	555.8 [10]	—	—
VO^0	835.6 [12]	621.6	1.34
VO^-	885.3 [12]	669.1	1.32

^a Values in the last column give the ratio of Si to Ge positions. Positions within brackets indicate bands for which assignment to the dimer is doubtful.

four preferential candidates for the dimer-related LVM bands in Ge, as summarised in Table 1.

More evidence to assign the bands may be obtained from a comparison with the observed dimer peaks in Si. A scaling factor of about 1.32 for oxygen modes in Ge with respect to Si may be predicted from the relative positions of the ν_3 mode of O_i in the two semiconductors. As shown in Table 1, three of the four modes selected have a counterpart in Si with a scaling factor very close to 1.32. Scaling of the lowest dimer mode of Si at 555.8 cm^{-1} predicts a mode around 420 cm^{-1} in Ge, however, in a wave number range where clear detection of small bands is difficult. On the other hand, no counterpart of the 766.0 cm^{-1} mode seems to exist in Si, throwing doubt on its correlation with the oxygen dimer.

Comparison of our experimental data with the calculated values for the staggered dimer in Ge in Ref. [2] results in an excellent agreement for the upper three dimer modes. The experimental modes at 525.5 , 780.3 and 817.9 cm^{-1} agree within only 2–4% with the calculated modes at 517 , 749 and 784 cm^{-1} . It may also be remarked that contrary to the situation in Si, the dimer bands in Ge display a normal temperature shift expected for LVMs.

3.2. Thermal donors

In Fig. 3, the annealing curve for the dimer is plotted together with those of the first three TDs. In order to compare integrated absorption also (i.e. concentration), results have been plotted for LVMs in a similar wave number range, i.e. the 525.5 cm^{-1} band for the dimer

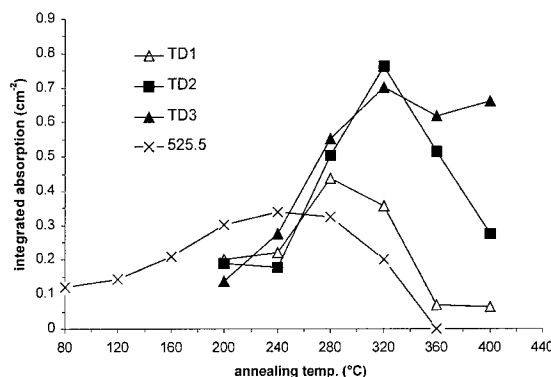


Fig. 3. Sequential appearance of oxygen dimer and thermal donor bands during annealing. The TD curves plotted represent the total absorption of a TD species in the “600” band, e.g. the sum of the neutral and double donor state absorption.

and the LVM lines in the “600” range for TD1, TD2 and TD3. The figure shows that the dimer appears in a sequence preceding the early TDs. This sequential appearance also seems to support our earlier identification of TD2 with a complex with four oxygens [6], which would imply that TD1 fitting between the dimer and TD2 would probably contain three oxygens. An interesting observation is that in the irradiated Ge, LVM from the TDs becomes visible in the “600” range already after 20 min annealing at $200\text{--}240^\circ\text{C}$. Even if a detailed comparison with the 350°C isothermal anneals of our previous study is difficult [6], it is obvious that the irradiation enhances not only the dimer concentration but also the TD formation. This seems logical if both kinds of defects would belong to the same agglomeration sequence. The presence of simple irradiation defects probably favours the oxygen agglomeration [10].

3.3. VO (A-centre)

In the as-irradiated Ge, the most prominent peak occurs at 621.6 cm^{-1} . It was attributed before by Whan [8] to the A-centre. A second prominent peak annealing out at the same temperature of $160\text{--}200^\circ\text{C}$ (Figs. 1 and 2) and that was not reported before, is observed at 669.1 cm^{-1} . This reminds of Si where the LVM of VO^0 and VO^- may be observed simultaneously depending on the resistivity. From our electrical data we calculate that the Fermi level is situated around $E_C - 0.25\text{ eV}$ during the annealing stages at which the two peaks are observed. Comparing this with the position of the VO-acceptor level in Ge at about $E_C - 0.25\text{ eV}$ [11], it seems reasonable to conclude that in our case, both charge states are also simultaneously present. Comparing again the positions of the corresponding bands in Si and Ge, we find once more a

scaling factor close to 1.32 for both peaks (Table 1). We accordingly assign the bands at 621.6 and 669.1 cm^{-1} to the anti-symmetric stretching LVM of the VO^0 and VO^- centre in Ge, respectively.

4. Conclusion

A major result of this study concerns the observation of LVM bands at 525.5, 780.9 and 817.9 cm^{-1} which are assigned to the oxygen dimer in Ge. The positions are in excellent agreement with observed counterparts in Si and with ab initio calculations. The enhancement of the formation of both the dimer and the early TDs as a consequence of irradiation, as well as their sequential appearance during isochronal annealing, strengthen the model of the dimer being a precursor of the TDs. Whether this also implies that the oxygen dimer in Ge represents a faster diffusion species than oxygen interstitials is less obvious, regarding the high diffusion coefficient of the latter in Ge [5]. A new band has been observed at 669.1 cm^{-1} with similar annealing as the band at 621.6 cm^{-1} due to the A-centre. The assignment of the bands to VO^- and VO^0 , respectively, is in agreement with the positions of similar bands in Si and with electrical data.

Experiments are in progress using ^{18}O -doped Ge in order to confirm the above assignments.

References

- [1] S. Öberg, C.P. Ewels, R. Jones, T. Hallberg, J.L. Lindström, L.I. Murin, P.R. Briddon, Phys. Rev. Lett. 81 (1998) 2930.
- [2] J. Coutinho, R. Jones, P.R. Briddon, S. Öberg, Phys. Rev. B 62 (16) (2000) 10824.
- [3] D.J. Chadi, Phys. Rev. Lett. 77 (1996) 861.
- [4] M. Pesola, J. von Boehm, R.M. Nieminen, Phys. Rev. Lett. 82 (1999) 4022.
- [5] P. Clauws, Mater. Sci. Eng. B 36 (1996) 213.
- [6] P. Clauws, P. Vanmeerbeek, Physica B 273–274 (1999) 557.
- [7] W. Kaiser, C.D. Thurmond, J. Appl. Phys. 32 (1961) 115.
- [8] R.E. Whan, Phys. Rev. 140 (2A) (1965) A690.
- [9] J.F. Becker, J.C. Corelli, J. Appl. Phys. 36 (1965) 3606.
- [10] J.L. Lindström, T. Hallberg, D. Åberg, B.G. Svensson, L.I. Murin, V.P. Markevich, Mater. Sci. Forum 258–263 (1997) 367.
- [11] N. Fukuoka, K. Atohe, M. Honda, K. Matsuda, Jpn. J. Appl. Phys. 30 (4) (1991) 784.
- [12] J.L. Lindström, L.I. Murin, V.P. Markevich, T. Hallberg, B.G. Svensson, Physica B 273–274 (1999) 291.



ELSEVIER

Physica B 308–310 (2001) 521–524

PHYSICA B

www.elsevier.com/locate/physb

Correlated to random transition of ionized impurity distribution in n-type Ge:(As, Ga)

Jiro Kato^a, Kohei M. Itoh^{a,*}, Eugene E. Haller^b

^a Department of Applied Physics and Physico-Informatics, Keio University, 3-14-1 Hiyoshi, Yokohama 223-8522 Japan

^b UC Berkeley and Lawrence Berkeley National Labs, Berkeley, CA 94720, USA

Abstract

We discuss the broadening of ground-state to bounded excited-state transitions of shallow donors in strongly compensated n-type Ge:(As,Ga) in the presence of electric fields and their gradients, arising from randomly distributed ionized impurities. Quantitative comparison of the experimentally obtained linewidths with Monte Carlo simulation results makes possible, a unique determination of the ionized impurity distribution in the samples. We present clear evidence for the random-to-correlated transition of the ionized impurity distribution as a function of the ionized impurity concentration and of temperature. © 2001 Published by Elsevier Science B.V.

Keywords: Impurity distribution; Compensated semiconductor; Impurity absorption

Many-body Coulombic interactions between randomly distributed positive and negative charges play important roles in a wide variety of physical systems. Such interactions become important especially when the charges are mobile and redistribute themselves in order to minimize the total Coulombic energy of the system. In this paper, it is demonstrated that the quantitative comparison of the experimental donor 1s–2p_± hydrogenic absorption linewidths and Monte Carlo simulations lead to an unambiguous determination of the ionized impurity distribution as a function of the ionized impurity concentration (N_I) and the temperature (T).

It has been expected theoretically that the ionized impurity distribution is correlated when the available thermal energy is sufficiently smaller than the correlation energy [1,2]. Electrons distribute themselves among donors in such a way as to reduce the total Coulombic energy, i.e., an energy gap known as “Coulomb gap” appears at the Fermi level in the density of the states of the donor band [3]. The correlated distribution is expected to dominate for the condition [1–3]

$$N_I = 2K \left(\frac{k_B T \kappa}{e^2} \right)^3 \quad (1)$$

with κ is the dielectric constant, K is the compensation ratio. The correlated distribution of the ionized impurities has been confirmed for the condition given by Eq. (1) in p-type Ge in our previous study [4].

When the thermal energy becomes larger than the correlation energy, electrons will be randomly distributed among donors, and the ionized impurity distribution is completely random. The random distribution is preferred for lower N_I since the larger distance between ions leads to weaker correlation. Larsen’s classic theory for the calculation of the linewidth assuming the random distribution is valid for the range [5,6]

$$N_I \leq 0.7 \times 10^{-5} a^{*-3}, \quad (2)$$

where a^* is the effective Bohr radius of donor impurities in units of cm.

The experimental determination of the transition temperature allows us to estimate the value of the correlation energy. The correlation energy (or equivalently the width of the Coulomb gap) becomes larger with increasing ionized impurity concentration N_I . While there have been many experiments to confirm the existence of the Coulomb gap, there has been very

*Corresponding author. Tel.: +81-45-566-1594; fax: +81-45-566-1587.

E-mail address: kitoh@appi.keio.ac.jp (K.M. Itoh).

little direct evidence for the random distribution of ionized impurities at low temperatures in semiconductors.

For our studies, we cut samples from a CZ-grown, n-type Ge:(As,Ga) single-crystal ingot. The concentrations of As and Ga vary as a function of the position along the ingot growth direction due to impurity segregation during growth. We have obtained a series of samples from various positions of the ingot and determined the concentrations N_D and N_A of As and Ga, respectively, using variable-temperature Hall effect measurements. The infrared absorption spectra were recorded with a BOMEM DA-8 Fourier transform spectrometer. The signal-to-noise ratio was improved by coadding 100–720 spectra. A composite silicon bolometer operating at $T = 4.2$ K was used as a detector. The samples were cooled in the OXFORD OPTISTAT cryostat and the sample temperature was monitored with a calibrated thermometer installed at the sample mount. A 0.1 μm black polyethylene film was placed in front of the samples to eliminate the above band-gap radiation.

The inset of Fig. 1 shows the absorption spectrum of a sample having $N_D = 3.03 \times 10^{13} \text{ cm}^{-3}$, $N_A = 1.75 \times 10^{13} \text{ cm}^{-3}$, i.e., $N_I \approx 2N_A = 3.50 \times 10^{13} \text{ cm}^{-3}$. The spectrum has been recorded at $T = 4$ K with a resolution of

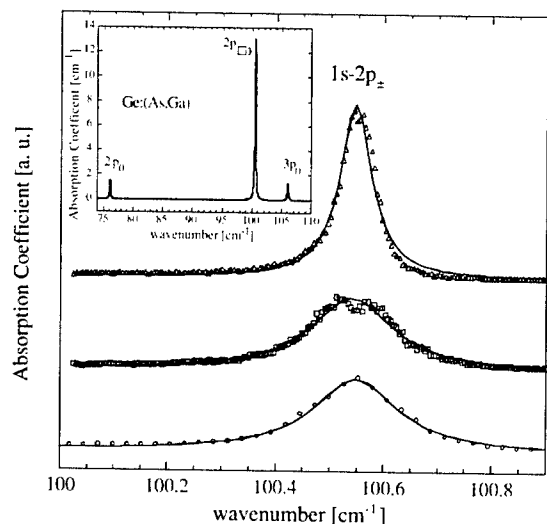


Fig. 1. The main frame shows the enlargement of the $1s-2p_{\pm}$ (100 cm^{-1}) absorption peak determined experimentally (\circ), calculated assuming random (\square) and correlated (\triangle) distributions of ionized impurities using the Monte Carlo method. The solid curves are the best fits to the experimental and calculated points assuming Lorentzian distributions. The inset shows As-donor absorption peaks recorded at $T = 4$ K with a sample having $N_I = 3.50 \times 10^{13} \text{ cm}^{-3}$. The three absorption peaks correspond to the As donor $1s-2p_0$ (76 cm^{-1}), $1s-2p_{\pm}$ (100 cm^{-1}), and $1s-3p_{\pm}$ (106 cm^{-1}) transitions.

0.026 cm^{-1} in the wavenumber range between 70 and 110 cm^{-1} . Three distinct peaks correspond to transitions of bound electrons of As in Ge from the $1s$ ground state to $2p_0$, $2p_{\pm}$, and $3p_0$ excited states, respectively. The main frame of Fig. 1 shows, from bottom to top, the enlargement of the $1s$ to $2p_{\pm}$ transition peaks; the experimental result (open circles), a Monte Carlo simulation assuming a random distribution of ionized impurities (open squares), and a Monte Carlo simulation assuming a correlated distribution of impurities (open triangles). The solid curves are Lorentzian fits to each set of data.

Fig. 2 shows FWHM vs. N_I at $T = 4$ K. The experimental data (filled circles) are compared with the theoretical linewidths assuming random (dashed line) and correlated (solid line) distributions of the ionized impurities. The intrinsic linewidth due to phonon lifetime broadening [7] for Ge has been found, experimentally, to be 0.066 cm^{-1} [8], which is negligibly small compared to the linewidths shown. Also $N_D < 1 \times 10^{15} \text{ cm}^{-3}$ for all of the samples employed, i.e., the broadening due to overlap of donor wavefunctions (concentration broadening) is negligible compared to the amount of electric-field broadening [9]. Therefore, it is appropriate to compare the experimentally found FWHM directly with the calculated widths assuming only an effect of the electric-field broadening. The comparison between the experimental results and theoretical estimates leads us to very interesting conclusions. Excellent agreement between the experimentally determined FWHM and the random theory for $N_I < 7.5 \times 10^{13} \text{ cm}^{-3}$ is clear evidence for the random distribution of ionized impurities in this low N_I region. When N_I is larger than $7.5 \times 10^{13} \text{ cm}^{-3}$, the experimental

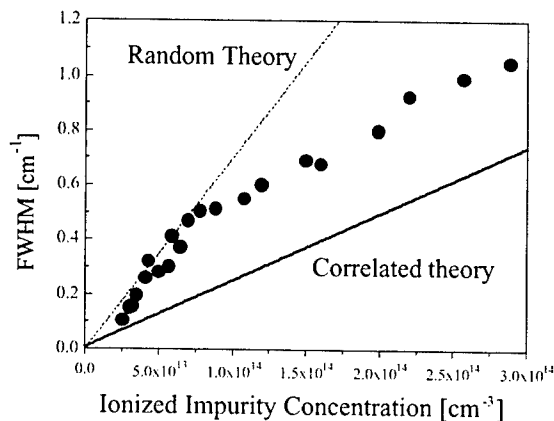


Fig. 2. Experimentally determined FWHM (filled circles) vs. N_I at $T = 4$ K. The dashed line is the prediction based on a random distribution of ions, while the solid line is the prediction based on a correlated distribution of ionized impurities at zero temperature.

data lie between the estimates of random theory and correlated theory. This implies that the ionized impurity distribution is somewhere between “completely random” and “completely correlated”. The Monte Carlo simulation for the correlated distribution shown in Fig. 2 has been performed for $T = 0$ K. However, the measurement was performed at finite temperature ($T = 4$ K) at which a certain degree of randomization of ionized impurities occurs due to the finite thermal energy. In this case, we expect the linewidth to have a value between the prediction of “completely random” and “completely correlated” distribution. Fig. 3 shows the comparison of the linewidths between $T = 4$ and 10 K. As expected, the linewidths at 4 and 10 K for the “completely random” region ($N_I < 7.5 \times 10^{13} \text{ cm}^{-3}$) are

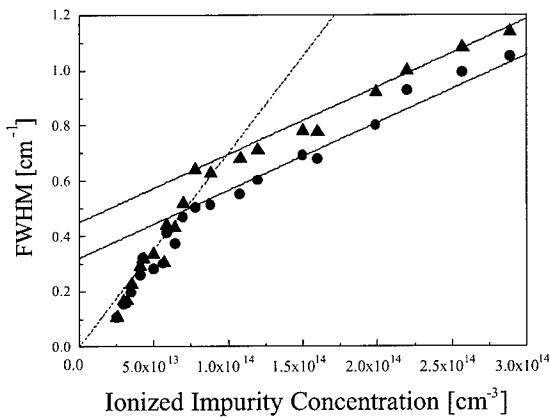


Fig. 3. Experimentally determined FWHM vs. N_I at $T = 4$ (●) and 10 K (▲).

the same while that of 10 K is broader than 4 K due to the larger degree of thermal randomization of the ionized impurity distribution. The critical ionized impurity concentration (N_{IC}), where the change of slope occurs in Fig. 3, shifts from $7.5 \times 10^{13} \text{ cm}^{-3}$ at $T = 4$ K, to $1.0 \times 10^{14} \text{ cm}^{-3}$ at $T = 10$ K. Eq. (2) predicts $N_{IC} = 1 \times 10^{13} \text{ cm}^{-3}$ for Ge at $T = 0$ K. Considering the fact that N_{IC} shifts to larger values for $T > 0$ K, the experimentally observed $N_{IC} = 7.5 \times 10^{13} \text{ cm}^{-3}$ at $T = 4$ K should be considered to be in excellent agreement with the prediction of Eq. (2). Fig. 4 shows the temperature dependence of the FWHM (■) for a sample having $N_I = 7.8 \times 10^{13} \text{ cm}^{-3}$, which is just above the critical concentration $N_{IC} = 7.5 \times 10^{13} \text{ cm}^{-3}$ for $T = 4$ K. We are interested in whether we observe a random to correlated transition with temperatures increasing from $T = 2$ K. Fig. 4 shows clearly that the FWHM increases in two steps; the first gradual increase occurs between $T = 5$ and 11 K and the second rapid increase takes place above $T = 14$ K. The second increase at $T > 14$ K is due to thermal ionization of donors as it matches with the increment of N_I (solid curve). The first gradual increase is due to the transition of the ionized impurity distribution from correlated to random, and the two plateaus in FWHM at $T = 2$ –5 K and 11–13 K represent characteristic FWHM for the two distributions. In order to support our claim that we have observed the transition, we shall estimate the critical temperature (T_c), for the transition, using the theory of Efros and Shklovskii and compare the result directly with our experimental observation. The energy of the Coulomb gap Δ for three dimensions is approximately [3];

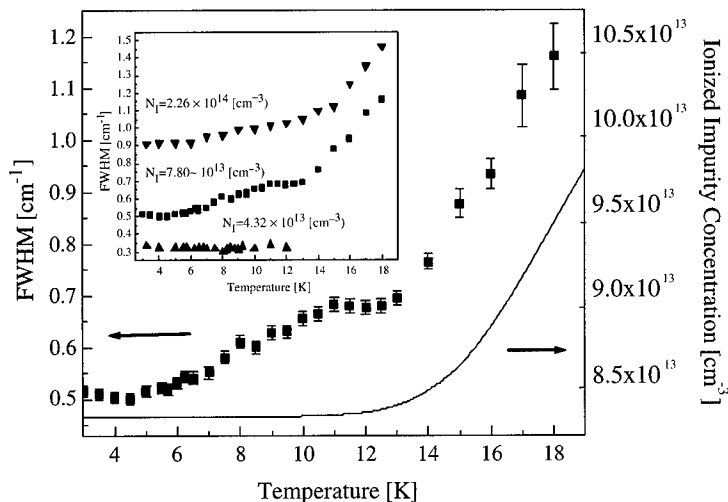


Fig. 4. The main frame shows FWHM vs. temperature for a sample having $N_I = 7.80 \times 10^{13} \text{ cm}^{-3}$. The solid curve is the ionized impurity concentration calculated with Eqs. (3) and (4). The inset shows the FWHM vs. temperature of three samples having $N_I = 4.32 \times 10^{13}$ (▲), 7.80×10^{13} (■), and $2.26 \times 10^{14} \text{ cm}^{-3}$ (▼).

$$\Delta = e^3 g_0^{1/2} / k^{3/2}, \quad (3)$$

where g_0 is the density of states at the Fermi level and can be estimated with

$$g_0 = KN_D k r_D / e^2. \quad (4)$$

$r_D = (3/4\pi N_D)^{1/3}$ is the distance between donors. Using Eqs. (3) and (4), $\Delta = 0.31$ meV has been obtained for the sample having $N_D = 7.8 \times 10^{13} \text{ cm}^{-3}$ in Fig. 4. To first order, we expect T_c to be of the same order as Δ , i.e., $T_c \approx 3.6$ K is what we estimate, based on theory. The experimentally found gradual increase starts around 4 K, in very good agreement with the theoretically estimated $T_c \approx 3.6$ K. The inset in Fig. 4 shows the temperature dependence of the FWHM for samples well below N_{IC} and well above N_{IC} . The width of the bottom curve ($N_D = 4.3 \times 10^{13}$) remains unchanged because its width is determined solely by the random distribution all the way up to 12 K. Above 12 K, the ionization of donors takes place and the peak disappears very quickly, i.e., it was not possible to determine the widths in this high temperature region. The FWHM of the bottom curve ($N_D = 4.3 \times 10^{13}$) for the temperature range 2–12 K agrees very well with the theoretical prediction of the random theory (the dashed line in Fig. 2). The FWHM of the top curve in the inset ($N_D = 2.26 \times 10^{14}$) for the temperature range shown is determined dominantly by the correlated distribution because the donor concentration is high enough for the neighboring ionized impurities to interact with one another. The FWHM increases with the increasing temperature because the partial randomization of the correlated distribution proceeds as was shown in Fig. 3.

Observation of the random-to-correlated transition of ionized impurity distributions as a function of tempera-

ture has been claimed before by Baranovskii et al. for GaAs [10–13]. However, analysis of their data shows that they observe an increase of FWHM due to ionization of donors and not due to the transition. As one can see in the inset of Fig. 4, it takes extreme fine-tuning of N_D and N_A in order to observe a clear signature of the transition with two distinct plateaus below the temperatures where ionization takes place. The precise control of both donors and acceptors at the level of 10^{13} cm^{-3} has been the key for the successful observation of the random-to-correlated transition of the ionized impurity distribution in semiconductors.

References

- [1] S.M. Kogan, N. Van Lien, *Fiz. Tekh. Poluprovodn.* 15 (1981) 44.
- [2] S.M. Kogan, N. Van Lien, *Sov. Phys. Semicond.* 15 (1981) 26.
- [3] B.I. Shklovskii, A.L. Efros, *Electronic Properties of Doped Semiconductors*, Springer, Berlin, 1984, p. 237.
- [4] K.M. Itoh, et al., *Phys. Rev. B* 53 (1996) 7797.
- [5] D.M. Larsen, *Phys. Rev. B* 8 (1973) 535.
- [6] D.M. Larsen, *Phys. Rev. B* 13 (1976) 1681.
- [7] K. Nishikawa, R. Barrie, *Can. J. Phys.* 41 (1963) 1135.
- [8] H. Navarro, et al., *Phys. Rev. B* 37 (1988) 10822.
- [9] W. Baltensperger, *Philos. Mag.* 44 (1953) 1355.
- [10] S.D. Baranovskii, et al., *Pis'ma Zh. Eksp. Teor. Fiz.* 46 (1987) 405.
- [11] S.D. Baranovskii, et al., *JETP Lett.* 46 (1987) 510.
- [12] S.D. Baranovskii, et al., *Fiz. Tekh. Poluprovodn.* 23 (1989) 1434.
- [13] S.D. Baranovskii, et al., *Sov. Phys. Semicond.* 23 (1989) 891.



ELSEVIER

Physica B 308–310 (2001) 525–528

PHYSICA B

www.elsevier.com/locate/physb

Ion-implantation and diffusion behaviour of boron in germanium

Suresh Uppal^{a,*}, A.F.W. Willoughby^a, Janet M. Bonar^b, Alan G.R. Evans^b,
Nick E.B. Cowern^c, Richard Morris^d, Mark G. Dowsett^d

^a Department of Engineering Materials, University of Southampton, Highfield, Southampton, SO17 1BJ, UK

^b Department of Electronics and Computer Science, University of Southampton, Highfield, Southampton, SO17 1BJ, UK

^c Philips Research Laboratories, Professor Holstlaan 4, 5656 AA Eindhoven, The Netherlands

^d Department of Physics, University of Warwick, Coventry CV4 7AL, UK

Abstract

Results are presented of implantation and diffusion study of boron (B) in germanium (Ge). B implantation was carried out in Ge with different energies and to different doses. High-resolution secondary ion mass spectroscopy was used to obtain concentration profiles after furnace annealing. The as-implanted profiles show a long tail possibly due to enhanced diffusion. A limited diffusion has been observed after furnace annealing. Using T-SUPREM, diffusivity value of $1.5(\pm 0.3) \times 10^{-16} \text{ cm}^2/\text{s}$ at 850°C has been extracted. This value is two orders of magnitude lower than previously reported values. The results question the change in diffusion mechanism of B diffusion in Si–Ge alloys from low Ge levels to high Ge levels. © 2001 Elsevier Science B.V. All rights reserved.

Keywords: Germanium; Boron; Ion implantation; Diffusion

1. Introduction

Potential application of silicon germanium (Si–Ge) alloys in HBTs, HFETs, and optoelectronic devices has motivated dopant diffusion studies in these alloys. The dominance of interstitials in diffusion of B in Si is well established from various studies [1] while recent defect injection studies confirm the same interstitially mediated diffusion in Si–Ge alloys up to 20% Ge [2]. Compared to Si, very little experimental work has been carried out in pure Ge or Si–Ge at high Ge levels. There are only two reports [3,4] of B diffusion in Ge which themselves disagree in diffusivity value by two orders of magnitude. Motivated by lack of knowledge of B diffusion in Ge and availability of better characterization techniques, along with ion implantation as method of introducing known amount of B, diffusion behaviour of B in Ge is studied. Furnace annealing is carried out and diffusivity

values have been calculated by fitting the experimentally obtained profiles.

2. Experimental procedure

Germanium single crystals, polished either on one or both sides with diameters 2" and 4" and a thickness of 300 μm were supplied by Eagle-Picher technologies, USA. The wafers were $\langle 111 \rangle$ and $\langle 100 \rangle$ oriented, n doped ($\leq 0.4 \Omega \text{ cm}$) or undoped ($> 30 \Omega \text{ cm}$). Dislocation density of all wafers was less than $5000/\text{cm}^2$. Wafers were cleaned with fuming nitric acid followed by rinsing in de-ionized (DI) water. ^{11}B ions were implanted into the polished side of the wafers with 5 and 20 keV to different doses ranging from 5×10^{13} to 6×10^{14} ions/ cm^2 . The ion beam was misoriented by 8° to the normal of the wafers. A silicon dioxide (SiO_2) layer was deposited on the implanted side of the wafers. This layer had two-fold function of protecting the vulnerable Ge surface during high temperature annealing and avoiding any out-diffusion of B atoms. The SiO_2 layer

*Corresponding author. Tel.: +44-2380-592351; fax: +44-2380-593016.

E-mail address: suresh@soton.ac.uk (S. Uppal).

was deposited by plasma enhanced chemical vapor deposition method at a temperature of $\sim 200^\circ\text{C}$ and had a thickness of approximately 2000 \AA . The samples were cleaned ultrasonically in DI water and methanol before annealing. Furnace annealing was carried out for temperature range $675\text{--}850^\circ\text{C}$ ($\pm 3^\circ\text{C}$) for different times. A reducing atmosphere of forming gas [a mixture of H_2 (5%) and N_2] flowing at a rate of 1 L/min was ambient for diffusion experiments. The SiO_2 layer was etched away using a standard HF etch after annealing. For determining the depth profiles an Atomika 4500 secondary ions mass spectroscopy instrument was used. A primary beam of oxygen (O_2^+) ions was used with 500 eV energy and at an angle of 25° to the normal of the wafer surface. An error of 10% can be associated with depth and concentration quantification from the raw SIMS data. A surface degradation was observed on annealing at higher temperatures and for longer times which made depth profiling using SIMS very difficult.

3. Results and discussions

Preliminary experiments were performed with implantation dose up to $5 \times 10^{14}\text{ ions/cm}^2$. The annealing carried out in forming gas ambient for temperatures up to 800°C for 24 h did not show any noticeable B movement from the as-implanted profile. Subsequently the temperature was raised to 850°C . A limited movement towards the end of the profiles was observed after annealing for 24 h. The profiles so obtained were analyzed quantitatively for diffusivity.

The measured boron profiles for implantation with two different energies of 5 and 20 keV in $\langle 111 \rangle$ Ge are presented in Fig. 1. The implantation dose used in each case is indicated in the figure. It also shows the profiles obtained from theoretical projected range and standard deviation values given by Gibbons et al. [5] using LSS calculations. Note that the values for 5 keV implant have been obtained by extrapolation. Similar implantation tails were observed for 5 and 20 keV implants in $\langle 111 \rangle$, and 20 keV implant in $\langle 100 \rangle$ direction. Comparing the peak concentration positions and theoretical values, we observe rough agreement in projected range although an implantation tail could be seen in all the as-implanted profiles. The implanted profiles were fitted using T-SUPREM assuming a dual-Pearson distribution. The parameters for fitting the as-implanted profiles were estimated from the experimentally obtained depth profiles. With 80% dose allocated to amorphous profile and 20% to channeling, the as-implanted profiles could be fitted very well. Similar tails have been observed for implanted B in Si where predominant contribution to the tail is from channeling. However, other implantation studies [6,7] have emphasized *radiation-enhanced diffusion* as dominant during B implantation in Ge at low

energies. The contribution of channeling, as obtained from fitting the implanted B profiles, is only 20% and thus it appears that enhanced diffusion is mainly responsible for the tails observed in our case as well.

The limited B diffusion was also analysed using T-SUPREM, which, as discussed above, could achieve a fit to the as-implanted profiles. These fitted profiles were taken as initial conditions for the diffusion calculations. The diffused distributions so obtained were compared to diffused SIMS profiles (850°C , 24 h) for the best fits to obtain values for solid solubility and diffusion coefficient, which were taken as parameters. For n type $\langle 111 \rangle$ Ge, $4.5 \times 10^{18}/\text{cm}^3$ and $1.8 \times 10^{-16}\text{ cm}^2/\text{s}$ values were obtained for solid solubility and diffusion coefficient, respectively. The values used for best fit of diffused profile for n type $\langle 100 \rangle$ were $6.5 \times 10^{18}/\text{cm}^3$ and $1.3 \times 10^{-16}\text{ cm}^2/\text{s}$ for solid solubility and diffusion coefficient, respectively. The experimental as-implanted and diffused profiles along with the fitted profiles are shown in Fig. 2. The solid solubility values agree with the values reported in literature [8]. The diffusivity calculation for $\langle 111 \rangle$ and $\langle 100 \rangle$ are also consistent. However, these diffusivity values are at least two orders of magnitude smaller than the minimum values reported in literature [9,10]. Hot probe measurements were also performed on samples as implanted and after heat treatment. Samples implanted with low dose were noticed to have a p–n junction formation in as-implanted state. However complete electrical activity for all doses studied could be observed only after the heat treatment.

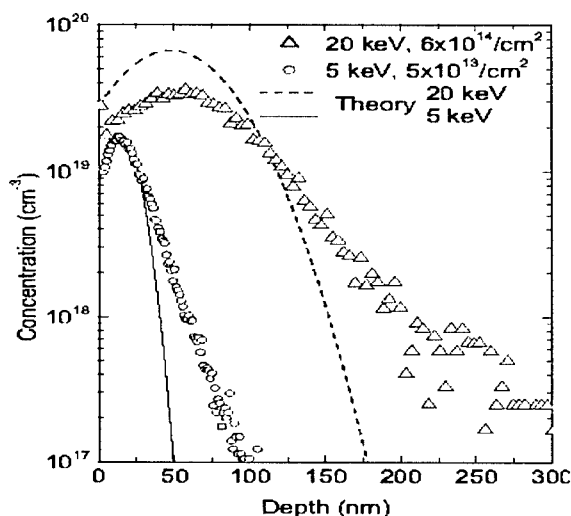


Fig. 1. Concentration profiles of as implanted B in $\langle 111 \rangle$ Ge for different energies. Also shown are the profiles obtained using LSS calculations for the two energies. The projected range and projected standard deviations for 5 keV implant were extrapolated from the data Gibbons et al. [5].

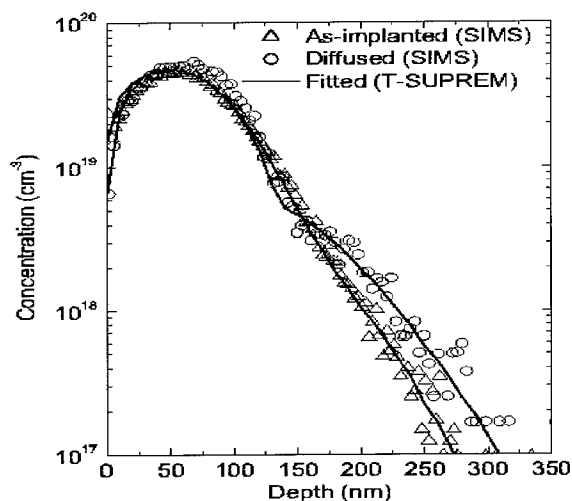


Fig. 2. SIMS B depth profiles of as implanted ($6 \times 10^{14}/\text{cm}^2$, 20 keV) and annealed (850°C, 24 h) sample. Using T-SUPREM, the best fit to diffused profile gave a diffusivity value of $1.3 \times 10^{-16} \text{ cm}^2/\text{s}$ for $n < 100$ Ge.

Various possibilities for the large discrepancy between the diffusivity values of this work and previous studies have been highlighted in a previous report [10]. It is important to note that the previous studies [3,4] were carried out by p–n junction and profiling by sheet resistance, rather than the SIMS profiling of total B in the present work. The possible cause for an immobile peak is precipitation of excess B since the solid solubility limit of B is crossed. The slower diffusion could be due to pairing/trapping of B with the implantation-induced defects (e.g. self-interstitial) however, Fang et al. [11] have shown that Arsenic implantation enhanced B diffusion in Si–Ge. The SiO_2 layer is believed to introduce point defects in Si which affects dopant diffusion. The presence of a SiO_2 layer on Ge surface might as well influence the dopant diffusion by injecting defects. Further studies are being carried out to resolve these issues.

B diffusivity as a function of Ge content for strained and relaxed Si–Ge obtained by various workers [11–15] is presented in Fig. 3. The diffusivity for strained as well as relaxed Si–Ge decreases rapidly with Ge content up to about 40% Ge. No consensus on the cause for this decrease in diffusivity has been reached. For Arsenic implantation in Si–Ge, a decrease in implantation-induced enhancement of B diffusivity with increase in the Ge concentration has been reported [11]. Based on a simple implantation-enhancement model, increase in the concentration of interstitials in thermal equilibrium with increase in Ge percentage has been hypothesized. Recent defect injection studies [2] have already shown that the mechanism responsible for B diffusion in Si–Ge alloys is interstitially mediated. Fang et al. [11] have concluded

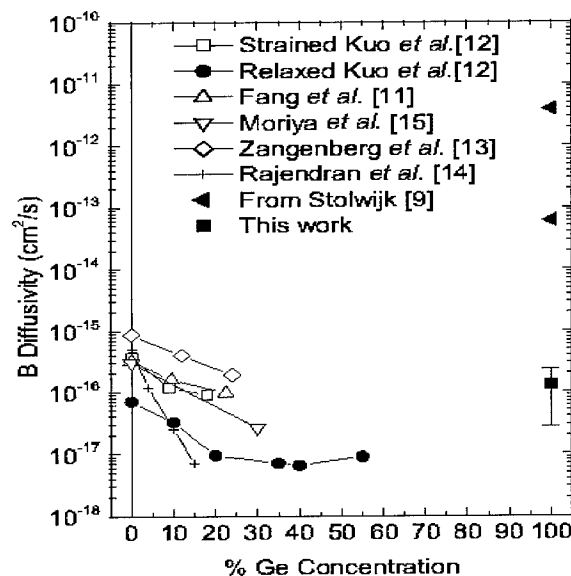


Fig. 3. Boron diffusivity as a function of Ge composition in Si–Ge alloys. Values for relaxed Si–Ge are for 800°C, other values being at 850°C. Our diffusivity value corrects the previous values by two orders of magnitude in pure Ge.

that decrease in the mobile B diffusivity, and not decrease in interstitial concentration, causes much of the decrease in B diffusivity in Si–Ge alloys with Ge content. This model also implies that it is unlikely that at high Ge levels diffusion of B will be dominated by vacancies as previously assumed for most Group III elements in Ge. Our present measurements suggest, in fact, that at Ge levels above 50%, there is at most a very small increase in diffusivity with Ge content (see Fig. 3), and imply no sharp change as assumed previously. Experiments are being carried out to answer these questions by better understanding of B diffusion process in pure Ge.

4. Summary

Boron implantation in Ge has resulted in profiles which differ from LSS calculation in terms of an implanted tail. The observed tails could be a result of radiation-enhanced diffusion. A slow diffusion for implanted B is observed. The diffusivity value has been calculated to be $1.5(\pm 0.3) \times 10^{-16} \text{ cm}^2/\text{s}$ at 850°C from the fitting of the diffused profiles which correct the previous values reported by at least 2 orders of magnitude. The cause for this slow diffusion is not directly apparent. Nevertheless, this new measurement suggests that there is little increase in B diffusivity from 50% to 100% Ge and calls into question the previously accepted view that the interstitially dominated diffusion

at low Ge level changes to a vacancy dominated mechanism at high Ge level.

References

- [1] W. Frank, U. Gösele, H. Mehrer, A. Seeger, Diffusion in silicon and germanium, in: G. E. Murch, A.S. Nowich (Eds.), *Diffusion in Crystalline Solids*, Academic Press, London, 1984 (Chapter 2).
- [2] J.M. Bonar, A.F.W. Willoughby, A.H. Dan, B.M. McGregor, W. Lerch, D. Loeffelmacher, G.A. Cooke, M.G. Dowsett, *J. Mater. Sci.: Mater. Electron.* 12 (2001) 219.
- [3] W.C. Dunlap Jr., *Phys. Rev.* 94 (1954) 1531.
- [4] W. Meer, D. Pommerrenig, *Z. Angew. Phys.* 6 (1967) 369.
- [5] J.F. Gibbons, W.S. Johnson, S.M. Mylroie, *Projected Range Statistics: Semiconductors and Related Materials*, Dowden, Hutchinson and Ross, Stroudsburg, 1975.
- [6] H. Herzer, S. Kalbitzer, in: I. Ruge, J. Graul (Eds.), *Proceedings of the Second International Conference on Ion Implantation in Semiconductors*, Springer, Berlin, (1972) p. 307.
- [7] M.I. Guseva, A.N. Mansurova, *Rad. Eff.* 20 (1973) 207.
- [8] B.L. Sharma, *Defect Diffus Forum* 70/71 (1990) 1.
- [9] N.A. Stolwijk, in: M. Schulz (Ed.), *Impurities and Defects in Group IV Elements and III–V Compounds*, Landolt-Börnstein, New Series, Vol. III/22b, Springer, Heidelberg, 1989, p. 456.
- [10] Suresh Uppal, A.F.W. Willoughby, Janet M. Bonar, Alan G.R. Evans, Nick E.B. Cowern, Richard Morris, Mark G. Dowsett, *J. Appl. Phys.*, in press.
- [11] Wingra T.C. Fang, Peter B. Griffin, James D. Plummer, in: Eugene A. Fitzgerald, Judy Hoyt, Keh-Yung Cheng, John Bean (Eds.), *Materials Research Society Symposium Proceedings*, 379 (1995), p. 379.
- [12] P. Kuo, J.L. Hoyt, J.F. Gibbons, J.E. Turner, D. Lefforge, in: Eugene A. Fitzgerald, Judy Hoyt, Keh-Yung Cheng, John Bean (Eds.), *Materials Research Society Symposium Proceedings*, 379 (1995), p. 373.
- [13] N.R. Zangenberg, J. Fage-Pedersen, J. Lundsgaard Hansen, A. Nylandsted Larsen, *Defect Diffus Forum* 194–199 (2001) 703.
- [14] K. Rajendran, W. Schoenmaker, *J. Appl. Phys.* 89 (2001) 980.
- [15] N. Moriya, L.C. Feldman, H.S. Luftman, C.A. King, J. Bevk, B. Freer, *Phys. Rev. Lett.* 71 (1993) 883.



ELSEVIER

Physica B 308–310 (2001) 529–534

PHYSICA B

www.elsevier.com/locate/physb

Vacancies and self-interstitials in germanium: a picture derived from radioactive probes

R. Sielemann^{a,*}, H. Hässlein^a, Ch. Zistl^a, M. Müller^a, L. Stadler^a, V.V. Emtsev^b^a *Hahn-Meitner-Institut Berlin GmbH, Glienicker Strasse 100, 14109 Berlin, Germany*^b *Joffe Institut St. Petersburg, Russia*

Abstract

Several experimental methods based on radioactive probes have been used and combined to study vacancies and self-interstitials in Ge. Central to the studies is the perturbed angular correlation spectroscopy. Defects are created and detected by electron irradiation with subsequent trapping at ^{111}In probe atoms and the neutrino-recoil technique. From combination of both types of techniques defect identification is achieved and numerous microscopic defect parameters of the isolated defects and defect–impurity pairs are extracted. Additional information on electrical levels is obtained by applying deep level transient spectroscopy (DLTS) to samples containing radioactive ^{111}In probes (radiotracer-DLTS).
© 2001 Elsevier Science B.V. All rights reserved.

Keywords: Germanium defects; Perturbed angular correlation; Deep level transient spectroscopy

1. Introduction

Though point defects in Ge have attracted intensive research for a long time and numerous results have been obtained, mostly by electrical and capacitance techniques [1,2], no microscopic identification of either vacancy or self-interstitial has yet been accomplished. Thus, a definite assignment of the collected data to the respective defects is still missing and interpretation of the results has remained largely speculative. It is clear, however, that a better knowledge would be of considerable interest not only for Ge itself but also with respect to Si for which a large amount of definite data exist [3].

Recently, another approach to identify and study the intrinsic defects in Ge has been presented. Several experimental techniques based on the radioactive probe nuclei have been employed. Primarily, the perturbed

angular correlation (PAC) technique has been used which is based on the fact that defects in the immediate vicinity of a radioactive probe atom (^{111}In) can be studied via the induced hyperfine interaction. In this way, structural and electronic defect properties can be obtained. Vacancies and self-interstitials were produced either by electron irradiation or by using the PAC probe itself as primary knock-on atom (PKA) effected by the emission of a neutrino in a preceding nuclear transmutation. From the combination of both types of experiments, identification of both the vacancy and the self-interstitial is achieved and numerous defect properties are obtained. A further experimental technique used is DLTS applied to Ge samples doped with radioactive ^{111}In probes.

In this contribution, we will first shortly present the experimental techniques. In the following, we list and discuss the properties of the vacancy and self-interstitial and how these properties were extracted from the various experiments. Finally, we touch recent results obtained by other experimental techniques and mention work in progress which calculates the geometrical structure and electronic properties of the relevant defect–probe pairs.

*Corresponding author. Tel.: +49-30-8062-2725; fax: +49-30-8062-2293.

E-mail address: sielemann@hmi.de (R. Sielemann).

2. Experimental techniques

2.1. Perturbed angular correlation spectroscopy (PAC)

The PAC method is based on the measurement of the nuclear quadrupole interaction of a radioactive probe nucleus with the charge distribution in its immediate environment. The charge distribution yields information on the probe's lattice site and defects, which might be situated around it in the form of an electric field gradient (EFG) tensor. The tensor parameters measured are the strength (frequency) ν_Q , the asymmetry parameter η and the crystallographic orientation which yields microscopic information on the probe-defect structure. In addition, the fraction of probes with a certain defect configuration can be determined. The probe nucleus used throughout the experiments is ^{111}In decaying to ^{111}Cd on which the hyperfine parameters are measured. A recent review of the PAC technique can be found in Ref. [4].

2.2. Defect production by electron irradiation

Vacancies and self-interstitials were produced in two different ways: either by irradiation with 1.2 MeV electrons or by the neutrino recoil technique. In the first case, irradiations of the samples were performed at cryogenic temperatures (in some cases at room temperature) to fluences of typically $5 \times 10^{16} \text{ e/cm}^2$. Following the irradiations, isochronal anneals were performed monitored by PAC to search for trapping at the ^{111}In probes.

2.3. Defect production by neutrino recoil

The direct neighbourhood between probe atom and defect is essential for PAC. A full exploitation of this fact is made by a defect production technique which is centered on the probe atom [5]. This is accomplished by using a probe atom which also serves as PKA. Fig. 1 shows the principle: instead of using ^{111}In as parent activity, the precursor ^{111}Sn is used. In the electron capture decay to ^{111}In a high energy neutrino is emitted which leads to a monoenergetic recoil of 29 eV on the ^{111}In probe. This is an energy close to or above the threshold T_d for single Frenkel pair formation in most materials in immediate vicinity of the ^{111}In probe. For Ge T_d is known to be about 20 eV.

2.4. Deep level transient spectroscopy (DLTS) on radioactive probes

A current weakness of DLTS is the fact that it does not contain information on the chemical nature and microscopic structure of an observed defect. This deficiency makes it difficult to correlate DLTS with

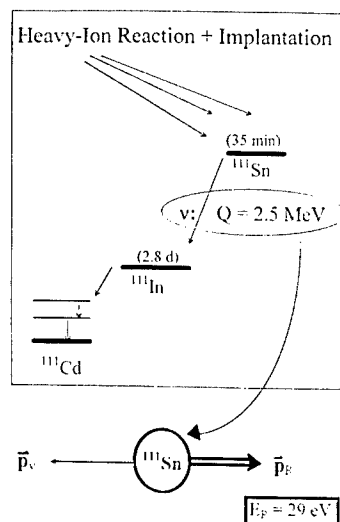


Fig. 1. Partial decay scheme illustrating the neutrino recoil effect. The neutrino emitted in the decay of ^{111}Sn carries an energy of 2.5 MeV leading to 29 eV recoil on the PAC probe ^{111}In .

structure sensitive methods. In recent developments, it was shown that information on the chemical nature can be added by applying DLTS to radioactive atoms [6]. In the present case, we have used samples like those prepared for PAC with radioactive ^{111}In probes subjected to electron irradiation and isochronal anneals. DLTS spectra were measured on these samples during a period of several days covering the decay of ^{111}In ($T_{1/2} = 2.8 \text{ d}$). One expects that the concentration of deep levels related to ^{111}In should decrease and those related to ^{111}Cd increase as function of time.

2.5. Probe production and recoil implantation

All methods described above are based on the incorporation of radioactive probe atoms in Ge [5]. This is done by a recoil implantation technique: A heavy ion beam of high energy (50–100 MeV) produces ^{111}In (or ^{111}Sn) atoms. In this process, the radioactive ions receive recoil energies between 1 and 10 MeV and become well separated from the primary heavy ion beam. The high recoil energies lead to implantation depths of typically 1–5 μm and low probe concentrations: typically between 10^{13} and 10^{14} cm^{-3} . Following implantation, the Ge samples are annealed at slightly above 600°C to remove the implantation damage and relax the probes to substitutional sites. This process is well monitored and leads to completely unperturbed probe incorporation.

3. Experimental results and discussion

3.1. Identification of vacancy and self-interstitial

Combining the results of the neutrino recoil experiments with those from the trapping experiments, identification of vacancy and self-interstitial is possible. In the recoil experiment, ^{111}Sn was implanted in p- and n-type samples with subsequent annealing of the implantation damage. Following this procedure, the probe is cooled to 4.2 K so that the decay of ^{111}Sn to ^{111}In takes place at this temperature. The result is shown in Fig. 2. 11% of the probes display an interaction frequency $\nu_{Q1} = 54 \text{ MHz}$ with axial symmetry ($\eta = 0$), showing that a defect is present at the probe. From additional experiments, the orientation of the probe-defect complex can be inferred to be in a $\langle 111 \rangle$ direction. This defect production is restricted to p-Ge, in n-type and intrinsic material no defect production occurs. Isochronal anneals show that the defect is stable to 205 K [7] and then disappears. Since the threshold for Frenkel pair formation is known to be around 20 eV, only one Frenkel pair, one vacancy and one interstitial can be produced. The probe atom as the PKA can either knock a neighbouring atom out of its site and take its position, leaving a vacancy behind (adjacent to the probe), or it may itself end up in an interstitial position. So the defect (54 MHz) connected with ν_{Q1} must be the association of the probe with a vacancy or represents the probe on some type of interstitial site. Theory has until recently not been able to calculate the EFGs pertaining to specific defect situations with sufficient accuracy, this situation, however, is presently changing [8,9]. Remedy of this ambiguity, however, can be obtained by combining the results from neutrino recoil with those from the trapping experiments described in the following.

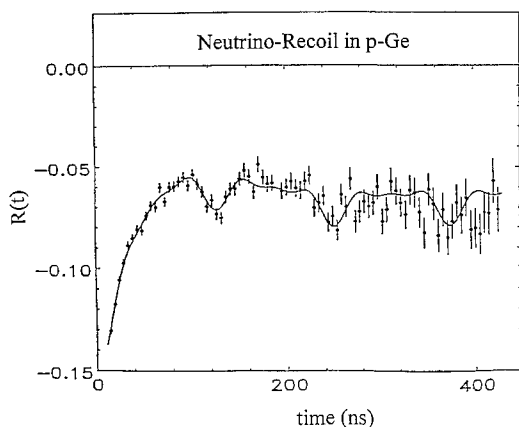


Fig. 2. PAC spectrum of $^{111}\text{In}/^{111}\text{Cd}$ measured at 4.2 K after neutrino recoil in p-Ge. The spectrum shows a defect with $\nu_{Q1} = 54 \text{ MHz}$.

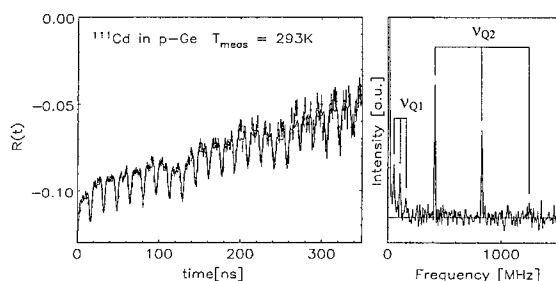


Fig. 3. PAC spectrum of $^{111}\text{In}/^{111}\text{Cd}$ and Fourier transform after electron irradiation in p-Ge measured at 293 K. The spectrum shows both ν_{Q1} and ν_{Q2} .

In these experiments, the ^{111}In -implanted and subsequently annealed samples were electron irradiated (mostly at 77 K). Isochronal annealing was executed and monitored by PAC in a range up to several hundred K. These experiments were performed with p-(Ga), n-(Sb) type, and also with high purity material. Depending on doping either one or two defects are trapped at the probes [10]: the already known defect from neutrino recoil (54 MHz) and a second one with $\nu_{Q2} = 420 \text{ MHz}$ ($\eta = 0$ and orientation $\langle 111 \rangle$), Fig. 3. Since $\nu_{Q1} = 54 \text{ MHz}$ occurs in both the recoil and the trapping experiment, the probe has to occupy a position compatible with both types of defect formation. This leaves only the substitutional site for the probe atom and identifies ν_{Q1} with a monovacancy nearest neighbour to the probe. For ν_{Q2} , such an identification is not possible since this defect is not produced by neutrino recoil. From extended series of experiments [10], it could be excluded that unintentional impurity trapping is observed. Thus, by exclusion of that possibility one can associate ν_{Q2} with a self-interstitial trapped at the probe in $\langle 111 \rangle$ direction. Additional corroboration of this identification will be discussed below.

3.2. Electrical properties of vacancy and self-interstitial

Given the above identification of vacancy and self-interstitial microscopic defect parameters can be extracted from the data [10]. The defects' trapping behaviour was studied as function of the carrier concentration (Fermi level) in n- and p-type material, see Fig. 4. The vacancy is observed only in p-Ge, the self-interstitial in p- and n-Ge but not in highly doped material. The entire trapping behaviour can be consistently explained when Fermi level-dependent charge states are assigned to the defects, keeping in mind that the shallow acceptor ^{111}In is always negative (or partly neutral in heavily p-doped material). Trapping of the vacancy in the form shown in Fig. 4 becomes understandable if an acceptor state for V at $E = E_V + 0.20 \text{ eV}$

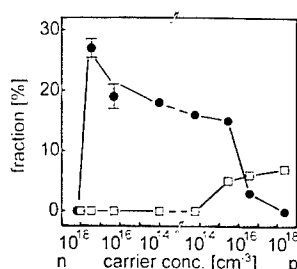


Fig. 4. Fractions of ^{111}In atoms forming complexes with vacancies (squares) and self-interstitials (circles) observed versus carrier concentration in n- and p-type Ge after electron irradiation at 77 K and subsequent warm-up to room temperature.

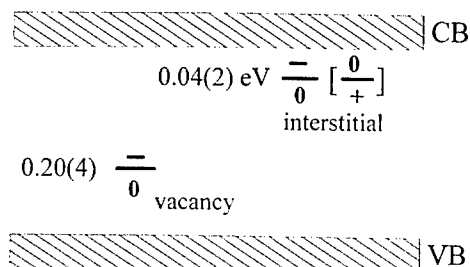


Fig. 5. Electrical levels of vacancy and self-interstitial in Ge as deduced from PAC. For the self-interstitial two options are possible: The acceptor represents the more likely case, see text.

exists, see Fig. 5. This leads to trapping at ^{111}In when V is neutral whereas in the negative state no trapping occurs due to Coulomb repulsion. Obviously, the trapping must be caused by elastic interaction between V and the strongly oversized ^{111}In atom in the Ge matrix. This reasoning becomes unique when the presence of the Ga dopants are simultaneously taken into account: vice versa with similar considerations, one can infer that the Ga doping atoms, being shallow acceptors like the In probes, do not (or very weakly) interact with Vs. Recent ab initio calculations also place an acceptor level for V in that energy region [11]. This is also in accordance with earlier evidence from electrical measurements [1].

For the self-interstitials' trapping at the probes, the data displayed in Fig. 4 leave two possible scenarios for the interstitials' charge states. Both need a level close to the conduction band, see Fig. 5. If this level were a donor, trapping might be explained as occurring between positive Is and the probes (Coulomb attraction), loss of trapping in highly doped n-Ge would then result from the neutralisation of I. Loss of trapping in p-type Ge would result from competitive Coulomb trapping at the Ga dopants. A second scenario might

assume the level close to the conduction band to be an acceptor. In this case, trapping would take place between neutral Is and the In probes. Loss of trapping in n-material would then result from the Coulomb repulsion when I turns negative. Loss of trapping in p-type Ge either from competitive trapping of the neutral Is with the Ga dopants or due to a second gap state of the Is in the lower half of the band gap which might render Is positive in highly doped material also leads to competitive trapping at Ga. The trapping data alone cannot decide between these two options. Recent ab initio calculations [12] indeed place an acceptor level close to the conduction band, which is also in accordance with earlier more indirect evidence [1]. If we accept that interpretation (scenario 2), an interesting question arises as to the origin of the interaction between a neutral I and a negative In atom while, on the other hand, there is practically no interaction between the Is and the donor dopants (Sb). This question is thoroughly discussed in Ref. [13].

3.3. Kinetic properties of vacancies and self-interstitials

Fig. 6 shows detailed annealing experiments in p-Ge following electron irradiation. Capture of the neutral vacancy and the interstitial (presumably also neutral, see above) occurs in a similar temperature range, 200(10) K for the vacancy and 220(10) K for the interstitial (for 15 min isochronal anneals). From several supporting arguments, we conclude that the capture processes are diffusion limited implying that both defects undergo long range migration with very similar activation energy, about 0.6(1) eV. This finding is somewhat surprising since interstitial migration is often assumed to occur at much lower temperatures. From the annealing behaviour shown in Fig. 6 the binding energy to the In probe can also be extracted: 0.5(1) eV for both I and V. With the given defect identification, the

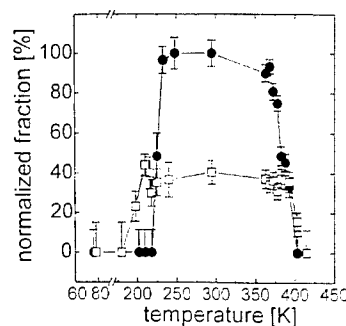


Fig. 6. Normalised fractions of ^{111}In atoms forming complexes with vacancies (squares) and self-interstitials (circles) observed versus annealing temperature after electron irradiation at 77 K in p-Ge.

production and thermal annealing of the neutrino recoil can also be understood. The recoil process leads to a vacancy-associated probe (v_Q) with a defect stability of only 205 K in contrast to the stability of this same pair occurring in the trapping reaction (about 400 K, see Fig. 6). This fact implies that the mechanisms erasing the pair are different: after recoil, the pair is annihilated by the close-by but not visible antidefect, the self-interstitial; after trapping, however, the pair disappears when the vacancy overcomes the binding to the probe and diffuses away. Both, free interstitial trapping (220 K, see Fig. 6) and pair annihilation by the close-by interstitial are rather close in temperature (the latter about 20 K lower) indicating that the processes are diffusion limited and not determined by barriers since eventual barriers should be quite different.

3.4. Electrical level of In–V pair

Since the probe–defect complexes (In–V, In–I, Cd–V, Cd–I) play such an important role in PAC, further electrical and structural information on these pairs is desirable. For electrical information DLTS is useful, however, even though quite a number of studies on radiation-induced defect–impurity pairs exist, interpretation of the data remained more or less speculative. We have, therefore, used DLTS on radioactive ^{111}In probes as described above. In this study, a level in p-Ge at $E = E_V + 0.33 \text{ eV}$ decreases in concentration with a half-life of 2.8 d and must, therefore, be related to the ^{111}In probe [14]. From PAC measured on the same sample, we can assign this level uniquely to the In–V defect, which is the only one appearing in the PAC spectra. Since the Cd–V level, into which the In–V level decays, is not observed in these spectra, we conclude that it must be situated in the upper half of the band gap. Levels associated with I are neither observed in p-type nor in n-type material, one reason might be that these levels are too shallow to be detected.

3.5. Structural properties of defect–impurity pairs

Since PAC always measures the properties of defect–probe pairs, structural information on the isolated defects is not directly available. Some information on the defect–probe pairs, however, can directly be gained by PAC-like symmetry properties and crystallographic orientation. This information was used in characterising the Cd–V and Cd–I pair. Another major source of information, the strength of the EFG (coupling constant v_Q) has in the past found little application in determining defect structures since it could not be reliably calculated for comparison with experiment. This situation, however, is about to change. Recently, ab initio methods have been used to calculate the geometric structure and resulting field gradients for defects and

defect pairs in semiconductors [8,9]. In the present case, the small electric field gradient (quadrupole coupling $v_Q = 54 \text{ MHz}$) obtained for the Cd–V pair has prompted us to suggest that the Cd probe might assume a position in the centre of a divacancy-like configuration (“split-vacancy”) analogous to the Sn-vacancy configuration in Si unravelled by Watkins [3]. This special configuration might also be involved in defect structures measured by PAC in Si [15–17] where defect frequencies in close analogy to Ge appear ($v_Q = 29$ and 451 MHz). Calculations for both Ge and Si are presently on the way [18] and seem to corroborate the identifications given for the vacancy and self-interstitial in the present work.

4. Conclusion

A combination of several experimental techniques based on radioactive probes has been used to study the fundamental defects, vacancy and self-interstitial in Ge. Identification of the defects could be achieved and a variety of microscopic defect parameters determined. Recently, published results obtained with positron annihilation spectroscopy [19] and X-ray techniques [20] confirm the conclusions of the present paper on the kinetic properties of V and I. Newly developed ab initio calculations of EFGs will allow to draw detailed structural information from the measured PAC parameters by comparison of experiment and theory in the near future [18].

Acknowledgements

Helpful work by R. Govindaraj in the preparation of this manuscript is gratefully acknowledged.

References

- [1] V.V. Emtsev, T.V. Mashovets, V.V. Mikhnovich, N.A. Vitovskii, *Radiat. Eff. Defects Solids* 111–112 (1989) 99.
- [2] J.C. Bourgoin, P.M. Mooney, F. Poulin, *Institute of Physics Conference Series*, Vol. 59, 1981, p. 33.
- [3] G.D. Watkins, *Mater. Sci. Forum* 143–147 (1994) 9.
- [4] Th. Wichert, *Hyperfine Interaction* 97–98 (1996) 135.
- [5] R. Sielemann, *Nucl. Instrum. Methods B* 146 (1998) 329.
- [6] N. Achtziger, W. Witthuhn, *Phys. Rev. Lett.* 75 (1995) 4484.
- [7] R. Sielemann, H. Hässlein, L. Wende, Ch. Zistl, *Physica B* 273–274 (1999) 565.
- [8] A. Settels, T. Korhonen, N. Papanikolaou, R. Zeller, P.H. Dederichs, *Phys. Rev. Lett.* 83 (1999) 4369.
- [9] S. Lany, P. Blaha, J. Hamann, V. Ostheimer, H. Wolf, Th. Wichert, *Phys. Rev. B* 62 (2000) R2259.

- [10] H. Hässlein, R. Sielemann, Ch. Zistl, *Phys. Rev. Lett.* 80 (1998) 2626.
- [11] A. Fazzio, A. Janotti, A.J.R. da Silva, R. Mota, *Phys. Rev. B* 61 (2000) R2401.
- [12] A.J.R. da Silva, A. Janotti, A. Fazzio, R.J. Baierle, *Phys. Rev. B* 62 (2000) 9903.
- [13] R. Sielemann, H. Hässlein, Ch. Zistl, *Physica B* 302–303 (2001) 101.
- [14] Ch. Zistl, R. Sielemann, H. Haesslein, S. Gall, D. Bräunig, J. Bollmann, *Mater. Sci. Forum* 258–263 (1997) 53.
- [15] D. Forkel, F. Meyer, W. Witthuhn, H. Wolf, M. Deicher, M. Uhrmacher, *Hyperfine Interaction* 35 (1987) 715.
- [16] Th. Wichert, M. Deicher, G. Gruebel, R. Keller, N. Schulz, K. Skudlik, *Appl. Phys. A* 48 (1989) 59.
- [17] H. Haesslein, et al., *Annual Report Hahn-Meitner-Institut, Bereich Schwerionenphysik*, 1990, p. 114.
- [18] P. Blaha, private communication.
- [19] A. Polity, F. Rudolf, *Phys. Rev. B* 59 (1999) 10025.
- [20] P. Ehrhart, H. Zillgen, *J. Appl. Phys.* 85 (1999) 3503.



ELSEVIER

Physica B 308–310 (2001) 535–538

PHYSICA B

www.elsevier.com/locate/physb

The interstitial boron and the boron–germanium complex in silicon–germanium crystals

J. Hattendorf^a, W.-D. Zeitz^{a,*}, N.V. Abrosimov^b, W. Schröder^b

^a Hahn-Meitner-Institut, Bereich Strukturforchung, Glienicker Strasse 100, D-14109 Berlin, Germany

^b Institut für Kristallzüchtung, Max-Born-Strasse 2, D-12489 Berlin, Germany

Abstract

The implantation behaviour of boron in silicon–germanium mixed crystals was studied. The β -NMR technique was used to measure electric field gradients at boron nuclei in defects. In addition, full-potential DFT calculations were performed to allow the interpretation on the basis of calculated bond lengths and electronic densities. Two defects were identified: a boron–germanium pair on lattice site in a relaxed silicon environment and a complex with interstitial boron. © 2001 Elsevier Science B.V. All rights reserved.

Keywords: Silicon–germanium crystals; Boron implantation; β -NMR; DFT calculations

Silicon–germanium crystals carry expectations for improved semiconductor devices. Although the phase diagram [1] and the band gaps for different compositions of $\text{Si}_{1-x}\text{Ge}_x$ [2] are known, investigations about growth properties and doping conditions are still relevant. The volume difference between silicon and germanium of about 4% makes it difficult to grow bulk materials in good quality, and the development of acceptors after boron implantation depends on the occupied lattice site. In order to contribute to the knowledge of boron defect centres, we have implanted radioactive ^{12}B into the mixed crystals. Combining β -NMR measurements with full-potential DFT calculations, we were able to identify and characterise two boron defect configurations.

In the experiment, we took advantage of the known nuclear properties of the radioactive ^{12}B isotope and its production process. The nuclear spin of the ground state is $I^\pi = 1^+$. Using 1.5 MeV deuterons in the $^{11}\text{B}(\text{d}, \text{p})^{12}\text{B}$ nuclear reaction on a thin target foil and choosing the appropriate recoil angle of 45° [3], we obtained a 10% polarisation of the nuclear spin in the implanted nuclear ensemble. This polarisation, which is correlated to the asymmetric ejection of electrons in the β -decay of ^{12}B , was detected by two detectors, one on each side of the

reaction plane. The boron-doped crystals were grown by the Czochralski method to make samples with germanium contents between 0% and 7% [4]. In order to be able to align each of the three low-index axes of the cubic lattice parallel to the external magnetic field \mathbf{B}_0 , the single crystals were prepared to have polished (110) surfaces.

In the combined interaction with the external magnetic field and the electric field gradient, the degenerate nuclear level is split with respect to the nuclear magnetic quantum number m . The sublevel position depends on the Larmor frequency ν_L and the quadrupole constant ν_Q which are defined by

$$h\nu_L = -(m/I)\mu\mathbf{B}_0, \quad h\nu_Q = eQV_{zz}. \quad (1)$$

V_{zz} is the greatest eigenvalue of the electric field gradient. For ^{12}B , the nuclear magnetic moment $\mu = 1.002\mu_B$ [5] and the quadrupole moment and its sign $Q = 13.2\text{ mb}$ [6,7] are known.

In the experiment, we frequently made use of transitions between the $m = -1$ and $m = +1$ sublevels, which can be observed if quadrupolar interactions are present. The transition frequency between these levels is calculated from second order perturbation theory [8]:

$$\begin{aligned} \nu_{-1 \leftrightarrow +1} &= 2\nu_L + \delta \\ \text{with } \delta &= (3/8)^2 \sin^2 \theta (3 \cos^2 \theta + 1) \nu_Q^2 / \nu_L. \end{aligned} \quad (2)$$

*Corresponding author. Tel.: + 49-30-80-622-916; fax: + 49-30-8062-2293.

E-mail address: zeitz@hmi.de (W.-D. Zeitz).

Here, θ is the angle between the directions of z and B_0 . The angular dependence of δ was used to determine the alignment of the field gradient in the lattice.

There are two configurations which were identified by their quadrupolar interaction: interstitial boron and boron on a lattice site with one germanium neighbour. Both these defects have C_{3v} symmetry around the $[111]$ axis of the lattice and are merely discriminated by the strength of the electric field gradient. This finding can be demonstrated in Fig. 1.

In principle, there are four $[111]$ directions in the T_d lattice which give rise to four resonances in the spectrum. As can be seen in Fig. 1, these resonances fall in one line if the $[100]$ axis of the crystal is aligned parallel to the external magnetic field. The resonance of the interstitial boron exhibits the greatest shift from the $2\nu_L$ value in the spectrum and is followed by the boron–germanium pair which has a weaker field gradient. The resonance line closer to $2\nu_L$ belongs to the substitutional boron atoms in the slightly distorted lattice.

The β -NMR resonance of the interstitial boron was observed first in pure silicon by Fischer et al. [9]. It is tempting to correlate this measured defect to the negative U-system which Watkins et al. [10,11] had described. Investigating different silicon-rich $Si_{1-x}Ge_x$ samples, we found that the resonance frequencies were independent of the germanium content. In all samples, a negative field gradient of $V_{zz} = -11.2(8) \text{ V/\AA}^2$ was measured, the value of which is in agreement with Fischer's result.

For the attributed defect complex, two different configurations are in discussion. Watkins suggested a positively charged boron which is located in the bond-centre between two silicon atoms [10], whereas recently DFT calculations [12] supported the configuration originally proposed by Tarnow et al. [13]. Here, a two-fold positively charged silicon in the interstitial is bonded to a negative boron which remains close to a regular lattice site. This configuration is shown in Fig. 2.

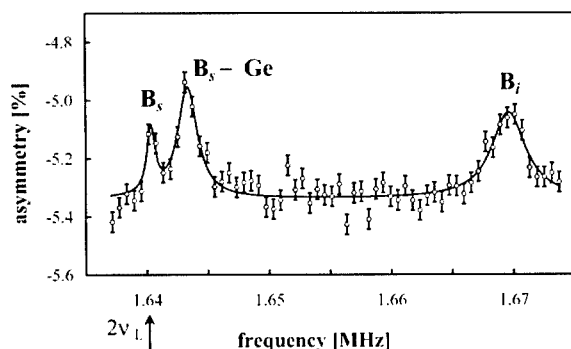


Fig. 1. Quadrupole resonances in the β -NMR spectrum for the $\nu_{-1/2 \rightarrow +1/2}$ transitions in a mixed crystal with 7at% germanium content at room temperature.

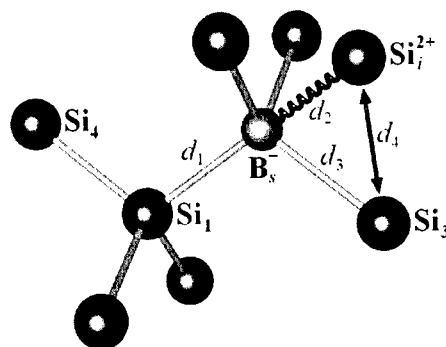


Fig. 2. Proposed configuration for interstitial boron.

In order to take the measured field gradient value to decide between the two configurations, we carried out the full-potential DFT calculations using the program package WIEN97 [14]. This code is based upon the density functional theory [15], the Kohn–Sham formalism [16] and the linearised augmented plane waves method [17]. For the exchange and correlation potential, the representation of Perdew et al. [18] was used. Additionally, a Newton algorithm was introduced to find the configuration in the minimum of energy.

The configurations were calculated in an array of 8, 9 atoms, respectively, which were subjected to the symmetry conditions mentioned above. In each Newton cycle these symmetries were maintained and, in addition, the bond-centre configuration of boron was to conserve the inversion symmetry. The atom positions were changed until the forces converged to a value lower than $0.5 \text{ mRy}/a_0$.

For both configurations, we found negative electric field gradients. An overview of the results of the measurements and calculations is given in Table 1. In the first two rows of the table, the bond lengths and the field gradients were calculated at the minimum of total energy, while in the last two rows, the field gradients were calculated by the WIEN code maintaining the bond lengths which are given in the reference papers. As an illustration of the results, contour plots of the calculated electronic charge densities in the $[110]$ planes of the lattice are shown in Figs. 3 and 4. For both configurations, the cigar-like enhanced charge densities around boron ions indicate negative field gradients.

Now we try to make a decision between the two proposed configurations from a comparison between the measured and calculated field gradients. It is obvious from the table that extremely short boron–silicon bonds and consequently high field gradient values are necessary to establish the bond-centre configuration. The calculated field gradient of $V_{zz} = -47.0 \text{ V/\AA}^2$ greatly exceeds the measured value. For Tarnow's configuration our calculation yielded $V_{zz} = -7.3 \text{ V/\AA}^2$. All boron–silicon bonds are found to be larger than 2.03 \AA . We

Table 1

Calculated bond lengths d_i and field gradients V_{zz} for different configurations of interstitial boron in comparison with the measured field gradient

Reference	d_1 (Å)	d_2 (Å)	d_3 (Å)	d_4 (Å)	V_{zz} (V/Å ²)
Bond-centre (this work)	1.85				−47.0
Complex (this work)	2.10	2.05	2.23	2.56	−7.3
Hakala [12]	2.08	2.03	2.19	2.51	−7.5
Tarnow [13]	2.08	2.07	2.51	2.51	−17.9
Experiment (this work)					−11.1(8)

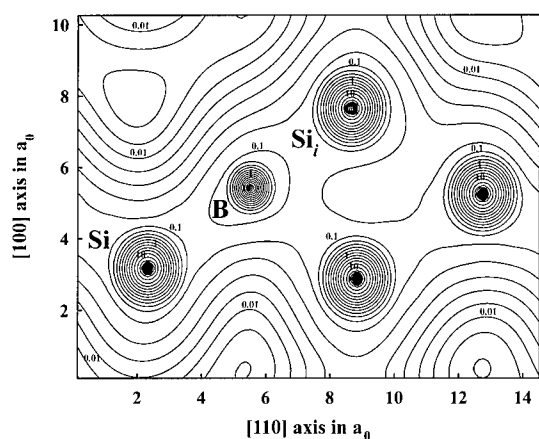


Fig. 3. Contour plot of the electronic charge density for Tarnow's configuration. The contour lines are shown in the [110]-plane in the dimension of (e/a_0^3).

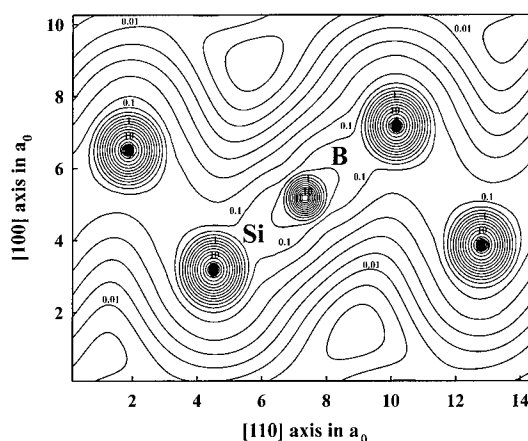


Fig. 4. Contour plot of the electronic charge density for the bond-centre configuration.

mention that, in this configuration, the field gradient significantly depends on the out-of-axis bond lengths and might be adjusted to the measured value by changing the lengths. In conclusion, we like to propose that the observed resonance is more likely caused by a defect configuration similar to Tarnow's suggestion.

In a second experiment, the details of which will be given in a forthcoming publication, we found the formation of boron–germanium pairs in silicon-rich mixed crystals. In the β -NMR measurements we found a field gradient of $V_{zz} = 3.8(3) \text{ V/Å}^2$. Our DFT calculations lead to a value of $V_{zz} = 3.1 \text{ V/Å}^2$ at the minimum of the total energy of the system. As this value is in reasonable agreement with the measured field gradient, the above attribution is considered to be confirmed. With reference to the undisturbed pure crystals, bonds are smaller when boron is the partner in the pair configurations. However, the boron–silicon bond does not go below $d = 2.16 \text{ Å}$. This result may be taken as a further support for the preference of Tarnow's configuration.

In conclusion, we point out that the combination of measurements and full-potential model calculations was necessary for the identification of defect complexes and

provided insight in the geometric and electronic structures of these defects.

References

- [1] R.W. Olesinski, G.J. Abbaschian, Bull. Alloy Phase Diag. 5 (1982) 180.
- [2] J. Weber, M.I. Alonso, Phys. Rev. B 109 (1989) 5683.
- [3] M. Tanaka, S. Ochi, T. Minamisono, A. Mizobuchi, K. Sugimoto, Nucl. Phys. A 263 (1976) 1.
- [4] N.V. Abrosimov, S.N. Rossolenko, W. Thieme, A. Gerhardt, W. Schröder, J. Crystal Growth 174 (1997) 182.
- [5] R.B. Firestone, V.S. Shirley (Eds.), Table of Isotopes, Wiley, New York, 1996.
- [6] T. Ohtsubo, Y. Nakayama, T. Izumikawa, S. Takeda, N. Nakamura, H. Tanji, T. Minamisono, Hyperfine Interactions 88 (1994) 25.
- [7] T. Yamaguchi, Hyperfine Interactions 120/121 (1999) 689.
- [8] A. Abragam, Principles of Nuclear Magnetism, Oxford University Press, Oxford, 1961.
- [9] B. Fischer, W. Seelinger, E. Diehl, K.-H. Ergezinger, H.-P. Frank, B. Ittermann, F. Mai, G. Welker, H. Ackermann, H.-J. Stöckmann, Mat. Sci. Forum 83-87 (1992) 269.
- [10] G.D. Watkins, Phys. Rev. B 12 (1975) 5824.

- [11] R.D. Harris, J.L. Newton, G.D. Watkins, *Phys. Rev. B* 36 (1987) 1094.
- [12] M. Hakala, M.J. Puska, R.M. Nieminen, *Phys. Rev. B* 61 (2000) 8155.
- [13] E. Tarnow, *Europhys. Lett.* 16 (1991) 449.
- [14] P. Blaha, K. Schwarz, J. Luitz, WIEN97, A Full Potential Linearized Augmented Plane Wave Package for Calculating Crystal Properties, Karlheinz Schwarz, Techn. Universität Wien, Austria, 1999, ISBN 3-9501031-0-4.
- [15] P. Hohenberg, W. Kohn, *Phys. Rev.* 136 (1964) B864.
- [16] W. Kohn, L.J. Sham, *Phys. Rev.* 140 (1965) A1133.
- [17] D.J. Singh, *Planewaves, Pseudopotentials and the LAPW-Method*, Kluwer Academic Publishers, Dordrecht, 1994.
- [18] J.P. Perdew, S. Burke, M. Ernzerhof, *Phys. Rev. Lett.* 77 (1996) 3865.

Interstitial oxygen in GeSi alloys

I. Yonenaga*, M. Nonaka, N. Fukata

Institute for Materials Research, Tohoku University, Katahira 2-1-1, Aoba-ku, Sendai 980-8577, Japan

Abstract

Interstitally dissolved oxygen atoms in the Czochralski-grown $\text{Ge}_{1-x}\text{Si}_x$ were investigated by the infrared spectroscopy together with the analysis by the secondary ion mass spectroscopy and the X-ray fine structure. In GeSi alloys in the whole composition range $0 < x < 1$, oxygen atoms occupy preferentially a bond-center site between Si atoms to make a Si–O–Si quasi-molecule leading to a typical 1106 cm^{-1} peak. The 1106 cm^{-1} peak shifts to low frequency side with an increase in Ge, possibly due to the expansion of Si–Si bonds. © 2001 Elsevier Science B.V. All rights reserved.

Keywords: Germanium–silicon alloys; Oxygen; Infrared spectroscopy; Crystal growth

1. Introduction

Germanium–silicon ($\text{Ge}_{1-x}\text{Si}_x$) alloy is a fully miscible solid solution of the diamond-base and has attracted keen interest as material for applications such as both microelectronic and opto-electronic devices with various unique properties due to the band gap and lattice parameter variations according to the composition [1]. GeSi alloy crystals have been successfully grown by the Czochralski technique from a melt prepared in a quartz crucible [1–5]. A large number of oxygen atoms are incorporated into the grown crystals due to the chemical reaction between Si melt and quartz crucible [4]. Oxygen is one of the most important impurities in Si from both the practical and fundamental points of view. It is well known that oxygen atoms dissolve interstitially in Si in the concentration of about 10^{18} cm^{-3} in maximum concentration and occupy a bond-off center site between Si atoms. Such a Si–O–Si quasi-molecule causes the anti-symmetric stretching vibration around 1106 cm^{-1} at room temperature. Similarly, in Ge, oxygen occupies the similar site to make a Ge–O–Ge [6], but the concentration is more than two orders of magnitude lower in Ge than in Si. Far less is known about oxygen impurities in GeSi except only for Si-rich cases higher than $x = 0.93$

as reported by Kaneta-Yamada et al. [7] and Wauters and Clauws [8].

This paper reports the infrared spectroscopy investigation of interstitially dissolved oxygen atoms in the Czochralski-grown $\text{Ge}_{1-x}\text{Si}_x$ alloy crystals in the complete composition range ($0 < x < 1$). The results are discussed together with the total oxygen concentration obtained by the secondary ion mass spectroscopy (SIMS) and the local atomic structure by the extended X-ray fine structure (XAFS) studies [9].

2. Experiments

High purity bulk crystals of $\text{Ge}_{1-x}\text{Si}_x$ alloys across the whole composition range $0 < x < 1$ were grown by the Czochralski technique at very low pulling rates ranging from 1 to 8 mm/h in a flowing Ar gas atmosphere. The details are described in previous papers [1–5]. Samples for experiments were prepared from the as-grown boules of both single crystals of GeSi alloy in the composition ranges $0 < x < 0.15$ and $0.85 < x < 1$ and polycrystals in the composition range $0.15 < x < 0.85$. The composition of the grown alloys was determined by means of energy dispersive X-ray (EDX) analysis.

The infrared absorption in the alloys was observed at room temperature (RT) and at 5 K by means of a Fourier transform infrared (FT-IR) spectrophotometer

*Corresponding author. Tel.: +81-22-215-2042; fax: +81-22-215-2041.

E-mail address: yonenaga@imr.edu (I. Yonenaga).

using JEOL-100 and BRUKER-IFS66 V apparatus with a liquid helium cryostat, respectively.

3. Results and discussion

Fig. 1 shows the infrared absorption spectra of the grown $\text{Ge}_{1-x}\text{Si}_x$ alloys of various Si content x , obtained at RT. The remarkable, broad peak was observed at the position centered around 1106 cm^{-1} , which originate on the anti-symmetric stretching vibration of interstitially dissolved oxygen atoms between Si atoms, Si–O–Si. The absorption coefficient $3\text{--}4\text{ cm}^{-1}$ was measured in Si-rich GeSi alloys, meaning that a large number of interstitial oxygen atoms are being included in the alloys. The peak intensity decreases with a decrease in the Si content x and then the peak almost disappears in the alloys with x lower than 0.23. In addition, with decreasing x the peak position shifts to the low wave number side. No peak at 855 cm^{-1} originating from Ge–O–Ge vibration was detected even in Ge-rich GeSi alloys. Moreover, there is no peak in the wave number range $1106\text{--}855\text{ cm}^{-1}$. At 5 K the main peak originating from Si–O–Si vibration shifts to the high frequency side and no other peak is observed in the above-mentioned wave number range. Thus, it seems that no peak originating into Si–O–Ge quasi-molecule exists in GeSi alloys.

Fig. 2 shows the absorption coefficient of the peak around 1106 cm^{-1} as a function of alloy composition. In the figure, the total amount of oxygen atoms in the GeSi alloys, determined by SIMS using Cs^+ induced at 10 kV, is also shown. The peak intensity corresponds well to the change of the total oxygen concentration determined by SIMS, which means that almost all the oxygen atoms in the alloys are present as interstitially dissolved atoms, but not as precipitates. As seen in Fig. 2, their dependences on the alloy composition fit well with the relation Ax^2 , where A is a constant. The results seem to show that the oxygen concentration depends strongly on

the ratio of Si–Si bonds in GeSi alloy with respect to the composition, if Si and Ge atoms occupy the lattice sites randomly. In fact, the XAFS investigations show the random substitutional site occupancy of Si and Ge atoms and no preferential ordering of the Ge–Ge dimer across the complete composition range [9]. We find that an oxygen atom preferentially occupies the bond-centered position of Si–Si bonds, forming Si–O–Si centers. Probably oxygen atoms have a stronger interaction with Si atoms than with Ge ones. From the correlation between the peak intensity and oxygen concentration, the calibration factor is estimated to be $5 \times 10^{17}\text{ cm}^{-2}$.

As seen in Fig. 3, the maximum peak around 1106 cm^{-1} shifts to the low wave number side linearly with the alloy composition in the complete range. In comparison with the previous results on Si-rich GeSi alloys reported by Kaneta-Yamada et al. [7] and Wauters and Clauws [8], also shown in the figure, the change rate is rather weak. The XAFS investigation [9] shows the following: First, the Ge–Ge and Ge–Si bond

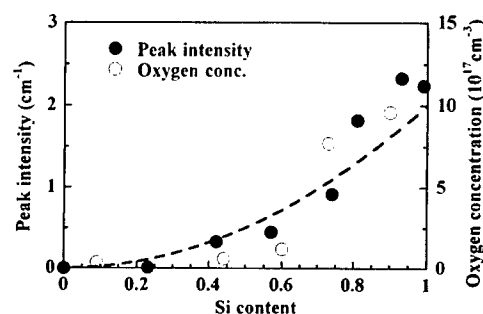


Fig. 2. The absorption coefficient of the peak around 1106 cm^{-1} as a function of alloy composition together with the oxygen concentration measured by SIMS. The broken line shows the ratio of Si–Si bonds in GeSi.

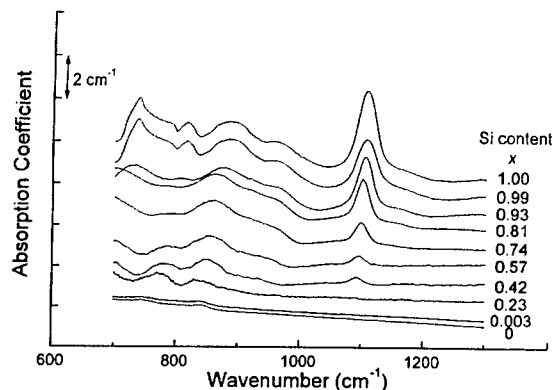


Fig. 1. Infrared absorption spectra of the as-grown $\text{Ge}_{1-x}\text{Si}_x$ alloys of various Si content x , measured at RT.

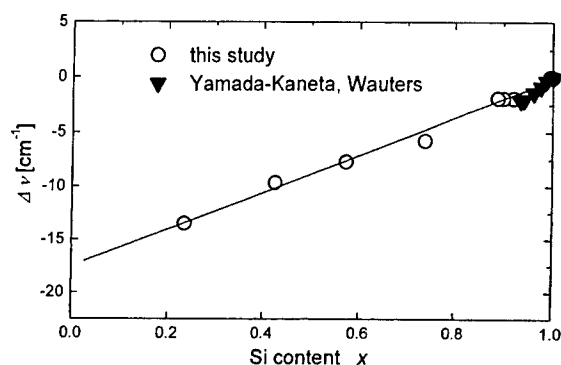


Fig. 3. Shift of the 1106 cm^{-1} peak as a function of alloy composition together with those reported by Yamada-Kaneta et al. [7] and Wauters and Clauws [8].

lengths in GeSi alloys increase linearly, being parallel to each other, with decreasing Si content. Possibly the Si–Si bonds, not investigated, have the same dependence on composition in analogy with the Ge–Ge and Ge–Si cases. Second, the bonding feature in bulk GeSi alloys is close, but not completely, to the Pauling limit [10] rather than the Vegard limit [11]. From these XAFS results, it is known that most of the strain in GeSi alloys may be accommodated by changes in the bond length and bond angle. Yamada-Kaneta et al. [7] and Wauters and Clauws [8] pointed out that the peak shift of 1106 cm^{-1} to lower wave numbers is attributed to Si–O–Si vibration perturbed on Ge atoms at second and third neighbor sites with changing coupling strength. Here, besides this mechanism an increase of the Si–Si bond length with the decrease of Si content may be included.

4. Conclusion

Interstitally dissolved oxygen atoms in $\text{Ge}_{1-x}\text{Si}_x$ crystals in the whole composition range ($0 < x < 1$) grown by the Czochralski method were investigated by means of FT-IR, SIMS and XAFS. Only a typical peak at 1106 cm^{-1} originating from the vibration of Si–O–Si molecule was detected for the complete composition range. Oxygen atoms are known to occupy preferentially a bond-center site between Si atoms and to make Si–O–Si quasi-molecules in GeSi alloys. The expansion

of Si–Si bonds with an increase in Ge content may lead to a shift of the 1106 cm^{-1} peak of the Si–O–Si vibration to lower wave numbers.

Acknowledgements

The authors are grateful to Dr. M. Sakurai of Tohoku University for supporting the XAFS investigation.

References

- [1] I. Yonenaga, *J. Mater. Sci.: Mater. Electron.* 10 (1999) 329.
- [2] I. Yonenaga, A. Matsui, S. Tozawa, K. Sumino, T. Fukuda, *J. Crystal Growth* 154 (1995) 275.
- [3] A. Matsui, I. Yonenaga, K. Sumino, *J. Crystal Growth* 183 (1998) 109.
- [4] I. Yonenaga, M. Nonaka, *J. Crystal Growth* 191 (1998) 393.
- [5] I. Yonenaga, *J. Crystal Growth* 198/199 (1999) 404.
- [6] P. Clauws, *Mater. Sci. Eng. B* 36 (1996) 213.
- [7] H. Yamada-Kaneta, C. Kaneta, T. Ogawa, *Phys. Rev. B* 47 (1990) 9338.
- [8] D. Wauters, P. Clauws, *Mater. Sci. Forum* 258–263 (1998) 103.
- [9] I. Yonenaga, M. Sakurai, *Phys. Rev. B* 64 (2001) 113206.
- [10] L. Pauling, *The Nature of the Chemical Bond*, Cornell University Press, Ithaca, NY, 1967.
- [11] L. Vegard, *Z. Phys.* 5 (1921) 17.



ELSEVIER

Physica B 308–310 (2001) 542–545

PHYSICA B

www.elsevier.com/locate/physb

Self-diffusion of ^{71}Ge in Si–Ge

A. Strohm^a, T. Voss^b, W. Frank^{a,b,*}, J. Räisänen^c, M. Dietrich^d^aMax-Planck-Institut für Metallforschung, Heisenbergstraße 1, D-70569 Stuttgart, Germany^bInstitut für Theoretische und Angewandte Physik, Universität Stuttgart, D-70550 Stuttgart, Germany^cDepartment of Physics, University of Jyväskylä, FIN-40351 Jyväskylä, Finland^dTechnische Physik, Universität des Saarlandes, D-66041 Saarbrücken, Germany

Abstract

The self-diffusivity D of implanted ^{71}Ge in relaxed, monocrystalline $\text{Si}_{1-y}\text{Ge}_y$ epi-layers has been measured as a function of temperature T ($894^\circ\text{C} \leq T \leq 1263^\circ\text{C}$) and composition y ($0 \leq y \leq 1$) by means of a radiotracer technique, where serial sectioning was done by ion-beam sputtering. For all compositions, the T -dependence of D is of Arrhenius type. The y -dependencies of both the diffusion enthalpy and the pre-exponential factor of D show a break at $y \approx 0.25$, which is ascribed to a transition from interstitialcy- ($y < 0.25$) to vacancy- ($y > 0.25$) mediated ^{71}Ge self-diffusion. © 2001 Elsevier Science B.V. All rights reserved.

PACS: 66.30.–h; 66.30.Fq; 81.05.Hd

Keywords: Si–Ge epi-layers; ^{71}Ge self-diffusion; Radiotracer technique; Transition from interstitialcy to vacancy mechanism

1. Introduction

Recently, a renaissance of Si–Ge alloys in semiconductor device technology has taken place because of the following reasons. Their charge carrier mobility and their band structure can be altered by changing the composition. For their device integration, the conventional and hence inexpensive silicon technology can be used.

A firm knowledge of the diffusion in Si–Ge alloys is highly desirable. On the one hand, doping with group-III and group-V elements for engineering the electric properties involves diffusion; on the other hand, the unintended in-diffusion of impurities has to be avoided.

Concerning diffusion in alloys, its dependencies on temperature and composition are of major interest. This is particularly so for Si–Ge, since different mechanisms of intrinsic-point-defect-mediated diffusion operate in its components [1]. This is due to the fact that under thermal-equilibrium conditions, in Ge, vacancies are the

only defect species, whereas in Si, vacancies and self-interstitials co-exist. More specifically, in Ge, self-diffusion takes place via vacancies in the entire regime of solid-state temperatures; in Si, self-diffusion is self-interstitial-controlled above about 1000°C and vacancy-controlled at lower temperatures. This implies that in Si–Ge, the mechanisms of self-diffusion change as a function of composition. This change can be investigated since the system Si–Ge does not have a gap of miscibility.

Already in 1974, McVay and DuCharme [2] published data on the self-diffusion of ^{71}Ge in polycrystalline Si–Ge. Within a research project of the present authors, the self-diffusivities of both ^{71}Ge and ^{31}Si in monocrystalline Si–Ge epi-layers are measured. First results on the diffusion of ^{71}Ge are presented in this paper.

2. Experiments

The specimens used in the present investigations were $7 \times 7 \text{ mm}^2$ platelets sawn out from the following three kinds of relaxed, monocrystalline $\text{Si}_{1-y}\text{Ge}_y$ epi-layers, all

*Corresponding author. Tel.: +49-711-689-1940; fax: +49-711-689-1922.

E-mail address: wfrank@mf.mpg.de (W. Frank).

of which were intrinsic and had been grown from the vapour phase on (100)-oriented substrates:

- (i) $\text{Si}_{0.95}\text{Ge}_{0.05}$, 10 μm thick, grown at 1100°C at the Institute of Electronics of the Academy of Sciences of Uzbekistan in Tashkent. The density of the threading dislocations in the epi-layers was estimated to be 10^{10}m^{-2} from the pit densities on Secco-etched surfaces by optical microscopy.
- (ii) $\text{Si}_{0.90}\text{Ge}_{0.10}$, 0.4 μm thick, and $\text{Si}_{0.75}\text{Ge}_{0.25}$, 1.05 μm thick, grown on the substrates after deposition of a 10 nm thick Si-buffer layer by Okmetic Ltd., Vantaa, Finland. The density of the threading dislocations in the epi-layers was found to be less than 10^9m^{-2} by transmission electron microscopy.
- (iii) $\text{Si}_{0.57}\text{Ge}_{0.43}$, 0.45 μm thick and virtually dislocation-free, grown on the substrates after deposition of an about 2 μm thick graded Si–Ge buffer layer at DaimlerChrysler Forschungszentrum, Ulm, Germany.

The diffusion studies were performed by means of a modified radiotracer technique, in which the ^{71}Ge -tracer atoms were implanted with an energy of 60 keV into the Si–Ge epi-layers in a non-channeling direction to depths between 30 and 40 nm at the mass separator of the Institut für Strahlen und Kernphysik at Bonn University, Germany, or at the on-line isotope separator (ISOLDE) of the European Organization for Nuclear Research (CERN) in Geneva, Switzerland.

The implanted specimens were cleaned in acetone, RCA I, RCA II, and citric acid, shortly dipped into HF, and finally rinsed with high-purity water. Then they were sealed up in HSQ-300 quartz ampoules under 15% H_2 –85% Ar atmosphere of 99.9999% purity, after these had been purified in HNO_3 – HCl (1:3) and HF. Next the specimens were isothermally diffusion-annealed in the temperature range of 894–1263°C. The durations of annealing lay in the regime from 2 h to 30 days, whose upper limit was dictated by the ^{71}Ge half-life of 11.2 days. Proceeding in this way guarantees that the thickness of the oxide growing on the epi-layers during diffusion annealing is less than 5 nm, and thus the implanted tracer atoms do not get stuck in the surface oxide.

After diffusion annealing, the ^{71}Ge distributions in the Si–Ge epi-layers were measured along the depth coordinate x perpendicular to the epi-layer surface $x = 0$. To this end, the specimens were serially sectioned by ion-beam sputtering at rates ranging from 6 to 10 nm/min. By sectionwise counting the ^{71}Ge atoms in the removed material, which was done by monitoring the radioactivity of the ^{71}Ge decay, it was possible to construct the ^{71}Ge concentration profiles $C(x)$ in the diffusion-annealed specimens. Implantation profiles in non-diffusion-annealed specimens were measured in the same way.

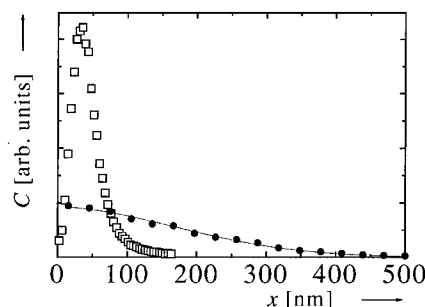


Fig. 1. ^{71}Ge -profiles in $\text{Si}_{0.95}\text{Ge}_{0.05}$ produced by 60 keV-implantation (\square) and subsequent diffusion annealing at 1095°C for 18 h (\bullet). The curve is a fit of an appropriate solution of the diffusion equation to the diffusion profile.

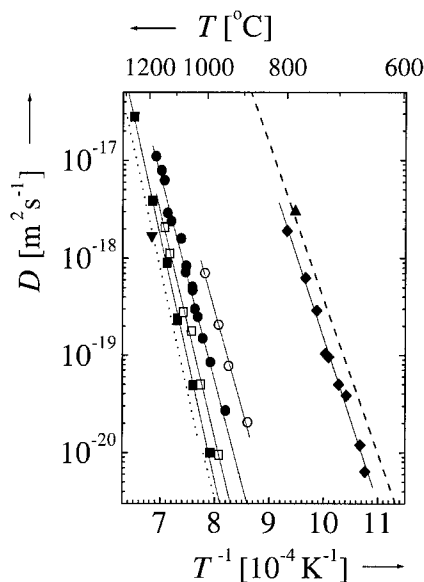


Fig. 2. Arrhenius presentation of self-diffusion coefficients of ^{71}Ge in $\text{Si}_{1-y}\text{Ge}_y$ (\blacktriangledown , $y = 0$, bulk; \cdots , $y = 0$, bulk [3]; \blacksquare , $y = 0.05$, epi-layers; \square , $y = 0.1$, epi-layers; \bullet , $y = 0.25$, epi-layers; \circ , $y = 0.43$, epi-layers; \blacklozenge , $y = 0.95$, bulk; $---$, $y = 1.0$, bulk [4]; \blacktriangle , $y = 1.0$, bulk).

3. Results

Examples of an implantation profile and a diffusion profile are presented in Fig. 1. By fitting an appropriate solution of the diffusion equation to the diffusion profiles, self-diffusion coefficients for ^{71}Ge in $\text{Si}_{1-y}\text{Ge}_y$, D , may be determined. The best fits were obtained for the semi-infinite-space ($x \geq 0$) solution, which contains the implantation profile for the corresponding Ge-content as initial condition, when total reflection of the diffusers at the surface $x = 0$ was assumed.

Fig. 2 shows D as a function of the diffusion temperature T for various compositions y . Obviously,

Table 1

Self-diffusion enthalpies H and pre-exponential factors D_0 of self-diffusion coefficients for ^{71}Ge in $\text{Si}_{1-y}\text{Ge}_y$ with various Ge-contents y

y	0.00	0.05	0.10	0.25	0.43	0.95	1.00
H (eV)	4.97	4.9	4.7	4.1	4.0	3.3	3.09
D_0 ($\text{m}^2 \text{s}^{-1}$)	0.25	0.4	0.04	0.0033	0.0029	0.01	0.00136

D obeys Arrhenius laws:

$$D = D_0 \exp(-H/kT), \quad (1)$$

for all compositions investigated (k = Boltzmann's constant). The corresponding diffusion enthalpies H and pre-exponential factors D_0 are compiled in Table 1. For comparison, data from the literature on the diffusion of ^{71}Ge in bulk Si ($y = 0$) [3] and bulk Ge ($y = 1$) [4] as well as own data on the ^{71}Ge -diffusion in (111)-oriented, highly dislocated, intrinsic bulk $\text{Si}_{0.05}\text{Ge}_{0.95}$ are included in Fig. 2 and Table 1. Apparently, these bulk-diffusion data are in accordance with our diffusion data on epi-layers. To demonstrate the agreement of our diffusion data with those of other authors [3,4], the ^{71}Ge -diffusivities in (111)-oriented bulk Si at 1200°C and in (100)-oriented bulk Ge at 748°C measured in the present work are also shown in Fig. 2.

The composition dependence of the ^{71}Ge -diffusion in $\text{Si}_{1-y}\text{Ge}_y$ is of particular interest. Fig. 3 illustrates how the diffusion enthalpy and the pre-exponential factor of the diffusion coefficient depend on the Ge-content. Either curve shows a break at the same Ge-content, viz., $y \approx 0.25$.

4. Discussion

The break in both the H - y and the D_0 - y curves we tentatively ascribe to the change from interstitial diffusion on the Si-side to vacancy diffusion on the Ge-side, which is expected according to Section 1. This interpretation is supported by other investigations to be reported below.

At first sight, the investigations of the ^{71}Ge -diffusion in polycrystalline Si-Ge of McVay and DuCharme, who also found breaks in the H - y and D_0 - y curves at a somewhat different composition ($y \approx 0.35$), seem to confirm our observations. However, one should bear in mind that several findings of McVay and DuCharme are not understood. For $y < 0.5$, the log D - x^2 plots of their diffusion profiles show a kink separating a steeper surface-near part from a deep-reaching tail, where the surface-near part shrinks with increasing Ge-content and disappears completely for $y > 0.5$. Evaluating the tails of their profiles, McVay and DuCharme found D -values, which for all temperatures and compositions distinctly exceed ours and those of other authors [3,4].

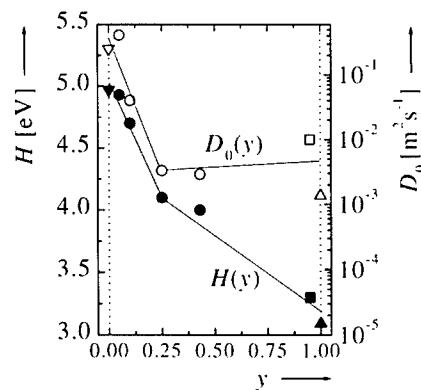


Fig. 3. Self-diffusion enthalpy H (full symbols) and pre-exponential factor D_0 (empty symbols) of the diffusion coefficient for ^{71}Ge in $\text{Si}_{1-y}\text{Ge}_y$ as functions of the Ge-content y (down-triangles, bulk [3]; circles, epi-layers; squares, bulk; up-triangles, bulk [4]).

These ambiguities raise doubts on whether McVay and DuCharme's data truly confirm our results.

Sb is a substitutional solute that, in contrast to ^{71}Ge , diffuses via vacancies in both Si [5] and Ge [6]. Hence, one expects that for Sb in $\text{Si}_{1-y}\text{Ge}_y$ neither occurs a break in the H - y nor in the D_0 - y curve. This has been tested in diffusion measurements of Sb in relaxed Si-Ge epi-layers by Nylandsted Larsen and Kringhøj [7]. Whereas the uncertainty of their D_0 -values inhibits to determine reliably the dependence of D_0 on y , H decreases monotonically from Si to Ge indeed.

Fischer et al. [8] have measured the diffusivity of ^{195}Au in $\text{Si}_{1-y}\text{Ge}_y$ up to $y = 0.24$. They found that in this composition range ^{195}Au undergoes kick-out-type diffusion. This involves exchanges of ^{195}Au between substitutional (Au_s) and interstitial (Au_i) sites according to



which are mediated by self-interstitials (I). Hence, even below 1000°C, where Fischer and collaborators' diffusion studies of ^{195}Au in Si-Ge were carried out, and up to a Ge-content of 24%, self-interstitials are present under thermodynamic equilibrium conditions. This result is compatible with our view that ^{71}Ge self-diffusion in $\text{Si}_{1-y}\text{Ge}_y$ is controlled by self-interstitials up to $y \approx 0.25$, where the curves in Fig. 3 show a break.

Further studies of diffusion in $\text{Si}_{1-y}\text{Ge}_y$ have been performed by Kuo et al. [9]. These authors report that

on the Si-side, in contrast to what is true for ^{71}Ge , for B-diffusion, H and D_0 increase with increasing Ge-content. This seeming conflict is resolved if, following Kuo et al., their B-data are interpreted in terms of a slowing down of the B-atoms by temporary trapping at Ge-sites. In fact, according to Koiwa [10], for this kind of retarded diffusion the $H - y$ and $D_0 - y$ dependencies observed by Kuo et al. are predicted.

Acknowledgements

The authors are grateful to N. Abrosimov, V.-M. Airaksinen, T. Hackbarth, and K. Lyutovich for the production of the Si–Ge material and to D. Eversheim for his assistance during the ^{71}Ge -implantation at Bonn University. Moreover, ^{71}Ge -implantations at ISOLDE, CERN, as well as financial support by the Academy of Finland (project 44875) and the HPRI Programme of the European Community are appreciated.

References

- [1] W. Frank, *Def. Diff. Forum* 75 (1991) 121.
- [2] G.L. McVay, A.R. DuCharme, *Phys. Rev. B* 9 (1974) 627.
- [3] G. Hettich, H. Mehrer, K. Maier, *Inst. Phys. Conf. Ser.* 46 (1979) 500.
- [4] M. Werner, H. Mehrer, H.D. Hochheimer, *Phys. Rev. B* 32 (1985) 3930.
- [5] P.M. Fahey, P.B. Griffin, J.D. Plummer, *Rev. Mod. Phys.* 61 (1989) 289.
- [6] W. Frank, U. Gösele, H. Mehrer, A. Seeger, in: G.E. Murch, A.S. Nowick (Eds.), *Diffusion in Crystalline Solids*, Academic Press, New York, NY, 1984, p. 63.
- [7] A. Nylandsted Larsen, P. Kringhøj, *Appl. Phys. Lett.* 68 (1996) 2684.
- [8] R. Fischer, W. Frank, K. Lyutovich, *Physica B* 273–274 (1999) 598.
- [9] P. Kuo, J.L. Hoyt, J.F. Gibbons, J.E. Turner, D. Lefforge, *Mater. Res. Soc. Symp. Proc.* 379 (1995) 373.
- [10] M. Koiwa, *Acta Metall.* 22 (1974) 1259.



ELSEVIER

Physica B 308–310 (2001) 546–549

PHYSICA B

www.elsevier.com/locate/physb

Low temperature muonium behaviour in Cz-Si and Cz-Si_{0.91}Ge_{0.09}

P.J.C. King^{a,*}, I. Yonenaga^b^a *ISIS Facility, Rutherford Appleton Laboratory, Chilton, Oxfordshire, OX11 0QX, UK*^b *Institute for Materials Research, Tohoku University, Sendai 980-8577, Japan*

Abstract

Observation of muon and muonium behaviour in semiconducting materials provides valuable insight into analogous hydrogen states and dynamics. We have used muon spin rotation, relaxation and resonance techniques to observe the low-temperature muon behaviour in Czochralski-grown silicon and bulk, Czochralski-grown silicon-germanium alloy materials. Low temperature relaxation of the rapidly moving tetrahedral muonium species and its conversion to a diamagnetic species is seen in the Cz material but not in the float zone silicon, suggesting site change and subsequent ionisation are promoted by the oxygen impurity. This is also the first time muon behaviour in a Si_{1-x}Ge_x alloy material has been presented. © 2001 Elsevier Science B.V. All rights reserved.

Keywords: Hydrogen; Muonium; Czochralski-silicon; Silicon-germanium

1. Introduction

Isolated hydrogen centres are difficult to study directly in semiconducting materials, yet an awareness of hydrogen behaviour is essential to enable its effects on electrical properties, diffusion and growth processes to be understood. One way of building up atomistic pictures of hydrogen behaviour is through observation of its analogue *muonium*, formed by implantation of positive muons. Implanted into a semiconducting material, muons behave like light proton isotopes, mimicking protons, isolated hydrogen or hydride ion species depending on how many electrons they pick up. Observation of muon and muonium (the isolated hydrogen atom analogue, μ^+e^- , Mu) behaviour therefore enables analogous hydrogen behaviour to be deduced [1].

The technique of μ SR—muon spin rotation, relaxation or resonance—involves implantation of spin polarised, positive muons followed by observation of the time evolution of the muon polarisation in the sample after implantation. Muons are unstable particles,

decaying after an average lifetime of 2.2 μ s to produce a positron, which is preferentially emitted in the instantaneous direction of the muon's spin at time of decay. Detection of these positrons therefore allows the evolution of the muon polarisation in the sample to be followed after implantation, informing on muon behaviour.

Observation of the muon response in semiconducting materials has enabled models of hydrogen behaviour to be built up. In silicon and germanium at low temperatures, three muon states are formed: a diamagnetic state (μ^+ or μ^-); a paramagnetic, isotropic muonium state which moves rapidly between tetrahedral sites (Mu_T); and an axially symmetric, immobile bond-centred paramagnetic species (Mu_{BC}). Detailed models for the dynamics of these states have been developed (for example [2]). Muons have recently provided the first experimental confirmation of a predicted shallow donor hydrogen state in ZnO [3], together with observation of shallow donor states in other II–VI materials [4].

The interaction between hydrogen and interstitial oxygen in Si is of particular interest, because of the ability of H to catalyse oxygen diffusion. The precise mechanism for this is not well understood, however, although it is believed that H adopts a bond centred site

*Corresponding author. Fax: +44-1235-445720.

E-mail address: philip.king@rl.ac.uk (P.J.C. King).

near to oxygen atoms in the Si lattice [5,6]. Comparison of the muon response between float zone and Czochralski material may enable information on oxygen–hydrogen interactions to be deduced.

This current study also includes data from a bulk, Cz-grown $\text{Si}_{1-x}\text{Ge}_x$ alloy. The recently developed ability to grow alloy material by the Czochralski technique [7] has opened up the possibility of exploring the bulk properties of this technologically important material. A more detailed comparison of alloy material with Cz-Si will be presented elsewhere; however, the alloy results shown here are the first presentation of the muon response from $\text{Si}_{1-x}\text{Ge}_x$ material.

2. Experimental

Muon behaviour in three samples is described: 300 μm thick, $\langle 111 \rangle$ oriented, 5 cm diameter prime undoped Czochralski silicon from Virginia Semiconductor, with n-type character and a measured resistivity of $885 \Omega \text{cm}^{-1}$ ($5 \times 10^{12} \text{carriers cm}^{-2}$); 330 μm thick, $\langle 111 \rangle$ oriented, 10 cm diameter float zone silicon from ShinEtsu Handotai with n-type character and a measured resistivity of $3300 \Omega \text{cm}^{-1}$ ($1.5 \times 10^{12} \text{carriers cm}^{-2}$); and $\langle 100 \rangle$ undoped Czochralski $\text{Si}_{0.91}\text{Ge}_{0.09}$ grown by Prof. I. Yonenaga in the form of a single wafer 2.5 cm across and about 500 μm in thickness.

Muon measurements were made at the ISIS pulsed muon facility. The muon spectrometers enable decay positrons to be detected using an array of scintillator detectors arranged in two groups, one forward and one backward of the initial muon polarisation direction. Forming the normalised difference in positron counts between these two detector groups enables a direct measurement of the time evolution of the muon polarisation in the sample after implantation to be made. Samples were mounted in exchange gas ^4He cryostats to allow temperatures from 5–300 K to be accessed.

Fig. 1 shows a typical plot of the muon polarisation as a function of time after muon implantation. This plot was taken from the Cz-Si sample at 25 K in an applied longitudinal field of 525 G. This plot was formed using

$$P = \frac{1}{a_0} \frac{F(t) - \alpha B(t)}{F(t) + \alpha B(t)},$$

where F and B are respectively the counts in the detectors forward and backward of the initial muon polarisation direction, and α is a factor to correct for small differences in efficiency and solid angle between the forward and backward detector sets. a_0 is the forward–backward detector asymmetry corresponding to full polarisation, typically about 0.24 on the ISIS muon instruments.

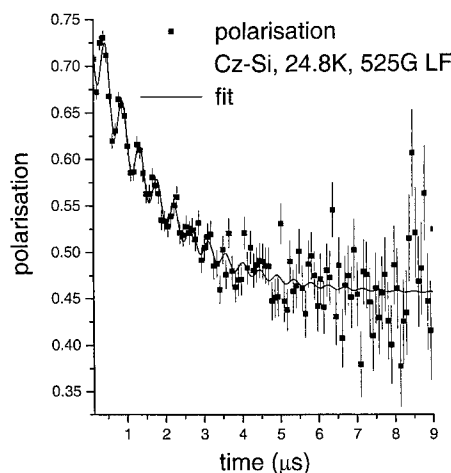


Fig. 1. Muon polarisation as a function of time in the Cz-Si sample at 24.8 K and a longitudinal field of 525 G. The exponential decrease is due to Mu_T relaxation; the oscillations are due to Mu_{BC} states with symmetry axis parallel to the field direction.

The features of the polarisation plot show the behaviour of the muon species in the sample. The main features in Fig. 1 are an overall decrease of the polarisation with time down to a constant value, on which is superimposed an oscillatory component. Dynamical processes involving muonium lead to an exponential relaxation of the muon polarisation after implantation; Fig. 1 has been fitted with a single exponential decay. States not involved in relaxation processes contribute a constant component. The oscillatory term in Fig. 1 is due to particular transitions within one of the muonium species, and can be fitted with a sinusoidal term whose amplitude decreases with time. All of the longitudinal field data in the current paper have been fitted with a single exponential decay (allowing the amplitude and relaxation rate of the component to be extracted) and a constant component, together with a single oscillatory term where needed.

3. Results

Fig. 2 shows the measured relaxation rate in applied longitudinal field as a function of temperature for the Cz-Si, $\text{Cz-Si}_{0.91}\text{Ge}_{0.09}$ and Fz-Si samples. For the $\langle 111 \rangle$ Cz-Si and Fz-Si samples, the applied field was 525 G. This field was chosen to allow oscillations caused by the avoidance of a level crossing in the Mu_{BC} energy levels, in Mu_{BC} species with symmetry axis parallel to the applied field diagram, to be observed; these can be seen in Fig. 1. Longitudinal field measurements at 525 G therefore allowed a very direct way of monitoring the behaviour of Mu_{BC} as a function of temperature. For the $\text{Cz-Si}_{0.91}\text{Ge}_{0.09}$ sample, the applied field was 100 G.

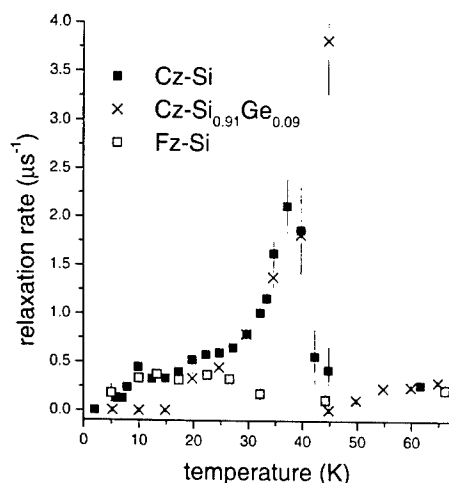


Fig. 2. Longitudinal field relaxation rate as a function of temperature from the Cz-Si and Fz-Si samples (both 525 G longitudinal field) and the Cz-Si_{0.91}Ge_{0.09} alloy material (100 G field).

The float zone silicon shows a small relaxation between 10 K and 30 K of about $0.3 \mu\text{s}^{-1}$; the rate stays low until above 100 K. The Cz-Si shows a similar behaviour below about 17 K, but then exhibits a very strong relaxation rising to a peak of $2\text{--}3 \mu\text{s}^{-1}$ at 40 K. Measurements as a function of applied field show the relaxing species to be Mu_T ; this is confirmed by the fact that the Mu_{BC} longitudinal field oscillations show little change over the temperature range shown in Fig. 2. Shown also in Fig. 2 is the relaxation rate from the Cz-Si_{0.91}Ge_{0.09} sample. This also exhibits a significant peak at around 40 K, again from the Mu_T species. The amplitudes of the relaxing components in the Cz-Si and Cz-Si_{0.91}Ge_{0.09} samples show peaks at around 30 K before falling to low values above 40 K.

Transverse field measurements can reveal the behaviour of promptly formed diamagnetic species—either μ^+ or μ^- —although delayed diamagnetic formation (for example, resulting from conversion of a paramagnetic species) is not seen in transverse data. Fig. 3 shows the transverse field amplitudes for the three samples as a function of temperature. Over the whole temperature region of Fig. 2 there is no significant increase in the prompt diamagnetic fractions in any of the samples. The rise shown by all three above 200 K is the result of Mu_{BC} ionisation.

Delayed formation of muon states can be seen using radio-frequency μSR . RF- μSR involves application of a static, longitudinal field to the sample, together with an RF pulse applied for the duration of data taking. Depolarisation is observed as the static field is swept through the resonance condition—in the case described here, the signal from diamagnetic muons has been measured. Fig. 4 shows the RF diamagnetic amplitude as a function of temperature for the three samples. At

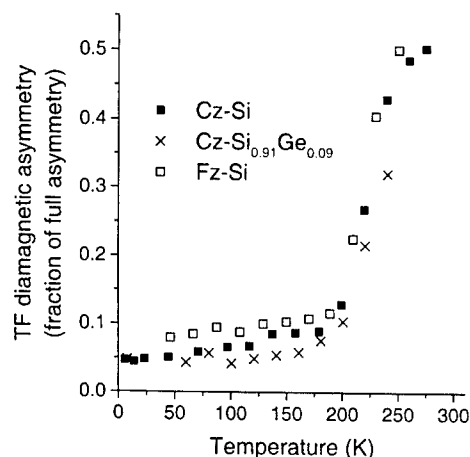


Fig. 3. Transverse field diamagnetic fractions as a function of temperature from the Cz-Si and Fz-Si samples (20 G transverse field used) and Si_{0.91}Ge_{0.09} alloy material (80 G field used).

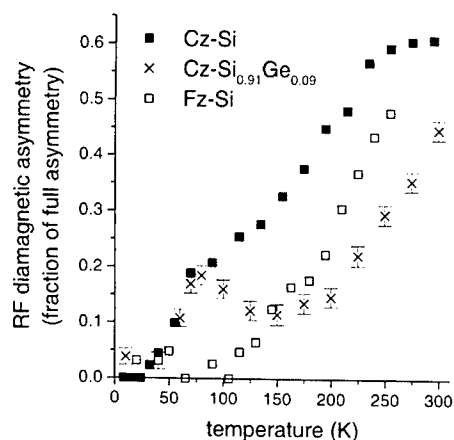


Fig. 4. Radio-frequency μSR diamagnetic fractions as a function of temperature from the Cz-Si, Fz-Si and Si_{0.91}Ge_{0.09} alloy materials.

low temperatures, below 100 K, there is no change in the signal from the Fz-Si; above 100 K, Mu_{BC} ionisation to a diamagnetic state is observed. In the two Cz samples, a significant increase in the diamagnetic signal is observed, starting at around 50 K. The diamagnetic species observed cannot be formed promptly, as it would appear in the transverse field data of Fig. 3 if so.

4. Discussion

The results described above reveal a Mu_T behaviour seen in the Cz samples that is not observed in the Fz-Si. The strong Mu_T relaxation seen at around 40 K, immediately followed by a rise in the RF diamagnetic amplitude, together with the transverse field diamagnetic

signal showing no change, all point to the mobile Mu_T species being involved in a process which initially leads to its relaxation, then to its conversion to a diamagnetic species. Whilst the temperature regime of this behaviour is around the region of donor ionisation, the carrier concentrations of the Cz-Si and Fz-Si are similar, so that such different behaviour between the samples based on donor behaviour would be surprising. The Mu_{BC} species in the Cz-Si is unaffected over the whole temperature range of Fig. 2 since no changes are observed in its longitudinal field precession signal. The visibility of this Mu_{BC} oscillation signal and the fact that it shows no temperature dependence is evidence that free carriers are not producing any spin-exchange relaxation, as would be seen at higher n-type doping levels. It seems likely that the Mu_T relaxation seen in the Cz samples is caused by interactions with oxygen impurity in this material; this would explain its absence in the Fz-Si. Previous authors [5,6] have reported the association of a bond centred Mu or H species with bond centred oxygen in Si. It is possible that the presence of oxygen facilitates the site change of muonium between the tetrahedral cage centres and the bond centres. The resultant modulation of hyperfine parameters in the course of diffusion is then the cause of the enhanced spin relaxation or depolarisation. A reduction in ionisation energy for bond centred muonium at these extrinsic sites, i.e. at the centre of a pre-stretched Si-Si bond, would then lead to the delayed formation of a diamagnetic species as seen in the RF data.

This paper is also the first time the muon response in a $\text{Si}_{1-x}\text{Ge}_x$ alloy has been reported. A more detailed analysis of the dealing specifically with the $\text{Si}_{0.91}\text{Ge}_{0.09}$ alloy material and with other alloy compositions will be presented in a future paper. In particular, whilst the transverse field diamagnetic plot (Fig. 3) suggests that the ionisation temperature for Mu_{BC} in the alloy material is relatively unaffected by the presence of 9% Ge, the RF diamagnetic behaviour for the alloy material shown in Fig. 4 is more complex in the 100–200 K region than in the Cz-Si and Fz-Si material and requires further investigation.

Acknowledgements

We gratefully acknowledge the EPSRC (grant GR/N64977) for funding muon beamtime at the ISIS facility to pursue this work.

References

- [1] B.D. Patterson, *Rev. Mod. Phys.* 60 (1) (1988) 69.
- [2] R.L. Lichti, et al., *Phys. Rev. B* 60 (3) (1999) 1734.
- [3] S.F.J. Cox, et al., *Phys. Rev. Lett.* 86 (12) (2001) 2601.
- [4] J.M. Gil, et al., *Phys. Rev. Lett.* 83 (25) (1999) 5294.
- [5] B. Bech Nielsen, et al., *Mater. Sci. Forum* 258 (1997) 391.
- [6] M. Schefzik, et al., *Philos. Mag. B* 79 (10) (1999) 1561.
- [7] I. Yonenaga, et al., *J. Phys. Chem. Solids* 62 (2001) 1313.



ELSEVIER

Physica B 308–310 (2001) 550–553

PHYSICA B

www.elsevier.com/locate/physb

Interaction of divacancies with Ge atoms in $\text{Si}_{1-x}\text{Ge}_x$

L. Khirunen^{a,*}, Yu. Pomozev^a, M. Sosnin^a, N. Abrosimov^{b,c}, W. Schröder^c

^a*Institute of Physics of the National Academy of Sciences of Ukraine, Prospect Nauki, 46, 03028 Kiev, Ukraine*

^b*Institute of Solid State Physics of Russian Academy of Sciences, 142432 Chernogolovka, Russia*

^c*Institute of Crystal Growth, D-12489 Berlin, Germany*

Abstract

It has been shown that during irradiation, the V_2 and $V_2\text{Ge}$ centers are formed and the absorption band that peaked at about 5560 cm^{-1} in as-irradiated $\text{Si}_{1-x}\text{Ge}_x$ samples is the superposition of two bands corresponding to the absorption by the V_2^0 and $V_2\text{Ge}$ centers. The contribution of the V_2^0 component to the absorption band in as-irradiated samples increases as the germanium content increases. A thermostability of the $V_2\text{Ge}$ centers is shown to be essentially higher than the one of the divacancy in silicon and increases with the germanium content. © 2001 Elsevier Science B.V. All rights reserved.

Keywords: $\text{Si}_{1-x}\text{Ge}_x$; Divacancies; Germanium

1. Introduction

It is known that the doping of semiconductors with isovalent impurities (IVI) can be employed to control defect–impurity interaction processes, which occur both during growth and under various external actions. Depending on the ratio of the covalent radii of the IVI and matrix atoms, they can suppress or enhance the effects associated with vacancies (V) or with interstitials (I) and change the reaction channels that are characteristic of Si. For example, the carbon in the Si interacts effectively with the I at irradiation and forms numerous defects of the I-type. The Ge and Sn influence the reactions involving the V. Earlier, we showed that a localization of the vacancy + oxygen (VO) centers near the Ge atom in the Si takes place [1]. In this paper, we report new data on the interaction of the divacancies with the Ge atoms in the $\text{Si}_{1-x}\text{Ge}_x$.

The divacancy (V_2) is known to be one of the main radiation defects both in single crystals and in thin layers of Si and $\text{Si}_{1-x}\text{Ge}_x$. It may be formed either as a primary radiation defect during irradiation or as a secondary defect as a result of the interaction of vacancies that

occurred during their thermally activated migration. The properties of the V_2 in the Si have been studied widely. The V_2 in the Si is known to be in four charge states, namely V_2^- , V_2 , V_2^+ , and V_2^{2+} [2–6]. Three absorption bands peaked at about 2500, 2760, and 5560 cm^{-1} correspond to the states V_2^- , V_2^+ , and V_2^0 , respectively. There are some papers on the V_2 in the $\text{Si}_{1-x}\text{Ge}_x$ solid solution. In Ref. [7], the V_2^0 in polycrystalline $\text{Si}_{1-x}\text{Ge}_x$ irradiated with neutrons and protons have been studied. It was found that, as the Ge concentration is increased, the 5560 cm^{-1} absorption band shifts to the low frequency side and this shift is supposed to correlate with the composition-related change in the lattice parameter. The authors also had marked the rise of the thermal stability of the V_2 in the Si-rich solid solutions and the decrease of the thermal stability in the Ge-rich samples. But in Refs. [8,9], in investigations of $\text{Si}_{1-x}\text{Ge}_x$ thin layers, it was shown that the thermal stability of the V_2 is not affected by variations in the composition of the $\text{Si}_{1-x}\text{Ge}_x$.

To the present day, the properties of the V_2 in the $\text{Si}_{1-x}\text{Ge}_x$ single crystals have been studied at Ge content less than 1 at%. Here, we report new data on the peculiarities of the V_2 formation (estimated on the 5560 cm^{-1} (V_2^0) absorption band) in the $\text{Si}_{1-x}\text{Ge}_x$ single crystals with the Ge content as high as 15 at%.

*Corresponding author. Tel.: +380-44-265-98-21; fax: +380-44-265-55-88.

E-mail address: lukh/a iop.kiev.ua (L. Khirunen).

2. Experimental results and discussion

The samples of boron-doped $\text{Si}_{1-x}\text{Ge}_x$ single crystals grown by the Czochralski method in the Institute of Crystal Growth (Berlin, Germany) [10,11] were investigated. The oxygen and carbon contents determined using infrared absorption lines 1107 and 604 cm^{-1} were $(7-9) \times 10^{17}$ and $(2-3) \times 10^{16}\text{ cm}^{-3}$, respectively. The Ge content was measured using the X-ray microanalyzer JCSA-733 and varied from 2 to 15 at%. To analyze the peculiarities of the Ge influence the properties of the V_2 the samples of Si that did not contain Ge and whose parameters were close to those of the $\text{Si}_{1-x}\text{Ge}_x$ were investigated.

The samples were irradiated by fast electrons with the energy 4 MeV at temperatures of about 300 and 90 K for doses $(3.5-6) \times 10^{17}\text{ e cm}^{-2}$. The samples were investigated just after irradiation and after following isochronous annealing ($t = 20\text{ min}$) in the temperature range $100-400^\circ\text{C}$. The processes of the formation and annealing of the divacancies (V_2^0 and V_2^+) and their dependence on the Ge content were studied by infrared Fourier spectroscopy.

The absorption spectra obtained for the samples irradiated at $T \approx 300\text{ K}$ with a dose $F_e \approx 5 \times 10^{17}\text{ e cm}^{-2}$ are shown in Fig. 1a, and the dependence of the band maximum position on the Ge content in Fig. 1b. As can be seen, a gradual shift of the V_2^0 absorption band towards low frequencies was observed at the increase of Ge content in the samples. The estimations of the V_2 concentrations from the intensity of the 5560 cm^{-1} band have shown that there is no noticeable influence of the Ge content on the efficiency of the V_2 formation. Note that previously, we have observed the decrease in the formation efficiency of the VO centers in these crystals [1].

Interesting features in the behavior of the V_2^0 absorption band were observed in the samples subjected to isochronous annealing. The results obtained for the crystals with the Ge content 3.5 at% are shown in Fig. 2a. One can see that in the temperature range $150-240^\circ\text{C}$, the high frequency wing of the absorption band anneals out, the maximum of the band shifts gradually to the lower frequency side, and the intensity of the band somewhat rises (Fig. 2a, curve 3 or V_2^*). These changes are observed in the same range of the annealing temperatures for all concentrations of the Ge used in the investigations. However, it should be noted that the shift of the absorption band on annealing decreases as the Ge content increases (Fig. 2b). In the reference Si samples, a larger part of the V_2 are annealed out in the temperature range of $150-240^\circ\text{C}$ (Fig. 3, curve 1) with the synchronous formation of additional VO centers. For all investigated $\text{Si}_{1-x}\text{Ge}_x$ samples no changes in the VO absorption region were observed after annealing in the temperature range $150-240^\circ\text{C}$.

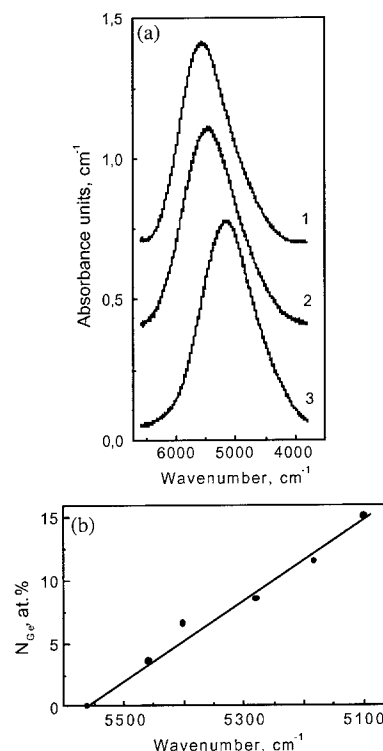


Fig. 1. The absorption spectra near 5560 cm^{-1} for the Si and $\text{Si}_{1-x}\text{Ge}_x$ measured at 300 K (a) and dependence of the band maximum position on the Ge content in the $\text{Si}_{1-x}\text{Ge}_x$ (b). $F_e \approx 5 \times 10^{17}\text{ e cm}^{-2}$. N_{Ge} (at%) for (a): 1—0; 2—3.5, and 3—11.5.

For higher annealing temperature ($T > 240^\circ\text{C}$), the intensity of the absorption band V_2^* at first does not change but later decreases gradually as a whole without any change in the maximum position (Fig. 2a, curves 4–7). The annealing behavior of the V_2^* band for the samples under investigation is shown in Fig. 3 (curves 2–5). As can be seen from Fig. 3, the annealing temperature of the V_2^* is higher than the one of the V_2 in Si and increases with increasing Ge content in the samples. These observations do not correlate with the results obtained by DLTS in Refs. [8,9], where it was shown that the thermal stability of the divacancies does not depend on the composition of the samples.

The V_2 are known to diffuse over the Si lattice during the annealing until they are trapped by the sinks. The diffusing V_2 effectively interact with the impurities with a formation of the complexes [1,12–14]. The observed features of the transformations of the band that peaked at about 5560 cm^{-1} on annealing of $\text{Si}_{1-x}\text{Ge}_x$ in the range of $150-240^\circ\text{C}$ (the annealing of the high frequency wing of the absorption band, shift of the band maximum position, increase in the

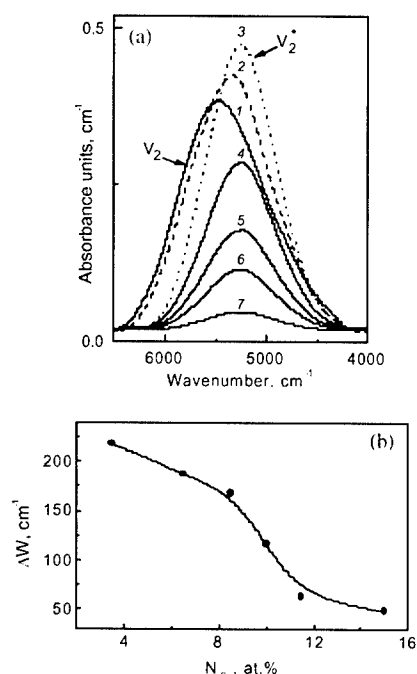


Fig. 2. The behavior of the absorption band near 5560 cm^{-1} during annealing of irradiated $\text{Si}_{0.965}\text{Ge}_{0.035}$ (a) and dependence of the band shift on the Ge content in the $\text{Si}_{1-x}\text{Ge}_x$ (b). T_{ann} ($^{\circ}\text{C}$) for (a): 1—before annealing; 2—180; 3—240; 4—310; 5—320; 6—330, and 7—335.

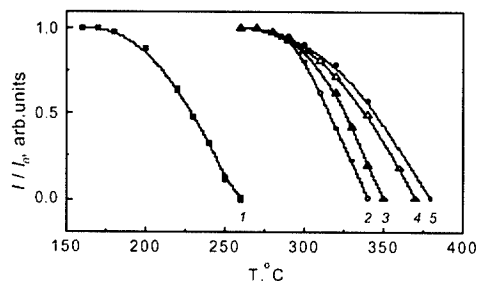


Fig. 3. The relative change in the intensity (I/I_0) of the absorption bands V_2^0 in the Si (1) and the V_2^* in the $\text{Si}_{1-x}\text{Ge}_x$ (2–5) at annealing. N_{Ge} (at%): 2—3.5; 3—6.5; 4—8.5, and 5—11.5.

intensity and the absence of the negative annealing stage of the VO centers) enable one to suggest that the observed V_2^* can be tentatively assigned to a new defect. Taking into account the fact that the Ge content in the samples under investigation is much larger than the concentration of all possible sinks one can assume that the diffusing V_2 interact with the Ge atoms and form $V_2\text{Ge}$ centers. As a result, V_2^* absorption band appears.

The decomposition of the absorption band that peaked at about 5560 cm^{-1} in as-irradiated $\text{Si}_{1-x}\text{Ge}_x$ samples shows that it is complicated and consists of two bands. One of the bands corresponds to the V_2^0 while another one corresponds to the V_2^* centers detected. The contribution of the V_2^* component to the absorption band increases as the Ge content increases, and at the Ge concentration about 15 at%, the contribution of the V_2^0 in the band peaked at about 5560 cm^{-1} is very small. This is probably the reason for the diminishing of the absorption band shift at annealing in the temperature range $150\text{--}240^{\circ}\text{C}$ with the increasing Ge content in the samples (Fig. 2b). Thus, the facts obtained testify that the V_2^* are formed during the irradiation also. Since the Ge atoms are the effective sinks for vacancies, the latter move towards the Ge atoms during irradiation and, evidently, associate with them into $V_2\text{Ge}$.

To confirm the complex structure of the absorption band that peaked in the vicinity of 5560 cm^{-1} in as-irradiated $\text{Si}_{1-x}\text{Ge}_x$, we have studied the samples irradiated at $T \leq 90\text{ K}$. At such irradiation temperatures, it is known that the GeV centers are effectively formed and almost all vacancies are captured by the Ge atoms. The last factor influences the formation rate of secondary V-related defects [15]. Fig. 4 shows the obtained spectra (measured at $T = 4.2\text{ K}$) for Si and $\text{Si}_{0.965}\text{Ge}_{0.035}$ irradiated with a dose of $6 \times 10^{17}\text{ e cm}^{-2}$ at $T \leq 90\text{ K}$. As can be seen, the band at $\sim 835\text{ cm}^{-1}$, corresponding to the VO centers is not observed in as-irradiated $\text{Si}_{0.965}\text{Ge}_{0.035}$ samples. However, any Ge noticeably influence absorption band that peaked at about 5560 cm^{-1} is not observed, although the efficiency of the secondary V_2 formation due to the vacancy–vacancy interactions in the CZ material is known to be lower than the efficiency of the VO formation at the energies and irradiation doses under investigation. Moreover, due to the high Ge content, the efficiency

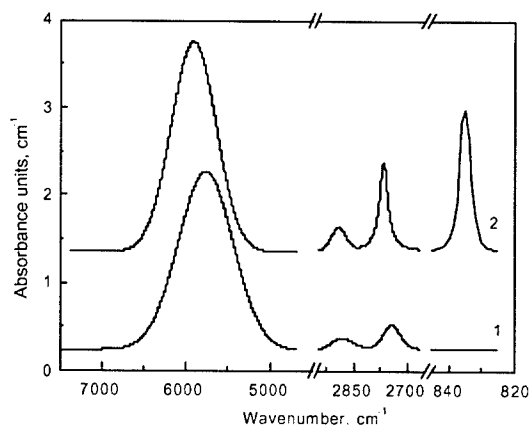


Fig. 4. The absorption spectra of the Si (2) and the $\text{Si}_{0.965}\text{Ge}_{0.035}$ (1) irradiated at $T \leq 90\text{ K}$ at a dose of $6 \times 10^{17}\text{ e cm}^{-2}$.

of the GeV centers formation is essentially larger than that for the secondary VO and V_2 centers. Thus, the influence of the Ge formation on the V_2 should be observed.

In the last experiment, we had the possibility of study the two charge states V_2^0 and V_2^+ (absorption band near 2760 cm^{-1} and its phonon-assisted high-energy satellite in Fig. 4) simultaneously. As it is seen from Fig. 4, the V_2^+ absorption band in the $\text{Si}_{0.965}\text{Ge}_{0.035}$ is shifted at $\sim 20\text{ cm}^{-1}$ to low frequencies as compared to the Si (note, that the 5560 cm^{-1} band shifts by $\sim 100\text{ cm}^{-1}$), some broaden, and the intensity of this band is lower than in the Si. A comparison of the areas under the V_2^+ curves shows that the concentration of the divacancies decreases in the $\text{Si}_{1-x}\text{Ge}_x$ as compared to the Si. As it has already been mentioned above, this decrease should be observed at low-temperature irradiation. Then we have carried out an isochronal annealing of samples and found that the annealing of the V_2^+ related absorption bands in the $\text{Si}_{1-x}\text{Ge}_x$ is similar to that in the Si. This band disappears in the temperature range of $180\text{--}260^\circ\text{C}$. This correlates with the results reported in Refs. [8,9]. All these obtained facts confirm our suggestion that the origin of the band that peaked at about 5560 cm^{-1} band is a complex one.

Thus, the experimental data obtained prove that the V_2 characteristic for the Si and complexes of the V_2 with the Ge atoms ($V_2\text{Ge}$) are formed in the $\text{Si}_{1-x}\text{Ge}_x$ single crystals during irradiation. The absorption band peaked at about 5560 cm^{-1} in as-irradiated $\text{Si}_{1-x}\text{Ge}_x$ is the superposition of two bands corresponding to absorption by these two centers. Note that the formation of the $V_2\text{Ge}$ during irradiation is, probably, one of the reasons for the suppression of the VO formation efficiency observed earlier [1].

Acknowledgements

This work was supported by the Science and Technology Center in the Ukraine (project No. 1646).

References

- [1] L.I. Khirunenko, Yu.V. Pomozev, M.G. Sosnin, V.I. Yashnik, N.V. Abrosimov, W. Schröder, M. Höne, *Fiz. Tekh. Poluprovodn.* 34 (2000) 1030.
- [2] G.D. Watkins, J.W. Corbett, *Phys. Rev.* 138 (1965) A543.
- [3] J.W. Corbett, G.D. Watkins, *Phys. Rev.* 138 (1965) A555.
- [4] R.C. Young, J.C. Corelli, *Phys. Rev. B* 5 (1972) 1455.
- [5] L.J. Cheng, J.C. Corelli, J.W. Corbett, G.D. Watkins, *Phys. Rev.* 152 (1966) 761.
- [6] B.G. Svensson, M. Willander, *J. Appl. Phys.* 62 (1987) 2758.
- [7] H.J. Stein, *J. Appl. Phys.* 45 (1974) 1954.
- [8] E.V. Monakov, A. Nylandsted Larsen, P. Kringhø, *J. Appl. Phys.* 81 (1996) 1180.
- [9] A.N. Larsen, *Solid State Phenom.* 69-70 (1999) 43.
- [10] N.V. Abrosimov, S.N. Rossolenko, V. Alex, A. Gerhardt, W. Schröder, *J. Crystal Growth* 166 (1996) 657.
- [11] N.V. Abrosimov, S.N. Rossolenko, W. Thieme, A. Gerhardt, W. Schröder, *J. Crystal Growth* 174 (1997) 182.
- [12] Y.H. Lee, J.C. Corelli, J.W. Corbett, *Phys. Letters* 60A (1977) 55.
- [13] J.L. Lindström, B.G. Svensson, *Mater. Res. Soc. Symp. Proc.* 59 (1986) 45.
- [14] G. Davies, E.C. Lightowers, R.C. Newman, A.S. Oates, *Semicond. Sci. Technol.* 2 (1987) 524.
- [15] A. Brelet, J. Charlemagne, *Proceedings of the International Conference on Radiation Effects in Semiconductors*, Gordon and Breach Science Publishers, London, NY, Paris, 1971, p. 161.



ELSEVIER

Physica B 308–310 (2001) 554–557

PHYSICA B

www.elsevier.com/locate/physb

High resolution minority carrier transient spectroscopy of defects in Si and Si/SiGe quantum wells

J.H. Evans-Freeman*, M.A. Gad

Centre for Electronic Materials, Department of Electrical Engineering and Electronics, UMIST, P.O. Box 88, Sackville St. Manchester, M60 1QD, UK

Abstract

High resolution Laplace minority carrier transient spectroscopy (LMCTS) has been used to study defects in gas source molecular beam epitaxy grown Si/Si_{0.855}Ge_{0.145} strained quantum wells. In LMCTS, the minority carrier emission transient is analysed and detailed emission properties of minority carrier traps which have similar energy can be characterised. The technique was evaluated by comparing LMCTS of a Au:H hole trap, G3, in n-type silicon with Laplace deep level transient spectroscopy of the same trap in p-type silicon. Both techniques confirm that this level consists of two states, as previously suggested in the literature. MCTS was then applied to the n-type Si/SiGe quantum well sample, and five-hole traps were observed. A level at 95 K in the MCTS spectrum was identified as a possible candidate for hole emission from the quantum wells. LMCTS showed that the emission rate of this hole trap exhibited only a slight temperature dependence compared to that exhibited by hole states associated with isolated point defects. This is attributed to holes tunnelling out of the quantum well assisted by the electric field present in the experiment. © 2001 Elsevier Science B.V. All rights reserved.

PACS: 73.29.Dx; 73.40.Gk

Keywords: Laplace MCTS; SiGe; Quantum wells

1. Introduction

Deep level transient spectroscopy (DLTS) is a commonly used technique to characterise the electrical activity of defects in semiconductors [1]. It yields a universal signature of the enthalpy of deep levels, but has some drawbacks. Only defect states in one half of the band gap can be easily characterised, and closely spaced energy levels are not resolvable because of the poor time constant resolution; both these problems have been addressed in recent years. To characterise deep states throughout the whole band gap, a complementary technique, minority carrier transient spectroscopy

(MCTS) [2] was developed, in which thermally stimulated minority carrier emission is measured and processed in the same way as DLTS. As an example of its use, it was reported [3] that Au:H complexes in silicon produce four deep levels, two in the upper half of the band gap and two in the lower, established by examining n- and p-type silicon [3]. The application of MCTS meant that all four new levels were observed in n-type Si [4]. MCTS can also be used to measure activation energies and capture cross sections, and can be combined with DLTS to examine carrier dynamics at recombination centres [5] but is difficult to use for depth profiling [6].

The problem of closely spaced levels has been addressed by the development of algorithms for analysing the components in the capacitance transient [7,8], and these have been used with considerable success to resolve some long standing defect problems in silicon

*Corresponding author. Tel.: +44-161-200-4796; fax: +44-161-200-4796.

E-mail address: j.evans-freeman@umist.ac.uk (J.H. Evans-Freeman).

[9–16]. This technique is termed Laplace DLTS (LDLTS) and produces an output of intensity as a function of emission rate.

In this paper, we report on application of the same algorithms to minority carrier emission transients, which we call Laplace MCTS (LMCTS). The technique is verified by applying it to minority carrier traps in n-type Si containing Au:H complexes. Earlier work had suggested that one of the Au:H states, G3, consisted of two closely spaced levels [3,4], based on detailed capture cross-section measurements [4]. G3 is a hole trap, therefore we have compared LMCTS of this trap in n-type Si with LDLTS of the trap in p-type Si. We have then applied the technique for the examination of hole emission from strained Si/SiGe/Si quantum wells (QWs). The majority of the band offset is in the valence band [17] and we have used MCTS and LMCTS to detect thermally stimulated hole emission from the wells. The results are compared with PL quenching experiments which yield the hole confinement energy.

2. Experimental

The samples containing Au:H complexes were either n-type CZ Si doped with $2 \times 10^{15} \text{ cm}^{-3}$ phosphorus or p-type Si doped with $2 \times 10^{15} \text{ cm}^{-3}$ boron. The gold diffusion and introduction of hydrogen (by wet chemical etching), is described elsewhere [4]. Gold Schottky diodes were evaporated onto the n-type Si, and titanium Schottky diodes were sputtered onto the p-type Si. The SiGe/Si QW structure was grown by gas source molecular beam epitaxy and consisted of 10 strained $\text{Si}_{0.855}\text{Ge}_{0.145}/\text{Si}$ QWs grown on a Si substrate. The Si cap layer was 199.8 nm, the wells were 5.7 nm thick, the barriers were 55 nm thick, and the layer was n-type because of a residual phosphorus level of about $1 \times 10^{16} \text{ cm}^{-3}$.

For the MCTS and LMCTS measurements, thin (20 nm) Au diodes were evaporated. Electrical measurements were carried out in a closed cycle cryostat between temperatures of 300 and 20 K. In MCTS, above band gap light is incident on the semitransparent Schottky diode, and creates electron-hole pairs. The wavelength of the light ensures that the extinction depth is greater than the depletion region width. Majority carriers are rejected from the depletion region, and it is predominantly minority carriers that are available for capture in the region. In the LMCTS experiment, the capacitance transient due to minority carrier emission was recorded up to 10,000 times at a fixed temperature in a high stability cryostat. For the photoluminescence (PL) measurements, the sample was attached to a cold finger inside a closed cycle cryostat and excited by using the 514.2 nm line of an argon ion laser. The signal was

detected using a liquid nitrogen cooled Ge detector and analysed by conventional lock-in techniques.

3. Results and discussion

When silicon containing Au:H complexes was characterised by DLTS and MCTS (not shown) the expected traps G1–G4 [3] due to Au:H complexes, and the Au acceptor and donor states were observed. In earlier work [3,4], it was noted that G3, at $E_v + 0.47 \text{ eV}$, exhibited different behaviour from the levels G1, G2 and G4. The annealing behaviour was different [3] and it exhibited a two-stage capture process [4]. The existence of two closely spaced levels in G3 is confirmed here by carrying out LDLTS and LMCTS. Fig. 1(a) shows LMCTS carried out at 225 K and Fig. 1(b) shows the LDLTS recorded at the same temperature in p-type Si. In both spectra two emission rates are observed. The relative intensities of the two emission rates are different between the n- and p-type samples, but this may reflect the differences observed and reported previously regarding G3 when it is in n- or p-type Si. These spectra confirm that LMCTS yields the same information at LDLTS.

Turning to the strained QW layer, PL at 5 K layer showed very clear zero phonon, transverse optical and transverse acoustic phonon peaks [18,19]. The hole confinement energy can be found by examining the PL quenching as a function of temperature [20]. This yielded an activation energy for thermal emission out of the wells of 110 meV, which is the depth above the Si valence band of the $n = 1$ heavy hole confined state.

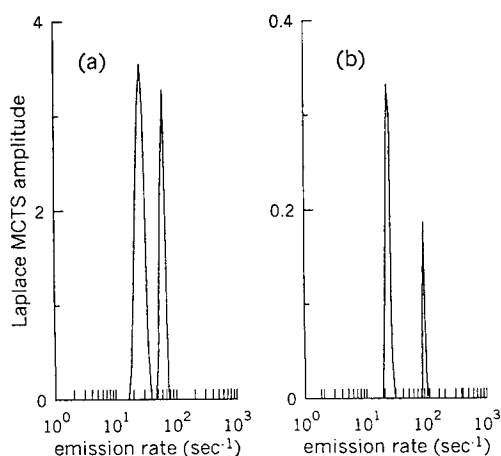


Fig. 1. (a) LMCTS carried out at 225 K of the trap G3 associated with Au:H complexes in n-type silicon, and (b) LDLTS of the same defect recorded at the same temperature in p-type Si.

In MCTS and LMCTS, the QWs capture holes during the fill pulse, the fill pulse creates a photocurrent through the diode, and the hole quasi-Fermi level varies with photon flux [6]. The calculation is further complicated by the presence of the QWs, because the quasi-Fermi level in them will depend upon the fraction of injected holes that are captured and reside in the wells. Difficulties in the calculation of the emission rates can easily be overcome if a few simple assumptions are made [21]. It can be assumed that all captured carriers will reside in the lowest confined energy state. This means that the experimental conditions are the same as during the PL experiment. It can also be assumed that the quasi-Fermi level in the QWs lies several kT above the confined heavy hole state, and will not affect the carrier dynamics during the emission process [22]. Hence, the emission rate for the holes out of the wells depends only upon the difference between the confined hole state energy and the valence band in the Si barrier.

It has been reported that at low temperatures (≤ 100 K) and relatively modest electric fields, $\geq 30 \text{ kVcm}^{-1}$, a plateau can be observed in the DLTS due to a constant emission rate of carriers out of QWs. This is attributed to tunnelling through a triangular potential barrier between the QW and the relevant carrier band [22]. Fig. 2 shows the MCTS spectrum of the Si/SiGe QW, in two halves for clarity. As an example of a point defect in this system, Fig. 3 shows the LMCTS spectra measured between 30 and 38 K, and shows that two emission rates are present. An Arrhenius plot of these two states, taken from the LDLTS data, yields activation energies of 50 ± 3 and 35 ± 3 meV. Both defects exhibit exponential filling, hence can be attributed to point defects. No Poole–Frenkel effect was observed.

The broad feature in Fig. 2 between 85 and 100 K is a strong candidate for the QW signal. The feature is

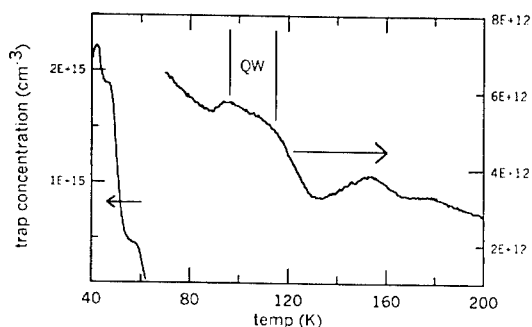


Fig. 2. MCTS spectrum of the $\text{Si}_{0.855}\text{Ge}_{0.145}/\text{Si}$ MQW sample, spectrum in two halves for clarity, at a rate window of 200 s^{-1} . The feature proposed to be due to hole tunnelling out of the wells is indicated.

almost plateau-like, in accordance with Ref. [22], and no other features in the MCTS spectrum have an activation energy of 110 meV. Fig. 4 shows the emission rate of this deep state between 100 and 112.3 K, and it is nearly constant. The best fit of the emission rate to temperature was by assuming a square root dependence upon the temperature, rather than a Boltzmann relationship. Other defects in the LMCTS spectrum of this sample do not exhibit this behaviour, and we therefore conclude that we are observing direct evidence of holes tunnelling out of SiGe QWs into the cladding layers.

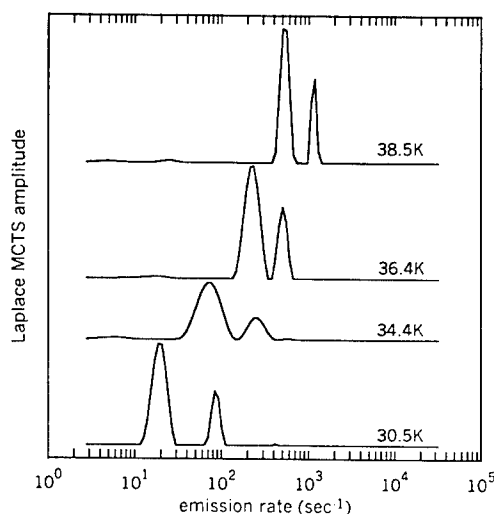


Fig. 3. Shows the LMCTS spectra of the $\text{Si}_{0.855}\text{Ge}_{0.145}/\text{Si}$ MQW sample measured between 30 and 38 K.

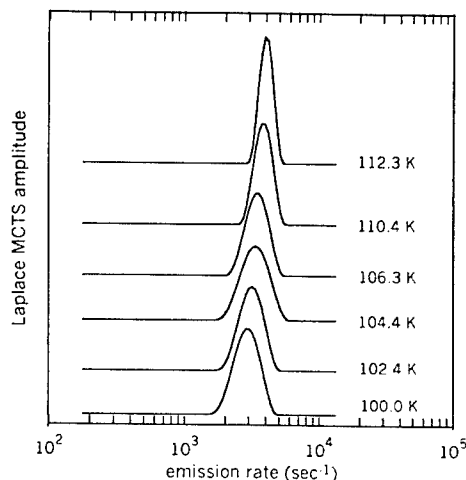


Fig. 4. LMCTS of the QW-related state, showing the nearly constant emission rate between 100 and 112.3 K.

4. Conclusions

A technique which uses the same analytical approach to the capacitance transient as LDLTS but examines the detailed emission properties of minority carrier traps, LMCTS, has been described. In LMCTS, minority carriers are injected into a depletion region by the application of a light pulse of suitable wavelength. LDLTS and LMCTS are complementary because traps in the whole of the band gap can be accessed in semiconductors of one polarity. To verify the technique, LMCTS in n-type Si containing Au:H complexes was compared to LDLTS of p-type Si containing the same complexes, and found to yield the same results. The LMCTS technique was then applied to n-type Si which contains 10 Si_{0.855}Ge_{0.145} strained QWs. Several hole traps were observed, but it was possible to identify a candidate for hole emission out of the QWs. When examined by LMCTS over a temperature range of 102–116 K, it was found that the emission rate for holes out of the QWs was only weakly dependent upon temperature. This indicates that this defect is not point-defect-like, and it is suggested that the nearly constant emission rate is due to holes tunnelling out of the QW. This is the first direct observation of this effect, which up till now could only be inferred from conventional DLTS spectra.

Acknowledgements

We acknowledge the EPSRC, UK for funding, and J Zhang at Imperial College for growing the MBE layer.

References

- [1] D.V. Lang, *J. Appl. Phys.* 45 (1974) 3023.
- [2] B. Hamilton, A.R. Peaker, D.R. Wight, *J. Appl. Phys.* 50 (1979) 6373.
- [3] E.Ö. Sveinbjörnsson, O. Engström, *Phys. Rev. B* 52 (1995) 4884.
- [4] J.A. Davidson, J.H. Evans, *Semicond. Sci. Technol.* 11 (1996) 1704.
- [5] R.H. Wu, A.R. Peaker, *Solid State Electron.* 25 (1982) 643.
- [6] J.A. Davidson, J.H. Evans, *J. Appl. Phys.* 81 (1997) 251.
- [7] L. Dobaczewski, P. Kaczor, I.D. Hawkins, A.R. Peaker, *J. Appl. Phys.* 76 (1994) 194.
- [8] J. Kang, H. Zhan, Q. Huang, *J. Crystal Growth* 210 (2000) 247.
- [9] L. Dobaczewski, P. Kaczor, M. Missous, A.R. Peaker, Z.R. Zytkeiwicz, *Phys. Rev. Lett.* 68 (1992) 2508.
- [10] P. Deixler, J. Terry, I.D. Hawkins, J.H. Evans-Freeman, A.R. Peaker, L. Rubaldo, D.K. Maude, J.-C. Portal, L. Dobaczewski, K. Bonde Nielsen, A. Nylandsted Larsen, A. Mesli, *Appl. Phys. Lett.* 73 (1998) 3126.
- [11] L. Rubaldo, P. Deixler, I.D. Hawkins, J. Terry, D.K. Maude, J.-C. Portal, J.H. Evans-Freeman, L. Dobaczewski, A.R. Peaker, *Mat. Sci. Eng. B* 58 (1999) 126.
- [12] A.R. Peaker, J.H. Evans-Freeman, L. Rubaldo, I.D. Hawkins, L. Dobaczewski, K. Vernon-Parry, *Physica B* 273–274 (1999) 243.
- [13] L. Dobaczewski, K. Goscinski, K. Bonde Nielsen, A.N. Larsen, J.L. Hansen, A.R. Peaker, *Phys. Rev. Lett.* 83 (1999) 4582.
- [14] K.B. Nielsen, L. Dobaczewski, K. Goscinski, R. Bendesen, O. Andersen, B. Bech Nielsen, *Physica B* 273–274 (1999) 167.
- [15] L. Dobaczewski, K.B. Nielsen, K. Goscinski, A.R. Peaker, A. Nylandsted Larsen, *Physica B* 273–274 (1999) 620.
- [16] L. Dobaczewski, K.B. Nielsen, K. Goscinski, O. Andersen, *Acta Phys. Pol. A* 98 (2000) 231.
- [17] R. People, J.C. Bean, *Appl. Phys. Lett.* 48 (1986) 538.
- [18] J.C. Sturm, H. Manoharan, L.C. Lechyshyn, M.L.W. Thewalt, N.L. Rowell, J.-P. Noël, D.C. Houghton, *Phys. Rev. Lett.* 66 (1991) 1362.
- [19] E.F. Gross, N.S. Sokolov, A.N. Titkov, *Sov. Phys. Solid State* 14 (1973) 1732.
- [20] D.C. Houghton, N.L. Rowell, J.-P. Noël, G. Aers, M. Davies, A. Wang, D.D. Perovic, *Silicon-Based Optoelectronic Materials Symposium, Mater. Res. Soc. Vol. 298, 1993, p. 3.*
- [21] L. Vescan, R. Apetz, H. Lüth, *J. Appl. Phys.* 73 (1993) 7427.
- [22] X. Letartre, D. Stiévenard, M. Lannoo, E. Barbier, *J. Appl. Phys.* 69 (1991) 7336.



ELSEVIER

Physica B 308–310 (2001) 558–560

PHYSICA B

www.elsevier.com/locate/physb

Alloy fluctuations in $\text{Si}_{1-x}\text{Ge}_x$ crystals

G. Kocher^{a,*}, W. Jantsch^a, N. Abrosimov^b, S. Egorov^c, A. Zabrodskii^c,
B. Andreev^d, H.G. Grimmeiss^e

^a *Institut für Halbleiter- und Festkörperphysik, JKU, Universität Linz, Altenbergstr. 69, 4040 Linz, Austria*

^b *Institut für Kristallzüchtung, FBV D-12489 Berlin, Germany*

^c *Ioffe Physico-Technical Institute, 194021 St. Petersburg, Russia*

^d *Institute Physics of Microstructures RAS, 603600 Nizhny Novgorod, GSP 105 Russia*

^e *University of Lund, S-221 00 Lund, Sweden*

Abstract

We have introduced S donors into SiGe alloys as probe atoms for a spectroscopic investigation of the local environment of these donors. Even for low Ge content ($x = 2.4\%$), we already observe strongly broadened lines for the intra-centre transitions, whereas the onset of the photo-ionisation stays at approximately the same energy, in contrast to expectations from a linear extrapolation of the impurity level from values of the pure compounds or from deformation potentials. We thus conclude that the S centres seen are located in the neighbourhood of significantly lower Ge content suggesting that Ge clusters may exist with much higher Ge content which, however, cannot be resolved in the photo-conductivity spectra. This finding, together with the observed line broadening demonstrates strong, non-statistical fluctuations in the alloy distribution. © 2001 Elsevier Science B.V. All rights reserved.

PACS: 61.66.Dk; 71.55.Ak

Keywords: Si–Ge; Alloy fluctuations; Deep donors

1. Introduction

It is quite common practice to describe alloys in terms of the so-called virtual crystal (VC) approximation. Within this VC model, it is assumed that all parameters of the alloy can be interpolated between the values of the pure constituents. There is, however, in general, very often a substantial mismatch in the bond length of the constituents and a tendency for phase segregation and cluster formation. As a consequence, there are substantial fluctuations of various parameters impairing the quality of the material with respect to both its optical and its transport properties. Proper characterisation methods are therefore needed in order to find ways for

optimising the material preparation. In this paper, we investigate the homogeneity of $\text{Si}_{1-x}\text{Ge}_x$ alloys for low x values ($x < 0.1$) making use of the photo-ionisation properties of chalcogen donors which are considered as local probes for their environment.

We investigated the influence of Ge contents in SiGe alloys on the highly localised states of deep impurities in silicon, in particular sulphur, using photothermal ionisation spectroscopy (PTIS). Chalcogen impurities in pure Si exhibit extremely sharp lines in the photo-conductivity spectra due to intra-centre transitions to excited states in the photo-conductivity spectra [1]. If these sharp lines could also be found in the alloys, one might be able to observe “alloy splitting” as it has been observed, e.g. for the DX centres in AlGaAs [2,3]. Due to the highly localised nature of the ground state of the DX centre, centres formed by substitutional donors exhibit different ground state energies depending on the different numbers of Al neighbours. For a group IV

*Corresponding author. Tel.: +43-732-2468-9649; fax: +43-732-2468-9696.

E-mail address: gudrun.kocher@jk.uni-linz.ac.at (G. Kocher).

donor, like Si_{Ga} , there are four possibilities: it can have $i = 0, \dots, 3$ Al neighbours after relaxation and the others will be Ga. Therefore, we expect a 4-fold splitting of the ground state which manifests itself in different emission energies. Here, the excited states are delocalized and thus they cause only broadening. The relative strength of the transitions gives a measure of the abundance of centres with different i . Consequently, in principle, it is possible to obtain information on the statistical distribution of the nearest neighbours.

For this work, we chose high quality, dislocation free bulk crystals of $\text{Si}_{1-x}\text{Ge}_x$ that show much lower line width in their rocking curves than MBE grown samples. We could not resolve, however, the intra-centre transitions even for the lowest Ge content investigated (2.4%). The photo-ionisation edge shows strong broadening but no shift in photon energy. We conclude thus that Ge clusters are formed and the VC approximation does not apply to SiGe alloys.

2. Experimental

$\text{Si}_{1-x}\text{Ge}_x$ wafers (bulk material) with low Ge content ($x \leq 0.1$) and either p- (boron) or n-type (phosphorous) doping between 10^{13} and 10^{15} cm^{-3} were additionally doped with sulphur (S) by means of diffusion. After the usual cleaning procedures, the samples were introduced into the first of two connected chambers of a quartz ampoule. In the second part, a mixture of Si-powder and S (approx. 100:1) was introduced. After evacuation and sealing off, the samples were put into a furnace for approx. 60 h at a diffusion temperature of 1100°C . In order to observe any line spectra due to S, p-type starting material had to be compensated which limits the initial doping level to less than about 10^{15} cm^{-3} (solid solubility of sulphur in Si).

Ohmic contacts were obtained by rubbing-on gallium. For the PTIS measurements, the sample itself was used as detector in a BOMEM DA8.22 Fourier spectrometer equipped with a Globar lamp and a KBr beamsplitter.

3. Discussion and conclusions

Typical PTIS spectra are given in Fig. 1 showing the threshold behaviour of the photo-ionisation for both Si and SiGe and there are sharp lines for pure Si ($x = 0$) which are superimposed on the absorption edge. For Si:S, we can clearly resolve the most prominent lines from the intra-centre transitions; the transitions to the excited states $1s(T_2)$, $2p_0$ and $2p_{\pm}$, respectively, are labelled 1, 2 and 3 (see Fig. 1). For a detailed discussion of these lines see Ref. [1]. This spectrum has been identified as that of isolated, substitutional S^0 . For a Ge concentration of 2.4%, the sharp lines are already

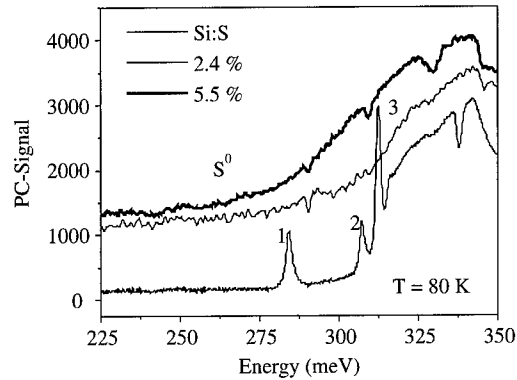


Fig. 1. Photo conductivity spectra for Si:S (lower trace) and SiGe:S with 2.4% Ge (middle trace) and 5.5% Ge (upper trace).

Table 1

Values of $-E_D$ as a function of Ge contents x for different methods

Ge content x	Experiment	Deformation potential	Linear extrapolation
0	318 [1]	318	318
0.024		329	322.3
0.055		341	328
0.1		360	335.2
1	280 [6]	280	280

completely smeared out and the ionisation edge appears broadened. The onset of the transitions into the continuum appears to stay at approximately the same energetic position (Fig. 1). This holds for a Ge content up to 10%.

The lattice mismatch between silicon and germanium is about 4% and drastically alters the band structure due to the built-in strain in the epitaxially grown $\text{Si}_{1-x}\text{Ge}_x$ films. In bulk crystals, strain will rather be induced statistically around some mean value. According to Herzog [4], the average lattice constant varies with Ge content x as

$$a_{av}(x) = 0.002733x^2 + 0.01992x + 0.5431(\text{nm}). \quad (1)$$

Using a_{av} , one can calculate the shift of the conduction band minima at the Δ -point using the deformation potential for the Δ_1 conduction band minimum [5]. Assuming that the deep ground state is hardly affected by the change in lattice constant, we obtain a value for the shift of E_D relative to the Δ_1 minimum (see Table 1). Another method to estimate the shift of the deep sulphur levels due to increasing Ge content would be a simple linear extrapolation (Fig. 2) using the experimentally

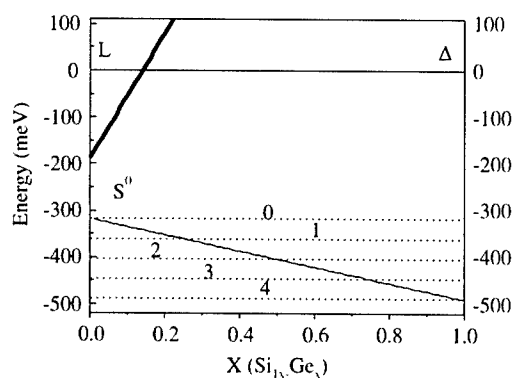


Fig. 2. Schematic diagram of the L- and A-conduction band edge as a function of x in $\text{Si}_{1-x}\text{Ge}_x$ alloys; in addition a linear extrapolation is given for the ground state level of S^0 between the values for the pure Si [1] and Ge [6]. The four dashed lines indicate the expected alloy splitting.

determined values for pure silicon [1] and pure germanium [6] as starting points which gives a shift of $\alpha = 1.72 \text{ meV per \%Ge}$.

In this extrapolation, we did not take into account the known bending of the conduction band edge [5]. Therefore the experimental values could be expected to lie somewhere in between the results of the two estimations. A summary of the energies for the neutral sulphur (S^0) level in pure Si and Ge as well as the expected shifts according to these two models for the various samples are given in Table 1. The variation in the threshold values derived from data in Fig. 1 is much smaller, however. We conclude thus that the S centres seen are surrounded by a significantly lower Ge content than suggested by the alloy concentration.

Considering all of the above and comparing it with our results, we conclude that the S centres seen are surrounded by a significantly lower Ge content than suggested by the alloy concentration. The fact, that we are not able to resolve single lines shows the existence of strain fluctuations. Using Eq. (1) and the result for α , we can estimate a lower limit for the fluctuation amplitude which is necessary to cause broadening bigger than the typical separation of the sharp intra-centre transitions. As a result, we estimate a fluctuation

amplitude Δx comparable to the mean value of the Ge concentration x .

The results obtained here indicate that the overwhelming majority of S donors are hardly affected by the presence of Ge. At 10% Ge content, the statistical probability for S to have one or two Ge neighbours is 30% and 5%, respectively. In other words, there is already a substantial probability for sulphur atoms to have Ge neighbours. We expect a strong effect of the nearest neighbours mostly for the deep, highly localised ground state. The strong shift of the ground state energy between Si and Ge ambience should manifest itself here. Since we do not observe it, we may conclude thus that S in our samples is surrounded almost exclusively by Si atoms and it feels the presence of Ge only via potential fluctuations caused by far distant Ge. A natural explanation for this observation is the existence of Ge clusters of high Ge content which, however, do not contain S donors at sizeable numbers. All our findings thus point to strong, non-statistical fluctuations in the alloy distribution.

Acknowledgements

This work was supported by the Fonds zur Förderung der Wissenschaftlichen Forschung, Vienna, the Royal Swedish Academy of Sciences, Stockholm and the BMBWK, Vienna.

References

- [1] E. Janzén, R. Stedman, G. Grossmann, H.G. Grimmeiss, *Phys. Rev. B* 29 (4) (1984) 1907.
- [2] P.M. Mooney, *Semicond. Sci. Technol.* 6 (10b) (1991) B1–B8.
- [3] Z. Willamowski, J. Kossut, W. Jantsch, G. Ostermayer, *Semicond. Sci. Technol.* 6 (10b) (1991) B34–B37.
- [4] H.-J. Herzog, in: E. Kasper (Ed.), *Properties of strained and relaxed silicon germanium*, INSPEC, London, 1995, ISBN 0 852968264, p.49.
- [5] C.G.v.d. Walle, *Semicond. Sci. Technol.* 6 (10b) (1991) 94.
- [6] H.G. Grimmeiss, L. Montelius, K. Larsson, *Phys. Rev. B* 37 (12) (1988) 6916.



ELSEVIER

Physica B 308–310 (2001) 561–564

PHYSICA B

www.elsevier.com/locate/physb

The new assignment of hyperfine parameters for deep defects in diamond

U. Gerstmann*, H. Overhof

AG Theoretical Physics, Physics Department, University of Paderborn, D-33095 Paderborn, Germany

Abstract

Hyperfine (hf) parameters calculated for the vacancy in diamond show deviations from the experimental data, that have been ascribed to the neglect of lattice relaxations. Extending the formalism to include lattice relaxations we have removed the discrepancies for the interactions with the nearest neighbor ligand nuclei. However, the disagreement for the interactions with the next neighbor shell apparently increased thereby. Extending our calculations to include all ligands up to the fifth shell we show that the hf interaction assigned to the next nearest neighbor shell at (2 2 0) must be reassigned to the (3 3 1) ligand shell instead. The same reassignment holds for substitutional Ni defects in diamond and for several deep donors in silicon, but apparently not for the silicon vacancy in SiC. © 2001 Elsevier Science B.V. All rights reserved.

Keywords: LSDA; Hyperfine interactions; Diamond; SiC

1. Introduction

The local spin density approximation of the density-functional theory (LSDA-DFT), most successful in determining the ground state properties of deep defects in semiconductors, can be applied to excited states as well, if these differ in symmetry from the ground state [1]. Total energies and hyperfine (hf) interactions for the 5A_2 excited state of the neutral vacancy in diamond show a similar accuracy as results for the 4A_2 ground state of the negatively charged vacancy [2]. The significant deviations of calculated hyperfine parameters assigned to interactions with the nearest and next nearest ^{13}C neighbor nuclei from the experimental data [3,4] have been ascribed to the neglect of lattice relaxations, as hf interactions probe the magnetization density at the nuclei, which certainly will be affected by lattice relaxations.

Several calculations show that for the neutral vacancy in diamond, there are only small deviations from a breathing mode relaxation, but the direction of this breathing relaxation is still controversial: Li and Low-

ther [5] report a 10% inward relaxation, Breuer and Briddon [6] obtain a 13% outward relaxation, whereas according to Zywietz et al. [7] and Messmer et al. [8] the outward relaxation is only about 7%.

To reinvestigate the influence of the lattice relaxation, we have included lattice relaxations into the calculation of hf interactions. We obtain an outward relaxation of 7% for the nearest neighbors. While this relaxation removes the discrepancies of the hf interactions with the nearest neighbor ligands, it even increases the disagreement observed for the interactions with the next shell of ligands observed experimentally. Extending our calculations to the fifth shell of ligands, we show that the hf interaction commonly assigned to the next nearest neighbors at (2 2 0) must be reassigned to the (3 3 1) ligand shell instead. A similar reassignment is necessary for substitutional Ni defects in diamond and for several deep donors in silicon, but certainly not for the silicon vacancy in SiC.

2. Computational

Reliable magnetization densities near the ligand nuclei are obtained by the linear muffin-tin orbitals method in

*Corresponding author. Tel.: +49-5251-602329; fax +49-5251-603435.

E-mail address: u.gerstmann@phys.upb.de (U. Gerstmann).

the atomic-spheres approximation (LMTO-ASA) [9]. In a Green's function approach, the problem of an isolated impurity in an otherwise perfect crystal separates into two parts. The Green's function $g^0(E)$ of the perfect crystal is constructed first. The Green's function $g(E)$ of the impurity problem is obtained from g^0 solving the Dyson equation

$$[1 + g^0(E)(\Delta P(E) - \Delta S)]g(E) = g^0(E). \quad (1)$$

Here $\Delta P = P - P^0$ is the perturbation of the potential function by the impurity while the matrix $\Delta S = S - S^0$ is the relaxation-induced change of the LMTO-ASA structure constants. Assuming $\Delta S = 0$ minimizes the size of the matrices and optimizes the performance of the numerical calculations, but is equivalent to a neglect of lattice relaxations.

In this work, we take into account the relaxation-induced changes of the structure constants ΔS in a next nearest neighbor approximation. We demonstrate the accuracy of the relaxation obtained from Eq. (1), taking the silicon vacancy in 3C-SiC as an example.

In all charge states the silicon vacancy in SiC is known to have T_d symmetry with a slight outward relaxation of the nearest neighbors. This is due to the small overlap of the strongly localized carbon dangling bonds [7]. Thus, pairing effects which could lead to Jahn-Teller distortions are rather small. Therefore, this defect is a perfect

example to compare the results of the extended Green's function method with results from supercell approaches (FHI96-MD [10,11], SCC-DFTB [12,13]). The relaxations of the nearest neighbor atoms calculated within our approach (Fig. 1) are slightly smaller than those predicted from first-principle supercell calculations [7,10]. Note that the different methods predict a similar dependence of the relaxation on the charge state of the defect.

For the negative silicon vacancy, experimental EPR data give similar ligand hf interactions for different SiC polytypes [14]. As shown in Table 1, the 6.1% outward relaxation of the nearest ^{13}C neighbor atoms obtained from our calculation removes the discrepancies between theory and experiment, reducing the isotropic hf parameter from 63.47 to 48.71 MHz — nearly the experimental value of 46.90 MHz (see Table 1). This gives us confidence to use the Green's function LMTO-ASA approach to calculate nearest neighbor relaxations for similar defects as well.

3. The vacancy in diamond

According to previous calculations [7,15], the relaxation of the next nearest neighbors of the vacancy in diamond is very small (<1% inward). We, therefore, shall discuss nearest neighbor breathing displacements exclusively. Furthermore, the states for which EPR spectra are reported are not subject to Jahn-Teller distortions.

Applying the LMTO-ASA Green's function method to all charge states of the vacancy in diamond we obtain the relaxations shown in Fig. 2. The breathing relaxation decreases from 11.5% outward relaxation for V^{2-} to 4.5% inward for V^{4-} . This is not compatible with results from supercell calculations: these predict quite different (8% [10,11] and about 4% [12,13]) outward relaxations that virtually do not depend on the charge state of the vacancy (see Fig. 2). Experimental EPR data with resolved ligand hf interactions are available for two different charge states, the neutral and the negative state. Fortunately both states, the 4A_2 ground state of V^- and the 5A_2 excited state of V^0 , are neither affected by Jahn-

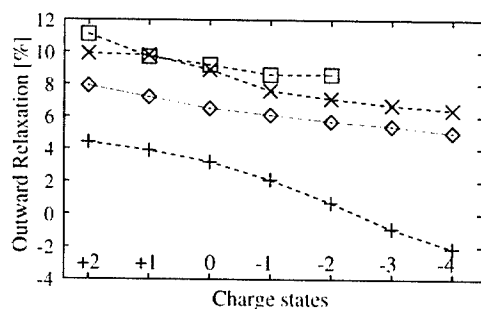


Fig. 1. T_d symmetry conserving relaxations for all charge states (+2 to -4) of the silicon vacancy in SiC in percent of the bondlength in the perfect crystal obtained by different calculations: present work (◇), SCC-DFTB supercells [12] (+), plane wave supercells [7] (□) and [10] (×).

Table 1

Calculated ligand hyperfine interaction constants (in MHz) for the relaxed V_{Si} in 3C-SiC compared with corresponding values for the unrelaxed structure and with experimental data [14]

	Δd (% d_0)	^{13}C (1 1 1) ligand		^{29}Si (2 2 0) ligand			^{13}C (1 1 3) ligand			^{13}C (3 3 1) ligand		
		<i>a</i>	<i>b</i>	<i>a</i>	<i>b</i>	<i>b'</i>	<i>a</i>	<i>b</i>	<i>b'</i>	<i>a</i>	<i>b</i>	<i>b'</i>
LSDA	0.0	63.47	13.72	4.07	-0.52	0.19	-1.57	0.11	0.09	3.38	1.15	0.04
LSDA	6.1	48.71	14.22	6.04	-0.23	0.20	-1.33	-0.10	0.09	3.68	1.22	0.07
Exp.		46.90	3.84	8.24	—	—						

Table 2

Ligand hyperfine interaction constants (in MHz) calculated for the relaxed 5A_2 excited state of V_C^{*0} compared with values calculated for the unrelaxed structure [2] and with experimental data from van Wyk et al. [4]. Also listed are corresponding data for the 4A_2 state of V_C^- compared with experimental data from Isoya et al. [3] and for Ni_C^- in diamond ([16,17]). The calculated hf interaction value of 13.5 MHz for ^{61}Ni nucleus (exp. value 17.1 MHz) is almost unaffected by the relaxation

Δd (% d_0)	^{13}C (1 1 1) ligand		^{13}C (2 2 0) ligand			^{13}C (1 1 3) ligand			^{13}C (3 3 1) ligand		
	<i>a</i>	<i>b</i>	<i>a</i>	<i>b</i>	<i>b'</i>	<i>a</i>	<i>b</i>	<i>b'</i>	<i>a</i>	<i>b</i>	<i>b'</i>
$V_C^{*0}(^5A_2)$											
LSDA 0.0	88.0	16.4	−4.7	1.20	0.20	−0.5	0.20	0.10	5.4	1.20	0.20
LSDA 6.7	58.9	17.7	−3.5	0.92	0.24	1.2	0.37	0.25	7.2	1.38	0.19
Exp.	53.73	18.70							6.36	1.20	—
$V_C^-(^4A_2)$											
LSDA 0.0	126.0	18.1	−3.2	1.2	0.3	0.4	0.20	0.20	6.7	1.2	0.3
LSDA 3.6	101.6	18.8	−2.1	0.96	0.26	1.3	0.36	0.32	8.1	1.31	0.21
Exp.	101.7	20.0							10.7	1.37	0.09
Ni_C^-											
LSDA 0.0	31.9	7.7	−4.1	0.4	0.1	0.7	1.20	0.20	7.2	1.2	0.3
LSDA 5.7	22.8	9.0	5.7	1.17	0.50	1.2	0.45	0.20	7.9	1.01	0.17
Exp.	18.85	9.32							8.63	1.04	0.05

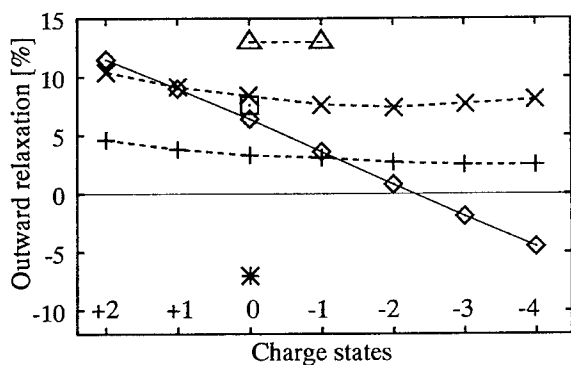


Fig. 2. Relaxations in the subspace of T_d symmetry for all charge states (+2 to −4) of the isolated vacancy in diamond in percent of the bondlength in the perfect crystal obtained by different calculations: present work (◇), SCC-DFTB supercells [12] (+), plane wave supercells [7] (□) and [10] (×), cluster calculations [6] (Δ). The result of a cluster calculation with a model potential [5] is denoted by an asterisk (*). Note that local density theory yields the ground state configurations for the charge states +2, −1, and −4 only.

Teller distortions nor by configuration interactions, since there are no further $a_1^1 t_2^2$ configurations that could be admixed to the orbital singlet states (see also Ref. [2,6]). This offers the possibility to check the LSDA spin densities for different atomic configurations against experimental ligand hf interaction data, and thereby to compare the consequences of the lattice relaxations predicted by different methods.

To this aim, we have calculated the hf parameters for the relaxed geometries predicted by our total energy calculations and by different supercell calculations. For

the 4A_2 state of the negative vacancy, the FHI-code leads to a relaxation of 7.8% [7,10]. This corresponds to an isotropic hf interaction of about 70 MHz, significantly less than the experimental value (101.7 MHz) with a deviation that is comparable in magnitude to the error found for the unrelaxed structure. In contrast, in this case the SCC-DFTB calculation [12] gives a geometry that leads to hf interactions (100.7 MHz) that are close to the experimental values. However, the SCC-DFTB calculations predict for the 5A_2 excited state a 3.8% outward relaxation, for which we obtain the isotropic hf value of 73.5 MHz, appreciably larger than the experimental value of 53.7 MHz.

The results of our present Green's function approach simultaneously explain the hf splittings due to the nearest neighbor ^{13}C ligands for both charge states as shown in Table 2. Predicted outward relaxations of 6.7% and 3.6% for the excited neutral and for the negative charge state of the vacancy, respectively, remove most of the discrepancies with the experimental data (see also Table 2).

This result can also be understood following a simple method for estimating the geometric structure of atoms from the hybridization ratio [18], as already used by van Wyk et al. [4]. From the hf parameters of the two defect states which differ by a factor of two, these authors estimate that for the neutral vacancy the displacement of the nearest neighbors must be 50% stronger than for the 4A_2 ground state of the negatively charged vacancy.

In contrast to the results for the nearest neighbors, the disagreement observed for the experimental data commonly assigned to the next nearest neighbor (2 2 0) shell increases if we include the lattice relaxations. Since, as mentioned above, the displacements of these atoms are

negligible, these discrepancies cannot be explained by our limitation of the lattice relaxation to the nearest neighbors. Comparing the experimental hf interactions with calculated results for shells which belong to the class of the (2 2 0) shell, we find satisfactory agreement for both the isotropic and the anisotropic interactions for the 5A_2 state as well as for the 4A_2 state, if we assign the experimental data to the (3 3 1) shell in both cases.

A closer look at Table 2 shows the same reassignment to hold for substitutional Ni defects in diamond as well. Here, the main argument against the (2 2 0) assignment comes from the fact that the experimental anisotropic hf interaction is nearly axial. We note in passing that with similar arguments, it can be shown that a comparable reassignment of the ligand hf interactions should be made for deep substitutional donors in silicon, but certainly not for the silicon vacancy in SiC, as can be seen in Table 1.

Acknowledgements

We are grateful to Eva Rauls and Balint Aradi for helpful discussions and for providing us with their unpublished results from numerous supercell calculations. Additionally, it is a pleasure to acknowledge financial support from the Deutsche Forschungsgemeinschaft (DFG) for this work.

References

- [1] U. von Barth, *Phys. Rev. A* 20 (4) (1979) 1693.
- [2] U. Gerstmann, M. Amkreutz, H. Overhof, *Phys. Rev. B* 60 (1999) R8446.
- [3] J. Isoya, H. Kanda, Y. Uchida, S.C. Lawson, S. Yamasaki, H. Itoh, Y. Morita, *Phys. Rev. B* 45 (1992) 1436.
- [4] J.A. van Wyk, O.D. Tucker, M.E. Newton, J.M. Baker, G.S. Woods, P. Spear, *Phys. Rev. B* 52 (1995) 12 657.
- [5] L.H. Li, J.E. Lowther, *Phys. Rev. B* 53 (1996) 11277.
- [6] S.J. Breuer, P.R. Briddon, *Phys. Rev. B* 51 (1995) 6984.
- [7] A. Zywickz, J. Furthmüller, F. Bechstedt, *Phys. Stat. Sol. B* 210 (1998) 13.
- [8] R.P. Messmer, G.D. Watkins, *Phys. Rev. B* 7 (1973) 2568.
- [9] O. Gunnarsson, O. Jepsen, O.K. Andersen, *Phys. Rev. B* 27 (1983) 7144.
- [10] B. Aradi, private communication, 2001.
- [11] M. Bockstedte, A. Kley, J. Neugebauer, M. Scheffler, *Comput. Phys. Commun.* 107 (1997) 187.
- [12] E. Rauls, private communication, 2001.
- [13] Th. Frauenheim, et al., *Phys. Stat. Sol. B* 217 (2000) 41.
- [14] T. Wimbauer, B. K. Meyer, A. Hofstaetter, A. Scharmann, H. Overhof, *Phys. Rev. B* 56 (1997) 7384.
- [15] J. Goss, R. Jones, P.R. Briddon, *Phys. Rev. B*, submitted for publication.
- [16] J. Isoya, H. Kanda, J.R. Norris, J. Tang, M.K. Bowman, *Phys. Rev. B* 41 (1990) 3905.
- [17] U. Gerstmann, M. Amkreutz, H. Overhof, *Phys. Stat. Sol. B* 217 (2000) 665.
- [18] O.D. Tucker, M.E. Newton, J.M. Baker, *Phys. Rev. B* 50 (1994) 15586.



ELSEVIER

Physica B 308–310 (2001) 565–568

PHYSICA B

www.elsevier.com/locate/physb

Transition metals in diamond: Do chemical trends arise from ab initio calculations?

Karl Johnston*, Alison Mainwood

Department of Physics, King's College, London, Strand, London, WC2R 2LS, UK

Abstract

The stability of transition metals as point defects in diamond is examined. Several impurities that have not been seen in diamond are modelled to understand whether they could be present, but are as yet, undetected. We model their solubility characteristics such as solvation enthalpies and entropies. The results indicate that the most likely transition metal impurities in diamond will be from metals with the greatest d-character. The most stable impurity is predicted to be nickel, in agreement with experimental work on these defects. The calculations also give credence to some of the models that have been proposed for these defects, in particular, that semi-divacancy defects relieve the strain imposed by these large impurity atoms. © 2001 Elsevier Science B.V. All rights reserved.

Keywords: Transition metals; Diamond; Stability

1. Introduction

The most common defects in diamond are either intrinsic or are those elements close to carbon in the periodic table such as N and B. Transition metals are an exception to this. The main reason for interest in them comes from synthetic samples where transition metals are used as solvent catalysts for the controlled production of industrial diamond. Synthetic stones now make up over 90% of the industrial diamond market [1]. One of the side effects of using metals in this way is that they become incorporated in the grown diamond as point defects; however, interestingly only two—Co and Ni—of the many used appear to form defects [2]. They have been identified unambiguously using optical and paramagnetic methods; the hyperfine information from EPR proving to be invaluable in the identification of the chemical species of the impurity [3,4]. There are three dominant lattice sites which are associated with these defects: interstitial, substitutional and “semi-divacancy” [4,5]. In a bid to answer some of the questions about which metals could form defects, we model the solvation enthalpy and entropy of transition metals impurities in

diamond. This helps us to gain an insight into the likelihood of more defects being identified.

In this study, we examine the metals that are most commonly used for the synthesis of diamond—iron, nickel and cobalt—and several on the first transition series, which are rarer—vanadium, manganese and copper. Because of the lack of a reliable pseudopotential for chromium, the full series cannot be modelled, but there will still be enough data to observe trends.

2. Method

The computer program AIMPRO [6] has been used to model many defect systems in a wide variety of materials. The typical clusters employed in this study were of 150 atoms, of which 70–90 were host/impurity atoms. Norm-conserving pseudopotentials for the carbon and metal atoms were used as derived by Bachelet et al. [7]. The metal atom was inserted in the centre of a cluster based around the site in question: substitutional, interstitial or semi-divacancy. The electronic wave functions were expanded in s- and p-Gaussian orbitals, centred on the nuclei, with the electron charge density fitted in the same way. These structures were then

*Corresponding author. Fax: +44-20-7848-2420.

E-mail address: karl.johnston@kcl.ac.uk (K. Johnston).

relaxed by first finding a self-consistent energy, then calculating the forces, and relaxing the system using a conjugate gradient function until an equilibrium point is reached. The runs have been repeated for clusters of varying sizes to see if the results obtained are size-independent; the typical variation is only of 1–2%. Vibrational properties of a defect centre can be obtained by diagonalising a dynamical matrix generated from the double derivatives of the total energy as described in Ref. [6]. These have an accuracy of about 10% although results are more unreliable close to the Raman frequency.

3. Stability of transition metals in diamond

The method that we use is primarily based on that of Mainwood and Stoneham [8]. Estimating the stability of the metal in the diamond requires dealing with several quantities: solvation enthalpies and entropies and long-range strain. The solvation enthalpy of a metal–carbon solution is estimated by using a similar Born–Haber relation to the one that appears in Ref. [8]:

$$E_{\text{Tot}}(MC_{n-x}) - E_{\text{Tot}}(C_n) - E_{\text{coh}}(M), \quad (1)$$

where $E_{\text{Tot}}(MC_{n-x})$ is the total energy of the cluster containing the metal; $E_{\text{Tot}}(C_n)$ is the total energy of the “pure” diamond and $E_{\text{coh}}(M)$ is the cohesive energy of the metal which is taken from the values given by Kittel [9]. This assumes that the transition metal is dissolved from the metal. The transition metal impurity will introduce strain into the lattice. This strain will effectively extend beyond the range of the cluster. Continuum elastic theory [10] predicts that this strain will fall off as the cube of the distance from the impurity. To estimate the strain, we use the technique of Safonov et al. [11]. This relates the strain components e_{ij} at a point (x_1, x_2, x_3) a distance, r , away as

$$e_{ij} = Ar^{-3}(\delta_{ij} - 3x_i x_j / r^2), \quad (2)$$

where δ_{ij} is the Kronecker delta. A is an elastic mismatch parameter. The total strain energy per unit volume is then given by Nye [12] as

$$\delta_{ij} = \frac{1}{2} \sum_{ij} c_{ij} e_i e_j, \quad (3)$$

where c_{ij} are the elastic moduli of diamond [13]. The long-range strain energy is shown for the various types of defects in Fig. 1. We see that, for the majority of metals, the strain is similar. However, there are some points to note. Generally, the semi-divacancy exhibits the lowest strain, supporting an intuitive feeling that moving a large substitutional atom to a semi-divacancy site should relieve strain in the lattice. This is most obvious for the copper impurity, where the substitutional impurity has very high strain whereas the

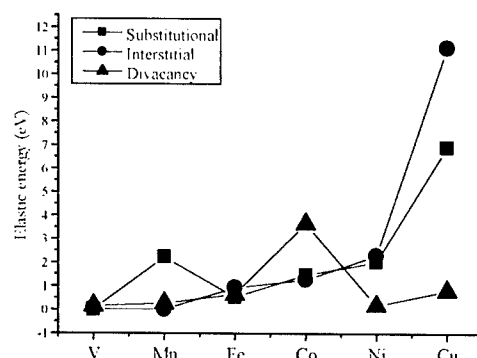


Fig. 1. The elastic strain energies for the various impurities under consideration in this paper. The divacancy impurity has generally the lowest long-range strain, in agreement with theoretical approaches describing the formation of this defect.

Table 1
Cohesive energies for the metals under consideration in this study^a

Metal	Cohesive Energy (eV atom ⁻¹)
V	5.31
Mn	2.92
Fe	4.28
Co	4.39
Ni	4.44
Cu	3.49

^a Values taken from Ref. [3] (Kittel).

transition to the divacancy results in considerably less strain.

The next component that describes the solubility is the solvation entropy. The main contribution to this is the vibrations of the atoms. In the case of a cluster, this means calculating the local vibrational modes due to the impurity have to be calculated, as described in Born and Huang [14], from which the solvation entropy is given by [8]

$$S_v = -k \ln \left\{ \frac{\prod_{i=1}^n v_{1i}}{\prod_{i=1}^n v_{0i}} \right\}, \quad (4)$$

where v_{1i} are the vibrations with the impurity present and v_{0i} when it is absent. The values of the contributions to the vibrational entropy are shown in Tables 1 and 2. When we take these in addition to the enthalpies, we arrive at an estimate for the Gibbs' free energy:

$$\Delta G = \Delta H - T \Delta S, \quad (5)$$

where ΔH is the change in enthalpy, and ΔS , that of entropy.

The results are shown in Figs. 2–4. It is clear from these figures that the impurities most likely to be found

Table 2

The vibrational entropies calculated for the interstitial and the substitutional impurities^a

Metal	Substitutional vibrational entropy (eV K ⁻¹)	Interstitial vibrational entropy (eV K ⁻¹)
V	-2.95E-06	9.60E-04
Mn	-2.88E-18	-1.16E-15
Fe	3.08E-04	2.17E-03
Co	1.23E-03	2.12E-03
Ni	6.99E-05	4.79E-04
Cu	-5.63E-04	2.58E-04

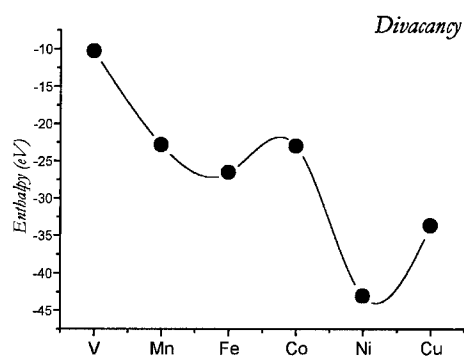
^a The values are small compared to the enthalpies (Figs. 2–4).

Fig. 2. The stability of the interstitial metal in the diamond lattice.

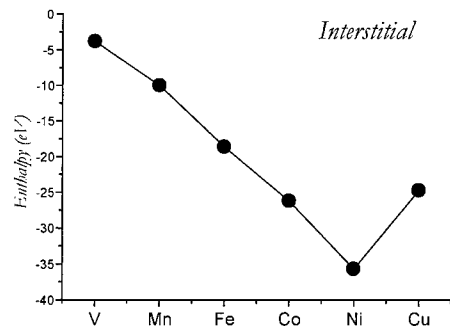


Fig. 3. The stability of the divacancy metal in diamond.

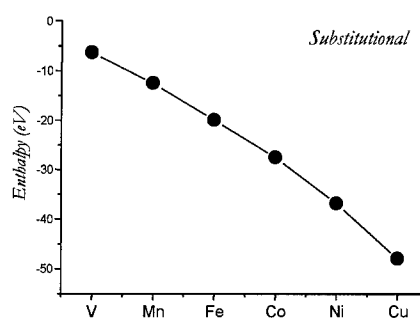


Fig. 4. The stability of the substitutional metal in diamond.

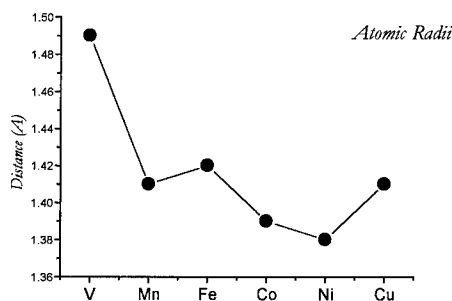


Fig. 5. The atomic radii of the metals under consideration. There is a definite similarity to the trend observed in the interstitial atoms.

in the diamond are those of increasing d-character. Nickel is predicted to be the most stable metal impurity in diamond, in agreement with experimental observation, where the vast majority of the work has been on identifying this metal in the various lattice sites mentioned in the introduction. The second most likely impurity is cobalt, which is also found experimentally. From the graphs, it would also appear that copper—admittedly a rarely used catalyst—would be a likely defect; in silicon, it is widely known as fast diffuser [15]. However, when we refer back to Fig. 1, the considerable

long-range strain that is introduced, reduces this likelihood for the substitutional and interstitial impurities, although not for the divacancy case. This supports a recent paper by Baker [7], which re-evaluates the EPR W36 centre in terms of its origin from a semi-divacancy copper defect. Intriguingly, iron does not appear to be very stable in diamond. Iron is an efficient solvent for graphite. As a result, almost all the solvent catalysts used to grow in diamond are iron alloys. Its non-stability as a point defect in diamond is therefore, surprising, although it is worth noting that no point defects containing iron have been unambiguously

identified in synthetic diamonds grown with iron or iron-alloy solvent catalysts. The interstitial metal results bear a strong resemblance to the atomic radii of the metals, as shown in Fig. 5. As this impurity does not bond to the lattice, it is the most similar to the unaffected metal in the diamond lattice, a fact borne out by the stability results.

References

- [1] More information can be obtained at <http://minerals.usgs.gov/minerals/pubs/commodity/diamond/>.
- [2] A.J. Neves, J.C. Lopes, Optical and EPR properties of transition metals in diamond, in: M.H. Nazare, A.J. Neves (Eds.), *Properties, Growth and Applications of Diamond*, INSPEC, 2000.
- [3] D.J. Twitchen, et al., *Phys. Rev. B* 61 (2000) 9.
- [4] J. Isoya, et al., *Phys. Rev. B* 41 (1990) 3905.
- [5] V. Nadolinny, A. Yeliseyev, *Diamond Relat. Mater.* 3 (1994) 1196.
- [6] R. Jones, P.R. Briddon, Identification of defects in semiconductors, in: M. Stavola (Ed.), *Semiconductors and Semimetals*, Vol. 51A, Academic Press, Boston, 1998 (Chapter 6).
- [7] J.M. Baker, *J. Phys. Cond. Matter* 13 (2001) 2053.
- [8] Alison Mainwood, A.M. Stoneham, *Philos. Mag. B* 37 (1978) 255.
- [9] C. Kittel, *Introduction to Solid State Physics*, 7th Edition, Wiley, New York, 1997.
- [10] J.D. Eshelby, in: F. Seitz, D. Turnbull (Eds.), *Solid State Physics, Advances in Research and Applications*, Vol. 3, Academic Press, New York, 1956, p. 79.
- [11] A.N. Safonov, G. Davies, E.C. Lightowers, *Phys. Rev. B* 54 (7) (1996) 4409.
- [12] J.F. Nye, *Physical Properties of Crystals*, OUP, Oxford, 1985.
- [13] M. Grimsditch, in: M.H. Nazare, A.J. Neves (Eds.), *Elastic Moduli of Diamond, Properties, Growth and Applications of Diamond*, INSPECC, London, 2001.
- [14] M. Born, K. Huang, *Dynamical Theory of Crystal Lattices*, Oxford University Press, Oxford, 1955.
- [15] G. Davies, The optical properties of luminescence centres in silicon, *Physics Reports*, Vol. 176, 1989.



ELSEVIER

Physica B 308–310 (2001) 569–572

PHYSICA B

www.elsevier.com/locate/physb

Annealing of monovacancies in electron and γ -irradiated diamonds

S. Dannefaer*, A. Pu, V. Avalos, D. Kerr

Department of Physics, University of Winnipeg, 515 Portage Avenue, Winnipeg, MB, Manitoba, Canada, R3B 2E9

Abstract

Diamonds were irradiated by either 2.3 MeV electrons or by ^{60}Co γ -rays. In the case of electron irradiation, positron annihilation and optical absorption showed that 30–35% of the monovacancies (positron lifetime of 145 ps) were removed by interstitials between 700 and 1020 K. Above 1020 K, divacancies were formed giving rise to TH5 optical absorption and a positron lifetime of 185 ps. Above 1120 K, TH5 absorption was replaced by absorption at 507/517 nm, but no change in the positron lifetime was observed. Annealing of the γ -irradiated type Ib diamonds differed substantially from that for the electron irradiated samples; 60% of the monovacancies were removed between 350 and 525 K. © 2001 Elsevier Science B.V. All rights reserved.

Keywords: Diamond; Vacancies; Annealing; Positron annihilation

1. Introduction

The purpose of this work is to investigate the mechanisms by which irradiation-produced monovacancies anneal out upon heat-treatment. Monovacancies were introduced either by 2.3 MeV electron irradiation or by ^{60}Co irradiation, where the latter type of irradiation causes damage due to Compton scattered electrons with a maximum energy of only 1.1 MeV. It will be shown that the annealing behaviour of monovacancies differs significantly between these two irradiation conditions.

2. Experimental

In Section 2.1 details of the samples and irradiations are given and in Section 2.2, a brief introduction to positron annihilation.

2.1. Experimental details

Two type IIa natural diamonds were electron irradiated by 2.3 MeV electrons to a dose of

$1.4 \times 10^{18} \text{ cm}^{-2}$ over a time period of 14 h at 281 K after which the positron source was sandwiched between the samples. The two ^{60}Co γ -irradiated samples were type Ib synthetic diamonds with a substitutional nitrogen concentration of 90 ppm. They were irradiated to an absorbed dose of 6 MGy (H_2O) accumulated during 7 days of irradiation at 300–350 K. Isochronal annealing (1/2 h) was done in air up to 700 K, while above this temperature a protective atmosphere of Ar was used.

Positron experiments were done with a lifetime spectrometer with a full-width at half-maximum of 170–175 ps and Doppler spectra were measured with an energy resolution of 1.2 keV. Data analysis was based on spectra containing $(6\text{--}10) \times 10^6$ counts. Optical measurements were done at 80 K in the wavelength range of 220–1100 nm.

2.2. Positron annihilation

In this work two positron techniques were used, lifetime spectroscopy and Doppler broadening. In the first technique vacancies are detected because positron trapped by vacancies have a longer lifetime than in the untrapped state (bulk) due to the smaller electron density in vacancies. In Doppler broadening experiments the electron momentum distribution is measured, and trapping by vacancies causes the positron to

*Corresponding author. Tel.: +1-204-786-9754; fax: +1-204-783-7981.

E-mail address: steen.dannefaer@uwinnipeg.ca (S. Dannefaer).

annihilate with electrons with a narrower momentum distribution than in the bulk: The so-called *S* parameter is designed to give a quantitative measure for this narrowing.

The rate by which positrons are trapped by vacancies (the so-called trapping rate) is linearly dependent on their concentration. In lifetime spectra this causes an increase in the intensity of the lifetime arising from the trapping, and for the *S* parameter in an increase in its value; a more detailed account of positron annihilation can be found in Ref. [1].

3. Results and discussion

The results for the electron irradiated samples are presented in Section 3.1 and those obtained for the γ -irradiated samples in Section 3.2.

3.1. Electron irradiation

Optical absorption of six zero-phonon lines were measured as a function of annealing temperature. The six lines were: 741 (GR1, arising from neutral monovacancies), 488 (TH5), 507 (M1), 517 (M2), 595, and 610 nm. The two latter lines were weak compared to the other lines and will not be considered further; the identifiers given in the parentheses originate from optical works. The four main optical absorption lines were quantified by integration over a 10 nm wide range centered at each line after a linear background subtraction for each of the lines. Fig. 1 shows the integrated absorption normalized to the maximum value for each of the four lines; the integrated absorptions of the 507/517 nm lines were identical.

Absorption due to neutral monovacancies (GR1) decreases by 30% up to 1020 K, with a hint of a 'stage' close to 820 K. The main annealing stage above 1020 K is accompanied by an increase in the 488 nm line (TH5) and during its subsequent decrease above 1110 K the 507/517 lines grow in, although faintly present already above 1000 K. It is noteworthy that the maximum value of the absorption of the 488 nm line equals, to within 10%, the sum of the maximum values for the 507/517 nm lines. This indicates that these three lines are closely related.

Positron lifetime results are presented in Fig. 2. Panel (a) shows that the irradiation-produced lifetime of 145 ± 3 for positrons trapped by monovacancies [1] is constant up to 1020 K. Above 1020 K the lifetime increases and levels off at 185 ± 3 ps, which shows that vacancy agglomeration occurs during the decrease in GR1 absorption.

In Fig. 2b is shown the fraction remaining of the trapping rate, i.e. its value at any of the annealing temperatures divided by its value before annealing.

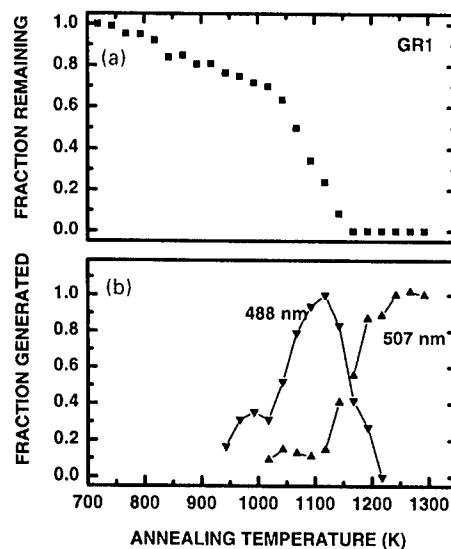


Fig. 1. Normalized optical absorption as a function of isochronal annealing temperature for electron irradiated samples. Panel (a) depicts that for GR1 and panel (b) for 488 (TH5) and 507 nm (M1); absorption at 517 nm (M2) is identical to that for 507 nm. Curves in panel (b) are merely guides to the eye.

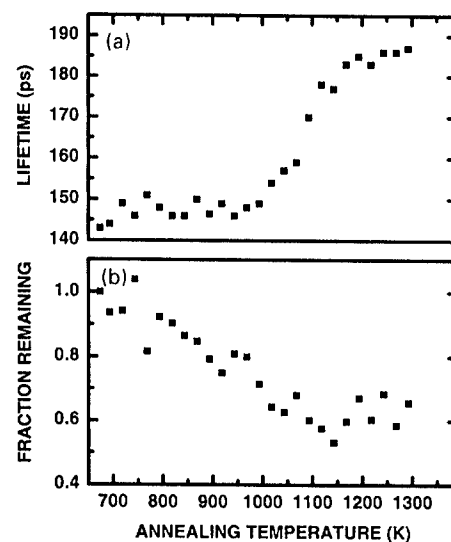


Fig. 2. Positron lifetime results obtained at 293 K as a function of isochronal annealing temperature for electron irradiated samples. Panel (a) shows the irradiation-produced lifetime and panel (b) the normalized trapping rate.

The fraction remaining of the trapping rate and the fraction remaining of GR1 decreased by the same amount up to 1020 K (30–35%), and since there was no evidence for vacancy agglomeration according to the

lifetime results (Fig. 2a), we conclude that monovacancies are removed due to migration of interstitials. Hunt et al. [2] have recently ascribed a 10% decrease in monovacancy concentration due to recombination with single (split) interstitials. This took place upon annealing to 750 K and is consistent with the decrease in GR1 absorption at 820 K observed in this work. However, interstitials with higher thermal stability are required for the further 20–25% reduction in monovacancy concentration up to 1020 K: This leaves 65–70% of the interstitials unaccounted for.

Above the annealing temperature of 1020 K, vacancy agglomeration is most likely due to creation of divacancies in view of theoretical calculations of the positron lifetime for divacancies [3] and of the emergence of the 488 nm line (TH5) and by the EPR signal (R4/W6) for divacancies [4].

The positron experiments show that the 507/517 nm lines are also associated with divacancies, since the positron lifetime did not vary during the changes in the absorption at 488/507/517 nm. Furthermore, the observation that the positron trapping rate (Fig. 2b) is constant throughout the changes in these lines (Fig. 1b) shows that divacancies are not lost during these processes.

Importantly, this implies that interstitials do not remove vacancies above 1020 K, and thus raises the question of where the remaining 65–70% of the interstitials went? An explanation could be that these interstitials were removed during irradiation by dislocations as well as by the large vacancy clusters commonly observed by positrons [1].

In summary, divacancies are confirmed to be created by monovacancy migration above 1020 K and we suggest that the 507/517 nm lines are associated with 'high' temperature forms of the divacancy.

3.2. γ irradiation

To further investigate the fate of interstitials, type Ib synthetic diamonds were irradiated with ^{60}Co γ -rays (1.13 and 1.3 MeV) to create monovacancies due to Compton scattered electrons of a maximum energy of 1.1 MeV. The idea is that such irradiation would create close vacancy–interstitial pairs (Frenkel pairs) which would curtail removal of interstitials by other defects, and consequently exhibit a different annealing behaviour than that arising from 2.3 MeV electron irradiation.

It should be pointed out that the γ -irradiated diamonds were of type Ib so monovacancies would be negatively charged and no absorption due to neutral monovacancies (GR1) was observed. Absorption from the negatively charged monovacancies, however, could not be observed due to the strong absorption from substitutional nitrogen.

Positron results are shown in Fig. 3 and display notable differences compared to the 2.3 MeV electron irradiated samples. According to panel (a) the radiation-produced vacancies give rise to a positron lifetime of 130 ± 3 ps, some 15 ps shorter than for the previous samples. The normalized trapping rate is shown in panel (b) of Fig. 3. It is remarkable that annealing of vacancies takes place at much lower temperatures than for the 2.3 MeV electron irradiated samples (cf. Fig. 2b). Another remarkable observation comes from the low temperature Doppler S parameter measurements between 8 and 300 K shown in Fig. 4. Negatively charged monovacancies should normally result in a strong decrease in the S parameter with increasing temperature, but here S is seen to increase slightly with temperature.

The defect inventory created by γ irradiation is quite different from that for 2.3 MeV electrons, and we

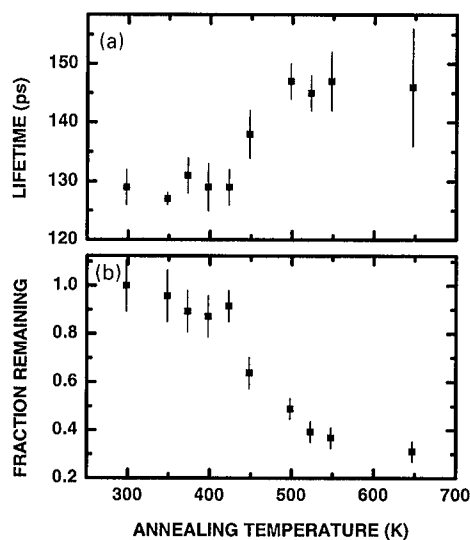


Fig. 3. Irradiation produced lifetime (panel (a)) and normalized trapping rate (panel (b)) for the γ -irradiated samples, as a function of annealing temperature. Measurements were made at 293 K.

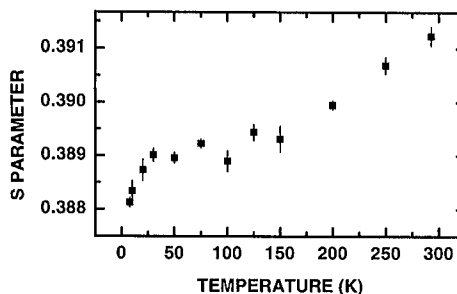


Fig. 4. S parameter as a function of measurement temperature for the γ -irradiated samples.

suggest that close vacancy–interstitial pairs $V I^+$ (Frenkel pairs) are created by γ radiation. This suggestion explains the low temperature annealing of the vacancies and the overall neutral charge of the Frenkel pair would account for the behaviour of the S parameter, while at the same time explain why no GR1 absorption is observed. Further experiments on γ -irradiated synthetic type IIa and type IIb diamonds are in progress.

4. Conclusion

Positron experiments confirm the association of the optical absorption line TH5 with the divacancy, and suggest that the absorption lines at 507 and 517 nm (M1 and M2, respectively) are also due to divacancies.

Damage arising from ^{60}Co γ irradiation, i.e. by electrons of maximum energy of 1.1 MeV, is suggested to be in the form of close vacancy–interstitial pairs with an overall neutral charge and stable only up to ~ 400 K.

Acknowledgements

We are indebted to Mr. C. Hunter, MDS Nordion Canada, for graciously providing the γ irradiations, to Dr. Uedono, Tsukuba, Japan for the type Ib diamonds, and to GIA, USA for the type IIa diamonds. This research was financially supported by the Natural Sciences and Engineering Council of Canada.

References

- [1] A. Pu, T. Bretagnon, D. Kerr, S. Dannefaer, *Diamond Relat. Mater.* 9 (2000) 1450.
- [2] D.C. Hunt, D.J. Twitchen, M.E. Newton, J.M. Baker, T.R. Anthony, W.F. Banholzer, S.S. Vagarali, *Phys. Rev. B* 61 (2000) 3863.
- [3] M.J. Puska, S. Mäkinen, M. Manninen, R.M. Nieminen, *Phys. Rev. B* 39 (1989) 7666.
- [4] D.J. Twitchen, M.E. Newton, J.M. Baker, T.R. Anthony, W.F. Banholzer, *Phys. Rev. B* 59 (1999) 12900.



ELSEVIER

Physica B 308–310 (2001) 573–576

PHYSICA B

www.elsevier.com/locate/physb

Defect-induced graphitisation in diamond implanted with light ions

A.A. Gippius^{a,*}, R.A. Khmel'nitsky^a, V.A. Dravin^a, A.V. Khomich^b

^a*P.N. Lebedev Physical Institute of the Russian Academy of Sciences, Leninsky Prospect 53, Moscow 119991, Russia*

^b*Institute of Radiotechnique and Electronics of the Russian Academy of Sciences, Mokhovaya Street 11, Moscow 103907, Russia*

Abstract

Optical absorption, interference and microscopy studies of diamond samples implanted with light ions (H^+ , D^+ and He^+) and annealed at various regimes revealed new features of irradiation induced graphitisation of diamond: the “low temperature” graphitisation directly related to vacancies, the specific mechanism of graphitisation accompanied by blistering in H^+ implanted samples and high temperature graphitisation stimulated by residual radiation damage. © 2001 Elsevier Science B.V. All rights reserved.

Keywords: Diamond; Ion implantation; Graphitisation

1. Introduction

Due to metastability of diamond (under ambient conditions the stable phase of crystalline carbon is graphite) it tends to transform to graphite under heat treatment and/or irradiation [1,2]. This puts a severe limitation on ion implantation doping. On the other hand ion-beam induced graphitisation opens new prospects of defect engineering [3].

In this paper we present the results of studies of formation of graphitised layers in diamond under various conditions of implantation with H^+ , D^+ and He^+ ions and annealing. The use of the light ions offers some advantage over heavier ions since the former produce buried graphitised layers at a considerable (~ 1000 nm) depth, which is essential for applications. It is shown that the phenomenon of radiation-induced graphitisation is more complicated than it was previously anticipated. Of particular interest are the data referring to implantation with hydrogen, which reveal a specific role of hydrogen in “conservation” of radiation damage.

2. Experimental

Polished (110) samples of IIa or intermediate (IIa–IIa) natural diamond were bombarded at room temperature by 350 keV H^+ , D^+ and He^+ ions with doses in the range $2\text{--}12 \times 10^{16} \text{ cm}^{-2}$. Implanted areas 0.75×1.75 mm in size were specified by masks. Annealing was performed at temperatures up to 1700°C in a graphite furnace. The formation of the graphitised layers was monitored by optical absorption, interference and microscopy.

3. Results

3.1. Radiation damage and graphitisation

In the case of implantation of light ions it can be thought that the radiation damage consists mainly of vacancies and interstitials. The latter are annealed at temperatures well below those characteristic of the process of graphitisation, which is thus determined by the amount and spatial distribution of vacancies.

In Fig. 1 the spatial distributions of implanted species and radiation damage (vacancies) calculated by Monte Carlo simulation are shown for the dose $3 \times 10^{16} \text{ cm}^{-2}$ of 350 keV H^+ , D^+ and He^+ ions. It is seen that the

*Corresponding author. Fax: +7-095-938-2251.

E-mail address: gippius@sci.lpi.ac.ru (A.A. Gippius).

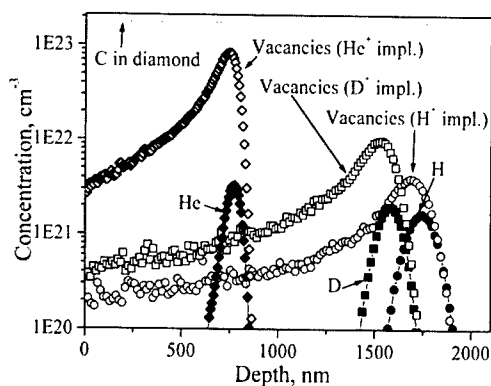


Fig. 1. Spatial distribution in diamond of the implanted species and radiation damage calculated by Monte Carlo simulation.

amount of radiation damage decreases with the decrease of ion mass (at the energy of 350 keV, the number of vacancies produced per implanted ion is 56, 12 and 5 for He^+ , D^+ and H^+ , respectively). According to the simple model there must be direct correlation between these numbers and corresponding critical doses for graphitisation. However, our studies have shown that this simple suggestion does not work, partly due to the interaction of radiation defects with each other and with implanted or background impurities neglected by Monte Carlo simulation.

3.2. D^+ and He^+ implantation

We have found much similarity between the data referring to D^+ and He^+ implantation, with proper dose scaling factor. That is why we concentrate on the results for D^+ implantation all the more because they are of particular interest in comparison with those for H^+ .

In Fig. 2 optical density spectra of diamond are shown for various conditions of implantation and annealing. It is seen that absorption of implanted samples (before annealing) is dominated by two broad bands at 600 and 290 nm. These bands (at room temperature) refer, respectively, to the GR1 and GR2-8 optical systems produced by neutral isolated vacancies [4]. In all D^+ and He^+ implanted samples the vacancy absorption bands practically disappear after annealing at 780°C.

In the samples implanted with $6\text{--}12 \times 10^{16} \text{ cm}^{-2}$ of D^+ ions, the disappearance of the vacancy absorption after annealing at 780°C and higher temperatures is accompanied by emergence of interference. This indicates that in the depth of the crystal a layer is formed (with is quite smooth judging from the great number of periods of the interference) with optical parameters different from those of the bulk material. Absorption spectra (after subtraction of the interference) are very

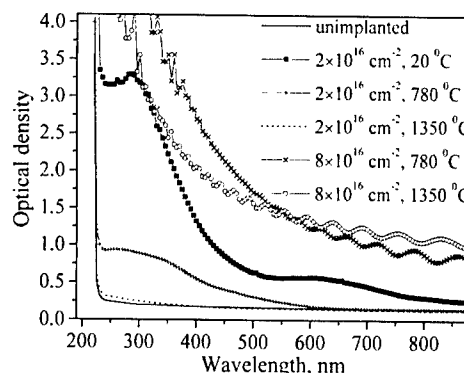


Fig. 2. Optical density spectra of diamond samples for various conditions of D^+ implantation and annealing.

similar to those of highly oriented pyrolytic graphite [5,6]. Basing upon these data combined with the sharp increase of conductivity of the buried layer at these conditions we can state that the graphitised layer is formed in the depth of implanted diamond and vacancies play the dominant role in its formation.

The depth of the layer determined from the analysis of the interference data does not change up to the annealing temperature 1460°C and decreases slightly with the increase of the dose: $1774 \pm 4 \text{ nm}$ for $6 \times 10^{16} \text{ cm}^{-2}$ and $1665 \pm 4 \text{ nm}$ for $12 \times 10^{16} \text{ cm}^{-2}$. These values are in satisfactory agreement with the data inferred from Fig. 1 though the discrepancy between the experiment and the theory is conspicuously worse than in the case of heavier ions.

In the annealing temperatures range 1460–1600°C, the layer increases in thickness but remains quite smooth. At 1660°C its optical density increases sharply and the interference disappears. In the microphoto of the sample it is seen that the graphitised layer is no longer smooth due to the growth in the “vertical” direction. At 1700°C the expanding graphitised layer reaches the surface of the sample. The graphitisation spreads also laterally from the boundary of the implanted areas into the undamaged part of the crystal. There are some points within this part where graphitisation starts without any stimulation by external agents.

Our results on D^+ implantation with doses $6\text{--}12 \times 10^{16} \text{ cm}^{-2}$ (as well as those for heavier ions with properly scaled doses) suggest that we deal with two different mechanisms of graphitisation: “low temperature” graphitisation starting at $\sim 800^\circ\text{C}$ and stimulated by vacancies and “high temperature” graphitisation in the range 1460–1700°C which is the combination of the process stimulated by the already (at lower temperatures) formed graphite phase and/or some residual defects and the spontaneous process dominating at 1660–1700°C without any evident external agents.

3.3. H^+ implantation

The results for H^+ implantation are quite different from those presented in 3.2 for D^+ . First of all, for the whole range of doses $2\text{--}12 \times 10^{16} \text{ cm}^{-2}$ no graphitization is observed after the annealing at 780°C , while vacancy related absorption disappears, just like in the case of D^+ implantation. Optical absorption due to residual radiation damage decreases with the increase of annealing temperature.

In samples implanted with H^+ doses 12, 10 and $8 \times 10^{16} \text{ cm}^{-2}$, starting from annealing temperatures 780°C , 1120°C and 1350°C , respectively, weak interference is observed. At the annealing temperatures above 1460°C the amplitude of the interference increases sharply indicating the formation of a graphitised layer. In this case we observe quite a peculiar kind of graphitisation accompanied by blistering, i. e. formation of bubbles filled with a gas (hydrogen). In Fig. 3 it is seen that the dark graphitised layer is broken into islands with dimensions $10\text{--}50 \mu\text{m}$ separated by light colored ungraphitised areas. The bubbles $\sim 100 \mu\text{m}$ in size are clearly seen. One of them (in the low right corner of the figure) is broken, its upper part has gone forming a pit with boundaries oriented along crystallographic axes. The phenomenon of blistering in diamond is similar to the one well known for silicon [7]. The implanted hydrogen atoms form relatively stable associations with radiation defects (passivation) immediately after implantation or at early stages of annealing. At the annealing temperatures higher than 1460°C these associations are broken providing both the lattice defects and free hydrogen atoms. The former stimulate the process of graphitisation while the latter can at these temperatures diffuse and form in the disordered layer (and only in this layer) the hydrogen filled bubbles of a

peculiar shape with lateral dimensions two order of magnitude larger than the thickness. Nonuniformity of the graphitised layer and the presence of the bubbles do not allow quantitative measurements of optical absorption. However the interference is quite strong and well resolved, this means that the graphite islands are all at the same depth, which can be accurately determined. This depth for H^+ implanted samples (1870 nm) is predictably higher than that for D^+ implantation (1770 nm) with the same ($\sim 15\%$) relative deviation from the data of theory.

4. Discussion

Among the results of the present work which need to be discussed is the difference in characteristics between the graphitisation processes induced by implantation of D^+ and H^+ . In the first case we observed the “low temperature” ($\sim 800^\circ\text{C}$) mode of graphitization which can be directly related to vacancies. On the other hand, in H^+ implanted samples this stage is absent, the graphitization is observed starting from the annealing temperature 1460°C and is accompanied by blistering.

Bearing in mind chemical identity of H and D (and consequently their ability to passivate lattice defects) it looks strange at first sight that there is no blistering in the case of D^+ implantation and no low temperature stage for H^+ implantation. The explanation might be in different amount of radiation damage produced by H^+ and D^+ (5 and 12 vacancies per ion, respectively, according to the Monte Carlo simulation data). With all the limitations of these estimates, with the lack of data referring to initial ($T < 800^\circ\text{C}$) stages of annealing (in particular, to the proportion of vacancies annihilated with interstitials) we might cautionary suggest that the passivation effect is more pronounced for H^+ implantation. In this case considerable fraction of radiation damage which survives the initial stage of annealing is passivated by hydrogen, so the amount of “unpassivated” damage is not enough to stimulate the “low temperature” graphitisation. The passivated component of radiation damage is “stored” up to the annealing temperature needed to break the associations of hydrogen atoms with defects (and to start both graphitisation and blistering). On the other hand, in D^+ implanted samples the passivated fraction of radiation damage is considerably lower, so the unpassivated damage (vacancies) can stimulate the “low temperature” graphitisation which represents a drastic change of the structure of the material, so it is now hardly pertinent to speak in terms of disruption (at higher temperatures) of what used to be associations of deuterium atoms with defects in diamond lattice. The absence of deuterium blistering in this case can be attributed both to its lower (compared to

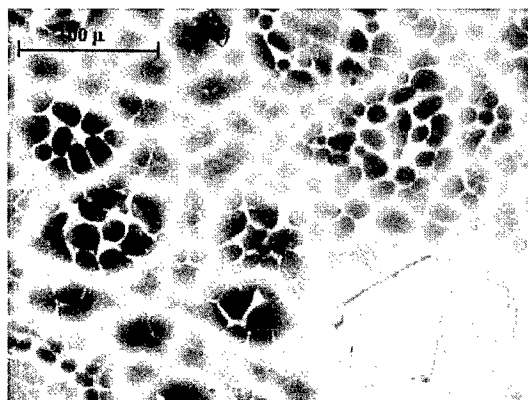


Fig. 3. Microphoto of island graphitization and blistering in the diamond sample implanted with $8 \times 10^{16} \text{ cm}^{-2}$ of H^+ and annealed at 1460°C .

hydrogen) diffusion coefficient in diamond and to its high solubility in graphite.

5. Conclusions

Our studies of graphitisation of diamond under various conditions of implantation and annealing have demonstrated that the process of graphitisation is more complicated than it was previously anticipated. Of particular interest are the “low temperature” graphitisation directly related to vacancies, the specific mechanism of graphitisation accompanied by blistering in H^+ implanted samples and high temperature graphitisation stimulated by residual radiation damage.

Acknowledgements

The authors gratefully acknowledge financial support by Russian Foundation for Basic Research (Project No.

01-02-16826). They are indebted to I. Vlasov who performed the microphotography of the samples.

References

- [1] M.S. Dresselhaus, R. Kalish, *Ion Implantation in Diamond, Graphite and Related Materials*, Springer, Berlin, 1992, p. 3.
- [2] J.F. Prins, T.E. Derry, *Nucl. Instr. and Meth. B* 166–167 (2000) 364.
- [3] A.A. Gippius, R.A. Khmelnskiy, V.A. Dravin, S.D. Tkachenko, *Diamond Relat. Mater.* 8 (1999) 1631.
- [4] G.B. Bokiy, G.N. Bezrukov, J.A. Kluev, A.M. Naletov, V.I. Nepsha, *Natural and Synthetic Diamonds*, Nauka, Moscow, 1986, p. 37.
- [5] A.N. Bekhterev, B.M. Zolotarev, *Opt.-Mekh. Promishlennost.* 12 (1986) 41.
- [6] J.M. Zhang, P.C. Eklund, *J. Mater. Res.* 2 (6) (1987) 860.
- [7] V.V. Kozlovskiy, V.A. Kozlov, V.N. Lomasov, *Fiz. Tekh. Poluprovodn.* 34 (2) (2000) 129.



ELSEVIER

Physica B 308–310 (2001) 577–580

PHYSICA B

www.elsevier.com/locate/physb

Modelling electron energy-loss spectra of dislocations in silicon and diamond

C.J. Fall^{a,*}, J.P.G. Goss^a, R. Jones^a, P.R. Briddon^b, A.T. Blumenau^{a,c},
T. Frauenheim^c

¹ School of Physics, University of Exeter, Exeter EX4 4QL, UK

² Department of Physics, University of Newcastle upon Tyne, Newcastle NE1 7RU, UK

³ Theoretische Physik, Universität Paderborn, D-33098 Paderborn, Germany

Abstract

Electron energy-loss spectroscopy (EELS) performed near dislocation cores is one of the few experimental techniques that can yield valuable information about the electronic levels associated with dislocations. In this study, using *ab initio* calculations, we model and predict low-loss and core-excitation EELS spectra acquired on various dislocation cores in silicon and diamond, and compare the results with bulk spectra. In diamond, we consider in particular 90° partial glide, undissociated 60° shuffle, and 30° partial dislocations. We find evidence of empty states localized on diamond shuffle dislocation cores and positioned below the bulk band edge, which modify the EELS spectrum. In silicon, we find changes—analogueous to those seen experimentally—in core-excitation EELS near stacking faults and partial glide dislocations. © 2001 Elsevier Science B.V. All rights reserved.

PACS: 71.55.-i; 78.20.Bh; 78.20.Ci

Keywords: Dislocation; EELS; Silicon; Diamond

The presence of dislocations in semiconductor crystals can strongly influence the electrical and optical properties of the material. The growth of polycrystalline CVD diamond, in particular, generates high densities of dislocations (up to 10^{12} cm^{-2}), which originate in the substrate-interface region and can propagate throughout the thin film [1]. The influence of these structural defects on the electrical and optical properties of the material is determined essentially by the nature of the atom bonding at the dislocation core. The atomic structure of dislocations, and their dissociation into partials, has been widely studied experimentally in silicon and diamond by transmission electron microscopy [2,3]. However, this technique does not yield any information about the electronic structure of the dislocation core. Spatially resolved electron energy-loss

spectroscopy (EELS) performed near dislocation cores can in principle yield valuable information about electronic levels associated with dislocations, both within and above the band gap. Recent EELS experiments performed near dislocations in Si [2] and diamond [4] have shown differences from bulk regions, but there are still issues regarding their interpretation. Such information could prove crucial to help resolve whether any electrical or optical activity is associated with undecorated dislocations. In this study, we perform first-principles simulations of a variety of dislocation cores, and, by means of a simple model, we identify extended defect structures that lead to changes in EELS spectra compared with the bulk regions.

We perform self-consistent *ab initio* simulations of dislocations in Si and diamond crystals within the local density approximation (LDA) to density functional theory, using the recently enhanced AIMPRO code [5]. The wave functions are expanded in a set of *s*, *p*, and *d* atom-centered Gaussian orbitals. We use

*Corresponding author Tel.: +44-1392-264-198; fax: +44-1392-264-111.

E-mail address: c.j.fall@exeter.ac.uk (C.J. Fall).

pseudopotentials to describe the ion cores [6]. A single dislocation is placed within a hydrogen-terminated nano-crystal in a supercell, thus imposing perfect periodicity along the [110] dislocation core. The supercells contain between 60 and 160 atoms, and are fully relaxed to their equilibrium positions. Initial relaxations of the dislocation cores are performed using the self-consistent charge density functional tight-binding method [7], with clusters of up to 500 atoms. The dislocation cores are then further optimized with AIMPRO to obtain accurate band structures.

Low-loss EELS results from electronic transitions between the valence bands (VB) and the conduction bands (CB). The signal obtained experimentally is usually interpreted as being representative of $-\text{Im } \epsilon(E)^{-1}$, where $\epsilon = \epsilon_1 + i\epsilon_2$ is the dielectric function and E is the energy loss. We calculate the imaginary part of the dielectric function in the dipole approximation [8,9]:

$$\epsilon_2(E) = \frac{4\pi e^2}{\Omega} \sum_{c,k} |\langle \Psi_k^c | r | \Psi_k^v \rangle|^2 \delta(E_k^c - E_k^v - E), \quad (1)$$

where Ω is the unit cell volume, and $|\Psi_k^{v,c}\rangle$ are VB and CB states, with energies $E_k^{v,c}$, respectively. The real part of the dielectric function is obtained through a Kramers–Kronig (KK) transformation.

Core-excitation EELS results from electronic transitions between deep core states and the CB. In view of the localization of the initial state on an atom, core EELS spectra are related to an angular momentum projected local density of states on the atom. If the initial core state $|\Psi_k^i\rangle$ is s-like (as for the diamond K-edge), the core EELS spectrum from an atom at \mathbf{R} is proportional to a p -projected local density of states at \mathbf{R} , written symbolically as

$$I_R(E) = \sum_{c,k} |\langle \Psi_k^c | p_R \rangle|^2 \delta(E_k^c - E_i - E), \quad (2)$$

where $E_i = E_a + \Delta V(\mathbf{R})$. E_i (E_a) is the core level for the solid (for the atom, respectively). To first-order perturbation, $\Delta V(\mathbf{R})$ is the difference in potential at the atomic core between the bulk and the atom. In Si, we find $\Delta V(\mathbf{R})$ varies by ± 0.15 eV near the dislocation, and, as a first approximation, we neglect it in the following. This level of theory makes no account of final state effects, which should in principle include interactions between the excited electron and the hole. However, as we show below, it allows a qualitative understanding of EELS spectra, and permits comparisons between bulk and defect regions to be made. The scissor operator is used to adjust calculated LDA band gaps to experimental ones. The Brillouin zone (BZ) integrations are performed using 1000–5300 k -points for bulk, and 50–150 k -points for supercells. Core EELS spectra are displayed with a Gaussian broadening of 0.4 eV for Si, and 0.8 eV for diamond. Low-loss EELS spectra are broadened

using a Lorentzian function, which conveniently allows an analytical KK transformation.

We start by considering the core-excitation EELS spectrum of bulk diamond, shown in Fig. 1, where we compare it with two experimental observations. Qualitative agreement between the computed and measured values is obtained and the peak positions are well described. Oscillations in the theoretical spectrum at high energies are calculational artifacts that result from convergence difficulties with the BZ integrations. Absorption seen experimentally below the band gap may be attributed primarily to surface effects, particularly for the experimental data acquired on diamond nano-crystals [11].

In Si and diamond, 60° glide dislocations dissociate into 30° and 90° partial dislocations [10,3]. These partial dislocations are believed to have reconstructed cores consisting entirely of four-fold co-ordinated atoms. In diamond, we have studied the low-loss and core-excitation EELS spectra of the undissociated 60° glide, as well as the 30° and 90° partial glide dislocations. A typical result for glide dislocations is shown in Fig. 2A, where we consider the lowest-energy form of the 90° partial, which possesses a double-period reconstruction along its core [10]. We find no evidence of gap states associated with the undecorated glide dislocations, and only small changes in the corresponding EELS spectra compared with bulk.

In diamond-structured semiconductors, the (111) planes of atoms are alternately separated by long and

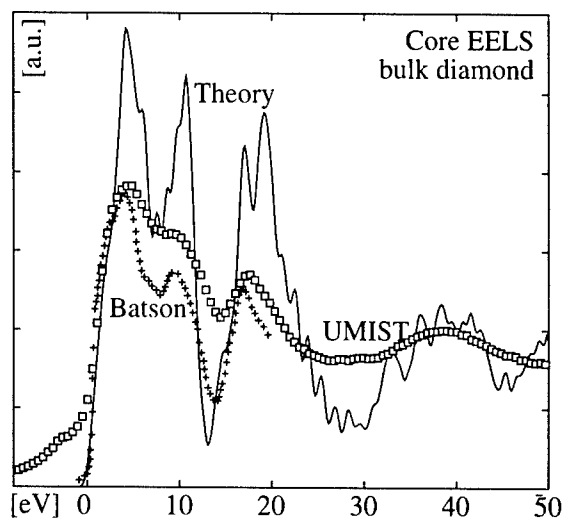


Fig. 1. Theoretical K-edge EELS spectrum of bulk diamond (solid line), compared with experimental data on type-IIb diamond from Bruley and Batson [4] (crosses) and on diamond nano-crystals from Gutiérrez-Sosa, et al. at UMIST [11] (squares). The results are given in arbitrary units, and the energy zero is set at the conduction band minimum (CBM), where the curves have been aligned.

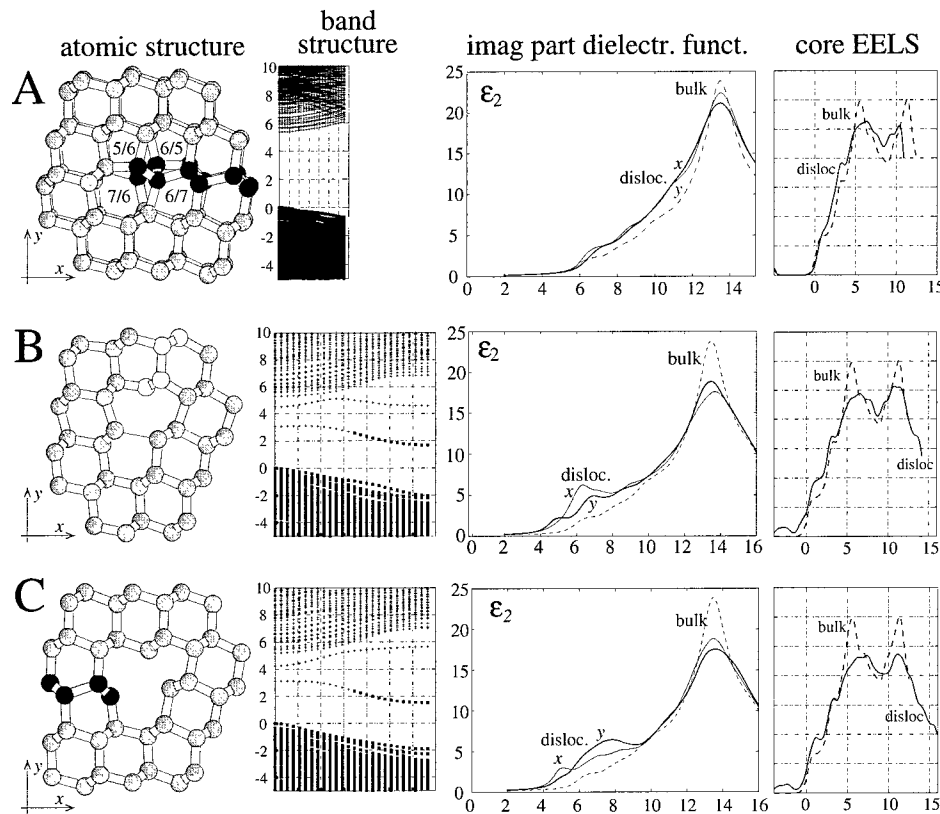


Fig. 2. Atomic structure, band structure along the dislocation core in the gap region, imaginary part of the dielectric function, and predicted K-edge EELS spectrum for a 90° glide partial dislocation with a double-period reconstruction (panel A), a 60° shuffle dislocation (panel B), and a 30° partial dislocation with an open core (panel C) in diamond. Lighter (darker) atoms indicate the stacking faults (inserted atoms, respectively). In view of the double-period reconstruction, the BZ of structure A is folded to half the thickness of those of structures B and C. In the band structures, squares indicate filled states and crosses indicate empty states of a neutral dislocation. The dielectric function is shown for incident beams polarized in the $[1\bar{1}\bar{2}]x$ (thin line) and $[1\bar{1}1]y$ (thick line) directions orthogonal to the dislocation axis. For core-excitation EELS spectra, the energy zero is set at the CBM. Energy scales are given in eV.

short distances. Shuffle dislocations differ from glide dislocations in that the removed half-plane of atoms terminates after a short, rather than a long, inter-plane separation. We have studied the undissociated 60° shuffle dislocation in diamond, shown in Fig. 2B, and its dissociation into 30° and 90° partials. Since shuffle dislocations can be obtained from glide dislocations by inserting (or equivalently removing) an extra row of atoms, several core structures of the dissociated shuffle dislocation are possible. One of these is shown in Fig. 2C, and corresponds to a 30° partial with an open core. This core structure could be obtained, for example, by the dissociation of Fig. 2B into Figs. 2A and C.

For diamond shuffle dislocations (Fig. 2B) and open-core partial dislocations (Fig. 2C), we find evidence of empty states localized on the dislocation cores below the conduction band edge. If core-excitation EELS is

performed on these dislocations, the empty gap states create supplementary absorption peaks below the conduction band minimum (CBM), which could account for the EELS experimental evidence [4]. Strong differences in the imaginary part of the dielectric function for the structures in Figs. 2B and C, compared with bulk regions, also lead to changes in the predicted low-loss EELS.

Turning to Si, we show in Fig. 3 the predicted EELS spectra acquired at an intrinsic stacking fault, at a 30° glide partial dislocation, and at a 90° glide partial dislocation with a double-period reconstruction. None of these defects possess deep gap levels. Experimental results of this kind have been obtained recently [2]. We note that there is a small predicted increase in the EELS spectrum around 0.5 eV above the CBM for the 90° partial, as also evidenced experimentally. The number

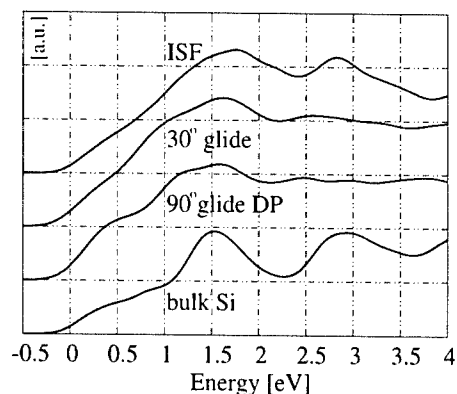


Fig. 3. Theoretical core-excitation EELS spectra for bulk, a 90° glide partial with a double-period (DP) reconstruction, a 30° glide partial, and an intrinsic stacking fault (ISF). These spectra are determined by averaging over core excitations calculated for several atoms bordering the defects. The energy zero is set at the CBM in each case.

and the positions of the first few peaks in the EELS spectra differ from one structure to the other, as also seen in the experiment. In view of the simple theoretical model used here, these results should be taken as a qualitative guide to the experimental observations.

In summary, we find that changes in the densities of empty states at shuffle dislocations create strong differences in both low-loss and core-excitation EELS of diamond. Reconstructed glide dislocations in dia-

mond, however, create only small differences in the EELS signal on and off the core. In silicon, similar small differences in core EELS are found near partial dislocations. Future developments of the theory, which are underway, will include accounting for the electron-hole interactions in core EELS.

The authors would like to thank A.Gutiérrez-Sosa, A.J. Harvey, and U. Bangert, for stimulating discussions and for providing experimental data on diamond.

References

- [1] J.E. Graebner, et al., *Phys. Rev. B* 50 (1994) 3702.
- [2] P.E. Batson, *Phys. Rev. Lett.* 83 (1999) 4409.
- [3] P. Pirouz, et al., *Proc. Roy. Soc. London A* 386 (1983) 241.
- [4] J. Bruley, P.E. Batson, *Phys. Rev. B* 40 (1989) 9888.
- [5] P.R. Briddon, R. Jones, *Phys. Stat. Sol. B* 217 (2000) 131.
- [6] G.B. Bachelet, D.R. Hamann, M. Schlüter, *Phys. Rev. B* 26 (1982) 4199.
- [7] M. Elstner, et al., *Phys. Rev. B* 58 (1998) 7260.
- [8] G.F. Bassani, G. Pastori Parravicini, in: R.A. Ballinger (Ed.), *Electronic States and Optical Transitions in Solids*, International Series of Monographs in the Science of the Solid State, Vol. 8, Pergamon Press, Oxford, 1975.
- [9] A.J. Read, R.J. Needs, *Phys. Rev. B* 44 (1991) 13071.
- [10] R.W. Nunes, J. Bennetto, D. Vanderbilt, *Phys. Rev. B* 58 (1998) 12563.
- [11] A. Gutiérrez-Sosa, U. Bangert, A.J. Harvey, private communication (unpublished).



ELSEVIER

Physica B 308–310 (2001) 581–584

PHYSICA B

www.elsevier.com/locate/physb

The variation of optical absorption of CVD diamond as a function of temperature

Clara Piccirillo^{a,*}, Gordon Davies^a, Alison Mainwood^a, C.M. Penchina^{a,b}

^a *Physics Department, King's College London, Strand, London WC2R 2LS, UK*

^b *Department of Physics, University of Massachusetts, Amherst, MA 01003-4525, USA*

Abstract

The infrared absorption of CVD diamond films is reported as a function of temperature in both intrinsic and boron-doped samples. In pure diamond, because of the inversion symmetry of the lattice, there is no one-phonon IR absorption, but there are bands corresponding to the interaction of the photon with two or more phonons. We fit the measured temperature dependence of the absorption by including the Bose–Einstein factors for the two phonons involved at each energy.

The infrared absorption of boron was measured in the range 500–5000 cm⁻¹ between 14 and 630 K. We show that the temperature dependence of the absorption can be understood in terms of thermal ionisation and thermal transitions between electronic states. © 2001 Elsevier Science B.V. All rights reserved.

Keywords: Diamond; Boron; Infrared absorption; Phonons

1. Introduction

Pure diamond has negligible absorption for photons with energies below the band gap at 5.47 eV except for the region in the infrared between 1500 and 4000 cm⁻¹ (0.18–0.5 eV) at low temperatures. Absorption of a photon to produce a single phonon is forbidden by symmetry, but the creation of two or more phonons gives a weak absorption. This has been studied to try to determine the energies of the phonons at high symmetry points in the Brillouin zone [1–4]. In this paper we interpret the temperature dependence of the absorption in terms of the phonons which contribute.

If the symmetry of the lattice is broken by the addition of impurities or dopants, then some one-phonon absorption is allowed. This is well known for nitrogen, where the one-phonon absorption is used to determine the concentration of the nitrogen and its complexes [5]. For the only effective-mass-like acceptor, boron, an infrared spectrum in the range 500–5000 cm⁻¹ (0.06–0.62 eV) is observed. This spectrum consists not only of

a one-phonon peak, but also of absorption due to electronic excitations between bound states of the boron, ionisation of the boron and transitions of holes between valence band states [6–8], all of which vary strongly with temperature.

2. Experimental details

Absorption measurements were made using a Perkin Elmer 1720 Fourier transform spectrometer. The sample was mounted in an Oxford Instruments flow cryostat for measurements down to 14 K. Measurements up to 620 K were made in a custom made cell fitted with a resistive coil heater that was in contact with the copper sample holder. A heat shield reduced the emission from the hot sample stage that could be radiated to the detector. The samples were CVD diamond plates of at least 8 mm square, to decrease the effect of emission from the sample mount.

Surveys of the boron-containing samples were made at room temperature using a Nicolet FTIR coupled to a microscope stage. No inhomogeneities were detected in the spectra recorded through 25 μm square apertures, on

*Corresponding author. Fax: +44-207-848-2420.

E-mail address: clara.piccirillo@kcl.ac.uk (C. Piccirillo).

a much smaller scale than the 3 mm diameter focus used for the temperature-dependent measurements. The samples were chosen so that the boron concentrations, determined by the calibration of Collins and Williams [9] from the absorption in the 2800 cm^{-1} absorption line, varied from $6.8 \pm 0.3 \times 10^{16}$ to $3.2 \pm 0.2 \times 10^{18}\text{ cm}^{-3}$. A pure sample of CVD diamond was used as a reference sample to remove the intrinsic absorption from the spectra.

3. Intrinsic absorption

Fig. 1 shows the intrinsic absorption at room temperature. The peaks identified in Ref. [4] are indicated. The two-phonon absorption in the range ~ 1400 – 2665 cm^{-1} sits on top of a very weak 3-phonon absorption, which has been removed in the analysis.

In order to conserve energy, the sum of the energies of the two phonons involved must equal the energy of the photon. To conserve momentum, the wave vectors of the two phonons must be equal and opposite, since the wave vector of a photon is negligible compared to that of the phonons. Two identical phonons cannot be created by a photon because that implies the creation of an electrical dipole, so two different branches of the phonon dispersion curves are required. The phonon dispersion curves for diamond (for example [10]) indicate that the energies at which one would expect high intensities are at the zone boundaries where there are large regions of k -space with phonons of near constant energy. In particular the zone boundaries at X, W, L and K show levelling out of at least some of the

phonon branches [10]. As examples of this, Vogelgesang et al. [4] have identified the prominent peaks labelled 9, 12 and 14 on Fig. 1 with transitions involving phonons at Σ along (110) branches, very close to K, and rather smaller features labelled 8 and 15 with the X and W points.

At higher temperatures the number of phonons created with energy E , varies as $(1 + n(E))$, where $n(E)$ is a Bose-Einstein factor. Hence, for any pair of phonons of energy E_1 and E_2 created by a photon of energy $(E_1 + E_2)$, the intensity of the absorption is proportional to [1]

$$(1 + n(E_1))(1 + n(E_2)). \quad (1)$$

Fig. 2 shows the absorption spectra at temperatures up to 598 K, showing a substantial increase in absorption at higher temperatures.

Using the identification of the phonons listed by Vogelgesang et al. [4], we have calculated the temperature dependence of the main features of the spectrum. Fig. 3 shows that several of the peaks, such as 3, 14 and 19, agree very well with experiment, but others, for example peaks 8, 9, and 12, do not. It is possible that the phonon branches involved in the absorption have been misidentified—for example reassigning the lower energy phonon involved in peaks 9 and 12 to $\Sigma^{(4)}(A)$ rather than $\Sigma^{(3)}(A)$ fits the temperature dependence satisfactorily.

4. Boron one-phonon absorption

The one-phonon absorption due to boron overlaps the intrinsic two and three phonon bands discussed above. Therefore, we have subtracted the intrinsic

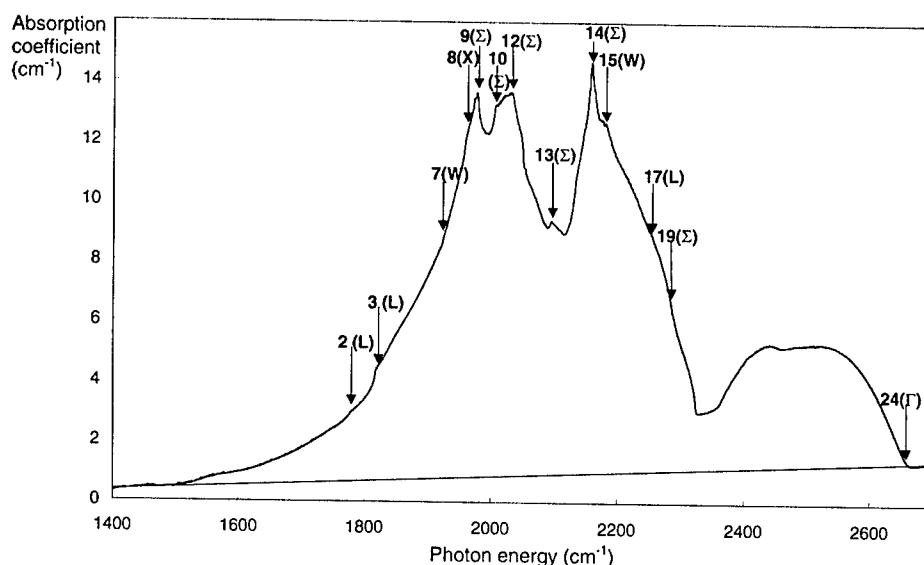


Fig. 1. Intrinsic absorption of diamond at room temperature in the two-phonon region. The peaks are labelled as in Ref. [4] and with the high symmetry points with which the relevant phonons are associated, as described in the text.

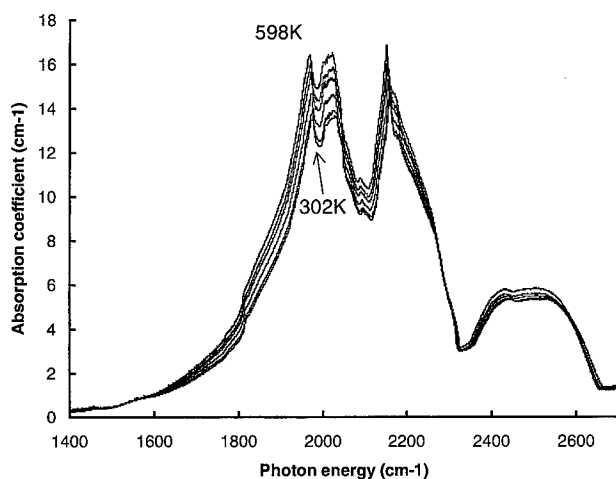


Fig. 2. The infrared absorption at temperatures of 302, 351, 448, 515, 556 and 598 K, showing the monotonic increase in absorption as the temperature rises.

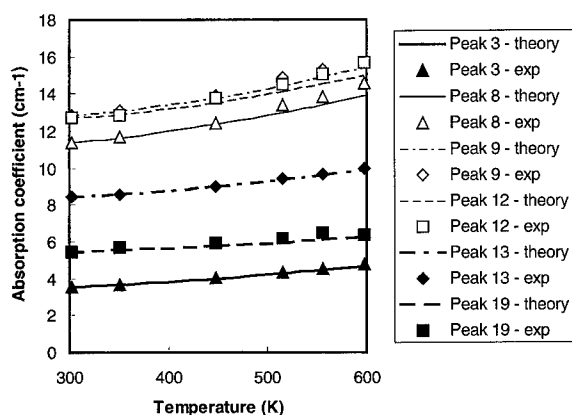


Fig. 3. The variation as a function of temperature of some of the peaks identified in Fig. 1. The lines show the theoretical fit (Eq. (1)) using the phonon energies listed in Ref. [4].

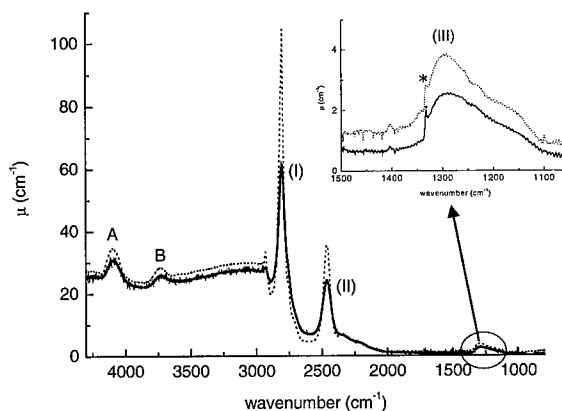


Fig. 4. The infrared absorption at 27 K (broken line) and 300 K (continuous line) in boron-doped diamond. The intrinsic absorption has been subtracted. The labelled features are explained in the text.

absorption spectrum recorded at the same temperature from each spectrum of the boron-containing samples. Spectra were acquired in the temperature range 14–620 K. Fig. 4 shows the infrared spectrum of one sample at room temperature compared with the spectrum at 27 K. The two peaks labelled I and II correspond to electronic transitions at the boron acceptor and the third peak (labelled III on Fig. 4) to the creation of a single phonon (allowed by the presence of the boron). Also noticeable is the increase of background absorption above about 3000 cm^{-1} due to ionisation of the boron and at lower energies due to the transitions of holes already in the valence band between valence band states. A Fano resonance at the Raman energy (1332.5 cm^{-1}) is marked in the inset in Fig. 4 by an asterisk.

In order to compare the data from the four samples, in Fig. 5a–c, the integrated areas under the three peaks I,

II and III, respectively, have been normalised by dividing by the integrated area extrapolated to zero temperature. Fig. 5a–c shows the variation with temperature for the three peaks. Each shows a decrease in absorption, A, at higher temperatures due, we can assume, to thermally induced effects, and can be fitted by the function:

$$A = \frac{1}{1 + b_1 \exp(-\Delta E_1/kT) + b_2 \exp(-\Delta E_2/kT)} \quad (2)$$

for peaks I and III, where k is Boltzmann's constant, and b_1 and b_2 are degeneracy parameters. The two activation energies are: $\Delta E_1 = 65 \pm 7\text{ meV}$ ($524 \pm 56\text{ cm}^{-1}$), $\Delta E_2 = 384 \pm 80\text{ meV}$ ($3100 \pm 40\text{ cm}^{-1}$) for peak I (Fig. 5a). For the one-phonon transition—peak III (Fig. 5c) the energy values were: $\Delta E_1 = 69 \pm 10\text{ meV}$ ($556 \pm 80\text{ cm}^{-1}$), $\Delta E_2 = 218 \pm 45\text{ meV}$ ($1760 \pm 360\text{ cm}^{-1}$).

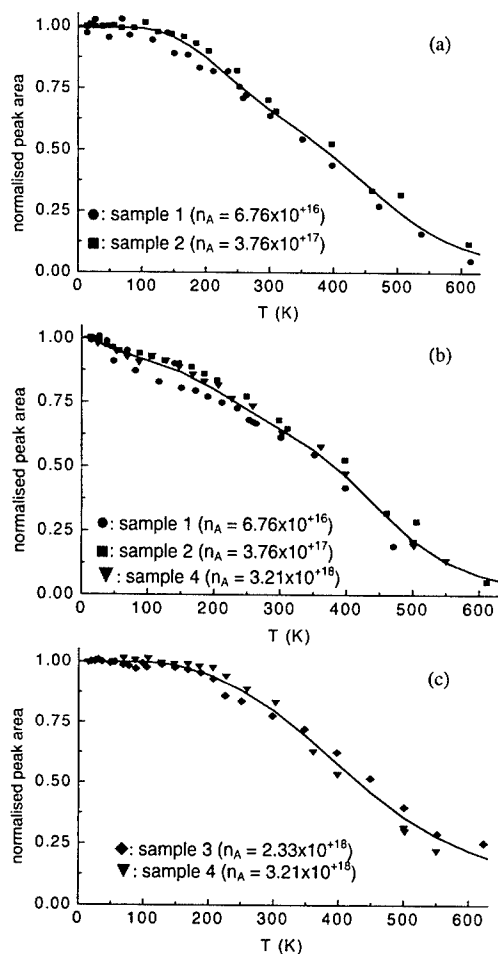


Fig. 5. The temperature dependence of the normalised integrated areas under the three peaks labelled (a) I, (b) II and (c) III in Fig. 4. The lines show the fit using Eqs. (2), (3) and (2), respectively.

For peak II (Fig. 5b), an additional transition at very low temperatures was evident and a third exponential was necessary to fit the data

$$A = \frac{1}{1 + b_1 \exp(-\Delta E_1/kT) + b_2 \exp(-\Delta E_2/kT) + b_3 \exp(-\Delta E_3/kT)} \quad (3)$$

The energies of the three processes were: $\Delta E_1 = 5 \pm 2$ meV (40 ± 16 cm⁻¹), $\Delta E_2 = 61 \pm 12$ meV (490 ± 100 cm⁻¹), $\Delta E_3 = 370 \pm 78$ meV (2980 ± 320 cm⁻¹).

The activation energies near 380 meV (3100 cm⁻¹) correspond to the ionisation of the acceptor, and the low energy one at ~ 5 meV (40 cm⁻¹) is probably the spin orbit splitting observed by Kim et al. [11]. The energies near 65 meV (520 cm⁻¹) have not been reported previously.

Phonon-assisted processes have been observed in B-doped diamond [12]. Strong infrared absorption peaks

at 506 ($347 + 159$) and 464 ($305 + 159$) meV, indicated the internal transition of the hole to excited states with the emission of one phonon of a typical optic phonon energy of 159 meV (1282 cm⁻¹)—they are marked with A and B, respectively, in Fig. 4. In the case of peak (III), the ionisation of the boron takes place with the absorption of one phonon—it can be seen that

$$\Delta E_{\text{ionis}} - \Delta E_{\text{phon}} = 380 - 159 = 221 \text{ meV} (1782 \text{ cm}^{-1})$$

This result is in agreement with the energy ΔE_2 for peak III.

5. Conclusions

The temperature dependence of the infrared absorption in intrinsic and boron-doped diamond has been studied in order to investigate the detailed processes involved. For pure diamond, the temperature dependence of the peaks in the two phonon band can be understood in terms of the phonons at high symmetry points in the Brillouin zone. In boron-doped diamond, the absorption peaks are due to internal electronic transitions and one-phonon excitations.

Acknowledgements

We thank De Beers Industrial Diamond Division (UK) and the Naval Research Laboratory, Washington, USA for the loan of samples. This project was supported by the EU RTN project: HPRN-CT-1999-00139.

References

- [1] G. Dolling, R.A. Cowley, Proc. Phys. Soc. London 88 (1966) 463.
- [2] J.L. Birman, Phys. Rev. 127 (1962) 1093.
- [3] J.L. Birman, Phys. Rev. 131 (1963) 1489.
- [4] R. Vogelgesang, et al., Phys. Rev. B 58 (1998) 5408.
- [5] G.S. Woods, in: G. Davies (Ed.), Properties and growth of diamond, INSPEC, IEE, London, 1994, p. 101.
- [6] A.T. Collins, Philos. Trans. R. Soc. London A 342 (1993) 233.
- [7] E. Gheeraert, et al., Phys. Stat. Sol. A 174 (1999) 39.
- [8] E. Gheeraert, A. Deneuville, J. Mambou, Diam. Relat. Mater. 7 (1998) 1509.
- [9] A.T. Collins, A.W.S. Williams, J. Phys. C4 (1971) 1789.
- [10] A.K. Ramdas, in: M.H. Nazare, A.J. Neves (Eds.), Properties, growth and applications of Diamond, INSPEC IEE, London, 2001, p. 3.
- [11] H. Kim, et al., Phys. Rev. B 57 (1998) 15315.
- [12] S.D. Smith, W. Taylor, Proc. Phys. Soc. London 79 (1962) 1142.



ELSEVIER

Physica B 308–310 (2001) 585–588

PHYSICA B

www.elsevier.com/locate/physb

Photoelectrical properties of the 1.682-eV and 3 H centres in diamond

Konstantin Iakoubovskii*, André Stesmans

Laboratorium Voor Halfgeleiderfysica, Semiconductor Physics Laboratory, Katholieke Universiteit Leuven, Celestijnenlaan 200 D, 3001 Heverlee-Leuven, Belgium

Abstract

A narrow (few meV halfwidth) dip was observed at 1.682 eV in the photocurrent (PC) spectra from diamond films grown by chemical vapour deposition (CVD). The shape of the dip matched that of the absorption line from the well-known 1.682 eV Si-related centre. However, optical absorption measurements show that it cannot be explained by straight absorption of light at the 1.682 eV centre. A similar appearance of narrow peaks was observed in PC and absorption spectra for the interstitial-related 3 H centre in this work and for the vacancy-related GR1-8 and ND1 lines previously. The phenomenon can be explained by suggesting involvement of electron transfer process: e.g., electrons from the excited states of a given centre are captured by the defects responsible for the background PC, thus PC-(in)activating the latter. © 2001 Elsevier Science B.V. All rights reserved.

Keywords: CVD diamond; Absorption; Photoconductivity; Vacancies

1. Introduction

Most diamond films grown by chemical vapour deposition (CVD) show an optical signal at 1.682 eV. It has been thoroughly characterised by optical absorption and luminescence techniques [1,2]. The results suggest it to correspond to a defect centre that has a C_2 symmetry axis and contains a Si atom and a vacancy. In samples grown on Si substrates, most of the 1.682 eV centres are concentrated within a 1- μ m-thick surface layer at the substrate side of the CVD film. The intensity of the 1.682 eV optical absorption peak can be enhanced up to 10 times by UV illumination, and the photo-induced changes decay on a time-scale of hours. Some photocurrent (PC) spectra from CVD diamond show a dip at 1.682 eV too, whose shape resembles the 1.682 eV absorption line. This observation was interpreted as self-absorption of incident light by the 1.682 eV centres [1,3].

In this report we demonstrate that self-absorption cannot explain the strength of the 1.682 eV PC dip. Alternatively, a simple model is proposed, which considers an electron transfer from the excited states of the 1.682 eV centres to the defects responsible for the background PC. It is suggested that this model can provide a natural explanation of the narrow lines observed in PC spectra of irradiated diamonds.

2. Experimental details

Polycrystalline diamond films with random orientation of the grains have been grown by microwave-assisted CVD on Si substrates [1]. The substrates were removed by acid etching. Thermally evaporated gold was used for electrical contacts. Preliminary experiments showed that this resulted in a low-resistive Ohmic contact at the rough growth side of the films and a highly resistive contact at the smooth substrate side. Therefore, two contacts were evaporated on the rough side of a 50- μ m-thick film, forming a gap-cell

*Corresponding author. Tel.: +32-16-327705; fax: +32-16-327987.

E-mail address: kostya.iak@fys.kuleuven.ac.be (K. Iakoubovskii).

configuration with contact spacing of 1 mm and contact width of 2 mm, being equal to the sample width. Wires were attached to the contacts using silver paint, which also masked all the film area, except for the $1 \times 2 \text{ mm}^2$ gap between the contacts. The sample was mounted on top of a $2 \times 2 \text{ mm}^2$ flat Si diode and illuminated by light from a 50 W halogen lamp passed through a monochromator. No narrow spectral features were found in the spectrum of the illumination source. In this arrangement, transmittance and PC spectra were simultaneously measured from the same sample area. For UV illumination, light from a pulsed N_2 laser, providing 100- μJ 3-ns pulses at 3.678 eV with a frequency of 35 Hz, was directed at the sample for 10 min. A DC voltage of 140 V was applied to the contacts. Applied voltage had no effect on the absorption spectra.

Some of the studied CVD samples have been irradiated by a dose of $10^{18} \text{ MeV neutrons/cm}^2$ at the Research reactor of the Moscow Engineering Physics Institute.

3. Results

Fig. 1 presents the room-temperature transmittance and PC spectra observed in the 1.62–1.74 eV range from an as-grown CVD film before and right after UV illumination. More extended spectra have been presented and analysed previously [1]. The background PC is a quasi-plateau, following a broadened threshold at $\sim 0.8 \text{ eV}$. The threshold is probably due to electron transitions from the valence band to a distribution of levels centred around $E_v + 0.8 \text{ eV}$, attributed to dangling bond related defects. The 1.682 eV dip is present both in transmittance and PC spectra, being less intense in the former. UV illumination induced the following

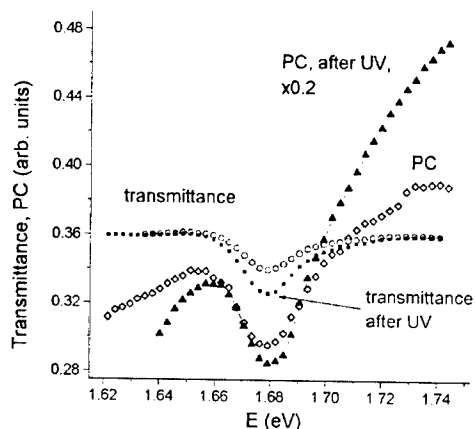


Fig. 1. Transmittance and photocurrent spectra (300 K) from as-grown CVD diamond film before and after UV irradiation.

changes: The amplitude of the transmittance dip increased 1.7 times. The background PC increased about 5 times, with an apparent change in slope. However, the relative intensity of the 1.682 eV dip in the PC spectrum remained constant within 20%.

Fig. 2 shows room-temperature transmittance and PC spectra in the 2.35–2.55 eV range from a neutron-irradiated CVD film. A dip at 2.463 eV, attributed to an interstitial-related 3H centre, is present in both spectra, being more pronounced in PC as was the case for the 1.682 eV dip in Fig. 1. The background PC originates from a threshold at $\sim 1 \text{ eV}$. Previous PC and photo-Hall studies of irradiated diamonds [4–6] reported detection of the narrow vacancy-related features ND1 and GR1, GR2... GR8 both in absorption and PC spectra, measured at 8 or 80 K. In the PC spectra the GR1 line with associated vibronic sideband was observed as dips, but the ND1 and GR2-8 systems were present as peaks. Attempts to reproduce those PC results in this work failed because of a strong decrease in PC signals when cooling the sample. Meanwhile, those peaks could not be resolved at room temperature.

No changes could be induced by UV illumination in the spectra of Fig. 2, however, the following observation has been made: The sample used for the Fig. 2 was subjected to isochronal (1 h) annealing at different temperatures in the range 200–1100°C. Annealing in the range 500–1000°C resulted in the apparent removal of the 3H absorption. However, it could be restored by the mentioned UV illumination. After annealing at $T = 1100^\circ\text{C}$ the 3H centre could not be seen either with or without UV illumination. This observation along with our previous results [7] shows that the interstitial-related 3H centre is stable up to the temperature of 1000°C, but not 400°C, as widely believed.

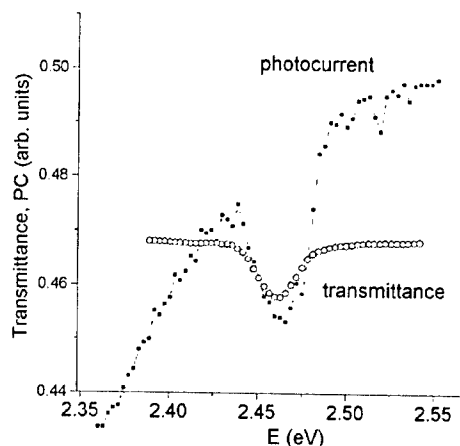


Fig. 2. Transmittance and photocurrent spectra (300 K) from neutron-irradiated CVD diamond film.

4. Discussion

The differences in the intensity of the 1.682 eV dip in the transmittance and PC spectra of Fig. 1 exclude self-absorption of light as the reason of the PC dip. The 1.682 eV transmittance line corresponds to *internal* resonant excitation of a Si-related centre. In order to explain the effect of such process on PC the following charge-transfer model is proposed. It assumes that electrons from the excited states of the 1.682 eV centres can be transferred to defects, termed X, responsible for the broadband background PC. Transfer of excitation between different defects is rather common for diamond [2,8]. The $E_V + 0.8$ eV levels of the X defects become populated and do not contribute anymore to PC, at least at energies below 4 eV. As a result, PC is selectively quenched at the energy of the 1.682 eV absorption line. By changing the relative concentrations and occupancies of the 1.682-eV and X centres it is possible to alter the relative intensities of the 1.682 eV dips in transmittance and PC spectra in a wide amplitude range. UV illumination could induce all those processes, but at non-equal rates, thus affecting differently the transmittance and PC spectra of Fig. 1.

The charge-transfer model can be directly transferred from the 1.682-eV to the 3H centre: Previous photo-Hall measurements reveal that the background PC from irradiated diamond in the 1–3 eV range corresponds to electron transitions from the valence band to a $E_V + 1$ eV level [5,6]. As in the case of the 1.682 eV centre, electron transfer from the excited state of the 3H centre to the $E_V + 1$ eV level can naturally explain resonant PC decrease at 2.463 eV (Fig. 2).

It is possible that the defects, responsible for the $E_V + 1$ eV level in irradiated diamond and for the $E_V + 0.8$ eV level in as-grown CVD films, have a common dangling bond related origin.

The charge-transfer model can also be applied to narrow peaks in PC from irradiated diamonds, attributed to the ND1 and GR1-8 absorption lines. The GR1-8 absorption peaks were unambiguously identified as due to the transitions from a common ground state to a series of excited states at neutral vacancy (V^0) in diamond, while the ND1 line is assigned to the internal excitation of V^- [9]. Photo-Hall measurements reveal that the GR2-8 and ND1 PC peaks correspond to p-type and n-type conductivity, respectively [5,9]. The sharpness of the features suggests that none of the corresponding defect levels situate within the valence or conduction band of diamond. Meanwhile, low temperature of those measurements (8–80 K) should have suppressed photothermal ionisation processes.

Currently tolerated explanations for the ND1 and GR2-8 PC peaks imply the following: The GR2-8 lines are attributed to a complex multi-electron excitation at V^0 (see [10,11] for details), which, along with the internal

excitation of V^0 , produces a hole in the valence band of diamond. For ND1 it is proposed that the excited state of V^- ($[V^-]^*$) is situated at the bottom of the conduction band, and the electronic states of the conduction band and of $[V^-]^*$ are orthogonal and thus are not mixed. Consequently, the ND1 line is sharp and electron transfer from $[V^-]^*$ to the conduction band is possible [12].

Both models are rather complex and require many assumptions about the microscopic properties of the vacancy in diamond. Here we would like to point to simpler alternatives:

PC dips at 1.673 eV (GR1) and 1.682 eV are both superimposed on a threshold originating from $E_V \rightarrow E_V + (\sim 1 \text{ eV})$ transitions, and consequently may be explained by the same charge-transfer mechanism, described in the first paragraph of the Discussion. Alternatively, the 1.673 eV PC dip can be caused by straight light absorption at the GR1 centre. The charge-transfer model can also apply to the n-type ND1 PC peak: Let us assume that there is an efficient electron transfer between the excited state of V^- and a defect Y, responsible for background n-type PC in the spectral range of ND1 absorption. Internal excitation of V^- will then produce more occupied Y centres, thus increasing the (n-type) PC in the spectral range of the ND1 absorption.

Apparently, the charge-transfer model does not apply to the GR2-8 lines, where PC *peaks* are observed for *p-type* conductivity. However, it is worth noting that PC is a function not only of carrier generation, but also of recombination rate. The latter can be strongly reduced by shallow traps that should be considered when interpreting the PC spectra. For example, it is easy to picture a mechanism, increasing the concentration of effective hole traps via electron transfer from the excited states of V^0 to some other defect. Such process would lead to increase in PC at energies of the GR2-8 absorption. A positive vacancy, produced upon electron removal from V^0 may even be considered as a candidate for such shallow trap. In our opinion, such mechanism can explain the GR2-8 PC peaks in a much easier way than the multi-electron excitation model [10,11].

5. Conclusion

A narrow-line structure, attributed to internal excitation of a deep centre, can be observed in photocurrent (PC) spectra and this is not a rare phenomenon in diamond. Straight absorption of incident light cannot account for the strength of the photocurrent features in many cases, in particular, for the 1.682 eV and 3H centres in diamond, considered in the present work. However, those features can be naturally explained by a model based on electron transfer from an excited state of

a deep centre to a defect responsible for the broad background PC band. This model can be applied to the unusual PC features associated with electron excitation of the negative and neutral vacancies in diamond. However, we would like to stress that the goal of the present paper is not to claim an unambiguous explanation of the vacancy-related narrow-line PC structure in diamond, but to draw attention to simple electron transfer mechanisms which may provide alternative to the existing quantum mechanical models.

Acknowledgements

Provision of CVD samples by M. Nesladek is gratefully acknowledged. Authors are indebted to N.N. Dogadkin for reactor irradiation and to the Belgian FWO for financial support.

References

- [1] K. Iakoubovskii, G.J. Adriaenssens, *Diamond Relat. Mater.* 9 (2000) 1349.
- [2] K. Iakoubovskii, G.J. Adriaenssens, N.N. Dogadkin, A.A. Shiryaev, *Diamond Relat. Mater.* 10 (2001) 18, and references therein.
- [3] L. Allers, A.T. Collins, *J. Appl. Phys.* 77 (1995) 3879.
- [4] R.G. Farrer, L.A. Vermeulen, *J. Phys. C* 5 (1972) 2762.
- [5] C.D. Clark, B.J. Parson, L.A. Vermeulen, *J. Phys. C* 12 (1979) 2597 and references therein.
- [6] L.A. Vermeulen, A. Halperin, *J. Phys. Chem. Solids* 42 (1981) 115.
- [7] K. Iakoubovskii, G.J. Adriaenssens, *Phys. Status Solidi (a)* 181 (2000) 59.
- [8] K. Iakoubovskii, G.J. Adriaenssens, *Phys. Rev. B* 61 (2000) 10174.
- [9] A. Mainwood, A.M. Stoneham, *J. Phys.: Condens. Matter* 9 (1997) 2453, and references therein.
- [10] A.M. Stoneham, *Mater. Sci. Eng. B* 11 (1992) 211.
- [11] A. Mainwood, A.M. Stoneham, *Mater. Sci. Eng. Forum* 239–241 (1997) 99.
- [12] A. Mainwood, personal communication.



ELSEVIER

Physica B 308–310 (2001) 589–592

PHYSICA B

www.elsevier.com/locate/physb

Photo-EPR studies on the AB3 and AB4 nickel-related defects in diamond

R.N. Pereira^{a,b,*}, W. Gehlhoff^b, N.A. Sobolev^a, A.J. Neves^a, D. Bimberg^b

^a Department of Physics, University of Aveiro, 3810-193 Aveiro, Portugal

^b Institute of Solid State Physics, TU Berlin, D-10623 Berlin, Germany

Abstract

We present electron paramagnetic resonance (EPR) and photo-EPR investigations on the AB3 and AB4 centers found in synthetic diamond crystals. We observed a strong increase of the AB4 EPR signal intensity when diamond samples were illuminated with monochromatic light for photon energies $h\nu > 2.06 \pm 0.02$ eV. Additionally, a quenching of the AB3 signal intensity was observed for photoexcitations at $h\nu > 2.26 \pm 0.02$ eV. The nature of the physical processes responsible for the observed photoinduced changes in both centers is discussed. © 2001 Elsevier Science B.V. All rights reserved.

Keywords: HPHT diamond; Nickel; EPR; Deep levels

1. Introduction

The identification and characterization of point defects continues to be a primary focus of research in diamond. Much of the current interest arises because of the influence of such defects on the performance of diamond in several applications. In diamond synthesized at high pressure and high temperature (HPHT), transition metals, especially Ni and Ni alloys, are used as solvent/catalysts. In such crystals Ni is incorporated as a dispersed impurity and several Ni-related defects are formed during the growth process. Nitrogen is the most abundant impurity both in natural and synthetic HPHT diamond, and is incorporated in different forms, predominantly as isolated substitutional N_s (N^0 : P1 EPR center [1]) and substitutional pairs (N_s-N_s). Electron paramagnetic resonance (EPR) studies on diamond grown from nickel solvent enriched with ^{61}Ni ($I = \frac{3}{2}$, natural abundance 1.2%) have directly proven the incorporation of nickel as a paramagnetic impurity with a spin $S = \frac{3}{2}$ (the W8 EPR center) [2,3]. In the recent years several paramagnetic defects with strong evidence of nickel participation were found by magnetic

resonance techniques [4–9]. Contrary to the available amount of information concerning the formation conditions and structure of these nickel-related centers, there is little knowledge about their energy levels in the diamond gap. For paramagnetic centers these energy levels can be determined by photoelectron paramagnetic resonance (photo-EPR). Photo-EPR studies involving the W8, P1, and AB5 ($S = 1$ [5]) centers have shown that the W8 photoquenching [10] is caused by the promotion of electrons to the conduction band, and that the energy level of the AB5 center is located at $E = E_c - 1.88$ eV [11]. The main advantage of the photo-EPR as a tool for the determination of defect level energies, as compared to other methods, is based upon the fact that it allows a direct correlation between the spectroscopically identified defects and their energy levels. This technique may provide also additional information about the optical behavior of paramagnetic centers, like their optical cross sections and their aptitude for capturing and recombining charge carriers.

Among the nickel-related defects in diamond, the AB3 and AB4 centers were found for the first time in samples that experienced a heat treatment after growth. Both centers have a spin $S = \frac{1}{2}$ and orthorhombic-I symmetry [6]. In this article we present new EPR and photo-EPR results on these nickel-related centers.

*Corresponding author. Fax: +351-2344-24965.

E-mail address: rui.pereira@fis.ua.pt (R.N. Pereira).

2. Experimental details

In this study we used diamond single crystals synthesized by H. Kanda at the National Institute for Research in Inorganic Materials (NIRIM), Japan. The samples were grown by the temperature gradient method at high pressure and high temperature using Ni as solvent/catalyst. Two of the diamond samples were annealed during 4 h at 1600°C under a stabilizing pressure of ~ 6 GPa. The samples were oriented either by growth facets or by faces polished along the main crystallographic planes.

EPR and photo-EPR measurements were carried out using a Bruker ESP 300E spectrometer operating both in X-band (9.5 GHz) and Q-band (34 GHz). Oxford Instruments helium gas flow and bath cryostat systems in the X- and Q-band, respectively, maintained the samples temperature at selected values between 4.2–100 K. The samples were always cooled down in the dark to guarantee a thermal equilibrium state prior to the illumination procedure in the photo-EPR experiments. A Xe lamp associated with a grating monochromator provided the monochromatic light source for sample illumination. This was done in the X-band through a hole at the used TE_{102} cavity, while in the Q-band the samples were irradiated via a 0.4 mm optical fiber inserted into the helium cryostat. The light from the monochromator was coupled into another 0.4 mm optical fiber at whose end we measured the spectral dependence of the photon flux. When illuminating the samples, the two fibers were connected.

3. Experimental results and discussion

3.1. AB4 center

The EPR spectrum of the AB4 center was for the first time detected in diamonds that were heat-treated after growth [6]. In the present study we only detect this center in the samples that were annealed at 1600°C. The AB4 EPR signal was observed both at room temperature and at temperatures between 4.2 and 100 K. For these samples a strong increase of the AB4 signal intensity was observed upon sample illumination.

In order to monitor the kinetics and the wavelength dependence of this photoinduced effect, we fixed the external magnetic field \mathbf{B} at the position of maximum intensity of the first derivative of one of the AB4 EPR lines and monitored the time dependence of the EPR signal intensity (I_{EPR}) upon monochromatic illumination. In order to avoid an erroneous evaluation of the photoinduced changes by monitoring overlapping EPR lines from different centers, we chose the well isolated lower magnetic field AB4 line for $\mathbf{B} \parallel \langle 011 \rangle$. The photoinduced changes in the AB4 signal intensity for

excitation photon energies $h\nu = 2.01, 2.05, 2.09$, and 2.14 eV are shown in Fig. 1. For a sequence of increasing photoexcitation energies $h\nu$, the difference ΔI_{EPR} between the photoinduced EPR signal intensity and the I_{EPR} measured prior to illumination was estimated through fitting the I_{EPR} vs. time data with exponential decay functions, see Fig. 1. The spectral dependence of ΔI_{EPR} determined from this fitting is presented in Fig. 2(a). The observed enhancement of the AB4 EPR signal intensity is interpreted as a result of a photo-

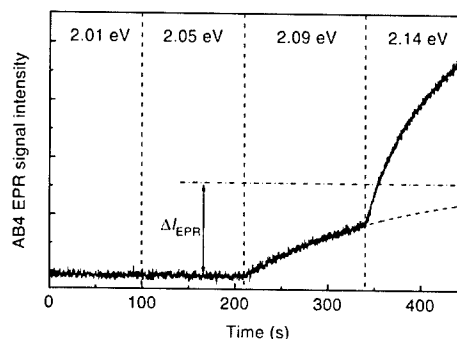


Fig. 1. Time dependence of the EPR signal intensity I_{EPR} of the AB4 center at $T = 100$ K for different excitation energies $h\nu$. Full curves represent experimental data and dashed curves are exponential fits.

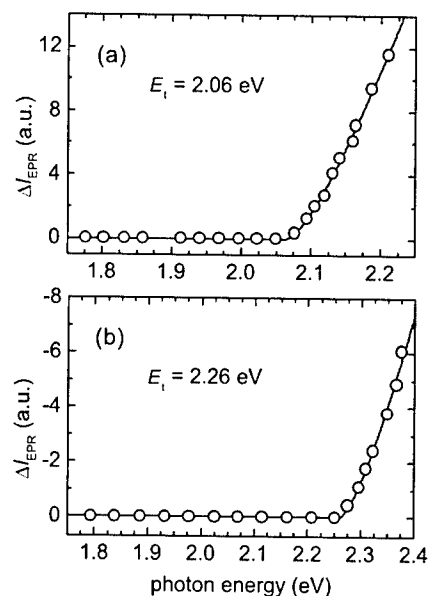


Fig. 2. (a) Spectral dependence of the EPR signal change ΔI_{EPR} (as defined in Fig. 1) for the AB4 center (enhancement) and (b) for the AB3 center (quenching). The measurement temperature is 100 K. The circles represent experimental data and the solid curves are fits to the data by Eq. (1).

ionization process occurring on a defect with localized states in diamond. Generally, the ionization energy E_i of a defect involved in such a photoionization transition (PT) can be determined from the spectral dependence of the corresponding optical cross section σ . The requirements for a correct determination of this dependence from the photo-EPR data were extensively discussed by Godlewski [12]. In the present work we used the saturation value method, which is based on the determination of the optical cross section of the photoionization transition through the spectral dependence of the ΔI_{EPR} values. This allowed us to consider different starting populations of the center under study for each photon energy, and overcomes the difficulty of ensuring the same starting signal intensity prior to each subsequent photoexcitation in the temperature range of our measurements. The calculation of the dependence of ΔI_{EPR} on the optical cross section for a given PT requires the solution of a complex system of kinetic equations that would consider all the excitation, recombination, and capture processes occurring in the sample. Our approach to this problem is based on the general principle that the ΔI_{EPR} values depend in the same way on the light intensity I and on the optical cross section σ , as these two quantities appear always together in the form of $\alpha = I \times \sigma$ in the kinetic equations that describe the photoionization process. In the photo-EPR study of the W8 and AB5 centers [11] we described in detail how the relation between the ΔI_{EPR} values and the optical cross section can be obtained. In the case of the AB4 photoexcitation we assume that the enhancement of the AB4 EPR signal intensity results from one dominant photoionization process. Considering besides that the data shown in Fig. 2(a) were obtained under experimental conditions of a linear dependence between ΔI_{EPR} and α , the optical cross section of the involved PT is linearly related to ΔI_{EPR} . Fitting the spectral dependence $\sigma(h\nu)$ of the AB4 photoexcitation by the Lucovsky formula for a purely electronic cross section [13]

$$\sigma(E_i, h\nu) \propto \frac{(h\nu - E_i)^{3/2}}{(h\nu)^3} \quad (1)$$

we found the ionization energy $E_i = 2.06 \pm 0.02$ eV, see Fig. 2(a).

The observed enhancement of the AB4 signal intensity can be caused by two type of processes: (i) a direct electron (hole) excitation from the AB4 centers to the conduction (valence) band, or (ii) an indirect process if electrons (holes) excited to the conduction (valence) band from another defect are then captured by the AB4 centers. The unambiguous determination of the process that governs the photoinduced increase of the AB4 EPR signal intensity is hindered by the fact that this spectrum could only be detected in one type of the available set of samples. The W8 and AB5 signals decrease in the same

samples for excitation energies $h\nu$ higher than 2.5 and 1.9 eV, respectively. However, the appearance of a strong photoinduced effect with a threshold at 2.06 eV only for the AB4 lines, together with the observation of different spectral dependencies for the photoinduced changes of other centers present in the same samples, indicate that a direct photoionization is the most probable process to explain the observed behavior of the AB4 center under illumination. Whether the increase of the AB4 signal is resulting from a direct (i) or an indirect (ii), it can occur either by electron or by hole ionization. The observation of the nitrogen donor signal (P1) prior to any illumination of the samples indicates that the Fermi level is located at or above the $N^{0/+}$ level. The position of this defect level in the diamond gap have been taken as $E = E_c - 1.7$ eV [14]. Therefore, the observed transition with the threshold at 2.06 eV is interpreted as promotion of electrons to the conduction band.

3.2. AB3 center

The EPR measurements at temperatures between 4.2 and 100 K reveal in all samples the presence of the AB3 EPR spectrum. This spectrum is not detectable at room temperature.

The intensity of the AB3 EPR lines in annealed diamonds decreases upon sample illumination with visible light. The time dependence of this process was recorded for different excitation wavelengths and the ΔI_{EPR} values were determined as described above for the AB4 center. The obtained spectral dependence of ΔI_{EPR} normalized to a constant photon flux is presented in Fig. 2(b). A photon energy threshold of about 2.3 eV was determined for the observed decrease of the signal intensity. Provided only one photoionization process is responsible for the decrease of the AB3 EPR signal intensity and taking into account that the experimental data shown in Fig. 2(b) were obtained under the condition of a linear dependence between ΔI_{EPR} and α , the optical cross section of the PT is linearly related to ΔI_{EPR} . The best fit of Eq. (1) to the curve shown in Fig. 2(b) is obtained for $E_i = 2.26 \pm 0.02$ eV.

This photoinduced effect on the AB3 center was only observed in annealed samples whereas in as-grown diamonds that exhibit the AB3 spectrum a sensitive change of the AB3 EPR signal intensity upon illumination was not detected. We see two possible explanations for this behavior of the AB3 center: (a) the decrease of the signal intensity results from the capture, from the conduction (valence) band, of electrons (holes) that were excited from another defect produced during the annealing process and located at 2.26 eV in the diamond gap; or (b) the direct photoionization of AB3 centers is observed and the photoexcitation effect in the as-grown samples is undetectable due to the small amount of

acceptor (donor) levels available to capture the photo-excited electrons (holes). The time dependence of I_{EPR} of the AB5 center measured at different photoexcitation energies for the same annealed samples have shown that by changing the photoexcitation energy from 2.23 to 2.32 eV a second process which overlaps with the photoquenching of the AB5 EPR signal sets in [11]. This process and that leading to the decrease of the AB3 signal intensity have possibly the same origin. As in the AB4 photoexcitation mechanism, the photoionization transition that leads to the changes in the AB3 signal intensity should involve the promotion of electrons to the conduction band, independently of process (a) or (b) occurs.

4. Conclusions

Photoionization processes involving the AB3 and AB4 paramagnetic centers were studied in as-grown and annealed diamond samples grown from a nickel solvent/catalyst. The strong increase of the AB4 EPR signal intensity observed by optical excitation with photon energies $h\nu \geq 2.06$ eV is interpreted as resulting from photoionization of AB4 defects located at 2.06 eV below the conduction band. The photoinduced decrease of the AB3 signal intensity evidences the presence of an acceptor state at $E = E_c - 2.26$ eV in HPHT diamond.

Acknowledgements

The authors would like to thank H. Kanda (NIRIM, Japan) for supplying the samples. The work was supported in part by “Acções Integradas Luso-

Alemãs”, Project No A-13/99. RNP thanks the Institute for Solid State Physics, TU-Berlin, for its hospitality and acknowledges the financial support from FCT under contract PRAXIS XXI/BD/18405/98, which made a longer stay in the Federal Republic of Germany possible.

References

- [1] W.V. Smith, P.P. Sorokin, I.L. Gelles, G.J. Lasher, *Phys. Rev.* 115 (1959) 1546.
- [2] M.I. Samoilovich, G.N. Bezrukov, V.P. Butuzov, *JETP Lett.* 14 (1971) 379.
- [3] J. Isoya, H. Kanda, J.R. Norris, J. Tang, M.K. Bowman, *Phys. Rev. B* 41 (1990) 3905.
- [4] V.A. Nadolinny, A.P. Yelisseyev, O.P. Yuryeva, B.N. Feygelson, *Appl. Magn. Reson.* 12 (1997) 543.
- [5] A.J. Neves, R. Pereira, N.A. Sobolev, M.H. Nazaré, W. Gehlhoff, A. Naeser, H. Kanda, *Diamond Relat. Mater.* 9 (2000) 1057.
- [6] A.J. Neves, R. Pereira, N.A. Sobolev, M.H. Nazaré, W. Gehlhoff, A. Naeser, H. Kanda, *Physica B* 273–274 (1999) 651.
- [7] J. Isoya, H. Kanda, Y. Uchida, *Phys. Rev. B* 42 (1990) 9843.
- [8] C.J. Noble, Th. Pawlik, J.-M. Spaeth, *J. Phys.: Condens. Matter* 10 (1998) 11781.
- [9] Th. Pawlik, C. Noble, J.-M. Spaeth, *J. Phys.: Condens. Matter* 10 (1998) 9833.
- [10] D.M. Hofmann, M. Ludwig, P. Christmann, D. Volm, B.K. Meyer, L. Pereira, L. Santos, E. Pereira, *Phys. Rev. B* 50 (1994) 17618.
- [11] R.N. Pereira, W. Gehlhoff, N.A. Sobolev, A.J. Neves, D. Bimberg, *J. Phys.: Condens. Matter* 13 (2001) in press.
- [12] M. Godlewski, *Phys. Stat. Sol. (A)* 90 (1985) 11.
- [13] G. Lucovsky, *Solid State Commun.* 3 (1965) 299.
- [14] G. Davies, *Physica B* 273–274 (1999) 15.



ELSEVIER

Physica B 308–310 (2001) 593–597

PHYSICA B

www.elsevier.com/locate/physb

Electrically detected magnetic resonance studies of phosphorus doped diamond

T. Graf^{a,*}, M.S. Brandt^a, C.E. Nebel^a, M. Stutzmann^a, S. Koizumi^b

^a Walter Schottky Institut, Technische Universität München, Am Coulombwall, D-85748 Garching, Germany

^b Advanced Materials Laboratory, National Institute for Materials Science, 1-1 Namiki, Tsukuba 305-0044, Japan

Abstract

Phosphorus doped n-type epitaxial diamond films have been studied by electron spin resonance (ESR) and electrically detected magnetic resonance (EDMR). At low electric field, the dominant defects influencing the electronic transport are carbon dangling bonds, while at higher fields the anisotropic spin resonance signal of a new phosphorus-related center with $g_{\perp} = 2.0026$, $g_{\parallel} = 2.0042$, $A_{\text{iso}} = 17.6$ G, and $A_{\text{aniso}} = 1.8$ G is observed. These results indicate that room temperature conductivity in this film is dominated by hopping via phosphorus-related defect centers rather than via hydrogenic donor states of phosphorus atoms on substitutional sites. © 2001 Elsevier Science B.V. All rights reserved.

PACS: 61.72.-y; 71.55.-i

Keywords: Diamond; Phosphorus; Doping; EDMR; Spin resonance

1. Introduction

As a potential semiconducting material, diamond has several outstanding properties. The major obstacle for the realisation of bipolar diamond-based electronic devices still is the lack of shallow n-type dopants. One possible candidate for a shallow donor state is substitutional phosphorus, which unfortunately is much harder to incorporate into diamond than into silicon because of the mismatch in atomic radii. Nevertheless, several groups have reported phosphorus incorporation into diamond. In epitaxial samples grown using phosphine as a dopant source, n-type conductivity was found with activation energies of the Hall carrier concentration of 0.4–0.6 eV [1]. For the same samples, infrared absorption peaks were observed at 0.52 and 0.56 eV and related to a photoionization onset in photoconductivity measurements [2]. The aim of the present paper is to investigate the microscopic structure of the phosphorus-related electronic states in these samples by electron spin

resonance (ESR) to obtain information on their ground state wavefunction.

ESR of phosphorus-related states in diamond has been observed in polycrystalline powders [3], in crystals grown from phosphorus catalyst [4], and in CVD films implanted during growth [5] or after growth with subsequential annealing [6]. In the crystalline films, isotropic hyperfine lines with a characteristic splitting of 27–28 G were observed and attributed to the $I = 1/2$ nuclear magnetic moment of substitutional ^{31}P . Unfortunately, these samples have a large number of implantation defects besides the phosphorus states so that n-type conductivity has not been confirmed yet. Only recently, 28 G split hyperfine lines were observed in these samples together with the characteristic infrared absorption at 0.52 and 0.56 eV also found in the samples of Ref. [1,2], suggesting that shallow states give rise to the ESR signal [6].

Conventional ESR of epitaxial diamond layers usually is dominated by the large density of well-known nitrogen P1 centers in the substrate [7]. We therefore have used electrically detected magnetic resonance (EDMR) experiments, which are sensitive to paramagnetic states in the path of conductivity only. Therefore,

*Corresponding author. Tel.: +49-89-289-12768; fax: +49-89-289-12737.

E-mail address: tobias.graf@wsi.tum.de (T. Graf).

background signals from the insulating substrate do not interfere with signals of the conductive film, allowing the selective investigation of paramagnetic states in the P-doped epilayer.

2. Experimental details

The diamond film under investigation has been prepared by plasma-assisted chemical vapor deposition. By addition of phosphine to the gas phase with relative concentrations of $(\text{PH}_3/\text{CH}_4) = 1000 \text{ ppm}$ and $(\text{CH}_4/\text{H}_2) = 0.075\%$, a doped epitaxial film with $1.5 \mu\text{m}$ thickness was deposited on the polished $[111]$ surface of a $2 \times 2 \times 0.5 \text{ mm}^3$ type Ib synthetic diamond, as described in Ref. [1]. The nominal phosphorus concentration of this film was $5 \times 10^{18} \text{ cm}^{-3}$, which is just below the concentration expected for the metal-insulator transition, at which the hyperfine satellites of the nuclear spin $I = 1/2$ of ^{31}P would collapse [5]. A detailed description of the growth as well as measurements of photoconductivity and infrared absorption can be found in Ref. [2] and references therein, where the present sample is labeled as #4. For the electrical measurements performed in this paper, coplanar interdigital Au contacts with $50 \mu\text{m}$ spacing were deposited on top of the epitaxial film.

As noted above, the nitrogen P1 center in the substrate dominates the conventional ESR of the sample. Its anisotropic ESR signal has been used to orient the sample with respect to the external magnetic field and for g -factor calibration. EDMR measurements were taken in a conventional X-band ESR spectrometer (Bruker ESP-300, TE₁₀₂ cavity) in combination with a Keithley 237 Source Measure Unit and a Stanford Research SR570 Low-Noise Current Preamplifier. The spectra shown have been recorded at room temperature, but have been observed similarly at 100 K as well. Above room temperature, the dark conductivity of the sample is thermally activated with the characteristic ionization energy of about 0.5 eV attributed to the substitutional phosphorus level [1]. In contrast, at room temperature and below, the dominant transport process is hopping at the Fermi level, which is expected to be a spin-dependent transport path similar to existing results in other materials [8]. Therefore, room temperature EDMR measurements seem to be a suitable tool to resolve the hyperfine interaction of electronic spins with the nuclear spins of ^{31}P and to extract from this hyperfine splitting microscopic parameters of the electron wavefunction at the donor sites.

3. Transport regimes and EDMR at low electric field

Fig. 1 shows the IV -characteristic of the film at room temperature in the dark. Above $\pm 20 \text{ V}$, the behavior is

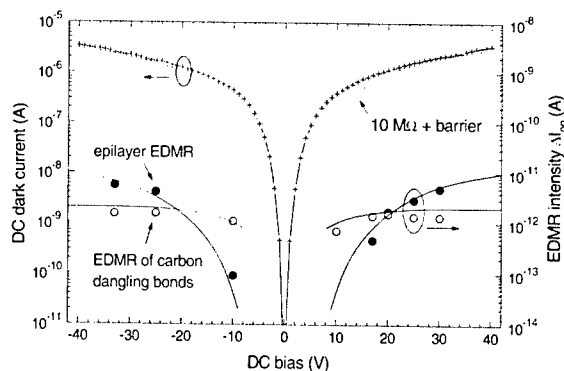


Fig. 1. Room temperature IV -characteristic of the phosphorus doped diamond film with $50 \mu\text{m}$ interdigit finger contacts. The dashed line indicates the IV characteristics of an ohmic resistor, which is offset from zero voltage due to barriers at the non-ideal contacts. Open and closed circles show the intensities of the two signal components in EDMR.

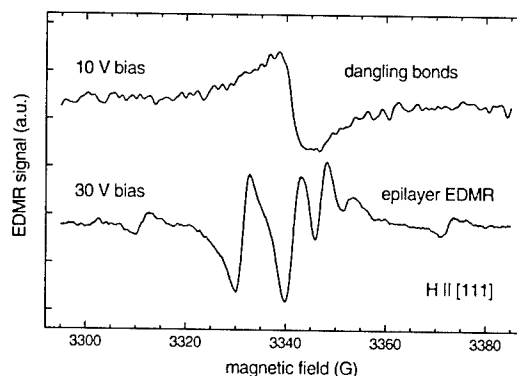


Fig. 2. EDMR spectra at 10 V bias and at 30 V bias corresponding to 2 and 6 kV/cm in the case of a homogeneous field distribution. In the regime of low electric field, carbon dangling bonds dominate spin-dependent transport, while at higher electric fields the signal shows a complex structure of several resonances.

almost ohmic as indicated by the dashed line that corresponds to a differential resistance of $10 \text{ M}\Omega$ and a conductivity of $10^{-6} \Omega^{-1} \text{ cm}^{-1}$, consistent with the reported data for n and μ [2]. In contrast, the IV -curve at lower bias voltages is nonlinear, indicating that the current is limited by some kind of barrier, such as the space charge region of a Schottky contact below breakthrough in reverse-bias. Obviously, any electrical measurement such as EDMR should be analyzed with regard to the bias voltage that determines the dominant resistance. In the regime of high voltages, the applied electric field is able to overcome the barriers so that the measured current is limited by the epilayer of interest, whereas in the low-field regime the space charge layers limit the overall current.

The different EDMR signatures observed at high and low bias voltages shown in Fig. 2 support this qualitative explanation. While in the high-field regime at 30 V bias, a complex anisotropic signal is observed that will be discussed in more detail below, the low-field signal at 10 V bias can be identified directly by its isotropic g -factor $g = 2.0028$ and the peak-to-peak linewidth $\Delta H_{pp} \sim 7$ G. These parameters are commonly associated with carbon dangling bonds in amorphous hydrogenated carbon [9] as well as in polycrystalline diamond [10], and in crystalline thin CVD diamond films after implantation [5,6]. EDMR of carbon dangling bonds has been demonstrated in polycrystalline CVD diamond films with high defect density [11]. In the present homoepitaxial film, EDMR sensitivity is enhanced as these defects limit conductivity through the space charge regions of the interdigital contacts. The sign of the EDMR signal at low electric fields indicates a resonant quenching of the current due to a spin-dependent capture process of conduction band electrons. In contrast, the signal at high electric field corresponds to resonant enhancement of the current, which is typical for hopping transport at the Fermi level.

At intermediate bias voltages, the two different components to conductivity give rise to a superposition of the two types of EDMR spectra. In Fig. 1, the maximum resonant current change ΔI_{pp} of both spectral contributions is shown separately, the full symbols indicating the resonant current change for the contribution attributed to the epilayer outside the space charge region and the open symbols indicating the change due to dangling bonds. According to the picture given above, the crossover between both regimes takes place at the interchange between ohmic and barrier-dominated transport. The normalized EDMR intensity is $\Delta\sigma/\sigma = \Delta I_{pp}/I_{DC} \sim 10^{-6}$ for these maximum components of the signals. As for the smaller features, $\Delta\sigma/\sigma < 10^{-7}$, massive signal averaging is required to completely resolve each spectrum.

4. Interpretation of the EDMR at high electric fields

In Fig. 3, EDMR spectra for the three fundamental crystal orientations with respect to the magnetic field H_0 perpendicular to the $[\bar{1}10]$ axis of rotation are shown. They have been recorded at a bias voltage of 30 V, which is appropriate to suppress the contribution from the contacts and to select paramagnetic states from the phosphorus doped film. Within the complex pattern of overlapping resonances, the outer pairs of hyperfine satellites are clearly identified as P1 hyperfine triplets. They are identical to the ESR signal of the substrate besides some broadening due to the experimental conditions of EDMR. Although the substrate has a higher thickness than the epilayer, its room temperature

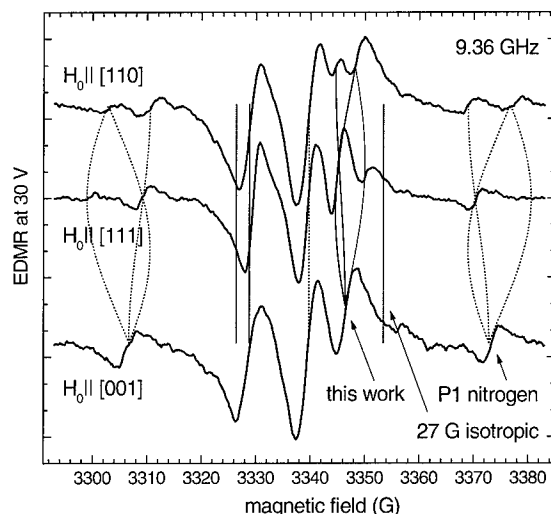


Fig. 3. EDMR at 30 V bias for three fundamental crystal orientations. The crystal rotation is performed around a $[\bar{1}10]$ axis, so that 0° rotation angle corresponds to $H_0 \parallel [111]$, $+35^\circ$ to $H_0 \parallel [110]$, and -55° to $H_0 \parallel [001]$. The outer transitions belong to P1 triplets that dominate the ESR signal of the Ib substrate. The inner set of lines is attributed to hyperfine satellites of a new phosphorus-related center. Also drawn are the positions of the 27 G hyperfine satellites reported for other P-doped diamond samples [5], but which are not found in this sample.

dark conductivity is too low for a contribution to the EDMR signal, suggesting the presence of deep P1 centers in the epitaxial film. Alternatively, microwave absorption of P1 centers in the substrate could lead to thermal crosstalk and to a resonant increase in conductivity.

In contrast, no significant absorption is detectable in ESR under identical conditions for the remaining resonance lines, so that these lines have to originate from spin-dependent transport at the Fermi level of the epilayer. Also indicated in Fig. 3 are the resonance positions for $\Delta H = 27$ G and $g = 2.0023$ which have been reported for ^{31}P -related centers in diamond earlier [5,6]. This hyperfine doublet is not observed in the present sample. Instead, we observe an isotropic line at 3329 G and an anisotropic set of lines at about 3347 G, more similar to the ESR signals reported in Refs. [3,4]. The interpretation of these lines as two independent resonances would result in g -factors of $g = 2.009$ and $g \sim 1.998$, which are well out of the narrow range of g -factors typical for diamond [12]. Therefore, the two resonances will be interpreted in the following as a set of hyperfine lines, although their anisotropy is not resolved completely on both sides. As indicated in Fig. 3, the difference can be simulated by g -factor anisotropy in addition to anisotropy of the hyperfine interaction. Both contributions have opposite

orientation at 3329 G, leading to a small total anisotropy and to overlapping lines for the satellites at lower magnetic field. In contrast, the anisotropy adds up for the 3347 G line. It is incompatible with the axial symmetry expected of surface states, which also might influence the conductivity [13]. Identical spectra have been observed for H_0 oriented parallel to $[1\ 1\ 1]$ and $[1\ 1\ \bar{1}]$. This is consistent with the C_{3v} symmetry of sp^3 orbitals in diamond. Spectra at intermediate angles also support the calculated line pattern included in Fig. 3, which simulates a C_{3v} -center with $g_{\perp} = 2.0026$, $g = 2.0042$, $A_{iso} = 17.6$ G, and $A_{aniso} = 1.8$ G. The pattern contains four symmetry related sites with $I = 1/2$, two of which coincide for the investigated axis of rotation. A more detailed analysis of the ESR parameters is hindered by the linewidth of $\Delta H_{pp} \sim 5$ G that leads to severe overlapping of the expected resonances. Nevertheless, the observed parameters are significantly different from those of the analysis of the powder pattern in polycrystalline samples $g = 2.0025$, $A_{iso} = 20.8$ G, and $A_{aniso} = 1.2$ G [3].

Up to now, all isotropic hyperfine constants reported for phosphorus in diamond are below 30 G, which can be converted into a probability density of the 3s orbital at the phosphorus atom of $<0.6\%$ [4]. Small ^{31}P hyperfine splittings have been discussed for several centers, for example a phosphorus-vacancy complex with low spin density on the central nucleus [14] or a complex similar to the N1 center with phosphorus in a positive charge state at the next-nearest neighbor site of an unpaired electron [4]. For substitutional donors, the spin density at the donor atom can be estimated by the effective mass theory. The effective electron masses in diamond are uncertain up to now, but seem to have the same anisotropy as the effective electron mass of silicon, with a ratio of $m_c^*/m_{si}^* \approx 1.5$ [15]. At the same time, the ratio of dielectric constants is $\epsilon_c/\epsilon_{si} = 5.7/11.7 \approx 0.5$. Both ratios cause a higher degree of localization at donor atoms in diamond compared to silicon, as the ionization energy scales like $E \propto m^*/\epsilon^2$, and the localization radius like $a \propto \epsilon/m^*$. Considering only changes of the hydrogen-like envelope of the donor electron wave function without detailed calculation of Bloch functions and central cell corrections, the hyperfine splitting scales roughly like $A \propto |\psi(0)|^2 \approx (m^*/\epsilon)^3$ [16]. The extrapolation from phosphorus donors in silicon to diamond predicts $A_c > 1000$ G, in contrast to the arguments based on relative electronegativities, which suggest a smaller hyperfine interaction in diamond compared to silicon [5]. The experimental ionization energy of 0.6 eV is significantly higher than the value $E \sim 0.2$ eV predicted from effective mass theory, indicating an even higher degree of localization and larger hyperfine splitting [15]. At the signal-to-noise level of the present EDMR experiments, no additional hyperfine pairs were detected within a

magnetic field range of ± 2000 G. Nevertheless, one has to keep in mind that EDMR of dark conductivity is limited to spin-dependent processes in paramagnetic states close to the Fermi level. Therefore, in partially compensated samples, EDMR experiments cannot exclude the existence of shallow phosphorus levels in the presence of deeper compensating centers, for example dangling bonds, P1 centers, or X_{P2} levels that were observed in similar samples by CPM at 0.81 eV [2].

5. Conclusions

ESR and EDMR experiments were performed on a P-doped diamond film exhibiting n-type conductivity. Two transport regimes have been studied separately: At low electric field, carbon dangling bonds limit dark current through barriers below the non-ideal contacts. At higher electric fields, a new ESR center with $g_{\perp} = 2.0026$, $g = 2.0042$, $A_{iso} = 17.6$ G, and $A_{aniso} = 1.8$ G was detected in the epilayer. It dominantly contributes to room temperature transport, but cannot be assigned to substitutional phosphorus donors. Most likely, the presence of compensating defects hinders the observation of substitutional phosphorus with EDMR of dark conductivity in these samples. Measurements of spin-dependent non-equilibrium processes like spin-dependent recombination could help to resolve this problem.

Acknowledgements

This work was supported by Deutsche Forschungsgemeinschaft (SFB 348 and Ne 524/2).

References

- [1] S. Koizumi, M. Kamo, Y. Sato, H. Ozaki, T. Inuzuka, Appl. Phys. Lett. 71 (1997) 1065.
- [2] K. Haenen, K. Meykens, M. Nesládek, G. Knuyt, C. Quaeys, L.M. Stals, S. Koizumi, E. Gheeraert, Phys. Status Solidi A 174 (1999) 53.
- [3] N.D. Samsonenko, V.V. Tokil, S.V. Gorban, Sov. Phys. Solid State 33 (1991) 1409.
- [4] J. Isoya, H. Kanda, M. Askaishi, Y. Morita, T. Ohshima, Diamond Relat. Mater. 6 (1997) 356.
- [5] M.E. Zvanut, W.E. Carlos, J.A. Freitas Jr., K.D. Jamison, R.P. Hellmer, Appl. Phys. Lett. 65 (1994) 2287.
- [6] N. Casanova, E. Gheeraert, A. Deneuville, C. Uzan-Saguy, R. Kalish, Phys. Status Solidi A 181 (2000) 5.
- [7] W.V. Smith, P.P. Sorokin, I.L. Gelles, G.J. Lasher, Phys. Rev. 115 (1959) 1546.
- [8] N. Kishimoto, K. Morigaki, K. Murakami, J. Phys. Soc. Jpn. 50 (1981) 1970.

- [9] R.C. Barklie, M. Collins, S.R.P. Silva, *Phys. Rev. B* 61 (2000) 3546.
- [10] X. Zhou, G.D. Watkins, K.M. McNamara Rutledge, R.P. Messmer, S. Chawla, *Phys. Rev. B* 54 (1996) 7881.
- [11] C.F.O. Graeff, E. Rohrer, C.E. Nebel, M. Stutzmann, H. Güttler, R. Zachai, *Mater. Res. Soc. Symp. Proc.* 423 (1996) 495.
- [12] J.H.N. Loubser, J.A. van Wyk, *Rep. Prog. Phys. (UK)* 41 (1978) 1201.
- [13] H. Kawai, *Surf. Sci. Rep.* 26 (1996) 205.
- [14] R. Jones, J.E. Lowther, J. Goss, *Appl. Phys. Lett.* 69 (1996) 2489.
- [15] E. Gheeraert, S. Koizumi, T. Teraji, H. Kanda, M. Nesládek, *Phys. Status Solidi A* 174 (1999) 39.
- [16] W. Kohn, J.M. Luttinger, *Phys. Rev. B* 97 (1995) 833.



ELSEVIER

Physica B 308–310 (2001) 598–603

PHYSICA B

www.elsevier.com/locate/physb

High-temperature high-pressure annealing of diamond Small-angle X-ray scattering and optical study

A.A. Shiryaev^{a,b,*}, M.T. Hutchison^{c,d}, K.A. Dembo^a, A.T. Dembo^a,
K. Iakoubovskii^c, Yu.A. Klyuev^f, A.M. Naletov^f

^a*Institute of Crystallography, Leninsky Pr. 57, 117333 Moscow, Russia*

^b*IRI, Delft University of Technology, Mekelweg 15, JB 2629 Delft, The Netherlands*

^c*Lunar and Planetary Laboratory, University of Arizona, Tucson, USA*

^d*Research School of Earth Sciences, Australian National University, Australia*

^e*Semiconductor Physics Laboratory, Katholieke Universiteit Leuven, Leuven, Belgium*

^f*VNIImaz, Moscow, Russia*

Abstract

Annealing of Ib and IIa diamonds at temperature of 1800°C and pressure of 7.2 GPa was performed. It is shown that for experiments with comparable total duration, the nitrogen aggregation rate is significantly slower for a single-run than for multiple-run annealing. Consequently, many previously reported multiple annealing experiments could overestimate the rate of nitrogen diffusion in diamond. Small-angle X-ray scattering reveals that three-dimensional defect clusters were formed during annealing. The size of clusters (27–57 nm) is similar in annealed natural IaA, IaB, IIa and synthetic Ib diamonds. The presence of clusters is unrelated to ‘platelets’ and contain little, if any, nitrogen. Optical results reveal that annealing resulted in decay of the 4N–2V (H4) defects into 2N–V (H3) and that the B nitrogen defect is not responsible for the N9 optical center. © 2001 Elsevier Science B.V. All rights reserved.

Keywords: Diamond; Annealing; Small-angle scattering; Luminescence

1. Introduction

Many physical and chemical properties of minerals depend on the concentration and type of point and extended defects present in their lattices. Diffusion of point defects can lead to creation of clusters and under favorable conditions even new phases can be formed. In this paper we report on a new type of extended defect formed in diamond during long continuous annealing at high pressure–high temperature (HPHT) conditions.

Oxygen, hydrogen and nitrogen are the principal impurities found in diamond. Nitrogen concentrations can be as high as 0.3 at%. Oxygen and hydrogen

concentrations can be comparable and, in some cases, higher than that of nitrogen. However, while most oxygen and hydrogen atoms reside in internal voids in the diamond lattice and within non-diamond inclusions, nitrogen predominantly forms integral lattice-bonded defects [1].

The common classification scheme for diamond is based on the principal nitrogen defect types as identifiable by infrared (IR) spectroscopy. In type Ib diamond nitrogen is dominantly present as single substitutional atoms, referred to as the C or P1 centers. Most synthetic diamonds belong to this type. HPHT annealing, performed either naturally or under laboratory conditions, leads to aggregation of single substitutional nitrogen atoms to the so-called A and B complexes in the order $C \rightarrow A \rightarrow B$ [2–4]. Diamonds with these defects are referred to as type IaA and IaB, respectively. Optical studies [5,6] combined with electron spin resonance

*Corresponding author. IRI, Delft University of Technology, Mekelweg 15, JB 2629 Delft, Netherlands. Tel.: +31-15-2786813; fax: +31-15-2786422.

E-mail address: a.shiryaev@mail.ru (A.A. Shiryaev).

(ESR) show that the A center is comprised of a pair of nearest-neighbor substitutional nitrogen atoms. The microscopic structure of the B defect is not so firmly established. Results obtained by ESR [7] and optical methods [8] suggest a complex of four nitrogen atoms in tetrahedral coordination around a vacancy.

In addition to these simple point defects, most diamonds are rich in more complex and variable extended defects. Besides dislocations, twins and stacking faults, one of the best-known examples is termed 'platelets'—planar (in {100} plane) defects containing carbon and nitrogen atoms. It is suggested that platelets are formed from interstitial carbon atoms as a result of their migration at high temperature [9,10]. Another abundant group of extended defects in diamonds is termed 'voidites', which are typically octahedral formations with a large scatter in size (1–30 nm) and with lower electron density than diamond. Their composition is uncertain, but N–C–H compounds are considered as probable constituents [11].

X-ray diffuse scattering [12] and high-resolution electron microscopy [13] show that Ia diamonds also contain planar {111} defects. Existence of sphere-like (isometric) clusters with diameter ~ 8 –9 nm [14,15] or larger [16] has been reported. Values for hardness and low-temperature thermal conductivity appear to depend on the presence of such clusters [17]. Extended defects can be produced during laboratory or natural HPHT annealing [3,17].

Recently, large defect clusters have been identified by small-angle X-ray scattering (SAXS) in natural IaB and natural and synthetic IaA diamonds [17]. Measurements reveal the presence of spherical defect clusters about 9 nm in diameter in IaB crystals. In type IaA diamonds, the scattering contrast is much weaker and the cluster sizes are more variable (10–60 nm). The composition of those clusters was not clear, although it has been suggested that they may have a significant nitrogen component [17]. The purpose of this paper is to clarify the composition of large spherical defects (clusters) observed by SAXS by their reproduction under laboratory conditions. We present results of SAXS and optical

measurements on synthetic nitrogen-bearing diamonds and on a natural low-nitrogen stone, annealed at HPHT conditions for different periods, and demonstrate that nitrogen, if present at all, is not a significant part of those clusters.

In laboratory experiments on nitrogen aggregation, diamonds are usually annealed in a sequence of several short runs at high temperatures (up to 2800°C) in order to increase diffusion rate. Mechanical stresses as well as changes in pressure–temperature parameters during conventional annealing experiments unavoidably influence defect diffusion. The situation is very different for the majority of natural diamonds, which are annealed at relatively stable upper mantle conditions, at modest temperatures ($<1400^\circ\text{C}$ [18]), but for time-scales of $\sim 10^9$ years. Therefore, in the present work we performed experimental runs with durations up to 960 h hoping to make a closer approximation to the conditions of annealing of diamonds in the Earth's mantle.

2. Experimental

Two synthetic nitrogenous Ib diamonds and one low-nitrogen (IIa) natural stone from the Juina district of Brazil have been used in this work. Synthetic diamonds were grown with a Ni-based catalyst. Nitrogen contents in them, determined by Fourier-transform IR spectroscopy (FTIR), are presented in Table 1. Nickel content of synthetic stones was measured using synchrotron-based X-ray fluorescence (beamline L, HASYLAB). Total Ni concentration was of the order of tens of atomic ppm. Optical measurements, discussed below, revealed that the concentration of Ni-related point defects was on the ppb level, and thus most of Ni was likely present as metallic inclusions. FTIR measurements of the type IIa stone showed a presence of <20 ppm of nitrogen and no Ni could be detected in it by optical absorption or luminescence.

HPHT experiments were carried out using the Walker-style 1000-ton multi-anvil press of the Lunar

Table 1
Defect parameters in annealed diamond samples

Sample number	Nitrogen type	Duration (h)	Total N content (at. ppm)	Nitrogen aggregation ^a (%)	SAXS cluster size (nm)
1 ^b	Ib	10 h 40'	250	25	57
2	Ib	10	240	7	57
3	Ib	100	250	14	44
4	Ib	960	255	10	44
5	IIa	100	20	—	27

^aNitrogen aggregation is a ratio of A center concentration to the total nitrogen content after annealing. It was below 1% before annealing.

^bSample 1 was annealed incrementally in five separate experiments run for 462, 2, 74, 76 and 25 min.

and Planetary Laboratory, University of Arizona. Runs were conducted at 7.2 GPa and $\sim 1800^\circ\text{C}$ using 14/8 mm assemblies. Durations ranged from 10 h to 40 days and are provided in Table 1. Diamond fragments of approximately 2 mm in maximum dimension were loaded into Pt capsules and packed with dry graphite. Pressures of 7.2 GPa were obtained at a ram force of 294 tons (US) following calibration by Richter and Drake [19] and are believed to approximate well to hydrostatic conditions. Temperatures were held at 1595°C as measured directly using $\text{WRe}_{26}/\text{WRe}_5$ thermocouples located on the edge of the heater, 2.0 mm from the hot spot where the diamonds were located. Equivalent power, which was found to be a reliable estimation of temperature, was held constant for experiments where thermocouples failed. Measurements using a similar assembly with the thermocouple located at the hotspot confirm a temperature gradient of $\sim 100^\circ\text{C}/\text{mm}$, and thus samples are concluded to have been subjected to temperatures of $1795 \pm 50^\circ\text{C}$. Experiments were quenched by disconnecting the power supply.

SAXS measurements were performed in the angular region of 15° – 1.2° . A small-angle AMUR-K X-ray diffractometer [20] with Kratki-collimator and linear position-sensitive detector were used with a Ni-mono-chromated Cu-anode X-ray fine focus tube as the source of X-rays. The experimental curves were normalized to the primary beam intensity by applying corrections for sample absorption coefficients and holder scattering. Calculation of the size distribution of scattering objects was performed using GNOM software [21]. All mean defect diameters reported in this study are obtained from solutions, stable against variations of a maximum size of scattering centers. The best agreement with the experimental data was achieved by approximation of scattering centers as a polydisperse system of hard spheres.

FTIR spectra were acquired with a Philips PU9800 spectrometer in the range 400 – 3500 cm^{-1} at a 2 cm^{-1} resolution. Deconvolution of spectra was performed using software provided by David Fisher (D.T.C.). Most samples cracked during the annealing and thus the IR spectra of treated samples were taken from irregularly shaped pieces. Instead of conventional transmission geometry, a superposition of transmitted and diffuse components was measured using a DRIFT sample holder. This could affect the analysis of IR spectra. However, no significant changes in total nitrogen content with annealing were observed in IR spectrum from any sample.

Optical absorption was measured in the range 1.2 – 5.6 eV at 77 and 300 K using a home-built spectrometer. For given sample thickness a sensitivity of $\sim 10^{-2}\text{ cm}^{-1}$ was achieved. Photoluminescence (PL) measurements were performed at 77 and 300 K under 3.68 eV or 2.41 eV excitation provided by N_2 or Ar^+ lasers,

respectively. For 2.41 eV excitation the spectra could be measured at energies above (anti-Stokes mode) and below (normal, Stokes mode) the excitation laser line. This allowed interference-free detection of the H3 system with a zero-phonon line at 2.463 eV under 2.41 eV excitation. PL spectra were scaled to the integrated diamond Raman peak. After normalization, the concentration of the detected PL centers could be estimated by comparison of the spectra with the standards, in which the concentration of those centers was calibrated by optical absorption using the data of Davies [8].

3. Results

3.1. Optical studies

Optical spectra measured on the Ib HPHT samples before annealing were rather featureless: Absorption measurements revealed only a broad spectrum, associated with the C centers and only the 2.56 eV system, attributed to the Ni_s defect [8], has been observed in PL. Luminescence intensity was relatively weak, suggesting that the corresponding defect is present on the ppb level. The PL intensity was the same in samples 1 and 2 being about 3 times stronger than in the samples 3 and 4. Only C-defect spectra were detected in IR absorption, which were used to deduce the nitrogen content in the samples (see Table 1).

After annealing the intensity of the C center absorption decreased and a threshold at 4 eV , associated with the A center, emerged in all Ib samples. The signature of this center was also seen in IR absorption spectra. Moreover, weak absorption appeared from the 1.945 eV system, which was associated with the negatively charged nitrogen–vacancy ($[\text{N}-\text{V}]^-$) complex [8]. By integrating the corresponding vibronic band the $[\text{N}-\text{V}]^-$ concentrations were inferred as 80, 80, 120 and 170 ppb with the uncertainty of 40% for samples 1, 2, 3 and 4, respectively. PL from all these samples became much brighter after annealing. Spectra under 3.68 eV excitation from the Ib HPHT samples 1 and 2 were dominated by the S2 and S3 systems, associated with different complexes involving one Ni and two or more nitrogen atoms [22]. Intensity of PL was the strongest in sample 1, an order of magnitude weaker in sample 2 and even more faint in samples 3 and 4. In accordance with the absorption results, PL spectra under 2.41 eV excitation revealed the 1.945 eV system, having about the same intensity in samples 1 and 2 and about twice as strong in samples 3 and 4. However, sample 1 in addition showed the H3 system with intensity comparable to that of the $[\text{N}-\text{V}]^-$ band. Meanwhile, the H3 luminescence was much weaker in sample 2 and undetectable in samples 3 and 4.

Along with the UV-visible absorption and PL results, IR measurements on annealed samples show that the degree of nitrogen aggregation decreases from sample 1 to 4. Along with the absorption, related to the A defect, a weak E-component appeared. This component has been previously reported in some natural Ia/Ib diamonds [23].

In type IIa diamond (#5) optical absorption measurements reveal a presence of the N9 center on the level ≤ 1 ppm. PL detected minute amounts (ppb level) of N3 as well as H3, H4, 536 nm and 576 nm centers. Analysis of the vibronic structure revealed that the 576 nm system is irrelevant to the 575-nm $[N-V]^0$ related center. Annealing did not produce any changes in the intensity of N9, N3, 536 nm and 576 nm systems. Meanwhile, the intensity of the H4 lines decreased while that of the H3 signals increased. Comparison of absorption spectra from the different pieces of sample 5, before and after annealing, with absorption spectra from natural IaB diamonds revealed that no correlation exists between the intensity of N9 absorption and the concentration of nitrogen in the B form. For example, strong N9 peaks were recorded in the IIa sample 5 with almost no (≤ 20 ppm) B defects. Along with the previous work [24] this result disproves a widely tolerated idea that the N9 center is related to the B nitrogen.

No platelets were observed in IR spectra of our samples either before or after annealing.

Comparison of optical results of each run shows that, unexpectedly, the aggregation of nitrogen was the highest in sample 1, which was annealed for only 10 h but in several steps (see Table 1). All samples, but #5, still contain an appreciable fraction of nitrogen in the C form after annealing and only a small fraction ($\leq 25\%$) of nitrogen converted to pairs (A defect). This result is at odds with many other works, where almost complete transformation of nitrogen (C \rightarrow A) could be achieved after few hours of annealing at similar conditions [2–4].

3.2. Small angle X-ray studies

An introduction to the theory and details of the SAXS technique can be found in Ref. [25]. All diamonds investigated in this work were examined by SAXS and showed no scattering prior to the annealing. This indicates the absence of defect clusters.

After 100 h or 960 h annealing of synthetic stones (3 and 4) SAXS signals appeared. The deduced gyration radius of scattering defects was rather close for both samples and is equal to 17 nm. The best agreement with the experimental curves was achieved using the hard sphere approximation. The diameter of the spherical defects in samples 3 and 4 were estimated as 44 nm. Despite the similarity of defects size in samples 1–4 the scattering in sample 4 was much more intense than in samples 1–3. This indicates a higher contrast of

electronic density of the clusters with the diamond matrix and/or higher concentration of clusters per unit volume of diamond.

Rather unexpectedly, strong scattering, comparable to that from sample 4, was observed in the annealed type IIa diamond (sample 5). The diameter of defects in it is, however, significantly smaller and is close to 27 nm. The difference between SAXS curves prior and after annealing is shown in Fig. 1.

After 10 h annealing of synthetic diamonds (both incremental and continuous, samples 1 and 2) SAXS curves were close to the background. Because the approximation of defects by the hard spheres satisfactorily fitted experimental curves from samples 3, 4 and 5 this model was also applied to the small signals in samples 1 and 2 and yielded a diameter of the spherical defects of ~ 57 nm. However, referring to the weakness of the experimental signals, we would stress the approximate nature of this result.

The sizes of defects responsible for SAXS in samples studied in this work are similar to those observed previously for annealed synthetic and natural IaA diamonds [17]. Our SAXS data show that there is no well-defined boundary between the defect and surrounding matrix. Similar results were obtained earlier from X-ray diffuse scattering [26].

One of the most important results of this study is that the contrast between scattering clusters and the diamond matrix as well as their size can be similar in nitrogen-rich and nitrogen-poor samples. The contrast between the electronic density of the defects and the diamond matrix is significant. For nitrogen-containing samples this contrast increases with the duration of annealing and the defects size possibly decreases with the annealing time, though the latter fact needs larger statistics. Significant changes in the X-ray scattering became observable in the IIa (low-nitrogen) diamond after much shorter annealing (100 h), than that for the nitrogen-containing sample #4 (960 h). However, the reason for this phenomenon could be that the IIa

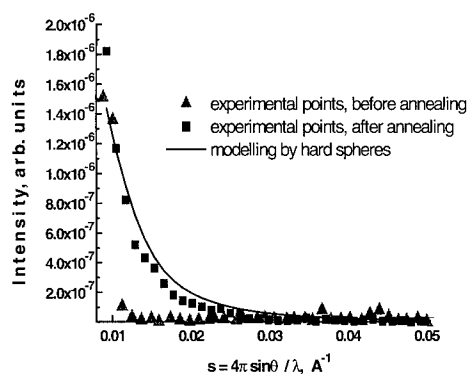


Fig. 1. Small-angle scattering from type IIa natural diamond.

diamond used in our study was natural and thus already significantly annealed. This explanation is supported by the fact that the small amount of nitrogen (<20 ppm) in this sample was present in the aggregated B form already before the experiment.

4. Discussion

Several factors can account for the observed small degrees of nitrogen aggregation and the differences between continuous and incremental runs. It is known that atoms of transition metals strongly increase nitrogen aggregation rate [27]. According to PL measurements, the concentration of Ni atoms was lowest in samples 3 and 4 which, combined with the longer durations of these experiments could explain the low aggregation rate observed for these samples compared to 1 and 2. However an additional mechanism is required to account for the differences in aggregation rate between samples 1 and 2 which contain the same quantities of nickel. During every HPHT annealing cycle some non-hydrostatic pressure component is present, especially when pressurizing and depressurizing the sample. This can result in production of vacancies, thus greatly facilitating nitrogen diffusion [28]. With annealing time, the majority of vacancies should disappear into a variety of sinks, and diffusion rates should subsequently decrease unless a new pressure load-release cycle occurs. We would conclude from these observations that many historical experiments on nitrogen aggregation could produce artificially high diffusion rates compared to natural settings which do not involve cyclical pressure changes.

One of the major results of this study is that continuous annealing leads to much lower nitrogen aggregation rate, than a series of short runs of comparable total duration. This should be taken into account when analyzing results of experiments on nitrogen aggregation.

Our experimental results also suggest that the observations by SAXS isometric clusters in diamond are not related [17] to previously reported extended defects in diamond, such as platelets or voidites. To the best of our knowledge, neither platelets nor voidites have ever been observed in IIa diamonds, whereas we have been able to produce the clusters in diamonds of that type. Additionally, the presence of defect clusters, differing from platelets, is indirectly supported by positron annihilation measurements [29,30]. The contrast of electronic density with the diamond matrix is much higher for platelets than for the clusters we observe, and additionally, the cluster contrast is sample dependent. It is reasonable to suggest that the variations of contrast could be related to different amounts of point defects inside the cluster. For example, pressure

increases the rate of interstitial-assisted diffusion [31]. If the clusters contain appreciable amount of interstitial atoms, then their contrast with the diamond matrix may depend on pressure during annealing. Pressure used in our experiments (7.2 GPa) is higher than average pressure experienced by most natural diamonds (4–5 GPa [18]). This could be an explanation why the SAXS contrast is higher for experimentally annealed samples than for natural IaB diamonds.

The similarity of SAXS patterns in annealed Ia and IIa diamonds does not obviate the possibility of nitrogen as a component of all clusters per se. For example, it was shown that 'man-made' voidites [32] and platelets [33] differ from 'natural' ones in terms of size, shape and probably, composition. Similarly there could be a large variety of ways to form observed extended defects. In several papers voidites formation was correlated with the platelet degradation [11,32], however, voidites have also been reported for diamonds without platelets or dislocation loops [34]. Despite the size differences, there is no evidence from SAXS measurements to suggest that the clusters in nitrogen-rich Ia and nitrogen-free IIa diamonds have different compositions. It is concluded therefore, that the clusters, observed in the present experiments, in addition to those observed previously for IaA and IaB stones [17], do not consist of nitrogen, but possibly contain carbon interstitials.

5. Conclusions

Annealing of Ib and IIa diamonds at temperature of ~1800°C and pressure of 7.2 GPa was performed. Long continuous runs (up to 40 days) were used in order to simulate the conditions of the upper mantle of the Earth and spectra obtained are similar to naturally annealed diamonds. It is shown that the nitrogen aggregation rate is significantly slower in single duration experiments than in those involving several runs, despite similar total time. It is therefore considered likely that many multiple-run annealing experiments described in literature over-estimate the rate of nitrogen diffusion in diamond. This conclusion has a significant bearing on the age/temperature relationships calculated for natural diamonds.

Three-dimensional clusters of defects were formed during our experiments, as detected by SAXS. Their size is similar to that of clusters previously observed in annealed natural and synthetic IaA and IaB diamonds. Nitrogen, if present at all, is not an important component of these clusters, but they may contain carbon interstitials. Generation of the observed clusters is independent of the formation of platelets.

Optical results reveal that HPHT annealing can lead to decay of the 4N–2V (H4) defects into 2N–V (H3) and that the N9 optical center is not the B nitrogen defect.

References

- [1] J.P.F. Sellschop, Nuclear probes, in: J.E. Field (Ed.), *The Properties of Diamond*, Academic Press, London, 1992.
- [2] R.M. Chrenko, R.E. Tuft, H.M. Strong, *Nature* 290 (1977) 40.
- [3] T. Evans, Z. Qi, *Proc. Roy. Soc. London A* 381 (1982) 159.
- [4] Yu.A. Klyuev, A.M. Naletov, V.I. Nepsha, L.D. Belimenko, V.A. Laptev, M.I. Samoilovich, *Russ. J. Phys. Chem.* 56 (1982) 323.
- [5] E.V. Sobolev, N.D. Samsonenko, V.E. Il'in, *J. Struct. Chem.* 10 (1969) 552.
- [6] G. Davies, *J. Phys. C* 9 (1976) L537.
- [7] J.A. van Wyk, G.S. Woods, *J. Phys.: Condens. Matter* 7 (1995) 5901.
- [8] G. Davies, *Physica B* 273–274 (1999) 15.
- [9] J.M. Baker, *Diam. Rel. Mater.* 7 (1998) 1282.
- [10] J.P. Goss, B.J. Coomer, R. Jones, T.D. Shaw, P.R. Briddon, S. Oberg, *Diam. Rel. Mater.* 10 (2001) 434.
- [11] P.B. Hirsch, P. Pirouz, J.C. Barry, *Proc. Roy. Soc. London A* 407 (1986) 168.
- [12] V.I. Lisoivan, *Fiz. Tverdogo Tela* 21 (1979) 240 (in Russian).
- [13] J.C. Walmsley, A.R. Lang, M.-L.T. Rooney, C.M. Welbourn, *Philos. Mag. Lett.* 55 (1987) 209.
- [14] Yu.A. Klyuev, A.M. Naletov, V.I. Nepsha, N.I. Epishina, T.A. Buligina, *Sov. Phys. Solid State* 19 (1977) 7.
- [15] A.M. Naletov, Yu.A. Klyuev, V.I. Nepsha, T.A. Buligina, N.I. Epishina, *Fiz. Tverdogo Tela* 19 (1977) 1529 (in Russian).
- [16] R.R. Ramanan, S.N.N. Goswami, K. Lal, *Acta Crystallogr. A* 54 (1998) 163.
- [17] A.A. Shiryaev, Yu.A. Klyuev, A.M. Naletov, A.T. Dembo, B.N. Feigelson, *Diam. Relat. Mater.* 9 (2000) 1494.
- [18] G.P. Bulanova, *J. Geochem. Explor.* 53 (1995) 1.
- [19] K. Richter, M.J. Drake, *Earth Planet. Sci. Lett.* 173 (1999) 361.
- [20] L.Yu. Mogilevsky, A.T. Dembo, D.I. Svergun, L.A. Feigin, *Kristallografia* 29 (1984) 581 (in Russian).
- [21] D.I. Svergun, *J. Appl. Crystallogr.* 25 (1992) 495.
- [22] V.A. Nadolinny, A.P. Yeliseyev, O.P. Yuryeva, B.N. Feigelson, *Appl. Magn. Res.* 12 (1997) 543.
- [23] C.D. Clark, S.T. Davey, *J. Phys. C* 17 (1984) 1127.
- [24] G. Davies, I. Summersgill, *Diam. Res.* 1 (1973) 6.
- [25] L.A. Feigin, D.I. Svergun, *Structure Analysis by Small-Angle X-ray and Neutron Scattering*, Plenum Press, New York, 1987.
- [26] A.M. Naletov, Ph.D. Thesis, Kiev, 1978 (unpublished).
- [27] I. Kiflawi, H. Kanda, D. Fisher, S.C. Lawson, *Diam. Rel. Mater.* 6 (1997) 1643.
- [28] A.T. Collins, *J. Phys. C* 11 (1978) L417.
- [29] A.A. Shiryaev, A. van Veen, H. Schut, A.C. Kruseman, O.D. Zakharchenko, *Radiat. Phys. Chem.* 58 (2000) 625.
- [30] A.A. Shiryaev, K. Iakoubovskii, A. van Veen, H. Schut, R. Escobar Galindo, O.D. Zakharchenko, Yu.A. Klyuev, F.V. Kaminsky, B.N. Feigelson, *Mater. Sci. Forum* 363–365 (2001) 40–46.
- [31] M. Aziz, *Appl. Phys. Lett.* 70 (1997) 2810.
- [32] T. Evans, I. Kiflawi, W. Lyuten, G. van Tendeloo, G.S. Woods, *Proc. Roy. Soc. London A* 449 (1995) 295–313.
- [33] I. Kiflawi, J. Bruley, W. Lyuten, G. van Tendeloo, *Philos. Mag. B* 78 (1998) 299.
- [34] G. van Tendeloo, W. Luyten, G.S. Woods, *Philos. Mag. Lett.* 61 (1990) 343.



ELSEVIER

Physica B 308–310 (2001) 604–607

PHYSICA B

www.elsevier.com/locate/physb

Volume expansion and stress tensors for self-interstitial aggregates in diamond

J.P. Goss^{a,*}, R. Jones^a, P.R. Briddon^b^a*School of Physics, University of Exeter, Exeter EX4 4QL, UK*^b*Department of Physics, University of Newcastle upon Tyne, Newcastle NE1 7RU, UK*

Abstract

We present the results of first principles local density functional calculations of the volume dilations and piezospectroscopic stress tensors for interstitial aggregates in diamond to facilitate correlation with the experimental centres. © 2001 Elsevier Science B.V. All rights reserved.

PACS: 61.72.Ji; 61.72.Bb; 71.20.Mq

Keywords: Diamond; Dilation; Stress tensor; Self-interstitials

1. Introduction

In the absence of any imposed stress, isolated point defects are equally distributed over all possible orientations. Applying a compressive stress across a particular face results in an increase in energy of those defects exerting a compressive stress on this face, and a decrease in the energy of those which impose a tensile stress. The increase in energy is $\Delta E = (\text{Tr } B_i \cdot \epsilon)$ where ϵ is the imposed strain tensor and B_i is the traceless energy-stress tensor for defects with orientation i . The equilibrium populations of defects aligned along a direction at temperature T is then proportional to $\exp(-\Delta E_i/kT)$. If the defects can be aligned by stress, then the fraction with orientation i can be measured and the B -tensor found. The tensor does not depend on an energy barrier between different orientations, but the barrier must be low enough that the defects can reorient in the stress field and thermal equilibrium be established. The tensor B can be obtained by the total energy methods and previous calculations have produced agreement with the experimental stress tensors for an

aggregate of four self-interstitials [1] and oxygen defects [2] in Si.

In this paper we apply the same techniques to the known interstitial centres in diamond. The single, di- and tri-self-interstitial defects have been observed via electron paramagnetic resonance (EPR), labelled R2, R1 and O3, respectively (Figs. 1 and 2(a)). Stress alignment data [8] has only been reported for R2. This has been investigated previously by theory, with good agreement between the calculated and measured B -tensors [3]. Encouraged by this success, we report in this paper B -tensors for a number of other self-interstitial aggregates.

2. Method

We use a local spin-density functional method, AIMPRO, in large supercells containing the defect [2,4]. Each interstitial defect is modelled by placing the appropriate number of extra carbon atoms into the centre of a supercell containing up to 216 host atoms.

To calculate the stress tensor of a defect, one first relaxes the volume of the supercell containing it. This provides information about dilatation which can be measured. Strains are then imposed across the surfaces

*Corresponding author. Tel.: +44-1392-264198; fax: +44-1392-264111.

E-mail address: goss@excc.ex.ac.uk (J.P. Goss).

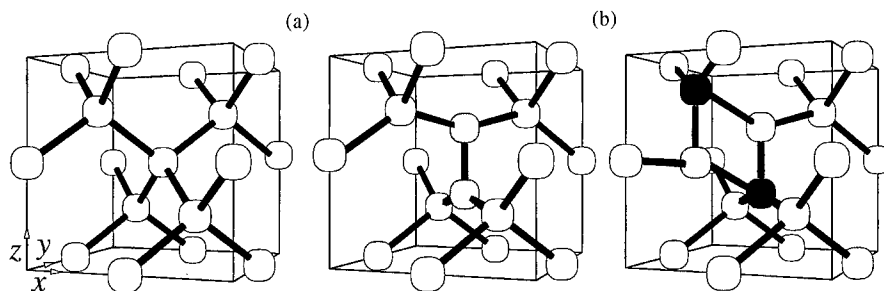


Fig. 1. Diagram showing the geometry of (a) I_1 (R2), and (b) I_2 (R1). Three- and four-fold coordinated interstitial atoms are shown grey and black, respectively.

of the relaxed supercell and the derivative of the energy with strain provides the components of the B -tensor.

The volume change caused by a defect can, in favourable cases, be measured and compared directly with calculations. We adopt the notation that the fractional change in volume is $\eta[X]/[C]$ for defect X , where $[C]$ is the number density of host sites. η has units of the volume per host atom, $V_{\text{ref}} = a_0^3/8$, and can be then be interpreted as the measured volume change caused by X . As an example A-centres (neighbouring substitutional nitrogen atoms) cause an increase in lattice parameter interpreted as $\eta = 0.11$ [5]. Calculations were carried out in a 64 atom cell containing an A-centre. Volume relaxation yields $\eta = 0.11$, in excellent agreement with the experimental data. This gives us the confidence in evaluating the volume changes associated with other defects.

3. Results

The structure of the single self-interstitial is a $[001]$ -oriented split-interstitial (Fig. 1(a)). For this centre we calculate $\eta = 1.9$, which is a factor of twenty times than that of the A-centre. Due to the high symmetry (D_{2d}), the B -tensor for a defect is given by a single term. For a z -oriented defect, the values of B_{xx} , B_{yy} and B_{zz} found from the 64 atom unit cell are 13.8, 13.8 and -27.6 eV, respectively. The B -tensor can be directly compared with experimental work on R2 [8], which implies $B_{xx} = B_{yy} = 12$ eV, $B_{zz} = -24$ eV.

The R1 EPR centre has been identified with one form of the di-interstitial (I_2) [6]. This consists of two parallel $[001]$ split-interstitial defects sited at nearest neighbour locations so that one pair of dangling bonds is reconstructed. This leaves the remaining pair parallel to a $[1\bar{1}0]$ direction as illustrated in Fig. 1(b). We have calculated the B -tensor and dilatation for I_2 . Since there are non-zero off-diagonal terms in the I_2 B -tensor, we diagonalise this matrix to find its principle values and

Table 1

Principal values and directions for the stress-energy tensors (eV per unit strain) of self-interstitial aggregates. The dilation constant per interstitial η/n is also given

Defect	η/n	B_1	B_2	B_3
I_1	1.9	-27.6	13.8	13.8
(R2)		$[001]$	$[100]$	$[010]$
I_2	1.7	-44.4	41.9	2.6
(R1)		23° to $[00\bar{1}]$	23° to $[110]$	$[1\bar{1}0]$
I_3	1.6	-89.7	45.9	43.8
(O3)		2° to $[001]$	2° to $[100]$	$[010]$
I_4	1.5	-120.5	60.3	60.3
		$[001]$	$[100]$	$[010]$

directions. The diagonal form of the B -tensor is given in Table 1, as well as the volume expansion in terms of η for this centre. Note that the volume dilation per interstitial is lower than that of I_1 , showing that as well as eliminating dangling bonds, aggregation of interstitials also reduces the local strain, and hence the formation energy.

One form of the tri-interstitial eliminates four of the dangling bonds leaving a pair of radicals. This is illustrated in Fig. 2(a), and can be understood as a next-nearest-neighbour di-interstitial in a (110) plane with an additional I_1 in the $(1\bar{1}0)$ plane also at the next-nearest-neighbour site. It possesses a C_2 axis along a cube direction. The D -tensor for the $S = 1$ defect is close to the O3 $S = 1$ EPR centre [7] which also has this symmetry. As before, the additional aggregation reduces the volume relaxation per interstitial (Table 1). The diagonalised B -tensor for I_3 is also given in Table 1.

The structure of the O3 EPR centre leads naturally to a stable form of I_4 shown in Fig. 2(b). This was originally suggested as a building block for $\{001\}$ platelets in diamond [9]. The bond angles only deviate by $\pm 9^\circ$ and bond lengths by $\pm 10\%$ from bulk values. The calculated η and B -tensor are listed in Table 1.

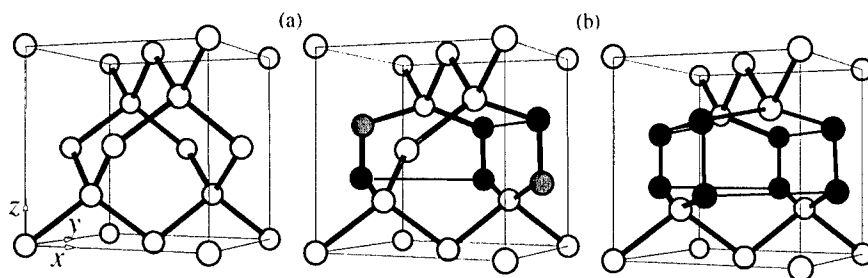


Fig. 2. Diagram showing the geometry of (a) I_3 (O3), and (b) I_4 . Three- and four-fold coordinated interstitial atoms are shown grey and black, respectively.

Note, the total volume relaxation for I_4 is close to that of only three isolated self-interstitials. The experimental value of B_3 for the corresponding defect in silicon is -28 eV [10]. Scaling this experimental value for I_4 in silicon by the ratio of the bulk moduli of diamond to silicon yields a value of $B_{3\pm} = -126.5$ eV, very close to the calculated value in this study.

Finally, it is useful to compare the volume changes of the interstitial defects with that of the vacancy in diamond. The level of theory employed cannot treat the individual multiplets of the vacancy, and in line with most previous work, we assume the defect is described by a single determinantal wave function. We used a 64 atom supercell from which we have removed a single atom. The atoms bordering the vacancy move outwards and form a cube of length 1.89 Å, but the net volume change of the entire supercell is practically zero, with $\eta < 0.01$. In fact, the only large deviations from bulk positions for the vacancy occur at the nearest neighbours. We conclude that the volume increase due to vacancies is very much less than that for interstitials, and in particular the effect on the lattice due to the single self-interstitial is at least one and probably several orders of magnitude larger than that due to the vacancy.

4. Discussion and conclusions

We have found volume increases and piezospectroscopic tensors B for several self-interstitial defects in diamond. The values of B found for the single interstitial agree very well with the measurements on the R2 EPR centre. To our knowledge, no other alignment studies have been carried out on other EPR centres linked with interstitials, although the R1 and O3 defects could potentially be directly measured. The volume displaced per interstitial diminishes as the aggregates get larger. This, along with the elimination of dangling bonds, contributes to the increased binding energy per interstitial with increasing aggregates size [3].

The very large magnitudes for the B -tensor elements of multi-interstitial defects imply that even for relatively small applied stresses a detectable polarisation of the defect orientation would be apparent, provided that any barrier to reorientation can be overcome.

Finally, it is clear that there is a vast disparity between the volume expansion arising from vacancy and interstitial related centres, of which I_1 is usually by far the dominant species. This means that any volume expansion measured for irradiated material by, for example, X-ray diffraction, arises from the single self-interstitial and not the vacancy. Such a volume effect should be discernible in X-ray experiments on heavily irradiated diamonds provided that the damage leaves the diamond essentially crystalline.

Acknowledgements

The authors would like to thank A.R. Lang, for helpful discussions.

References

- [1] B.J. Coomer, J.P. Goss, R. Jones, S. Öberg, P.R. Briddon, *J. Phys.: Condens. Matter* 13 (2001) L1.
- [2] J. Coutinho, R. Jones, P.R. Briddon, S. Öberg, *Phys. Rev. B* 62 (2000) 10824.
- [3] J.P. Goss, B.J. Coomer, R. Jones, T.D. Shaw, P.R. Briddon, M. Rayson, S. Öberg, *Phys. Rev. B* 63 (2001) 195208.
- [4] R. Jones, P.R. Briddon, in: M. Stavola (Ed.), *Identification of Defects in Semiconductors, Semiconductors and Semimetals*, Vol. 51A, Academic Press, Boston, 1998 (Chapter 6).
- [5] A.R. Lang, G. Pang, *Philos. Trans. Roy. Soc. London, Ser. A* 356 (1998) 1397.
- [6] D.J. Twitchen, M.E. Newton, J.M. Baker, O.D. Tucker, T.R. Anthony, W.F. Banholzer, *Phys. Rev. B* 54 (1996) 6988.

- [7] D. Hunt, D. Twitchen, M.E. Newton, J.M. Baker, 1999, private communication.
- [8] D.C. Hunt, D.J. Twitchen, M.E. Newton, J.M. Baker, T.R. Anthony, W.F. Banholzer, S.S. Vagarali, Phys. Rev. B 61 (2000) 3863.
- [9] P. Humble, Proc. Roy. Soc. London, Ser. A 381 (1982) 65.
- [10] K.L. Brower, Phys. Rev. B 14 (1976) 872.



ELSEVIER

Physica B 308–310 (2001) 608–611

PHYSICA B

www.elsevier.com/locate/physb

Modeling fluorescence of single nitrogen–vacancy defect centers in diamond

A.P. Nizovtsev^{a,*}, S.Ya. Kilin^a, C. Tietz^b, F. Jelezko^b, J. Wrachtrup^b

^a*Institute of Physics, Belarus National Academy of Science, 220072 Minsk, Byelorussia*

^b*Institute of Physics, University of Stuttgart, Stuttgart, Germany*

Abstract

Based on new spectroscopic information retrieved by experiments on individual Nitrogen–Vacancy (NV) defect centers in diamond, we introduced the five-level photophysical model of the center and demonstrate its applicability to describe consistently different experiments on single NV centers. The model takes into account the triplet–triplet character of the optical transition $^3A \rightarrow ^3E$ (637 nm) of the center and the presence of a metastable singlet state 1A . Supposing optical excitation rates B_T from spin substates $T = X, Y, Z$ of the ground 3A state as well as the fluorescence emission rates A_T to these substates to be different ($B_Z/B_X \approx 11$, $B_X = B_Y$ while $A_Z/A_X \approx 18$, $A_X = A_Y$), we were able to fit consistently the experimental data obtained for green-laser-excited single NV centers at room-temperature: (i) lineshapes of fluorescence-detected magnetic resonance at 2.88 GHz in the ground 3A state and their changes due to the strains in the diamond crystal, (ii) fluorescence saturation and (iii) photon antibunching/bunching in the fluorescence light emitted by a single NV center. © 2001 Elsevier Science B.V. All rights reserved.

Keywords: Single defect; Quantum optics; Optically detected magnetic resonance

1. Introduction

Recently the nitrogen–vacancy (NV) defect center in diamond has been observed [1] and studied in detail spectroscopically [2–5] as an individual quantum object using single molecule spectroscopy (SMS) (see, e.g. Ref. [6] for review). The centers consist of a nitrogen atom (N) and a vacancy (V) in adjacent lattice sites. At low NV concentration (≤ 1 center per μm^3) they are well separated spatially and can be detected individually [1] using scanning confocal microscopy. Therefore, exciting individual NV centers and counting emitted fluorescence photons with an appropriate photon detector, one can measure the average fluorescence intensity $\langle I_0 \rangle$ and the second order fluorescence intensity correlation function $g^{(2)}(\tau) = \langle I_0(t)I_0(t+\tau) \rangle / \langle I_0 \rangle^2$, study their variations from center to center and their changes under additional external influences. Experiments of such kind [1–5] have provided new insight into the photodynamics of the

center and contributed new information to the characterisation of the defect which has a long history based on conventional high-resolution spectroscopic techniques (see, e.g. Refs. [7–9] for review and references). In particular, it has been established [10] that under green/blue optical excitation the centers exhibit strong red fluorescence (yield $\phi = 0.96$) due to dipole-allowed E–A optical transitions with a zero-phonon line (ZPL) at 1.945 eV ($\lambda \approx 637$ nm) and a phonon-assisted band spaced ~ 300 meV apart. The essential feature of the NV center is that its electronic ground state is a spin triplet 3A [7–9,11]. At zero field the state 3A is split by crystal field into a doublet X, Y ($m_s = \pm 1$) and a singlet Z ($m_s = 0$) separated by 2.88 GHz. In turn, the excited electronic triplet state 3E of the center has a rather complicated fine structure [12] originating from spin–spin and spin–orbit interactions as well as from the strain in the crystal. Additionally, the center has a metastable singlet state 1A [13] to which it can escape from the fluorescent 3E state through intersystem crossing (ISC). Optical illumination generates the non-Boltzman distribution of populations of the ground 3A

*Corresponding author. Fax: +375-172-84-08-79.

E-mail address: apniz@dragon.bas-net.by (A.P. Nizovtsev).

state spin sublevels X, Y and Z due to transitions in the optical pumping circle that do not conserve spin projections. As a result, optically excited NV centers exhibit a strong ESR signal at 2.88 GHz. In turn, microwaves (MW) at ~ 2.88 GHz modify the populations of the spin sublevels which results in changes of the fluorescence intensity emitted by the optically excited center, thus providing the basis for a variety of fluorescence-detected magnetic resonance (FDMR) phenomena [7–9,11].

Experiments [1–5] with single NV centers which eliminate completely the effects of inhomogeneous broadening and ensemble averaging allowed (i) to measure the absolute value ($\sim 10\%$) of the FDMR effect [1], (ii) to study the fluorescence saturation [1–5] (saturation power of 1.3 mW has been determined at focused laser beam diameter $\sim 1.6 \mu\text{m}$), (iii) to observe antibunching of the fluorescence photons emitted by the center [3–5]. All the above experiments have been done at room-temperature and under green-laser optical excitation. In Refs. [3–5] the NV center photokinetics has been analysed in terms of the simplest three-level model that ignores the triplet character of the ground 3A state of the center. Here we introduce a more realistic five-level model which allows to describe consistently a wide range of optical and FDMR experiments dealing both with single NV centers and with their ensemble. The model is practically important for quantum optics

due to recent suggestions to use the single NV center as a single-photon emitter [3–5] as well as to a construct quantum computer using ^{13}C nuclear spins in vicinity of the center [14].

2. Five-level model of the NV center

The basic idea of the model for the green-laser-excited NV center is illustrated in Fig. 1 where the left part shows double-well potentials (DWP) for the ground 3A and excited 3E electronic states of the center calculated in Ref. [15] using a simple analytical expression for DWP to fit the experimental fluorescence spectra for few single NV centers [1]. Due to different positions of the DWPs minima, the most effective optical excitation of the center is provided by green/blue optical radiation. Internal conversion (IC) transfers the center to the fluorescing zero-phonon vibrational substate of the N atom in the upper DWP. Transitions to the vibrational states in the ground DWP form the fluorescence spectrum with the outer left transition in the Fig. 1 contributing to the ZPL, while the other ones contribute to the phonon sideband. Fast IC destroys completely the optical coherence, allowing to describe laser excitation of the center in terms of Einstein coefficients $B = bI_{\text{opt}}$. Moreover, it makes it possible not to consider the details of the fast

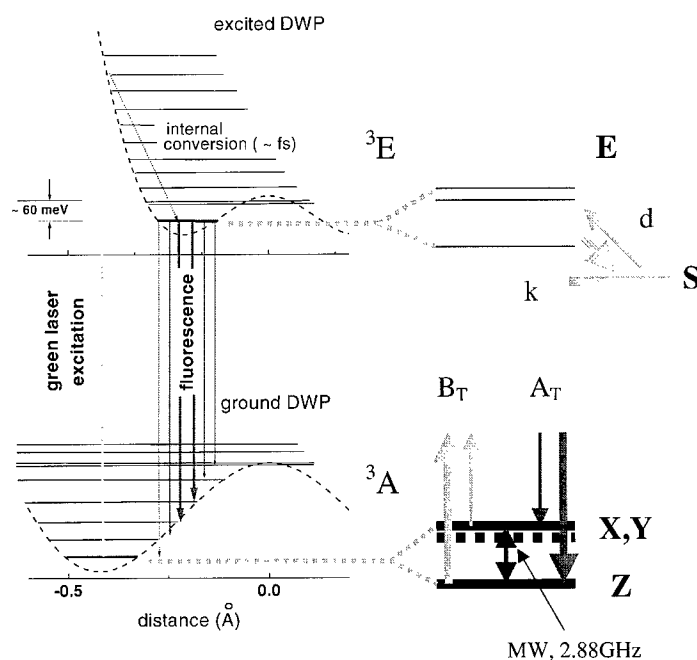


Fig. 1. Left: Double-well potentials for ground and excited electronic states of the center as well as respective vibrational energies of the N atom within the DWPs calculated in Ref. [15]. The figure takes into account a possible tunneling of the N atom into the vacancy. Right: Spin-triplet substructure of ground 3A and fluorescing excited 3E states and the presence of 'metastable' singlet 1A state S of the center. The five-level photophysical model of the center incorporates the states E, S, X, Y and Z.

movement of the center over intermediate vibrational states and consider only final zero-phonon states. In doing so we will neglect the complicated substructure of the excited state of the NV center [12] and consider it as a single fluorescing state E. On the other hand, to be able to describe the FDMR phenomena within the model we will consider the ground triplet electronic state of the center as consisting of three spin substates X, Y and Z. Additionally, our five-level model incorporates the singlet state 1A which is indicated on the right part of Fig. 1 as state S. According to Dräbenstedt et al. [2] the state S lies at 37 meV lower than the E state. Due to ISC transition the center can be shelved into this state with rate k . Opposite deshelling transitions SE will be taken into account by rate $d = d_T + d_{opt}$ consisted of the contribution d_T due to a phonon absorption as well as the contribution d_{opt} describing possible optical excitation of the center into higher singlet states followed there by ISC transition to the triplet manifold [2].

In general, optical excitation rates B_T from different spin substates $T = X, Y, Z$ as well as the spontaneous emission rates A_T to these substates are different for different substates T. The reasons are the spin-projection selection rules for excitation as well as the simplified description of the excited-state spin manifold as a single level. In particular, different spin sublevels of the excited electronic state are characterized by spin-selective rates for ISC transitions to and from the singlet state S resulting in their different populations. Effectively, these different populations, in combination with selection rules for emission, result in different rates of arrival of the center at the sublevels X, Y, Z by spontaneous emission. Clearly, the total fluorescence rate $A = 13.7$ MHz [16] is $A = A_X + A_Y + A_Z$. Due to symmetry considerations we will suppose spin subsubstates X and Y to be optically equivalent: $B_X = B_Y$ and $A_X = A_Y$.

The density matrix equations for the model can be written straightforwardly using respective rates B_T , A_T , k and d to describe optical and ISC transitions while considering the interaction of a triplet spin with MWs with all necessary details i.e. taking into account MW-induced coherences in terms of density matrix elements ρ_{XZ} , ρ_{YZ} and ρ_{XY} . In the representation rotating with the MW frequency ω , one gets a set of 11 by 11 linear differential equations with constant coefficients. In these equations essential parameters for MW-spin interaction are the Rabi frequency $W = W_{XZ} = W_{YZ} = -mB^\pm$ (m is magnetic dipole matrix element for transitions X(Y)-Z, and B^\pm are MW field amplitudes) and the detuning $\varepsilon = \omega_{XZ} - \omega$, $\varepsilon - \Delta = \omega_{YZ} - \omega$. Decay of coherence (e.g. of the element ρ_{XZ}) is described in these equations by the rate $\Gamma_{XZ} = K_{XZ} + (L_{XZ} + L_{XY} + L_{ZY} + L_{ZX})/2 + (B_X + B_Z)/2$ where K_{XZ} is the rate of pure spin dephasing due to fluctuating nuclear spins

around the NV center, $L_{TT'}$ takes into account spectral diffusion and spin-lattice relaxation and the final term, proportional to the optical intensity ($B_T = b_T I_{opt}$), results from finite lifetimes of spin substates due to optical excitation.

Under steady-state conditions the equations of the model can be solved analytically. The fluorescent state population ρ_{EE}^{st} is calculated to determine the average fluorescence intensity $\langle I_{fluor} \rangle = A\rho_{EE}^{st}$ and to describe the fluorescence saturation with optical power P_{opt} and the FDMR lineshape, i.e. the dependence of $\langle I_{fluor} \rangle$ on the MW frequency ω . The second order correlation function has been calculated according to $g^{(2)}(\tau) = [A_X\rho_{EEXX}(\tau) + A_Y\rho_{EEYY}(\tau) + A_Z\rho_{EEZZ}(\tau)] / A\rho_{EE}^{st}$, where $\rho_{EETT}(\tau)$ are the transient solutions for $\rho_{EE}(\tau)$ with the initial condition that at time $t = 0$ the center is in the state T. The weight coefficients A_T/A are the probabilities for the center to be in the state T after the emission of the first photon at the moment $t = 0$.

Analysis has shown that a consistent description of the experiments [1–5] can be done if one supposes that the induced absorption rates $B_X (= B_Y)$ and B_Z for the green-laser excited NV center differ by a factor of ~ 11 ($B_Z/B_X \sim 11$), while the fluorescence rates $A_X (= A_Y)$

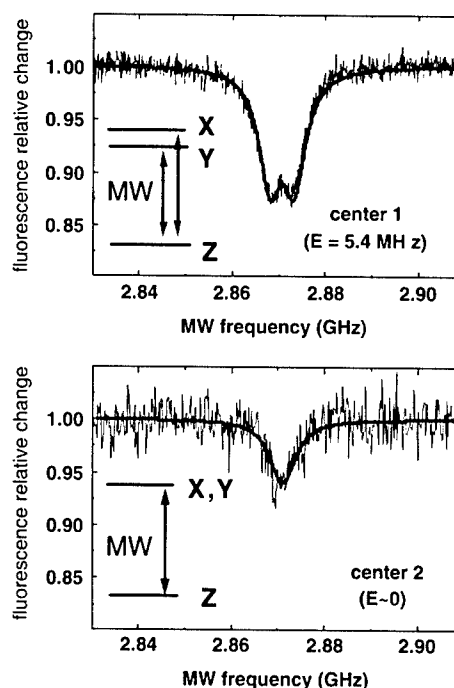


Fig. 2. Experimental FDMR lineshapes for two individual NV centers [1] and those calculated using the five-level model of Fig. 1 with parameter values indicated in the text. Center 2 exhibits ideal C_{3v} symmetry (zero-field splitting $\Delta = \omega_{XZ} - \omega_{YZ} = 0$) while for center 1 this symmetry is broken due to influence of strain ($\Delta = 5.4$ MHz).

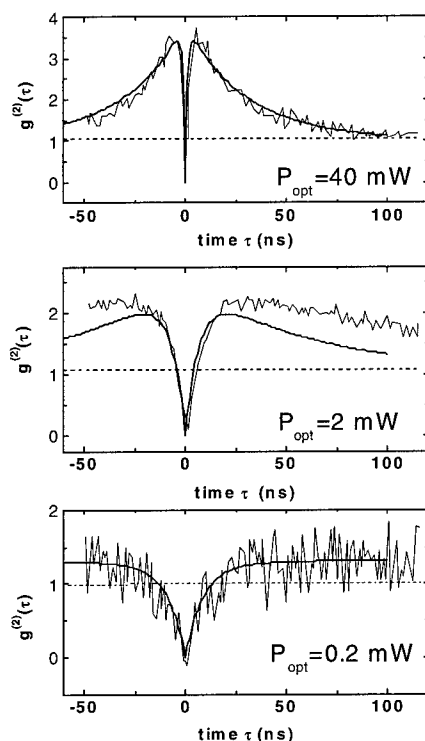


Fig. 3. Noise-corrected experimental $g^{(2)}(\tau)$ functions measured in Refs. [3–5] at different optical powers P_{opt} and those calculated using five-level model of Fig. 1 at parameter values indicated in the text.

and A_Z to these sublevels differ by a factor of 18 ($A_Z/A_X \sim 18$). At room temperature ISC shelving/deshelving rates are high enough: $k \sim A/3$; $d \sim A/10$ with optical deshelling d_{opt} to be negligible. The model with these parameters predicts optical alignment of the center (under low-intensity optical illumination) at which most of population is in Z substate: $\rho_{ZZ}^{\text{st}} \sim 0.4$, $\rho_{XX}^{\text{st}} = \rho_{YY}^{\text{st}} \sim 0.3$, $\rho_{SS}^{\text{st}} \sim 0.006$. The model gives the experimentally monitored value $\sim 10\%$ of the FDMR effect and fits well the FDMR lineshapes (Fig. 2). Using the laser beam diameter as an additional fitting parameter and taking the experimental value of $\sim 0.15\%$ for the fluorescent photon detection efficiency we were able to fit well the experimental data of Refs. [3–5] for the fluorescence saturation behavior, the saturation power $P_{\text{opt}} = 1.3 \text{ mW}$ and the saturated fluores-

cence intensity $\sim 5 \text{ kcounts/s}$. Finally, the correlation functions $g^{(2)}(\tau)$, calculated within the model, fit rather well the noise-corrected experimental ones [3–5], demonstrating strong photon antibunching at short times (Fig. 3). Preliminary analysis shows that additionally the model with the above parameters describes well experimental data on FDMR transients, obtained previously [11] for NV ensemble.

Acknowledgements

This work is supported in part by DFG grants 28-8/2 and 28-6/1.

References

- [1] A. Gruber, A. Dräbenstedt, C. Tietz, L. Fleury, J. Wrachtrup, C. von Borczyskowski, *Science* 276 (1997) 2012.
- [2] A. Dräbenstedt, L. Fleury, C. Tietz, F. Jelezko, S. Kilin, A. Nizovtsev, J. Wrachtrup, *Phys. Rev. B* 60 (1999) 11503.
- [3] C. Kurtsiefer, S. Mayer, P. Zarda, H. Weinfurter, *Phys. Rev. Lett.* 85 (2000) 290.
- [4] R. Brouri, A. Beveratos, J.-Ph. Poizat, Ph. Grangier, *Opt. Lett.* 25 (2000) 294.
- [5] A. Beveratos, R. Brouri, J.-P. Poizat, Ph. Grangier, *quant-ph/0010044* (2000).
- [6] T. Basché, W.E. Moerner, M. Orrit, U. Wild (Eds.), *Single-Molecule Optical Detection, Imaging and Spectroscopy*, VCH, Weinheim, 1997.
- [7] G. Davies, N.B. Manson, in: G. Davies (Ed.), *Properties and Growth of Diamond*, INSPEC, London, 1994, p. 173.
- [8] E. Van Oort, Ph.D. Thesis, Amsterdam University, 1990.
- [9] A. Dräbenstedt, Ph.D. Thesis, University of Jena, 1999.
- [10] G. Davies, M.F. Hammer, *Proc. R. Soc. London A (UK)* 348 (1976) 285.
- [11] E. van Oort, N.B. Manson, M. Glasbeek, *J. Phys. C* 21 (1988) 4385.
- [12] J.P.D. Martin, *J. Lumin.* 81 (1999) 237.
- [13] D.A. Redman, S. Brown, R.R. Sands, S.C. Rand, *Phys. Rev. Lett.* 67 (1991) 3420.
- [14] J. Wrachtrup, S.Ya. Kilin, A.P. Nizovtsev, *Opt. Spectrosc.* 91 (2001) 460.
- [15] S.Ya. Kilin, A.P. Nizovtsev, T.M. Maevskaya, A. Dräbenstedt, J. Wrachtrup, *J. Lumin.* 86 (2000) 201.
- [16] A.T. Collins, M.F. Thomaz, M.I.B. Jorge, *J. Phys. C* 16 (1983) 2177.



ELSEVIER

Physica B 308–310 (2001) 612–615

PHYSICA B

www.elsevier.com/locate/physb

Irradiation effects in semiconducting diamonds

N. Kristianpoller*, D. Weiss, R. Chen

*School of Physics & Astronomy, Raymond and Beverly Sacker Faculty of Exact Sciences, Tel-Aviv University,
Ramat-Aviv, Tel-Aviv 69978, Israel*

Abstract

Effects of X-ray, β and UV irradiation on semiconducting diamonds (type IIb) were studied and compared with those induced at the same conditions in natural (type Ia) and in synthetic diamonds. Methods of optical absorption, of X-ray and light induced luminescence, of thermoluminescence (TL) as well as of optically stimulated luminescence and optically stimulated thermoluminescence (OSL and OSTL) were used for the investigations. The IIb diamonds showed in the UV a weak absorption band at 260 nm and a sharp increase of absorption below 230 nm, while in the Ia samples the absorption increased sharply below 300 nm and absorption bands appeared near 310, 385 and 415 nm. In the X-ray induced luminescence of all samples an emission band appeared near 440 nm; in the Ia samples, additional band was recorded near 500 nm and a very weak one at about 360 nm. In all samples TL could be excited by X-ray, β as well as by 360-nm UV radiation; and in the IIb diamond also by 225 and 470 nm. In the TL of IIb diamonds main emission bands appeared at 475 and 665 nm, and in the OSTL of the Ia samples at 650 nm. The thermal activation energies were evaluated and found to be of about 0.36, 0.52 and 0.67 eV at the 360, 420 and 520 K peaks, respectively. The main TL peaks appeared in all samples above RT at the same temperatures and with the same thermal activation energies. The results indicate that these TL peaks are due to the same radiation induced trapping levels in all investigated types of diamonds, while in the emission of the various samples different luminescence centers are involved. The TL reached in all investigated samples saturation for relatively low radiation doses. © 2001 Elsevier Science B.V. All rights reserved.

PACS: 78.30.Am; 78.60.Kn; 78.60.Ya

Keywords: Diamond; Irradiation effects; Radiation defects

1. Introduction

Irradiation effects and formation of radiation induced defects in diamonds have been studied for several decades. Most of these studies concentrated on natural—type Ia diamonds; in some studies also semiconducting—type IIb diamonds were investigated (e.g.: [1–4]). More recently also synthetic diamonds [5] as well as diamond films grown by chemical vapor deposition technique (CVD) [6] were applied for these studies. Some of the CVD diamonds were also found to be highly suitable for application in radiation dosimetry [7].

In the present work, effects of X-ray, β and UV irradiation were studied in semiconducting diamonds (type IIb) and compared with those induced at the same conditions in natural (type Ia) and in synthetic-boron containing diamonds. Methods of optical absorption, of X-ray and light induced luminescence (XL and PL) of thermoluminescence (TL) as well as of optically stimulated luminescence and optically stimulated thermoluminescence (OSL and OSTL) were applied for the studies.

2. Experimental techniques

The X-ray irradiations were performed with a W-tube (40 kV, 15 mA) and the β irradiations with a ^{90}Sr source of a 1.5 Gy/min dose rate. The UV irradiations were

*Corresponding author. Tel.: +972-3-6408684; fax: +972-3-6429306.

E-mail address: nahum@post.tau.ac.il (N. Kristianpoller).

carried out with a Xe lamp (150 W) and a grating monochromator. The β irradiations were carried out at room temperature (RT) and the X and UV irradiations at various temperatures between 80 and 300 K. The TL measurements above RT were carried out in a TL compartment, flushed by N_2 gas; the heating rate above RT was 5 K/s. For the low temperature absorption, luminescence and thermoluminescence measurements the samples were kept in liquid nitrogen vacuum cryostat and for the TL measurements they were heated at a rate of 20 K/min. The OSTL and OSL were stimulated at various temperatures between 80 and 400 K by monochromatic light in samples which had previously been exposed to X or β radiation. The optical absorption was measured with a Cary 17 spectrophotometer. The PL, OSL, TL and OSTL measurements were taken with Aminco-Bowman/2 luminescence-spectrometer.

3. Results and discussion

3.1. Optical absorption

The I Ib diamonds showed in the UV a weak absorption band near 260 nm and a sharp increase of absorption below 230 nm. In the Ia samples the absorption increased sharply below 300 nm and an additional absorption band appeared on the absorption tail at 310 nm and weaker bands at 385 and 415 nm.

3.2. XL, PL and OSL

During X-ray irradiation at RT, a luminescence band was recorded in the I Ib samples at 450 nm. At liquid nitrogen temperature (LNT) an XL emission band appeared in these samples at 435 nm and was narrower and by an order of magnitude stronger than at RT. In the Ia type diamonds a main XL band was recorded at RT at 445 nm with a shoulder at 500 nm and a weaker band at 360 nm. By cooling to LNT the main 445 nm band intensity increased by a factor of three. In Fig. 1, XL emission spectra of the various types of diamonds are given. No photoluminescence could be detected by UV excitation in the I Ib and in the synthetic diamonds neither before nor after prolonged exposure to ionizing radiation. In Ia samples, which had previously been exposed to ionizing radiation, a luminescence emission could be excited by UV light. This luminescence disappeared after heating to about 800 K and is therefore attributed to an OSL emission, where carriers are trapped by ionizing X-ray or β irradiation at certain defect levels and then optically stimulated by UV or even visible light. These results also indicate that the defects, induced by ionizing radiation, become unstable at about 800 K. The main OSL emission band was at

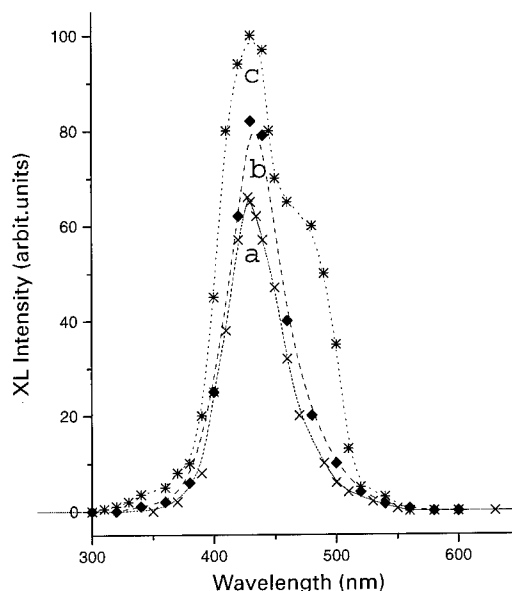


Fig. 1. X-ray induced emission spectra of various samples measured at LNT: (a) a synthetic diamond, (b) a semiconducting I Ib and (c) a natural Ia diamond.

340 nm and had a stimulation maximum at the absorption peak at 310 nm. An additional broad band was recorded in the Ia samples between 420 and 480 nm; this broad band is apparently composed of two spectral components at 435 and 475 nm. The 340 nm emission band could also be excited by longer wavelengths up to about 550 nm. This finding supports the conclusion that this emission is due to a process of optical stimulation. The intensity of all these OSL emission bands increased markedly by cooling from RT to LNT.

3.3. TL and OSTL

In all samples, TL could be excited by X, β as well as by UV radiation. TL peaks above RT appeared in the various samples at 360, 420 and 520 K. The relative intensities of the various peaks differed and in some samples additional peaks were recorded at about 480 and 550 K. The thermal activation energies at the main TL peaks were evaluated by the “initial rise” and “different heating rate” method (Booth formula) [8]. The values of the thermal energies were found to be in all samples about 0.36, 0.52 and 0.67 eV at the 360, 420 and 520 K peaks respectively.

After irradiation at LNT, different TL peaks appeared in the various samples. After X irradiation, the main peak appeared in the I Ib samples at 265 K, and a weaker one at 145 K. In the Ia samples TL peaks appeared after

LNT irradiation at 180, 225, 260 and 300 K. In the synthetic samples, TL peaks were recorded at 145, 240, 300 and 355 K. The 355 K peak is probably the same as the 360 K peak, which appears after RT irradiation. This 360 K peak decays very fast at RT (about 75% of its initial intensity in 1 min); this is apparently due to thermal fading.

In all examined diamonds, TL could also be excited by UV light and the dependence of the excitation efficiency on the wavelength of the exciting light was measured. TL excitation spectra of the main 360 K peak had in all samples a maximum at 365 nm. In the IIB samples the UV excitation spectrum had an additional main maximum at 225 nm and at LNT also at 470 nm. In the IIB diamonds, the main peak appeared by 225 nm excitation at 265 K and by 365 nm excitation at 285 K. TL excitation spectra are shown in Fig. 2. In Ia diamonds that had previously been X-ray or β irradiated at RT and subsequently illuminated at LNT with light of 310 nm glow peaks were recorded during heating from LNT to RT at 116 and 285 K. These glow peaks could not be excited by 310 nm UV light in un-irradiated Ia diamond samples and not in X or β irradiated samples that were heated to 800 K before exposure to the 310 nm illumination. These 116 and 285 K glow peaks excited by the 310 nm illumination are therefore attributed to a process of OSTL. In this process, carriers which were trapped by the ionizing radiation in deep traps at RT, are subsequently stimulated by the illuminating light and

transferred to shallower traps; the OSTL is emitted during their thermal release and radiative recombination. It may be noted that the wavelength of 310 nm was also optimal for the stimulation of OSL in pre-irradiated Ia samples. In the pre-irradiated synthetic diamonds, illumination with 500 nm caused the optical bleaching of the 520 K TL peak and the rise of the 420 K peak; this is also attributed to a photo-transfer from a deep trap to a shallower one. No OSTL was recorded in the IIB samples.

The spectral composition of the TL emission was measured at the main glow peaks. In the TL emission of type IIB diamonds, the main bands appeared at 475 and 665 nm. The emission of the main OSTL peak in the Ia diamonds was at 650 nm. Emission spectra measured at the main glow peaks are shown in Fig. 3. The fact that different emission bands appeared in the various examined diamonds indicate that different luminescence centers are involved in the emission of these samples. The finding that the main TL peaks appeared in the various samples at the same temperatures and with the same thermal activation energies indicate that these TL peaks are due to the same radiation induced trapping levels.

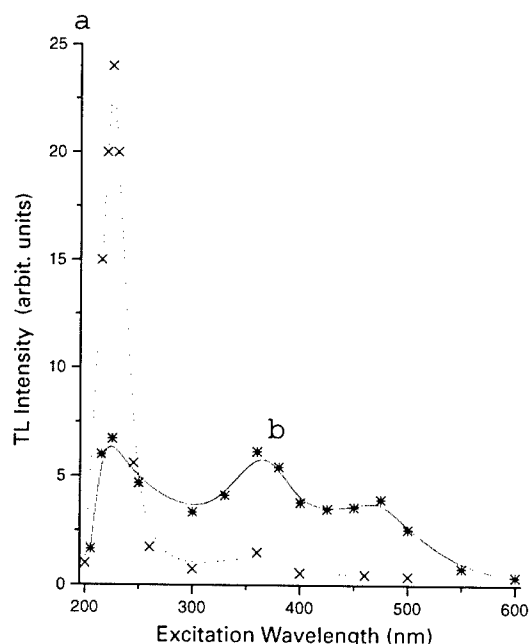


Fig. 2. TL excitation spectra of: IIB diamond at (a) RT, (b) LNT.

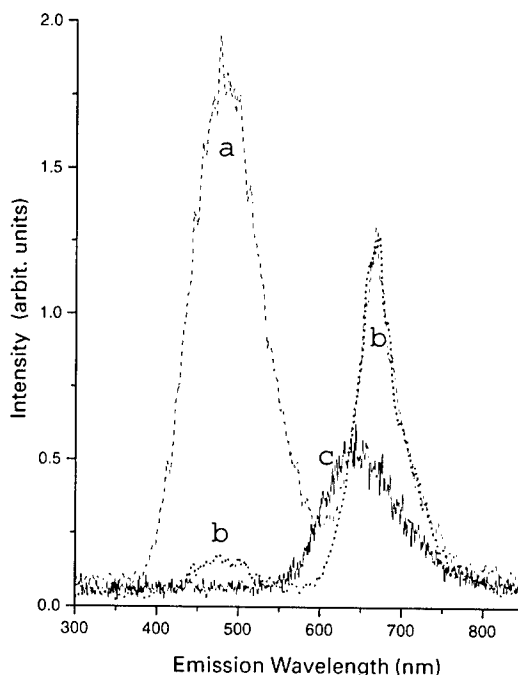


Fig. 3. TL Emission spectra of IIB diamond recorded after UV irradiation at LNT with: (a) 225 nm, (b) 360 nm UV light and (c) emission spectrum of Ia diamond, recorded at the 116 K OSTL peak after X irradiation at RT and 310 nm illumination at LNT.

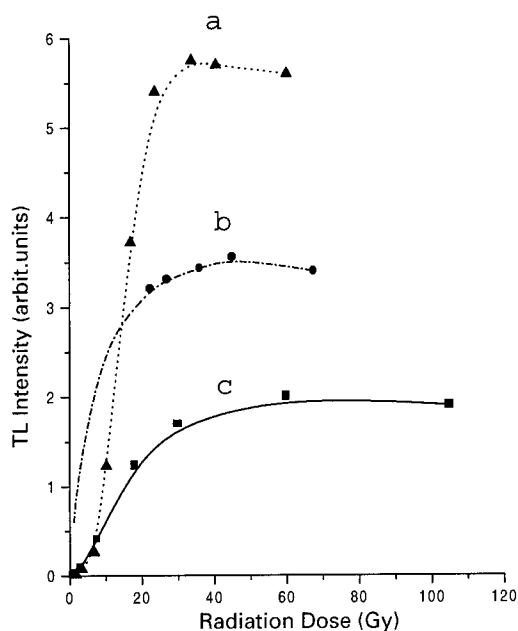


Fig. 4. Dependence of the TL intensity on beta dose of: (a) Ia diamond (enlarged $\times 10$), (b) IIb diamond and (c) synthetic diamond.

The dependence of the TL intensity on the dose of the exciting radiation were also measured. The dependence

of the TL intensity on the dose of the exciting β radiation is shown in Fig. 4 for the various investigated types of diamonds. It can be seen that the TL intensity reaches in these samples saturation for relatively low doses. A similar behavior of dose dependence was also recorded for UV excited TL. This behavior is not favorable for application in TL dosimetry, but may be different for other types of synthetic diamonds.

References

- [1] A. Halperin, J. Nahum, *J. Phys. Chem. Solids* 18 (1961) 297.
- [2] P.J. Dean, *Phys. Rev.* 139A (1965) 588.
- [3] R. Chen, S.A.A. Winer, N. Kristianpoller, *J. Chem. Phys.* 60 (1974) 4804.
- [4] P. Klein, M.D. Crossfield, H.A. Freitas Jr., A.T. Collins, *Phys. Rev. B* 51 (1995) 9634.
- [5] R. Zeisel, C.E. Nebel, M. Stutzmann, *J. Appl. Phys.* 84 (1998) 6105.
- [6] A. Bizarri, B. Bogani, M. Bruzzi, S. Sciortino, *Nucl. Instr. and Meth. A* 426 (1999) 169.
- [7] M. Benabdesselam, P. Iaconi, D. Briand, J.E. Butler, *Diamond Relat. Mater.* 9 (2000) 1013.
- [8] R. Chen, S.W.S. McKeever, *Theory of Thermoluminescence and Related Phenomena*, World Scientific Publ. Co., Singapore, 1997, pp. 12, 101–113.



ELSEVIER

Physica B 308–310 (2001) 616–620

PHYSICA B

www.elsevier.com/locate/physb

Nickel related defects in diamond: the 2.51 eV band

M.H. Nazaré*, J.C. Lopes, A.J. Neves

Departamento de Física, Universidade de Aveiro, 3810 Aveiro, Portugal

Abstract

Optical and magnetic properties of nickel related defects in as-grown diamond are reviewed. Published and new data on the problem of negatively charged substitutional nickel are presented and discussed. We show that the 2.51 eV absorption band occurs at the Ni_i^- , the spin-orbit and the Jahn–Teller interactions playing important roles in the optical properties of the defect. © 2001 Elsevier Science B.V. All rights reserved.

Keywords: Diamond; Nickel; Spin-orbit; Optical properties

1. Introduction

Transition metals (TMs), namely nickel, cobalt, iron, manganese and most of the first TM series, are used as solvent catalysts during the growth of diamond; hence the metals can become incorporated in the diamond, at atomic level, as point defects. However, only nickel and cobalt are known to exist in this way [1–3], i.e. bonded to the diamond lattice; the other TMs appear to resist incorporation or avoid detection. Nickel is now known to form optical and paramagnetic centres, and to have complex interactions with nitrogen. The observed properties of Ni related centres strongly depend on the nitrogen concentration ([N]) in the diamond. In as-grown high-pressure high-temperature diamond, either interstitial or substitutional Ni is observed, depending on the concentration of neutral nitrogen, $[\text{N}^0]$, which controls the Fermi energy and hence the charge state of the active centres.

In as-grown diamonds with $[\text{N}] < 10$ ppm, two Ni interstitial EPR centres are observed. The NIRIM1 has an isotropic g -factor, and is assumed to be a tetrahedral Ni_i^+ atom; the NIRIM2 has $g_{\perp} \sim 0$ and $g = 2.3285$, and is assumed to be Ni_i^+ in trigonal symmetry [4]. Also, nickel related absorption bands occur at 1.2, 1.4 and 3.1 eV. The 1.4 eV system, which can be detected in luminescence as well, consists of a zero-phonon doublet,

at 1.401 and 1.404 eV. The splitting of the ground state was accounted for in terms of spin-orbit (S–O) interaction. Fine structure in each of the doublet has shown to be due to isotopic splitting and is consistent with one nickel atom per optical centre [5]. Uniaxial stress and Zeeman measurements have led to the conclusion that the defect has trigonal symmetry and that both the ground doublet and the excited singlet have effective spins $S = \frac{1}{2}$; the g -values, determined from the Zeeman data for the ground state of the doublet, agree with the g -values of the EPR study of the NIRIM2 defect. Therefore, it was then concluded, and recently confirmed [6,7], that the centre concerned is an interstitial positive Ni ion, Ni_i^+ , in a trigonal environment.

In as-grown diamonds with $[\text{N}] > 50$ ppm, an isotropic EPR signal (W8) with $g = 2.0319$ has been identified with the negative charge state of isolated substitutional nickel, Ni_s^- [8]. Optical features typical of these diamonds are two centres with zero-phonon lines (ZPLs) at 1.885 and 2.51 eV. The 1.885 eV defect has rhombic-I symmetry and, given the circumstantial evidence, it was suggested to occur at a Ni–N complex [9]. Absorption at 1.885 and at 2.51 eV has been tentatively correlated with the strength of the W8 signal [10], however, no definite answer was produced.

In this paper, using high-resolution absorption data and uniaxial stress measurements, we show that the 2.51 eV ZPL is consistent with a transition from a $^4\text{A}_2$ ground state into a $^4\text{T}_2$ excited state at a tetrahedral

*Corresponding author. Fax: +351-2344-24965.

E-mail address: mhnazare@fis.ua.pt (M.H. Nazaré).

defect; such a transition is forbidden by symmetry, but becomes allowed through S–O induced mixing of the excited and fundamental states. Furthermore, we show that S–O interaction splits the excited state, giving rise to the fine structure observed in the ZPL. In view of the results we propose that in fact the 2.51 eV absorption band occurs at the negatively charged substitutional nickel (Ni_s^-) that is the same defect where the W8 EPR signal occurs.

2. Experimental details

The samples used in this work were synthetic diamond grown by the Japanese Institute for Research in Inorganic Materials. Absorption measurements were made using a 100 W quartz-halogen tungsten lamp. Light from the sample was analysed and detected by a SPEX monochromator fitted with a 1200 grooves/mm grating and an RCA photomultiplier. Uniaxial stresses were applied using oil driven push rods, the samples being cooled by liquid nitrogen or liquid helium.

3. The 2.51 eV zero-phonon line shape

The 2.51 eV absorption band is depicted in Fig. 1. The ZPL is a multiplet spanning about 1.5 meV. Previous work [11] showed that the fine structure must be due to a split excited state and cannot be accounted for in terms of isotopic splitting originated by the different abundances of the Ni isotopes. The same work reported uniaxial stress measurements carried out at 77 K (at this temperature no fine structure can be detected), suggesting that the 2.51 eV centre has tetrahedral symmetry, the ZPL occurring between T_2 states. However no obvious explanation was advanced for the lack of splitting under stress of the ground state, nor for the unfitting predictions regarding the relative intensities. These discrepancies can be clarified in a model that considers

the 2.51 eV band to occur between the ground and first excited states, predicted by crystal field theory, of the Ni_s^- , that is between a 4A_2 ground state and a 4T_2 excited state. Although such transition is symmetry forbidden, S–O interaction makes it possible through mixing the excited 4T_2 state with the 4A_2 ground state; such being the case, and loosely speaking, the splitting pattern under stress would look like that of a transition between two T_2 states, where the ground state is not split. We now show that the fine structure can also be consistently accounted for in terms of the above model.

The Hamiltonian for a TM ion of the d^n configuration, placed in a cubic crystal field, can be written as

$$H = H_{\text{cub}} + H_{\text{S-O}}, \quad (1)$$

the two terms representing the crystal field and the S–O interaction, respectively.

At a site of tetrahedral symmetry, the lowest free ion term, 4F , of Ni_s^- ($3d^7$) is split by the crystalline field into an orbital ground state 4A_2 (Γ_2) at $-720B_4$, a 4T_2 (Γ_5) state at $-120B_4$ and a 4T_1 (Γ_4) state at $360B_4$. First order S–O interaction splits the 4T_2 state into $J = 1/2$ (Γ_7) at $5\lambda/2$, $J = 3/2$ (Γ_8) at λ and $J = 5/2$ ($\Gamma_8 + \Gamma_6$) at $-3\lambda/2$; second orders effects further split the $J = 5/2$ states.

The S–O splitting of a cubic term can be described by the effective Hamiltonian of second order in L and S [12]:

$$H_{\text{S-O}} = \lambda(\mathbf{L} \cdot \mathbf{S}) + \kappa(\mathbf{L} \cdot \mathbf{S})^2 + \rho(L_X^2 S_X^2 + L_Y^2 S_Y^2 + L_Z^2 S_Z^2). \quad (2)$$

Here, S is the spin (3/2) and L is the effective orbital-momentum operator within the cubic term ($L = 1$ for a T_2 term). The 4T_2 excited state can be written as the product of a spatial ($|T_{2i}\rangle$, $i = x, y, z$) and a spin ($|a_j\rangle$, $j = -3/2, \dots, +3/2$) part transforming as the Γ_5 and Γ_8 representations of the T_d double group respectively. In this basis set, the secular matrix of the Hamiltonian in Eqs. (1) and (2) can be written as

$$\begin{bmatrix} 3\beta + \Delta & 0 & -\sqrt{3}\beta/2 & 0 & i\delta/4 & 0 & i\sqrt{3}\kappa/2 & 0 & 0 & \sqrt{3}\gamma/4 & 0 & 0 \\ 0 & 2\beta + \Delta & 0 & -\sqrt{3}\beta/2 & 0 & i\delta/4 & 0 & i\sqrt{3}\kappa/2 & -\sqrt{3}\eta/4 & 0 & \lambda - \kappa/2 & 0 \\ -\sqrt{3}\beta/2 & 0 & 2\beta + \Delta & 0 & -i\sqrt{3}\kappa/2 & 0 & -i\delta/4 & 0 & 0 & \delta/2 & 0 & \sqrt{3}\eta/2 \\ 0 & -\sqrt{3}\beta/2 & 0 & 3\beta + \Delta & 0 & -i\sqrt{3}\kappa/2 & 0 & -i\delta/4 & 0 & 0 & \sqrt{3}\gamma/4 & 0 \\ -i\delta/4 & 0 & i\sqrt{3}\kappa/2 & 0 & 3\beta + \Delta & 0 & \sqrt{3}\beta/2 & 0 & 0 & i\sqrt{3}\gamma/4 & 0 & 0 \\ 0 & -i\delta/4 & 0 & i\sqrt{3}\kappa/2 & 0 & 2\beta + \Delta & 0 & \sqrt{3}\beta/2 & -i\sqrt{3}\eta/4 & 0 & i\delta/2 & 0 \\ i\sqrt{3}\kappa/2 & 0 & i\delta/4 & 0 & \sqrt{3}\beta/2 & 0 & 2\beta + \Delta & 0 & 0 & i\delta/2 & 0 & i\sqrt{3}\eta/4 \\ 0 & i\sqrt{3}\kappa/2 & 0 & i\delta/4 & 0 & \sqrt{3}\beta/2 & 0 & 3\beta + \Delta & 0 & 0 & i\sqrt{3}\gamma/4 & 0 \\ 0 & -\sqrt{3}\eta/4 & 0 & 0 & 0 & i\sqrt{3}\eta/4 & 0 & 0 & 3\beta/2 + \Delta & 0 & 0 & 0 \\ -\sqrt{3}\gamma + 4 & 0 & \delta/2 & 0 & -i\sqrt{3}\gamma + 4 & 0 & i\delta/2 & 0 & 0 & 7\beta/2 + \Delta & 0 & 0 \\ 0 & \lambda - \kappa/2 & 0 & \sqrt{3}\gamma + 4 & 0 & i\delta/2 & 0 & i\sqrt{3}\gamma + 4 & 0 & 0 & 7\beta/2 + \Delta & 0 \\ 0 & 0 & \sqrt{3}\eta + 4 & 0 & 0 & 0 & i\sqrt{3}\eta + 4 & 0 & 0 & 0 & 0 & 3\beta/2 + \Delta \end{bmatrix}$$

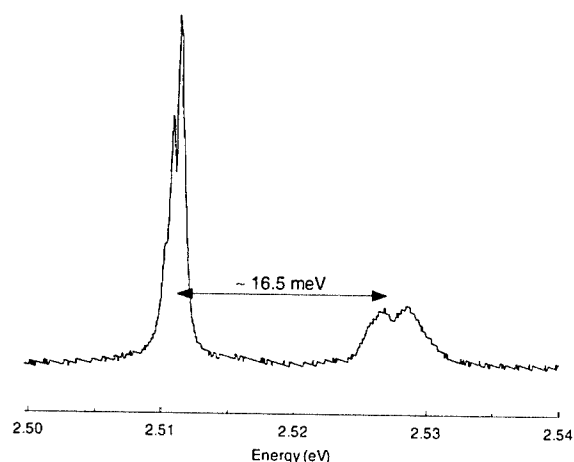


Fig. 1. The 2.51 eV absorption band, recorded at 4 K. The zero-phonon line is a multiplet spanning about 1.5 meV.

Here, $\beta = \kappa + \rho$, $\delta = \kappa - 2\lambda$, $\gamma = 3\kappa - 2\lambda$, $\eta = \kappa + 2\lambda$ and $\Delta = 600B_4$ are the energy separation between the ground (4A_2) and the first excited state (4T_2) before S–O interaction. Fitting the eigenvalues of the above matrix to the measured energy values and the intensity ratio of the components in the ZPL, calculated using the eigenvectors, to the measured ones, yields the following set of values for the parameters (all but the first in meV):

$$\begin{aligned} \Delta &= 2.5105 \text{ eV}, \quad \lambda = -0.163, \\ \kappa &= -0.326, \quad \rho = 0.532. \end{aligned} \quad (3)$$

Fig. 2 shows a comparison between the experimental zero-phonon band shape and the calculated one,

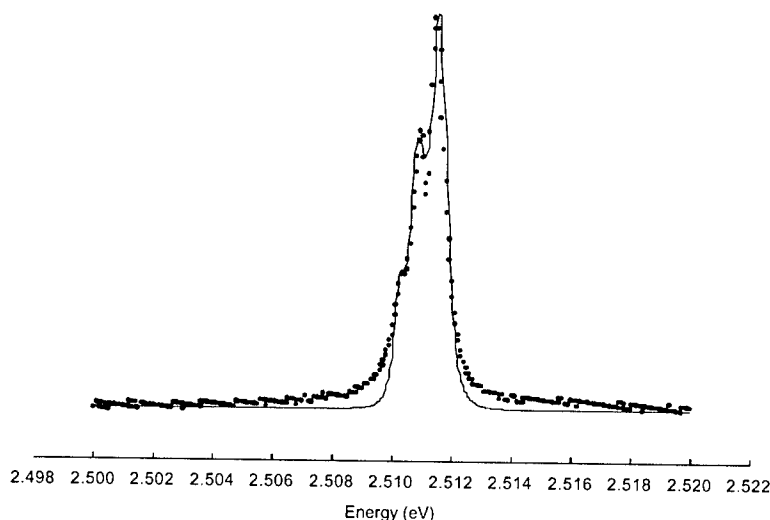


Fig. 2. Comparison between the experimental (points) zero-phonon band shape (the same as in Fig. 1) and the calculated one (line). A bi-Lorentzian shape for each component has been assumed. The values of the parameters (see text) were: $\Delta = 2.5105$ eV and (in meV) $\lambda = -0.163$, $\kappa = -0.326$ and $\rho = 0.532$.

assuming a bi-Lorentzian shape for each component of the ZPL, $I(\nu) = a/[b + (\nu - \nu_0)^2]^2$, and using the values in Eq. (3) to calculate the intensity (a) and the energy (ν_0) of each component. The width (b) of each component was measured experimentally.

4. Uniaxial stress results

The effects on the energies of the ZPLs of uniaxial compressions of up to 2 GPa applied along the $\langle 001 \rangle$, $\langle 111 \rangle$ and $\langle 110 \rangle$ axes, with the crystal cooled to 4 K, are shown in Fig. 3. The data are consistent with the 2.51 eV ZPLs being transitions from a 4A_2 ground state into a 4T_2 excited state in the centre of tetrahedral symmetry. The excited state is split into a quartet by S–O interaction taken to second order.

Since the strains used in the experiments are small, the stress-induced change in the Hamiltonian is linear in the stress tensor components σ_{ij} , and can be written as:

$$\begin{aligned} \Delta H &= C_A(\sigma_{xx} + \sigma_{yy} + \sigma_{zz}) + C_{Et}(2\sigma_{zz} - \sigma_{xx} - \sigma_{yy}) \\ &\quad + C_{Ec}\sqrt{3}(\sigma_{xx} - \sigma_{yy}) + C_{yz}\sigma_{yz} + C_{zx}\sigma_{zx} + C_{xy}\sigma_{xy}. \end{aligned} \quad (4)$$

Here the electronic operators C_A, \dots, C_{xy} transform as shown by the subscripts in the tetrahedral point group. In terms of the basis set we define matrix elements $B = 2\langle T_{2x} | C_{Et} | T_{2x} \rangle / \sqrt{3}$ and $C = \langle T_{2x} | C_{xy} | T_{2y} \rangle$.

In the experiments it is not possible to separate the effects of totally symmetric stresses σ_{ij} on the excited T_2 and ground A_2 states, hence we define the parameter $A = \langle T_{2x} | C_A | T_{2x} \rangle - \langle A_2 | C_A | A_2 \rangle$. The analysis is simplified by noting that there are no matrix elements of the stress perturbation between states of different spins.

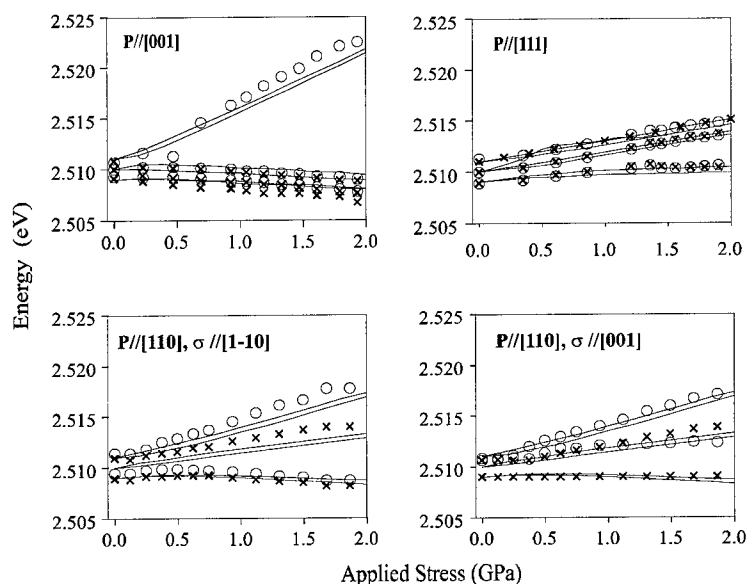


Fig. 3. Theoretical (lines) and experimental stress-induced splittings of the 2.52 eV zero-phonon line at 4 K (experimental points for $P//[110]$ were obtained at 77 K).

The lines in Fig. 3 have been calculated using this theory with the parameters: $A = 1.45$ meV/GPa, $B = 2.15$ meV/GPa, and $C = -1.93$ meV/GPa. The agreement between the predictions and the data establishes that the defect has tetrahedral symmetry, and that the 2.51 eV transition occurs between 4A_2 and 4T_2 states. Spin-orbit interaction admixes the ground and excited states, which makes the transition possible, and also produces the fine structure splitting.

5. Discussion

The work of Isoya et al. [8] shows that the $g = 2.0319$ EPR signal is from a Ni^- ($3d^7$) located at a substitutional site in diamond, with an effective spin $S = 3/2$. We have shown that the fine structure and behaviour under applied stress of the 2.51 eV ZPL is consistent with a transition occurring between 4A_2 and 4T_2 states at a tetrahedral defect. These have the predicted symmetry and order of the crystal field split states originated from a 4F term of the d^7 electronic configuration expected for the Ni_s^- ion in diamond, hence the conclusion that both the EPR signal and the 2.51 eV optical transition originate at the same defect.

The orbital degeneracy of the excited state implies that it is unstable against distortions, which lower its symmetry and lift the electronic degeneracy. This type of instability, first studied by Jahn and Teller, couples the electronic and vibrational motions lowering the energy of the symmetrical configuration by E_{JT} . If the Jahn–

Teller and the S–O interactions are comparable, it has been shown that the Jahn–Teller coupling partially quenches the first order S–O interaction within the T_2 state, reducing it by a factor $Q \cong \exp[-3/2(E_{JT}/\hbar\omega)]$, where $\hbar\omega$ is the average energy for the effective phonons, while it may either diminish or enhance the second order S–O interactions within this state [13,14]. The g -value for the ground state is related to $A = 2\lambda$ through $g = g_e - 8A/4$; this gives for λ , within the ground state, a value of -4.7 meV, about 30 times larger than the S–O coupling parameter within the 4T_2 state. This indicates the importance of Jahn–Teller coupling to understand fully the optical properties of the Ni_s^- .

References

- [1] A.T. Collins, H. Kanda, R.C. Burns, *Philos. Mag.* B 61 (1990) 797.
- [2] S.C. Lawson, et al., *J. Appl. Phys.* 79 (1996) 4348.
- [3] K. Johnston, et al., *Diamond Relat. Mater.* 9 (2000) 424.
- [4] J. Isoya, H. Kanda, Y. Uchida, *Phys. Rev. B* 42 (1990) 9843.
- [5] G. Davies, A.J. Neves, M.H. Nazaré, *Europhys. Lett.* 9 (1989) 47.
- [6] M.H. Nazaré, A.J. Neves, G. Davies, *Phys. Rev. B* 43 (1991) 14196.
- [7] P.W. Mason, F.S. Ham, G.D. Watkins, *Phys. Rev. B* 60 (1999) 5417.
- [8] J. Isoya, H. Kanda, J.R. Norris, M.K. Bowman, *Phys. Rev. B* 41 (1990) 3905.

- [9] M.H. Nazaré, L.M. Rino, H. Kanda, *Mater. Sci. Eng. A* 209 (1996) 302.
- [10] A.T. Collins, et al., *Diamond Relat. Mater.* 7 (1998) 333.
- [11] M.H. Nazaré, J.C. Lopes, H. Kanda, *Mater. Res. Soc. Symp. Proc.* 339 (1994) 625.
- [12] M.D. Sturge, *Phys. Rev. B* 1 (1970) 1005.
- [13] F.S. Ham, *Phys. Rev.* 138 (1965) A1727.
- [14] G.A. Slack, F.S. Ham, R.M. Chrenko, *Phys. Rev.* 152 (1966) 376.



ELSEVIER

Physica B 308–310 (2001) 621–624

PHYSICA B

www.elsevier.com/locate/physb

Positively charged carbon vacancy in 6H–SiC: EPR study

V.Ya. Bratus^{a,*}, I.N. Makeeva^a, S.M. Okulov^a, T.L. Petrenko^a, T.T. Petrenko^a,
H.J. von Bardeleben^b

^a*Institute of Semiconductor Physics NASU, 45, Prospect Nauky, 03028 Kyiv, Ukraine*

^b*Groupe de Physique des Solides, Universités Paris 6&7, 2, Place Jussieu, 75251 Paris, France*

Abstract

The low-temperature X-band EPR study of Ky1 and Ky2 centers assigned to positively charged carbon vacancy (V_C^+) in two quasicubic sites of 6H–SiC crystal is presented. The C_s symmetry, spin $S = 1/2$ and close coincidence of the g -tensor components have been revealed. The principal values of g -tensor are determined as $g_z = 2.0048$, $g_x = 2.0022$ and $g_y = 2.0037$ for Ky2 defect, where z - and x -directions reside in the $(1\ 1\ \bar{2}\ 0)$ plane and the z -axis makes up an angle 65° with the c -axis. The same residence of z - and x -axis and an angle 59° are found for Ky1 center with $g_z = 2.0058$, $g_x = 2.0025$ and $g_y = 2.0023$. For Ky2 center, the principal values and corresponding directional cosines of the hyperfine (HF) interaction tensor A are determined for four Si atoms in the nearest neighborhood of the defect. Ky3 center is tentatively proposed as V_C^+ defect in quasihexagonal site of 6H–SiC. The results of ab initio DFT calculations using cubic $C_{18}Si_{16}H_{36}$ and hexagonal $C_{18}Si_{20}H_{40}$ clusters corroborate the main features of proposed V_C^+ defect models including the point symmetry and values of HF parameters. © 2001 Elsevier Science B.V. All rights reserved.

Keywords: Intrinsic defect; Carbon vacancy; Silicon carbide; EPR

1. Introduction

Positively charged carbon vacancy V_C^+ was originally identified in p-type cubic SiC based on the intensity ratio of all hyperfine satellite lines to the main lines [1]. An EPR spectrum labeled T5 belongs to a paramagnetic defect with D_2 symmetry, spin $S = 1/2$ and axially symmetric HF tensor along $\langle 1\ 1\ 1 \rangle$ axis, $A_{||} = -18.9 \times 10^{-4} \text{ cm}^{-1}$ and $A_{\perp} = -13.8 \times 10^{-4} \text{ cm}^{-1}$. In the recent publications a variety of carbon vacancy-related defects have been found in electron irradiated p-type 4H- and 6H–SiC [2–6]. Some of them with the HF constants being about twice as large as for T5 center have also been attributed to V_C^+ center [4–6]. Subsequently, a revision of T5 nature as the $(V_C + 2H)$ complex has been proposed in Ref. [7].

As was found in our previous work [4], three carbon vacancy-related defects labeled Ky1, Ky2 and Ky3 are

detected in boron-doped 6H–SiC crystals after a high dose 2 MeV electron irradiation. The spin Hamiltonian parameters for $T \geq 77 \text{ K}$ were found for Ky1, Ky2 and Ky3 defects when some indications of motional averaging were observed [4]. However, the ultimate elucidation of defect nature requires the knowledge about its low-temperature symmetry. In this paper, we focus on the X-band EPR study of Ky1 and Ky2 centers at 4.2 K.

2. Experimental

The samples for electron irradiation were high quality Lely-grown 450 μm thick crystals of 6H–SiC with boron content of about $4 \times 10^{17} \text{ cm}^{-3}$. The electron irradiation was performed at 77 K with 2.0 MeV electron beam parallel to the crystal c -axis up to the dose of $1 \times 10^{18} \text{ cm}^{-2}$. The X-band EPR spectra of carbon vacancy-related defects were measured at 4.2 K at microwave power level of 40 nW. The angular variations were studied for a rotation of the magnetic field in three mutually perpendicular $(1\ 1\ \bar{2}\ 0)$, $(1\ \bar{1}\ 0\ 0)$ and $(0\ 0\ 0\ 1)$

*Corresponding author. Fax: +380-44-265-8342.

E-mail address: endor@div5.semicond.kiev.ua
(V.Y. Bratus).

crystal planes. The g -values were determined with a precision of $\Delta g = \pm 0.0001$ via a microwave frequency counter and a calibration of the magnetic field by a proton NMR probe.

3. Results and discussion

Six-line EPR spectra observed for Ky1 and Ky2 centers for rotation of the magnetic field in $(11\bar{2}0)$ crystal plane indicate C_s symmetry, spin $S = 1/2$ and a close coincidence of the g -tensor components. Distinctly oriented defects are magnetically equivalent in couples when magnetic field is rotated in $(1\bar{1}00)$ plane and three-line spectrum is detected for either center as shown in Fig. 1a. The spectrum Ky3 is only observed at a higher temperature, $T \geq 30$ K. Fig. 2 shows the angular variations of Ky1 and Ky2 central lines in three mutually perpendicular $(11\bar{2}0)$, $(1\bar{1}00)$ and (0001) crystals planes. From these dependences, the principal

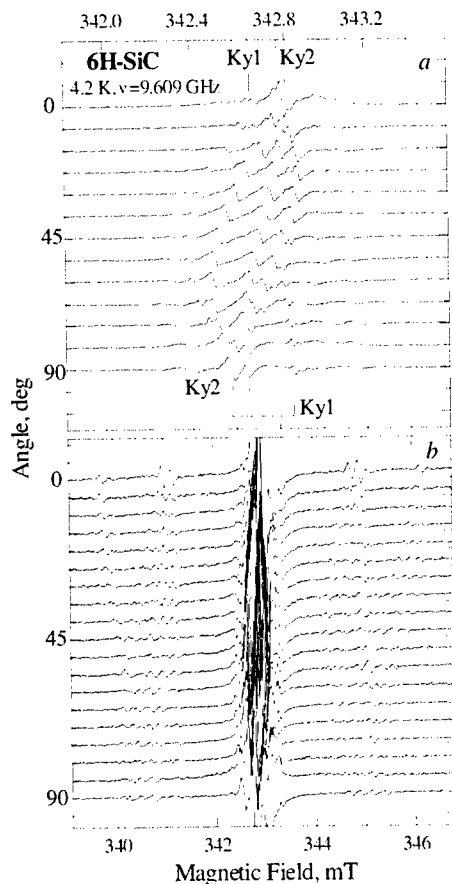


Fig. 1. EPR spectra of electron-irradiated 6H-SiC $\langle B \rangle$ for a rotation of the magnetic field in $(1\bar{1}00)$ plane: a, central lines and b, hyperfine satellites of Ky2. $T = 4.2$ K, $\nu = 9.609$ GHz. Angle 0° corresponds to the direction of magnetic field $B \parallel c$.

values of g -tensor have been determined as $g_z = 2.0048$, $g_x = 2.0022$ and $g_y = 2.0037$, where z and x directions reside in the $(11\bar{2}0)$ plane and the z -axis makes up an angle 65° with the c -axis as shown in Fig. 3. The same residence of z - and x -axis and an angle 59° are found for Ky1 center, $g_z = 2.0058$, $g_x = 2.0025$ and $g_y = 2.0023$. Spin Hamiltonian parameters corresponding to HF

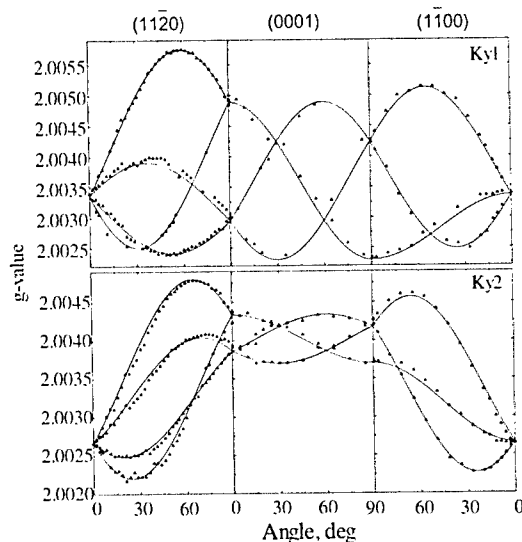


Fig. 2. EPR angular variations of Ky1 and Ky2 centers in 6H-SiC for rotation of the magnetic field in three mutually perpendicular crystal planes. $T = 4.2$ K, $\nu = 9.609$ GHz. The triangles are the experimental points, and the solid curves were calculated with the spin Hamiltonian parameters listed in the text.

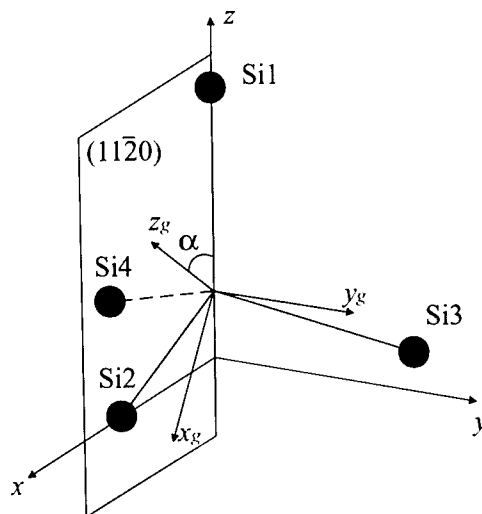


Fig. 3. Directions of the g -tensor principal axes for Ky1 and Ky2 centers in 6H-SiC.

Table 1
Experimentally determined hyperfine parameters of Ky2 center in 6H-SiC

Ligand atom	Principal values of HF tensor (MHz)	Directional cosines corresponding to $A_{ }$
Si1	$A_{ } = 180.7 \pm 0.2$ $A_{\perp} = 119 \pm 1$	$l = (-0.13 \pm 0.01; 0.00; 0.991 \pm 0.001)$
Si2	$A_{ } = 129.5 \pm 0.6$ $A_{\perp} = 87 \pm 1$	$l = (0.85 \pm 0.01; 0.00; -0.53 \pm 0.01)$
Si3	$A_{ } = 153.7 \pm 0.3$ $A_{\perp} = 108 \pm 1$	$l = (0.60 \pm 0.02; 0.77 \pm 0.02; 0.22 \pm 0.01)$
Si4	$A_{ } = 153.7 \pm 0.3$ $A_{\perp} = 108 \pm 1$	$l = (0.60 \pm 0.02; -0.77 \pm 0.02; 0.22 \pm 0.01)$

interaction with nuclei of four Si atoms in the nearest neighborhood are determined just for the Ky2 defect and presented in Table 1. Each of these nuclei is characterized by quasixial HF tensor and an angle α between principal axis associated with $A_{||}$ and direction from the undistorted position of a Si atom to the center of the defect. The directional cosines listed in Table 1 correspond to α values in the range of 8–12°.

Due to longer then for Ky2 center spin-relaxation time, low intensity of the Ky1 spectrum precludes from the determination of its HF parameters at 4.2 K. The close values of HF parameters for Ky1 and Ky2 centers were found at 77 K, where their spectra have the same intensities [4]. Thus, from the identical spin and close values of the g -tensors and HF parameters, it is tempting to suggest that Ky1 and Ky2 spectra originated from the same carbon vacancy-related defect in two quasicubic sites of 6H-SiC crystal. In previous paper [4], this suggestion was supported by cluster calculations of the point symmetry and HF parameters with tetrahedral 52-atom clusters $\text{Si}_4\text{C}_{12}\text{H}_{36}$ and $\text{Si}_3\text{BC}_{12}\text{H}_{36}$ and geometry optimization at UHF/6-31G(d) level of theory [8] with fixed H atoms. In our new approach [9], the geometry optimization of larger 70-atom $\text{C}_{18}\text{Si}_{16}\text{H}_{36}$ cubic cluster has been performed with higher density functional level of theory and all electron split valence Gaussian basis set 6-311G(d) with polarization d-functions for both Si and C atoms. The D_{2d} point symmetry and the same $A_{||} \cong -166$ MHz, $A_{\perp} \cong -97$ MHz hyperfine parameters for all the four nearest Si atoms have been obtained. Relatively slight deviation of experimentally determined HF tensor from the D_{2d} point symmetry and close coincidence with theoretical values demonstrate a rather small perturbation of V_C^+ in quasicubic sites of 6H-SiC by axial crystal field.

The assignment of Ky1 and Ky2 centers to V_C^+ defect in two quasicubic sites of 6H-SiC lattice generates a question regarding the microscopic structure of V_C^+ in hexagonal site. As was pointed out earlier [4], the HF structure of Ky3 spectrum involves three doublets with an intensity ratio 1:1:2 (Fig. 4) analogous to Ky1 and Ky2 spectra. Additional observation of similar hyperfine structure on low-field HF line of Ky3 spectrum (Fig. 4c)

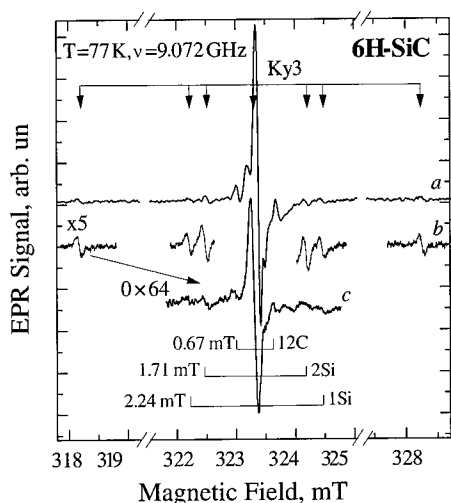


Fig. 4. X-band EPR spectrum of electron-irradiated 6H-SiC $\langle B \rangle$ for orientation of the magnetic field B parallel to the $[1\bar{1}00]$ direction (a). The details of hyperfine structure of Ky3 defect central line (b) and low-field HF line (c) are also shown, $T = 77$ K, $\nu = 9.072$ GHz.

suggests that this defect can be a candidate for V_C^+ in hexagonal site. Preliminary calculations of V_C^+ hyperfine parameters with 78-atom hexagonal cluster [9] reveal the dramatic changes of spin density distribution over four nearest Si atoms as compared to the cubic cluster. The major part of spin density is localized on Si1 and Si2 atoms located in a symmetry plane, see Fig. 3. Curiously, it has been found that the largest HF parameters take place for Si1 atom lying along the c -axis and equal to $A_{||} \cong -164 \times 10^{-4} \text{ cm}^{-1}$ and $A_{\perp} \cong -99 \times 10^{-4} \text{ cm}^{-1}$ in close agreement with the experimental values [4].

Notice that EI6 defect having the similar parameters as Ky3 center has been tentatively attributed to carbon antisite Si_C^+ [5]. However, five HF doublets should be observed in this case in accordance with the number of silicon atoms for such a defect.

In conclusion, the C_s point symmetry and parameters of spin Hamiltonian have been found from a low-temperature study of positively charged carbon vacancy in two quasicubic sites of 6H-SiC crystal. Ky3 center is

tentatively proposed as V_C^+ defect in quasihexagonal site of 6H-SiC. The results of ab initio DFT calculations using cubic $C_{18}Si_{16}H_{36}$ and hexagonal $C_{18}Si_{20}H_{40}$ clusters corroborate the main features of proposed V_C^+ defect models including the point symmetry and values of HF parameters.

Acknowledgements

The support of INTAS 97-2141 Grant and French-Ukrainian project 9350 are gratefully acknowledged.

References

- [1] H. Itoh, M. Yoshikawa, I. Nashiyama, S. Misawa, H. Okumura, S. Yoshida, *J. Electr. Mater.* 21 (1992) 707.
- [2] D. Cha, H. Itoh, N. Morishita, A. Kawasuso, T. Ohshima, Y. Watanabe, J. Ko, K. Lee, I. Nashiyama, *Mater. Sci. Forum* 264–268 (1998) 615.
- [3] N.T. Son, W.M. Chen, J.L. Lindström, B. Monemar, E. Janzén, *Mater. Sci. Eng. B* 61–62 (1999) 202.
- [4] V.Ya. Bratus', I.N. Makeeva, S.M. Okulov, T.L. Petrenko, T.T. Petrenko, H.J. von Bardeleben, *Mater. Sci. Forum* 353–356 (2001) 517.
- [5] N.T. Son, P.N. Hai, E. Janzén, *Mater. Sci. Forum* 353–356 (2001) 499.
- [6] N.T. Son, P.N. Hai, E. Janzén, *Phys. Rev. B* 63 (2001) 201201.
- [7] A. Gali, B. Aradi, P. Deák, W.J. Choyke, N.T. Son, *Phys. Rev. Lett.* 84 (2000) 4926.
- [8] M.J. Frisch, et al., in these Proceedings (ICDS-21), Gaussian 94, Revision E.1, Gaussian, Inc., Pittsburgh PA, 1995.
- [9] T.T. Petrenko, T.L. Petrenko, V.Ya. Bratus', J.L. Monge, *Physica B* 308–310 (2001).



ELSEVIER

Physica B 308–310 (2001) 625–628

PHYSICA B

www.elsevier.com/locate/physb

The annealing product of the silicon vacancy in 6H–SiC

Th. Lingner^{a,*}, S. Greulich-Weber^a, J.-M. Spaeth^a, U. Gerstmann^b,
E. Rauls^b, H. Overhof^b

^aFB6-Experimental Physics, University of Paderborn, Warburgerstrasse 100, D-33098 Paderborn, Germany

^bTheoretical Physics, University of Paderborn, Warburgerstrasse 100, D-33098 Paderborn, Germany

Abstract

Radiation-induced defects in 6H-silicon carbide were investigated with electron paramagnetic resonance (EPR), the magnetic circular dichroism of the absorption (MCDA) and MCDA-detected EPR (MCDA-EPR). In irradiated samples, annealed beyond the annealing temperature of the isolated silicon vacancy (V_{Si}), we observed photo-EPR spectra of spin $S = 1$ centers, having the symmetry of nearest neighbor pair defects. By MCDA-EPR, they were associated to optical transitions with photon energies between 999 and 1075 meV. The hyperfine structure of the EPR spectra shows the presence of one single carbon and several silicon ligands. The experimental results are interpreted with the help of total energy and spin density data obtained from the standard local-density approximation of the density-functional theory, using relaxed defect geometries obtained from the self-consistent charge density-functional theory based tight binding scheme. The only model that explains all experimental findings is the photo-excited spin triplet state of the carbon antisite–carbon vacancy pair ($C_{Si}-V_C$) in the doubly positive charge state. We conclude that the $C_{Si}-V_C$ defect is formed from V_{Si} as an annealing product by the movement of a carbon neighbor into the vacancy. © 2001 Elsevier Science B.V. All rights reserved.

Keywords: Silicon carbide; Vacancies; Antisite; Electron paramagnetic resonance

1. Introduction

The silicon vacancy (V_{Si}) is a basic defect in silicon carbide (SiC) which can be introduced during crystal growth or by irradiation with high-energy particles, e.g. during ion implantation. The negatively charged V_{Si} has been identified by electron paramagnetic resonance (EPR). It anneals out at 750°C with an activation energy of 2.2 ± 0.3 eV [1]. In elemental semiconductors, a lattice vacancy can anneal out by moving through the lattice. In a compound semiconductor like SiC, the situation is more complicated, because chains of antisite defects must be created if the vacancy moves by nearest neighbor hops. It has recently been proposed that the first step in such an annealing process, the transforma-

tion of V_{Si} into the $C_{Si}-V_C$ antisite-vacancy pair, is a quite probable process [2]. Here, we provide experimental evidence for the presence of the pair after annealing.

2. Experimental

The nitrogen-doped (10^{18} cm^{-3}) 6H–SiC samples were grown by the sublimation sandwich method. They were irradiated with reactor neutrons at a dose of $2 \times 10^{18} \text{ cm}^{-2}$ and then annealed for 2 min at 600°C, 1000°C and 1200°C, respectively. One sample of the same batch was left unirradiated, and another sample was irradiated but not annealed. EPR was measured with X-band (9.8 GHz) at 7 K. The samples were illuminated in situ with the light of a halogen lamp. The paramagnetic part of the magnetic circular dichroism (MCDA) is proportional to the spin polarization of the ground state of the optical transition. Saturating

*Corresponding author. Tel.: +49-5251-60-2749; fax: +49-5251-60-3247.

E-mail address: lingner@physik.uni-paderborn.de (T. Lingner).

EPR transitions change the spin polarization which is observed as a decrease of the MCDA signal intensity (MCDA-EPR).

3. Computational

We used the self-consistent linear muffin-tin orbitals method in the atomic spheres approximation (LMTO-ASA), treating exchange and correlation effects within the framework of the local spin density approximation of the density-functional theory (LSDA-DFT) [3]. The atomic positions of the relaxed structure were obtained from additional calculations within the self-consistent charge density-functional theory based tight-binding (SCC-DFTB) scheme [4]. In a $(5 \times 6 \times 1)$ supercell model of the 6H polytype containing 300 atoms, the defect and its nearest and next nearest neighbors were relaxed. The relaxation energies were added to the LMTO total energies. Starting from the relaxed structures obtained from SCC-DFTB, the hyperfine (HF) interactions were calculated within an extended version of the LMTO-ASA Green's function method. For further details of this combined approach, see also Ref. [5].

4. Results and discussion

The EPR signal of neutron-irradiated and annealed 6H-SiC consists of six spin-triplet spectra. The angular dependence (Fig. 1) was analyzed using the usual spin Hamiltonian for $S = 1$ including fine structure (Table 1). For three of the centers (P6a, b and c), the principal axis z of the fine structure tensor is parallel to the c -axis of

Table 1

EPR parameters, angle θ between the principal axis of the fine structure tensor and the c -axis, and optical transition energies of the P6/P7 centers^a

Center	g	D (10^{-4} cm^{-1})	E (10^{-4} cm^{-1})	θ (deg)	$h\nu$ (meV)
P6a	2.003	456	0	0	1075
P6b	2.003	447	0	0	1048
P6c	2.003	430	0	0	1011
P7a	2.003	449	-4	71.2	1049
P7b	2.003	441	46	70.0	1030
P7c	2.003	416	-1	70.5	999

^a The notations P6 and P7 for the axial ($\theta = 0^\circ$) and the basal ($\theta \approx 71^\circ$) orientations is adopted from Ref. [6]. D is axially symmetric, E the anisotropic fine structure constant [9].

the crystal (axial orientations). The z -axis of the other three centers (P7a, b and c) is oriented in the six $\{11\bar{2}0\}$ planes at an angle θ to the c -axis (basal orientations). The angle θ is close to the ideal tetrahedral angle (70.529°). The letters a, b and c denote three different spectra of each orientation, which are thought to arise from the defect at the three inequivalent lattice sites in 6H-SiC. Similar spectra have been measured by EPR [6] and PL-EPR [7], but only two lattice sites have been identified so far [7].

The P6/P7 spectra were present in the samples annealed at 600°C , 1000°C and 1200°C . Their highest intensity was observed after a 1000°C anneal. They were not found in the unannealed and in the unirradiated samples. All EPR spectra emerged only during illumination with photon energies above $1.1 \pm 0.1 \text{ eV}$ and hence, belong to a photo-excited state.

The MCDA and photoluminescence (PL) spectra of the unannealed and the 600°C -annealed sample showed optical transitions of the V_{Si} -related defect reported in Ref. [8]. This signal is absent after a 1000°C anneal. Instead, MCDA lines between 1 and 1.1 eV are observed (Fig. 2). In each of these MCDA lines, a single EPR spectrum from Table 1 was detectable with MCDA-EPR. The higher the value of D , the larger is the photon energy of the optical transition observed.

The HF splitting of the P6c EPR signal (Fig. 3) indicates the presence of one single ^{13}C nucleus ($A = 48 \text{ MHz}$, intensity of one HF line $0.7 \pm 0.2\%$ of the central line) and four to eight ^{29}Si neighbors ($A = 12 \text{ MHz}$, intensity $15 \pm 5\%$ of the central line). The ^{29}Si -related HF lines are broadened and may contain contributions from different Si neighbor shells with similar HF constants.

The symmetry characteristic for a nearest neighbor pair defect and the intrinsic nature of the defect, limit the possible models to the vacancy pair ($V_{\text{Si}}-V_{\text{C}}$), the antisite pair ($\text{C}_{\text{Si}}-\text{Si}_{\text{C}}$) and the vacancy-antisite pairs

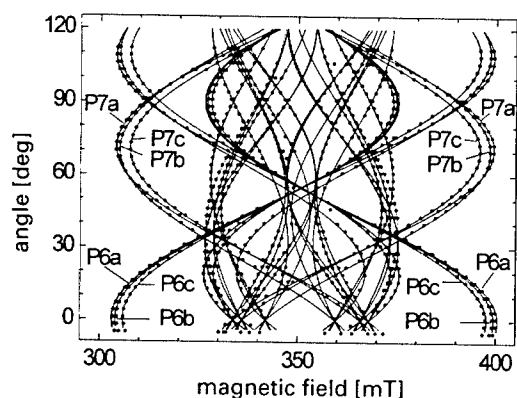


Fig. 1. Angular dependence of the P6/P7 EPR-spectra in 6H-SiC, measured at $T = 7 \text{ K}$ in X-band (9.87 GHz). Dots indicate the experimental data. The solid lines are calculated curves using the parameters given in Table 1.

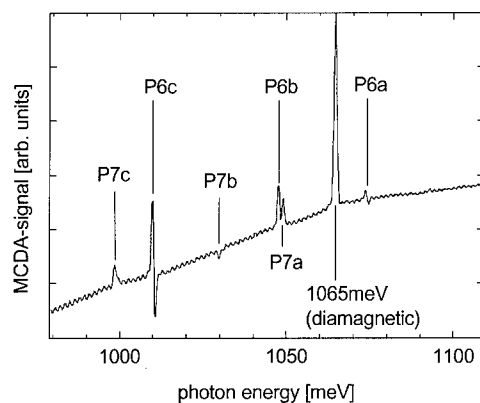


Fig. 2. MCDA spectrum of neutron-irradiated and at $T_{\text{ann}} = 1000^\circ\text{C}$ -annealed 6H-SiC, measured under additional excitation of the sample with an Ar-ion laser. In each of the P6/P7 MCDA lines, one of the EPR spectra from Table 1 was measured with MCDA-EPR.

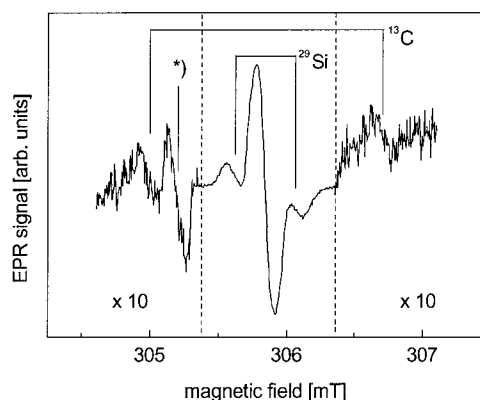


Fig. 3. Hyperfine structure of the P6c low field line for $\mathbf{B} \parallel \mathbf{c}$. The line marked with an asterisk belongs to a different defect.

$\text{V}_{\text{Si}}\text{-SiC}$ and $\text{C}_{\text{Si}}\text{-V}_{\text{C}}$. Only $\text{C}_{\text{Si}}\text{-SiC}$ and $\text{C}_{\text{Si}}\text{-V}_{\text{C}}$ have one prominent C nucleus. The antisite pair $\text{C}_{\text{Si}}\text{-SiC}$ has excitation energies $< 0.2\text{ eV}$ and can, therefore, by no means explain the optical transitions of the P6/P7 centers ($\sim 1\text{ eV}$).

The formation energy of $\text{C}_{\text{Si}}\text{-V}_{\text{C}}$ is lower than that of V_{Si} for most charge states (Fig. 4). The calculated energy barrier for the formation of $(\text{C}_{\text{Si}}\text{-V}_{\text{C}})^0$ from V_{Si}^0 (1.7 eV, [2]) is close to the experimentally observed activation energy for the annealing of V_{Si}^0 ($2.2 \pm 0.3\text{ eV}$, [1]). $\text{C}_{\text{Si}}\text{-V}_{\text{C}}$ is, therefore, expected to be formed from V_{Si} as an annealing product.

In C_{3v} symmetry, $\text{C}_{\text{Si}}\text{-V}_{\text{C}}$ has an $a_1(\text{s})$ level in the valence band, an $a_1(\text{p})$ and an $e(\text{p})$ level in the band gap (Fig. 5). The ground state of $(\text{C}_{\text{Si}}\text{-V}_{\text{C}})^{2+}$ is a singlet 1A_1 ($a_1(\text{s})\uparrow\downarrow$). Photon energies above 1.15 eV (exp.: 1.1 eV)

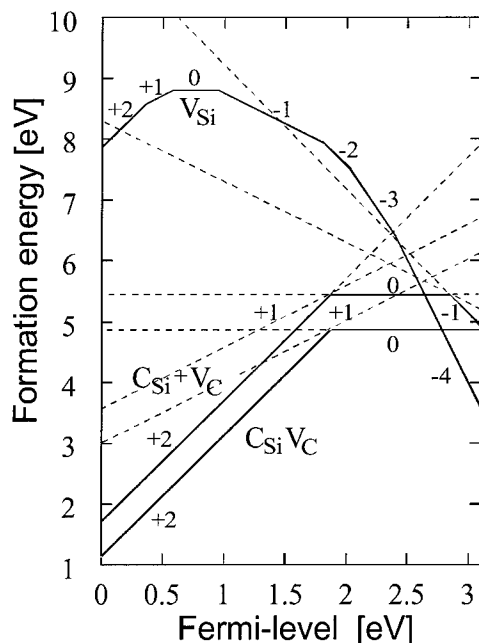


Fig. 4. Formation energies of the silicon vacancy (V_{Si}), the carbon-antisite carbon-vacancy pair ($\text{C}_{\text{Si}}\text{V}_{\text{C}}$), and sum of formation energies of the isolated carbon antisite and the isolated carbon vacancy ($\text{C}_{\text{Si}} + \text{V}_{\text{C}}$).

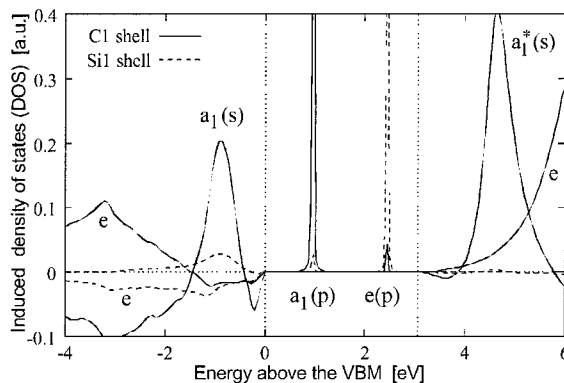


Fig. 5. Induced density of states for the diamagnetic ground state of the $\text{C}_{\text{Si}}\text{-V}_{\text{C}}$ pair in the charge state +2.

can excite one electron from the $a_1(\text{s})$ level into the $a_1(\text{p})$ level, forming the 1A_2 ($a_1(\text{s})\uparrow a_1(\text{p})\downarrow$) state. A non-radiative transition to the energetically lower metastable triplet state 3A_2 ($a_1(\text{s})\uparrow a_1(\text{p})\uparrow$) is possible with help of phonons. This 3A_2 state gives rise to the P6/P7 EPR spectra observed experimentally. The MCDA is explained by the excitation of the $a_1(\text{p})$ electron into the $e(\text{p})$ state ($a_1(\text{s})\uparrow e(\text{p})\uparrow$). The calculated photon energy (1.52 eV) is in reasonable agreement with the experimental values (1.0–1.1 eV).

The calculated HF interaction with the C_{Si} approaches the experimental value when C_{Si} relaxes 22% away from V_C . This is close to the relaxation predicted by SCC-DFTB (16%). The three Si neighbors of V_C and three next nearest neighbors of C_{Si} (in the direction of the defect axis) contribute to the silicon HF interaction with similar constants, explaining the observed HF lines (6 ± 2 inequivalent Si nuclei).

A similar excitation scheme as for $(C_{Si}-V_C)^{2+}$ is possible for $(C_{Si}-V_C)^0$, but, in this case, the $e(p)$ state is occupied in the metastable triplet state $^3E(a_1(s)\uparrow\downarrow a_1(p)\uparrow e(p)\uparrow)$ and gives rise to a large HF interaction with the Si neighbors of V_C (> 150 MHz), which, by far, exceeds the experimentally observed value. Thus, this charge state must be ruled out. For a more detailed discussion, see Ref. [5].

In summary, we have identified the $C_{Si}-V_C$ pair in 6H-SiC in the doubly positive charge state on all inequivalent lattice sites and in all orientations. The $C_{Si}-V_C$ pair is the ideal candidate for the annealing product of V_{Si} . The bad news, though, is that the $C_{Si}-V_C$ defect is electrically and optically active. It has a charge transfer level just above midgap. Thus, at least a second anneal step is required to remove the electrical activity of silicon vacancy-related defects.

References

- [1] H. Itoh, M. Yoshikawa, I. Nashiyama, S. Misawa, H. Okumura, S. Yoshida, *IEEE Trans. Nucl. Sci.* 37 (1990) 1732.
- [2] E. Rauls, Th. Lingner, Z. Hajnal, S. Greulich-Weber, Th. Frauenheim, J.-M. Spaeth, *Phys. Stat. Sol. B* 217/2 (2000) R1.
- [3] O. Gunnarsson, O. Jepsen, O.K. Andersen, *Phys. Rev. B* 27 (1983) 7144.
- [4] Th. Frauenheim, et al., *Phys. Stat. Sol. B* 217 (2000) 41.
- [5] Th. Lingner, S. Greulich-Weber, J.-M. Spaeth, U. Gerstmann, H. Overhof, E. Rauls, Z. Hajnal, Th. Frauenheim, *Phys. Rev. B*, submitted for publication.
- [6] V.S. Vainer, V.A. Il'in, *Sov. Phys. Sol. State* 23 (1981) 2126.
- [7] N.T. Son, P.N. Hai, M. Wagner, W.M. Chen, A. Ellison, C. Hallin, B. Monemar, E. Janzén, *Semicond. Sci. Technol.* 14 (1999) 1141.
- [8] E. Sörman, N.T. Son, W.M. Chen, O. Kordina, C. Hallin, E. Janzén, *Phys. Rev. B* 61 (2000) 2613.
- [9] J.-M. Spaeth, J.R. Niklas, R.H. Bartram, *Structural Analysis of Point Defects in Solids, Solid State Sciences* 43, Springer, Heidelberg, 1992.



ELSEVIER

Physica B 308–310 (2001) 629–632

PHYSICA B

www.elsevier.com/locate/physb

Illumination effects in irradiated 6H n-type SiC observed by positron annihilation spectroscopy

F. Redmann^{a,*}, A. Kawasuso^{a,b}, K. Petters^a, H. Itoh^b, R. Krause-Rehberg^a

^a Martin-Luther-Universität Halle-Wittenberg, Fachbereich Physik, D-06099 Halle, Germany

^b Japan Atomic Energy Research Institute, 1233, Watanuki, Takasaki, Gumma 370-1292, Japan

Abstract

In the present study, we used positron annihilation spectroscopy to investigate defects after electron irradiation in 6H n-type SiC. The density of vacancy-type defects strongly increased during this treatment. An isochronal annealing experiment was performed, and the main recovery stage was found to be between 1000°C and 1400°C. This corresponds to the annealing range of the E_1/E_2 defect, which was also found by a correlated positron and DLTS study in 6H-SiC epilayers after electron irradiation (J. Appl. Phys. 80 (1996) 5639). Optical excitation experiments during the positron experiment show that the observed defect has an ionization level at about $E_c - 0.47$ eV, which is similar to the level $E_c - 0.44$ eV obtained by DLTS for the E_1/E_2 defect (Appl. Phys. Lett. 74 (1999) 839). Doppler-coincidence experiments suggest that the observed vacancy is surrounded by C atoms, so that most probably the Si vacancy (isolated or bound to an impurity or another defect) is the dominating defect after electron irradiation. © 2001 Elsevier Science B.V. All rights reserved.

Keywords: SiC; Annealing; Radiation defects; Positron annihilation

1. Introduction

Electrical and optical properties of defects in semiconductors play an important role in SiC based wide band gap electronic devices. One way to introduce defined defects in SiC is electron irradiation. Irradiated SiC was studied by several experimental methods to characterize the introduced defects (DLTS, PL, ESR). In order to study open-volume defects, we performed positron lifetime experiments for n-type 6H SiC irradiated with 2 MeV electrons (dose: 1×10^{17} and $3 \times 10^{17} \text{ cm}^{-2}$). The positron lifetime was found to increase after irradiation indicating the presence of vacancy-type defects. Annealing experiments were performed to observe the disappearing or agglomeration of vacancies. The excitation of electrons to the conduction

band due to illumination shows different annealing behavior dependent on the irradiation dose. Additional Doppler broadening coincidence experiments were performed to get information about the chemical environment of the vacancies observed by positrons.

2. Experimental details

N-doped SiC bulk wafers ($[N] = 1 \times 10^{17} \text{ cm}^{-3}$) of a thickness of 0.3 mm were purchased by the Nippon Steel Company and irradiated in the Japan Atomic Energy Research Institute (JAERI) with 2 MeV electrons for two different doses (1×10^{17} and $3 \times 10^{17} \text{ cm}^{-2}$) at room temperature. The size of the samples is $5 \times 5 \text{ mm}^2$. A conventional positron emitter $^{22}\text{NaCl}$ (10–90 μCi) was used as positron source. It was encapsulated with 4 μm of aluminum foil. Due to the high kinetic energy of positrons ($E_{\text{max}} = 0.54 \text{ MeV}$), 2% of them get through the thin samples. To prevent the annihilation of positrons in the sample holder, an additional piece of SiC was arranged on both sides of the sandwich. The

*Corresponding author. Univ. Halle, FB Physik, Fr.-Bach-Platz 6, D-06108 Halle, Germany. Tel.: +49-345-552-5571; fax: +49-345-552-7160.

E-mail address: pshcg@ra.physik.uni-halle.de (F. Redmann).

positron lifetime measurements were performed with a conventional fast-fast positron lifetime spectrometer (FWHM = 260 ps) in the temperature range of 15–600 K. The illumination experiment using an optical cryostat was carried out in the same temperature range. The effect of illumination on positron lifetime was examined using white and monochromatic light ($h\nu = 0.3$ – 3.2 eV). In the range between 100°C and 1300°C , the samples were annealed in a furnace under vacuum and up to 1700°C under ambient argon atmosphere to avoid the sublimation of silicon from the surface. Doppler broadening coincidence experiments were performed using two Ge-detectors with a resulting resolution function of about 1 keV.

3. Results and discussion

Fig. 1 shows the difference of the average lifetime of low-dose electron irradiated 6H SiC (dose: $1 \times 10^{17} \text{ cm}^{-2}$) with monochromatic light and in darkness as a function of photon energy. The direct transition of electrons from the valence band to the conduction band causes the disappearance of the illumination effect above a photon energy of 3 eV. It is found that the average lifetime increases from 0.4 eV and tends to saturate above 1 eV. This could be explained as the internal transition of electrons from localized levels to the

conduction band (fundamental absorption). The lower threshold energy for the appearance of the illumination effect is associated with the position of the energy level of defects in the band gap acting as a trapping center for positrons. According to the Lucowsky model [7], the threshold energy is determined to be $E = 0.47$ eV from the fitting as shown in Fig. 1. DLTS studies showed that the energy level of E_1/E_2 is located at 0.35–0.44 eV below the conduction band [2,6]. In the case of an indirect transition from the ground state to the conduction band [2], the small difference of these two energies allows us to conclude that the observed threshold energy (0.47 eV) might be related to the E_1/E_2 level.

Fig. 2 shows the isochronal annealing behavior of average positron lifetime in darkness measured at 20 K. From this figure, two annealing steps are seen: the first is from room temperature to 250°C and the second is above 1000°C . The first step can be explained as the recombination of Frenkel pairs and the annealing of carbon vacancies, which are mobile below 300°C . Considering that pure silicon vacancies are mobile at 600 – 800°C [5], the higher thermal stability of trapping centers can be explained as a creation of complexes involving Si vacancies. This could be inferred due to the nearly constant defect-related lifetime (190 ± 5 ps) determined by decomposition of positron lifetime spectra in the range of annealing temperature from 400°C to

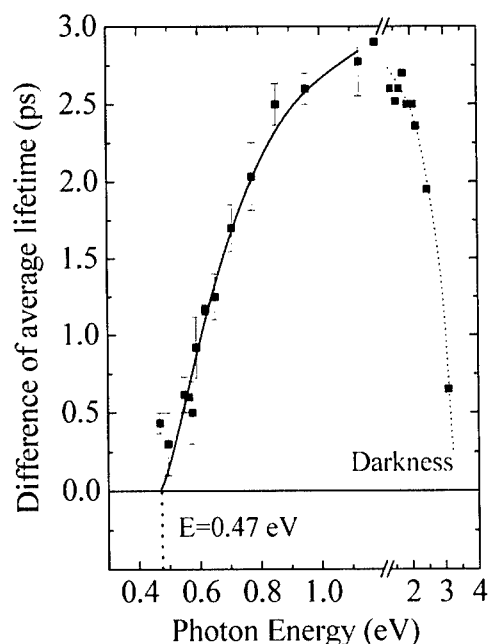


Fig. 1. Difference of average positron lifetime under illumination and in darkness as a function of photon energy.

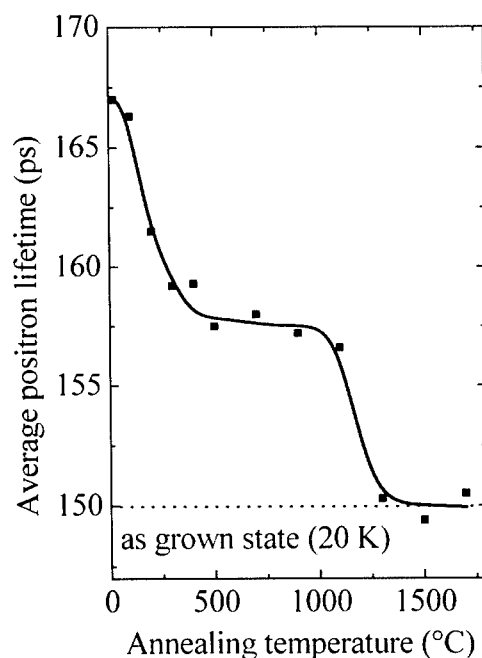


Fig. 2. Average positron lifetime as a function of annealing temperature for electron irradiated 6H n-type SiC (dose: $1 \times 10^{17} \text{ cm}^{-2}$).

1200°C. Above 1300°C, all detectable vacancy-type defects disappear [1]. Based on theoretical calculations [3] and a positron lifetime experiment combined with electron spin resonance [4], the lifetime of positrons at silicon vacancies is 187–193 ps. Thus, it seems that the major positron trapping center is related to silicon vacancies. It is important to note that the E_1/E_2 defects observed in DLTS experiments also disappear in the same temperature region [6]. Thus, we conclude that the E_1/E_2 center is decorated with a silicon vacancy. The annealing behavior under illumination shows very similar characteristics [8], so that introduced vacancy-type defects due to electron irradiation are responsible for the illumination effect.

Fig. 3 presents the annealing characteristics of average positron lifetime for the electron irradiated 6H n-type SiC with a dose of $3 \times 10^{17} \text{ cm}^{-2}$ for two different measurement temperatures. For the low-temperature measurements, the annealing characteristics show a very similar behavior in case of illumination and darkness. The effect of illumination decreases slightly due to the annealing temperature. The annealing behavior can be divided into four steps. The first step is the recombination of Frenkel pairs, which drastically reduces the average lifetime below 200°C annealing temperature. Then, a bright shoulder follows up to 500°C where carbon vacancies will become mobile and anneal out [1]. The average lifetime increases near 800°C due to the

building of complexes with silicon vacancies, and after 1200°C most of the introduced vacancy-type defects annealed out. The high-temperature measurements show a completely different annealing behavior. No illumination effect is to be seen up to an annealing temperature of 600°C. Above this temperature, the average lifetime is higher under illumination, which was not observed for the low-temperature measurements. The last picture in Fig. 3(c) shows the difference of average lifetime under illumination and in darkness. It shows that a small increase of average lifetime appears in the mobility range of the two kinds of vacancies.

The decomposition of positron lifetime spectra for the annealing temperature 800°C is displayed in Fig. 4. It demonstrates that for a measurement temperature of 300 K, two different types of defects act as trapping centers for positrons. Under illumination, the defect-related lifetime τ_2 has a value of 190 ± 10 ps similar to the silicon vacancy [3]. In darkness, an additional defect (unknown defect with an ionization energy, $E > 100 \text{ meV}$) acts as a trap ($\tau_2 = 165 \pm 10$ ps) in competition with the silicon vacancy. The decomposed lifetime is a mixture of these two defects where the value of positron lifetime for the silicon vacancy approaches the high measurement temperature. The above mentioned deep center must change its charge state (negative to neutral) due to the excitation of electrons from the deep level to the conduction band.

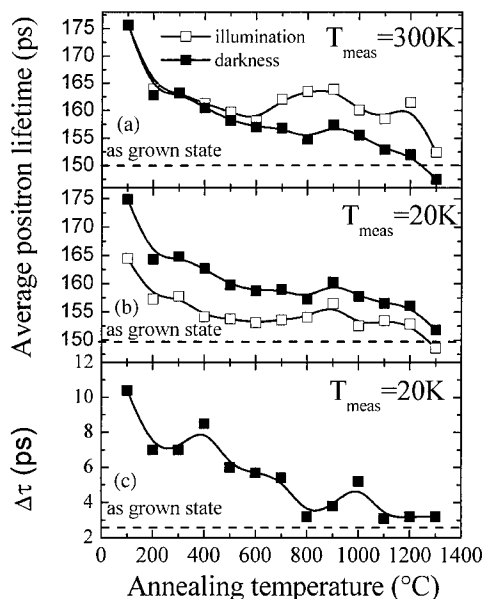


Fig. 3. Average positron lifetime as a function of annealing temperature for electron irradiated 6H n-type SiC (dose: $3 \times 10^{17} \text{ cm}^{-2}$) under illumination and in darkness. The picture (c) shows the difference of average lifetime between darkness and illumination for the measurement temperature of 20 K.

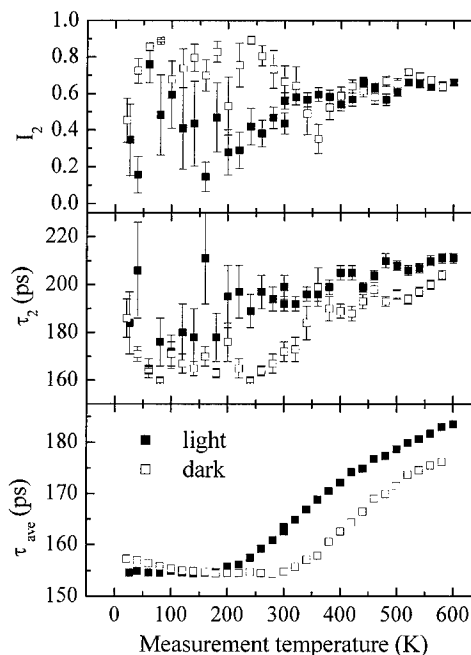


Fig. 4. Positron lifetime as a function of measurement temperature for 6H n-type SiC annealed at 800°C (irradiation dose: $3 \times 10^{17} \text{ cm}^{-2}$).

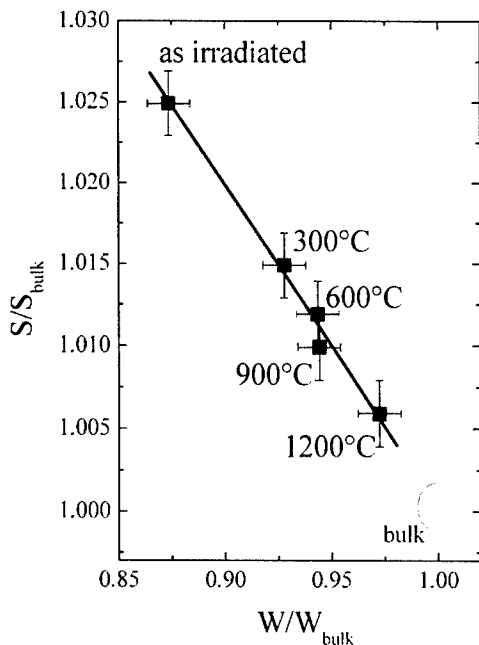


Fig. 5. Doppler broadening line-shape parameters S and W of the 511 keV annihilation peak as a function of annealing temperature (irradiation dose: $3 \times 10^{17} \text{ cm}^{-2}$).

Fig. 5 shows the annealing behavior for the Doppler broadening spectroscopy. The W -parameter is sensitive for the chemical environment of the trapping center. The S -parameter represents the open-volume space and the concentration of open-volume defects. The straight line found during annealing allows us to conclude that only monovacancies anneal out and no additional vacancy type defect is involved [10]. After 1200°C annealing some defects remain which cannot be isolated monovacancies [4]. This indicates that silicon vacancies and complexes with silicon vacancies are the major trapping centers.

4. Conclusions

In summary, we performed positron lifetime measurements with n-type 6H SiC after 2 MeV electron

irradiation for two different doses in darkness and under illumination. After the 1300°C annealing, vacancy-type defects and the illumination effect disappear. The annealing behavior in darkness shows very similar behavior to the E_1/E_2 centers observed by DLTS measurements [9]. Thus, we conclude that the observed defect contains silicon vacancies. The determined threshold energy of 0.47 eV for the illumination effect further supports this assumption. In the case of high-dose irradiation more than one optical active trapping center was found for the measurement temperature of 300 K. To clarify the structure of possible complexes with silicon vacancies, further experiments are necessary.

Acknowledgements

We thank T. Frank and M. Weidner (Univ. Erlangen-Nürnberg, Germany) for their help in sample treatment.

References

- [1] A. Kawasuso, H. Itoh, S. Okada, H. Okumura, J. Appl. Phys. 80 (1996) 5639.
- [2] C.G. Hemmingson, N.T. Son, E. Janzén, Appl. Phys. Lett. 74 (1999) 839.
- [3] G. Brauer, W. Anwand, E.-M. Nicht, Phys. Rev. B 54 (1996) 2512.
- [4] A. Kawasuso, H. Itoh, N. Morishita, M. Yoshikawa, T. Ohshima, I. Nashiyama, S. Okada, H. Okumura, S. Yoshida, Appl. Phys. A 67 (1998) 209.
- [5] H. Itoh, N. Hayakawa, I. Nashiyama, E. Sakuma, J. Appl. Phys. 66 (1989) 4529.
- [6] H. Zhang, G. Pensl, Electrochem. Soc. Ext. Abstracts 89-2 (1989) 699.
- [7] G. Lucowsky, Solid State Commun. 3 (1965) 299.
- [8] F. Redmann, A. Kawasuso, K. Petters, R. Krause-Rehberg, H. Itoh, Mat. Science Forum 363 (2000) 126.
- [9] M. Weidner, et al., in these Proceedings (ICDS-21), Physica B 308–310 (2001).
- [10] R. Krause-Rehberg, H.S. Leipner, Positron Annihilation in Semiconductors, Springer, Berlin, 1999.



ELSEVIER

Physica B 308–310 (2001) 633–636

PHYSICA B

www.elsevier.com/locate/physb

Formation and annihilation of intrinsic-related defect centers in high energy electron-irradiated or ion-implanted 4H- and 6H-silicon carbide

M. Weidner^{a,*}, T. Frank^a, G. Pensl^a, A. Kawasuso^{b,c}, H. Itoh^b,
R. Krause-Rehberg^c

^a*Institute of Applied Physics, University of Erlangen-Nürnberg, Staudtstrasse 7/A3, D-91058, Erlangen, Germany*

^b*Japan Atomic Energy Research Institute, Takasaki, Japan*

^c*Fachbereich Physik, University of Halle-Wittenberg, Halle, Germany*

Abstract

Intrinsic-related defect centers (IRDCs) in 4H-/6H-SiC are generated by implantation of helium ions, protons or by irradiation of high energy electrons. The formation and thermal stability of these centers are studied by deep level transient and positron annihilation spectroscopy subsequent to anneals at 600–1800°C. It turns out that the formation of IRDCs depends on the injected particle. Further we have identified defect centers which show identical temperature dependence of DLTS defect concentrations and positron capture rates. © 2001 Elsevier Science B.V. All rights reserved.

Keywords: 4H-SiC; 6H-SiC; Intrinsic-related defect centers; DLTS; PAS

1. Introduction

Ion implantation, which is an important tool to dope silicon carbide (SiC) with donors and acceptors, not only causes lattice damage but is also accompanied by an unintentional local disturbance of the stoichiometry of SiC. Based on the different masses of silicon (Si) and carbon (C) atoms, the heavier Si atoms accumulate close to the surface while the lighter C atoms are knocked on deeper into the bulk. This effect may, in addition, enhance the formation of intrinsic-related defect centers (IRDCs). For a survey of IRDCs in ion-implanted or electron-irradiated SiC, see e.g. Refs. [1–3].

In this paper, we conduct a detailed study of the formation and annihilation of IRDCs in helium (He⁺), proton (H⁺) or 2 MeV electron (e[−]) damaged and

subsequently annealed n-type 4H-/6H-SiC. Deep level transient spectroscopy (DLTS) and positron annihilation spectroscopy (PAS) are applied to determine defect concentrations and positron capture rates, respectively. It is the aim to examine whether the formation of IRDCs differs for the different generation processes and whether part of the observed defects are vacancy-related.

2. Experimental

Nitrogen (N)-doped epitaxially grown SiC layers of 4H and 6H polytype, respectively, are used for these investigations (CREE, $[N_N - N_{Comp}] = 5 \times 10^{15} \text{ cm}^{-3}$). Square-shaped samples with an area of 5 mm × 5 mm are cut from the wafers. Intrinsic defect centers are generated by irradiation of 2 MeV electrons (e[−] current = 0.5 mA, fluence = 10^{15} cm^{-2}) or by implantation of 2 MeV protons (Gaussian H⁺-profile with $R_p = 25 \mu\text{m}$

*Corresponding author. Fax: +49-9131-852-8423.

E-mail address: michael.weidner@physik.uni-erlangen.de (M. Weidner).

(calculated by TRIM.C), H^+ current = 30 nA, fluence = 10^{13} cm^{-2}) or helium ions (box profile generated by multiple implantation of He^+ ions with energies ranging from 30 to 950 keV, He^+ current = 50 nA, total He^+ fluence = $8 \times 10^{12} \text{ cm}^{-2}$). The e^- -irradiated and He^+ -implanted samples are sequentially exposed to anneals at temperatures, T_a , ranging from 600°C to 1700°C for 30 min. They are characterized by DLTS subsequent to each heat treatment (similar processed samples were investigated by PAS, see Ref. [4]). In contrast each H^+ -implanted sample is isochronally annealed for 30 min at one fixed temperature. Anneals up to 1000°C are performed under vacuum in a rapid isothermal annealing (RIA)-system. Above 1000°C the samples are put into a SiC container and annealed under 1 atm Ar pressure in a resistance-heated graphite furnace. Subsequent to heat treatments above 900°C, a surface layer of 100 nm is etched off by reactive ion etching (RIE). Schottky contacts are fabricated by evaporation of nickel (Ni) through a shadow mask (contact diameter varies between 0.35 and 1 mm); large area Ohmic contacts (Ni) are evaporated on the backside of the samples. Prior to each annealing step the contacts are removed. DLTS spectra are taken in a temperature range from 90 to 700 K. The filling pulse width is 20 ms and the rate window is chosen between 0.25 and 32 ms. Defect concentrations are determined from the height of the DLTS peaks.

3. Results and discussion

Although all the observed DLTS spectra show identical features (IRDC-related peaks), the abundance of defect centers and their formation strongly depend on the particular injected particles. Fig. 1 shows DLTS spectra taken on an e^- -irradiated and annealed ($T_a = 900^\circ\text{C}$, $t_a = 30 \text{ min}$) 4H- (solid curve) and 6H-SiC (dotted curve) epilayer, respectively. The dominant-

ing peaks in the spectrum of the 4H-SiC epilayer (related to the y-axis on the left) are attributed to electron traps like the ET1-, ET3- and $Z_1/Z_2(4H)$ -center [5]. The activation energies and generated concentrations of these IRDCs are summarized in Table 1. Their chemical composition and microscopic structure are not known. Similar electron traps are described in Ref. [2]. In addition, the titanium (Ti) acceptor is observed at about 90 K. Ti is an omnipresent contamination in SiC due to graphite parts. In the case of the 6H-SiC polytype (related to the y-axis on the right), the E_1/E_2 - and $Z_1/Z_2(6H)$ -center prevail (for activation energies and concentrations, see Table 1).

The formation of the observed IRDCs in 4H-/6H-SiC strongly depends on the injected particles. As an example the annealing behavior of $Z_1/Z_2(4H)$ -centers in n-type 4H-SiC generated by He^+ -ions, H^+ -ions and high energy electrons, respectively, is displayed in Fig. 2. The implantation/irradiation parameters are selected in such a way that (a) the He^+ implantation generates a vacancy profile to a depth of 2.2 μm with a mean

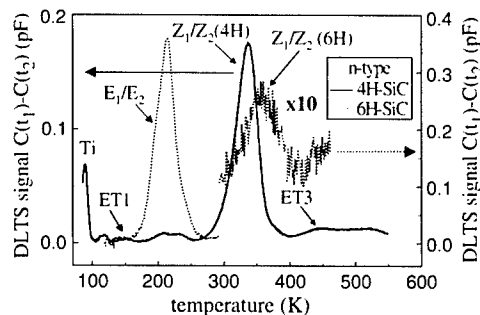


Fig. 1. DLTS spectra taken on an e^- -irradiated and annealed ($T_a = 900^\circ\text{C}$, $t_a = 30 \text{ min}$) 4H- (solid curve) and 6H-SiC (dotted curve) epilayer, respectively. The corresponding defect parameters are summarized in Table 1.

Table 1

Ionization energy, concentration and thermal stability of intrinsic-related defect centers generated by implantation of He^+ -, H^+ -ions and by irradiation of 2 MeV electrons in 4H-/6H-SiC

Defect	Ionization energy (meV) for $\sigma \sim T^0/T^{-2}$	Concentration (cm^{-3}) (subsequent to anneal at $900^\circ\text{C}/30 \text{ min}$)	Thermal stability ($^\circ\text{C}$)
4H-SiC			
ET1	220/245	6.1×10^{12}	RT–1300
ET3	660/740	1.9×10^{13}	RT–1300
$Z_1/Z_2(4H)$	590/650	2.3×10^{14}	400–1700
6H-SiC			
E_1/E_2	0.42/0.46	3.6×10^{13}	RT–1200 (?)
$Z_1/Z_2(6H)$	660/720	1.9×10^{13}	RT–1700

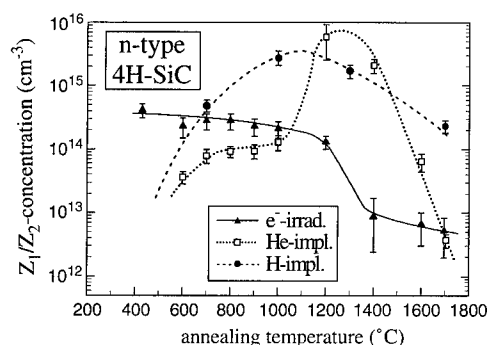


Fig. 2. Annealing behavior of Z_1/Z_2 -centers in n-type 4H-SiC generated by implantation of He^{+} - and H^{+} -ions or by irradiation of 2 MeV electrons. The annealing time t_a at fixed temperature is 30 min. High Z_1/Z_2 -concentrations are determined by temperature-dependent $C-V$ measurements.

concentration of $2 \times 10^{18} \text{ cm}^{-3}$ (calculated by TRIM-C), (b) the H^{+} ions accumulate in a depth of approx. 25 μm and can, therefore, not directly affect the formation of IRDCs in the investigated zone and (c) the 2 MeV electrons generate an almost homogeneous intrinsic defect concentration through the whole bulk of the SiC wafer. The temperature during ion implantation/ e^{-} irradiation is in each case below 50°C; this low temperature avoids annealing of lattice damage during irradiation. In He^{+} - and H^{+} -implanted samples, the Z_1/Z_2 -center is not observable directly after the implantation; its formation requires an annealing step at temperatures above 600°C. The Z_1/Z_2 -concentration increases with increasing annealing temperature and reaches a maximum value in the temperature range between 1100°C and 1200°C. This observation is also true for heavier ion masses (see Ref. [3]). Irradiation with 2 MeV electrons generates the $Z_1/Z_2(4\text{H})$ -center without additional anneal. We suggest that the number of displacements per injected particle is much lower for electrons than for ions. Therefore, isolated intrinsic defects must be formed in ion-implanted layers by additional heat treatments. Annihilation of the $Z_1/Z_2(4\text{H})$ -center occurs at temperatures $T_a > 1200^\circ\text{C}$ in all three cases.

Our experimental results are in contrast with data published by Storasta et al. [6], who reported that the maximum concentration of $Z_1/Z_2(4\text{H})$ -centers generated by H^{+} -ions (2.9 MeV) does not show any distinct change with the annealing temperature up to 1300°C.

The concentration of ET1 , ET3 and $Z_1/Z_2(4\text{H})$ -centers as well as that of E_1/E_2 - and $Z_1/Z_2(6\text{H})$ -centers in electron-irradiated n-type 4H- and 6H-SiC samples, respectively, as a function of the annealing temperature is displayed in Figs. 3 and 4. The annealing steps (30 min each) have been sequentially conducted. Up to 1000°C

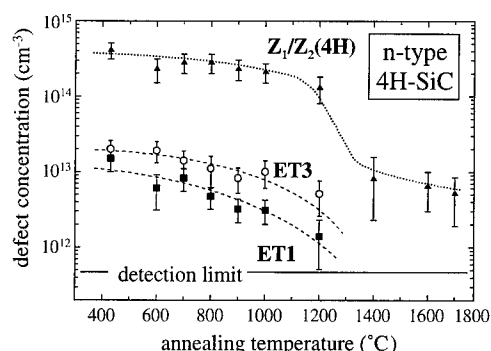


Fig. 3. Annealing behavior of ET1 -, ET3 - and Z_1/Z_2 -centers in n-type 4H-SiC generated by irradiation of 2 MeV electrons. The annealing steps ($t_a = 30$ min at each applied temperature) have been sequentially conducted.

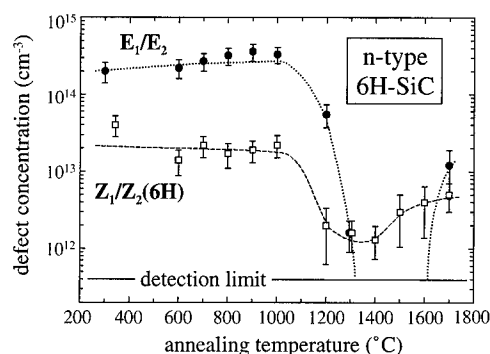


Fig. 4. Annealing behavior of E_1/E_2 - and Z_1/Z_2 -centers in n-type 6H-SiC generated by irradiation of 2 MeV electrons. The annealing steps ($t_a = 30$ min at each applied temperature) have been sequentially conducted.

the defect concentrations are not affected by the heat treatments. For temperatures $T_a > 1000^\circ\text{C}$, the concentrations strongly decrease. For $T_a > 1300^\circ\text{C}$, ET1 - and ET3 -centers are no longer detectable with our DLTS system. $Z_1/Z_2(4\text{H})$ -centers in the 4H polytype and E_1/E_2 - and $Z_1/Z_2(6\text{H})$ -centers in the 6H polytype show qualitatively a similar annealing behavior. In the temperature range from 1300°C to 1600°C, the concentration of these centers is strongly reduced (the DLTS signal of E_1/E_2 -centers is below the detection limit). Subsequent to anneals at $T_a > 1400^\circ\text{C}$, these defect concentrations begin to increase again. They are still detectable at a few 10^{12} cm^{-3} subsequent to a heat treatment at 1700°C (for the temperature range of thermal stability of defects, see Table 1, last column). These results are reproducible and have been repeated with a series of samples. The formation and dissociation of intrinsic-related defects in this temperature range appear to be extremely complex. Most of the intrinsic-

related defect complexes are dissolved in this temperature range and serve as a source for Si and C interstitials and/or vacancies. This increase in intrinsic defects may lead to the observed slight recovery of $Z_1/Z_2(4H)$, E_1/E_2 - and $Z_1/Z_2(6H)$ -centers.

PAS investigations on identically processed 6H-SiC samples (not shown here, see Ref. [4]) also result in a decrease of the positron capture rate of the particular defect centers at annealing temperatures above 1000°C. The clear temperature correlation between DLTS concentrations and positron capture rates strongly indicates that the centers under discussion ($Z_1/Z_2(4H)$ -center in 4H-SiC, E_1/E_2 - and $Z_1/Z_2(6H)$ in 6H-SiC) are vacancy-related.

4. Summary

Intrinsic-related defect centers are generated in 4H-/6H-SiC by implantation of He^+ -ions or protons or by irradiation of high energy electrons. The formation and annihilation of IRDCs is studied as a function of annealing temperature in the range from 600°C to 1700°C. The formation process of IRDCs depends on the injected particle. Implantation of ions (e.g. H^+ , He^+) requires an annealing step above 600°C to form IRDCs. In the 4H- and 6H-SiC polytypes ET1, ET3, $Z_1/Z_2(4H)$ and E_1/E_2 , $Z_1/Z_2(6H)$, respectively, are the dominating centers; they partially resist heat treatments up to 1700°C. In electron-irradiated samples, these defects are already present at maximum concentration without additional anneal. Based on the comparison of

DLTS and PAS results taken on identically processed 4H-/6H-SiC samples, it is concluded that vacancies participate in the investigated defect complexes.

Acknowledgements

The support of this work by the German Science Foundation (Sonderforschungsbereich 292) and the Humboldt Foundation is gratefully acknowledged.

References

- [1] T. Dalibor, G. Pensl, H. Matsunami, T. Kimoto, W.J. Choyke, A. Schöner, N. Nordell, *Phys. Stat. Sol. (a)* 162 (1997) 199.
- [2] C. Hemmingsson, N.T. Son, O. Kordina, J.P. Bergman, E. Janzén, *J. Appl. Phys.* 81 (1997) 6155.
- [3] Th. Frank, M. Weidner, H. Itoh, G. Pensl, *Mater. Sci. Forum* 353–356 (2001) 439.
- [4] A. Kawasuso, M. Weidner, F. Redmann, T. Frank, P. Sperr, R. Krause-Rehberg, G. Pensl, Vacancies in He-implanted 4H and 6H SiC epilayers studied by positron annihilation, in these Proceedings (ICDS-21), *Physica B* 308–310 (2001).
- [5] T. Dalibor, C. Peppermüller, G. Pensl, S. Sridhara, R.P. Devaty, W.J. Choyke, A. Itoh, T. Kimoto, H. Matsunami, *Inst. Phys. Conf. Ser.* 142 (1996) 517.
- [6] L. Storasta, F.H.C. Carlsson, S.G. Sridhara, J.P. Bergman, A. Henry, T. Egilsson, E. Hallén, E. Janzén, *Appl. Phys. Lett.* 78 (2001) 46.

Calculation of hyperfine parameters of positively charged carbon vacancy in SiC

T.T. Petrenko^{a,*}, T.L. Petrenko^a, V.Ya. Bratus^a, J.L. Monge^b

^a *Institute of Semiconductor Physics, National Academy of Sciences of Ukraine, Prospect Nauky 45, Kyiv 03028, Ukraine*

^b *Groupe de Physique des Solides, Universités Paris 6&7, UMR 75-88 au CNRS, Tour 23, 2, Place Jussieu, 75251 Paris Cedex 05, France*

Abstract

Theoretical simulation of hyperfine parameters for the nearest and next-nearest neighbor atoms of V_C^+ in SiC has been performed for the cubic and hexagonal clusters. The gradient-corrected all-electron DFT calculations with Becke's three-parameter functional have been performed by the use of split valence basis of Gaussian functions with d-functions. High performance of such approximations for the calculation of the hyperfine parameters of the well-known vacancy-related centers in SiC and Si has been demonstrated. We have found the D_{2d} local symmetry for the V_C^+ in the SiC cubic cluster. In hexagonal-like cluster, the D_{2d} symmetry is lowered to the C_s one. The symmetry plane contains the c -axis and one of the transverse bonds. Four Si atoms of the first shell become essentially inequivalent and have different hyperfine parameters. Two in-plane Si atoms concentrate the major part of the spin density and out-of-plane Si atoms exhibit relatively small hyperfine parameters. © 2001 Elsevier Science B.V. All rights reserved.

PACS: 71.15.M; 61.72.J; 76.30.M

Keywords: Carbon vacancy; SiC; Hyperfine parameters; DFT calculation

1. Introduction

Vacancy-related defects in electron-irradiated SiC polytypes have been the subject of extensive experimental investigations during the last three decades. The microscopic models of such defects, as a rule, are deduced from hyperfine parameters (HFPs) and corresponding relative intensities of the EPR lines originated from the ^{13}C and ^{29}Si isotopes located in different shells. The vacancy-related centers exhibit a great variety of properties depending on the doping of the crystal, dose of irradiation, energy of a beam and type of the particles. However, the experimental data and simple considerations are not enough to advance the adequate and unique microscopic models. In particular, magnetic resonance experiments themselves do not permit the

determination of a charge state of the defect. As a consequence, only a negatively charged isolated silicon vacancy is reliably identified at the present time. This identification is based on the experimental ENDOR determined value of the spin, $S = \frac{3}{2}$, and HFPs for the atoms of the first and second shells together with the first-principles calculation of the HFPs [1]. Ab initio plane-wave pseudopotential calculation for the fully relaxed silicon and carbon vacancies was performed in Ref. [2] for various charge and spin states using the local-spin-density approximation. However, these calculations gave no information except the spin states and point symmetry suitable for the assignment of these defects. On the other hand, the calculated HFPs generally are very sensitive to the level of theory used for the computation and an agreement with experimental results will suggest the quality of calculations.

In the last decade, several EPR spectra [3–7] with sufficiently different HFPs were tentatively assigned to the positively charged carbon vacancy V_C^+ in the SiC polytypes. Thus, for an unambiguous assignment, one

*Corresponding author. Tel.: +380-44-265-8275; fax: +380-44-265-8342.

E-mail address: endor@div51.semicond.kiev.ua (T.T. Petrenko).

must perform a high-accuracy simulation of the hyperfine interactions at least with four silicon atoms of the first shell. The present work deals with the cluster DFT calculation of the symmetry and tensor of hyperfine interaction with atoms of the first and second shells of the V_C^- in purely cubic and hexagonal lattice sites of the SiC.

2. Computational method

It is well known that accurate calculation of the HFPs requires high-level post-Hartree–Fock treatment. Due to the local nature of the hyperfine interaction, the calculated parameters are sensitive to the basis set size, electron correlation and optimized geometry. In recent years, the high performance of the DFT-based calculations of the spin densities with gradient-corrected functionals was shown for the molecular systems containing atoms of the second and third rows. The most extensively employed is the B3LYP functional, which is a combination of Becke's three-parameter hybrid exchange functional with the Lee–Yang–Parr nonlocal correlation functional [8,9]. To apply such a method of calculation we have used the $C_{18}Si_{16}H_{36}$ and $C_{18}Si_{20}H_{40}$ clusters as the model systems for a simulation of the carbon vacancy (see Fig. 1). The first one simulates the purely cubic site in 3C–SiC and the second one—hexagonal site (h-site). To check the validity of such an approach for the reproducing of observed HFPs of vacancy-related centers we have performed test calculations for well-known defects such as the V_{Si}^- in cubic SiC ($S = \frac{3}{2}$, T_d symmetry) and the V_{Si}^- in silicon ($S = \frac{1}{2}$, D_{2d} symmetry). For this purpose, the $Si_{18}C_{16}H_{36}$ and $Si_{34}H_{36}$ clusters have been used. For the calculations of all the above-mentioned defects in cubic clusters, the all-electron split valence Gaussian basis set 6-311G(d) with polarization d-functions has been applied for both Si and C atoms. To save the computational time we have used STO-3G basis for the capped bond hydrogen atoms which were fixed during the total energy minimization.

The pseudopotentials with corresponding basis sets (31G for C and 21G(d) for Si atoms beyond the first and second shells) have been used for calculations with hexagonal cluster [10,11]. For the first and second shells, the all-electron 6-311G(d) basis has been used for the correct description of the spin density distribution in the actual region.

The isotropic hyperfine coupling constant a_{iso} and components T_{ij} of the traceless tensor of anisotropic hyperfine interaction (AHFI) with nucleus N have been calculated according to the relations

$$a_{iso}^{(N)} = \frac{4\pi}{3} g\beta g_N \beta_N \langle S_z \rangle^{-1} \rho^S(R_N), \quad (1)$$

$$T_{ij}^{(N)} = \frac{1}{2} g\beta g_N \beta_N \langle S_z \rangle^{-1} \int \rho^S(r) \tau_{ij}(r - R_N) dr, \quad (2)$$

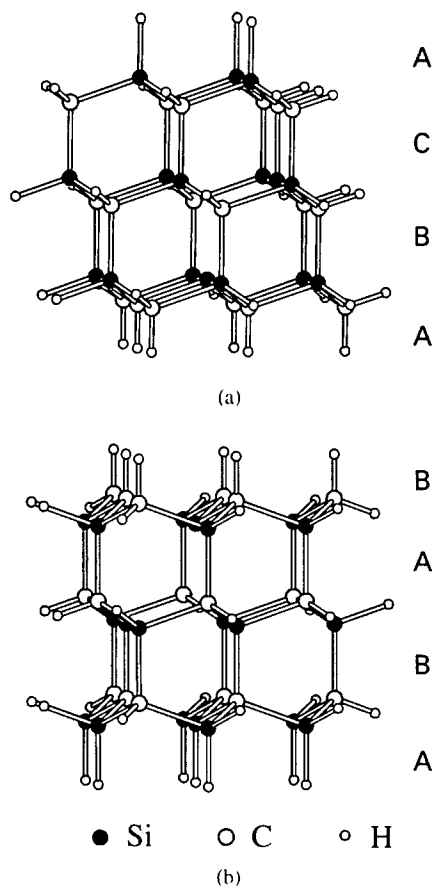


Fig. 1. Clusters used for a calculation of the HFPs of vacancy-related centers: a—cubic $C_{18}Si_{16}H_{36}$ cluster and b—hexagonal $C_{18}Si_{20}H_{40}$ cluster.

where $\tau_{ij}(r - R_N) = r_{kN}^{-5}(r_{kN}^2 \delta_{ij} - 3r_{kN,i}r_{kN,j})$ and $\rho^S(r)$ is the spin density.

3. Results of calculations and discussion

The results of our calculations of the HFPs for the first and second shells are presented in Table 1 for several vacancy-related defects. In this table, for example, the notation $Si_2(I)$ designates the second symmetry inequivalent silicon atom of the first shell and so on. T_{11} , T_{22} and T_{33} are the principal values of the AHFI tensor calculated according to Eq. (2).

The T_d point symmetry for the V_{Si}^- in the 3C–SiC and the D_{2d} point symmetry for the V_{Si}^- in the silicon were obtained in agreement with the experiment [1,12]. It is well known for the negatively charged vacancy in silicon [13] that a strong dependence of the calculated point

Table 1
Calculated hyperfine parameters for the vacancy-related centers in the SiC and Si crystals^a

Defect	Atom(number of shell)	a_{iso}	T_{11}	T_{22}	T_{33}
V_{Si}^- in 3C–SiC	C(I)	14.18 (± 16.2)	11.00 (± 10.5)	–5.50 (∓ 5.25)	–5.50 (∓ 5.25)
	Si(II)	2.82 (± 2.73)	–0.22 (0.0)	0.06 (0.0)	0.16 (0.0)
V_{Si}^+ in silicon	Si(I)	–33.96 (± 34.5)	–14.86 (± 9.4)	7.68 (∓ 4.7)	7.18 (∓ 4.7)
V_{C}^+ in 3C–SiC	Si(I)	–40.05	–15.27	6.75	8.52
	C ₁ (II)	7.87	2.34	–1.22	–1.12
	C ₂ (II)	–1.03	0.78	–0.43	–0.35
V_{C}^+ in h-sites of SiC	Si ₁ (I)	–120.29	–43.30	21.77	21.53
	Si ₂ (I)	–60.19	–21.12	11.50	9.62
	Si ₃ (I)	4.85	2.13	–1.37	–0.76
	C ₁ (II)	3.76	1.25	–0.71	–0.54
	C ₂ (II)	8.34	3.50	–1.79	–1.71
	C ₃ (II)	1.74	0.79	–0.64	–0.15
	C ₄ (II)	–0.44	–0.41	0.36	0.05
	C ₅ (II)	0.32	0.54	–0.50	–0.04
	C ₆ (II)	10.37	3.70	–1.97	–1.73
	C ₇ (II)	5.61	1.73	–1.24	–0.49

^aThe available experimental data are shown in parentheses. All values are given in 10^{-4}cm^{-1} .

symmetry and the HFPs on the cluster size occurs. However, our calculations show that for the positively charged vacancy in silicon, this is not the case. One may point out the good agreement of calculated and experimental values of the HFPs for both defects, used for the test calculations.

For the V_{C}^+ in cubic SiC, cluster calculations give D_{2d} point symmetry in agreement with the local-spin-density pseudopotential calculations with supercell approach [2]. Our calculations show that in this case, hyperfine splittings are sufficiently greater as compared to those ones for the T5 center [3]. Thus, the tentative assignment of this center to the V_{C}^+ must be revised. It is interesting to note that calculations with smaller $\text{Si}_4\text{C}_{12}\text{H}_{36}$ cluster give the same point symmetry D_{2d} and show small deviation of the HFPs for the Si atoms of the first shell from those for the larger cluster. For the V_{Si}^- in 3C–SiC we have found the more sufficient dependence of the calculated HFPs on the cluster size. Nevertheless, it may be deduced that the used cluster size is a good compromise between the precision of calculations and the CPU time.

For the V_{C}^+ in hexagonal cluster, the calculated point symmetry is C_s . In this case, the distance between the Si₁(I) atom (longitudinal bond) and Si₂(I) (transverse bond) is elongated up to 3.32 Å as compared to 3.086 Å in a perfect lattice. At the same time, the distance between two other atoms of the first shell is 2.28 Å. As a consequence of such a reconstruction, dramatic changes

in the spatial distribution of the spin density occur as compared to the purely cubic sites. Specifically, the major part of the spin density is localized on the Si₁(I) and Si₂(I) atoms located in the symmetry plane (see Table 1). Two symmetry equivalent atoms labeled Si₃(I) and located out of the symmetry plane, contain sufficiently smaller part of the spin density. Moreover, a sign of the spin density on the Si₃(I) atoms is negative. Thus, for the V_{C}^+ in the h-sites, one can expect dramatic changes of the hyperfine splittings originated from atoms of the first shell as compared to the purely cubic sites.

For the V_{C}^+ located in the quasicubic lattice sites in the hexagonal SiC polytypes, an intermediate behavior of the spin density distribution is suggested. In this case, one may regard the quasicubic lattice sites as slightly perturbed ones in 3C–SiC. Fig. 2 represents the comparison of the calculated HFPs for the Si atoms of the first shell in cubic cluster with available experimental data assigned to the V_{C}^+ defect with the C_s point symmetry in quasicubic sites of 6H–SiC [14]. One may see that for the Si₁ atom (longitudinal bond), the isotropic hyperfine interaction increases, while for the Si₂ atom (a transverse bond in a symmetry plane) it decreases as compared to the one for the 3C–SiC. At the same time, the values of a_{iso} for the Si₃ and Si₄ out-of-plane symmetry equivalent atoms remain practically unchanged. It may be assumed that large relative (but not absolute) deviation of calculated principal values of the AHFI tensor from

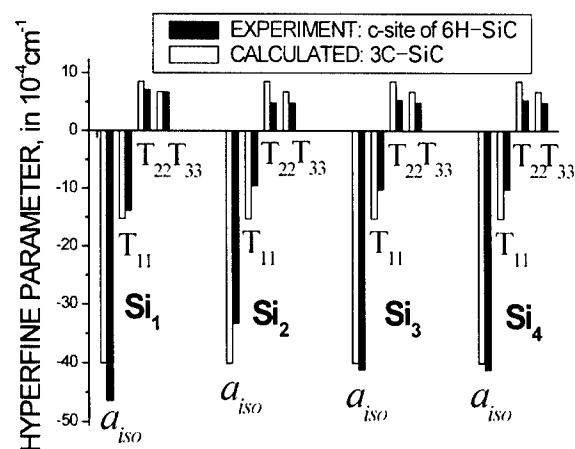


Fig. 2. Comparison of the HFPs for the first shell of the V_C^+ defect in the purely cubic sites (calculated) and quasicubic site in the 6H-SiC (experiment).

experimental ones may be caused by the used approximations as well as by influence of the specific crystal environment in 6H-SiC.

Notice that for all the considered defects listed in Table 1, the sign of the spin density on the atoms of the first shell is positive, with one exception for the $Si_3(I)$ atoms in hexagonal cluster. The spin density on the atoms of the second shell is also negative in some cases. This clearly demonstrates the significance of the spin polarization effects which are responsible for the negative spin densities.

Acknowledgements

The support of French-Ukrainian project 9350 and the Calculation Center CCR at Jussieu are gratefully acknowledged.

References

- [1] T. Wimbauer, B.K. Meyer, A. Hofstaetter, A. Scharmann, H. Overhof, Phys. Rev. B 56 (1997) 7384.
- [2] A. Zywiez, J. Furthmüller, F. Bechstedt, Phys. Rev. B 59 (1999) 15166.
- [3] H. Itoh, M. Yoshikawa, I. Nishiyama, S. Misawa, H. Okumura, S. Yoshida, J. Electron. Mater. 21 (1992) 707.
- [4] V.Ya. Bratus', et al., Mater. Sci. Forum 353–356 (2001) 517.
- [5] D. Cha, H. Itoh, N. Morishita, A. Kawasuso, T. Ohshima, Y. Watanabe, J. Ko, K. Lee, I. Nishiyama, Mater. Sci. Forum 264–268 (1998) 615.
- [6] N.T. Son, W.M. Chen, J.L. Lindström, B. Monemar, E. Janzén, Mater. Sci. Eng. B 61–62 (1999) 202.
- [7] N.T. Son, P.N. Hai, E. Janzén, Mater. Sci. Forum 353–356 (2001) 499.
- [8] M.J. Frisch, et al., Gaussian 98, Revision A.7, Gaussian Inc., Pittsburgh PA, 1998.
- [9] A.D. Becke, J. Chem. Phys. 98 (1993) 5648.
- [10] W.J. Stevens, H. Basch, M. Krauss, J. Chem. Phys. 81 (1984) 6026.
- [11] W.R. Wadt, P.J. Hay, J. Chem. Phys. 82 (1985) 284.
- [12] G.D. Watkins, J. Phys. Soc. Japan 18 (Suppl. 2) (1963) 22.
- [13] M.J. Puska, S. Pöykkö, M. Pesola, R.M. Nieminen, Phys. Rev. B 58 (1998) 1318.
- [14] V.Ya. Bratus', et al., in these Proceedings (ICDS-21), Physica B 308–310 (2001).



ELSEVIER

Physica B 308–310 (2001) 641–644

PHYSICA B

www.elsevier.com/locate/physb

DLTS study of defects in 6H- and 4H-SiC created by proton irradiation

D.V. Davydov^{a,*}, A.A. Lebedev^a, V.V. Kozlovski^b, N.S. Savkina^a,
A.M. Strel'chuk^a

^a A.F. Ioffe Physicotechnical Institute, Russian Academy of Sciences, Polytekhnicheskaya 26, St. Petersburg 194021, Russia

^b St. Petersburg State Technical University, St. Petersburg 194027, Russia

Abstract

Experiments on proton irradiation with energy of 150 KeV, 8 MeV and 1 GeV were made. Capacitance–voltage characteristics measured at 650 K showed that 8 MeV and 1 GeV proton irradiation of 6H-SiC leads to an increase of uncompensated donor concentration. However, donor concentration in 6H-SiC remains unaffected after 150 keV proton irradiation. Deep centers were investigated by deep levels transient spectroscopy (DLTS). Results of $C-V$ measurements are interpreted using DLTS data. The results obtained show the possibility of using proton irradiation for producing local high-resistance regions in SiC devices not intended for high-temperature applications. © 2001 Elsevier Science B.V. All rights reserved.

Keywords: SiC; Proton irradiation; DLTS

1. Introduction

There is several reports on formation of SiC layers semi-insulating (SI) at room temperature (RT) by means of proton irradiation [1–3]. However, the parameters and concentrations of radiation defects (RD) formed during irradiation have not been studied. In other works [4,5] RD parameters were studied but the compensation appearing in the course of irradiation was not analyzed.

The aim of this work was to fabricate SI 6H- and 4H-SiC layers by proton irradiation with different energies, compare their electrical properties, and determine the parameters of RDs responsible for the compensation. The samples were studied with capacitance–voltage ($C-V$) characteristics and deep levels transient spectroscopy (DLTS) methods.

2. Experiment

Silicon carbide p^+-n structures and epitaxial layers commercially produced by CREE Research, Inc., or fabricated at the Ioffe Institute by sublimation epitaxy (SE) [6] were used. The n-type layer thickness was about 5 μm ; that of the p-type layer: about 1 μm ; and substrate thickness: about 400 μm . The diameter of Schottky barriers or mesa structures of the diodes was in the range 600–700 μm . The concentration of uncompensated donors in the n-type layer ($N_d - N_a$) was $(0.8-4) \times 10^{16} \text{ cm}^{-3}$, that in the substrate, $(3-5) \times 10^{18} \text{ cm}^{-3}$, and concentration of acceptors in the p-type layer: $\sim 5 \times 10^{18} \text{ cm}^{-3}$. Thus, the doping level in the substrate and p-type emitter exceeded by no less than two orders of magnitude that in the n-type base layer.

A set of 6H- and 4H-SiC samples ($p-n$ structure and Schottky diodes) were step by step irradiated with 8 MeV protons. Total irradiation dose (D) was changed from $1 \times 10^{14} \text{ cm}^{-2}$ to $2 \times 10^{16} \text{ cm}^{-2}$. Two sequential 1 GeV proton irradiations with D of 3×10^{14} and $9 \times 10^{14} \text{ cm}^{-2}$ were made on one 6H-SiC SE sample

*Corresponding author. Tel.: +7-812-247-9930; fax: +7-812-247-6425.

E-mail address: dd@pop.ioffe.rssi.ru (D.V. Davydov).

with Schottky diodes. The epilayer was nonuniformly doped— $N_d - N_a$ varied from 5×10^{14} to $8 \times 10^{15} \text{ cm}^{-3}$ at the surface and at $7 \mu\text{m}$ depth, respectively. Furthermore, three 6H-SiC SE samples having initial $N_d - N_a$ value of $4 \times 10^{16} \text{ cm}^{-3}$ were irradiated with 150 keV protons with doses of 10^{11} , 10^{12} , and 10^{13} cm^{-2} . All irradiations were carried out at RT.

The C - V characteristics were measured on a bridge C - V setup on a frequency of 10 kHz. A study of 8 MeV irradiated samples demonstrated a decline in the $N_d - N_a$ value measured at RT, with $N_d - N_a$ markedly increasing on heating a structure to 650 K. For 6H-SiC the $N_d - N_a$ value measured at 650 K was even higher than that in the initial structures prior to irradiation. With increasing irradiation dose, this difference became more pronounced (Figs. 1 and 2). Irradiation of lightly doped samples with D of 10^{16} cm^{-2} led to formation of SI layers with specific resistivity of about $10^9 \Omega\text{cm}$ at RT.

Typical C - V characteristics measured after 150 keV proton irradiation are shown on Fig. 3. At high reverse bias the characteristic is similar to initial one; but irradiation resulted in appearance of flat region at low bias voltages where the capacitance does not depend on voltage, and its value corresponds to depleted region width of $\sim 1 \mu\text{m}$. We attribute this to formation of a SI layer due to the irradiation. The characteristics measured at 100 K shift right along the voltage axis. Increase of the temperature to about 500 K led to recovery of initial C - V characteristics of the diodes. The shape of the characteristics were the same for all the samples (all the irradiation dose values).

First 1 GeV irradiation did not noticeably influence on C - V characteristics. However, after the second irradiation ($D = 1.2 \times 10^{15} \text{ cm}^{-2}$) RT capacitance became independent on voltage (the epilayer became SI). C - V characteristic measured at temperature of 500 K after second irradiation was linear (Fig. 4); it revealed

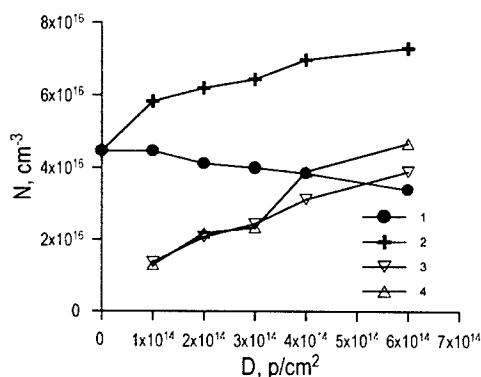


Fig. 1. 6H-SiC: $N_d - N_a$ measured at $T = 300 \text{ K}$ (1) and $T = 650 \text{ K}$ (2), difference of them (3), and concentration of the center located at $E_c - 1.22 \text{ eV}$ (4) vs. the irradiation dose.

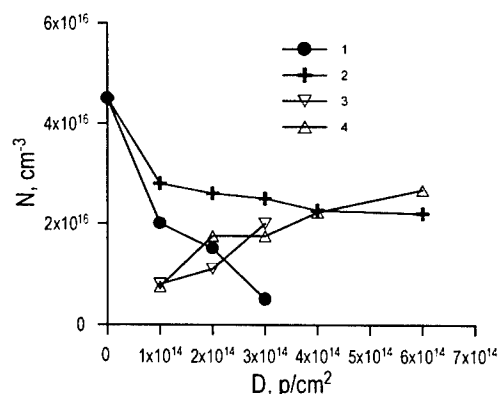


Fig. 2. 4H-SiC: $N_d - N_a$ measured at $T = 300 \text{ K}$ (1) and $T = 650 \text{ K}$ (2), difference of them (3), and total concentration of the centers RD_1 , RD_2 , RD_3 , and RD_4 (4) vs. the irradiation dose.

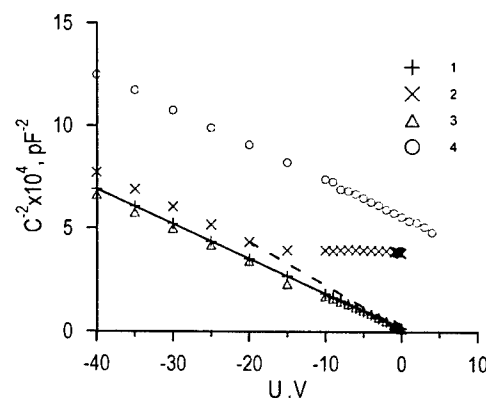


Fig. 3. C - V characteristics of n-6H-SiC epilayer before irradiation (1) and after 150 keV irradiation with dose of 10^{13} cm^{-2} measured at RT (2), 500 K (3), and 100 K (4).

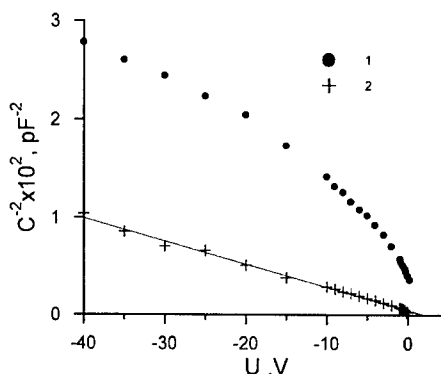


Fig. 4. C - V characteristics of unirradiated n-6H-SiC epilayer (1) and one measured at temperature of 500 K after 1 GeV proton irradiation ($D = 1.2 \times 10^{15} \text{ cm}^{-2}$) (2).

uniform doping with $N_d - N_a$ of $7 \times 10^{15} \text{ cm}^{-3}$ which exceeds much the initial one.

Six electron traps were found in DLTS spectra of n-type 6H-SiC samples irradiated with 8 MeV protons. Most of them were observed in electron-irradiated samples [7] or had parameters close to intrinsic structural defects. Two of the observed centers (with position in the band gap $E_c - 0.16 - 0.2 \text{ eV}$ and $E_c - 0.5 \text{ eV}$) were completely annealed out at 500–650 K. Sample with p-n junction was annealed at 800 K what resulted in small increase of the center $E_c - 0.7 \text{ eV}$ concentration.

DLTS investigation of electron traps in n-type 4H-SiC revealed 5 deep centers. Most of these were found in samples implanted with He^+ ions [4] or had parameters close to those of intrinsic defects. One of the observed centers ($E_c - 0.18 \text{ eV}$) was completely eliminated by annealing at 500–650 K.

Tables 1 and 2 list ionization energies of the observed centers, their estimated electron capture cross-sections (σ_n) and concentrations after irradiation with a dose of $2 \times 10^{14} \text{ cm}^{-2}$. For both of the polytypes studied, no pronounced difference was observed between the spectrum of deep centers formed in CREE epitaxial layers (CVD) and those grown by SE. The introduced RDs were completely annealed out at $\leq 2100 \text{ K}$.

In 6H-SiC epilayer irradiated with 1 GeV protons with dose of $3 \times 10^{14} \text{ cm}^{-2}$ DLTS revealed only two deep

electron traps: $E_c - 0.35 - 0.4 \text{ eV}$ (E_1/E_2) and $E_c - 1.2 \text{ eV}$ (R-center) in concentrations of $1 \times 10^{13} \text{ cm}^{-3}$ and $5 \times 10^{13} \text{ cm}^{-3}$, respectively. The R-center introduction rate was equal to 70 cm^{-1} for 8 MeV, and 0.17 cm^{-1} for 1 GeV protons.

3. Discussion and conclusion

As shown by the DLTS study, both 8 MeV and 1 GeV proton irradiation creates in n-type 6H-SiC a defect with the highest introduction rate ($E_c - 1.22 \text{ eV}$) with parameters close to those of the known structural defect—R center [8]. As follows from the parameters of the center located at $E_c - 1.22 \text{ eV}$, the recharging time (τ) for this center is of about two weeks at 300 K. Thus, the charge state of this and deeper lying centers does not change during $C-V$ measurements at RT. At the same time, the τ value for the center which is the closest to this level, ($E_c - 0.8 \text{ eV}$), is 3.3 s. Hence, the center $E_c - 0.8 \text{ eV}$ (and all shallower centers) can be considered completely ionized in $C-V$ measurements at RT.

In n-type 4H-SiC, several deep centers with ionization energy in the range of 0.96–1.5 eV are formed. The time constant of charge exchange for the $\text{RD}_{1,2}$ center is $5 \times 10^3 \text{ s}$ at RT. Similarly to the case of 6H-SiC, the charge state of these and deeper centers remains unchanged in the course of RT $C-V$ measurements. At

Table 1
Parameters of RDs observed in 6H-SiC

Parameters of observed RDs				Identification	
$E_c - E_0$ (eV)	σ_n (cm^2)	N_g (cm^{-3})	T_{ann} (K)	Electron irradi. [7]	Intrinsic defects
0.16–0.2	6×10^{-17}	3×10^{14}	< 650	L_1	E_1/E_2 [4]
0.36/0.4	2×10^{-15}	3.3×10^{15}	< 650	L_3/L_4	
0.5	5×10^{-15}	2.2×10^{15}		L_6	
0.7	4×10^{-15}	1.3×10^{15}	< 650	L_7/L_8	Z_1/Z_2 [4]
0.8	4×10^{-15}	6×10^{14}		L_9	
1.1–1.22	2×10^{-15}	2×10^{16}		L_{10}	

Table 2
Parameters of RDs observed in 4H-SiC

Parameters of observed RDs				Identification	
$E_c - E_0$ (eV)	σ_n (cm^2)	N_g (cm^{-3})	T_{ann} (K)	Implantation of He^+ [4]	Intrinsic defects
0.18	6×10^{-15}	2×10^{14}	< 650	P_1/P_2	Z_1 [4]
0.63–0.7	5×10^{-15}	5×10^{15}		Z_1	
0.96	5×10^{-15}	6.3×10^{15}		$\text{RD}_{1,2}$	
1.0	1×10^{-16}	6.3×10^{15}		RD_3	1.1 eV [9]
1.5	2×10^{-13}	5×10^{15}		RD_4	

the same time, the time τ for the Z_1 center, the closest to the mentioned above levels, as low as 3.6×10^{-2} s at RT.

At temperature of 650 K all known electron traps become ionized. Thus, the difference between the $N_d - N_a$ values measured at 300 and 650 K must be equal to the concentration of the center located at $E_c - 1.22$ eV for 6H-SiC and sum of $RD_{1,2}$, RD_3 , and RD_4 concentrations for 4H-SiC, determined from DLTS spectra. As seen from Figs. 1 and 2, this equality agrees well with experiment.

Most pronounced feature of 150 keV proton irradiation is insensitivity of the $C-V$ characteristics to dose of irradiation. This fact together with identity of the $C-V$ characteristics measured at 500 K after irradiation and ones of unirradiated samples means that the introduction rate of acceptor-like hole traps is equal to the one of donor-like electron traps. That is, 150 keV irradiation does not lead to change of charge density in space charge region of Schottky diodes at RT and higher temperatures. At the same time, at 100 K relatively shallow RDs are characterized by high τ and remains filled with electrons and, hence, their negative charge causes the shift of $C-V$ characteristics. Using approach described above (8 MeV protons) we estimated the R-center concentration. We extrapolate RT $C-V$ characteristic as shown in Fig. 4 (dashed curve) and obtained R-center concentration of $7 \times 10^{15} \text{ cm}^{-3}$. Hence, the R-center introduction rate by 150 keV proton irradiation is of about 700 cm^{-1} .

In conclusion, SI layers of 6H and 4H-SiC were created by proton irradiation with energies of 1 GeV, 8 MeV, 150 keV and 8 MeV, respectively. At the same time, it is shown that 1 GeV and 8 MeV irradiation of n-6H-SiC leads to increase of uncompensated donor concentration. Irradiation with energy of 150 keV leads only to capturing of electrons by

RD levels, but not to change in $N_d - N_a$ value. The introduction rate of the deepest RD in n-6H-SiC—R center was found to be 0.17, 70, and 700 cm^{-1} for 1 GeV, 8 MeV, and 150 keV protons, respectively. In 4H-SiC we obtained decrease of $N_d - N_a$ value after 8 MeV proton irradiation.

The obtained results may be applicable for creating local high-resistance SiC regions in technology of devices not intended for operation at high temperature, e.g., radiation detectors.

Acknowledgements

This work was partly supported by the grant INTAS-9730834.

References

- [1] A.O. Konstantinov, V.N. Kuzmin, L.S. Lebedev, D.P. Litvin, A.G. Ostroumov, V.I. Sankin, V.V. Semenov, *Zh. Tekhnich. Phys.* 54 (1984) 1622 (in Russian).
- [2] G.C. Rybicki, *J. Appl. Phys.* 78 (1995) 2996.
- [3] R.K. Nadela, M.A. Capano, *Appl. Phys. Lett.* 70 (1997) 886.
- [4] T. Dalibor, G. Pensl, H. Matsunami, T. Kimoto, W.J. Choyke, A. Schoner, N. Nordel, *Phys. Stat. Sol. (A)* 162 (1997) 199.
- [5] W. Puff, P. Mascher, A.G. Balogh, H. Baumann, *Mater. Sci. Forum* 258-263 (1997) 733.
- [6] N.S. Savkina, A.A. Lebedev, D.V. Davydov, A.M. Strel'chuk, A.S. Tregubova, M.A. Yagovkina, *Mater. Sci. Eng. B* 61-62 (1999) 165.
- [7] V.S. Ballandovich, *Sov. Phys. Semicond.* 33 (1999) 1188.
- [8] M.M. Anikin, A.S. Zubrilov, A.A. Lebedev, A.M. Strel'chuk, A.E. Cherenkov, *Sov. Phys. Semicond.* 25 (1991) 519.
- [9] W.C. Mitchel, et al., *Mater. Sci. Forum* 338-342 (2000) 21.



ELSEVIER

Physica B 308–310 (2001) 645–648

PHYSICA B

www.elsevier.com/locate/physb

Interstitial-based vacancy annealing in 4H–SiC

E. Rauls^{a,*}, T.E.M. Staab^b, Z. Hajnal^a, Th. Frauenheim^a^a *Universität Paderborn, Fachbereich Theoretische Physik, Warburger Str. 100, 33100 Paderborn, Germany*^b *Laboratory of Physics, Helsinki University of Technology, Finland*

Abstract

The migration of carbon interstitials through the 4H–SiC lattice and their recombination with vacancies has been investigated theoretically within the self-consistent charge density functional based tight-binding (SCC-DFTB) method. For vacancy–interstitial pairs created by irradiation, the capture radius of silicon and carbon vacancies has been examined, showing that interstitial migration through the otherwise perfect lattice starts getting important for distances larger than four nearest-neighbor atomic distances. © 2001 Elsevier Science B.V. All rights reserved.

PACS: 61.72.Ji; 67.80.Mg; 71.15.Mb

Keywords: SiC; Interstitials; Diffusion; Vacancies

1. Introduction

Many defects in SiC have a strong influence on the electrical properties of the material. A detailed understanding of their structure and behavior due to radiation or a change in temperature is crucial to the application of SiC as material for high-power devices [1]. In spite of the great amount of experimental as well as theoretical work in this field, many defects in SiC are still not very well understood—among these are the most simple defects, single silicon and carbon vacancies. It is still an open question as to what happens on the microscopic scale, when the EPR-signals of these vacancies vanish after annealing of the crystal at certain temperatures [2]. The assignment of the signal made in Ref. [2] to a single carbon vacancy in 3C–SiC is still controversially discussed and the signal might instead belong to a defect complex involving the carbon vacancy. For example in Ref. [3], the authors investigated this problem with positron lifetime spectroscopy, and report the vanishing of the carbon vacancy in the temperature range of 400–650°C. Nevertheless, a migration process

in the SiC-lattice has to be found, for which the activation energy can explain the extremely low temperatures which are in the discussion to be the annealing temperature of V_C .

The first process one may think of is that the vacancies themselves become mobile and migrate on their sublattices to surfaces or dislocations. The energies needed for activating these processes were calculated to be 4.8 eV for V_{Si} and 5.2 eV for V_C —much too high to explain the experimental results [2].

Another process that could cause the signals to vanish is the formation of defect complexes, possibly leading to significantly different signals. The silicon vacancy can be annealed out by one of its carbon neighbors migrating into the vacancy, thus forming a $C_{Si}-V_C$ pair defect, which has already been described experimentally and theoretically [4,5]. The calculated activation barrier of 1.7 eV can explain the 750°C annealing stage found in Ref. [2]. The analogue process for the carbon vacancy, though, is not possible, since the Si_C-V_{Si} pair defect has been calculated to be unstable, recombining to V_C without a barrier [4,6]. The annealing of carbon vacancies must therefore be attributed to a more complicated mechanism.

In this work, we investigated several processes involving silicon and carbon interstitials, which, by irradiation of the sample, are created in comparable

*Corresponding author. AG Theoretical Physics, Physics Department, University of Paderborn, D-33095 Paderborn, Germany. Tel.: +49-5251-602378; fax: +49-5251-603435.

E-mail address: rauls@phys.upb.de (E. Rauls).

amounts to silicon and carbon vacancies. The number of carbon and silicon atoms that are moved from their lattice sites depends on the irradiation energy. This determines also the average distances of the created interstitial–vacancy pairs. As shown in Ref. [7], low irradiation energies (in the range of 100 keV) lead to close Frenkel pairs. In samples irradiated with energies at 300 keV, carbon interstitials and carbon vacancies are spatially separated, while silicon atoms due to their higher mass still form close Frenkel pairs. Only when using high irradiation energies in the range of 2 MeV, the silicon interstitials and silicon vacancies are separated as well [7].

Hence, two different situations have to be considered: If being separated by just a few atomic distances, vacancy and interstitial are not independent of each other and the vacancy might capture the interstitial, resulting in a strong lowering of the total energy of the whole structure. On the contrary, higher irradiation energies cause the pairwise created interstitials and vacancies to be much farther separated. Here, for the recombination process, the determining quantity is the activation barrier for the migration of the interstitials through the lattice, before reaching the capture radius of a vacancy.

In this paper, we focus on the case of low irradiation energies, i.e. slight separation of vacancy and interstitial. Here, the question arises as to how long-ranged the influence of the vacancy on the interstitial is. By calculating the energy barriers for several structures with a vacancy and a carbon interstitial in different distances, we investigated up to which atomic distance interstitial recombination with the vacancy is the dominating process, before migration from one lattice site to the next prevails.

Our calculations with the self-consistent charge density functional based tight binding (SCC-DFTB) method have been performed in a $(5 \times 6 \times 1)$ supercell of 4H-SiC containing 240 atoms. Saddle point geometries and diffusion paths were obtained using a constraint conjugate gradient [8] and an uphill activation relaxation technique (ART) [9] followed by steepest descent relaxations into both minima.

2. Migration of C-interstitials

Carbon interstitials are stable as split interstitials on both carbon and silicon sites: on the carbon site as $(CC)_C$ and on the silicon site in the form of a mixed split interstitial $(CSi)_{Si}$. For neutral silicon interstitials only $(SiSi)_{Si}$ is a stable configuration in 4H-SiC. Consequently, the migration of carbon interstitials in 4H-SiC can, in contrast to the silicon interstitials, take place on both silicon and carbon sublattices.

The migration mechanism from $(CC)_C$ to $(CSi)_{Si}$ has been investigated for different charge states in the 3C polytype in Ref. [10]. Since the local environment is very

similar in the different polytypes, the results are not expected to vary significantly over the different cubic or hexagonal polytypes. For comparison, we have performed test calculations for several intrinsic defects in 3C- and 4H-SiC. In 3C-SiC, formation energies and diffusion barriers calculated within the SCC-DFTB scheme differ from the ab initio results in most cases by less than 0.2 eV. The differences between formation energies of the same defect in 3C-SiC and 4H- or 6H-SiC are for simple defects like vacancies or antisites, of the same order of magnitude.

In the case of the neutral $(CSi)_{Si}$ split interstitial, however, we find the formation energy to be 2.2 eV higher than that of $(CC)_C$. This clearly deviates from the ab initio result of ≈ 0.5 eV given in Ref. [10]. The energy barrier between these two configurations is found to be only 0.1 eV for the additional C-atom moving from the Si- to the C-site. Thus, the stability of $(CSi)_{Si}$ is underestimated in SCC-DFTB compared to the ab initio calculations. An explanation for the described discrepancies of these results may be found in the choice of the basis. In the SCC-DFTB calculations a minimal (sp-) basis has been used, which probably does not describe the overcoordinated Si-atoms occurring in the $(CSi)_{Si}$ structures correctly. To further investigate this open question, calculations with an extended spd-basis are currently under way. Hence, we limit the presentation of our results in this paper to structures, where this problem does not occur.

For a migration on the C-sublattice only, the split carbon interstitial has to move from one C-site to another, the inequivalent lattice sites in the hexagonal polytypes of SiC, this migration mechanism to a second nearest neighbor site depends on the crystal direction. The directions for which the migration paths have been calculated are depicted by arrows in Fig. 1.

Furthermore, the orientation of the interstitial has to be considered. For the interstitial oriented as in Fig. 1, the distance from one of the interstitial atoms to the second nearest neighbor is slightly shorter in the direction of the *c*-axis than along $[10\bar{1}0]$ or $[11\bar{2}0]$. Fig. 2 shows the diffusion paths for the three different crystal directions. The lowest barrier (2.9 eV) is found for a migration along (0001) .

This energy barrier is rather high and a migration process consisting of several of these steps can certainly not explain an annealing process starting at the experimentally observed temperatures around 200°C [2]. Thus, some other process has to be considered—possibly including a change of the sublattice. Such processes are currently being investigated and will be published elsewhere.

As already stated above, in case of low irradiation energies interstitials and vacancies will not be separated so much that they could be treated as isolated defects. With decreasing distance the influence of the vacancy on

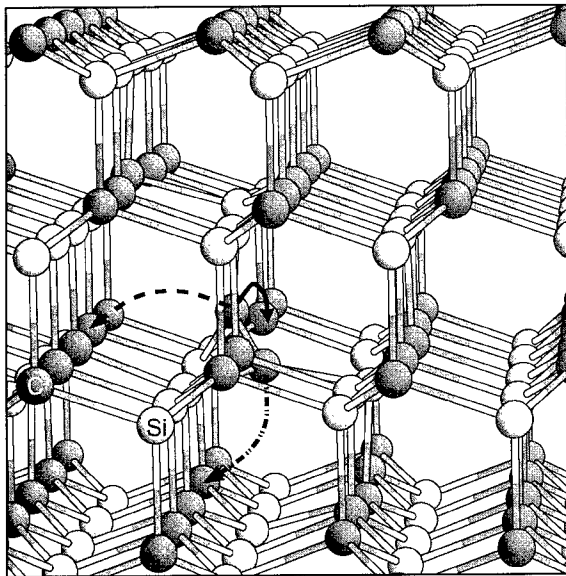


Fig. 1. $(CC)_C$ in a 4H-SiC lattice. The arrows show the directions for which the migration paths are shown in Fig. 2. Solid arrow: migration along $[10\bar{1}0]$, dashed arrow: $[11\bar{2}0]$, dash-dotted arrow: $[0001]$.

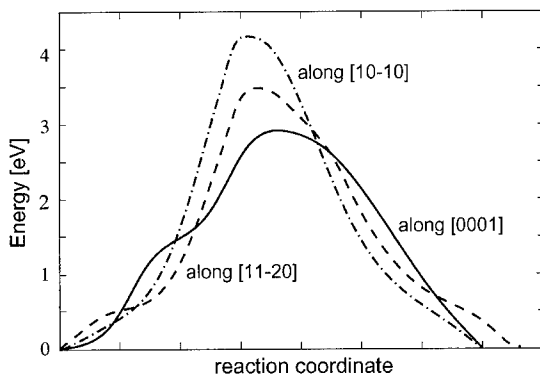


Fig. 2. Diffusion paths for the movement of $(CC)_C$ to the next C-lattice site depending on the three lattice directions.

the interstitial grows, and activation barriers for recombination will decrease. For $(CC)_C$ this has been investigated up to a fourth nearest neighbor distance between vacancy and interstitial site.

3. Recombination with vacancies

The mechanisms presented in this section apply in two cases: if created by high irradiation energies, the interstitial may start its migration process as described above on the carbon sublattice. After several of these steps or in case of lower irradiation energies, the

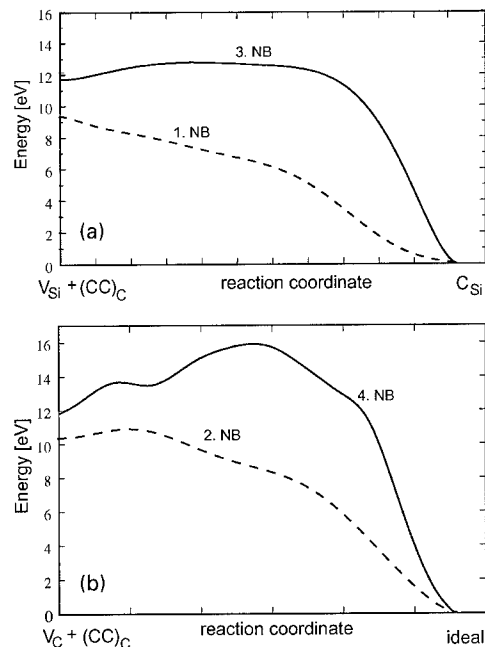


Fig. 3. Recombination of $(CC)_C$ with (a) V_{Si} and (b) V_C in several different distances. In (a), the energy during the migration process of the interstitial into the vacancy starting from a first neighbor (dashed line) or a third neighbor (solid line) position is shown. The structure $(CC)_C + V_{Si}^{1.NB}$ is metastable and recombines directly during relaxation. In (b) the same is shown for the carbon vacancy and the interstitial starting from a second (dashed) and a (fourth) neighbor distance, respectively.

interstitial reaches the capture area of either a silicon or a carbon vacancy. Then the height of the migration barriers for a direct recombination process compared to the barriers for the migration through the lattice determines whether migration continues by jumps along lattice sites or interstitial and vacancy recombine directly. The calculated diffusion curves are shown in Fig. 3.

Approaching the first neighbor site of V_{Si} , the C-interstitial becomes unstable and recombines with the vacancy without an energy barrier, see the dashed curve in Fig. 3(a). The resulting structure is a carbon antisite: $(CC)_C + V_{Si}^{1.NB} \rightarrow C_{Si}$, which is invisible by EPR and should, thus, explain the vanishing of the signals. For $(CC)_C$ at a second neighbor site to a carbon vacancy the barriers are with 0.5 eV still very low, see the dashed line in Fig. 3(b). For a third neighbor distance to V_{Si} we calculated a barrier of 1.08 eV (solid curve in Fig. 3(a)), which is still much lower than the lowest energy barrier for a migration on the C-sublattice (2.9 eV). In a fourth neighbor distance to V_C , the barrier approaches 4 eV (solid curve in Fig. 3(b)). Thus, starting from this position, the interstitial is unlikely to choose this

migration mechanism, but instead moves to a second neighbor C-site near the vacancy, and starts the described recombination process from this site. Thus, the lattice migration mechanism determines the necessary activation energy of the recombination. The influence of the vacancy on the interstitial is already negligible for a fourth neighbor separation. This is reflected by the formation energies of these structures, as well. For a fourth neighbor distance of these systems of a vacancy and a C-interstitial the limit for the sum of formation energies of an isolated vacancy and an isolated $(CC)_C$ is reached.

4. Conclusion

It has been investigated as to how interstitials, especially the carbon split interstitial $(CC)_C$, can contribute to the annealing of silicon and carbon vacancies in 4H-SiC. For migration on the carbon sublattice, diffusion paths along the three crystal directions have been calculated. The lowest activation barrier has been found for a migration along the c -axis of the crystal. Furthermore, the capture radius of vacancies has been examined by calculating activation barriers for a recombination with $(CC)_C$. We find that

such a process is favorable if $(CC)_C$ has approached at least a third nearest neighbor distance to the vacancy.

References

- [1] Silicon carbide, *Phys. Stat. Sol. B* 202 (1997).
- [2] H. Itoh, M. Yoshikawa, I. Nashiyama, S. Misawa, H. Okumura, S. Yoshida, *J. Electron. Mater.* 21 (7) (1992) 707.
- [3] C.C. Ling, C.D. Beling, S. Fung, *Phys. Rev. B* 62 (2000) 8016.
- [4] E. Rauls, Th. Lingner, Z. Hajnal, S. Greulich-Weber, Th. Frauenheim, J. Spaeth, *Phys. Stat. Sol. B* 217/2 (2000) R1.
- [5] Th. Lingner, U. Gerstmann, E. Rauls, S. Greulich-Weber, J. Spaeth, H. Overhof, Z. Hajnal, Th. Frauenheim, *Phys. Rev. B*, submitted for publication.
- [6] M. Bockstedte, O. Pankratov, *Mater. Sci. Forum* 338–342 (2000) 949.
- [7] H.J. von Bardeleben, J.L. Cantin, L. Henry, M.F. Barthe, *Phys. Rev. B* 62 (16) 10,841.
- [8] M. Kaukonen, R.M. Nieminen, P. Sitch, G. Jungnickel, D. Porezag, Th. Frauenheim, S. Pöykkö, *Phys. Rev. B* 57 (1998) 9965.
- [9] G.T. Barkema, N. Mousseau, *Phys. Rev. Lett.* 77 (1996) 4358.
- [10] A. Mattausch, M. Bockstedte, O. Pankratov, *Mater. Sci. Forum* 353–356 (2001) 323.



ELSEVIER

Physica B 308–310 (2001) 649–651

PHYSICA B

www.elsevier.com/locate/physb

The ground state of silicon vacancies in 6H–SiC and 15R–SiC

Th. Lingner*, S. Greulich-Weber, J.-M. Spaeth

FB6-Experimental Physics, University of Paderborn, Warburger Str. 100, 33098 Paderborn, Germany

Abstract

We investigated irradiated 6H–silicon carbide (SiC) and 15R–SiC with the magnetic circular dichroism of the absorption (MCDA) and MCDA-detected electron paramagnetic resonance (EPR). In neutron- and electron-irradiated 6H–SiC, we observed two MCDA transitions at photon energies of 1.435 and 1.369 eV. Photoluminescence (PL) lines at these photon energies (the so-called V1 and V3 lines) are presently assigned to the neutral silicon vacancy at the two quasicubic lattice sites in 6H–SiC. In electron-irradiated 15R–SiC, which has three inequivalent quasicubic lattice sites, we observed three MCDA lines at 1442, 1438 and 1373 meV, respectively. At the photon energy expected for the hexagonal site in 6H–SiC (the so-called V2 PL line), no MCDA signal was observed. From the temperature and field dependence of the MCDA, a spin $S = \frac{1}{2}$ of the quasicubic sites was determined. EPR spectra detected via these MCDA lines consist of single EPR lines at $g = 2.005(2)$. We conclude that the ground state of V_{Si} giving rise to these optical transitions is paramagnetic with $S = \frac{1}{2}$, which is predicted theoretically for the ground state of the triply negative charge state. The previous assignment of the optical transitions to the neutral charge state must, therefore, be corrected. © 2001 Elsevier Science B.V. All rights reserved.

Keywords: Silicon carbide; Vacancies; Electron paramagnetic resonance; Magnetic circular dichroism of the absorption

1. Introduction

Radiation-induced point defects in silicon carbide (SiC) have been studied for many years. But not even one of the most basic defects, the isolated silicon vacancy, is yet fully understood.

Photoluminescence (PL) spectra with zero phonon lines (ZPL) between 1.3 and 1.5 eV (the so-called V1, V2 and V3 lines) are frequently observed in irradiated 4H–SiC and 6H–SiC [1]. The number of ZPLs corresponds to the number of inequivalent lattice sites (two quasicubic and one hexagonal in 6H–SiC, and one quasicubic and one hexagonal in 4H–SiC). The intensity of the spectra is reduced after annealing above 750°C [1]. Sörman et al. detected several spin-triplet systems via the ZPLs with optically detected magnetic resonance

(ODMR) [1]. It was suggested that the ZPLs originate from the silicon vacancy in the neutral charge state. Later, Wagner et al. performed Zeeman experiments on these ZPLs [2]. No splitting of the lines in a magnetic field was observed, thus, it was concluded that the ground state and the excited states of the PL transitions in question were singlets and that the ODMR signals of the triplet systems had been detected indirectly via a shunt process [2,3].

To obtain information on the ground state of these optical transitions, we investigated irradiated 6H–SiC and 15R–SiC with the magnetic circular dichroism of the absorption (MCDA) and MCDA-detected electron paramagnetic resonance (MCDA-EPR). The MCDA technique is especially suited to investigate the ground state of an optical transition, because the MCDA signal of a paramagnetic center is proportional to the spin polarization of the ground state [3]. Saturation of the EPR transitions between the Zeeman levels of the ground state reduces the spin polarization and can be detected as a decrease in the MCDA signal (MCDA-EPR).

*Corresponding author. Tel.: +49-5251-60-2749; fax: +49-5251-60-3247.

E-mail address: lingner@physik.uni-paderborn.de (Th. Lingner).

2. Experimental results

The MCDA spectrum of neutron- or electron-irradiated 6H-SiC (Fig. 1a) consists of two ZPLs at photon energies close to the energies of the V1 and V3 luminescence lines (Table 1). Such MCDA spectra were observed in n-type electron-irradiated, unannealed 6H-SiC as well as in neutron-irradiated and afterwards annealed ($T_{\text{ann}} = 600^\circ\text{C}$) n-type 6H-SiC. The MCDA lines disappeared after a 1000°C anneal. A similar MCDA-spectrum, but with three zero-phonon lines instead of two, was measured in electron-irradiated, unannealed n-type 15R-SiC (Fig. 1b). The intensities of the MCDA lines are field and temperature dependent and originate, therefore, from a paramagnetic ground state.

MCDA-EPR signals as in Fig. 2 were detected in all MCDA lines. The two 6H-SiC MCDA-EPR spectra consist of a single line at $g = 2.005(1)$. No anisotropy, fine structure, or hyperfine structure was resolved. However, the line is wide enough to contain a hyperfine structure as reported in Ref. [1]. MCDA-EPR

spectra with a single line at $g = 2.005(2)$ were also measured in 15R-SiC in the k_1 , k_2 and k_3 (quasicubic) MCDA lines. The spin S of the ground state can be determined from the temperature and field dependence of the MCDA intensity, using the Brillouin function [3]. We obtain $S = \frac{1}{2}$.

3. Discussion

In 6H-SiC, there are two and in 15R-SiC, there are three inequivalent quasicubic sites. We, therefore, tentatively attribute the three MCDA lines observed in 15R-SiC to the silicon vacancy at the three quasicubic sites.

The MCDA-EPR spectra measured in the V1 and V3 MCDA lines of 6H-SiC are not the spin triplet spectra reported in Ref. [1], which would be split by 2 mT. Assuming that according to Ref. [1], the luminescence ZPL assignment to the silicon vacancy at the different sites is correct, the ground state of the optical transitions of the quasicubic sites is indeed paramagnetic in contrast to Ref. [2], but its EPR spectrum is not the triplet spectrum reported in Ref. [1].

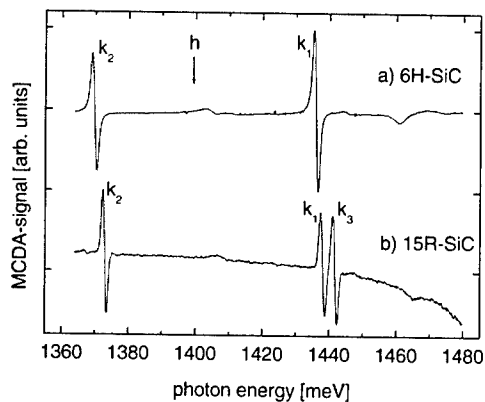


Fig. 1. MCDA spectrum of (a) neutron-irradiated 6H-SiC and (b) electron-irradiated 15R-SiC, measured with the magnetic field ($B = 2\text{ T}$) being parallel to the c -axis of the crystal at $T = 1.5\text{ K}$. The arrow indicates the position of the V2 luminescence ZPL for the hexagonal site in 6H-SiC as given in Ref. [1].

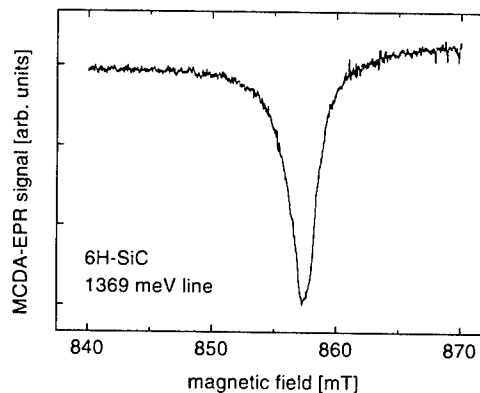


Fig. 2. MCDA-EPR-spectrum measured on the 1369 meV MCDA line of neutron-irradiated 6H-SiC at $T = 1.5\text{ K}$. The microwave frequency was 24.05 GHz. The magnetic field direction was parallel to the c -axis of the crystal.

Table 1
Zero phonon lines of the silicon vacancy in different polytypes of SiC

Site (label)	Photon energy (meV)			
	15R-SiC MCDA	6H-SiC MCDA	6H-SiC PL [2]	4H-SiC PL [2]
h_1 (V2)	—	—	1398	1352
h_2	—	—	—	—
k_1 (V1)	1438 ± 1	1435 ± 1	1433	1438
k_2 (V3)	1373 ± 1	1369 ± 1	1368	—
k_3	1442 ± 1	—	—	—

A spin $S = \frac{1}{2}$ ground state is possible for the silicon vacancy in the charge states +1 and -3 [4]. As the luminescence lines are always observed in n-type material [1,2] together with the EPR signal of the nitrogen donor [1], the charge state +1 is unlikely.

In tetrahedral symmetry, the silicon vacancy in SiC has an a_1 level and a higher lying t_2 level in the band gap [6]. The charge state $-3(a_1^2 t_2^5)$ has allowed optical transitions in the 1.4 eV range, as one electron from the a_1 level state can be optically excited into the t_2 level [6].

The absence of an MCDA signal at the position of the V2 line (which is assigned to the hexagonal sites [1]) in our samples can be explained by the silicon vacancies at the hexagonal sites being in the diamagnetic charge state $-4(a_1^2 t_2^6)$, while the vacancies at the quasicubic sites are at the same time in the charge state -3. This would mean that the charge transfer level $-3/-4$ of the quasicubic sites is above the charge transfer level $-3/-4$ of the hexagonal sites, and the Fermi level is in between these charge transfer levels. Such differences in charge transfer levels between the sites have been predicted theoretically [4,5].

In summary, we have to conclude that if the assignment of the V1, V2 and V3 PL lines to the silicon vacancy at the different sites according to Ref. [1] is correct, then the charge state giving rise to the V1 and

V3 luminescence lines of Table 1 is not zero but -3 with $S = \frac{1}{2}$. The previous assignment of the luminescence ZPLs to the neutral charge state of the silicon vacancy [1] must, therefore, be corrected.

Acknowledgements

We thank Dr. E.N. Kalabukhova from the Institute of Semiconductor Physics, Kiev, Ukraine, for providing the neutron-irradiated samples.

References

- [1] E. Sörman, N.T. Son, W.M. Chen, O. Kordina, C. Hallin, E. Janzén, *Phys. Rev. B* 61 (2000) 2613.
- [2] M. Wagner, B. Magnusson, W.M. Chen, E. Janzén, *Phys. Rev. B* 62 (2000) 16555.
- [3] J.-M. Spaeth, J.R. Niklas, R.H. Bartram, *Structural Analysis of Point Defects in Solids*, Solid State Sciences 43, Springer, Heidelberg, 1992.
- [4] L. Torpo, R.M. Nieminen, K.E. Laasonen, S. Pöykkö, *Appl. Phys. Lett.* 74 (1999) 221.
- [5] A. Zywietz, J. Furthmüller, F. Bechstedt, *Phys. Rev. B* 59 (1999) 15166.
- [6] U. Gerstmann, University of Paderborn, Private communication, 2001.



ELSEVIER

Physica B 308–310 (2001) 652–655

PHYSICA B

www.elsevier.com/locate/physb

Positron annihilation study of vacancy-type defects in silicon carbide co-implanted with aluminum and carbon ions

Takeshi Ohshima^{a,*}, Akira Uedono^b, Hiroshi Abe^a, Z.Q. Chen^{b,1}, Hisayoshi Itoh^a,
Masahito Yoshikawa^a, Koji Abe^c, Osamu Eryu^c, Kenshiro Nakashima^c

^a Japan Atomic Energy Research Institute, 1233 Watanuki, Takasaki, Gunma 370-1292, Japan

^b Institute of Applied Physics, University of Tsukuba, Tsukuba, Ibaraki 305-8573, Japan

^c Department of Electrical and Computer Engineering, Nagoya Institute of Technology, Nagoya 466-8555, Japan

Abstract

Co-implantation of Al ($2 \times 10^{18}/\text{cm}^3$) and C ($1 \times 10^{18}/\text{cm}^3$), Al/C, into 6H-SiC and subsequent annealing up to 1650°C were performed. Vacancy-type defects in the implanted layers were studied by positron annihilation spectroscopy. The mean size of vacancy-type defects produced by Al/C-implantation is found to be close to the size of divacancy. The mean size of vacancy-type defects is hardly changed by annealing below 600°C, and vacancy clustering occurs in an annealing temperature range between 600°C and 1000°C. At annealing temperatures between 1000°C and 1400°C, the mean size of vacancy-type defects decreases, and the major vacancy defects are annealed out above 1400°C. No significant difference is observed in the annealing behavior of vacancy-type defects between samples implanted with Al/C and only Al. © 2001 Elsevier Science B.V. All rights reserved.

Keywords: Silicon carbide; Co-implantation; Vacancy-type defects; Positron annihilation

1. Introduction

Silicon carbide (SiC) is regarded as a promising candidate for high-power and high-frequency devices owing to its excellent thermal and electrical properties [1,2]. In addition, since SiC has a strong radiation resistance [3,4], it is expected to be applied to electric devices used in radiation fields. For the fabrication of SiC devices, one of the key issues is the development of a selective impurity-doping technique. Donor or acceptor impurities have very low diffusion coefficients in SiC, and thus, thermal diffusion methods are not applicable for impurity doping into SiC. Therefore, ion implantation is considered as the most suitable technique. Since residual defects in implanted SiC layers act as carrier traps and/or scattering centers [5], understanding of

their annealing behavior is quite important. In previous studies [6,7], it was reported that the electrical activation of acceptors such as aluminum (Al) and boron in SiC was enhanced by co-implantation of carbon (C) ions. However, defects in co-implanted layers and their annealing behavior have not yet been clarified. In this study, we have investigated vacancy-type defects in 6H-SiC co-implanted with Al and C (Al/C) ions by positron annihilation spectroscopy (PAS) using monoenergetic positron beams.

2. Experiments

The samples used in this study were 5 µm thick n-type 6H-SiC epitaxial films grown on 6H-SiC substrates (3.5° off, Si-face). The net donor concentration of the epitaxial layer was $5 \times 10^{15} \sim 1 \times 10^{16}/\text{cm}^3$. Five-fold implantation of Al (20, 50, 110, 200 and 340 keV) was carried out at room temperature (RT) to form a box profile (depth: 0.5 µm) with a mean Al concentration of

*Corresponding author. Tel.: +81-27-346-9323; fax: +81-27-346-9687.

E-mail address: ohshima@taka.jaeri.go.jp (T. Ohshima).

¹Permanent address: Department of Physics, Wuhan University, Wuhan 430072, People's Republic of China.

$2 \times 10^{18}/\text{cm}^3$. A box profile of C atoms ($1 \times 10^{18}/\text{cm}^3$, $0.5 \mu\text{m}$ thick) was also formed by five-fold C-implantation (20, 60, 120, 190 and 270 keV) at RT or 800°C . The samples were annealed for 30 min up to 1650°C in argon (Ar) atmosphere after implantation. The hole concentration in Al-implanted layers was determined from the Hall measurements at RT.

PAS was carried out at the University of Tsukuba [8]. Doppler broadening profiles of annihilation γ -rays as a function of incident positron energy, E , were obtained by using monoenergetic positron beams. A spectrum of annihilation γ -rays (total counts of 5×10^5) was obtained using a Ge detector for each positron energy. The relationship between the S parameter (the ratio of the counts in $511 \pm 0.75 \text{ keV}$ to the total counts) and E (S - E curve) was analyzed with a computer code VEPFIT [9], which can solve a one-dimensional diffusion equation for positrons. The region sampled by positrons in ion-implanted 6H-SiC was divided into two or three blocks. From the calculations using the diffusion equation, the fractions of positrons annihilated at the surface, $F_s(E)$, and those in the i th block, $F_i(E)$, ($F_s(E) + \sum F_i(E) = 1$), were determined. The observed S - E curves were fitted to the following expression:

$$S(E) = S_s F_s(E) + \sum S_i F_i(E), \quad (1)$$

where S_s and S_i are the characteristic values of the S parameter for positrons annihilated at the surface and the i th block, respectively. The position of the boundary for each block and the diffusion length of positrons in each block were also determined by fitting. Details of the PAS measurements and analysis procedures have been reported in Ref. [8].

3. Results and discussion

Fig. 1 shows the depth profiles of S obtained for the 6H-SiC sample implanted with Al/C at RT and those subsequently annealed at 1000°C and 1300°C . For reference, the depth profile of Al atoms after implantation is also indicated. The S values are normalized by the S_b obtained for unimplanted 6H-SiC (S/S_b). The S values in shallow and deep damaged regions are referred to as S_{shallow} and S_{deep} , respectively. The positions of their boundaries are depicted as “the interface between the shallow and the deep blocks ($D_{s/d}$)” and “the interface between the deep block and the defect-free region ($D_{d/f}$)”. For the as-implanted sample, S_{shallow} and S_{deep} are obtained to be 1.075 and 1.065, respectively. This indicates that the open volume of vacancies in the shallow block, whose thickness is almost the same as the Al box profile, is larger than that in the deep block. Brauer et al. [10] reported that the normalized S value for divacancies, $V_{\text{Si}}V_{\text{C}}$, consisting of a silicon vacancy, V_{Si} , and a carbon vacancy, V_{C} , in 6H-SiC was 1.05. The

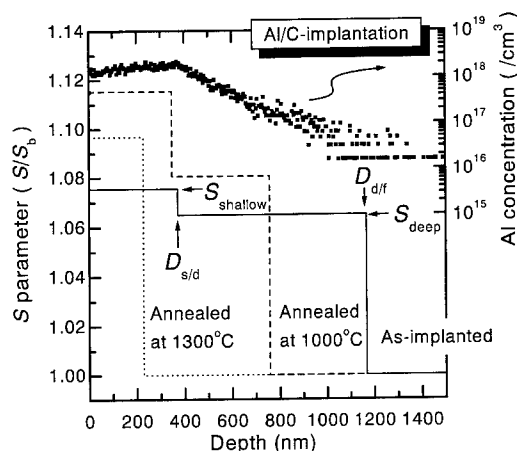


Fig. 1. Depth profile of S parameters obtained for 6H-SiC implanted with Al/C at RT and those subsequently annealed at 1000°C and 1300°C . The depth profile of Al atoms after implantation, which is determined from secondary ion mass spectroscopy, is also shown in the figure. The S values are normalized by the S_b obtained for the unimplanted one (S/S_b).

normalized S , which depends on the mean size of vacancy-type defects, was also reported to be 1.105 for $2-V_{\text{Si}}V_{\text{C}}$ or $3-V_{\text{Si}}V_{\text{C}}$ [10,11]. Taking into account the fact that several species of vacancy-type defects coexist in ion-implanted layers, we can say that the mean size of the residual vacancy-type defects in 6H-SiC implanted with Al/C at RT is close to the size of $V_{\text{Si}}V_{\text{C}}$. After annealing at 1000°C , S_{shallow} remarkably increases to be 1.115 whereas such a drastic increase is not observed in S_{deep} . This result indicates that large vacancy clusters are formed in the shallow block and that clustering of vacancies is suppressed in the deep block. No significant change of $D_{s/d}$ and a large shift of $D_{d/f}$ toward the surface suggest that damages are not annealed in the shallow region but recover in the deep region at 1000°C . A similar annealing behavior was reported in 6H-SiC implanted with phosphorus, P [11,12]. For the sample annealed at 1300°C , the S - E curve can be fitted using two blocks. A decrease of S_{shallow} and a further shift of $D_{d/f}$ toward the surface are observed. This result indicates that the mean size of vacancy-type defects decreases and further recovery of the damaged layer takes place on annealing at 1300°C .

Figs. 2 (a) and (b) show the annealing temperature dependence of S parameters and the position of the interface, respectively, for the samples implanted with Al and Al/C. No significant difference in the changes of S parameters and interface positions due to annealing is observed among all samples. Both S_{shallow} and S_{deep} are hardly changed by annealing up to 600°C . No significant change of $D_{s/d}$ and $D_{d/f}$ are observed below 600°C . Those results show that vacancy-type defects hardly migrate in this annealing temperature range. Between

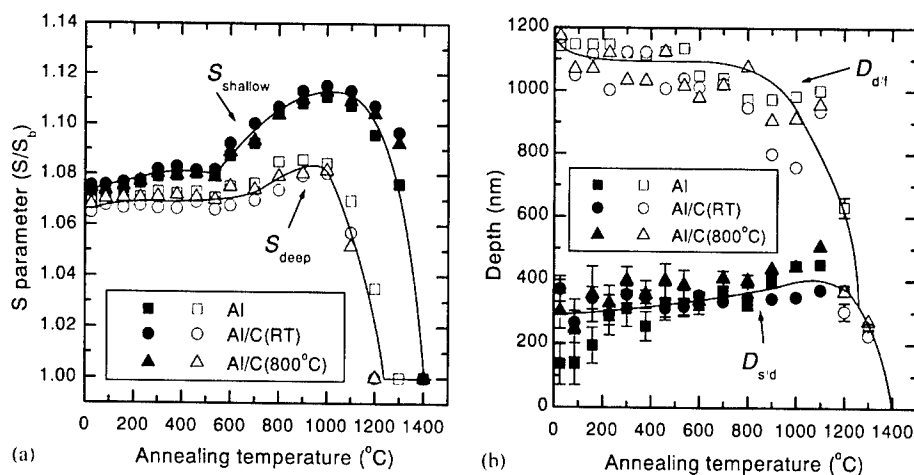


Fig. 2. (a) Annealing temperature dependence of S_{shallow} and S_{deep} obtained in 6H-SiC implanted with Al/C and Al ions. Al-implantation into all samples was carried out at RT. Squares, circles and triangles represent the results obtained in samples implanted with only Al, Al/C at RT, and Al/C at 800°C, respectively. Closed and open symbols represent S_{shallow} and S_{deep} , respectively. The S values are normalized by the S_0 obtained in the unimplanted sample (S/S_0). (b) Annealing temperature dependence of $D_{s/d}$ and $D_{d/r}$ obtained in 6H-SiC implanted with Al/C and Al ions. Closed and open symbols represent $D_{s/d}$ and $D_{d/r}$, respectively.

600°C and 1000°C, S_{shallow} remarkably increases with annealing temperature, though an increase of S_{deep} is not so large for all samples. In this temperature range, no significant shift of $D_{s/d}$ is observed in contrast to the shift of $D_{d/r}$. Those results suggest that clustering of vacancies occurs via the partial migration of vacancies from a deep region. The S_{shallow} and S_{deep} for all samples decrease with raising annealing temperature above 1000°C. A considerable shift of $D_{d/r}$ toward the surface is observed in this range. After annealing at 1400°C, the $S-E$ curves for all implanted samples are comparable to that for unimplanted sample, indicating that the concentration of vacancy-type defects are reduced below the detection limit of PAS by annealing at 1400°C. The results obtained above 1000°C are explained by annealing of damaged layers at such high temperatures. Similar observations were reported in P-implanted 6H-SiC [11,12]. The results of Hall measurements indicated the enhancement of the electrical activation of Al acceptors due to co-implantation, which is shown in Table 1. Taking into account the fact that the removal of vacancy-type defects by annealing at 1400°C is observed in all samples, the enhancement of the Al acceptor activation due to the co-implantation is not attributable to remaining defects which act as carrier traps. This supports the site competition model [6], i.e., the improvement of the electrical activation of Al is due to an increase of the number of Al atoms residing at Si sublattice sites, which act as shallow acceptors. However, the mechanism of the further improvement of the electrical activation of Al by co-implantation of C at elevated temperature is still unclear. To clarify this point, further investigations are necessary.

Table 1

Hole concentration (RT) in samples implanted with Al and Al/C. The samples were subsequently annealed at 1650°C in Ar

Ion species/ substrate temperature	Ion species/ substrate temperature	Hole concentration (/cm ³)
Al/RT		3×10^{16}
Al/RT	C/RT	4×10^{16}
Al/RT	C/800°C	8×10^{16}

4. Summary

Co-implantation of Al ($2 \times 10^{18}/\text{cm}^3$) and C ($1 \times 10^{18}/\text{cm}^3$) into 6H-SiC and subsequent annealing up to 1650°C were carried out. Vacancy-type defects in implanted layers were studied by PAS using monoenergetic positron beams. The mean size of vacancy-type defects in the sample implanted with Al/C or only Al is found to be close to the size of $V_{\text{Si}}V_{\text{C}}$. No significant difference in the annealing behavior of vacancy-type defects is observed between Al/C- and only Al-implanted samples. The mean size and depth profile of vacancy-type defects do not change significantly by annealing up to 600°C. Clustering of vacancies takes place by annealing between 600°C and 1000°C. Vacancy-type defects are annealed at temperatures above 1000°C and most of them are annealed out at 1400°C. Concerning the electrical properties of implanted layers, the electrical activation of Al acceptors is enhanced by co-implantation of C. The enhancement can be

explained by the site competition model, which has no discrepancy with the results obtained for defects remaining in SiC implanted with Al/C and Al.

References

- [1] W.E. Nelson, et al., *J. Appl. Phys.* 37 (1996) 333.
- [2] D.K. Ferry, *Phys. Rev. B* 12 (1975) 2361.
- [3] H. Itoh, et al., *IEEE Trans. Nucl. Sci.* NS-37 (1990) 1732.
- [4] T. Ohshima, et al., *Jpn. J. Appl. Phys.* 37 (1998) L1002.
- [5] G.C. Rybicki, *J. Appl. Phys.* 78 (1995) 2996.
- [6] H. Itoh, et al., *Mater. Sci. Forum* 264–268 (1998) 685.
- [7] T. Ohshima, et al., *Mater. Sci. Forum* 353–356 (2001) 575.
- [8] A. Uedono, et al., *Jpn. J. Appl. Phys.* 35 (1996) 5986.
- [9] A. van Veen, et al., *Appl. Surf. Sci.* 85 (1995) 216.
- [10] G. Brauer, et al., *Phys. Rev. B* 54 (1996) 3084.
- [11] A. Uedono, et al., *Jpn. J. Appl. Phys.* 37 (1998) 2422.
- [12] T. Ohshima, et al., *Appl. Phys. A* 67 (1998) 407.



ELSEVIER

Physica B 308–310 (2001) 656–659

PHYSICA B

www.elsevier.com/locate/physb

Interstitials in SiC: a model for the D_{II} center

Alexander Mattausch*, Michel Bockstedte, Oleg Pankratov

Lst. für. Theor. Festkörperphysik, Universität Erlangen–Nürnberg, Staudtstrasse 7, D-91058 Erlangen, Germany

Abstract

In photo luminescence experiments, the D_{II} center shows strong carbon-like vibrational modes above the highest bulk phonon mode. We have performed ab initio DFT calculations of the localized vibrational modes (LVM) of defects in SiC possessing carbon–carbon bonds. Among these defects, only the carbon split interstitial–antisite complex is found to exhibit a LVM spectrum compatible with that of the D_{II} center. The formation energy of this complex compares to the formation energy of the most abundant interstitial defects, namely the carbon split interstitial and the carbon–silicon split interstitial. We find a high binding energy of 3.6 eV and above. © 2001 Elsevier Science B.V. All rights reserved.

PACS: 61.72.Ji; 63.20.Mt; 61.72.Cc

Keywords: Silicon carbide; Point defects; D_{II} center; LVM

1. Introduction

For decades the D_I and D_{II} centers in SiC have been subject to thorough investigation. Though generated via ion implantation and subsequent annealing, both centers do not depend on the particular dopant and polytype and are stable at temperatures up to 1700°C and 1300°C, respectively. These properties indicate that the centers are intrinsic defects. While the microscopic structure of the D_I center still remains unclear, a di-interstitial configuration has been proposed for the D_{II} center by Patrick and Choyke [1,2]. This suggestion is based on photo luminescence experiments that exhibit five localized vibrational modes (LVM) above the highest SiC bulk phonon spectrum and two additional modes within the phonon band gap. The LVM-frequencies reach up to 40 THz, which is the same value as the highest phonon mode in diamond. For this reason, short carbon bonds have been suggested as the origin of these LVMs.

2. Ab initio calculation of LVMs and defect formation energy

We have analyzed the phonon frequencies of several possible candidates for the D_{II} center by employing density functional theory within the local density approximation and using norm-conserving pseudopotentials. The full dynamic matrix of the supercells with 64 atoms (3C–SiC) and 128 atoms (4H–SiC) has been calculated and diagonalized. This matrix is defined as

$$\Phi_{ij} = \frac{1}{\sqrt{m_i m_j}} \frac{\partial^2 E}{\partial Q_i \partial Q_j} = \frac{1}{\sqrt{m_i m_j}} \frac{\partial F_i}{\partial Q_j}.$$

With small displacements we numerically calculate the derivative $\partial F_i / \partial Q_j$. However, we have found sizable anharmonic effects. To obtain proper harmonic force constants, we have considered three different displacements for each atom and extracted the linear factor in a polynomial expansion of the forces. The forces have been calculated with software package FHI96SPIN [3]. A cut-off energy of 30 Ry and a special k-point-set to sample the Brillouin zone have been employed (except when the Jahn–Teller effect comes into play, then the Γ -point has been used). The forces have been converged to

*Corresponding author. Fax: +49-9131-85-28833.

E-mail address: alexander.mattausch@physik.uni-erlangen.de (A. Mattausch).

a relative accuracy of up to 10^{-4} . The resulting phonon spectra for the analyzed defects reveal vibrational modes in the band gap and above the highest bulk phonon mode which can be identified by comparison with a calculated bulk phonon spectrum. For the bulk spectrum, we find a slightly too small phonon band gap with 19.2 THz for the lower band edge (L and X point) versus 18.5 THz experimentally and 22.0 THz for the upper band edge at the L-point (23.1 THz experimentally). For the optical modes (LO, TO) at the Γ point we find 27.9 THz. In our calculation, we cannot distinguish between the TO and the LO mode at the Γ point (24.1 and 29.1 THz experimentally) due to the incompatibility of the macroscopic polarization of the crystal with the periodic boundary conditions imposed on the defect cell. This shortcoming, though, does not have any implications for the calculation of the localized defect modes. The results on defect energetics in 3C-SiC have been published previously [4].

3. Candidates for the D_{II} center

The relevant defect models for the D_{II} spectrum need a diamond-like environment to provide LVMs with frequencies as high as those experimentally found. The originally suggested di-interstitial is indeed a short carbon dimer, but we find a formation energy of approximately 12 eV which is much higher than that of other intrinsic defects. The most abundant defects with carbon bonds are the carbon antisite (C_{Si}), the carbon split interstitial $C_{sp}<100>$ (two carbon atoms sharing a carbon lattice site), the carbon–silicon split interstitial $C_{sp,Si}<100>$ (a carbon and a silicon atom on a silicon site) and the carbon split interstitial–antisite complex

$C_{sp,C_{Si}}<100>$ (two carbon atoms sharing a silicon site). The geometries of these defects are shown in Fig. 1.

In their undistorted structure, all split interstitials show degenerate defect levels in the electronic band gap. By occupying these levels, the Jahn–Teller effect causes a reduction of the symmetry and a splitting of these levels. In order to avoid the Jahn–Teller effect initially, we have considered the charge state 2^+ , in which the defect levels are unoccupied. For further investigation of $C_{sp,C_{Si}}<100>$, also the charge state 1^+ including Jahn–Teller distortion has been investigated. The carbon antisite C_{Si} exists only in the neutral charge state.

4. LVMs of D_{II} candidates

We have listed the results for all analyzed defects in 3C-SiC in Table 1. The antisite C_{Si} is the second most abundant carbon defect in SiC. Though it is surrounded by carbon neighbors, the phonon spectrum only shows a splitting of the bulk modes. The nearest neighbor atoms relax inwards and a shortening of the bonds can be identified, but they are still too distant to allow for the localized modes found in the D_{II} spectrum.

The carbon split interstitial $C_{sp}<100>$ has a carbon dimer (we find a distance between the two carbon atoms of approximately 2 Bohr) and is therefore closely related to the originally suggested carbon di-interstitial. It is the most abundant interstitial defect in SiC. The phonon spectrum, though, only shows a single LVM above the bulk spectrum with a frequency of 53 THz. The bonds to the neighboring silicon atoms are weak, the vibration decouples from its nearest neighbors and the split interstitial shows the behavior of a single C_2 molecule, which has a highest vibrational mode of 48.3 THz. Our

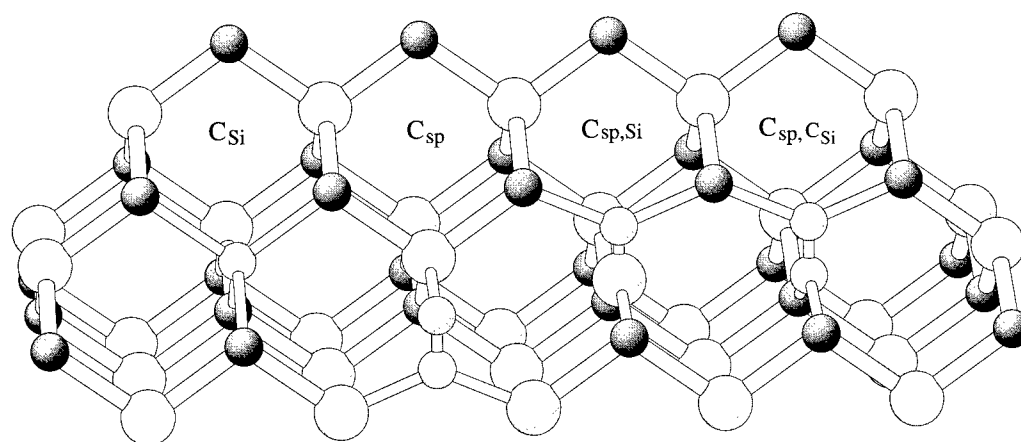


Fig. 1. Atomic structure of the investigated defects. From left to right: carbon antisite C_{Si} , carbon split interstitial $C_{sp}<100>$, carbon–silicon split interstitial $C_{sp,C_{Si}}<100>$, carbon split interstitial–antisite complex $C_{sp,C_{Si}}<100>$.

Table 1
Frequencies of LVMs of analyzed defects (3C–SiC) in THz

Mode	C_{Si}	$C_{sp}^{2+} \langle 100 \rangle$	$C_{sp, Si}^{2+} \langle 100 \rangle$	$C_{sp, C_{Si} \langle 100 \rangle}^{2+}$	$C_{sp, C_{Si} \langle 100 \rangle}^{1+}$	D_{II} [1]
Gap (2)	multiply	19.5	19.7	20.0	20.6	20.3
Gap (3)	gap modes	21.5	21.3	21.4	21.1	21.5
Mode B	—	—	—	28.4	28.1	30.9
Mode C	—	—	—	30.6	30.7	31.7
Mode D	—	—	31.4	35.7	35.1	35.3
Mode E	—	—	35.1	35.7	36.5	36.8
Mode F	—	53.0	38.1	43.4	43.2	39.8

calculated result is higher than this value. However, significant anharmonicity already for small displacements is present as the saddle point for a migration of one of the atoms lies very close to the defect geometry. The silicon–carbon split interstitial $C_{sp, Si} \langle 100 \rangle$ is surrounded by carbon neighbors. This defect has the second lowest formation energy of all interstitial defects. Carbon bonds exist between the carbon atom of the split interstitial and its two nearest neighbor atoms. A more complex vibrational spectrum is hence expected. Indeed, we find three non-degenerate LVMs above the highest bulk mode. However, the number of LVMs does not match those of the D_{II} center. Since the defect's saddle point for migration also lies close to the defect geometry, anharmonicity should be relevant.

The carbon split interstitial–antisite complex $C_{sp, C_{Si} \langle 100 \rangle}$ is a stable defect complex with a formation energy comparable to that of the split interstitials. We find a high binding energy of 3.6 eV for the charge state 2^+ , rising up to 4.4 eV for the neutral charge state. Hence this complex should be stable up to high temperatures. The phonon spectrum shows five LVMs above the highest SiC bulk mode, with frequencies in agreement with the D_{II} spectrum. Furthermore, two gap modes can be identified. The amplitudes of the high frequency modes are well localized to the defect molecule comprised of the split interstitial and the neighboring carbon atoms. In the charge state 2^+ the modes D and E are degenerate (c.f. Table 1), whereas the D_{II} spectrum shows two distinct lines for this frequency region. This can be explained by symmetry. In the charge state 2^+ the defect's point group is D_{2d} and the defect possesses an unoccupied degenerate defect level in the electronic band gap. This changes for the charge state 1^+ . The degenerate orbitals become occupied and a Jahn–Teller distortion lowers the symmetry of the defect to C_{2v} . This implies a symmetry induced splitting of the vibrational modes. Indeed, for the charge state 1^+ we find five non-degenerate phonon modes in good agreement with the D_{II} spectrum. The transition level for this charge state $E(+ + / +)$ lies 0.4 eV above the valence band, allowing for the existence of this defect in C_{2v} already in p-type material. In the charge

state 2^- all defect states are occupied, a Jahn–Teller effect does not occur and the defect has D_{2d} symmetry again. The transition level $E(-/-)$ is 1.5 eV above the valence band, well above mid-gap. Thus this defect exists in C_{2v} symmetry over a wide range of doping conditions—in p-type material as well as in n-type material.

Considering the defect molecule only, we find a similar result for 4H–SiC. For the charge state 2^+ the phonon spectrum of this defect shows five non-degenerate LVMs above the highest SiC bulk mode with frequencies comparable to those in 3C–SiC. The splitting of the LVMs D and E results from the lower symmetry of 4H–SiC. Our findings suggest an independence of the vibrational spectrum of the polytype for this defect.

5. Kinetic aspects

It is well-known from experiments that the concentration of the D_{II} center increases during the annealing and the spectrum persists to temperatures up to 1300°C. This suggests that the formation of the D_{II} center is kinetically driven and that it possesses a high binding energy. During implantation, an excess concentration of interstitials and vacancies is created. Considering diffusion processes [5], it is possible to construct a formation mechanism for the $C_{sp, C_{Si} \langle 100 \rangle}$ complex. The first step in this process is the formation of a carbon antisite. A possible process may start with a silicon vacancy. This defect is unstable against transformation into a carbon vacancy–antisite complex with a barrier of 1.6 eV in p-type material. As already noted, the carbon split interstitial is the most abundant interstitial defect in SiC. It also has a very low migration barrier of 1.7 eV. Such an interstitial can now recombine with the carbon vacancy of the vacancy–antisite complex to form an isolated carbon antisite. A further carbon split interstitial is now needed for the formation of the split interstitial–antisite complex. Due to its high binding energy of 3.6 eV and above, an attraction between the individual defects can be assumed.

From the above, we expect for $C_{sp,C_{Si}}\langle 1\ 0\ 0 \rangle$ the annealing kinetics comparable to that of the D_{II} center.

6. Summary

We have analyzed the phonon spectra of carbon related intrinsic point defects in order to identify the localized vibrational modes. For the carbon split interstitial–antisite complex $C_{sp,C_{Si}}\langle 1\ 0\ 0 \rangle$ we find good agreement between our calculated phonon frequencies and the D_{II} spectrum from PL-experiments. Its high binding energy suggests a high thermal stability. The other investigated defects do not show compatible phonon spectra. Besides, the high mobility of both split interstitials does not agree with the high thermal stability of the D_{II} spectrum. A possible annealing kinetics for this complex has been discussed.

Acknowledgements

This work has been supported by the Deutsche Forschungsgemeinschaft, Sonderforschungsbereich 292.

References

- [1] L. Patrick, W.J. Choyke, *J. Phys. Chem. Solids* 34 (1973) 565.
- [2] S.G. Sridhara, et al., *Mater. Sci. Forum* 264–268 (1998) 493.
- [3] M. Bockstedte, et al., *Comput. Phys. Commun.* 107 (1997) 187.
- [4] M. Bockstedte, O. Pankratov, *Mater. Sci. Forum* 338–342 (2000) 949.
- [5] A. Mattausch, M. Bockstedte, O. Pankratov, *Mater. Sci. Forum* 353–356 (2001) 323.



ELSEVIER

Physica B 308–310 (2001) 660–663

PHYSICA B

www.elsevier.com/locate/physb

Vacancies in He-implanted 4H and 6H SiC epilayers studied by positron annihilation

A. Kawasuso^{a,*}, M. Weidner^b, F. Redmann^a, T. Frank^b, P. Sperr^c,
R. Krause-Rehberg^a, W. Triftshäuser^c, G. Pensl^b

^a Martin-Luther-Universität, Friedemann-Bach-Platz 6, D-06108 Halle, Germany

^b Universität Erlangen-Nürnberg, Staudtstrasse 7, D-91058 Erlangen, Germany

^c Universität der Bundeswehr München, D-85577 Neubiberg, Germany

Abstract

Defects in epitaxially grown 4H and 6H SiC induced by He-implantation have been studied by positron annihilation and deep level transient spectroscopy. Two major annealing processes of vacancy-type defects appeared at 500–800°C and above 1000°C irrespective of polytype and conduction type. In n-type samples, the latter process is dominated by two different types of defects. In n-type 6H SiC, $Z_{1/2}$ levels emerged after annealing at 800°C. The $Z_{1/2}$ levels disappeared around 1100°C with an appearance of $E_{1/2}$ levels. The $E_{1/2}$ levels are eventually annealed at 1500–1700°C. Similar annealing behavior was observed for the corresponding levels in n-type 4H SiC, i.e., $RD_{1/2}$ and $Z_{1/2}$ levels. The overall annealing behavior of vacancy-type defects by positron annihilation and the deep levels are in good agreement above 800°C suggesting that the above deep levels are related to the vacancy-type defects. © 2001 Elsevier Science B.V. All rights reserved.

Keywords: SiC; Positron annihilation; DLTS; Vacancies

1. Introduction

Ion-implantation is an indispensable technique for the selective doping of SiC because of the extremely small diffusion constants of the dopant impurities. Residual defects induced by post-implantation annealing prevent the full activation of dopant impurities. After ion bombardment a series of deep levels have so far been observed in SiC [1]. In particular, two major peaks termed $E_{1/2}$ and $Z_{1/2}$ in 6H SiC and $Z_{1/2}$ and $RD_{1/2}$ in 4H SiC are important after a high temperature annealing above 1000°C [2]. These levels are thought to have the following correspondence: $E_{1/2}:6H \leftrightarrow Z_{1/2}:4H$ and $Z_{1/2}:6H \leftrightarrow RD_{1/2}:4H$ [1]. That is, the corresponding defects in these polytypes have the same atomic structures. Their origins are still unknown.

In this work, we investigated the annealing processes of vacancy-type defects in 4H and 6H SiC epilayers after He-implantation using positron annihilation spectroscopy (PAS). Deep level transient spectroscopy (DLTS) measurements have also been carried out on the same wafers [3]. From the correlation between PAS and DLTS data, we confirmed that $E_{1/2}$ and $Z_{1/2}$ levels in 6H SiC and $Z_{1/2}$ and $RD_{1/2}$ levels in 4H SiC are originating from vacancy-type defects.

2. Experimental

Samples were cut from chemical vapor deposition (CVD) grown 4H and 6H SiC films doped with nitrogen (n-type) or aluminum (p-type) with approximately 5 μm thick on the respective substrates. The net doping concentration was approximately $5 \times 10^{15} \text{ cm}^{-3}$. In order to generate a box-shape defect profile in the epilayers, the samples were implanted with He ions at

*Corresponding author. Japan Atomic Energy Research Institute, Watanuki, 1233, Takasaki, Gunma, 370-1292, Japan. Fax: +81-27-346-9687.

E-mail address: ak@taka.jaeri.go.jp (A. Kawasuso).

energies (doses) of 30 keV ($8 \times 10^{11} \text{ cm}^{-2}$), 100 keV ($9.5 \times 10^{11} \text{ cm}^{-2}$), 210 keV ($9.5 \times 10^{11} \text{ cm}^{-2}$), 350 keV ($9.5 \times 10^{11} \text{ cm}^{-2}$), 500 keV ($9.5 \times 10^{11} \text{ cm}^{-2}$), 650 keV ($1 \times 10^{12} \text{ cm}^{-2}$), 800 keV ($1.1 \times 10^{12} \text{ cm}^{-2}$) and 950 keV ($1.3 \times 10^{12} \text{ cm}^{-2}$) at room temperature. Isochronal annealing was conducted from 100°C to 1700°C for 30 min in vacuum or dry argon ambient. Positron annihilation Doppler broadening measurements were performed with the positron beam at an incident energy (E) below 40 keV. The energy windows for the peak intensity (S -parameter) and tail intensity (W -parameter) are 511.0 ± 0.9 and 516.0 ± 6.0 keV, respectively. Positron lifetime measurements were also carried out with a pulsed beam at $E = 17$ keV. The time resolution of the spectrometer was approximately 260 ps. All the unimplanted samples showed a unique S -parameter at $E > 15$ keV. Only one lifetime component (140–145 ps), which agreed with the SiC bulk lifetime [4], was found in unimplanted p-type samples though the spectra of unimplanted n-type samples that were strongly modulated due to the positron reemission effect. Thus, we use unimplanted p-type samples as references and suppose that S -parameter at $E > 15$ keV represents the bulk value.

3. Results and discussion

Fig. 1 shows the positron lifetime spectra for He-implanted samples with a reference sample (unimplanted p-type 6H). The positron lifetime shows a similar increase after implantation in both polytypes and conduction types. The average lifetime after implantation is determined to be approximately 210 ps for all the

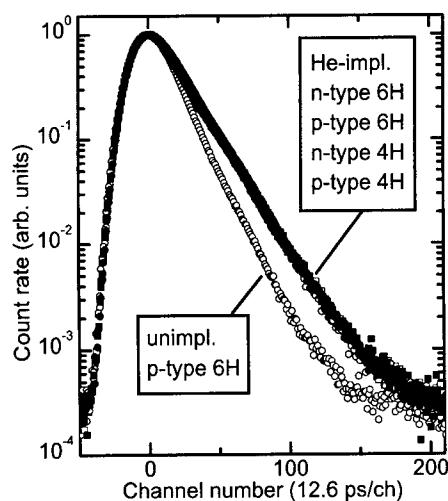


Fig. 1. Positron lifetime spectra of an unimplanted p-type 6H SiC (as a reference) and of He-implanted samples.

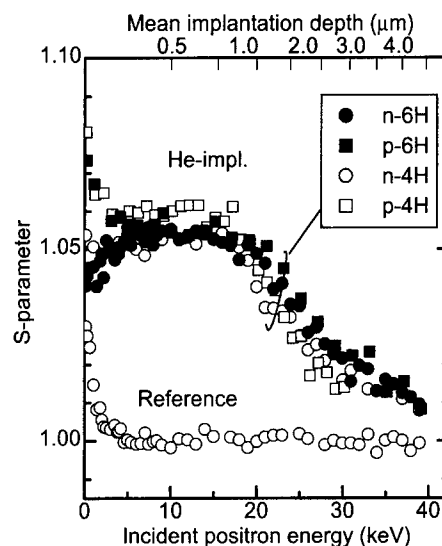


Fig. 2. S -parameter for the reference sample (unimplanted p-type 6H SiC) and for the He-implanted samples as a function of incident positron energy. The S -parameter is normalized to that of the reference sample at $E > 15$ keV.

samples. Two-component analyses gave rise to the defect-related lifetime (τ_2) of 236 ± 8 ps with an intensity of 60–70%. Fig. 2 shows S -parameter after implantation (normalized to the bulk S -parameter) with that of the reference sample as a function of incident positron energy. After implantation, S -parameter increases homogeneously from the unimplanted level at $3 \text{ keV} < E < 17 \text{ keV}$ and approaches the bulk value with increasing energy. This indicates that vacancies are homogeneously distributed in the implanted region. The depth profiles of vacancies determined by the VEPFIT program considering the one-dimensional diffusion of positrons [5] actually agreed with that calculated from SRIM simulation [6]. The average S -parameter in the implanted region is 1.056. There are no significant differences between different polytypes and conduction types in both lifetime spectra and S - E relations. The absence of polytype dependence on S -parameter and lifetime shows that the same types of vacancies are generated as positron trapping centers irrespective of the polytype. The absence of conduction type dependence can be explained as the shift of the Fermi level towards the mid-gap in both n- and p-type samples so that positron-trapping centers are retained in the same charge states. The observed S -parameter (~ 1.06) and positron lifetime ($\tau_2 = 236$ ps) in the damage region greatly exceed the specific values for isolated silicon vacancies (1.028–1.031 [7] and ~ 190 ps [8], respectively). This shows that both single vacancies and further vacancy agglomerates, such as divacancies, are

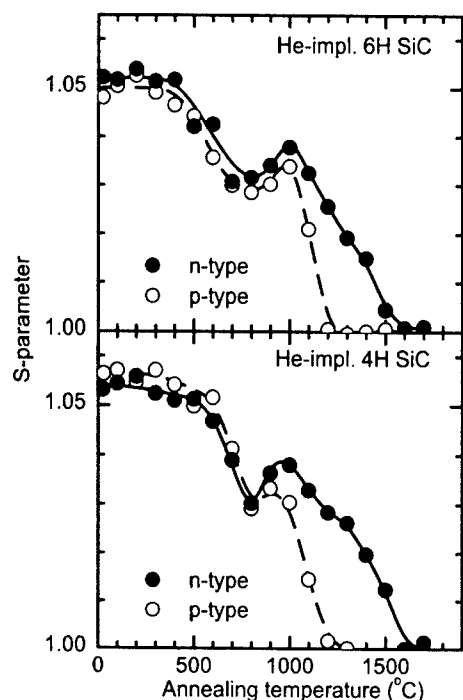


Fig. 3. S -parameter for He-implanted samples as a function of annealing temperature.

generated by implantation. This is naturally understood in terms of nuclear collisions near the ranges of He ions.

Fig. 3 shows the annealing behavior of the S -parameter in the damage region determined by the VEPFIT analysis. The annealing behaviors for 4H and 6H samples are quite identical. This again shows that the similar damages are created in both polytypes. One may divide the annealing process of S -parameter into three parts: (i) the first decrease at 500–700°C; (ii) a slight increase around 1000°C and (iii) a final recovery above 1100°C. In the first part, the defect-related positron lifetime was similar to that for the as-implanted sample ($\tau_2 = 236$ ps), while the intensity decreased from approximately 70% to 50%. The first annealing process is primarily interpreted as the disappearance of as the single vacancies. This is in good agreement with the previous report that isolated silicon and carbon vacancies are mobile below 1000°C [9]. The increase of the S -parameter in the second part implies the generation of complex defects. Probably, a part of mobile vacancies agglomerates or combines with other defects. The former two processes are commonly observed for both conduction types suggesting a lesser influence of dopant impurities. The S -parameter for the p-type samples decreases steeply around 1100°C and reaches the unimplanted level already at 1200°C. Contrary to this steep recovery for the p-type samples, the n-type

samples show a somewhat broad feature. This means that another type of defects, which cannot be seen in p-type samples, is detected in n-type samples above 1200°C. There are two possible ways to explain this result: (i) Only one type of defect exists in p-type samples, while two types of defects (one of them is common to p-type) exist in n-type, or (ii) Two types of defects acting as positron trapping centers exist in both n- and p-type samples. One of them, which has a higher thermal stability, is not detected in p-type samples due to the recovery of the Fermi level accompanying the disappearance of the majority of defects so as to charge positron-trapping centers more negatively and positively in n- and p-type samples, respectively. It is rather difficult to decide which of the above possibilities actually occur. However, in any case, two different types of defects contribute to the annealing process of n-type samples above 1000°C. The increase of S -parameter at 1000°C was not observed in the case of electron-irradiated samples [10]. It is assumed that He-implantation causes much more complicated damage structures than electron irradiation. Therefore, we suppose that such an effect preferentially appears with higher amount of damages. The final recovery of S -parameter above 1200°C for n-type samples is also observed in the electron-irradiated samples. Thus, the same type of defects should be responsible for this annealing process in He-implanted and electron-irradiated samples. From the detailed analyses of the electron-irradiated samples, we proposed that complex defects related to silicon vacancies are important. It is interesting to note that even in the case of He-implantation, which may resulting in a heavier damage than electron irradiation, all the vacancy-type defects detected by positron annihilation vanish after annealing at 1700°C as well as in electron irradiation case.

We compare the above-described positron annihilation and DLTS experiments. After annealing above 700°C, $E_{1/2}$ and $Z_{1/2}$ levels in 6H and $Z_{1/2}$ and $RD_{1/2}$ levels in 4H are observed [3]. The concentrations of these levels are determined by $C-V$ characteristics. Fig. 4 shows the annealing behavior of these levels with the respective S -parameters. The concentrations of $Z_{1/2}$ in 6H and $RD_{1/2}$ in 4H samples slightly increase at 1000°C and drastically decrease until 1200°C. The concentrations of $E_{1/2}$ in 6H and $Z_{1/2}$ in 4H increase from 1000°C along with the decreases of $Z_{1/2}$ in 6H and $RD_{1/2}$ in 4H and finally decrease above 1400°C. One can immediately find that these successive annealing behaviors of $E_{1/2}$ and $Z_{1/2}$ levels in 6H and $Z_{1/2}$ and $RD_{1/2}$ levels in 4H are in good agreement with what we observed for the S -parameter. That is, increase in the concentrations of $Z_{1/2}$ in 6H and $RD_{1/2}$ levels in 4H closely matches with that of S -parameter at 1000°C. The decrease in the concentrations of $E_{1/2}$ in 6H and $Z_{1/2}$ levels in 4H coincides with the final recovery of S -parameter at

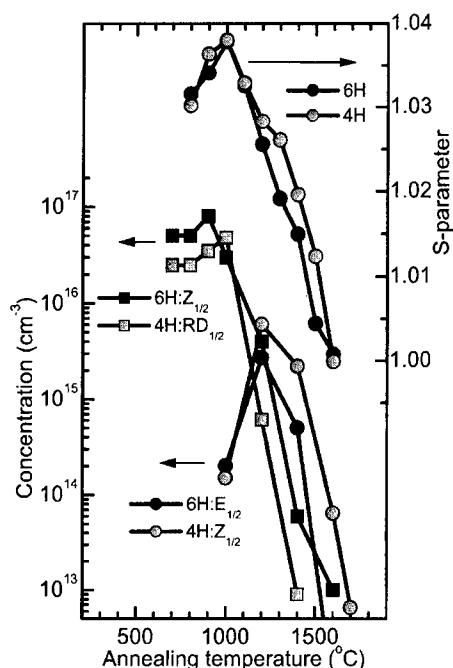


Fig. 4. Annealing behavior of the S -parameter and concentrations of the observed deep levels ($E_{1/2}$ and $Z_{1/2}$ levels in 6H and $Z_{1/2}$ and $RD_{1/2}$ levels in 4H SiC) for He-implanted samples in the annealing temperature range above 800°C.

1200°C. Thus, the above electronic levels should be related to vacancy-type defects detected by positron annihilation. Recently, we also proposed that $E_{1/2}$ in 6H and $Z_{1/2}$ in 4H should be silicon-vacancy-related defects using electron-irradiated epilayers [10]. This proposal is again supported here.

4. Summary

In summary, we investigated the annealing process of vacancy-type defects in 4H and 6H SiC CVD epilayers after He-implantation. There are no essential differences

between 4H and 6H samples in their annealing process. From the comparison between n- and p-type samples, it was found that two types of vacancies contribute to the annealing process above 1000°C in n-type samples. The overall annealing behavior for vacancy-type defects agrees with the successive annealing of $Z_{1/2}$ and $E_{1/2}$ levels in 6H and $Z_{1/2}$ and $RD_{1/2}$ levels in 4H SiC.

Acknowledgements

One of the author (A.K.) thanks the Alexander von Humboldt Stiftung for their financial support to promote this research project.

References

- [1] T. Dalibor, G. Pensl, H. Matsunami, T. Kimoto, W.J. Choyke, A. Schöner, N. Nordell, Phys. Stat. Sol. A 162 (1997) 199.
- [2] T. Frank, G. Pensl, S. Bai, R.P. Devaty, W.J. Choyke, Mater. Sci. Forum 338–342 (2000) 753.
- [3] M. Weidner, et al., in these Proceedings (ICDS-21), Physica B 308–310 (2001).
- [4] G. Brauer, W. Anward, E.-M. Nicht, J. Kuriplach, M. Šob, N. Wagner, P.G. Poleman, M.J. Puska, T. Korhonen, Phys. Rev. B 54 (1996) 2512.
- [5] A. van Veen, H. Schut, M. Clement, J.M.M. de Nijs, A. Kruseman, M.R. Ijpma, Appl. Surf. Sci. 85 (1995) 216.
- [6] A. Kawasuso, F. Redmann, R. Krause-Rehberg, P. Sperr, M. Weidner, T. Frank, G. Pensl, H. Itoh, Mater. Sci. Forum 353–356 (2001) 537.
- [7] A. Kawasuso, F. Redmann, R. Krause-Rehberg, M. Yoshikawa, K. Kojima, H. Itoh, Phys. Stat. Sol. B 223 (2001) R8.
- [8] A. Kawasuso, H. Itoh, N. Morishita, M. Yoshikawa, T. Ohshima, I. Nashiyama, S. Okada, H. Okumura, S. Yoshida, Appl. Phys. A 67 (1998) 209.
- [9] H. Itoh, A. Kawasuso, T. Ohshima, M. Toshikawa, I. Nashiyama, S. Tanigawa, S. Misawa, H. Okumura, S. Yoshida, Phys. Stat. Sol. A 162 (1997) 173.
- [10] A. Kawasuso, et al., J. Appl. Phys., to be published.



ELSEVIER

Physica B 308–310 (2001) 664–667

PHYSICA B

www.elsevier.com/locate/physb

Vacancy type defects in Al implanted 4H–SiC studied by positron annihilation spectroscopy

J. Slotte^{a,*}, K. Saarinen^a, A.Yu. Kuznetsov^b, A. Hallén^b^a *Laboratory of Physics, Helsinki University of Technology, P.O. Box 1100, FIN-02015 HUT, Finland*^b *Royal Institute of Technology, Department of Electronics, Electrum 229 SE-164 40, Kista-Stockholm, Sweden*

Abstract

Vacancy-type defects produced by 100 keV Al⁺ ion implantation in epitaxial 4H–SiC have been studied by positron annihilation spectroscopy. The implantation dose varied from 3×10^{13} to 1×10^{15} /cm² and the implantation temperature was 25–800°C. From the experimental results it is clear that the implantation at elevated temperatures reduces the number of vacancy type defects. Furthermore, the defect-cluster size depends on the implantation temperature, suggesting that the vacancies involved are mobile. The positron annihilation experiments also suggest that the defect profile extends deeper into the samples than expected from the deposited energy distribution and from previous Rutherford backscattering/channeling measurements. © 2001 Elsevier Science B.V. All rights reserved.

Keywords: Vacancies; Implantation; Positron annihilation

1. Introduction

During the last decade much interest has been drawn towards silicon carbide, due to its versatility as a base for electronic and optoelectronic devices. Owing to its material properties, SiC devices can operate under extreme conditions, e.g. high electric power, high temperatures, etc. It has previously been shown that Al implantation is an adequate technique to produce sharp p[−] doped regions in SiC [1–3]. An evident disadvantage of this technique is the production of implantation induced defects, such as vacancies and interstitials. In order to maintain the electrical properties of the crystal these defects have to be annealed. These anneals often require very high temperatures [4], but if the implantation damage is too heavy, the electrical properties of the crystal cannot be restored [5]. In order to reduce the implantation damage and allow point defects to recombine, the implantation can be performed at elevated temperatures.

Positron annihilation spectroscopy (PAS) has successfully been used to identify and characterize vacancy-type point defects in semiconductors [6]. In this study we apply PAS in the Doppler broadening mode to study ion implantation induced defects in 4H–SiC. Previous studies have identified the silicon and carbon mono-vacancies in irradiated SiC [7] and some studies on implantation related defects have also been done [8,9]. The PAS results are compared to measurements done with Rutherford backscattering spectrometry (RBS) in the channeling mode from the same samples.

2. Experimental

The samples used in this study were epitaxial 4H–SiC layers with thicknesses of more than 10 μm grown by chemical vapour deposition on 4H n-type SiC substrates. The samples were implanted with 100 keV Al⁺ ions, the dose varied between 3×10^{13} and 1×10^{15} /cm². The implantation temperature was 25–800°C.

In order to study the vacancy-type defect distributions in the implanted samples, we used a monoenergetic positron beam. Positron spectroscopy is a powerful tool to study vacancy-type defects. Positrons in materials

*Corresponding author. Tel.: +358-9-451-3111; fax: +358-9-451-3116.

E-mail address: jonatan.slotte@hut.fi (J. Slotte).

science can either be taken directly from a β^+ source or, as in this case, be moderated and then accelerated to the desired implantation energy. After thermalization the positron diffuses in the sample until it annihilates with an electron. Neutral and negative vacancy-type defects in the lattice act as positron traps. When a positron is trapped by such a defect, its lifetime increases and the positron–electron momentum distribution narrows due to reduced electron density.

The momentum of the annihilating positron–electron pair can be detected as Doppler broadening of the 511 keV annihilation line. In order to detect this broadening we used a Ge detector with a energy resolution 1.3 keV at 511 keV. The shape of the broadened annihilation line is usually described by the parameters S and W . The low momentum parameter S is the fraction of counts in the central part of the line and thus it describes annihilation with low momentum valence electrons. Correspondingly W is the high momentum parameter obtained as the fraction of counts in the wing region of the annihilation line and it thus describes annihilation mainly with core electrons. Consequently an increase/decrease in S/W parameter indicates the presence of vacancy-type defects. The measured S/W parameter is a superposition of the S/W parameter of the bulk and the parameters of the different defects in the sample. Near the surface, the annihilation of the positron at the surface also has to be accounted for. This gives the following equations for the S/W parameter:

$$S = \eta_B S_B + \sum \eta_{Di} S_{Di}, \quad (1)$$

$$W = \eta_B W_B + \sum \eta_{Di} W_{Di}. \quad (2)$$

If a sample contains only one type of defect, the S – W plot of the measurement should form the segment of a line between the defect and the bulk state.

3. Results and discussion

Fig. 1 shows the S and W parameters as a function of positron implantation energy for Al⁺ implantations at 25°C (3×10^{13} and 5×10^{14} Al/cm²) and at 800°C (5×10^{14} Al/cm²). The mean positron implantation depth is also indicated in the figure. As can be seen for the samples implanted at RT, the S and W parameters behave as expected in the implanted region, i.e. higher dose results in higher S parameter. A previous work [10] where the implantation damage was studied by RBS/channeling showed that for samples implanted with 1×10^{15} /cm² Al at RT the sample was almost amorphized to a depth of approximately 300 nm. This trend can also be seen in the large S parameter values obtained near the maximum of the Al implantation profile for the samples measured with PAS. For the sample implanted at 800°C

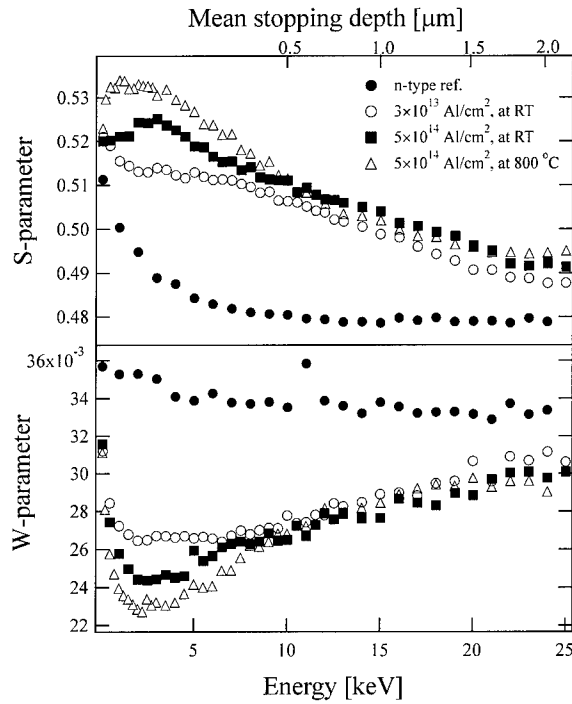


Fig. 1. S and W parameters as a function of positron implantation energy for samples implanted at room temperature and at 800°C. The doses are indicated in the figure as well as the mean positron implantation depth.

in Fig. 1 the elevated implantation temperature does not seem to have a positive effect on the reduction of implantation induced defects. However, as we will show the high S parameter values obtained in the samples implanted at elevated temperatures is due to defect clustering.

Fig. 2 shows the S – W plot for the sample implanted at 800°C, in the figure the S/W parameters of the silicon vacancy [11] is also shown. As can be seen the parameters fall on the same line, suggesting that only one type of defect of the same kind is present in the sample, also the S/W parameters of the Si vacancy fall on this line. Since some measured S parameters are higher and some measured W parameters are lower than that for the Si vacancy and still on the same line we do not think that this is a sign of a single vacancy type present in the samples. Rather mono-vacancies and larger vacancy-type defects coexist. Since the carbon atom is much smaller than the silicon atom and has much fewer electrons, the influence of the carbon atoms on the S and W parameters is insignificant. This results in the parameters falling on the same line. In Fig. 2 is also shown the turning point from the bulk–defect line to the defect–surface state line for the samples implanted with 5×10^{14} Al/cm² at 400°C as well as the turning

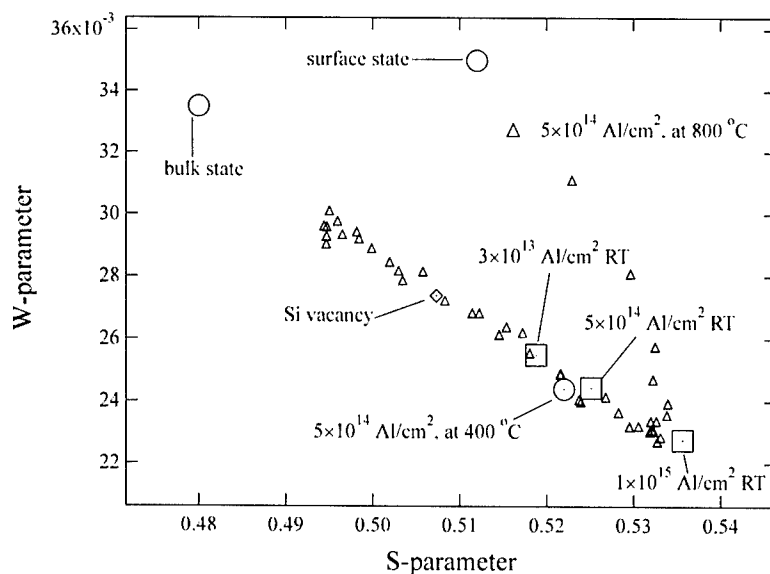


Fig. 2. S - W plot for the sample implanted at 800°C with $5 \times 10^{14} \text{ Al/cm}^2$. The parameters for the silicon vacancy are from Ref. [11]. In the figure is also shown the turning points from the bulk-defect line to the defect-surface line for different implantations.

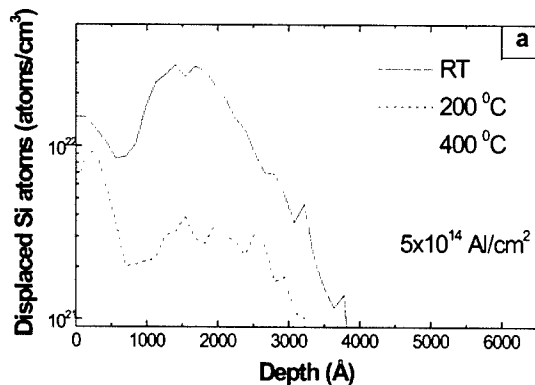


Fig. 3. Displaced silicon atoms versus depth calculated from RBS/channeling measurements for samples implanted with $5 \times 10^{14} \text{ Al/cm}^2$ at RT, 200°C and 400°C [10].

points for samples implanted with 3×10^{13} , 5×10^{14} and $1 \times 10^{15} \text{ Al/cm}^2$ at RT. As can be seen the turning point moves to higher S parameters value/lower W parameter value with increasing temperature, indicating increasing defect size. From the turning points of the samples implanted at room temperature, Fig. 2 also indicate, as expected, that the amount of damage increases with increasing implantation dose.

Fig. 2 can be compared to the RBS/channeling result shown in Fig. 3. The concentration of displaced silicon atoms is decreasing with increasing implantation temperature. For samples implanted at temperatures above 400°C the RBS/channeling analysis is not sensitive

enough to detect displaced atoms. A quick comparison of Figs. 2 and 3 could results in the interpretation that the PAS and channeling results contradict each other, since the PAS study indicate more/larger defects with increasing implantation temperature and the channeling analysis indicate a decrease in defects with increasing implantation temperature. However, PAS is sensitive to vacancy-type defects and channeling is sensitive to displaced atoms. The correct interpretation of Figs. 2 and 3 is that with increasing implantation temperature, the recombination of vacancies and interstitials created in the implantation process is increasing, but at the same time vacancy migration results in vacancy clustering and thus in larger vacancy-type defects and in the turning point moving to higher S parameter values.

When Fig. 1 is compared to the Srim 98 [12,13] simulation of the Al implantation in Fig. 4 and to the RBS/channeling measurement in Fig. 3, the following observation can be done: The S/W parameters do not reach the bulk value even at the maximum positron implantation energy of 25 keV for any of the implanted samples. At this energy less than 5% of the implanted positrons annihilate in the Al implanted region, these 5% include the positron diffusion length of approximately 200 nm in bulk SiC [8]. This is not enough to cause the relatively high S parameter at 25 keV. Evidently, the defect distribution extends deeper in the sample than expected from Figs. 3 and 4. At this stage we can only speculate over the phenomenon behind this effect, but a possible explanation could be the channeling effect combined with the feeding effect [14]. Previous studies of Al implantation in 6H-SiC in channelled

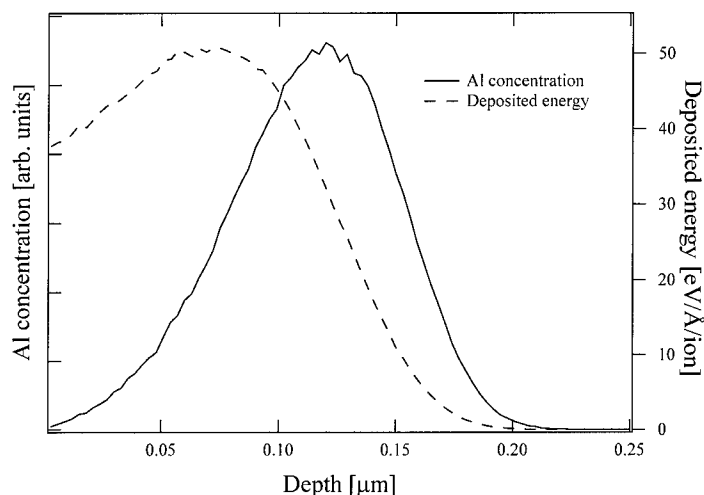


Fig. 4. Srim 98 simulation of the Al^+ 100 keV implantation.

directions have shown that the range is significantly extended when compared to random implantation [15]. Another explanation would be an electric field which would drive the positrons into annihilating in the implanted region, this would distort the interpretation of the results in Fig. 1. However, this does not seem likely since the Al need to be activated in order to produce this electric field and the annealing temperatures needed for this are significantly higher than the implantation temperatures used in our experiments.

4. Conclusions

We have studied the formation of vacancy-type defects in Al implanted 4H-SiC, both as a function of implantation dose and implantation temperature. As expected the amount of damage induced in the samples depend on the implantation dose. The results also indicate that the defect distributions extend deeper into the samples than expected. Further studies are planned to verify and investigate this phenomenon. The recovery process of the samples implanted at elevated temperatures shows signs of vacancy migration and vacancy clustering.

References

- [1] M.V. Rao, P. Griffiths, O.W. Holland, G. Kelner, J.J.A. Freitas, D.S. Simons, P.H. Chi, M. Ghezzi, J. Appl. Phys. 77 (1995) 2479.
- [2] T. Kimoto, A. Itoh, N. Inoue, O. Takamura, T. Yamamoto, T. Nakajima, H. Matsunami, Mater. Sci. Forum 264–268 (1998) 675.

- [3] T. Troffer, M. Schadt, T. Frank, H. Itoh, G. Pensl, J. Heindl, H.P. Strunk, M. Maier, Silicon Carbide: A Review of Fundamental Questions and Applications to Current Device Technology, Akademie-Verlag GmbH, Berlin, 1997, p. 277.
- [4] E. Wendler, A. Heft, W. Wesch, Nucl. Instr. and Meth. B 141 (1998) 105.
- [5] T. Kimoto, N. Inoue, H. Matsunami, Phys. Stat. Sol. A 162 (1997) 263.
- [6] K. Saarinen, P. Hautojärvi, C. Corbel, in: M. Stavola (Ed.), Identification of Defects in Semiconductors, Academic Press, New York, 1998.
- [7] M.A. Müller, A.A. Rempel, K. Reichle, W. Sprengel, J. Major, H.E. Schaefer, Mater. Sci. Forum 363–365 (2001) 70.
- [8] A. Uedono, H. Itoh, T. Ohshima, Y. Aoki, M. Yoshikawa, I. Nashiyama, H. Okumura, S. Yoshida, T. Moriya, T. Kawano, S. Tanigawa, Jpn. J. Appl. Phys. 35 (1996) 5986.
- [9] A. Uedono, H. Itoh, T. Ohshima, R. Suzuki, T. Ohdaira, S. Tanigawa, Y. Aoki, M. Yoshikawa, I. Nashiyama, T. Mikado, H. Okumura, S. Yoshida, Jpn. J. Appl. Phys. 36 (1997) 6650.
- [10] A.Y. Kuznetsov, M. Janson, A. Hallén, B.G. Svensson, C. Jagadish, unpublished.
- [11] L. Henry, M.-F. Barthe, S. Arpiainen, K. Saarinen, P. Hautojärvi, unpublished.
- [12] J.F. Ziegler, private communication.
- [13] J.F. Ziegler, J.P. Biersack, U. Littmark, The Stopping and Range of Ions in All Elements, Pergamon, New York, 1985.
- [14] B.R. Appleton, C. Erginsoy, W.M. Gibson, Phys. Rev. 161 (1967) 330.
- [15] E. Morvan, P. Godignon, M. Vellvehi, A. Hallén, M. Linnarsson, A.Y. Kuznetsov, Appl. Phys. Lett. 74 (1999) 3990.



ELSEVIER

Physica B 308–310 (2001) 668–670

PHYSICA B

www.elsevier.com/locate/physb

Negatively charged vacancy defects in 6H–SiC after low-energy proton implantation and annealing

M.-F. Barthe^{a,*}, D.T. Britton^b, C. Corbel^a, A. Hempel^b, L. Henry^a, P. Desgardin^a,
W. Bauer-Kugelmann^c, G. Kögel^c, P. Sperr^c, W. Triftshäuser^c

^a CERI-CNRS, 3A Rue de la Férollerie, F-45071 Orléans, France

^b Department of Physics, University of Cape Town, Rondebosch 7701, South Africa

^c Universität der Bundeswehr München, I.N.F., D-85577 Neubiberg, Germany

Abstract

We have used pulsed-slow-positron-beam-based positron lifetime spectroscopy to investigate the nature of acceptors and charge states of vacancy-type defects in low-energy proton-implanted 6H–SiC(H). We can infer from the temperature dependence of the lifetime spectra that neutral and negatively charged vacancy clusters exist in the track region. Depending on annealing, they give rise to positron lifetimes of 257 ± 2 , 281 ± 4 and 345 ± 2 ps, respectively. The 281 ps cluster has likely an ionization level near the middle of the band gap. By comparison with theory, the 257 and 280 ps are identified as $(V_C-V_{Si})_2$ and $(V_C-V_{Si})_3$ clusters, respectively. In addition, other acceptors of ionic type act as strong trapping centers at low temperature ($T < 150$ K). Neutral monovacancy-like complexes are also detected with a lifetime of 160 ± 2 after 900 °C annealing. © 2001 Elsevier Science B.V. All rights reserved.

Keywords: Slow positron annihilation; Silicon carbide; Proton implantation; Vacancy defects

Silicon Carbide is a large band gap semiconductor, with fast switching times suitable for high power and high temperature applications. It occurs in different polytypes [1], the hexagonal 4H and 6H ones are the most important for microelectronic applications. Defects in the different SiC polytypes have been studied by different techniques, including deep level transient spectroscopy [1,2], electron spin resonance [1,3] and positron annihilation spectroscopy [4–11]. In 6H–SiC, passivation [12], doping [13] and the Smart Cut process [14,15] have been all achieved using hydrogen implantation. However, the role and type of defects controlling the electrical properties in 6H–SiC(H) is far from fully understood.

We use positron annihilation to investigate the nature of acceptors and the charge states of vacancy-induced

defects in 6H–SiC. We focus here on the track region of low-energy protons after 900 °C and 1300 °C annealing.

The two studied layers were initially 4 μm thick n-type 10^{17} cm^{-3} nitrogen doped 6H–SiC grown epitaxially on n-type ($3.5 \times 10^{18} \text{ cm}^{-2}$) substrates from CREE. As detailed in Ref. [16], they were implanted with approximately $4 \times 10^{16} \text{ cm}^{-2} \text{ H}^+$ at 1 μm depth and then annealed at 900 °C (H900) and 1300 °C (H1300). After annealing, the doping of the initially n-type epitaxial layers was still compensated, indicating the presence of acceptor-like defect states surviving the annealing.

Slow positron beam based Doppler broadening spectroscopy, which gives information on the electron momentum distribution, has been used to investigate the defect distribution as a function of depth at room temperature. In both layers the fitting by VEPFIT of the data in Fig. 1 reveals three broadly different regions: the track region, between the surface and the hydrogen peak at 1 μm; the cascade region, around the hydrogen peak at 1 μm; and the beyond cascade region. In H900, the track region is homogeneous and the size of vacancy

*Corresponding author. Tel.: +33-2-38-255429; fax: +33-2-38-630271.

E-mail address: barthe@cns-orleans.fr (M.-F. Barthe).

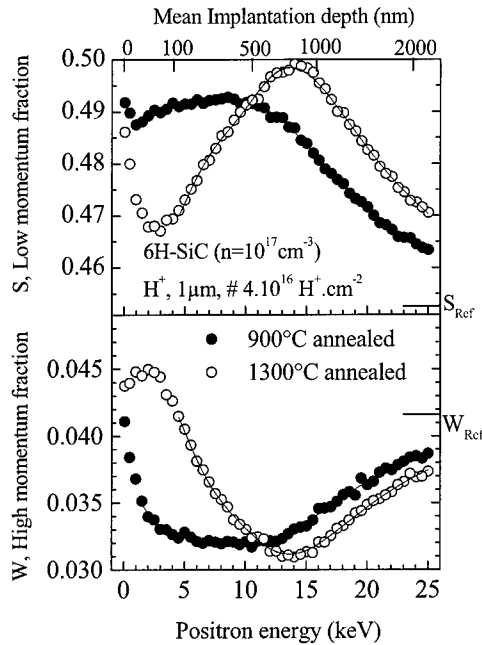


Fig. 1. Low momentum fraction $S = N_A([0 - |2.88|] \times 10^{-3} m_0 c) / N_A([0 - |27.32|] \times 10^{-3} m_0 c)$ and high momentum fraction $W = N_A([11.27] - |27.32| \times 10^{-3} m_0 c) / N_A([0 - |27.32|] \times 10^{-3} m_0 c)$ as a function of positron beam energy in H^+ implanted 6H-SiC layers annealed at 900°C or 1300°C. The mean implantation depth in SiC is $z(E) \text{ (nm)} = 9.17 \times E^{1.7} \text{ (keV)}$ [19]. A modified version of VEPFIT is used to consistently fit (dots lines) the $S(W)$ curves from 2.5 keV in the annealed layers with a model of several homogeneous layers (3 for H900 and 4 for H1300, see details in Ref. [16]).

defects is big as suggested by the high value of the low momentum annihilation fraction (S) and the low value of the high momentum annihilation fraction (W) found in the fitting ($S/S_{\text{ref}} = 1.088$, $W/W_{\text{ref}} = 0.766$). After 1300°C annealing the track region is divided into 2 regions: the first region from the surface to around $0.3 \mu\text{m}$ is less damaged than the second region extending from 0.3 to $1.05 \mu\text{m}$.

The positron lifetime measurements were performed using the pulsed low-energy positron system at the Universität der Bundeswehr München [17]. The positron lifetime spectra $N(t, E, T)$ were recorded as a function of the incident positron energy E (see details in Ref. [20]) for different temperatures T between 75 and 375 K for H900 and 300 K for H1300. We could use a conventional analysis of the lifetime spectra in terms of exponential components due to the short positron diffusion length in these layers: the energy dependence reflects only the stopping profile in the track region and the surface contribution vanishes quickly at energy $\geq 5 \text{ keV}$. The lifetime spectra in 6H-SiC could be decomposed into a sum of two exponential decay

components (I_1, τ_1) , (I_2, τ_2) (see details in Ref. [20]) where the mean lifetime $\tau(E, T) = [1 - I_2(E, T)] \times \tau_1(E, T) + I_2(E, T) \times \tau_2(E, T)$ is equal to the center of mass. In both layers, the mean lifetime τ as a function of E exhibits a plateau in the energy range corresponding to the proton track region 6–10 keV in H900 and 9–13 keV in H1300. In these energy ranges the positron mean lifetimes are temperature dependent and vary from $255 \pm 2 \text{ ps}$ at 300 K to $247 \pm 1 \text{ ps}$ at 75 K in H900 and from, respectively, 276 ± 5 – $235 \pm 2 \text{ ps}$ in H1300. One can thus conclude that positrons in the track region see a homogeneous distribution of vacancy-type defects where the trapping rates vary with temperature. To investigate the vacancy distribution, we monitor the temperature dependence of the lifetime spectra, in the track region 180–600 nm sampled by 8–10 keV positrons [19].

In the two layers, the values $\tau^*(T) = [(I_1(T)/\tau_1(T) + I_2(T)/\tau_2(T))^{-1}]$ are calculated to check the validity of the one defect trapping model. At all temperatures the $\tau^*(T)$ values are much longer than the lifetime 141 ps in 6H-SiC lattice [6–8]. This indicates that positrons are trapped by different types of defects [18]. In both layers the lifetime $\tau_2(T)$ vary from a low to a high temperature plateau. It sharply increases by 24 ps from 257 ± 2 to $281 \pm 4 \text{ ps}$ in the range 175–225 K in H900. It strongly increases by 60 ps from 285 ± 5 to $345 \pm 2 \text{ ps}$ in the range 150–250 K in H1300. The variation of $\tau_2(T)$ with temperature indicates that different types of vacancy clusters exist after annealing. Assuming that the charge of defects is constant as a function of temperature in the semi-insulating layers, we conclude that a small cluster is detected at low temperature and a bigger one at high temperature. The trapping coefficient of vacancy-clusters is known to increase with the size of the cluster [18]. In order to compete with the trapping in the biggest defect, the trapping coefficient μ at the smallest cluster has to increase when temperature decreases. This property is fulfilled for negatively charged defects where μ is known to change in $T^{-1/2}$ [18]. We propose that, the low temperature τ_2 lifetimes values, 257 ps in H900 (Fig. 2c) and 280 ps in H1300 (Fig. 2g), arise from negatively charged vacancy clusters. The τ_2 lifetimes values, 280 ps in H900 and 345 ps in H1300 observed at high temperature, arise from neutral vacancy clusters. Another interesting point is that the 280 ps lifetime arises from a neutral defect above 225 K in H900 and from a negatively charged defect below 150 K in H1300. This suggests that the 280 ps lifetime is due to a defect which has an ionization level ~ 0 near the middle of the band gap. The Fermi level is above the ionization level in the H1300 where a higher fraction of defects than in H900 is expected to recover. We assigned the 257 and 280 ps lifetimes to $(V_C - V_{Si})_2$ and $(V_C - V_{Si})_3$ clusters, respectively, on the basis of calculations using the superimposed atomic model [9].

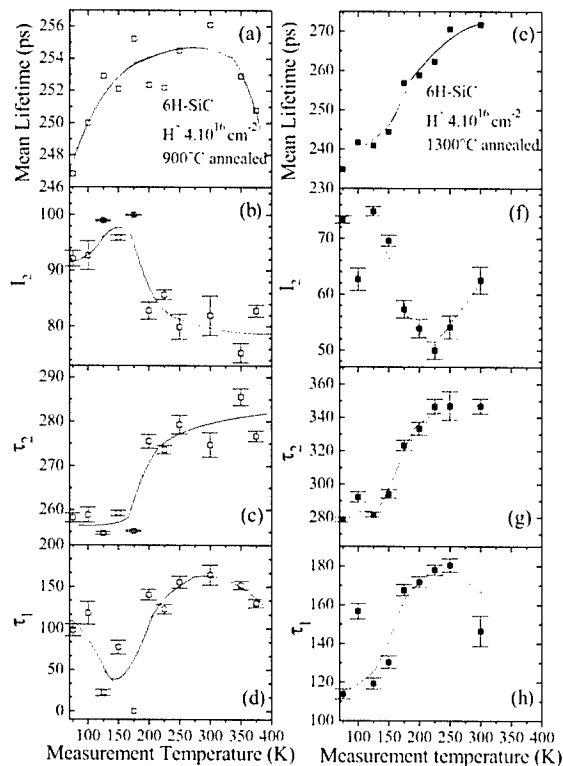


Fig. 2. Temperature dependence of the positron lifetime parameters in 6H-SiC implanted with a proton fluence of $4 \times 10^{16} \text{ cm}^{-2}$ at $1 \mu\text{m}$ and annealed at 900°C (\square) and 1300°C (\blacksquare). The values are a weighted average of data around an incident positron energy of 9 keV, probing a depth range between 180 and 620 nm: (a) and (e) mean lifetime, (b) and (f) intensity of the longest component, (c) and (g) its lifetime and finally (d) and (h) lifetime of the shortest component for H900 and H1300 samples, respectively. The solid lines are guides to the eye.

The $\tau_1(T)$ values (Fig. 2d and h) are longer or close to the lifetime 140 ps in 6H-SiC lattice at 75 K and above 200 K in H900 and at all temperatures in H1300. It means that the short component $\tau_1(T)$ is due to annihilations in a mixing of vacancy-like defects and negative ions. The 160 ps lifetime in H900 corresponds to neutral vacancy-like defects. At low temperature, the values τ_1 indicate that the negative ions become active traps. In both annealed layers, the lifetimes $\tau_2(E, T)$ are much higher than the value 243 ± 1 ps in as-implanted 6H-SiC(H) (to be published). This increase indicates that the size of the vacancy clusters trapping positrons increases as the annealing temperature increases from room temperature to 1300°C . Assuming that the 243 ps clusters cannot diffuse, the growth of the cluster size implies that, during annealing, small vacancy clusters emit mono-vacancies to the benefit of bigger clusters. We propose that, during the vacancy diffusion induced

by cluster reorganization, mono-vacancies get trap at nitrogen atoms due to the high nitrogen concentration in these layers. It follows that the positron trapping at the vacancy–nitrogen complex can give rise to the 160 ps lifetime.

In summary, we have identified two negative charge states of the $(V_C-V_{Si})_2$ and $(V_C-V_{Si})_3$ clusters that we have associated to the 257 and 280 ps lifetime by comparison with lifetimes calculations. We proposed that the $(V_C-V_{Si})_3$ cluster has a ionization level 0/- near the middle of the band gap. We associate the lifetimes of 160 ps to a neutral vacancy-like complex and of 345 ps to a neutral vacancy-cluster.

References

- [1] G. Pensl, W.J. Choyke, *Physica B* 185 (1993) 264.
- [2] M.O. Aboelfotoh, J.P. Doyle, *Phys. Rev. B* 59 (1999) 10823.
- [3] L.A. de, S. Balona, J.H. Loubser, *J. Phys. C* 3 (1970) 2344.
- [4] H. Itoh, N. Hayekawa, I. Nashiyama, E. Sakuma, *J. Appl. Phys.* 66 (1989) 4529.
- [5] A. Rempel, H.-E. Schaefer, *Appl. Phys. A* 61 (1995) 51.
- [6] W. Puff, P. Mascher, A.G. Balogh, H. Baumann, *Mater. Sci. Forum* 258-63 (1997) 733.
- [7] A. Kawasuso, H. Itoh, T. Ohshima, K. Abe, S. Okada, *J. Appl. Phys.* 82 (1997) 3232.
- [8] S. Dannefaer, *Appl. Phys. A* 61 (1995) 59.
- [9] G. Brauer, W. Anwand, P.G. Coleman, A.P. Knights, F. Plazaola, Y. Picaud, W. Skorupa, J. Störmer, P. Willutzki, *Phys. Rev. B* 54 (1996) 3084.
- [10] A. Polity, S. Huth, M. Lausmann, *Phys. Rev. B* 59 (1999) 10603.
- [11] C.C. Ling, A.H. Deng, S. Fung, C.D. Beling, *Appl. Phys. A* 70 (2000) 33.
- [12] N. Achtziger, J. Grillenberger, W. Witthuhn, *Appl. Phys. Lett.* 73 (1998) 945.
- [13] A.M. Strel'chuk, A.A. Lebedev, V.V. Kozlovski, N.S. Savkina, D.V. Davydov, V.V. Solov'ev, M.G. Rastegaeva, *Nucl. Instrum. Methods B* 147 (1999) 74.
- [14] M. Bruel, *Electr. Lett.* 31 (14) (1995) 1201.
- [15] L. Di Cioccio, Y. Le Tiec, C. Jaussaud, E. Hugonnard-Gruyère, M. Bruel, *Mater. Sci. Forum* 264 (1998) 765.
- [16] M.-F. Barthe, L. Henry, C. Corbel, G. Blondiaux, K. Saarinen, P. Hautojärvi, E. Hugonnard, L. Di Cioccio, F. Letertre, B. Ghyselen, *Phys. Rev. B* 62 (2000) 16638.
- [17] W. Bauer-Kugelmann, Technische Weiterentwicklungen am gepulsten Positronen-strahlsystem PLEPS, Dr. Ing. Thesis, Universität der Bundeswehr München, 2000.
- [18] C. Corbel, P. Hautojärvi, in: A. Dupasquier, A.P. Mills Jr. (Eds.), *Positron Spectroscopy of Solids*, IOS Press, Amsterdam, 1995, p. 533.
- [19] E. Soininen, J. Mäkinen, D. Beyer, P. Hautojärvi, *Phys. Rev. B* 46 (1992) 13104.
- [20] D.T. Britton, M.F. Barthe, C. Corbel, A. Hempel, L. Henry, P. Desgardin, W. Bauer-Kugelmann, G. Kögel, P. Sperr, W. Trifthäuser, *App. Phys. Lett.* 78 (9) (2001) 1234.



ELSEVIER

Physica B 308–310 (2001) 671–674

PHYSICA B

www.elsevier.com/locate/physb

Electron paramagnetic resonance studies of a carbon vacancy-related defect in as-grown 4H–SiC

V.V. Konovalov^{a,*}, M.E. Zvanut^a, V.F. Tsvetkov^b, J.R. Jenny^b, St.G. Müller^b,
H.McD. Hobgood^b

^a Physics Department, University of Alabama at Birmingham, CH310, Birmingham, AL 35294-1170, USA

^b Cree Inc., Durham, NC 27703, USA

Abstract

An intrinsic defect (ID) has been identified in as-grown 4H–SiC by electron paramagnetic resonance (EPR). The EPR parameters of an ID measured in our nominally semi-insulating material are similar to the literature data of the EI5 defect produced in p-type 4H and 6H–SiC by 2.5 MeV electrons and assigned to the carbon vacancy (N.T. Son, P.N. Hai, E. Jansen, Phys. Rev. B 63 (2000) 201201). However, comparison of the ID and EI5 centers reveals that the as-grown and radiation-induced centers exhibit different annealing behavior. Photo-induced EPR locates the ID level 0.9 eV above the valence band edge. © 2001 Elsevier Science B.V. All rights reserved.

PACS: 61.72.Hh; 61.72.Ji

Keywords: 4H–SiC; EPR; Intrinsic defect; Carbon vacancy

1. Introduction

Deep level defects are known to control the conductivity and carrier lifetime in semiconductors [1–3]. For example, semi-insulating 4H–SiC is produced by doping with amphoteric vanadium, which provides the donor ($E_v + 1.6$ eV) and acceptor ($E_c - 0.8$ eV) levels [4,5]. Intrinsic defects (IDs) produced by high energy irradiation or during the crystal growth may also influence the doping efficiency [6]. However, many radiation-induced defects are thermally unstable and anneal at 200–800°C [4,5,7,8]. Such defects may not be suitable for making SiC for high temperature applications. On the other hand, defects formed during a 1500–2200°C growth process may possess the natural high temperature stability.

An ID in high-purity 4H–SiC has been detected by electron paramagnetic resonance (EPR) [9]. The EPR spectrum is similar to the EI5 center produced by

2.5 MeV electron irradiation of p-type 4H and 6H–SiC [10]. The EI5 center has C_{3v} symmetry and was assigned to the positively charged carbon vacancy (V_C^+) with an electron spin $S = \frac{1}{2}$. Recently, Cree Inc. announced the production of high-quality semi-insulating 4H–SiC without using vanadium, and it is possible that an ID reported in Refs. [9,10] is responsible for the charge compensation in that material [11].

The present paper reports an EPR study of the ID center in as-grown, semi-insulating 4H–SiC. The paper focuses on a comparison of the ID and EI5 centers and briefly discusses the position of the ID level in the SiC band gap.

2. Results and discussion

High-purity, as-grown (0001) 4H–SiC wafers grown by the seed sublimation method and provided by Cree Inc. were used in this study. The samples were $0.35 \times 3 \times 15$ mm³ bars cut along the (1100) plane. The EPR spectra were recorded using a Bruker 200 spectrometer (9.75 GHz) equipped with an Oxford ESR

*Corresponding author. Fax: +1-205-934-8042.

E-mail address: vkono@uab.edu (V.V. Konovalov).

900 flow cryostat. The reproducibility of the EPR signal amplitude was $\pm 5\%$ and the error in the g -value determination was $\pm 5 \times 10^{-5}$. When measured in the dark, we can distinguish between three types of samples according to their EPR spectra: (1) nominally n-type samples exhibiting only the N donor signal; (2) nominally p-type material exhibiting only the shallow B acceptor signal and (3) nominally semi-insulating samples exhibiting only the anisotropic ID center. The density of N (B) in sample set 1 (2) was 10^{14} – 10^{15} cm^{-3} . All samples contain a 3 G wide isotropic line at $g = 2.003$ which is similar to the surface damage signal [12]. Additional support for the surface origin of this line was provided by a 1 h 850°C anneal in air, which reduced the line intensity by a factor of 3 but did not affect the other EPR signals. Except for Mn with concentration $\leq 10^{13} \text{ cm}^{-3}$, none of the other common impurities such as V, Cr, Ti, etc. [3,13] were detected.

Figs. 1a and b show the dark EPR spectra of the ID at 77 K and the angular dependence of the zero-crossings upon rotating the magnetic field in the (11 $\bar{2}$ 0) plane. The $B_{\parallel c}$ -axis spectrum consists of a 0.4 G wide central line A, a smaller line B and 6 pairs of satellite lines. When the sample is rotated from the position $\theta = 0^\circ$ ($B_{\parallel c}$ -axis), the lines 2–2' and 3–3' split into 3 and 2 smaller lines, respectively, with intensities approximately 3 and 2 times less than those of the initial lines at $\theta = 0^\circ$. The A, 1–1' and 2–2' overall line intensities do not depend on the angle (taking into account the line splitting). However, the intensities of the 5–5' and 6–6' lines are reduced at $\theta > 25^\circ$, which suggests an anisotropic line width. At 4 K, the ID spectrum is similar to the 77 K one, but lines B and 3–3' disappear, and upon rotating the sample line A splits into 2 lines at 90 and into 3 lines at intermediate angles.

The measured angular dependence of the ID-1 spectrum can be simulated using axial g - and hyperfine (hf) A -tensors, depending on the angle [14]:

$$g = (g_{\parallel}^2 \sin^2 \theta + g_{\perp}^2 \cos^2 \theta)^{1/2} \quad (1)$$

$$A = (A_{\parallel}^2 \sin^2 \theta + A_{\perp}^2 \cos^2 \theta)^{1/2}, \quad (2)$$

For lines A, 1–1' and 4–4', relations (1) and (2) fit the g and A angular dependencies with the parameters presented in Table 1. Unfortunately, our present samples are not suitable to rotation in two additional planes; thus, the full g - and hf-tensors were not determined. We plan to complete that study in the near future.

From the similarity of angular dependence and their effective g -values, 1–1', 2–2', 5–5' and 6–6' lines can be assigned to the hf splitting of the central line A due to the nuclei with spin $I = \frac{1}{2}$. We will denote this set of lines as ID-1 center. Also, the similarity of the g -values suggests that the 4–4' lines are associated with B forming an ID-2 center, and the 3–3' pair make-up an ID-3

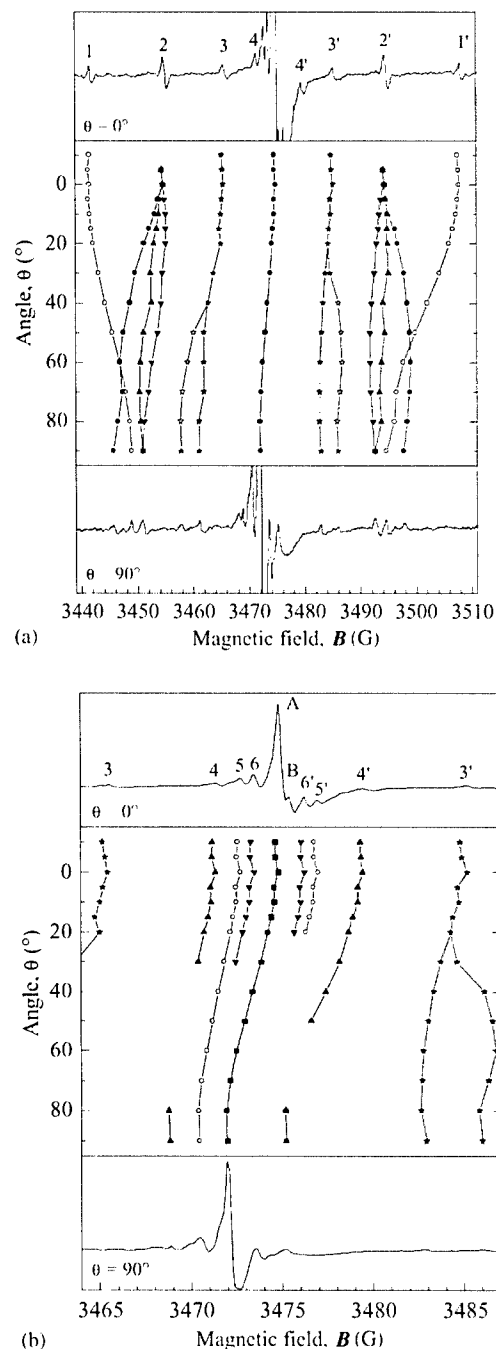


Fig. 1. (a) The upper and lower frames show the dark EPR spectra of the 4H-SiC obtained at 77 K for $B_{\parallel c}$ -axis and $B_{\perp c}$ -axis, respectively. The middle frame displays the angular dependence of the zero-crossings measured for rotation of the magnetic field (B) in the (11 $\bar{2}$ 0) plane. (b). The extended central part of Fig. 1a.

center. Individual satellite lines of the ID-1 center can be assigned to the magnetic nuclei using the line intensities and the natural abundance of magnetic isotopes ^{29}Si

Table 1

The EPR parameters of the ID lines in 4H-SiC at 77 K. For each pair of lines $x-x'$, the g -value was calculated from the mid-field magnetic field position

	Lines							
	A	B	1-1'	2-2'	3-3'	4-4'	5-5'	6-6'
g_{\parallel}	2.00334	2.0028	2.0033	2.0033	2.0087	2.00285	2.00334	2.00334
g_{\perp}	2.00495	—	2.0050	—	—	2.0048	—	—
A_{\parallel} (G)	—	—	66.4	39.74	19.6	8.08	4.24	2.78
A_{\perp} (G)	—	—	45.7	42–52	25–28	6.4	4.78	2.84
Center	ID-1	ID-2	ID-1	ID-1	ID-3	ID-2	ID-1	ID-1
Model			$1 \times {}^{29}\text{Si}$	$3 \times {}^{29}\text{Si}$			$12 \times {}^{13}\text{C}$	$6 \times {}^{29}\text{Si}$

(4.67%) and ${}^{13}\text{C}$ (1.11%). The pairs 1-1', 2-2', 5-5' and 6-6' were assigned to the $1 \times {}^{29}\text{Si}$, $3 \times {}^{29}\text{Si}$, $12 \times {}^{13}\text{C}$ and $6 \times {}^{29}\text{Si}$ magnetic nuclei, respectively (see Table 1). The lines B and 4-4' form a triplet which can be assigned to a defect interacting with an $I = 1$ nucleus such as nitrogen.

The EPR parameters for the ID-1 center in our semi-insulating 4H-SiC (see Table 1) coincide with parameters of the EI5 center produced by 2.5 MeV electron irradiation in p-type 4H and 6H-SiC [10]. In agreement with the model presented in Ref. [10], our assignment of neighboring atoms corresponds to the deformed carbon vacancy with C_{3v} symmetry with 1 unique and 3 equivalent Si nearest neighbors (NN). In addition, we assigned the 5-5' and 6-6' lines not reported in the earlier work to 12C and 6Si next nearest neighbors (NNN) of the vacancy (see Fig. 2). Non-equivalency of the 4 NN Si atoms may result from a Jahn-Teller distortion of the charged vacancy, where the upper Si atom is shifted along the c -axis (Fig. 2). A larger hf splitting on the unique Si atom (66.4 G) compared to the 3 lower plane Si atoms (39.7 G) suggests that more electron spin density is localized in the upper plane. This would explain why the hf splitting of the Si NNN is due to only 6 atoms, presumably the 6 upper plane Si atoms. When the angular dependence is measured at 4 K, the central line A exhibits splitting not apparent at 77 K. The behavior suggests that the electron spin density becomes more localized at lower temperature. The temperature dependence merits further investigation.

Despite the similarity of their EPR spectra, the ID-1 and EI5 centers exhibit several differences: (1) In our work, ID-1 is seen only in samples which do not exhibit a B or N signal under dark conditions (the semi-insulating samples), while EI5 is observed in the p-type irradiated SiC. (2) The ID-1 intensity did not change after the 850°C anneal, but the EI5 intensity decreased at least several times by 500°C. (3) The ID-1 can be observed between 4 and 300 K, but the EI5 disappears below 25 K. Detection of the defect in our semi-insulating SiC weakens earlier arguments that the charge state of the vacancy is positive which was based on the

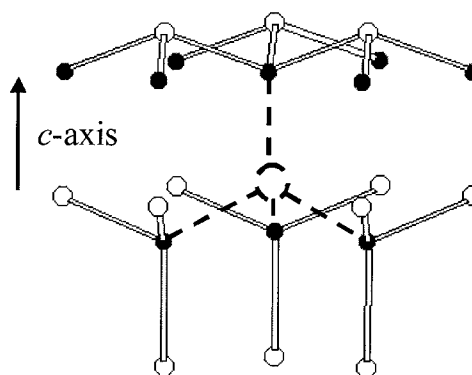


Fig. 2. A schematic of a carbon vacancy in SiC. The Si atoms are indicated by black circles and the C atoms by white circles.

observation of the EI5 in p-type material [10]. Another possibility for a carbon vacancy with $S = \frac{1}{2}$ is a negative charge state, V_C^- . The different annealing behavior could be caused by the presence of interstitial carbon trapped not far from the radiation-induced carbon vacancy, favoring defect annihilation as the sample is heated. The thermal instability observed for the radiation-induced carbon vacancy above 500°C suggests that material containing this defect will not be suitable for high temperature applications. Finally, the disappearance of the EI5 center below 25 K may be attributed to the presence of an additional level close to the vacancy in irradiated SiC. Clearly, our data demonstrates significant differences between the as-grown and radiation-induced vacancies which deserve further exploration.

The dependence of the photo-induced EPR signals on the photon energy has been used to locate the energy level of the ID-1 with respect to the band edges [15]. The illumination with sub-band gap light (750–1500 nm) quenched the ID-1 signal and produced an approximately equal amount of shallow paramagnetic boron. Electrons are excited from the valence band to the ID level making it non-paramagnetic and the hole formed

in the valence band is captured by a B acceptor making it paramagnetic. A model based on the photo-induced EPR data places the ID defect level 0.9 eV above the valence band.

3. Conclusion

Our work has identified an intrinsic defect (ID-1) in as-grown nominally semi-insulating 4H-SiC with EPR parameters similar to the EI5 center found by others in p-type 4H and 6H-SiC irradiated with 2.5 MeV electrons. The EI5 has been assigned to the positively charged carbon vacancy, V_C^+ , with electron spin $S = \frac{1}{2}$ [10]. Although analysis of data for the ID-1 is in agreement with the carbon vacancy model, detection of the center in our semi-insulating material makes the charge state assignment less certain. The ID-1 and EI5 centers demonstrate different thermal annealing behavior. The former is stable until at least 850°C, while the latter begins to anneal below 500°C. The annealing of the EI5 may be caused by the release of radiation-induced interstitial carbon trapped in the vicinity of the vacancy. The disappearance of the EI5 center below 25 K, in contrast to the persistence of the ID at 4 K, suggests the presence of an additional level close to the vacancy in irradiated SiC. Photo-induced EPR identified the ID defect as a deep level 0.9 eV above the valence band edge.

Acknowledgements

The work was supported by the US Office of Naval Research.

References

- [1] S. Greulich-Weber, *Phys. Stat. Sol.* 210 (1998) 415.
- [2] P.G. Baranov, *Defect Diffus. Forum* 148–149 (1997) 129.
- [3] A.A. Lebedev, *Semiconductors* 33 (1999) 107.
- [4] J. Schneider, H.D. Müller, K. Maier, W. Wilkening, F. Fuchs, A. Dörnen, S. Leibenzeder, R. Stein, *Appl. Phys. Lett.* 56 (1990) 1184.
- [5] J.R. Jenny, M. Skowronski, W.C. Mitchell, H.M. Hobgood, R.C. Glass, G. Augustine, R.H. Hopkins, *Appl. Phys. Lett.* 68 (1996) 1963.
- [6] C. Wang, J. Bernholc, R.F. Davis, *Phys. Rev. B* 38 (1988) 12752.
- [7] E. Sörman, T.N. Son, W.M. Chen, O. Kordina, C. Hallin, E. Janzen, *Phys. Rev. B* 61 (2000) 2613.
- [8] M. Okada, K. Atobe, M. Nakagawa, S. Kanazawa, I. Kanno, I. Kimura, *Nucl. Instr. and Meth. B* 166–167 (2000) 399.
- [9] V.V. Konovalov, B. Geislinger, M.E. Zvanut, *Proceedings of the APS Spring Meeting*, Washington, DC, USA, April 28–May 1, 2001 (abstract).
- [10] N.T. Son, P.N. Hai, E. Jansen, *Phys. Rev. B* 63 (2001) 201201.
- [11] J.R. Jenny, S.G. Muller, A. Powell, M. Brady, V.F. Tsvetkov, H.M. Hobgood, R.C. Glass, C.H. Carter, *Proceedings of the 43rd Electronic Material Conference*, University of Notre Dame, Indiana, USA, June 27–29, 2001 (abstract).
- [12] G.K. Walters, T.L. Estle, *J. Appl. Phys.* 32 (1961) 1854.
- [13] J. Baur, M. Kunzer, J. Schneider, *Phys. Stat. Sol.* 162 (1997) 153.
- [14] J.A. Weil, J.R. Bolton, J.E. Wertz, *Electron Paramagnetic Resonance*, Wiley-Interscience, New York, 1994.
- [15] V.V. Konovalov, M.E. Zvanut, *Appl. Phys. Lett.* (2001), submitted for publication.



ELSEVIER

Physica B 308–310 (2001) 675–679

PHYSICA B

www.elsevier.com/locate/physb

Defects in 4H silicon carbide

J.P. Bergman*, L. Storasta, F.H.C. Carlsson, S. Sridhara, B. Magnusson,
E. Janze'n

Department of Physics and Measurement Technology, Linköping University, S-58183 Linköping, Sweden

Abstract

We present experimental results related to several different intrinsic defects that in different ways influence the material properties and are therefore technologically important defects. This includes the so-called D1 defect which is created after irradiation and which is temperature stable. From the optical measurements we were able to identify the D1 bound exciton as an isoelectronic defect bound at a hole attractive pseudo-donor, and we have been able to correlate this to the electrically observed hole trap HS1 seen in minority carrier transient spectroscopy (MCTS). Finally, we describe the formation and properties of a critical, generated defect in high power SiC bipolar devices. It is identified as a stacking fault in the SiC basal plane. It can be seen as a local reduction of the carrier lifetime, in triangular or rectangular shape, which explains the enhanced forward voltage drop in the diodes. The entire stacking faults are also optically active as can be seen as dark triangles and rectangles in low temperature cathodo-luminescence, and the fault and their bounding partial dislocations are seen and identified using synchrotron topography. © 2001 Elsevier Science B.V. All rights reserved.

Keywords: SiC; Defects; Stacking faults

1. Introduction

During the last decade silicon carbide has attracted increasing interest. The reason for this is that SiC has material properties which makes it attractive for device applications. This includes particularly high power devices, high frequency devices and sensor devices needed to operate at high temperatures or in harsh environments. In the recent years, SiC has also been important as substrate material for the growth of epitaxial nitride structures.

The increasing interest in SiC was related to the development of commercially available substrate material, first conducting substrates in the 6H polytype and later the 4H polytype were followed by semi-insulating substrates. This was followed by the development of epitaxial growth techniques, like the hot wall CVD technique to grow thick low doped layers needed for high voltage bipolar components and thin well con-

trolled n- and p-type doped layers for sensors or MESFET applications. Currently, one of the main obstacles for SiC devices to reach a larger production scale is to understand and to control the residual defects in the material.

SiC is consequently a very interesting material for defect studies. From a fundamental point of view the polytype formation provides a unique possibility of studying the same defects in different lattice matrixes, where the large and indirect bandgap provides narrow emission lines and a large number of possible bandgap states. The defects are also of large applied interest which provides further motivation for detailed defects studies.

In this presentation, we will describe some of the most interesting and important defects in our opinion, both from a scientific and applied point of view. We will focus on three different types of defects, which are all of intrinsic nature. The first are the intrinsic defects with associated bound excitons in the near bandgap region. These are created by all kinds of irradiation, including ion-, electron-, neutron- and proton-irradiations, but

*Corresponding author. Fax: +46-13-142337.

E-mail address: ped@ifm.liu.se (J.P. Bergman).

can sometimes also be seen in as-grown material. The fact that some of those are temperature stable and can be produced by ion-implantation makes them of applied interest since they will remain after such a process step and influence the performance of the device. The second type of intrinsic defects is seen by absorption and photoluminescence in semi-insulating material grown by high temperature CVD (HTCVD). This material has very low concentrations of Vanadium which is the usual dopant in semi-insulating SiC, and it is believed that these yet unidentified deep intrinsic defects are giving the HTCVD material its semi-insulating properties. Finally, we will discuss the effect of intrinsic structural defects, such as dislocations and stacking faults, in SiC.

The results discussed are all on 4H SiC, even if several of the defects are present with similar properties also in the other polytypes. All material is grown by hot wall CVD or high temperature CVD.

2. Near bandgap bound excitons at intrinsic defects

The low temperature near bandgap photoluminescence (PL) emission from 4H epitaxial SiC layers is normally dominated by the recombination of free excitons (FE) and of bound excitons (BE) at the neutral nitrogen donor, and in the case of p-type or compensated material of excitons bound at the Al acceptor. After particle irradiation, with ions, electrons, neutrons or protons, additional emissions, labeled as the Ea spectra [1], appear which dominate the near bandgap spectrum. It consists of about 40 sharp no-phonons lines at energy between 2.8 and 2.9 eV, accompanied by a broad phonon assisted structure, as shown in Fig. 1. Using temperature dependent measurements, photoluminescence excitation spectroscopy and time resolved

spectroscopy [2] the lines have been shown to come in groups of two to four lines, with one ground state and several excited states, giving approximately 12 groups of emissions. The time resolved measurements have shown that the decay times of the ground state emissions are relatively long with values of several hundred microseconds at low temperatures. The decay from the excited states is considerably faster with decay times in the order of a few microseconds. The fact that the excited states can be seen at low temperatures indicates a very slow relaxation process down to the ground state. The measured decay time could either be the time for the relaxation or the time for the recombination rate of the bound excitons, or a combination of both. The slow times also indicate that there is no competing Auger process as observed for the donor bound and acceptor bound excitons. The bound excitons in the Ea series are therefore believed to be electron hole pairs bound at isoelectronic defect centers. About half of the lines can be observed after low energy (200 keV) electron irradiation that is below the displacement energy of creating Si vacancies (225–250 keV) [3] and no Si vacancy-related signal is either seen in the IR. This indicates that these lines are related to carbon centers, where a vacancy-interstitial pair could be a good candidate, but this remains to be proven. The fact that the high-energy lines are not observed after low energy irradiation indicates that these might be Si related, but their absence could also be an intensity or irradiation dose effect. A fact is, however, that the defects anneal at different temperatures starting from 750 °C and are completely quenched at 1200 °C.

When the Ea spectrum disappears, it is replaced by the emission labeled as D1, Fig. 2. This is not seen directly after irradiation but is sometimes seen as a

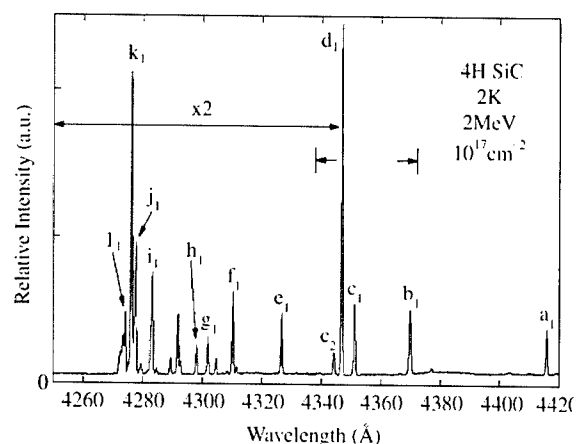


Fig. 1. A low temperature photoluminescence spectra of 4H SiC showing the Ea spectrum, present after particle irradiation.

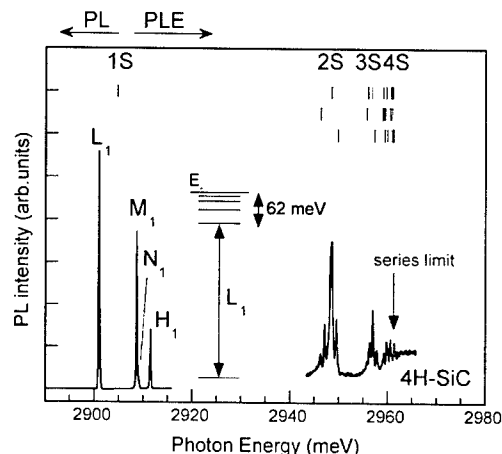


Fig. 2. A photoluminescence (PL) and photoluminescence excitation (PLE) spectra of 4H SiC showing the D1 spectrum, observed after particle irradiation and high temperature annealing.

residual emission in as-grown material. The D1 center is stable up to CVD growth temperatures and should be considered as a process induced defect that will remain and influence any device. In the turn-over range between the Ea and the D1 spectrum, i.e. at annealing temperatures between 800°C and 1200°C, a new and so far not further studied emission is observed at 4340 Å [4]. The D1 spectra has previously been studied in detail using PL [5,6], PL excitation, temperature dependent PL [5], time resolved PL [5] and Zeeman measurements [6], and recently the properties and the electronic structure have been studied in detail [7]. The PL and PLE spectrum are shown in Fig. 2. The ground state (L1) has two strong excited states (M1 and H1). A series of lines is observed at higher energies. The final states of the transitions corresponding to these lines were interpreted as effective-mass-like excited electron states well described by exciton theory. This was interpreted as the D1 defect being a pseudo-donor, where the defect has a neutral state in the bandgap, which contains no charge particles but still has a hole attractive potential, either from the electronegativity difference or from the local strain field. Once a hole is bound the defect is positively charged and attracts an electron via Coulomb interaction. The observed BE emission from the D1 defect is the recombination between the loosely bound electron and the strongly localized hole at the defect. At higher temperatures, the electron can be thermally emitted to the conduction band. This model of the D1 BE predicts an energy level for the primarily bound hole about 0.35 eV above the valence band. This level, denoted as HS1, has recently [8] been observed using minority carrier transient spectroscopy (MCTS). The correlation between the D1 and the HS1 hole trap was further shown by comparing the relative PL intensities and hole trap concentrations as a function of annealing temperature. This result also shows that the D1 is not correlated with the Z1/2 electron trap seen in DLTS as was previously assumed.

All characteristic properties of the D1 defect are also observed for the BE in the Ea spectrum and for the 4340 Å BE, and it is also very natural to assume that these BEs are related to similar isoelectronic defects described within a similar pseudo-donor model.

None of the above described BE have been correlated with the defects observed by ODMR or EPR, and their atomistic structure has to be determined.

3. Deep intrinsic defects

Another important defect that at the moment is subject to an extensive study, is the deep probably intrinsic defect that imparts semi-insulating properties to SiC. Generally, semi-insulating properties can be obtained by introducing vanadium, but in our high

temperature CVD (HTCVD) process low doped and semi-insulating material can be obtained without the intentional introduction of deep defects. The origin of the residual defects causing this is not yet fully understood but the presence of deeper defect states has been seen using FTIR and PL spectroscopy.

In Fig. 3 an FTIR absorption spectrum of an as-grown 4H SiC sample is shown. In this sample, a yet unidentified defect line (UD1) is observed. These lines are also seen in HTCVD grown semi-insulating 6H SiC and sometimes in commercial p-type substrates. The UD-1 center consists of two narrow no-phonon lines with different polarization [9]. The linewidth of UD1 lines is less than 0.5 meV, which is typical for luminescence lines in the infrared originating from deep defects in SiC. In other samples, some weaker additional lines were also observed [10].

The UD1 defect is temperature stable for annealing temperatures up to 1600°C, HTCVD material showing this line has very good semi-insulating properties with resistivities above $10^{10} \Omega \text{cm}$ measured at 200°C. The resistivity does not change after high temperature annealing.

Using the HTCVD technique it is also possible to grow crystals where the Si vacancy is the dominating observable defect. Also, these samples have semi-insulating properties but are not as stable after high temperature annealing as samples with the UD1 defect dominating. The reduction of the measured resistivity

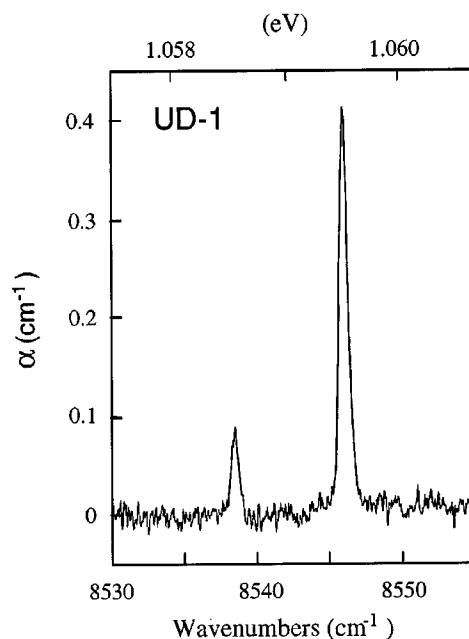


Fig. 3. Infrared absorption measurement of semi-insulating HTCVD grown 4H SiC. The spectrum was recorded at low temperature (10 K) using the FT technique.

after 1600°C annealing corresponds to the decrease of the Si vacancy signal. However, we have found that the Si vacancy does not have the same annealing behavior in as-grown material as in irradiated material. In our samples, the Si_V is stable at 800°C, a temperature where it anneals out in irradiated samples. A reason for this could be that the disappearance of the Si_V is related to the diffusion of Si interstitials (Si_I). In irradiated material these species are created in an equal number, and possibly, at a very close distance to the vacancies. When the interstitial becomes mobile it has a very high possibility to annihilate with the vacancy. In as-grown material it is, however, not obvious that interstitials are present in a corresponding number to the vacancies, thus the annihilation of Si_V could be caused by a completely different mechanism.

4. Structural defects

Structural defects in the form of dislocations and other extended defects are always present in every semiconductor material except Si. There is, however, relatively very little knowledge about the electronic properties and influence of extended defects. In SiC, the so-called micropipes have been of major concern for several years. These are open hollow core screw dislocations which were shown to be detrimental to device operations. In recent years, the micropipe density could be considerably reduced and they are now no more considered as a serious problem. Attention has instead been focused on other dislocations, and their influence has for example been seen in large area carrier lifetime mappings [10]. These mappings have shown a correlation between extended defects such as small angle boundaries and screw dislocations with measured minority carrier lifetime. This indicates that extended structural defects are active as recombination centers in SiC.

A second and more important influence of structural defects in the form of stacking faults has recently been shown. In this case, a change in the electrical performance, in the form of an increase of the forward voltage drop, of bipolar devices was observed [11]. A material study showed that structural defects were created during the device operation [12]. These defects were identified as stacking faults in the epitaxial layer. The stacking faults are in the basal plane $[0001]$ and propagate through the entire epitaxial layer, which is grown on an 8° off angle from the basal plane. Since a typical epitaxial layer is about 30 µm thick the stacking fault has a height, as seen from the top, of about 250 µm, and typically has a triangular shape. This is macroscopically observable with different techniques, such as lifetime mapping, cathodo-luminescence, X-ray topography and electro-luminescence. Fig. 4b. shows a panchromatic CL image over the area where a diode was processed. The stacking faults are seen as darker triangles gradually reduced towards one direction corresponding to the extension of the basal plane into the epitaxial layer. The stacking faults are only seen on diodes stressed with a high forward current, and are not present in the original epitaxial layer.

Stacking faults are also observed and identified using synchrotron white beam XRD (SWBXT) as can be seen in Fig 4b, that shows the same diode as in Fig 4a. The boundaries of the diodes are clearly seen, probably due to the stress introduced between the p+ layer and the n-base layer. White dots in the image are elementary screw dislocations, while no micro-pipes are observed on this image. A clear correlation between the structural defects observed with SWBXT and the optical features seen in CL can be seen by comparing Fig. 4a and b.

A more detailed spectral analysis using CL and PL shows that a new and previously not reported emission band is related to the stacking faults, as shown in Fig. 5. This emission is observed in the entire stacking fault area and increases in intensity with increasing temperature. The emission has an intensity maximum at about

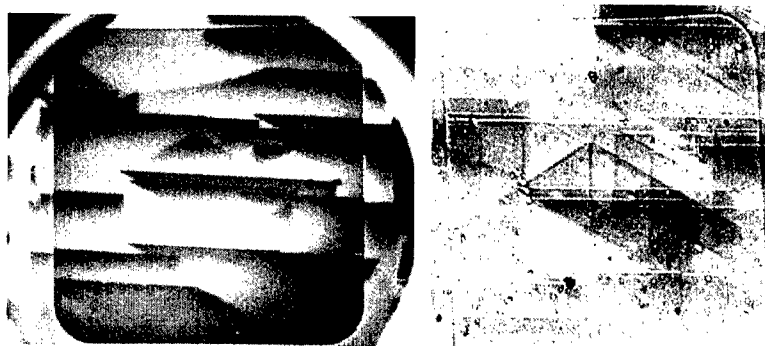


Fig. 4. Panchromatic cathodoluminescence image (left) of stacking faults generated in bipolar diodes. SWBXT image (right) of the same diode showing the stacking faults as dark triangles. The white spot is an elementary screw dislocation.

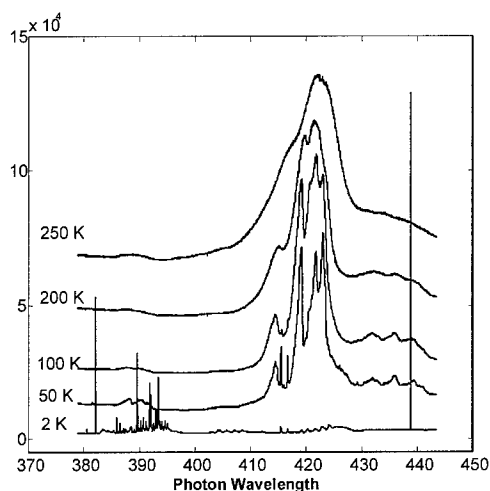


Fig. 5. PL spectra measured at different temperatures on an epitaxial layer where a stacking fault has been identified using CL or SWBXT. The emission in the range from 415 to 430 nm is attributed to recombinations at the stacking fault.

150 K, and is thermally quenched at higher temperatures with an activation energy of 280 meV.

We propose that the stacking fault in 4H SiC gives rise to a local potential fluctuation corresponding to a reduction of the bandgap. This potential attracts and binds carriers and excitons which then recombine with phonon participation and give rise to the observed emission. Since the stacking fault has a two-dimensional extension this will give a “quantum well” situation. The temperature quenching of the emission is related to the thermal escape of carriers from the “well”.

5. Summary

We have described and shown the properties of several types of intrinsic defects in SiC. These defects

are interesting both from a fundamental physics point of view as well as from an applied point of view since they have a strong influence on the properties of the material. Even if several defects are observed, there is very little detailed knowledge, especially on the atomistic defect identification, their electronic structure, and their influence on the material properties.

The importance of structural extended defects such as dislocations and stacking faults have been shown, and the study and further understanding of such defects will be of high priority in the future.

References

- [1] T. Egilsson, A. Henry, I.G. Ivanov, J.L. Lindström, E. Janzen, *Phys. Rev. B* 59 (1999) 8008.
- [2] S.G. Sridhara, P.O.Å. Person, F.H.C. Carlsson, J.P. Bergman, E. Janzen, G. Evans, J.W. Steeds, *Proceedings of the Material Research Society*, 2000.
- [3] J.W. Steeds, G. Evans, *Mat. Sci. Forum* 353–356 (2001) 381.
- [4] F.H.C. Carlsson, L. Storasta, B. Magnusson, K. Sköld, J.P. Bergman, E. Janzen, *Mat. Sci. Forum* 353–356 (2001) 555.
- [5] T. Egilsson, J.P. Bergman, I.G. Ivanov, A. Henry, E. Janzen, *Phys. Rev. B* 59 (1999) 1956.
- [6] L. Patrick, W. J. Choyke, *Phys. Rev. B* 5 (1972) 3253.
- [7] T. Egilsson, Ph.D. Thesis No. 588, Linköping University, 1999.
- [8] L. Storasta, F.H.C. Carlsson, S. Sridhara, J.P. Bergman, A. Henry, T. Egilsson, A. Hallen, E. Janzen, *Appl. Phys. Lett.* 78 (2001) 46.
- [9] B. Magnusson, A. Ellison, L. Storasta, E. Janzen, *Proceedings of the Material Research Society*, 2000.
- [10] B. Magnusson, A. Ellison, F.H.C. Carlsson, N.T. Son, E. Janzen, *Mat. Sci. Forum* 353–356 (2001) 365.
- [11] J.P. Bergman, H. Lendenmann, P.Å. Nilsson, U. Lindefelt, P. Skytt, *Mat. Sci. Forum* 353–356 (2001) 299.
- [12] H. Lendenmann, F. Dahlquist, N. Johansson, R. Söderholm, P.A. Nilsson, J.P. Bergman, P. Skytt, *Mat. Sci. Forum* 353–356 (2001) 727.



ELSEVIER

Physica B 308–310 (2001) 680–683

PHYSICA B

www.elsevier.com/locate/physb

Neutral and negatively charged silicon vacancies in neutron irradiated SiC: a high-field electron paramagnetic resonance study

P.G. Baranov^a, E.N. Mokhov^a, S.B. Orlinskii^{b,*}, J. Schmidt^b

^a *A.F. Ioffe Institute, Russian Academy of Sciences, St. Petersburg, Russia*

^b *Huygens Laboratory, Leiden University, Niels Bohrweg 2, Leiden 2300 RA, The Netherlands*

Abstract

High-field pulsed and continuous-wave electron paramagnetic resonance (EPR) techniques at 95 GHz have been used to investigate radiation defects in neutron-irradiated SiC. In the temperature range between 1.2 and 300 K three types of EPR spectra were observed in 4H- and 6H-SiC crystals that are attributed to the neutral silicon vacancy, the negatively charged silicon vacancy, and the carbon vacancy. In the EPR spectra of V_{Si}^- in 4H- and 6H-SiC an anisotropic splitting of the EPR lines is observed. This splitting is assumed to arise from small differences in the g -tensor of the quasi-cubic (k) and hexagonal (h) sites. The g -factor for the k site $g(k)$ is found to be isotropic with $g(k) = 2.0032$ and the g -factor of the h -site is found to be slightly anisotropic with $g(h) = g(k) - 0.00004$ and $g_{\perp}(h) = g(k) - 0.00002$. The 95 GHz EPR spectra at 1.4 K show that the ground state of V_{Si}^0 is a triplet state. Additional 9.5 GHz EPR experiments reveal signals that are attributed to the carbon vacancy on the basis of the observed hyperfine splitting. The results demonstrate that V_{Si}^- , V_{Si}^0 and V_{C} are dominant defects after neutron irradiation of SiC to doses up to 10^{19} cm^{-2} . © 2001 Elsevier Science B.V. All rights reserved.

PACS: 61.80.Fe; 61.72.Ji

Keywords: SiC; Vacancies; EPR

1. Introduction

The primary defects that can be produced in the binary compound SiC are vacancies, interstitials and antisites. In contrast to silicon [1] the primary defects in SiC seem to be stable at and even far above room temperature. The principal experimental tools for the identification and study of the defects in SiC are electron paramagnetic resonance (EPR) and optically detected magnetic resonance (ODMR) [2–15]. EPR investigations have revealed two charge states of the Si vacancy [5–7,9–12] but the identification of carbon vacancies is presently still under debate [14,15]. In addition sophisticated EPR

investigations have shown the existence of Si-related Frenkel pairs in SiC [13].

The dominant EPR spectrum with a g -factor $g = 2.0032$ that can be observed in irradiated 4H- and 6H-SiC crystals up to room temperature was attributed to the negatively charged isolated silicon vacancy V_{Si}^- with $S = \frac{3}{2}$ [5–7,9,12]. An anisotropic hyperfine (hf) structure caused by the interaction with the four nearest-neighbor carbon atoms (the first shell) and an almost isotropic hyperfine structure caused by the interaction with 12 next-nearest-neighbor silicon atoms (the second shell) were observed in the EPR spectra. No site dependence was detected for V_{Si}^- .

The second type of EPR spectra that was observed by several groups [4,8,10–12] is related to a center with a triplet state ($S = 1$) with an isotropic g -factor $g = 2.0032$ and a site-dependent zero-field splitting parameter D . In Refs. [8,10,11] these spectra were detected by ODMR by

*Corresponding author. Fax: 31-71-527-5819.

E-mail address: orlinski@molphys.leidenuniv.nl (S.B. Orlinskii).

monitoring the zero-phonon lines (ZPL's) at 1.438 and 1.352 eV in 4H-SiC and at 1.433, 1.398, and 1.368 eV in 6H-SiC. The authors of [10,11] were the first to attribute these EPR spectra to the neutral Si vacancy (V_{Si}^0) on the basis of the characteristic hf structure with the 12 Si atoms of the second shell that looked similar to the hf structure for the negatively charged isolated silicon vacancy V_{Si}^- . The assignment of the triplet EPR and ODMR spectra to the various sites was made on the assumption that the hexagonal site experiences a stronger axial crystal field than in the quasi-cubic sites. However, it remains unclear why the zero-field splitting for the hexagonal site is larger in the 6H polytype than in the 4H polytype that exhibits a larger axial crystal field. In addition, the order of the ZPL in the 6H polytype, with the ZPL for the hexagonal site placed between the two quasi-cubic lines, is not clear.

In the case of the negatively charged silicon vacancy V_{Si}^- , there is now consensus between theory and experiment [5,6,9] that the ground state corresponds to the high-spin configuration. In the case of the neutral isolated silicon vacancy V_{Si}^0 however, there exist two opposite points of view that support respectively a singlet [4,10,11,16,17] and a triplet [12,18,19] ground state. In particular, the theoretical studies predict a spin singlet [16,17] as well as a spin triplet [18,19] for the ground state of V_{Si}^0 . This raises the question of whether the triplet spectrum observed by several groups belongs to the ground state or a thermally populated excited state.

In this contribution, we present the results of a series of EPR measurements on V_{Si}^- and V_{Si}^0 in neutron irradiated 4H- and 6H-SiC at 9 GHz (X-band) and 95 GHz (W-band) at temperatures ranging from 1.4 to 300 K. The EPR results at 1.4 K show that the ground state of V_{Si}^0 corresponds to a triplet state. Further the EPR spectra at 95 GHz of V_{Si}^- in 4H- and 6H-SiC confirm that the spin multiplicity $S = \frac{3}{2}$ and that the signals from defects in the different sites can be resolved even for this system with a g -tensor that deviates only slightly from that of a free electron.

2. Experimental

The samples used in this study were Lely grown n -type 4H-SiC and 6H-SiC crystals with concentrations of uncompensated nitrogen in the range of 10^{16} – 10^{17} cm $^{-3}$. These samples were irradiated at room temperature with neutrons with doses ranging from 10^{15} to 10^{20} cm $^{-2}$. The advantage of the n -irradiated samples is that the irradiation produces a homogeneous distribution of defects in the sample. EPR measurements were performed on a homemade W-band (95 GHz) pulsed electron spin echo (ESE) spectrometer over a temperature range between 1.4 and 300 K [20] and on a Bruker

X-band (9.5 GHz) and W-band (95 GHz) continuous wave (cw) EPR spectrometer. The samples having the shape of platelets with sizes of about $4 \times 8 \times 0.1$ mm 3 for X-band and $0.4 \times 0.8 \times 0.1$ mm 3 for W-band were oriented for rotation in the $\{11\bar{2}0\}$ plane.

3. Results and discussion

In Fig. 1 the angular dependences of the ESE detected EPR spectra at W-band at 190 K (a) and 1.4 K (b) of the n -irradiated 4H-SiC (10^{18} cm $^{-2}$) sample are presented. The experimental spectra are only shown for the orientation with the magnetic field parallel and perpendicular to the c -axis. In 6H-SiC similar spectra and angular dependences were observed. It is seen that the triplet EPR signals are very strong. Note that the triplet EPR lines for $B_0 \parallel c$ (Fig. 1b) at high field is much stronger than at low field (the reverse is true for $B_0 \perp c$) as a result of the high spin polarization at 1.4 K and 95 GHz. This effect allows us to decide that the

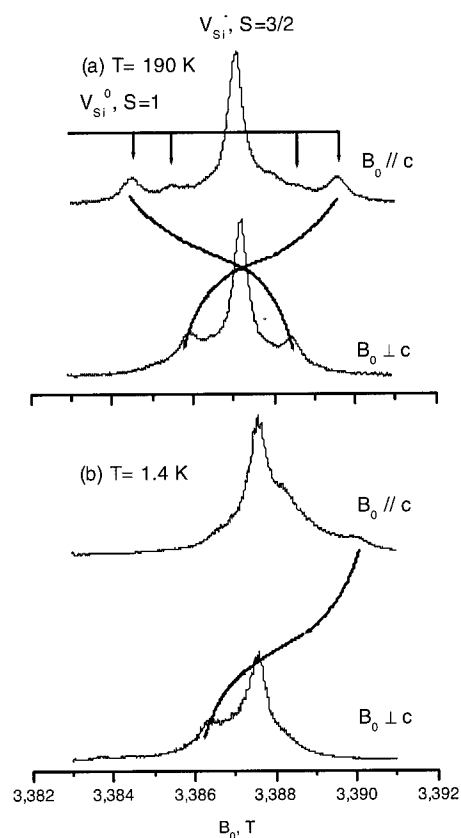


Fig. 1. Angular dependences of the 95 GHz EPR spectra observed in n -irradiated 4H-SiC (10^{18} cm $^{-2}$) at 190 K (a) and 1.4 K (b). The central line is related to V_{Si}^- whereas the outer, orientation-dependent lines are caused by the triplet state of V_{Si}^0 .

D -parameter is positive. We conclude, especially from the results at 1.4 K that the ground state of V_{Si}^0 corresponds to a triplet state.

In Fig. 2 the cw W-band EPR spectra of V_{Si}^- are shown as observed at 300 K in n-irradiated 4H-SiC (10^{18} cm^{-2}) with the magnetic field parallel and perpendicular to the c -axis. The spin multiplicity of V_{Si}^- was determined as $S = \frac{3}{2}$ by measuring the difference in amplitude of two $2\pi/3$ mw-pulses needed for the maximum echo signals of V_{Si}^- ($S = \frac{3}{2}$) and V_{Si}^0 ($S = 1$). A very small splitting is observed that is more pronounced with the magnetic field parallel to the c -axis. This splitting is assumed to arise from the small difference of the g -tensors in the quasi-cubic and hexagonal sites. The anisotropy of the g -tensors is only of the order of 10^{-5} but becomes visible owing to the high magnetic field of 3.4 T used for the 95 GHz EPR measurements. The g -tensor for the k site is found to be isotropic with $g(k) = 2.0032$ and the g -factor of the h -site is found to be slightly anisotropic with $g_{\parallel}(h) - g(k) = 0.00004$ and $g_{\perp}(h) - g(k) = 0.00002$. The assignment of the sites is based on the expectation that a defect at an hexagonal site experiences a stronger axial crystal field than a defect in quasi-cubic site. To derive the sign and the value of these small changes in position of the line we used the EPR signal of the V_{Si}^- vacancy in n-irradiated cubic 3C-SiC as a g -marker because in this crystal the g -tensor is isotropic.

In Fig. 3, we present the cw X-band EPR spectrum observed at 40 K in n-irradiated 4H-SiC (10^{18} cm^{-2}) with the magnetic field parallel and perpendicular to the c -axis that we attribute to the carbon vacancy. A closer inspection of the spectra reveals a hf structure when the magnetic field is parallel to the c -axis. This hf structure can be explained by the presence of a set of four Si atoms in the first neighbouring shell (one non-equivalent

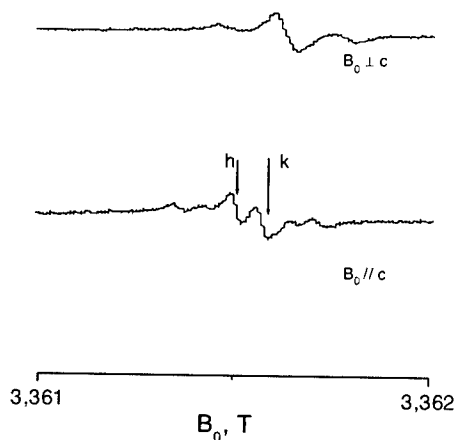


Fig. 2. CW 95 GHz EPR spectra of the V_{Si}^- vacancy observed at 300 K in n-irradiated 4H-SiC (10^{18} cm^{-2}) for the magnetic field parallel and perpendicular to the c -axis.

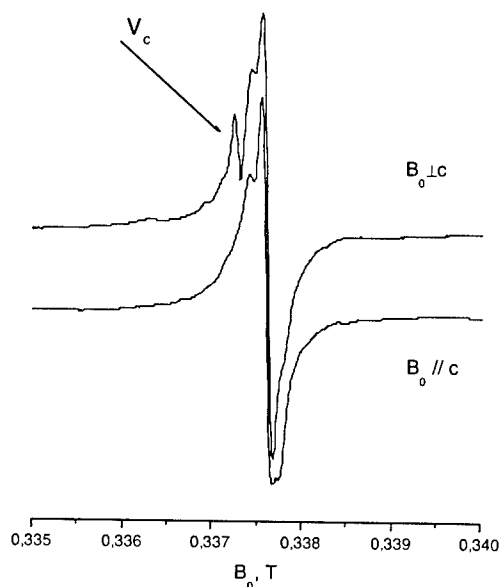


Fig. 3. CW 9.5 GHz EPR spectra observed at 40 K in n-irradiated 4H-SiC (10^{18} cm^{-2}) with the magnetic field parallel (a) and perpendicular (b) to the c -axis. The central EPR line of V_c is indicated by an arrow.

and three equivalent) and 12 C atoms in the second shell. With the magnetic field perpendicular to the c -axis the hf structure caused by the Si nuclei in the first shell can be recognized. The g -tensor and hf splitting with the Si atoms in the first shell are identical to the parameters obtained by Son et al. and Bratus' et al. [14,15] for electron-irradiated SiC crystals that were attributed to the carbon vacancy-related defect. The small linewidth allowed us to study in more detail the central part of the spectrum. An additional weaker hf structure was observable that allowed us to further support our assignment. In case of an isolated carbon vacancy the additional hf structure is expected to be caused by the interaction with 12 carbon atoms in the second shell.

4. Conclusions

Our EPR and ESE studies show that V_{Si}^- , V_{Si}^0 and V_c are the dominant defects in SiC generated by neutron irradiation with doses up to 10^{19} cm^{-2} . For the V_c defect it could not be decided whether this defect is positively or negatively charged. The simultaneous observation of all of these defects show that the positions of their energy levels are close and all lie in the bandgap.

The 95 GHz EPR results at 1.4 K prove that the ground state of V_{Si}^0 correspond to a spin triplet state. The zero-field splitting parameter is found to be positive.

In the EPR spectra of V_{Si}^- in 4H- and 6H-SiC a splitting of the EPR lines is observed that is assumed to

arise from small differences in the g -tensor of this defect in the quasi-cubic and hexagonal sites. Pulsed EPR experiments confirm that the spin multiplicity of V_{Si}^- is $S = \frac{3}{2}$ in agreement with the previous ENDOR measurements [1].

The EPR parameters of V_c are identical to those of Son et al. and Bratus' et al. [14,15]. The weak hf structure observed on the central line could be explained as arising from 12 carbon atoms in the second shell and served to further confirm the assignment as an isolated carbon vacancy.

Acknowledgements

This work was supported financially by the Technology Foundation STW with financial support of the "Nederlandse Organisatie voor Wetenschappelijk Onderzoek" (NWO). Further support was provided by NWO under grant No. B-67-286.

References

- [1] G. Watkins, in: S.T. Pantelides (Ed.), *Deep Centers in Semiconductors*, Gordon and Breach, New York, 1986, p. 147.
- [2] L.A.deS. Balona, J.H.N. Loubser, *J. Phys. C* 3 (1970) 2344.
- [3] N.M. Pavlov, et al., *Sov. Phys. Semicond.* 9 (1975) 845.
- [4] V.S. Vainer, V.A. Il'in, *Soviet Phys.* 23 (1981) 2126.
- [5] H. Itoh, M. Yoshikawa, I. Nashiyama, S. Misawa, H. Okumura, S. Yoshida, *IEEE Trans. Nucl. Sci.* 37 (1990) 1732.
- [6] H. Itoh, et al., *Phys. Stat. Sol. (a)* 162 (1997) 173.
- [7] J. Schneider, K. Maier, *Physica B* 185 (1993) 199.
- [8] M. Kunzer, Ph.D Thesis, University of Freiburg, Germany, 1995.
- [9] T. Wimbauer, et al., *Phys. Rev. B* 56 (1997-II) 7384.
- [10] E. Sörmann, et al., *Phys. Rev. B* 61 (2000-II) 2613.
- [11] Mt. Wagner, B. Magnusson, W.M. Chen, E. Janzen, E. Sormann, C. Hallin, J.L. Lidstrom, *Phys. Rev. B* 62 (2000-II) 16555.
- [12] H.J. von Bardeleben, J.L. Cantin, G. Battistig, I. Vickridge, *Phys. Rev. B* 62 (2000-I) 10126.
- [13] H.J. von Bardeleben, J.L. Cantin, L. Henry, M.F. Barthe, *Phys. Rev. B* 62 (2000-II) 10841.
- [14] N.T. Son, et al., *Materials Science Forum*, Trans. Tech. Publications, Switzerland, Vols. 353–356, 2001, p. 499.
- [15] V.Ya. Bratus', et al., *Materials Science Forum*, Trans. Tech. Publications, Switzerland, Vols. 353–356, 2001, p. 517.
- [16] F.P. Larkin, A.M. Stoneham, *J. Phys. C* 3 (1970) L112.
- [17] P. Deak, J. Miro, A. Gali, L. Udvardi, H. Overhof, *Appl. Phys. Lett.* 75 (1999) 2103.
- [18] L. Torpo, R.M. Nieminen, K.E. Laasonen, S. Poykko, *Appl. Phys. Lett.* 74 (1999) 221.
- [19] A. Zywiets, J. Furthmuller, F. Bechstedt, *Phys. Rev. B* 59 (1999-I) 15166.
- [20] J.A.J. Disselhorst, H.J. van der Meer, O.G. Poluektov, J. Schmidt, *J. Magn. Reson.* 115 (1995) 183.



ELSEVIER

Physica B 308–310 (2001) 684–686

PHYSICA B

www.elsevier.com/locate/physb

Detection of defects in SiC crystalline films by Raman scattering

S. Nakashima^{a,b,*}, Y. Nakatake^a, Y. Ishida^b, T. Talkahashi^b, H. Okumura^b

^aDepartment of Electrical and Electronics Engineering, Miyazaki University, Gakuen KibanadaiNishi, Miyazaki 889-2192, Japan

^bNational Institute of Advanced Industrial Science and Technology, Central 2, 1-1-1 Umezono, Tsukuba, Ibaraki 305-8563, Japan

Abstract

Defects in SiC films and bulk crystals are detected by Raman scattering. It is found that the observation of defect activated transverse optic bands at a Raman forbidden configuration is useful for the detection of small amount of defects. The shape of the defect activated Raman band is discussed in relation to structures of the defects. © 2001 Elsevier Science B.V. All rights reserved.

Keywords: SiC; Raman scattering; Defects; Stacking faults

1. Introduction

Defects in crystals occur during crystal growth and processing of the device fabrication. The defects can be examined by various techniques, such as X-ray diffraction, electron microscopy, ion beam analyses, optical spectroscopy, resonance spectroscopy in magnetic fields and so on. The optical spectroscopies have widely been used for characterization of defects, because it is a non-destructive method and no contact is required. Raman spectra are sensitive to the phonon properties, which reflect the microscopic structures of crystals, and have been actively used to obtain information on the nature and microscopic structure of defects. In the present work, we have tried to establish a Raman scattering technique for sensitive detection of defects in SiC crystals.

2. Defect activated Raman scattering

For the phonon Raman scattering process, the wave vector selection (conservation) rule and the polarization selection rule hold strictly in perfect crystals. The former rule restricts the wave vector of the phonons detected in

the Raman scattering process to almost zero when visible laser light is used as an excitation source [1,2]. This is a reason why sharp phonon Raman bands are observed nevertheless there are a number of phonons with different frequencies and wave vectors in crystals. The defects produce a loss of the periodicity, reduction of the crystal symmetry and a topological disorder of crystals. Therefore, they induce a breakdown of the selection rules for the wave vector, the polarization and a reduction of the phonon lifetime. For SiC crystals containing stacking faults (stacking errors), which are typical defects in SiC crystals, the partial breakdown of the wave vector selection rule causes the activation of phonon modes with wave vectors different from $q = 0$, and thereby gives rise to an asymmetric band shape [3]. The breakdown of the polarization selection rule causes the appearance of Raman bands at a forbidden configuration, and the reduction of the phonon lifetime due to the defects causes a broadening of phonon Raman bands. Accordingly, one can characterize defects using Raman parameters as bandwidth, intensity, frequency shift and polarization properties of the Raman bands.

In the past, the Raman study of defects was limited to crystals which contain a high density of defects and impurities, because the sensitivity of the systems for detection of defects was not high enough and also the spectral analysis was not well established so far.

*Corresponding author. Fax: +81-298-61-5434.

E-mail address: nakashima-s@aist.go.jp (S. Nakashima).

However, the recent development in multichannel detectors has enabled us to detect small amounts of defects in crystals. More recently, an attempt to analyze such weak defects was tried for 6H-SiC crystals [4]. In the present work, we developed a Raman scattering technique for sensitive detection of defects in crystals and applied this technique to SiC, especially 3C-SiC having a zinc blende structure.

3. Detection of defects in 3C-, 4H- and 6H-SiC

Samples were irradiated by laser beams (488 nm) with a power level of 200 mW through an objective lens with a numerical aperture of 0.45. Scattered light was dispersed using a triple spectrometer with $f = 0.6$ m and then detected by a cooled CCD detector.

We observed Raman spectra of a 3C-SiC film at the back scattering geometry using the (001) face. The heteroepitaxial films used in this experiment were grown on Si (001) and then removed from the substrate. These films contained stacking faults, dislocations and anti-phase boundaries at around the interface of SiC and Si. The transverse optic (TO) and LO modes are Raman forbidden and allowed, respectively, at this scattering geometry. On the other hand, for the back scattering geometry using the (110) surface, the TO and LO bands are Raman active and forbidden, respectively. As shown in Fig. 1(a), the intensity of the TO band is very weak at this forbidden geometry, being a percentage of the intensity at the allowed geometry. We obtained TO signals with a good signal noise ratio after a long exposure to the CCD detector. As shown in Fig. 1(b), the TO band has a tail at the low frequency side for the forbidden configuration. For comparison, we show also a Raman spectrum of the TO band at 796 cm^{-1} measured for the (110) cross section. The shape of the forbidden band at the high frequency side is almost the same as that of the allowed band. This result indicates that the asymmetric TO band observed at the forbidden geometry results from the breakdown of the wave vector and polarization selection rules due to the stacking faults. At some places, a broadening at the high frequency side is found for the forbidden TO band. This fact indicates that the defects and the stacking faults accompanying partial dislocations make the phonon lifetime short and contribute to the broadening of the phonon Raman bands.

To confirm that the observed TO band at the forbidden configuration is activated by defects, we investigated TO bands in various places in several 3C-SiC heteroepitaxial films and obtained the bandwidth as a function of the intensity. As shown in Fig. 2, there is a strong correlation between the band width and intensity: The band width increases almost linearly with increasing intensity.

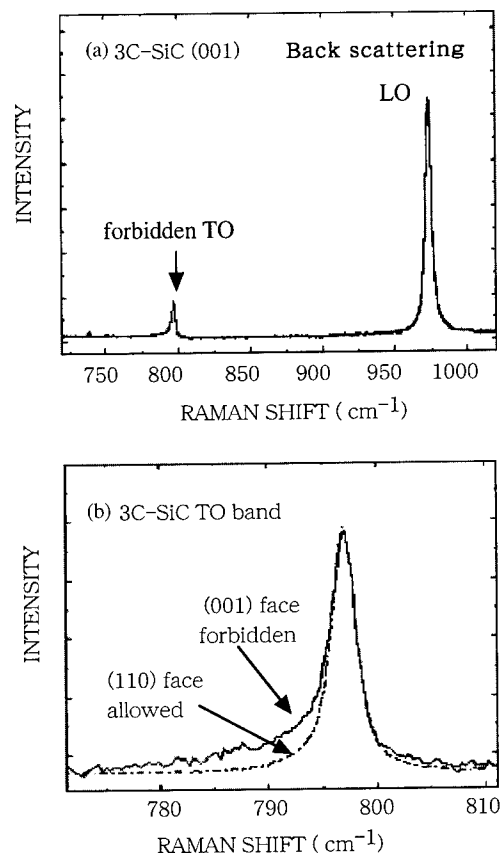


Fig. 1. (a) Raman spectrum of a 3C-SiC film taken at the back scattering geometry and (b) the spectrum of the forbidden TO band obtained by long time exposure of the CCD detector. The dashed line is a spectrum measured using the (110) face.

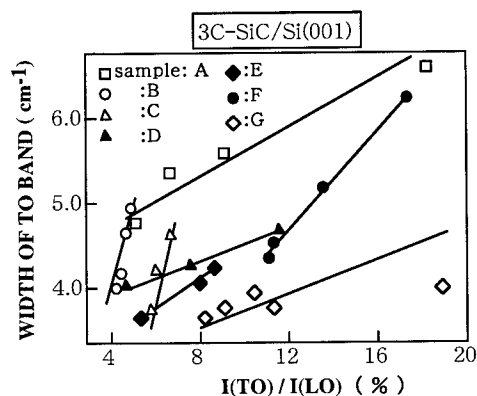


Fig. 2. The width of the forbidden TO band in 3C-SiC/Si(001) is plotted versus the intensity I of the TO band, normalized to the LO band.

It should be noted that the phonon polariton mode, which arises from reflected light from the back surface of the thin films, prevents observation of the defect induced

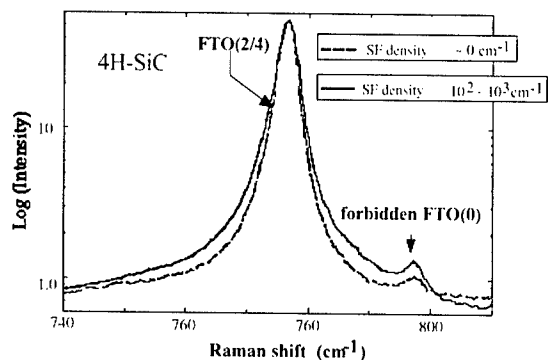


Fig. 3. Raman spectra of TO bands in the 4H polytype crystals, containing stacking faults.

TO bands. A cross polarization geometry ($e_i \perp e_s$, $e_i \parallel \langle 110 \rangle$) was used to avoid this phonon polariton mode.

The TO mode at 796 cm^{-1} in 6H- and 4H-SiC corresponds to phonon mode at the Γ point in 3C-SiC

and is called FTO(0) mode. This mode is forbidden for the back scattering geometry using the (0001) face. However, the FTO(0) band appears weakly for these polytypes containing stacking faults as shown in Fig. 3, where the result for the 4H polytype is shown. The appearance of the FTO(0) band in 6H-SiC is considered to be due to the breakdown of the wave vector selection rule by stacking faults as interpreted in Ref. [4].

References

- [1] S. Nakashima, K. Tahara, Phys. Rev. B 40 (1989) 6345.
- [2] S. Nakashima, M. Hangyo, Solid State Commun. 80 (1991) 21.
- [3] S. Nakashima, H. Ohta, M. Hangyo, B. Palosz, Philos. Mag. B 70 (1994) 971.
- [4] S. Nakashima, Y. Nakatake, H. Harima, M. Katsuno, N. Ohtani, Appl. Phys. Lett. 77 (2000) 3612.



ELSEVIER

Physica B 308–310 (2001) 687–690

PHYSICA B

www.elsevier.com/locate/physb

Electrical and optical properties of erbium-related centers in 6H silicon carbide

O. Klettke^{a,*}, S.A. Reshanov^a, G. Pensl^a, Y. Shishkin^b, R.P. Devaty^b,
W.J. Choyke^b

^a*Institute of Applied Physics, University of Erlangen-Nürnberg, Staudtstr. 7/A3, D-91058 Erlangen, Germany*

^b*Department of Physics and Astronomy, University of Pittsburgh, Pittsburgh, PA, USA*

Abstract

Implants of Er, Al and N with energies ranging from 120 keV to 2 MeV were carried out in n- and p-type 6H-SiC. The aim is to identify electrically active defects in the bandgap which can be associated with the 1.54 μm Er^{3+} luminescence in 6H-SiC. Measurements are conducted by means of deep level transient spectroscopy (DLTS) as well as low temperature photoluminescence (LTPL). In n-type 6H-SiC implanted with Er, we find well known DLTS damage levels whereas strong characteristic lines of Er^{3+} , near 1.54 μm , are seen in the photoluminescence. In p-type 6H-SiC implanted with Er two DLTS peaks can be uniquely associated with the Er^{3+} , on the other hand, *no* luminescence is observed. Conversion of such p-type 6H-SiC into n-type, by nitrogen implantation, recovers the photoluminescence. We conclude that the Er-associated defect levels in the lower half of the gap are likely not involved in the energy transfer mechanism which is responsible for the 1.54 μm luminescence. © 2001 Elsevier Science B.V. All rights reserved.

Keywords: Erbium-related centers; 6H silicon carbide; DLTS; LTPL

1. Introduction

A number of electrical and optical experiments on various polytypes of SiC, doped with Er, by means of ion implantation or during growth have been reported in the literature [1–4]. It is the purpose of this report to further elucidate the nature of the defect centers that are believed to play a part in the energy transfer process which ultimately leads to the observed Er^{3+} spectra. DLTS and LTPL measurements are applied to n- and p-type 6H-SiC to clarify this issue.

2. Experimental

To achieve a rectangular Er profile to a depth of 0.4 μm , we conducted a sevenfold Er^{3+} -implantation

with integral fluences of 9×10^{10} to $3 \times 10^{12} \text{ cm}^{-2}$ resulting in a mean concentration of 1.6×10^{16} to $4 \times 10^{17} \text{ cm}^{-3}$ as calculated by the TRIM cascade program. As reference element for the implantation damage Xe was implanted in corresponding concentrations. For changing the conduction type from p- to n-type, nitrogen implantations were performed with a resulting average concentration of $3 \times 10^{17} \text{ cm}^{-3}$. Aluminum implants were used to influence the net acceptor concentration of the epilayers. The anneals were performed at atmospheric pressure in a furnace with a closed SiC crucible (1700°C anneal) under argon ambient.

Prior to the preparation of Schottky contacts, a reactive ion etching (RIE) process was performed to remove the surface damage, after that a standard chemical cleaning of the sample was performed using acetone, aqua regia and hydrofluoric acid. For the DLTS investigations, Schottky contacts with a diameter of 1.0 mm were fabricated by evaporation of nickel. The DLTS spectra were taken in a temperature range of 100–700 K with a digital DLTS system (FT1020 by

*Corresponding author. Tel.: +49-9131-852-8427; fax: +49-9131-852-8423.

E-mail address: mpap05@physik.uni-erlangen.de (O. Klettke).

PhysTech). For the figures in this paper a double box-car correlation was chosen, defining the temperature position of the peaks. The net donor concentration was determined at room temperature ($f = 1$ MHz) by the $C-V$ method.

3. Results

DLTS spectra were taken on n-type and p-type 6H-SiC epilayers which were implanted with different Er^{3+} doses (Table 1). To separate implantation-induced defects from those which were caused by Er-related levels in the bandgap, Xe was implanted as the noble gas with an atomic-mass close to that of erbium. After implantation all samples were annealed in the same way at 1700°C for 30 min.

Fig. 1a shows the DLTS spectrum of a n-type sample implanted with Er^{3+} (curve 2) in comparison with the same material implanted with the electrically inactive Xe (curve 3) and the non-implanted epilayer (curve 1). In the non-implanted sample no electrically active defects could be found in the upper half of the bandgap. In contrast, the Er-implanted as well as the Xe-implanted sample show three pronounced peaks. The temperature positions and the calculated activation energies, shown in Table 2, when compared with reference [5] show that these defects are identical to the well-known intrinsic defects ID_6 , ID_7 and Z_1/Z_2 . No Er-related defect level was detected in n-type material.

On the other hand for the p-type epilayers (Fig. 1b) where no intrinsic defects have been observed as yet, a strong peak at 330 K named $\text{Er}(\text{p})_1$ was observed in the DLTS spectrum. This peak could not be seen in the non-implanted epilayer as well as in the Xe-implanted sample. This is a strong evidence that this peak is related to a defect center caused by erbium. More over

the peak height, which is proportional to the concentration of the defect, scales linearly with the implanted Er^{3+} dose. A five time higher implanted Er concentration results in a five times higher peak. The same is true for the smaller $\text{Er}(\text{p})_2$ peak at 370 K. Thus two Er-related deep centers are detected in p-type material.

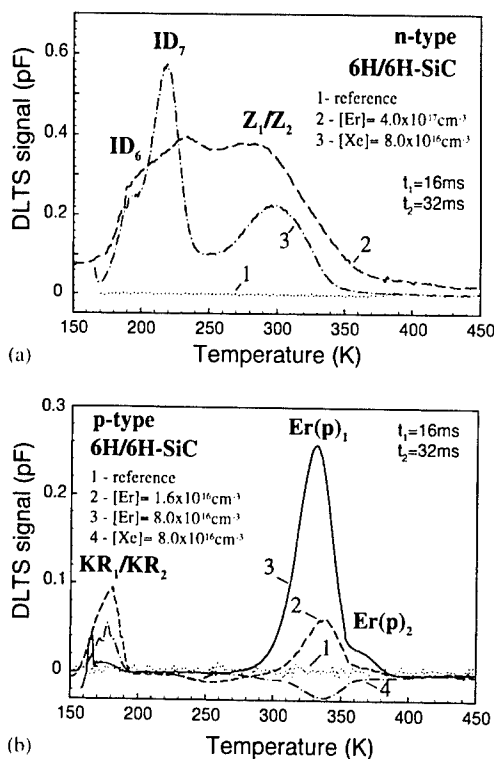


Fig. 1. (a) DLTS spectra taken on n-type 6H-SiC epilayers. Curve 1 is a none implanted epilayer. (b) DLTS spectra taken on p-type 6H-SiC epilayers. Curve 1 is a none implanted epilayer.

Table 1
Parameters of investigated 6H-SiC epilayers

Sample No.	Conductivity type of epilayer	Doping level of epilayer (cm^{-3})	Implanted elements (cm^{-3})			
			Er	Al	Xe	N
01	p	3.4×10^{15}	—	—	—	—
12	p		1.6×10^{16}	—	—	—
02	p		8.0×10^{16}	—	—	—
05	p		—	—	8.0×10^{16}	—
23	p		1.6×10^{16}	—	—	3.0×10^{17}
24	p	5.0×10^{17}	1.6×10^{16}	4.0×10^{17}	—	3.0×10^{17}
08	n		—	—	—	—
09	n		8.0×10^{16}	—	—	—
10	n		4.0×10^{17}	—	—	—
11	n		—	—	3.0×10^{16}	—

Table 2

Trap parameters of defect centers observed in DLTS spectra of Er-implanted 6H-SiC samples

Defect	Conductivity type	Peak temperature (K) ($t_1/t_2 = 16/32$ ms)	Activation energy (meV)
ID ₆	n	190	414 ± 15
ID ₇	n	220	463 ± 25
Z ₁ /Z ₂	n	300	550 ± 60
KR ₁ /KR ₂	p	170/180	450 ± 100
Er(p) ₁	p	335	789 ± 25
Er(p) ₂	p	365	780 ± 35

An interesting feature of these DLTS measurements is that the peaks KR₁/KR₂ near 170 K (Table 2) appear in the Er- as well as in the Xe-implanted samples in p-type material. None of these defects have been published in the literature to our knowledge.

2, 77 and 295 K photoluminescence measurements were taken on n- and p-type epi-grown 6H-SiC implanted with various fluences of Er and subsequently annealed at 1700°C for 30 minutes. In Fig. 2 (a), we have implanted $8 \times 10^{16} \text{ cm}^{-3}$ Er into p-type 6H-SiC and no $1.54 \mu\text{m}$ $^4\text{I}_{13/2}$ to $^4\text{I}_{15/2}$ transitions ($1.54 \mu\text{m}$) are observed. In contrast in panel (c) of this figure, we have a strong $1.54 \mu\text{m}$ spectrum despite a five-fold reduction of the Er fluence and using twice the resolution as in panel (a). To further demonstrate the dependence on the n- and p-type doping, we have taken an n-type sample implanted with the same fluence as in panel (c) and further implanted it with Al ions to compensate some of the N donors. We see the result in panel (b) where the $1.54 \mu\text{m}$ spectrum is considerably weaker despite using a lower resolution than in panel (c). These experiments clearly indicate that the Er^{3+} spectra are seen in n-type and not in p-type Er-implanted 6H-SiC.

4. Discussion

Our DLTS measurements on n- and p-type 6H-SiC clearly show that the defect levels that are found in Er-implanted n-type material can be attributed to well-known defect centers, however, in Er implanted p-type material two DLTS peaks can definitely be associated with Er. On the other hand, the optical data clearly shows that the Er^{3+} $1.54 \mu\text{m}$ spectra in 6H-SiC are confined to n-type material. A model was given in Ref. [2] which proposed that the excitation of the Er^{3+} 4f electrons occurs through the collapse of an exciton at an Er-related defect in the upper half of the gap. Our new results appear to require a revision of this model in so far that the defect at which

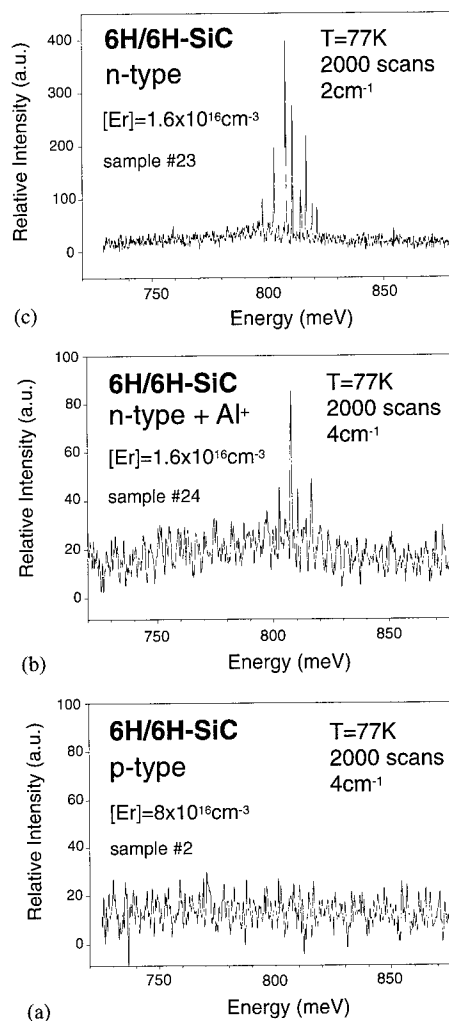


Fig. 2. LTPL signals taken at 77 K of Er-implanted 6H-SiC epilayers with different doping levels and conductivity types.

the energy transfer to the 4f electrons occurs is one of the well-known damage defects rather than an Er-related defect. Whether the Er defects found in the lower half of the gap (p-type 6H-SiC) play any role in the energy transport to the 4f electrons is presently unknown.

Acknowledgements

The support of this work by the German Science Foundation (Sonderforschungsbereich 292) is gratefully acknowledged.

Y. Shishkin, R.P. Devaty and W.J. Choyke wish to thank the ONR and NASA-Glenn Res. Center for partial support of this work.

References

- [1] W.J. Choyke, R.P. Devaty, L.L. Clemen, M. Yoganathan, G. Pensl, Ch. Hässler, *Appl. Phys. Lett.* 65 (1994) 1668.
- [2] W.J. Choyke, R.P. Devaty, M. Yoganathan, G. Pensl, J.A. Edmond, *Proceedings of the 7th International Conference Shallow-Level Centers in Semiconductors*, World Scientific Publ. Co., Singapore, 1997, p. 297.
- [3] Y. Shishkin, W.J. Choyke, R.P. Devaty, N. Achtziger, Th. Opfermann, W. Witthuhn, *Mater. Sci. Forum* 338–342 (2000) 639.
- [4] R.A. Babunts, V.A. Vetrov, I.V. Il'in, E.N. Mokhov, N.G. Romanov, V.A. Khramtsov, P.G. Baranov, *Phys. Solid State* 42 (2000) 829.
- [5] T. Dalibor, G. Pensl, H. Matsunami, T. Kimoto, W.J. Choyke, A. Schöner, N. Nordell, *Phys. Stat. Sol. A* 162 (1997) 199.



ELSEVIER

Physica B 308–310 (2001) 691–694

PHYSICA B

www.elsevier.com/locate/physb

Contactless studies of semi-insulating 4H–SiC

W.E. Carlos^{a,*}, W.J. Moore^b, G.C.B Braga^c, J.A. Freitas Jr.^a, E.R. Glaser^a,
B.V. Shanabrook^a

^aNaval Research Laboratory, Code 6862, Washington, DC 20375, USA

^bSFA, Inc., Largo, MD 20774, USA

^cInstitute of Physics, Universidade de Brasilia, Brasilia, Brazil

Abstract

Semi-insulating (SI) silicon carbide is important for applications in high-power, high-frequency electronics, such as SiC MESFETs and GaN FETs. In this work, we discuss the use of low-temperature electron paramagnetic resonance (EPR), room- and low-temperature FTIR and photoluminescence as potential screening probes. In addition, the improved materials quality enhances the resolution of such spectroscopic measurements to better understand the material. The EPR spectra reveal the expected V^{4+} as well as the shallow boron center, suggesting inhomogeneities in the B and/or V distribution. We observe significant reduction in the free-carrier absorption compared with n-type material and the intra-3d-shell $E_2-^2T_2$ IR absorption. In addition, we observe an N-related gap mode which may serve as a quantitative probe of the N content. The photoluminescence from the V-doped sample exhibits weak donor-bound excitons and shows a broad structured band near 3.0 eV related to recombination between photoneutralized N-donors and photoneutralized acceptors. Published by Elsevier Science B.V.

PACS: 71.55.Ht; 76.30.Lh; 78.30.Am; 78.55.Hx

Keywords: Silicon carbide; Semi-insulating; EPR; IR

1. Introduction

Silicon carbide has become an important semiconductor for high power, high frequency and high temperature devices [1,2] and 4H–SiC has emerged as the superior polytype, owing to a wider band gap and higher mobilities. Semi-insulating (SI) substrates are required for a number of these applications and, as with SI GaAs and InP in which optical absorption plays an important role in wafer screening [3], contactless, nondestructive methods are needed to select acceptable wafers. The improved materials quality (from a number of different growers) has opened the door to renewed application of spectroscopic probes. The spectral lines are often sharper and with the decrease in the residual

defects and impurities, additional centers become important to the electronic properties of the materials. In this paper, we discuss the application of a number of spectroscopic probes to these materials with the overall goal of developing useful contactless screening techniques as well as a better understanding of the defects important to this material.

2. Electron paramagnetic resonance

The electron paramagnetic resonance (EPR) measurements were all performed in a Bruker 9.5 GHz spectrometer, typically at 4–20 K. The signal due to the V^{4+} is seen in Fig. 1. The $V^{5+}-V^{4+}$ transition occurs near mid-gap, pinning the Fermi level there [4]. As has been previously reported [4], there are two ^{51}V ($I = 7/2$, 100% abundant) hyperfine split octets due to the V_{Si} on the cubic and hexagonal sites, as indicated in Fig. 1.

*Corresponding author. Tel.: +1-202-404-4573; fax: +1-202-767-0546.

E-mail address: carlos@bloch.nrl.navy.mil (W.E. Carlos).

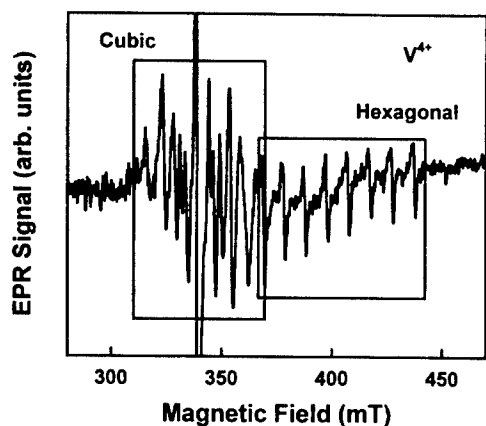


Fig. 1. The EPR spectrum of the V^{4+} ion in the SiC. There is no indication of the V^{3+} ; the central line is due to boron acceptors that are discussed in the text. B is parallel to c .

In addition to the expected V^{4+} signal, we observe the shallow boron signal in this sample, as seen in Fig. 2. This is unanticipated because the electron from the V^{4+} is expected to compensate the B acceptors. Considerable effort was applied to assure that the sample was in thermal equilibrium: e.g., the sample was left in the dark at room temperature overnight and no change was observed in the signal. We, therefore, conclude that there are nonuniform regions of the sample where the V does not completely compensate the B and, in those regions, the Fermi level is nearer the boron acceptor level (~ 300 meV above the valence band) rather than near the mid-gap. The boron spectrum is extremely sharp and this presents us with some opportunities to better understand this center. The integrated intensity of the boron lines on the cubic site is almost an order of magnitude larger than that for the hexagonal site (particularly apparent for $B \parallel c$), suggesting that the energy level of the cubic site is deeper than that of the hexagonal site. This is in general agreement with the thinking of Evwaraye et al. [5] and Duijin-Arnold et al. [6] who have argued that the hexagonal site is the shallowest. This could be the most definitive measurement of which of the two levels is deepest since the EPR provides a fingerprint and an intensity measurement. However, there is one caveat. In some SI samples, it does appear that the B on the hexagonal site has a stronger signal. Furthermore, we are assuming that the B occupies the cubic and hexagonal sites with equal probability and it may be that under certain growth conditions one or the other is preferred. Clearly, additional careful measurements are required to resolve this apparent contradiction.

In addition to the two sets of four lines (one for each site), we also observe a number of weaker lines which are not commonly observed in simple EPR for isolated B in

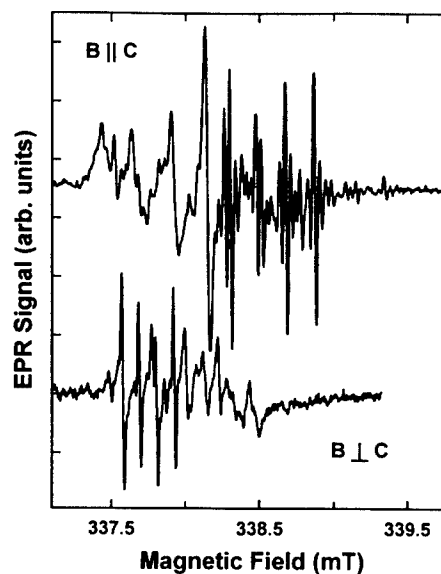


Fig. 2. The EPR signal of the shallow B acceptor for B perpendicular (bottom) and B parallel (top) to the c -axis. The sharp lines to the right in the upper plot and to the left in the lower one are due to the hexagonal site while the other structure is due to the cubic site.

the SiC. These are especially apparent for the hexagonal site. Some of the structures between the ^{11}B hyperfine split lines may be due to hyperfine splitting due to the ^{10}B ($I = 3$, 20% abundant and with a nuclear moment about $\frac{1}{3}$ that of the ^{11}B) and positions for those lines are marked in Fig. 3. The superhyperfine structure from the neighboring ^{29}Si could also account for some of the structure. We also note that the lines are exceptionally sharp ($\sim 10 \mu\text{T}$) and so, much more detail is observed in conventional EPR than has typically been seen and the data clearly require further analysis.

3. Infrared spectroscopy

Near-infrared studies were conducted at room temperature with a Bomem MB-155 FTIR. Samples were wedged to minimize interference effects. In Fig. 4, we compare the near-IR transmission for an SI vanadium-doped sample with an n-type sample. We observe the $V E_2-^2T_2$ intra-3d-shell IR absorption in the SI sample (expanded and shown in the dashed ellipse in Fig. 4). This is a signature of the SI vanadium-doped material in that the V must be in the neutral state. This is not seen in the n-type sample, where the absorption is dominated by free-carrier absorption. The free carriers absorb radiation at low-infrared frequencies (long wavelengths). This absorption can be used as a nondestructive

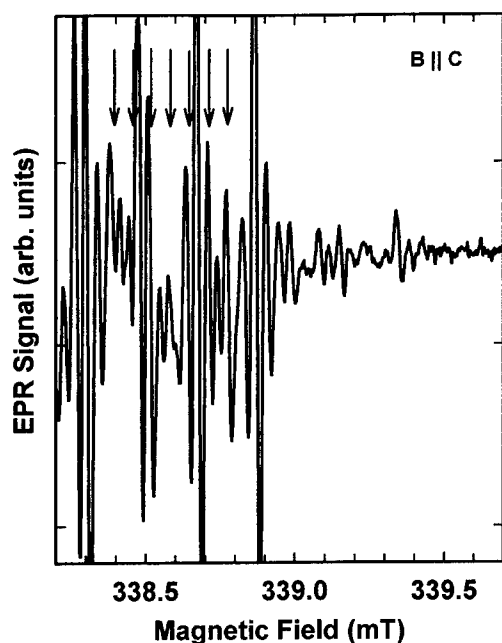


Fig. 3. The weak multi-line spectrum of the shallow B-center with **B** perpendicular to the **c**-axis. The arrows indicate the positions of the ^{10}B hyperfine structure.

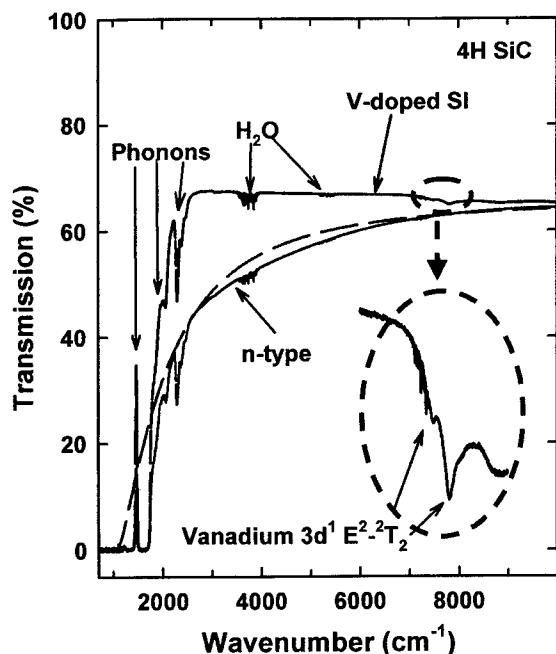


Fig. 4. The near-IR absorption spectra for a V-doped SI sample and an n-type sample. The dashed line is a fit of the free-carrier absorption with $n = 1 \times 10^{18} \text{ cm}^{-3}$ and $\mu = 200 \text{ cm}^2 \text{ V}^{-1} \text{ s}$. The intra-3d-transition is expanded and shown in the ellipse.

measurement of carrier concentration of conductive wafers. The sample here is strongly absorbing below the TO phonon frequency ($\sim 780 \text{ cm}^{-1}$) but can be modeled above the TO phonon to extract an indicated carrier concentration of $1 \times 10^{18} \text{ cm}^{-3}$. The SI wafers are transparent below the TO phonon frequency and intermediate resistivity wafers can be studied below the TO phonon frequency to extract similar information.

Between the optical and acoustic phonons, we observe a localized nitrogen gap mode at 611 cm^{-1} as shown for two 4H samples in Fig. 5. This study was carried out near 4.2 K with a Bomem DA8 FTIR and again the sample was wedged to minimize interference. The one sample has a relatively high nitrogen concentration while the second is semi-insulating with over an order of magnitude less nitrogen. SIMS measurements are currently under way to further quantify this technique that could provide a relatively quick nondestructive probe of the N content in a wafer.

4. Photoluminescence spectroscopy

The photoluminescence (PL) spectra were obtained with samples in a cryostat at 6 K. The 325 nm line of a HeCd laser was used for excitation and the PL was analyzed by a 0.85 m double spectrometer and detected with a UV-sensitive photomultiplier. The low temperature PL spectrum of N-doped 4H-SiC is dominated by recombination processes involving N-donor-bound

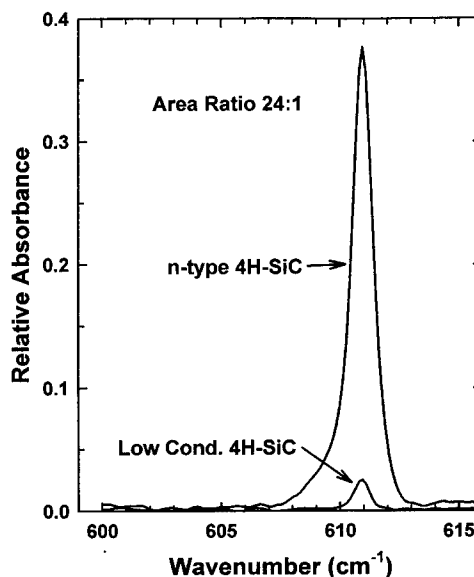


Fig. 5. The IR absorption due to a nitrogen gap mode for two samples. The ratio of intensities indicates a factor of 24 difference in the N concentration.

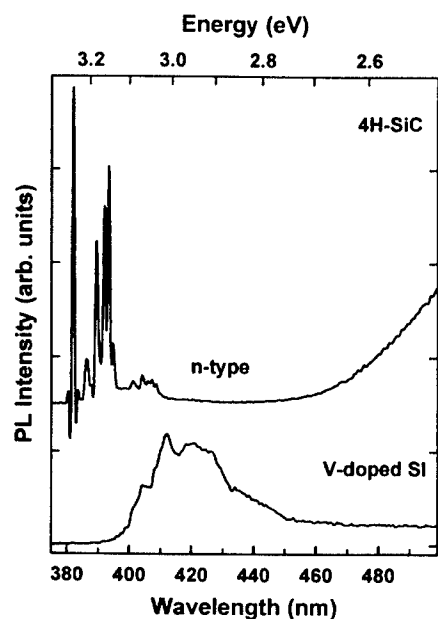


Fig. 6. A comparison of the PL for an n-type sample (top) and an SI V-doped sample (bottom).

excitons. The samples doped with V show a considerable quenching of the band edge emission related to the N-donors as shown in Fig. 6. This is attributed to the high degree of compensation of the N-donors. A broad structured emission band near 3.0 eV is also found in the V-doped sample. This PL has been ascribed to a recombination process involving photoneutralized N-donors and photoneutralized acceptors [7]. Optically Detected Magnetic Resonance experiments are under way to provide more detailed information on the nature of this PL.

5. Summary

We have shown that we can apply a number of spectroscopic measurements such as the EPR, FTIR and PL to analyze V-doped 4H-SiC samples and define their

semi-insulating character. Notably, the observation of an EPR signal due to shallow B suggests that V and/or B are not uniformly distributed resulting in inhomogeneities in the Fermi level relative to the valence band. In addition, we observe super-hyperfine structure on the boron center due to the ^{29}Si and/or ^{51}V . In the near IR we observe the V E_2 - T_2 intra-3d-absorption in the SI sample and, as expected, a significant decrease in free-carrier absorption. A nitrogen gap mode is observed and may serve as a measure of N concentration. In V-doped samples, the excitonic emission is quenched and a broad PL band at ~ 3 eV is observed.

Acknowledgements

This work was supported by the Office of Naval Research (ONR) and samples were supplied by John Zolper of ONR.

References

- [1] T.P. Chow, Mat. Sci. Forum 338–342 (2000) 1155.
- [2] P.G. Neudeck, Mat. Sci. Forum 338–342 (2000) 1161.
- [3] L. Breivik, M.R. Brozel, D.J. Stirland, S. Tuzemen, Semi. Sci. Tech. 7 (1992) A.
- [4] J. Baur, M. Kunzer, J. Schneider, Phys. Stat. Sol. A 162 (1997) 1553.
- [5] A.O. Ewvaraye, S.R. Smith, W.C. Mitchell, H.McD. Hobgood, Appl. Phys. Lett. 71 (1997) 1186.
- [6] A. van Duijn-Arnold, J. Mol, R. Verberk, J. Schmidt, E.N. Mokhov, P.G. Baranov, Phy. Rev. B 60 (1999) 15829.
- [7] St.G. Müller, D. Hofmann, A. Winnacker, E.N. Mokhov, Yu.A. Vodakov, Proceedings of the 1995 Silicon Carbide and Related Materials Conference, Institute of Physics Conference Series No. 142, Institute of Physics, Bristol, UK, 1996, p. 361.



ELSEVIER

Physica B 308–310 (2001) 695–697

PHYSICA B

www.elsevier.com/locate/physb

Influence of annealing temperature upon deep levels in 6 H SiC

F. Perjeru^{a,*}, R.L. Woodin^b, M.E. Kordesch^a^a 251A Clippinger Laboratory, Department of Physics and Astronomy, Ohio University, Athens OH 45701, USA^b Extreme Devices, Inc., 3500 ComSouth Drive, Austin TX 78744, USA

Abstract

The evolution of deep levels that depend upon annealing temperature is investigated for *p*-type 6 H SiC–Al Schottky barriers. Several samples, cut from the same wafer, have been annealed at 400°C, 600°C and 800°C, in air, while on one sample no annealing has been done. Deep level transient spectroscopy (DLTS) has been used to investigate deep levels in all four sets of samples. The results show that only electron traps can be detected in the temperature range 220–440 K. Defects with activation energies having values between 0.12–0.37 eV are detected by DLTS. © 2001 Elsevier Science B.V. All rights reserved.

PACS: 73.20.Hb; 73.61.Ey; 73.40.Vz

Keywords: SiC; Defects; DLTS

1. Introduction

Silicon carbide (SiC)-based semiconductor electronic devices and circuits are presently being developed for use in high-temperature, high-power, and/or high-radiation conditions under which conventional semiconductors cannot adequately perform. Silicon carbide is expected to enable significant improvements to a variety of applications and systems, such as high-voltage switching [1–3] and powerful microwave electronics for radar and communications [4].

Due to the fact that SiC has a low diffusion coefficient of the impurities, the commonly used process to dope the material is by ion implantation. There is radiation damage left which introduces electrically active defects. For example, Al implantation in 6H–SiC introduces both deep acceptor ($E_T = E_V + 0.26$ eV) and donor ($E_T = E_C - 0.44$ eV) states [5,6].

Doping the material with Al or N during growth is used to obtain *p*- and *n*-type material, respectively, resulting also in defect creation. One of the resulting defects, due to N residing at the C lattice site, has activation energies in the range 0.08–0.150 eV [7].

Other defects are created as a result of incorporation of residual impurities present in the growth systems. Independent of the polytype, B residing at a Si lattice site forms a deep level at approximately $E_V + 0.30$ eV, while a complex of one B atom at a C site and a neighboring intrinsic defect such as V_{Si} and V_C , forms a deep level (D defect) at approximately $E_C - 0.65$ eV [8,9]. Vanadium forms deep levels at 0.35, 0.7 eV and near midgap in 4H- and 6H–SiC material [10].

The large number of defects investigated by numerous groups, cited above, indicates that growth conditions as well as post-growth processing of the substrates might play an important role in the creation and evolution of the deep defects in SiC.

The material used in this study, 6H–SiC acquired from Cree Corp., doped with Al ($p = 3.6 \times 10^{18} \text{ cm}^{-3}$) has been cut in four pieces. Three of these have been annealed in air for 30 min at 400°C, 600°C and 800°C, respectively, while on the fourth piece no heat treatment has been applied. After annealing, all samples have been cleaned in HF: deionized water (1:2) for 5 min, then rinsed in deionized water and dried in inert gas. After cleaning, the samples have been placed in a standard Edwards evaporator system for Al Schottky contact deposition through masks with circular dots with diameters of 0.5 mm. On each sample, 12 dots have

*Corresponding author. Fax: +1-740-593-0433.

E-mail address: perjeru@helios.phy.ohiou.edu (F. Perjeru).

been deposited resulting in the formation of 12 Schottky barriers (thickness of the contact 400 nm). Ohmic contacts have been formed by evaporation of Al on the back of the samples (contact thickness of approximately 1000 nm).

To test the properties of the Schottky barriers thus obtained, current–voltage measurements (I – V) were performed at 300 K using a Keithley236 source measure unit. Capacitance–voltage (C – V) and deep level transient spectroscopy (DLTS) measurements were performed in vacuum at a pressure of 1×10^{-3} Torr and at a frequency of 1 MHz using a SULA Technologies DLTS. DLTS analysis have been performed for several junctions on each sample in the temperature range 220–440°K. A reverse bias of 3–5 V was applied to the junctions. The traps were filled by decreasing the bias to 0 V. The duration of the filling pulse was 5 ms.

2. Results

I – V measurements were performed for each barrier on every sample. The junctions were characterized by ideality factors close to 2, and leakage currents of the order of 2.0×10^{-8} A cm $^{-2}$ at 5 V reverse bias. From C – V measurements, values for the built-in voltages of 3.3 eV and $(1.3\text{--}1.4) \times 10^{18}$ cm $^{-3}$ for the carrier concentration were obtained. Within the depth sampled by the spreading charge region, 200 nm from the surface, the free carrier concentration remained constant.

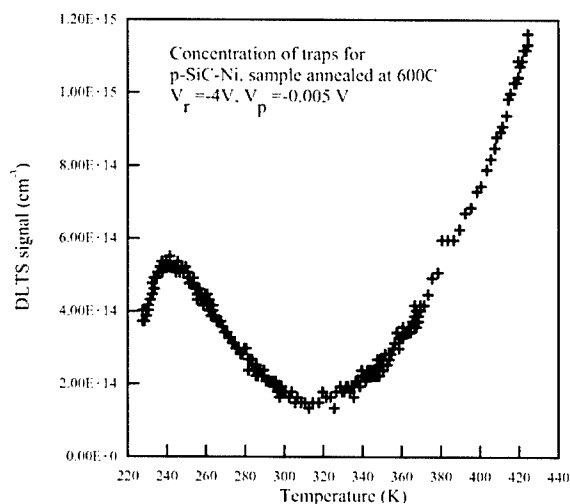


Fig. 1. DLTS for p-type SiC annealed at 600°C. There are signatures from two defects, both electron traps. One trap cannot be followed using the available rate windows to be able to extract the activation energy.

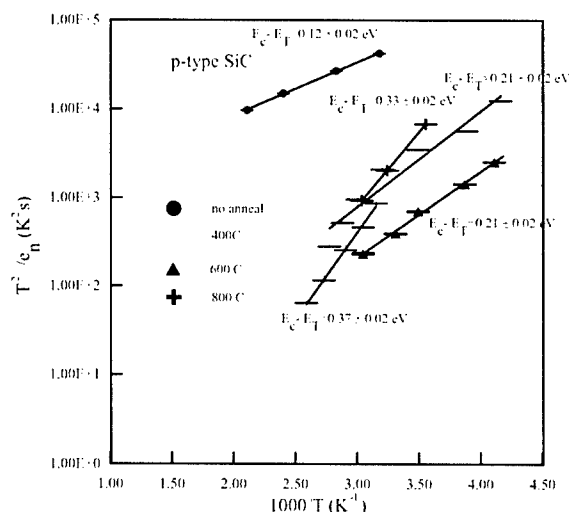


Fig. 2. Activation energies for traps in p-type SiC.

An example of DLTS spectrum on a sample that has been annealed at 600°C is shown in Fig. 1. The activation energy was determined from Arrhenius plots for all defects (using a temperature independent capture cross-section approximation). DLTS results for all samples are shown in Fig. 2 and are listed in Table 1. It has been seen that only electron traps are active in the temperature range investigated and that more than one trap is present for all samples. For one trap the activation energy could not be extracted because a temperature higher than could possibly be used was necessary, as seen in Fig. 1.

For the sample annealed at 400°C it has been observed that besides the trap that cannot be reached, depending upon the rate window chosen, there are two traps that occur in the same temperature range, with activation energies of $E_c - E_T = 0.37 \pm 0.02$ and (0.21 ± 0.02) eV, respectively. Both are electronic traps. All traps have uniform distribution within the region of the bulk sampled (200 nm).

3. Discussion

In terms of I – V and C – V measurements, the results are similar with those obtained by other groups on similar samples [11–13]. In general, for SiC is not trivial to obtain ideality factors close to unity. The process in general requires extensive cleaning and etching of the surface oxides [11,14].

The defects found in this study have minority carrier DLTS signatures and are therefore, electron traps. Some defects have been detected by other groups, for

Table 1
Activation energies and concentrations for traps in p-type SiC

	As grown	400°C	600°C	800°C
Name and activation energy (eV)	PE1 0.12 ± 0.2	PE2 0.21 ± 0.2 PE3 0.37 ± 0.2	PE4 0.21 ± 0.2	PE5 0.33 ± 0.2
Concentration (cm^{-3})	PE1 $(2-3) \times 10^{14}$	PE2 $(3-4) \times 10^{15}$ PE3 $(1-3) \times 10^{15}$	PE4 $(5-6) \times 10^{14}$	PE5 $(1-1.5) \times 10^{15}$

example, the PE1 defect, which is close to the L1 electron trap found by Ballandovich [15]. The PE2 and PE4 defects, present in the samples annealed at 400°C and 600°C are probably the same defect with an intrinsic nature, especially since after annealing at temperatures higher than 600°C their signature is no longer present. This conclusion is further supported by the fact that the concentration of this defect decreases with annealing temperature, from $(3-4) \times 10^{15} \text{ cm}^{-3}$ at 400°C, to $(5-6) \times 10^{14} \text{ cm}^{-3}$ at 600°C. It is known that simple point defects, such as single vacancies and Frenkel pairs are annealed out in the range 100–750°C [15].

The PE3 and PE5 defects might be different defects, especially since they are active at different temperatures. A defect with activation energy of $E_C - 0.32 \text{ eV}$, has been detected by Kobayashi et al. [16] as well, but no hypothesis has been formulated regarding its nature [16]. Vanadium impurities are found to introduce defects with activation energy of $E_C - E_V = 0.35 \text{ eV}$ [10]. Either PE3 and PE5 might be related to such residual V impurities. Another hypothesis regarding these two defects is that they could be related to deep center observed by Zhang et al. [17], which showed that actually there are two centers, and that it is difficult to resolve the energy position of these centers when recording DLTS spectra. Based on data in which T^2 corrections were used, the activation energy was calculated to be 0.35–0.39 eV [15]. In these conditions, both PE3 and PE5 might be related to these centers.

One defect that appears at higher temperatures could not be reached with the experimental apparatus and samples. This could be a defect with activation energy $> 1 \text{ eV}$ below the conduction band. Such defects have been observed by Kobayashi et al. [16]. The fact that no other defects have been detected in this temperature range could be a consequence of their concentration being below the detection limit of our apparatus.

In conclusion, defects in p-type 6H-SiC samples have been investigated and results displayed in Table 1. Several defects were found, depending upon the annealing temperature of the sample. From carrier concentration and activation energy, some of the defects have been tentatively associated with defects published in literature.

Acknowledgements

This work is supported by BMDO URISP grant N00014-96-1782 entitled “Growth Doping and Contacts for Wide Band-Gap Semiconductors” and Grant N00014-99-1-0975 entitled “Band-Gap Engineering of the Amorphous In-Ga-Al Nitride Semiconductor Alloys for Luminescent Devices from the Ultraviolet to the Infrared”.

References

- [1] N.G. Hingorani, K.E. Stahlkopf, High-Power Electronics, Sci. Am. 269 (1993) 78.
- [2] M. Bhatnagar, B.J. Baliga, Comparison of 6H-SiC, 3C-SiC, and Si for Power Devices, IEEE Trans. Electron Devices 40 (1993) 645.
- [3] B.J. Baliga, Power semiconductor devices for variable-frequency drives, Proc. IEEE 82 (1994) 1112.
- [4] R.J. Trew, J.-B. Yan, P.M. Mock, Proc. IEEE 79 (1991) 598.
- [5] S. Fung, M. Gong, C.D. Beling, G. Brauer, H. Wirth, W. Skorupa, J. Appl. Phys. 84 (2) (1998) 1152.
- [6] T. Troffer, M. Schada, T. Frank, H. Itoh, G. Pensl, Jheindl, H.P. Strunk, M. Mayer, Phys. Stat. Sol. A 162 (1997) 277.
- [7] G. Pensl, W.J. Choyke, Physica B 185 (1993) 264.
- [8] T. Frank, T. Troffer, G. Pensl, N. Nordell, S. Karlsson, A. Schoner, Silicon Carbide, III-Nitrides and Related Materials, (1998) pp. 681–684.
- [9] W. Suttrop, G. Pensl, P. Lanig, Appl. Phys. A 51 (1990) 231.
- [10] W.C. Mitchel, R. Perrin, J. Goldstein, M. Roth, M. Ahouja, S.R. Smith, A.O. Ewvaraye, J.S. Solomon, G. Landis, et al., Silicon Carbide and Related Materials Parts 1,2, Vol. 264(2) 1998 pp. 545–548.
- [11] L.M. Porter, R.F. Davies, Mater. Sci. Eng. B 34 (1995) 83.
- [12] C.A. Mead, W.G. Spitzer, Phys. Rev. 134 (1964) A713.
- [13] K. Yasuda, T. Hayakawa, M. Saji, IEEE Trans. Electron. Devices ED-34 (1987) 2002.
- [14] S.Y. Wu, R.B. Campbell, Solid-State Electron. 17 (1974) 683.
- [15] V.S. Ballandovich, Semiconductors 33 (11) (1999) 1188.
- [16] S. Kobayashi, S. Imai, Y. Hayami, M. Kushibe, T. Shinohe, H. Okushi, Silicon Carbide and Related Materials-1999 Parts 1,2, Vol. 338(3) (2000) pp. 757–760.
- [17] H. Zhang, G. Pensl, P. Glasow, S. Levenzeder, ECS Extended Abstr. 82 (2) (1987) 714.



ELSEVIER

Physica B 308–310 (2001) 698–701

PHYSICA B

www.elsevier.com/locate/physb

EPR and photoluminescence studies of semi-insulating 4H-SiC samples

E.N. Kalabukhova^{a,*}, S.N. Lukin^a, W.C. Mitchel^b, A. Saxler^b, R.L. Jones^b

^a *Institute of Semiconductor Physics, NASU, PR. Nauki 45, 03028, Kiev, Ukraine*

^b *Air Force Research Laboratory, AFRL/MLPS, W-PAFB, OH 45433-7707, USA*

Abstract

Several samples of semi-insulating (s.-i.) 4H-SiC have been studied by Electron Paramagnetic Resonance (EPR) at 37 GHz and by photoluminescence (PL). One set of samples revealed EPR spectra of vanadium. The signs of fine structure constants D were determined, at 4.2 K, to be positive. In the second set of samples the EPR signals from nitrogen, boron and a deep center, P, with $g_{\parallel} = 2.0048$ and $g_{\perp} = 2.0030$ appeared in the EPR spectrum after photo excitation of the sample. The P center is postulated to be the deep donor reported previously to be a dominant center in s.-i. 4H-SiC. Intercenter charge transfer processes between nitrogen and the P center are shown to be very efficient. Both sets of samples revealed the well known vanadium intracenter PL emission lines near 0.95 eV. In addition, a broad band located at 2.43 eV along with sharp near-band-edge luminescence lines has been observed for the samples containing large amounts of vanadium and at 2.38 eV with a shoulder at 2.14 eV in the samples with low levels of vanadium. © 2001 Elsevier Science B.V. All rights reserved.

Keywords: Semi-insulating SiC; Photo EPR; Photoluminescence

1. Introduction

There is currently interest in deep levels in SiC for the production of semi-insulating (s.-i.) substrates for microwave devices. Although considerable progress has been made in the technology of s.-i. SiC material, information on the dominant recombination centers, including their nature, energy levels and influence on the s.-i. properties of SiC, is limited. Mitchel et al. [1] have demonstrated that, in addition to vanadium, another level at $E_C - 1.1$ eV may dominate some s.-i. material. This level must be taken into consideration as lifetime limiting recombination center as well as a deep level responsible for the s.-i. feature of this material.

2. Experimental

To investigate the deep levels in SiC, two sets of s.-i. 4H samples have been studied by photo EPR

and photoluminescence (PL). Photo EPR measurements using photo excitation and photo quenching techniques are a good method for determining the charge state of impurities and defects. Also, conclusions about the level positions in the band gap of the defects and impurities, and on charge exchange processes, can be obtained. Photoluminescence provides further information on the electronic levels present in the material through the recombination of free carriers.

The samples were bulk semi-insulating 4H-SiC grown by physical vapor transport. The first set had high vanadium concentrations as determined by SIMS ($> 10^{17} \text{ cm}^{-3}$) while the second set had a smaller concentration ($< 10^{16} \text{ cm}^{-3}$).

EPR measurements were performed on Q-band EPR spectrometer. The photo excitation and quenching experiments were performed using a 250 W high-pressure mercury vapor lamp and a 100 W halogen lamp combined with interference filters and a prismatic monochromator for a wavelength range of 380–1000 nm.

*Corresponding author. Fax: +380-44-243-48-93.

E-mail address: katia@i.kiev.ua (E.N. Kalabukhova).

3. Results

Prior to illumination, the first set of samples revealed the EPR spectra of vanadium in the $V^{3+}(3d^2)$ charge state ($S = 1$, $I = 7/2$) from the cubic and hexagonal sites in the temperature interval from 4.2 to 77 K. The two hyperfine octets arising from cubic site V taken at 4.2 K and 37 GHz for $H \parallel c$ are shown in Fig. 1. The parameters of the spin Hamiltonian obtained from an analysis of the angular dependence of the EPR spectra for a rotation of the magnetic field in the $(1\bar{1}0)$ plane, listed in Table 1, are very similar to those obtained in Ref. [2] at 9 GHz. The signs of the fine structure parameters D were determined to be positive for the two V spectra from the difference in the intensity of the low and high field resonance transitions which, as seen in Fig. 1, are enhanced by raising the frequency and lowering the temperature to 4.2 K.

After illumination with above-band-gap UV light, two lines at $g_{\parallel}^h = 2.0019$ and $g_{\parallel}^k = 2.0063$ appeared in the EPR spectrum. These lines are due to the boron acceptor on hexagonal and cubic sites [3]. At the same

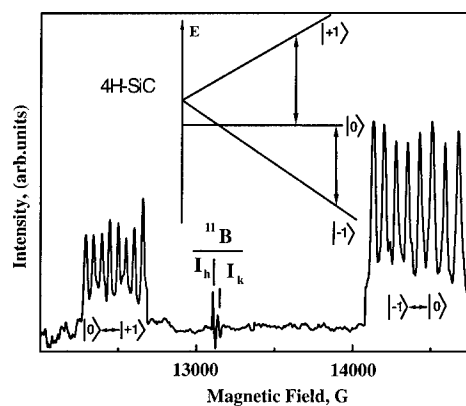


Fig. 1. Vanadium $V^{3+}(3d^2)$ EPR spectrum in s.i. 4H-SiC measured at $T = 4.2$ K, 37 GHz and $H \parallel c$. The two hyperfine octets belong to the $V^{3+}(3d^2)$ cubic site. The energy level scheme for a triplet system in a static magnetic field is shown for $D > 0$.

Table 1

Parameters of vanadium $V^{3+}(3d^2)$ EPR spectra in 4H-SiC, measured at 4.2 K and 37 GHz

	I_h	I_k
g_{\parallel}	1.962 ± 0.008	1.959 ± 0.005
g_{\perp}	1.958 ± 0.008	1.958 ± 0.005
D (GHz)	10.5 ± 0.1	2.65 ± 0.05
A_{\perp} (G)	63.0 ± 1.0	64.0 ± 1.0
A_{\parallel} (G)	68 ± 1.5	65 ± 1.5

time, the vanadium spectrum itself does not change with illumination.

In the dark, the second set of samples showed only a weak cubic site boron EPR signal without the vanadium lines. Excitation of the sample with UV light resulted in the neutralization of the shallow donors and acceptors and as a result the EPR signals from nitrogen and boron appeared. Fig. 2 shows the EPR spectrum measured at 37 GHz and 77 K during illumination with UV light. The spectrum consists of two lines with unresolved hyperfine structure due to the two inequivalent sites of shallow boron, I_k^B with $g_{\perp} = 2.0046$ and I_h^B with $g_{\perp} = 2.0070$ corresponding to the two inequivalent sites, which have C_{3v} symmetry at temperatures higher than 50 K [3] and cubic site nitrogen, I_k^N , which is easily recognized by the characteristic three line hyperfine pattern and $g_{\perp} = 2.0013$ [4].

After the UV light was turned off, the hexagonal and cubic boron resonances decreased slowly to about 0.4 and 0.7 of their values under illumination, respectively. The nitrogen EPR lines decayed to about 0.07 of their value under illumination after 21 h in the dark. At the same time, as was seen in Fig. 2b, a new single line, labeled I_p , with $S = 1/2$, and $g_{\parallel} = 2.0048$, $g_{\perp} = 2.0030$ appeared in the EPR spectrum. The intensities of the photo-induced EPR signals indicate that the lifetimes of electrons and holes at $T = 77$ K are very long and that the recombination rate of the photo-excited carriers is

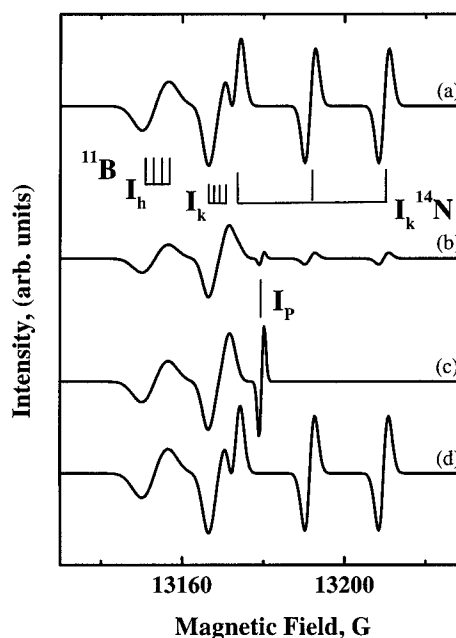


Fig. 2. Photoresponse of EPR spectra in s.i. 4H-SiC measured at 77 K and $H \parallel c$. (a) UV light excitation; (b) spectra 21 h after UV illumination; (c) visible light excitation; (d): UV quenching of visible light induced signal.

very small. The nitrogen and boron resonances can be quenched by shining below-band-gap light of various wavelengths on the sample. The time dependence of the decay of the nitrogen resonance line for four different quenching photon energies is plotted in Fig. 3. This figure shows that a substantial enhancement of the recombination rate of the photo-created carriers starts at about $\Delta E_q = 2.36$ eV, which corresponds to the energetic distance of the deep donor level from the valence band: $E_g = \Delta E_q + \Delta E_{DL} \cong 2.36$ eV + 0.9 eV $\cong 3.26$ eV. Starting from 2.36 eV the number of the electrons released from nitrogen increase and hence the donor–acceptor recombination process becomes more efficient. During quenching, the I_P line first appears when the intensity of the nitrogen EPR line decays to about 0.3 of its light-on value, independent of the energy of the quenching light. This indicates that the release of electrons from nitrogen is responsible for the appearance of the P center in the quenched EPR spectra.

The I_P line also appeared in the EPR spectrum after direct excitation with below-band-gap light as shown in Fig. 2c. When the below-band-gap light was turned off, I_P and the boron lines persisted for more than 14 h without a noticeable change in intensity, showing that no recombination processes occurred between the P center and boron. Subsequent illumination of the sample with UV light quenched the P center, restored the nitrogen EPR spectrum and enhanced the boron line to

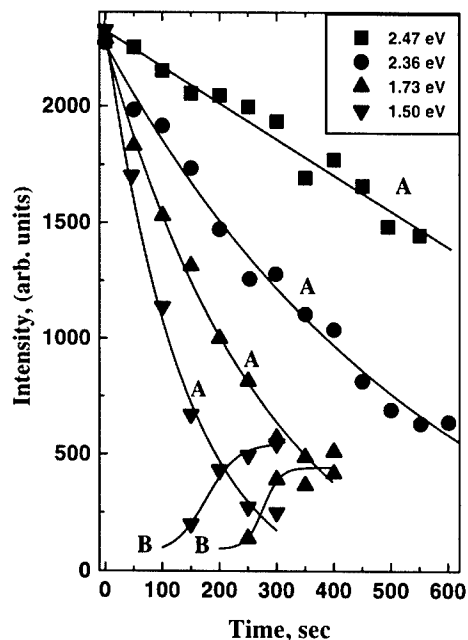


Fig. 3. Time dependence of the decay and rise of the nitrogen (A) and P center (B) EPR resonance lines for four different quenching photon energies.

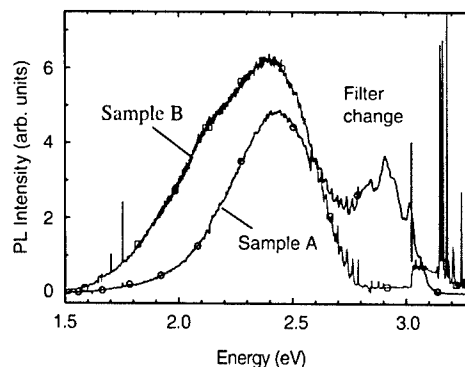


Fig. 4. PL spectra for two 4H-SiC samples. Sample A contains vanadium while V is undetectable by SIMS in sample B. The feature labeled figure caption is an artifact due to a change in filters during the experiment.

its maximum intensity, as seen in Fig. 2d. The rise and decay times of the intensity of the EPR signals of nitrogen, boron and the P center were found to depend on the intensity of the irradiating UV light. Under low intensity UV illumination the nitrogen and boron EPR lines increased slowly to their maximum values approximately for 15 min while the I_P line completely vanished for this time, showing a correlation between the rise and decay of the EPR signals of nitrogen and the P center.

In the PL experiments, both sets of samples revealed spectra in the 0.95 eV region from the intra-3d-shell transitions of vanadium which show the polytype to be 4H [2]. In addition, as shown in Fig. 4, a broad band near 2.4 eV has been observed along with the typical near-band-edge sharp luminescence lines. For the first set of samples, which contains higher concentrations of V, the peak position of the 2.4 eV band is located at 2.43 eV. For the sample in which SIMS was unable to detect V, the peak shifts to 2.38 with a shoulder at 2.10 eV.

4. Discussion

The excitation and quenching spectra of the nitrogen and boron EPR signals may be explained by a recombination process between nitrogen and boron that involves the P center. The P center, observed only in the second set of samples after illumination, is suggested to be a donor due to the sense of the g -anisotropy (i.e. $g_{\parallel} > g_{\perp}$) which coincides with that found for donor paramagnetic centers in SiC. Since the P center showed a slight anisotropy ($\Delta g = 1.8 \times 10^{-3}$) compared to that for nitrogen ($\Delta g = 4.5 \times 10^{-3}$) it was concluded that the P center should have an energy level deeper than nitrogen [4].

The excitation and quenching EPR spectra can be understood as due to two competing processes. One is the recombination process between nitrogen and boron and second is the charge transfer process occurring between shallow nitrogen and deep donors resulting in the appearance and subsequent disappearance of I_P in the quenched EPR spectra. As was shown in Ref. [5] the efficiency of the intercenter charge transfer process in SiC is enhanced by increasing the concentration of deep donors and by lowering the Fermi level to midgap after which the nitrogen donors tends to interact less with the conduction band and more with states below them.

It should be noted that the lifetime of electrons trapped on the P center is very long, 15–20 h. Taking into account that the boron lines also persist in the quenched EPR spectrum, we conclude that the recombination between nonequilibrium carriers is impeded by the presence of P center. Thus, the P center is strongly involved in the trapping and recombination (TR) process and is possibly the dominant lifetime controlling defect at low temperature in these samples.

The luminescence properties of the samples were found to correlate with the paramagnetic properties. As seen in Fig. 4, the samples with the lowest intensity vanadium PL band exhibited a shoulder peaking at about 2.14 eV, which is close to band gap, minus the activation energy of the P center. The Fermi level in these samples was pinned at the 1.1 eV level.

References

- [1] W.C. Mitchel, et al., *Appl. Phys.* 86 (1999) 5040.
- [2] J. Schneider, et al., *Appl. Phys. Lett.* 56 (1990) 1184.
- [3] S. Greulich-Weber, et al., *Semicond. Sci. Technol.* 13 (1998) 59.
- [4] E.N. Kalabukhova, et al., *Sov. Phys. Sol. State* 32 (1990) 482.
- [5] E. Sörman, et al., *Proceedings of the 23rd International Conference on the Physics of Semiconductors (ICPS)*, World Scientific Publishing Co Pte Ltd., M. Scheffler (Ed.), 1996, p. 2665.



ELSEVIER

Physica B 308–310 (2001) 702–705

PHYSICA B

www.elsevier.com/locate/physb

Defect correlated emission and electrical properties of 4H- and 6H-SiC epitaxial layers doped by nuclear transmutation doping (NTD)

H. Heissenstein*, H. Sadowski, R. Helbig

University of Erlangen-Nürnberg, Lehrstuhl für Angewandte Physik, Staudtstr. 7/A3, D-91058 Erlangen, Germany

Abstract

We have investigated 4H-SiC and 6H-SiC epitaxial layers after doping by nuclear transmutation doping (NTD). N-type layers on n-type substrates were characterized by low-temperature photoluminescence (LTPL) and p-type layers on p-type substrates with I - V , C - V and Hall effect measurements. Resulting from irradiations with thermalized neutrons of different energy spectra the samples were doped with phosphorous. Our experiments show defects which are generated by fast neutrons which inevitably exist in the energy spectra of reactor neutrons. We characterized samples by LTPL at temperatures of measurement between 2 and 72 K in the visible range as irradiated and annealed up to 1200°C. I - V curves of pn-junctions which are annealed at 1500°C and 1600°C with varied fluences of fast neutrons are presented. © 2001 Elsevier Science B.V. All rights reserved.

PACS: 78.55.Ap; 61.80.Hg; 61.82.Fk

Keywords: SiC; LTPL; NTD; Neutrons

1. Introduction

Nuclear transmutation doping (NTD) of SiC is based on the reaction [$^{30}\text{Si}(n,\gamma)^{31}\text{Si} \xrightarrow{\beta^-} ^{31}\text{P}$] and therefore, it is basically useful to produce the phosphorous donor in volumes of SiC. The phosphorous doping of SiC also was analysed after ion-implantation [1]. First attempts applying NTD on SiC were made with respect to the behaviour of SiC in radiative environments [2] and in order to get higher doping levels for ESR-investigations [3]. In the last years NTD is introduced in SiC technology as doping technique [4–6]. The electrical characteristics of irradiated samples are influenced by defects due to fast neutrons, which are incorporated inevitably by NTD using neutrons with energy spectra from nuclear reactors [4].

2. Experimental

We irradiated different 4H and 6H epitaxial layers on Cree Substrates (n- and p-type) in different positions of several reactors with a fluence of thermal neutrons of $4 \times 10^{19} \text{ cm}^{-2}$ and fluences of fast neutrons (energy $> \text{MeV}$) of $8 \times 10^{16} \text{ cm}^{-2}$ and $5 \times 10^{15} \text{ cm}^{-2}$.

The samples were characterized after irradiation and after different annealing steps (for details of sample preparation see [4]). We investigated low-temperature photoluminescence (LTPL) (for apparatus details [7]) with a HeCd laser at 325 nm for excitation. The studies of the electrical behaviour were carried out after preparing mesadiodes of 6 mm in diameter without any special surface or edge preparation techniques. The mesadiodes were contacted by aluminum on the n-type layer and by Ni on the p-type substrate. Diodes prepared from the same chip were annealed at 1400°C, 1500°C, 1600°C to generate the pn-junctions in the previously p-type on p-type samples. I - V measurements

*Corresponding author. Fax: +49-91-31-85-284-23.

E-mail address: hans.heissenstein@gmx.de (H. Heissenstein).

were carried out with a Keithley 6517 and a curvetracer Sony 370 A.

3. Results

LTPL is a powerful tool for non-destructive characterization of samples. Directly after irradiation LTPL spectra are to be detected if the applied fluence of fast neutrons is low (e.g. $<10^{16} \text{ cm}^{-2}$). For samples irradiated with higher fluences of fast neutrons luminescence is not detectable until applying annealing temperatures above 1000°C .

At samples with low applied fluences of fast neutrons we measured the emission after NTD and after several annealing steps. In addition the emission spectra for increasing temperatures from 2 up to 72 K were measured.

In the visible region, there is a small band of lines in both polytypes which is shifted on the energy scale towards each other (Fig. 1) corresponding to the different energy gaps. There is another emission band strongly correlated to defects in the near IR [5, 6H: 8] which shall not be discussed here.

The experiments where the temperature of the measurements is directly increased after NTD show impressive changes between 6, 7 and 21 K, respectively (Fig. 2 for 4H; Fig. 3 for 6H). Obviously the lines can be divided into three groups. First there are stable (s) lines over a wide range of temperatures, other lines vanish (v) with increasing temperature and there are rising (r) ones. In both polytypes there are groups of lines of type v (4H: lines at 4250, 4274, 4278, 4284, 4290, 4294, 4299, 4306, 4311, 4328, 4346, 4348, 4352 (Å); 6H: lines at 4711, 4719, 4724, 4728, 4738, 4741, 4745, 4750, 4755, 4759, 4767 (Å)) at the high-energetic side and at the low-energetic side (4H: 4384, 4389, 4405, 4417 (Å); 6H: 4831, 4836, 4843, 4846, 4849, 4854, 4857, 4862, 4867, 4896, 4904 (Å)). The stable lines are in 4H: 4372, 4466,

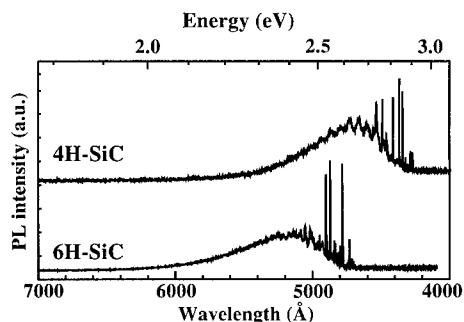


Fig. 1. LTPL spectra (at 2 K) in the visible range of photoluminescence of 4H- and 6H-SiC directly after neutron irradiation.

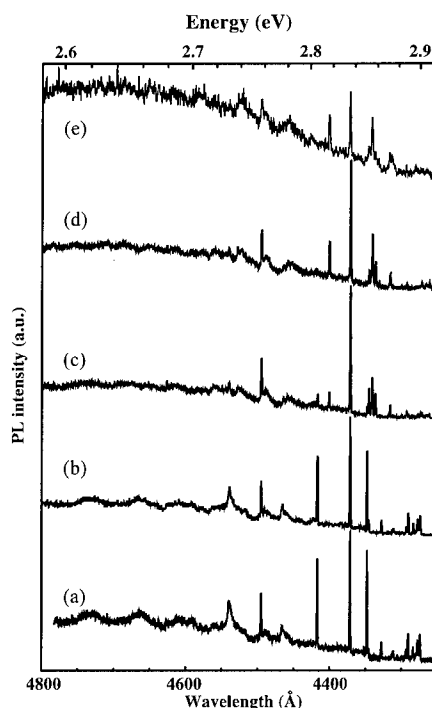


Fig. 2. LTPL spectra of 4H-SiC directly after neutron irradiation at different temperatures of measurement: (a) 2 K, (b) 7 K, (c) 21 K, (d) 43 K, and (e) 68 K.

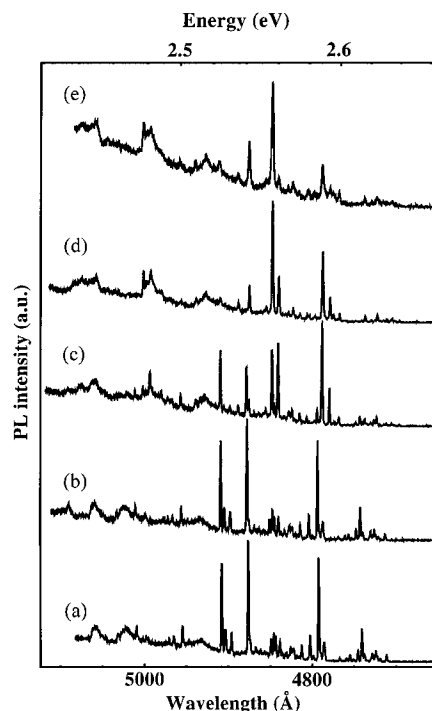


Fig. 3. LTPL spectra of 6H-SiC directly after neutron irradiation at different temperatures of measurement: (a) 2 K, (b) 6 K, (c) 21 K, (d) 43 K, and (e) 72 K.

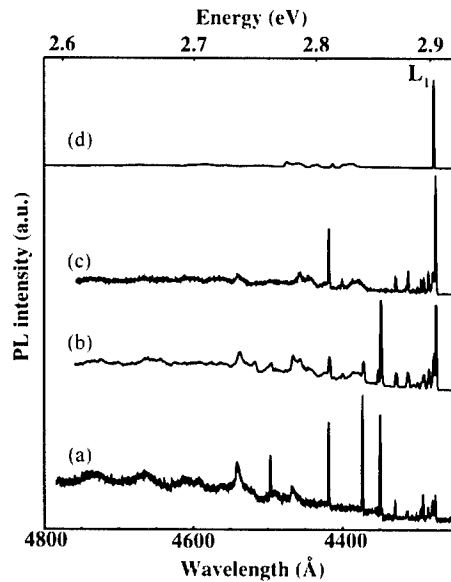


Fig. 4. LTPL spectra at 2 K of 4H-SiC directly after neutron irradiation and after different annealing temperatures: (a) as irr., (b) 600 °C, (c) 700 °C, and (d) 1200 °C.

4495 (Å) and in 6H: 4792, 4875, 4908 (Å). At 21 K we detect type r (4H: 4262, 4266, 4273, 4288, 4293, 4301, 4316, 4332, 4337, 4341, 4346, 4372 (Å); 6H: 4766, 4777, 4839, 4846 (Å)).

Furthermore we measured spectra after annealing at low temperatures (Fig. 4 for 4H; Fig. 5 for 6H). Most lines arise after annealing at less than 600 °C, only few decrease in this range. After annealing above 1000 °C all these lines are vanishing and only the well known D_1 -defect [9] is detected. The D_1 -defect correlated emission consists in 4H-SiC of one line L_1 (4276 Å). In 6H-SiC it consists of three lines L_1 (4724 Å), L_2 (4789 Å), L_3 (4825 Å). Amazingly the D_1 -defect emission arises already at annealing temperatures < 600 °C. Especially in 6H-SiC in the well-known intensity distribution between the three lines; due to the fact that in 6H-SiC one hexagonal lattice site and two cubic lattice sites exist, whereas in 4H-SiC one cubic lattice site and one hexagonal site exist. Thus in 6H-SiC more emission lines are expected. But the experimental result that in 4H-SiC only one emission line for the D_1 -defect was observed is still not understood.

After small applied fluences of fast neutrons the well-known intensity distribution of the L lines dominates the LTPL spectrum at annealing temperatures above 1000 °C. After higher fluences of fast neutrons (approx. 10^{18} cm^{-2}) the distribution has changed [4] and after further annealing the distribution of the L-lines changes to the well-known spectrum.

After irradiation both spectra (Figs. 4 and 5) show three intensive lines (4H: 4348, 4372, 4417 (Å); 6H: 4792, 4876, 4908 (Å)). At the high energetic part of the spectra

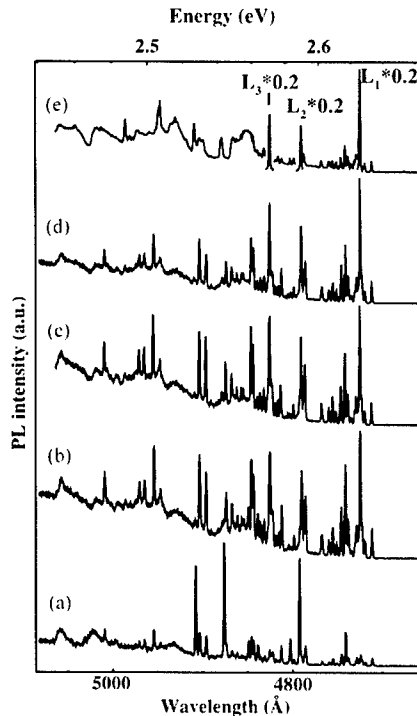


Fig. 5. LTPL spectra at 2 K of 6H-SiC directly after neutron irradiation and after different annealing temperatures: (a) as irr., (b) 700 °C, (c) 750 °C, (d) 800 °C, and (e) 1000 °C—here the intensity of the D_1 -defect is reduced by a factor of five.

there is a group of weak lines (after the thermal behaviour designed as type v). In 6H-SiC we find in between the strong lines some weaker ones at 4796, 4803, 4813, 4816, 4818, 4822, 4825, 4831, 4836, 4839, 4843, 4846, 4849, 4854, 4857, 4862, 4867, 4891, 4896, 4904 (Å). As well at the lower energetic side (4H: 4466, 4495; 6H: 4932, 4937, 4947, 4955, 4960, 4965, 4970, 4974, 4980, 4983, 4987, 4991, 4997, 5002, 5009, 5023, 5031, 5057 (Å)).

Electrical measurements on 4H-SiC pn-junctions (Fig. 6) were carried out, demonstrating that the pn-junction generated with few fast neutrons has in forward direction below the built-in potential a very low current density. The sample with a higher applied fluence of fast neutrons shows after annealing at 1500 °C a comparably low forward current density even above the built-in potential. After annealing at 1600 °C there is no current flow beneath the built-in potential within the detection limit.

4. Discussion

After irradiation with thermal neutrons the SiC samples are expected to have numerous defects of

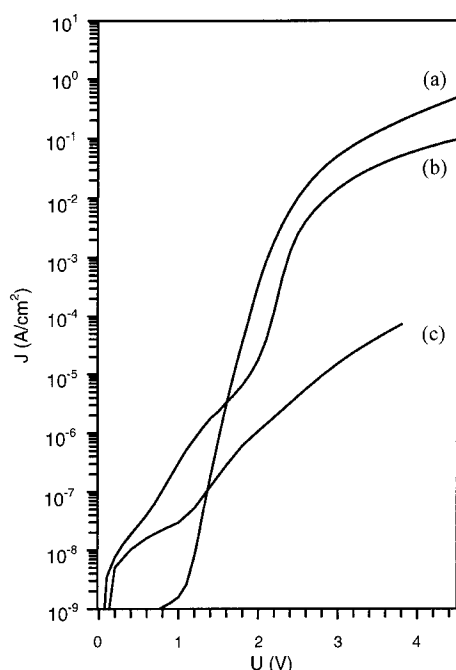


Fig. 6. Current density over voltage in forward direction for samples with equal net doping but with different applied fluences of fast neutrons and different annealing temperatures: (a) $8 \times 10^{16} \text{ cm}^{-2}$ fast neutrons and 1600°C , (b) $5 \times 10^{15} \text{ cm}^{-2}$ and 1500°C , (c) $8 \times 10^{16} \text{ cm}^{-2}$ and 1500°C .

different nature. Applying thermal energy with different annealing temperatures the SiC becomes the chance to reorganize the defects in terms of the formation energies of single defects. This process ends with a nearly ideal structure and with some residual complex defect structures. In this sense, it is not surprising that one gets first a big zoo of lines from LTPL investigations which end up in the D_1 -defect above 1000°C . But it is amazing that SiC, praised to show long time stability up to 700°C [10,11], obviously begins to recover defects at much lower temperatures, if radiation defects are previously introduced.

Additionally we found pn-junctions with nearly ideal I - V curves in forward direction after annealing at 1600°C . After an annealing step of 1400°C with the

applied fluence of fast neutrons of $8 \times 10^{16} \text{ cm}^{-2}$ the pn-junction is not created yet. After 1500°C annealing the comparison of samples with applied fluences of fast neutrons which differ by a factor of 16 show a big difference in forward direction although the fast fluence is just a factor 2×10^{-3} of the thermal fluence necessary for doping.

Acknowledgements

We thank the irradiation groups of the FRG and the FRJ and the BER-reactors at the GKSS, KFA, HMI in Geesthacht, Jülich, Berlin for good cooperation. Further we thank Dr. K.P. Frohmader and Mr. Wadehn for their support with photolithography.

References

- [1] M.A. Capano, J.A. Cooper, M.R. Melloch, A. Saxler, W.C. Mitchel, *J. Appl. Phys.* 87 (2000) 8773.
- [2] M.A. Il'in, M.G. Kosaganova, V.N. Solomatin, Yu.V. Barinov, Yu.V. Bulgakov, *Sov. Phys. Semicond.* 5 (1971) 506.
- [3] E.N. Kalabukhova, S.N. Lukin, E.N. Mokhov, *Phys. Sol. State* 35 (1993) 361.
- [4] H. Heissenstein, C. Peppermüller, R. Helbig, *J. Appl. Phys.* 83 (1998) 7542.
- [5] H. Heissenstein, H. Sadowski, C. Peppermüller, R. Helbig, *Mater. Sci. Forum* 338–342 (2000) 853.
- [6] S. Tamura, T. Kimoto, H. Matsunami, M. Okada, S. Karazawa, I. Kimura, *Mater. Sci. Forum* 338–342 (2000) 849.
- [7] C. Peppermüller, R. Helbig, A. Schoener, K. Rottner, *Appl. Phys. Lett.* 70 (1997) 1014.
- [8] N.T. Son, E. Sörman, M. Singh, W.M. Chen, C. Hallin, O. Kordina, B. Monemar, J.L. Lindström, E. Janzen, *Diamond Relat. Mater.* 6 (1997) 1372.
- [9] W.J. Choyke, L. Patrick, *Phys. Rev. B* 5 (1972) 3253.
- [10] A. Lloyd Spetz, A. Baranzahi, P. Tobias, I. Lundström, *Phys. Stat. Sol. A* 162 (1997) 493.
- [11] A.K. Agarwal, P.A. Ivanov, M.E. Levinshtein, J.W. Palmour, S.L. Rumyantsev, S.H. Ryu, M.S. Shur, *Mater. Sci. Forum* 353–356 (2001) 703.



ELSEVIER

Physica B 308–310 (2001) 706–709

PHYSICA B

www.elsevier.com/locate/physb

Characterization of deep centers in bulk n-type 4H–SiC

Z.-Q. Fang^{a,b}, D.C. Look^{a,b}, A. Saxler^a, W.C. Mitchel^{a,*}^a Air Force Research Laboratory, AFRL/MLPS, W-PAFB, 3005 P. St. Rm243, OH 45433-7707, USA^b Semiconductor Research Center, Wright State University, Dayton, OH 45435, USA

Abstract

Nitrogen-related shallow centers and defect- and impurity-related deep centers in nitrogen doped bulk n-type 4H–SiC were characterized by high temperature Hall effect and deep level transient spectroscopy (DLTS) measurements. Two nitrogen centers at $E_c - 0.048$ and -0.098 eV, with a concentration close to each other, and a poorly resolved deep donor level, with activation energy of 0.58 eV, were found by fitting the Hall-effect data. A dominant DLTS deep center is observed at $E_c - 0.61 - 0.63$ eV due to electric field effect, with a concentration of $\sim 1.2 \times 10^{15} \text{ cm}^{-3}$. The center is believed to be the Z_1 center (also called $Z_1/Z_2(4H)$), which is often observed in as-grown and implanted or irradiated 4H–SiC epilayers and is speculated to be a vacancy-type defect. Correlation between the Hall effect deep donor and Z_1 suggests that Z_1 is donor-like. © 2001 Elsevier Science B.V. All rights reserved.

Keywords: Bulk 4H–SiC; Nitrogen levels; Intrinsic and extrinsic defects; DLTS

1. Introduction

Silicon carbide (SiC) is of interest for high-temperature, high-power, and high-frequency devices. Besides shallow dopants, intrinsic and extrinsic defects are present in SiC, giving rise to deep centers in the band gap. These deep centers may act as electron and hole traps or recombination centers, and affect the performance of devices. Electrical data obtained mainly from deep level transient spectroscopy (DLTS) studies on intrinsic deep centers and extrinsic deep centers in the 3C-, 4H-, and 6H–SiC polytypes have been well reviewed [1,2]. Most of the materials mentioned in the reviews are epilayers, grown by chemical vapor deposition (CVD). It is desirable to study deep centers in the substrates as well and to understand their origins. In this study, Schottky barrier diodes (SBDs) made on a bulk n-type 4H–SiC sample were characterized by capacitance–voltage ($C-V$), DLTS measurements, and temperature dependent Hall effect (TDH) measurements were

performed on an adjacent sample. From fitting Hall-effect data, two nitrogen related centers at near $E_c - 0.05$ and -0.1 eV, and a poorly resolved deep donor level with activation energy of 0.58 eV can be revealed. A dominant DLTS deep center at $E_c - 0.61 - 0.63$ eV, with a concentration of $\sim 1.2 \times 10^{15} \text{ cm}^{-3}$, was found and is believed to be related to the intrinsic defect-related Z_1 center (also referred to as $Z_1/Z_2(4H)$). This is believed to be the first correlation between DLTS and Hall effect for a deep level in SiC. Also, the correlation suggest that, contrary to previous reports, the Z_1 level is donor-like.

2. Experimental and results

The samples used in this study were cut from an n-type 4H–SiC boule, grown along the c -axis by physical vapor transport technique at Cree Inc. A square sample approximately 0.75 cm on a side was cut for resistivity and Hall effect measurements. Contacts were Au on Ni/Cr annealed at 925°C. For the SBD sample, Schottky contacts were unannealed Al dots with diameters of 500 μm , which were surrounded by a large area Al ohmic contact. A Bio-Rad DL4600 system with a 100 mV test signal at 1 MHz was used to take $C-V$ and DLTS data.

*Corresponding author. Tel.: +1-937-255-4474; fax: +1-937-255-4913.

E-mail address: william.mitchel@wpafb.af.mil (W.C. Mitchel).

To determine the activation energy E_T of deep centers, the DLTS spectra were taken at different rate windows, from 4 to 200 s⁻¹, and were analyzed by the standard Arrhenius technique.

TDH measurements from 40 to 1000 K were made at a magnetic field of 5 KG. The electron concentration is plotted as a function of the reciprocal temperature in Fig. 1. From a least-squares fit of the charge neutrality equation, we are able to determine nitrogen donor activation energies and concentrations. The activation energies of nitrogen donors, N_h and N_c , substituting at hexagonal and cubic lattice sites, were found to be 0.048 and 0.098 eV, respectively. The corresponding nitrogen donor concentrations are 4.7×10^{16} and 4.3×10^{16} cm⁻³, with a ratio of concentrations (N_h/N_c) close to unity, which is expected for 4H-SiC [3]. In addition to two shallow nitrogen levels, a deep level with a concentration in the 10^{15} – 10^{16} cm⁻³ range and an activation energy of 0.58 eV can be poorly resolved.

Al-Schottky diodes show low leakage currents (~ 400 nA) at a reverse bias of -10 V, which enabled us to perform measurements at higher reverse biases and to observe electric-field effect on deep centers. To determine the near-surface carrier concentrations, we measured C - V characteristics at different temperatures, and carried out $1/C^2$ vs. V analyses. Plots of $1/C^2$ vs. V , obtained at temperatures of 200–400 K, are very good straight lines. Assuming a dielectric constant of 9.7 for 4H-SiC, the carrier concentrations at 200, 300, and 400 K are 4.1, 4.2, and 4.3×10^{16} cm⁻³, respectively. As compared to Hall-effect data, C - V results show a weaker temperature dependence, which we do not understand at present. From the intercept at $1/C^2 = 0$, 1.25 V at 300 K, the barrier height of Al on the n-type 4H-SiC was determined to be 1.43 eV. A typical DLTS

spectrum, measured at a reverse bias (V_b) of -9 V, a forward filling pulse height (V_f) of 0 V, and a filling pulse width (W_f) of 1 ms, is shown in Fig. 2. We see a dominant trap C at around room temperature, and some other traps at high temperatures (A and B) and at low temperatures (trap D and unsolved traps E, and F). The concentration of trap C can be as high as 1×10^{15} cm⁻³, while the concentrations of other traps are in low 10^{14} cm⁻³ range. Arrhenius plots of T^2/e_n vs. $10^3/T$ for traps A, B, C, and D are presented in Fig. 3, from which their activation energies were determined to be 0.89, 0.74, 0.61, and 0.40 eV, respectively. To investigate the electric-field effect on the dominant center, we performed DLTS measurements in two different ways. One set of spectra was measured by varying V_f , but keeping V_b (-9.0 V) unchanged; and the other by changing V_b , but keeping V_f constant at 0 V. The resultant DLTS spectra, measured as a function of V_f and V_b , are shown in Figs. 4a and b, respectively. In two cases, we see a peak shift of the dominant center to lower temperatures, as V_f increases from -6 to $+1$ V (Fig. 4a), and as V_b changes from -2 to -9 V (Fig. 4b). Both shifts

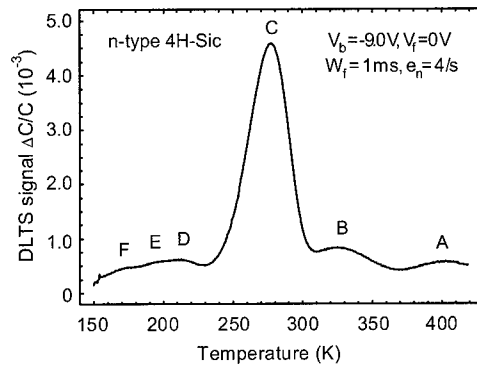


Fig. 2. Typical DLTS spectrum measured at the temperature range from 150 to 420 K.

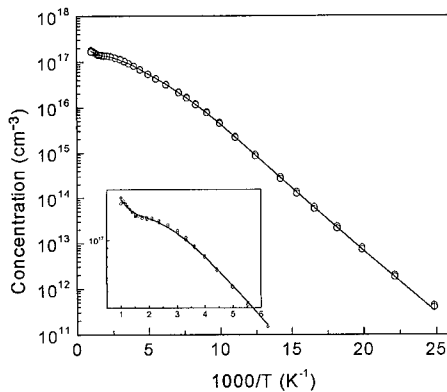


Fig. 1. Carrier concentration vs. inverse temperature from Hall effect. Solid line is fit to charge neutrality equation for three donor levels. Inset: expanded view of high temperature data showing presence of deep level after full activation of the nitrogen levels.

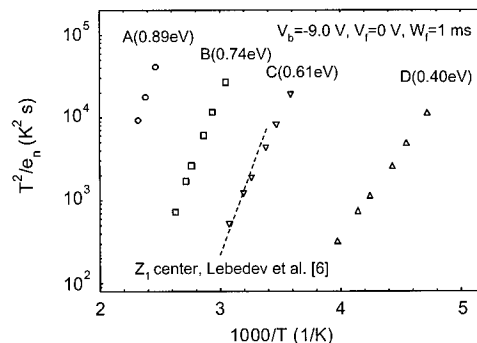


Fig. 3. Arrhenius plots of T^2/e_n for deep centers observed in the bulk 4H-SiC sample.

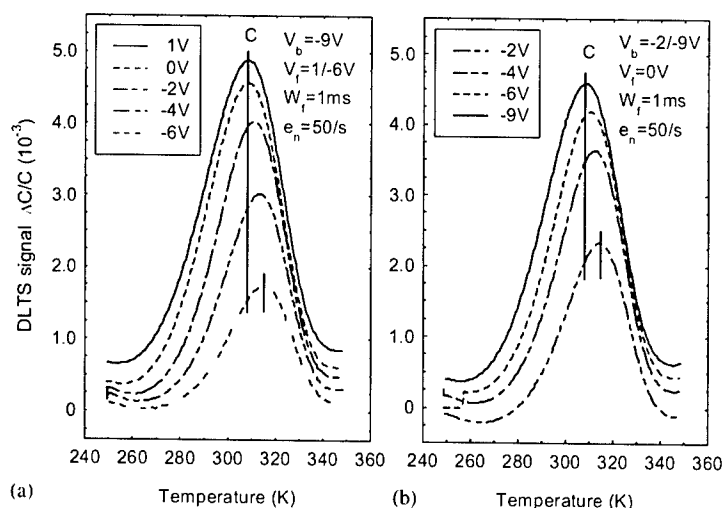


Fig. 4. DLTS spectra measured (a) as a function of V_f and keeping V_b (-9 V) unchanged; and (b) as a function of V_b and keeping V_f (0 V) constant.

correspond to an increase of average electric field in the depletion region. Under a high electric field, a trap peak should shift to lower temperatures due to the effective lowering of the potential well. The activation energies of the dominant trap were determined to be 0.61 eV for the high average field case, and 0.63 eV for the low average field case. The average electric fields are 3.5×10^5 V cm $^{-1}$ for the former case and $<1 \times 10^5$ V cm $^{-1}$ for the latter case.

3. Discussion

A center at $E_c - (0.63\text{--}0.68)$ eV, named the Z_1 center, has been reported in previous DLTS studies on 4H-SiC epilayers [1,2]. This defect has activation energy similar to that of a double-peak trap in bulk 6H-SiC, named the Z_1/Z_2 center, discovered by Zhang et al. [4]. In high quality CVD-grown 4H-SiC epilayers, Kimoto et al. [5] revealed that the Z_1 center was the only residual defect with concentrations in the 10^{13} cm $^{-3}$ range. While in 4H-SiC epilayers, Lebedev et al. [6] reported that the Z_1 concentration was shown to fall with decreasing net donor concentration and to be lower in layers with a high dislocation density. Here, in this study with n-type bulk 4H-SiC, we found a dominant trap with activation energy similar to that of Z_1 center and with a higher concentration compared to that in the epilayers. By trap fingerprint comparison (see Fig. 3), we believe that the dominant trap here is due to the Z_1 center. To understand the nature of the Z_1 center, many ion-implantation and irradiation studies have been performed [2]. It has been demonstrated that the Z_1 center, induced by H^+ -implantation, is acceptor-like and is

thermally stable up to 2015°C [7]. However, a recent report indicated that Z_1 (or $Z_{1/2}$) centers, generated by 2.9 MeV H^+ -irradiation, show a concentration drop at annealing temperature of 1300°C [8]. A current consensus is that the Z_1 center is related to a vacancy-type defect, however, whether it is a C-Si nearest-neighbor divacancy [9] or a C vacancy [10] is still an open question. The conclusion of acceptor-like nature of Z_1 was deduced from double DLTS investigations, where the peak position of Z_1 showed no change with varying electric field [7]. This observation is in contrast with what we found in this study. The fact that the activation energy of trap C shows a clear dependence on electric field implies that the Z_1 center might consist of two components, each with an opposite charge state. The fact that the Z_1 center is the only deep center observed in this material with concentration high enough to correspond to the deep donor seen in Hall effect experiments suggests that the two experiments are observing the same defect level. This suggests that Z_1 is donor-like, since an acceptor-like defect would not be observed in Hall effect in n-type material.

Transition metals produce electrically active deep centers in the band gap of semiconductors. In an early study of SiC substrates, V, Cr, Fe and Ti were found in high concentration compared to other residual impurities [11]. By V^{3+} - and Ti^{3+} -implantation [2], and Cr-isotope doping [12], the deep centers, induced by these metals in 4H-SiC epilayers, were characterized by DLTS. Vanadium is an amphoteric impurity, leading to formation of both donor and acceptor levels. An acceptor-like deep center V_1/V_2 at $E_c - (0.88\text{--}0.97)$ eV in V^+ -implanted 4H-SiC epilayers was reported [2]. Recently, V doping, known as a compensating donor,

was demonstrated to be useful in growth of semi-insulating SiC crystals [13]. Three Cr-related deep centers at $E_c-0.15$, -0.18 and -0.74 eV were reported [12]. By comparing with these literature data, two deep traps found in this study, A at $E_c-0.89$ eV and B at $E_c-0.74$ eV, might be due to residual impurities V and Cr, respectively. The trap D and unsolved traps, E and F, at or below $E_c-0.40$ eV, might be related to impurity-defect complexes or simply intrinsic defects, as suggested in Ref. [2].

4. Summary

Nitrogen-related centers and deep centers in nitrogen doped bulk 4H-SiC were characterized by TDH and DLTS measurements. Two nitrogen-related centers, each with a concentration of $\sim 4.5 \times 10^{16} \text{ cm}^{-3}$, were found at $E_c-0.048$ eV and $E_c-0.098$ eV, respectively. A poorly resolved deep center with activation energy of 0.58 eV was also revealed by the TDH measurement. A dominant DLTS center in the material is at $E_c-0.61-0.63$ eV and with a concentration of $\sim 1.2 \times 10^{15} \text{ cm}^{-3}$, which shows a clear electric field effect and is believed to be an intrinsic defect-related Z_1 center. The Z_1 center is believed to be donor-like. Two deeper centers, observed at $E_c-0.74$ and -0.89 eV and with concentrations in the low- 10^{14} cm^{-3} range, might be due to residual impurities Cr and V, respectively. Other centers, found at or below $E_c-0.40$ eV and with concentrations also in the low 10^{14} cm^{-3} range, are thought to be associated with defect-impurity complexes.

Acknowledgements

The work of Z.-Q. F. and D.C. L. was supported by the Air Force Office of Scientific Research (AFOSR), under

Contract No. F49620-00-1-0347, and the Air Force Research Laboratory, under Contract No. F33615-00-C-5402.

References

- [1] A.A. Lebedev, *Semiconductors* 33 (1999) 107.
- [2] T. Dalibor, G. Pensl, H. Matsunami, T. Kimoto, W.J. Choyke, A. Schöner, N. Nordell, *Phys. Status Solidi A* 162 (1997) 199.
- [3] W. Götz, A. Schöner, G. Pensl, W. Suttrop, W.J. Choyke, R. Steine, S. Leibenzeder, *J. Appl. Phys.* 73 (1993) 3332.
- [4] H. Zhang, G. Pensl, A. Dröner, S. Leibenzeder, *ECS Extended Abstracts* 89 (2) (1989) 699.
- [5] T. Kimoto, A. Itoh, H. Matsunami, S. Sridhara, L.L. Clemen, R.P. Devaty, W.J. Choyke, T. Dalibor, C. Peppermüller, G. Pensl, *Appl. Phys. Lett.* 67 (1995) 2833.
- [6] A.A. Lebedev, D.V. Davydov, N.S. Savkina, A.S. Tregubova, M.P. Shcheglov, R. Yakimova, M. Syväjärvi, E. Janzén, *Semiconductors* 34 (2000) 1133.
- [7] T. Dalibor, C. Peppermüller, G. Pensl, S. Sridhara, R.P. Devaty, W.J. Choyke, A. Itoh, T. Kimoto, H. Matsunami, *Inst. Phys. Conf. Ser.* 142 (1996) 517.
- [8] L. Storasta, F.H.C. Carlsson, S.G. Sridhara, J.P. Bergman, A. Herry, T. Egilsson, A. Hallén, E. Janzén, *Appl. Phys. Lett.* 78 (2001) 46.
- [9] L. Patrick, W.J. Choyke, *Phys. Rev. B* 5 (1972) 3253.
- [10] A.A. Lebedev, A.I. Veinger, D.V. Davydov, V.V. Kozlovskii, N.S. Savkina, A.M. Strel'chuk, *Semiconductors* 34 (2000) 1058.
- [11] A. Uddin, H. Mitsuhashi, T. Uemoto, *Jpn. J. Appl. Phys. Part 2*, 33 (1994) L908.
- [12] N. Achtziger, J. Grillenberg, W. Witthuhn, *Mat'ls Sci. Forum* 264–268 (1998) 541.
- [13] H.McD. Hobgood, R.C. Glass, A. Augustine, R.H. Hopkins, J. Jenny, M. Skowronski, W.C. Mitchel, M. Roth, *Appl. Phys. Lett.* 66 (1995) 1364.



ELSEVIER

Physica B 308–310 (2001) 710–713

PHYSICA B

www.elsevier.com/locate/physb

Photoluminescence study of beryllium implantation induced intrinsic defects in 6H-silicon carbide

S. Fung^{a,*}, X.D. Chen^a, C.D. Beling^a, Y. Huang^a, Q. Li^a, S.J. Xu^a, M. Gong^b,
T. Henkel^c, H. Tanoue^c, N. Kobayashi^c

^aDepartment of Physics, University of Hong Kong, Hong Kong, People's Republic of China

^bDepartment of Physics, Sichuan University, Chengdu, People's Republic of China

^cElectrotechnical Laboratory, Tsukuba, Ibaraki 305-8568, Japan

Abstract

Beryllium was implanted into both n- and p-type 6H-SiC and the samples were subsequently annealed at 1600 °C. Photoluminescence (PL) measurements were performed and PL lines at 420 and 472 nm were observed. The PL lines at around 420 nm have been detected from various ion implanted SiC samples and have been attributed to transitions involving some implantation induced intrinsic defect labeled as D_{II}. The present observation of the PL lines at 420 nm from Be implanted 6H-SiC supports the intrinsic model that D_{II} might be a carbon-di-interstitial defect. The lines at 472 nm labeled as D_I in the PL spectra have previously been identified as divacancy defect (V_{Si} – V_C). We note that it was suggested that the electron traps labeled Z₁/Z₂ observed in deep level transient spectroscopy (DLTS) were due to the same divacancy defect. In our experiments, while the D_I series PL lines are prominent, DLTS results from the same samples show no Z₁/Z₂ related peaks. The PL and DLTS results seem to be against the possibility that Z₁/Z₂ arise from the same defect. © 2001 Elsevier Science B.V. All rights reserved.

Keywords: Photoluminescence; Beryllium; Defects; 6H-SiC; Implantation

1. Introduction

Ion implantation is an important process for silicon carbide (SiC) device technology as it allows selective doping of n- and p-type dopants. The detection and identification of dopants and implantation induced defects is one of the major tasks in order to control the characteristics of SiC material for device design and fabrication. Together with the electrical methods such as the Hall effect and deep level transient spectroscopy (DLTS), the optical photoluminescence (PL) method is powerful and successful in this kind of investigation.

SiC doped with aluminum (Al), gallium (Ga), and boron (B), etc. has been intensively investigated by using electrical and optical measurement methods in the past

[1–6]. Recently, beryllium (Be) was successfully applied in the fabrication of SiC diodes [7,8]. A better forward characteristics was obtained in comparison with Al and B implanted pn junctions [7]. Electrical measurements such as current–voltage, DLTS, Hall effect on Be implanted or diffused 6H-SiC have been reported [7–9]. However, data from optical measurement like PL are relatively scarce. Be has been reported to be an effective luminescence activator when diffused into 6H-SiC [10]. Further, more than three series of PL lines were detected and are thought to be related to Be implantation [7]. Detailed assignment concerning the PL lines from either Be dopant or implantation induced intrinsic defects is still lacking. In the present work, Be was implanted into both n- and p-type 6H-SiC with both high and low doses at room temperature followed by annealing at 1600 °C. In this article, we report PL observations of the Be implantation induced intrinsic defects in 6H-SiC samples.

*Corresponding author. Fax: +86-852-2859-8972.

E-mail address: sfung@hkucc.hku.hk (S. Fung).

2. Experiment

The SiC samples used in our experiment are commercially available epiwafers from CREE Research Inc. For the starting n-type 6H-SiC (0001), a 10- μm -thick nitrogen doped epilayer was grown on n⁺-type 6H-SiC substrate with chemical vapor deposition (CVD). The nitrogen (N) donor concentrations were 1×10^{16} and $8 \times 10^{17} \text{ cm}^{-3}$ in the epilayer and the substrate, respectively. For the p-type 6H-SiC (0001), there is a 5- μm -thick Al doped epilayer grown on p⁺-type 6H-SiC substrate. The Al acceptor concentrations were 1×10^{16} and $1 \times 10^{18} \text{ cm}^{-3}$ in the epilayer and substrate, respectively. 50–590 keV Be implantation was carried out at room temperature to obtain a box-shaped profile with a mean concentration of Be about $1 \times 10^{19} \text{ cm}^{-3}$ (termed “high-dose Be” implantation hereafter) both into n- and p-type samples. To repair the implantation induced damage and activate the Be dopant, post-implantation annealing was performed in flowing argon gas at 1600°C for 1 min using a rapid thermal annealing (RTA) system.

For a comparison study, a lower Be concentration of about $1 \times 10^{18} \text{ cm}^{-3}$ (termed “low-dose Be” implantation hereafter) were also implanted into both n- and p-type 6H-SiC samples. The same multiple energy implantation schedule as for the high-dose Be implantation was employed. RTA was performed at 1600°C for 30 s under similar conditions as stated previously. Table 1 presents an overview of the preparation parameters for the different samples.

For PL measurements, the excitation was done with a He–Cd laser operating at a wavelength of 325 nm. PL measurement was performed at temperature $T = 3.5 \text{ K}$. The PL emission was analyzed with a SPEX750 M single gratings (1200 lines/mm) monochrometer and detected with a Hamamatsu R928 photomultiplier.

3. Results and discussion

A comparison of the PL spectra at 3.5 K of the high- and low-dose Be implanted n- and p-type 6H-SiC samples is shown in Fig. 1. The lines labeled by 4N₀ from n-type samples are related to bound exciton

recombination at a four-particle neutral nitrogen donor at the three inequivalent lattice sites. On the other hand, the PL lines labeled by 4Al₀ from p-type samples are attributed to the bound exciton recombination at a four-particle neutral Al acceptor lattice sites of the 6H-SiC unit cell. Both groups of PL lines have been intensively investigated and clearly identified in previous literatures [1,2], and are commonly used as indicators for the presence of N and Al dopants in SiC, respectively.

The PL peak at around 420 nm is detected in both n- and p-type Be implanted samples. At higher spectral resolution, the 420 nm peak can be resolved into at least two lines at 420.3 and 420.5 nm. Compared with 4N₀ or 4Al₀, the PL line intensity are stronger in high-dose Be implanted samples, indicating the dependence on the ion implantation doses. It should be noted that there is a weak line relative to 4N₀ at 420.3 nm in the PL spectra of the control samples as also reported in most literatures [1,2], which was labeled by I₇₇ at the same wavelength. The I₇₇ line was identified as a recombination at a free exciton (FE). It is a good indicator of

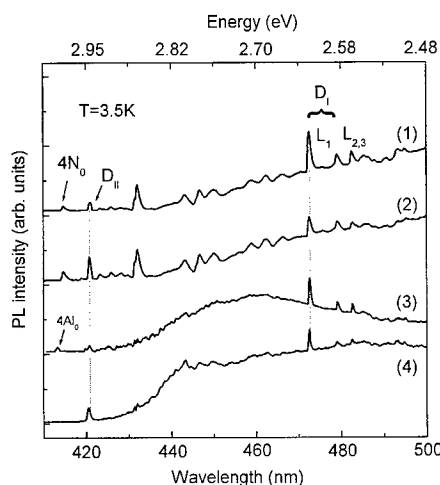


Fig. 1. PL spectra of Be implanted n- and p-type 6H-SiC. (1) Low-dose Be implanted n-type 6H-SiC; (2) High-dose Be implanted n-type 6H-SiC; (3) Low-dose Be implanted p-type 6H-SiC; (4) High-dose Be implanted p-type 6H-SiC. Implantation was at room temperature and annealing was carried out at 1600°C.

Table 1

Preparation conditions of various Be implanted n- and p-type 6H-SiC samples

Sample number	1	2	3	4
Sample type before implantation	n-type	n-type	p-type	p-type
Sample terms as mentioned in the text	Low-dose Be n-type	High-dose Be n-type	Low-dose Be p-type	High-dose Be p-type
Mean con. of Be (atoms/cm ³)	$\sim 1 \times 10^{18}$	$\sim 1 \times 10^{19}$	$\sim 1 \times 10^{18}$	$\sim 1 \times 10^{19}$
Duration of annealing at 1600°C	30 s	1 min	30 s	1 min

crystal quality [11]. However, in the present Be implantation experiment, the PL lines at 420.3 and 420.5 nm which depend on the ion doses should be attributed to Be implantation induced new PL activator rather than the I_{77} free exciton with the same wavelength.

Recently, based on the observation of the same spectrum in different ion implanted 6H-SiC samples, the PL lines were proposed to be due to an intrinsic defect labeled as D_{II} induced by ion implantation. Moreover, together with the observation of high energy localized modes beyond the lattice limit of 120 meV, the D_{II} center was suggested to be carbon-di-interstitial [6]. The present PL spectrum of Be implanted 6H-SiC gives further information and strongly supports the intrinsic modes of D_{II} center induced by ion implantation. Subsequently, the high intensity of 420.3 and 420.5 nm lines from high-dose Be implantation samples is expected since high-dose ion implantation will produce more such defect centers.

The PL emission lines labeled as L_1 , L_2 , and L_3 at around 472 nm are prominent in the PL spectrum as shown in Fig. 1. These lines called D_I -center were regularly found in 6H-SiC after implantation of ions, electrons, etc. and subsequent annealing at $T > 900^\circ\text{C}$. [1,2] Although the microscopic structure of this D_I -center is still a matter for discussion, there is a mounting evidence that it is due to the $V_{Si}-V_C$ divacancy [12]. On the other hand, it should be pointed out that deep levels at $E_c-0.62/0.72$ eV labeled as Z_1/Z_2 in DLTS spectra have been reported and speculated as the same as divacancy ($V_{Si}-V_C$) on inequivalent lattice sites in as-grown, high-energy particle irradiated or ion implanted SiC [13,14]. Zhang et al. demonstrated that the Z_1/Z_2 centers can be generated either by irradiation with high-energy electrons or by ion implantation and that it is thermally stable up to at least 1700°C [13]. However, recently the identification was questioned based on the studies of thermal annealing behaviors of Z_1/Z_2 that almost disappear with post-irradiation annealing temperature below 1000°C [14,15]. In the present experiment, we have conducted DLTS study of the identical samples. Fig. 2 displays the DLTS spectrum of the low-dose Be implanted 6H-SiC with post-implantation annealing at 1600°C . It can be seen that no obvious DLTS peaks related to Z_1/Z_2 was observed. However, as shown in Fig. 1, the L_1 , L_2 and L_3 lines of D_I -center are dominant in the PL spectra from all samples. These results are consistent with those observed for helium ion implanted n-type 6H-SiC using DLTS and PL techniques by Frank et al. [14] and strongly support the argument against that of Z_1/Z_2 and D_I -center was due to the same defect.

The microstructure of Z_1/Z_2 is still a matter for discussion. Aboelfotoch et al. reported that the two levels at $E_c-0.62/0.64$ eV which were associated with the

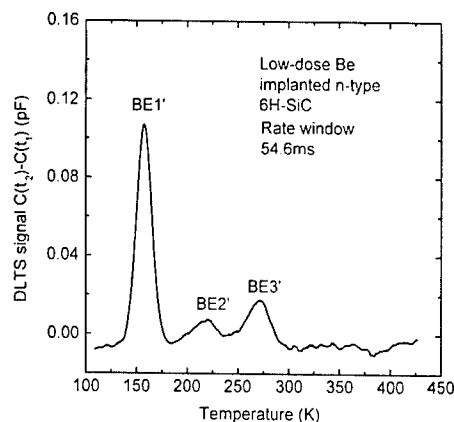


Fig. 2. DLTS spectrum of beryllium (low-dose Be) implanted n-type 6H-SiC with subsequent annealing at 1600°C .

Z_1/Z_2 centers in electron-irradiated n-type 6H-SiC were annealed out at around 850°C [16]. Based on the thermal annealing behaviors the two levels were assigned to be a defect involving a silicon vacancy occupying inequivalent sites in the 6H-SiC lattices.

Acknowledgements

The work described in this paper was partially supported by the grants from the Research Grant Council of the Hong Kong Special Administrative Region, China (under project no. HKU7137/99P).

References

- [1] G. Pensl, W.J. Choyke, Phys. B 185 (1993) 264.
- [2] P.R. Devaty, W.J. Choyke, Phys. State Sol. A 162 (1997) 5.
- [3] M. Ikeda, H. Matsunami, T. Tanaka, Phys. Rev. B 22 (1980) 2842.
- [4] A. Henry, C. Hallin, I.G. Ivanov, J.P. Bergman, O. Kordina, U. Lindefelt, E. Janzén, Phys. Rev. B 53 (1996) 13503.
- [5] C. Peppermüller, R. Helbig, K. Rottner, A. Schöner, Appl. Phys. Lett. 70 (1997) 1014.
- [6] S.G. Sridhara, D.G. Nizhner, R.P. Devaty, W.J. Choyke, T. Dalibor, G. Pensl, T. Kimoto, Mater. Sci. Forum 264 268 (1998) 493.
- [7] N. Ramungul, V. Khemka, Y. Zheng, R. Patel, T.P. Chow, IEEE Tran. ED 46 (1999) 465.
- [8] X.D. Chen, S. Fung, C.D. Belling, M. Gong, T. Henkel, H. Tanoue, N. Kobayashi, J. Appl. Phys. 88 (2000) 4558.
- [9] Y.A. Vadakov, G.A. Lomakina, E.N. Mokhov, V.G. Oding, E.I. Radovanova, Sov. Phys. Solid State 20 (1978) 258.
- [10] V.I. Sokolov, V.V. Makarov, E.N. Mokhov, G.A. Lomakina, Y.A. Vadakov, Sov. Phys. Solid State 10 (1969) 2383.

- [11] A. Henry, O. Kordina, C. Hallin, C. Hemmingsson, E. Janzén, *Appl. Phys. Lett.* 65 (1994) 2457.
- [12] L. Patrick, W.J. Choyke, *Phys. Rev. B* 5 (1972) 3253.
- [13] H. Zhang, G. Pensl, A. Dömer, S. Leibenzeder, *The Electrochemical Society, Extended Abstract* 89 (2) (1989) 699.
- [14] T. Frank G. Pensl, S. Bai, R.P. Devaty, W.J. Choyke, *Proceedings of the 11th International Conference on Silicon Carbide and Related Materials (ICSCRM'99)*, NC, 1999.
- [15] M. Gong, S. Fung, C.D. Beling, Z. You, *J. Appl. Phys.* 85 (1999) 7604.
- [16] M.O. Abouelfotoh, J.P. Doyle, *Phys. Rev. B* 59 (10) (1999) 823.



ELSEVIER

Physica B 308–310 (2001) 714–717

PHYSICA B

www.elsevier.com/locate/physb

Luminescence characterization of titanium related defects in 6H–SiC

Yu.M. Suleimanov^a, I. Zaharchenko^a, S. Ostapenko^{b,*}^aTaras Shevchenko University, Kiev, Ukraine^bCenter for Microelectronics Research, University of South Florida, 4202 E Fowler Avenue, Tampa, FL 33620, USA

Abstract

Photoluminescence (PL), thermally stimulated luminescence (TSL) and their photo-excitation spectra in hexagonal type SiC were studied between the temperatures of 5 and 300 K. Titanium related TSL glow peak is observed close to 140 K in compensated crystals 6H–SiC with corresponding thermal ionisation energy of a trap close to 170 meV. The spectral distribution of TSL has a maximum at 1.8 eV in 6H–SiC and 2.43 eV in 4H–SiC. A specific structure in the photo-excitation spectrum of PL close to the exciton gap $E_{\text{ex}} = 3.023$ eV is revealed, exclusively in 6H–SiC material. This indicates an essential role of excitons in the resonance energy transfer to the Ti-related centers in silicon carbide. The results are discussed in a model of isoelectronic centers composed of either individual Ti atoms or Ti–N pair representing a complex of the electronic trap and recombination center. © 2001 Elsevier Science B.V. All rights reserved.

Keywords: Defect state; Silicon carbide; Transition metals; Titanium

1. Introduction

In the photoluminescence (PL) spectrum of silicon carbide (SiC) a broad 'green' band with maximum at 2.43 eV is observed [1]. This band is accompanied with a set of narrow lines on the short-wavelength shoulder at low temperatures. These lines have been named as ABC-spectrum and has a relevance to Ti impurity. The PL spectrum of the green band is similar in SiC polytypes while the ABC-spectrum is various. The origin of the green luminescence in 6H–SiC has been a subject of numerous investigations. Three narrow zero-phonon lines (ZPLs) A_0 , B_0 and C_0 were interpreted as bound exciton recombination at a neutral isoelectronic center [2], which was finally attributed to Ti impurity [3]. Until now the interpretation of Ti-related PL spectrum is controversial. The most comprehensive results on the electronic structure of luminescence center can be obtained with the methods of magnetic resonance, specifically optically detected magnetic resonance

(ODMR). Initial identification of the Ti as isolated impurity atom was performed using ODMR [4]. EPR identification of titanium–nitrogen pairs (Ti–N)⁰ in 6H–SiC was made in Ref. [5]. In these papers, authors found a correlation between excited triplet states [4] or three signals with the spin $\frac{1}{2}$ [5] and A_0 , B_0 , and C_0 lines of luminescence spectrum.

We report on PL, thermally stimulated luminescence (TSL) and photoluminescence excitation (PLE) study in 6H– and 4H–SiC crystals. PLE spectroscopy is applied to reveal details of electronic energy transfer within complex PL center.

2. Experiment

Applying the procedure of a selective photoexcitation, we used two grating spectrometers, one of them coupled with xenon or tungsten lamp was used as an excitation source and the second spectrometer coupled to photomultiplier served for PL spectroscopy. The system recorded PL and PLE spectra with a resolution of 0.015 and 0.04 nm, respectively. Combining polarization of the excitation light and the luminescence, we

*Corresponding author. Tel.: +1-813-974-2031; fax: +1-813-974-3610.

E-mail address: ostapenko@eng.usf.edu (S. Ostapenko).

deconvoluted the green PL band in both polytypes of SiC into three elementary spectra assigned as A, B, and C series. PLE spectra of the individual ZPLs A₀, B₀, and C₀ were obtained separately. These data are consistent with ODMR results [4].

Fig. 1 shows the high-energy parts of the 'elementary' PL spectra and low-energy part of PLE spectrum for each of A, B and C series. These spectra can be attributed to intra-center transitions of two types of defects. One of these defects is an isolated impurity atom of Ti (A spectrum and C spectrum), and the other defect includes nearest neighbour Ti–N pair (B spectrum).

To observe TSL signal, a sample was illuminated with 337 line of the N₂ laser at 77 K. After initial 60 s decay, the sample was heated up at rates of 0.5 or 0.2 K/s. PL and TSL signals were recorded on the 0.4 m spectrometer with a resolution of 3 nm to obtain the spectral distribution of TSL. Fig. 2 shows low-temperature parts of glow curves n- and p-type samples with different compensation. All samples except n-type 6H–SiC were compensated by Ti impurity. The solid curves is for 6H polytype and the dashed curve corresponds to 4H–SiC. Solid and dotted glow curves represent spectrum in the region of 1.8 eV maximum, while the dashed curves in the region of 2.43 eV. Only one band with the maximum at 1.8 eV is observed in TSL of 6H–SiC. TSL spectra in 4H–SiC:Ti impurity are identical to the PL spectrum

with the maximum at 2.43 eV (Fig. 2). Spectral distributions of PL and TSL are shown in the insert.

3. Discussion

Performed experiments, especially on selective photo-excitation, revealed details of processes of the excitation and luminescence in Ti-related centers in SiC. PL spectra assigned as A and C, can be connected with different hole transitions in the bound exciton state of the same center (A-center) involving an isolated Ti atom. Such excitons are the excited states of the pseudo ion Ti (dⁿ) if a Colomby coupled hole is formed from Bloch waves of the valence band near the charged Ti (dⁿ⁺¹) ion (an excited state of the type of an 'acceptor exciton'—[dⁿ⁺¹ × h] in denotation of Ref. [6]).

We established that PLE series showed by dotted line in Fig. 1c as three maxima at 2.911, 2.930, and 2.949 eV is connected with excitation of C-spectra PL. Two other PLE series with identical energy interval of 19 meV have maxima at 2.868, 2.8865, 2.905, 2.9245, 2.944 eV (noted by single arrows) and 2.861, 2.880, 2.900 eV. These lines can be connected with the excitation of A spectrum. The head lines of these series at 2.911, and 2.868, 2.861 eV correspond the excitation of electron from different valence bands-Γ₇ (P_z) and Γ₉, respectively, into the

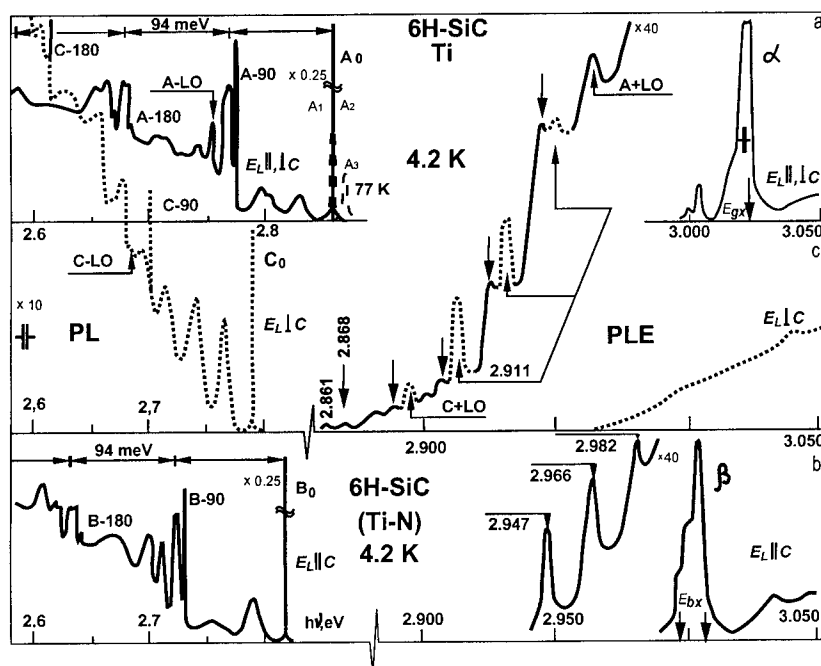


Fig. 1. PL spectra of elementary series composing green PL band in 6H–SiC:Ti (left). Low-energy region of PLE spectrum measured of the maximum of these band (right). Polarisation of excitation is $E_E \perp c$, polarisation of luminescence is performed—in two components $E_L \perp c$ and $E_L \parallel c$. c -direction of the crystallographic axis. Maximum in PLE spectra taken for $E_L \parallel c$ turned out to be connected to the excitation of the B spectrum, while the maxima marked by dotted lines in this spectrum taken for $E_L \perp c$ are connected with excitation of C-spectrum.

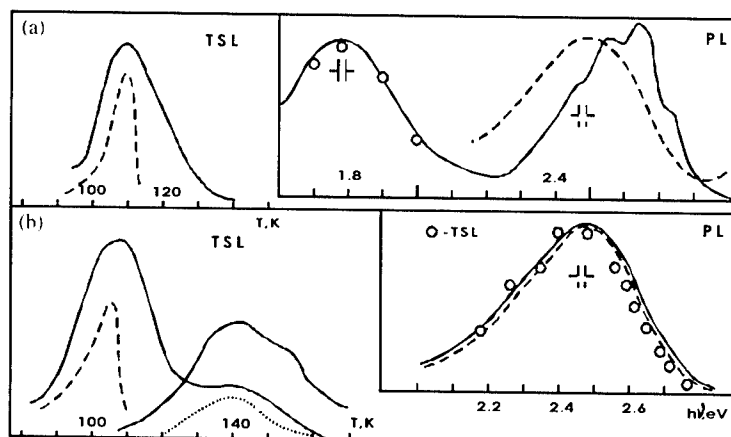


Fig. 2. Low-temperature parts of TSL glow curves of 6H –(solid and dotted lines) and 4H-(dashed lines) SiC corresponds to (a) n-type and (b) p-type conductivity. Dotted curve represents TSL after emptying of the nitrogen traps. In insert the spectral distribution of PL and TSL (circles).

d-orbitals of Ti (d^n). Indeed, these head lines are separated by 43–50 meV which is close to 53 meV $\Gamma_7 - \Gamma_9$ crystal field splitting Δ_{CR} in 6H-SiC. The energy separation of two PLE series 2868–2861 = 7 meV is very close to spin-orbit splitting of the Γ_9 valence band ($\Delta_{so} = 7.1$ meV [4]). Differences in the vibration structure of C and A luminescence spectra can be explained by different coupling of holes [4]. In such interpretation, vibration modes dominating in the PL spectra are determined by the symmetry of the hole wave function in the final state of optical transitions within A-center. Specifically 24.4 meV phonon replica in C spectrum shows a vibration structure of final states of this center with the hole corresponding to the $A_1(P_z)$ valence band symmetry. We suggest that three equally separated at 19 meV maxima in PLE spectrum at 2.947, 2.966, and 2.982 eV correspond to a softer vibration mode of electronic excited state in A center.

The continuous background under the structure of the discussed PLE spectrum is presumably a spectral distribution of the photo-excitation cross section of electrons (d^n/d^{n+1}) into d-orbitals of Ti impurity. The long-wavelength cut-off in this background at the energy at about 2.90 eV represents the level of Ti-related deep acceptor A^0/A^- above the valence band. This acceptor level links to the electron trap with energy $E_{trap} \approx 170$ meV estimated from TSL glow peak at the temperature 140 K (Fig. 2b). We suggest that a complex of the ionized $(Ti^0-N^+)^+$ pair is involved in PL and TSL. Indeed, ABC-spectra in 6H-SiC is observed only in p-type crystals, but EPR of $(Ti-N)$ pair-only in n-type. The photo-EPR spectra of a neutral $(Ti-N^+)^0$ were observed in highly compensated n-type SiC under broad band illumination [5]. The energy position of the Ti-related glow peak in 6H-SiC is consistent with the Ref. [5] where the energy level of $(Ti-N)^0$ pairs attributed to the level of nitrogen donor in this polytype.

In our study the glow peak with the maximum near 110 K (Fig. 2a and b) is connected with nitrogen trap with activation energy of 140 meV. A similar model of isoelectronic complex composed of deep acceptor and an electron trap was developed in GaP:N [7].

In 4H-polytype only one glow maximum in the region of 77–120 K is observed both in n-type and p-type Ti-doped crystals. The initial temperature of photo-excitation has to be reduced below than 77 K [8] to correctly estimate a depth of corresponding trap. We noticed the coincidence of PL and TSL spectra, which indicate a difference in the depth of the trap and level of excited state of Ti-related center in 4H-SiC.

Besides the band-to-band excitation, there are two possibilities of the photoexcitation of A-spectrum: (1) direct excitation to the lowest excited state of the A-center and (2) indirect excitation-to the level of deep acceptor, d^n/d^{n+1} . We found an efficient PL excitation through the α -maximum in PLE spectra of 6H-SiC (see Fig. 1a). This α -maximum is location in the region of the excitonic band gap, for this polytype $E_{gx} = 3.023$ eV. It is important, that in PLE of 4H-SiC the structure in the region of E_{gx} of this polytype (3.265 eV) is also exhibited however excitation efficiency is much lower. Individual lines in PLE spectra in the region of photon energies corresponding to the values of E_{gx} in both polytypes can be explained as free exciton scattering on titanium atoms. Indeed, substitution Ti, which is an isoelectronic impurity in SiC, can substantially change the exciton quasi-momentum by elastic scattering due to a short-range potential of Ti-center.

The PLE efficiency of A_0 line in 6H-SiC is of the order of magnitude higher in the α -maximum than under band-to-band excitation [9]. This can be explained by coincidence of the free exciton energy ($E_{gx} = 3.023 \pm 0.01$ eV) and the energy of the excited electronic state of the 'A-center' in 6H-SiC polytype

only. A mechanism of the resonance energy transfer from the free excitons to A-center is involved. The high efficiency of non-radiative energy transfer in isoelectronic impurities of rare-earth metals in II–VI compounds was shown in [10]. The spectral structure in PLE spectrum of the A_0 line in the 3.023–3.150 eV region represents electron transitions at the exciton states with the emission of phonons [11] and proved the participation of the free excitons in the excitation process of A-center.

A direct evidence on existence of (Ti–N) pair was presented by EPR in Refs. [5,12]. A strong β maximum at 3.003 eV (see Fig. 1b) in PLE spectra of B_0 line in the region of ZPL of the excitons bounded to the neutral N donors ('D₀X' complexes in terms of Ref. [2]), can be attributed to the (Ti–N) pair. Cross relaxation study between the excited triplet states of titanium and the ground state of nitrogen donors [13], also supports this identification. This study demonstrates an essential role of excitons in the resonance energy transfer to Ti-related centers in silicon carbide.

Acknowledgements

We thank S. Teslenko and K.A. Kikoin for tight collaboration and fruitful discussion.

References

- [1] D.R. Hamilton, W.J. Choyke, L. Patrick, *Phys. Rev.* 131 (1963) 127.
- [2] P.J. Dean, R.L. Hartman, *Phys. Rev. B* 5 (1972) 4911.
- [3] L. Patrick, W.J. Choyke, *Phys. Rev. B* 10 (1973) 5091.
- [4] K.M. Lee, L.S. Dange, G.D. Watkins, W.J. Choyke, *Phys. Rev. B* 32 (1985) 2273.
- [5] V.S. Vainer, V.A. Il'in, V.A. Karachinov, et al., *Sov. Phys.-Solid State* 281 (1986) 201.
- [6] K.A. Kikoin, V.I. Sokolov, V.N. Flerov, et al., *Sov. Phys. JETP* 56 (1982) 1354.
- [7] I.A. Buyanova, S. Ostapenko, M.K. Sheinkman, *Sov. Phys. Semicond.* 20 (1986) 1123.
- [8] Th. Stiasny, R. Helbig, *Inst. Phys. Conf. Ser.* 142 (1996) 389.
- [9] Yu.M. Suleimanov, S.I. Teslenko, *Sov. Phys. Semicond.* 11 (1977) 958.
- [10] D.J. Robbins, P.J. Dean, *Adv. Phys.* 27 (1978) 499.
- [11] R.B. Hemfreys, D. Bimberg, W.J. Choyke, *Solid State Commun.* 39 (1981) 163.
- [12] K. Majer, H.D. Muller, J. Schneider, *Mater. Sci. Forum* 83–87 (1992) 1183.
- [13] K.M. Lee, G.D. Watkins, *Phys. Rev. B* 26 (1982) 26.



ELSEVIER

Physica B 308–310 (2001) 718–721

PHYSICA B

www.elsevier.com/locate/physb

Beryllium implantation induced deep levels in 6H-silicon carbide

X.D. Chen^{a,*}, S. Fung^a, C.D. Beling^a, M. Gong^b, T. Henkel^c,
H. Tanoue^c, N. Kobayashi^c

^aDepartment of Physics, University of Hong Kong, Hong Kong, People's Republic of China

^bDepartment of Physics, Sichuan University, Chengdu, People's Republic of China

^cElectrotechnical Laboratory, Tsukuba, Ibaraki 305-8568, Japan

Abstract

Beryllium has been implanted into both n- and p-type 6H-silicon carbide (SiC) with high and low doses. Upon subsequent annealing at 1600°C, Beryllium implantation induced deep levels have been investigated by deep level transient spectroscopy. Five deep level centers labeled as BE1–BE5 were detected from high dose beryllium implantation produced pn junctions. A comparative study of low dose beryllium implanted n-type 6H-SiC sample proved that the BE1–BE3 centers were electron traps located at 0.34, 0.44, and 0.53 eV, respectively below the conduction band edge. At the same time, the BE4 and BE5 centers were found to be hole traps situated at 0.64 and 0.73 eV, respectively, above the valence band edge. In the case of beryllium implanted p-type 6H-SiC, four hole traps labeled as BEP1, BEP2, BEP3, and BEP4 have been observed. The observed levels of the hole traps BEP1 and BEP2 at 0.41 and 0.60 eV, respectively, above the valence band agree well with those from the Hall effect data from material with beryllium acting as doubly charged acceptor. The other hole traps BEP3 and BEP4 at 0.76 and 0.88 eV, above the valence band, respectively, are thought to be due to beryllium implantation induced defects or complexes. © 2001 Elsevier Science B.V. All rights reserved.

Keywords: Deep level defect; Beryllium; 6H-silicon carbide; Implantation

1. Introduction

Beryllium (Be) is known as a doubly charged acceptor in silicon carbide (SiC). The acceptor levels, 0.42 and 0.60 eV were determined at the first attempt by Hall measurements on 6H-SiC bulk material [1]. Recently, Be was successfully applied in the fabrication of SiC diodes. A better forward characteristic was obtained in comparison with pn junctions produced by boron (B) and aluminum (Al) implantation [2]. On the other hand, Be may also act as a donor in SiC when residing on the interstitial sites, although, the donor levels are not known [3]. However, the knowledge about the physics of the Be dopant in SiC is still very limited.

2. Experiment and results

The 6H-SiC used in this work was purchased from CREE Research Inc. in the form of 10 µm thick nitrogen doped (0001) oriented epilayers grown on n⁺ type SiC substrates. The nitrogen donor concentrations were 1×10^{16} and $8 \times 10^{17} \text{ cm}^{-3}$ in the epilayer and the substrate, respectively. 50–590 keV Be implantation (termed as high-dose Be implantation hereafter) was carried out to obtain a box-shaped profile with a mean Be concentration of about $1 \times 10^{19} \text{ cm}^{-3}$. To repair the implantation induced damage and to electrically activate the dopant, samples were annealed in flowing argon gas at 1600°C for 1 min using a rapid thermal annealing (RTA) system.

For a comparative study, 6H-SiC samples with a lower Be concentration of about $1 \times 10^{18} \text{ cm}^{-3}$ (termed

*Corresponding author. Fax: +852-28598972.

E-mail address: sfung@hkucc.hku.hk (S. Fung).

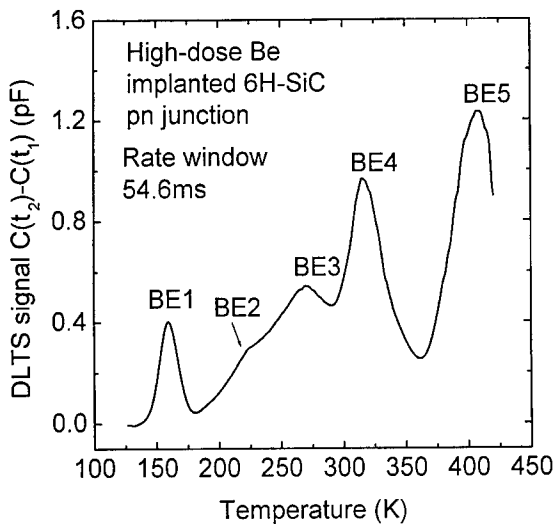


Fig. 1. DLTS spectrum recorded on the high-dose Be implanted 6H-SiC pn junction samples.

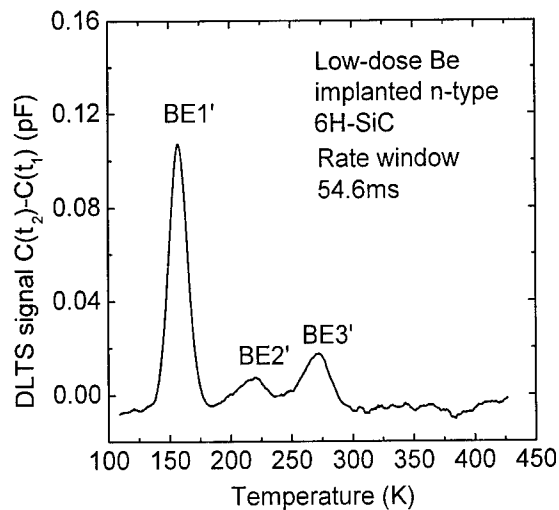


Fig. 2. DLTS spectrum recorded on the low-dose Be implanted n-type 6H-SiC.

low-dose Be implantation hereafter) were implanted into n- and p-type 6H-SiC samples, respectively. The same multiple energy implantation schedule as for the high-dose implantation was applied. RTA was performed at 1600°C for 30 s under similar conditions as stated above.

A typical majority carrier spectrum is shown in Fig. 1. Five peaks labeled as BE1, BE2, BE3, BE4, and BE5 were observed in the deep level transient spectroscopy (DLTS) measurement temperature range of 100–450 K. To check whether these traps were induced by Be implantation, a control measurement was performed on a schottky contact on unimplanted n-type epilayer. None of the above traps were detected indicating that all the traps described above were induced by the Be implantation process.

It should be pointed out that for the high-dose Be implanted samples, the Hall measurements indicated a weak p-type conduction in the Be implanted layer, the free hole concentration in the p-region and the free electron concentration in the n-region of the pn junction were of the same order of magnitude. Under reverse bias conditions it is thus reasonable to expect that the width of the depletion layer in the p-region is comparable with the one in the n-region. Consequently, the observed DLTS peaks may arise either from hole traps in the p-region or electron traps in the n-region of the pn junction. A definitive assignment is not possible without further information about these traps. Therefore, the n-type low-dose Be implanted samples was additionally prepared. A typical DLTS spectrum of these samples is shown in Fig. 2, all the three levels are attributed to electron traps. Since the energy level and the temperature position of the DLTS peak BE1' (see Fig. 2) are in excellent agreement with those of BE1 (see Fig. 1), BE1'

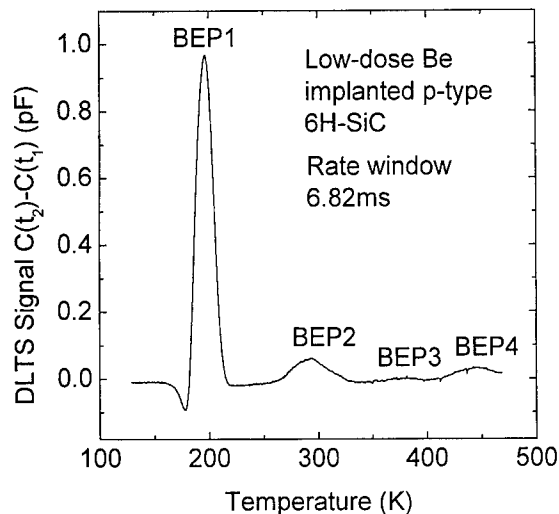


Fig. 3. DLTS spectrum recorded on the low-dose Be implanted p-type 6H-SiC.

and BE1 are attributed to the same defect center. Likewise BE2' and BE3' are assumed to be related to the overlapping peaks BE2 and BE3 because of their very similar energy levels. Hence, it is unambiguously clear that three (BE1, BE2, and BE3) of the five deep level traps observed in the high-dose Be implanted sample are electron traps arising from the n-region while the other traps (BE4, BE5) are assumed to be hole traps from the p-region of the pn junction.

Fig. 3 shows the DLTS spectrum of Be implanted p-type 6H-SiC. Four deep levels labeled as BEP1, BEP2, BEP3, and BEP4 as hole traps are observed in a

Table 1

Energy levels E_T , capture cross sections σ_T , and concentrations N_T of the deep level traps determined using DLTS data of the high- and low-dose Be implanted 6H-SiC samples

	E_T (eV)	σ_T (cm ²)	N_T (cm ⁻³)
BE1	$E_C - 0.34$	$\sim 10^{13}$	$4\text{--}10 \times 10^{13}$
BE2	$E_C - 0.44$	$\sim 10^{14}$	$1\text{--}6 \times 10^{13}$
BE3	$E_C - 0.53$	$\sim 10^{14}$	$3\text{--}8 \times 10^{13}$
BE4	$E_V + 0.64$	$\sim 10^{16}$	$4\text{--}6 \times 10^{14}$
BE5	$E_V + 0.73$	$\sim 10^{16}$	$2\text{--}7 \times 10^{14}$
BEP1	$E_V + 0.41$	$\sim 10^{13}$	$4\text{--}10 \times 10^{14}$
BEP2	$E_V + 0.60$	$\sim 10^{15}$	$1\text{--}6 \times 10^{13}$
BEP3	$E_V + 0.76$	$\sim 10^{16}$	$1\text{--}3 \times 10^{13}$
BEP4	$E_V + 0.88$	$\sim 10^{17}$	$2\text{--}6 \times 10^{13}$

temperature range of 180–450 K. At temperatures below $T = 180$ K, the DLTS peak shape is strongly affected by the increased series resistance due to the free carrier freeze-out of the shallow Al dopant. The energy levels, capture cross sections, and concentrations of the defect centers determined are summarized in Table 1.

3. Discussion

Recent DLTS studies on electron-irradiated [4–6] and deuterium-implanted [5] n-type 6H-SiC have demonstrated the existence of two overlapping levels at $E_C - 0.33$ and 0.34 eV that were designated as E_1 and E_2 , respectively. Our previous DLTS investigations on electron-irradiated 6H-SiC revealed several deep level traps. Two of them (labeled as ED₃ and ED₄) were attributed to the E_1/E_2 center [6]. The fact that the BE1 peak is so close in energy to those of the E_1/E_2 doublet is suggestive that the two are one and the same defect with the perturbations present on the center close to the pn junction perhaps causing the doublet to smear into a single peak. Such a view, however, meets with some difficulty when it is realized that the peak maximum temperatures of BE1 and ED₃ differ by 50 K and the calculated cross-section by two orders of magnitude. This makes it unlikely that BE1 and E_1/E_2 are the same defect.

An alternative explanation for BE1 is that it is associated with interstitial Be. It is known that Be may act as a donor when residing on interstitial positions [3]. Further, there is strong evidence indicating that Be diffuses via interstitial sites [3,7,8]. Since a deep diffusion tail into the epilayer is observed after RTA, there is definite evidence for fast interstitial diffusion of Be and thus by inference the related donor site [7,8]. It may tentatively be argued that Be is residing on an interstitial site that leads to the BE1 center. Clearly, further theoretical investigations will be necessary to test this possibility.

The trap BE3, the energy level of which has been determined as $E_C - 0.53$ eV, is similar to the defect level was previously found in electron irradiated 6H-SiC by several groups [4,5]. On the other hand, Dalibor et al. observed a trap labeled as ID₇ at $E_C - 0.50$ eV after vanadium as well as titanium implantation followed by an annealing process at 1700°C [9]. This defect level was ascribed to an implantation induced intrinsic defect center. Due to the different annealing behavior, the defect associated with the ID₇ center must be different from the one observed in electron irradiated material. We believe that the BE3 and ID₇ levels originate from the same defect, i.e., an intrinsic defect center induced by the implantation process. The peak BE2 in the DLTS spectrum is very weak and overlapped by the peak BE3, which limits the precision of the calculated parameters. Therefore, the question whether the trap BE2 is to be associated with an implantation induced intrinsic defect or a Be induced defect cannot be answered at present.

In the case of the low-dose Be implanted Al doped p-type 6H-SiC samples, the Fermi-level should mainly be controlled by the acceptor level of Al dopant. Therefore, the doubly charged states of Be may be observed in Be implanted p-type samples by using DLTS technique. The energy levels of BEP1 and BEP2, respectively at $E_V + 0.41$ and 0.60 eV determined from the current experiment are consistent with the Hall effect result determined in Be diffused 6H-SiC samples [1]. Thus, we can conclude that the BEP1 and BEP2 traps are attributed to the doubly charged states of substitutional Be acting as acceptor. On the other hand, the BE4 center located at $E_V + 0.64$ eV from the p-side of Be implanted pn junction may also arise from the second charge state of the Be acceptor. The different measurement techniques and purities of the samples are assumed to be responsible for the small discrepancy between the DLTS and the Hall result ($E_V + 0.60$ eV) reported in the past [1].

Considering the hole trap BEP3, energy level was determined to be 0.76 eV above the valence band. Though comprehensive investigations on intrinsic defects in p-type 6H-SiC are still lacking, a defect level labeled as H2 at a similar energy position was found in electron irradiated material by our group [10]. It was demonstrated that the defect associated with H2 anneals out at about 350°C. As stated earlier, the current Be implanted 6H-SiC samples were annealed at temperature $T = 1600^\circ\text{C}$, the different thermal annealing behaviors seem to argue against the assignment of BEP3 as H2 in the p-type 6H-SiC. However, it should be pointed out that the DLTS signal of BEP3 is very weak (as shown in Fig. 3), and the low-dose Be implanted p-type samples were annealed at 1600°C for 30 s. It does not preclude the possibility that BEP3 may arise from an intrinsic defect due to the very short annealing duration used for the low-dose Be implanted SiC samples.

The BEP4 at $E_V + 0.88$ eV determined from p-type sample and the BE5 at $E_V + 0.73$ eV detected from the p-side of pn junction are determined as hole traps induced by Be implantation. Since there was no similar energy levels observed from electron irradiated or boron and gallium implanted p-type 6H-SiC experiments, we assign the two levels to be beryllium-related defects. Recently, several deep Be related centers were found by electron paramagnetic resonance (EPR) investigation on 6H-SiC crystal doped by diffusion technique [11]. The BEP4 and BE5 centers may be associated with these defects which were found to resemble the deep B center in terms of electronic and magnetic properties [12].

Acknowledgements

The work described in this paper was partially supported by the grants from the Research Grant Council of the Hong Kong Special Administrative Region, China (under project No. HKU7137/99P).

References

- [1] Y.P. Maslakovets, E.N. Mokhov, Y.A. Vodakov, G.A. Lomakina, *Sov. Phys. Solid State* 10 (1968) 634.
- [2] N. Ramungul, Y.P. Zheng, R. Rupal, T.P. Chow, *IEEE Trans. Electron Devices* ED-46 (1999) 465.
- [3] Y.A. Vodakov, G.A. Lomakina, E.N. Mokhov, V.G. Oding, E.I. Radovanova, *Sov. Phys. Solid State* 20 (1978) 258.
- [4] C. Hemmingsson, N.T. Son, O. Kordina, E. Janzen, *J. Appl. Phys.* 84 (1998) 704.
- [5] M.O. Aboelfotoh, J.P. Doyle, *Phys. Rev. B* 59 (10) (1999) 823.
- [6] M. Gong, S. Fung, C.D. Beling, Z. You, *J. Appl. Phys.* 85 (1999) 7604.
- [7] X.D. Chen, S. Fung, C.D. Beling, M. Gong, T. Henkel, Y. Tanaka, N. Kobayashi, H. Tanoue, *J. Appl. Phys.* 88 (2000) 4558.
- [8] T. Henkel, Y. Tanaka, N. Kobayashi, H. Tanoue, S. Hishita, *Appl. Phys. Lett.* 78 (2001) 231.
- [9] T. Dalibor, G. Pensl, H. Matsunami, T. Kimoto, W.J. Choyke, A. Schoener, N. Nordell, *Phys. Stat. Sol. A* 162 (1997) 199.
- [10] M. Gong, S. Fung, C.D. Beling, Z. You, *J. Appl. Phys.* 85 (1999) 7120.
- [11] A. van Duijn-Arnold, J. Schmidt, O.G. Poluektov, P.G. Baranov, E.N. Mokhov, *Phys. Rev. B* 60 (1999) 15799.
- [12] A. van Duijn-Arnold, T. Ikoma, O.G. Poluektov, P.G. Baranov, J. Schmidt, *Phys. Rev. B* 57 (1998) 1607.



ELSEVIER

Physica B 308–310 (2001) 722–725

PHYSICA B

www.elsevier.com/locate/physb

Passivation of p-type dopants in 4H-SiC by hydrogen

B. Aradi^{a,*}, A. Gali^a, P. Deák^a, N.T. Son^b, E. Janzén^b^a Department of Atomic Physics, Budapest University of Technology and Economics, Budafoki út 8, H-1111 Budapest, Hungary^b Department of Physics and Measurement Technology, University of Linköping, Linköping, S-58183 Sweden

Abstract

Experimental investigations showed passivation of the p-type dopants B and Al in 4H-SiC by the formation of B + H and Al + H complexes. The dissociation energies of these complexes differed by 0.9 eV. Ab initio supercell calculations have been performed to investigate the interaction of H with B and Al in hexagonal 4H-SiC. The total energy, geometry and electronic structure of the possible complexes have been determined. Site dependencies have also been investigated. The most stable configurations were found with H at a bond center site next to B at the Si site, and with H at the antibonding site of a carbon atom which is first neighbor to Al at a Si site. Both the $B_{Si} + H_{BC}$ and the $Al_{Si} + H_{ABc}$ complexes turned out to be electrically inactive. The different structure of the passivated complexes explains the observed difference in their dissociation energy: the calculated difference of the binding energies of these complexes is 0.9 eV, which agrees well with the experimental finding. © 2001 Elsevier Science B.V. All rights reserved.

PACS: 71.15.Mb; 71.55.Ht; 61.72.Bb; 61.72.Ji; 61.72.Ww

Keywords: SiC; Passivation; Aluminum; Boron; Hydrogen

1. Introduction

Hydrogen is one of the most common impurities in semiconductors, introduced by both wet and dry etching among other methods. Due to its ability to passivate dopants or to compensate them by forming electrically active centers, its properties have been studied in various semiconductors. Silicon carbide (SiC) is one of the most promising wide band gap semiconductors for building high-power, low-loss electronic devices. Hydrogen has a special importance with regard to the doping of this semiconductor: due to the slow diffusion under 1300°C, doping is very often carried out in growth. This is most often done using chemical vapor deposition (CVD) from precursor molecules (e.g. C_3H_8 , SiH_4 , B_2H_6 or $Al(CH_3)_3$) diluted in H_2 carrier gas, causing an unavoidable hydrogen contamination in the epitaxially grown sample.

The most important p-type dopants of silicon carbide are boron and aluminum. The behavior of aluminum is

relatively predictable, it substitutes a silicon atom in the lattice (Al_{Si}) and produces a shallow acceptor level between $E_V + 0.19$ – 0.25 eV in the different polytypes [1]. Boron has been reported to occupy both the silicon and the carbon site, alas with preference for the Si site [2]. It produces a shallow and a deep acceptor level with (0/–) occupation levels at $\sim E_V + 0.30$ eV and $\sim E_V + 0.55$ eV, respectively, in the 4H polytype [3,4]. Although no conclusive proof has yet been shown, B_{Si} is usually associated with the shallow acceptor.

For boron doped 6H-SiC samples it was shown with SIMS (secondary ion mass spectrometry) and PL (photoluminescence spectroscopy) [5,2] that hydrogen is incorporated during epitaxial growth. Those samples showed strong decrease in the carrier concentration due to hydrogen. Experiments introducing hydrogen by implantation [6] or low-temperature plasma anneal [7] showed a passivation of the p-type doping by the formation of Al + H and B + H complexes. The observed dissociation energies for these complexes (1.61 and 2.51 eV for Al + H and B + H, resp. [8]) differ by 0.9 eV, suggesting that the atomic configurations of the two complexes are significantly different.

*Corresponding author. Fax: +36-1-4634357.

E-mail address: ab007@hszk.bme.hu (B. Aradi).

2. Method

First-principles calculations using the local density approximation (LDA) to density-functional theory were carried out using a plane wave basis. The Ceperley–Alder exchange-correlation functional was used as parametrized by Perdew and Zunger. Atomic cores were represented through norm conserving Troullier–Martins pseudopotentials. The basis included plane waves with kinetic energy up to 36 Ry. This makes the relative stability of the calculated complexes converge within 0.05 eV. Integration over the Brillouin zone of the supercells was carried out through a summation on the $2 \times 2 \times 2$ Monkhorst–Pack (MP) mesh. The defective solid was modeled with a 96 atom supercell ($2\sqrt{3} \times 2\sqrt{3} \times 1$) enabling symmetry constrained relaxation of the atoms within the first three shells around the defect. The calculation had been carried out with the FHI98MD code [9]. LDA is known to underestimate the width of the gap. To correct that a posteriori, the conduction band has been rigidly shifted to reproduce the experimental gap. Defect levels in the gap had been shifted proportional to their overlap with the conduction band states of the perfect lattice [10]. In the case of occupied defect levels, this gives rise to a correction in the total energy as well. Details and references are given in Ref. [11].

3. Hydrogen in 4H-SiC

To find the stable geometry for the neutral interstitial hydrogen, we started hydrogen from the different antibonding and bond center positions using initial Si–H and C–H distances that we have obtained earlier for interstitial hydrogen in 3C-SiC [11]. The most stable configuration turned out to be hydrogen in an antibonding position behind a silicon atom ($H_{AB_{Si}}$). The geometry of the stable configuration is shown in Fig. 1.

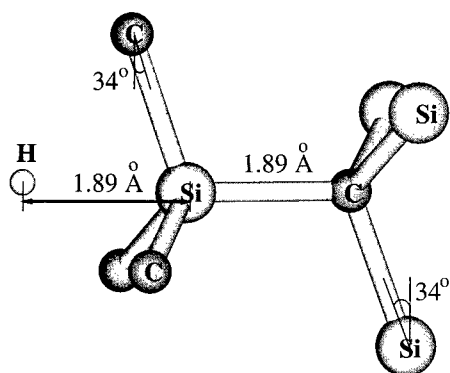


Fig. 1. Geometry of the $H_{AB_{Si}}$ complex.

The stable $H_{AB_{Si}}$ complex causes a single occupied defect level at $E_V + 1.45$ eV.

Calculation of the negatively charged interstitial hydrogen showed hydrogen to be most stable staying behind the silicon atom in an antibonding position. The hydrogen–silicon distance decreases to 1.76 Å, while the silicon–carbon bond gets weakened by the additional electron, and increases to 1.96 Å. In the positively charged state, hydrogen prefers the antibonding site of carbon at a distance of 1.15 Å. The positively charged hydrogen weakens the bond of the carbon atoms to its silicon neighbors: the bond lengths increase to 1.95–1.96 Å.

A Comparison of the total energies of the stable interstitial hydrogen complexes in the different charge states (shown in Fig. 2) predicts a negative U behavior for hydrogen in 4H-SiC, with a (+/–) occupation level at $E_V + 2.3$ eV. Accordingly, interstitial hydrogen is an amphoteric defect in 4H-SiC, being (unlike in 3C-SiC) a deep electron and hole trap as well. It is positively charged in the p-type material and, therefore attracted by the negatively charged acceptors.

4. Passivation of boron and aluminum by hydrogen

We have investigated the complexes of hydrogen with the p-type dopant B_{Si} in 4H-SiC. Among the investigated $B_{Si} + H$ complexes those with hydrogen in a bond center position between the substitutional boron and one of its carbon ($B_{Si} + H_{BC}$) neighbor turned out to be most stable. The geometry for the complex is shown in Fig. 3. As it can be seen, the hydrogen bonds to the carbon atom (having a typical C–H distance of ~ 1.1 Å) and pushed the boron in an almost planar configuration. All of these complexes turned out to be electrically inactive, meaning that the complex has no level in the gap. The next stable complex contains hydrogen at an antibonding position behind one of the carbon neighbors of the substituting boron.

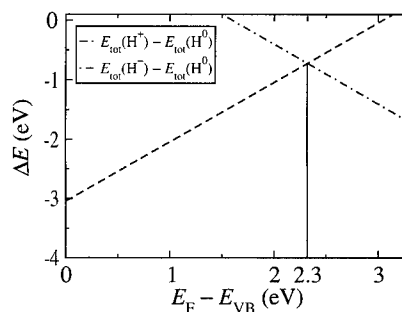
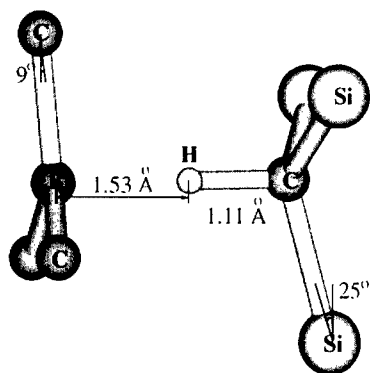
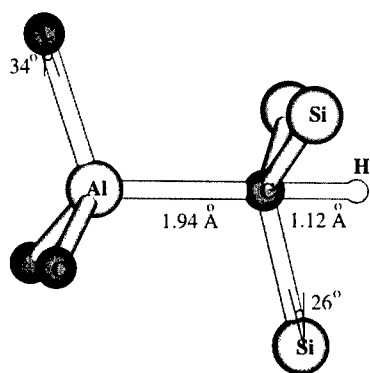


Fig. 2. Stability of the charge states of interstitial atomic H with respect to the neutral state in 4H-SiC as a function of the Fermi level in the gap.

Fig. 3. Geometry of the $B_{Si} + H_{BC}$ complex.Fig. 4. Geometry of the $Al_{Si} + H$ complex.

To investigate the interaction of hydrogen with aluminum in 4H-SiC, we performed a similar calculation for aluminum as for boron. In the energetically most favorable complex, the hydrogen is at an antibonding position to one of the first neighbor carbon atoms of the substituting aluminum ($Al_{Si} + H_{AB_C}$). The geometry of this complex is shown in Fig. 4. The hydrogen bonds here also to the carbon atom, however, from the antibonding site. The $Al_{Si} + H_{BC}$ configuration, containing a bond center hydrogen between the Al and the C atom is less stable, the difference to the $Al_{Si} + H_{AB_C}$ complex is about 0.3 eV. Obviously, hydrogen would prefer to have a bond center position, to have a "normal" bond with carbon as in the case of boron, but since aluminum is too big, this configuration involves too much relaxation, making it energetically less favorable. Similar to boron, the complex forming with hydrogen causes passivation of Al, since all of these complexes turned out to be electrically inactive.

5. Dissociation of the dopant-hydrogen complexes

To calculate the dissociation energy of the passivated complexes, one has to consider that hydrogen is

positively charged in p-type silicon carbide, while the acceptors are negative. Therefore, the reaction for the dissociation would be



where the variable X stands for the different p-type dopants (B and Al in our case). By subtracting from the sum of the total energies of the dopant X in the negative charge state and the hydrogen in the positive charge state the sum of the total energies of a neutral $X + H$ complex and a perfect supercell, one obtains the binding energy which is a lower limit for the dissociation energies. (The dissociation energy is equal to the binding energy *plus* the activation energy of the diffusion.)

By calculating the binding energy for the $B_{Si} + H_{BC}$ and the $Al_{Si} + H_{AB_C}$ complexes in this way we obtain 1.6 and 0.7 eV, respectively. The difference between them can be explained with the bonding configuration of hydrogen: in the case of $B_{Si} + H$, hydrogen is the fourth neighbor of the more or less tetrahedral coordinated carbon atom, giving rise to a strong C-H bond, while in the case of aluminum, hydrogen bonds weakly to the carbon atom from an antibonding position.

The experimental values for the dissociation energy are 2.51 and 1.61 eV for B and Al, respectively. The difference to our binding energies are 0.9 eV in both cases. This value can be interpreted as an approximate activation energy of diffusion. (For neutral H Kaukonen et al. have obtained a migration barrier of 0.7 eV, Ref. [12]). The difference of the binding energies are equal to the observed difference of dissociation energies.

6. Summary

Using *ab initio* LDA supercell calculations we investigated the interaction of hydrogen with the boron and aluminum dopants in 4H-SiC. We showed that the interstitial hydrogen has a negative U behavior in 4H-SiC and is a deep electron and hole trap. In p-type SiC it is positively charged and, therefore attracted by the negatively charged boron and aluminum dopants. Our calculations showed that these dopants can be passivated by forming complexes with the hydrogen. The difference in the structures of the most stable electrically inactive $B_{Si} + H_{BC}$ and $Al_{Si} + H_{AB_C}$ complexes explain the experimentally observed difference between the dissociation energies of the $B + H$ and $Al + H$ complexes.

Acknowledgements

The fruitful discussions with A.W.R. Leitch and E. van Wyk are appreciated. Support from the Hungarian OTKA Grant No. T032174 and the bilateral

programs between Hungary and Sweden (IVA-MTA Grant No. 36) and Hungary and South Africa (DAK 7/98) are appreciated. This work was also supported by grants from the Pittsburgh Supercomputer Center (PHY970000) and the Swedish National Supercomputer Center (2000018).

References

- [1] O. Madelung (Ed.), *Data in Science and Technology: Semiconductors (Group IV. Elements and III–V Compounds)*, Springer, Heidelberg, 1991, p. 56.
- [2] D.J. Larkin, *Phys. Stat. Sol. B* 202 (1997) 305.
- [3] W. Suttrop, G. Pensl, P. Lanig, *Appl. Phys. A* 51 (1990) 231.
- [4] S.G. Sridhara, L.L. Clemen, R.P. Devaty, W.J. Choyke, D.J. Larkin, H.S. Kong, T. Troffer, G. Pensl, *J. Appl. Phys.* 83 (1998) 7909.
- [5] D.J. Larkin, *J. Electron. Mater.* 24 (1995) 289.
- [6] M.S. Janson, A. Hallén, M.K. Linnarsson, N. Nordell, S. Karlsson, B.G. Svensson, *Mater. Sci. Forum* 353–356 (2001) 427.
- [7] M.E. Samiji, A. Venter, M.C. Wagener, A.W.R. Leitch, *J. Phys.: Condens. Matter* 13 (2001) 1.
- [8] M.S. Janson, A. Hallén, M.K. Linnarsson, B.G. Svensson, *Phys. Rev. B*, to be published.
- [9] M. Bockstedte, A. Kley, J. Neugebauer, M. Scheffler, *Comp. Phys. Commun.* 107 (1997) 187.
- [10] G.A. Baraff, M. Schlüter, *Phys. Rev. B* 30 (1984) 1853.
- [11] B. Aradi, A. Gali, P. Deák, J.E. Lowther, N.T. Son, E. Janzén, W.J. Choyke, *Phys. Rev. B* 63 (2001) 245202.
- [12] M. Kaukonen, C.J. Fall, P.R. Briddon, R. Jones, *J. Phys.: Condens. Matter* 13.



ELSEVIER

Physica B 308–310 (2001) 726–729

PHYSICA B

www.elsevier.com/locate/physb

First-principles studies of Ti impurities in SiC

K.O. Barbosa, W.V.M. Machado, L.V.C. Assali*

Departamento de Física dos Materiais e Mecânica, Instituto de Física da Universidade de São Paulo, CP 66318, CEP 05315-970, São Paulo, SP, Brazil

Abstract

In this work we perform a theoretical investigation on the atomic structure, atomic geometry, and formation energy of isolated substitutional and interstitial Ti impurities in cubic silicon carbide (3C-SiC), using the spin-polarized full-potential linearized augmented plane wave method. For each configuration, the atoms around the impurity site are allowed to relax without any constraints, following the damped Newton dynamics scheme. The overall structural stability is analyzed in the light of the electronic structure and the bonding features. © 2001 Elsevier Science B.V. All rights reserved.

PACS: 71.55.-i; 71.55.Hi

Keywords: Transition metals; Silicon carbide; Ab initio methods

1. Introduction

Silicon carbide (SiC) is a wide band gap semiconductor that is finding a place which is difficult to fill with the presently available Si or GaAs technology. One of the aspects that makes SiC fascinating from a fundamental point of view is that in some sense SiC is not a single semiconductor but a whole class of semiconductors because of its polytypism [1]. The material can crystallize in many different but closely related crystal structures. Since its discovery [2], more than 200 polytypes have been determined [3]. The most extreme polytypes are the zinc-blende 3C-SiC with pure cubic stacking of Si-C bilayers in the [111] direction and the wurtzite 2H-SiC with pure hexagonal stacking in the [0001] direction. The pure crystals indirect band gap varies in the range of 2.4 eV for 3C-SiC to 3.3 eV for 2H-SiC. Due to the existence of these polytypes, a variety of impurity sites exist since there are two different sublattices and no equivalent cubic (k) and hexagonal (h) sites in the sublattices. It is known that not only the electronic properties of SiC crystals are influenced by the different

stacking order but also those of the defects and impurities.

The study of 3dⁿ transition metal (TM) point defects in SiC is very important because they can be incorporated in SiC by doping or can be present in the material as residual impurities [4,5] and, as in Si, they play an important role in the crystal electric and magnetic properties. The TM impurity properties would vary if it is built in C or Si sites or in an interstitial site, and vary also from polytype to polytype.

Theoretically, there are few studies involving TM impurities in SiC. The aim of this work is to describe the electronic and atomic structure, the spin state, and the energetics for the Ti impurity in 3C-SiC. In order to understand the effects of the Ti impurity in the material properties we studied, using a total energy method with atomic relaxation, isolated substitutional Ti impurity in a Si site (Ti_{Si}^{Si}) and in a C site (Ti_C^C), as well as tetrahedral interstitial isolated Ti impurity surrounded by four C atoms (Ti_i^C) and surrounded by four Si atoms (Ti_i^{Si}) in 3C-SiC. A 54-atom supercell approach is used to describe the impurity located in different atomic and interstitial sites. The calculations are performed within the framework of the density functional theory (DFT) [6,7], using the full-potential linearized augmented plane wave (FP-LAPW) method [8], implemented into the

*Corresponding author. Tel.: +55-11-3818-7041.

E-mail address: lassali@macbeth.if.usp.br (L.V.C. Assali).

package WIEN97 [9], using the exchange-correlation potential of Perdew et al. [10].

2. Results

2.1. Perfect crystal 3C–SiC

The properties of the zinc-blende 3C–SiC material parameters are obtained using $RK_{\max} = 8$, the smallest *muffin-tin* radius of the host atoms times the largest reciprocal lattice vector in plane wave expansion ($R_{\text{Si}} = 1.5a_0$ and $R_{\text{C}} = 1.2a_0$), that corresponds to a cutoff energy of 44 Ry. In the atomic regions a spherical harmonic basis set is used with azimuthal quantum number up to $\ell = 10$ and a nonspherical contribution up to $\ell_{\text{ns}} = 4$. The carbon 1s, 2s wave functions and the silicon 1s, 2s wave functions are considered as core states. The k-mesh in the full Brillouin zone (BZ) consists of $6 \times 6 \times 6$ Monkhorst–Pack points, which are reduced to 28 k points in the irreducible edge of the BZ. The self-consistent iterations were considered to be converged when both the total energy and the total charge in the atomic spheres were stable within 10^{-4} eV per unit cell and 10^{-4} electron charges per atom, respectively. Minimizing the total energy with respect to changes in the volume of the unit cell, the computed primitive 3C–SiC unit cell constant is $a = 4.38$ Å. The obtained energy/SiC is -656.304 Ry.

The computed electronic and structural properties of 3C–SiC, using the optimized lattice parameter, are shown in Table 1 and are in good agreement with experiments [11].

For the perfect supercell, convergence with respect to k points was checked. It was used the Γ , L and a $2 \times 2 \times 2$ grid for k-space integrations and no difference in the electronic properties of the material was verified and the total energy was converged within 0.02 eV/atom. We must note that 27 points of the unit cell BZ are sampled in just one point. The points 1 Γ , 6 Δ ($\frac{2}{3}, 0, 0$), 12 Σ ($\frac{2}{3}, \frac{2}{3}, 0$), and 8 Λ ($\frac{1}{3}, \frac{1}{3}, \frac{1}{3}$) of the unit cell BZ are all equivalent to the Γ point of the 54-atom supercell BZ. All properties displayed in Table 1, for the unit cell, are reproduced by the perfect supercell.

2.2. Electronic structure of Ti impurities

For an impurity supercell with a Ti impurity, the self-consistent iterations were considered to be converged when both the total energy and the total charge in the atomic spheres were stable within 10^{-4} eV and 10^{-5} electron charges per atom, respectively. The atoms were assumed to be in their fully relaxed positions when the forces acting on ions were smaller than 0.05 eV/Å.

Fig. 1 displays, schematically, the impurity-induced energy levels based on Kohn–Sham eigenvalues for the neutral $\text{Ti}_{\text{Si}}^{\text{Si}}$, $\text{Ti}_{\text{Si}}^{\text{C}}$, $\text{Ti}_{\text{C}}^{\text{Si}}$, and $\text{Ti}_{\text{C}}^{\text{C}}$ centers at Γ . The full lines indicate the energy level with ‘up’ spin and the dotted lines with ‘down’ spin. The occupation of the energy levels is represented by the numbers of \uparrow (spin up) and \downarrow (spin down) arrows, respectively. In the crystal field, the Ti 3d-derived states split into twofold degenerate e levels and threefold degenerate t_2 levels, which are displayed in Fig. 1.

The $\text{Ti}_{\text{Si}}^{\text{Si}}$ center (substitutional Ti impurity in the Si site) introduces no energy levels in the band gap region. The energy levels related to Ti impurity are unoccupied resonant levels in the conduction band, where the e energy levels lie below the t_2 energy levels. Therefore, when a Si atom is replaced by a Ti atom, the latter undergoes a p–d hybridization, bonding to the nearest-neighbor C atoms, causing the band structure of the 3C–SiC material to be restored. Furthermore, we can say that the $\text{Ti}_{\text{Si}}^{\text{Si}}$ center reconstructs the Si vacancy dangling bonds, showing little influence in the band structure of the perfect material. On the other hand, one can understand these results on comparing them with the electronic structure of a substitutional Ti impurity in diamond [12] that shows no energy levels in the band gap. As the Ti impurity replacing a Si atom in 3C–SiC has four C atoms as nearest-neighbors, its electronic structure is quite similar to that of the substitutional Ti impurity in diamond. The Ti atom, which has an electronegativity similar to that of a Si atom and smaller than that of a C atom, interacts mainly with the nearest-neighbor C atoms through a p–d hybridization. The neutral $\text{Ti}_{\text{Si}}^{\text{Si}}$ center shows a closed-shell configuration, leading to an effective spin $S=0$. The point structure of the center has a T_d symmetry with a small relaxation where the

Table 1
Electronic properties of 3C–SiC^a

	a (Å)	E_g (eV)	B (Mbar)	E_{VB} (eV)	E_c (eV)	E_{so} (meV)
	4.38	1.32	2.2	15.4	12.9	13
Exp.	4.36	2.46	2.24	≈ 15	12.67	10.3

^a Lattice parameter a , energy band gap, E_g ; bulk modulus, B ; valence bandwidth, E_{VB} ; cohesive energy, E_c ; spin–orbit splitting, E_{so} .

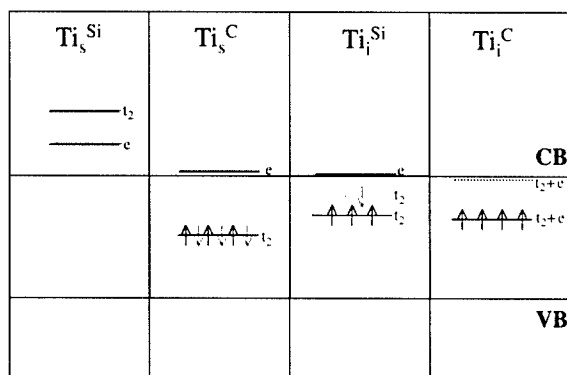


Fig. 1. Schematic representation of the Ti 3d-related impurity energy levels in the band gap region for the neutral $\text{Ti}_\text{Si}^\text{Si}$, $\text{Ti}_\text{Si}^\text{C}$, $\text{Ti}_\text{i}^\text{Si}$, and $\text{Ti}_\text{i}^\text{C}$ centers at Γ ($E_\text{g} = 2.4\text{ eV}$). The full lines indicate the energy levels with 'up' spin and the dotted lines with 'down' spin. The occupation of the energy levels is represented by the numbers of \uparrow (spin up) and \downarrow (spin down) arrows, respectively.

four nearest-neighbor C atoms undergo an outward relaxation of 0.1 Å.

The $\text{Ti}_\text{Si}^\text{C}$ center (substitutional Ti impurity in the C site) introduces totally occupied t_2 energy levels in the band gap region and resonant unoccupied e energy levels in the conduction band. Therefore, when a C atom is replaced by a Ti atom, the latter does not bond to the four nearest-neighbor Si atoms and does not reconstruct the C vacancy dangling bonds. Therefore, different from the substitutional Ti impurity in Si crystal [13], the interactions between Ti and the nearest-neighbor C atoms cause a crystal field splitting so that the t_2 energy levels lie below the e levels. The neutral $\text{Ti}_\text{Si}^\text{C}$ center shows a closed-shell configuration, leading to an effective spin $S = 0$. The point symmetry of the center is T_d where the four nearest-neighbor Si atoms and the 12 near-nearest-neighbor C atoms show an outward relaxation of 0.5 and 0.1 Å, respectively.

The $\text{Ti}_\text{i}^\text{Si}$ center (interstitial Ti impurity tetrahedrally surrounded by four Si atoms) introduces occupied t_2 energy levels, with up spin, and partially occupied t_2 energy level, with down spin, in the band gap region, and resonant unoccupied e energy levels with up and down spins in the conduction band. This center shows a low-spin configuration with an effective spin $S = 1$. The center point symmetry is approximately T_d where the four nearest-neighbor Si atoms and the six near-nearest-neighbor C atoms show an outward relaxation of 0.2 and 0.1 Å, respectively.

The $\text{Ti}_\text{i}^\text{C}$ center (interstitial Ti impurity tetrahedrally surrounded by four C atoms) introduces degenerate energy levels, $t_2 + e$, with spin up, in the band gap region (Ti 3d-related state) and unoccupied energy levels, with down spin, in the conduction band. The crystal field splitting is practically null and the center

shows a high-spin configuration with an effective spin $S = 2$. The center point symmetry is approximately T_d where the four nearest-neighbor C atoms and the six near-nearest-neighbor Si atoms show an outward relaxation of 0.1 and 0.2 Å, respectively.

2.3. Impurity formation energies and chemical potentials

At equilibrium and in the dilute limit, the concentration of an impurity in a crystal depends upon its free energy of formation

$$[D_i] = N_\text{sites} \exp\{-\Delta G_f/k_B T\}, \quad (1)$$

where N_sites is the number of sites, per unit volume, in the crystal where the impurity can occur, k_B is the Boltzmann constant, T is the temperature, and ΔG_f is given by

$$\Delta G_f = \Delta E_f - T\Delta S_f + P\Delta V_f. \quad (2)$$

Here, ΔE_f is the total energy variation, ΔS_f and ΔV_f are the entropy and volume variation when the impurity is introduced into the system under pressure P .

The formation energy of a charged point defect in SiC, ΔE_f^q is computed as

$$\Delta E_f^q = E(n_\text{Si}, n_\text{C}, n_\text{Ti}, q) - n_\text{Si}\mu_\text{Si} - n_\text{C}\mu_\text{C} - n_\text{Ti}\mu_\text{Ti} - q(\mu_\text{e} + E_\text{F}), \quad (3)$$

where $E(n_\text{Si}, n_\text{C}, n_\text{Ti}, q)$ is the total supercell energy with n_Si silicon atoms, n_C carbon atoms, and n_Ti Ti impurity atoms; μ_Si , μ_C , and μ_Ti are the external chemical potentials for Si, C, and Ti, respectively; q is the charge state of the defect. The electron chemical potential μ_e gives the position of the Fermi level in the band gap relative to the top of the valence band E_V . Silicon and carbon chemical potentials are not independent but are under the constraint

$$\mu_\text{Si} + \mu_\text{C} = \mu_\text{SiC(Bulk)} \quad (4)$$

that represents the equilibrium of a pair of atoms in the SiC crystal. $\mu_\text{SiC(Bulk)}$ is the chemical potential of the SiC pair in the bulk SiC compound. The allowed range of μ_Si and μ_C is determined from the heat formation ΔH_f defined as

$$\Delta H_f^{\text{SiC}} = \mu_\text{SiC(Bulk)} - \mu_\text{Si(Bulk)} - \mu_\text{C(Bulk)}, \quad (5)$$

where $\mu_\text{Si(Bulk)}$ and $\mu_\text{C(Bulk)}$ are the total energies per atom for Si and C crystals in the diamond structure, respectively. The calculated heat formation energy for SiC is -0.59 eV/SiC . This value is in good agreement with the experimental -0.68 eV/SiC enthalpy of formation [11]. In accordance with the preparation condition, the Si and C chemical potentials fluctuations vary according to

$$\mu_\text{Si} = \mu_\text{Si(Bulk)} + \lambda\Delta H_f^{\text{SiC}}, \quad (6)$$

$$\mu_\text{C} = \mu_\text{C(Bulk)} + (1 - \lambda)\Delta H_f^{\text{SiC}} \quad (7)$$

Table 2
Formation energies (ΔE_f), in units of eV, of the Ti impurity in 3C–SiC for different sites

Impurity	$\Delta E_f (\mu_{\text{Si}} = \mu_{\text{Si(Bulk)}})$	$\Delta E_f (\mu_{\text{Si}} = \mu_{\text{Si(Bulk)}} + \Delta H^{\text{SiC}})$
$\text{Ti}_{\text{S}}^{\text{Si}}$	6.9	6.9
$\text{Ti}_{\text{S}}^{\text{C}}$	14.1	15.3
$\text{Ti}_{\text{I}}^{\text{Si}}$	15.5	16.1
$\text{Ti}_{\text{I}}^{\text{C}}$	16.0	16.6

λ being a parameter ranging from 0 (Si-rich condition) to 1 (C-rich condition).

Table 2 presents the formation energies (ΔE_f) of the Ti impurity in 3C–SiC, in the limits of the silicon chemical potential, for different sites.

The results indicate that the substitutional sites are more stable than the interstitial ones and that substitutional Ti is more favorable in the Si sublattice than in the C sublattice.

3. Conclusion

We have performed ab initio total energy calculations of isolated Ti impurities in 3C–SiC, using the FP-LAPW method, the damped Newton dynamics scheme, and the supercell approach.

The electronic structure results show that the bonding features are quite different for the substitutional Ti impurity if it is built in Si or C sites. The $\text{Ti}_{\text{S}}^{\text{Si}}$ center reconstructs the Si vacancy dangling bonds and shows no energy levels in the band gap. On the other hand, the $\text{Ti}_{\text{S}}^{\text{C}}$ center does not reconstruct the C vacancy dangling bonds, showing fully occupied t_2 energy levels in the band gap region. For the interstitial Ti impurities the results show that when Ti impurity is surrounded tetrahedrally by Si atoms ($\text{Ti}_{\text{I}}^{\text{Si}}$) the exchange splitting drives the center to a low-spin configuration while for the Ti impurity surrounded tetrahedrally by C atoms ($\text{Ti}_{\text{I}}^{\text{C}}$) the crystal field splitting is practically null and the exchange splitting drives the center to a high-spin configuration. Although the relaxations are small for all centers studied here, our results show that they are important to compute values related to hyperfine parameters.

The formation energy results indicate that the Ti impurity in 3C–SiC in substitutional sites are more stable than in interstitial sites. Moreover, the Si site sublattice is the more stable one.

We can conclude from our results that isolated Ti impurity in 3C–SiC crystal is more stable as a substitutional impurity in the Si sublattice and, in this microscopic structure, it presents no band gap energy levels, in agreement with experimental evidences [14].

Acknowledgements

KOB and LVCA acknowledge the financial support from FAPESP and CNPq. The calculations were partially performed at the LCCA-CCE of the Universidade de São Paulo.

References

- [1] A.P. Verma, P. Krishna, Polymorphism and Polytypism in Crystals, Wiley, New York, 1966.
- [2] H. Baumhauer, Z. Kristallogr. 50 (1912) 33.
- [3] N.W. Jepps, T.F. Page, Prog. Crystal. Growth Charact. 7 (1983) 259.
- [4] S.T.G. Muller, D. Hoffman, A. Winnacker, E.N. Mokhov, Yu.A. Vodakov, in: S. Nakashima, H. Matsunami, S. Yoshida (Eds.), Silicon Carbide and Related Materials, 1995.
- [5] N.T. Son, E. Sorman, W.M. Chen, O. Kordina, B. Monemar, E. Jansen, Appl. Phys. Lett. 65 (1994) 2687.
- [6] P. Hohenberg, W. Kohn, Phys. Rev. B 136 (1964) 864.
- [7] W. Kohn, L.J. Sham, Phys. Rev. A 140 (1965) 1133.
- [8] D.J. Singh, Planewaves, Pseudopotentials and the LAPW method, Kluwer Academic, Norwell, 1994.
- [9] P. Blaha, K. Schwarz, J. Luitz, WIEN97, A Full Potential Linearized Augmented Plane Wave Package for Calculating Crystal Properties, Karlheinz Schwarz, Techn. Universitat WIEN, Austria, 1999, ISBN 3-9501031-0-4.
- [10] J.P. Perdew, S. Burke, M. Ernzerhof, Phys. Rev. Lett. 77 (1996) 3865.
- [11] Landolt-Börnstein, in: O. Madelung, M. Schulz, H. Weiss (Eds.), Numerical Data and Functional Relationships in Science and Technology, Vol. 17, Springer, New York, 1982.
- [12] L. Paslovsky, J.E. Lowter, T.L. Nam, R.J. Keddy, J. Lumin. 55 (1993) 167.
- [13] F. Beeler, O.K. Andersen, M. Scheffler, Phys. Rev. B 41 (1990) 1603.
- [14] A.A. Lebedev, Semiconductors 33 (1990) 107.



ELSEVIER

Physica B 308–310 (2001) 730–733

PHYSICA B

www.elsevier.com/locate/physb

Deep level defects in sublimation-grown 6H silicon carbide investigated by DLTS and EPR

K. Irmscher^{a,*}, I. Pintilie^b, L. Pintilie^b, D. Schulz^a

^a *Institut für Kristallzüchtung, Max-Born-Str. 2, D-12489 Berlin, Germany*

^b *National Institute of Materials Physics, Bucharest-Magurele, P.O. Box MG-7, R-76900, Romania*

Abstract

6H-SiC bulk single crystals grown by physical vapor transport (PVT) were investigated by deep-level transient spectroscopy (DLTS) and electron paramagnetic resonance (EPR). One of the observed deep level defects was identified as isolated tungsten on Si sites by EPR. The electron spin of $\frac{1}{2}$ could be explained by W^{5+} ($5d^1$). This is equivalent to the single positive charge state of a double donor when taking into account the Fermi level position in the n-type samples. The interpretation is also consistent with the DLTS detection of a W related deep level which showed a behavior of the capture of electrons and holes that hints at a double donor. In addition a tantalum related deep level is tentatively discussed. W and Ta were incorporated on electrically active sites in 6H-SiC only in low concentrations ($2\text{--}4 \times 10^{14} \text{ cm}^{-3}$) during crystal growth by PVT. © 2001 Elsevier Science B.V. All rights reserved.

PACS: 61.72.Ss; 71.55.Ht; 78.30.He

Keywords: 6H-SiC; DLTS; EPR; Tungsten; Tantalum

1. Introduction

The high temperatures during the PVT growth of 6H-SiC crystals bear the risk of unintentional impurity incorporation and incomplete annihilation of intrinsic point defects. Many of these impurities and defects form deep levels which can alter the electrical properties of the crystal by their action as compensation or recombination centers. Therefore, we investigated our 6H-SiC PVT crystals by DLTS and EPR to find out which deep levels are present, their concentration and electrical parameters as well as their structural and chemical identity. Especially, we were interested if tungsten and tantalum, which are potential impurities in our crystal growth process, were incorporated as deep level defects. Recent investigations of W and Ta implanted SiC by radiotracer DLTS revealed deep levels which could unambiguously assigned to W and Ta related defects, respectively [1,2].

However, such experiments cannot prove whether the chemically identified impurity is incorporated on a substitutional or an interstitial site, and if it is isolated or associated with other defects.

We report about the EPR identification of W substituting for Si in 6H-SiC and its assignation to a deep double donor level for the first time. A tentative correlation of the measurements in the case of Ta is also given.

2. Experimental details

6H-SiC bulk single crystals 30 mm in diameter were grown by physical vapor transport using 6H(0001)-SiC seeds with about 3° off-orientation. The sublimation of the SiC source took place at about 2200°C in an inductively heated crucible made of graphite [3]. For the most investigated crystal of this report 5 wt% of metallic tantalum was added to the source powder without deterioration of the resulting crystal quality. Furthermore, this crystal was only unintentionally doped with nitrogen and we obtained n-type samples in the mid 10^{16} cm^{-3} range.

*Corresponding author. Tel.: +49-30-6392-3090; fax: +49-30-6392-3003.

E-mail address: irmscher@ikz-berlin.de (K. Irmscher).

The DLTS measurements were performed using a commercial digital system in the capacitance detecting mode (DL8000, BioRad) equipped with a liquid nitrogen cryostat for temperature scans from 90 to 550 K. We have extended the system by an ultraviolet laser excitation source (Crystal GmbH) emitting at a wavelength of 355 nm to enable minority carrier pulses. As test structures semitransparent Schottky contacts obtained by Ni evaporation were used.

The EPR spectrometer (ESP300E, Bruker) works at X-band (9.4 GHz). The sample temperature can be varied between 4 and 300 K by means of a helium-flow cryostat (Oxford Instruments).

3. Results and discussion

3.1. EPR

In the EPR spectra the shallow nitrogen donor signals dominated and the known resonances of transition metals (TM's) in SiC [4,5] could not be detected. The latter was not surprising since former studies of the incorporation of selected TM's in our crystals revealed only low chemical concentrations, e.g. for vanadium around 10^{14} cm^{-3} [6].

Fig. 1(a) shows a typical EPR spectrum without illumination of the sample for the direction of the static magnetic induction \mathbf{B} parallel to the c -axis of the crystal. At the measurement temperature of 4 K and the used microwave power (0.2 mW) the N donor signal is strongly suppressed by saturation and an extremely narrow line (peak-to-peak line width of about 0.03 mT) labeled W^{5+} is visible at a resonance field of 335.7 mT. There are further lines, which could not be analysed up to now because of their low intensities for arbitrary directions of the magnetic induction. However the pair

of line groups labeled $\text{Ta}^{3+?}$ at about 320 and 350 mT, respectively, most probably originates from a defect with an electron spin $S = 1$, an axial fine structure and a complicated hyperfine interaction. These characteristics are to be expected for the ^{181}Ta isotope (natural abundance of nearly 100%) with nuclear spin $I = \frac{7}{2}$ and a very large nuclear electric quadrupole moment. The effect of near band gap light on the EPR spectrum is shown in Fig. 1(b). The lines of W^{5+} and $\text{Ta}^{3+?}$ almost disappear whereas new ones arise. This behavior proves that the underlying defects possess energy levels within the band gap. Among the new resonances the ones at about 302 and 368 mT labeled $\text{W}^{4+?}$ can be described by a spin $S = 1$. The identities suggested by the labels with question marks are only working hypotheses and need justification by further investigations.

Fig. 2 shows the spectrum of W^{5+} for \mathbf{B} parallel to c on an expanded scale. The central line exhibits an additional structure, which is assumed to arise from a super hyperfine (shf) interaction with ligand nuclei. The pair of outer lines, on which this shf structure is also present, is thought to be a result of a hyperfine (hf) interaction of the electron spin of an impurity ion with its own nuclear magnetic moment. The ratio of the sum of the two outer line intensities to the total intensity, i.e. central line plus two outer lines, amounts to 14.3%. Among the impurities which are possible candidates for an unintentional incorporation during crystal growth only tungsten has an isotope (^{183}W) with nuclear spin $I = \frac{1}{2}$ and a natural abundance of 14.3% while the other W isotopes (with even numbered atomic masses) have zero nuclear spin. Therefore tungsten is the most probable chemical identification of the impurity in question. Concerning the electron spin, we can conclude from the anisotropy of the spectrum and the missing fine structure that it must be $S = \frac{1}{2}$. The incorporation of W on interstitial sites or on substitutional carbon sites is

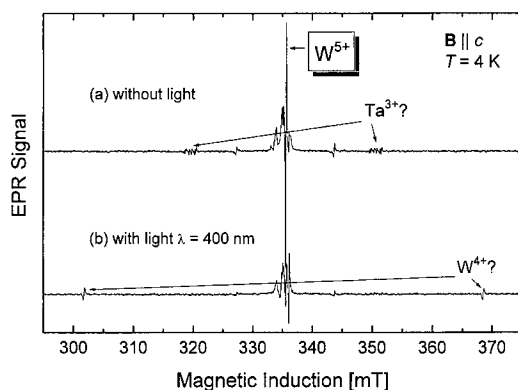


Fig. 1. Typical EPR spectrum of an as-grown 6H-SiC crystal for the direction of the static magnetic induction parallel to the c -axis, (a) without illumination and (b) with near band gap light excitation.

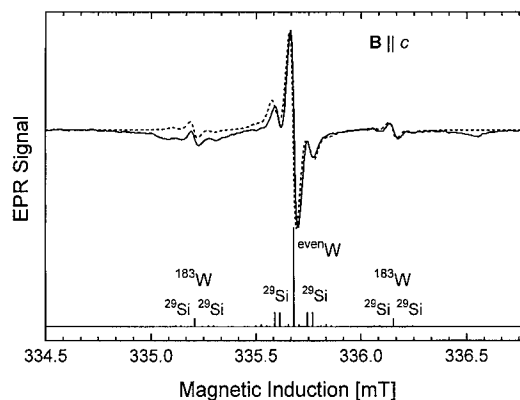


Fig. 2. Measured (solid line) and simulated (dashed line) EPR spectrum of W^{5+} on a Si site in 6H-SiC. The calculated stick spectrum (bottom) was convoluted with Lorentzian lines of 0.036 mT peak-to-peak width.

incompatible with the observed shf structure as checked by trial simulations of the spectrum. Hence, W substituting for Si is more obvious. Then four electrons are spent for the bonds and the $5d^1$ electron configuration of W^{5+} can be assumed in agreement with $S = \frac{1}{2}$. This is equivalent to the single positive charge state of a donor. All features of the spectrum can be adequately described by the spin Hamiltonian

$$H = \mu_B \mathbf{B} \mathbf{g} \mathbf{S} + \mathbf{S} \mathbf{A} \mathbf{I}^W + \sum_{i=1}^{12} \mathbf{S} \mathbf{A}_i \mathbf{I}_i^{\text{Si}} \left(+ \sum_{i=1}^4 \mathbf{S} \mathbf{A}_i \mathbf{I}_i^{\text{C}} \right) \quad (1)$$

and $S = \frac{1}{2}$. The first term describes the electronic Zeeman interaction and determines the anisotropy of the central resonance line. The hf interaction with the ^{183}W nucleus is represented by the second term of Eq. (1) and accounts for that 14.3% of the total line intensity is split into two lines. The third term contains the shf interaction with the nuclear spin possessing isotopes of the 12 next-nearest Si neighbors which gives rise to the substructure of the resonance lines when taking into account that in natural composition only 4.7% of the Si isotopes have a nuclear spin (^{29}Si). The shf interaction with the four nearest C neighbors, included in Eq. (1) by the term in parentheses, could not be detected because of too low intensity compared to the N donor background signal. Only the nuclei of the isotope ^{13}C (natural abundance 1.1%, $I = \frac{1}{2}$) take part in this interaction. The parameters of the spin Hamiltonian are summarized in Table 1. For the simulation of the spectrum (Fig. 2) it was, compatible with $\mathbf{B} \parallel c$, necessary to divide the 12 next-nearest Si neighbors into two groups of 6 magnetically equivalent atoms in each case with shf splitting constants of 0.13 and 0.18 mT, respectively.

3.2. DLTS

In Fig. 3 a typical DLTS spectrum of an as-grown 6H-SiC crystal, the same one as investigated by EPR, is shown for a time window of 20 ms, which corresponds to an emission time constant of about 8 ms at the DLTS peak maximum. Most of the observed deep levels have already been reported by other authors [7,8]. The activation energies and capture cross sections were

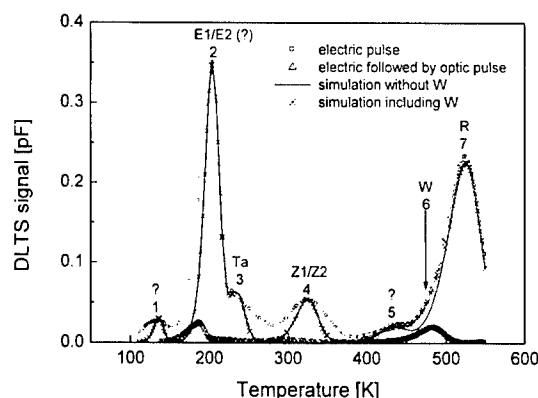


Fig. 3. Typical DLTS spectrum of an as-grown 6H-SiC crystal in comparison to a spectrum obtained when UV light pulses were included in the excitation and to simulations.

Table 2

Parameters of the deep levels observed in as-grown, n-type 6H-SiC crystals

Peak	$E_C - E_T$ (eV)	σ_n (10^{-14} cm^2)	N_T (10^{14} cm^{-3})	Related defects
1	0.28	2	2.4	?
2	0.42	1–2	33	E_1/E_2 [7,8]
3	0.49	1–2	4.5	Ta [2]
4	0.69	1–2	5.3	Z_1/Z_2 [7]
5	0.95	1–2	1.6	?
6	1.16	14–18	2.3	W [1,2]
7	1.23	4–6	31	R [7,8]

obtained from an Arrhenius plot analysis. The trap concentrations were corrected for the influence of the so-called transition region. These data are summarized in Table 2 together with possible defect assignments. The deep levels E_1/E_2 , Z_1/Z_2 and R are most probably related to intrinsic defects [7,8], whereas the temperature positions labeled Ta and W in Fig. 3 were proven to be the peak positions of tantalum and tungsten related defects, respectively [1,2]. Since Ta and W related defects could not completely identified by the experimental DLTS spectrum simulations based on the deep level parameters (Table 2) were carried out. In Fig. 3 the simulation, including all deep levels for which a parameter evaluation was possible, shows that the shoulder at about 240 K can be assigned to the Ta related defect with a concentration of about $4 \times 10^{14} \text{ cm}^{-3}$. For the W related defect an additional simulation excluding the level in question was calculated to support that its presence with a concentration of about $2 \times 10^{14} \text{ cm}^{-3}$ much better fits the measurement. Finally, a DLTS spectrum was recorded using an electric (i.e. voltage) pulse followed by an optic one from the UV

Table 1

Spin Hamiltonian parameters of W^{5+} in 6H-SiC

	G	$A(^{183}\text{W})$ (mT)	$A(^{29}\text{Si})$ (mT)
$B \parallel c$	2.0023	0.947	0.13–0.18
$B \perp c$	2.0035	0.91	0.15

laser. All deep electron traps which have a not too low hole capture cross section should be cleared. For two peaks (Fig. 3) this was not the case. Especially, the peak at about 480 K mainly consists of the W related defect with its full concentration. Hence, the hole capture cross section of this level is very low, whereas its electron capture cross section, in accordance with the Arrhenius plot analysis given here (Table 2) and in Ref. [1], should be very large. This behavior suggests a double donor state for the W related deep level.

4. Conclusions

Isolated tungsten on Si sites in 6H-SiC was identified by EPR for the first time. The anisotropy and the splitting pattern of the observed resonance lines could be interpreted by W^{5+} ($5d^1$, $S = \frac{1}{2}$). This is equivalent to a single positively charged donor. By DLTS a W related deep level was detected at about $E_C - 1.16$ eV. Its capture behavior for electrons and holes hints at a double donor level. Since this level is occupied by one electron in our n-type samples the resulting charge state is consistent with the EPR observation. Further support of our interpretation of the W related defect comes from theory [9,10]. Overhof calculated the charge transfer energy levels for several isolated TM's at different high-symmetry positions in 3C-SiC. There are theoretical [9] and experimental [7] arguments that these energies are relatively insensitive to the polytype and that the valence band edge can be used as reference level. Especially for isolated W on a Si site a double donor level at $E_V + 1.94$ eV, a single donor level at $E_V + 2.98$ eV and a single acceptor level at $E_V + 4.15$ eV were obtained [10]. The double donor level fits very well with the energy position determined by DLTS when using a gap

energy of 3.03 eV for 6H-SiC. Furthermore the charge state assigned by EPR and DLTS agrees with theory.

The W related defect detected by radiotracer DLTS in implanted samples [1] is the same one as in our as-grown samples, i.e. it is not a defect complex. However the assignation to a single acceptor given in [1] is incorrect.

The DLTS results for the Ta related deep level in an ion implanted sample [2] agree with ours for Ta in as-grown crystals. Therefore a complex of Ta with residual radiation damage can be excluded for the radiotracer DLTS experiments of [2].

W and Ta were incorporated on electrically active sites in 6H-SiC only in low concentrations of $2.4 \times 10^{14} \text{ cm}^{-3}$ during PVT growth.

References

- [1] N. Achtziger, G. Pasold, R. Sielemann, C. Hülsen, J. Grillenberger, W. Witthuhn, *Phys. Rev. B* 62 (2000) 12888.
- [2] J. Grillenberger, N. Achtziger, G. Pasold, R. Sielemann, W. Witthuhn, *Mater. Sci. Forum* 353–356 (2001) 475.
- [3] D. Schulz, K. Irmscher, J. Dolle, W. Eiserbeck, T. Müller, H.-J. Rost, D. Siche, G. Wagner, J. Wollweber, *Mater. Sci. Forum* 338–342 (2000) 87.
- [4] J. Baur, M. Kunzer, J. Schneider, *Phys. Stat. Sol. (A)* 162 (1997) 153.
- [5] P.G. Baranov, I.V. Ilyin, E.N. Mokhov, V.A. Khramtsov, *Mater. Sci. Forum* 353–356 (2001) 529.
- [6] D. Schulz, G. Wagner, J. Dolle, K. Irmscher, T. Müller, H.-J. Rost, D. Siche, J. Wollweber, *J. Crystal Growth* 198/199 (1999) 1024.
- [7] T. Dalibor, G. Pensl, H. Matsunami, T. Kimoto, W.J. Choyke, A. Schöner, N. Nordell, *Phys. Stat. Sol. (A)* 162 (1997) 199.
- [8] A.A. Lebedev, *Semiconductors* 33 (1999) 107.
- [9] H. Overhof, *Mater. Sci. Forum* 258–263 (1997) 677.
- [10] H. Overhof, private communication.



ELSEVIER

Physica B 308–310 (2001) 734–737

PHYSICA B

www.elsevier.com/locate/physb

Diffusion of boron in silicon carbide

K. Rüschemschmidt^{a,*}, H. Bracht^a, M. Laube^b, N.A. Stolwijk^a, G. Pensl^b

^a*Institut für Materialphysik, University of Münster, Wilhelm-Klemm Str. 10, D-48149 Münster, Germany*

^b*Institut für Angewandte Physik, University of Erlangen-Nürnberg, Staudtstrasse 7, D-91058 Erlangen, Germany*

Abstract

We have performed diffusion experiments with B-implanted 6H-SiC at temperatures between 1700°C and 2100°C. After diffusion, B concentration profiles were measured by means of secondary ion mass spectrometry. Accurate modeling of B diffusion is achieved on the basis of a kick-out diffusion mechanism which only involves point defects on the Si sublattice. Fitting of our experimental profiles yields data for the B interstitial-controlled B diffusion coefficient which are in good agreement with literature data. Moreover, the analysis of B diffusion provides data for the Si interstitial-controlled B diffusion coefficient which is interrelated with the Si self-interstitial contribution to Si diffusion in SiC. This contribution is found to be two orders of magnitude lower than an extrapolation of Si diffusion data reported in the literature. © 2001 Elsevier Science B.V. All rights reserved.

PACS: 61.72.Ji; 66.30.Dn; 66.30.Hs; 66.30.Jt

Keywords: Silicon carbide; Boron diffusion; Si self-interstitial; Kick-out mechanism

1. Introduction

SiC is a promising wide band gap semiconductor for high-temperature, high frequency, and high voltage electronic applications (see e.g. Ref. [1]). B like Al behaves as an acceptor in SiC but diffuses more rapidly in SiC than Al. Implantation of B in SiC is generally used for selective area doping [2]. This implantation process induces native point defects in concentrations exceeding the equilibrium value and can cause transient enhanced diffusion of B towards the surface and into the undamaged region of the SiC substrate during a subsequent high-temperature treatment. A preanneal at 900°C for 2 h has been shown to effectively reduce this transient enhanced B diffusion [3,4].

The fast diffusion of B compared to Al may seem unusual since B like Al is considered to be mainly dissolved on Si lattice sites in SiC. However, assuming that B diffuses via interstitial–substitutional exchange mechanisms



namely the dissociative mechanism and the kick-out mechanism, respectively, the fast diffusion of B is a consequence of a non-neglectable fraction of B in a highly mobile interstitial configuration B_i . V_{Si} , B_{Si} , and Si_i denote a vacancy on a Si lattice site, B dissolved on a Si lattice site, and a Si self-interstitial, respectively.

The B profiles shown in this work are considered to reflect B diffusion under near-equilibrium conditions and provide strong evidence that B diffusion at temperatures between 1700°C and 2000°C is mediated by the kick-out mechanism. Compared to a recent paper on B diffusion in SiC [5], we extend the present measurements to a wider temperature range. Additionally we have found evidence that a substantial fraction of B within the damaged region of the implanted sample may be not electrically active and hence some B atoms are not dissolved as isolated defects on Si lattice sites.

2. Experimental

A SiC wafer with a 10 μm thick Al-doped ($4.8 \times 10^{15} \text{ cm}^{-3}$) epitaxial SiC layer grown on an Al-doped

*Corresponding author.

E-mail address: kathrinr@uni-muenster.de (K. Rüschemschmidt).

substrate with a resistivity of $2.10 \Omega \text{ cm}$ was cut into stripes of 5 mm width with various length. These stripes were subsequently subjected to a five-fold B implantation at energies ranging from 20 to 200 keV and doses between 2.7×10^{13} and $7.3 \times 10^{13} \text{ cm}^{-2}$. The implantation results in a box-shaped as-implanted B profile with a B concentration of about $5 \times 10^{18} \text{ cm}^{-3}$. After implantation the sample stripes were preannealed at 900°C for 2 h to reduce the implantation damage and thus the transient enhanced diffusion of B during the high-temperature diffusion anneal. After the implantation and the preanneal, SiC samples, $5 \times 5 \text{ mm}^2$ in size, were cut and rinsed in organic solvents and placed in a high-temperature furnace for annealing at temperatures between 1700°C and 2100°C . This furnace was specially designed by Gero Hochtemperaturöfen GmbH for annealing of small samples at temperatures up to 2500°C . Various temperature programs are possible which include heating to a single set point and more sophisticated temperature profiles with different temperature ramps. It takes about 1 h to reach a fixed temperature of e.g. 2000°C . The water cooled double-wall vacuum chamber is purged with argon during annealing.

For our diffusion experiments the sample holder is driven into the region of maximum temperature after the set point is reached. The diffusion process is terminated by pulling the sample holder out of the high-temperature area. The distribution of B in the as-grown and annealed samples were measured with secondary ion mass spectrometry (SIMS). The recorded secondary ion counts were converted to concentrations by using B-implanted SiC calibration samples. The depths of the craters left from the analysis were determined with a surface profilometer.

3. Results and discussion

Fig. 1 shows concentration profiles of B after diffusion at 1700°C , 1800°C and 2100°C . Similar B profiles after diffusion at 1900°C and 2000°C are illustrated in Fig. 2. All profiles measured after diffusion at temperatures between 1700°C and 2000°C show a B concentration near the surface which is lower than 10^{18} cm^{-3} , a maximum concentration of $2\text{--}3 \times 10^{18} \text{ cm}^{-3}$ at about 300 nm within the damaged region of the implanted layer, and a pronounced B profile tail which extends several microns into the undamaged SiC substrate. Contrary to these findings annealing at 2100°C causes B to diffuse out of the sample and to accumulate near the surface. Moreover, B diffusion into the undamaged SiC substrate is not observed. This sample reveals an interesting pattern under an optical microscope which could originate from B segregation. We currently analyze this sample and the other B-diffused SiC crystals

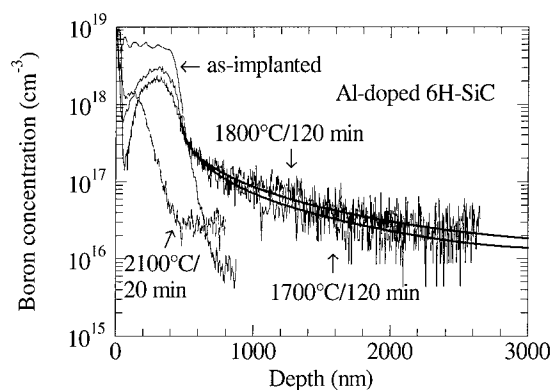


Fig. 1. Concentration depth profiles of B measured with SIMS (thin solid line) before (as-implanted) and after diffusion at 1700°C (120 min), 1800°C (120 min), and 2100°C (20 min) in Al-doped 6H-SiC. The thick solid lines represent the simulations on the basis of the kick-out mechanism.

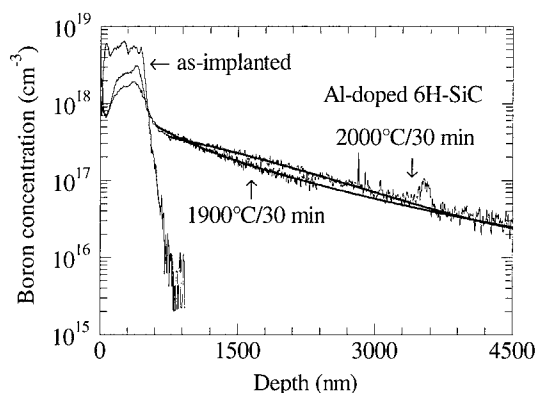


Fig. 2. Concentration depth profiles of B measured with SIMS (thin solid lines) before (as-implanted) and after diffusion at 1900°C (30 min) and 2000°C (30 min) in Al-doped 6H-SiC. The thick solid lines represent the simulations on the basis of the kick-out mechanism.

with transmission electron microscope (TEM) to detect the possible existence of B precipitates within the B-implanted layer. Taking the B profile at 2100°C as indication that B segregation very likely takes place within the damaged region, we believe that the corresponding B profile measured with SIMS does not reflect the actual distribution of isolated B on Si lattice sites. Hence for modeling the B distribution in the undamaged SiC substrate we neglected the first 500 nm of the B profiles. Furthermore we assumed that the B-implanted near-surface layer serves as an infinite source for B diffusion into the SiC substrate as long as the B concentration in this region is sufficiently high. All B diffusion profiles in 6H-SiC are accurately described on the basis of the kick-out reaction (2) (see thick solid lines in Figs. 1 and 2) whereas the dissociative mechanism

expressed by reaction (1) does not provide an accurate fit to the experimental profiles as demonstrated recently [5]. It is noted that the shape of the B diffusion profile slightly changes from convex to concave with increasing temperature. This observation is consistent with the kick-out diffusion model and reveals that B diffusion at temperatures below 2000°C is controlled by Si self-interstitials Si_i whereas B interstitials B_i control B diffusion at 2000°C.

Modeling of the B diffusion profiles yields data for the effective B and Si diffusion coefficients $D_{\text{B}_i}^*$ and $D_{\text{Si}_i}^*$, respectively, which are interrelated with the products $C_X^{\text{eq}} D_X$, $X \in \{\text{B}_i, \text{Si}_i\}$ between the equilibrium concentration and diffusivity of the respective point defects according to

$$D_{\text{B}_i}^* = \frac{C_{\text{B}_i}^{\text{eq}} D_{\text{B}_i}}{C_{\text{B}_i}^{\text{eq}}}, \quad (3)$$

$$D_{\text{Si}_i}^* = \frac{C_{\text{Si}_i}^{\text{eq}} D_{\text{Si}_i}}{C_{\text{B}_i}^{\text{eq}}}, \quad (4)$$

where $C_{\text{B}_i}^{\text{eq}}$ represents the solubility of B on the Si sublattice. We assume that this solubility is given by the B concentration measured with SIMS at the interface between the damaged and the undamaged region of the SiC epilayer. Data deduced for $D_{\text{B}_i}^*$ and shown in Fig. 3 are in good agreement with earlier results given by Mokhov et al. [6] which are thus considered to represent the B_i -controlled B diffusion characterized by $D_{\text{B}_i}^*$. The data extracted for $D_{\text{Si}_i}^*$ and $C_{\text{B}_i}^{\text{eq}}$ enables us to calculate

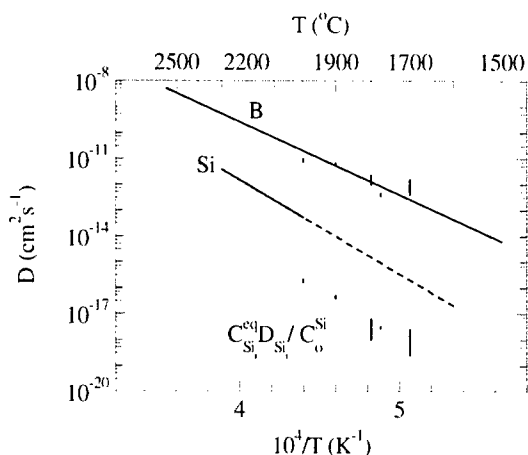


Fig. 3. Temperature dependence of B and Si diffusion coefficients D_{B_i} and D_{Si_i} (solid lines) in 6H-SiC reported in the literature [6,7] in comparison to our results. B diffusion data indicated by the upper solid bars were obtained from fitting the experimental B profiles shown in Figs. 1, 2 and 4. The lower solid bars represent the Si self-interstitial contribution to Si self-diffusion which is compared to Si tracer data extrapolated from high-temperatures (dashed line).

the Si self-interstitial contribution $C_{\text{Si}_i}^{\text{eq}} D_{\text{Si}_i} / C_{\text{O}_i}^{\text{Si}}$ of Si diffusion in SiC. This contribution is shown in Fig. 3 in comparison to the directly measured Si diffusion coefficient in 6H-SiC [7]. The Si self-interstitial contribution to Si diffusion in SiC is about two orders of magnitude lower than an extrapolation of the Si diffusion data to lower temperatures. This may suggest that Si diffusion is mainly mediated by vacancies on the Si sublattice. Consequently the vacancy contribution to Si diffusion should be two orders of magnitude higher than the Si self-interstitial contribution. In this case, one would expect that the interstitial-substitutional exchange via Si vacancies, that is, the dissociative mechanism mediates B diffusion in SiC. This, however, is in contrast with the shape of the B profiles which clearly points to B diffusion mediated by the kick-out mechanism. This conflict leaves some doubt about the accuracy of the earlier measured Si diffusion coefficients and may be solved by novel Si tracer-diffusion experiments that are currently in progress at our laboratory.

For modeling B diffusion in SiC, we recently assumed that B is completely electrically activated even within the ion-implanted region of the SiC layer [5]. Since this appears to be questionable now, we have considered in this paper that a substantial fraction of B within the damaged region is clustered and that actually the B concentration at the interface between the B implanted layer and the undamaged region equals the equilibrium concentration of B on Si lattice sites for the pertaining experimental conditions. Taking this approach for modeling B diffusion in SiC, all conclusions given in Ref. [5] remain valid. Only the values extracted for $D_{\text{B}_i}^*$ and $C_{\text{Si}_i}^{\text{eq}} D_{\text{Si}_i} / C_{\text{O}_i}^{\text{Si}}$ are slightly lower (by about a factor of 3) than the values earlier reported [5]. Moreover, B diffusion in N-doped 4H-SiC is also accurately described on the basis of this approach as demonstrated by Fig. 4.

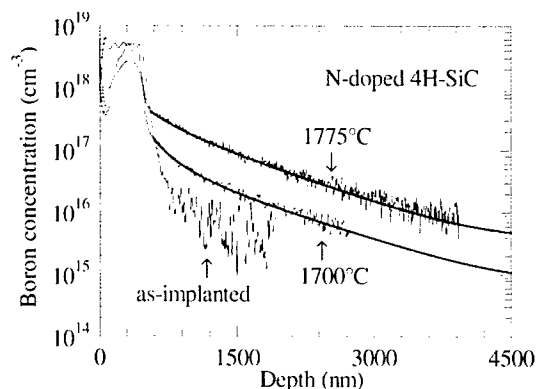


Fig. 4. Concentration depth profiles of B measured with SIMS (thin solid lines) before (as-implanted) and after diffusion at 1700°C and 1775°C for 60 and 180 min, respectively, in N-doped 4H-SiC. The thick solid lines represent simulations on the basis of the kick-out mechanism.

Modeling of these profiles yields data for the B and Si related diffusion coefficients which are equal to the results obtained from B diffusion in Al-doped 6H-SiC. This shows that the diffusion of B and Si in 6H-SiC and 4H-SiC is similar and does not depend very strongly on the conduction type of the SiC material, at least for the moderate doping concentrations under consideration.

4. Conclusions

The diffusion of B in 6H-SiC at temperatures between 1700°C and 2000°C is accurately described on the basis of the kick-out diffusion mechanism (see Eq. (2)). Values obtained for the B_i-controlled diffusion coefficient $D_{B_i}^*$ are in good agreement with literature data. The deduced Si self-interstitial contribution to Si self-diffusion is lower than data reported for Si diffusion in SiC which leaves some doubt about the accuracy of the Si diffusion data given in the literature. In order to investigate the interrelation between B and Si diffusion in more detail Si tracer-diffusion experiments exploring the temperature range between 1700°C and 2200°C should be performed. Annealing of B-implanted SiC at 2100°C seems to result in a pronounced outdiffusion of B and a segregation of B near the surface. TEM analyses of all samples are in

progress to characterize the precipitates which may exist after B-implantation and subsequent annealing.

Acknowledgements

We gratefully acknowledge financial support by the Deutsche Forschungsgemeinschaft.

References

- [1] M.V. Rao, J.A. Gardner, P.H. Chi, O.W. Holland, G. Kelner, J. Kretchmer, M. Ghezzi, *J. Appl. Phys.* 81 (1997) 6635.
- [2] T. Troffer, M. Schadt, T. Frank, H. Itoh, G. Pensl, J. Heindl, H.P. Strunk, M. Maier, *Phys. Stat. Sol. A* 162 (1997) 277.
- [3] M. Laube, G. Pensl, H. Itoh, *Appl. Phys. Lett.* 74 (1999) 2292.
- [4] M. Laube, G. Pensl, *Mat. Sci. Forum.* 338–342 (2000) 941.
- [5] H. Bracht, N.A. Stolwijk, M. Laube, G. Pensl, *Appl. Phys. Lett.* 77 (2000) 3188.
- [6] E.N. Mokhov, E.E. Goncharov, G.G. Ryabova, *Sov. Phys. Semicond.* 18 (1984) 27.
- [7] J.D. Hong, R.F. Davis, D.E. Newbury, *J. Mater. Sci.* 16 (1981) 2485.



ELSEVIER

Physica B 308–310 (2001) 738–741

PHYSICA B

www.elsevier.com/locate/physb

Identification of arsenic antisite defects with EL2 by nanospectroscopic studies of individual centers

Akira Hida*, Yutaka Mera, Koji Maeda

Department of Applied Physics, School of Engineering, The University of Tokyo, Tokyo, Japan

Abstract

The bistable behavior of point defects, presumably considered to be arsenic antisite defects, in low-temperature-grown GaAs crystals was studied experimentally by using scanning tunneling microscopy (STM) coupled with spectroscopic measurements in the nanometer scale (nanospectroscopy). At room temperature, the photoabsorption detected at the individual defects by measuring the reduction of the tunneling current flowing out of the filled gap states associated with them exhibits spectroscopic features quite similar to those observed in bulk GaAs crystals containing EL2 centers. At 90 K, optical excitation causes transformation of the individual defects from the normal state to a metastable state devoid of gap states. The metastable state is recovered to the normal state by injecting electrons from the STM tip into the defects. The excitation spectrum of the defect transformation was very close to that observed in photoquenching of the EL2 centers. These facts strongly indicate that, if the present defects are isolated arsenic antisite defects (As_{Ga}), the EL2 centers in bulk GaAs crystals are truly As_{Ga} . © 2001 Published by Elsevier Science B.V.

Keywords: As antisite defect; EL2; Scanning tunneling microscopy; GaAs

The midgap deep level center EL2 in GaAs has long been a well-known defect drawing great attention [1] not only of the technological importance as a center responsible for obtaining semi-insulating GaAs bulk crystals, but also of the academic concern on the peculiar behaviors of the bistable transformation, one of the most remarkable features of EL2. Particularly the so-called photoquenching effect, the reduction of photoabsorption induced by light illumination at low temperatures, stimulated intensive studies on the microscopic mechanism. Phenomenologically, the photoquenching effect has been interpreted by the configuration coordinate diagram as illustrated in Fig. 1(a) proposed by Vincent et al. [2]: the intracenter optical excitation from the normal state (neutral EL2) to an excited state being resonant with the conduction band relaxes along the adiabatic potential of a

metastable state (neutral EL2*) with a large atomic displacement. The problem that remained was on the atomistic structures of the defect in the bistable states.

Many experimental facts and some theoretical calculations [3,4] strongly suggested that the EL2 centers are isolated arsenic antisite defect (As_{Ga}). In this framework, the photoquenching effect could be interpreted in terms of the Jahn–Teller distortion that breaks the on-center symmetry of the antisite As atom to a lower symmetry by displacing the As along the $[111]$ direction to an interstitial site (off-center site) as illustrated in Fig. 1(b). However, the microscopic identification of EL2 as isolated As antisites remained somewhat controversial since there has been no direct experimental evidence for the atomistic structure of EL2.

In this report, we present a direct proof for the identity of EL2 with isolated As antisites by showing the photoabsorption property and the bistable behavior of individual point defects, presumably isolated As antisites, abundantly observed by cross-sectional STM in low-temperature-grown (LT-) GaAs [5]. The present STM instrumentation coupled with optical spectroscopic

*Corresponding author. Department of Applied Physics, School of Engineering, The University of Tokyo, Tokyo, Japan. Fax: +81-3-5841-8888.

E-mail address: hida@exp.t.u-tokyo.ac.jp (A. Hida).

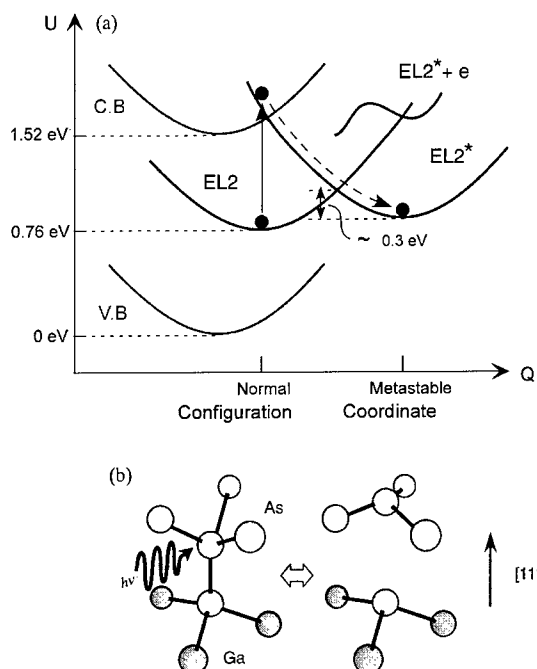


Fig. 1. (a) The configuration coordinate diagram suggested for EL2 [2] and (b) an isolated arsenic antisite (As_{Ga}) model [3,4] for EL2 suggested to explain, especially, the photoquenching effect.

measurements with nano-scale resolution (nanospectroscopy [6–8]) allowed us to show that individual single defects exhibit an infrared photoabsorption spectrum quite similar to that of EL2, and a photo-induced transformation with an excitation spectrum very close to that obtained for the photoquenching effect.

The LT-GaAs undoped film of 200 nm in thickness was grown homoepitaxially on a Si-doped n-type GaAs (001) substrate ($n \sim 10^{18} \text{ cm}^{-3}$) at 250°C in a VG-SEMICON VG80H molecular beam epitaxy (MBE) system. A clean (110) surface was prepared by cleaving a wafer piece in the ultra-high vacuum (UHV) STM chamber (UNISOKU, a custom model, base pressure $< 2 \times 10^{-8} \text{ Pa}$) and probed with a Pt–Ir tip.

Other than the instrumentation for the conventional scanning tunneling spectroscopic (STS) measurements [9], the present experimental set-up, schematically shown in Fig. 2, contained implements for photo-spectroscopic measurements as well. The monochromatic light from a monochromator was used to illuminate the sample surface at various photon energies.

For photoabsorption measurements, the light was chopped and the induced change of the tunneling current that occurs anyhow reflecting the photoabsorption of the sample were detected by a lock-in amplifier tuned at the chopping frequency. The photoabsorption

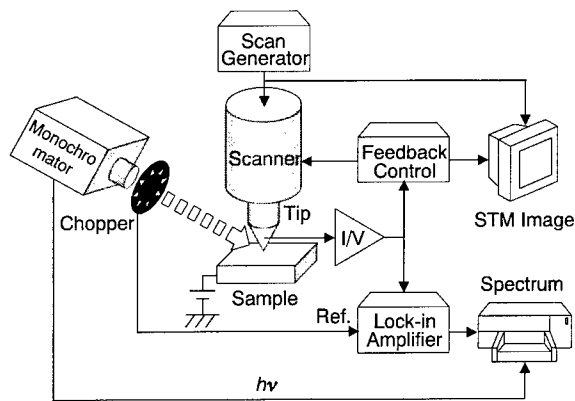


Fig. 2. The schematic diagram of the experimental setup for photoabsorption nanospectroscopy. A change in the tunneling current induced by photoabsorption of a defect is detected by a lock-in amplifier as a modulation signal synchronizing with the chopped light from a monochromator. The photoabsorption spectrum can be obtained by measuring the output of the lock-in amplifier as a function of the photon energy of the light.

signals could be generated by various mechanisms. Here we consider a case in which the STM tip positioned above a defect site is biased to extract electrons from the electronic level associated with the defect. When the electron occupying the defect level is optically pumped to an unoccupied upper level, the tunneling current will be reduced since the electron occupancy is decreased. Therefore, the photon energy dependence of the modulated signal of the tunneling current (ΔI) detected by the lock-in amplifier represents the photoabsorption spectrum of the defect. In the present experiments, the chopping frequency was chosen to be 1 kHz, high enough for the thermal expansion effect [7] to be suppressed and for the current modulation to be undamped by the STM feedback control. The photoabsorption measurements were performed at room temperature.

For inducing photoreactions that are to be detected in STM images, the sample was illuminated continuously in order to avoid thermal disturbance caused by light chopping. The spectroscopic measurements of the photoreaction rate were conducted at 90 K, low enough for the photoquenching effect to be observed. Excitation spectra of the photoreaction were obtained by measuring the mean rate of the atomic reaction that was detected in the repetitively acquired STM images of the same surface that was continuously subject to illumination with various photon energies.

Fig. 3(a) shows an STM image of the representative defects observed at room temperature in the cross-section of the LT-GaAs samples. The defects have characteristic contrasts appearing the same as those first reported by Feenstra et al. [10] and later cited by Jaeger

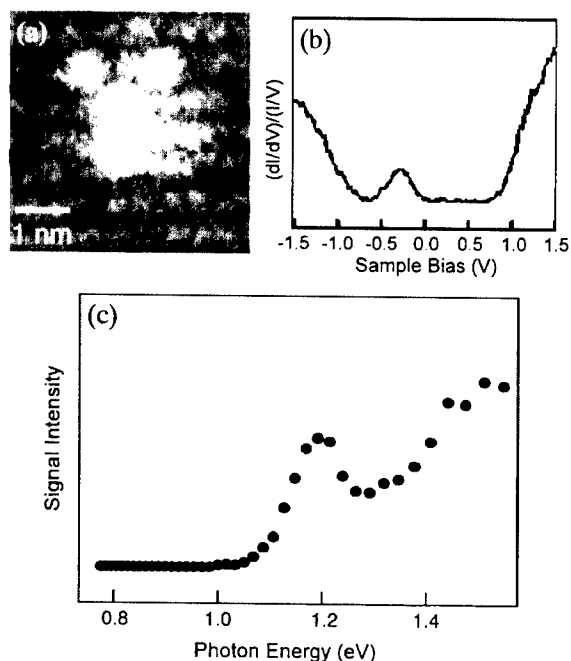


Fig. 3. (a) A typical STM image of a defect observed in an LT-GaAs epi-layer at room temperature and (b) the STS spectrum obtained at the defect site exhibiting a distinct midgap donor level. (c) The photoabsorption spectrum obtained with a tip fixed above one of the defects and setting the sample bias voltage at -0.5 V with respect to the tip so that the tunneling current is supplied from the midgap level if occupied. Note the spectrum is quite similar to the infrared absorption spectra observed in bulk GaAs crystals containing EL2 centers [1].

and Weber [11]. The STS spectra (Fig. 3(b)) obtained at these defects show that they commonly possess a deep donor level around the midgap energy, consistent with the previous report by Feenstra et al. [10].

The photoabsorption spectrum obtained by positioning the tip at the defect site and fixing the sample bias voltage at -0.5 V to extract electrons from the midgap level is shown in Fig. 3(c). The optical spectrum is characterized by the threshold around 1.05 eV followed by the gradually increasing infrared absorption background up to 1.4 eV, and a clear hump around 1.2 eV.

At 90 K, we found that prolonged light illumination causes a transformation of the majority of the point defects from the normal state (Fig. 4(a)) to a state quite different in the STM image (Fig. 4(b)). The STS spectra in the transformed state exhibited no gap levels in contrast to the initial normal state (Fig. 4(c)) as shown in Fig. 4(d). Though the transformed state persisted for long time if kept intact other than illumination, we found that the defect contrasts and the STS spectrum are recovered to the normal state immediately when we injected tunneling electrons to the defect at an appro-

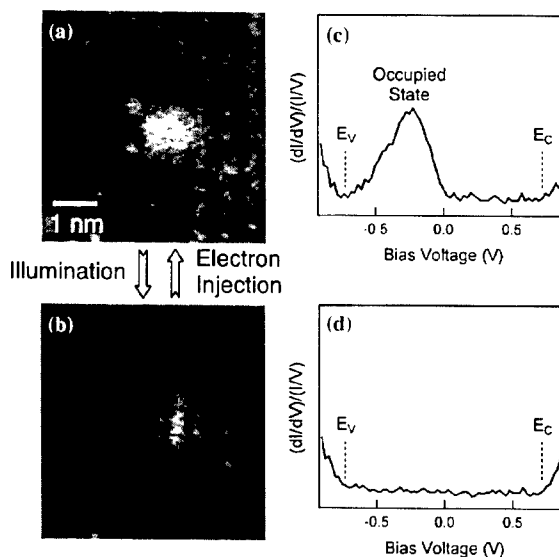


Fig. 4. (a) A typical STM image in the normal state and (b) the STM image in the metastable state transformed from the normal one by light illumination at 90 K (The images were taken at $V_s = -2.3$ V and $I_t = 100$ pA). The metastable state is recovered by injection of electrons from the tip to the defect. The STS spectrum at the defect site in the normal state (c) and in the metastable state (d). In the metastable state the midgap level disappears. Such bistable behaviors were not observed at room temperature.

prate positive sample bias. Taking full advantage of this effect of electron injection allowing 'initialization' of the defect state, we could conduct such experiments that after 'initialized' the defect state by the electron injection, we repeated STM observations under a 'non-destructive' imaging condition ($V_s = -2.3$ V, $I_t = 100$ pA) and as a function of the number of scans (time) we counted the number of the defects that changed the contrasts by the effect of the continuous light illumination. We repeated such experiments for various photon energies and obtained an excitation spectrum of such transformation as shown in Fig. 5.

The infrared absorption spectrum shown in Fig. 3(c) is quite similar to that obtained by macroscopic photoabsorption measurements on GaAs crystals containing EL2 centers. However, we should not hastily conclude that the defects probed with the STM tip are the EL2 centers, because the tunneling current flowing through the defect level probed directly by the STM tip must be supplied by hopping conduction via other centers densely populated in the crystals as pointed out by Grandidier et al. [14]. In other words the spectrum might simply reflect the photoabsorption of the centers along the conduction path rather than the defect at the surface observed by STM.

Nevertheless, the photo-induced transformation of the defects observed at 90 K is quite consistent with the

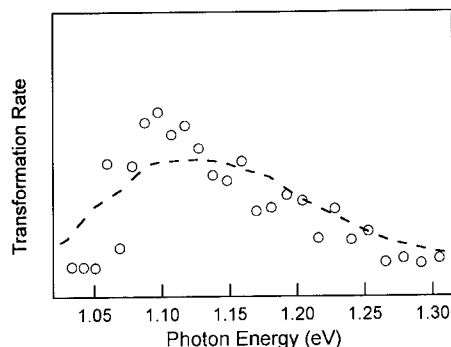


Fig. 5. The Excitation spectrum of the photo-induced transformation from the normal state to the metastable state. The spectrum is very close to that (broken line) measured by Fisher et al [15] for the macroscopic photoquenching effect of EL2 centers, indicating that the defects observed in the present experiments are EL2.

photoquenching behavior of EL2. The absence of the photo-transformation at room temperature and the long lifetime of the transformed state at the low temperature indicate that the transformed state is metastable. The excitation spectrum of this transformation is very close to that reported by Fisher [15] for the normal to metastable transition of EL2 centers that was studied by macroscopic measurements. The ambiguity discussed above in the interpretation of the local photoabsorption detected by the present method does not exist in the photo-transformation experiments because the transformation does not need the presence of other defects. Also the electron-injection-induced recovery of the metastable state to the normal state is consistent with another feature observed in EL2 [3,16,17]. Therefore, we can safely conclude that the defects observed are EL2 centers.

The defects in LT-GaAs giving the characteristic contrasts were identified by ab-initio calculations of STM images [12,13] to isolated As_{Ga} embedded in the first few layers beneath the (110) surface. The isolated arsenic antisites (As_{Ga}) model of EL2 has achieved successful interpretation for the bistable behaviors of EL2 including the photoabsorption, the photo-transformation and the electron-injection-induced recovery (the

process being illustrated in the coordination diagram in Fig. 1(a) [3]). The STM image of an isolated As_{Ga} in the metastable state was calculated by Zhang [13], but the bias polarity is different from that used in the present study (Note imaging with positive sample biases causes the structural recovery). Although the defect image shown in Fig. 4(b) is one obtained for the first time for the EL2 centers at the metastable state, the direct verification of the validity of the isolated As_{Ga} model was not possible at present from the image comparison. If reasonably we can assume that the present defects are isolated As_{Ga} , we can conclude that the atomic structure of EL2 is isolated As_{Ga} .

Acknowledgements

This work has been supported by Grant-in-Aid on Priority Area (Atomic Manipulation by Electronic Excitations #11222101 & #11222201) from the MEXT of Japan.

References

- [1] G.M. Martin, et al., in: S.T. Pantelides (Ed.), *Deep Centers in Semiconductors*, Gordon and Breach, New York, 1986, p. 399.
- [2] G. Vincent et al., *J. Appl. Phys.* 53 (1982) 3643.
- [3] J. Dabrowski, et al., *Phys. Rev. Lett.* 60 (1988) 2183.
- [4] D.J. Chadi, et al., *Phys. Rev. Lett.* 60 (1988) 2187.
- [5] G. Binnig, et al., *Helv. Phys. Acta.* 55 (1982) 726.
- [6] A. Hida, et al., *Appl. Phys. Lett.* 78 (2001) 3029.
- [7] A. Hida, et al., *Appl. Phys. Lett.* 78 (2001) 3190.
- [8] A. Hida, et al., *Solid State Phenom.* 78–79 (2001) 419.
- [9] R.M. Feenstra, et al., *J. Vac. Sci. Technol. B* 5 (1987) 923.
- [10] R.M. Feenstra, et al., *Phys. Rev. Lett.* 71 (1993) 1176.
- [11] N.D. Jaeger, E.R. Weber, *Semicond. Semimet.* 51B (1999) 261.
- [12] R.B. Capaz, et al., *Phys. Rev. Lett.* 75 (1995) 1811.
- [13] S.B. Zhang, *Phys. Rev. B* 60 (1999) 4462.
- [14] B. Grandidier, et al., *Appl. Phys. Lett.* 76 (2000) 3142.
- [15] D.W. Fisher, *Appl. Phys. Lett.* 50 (1987) 1751.
- [16] E.R. Weber, et al., *J. Appl. Phys.* 53 (1982) 6140.
- [17] A. Mittoneau, et al., *Solid State Commun.* 30 (1979) 157.



ELSEVIER

Physica B 308 310 (2001) 742–744

PHYSICA B

www.elsevier.com/locate/physb

Study of As self-diffusion in GaAs using sulfur as a tracer

N. Engler^{a,*}, H.S. Leipner^b, R.F. Scholz^{a,c}, P. Werner^a, U. Gösele^a

^aMax Planck Institute of Microstructure Physics, Weinberg 2, D-06120 Halle, Germany

^bMartin Luther University Halle-Wittenberg, Hoher Weg 8, D-06120 Halle, Germany

^cFractal AG, Gröbern 25, D-06434 Quedlinburg, Germany

Abstract

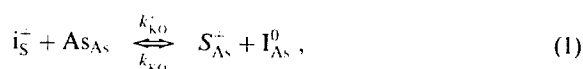
The diffusion of sulfur was investigated in order to study arsenic self-diffusion. From in-diffusion experiments the effective diffusion coefficients of sulfur and arsenic were determined in the temperature range between 750°C and 1100°C. For this purpose, different surface concentrations of sulfur were provided to establish the diffusion model. The simulations show that As self-interstitials are responsible for the diffusion of sulfur under thermal non-equilibrium of native point defects. The self-diffusion coefficient and the solubility of As self-interstitials were determined. © 2001 Elsevier Science B.V. All rights reserved.

PACS: 66.30.Jt; 66.30.Lw; 71.55.Eq; 72.80.Ey; 81.05.Ea; 85.40.Ky

Keywords: As self-diffusion; Sulfur diffusion; GaAs

1. Introduction

Dopant diffusion on the group-III sublattice of GaAs was extensively studied in the past, because most of the common dopants are dissolved on this sublattice. In the last few years, the diffusion on the group-V sublattice has become more and more important. Carbon as an acceptor for base doping of HBTs is dissolved on the As sublattice as well as nitrogen for active layer doping of VCSELs. Therefore, reliable diffusion data for this sublattice are necessary. Sulfur, which is a donor, can be used as a vehicle to study dopant diffusion and additionally As self-diffusion on the group-V sublattice of GaAs. Therefore, several experiments and simulations were performed to investigate diffusion depth profiles. It is known that the diffusion behavior of S in GaAs can be described within the kick-out diffusion model [1],



where i_S^+ denotes interstitially dissolved S, S_{As}^+ substitutionally dissolved S and I_{As}^0 an As self-interstitial. k_{KO}^+ and k_{KO}^- are the reaction constants in forward and backward direction. The backward reaction constant is given according to [2] as a diffusion controlled value,

$$k_{KO}^- = 4\pi r_c D_{I_{As}}. \quad (2)$$

In Eq. (2) r_c is the capture radius and $D_{I_{As}}$ the diffusion constant of As self-interstitials. The shape of the diffusion profile and the depth distribution can be controlled by the amount of S at the sample surface. At low concentrations the diffusion is governed by the kick-out diffusion under thermal equilibrium of native point defects. For a high S concentration at the surface the diffusion of S is mainly determined by the diffusion of the As self-interstitials. Based on this thermal non-equilibrium of native point defects self-diffusion of As can be described by simulations.

2. Experiments

For the experiments, undoped semi-insulating Bridge-man-grown GaAs with a low dislocation density was

*Corresponding author.

E-mail address: engler@mpi-halle.mpg.de (N. Engler).

used. After cleaning the samples were added into pre-cleaned quartz tubes. In order to establish an arsenic vapor pressure during the annealing procedure metallic arsenic was added to the ampoule in an amount needed for a 1 bar partial vapor pressure. Sulfur was dissolved in benzene to provide a small concentration and filled into the ampoule before evacuating down to 2×10^{-6} Torr and sealing. The experiments were performed in the temperature range between 750°C and 1100°C with different concentrations of S provided during the annealing procedure. After annealing the samples were quenched to room temperature. The depth profiles of sulfur were recorded by secondary ion mass spectrometry (SIMS) and analyzed by simulating the diffusion according to the 2nd Fickian Law and the kick-out model with the process simulator Zombie [3].

3. Results and discussion

Fig. 1 shows the depth profiles after in-diffusion at 850°C for 4 h. Providing a low S surface concentration of $c_{\text{S}}^{\text{surf}} = 2 \times 10^{18}$, represented by circles, the diffusion occurs under conditions closed to thermal equilibrium of native point defects. This can be described by the relation of the transport capacities, given by the product of the diffusion coefficient and the solubility of the mobile species,

$$D_{\text{IS}} c_{\text{IS}}^{\text{eq}} \approx D_{\text{IAS}} c_{\text{IAS}}^{\text{eq}}. \quad (3)$$

In this case, only a slight supersaturation of As self-interstitials has been established. The second profile with a surface concentration of $c_{\text{S}}^{\text{surf}} = 2.2 \times 10^{20}$ shows a non-equilibrium behavior of native point defects. The relation of the transport capacities is given by

$$D_{\text{IS}} c_{\text{IS}}^{\text{eq}} \gg D_{\text{IAS}} c_{\text{IAS}}^{\text{eq}}. \quad (4)$$

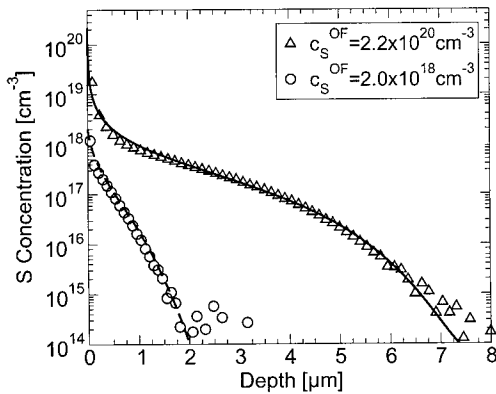


Fig. 1. In-diffusion profiles of sulfur after annealing at 850°C for 4 h. The surface concentration of S was varied between 2×10^{18} and $2.2 \times 10^{20} \text{ cm}^{-3}$. The symbols represent the total concentration measured by SIMS and the lines are the simulated concentration of substitutionally dissolved sulfur.

Under thermal non-equilibrium of native point defects the diffusion progress is controlled by the slower diffusing point defect. These experiments and simulations have shown that As self-interstitials are the diffusion controlling point defects. From the simulations, we were able to extract the diffusion coefficient and the solubility of the IAS according to the relation

$$D_{\text{AS}}^{\text{eff}} = \frac{D_{\text{IAS}} c_{\text{IAS}}^{\text{eq}}}{c_{\text{SAS}}^{\text{eq}}}. \quad (5)$$

For the simulations $D_{\text{AS}}^{\text{eff}}$ was kept constant and the solubility $c_{\text{SAS}}^{\text{eq}}$ is given by the surface concentration of sulfur.

Fig. 2 represents the effective diffusion coefficients of As and S. The As self-diffusion coefficient was determined as

$$D_{\text{AS}}^{\text{eff}} = (8.54 \pm 1.88) \times 10^{-1} \times \exp\left(-\frac{4.01 \pm 0.19 \text{ eV}}{k_{\text{B}} T}\right) \text{ cm}^2 \text{ s}^{-1} \quad (6)$$

and the effective diffusion coefficient of sulfur as

$$D_{\text{S}}^{\text{eff}} = (8.95 \pm 1.08) \times 10^{-4} \times \exp\left(-\frac{2.29 \pm 0.11 \text{ eV}}{k_{\text{B}} T}\right) \text{ cm}^2 \text{ s}^{-1}. \quad (7)$$

The value for As is in a good agreement with the effective As self-diffusion coefficient determined by Stolwijk et al. [4] and the value for sulfur with that reported by Young and Pearson [5]. For all simulations, the conditions

$$c_{\text{S}}^{\text{eq}} \gg c_{\text{IS}}^{\text{eq}} \quad \text{and} \quad c_{\text{IAS}}^{\text{eq}}; c_{\text{IS}}^{\text{eq}} \leq n_{\text{i}} \quad (8)$$

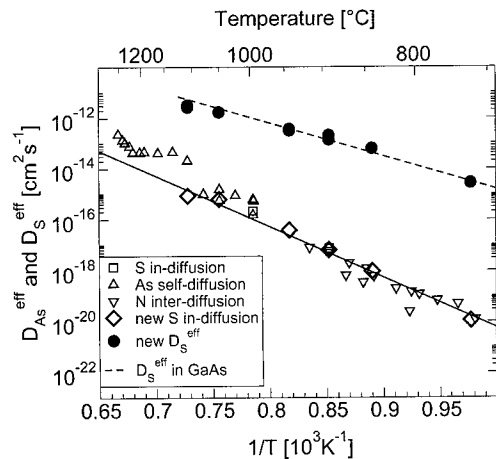


Fig. 2. Effective diffusion coefficients of As from S in-diffusion experiments [1], As tracer diffusion [7,8], N inter-diffusion [9,4] and this work. Additionally, the effective S diffusion coefficient is shown as symbols (this work) in comparison with literature data [5].

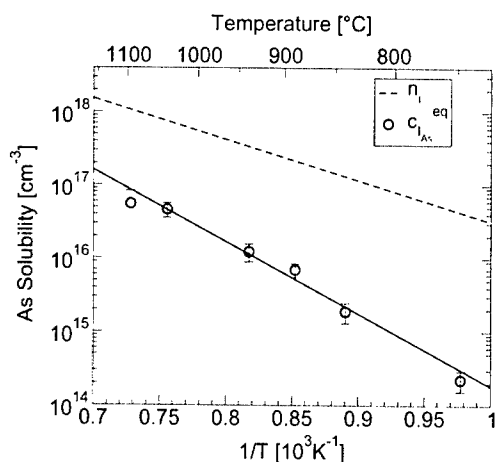


Fig. 3. Solubility of As self-interstitials. The values were determined from experiments under non-equilibrium conditions. The dashed line represents the intrinsic carrier concentration [6].

were established to calculate the diffusion parameters. n_i represents the intrinsic carrier concentration and is given in Ref. [6]. To determine the diffusion coefficients the set of partial differential equations for every point defect in Eq. (1) was solved numerically by the simulation program Zombie [3]. In all simulations, the As self-interstitials are assumed to be neutral. For these conditions, the solubility of the As self-interstitials as a function of the inverse temperature is shown in Fig. 3. Additionally, the intrinsic carrier concentration according to [6] is shown in this figure. The solubility of As self-interstitials was determined as

$$c_{I_{As}}^{eq} = (1.2 \pm 1.31) \times 10^{24} \times \exp\left(-\frac{1.95 \pm 0.13 \text{ eV}}{k_B T}\right) \text{ cm}^{-3}. \quad (9)$$

The values calculated in Eq. (9) are in agreement with the condition described in Eq. (8).

4. Conclusion

After sulfur in-diffusion experiments we investigated depth profiles of sulfur using SIMS and theoretically by simulations. Based on these investigations we determined the effective diffusion coefficients of S and As. Additionally, from non-equilibrium profiles we extracted the diffusion coefficient as well as the solubility of As self-interstitials.

Acknowledgements

This project was partly supported by Kultusministerium Sachsen-Anhalt (FKZ 2169A/0085B) and DFG (GK415).

References

- [1] M. Uematsu, P. Werner, M. Schultz, T. Tan, U. Gösele, *App. Phys. Lett.* 67 (19) (1995) 2863.
- [2] T. Waite, *Phys. Rev.* 107 (2) (1957) 463.
- [3] W. Jüngling, P. Pichler, S. Selberherr, E. Guerrero, H. Pötzel, *IEEE Trans. Electron. Dev.* ED-32 (1985) 156.
- [4] N. Stolwijk, G. Bösker, J. Thordson, U. Södervall, T. Andersson, C. Jäger, W. Jäger, *Physica B* 273–274 (1999) 685.
- [5] A. Young, G. Pearson, *J. Phys. Chem. Solids* 31 (1970) 517.
- [6] J. Blakemore, *J. Appl. Phys.* 53 (1) (1982) 520.
- [7] B. Goldstein, *Phys. Rev.* 121 (1961) 1305.
- [8] H. Palfrey, M. Brown, A. Willoughby, *J. Electron. Mater.* 12 (5) (1983) 864.
- [9] G. Bösker, N. Stolwijk, J. Thordson, U. Södervall, T. Andersson, *Phys. Rev. Lett.* 81 (16) (1998) 3443.



ELSEVIER

Physica B 308–310 (2001) 745–748

PHYSICA B

www.elsevier.com/locate/physb

On the microscopic structure of the EL6 defect in GaAs

Th. Steinegger^a, B. Gründig-Wendrock^c, M. Jurisch^b, J.R. Niklas^{c,*}

^a Infineon Technologies AG, München, Germany

^b Freiburger Compound Materials GmbH, Freiberg, Germany

^c Technical University Bergakademie Freiberg, Silbermannstr. 1, 06596 Freiberg, Germany

Abstract

Among the intrinsic defects in GaAs the EL6 gains more attention due to its properties as a non-radiative recombination centre. Also, for an efficient defect engineering its atomistic structure becomes an important question. There are many suggestions for this structure in the literature, however, nothing definite is known so far. From a combination of results from PICTS experiments to measure the EL6 concentration, positron annihilation, infrared absorption and laser scattering tomography arguments are put forward which point to a structure $\text{As}_{\text{Ga}}\text{-V}_{\text{As}}$ for the EL6. © 2001 Elsevier Science B.V. All rights reserved.

Keywords: GaAs; Defects; PICTS

1. Introduction

Among the intrinsic defects in GaAs, the midgap double donor EL2 is the most prominent and the most important one since it enables the GaAs to become semi-insulating (SI) by overcompensating shallow acceptors which, in turn, compensate shallow or medium deep donors. Progress in GaAs technology made it more and more possible to reduce the concentrations of extrinsic impurities and at the same time other, so far, less considered intrinsic defects like the EL6 gain attention. Moreover, it turned out that the EL6 plays an important role as a recombination centre determining the lifetime of excess carriers [1,2]. For these reasons, also the atomistic structure of this defect becomes an increasingly important factor from a basic point of view and also for the optimisation of defect engineering. However, so far, almost nothing is known definitely about the structure of the EL6. Since no spin resonance experiments are available for the EL6 there are only cumbersome indirect ways to first ideas of its structure. Many suggestions are found in the literature: $\text{V}_{\text{Ga}}\text{-V}_{\text{As}}$ [3–6]; $\text{V}_{\text{Ga}}\text{-As}_i$ or $\text{V}_{\text{Ga}}\text{-X}$ [7,8]; $\text{As}_{\text{Ga}}\text{-X}$ [9]; $\text{As}_{\text{Ga}}\text{-As}_i$ or

$\text{As}_i\text{-X}$ [10,11] and finally $\text{V}_{\text{As}}\text{-X}$, $\text{As}_{\text{Ga}}\text{-V}_{\text{As}}$ or $\text{V}_{\text{Ga}}\text{-As}_i\text{-V}_{\text{As}}$ [12–16]. The aim of this work is to find arguments for or against of some of these models using results of IR-absorption experiments [17], laser scattering tomography (LST) [18], positron annihilation (PA) [19], and finally, photo-induced current transient spectroscopy (PICTS) [20]. It is well known for GaAs that different annealing procedures greatly influence the concentration of Ga and As interstitials or vacancies and various intrinsic defects. This is reflected by the results of the above mentioned experiments giving rise to arguments for falsification or verification of structural models of the EL6.

2. Annealing procedures

Special annealing procedures with different temperature–time regimes were used for the GaAs samples investigated. These procedures are usually characterised by the following four steps: (a) A homogenisation at 1453 K resolves As precipitates and atmospheres of structural defects. (b) In the following regime of cooling down, an As supersaturation takes place with the formation of As nuclei. (c) During the subsequent temperature–time regime precipitates grow, additional

*Corresponding author. Tel.: +49-3731-39-2860; Fax: +49-3731-39-4314.

E-mail address: niklas@physik.tu-freiberg.de (J.R. Niklas).

As nuclei are formed and excess As interacts with other defects. (d) Finally, quenching to room temperature stabilises the defect structures thus obtained.

For the following experiments, a more special annealing regime was used. After the homogenisation at 1453 K for 20 h (warm-up rate 1 K/min) and subsequent quenching to room temperature, a second heating with 52 K/min to 1073 K was performed. Each sample was kept at this temperature for a well defined time ranging from 10 to 7200 min before recycling to room temperature again. All measurements took place at room temperature or below and therefore each measurement point in the following figures corresponds to a new sample. The samples treated this way differ clearly also by their EL6 content.

3. Experimental results

The relative concentrations of the EL6 defect were measured by PICTS. This type of spectroscopy delivers results similar to those of DLTS. However, in contrast to DLTS, no capacitance transients of a junction are evaluated but only photoconductivity transients due to a thermal re-emission of carriers out of levels which were filled by a preceding light pulse. This spectroscopy requires no co-doping with shallow levels and is therefore applicable also to high resistive SI material. However, as a drawback, PICTS furnishes no precise information about absolute concentrations of defects but only good values for relative defect concentrations for the same defect as a function of different preparations. Results of PICTS experiments are shown in Fig. 1, where the concentration of the EL6 is plotted versus annealing time, t , at 1073 K. The data indicate a drop of the EL6 concentration by about one order of magnitude

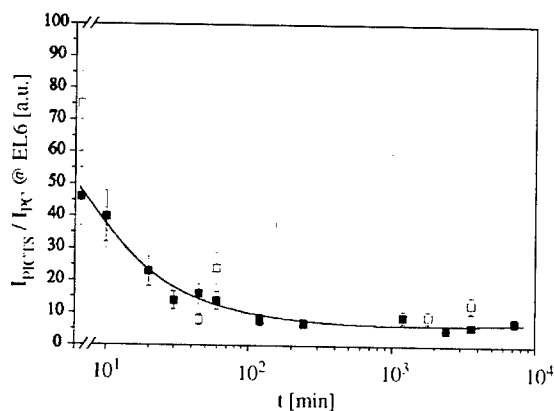


Fig. 1. Concentration of EL6 as measured by PICTS as a function of annealing time. Each dot corresponds to a new sample. Full squares, medium pressure GaAs (inert gas pressure during LEC crystal growth); open squares, low pressure GaAs.

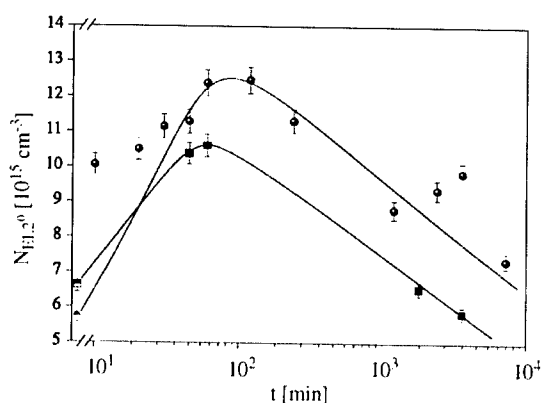


Fig. 2. Concentration of EL2⁰ as a function of annealing time. Upper curve, medium pressure GaAs; lower curve, low pressure GaAs.

with annealing. It should be stressed that the EL6 concentration is no longer diminished for annealing times longer than 60 min. After this time it remains constant at a value of about 10% of its starting value right after quenching. Fig. 2 reflects the annealing behaviour of the EL2⁰ as measured by IR-absorption. With increasing annealing time the concentration of the EL2⁰ increases by roughly a factor of 2 until a maximum at 60 min and then it decreases again. Fig. 3 shows the concentration of V_{Ga} by PA. These data must be taken with some care. There is a detection limit due to background signals as indicated by the horizontal line. The actual V_{Ga} concentrations for the higher annealing times might be well below this line. The concentration of precipitates was measured by LST. The data indicate a continuous increase with annealing time.

4. Interpretation of results and discussion

It is generally accepted that the structure of the EL2 is basically As_{Ga} . Based on ODENDOR-experiments an additional As_i in [1 1 1] direction was put forward [21], it was, however, also shown that the ODENDOR results published do not necessarily require the assumption of this As_i and that this assumption is moreover in contradiction to the corresponding ODEPR spectrum [22]. This controversy, however, does not substantially affect the following arguments. For the interpretation of the results, it is most important that the concentration of the EL2 exhibits a maximum at an annealing time of about 60 min and that exactly after this time the concentration of the EL6 does no longer change. It would be hard to believe that this behaviour could occur if the structures of the EL2 and EL6 were completely unrelated to each other. This is one argument to assume that the structure of the EL6 contains a unit As_{Ga} like in

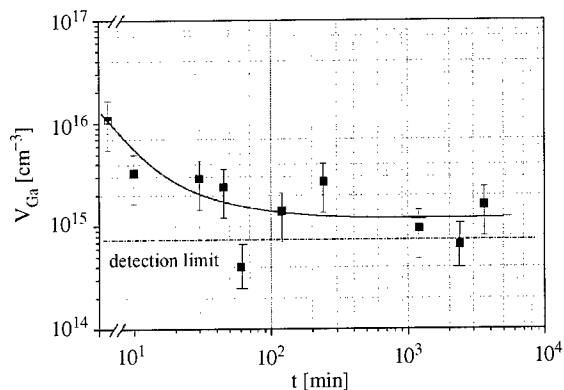


Fig. 3. Concentration of Ga-vacancies as obtained by positron annihilation as a function of annealing time (medium pressure GaAs).

$\text{As}_{\text{Ga}}\text{-V}_{\text{As}}$ or $\text{As}_{\text{Ga}}\text{-As}_i$ rather than a unit V_{Ga} . The structure As_{Ga} is apparently very stable as indicated by the relatively high concentration in the order $10^{16}/\text{cm}^3$ of the EL2 right after quenching from 1453 K (so-called as-grown state). Under the same conditions the concentration of the EL6 is estimated to be in the order $10^{15}/\text{cm}^3$ [23] indicating a likewise lower stability for this defect. The increase of the EL2 concentration with annealing time by roughly a factor of 2 corresponds well to the decrease of the V_{Ga} from about $10^{16}/\text{cm}^3$ to 'zero' (note PA detection limit): 'All' V_{Ga} are occupied by former As_i to form EL2 at an annealing time where the EL2 concentration reaches its maximum. Due to the high stability of the EL2 the concentration of still existing V_{Ga} in the equilibrium between EL2 and V_{Ga} together with As_i should be, therefore, extremely small, much smaller than the observed concentration of the EL6. This is taken as a further argument not to assume V_{Ga} as an integral part of the EL6.

Assuming now $\text{As}_{\text{Ga}}\text{-V}_{\text{As}}$ for the EL6 gives a much more consistent picture. EL6 is converted to EL2 which contributes to the increase of the EL2 for the lower annealing times. Later the EL6 concentration is stabilised by the equilibrium between $\text{As}_{\text{Ga}}\text{-V}_{\text{As}}$ (EL6) together with As_i and As_{Ga} (EL2). At the higher annealing times the EL2 may be destroyed by more and more accumulation of further As converting EL2 defects to As precipitates. At least in the beginning of this process the EL6 equilibrium is not affected too much since both the EL2 and the As_i concentrations are diminished when forming As precipitates.

The above arguments are indeed not yet able to really establish the structure $\text{As}_{\text{Ga}}\text{-V}_{\text{As}}$ for the EL6. However, there are clear hints towards this assumption to motivate further more specific experiments like spatially resolved defect analyses to account for the cellular structure of

the GaAs. Such special PICTS experiments are underway.

Acknowledgements

The authors wish to thank R. Krause-Rehberg, University Halle-Wittenberg, Germany for the PA-investigations

References

- [1] H.Ch. Alt, M. Muellenborn, G. Packeiser, in: A.G. Milnes, C.J. Miner (Eds.), *Proceedings of the Sixth Conference on Semi-Insulating III-V Materials*, Toronto, Canada, Adam Hilger, Bristol, UK, 1990, pp. 309–316.
- [2] M. Muellenborn, H.Ch. Alt, A. Heberle, *J. Appl. Phys.* 69 (1991) 4310.
- [3] Z.-Q. Fang, T.E. Schlesinger, A.G. Milnes, *J. Appl. Phys.* 61 (1987) 5047.
- [4] W. Fengmei, Z. Zhouying, *Rare Metals* 15 (1996) 191.
- [5] S.-K. Min, E.K. Kim, H.Y. Cho, *J. Appl. Phys.* 63 (1988) 4422.
- [6] C.V. Reddy, S. Fung, C.D. Beling, *Phys. Rev. B* 54 (1996) 11290.
- [7] J. Darmo, F. Dubecky, P. Kords, A. Foerster, *Appl. Phys. Lett.* 72 (1998) 590.
- [8] K. Mojeiko-Kotlinska, H. Scibior, I. Brylowska, M. Subotowicz, *Phys. Stat. Sol. A* 138 (1993) 217.
- [9] M. Levinson, in: A. Christou, H.S. Rupprecht (Eds.), *Proceeding of the 14th International Symposium on Gallium Arsenide and Related Compounds*, Institute of Physics Conference Series, Vol. 91, Heraklion, Crete, IOP Publishing Ltd., Bristol, UK, 1987, pp. 73–76.
- [10] K. Yasutake, H. Kakiuchi, A. Takeuchi, K. Yoshii, H. Kawabe, *J. Mater. Sci.* 8 (1997) 239.
- [11] N.M. Haegel, A. Winnacker, K. Leo, W.W. Ruehle, S. Gisdakis, *J. Appl. Phys.* 62 (1987) 2946.
- [12] T. Hashizume, H. Nagabuchi, *Semicond. Sci. Technol.* 4 (1989) 427.
- [13] Z.-Q. Fang, D.C. Look, *J. Appl. Phys.* 73 (1993) 4971.
- [14] Z.-Q. Fang, D.C. Look, S. Kuisma, K. Saarinen, P. Hautajarvi, in: C. Fontaine (Ed.), *Proceedings of the Ninth Conference on Semiconducting and Insulating Materials*, Toulouse, France, IEEE Inc., Piscataway, USA, 1996, pp. 149–154.
- [15] Z.-Q. Fang, D.C. Look, H. Yamamoto, H. Shimakura, *Appl. Phys. Lett.* 69 (1996) 3417.
- [16] Z.-Q. Fang, D.C. Look, *Mater. Res. Soc. Symp. Proc.* 442 (1997) 405.
- [17] F.X. Zach, A. Winnacker, *Jpn. J. Appl. Phys.* 28 (1989) 957.
- [18] M. Naumann, J. Donecker, DGKK-Arbeitskreis tagung GaAs, InP und SiC, Erlangen, March 22, 2000.
- [19] R. Krause-Rehberg, H.S. Leipner, *Positron Annihilation in Semiconductors—Defect Studies*, in: M. Cardona, P. Fulde, K. von Klitzing, R. Merlin, H.-J. Queiser, H. Stoermer (Eds.), *Springer Series in Solid-State Sciences*, Vol. 127, Springer, Berlin, Germany, 1999.

- [20] P. Blood, J.W. Orton, *The Electrical Characterization of Semiconductors: Majority Carriers and Electron States*, Academic Press, London, UK, 1992.
- [21] B.K. Meier, D.M. Hoffmann, J.-M. Spaeth, *Mater. Sci. Forum* 10–12 (1986) 311.
- [22] F. Wirbeleit, J.R. Niklas, in: G. Davies (Ed.), *Proceeding of the 19th International Conference on Defects in Semiconductors*, Aveiro, Portugal, *Mater. Sci. Forum* 253–263 (1997) 987–992.
- [23] S. Reichelmaier, K. Lochnert, M. Baumgartner, *Jpn. J. Appl. Phys.* 27 (1988) 2329.



ELSEVIER

Physica B 308–310 (2001) 749–752

PHYSICA B

www.elsevier.com/locate/physb

Magneto-optical and ODEPR investigations of native defects in substrate-free LT-MBE grown GaAs

I. Tkach^{a,*}, K. Krambrock^b, C. Steen^c, P. Kiesel^c, J.-M. Spaeth^a

^a *Fachbereich Physik, Universität Paderborn, 33095 Paderborn, Germany*

^b *Departamento de Física, UFMG, 30.123-970 Belo Horizonte, MG, Brazil*

^c *Institut für Technische Physik I, 91058 Erlangen, Germany*

Abstract

As-grown substrate-free LT-GaAs (200°C) and annealed samples (up to 660°C) have been investigated with magnetic circular dichroism of absorption (MCDA) and optically detected electron paramagnetic resonance (MCDA-EPR) in K- and W-bands. MCDA-EPR spectra of all samples reveal several As_{Ga}-related defects with different excitation spectra, that indicate their different structures in as-grown and annealed material. A strong change occurs in samples annealed above 400°C. The ODEPR spectra show another yet unknown defect which we attribute to a Ga vacancy-related defect. Samples annealed at 500°C exhibit EL2-like MCDA spectra. From the above band gap MCDA spectra of the EL2-like defects evidence is found for their low symmetry. The bleaching properties and spin-lattice relaxation times of the different As_{Ga}-related defects were investigated and compared with the properties of the EL2 defect in bulk semi-insulating GaAs. © 2001 Elsevier Science B.V. All rights reserved.

Keywords: LT-GaAs; As_{Ga}-related defect; Lift-off; MCDA-EPR

1. Introduction

The non-stoichiometry of LT-GaAs (As-rich) is a reason of really unique properties which have found many applications. The ultra short lifetimes of photo-generated carriers (< 1 ps), semi-insulating (SI) behavior after annealing and other useful properties influenced the development of different devices working in THz region [1]. Most of these features are caused by native point defects, mainly As_{Ga}-related defects, in extremely high concentrations (10^{18} – 10^{20} cm⁻³) which control the optical and electrical properties [2].

In general, in As-rich LT-GaAs three native point defects (or complexes between them) are favored: As antisite (As_{Ga})-like defects, Ga-vacancies (V_{Ga}) and As interstitials (As_i). Evidence was found for all of them [3–5], but their role and identification is still questioned, especially in connection with dramatic changes of the properties after annealing. The concentration and probably also the microscopic structure of the native

defects are influenced by annealing, which is often required in device processing. The question arises whether the defects are only modified by the annealing with respect to strain or charge states or whether different defects exist in as-grown and annealed material.

The dominant deep donor in LT-GaAs is regarded to be an As_{Ga}-related defect, a defect similar to the well-known EL2 defect which is responsible for the compensation of SI bulk GaAs. The optical and electrical properties of the EL2 defect are well known and have been extensively investigated. However, the mechanism of its metastability as well as its microscopic structure have still remained controversial issues. Similar bleaching behavior was observed for As_{Ga}-related defects in LT-GaAs, although less effective, and together with the SI properties supported somehow the suggestion that native defects in LT-GaAs are EL2-like defects [6,7].

In this paper we present and discuss experimental results which were obtained with magnetic circular dichroism of the optical absorption (MCDA) and MCDA detected electron paramagnetic resonance (MCDA-EPR) of substrate-free GaAs layers grown by

*Corresponding author. Fax: +49-5251-603247.

E-mail address: sp-it@physik.uni-paderborn.de (I. Tkach).

MBE at low substrate temperature ($\sim 200^\circ\text{C}$) and annealed after growth at different temperatures. Investigations were performed within a wide range of photon energies (0.7–1.8 eV) and MCDA-EPR in K- and W-microwave frequency bands (~ 24 and ~ 94 GHz, respectively) has been measured. Furthermore, the bleaching properties of As_{Ga} -related defects in LT-GaAs and of EL2 defects in SI bulk GaAs have been investigated for comparison. Experimental details can be found elsewhere [8].

The LT-MBE GaAs samples were grown in the University of California (Santa Barbara, USA) and in the University of Erlangen, Germany (Institut für Technische Physik). The temperature of the GaAs substrate was about 200°C . The thickness of the layers varied from 0.5 to $1\ \mu\text{m}$. After growth the samples were annealed in N_2 atmosphere at different temperatures from 200°C up to 660°C with minimal temperature steps of 50°C . To suppress the As evaporation, the surface of the samples was laid face down onto a GaAs substrate during annealing. After annealing the samples were prepared with a lift-off technique where the MBE films were separated from the GaAs substrate and glued onto glass plates [9]. This procedure was performed in the University of Erlangen.

2. Experimental results and discussion

ODEPR spectra of as-grown (200°C) and annealed (500°C) LT-GaAs measured via the MCDA at 0.93 and 1.12 eV are shown in Figs. 1a and b, respectively. The spectra are detectable in four different series of samples in different MCDA bands with exception of the samples annealed above 600°C , in which the MCDA-EPR

spectra of the LT-GaAs disappear. The MCDA-EPR spectra show mainly the four line hyperfine (hf)-split spectra due to As_{Ga} -related defects (nuclear spin of ^{75}As is $I = \frac{3}{2}$) [10]. The spectra are isotropic. Important to note are the large line widths ($W_{1/2}$) of about 40–50 mT of each hf line consistent with conventional EPR measurements of such samples [11]. The hf lines are broader than those measured for the EL2 defects in SI bulk GaAs (~ 38 mT). The g -values range from 2.030 to 2.041 for samples annealed at different temperatures. The central ^{75}As hf interaction of 2630 MHz is nearly constant.

The difference in intensity of the four hf lines does not disappear even at lowest microwave power levels ($\sim \mu\text{W}$), where forbidden transitions are suppressed definitely [15]. Therefore, one has to assume that a superimposed MCDA-EPR spectrum with a large line width and g factor of about 2.04 is also measured. It has the typical line shape (dashed curve 1 in Fig. 1) as was observed for different intrinsic acceptors in bulk GaAs [12]. It should be noted that the new spectrum was detected both in the as-grown and the annealed samples. We attribute the new MCDA-EPR line to V_{Ga} -related defects for the following reasons: (i) V_{Ga} is very probable in As-rich high non-stoichiometric LT-GaAs and (ii) positron annihilation experiments detect high concentrations of V_{Ga} defects in the same material [5]. V_{Ga} is a multiple acceptor with a T_2 ground state in the band gap of GaAs and is compensated by As_{Ga} -related donors. V_{Ga} -related defects with trigonal symmetry were detected and identified earlier in electron-irradiated GaAs [13,14]. The measured spectrum is compatible with the V_{Ga} (trigonal) for B [100] with a g -value of about 2.04 and a shf interaction with one ^{75}As neighbor of about 540 MHz.

In addition to the V_{Ga} -related defects another MCDA-EPR spectrum was observed for samples annealed above 450°C exposing the material to light with a photon energy above 1.12 eV (dashed curve 2 in Figs. 1b and c). It has a g -factor of about 1.98. Unfortunately, the large line widths and high intensity of the As_{Ga} -related spectra prevent the reliable identification of the defect. Neither the tagged MCDA technique nor high-frequency (91 GHz) MCDA-EPR (Fig. 1c) measurements could separate the different spectra.

The small differences in the MCDA-EPR parameters of the As_{Ga} -related defects could be an indication that different As_{Ga} -related defects exist in as-grown and annealed material. Rather strong evidence for that was obtained with the tagged MCDA technique, where when setting the EPR resonance conditions to a particular ODEPR line and varying the optical wavelength the EPR line of the defect can be correlated with its optical properties [8]. Fig. 2 shows such excitation spectra for the as-grown sample (Fig. 2a) and for the 500°C

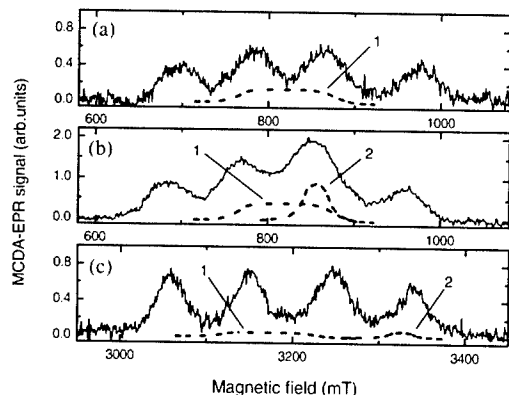


Fig. 1. (a) MCDA-EPR spectrum of as-grown (200°C) LT-GaAs measured at 24.0 GHz with photon energy of 0.92 eV at 1.5 K. (b) MCDA-EPR of annealed (500°C) LT-GaAs measured with light energy of 1.12 eV at 23.5 GHz and temperature of 1.5 K and (c) the same spectrum measured at 91 GHz (W-band).

annealed sample (Fig. 2b). Clearly the spectra are different. From earlier investigations of several different As_{Ga} -related defects in electron-irradiated GaAs it is known that most of them have nearly indistinguishable MCDA-EPR spectra, but different tagged MCDA spectra which serve as their fingerprints [15]. MCDA-detected electron nuclear double resonance experiments confirmed evidently the difference in the microscopic structure of the defects [15,16]. We conclude therefore that we deal with different As_{Ga} -related defects in as-grown and annealed LT-GaAs. Furthermore, one can notice the similarity of the MCDA spectrum of the annealed (500°C) LT-GaAs sample and the MCDA spectrum of the EL2 defect (dashed line), which appears in SI bulk GaAs (Fig. 2b). The critical annealing temperature lies near 400°C, where the MCDA and MCDA-EPR spectra nearly disappear. This behavior has been observed in different series of samples. It may indicate that the Fermi level position is shifted because of the recombination of defects or reconstruction of the microscopic structure of defects, which affect their electronic levels in the band gap.

Of particular interest are also the MCDA transitions at photon energies above the band gap of GaAs (Fig. 2). The preparation of the LT-GaAs films with the lift-off technique enabled us to perform MCDA and MCDA-EPR measurements without the influence of the GaAs substrate and very importantly, to measure above the band gap. For example, in as-grown LT-GaAs, a MCDA-EPR signal was detected using the photon energy of 1.69 eV (730 nm). For the isolated As_{Ga} defect the MCDA spectrum, which shows a single derivative-like shape, has been interpreted as belonging to a transition from the A_1 ground state to a localized excited T_2 state in the conduction band [17]. For the EL2 defect and also for the EL2-like defects in LT-GaAs more

transitions are observed, which are probably explained by a symmetry reduction which splits the excited state T_2 confirming previous MCDA-EPR/ENDOR results that EL2 is not the isolated As_{Ga} defect [18].

Of interest are also the different spin-lattice relaxation times T_1 measured for the different As_{Ga} -related defects. The MCDA depends only on the longitudinal magnetization, therefore only on T_1 [8]. From such measurements a difference between the As_{Ga} -related defects in as-grown and annealed material was found. T_1 of the defects in as-grown material was measured to be ~ 0.7 – 1 s at 1.5 K, while in annealed samples at 500°C it is ~ 3.5 – 4 s. The latter value is almost the same as that measured for EL2 defects in SI bulk GaAs. Interesting to note is that As_{Ga} -related defects in LT-GaAs (200°C) on substrate studied earlier showed T_1 times of < 100 ms [10]. It seems that the lattice mismatch between substrate and layer induce additional strains which reduce the T_1 times similarly to observations in plastically deformed GaAs.

For comparison of EL2 defects in bulk GaAs and As_{Ga} -related defects in annealed LT-GaAs the metastable properties have also been investigated under light illumination at low temperatures. It has been argued that the As_{Ga} -related defects in LT material are modified EL2 defects because of the lattice strain caused by the As excess. Inspecting the bleaching behavior of the native defects in as-grown and annealed LT-GaAs we have observed rather complicated bleaching dynamics which depend strongly on annealing. Our investigations confirm that the bleaching efficiency for the As_{Ga} -related defects in LT GaAs is shifted to higher photon energies, what has been observed previously also by different techniques [6]. The shift in photon energy depends on the annealing temperature and seems to be maximal for as-grown samples with lowest bleaching efficiency. When exposing the samples to light which was usually used to bleach the EL2 defect ($h\nu \sim 1.2$ eV), we have observed the opposite effect, namely enhancement of the MCDA-EPR spectra. This can be related to recharging from the diamagnetic (As_{Ga}^0) to the paramagnetic (As_{Ga}^+) charge states. The maximal enhancement was detected for as-grown LT-GaAs. Exposing the material to white light during 4 h only $\sim 32\%$ of the total MCDA of the defects in samples annealed at 500°C could be bleached. For as-grown material this value is even less (near 10%), which indicates that most of the As_{Ga} -related defects are unbleachable. It seems likely that we deal with As_{Ga} -related defects in different local environments and structures.

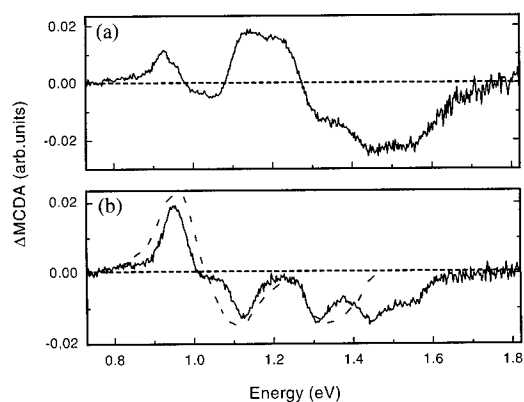


Fig. 2. Tagged MCDA spectra of As_{Ga} -related defects in (a) as-grown (200°C); (b) annealed at 500°C LT-GaAs. Measurement temperature 1.5 K, microwave frequency 24.8 GHz, resonance field B of 700 mT.

3. Summary

MCDA and MCDA-EPR spectra of different As_{Ga} -related defects in as-grown and annealed LT-GaAs have

been observed. A critical annealing temperature has been determined to be about 400°C. In samples annealed near 500°C EL2-like defects were detected, whereas for annealing at 600°C and above As_{Ga}-related MCDA-EPR spectra disappeared. The MCDA-EPR spectra superimposed on the spectra of the As_{Ga}-related defects were attributed to V_{Ga}-related defects, consistent with positron annihilation experiments. The lift-off sample preparation technique allowed the observation of the MCDA bands of the As_{Ga}-related defects with photon energies exceeding the band gap energy of GaAs. These transitions were attributed to localized excited states in the conduction band, which are indicative of low symmetry defects where the T₂ excited state of the isolated As_{Ga} is split. The EL2-like defects observed in 500°C annealed LT-GaAs show nearly the same tagged MCDA spectra as those of EL2 defects in SI bulk GaAs and a maximum bleaching efficiency. Therefore, their structure should be similar. The large MCDA-EPR line widths of these defects are explained by local disorder and strain in the samples.

Acknowledgements

The authors wish to thank the Deutsche Forschungsgemeinschaft (DFG) for financial support. One of us,

Dr. Klaus Krambrock, acknowledges a grant from the Brazilian agency CAPES (Grant No. BEX 0356/00-0).

References

- [1] M.O. Manasreh, et al., *Phys. Rev. B* 41 (1990) 10272.
- [2] H.-J. Sun, et al., *Appl. Phys. Lett.* 60 (1992) 718.
- [3] K.M. Yu, et al., *J. Appl. Phys.* 72 (1992) 2850.
- [4] J. Gebauer, et al., *Appl. Phys. Lett.* 71 (1997) 638.
- [5] J. Gebauer, et al., *J. Appl. Phys.* 87 (2000) 8368.
- [6] M. Kaminska, et al., *Mater. Sci. Forum* 83–87 (1992) 1033.
- [7] G. Kowalski, et al., *Mater. Sci. Eng. B* 22 (1993) 27.
- [8] J.-M. Spaeth, et al., *Structural Analysis of Point Defects*, Springer, Berlin, 1992.
- [9] E. Yablonovitch, et al., *Appl. Phys. Lett.* 51 (1987) 2222.
- [10] K. Krambrock, et al., *Semicond. Sci. Technol.* 7 (1992) 1037.
- [11] H.J. von Bardeleben, et al., *Phys. Rev. B* 45 (1992) 3372.
- [12] K. Krambrock, et al., *Mater. Sci. Forum* 38–41 (1989) 863.
- [13] Y.Q. Jia, et al., *Phys. Rev. B* 45 (1992) 1645.
- [14] K. Krambrock, et al., *Solid State Commun.* 93 (1995) 285.
- [15] F.K. Koschnick, et al., *Phys. Stat. Sol. B* 216 (1999) 817.
- [16] J.-M. Spaeth, et al., *Mater. Sci. Forum* 143–147 (1994) 217.
- [17] K. Krambrock, et al., *Phys. Rev. B* 45 (1992) 1481.
- [18] J.-M. Spaeth, et al., *Festkörperprobleme* 33 (1993) 111.



ELSEVIER

Physica B 308–310 (2001) 753–756

PHYSICA B

www.elsevier.com/locate/physb

On the problem of the EL2 structure in semi-insulating GaAs: high-frequency ODEPR/ODENDOR measurements in W-band

I. Tkach^{a,*}, K. Krambrock^b, J.-M. Spaeth^a

^a *Fachbereich Physik, Universität Paderborn, D-33095 Paderborn, Germany*

^b *Departamento de Física, UFMG, 30.123-970 Belo Horizonte, MG, Brazil*

Abstract

For almost two decades the structure model of the EL2 defect in semi-insulating (SI) GaAs has been controversially discussed. Neither the isolated As_{Ga} with T_d symmetry, nor the $\text{As}_{\text{Ga}}\text{--As}_i$ pair model nor any other As_{Ga} -related defect model could be unambiguously established. The reason was that the analysis of previous optically detected electron nuclear double resonance (ODENDOR) and optically detected electron paramagnetic resonance (ODEPR) spectra measured at 24 GHz was difficult and not unambiguous because of forbidden transitions, pseudo-dipolar couplings and higher order effects. However, the ODEPR spectra of the EL2 defect measured in W-band (93 GHz) can be fitted by first order perturbation calculation of the spin Hamiltonian thus allowing a much simpler analysis compared to X- or K-band. From ODEPR measurements in different SI GaAs samples both in K- and W-band we show that the ODEPR spectra of the EL2 defect together with the K-band ODENDOR data are not consistent with the $\text{As}_{\text{Ga}}\text{--As}_i$ pair model, but the highly symmetric isolated As_{Ga} model has to be excluded as well. First ODENDOR measurements in W-band are also reported. © 2001 Elsevier Science B.V. All rights reserved.

Keywords: GaAs; EL2; EPR; ENDOR

1. Introduction

The microscopic structure of the dominant deep donor EL2 in semi-insulating (SI) GaAs with its fascinating metastable properties is still not fully understood. Two microscopic models are mainly discussed (i) the isolated As_{Ga} model having T_d symmetry and the (ii) $\text{As}_{\text{Ga}}\text{--As}_i$ pair defect. The first model was based on piezospectroscopic studies of optical transitions of the EL2 defect [1] and favored by theory to explain the metastable state [2,3]. The second model was proposed from a combined study of electron paramagnetic resonance (EPR) and deep level transient spectroscopy (DLTS) [4] and supported by optically detected electron nuclear double resonance (ODENDOR) [5]. In 1992, ODENDOR studies of electron irradiation-induced

As_{Ga} -related defects revealed an As antisite defect which was attributed to the isolated As_{Ga} defect with higher symmetry (T_d) compared with EL2 [6]. In 1997, the model of the EL2 defect as an $\text{As}_{\text{Ga}}\text{--As}_i$ pair defect was questioned by a calculation of the width of the EPR lines measured in X- and K-band [7].

In principle, for each defect model derived by ENDOR, which allows the determination of the hyperfine (hf), super-hyperfine (shf) and quadrupole interaction tensors for many neighboring nuclei, the EPR line width has to be explained by a calculation using these ENDOR parameters. This is necessary because ENDOR permits only the determination of the ‘chemical’ nature and the symmetry and principal values of the interaction tensors of the neighboring nuclei, but not their numbers, i.e. how many members are in a shell [8]. The calculation of the EPR spectrum from the ENDOR parameters is necessary to confirm a proposed defect model. The analysis of previous

*Corresponding author. Fax: +49-5251-603247.

E-mail address: sp-it@physik.uni-paderborn.de (I. Tkach).

optically detected electron paramagnetic resonance (ODEPR) and ODENDOR spectra in K-band was very difficult because of forbidden transitions, pseudo-dipolar couplings and higher order effects in the spectra. The same holds for conventional X-band (10 GHz) EPR measurements. The EPR (and ENDOR) spectra would have to be calculated using exact diagonalization of the appropriate spin Hamiltonian with prohibitive large spin matrices preventing a satisfactory calculation.

We present the results of W-band (93–95 GHz) high-field/high-frequency ODEPR investigations of the EL2 defect in SI GaAs samples grown either by the liquid encapsulated Czochralski (LEC) or the horizontal Bridgman (HB) technique. The samples were cut to dimensions of $1.5 \times 1.5 \times 3.0 \text{ mm}^3$ and orientated by X-ray Laue analysis along the [001], [110] and [111] crystallographic axes. It is shown that the high-field ODEPR spectra can be described by first order perturbation calculation of the spin Hamiltonian thus allowing a much simpler analysis compared to X- or K-band spectra. First results of very recent ODENDOR measurements in W-band are also reported. The results are discussed with respect to the proposed EL2 structure models.

2. Experimental results

Fig. 1 shows the typical four-line hf-split ODEPR spectra of the EL2 defect in SI GaAs measured for $B_0 \parallel [001]$ in K-band (a) and W-band (b), respectively. The spectra were monitored with the magnetic circular dichroism of the absorption (MCDA) at 1.5 K in MCDA band centered at 0.94 eV. The observed hf splitting is due to the central ^{75}As nucleus of the antisite

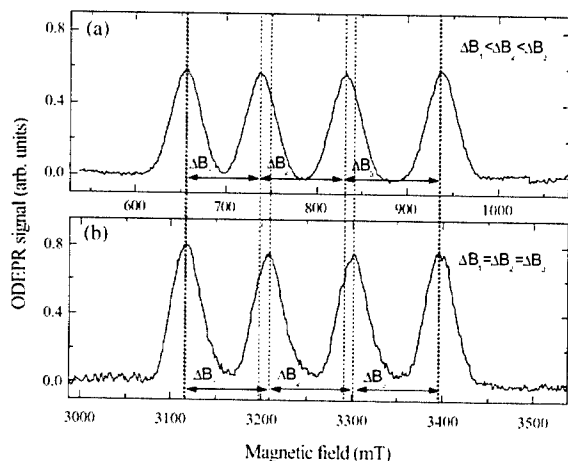


Fig. 1. ODEPR spectra of the EL2 defect in GaAs measured in (a) K-band (24 GHz) and (b) W-band (93 GHz) for $B \parallel [001]$ at 1.5 K.

($I = 3/2$, 100% abundance) and is described by an isotropic hf constant of $2656 \pm 30 \text{ MHz}$ in agreement with the previously determined one from K-band. However, the four hf lines measured in W-band are equidistant (93 mT separation) in contrast to the K-band spectra where the hf line separation increases with increasing magnetic field.

The angular dependence of the ODEPR line widths measured in W-band is shown in Fig. 2. The center line positions of the hf ODEPR lines are isotropic. But the ODEPR line width varies by about 2.5 mT with the orientation of the samples. It is smallest for $B_0 \parallel [001]$ and largest for $B_0 \parallel [111]$, both in K- and W-band spectra. The ODEPR line widths in W-band are smaller by about 2 mT compared to K-band measurements. This result is expected because of reduced contributions of forbidden transitions in W-band. For example, ODEPR line widths measured very carefully with the lowest microwave power levels for $B_0 \parallel [001]$ are $38.0 \pm 0.8 \text{ mT}$ and $35.7 \pm 0.8 \text{ mT}$, in K- and W-band, respectively.

Fig. 3 shows the very first ODENDOR measurements in W-band for $B_0 \parallel [110] + 20^\circ$ (20° off $[110]$ in a (001) plane) setting B_0 into the flanks of two of the ^{75}As hf lines. Compared to the many ENDOR lines in K-band [5] due to higher order effects there are less lines. All lines are due to ^{75}As and $m_s = -1/2$ ('sum' frequencies) as seen from the lines shifts when varying B_0 . No further sample orientations could yet be measured. Further work is in progress.

3. Discussion

Wirbeleit et al. [7] have performed calculations of the EPR/ODEPR line width of the EL2 defect using an exact diagonalization of the spin Hamiltonian and

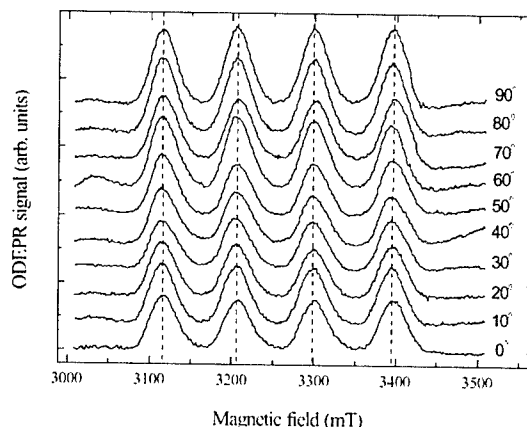


Fig. 2. Angular dependence of the ODEPR line widths of the EL2 defect in SI GaAs measured in W-band for rotation of the magnetic field in the (011) plane. 0° corresponds to $B \parallel [001]$ and 90° to $B \parallel [111]$.

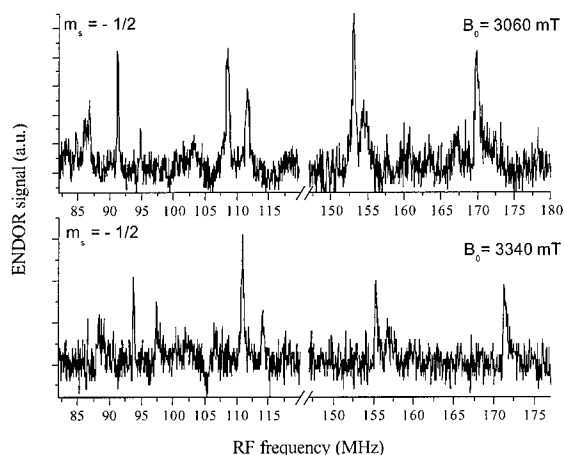


Fig. 3. ODENDOR spectra measured in W-band (93 GHz) for $B_0 \parallel [1\ 1\ 0] + 20^\circ$ (20° in $(0\ 0\ 1)$ plane) for two B_0 values. All lines are due to ^{75}As nuclei.

compared the results with experimental spectra. Unfortunately, Wirbeleit et al. did not publish absolute values for the line widths. They concluded, that the $\text{As}_{\text{Ga}}\text{--As}_i$ pair model for the EL2 defect was wrong and that the half width calculated with the ENDOR parameters without the As interstitial is consistent with the EPR line width, i.e. they favored the isolated As_{Ga} antisite model. However in their calculations Wirbeleit et al. used some approximations: (i) they considered only off-diagonal elements of the spin matrices near the diagonal and (ii) they neglected the central ^{75}As hf interaction. Unfortunately, a calculation of the EPR spectra never appeared using their full diagonalization procedure.

The equidistance of the four-line hf-split ODEPR spectrum measured in W-band indicates that the spectrum can be calculated in the first order perturbation theory approximation, i.e. the Zeeman interaction is much stronger than the hf interaction of the central ^{75}As nucleus. Thus, the W-band ODEPR spectra are much simpler to analyze in comparison with X- or K-band spectra because forbidden transitions of type $\Delta m_I = \pm 1$ are less probable. The transition probability of the forbidden transitions is proportional to $(1/B_0)^2$. Therefore, their intensities in W-band are reduced by more than one order of magnitude compared to K-band measurements (see also Ref. [9]).

In W-band in first order perturbation theory all nuclei can be treated independently. One needs only to know their shf interaction constants and their nuclear spin quantum numbers. With the knowledge of the ODENDOR line width which is about 1 MHz as measured for the EL2 defect in K-band, all allowed EPR transitions can be summed up to give the total ODEPR spectrum in first order.

For the line width calculations the ODENDOR parameters of Ref. [5] have been used, i.e. $g = 2.04$, $a = 2656$ MHz (central ^{75}As nucleus), and the shf parameters: $a = 167.8$ MHz, $b = 53.9$ MHz (4 next nearest As neighbors); $a = 35.2$ MHz, $b = -1.3$ MHz (3 second nearest As neighbors); $a = 19.5$ MHz, $b = 3.2$ MHz (9 second nearest As neighbors). In order to examine of the two structure models, isolated As_{Ga} versus $\text{As}_{\text{Ga}}\text{--As}_i$ pair defect, for the latter the As interstitial was considered with its shf parameters $a = 215$ MHz and $b = 44$ MHz [5]. Anisotropic shf interaction parameters b have been included in the calculations for orientations different from $[0\ 0\ 1]$. The quadrupole interactions of the neighboring nuclei can be neglected in first order [8].

Calculating the full half width ($W_{1/2}$) of the ODEPR spectra for the isolated As_{Ga} model we obtain 33.7, 36.0 and 39.1 mT for the $[0\ 0\ 1]$, $[1\ 1\ 0]$ and $[1\ 1\ 1]$ orientations, respectively. Considering the interaction with an additional As interstitial in the $\text{As}_{\text{Ga}}\text{--As}_i$ model we obtain 39.5, 41.3 and 42.8 mT. The measured line widths in W-band are 35.7, 36.8 and 38.0 mT, respectively, with an error of ± 0.8 mT. In the literature a value of 33.0 mT has been published for the peak-to-peak line width (W_{pp}) of the conventional EPR spectrum of the EL2 defect for $B_0 \parallel [0\ 0\ 1]$ in X-band [10], which corresponds to 38.0 mT for $W_{1/2}$ in agreement with K-band ODEPR measurements.

The result can be summarized as follows: (i) the experimental (W-band) ODEPR line widths lie between the calculated ones for the isolated and the $\text{As}_{\text{Ga}}\text{--As}_i$ pair model; (ii) the measured variation of the line width with orientation of the samples is smaller than the calculated one both for the isolated and for the pair model; (iii) the ODEPR line width in W-band is smaller by 2 mT compared to the K-band line width and (iv) the ODEPR line width measured in K-band is in agreement with X-band conventional EPR measurements. The first result can be explained if we assume that the high shf values determined for the As interstitial from the ODENDOR measurements [5] are not correct. The corresponding ODENDOR lines with very low intensity may have been due to forbidden transitions and were wrongly interpreted. From the second result a lower symmetry than C_{3v} could be suggested because in that case the measured line width variation ΔW is smaller as the calculated one for both the isolated as well as for the pair defect. The third result is consistent with a predicted reduction of forbidden transition probabilities at higher magnetic fields B_0 . The last point means that conventional EPR and ODEPR detect the same defect.

Thus, when calculating the ODEPR spectra of the EL2 defect in first order perturbation theory with the ODENDOR parameters of Ref. [5] and comparing the results with the new W-band experimental results we can exclude the $\text{As}_{\text{Ga}}\text{--As}_i$ model as the model for EL2. An

additional As_i with $a = 215 \text{ MHz}$ and $b = 44 \text{ MHz}$, respectively, leads to larger line widths compared to the isolated As_{Ga} model. However, when comparing the measured and calculated line shapes the EL2 defect can not be the isolated As_{Ga} antisite defect with T_d symmetry either. The resulting line width would be too small. This conclusion is supported by other experimental information such as its MCDA line shape in comparison with other As_{Ga} -related defects [11], the ODENDOR spectra of the higher As neighbor shells and the observation that the isolated As_{Ga} defect is produced in SI GaAs by low temperature electron irradiation and not stable at room temperature [6].

The first W-band ODENDOR spectra for $B_0 \parallel [110] + 20^\circ$ show at least 8 lines belonging to ^{75}As and $m_s = -1/2$, all in a frequency range where nearest neighbors are measured (further neighbors would be at much lower frequencies). For an isolated As_{Ga} -defect with T_d -symmetry including a quadrupole interaction ($I = 3/2$) at most 2 triplets, that is only 6 lines would be measured for B_0 in a $\{001\}$ plane. There are, however, more lines. The observed pattern can not be due to a tilt of the sample either. Thus, with all precaution, because an angular dependence has not yet been measured, it looks as if the EL2 defect is a perturbed As_{Ga} defect in which not all nearest As neighbors are equivalent.

4. Conclusions

From ODEPR measurements of the EL2 defect in W-band and calculations of the ODEPR spectra we can conclude that the $\text{As}_{\text{Ga}}\text{--As}_i$ model assuming an additional As interstitial is not consistent with the observed ODEPR line widths. However, the EL2 cannot be the

highly symmetric isolated As_{Ga} defect either. Thus, EL2 must be an As_{Ga} -related defect with lower than T_d symmetry. The cause for the symmetry lowering, however, should only contribute a very small shf interaction. For example, a vacancy as suggested in Ref. [11] could cause a nonequivalence in nearest neighbor shf interactions and thus explain the experimental line width in W-band. The first W-band ENDOR measurements seem to support this.

Acknowledgements

The authors wish to thank the Deutsche Forschungsgemeinschaft DFG for financial support. One of us, Klaus Krambrock, acknowledges a grant from the Brazilian agency CAPES (grant number BEX 0356/00-0).

References

- [1] M. Kaminska, et al., Phys. Rev. Lett. 55 (1985) 2204.
- [2] J. Dabrowski, et al., Phys. Rev. Lett. 60 (1988) 2183.
- [3] D.J. Chadi, et al., Phys. Rev. Lett. 60 (1988) 2187.
- [4] H.J. von Bardeleben, et al., Phys. Rev. B 34 (1986) 7192.
- [5] B.K. Meyer, et al., Phys. Rev. B 36 (1987) 1332.
- [6] K. Krambrock, et al., Phys. Rev. B 45 (1992) 1481.
- [7] F. Wirbeleit, et al., Mater. Sci. Forum 258–263 (1997) 987.
- [8] J.-M. Spaeth, et al., in: H.-J. Queisser (Ed.), Structural Analysis of Point Defects in Solids, Springer, Heidelberg, 1992.
- [9] F.K. Koschnik, et al., Phys. Stat. Sol. (B) 216 (1999) 817.
- [10] B. Dischler, et al., Phys. Rev. Appl. 23 (1988) 779.
- [11] J.-M. Spaeth, et al., Festkörperprobleme 33 (1994) 111.



ELSEVIER

Physica B 308–310 (2001) 757–760

PHYSICA B

www.elsevier.com/locate/physb

Capture kinetics at deep-level defects in lattice-mismatched GaAs-based heterostructures

O. Yastrubchak^a, T. Wosiński^{a,*}, A. Makosa^a, T. Figielski^a, A.L. Tóth^b

^a Institute of Physics, Polish Academy of Sciences, Al. Lotnikow 32/46, 02-668 Warsaw, Poland

^b Research Institute for Technical Physics and Materials Science, Hungarian Academy of Sciences, Budapest 1525, Hungary

Abstract

Two deep-level traps associated with lattice-mismatch induced defects in GaAs/InGaAs heterostructures have been revealed by means of deep-level transient spectroscopy (DLTS). An electron trap, at $E_c - 0.64$ eV, has been attributed to electron states associated with threading dislocations in the ternary compound while a hole trap, at $E_v + 0.67$ eV, has been ascribed to misfit dislocations at the heterostructure interface. Detailed investigation of the dependence of DLTS-line amplitude and its shape on the filling time of the traps with charge carriers allowed us to specify the type of electronic states related to both traps. In terms of the model of electronic states associated with extended defects, which takes into account the rate at which the states reach their internal electron equilibrium, we relate the electron trap to “localized” states and the hole trap to “bandlike” ones. © 2001 Elsevier Science B.V. All rights reserved.

Keywords: Semiconductor heterostructures; Dislocations; Deep levels; Capture kinetics

1. Introduction

Lattice-mismatched GaAs-based heterostructures are of continual interest because of their application in high-speed and optoelectronic devices. Epitaxial growth of those heterostructures is accompanied by a strain in the epitaxial layer that results from a difference in lattice parameters between the substrate and the layer. If the thickness of the layer exceeds its critical value the strain is relieved by the formation of misfit dislocations. In heteroepitaxial semiconductor systems with zinc-blende structure and small lattice mismatch, grown on (001)-oriented substrates, orthogonal arrays of regular 60° misfit dislocations are formed at the interface [1]. The misfit dislocations are accompanied by threading dislocations which propagate into the epitaxial layer. Both kinds of dislocations can give rise to energy levels in the band gap which act as recombination centres or traps for free carriers. Due to translational symmetry along dislocation lines, one-dimensional energy bands rather

than isolated localized electron states are expected to be associated with the dislocation cores.

In our recent paper [2], we revealed, by means of deep-level transient spectroscopy (DLTS), three deep-level traps associated with lattice-mismatch induced defects in two types of GaAs-based heterostructures: GaAs/GaAsSb and GaAs/InGaAs. In this communication we report new results of systematic investigation of kinetics for capture of charge carriers into the trap states. They give a new insight into the nature of the electronic states associated with two of the traps, which have been related to lattice-mismatch induced dislocations.

2. Samples

We investigated GaAs/InGaAs heterostructures, with the In content of 2%, grown by molecular beam epitaxy (MBE). The InGaAs layer of 1 µm thickness was grown on n⁺-type GaAs buffer layer doped with Si. The InGaAs layer was Si doped to a thickness of 0.3 µm and its upper part was Be doped to p-type at the concentration of 10¹⁶ cm⁻³, so that an n⁺-p junction was formed in the layer of the ternary compound. The junction

*Corresponding author. Fax: +48-22-843-0926.

E-mail address: wosin@ifpan.edu.pl (T. Wosiński).

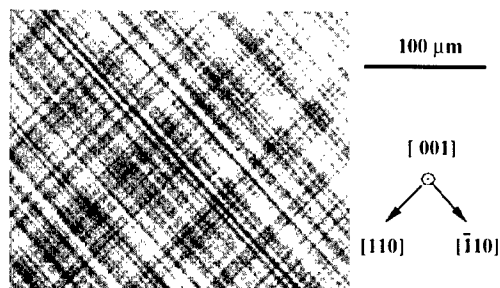


Fig. 1. Distribution of misfit dislocations at the interface of $n^+ - p$ GaAs/In_{0.02}Ga_{0.98}As heterojunction revealed by means of EBIC technique in a scanning electron microscope.

position was shifted from the heterointerface towards the InGaAs side by 0.3 μm .

A difference in lattice constant between GaAs and the ternary compound, of about 0.2%, resulted in the generation of a two-dimensional network of misfit dislocations lying along two orthogonal $\langle 110 \rangle$ directions at the (001) interface. Such a dislocation network which has been revealed by means of an electron-beam induced current (EBIC) technique in a scanning electron microscope is shown in Fig. 1. Here, the misfit dislocations are visible as dark lines owing to enhanced recombination rate of electron-hole pairs generated by an electron beam.

3. DLTS results

The spectrum of lattice-mismatch induced defects has been studied by means of DLTS using $p - n$ junctions formed in the epilayers. This allowed for investigation of both electron traps in the upper half of the band gap and hole traps in the lower half.

One electron trap, called ED1, has been revealed in the DLTS spectrum measured under typical bias conditions, i.e. under reverse quiescent bias, which was decreased to zero during the filling pulse, Fig. 2. This trap, with a deep level at $E_c - 0.64 \text{ eV}$ as determined from the slope of the Arrhenius plot shown in Fig. 3, has been attributed to threading dislocations in the layer of ternary compound close to the plane of $p - n$ junction [2]. The ED1 trap had been, for the first time, revealed by means of DLTS in plastically deformed bulk GaAs at $E_c - 0.68 \text{ eV}$ and related to electron states associated with 60° dislocations [3]. The same trap was then found in several MOVPE-grown GaAs/InGaAs heterostructures by Watson et al. [4] and by Panepinto et al. [5], who ascribed the trap to misfit dislocations generated either at the interface [4] or in GaAs buffer layer close to the interface [5].

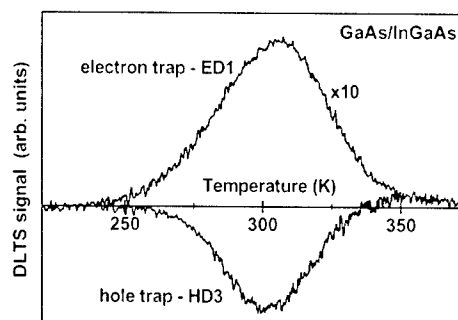


Fig. 2. DLTS spectra measured at a rate window of 48 s^{-1} for the $n^+ - p$ GaAs/InGaAs heterojunction. The upper spectrum was recorded under reverse-bias conditions while the lower one was detected under forward-bias injection. Note the scale expansion for the upper spectrum.

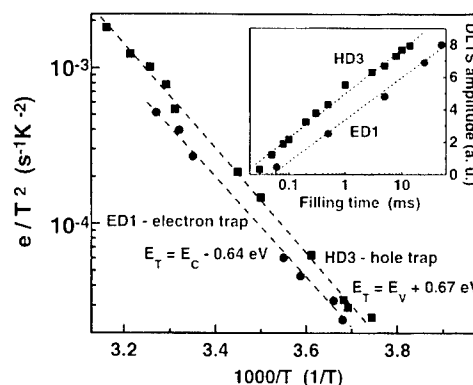


Fig. 3. Temperature dependence of the thermal emission rates (Arrhenius plots) for the traps revealed in the GaAs/InGaAs heterojunction. Energy positions of the trap levels, evaluated from the Arrhenius plots, are written in the figure. The inset shows DLTS peak amplitudes of ED1 and HD3 traps versus filling-pulse duration.

We have also identified the ED1 trap in GaAs/GaAsSb heterostructures with different Sb content (0–3%) and attributed it to threading dislocations present in the GaAsSb epilayer [2,6]. The activation energies for the electron emission from the ED1 traps, obtained for various heterostructures, decrease with an increase of the Sb or In content in the epitaxial layer similar to the manner in which the band-gap energy in the ternary compound decreases [2]. This relation implies that the energy level position of the trap with respect to the top of the valence band remains the same in each material, suggesting that the defect state is composed primarily of the valence band states. A similar dependence of the trap activation energy on the band gap energy has recently been found by Pal et al. [7] for the electron trap, attributed to threading dislocations in MBE-grown InGaAs layers with higher (10–30%) In mole fractions.

On the other hand, our DLTS measurements performed under injection conditions, i.e. under zero quiescent voltage and forward-bias filling pulse, revealed one hole trap (Fig. 2), called HD3, with a deep level at $E_v + 0.67$ eV (Fig. 3). We relate the trap, which has been detected only when the DLTS-active region comprises the interface, to defects associated with the lattice-mismatched interface, most probably to misfit dislocations lying at the interface. We revealed the same hole trap in the DLTS spectra of lattice-mismatched GaAs/GaAsSb heterostructures; however, the precise evaluation of its activation energy was strongly disturbed owing to the position of its DLTS line on the high-temperature slope of another line in those heterostructures [2]. Probably the hole trap recently found by Du et al. [8] in lattice-mismatched GaAs/InGaAs heterostructures with various In mole fractions and layer thicknesses is the same as HD3. That trap, labelled H4 by the authors, with the DLTS activation energy between 0.67 and 0.73 eV, has been related to misfit dislocations at the interface by comparing the DLTS spectra in various heterostructures with the distribution of dislocations revealed by means of transmission electron microscopy (TEM).

4. Capture kinetics

The principal argument for the assignment of the traps to dislocations was logarithmic kinetics for capture of charge carriers into the trap states. Such kinetics results from the Coulomb interaction between a charge carrier just being captured and other charges already captured at the dislocation line [9]. This interaction manifests itself in DLTS measurements in a linear dependence of the signal amplitude on the logarithm of the filling-pulse duration [3], as shown for the ED1 and HD3 traps over several orders of magnitude of that duration; see the inset of Fig. 3. In contrast, isolated point defects or impurities exhibit exponential capture kinetics.

Recently, Schröter et al. [10,11] proposed that electronic states associated with extended defects in semiconductors can be classified as *localized* or *bandlike* by taking into account the rate R_i , at which the states reach their internal electron equilibrium. The internal equilibration rate, when compared to the carrier emission rate from the defect R_e and the capture rate R_c , allows us to distinguish between *localized* states ($R_i \ll R_e, R_c$) and *bandlike* ones ($R_i \gg R_e, R_c$). The authors demonstrated, by computer simulation of DLTS spectra induced by the two types of states, that can be distinguished on the grounds of dependence of their DLTS-line shape on the filling time.

For *localized* states the DLTS-line maximum stays constant while changing the filling-pulse duration,

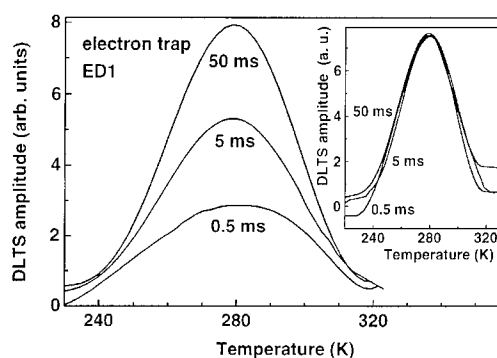


Fig. 4. DLTS line for the ED1 trap and its dependence on filling-pulse duration, whose values are written in the figure, measured at a rate window of 2 s^{-1} . In the inset, the line amplitude is normalized to the same height.

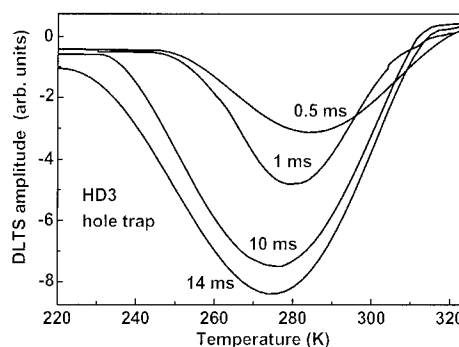


Fig. 5. DLTS line for the HD3 trap and its dependence on filling-pulse duration, written in the figure, measured at a rate window of 2 s^{-1} .

whereas the line amplitude exhibits a linear dependence on the logarithm of the filling time. Such behaviour has been found for the ED1 trap as shown in Fig. 4. This finding is in agreement with the results of Panepinto et al. [5] for the same electron trap, labelled EG4 in Ref. [5]. It has also been shown that the DLTS signal associated with 60° dislocations in plastically deformed Si can be described by this type of electronic states [10].

On the contrary, in the case of *bandlike* states, variation of filling-pulse duration results in broadened DLTS lines whose maximum shifts towards lower temperature on increasing that duration and whose high-temperature sides coincide. This is the case of the HD3 trap as demonstrated in Fig. 5. Possibly, the electronic states associated with misfit dislocations belong to *bandlike* states because of a higher regularity of those dislocations as compared with the threading ones. To this category of states belong also electronic states associated with dislocation rings bounding nanoscale NiSi_2 precipitates in silicon [11].

5. Conclusions

One electron trap and one hole trap have been found with the DLTS technique in lattice-mismatched GaAs/InGaAs heterostructures. The electron trap, called ED1, has been attributed to threading dislocations in the layer of ternary compound, whereas the hole trap, HD3, has been related to misfit dislocations lying at the heterostructure interface. A thorough analysis of the dependence of DLTS-line shape of the traps on the filling time allowed us to specify the type of electronic states related to both traps. We relate the ED1 electron trap to *localized* states and the HD3 hole trap to *bandlike* ones.

Acknowledgements

The authors would like to thank B.F. Usher (Melbourne) for growing the heterostructures investigated. This work has been partly supported by the Committee for Scientific Research of Poland under Grant No. 2 P03B 063 19.

References

- [1] X.W. Liu, A.A. Hopgood, B.F. Usher, H. Wang, N.S. Braithwaite, J. Appl. Phys. 88 (2000) 5975.
- [2] T. Wosiński, O. Yastrubchak, A. Mąkosa, T. Figielski, J. Phys.: Condens. Matter 12 (2000) 10153.
- [3] T. Wosiński, J. Appl. Phys. 65 (1989) 1566.
- [4] G.P. Watson, D.G. Ast, T.J. Anderson, B. Pathangey, Y. Hayakawa, J. Appl. Phys. 71 (1992) 3399.
- [5] L. Panepinto, U. Zeimer, W. Seifert, M. Seibt, F. Bugge, M. Weyers, W. Schröter, Mater. Sci. Eng. B 42 (1996) 77.
- [6] T. Wosiński, A. Mąkosa, T. Figielski, J. Raczyńska, Appl. Phys. Lett. 67 (1995) 1131.
- [7] D. Pal, E. Gombia, R. Mosca, A. Bosacchi, S. Franchi, J. Appl. Phys. 84 (1998) 2965.
- [8] A.Y. Du, M.F. Li, T.C. Chong, S.J. Xu, Z. Zhang, D.P. Yu, Thin Solid Films 311 (1997) 7.
- [9] T. Figielski, Solid State Electron. 21 (1978) 1403.
- [10] W. Schröter, J. Kronewitz, U. Gnauert, F. Riedel, M. Seibt, Phys. Rev. B 52 (1995) 13726.
- [11] F. Riedel, W. Schröter, Phys. Rev. B 62 (2000) 7150.



ELSEVIER

Physica B 308–310 (2001) 761–764

PHYSICA B

www.elsevier.com/locate/physb

Passivation of growth defects in GaAs/AlGaAs multiple quantum well structures by CF₄ plasma

T.S. Shamirzaev^{a,*}, K.S. Zhuravlev^a, A.Yu. Kobitski^{a,b}, H.P. Wagner^b,
D.R.T. Zahn^b

^a *Institute of Semiconductor Physics, Pr. Lavrent'eva 13, 630090 Novosibirsk, Russia*

^b *Institut für Physik, TU Chemnitz, Chemnitz, Germany*

Abstract

The effect of low-energy plasma treatment on GaAs/AlGaAs multiple quantum wells structures has been studied by CW and time-resolved photoluminescence. An increase of the photoluminescence intensity of quantum wells below the plasma damaged region is observed. The concentration of nonradiative centers in these QWs is reduced by a factor of 30 after a 40 s exposure to a CF₄ plasma. © 2001 Elsevier Science B.V. All rights reserved.

Keywords: Plasma treatment; Defect passivation; Photoluminescence

Low-energy fluoride-based plasmas are widely used in III–V semiconductor device fabrication for selective removal of dielectric films from the surface of the structures. During this reactive ion etching (RIE) process, overetching is a common practice to ensure complete removal of the dielectric films. Inevitably, semiconductor materials below the dielectric films have to be exposed to the plasma leading to damage of the near-surface region and as a result both the electrical and the optical properties of the materials deteriorate significantly [1–7]. In order to exploit the full potential of the plasma treatment and to develop new processes for future applications it is necessary to understand the cause and effect of this damage. Wang et al. [8] have proposed to detect the RIE induced effects utilizing the photoluminescence (PL) properties of AlGaAs/GaAs multiple quantum well (MQW) structures. To increase the detection sensitivity of point defects generated by RIE, Ooi et al. [9] have used a quantum well intermixing technique. Both publications report on a reduction of the PL intensity generated by near-surface QWs which are damaged by the RIE process. In our investigations

not only a reduction of the near-surface PL is observed, in addition we also detected an increase of the PL intensity from QWs lying below the damaged region after the structure is treated using a CF₄ plasma.

The AlGaAs/GaAs MQW structures used in this study were grown by molecular beam epitaxy. A 1.0 μm undoped GaAs layer was grown on a (100) semi-insulating GaAs substrate, followed by a 0.5 μm undoped Al_{0.3}Ga_{0.7}As layer, and GaAs QWs of different widths were grown on top of this layer. In particular the region contains six QWs with 2.2, 2.8, 3.4, 4.2, 5.6 and 8.5 nm wide wells, which are separated by 24 nm Al_{0.3}Ga_{0.7}As barriers. The sample was capped by a 10 nm GaAs layer. Furthermore a short-period AlAs/GaAs superlattice was introduced within the 0.5 μm Al_{0.3}Ga_{0.7}As layer to trap impurities which are segregated during growth on the AlGaAs surface [10–13] and point defects originating from the substrate [14]. For the plasma treatments CF₄ gas was used. The plasma power density was kept at 0.5 W cm⁻² with an operating pressure of 0.07 Torr and direct current self-bias of approximately –300 V. The exposure time was varied from 5 to 600 s. In order to avoid sample heating during extended plasma treatment the plasma was extinguished after 120 s exposure and the sample was cooled. A 632.8 nm He–Ne laser with a power density of

*Corresponding author. Fax: +7-3832-33-27-71.

E-mail address: timur@thermo.isp.nsc.ru
(T.S. Shamirzaev).

20 W cm^{-2} was used to perform continuous wave PL measurements. Since the absorption coefficient at 632.8 nm is about $3 \times 10^4 \text{ cm}^{-1}$ and $1 \times 10^4 \text{ cm}^{-1}$ in GaAs and $\text{Al}_{0.3}\text{Ga}_{0.7}\text{As}$ ($T = 77 \text{ K}$), respectively, approximately 3% of the illuminated light is absorbed in each QW. The details of the equipment used for time resolved PL measurements were described elsewhere [15].

Fig. 1 presents 77 K PL spectra of the structure obtained before and after an exposure to CF_4 plasma. The PL peak at 822 nm (1.507 eV) originates from band to band recombination in the GaAs layer and the other peaks are due to $1\text{e}hh$ transitions in the quantum wells. The 2.2, 2.8, 3.4, 4.2 and 5.6 nm QWs in the as-grown sample reveal a high PL intensity, only the 8.5 nm QW (which is nearest to the substrate) shows a low PL intensity. Note that at liquid helium temperature all the QWs show the same PL intensities, therefore, the amount of the excitation light absorbed by the 8.5 nm QW is approximately the same as in the others. After 60 s exposure to the CF_4 plasma the PL signal originating from the surface near QW completely disappears, while the PL signal generated in the 3.4, 4.2 and 5.6 nm QWs remains unchanged. Unexpectedly the PL signal arising from the 8.5 nm QW is increased by more than one order of magnitude and lines up with the intensities of the 3.4, 4.2 and 5.6 nm QWs. No shift in the PL peaks of the QWs is observed.

Fig. 2 shows the PL peak intensities of all QWs after CF_4 plasma exposure. The PL intensities were normalized relative to the intensities obtained from as-grown QWs. Since the GaAs layer is far enough away from the sample surface to remain undamaged under the plasma

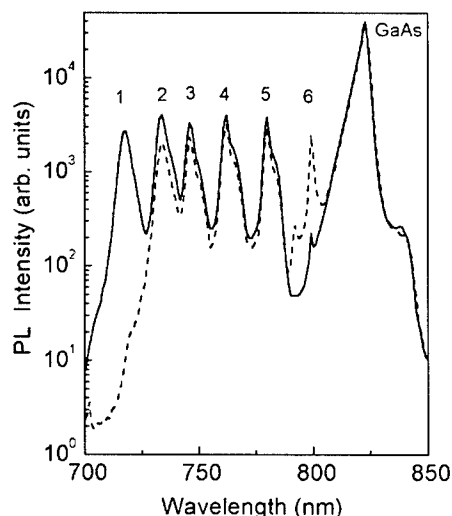


Fig. 1. PL spectra of the GaAs/GaAlAs MQW structures obtained before (solid line) and after (dashed line) a 60 s CF_4 plasma exposure. Numbers label the PL originating from the following QWs: 1–2.2, 2–2.8, 3–3.4, 4–4.2, 5–5.6, and 6–8.5 nm.

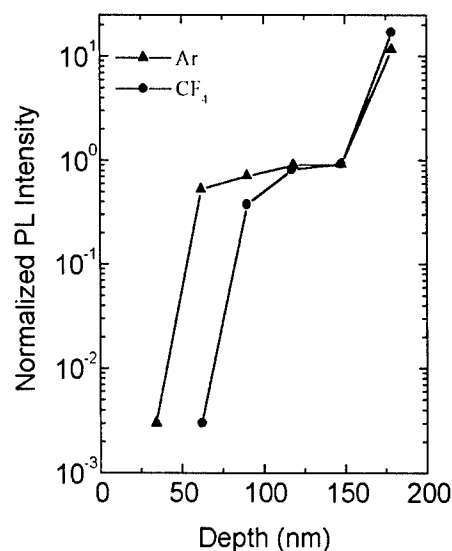


Fig. 2. Normalized QW PL intensity vs depth in the structures exposed for 60 s in the CF_4 and Ar plasmas.

treatment its PL was used as a reference. Fig. 2 clearly shows that the CF_4 plasma causes PL degradation in the near surface region and also induces an increase of the PL intensity of deeper lying QWs below this region. A clear PL enhancement is observed in the QW, which reveals a low initial PL intensity in as-grown samples. The low PL intensity is thereby attributed to the segregation of impurity atoms and point defects at QW interfaces during growth, which act as traps or nonradiative recombination centers. Possible reasons for the plasma-induced increase of the PL intensity would be an annihilation or significant transformation of the nonradiative centers due to interaction with some plasma-induced highly mobile defects.

During plasma exposure an implantation of incident species (ions of plasma, elements from walls of the reactor) and a generation of point defects, such as vacancies and interstitial atoms, occurs in the near-surface region of the structures. It is well known that fluoride and hydrogen can passivate the dangling or defective bonds acting as traps or nonradiative recombination centers in amorphous silicon [16]. Moreover, it was shown [17–19] that the incorporation of hydrogen in III–V semiconductor structures leads to the passivation of deep nonradiative centers and to enhancement of PL efficiency. Therefore we first assumed that implanted fluoride could penetrate into the GaAs/AlGaAs MQW structures and passivate the growth defects. In order to prove this assumption we compared the influence of Ar and Kr plasmas on the PL intensity obtained from the MQW structures. The normalized PL intensities of QWs, which are treated by an Ar plasma are shown in Fig. 2 as full triangles. From comparison it becomes

evident that the nature of the PL enhancement is independent from the plasma gas used. We therefore conclude that the observed PL increase is caused by plasma-induced, highly mobile point defects and not by a fluoride passivation. After low-temperature annealing (400°C in Ar atmosphere for 60 s) a depassivation occurs, and the PL intensity of the deeper lying QW drops again. However, a second plasma treatment once more leads to the passivation of the growth defects.

Fig. 3 shows the normalized PL intensity as a function of CF₄ exposure time. This figure demonstrates that the PL intensity arising from the 8.5 nm QW significantly increases after only a $\tau_0 = 20$ s exposure to the plasma, a further prolongation of the exposure time hardly increases the PL intensity. Moreover, Fig. 3 shows that the prolongation of the exposure time up to 10 min enlarges the near-surface damaged region. In order to estimate a diffusion coefficient (D) of the plasma-induced point defects, which cause the increase in the PL intensity in the deepest QW we use the diffusion length relationship $d = (Dt)^{1/2}$, where t is the exposure time and $d = 17$ nm is the distance of 8.5 nm QW from the surface. We took t equal to τ_0 and obtained the D value of about 10^{-11} cm² s⁻¹. It should be noted that the measured values of the defect diffusion coefficient are too high, particularly taking into account that during the plasma treatment the temperature of the samples did not exceed 50°C. It seems likely that an excitation of the crystal by ultraviolet, X-rays, and energetic electrons generated in the plasma enhances diffusion of the defects in MQW structures. Investigations of these effects are in progress now.

In order to estimate the change of the growth defect concentration in the 8.5 nm QW we measured the PL lifetime in this QW before and after a 40 s exposure to plasma as a function of the temperature. Jin et al. [20] obtained the following equation that connect the PL decay lifetime (τ) with the bath temperature (T) and the

nonradiative recombination probability (R_{nr}).

$$\tau(T) = (p_0 + n_c(T)) / (p_0 R_r(T) + n_c(T) R_{nr}(T)), \quad (1)$$

$$R_r(T) = B n_c(T) + R_x,$$

$$R_{nr}(T) = R_0 + R_s \exp[-E_A/kT],$$

$$n_c(T) = [m_e m_h / (m_e + m_h)] [kT / \pi \hbar^2] \exp[-E_x/kT],$$

where $1/R_x$ is the intrinsic exciton radiative lifetime, B is the rate of the band-to-band radiative recombination of the free carriers, R_0 is the nonradiative recombination probability, which is proportional to the concentration of nonradiative centers, $n_c = np/n_x$, where n , p , n_x are the electron, hole, and exciton concentration, respectively, E_x is the exciton binding energy, E_A is the activation energy of nonradiative recombination, p_0 is the concentration of the free holes, $m_e = 0.065m_0$ and $m_h = 0.5m_0$ are respectively electron and hole effective masses, which are taken as equal to bulk GaAs masses independently of the QW size.

The experimental values of the PL decay lifetime measured at different temperatures in the 8.5 nm QW and the calculated lifetime dependence using Eq. (1) are shown in Fig. 4. The best coincidence between the experiment and calculation has been obtained for the following parameters which were fixed for both as-grown and exposed structures: $E_x = 8$ meV, $E_A = 90$ meV, $B = 10^{-10}$ cm² c⁻¹, $p_0 = 5 \times 10^9$ cm⁻², $R_s = 1.2 \times 10^{10}$ c⁻¹, $R_x = 1.8 \times 10^9$ c⁻¹. The factor R_0 , proportional to the concentration of nonradiative centers, changes from 1.17×10^9 c⁻¹ in the as-grown structure to 4.2×10^7 c⁻¹ in the plasma treated structure. Therefore,

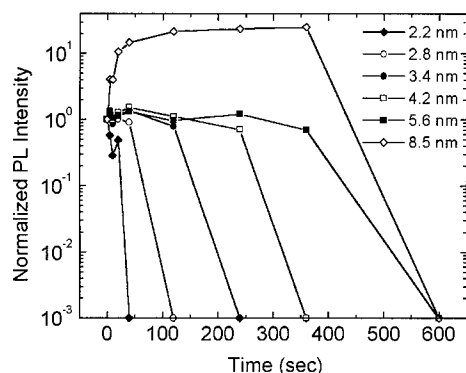


Fig. 3. Variation of the normalized PL intensities originating from the QWs in the structure as a function of CF₄ plasma exposure time.

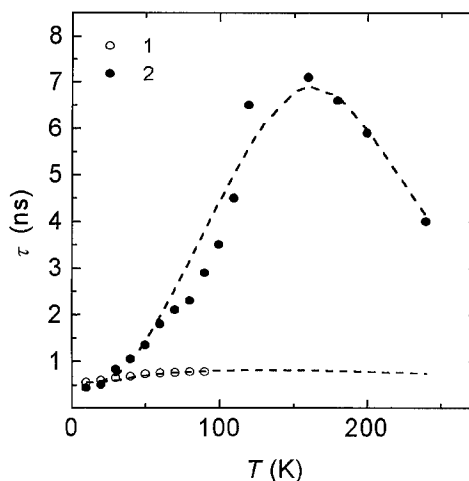


Fig. 4. PL decay lifetime of the 8.5 nm QW as a function of the bath temperature. Symbols mark (1) as-grown structure, (2) the same structure after 40 s exposure in CF₄ plasma. Dashed lines show the calculated dependence according to Eq. (1).

the defect concentration is decreased by a factor of about 30 after exposure to CF_4 plasma.

In conclusion we have examined the effect of a CF_4 plasma exposure on the PL properties of GaAs/AlGaAs MQW structures and observed a plasma induced quenching of the QW PL in the near surface region. Unexpectedly, the CF_4 plasma causes a remarkable increase of the PL intensity in the QW below this region. We explain this PL enhancement by a passivation of nonradiative growth defects which is induced by plasma generated highly mobile point defects.

References

- [1] W. Beinstingl, R. Christanell, J. Smoliner, C. Wirner, E. Gornik, G. Weimann, W. Schlapp, *Appl. Phys. Lett.* 57 (1990) 177.
- [2] C. Juang, J.K. Hsu, I.S. Yen, H.S. Shiau, *J. Appl. Phys.* 72 (1992) 684.
- [3] K.L. Seaward, N.J. Moll, W.F. Stickle, *J. Electron. Mater.* 19 (1990) 385.
- [4] S.J. Pearton, U.K. Chakrabarti, F.A. Baiocchi, *Appl. Phys. Lett.* 55 (1989) 1633.
- [5] S.J. Yun, S.J. Park, M.C. Paek, J.Y. Lee, *J. Electrochem. Soc.* 137 (1990) 2634.
- [6] K. Ohtsuka, T. Ohishi, Y. Abe, H. Sugimoto, T. Matsui, *J. Appl. Phys.* 70 (1991) 2361.
- [7] O.J. Glembocki, B.E. Taylor, E.A. Dobisz, *J. Vac. Sci. Technol. B* 9 (1991) 3546.
- [8] H.F. Wong, D.L. Green, T.Y. Liu, D.G. Lishan, M. Bellis, E.L. Hu, P.M. Petroff, P.O. Holtz, J.L. Merz, *J. Vac. Sci. Technol. B* 6 (1988) 1906.
- [9] B.S. Ooi, A.C. Bryce, C.D.W. Wilkinson, J.H. Marsh, *Appl. Phys. Lett.* 64 (1994) 598.
- [10] T. Achtnich, G. Burri, M.A. Py, M. Illegems, *Appl. Phys. Lett.* 50 (1987) 1730.
- [11] M.T. Ason, S.N.G. Chu, M. Geva, R.E. Leibenguth, *Appl. Phys. Lett.* 59 (1991) 976.
- [12] N. Chand, S.N.G. Chu, M. Geva, *Appl. Phys. Lett.* 59 (1991) 2874.
- [13] T. Achtnich, G. Burri, M. Illegems, *J. Vac. Sci. Technol. A* 7 (1989) 2537.
- [14] P.M. Petroff, R.C. Miller, A.C. Gossard, W. Wiegmann, *Appl. Phys. Lett.* 44 (1984) 217.
- [15] T.S. Shamirzaev, K.S. Zhuravlev, A.I. Toropov, A.K. Bakarov, A. Yu. Kobitsky, H.P. Wagner, D.R.T. Zahn, *Phys. Rev. B*, to be published.
- [16] J.D. Joannopoulos, G. Lucovsky (Ed.), *The Physics of Hydrogenated Amorphous Silicon I, Topics in Applied Physics*, Vol. 55, Springer, Berlin, 1984.
- [17] W.C. Dautremont-Smith, J.C. Nabity, V. Swaminathan, M. Stavola, J. Chevallier, C.W. Tu, S.J. Pearton, *Appl. Phys. Lett.* 49 (1986) 1089.
- [18] S.J. Pearton, *Appl. Phys. A* 43 (1987) 153.
- [19] L. Pavesi, F. Martelli, D. Martin, F.K. Reinhart, *Appl. Phys. Lett.* 54 (1989) 1522.
- [20] S. Jin, A. Li, *J. Appl. Phys.* 81 (1997) 7357.



ELSEVIER

Physica B 308–310 (2001) 765–768

PHYSICA B

www.elsevier.com/locate/physb

Exciton localization dynamics due to intrinsic interface defects within growth island terraces of all-binary GaAs/AlAs quantum wells

K. Fujiwara^{a,*}, K.H. Ploog^b

^a *Kyushu Institute of Technology, Tobata, Kitakyushu 804-8550, Japan*

^b *Paul-Drude-Institut für Festkörperelektronik, Hausvogteiplatz 5-7, 10117 Berlin, Germany*

Abstract

The localization dynamics of excitons within growth island terraces of a narrow GaAs single quantum well confined by all-binary GaAs/AlAs short-period superlattices is investigated by time-resolved photoluminescence (PL) spectroscopy. Under resonant photoexcitation into the ground light-hole exciton state of the dominant terrace, as confirmed by PL excitation spectra, we clearly observe an enhancement of the fundamental free heavy-hole exciton emission as well as the localized excitons associated with the terrace. The time evolution of the split PL line-shape indicates the coexistence of distinct free and localized excitons in the ps time domain, revealing transfer from the free to localized excitons within the terrace in addition to the transfer between the island terraces. These results directly evidence that the binary–binary heterointerface contains intrinsic interface defects within the terraces and that the split PL line-shape dynamically evolves due to confinement potential fluctuations on the island terraces in agreement with the bimodal interface nano-roughness model. © 2001 Elsevier Science B.V. All rights reserved.

Keywords: GaAs quantum well; Interface defects; Photoluminescence; Exciton

1. Introduction

In narrow quantum wells prepared by growth interrupted molecular beam epitaxy, split two-dimensional exciton lines are observed in photoluminescence (PL) spectra, which reflect the formation of uniform and flat monolayer (ML) growth islands whose lateral terrace size is larger than the exciton Bohr radius [1–6]. However, recent analyses [7–13] of the detailed PL line-shape and atomic-scale characteristics indicate that the interface heterostructure within the terraces is not always perfectly abrupt but contains a number of intrinsic defects due to atomic displacement in the group III sublattice. Therefore, a microscopic roughness, called nano-roughness exists on the macroscopically flat island terraces. In this paper, the localization dynamics of excitons within growth islands of a narrow GaAs single quantum well (SQW) confined by all-binary GaAs/AlAs

short-period superlattices is investigated by time-resolved PL spectroscopy to provide further evidences for the nano-roughness. Under resonant photoexcitation into the ground light-hole exciton state of the dominant terrace, we clearly observe an enhancement of the fundamental free heavy-hole exciton emission associated with the terrace by measuring the time evolution of the split PL line-shape. The PL line-shape thus shows the coexistence of distinct free and localized excitons in the ps time domain, revealing the transfer from free to localized excitons within the terrace. These results under resonant photoexcitation conditions directly evidence that the binary–binary heterointerface contains intrinsic interface defects within the SQW island terraces.

2. Experimental

The GaAs SQW sample was grown by a molecular beam epitaxy (MBE) with growth interruption for 2 min

*Corresponding author. Fax: +81-93-884-3221.

E-mail address: fujiwara@ele.kyutech.ac.jp (K. Fujiwara).

at 670 °C under arsenic exposure at each interface. The well width (L_z) of the different SQW growth islands approximately range from 22 (6.2 nm), 21 (5.9 nm), 20 (5.7 nm) and 19 (5.4 nm) MLs, named A, B, C and D, respectively. The SQW layer is separated by all-binary GaAs/AlAs superlattice layers ($L_z/L_B = 3.4/1.2$ nm, 40 periods). The detailed sample heterostructure has been described previously [5,6]. The low intensity cw PL and PL excitation (PLE) measurements were carried out at 6 K using monochromatized radiation from a halogen lamp, for excitation, and a photon counting system, for detection. Spectrally and temporally resolved PL experiments were performed at 15 K by using a streak-camera based system for detection, and a pyridine 2 dye laser synchronously pumped by a mode-locked Ar⁺ laser for excitation. The narrow GaAs SQW sample was mounted in a temperature variable cryostat and directly excited by 10 ps optical pulses with a wavelength of 755 nm (1.642 eV) at which the light-hole exciton is resonantly excited in the dominant terrace C. The average excitation power was 34 mW which corresponds to an excitation power density of a few W/cm².

3. Results and discussion

The PL and PLE spectra from the GaAs SQW sample are shown in Fig. 1. The PL spectrum was measured using an excitation wavelength of 600 nm, while the PLE spectrum was obtained by setting the PL detection wavelength at 777 nm. Three PL structures are observed, which are associated with terraces A, B and C. The PLE spectrum reveals three distinct resonances associated with the 1s heavy-hole (1hh) excitons (as well as the light-hole (1lh) excitons) for terraces B, C and D. The strongest PL peak B is red-shifted by 9.8 meV from the main exciton resonance peak C (Stokes-shift) with a narrow, but finite line-width of about 2 meV (FWHM). We note that a doublet PL structure with about 3 meV splitting is seen for the dominating terrace C, while additional shoulders or tails are also observed on the longer wavelength (lower energy) side. The higher energy PL structure of terrace C coincides with the PLE peak position. The energy separations between the PLE peaks, B and C and C and D, are found to be 6.0 and 6.9 meV, respectively. These values correspond to well-width changes of 0.75 and 0.80 ML and are smaller than the calculated energy gap changes (8.0 meV/8.9 meV) by one ML. In addition, the PL peak position of terrace B is also red-shifted by 3.8 meV from the corresponding PLE peak as assigned in Fig. 1. This PL red-shift, which is also valid for terrace C, is due to the exciton center-of-mass motion (exciton intra-terrace transfer) from the free to localized excitons in terraces B and C in addition to the inter-terrace transfer (from C to B) during the radiative recombination processes. The

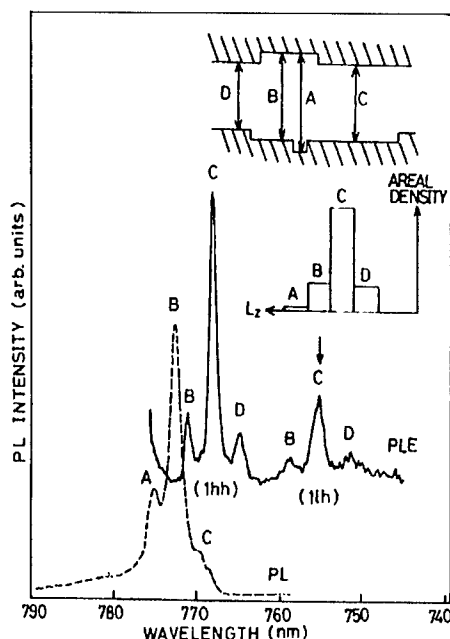


Fig. 1. cw PL (dashed) and PLE (solid) spectra of the 19–22 ML GaAs single quantum well. The excitation wavelength for PL is 600 nm while for PLE the PL detection is set at 777 nm. The inset figures schematically show the spatial configuration of the well and the areal density distribution of the SQW growth islands.

PL emission from terrace D was not observed in the cw PL spectrum of Fig. 1.

Fig. 2 shows the time evolution of transient PL spectra for the GaAs SQW as a function of delay time under 1lh exciton resonant photoexcitation of the main terrace C. In Fig. 2, the PL spectra (a)–(g) were measured at 14, 94, 174, 254, 414, 574 and 814 ps, respectively, after the excitation pulse averaged over 80 ps each. The PL intensity is vertically shifted for clear comparison and normalized to the highest peak intensity in each spectrum. In spectrum (a), the PL intensity distribution is dominated by emissions from terrace C over those from other terraces. In addition, a small PL signal from terrace D is observed on the higher energy side in the early stage. Within the emission band C, a doublet structure similar to the one seen in Fig. 1 is now more clearly observed in Fig. 2(a), and the short wavelength (high energy) peak is drastically enhanced in intensity. This is obviously due to the resonance enhancement effects on the photoexcitation in terrace C, i.e., more excitons are selectively generated in the spatial region of terrace C. With increasing delay time, the relative PL intensity from terrace C decreases generally, while the PL intensity from terrace B increases. For example, in the spectrum (c) after 174 ps, the strongest emission is already shifted to the lower energy peak B,

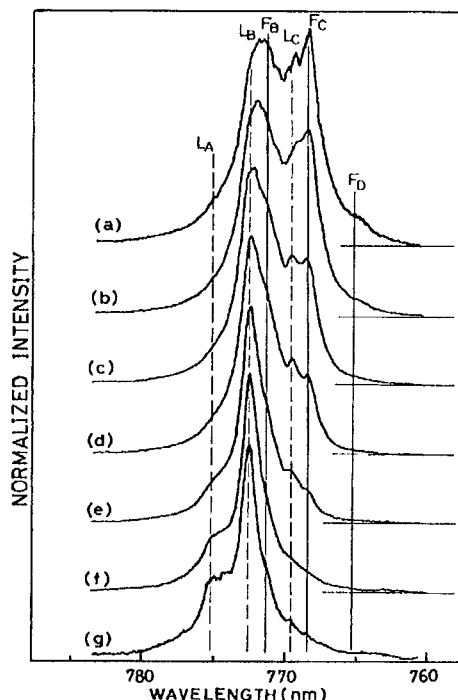


Fig. 2. Normalized PL spectra of the GaAs single quantum well as a function of time after pulsed excitation. The transient spectra (a)–(g) are detected at 14 (a), 94 (b), 174 (c), 254 (d), 414 (e), 574 (f) and 814 ps (g) after the 10 ps excitation pulse averaged over 80 ps each. The peak positions, F_i (L_i) ($i = A, B, C$ and D) of the free (localized) excitons are indicated by vertical solid (dashed) lines.

revealing the exciton transfer from terrace C to B. In the lowest spectrum (g), the PL intensity of terrace B dominates, while the emission intensity from terrace A is higher than terrace C. We also note that the emission band B has a doublet structure in Fig. 2, although the spectral separation is not so clear like the one for terrace C. Considering this doublet the dominating PL peak (B) in (g) is sharper than the one in (a), which indicates that the free excitons with the high energy emission component are significantly transferred to the localized states after 814 ps. These dynamical changes of the PL intensity in Fig. 2 indeed reflect the fact that during radiative recombination the excitons are moving in real space from terrace C to B, as schematically illustrated in Fig. 3.

The most important point we would like to stress here is, however, that the PL emission lines in the transient spectra clearly exhibit an additional doublet structure within the terraces, while their relative intensities of the different peaks evolve due to changes in the exciton population (see Fig. 3). In order to compare the cw PL and PLE peak positions, the measured peak wavelengths are indicated by solid (dashed) vertical lines for the free

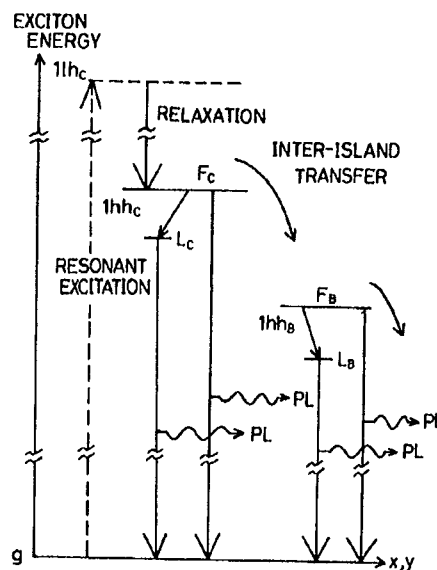


Fig. 3. Schematic model for the exciton energy distribution of the free and localized exciton states under resonant excitation into the ground light-hole exciton of the dominant terrace C.

(localized) excitons in Fig. 2 for the terraces A, B, C and D. A clear correlation is seen between the cw PL/PLE peak energies and those from the transient PL spectra, although the free exciton peak A cannot be resolved for PLE. This allows one to assign the transient PL fine structures to the free and localized $1hh$ excitons in the terraces.

Here we use excitons as a probe to examine the interface potential fluctuations whose lateral length scale is less than the exciton Bohr radius. Hence, the energy splitting of the doublet structure is naturally explained by the interface nano-roughness, which causes the confinement energy changes by a fractional ML (0.3 ML/3.8 meV). This is also valid for the case between the terraces, since the energy splitting is only partial, equivalent to 0.75–0.8 ML. The reduction of the probe size by increasing the quantum confinements thus makes it possible to visualize miniature-size intrinsic defects by a discrete exciton level, i.e., isoelectric trap sites for localized excitons. The experimental results presented here directly show the existence of nano-roughness within the macroscopically flat island terraces, which supports the bimodal interface roughness model [8].

4. Conclusion

In summary, PL transients in a narrow GaAs single quantum well with growth islands confined by all-binary GaAs/AlAs short-period superlattices have been inves-

tigated using resonant photoexcitation at the ground light-hole exciton level to the dominant island terrace. The transient PL spectra reveal two types of dynamical Stokes shifts due to intra- and inter-terrace exciton transfers. The finely split line-shape of the PL doublet structure directly evidences the existence of localized excitons formed within the terraces due to the confinement potential fluctuations. This reflects the existence of intrinsic interface defects caused by atomic displacements with respect to the sublattice. The discrete change of the PL peak energy with increasing delay time indicates the existence of a small-scale nano-roughness within the macroscopically flat quantum well island terraces.

References

- [1] C. Weisbuch, R. Dingle, A.C. Gossard, W. Wiegmann, *Solid State Commun.* 38 (1981) 709.
- [2] H. Sakaki, M. Tanaka, J. Yoshino, *Jpn. J. Appl. Phys.* 24 (1985) L417.
- [3] T. Fukunaga, K.L.I. Kobayashi, H. Nakajima, *Jpn. J. Appl. Phys.* 24 (1985) L510.
- [4] B. Deveaud, T.C. Damen, J. Shah, *Appl. Phys. Lett.* 51 (1987) 828.
- [5] K. Fujiwara, et al., *J. Appl. Phys.* 66 (1989) 148.
- [6] K. Fujiwara, et al., *Phys. Rev. B* 40 (1989) 9698.
- [7] D. Gammon, B.V. Shanabrook, D.S. Katzer, *Phys. Rev. Lett.* 67 (1991) 1547.
- [8] C.A. Warwick, R.F. Kopf, *Appl. Phys. Lett.* 60 (1992) 386.
- [9] U. Jahn, et al., *J. Cryst. Growth* 150 (1995) 43.
- [10] J. Behrend, et al., *Phys. Rev. B* 53 (1996) 9907.
- [11] K. Fujiwara, et al., *Phys. Rev. B* 43 (1991) 13978.
- [12] K. Fujiwara, et al., *Phys. Rev. B* 56 (1997) 1081.
- [13] R. Klann, H.T. Grahn, K. Fujiwara, *Phys. Rev. B* 51 (1995) 10232.



ELSEVIER

Physica B 308–310 (2001) 769–771

PHYSICA B

www.elsevier.com/locate/physb

Metastable irradiation induced defects in Be doped $\text{Al}_{0.5}\text{Ga}_{0.5}\text{As}$ MBE layers

J. Szatkowski^{a,*}, E. Placzek-Popko^a, A. Hajdusianek^a, A. Johansen^b,
C. Soerensen^b

^a *Institute of Physics, Wroclaw University of Technology, Wybrzeze Wyspianskiego 27, 50-370 Wroclaw, Poland*

^b *Oersted Laboratory, University of Copenhagen, Copenhagen, Denmark*

Abstract

It has been shown that He^{++} ions irradiation introduces in Be doped $\text{Al}_{0.5}\text{Ga}_{0.5}\text{As}$ MBE layers some metastable defects. After sample illumination at liquid nitrogen ambient with photons of energy below the band gap energy persistent photocapacitance was observed. DLTS measurements performed in darkness after such illumination revealed the presence of additional deep level with energy activation equal to 0.24 eV. © 2001 Elsevier Science B.V. All rights reserved.

Keywords: Deep levels; AlGaAs; α -irradiation

1. Introduction

Defects in semiconductors play important role as they control operation of semiconducting devices. It is well-known that irradiation introduces or increases the number of defects in semiconductors. This impact is of premium importance for the devices exposed to irradiation, as in the case of those applied in extraterrestrial space. On the other hand studying defects introduced by irradiation gets insight into physics of defects.

Some defects introduced during light-ion irradiation of semiconductors can be metastable. Metastability refers to the reversible transformation of defects from one structural configuration to another. Their formation can strongly depend on heat treatment or biasing condition during heating or cooling of the sample. Metastable defects are important for both fundamental physics and device applications as they can affect semiconductor properties. In some cases the metastability follows a large lattice relaxation and is

explained with the help of configuration coordinate diagram.

Whereas metastable defects introduced in n-type GaAs during α irradiation have been widely investigated [1] there is very little information about irradiation induced metastable defects in p-type GaAs and related $\text{Al}_x\text{Ga}_{1-x}\text{As}$ mixed crystals. Recently, observation of metastability in p-type GaAs has been reported [2].

In the present paper the influence of He^{++} ion radiation on defects in beryllium doped p-type MBE layers has been studied by DLTS and photocapacitance method. It was found that irradiation introduced a metastable defect which manifests itself after light illumination in nitrogen temperatures. Metastability due to this defect is similar to the metastability observed in many II–VI and III–V semiconducting crystals. The “signature” of the defect has been determined.

2. Experiment

The samples under study were Be doped to obtain p-type $\text{Al}_{0.5}\text{Ga}_{0.5}\text{As}$. Their net acceptor concentration was equal to $1 \times 10^{16} \text{ cm}^{-3}$. The wafer from which the samples were made was grown on a semi-insulating

*Corresponding author. Tel.: +48-71-320-2642; fax: +48-71-328-3696.

E-mail address: jasza@rainbow.if.pwr.wroc.pl (J. Szatkowski).

[001] GaAs substrate in a Varian Gen II MBE-machine. Metal-semiconductor structures were realised in order to perform DLTS studies. Detailed description of the sample and contact processing is given in Ref. [3]. The samples with contacts processed were exposed to He ion bombardment. The irradiation was performed at Copenhagen University's accelerator laboratory with 0.3 MeV He^{++} ions of fluences equal to 10^{11} and 10^{12} cm^{-2} . Capacitance and DLTS measurements were collected with 1 MHz capacitance bridge and a lock-in system. Applied temperature range was equal to 77–350 K.

3. Results and discussion

In Fig. 1 the DLTS signal temperature scans are shown for reference sample and irradiated with two different doses of He^{++} ion fluences: 10^{11} and 10^{12} cm^{-2} . The data for non-irradiated sample had to be multiplied 10 times and for the sample irradiated with lower fluence—5 times so that it was possible put the data together in one figure with those for higher dose.

DLTS signal peaks labeled as H1 and H3 are visible on each of the curves. Increasing ion fluence however magnifies more the second one. Level H2 remains unaffected by radiation, as it disappears gradually with increasing fluence, hidden inside the signal related to the trap H3. The peak labeled as H4 becomes barely distinguishable with increasing fluence due to the new giant peak H5. Another new peak appeared, the one which is partly included on the high temperature side of the scan. Properties of the traps determined for both non-irradiated and irradiated samples by fitting theoretical DLTS signal to experimental data have been presented elsewhere [4].

It was found, that irradiation introduced also some metastable defects. The presence of a metastable defect in a semiconductor manifests itself in persistent photo-

conductivity or persistent photocapacitance effects. These effects are observed when the sample is exposed to illumination at sufficiently low temperature. For metastable defects, illumination increases conductivity or capacitance and this state persists for a long time period after turning off the light. Both conductivity and capacitance return to their 'dark' values after warming up the samples above certain temperature. In order to explain the effect it is assumed that after illumination the metastable defect undergoes transformation and return to its initial state is not possible due to energetic barrier for carrier recapture. Warming the sample allows overcoming of the barrier and return to the ground state. Persistent photocapacitance was observed for the He^{++} irradiated samples of Be doped $\text{Al}_{0.5}\text{Ga}_{0.5}\text{As}$ studied here. After applying for several minutes at liquid nitrogen 'below band gap' illumination, increase in capacitance has been observed. After turning off the light, the capacitance remained unchanged for many hours. The quenching of the effect might be achieved by warming the sample above 200 K. The optical threshold for the persistent photoeffect was found to be equal to 1 eV, approximately. The effect of persistent photocapacitance is shown in Fig. 2. Both curves representing (i) capacitance measured without illumination, and (ii) after illumination at 77 K coincide at 200 K, approximately.

Besides the persistent photocapacitance, another metastable effect has been observed for the irradiated samples. It was found that for the samples exposed for several minutes to illumination at 77 K additional minimum appeared on DLTS temperature scan run in darkness. Above minimum was observed after sample illumination with photons energy higher than 1 eV. In Fig. 3. DLTS signal vs. temperature dependence is shown with wavelength taken as a parameter. It is clearly seen that for wavelengths lower than $1.3 \mu\text{m}$ a new minimum appears within 150–200 K temperature range i.e. new deep level is created by photons.

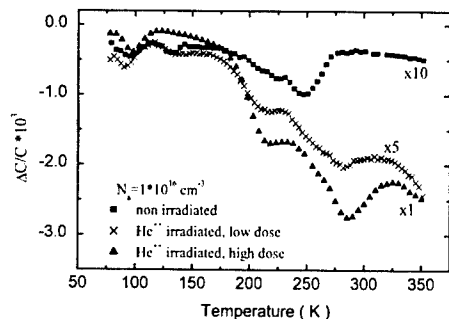


Fig. 1. DLTS signal temperature scans for beryllium doped $\text{Al}_{0.5}\text{Ga}_{0.5}\text{As}$ MBE layers. Lock-in frequency was equal to 69 Hz.

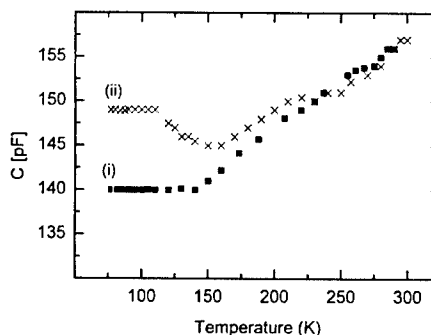


Fig. 2. Curve (i) capacitance measured without illumination, and curve (ii) capacitance measured also in darkness but after initial illumination at 77 K for several minutes.

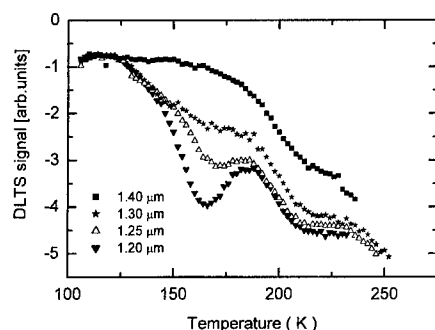


Fig. 3. “Dark” DLTS temperature scans taken after exposing the sample for several minutes at 77 K to monochromatic illumination of different wavelengths.

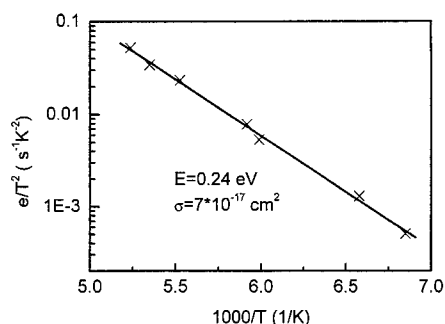


Fig. 4. Arrhenius plot of the DLTS trap appearing after illumination of the irradiated samples with photons of energy higher than 1 eV.

Arrhenius plot related to the new level is shown in Fig. 4. Solid line is the best square fit to the experimental data. The plot results in activation energy equal to 0.24 eV and apparent capture cross section $\sigma = 7 \times 10^{-17} \text{ cm}^2$.

As optical thresholds for persistent photoeffect and appearance of a new DLTS minimum were equal to 1 eV, it was tempting to propose, that both effects are related to the same origin. Let us assume therefore, that illumination changes charge state of some metastable defect by light induced emission of holes and in effect transformation of the defect into another defect takes place. At low temperature, say close to 77 K, return to the initial state is not possible and persistent photocapacitance is observed. It should be pointed out here,

that emission of holes to the valence band is considered here, as for a metal—p-type semiconductor junction this process is accompanied by increase of a negative charge within depletion region of the junction and increase of its capacitance. This new defect accompanies creation of additional deep level within band gap which can be visible in DLTS. It is clear now, that the DLTS signal is observed only after illumination by photons of energy higher than energetic distance of the ground state of the defect.

Physical origin of such a defect can be different. One of the possibilities is creation of a complex composed of a mobile (due to irradiation) host atom, attracting (after hole emission) some element. Another, transformation of the same defect accompanied by lattice relaxation, like in the case of DX centers in III–V and II–VI compounds.

4. Conclusions

In present paper the results of DLTS studies and photocapacitance measurements are given for He^{++} irradiated Be doped $\text{Al}_{0.5}\text{Ga}_{0.5}\text{As}$ MBE layers. Comparison of DLTS studies with those made for unirradiated samples let us assume, that irradiation introduced metastable centers. In effect, persistent photocapacitance was observed and additional DLTS minimum on DLTS temperature scan related to new deep level emerged after exposing the samples to illumination at 77 K. As optical thresholds for persistent photoeffect and creation of the new deep level were equal we assumed that new level is related to metastable defect created by irradiation.

References

- [1] M.J. Legodi, F.D. Aurret, S.A. Goodman, *Physica B* 273–274 (1999) 762 and references therein.
- [2] Z.Q. Fang, J.W. Kim, P.W. Yu, *Appl. Phys. Lett.* 78 (2001) 2526.
- [3] J. Szatkowski, E. Płaczek-Popko, K. Sierański, O.P. Hansen, *J. Appl. Phys.* 86 (1999) 1433.
- [4] J. Szatkowski, E. Płaczek-Popko, K. Sierański, A. Johansen, J. Fiałkowski, *Nucl. Instrum. Methods B* 178 (2001) 252.



ELSEVIER

Physica B 308–310 (2001) 772–775

PHYSICA B

www.elsevier.com/locate/physb

Raman probing of the wave function of collective excitations in the presence of disorder

Yu.A. Pusep^{a,*}, S.S. Sokolov^{b,c}, W. Fortunato^b, J.C. Galzerani^b, J.R. Leite^d

^a Departamento de Física e Ciência dos Materiais, Instituto de Física de São Carlos, Universidade de São Paulo, Av. Trabalhador São Carleone, 400, 13566-560 São Carlos, SP, Brazil

^b Departamento de Física, Universidade Federal de São Carlos, CP 676, 13565-905 São Carlos, Brazil

^c Institute for Low Temperature Physics and Engineering, 61164 Kharkov, Ukraine

^d Instituto de Física da Universidade de São Paulo, 05315-970 São Paulo, Brazil

Abstract

The spatial extents of the wave functions of the collective plasmon–LO phonon excitations were studied as a function of the doping concentration and the temperature in the AlGaAs alloy. A strong increase of the localization length was found with the increase of doping, while a decrease of the localization length was detected with the increase of the doping level at higher electron densities. A theoretical analysis based on the variational principle showed that the ionized impurities are responsible for the observed decrease of the localization length. © 2001 Elsevier Science B.V. All rights reserved.

Keywords: AlGaAs alloys; Plasmons; Localization

1. Introduction

The problem of the interaction of the carriers with the crystal imperfections such as impurity centers, native defects, phonons, etc., is of great importance in solid state physics. In the case of a weak interaction, this problem is usually treated in a semiclassical approach, when an electron can be represented by a point particle in a well-defined Bloch state $\Psi(\mathbf{q})$. The Born approximation is then used to determine the scattering rate $W(\mathbf{q}, \mathbf{q}')$, which defines the probability of the electron in a state \mathbf{q} to be scattered into a state \mathbf{q}' [1]. This approximation is basically valid when the potential energy of the interaction is small in comparison with the particle kinetic energy. An additional consequence of the scattering is the decay of the wave function of the scattered particle. This decay is negligible when the interaction is weak; however, for a strong interaction the uncertainty in the determination of the particle wave number δq —associated with the spatial localization of the particle $L_c(\delta q \propto L_c^{-1})$ —can be large enough, being a

significant part of the Brillouin zone. In this case, the Born approximation fails and a more general approach to treat the scattering process, which would take into account the modification of the wave function, should be used.

In recent papers, we have already shown that in disordered solids, where the Raman selection rules are relaxed, Raman scattering serves as a tool to study the spatial extent of the collective excitations involved, such as phonons, plasmons and coupled plasmon–phonon modes [2,3]. In many aspects, the dynamic properties of the single particle excitations and of the collective excitations are similar. In particular, as the single electron, the plasmons reveal a localization when undergoing a random potential [4]. Therefore, the investigation of the spatial extent of the localized plasmon can shed some light on the behavior of the wave function of the localized electrons.

In this paper, we present a systematic study of the influence of imperfections on the propagation and localization of collective plasmon-like excitations in the AlGaAs alloys. We show that already at rather moderate doping levels the impurities strongly modify the wave functions of the plasmons, giving rise to their

*Corresponding author. Fax: +55-16-2739827.

E-mail address: pusep@if.sc.usp.br (Y.A. Pusep).

localization. A simple theoretical model was developed to account for the interaction of the plasmons with the impurities. In addition, a significant increase of the plasmon localization caused by the interaction with phonons was found with the increase of the temperature.

2. Experimental

$\text{Al}_{0.11}\text{Ga}_{0.89}\text{As}$ alloys doped with Si were grown by molecular beam epitaxy on (100) oriented GaAs substrates. The electron concentrations were obtained both by Hall and capacitance measurements. Unpolarized back-scattered Raman spectra were performed at $T = 10\text{ K}$ with a “Instruments S.A. T64000” triple grating spectrometer supplied with a CCD detector cooled by nitrogen; the 5145 Å line of an Ar^+ laser was used for excitation.

Some selected Raman spectra of the $\text{Al}_{0.11}\text{Ga}_{0.89}\text{As}$ alloy are demonstrated in Fig. 1 where the data concerning the AIA-like mode are presented. The values of the parameters characterizing the AIA-like coupled

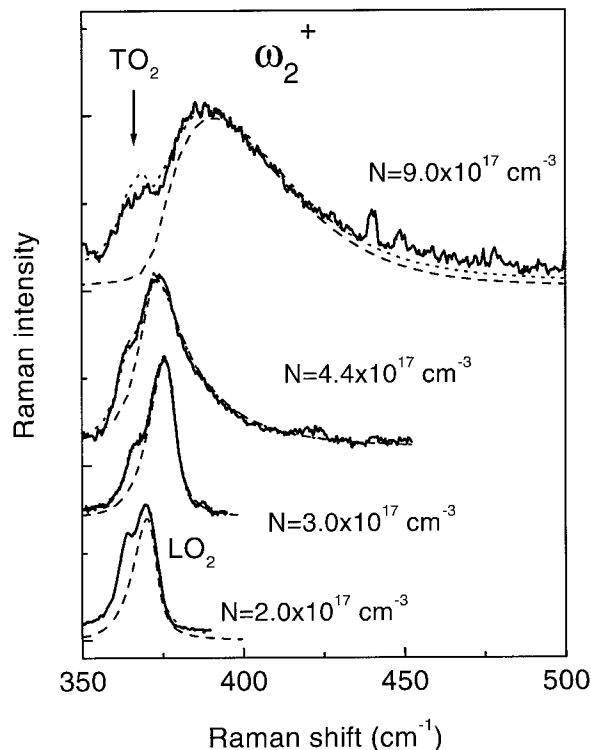


Fig. 1. Raman spectra of the $\text{Al}_{0.11}\text{Ga}_{0.89}\text{As}$ alloys with different electron concentrations measured at $T = 10\text{ K}$ in the frequency range of the AIA-like optical phonons (solid lines). The dotted lines show the full calculated spectra, while the separate contributions of the collective plasmon-LO phonon excitations are plotted by dashed lines.

modes (the mode frequencies, the damping constants and the localization lengths) were determined by the fitting of the experimental Raman spectra as in [3].

The parameters of the collective excitations of interest measured in the alloys with different electron concentrations are shown in Fig. 2. The whole interval of the electron densities studied here can be divided into the following three ranges, where different behaviors of the collective excitations were found:

- (i) Low electron densities range. Here, with the increase of the doping level, the LO phonons are transformed into the coupled plasmon-LO phonon excitations. This process is accompanied by the increase of the intensities of the relevant Raman lines which takes place because the active volume of the excitations contributing to the Raman process rapidly increases when changing from phonons to plasmons. This increase of the active volume of the excitations contributing to Raman scattering is

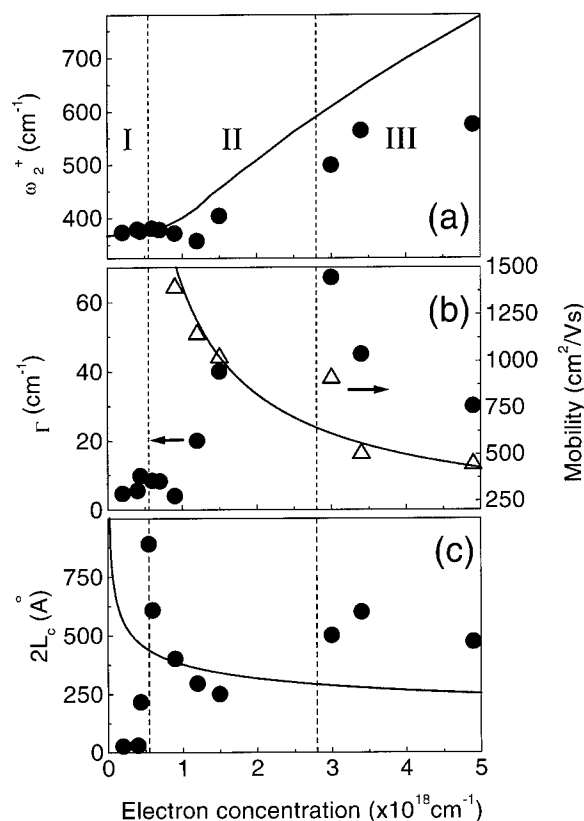


Fig. 2. Dependencies of the frequency ω_2 , the damping constant (Γ) and the localization length ($2L_c$) of the AIA-like collective plasmon-LO phonon excitations on the electron density measured in the $\text{Al}_{0.11}\text{Ga}_{0.89}\text{As}$ alloy at $T = 10\text{ K}$. The values of the Hall mobilities (μ) are shown in (b) by triangles. The solid lines are the calculated dependencies $\omega_2(N)$ (a) $\mu(N)$ (b) and $2L_c(N)$ (c) as explained in the text.

directly seen in the increase of the localization length (L_c) presented in Fig. 2(c).

- (ii) Intermediate electron densities range. In this range, the collective modes mostly acquire a plasmon character, which is revealed in the corresponding asymmetry of the Raman lines [2] and in the blue shift of the mode frequency. The dependence of the frequency ω_2^+ on the electron density calculated in the $\text{Al}_{0.11}\text{Ga}_{0.89}\text{As}$ alloy is shown in Fig. 2(a) by a solid line. At such doping levels, the scattering of the plasmons by the impurity silicon atoms dominates, resulting in the increase of the damping constant (Γ) and in the decrease of the localization length (L_c) of the studied collective excitations.
- (iii) High electron densities range, where the effects of the correlation caused by the electron-electron interaction—which have already been found in the disordered GaAs/AlGaAs superlattices—become significant, resulting in the formation of the coherent spatial clusters [5,6] and, as a consequence, in the narrowing of the Raman lines (the decrease of the damping constant Γ) and in the increase of the localization length with the increase of the doping levels.

It ought to be pointed out that the relatively small values of the localization lengths of the collective coupled plasmon-LO phonon excitations (comparable with the interelectron distances) obtained in the highly doped samples mean that in this case, the collective excitations are mostly represented by the LO phonon-like vibrations, probably strongly coupled only with the neighboring electrons.

3. Theoretical analysis and discussion

In the range of the intermediate electron densities (range II in Fig. 2), where the scattering dominates in the origin of the spatial extents of the coupled plasmon-like excitations and the above discussed electron-electron correlations are still not significant, the modification of the wave function of the plasmons can be calculated taking into account the interaction of the plasmons with the impurities.

As it was mentioned in the introduction, in the presence of disorder collective excitations can be represented as a superposition of plane waves with the wave vectors distributed in a finite interval δq . In this case, according to the model successfully used for the optical phonons in microcrystalline silicon [7] one can present the wave function in the form of a Gaussian:

$$\varphi(r) = \frac{2\sqrt{2}}{\pi^{3/4}L_c^{3/2}} \exp\left(-\frac{2\pi^2}{L_c^2}\right), \quad (1)$$

which means the effective localization at $|r| < L_c$.

In order to calculate the variation of the localization length caused by the interaction with the scattering potential of the ionized impurities, we developed the following approach. We start with the wave function written in the form of a Gaussian (1), which is equivalent to the representation of the collective excitations as noninteracting quasiparticles with an effective charge e^* and a mass M^* , spatially localized in a sphere of radius L_c . This wave function, coinciding with a spherically symmetric ground state wave function of a 3D harmonic oscillator allows us to write the effective Hamiltonian of the collective excitations as

$$\hat{H}_{\text{eff}} = -\frac{\hbar^2}{2M^*} \frac{1}{r^2} \frac{\partial}{\partial r} \left(r^2 \frac{\partial}{\partial r} \right) + \frac{8\hbar^2}{M^*L_c^4} r^2, \quad (2)$$

where the wave function $\varphi(r)$ is the eigenfunction H_{eff} for $L_c = L_0 = 2\sqrt{\hbar/M^*\omega_0}$, which is the localization length of the harmonic oscillator with a resonance frequency ω_0 . In our case, L_0 has a meaning of the localization length of the plasmon-like excitations in the absence of impurities (in an undoped alloy). The interaction of the plasmon with impurities transforms H_{eff} into

$$\hat{H}_{\text{pl}} = \hat{H}_{\text{eff}} + U_{\text{imp}}(r), \quad (3)$$

$$U_{\text{imp}}(r) = \frac{Ze^*}{\epsilon} \sum_j \frac{e^{-q_0|r-r_j|}}{|r-r_j|}. \quad (4)$$

Here, Ze is the effective charge of the ionized impurities, e is the electron charge, ϵ is the medium dielectric constant. The exponential dependence of $U_{\text{imp}}(r)$ is associated with the screening action of the electrons located between the plasmon and the charge center interacting with it. The screening parameter is q_0 .

The wave function given by Eq. (1) is not the eigenfunction of the operator H_{pl} . We can, however, treat it as a trial function of the Schrödinger equation for the plasmon depending on the Hamiltonian H_{pl} and containing L_c as a variational parameter. Using the interaction in the form presented by Eq. (4) we calculated the ground state energy:

$$E_0 = \frac{N_i e^2 L_c^3}{4\epsilon} \left[\exp\left(-\frac{q_0 L_c - 1}{4}\right) \text{erfc}\left(-\frac{q_0 L_c - 1}{4}\right) - \exp\left(-\frac{q_0 L_c + 1}{4}\right) \text{erfc}\left(-\frac{q_0 L_c + 1}{4}\right) \right], \quad (5)$$

where N_i is the concentration of the ionized impurities correspondingly.

The value L_c of interest can be found from the condition of the minimum of the E_0 as a function of L_c :

$$\frac{\partial E_0}{\partial L_c} = 0. \quad (6)$$

As it is seen from Eq. (5) the value E_0 depends on the impurity and on the electron concentrations causing the corresponding dependence of the localization length

calculated from Eq. (6). The results of the numerical calculations of L_c fulfilled by Eq. (6) are presented in Fig. 2(c) by a solid line. A reasonable agreement between our calculations and the experimental data obtained for the $\text{Al}_{0.11}\text{Ga}_{0.89}\text{As}$ alloys was observed. It should be emphasized that no fitting parameters except the localization length of the plasmon-like excitation in the undoped alloy (L_0) were used in the calculation of the localization lengths presented in Fig. 2(c); the best correspondence with the experimental data was obtained with $L_0 = 4000 \text{ \AA}$.

4. Conclusions

The localization dynamic properties of the collective coupled plasmon-LO phonon excitations were studied in the doped AlGaAs alloys. It was shown that the plasmon-like excitations in the doped AlGaAs alloy are strongly influenced by the ionized impurities

revealing a decrease of the localization length with the increase of the doping level.

Acknowledgements

The financial support from FAPESP is gratefully acknowledged.

References

- [1] J. Singh, *Physics of Semiconductors and their Heterostructures*, McGraw-Hill Inc., New York, 1993.
- [2] Yu.A. Pusep, et al., *Phys. Rev. B* 58 (1998) 10683.
- [3] Yu.A. Pusep, et al., *Phys. Rev. B* 60 (2000) 4441.
- [4] S. Das Sarma, et al., *Phys. Rev. Lett.* 56 (1986) 1280.
- [5] Yu.A. Pusep, *J. Phys.: Condens. Matter* 12 (2000) 353.
- [6] Yu.A. Pusep, et al., *Phys. Rev. B* 63 (2001) 115311.
- [7] H. Richter, et al., *Solid State Commun.* 39 (1981) 625.



ELSEVIER

Physica B 308–310 (2001) 776–779

PHYSICA B

www.elsevier.com/locate/physb

Deep-level transient spectroscopy study of electron traps in rapid thermally annealed SiO₂-capped n-type GaAs layers grown by metalorganic chemical vapour deposition

P.N.K. Deenapanray^{a,*}, M. Lay^a, D. Åberg^b, H.H. Tan^a, B.G. Svensson^{b,c},
F.D. Aurret^d, C. Jagadish^a

^a *Department of Electronic Materials Engineering, Research School of Physical Sciences and Engineering, RSPSE, Australian National University, Canberra ACT 0200, Australia*

^b *Solid State Electronics, Royal Institute of Technology, P.O. Box E229, S-164 40 Kista-Stockholm, Sweden*

^c *Department of Physics/Physical Electronics, University of Oslo, P.B. 1032 Blindern, N-0316 Oslo, Norway*

^d *Department of Physics, University of Pretoria, Pretoria 0002, South Africa*

Abstract

Three dominant electron traps S1 ($E_c - 0.23$ eV), S2* ($E_c - 0.53$ eV), and S4 ($E_c - 0.74$ eV) are introduced in SiO₂/n-GaAs after rapid thermal annealing (RTA). A defect S3 ($E_c - 0.72$ eV) is observed in uncapped and annealed samples only. The S2* arises from the superposition of two defects, of which S2 ($E_c - 0.46$ eV) can be resolved using filling pulse widths < 1 ms. The intensities of S1, S2*, and S4 show Arrhenius-like dependencies on the RTA temperature. We argue that the defects are formed as a result of an increase in the ratio of As : Ga in the near-surface region of the GaAs layers. The electronic and annealing properties of S4 show that it is a member of the EL2 family of defects. The removal of S1 and S2*, as well as the introduction of secondary defects, during isochronal annealing experiments is also discussed. © 2001 Elsevier Science B.V. All rights reserved.

Keywords: Deep-level transient spectroscopy; GaAs; Impurity-free disordering; Defects

1. Introduction

Impurity-free Disordering (IFD) using SiO₂ capping layers has recently been used to engineer the bandgap of GaAs-based heterostructures for the monolithic integration of optoelectronic devices (for a comprehensive review of impurity-free disordering see, Ref. [1]). IFD proceeds via the diffusion of point defects, namely the vacancies, on the group III sublattice in the GaAs-based system [1,2]. Excess vacancies (V_{Ga}) are generated at the SiO₂/GaAs interface by the out-diffusion of Ga atoms into the dielectric layer. The controlled modification of semiconductor properties using such defect engineering

can be better understood and improved by investigating the defects created during capped annealing. In this paper, we report on the electronic and annealing properties of electron traps introduced in rapid thermally annealed (RTA) SiO₂-capped n-GaAs epilayers using deep level transient spectroscopy (DLTS).

2. Experimental procedure

Epitaxial GaAs layers of (100) orientation and doped with 1×10^{16} Si cm⁻³ were used. The 4 μm thick epitaxial layers were grown by MOCVD on n⁺-GaAs substrates. The epitaxial side of the samples were capped with 200 nm SiO₂ by plasma-enhanced chemical vapor deposition. RTA was performed on both SiO₂-capped and uncapped GaAs samples at 800 °C, 850 °C or 900 °C for 30 s under Ar flow. After removing the SiO₂ layer,

*Corresponding author. Tel.: +61-2-6249-0374; fax: +61-2-6125-0511.

E-mail address: pnk109@rsphysse.anu.edu.au (P.N.K. Deenapanray).

selected samples were annealed for 20 min at various temperatures. Annealing up to 400°C was carried out in an Ar atmosphere, while annealing above 400°C was performed under an arsine ambient. DLTS measurements were made on Au Schottky barrier diodes deposited by resistive evaporation on the chemically cleaned layers. Reverse bias and filling pulse conditions were adjusted so that the depth region between 0.35 and 0.60 μm of each sample was probed during the DLTS measurements.

3. Results and discussion

The as-grown n-GaAs epilayers used in this study contained only the EL2 ($E_c - 0.79\text{ eV}$) with concentrations $\sim 1 \times 10^{13}\text{ cm}^{-3}$ [spectrum (a) in Fig. 1]. IFD created electron traps S1 ($E_c - 0.23\text{ eV}$), S2* ($E_c - 0.53\text{ eV}$), and S4 ($E_c - 0.74\text{ eV}$) as shown in spectrum (c) of Fig. 1. In addition to S1, S2*, and EL2, a defect S3 ($E_c - 0.72\text{ eV}$) is only observed in samples annealed without SiO_2 capping. It should, however, be noted that the presence of S3 in IFD samples could be masked by the much larger defect peak S4. Defect S4 is observed only in SiO_2 -capped and annealed samples, and its shallower peak position suggests that it is not the EL2. A comparison of spectra (b) and (c) reveals that although S1 and S2* are generated thermally (i.e. without SiO_2 capping), their concentrations are much increased by IFD. Spectra (d) and (e) were taken from samples annealed at 400°C and

500°C, respectively, following initial IFD at 900°C for 30 s. These spectra show the creation of secondary defects during post-IFD annealing, which will be further discussed later.

We have performed variable-filling-pulse-width (t_p) measurements on S2* ($\sim 221\text{ K}$). Defect peak S2* is, in fact, a superposition of two discrete defects with different capture cross-sections, as evidenced by the two thresholds and the plateau in Fig. 2. In the present study, we detect the superposition of both defects, i.e. S2*, since we have used $t_p = 150\text{ ms}$. In a previous study, we used $t_p = 0.2\text{ ms}$ and determined an activation energy ($E_c = 0.46\text{ eV}$) for S2 [3]. We showed that S2 had an electronic “signature” similar to Si-related defects observed in n-GaAs epilayers grown on Si substrates. Furthermore, S2 was created with an activation energy $\sim 4.4\text{ eV}$, which is in the range 4.02–4.91 eV reported in the literature for the activation energy of group III interdiffusion coefficients in GaAs/AlGaAs and GaAs/InGaAs quantum well heterostructures [3]. Following these observations, S2 has been speculated to be the $\text{V}_{\text{Ga}}\text{--Si}_{\text{Ga}}$ complex [3]. The results shown in Fig. 2 indicate that the individual depth profiles of the two overlapping electron traps comprising S2* can be separated using different pulse widths, in a fashion similar to the recently reported deconvolution of overlapping vacancy (VO) and interstitial-related ($\text{C}_i\text{--C}_s$) defects in ion implanted n-type Si [4].

We now turn to the influence of RTA temperature on the creation of electron traps in SiO_2 -capped n-type GaAs epilayers. RTA was performed at 800°C, 850°C, or 900°C for 30 s under Ar flow. The peak intensities of S1, S2*, and S4 exhibit Arrhenius-like dependencies on the RTA temperature, $1000/T_{\text{RTA}}$, as depicted in Fig. 3. There is the consensus that defects created in

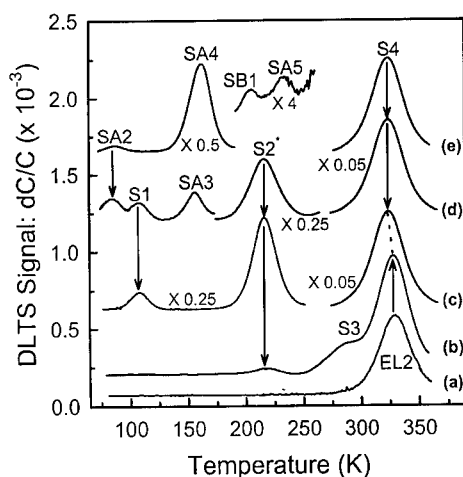


Fig. 1. DLTS spectra from uncapped (b) and (c) SiO_2 -capped and annealed n-GaAs. RTA was performed for 30 s at 900°C using proximity capping. Only defect EL2 (a) was present in the as-grown epilayers. Spectra (d) and (e) were taken from samples annealed at 400°C and 500°C for 20 min following impurity-free disordering at 900°C.

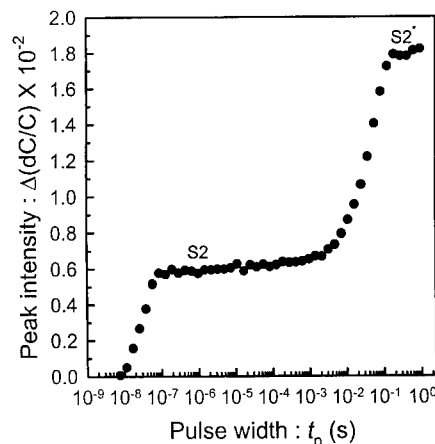


Fig. 2. Intensity of defect peak at $\sim 221\text{ K}$ (S2*) as a function of the filling pulse width, t_p .

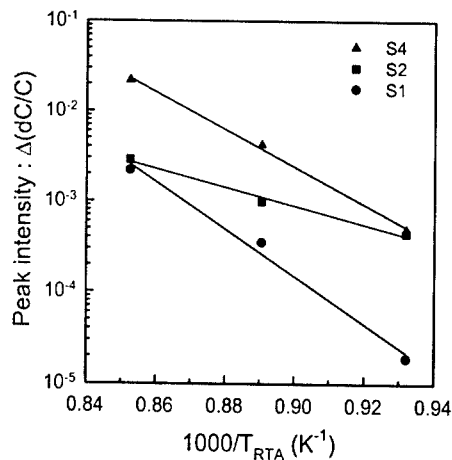


Fig. 3. Arrhenius-type dependence of defects creation on RTA temperature, T_{RTA} .

SiO₂-capped GaAs during annealing relate to the outdiffusion of Ga atoms into the capping layer [1,2]. It is pointed out here that the diffusivity of Ga atoms in SiO₂ also shows an Arrhenius-like relationship with the inverse of temperature [5]. The results shown in Fig. 3, therefore, provide the conclusive evidence that the introduction of S1, S2*, and S4 in our n-type GaAs epitaxial layers is directly related to the outdiffusion of Ga atoms into the SiO₂ capping layer during RTA. An exponential increase in the outdiffusion of Ga atoms into the SiO₂ layer with the RTA temperature results in an exponential increase in the concentration of V_{Ga} . The consequent increase in the ratio of As:Ga in the near-surface region of n-GaAs gives rise to the exponential increase in both As_{Ga} and As_i . We, therefore, propose that defects S1, S2*, and S4 are related to V_{Ga} , As_i , As_{Ga} , or complexes thereof. Similar to the results in Fig. 2, variable-filling-pulse-width measurements have shown that S2* was ~3 times larger than S2 in samples annealed at 800°C or 850°C.

Although defects are necessary to engineer the bandgap in GaAs-based heterostructures, they may also have detrimental effects on device performance. For instance, deep levels, especially those close to the middle of the bandgap, may act as efficient recombination centres [6]. In addition to increasing the leakage current of devices (due to free carrier compensation and increased generation/recombination of carriers), non-radiative recombination centres may also decrease the excitonic behaviour of optical devices [7]. Hence, it is desirable to study the removal kinetics of deep levels for the optimisation of device performance. DLTS spectra (d) and (e) in Fig. 1 show that the removal of defects S1 and S2* are accompanied by the creation of secondary defects. Fig. 4 summarises the isochronal annealing behaviour of defects S1 and S2*, together with the

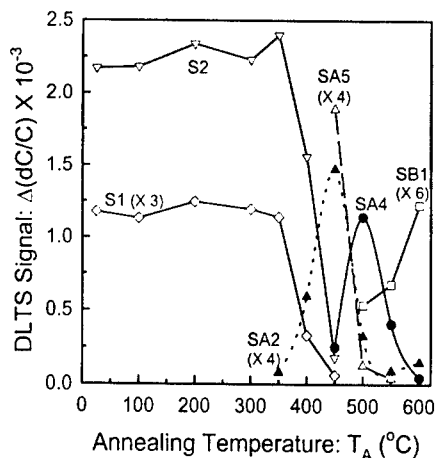


Fig. 4. Isochronal annealing behaviour of defects.

creation of secondary defects. The change in the intensity of S4 is not shown, but it remained unchanged up to 600°C [spectra (c), (d), and (e) in Fig. 1]. We have previously proposed that S4 was a member of the EL2 family of defects [8]. The intensities of S1 and S2* remained unchanged up to 350°C. Their dramatic removal above 350°C is accompanied by the introduction of a host of secondary defects, including SA2, SA3, SA4, and SB1. The defect SA3 could be detected only at 350°C and 400°C, because it is completely masked by the defect peak SA4 at the higher annealing temperatures. Defect SA5 could be resolved at 450°C after a significant reduction in S2*. It is worth noting here that SA5 may well not be a secondary defect, but one of the constituents of S2*. A defect peak, SB1, which increases with the increasing annealing temperature > 500°C, can also be observed when S2* has been removed. Although the secondary defects may be related to complexes involving V_{Ga} and As_i , when S1 and S2 dissociate, their identities remain unknown. Table 1 summarises the electronic signatures of all electron traps observed in this study (capture cross-sections obtained from extrapolation of the Arrhenius plots).

4. Conclusions

In summary, we have investigated the electronic and isochronal annealing properties of defects created in n-GaAs epilayers by impurity-free disordering. The creation of defects S1, S2*, and S4 is related to the outdiffusion of Ga atoms into the SiO₂ layer during RTA at 800–900°C. We have provided the evidence that S2* arises from the superposition of two discrete traps, including S2. The generation of excess V_{Ga} in the near-surface region of n-GaAs epilayers during RTA also

Table 1
Summary of the electronic properties of defects detected in this study

Defect	Activation energy (eV)	Capture cross-section (cm ²)	Remarks
S1	0.23 ± 0.02	7 × 10 ⁻¹⁵	Electric field dependent [8]
S2*	0.53 ± 0.03	4 × 10 ⁻¹³	Composed of 2 defects, including S2 [3]
S4	0.74 ± 0.04	6 × 10 ⁻¹³	Member of EL2 family of defects [8]
SA2	0.16 ± 0.02	6 × 10 ⁻¹³	
SA3	0.39 ± 0.02	2 × 10 ⁻¹³	
SA4	0.37 ± 0.02	7 × 10 ⁻¹⁴	
SA5	0.51 ± 0.02	6 × 10 ⁻¹⁵	Could be a component of S2*?
SB1	0.51 ± 0.02	2 × 10 ⁻¹³	

creates an excess of As_i and As_{Ga}. We have, therefore, proposed that S1, S2*, and S4 are related to either V_{Ga}, As_i, As_{Ga}, or complexes thereof. S1 and S2* are thermally stable up to 350°C, and their dissociation at higher annealing temperatures gives rise to several secondary defects. S4 is stable up to 600°C, which is typical of the annealing behaviour of a member of the EL2 family of defects.

Acknowledgements

Financial support from the Swedish Foundation for International Cooperation in Research and Higher Education (STINT) is gratefully acknowledged.

References

- [1] E.H. Li (Ed.), *Semiconductor Quantum Wells Intermixing, Optoelectronic Properties of Semiconductors and Superlattices*, Vol. 8, Gordon and Breach, Amsterdam, 2000.
- [2] A. Pépin, et al., *J. Vac. Sci. Technol. B* 15 (1997) 142.
- [3] P.N.K. Deenapanray, et al., *Appl. Phys. Lett.* 77 (2000) 696.
- [4] P. Pellegrino, et al., *Appl. Phys. Lett.* 78 (2001) 3442.
- [5] J.W. Mayer, S.S. Lau, *Electronic Materials Science: For Intergrated Circuits in Si and GaAs*, Macmillan, New York, 1990, p. 208.
- [6] S.M. Sze, *Physics of Semiconductor Devices*, 2nd Edition, Wiley Eastern, New Delhi, 1987, pp. 35–38.
- [7] P.N.K. Deenapanray, et al., *J. Electrochem. Soc.* 147 (2000) 1950.
- [8] P.N.K. Deenapanray, et al., *J. Appl. Phys.* 88 (2000) 5255.



ELSEVIER

Physica B 308–310 (2001) 780–783

PHYSICA B

www.elsevier.com/locate/physb

Acceptor–hydrogen complexes in semiconductors under pressure

M.D. McCluskey^{a,*}, K.K. Zhuravlev^a, B.R. Davidson^b, R.C. Newman^b^a *Department of Physics, Washington State University, Pullman, WA 99164-2814, USA*^b *Interdisciplinary Research Centre for Semiconductor Materials, Imperial College of Science, Technology, and Medicine, London SW7 2BZ, UK*

Abstract

The structure of acceptor–hydrogen complexes is a subject of fundamental and technological interest. To probe the interactions between hydrogen, the acceptor, and the surrounding host atoms, hydrostatic pressure may be applied over a wide range. Using infrared spectroscopy at liquid-helium temperatures, we have observed carbon and carbon–hydrogen local vibrational modes (LVMs) in InP at hydrostatic pressures as high as 5.5 GPa. For pressures beyond 4.5 GPa, the carbon–hydrogen mode was not observed, perhaps as a result of a transformation of the complex into a different configuration. The LVM arising from carbon substitutional impurities varies linearly with pressure, whereas the shift of the carbon–hydrogen mode has a positive curvature. Both of these observations are in qualitative agreement with the pressure dependence of LVMs in GaAs. While the substitutional carbon impurities show very similar pressure shifts in the two materials, the linear pressure coefficient of the carbon–hydrogen stretch mode in InP is nearly three times that in GaAs. © 2001 Elsevier Science B.V. All rights reserved.

Keywords: Hydrogen; Local vibrational modes; Infrared; Pressure

Hydrostatic pressure is an important experimental parameter that can be tuned over a wide range in order to obtain insight into the properties of solids [1]. The development of high-pressure diamond anvil cells (DACs) has led to extensive experimental research on the properties of high-density molecular solids [2] and semiconductors [3]. In a DAC, a sample is placed in a pressure-transmitting ambient, such as liquid nitrogen or alcohol mixtures. Pressures up to several hundred GPa (1 GPa = 10 kbar = 10^{-2} Mbar = 9870 atm) have been achieved.

DACs are well suited to infrared (IR) spectroscopy. Diamonds are transparent over a wide spectral range, although type I diamonds contain nitrogen impurities that strongly absorb from 1000 to 1500 cm^{-1} . Type II-A diamonds does not contain this absorption band. In addition, all diamonds contain a two-photon absorption band around 2100 cm^{-1} . N_2 , Ar, or He are typically used

as the ambient, since, unlike alcohol mixtures, they are transparent to IR light. In N_2 , a vibrational mode of CO_2 impurities is sensitive to pressure and is used as a precise in situ pressure calibration for IR absorption experiments [4]. This calibration has been established up to a pressure of 7 GPa.

To measure the IR spectra of semiconductors under pressure, a custom diamond anvil cell has been designed and fabricated (Fig. 1). In this cell, force is applied by six Allen screws, which squeeze together a piston and cylinder [5]. The diamonds are supported by flat and hemispherical backing plates made from tungsten carbide. An off-axis parabolic mirror efficiently focuses the collimated IR beam onto the sample. A photoconducting Ge:Cu detector is placed in close proximity to the sample, so that a large fraction of the transmitted IR light is collected. The entire assembly is placed in a Janis STVP-100 liquid-helium cryostat and kept at a temperature of 6–12 K. The low temperatures are advantageous for two reasons. First, the local vibrational mode (LVM) lines sharpen with decreasing

*Corresponding author. Fax: +1-509-335-7816.

E-mail address: mattmcc@wsu.edu (M.D. McCluskey).

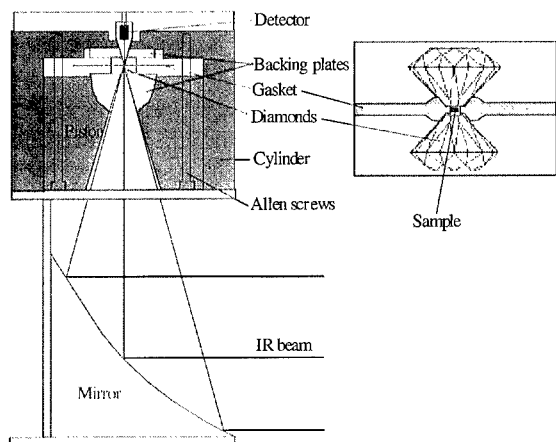


Fig. 1. Cross section of DACs used for IR spectroscopy. The diamonds, gasket, and sample are shown in the inset.

temperature. Second, the sensitive, low-noise Ge:Cu detector operates at liquid-helium temperatures.

LVM spectroscopy is a useful technique for determining the microscopic structure of impurities and defects in semiconductors [6–8]. LVMs of impurities are localized in real and frequency space [9], giving rise to sharp IR absorption peaks at liquid-helium temperatures [8]. Hydrogen, for example, typically has LVM frequencies 5–10 times the maximum phonon frequency and has narrow IR absorption peaks [10–12]. After the discoveries that hydrogen passivates donors [13] and acceptors [14] in GaAs, numerous hydrogen-related complexes have been observed in compound semiconductors [10,15]. In this paper, we review measurements of the dependence of carbon and carbon–hydrogen LVMs in GaAs and InP under large hydrostatic pressures.

The effect of pressure on LVMs in semiconductors has only recently been studied and has shown interesting results. Pressure has been applied, in conjunction with LVM spectroscopy, to probe DX centers in GaAs [16], resonant interactions in AlSb [17], hydrogen-related complexes in GaAs [18] and InP [19] and interstitial oxygen in silicon [20]. It is hoped that hydrostatic pressure may be used to differentiate between different hydrogen configurations that have the same symmetry (e.g., bond-centered vs. antibonding).

Samples discussed in this paper were carbon-doped and grown by metalorganic chemical vapor deposition on semi-insulating substrates. For the case of InP:C, it has been shown [21] that approximately half of the carbon impurities are paired with hydrogen ($C_p\text{--}H$) while the other half are substitutional carbon acceptors (C_p) that are compensated by donors. At liquid-helium temperatures, the $C_p\text{--}H$ stretch mode and C_p mode have frequencies of 2703 and 547 cm^{-1} , respectively. It was proposed [21] that the hydrogen attaches directly to the

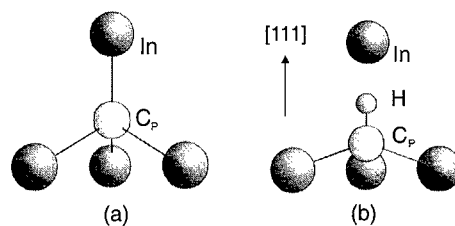


Fig. 2. Schematic diagrams of (a) substitutional carbon acceptor (C_p) and (b) carbon–hydrogen pair ($C_p\text{--}H$), in InP.

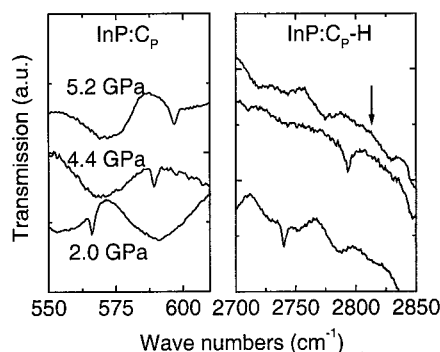


Fig. 3. IR spectra of InP:C, H for three different pressures, at a temperature of 9 K. The arrow indicates where the $^{12}\text{C}_p\text{--}H$ peak should be, by extrapolation from the lower pressure data.

carbon acceptor, in a $[111]$ bond-centered orientation, adjacent to a host indium atom (Fig. 2). This bond-centered model is believed to apply for all known $C_v\text{--}H$ pairs in III–V semiconductors [22].

IR spectra for several different pressures are shown in Fig. 3. In this figure, the spectra were taken during a decrease in pressure. The pressure was increased and decreased several times, and no evidence of hysteresis was observed. Both the C_p and $C_p\text{--}H$ peak frequencies increase with increasing pressure. For pressures beyond approximately 4.5 GPa, the $C_p\text{--}H$ peak was not observed. The arrow in Fig. 3 indicates where the peak should be, by extrapolation from the lower pressure data. The disappearance of this peak may be due to nonhydrostatic stresses that cause significant line broadening. It is not clear, however, why the carbon LVM would not be affected to the same degree. A second possibility is that the $C_p\text{--}H$ complex transforms into a different configuration at high pressures, since there is no associated change in the C_p LVM. However, no new peak is observed, so that the location of the “missing hydrogen” is currently an unsolved mystery.

The pressure-dependent shifts of InP two-phonon modes and C_p LVM were measured. The two-phonon modes have been identified previously as 2 TO and LO+TO modes [23]. In the range of pressures studied,

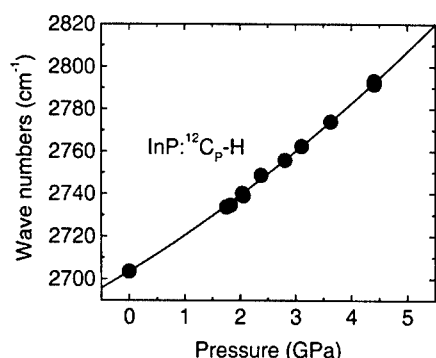


Fig. 4. InP: $^{12}\text{C}_\text{p}$ -H stretch-mode frequency as a function of pressure. The solid line is a polynomial least-squares fit to the data [Eq. (5)].

the frequencies of the phonon modes and C_p LVM vary linearly with pressure. Least-squares linear fits yield the following expressions:

$$\nu(\text{InP}:^{12}\text{C}_\text{p}) = 546.9 + 9.5P, \quad (1)$$

$$\nu(\text{InP}, 2\text{TO}) = 631.6 + 10.7P, \quad (2)$$

$$\nu(\text{InP}, \text{LO} + \text{TO}) = 659.0 + 10.8P, \quad (3)$$

where the frequencies ν are in cm^{-1} and pressures P are in GPa. The similarity between the phonon and LVM shifts is consistent with a mass-defect model, in which the properties of the bonds are not affected by the substitution of an impurity. The pressure dependence of the carbon LVM is similar to that in GaAs (Ref. [18]):

$$\nu(\text{GaAs}:^{12}\text{C}_\text{As}) = 582.7 + 9.3P, \quad (4)$$

The C_p -H stretch-mode frequency is plotted as a function of pressure in Fig. 4. The plot shows a slight positive curvature. A least-squares quadratic fit yields

$$\nu(\text{InP}:^{12}\text{C}_\text{p}-\text{H}) = 2703.4 + 16.4P + 0.9P^2. \quad (5)$$

A positive curvature was also observed in GaAs: C, H stretch modes [18]:

$$\nu(\text{GaAs}:^{12}\text{C}_\text{As}-\text{H}) = 2635.2 + 6.0P + 1.1P^2. \quad (6)$$

While the quadratic terms are similar, the linear term for InP: C_p -H is nearly three times that for GaAs: C_As -H. The reason for this significant difference is not obvious. One contributing factor may be the weaker C_p -In bond compared with the C_As -Ga bond [24,25]. The weaker bond would allow for a larger displacement of the C_p -H pair toward the plane of the three neighboring In atoms, allowing us to speculate that this could lead to a larger rate of change of the LVM frequency with increasing pressure.

In summary, we have measured the pressure dependence of LVM frequencies in InP. As in the case of AlSb: ^{12}C [4], GaAs: ^{28}Si [16], GaAs: ^{12}C , and GaAs: ^{13}C [18], we find that the InP: $^{12}\text{C}_\text{p}$ LVM

frequency varies linearly with pressure. The pressure-dependent shift of the InP: $^{12}\text{C}_\text{p}$ -H stretch mode has a positive curvature, as in the case of GaAs. This result supports the hypothesis that bond-centered hydrogen complexes generally exhibit positive curvatures in their frequency vs. pressure plots. In the future, hydrostatic pressure may prove to be a useful technique for differentiating between bond-centered and antibonding configurations. For instance, the different theoretical models proposed for Mg-H complexes in GaN should predict different pressure-dependent LVM shifts, allowing us to test the models experimentally.

The authors wish to acknowledge E.E. Haller and J. Beeman (Lawrence Berkeley National Laboratory) for providing the Ge:Cu detector and S. Watson (Washington State University) for construction of the diamond-anvil cells. This work was supported by the US National Science Foundation through Grant No. DMR-9901625 and the EPSERC, UK on Grant No. GR/K 96977. Support was also provided by WSU's Institute for Shock Physics through the DOE, Grant No. DE-FG03-97SF21388.

References

- [1] A. Jayaraman, *Rev. Modern Phys.* 55 (1983) 65.
- [2] A. Polian, P. Loubeyre, N. Boccara, *Simple Molecular Systems at Very High Density*, Plenum Press, New York, 1989.
- [3] W. Paul, in: T. Suski, W. Paul (Eds.), *Semiconductors and Semimetals* 54, Academic Press, New York, 1998 (Chapter 1).
- [4] M.D. McCluskey, L. Hsu, L. Wang, E.E. Haller, *Phys. Rev. B* 54 (1996) 8962.
- [5] G.Yu. Machavariani, M.P. Pasternak, G.R. Hearne, G.Kh. Rozenberg, *Rev. Sci. Instrum.* 69 (1998) 1423.
- [6] R.C. Newman, *Adv. Phys.* 18 (1969) 545.
- [7] M. Stavola, in: M. Stavola (Ed.), *Semiconductors and Semimetals* 51B, Academic Press, New York, 1999 (Chapter 4).
- [8] M.D. McCluskey, *Appl. Phys. Rev.* 87 (2000) 3593.
- [9] A.S. Barker Jr., A.J. Sievers, *Rev. Mod. Phys.* 47 (1975) S1.
- [10] J.I. Pankove, N.M. Johnson (Ed.), *Semiconductors and Semimetals* 34, Academic Press, New York, 1991.
- [11] S.J. Pearton, J.W. Corbett, M. Stavola, *Hydrogen in Crystalline Semiconductors*, Springer, Berlin, 1992.
- [12] E.E. Haller, in: S. Mahajan (Ed.), *Handbook on Semiconductors* 3b, North-Holland, Amsterdam, 1994, p. 1515.
- [13] J. Chevallier, W.C. Dautremont-Smith, C.W. Tu, S.J. Pearton, *Appl. Phys. Lett.* 47 (1985) 108.
- [14] N.M. Johnson, R.D. Burnham, R.A. Street, R.L. Thornton, *Phys. Rev. B* 33 (1985) 1102.
- [15] N. Nickel (Ed.), *Semiconductors and Semimetals*, Vol. 61, Academic Press, New York, 1999.
- [16] J.A. Wolk, M.B. Kruger, J.N. Heyman, W. Walukiewicz, R. Jeanloz, E.E. Haller, *Phys. Rev. Lett.* 66 (1991) 774.

- [17] M.D. McCluskey, E.E. Haller, W. Walukiewicz, P. Becla, Solid State Commun. 106 (1998) 587.
- [18] M.D. McCluskey, E.E. Haller, J. Walker, N.M. Johnson, J. Vetterhöffer, J. Weber, T.B. Joyce, R.C. Newman, Phys. Rev. B 56 (1997) 6404.
- [19] M.D. McCluskey, K.K. Zhuravlev, B.R. Davidson, R.C. Newman, Phys. Rev. B 63 (2001) 1 25 202.
- [20] M.D. McCluskey, E.E. Haller, Phys. Rev. B 56 (1997) 9520.
- [21] B.R. Davidson, R.C. Newman, C.C. Button, Phys. Rev. B 58 (1998) 15 609.
- [22] M.D. McCluskey, E.E. Haller, in: N. Nickel (Ed.), Semiconductors and Semimetals 61, Academic Press, New York, 1999 (Chapter 9).
- [23] E.T.M. Kernohan, R.T. Phillips, Solid State Commun. 100 (1996) 245.
- [24] M.J. Ashwin, R.E. Pritchard, R.C. Newman, T.B. Joyce, T.J. Bullough, J. Wagner, C. Jeynes, S.J. Breuer, R. Jones, P.R. Briddon, S. Öberg, J. Appl. Phys. 80 (1996) 6754.
- [25] R.C. Newman, B.R. Davidson, R.S. Leigh, M.J.L. Sangster, C.C. Button, Physica B 273–4 (1999) 827.



ELSEVIER

Physica B 308–310 (2001) 784–787

PHYSICA B

www.elsevier.com/locate/physb

Donor–acceptor recombination in δ -doped type II GaAs/AlAs superlattices

D.V. Gulyaev*, A.M. Gilinsky, A.I. Toropov, A.K. Bakarov, K.S. Zhuravlev

Institute of Semiconductor Physics, pr. Lavrentieva 13, 630090 Novosibirsk, Russia

Abstract

The results of a study of peculiarities of donor–acceptor recombination in δ -doped type II GaAs/AlAs superlattices are presented. The binding energies of donors and acceptors in the superlattices have been determined. The possibility of donor–acceptor recombination in superlattices with impurities separated by several undoped layers has been demonstrated. © 2001 Elsevier Science B.V. All rights reserved.

Keywords: Superlattice; Photoluminescence; Impurity

Recently type II quantum wells (QWs) and superlattices (SLs), the characteristics of which strongly differ from those of type I QWs and SLs, were investigated both theoretically and experimentally. The investigation of recombination mechanisms in superlattices with type-II band alignment is gaining not only a fundamental, but also an applied importance today. It was shown recently that Auger recombination, which is the major channel of nonradiative recombination at high temperatures and excitation densities, can be suppressed in type II structures [1], which could promote creation of low-threshold lasers [2] on the basis of such structures. The fundamental excitonic recombination has been investigated in type II SLs in detail, while radiative recombination through impurity levels has been studied only scarcely. In this work we report the results of a study of donor–acceptor recombination (DAR) in δ -doped type II GaAs/AlAs superlattices.

The study was performed on δ -doped short-period GaAs/AlAs superlattices grown by molecular beam epitaxy on (100) GaAs substrates at a substrate temperature of 600°C. The SLs consisted of 40 periods of GaAs and AlAs layer pairs grown on top of a 0.5 μ m GaAs buffer layer. The SL layer thicknesses ranged from 5 to 11 monolayers. The doping of the SLs was

performed with δ -layers of acceptors (beryllium) placed in the GaAs layers and δ -layers of donors (silicon) in the AlAs layers. The δ -layers were formed either symmetrically in the center of SL layers, or two monolayers apart from the direct heterointerface (AlAs on GaAs), and could be separated one from another with several undoped layers of the SL.

Steady-state photoluminescence (PL) was excited by an Ar⁺ laser with a wavelength of 488 nm. The excitation intensity was varied in the range 2–100 W/cm². Nonstationary PL was excited by a nitrogen laser with a pulse duration of 10 ns and a repetition frequency 1 kHz. Spectra and PL kinetics were recorded by a double grating spectrometer equipped with a cooled S-20 cathode photomultiplier operated in the photon counting mode.

The low-temperature steady-state PL spectra of non-center-doped (GaAs)₇(AlAs)₉ SLs (7 monolayers of GaAs and 9 monolayers of AlAs per period) with different doping concentrations are shown in Fig. 1. The line of X₂ excitons consisting from electrons in the X₂ valley of the conduction band of AlAs and holes in the Γ valley of the valence band of GaAs dominates in the spectrum of the structure with the lowest doping level of 5×10^{10} cm⁻² (upper spectrum), accompanied by its phonon replicas Y1 and Y2. The line Y1 is separated by 27 meV from the X₂ line, which corresponds to the energy of LA phonons in GaAs and AlAs, and the line

*Corresponding author. Fax: +7-3832-332771.

E-mail address: zhur@thermo.isp.nsc.ru (D.V. Gulyaev).

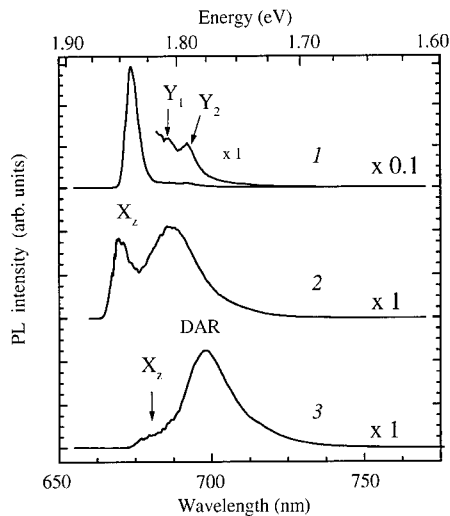


Fig. 1. Steady-state PL spectra of δ -doped type II $(\text{GaAs})_7(\text{AlAs})_9$ superlattices. Doping levels: 1— 5.5×10^{10} , 2— 2×10^{11} , and 3— $7.5 \times 10^{11} \text{ cm}^{-2}$. Measurement temperature $T = 4.2 \text{ K}$.

Y_2 is separated by 49 meV, which corresponds to the LO phonon energy in AlAs.

When the impurity concentration reaches 10^{11} cm^{-2} , a new broad line emerges in the spectrum 50–100 meV below the X_z exciton line, similar to the line which was earlier identified in the spectra of uniformly doped SLs as a line of interimpurity transitions between donors located in the AlAs layers and acceptors in the GaAs layers of an SL [3]. When the impurity concentration is greater than $2 \times 10^{11} \text{ cm}^{-2}$, this line becomes dominating in the spectrum. The increase of the intensity of the new line with doping concentration increase confirms its assignment to the donor–acceptor recombination mechanism.

To reveal the peculiarities of donor–acceptor recombination in δ -doped type II SLs and to determine the carrier binding energies the steady state and nonstationary PL spectra of samples with different layer thicknesses were measured at different temperatures and excitation intensities.

The new line displayed a red shift in the spectrum with a decrease in the excitation intensity, as is the case for DAR in bulk semiconductors. Fig. 2 shows the dependence of the position of the new line on excitation intensity for samples with different layer thicknesses. The magnitude of the red shift is larger than in bulk material and depends on the SL layer thicknesses: in the $(\text{GaAs})_7(\text{AlAs})_7$ SL the shift reaches 20 meV when the excitation intensity is changed by 10 times, while in the $(\text{GaAs})_{11}(\text{AlAs})_{11}$ SL the shift amounts to 15 meV. In comparison, in bulk AlAs a 10-fold excitation intensity increase results in a 10 meV shift of the DAR line [4].

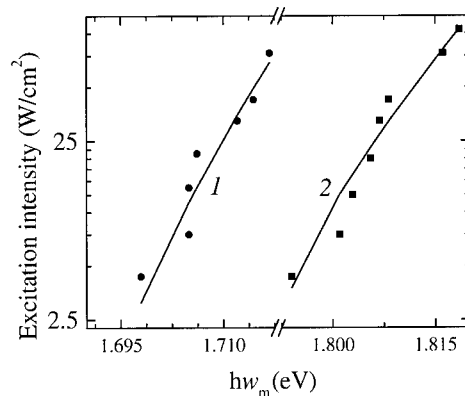


Fig. 2. Dependence of the donor-acceptor PL line position on excitation intensity for the $(\text{GaAs})_7(\text{AlAs})_7$ SL (curve 1) and $(\text{GaAs})_{11}(\text{AlAs})_{11}$ SL (curve 2) at $T = 4.2 \text{ K}$.

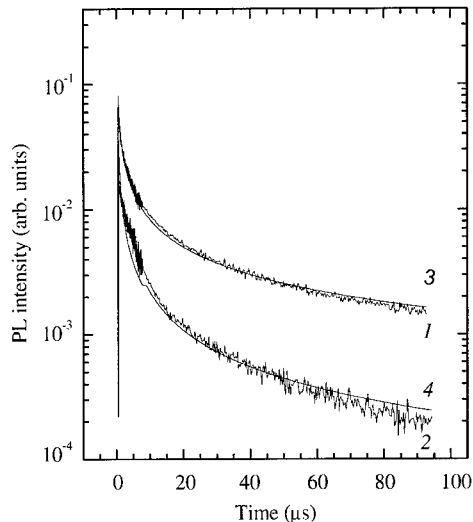


Fig. 3. Decay curves of the donor-acceptor PL line for the $(\text{GaAs})_{11}(\text{AlAs})_{11}$ SL (curve 1) and $(\text{GaAs})_7(\text{AlAs})_7$ SL (curve 2) and their power-law fits (curves 3 and 4, respectively). Measurement temperature $T = 6 \text{ K}$.

After a transient excitation the integrated intensity I of the new line exhibits a microsecond-scale decay which follows a power-law $I(t) \sim 1/t^\gamma$ (Fig. 3). The value of the exponent γ depends on the SL layer thicknesses: it was found to be smaller in the $(\text{GaAs})_7(\text{AlAs})_7$ SL ($\gamma = 0.73$) than in the $(\text{GaAs})_{11}(\text{AlAs})_{11}$ sample ($\gamma = 0.93$). It is necessary to note that γ does not change with the sample temperature increased in the range up to $\approx 50 \text{ K}$. The line displays a red shift in the time-resolved spectrum with delay time.

Fig. 4 shows a typical dependence of the integrated intensity and position of the DAR line on temperature

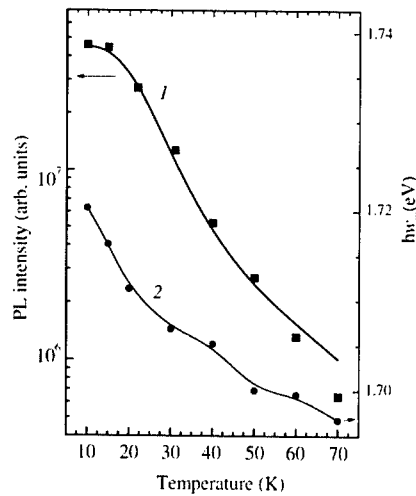


Fig. 4. Temperature dependencies of the donor-acceptor line intensity and position taken on the $(\text{GaAs})_{11}(\text{AlAs})_{11}$ SL sample.

(T). It is seen that the DAR line is red-shifting with temperature faster than the band gap is decreasing. The intensity of the DAR line decreases exponentially with temperature increase. The decrease of the DAR line intensity is apparently connected with ionization of the smaller binding energy impurity in a pair (in bulk AlAs the binding energy of the silicon donors is equal to 80 meV [4,5] and the binding energy of the beryllium acceptors in bulk GaAs is 30 meV [6]). To determine the acceptor binding energy the temperature dependence of the integrated intensity of the DAR line was approximated with the relationship $I(T) = I_0/[1 + A \exp(-E_A/kT)]$, where I_0 is the intensity at 4.2 K, A is a constant, E_A is the acceptor activation energy, and k is the Boltzmann's constant. The activation energy value obtained from the fit equals to 12.5 ± 0.5 meV independently on the layer thickness and position of impurity δ -layers. This value disagrees with the results obtained in experiments with beryllium in quantum wells of similar thickness, where its activation energy is equal to 40 meV [6]. The smaller value of the thermal activation energy in δ -doped SLs may be caused by Coulomb interaction between the acceptor and donor in a pair. To determine the binding energy of silicon donors the experimental dependence of the position of the DAR line maximum on the excitation intensity J at $T = 4.2$ K was approximated by the theoretical dependence obtained in Ref. [7] for the three-dimensional case:

$$J = D \left\{ \frac{[h\omega_m - E_g + (E_A + E_D)]^3}{[2(E_g - (E_A + E_D) - h\omega_m) + e^2/(eR_B)]} \right\} \\ \times \exp \left\{ \frac{-2e^2/(eR_B)}{[h\omega_m - E_g + (E_A + E_D)]} \right\},$$

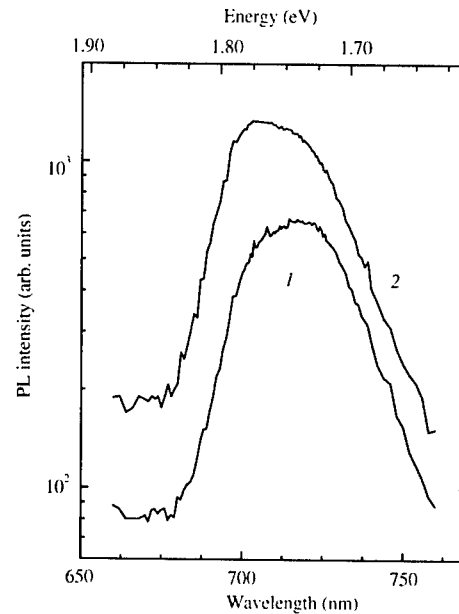


Fig. 5. Steady-state PL spectra of the $(\text{GaAs})_7/(\text{AlAs})_9$ superlattice with dopant δ -layers located near the AlAs/GaAs heterointerface. Spectra 1 and 2—excitation intensities of 15 and 30 W/cm^2 , respectively. Doping level $5 \times 10^{11} \text{ cm}^{-2}$.

where $h\omega_m$ is the position of the DAR line maximum, ϵ is the permittivity of the medium chosen to be 11.3, E_g is the band gap which was taken to be equal to the distance between the lowest electron quantization level in the AlAs layer and the lowest heavy hole level in the GaAs layer, $E_A + E_D$ is the sum of the binding energies of acceptor and donor, R_B is the acceptor Bohr radius, D is a proportionality factor, and e is the electron charge. The sum $E_A + E_D$ in SLs determined by the fit equal to 150 meV in the $(\text{GaAs})_7(\text{AlAs})_7$ SL and 140 meV in the $(\text{GaAs})_{11}(\text{AlAs})_{11}$ SL. The binding energy of donors in the AlAs layers can then be deduced from these data. Taking into account that the found acceptor binding energy may have decreased because of the Coulomb interaction and taking it equal to the binding energy of beryllium in a single QW, that is 40 meV, we obtain the binding energy of silicon in the AlAs layers of the $(\text{GaAs})_7(\text{AlAs})_7$ SL of 110 meV, and 100 meV in the $(\text{GaAs})_{11}(\text{AlAs})_{11}$ SL. It is seen that the donor binding energies in SLs obtained in the current work exceed the values reported for AlAs, which may be caused by the influence of the SL potential on the binding energy.

Next, the DAR in SLs with the dopant layers located near the heterointerfaces was studied. We found that in these asymmetric SLs the DAR line exhibits a complex structure and consists of two strongly overlapping bands separated by approximately 40 meV (Fig. 5). We believe that the appearance of the two bands is caused by the

possibility of carrier recombination in both directions—through both the direct and inverted heterointerfaces in such SLs.

To evaluate the distance between the dopant layers through which the interimpurity recombination is still possible, we separated the n- and p- δ -doped layers of the SL with several undoped layers. We found that the DAR line is observed in SLs where impurities are separated by two and even by four undoped SL layers, or by 4.3 nm and 7.2 nm, respectively.

The large shift of the DAR line with the excitation intensity that we observed (Fig. 2) is one of the peculiarities of donor–acceptor recombination in type II SLs. The larger line shift in comparison with the bulk data is explained by the increased impurity binding energies in SLs [8–10].

The increase of shallow impurity binding energies in an SL should be accompanied by a decrease of the recombination rate of a DAR line. On the contrary, a decrease of the distance between the δ -layers should increase the DAR rate. However, we observed that in the (GaAs)₁₁(AlAs)₁₁ SL the DAR decay is faster than in the (GaAs)₇(AlAs)₇ sample (Fig. 3). We therefore conclude that the effect of the SL potential on the impurity wavefunctions turns out to be stronger than the influence of the change of the distance between impurity δ -layers in the SL layers.

In summary, the following peculiarities of donor–acceptor recombination have been experimentally observed in δ -doped type II GaAs/AlAs superlattices: (1) the magnitude of the DAR line shift with excitation intensity is greater than in 3D, and (2) the DAR line decay kinetics is described by a power-law $1/t^\gamma$ with the power γ being dependent on the SL layer

thickness. The carrier binding energies of donors and acceptors in SLs have been determined. The possibility of donor–acceptor recombination in SLs with impurities separated by several undoped SL layers has been demonstrated.

The authors gratefully acknowledge the support of this work by the joint Russian-Ukraine program ‘Nanophysics and Nanoelectronics’ (Grant No. 2000-1f) and the program ‘Physics of Solid State Structures’ of MNTP (Grant No. 99-1133).

References

- [1] G.G. Zegrya, A.D. Andreev, *Appl. Phys. Lett.* 67 (1995) 2681.
- [2] V.G. Litovchenko, D.V. Korbutyak, A.L. Bercha, H.T. Graham, K.H. Ploog, *Proceedings of the 25th International Conference on the Physics of Semiconductors*, Japan, 2000, p. D092.
- [3] K.S. Zhuravlev, A.M. Gilinsky, T.S. Shamirzaev, V.V. Preobrazhenskii, B.R. Semyagin, M.A. Putyato, S.S. Chipkin, *Phys. Solid State* 40 (1998) 1577.
- [4] S. Lassen, R. Schawabe, J.L. Staehli, *Sem. Sci. Technol.* 10 (1995) 903.
- [5] N. Chand, T. Henderson, J. Klem, W.T. Masselink, R. Fischer, Y. Chang, H. Morkoc, *Phys. Rev. B* 30 (1984) 4481.
- [6] B. Podor, *Phys. Stat. Sol.* 43 (1992).
- [7] E. Zacks, A. Halperin, *Phys. Rev. B* 6 (1972) 3072.
- [8] G. Weber, *Appl. Phys. Lett.* 67 (1995) 1447.
- [9] G.N. Carniero, G. Weber, *Phys. Rev. B* 58 (1998) 7829.
- [10] W.T. Masselink, Y.-C. Chang, H. Morcos, D.C. Reynolds, C.W. Litton, K.K. Bajaj, P.W. Yu, *Solid-State Electron.* 29 (1986) 205.



ELSEVIER

Physica B 308–310 (2001) 788–791

PHYSICA B

www.elsevier.com/locate/physb

The DX⁻-centre formation at high electric fields in planar-doped GaAs : Si

M. Asche^{a,*}, O.G. Sarbey^b^aGreifswalderstr. 88, D-10409 Berlin, Germany^bInstitute of Physics, Prospekt Nauki 46, Kiev, Ukraine

Abstract

Investigating current transients, it is established that in the dark at low temperatures resonant energy levels in the conduction band can be transformed in the presence of hot electrons into metastable centres. There exist critical lower thresholds with respect to the applied electric field and the Si_{Ga}-concentration. These facts can be explained by carrier heating. It leads to a change of the potential wells. Due to their significant deepening more electrons are in subband states above the energy of the DX⁻-centre and therefore allow the formation of metastable centres. The hot carriers also decrease the screening of the interaction between neighbouring Si_{Ga}-atoms. © 2001 Elsevier Science B.V. All rights reserved.

PACS: 72.20.Ht; 72.20.Jv; 72.80.Ey

Keywords: DX centres; Hot electrons; Quantum well; Transport process

1. Introduction

In homogeneously doped GaAs:Si, the DX-centre with 2 bound electrons and the Si atom shifted in $\langle 111 \rangle$ -direction towards an interstitial site [1,2] could explain the essential difference between the thermal and optical activation and persistent photoconductivity. This model provoked many discussions, and the description of some experimental results by such a centre was not always unambiguous.¹ However, in IR spectroscopy under high pressure a new line was detected and connected with the DX-centre [3]. Another proof of the model is the results of positron annihilation experiments, which exhibited a small “vacuum” at the Si_{Ga} site, when the DX⁻-centre had been created, vanishing again when destroyed [4].

In highly doped delta-layers, in which group IV impurities are deposited on cation sites of III–V semiconductors, the wave functions of the donors and the conduction band edge overlap, and there are deep potential wells formed, in which the motion of the electrons is restricted perpendicular to the plane. Nevertheless, the DX-centres due to their localized wave function might be formed in delta layers. It had been suggested that DX⁻-centres could be responsible for the well-known discrepancy between the concentrations of active donors and nominal deposited Si-atoms (e.g. Ref. [5]), since it was expected that in such planar structures due to the high electron concentration the Fermi level can reach the energy of the resonant states. However, in Ref. [6] the broadening of the potential wells at high donor concentration and growth temperature was shown to inhibit the DX⁻-centre formation in the absence of pressure in contrast to a narrow potential profile. Yet persistent photoconductivity observed in a layer with a sheet donor concentration of 10^{13} cm^{-2} seemed to prove the existence of DX-centres [7]. Probably the different results are connected with the strong dependence of properties of delta-layers on the

*Corresponding author.

E-mail address: marion.asche@freenet.de (M. Asche).

¹ Fits to experimental data neglecting the correlation between positively and negatively charged ions seemed to favour the AI type.

growth conditions. The occupation of resonant states due to an electron heating in high electric fields and the formation of DX⁻-centres in GaAs/AlGaAs heterostructure was thought to be the origin of a current decrease [8], yet it was probably connected with the Si dopants in the barriers of the MODFETs.

2. Experiments and results

We investigated GaAs:Si under the influence of high electric field pulses—of 240 ns duration each in order to eliminate Joule heating—applied within the doping plane to explore the enhanced average energy of the carriers for a possible formation of metastable centres. The measurements were performed in the dark in liquid nitrogen or helium baths.

Our GaAs:Si structures were grown by molecular beam epitaxy at comparatively high temperatures (550°C and 610°C) and low equivalent As partial pressure [9]. The main differences of the presented four structures are the substrate orientations and dopant concentrations: (001) for the first pair (A,B) with a doping of $7 \times 10^{12} \text{ cm}^{-2}$ and a second pair (C,D) 2° misoriented towards the (111)-Ga plane with a deposition of nominal $1.4 \times 10^{14} \text{ cm}^{-2}$ Si atoms by interrupted growth technique. The latter structures were especially grown under those conditions to obtain “wires” of Si pairs along the edges of the terraces [10]. They differ from each other by a reduced temperature during overgrowth for C. However, concerning our high field transport investigations, all the structures behave in a similar way as long as the concentration of electrically active donors is not below $3 \times 10^{12} \text{ cm}^{-2}$.

The results exhibit five particularities:

1. In the course of the applied high field pulses the current decreases remarkably as shown for type D in Fig. 1 with electric field strength as parameter. For decreased doping down to $7 \times 10^{12} \text{ cm}^{-2}$ and an estimated lower limit of conducting electrons by Hall measurements of 3.5×10^{12} – $5 \times 10^{12} \text{ cm}^{-2}$ by Shubnikov–De Haas measurements—(type B) the saturated current change was approximately alike, while for somewhat less electrically active donors (type A) it gained only a value of some percent, and no effect at all was to be seen for a less doped structure with only $4 \times 10^{12} \text{ cm}^{-2}$ Si atoms.²

2. A current decrease occurs realised only if the applied field is higher than a certain threshold field. The latter strongly depends on the concentration of electrically active donors being about 6 kV/cm for

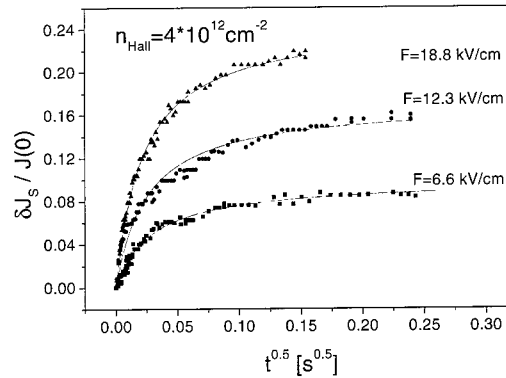


Fig. 1. Current change as a function of applied field pulses normalised to its initial value for structure D with an Si doping concentration of $1.4 \times 10^{14} \text{ cm}^{-2}$ and a lower limit of electron concentration estimated as $4 \times 10^{12} \text{ cm}^{-2}$ by Hall measurements.

3. The new current value remains unchanged for days at low temperature. Besides a recovery to its initial value by thermal activation above 130 K or an optical excitation with an energy above 0.9 eV [11]—also typical for homogeneously doped GaAs—the conductivity can be partly restored by lower electric fields than used to form the centres.

4. In the beginning of the applied heating field the current changes proportional to the square root of time. Therefore, in order to analyse the data they were presented in dependence on $t^{1/2}$ and a fitting procedure with one of the expressions

$$\delta j(t)/j(0) = \delta j_s/j(0) \times \sqrt{t/\tau} / (1 + \sqrt{t/\tau})$$

or

$$\delta j(t)/j(0) = \delta j_s/j(0) \times \{1 - \exp(-\sqrt{t/\tau})\}$$

was used. The values of the time constants do not depend on the chosen fitting procedure and those of the saturation value of the normalised current changes only up to 10%. Then $\delta j_s/j(0)$ and τ obtained from the transients are shown in Fig. 2a and b as functions of the applied field. They can be presented by

$$\delta j_s/j(0) = \delta j_s(\infty)/j(0) \times \left\{ 1 - \exp\left(-\frac{F - F_0}{F_j}\right) \right\},$$

$$\tau = \tau(\infty) / \left\{ 1 - \exp\left(-\frac{F - F_0}{F_\tau}\right) \right\},$$

i.e., both expressions with a threshold field F_0 , and $j_s(\infty)$ as well as $\tau(\infty)$ denoting the values for $F \rightarrow \infty$.

5. For lower lattice temperature (helium bath) the characteristic features remain qualitatively the same,

²Remember that $4 \times 10^{12} \text{ cm}^{-2}$ is equivalent to about $8 \times 10^{18} \text{ cm}^{-3}$, while in homogeneously doped GaAs with pressure the DX⁻-centre was observed down to 10^{17} cm^{-3} .

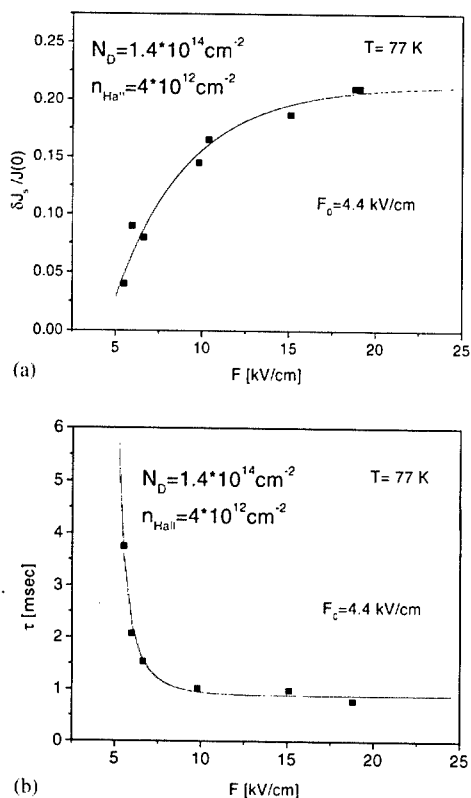


Fig. 2. Normalised saturation current change (a) and time constant for the current decrease (b) as functions of applied field obtained by fitting procedures.

only the normalised current change at a given field strength is somewhat bigger.

Besides, the field dependences of the currents before and after creation of centres almost coincide, when normalised in the region of highest applied fields, and allow to conclude that the high field mobilities do not differ remarkably. Therefore, the normalised saturation current change equals the normalised carrier concentration change. Consequently the concentration of created DX^- -centres can be determined.

3. Discussion

Particularity 3 is an evidence that in our experiments metastable DX^- -centres are the cause of current decrease. To form these centres it is necessary to populate the resonant levels of Si in the Γ -conduction band. The carrier heating in strong electric fields, firstly, changes the form of the potential well as well as the energy of its bottom and, secondly, weakens the screening of the interaction of charged ions, consequently decreasing the energy difference between

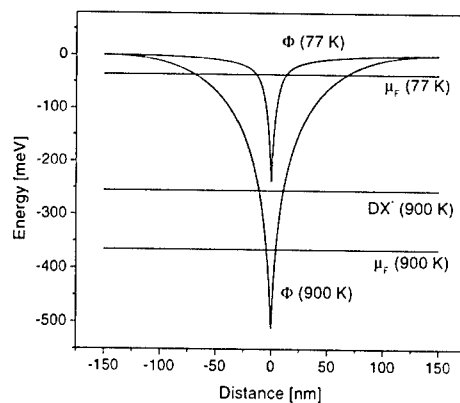


Fig. 3. Self-consistently calculated potential Φ as well as quasi-Fermi level μ_F for $7 \times 10^{12} \text{ cm}^{-2}$ donors at electron temperatures of 77 and 900 K, respectively, and the energy level of DX^- for 900 K (being still positive for 77 K).

positively and negatively charged Si-ions. We estimated both the factors by self-consistent calculations of the energy levels and the quasi-Fermi energy in the two-dimensional potential well in local-density approximation as functions of electron temperature (Fig. 3). Then taking the energy of the resonant level equal to 280 meV we found that with increased heating more electrons in the Γ -subbands occupy states above the resonant level, and become able to initiate the creation of the DX^- -centre. The strong dependence of that fraction of electrons on donor concentration and field strength is responsible for both the apparent thresholds (particularities 1 and 2). Since the electron temperature at the high electric fields used in our experiments only weakly depends on the lattice temperature, particularity 5 follows.

4. Conclusion

We state that DX^- -centres can be formed in planar-doped GaAs by high electric fields since the potential wells are significantly deepened by carrier heating. Furthermore, the weakened screening can favour a shift of the Si-atom from the lattice site towards an interstitial site.

Acknowledgements

We thank R. Hey and M. Hörcke for the growth of the structures, H. Kostial and E. Wiebicke for technological processing, and L. Däweritz and M. Ramsteiner for discussions of the Si arrangement in the planar doping layers.

References

- [1] D.J. Chadi, K.J. Chang, *Phys. Rev. Lett.* 61 (1988) 873.
- [2] D.J. Chadi, K.J. Chang, *Phys. Rev. B* 39 (1989) 1006.
- [3] J.A. Wolk, et al., *Phys. Rev. Lett.* 66 (1991) 774.
- [4] J. Mäkinen, et al., *Phys. Rev. Lett.* 71 (1993) 3154.
- [5] R.C. Newman, *Semicond. Sci. Technol.* 9 (1994) 1749.
- [6] A. Zrenner, et al., *Semicond. Sci. Technol.* 3 (1988) 1203.
- [7] S. Arscott, et al., *Semicond. Sci. Technol.* 7 (1992) 620.
- [8] T.N. Theiss, et al., *Appl. Phys. Lett.* 49 (1986) 1542.
- [9] R. Stasch, et al., *J. Appl. Phys.* 77 (1995) 4463.
- [10] L. Däweritz, et al., *J. Crystal Growth* 150 (1995) 214.
- [11] R. Stasch, et al., *J. Phys.: Condens. Matter* 8 (1996) 3215.



ELSEVIER

Physica B 308–310 (2001) 792–795

PHYSICA B

www.elsevier.com/locate/physb

Study of vacancy-type defects after Cu diffusion in GaAs

V. Bondarenko*, K. Petters, R. Krause-Rehberg, J. Gebauer, H.S. Leipner

Martin-Luther-Universität Halle-Wittenberg, Fachbereich Physik, D-06099 Halle, Germany

Abstract

Semi-insulating GaAs was contaminated by Cu. For this purpose, a thin Cu layer (30 nm) was deposited by evaporation. The diffusion and the homogeneous distribution of the Cu was performed during an annealing step at 1100 °C under defined As vapour pressures. The samples were quenched to room temperature. During a subsequent isochronal annealing experiment, vacancy clusters were found to be created, grown, and finally disappeared. The number, size, and distance depend on the annealing temperature and quenching speed. Positron lifetime measurements show that the clusters contain more than 10 vacancies. Moreover, Doppler-coincidence spectroscopy shows clearly that the clusters are surrounded by Cu atoms. The association of Cu-rich precipitates and voids with a diameter of up to 50 nm could be evidenced by analytical transmission electron microscopy. The smaller clusters have a crystallographic shape, while larger voids are spherical with a Cu-rich shell. The particles are frequently bound to dislocations. A possible model related to the out-diffusion of copper and the agglomeration of the formed vacancies is discussed. © 2001 Elsevier Science B.V. All rights reserved.

PACS: 78.70.Bj; 61.72.Ji; 68.35.Dv

Keywords: GaAs; Cu diffusion; Vacancy clusters; Positron annihilation; TEM

1. Introduction

Copper is one of the most common unintentional impurities in semiconductors. It diffuses rapidly even at low temperatures by interstitial diffusion process (the so-called kick-out mechanism) [1]. The diffusion coefficient in GaAs was reported to be as high as $D = 1.1 \times 10^{-5} \text{ cm}^2 \text{ s}^{-1}$ at 500 °C [2]. The solubility was found also to be rather high $\sim 2 \times 10^{16} \text{ cm}^{-3}$ at 500 °C and $7 \times 10^{18} \text{ cm}^{-3}$ at 1100 °C [2].

In GaAs copper acts as a double acceptor, being incorporated at a substitutional lattice site as a Cu_{Ga} . But in spite of high solubility only a small fraction of the total Cu concentration is electrically active as acceptor after cooling to room temperature. The major part forms Cu–Ga precipitates [3].

In an earlier work [4] it was shown that vacancy clusters are formed during the post-annealing of the GaAs contaminated with Cu by diffusion. It was assumed that the copper atoms surround these clusters. The present paper is the continuation of the previous positron annihilation study of the Cu in- and out-diffusion in GaAs. The presence of Cu precipitates–vacancy cluster complexes was confirmed by transmission electron microscopy (TEM) and Doppler coincidence spectroscopy. We will show also that Cu out-diffusion depends on the in-diffusion conditions, in particular on the arsenic pressure during Cu diffusion.

2. Experimental details

Undoped semi-insulating GaAs samples of thickness 0.4 mm were covered by 30 nm Cu by evaporating it under UHV conditions. This corresponds to a volume concentration of $6 \times 10^{18} \text{ cm}^{-3}$ which is approximately the upper solubility limit of Cu in GaAs. The thickness of the deposited layer was controlled by a thickness

*Corresponding author. Univ. Halle, FB Physik, Fr.-Bach-Platz 6, D-06108 Halle, Germany. Tel.: +49-345-552-5570; fax: +49-345-552-7160.

E-mail address: bondarenko@physik.uni-halle.de (V. Bondarenko).

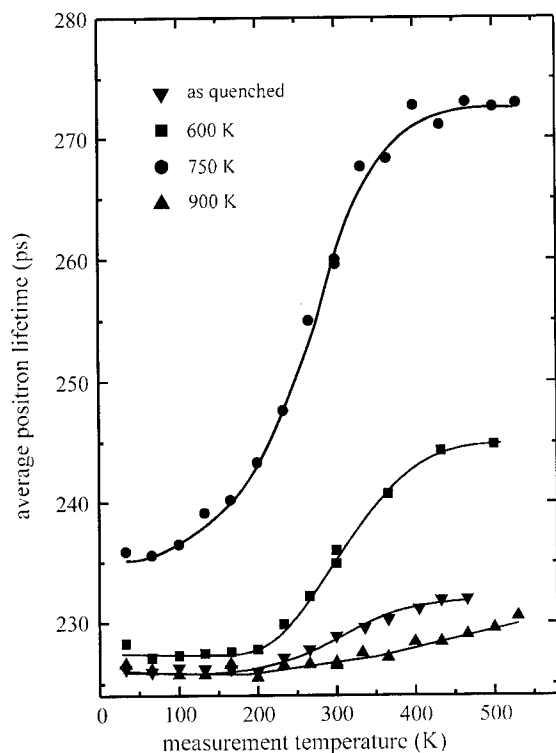


Fig. 1. Average positron lifetime as a function of sample temperature in undoped GaAs. Prior to the experiment, about $6 \times 10^{18} \text{ cm}^{-3}$ Cu atoms were introduced by evaporating 30 nm Cu to the sample surface and by a subsequent annealing at 1100°C under 2.62 bar of As pressure (3 h, quenched into water). The lifetime experiment was performed after each annealing step as indicated in the figure.

measurement device (frequency shift of a crystal oscillator). After Cu deposition at one surface, the samples were annealed in a two-zone furnace at 1100°C (sample temperature) under different arsenic pressure (0.2–10 bar) for 3 h corresponding to a Cu diffusion length of about 1.5 cm. After annealing, the samples were quenched in the quartz ampoules into water at room temperature. The samples were measured in the as-quenched state by Hall effect and thermoprobe measurements. Thereafter, the samples were isochronally annealed in the temperature range up to 900 K. The samples were cooled down slowly after each annealing step. After each annealing step positron annihilation lifetime, Doppler-broadening spectroscopy, and Hall-effect measurements were performed. The resolution of the spectrometers was 240 ps and 1.4 keV, respectively. The GaAs crystals were oriented with their (110) axis towards the Ge detector. The samples were investigated with TEM and energy dispersive X-ray spectroscopy (EDX).

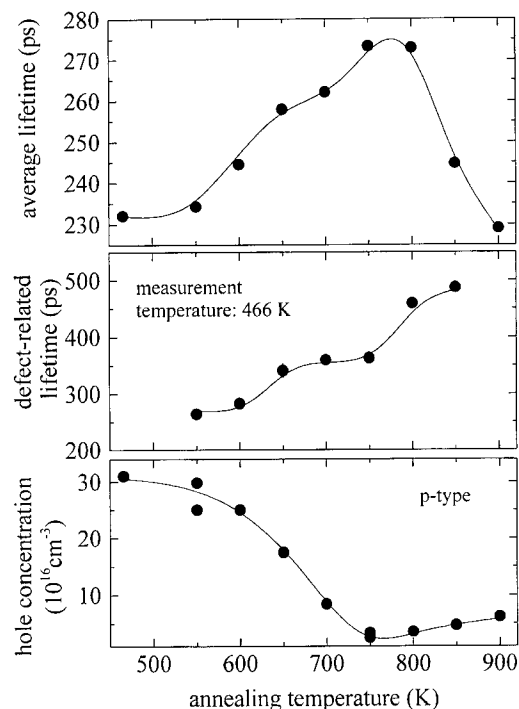


Fig. 2. Positron lifetime results of the annealing experiments of undoped semi-insulating GaAs sample after in-diffusion of $6 \times 10^{18} \text{ cm}^{-3}$ Cu atoms at the 2.62 bar As vapour pressure: (a) average positron lifetime. (b) defect-related lifetime. The spectra were measured at 466 K. (c) Hall-effect measurements after each annealing step.

3. Results and discussion

Our semi-insulating undoped GaAs sample did not show any positron trapping. After Cu in-diffusion a small increase in the average positron lifetime in the high-temperature region was observed. In Fig. 1 the temperature-dependent measurements of the average positron lifetime after different annealing steps are shown. All the curves demonstrate a strong decrease of the average lifetime at low temperatures. This is a typical dependence for shallow positron traps, which tend to trap positrons in the extended region of the Coulombic potential, reflecting thereby the properties of the bulk [5]. At high temperatures, the existence of shallow traps can be neglected due to the high detrapping rate. In the case of copper in-diffusion these traps must be the Cu acceptors, whose concentration is up to $3 \times 10^{17} \text{ cm}^{-3}$ according to the Hall-effect measurements (Fig. 2c).

During the first annealing steps, average positron lifetime increases significantly up to the value of 273 ps, indicating the presence of vacancy-type defects. With a further increase of the annealing temperature we observed a rapid decrease of the average positron

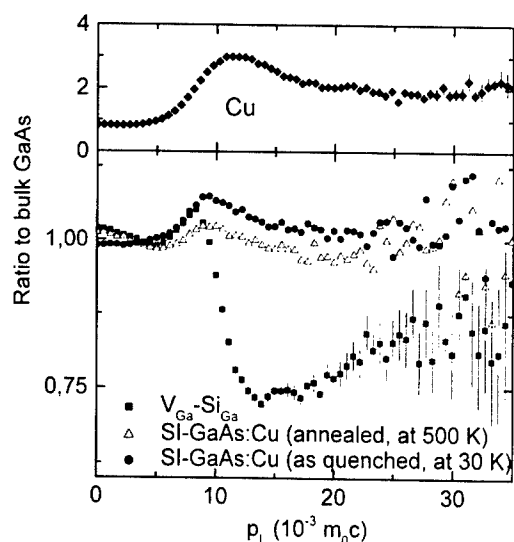


Fig. 3. High momentum part of the positron annihilation momentum distribution, normalized by taking the ratio to GaAs:Zn reference values. In the upper part the spectrum for pure copper is shown, lower part represents spectra for GaAs:Si, GaAs:Cu after quenching from the diffusion temperature and after post-annealing at 500 K.

lifetime. This annealing behaviour of the average and defect-related lifetime is presented in Fig. 2a and b. It can be seen that the open volume of the detected objects increases during annealing. The defect-related lifetime is much higher than that for monovacancy (250–260 ps) [5] and may only be explained by positron trapping at large microvoids. The value of 480 ps corresponds to the clusters, which contain more than 10 vacancies. It was assumed that these clusters are decorated by Cu precipitates [4]. However, this cannot be concluded from positron lifetime results alone.

Fig. 3 shows the high momentum part of the positron annihilation momentum distribution, normalised to the GaAs:Zn reference. The upper part presents the curve for pure Cu, the lower contains three curves: one for $\text{Si}_{\text{Ga}}\text{-V}_{\text{Ga}}$ complex, corresponding to the Ga monovacancy, and the other two for GaAs contaminated with Cu in as-quenched state and after annealing at 500 K. It is obvious that the shape of GaAs:Cu momentum distribution is very similar to the one for pure Cu. This means that copper atoms surround the observed positron trapping centres.

The presence of such vacancy cluster–Cu precipitate complexes was found also by TEM performed together with the EDX measurements in all the samples after Cu in-diffusion and after further annealing. The results are presented in Fig. 4. One can see large vacancy clusters (light spot on the picture) surrounded by copper atoms and neighbored by a copper precipitate. These clusters

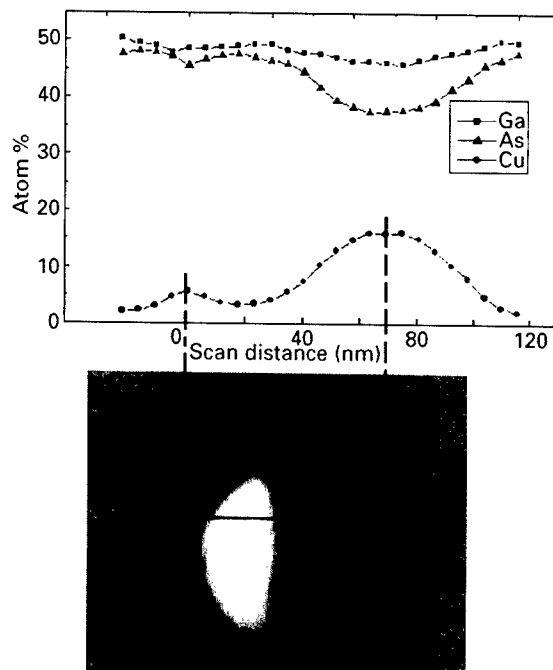


Fig. 4. (a) EDX scan measurements of the vacancy cluster–Cu precipitate complex in GaAs formed after Cu in-diffusion. (b) Transmission electron microscope image of this complex. The line on the picture indicates the scanned position of the EDX measurements.

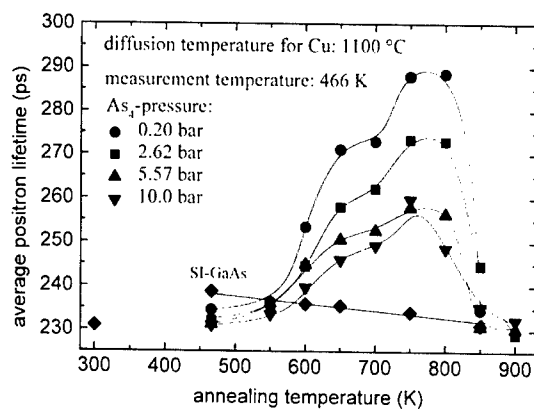


Fig. 5. Average positron lifetime vs. annealing temperature for samples contaminated with Cu at different As vapour pressure (pressure is indicated). The measurements were performed at 466 K. Also the data for undoped SI–GaAs without Cu contamination are presented for comparison.

were observed for all samples after copper in-diffusion and after each annealing step. However, the distance between them is much higher than the mean positron diffusion length, so they should be invisible for positron annihilation. The large voids were earlier also found in GaAs after Zn in-diffusion [6].

Thus, we have two types of cluster–copper complexes: the relatively small number of large clusters after in-diffusion of copper, and the large number of smaller clusters after the applied annealing procedure, that are formed during out-diffusion of copper atoms. That means that Cu_{Ga} atoms dissolved during the annealing begin to leave their sites and form precipitates which are connected with vacancy clusters. This out-diffusion process can be seen clearly in Fig. 2c where the minimum of the hole concentration corresponds to the maximum of the defect-related lifetime, i.e. to the maximum size of the vacancy clusters. The origin of these clusters is easy to understand taking into account that the atomic density of GaAs ($4.43 \times 10^{22} \text{ cm}^{-3}$) is two times smaller than the atomic density of Cu ($8.48 \times 10^{22} \text{ cm}^{-3}$). Therefore, when Cu leaves the Ga sublattice and forms precipitates some open-volume defects must be formed. In the first place these are Ga vacancies. But according to the large defect lifetime, vacancies in both sublattices must be involved. That means that As atoms must go into the interstitial region. If it is so this process should be dependent on the quantity of the excess As in GaAs, i.e. on the stoichiometry. This was indeed observed.

Fig. 5 shows the results of the same annealing experiments for the samples that were contaminated with Cu at different As pressures (0.2–10 bar). The lower the As pressure during in-diffusion is (As deficiency), the easier the arsenic goes into the interstitial region, and the more remarkable is the process of voids formation (the maximum of the average positron lifetime is higher).

After annealing at 850 K the vacancy signal for all of the samples disappears. It is possible that the small vacancy clusters are dissolved at this temperature. But in this case the hole concentration should have a sharp increase at this temperature. That was not observed (Fig. 2c). Another probable reason is that small clusters combine with each other forming large voids with the distance between them being much longer than the mean positron diffusion length and thus become invisible for positron annihilation.

4. Conclusion

Positron annihilation together with electron microscopy and electrical measurements was used to study

undoped semi-insulating GaAs after Cu in-diffusion and during Cu out-diffusion. To summarize our experimental finding we can state the following:

- large vacancy clusters surrounded by Cu atoms and neighboured by Cu precipitates are formed during Cu in-diffusion and cooling; almost no positron trapping is found after quenching from diffusion temperature,
- during annealing, vacancy clusters decorated with Cu atoms are formed and grow up to a size more than 10 vacancies with increasing annealing temperature,
- according to the Hall-effect measurements the process of formation of these clusters relates to the Cu out-diffusion,
- as far as the vacancies in both sublattices must be involved the creation of the open-volume defects should be dependent on the stoichiometry of the GaAs system. A smaller quantity of excess As should support the formation of vacancy cluster, i.e. it is more simple for As atoms to go into interstitial region,
- with annealing at temperatures higher than 850 K the vacancy clusters grow and the distance between them becomes larger than the diffusion length of they positron: they become invisible for positron annihilation.

References

- [1] F.C. Frank, D. Turnbull, *Phys. Rev.* 104 (1956) 617.
- [2] R.N. Hall, J.H. Racette, *J. Appl. Phys.* 35 (1964) 379.
- [3] R. Leon, P. Werner, K.M. Yu, M. Kaminska, E.R. Weber, *Appl. Phys. A* D61 (1995) 7.
- [4] R. Krause-Rehberg, K. Petters, J. Gebauer, *Physica B* 273–274 (1999) 714.
- [5] R. Krause-Rehberg, H.S. Leipner, *Positron Annihilation in Semiconductors*, Springer, Berlin, 1999.
- [6] T.Y. Tan, U. Gösele, S. Yu, *Crit. Rev. Solid State Mater. Sci.* 17 (1991) 47.



ELSEVIER

Physica B 308–310 (2001) 796–799

PHYSICA B

www.elsevier.com/locate/physb

Luminescence properties of Dy-doped GaAs grown by organometallic vapor phase epitaxy

Y. Fujiwara^{a,*}, T. Koide^a, S. Jinno^a, Y. Isogai^a, Y. Takeda^{a,b}

^a *Department of Materials Science and Engineering, Graduate School of Engineering, Nagoya University, Furo-cho, Chikusa-ku, Nagoya 464-8603, Japan*

^b *CREST, JST (Japan Science and Technology), Furo-cho, Chikusa-ku, Nagoya 464-8603, Japan*

Abstract

Photoluminescence (PL) properties of GaAs doped with Dy by organometallic vapor phase epitaxy (OMVPE) have been investigated. In measurements at 4.2 K, characteristic luminescence has been successfully observed at around 1.1, 1.3, 1.7 and 2.8 μm , which is assigned to the intra-4f shell transition of Dy^{3+} ions. The Dy-related PL intensity depends strongly on growth temperature, though the spectrum is almost invariant. The intensity decreases with increasing growth temperature, while the Dy concentration remains almost constant against the growth temperature. This indicates that the formation of optically active atom configurations around Dy ions is suppressed at higher growth temperatures. Furthermore, new Dy-related emission lines appear in the Dy-doped GaAs with Er. © 2001 Elsevier Science B.V. All rights reserved.

Keywords: Dysprosium; GaAs; Intra-4f shell transition; Dy–Er center

1. Introduction

There has been a strong interest in rare-earth (RE) doped semiconductors because of their potential to combine sharp RE luminescence with the convenience of electrical excitation via the semiconductor host. One important feature of RE luminescence is that the emission wavelength is largely independent on both the host material and temperature, because the filled outer 5s and 5p electron shells screen the inner 4f electrons from interaction with the host. Er-doped semiconductors have been of particular interest. The intra-4f shell transition from the first excited state ($^4\text{I}_{13/2}$) to the ground state ($^4\text{I}_{15/2}$) of Er^{3+} ions results in emission at 1.5 μm . The wavelength of 1.5 μm lies in the range of minimum transmission loss in silica-based fibers.

We have intensively investigated Er-doped III–V semiconductors by organometallic vapor phase epitaxy

(OMVPE). In Er-doped InP, it has been found that there is a threshold growth temperature between 550°C and 580°C for Er incorporation into InP. The majority of Er atoms substitute In sublattice in the lower-temperature grown InP, exhibiting high luminescence efficiency [1,2]. In Er, O-codoped GaAs, the Er-related PL spectrum was dominated by seven emission lines under host-excited conditions at a low temperature [3,4]. The Er center has been identified as an Er atom located at the Ga sublattice with two adjacent O atoms (hereafter referred as Er–2O) [4]. The dependence of the Er-related PL spectra on the growth temperature also revealed the existence of a threshold growth temperature (543–585°C) [5]. Above the threshold growth temperature, the formation of the Er–2O center was suppressed greatly. Er-doped GaP produced several new emission lines by the addition of O_2 to the growth ambient. Some of them were quite similar to those due to an Er–2O center in Er, O-codoped GaAs, indicating that a similar atom configuration with two O atoms is successfully formed around Er ions in GaP [6].

Now we have paid particular attention to Dy among RE elements because it can potentially exhibit 1.3 and

*Corresponding author. Tel.: +81-52-789-3368; fax: +81-52-789-3239.

E-mail address: fujiwara@numsc.nagoya-u.ac.jp (Y. Fujiwara).

2.8 μm emissions [7]. The wavelengths are technologically important for communication and medical applications, respectively. The other interesting viewpoint is that Dy is a well-known magnetic element. Dy ions doped in semiconductors have a feasibility to introduce the new degree of freedom induced by the interaction among carriers and the magnetic ions into semiconductor electronics. Recently, we described the first results on OMVPE growth of Dy-doped GaAs and observation of Dy-related luminescence in the infrared region [8]. However, the Er-related luminescence was also observed in the samples which originated from Er ions doped unintentionally by the contamination of the OMVPE growth system.

In this article, we report mainly on the Dy-related luminescence in Er-free Dy-doped GaAs and its dependence on the growth temperature.

2. Experimental

A low-pressure growth system with a vertical quartz reactor was utilized in this work [9]. TEGa and TBAs were used as source materials for GaAs growth. Dy was doped with trimethylcyclopentadienyldysprosium ($\text{Dy}(\text{CH}_3\text{C}_5\text{H}_4)_3$, $\text{Dy}(\text{MeCp})_3$). The Dy source was maintained mainly at a constant temperature of 100°C and introduced into the reactor by an H_2 flow through a source cylinder. The growth temperature was in the range of 530–610°C. The substrates for the growth were undoped or Si-doped (001)-oriented GaAs.

PL measurements were carried out mainly with the samples directly immersed in liquid He at 4.2 K. The photoexcitation source was a cw mode Ar^+ laser with a beam diameter of 1 mm and an incident power of 200 mW. The luminescence of the samples was dispersed using 0.91 m grating monochromator and detected with a liquid nitrogen-cooled Ge pin using a chopper and a lock-in amplifier.

3. Results and discussion

3.1. Dy-doped GaAs

Specular surface was successfully obtained in all Dy-doped GaAs grown in this work.

In-depth profiles of Dy concentration in GaAs layers were characterized by SIMS measurements. The measurements were performed using Cs^+ and O^+ as primary ions, accelerated at 6 kV, respectively. Dy concentration in the layers was evaluated in comparison with the ion intensity of Dy^{164} , which was calibrated using GaAs implanted at 180 keV with a Dy dosage of $5 \times 10^{14} \text{ cm}^{-2}$.

The resultant profiles exhibited a uniform Dy distribution along the growth direction in all the layers. Dy concentration in the layers was obtained in the range of 10^{17} – 10^{19} cm^{-3} , which was well controlled and increases with the H_2 flow rate through a Dy source cylinder and the cylinder temperature. The Dy concentration was almost independent of the growth temperature.

3.2. Dy-related luminescence in GaAs

In PL measurements at 4.2 K, characteristic luminescence was observed at around 1.1, 1.3, 1.7 and 2.8 μm . In comparison of results on Dy-doped oxides and fluorides [7], the luminescence can be assigned to intra-4f shell transitions between the Dy^{3+} states split by the spin-orbit interaction; (${}^6\text{H}_{7/2}$, ${}^6\text{F}_{9/2} \rightarrow {}^6\text{H}_{15/2}$), (${}^6\text{H}_{9/2}$, ${}^6\text{F}_{11/2} \rightarrow {}^6\text{H}_{15/2}$), (${}^6\text{H}_{11/2} \rightarrow {}^6\text{H}_{15/2}$) and (${}^6\text{H}_{13/2} \rightarrow {}^6\text{H}_{15/2}$) in order from the shorter wavelength side, respectively.

3.3. Growth temperature dependence of Dy-related luminescence

The Dy-related PL intensity depended strongly on the growth temperature, though the spectrum was almost invariant. Figs. 1–3 show the growth temperature dependence of Dy-related PL spectra around 1.1, 1.3 and 1.7 μm in Dy-doped GaAs. The intensity decreases with increasing growth temperature. SIMS measurements revealed that the Dy concentration is in the range of 10^{17} cm^{-3} and remains almost constant against the growth temperature. This indicates that the formation of optically active atom configurations around Dy ions is suppressed at higher growth temperatures. Similar

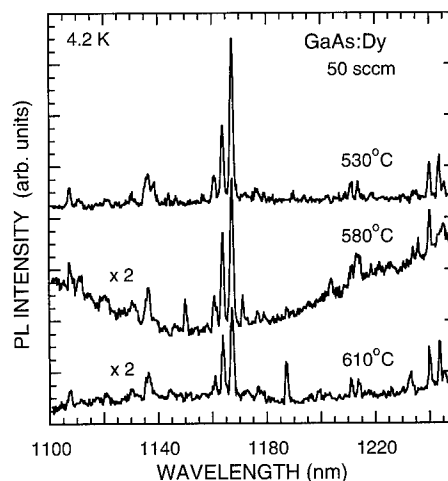


Fig. 1. Growth temperature dependence of the 1.1 μm PL spectra in Dy-doped GaAs. The PL intensity decreases with increasing growth temperature, while the spectrum is almost invariant.

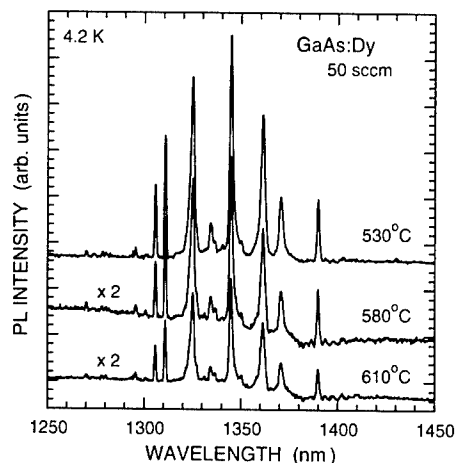


Fig. 2. Growth temperature dependence of the 1.3 μm PL spectra in Dy-doped GaAs. The behavior is quite similar to that of the 1.1 μm luminescence.

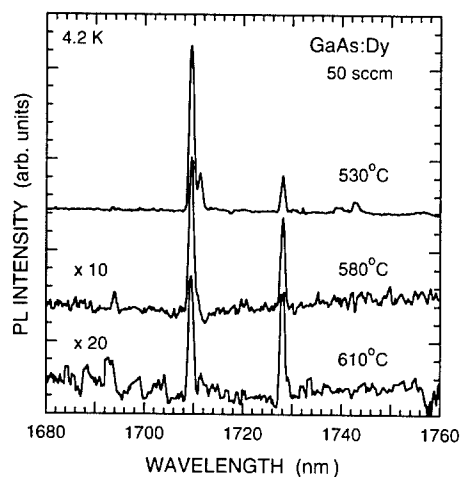


Fig. 3. Growth temperature dependence of the 1.7 μm PL spectra in Dy-doped GaAs. The reduction in PL intensity against the increase in growth temperature is much larger than those of the 1.1 and 1.3 μm luminescence. This indicates that the 1.7 μm luminescence originates from a center different from a center for the 1.1 and 1.3 μm luminescence.

behavior was previously reported in Er-doped InP and GaAs [1,5].

The reduction ratio of the PL intensity against the increase in growth temperature is different for the three luminescence and it is classified into two groups. For the 1.1 and 1.3 μm luminescence, the reduction is quite moderate and their intensities are proportional each other. For the 1.7 μm luminescence, on the other hand, the intensity decreases steeper with increasing growth temperature. These observations suggest that the 1.7 μm

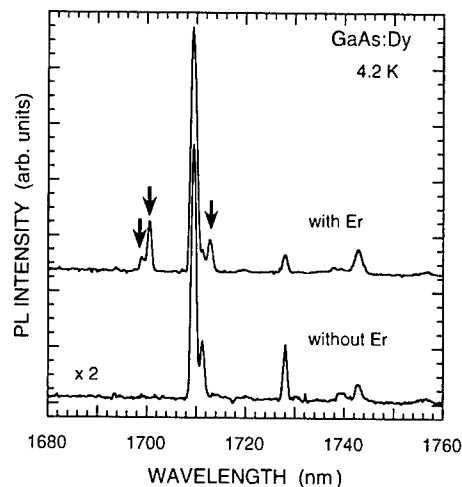


Fig. 4. Comparison of the 1.7 μm PL spectra in Er-free and Er-contaminated Dy-doped GaAs. Dy and Er concentrations are in the range of 10^{17} cm^{-3} . New emission lines appear in the sample with Er, indicating the formation of Dy-Er centers.

luminescence originates from a Dy center different from that for the 1.1 and 1.3 μm luminescence.

3.4. Dy-related luminescence in Dy-doped GaAs with Er

In comparison of PL spectra in Er-free and Er-contaminated Dy-doped GaAs, we have observed several new emission lines in the sample with Er. Fig. 4 shows the result for the 1.7 μm luminescence. New emission lines appear clearly in the sample with Er, which are shown by arrows, reflecting the formation of Dy-Er centers.

The appearance of the Dy-Er emission lines indicates the existence of Dy ions with Er at least in the second-nearest neighborhood. Dy and Er concentrations are, however, in the range of 10^{17} cm^{-3} in the sample with Er. Therefore, the formation of Dy-Er centers in spite of such low concentrations suggests strongly the presence of attractive interaction between Dy and Er ions in GaAs.

4. Conclusions

We have investigated luminescence properties of Dy-doped GaAs grown by OMVPE. SIMS measurements revealed a uniform Dy distribution along the growth direction. Dy concentration in the layers was obtained in the range of 10^{17} – 10^{19} cm^{-3} , which was well controlled and increased with the H_2 flow rate through a Dy source cylinder and the cylinder temperature. The Dy concentration was almost independent of the growth temperature. In PL measurements at 4.2 K, characteristic luminescence was observed successfully at around

1.1, 1.3, 1.7 and 2.8 μm . The luminescence was assigned to intra-4f shell transitions between the Dy^{3+} states split by the spin-orbit interaction; (${}^6\text{H}_{7/2}$, ${}^6\text{F}_{9/2} \rightarrow {}^6\text{H}_{15/2}$), (${}^6\text{H}_{9/2}$, ${}^6\text{F}_{11/2} \rightarrow {}^6\text{H}_{15/2}$), (${}^6\text{H}_{11/2} \rightarrow {}^6\text{H}_{15/2}$) and (${}^6\text{H}_{13/2} \rightarrow {}^6\text{H}_{15/2}$) in order from the shorter wavelength side, respectively. The Dy-related PL intensity depended strongly on the growth temperature, though the spectrum was almost invariant. The intensity decreased with increasing growth temperature, while the Dy concentration remained almost constant against the growth temperature. This indicates that formation of optically active atom configurations around Dy ions is suppressed at higher growth temperatures. The reduction ratio of the PL intensity against the increase in growth temperature was classified into two groups, 1.1 and 1.3 μm luminescence, and 1.7 μm luminescence. It suggests that the 1.7 μm luminescence originates from a Dy center different from that for the 1.1 μm and 1.3 μm luminescence. Furthermore, new Dy-related emission lines appeared in Dy-doped GaAs with Er, reflecting the formation of Dy–Er centers.

Acknowledgements

The authors would like to thank Hitachi Cable Ltd. for GaAs substrates. This work was supported in

part by Grant-in-Aids for Scientific Research (A)(2) No. 13305022, for Scientific Research (B)(2) No. 11450119 and No. 13555002, for Exploration Research No. 13875062 from the Ministry of Education, Culture, Sports, Science and Technology, and by the Inamori Foundation.

References

- [1] Y. Fujiwara, N. Matsubara, J. Tsuchiya, T. Ito, Y. Takeda, *Jpn. J. Appl. Phys.* 36 (1997) 2587.
- [2] H. Ofuchi, D. Kawamura, N. Matsubara, M. Tabuchi, Y. Fujiwara, Y. Takeda, *Microelectron. Eng.* 43/44 (1998) 745.
- [3] K. Takahei, A. Taguchi, *J. Appl. Phys.* 74 (1993) 1979.
- [4] K. Takahei, A. Taguchi, Y. Horikoshi, J. Nakata, *J. Appl. Phys.* 76 (1994) 4332.
- [5] Y. Fujiwara, T. Kawamoto, T. Koide, Y. Takeda, *Physica B* 273–274 (1999) 770.
- [6] Y. Fujiwara, T. Koide, Y. Takeda, *Mater. Sci. Eng. B* 81 (2001) 153.
- [7] L.F. Johnson, H.J. Guggenheim, *Appl. Phys. Lett.* 23 (1973) 96.
- [8] T. Koide, Y. Isogai, Y. Fujiwara, Y. Takeda, *Physica E* 10 (2001) 406.
- [9] Y. Fujiwara, S. Furuta, K. Makita, Y. Ito, Y. Nonogaki, Y. Takeda, *J. Cryst. Growth* 146 (1995) 544.



ELSEVIER

Physica B 308–310 (2001) 800–803

PHYSICA B

www.elsevier.com/locate/physb

Investigation of Cu-related deep levels in semi-insulating GaAs by PICTS

G. Zychowitz^a, W. Siegel^a, T. Steinegger^b, G. Kühnel^{a,*}, J.-R. Niklas^a

^a*Institut für Experimentelle Physik, TU Bergakademie Freiberg, Silbermannstr. 1, D-09596 Freiberg, Germany*

^b*Infineon Technologies, D-81669 München, Germany*

Abstract

Cu diffusion into semi-insulating GaAs was performed at 1150°C. The PICTS spectra of the diffused GaAs show several Cu-related peaks. The height of the characteristic low-temperature peak (Cu_A , $T \approx 150$ K) is proportional to the total Cu concentration determined by AES. The appearance and the peak heights of further Cu-related peaks in the spectra are obviously a function of the Cu concentration. © 2001 Elsevier Science B.V. All rights reserved.

Keywords: GaAs; PICTS; Copper; Diffusion

1. Introduction

It is well known that Copper is a very quickly diffusing impurity in semiconductors. However, in most cases it is undesired, because Cu forms deep levels, e.g. in Si and GaAs.

Using both TDH (temperature dependent Hall effect) [1,2] and DLTS (deep level transient spectroscopy) [2,3] measurements in p-type Cu-diffused GaAs two Cu-related acceptor levels and hole traps, respectively, were detected: Cu_A with an activation energy of 0.15–0.17 eV and Cu_B with 0.44–0.49 eV.

By DLTS measurements on n-type Cu-diffused GaAs a drastic reduction of the intrinsic defects EL2 and EL6 enhancing with increasing diffusion temperature 500–650°C was found [4].

For the detection of Cu-related levels in semi-insulating (SI) GaAs, photo-induced current transient spectroscopy (PICTS) [5] and thermally stimulated currents (TSC) [6,7] were used. Also, in this case two Cu-related levels with activation energies of 0.14–0.20 and 0.40–0.43 eV, respectively, were observed. Additionally, a level with 0.51–0.52 eV has been found. However,

there are some discrepancies in the results concerning Cu in GaAs. Thus, for instance, no clear dependence of the heights of the Cu-related peaks in the spectra on the concentration of the in-diffused Cu was observed [5].

The aim of this work was to investigate Cu-diffused SI GaAs by PICTS and to correlate the dependence of measured spectra on the copper concentration decreasing with the depth below the Cu-covered surface.

2. Experimental

Starting material for the diffusion experiment was a cylindrical block of undoped LEC SI GaAs ($\rho = 5 \times 10^7 \Omega \text{cm}$) with a diameter of 25 mm and a length of 56 mm. Cu was deposited on one front of the block by evaporation of few droplets of a CuCl_2 solution ($[\text{Cu}]_{\text{surface}} \approx 3 \times 10^{17} \text{cm}^{-2}$) to give a low concentration. After diffusion at 1150°C (20 h), the block was cut into 44 wafers of 1 mm thickness parallel to the Cu-coated surface. Cu concentrations were determined by atom emission spectroscopy (AES). Electrical properties were obtained by conductivity and Hall effect measurements. Samples of dimensions $6 \times 3 \times 0.6 \text{mm}^3$ with Sn contacts alloyed at 400°C were used for the PICTS measurements. Optical excitation was made with a LED

*Corresponding author. Fax: +49-3731-39-4314.

E-mail address: guenter.kuehnel@physik.tu-freiberg.de (G. Kühnel).

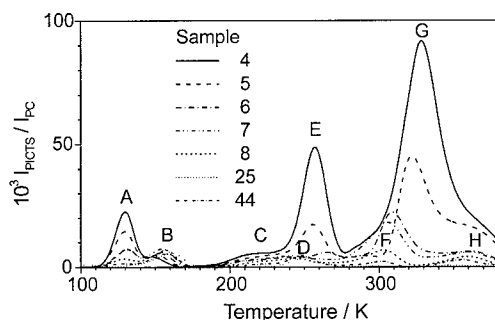


Fig. 1. Normalized PICTS spectra (initial delay $t_1 = 14$ ms) of Cu-diffused SI GaAs. The samples were prepared from different depths below the Cu-covered surface.

($\lambda = 950$ nm, $t_p = 40$ ms). The current transients were evaluated using window technique with a constant ratio $t_2/t_1 = 2.7$ varying t_1 between 0.28 and 140 ms. For the determination of relative concentrations, the PICTS signal I_{PICTS} was normalized with the infrared photo-current I_{ph} at the same photon flux.

3. Results

An influence of the Cu diffusion on the electrical properties of the GaAs block was detected to a depth of about 10 mm below the Cu-deposited surface. The uppermost samples (near to the surface) were high-resistivity p-type and the following were n-type and had resistivities decreasing from $7 \times 10^8 \Omega\text{cm}$ down to the starting level of $5 \times 10^7 \Omega\text{cm}$.

Fig. 1 shows normalized PICTS spectra of five SI samples (No. 4–8) from the diffusion region. Additionally, spectra of a sample (25) from the middle of the block as well as of a sample (44) from the surface opposite to the Cu-deposited one are given.

In samples 25 and 44, characteristic peaks (B, D) appear at about 160 and 250 K (at $t_1 = 14$ ms) which can be attributed to the electron traps EL6 and EL3 (DLTS signature) [8].

The PICTS spectra of the SI samples 4–8 show clear changes due to the Cu diffusion and a pronounced depth dependence. Peak A with the lowest maximum temperature (130 K at $t_1 = 14$ ms) decreases monotonously with the distance of the sample from the Cu surface (Fig. 2). Sample 25 was obviously not influenced by the Cu diffusion because peak A is absent. However, in sample 44 from the opposite surface the peak appears with a small height. According to its maximum temperature, the 130 K peak should correspond to the Cu_A level reported by other authors. However, the Arrhenius plot $\ln T^2/e$ versus $1/T$ yields for the activation energy of this peak in different samples values between 0.27 and

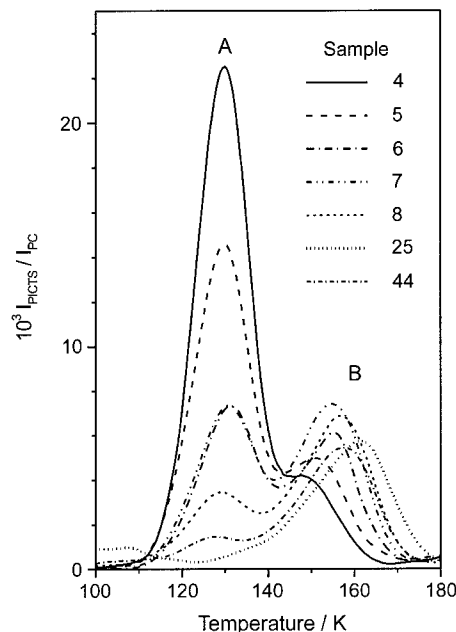


Fig. 2. Low-temperature part of the PICTS spectra of Fig. 1 including the Cu-related peak A and peak B (EL6).

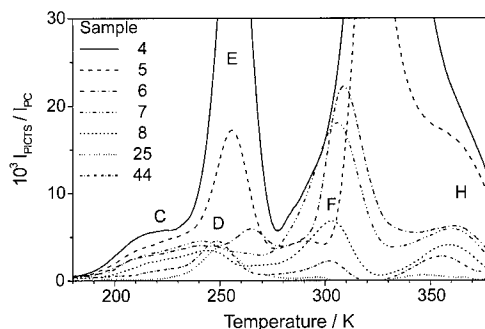


Fig. 3. High-temperature part of the PICTS spectra of Fig. 1 including the Cu-related shoulder C, the Cu-related peaks E–H as well as peak D (EL3).

0.30 eV which are clearly higher than the values given by other authors for Cu_A .

As the next deeper Cu-related level (shoulder C) with a characteristic temperature of 215 K ($t_1 = 14$ ms) appears which shows a likewise clear depth correlation as the 130 K peak (Fig. 3).

The normalized PICTS peak height $I_{\text{PICTS}}/I_{\text{ph}}$ is under certain conditions proportional to the concentration of the corresponding trap. However, the determination of absolute trap concentrations by PICTS is only conditionally possible. By plotting $I_{\text{PICTS}}/I_{\text{ph}}$ of peak A and of shoulder C versus the total Cu concentration

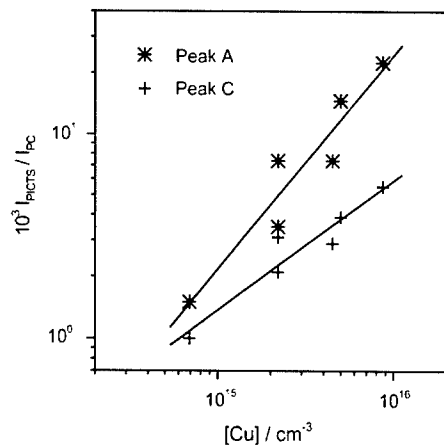


Fig. 4. Normalized peak heights of peaks A and C versus Cu concentration determined by atom emission spectroscopy.

determined by AES (Fig. 4), a linear dependence results for peak A and a relation $I_{\text{PICTS}}/I_{\text{ph}} \sim [\text{Cu}]^{0.5}$ for shoulder C. From the former dependence the limit for the detection of Cu via the 130 K peak can be estimated to about $2 \times 10^{14} \text{ cm}^{-3}$ under these conditions.

Further Cu-related peaks (E–H) appear in the PICTS spectra which obviously depend on the Cu concentration. At moderate Cu concentrations (samples 6–8) peaks F and H at about 300–310 and 355–365 K, respectively, were observed (Fig. 3). The Arrhenius plot yielded activation energies of 0.87 ± 0.02 and 0.9 ± 0.1 eV for F and H, respectively. In samples 4 and 5, near to the surface two other peaks (E and G) occur at about 255 and 320 K, partly much higher than the 130 K peak (Fig. 1). Their activation energies were determined to be 0.64 ± 0.01 and 0.8 ± 0.1 eV, respectively.

Concerning peak B (EL6) with the maximum temperature between 155 and 163 K it can be stated that it is only moderately influenced by the Cu diffusion at 1150°C.

4. Discussion

In the Cu-diffused SI-GaAs samples, a clear correlation of the normalized peak height of the low-temperature peak A in the PICTS spectrum with the total Cu concentration determined by AES was found. Also, the shoulder C at about 215 K increases clearly with increasing Cu concentration. From this correlation, it can be deduced that PICTS allows a sensitive detection of Cu in GaAs as residual impurity arising, e.g. from Cu contamination by annealing or by other device processing techniques. The detection limit for Cu ($\approx 2 \times 10^{14} \text{ cm}^{-3}$) estimated from the plot of the

normalized peak heights, $I_{\text{PICTS}}/I_{\text{ph}}$, of Cu_A versus $[\text{Cu}]_{\text{AES}}$ corresponds to the total Cu concentration. However, the detection limit of the Cu_A level itself is clearly lower due to the existence of further Cu related levels.

Leon et al. [2] concluded from the comparison of the Cu_A concentration taken from the hole concentration of p-type Cu-diffused GaAs samples, determined by Hall effect at 300 K, with the total Cu concentration obtained by SIMS (secondary ion mass spectrometry) that only a small percentage of Cu was electrically active. However, this conclusion is doubtful because on the one hand, the hole concentration at 300 K in Cu-dominated GaAs samples is not identical with N_A and on the other hand, further Cu levels exist beside Cu_A .

The Arrhenius plot for the Cu_A peak deviates clearly from a straight line what can be caused, e.g. by a non-exponential transient and/or by the contribution of more than one levels to the analysed peak. This yields a reference to the difference between the activation energies obtained in this work (0.27–0.30 eV) and those obtained by other authors (0.14–0.20 eV).

Further four Cu related peaks appear in the PICTS spectra, but their occurrence depends on the Cu concentration.

Concerning the interaction of Cu with intrinsic defects present in the starting material only a weak lowering of the EL6 peak was observed at $[\text{Cu}] > 5 \times 10^{15} \text{ cm}^{-3}$. A similar behaviour shows the EL2 defect. This finding is in contradiction to the result of Yang et al. [4] mentioned above that the concentrations of EL6 and EL2 are drastically reduced after diffusion at 500–650°C. This discrepancy we attribute mainly to the different conditions (temperature, time, As vapour pressure) used for Cu diffusion by the authors and by Yang et al., respectively, because the interaction of Cu with the intrinsic defects in GaAs is obviously a function of temperature and thermal history.

Summarizing, it can be stated that there is a clear correlation between several peaks of PICTS spectra of Cu-diffused SI GaAs and the concentration of the in-diffused Cu.

However, there exist still obscurities concerning the variety of Cu-related levels and the interaction of Cu with intrinsic defects in GaAs. We believe that they are partly caused by different temperatures and Cu concentration used in the diffusion (or annealing) experiments. Therefore, further work is necessary to clear up these discrepancies.

References

- [1] R.N. Hall, J.H. Racette, J. Appl. Phys. 35 (1964) 379.
- [2] R. Leon, P. Werner, K.M. Yu, M. Kaminska, E.R. Weber, Appl. Phys. A 61 (1995) 7.

- [3] K. Leosson, H.P. Gislason, *Mater. Res. Soc. Symp. Proc.* 442 (1997) 453.
- [4] B.H. Yang, T. Egilsson, H.P. Gislason, in: M. Godlewski (Ed.), *Semi-Insulating III–V Materials*, Warsaw, Poland, 1994, World Scientific, Singapore, 1994, p. 263.
- [5] C.C. Tin, C.K. Teh, F.L. Weichman, *J. Appl. Phys.* 63 (1988) 355.
- [6] K. Kuriyama, K. Tomizawa, S. Uematsu, H. Takahashi, *Appl. Phys. Lett.* 65 (1994) 746.
- [7] Z.-Q. Fang, D.C. Look, R.L. Jones, *J. Electron. Mater.* 26 (1997) L29.
- [8] K. Yasutake, H. Kakiuchi, A. Takeuchi, K. Yoshii, H. Kawabe, *J. Mater. Sci.* 8 (1997) 239.



ELSEVIER

Physica B 308–310 (2001) 804–807

PHYSICA B

www.elsevier.com/locate/physb

The effect of Si site-switching in GaAs on electrical properties and potential fluctuation

H.G. Svavarsson, J.T. Gudmundsson, G.I. Gudjonsson, H.P. Gislason*

Science Institute, University of Iceland, Dunhaga 3, IS-107 Reykjavik, Iceland

Abstract

Si-doped GaAs layers were grown p-type at 700°C and n-type at 840°C by liquid phase epitaxy. Thermal annealing of the p-type samples at temperatures around 840°C converted the samples to n-type. We compare the as-grown and annealed samples by means of photoluminescence and temperature-dependent Hall and conductivity measurements. Highly doped samples converted to n-type through annealing become highly compensated. Their Hall mobility also increases more than an order of magnitude. Samples grown n-type at 840°C show up to three times higher mobility than the annealed ones. The compensation in each case was monitored through the shift of the photoluminescence bands with excitation intensity, up to 24 meV per decade of increase in the excitation power density for the highest compensation ratio. © 2001 Elsevier Science B.V. All rights reserved.

PACS: 78.55.Cr

Keywords: GaAs; Si-doping; Site-switching; Fluctuating potential

1. Introduction

At high growth temperatures, Si-doped GaAs samples grown by liquid-phase-epitaxy (LPE) are n-type but highly compensated, while at lower growth temperatures they are p-type [1–4]. The actual crossover-temperature depends on silicon concentration and crystal orientation [5]. Gallium arsenide grown by LPE from gallium melt is expected to be low in gallium vacancies and possibly high in arsenic vacancies [6]. Under these conditions, Si should predominantly be a shallow acceptor on As site. However, growth at high temperatures evidently favors Si on Ga sites. In the present investigation, we study the highly compensated regime of GaAs:Si and potential fluctuations resulting from insufficient screening of ionized impurities by free carriers [7]. In highly compensated semiconductors, the fixed charge may

be randomly distributed and donor- and acceptor-rich regions may appear locally. Under normal circumstances, such fluctuations in the local potential are screened by mobile carriers, while the screening is insufficient in highly compensated samples. In photoluminescence (PL) measurements, potential fluctuations are manifested by a downward shift in photon energy of the near bandgap PL bands through localization of the charge carriers, as well as a shift of the localized PL bands to higher energy with increasing excitation power density. In GaAs, such fluctuations have been studied by photoluminescence in Li-compensated material [8] and highly Ge-doped material [9]. Here, we report on photoluminescence measurements of potential fluctuations in Si-doped GaAs, which has been converted from as-grown p-type to n-type by annealing above a certain transition temperature. Furthermore, we also correlate the defect density with the temperature-dependent Hall mobility of the majority carriers and compare the results from annealed samples with samples directly grown n-type.

*Corresponding author. Tel.: +354-525-4800; fax: +354-552-8911.

E-mail address: hafliði@hi.is (H.P. Gislason).

2. Sample preparation and experiment

We grew about 1 μm thick GaAs films by liquid phase epitaxy on a semi-insulating GaAs (100) substrate. Four LPE batches were made. Keeping other growth conditions the same, the Si/Ga mass ratio in the growth solutions was altered from $(0.1\text{--}2.1)\times 10^{-3}$ or $(0.3\text{--}5.2)\times 10^{-3}$ mole fraction Si. Two GaAs samples were grown at 700°C, one with low Si concentration (sample #1), and another with higher Si concentration (sample #2). The other two LPE samples were grown at 840°C, one with low Si (sample #3) and the other with high Si (sample #4).

One piece of each sample #1 and #2 were baked in quartz ampoules at 840°C for 24 h with a subsequent quenching in liquid nitrogen. The sample derived from sample #1 was labeled #1a and similarly the one derived from sample #2 was labeled #2a. Table 1 summarizes the resulting data from the samples. To suppress arsenic vacancy V_{As} formation during baking, we placed a controlled amount of solid As into the ampoule prior to evacuation, giving an As gas pressure slightly below 1 bar at the baking temperature. Details of the sample preparation procedure are published elsewhere [10].

The free carrier concentration of the majority carriers and their Hall mobility were obtained by Hall measurements in the van der Pauw configuration. The Hall coefficient R_{H} was calculated from the slope of the Hall voltage versus the magnetic field in the range of 0–0.5 T, and an average of four values in each point was taken where the two pairs of contacts were interchanged and the current reversed. The conductivity was measured by the van der Pauw technique [11]. Then the Hall mobility is given by $\mu_{\text{H}} = R_{\text{H}}/\rho$, where ρ is the conductivity.

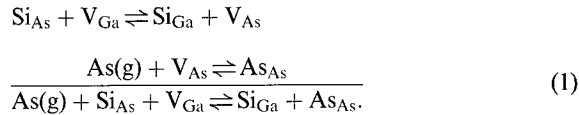
Photoluminescence measurements were performed at 14 K using the 532 nm line of a Verdi Nd:YVO4 laser from coherent as an excitation source. The excitation intensity was varied over several decades, from 0.001 to 0.1 W, and the laser beam was focused on an area of $\sim 1 \text{ mm}^2$. For each series of excitation intensities the area was kept constant. The PL signal was detected via a double 0.85 m Spex 1404 grating monochromator using a cooled Ge detector.

3. Results and discussion

3.1. Annealing experiment

Both LPE samples grown at 700°C were p-type. Annealing of p-type samples around a crossover-temperature makes them highly compensated and eventually n-type at still higher temperatures. The compensation ratio is defined $N_{\text{A}}^{-}/N_{\text{D}}^{+}$ for n-type but $N_{\text{D}}^{+}/N_{\text{A}}^{-}$ in the case of p-type material [12], where N_{A}^{-} is the concentration of ionized acceptors and N_{D}^{+} that of ionized donors. This ratio can be varied with the annealing temperature. Annealing at 840°C converted samples #1 and #2 to n-type with rather similar electron concentration, sample #1a with $n = 3.9 \times 10^{17} \text{ cm}^{-3}$ and sample #2a with $n = 1.9 \times 10^{17} \text{ cm}^{-3}$. We note that in addition to the type conversion, there is a significant difference in the compensation ratio of sample #2 before and after annealing, since the net electron concentration in sample #2a is only about 10% of the original hole concentration. In the less Si-doped sample #1 the carrier concentration before and after annealing remains the same within a factor of two.

The type conversion from p- to n-type upon annealing may be caused by site-switching of silicon on arsenic site Si_{As} to form silicon on gallium site Si_{Ga} in As ambient gas according to the equation



Driving the reaction to the right by increasing the ambient As gas pressure, either during growth or through annealing increases the concentration of Si_{Ga} according to Eq. (1).

3.2. Photoluminescence measurements

In the as-grown sample #1 with low Si concentration, the spectrum is dominated by a broad PL band peaking around 1.445 eV for the lowest excitation intensity level

Table 1

The carrier concentration, mobility and conductivity obtained by Hall measurements at room temperature and PL peak shift with excitation intensity measured at 14 K in as-grown and annealed samples

Low Si-doping level				High Si-doping level			
Sample	Carrier conc. (cm^{-3})	Shift (meV/dec.)	Mobility ($\text{cm}^2/\text{V s}$)	Sample	Carrier conc. (cm^{-3})	Shift (meV/dec.)	Mobility ($\text{cm}^2/\text{V s}$)
#1	$p = 1.6 \times 10^{17}$	6	110	#2	$p = 2.0 \times 10^{18}$	5	20
#1a	$n = 3.9 \times 10^{17}$	2–5	880	#2a	$n = 1.9 \times 10^{17}$	24	820
#3	$n = 1.4 \times 10^{16}$	8	2500	#4	$p = 3.9 \times 10^{17}$	8	50

used, I_{\min} [10]. Increasing the excitation intensity shifts the peak position around 6 meV per decade of change, which we interpret as a shift caused by insufficient screening of ionized impurities. Annealing at 840 °C dramatically changes the spectrum. The intensity becomes much smaller and a weak band at 1.385 eV at I_{\min} shows a shift of 2–5 meV per decade of change in intensity.

The photoluminescence spectrum of the as-grown sample #2 with high Si concentration exhibits a broad, strong peak at 1.435 eV for an excitation level of I_{\min} . This peak shows a rather similar shift with excitation intensity as found in sample #1. In this sample, the annealing produces a strong shift in the PL spectrum as illustrated in Fig. 1. A broad peak around 1.35 eV at I_{\min} shifts some 24 meV per decade of change.

The shift rate of the two as-grown samples #3 (low Si concentration) and #4 (high Si concentration) is similar, close to 8 meV. Fig. 1 summarizes the dependence of the peak positions of the six as-grown and annealed samples on the excitation intensity. Table 1 also includes the observed shift rate of the PL bands. The localization caused by the potential fluctuation can be described as a lowering of the photon energy of PL transitions by twice the depth of a potential well [7]. In n-type semiconductors, this potential well depth is directly proportional to the ratio $N_t^{2/3}/n^{1/3}$ with p replacing n in p-type semiconductors. Here, N_t is the total concentration of charged impurities in the material which are assumed to have a Gaussian distribution. Hence, the well depth increases with increasing concentration of charged impurities, N_t , but decreases with increasing concentration of free charge carriers. Therefore, in the presence of potential fluctuations, one expects to find a shifting PL band at lowest photon energies in highly compensated semiconductors with a high original shallow

doping. Also, one expects a shift to higher energies with increased excitation intensity which increases the concentration of photo-excited carriers. This is indeed what we observe.

Comparing the as-grown spectra of samples #1 and #2, we see that the shift rate with excitation intensity in Fig. 1, is comparable for both samples while the peak position is somewhat lower in energy for sample #2 which has a higher Si concentration. This is in general agreement with the higher concentration of ionized impurities, although the higher concentration of free carriers in sample #2 reduces the corresponding well depth.

The type conversion from p- to n-type through annealing illustrates a way of obtaining a striking range of compensation ratios. A significant difference between the two samples is evident upon annealing as shown in Fig. 1. The highly doped sample #2a shows a substantial shift, whereas the shift rate of the weakly doped sample remains low. Although the electron concentration of the two samples after annealing is rather similar, the large shift of the PL band in sample #2a is typical of a high concentration of compensated ionized impurities. The PL shift accompanies a reduction of the free carrier concentration by a factor of 10 in addition to the type conversion. The measured Hall concentration in the as-grown sample #2 can, therefore, be concluded to reflect the true Si_{Ga} concentration and a low compensation ratio, whereas the Si_{Ga} and Si_{As} concentrations become roughly similar upon annealing, with a compensation ratio approaching one as a consequence.

3.3. Electrical measurements

In Fig. 2, the Hall mobilities of the three samples with low Si-doping level, are compared. Sample #3 is n-type

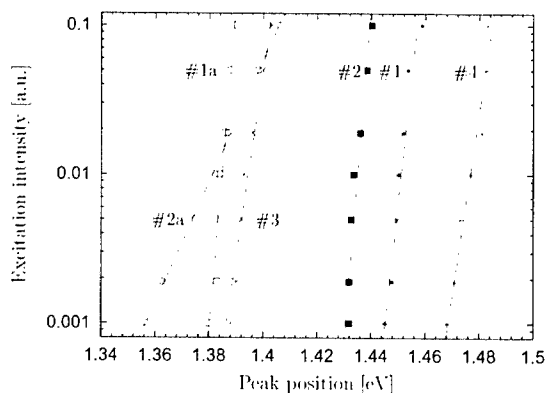


Fig. 1. PL peak position for different excitation intensity for the six samples. The slope of each curve represents the shift rate with excitation intensity.

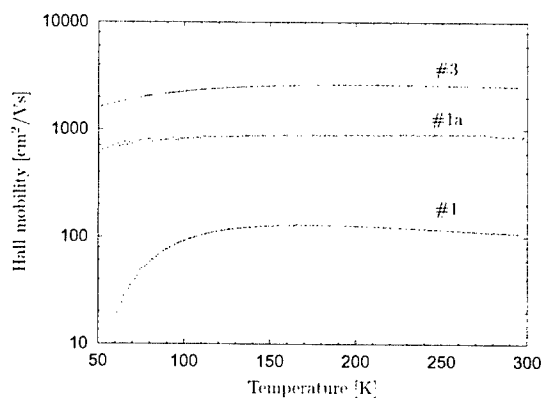


Fig. 2. The Hall mobility of low Si-doped GaAs as a function of temperature. Sample #1 is p-type GaAs, as-grown at 700 °C; #1a is n-type GaAs, grown at 700 °C and annealed at 840 °C; #3 is n-type GaAs as-grown at 840 °C.

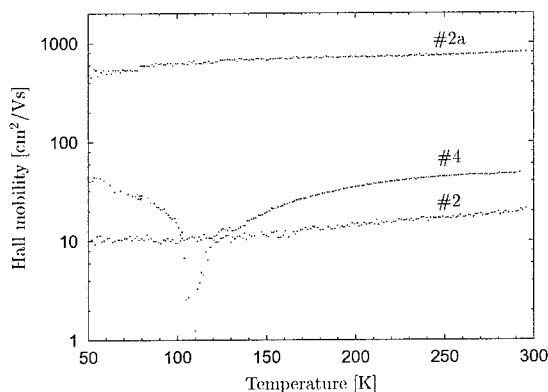


Fig. 3. The Hall mobility of high Si-doped GaAs as a function of temperature. Sample #2 is p-type GaAs, as-grown at 700°C; #2a is n-type GaAs, grown at 700°C and annealed at 840°C; #4 is GaAs as-grown at 840°C and is n-type below 105 K.

and has a Hall mobility of around 2500 cm²/Vs at room temperature, whereas sample #1 grown at 700°C is p-type with a Hall mobility of 110 cm²/Vs. After annealing at 840°C, the sample grown at 700°C has converted to n-type and its mobility increased nearly one order of magnitude, to 880 cm²/Vs at room temperature (sample #1a).

Fig. 3 shows the Hall mobility data for samples grown and annealed at the same temperatures as in Fig. 2 but at ~ 20 times higher doping level. Here, the annealed sample #2a has the highest Hall mobility, 850 cm²/Vs. Hall measurements show that the highly doped sample #4 exhibits p-type behavior at elevated temperatures but n-type behavior below 105 K. The minimum in the mobility curve for sample #4 is an artifact due to the Hall overshoot when $p = n(\mu_n/\mu_p)^2$ where the electrons and holes attempt to cancel the contributions of each other towards the Hall effect [13]. Here μ_n is the mobility of electrons and μ_p is the mobility of holes. Sample #3, grown at 840°C is n-type, whereas sample #4, grown at the same temperature but with much higher Si-concentration, is p-type above 105 K and n-type below. At this temperature the number of ionized donors and acceptors is equal.

Even though the mobility of samples #1 and #2 significantly increases upon annealing, it is still several times lower than that of sample #3. Most likely, the number of scattering centers has grown by the annealing. Presumably they include Ga vacancies and, to some extent, antisite defects.

4. Conclusion

Annealing at temperatures close to a transition temperature of 840°C resulted in closely compensated samples as verified by a shift of localized PL bands with excitation intensity. The presence of potential fluctuations is manifested through a shift of the PL peak position of up to 24 meV per decade of increase in the excitation power density. Furthermore, the annealing of p-type samples converted them into n-type with ~ 10 times higher mobility. We have correlated the observation of potential fluctuations with a possible site-switching of Si from As sites to Ga sites. Our results strongly suggest that the type conversion from p- to n-type may in fact be caused by such site-switching.

Acknowledgements

This work was partially supported by the Icelandic Research Council and The University of Iceland Research Fund.

References

- [1] W.G. Spitzer, W. Allred, J. Appl. Phys. 39 (1968) 4999.
- [2] W.G. Spitzer, M.B. Panish, J. Appl. Phys. 40 (1969) 4200.
- [3] M.J. Ashwin, R. Addinall, M.R. Fahy, R.C. Newman, I. Silier, E. Bauser, Mater. Sci. Forum 143–147 (1994) 265.
- [4] R.C. Newman, Semicond. Sci. Technol. 9 (10) (1994) 1749.
- [5] S.K. Ghandi, VLSI Fabrication Principles: Silicon and Gallium Arsenide, Wiley, New York, 1983, p. 275.
- [6] A.G. Milnes, in: P.W. Hawkes (Ed.), Advances in Electronics and Electron Physics, Vol. 61, Academic Press, New York, 1983, p. 63.
- [7] B.I. Shklovskii, A.L. Efros, Electronic Properties of Doped Semiconductors, Springer, Berlin, 1984.
- [8] H.P. Gislason, B.H. Yang, M. Linnarsson, Phys. Rev. B 47 (1993) 9418.
- [9] M. Watanabe, A. Watanabe, M. Suezawa, Physica B 273, 274 (1999) 750.
- [10] H.G. Svavarsson, J.T. Gudmundsson, G.I. Gudjonsson, H.P. Gislason, Phys. Scripta (2001), accepted for publication in Phys. Scripta.
- [11] L.J. van der Pauw, Philips Res. Rep. 13 (1958) 1.
- [12] S.K. Ghandi, VLSI Fabrication Principles: Silicon and Gallium Arsenide, Wiley, New York, 1983, p. 32.
- [13] K. Seeger, Semiconductor Physics, 5th Edition, Springer, Berlin, 1991, p. 59.



ELSEVIER

Physica B 308–310 (2001) 808–811

PHYSICA B

www.elsevier.com/locate/physb

Incorporation and thermal stability of defects in highly p-conductive non-stoichiometric GaAs:Be

P. Specht^{a,*}, M.J. Cich^a, R. Zhao^a, J. Gebauer^a, M. Luysberg^b, E.R. Weber^a

^aDepartment of Materials Science & Engineering, University of California at Berkeley, LBNL, Bldg. 66-222, One Cyclotron Road, Berkeley, CA 94720, USA

^bInstitute of Solid State Research, Research Center Jülich, D-52425 Jülich, Germany

Abstract

Non-stoichiometric GaAs is known to contain a high concentration of native point defects. The dominant defect in the epilayers is the arsenic antisite (As_{Ga}), a deep double donor, which is incorporated at low growth temperatures (commonly between 200°C and 300°C) in molecular beam epitaxy (MBE). Consequently, p-doping of non-stoichiometric GaAs is difficult because large concentrations of acceptors are compensated by the As_{Ga} . Recently, we found that despite this compensation effect we can achieve p-conductive GaAs:Be with almost one order of magnitude higher Be-doping than previously obtained in MBE grown GaAs. The kinetics of dopant incorporation during MBE growth at these low growth temperatures seem to allow pushing the doping concentration further beyond thermal equilibrium. The epilayers, which are about 1 μm thick, are pseudomorphic with a lattice mismatch to the substrate of up to $\Delta c/c = -0.4\%$. They remain free of structural defects such as dislocations and stacking faults. After annealing at 600°C only the highest doped epilayers show a reduction in the Be concentration although the layers remain ultrahigh p-conductive. The increased incorporation of Be as well as its unusual stability in non-stoichiometric GaAs is likely influenced by the native defects in these layers, double positively charged As_{Ga} defects and probably neutral gallium vacancies (V_{Ga}). This novel material which is solely achievable through low-temperature growth may significantly enhance III–V semiconductor applicability due to ultrahigh doping capability with increased thermal stability. © 2001 Elsevier Science B.V. All rights reserved.

Keywords: Non-stoichiometric GaAs; Be doping; Thermal stability; Native point defects

1. Introduction

Low-temperature (LT) molecular beam epitaxy (MBE)-grown III–V semiconductors have found many applications as highly resistive buffer layers for FETs [1], as radiation hardened layer for satellite technology [2] and in ultrafast opto-electronics [3–6]. Conductive LT-layers, however, never reached satisfying conduction because of the presence of electrically active, native defects, namely arsenic antisites (As_{Ga}) and gallium vacancies (V_{Ga}). The As_{Ga} defects, electrically active as deep double donors, which can be incorporated in

concentrations as high as $10^{20}/\text{cm}^3$ [7] compensate p-dopants (commonly Be or C) and also lead to a reduced mobility of the active carriers, usually electrons [8]. N-type conduction was identified to be dominated by nearest-neighbor hopping [9,10]. P-conduction was observed in highly compensated epilayers with low dopant activation or in the so-called stoichiometric LT-GaAs with Be doping concentrations up to $10^{19}/\text{cm}^3$ only [7,11].

The addition of Beryllium to a GaAs epilayer leads to a smaller lattice constant for high doping concentrations because the Beryllium which is commonly incorporated on the Ga-sublattice is smaller than the host atom Ga. At low growth temperatures this effect is compensated by the introduction of larger native point defects, the As_{Ga} antisite defects. These defects are also located in

*Corresponding author. Tel.: +1-510-495-2934; fax: +1-510-486-4995.

E-mail address: specht@socrates.berkeley.edu (P. Specht).

the Ga-sublattice and dilate the epilayer lattice if present in large concentrations [7]. The strain compensation between the small Be_{Ga} and the larger As_{Ga} defects is expected to thermally stabilize the defects [12]. Even more important than this stabilization is the fact that the maximum concentration of Be which can be incorporated into LT-GaAs epilayers is largely enhanced. In this contribution, the electronic properties of the highly strained epilayers with several $10^{20}/\text{cm}^3$ Be incorporation are investigated. It is studied how the maximum free hole concentration and their thermal stability as well as the stability of the Be dopant atoms depend on the growth conditions.

2. Experimental

Be-doped LT-GaAs layers were grown by MBE on (100) GaAs wafers grown by Vertical Gradient Freeze (VGF substrates, AXT, Fremont, CA) at As/Ga beam equivalent pressure ratios of 20 (As-rich conditions) and a growth rate of $1\mu\text{m/h}$. The growth temperature measured by diffuse reflectance spectroscopy (Thermionics NW, Hayward, CA) was varied from 210°C to 300°C . Nominal Be doping levels between 1×10^{19} and $2 \times 10^{21}/\text{cm}^3$ were attempted. Be concentrations were determined by SIMS analysis at Applied Microanalysis Lab. in Santa Clara, CA. The wafers were annealed in proximity to a sacrificial GaAs substrate at 600°C for 30 min in nitrogen ambient. The structural properties were investigated by X-ray diffraction using (004) reflection conditions and in JEOL 4000EX and JEOL 4000FX transmission electron microscopes operated at 400 kV. For the latter technique samples were prepared in cross section by conventional techniques including Ar ion milling. Free carrier concentrations were determined with both electrochemical capacitance voltage profiling (ECV) and Hall effect measurements in Van der Pauw geometry. For more details on MBE growth see Refs. [13,14] for the electrical measurements.

3. Results and discussion

The lattice mismatch between the GaAs substrate and the epilayer gives a first indication for the large concentrations of incorporated Be acceptors in LT-GaAs:Be. With increasing Be concentration the epilayer lattice constant decreases resulting in lattice matching to the substrate [15]. For higher doping concentrations the lattice mismatch becomes negative and duplicates approximately the data from GaAs:Be grown at 580°C if extrapolated to high Be concentrations as can be seen in Fig. 1. It was concluded that the Be in the LT-grown epilayer is mainly incorporated on the Ga-sublattice resulting in a similar lattice mismatch to the GaAs

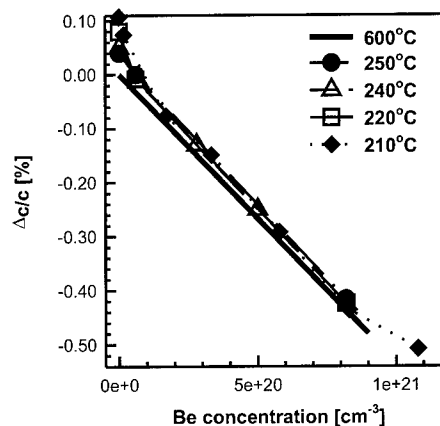


Fig. 1. Lattice mismatch in growth direction, $\Delta c/c$, between GaAs substrate and LT-GaAs epilayer dependent on Be-doping. The solid line, 600°C growth temperature, is extrapolated for Be doping levels above $10^{20}/\text{cm}^3$.

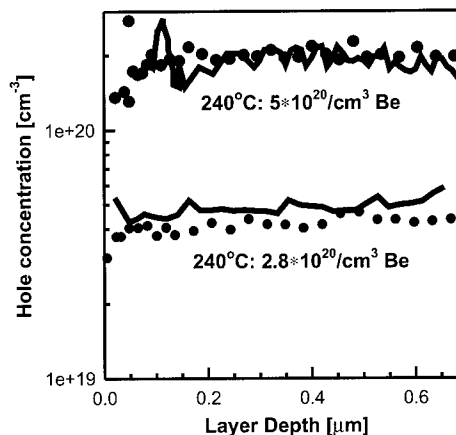


Fig. 2. ECV profiles of as-grown (dots) and at 600°C annealed (lines) LT-GaAs:Be epilayers. The large variation of $[p]$, especially at the surface of the higher doped layer, is mainly due to inhomogeneous etching. The free hole concentration does not change upon annealing.

substrate as it would theoretically occur in GaAs:Be grown at 580°C by MBE. Even at Be concentrations of about $8 \times 10^{20}/\text{cm}^3$ the lattice mismatch in growth direction, $\Delta c/c$, follows this extrapolated reference line. In cross-sectional TEM analysis no structural defects were found, the epilayers are grown pseudomorphic. The $1\mu\text{m}$ thick epilayer with a lattice mismatch of $\Delta c/c = -0.42\%$ shows a slightly broadened (004) peak in X-ray diffraction with a doubled FWHM if compared to the substrate, probably due to a bending effect.

The ECV profiles of two epilayers ($[\text{Be}] = 5 \times 10^{20}$ and $2.8 \times 10^{20}/\text{cm}^3$, $T_g = 240^\circ\text{C}$, Fig. 2) show the thermal stabilization of the hole concentrations upon annealing

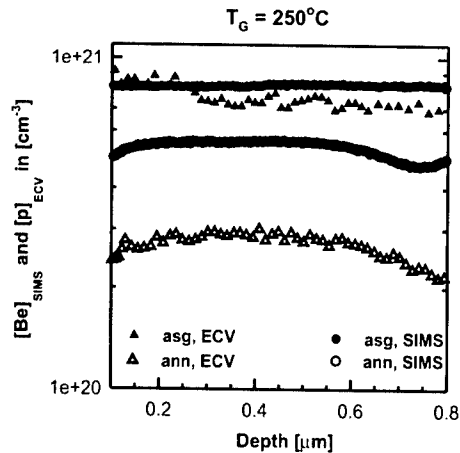


Fig. 3. ECV (triangles) and SIMS (dots) profiles of a LT-GaAs:Be epilayer grown at 250°C with $8 \times 10^{20}/\text{cm}^3$ Be. The as-grown layer shows almost complete Be activation. Upon annealing at 600°C (open symbols), both the total Be concentration (SIMS) and the free hole concentration (ECV) are significantly reduced.

at 600°C (overgrowth condition). Only 10% of the Be contributes to the hole concentration in the lower doped sample which increases to over 40% in the higher doped layer. However, it shall be noted that the dopant activation presented here already exceeds the maximum hole concentration observable in GaAs:Be. Assuming the native point defects, As_{Ga} double donors, are compensating the Be_{Ga} , more than $1 \times 10^{20}/\text{cm}^3$ $\text{As}_{\text{Ga}}^{2+}$ have to be present in these layers. It is noted that such high concentrations of As_{Ga} defects were measured before in undoped, pseudomorphically grown LT-GaAs. Upon annealing at 600°C neither the total Be concentration, $[\text{Be}]$, nor the concentration of free holes $[p]$, changes and, consequently, also the lattice mismatch remains stable. This also indicates that the Be is not likely to be present as interstitials in large concentrations since Be interstitials are known to be fast diffusers and that the compensating antisite defects are thermally stable under these annealing conditions.

Fig. 3 depicts ECV and SIMS results of an epilayer grown at 250°C. An even higher doping concentration of $[\text{Be}] = 8 \times 10^{20}/\text{cm}^3$ is achieved. The average concentration of compensated Be is significantly lower than in the lower doped epilayers. Consequently, if As_{Ga} defects are present in this layer, their concentration must be significantly lower with a maximum value of about $4 \times 10^{19}/\text{cm}^3$ $\text{As}_{\text{Ga}}^{2+}$. Hall measurements of the as-grown layer confirmed the ECV results. Additionally, a hole mobility of $27 \text{ cm}^2/\text{Vs}$ was measured which agrees well with the extrapolated value for such high Be amounts. During annealing, part of the Be diffuses out of the epilayer. Simultaneously, the free hole concentration is

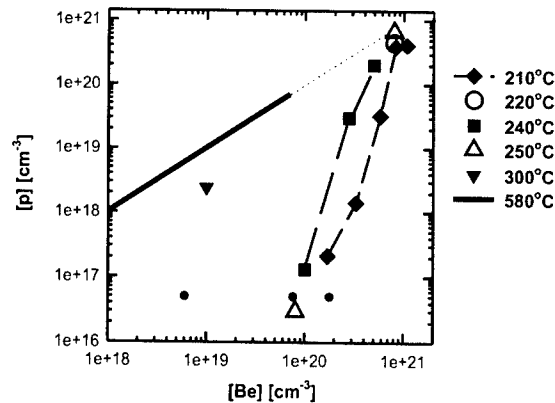


Fig. 4. Free hole concentrations achieved in GaAs:Be. The plot for high temperature grown MBE GaAs (solid line) is shown extrapolated (dotted line) for easier comparison with LT-growth. The small dots at hole concentration levels of $5 \times 10^{16}/\text{cm}^3$ represent the theoretically expected values for 300°C/240°C/210°C growth temperature, from left to right, respectively (Fermi Level calculation for constant native defect concentration for each T_g).

reduced. Roughly half of the remaining Be is still electrically active after annealing with only 30% of the inactive Be explicable due to the maximal present native defect concentration $[\text{As}_{\text{Ga}}^{2+}]$. This indicates that part of the Be is likely to be incorporated on interstitial sites and/or has formed Be clusters.

Fig. 4 summarizes the achieved free hole concentrations in 580°C grown GaAs and in various LT-GaAs epilayers. The maximal free carrier concentration is almost one order of magnitude larger in LT-GaAs than in GaAs grown at 580°C, retaining reasonable carrier mobility. Ultrahigh conductivity is achieved in a growth temperature range of at least 40°C although the maximum free hole concentrations vary with the growth temperature. In the p-conductive layers Be is by far more stable in LT-GaAs, a fact which was already observed for semi-insulating LT-GaAs:Be epilayers [12,15].

Reasons for both the enhanced incorporation of Be and its higher thermal stability in LT-GaAs are still under discussion. For low growth temperatures Be may simply be kinetically buried in the epilayer. It is still unclear why Be diffusion and precipitation seems to be suppressed resulting in stabilized high free carrier concentrations in the epilayers. Beryllium is known to diffuse fast on interstitial sites in GaAs which may certainly be suppressed in an up to 2% more dense crystalline structure. However, our observations rather indicate a correlation between a large compensation and a high thermal stabilization of Be. A lower compensation in the most dense epilayer resulted in insufficient Be stabilization. Because of our assumption that antisite

defects are responsible for the electrical compensation, the behavior of these native defects shall be investigated in more detail.

The As_{Ga} defects in ultrahigh Be-doped LT-GaAs can be indirectly estimated through the amount of compensated Be in the as-grown layers. For the other native defect, the gallium vacancy V_{Ga} , a concentration reduction and clustering is seen in ultrahigh Be-doped layers measured by positron annihilation spectroscopy. Details about this measurement technique can be found in Ref. [16]. It is likely that simultaneously the As_{Ga} defect concentration increases as it would in GaAs with a lowered Fermi energy level. From the amount of compensated Be an increase in antisite defects to concentrations of about $10^{20}/\text{cm}^3$ is expected. Therefore, we propose that the strain field of the As_{Ga} , whose average distance in LT-GaAs can be as low as 1.7 nm or 3 unit cells in the GaAs lattice, is mainly responsible for the thermal stabilization of the Be atoms. The As_{Ga} defects themselves may be thermally stabilized because the V_{Ga} assisted diffusion of As is suppressed in the ultrahigh Be-doped layers due to the lack of single V_{Ga} .

4. Summary

Ultrahigh p-conductive LT-GaAs:Be epilayers were grown with free hole concentrations as high as $7 \times 10^{20}/\text{cm}^3$. After annealing at 600°C about $2 \times 10^{20}/\text{cm}^3$ holes remain in the epilayers which are highly strained. The effect of ultrahigh Be-doping is fairly growth temperature insensitive within at least a 40°C temperature range, although the maximum amount of free holes is dependent on the growth temperature. A suppressed Be diffusion is observed, which is likely to be caused by residual As_{Ga} antisite defects, which are themselves thermally stabilized due to the lack of native single V_{Ga} . These highly p-doped epilayers may find an application for example as base layer in an AlGaAs/GaAs HBT. A considerably increased electron efficiency in the emitter due to a reduced bandgap and decreased resistivity of the base layer can benefit the clock rates in IC's. The minority carrier lifetime and mobility in such layers still has to be investigated.

Acknowledgements

This work has been supported by the Air Force Office of Scientific Research under grant no. F49620-98-1-0135. We appreciate the use of the Integrated

Materials Laboratories at UC Berkeley. Positron Annihilation Spectroscopy was performed at the Martin-Luther Universität in Halle, Germany. We thank Dr. R. Krause-Rehberg for his support. One of us, J.G., acknowledges a Feodor-Lynen Fellowship of the Alexander von Humboldt Foundation.

References

- [1] D.C. Look, *J. Appl. Phys.* 70 (1991) 3148.
- [2] T.R. Weatherford, P.W. Marshall, C.J. Marshall, D.J. Fouts, B. Mathes, M. LaMaccia, *IEEE Trans. Nucl. Sci.* NS-44 (1997) 2298.
- [3] S. Gupta, J.F. Whitaker, G.A. Mourou, *IEEE J. Quantum Electron.* 28 (1992) 2464.
- [4] H.S. Loka, P.W.E. Smith, *IEEE Phot. Tech. Lett.* 10 (1998) 1733.
- [5] U. Keller, K.J. Weingarten, F.X. Kärtner, D. Kopf, B. Braun, I.D. Jung, R. Fluck, C. Hönniger, N. Matuschek, J. Aus der Au, *IEEE J. Selected Top. Quantum Electron.* 2 (1996) 435.
- [6] R. Takahashi, Y. Kawamura, H. Iwamura, *Appl. Phys. Lett.* 68 (1996) 153.
- [7] X. Liu, A. Prasad, J. Nishio, E.R. Weber, Z. Liliental-Weber, W. Walukiewicz, *Appl. Phys. Lett.* 67 (1995) 279.
- [8] R.E. Pritchard, S.A. McQuaid, L. Hart, R.C. Newman, J. Mäkinen, H.J. von Bardeleben, M. Missous, *J. Appl. Phys.* 78 (1995) 2411.
- [9] D.C. Look, D.C. Walters, M.O. Mansreh, J.R. Sizelove, C.E. Stutz, K.R. Evans, *Phys. Rev. B* 42 (1990) 3578.
- [10] M. Kaminska, E.R. Weber, in: E.M. Anastassakis, J.D. Joannopoulos (Eds.), *Proceedings of the 20th International Conference on the Physics of Semiconductors*, World Scientific, 1990, p. 473.
- [11] D.E. Bliss, W. Walukiewicz, J.W. Ager, E.E. Haller, K.T. Chan, S. Tanigawa, *J. Appl. Phys.* 71 (1992) 1799.
- [12] P. Specht, S. Jeong, H. Sohn, M. Luysberg, A. Prasad, J. Gebauer, R. Krause-Rehberg, E.R. Weber, *Mater. Sci. Forum* 258–263 (1997) 951.
- [13] M. Luysberg, H. Sohn, A. Prasad, P. Specht, Z. Liliental-Weber, E.R. Weber, J. Gebauer, R. Krause-Rehberg, *J. Appl. Phys.* 83 (1998) 561.
- [14] M.J. Cich, R.C. Lutz, R. Zhao, P. Specht, E.R. Weber, *MRS Symp. Proc.* 570 (1999) 129.
- [15] P. Specht, R.C. Lutz, R. Zhao, E.R. Weber, *Growth and Characterization of p-doped LT-GaAs*, in: T. Marek, S. Malzer, P. Kiesel (Eds.), *Physik Mikrostrukturierter Halbleiter*, vol. 6, Erlangen-Nürnberg, 1998, p. 15.
- [16] J. Gebauer, F. Börner, R. Krause-Rehberg, T.E.M. Staab, W. Bauer-Kugelmann, G. Kögel, W. Triftshäuser, P. Specht, R.C. Lutz, E.R. Weber, M. Luysberg, *J. Appl. Phys.* 87 (2000) 8368.



ELSEVIER

Physica B 308–310 (2001) 812–815

PHYSICA B

www.elsevier.com/locate/physb

Native point defects in non-stoichiometric GaAs doped with beryllium

J. Gebauer^{a,b,*}, R. Zhao^a, P. Specht^a, F. Börner^b, F. Redmann^b,
R. Krause-Rehberg^b, E.R. Weber^a

^aDepartment of Materials Science and Engineering, University of California at Berkeley, Berkeley CA 94720, USA

^bFachbereich Physik, Martin-Luther-Universität Halle-Wittenberg, D-06099 Halle, Germany

Abstract

Native point defects in non-stoichiometric GaAs layers doped with Be were observed. Ga vacancies were identified by positron annihilation. As_{Ga} antisite defects were investigated by near infrared absorption and magnetic circular dichroism of absorption, respectively. We found the properties of the As_{Ga} antisites very similar to that of As_{Ga} in bulk GaAs, i.e. they exhibit the same MCDA spectra and quenching behavior. The concentration of native point defects was not influenced by the Be doping. Therefore, the thermal stability of non-stoichiometric GaAs:Be can not be explained with a different incorporation of native defects. © 2001 Elsevier Science B.V. All rights reserved.

Keywords: LT-GaAs; Ga-vacancy; Arsenic antisite; MCDA

1. Introduction

Non-stoichiometric GaAs layers grown by molecular beam epitaxy (MBE) at low temperatures (LT-GaAs) attracted a large interest due to their unique properties, i.e. ultrafast carrier recombination and semi-insulating behavior after annealing. During the growth at low temperatures, a large As excess is incorporated in form of point defects [1,2]. The properties of (undoped) LT-GaAs are dominated by As_{Ga} antisites incorporated in concentrations up to 10^{20} cm^{-3} while V_{Ga} (with densities in the 10^{18} cm^{-3} range) is responsible for the compensation of positive As_{Ga} [3].

The major drawback of undoped LT-GaAs, however, is its thermal instability which restricted applications so far. Recently, doping with Be was found to thermally stabilize As_{Ga} defects therewith opening new prospects for the application of non-stoichiometric GaAs layers [4]. The origin of the thermal stability is uncertain. Ga

vacancies are believed to mediate the diffusion of As_{Ga} , thus, it has been suggested that Be doping reduces the concentration of V_{Ga} thereby suppressing the outdiffusion of excess As [5]. However, this hypothesis is supported by very few experiments [5,6]. Another possible explanation involves the formation of defect complexes such as $\text{As}_{\text{Ga}}\text{--Be}_{\text{Ga}}$ which would hinder the diffusion of As_{Ga} . In this work, we investigate the native point defects in LT-GaAs:Be and their concentration in relation to the doping concentration in order to understand the properties and thermal stability of that material.

2. Experimental

Non-stoichiometric GaAs layers were grown by MBE under arsenic-rich conditions with an As/Ga beam equivalent pressure (BEP) of 20 at temperatures from 200°C to 300°C. The Be doping concentration varied up to $8 \times 10^{19} \text{ cm}^{-3}$. The growth rate was 1 $\mu\text{m/h}$ and the layer thickness 1–1.5 μm . Positron annihilation spectroscopy (PAS) employing slow monoenergetic positrons was used to investigate vacancy defects [7]. Positron

*Corresponding author. Lawrence Berkeley National Lab., Bldg. 66, Rm. 222, 1 Cyclotron Road, Berkeley CA 94720, USA. Tel.: +1-510-486-5305; fax: +1-510-486-4995.

E-mail address: jgebauer@lbl.gov (J. Gebauer).

trapping in vacancy defects can be observed as a change of the shape of the 511-keV annihilation peak, characterized by the lineshape parameters S and W . The experimental details are the same as in Ref. [8]. As_{Ga} antisites were observed by near infrared absorption (NIRA) and magnetic circular dichroism of absorption (MCDA). The experimental details of the absorption techniques are described in Ref. [2].

3. Detection of Ga vacancies by positron annihilation

PAS measurements as a function of incident positron energy showed results very similar to those reported earlier for undoped LT-GaAs [8]. Most important, the S parameter characteristic for the LT-GaAs layers was significantly higher than that one in defect free GaAs. This shows clearly positron trapping at vacancy defects. In order to identify the defects, we analyzed the correlation between S and W parameter. For all our LT-GaAs:Be samples, the data followed the same linear variation, previously shown to be due to Ga monovacancies [8]. Other defects in GaAs, e.g. vacancy cluster or As vacancies exhibit significantly different annihilation characteristics than V_{Ga} . Therefore, the vacancies in LT-GaAs:Be are also Ga monovacancies.

With that knowledge, we determined the V_{Ga} concentration from the S parameter characteristic for the respective LT-GaAs:Be layer from $c_v = \lambda_b \times (S - S_b) / (\mu_v(S_d - S))$. $\lambda_b = (229 \text{ ps})^{-1}$ is the annihilation rate in defect-free GaAs and $\mu_v = 10^{15} \text{ s}^{-1}$ is the trapping coefficient for V_{Ga} [7]. The S parameter S_d , specific for annihilation in V_{Ga} , is 1.017 [8]. In Fig. 1, we show the resulting V_{Ga} concentrations as a function of the Be concentration for LT-GaAs grown at different temperatures. The V_{Ga} concentration is independent on

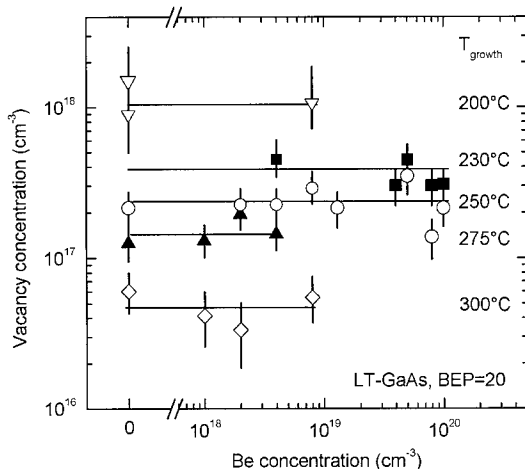


Fig. 1. Concentration of V_{Ga} in LT-GaAs:Be as a function of the Be concentration. Lines are guide to the eyes.

Be doping up to the highest doping level investigated. Thus, Be doping has no influence on the incorporation of Ga vacancies during the MBE growth of GaAs at low temperatures.

4. Optical absorption spectroscopy of As_{Ga} antisites

Optical absorption spectroscopy was the major experimental tool to investigate As_{Ga} defects in LT-GaAs layers [1,2]. Nevertheless, considerable uncertainty remained because several features of As_{Ga} defects known from bulk GaAs were not observed in LT-GaAs. Often only a part of the As_{Ga} in LT-GaAs was found to be quenchable (if any at all) [2,9] while this property is one of the major fingerprints of As_{Ga}^0 in bulk GaAs. Moreover, the MCDA spectra of As_{Ga} defects in LT-GaAs, known to be sensitively dependent on the detailed microscopic structure of the defect, often seemed different from that known from bulk GaAs [2,10]. This section will therefore focus on a detailed investigation of the As_{Ga} related MCDA spectra in LT-GaAs.

In Fig. 2 (a), MCDA spectra from LT-GaAs and SI bulk GaAs are compared. The spectrum obtained from SI GaAs exhibits the one derivative, one bell shaped structure typical for the paramagnetic As_{Ga}^+ defects [11]. The spectrum in undoped LT-GaAs exhibits a similar negative band at $\sim 0.95 \text{ eV}$ but has also a negative band at $\sim 1.2 \text{ eV}$, significantly different from the two positive

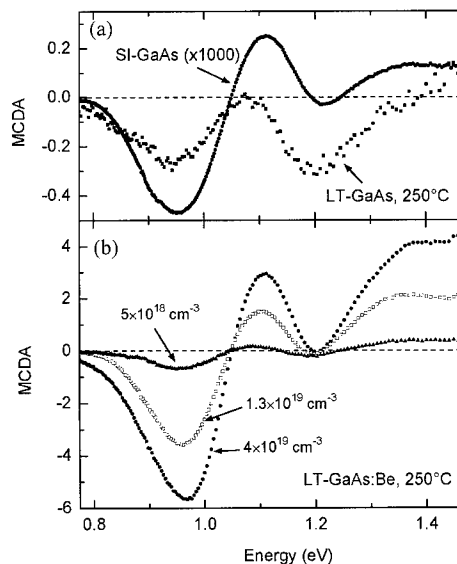


Fig. 2. MCDA spectra of As_{Ga} defects in GaAs measured at $T = 1.8 \text{ K}$ and $B = 2 \text{ T}$ (a) Spectra from semi insulating bulk GaAs and undoped LT-GaAs grown at 250°C . (b) Spectra from Be doped LT-GaAs grown at 250°C with different Be concentrations as indicated.

bands in bulk GaAs. In contrast, the spectra from LT-GaAs:Be (Fig. 2b) are very similar to that in bulk GaAs. The MCDA band at 0.95 eV is known to be proportional to the As_{Ga}^+ concentration [11]. In Fig 2 (b) its intensity is directly proportional to the Be doping, indicating that the As_{Ga}^+ compensate the Be acceptors. Thus, $[As_{Ga}^+]$ is close to the Be concentration (e.g. $\sim 3 \times 10^{19} \text{ cm}^{-3}$ in the highest doped sample).

It has been shown that As_{Ga} in its neutral charge state posses a characteristic MCD signal [12], albeit with lower intensity than that of As_{Ga}^+ . According to theory, the spectrum due to the paramagnetic As_{Ga}^+ has a strong temperature dependence while the spectrum due to the diamagnetic As_{Ga}^0 is independent on temperature [13]. Therefore, we performed MCDA measurements at a higher temperature (125 K) in order to separate diamagnetic and paramagnetic spectra. In Fig. 3, such measurements are shown for (a) LT-GaAs:Be and (b) the undoped LT-GaAs sample from Fig 2. The spectra measured at 125 K have the same features in both samples, i.e. two negative bands at 1.2 and 0.94 eV with intensity ratio of ~ 1.8 . The spectrum is the same as the diamagnetic spectrum due to As_{Ga}^0 previously observed in bulk GaAs [12]. Similar measurements were done for a larger set of samples. The intensity of the two bands was directly proportional to the absorption coefficient at 1.2 eV, i.e. to the As_{Ga}^0 concentration. It is especially

notable that the diamagnetic spectrum is very similar to the MCDA which can be photoquenched. Thus, As_{Ga}^0 in our layers is fully quenchable, in contrast to previous results that As_{Ga} in LT-GaAs is not or only partly quenchable [2,9].

In Fig. 3, we show also the paramagnetic spectra obtained by subtracting the diamagnetic spectra from the total MCDA. In both cases, they are very similar to that of As_{Ga}^+ in bulk GaAs shown in Fig. 2. The total MCDA spectrum from undoped LT-GaAs can therefore be explained by the superposition of diamagnetic (due to As_{Ga}^0) and paramagnetic MCDA (due to As_{Ga}^+). For the undoped LT-GaAs sample in Figs. 2 and 3, $[As_{Ga}^0]$ is $\sim 3 \times 10^{19} \text{ cm}^{-3}$, significantly larger than $[As_{Ga}^+]$ ($\sim 6 \times 10^{17} \text{ cm}^{-3}$). Therefore, the diamagnetic spectrum dominates for this particular sample, explaining the overall shape of the MCDA spectrum.

The detailed investigation of the MCDA spectra in LT-GaAs shows that the As_{Ga} antisites in both charge states have properties very similar to that in bulk GaAs. We found this finding to be true for undoped as well as for Be doped LT-GaAs. Our data provide therefore no evidence that Be forms a complex with the As_{Ga} antisites.

With these results, we can now determine the As_{Ga} antisite concentration. $[As_{Ga}^+]$ increases with the Be doping because of charge compensation, but the total As_{Ga} concentration (i.e. $[As_{Ga}^0] + [As_{Ga}^+]$) is independent on Be doping. In Fig. 4, $[V_{Ga}]$ is plotted vs. the total $[As_{Ga}]$. $[V_{Ga}]$ is $\sim 1\%$ of the total $[As_{Ga}]$ in all samples (solid line). The data agree with previous results from undoped LT-GaAs. Therefore, doping with Be has no influence on the incorporation of *all* native point defects in LT-GaAs.

5. Discussion and summary

Our results exclude that a different incorporation of native point defects, especially V_{Ga} , is responsible for the thermal stability of LT-GaAs:Be. It has been suggested that $[V_{Ga}]$ should be reduced in LT-GaAs:Be because the Fermi level effect reduces the formation energy of V_{Ga} in p-doped GaAs [5]. However, the formation energy governs defect concentrations preferably in thermal equilibrium. Contrary, MBE growth at low temperature is a non-equilibrium process where defect concentrations are governed mainly by the growth kinetics.

The incorporation of As_{Ga} in undoped LT-GaAs has been explained by the evaporation and absorption of the incoming atomic species. With decreasing temperature, reduced As desorption leads to an increased $[As_{Ga}]$ concentration while the reduced Ga diffusivity at the surface leads to an increase of $[V_{Ga}]$ [14]. The universal relationship between $[V_{Ga}]$ and $[As_{Ga}]$ shown in Fig. 4 suggests the same growth mechanism also for

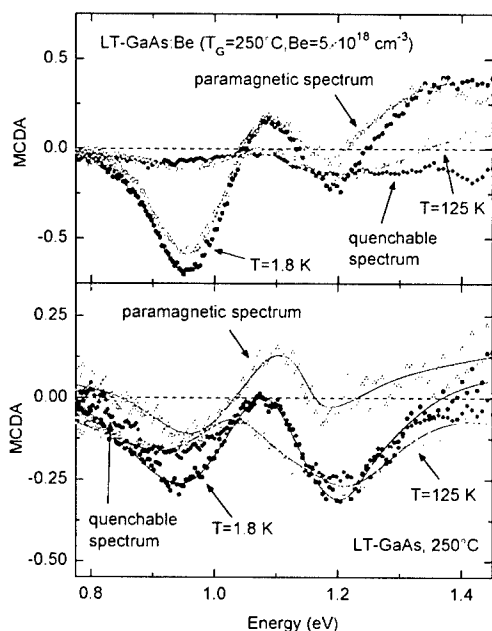


Fig. 3. MCDA spectra of LT-GaAs:Be (a) and undoped LT-GaAs (b) measured at 1.8 and 125 K. The spectra are compared to the MCDA quenchable at 1.8 K and to the paramagnetic MCDA obtained as the difference between the spectra at 1.8 and 125 K.

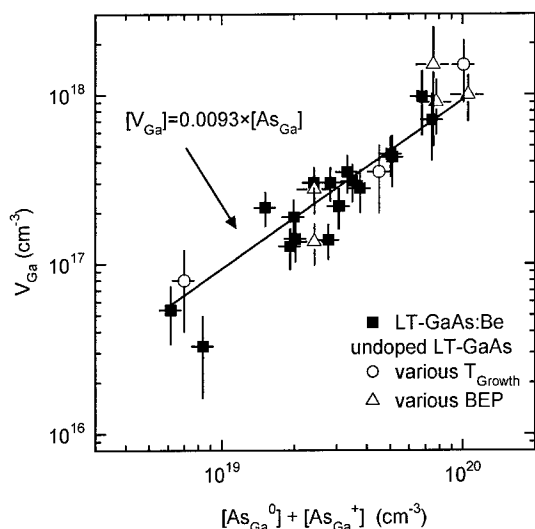


Fig. 4. Concentration of V_{Ga} as a function of the total As_{Ga} concentration (sum of $[\text{As}_{\text{Ga}}^0]$ and $[\text{As}_{\text{Ga}}^+]$) in LT-GaAs doped with Be (■) in comparison to undoped LT-GaAs grown at different temperatures with a BEP of 20 (○, Ref. [3]) and to undoped LT-GaAs grown at 200°C with variable BEP (△, Ref. [8]).

LT-GaAs:Be. The PAS and MCDA results gave no evidence for the formation of Be containing complexes. This indicates that the Be does not interact with the other defects. Because the Ga or As concentration at the surface is still much higher than the Be concentration, the defect concentrations will then be governed by the same kinetically factors as in undoped material.

Finally, we address the issue of thermal stability of LT-GaAs:Be. While we exclude that type and concentration of native point defects are changed it is known that the small Be atoms compensate the lattice strain caused by As_{Ga} antisites. Because thermal stabilization is best in layers where the net amount of strain is lowest [4], we conclude that the most likely explanation for

thermal stabilization in LT-GaAs:Be is strain compensation.

In summary, we studied native defects in non-stoichiometric LT-GaAs doped with Be. We found the same defects as in undoped LT-GaAs, i.e. As_{Ga} antisites and Ga vacancies. The As_{Ga} exhibited the same features as As_{Ga} defects in bulk GaAs, i.e. they have similar MCDA spectra and could be fully quenched. The concentration of native defects was not influenced by the Be doping and depends only on the growth conditions. Our results suggest that the most likely explanation for thermal stability of LT-GaAs:Be is the compensation of lattice strain by the Be atoms.

Acknowledgements

J.G. gratefully acknowledges a Feodor Lynen Fellowship of the Alexander von Humboldt Association. This work was supported by the AFOSR, grant No. F49620-98-1-0135. MBE growth was performed in the Integrated Materials Laboratory at UC Berkeley.

References

- [1] M. Kaminska, et al., Appl. Phys. Lett. 54 (1989) 1881.
- [2] X. Liu, et al., Appl. Phys. Lett. 65 (1994) 3002.
- [3] M. Luysberg, et al., J. Appl. Phys. 83 (1998) 561.
- [4] P. Specht, et al., J. Vac. Sci. Technol. B 17 (1999) 1200.
- [5] D.E. Bliss, et al., Appl. Phys. 71 (1992) 1699.
- [6] T. Laine, et al., J. Appl. Phys. 86 (1999) 1888.
- [7] R. Krause-Rehberg, H.S. Leipner, Positron Annihilation in Semiconductors, Springer, Berlin, 1999.
- [8] J. Gebauer, et al., J. Appl. Phys. 87 (2000) 8368.
- [9] K. Krambrock, et al., Semicon. Sci. Technol. 7 (1992) 1037.
- [10] W. Jost, et al., Semicon. Sci. Technol. 7 (1992) 1386.
- [11] B.K. Meyer, et al., Phys. Rev. Lett. 52 (1984) 851.
- [12] K.H. Wietzke, et al., Appl. Phys. Lett. 71 (1997) 2133.
- [13] P.J. Stephens, Adv. Chem. Phys. 35 (1976) 197.
- [14] S. Muthuvenkatraman, et al., J. Appl. Phys. 83 (1998) 5845.



ELSEVIER

Physica B 308–310 (2001) 816–819

PHYSICA B

www.elsevier.com/locate/physb

Rhodium-related deep levels in n-type MOCVD GaAs

M. Zafar Iqbal^{a,*}, A. Majid^a, S. Haidar Khan^a, Akbar Ali^a, Nasim Zafar^a,
A. Dadgar^b, D. Bimberg^b

^a Semiconductor Physics Laboratory, Department of Physics, Quaid-i-Azam University, Islamabad 45320, Pakistan

^b Institut für Festkörperphysik, Technische Universität, Hardenbergstr. 36, 10623 Berlin, Germany

Abstract

Preliminary results on the study of deep levels associated with 4d-transition metal, rhodium, in crystalline GaAs grown by metal-organic chemical vapour deposition (MOCVD) technique are reported for the first time. Deep level transient spectroscopy on n-type GaAs doped in situ with Rh during MOCVD growth reveals a broad majority carrier emission peak. The peak corresponds to a band of deep levels extending over the energy range 0.57–0.65 eV below the conduction band edge with lower-energy states having lower electron capture cross-sections. The deep levels show a pronounced dependence of electron emission rate on the junction electric field. Minority carrier (hole) emission spectra at zero bias show a pronounced Rh-related deep-level peak with a low-temperature shoulder. The dominant level in the lower half-gap is found to have a position $E_v + 0.44$ eV, with a field-dependent emission rate signature. © 2001 Elsevier Science B.V. All rights reserved.

Keywords: Transition metals; GaAs; DLTS; MOCVD

1. Introduction

The study of transition metal (TM) impurities is a subject of continuing importance in semiconductor physics owing to their fundamental and technological importance. In this regard, the role of heavier, 4d- and 5d-TM impurities is of particular importance in compound semiconductors as shown by our recent work on InP [1–3]. For example, the 5d-TM ruthenium (Ru) has been shown to provide a thermally stable, compensator dopant for producing semi-insulating InP needed for InP-based semiconductor technology [2]. This paper reports the results of the first ever DLTS investigation of the 4d-TM impurity rhodium (Rh) in GaAs, to our knowledge.

2. Material and samples

Epitaxial layers of n-type GaAs grown by low pressure, metal-organic chemical vapour deposition

(LP-MOCVD) doped in situ with Rh have been used in this study. The temperature and pressure during growth were 720 °C and 20 mbar, respectively. p^+ -layers doped with Zn were grown on these layers by metal-organic chemical vapour deposition (MOCVD) in the same reactor to fabricate mesa p^+ -n-junction diodes suitable for performing DLTS investigations, after providing appropriate metallic ohmic contacts on the two sides by vacuum evaporation. A sensitive deep-level spectrometer based on lock-in detection system has been used for DLTS measurements from 77 K upwards in temperature. Identically prepared reference samples without any intentional Rh doping were used to identify the Rh-related deep-level defects in Rh-doped samples.

3. Results

3.1. Majority carrier deep levels

The typical DLTS spectra for majority carrier (electron) emission obtained from the reference and Rh-doped samples are shown in Fig. 1. While no

*Corresponding author. Tel.: +92-51-2829537; fax: 92-51-9210256.

E-mail address: mzi8149@yahoo.com (M. Zafar Iqbal).

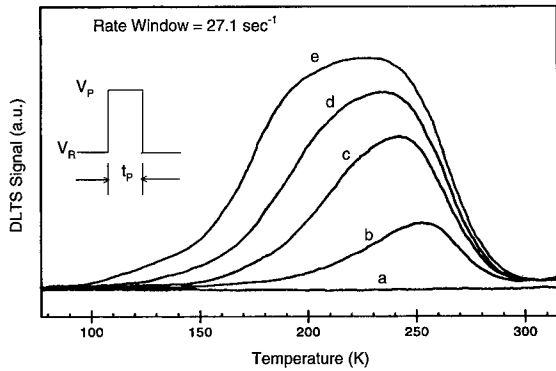


Fig. 1. Majority carrier (electron) emission DLTS spectra of (a) p^+n -GaAs reference sample at 500 μ s capture pulse width. (b)–(e) Rh-doped p^+n -GaAs at (b) 5 μ s, (c) 50 μ s, (d) 500 μ s and (e) 5 ms capture pulse widths, respectively. $V_R = -2.0$ V and $V_P = -0.5$ V for all spectra.

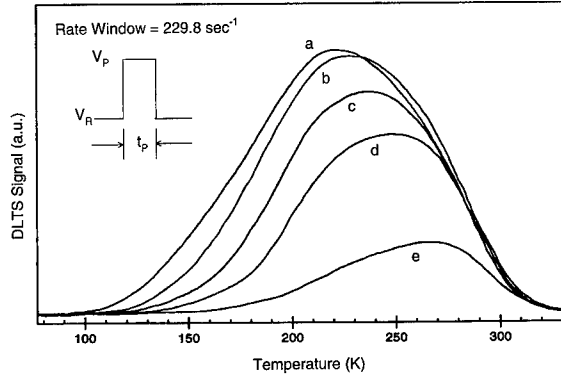


Fig. 2. Majority carrier (electron) emission DLTS spectra for Rh-doped n -GaAs at different reverse biases (V_R) showing the effect of electric field: (a) $V_R = -5$ V, (b) -4 V, (c) -3 V, (d) -2 V, (e) -1 V; $V_P = -0.5$ V and $t_p = 500$ μ s for all spectra.

significant deep level emission signal is observed from the reference samples in the temperature range used, the Rh-doped samples show a prominent, broad peak corresponding to electron emission to the conduction band. This peak shows a strong increase in the width and height, with a pronounced broadening towards low-temperature end, as the width of the electron capture pulse is increased from 5 μ s to 5 ms, as shown in Fig. 1. This clearly shows that Rh introduces a band of deep-level states in the upper half-gap with lower-energy levels having lower electron capture cross-sections as compared to the higher-energy (deeper) states. DLTS scans at different applied quiescent biases show a significant shift in the peak position towards lower temperatures with the increase of the junction electric field along with the accompanying broadening, as shown in Fig. 2. This is a clear indication that most of the Rh-related deep levels comprising the broad peak have field-dependent emission rates. Attempts to resolve this band into component peaks, at least at the high-temperature end, by using smaller capture pulse widths did not yield clear single peaks when tested against theoretical DLTS line-shape formula [4,5]. The DLTS spectra for low (250 ns) and high (500 μ s) capture pulse widths are shown in Fig. 3. In view of the strong electric field dependence, double-correlation DLTS (DDLTS) was used to obtain information on the limiting positions of the energy levels comprising the above-mentioned band. The Arrhenius plots of the electron emission rate data so obtained for these limiting cases, given in the inset of Fig. 3, show the activation energies of the levels corresponding to the low- and high-temperature ends of the emission band to be approximately 0.57 and 0.65 eV, respectively, at an electric field of $\sim 6 \times 10^4$ V/cm. The respective apparent electron capture cross-sections for these two ends of the band, obtained from

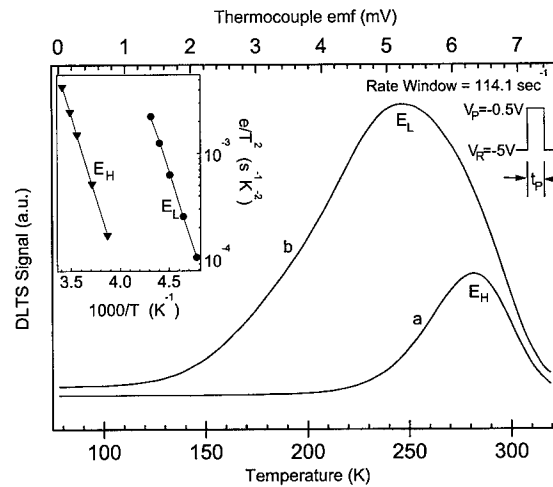


Fig. 3. Majority carrier (electron) emission DLTS spectra for Rh-doped sample at (a) 250 ns and (b) 500 μ s pulse width. The inset shows the Arrhenius plots, obtained in the DDLTS mode for the peaks E_L and E_H corresponding to the low- and high-temperature ends, respectively, of the emission band.

the intercepts of the Arrhenius plots of the respective emission rate signatures, are given in Table 1.

3.2. Minority carrier deep levels

Fig. 4 shows DLTS spectra obtained with minority carrier injection at zero volt quiescent bias. High injection (+2.0 V) and large pulse width (500 μ s) spectrum, trace (a), clearly shows a prominent, broad negative peak with a shoulder at the lower-temperature end, corresponding to at least two deep-level states in

Table 1
Characteristics of deep levels observed in n-GaAs:Rh

Deep level position (eV)	Capture cross-section $\sigma(\tau)(\times 10^{-12} \text{ cm}^2)$
$E_c - 0.57^a$	5.17
$E_c - 0.65^a$	4.08
$E_v + 0.44$	0.33

^aThese levels correspond to the low- and high-temperature ends of the DLTS emission band.

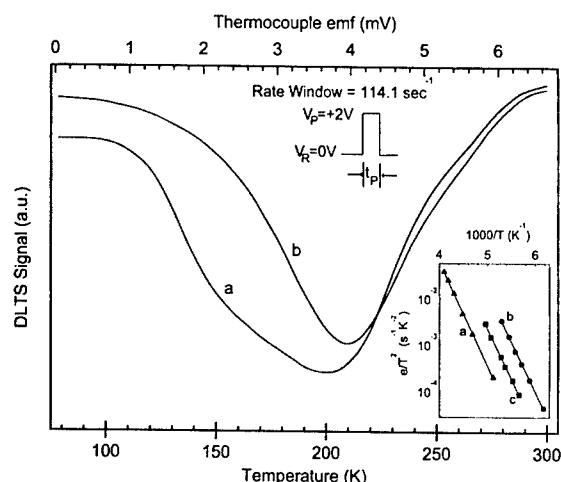


Fig. 4. Minority carrier (hole) emission DLTS spectra for Rh-doped n-GaAs at two different pulse widths (a) 500 μs and (b) 0.5 μs . The inset shows Arrhenius plots of minority carrier emission peak observed under the following conditions: (a) DLTS mode: $V_R = 0 \text{ V}$, $V_P = +2.0 \text{ V}$, $t_P = 250 \text{ ns}$; (b) DDLTS mode: $V_R = -5 \text{ V}$, $V_{P1} = +2.0 \text{ V}$, $V_{P2} = 0 \text{ V}$, $t_P = 500 \mu\text{s}$ and (c) DDLTS mode: $V_R = -1 \text{ V}$, $V_{P1} = +2.0 \text{ V}$, $V_{P2} = 0 \text{ V}$, $t_P = 500 \mu\text{s}$.

the lower half-gap of our material. Lowering the injection pulse width leads to the disappearance (or strong reduction in the strength) of the shoulder, as shown by trace (b) in Fig. 4, indicating a significantly lower hole capture cross-section for the lower-energy deep-level component. The measured hole emission-rate signature of the dominant minority carrier deep level is shown as plot (a) in the inset of Fig. 4, yielding an activation energy of $\sim 0.44 \text{ eV}$ for this level. It is pertinent to point out that the minority carrier injection scans with non-zero quiescent reverse bias (V_R) show either no negative peak (for $V_R < -2 \text{ V}$), or a much smaller (by a factor of 2, approximately) negative peak (for $V_R > -2 \text{ V}$) superposed on the dominant majority carrier emission band, while the injection DLTS spectrum at zero quiescent bias shows only the minority

carrier peak, as expected. However, DDLTS using an injection pulse followed by a zero volt majority carrier excitation pulse, which would eliminate at least a major part of the majority carrier emission peaks, if not completely, would circumvent this problem and clearly show minority carrier emission peaks even at non-zero quiescent reverse bias. This is indeed what is observed, allowing measurement of the emission rate signature at an applied reverse bias, which is also included in the inset of Fig. 4 (plot b). Plot (c) in the same inset is the emission rate signature for the same peak measured in the DDLTS mode at a lower applied bias of -1 V , keeping all other parameters the same as for plot (b). This clearly shows that this hole-emitting level has a strongly field-dependent emission rate.

DLTS investigations on the reference diodes show much smaller minority carrier emission features in similar (but not identical) temperature regions. However, while the higher-temperature peak is too weak to allow detailed measurements, careful measurements show that the lower-temperature peak in these samples has a significantly different emission rate signature than that of the minority carrier emission peak in the Rh-doped samples. The minority carrier emission peaks seen in Rh-doped GaAs are either exclusively Rh-related or combined with the much smaller peaks, corresponding to deep levels in close-by positions in the band gap, seen in the reference samples. The much stronger hole emission peaks in the Rh-doped samples may, thus, originate from isolated Rh impurity or some complexes of Rh with the pre-existing/growth-related inadvertent defects in the as-grown MOCVD material. Unambiguous resolution of these aspects and some other unusual properties of the small minority carrier peaks in the reference samples require detailed further work, which is in progress.

4. Conclusions

In conclusion, Rh impurity is seen to introduce deep-level defect states in the bandgap of n-type GaAs crystals grown by LP-MOCVD at energy positions extending from $E_c - 0.57$ to $E_c - 0.65 \text{ eV}$ in the upper-half gap. Most of this band of levels appear to have electric field dependent emission characteristics. In the lower-half gap, a Rh-related deep level at $E_v + 0.44 \text{ eV}$ is found to dominate the DLTS spectrum. In addition, unresolved hole-emitting deep-level signals are also observed both on the lower- and higher-temperature sides of this dominant peak in the hole emission spectra. The 0.44 eV hole level is also found to exhibit electric field dependent emission rate signature. Theoretical efforts to resolve the majority carrier deep-level band and detailed quantitative analysis of the field dependence of these components are in progress.

Acknowledgements

This collaborative study was partially supported by the Commission of European Communities project No. CII-CT93-0076.

References

- [1] A. Dadgar, D. Ammerlann, A. Näser, R. Heitz, M. Kuttler, D. Bimberg, N. Babar, J.Y. Hyeon, H. Schumann, *Phys. Rev. B* 53 (1996) 7190.
- [2] A. Dadgar, O. Stenzel, A. Näser, M. Zafar Iqbal, D. Bimberg, H. Schumann, *Appl. Phys. Lett.* 73 (1998) 3818.
- [3] L. Köhne, A. Dadgar, D. Bimberg, M. Zafar Iqbal, U.S. Qurashi, T. Gründemann, H. Schumann, *Phys. Stat. Sol. (A)* 171 (1999) 512.
- [4] G.L. Miller, D.V. Lang, L.C. Kimerling, *Ann. Rev. Mater. Sci.* 7 (1977) 377.
- [5] D.V. Lang, in: P. Bräunlich (Ed.), *Thermally Simulated Relaxation in Solids*, Springer, Berlin, 1979, pp. 93–133.



ELSEVIER

Physica B 308 310 (2001) 820–822

PHYSICA B

www.elsevier.com/locate/physb

Stress-induced transformation of defects in homoepitaxial beryllium-doped GaAs thin films

J. Bak-Misiuk^{a,*}, A. Misiuk^b, K.S. Zhuravlev^c, J.Z. Domagala^a, J. Adamczewska^a,
V.V. Preobrazhenskii^c

^a*Institute of Physics, Polish Academy of Sciences, Al. Lotników 46, 02-668 Warsaw, Poland*

^b*Institute of Electron Technology, 02-668 Warsaw, Poland*

^c*Institute of Semiconductor Physics, RAS, Novosibirsk, Russia*

Abstract

The effect of beryllium doping on defect structure of the 1.5 μm thick GaAs:Be films grown by MBE on GaAs substrate as well as the effect of high temperature–high pressure treatment (HT–HP) on structural changes in that material were investigated by X-ray, electrical and SIMS methods. For As-grown GaAs:Be with Be concentration $\leq 2.7 \times 10^{19} \text{ cm}^{-3}$, the Be doping-related decrease of lattice parameter, a , corresponded to that calculated from the Vegard law, accounting for the effect of holes on that parameter. For GaAs:Be with the higher Be concentration, a decrease of the a value was lower than that calculated. This effect can be explained assuming creation of Be inclusions. © 2001 Elsevier Science B.V. All rights reserved.

Keywords: GaAs:Be; High hydrostatic pressure; Beryllium inclusion; X-ray

1. Introduction

Heavily doped p-type GaAs makes it easier to produce ohmic contact and is very desirable in device structures such as tunnel diodes or heterojunction bipolar transistors. Beryllium is the most frequently used dopant for preparing p-type GaAs. Beryllium incorporation in GaAs produces a shallow donor at about 19 meV level above the valence band.

Doping with electrically active atoms changes the lattice constant of the semiconductors owing two factors: (i) size effect and (ii) presence of free charges. The effect of inclusions on the lattice constant ought to be also taken into account for the case of highly doped semiconductor. Linear dependence of the lattice constant value on the beryllium concentration has been reported [1].

As it follows from recent investigations of the high temperature–high hydrostatic pressure, HT–HP, effect on strained, hydrogen- and oxygen-implanted silicon, Si:H and Si:O [2–4] and on the thin AlGaAs layers deposited on the GaAs substrate [5], the HT–HP treatment can result in:

- (i) change of thin layer strain;
- (ii) change of components diffusivity;
- (iii) creation of additional nucleation sites for newly created bulk and interface defects;
- (iv) change of dislocation mobility; and
- (v) creation of defects at the thin film/matrix boundary.

An influence of enhanced hydrostatic pressure of ambient gas on the layer strain can be neglected for the GaAs:Be/GaAs samples due to similar bulk moduli [5] of the layer and substrate materials. It means that the GaAs:Be lattice parameter value after the HT–HP treatment would depend mainly on the primary defect structure of the layer material. Therefore, the HT–HP treatment was applied in our work to obtain information on the defect structure of the GaAs:Be layer modified by beryllium doping.

*Corresponding author. Tel.: +48-22-8436-034; fax: +48-22-8430-926.

E-mail address: bakmi@ifpan.edu.pl (J. Bak-Misiuk).

2. Experimental

The epitaxial GaAs:Be layers were grown on the semi-insulating (100)-oriented GaAs substrates at 870 K with a growth rate of 1.0 $\mu\text{m}/\text{h}$ in the Katun's MBE system. The layers thickness was equal to 1.5 μm . The GaAs:Be layers were separated from the GaAs substrate by a 100 nm thick superlattice comprising five pairs of (AlAs)/(GaAs) subsequent layers, each layer with 10 nm thickness. The GaAs:Be layers were covered by a 30 nm thick capping AlAs layer.

The Be and carrier (hole) concentrations were determined by secondary ions mass spectrometry, SIMS and Van der Pauw measurements, respectively. The last measurements were performed at room and liquid nitrogen temperatures.

The GaAs:Be/GaAs structures were HT–HP treated for 1 h under 1.2 GPa argon pressure at 870 K, the same temperature as that of layer growth.

The lattice constant of the layer material, before and after the HT–HP treatment, was determined by the Fewster method [6] using X-ray high-resolution diffractometer. A set of high Bragg angle reflections (006, 335 and 117) was used. The relaxed lattice parameter of the layer material, a_{relax} , was calculated using the following equation:

$$a_{\text{relax}} = (a_{\perp} + 2Ca_{\parallel}) / (1 + 2C), \quad (1)$$

where a_{\perp} is the lattice parameter perpendicular to the layer/substrate interface, a_{\parallel} is the lattice parameter parallel to that interface and $C = (1 - \nu)/(1 + \nu)$, where ν is the Poisson ratio, equal to 0.311 for GaAs.

3. Results and discussion

The Hall and SIMS data for investigated samples are given in Table 1. The designations correspond to GaAs:Be with different Be concentration.

Beryllium is substitutionally incorporated into the Ga sublattice where it becomes an acceptor. A decrease of hole concentration with decreasing temperature was observed for the 906 and 907 layers (Table 1). The

hole concentration at 77 K was the same as the Be concentration in the Ga sublattice. However, it was not possible to determine the nature and concentration of deeper acceptors revealed at 300 K. It is necessary to notice that similar deep acceptors were reported earlier for the undoped MBE grown GaAs layers [7].

As it follows from the data in Table 1, the SIMS-detected Be concentration was higher than that determined by the Van der Pauw method. It means that the Be concentration in the GaAs:Be layers was higher than that corresponding to Be incorporated into the Ga sublattice. That additional Be atoms occupy interstitial positions or create the Be composed inclusions. The similar effect was reported also for GaAs:Si [8]. In the case of sample 907, the Be concentration in the Ga sublattice was lower than that for the 906 sample; however, the Be concentration, determined by SIMS, was higher, quite opposite to before mentioned observation. It means that the creation of Be inclusions or/and of Be interstitials is not directly dependent on the Be concentration.

The change of the relaxed lattice constant of the layer material is given in Table 2.

For all investigated layers, the parallel lattice constant of GaAs:Be, a_{\parallel} , was equal to the lattice constant of GaAs substrate. However, the decreased perpendicular and relaxed lattice parameters were detected for all investigated GaAs:Be layers (the lattice constant of GaAs equals to 5.65332 Å). The relative change of lattice parameter, a , for the p-type semiconductor of the zinc blend structure, related to the size and hole concentration effects, is given by the formula [9–11]

$$\Delta a/a = \beta_s N_d + \beta_p N_p, \quad (2)$$

where N_d is the Be dopant concentration in the Ga sublattice (N_d is equal to the hole concentration at 77 K—see Table 1), N_p the hole concentration in the top of valence band (we took into account the hole concentration at 300 K—Table 1), β_s and β_p describe

Table 1
Hall and SIMS data for As-grown GaAs:Be samples^a

Data	N_p (10^{19} cm^{-3})		c_{Be} (10^{19} cm^{-3})
	300 K	77 K	
Sample			
903	0.5	0.5	0.5
905	2.6	2.7	5
906	8	7	18
907	9.2	5.8	21.5

^a Concentration of holes, N_p , and beryllium concentration, c_{Be} , at 300 and 77 K, respectively.

Table 2
Decrease of calculated and experimentally determined relaxed lattice parameter, Δa_{relax} , for As-grown GaAs:Be (in comparison to a_{GaAs}), and increase of the lattice parameter after the HT–HP treatment, $\Delta a'_{\text{relax}}$, in comparison to lattice parameter a of the As-grown GaAs:Be samples

Samples	As-grown $\Delta a \pm 0.5 \times 10^{-4}$ (Å)		After HT–HP $\Delta a' \pm 0.5 \times 10^{-4}$ (Å)
	Exp.	Calc.	Exp.
903	–1	–0.5	<0.5
905	–3.7	–3.8	1
906	–8.6	–10.1	1.5
907	–6	–9.2	2

the size effect (corresponding to the Vegard law) and the effect of presence of holes:

$$\beta_s = 4(R_d - R_s)/\sqrt{3}aN_0 = 2.03 \times 10^{-24}, \quad (3)$$

$$\beta_p = D/3B = 0.4978 \times 10^{-24}, \quad (4)$$

where $N_0 = 2.21 \times 10^{22} \text{ cm}^{-3}$ is the Ga density in a non-doped GaAs, R_d and R_s the covalent radii of Be (1.11 Å) and of Ga (1.22 Å), respectively, B the bulk modulus of GaAs, equal to $7.5 \times 10^6 \text{ N/cm}^{-2}$, D the deformation potential of the top valence band, equal to 0.7 eV.

As it follows from Table 2, the experimentally detected decrease of the relaxed lattice constant is smaller than that calculated from the formula (2). This effect is probably caused by the creation of Be-related defects. If such Be containing inclusions are created during the layer growth, the HT–HP treatment would influence the defect structure of GaAs:Be and so the treatment-induced lattice parameter changes would be observed.

Indeed, the GaAs:Be samples subjected to the HT–HP treatment indicate an increase of the lattice parameters (Table 2). The HT–HP treatment, due to the different (in respect to that of the matrix material) compressibility and thermal expansion of the Be containing inclusions, results in creation of additional defects influencing the lattice parameter value. It is known that, at sufficiently severe HT–HP conditions, the stress at the precipitate/matrix material can reach the critical value for emitting dislocations loops and other defects [12].

Our results suggest that a part of Be atoms create, during the GaAs:Be layer growth, some Be containing defects. Just their presence is the most probable explanation of the HT–HP induced effects in the GaAs:Be samples.

4. Conclusions

The Be containing defects (inclusions ?) were detected in the GaAs:Be samples with the Be concentration higher than $2 \times 10^{19} \text{ cm}^{-3}$. The increased lattice constant

value was detected for GaAs:Be after the treatment at 870 K, 1.2 GPa. It was shown that effects of the HT–HP treatment can be considered as a specific indicator of the primary defect state of the GaAs:Be samples.

Acknowledgements

This work was partially supported by the grants of Polish Committee for Scientific Research, No. 2 PO3B-14018 (at 2000–2002) and 8T11B 072 19. The authors thank Prof. A. Barcz from the Institute of Electron Technology, Warsaw for the SIMS measurements.

References

- [1] J.L. Lievin, F. Alexandre, *Electron. Lett.* 21 (1985) 413.
- [2] A. Misiuk, *Phys. Mech.* 1 (2000) 119.
- [3] A. Misiuk, H.B. Surma, I.V. Antonova, V.P. Popov, J. Bak-Misiuk, M. Lopez, A. Romano-Rodriguez, A. Barcz, J. Jun, *Solid State Phenomena* 69–79 (1999) 345.
- [4] A. Misiuk, A. Barcz, J. Ratajczak, M. Lopez, A. Romano-Rodriguez, J. Bak-Misiuk, H.B. Surma, J. Jun, I.V. Antonova, V.P. Popov, *Mater. Sci. Eng. B* 73 (2000) 134.
- [5] J. Bak-Misiuk, J. Domagala, A. Misiuk, J. Sadowski, Z.R. Zytkeiwicz, J. Trela, I.V. Antonova, *Thin Solid Films* 380 (2000) 117.
- [6] P.F. Fewster, N.L. Andrew, *J. Appl. Crystallogr.* 28 (1995) 451.
- [7] K.S. Zhuravlev, A.K. Kalagin, N.T. Moshegov, A.I. Toporov, T.S. Shamirzaev, O.A. Shegai, *Semiconductors* 32 (1996) 892.
- [8] V.P. Kladko, L.I. Datsenko, J. Bak-Misiuk, S.I. Olichowski, V.F. Maluchin, I.V. Prokopenko, V.B. Molodkin, Z.V. Maksimenko, *J. Phys. D.* 34 (2001) A87.
- [9] T. Figielski, *Phys. Stat. Sol.* 1 (1961) 306.
- [10] Wei Li, M. Pessa, *Phys. Rev B* 57 (1997) 14 627.
- [11] M. Leszczynski, J. Bak-Misiuk, J. Domagala, J. Muszalski, M. Kaniewska, J. Marczewski, *Appl. Phys. Lett.* 67 (1995) 5399.
- [12] J. Jung, *Philos. Mag. A* 30 (1984) 257.



ELSEVIER

Physica B 308–310 (2001) 823–826

PHYSICA B

www.elsevier.com/locate/physb

Carbon incorporation during growth of GaAs at low temperatures

J. Herfort^{a,*}, W. Ulrici^a, M. Moreno^a, M. Luysberg^b, K.H. Ploog^a

^a Paul-Drude-Institut für Festkörperelektronik, Hausvogteiplatz 5-7, D-10117 Berlin, Germany

^b Institut für Festkörperforschung, Forschungszentrum Jülich, 52425 Jülich, Germany

Abstract

Heavily C-doped GaAs layers grown by solid-source molecular beam epitaxy at low substrate temperatures, $195^{\circ}\text{C} < T_G < 375^{\circ}\text{C}$, are investigated using infrared absorption measurements. The heavy C-doping (about $2 \times 10^{19} \text{ cm}^{-3}$) causes a compensation of the strain created by the simultaneously formed As antisite defects, As_{Ga} . The contents of As_{Ga} and substitutionally incorporated carbon, C_{As} , are determined as a function of T_G . Additionally, for $T_G < 400^{\circ}\text{C}$ the local vibrational mode absorption lines of four C-containing complexes are found. These lines, located at frequencies around 1800 cm^{-1} , are most likely due to C–C stretching modes. For $T_G < 250^{\circ}\text{C}$ the C-complexes are responsible for the strain compensation, as no C_{As} is detectable. After annealing at 600°C the content of C_{As} is not changed, but the C-complexes completely disappear. © 2001 Elsevier Science B.V. All rights reserved.

Keywords: LT-GaAs; Carbon; Local vibrational modes; Molecular beam epitaxy

1. Introduction

GaAs grown by molecular beam epitaxy (MBE) at low substrate temperatures (LT-GaAs) has gained increasing interest because of its special properties which lead to a wide range of opto-electronic applications [1–3]. Most attractive are the ultrashort carrier trapping times and, upon annealing, very high resistivities [4,5]. These properties are explained by the presence of a very high content of As_{Ga} antisite defects formed during the growth. Carrier trapping times even shorter than in undoped material are expected for p-doped LT-GaAs owing to the higher concentration of charged antisite defects [6,7]. Furthermore, strain compensation is achievable, as the lattice expansion created by the As_{Ga} can be compensated by the lattice contraction created by the acceptors. These efforts have been concentrated on Be-doped LT-GaAs [8–10]. Compared to carbon, however, Be has a much higher diffusion coefficient [11] which can lead to undesirable diffusion

and precipitation at high doping levels although this might be less pronounced for growth at low temperatures [6].

C incorporation in LT-GaAs has been studied by Liu et al. [12] using a CBr_4 gas source. They found that the C-doping is unavoidably accompanied by a significant unfavorable bromine incorporation. In a recent paper [13] we have investigated the C incorporation into LT-GaAs layers grown by solid source MBE at different growth temperatures T_G and C concentrations. From double crystal X-ray diffraction (DCXRD) measurements on LT-GaAs:C with $p = 2.5 \times 10^{19} \text{ cm}^{-3}$, it was derived that layers grown at $T_G \approx 220^{\circ}\text{C}$ are almost lattice matched to the GaAs substrate [13]. The good quality of these layers was evidenced by the interference fringes appearing in the X-ray rocking curves. Below (above) this growth temperature, the tensile (compressive) strain produced by As_{Ga} and C_{As} , respectively, is detected. Here, we investigate by infrared absorption measurements on such LT-GaAs:C layers, how the incorporation of C_{As} and As_{Ga} , and the formation of C-containing complexes depends on T_G and how this is affected by subsequent annealing.

*Corresponding author. Fax: +49-30-20377-201.

E-mail address: herfort@pdi-berlin.de (J. Herfort).

2. Experimental details

Two sets of LT-GaAs:C samples were grown by MBE on semi-insulating GaAs(001) substrates at various growth temperatures T_G , between 195 and 375°C. The C-concentrations for the two sets as determined from Hall effect measurements of reference samples grown at high T_G , i.e. 550°C, were 1.2×10^{18} and $2.5 \times 10^{19} \text{ cm}^{-3}$, respectively. Secondary-ion mass spectroscopy (SIMS) revealed that the total carbon content $[C_T]$ is apparently larger by about a factor of 4 in case of the higher doping concentration, but most important, it remains constant when T_G is decreased.

The LT-GaAs:C layers with a thickness of about 300 nm were deposited with a growth rate of 0.5 $\mu\text{m/h}$ after growing a 200 nm thick GaAs buffer layer at 570°C. The As₄:Ga BEP ratio was about 20 to have stable arsenic rich conditions. For more details of the sample growth we refer to Ref. [13]. One piece of each sample was subsequently annealed in the growth chamber at 600°C for 20 min under As overpressure. The infrared absorption experiments have been performed with a Bruker IFS 120 HR Fourier-transform spectrometer operating with spectral resolutions of 0.2–2 cm^{-1} with the samples kept at $T = 80 \text{ K}$ in a cryostat.

3. Results and discussion

In Fig. 1 the absorption features measured at $T = 80 \text{ K}$ on LT-GaAs:C layers in the frequency region

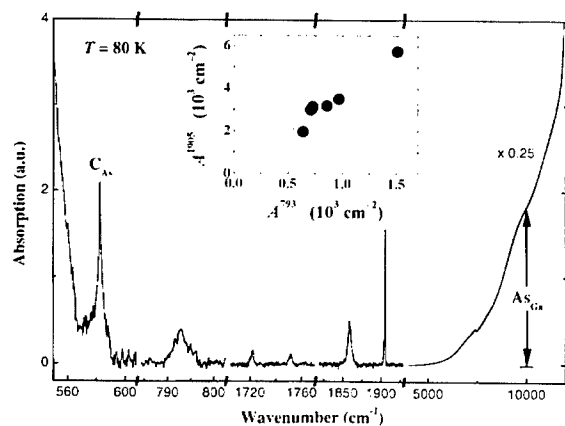


Fig. 1. Infrared absorption spectra measured at $T = 80 \text{ K}$ on LT-GaAs:C samples grown at different substrate temperatures $210^\circ\text{C} < T_G < 280^\circ\text{C}$. Different parts are measured on samples grown at different T_G to show all investigated vibrational absorption lines. The inset shows the correlation between the integrated intensities A of the vibrational absorption lines at 793 and 1905 cm^{-1} .

from the two-phonon cut-off at $\approx 550 \text{ cm}^{-1}$ up to the electronic edge of GaAs at $\approx 12\,000 \text{ cm}^{-1}$ are summarized. These spectra were measured on the set of samples with high C content ($p = 2.5 \times 10^{19} \text{ cm}^{-3}$). At high wavenumbers the broad absorption with the EL2-like spectral shape can be seen which is due to electronic transitions from the As_{Ga}^0 midgap level into the conduction band of GaAs as characteristic for LT-GaAs [14]. This absorption allows evaluating the concentration of neutral As_{Ga}^0 antisite defects $[\text{As}_{\text{Ga}}^0]$, using the known photoionization cross sections [15] of As_{Ga} in single crystalline bulk GaAs. The local vibrational mode (LVM) absorption line at 582.5 cm^{-1} due to substitutional carbon, C_{As} , can be well detected. However, in contrast to bulk GaAs with low C_{As} content, the isotope structure due to the surrounding ^{69}Ga and ^{71}Ga is not resolved, and the half-width of the line is larger and increases with decreasing T_G . This broadening is probably caused by strain due to the presence of a high concentration of nonstoichiometric defects in LT-GaAs. Nevertheless, the concentration of C atoms on arsenic sites $[\text{C}_{\text{As}}]$ can be determined using the calibration factor $f = 7 \times 10^{15} \text{ cm}^{-1}$ [16] for the integrated intensity of the LVM absorption line at 582.5 cm^{-1} .

The concentrations of As_{Ga}^0 and C_{As} determined for as-grown layers with high C content ($p = 2.5 \times 10^{19} \text{ cm}^{-3}$) at different substrate temperatures T_G are shown in Fig. 2. As can be seen, $[\text{As}_{\text{Ga}}^0]$ increases strongly with decreasing T_G in the same manner, as

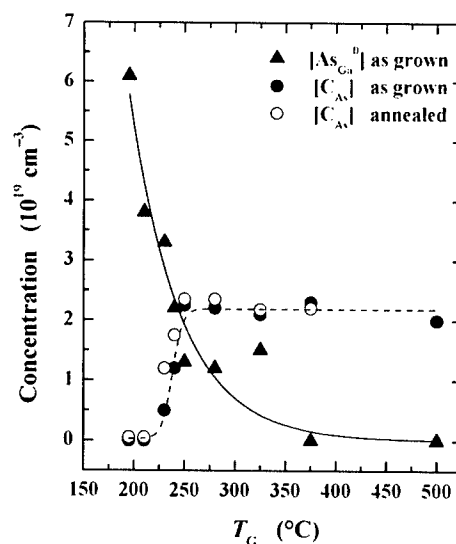


Fig. 2. Concentration of arsenic antisite defects $[\text{As}_{\text{Ga}}^0]$ and substitutionally incorporated carbon $[\text{C}_{\text{As}}]$ in LT-GaAs as a function of the growth temperature T_G for as-grown layers (full symbols) and after annealing at 600°C (open symbols). The C concentration corresponds to $2.5 \times 10^{19} \text{ cm}^{-3}$.

it is known for undoped LT-GaAs [5]. On the other hand, below $T_G = 250^\circ\text{C}$ a drastic decrease of $[C_{As}]$ is observed. A qualitative similar behavior is found for the LT-GaAs:C layers with lower C content ($p = 1.2 \times 10^{18} \text{ cm}^{-3}$). Annealing at 600°C reduces the $[As_{Ga}^0]$ below the detection limit (here $< 10^{19} \text{ cm}^{-3}$) for all T_G in the same manner as for undoped LT-GaAs. The concentration of C_{As} , however, remains unchanged after annealing at 600°C for all samples. This is expected (and desired) because of the low diffusion coefficient of C in GaAs [11] causing C to be immobile at this temperature.

From Fig. 1 it can be seen that in the frequency region from 700 to 2000 cm^{-1} additional five LVM lines with small half width Γ are detected for low T_G , never observed before in LT-GaAs or bulk GaAs. Three of them are quite intense (their integrated intensities are comparable with that of C_{As} at $T_G > 250^\circ\text{C}$) and located at 792.9 cm^{-1} ($\Gamma = 1.5 \text{ cm}^{-1}$), 1859.0 cm^{-1} ($\Gamma = 4.8 \text{ cm}^{-1}$), and 1905.3 cm^{-1} ($\Gamma = 0.9 \text{ cm}^{-1}$). The inset in Fig. 1 shows that the intensities of the narrow lines at 793 and 1905 cm^{-1} are correlated, indicating that they are caused by a single defect called C_{LT}^A . In Fig. 3 the integrated intensities A of the three lines are shown as measured for the samples grown at different T_G . For low $T_G < 240^\circ\text{C}$ only the lines of defect C_{LT}^A are measured and they decrease in the region $240^\circ\text{C} < T_G < 375^\circ\text{C}$. On the other hand, in this region of T_G the line at 1859 cm^{-1} grows up, which is obviously due to a different center called C_{LT}^B . The dashed line for C_{LT}^B in Fig. 3 means that for $T_G = 550^\circ\text{C}$ also this center was not detectable. It should be noted that C_{LT}^A is

observed also in the LT-GaAs:C layers with lower C content ($p = 1.2 \times 10^{18} \text{ cm}^{-3}$), but the intensity of the 1905 cm^{-1} line is lower by a factor of ≈ 50 (Γ amounts to only 0.3 cm^{-1}). There are another two LVM lines shown in Fig. 1 at 1721.8 cm^{-1} ($\Gamma = 2.0 \text{ cm}^{-1}$) and 1751.9 cm^{-1} ($\Gamma = 3.5 \text{ cm}^{-1}$) which are detected only in samples grown at $T_G < 240^\circ\text{C}$. Their intensities are smaller by a factor of about 10 compared with the other three lines. Annealing at 600°C causes the complete disappearance of all the five LVM absorption lines, i.e., the responsible centers are destroyed at this temperature without any detectable increase of $[C_{As}]$.

These results suggest that in LT-GaAs:C grown at $T_G < 250^\circ\text{C}$ carbon is not incorporated substitutionally on As sites but in the form of at least three different complexes giving rise to the observed LVM absorption lines. For $250^\circ\text{C} < T_G < 400^\circ\text{C}$ two complexes coexist. These complexes, however, have still to be part of the GaAs lattice, as they contribute to the strain compensation as derived from the DCXRD experiments [13]. Especially in the region around $T_G = 220^\circ\text{C}$, where complete strain compensation is observed, this compensation must arise from these complexes rather than from C_{As} . The formation of As precipitates seems also to be affected by the different C incorporation since we observe As precipitates in annealed LT-GaAs:C with $p = 2.5 \times 10^{19} \text{ cm}^{-3}$ for $T_G = 210^\circ\text{C}$ whereas for $T_G = 250^\circ\text{C}$ no precipitates could be resolved by transmission electron microscopy.

Concerning the structure of the C complexes the following arguments must be considered. They certainly contain C, as they are observed only in C-doped LT-GaAs. Other defects must be involved which at $T = 600^\circ\text{C}$ can diffuse away from or onto the complexes to destroy or convert them. Due to the high content of the complexes (several 10^{19} cm^{-3}), these defects can only be As_{Ga} , interstitial As_i , and possibly vacancies.

As for the assignment of the vibrational lines, two types of bonds are possible taking into account the described experimental results. First, the complexes consist of a C–As core, i.e., the C–As vibration is responsible for the lines, where the manifold comes from the possibility to have additional defects in the neighborhood. The destruction by annealing might be explained by the diffusion away of As to form As precipitates. However, there are experiments [17] and calculations [18,19] for the C_{As} – As_i complex in bulk GaAs. These results suggest that the frequencies of the C–As vibrations are around 600 cm^{-1} , i.e., considerably smaller than those observed here.

Second, the complexes consist of a C–C core and the lines are due to C–C vibrations. In this case, the destruction of the complexes during annealing at 600°C by C diffusion is not possible. However, As_{Ga} and/or As_i can diffuse at this temperature onto the C–C complexes forming As-precipitates containing C-inclusions, which

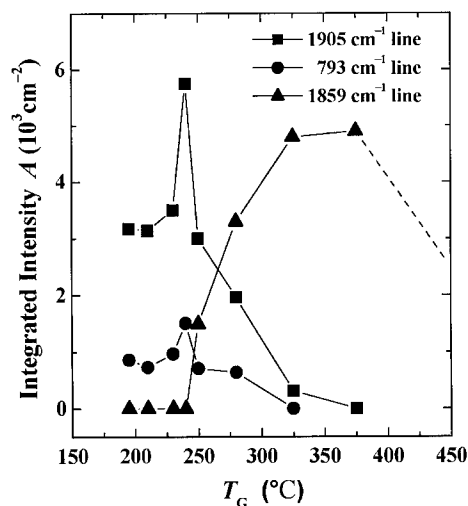


Fig. 3. Integrated intensities A of the vibrational absorption lines at 793 , 1859 , and 1905 cm^{-1} measured in LT-GaAs:C layers grown at different temperatures T_G . C concentration as in Fig. 2.

causes also a disappearance of the complexes. The vibrational frequencies of the C–C molecule in the gas phase are around 1800 cm^{-1} [20]. In highly carbon doped GaAs [21] and AlAs [22] two dicarbon centers have been detected by Raman scattering with their C–C stretching modes around 1750 and 1856 cm^{-1} . These centers were interpreted as $(\text{C-C})_{\text{As}}$ complexes having two different orientations. Therefore, the frequencies of the absorption lines due to the complexes in LT-GaAs:C are quite accurate by the region of the known C–C vibrations. This suggests that most probably C–C complexes with slightly different surroundings be formed in LT-GaAs:C during the growth. The line at 793 cm^{-1} can be interpreted as a bending mode of $\text{C}_{\text{LT}}^{\text{I}}$ with its stretching mode at 1905 cm^{-1} . The stretching modes of the $(\text{C-C})_{\text{As}}$ complexes in GaAs and AlAs [21,22] have no dipole moment and are, therefore, detectable only by Raman scattering. In LT-GaAs:C, however, the C–C bonds are certainly disturbed by adjacent intrinsic defects (As_{Ga} , As_{i} , vacancies) which cause a redistribution of the symmetric electron density around the C–C bond, so that a dipole moment of the C–C vibrations is induced and they become infrared active. Such an effect has been convincingly demonstrated for the vibrations of the H_2 molecule in Si disturbed by interstitial oxygen [23].

Acknowledgements

Part of this work has been supported by the German Bundesministerium für Bildung und Forschung.

References

- [1] F.W. Smith, A.R. Calawa, C.L. Chen, M.J. Manfra, L.J. Mahoney, *IEEE Electron Dev. Lett.* 9 (1988) 77.
- [2] J.F. Whitaker, *Mater. Sci. Eng. B* 22 (1993) 61.
- [3] J. Herfort, G. Apostolopoulos, K.-J. Friedland, H. Kostial, W. Ulrici, L. Däweritz, M. Leitner, P. Glas, K.H. Ploog, *Jpn. J. Appl. Phys.* 39 (2000) 2452.
- [4] D.C. Look, D.C. Walters, G.D. Robinson, J.R. Sizelove, M.G. Mier, C.E. Stutz, *J. Appl. Phys.* 74 (1993) 306.
- [5] X. Liu, A. Prasad, J. Nishio, E.R. Weber, Z. Lilienthal-Weber, W. Walukiewicz, *Appl. Phys. Lett.* 67 (1995) 279.
- [6] P. Specht, R.C. Lutz, R. Zhao, E.R. Weber, W.K. Liu, K. Bacher, F.J. Towner, T.R. Steward, M. Luysberg, *J. Vac. Sci. Technol. B* 17 (1999) 1200.
- [7] M. Haiml, U. Siegner, F. Morier-Genoud, U. Keller, M. Luysberg, P. Specht, E.R. Weber, *Appl. Phys. Lett.* 74 (1999) 1269.
- [8] D.E. Bliss, W. Walukiewicz, K.T. Chan, J.W. Ager III, S. Tanigawa, E.E. Haller, *Mater. Res. Soc. Symp. Proc.* 241 (1992) 93.
- [9] M.R. Melloch, N. Otsuka, K. Mahalingham, C.L. Chang, J.M. Wodall, *J. Appl. Phys.* 72 (1992) 3509.
- [10] P. Specht, H. Sohn, M. Luysberg, A. Prasad, J. Gebauer, R. Krause-Rehberg, E.R. Weber, *Mater. Sci. Forum* 258–263 (1997) 951.
- [11] K. Mochizuki, T. Nakamura, *Appl. Phys. Lett.* 65 (1994) 2066.
- [12] W.K. Liu, D.I. Lubyshev, P. Specht, R. Zhao, E.R. Weber, J. Gebauer, A.J. SpringThorpe, R.W. Streater, S. Vijarnwannaaluk, W. Songprakob, R. Zallen, *J. Vac. Sci. Technol. B* 18 (2000) 1594.
- [13] J. Herfort, W. Ulrici, M. Moreno, K.H. Ploog, *J. Crystal Growth* (2001), in press.
- [14] M.O. Manasreh, D.C. Look, K.R. Evans, C.E. Stutz, *Phys. Rev. B* 41 (1990) 10272.
- [15] P. Silverberg, P. Omling, L. Samuelson, *Appl. Phys. Lett.* 52 (1988) 1689.
- [16] H.Ch. Alt, B. Dischler, *Appl. Phys. Lett.* 66 (1995) 1689.
- [17] G.A. Gledhill, S.B. Upadhyay, M.J.L. Sangster, R.C. Newman, *J. Mol. Struct.* 247 (1991) 313.
- [18] M.J.L. Sangster, R.C. Newman, G.A. Gledhill, S.B. Upadhyay, *Semicond. Sci. Technol.* 7 (1992) 1295.
- [19] R. Jones, S. Öberg, *Semicond. Sci. Technol.* 7 (1992) 855.
- [20] K.P. Huber, G. Herzberg, in: G. Herzberg (Ed.), *Molecular Spectra and Molecular Structure*, Van Nostrand Reinhold, New York, 1979, p. 114.
- [21] J. Wagner, R.C. Newman, B.R. Davidson, S.P. Westwater, T.J. Bulloch, T.B. Joyce, C.D. Latham, R. Jones, S. Öberg, *Phys. Rev. Lett.* 78 (1997) 74.
- [22] B.R. Davidson, R.C. Newman, C.D. Latham, R. Jones, J. Wagner, C.C. Button, P.R. Briddon, *Phys. Rev. B* 60 (1999) 5447.
- [23] R.E. Pritchard, M.J. Ashwin, J.H. Tucker, R.C. Newman, E.C. Lightowers, M.J. Binns, S.A. McQuaid, R. Falster, *Phys. Rev. B* 56 (1997) 13118.



ELSEVIER

Physica B 308–310 (2001) 827–830

PHYSICA B

www.elsevier.com/locate/physb

Study of depth distribution of metastable hydrogen-related defects in n-type GaAs

O.A. Soltanovich^{a,*}, E.B. Yakimov^a, V.A. Kagadei^b, L.M. Romas^b

^a *Institute of Microelectronics Technology RAS, 142432 Chernogolovka Moscow district, Chernogolovka, Russia*

^b *Research Institute of Semiconductor Devices, Tomsk, Russia*

Abstract

Depth distribution and annealing behavior of deep level defects in epitaxial n-GaAs exposed by atomic hydrogen treatment are investigated. By the analysis of hydrogen-related metastable defect M3/M4 and EL2 center depth profiles it is shown that M3 defect contains one hydrogen atom and the relation of M3 defect with EL2 is quantitatively confirmed. The reversible changes of space charge density under metastable transition are revealed. It is shown that these changes are determined by the second component of M4 defect that is one more metastable hydrogen-related defect could be assumed. © 2001 Elsevier Science B.V. All rights reserved.

Keywords: GaAs; Hydrogen; M3/M4 defects; Metastability

1. Introduction

The nature and properties of metastable M3/M4 defects firstly observed in n-GaAs grown by metal-organic chemical-vapor deposition (MOCVD) [1,2] were extensively studied [3–7]. It was shown that these defects are hydrogen-related [3] and that their formation correlates with the existence of arsenic antisite [4] or EL2 center [5,6], which are the most probable precursors for the M3/M4 defects.

In spite of the studies, the knowledge concerning the formation and behavior of M3/M4 defects is still incomplete. So, the relationship between EL2 centers and M3/M4 defects was not quantitatively supported. In addition, in the most studies the concentration of M4 defect essentially exceeds that of M3 and can be even higher than the initial EL2 concentration. To explain this contradiction, it was assumed [6] that the deep level transient spectroscopy [8] (DLTS) peak related to M4 consisted of two components. Recently, these two components were separated [7] by the isothermal constant-capacitance-voltage transient spectroscopy (CCVTS) [9]. One of these components was assumed

to be the second metastable state of M3 defect while the origin of other one is unclear up to now. Moreover, in the mentioned works the “average concentration over some region” was used for the comparison of M3, M4 and EL2 concentrations that could lead to wrong conclusions if the defects have the different depth distribution. To avoid the confusions and to obtain the complete picture of defect transformations, the accurate depth profiling is required.

In the present work, the depth distributions of all electrically active deep level (DL) defects after each step of sample treatment (hydrogenation, reverse bias (RBA) and zero bias annealing (ZBA)) are studied by DLTS and capacitance-voltage (CV) profiling. The analysis of depth profiles quantitatively confirms that EL2 is a precursor for the M3 formation. It is shown that the M3 center contains one atom of hydrogen. It is found that changes in free carrier concentration under the metastable transition are determined by second metastable component of M4 defect.

2. Experimental

The samples of Sn doped n-GaAs with the carrier concentration $(4\text{--}5) \times 10^{15} \text{ cm}^{-3}$ grown by the metal-

*Corresponding author. Fax: +7-095-962-8047.

E-mail address: solt@ipmt-hpm.ac.ru (O.A. Soltanovich).

organic vapor-phase-epitaxy (MOVPE) on (100) n^+ -GaAs:Te substrates were used for atomic hydrogen exposure. Ohmic contacts were made by the electrochemical deposition of GeNi+Au with subsequent annealing at 450°C for 5 min. Before the hydrogen treatment a native oxide was removed in the mixture $\text{NH}_4\text{OH}:\text{H}_2\text{O}$ (1:5) and a 5 nm SiO_2 film was deposited on the surface to avoid the direct impact of hydrogen atoms. The samples were treated in atomic hydrogen flow produced by the arc-reflected-discharge-based source with a hollow cathode and a self-heating electrode [10]. The samples were placed at the distance of 12 cm from the source of atomic hydrogen that prevents a surface damage. Sample temperature during the treatment was 200°C or 300°C (below referred to as samples 2 and 3, respectively) and the exposure time was 45 min. The Schottky diodes for the CV and DLTS measurements with an area of $1.95 \times 1.95 \text{ mm}^2$ were formed by thermal evaporation of Au through the windows opened in SiO_2 . Control samples were made by the same procedure excluding the atomic hydrogen treatment.

Annealing (400 K, 15 min) under 10 V reverse or zero bias was used to stimulate the transitions between the metastable states of M3/M4 defect. Depth distributions of all DL defects were controlled by the DLTS technique. To avoid defect transformations under DLTS spectra recording, the temperature during measurements did not exceed 310 K. The isothermal capacitance transient spectroscopy (ICTS) [11] at 295 K with following computer processing of capacitance transient was used for EL2 profiling. The changes in free carrier concentration profiles were controlled by the CV technique.

3. Results and discussion

3.1. DL defects introduced under atomic hydrogen treatment

Two DL defects with energy levels $E_C-0.39 \text{ eV}$ and $E_C-0.80 \text{ eV}$ are found in the DLTS spectra of control sample (Fig. 1, curve 1). The deeper level corresponds to well-known EL2 center while the shallower one is similar to EL5 [12]. Hydrogenation leads to an appearance of three DL in the DLTS spectra while the EL2 peak amplitude is significantly decreased. The most prominent of arising peaks ($E_C-0.54 \text{ eV}$) disappears under following RBA while the other large peak ($E_C-0.29 \text{ eV}$) appears (Fig. 1, curves 2, 3). These changes are reversible under subsequent ZBA and RBA. Parameters and behavior of these traps completely correspond to those of known metastable M3/M4 defects. The changes in EL2 concentration under annealing are negligible in

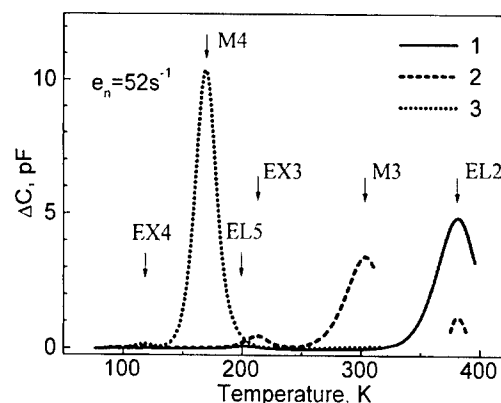


Fig. 1. DLTS spectra of n-GaAs samples after hydrogenation and RBA. 1—control sample, 2—after hydrogenation (sample 3), 3—after hydrogenation and RBA (sample 3). The EL2 peak amplitude after hydrogenation is obtained from ICTS.

comparison with the EL2 decrease due to hydrogenation.

Concentrations of other two peaks with energy levels $E_C-0.46 \text{ eV}$ and $E_C-0.19 \text{ eV}$ (EX3 and EX4 in Fig. 1) are found to decrease with a depth therefore they also could be associated with hydrogen. But because of rather small concentration and annealing behavior revealed, they unlikely participate in transformations of EL2 and M3/M4 defects and will not be discussed here.

3.2. Depth profiles of DL defects in hydrogenated samples

One can see (Fig. 2a) that the tails of M3 profiles and a depth dependence of the difference between the shallow donor concentrations in the bulk and in the hydrogenated near-surface layers ΔN_d for both type of samples (2 and 3) can be approximated by the exponential law. As shown in Ref. [13], if the hydrogen concentration decays exponentially (that is often the case for the strong hydrogen capture), the tail part of hydrogen-related defect depth distribution is described as $NH_i \propto \exp(-ix/L_0)$, where NH_i is the concentration of centers containing i hydrogen atoms, x is the depth from the surface, L_0 is the characteristic length of hydrogen depth distribution in the crystal. Since L_0 can be estimated from the distribution of ΔN_d , the comparison of hydrogen-related defect profile with that of ΔN_d allows to derive the number of hydrogen atoms in the complex.

The values of ΔN_d and L_0 in the samples 2 and 3 are different (see Fig. 2a). But for the both samples the slopes of the M3 depth profile in semi-logarithmic scale are close to that of corresponding ΔN_d profiles. Since shallow donors are known to be passivated by one hydrogen atom [14], it can be concluded that M3 center also contains one hydrogen atom.

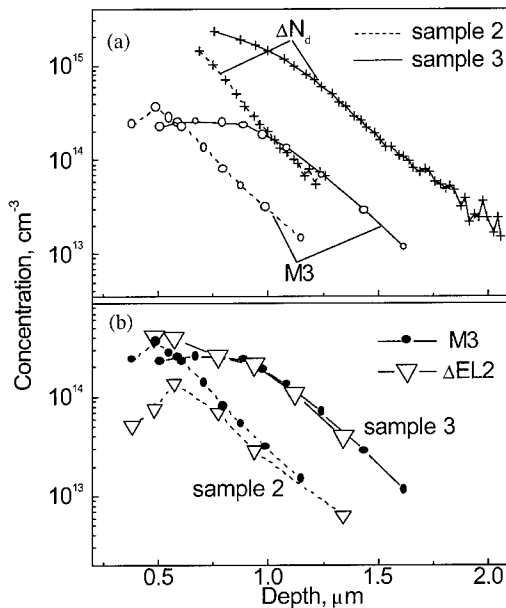


Fig. 2. Depth profiles in as-hydrogenated samples 2 and 3. (a) M3 and passivated shallow donors ΔN_d ; (b) M3 and the EL2 deficiency caused by hydrogenation.

As seen in Fig. 2b, the EL2 deficiency caused by hydrogenation ($\Delta EL2$) rather well coincides with the M3 depth profile for the samples with different hydrogen profiles. This evidences that EL2 or products of its dissociation participate in the M3/M4 formation and quantitatively confirms the conclusion made in Refs. [5,6].

3.3. Two metastable components of M4 defect

As seen in Fig. 3, the M4 concentration essentially exceeds that of M3 near the surface but this difference comes to be rather small at higher depths. This corresponds to the assumption [6,7] that M4 consists of two components which below will be referred to as M4a (the other metastable state of M3 defect) and M4b, and shows that the concentration of M4b component also decreases with the depth. Since the total M4 concentration near the surface is higher than that of EL2 in the control sample (see Fig. 3), M4b defect could not be related to EL2 center.

It is found that the reversible changes in a free carrier concentration accompany the metastable transition (Fig. 4). Under RBA when M4 peak appears the free carrier concentration is increased by $\Delta N_{RBA}(x)$. Under ZBA, when M4 peak disappears and M3 peak is recovered, the carrier concentration decreases to that before RBA. The sum of ΔN_{RBA} and M3 depth profiles well coincides with the profile of M4 (see Fig. 3). It brings us to the conclusion that the changes in carrier

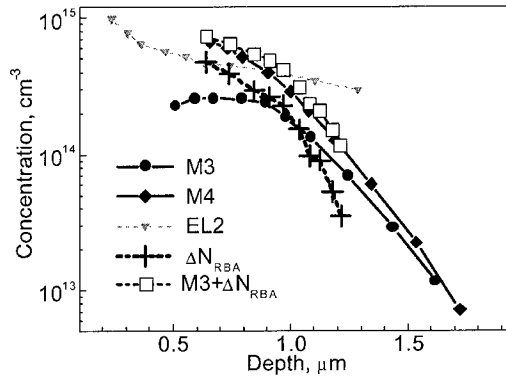


Fig. 3. Depth profiles of M3 and M4 defects in the sample 3 in comparison with that of EL2 in control sample and with the ΔN_{RBA} profile in sample 3.

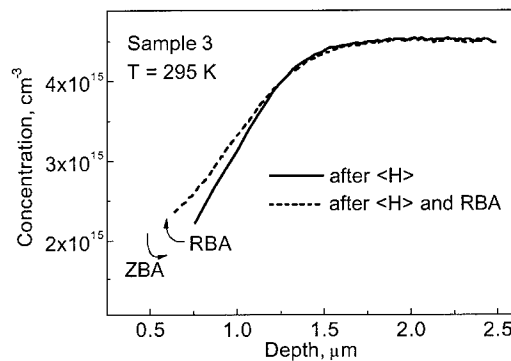


Fig. 4. The reversible changes in free carrier concentration in hydrogenated n-GaAs under the metastable transition.

concentration under metastable transition are determined by the M4b component. It should be noted that the metastable behavior of charge density was observed in Ar-plasma-irradiated n-GaAs [15] but no correlation with the changes in DL spectra was established.

The analysis of the possible (donor or acceptor) nature of the regarded defects based on value and sign of ΔN_{RBA} gives an additional information about the second metastable state of M4b. As M3 was identified as a donor [2,7], two possible models satisfy our experimental data. If both M4a and M4b defects are donors, then the second metastable state of M4b (let us call it M3b) is electrically neutral, i.e. it is electrically inactive or has a donor level in the lower half of the gap. If M4a is a donor and M4b is an acceptor, then M3b should be an acceptor with the energy level in the lower half of the gap that leads to a compensation of shallow donors. Taking into account that one of the M4 defect components was shown to be a donor while the other one an acceptor [7], the second model looks more preferable.

Thus, the existence of another metastable hydrogen-related defect different from M3/M4a could be assumed. This defect is revealed as M4b in one state and, more probably, has an acceptor DL in the lower half of the gap in the other one. The depth profile of M4b component obtained as difference of M4 and M3 defect depth distributions is steeper than that of M3. Thus, M4b should contain more than one hydrogen atom.

4. Conclusion

New data concerning metastable hydrogen-related defects M3/M4 are obtained from the analysis of the results of DLTS and CV profiling. It is shown that M3 defect contains one hydrogen atom and that EL2 defect or products of its dissociation participate in formation of M3. The reversible changes of free carrier concentration under metastable transition are revealed. It is shown that these changes are associated with the changes in the M4b component charge state and the existence of one more metastable hydrogen-related defect can be assumed.

References

- [1] W.R. Buchwald, N.M. Johnson, L.P. Trombetta, *Appl. Phys. Lett.* 50 (1987) 1007.
- [2] W.R. Buchwald, G.J. Gerardi, E.H. Poindexter, N.M. Johnson, H.G. Grimmeiss, D.J. Keeble, *Phys. Rev. B* 40 (1989) 2940.
- [3] A.W.R. Leitch, Th. Prescha, J. Weber, *Phys. Rev. B* 45 (1992) 14400.
- [4] A.S. Tabata, M.A.A. Pudensi, A.M. Machado, *J. Appl. Phys.* 65 (1989) 4076.
- [5] T. Okumura, T. Shinagawa, *Mater. Res. Soc. Symp. Proc.* 513 (1998) 257.
- [6] T. Shinagawa, T. Okumura, *Jpn. J. Appl. Phys.* 37 (1998) 1939.
- [7] Y. Tokuda, K. Kamiya, T. Okumura, *J. Appl. Phys.* 88 (2000) 1943.
- [8] D.V. Lang, *J. Appl. Phys.* 45 (1974) 3023.
- [9] J.-J. Shiao, A.L. Fahrenbruch, R.H. Bube, *J. Appl. Phys.* 61 (1987) 1340.
- [10] V.A. Kagadei, D.I. Proskurovsky, *J. Vac. Sci. Technol. A* 16 (1998) 2556.
- [11] H. Okushi, Y. Tokumaru, *Jpn. J. Appl. Phys.* 19 (1980) L335.
- [12] G.M. Martin, A. Mitonneau, A. Mircea, *Electron. Lett.* 13 (1977) 191.
- [13] N. Yarykin, J.-U. Sachse, H. Lemke, J. Weber, *Phys. Rev. B* 59 (1999) 5551.
- [14] S.J. Pearton, J.W. Corbett, M. Stavola, *Hydrogen in Crystalline Semiconductors*, Springer-Verlag, Heidelberg, 1992, pp. 83–88.
- [15] K. Wada, H. Nakanishi, *Mater. Sci. Forum* 258–263 (1997) 1051.



ELSEVIER

Physica B 308–310 (2001) 831–834

PHYSICA B

www.elsevier.com/locate/physb

Zinc diffusion enhanced Ga diffusion in GaAs isotope heterostructures

H. Bracht^{a,*}, M.S. Norseng^b, E.E. Haller^b, K. Eberl^c

^a *Institut für Materialphysik, University of Münster, Wilhelm-Klemm Str. 10, 48149 Münster, Germany*

^b *Lawrence Berkeley National Laboratory and University of California at Berkeley, MS 2-200, 1 Cyclotron Rd, Berkeley, CA 94720, USA*

^c *Max-Planck Institut für Festkörperforschung, Heisenbergstr. 1, 70569 Stuttgart, Germany*

Abstract

We have investigated the simultaneous diffusion of Zn and Ga in a ⁶⁹GaAs/⁷¹GaAs isotope multilayer structure at temperatures between 618°C and 714°C. Diffusion profiles of Zn, ⁶⁹Ga, and ⁷¹Ga were measured with secondary ion mass spectrometry. Accurate modeling of the simultaneous diffusion of Zn and Ga is achieved on the basis of a Ga vacancy and Ga interstitial controlled mode of Zn diffusion. This result is at variance with the generally accepted model of Zn diffusion via Ga self-interstitials. We discuss the consequences of our approach against the background of Zn and Cd diffusion experiments performed earlier. © 2001 Elsevier Science B.V. All rights reserved.

PACS: 61.72.Ji; 66.30.Dn; 66.30.Hs; 66.30.Jt

Keywords: Gallium arsenide isotope structure; Gallium self-diffusion; Zinc diffusion; Zinc-induced interdiffusion

1. Introduction

Following the conclusions of Gösele and Morehead [1] and more recent results of Yu et al. [2] and Bösker et al. [3], Zn diffuses in GaAs via the kick-out mechanism



Zn_i^+ , Zn_{Ga}^- , and $\text{I}_{\text{Ga}}^{2+}$ denote, interstitial Zn, Zn occupying a Ga lattice site, and a Ga self-interstitial, respectively, with charge states indicated by the corresponding superscripts. In addition to a contribution of $\text{I}_{\text{Ga}}^{2+}$, a contribution of $\text{I}_{\text{Ga}}^{3+}$ was proposed by Bösker et al. [3].

The research effort aimed at understanding the diffusion behavior of Zn stems, in part, from the discovery of Zn-induced disordering of AlAs/GaAs superlattice structures [4]. A qualitative simulation of Zn-induced interdiffusion of AlAs/GaAs layers on the

basis of reaction (1) has been performed by Zimmermann et al. [5]. These authors concluded that the enhanced Al–Ga interdiffusion is mainly caused by the increase in the equilibrium concentration of $\text{I}_{\text{Ga}}^{2+}$ with increasing Zn doping. However, a more quantitative analysis of Zn-induced AlAs/GaAs layer disordering is difficult because the Al–Ga interdiffusion is concentration-dependent [6]. Moreover, little is known about Zn diffusion in AlAs. These drawbacks are overcome by studying Zn diffusion in ⁶⁹GaAs/⁷¹GaAs multilayer isotope structures.

2. Experimental

An undoped GaAs isotope superlattice with 10 periods of ⁶⁹GaAs/⁷¹GaAs layers was grown by molecular beam epitaxy on a semi-insulating GaAs substrate at 580°C. The thickness of each GaAs isotope layer is about 45 nm. Rectangular samples, 1 × 3–4 mm² in size, were cut and rinsed in organic solvents, etched in diluted HCl and purged with deionized water. The isotope samples were placed on a

*Corresponding author. Tel.: +49-251-833-9004; fax: +49-251-833-8346.

E-mail address: bracht@uni-muenster.de (H. Bracht).

polished semi-insulating GaAs carrier wafer and sealed in evacuated quartz ampoules together with about 30 mg of a Ga–Zn alloy. Alloys with 10 and 20 at% Zn were used as diffusion source to alter the Zn partial pressure and hence the concentration of Zn at the sample surface. Diffusion anneals were performed at temperatures between 618°C and 714°C. The temperature was controlled with an accuracy of ± 2 K. The diffusion process was terminated by rapidly cooling the ampoule with water down to room temperature. After annealing the surface of the samples remained specular.

Concentration profiles of Zn, ^{69}Ga , and ^{71}Ga were measured with secondary ion mass spectrometry (SIMS) (CAMECA IMS-3f) using a Cs^+ ion-beam with an energy of about 2 keV. The depths of the craters left from the SIMS analysis were measured with a surface profilometer with an accuracy of about 10%. The secondary ion counts of Zn, ^{69}Ga and ^{71}Ga were converted into concentrations taking into account Zn-implanted GaAs calibration standards and the known compositions of the stable Ga isotopes in natural GaAs. Additionally, the Zn-diffused GaAs carrier wafers were analyzed with electrochemical capacitance voltage (ECV) profiling to determine the maximum Zn-doping level.

3. Experimental results

Fig. 1 shows concentration profiles of Zn and Ga after annealing at 666°C for 180 min utilizing a 10% Ga–Zn

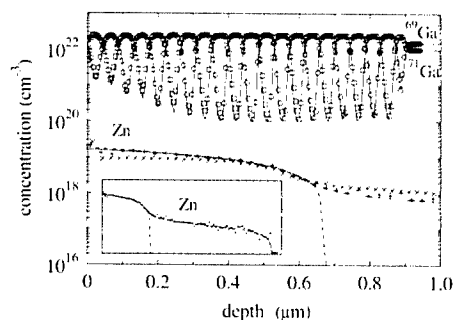


Fig. 1. Concentration depth profiles of ^{69}Ga (○), ^{71}Ga (□) and Zn (+) measured with SIMS after diffusion of Zn in a GaAs isotope heterostructure at 666°C for 180 min utilizing a 10 at% Ga–Zn alloy source. The concentration of electrically active Zn (×) measured by means of ECV profiling is shown for comparison. For clarity only very second data point is plotted. The solid lines represent simulations of Zn and Ga diffusion which were performed on the basis of reactions (2)–(4). The inset shows the whole Zn profile with a penetration depth of about 2.3 μm. The dashed line represents a simulation of Zn diffusion on the basis of reaction (1).

source. Within experimental accuracy the concentrations of total and electrically active Zn are identical. Similar Zn and Ga profiles were obtained after diffusion at 618°C, 666°C and 714°C. All Zn profiles exhibit a kink-and-tail shape (see inset of Fig. 1). Enhanced Ga diffusion is only observed across the near-surface kink of the Zn profile.

4. Discussion

In accord with earlier Zn diffusion studies [2,3], we attempted to describe the simultaneous diffusion of Zn and Ga on the basis of reaction (1). Partial differential equations which consider the diffusion and reaction of the point defects involved and a differential equation for Ga diffusion were solved numerically. Assuming that under the considered Zn-doping conditions I_{Ga}^{2-} mainly controls Ga diffusion, the experimental Ga profiles could be reproduced (not shown in Fig. 1). However, the calculated Zn profile only describes the near-surface kink of the experimental profile. The profile tail at Zn concentrations of about 10^{18} cm^{-3} and below is not reproduced (see dashed line in Fig. 1). All experiments were first analyzed on the basis of reaction (1), although it is obvious that the Zn profiles cannot be completely described. Solid symbols in Fig. 2a and b show the I_{Ga}^{2-} - and Zn-related diffusion coefficients, respectively, obtained from this analysis. Fig. 2a reveals that the I_{Ga}^{2-} contribution to Ga self-diffusion (see solid circles) is in good agreement with results reported by Yu et al. [2] (see lower solid and dashed line). This may indicate that the Zn profiles analyzed by Yu et al. actually also have an extended tail. Unfortunately, this cannot be verified because the profiles analyzed by Yu et al. extend only to concentrations of 10^{18} cm^{-3} .

Fig. 2b illustrates that the Zn diffusion coefficients (see solid square) which were obtained on the basis of reaction (1) systematically deviate from literature data (see solid and dashed line). This deviation shows that Zn diffusion is systematically underestimated in the case when the tail of the experimental Zn profile is ignored.

Kink-and-tail profiles of Zn are known to develop in the very high Zn concentration region ($C_{\text{Zn}} \geq 10^{20} \text{ cm}^{-3}$). These profiles are associated with the formation of voids and interstitial-type dislocation loops [2,8–11]. After Zn diffusion the dopant concentration profile in our isotope samples looks similar to the profile of Zn-diffused natural GaAs samples which contain no voids or dislocation loops [3]. These profiles given by Bösker et al. [3] also reveal a kink-and-tail shape although no extended defects were detected. The authors proposed that Zn diffusion is controlled not only by I_{Ga}^{2-} but also by I_{Ga}^{3+} and they could fit their experimental profiles fairly well. However, a major drawback of their diffusion model is that the high equilibrium concentra-

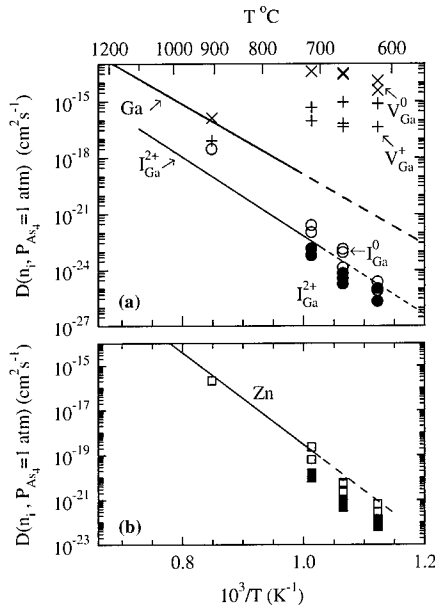
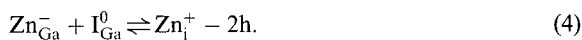


Fig. 2. Temperature dependence of (a) V_{Ga} and I_{Ga} contributions to Ga diffusion and (b) Zn diffusion in GaAs. Data were obtained from modeling the simultaneous diffusion of Zn and Ga in isotope heterostructures and from fitting the Zn profile shown in Fig. 3. All data were reduced to electronically intrinsic conditions and an As_4 pressure of 1 atm. (a): I_{Ga}^{2+} (thin solid line: [2], \bullet : this work), I_{Ga}^0 (\circ : this work), V_{Ga}^0 (\times : this work), and V_{Ga}^+ ($+$: this work) contributions to Ga diffusion in comparison to the direct measured Ga diffusivity (thick solid line: [7]). (b): Zn diffusivity obtained from modeling Zn diffusion on the basis of reaction (1) (\blacksquare) or reactions (2)–(4) (\square). Solid and dashed lines represent the Zn diffusivity under isoconcentration conditions [2].

tion of I_{Ga}^{2+} , which is required to reproduce the tail of the Zn profile, leads to almost complete electrical compensation of the Zn acceptors near the diffusion front [3]. Had the authors considered compensation, the calculated Zn profile would not be as steep at the diffusion front as the profile observed experimentally.

Systematic simulations of Zn diffusion show that kink-and-tail profiles can be described by



V_{Ga}^0 , V_{Ga}^+ , I_{Ga}^0 , and h denote neutral and singly positively charged Ga vacancies, neutral Ga self-interstitials, and holes, respectively. On the basis of this model the kink-and-tail Zn profile as well as the interdiffusion of the $^{69}\text{GaAs}/^{71}\text{GaAs}$ layers are reproduced as demonstrated by the solid lines in Fig. 1. Moreover, this approach solves the compensation

problem associated with the $I_{\text{Ga}}^{2+,3+}$ controlled diffusion mode proposed by Bösker et al. [3,12] for Zn and Cd diffusion in GaAs whose diffusion, as shown in Fig. 3, is also accurately described by reactions (2)–(4). On the basis of this approach the near surface kink is a consequence of a V_{Ga}^0 and V_{Ga}^+ controlled mode of dopant diffusion whereas the tail of the profiles is determined by I_{Ga}^0 . Accordingly, the interdiffusion of the $^{69}\text{GaAs}/^{71}\text{GaAs}$ layers, which is limited to the near-surface kink of the Zn profile (see Fig. 1), should be controlled by V_{Ga}^0 and V_{Ga}^+ .

In order to test the consistency of our Zn diffusion model, the values obtained from fitting our experimental profiles are shown in Figs. 2a and b in comparison to data from Ga self-diffusion and Zn diffusion under isoconcentration conditions, respectively. Based on the generally accepted interpretation that Ga diffusion in intrinsic GaAs is mainly controlled by Ga vacancies [7], the I_{Ga}^0 component of Ga diffusion is lower than Ga self-diffusion. Fitting of the Zn and Cd profiles shown in Fig. 3 yields values for the I_{Ga}^0 component of Ga diffusion which are mutually consistent within a factor of 3. Moreover, Fig. 2b indicates that the Zn diffusivity is in excellent agreement with data of Zn diffusion under isoconcentration conditions. However, the V_{Ga}^0 and V_{Ga}^+ components which were obtained from fitting the simultaneous diffusion of Zn and Ga in the GaAs isotope superlattice exceed Ga self-diffusion (see Fig. 2a). On the other hand, data for these components used to model the Zn and Cd profiles for As-rich conditions shown in Fig. 3 are in acceptable agreement with Ga self-diffusion whereas the Cd profile for Ga-rich condition yields a V_{Ga}^0 component which is two orders of magnitude higher than the value for As-rich conditions. This shows that the V_{Ga} component of Ga diffusion deduced from Zn diffusion under Ga-rich conditions and reduced to standard conditions (electronically intrinsic conditions and an As_4 pressure of 1 atm) exceeds the data for the directly measured Ga

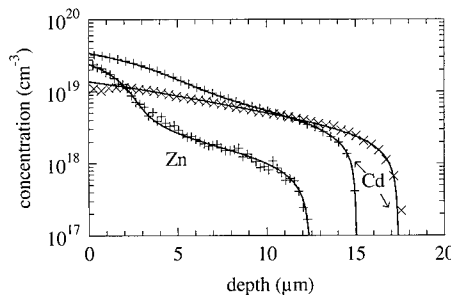


Fig. 3. Concentration depth profiles of Zn after annealing at 906°C for 29 h under an As_4 pressure of 0.5 atm [3] and of Cd after annealing at 907°C for 7 d under Ga-rich (\times) and As-rich ($+$) ambients [12]. Solid lines represent best fits on the basis of reactions (2)–(4).

self-diffusion. This finding is taken as an evidence that reactions (2)–(4) very likely not represent the actual mechanisms which control the interference between Zn and Ga diffusion and the diffusion of Zn and Cd in GaAs although these reactions provide a remarkable good fit to the experimental profiles. It is noteworthy that our approach also describes the diffusion profiles of Zn in GaSb [13] and GaP [14] more accurately than reaction (1). However, Zn diffusion in GaSb is accurately described by reaction (4) only yielding data for the I_{Ga}^0 component of Ga diffusion which are consistent with the directly measured Ga diffusion coefficients [13]. On the other hand, modeling of Zn diffusion in GaP on the basis of reactions (2) to (4) yields V_{Ga}^0 and V_{Ga}^+ components which also exceed data for Ga diffusion in GaP [14].

5. Conclusions

Accurate modeling of the interference between Zn and Ga diffusion in GaAs isotope heterostructures and of recent Zn and Cd diffusion profiles given in the literature suggests that V_{Ga}^0 , V_{Ga}^- and I_{Ga}^0 rather than I_{Ga}^{2+} and I_{Ga}^{3+} control Zn and Cd diffusion. On the basis of this model, the Zn-induced interdiffusion of $^{69}\text{GaAs}/^{71}\text{GaAs}$ layers seems to be controlled by V_{Ga}^0 and V_{Ga}^- . However, the V_{Ga}^0 and V_{Ga}^- contributions to Ga diffusion exceed the data for Ga self-diffusion even after a reduction to standard conditions whereas corresponding data for I_{Ga}^0 are consistent with Ga self-diffusion. The physical reason for this deviation, which appears to be limited to Ga-rich and heavy p-type doping conditions, is not yet known but indicates that the proposed diffusion model needs to be improved. An improved model can be based on reactions similar to those considered in this paper but may involve e.g. $V_{\text{Ga}}V_{\text{As}}$ or ZnV defect pairs or even more complex defects. Although a consistent interpretation of Zn diffusion in GaAs is not yet evident, our results on the interference of Zn and Ga diffusion put the earlier interpretation of Zn and Cd diffusion in GaAs into question and will stimulate further investigations.

Acknowledgements

H.B. acknowledges a Feodor Lynen fellowship from the Alexander von Humboldt-Stiftung and is indebted to N.A. Stolwijk for valuable discussions. This work was supported in part by the Director, Office of Energy Research, Office of Basic Energy Sciences, Materials Sciences Division of the US Department of Energy under Contract No. DE-AC03-76SF00098, by US NSF Grant DMR-97 32707, by the Fond der Chemischen Industrie and by a Max-Planck Research Award.

References

- [1] U. Gösele, F. Morehead, J. Appl. Phys. 52 (1981) 4617.
- [2] S. Yu. T.Y. Tan, U. Gösele, J. Appl. Phys. 69 (1991) 3547.
- [3] G. Bösker, N.A. Stolwijk, H.-G. Hettwer, A. Rucki, W. Jäger, U. Södervall, Phys. Rev. B 52 (1995) 11927.
- [4] W.D. Laidig, N. Holonyak Jr., M.D. Camras, K. Hess, J.J. Coleman, P.D. Dapkus, J. Bardeen, Appl. Phys. Lett. 38 (1981) 776.
- [5] H. Zimmermann, U. Gösele, T.Y. Tan, J. Appl. Phys. 73 (1993) 150.
- [6] H. Bracht, E.E. Haller, K. Eberl, M. Cardona, Appl. Phys. Lett. 74 (1999) 49.
- [7] H. Bracht, M. Norseng, E.E. Haller, K. Eberl, M. Cardona, Solid State Commun. 112 (1999) 301.
- [8] H.R. Winteler, Helv. Phys. Acta 43 (1970) 496.
- [9] H.R. Winteler, Helv. Phys. Acta 44 (1971) 451.
- [10] M. Luysberg, W. Jäger, K. Urban, M. Schänzer, N.A. Stolwijk, H. Mehrer, Mater. Sci. Eng. B 13 (1992) 137.
- [11] W. Jäger, A. Rucki, K. Urban, H.-G. Hettwer, N.A. Stolwijk, H. Mehrer, T.Y. Tan, J. Appl. Phys. 74 (1993) 4409.
- [12] G. Bösker, N.A. Stolwijk, H. Mehrer, U. Södervall, W. Jäger, J. Appl. Phys. 86 (1999) 791.
- [13] S.P. Nicols, H. Bracht, M. Benamara, Z. Liliental-Weber, E.E. Haller, Physica B, in these Proceedings (ICPS-21), Physica B 308–310 (2001).
- [14] J. Pöpping, N.A. Stolwijk, U. Södervall, Ch. Jäger, W. Jäger, Physica B, in these Proceedings (ICPS-21), Physica B 308–310 (2001).



ELSEVIER

Physica B 308–310 (2001) 835–838

PHYSICA B

www.elsevier.com/locate/physb

Vibrational modes of a hydrogen-impurity centre in LEC-GaAs

W. Ulrici^{a,*}, M. Jurisch^b^a Paul-Drude-Institut für Festkörperelektronik, Hausvogteiplatz 5-7, D-10117 Berlin, Germany^b Freiburger Compound Materials GmbH, Am Junger Löwe Schacht 5, D-09599 Freiberg, Germany

Abstract

Two sharp vibrational absorption lines at 3079.2 and 983.3 cm⁻¹ are investigated, occurring in semi-insulating LEC-grown GaAs with their intensities strictly correlated. After doping with deuterium, two additional correlated lines appear at 2288.3 and 729.1 cm⁻¹. These lines are due to the stretching and wagging mode of a single hydrogen (or deuterium) atom bonded to a light impurity atom, most probably oxygen. Illumination with sub-band gap light at $T < 100$ K results in a decrease of the intensity of the four lines and the simultaneous appearance of four new ones. This effect is explained as due to the recharging of the hydrogen centre by capturing photogenerated holes. The centre forms an electronic level in the gap between E_v and about $E_v + 0.5$ eV. © 2001 Elsevier Science B.V. All rights reserved.

PACS: 61.72.-Y; 63.20.Pw; 78.30.Fs

Keywords: GaAs; Hydrogen; Deuterium; Vibrational modes

1. Introduction

Hydrogen is a residual impurity in the III–V materials grown by the liquid encapsulation Czochralski (LEC) technique. The LEC-GaAs crystals with diameters up to 6 in are grown for semi-insulating substrates used in the production of microelectronic devices. The synthesis and growth of the GaAs also imply the unavoidable presence of further light-element impurities such as carbon, boron, nitrogen, and oxygen in the grown material. The origin of hydrogen in the material is the water-containing boric oxide (B₂O₃) encapsulant.

By the FT-IR spectroscopy, several vibrational absorption lines have been detected on LEC-GaAs in the frequency region above 3000 cm⁻¹ [1,2]. The high frequencies indicate that the stretching modes of bonded hydrogen must be responsible for these lines. One of these lines at 3300.0 cm⁻¹ ($T = 7$ K) could be identified as due to an (O–H) centre by the detection of the ¹⁸O-isotope satellite. This O–H bond can orient along two

nonequivalent crystallographic directions as derived from uniaxial-stress experiments [1]. Another two lines at 3235.2 and 3108.0 cm⁻¹ have been tentatively assigned to two centres with hydrogen bonded to interstitial oxygen (O_i) because of the nearly identical properties with two lines found in GaP [3] and the same structure of the O_i centres in GaAs and GaP [4,5].

The most important experiment to clarify the nature of a hydrogen-containing centre is the additional doping with deuterium. The appearance of the isotope-shifted deuterium line proves the hydrogen identity, and the number of the additional lines gives information about the number of hydrogen atoms involved in the centre. In this paper, we investigate the vibrational absorption line at 3079.2 cm⁻¹ (line 4 in Ref. [1]) and the associated wagging mode, their deuterium analogues, and the photoinduced recharging of the responsible hydrogen centre.

2. Experimental details

The undoped semi-insulating GaAs samples were grown by the LEC-technique from p-BN crucibles under

*Corresponding author. Fax: +49-30-20377-515.

E-mail address: ulrici@pdi-berlin.de (W. Ulrici).

N_2 or argon inert gas. Additionally, undoped polycrystalline GaAs was investigated, which has been synthesized in a separate high-pressure equipment using p-BN crucibles under 70 bar N_2 or Ar inert gas. In order to introduce deuterium into the ingots, the boric oxide encapsulant was wetted with heavy water in both kinds of preparation. In this study, mainly those samples were investigated containing the isolated interstitial oxygen (O_i) [4] and the off-centre substitutional oxygen (oc- O_{As}) [6] impurities with an amount of about 10^{15} – 10^{16} cm^{-3} . The infrared absorption experiments have been performed with a Bruker IFS 120 HR Fourier-transform spectrometer operating with resolutions of 0.02–0.1 cm^{-1} . The samples were held at $T = 7$ or 80 K in an Oxford Instruments cryostat Optistat^{CF}.

3. Vibrational modes

In Fig. 1a, the very narrow vibrational absorption line at 3079.2 cm^{-1} is shown together with a vibrational line at 983.3 cm^{-1} , which has also been reported earlier in Refs. [1,7]. Fig. 2 demonstrates that the integrated intensities A of both lines are strictly correlated, indicating that both lines are caused by the same centre. The intensity ratio $A^{983}/A^{3079} \approx 2$ and their frequency ratio of about 0.3 suggest that these two lines are the

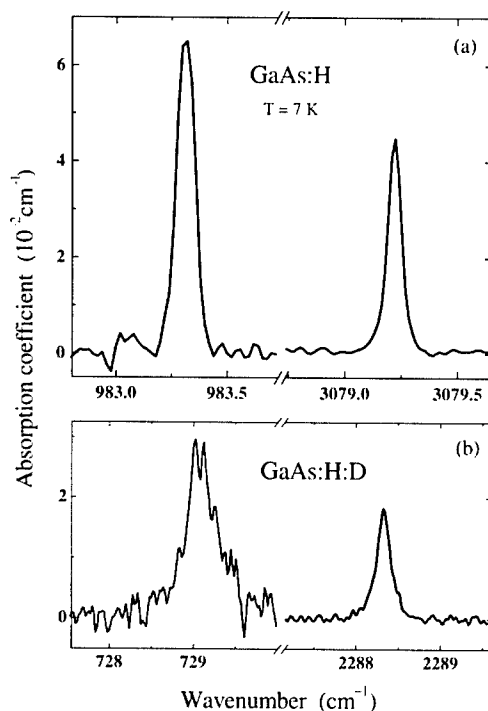


Fig. 1. The infrared absorption spectra measured at $T = 7$ K on the GaAs:H (a) and the GaAs:H:D (b).

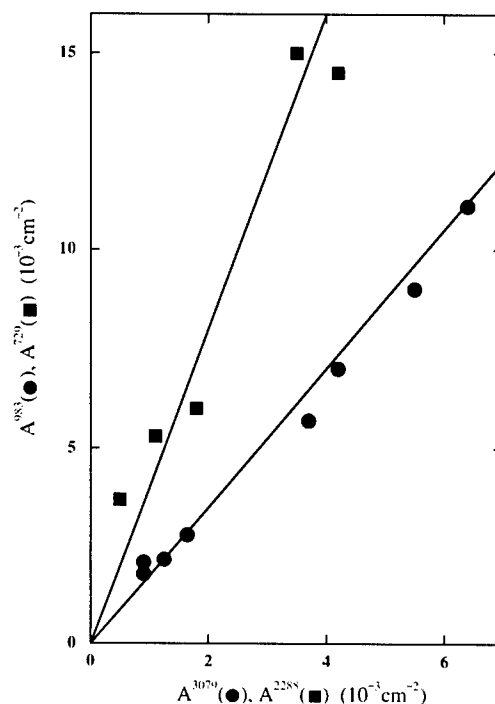


Fig. 2. The correlation between the integrated intensities A of the 3079 and 983 cm^{-1} H-lines (circles) and the 2288 and 729 cm^{-1} D-lines (squares). The points represent different samples.

stretching mode (3079 cm^{-1}) and the twofold degenerate wagging mode (983 cm^{-1}) of a bonded hydrogen atom located in an antibonding position. To check this assumption, GaAs samples containing both hydrogen and deuterium were investigated. In addition to the mentioned lines at 3079 and 983 cm^{-1} , two new lines are measured on the GaAs:H:D samples at 2288.3 and 729.1 cm^{-1} (see Fig. 1b). These lines are assigned to the corresponding stretching and wagging mode of D replacing H in the centre as can be derived from their frequency ratio $r = \omega(H)/\omega(D) \approx 1.347$ (see Table 1) and from the correlation of the integrated intensities $A^{729}/A^{2288} \approx 4$ (see Fig. 2). The result that in the GaAs:H:D samples only two D-modes are measured besides the two H-modes proves that the centre responsible for these lines contains only a single hydrogen atom. The rather low r -values indicate that the H(D) atom cannot be bonded to lattice atoms (Ga or As), but must be bonded to a light impurity atom Z with a mass $M_Z < 20 \text{ amu}$. The centre is provisionally labelled (Z–H). The lines at 3079, 2288, and 983 cm^{-1} could be measured up to $T = 300 \text{ K}$ proving their vibrational nature. Whereas the H- and D- stretching modes shift only very weakly ($d\omega/dT \approx 1 \times 10^{-3} \text{ K}^{-1} \text{ cm}^{-1}$), the frequency of the H-wagging mode exhibits a

Table 1

The maximum frequencies ω and half-widths Γ of the absorption lines due to the stretching (top) and wagging modes (bottom) of the (Z–H) centre measured at $T = 7$ K. The data for (Z–H)* are those of the photoinduced recharged state

Mode	ω (cm ⁻¹)	Γ (cm ⁻¹)	$r = \omega(\text{H})/\omega(\text{D})$
Z–H	3079.2	0.04	
(Z–H)*	3099.0	0.25	
Z–D	2288.3	0.20	1.3456
(Z–D)*	2301.9	0.15	1.3463
Z–H	983.3	0.05	
(Z–H)*	972.5	0.3	
Z–D	729.1	0.4	1.3488
(Z–D)*	723.6	1	1.344

considerable shift to lower energies ($d\omega/dT = -1 \times 10^{-2} \text{ K}^{-1} \text{ cm}^{-1}$).

Illumination of the samples with light at low temperatures (<100 K) results in a decrease of the intensity of the four absorption lines. Simultaneous to this decrease, a set of four new lines appears at slightly shifted frequencies summarized in Table 1. This effect has already been reported for the H-lines in Refs. [1,8]. The r -values for the lines appearing under illumination are the same as those in the dark confirming that the new lines are due to a photoinduced state called (Z–H)*. It has to be clarified whether (Z–H)* is a different charge state or a metastable excited state of (Z–H). The decrease of the integrated intensity of the (Z–H) and (Z–D) lines under illumination (A_{ill}) was measured as a function of the photon energy $h\nu_{\text{exc}}$. This decrease, normalized to the line intensity A_{dark} measured in the dark, is shown in Fig. 3 investigated on two types of samples with different positions of the Fermi level E_F . It should be noted that each data point in Fig. 3 is measured after long-time illumination ($\approx 10^4$ s, cf. Ref. [8]). As can be seen, the onsets as well as the spectral shapes of the decrease are different for the two kinds of samples. However, the intensity of the (Z–H) and (Z–D) lines decreases nearly by the same amount at each distinct $h\nu_{\text{exc}}$ value confirming once again the correlation between the stretching and wagging modes.

In the course of the present study, we also observed the line at 3000.0 cm^{-1} on the GaAs:H:D samples, which has been identified by Pajot and Song [1] as due to an (O–H) centre. To make a distinction between the different hydrogen centres, this centre will be called here (O–H)^A. Together with this line, one corresponding line due to the deuterium containing centre (O–D)^A was found at 2455.0 cm^{-1} . For the new line appearing under illumination (photon energy 1.2 eV) at 3296.4 cm^{-1} [1], its deuterium counterpart was detected at 2451.6 cm^{-1} (all frequencies measured at $T = 7$ K).

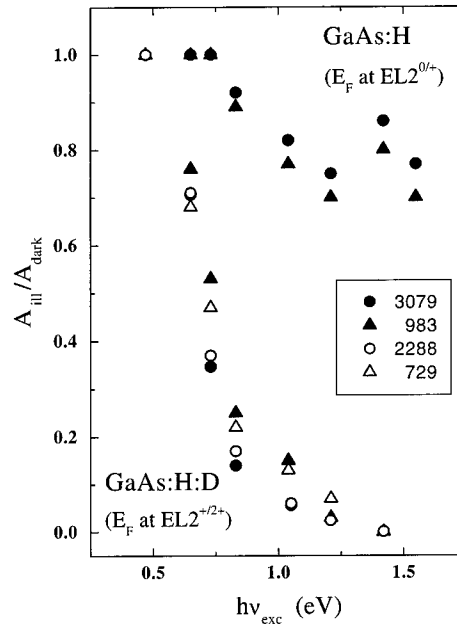


Fig. 3. The normalized integrated intensity $A_{\text{ill}}/A_{\text{dark}}$ of the absorption lines of Fig. 1 under illumination with different photon energies $h\nu_{\text{exc}}$ measured at $T = 80$ K on two samples with different Fermi-level positions E_F .

These results prove that the (O–H)^A centre contains only one hydrogen atom.

4. Discussion

From the experimental results, especially those of the GaAs:H:D, it is clearly evident that the investigated vibrational lines of the (Z–H) centre are due to the stretching and wagging mode of one hydrogen atom bonded to a light impurity atom Z. The rather high frequency of the wagging mode (about one-third of that of the stretching mode) indicates that the H atom should be located in an antibonding position. Among the four possible candidates for Z in LEC-GaAs (C, B, N, and O), carbon and boron can be definitely ruled out by spectroscopic arguments. The (Z–H) centre was detectable only in the samples containing sufficient isolated oxygen centres (oc-O_{As} and O_i). This suggests the assumption that Z is oxygen. However, as in all investigated samples the N–H centre [9] was also found; N cannot be completely excluded as the partner in the (Z–H) centre.

The spectral dependence of the photoinduced change (Fig. 3) gives information about the nature of this change. The sample with its Fermi level at the EL2^{0/+} mid-gap level ($E_v + 0.78 \text{ eV}$) shows the onset of the photoinduced decrease at about 0.8 eV, and its spectral

shape is roughly that of the photoionization cross-section σ_{p1} of the transition $EL2^- + h\nu \rightarrow EL2^0 + \text{hole}_{vb}$ [10]. However, the sample with E_F at the $EL2^{+2+}$ level ($E_v + 0.54$ eV) shows the onset of the photoinduced decrease at about 0.5 eV, and the spectral dependence corresponds to that of the photoionization cross-section σ_{p2} of the transition $EL2^{2-} + h\nu \rightarrow EL2^- + \text{hole}_{vb}$ [11]. Obviously, in both kinds of samples, the holes in the valence band created by these transitions will be captured by the (Z–H) centre forming the state (Z–H)*, which is, therefore, a recharged state (Z–H)⁺. These results suggest that the (Z–H) centre forms an electronic level (Z–H)/(Z–H)⁺ in the region between E_v and $E_v + 0.5$ eV within the gap of the GaAs. This conclusion is supported by the measurements on a p-type GaAs:H sample exhibiting both lines at 3079 cm^{-1} (Z–H) and 3099 cm^{-1} (Z–H)⁺ without illumination. Finally, the maximum concentration of the (Z–H) centre detected in the LEC-GaAs is in the region between 10^{13} and 10^{14} cm^{-3} , if the calibration factor for the C–H stretching mode [12] is used.

References

- [1] B. Pajot, C. Song, *Phys. Rev. B* 45 (1992) 6484.
- [2] B. Pajot, C. Song, C. Porte, *Mater. Sci. Forum* 83–87 (1992) 581.
- [3] W. Ulrici, M. Czupalla, M. Seifert, *Phys. Stat. Sol. B* 210 (1998) 551.
- [4] C. Song, B. Pajot, C. Porte, *Phys. Rev. B* 41 (1990) 12330.
- [5] W. Ulrici, B. Clerjaud, D. Côte, *Physica B* 273–274 (1999) 807.
- [6] H.Ch. Alt, *Phys. Rev. Lett.* 65 (1990) 3421.
- [7] C. Song, B. Pajot, F. Gendron, *J. Appl. Phys.* 67 (1990) 7307.
- [8] C. Song, B. Pajot, W.K. Ge, D.S. Jiang, *Phys. Rev. B* 52 (1995) 4864.
- [9] B. Clerjaud, D. Côte, W.S. Hahn, A. Lebkiri, W. Ulrici, D. Wasik, *Phys. Stat. Sol. A* 159 (1997) 121.
- [10] P. Silverberg, P. Omling, L. Samuelson, *Appl. Phys. Lett.* 52 (1988) 1689.
- [11] P. Omling, P. Silverberg, L. Samuelson, *Phys. Rev. B* 38 (1988) 3606.
- [12] B.R. Davidson, R.C. Newman, T.B. Joyce, T.J. Bullogh, *Semicond. Sci. Technol.* 11 (1996) 455.



ELSEVIER

Physica B 308–310 (2001) 839–842

PHYSICA B

www.elsevier.com/locate/physb

Nitrogen solubility and N-induced defect complexes in epitaxial GaAs:N

S.B. Zhang*, Su-Huai Wei

National Renewable Energy Laboratory, 1617 Cole Blvd., Golden, CO 80401, USA

Abstract

Previous calculations suggested low-equilibrium N solubility in bulk GaAs. In epitaxial growth, however, N solubility can be significantly enhanced to as much as a few %. First-principles total-energy calculations show that this large difference is due to the lack of low-energy nucleation sites of GaN during epitaxy. As a result, the atomic chemical potential of N can be significantly larger. This gives rise to new defect physics distinctly different from those in GaAs. © 2001 Elsevier Science B.V. All rights reserved.

Keywords: Impurity solubility; Doping; Impurity-defect complexes

Substitution by first-row elements in semiconductors is an interesting problem. For example, with a few percent of N, the bandgap of $\text{GaAs}_{1-x}\text{N}_x$ dilute alloy can be significantly smaller than GaAs [1]. As such, $\text{GaAs}_{1-x}\text{N}_x$ is a potential candidate for infrared lasers and as an absorber for high-efficiency tandem solar cells. It is also a natural buffer layer for the epitaxial growth of cubic-phase GaN on GaAs, thus integrating two important optoelectronic materials. However, the doping mechanism of GaAs:N is largely unknown. The thermodynamic solubility of N in bulk GaAs is exceedingly low ($[\text{N}] < 10^{14} \text{ cm}^{-3}$ at $T = 650^\circ\text{C}$) [1–3] due to the formation of a fully relaxed, secondary GaN phase; yet, single-phase epitaxial films grown at $T = 400\text{--}650^\circ\text{C}$ with $[\text{N}]$ as high as $\sim 10\%$ have been reported [4–9]. To explain this giant eight orders of magnitude difference in GaAs:N, surface-reconstruction-induced subsurface strain has been implicated [3]. However, the calculated $[\text{N}]$ by this model is four orders of magnitude too small. Another puzzle about GaAs:N with high $[\text{N}]$ is the considerable degradation of the minority carrier lifetimes [10,11], not seen in ordinary binaries.

Recently, we suggested [12] by first principles calculations that the formation of the secondary GaN phase could be suppressed during epitaxial growth. This is because having well-defined growth surface often eliminates many defective, therefore chemically active, sites for secondary phase nucleation. Indeed, a key factor in fabricating high $[\text{N}]$ homogeneous GaAs:N films is to eliminate the formation of GaN precipitates, as well as the amorphous phase of GaN on the epitaxial surface [11]. As such, there exists a new region of the atomic chemical potentials ($\mu_{\text{Ga}}, \mu_{\text{As}}, \mu_{\text{N}}$), available for epitaxial growth but not for equilibrium bulk growth. The chemical potentials are the energies of individual atoms in the reservoirs (such as in the gas sources) that affect impurity substitutional energy [13]. As a result, the calculated maximum solubility $[\text{N}]$ at $T = 650^\circ\text{C}$ is about 4%, instead of $< 10^{14} \text{ cm}^{-3}$ for equilibrium growth. Because defect formation energies are also functions of the chemical potentials, defect physics at high N concentration is qualitatively different from defect physics at low $[\text{N}]$. For example, the dominant charge-neutral defect is no longer the As antisite in GaAs but the N–N split interstitial in GaAs:N. While the As antisite has a doubly occupied (and relatively benign) mid-gap state, the N–N split interstitial has a singly occupied mid-gap state. Thus, depending on the capture

*Corresponding author. Tel.: +1-303-384-6622; fax: +1-303-384-6432.

E-mail address: szhang@nrel.gov (S.B. Zhang).

cross sections the split interstitial could be a deep trap for both electrons and holes. This suggests a microscopic mechanism for the so-far mysterious degradation of the minority carrier lifetimes in epitaxial GaAs:N.

Equilibrium N solubility: Physically, the solubility limit is reached when N starts to precipitate into GaN. The formation energy of a charge-neutral defect is defined [13] as

$$\Delta H_f = E_{\text{tot}}(\text{Defect}) - E_{\text{tot}}(\text{Host}) + n_{\text{Ga}}\mu_{\text{Ga}} + n_{\text{As}}\mu_{\text{As}} + n_{\text{N}}\mu_{\text{N}}, \quad (1)$$

where $E_{\text{tot}}(\text{Host})$ is the total energy of a supercell containing 32 GaAs, $E_{\text{tot}}(\text{Defect})$ is the total energy for the same supercell but with a defect, and $n = (n_{\text{Ga}}, n_{\text{As}}, n_{\text{N}})$ is the number of particles being removed (upon the defect formation) from the host to a reservoir of chemical potentials $\mu = (\mu_{\text{Ga}}, \mu_{\text{As}}, \mu_{\text{N}})$. If we set the energies of bulk Ga, bulk As, and N_2 gas as the reference zeros, then the chemical potentials satisfy

$$\mu_{\text{Ga}} \leq 0, \quad \mu_{\text{As}} \leq 0 \quad \text{and} \quad \mu_{\text{N}} \leq 0. \quad (2)$$

This happens because if $\mu > 0$, an elemental solid (or gas) will spontaneously form that hinders any further increase of μ . For GaAs to be thermodynamically stable, it also requires that $\mu_{\text{Ga}} + \mu_{\text{As}} = \mu_{\text{GaAs}} = \Delta H(\text{GaAs}) = -0.62 \text{ eV}$. Thus, defect formation energies in GaAs:N are functions of only two independent variables, $(\mu_{\text{As}}, \mu_{\text{N}})$, satisfying (see Fig. 1)

$$-0.62 \text{ eV} \leq \mu_{\text{As}} \leq 0 \quad \text{and} \quad \mu_{\text{N}} \leq 0. \quad (3)$$

Spontaneous formation of the secondary bulk GaN phase puts a further restriction on the chemical

potentials, namely

$$\mu_{\text{Ga}} + \mu_{\text{N}} \leq \mu_{\text{GaN}}. \quad (4)$$

Because $\mu_{\text{GaN}} = \Delta H(\text{GaN}) = -1.57 \text{ eV}$, the upper limit for μ_{N} is not $\mu_{\text{N}}^{\text{max}} = 0$ in Eq. (3), but $\mu_{\text{N}}^{\text{max}} = \mu_{\text{GaN}} - \mu_{\text{Ga}} = \mu_{\text{GaN}} - (\mu_{\text{GaAs}} - \mu_{\text{As}}) = -1.57 + 0.62 + \mu_{\text{As}} = -0.95 \text{ eV}$ at $\mu_{\text{As}} = 0$. This defines the “original region” in Fig. 1. Nitrogen substitution is a special case of Eq. (1)

$$\Delta E_{\text{sub}} = \Delta E_{\text{tot}} - \mu_{\text{N}} + \mu_{\text{As}}, \quad (5)$$

where $\Delta E_{\text{tot}} = E_{\text{tot}}(\text{N}_{\text{As}}) - E_{\text{tot}}(\text{GaAs})$. The higher the $\mu_{\text{N}}^{\text{max}}$ (and the lower the $\mu_{\text{As}}^{\text{min}}$), the lower the minimum $\Delta E_{\text{sub}}^{\text{min}}$ is. The calculated $\Delta E_{\text{sub}}^{\text{min}}$ is 1.64 eV, which accounts for the low [N] in equilibrium grown GaAs:N.

Surface enhanced solubility: In the epitaxial growth, relaxed GaN phase can form only if both of the following conditions are satisfied: (1) Formation of the GaN phase at the surface is energetically favored (namely, spontaneously). (2) The size (and/or thickness) of the surface GaN cluster exceeds the critical size for dislocation formation. Condition (1) proceeds condition (2) and sets the physical limit on μ_{N} in epitaxial GaAs:N [cf. Eq. (4)]:

$$\mu_{\text{Ga}} + \mu_{\text{N}} \leq \mu_{\text{GaN}}^{\text{Surf}}, \quad (6)$$

where $\mu_{\text{GaN}}^{\text{Surf}} = \Delta H^{\text{Surf}}$ is the heat of formation of the GaN layer on a specific surface. The spontaneous formation of the GaN layer is equivalent to having the single nitrogen substitutional energy $\Delta E_{\text{sub}}^{\text{Surf}}$ [cf. Eq. (5)] equal zero. Thus, to find the N solubility in epitaxial GaAs:N films, we first solve

$$\Delta E_{\text{sub}}^{\text{Surf}}(\mu_{\text{As}}^{\text{min}}, \mu_{\text{N}}^{\text{max}}) = 0 \quad (7)$$

to find $(\mu_{\text{As}}^{\text{min}}, \mu_{\text{N}}^{\text{max}})$ using a $\beta 2(2 \times 4)$ surface reconstruction [14], as detailed in Ref. [12]. Second, we plug $(\mu_{\text{As}}^{\text{min}}, \mu_{\text{N}}^{\text{max}})$ into Eq. (5) to determine $\Delta E_{\text{sub}}^{\text{min}}$, as shown in Fig. 2. The corresponding [N] is calculated to be 4% at $T = 650^\circ$.

Nitrogen-induced defects: At the high N concentration, the defect physics changes from low [N] in two fundamental ways: (1) the dominant defects are no longer the same, (2) the electronic properties of the leading defects are qualitatively different. The calculations were done with a 64-atom supercell and a 25 Ry plane-wave cutoff energy. All the atoms are relaxed. More details can be found in Ref. [13]. Several defects are shown in Fig. 3. (1) The N–N split interstitial. Here, an N_2 molecule replaces an As atom. Each N is threefold co-ordinated. The N–N is important because of the exceptionally strong N–N bond, at the same time the strong Ga–N bonds, and the small size of the N atom. The calculated N–N bondlength is 1.39 Å, compared to 1.10 Å for N_2 molecule. The calculated Ga–N bondlength is 2.01 Å, compared to 1.95 Å for bulk GaN. The calculated N–N–Ga and Ga–N–Ga bondan-

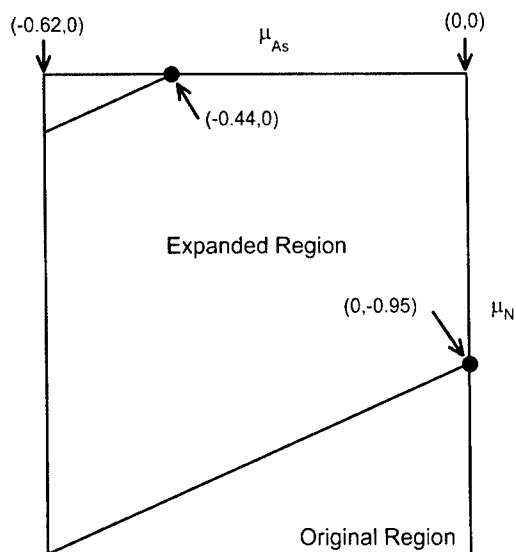


Fig. 1. The physically accessible region of the chemical potentials, $(\mu_{\text{As}}, \mu_{\text{N}})$, is shown.

gles are 114° and 132° , respectively. (2) The N–As split interstitial. Here, the calculated N–As bondlength is

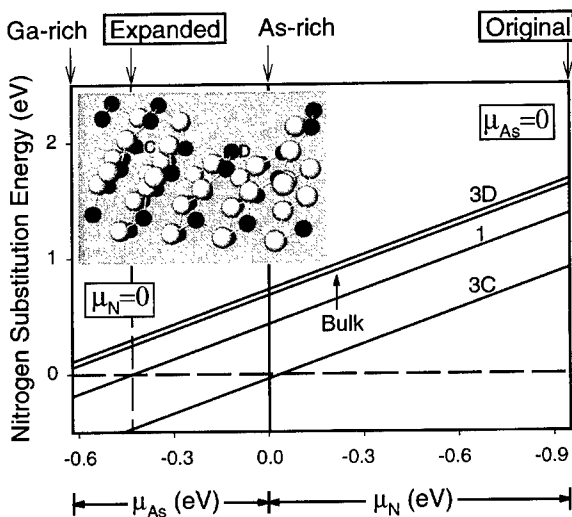


Fig. 2. N substitutional energies ΔE_{sub} as functions of $(\mu_{\text{As}}, \mu_{\text{N}})$. The inset is the GaAs(2×4) surface, indicating the various substitution sites. The anion is denoted by a dark circle while Ga is denoted by a light circle.

1.85 Å, the Ga–As bondlength is 2.37 Å, and the Ga–N bondlength is 1.94 Å, respectively, compared with 1.62 Å for diatomic N–As, 2.44 Å for bulk GaAs and 1.95 Å for bulk GaN. All the calculated bondangles are within the range of 103 – 144° . (3) The $(\text{As}_{\text{Ga}}-\text{N}_{\text{As}})_{\text{nn}}$ pair, where nn stands for nearest neighbor. The N_{As} attracts the As_{Ga} because N_{As} is associated with compressive strain due to the small size of N, while As_{Ga} is associated with tensile strain due to two extra electrons in the non-bonding orbital. The $(\text{As}_{\text{Ga}}-\text{N}_{\text{As}})_{\text{nn}}$ pair has a 0.5-eV binding energy. Thus, at high [N] the formation of $(\text{As}_{\text{Ga}}-\text{N}_{\text{As}})_{\text{nn}}$ may eliminate isolated As_{Ga} . The N–As separation in the nn-pair is 2.86 Å, 47% larger than the sum of atomic radii. Hence, the nn-pair, where both N and As are threefold coordinated, is qualitatively different from any other distant $\text{As}_{\text{Ga}}-\text{N}_{\text{As}}$ pairs. (4) The $(\text{V}_{\text{Ga}}-\text{N}_{\text{As}})_{\text{nn}}$ pair. Despite being the nearest neighbor, the binding energy (<0.05 eV) is negligible.

Fig. 4(a) shows the charge-neutral defect formation energy ΔH_f as a function of atomic chemical potentials. At the N solubility limit $[(\mu_{\text{As}}^{\text{min}}, \mu_{\text{N}}^{\text{max}}) = (-0.44, 0 \text{ eV})]$, the dominant defect in GaAs:N is the $(\text{N}-\text{N})_{\text{spl}}$ split-interstitial, not the As_{Ga} in GaAs. The calculated $\Delta H_f(\text{N}-\text{N})_{\text{spl}} = 1.52 \text{ eV}$ is considerably smaller than As_{Ga} (2.24 eV), $(\text{As}_{\text{Ga}}-\text{N}_{\text{As}})_{\text{nn}}$ (1.96 eV), and $(\text{N}-\text{As})_{\text{spl}}$

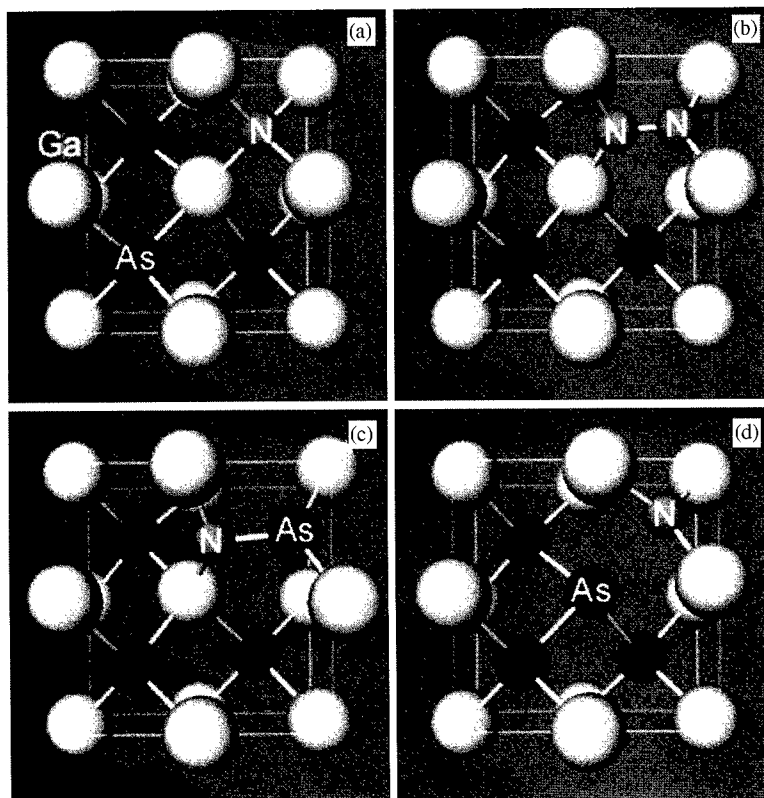


Fig. 3. Atomic structures for (a) N_{As} , (b) N–N, (c) N–As split interstitials, and (d) $(\text{As}_{\text{Ga}}-\text{N}_{\text{As}})_{\text{nn}}$ complex. As is the dark circle, Ga is the light circle, and N is labeled.

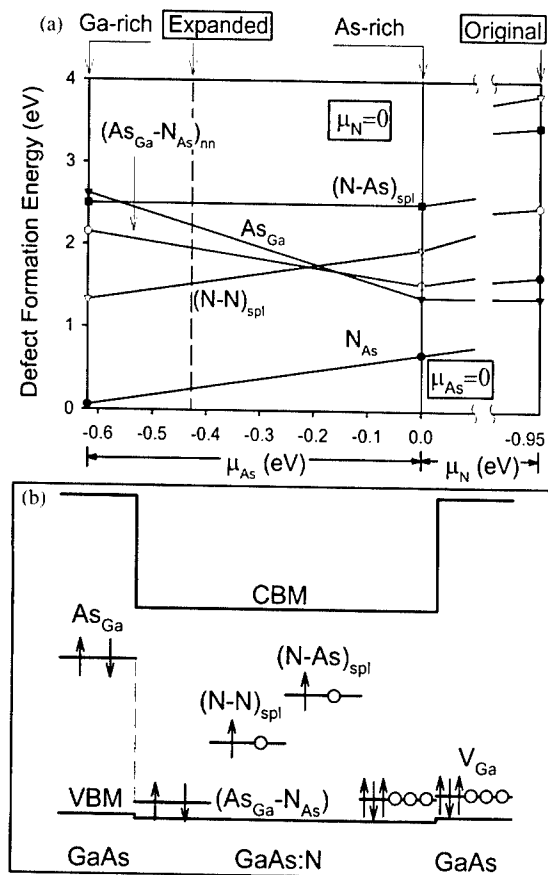


Fig. 4. (a) Defect formation energies. The ordinates and legends are the same as in Fig. 2. (b) Calculated single-particle defect energy levels with electron occupation indicated by arrows.

(2.49 eV). This gives an $(N-N)_{spl}$ concentration at $T=650^\circ\text{C}$ of $[C]=1 \times 10^{14} \text{ cm}^{-3}$. In the relative N-poor conditions $[(\mu_{As}, \mu_N) = (0, -0.95 \text{ eV})]$, the most abundant defects are As_{Ga} (1.38 eV), N_{As} (1.64 eV) and $(As_{Ga}-N_{As})_{nn}$ (2.47 eV), instead.

Fig. 4(b) shows the calculated single-particle gap states, along with the bandgaps of bulk GaAs and GaAs:N at $x=3.125\%$ (i.e., one N in a 64-atom supercell). Inside GaAs, As_{Ga} forms a mid-gap double donor state, whereas V_{Ga} forms several shallow acceptor states. Inside GaAs:N, the As_{Ga} mid-gap state disappears with the formation of the $(As_{Ga}-N_{As})_{nn}$ pairs:

the N_{As} state near the conduction band minimum (CBM) pushes down the As_{Ga} gap state to near the valence band maximum (VBM). On the other hand, the effect of N_{As} on V_{Ga} is negligible. Both $(N-N)_{spl}$ and $(N-As)_{spl}$ have a deep level (0.38 and 0.62 eV above the VBM or 0.66 and 0.42 eV below the CBM, respectively) with single electron occupancy. Assuming reasonable capture cross sections, we anticipate that the split interstitials will be important recombination centers for the minority carrier.

In summary, we showed that one can significantly increase the N chemical potential and subsequently the N solubility in epitaxial GaAs:N. At such high N concentration, the physics of defects changes qualitatively from that of GaAs. Nitrogen split interstitials, which are potentially detrimental to minority carrier lifetimes, could become important. This work is supported by the U.S. DOE under contract No. DE-AC36-99GO10337.

References

- [1] S.-H. Wei, A. Zunger, *Phys. Rev. Lett.* 76 (1996) 664.
- [2] I.-H. Ho, G.B. Stringfellow, *J. Crystal Growth* 178 (1997) 1.
- [3] S.B. Zhang, A. Zunger, *Appl. Phys. Lett.* 71 (1997) 677.
- [4] D.J. Welford, J.A. Bradley, K. Fry, J. Thompson, in: J.D. Chadi, W.A. Harrison (Eds.), *Proceedings of the 17th International Conference on the Physics of Semiconductors*, Springer, New York, 1984, p. 627.
- [5] M. Weyers, M. Sato, *Appl. Phys. Lett.* 62 (1993) 1396.
- [6] M. Kondow, K. Uomi, T. Kitatani, S. Watahiki, Y. Yazawa, *J. Crystal Growth* 164 (1996) 175.
- [7] Y. Qiu, S.A. Nikishin, H. Temkin, N.N. Faleev, Y.A. Kudriavtsev, *Appl. Phys. Lett.* 70 (1997) 3242.
- [8] W.G. Bi, C.W. Tu, *Appl. Phys. Lett.* 70 (1997) 1608.
- [9] K. Uesugi, I. Suemune, *J. Crystal Growth* 189/190 (1998) 490.
- [10] A. Moto, S. Tanaka, N. Ikoma, T. Tanabe, S. Takagishi, M. Takahashi, T. Katsuyama, *Jpn. J. Appl. Phys.* 38 (Part 1) (1999) 1015.
- [11] J.F. Geisz, D.J. Friedman, J.M. Olson, S.R. Kurtz, B.M. Keyes, *J. Crystal Growth* 195 (1998) 401, and private communications.
- [12] S.B. Zhang, S.-H. Wei, *Phys. Rev. Lett.* 86 (2001) 1789.
- [13] S.B. Zhang, J.E. Northrup, *Phys. Rev. Lett.* 67 (1991) 2339.
- [14] J.E. Northrup, S. Froyen, *Phys. Rev. B* 50 (1994) 2015.



ELSEVIER

Physica B 308–310 (2001) 843–845

PHYSICA B

www.elsevier.com/locate/physb

Plasmon-like oscillations of the electrons localized by the DX centers in doped $\text{Al}_x\text{Ga}_{1-x}\text{As}$

Yu.A. Pusep*, A.J. Chiquito, W. Fortunato, J.C. Galzerani

Universidade Federal de São Carlos, 13565-905 São Carlos SP, Brazil

Abstract

Raman scattering of the plasmon-like coupled excitations, which permits to detect both the polarization of free and localized electrons was explored in the heavily doped $\text{Al}_x\text{Ga}_{1-x}\text{As}$ alloys. Complementary information about the localized electrons was obtained by the electric measurements: the temperature dependencies of the Hall concentrations and mobilities and the photoexcited DC conductivities. It was shown that the characteristic decrease of the Hall concentration observed with the increase of the concentration of Al in alloys was accompanied by a corresponding decrease of the frequency of the plasma oscillations of free electrons. The observed decreases of both the Hall conductivity and the plasma frequency were caused by the DX centers. © 2001 Elsevier Science B.V. All rights reserved.

Keywords: Plasmons; Localization; AlGaAs alloys

Two fundamentally distinct states of the matter will be discussed here. They are an insulator and a conductor which are distinguished at zero temperature by the different behavior of DC conductivity: it vanishes for an insulator and remains finite for a conductor. Another important property which allows to distinguish insulators and conductors is the macroscopic polarization (essential in insulators and negligible in conductors). Both, the DC conductivity and the polarization can be used to determine the metal-to-insulator transition—a phenomenon, which occurs when the localization length of electrons reveals different behavior: it diverges for metals and is a finite quantity for insulators [1].

In this work, we studied the localization properties of electrons in $\text{Al}_x\text{Ga}_{1-x}\text{As}$ alloys and compared it with those of the GaAs/AlAs superlattices where the metal-to-insulator transition can be achieved. In the $\text{Al}_x\text{Ga}_{1-x}\text{As}$ alloys doped with Si, the strong localization of electrons is provided by the deep DX centers [2],

number of which depends on the contents of alloy. While, the alteration of the widths of the barriers results in a change of the coupling between electrons in adjacent wells thus, presenting a possibility to produce an insulator (thick barriers) and a metal (thin barriers) states of the electron system in superlattices. We demonstrate that the alterations of both the DC conductivity and the polarization which occur when the metal-to-insulator transition takes place, are strongly coupled with the character of the state of the electron system in the samples under investigation.

The photoresistance and the Hall measurements were utilized in order to study the DC conductivity, while the Raman scattering of the plasmon-LO phonon coupled excitations was performed to explore the electric polarization of the electrons.

The current source Keithley-237 was used for the electrical measurements; the tungsten lamp was utilized for the optical excitation during the electrical measurements. The unpolarized back-scattered Raman spectra were performed at $T = 10\text{ K}$ with a “Instruments S.A. T64000” triple grating spectrometer supplied with a CCD detector cooled by nitrogen; the 4764 Å line of an Ar^+ laser was used for excitation. The closed circle cryostats Janis-350CS were used to cool the samples.

*Corresponding author. Departamento de Física e Ciência dos Materiais, Instituto de Física de São Carlos, Universidade de São Paulo, Av. Trabalhador São Carlense, 400, 13566-560 São Carlos-SP-Brazil. Fax: +55-16-2739827.

E-mail address: pusep@ifsc.usp.br (Y.A. Pusep).

The $\text{Al}_x\text{Ga}_{1-x}\text{As}$ alloys and the GaAs/AlAs superlattices both doped with Si were grown on the (001) oriented GaAs substrates by molecular beam epitaxy.

The Raman spectra of the $\text{Al}_x\text{Ga}_{1-x}\text{As}$ alloys with different contents of Al (x), nominally doped with the concentration of $N_{\text{Si}} = 2 \times 10^{18} \text{ cm}^{-3}$, together with the Hall data are shown in Fig. 1. The LO mode of GaAs originated from the depletion surface layer was detected at 295 cm^{-1} together with two plasmon-LO phonon modes: the low-frequency acoustic mode ω^- and the high-frequency optic one ω^+ . As expected, three coupled modes were found in the $\text{Al}_x\text{Ga}_{1-x}\text{As}$ alloy with $x = 0.2$: the acoustic ω^- mode, and two optic ω_1^+ (GaAs-like) and ω_2^+ (AlAs-like) modes. In addition, the LO_1 GaAs-like mode of the depletion layer was observed at 286 cm^{-1} . The GaAs-like (TO_1 and LO_1) and the AlAs-like (TO_2 and LO_2) bulk optical phonons, evidencing the absence of the plasmons, were found in the $\text{Al}_x\text{Ga}_{1-x}\text{As}$ alloys with $x = 0.4$. The Hall data shown in Fig. 1(b) reveal the strong decrease of the concentration of the electrons and their mobilities with the increase of the Al contents. The thick arrows in Fig. 1(a) show the frequency positions of the high-frequency coupled modes calculated with the Hall concentrations in the corresponding alloys.

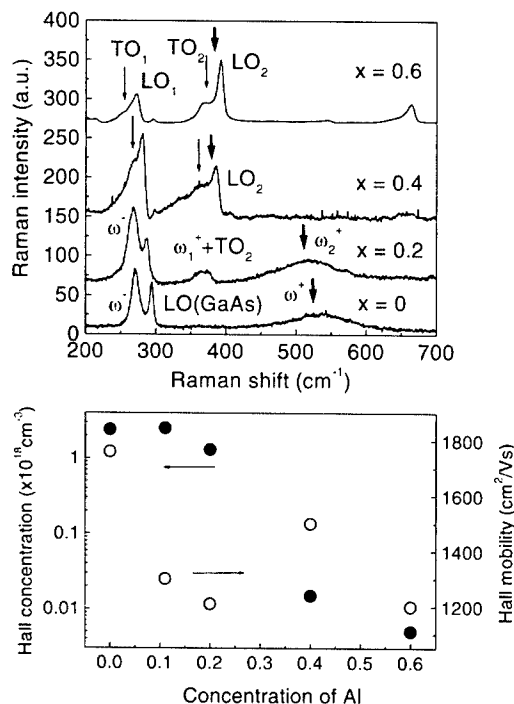


Fig. 1. (a) Raman spectra and (b) the Hall data of the $\text{Al}_x\text{Ga}_{1-x}\text{As}$ alloys with the nominal doping concentration $N_{\text{Si}} = 2 \times 10^{18} \text{ cm}^{-3}$ measured at $T = 10 \text{ K}$. The thick arrows show the calculated frequencies of the coupled plasmon-LO phonon modes.

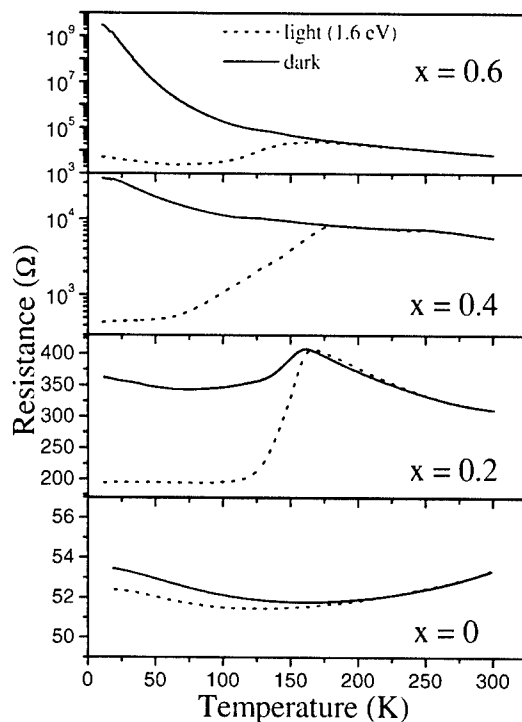


Fig. 2. Dependencies of the resistance on the temperature measured in the $\text{Al}_x\text{Ga}_{1-x}\text{As}$ alloys with the nominal doping concentration $N_{\text{Si}} = 2 \times 10^{18} \text{ cm}^{-3}$ with the illumination (dashed lines) and in the dark (solid lines).

The results of the photoresistance measurements, clearly showing the presence of the DX centers are plotted in Fig. 2. The low temperature resistance was found smaller in the optically excited samples than in the dark. The difference between the illuminated resistance and the dark one increased with the increase of the concentration of Al. According to Ref. [2], the difference between the illuminated and dark resistances is caused by the optical excitation of the electrons localized by the DX centers. Clearly is seen in Fig. 2, that the concentration of the DX centers increased with the increase of the concentration of Al in the $\text{Al}_x\text{Ga}_{1-x}\text{As}$ alloy resulting in the increase of a number of the localized electrons. This caused the decrease of the Hall concentration and of the plasma frequency which is observed in Fig. 1.

The localization of electrons resulting in the decrease of the superlattice plasma frequency (the frequency of the plasmons polarized along the superlattice axis) was observed in the doped GaAs/AlAs superlattices with thin enough thicknesses of the barriers. The Raman spectra of some of the superlattices with different thicknesses of the barriers are depicted in Fig. 3. In the superlattices $(\text{GaAs})_{l_1}(\text{AlAs})_{l_2}$, where the numbers denote the thicknesses of the corresponding layers expressed in the monolayers, all the three expected

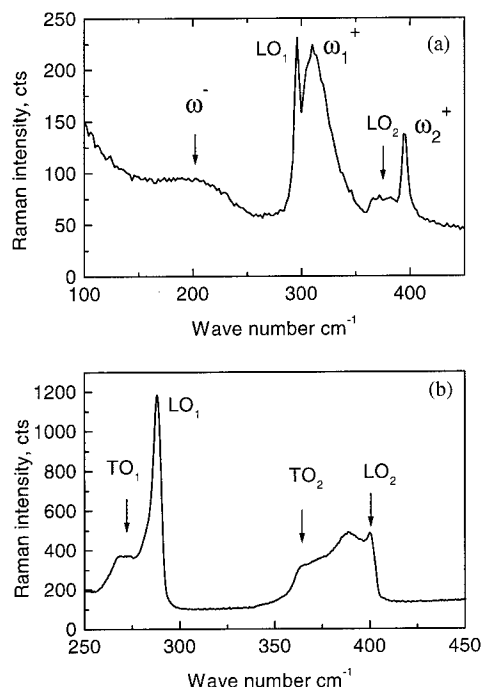


Fig. 3. Raman spectra of the (a) $(GaAs)_{17}(AlAs)_2$ ($N = 7.0 \times 10^{17} \text{ cm}^{-3}$) and (b) $(GaAs)_5(AlAs)_5$ ($N = 5.0 \times 10^{18} \text{ cm}^{-3}$) doped superlattices measured at $T = 10 \text{ K}$.

plasmon-LO phonon coupled modes were found. Calculations made by the envelope function approximation show that in this superlattice the lowest broad miniband (with the width $W_{SL} = 65 \text{ meV}$) is formed by the Γ electron states of the wells and the barriers. While, in the $(GaAs)_5(AlAs)_5$, as in the $Al_xGa_{1-x}As$ alloys with $x = 0.4$, no evidences of the plasmons were found; instead, the GaAs-like and the AlAs-like TO and LO phonons were observed even in heavily doped samples.

According to the calculations, in this superlattice the very narrow lowest miniband ($W_{SL} = 2 \text{ meV}$) is formed by the X electron states. The width of the miniband is considered as a measure of the coupling between the electrons in the wells of a superlattice; or equivalently, as a measure of the electron localization. Therefore, the broad minibands of the $(GaAs)_{17}(AlAs)_2$ superlattices provided free motion of electrons along the superlattice axis and as a consequence, the superlattice plasmons were observed. While, in the $(GaAs)_5(AlAs)_5$ the narrow minibands resulted in a strong modulation of the electron density along the superlattice axis producing

the localization of electrons in the wells. As a consequence, no superlattice plasmons were observed.

In this work we studied the Raman scattering of the plasmon-like coupled excitations, which permits to detect both the polarization of free and localized electrons in the heavily doped $Al_xGa_{1-x}As$ alloys. Complementary information about the localized electrons was obtained by the electric measurements: the temperature dependencies of the Hall concentrations and mobilities and the photoexcited DC conductivities. It was shown that the characteristic decrease of the Hall concentration observed with the increase of the concentration of Al in alloys was accompanied by a corresponding decrease of the frequency of the plasma oscillations of free electrons. The measurements of the conductivity caused by the photoexcited electrons revealed the presence of the DX centers with the concentration strongly increasing with the increase of the concentration of Al. Thus, it was shown that the observed decreases of both the Hall conductivity and the plasma frequency were caused by the DX centers. The Raman spectra of the $Al_xGa_{1-x}As$ alloys with different x were compared with those of the GaAs/AlAs superlattices with various strengths of the coupling between the wells. It was shown that the decrease of the coupling between the wells of the superlattices acts similar to the increase of the contents of Al in the alloys both decreasing the plasma frequency of free electrons. In the superlattices, the electrons become more localized in the wells with the decrease of the coupling between them, while in the alloys, the DX centers are responsible for the analogous electron localization. In addition, an evidence of the formation of the coherent clusters was found in the Raman spectra of both the doped $Al_xGa_{1-x}As$ alloys and the doped GaAs/AlAs superlattices.

Acknowledgements

The financial support from CNPq, FAPESP and CAPES is gratefully acknowledged.

References

- [1] I. Souza, T. Wilkens, R.M. Martin, Phys. Rev. B 62 (2000) 1666.
- [2] P.M. Mooney, J. Appl. Phys. 67 (1990) R1.



ELSEVIER

Physica B 308–310 (2001) 846–849

PHYSICA B

www.elsevier.com/locate/physb

Defect engineering in III–V ternary alloys: effects of strain and local charge on the formation of substitutional and interstitial native defects

A. Amore Bonapasta^{a,*}, P. Giannozzi^b

^aCNR, Istituto di Chimica dei Materiali (ICMAT), Via Salaria Km 29.5, CP 10, 00016 Monterotondo Stazione, Italy

^bINFM, Scuola Normale Superiore, Piazza dei Cavalieri 7, I-56126 Pisa, Italy

Abstract

The effects of external and internal strains and of defect charges on the formation of vacancies, antisites and interstitials in GaAs and $\text{In}_{0.5}\text{Ga}_{0.5}\text{As}$ have been investigated by *first principles* density functional methods. Present results show that strain and doping permit a *defect engineering* of III–V semiconductors. Specifically, they predict that doping may have major effects on the formation of antisites while vacancies may be favored only by extreme conditions of compressive strain. Interstitials may be moderately favored by doping and tensile strain. © 2001 Elsevier Science B.V. All rights reserved.

Keywords: Defects; Theoretical methods; III–V semiconductors

1. Introduction

Investigations on the formation of defects in III–V semiconductors have been stimulated by an increasing interest in the *defect engineering* of semiconductors, namely, a controlled introduction of defects aimed to tuning the material properties. As an example, materials for ultrafast optical devices have been obtained by growing GaAs or InGaAs at low temperature (LT) by molecular beam epitaxy (MBE) [1,2]. This growth should favor the formation of As antisites [3] and Ga vacancies. A key quantity describing the behavior of defects is represented by the defect formation energy [4,5]. Defect formation energies depend on the chemical potentials (μ_{Ga} , μ_{As}) and on the electron chemical potential, μ_e , which defines the reservoir of electrons [4,5]. In a supercell approach, the formation energy Ω_D of a defect D in GaAs may be written as in Ref. [4]:

$$\Omega_D = E_D - n_e \mu_e - n_{\text{Ga}} \mu_{\text{Ga}} - n_{\text{As}} \mu_{\text{As}}, \quad (1)$$

where E_D is the energy of a supercell containing n_{Ga} Ga atoms, n_{As} As atoms, and one D defect and n_e is the number of electrons transferred from an electron reservoir with a chemical potential μ_e to the defect D in a given charge state. In equilibrium, several restrictions apply to the chemical potentials [4]: $0 \leq \mu_e \leq E_g$ and $-\Delta H \leq \Delta\mu \leq \Delta H$, where $\Delta\mu$ is the chemical potential difference $(\mu_{\text{Ga}} - \mu_{\text{As}}) - (\mu_{\text{Ga(B)}} - \mu_{\text{As(B)}})$, $\mu_{\text{X(B)}}$ is the chemical potential of the X species in the bulk, E_g is the energy gap and ΔH is the heat of formation of GaAs [4]. $\Delta\mu = -\Delta H$ and $\Delta\mu = \Delta H$ correspond to the As-rich limit and the Ga-rich limit case, respectively, i.e., to different growth conditions which may affect the formation of defects. Different values of μ_e are related, instead, to different doping levels, $\mu_e = 0$ corresponding to a Fermi level at the top of the valence band. In the case of InGaAs, further restrictions apply to the chemical potentials of the cations [5]. In a previous paper [6], the formation of defects favored by As-rich conditions, i.e., gallium vacancies (V_{Ga}) and arsenic antisites (As_{Ga}), has been investigated in GaAs and $\text{In}_{0.5}\text{Ga}_{0.5}\text{As}$. This investigation has been extended here to defects favored by Ga-rich conditions, i.e., arsenic vacancies (V_{As}) and

*Corresponding author. Fax: +39-6-9067-2316.

E-mail address: aldo.amore@mlib.cnr.it (A. Amore Bonapasta).

gallium antisites (Ga_{As}) and to the interstitials Ga_i , In_i , As_i , in the same materials.

2. Methods

The defect energy E_D and the total energies related to the $\mu_{X(B)}$ potentials have been calculated in the local density approximation [7] by using supercells, separable ab-initio pseudopotentials [8], planewave basis sets, the special-points technique for k -space integration [9], and the exchange-correlation functional of Ceperley–Alder [10]. The geometry of a given supercell has been fully relaxed by minimizing the forces on the atoms. Convergence tests have been carried out by using plane-wave cutoffs ranging from 12 to 20 Ry, supercells of 32 and 64 atoms, and k -point meshes equivalent to a (4, 4, 4) or (8, 8, 8) Monkhorst-Pack mesh in the zinc-blend unit cell. The results presented here have been achieved by using 64-atom supercells, the (4, 4, 4) k -point Monkhorst-Pack mesh in the zinc-blend unit cell, and cutoffs of 18 Ry.

3. Results and discussion

Generally, a ternary alloy may be assumed to be given by a binary compound where a fraction of the cations have been substituted with cations of a different species. In the case of GaAs and $\text{In}_{0.5}\text{Ga}_{0.5}\text{As}$, this substitution induces two competing effects: (i) increase of the lattice constant (a_0); (ii) emergence of an *internal strain*. These effects have been investigated separately by introducing two model materials, “strained” GaAs, with a_0 extended to that of $\text{In}_{0.5}\text{Ga}_{0.5}\text{As}$ (GaAs-ext), and “strained” $\text{In}_{0.5}\text{Ga}_{0.5}\text{As}$, with a_0 contracted to that of bulk GaAs ($\text{In}_{0.5}\text{Ga}_{0.5}\text{As-ctd}$). These model materials provide also a first, qualitative estimate of the effects of an external

strain on the formation of vacancies and antisites, although they do not fully reproduce the structure of strained, pseudomorphic heterostructures grown by MBE. The previous investigation of the As_{Ga}^0 , $\text{As}_{\text{Ga}}^{+2}$, V_{Ga}^0 and $\text{V}_{\text{Ga}}^{-3}$ defects in the above four materials [6] has suggested that *doping* and *strain* may have major effects on the defect formation when the *defect electronic states are closely related to bonding (or antibonding) interactions* between the atoms around the defect site, which implies that the *local charge* on the defect is closely related to its *local geometry*. This picture is supported by the formation energies calculated here for the Ga_{As} , V_{As} and interstitial defects, see Table 1. Both the Ga_{As} and V_{As} defects induce one electronic level in the energy gap. The V_{As} defect has also two electrons occupying a level close to the top of the valence band. Ga_{As} is a double acceptor, while V_{As} may have an amphoteric behavior. The occupancy levels estimated for these defects indicate that the Ga_{As}^0 and $\text{V}_{\text{As}}^{+1}$ are stable charge states when $\mu_e = 0$. When the Fermi level is at midgap ($\mu_e = E_g/2$), the stable states are, instead, $\text{Ga}_{\text{As}}^{-2}$ and V_{As}^0 . When the Fermi level is at the bottom of the conduction band ($\mu_e = E_g$), the $\text{V}_{\text{As}}^{-1}$ state of the defect has formation energies close to (or smaller than) those of the neutral defect, see Table 1. In the case of Ga_{As}^0 , the length of the $\text{Ga}_{\text{As}}\text{--Ga}$ and $\text{Ga}_{\text{As}}\text{--In}$ bonds formed by the defect with its nearest neighbor (NN) atoms is reported in Table 2. In GaAs, the atomic arrangement around the defect has a C_{3v} symmetry induced by the formation of *three* stable $\text{Ga}_{\text{As}}\text{--Ga}$ bonds and by a non-bonding interaction of the Ga_{As} with the fourth NN Ga atom. In GaAs-ext, the increased a_0 leads only to an increase of the distance between the not bonded Ga atom and the Ga_{As} , which reduces Ω_D . In $\text{In}_{0.5}\text{Ga}_{0.5}\text{As}$, the internal strain breaks the C_{3v} symmetry. Furthermore, only two stable bonds are formed having lengths of 2.30 and 2.48 Å, see Table 2. This change of the local geometry of the defect agrees with the increase of Ω_D . Finally, in $\text{In}_{0.5}\text{Ga}_{0.5}\text{As-ctd}$,

Table 1
Defect formation energies of the different defects investigated in the present work (see the text)^a

Defect	GaAs	GaAs-ext	$\text{In}_{0.5}\text{Ga}_{0.5}\text{As}$	$\text{In}_{0.5}\text{Ga}_{0.5}\text{As-ctd}$	μ_e
Ga_{As}^0	2.85	2.40	2.86	2.43	0
$\text{Ga}_{\text{As}}^{+2}$	1.17	1.18	1.80	1.26	$E_g/2$
$\text{Ga}_{\text{As}}^{-2}$	−0.32	−0.12	0.88	0.16	E_g
$\text{V}_{\text{As}}^{-1}$	2.25	3.16	2.14	−0.13	E_g
V_{As}^0	2.08	3.29	2.52	0.58	$E_g/2$
$\text{V}_{\text{As}}^{+1}$	1.11	1.88	1.52	−0.11	0
Ga_i^{+1}	2.08	1.17	1.60	2.03	0
Ga_i^{-1}	2.75	1.81	2.55	2.84	E_g
As_i^{+1}	2.13	0.75	1.56	2.32	0
As_i^{-1}	1.61	0.65	1.68	2.22	E_g

^a The last column gives the value of the electronic chemical potential μ_e . The zero of μ_e is taken at the top of the valence band. E_g is the energy gap. All values are given in eV.

Table 2

Length of the Ga_{As}-Ga and Ga_{As}-In bonds formed by the defect with its NN atoms^a

Defect	GaAs	GaAs-ext	In _{0.5} Ga _{0.5} As	In _{0.5} Ga _{0.5} As-ctd
Ga _{As} ⁰	(3 × 2.31, 2.89)	(3 × 2.38, 3.41)	(2.64, 2.48, 2.30, 2.68)	(2.59, 2.41, 2.22, 2.56)
Ga _{As} ²⁻	4 × 2.29	4 × 2.38	(2.46, 2.46, 2.27, 2.44)	(2.38, 2.37, 2.19, 2.36)
V _{As} ¹⁻	(2 × 2.75, 4 × 3.54)	(2 × 3.08, 4 × 3.88)	(3.00, 2.90, 2 × 3.76, 2 × 3.58)	(2.66, 2 × 3.53, 2.81, 2 × 3.27)
V _{As} ⁰	6 × 3.63	6 × 4.15	(3.16, 2 × 3.58, 3.60, 2 × 3.93)	(2.80, 2.95, 2 × 3.55, 2 × 3.24)
V _{As} ¹⁻	6 × 3.85	6 × 4.32	(3 × 3.60, 3 × 4.16)	(3 × 3.15, 2 × 3.65, 3.36)
Ga _i ¹⁻	2 × 2.55	2 × 2.63	(2.73, 2.59)	(2.68, 2.54)
Ga _i ¹	(2.44, 2 × 2.57)	(2.52, 2 × 2.66)	(2.55, 2.50, 2.47)	(2 × 2.44, 2.47)
As _i ¹⁻	(2 × 2.42, 2.26)	(2 × 2.47, 2.30)	(2.44, 2.46, 2.29)	(2.40, 2.39, 2.30)
As _i ¹	(2 × 2.51, 2.28)	(2 × 2.58, 2.33)	(2.48, 2.54, 2.61)	(2.45, 2.41, 2.61)

^a X–X distances (X = Ga or In) between a Ga antisite and its nearest neighbors (NN) are reported in the upper part of the table together with the X–X distances between the NN of an arsenic vacancy. Ga–In and In–In distances are given in italic and bold characters, respectively. Y–Y distances (Y = Ga or As) between an interstitial atom and its NN are reported in the lower part of the table. Ga–In, Ga–As and In–As distances are given in italic, bold and bold-italic characters, respectively. *n* distances with an equal value *d* are represented by *n* × *d*. The distances should be compared with those given by covalent radii of Ga, In and As (1.26, 1.44 and 1.2 Å, respectively). All values are given in Å.

the contraction of *a*₀ favors a bonding interaction of Ga_{As} with its NN atoms, thus leading to a reduction of the formation energy. In the case of Ga_{As}²⁻ defect, in GaAs this defect forms *four* stable Ga_{As}-Ga bonds, thus indicating that *the defect electronic states are closely related to bonding interactions* between the Ga_{As} and its NN atoms. As a consequence, the Ga_{As}²⁻ formation energy results to be significantly affected by the position of the Fermi level, as shown by the large reduction of its value in the case of $\mu_c = E_g$ (i.e., n-type doping). Furthermore, strain has appreciable effects on the Ga_{As}²⁻ formation energy like for the neutral defect. Similar results were found for the As_{Ga}²⁺, which are favored by p-type doping. In the case of V_{As}⁰, generally the vacancy dangling bonds are not involved in an internal reconstruction. However, the three electrons of the vacancy may give rise to some bonding interaction in the presence of a compressive strain. This defect is characterized therefore by a small coupling between local charge and local geometry. In fact, an analysis of the results reported in Table 1 and 2 for the different charge states of V_{As} shows that the doping and strain have smaller effects on the formation energies of arsenic vacancies. Similar results were found in the case of gallium vacancies. In the case of interstitials, it as to be taken into account that the Ga_i¹⁻ occupies a tetrahedral site, while the Ga_i¹, As_i¹⁻ and Ga_i¹ are characterized by an (110)-split, (110)-split and (100)-split geometries [11], respectively. The results given in the Tables show a common behavior of these defects. They are favored by an increase of the lattice constant and hindered by an internal strain because they need to relax their local geometry. As a related effect, changes of the local charge (as induced by different doping) have limited effects on the reduction of the formation energies.

4. Conclusions

Previous and present results on the formation of antisites and vacancies show that these defects have quite different behaviors when vacancies do not give rise to internal reconstruction. In that case, indeed, antisites are characterized by stronger relationships between defect levels and bonding interactions involving the defect. This implies that antisites are more sensitive to lattice and local-charge rearrangements than vacancies. As a consequence, an *efficient defect engineering* seems possible for *antisites*, difficult for *vacancies*. In fact, in the case of Ga (As) antisites, a n-type (p-type) doping and a compressive (tensile) strain permit to reach very small formation energy values. On the other hand, both gallium and arsenic vacancies reach small formation energies only in extreme conditions of compressive strain. Interstitials present an intermediate behavior with respect to that of antisites and vacancies.

References

- [1] S.D. Benjamin, H.S. Loka, A. Othonos, P.W.E. Smith, Appl. Phys. Lett. 68 (1996) 2544.
- [2] R. Takahashi, Y. Kawamura, T. Kagawa, H. Iwamura, Appl. Phys. Lett. 65 (1994) 1790.
- [3] M. Kaminska, E.R. Weber, in: Semiconductors and Semimetals, Vol. 38, Academic, New York, 1993, pp. 59–89.
- [4] S.B. Zhang, J.E. Northrup, Phys. Rev. Lett. 67 (1991) 2339.
- [5] Sun-Ghil Lee, K.J. Chang, Phys. Rev. B 53 (1996) 9784.
- [6] A. Amore Bonapasta, P. Giannozzi, Phys. Rev. Lett. 84 (2000) 3923.

- [7] R.M. Martin, in: J.T. Devreese, P. Van Camp (Eds.), *Electronic Structure, Dynamics and Quantum Structural Properties of Condensed Matter*, Plenum, New York, 1985.
- [8] R. Stumpf, X. Gonze, M. Scheffler, Research Report of the Fritz-Haber-Institut, Berlin (FRG), April 1990.
- [9] H.J. Monkhorst, J.D. Pack, *Phys. Rev. B* 13 (1976) 5188.
- [10] D.M. Ceperley, B.J. Alder, *Phys. Rev. Lett.* 45 (1980) 566.
- [11] D.J. Chadi, *Phys. Rev. B* 46 (1976) 9400.



ELSEVIER

Physica B 308–310 (2001) 850–853

PHYSICA B

www.elsevier.com/locate/physb

Interplay of nitrogen and hydrogen in $\text{In}_x\text{Ga}_{1-x}\text{As}_{1-y}\text{N}_y/\text{GaAs}$ heterostructures

A. Polimeni^{a,*}, G. Baldassarri Höger von Högersthal^a, M. Bissiri^a, V. Gaspari^a,
F. Ranalli^a, M. Capizzi^a, A. Frova^a, A. Miriametro^a, M. Geddo^b, M. Fischer^c,
M. Reinhardt^c, A. Forchel^c

^a *Istituto Nazionale di Fisica della Materia, Dipartimento di Fisica, Università degli Studi di Roma "La Sapienza", Piazzale A. Moro 2, I-00185 Roma, Italy*

^b *Istituto Nazionale di Fisica della Materia, Dipartimento di Fisica, Università degli Studi di Parma, Viale delle Scienze 7a, 43010 Fontanini (Parma), Italy*

^c *Universität Würzburg, Technische Physik, Am Hubland, 97074 Würzburg, Germany*

Abstract

Photoluminescence and photoreflectance spectroscopy are used to investigate the electronic properties of $\text{In}_x\text{Ga}_{1-x}\text{As}_{1-y}\text{N}_y/\text{GaAs}$ heterostructures treated with low-energy atomic hydrogen. With increasing hydrogen doses, the $\text{In}_x\text{Ga}_{1-x}\text{As}_{1-y}\text{N}_y$ optical gap blue-shifts until it reaches the value of a corresponding N-free reference sample. This effect is ascribed to the formation of N–H bonds, which leads to an electronic passivation of N and, hence, to a reopening of the material band gap. Thermal annealing of the samples restores the band gap the $\text{In}_x\text{Ga}_{1-x}\text{As}_{1-y}\text{N}_y$ had before hydrogenation and gives an activation energy for the dissociation of N–H complexes equal to 2.28 eV. © 2001 Elsevier Science B.V. All rights reserved.

Keywords: Isoelectronic impurities; $\text{In}_x\text{Ga}_{1-x}\text{As}_{1-y}\text{N}_y$; Hydrogen; Optical properties

1. Introduction

Nitrogen introduction in $\text{In}_x\text{Ga}_{1-x}\text{As}$ -based materials leads to striking effects on the band structure of the host material, the most relevant being a large band gap reduction for increasing N concentration [1]. A model based on quantum repulsion between the states of the conduction band minimum of the host material and a N-related level resonant with the former states has been firstly proposed in order to explain the dependence of the $\text{In}_x\text{Ga}_{1-x}\text{As}_{1-y}\text{N}_y$ band gap on nitrogen content [2]. On the other hand, pseudopotential supercell calculations show that the N-mediated coupling between the host crystal band edge states (F , L , and X) also accounts for the band gap decrease of $\text{In}_x\text{Ga}_{1-x}\text{As}_{1-y}\text{N}_y$ with y [3]. Regardless of the exact mechanism leading to the

strong modification of the $\text{In}_x\text{Ga}_{1-x}\text{As}$ conduction band subsequent to N incorporation, the observed effects originate from the large mismatch in size and electro-negativity between N and its lattice neighbors.

In this work, we exploit the high diffusivity and strong chemical activity of atomic hydrogen in order to perturb the nitrogen bond with the cation sublattice atoms. By means of photoluminescence (PL) and photoreflectance (PR) measurements, we show that the insertion of H in $\text{In}_x\text{Ga}_{1-x}\text{As}_{1-y}\text{N}_y/\text{GaAs}$ single quantum wells (QWs) increases the band gap to the value the material had before N incorporation, i.e., the value of a reference QW without nitrogen. Thermal annealing at 550°C restores, instead, the optical properties the $\text{In}_x\text{Ga}_{1-x}\text{As}_{1-y}\text{N}_y/\text{GaAs}$ QW had before hydrogenation. We discuss these results in terms of the formation (dissociation) of N–H bonds which decreases (increases) the effective N content and consequently increases (decreases) the band gap energy of the well.

*Corresponding author. Fax: +39-6-4957697.

E-mail address: polimeni@romal.infn.it (A. Polimeni).

A number of $\text{In}_x\text{Ga}_{1-x}\text{As}_{1-y}\text{N}_y/\text{GaAs}$ single QWs grown by solid source molecular beam epitaxy have been investigated. N_2 cracking was achieved by using a radio frequency plasma source. Indium and nitrogen concentrations in the samples are $x = 0.0 - 0.41$ and $y = 0.0 - 0.052$, respectively. The N concentration has been determined by a combined analysis of X-ray diffraction and optical data. For each subset of quantum wells having the same indium content and well width, L , but differing in terms of the nitrogen concentration, a reference sample without nitrogen has been grown. L ranges from 6.0 to 8.0 nm. All samples have a 100 nm thick GaAs capping layer. Post-growth treatment with atomic hydrogen was obtained by ion-beam irradiation from a Kaufman source with the samples kept at 300°C. The ion energy was about 100 eV and the current density was few tens of $\mu\text{A}/\text{cm}^2$. Several hydrogen doses ($d_H = 1, 5, 50, 270$, and $690 \times 10^{16} \text{ ions}/\text{cm}^2$) have been used in this study. One hour thermal annealing was performed at 10^{-6} Torr at temperatures ranging between 220°C and 550°C. PL was excited by the 515 nm line of an Ar^+ laser, dispersed by a single 1 m monochromator and detected by a cooled Ge detector. PR measurements were performed at near normal incidence. The probe source was a 100 W halogen lamp, the excitation source was an He–Ne laser (power 2 mW) chopped at 220 Hz.

Fig. 1 shows the PR spectra at $T = 90 \text{ K}$ of an $\text{In}_{0.32}\text{Ga}_{0.68}\text{As}_{0.973}\text{N}_{0.027}/\text{GaAs}$ QW (gray full dots), of the same sample irradiated with hydrogen at $d_H = 6.9 \times 10^{18} \text{ ions}/\text{cm}^2$ (black full dots), and of the N-free reference QW (open dots). The dashed lines are a simulation of the PR data based on the model of Ref. [4]. In PR, two transitions are observed and attributed to heavy (HH)- and light (LH)-hole excitons. Firstly, it can be noted how the presence of a few percent (0.027) of nitrogen results in an HH energy red-shift of about 0.17 eV. A similar energy shift is found for the light-hole exciton ($\sim 0.19 \text{ eV}$). H treatment leads, instead, to a blue-shift of both HH- and LH-hole excitons, as well as to a change on the low energy side of the HH exciton transition lineshape, which suggests the insurgence of an H-related level in the QW band gap. In the N-free QW (not shown here), H irradiation does not affect the energy of the exciton-related transitions, which gain a factor 10 in intensity because of likely passivation of surface states. Also, PR linewidth broadens upon hydrogenation indicating an increase of microscopic disorder. We point out that heat treatment like that experienced during H irradiation, but in absence of H, has no effect on the sample linewidth and peak energy.

The band gap reopening subsequent to the H treatment described above has been observed in all samples considered ($y = 0.007 - 0.052$). We will focus then on the results obtained in a QW with $x = 0.34$, $y = 0.007$, and $L = 7.0 \text{ nm}$ and its corresponding N-free reference.

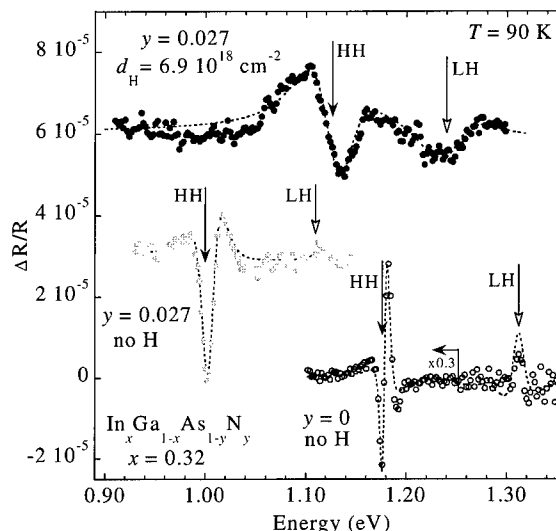


Fig. 1. Photoreflectance spectra at $T = 90 \text{ K}$ of an untreated $\text{In}_{0.32}\text{Ga}_{0.68}\text{As}_{0.973}\text{N}_{0.027}/\text{GaAs}$ QW (gray full dots), of the same sample irradiated with hydrogen at $d_H = 6.9 \times 10^{18} \text{ ions}/\text{cm}^2$ (black full dots), and of the N-free reference QW (open dots). The dashed lines are a simulation to the data by means of the model of Ref. [4]. HH and LH indicate the heavy- and light-hole exciton transitions, respectively. Vertical arrows indicate the transition energies as determined by the simulation procedure.

Fig. 2 shows the room temperature PL spectra recorded on a N-containing QW (continuous lines) treated with different hydrogen doses (graphs (a)–(c)). Graphs (b')–(d) show the effect of thermal annealing performed on the same QW hydrogenated at $d_H = 5.0 \times 10^{17} \text{ ions}/\text{cm}^2$ (graph (b)). For comparison purposes, the PL spectra of the N-free reference QW (dashed lines) treated and untreated with hydrogen are also shown. Let us consider the effects of hydrogen treatment first. In the nitrogen containing QW, the PL peak shifts towards higher energy for increasing hydrogen doses until it saturates at the value it has in the N-free QW, whose peak energy does not change with d_H (see dashed lines in the figure). As observed in the PR spectra of Fig. 1, hydrogen treatment leads also to an increased microscopic disorder, mainly in the N-containing QW, whose PL linewidth is appreciably broader than that of the reference QW even at the lowest d_H .

The effects of hydrogen treatment can be reversed by thermally annealing the sample. The N-containing QW hydrogenated at a dose $d_H = 5.0 \times 10^{17} \text{ ions}/\text{cm}^2$ (graph (b)) has been annealed at various temperatures ranging from 220°C to 550°C. Fig. 2 shows the room temperature PL spectra for increasing T_a (graphs (b')–(d)). The PL band of the hydrogenated $y = 0.007$ QW moves

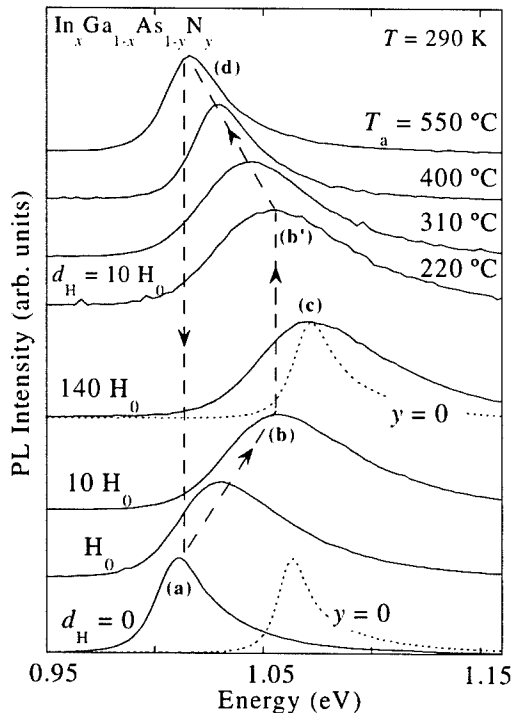


Fig. 2. Graphs (a)–(c): Room temperature peak normalized photoluminescence spectra of hydrogenated $\text{In}_{0.34}\text{Ga}_{0.66}\text{As}_{1-y}\text{N}_y/\text{GaAs}$ QWs with $y = 0.007$ (continuous lines), and $y = 0.0$ (dashed lines) for different hydrogen doses d_{H} ($H_0 = 5.0 \times 10^{16}$ ions/cm²). Graphs (b')–(d): Room temperature peak normalized photoluminescence spectra of the $\text{In}_{0.34}\text{Ga}_{0.66}\text{As}_{0.993}\text{N}_{0.007}$ QW hydrogenated at $d_{\text{H}} = 10 H_0$ and annealed at different temperatures, T_{a} . Laser power density $P = 70 \text{ W/cm}^2$ for all spectra.

towards lower energy until its lineshape nearly coincides with the PL spectrum of the H-free, not annealed, $y = 0.007$ QW (compare graphs (a) and (d)); instead, the PL band of the reference QW (not shown here) is not affected by the annealing process.

We can account for the band gap opening induced by H in $\text{In}_x\text{Ga}_{1-x}\text{As}_{1-y}\text{N}_y$ in the framework of H bonding to point defects in semiconductors [5]. The charge transfer from the group III atoms towards the strong electronegative N atoms favors the formation of H–N bonds in $\text{In}_x\text{Ga}_{1-x}\text{As}_{1-y}\text{N}_y\text{:H}$. This is consistent with theoretical predictions of an N antibonding equilibrium position for H^+ in p-type GaN [6].¹ A “molecular orbital” formed by hydrogen and nitrogen leads to a bonding level with electronic properties different from and with an energy level lower than those of the original N level. This neutralizes the N electrical activity with a decrease of the effective number of N atoms and an

¹Nominally, undoped GaAs grown by molecular beam epitaxy is generally slight p-type due to the residual C in the growth chamber.

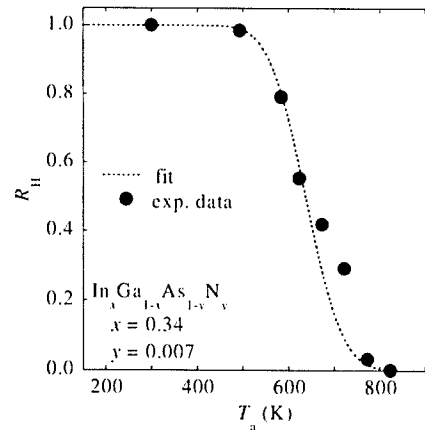


Fig. 3. Dependence of the residual percentage of H, R_{H} , left into an $\text{In}_{0.34}\text{Ga}_{0.66}\text{As}_{0.993}\text{N}_{0.007}$ QW hydrogenated at $d_{\text{H}} = 5.0 \times 10^{17}$ ions/cm² and annealed for one hour at temperature T_{a} . The dashed line is a simulation to the data by means of Eq. (1), which gives a value of the activation energy for the dissociation of the N–H complexes equal to $2.28 \pm 0.26 \text{ eV}$.

increase of the band gap. Thermal annealing breaks the H–N bonds, thus increasing back the effective number of N atoms, accordingly with the results shown in Fig. 2.

In order to determine the bond strength of the H–N complexes we analyzed the shift of the PL peak energy as a function of the annealing temperature, T_{a} . We assume zero residual hydrogen when the $\text{In}_x\text{Ga}_{1-x}\text{As}_{1-y}\text{N}_y$ QW emission energy coincides with the same quantity measured in the H-free sample (i.e., $T_{\text{a}} > 800 \text{ K}$). Instead, the not-annealed hydrogenated $\text{In}_x\text{Ga}_{1-x}\text{As}_{1-y}\text{N}_y$ QW corresponds to residual H equal to one. For a given T_{a} value, we (i) first estimate the effective N content from the PL peak energy;² (ii) then obtain the residual hydrogen assuming that each H atom interacts with a single N atom [7]. The results of this analysis are shown in Fig. 3. If R_{H} is the residual percentage of H atoms present in the sample after annealing, we can estimate the activation energy of dissociation for N–H complexes, E_{a} , by using [8]

$$R_{\text{H}} = \int_0^1 e^{-t_{\text{a}} f(E, T_{\text{a}}) G(E - E_{\text{a}})} dE, \quad (1)$$

where $f(E, T_{\text{a}}) = \exp(-E/k_{\text{B}}T_{\text{a}})$ and $G(E - E_{\text{a}})$ is a Gauss function introduced for taking into account a distribution of activation energies around a mean value, E_{a} . t_{a} is the annealing time (one hour in this case) and ν is the attempt frequency equal to 93 THz, as derived

²For determining the effective N concentration, we used $E_{\text{p}}(y \neq 0) = E_{\text{p}}(y = 0) - 2.2 y^{0.7}$, where E_{p} is the PL peak energy in eV. The above formula has been obtained by means of a fit to the experimental E_{p} 's measured in the untreated $\text{In}_x\text{Ga}_{1-x}\text{As}_{1-y}\text{N}_y$ samples.

from the N–H stretch frequency measured in $\text{In}_x\text{Ga}_{1-x}\text{As}_{1-y}\text{N}_y$ [9]. The dashed line shown in Fig. 3 is a fit of R_H to the data, which yields $E_a = 2.28 \text{ eV}$ and a standard deviation for $G(E - E_a)$ equal to 0.26 eV . The E_a value found here may be compared with those found typically for H-donor complexes in GaAs ($\sim 2.1 \text{ eV}$) [10] and Si ($\sim 1.4 \text{ eV}$) [8], and H-acceptor complexes in GaN ($\sim 2.2 \text{ eV}$) [11].

To conclude, we have shown that hydrogen strongly perturbs the electronic properties of $\text{In}_x\text{Ga}_{1-x}\text{As}_{1-y}\text{N}_y$, restoring the band gap energy to the value it has in the N-free crystal. We account for this effect by the formation of H–N bonds, which effectively diminish the N content of the samples. Therefore, present results indicate that the N-associated wavefunction in $\text{In}_x\text{Ga}_{1-x}\text{As}_{1-y}\text{N}_y$ maintains a strongly impurity-like character up to $y = 0.052$. Therefore, the so-called “alloy” limit may have not been fully reached even for such high N contents.

References

- [1] I.A. Buyanova, W.M. Chen, B. Monemar, *MRS Internet J. Nitride Semicond. Res.* 6 (2) (2001) 1.
- [2] W. Shan, W. Walukiewicz, J.W. Ager III, E.E. Haller, J.F. Geisz, D.J. Friedman, J.M. Olson, S.R. Kurtz, *Phys. Rev. Lett.* 82 (1999) 1221.
- [3] P.R.C. Kent, A. Zunger, *Phys. Rev. Lett.* 82 (1999) 1221.
- [4] D.E. Aspnes, *Surf. Sci.* 37 (1973) 418.
- [5] G.G. DeLeo, W.B. Fowler, in: J.I. Pankove, N.M. Johnson (Eds.), *Semiconductors and Semimetals*, Vol. 34, Academic Press, New York, 1991.
- [6] J. Neugebauer, C.G. Van de Walle, *Phys. Rev. Lett.* 75 (1995) 4452.
- [7] A. Polimeni, G. Baldassarri Höger von Högersthal, M. Bissiri, Capizzi, M. Fischer, M. Reinhardt, A. Forchel, *Phys. Rev. B* 63 (2001) 201304.
- [8] K. Bergman, M. Stavola, S.J. Pearton, J. Lopata, *Phys. Rev. B* 37 (1988) 2770.
- [9] S. Kurtz, J. Webb, L. Gedvilas, D. Friedman, J. Geisz, J. Olson, R. King, D. Joslin, N. Karam, *Appl. Phys. Lett.* 78 (2001) 748.
- [10] S.J. Pearton, W.C. Dautremont-Smith, J. Chevallier, C.W. Tu, D. Cummings, *J. Appl. Phys.* 59 (1986) 2821.
- [11] S.J. Pearton, J.C. Zolper, R.J. Shul, F. Ren, J. Appl. Phys. 86 (1999) 1.



ELSEVIER

Physica B 308–310 (2001) 854–857

PHYSICA B

www.elsevier.com/locate/physb

Mechanism of zinc diffusion in gallium antimonide

S.P. Nicols^{a,b,*}, H. Bracht^c, M. Benamara^b, Z. Liliental-Weber^b, E.E. Haller^{a,b}

^a University of California at Berkeley, 1 Cyclotron Road MS 2-200, Berkeley, CA 94720, USA

^b Lawrence Berkeley National Laboratory, Berkeley, CA 94720, USA

^c Institut für Materialphysik, University of Münster, Münster, Germany

Abstract

Zn diffusion experiments in GaSb at temperatures between 500°C and 650°C were performed using Ga–Zn alloy sources. For surface Zn concentrations exceeding 10^{20} cm^{-3} , extended defects were detected using cross-sectional transmission electron microscopy (TEM). These defect networks correlate directly with the observed kink and tail profile shape. For lower Zn doping levels the kink disappears. The profiles of these samples reflect the diffusion behavior of Zn in virtually defect-free GaSb and are accurately described by a Ga interstitial controlled mode of Zn diffusion via the kick-out mechanism. Neutral and singly positively charged Ga interstitials mediate Zn diffusion at Zn doping levels of $1\text{--}2 \times 10^{19}$ and $3\text{--}10 \times 10^{19} \text{ cm}^{-3}$, respectively. The contribution of neutral Ga interstitials to Ga diffusion deduced from fitting experimental Zn profiles is in agreement with the directly measured Ga self-diffusion coefficient in GaSb isotope heterostructures. This provides strong evidence that Ga diffusion in undoped GaSb under Ga-rich conditions is mainly mediated by neutral Ga interstitials. Published by Elsevier Science B.V.

Keywords: Zinc diffusion; Gallium antimonide; Kick-out model; Ga self-interstitial

1. Introduction

The understanding of both self- and foreign-atom diffusion in semiconductor systems is of fundamental importance. Diffusion in semiconductors is mediated by native point defects in the crystalline lattice. Diffusion is one of only a few methods that can provide information on point defect properties such as equilibrium concentrations, formation and migration energies, as well as charge states. From the technological point of view, diffusion processes govern the dopant profiles that form the junctions in all microelectronic devices. As devices are engineered with ever shrinking dimensions and higher dopant concentrations, the quantitative understanding and control of diffusion becomes more and more important.

Research in the GaSb system has recently intensified due to applications in high speed electronics as well as infrared lasers, detectors, and photovoltaics. Particular success has been seen in GaSb based heterojunction

bi-polar transistors (HBTs), where switching speeds exceeding 250 GHz have been reported [1]. We have recently shown that Sb diffuses about 1000 times more slowly than Ga in intrinsic GaSb, all the way up to the melting point [2,3]. This atypically low value for Sb self-diffusion makes GaSb a very interesting material from the diffusion and point defect standpoint.

In order to learn more about the influence of the Fermi level position on diffusion in GaSb, we have performed Zn doping experiments. Kyuregyan and Stuchebnikov [4] first showed that Zn diffusion from a constant surface concentration source cannot be described by the complementary error function. Instead, the diffusion coefficient is a function of the local zinc concentration. Since this publication, many groups have published results further exploring these initial findings, but no clear identification of the diffusion mechanism of Zn in GaSb has been made [5–10]. Conibeer et al. propose that Zn diffuses via a substitutional-interstitial mechanism [8], yet they lack sufficient evidence to support either the vacancy (Frank and Turnbull [11]) or kick-out (Gösele and Morehead [12]) mechanism.

*Corresponding author. Fax: +1-510-486-5530.

E-mail address: spnicols@lbl.gov (S.P. Nicols).

This work aims to identify the diffusion mechanism of Zn in GaSb and to apply this knowledge towards a more complete understanding of Ga diffusion in this compound semiconductor than can be achieved by self-diffusion studies alone.

2. Experimental

Cz-grown undoped p-type GaSb wafers (100) from Atomergic Chemetals Corp. with a carrier concentration of $1\text{--}2 \times 10^{16} \text{ cm}^{-3}$ were used for Zn diffusion experiments. Ga–Zn alloys with 2–20 at% Zn were made by annealing Zn (99.9999%) with Ga (99.9999%) at 750°C for 2 days in evacuated ampoules. Prior to the diffusion anneal, rectangular samples of approximately 15 mm^2 GaSb were cleaned first with organic solvents, followed by a 30 s HCl etch and a 10 s HF etch. Samples were sealed in quartz ampoules with base pressures of below 2×10^{-5} Torr along with approximately 5 mg of Ga–Zn alloy as Zn source. The samples were annealed in a resistively heated furnace where the temperature can be controlled to $\pm 2 \text{ K}$. Termination of the annealing process was carried out through quenching the ampoule in water at room temperature.

Cross-sectional transmission electron microscopy (TEM) was performed at the National Center for Electron Microscopy at the Lawrence Berkeley National Laboratory.

Secondary ion mass spectrometry (SIMS) with a Cameca IMS-3f was used to measure elemental profiles. A Cs^+ ion beam with energies of 2–3 keV was used to obtain the diffusion profiles of ^{64}Zn while monitoring ^{69}Ga to assure a constant etch rate in the matrix. In order to achieve good depth resolution, only those samples having a specular surface after annealing were used for the SIMS analysis. Crater depth measurements were done using a surface profilometer with an accuracy of 5%. Secondary ion counts were converted into concentrations using a Cz-grown Zn doped GaSb wafer from University Wafer with a bulk Zn concentration of $1\text{--}2 \times 10^{18} \text{ cm}^{-3}$.

3. Experimental results

SIMS depth concentration profiles of Zn were obtained showing two characteristic shapes. Fig. 1 gives examples of both the kink and tail and box type diffusion profiles. The kink and tail profiles are clearly identifiable by their kink located behind the diffusion front while this characteristic is missing in the box profiles. The kink and tail profiles were observed in all samples showing Zn surface concentrations in excess of 10^{20} cm^{-3} while box profiles were observed in all samples showing surface concentrations below 10^{20} cm^{-3} .

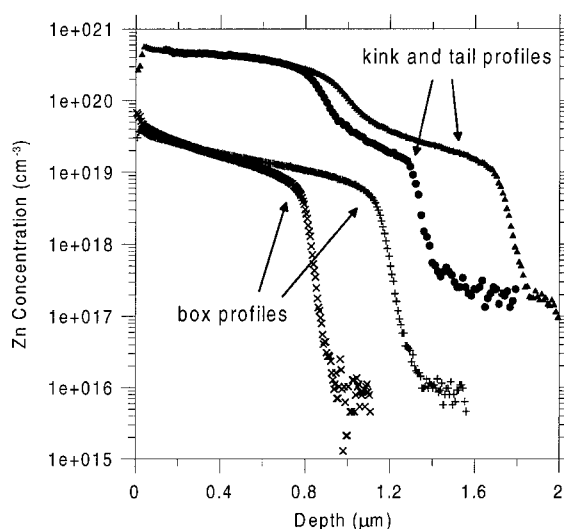


Fig. 1. Two examples each of kink and tail and box shaped Zn diffusion profiles in GaSb as measured by SIMS. Annealing schedules and Zn sources are as follows: 4% Zn/96% Ga source, 30 min at 640°C (\times); 4% Zn/96% Ga source, 114 min at 638°C ($+$); 20% Zn/80% Ga source, 60 min, 550°C (\bullet); 3% Zn/39% Ga/58% Sb source, 917 min at 576°C (\blacktriangle).

Cross-sectional TEM was carried out on representative samples showing box as well as kink and tail profiles to determine the presence of any extended defects which would make the samples unsuitable for these diffusion studies. The box shaped diffusion profiles were all found to be free of extended defects in the area of diffusion, while a loose network of dislocations coincident with the high concentration kink was observed in the kink and tail samples. An example of this can be seen in Fig. 2 where the SIMS profile and TEM are overlaid with matching depth axes for comparison. Two defective regions are clearly visible in the TEM, the first being approximately 450 nm below the surface, and the second near 800 nm. The defect band at 800 nm is formed by $\frac{1}{2}\langle 110 \rangle$ type dislocations.

4. Discussion

The presence of extended defects in the samples with kink and tail profiles made them unsuitable for this diffusion study. The observation that the deeper defect band coincides nearly exactly with the kink suggests that they are directly interrelated. No kink and tail type profiles were used in any of our modeling.

Extensive modeling was carried out on a number of profiles showing the box shape. In all models, it is assumed that Zn diffuses interstitially as a singly positively charged specie, while being present as a

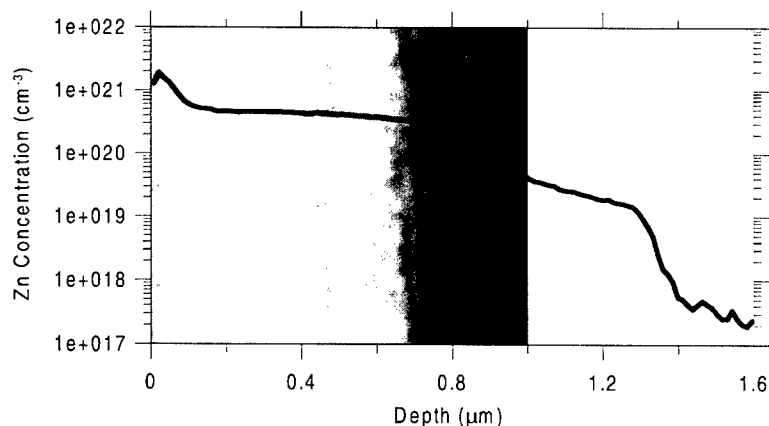


Fig. 2. Composite SIMS profile and TEM micrograph with common depth axis of a sample annealed at 550 °C for 60 min using a 20% Zn/80% Ga source. SIMS clearly shows a kink and tail diffusion profile while the TEM shows two defective regions approximately 450 and 800 nm from the surface.

singly ionized acceptor in the Ga substitutional position. Accurate modeling of the box profiles is achieved within the Ga interstitial controlled mode of Zn diffusion via the kick-out mechanism. For surface concentrations of $1\text{--}2 \times 10^{19} \text{ cm}^{-3}$, very good fits are obtained assuming that neutral Ga interstitials are the mediating defects. Hence the reaction considered for modeling these Zn profiles reads



For surface concentrations exceeding $2 \times 10^{19} \text{ cm}^{-3}$, reaction (1) does not ensure an accurate fit to the Zn distribution at the diffusion front. Examples of these two conditions can be seen in Fig. 3. At the higher surface concentration we believe that the Fermi level drops low enough to ionize the neutral Ga interstitials into a singly positively charged donor state via the following reaction:



The kick-out reaction is thus no longer described only by (1), but by a combination of (1) and the following reaction



The shallower diffusion front observed for these samples is very likely related to a lower effective rate constant for the Zn_i to Zn_{Ga} exchange active at this doping level.

Diffusivity data can be extracted directly from the accurate fittings achieved in the surface concentration range of $1\text{--}2 \times 10^{19} \text{ cm}^{-3}$. Reduced Zn diffusivity data (Zn concentration independent) were used to calculate D_0 and Q for Zn diffusion under intrinsic conditions as $1.4 \times 10^{10} \text{ cm}^2/\text{s}$ and 4.3 eV, respectively. The fitting also yielded data for the Ga interstitial contribution to Ga self-diffusion. The I_{Ga}^0 contribution equals the directly measured Ga self-diffusion under Ga-rich conditions [2]

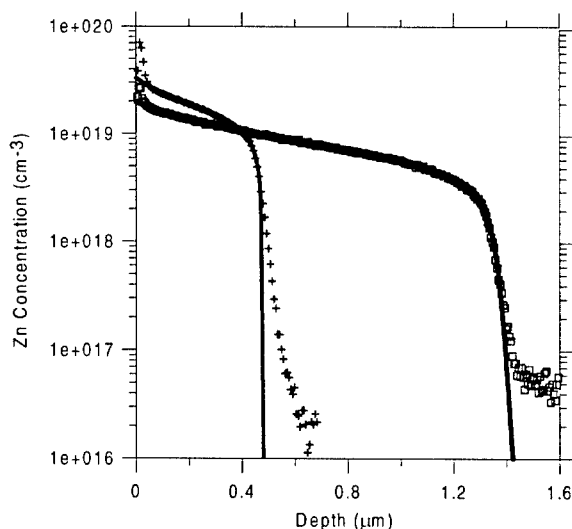


Fig. 3. SIMS profiles (□, +) and fits (solid lines) based on neutral Ga interstitial controlled mode of the kick-out mechanism. The samples were annealed at 609 °C for 500 min (□) and 561 °C for 921 min (+) using a 2% Zn/98% Ga source.

within a factor of 2. This indicates that Ga self-diffusion is very likely mediated by neutral Ga interstitials. The Zn and Ga diffusion data is summarized in Fig. 4. At this time we cannot completely exclude that singly positively charged Ga interstitials also contribute to Zn diffusion at Zn doping levels of $1\text{--}2 \times 10^{19} \text{ cm}^{-3}$. More extensive modeling of Zn diffusion must be performed to determine the contributions of reactions (1) and (3) to Zn diffusion and thereby the individual contributions of neutral and singly positively charged Ga interstitials to Ga self-diffusion.

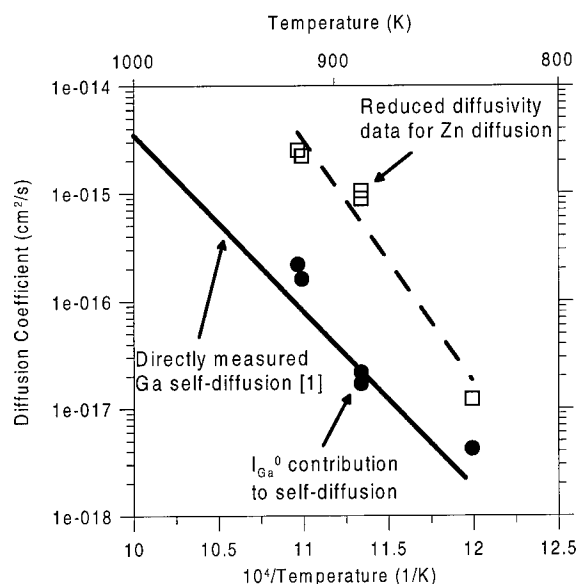


Fig. 4. Ga and Zn diffusion data extracted from Zn diffusion profiles. Contribution of neutral Ga interstitial to Ga self-diffusion (●) as extracted from box profile diffusion profiles compared to directly measured Ga self-diffusion data [2] (solid line). Reduced Zn diffusivity (□) and best fit using exponential form (dashed line).

The deviation from Arrhenius behavior observed in the diffusivity data can be explained by the limited accuracy of the Zn surface concentration. All values determined for the effective diffusivity of I_{Ga}^0 and the reduced Zn diffusivity are reduced by the equilibrium concentration of Zn adjusted at the surface. Hence the accuracy of the diffusivity data depends on an accurate determination of the Zn surface concentration.

5. Conclusion

Kink and tail Zn diffusion profiles in GaSb are shown to correlate with the presence of a dislocation network behind the diffusion front for Zn surface concentrations exceeding 10^{20} cm^{-3} . Defect-free samples with box shape diffusion profiles are found for Zn surface concentrations below 10^{20} cm^{-3} . Accurate modeling of the box shaped diffusion profiles is only achieved with the kick-out mechanism for Zn diffusion. Neutral Ga

interstitials are considered to mediate Zn diffusion for Zn surface concentrations of $1\text{--}2 \times 10^{19} \text{ cm}^{-3}$, while singly positive charged Ga interstitials begin to contribute at concentrations above $3 \times 10^{19} \text{ cm}^{-3}$. The deduced contribution of neutral Ga interstitials to Ga self-diffusion equals the directly measured Ga self-diffusion within a factor of 2, indicating that Ga self-diffusion is very likely mediated by the neutral Ga interstitial.

Acknowledgements

H.B. acknowledges a Feodor Lynen fellowship of the Alexander von Humboldt-Stiftung. This work was supported in part by the Director, Office of Science, Office of Basic Energy Sciences, Materials Sciences Division of the US Department of Energy under Contract No. DE-AC03-76SF00098, by US NSF Grant No. DMR-97 32707, and by the Fond der Chemischen Industrie.

References

- [1] M.W. Dvorak, O.J. Pitts, S.P. Watkins, C.R. Bolognesi, International Electron Devices Meeting 2000, IEEE Piscataway, NJ, USA, 2000, p. 178.
- [2] H. Bracht, S.P. Nicols, W. Walukiewicz, J.P. Silveira, F. Briones, E.E. Haller, *Nature* 408 (2000) 69.
- [3] H. Bracht, S.P. Nicols, E.E. Haller, J.P. Silveira, F. Briones, *J. Appl. Phys.* 89 (2001) 5393.
- [4] A.S. Kyuregyan, V.M. Stuchechnikov, *Sov. Phys.—Semicond.* 4 (1971) 1365.
- [5] S.F. Da Cunha, J. Bougnot, *Phys. Status Solidi A* 22 (1974) 205.
- [6] V.S. Sundaram, P.E. Gruenbaum, *J. Appl. Phys.* 73 (1993) 3787.
- [7] G.J. Conibeer, A.F.W. Willoughby, C.M. Hardingham, V.K.M. Sharma, *Mater. Sci. Forum* 143 (1994) 1427.
- [8] G.J. Conibeer, A.F.W. Willoughby, C.M. Hardingham, V.K.M. Sharma, *J. Electron. Mater.* 25 (1996) 1108.
- [9] A.W. Bett, S. Keser, O.V. Sulima, *J. Crystal Growth* 181 (1997) 9.
- [10] J. Mimkes, V. Šestáková, K.M. Nassr, M. Lübbers, B. Štěpánek, *J. Crystal Growth* 187 (1998) 355.
- [11] F.C. Frank, D. Turnbull, *Phys. Rev.* 104 (1956) 617.
- [12] U. Gösele, F. Morehead, *J. Appl. Phys.* 52 (1981) 4617.



ELSEVIER

Physica B 308–310 (2001) 858–861

PHYSICA B

www.elsevier.com/locate/physb

Carbon-doped MOCVD InP is semi-insulating up to 700°C

R.C. Newman^{a,*}, B.R. Davidson^a, J. Wagner^b, M.J.L. Sangster^c, R.S. Leigh^c^aCEMD, The Blackett Laboratory, Imperial College, Prince Consort Road, London SW7 2BZ, UK^bFraunhofer-IAF, Tullastrasse 72, D-71908, Freiburg, Germany^cJ.J. Thomson Physical Laboratory, Reading University, P.O. BOX 220, Reading RG6 6AF, UK

Abstract

InP:C layers grown by metal organic vapour phase epitaxy at 500°C and doped with CCl₄ remain semi-insulating following anneals up to 700°C. The compensation of grown-in C_P acceptors ([C_P] ~ 5 × 10¹⁸ cm⁻³) is attributed to the presence of C–C deep donor defects, revealed by Raman scattering. [C_P] and the concentration of grown-in C_P–H pairs both decrease with increasing temperatures. C_{In}, V_{In}H₄ or P_{In} shallow donors are not detected. Reductions in the internal random electric fields upon annealing lead to narrowing of the C_P localised vibrational mode. Samples annealed at 800°C become lightly n-type (~ 10¹⁶ cm⁻³). © 2001 Elsevier Science B.V. All rights reserved.

PACS: 81.15.Gh; 81.05.Ea; 66.30.Jt; 63.20.Pw

Keywords: Annealed InP:C; (C–C) precipitates in InP:C; InP:C Raman scattering

1. Introduction

Semi-insulating layers of carbon-doped InP can be grown on (100) InP substrates by metal organic vapour phase epitaxy (MOVPE) at 500°C, using PH₃ and In(CH₃)₃ precursors and CCl₄ as the dopant source [1,2]. We shall discuss measurements made on such layers with a thickness of 8 × 10⁻⁴ cm and an incorporated carbon concentration, [C] ~ 10¹⁹ cm⁻³, determined by secondary ion mass spectrometry (SIMS). These measurements also reveal hydrogen concentrations [H] ~ 5 × 10¹⁸ cm⁻³ but the concentrations of all other elements are much smaller [2]. The strengths of infrared (IR) active localised vibrational modes (LVMs) originating from the layers confirm the SIMS data since we find [H–C] = 5.4 × 10¹⁸ and [C] = 5.8 × 10¹⁸, assuming the two unknown calibration factors, (*f*), to be similar to those for the corresponding centres in GaAs. The separation of the LVM frequencies of the ¹²C and ¹³C

(1.1% naturally abundant) modes is incompatible with an assignment to C_{In} donors but is consistent with the interpretation of C_P acceptors [2]. Three other modes were assigned to H–¹²C_P pairs by comparing their dispositions and relative strengths with the modes of H–C_{As} pairs in GaAs [3]. This assignment is now confirmed by demonstrating correlations of the line strengths in InP samples following anneals at temperatures up to 800°C, that lead to reductions of [C_P] and the complete loss of [H–C_P] pairs.

There has been an outstanding need to identify the incorporated donors or traps that compensate C_P acceptors in the InP epitaxial layers. LVMs from V_{In}H₄ defects (2316 cm⁻¹) were present in the as-grown substrates [4] but any additional V_{In}H₄ absorption (not detected) from the epitaxial layer was smaller by a factor of at least 10² than that required to effect compensation: our measurements do not reveal LVMs of P_{In} antisite defects or C_{In} centres. However, we now show that Raman scattering measurements reveal high frequency modes, analogous to those of deep donor di-carbon pair defects (C–C), present as dumbbells occupying As lattice sites in highly carbon-doped GaAs and AlAs [5,6]. Anneals lead to increases of [C–C] in InP as [C_P] and [H–C_P] decrease.

*Corresponding author. Tel.: +44-207-594-6692; fax: +44-207-581-3817.

E-mail address: r.newman@ic.ac.uk (R.C. Newman).

¹23 Betchworth Ave. Earley, Reading, Berks. RG6 7RH, UK.

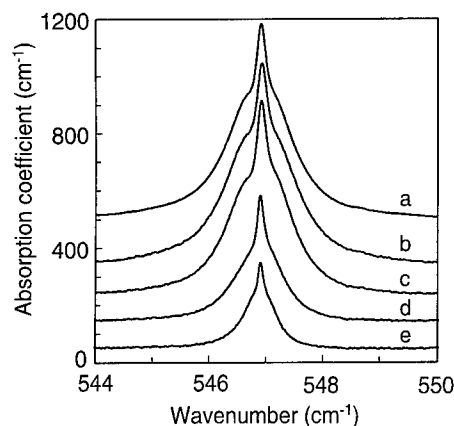


Fig. 1. Profiles of the $^{12}\text{C}_\text{P}$ IR LVM, after growth, *a*, and following anneals at increasing temperatures, *b*, *c*, *d*, *e*, at 500°C, 600°C, 700°C and 800°C.

The $^{12}\text{C}_\text{P}$ and $^{13}\text{C}_\text{P}$ LVMs are located in a gap in the density of two-phonon states of InP, so that decay of their excitations must involve the formation of three (or more) InP lattice modes [2]. Their linewidths Δ were expected to be small ($\sim 0.1\text{ cm}^{-1}$) but the observed profiles for $^{12}\text{C}_\text{P}$ show a very sharp central peak with two 'shoulders' (Fig. 1). The splitting of the three-fold degenerate first excited vibrational state of ionised acceptor carbon atoms is caused by internal electric fields that have random strengths and orientations, arising from all other incorporated acceptors and donors [7,8]. There are no mobile electrons to effect screening since the material is semi-insulating. We show that reductions of $[\text{C}_\text{P}]$ in annealed samples leads to reduced LVM linewidths as the strength of the internal fields decreases, probably with decreases of strain.

2. Experimental details

Details of as-grown samples (see [2]) have been outlined in Section 1. These samples were then subjected to rapid transient anneals for 5 min at 500°C, 600°C, 700°C or 800°C in flowing argon, leading to changes in $[\text{C}_\text{P}]$ and $[\text{H-C}_\text{P}]$ (Table 1). The samples were coated with a thin layer of SiO_2 from a plasma source to prevent destruction of the epitaxial InP:C layers during the anneals and the SiO_2 was subsequently removed with HF acid. IR measurements were made with a Bruker IFS 120 HR spectrometer operated at a spectral resolution of 0.02 cm^{-1} and a sample temperature of $\sim 10\text{ K}$. Raman measurements were made from the (100) growth surface of samples cooled to 77 K. The back scattering geometry was used and the scattered light from a Kr^+ ion laser with $h\nu_\text{L} = 3.00$ or 3.05 eV was analysed with a triple spectrometer and a charge coupled detector array for the spectral ranges between

Table 1

Values of $[\text{C}_\text{P}] \times 10^{18}\text{ cm}^{-3}$ and $[\text{H-C}_\text{P}] \times 10^{18}\text{ cm}^{-3}$ using IR calibration factors $f(\text{C}_\text{P}) = 7 \times 10^{15}\text{ cm}^{-1}$ and $f(\text{H-C}_\text{P}) = 2 \times 10^{15}\text{ cm}^{-1}$, respectively [2], and the parameter, γ , following heat treatments of samples [10]

Anneal <i>T</i> (°C)	$[\text{C}_\text{P}]$ 546.9 cm^{-1}	$[\text{H-}^{12}\text{C}_\text{P}]$ 2703 cm^{-1}	γ (cm^{-1})
As-grown	5.8	5.4	0.07
500°C	6.6	4.6	0.08
600°C	5.3	2.6	0.06
700°C	2.5	0.7	0.04
800°C	1.3	0.0	0.04

60–2200 and 3000–4500 cm^{-1} : the partial breakdown of selection rules implies some roughening of the sample surfaces. Hall measurements were made at room temperature using the van der Pauw geometry with indium dot contacts made at a temperature below 350°C.

3. IR and Raman measurements of the modes of isolated carbon atoms and H-C_P pairs

Increases of $[\text{C}_\text{P}]$ and decreases of $[\text{H-C}_\text{P}]$ in samples heated at 500°C (the growth temperature) are attributed to out-diffusion of hydrogen (Table 1). At higher temperatures, there are systematic reductions of both $[\text{C}_\text{P}]$ and $[\text{H-C}_\text{P}]$, implying a loss of carbon acceptors from substitutional sites and further out-diffusion of H-atoms.

Three of the four IR-active modes of the H-C_P centres are detected for samples annealed at temperatures up to 700°C, namely the A_1^- -anti-symmetric stretch mode at 2703.3 cm^{-1} , the A_1^+ -symmetric stretch mode at 413.5 cm^{-1} and the transverse *E*-mode (also identified by Raman scattering) at 521.1 cm^{-1} with dominant carbon vibrational displacements. The second *E*-mode, with dominant H-displacements, is not detected but the corresponding line in GaAs is also very weak [3]. The measurements establish the correlation of the three lines (Fig. 2), supporting the assignment of paired substitutional carbon atoms to phosphorus lattice sites. Weak satellite lines detected at 2756 and 2818 cm^{-1} are tentatively attributed to centres with a hydrogen atom paired to two adjacent substitutional carbon atoms (cf. data for highly carbon-doped GaAs [9]). The samples remain semi-insulating after anneals at 600°C and 700°C, but an anneal at 800°C leads to low conductivity with $n \sim 10^{16}\text{ cm}^{-3}$ that is two orders of magnitude smaller than the remaining $[\text{C}_\text{P}] = 1.3 \times 10^{18}\text{ cm}^{-3}$. Related Raman scattering measurements of C_P and H-C_P pairs are discussed elsewhere [10].

Of greater importance is the presence of lines at 1785 and 1814 cm^{-1} detected by Raman scattering from

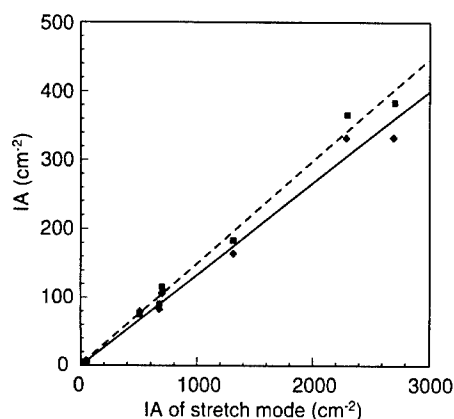


Fig. 2. Correlations of the IR strengths (integrated absorption IAs) of the LVMs at 521 cm^{-1} (squares, E -mode) and 414 cm^{-1} (diamonds, A_1^- -mode) as a function of the IA of the LVM at 2703 cm^{-1} (A_1^- , stretch mode) for as-grown and annealed samples: additional points are for other samples with $[C_P] = 2.5 \times 10^{18}$ and $[H-C_P] = 1.4 \times 10^{18}\text{ cm}^{-3}$ [10]. The dashed (solid) line is a fit to the square points (diamonds) with a gradient of 0.150 (0.134).

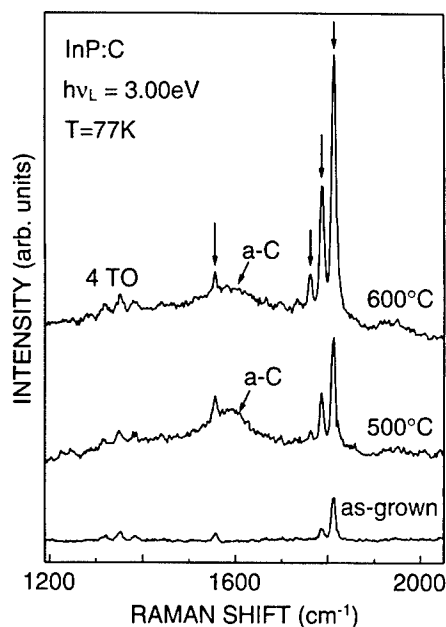


Fig. 3. Raman spectra from as-grown and annealed InP:C samples with lines due to carbon complexes marked by arrows and where $a\text{-C}$ denotes scattering from amorphous carbon. The spectral resolution was 7 cm^{-1} .

as-grown samples (Fig. 3). The strengths of these modes increase with a constant ratio following anneals at 500 and 600°C and a small third line at 1764 cm^{-1} emerges and becomes stronger. Another line at 1558 cm^{-1} also appears, together with a broad band, centred at 1580 cm^{-1} with $\Delta \sim 70\text{ cm}^{-1}$, characteristic of precipi-

tated amorphous carbon. Similar scattering occurs in samples that were etched to remove the surface of the epitaxial layer, demonstrating that precipitation of carbon occurs in the InP bulk. There are no significant changes following the 700°C anneal but the lines discussed are no longer resolved after the 800°C anneal because of strong background scattering and/or luminescence in the range $1000\text{--}2000\text{ cm}^{-1}$. Raman scattering from hydrogen (H_2) is not detected in the frequency range $3000\text{--}4500\text{ cm}^{-1}$.

The structure of the C_P LVM (Fig. 1) can be fitted to theoretical profiles [7,8] that predict the sharp central feature to be logarithmically divergent in the absence of strain. In practice, all of the sharp lines that go together to form the profile are broadened by inhomogeneous strain from point defects and dislocations, limited instrumental resolution and three-phonon decay. This broadening is characterised by a half width at half height, γ . The reductions in γ that follow sample anneals (Table 1) are attributed to reductions of $[C_P]$ and $[H-C_P]$, with the implication that the resulting C–C defects and amorphous carbon produce smaller strains. We note that the smallest value of $\gamma = 0.04\text{ cm}^{-1}$ (Table 1) is not limited by the IR resolution of 0.02 cm^{-1} , (corresponding to $\gamma = 0.01\text{ cm}^{-1}$).

4. Discussion and conclusions

The assignment of Raman LVMs lines in the range $1763\text{--}1814\text{ cm}^{-1}$ to $(^{12}\text{C}\text{--}^{12}\text{C})_P$ pairs in InP:C is inferred by comparisons with corresponding lines observed in annealed GaAs:C and AlAs:C. Two sets of transitions, each showing $^{12}\text{C}\text{--}^{12}\text{C}$, $^{12}\text{C}\text{--}^{13}\text{C}$ and $^{13}\text{C}\text{--}^{13}\text{C}$ pairs, are observed in GaAs that contains $[^{12}\text{C}_{\text{As}}] = [^{13}\text{C}_{\text{As}}]$ [5]. Theory shows that the two types of (C–C) pairs, labelled T1 and T2 (also observed in AlAs), are both deep donors that occupy vacant As-lattice sites but with two nonequivalent molecular orientations [5]. The two Raman transitions have separations of 87 and 96 cm^{-1} for GaAs and AlAs, respectively, and a common mean frequency of 1800 cm^{-1} ; for comparison, the two strong lines in InP:C at 1784.9 and 1814.0 cm^{-1} have a smaller separation of 25 cm^{-1} but the same mean frequency of 1800 cm^{-1} . We therefore attribute the compensation of the carbon acceptors in epitaxial InP layers predominantly to H–C pairs and to di-carbon deep donors occupying P-lattice sites. During anneals substitutional carbon atoms must jump to interstitial sites and diffuse to form di-carbon defects [11] and larger amorphous carbon precipitates. The continued loss of C_P atoms with the formation of $(\text{C}\text{--}\text{C})_P$ donors is expected eventually to cause the samples to become lightly n-type when an excess of the defects occurs. The possibility that some C_{In} and P_{In} donors are present is not ruled out as their LVMs may be obscured by strong intrinsic

absorption and/or scattering from the InP lattice (the frequencies are not known): we state only that there is no evidence for their presence. Additionally, phosphorus vacancies are expected to be deep hole traps but they have not been detected.

In conclusion, our analyses now lead to significant steps in understanding the semi-insulating property of the InP layers that may have future technological applications [1].

Acknowledgements

We thank J.C. Clark and G. Hill (Sheffield University) for coating the samples with SiO₂. B.R.D. and R.C.N. thank the EPSRC, UK for their support (Grant GR/K 96977).

References

- [1] N.F. Gardner, Q.H. Hartman, J.E. Baker, G.E. Stillman, *Appl. Phys. Lett.* 67 (1995) 3004.
- [2] B.R. Davidson, R.C. Newman, C.C. Button, *Phys. Rev. B* 58 (1998) 15 609.
- [3] B.R. Davidson, R.C. Newman, T.J. Bullough, T.B. Joyce, *Phys. Rev. B* 48 (1993) 17 106.
- [4] R. Darwich, B. Pajot, B. Rose, D. Bobein, B. Theys, R. Rhabi, C. Porte, F. Genson, *Phys. Rev. B* 48 (1993) 17 776.
- [5] J. Wagner, R.C. Newman, B.R. Davidson, S.P. Westwater, T.J. Bullough, T.B. Joyce, C.D. Latham, R. Jones, S. Öberg, *Phys. Rev. Lett.* 78 (1997) 74.
- [6] B.R. Davidson, R.C. Newman, C.D. Latham, R. Jones, J. Wagner, C.C. Button, P.R. Briddon, *Phys. Rev. B* 60 (1999) 5447.
- [7] R.S. Leigh, M.J.L. Sangster, R.C. Newman, *Phys. Rev. B* 60 (1999) 10851.
- [8] R.C. Newman, B.R. Davidson, R.S. Leigh, M.J.L. Sangster, C.C. Button, *Physica B* 273–4 (1999) 827.
- [9] Y. Cheng, M. Stavola, C.R. Abernathy, S.J. Pearton, W.S. Hobson, *Phys. Rev. B* 49 (1994) 2469.
- [10] R.C. Newman, B.R. Davidson, J. Wagner, M.J.L. Sangster, R.S. Leigh, *Phys. Rev. B* 63 (2001) 20 5 307.
- [11] C.D. Latham, R. Jones, M. Haugk, Th. Frauenheim, P.R. Briddon, *Physica B* 273–274 (1999) 784.



ELSEVIER

Physica B 308–310 (2001) 862–865

PHYSICA B

www.elsevier.com/locate/physb

Motional properties of positive muonium in gallium III–V compounds

R.L. Lichti^{a,*}, K.H. Chow^b, B. Hitti^c, E.A. Davis^d, S.K.L. Sjøe^a, S.F.J. Cox^{e,f}

^a Physics Department, Texas Tech University, Lubbock, TX 79409-1051, USA

^b Physics Department, University of Alberta, Edmonton, AB, Canada T6G 2J1

^c TRIUMF, 4004 Wesbrook Mall, Vancouver, BC, Canada V6T 2A3

^d Department of Physics and Astronomy, University of Leicester, Leicester, LE1 7RH, UK

^e ISIS Facility, Rutherford Appleton Laboratory, Chilton OX11 0QX, UK

^f Department of Physics and Astronomy, University College London WCE 6BT, UK

Abstract

The motion of Mu^+ defect centers is investigated in heavily Zn-doped p-type GaAs, GaP, and GaSb using zero-field muon spin depolarization. Hop rates extracted from dynamic Kubo–Toyabe relaxation functions show activated motion above 200 K and changes in site or dynamics within 50 K of the onset. Barrier energies are extracted for the mobile centers. A second Mu^+ state at T_V sites is suggested by these results. Additional diamagnetic states are present implying interactions with Zn acceptors involving mobile states, Mu_T^0 at low T and Mu^+ at high T . © 2001 Elsevier Science B.V. All rights reserved.

PACS: 66.30.Jt; 71.55.Eq; 76.75.+i

Keywords: Muonium; Hydrogen mobility; GaAs; GaP; GaSb

1. Introduction

The effectiveness of hydrogen passivation reactions in semiconducting materials depends to a large extent on properties of the isolated hydrogen precursors. Hydrogen is ordinarily a deep compensating defect, thus, the equilibrium charge state for an isolated hydrogen is appropriate for a Coulomb interaction with the dominant dopant leading to hydrogen passivation. Thus, at ordinary temperatures where dopants are ionized, the mobility of oppositely charged hydrogen impurities may control the reaction rates.

Much of the experimental information on isolated hydrogen impurities has come from investigations of its muonium counterpart (Mu) formed when positive muons are implanted into a semiconductor. Muonium

forms defect states very similar to those of hydrogen, and although care must be taken when inferring motional properties of H from measurements on Mu due to the factor of nine mass difference, the dynamics of Mu^\pm states can serve as a qualitative guide to behavior of H^\pm centers. Preliminary data [1] on Mu^+ and Mu^- in GaAs showed the onset of motion for Mu^+ near 200 K and that Mu^- remains stationary to 500 K, consistent with drift properties inferred for hydrogen in GaAs [2–5]. Subsequently, we obtained a barrier of 0.7 eV for motion of Mu^- [6]. However, the neutral Mu_T^0 center is several orders of magnitude more mobile than either charged state [7], and we concluded that diffusion of H is controlled by transitions into and out of this highly mobile state [6].

We recently examined the motion of Mu^- in p-type Zn-doped GaAs and demonstrated trapping of Mu^+ at the Zn acceptor above room temperature [8]. In that work we characterized the motion of Mu^+ as hops among bond-center (BC) sites with barrier of 0.15 eV.

*Corresponding author. Tel.: +1-806-742-3697; fax: +1-806-742-1182.

E-mail address: XBRLL@ttacs.ttu.edu (R.L. Lichti).

However, more detailed examination of the data strongly suggests that the motion is not a simple activated process, and that a change in dynamics occurs about 50 K above the onset. In the present contribution, we pursue details of these data for p-type GaAs and examine two other Ga-based materials to understand general features of H^+ dynamics in III–V compounds as elucidated by changes to muon depolarization associated with Mu^+ motion.

Before examining the data and results, we point out a few qualitative features pertinent to Mu^+ motion. First, the BC structure for Mu in a III–V compound is asymmetric in both the positive and neutral charge state [9]. For Mu^+ , this asymmetry and the weakly ionic nature of the host bonds imply that, the bond with Ga should be weaker than that with the Group-V element. Consequently, the lowest temperature motion is likely to be among four BC sites with the Mu^+ staying attached to a single Group-V atom. Second, bond ionicity implies that the tetrahedral site with group-V neighbors (T_V) is negatively charged and thus attractive for Mu^+ . At elevated temperatures a metastable T_V region could serve as the main Mu^+ location during diffusion, which would likely proceed through BC. Alternatively, and at lower temperatures, global motion may be BC-to-BC through an off-center site within T_V regions [9]. Zero-point motion will centralize Mu^+ at T_V if it remains in that general region for any length of time, although it might not do so for H^+ [10]. Furthermore, lattice dynamics can shift stability from BC to a T site [11]. These features suggest the possibility of three distinctly different types of motion for Mu^+ as a function of increasing temperature: local hops among four BC sites, BC-based diffusion, and perhaps eventually T_V -based diffusion.

2. Zero-field data and analysis

Fig. 1 shows typical zero-field depolarization data used in the present study, specifically from p-type Zn-doped GaP, analyzed as either one or two dynamic Kubo–Toyabe (KT) relaxation functions. Our standard procedure was to initially fit each curve as a single dynamic KT signal with all parameters free, then to fix the width parameter Δ_{KT} to an average over the region where these fits imply a “static” center (see later discussion) and perform a second round of fits to obtain good hop rates. In some circumstances, as for 230 K in Fig. 1, a single dynamic KT function fails to produce a good fit; in which case a second static KT component was added, followed by freeing the second hop rate if required. This procedure yields very good fits, but may not give a unique component separation.

Figs. 2 and 3, along with Table 1, summarize the results of this analysis. The temperature-dependent amplitudes of component signals for GaP are displayed

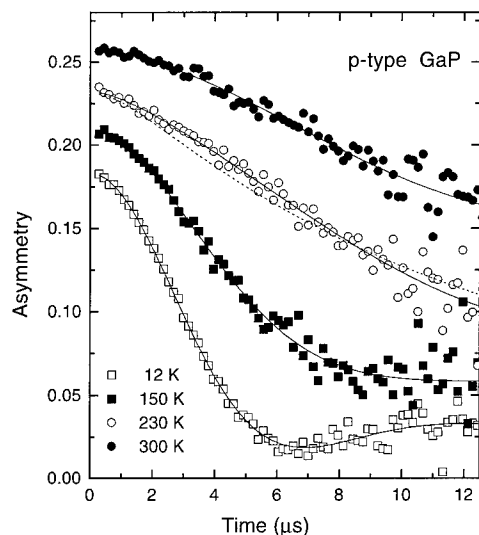


Fig. 1. Zero-field muon spin depolarization curves at selected temperatures for p-type GaP:Zn offset for clarity. Fits are for two Kubo–Toyabe signals, except for Mu_{BC}^+ alone at 150 K. Dashed line for 230 K is a Mu_{BC}^+ fit for comparison.

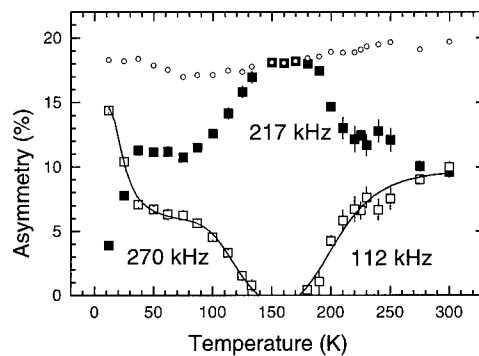


Fig. 2. Amplitudes for the different zero-field signals in GaP. State assignments are in Table 1.

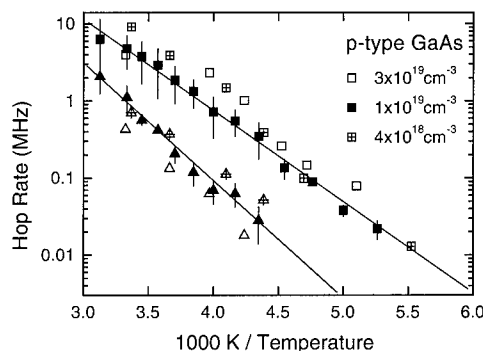


Fig. 3. Hop rates extracted for Mu^+ in GaAs with BC (squares) and T_V (triangles) as separate signals. Fitted energies are in Table 1.

Table 1

Assignment of states to static KT widths within the model presented, and the motion-related parameters obtained for Mu^+ in Ga-based III–V compounds

State and parameter	GaAs	GaP	GaSb
Mu_{BC}^+ state:			
Static width, Δ_{BC} (kHz)	199(3)	217(4)	231(3)
Tunneling rate, v_0 (kHz)	68(27)	262(15)	63(8)
Hop barrier, E'_{BC} (meV)	222(8)	215(14)	330(50)
Hop prefactor, v'_{BC} (MHz)	3×10^4	3×10^5	2×10^5
$\text{Mu}_{\text{T}_\text{V}}^+$ state:			
Static width, $\Delta_{\text{T}_\text{V}}$ (kHz)	122(4)	112(2)	150(30)
Hop barrier, E'_{T_V} (meV)	260(30)		
Hop prefactor, v'_{T_V} (MHz)	2×10^5		
Low- T Mu–Zn pair:			
Static width, Δ_{Zn} (kHz)		270	
High- T Mu–Zn pair:			
Static width, Δ'_{Zn} (kHz)	87(1)		63(6)

in Fig. 2. A second signal, tentatively assigned to a Mu^+ at a T_P site, is definitely required above 220 K. For GaAs a second signal is also suggested by a small change in barrier energy near 230 K when a single KT signal is used [8]. Hop rates for Mu^+ states in GaAs from a two signal analysis up to 320 K are shown in Fig. 3. The GaSb data do not show a second isolated Mu^+ state quite as convincingly, and Mu_T^0 ionizes at approximately the same temperature increasing the mobile Mu^+ amplitude.

3. Discussion

As indicated in the introduction, III–V bonding properties and structural asymmetry of BC states suggest a second site and three distinct motions for Mu^+ in zincblende materials. The most straightforward interpretation of the GaAs results presented here support that picture of the dynamics; however, several caveats need to be stated. We have used the Kubo–Toyabe relaxation function in its static form as characteristic of a stationary Mu_{BC}^+ center. This function assumes that a large number of nuclear moments contribute equally to local magnetic fields at the muon location. In reality, these fields are dominated by the two nearest neighbors for a BC site, giving a slightly different functional form [12]. The slow hop rates found at low temperatures might simply represent these differences; and, although very high-statistics data could answer that question, we currently have no points with the necessary statistics. If one accepts the static KT function as properly characterizing a stationary Mu_{BC}^+ , the low- T hop rates imply temperature-independent

dynamics. This is typical of a tunneling process and consistent with expectations for low- T hops among four BC orientations around a central atom. In this picture, the onset of activated dynamics represents detachment from the central atom and global hopping motion among BC sites, and the additional change in dynamics signals the switch to T-site based diffusion. The state labels in Table 1 are based on this model of Mu^+ behavior. Conversion to T-site motion in this analysis starts by 225 K and is nearly complete by 300 K. If the low- T dynamics are incorrect, an alternative is that the 200 K onset represents thermally assisted local tunneling, with the additional change in dynamics assigned to diffusive motion.

A second complication is that an increase in depolarization rates is observed above 300 K for p-type GaAs and GaSb (the high- T data do not yet exist for GaP). Such increases may signal either muonium charge-state cycling or trapping of the mobile state. In GaAs, where we have extensively investigated the high- T behavior, Mu^+ traps at an ionized Zn^- and we obtained $\Delta_{\text{KT}} = 86.5(\pm 8)$ kHz for the complex. This value differs considerably from that assigned to the second Mu^+ state for 220–300 K (Table 1). Furthermore, the hop rates are too small for Mu^+ to encounter an acceptor on average over much of this range: evidence of the trapped state is present only above 290 K in the current analysis. We therefore discount interaction with another impurity as the explanation of changes occurring just above the onset of activated dynamics.

Formation of a different state immediately above the onset of motion was also observed [13] in p-type InP, where the new state was interpreted as Mu^+ in the T_P interstitial cage based on observed Δ_{KT} values compared to local fields expected for various sites. The present data for GaP yield a value for Δ_{KT} almost identical to that for InP, lending additional credence to the T_V site interpretation. The difference between results for InP and GaP compared to GaAs is that this state is mobile from its initial formation in GaAs. Additional support for two sites comes from $\text{Mu}^0 \leftrightarrow \text{Mu}^+$ charge-cycle data in semi-insulating GaAs [14] which also suggests two different Mu^+ states.

Finally, we turn to the additional low- T state in p-type GaP. A similar situation is seen in n-type GaP and reported [15] for n-type GaAs as well. In the latter case, Mu_T^0 QLCR spectra are seen only above 150 K and low- T depolarization rates imply interaction of the mobile Mu_T^0 with donors, leading to a Mu–donor complex. We suggest that a similar low- T charge-exchange interaction and formation of a Mu–acceptor complex is present for p-type GaP. The reaction we envision is $\text{Mu}^0 + \text{A}^0 \rightarrow \text{Mu}^+ + \text{A}^-$ with the final state most likely a bound complex. The rate of this reaction would be reduced when the acceptors thermally ionize, roughly consistent with the results in Fig. 2.

In conclusion, we have presented zero-field muon spin depolarization data related to Mu^+ defect centers in GaAs, GaP and GaSb which support the possibility of a second Mu^+ site and three distinctly different types of motional dynamics. In addition, interactions are inferred for mobile Mu_T^0 centers with neutral acceptors at low temperatures and mobile Mu^+ centers with ionized acceptors at elevated temperatures, both of which can lead to formation of Mu–acceptor complexes in analogy to hydrogen passivation.

Acknowledgements

This work was supported by the Robert A. Welch Foundation (D-1321 [rll]) and by the UK EPSRC (GR/R25361 [sfjc, ead]).

References

- [1] T.R. Adams, et al., *Philos. Mag. B* 72 (1995) 183.
- [2] A.J. Tavendale, et al., *Appl. Phys. Lett.* 56 (1990) 1457.
- [3] N.M. Johnson, et al., *Phys. Rev. B* 48 (1993) 18 308.
- [4] G. Roos, et al., *Appl. Phys. Lett.* 59 (1991) 461.
- [5] A.W.R. Leitch, et al., *Phys. Rev. B* 44 (1991) 1375.
- [6] K.H. Chow, et al., *Phys. Rev. Lett.* 76 (1996) 3790.
- [7] R. Kadono, et al., *Hyperfine Interactions* 64 (1990) 635.
- [8] K.H. Chow, et al., *Phys. Rev. Lett.* (2001), to be published.
- [9] S.K. Estreicher, *Mater. Sci. Eng. R* 14 (1995) 319.
- [10] T. Miyake, et al., *Phys. Rev. Lett.* 81 (1998) 1873.
- [11] R. Ramirez, C.P. Herrero, *Phys. Rev. Lett.* 73 (1994) 126.
- [12] M. Celio, P.F. Meier, *Phys. Rev. B* 27 (1983) 1908.
- [13] R.L. Lichti, et al., *Hyperfine Interactions* 105 (1997) 333.
- [14] T.L. Estle, et al., *Mater. Sci. Forum* 258–263 (1997) 849.
- [15] E.S. Bates, et al., *Physica B* 289–290 (2000) 550.



ELSEVIER

Physica B 308 310 (2001) 866–869

PHYSICA B

www.elsevier.com/locate/physb

Substitutional incorporation of arsenic from GaAs substrates into MOVPE grown InSbBi thin films

M.C. Wagener, J.R. Botha, A.W.R. Leitch*

Department of Physics, University of Port Elizabeth, P.O. Box 1600, Port Elizabeth 6000, South Africa

Abstract

The substitutional incorporation of As from the GaAs substrate during the MOVPE growth of InSbBi layers has been verified by resonant Raman scattering measurements. The anticipated reduction in the energy gap was also confirmed by infrared spectroscopy. The detection of an In–As LO phonon mode, as well as the absence of an In–Bi phonon mode, established that no Bi was substitutionally incorporated into the layers and that the previously observed lattice contraction and band gap reduction are entirely attributed to As incorporation. © 2001 Published by Elsevier Science B.V.

Keywords: InSbBi; Arsenic; Raman scattering

1. Introduction

The III–V compound $\text{InSb}_{1-x}\text{Bi}_x$ has received attention as a candidate for infrared detectors operating in the 8–14 μm wavelength range [1–4]. The band gap of InSbBi can in principle be reduced from that of InSb (0.167 eV at 300°C) to that of the semi-metal InBi (–1.5 eV at 300°C). Although only a small concentration of Bi is required to decrease the band gap into the desired range, the large miscibility gap of the material has necessitated the use of non-equilibrium growth techniques. A recent series of papers by Lee et al. [3,5] demonstrated the low pressure MOVPE growth of InSbBi at 456°C. Seventy-seven Kelvin photoconductive spectral response measurements clearly indicated an extension of the absorption edge from that of InSb (5.5 μm) to 9.3 μm for layers grown on GaAs substrate. A peculiarity of these results was the observed lattice contraction of the InSbBi epilayers, instead of the expected lattice dilation [6]. This was tentatively attributed to a cubic-to-tetragonal phase transformation as Bi incorporates into the lattice.

In a report by Wagener et al. [4], the crystalline properties of InSbBi layers grown on GaAs substrates were shown to dramatically differ from layers grown on InSb substrates. The observed lattice contraction observed for layers grown on GaAs substrates was attributed to the incorporation of As from the substrate during growth. The incorporation of As was found to be directly attributed to the interaction between Bi and the GaAs substrate. The concentration of As incorporated into the epilayers also increased with the increased availability of Bi in the reactor, with concentrations as high as 35 mol% InAs being incorporated. Besides causing lattice contraction, the presence of As was also anticipated to dramatically alter the optical properties of the material. In this paper, the incorporation of As in these layers has been investigated by infrared absorption and Raman spectroscopy.

2. Experimental

The InSbBi layers were grown in a horizontal MOVPE reactor at atmospheric pressure. TMSb, TMIn and TMBi were used as precursors. Layers were grown on both InSb and GaAs substrates (orientated 2° off the (100) towards <110>) at a temperature of 455°C.

*Corresponding author. Tel.: +27-41504-2579; fax: +27-41504-2573.

E-mail address: phaaw@upe.ac.za (A.W.R. Leitch).

A 0.5 μm thick InSb buffer layer was grown before introducing TMBi into the reactor. The layers were grown at a rate of 2.1 $\mu\text{m}/\text{h}$, with the total epilayer thickness of approximately 2.6 μm . The TMIn flow rate was maintained at 5.6 $\mu\text{mol}/\text{min}$ and the Bi to group V ratio in the vapour (Bi/V) was varied between 0 and 0.1. The infrared absorption edges of the layers were determined by Fourier transform infrared spectroscopy using a Nicolet Magma 550 spectrometer. Resonant Raman scattering measurements of the near-surface region were also obtained using a Jobin–Yvon T640000 Raman spectrometer and CCD detector. The acquisition optics was configured in the triple subtractive mode, giving a resolution of roughly 1 cm^{-1} . The 647.1 nm line of a Kr^+ -ion laser was used in the backscattering configuration. The particular incident photon energy was chosen since it coincides with the second direct critical point, the E_1 energy gap = 1.86 eV [7]. The resulting resonance effect was found to greatly enhance the Raman scattering signal. The laser spot size was roughly 2 μm in diameter, with the incident power maintained at 590 mW (measured at the laser).

3. Results and discussion

If As is incorporated substitutionally on the group V lattice sites of InSb, additional phonon modes, related to the In–As bond, are expected. Fig. 1 depicts the Raman scattering spectra of InSbBi layers grown with a V/III = 2 and a Bi/V ratio = 0.1. Fig. 1(a) shows the expected LO-phonon peak at 190.2 cm^{-1} and TO-phonon mode at 183.3 cm^{-1} for layers grown on InSb substrates. Except for the peaks at 72 and 99 cm^{-1} , the spectrum is essentially the same as for an InSb layer grown on InSb substrate [7]. This agrees with previous

X-ray diffraction (XRD) measurements [4], which showed that layers grown on InSb substrates contained no substitutional Bi. The Raman scattering spectrum for the InSbBi layer grown on GaAs substrate (Fig. 1(b)) has, however, an additional peak at roughly 211 cm^{-1} . Since As is expected to be present in these layers, the extra peak is ascribed to the In–As vibrational mode. Although the ν_{InAs} TO phonon mode for bulk InAs is $218.6 \pm 0.2\text{ cm}^{-1}$ [8], the presence of Sb neighbouring atoms in the InAsSb alloy is expected to shift the InAs-phonon modes towards lower frequencies.

A Raman study by Li et al. [9] revealed that $\text{InAs}_{1-x}\text{Sb}_x$ displays a two-mode behaviour over the entire composition range, with the InAs-like LO phonon frequency having a composition dependence of $\nu_{\text{InAs}} (\text{cm}^{-1}) = 238 - 32x$. An InAs-like LO mode at 211 cm^{-1} would then correspond to a composition of roughly 16 mol% InAs, significantly less than the concentration of 36 mol% InAs measured by XRD. Although less pronounced, the InSb-like LO phonon mode also has a linear dependence on composition, with $\nu_{\text{InSb}} (\text{cm}^{-1}) = 177 + 12x$. For a composition of 16 mol% InAs, the InSb-like LO mode is therefore expected to decrease by only 1.9 cm^{-1} . Due to the high absorption coefficient of InSb at 647.1 nm, the observed scattering originates from a region extending roughly 500 Å below the surface. The expected decrease in the As concentration towards the surface [4], together with the high vapour pressure of As, will produce a near-surface As concentration notably lower than that measured by XRD. Based on the above discussion, the peaks measured in Fig. 1(b) at 190.0 and 182.8 cm^{-1} are labelled with the InSb-like LO and TO phonon modes, respectively, and the peak at 211 cm^{-1} with the InAs-like LO phonon mode.

The InAs-like LO peak position showed a very weak dependence on the Bi/V ratio and consequently the As concentration. Fig. 2 shows the Raman spectra for layers grown with significantly different Bi/V ratios (and hence As concentrations) on GaAs substrates. The As concentrations determined by XRD were 11 and 36 mol% InAs for Figs. 2 (a) and (b), respectively. The similarity of the InAs-like LO peak positions is probably due to similar As concentrations in the near-surface region, as well as a slight insensitivity to changes in composition. The InSb-like TO mode was also found to be enhanced with higher Bi/V ratios (or As concentrations). This can either be attributed to a deterioration in crystallinity, since increased Bi/V ratios produced broader XRD peaks [4], or to the presence of alloy disorder with the addition of a second group V atom [9].

The LO and TO vibrational modes for InBi are 161 and 155 cm^{-1} , respectively [10]. No phonon mode was, however, observed in this region. This, therefore, clearly illustrates that the lattice contraction related to growth on GaAs substrates only requires that Bi be present

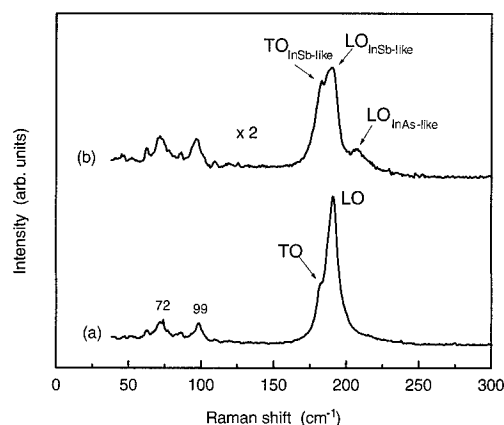


Fig. 1. Room temperature Raman spectra of an InSbBi epilayer grown on (a) InSb and (b) GaAs substrate. The epilayers were grown with a V/III = 2 and a Bi/V ratio = 0.1.

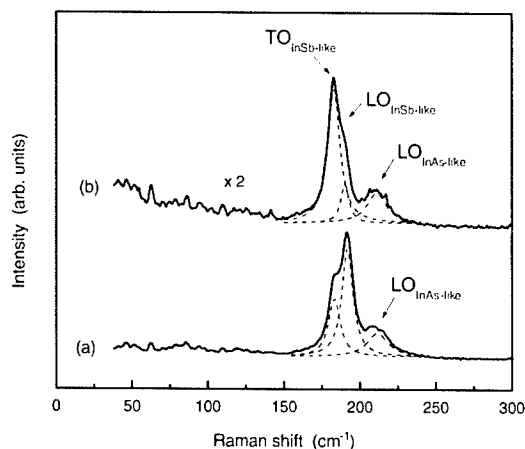


Fig. 2. Room temperature Raman spectra of an InSbBi epilayer grown on GaAs substrate with a V/III = 2 and a Bi/V ratio of (a) 0.01 and (b) 0.1. The deconvolution of the spectra has been obtained by fitting three Lorentzian functions.

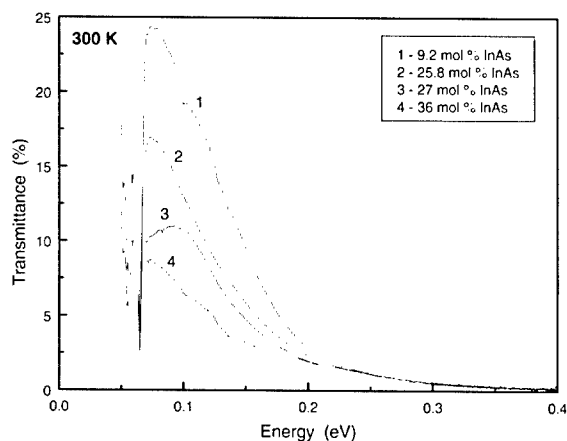


Fig. 3. Room temperature infrared transmittance curves of 2.1 μm thick $\text{InAs}_{1-x}\text{Sb}_x$ layers resulting from As incorporation from the GaAs substrate. The compositions have been determined by XRD.

during the growth, with Bi having no direct influence on the epitaxial properties of the epilayers. The two extra peaks shown in Figs. 1 and 3 (positioned at 72 and 99 cm^{-1}) were measured in only two of the samples. The Raman spectrum of Bi has a prominent mode at 141 cm^{-1} [10]. It is, therefore, unlikely that the two peaks are attributed to Bi precipitates within the material [4]. Since the two peaks have been detected in layers grown on both InSb and GaAs substrates, it is also unlikely that they are related to the incorporation of As or Ga. Their origin therefore remains unclear.

The Raman scattering measurements clearly corroborate the incorporation of As into the epilayers, which

was inferred from the lattice contraction measured by XRD [4]. Besides lattice contraction, the substitutional incorporation of As is also expected to alter the energy gap of the material: the 300 K energy gap decreases with increasing As concentrations, reaching a minimum of 0.12 eV (absorption edge of roughly 12 μm) at 35 mol% InAs. The epilayers in which As has been incorporated are therefore capable of having significantly increased absorption cut-off wavelengths. Fig. 3 shows the room temperature transmittance spectra of InAsSb layers resulting from As incorporation from the GaAs substrate. The layers were grown with different V/III and Bi/V ratios. The compositions, which were determined by XRD, increased from 9.2 to 36 mol% InAs as the Bi/V ratio was increased from 4.4×10^{-4} to 0.1. The high surface roughness of these layers produced significant photon scattering. As a result, it was not possible to calculate sensible values for the absorption coefficient. What is clear, however, is that the absorption edge of the InAsSb layers shifts to lower energies (longer wavelengths) as the As concentration increases. The overall reduction in transmittance with increasing composition is ascribed to the increased surface roughness of the layers. The sharp drop in transmittance below 0.07 eV is due to the low response of the IR detector in this wavelength region.

4. Conclusions

Even though the original objective was to reduce the energy gap by incorporating Bi into the InSb lattice, no direct evidence of substitutional Bi could be found. Instead, a reduction in the energy gap was achieved by the interaction of Bi with the GaAs substrate, which consequently led to the substitutional incorporation of As into the layers. This was successfully verified by the observed In-As vibrational mode, as well as by the extension of the absorption edge to longer wavelengths. Care should, therefore, be taken with growth studies involving Bi, as well as possibly other heavy metals, i.e. thallium, with special attention given to variations in the properties of layers grown on different substrates.

Acknowledgements

The financial assistance of the South African National Research Foundation is gratefully acknowledged.

References

- [1] A.J. Noreika, et al., *J. Appl. Phys.* 53 (1982) 4932.
- [2] T.P. Humphreys, et al., *Appl. Phys. Lett.* 53 (1988) 142.

- [3] J.J. Lee, et al., Appl. Phys. Lett. 70 (1997) 3266.
- [4] M.C. Wagener, et al., J. Cryst. Growth 213 (2000) 51.
- [5] J.J. Lee, et al., Appl. Phys. Lett. 71 (1997) 2298.
- [6] K.T. Huang, et al., J. Appl. Phys. 75 (1994) 2857.
- [7] V.P. Gnezdilov, et al., Phys. Rev. B 48 (1993) 11 234.
- [8] N. Herres, et al., Phys. Rev. B 53 (1996) 15 688.
- [9] Y.B. Li, et al., Semicond. Sci. Technol. 7 (1992) 567.
- [10] P. Verma, et al., J. Appl. Phys. 89 (2001) 1657.



ELSEVIER

Physica B 308–310 (2001) 870–873

PHYSICA B

www.elsevier.com/locate/physb

Deep-level defects in MBE-grown Ga(As,N) layers

P. Krispin^{a,*}, S.G. Spruytte^b, J.S. Harris^b, K.H. Ploog^a

^a Paul-Drude-Institut für Festkörperelektronik, Hausvogteiplatz 5-7, 10117 Berlin, Germany

^b Solid State and Photonics Laboratory, Stanford University, Stanford, CA 94305, USA

Abstract

Deep levels are examined in the whole band gap of strained Ga(As,N) with 3% GaN composition by deep-level transient Fourier spectroscopy on as-grown as well as annealed GaAs/Ga(As,N)/GaAs heterojunctions grown by molecular beam epitaxy. In the lower half of the band gap, there are only hole traps, which are not associated with nitrogen-related defects. For n-type structures, we find in as-grown samples a huge concentration of an electron trap at $E_C - 0.25$ eV, which is most likely connected with the nitrogen split interstitial defect (N–N)_{As}. The concentration of this giant trap can be strongly reduced by rapid thermal annealing. © 2001 Elsevier Science B.V. All rights reserved.

Keywords: MBE-grown Ga(As,N); Hole and electron traps; Post-growth treatment

1. Introduction

Group-III-arsenide-nitrides grown on GaAs substrates are promising materials for optoelectronic devices. Ga(As,N) layers are of special interest, because the band gap decreases drastically with increasing GaN composition [1–3]. In contrast to the optical properties, the electrical characteristics of Ga(As,N) layers have been hardly studied. We have recently shown that p-type GaAs/Ga(As,N) interfaces exhibit a very small valence band offset ΔE_V [4]. For a GaN composition of 3%, ΔE_V values of (11 ± 2) meV have been determined. For the same composition, the conduction band offset ΔE_C has been found from n-type GaAs/Ga(As,N) heterostructures to be $-(400 \pm 10)$ meV [5]. Thus, the Ga(As,N)/GaAs heterointerface is definitely of type I, in accordance with first principle calculations [6].

Crystal quality and luminescence efficiency of Ga(As,N) layers deteriorate unfortunately for larger GaN mole fractions. Both can be remarkably improved by postgrowth heat treatment [7]. The degradation and anneal mechanisms are still controversially discussed. The presence of N-related deep-level defects has been often postulated, but not explored yet. We therefore use

deep-level transient Fourier spectroscopy (DLTFS) [8] on p- and n-type GaAs/Ga(As,N)/GaAs heterojunctions grown by molecular beam epitaxy (MBE) to examine the spatial distribution of hole and electron traps in as-grown as well as annealed structures. The main hole traps in as-grown and annealed Ga(As,N) layers with a GaN mole fraction of 3% are due to Cu and Fe impurities with concentrations in the 10^{15} cm⁻³ range. For as-grown, n-type Ga(As,N), substantial densities above 10^{17} cm⁻³ are estimated for an electron trap at about 0.25 eV below the conduction band edge E_C . The corresponding defect is of intrinsic origin and probably associated with nitrogen split interstitials (N–N)_{As}. Its concentration can be drastically reduced by rapid thermal annealing (RTA).

2. Experimental details

p- and n-type GaAs/Ga(As,N)/GaAs heterostructures were grown by elemental source MBE on p⁺- and n⁺-type GaAs(001) substrates, respectively. Dimeric arsenic and atomic nitrogen were provided by a thermal cracker and a radio frequency (RF) nitrogen plasma cell, respectively. Details of the growth [7] and of the carrier distribution [4,5] in the investigated heterostructures have been published previously. Deep-level spectra were

*Corresponding author. Tel.: +49-30-20377-399; fax: +49-30-20377-515.

E-mail address: krispin@pdi-berlin.de (P. Krispin).

measured with a computer-controlled Bio-Rad DL8000 system based on the DLTFs technique [8]. For this paper, temperature scans of the first sine coefficient b_1 were evaluated with a period of 1 s. RTA was performed after growth for 60 s at 760°C with a GaAs proximity cap under N₂ atmosphere.

3. Results and discussion

3.1. p-type GaAs/Ga(As,N)/GaAs structures

For an as-grown, p-type GaAs/Ga(As,N)/GaAs structure, deep-level spectra are shown in Fig. 1 as relative capacitance changes $\Delta C/C$ vs. temperature under various bias conditions. Fig. 1 exhibits a sequence of distinct peaks labeled Hk1 to Hk5, which are observed in all as-grown heterostructures. Their respective thermal activation energies are found to be about 0.17, 0.39, 0.36, 0.55, and 0.69 eV. The peak heights strongly change with bias. Since different bias conditions lead to deep-level responses from different depths below the MS contact, Fig. 1 shows that the concentration of all hole traps strongly varies with position. A further striking property of the level responses concerns the

shift of the DLTFs peak temperatures. For example, the signal of the hole trap Hk4 is observed in the lower bias range (curves 3 and 4) at 260 K. This peak shifts at intermediate bias values towards 250 K (curves 5 and 6) and then back to 260 K at sufficiently high reverse biases (curves 7 and 8). Such a behavior is characteristic for a defect with composition-dependent features. Very small differences of the thermal activation energy E_{th} are expected for hole traps linked to the same defect in GaAs and in Ga(As,N), because the band offset ΔE_V is only 11 meV [4]. For level Hk4, the DLTFs peaks in Fig. 1 at low, intermediate, and high reverse biases can be associated with the same defect in the upper GaAs, the Ga(As,N), and the bottom GaAs layers, respectively. Detailed depth profiles of the level concentration (not shown) emphasize that the switch from one to the other peak position occurs for all hole traps at the GaAs/Ga(As,N) interfaces.

Levels Hk2 and Hk5 are identical to the well-known hole traps A and B, which are the dominant levels in GaAs grown by liquid phase epitaxy [9]. They originate from the Ga_{As} antisite defect [9,10]. In particular, the hole trap Hk5 is observed in this study being spatially localized at the surface of the GaAs top layer (see curves 1–3 in Fig. 1). It is a general phenomenon that Ga_{As} antisite defects are formed during epitaxial GaAs growth near the p-type surface [11], because the defect formation energy, which depends strongly on the position of the Fermi level [12], becomes smaller at the surface.

The levels Hk3 and Hk4 exhibit properties identical to those well-known hole traps in GaAs, which are associated with Cu and Fe atoms on Ga sites, respectively [13,14]. Their occurrence in Ga(As,N) is apparently linked with the operation of the RF plasma source or the nitrogen purity. All dominant hole traps can be removed by annealing.

3.2. n-type GaAs/Ga(As,N)/GaAs structures

For an as-grown, n-type GaAs/Ga(As,N)/GaAs structure, deep-level spectra are plotted in Fig. 2 for varying bias conditions. The presence of a giant electron trap labeled Ek1 is obvious below 200 K. Its peak position is constant at low reverse biases (curves 1–3) and shifts to higher temperatures for higher reverse biases. The thermal activation energy E_{th} of this dominant level changes from 0.25 (curve 1) to 0.49 eV (curve 7). At higher reverse biases, level Ek1 disappears, and three minor electron traps Ek2, Ek3, and Ek4 emerge with energies of about 0.60, 0.67, and 0.75 eV, respectively. They disappear for even higher reverse biases (curve 10 in Fig. 2).

To determine the location of measured DLTFs responses, depths are commonly determined from the voltage-dependent capacitance of the MS contact

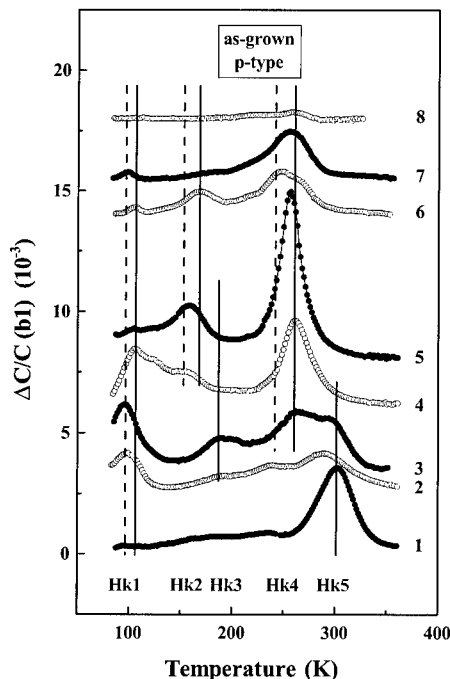


Fig. 1. Deep-level spectra for an as-grown, p-type heterostructure. The spectra 1–8 correspond to increasing reverse biases. The pulse height was 0.5 V. For the hole traps Hk1 to Hk5 in Ga(As,N) and GaAs, the temperature positions of the DLTFs peaks are marked by dashed and solid lines, respectively.

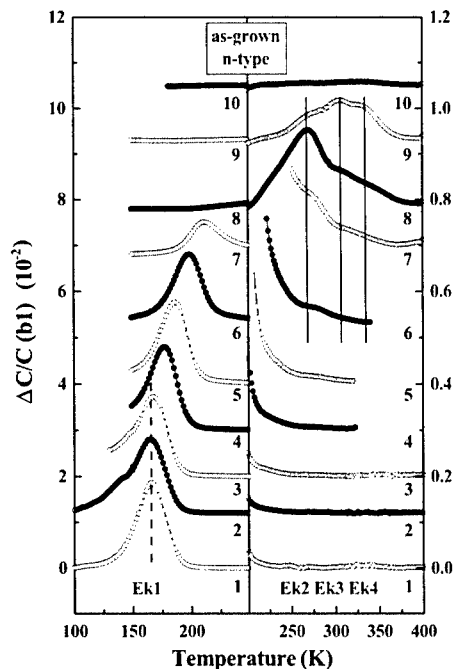


Fig. 2. Deep-level spectra for an as-grown n-type heterostructure. The spectra 1–10 correspond to increasing reverse biases. Curves 1 and 10 were measured at –2 and –6.5 V, respectively. The pulse height was 0.5 V.

including the λ -effect [15]. We, however, find for n-type heterostructures an admittance dispersion (see Ref. [5]). The capacitance therefore depends additionally on frequency and temperature (not shown). This admittance dispersion is due to the diffusion barrier at the GaAs/Ga(As,N) interfaces, which originates from the relatively large conduction band offset of 400 meV [5]. The potential distribution around the Ga(As,N) layer is illustrated in Fig. 3. Dots in Fig. 3 mark for each bias the thickness obtained from the capacitance.

In the bias range between –2 and –3 V, the peak position of the trap Ek1 remains at 170 K (curves 1–3 in Fig. 2), and the capacitance is dominated by electrons in the Ga(As,N) layer (cf. Fig. 3). However, there is a further (smaller) contribution to the capacitance at the edge of the depletion layer in GaAs close to the Ga(As,N)-on-GaAs interface (see, vertical dashed line at 725 nm in Fig. 3). The signal of the electron trap Ek1 is related to this part of the measured capacitance. Including the band offset, the λ -correction for the level Ek1 is about 200 nm (double arrow in Fig. 3). We can therefore conclude that the giant trap Ek1 is located in the Ga(As,N) layer. Its concentration is estimated to be above $1 \times 10^{17} \text{ cm}^{-3}$.

As long as the capacitance is dominated by the electrons in Ga(As,N), the Ek1 signal originates from

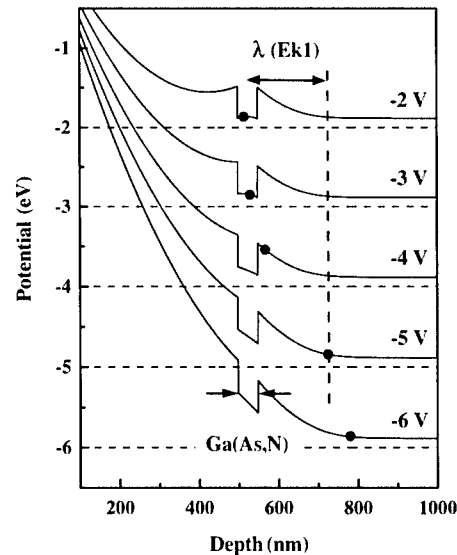


Fig. 3. Band diagram of investigated n-type GaAs/Ga(As,N)/GaAs structures as obtained from solutions of the Poisson equation for several reverse biases. The Fermi level for each bias is given by a horizontal dashed line. Dots mark for each bias the thickness obtained from the capacitance. The edge of the depletion layer in the bottom GaAs layer is marked by the vertical dashed line at 725 nm. For level Ek1, the λ value is indicated by a double arrow.

the Ga(As,N) layer. Its peak position and height remain constant with increasing reverse bias (curves 1–3 in Fig. 2). In the bias range from –3 to –5 V, the capacitive contribution of the electrons in the Ga(As,N) layer becomes weaker and the capacitance is more and more governed by the depletion layer edge in the bottom GaAs layer (dashed line at 725 nm in Fig. 3). Under these conditions, the DLTS peaks of the electron trap Ek1 are due to the interface region, where the GaN mole fraction decreases with increasing reverse bias. We observe a shift of the DLTS peak to higher temperatures and a decrease of the trap concentration (curves 4–7 in Fig. 2). The level Ek1 in the Ga(As,N) band gap reflects the increase of the conduction band edge energy with decreasing GaN composition. The electron trap Ek1 is probably associated with the split interstitial defect $(\text{N-N})_{\text{As}}$. As-grown Ga(As,N) layers contain a significant concentration of interstitial nitrogen [16], in agreement with the theoretical prediction that nitrogen split interstitials are the dominant defects in Ga(As,N) [17].

Deep-level spectra of the same GaAs/Ga(As,N)/GaAs structure after annealing are displayed in Fig. 4. The concentration of the electron trap Ek1 in Ga(As,N) is drastically reduced by RTA. We believe that the underlying defect is annihilated by reactions between

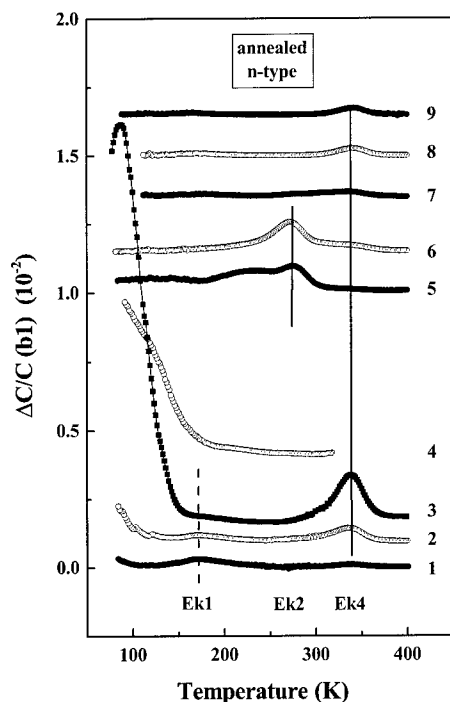


Fig. 4. Deep-level spectra for the same n-type heterostructure as in Fig. 2, but after annealing. The spectra 1–9 correspond to increasing reverse biases. Curves 1 and 9 were measured at -2 and -6 V, respectively. The pulse height was 0.5 V.

intrinsic defects. It is obvious that all partners, which are desired for the complete recombination, are available in the Ga(As,N) region. An additional level with an energy below 100 meV appears after annealing under certain bias conditions (peak at 100 K in Fig. 4). By heat treatment, the traps Ek2 and Ek4 are additionally generated in the GaAs top layer (see, curves 2 and 3 in Fig. 4). The level Ek3 is missing after annealing.

4. Conclusions

Deep levels have been examined in the whole band gap of strained Ga(As,N) with 3% GaN composition. In the lower half of the band gap of MBE-grown material, there is no indication for hole traps, which could be

associated with nitrogen-related defects. For n-type structures, we find in as-grown samples, however, a very high concentration of an electron trap at $E_C - 0.25$ eV, which is most likely connected with a nitrogen split interstitial defect on As site. According to thermodynamic calculations, this interstitial defect is dominant in Ga(As,N) [17]. However, the calculated trap level is 0.66 eV below the conduction band, in contrast to the experimental value of 0.25 eV. The concentration of this giant trap can be strongly reduced by annealing. Since the capture cross section of this level is about 10^{-17} cm², it cannot be the recombination center, which causes the degradation of the luminescent properties of Ga(As,N) at higher GaN compositions.

Acknowledgements

The authors would like to thank H.T. Grahn for helpful comments and a careful reading of the manuscript. We are grateful for the technical assistance of H. Kostial and E. Wiebicke.

References

- [1] M. Weyers, et al., Jpn. J. Appl. Phys. 31 (Part 2) (1992) L853.
- [2] M. Weyers, M. Sato, Appl. Phys. Lett. 62 (1993) 1396.
- [3] S.-H. Wei, A. Zunger, Phys. Rev. Lett. 76 (1996) 664.
- [4] P. Krispin, et al., J. Appl. Phys. 88 (2000) 4153.
- [5] P. Krispin, et al., J. Appl. Phys. 90 (2001) 2405.
- [6] L. Bellaiche, et al., Phys. Rev. B 54 (1996) 17568.
- [7] S.G. Spruytte, et al., in: R. Feenstra, T. Myers, M.S. Shur, H. Amano (Eds.), Materials Research Society Symposium Proceedings 595 (2000) W8.4.1.
- [8] S. Weiss, R. Kassing, Solid State Electron. 31 (1988) 1733.
- [9] Z.-G. Wang, et al., J. Phys. C 17 (1984) 259.
- [10] P. Krispin, J. Appl. Phys. 65 (1989) 3470.
- [11] P. Krispin, et al., Physica B 273–274 (1999) 693.
- [12] S.B. Zhang, J.E. Northrup, Phys. Rev. Lett. 67 (1991) 2339.
- [13] N. Kullendorff, et al., J. Appl. Phys. 54 (1983) 3203.
- [14] M. Kleverman, et al., J. Appl. Phys. 54 (1983) 814.
- [15] D. Pons, Appl. Phys. Lett. 37 (1980) 413.
- [16] S.G. Spruytte, et al., J. Appl. Phys. 89 (2001) 4401.
- [17] S.B. Zhang, S.-H. Wei, Phys. Rev. Lett. 86 (2001) 1789.



ELSEVIER

Physica B 308–310 (2001) 874–876

PHYSICA B

www.elsevier.com/locate/physb

Effects of structural defects on the activation of sulfur donors in $\text{GaN}_x\text{As}_{1-x}$ formed by N implantation

J. Jasinski^{*1}, K.M. Yu, W. Walukiewicz, Z. Liliental-Weber, J. Washburn

Materials Science Division, Lawrence Berkeley National Laboratory, 1 Cyclotron Road, MS 62-203, Berkeley, CA 94720, USA

Abstract

The effects of structural defects on the electrical activity of S-doped $\text{GaN}_x\text{As}_{1-x}$ layers formed by S and N co-implantation in GaAs are reported. S and N ions were implanted to the depth of about $0.4\text{ }\mu\text{m}$. Electrochemical capacitance voltage measurements on samples annealed at 945°C for 10 s show that in a thin ($<0.1\text{ }\mu\text{m}$) surface layer the concentration of active shallow donors is almost an order of magnitude larger in S and N co-implanted samples than in samples implanted with S alone. The activation efficiency of S donors also shows a broad minimum at a depth of about $0.2\text{ }\mu\text{m}$ below the surface. The results of these electrical measurements are correlated with the distribution of structural defects revealed by transmission electron microscopy (TEM). The TEM micrographs show that in addition to a band of dislocation loops commonly found in ion implanted GaAs, an additional band of small voids is observed in samples co-implanted with S and N. The location of this band correlates well with the region of reduced electrical activation of S donors, suggesting that the formation of the voids through N accumulation results in a lower concentration of “active”, substitutional N atoms. Published by Elsevier Science B.V.

Keywords: $\text{GaN}_x\text{As}_{1-x}$; TEM; Microstructure; Implantation

Incorporation of a small amount of N (up to $\sim 5\%$) into III-V semiconductors leads to a dramatic reduction of the energy gap of the resulting group III-N_x-V_{1-x} alloys. The effect has been observed experimentally in a large variety of III-N-V alloys including, GaNAs [1–4], GaInNAs [3,5], GaNP [6,7], InNP [8,9], and AlGaInAs [10]. The issue of the N-induced band gap reduction has been addressed by a number of recent theoretical studies [3,5–8]. It has been shown, based on the band anticrossing model [11,12], that the N-induced downward shift of the conduction band edge and a large increase in the electron effective mass lead to great improvements in the electrical activation of group VI donors [13]. The enhanced electrical activation was observed in the as-grown selenium-doped GaInNAs [14] as well as in sulfur implanted $\text{GaN}_x\text{As}_{1-x}$ [15]. A large increase in the

electrical activation of sulfur (S) co-implanted with nitrogen in GaAs has also been observed [16]. In the case of N and S co-implanted GaAs, however, the increase in the electrical activation of sulfur donors was measured only in the near-surface region. In order to understand the mechanism leading to such a behavior, we performed detailed structural studies using transmission electron microscopy (TEM) to make it possible to correlate the structural defect distribution with depth profiles of electrical measurements.

In this study we used two GaAs wafers. The first one was implanted only with S and the second was co-implanted with S and N. Multiple energy ion implantation was used in both cases, resulting in $\sim 0.4\text{ }\mu\text{m}$ thick layers with $\sim 3.3 \times 10^{20}\text{ 1/cm}^3$ of N and $\sim 0.2\text{ }\mu\text{m}$ thick layers with $\sim 6 \times 10^{19}\text{ 1/cm}^3$ of S. After implantation, wafers were covered by other GaAs wafers (in order to prevent As outdiffusion) and annealed at 945°C for 10 s by rapid thermal annealing (RTA) in a flowing N_2 ambient. Cross-sectional TEM specimens were prepared by the standard method of mechanical thinning followed

^{*}Corresponding author. Fax: +1-510-486-4995.

E-mail address: jbjasinski@lbl.gov (J. Jasinski).

¹Also with: Institute of Experimental Physics, Warsaw University, Hoza 69, 00-681 Warsaw, Poland

by ion milling. TEM studies were carried out using a TOPCON 002B microscope operated at 200 kV.

TEM studies performed on these wafers showed the presence of subsurface layers of post-implant damage. The distribution of structural defect present in these layers studied using bright field TEM images of both materials is shown in Fig. 1. In the sample implanted with S only [see Fig. 1(a)], a highly defective layer containing stacking faults, a dislocation network and small angle grain boundaries was observed below the surface. The thickness of this layer varied within the range: $\sim 0.05\text{--}0.10\text{ }\mu\text{m}$. Below this layer to a depth of $\sim 0.2\text{ }\mu\text{m}$ a high quality crystal layer was observed. However, in the middle of this layer at a depth of about $0.13\text{ }\mu\text{m}$ below the surface, a narrow band of tiny defects was present. High resolution electron microscopy studies suggested that they were stacking fault tetrahedra. Such defects have been previously reported in implanted GaAs [17,18]. The main structural feature visible in this sample was a band of defects present in a layer at a depth from ~ 0.2 to $\sim 0.3\text{ }\mu\text{m}$ below the surface. These defects were the dislocation loops with an average size of $\sim 10\text{ nm}$, located on $\{111\}$ planes surrounding extrinsic stacking faults. Such a band of dislocation loops is a typical feature in the implanted and then annealed GaAs.

TEM studies of the S and N co-implanted samples [see Fig. 1(b)] showed different structural features compared to those observed in the sample implanted with S only. The only similarity was the presence of the band of dislocation loops at the depth of $\sim 0.2\text{--}0.3\text{ }\mu\text{m}$ below the surface. This band was slightly narrower and the loops were larger (with an average size of $\sim 15\text{ nm}$) than in the sample implanted only with S. There were pits observed at the surface of the sample co-implanted with N and S, probably originating from very high annealing temperature or stacking fault formation. In this sample, a broad layer containing a high density of small voids (of an average size of about $4\text{--}5\text{ nm}$) was observed. They were located mostly in a layer extending

from $\sim 0.1\text{ }\mu\text{m}$ to $\sim 0.3\text{ }\mu\text{m}$ below the surface. Their concentration rapidly decreased outside this area.

The observed distribution of structural defects correlated well with electrical measurements performed on these samples. Depth profiles of free electron concentration obtained for these materials by electrochemical capacitance voltage (ECV) are shown in Fig. 2. The calculated distributions of implanted species are also shown in this figure. One can observe from these results that the electron concentration profile measured for the sample implanted only with S differs drastically from that obtained for the one co-implanted with S and N. For both samples, these line profiles have a qualitatively similar shape. In the near-surface region for a thickness of about $0.1\text{ }\mu\text{m}$ there is a maximum of electron concentration. Then as the distance from the surface increases this concentration rapidly decreases, resulting in a characteristic dip visible on these profiles. Despite these qualitative similarities there is a significant difference between the two profiles. In the co-implanted sample, the density of free electrons in the near-surface region is almost an order of magnitude higher than in the sample implanted with S only. On the other hand, the depth of the dip measured for the co-implanted sample is much larger than in the sample with S only. In addition, this dip is much broader ($0.2\text{ }\mu\text{m}$ compared to $0.1\text{ }\mu\text{m}$) in the co-implanted sample.

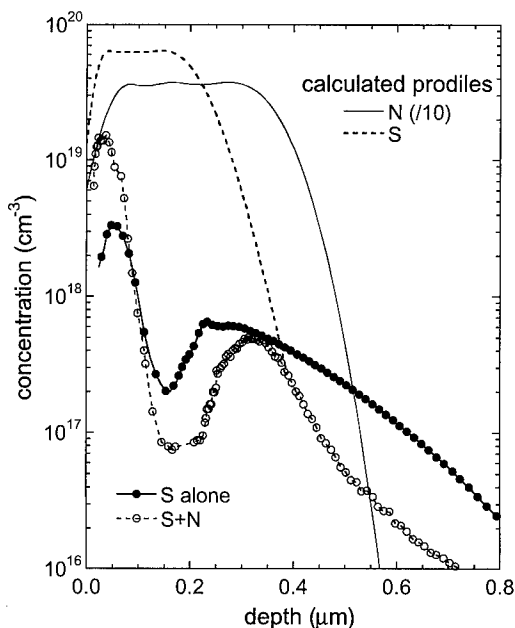


Fig. 2. ECV measured net donor concentration profiles for the GaAs samples implanted with S alone and S+N after RTA at 945°C for 10 s. The calculated atomic depth profiles for both S and N are also shown.

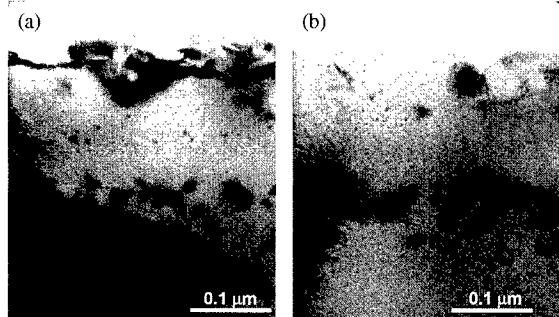


Fig. 1. TEM micrographs of GaAs samples implanted with S (a), and co-implanted with S and N (b).

A comparison of the measured free electron concentration profiles with structural defect distributions shows a correlation between these results. In the sample implanted only with S, the dip in the electrical profile correlates well with the location of the band of dislocation loops. It is likely that a significant fraction of the S implanted into this region becomes inactive by accumulating around the dislocation cores. This mechanism is probably also partially responsible for the reduced electrical activation of S in the co-implanted sample. However, it seems that in this case the presence of voids is an even more important mechanism for reducing the electrical activity of S. These voids were most likely formed as agglomerates of vacancies filled with N and acted as defect centers compensating for electrical activity of S donors. This argument is supported by the observed very large activation efficiency of S donors in the void-free region within the $\sim 0.1 \mu\text{m}$ layer near the surface, where N is incorporated into the As sublattice forming a layer of $\text{GaN}_{1-x}\text{As}_x$ alloy.

In summary, structural defect distributions, observed by TEM in GaAs implanted with S and co-implanted with S and N, were correlated with electrical measurements performed on the same samples. It was found in the co-implanted sample that besides the typical implantation induced structural defects, voids are formed in the material. We believe that these voids were filled with N and were responsible for the reduced activation of S donors. On the other hand, experimental results indicate that large N-induced enhancement of the donor activation efficiency can only be realized in the void-free region, where $\text{GaN}_{1-x}\text{As}_x$ alloy was formed.

Acknowledgements

This work was supported by the Director, Office of Science, Office of Basic Energy Sciences, Division of Materials Sciences, of the US Department of Energy under Contract No. DE-AC03-76SF00098. The authors would like to thank W. Swider for her excellent TEM sample preparation. Use of the facilities at the National Center for Electron Microscopy at Lawrence Berkeley National Laboratory is greatly appreciated.

References

- [1] M. Weyers, M. Sato, H. Ando, *Jpn. J. Appl. Phys.* 31 (1992) L853.
- [2] S. Sakai, Y. Ueta, Y. Terauchi, *Jpn. J. Appl. Phys.* 32 (1993) 4413.
- [3] M. Kondow, K. Uomi, K. Hosomi, T. Mozume, *Jpn. J. Appl. Phys.* 33 (1994) L1056.
- [4] K. Uesugi, N. Morooka, I. Suemune, *Appl. Phys. Lett.* 74 (1999) 1254.
- [5] J.F. Geisz, D.J. Friedman, J.M. Olson, S.R. Kurtz, B.M. Keyes, *J. Cryst. Growth* 195 (1998) 401.
- [6] J.N. Baillargeon, K.Y. Cheng, G.E. Hofer, P.J. Pearah, K.C. Hsieh, *Appl. Phys. Lett.* 60 (1992) 2540.
- [7] W. Shan, W. Walukiewicz, K.M. Yu, J. Wu, J.W. Ager, E.E. Haller, H.P. Xin, C.W. Tu, *Appl. Phys. Lett.* 76 (2000) 3251.
- [8] W.G. Bi, C.W. Tu, *J. Appl. Phys.* 80 (1996) 1934.
- [9] K.M. Yu, W. Walukiewicz, W. Shan, J. Wu, J.W. Beeman, J.W. Ager III, E.E. Haller, H.P. Xin, C.W. Tu, *Appl. Phys. Lett.* 78 (2001) 1077.
- [10] W. Shan, K.M. Yu, W. Walukiewicz, J.W. Ager, E.E. Haller, M.C. Ridgway, *Appl. Phys. Lett.* 75 (1999) 1410.
- [11] W. Shan, W. Walukiewicz, J.W. Ager III, E.E. Haller, J.F. Geisz, D.J. Friedman, J.M. Olson, S.R. Kurtz, *Phys. Rev. Lett.* 82 (1999) 1221.
- [12] W. Walukiewicz, W. Shan, J.W. Ager III, D.R. Chamberlin, E.E. Haller, J.F. Geisz, D.J. Friedman, J.M. Olson, S.R. Kurtz, in: V.K. Kapur, R.D. McDonnell, D. Carlson, G.P. Ceasar, A. Rohatgi (Eds.), *Photovoltaics for the 21st Century*, Electrochemical Society Press, Pennington, 1999, p. 190.
- [13] A. Lindsay, E.P. O'Reilly, *Solid State Commun.* 112 (1999) 443.
- [14] K.M. Yu, W. Walukiewicz, W. Shan, J.W. Ager III, J. Wu, E.E. Haller, J.F. Geisz, D.J. Friedman, J.M. Olson, *Phys. Rev. B* 61 (2000) R13337.
- [15] K.M. Yu, W. Walukiewicz, W. Shan, J. Wu, J.W. Ager III, E.E. Haller, J.F. Geisz, M.C. Ridgway, *Appl. Phys. Lett.* 77 (2000) 2858.
- [16] K.M. Yu, W. Walukiewicz, W. Shan, J. Wu, J.W. Beeman, J.W. Ager III, E.E. Haller, *Appl. Phys. Lett.* 77 (2000) 3607.
- [17] E. Morita, J. Kasahara, S. Kawado, *Jpn. J. Appl. Phys.* 24 (1985) 1274.
- [18] W.G. Opyd, J.F. Gibbons, A.J. Mardinly, *Appl. Phys. Lett.* 53 (1988) 1515.



ELSEVIER

Physica B 308–310 (2001) 877–880

PHYSICA B

www.elsevier.com/locate/physb

Incorporation of nitrogen in GaAsN and InGaAsN alloys investigated by FTIR and NRA

H.Ch. Alt^{a,*}, A.Yu. Egorov^b, H. Riechert^b, J.D. Meyer^c, B. Wiedemann^c

^a Engineering Physics, FHM—Munich University of Applied Sciences, Postfach 200113, 80001 München, Germany

^b Infineon Technologies, Corporate Research Photonics, München, Germany

^c Institute for Nuclear Physics, University of Frankfurt, Frankfurt, Germany

Abstract

InGaAsN layers grown by molecular beam epitaxy were investigated using Fourier transform infrared absorption spectroscopy. The nitrogen-related local mode at 471 cm^{-1} is used as a quantitative tool to assess the substitutional nitrogen fraction. Evidence is presented that nitrogen in the quaternary alloy is bonded only to gallium atoms as in GaAsN. No change in the local environment of nitrogen is observed after annealing. From nuclear reaction analysis of GaAsN under channeling conditions it is confirmed that the major fraction of nitrogen atoms ($>95\%$) is localized on string positions. © 2001 Elsevier Science B.V. All rights reserved.

Keywords: InGaAsN; Nitrogen; FTIR; NRA

1. Introduction

Adding of a small amount of nitrogen to GaAs during epitaxial growth leads to a large shrinkage of the band gap of about 100 meV per percent of nitrogen [1]. Contrary to the low concentrations of nitrogen found in bulk GaAs, being even in polycrystalline material in the lower 10^{16} cm^{-3} range at a maximum [2], alloy compositions of $\text{GaAs}_{1-x}\text{N}_x$ layers with x up to several percent can be grown by molecular beam epitaxy (MBE) as well as metalorganic vapor phase epitaxy (MOVPE). The simultaneous addition of indium, leading to the quaternary system InGaAsN, further reduces the band gap. Therefore optical emission in the $1.3\text{--}1.55\text{ }\mu\text{m}$ range, most interesting for optical fiber-based communication systems, can be expected [3]. Several groups reported recently on the observation of long-wavelength laser activity in such layers [4–6], culminating in the first vertical-cavity surface-emitting laser (VCSEL) working under CW conditions at room temperature [7].

In spite of this rapid technological progress, the theoretical understanding of the remarkable effects of nitrogen in these ternary and quaternary dilute alloy systems is still under debate [8–12]. Partly, this is related to the fact that it is experimentally not clear whether a true random alloy exists or some nitrogen-related ordering occurs, especially in the case of the quaternary InGaAsN. Experimental methods typically used for characterization are mass spectrometry, photoluminescence (PL) or X-ray diffraction (XRD). These methods are not selective with respect to the nitrogen species of interest, which is nitrogen on the anion site. Fourier transform infrared (FTIR) absorption spectroscopy can provide valuable information in this context. It is known that nitrogen in GaAs gives rise to a local vibrational mode (LVM) at 471 cm^{-1} which is due to isolated substitutional nitrogen, N_{As} [13]. The frequency of a LVM is a sensitive tool for the environment of a defect as it is dependent on the bond strength and the mass of the nearest neighbors [14]. It is the purpose of this paper to use FTIR absorption spectroscopy in combination with nuclear reaction analysis (NRA) under channeling conditions to resolve microscopic details of the local environment of nitrogen in these diluted alloys.

*Corresponding author. Tel.: +49-89-1265-1292; fax: +49-89-1265-1480.

E-mail address: hchalt@fh-muenchen.de (H.Ch. Alt).

2. Experimental

GaAs_{1-x}N_x and In_yGa_{1-y}As_{1-x}N_x layers were grown by solid-source MBE on semi-insulating GaAs (001) substrates. A radio frequency-coupled plasma source was used to generate the reactive nitrogen species from N₂. Ternary alloys were grown up to 3 μm thick. Quaternary alloys were produced as multiple-quantum-well (MQW) structures with up to 5 quantum wells of up to 10 nm thickness. The nitrogen content *x* was between 0.003 and 0.027 (according to X-ray diffraction [1]), the indium content *y* between 0.3 and 0.4. Standard annealing was performed in situ at 750°C, for comparative purposes some of the samples were annealed ex situ under similar conditions. InAs wafers of low conductivity were implanted with 3-MeV singly charged nitrogen ions. Three different sets of samples were generated: (i) 2×10^{16} ¹⁴N⁺/cm², (ii) 2×10^{16} ¹⁵N⁺/cm², (iii) 1×10^{16} ¹⁴N⁺/cm² + 1×10^{16} ¹⁵N⁺/cm².

FTIR measurements were carried out with a vacuum instrument (Bruker IFS 113v) using a globar source and a tri-glycine sulphate (TGS) detector. Due to the pronounced features of the two-phonon absorption in the GaAs substrate, subtraction of the spectrum of a reference sample was necessary. GaAsN layers were investigated by NRA under channeling conditions. The normalized yield of the ¹⁴N(*d*,α)¹²C nuclear reaction was measured as a function of the angle of incidence. The deuteron energy was 1.4 MeV.

3. Results and discussion

A typical low-temperature (77 K) FTIR absorption difference spectrum of an In_yGa_{1-y}As_{1-x}N_x MQW structure (*x* = 0.018, *y* = 0.35) with 5 quantum wells of a thickness of 10 nm each is shown in Fig. 1. A sharp band is found at 471.4 cm⁻¹. The band position is identical to the N-related LVM in bulk GaAs [2]. By implantation of ¹⁴N and ¹⁵N it has been proved that this band is due to the isolated nitrogen impurity on the anion lattice site, N_{As} [13]. The FWHM of about 3.0 cm⁻¹ is smaller than in the ternary alloy GaAsN and not much larger than in bulk crystals (2.0 cm⁻¹). This is indicative for the high quality of the MBE layer. After annealing no change is observed neither in the strength nor in the position of the band. This is in contrast to the behavior reported for InGaAsN layers grown by MOCVD [15]. The effect of annealing is, as usually observed, a large increase of the PL intensity. Evidently, this enhancement is not related to a substantial redistribution of the substitutional nitrogen fraction itself, but probably is caused by annealing of nonradiative recombination centers [16]. It should be mentioned that the 471 cm⁻¹ band was also detected by Raman spectroscopy [17,18].

For different in situ or ex situ annealed In_yGa_{1-y}As_{1-x}N_x MQW structures (0.3 ≤ *y* ≤ 0.4), the area under the absorption band, the integrated absorption (IA), is plotted versus the nitrogen content as determined by XRD on GaAsN layers produced by similar MBE growth conditions (Fig. 2). For *x* ≤ 0.02 reasonable agreement is found with the calculated IA

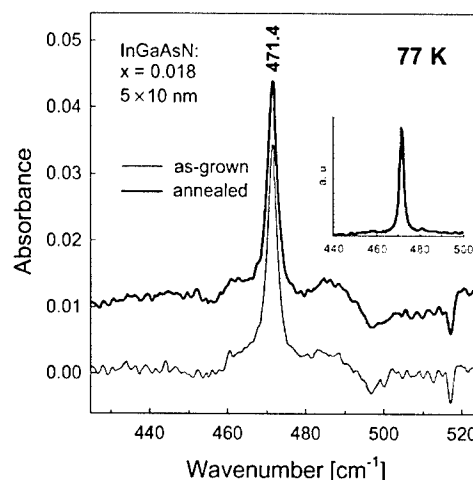


Fig. 1. Low-temperature FTIR absorption spectra of an In_yGa_{1-y}As_{1-x}N_x MQW structure with *y* = 0.35 and *x* = 0.018 before and after (ex situ) annealing. The reference spectrum has been subtracted. The spectrum of annealed sample has been displaced vertically for clarity. The inset shows the N_{As} LVM of a nitrogen-rich GaAs bulk crystal for comparison.

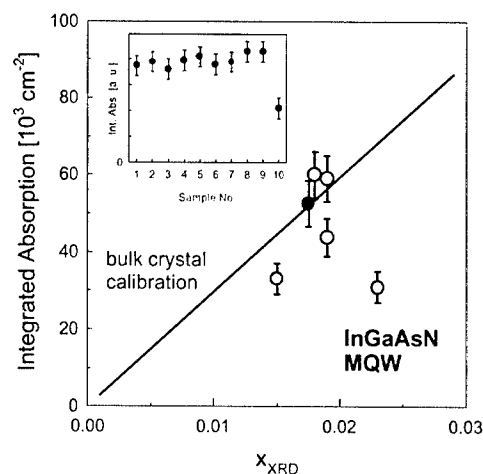


Fig. 2. IA of the 471 cm⁻¹ band in different In_yGa_{1-y}As_{1-x}N_x MQW structures (0.3 ≤ *y* ≤ 0.4) as a function of the nitrogen content determined by XRD. The straight line is calculated using the calibration factor derived from mass spectrometry in bulk GaAs crystals (Ref. [2]). The inset shows the lateral variation of the IA along the (100) direction of a 75-mm wafer (sample with full circle in the main graph).

based on the IR calibration factor of $7.4 \times 10^{15} \text{ cm}^{-1}$ derived from mass spectrometry on nitrogen-rich bulk GaAs crystals [2]. For higher x values considerable deviations exist, as previously observed in GaAsN layers [13]. It should be noted that recently also deviations were reported from Vegard's law, which is the basis for the XRD determination of the nitrogen content, for $x > 0.015$ in $\text{GaAs}_{1-x}\text{N}_x$ [19]. We found no dependence of the N content on the In content in the limited variation range for the In content ($0.3 \leq y \leq 0.4$). This is in agreement with the conclusions drawn by other groups for MBE material [20]. In any case, the FTIR method provides a sensitive tool to assess quantitatively the substitutional nitrogen content in MBE MQW structures. For the first time, it could be proved directly that, up to moderate x values of about 0.02, nitrogen is incorporated predominantly on the anion lattice site.

This picture is corroborated by the NRA investigation on selected $\text{GaAs}_{1-x}\text{N}_x$ layers produced by similar MBE growth conditions. In Fig. 3 the result is shown for a layer with a thickness of $0.35 \mu\text{m}$ and a total chemical nitrogen content of 0.6%. The normalized yield of the $^{14}\text{N}(d,\alpha)^{12}\text{C}$ nuclear reaction was measured as a function of the angle of incidence. Using a kinematical model for the reaction between deuterons and nitrogen atoms, the area projection of the N concentration in the GaAs lattice was calculated. N is predominantly localized on string positions. However, the half width of the distribution is larger than the thermal oscillation amplitude of the matrix atoms ($\langle u_{\text{th}} \rangle \approx 0.1 \text{ \AA}$). The

fraction of nitrogen atoms on interstitial sites is estimated to be less than 5%.

Using Monte Carlo simulations for the quaternary system InGaAsN, it was predicted that nitrogen should bond preferably with In atoms [21]. The argument is that the low-strain configuration N-In is energetically more favorable than N-Ga, in spite of the fact that the N-Ga bond energy is higher. Also experimentally some indications were presented that local correlations between nitrogen and indium occur [15,22]. Our FTIR results do not support such a behavior. The LVM frequency of N_{As} in InGaAsN is the same as in pure GaAs (Fig. 1). For nitrogen surrounded by indium a considerable lowering of the LVM frequency is expected. First indication is the LO phonon frequency being in InAs only 254 cm^{-1} compared to 296 cm^{-1} in GaAs. The so-far unknown frequency of the corresponding N_{As} LVM in InAs was studied by implantation of ^{14}N and ^{15}N into bulk crystals (Fig. 4). The result is similar to the same experiment in GaAs [13]. Two LVMs are observed at 443 ± 0.5 and $429 \pm 0.5 \text{ cm}^{-1}$ being due to ^{14}N and ^{15}N , respectively. The close correspondence to the same experiment in GaAs leaves no doubt that these bands are the LVMs of $^{14}\text{N}_{\text{As}}$ and $^{15}\text{N}_{\text{As}}$ in InAs, respectively. The frequency lowering amounts to 6.3% relative to GaAs. Cluster calculations have shown that already the inclusion of nearest neighbors leads to a very good approximation of the true LVM frequency [23]. Therefore a NIn_4 complex in InGaAsN should show a LVM frequency which is close to the frequency of N_{As} in bulk InAs. In a random

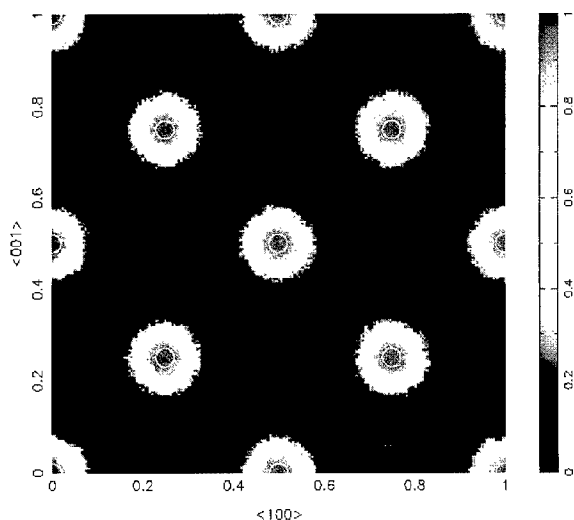


Fig. 3. Area projection of the ^{14}N content derived from NRA. The $\text{GaAs}_{1-x}\text{N}_x$ layer investigated has a thickness of $0.35 \mu\text{m}$ and a total chemical nitrogen content of 0.6%. The half width of the distribution is larger than the thermal oscillation amplitude of the matrix atoms ($\langle u_{\text{th}} \rangle \approx 0.1 \text{ \AA}$; indicated by white circle).

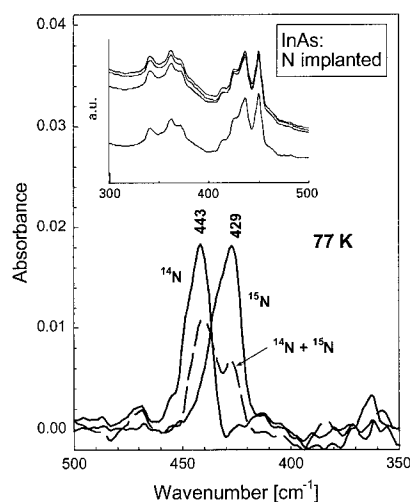


Fig. 4. FTIR absorption spectra of nitrogen-implanted InAs samples. The difference spectra shown were obtained after subtraction of the reference spectrum and a flat baseline. The inset shows from bottom to top the uncorrected spectra of unimplanted reference sample, the ^{14}N -, $^{14}\text{N}/^{15}\text{N}$ -, and the ^{15}N -implanted sample.

alloy with $y = 0.35$, the probability that 0, 1, 2, 3, and 4 nearest-neighbor indium atoms surround a nitrogen atom on the anion site, is 0.179, 0.384, 0.311, 0.111, and 0.015, respectively. From theory, these complexes have 9 different LVM frequencies which are essentially spread between the LVM frequencies of NGa_4 and NIn_4 [24]. No such bands are observed. Therefore, it is concluded that in the MBE grown InGaAsN MQW structures investigated nitrogen is surrounded only by nearest-neighbor gallium atoms.

4. Conclusion

Independent from the indium content, nitrogen in $\text{In}_y\text{Ga}_{1-y}\text{As}_{1-x}\text{N}_x$ layers grown by MBE is incorporated predominantly as substitutional N_{As} for $x < 0.02$. No redistribution or precipitation is found after annealing. Contrary to theoretical predictions, the local environment is determined by 4 nearest-neighbor gallium atoms.

References

- [1] M. Weyers, M. Sato, H. Ando, *Jpn. J. Appl. Phys.* 31 (1992) L853.
- [2] H.Ch. Alt, B. Wiedemann, K. Bethge, *Materials Science Forum*, Vols. 258–263 (Trans Tech, Zurich, 1997), p. 867.
- [3] M. Kondow, et al., *IEEE J. Sel. Top. Quantum Electron.* 3 (1997) 719.
- [4] K. Nakahara, et al., *Electron. Lett.* 32 (1996) 1585.
- [5] D. Mars, et al., *J. Vac. Sci. Technol. B* 17 (1999) 1272.
- [6] S. Sato, S. Satoh, *Electron. Lett.* 34 (1998) 1495.
- [7] G. Steinle, A.Yu. Egorov, H. Riechert, *Electron. Lett.* 37 (2001) 93.
- [8] S.-H. Wei, A. Zunger, *Phys. Rev. Lett.* 76 (1996) 664.
- [9] W. Shan, et al., *Phys. Rev. Lett.* 82 (1999) 1221.
- [10] E.D. Jones, et al., *Phys. Rev. B* 60 (1999) 4430.
- [11] T. Mattila, S.-H. Wei, A. Zunger, *Phys. Rev. B* 60 (1999) R11245.
- [12] A. Al-Yacoub, L. Bellaiche, *Phys. Rev. B* 62 (2000) 10847.
- [13] H.Ch. Alt, et al., *Appl. Phys. Lett.* 77 (2000) 3331.
- [14] R.C. Newman, *Infra-red Studies of Crystal Defects*, Taylor & Francis, London, 1973.
- [15] S. Kurtz, et al., *Appl. Phys. Lett.* 78 (2001) 748.
- [16] S.G. Spruytte, et al., *J. Appl. Phys.* 89 (2001) 4401.
- [17] T. Prokofyeva, et al., *Appl. Phys. Lett.* 73 (1998) 1409.
- [18] J. Wagner, et al., *Appl. Phys. Lett.* 77 (2000) 3592.
- [19] W. Li, M. Pessa, J. Likonon, *Appl. Phys. Lett.* 78 (2001) 2864.
- [20] E. Tournic, et al., *Appl. Phys. Lett.* 77 (2000) 2189.
- [21] K. Kim, A. Zunger, *Phys. Rev. Lett.* 86 (2001) 2609.
- [22] B.Q. Sun, et al., *Appl. Phys. Lett.* 77 (2000) 4148.
- [23] R.S. Leigh, R.C. Newman, *Semicond. Sci. Technol.* 3 (1988) 84.
- [24] M.J.L. Sangster, et al., *Semicond. Sci. Technol.* 7 (1992) 1295.



ELSEVIER

Physica B 308–310 (2001) 881–883

PHYSICA B

www.elsevier.com/locate/physb

Partly filled impurity band formation in compensated InP : Mn

S.B. Mikhlin*, K.F. Shtel'makh

*Experimental Physics Department, Saint Petersburg State Technical University, Russian Federation, Politechnicheskay 29,
195251 St. Petersburg, Russia*

Abstract

In this work, we present the results of the study of a compensated InP slightly doped with manganese. In this material, a large drop of resistivity (more than 10^4) with temperature decrease (120–100 K) has been observed. In order to clarify the mechanism of this effect we have undertaken the following: Hall effect and magneto-resistance measurements; magnetic susceptibility measurements; measurements of EPR and NMR; and optical absorption measurements. The main results of our investigations are (1) a peculiarity of NMR results corresponds with that of the Hall effect data and (2) non-paramagnetic behavior of an ^6S -state ESR signal in the temperature region 30–300 K. The main idea that explains these results exploits the non-symmetrical character of the manganese d^4 state. The impurity subband formation is due to the electron tunneling between the neutral non-relaxed manganese centers at temperatures below 120 K. We present some ideas in order to observe this effect in other A^3B^5 semiconductors doped with manganese. © 2001 Elsevier Science B.V. All rights reserved.

Keywords: InP : Mn; Conductivity; NMR; ESR; Impurity subband

1. Introduction

Manganese in A^3B^5 compounds is one of the most interesting impurities. Many unusual effects have been observed in heavy doped materials [1–2], and mostly, they are due to the interactions of the d-shells of the manganese impurities. Commonly, the lesser the d-element concentration we have in samples, the weaker effects we observe. The particular effect for such compounds is observed in the slightly doped samples of InP : Mn. A giant resistivity drop has been observed [3] under the temperature decrease in the slightly doped highly compensated samples. In this work, we continue the investigation of this phenomenon paying special attention to (a) the results obtained by EPR and (b) the comparison of the Hall effect data with NMR data.

2. Sample preparations

The InP : Mn single crystals grown by a liquid encapsulated Chokhralsky method have been used. Manganese has been added to the melt under the growth of the crystals. The very beginning of the ingot of n-type, the middle part of the ingot and its end have the conductivity of p-type (the distribution coefficient of $\text{Mn} < 1$). The total Mn content estimated by spectrochemical analysis has been varied over the range 5×10^{16} – $2 \times 10^{17}/\text{cm}^3$ for samples having an unusual conductivity. The non-controlled donor concentration was about $2 \times 10^{16}/\text{cm}^3$, the sample contacts were made by In–Ni(3%) alloy.

3. Experimental results

The results of Hall effect measurements for two samples are shown in Fig. 1. The manganese acceptor ionization energy, defined by $n(T)$ curve in the temperature range from 300 to 160 K, is $E_{\text{IH}} = (200 \pm 5) \text{ meV}$. The same energy determined by the $\rho(T)$ curve is equal

*Corresponding author. Tel.: +7-812-552-7574; fax: +7-812-552-7574.

E-mail address: mikhlin@tuexp.stu.neva.ru (S.B. Mikhlin).

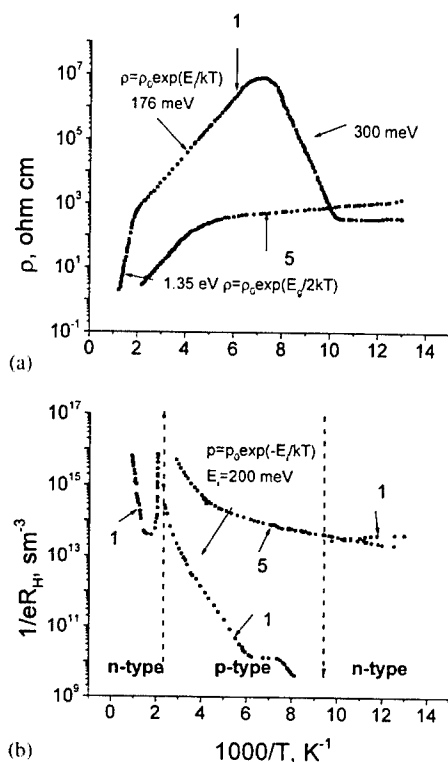


Fig. 1. Temperature dependencies of resistivity (a) for InP samples doped with different Mn concentrations: sample 1– $5 \times 10^{16}/cm^3$, sample 5– $5 \times 10^{17}/cm^3$, and carrier concentrations (b) for the same samples. Dashed lines show n–p–n conversion with temperature.

to 180 and 157 meV for the samples 1 and 5, respectively. The activation energy (1.35 eV) defined from $\rho(T)$ curve over the temperature range from 500 to 800 K correlates well with the forbidden gap energy E_g . A giant exponential drop of resistivity in the temperature range from 120 to 100 K has an activation energy of 300 ± 2 meV. In spite of p→n conversion, the carrier mobility changes the value from $70 cm^2/Vs$ only to 450 – $2500 cm^2/Vs$. It should be noted that the difference in electron mobility for the subband ($T < 100$ K) 450 – $2500 cm^2/Vs$ is much less than the corresponding value known for n-InP (77 K) $40,000 cm^2/Vs$. The magneto-resistivity has not changed significantly demonstrating a weak linear dependence in the temperature range from 200 to 77 K.

The optical absorption was measured at 300 K and the results were described well by Lukovsky's formula with the threshold $E_{IO} = 249 \pm 6$ meV. So, we have observed the difference $E_{IO} - E_{IH} \cong 50$ meV.

The results of EPR studies obtained for the temperature range 3.8–150 K are shown in Fig. 2. At low temperatures, the EPR spectrum consists of one broad line having the unresolved super fine

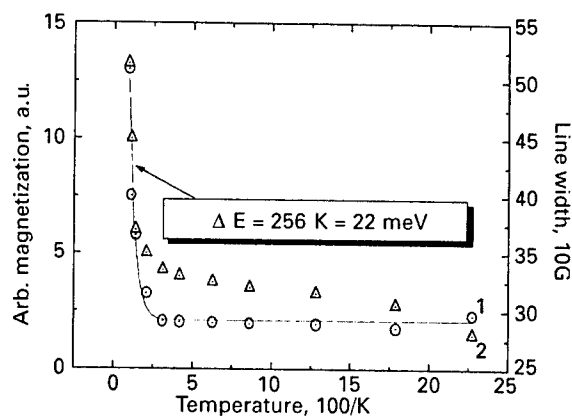


Fig. 2. The dependence of the relative magnetisation (circles) and the linewidth (triangles) on temperature for sample 1.

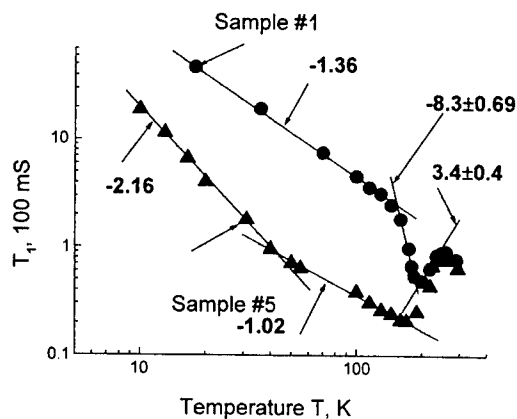


Fig. 3. The temperature dependence of the relaxation time T_1 for samples 1 and 5.

structure ($g = 1.99 \pm 0.03$). The relative magnetization which is proportional to a magnetic state population in 4–110 K temperature range increases exponentially with the activation energy $\Delta E = 22$ meV. This increase is defined mainly by the temperature variation of the linewidth. The shift of the spectrum to the range of lower magnetic fields has been observed for the temperature interval from 30 to 110 K (the g factor is 2.07 ± 0.03). The Curie-Weiss-law behavior with $\theta = -1.9$ K has been observed for the magnetic susceptibility.

The temperature dependences of NMR relaxation time T_1 for two samples [4] are shown in Fig. 3. The NMR measurements were carried out on ^{115}In nucleus at 8 MHz. The value of T_1 has been varied as $T^{3.4}$ dependence for both samples (1 and 5) in the temperature range from 250 to 200 K. It is important to note that in the temperature range from 185 to 160 K the differences between the two samples have been revealed:

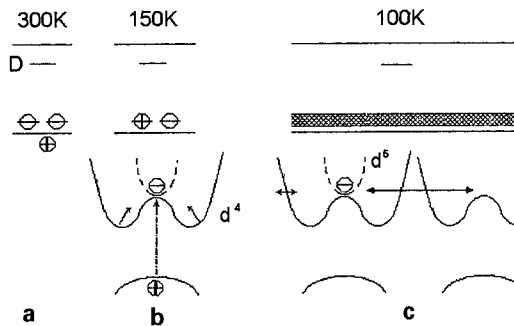


Fig. 4. An illustration of electron and hole transport in InP:Mn at different temperatures: 300 K—a (all manganese acceptors are ionized); 150 K—b (a part of manganese acceptors are ionized, the others are not) and 120 K—c.

for the heavy doped sample, T_1 continues to decrease, while for the low doped sample the value of T_1 increases as $T^{-8.3}$. For the last sample at temperatures less than 140 K, we have $T_1 \sim T^{-1.36}$. For temperatures less than 120 K we have observed the resonance frequency shift up to 1 G at 100 K which indicates the change of the relaxation mechanism [5].

4. Discussion

In contrast to the Mn impurity center in GaAs [6] for the similar center in InP we see quite significant Stokes shift. This clearly shows the non-central character of neutral Mn state (d^4 or d^5 + hole; the profile of Mn potential is shown by solid line in the central part of Fig. 4). We can explain the transport effects by the model which is illustrated in Fig. 4. At room temperature, all manganese centers are ionized (Fig. 4a) and there is no possibility for electron tunneling between them. With the temperature decrease up to ~ 150 K (Fig. 4b) one part of the Mn centers is ionized owing to the presence of the non-controlled shallow donors; the other part of the Mn centers is not ionized (strongly compensated samples have approximately equal

amounts of different Mn states; the compensation ratio $\alpha = \text{Nd/Na}$ is about 0.5). At this temperature (150 K), after the electron tunneling into non-central quantum well the d^4 Mn center relaxes into the state having the energy minimum produced by the d^5 state. The lattice relaxation is fast enough for the tunneling through the relaxed states produced under a strong phonon interaction. The further temperature decrease up to 100 K (Fig. 4c) leads to slowing down the processes of relaxation (Fig. 3) which in turn causes the electron tunneling between the non-relaxed Mn centers. The possibility exists whether the minimum of ^6S (d^5) state (dashed lines in Fig. 4) is above or coincides with the local maximum of d^4 state. The effect might be observed in GaAs:Mn having lower Mn concentration (10^{15} – $10^{16}/\text{cm}^3$) and the compensation ratio of about 0.5.

The conductivity at low temperatures (below 120 K), as a whole, exhibits an electron transport over the partly filled impurity subband. The electron mobility in the subband depends on the compensation ratio α (Nd/Na).

Acknowledgements

We gratefully thank our colleague Dr. V.P. Maslov for help in NMR studies.

References

- [1] T. Hayashi, M. Tanaka, T. Nishinaga, H. Shimada, *J. Appl. Phys.* 81 (1997) 4865.
- [2] A. Oiwa, S. Katsumoto, A. Endo, M. Hirasawa, Y. Iye, F. Matsukura, A. Shen, Y. Sugawara, H. Ohno, *Physica B* 249–251 (1998) 775.
- [3] E. Vavilov, L. Zacharenkov, S. Mikhlin, *Fizika i tehnika poluprovodnikov* 21 (1987) 1336.
- [4] M.N. Barbashov, V.P. Maslov, V.F. Masterov, *Fizika tverdogo tela* 25 (1983) 1130.
- [5] C.D. Jeffries, *Dynamic Nuclear Orientation*. Intersciens Publishers, Wiley, NY, 1963, p. 250.
- [6] B. Clerjaud, *J. Phys. C: Sol. State Phys.* 18 (1985) 3615.



ELSEVIER

Physica B 308 310 (2001) 884–887

PHYSICA B

www.elsevier.com/locate/physb

Optically induced Auger recombination of Yb^{3+} in p-type InP

M.A.J. Klik^{a,*}, I.V. Bradley^{b,c}, J.-P.R. Wells^{b,c}, T. Gregorkiewicz^a^a Van der Waals–Zeeman Institute, University of Amsterdam, Valckenierstraat 65, NL-1018 XE Amsterdam, Netherlands^b FOM Institute for Plasma Physics 'Rijnhuizen', P.O. Box 1207, NL-3430 BE Nieuwegein, Netherlands^c Department of Physics, Heriot Watt University, Edinburgh EH14 4AS, UK

Abstract

The effects of mid-infrared (MIR) radiation on the photoluminescence (PL) of Yb^{3+} in p-type InP have been investigated in the wavelength range of 7–17 μm . It has been found that effective quenching of the luminescence intensity can be observed during the 4 μs length of the MIR pulse. The effect is explained by an Auger process of energy transfer between the Yb^{3+} excited state and free holes that are ionized from the acceptors in the host. From the dependence of the luminescence quench amplitude on the MIR wavelength, the acceptor is identified as Zn, which is the residual acceptor in the investigated sample. © 2001 Elsevier Science B.V. All rights reserved.

PACS: 78.55.Cr; 32.80.Hd; 71.20.Eh

Keywords: Ytterbium; InP; Photoluminescence; Free electron laser

1. Introduction

Rare-earth (RE) doped semiconductors show sharp and temperature-stable luminescence due to the RE intra-4f-shell transitions. These properties are attractive for fabricating light-emitting devices that are insensitive to the host environment. However, the luminescence efficiency rapidly decreases at elevated temperatures, the effect known as thermal quenching. A good understanding of the luminescence mechanisms and the excitation pathways of the RE ions in semiconductor hosts is necessary to overcome this problem.

The Yb-doped InP has been widely used to investigate the excitation and de-excitation processes of the REs in semiconductors, because the Yb ions in the InP form a single kind of luminescence center and have only one excited state. It is believed that the Yb ion gives rise to an acceptor-like electron (AE) trap at 30 meV below the conduction band [1]. The recombination energy of an electron localized at the AE trap with a free hole can be

transferred to the 4f-shell of ytterbium, which excites the ion from the $^2\text{F}_{7/2}$ to the $^2\text{F}_{5/2}$ state.

The majority of information currently available on the excitation and de-excitation mechanisms of the REs in semiconductors is based on results obtained from temperature quenching of photoluminescence (PL) intensity and the decay characteristics of the excited state. However, processes governed by larger activation energies can only be observed at higher temperatures and, therefore, lower PL intensity. Two-beam experiments, with an intense mid-infrared (MIR) beam operating parallel to an above-band-gap photoexcitation, can be used to avoid this problem and study selectively energy transfer processes at low temperature, where the PL intensity is still high [2].

2. Experiment

The experiments were performed at the free-electron-laser (FEL) users facility in Nieuwegein, the Netherlands. The samples under investigation were grown by liquid phase epitaxy (LPE). The InP:Yb layer was grown in a graphite sliding-boat system by a super-cooling process at high growth temperatures of up to

*Corresponding author. Tel.: +31-20-525-5644; fax: +31-20-525-5788.

E-mail address: mklik@science.uva.nl (M.A.J. Klik).

800°C [3]. The Yb-concentration in the In growth melt was 0.2 percent mole fraction. The crystal exhibited p-type conductivity with a carrier concentration of $p = 7 \times 10^{16} \text{ cm}^{-3}$ at 300 K, with Zn being the residual acceptor. The samples were mounted inside an Oxford Instruments flow-cryostat and cooled down to 4.2 K. For band-to-band excitation, the samples were illuminated with the second harmonic (532 nm) of a Nd:YAG laser with a repetition rate of 5 Hz and a pulse length of 100 ps. A MIR ‘macropulse’ from the FEL provided the secondary excitation of a 4–6 μs length and an (adjustable) wavelength of 7–17 μm . The time delay between the Nd:YAG and the MIR pulses can be varied from –90 to +90 ms. A 7 μm cut-off filter was placed in the MIR beam to avoid penetration of shorter wavelengths from higher harmonics in the FEL. Both beams illuminated an area circular in shape and with a diameter of $\sim 5 \text{ mm}$. The emerging PL was gathered using a single grating monochromator and a near-infrared photomultiplier tube with a flat response from 300 to 1600 nm.

3. Results and discussion

Time-resolved measurements of the intra-4f-shell PL of Yb have been performed for various delay times Δt between the Nd:YAG pulse and the onset of the FEL pulse. Both enhancement and quenching of the PL signal could be observed, depending on Δt being positive (FEL before YAG) or negative.

3.1. Quench of luminescence

Fig. 1 shows the effect of the FEL pulse (depicted for reference at the lower part of the image) on the Yb^{3+} luminescence signal for a delay time of $\Delta t = -1, 2$ and

4 μs . It can be seen that quenching of the PL only occurs during the FEL pulse. This observation excludes thermal heating of the crystal lattice, which has a relaxation time of milliseconds, as a possible explanation for this intensity quenching effect. The ratio of the PL intensity observed with and without the FEL pulse, hereafter called the ‘quenching ratio’, is constant for all positive delay times for a given photon flux and a fixed wavelength of the MIR pulse. From this, we conclude that the quenching amplitude is proportional to the number of excited Yb^{3+} ions. The possible mechanisms that can explain this dependence are an optically induced back-transfer [4] effect and an Auger process, involving energy transfer from the excited Yb^{3+} ions to free or bound carriers. However, a back-transfer mechanism should not show saturation with the FEL photon-flux, as observed in our experiments. A localized Auger effect has been proposed as a PL quenching mechanism for the n-type InP:Yb as follows [5]. After excitation of the 4f-shell of Yb^{3+} by the recombination of the electron–hole pair, the AE trap becomes empty. These empty traps can again capture electrons from distant shallow donors. The energy of the excited 4f-shell can now be used to bring this electron to the conduction band in a localized Auger process, de-exciting the Yb^{3+} ion. This mechanism was used to explain the initial fast non-exponential decay observed in the InP:Yb intra-4f-shell luminescence in samples with high shallow donor concentrations [6]. For p-type materials, a similar model was proposed to explain the temperature quenching which involves holes captured at the acceptors receiving the relaxation energy of the 4f-shell. Similar to thermal ionization, the holes on these acceptors in the InP host can also be ionized by the MIR radiation. Therefore, the concentration of the bound holes will decrease with increasing FEL photon-flux. Taking into account our observation of an increase of PL quenching with increasing FEL photon-flux, it is more probable that a free-hole Auger process is responsible for the observed effect. It is reasonable to assume that a steady free-hole concentration exists during the FEL pulse, even at low temperatures. This concentration p will depend on the photon flux of the MIR pulse, the ionization cross-section of the shallow acceptor centers for a particular FEL wavelength and the shallow acceptor concentration in the sample. The intensity of the Yb^{3+} intra-4f-shell luminescence during the Auger quenching process can be described by

$$Y^*(t) = Y(t_1) \exp\left(\left(-\frac{1}{\tau} + C_A p\right)t\right)$$

$$\text{for } t_1 < t < t_2,$$

where t_1 and t_2 denote the time during which the FEL is on, $Y(t_1)$ is the luminescence intensity at time t_1 , τ is the effective lifetime of the Yb^{3+} excited state and C_A

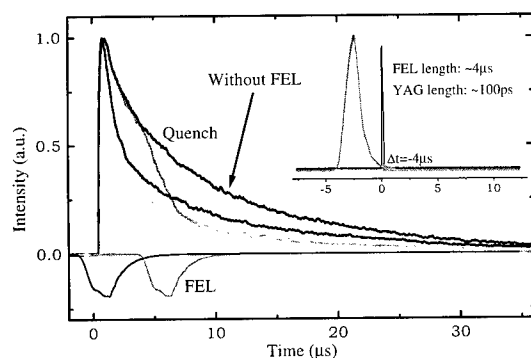


Fig. 1. The quenching of the Yb^{3+} PL observed under Nd:YAG excitation for three different delay times of the MIR pulse. The relative position at $t = 0$ is indicated in the inset.

the Auger coefficient describing the energy transfer to the ionized holes p . Calculating the ratio between the integrated 4f-shell luminescence for a luminescent transient with and without the FEL, we find

$$\ln \frac{Y^*(t)}{Y(t)} = -C_A p(t_2 - t_1) \quad \text{for } t > t_2.$$

The dependence of the quenching on the MIR photon-flux is depicted in Fig. 2. For two different wavelength settings of the FEL, the dependencies can be fitted with an exponentially decaying curve with an offset of 0.29, meaning that the quenching saturates when 71 percent of the signal has disappeared. Following the assumed mechanism, this saturation appears as a result of the exhaustion of holes bound to the acceptors. As can be seen from the picture, the photon-flux dependence of the quenching effect can be described with a single exponentially decaying curve for a low photon flux. Therefore, we can calculate the expected dependence of the quenching ratio $Q(t) = Y^*(t)/Y(t)$ on the FEL wavelength:

$$Q(\lambda) = \exp(-C_A P(\lambda) N_A \sigma(\lambda) \tau_{\text{H}}(t_2 - t_1)) \quad \text{for } t > t_2,$$

with $P(\lambda)$ the photon flux of the FEL at wavelength λ , $\sigma(\lambda)$ the ionization cross-section of the acceptor as a function of the FEL wavelength, N_A the number of acceptors and τ_{H} the effective lifetime of a hole. Fig. 3a shows this dependence for a value $\sigma(\lambda)$ that is taken to be constant over the wavelength range of the scan (black) and the measured dependence (gray). The value of $\sigma(\lambda)$ can now be calculated as follows:

$$\sigma(\lambda) = -\frac{\ln Q(\lambda)}{C_A P(\lambda) N_A \sigma(\lambda) \tau_{\text{H}}(t_2 - t_1)}.$$

This is shown in Fig. 3b, with the curve normalized to the value at $\lambda_{\text{FEL}} = 11 \mu\text{m}$; we conclude a clear

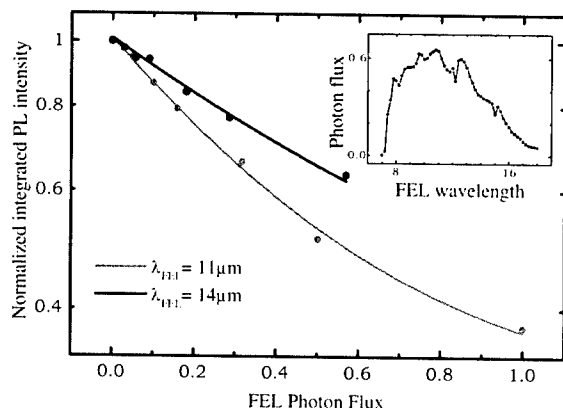


Fig. 2. The quenching ratio as a function of the MIR pulse photon flux for two different MIR wavelengths. The dependence of the photon flux of the MIR pulse on the wavelength is depicted in the inset.

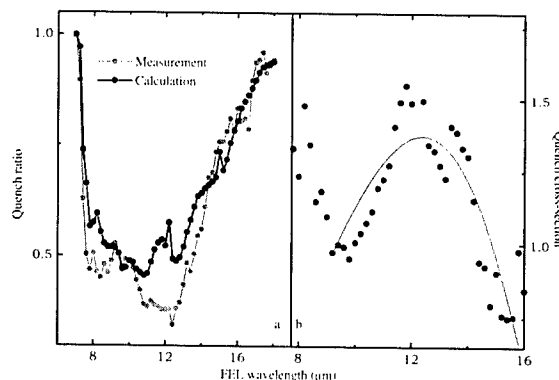


Fig. 3. (a) Calculated (black) and measured (gray) wavelength dependence of the quenching effect as a function of the MIR wavelength. (b) Ionization cross-section of the shallow acceptors as a function of the MIR wavelength. The data can be fitted with a curve corresponding to a trap characterized by a Coulomb potential and ionization energy of 70 meV.

dependence on the FEL wavelength, which has a maximum corresponding to an optical quantum energy of ~ 100 meV.

It has been shown that the photoionization cross-section of a trap can be described as [7]

$$\sigma = m \frac{(h\nu - E_D)^{3/2}}{(h\nu)^{3+2\gamma}},$$

with m a constant and $h\nu$ and E_D the energy of the ionizing beam and the trap ionization energy, respectively. The parameter γ depends on the form of the binding potential, and has a value between 0 (δ -like potential) and 1 (Coulomb potential). As illustrated in the figure, experimental data are best fitted to the ionization of a trap characterized by a Coulomb potential and (optical) ionization energy of $E_D \approx 70$ meV. This value is in good agreement with the position of the Zn acceptor as determined from the donor-acceptor/free-to-bound recombination observed in the same sample at 902 nm. It is therefore highly likely that in the present experiment, the MIR induced ionization of the Zn acceptor is observed.

For the regime where the quenching is saturated to 71 percent, we can estimate the hole concentration to be equal to that at room temperature. From the sample parameters of $2 \times 10^{20} \text{ cm}^{-3}$ for the Yb concentration and $7 \times 10^{16} \text{ cm}^{-3}$ for the free-hole concentration, we calculate an Auger coefficient value for the energy transfer to free holes of $C_A \approx 3 \times 10^{-12} \text{ cm}^{-3} \text{ s}^{-1}$.

3.2. Enhancement of luminescence

A considerable enhancement of the Yb^{3+} PL was found when applying the FEL before the band-to-band excitation with the Nd:YAG laser. The enhancement

effect was present for delay times up to -15 ms, which suggest a process with a long relaxation time. This could be due to the lattice heating and will not be discussed here.

A more complete treatise of the enhancement effect will be published elsewhere [8].

4. Conclusion

Two effects of the MIR radiation on the intra-4f-shell luminescence of the Yb in p-type InP have been investigated. It was found that an intense pulse of a FEL with a photon energy corresponding to 70–170 meV applied before the above-band excitation induced an enhancement of the intra-4f-shell PL intensity, most probably due to heating of the crystal matrix. Applying the FEL after the above-band excitation was found to quench the PL luminescence up to 70

percent. The observations were explained as a free-hole Auger process, for which we calculated an Auger coefficient of $3 \times 10^{-12} \text{ cm}^{-3} \text{ s}^{-1}$. The dependence of the quenching effect amplitude on the FEL wavelength suggests that the FEL induced ionization of the dominant acceptor Zn provides free holes participating in the Auger energy transfer.

References

- [1] P.S. Whitney, et al., *Appl. Phys. Lett.* 53 (1988) 2074.
- [2] I. Tsimperidis, et al., *Phys. Rev. Lett.* 81 (1998) 4748.
- [3] W. Körber, et al., *J. Crystal Growth* 79 (1986) 741.
- [4] A. Taguchi, et al., *J. Appl. Phys.* 76 (1994) 7288.
- [5] A. Taguchi, et al., *J. Appl. Phys.* 70 (1991) 5604.
- [6] K. Takahei, et al., *J. Appl. Phys.* 66 (1989) 4941.
- [7] J.M. Langer, et al., *Phys. Stat. Sol. B* 66 (1974) 537.
- [8] M.A.J. Klik, T. Gregorkiewicz, to be published.



ELSEVIER

Physica B 308–310 (2001) 888–890

PHYSICA B

www.elsevier.com/locate/physb

Dopant interactions and Mg segregation in $(\text{Al}_x\text{Ga}_{1-x})_{0.5}\text{In}_{0.5}\text{P}$ heterostructures

P.N. Grillo^{a,*}, S.A. Stockman^a, J.-W. Huang^a, Y.L. Chang^b

^aLumiLeds Lighting, US LLC, 370 W. Trimble Road 91-ML, San Jose, CA 95131, USA

^bAgilent Technologies, Palo Alto, CA 94888, USA

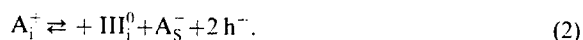
Abstract

Acceptor atoms are experimentally observed to accumulate in the low bandgap layers of III–V heterostructures while being depleted from the high bandgap layers. Such acceptor segregation can be explained by considering the space charge neutrality condition in conjunction with hole segregation across the heterointerface. This approach reveals that the acceptor concentration ratio varies exponentially with valence band offset across the heterointerface, and further demonstrates that such acceptor segregation is suppressed by counterdoping the high bandgap layer with donor atoms. The same model can be used to explain enhanced acceptor solubility and suppressed acceptor diffusion in uniform composition samples that are counterdoped with donors. In each of these cases, the dopant concentrations (and hence dopant diffusion) are determined by the thermal equilibrium requirement that the Fermi energy be spatially invariant. © 2001 Elsevier Science B.V. All rights reserved.

Keywords: Acceptor diffusion; Acceptor segregation; Counterdoping

1. Introduction and experiment

Although III–V semiconductors offer extensive design flexibility compared to Si based devices, the benefits of III–V devices are often compromised by the rapid diffusion of p-type dopants, which makes p–n junction placement difficult to control. The present understanding of this rapid acceptor diffusion is based upon the charge states of the interstitial and substitutional acceptor atoms, and upon the native defects (group III self interstitials, III_i^0 , or group III vacancies, III_v^0) and free holes, h^+ , that mediate the exchange of acceptor atoms between interstitial and substitutional sites [1].



Since the diffusion rate of the interstitial group II atom, A_i^+ , is assumed to far exceed that of the substitutional group II atom, A_s^- , acceptor diffusion is thought to

occur through the conversion of group II atoms from substitutional sites to interstitial sites. Given the assumption that acceptors diffuse as interstitial atoms, Eqs. (1) and (2) demonstrate the dependence of acceptor diffusion on the hole (acceptor) concentration. In fact, it can be shown from Eqs. (1) and (2) that the acceptor diffusion coefficient varies as the square of the acceptor concentration. In contrast to this rapid acceptor diffusion, donors are thought to diffuse by a different mechanism in III–V semiconductors, resulting in a linear dependence of donor diffusion coefficient on donor concentration [2].

While the above discussion explains rapid acceptor diffusion in III–V semiconductors, a variety of related, yet less understood phenomena have been reported in the literature. These observations include acceptor segregation in III–V heterostructures, where acceptors diffuse from regions of low concentration into regions of high concentration [2–6], as well as reduced acceptor diffusion and enhanced acceptor incorporation in the presence of donor species [4,7–9]. While the effect of such donor species on acceptor diffusion in III–V semiconductors is clear due to its impact on the hole

*Corresponding author. Fax: +1-408-435-6335.

E-mail address: pat.grillot@lumileds.com (P.N. Grillo).

concentration, its impact on acceptor incorporation is more subtle. We believe that this effect is fundamentally related to acceptor segregation, however, and it is our intent to demonstrate this connection in this paper.

To investigate these effects, six double heterostructure $(\text{Al}_x\text{Ga}_{1-x})_{0.5}\text{In}_{0.5}\text{P}$ samples were fabricated as described elsewhere [6]. These samples consisted of an n-type $\text{Al}_{0.5}\text{In}_{0.5}\text{P}$ lower confining layer, an $(\text{Al}_x\text{Ga}_{1-x})_{0.5}\text{In}_{0.5}\text{P}$ active layer (AL), and a p-type $(\text{Al}_x\text{Ga}_{1-x})_{0.5}\text{In}_{0.5}\text{P}$ upper confining layer (CL) all grown lattice matched on GaAs. Two different AL compositions (7% and 28% Al) and three different CL compositions (40%, 60%, and 100% Al) were used in this sample set. $(\text{Al}_x\text{Ga}_{1-x})_{0.5}\text{In}_{0.5}\text{P}$ is an ideal choice for such acceptor segregation studies since it is lattice matched to GaAs, and has a valence band energy that varies linearly with Al composition, x .

$$E_V(x) = E_V(0) - 0.241x. \quad (3)$$

2. Results

Various acceptor species, including Mg, Zn, Be, and Mn have previously been shown to segregate across a heterointerface in $(\text{Al}_x\text{Ga}_{1-x})_{0.5}\text{In}_{0.5}\text{P}/\text{GaAs}$ samples, similar to that shown in Fig. 1 for the six AlGaInP samples described above [2,6]. Note that the extent of this Mg segregation increases with increasing change in Al composition, dx , across the AL/CL interface. This Mg segregation can be understood by considering the segregation of free holes in such heterostructures. In a uniform composition, non-degenerate semiconductor, the free hole concentration is given by

$$p = N_V \exp[-(E_F - E_V)/kT]. \quad (4)$$

These holes will segregate across a heterointerface, however, and accumulate in the layer of lowest hole energy. Using the thermal equilibrium requirement that $E_{\text{FAL}} = E_{\text{FCL}}$, it is straightforward to show that the hole concentration ratio between layers AL and CL is given by

$$p_{\text{AL}}/p_{\text{CL}} = (m_{\text{hAL}}^*/m_{\text{hCL}}^*)^{3/2} \exp(\Delta E_V/kT), \quad (5)$$

where m_{hAL}^* and m_{hCL}^* are the hole effective masses in the AL and CL, respectively, and $\Delta E_V = E_{\text{VAL}} - E_{\text{VCL}}$. From the space charge neutrality condition, $p + N_D^+ = n + N_A^-$, it is apparent that the spatial separation of the positively charged holes and negatively charged acceptors will give rise to an electric field across the heterointerface, and given sufficient thermal energy for the acceptors to diffuse, the acceptors should achieve a similar segregation ratio. In fact, for a p-type semiconductor where $p \gg n$, the space charge neutrality condition reduces to $p = N_A^- - N_D^+$, which implies that

$$N_A^- - N_D^+ = N_V \exp[-(E_F - E_V)/kT]. \quad (6)$$

Under the additional condition that $N_A^- \gg N_D^+$, the ratio of Eq. (6) for layers AL and CL gives

$$N_{\text{AAL}}^-/N_{\text{ACL}}^- = (m_{\text{hAL}}^*/m_{\text{hCL}}^*)^{3/2} \exp(\Delta E_V/kT). \quad (7)$$

For the case in Fig. 1, where both the AL and CL are p-type, and $N_A^- \gg N_D^+$, the acceptor concentration ratio at the AL/CL interface should obey Eq. (7). Using the compositional dependence of m_{h}^* for $(\text{Al}_x\text{Ga}_{1-x})_{0.5}\text{In}_{0.5}\text{P}$, the results of Eq. (7) and Fig. 1 are compared in Fig. 2.

$$m_{\text{h}}^*(x) = (0.62 + 0.05x)m_0. \quad (8)$$

This comparison in Fig. 2 reveals close agreement between experiment and theory, thus indicating that Eq. (7) accurately describes the acceptor segregation that has been reported in the literature by numerous authors [2–6]. This acceptor segregation can be suppressed, however, if the p-type CL is counterdoped with a donor species, as in Fig. 3. Such reduced acceptor

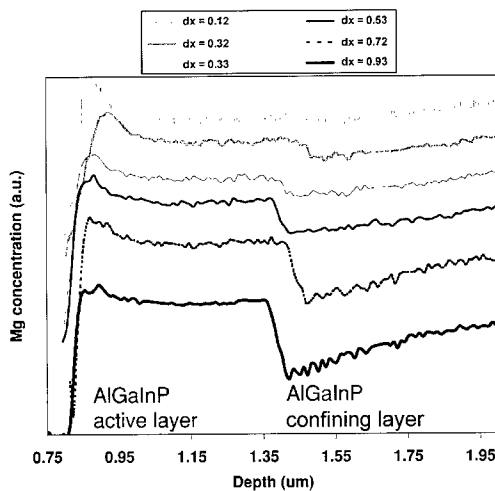


Fig. 1. Mg segregation in six $(\text{Al}_x\text{Ga}_{1-x})_{0.5}\text{In}_{0.5}\text{P}$ heterostructures with various compositional offsets, $dx = x_{\text{CL}} - x_{\text{AL}}$, across the AL/CL heterointerface.

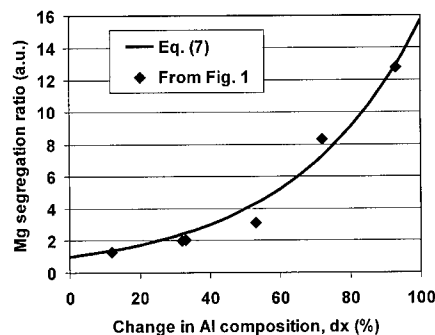


Fig. 2. Comparison of the Mg segregation ratio from Eq. (7) and from Fig. 1.

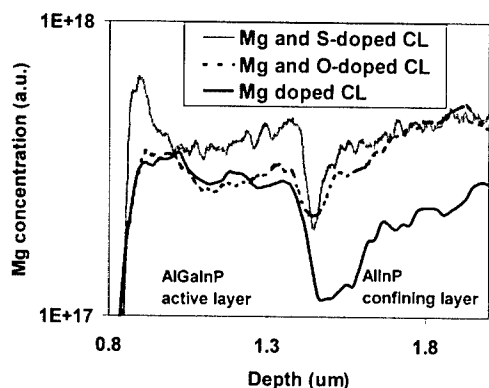


Fig. 3. Counterdoping the p-type CL with a donor species (O or S) reduces acceptor segregation.

segregation in the presence of compensating donor species is similar to previous reports of reduced acceptor diffusion and increased acceptor incorporation in III–V semiconductors that are simultaneously doped with both a donor species and an acceptor species. The key to understanding these three effects (enhanced acceptor incorporation, reduced acceptor diffusion, and reduced acceptor segregation) is apparent from Eqs. (6) and (7), in conjunction with the acceptor solubility equation,

$$[A_S^-] = C_0 \exp[(E_F - E_A)/kT], \quad (9)$$

where E_A is the ionized acceptor energy level and C_0 is the acceptor solubility when $E_F = E_A$ [10]. For example, counterdoping a p-type semiconductor with donors tends to increase $E_F - E_A$ in Eq. (9), which increases the solubility of the substitutional acceptor, $[A_S^-]$, and hence increases acceptor incorporation. This increase in the solubility of the substitutional acceptors will decrease the conversion of group II atoms from substitutional sites to interstitial sites, however, thus reducing acceptor diffusion. For the case in Fig. 3, where the CL is doped with both donors and acceptors, while the AL is doped only with acceptors, the donors will reduce acceptor segregation since they will not diffuse during thermal processing. This effect can be quantified by revisiting Eq. (7), where N_{AAL}^-/N_{ACL}^- must now be replaced by $N_{AAL}^-/(N_A^- - N_D^-)_{CL}$. While the theoretical basis for this technique is therefore quite simple, counterdoping is useful in helping to control both acceptor segregation and p–n junction location. A heterointerface is not necessary for this discussion to apply, however, as can be seen by setting $\Delta E_V = 0$ and $m_{hAL}^* = m_{hCL}^*$ in Eq. (7). Thus, one obtains $N_{AAL}^- = (N_A^- - N_D^-)_{CL}$. In thermal equilibrium, space charge neutrality thus requires that a sudden increase

in donor concentration must result in a sudden increase in acceptor concentration, i.e., enhanced acceptor incorporation. Hence, the equilibrium requirement of spatially invariant E_F explains reduced acceptor diffusion and enhanced acceptor incorporation in both uniform composition and heterostructure III–V semiconductors that are counterdoped with donors. The same effect of enhanced acceptor incorporation and suppressed acceptor diffusion can thus be achieved either by using spatially varying composition, or spatially varying doping compensation.

3. Conclusions

Acceptor segregation in semiconductor heterostructures was shown to depend exponentially on the valence band offset at the heterointerface, as explained by the space charge neutrality condition in conjunction with hole segregation across the heterointerface. This model also explains reduced acceptor diffusion, reduced acceptor segregation, and enhanced acceptor incorporation in the presence of compensating donor species. Thus, donor counterdoping is a useful technique to help control p–n junction location in both uniform composition and heterostructure III–V devices.

Acknowledgements

The authors are very grateful to H. Bracht for helpful communications.

References

- [1] U. Gosele, F. Morehead, *J. Appl. Phys.* 52 (1981) 4617.
- [2] D.G. Deppe, N. Holonyak Jr., *J. Appl. Phys.* 64 (1988) R93.
- [3] F. Dildy, R. Treichler, M.-C. Amann, M. Schier, G. Ebbinghaus, *Appl. Phys. Lett.* 55 (1989) 876.
- [4] E. Veuhoff, H. Baumeister, J. Rieger, M. Gorgel, R. Treichler, *J. Electron. Mater.* 20 (1991) 1037.
- [5] H. Bracht, W. Walukiewicz, E.E. Haller, *Mater. Res. Soc. Symp. Proc.* 490 (1998) 93.
- [6] P.N. Grillo, S.A. Stockman, J.-W. Huang, H. Bracht, Y.L. Chang, *J. Appl. Phys.*, submitted for publication.
- [7] C. Blaauw, F.R. Shepherd, D. Eger, *J. Appl. Phys.* 66 (1989) 605.
- [8] C. Blaauw, L. Hobbs, *Appl. Phys. Lett.* 59 (1991) 674.
- [9] P.N. Grillo, S.A. Stockman, J.-W. Huang, S.S. Yi, *J. Electron. Mater.*, submitted for publication.
- [10] R.L. Longini, R.F. Greene, *Phys. Rev.* 102 (1956) 992.



ELSEVIER

Physica B 308–310 (2001) 891–894

PHYSICA B

www.elsevier.com/locate/physb

Luminescence properties of Er,O-codoped GaAs/GaInP double heterostructures grown by organometallic vapor phase epitaxy

A. Koizumi^{a,*}, N. Watanabe^a, K. Inoue^a, Y. Fujiwara^a, Y. Takeda^{a,b}

^a Department of Materials Science and Engineering, Graduate School of Engineering, Nagoya University, Furo-cho, Chikusa-ku, Nagoya 464-8603, Japan

^b CREST, JST (Japan Science and Technology), Furo-cho, Chikusa-ku, Nagoya 464-8603, Japan

Abstract

Er,O-codoped GaAs/GaInP double heterostructures (DHS:Er,O) were grown by organometallic vapor phase epitaxy and the intra-4f shell transitions of Er ions were investigated by photoluminescence (PL) measurements. Er,O-codoping was carried out with trisdipivaloylmethanatoerbium ($\text{Er}(\text{DPM})_3$) as an Er source and an addition of O_2 diluted with Ar to a reactor. Er,O-codoped GaAs (GaAs:Er,O) and GaInP layers were all grown at 550°C. In-depth profiles showed a uniform distribution of Er and O along the growth direction in the GaAs:Er,O active layer. The Er concentration in the GaAs:Er,O active layer was evaluated to be about $5 \times 10^{17} \text{ cm}^{-3}$. In 4.2 K PL measurements, DHS:Er,O sample exhibited Er–2O lines and the intensity was approximately three times stronger than that of GaAs:Er,O sample. This suggests that photoexcited carriers confined in the GaAs:Er,O active layer contribute effectively to excitation of Er. © 2001 Elsevier Science B.V. All rights reserved.

Keywords: Erbium; Oxygen; Double heterostructures; Organometallic vapor phase epitaxy

1. Introduction

Recently, there has been a wide scientific and technological interest in semiconductors doped with rare-earth (RE) impurities. RE isoelectronic impurity incorporated into semiconductors shows sharp and temperature-stable intra-4f-shell luminescence. This stability occurs because the filled outer 5s and 5p electron shells screen transitions within the inner 4f electron shell from interaction with the host. These properties are attractive for fabricating optical devices such as semiconductor lasers and optical amplifiers.

Special attention has been paid to Er ions in III–V semiconductors. Er doping in III–V semiconductors produces sharp luminescence at around 1.54 μm due to

intra-4f-shell transition from the first excited state ($^4\text{I}_{13/2}$) to the ground state ($^4\text{I}_{15/2}$) of Er ions. The emission is coincident with the minimum loss wavelength region of silica-based fibers. However, it has been found that Er ions doped in semiconductors show various fine structures, depending on doping conditions. This indicates that various kinds of Er centers with different atom configurations are formed simultaneously in a semiconductor because the fine structures of photoluminescence (PL) spectra reflect atomic configurations around Er ions. Selective formation of highly efficient Er centers for luminescence has been strongly desired for applications of Er-related luminescence to light-emitting devices.

Oxygen (O) has been found to play an important role in the production of efficient Er-related luminescent centers in GaAs. Er,O-codoped GaAs (GaAs:Er,O) produces a strong emission intensity and simple PL spectrum predominantly from one kind of Er center [1]. The Er center has been identified as an Er atom located

*Corresponding author. Tel.: +81-52-789-3620; fax: +81-52-789-3239.

E-mail address: koizumi@mercury.numse.nagoya-u.ac.jp (A. Koizumi).

at the Ga sublattice with two adjacent O atoms (Er–2O center) [2]. The dependence of the PL spectra on growth temperature revealed the existence of a threshold growth temperature between 560°C and 580°C for Er incorporation into GaAs [3].

For optical device applications, Er should be introduced in confinement structures such as double heterostructures (DHS). In these structures, a GaAs:Er,O layer should be sandwiched between layers of a different semiconductor. The growth of $\text{Ga}_{0.51}\text{In}_{0.49}\text{P}$ (hereafter GaInP) is very attractive as an aluminum-free alternative to the conventional $\text{Al}_x\text{Ga}_{1-x}\text{As}$ -based materials. The aluminum-free GaAs/GaInP material system has advantages over the GaAs/ $\text{Al}_x\text{Ga}_{1-x}\text{As}$ material system, such as the low reactivity of GaInP to O.

In this paper, we report the results on fabrication of GaAs:Er,O/GaInP double heterostructures (DHS:Er,O) grown by organometallic vapor phase epitaxy (OMVPE) and its luminescence properties.

2. Experimental

GaAs:Er,O and DHS:Er,O samples used in this study were fabricated by a low-pressure growth system with a cold-wall quartz 4-barrel reactor [4]. The reactor pressure was 0.1 atm. The substrates were semi-insulating and Si-doped GaAs was oriented in the (100) direction. Triethylgallium (TEGa), trimethylindium (TMIn), tertiarybutylarsine (TBAs) and tertiarybutylphosphine (TBP) were used as sources. Er doping was carried out with trisdipivaloylmethanatoerbium ($\text{Er}(\text{C}_{11}\text{H}_{19}\text{O}_2)_3$, $\text{Er}(\text{DPM})_3$) as an Er source which was introduced into the reactor by a H_2 flow through the Er source cylinder. The rate of the H_2 flow was kept at 125 sccm. Ar gas with 38.4 ppm of $^{18}\text{O}_2$ was used as an additional O_2 source [3]. The O_2 content in growth ambient was set at 0.2 ppm.

Growth sequence for GaAs–GaInP interface used in this work is as follows. At the beginning of the layer growth, group-V gas was switched on first for 1 s and then group-III gas was switched on. At the end of layer growth, the group-III gas was switched off and growth was interrupted under the group-V gas to change TEGa flow rate and substrate temperature. In the growth of GaAs/GaInP DHS, we used two growth sequences (sequences A and B). Variations of gas flow and growth temperature for the sequences are schematically drawn in Fig. 1. In sequence A, GaInP and GaAs layers were grown at 580°C and 540°C, respectively. The temperatures were optimum growth temperatures for GaInP and GaAs:Er,O, respectively. In sequence B, GaAs and GaInP layers were all grown at 550°C. The crystal quality of the DHS was characterized by PL measurements at 77 K using the DHS having 200 nm-thick GaAs without Er,O-codoping and 200 nm-thick GaInP cladding layer.

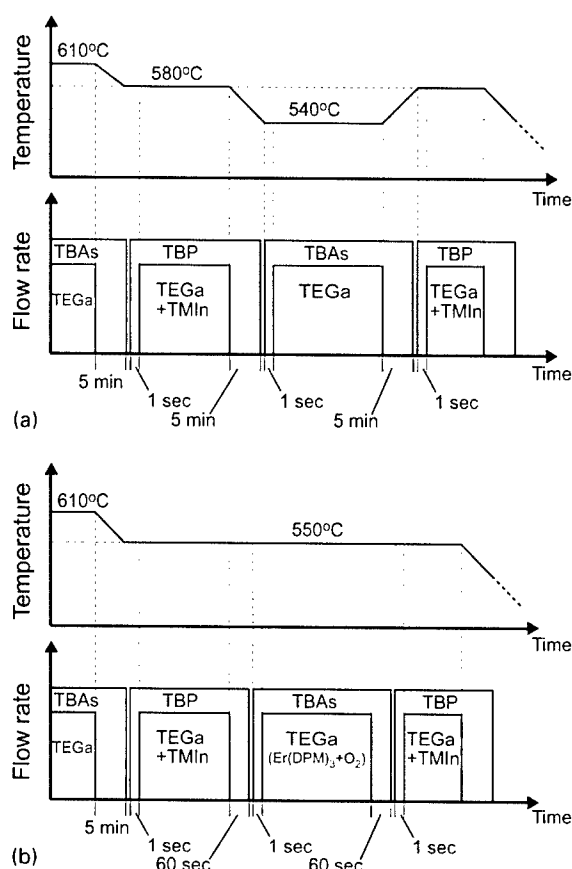


Fig. 1. Variations of gas flow and growth temperature for (a) sequence A and (b) sequence B. In sequence A, GaInP and GaAs layers were grown at 580°C and 540°C, respectively. In sequence B, on the other hand, these layers were all grown at 550°C.

The measurements were carried out with a 514.5 nm beam of Ar-ion laser and an Si-type detector cooled by dry ice.

The structure and growth conditions of DHS:Er,O samples are as follows. All the samples were initiated by the growth of a 150 nm thick GaAs buffer layer at 610°C. Then, 1 μm -thick GaInP cladding layer, 1 μm -thick GaAs:Er,O active layer and 0.6 μm -thick GaInP cladding layer were grown with sequence B. These thicknesses were evaluated using undoped GaAs/GaInP DHS samples by a scanning electron microscope (SEM). As a reference sample, GaAs:Er,O was grown under the same doping conditions as the active layer of DHS:Er,O.

PL measurements of Er-related luminescence were carried out mainly with the samples directly immersed in liquid He at 4.2 K. The photoexcitation source was a CW-mode semiconductor laser diode, operating at 660 nm, with an incident power of 30 mW. The photon energy is below the band-gap of the GaInP cladding

layer, which enabled us to excite the GaAs active layer directly. The luminescence of the sample was dispersed using a 0.91 m grating monochromator and detected with a liquid nitrogen-cooled Ge p-i-n photodiode using a chopper and a lock-in technique.

For measurements of concentration profiles by secondary ion mass spectroscopy (SIMS), an O^+ ion and a Cs^- ion were used as primary ions for Er and O, respectively.

3. Results and discussion

3.1. PL characterization of undoped GaAs/GaInP DHS

It is well known that making a high-quality GaInP–GaAs interface is very difficult via OMVPE growth because of the problems in As–P substitution and indium memory effects in reactor gas switching [5–13]. Characteristics of GaInP–GaAs interface strongly depend on the growth sequence for the interface. Fig. 2(a) shows 77 K PL spectrum of undoped DHS grown with sequence A. The spectrum has one peak at wavelength of 884 nm with the full-width at half-maximum (FWHM) of 54 meV. The wavelength of 884 nm is longer than those of the near-band-edge emissions from GaAs. Several researchers have also reported a similar broad peak at wavelengths between 850 and 930 nm in low-temperature PL spectra of GaAs/GaInP heterostructures [10,12].

Fig. 2(b) shows PL spectrum of a sample grown with sequence B. The spectrum is dominated by a peak

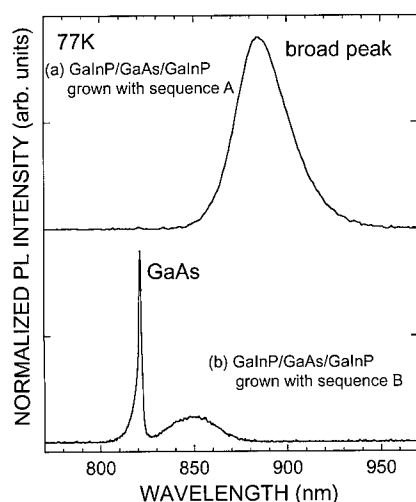


Fig. 2. 77 K PL spectra in undoped GaAs/GaInP DHS grown with (a) sequence A and (b) sequence B. An interface-related peak at 884 nm disappears in the sample grown with sequence B.

corresponding to the near-band-edge emission from GaAs. Also, a broad peak is weakly observed at 850 nm. This result suggests that photoexcited carriers injected in GaAs active layer recombine effectively in GaAs layer. Therefore, we can conclude that samples grown with sequence B have good quality of GaAs–GaInP interface compared with sequence A.

3.2. SIMS profiles in DHS:Er,O sample

DHS:Er,O samples were prepared with sequence B. In-depth profiles of Er, O, Ga and As for DHS:Er,O are shown in Fig. 3. For the DHS:Er,O sample, a distinct GaAs/GaInP DHS is seen in the SIMS profile. The profile reveals a uniform distribution of Er and O along the growth direction in the GaAs:Er,O active layer. Furthermore, in GaInP cladding layers, Er concentration is below the SIMS detection limit and O concentration is at the background level. Er concentration in GaAs:Er,O active layer, calibrated by using an Er-implanted GaAs sample, was evaluated to be about $5 \times 10^{17} \text{ cm}^{-3}$. This Er concentration was the same as GaAs:Er,O reference sample.

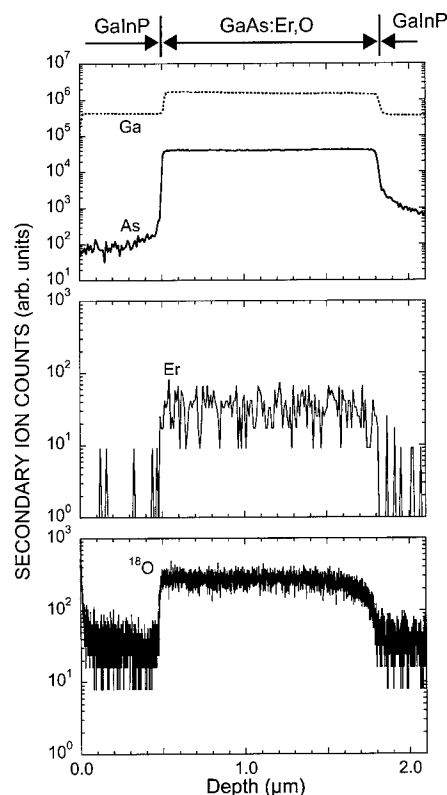


Fig. 3. In-depth profiles of Er, O, Ga and As for DHS:Er,O. Er and O are introduced selectively in the GaAs:Er,O active layer.

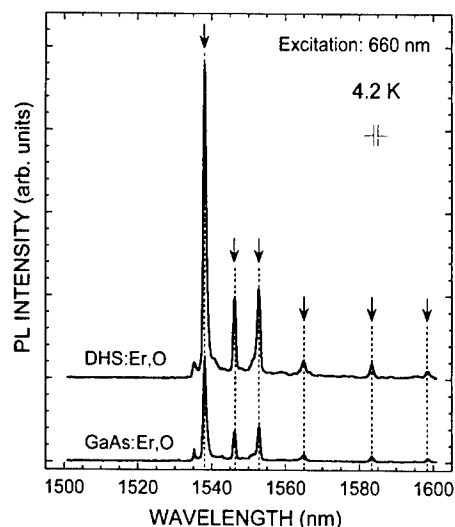


Fig. 4. 4.2 K Er-related PL spectra in (a) DHS:Er,O and (b) GaAs:Er,O. As shown by arrows, the spectrum is dominated by the Er-2O lines, indicating that an Er-2O center is selectively formed in GaAs:Er,O active layer of DHS:Er,O.

3.3. Er-related luminescence in DHS:Er,O

In Fig. 4, the 4.2 K $^4I_{13/2} \rightarrow ^4I_{15/2}$ Er-related luminescence from DHS:Er,O sample is compared with the luminescence from the GaAs:Er,O reference sample. The spectrum of DHS:Er,O shows identical positions of Er-related PL lines as in the GaAs:Er,O. Vertical arrows denote the Er-2O lines. This indicates that Er-2O centers are selectively formed in GaAs:Er,O active layers of DHS:Er,O. The intensity of the Er-related luminescence is approximately three times stronger than that of GaAs:Er,O sample. These results suggest that carriers photoexcited in the GaAs:Er,O region contribute effectively to excitation of Er because GaInP cladding layers confine the carriers and eliminate the surface recombination.

4. Conclusion

We have successfully grown Er,O-codoped GaAs/GaInP double heterostructures. In-depth profiles of Er and O exhibited a uniform distribution along the growth direction in the GaAs:Er,O active layer. The Er-related luminescence indicated that Er-2O centers

are selectively formed in GaAs:Er,O active layer. The intensity of Er-related luminescence was about three times higher than the GaAs:Er,O sample grown under the same doping conditions and Er concentration as in the GaAs:Er,O active layer of DHS:Er,O. These results are interpreted easily by the advantage of the DHS: confinement of photoexcited carriers and elimination of surface recombination.

Acknowledgements

The authors would like to thank Hitachi Cable Ltd. for GaAs substrates. This work was supported in part by Grant-in-Aids for Scientific Research (A)(2) No. 13305022, for Scientific Research (B)(2) No. 11450119 and No. 13555002, for Exploration Research No. 13875062 from the Ministry of Education, Science, Sports and Culture.

References

- [1] K. Takahei, A. Taguchi, J. Appl. Phys. 74 (1993) 1979.
- [2] K. Takahei, A. Taguchi, Y. Horikoshi, J. Nakata, J. Appl. Phys. 76 (1994) 4332.
- [3] Y. Fujiwara, T. Kawamoto, T. Koide, Y. Takeda, Physica B 273–274 (1999) 770.
- [4] Y. Fujiwara, S. Furuta, K. Makita, Y. Ito, Y. Nonogaki, Y. Takeda, J. Crystal Growth 146 (1995) 544.
- [5] T. Nittono, S. Sugitani, F. Hyuga, J. Appl. Phys. 78 (1995) 5387.
- [6] M. Razeghi, Ph. Maurel, F. Omnes, M. Defour, C. Boothroyd, W.M. Stobbs, M. Kelly, J. Appl. Phys. 63 (1988) 4511.
- [7] F. Omnes, M. Razeghi, Appl. Phys. Lett. 59 (1991) 1034.
- [8] X. He, M. Razeghi, Appl. Phys. Lett. 61 (1992) 1703.
- [9] D.P. Bour, J.R. Shealy, S. Mckernan, J. Appl. Phys. 63 (1988) 1241.
- [10] F.E.G. Guimaraes, B. Elsner, R. Westphalen, B. Spangenberg, H.J. Geelen, P. Balk, K. Heime, J. Crystal Growth 124 (1992) 199.
- [11] R. Bhat, M.A. Koza, M.J.S.P. Brasil, R.E. Nahory, C.J. Palmstorm, B.J. Wilkens, J. Crystal Growth 124 (1992) 576.
- [12] C.Y. Tsai, M. Moser, C. Geng, V. Harle, T. Forner, P. Michler, A. Hangleiter, F. Scholz, J. Crystal Growth 145 (1994) 786.
- [13] W. Seifert, N. Carlsson, M.E. Pistol, L. Samuelson, J. Crystal Growth 145 (1994) 758.



ELSEVIER

Physica B 308–310 (2001) 895–898

PHYSICA B

www.elsevier.com/locate/physb

Diffusion of zinc in gallium phosphide under defect-free phosphorus-rich conditions

J. Pöpping^a, N.A. Stolwijk^{a,*}, U. Södervall^b, Ch. Jäger^c, W. Jäger^c

^a *Institut für Materialphysik, University of Münster, Wilhelm-Klemm-Strasse 10, D-48149 Münster, Germany*

^b *Department of Microelectronics and Nanoscience, Chalmers University of Technology, S-41286 Göteborg, Sweden*

^c *Center for Microanalysis, Faculty of Engineering, Christian-Albrechts-University Kiel, Kiel, Germany*

Abstract

We investigated diffusion of Zn into GaP for P-rich conditions between 803°C and 1097°C to obtain information about the diffusion mechanism and the participating native point defects. Extremely diluted Zn sources were employed so as to avoid the formation of microstructural defects during diffusion. Penetration profiles measured by secondary ion mass spectroscopy and electrochemical capacitance–voltage profiling are in mutual accordance. The profiles are well described within the framework of interstitial-substitutional diffusion yielding not only Zn diffusion coefficients but also transport coefficients for the Ga-related native point defects involved. The latter data are compared with self-diffusion data related to the Ga sublattice in GaP. © 2001 Elsevier Science B.V. All rights reserved.

PACS: 61.72.Ji; 66.30.Dn; 66.30.Hs; 66.30.Jt

Keywords: Gallium phosphide; Self-interstitials; Vacancies; Zinc diffusion

1. Introduction

For GaAs there has been considerable recent progress in the understanding of diffusion processes [1] whereas diffusion in GaP is still poorly investigated. The progress for GaAs resulted to a large extent from experiments with hybrid impurities such as Cd [2] and N [3] which interchange between interstitial and substitutional sites under participation of native point defects. For obtaining quantitative information about the native-defect transport coefficients it proved to be advantageous when the hybrid impurity diffusion takes place under conditions virtually free of microstructural defects acting as sinks or sources for vacancies and self-interstitials.

In the present GaP study, Zn was chosen as hybrid impurity interacting with the Ga sublattice. Virgin GaP was exposed to Zn in diluted form so as to avoid

extreme diffusion-induced deviations from point-defect equilibria leading to agglomeration and precipitation processes [4,5].

2. Experimental

As base material we used $\langle 100 \rangle$ -oriented, nominally undoped GaP with a negligibly low density of dislocations and other extended defects. Samples of typically $6 \times 6 \text{ mm}^2$ were cut from 1 mm thick wafers and, after etching and cleaning, enclosed in Ar-flushed, evacuated quartz ampoules of about 3.5 cm^3 inner volume. Crushed Zn-diffusion-doped GaP was included as diffusion source while elemental phosphorus ($\approx 3 \text{ mg}$) was added to establish a P_4 partial pressure close to 1 atm. The ampoules were inserted into a pre-heated resistance furnace, isothermally annealed, and water quenched.

Zn depth profiles were monitored by secondary ion mass spectroscopy (SIMS) in a Cameca ims-6f instrument using O_2^+ primary ions and the state-of-the-art procedures characteristic of an in-depth analysis mode.

*Corresponding author. Tel.: +49-251-83-39013; fax: +49-251-83-38346.

E-mail address: stolwijk@nwz.uni-muenster.de (N.A. Stolwijk).

Conversion of mass counts to Zn concentration was based on calibration with a GaP:Zn implantation standard. The penetration depth scale was calibrated within about 5% error by measuring the SIMS crater depth with a surface profilometer. In each case, the Zn-induced hole distribution was analysed on a second GaP sample originating from the same diffusion ampoule by using a Biorad electrochemical capacitance–voltage (ECV) profiler.

Depth profiling was accompanied by transmission electron microscope (TEM) examination of a third, identically treated sample in a Philips CM30 instrument at 300 kV. Electron-transparent sample cross-sections were prepared using mechanical thinning followed by ion-beam thinning, thus allowing for the microstructural characterisation of the Zn-diffused regions.

3. Results

The TEM investigations showed the Zn-diffused samples to be free of crystal defects like the original GaP wafer material. This strongly supports the view that the diffusion proceeded under virtually ideal conditions in which only the sample surface acts as source or sink for point defects.

Figs. 1 and 2 show depth profiles arising from SIMS and ECV analysis after diffusion at 1097°C and 803°C, respectively. It is seen that the ECV-resolved hole concentration closely follows the SIMS-resolved Zn concentration. Within error tolerances this is consistent with the view that every Zn atom accommodated by the Ga sublattice (Zn_{Ga}^-) generates one electronic hole, and moreover, that the concentrations of interstitial Zn, i.e., Zn_{i}^+ , and the native point defects are negligibly small with respect to the Zn_{Ga}^- concentration.

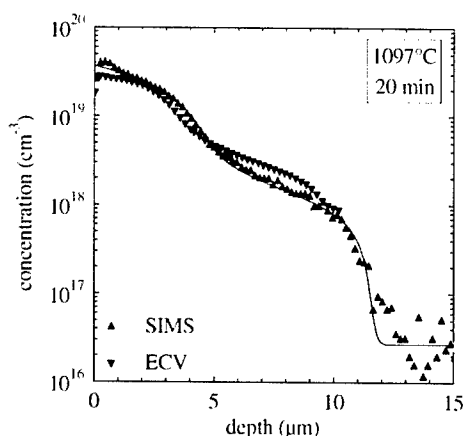


Fig. 1. SIMS depth profile of Zn in GaP after diffusion at 1097°C and corresponding hole distribution from ECV analysis. Solid-lines fits are based on Eqs. (1)–(3).

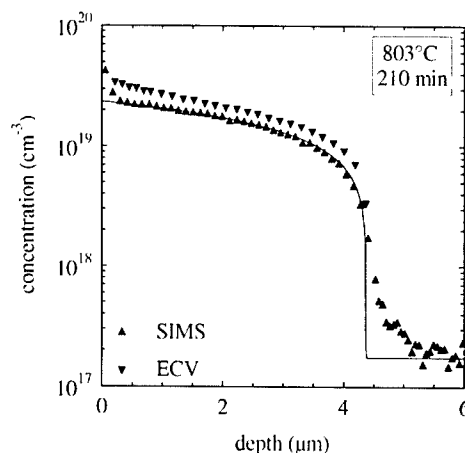


Fig. 2. Similar to Fig. 1 but after diffusion at 803°C.

At the highest temperature investigated, i.e. 1097°C, the Zn profile reveals two distinct steps (Fig. 1). With decreasing temperature the near-surface profile step increases relative to the great-depth profile step, so that finally at 803°C, the latter is hardly visible anymore (Fig. 2). The varying 'kink-and-tail' profile shape is reproduced by an interstitial-substitutional (i-s) diffusion model involving Ga-related point defects as documented by the solid lines in Figs. 1 and 2. The same model also describes Zn diffusion into GaAs [6].

4. Modeling

The simplest i-s diffusion model which accounts for all relevant features of the measured profiles as well as for earlier data on Zn in GaP [7,8] involves neutral Ga interstitials (I_{Ga}^0) in addition to neutral and singly positively charged Ga vacancies ($\text{V}_{\text{Ga}}^0, \text{V}_{\text{Ga}}^+$), i.e.,



Electronic holes h participate in these quasi-chemical reactions in order to maintain local charge neutrality under the extrinsic doping conditions in the Zn-diffused region. Profiles were simulated by solving the partial differential equations based on Eqs. (1)–(3). In the actual simulation, reaction (3) was replaced by $\text{Zn}_{\text{i}}^+ + \text{V}_{\text{Ga}}^+ \rightleftharpoons \text{Zn}_{\text{Ga}}^- + 3\text{h}$ being the 'sum' of Eqs. (2) and (3), i.e., for computational reasons. This does not affect the numerical results, provided that all reactions rates are chosen sufficiently large to virtually maintain local equilibrium among the point defects in terms of the mass action law. On the other hand, equilibrium and starting concentrations of the native defects were taken

low enough so that they do not explicitly enter the calculations. In this limiting case, the profiles are exclusively diffusion controlled.

In fitting the Zn_s profiles to the SIMS measurements (see solid lines in Figs. 1 and 2) we also obtained the depth distributions of the other species involved. This is illustrated in Fig. 3 for the 1097°C case. The vacancy annihilation and the self-interstitial generation by the Zn_i -to- Zn_s exchange leads to in-diffusion of V_{Ga}^0 , V_{Ga}^+ and out-diffusion of I_{Ga}^0 , respectively. This is also evident from Fig. 4 displaying the self-interstitial supersaturation ($S > 1$) and the corresponding vacancy undersaturation ($S < 1$). Here the local supersaturation parameter $S = C(x)/C^{eq}[p(x)]$ accounts for the dependence of the point-defect equilibrium concentration C^{eq}

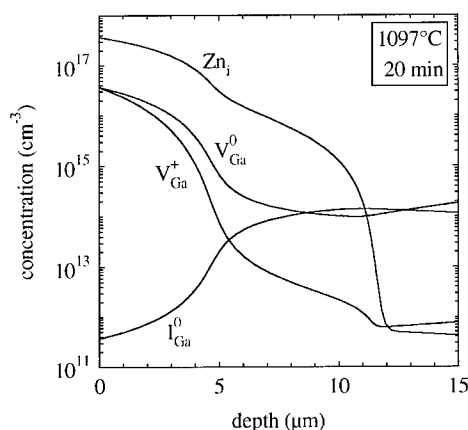


Fig. 3. Point-defect profiles associated with the Zn_s solid-line fit in Fig. 1.

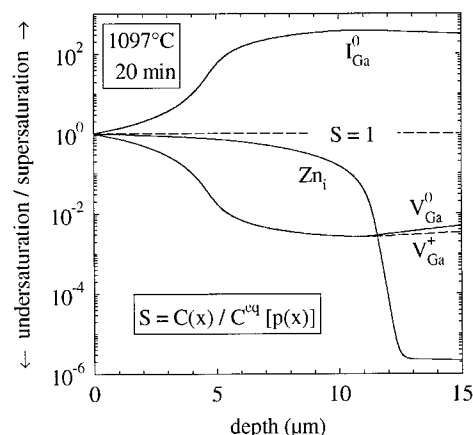


Fig. 4. Diffusion-induced super- or undersaturation of point defects associated with the Zn_s solid-line fit in Fig. 1.

on the local hole concentration $p(x)$ which, in turn, is practically equal to the Zn_s concentration C_s .

5. Diffusion coefficients

Fig. 5 exhibits the Zn-related diffusivity resulting from profile fitting in comparison to earlier data on GaP [4,7,8] and to similar data for GaAs [9]. Within the i-s diffusion model this 'effective' diffusivity is a complex quantity which comprises the individual diffusivity of Zn_i and the ratio of mobile (Zn_i) to immobile (Zn_s) atoms [2,4]. For the sake of comparability all data have been reduced to electronically intrinsic conditions ($p = n_i$) and a standard P_4 partial pressure of 1 atm [2,4]. Zn diffusion in intrinsic GaP is much slower than in p-type crystals (Fermi-level effect) while for the present 'P-rich' data the normalisation to standard pressure only leads to corrections of less than 15%. Altogether a fair agreement among the various GaP : Zn data is observed in Fig. 5, at least at the higher temperatures.

Fig. 6 compares the Ga-defect-related transport coefficients obtained in this work with the Ga tracer diffusivity D_{Ga}^T measured on GaP isotope heterostructures [10]. For instance, the I_{Ga}^0 -related data are given by the product of the I_{Ga}^0 diffusivity and the I_{Ga}^0 equilibrium concentration normalised to the Ga lattice-site density [2,4]. This represents the I_{Ga}^0 component of the ('overall') Ga tracer diffusivity (neglecting minor geometrical correlation effects). Fig. 6 reveals that the I_{Ga}^0 -related Ga diffusivity is not far from D_{Ga}^T but in any case below D_{Ga}^T , as it should be for a partial component. In contrast, the V_{Ga}^0 and V_{Ga}^+ components lie distinctly above D_{Ga}^T . This clearly violates the consistency among the different sets of data, which should

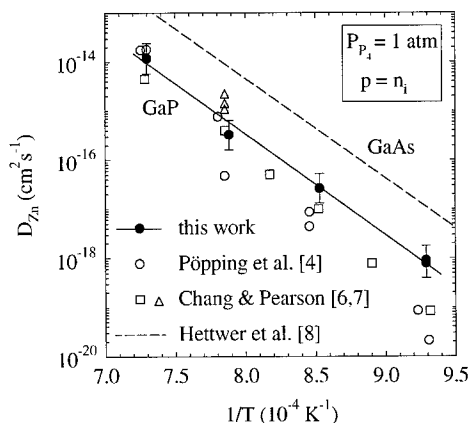


Fig. 5. Zn diffusion coefficient in GaP as a function of inverse temperature. Solid-line fit of present data: $9.5 \exp(-4.08 \text{ eV}/k_B T) \text{ cm}^2 \text{ s}^{-1}$.

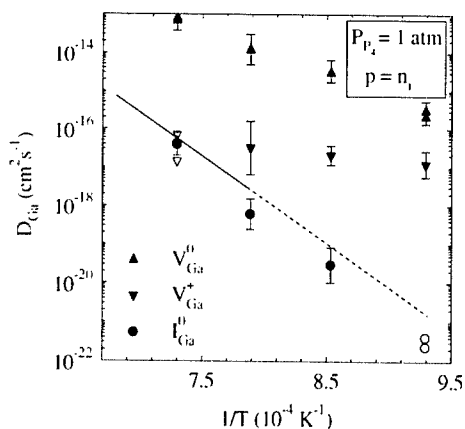


Fig. 6. Ga diffusivity components of various native point defects in GaP deduced from Zn diffusion profiles in comparison with Ga tracer data D_{Ga}^T (solid line).

be all representative for intrinsic GaP under P-rich conditions.

6. Conclusions and outlook

The present work represents the first study of Zn diffusion in GaP under well-established defect-free conditions. A good description of the measured 'kink-and-tail' profiles is obtained within an i-s diffusion model involving I_{Ga}^0 , V_{Ga}^0 , and V_{Ga}^- . Profile fitting yields the Ga self-diffusion components related to these native point defects. However, a discrepancy with existing Ga tracer diffusion data becomes manifest. This discrepancy gives rise to the following questions: (i) Does the presently chosen diffusion conditions allow for thermal equilibrium among the various atomic species and point

defects to be established near the surface of heavily Zn-doped GaP? (ii) Does the Ga tracer data from the epitaxially grown isotope heterostructures correspond to the assumed equilibrium conditions? (iii) Are more complex mobile defects like e.g. $V_{\text{Ga}}-V_{\text{P}}$ divacancies involved in the diffusion process? These open questions will stimulate further research on diffusion in GaP and other III–V compounds.

Acknowledgements

We thank H. Bracht for fruitful discussions and help in the simulations. Organisational support by H. Mehrer is gratefully acknowledged. This work was sponsored by the Deutsche Forschungsgemeinschaft.

References

- [1] N.A. Stolwijk, G. Bösker, J. Pöpping, Defect Diffusion Forum 194–199 (2001) 687.
- [2] G. Bösker, N.A. Stolwijk, H. Mehrer, U. Södervall, W. Jäger, J. Appl. Phys. 86 (1999) 791.
- [3] N.A. Stolwijk, G. Bösker, J.V. Thordson, T.G. Andersson, U. Södervall, Ch. Jäger, W. Jäger, Physica B 273–274 (1999) 685.
- [4] J. Pöpping, N.A. Stolwijk, G. Bösker, Ch. Jäger, W. Jäger, U. Södervall, Defect Diffusion Forum 194–199 (2001) 723.
- [5] Ch. Jäger, W. Jäger, J. Pöpping, G. Bösker, N.A. Stolwijk, J. Electron Microsc. 48 (2000) 1037.
- [6] H. Bracht, M.S. Norseng, E.E. Haller, K. Eberl, in these proceedings (ICDS), Physica B 308–310 (2001).
- [7] L.L. Chang, G.L. Pearson, J. Appl. Phys. 35 (1964) 374.
- [8] L.L. Chang, G.L. Pearson, J. Appl. Phys. 35 (1964) 1960.
- [9] H.-G. Hettwer, N.A. Stolwijk, H. Mehrer, Defect Diffusion Forum 143–147 (1997) 1117.
- [10] Lei Wang, J.A. Wolk, E.E. Haller, J.W. Erickson, M. Cardona, T. Ruf, J.P. Silveira, F. Briones, Appl. Phys. Lett. 70 (1997) 1831.



ELSEVIER

Physica B 308–310 (2001) 899–903

PHYSICA B

www.elsevier.com/locate/physb

Defect analysis and engineering in ZnO

Chris G. Van de Walle*

Xerox Palo Alto Research Center, 3333 Coyote Hill Road, Palo Alto, CA 94304, USA

Abstract

Zinc oxide has numerous applications in electronic and optoelectronic devices. Progress is currently hampered by a lack of control over electrical conductivity: ZnO is typically n-type conductive, the cause of which has been widely debated. A first-principles investigation, based on density functional theory, shows that native defects are unlikely to be the cause of the unintentional n-type conductivity. Detailed results for the oxygen vacancy show that it is a *deep* donor, and that its paramagnetic state is metastable. An investigation of likely donor impurities reveals that hydrogen acts as a shallow donor. Experimental results are discussed in the light of these new insights. © 2001 Elsevier Science B.V. All rights reserved.

Keywords: ZnO; Doping; Native defects; Hydrogen

1. Introduction

Zinc oxide is a wide-band-gap semiconductor with numerous technological applications. Its strongly non-linear resistance makes it useful for varistors, its large piezoelectric constants enable applications in transducers, and its luminescence is used in phosphors. The properties of ZnO surfaces are sensitive to the presence of adsorbates, allowing applications as sensors. ZnO also exhibits large optical nonlinearities that can be exploited in optical devices, and a high thermal conductivity that makes it suitable as a substrate for growth of other materials, including GaN. ZnO has a band gap of 3.4 eV, very close to that of GaN. It thus lends itself to similar applications as GaN in optoelectronics, i.e., light emitting diodes and lasers in the blue and UV region of the spectrum. Efficient excitonic emission should be possible at room temperature due to the large exciton binding energy (60 meV). For comparison, the exciton binding energy in GaN is 25 meV. Optically pumped lasing has already been reported in ZnO platelets [1], thin films [2], clusters consisting of ZnO nanocrystals [3], and ZnO nanowires [4].

ZnO can be grown with a variety of techniques, including vapor-phase transport [5], hydrothermal growth [6], chemical vapor deposition (MOCVD) [7], laser ablation [8] and sputtering [9]. Most of these growth techniques produce ZnO that is highly n-type. This high level of n-type conductivity is very useful for some applications, such as transparent conductors—but in general, it would be desirable to have better control over the conductivity. In particular, the ability to reduce the n-type background and to achieve p-type doping would open up tremendous possibilities for device applications, in general, and for light-emitting diodes and lasers, in particular.

Because of its widespread occurrence, the unintentional n-type conductivity has conventionally been attributed to native defects. In particular, zinc interstitials (Zn_i) and oxygen vacancies (V_O) are expected to act as donors, and have frequently been invoked as the source of high carrier concentrations. Recent first-principles investigations [10,11], however, have revealed that none of the native defects exhibits characteristics consistent with a high-concentration shallow donor. Zinc interstitials have high formation energies and low diffusion barriers; they are thus unlikely to be incorporated in a stable fashion. As to oxygen vacancies, the main problem is that they are *deep* rather than shallow donors. We will discuss their electronic and structural

*Tel.: +1-650-812-4163; fax: +1-650-812-4140.

E-mail address: vandewalle@parc.xerox.com
(C.G. Van de Walle).

properties in more detail in Section 3. Our numerical results on native defects are very similar to those of Zhang et al. [12], but we differ in the interpretation of those results.

Having concluded that native defects are *not* the cause of n-type conductivity, we must turn to extrinsic sources, i.e., impurities that are unintentionally incorporated. We have proposed that hydrogen is an excellent candidate for such an impurity [13]. Hydrogen is ubiquitous and very difficult to remove from the crystal growth environment. It also forms a strong bond with oxygen, providing a powerful driving force for its incorporation in the ZnO crystal. The resulting O–H bonding unit can, in fact, be regarded as a new type of dopant atom, the addition of the proton turning the oxygen into an element behaving more like fluorine. Details of the behavior of hydrogen in ZnO are discussed in Section 4. We will discuss experimental evidence for this proposal, including some very recent results for muonium, a pseudo-isotope of hydrogen [14,15].

2. Methods

Our first-principles calculations are based on density-functional theory (DFT) within the local density approximation (LDA) [16,17] and the pseudopotential plane-wave method [18]. We have studied both the zinc-blende (ZB) and the wurtzite (WZ) structure; the latter is the stable phase for ZnO. Properties of native defects and impurities are very similar in both phases; unless specifically mentioned, the results below are for WZ. Our defect and impurity studies were carried out in supercells containing up to 96 atoms for the WZ structure and up to 64 atoms for the ZB structure, using 2 or 3 special k-points in the irreducible part of the Brillouin zone. Effects of the Zn 3d states were included using the nonlinear core correction (nlcc) [19], using an energy cutoff of 40 Ry. Test calculations with explicit inclusion of the Zn 3d electrons as valence electrons (with a 70 Ry cutoff) confirmed the validity of the conclusions obtained with the nlcc.

Formation energies are foremost among the quantities that can be derived from the first-principles calculations. In equilibrium, the formation energy E^f determines the concentration c of the impurity in the semiconductor through the expression

$$c = N_{\text{sites}} \exp(-E^f/kT), \quad (1)$$

where N_{sites} is the number of sites in the lattice where the impurity can be incorporated, k is Boltzmann's constant, and T is the temperature. The formation energy of a hydrogen interstitial in charge state q is defined as

$$E^f(\text{H}^q) = E^{\text{tot}}(\text{H}^q) - E^{\text{tot}}(\text{bulk}) - \mu_{\text{H}} + qE_{\text{F}}, \quad (2)$$

where $E^{\text{tot}}(\text{H}^q)$ is the total energy derived from a supercell calculation for the hydrogen interstitial, and $E^{\text{tot}}(\text{bulk})$ is the total energy for a supercell containing only bulk ZnO. μ_{H} is the hydrogen chemical potential, i.e., the energy of the reservoir with which H atoms are exchanged. For presentation purposes, we will fix the value of μ_{H} to half the energy of an H_2 molecule. E_{F} , finally, is the Fermi level, i.e., the chemical potential of the reservoir with which electrons are exchanged.

Defects and impurities often introduce levels in the band gap; these *transition levels* can be obtained based on our calculated total energies. The transition level $\epsilon(q+1/q)$ is defined as the Fermi-level position for which the formation energies of charge states $q+1$ and q are equal. It is well known that DFT produces band gaps significantly smaller than experiment. When performing calculations for defects and impurities, the band-gap error introduces uncertainty in the position of the transition levels. We have addressed this uncertainty by comparing results obtained with the nlcc approach with those including full treatment of the 3d states. Such a comparison highlights the systematics in the behavior of the defect levels.

3. Oxygen vacancies

Our calculations show that the defects that are favored by Zn-rich conditions (V_{O} , Zn_{i} , and Zn_{O}) all behave as donors. Among these, the oxygen vacancy has the lowest formation energy. The oxygen vacancy has frequently been invoked as the source of n-type conductivity in ZnO. Our results indicate that this assignment cannot be correct. First of all, the formation energy of V_{O} is quite high under n-type conditions, even under Zn-rich conditions. More importantly, however, the oxygen vacancy is a *deep* rather than a *shallow* donor. Our calculated energies for the various charge states of V_{O} are shown in Fig. 1.

We find that the oxygen vacancy is a “negative- U ” center, implying that $\epsilon(2+/+)$ lies above $\epsilon(+/0)$ in the band gap. As the Fermi level moves upward, the charge-state transition is thus directly from the $2+$ to the 0 charge state, at an energy about 2.7 eV above the valence band. It is clear that the oxygen vacancy cannot provide electrons to the conduction band in a stable manner, and therefore it cannot be a source of n-type conductivity.

An alternative way to express the negative- U behavior of V_{O} is to say that V_{O}^- is always higher in energy than either V_{O}^{2-} or V_{O}^0 , for any Fermi-level position. The positive charge state is thus never thermodynamically stable. This is an important finding, because it is the positive charge state, with its unpaired electron, that is detectable by magnetic resonance techniques. We thus

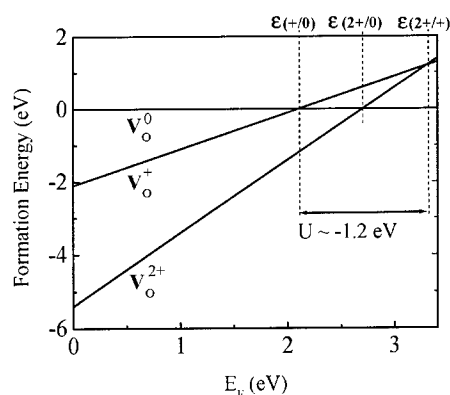


Fig. 1. Relative formation energies of various charge states of oxygen vacancies in ZnO as a function of Fermi level, obtained from DFT-LDA calculations. The formation energy of the neutral charge state is chosen as the reference, and the zero of Fermi energy is chosen at the top of the valence band. Transition levels and the value of U are indicated.

do not expect to observe an electron paramagnetic resonance (EPR) signal associated with V_O under thermodynamically stable conditions. It is, of course, possible to create oxygen vacancies in the $+$ charge state in a metastable manner, for instance by excitation with light. Once generated, V_O^+ does not immediately decay into the $2+$ or 0 charge state because of energetic barriers. These barriers are associated with the large lattice relaxations that occur around the oxygen vacancy; these relaxations are very different for the different charge states. We thus expect that at low enough temperatures EPR signals due to V_O^+ may be observed upon excitation, but if the excitation is removed and the temperature is raised, these signals will decay.

These theoretical results shed light on a rather confused situation in the experimental literature, which contains numerous reports of EPR measurements on oxygen vacancies. Space does not permit to provide a comprehensive list of references here, but the observations fall into two broad categories: those with g values ≈ 1.96 , and those with $g \approx 1.99$. In our opinion, it is the $g \approx 1.99$ signal that corresponds to V_O . Smith and Vehse [20] reported that the $g \approx 1.99$ center is light sensitive, and they also observed hyperfine interactions with the Zn neighbors of the vacancy. Similar hyperfine structure was observed by Gonzalez et al. [21]. Soriano and Galland [22] subsequently showed that illumination is necessary to observe the $g \approx 1.99$ line, and measured its decay after illumination is turned off. The light sensitivity and metastability are consistent with our results for the oxygen vacancy.

With regard to the $g \approx 1.96$ signal, a table with reported results up to 1970 can be found in Ref. [23].

Numerous authors have attributed the $g \approx 1.96$ line to oxygen vacancies; however, the evidence for this was much less convincing than in the case of the $g \approx 1.99$ line. It is much more likely that the $g \approx 1.96$ signal is associated with electrons in the conduction band or in a donor band, as originally proposed by Müller and Schneider [24].

4. Hydrogen in ZnO

The behavior of hydrogen in ZnO is highly unusual. In all other semiconductors studied to date, hydrogen has been found (theoretically as well as experimentally) to act as an *amphoteric* impurity [25,26]: in p-type material, hydrogen incorporates as H^+ , and in n-type material as H^- , always counteracting the prevailing conductivity of the material. This amphoteric behavior precludes hydrogen from acting as a dopant, i.e., from being a *source* of conductivity of the material. In ZnO, however, we find that hydrogen occurs exclusively in the positive charge state, i.e., it always acts as a donor.

The calculated formation energy for H in ZnO is displayed in Fig. 2. The lowest energy position for H^+ is at the bond-center (BC) site, with the antibonding (AB_O) position slightly higher in energy. H^0 and H^- are never stable in ZnO. We obtained this result by carefully checking the nature of the energy level in the band structure that is occupied with one or two electrons in the H^0 and H^- calculations. When H is at the AB_{Zn} site, the corresponding state is indeed localized near the H atom; but at this site, the energies of H^0 and H^- are always higher than that of H^+ , for all Fermi-level positions. When H is at the BC or AB_O sites, the occupied state turns out to be an *extended* state. Correct calculations for H^0 and H^- should therefore *not* place

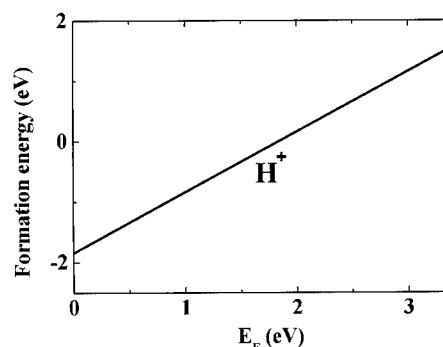


Fig. 2. Formation energy of interstitial hydrogen in ZnO as a function of Fermi level, obtained from DFT-LDA calculations and referenced to the energy of a free H_2 molecule. Zero-point energies are included. The zero of Fermi energy is chosen at the top of the valence band.

electrons in this state—the actual hydrogen-induced energy level occurs higher in the band structure. When these considerations are taken into account, AB_O and BC are found to be even higher in energy than AB_{Zn} for both H^0 and H^- .

Coming back to the positive charge state, we note that H^+ prefers sites where it can strongly bind to an oxygen atom, forming an O–H bond with a length of 0.99–1.01 Å. Large lattice relaxations occur around the hydrogen interstitial; in particular, for the BC configuration the Zn atom moves outward over a distance equal to 40% of the bond length (0.8 Å), to a position slightly beyond the plane of its nearest neighbors. Simultaneously, the O atom moves outwards by 11% of the bond length. For the AB configuration, the relaxation of both Zn and O amounts to about 20% of the bond length.

Interestingly, such large relaxations are not unique to hydrogen. We have performed calculations for fluorine in ZnO, which we find to be a shallow donor, in agreement with experiment [27]. For F^+ , we find a large displacement of one of the neighboring Zn atoms away from the F atom, by 25% of the bond length; the F atom itself moves outward by 12% of the bond length. The bond between the F atom and one of its Zn neighbors is thus effectively broken. Such large relaxations are usually thought of as giving rise to deep (localized) states, but here we find that F still behaves as a shallow donor.

Hydrogen is, of course, a very plausible impurity to be unintentionally incorporated during growth or processing. Hydrogen can indeed be present in all of the growth techniques mentioned in Section 1. Experimental indications for hydrogen's behavior as a donor in ZnO were reported in the 1950s [28–30]. ZnO was, in fact, the first semiconductor in which the properties of hydrogen were systematically studied. Those results, however, went largely unnoticed during the upsurge in research activity on hydrogen in semiconductors that started about 30 years later. Thomas and Lander [29] observed an increase in n-type conductivity when H diffuses into ZnO. They actually used the measured conductivity as a function of temperature to derive the solubility of H in ZnO, and found the heat of the reaction $H_2 \times (\text{gas}) \rightarrow 2H^+ + 2e^-$ to be 3.2, or 1.6 eV per hydrogen. This value should correspond (within small correction terms) to the formation energy for H^- in ZnO as defined above and plotted in Fig. 2. For $E_F = E_c$, this formation energy is 1.56 eV, in very good agreement with the experimental value.

More recent experiments have also proved consistent with the nature of hydrogen as a donor. An increase in conductivity upon exposure to H_2 was observed by Baik et al. [31], and by Kohiki et al. [32] who introduced hydrogen by proton implantation followed by annealing at 200°C.

Finally, we mention the very recent results obtained with the muon spin rotation technique [14,15]. Muonium is a pseudo-isotope of hydrogen and is expected to exhibit a very similar electronic structure. Muonium in ZnO was observed to exhibit all characteristics of a shallow donor (including ionization behavior consistent with a level close to the conduction band, and a delocalized wave function), confirming the model that H acts as a shallow donor.

Controlling the background n-type conductivity is an essential first step towards achieving p-type doping. Nitrogen seems to be a good candidate acceptor, and, interestingly, the simultaneous incorporation of hydrogen may actually be beneficial for achieving p-type doping. As previously discussed in the context of p-type doping of GaN [33], hydrogen has the beneficial effect of increasing acceptor solubility and suppressing compensation by native defects. Whether this type of dopant engineering also works in the case of ZnO will depend on the binding and dissociation energies of N–H complexes, and on the barriers that need to be overcome to remove H from the vicinity of the acceptors during a post-growth anneal.

5. Conclusions

We have reported first-principles results for native defects and for hydrogen in ZnO. We argue that native defects do not provide a consistent explanation for the observed n-type conductivity, pointing towards an extrinsic impurity as the cause. In particular, we note that the oxygen vacancy is a *deep* acceptor, with metastable behavior consistent with the experimentally observed $g \approx 1.99$ EPR center. As to the nature of the unintentional impurity, we propose that hydrogen is a plausible candidate.

Acknowledgements

I gratefully acknowledge collaborations with A. Kohan, G. Ceder, C. Stampfl, M. Fuchs, D. Vogel, and J. Pollman. Thanks are due to J. McCaldin for stimulating me to investigate ZnO, and to W. Carlos, E. Glaser, and J. Neugebauer for helpful discussions. I gratefully acknowledge the financial support of the Alexander von Humboldt Foundation and the hospitality of the Fritz-Haber-Institut and Paul-Drude-Institut, Berlin.

References

- [1] D.C. Reynolds, D.C. Look, B. Jogai, Solid State Commun. 99 (1996) 873.
- [2] D.M. Bagnall, et al., Appl. Phys. Lett. 70 (1997) 2230.
- [3] H. Cao, et al., Appl. Phys. Lett. 76 (2000) 2997.

- [4] M.H. Huang, et al., *Science* 292 (2001) 1897.
- [5] D.C. Look, et al. *Solid State Commun.* 10599 (1998) 199.
- [6] M. Suscavage, et al., *MRS Internet J. Nitride Semicond. Res.* 4S1 (1999) G340.
- [7] S.Y. Myong, et al., *Jpn. J. Appl. Phys.* 36 (1997) L1078.
- [8] H. Kordi Ardakani, *Thin Solid Films* 287 (1996) 280.
- [9] A. Valentini, et al., *J. Appl. Phys.* 73 (1993) 1143.
- [10] A.F. Kohan, G. Ceder, D. Morgan, C.G. Van de Walle, *Phys. Rev. B* 61 (2000) 15019.
- [11] C.G. Van de Walle, unpublished.
- [12] S.B. Zhang, S.-H. Wei, A. Zunger, *Phys. Rev. B* 63 (2001) 075205.
- [13] C.G. Van de Walle, *Phys. Rev. Lett.* 85 (2000) 1012.
- [14] S.F.J. Cox, et al., *Phys. Rev. Lett.* 86 (2001) 2601.
- [15] K. Shimomura, et al., in these Proceedings (ICDS-21), *Physica B* 308–310 (2001).
- [16] P. Hohenberg, W. Kohn, *Phys. Rev.* 136 (1964) B864.
- [17] W. Kohn, L.J. Sham, *Phys. Rev.* 140 (1965) A1133.
- [18] M. Bockstedte, et al., *Comput. Phys. Commun.* 107 (1997) 187.
- [19] S.G. Louie, S. Froyen, M.L. Cohen, *Phys. Rev. B* 26 (1982) 1739.
- [20] J.M. Smith, W.E. Vehse, *Phys. Lett.* 31A (1970) 147.
- [21] C. Gonzalez, D. Galland, A. Herve, *Phys. Stat. Sol. B* 72 (1975) 309.
- [22] V. Soriano, D. Galland, *Phys. Stat. Sol. B* 77 (1976) 739.
- [23] K.M. Sancier, *Surf. Sci.* 21 (1970) 1.
- [24] K.A. Müller, J. Schneider, *Phys. Lett.* 4 (1963) 288.
- [25] J.I. Pankove, N.M. Johnson (Eds.), *Hydrogen in Semiconductors, Semiconductors and Semimetals*, Vol. 34, Academic Press, Boston, 1991.
- [26] C.G. Van de Walle, N.M. Johnson, in: J.I. Pankove, T.D. Moustakas (Eds.), *Gallium Nitride (GaN) II, Semiconductors and Semimetals*, Vol. 57, Academic Press, Boston, 1998, p. 157.
- [27] J. Hu, R.G. Gordon, *Sol. Cells* 30 (1991) 437.
- [28] E. Mollwo, *Z. Phys.* 138 (1954) 478.
- [29] D.G. Thomas, J.J. Lander, *J. Chem. Phys.* 25 (1956) 1136.
- [30] J.J. Lander, *J. Phys. Chem. Solids* 3 (1957) 87.
- [31] S.J. Baik, et al., *Appl. Phys. Lett.* 70 (1997) 3516.
- [32] S. Kohiki, et al., *Appl. Phys. Lett.* 64 (1994) 2876.
- [33] J. Neugebauer, C.G. Van de Walle, *Appl. Phys. Lett.* 68 (1996) 1829.



ELSEVIER

Physica B 308–310 (2001) 904–907

PHYSICA B

www.elsevier.com/locate/physb

Electronic structure and ferromagnetism of transition-metal-impurity-doped zinc oxide

K. Sato*, H. Katayama-Yoshida

Department of Condensed Matter Physics, The Institute of Scientific and Industrial Research, Osaka University, 8-1 Mihogaoka, Ibaraki, Osaka 567-0047, Japan

Abstract

The ferromagnetism in ZnO-based diluted magnetic semiconductors (DMSs) is investigated based on the first principles calculations. The electronic structure of a ZnO-based DMS is calculated using the Korringa–Kohn–Rostoker method combined with the coherent potential approximation based on the local density approximation. The stability of the ferromagnetic state compared with that of the spin-glass state is systematically investigated by calculating the total energy difference between them. It is found that the ferromagnetic state is more stable than the spin-glass state in V-, Cr-, Fe-, Co- or Ni-doped ZnO without any additional carrier doping treatments. In the case of the Mn-doped ZnO, the spin-glass state is stable at a carrier concentration of 0%, but the ferromagnetic state is stabilized by the hole doping treatment. Analyzing the calculated density of states, it is proposed that the origin of the stabilization of the ferromagnetism is a double-exchange mechanism. © 2001 Elsevier Science B.V. All rights reserved.

PACS: 75.50.p

Keywords: ZnO; Transition metal; Ferromagnetism; Double-exchange mechanism

1. Introduction

Since the successful synthesis of ferromagnetic (In, Mn)As and (Ga, Mn)As, diluted magnetic semiconductors (DMSs) have been studied extensively to realize semiconductor spin electronics (spintronics) [1]. From the industrial viewpoint, it is indispensable to fabricate a ferromagnetic DMS whose Curie temperature (T_C) is higher than the room temperature. Recently, some new high- T_C DMSs were proposed based on experimental [2–4] and theoretical [5–9] studies. However, in order to develop spintronics as a practical technology, it is still necessary to explore a new candidate of functional DMS whose magnetic property is controllable by changing the external field or carrier concentration.

In this paper, the magnetism of (Zn, TM)O, where TM is one of the 3d-transition metals, is investigated

based on the first principles calculations [6–9], and a materials design of new ferromagnetic ZnO-based DMSs is proposed. Recently, ZnO attracted much attention because of its low cost, abundance and being environmentally friendly. Besides, ZnO has a wide band-gap energy of 3.3 eV and a large exciton binding energy of 60 meV, so it is one of the most promising substances for optoelectronics. Jin et al. experimentally showed that 3d-TM was soluble up to several tens (%) in ZnO [10]. Moreover, Joseph et al. successfully prepared p-type ZnO thin films by using the codoping method [11]. Therefore, it is worth investigating the carrier-induced ferromagnetism in the ZnO-based DMSs.

2. Calculation

The electronic structure of the TM-doped ZnO is performed based on the local spin density approximation with the parameterization by Moruzzi et al. [12]. The relativistic effect is taken into account by the scalar

*Corresponding author. Tel.: +81-6-6879-8536; fax: +81-6-6879-8539.

E-mail address: ksato@cmp.sanken.osaka-u.ac.jp (K. Sato).

relativistic approximation. We employ the muffin-tin approximation to describe the crystal potential, and the wave functions in each muffin-tin sphere are expanded with real harmonics up to $l = 2$, where l is the angular momentum defined at each muffin-tin sphere. Throughout the present calculations, lattice constants of doped ZnO are fixed to those of pure ZnO, which are $a = 3.24950 \text{ \AA}$, $c = 5.2069 \text{ \AA}$ and the internal coordinate $u = 0.345$ [13]. These lattice constants lead to muffin-tin radii of 0.941 and 0.855 \AA for the Zn and O, respectively, to touch muffin-tins with each other. Fifty-two independent k -points in the first Brillouin zone are used in the calculations.

ZnO-based DMSs are described within the framework of the coherent potential approximation to take disorder into account [14]. Owing to this treatment, it is possible to simulate the random distribution of the TM-impurities in an *ab initio* manner. In ZnO, the TM impurity has almost saturated magnetic moment. In this case, there are two directions of the magnetic moment along the quantization axis, i.e., up and down directions. Consequently, there are two self-consistent solutions for the electronic structure of the ZnO-based DMS. One is the ferromagnetic state in which all of the magnetic moments are parallel with each other. This is written as $(\text{Zn}, \text{TM}_x^{\text{up}})\text{O}$, where x is the concentration of the TM. The other is the spin-glass state in which the magnetic moments are pointed randomly at each other, therefore, the system has no magnetization. This is written as $(\text{Zn}, \text{TM}_{x/2}^{\text{up}}, \text{TM}_{x/2}^{\text{down}})\text{O}$. Comparing the total energy of the ferromagnetic state with that of the spin-glass state, it is possible to judge which state is more stable. Naively, the total energy difference between these two states corresponds to T_C .

3. Results and discussion

3.1. Chemical trend

First, the chemical trend in the magnetic states of the ZnO-based DMSs is investigated. The stability of the ferromagnetic state in $(\text{Zn}, \text{TM})\text{O}$ is studied as a function of atomic number of the TM impurity without any additional carrier doping treatments. V, Cr, Mn, Fe, Co and Ni are chosen as TM impurities. Calculated energy differences per one formula unit are shown in Fig. 1. The TM concentrations are 5%, 10%, 15%, 20% and 25%. As shown in the figure, $(\text{Zn}, \text{TM})\text{O}$ is ferromagnetic except for Mn, and the ferromagnetic states are very much stable. For example, in 25% V-doped ZnO, an energy difference of 1.36 mRy is expected. This is larger than the energy difference of 0.12 mRy in 5% Mn-doped GaAs. Taking into account that the T_C of 5.5% Mn-doped GaAs is 110 K [15], it is suggested that the ZnO doped with V, Cr, Fe, Co or Ni

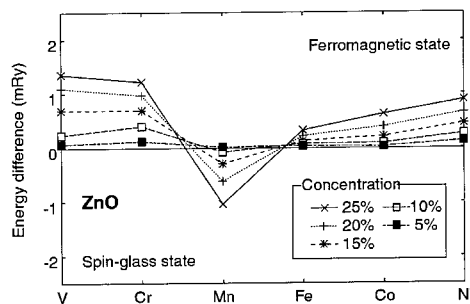


Fig. 1. The stability of the ferromagnetic states in ZnO-based DMSs. V, Cr, Mn, Fe, Co or Ni is doped as a magnetic impurity. The vertical axis is the energy difference per one formula unit between the ferromagnetic and the spin-glass state. A positive energy difference indicates that the ferromagnetic state is more stable than the spin-glass state.

is a candidate for high- T_C ferromagnetic DMS. It has been shown experimentally that TM-doped ZnO is transparent with visible ray [10], therefore, a material design of transparent ferromagnets with ZnO-based DMSs is proposed based on the present calculations.

Recently, some experiments have been performed to confirm the present materials design, and the ferromagnetic behavior was reported in $(\text{Zn}, \text{Co})\text{O}$ [16] and $(\text{Zn}, \text{Ni})\text{O}$ [17] above room temperature. On the other hand, the ferromagnetic interaction was not detected by the magneto-optical experiment [18]. Further experimental efforts are needed to make the magnetism in the ZnO-based DMSs clear.

In order to elucidate the mechanism underlying the ferromagnetism in the ZnO-based DMSs, density of states (DOS) of the ZnO-based DMS is calculated. In Fig. 2, the total DOS per unit cell and partial DOS of 3d-states per atom at each TM site in the ferromagnetic state are shown. The TM atoms are doped up to 25%. The host valence band consists of Zn-3d bands, which appear at approximately 0.5 Ry below the Fermi level (E_F) as a peak whose width is 0.15 Ry, and O-2p band, which distributes from -0.4 to -0.2 Ry. Between the valence band and the conduction band, there are impurity-3d states. These impurity states show large exchange splitting, and they are gradually occupied as increasing the atomic number of impurity. Since the exchange splitting is larger than the crystal field splitting, all the TMs are in high spin states. In particular, the half-metallic DOS are realized in the V-, Cr-, Fe-, Co- and Ni-doped ZnO.

In Fig. 2(c), it is shown that the Mn impurity has d^5 electron configuration due to the substitution of Zn^{2+} by Mn^{2+} . In this case, it is suggested that the anti-ferromagnetic super-exchange interaction between the Mn ions stabilize the spin-glass state. On the other hand, V^{2+} , Cr^{2+} , Fe^{2+} , Co^{2+} and Ni^{2+} have d^3 , d^4 , d^6 , d^7

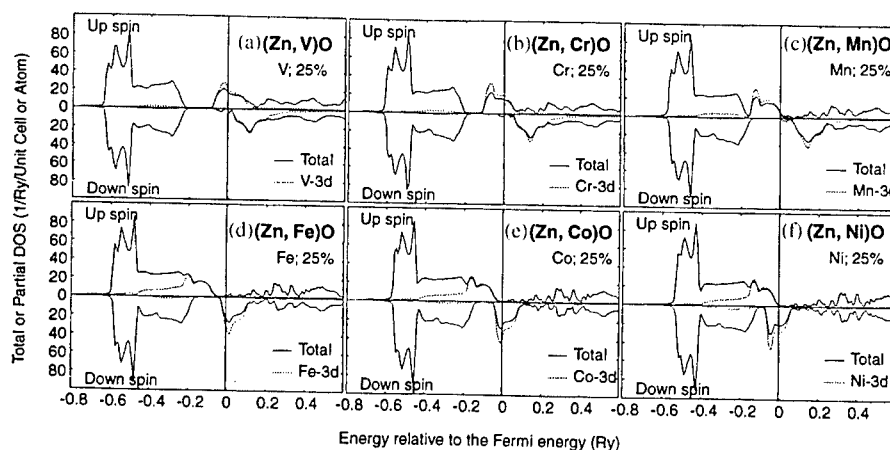


Fig. 2. Total DOS per unit cell (solid line) and partial density of d-states per TM atom at the TM site (dotted line) in (a) (Zn, V)O, (b) (Zn, Cr)O, (c) (Zn, Mn)O, (d) (Zn, Fe)O, (e) (Zn, Co)O and (f) (Zn, Ni)O in the ferromagnetic state. The TM atoms are doped up to 25%. The energy is relative to the Fermi energy.

and d^8 electronic configurations, respectively, therefore, 3d-band of the up- or the down-spin states are not fully occupied. In these cases, the 3d-electron in the partially occupied 3d-orbitals of the TM is allowed to hop to the 3d-orbitals of neighboring TM, if neighboring TM ions have parallel magnetic moments. As a result, the d-electron lowers its kinetic energy by hopping in the ferromagnetic state. This is the so-called double-exchange mechanism. Akai had already pointed out this mechanism in his paper on the magnetism in the (In, Mn)As [19]. From this point of view, the magnetism in ZnO-based DMSs is well-understood [6–9].

3.2. Carrier-induced ferromagnetism

In this section, the magnetism in the ZnO-based DMSs under carrier doping treatment is investigated [6,7]. Fig. 3 shows energy difference per one unit cell (two formula units) between the ferromagnetic and the spin-glass state in the Mn-doped ZnO as a function of the carrier concentration. In the (Zn, Mn)O, the spin-glass state is realized because there is no itinerant carrier and there is no contribution of the double-exchange interaction with the ferromagnetism. While increasing the hole concentration by N-doping, the ferromagnetic state is stabilized as shown in Fig. 3, namely, it is suggested that the carrier-induced ferromagnetism will be observed in the (Zn, Mn)O as is in the (Ga, Mn)As. Moreover, energy difference is large compared with that of the (Ga, Mn)As and a high- T_C is expected. On the contrary to the hole doping, electron doping does not stabilize the ferromagnetic state as shown in Fig. 3. The Zn atoms are substituted by Ga atoms to dope electrons. Due to the large hybridization of the N-2p states with

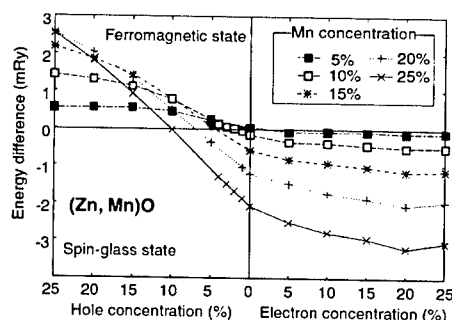


Fig. 3. Stability of the ferromagnetic state in Mn-doped ZnO-based DMSs as a function of the carrier concentration. The vertical axis is the energy difference between the ferromagnetic and the spin-glass state per two formula units. A positive energy difference indicates that the ferromagnetic states are more stable than the spin-glass state. The horizontal axis is the concentration of the holes or electrons.

the Mn-3d states, holes are itinerant in keeping with its d-character, therefore the kinetic energy is lowered so efficiently that the ferromagnetic state is stabilized by the double-exchange mechanism. On the other hand, the doped electrons never go into the Mn-3d states but into the host conduction band, therefore, the double-exchange mechanism does not work to stabilize the ferromagnetism.

The magnetism of the (Zn, Fe)O, (Zn, Co)O and (Zn, Ni)O under carrier doping treatment is also investigated [7]. In these systems, the ferromagnetic states are stabilized much more by electron doping. Considering that the n-type ZnO is easily available and the intrinsic defects such as the O-vacancies and Zn-interstitials work as a donor, it is concluded that the (Zn, Fe)O, (Zn, Co)O and (Zn, Ni)O are promising

candidates for high- T_C ferromagnets. It is also suggested that the (Zn,Mn, Fe)O, (Zn,Mn,Co)O or (Zn, Mn,Ni)O may show carrier-induced ferromagnetism under electron doping by adjusting the ratio of Mn to Fe, Co or Ni. It is strongly encouraged to perform the first principles materials design along this idea.

4. Conclusion

In this paper, the magnetism in ZnO-based DMSs is investigated by the first principles calculations. It is proposed that high- T_C ferromagnetic DMSs are available in V-, Cr-, Fe-, Co- and Ni-doped ZnO-based DMSs. As for controlling the magnetism of the ZnO-based DMSs, it is shown that the Mn-doped ZnO changes its magnetic states from the spin-glass state to the ferromagnetic state with increasing hole concentration. It is also shown that it is possible to raise the T_C of Fe-, Co- and Ni-doped ZnO by electron doping. Analyzing the calculated DOS, it is proposed that the mechanism to stabilize the ferromagnetic state is the double-exchange mechanism. We believe that new ideas which contribute to the spintronics will be triggered under the guidance of the present materials design.

Acknowledgements

This research was partially supported by the JSPS Research for the Future Program in the Area of Atomic-Scale Surface and Interface Dynamics, a Grant-in-Aid for Scientific Research on Priority Areas (A) and (B), and SANKEN-COE from the Ministry of Education, Culture, Sports, Science and Technology. One of the authors (K.S.) acknowledges financial support to JSPS. We used KKR-CPA band structure calculation package of MACHIKANEYAMA2000 developed by Professor Hisazumi Akai in Osaka University.

References

- [1] H. Ohno, *Science* 291 (2001) 840.
- [2] G.A. Medvedkin, T. Ishibashi, T. Nishi, K. Hayata, Y. Hasegawa, K. Sato, *Jpn. J. Appl. Phys.* 39 (2000) L949.
- [3] H. Akinaga, T. Manago, M. Shirai, *Jpn. J. Appl. Phys.* 39 (2000) L1118.
- [4] Y. Matsumoto, M. Murakami, T. Shono, T. Hasegawa, T. Fukumura, M. Kawasaki, P. Ahmet, T. Chikyow, S. Koshihara, H. Koinuma, *Science* 291 (2001) 854.
- [5] T. Dietl, H. Ohno, F. Matsukura, J. Cibert, D. Ferrand, *Science* 287 (2000) 1019.
- [6] K. Sato, H. Katayama-Yoshida, *Jpn. J. Appl. Phys.* 39 (2000) L555.
- [7] K. Sato, H. Katayama-Yoshida, *Jpn. J. Appl. Phys.* 40 (2001) L334.
- [8] K. Sato, H. Katayama-Yoshida, *Jpn. J. Appl. Phys.* 40 (2001) L485.
- [9] K. Sato, H. Katayama-Yoshida, *Jpn. J. Appl. Phys.* 40 (2001) L651.
- [10] Z. Jin, M. Murakami, T. Fukumura, Y. Matsumoto, A. Ohtomo, M. Kawasaki, H. Koinuma, *J. Crystal Growth* 214/215 (2000) 55.
- [11] M. Joseph, H. Tabata, T. Kawai, *Jpn. J. Appl. Phys.* 38 (1999) L1205.
- [12] H. Akai, M. Akai, S. Blügel, B. Drittler, H. Ebert, K. Terakura, R. Zeller, P.H. Dederichs, *Progr. Theor. Phys. Supplement* 101 (1990) 11.
- [13] R.W.G. Wyckoff, *Crystal Structures*, Vol. 1, 2nd Edition, Wiley, New York, 1986, p. 112.
- [14] H. Akai, *J. Phys.: Condens. Matter* 1 (1989) 8045.
- [15] F. Matsukura, H. Ohno, A. Shen, Y. Sugawara, *Phys. Rev. B* 57 (1998) R2037.
- [16] K. Ueda, H. Tabata, T. Kawai, *Appl. Phys. Lett.* 79 (2001) 988.
- [17] T. Wakano, N. Fujimura, Y. Morinaga, N. Abe, A. Ashida, T. Ito, *Physica E* 10 (2001) 260.
- [18] K. Ando, H. Saito, Zhengwu Jin, T. Fukumura, M. Kawasaki, Y. Matsumoto, H. Koinuma, *J. Appl. Phys.* 89 (2001) 7284.
- [19] H. Akai, *Phys. Rev. Lett.* 81 (1998) 3002.



ELSEVIER

Physica B 308–310 (2001) 908–911

PHYSICA B

www.elsevier.com/locate/physb

Magnetic resonance experiments on the green emission in undoped ZnO crystals

F. Leiter*, H. Zhou, F. Henecker, A. Hofstaetter, D.M. Hofmann, B.K. Meyer

I. Physikalisches Institut, Justus-Liebig-Universität, Heinrich-Buff-Ring 16, D-35625 Giessen, Germany

Abstract

Optically detected magnetic resonance shows that a broad, green emission band in ZnO at 2.45 eV originates from a spintriplet-recombination characterised by $g_{\parallel c} = 1.984$ and $g_{\perp c} = 2.025$ (parallel and perpendicular to the crystallographic c -axis, respectively) and a zero-field splitting of $D = 260 \times 10^{-4} \text{ cm}^{-1}$. These parameters and the polarisation properties of the emission are very similar to the anion vacancies in CaO but not compatible with the Zeeman results on ZnO:Cu. © 2001 Elsevier Science B.V. All rights reserved.

Keywords: ZnO; Optically detected magnetic resonance; Anion vacancies

1. Introduction

The recently reported ability to dope ZnO p-type has stimulated renewed interest in this material system as it opens novel possibilities for opto-electronic emitters in the blue spectral range [1]. Successful doping typically requires a detailed knowledge on the presence of residual impurities as well as on the formation of intrinsic defects because in many cases these defects counteract in the desired conductivity type or have severe influence on the optical properties of the material. For ZnO an emission in the green spectral range is commonly reported, but the responsible defects are not identified. Cu present in ZnO as a residual impurity was shown to create an emission in the green spectral range. The Cu related emission band exhibits a pronounced LO-phonon structure [2] and detailed structural information is available from Zeeman experiments [3]. But more frequently a broad emission is observed without any phonon structure, and intrinsic defects such as O- or Zn-vacancies are discussed as the origin of this recombination [4].

We used nominally undoped ZnO crystals and Cu doped ZnO crystals for our optically detected magnetic resonance (ODMR) investigation and will show that the origin of the unstructured green emission band in the undoped crystals is a spintriplet system with properties similar to the anion vacancies in CaO and MgO.

2. Experimental details

For our photoluminescence (PL) and ODMR experiments we used undoped n-type ZnO single crystals, which are commercially available from Eagle-Picher. The electrical properties are very similar to the samples investigated by Look et al. [5] which originates from the same supplier. The total shallow donor concentration is about $1 \times 10^{17} \text{ cm}^{-3}$. The ODMR measurements were carried out with a 24 GHz microwave bridge with 200 mW maximum output power. The sample is placed in a TE₀₁₁ resonator immersed in liquid helium at 1.5 K being part of a 4 T superconducting magnet system. The luminescence is excited by a HeCd laser (325 nm, 35 mW) and analysed by a 1/4 m monochromator in connection with a photomultiplier tube. A photo-elastic modulator (PEM) operating at 42 kHz in connection with a linear-polarizer allows to measure the difference of the left- and right-circular polarized components of the emitted light, i.e. the magnetic circular polarisation of the emission

*Corresponding author. Tel.: +49-641-9933-112; fax: +49-641-9933-119.

E-mail address: frank.h.leiter@physik.uni-giessen.de (F. Leiter).

(MCPE). Either, the frequency of the PEM or the amplitude modulation frequency of the microwave power served as the reference for lock-in detection.

3. Results

Fig. 1a shows the low temperature PL spectra of the undoped ZnO sample. At high energies bound exciton emissions are dominating, followed by LO-phonon replica. In the spectral range below 2.75 eV the unstructured “green” emission is visible. The intensity maximum of the emission is at 2.45 eV and its full width at half maximum is 320 meV. For comparison we show in Fig. 1b the emission of a Cu doped ZnO sample in this spectral range. Although the emission maximum of the Cu related band is almost the same as that observed in the undoped sample its LO-phonon structure is clearly visible and gives evidence that the two emissions are of different origin.

Following the temperature dependence of the green emission in undoped ZnO (Fig. 2) we find that it maintains its peak position up to 300 K, while the excitonic recombination follows the shrinkage of the bandgap of ZnO. This is a typical feature of a recombination within a localised defect, i.e. the ground and excited states are only very weakly coupled to the band properties of the host crystal.

In order to get further insight in the nature of the green emission in the undoped samples we performed ODMR. From ODMR experiments monitoring the emission intensity and modulating the microwave power spectra such as shown in Fig. 3a are obtained. In phase with the microwave modulation frequency two resonances are observed which enhance the emission

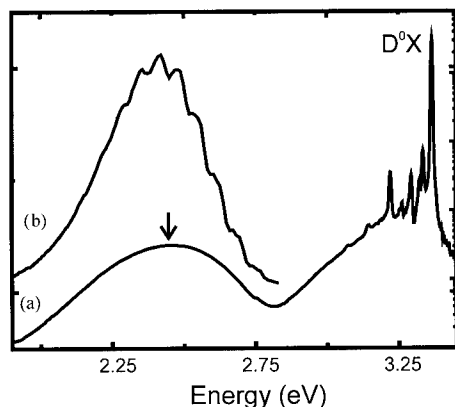


Fig. 1. Photoluminescence spectrum of undoped ZnO (spectrum (a)), the arrow indicates the peak position of the green emission on which the ODMR results were obtained. Spectrum (b) shows the phonon structured emission observed in Cu doped ZnO samples (5 K, 325 nm HeCd laser).

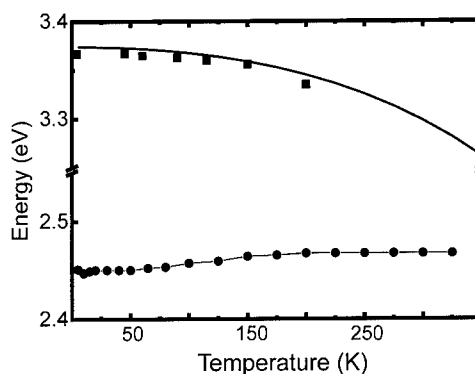


Fig. 2. Dependence of the peak position of the donor bound exciton (D^0X) and the 2.45 eV emission on temperature. The D^0X follows the shrinkage of the bandgap (drawn line), while the 2.45 eV emission maintains its peak position.

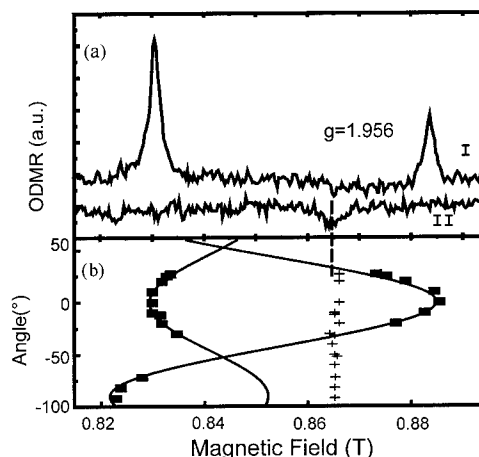


Fig. 3. (a) Optically detected magnetic resonance spectra measured on the 2.45 eV emission: (I) “in phase” with the microwave pulses, (II) “90° phase”. (b) Angular dependence of the ODMR signals (0° : $B_0 \parallel c$, 90° : $B_0 \perp c$).

intensity of the order of 1% (spectrum I), while with a 90° phase shift a third signal is detected (spectrum II). This behaviour is observed independent of the microwave modulation frequency which could be set in the range from 30 Hz to 5 kHz.

These observations indicate that the two signals are of different origin. This is also evident from the orientation dependence of the resonances in respect to the magnetic field (B_0) (Fig. 3b). The small signal is isotropic and the corresponding g -value is $g = 1.956$, i.e. the g -value of shallow donors in ZnO [6]. The reported small anisotropy of the signal originating from the wurtzite crystal structure of ZnO is not resolvable in our ODMR experiments. The two intense resonances show the characteristic angular dependence of a spin-triplet system ($S = 1$). The orientation dependence is explained

by the solution of the spin Hamiltonian:

$$H = \mu_B \mathbf{B}_0 g \mathbf{S} + D[S_z^2 - 1/3S(S+1)] \quad (1)$$

with $g_{\parallel} = 1.984$ and $g_{\perp} = 2.025$, and a fine-structure splitting D of $D = 260 \times 10^{-4} \text{ cm}^{-1}$.

It was proven that the triplet resonances are detectable only in the energy range of the green emission. The shallow donor is also detectable in the excitonic range, but as an emission enhancing signal. This indicates that the shallow donor signal appears in the green emission by a spin dependent energy transfer process.

Further proof for the triplet nature of the recombination were obtained from ODMR experiments monitoring the MCPE (Fig. 4). The MCPE intensity shows the expected increase with increasing magnetic field, and the two triplet related resonances (marked by arrows) are now observed as MCPE enhancing and decreasing signals. At low magnetic fields an additional resonance is seen (labeled Level Anti-Crossing (LAC)). It is observable even without applying any microwaves during the measurement. The sign of the triplet resonances and the appearance of the LAC signals are fully explained by the level scheme shown in the inset of Fig. 4. The circular polarised components of the emission arise from the magnetic sublevels $| -1 \rangle$ and $| +1 \rangle$. Due to the selection rules for dipole transitions we can expect the $| 0 \rangle$ state to have the highest population, between the $| -1 \rangle$ and $| +1 \rangle$ levels we assume a thermalised population. The latter is justified by the intensity dependence of the MCPE in respect to B_0 , which follows the expected Brillouin-function behaviour for an $S = 1$ system. For the ODMR transition equalising the population differences between the $| +1 \rangle$ and $| 0 \rangle$ levels we thus expect a decrease of the MCPE and for the $| -1 \rangle$ to $| 0 \rangle$ an enhanced MCPE intensity. The LAC signal is caused by the “crossing” of the $| 1 \rangle$ with the $| 0 \rangle$ state and is a direct measure of fine

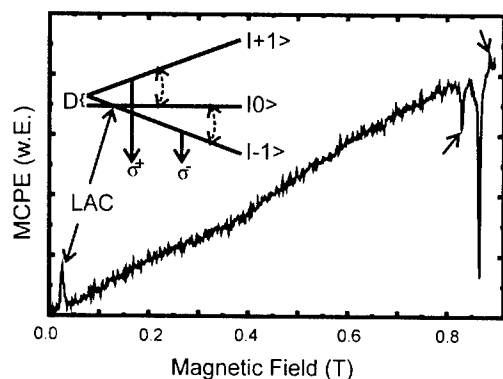


Fig. 4. Optically detected magnetic resonance spectrum detected on the magnetic circular polarisation emission (MCPE) of the 2.45 eV recombination in undoped ZnO. The inset shows the level scheme of the triplet explaining the magnetic resonance positions.

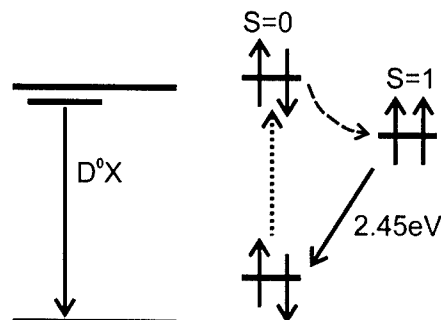


Fig. 5. Recombination model for the 2.45 eV recombination in undoped ZnO. For details see text.

structure splitting D . Further the observation of the LAC in connection with the sign of the ODMR resonances allows to determine the sign of D which is positive in our case. Remarkable is the strong influence of the shallow donor resonance on the MCPE of the triplet recombination. It gives further evidence that the population of the $| \pm 1 \rangle$ sublevels of the triplet is strongly dependent on the population of the magnetic sublevels of the shallow donor, i.e. a spin dependent energy transfer process.

Discussing the origin of the triplet emission we find similarities to the anion vacancies (F-centres) in CaO and MgO [7]. The ground state of the centre is a singlet state with two electrons, the neutral oxygen vacancy. Excitation with light leads to an excited singlet state, from which the electrons can relax into the triplet $S = 1$ state, causing the ODMR signals (see Fig. 5). The optical cycle is closed by radiative recombination back to the $S = 0$ groundstate. Such a cycle also explain our ODMR results as well as the constant emission energy of the green band with temperature. Above bandgap excitation seems to excite simultaneously the excitonic and the oxygen vacancy recombinations.

It should be noted that we failed to detect any ODMR signals on the LO-phonon structured emission in the Cu doped samples and that the ground and excited state g -values obtained by Zeeman spectroscopy for the green Cu emission are incompatible to the results obtained here.

In summary, our experimental results on the green unstructured emission band at 2.45 eV observed in undoped ZnO show that it is a spintriplet recombination with properties very similar to anion vacancies in ionic crystals. We thus conclude that it originates from the oxygen vacancy in ZnO.

References

- [1] K. Minegishi, Y. Koiwai, Y. Kikuchi, K. Yano, M. Kasuga, A. Shimizu, Jpn. J. Appl. Phys. 36 (1997) L1452.
- [2] R. Kuhnert, R. Helbig, J. Lumin. 26 (1981) 203.

- [3] I. Broser, R.K. Germer, H.J. Schulz, K. Wisznewski, *Solid State Electron.* 21 (1978) 1597.
- [4] A.F. Kohan, G. Ceder, D. Morgan, C.G. Van de Walle, *Phys. Rev. B* 61 (2000) 15019.
- [5] D.C. Look, D.C. Reynolds, J.R. Sizelove, R.L. Jones, C.W. Litton, G. Cantwell, W.C. Harsch, *Solid State Commun.* 105 (1998) 399.
- [6] J. Schneider, A. Räuber, *Z. Naturforsch. A* 16 (1961) 712.
- [7] P. Edel, C. Hennies, Y. Merle, D'Aubigné, R. Romestain, Y. Twarowski, *Phys. Rev. Lett.* 28 (1972) 1268.



ELSEVIER

Physica B 308 310 (2001) 912–915

PHYSICA B

www.elsevier.com/locate/physb

First-principles study of the compensation mechanism in N-doped ZnO

Eun-Cheol Lee, Y.-S. Kim, Y.-G. Jin, K.J. Chang*

Department of Physics, Korea Advanced Institute of Science and Technology, 373-1 Kusung-dong Yusung-Ku, Taejeon 305-701, South Korea

Abstract

Based on first-principles electronic structure calculations for N-related and native point defects in Zinc Oxide (ZnO), we propose a mechanism for the compensation of N acceptors. As compared to a normal N_2 source, the use of an active plasma N_2 gas generally increases the N solubility limit, because the N chemical potential is enhanced. However, whenever a pure N source is used, N acceptors are greatly compensated by donor defects, which may explain the difficulty in achieving low-resistance p-type ZnO. Major compensating donors for N acceptors are found to be different at low and high N doping levels, and also depend on the type of N_2 gas source. © 2001 Elsevier Science B.V. All rights reserved.

PACS: 71.55.Gs; 61.72.Vv; 61.72.Bb; 61.72.Ji

Keywords: ZnO; Nitrogen; Compensation

Very recently, zinc oxide (ZnO) has attracted much attention because of its wide applications for various optoelectronic devices. This material has a direct band gap of 3.3 eV and a large exciton binding energy of 60 meV, and efficient excitonic UV laser actions have been demonstrated at room temperature [1]. In addition, ZnO has been shown to be ferroelectric or antiferromagnetic by doping Li or Mn impurities [2,3]. For practical applications for optoelectronic devices based on p–n junctions such as laser diodes, both n- and p-type ZnO are needed. Undoped ZnO exhibits intrinsic n-type conductivity, and low-resistance n-type doping with electron concentrations as high as 10^{21} cm^{-3} was achieved [4]. However, it is very difficult to dope p-type in ZnO like other wide band-gap semiconductors, ZnSe and GaN. Although N is considered to be a good shallow p-type dopant among group IV acceptors [5], p-type doping in ZnO have been failed using a pure nitrogen source, while acceptor concentrations as high

as 10^{18} cm^{-3} have been obtained for ZnSe using an N_2 plasma source [6]. Thus, it appears that N acceptors are more strongly compensated in ZnO, compared with ZnSe. On the other hand, it has been reported that ZnO can be p-type by codoping N with H or Ga impurities [7,8].

In this work, we investigate the electronic structure of various defects including point defects and N-related defect complexes in ZnO using a first-principles pseudo potential method within the local-density-functional approximation (LDA). To find major compensating species for N acceptors, we calculate the formation energies and defect concentrations depending on stoichiometry and N gas source. For a normal N_2 gas as a doping source, N acceptors are mainly compensated by O-vacancies and N-acceptor–Zn-anti-site complexes. When an active N_2 plasma is used, the N solubility limit is increased. However, it is still difficult to achieve high hole carrier densities due to the compensation by N_2 molecules at O sites and $N_O-(N_2)_O$ complexes.

The total energies of native and N-related defects are calculated using the first-principles pseudopotential

*Corresponding author. Tel.: +82-42-869-2531; fax: +82-42-869-2510.

E-mail address: kchang@mail.kaist.ac.kr (K.J. Chang).

method within LDA [9]. The details of our calculation method are given elsewhere [10].

Since atomic N has five valence electrons, it acts as an acceptor at a substitutional O site in ZnO. To find possible donor defects which compensate for N acceptors in ZnO, we first examine the electronic structure of native point defects such as vacancies (V_O and V_{Zn}), interstitials (Zn_i and O_i), and antisites (Zn_O and O_{Zn}). We find that Zn_i and Zn_O behave as a shallow double donor, because their single particle donor levels are mainly composed of the Zn-4s orbitals, which derive the conduction band minimum (CBM) state. Other calculations [11] also reported that Zn_i and Zn_O are shallow donors, and experimentally, Zn_i was shown to behave as a shallow donor [12]. The single particle donor level of V_O is located well below the CBM state, corresponding to the A_1 state of the Zn-4s orbitals in the neighborhood of V_O . In fact, since the V_O donor level is characterized by the hybridization of the Zn-4s and O-2p orbitals, V_O is likely to be a deep donor [10]. In the 2+ charge state of V_O , the surrounding Zn atoms are relaxed outward by 0.34–0.42 Å from the vacancy site. The $(2+/0)$ transition level of V_O is found to lie at 0.73 eV below the CBM state, indicating that V_O becomes a negative-U defect. We investigate various configurations of O_i , and find that a split-interstitial configuration gives rise to a donor level, while O_i at an octahedral site behaves as an acceptor, with the acceptor level lying close to the valence band maximum (VBM). Since V_{Zn} and O_{Zn} are acceptors, they are not responsible for the compensation of N acceptors. Compared with the measured value of 3.3 eV, the calculated LDA band gap of 0.90 eV is severely underestimated, similar to other calculations [13,11], which treat the Zn-3d electrons as valence states. Since the underestimation of the LDA gap may cause errors up to 2.5 eV in the formation energies of donors, we include a band gap correction for shallow donors such as Zn_i and Zn_O . For V_O , we test the transition levels lying between 1.1 eV above the VBM and the CBM, and find that main compensating species for N acceptors remain unchanged.

Besides the native donor defects, N-related donor defects play an important role in the compensation for N acceptors. Low-energy defect complexes between native defects and N acceptors are easily formed when the densities of individual defects are sufficiently high. We find that N_O - Zn_i , N_O - Zn_O , N_O - V_O , and N_O - O_i complexes are single donors. In these complexes, N_O - Zn_i and N_O - Zn_O have large binding energies of 1.06 and 1.52 eV, respectively, while the binding energies of N_O - V_O and N_O - O_i are 0.60 and 0.31 eV, respectively. Other important N-related donors are N_2 molecules at O sites [$(N_2)_O$] and N-acceptor- $(N_2)_O$ complexes [N_O -(N_2) $_O$]. For the $(N_2)_O$ complex, the N-N bond is very strong whereas interactions between the N and surrounding Zn atoms are extremely weak. Thus, two valence electrons

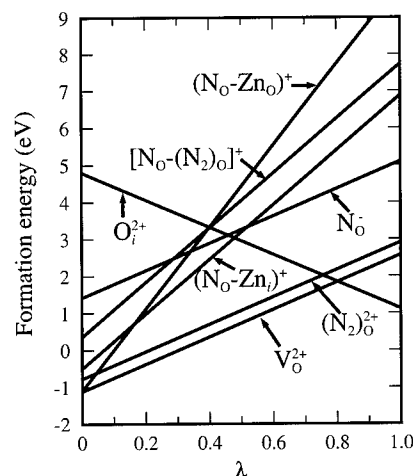


Fig. 1. Defect formation energies as a function of the stoichiometric parameter λ for the p-type condition ($\mu_e = 0$) when a normal N_2 gas source is used.

from the neighboring Zn atoms are almost in a nonbonding state, resulting in a double donor state. Similarly, an $(N_2)_{Se}$ molecule at a Se site in ZnSe is known to act as a shallow double donor [14].

We investigate the dominant compensating species for N acceptors under growth conditions using normal and plasma N_2 gas sources, assuming the p-type condition ($\mu_e = 0$). The stoichiometric condition of ZnO is represented by a single parameter λ , lying between 0 and 1 under extreme Zn- and O-rich conditions, respectively. Among the native donor defects, V_O or O_i has the lowest formation energy, depending on the stoichiometric condition. The formation energy of Zn_i is higher by 0.26 eV than for V_O . We find that the energy of the N_O - Zn_i complex is lower than those for N_O - V_O and N_O - O_i , independent of λ . However, going to the extreme Zn-rich condition, the energy of N_O - Zn_O becomes lower than for N_O - Zn_i . For defects purely composed of N atoms, N_O -(N_2) $_O$ becomes more stable than $(N_2)_O$, as the N chemical potential increases. Fig. 1 shows the formation energies of the N acceptor and several important compensating donors as a function of λ , when a normal N_2 gas source is used. In this case, μ_N is fixed to satisfy the extreme N-rich condition, i.e., $\mu_N = \mu_{N_2}/2$. The formation energies are drawn only for the lowest-energy states, i.e., the 1+ and 2+ charge states for single and double donors, respectively, which are expected to have no errors despite the underestimation of the LDA band gap. We find that V_O has the lowest formation energy for stoichiometric conditions of $\lambda < 0.8$, while O_i is stabilized for $\lambda > 0.8$. Since the maximum amount [N] of incorporated N impurities is below 10^{10} cm^{-3} for $\lambda > 0.62$ (see Fig. 2), O_i is not an important compensating donor when practical N doping levels are considered. For all the stoichiometric

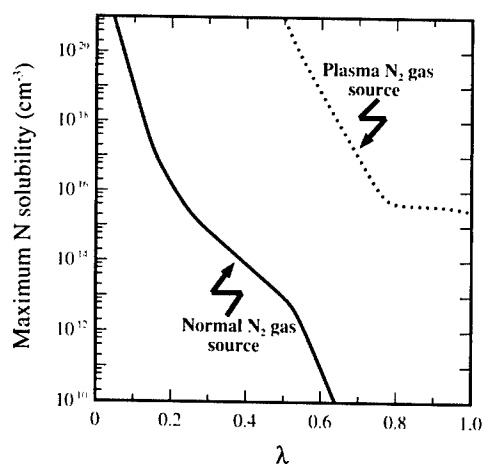


Fig. 2. Maximum N solubilities are plotted as a function of λ for normal and plasma N_2 gas sources.

conditions, the formation energy of the N acceptor is always higher by 2.53–3.99 eV than that of the lowest-energy donor, which explains the difficulty in achieving low-resistance p-type ZnO. The $(N_2)_O$ is higher by 0.34 eV than for V_O . Under the extreme Zn-rich condition, the formation energies of N_O-Zn_O and N_O-Zn_i are higher by 0.02 eV and 0.62 eV, respectively, than for V_O . However, as μ_c increases, N_O-Zn_O and N_O-Zn_i become energetically more stable than V_O . For example, for $\mu_c = 1.0$ eV, the formation energies of N_O-Zn_O and N_O-Zn_i are lower by 0.98 and 0.38 eV, respectively, than for V_O . When we vary μ_c , which is in fact determined by the charge neutrality condition [10], we find that the major compensating donor is V_O at low N doping levels, while it is the N_O-Zn_O complex at high doping levels.

When an active N_2 source is used, the N solubility increases greatly under O-rich conditions, as shown in Fig. 2, where native point defects and N-acceptor-native-defect complexes are rarely formed. Then, the p-type doping efficiency is expected to increase. Under the O-rich condition of $\lambda = 0.6$, the maximum N concentration is found to increase from 10^{11} to $7 \times 10^{18} \text{ cm}^{-3}$. To simulate theoretically the active N_2 source, we choose μ_{N_2} , which is higher by about 1.5 eV than that for N_2 molecules ($\mu_{N_2}/2$). This N chemical potential is determined by assuming that equal amounts of N_2 molecules are in the ground and excited states; the energy of an excited N_2 molecule in the $^3\Sigma_u^+$ state is higher by 3.09 eV per N atom, as compared to the ground state ($^1\Sigma_g^+$). In this case, as shown in Fig. 3, $(N_2)_O$ or $N_O-(N_2)_O$ has the lowest formation energy, depending on λ . For all the stoichiometric conditions, the formation energies of the N acceptor is higher by 3.74–4.15 eV than for the major compensating donor. Thus, N acceptors are still compensated sig-

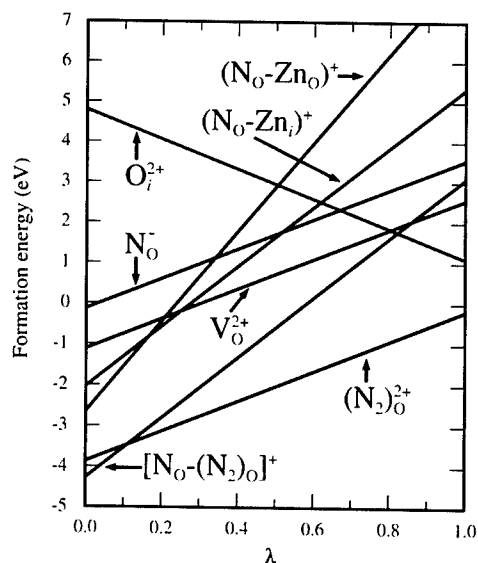


Fig. 3. Defect formation energies as a function of λ for the p-type condition ($\mu_c = 0$) when a plasma N_2 gas source is used.

nificantly, although the N solubility is increased using an active N_2 source. This result indicates that it is unlikely to enhance the p-type doping efficiency even if an active N_2 source is used. This feature also explains the failure of obtaining low-resistance p-type ZnO with a plasma N_2 source [15].

In conclusion, we find a mechanism for the compensation of N acceptors in ZnO, based on the first-principles pseudopotential calculations. When a normal N_2 gas source is used, N acceptors are mainly compensated by O vacancies at low N doping levels, while main compensating donors are defect complexes of N acceptors and native donors at high doping levels. An active plasma N_2 source increases the N solubility, however, the doping efficiency is found to be still low because of the compensation effect by N_2 molecules at O sites and $N_O-(N_2)_O$ complexes.

Acknowledgements

This work was supported by the supercomputing center in KISTI, which provided Cray T3E computing times.

References

- [1] D.M. Bagall, et al., Appl. Phys. Lett. 70 (1997) 2230.
- [2] A. Onodera, et al., Jpn. J. Appl. Phys. Part 1 35 (1996) 5160.
- [3] T. Fukumura, et al., Appl. Phys. Lett. 78 (2001) 958.
- [4] T. Minami, et al., Jpn. J. Appl. Phys. 24 (1985) L781.

- [5] A. Kobayashi, O.F. Sankey, J.D. Dow, *Phys. Rev. B* 28 (1983) 946.
- [6] R.M. Park, et al., *Appl. Phys. Lett.* 57 (1990) 2127.
- [7] K. Minegishi, et al., *Jpn. J. Appl. Phys.* 36 (1997) L1453.
- [8] M. Joseph, H. Tabata, T. Kawai, *Jpn. J. Appl. Phys.* 38 (1999) L1205.
- [9] P. Hohenberg, W. Kohn, *Phys. Rev. B* 136 (1964) 864.
- [10] E.-C. Lee, Y.-S. Kim, Y.-G. Jin, K.J. Chang, *Phys. Rev. B* 64 (2001) 85120.
- [11] S.B. Zhang, S.-H. Wei, A. Zunger, *Phys. Rev. B* 63 (2001) 75205.
- [12] D.C. Look, J.W. Hemsky, J.R. Sizelove, *Phys. Rev. Lett.* 82 (1999) 2552.
- [13] A.F. Kohan, et al., *Phys. Rev. B* 61 (2000) 15019.
- [14] B.-H. Cheong, C.H. Park, K.J. Chang, *Phys. Rev. B* 51 (1995) 10610.
- [15] Y. Sato, S. Sato, *Thin Solid Films* 281–282 (1996) 445.



ELSEVIER

Physica B 308–310 (2001) 916–919

PHYSICA B

www.elsevier.com/locate/physb

Control of valence states for ZnS by triple-codoping method

Tetsuya Yamamoto^{a,*}, Seiichi Kishimoto^{b,c}, Seishi Iida^c^aDepartment of Electronic and Photonic Systems Engineering, Kochi University of Technology, 185 Miyakuchi, Tosayamada-cho, Kami-gun, Kochi 782-8502, Japan^bKochi National College of Technology, Monobe-otsu 200-1, Nankoku, Kochi 783-8508, Japan^cDepartment of Electrical Engineering, Nagaoka University of Technology, Kamitomioka 1603-1, Nagaoka 940-2188, Japan

Abstract

We use In species as reactive codopants for N acceptors to realize p-type ZnS. We find a change in the impurity states of N acceptors between ZnS:N and ZnS:(2N, In), based on the calculated results using ab initio electronic band structure calculations: while we find highly localized states of N acceptors for ZnS:N, we verify delocalized states for ZnS:(2N, In). © 2001 Elsevier Science B.V. All rights reserved.

Keywords: Blue-Ag emission; Codoping; ZnS

1. Introduction

In this paper, a materials design using a triple-codoping method for the fabrication of low-resistivity p-type zinc sulfide (ZnS) with blue-Ag emission is proposed in order to realize highly efficient blue-light-emitting diodes (LED) and blue injection-laser diodes (LD). ZnS has a large band gap of 3.68 eV at room temperature. Ag impurities, which are Zn-substituting species, are well known to be the blue-Ag center (usually called *activator*) [1,2]. In order to realize the blue emission of approximately 440 nm (2.81 eV), it is necessary to introduce donors as *coactivators* into ZnS films. Conductivity control is a necessary prerequisite for device applications: ZnS must be doped with acceptors in order to realize p-type ZnS films. To date, we have reported on p-type ZnS doped with N acceptors (ZnS:N) [3,4] and the triple-codoped p-type ZnS:(Ag, In, and N) [5]. Vapor-phase epitaxial (VPE) ZnS:(Ag, In, and N) layers were grown on semi-insulating (SI) GaAs(100) substrates with hydrogen carrier gas flow. The source material was a luminescent-grade unactivated ZnS powder [5]. Based on photoluminescence

spectra, an emission at 436 nm was found to be dominant for the ZnS:(Ag, In and N) layer and it shifted to a shorter wavelength with increasing excitation intensity; this is the characteristic feature of donor–acceptor pair-type recombinations [5]. Hall-effect measurements at room temperature revealed free hole concentration and mobility values of $(0.56\text{--}1.4) \times 10^{19} \text{ cm}^{-3}$ and $11\text{--}25 \text{ cm}^2 \text{ V}^{-1} \text{ s}^{-1}$, respectively, for ZnS:(Ag, In and N) [5]. Moreover, the hole concentrations of the triple-codoped layers did not show temperature dependence, indicating that the impurity bands are formatted [5].

Svob et al. have reported p-type ZnS:N with hole concentrations up to 10^{18} cm^{-3} [6]. They found that the energy levels of the N acceptors are slightly deep, about 0.19 eV above the valence band [6]. Sufficiently, high free hole concentrations at room temperature should be realized by the codoping method previously proposed by us [7–9].

The purpose of this study is to investigate the effects of In codopants on the N states of ZnS codoped with N and In species based on ab initio electronic band structure calculations.

2. Methodology

The results of our band structure calculations for ZnS crystals with zincblende structures were based on the

*Corresponding author. Tel.: +81-887-57-2112; fax: +81-887-57-2120.

E-mail address: yamateko@ele.kochi-tech.ac.jp (T. Yamamoto).

local density approximation (LDA) treatment of electronic exchange and correlation [10–12] and on the augmented spherical wave (ASW) formalism for the solution of effective single-particle equations [13]. For these calculations, the atomic sphere approximation (ASA) with a correction term was adopted. For undoped ZnS crystals, the Brillouin zone integration was carried out for 84-k points in an irreducible wedge and for 24-k points for doped and codoped ZnS crystals. For valence electrons, we employed the outermost s, p and d orbitals of Zn and S atoms and the outermost s and p orbitals of In and N atoms. The Madelung energy, which reflects the long-range electrostatic interaction within the system, was assumed to be restricted to the sum over monopoles.

We studied the crystal structures of doped and codoped ZnS under periodic boundary conditions by generating supercells having 64 atoms that contain the object of interest: (1) for ZnS:N, we replaced one of the 32 sites of S atoms with an N site; (2) for ZnS:In, we replaced one of the 32 sites of Zn atoms with an In site; (3) for ZnS codoped with N and In (ZnS:(N, In)), we replaced one of the 32 sites of S atoms with a N site and one of the 32 sites of Zn atoms with an In site. First, we calculated the total energy for all cases to be considered for ZnS:(N, In). Second, we determined the crystal structure of the material under the condition that the total energy is minimized. The total energy calculations show that the formation of a N–In pair which occupies nearest-neighbor sites in the crystal is energetically favorable. Finally, to determine the crystal structure of ZnS:(2N, In), we replaced one of the remaining 31 sites of S with another N site for ZnS:(N, In), as mentioned above. Under the same total energy condition as that of ZnS:(N, In), we determined the crystal structure for ZnS:(2N, In). We find that the formation of the cluster, N–In–N, which occupies nearest-neighbor sites, is energetically favorable based on the total energy calculations. The difference in the total energy between the crystal structure having the lowest total energy and the one having the second-lowest total energy, such as the In–N pair and another N which occupy the second-nearest-neighbor sites from the In sites, is 832 meV. In this treatment, we ignore the effects of relaxation due to the dopants.

3. Results and discussion

We show the total density of states (DOS) for undoped ZnS crystals as a standard reference, for ZnS:N, and for ZnS:(In, 2N), in Fig. 1. The S 3s states are included in the calculation as valence states, but those which are located between -12.04 and -13.31 eV are omitted in the Fig. 1. Energy is measured relative to the Fermi level (E_F). For undoped ZnS, zero energy

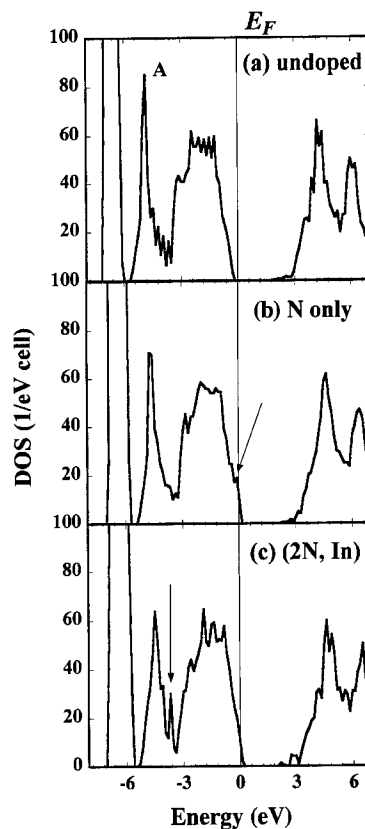


Fig. 1. Total DOS for (a) undoped, (b) N-doped and (c) (2N, In)-codoped ZnS. Energy is shown relative to the Fermi level (E_F).

indicates the top of the valence band. The calculated band gap of undoped ZnS is 2.08 eV. In general, the band-gap values calculated based on the LDA are less than the values obtained by optical experiments. Inaccuracy in determining the optical band gap has little influence on the present discussion.

Fig. 1(a) shows two groups in the valence band. The first group includes bands from -7.01 to -6.16 eV with strong d characteristics originating mostly from d states at Zn sites; the second group, located in the upper valence band above approximately -5.61 eV, mainly originates from the S 3p states. The letter A at -4.97 eV refers to a strong interaction between S p states and Zn s states. From approximately -3.5 eV to the top of the valence band, S p states mainly contribute to the DOS. The lowest conduction bands, antibonding states of the interaction stated above, have a strong Zn 4s contribution; there are charge transfers from Zn 4s to S 3s and 3p due to the mixing between the s and p states at S sites and the s states at Zn sites. As a result, the s and p states of the surrounding Zn shift the center of gravity of the local DOS at the S sites towards the lower energy region. In the following, we discuss the stability of the ionic

charge distributions in ZnS doped with acceptors or donors in terms of the change of electrostatic energy, the Madelung energy.

Fig. 1(b) shows that a hole is generated at the top of the valence band. The arrow in Fig. 1(b) at -0.1 eV refers to a sharp DOS peak induced by N doping. The peak originates in a very localized N-impurity state of which the center of gravity of the DOS at N sites shifts to a higher energy region due to the strong repulsive potential. This indicates that N doping generates a slightly deeper acceptor level above the valence band, which explains the experimental data well [6]. It is necessary that the N-impurity state change to a delocalized state for the realization of low-resistivity p-type ZnS.

For ZnS:(In, 2N), no sharp DOS peak is observed, as shown in Fig. 1(c). The arrow at -3.67 eV indicates a DOS peak resulting from the interaction between p states at S sites close to the In site and s states at the Zn site which occupies the nearest-neighbor site from the S sites and second-nearest-neighbor sites from the In atoms. We predict an increase in DOS around the corresponding energy regions for ZnS:(2N, In) compared with undoped and only N-doped ZnS, which can be verified by X-ray photoemission spectroscopy (XPS).

Next, we show the DOSs at N sites for ZnS:N in Fig. 2(a) and for ZnS:(2N, In) in Fig. 2(b) in order to illustrate what happens to the electronic structures, i.e., N-impurity states, near the top of the valence band upon In-codoping. They show that the impurity states at N sites change markedly from localized states, as presented in Fig. 2(a) for only N-doped ZnS, to delocalized states, as presented in Fig. 2(b) for p-type codoped ZnS. Based on the analysis of the DOS at the E_F for ZnS:N, we determined that the ratio of the partial DOS of p-states at the N sites to the total DOS at the E_F is 22%. The other DOS at the E_F is the sum of those at the S sites in the vicinity of the N sites. This indicates a small radius of the N-acceptor orbital. In other words, the Bohr radius of the N acceptors is very small, resulting in the high ionization energies due to the heavy effective mass of holes. In addition, the Madelung energy increased by 1.19 eV compared to undoped ZnS. We propose the following codoping method [7–9]: a deliberate codoping of the donors is essential for the delocalization of the impurity states at the acceptors and the stabilization of the ionic charge distributions in p-type highly doped semiconductors. The donor is not the p-type killer but a good by-player that activates acceptors, i.e., the reactive codopant.

From the calculations of the DOS at the E_F , we determined that the ratio of the sum of partial DOSs of p-states at the two N sites to the total DOS at the E_F is 9.2%; note that the partial DOSs not only at the S sites in the vicinity of the N sites but also at the more distant

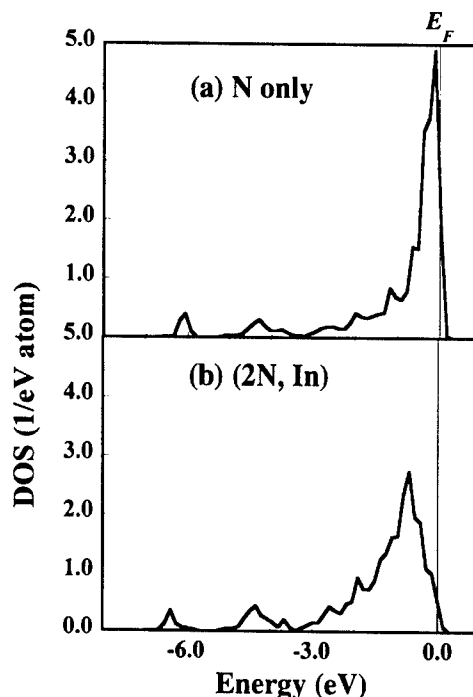


Fig. 2. Decomposed DOS at the N sites for (a) ZnS doped with N only and (b) ZnS codoped with In and 2N species. p states at the N sites are presented.

S sites contribute to the total DOS at the E_F for ZnS:(2N, In). The simultaneous codoping of In as the reactive codopant and N as the acceptor into ZnS causes a large radius of the N-acceptor orbital, resulting in the low effective mass of the hole, which is a consequence of the broadened impurity band. Considering the acceptor ionization energy given by hydrogenic calculations based on the Bohr theory, it is reasonable to predict that the N-acceptor ionization energy will decrease very well. This explains experimental data for the Hall measurement of ZnS:(Ag, In, and N) [5].

There remains one further factor concerning the effects of the In-codoping on ZnS:N that we need to consider. The Madelung energy of ZnS:(2N, In) decreased significantly by 30 eV compared with that for ZnS:N, which is due to a large charge transfer from In to N atoms. This decrease causes stabilization of the ionic charge distributions of the codoped materials according to the ionic picture. We verified the same effects of the codoping on the N-acceptor states for ZnS:(2N, Ga) as those discussed above for ZnS:(2N, In). Taking into consideration that the ZnS under investigation does not have a wurtzite structure, which is favored by more ionic compounds, but a zincblende structure, the optimum amount of In or Ga to be codoped must be determined by further experiments.

4. Conclusion

Simultaneous codoping using N as the acceptor and In as the reactive donor is very effective for the fabrication of low-resistivity p-type ZnS. The main role of In is to delocalize the N-impurity state by improving the incorporation of N species into ZnS. We propose a model for ZnS:(Ag, In, and N) in which some of the In species act as *coactivators* with Ag *activators* and other In species act as *reactive codopants* with N acceptors.

Acknowledgements

T. Y. thanks Dr. Jürgen Sticht for technical support. We used the ESOCS code of accelrys.

References

- [1] K. Era, S. Shionoya, Y. Washizawa, J. Phys. Chem. Solids 29 (1968) 1827.
- [2] K. Era, S. Shionoya, Y. Washizawa, H. Ohmatsu, J. Phys. Chem. Solids 29 (1968) 1843.
- [3] S. Iida, T. Yatabe, H. Kinto, Jpn. J. Appl. Phys. 28 (Part 2) (1989) L535.
- [4] S. Iida, T. Yatabe, H. Kinto, M. Shinohara, J. Crystal Growth 101 (1990) 141.
- [5] S. Kishimoto, T. Hasegawa, H. Kinto, O. Matsumoto, S. Iida, J. Crystal Growth 214/215 (2000) 556.
- [6] L. Svob, C. Thiandoume, A. Lusson, M. Bouanani, Y. Marfing, O. Gorochoy, Appl. Phys. Lett. 76 (2000) 1695.
- [7] T. Yamamoto, H. Katayama-Yoshida, Mater. Res. Soc. Proc. 426 (1996) 201.
- [8] T. Yamamoto, H. Katayama-Yoshida, Jpn. J. Appl. Phys. 36 (1997) L180.
- [9] T. Yamamoto, H. Katayama-Yoshida, Jpn. J. Appl. Phys. 38 (1999) L166.
- [10] W. Kohn, L.J. Sham, Phys. Rev. 140 (1965) A1133.
- [11] L. Hedin, B.I. Lundquist, J. Phys. C4 (1971) 3107.
- [12] U. von Barth, L. Hedin, J. Phys. C5 (1972) 1629.
- [13] A.R. Williams, J. Kübler, C.D. Gelatt, Phys. Rev. B19 (1979) 6094.



ELSEVIER

Physica B 308–310 (2001) 920–923

PHYSICA B

www.elsevier.com/locate/physb

Probing the shallow-donor muonium wave function in ZnO and CdS via transferred hyperfine interactions

J.S. Lord^a, S.P. Cottrell^a, P.J.C. King^a, H.V. Alberto^b, N. Ayres de Campos^b,
J.M. Gil^b, J. Piroto Duarte^b, R.C. Vilão^b, R.L. Lichti^c, S.K.L. Sjue^c,
B.A. Bailey^{c,f}, A. Weidinger^d, E.A. Davis^e, S.F.J. Cox^{a,f,*}

^aISIS Facility, Rutherford Appleton Laboratory, Chilton, Oxfordshire, OX11 0QX, UK

^bPhysics Department, University of Coimbra, P-3004 516 Coimbra, Portugal

^cDepartment of Physics, Texas Tech University, Lubbock, TX 79409-1051, USA

^dHahn-Meitner Institut Berlin, Glienickestrasse 100, D-14109 Berlin, Germany

^eDepartment of Physics and Astronomy, University of Leicester, Leicester LE1 7RH, UK

^fDepartment of Physics and Astronomy, University College London, London WC1E 6BT, UK

Abstract

The assignment of muon spin rotation spectra to muonium counterparts of hydrogen shallow-donor states is reviewed in four II–VI widegap semiconductors, CdS, CdSe, CdTe and ZnO. The existence of extended electronic orbitals is argued from the muon–electron hyperfine parameters and supported by the new muon spin repolarization data for CdS and ZnO, characterizing the superhyperfine parameters on the sparse Cd and Zn dipolar nuclei. The possibility of a more tightly bound electron occupying a compact orbital is reasonably excluded in these materials, contrasting with the muonium state in HgO. © 2001 Elsevier Science B.V. All rights reserved.

PACS: 71.55.Gs; 78.75.+i; 76.70.–r; 76.20.+q

Keywords: Hydrogen; Muonium; Shallow donors; ZnO; CdS

Muonium, the light pseudo-isotope of hydrogen, provides an experimentally accessible model for interstitial hydrogen in the II–VI compounds, as in other semiconductors. In these experiments, positive muons are implanted in the materials, where they are expected to adopt the same crystallographic sites as protons. In the Cd chalcogenides, and in ZnO, the implanted muons bind electrons weakly into a muonium state which has all the characteristics of a hydrogenic shallow donor [1–3]. The ZnO result is especially significant in that it confirms the theoretical prediction for protium [4]. Parameters characterizing the defect centres are given in Table 1. The muon–electron hyperfine parameters in these materials are exceedingly low, suggestive of an extended electron wave function. They were measured directly from the frequency splittings of the muon spin

rotation (μ SR) spectra in the Paschen–Back régime, i.e. in a magnetic field (applied transverse to the initial muon polarization) sufficient to decouple the muon and electron spins. The temperature dependences of the μ SR signals are also suggestive of ionization or dissociation of shallow-donor states: the activation energies deduced from the detailed temperature dependences of the signal amplitudes are fully consistent with estimates of these quantities in the effective-mass model.

Despite the overall consistency of this picture, the shallow-donor interpretation should be distinguished from a possible alternative model in which the electron wave function is more compact, but in which the spin density on the proton or muon is small due to some symmetry of the singly occupied orbital or special feature of the local bonding. Such a molecular–radical species would be tightly bound and unlikely to dissociate at cryogenic temperatures, but the disappearance of its

*Corresponding author. Fax: +44-1235-445477.

Table 1
Experimental hyperfine parameters and donor-level depths for the four shallow muonium states so far identified^a

	A_μ (kHz)	D_μ (kHz)	T_1 (K)	E_d^{exp} (meV)	E_d^{theo} (meV)
CdS	244 ± 5	91 ± 6	22 ± 2	26 ± 6	33
CdSe	87 ± 4	< 40	12 ± 2	20 ± 4	19
CdTe	261 ± 4	< 50	13 ± 2	16 ± 4	11
ZnO	500 ± 20	260 ± 20	38 ± 2	58 ± 6	52

^a The slightly anisotropic hyperfine interactions are expressed as isotropic (contact) and traceless (dipolar) components. The contact terms A_μ are four orders of magnitude smaller than the free-muonium hyperfine constant, which is isotropic and equal to 4.5 GHz. Donor depths are derived assuming equilibrium statistics; if the process involved is, in fact, direct ionization to the conduction band, the corresponding activation energies are about half these values. Shown for comparison are the shallow-donor depths calculated in the simple effective-mass model.

hyperfine signature might be attributed to spin-exchange depolarization, when extrinsic carriers are released by the ionization of other defects or impurities.

In this paper we present new information on the local electronic structure of the muonium states in ZnO and CdS, namely estimates of the transferred hyperfine interactions on surrounding nuclei. We refer to these as superhyperfine interactions, reserving the term hyperfine for the central muon, and probe them in these experiments by examining the muon response in low longitudinal fields, i.e. in magnetic fields applied parallel to the initial muon polarization. Host nuclei carrying a dipole moment are sparse in these materials but a measurement of how electron spin density is distributed over them would, in principle, allow a mapping of the wavefunction. In CdS, the relevant isotopes are ¹¹¹Cd and ¹¹³Cd, both with spin $\frac{1}{2}$ and a combined natural abundance of 25%. At below 1% abundance, ³³S can reasonably be neglected even though the muon may bond or antibond to S atoms. In ZnO, ⁶⁷Zn has spin $\frac{5}{2}$ and 4.1% abundance; no feature is likely to be observable in μ SR spectra from ¹⁷O in natural abundance although a study of samples enriched in this isotope would be worthwhile.

In Fig. 1, we show examples of the expectations of longitudinal-field measurements. The simulated quantity is muon polarization averaged over certain time windows and the field dependences are variously known as repolarization, decoupling or quenching curves. Fig. 1(a) is for ZnO and includes a simulation for muon–electron coupling alone (using the parameters of Table 1 from the transverse-field experiments). In this particular case, i.e. in the absence of nuclear superhyperfine couplings, it may be seen that the contact interaction is rapidly decoupled, in fields of order $A_\mu(2\pi/\gamma_e) = 0.02$ mT, and that the main feature is a level crossing resonance at a field close to $A_\mu(\pi/\gamma_\mu) = 1.8$ mT. The resonance occurs where the applied field “tunes out” the parallel hyperfine field, leaving the muon spin precessing around transverse components: an

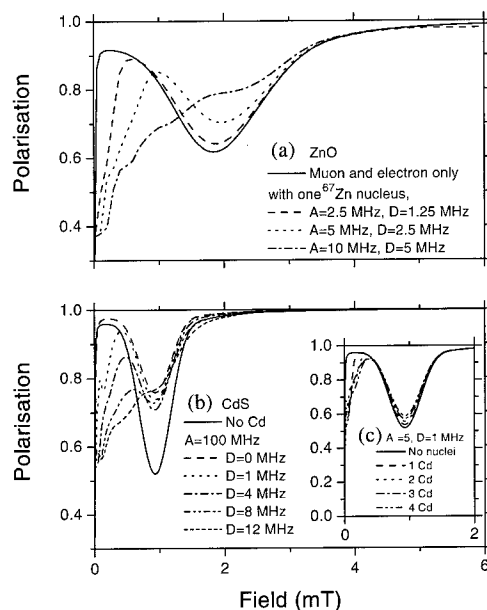


Fig. 1. Simulated muon spin repolarization curves for (a) ZnO and (b) CdS. The solid lines are in each case for the two-spin system of muon and electron only, using the hyperfine parameters as determined experimentally (Table 1). The broken lines are simulations including couplings to a third spin—⁶⁷Zn in (a) and ¹¹¹Cd in (b)—for various combinations of contact (A) and dipolar (D) superhyperfine couplings. The evolution of polarization is averaged over the time interval 0.8–8 μ s in (a) and 8–16 μ s in (b) for comparison with the experimental data of Fig. 2, where the level-crossing resonance is more prominent in the later time window. The inset to (b) shows an approximately \sqrt{N} dependence when more than one nuclear spin with identical coupling parameters are included.

oscillatory signal at the dipolar frequency is indeed visible in the time-domain signal at this field, confirming the parameters. Addition of superhyperfine interaction with, to begin with, a single ⁶⁷Zn nucleus, modifies both the strength of the resonance and the form the initial

repolarization. Simulations are shown for CdS in Fig. 1(b) and (c), where the corresponding level-crossing resonance falls around 0.9 mT. Varying the parameters independently, the strength of the resonance is found to be most sensitive to the nuclear contact interaction, up to a certain value beyond which there is no further suppression (roughly 100 MHz for CdS); the initial repolarization, on the other hand, is sensitive to both the dipolar component of nuclear coupling and to the number N of coupled nuclei, the decoupling field varying roughly as \sqrt{N} .

Experimental repolarization curves for comparison with these simulations are shown in Fig. 2. Here polarization is measured as usual via the muon decay asymmetry (a summary account is given in an accompanying paper [5]; these signals were recorded using the μ SR instrument at ISIS. Data for two different time windows are shown, indicating that the cross relaxation occurs on the timescale of several microseconds and that the hyperfine level-crossing resonance is more or less obscured by superhyperfine decoupling according to the time window and the relative strengths of the interactions in the two materials. Cross relaxation to the host nuclei is certainly mediated by the paramagnetic

electron, since measurements above the ionization temperature show close to maximum asymmetry throughout this field range. (That is, cross-relaxation due to purely nuclear–dipolar couplings in the diamagnetic or dissociated state is weak.) Below the ionization temperature it is apparent that the initial repolarization is more gradual than can be accounted for by the muon hyperfine parameters alone and that the form and strength of the level-crossing resonances, though visible, are greatly modified. The following conclusions can be drawn.

From the muon dipolar parameters D_μ in Table 1, we can state that major spin density (1 Bohr magneton) must either be localized at a distance greater than 1.5 nm from the muon in ZnO (and at even larger distances in the other materials) or else it must be distributed so that the dipolar term almost vanishes by symmetry. This already argues against a compact molecular radical comparable with bond-centred hydrogen or muonium in Si or GaAs, for which the (muonium) dipolar parameters are 51 and 86 MHz, respectively [6]. Such a compact state may well be formed in HgO, for which the hyperfine and ionization parameters are all quite large ($A_\mu = 15$ MHz, $D_\mu = 5$ MHz, $T_i = 150$ K, $E_d^{\text{exp}} = 300$ meV [7,8]) but we can reasonably exclude it for the materials of Table 1. For ZnO and CdS we can also state that all the muons which form paramagnetic centres are subject to the same superhyperfine interactions: there are not different components to the μ SR signals according to the isotopic abundance of near neighbours.

Pending simulations for a large number of coupled nuclei, with a distribution of coupling strengths, the following estimate of characteristic superhyperfine parameters may be made. We treat the electron spin density as distributed equally over N cations (spin density on the muon itself being so small). If the free-atom coupling for the cation in question is A_0 in frequency units and the isotopic abundance of the dipolar nuclei is c , there are cN interactions to be decoupled, each of A_0/N . The characteristic contact interaction to be decoupled may therefore be estimated as $\sqrt{cN}(A_0/N) = \sqrt{c/N}A_0$, and likewise for the dipolar parameter. We use the values of the atomic couplings given by Moreton and Preston [9]: $A_0 = 2087$ MHz for $4s(^{67}\text{Zn})$, 13650 MHz for $5s(^{111}\text{Cd})$. (The value for ^{113}Cd is not given by these authors, so we take it equal to that for ^{111}Cd ; dipolar parameters corresponding to occupation of the atomic p orbitals are not given for these elements.) Setting N equal to the number of cations contained within the effective Bohr radius of a hydrogenic shallow donor, we obtain parameters as in Table 2.

These values of $A_0\sqrt{c/N}$, the effective contact superhyperfine interactions to be decoupled, are not inconsistent with the repolarization curves of Fig. 2 if the accompanying dipolar parameters are about 5 MHz in ZnO and 10 MHz in CdS. The present model of

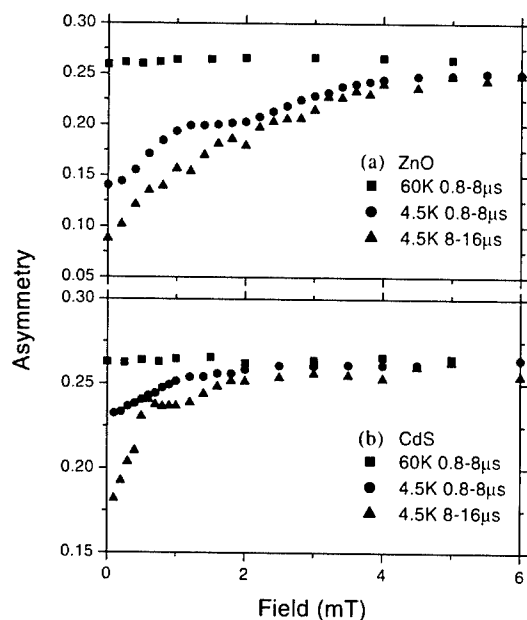


Fig. 2. Muon spin repolarization data for (a) ZnO and (b) CdS, for the temperatures and time windows indicated. The time evolution of muon polarization or relaxation function in response to Zeeman, hyperfine and superhyperfine interactions, is averaged over these time windows and expressed as muon decay asymmetry. According to the relative strengths of the various parameters, the level-crossing resonance due to the muon hyperfine interactions alone is more prominent in the early or late windows.

Table 2
Decoupling parameters as described in the text^a

	A_0 (MHz)	c	a^* (nm)	N	cN	A_0/N (MHz)	$A_0\sqrt{c/N}$ (MHz)
ZnO	2087	0.041	1.7	2000	80	1	10
CdS	13650	0.25	3.4	3000	750	5	100

^a a^* is the effective Bohr radius of hydrogenic shallow donors in these materials, calculated from electron effective mass and dielectric constant.

equivalent nuclear couplings is crude and these values may only indicate orders of magnitude. A more sophisticated treatment of the shallow-donor model would evidently involve simulating the muon response to a distribution of superhyperfine interactions. With individual couplings varying with radius according to a hydrogenic spin-density function $\rho(r) = \rho_0 \exp(-2r/a^*)$, the expected distribution has the form $P(\rho) \propto (\ln \rho)^2 / \rho$ (with limits $0 < \rho < \rho_0$). Our estimates of the typical couplings do suggest, however, that resonant cross-relaxation with the nearer nuclei (at fields given approximately by $(A_\mu - A_n)(\pi/(\gamma_{\text{mu}} - \gamma_n))$ [10]) may be accessible—the low isotopic abundance making these resolvable, if weak. Pending this more sophisticated treatment, and a search for these resonances, we can at least reasonably exclude a tightly bound and compact electronic orbital interacting with a small number of cation nuclei. The present data are more compatible with an extended electronic orbital.

Acknowledgements

This work was supported by EPSRC grant GR/R 25361 (UK) and by the POCTI Programme (FCT funding and Project POCTI/35334/FIS/2000, Portugal).

References

- [1] J.M. Gil, H.V. Alberto, R.C. Vilão, J. Piroto Duarte, P.J. Mendes, L.P. Ferreira, N. Ayres de Campos, A. Weidinger, J. Krauser, Ch. Niedermayer, S.F.J. Cox, Phys. Rev. Lett. 83 (1999) 5294.
- [2] S.F.J. Cox, E.A. Davis, S.P. Cottrell, P.J.C. King, J.S. Lord, J.M. Gil, H.V. Alberto, R.C. Vilão, J. Piroto Duarte, N. Ayres de Campos, A. Weidinger, R.L. Lichti, S.J.C. Irvine, Phys. Rev. Lett. 86 (2001) 2601.
- [3] J.M. Gil, H.V. Alberto, R.C. Vilão, J. Piroto Duarte, N. Ayres de Campos, A. Weidinger, J. Krauser, E.A. Davis, S.P. Cottrell, S.F.J. Cox, Phys. Rev. B 64 (2001) 075–205.
- [4] C.G. Van de Walle, Phys. Rev. Lett. 85 (2000) 1012.
- [5] P.J.C. King, I. Yonenaga, in these Proceedings (ICDS), Physica B 308–310 (2001).
- [6] S.F.J. Cox, M.C.R. Symons, Chem. Phys. Lett. 126 (1986) 516.
- [7] J.M. Gil, H.V. Alberto, R.C. Vilão, J. Piroto Duarte, N. Ayres de Campos, A. Weidinger, E.A. Davis, S.F.J. Cox, J. Phys.: Condens. Matter. 13 (2001) L613.
- [8] S.F.J. Cox, E.A. Davis, P.J.C. King, J.M. Gil, H.V. Alberto, R.C. Vilão, J. Piroto Duarte, N. Ayres de Campos, R.L. Lichti, J. Phys.: Condens. Matter. 13 (2001) 9001.
- [9] J.R. Morton, K.F. Preston, J. Magn. Reson. 30 (1978) 577.
- [10] R.F. Kiefl, et al., Phys. Rev. A 34 (1986) 681.



ELSEVIER

Physica B 308–310 (2001) 924–927

PHYSICA B

www.elsevier.com/locate/physb

Investigation of the defect structure in $\text{Cd}_{1-x}\text{Zn}_x\text{Te}$ by positron lifetime spectroscopy

M. Martyniuk, P. Mascher*

*Department of Engineering Physics, Centre for Electrophotonic Materials and Devices, McMaster University,
Hamilton, Ont., Canada L8S 4L7*

Abstract

Positron lifetime spectroscopy has been employed to explore grown-in defects in $\text{Cd}_{1-x}\text{Zn}_x\text{Te}$ (CZT) as a function of increasing Zn content. We find that with the increase of Zn content, both the average positron lifetime τ_{Avg} , and the lifetime in the bulk τ_{Bulk} , change smoothly from values typical for CdTe to those for ZnTe. In all samples, a defect-related lifetime component, τ_{D} , could be resolved with values decreasing from 347 ps in CdTe to 333 ps in ZnTe. This lifetime component is attributed to neutral $\text{Na}_{(\text{Cd,Zn})}\text{-V}_{\text{Te}}$ complexes in concentrations of around 10^{16} cm^{-3} , with a transition energy level below 0.19 eV above the valence band. It is established that these complexes are not connected to the p-type conductivity and their general characteristics are independent of the Zn content. This picture holds for stoichiometrically grown CZT and is independent of the growth method, whereas growth under Cd-rich conditions introduces a neutral impurity- V_{Te} complex with higher concentrations as compared to growth from stoichiometric conditions. © 2001 Elsevier Science B.V. All rights reserved.

Keywords: Cadmium zinc telluride; Defects; Positron annihilation spectroscopy

1. Introduction and experimental details

Certain characteristics of $\text{Cd}_{1-x}\text{Zn}_x\text{Te}$ (CZT) make this material an attractive choice for a variety of applications that stretch from X-, and γ -ray detectors to optoelectronic devices. Pre-existing native defects, however, appear to be the key reasons for its limited success to date. In this paper, we exploit positron lifetime spectroscopy (PLS) in an investigation aimed at exploring grown-in defects in CZT as a function of increasing Zn content, as well as the influence of growth conditions.

The series of samples used to study the influence of the Zn content were grown under stoichiometric conditions by the physical vapor transport technique (PVT) [1].

They exhibited p-type conductivity and consisted of CdTe, CZT ($x = 0.05, 0.10, 0.14, 0.15, 0.20$, and 0.25) and ZnTe. Two sets of samples were investigated: as-grown, exhibiting low resistivity, and annealed under cation overpressure, resulting in high resistivity. The values of various physical parameters are gathered in Table 1.

An additional three CZT ($x = 0.05$) samples, grown by the Bridgman method, were investigated to reveal the influence of the growth conditions. Two samples were grown under Cd-rich conditions; one was In doped ($[\text{In}] = 2 \times 10^{14} \text{ cm}^{-3}$), the other was undoped. The third sample was undoped and grown under stoichiometric conditions. PLS experiments were performed at temperatures between room temperature and 15 K. For details of the positron annihilation technique, the reader is referred to a recent comprehensive publication [2]. The details of the experimental set-ups as well as the data acquisition and analysis are given in Ref. [3].

*Corresponding author. Tel.: +1-905-525-9140 ext. 24963; fax: +1-905-527-8409.

E-mail address: mascher@mcmaster.ca (P. Mascher).

Table 1

Physical parameters of samples used to study the influence of the Zn content in CZT. Annealing was performed for 2–3 weeks under Cd overpressure at 720°C for CZT and under Zn overpressure at 820°C for ZnTe [1]

Physical parameter	CZT	ZnTe
<i>As-grown crystals ('low resistivity')</i>		
Etch pit density (cm ⁻²)	5×10^3 – 10^4	5×10^3 – 10^4
Resistivity (p-type) (Ωcm)	10 – 10^2	10 – 10^2
Free hole concentration (cm ⁻³)	10^{16}	10^{16}
<i>After annealing ('high resistivity')</i>		
Resistivity (Ωcm)	10^6 – 10^7	10^6 – 10^7
Free hole concentration (cm ⁻³)	$< 10^{14}$	$< 10^{14}$
Net acceptor concentration (cm ⁻³)	$< 10^{16}$	$< 10^{15}$

2. Results and discussion

2.1. Influence of Zn content in CZT

All of the obtained spectra required at least two lifetime components to be satisfactorily fitted and the one-defect-type trapping model [4] was utilized in the calculation of the annihilation parameters. Fig. 1 shows the positron average, τ_{Avg} , and bulk, τ_{Bulk} , lifetimes for low and high resistivity samples as a function of Zn content. Both parameters change smoothly from values typical for CdTe to those for ZnTe as the Zn content increases. τ_{Bulk} values are in agreement with previously published results [5–8] and theoretical predictions [9,10]. No significant difference was detected between the low and high resistivity CdTe and CZT ($x \leq 0.25$) samples. In the case of ZnTe, the τ_{Avg} values for the two ZnTe samples are significantly different suggesting different characteristics of the open volume defects in low resistivity ZnTe, as compared to high resistivity ZnTe.

A defect-related lifetime, τ_{D} , was resolved in all samples, indicating the presence of open volume defects

in significant concentrations. Its dependence on the Zn content is shown in Fig. 2a for both low and high resistivity samples. No significant difference was found in the values of τ_{D} before and after annealing, but there is a linear decreasing tendency with increasing Zn content from around 347 ps for CdTe to 333 ps for ZnTe. This change is directly linked to the change in the unit cell volume. Specifically, positrons 'see' a slightly smaller open volume as the lattice constant decreases with the increase in Zn content.

The ratio of the defect-related lifetime to the bulk lifetime, $\tau_{\text{D}}/\tau_{\text{Bulk}}$, can be used to estimate the size of the detected open volume. A ratio of less than 1.20 is typical for an open volume of a monovacancy, whereas a ratio of 1.3–1.5 is typically assigned to an open volume of a divacancy defect. In our case, $\tau_{\text{D}}/\tau_{\text{Bulk}}$ is between 1.20 and 1.25 for CdTe and ZnTe, respectively, for both resistivity cases (Fig. 2b). Its assignment to a mono- or a divacancy thus is somewhat uncertain, but favors a monovacancy-size open volume.

Identification of the detected defects as isolated intrinsic monovacancies can be ruled out with the help of the band diagram shown in Fig. 3, where defect

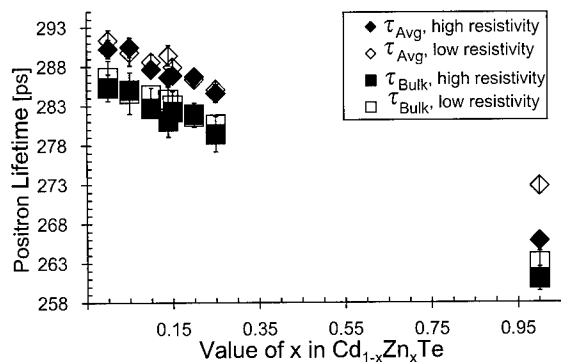


Fig. 1. Positron average and bulk lifetimes as a function of the Zn content measured in CZT.

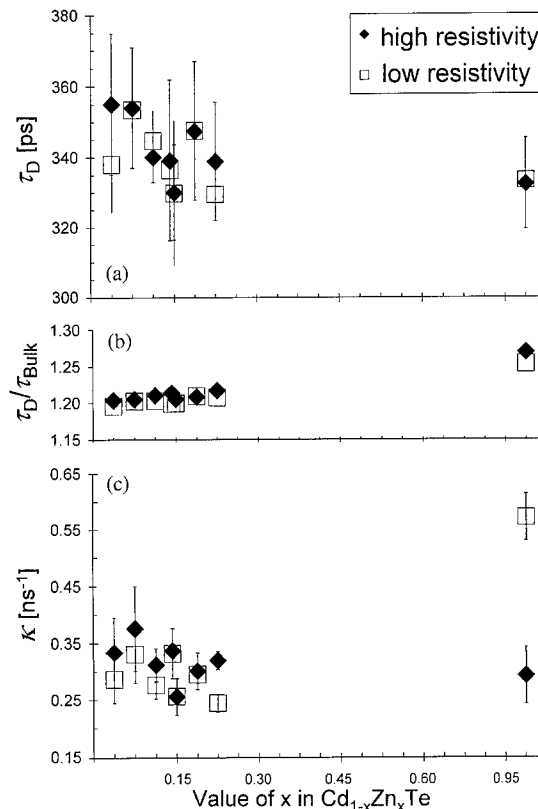


Fig. 2. Defect related lifetime (a), ratio of defect related lifetime to the bulk lifetime (b), and position trapping rate (c) as a function of the Zn content in CZT.

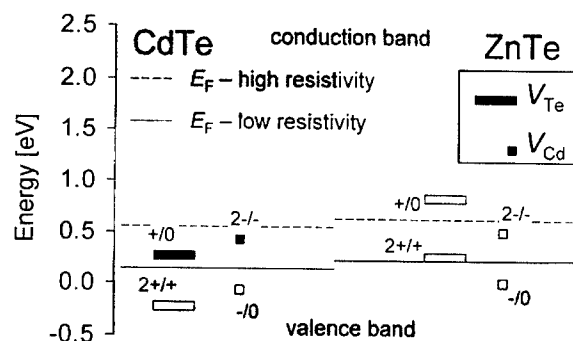


Fig. 3. Transition energy levels for isolated intrinsic anion, V_{Te} (—) and cation, $V_{(Cd,Zn)}$ (■) monovacancies in CdTe and ZnTe. Full symbols: experimental data; open symbols: experimentally not confirmed, based on chemical trends and theoretical predictions. Positions of the energy levels are shown to undergo a smooth transition in CZT with the increase in the Zn content [12]. Fermi levels for low and high resistivity samples are also indicated. The energy scale is relative to the top of the valence band in CdTe.

energy levels [12] are indicated. As a first step, we proceed with the elimination of positive vacancies (as they are not detectable with positron techniques), as well as the ones with energy levels in the valence band. This eliminates V_{Te}^+ , V_{Te}^{2+} , V_{Zn}^0 , and V_{Cd}^0 . Negative vacancies can be ruled out as none of the annihilation parameters exhibited any marked temperature dependence down to 15 K, indicating that the defects are electrically neutral in all the samples. Thus V_{Cd}^- , V_{Cd}^{2-} , V_{Zn}^- , and V_{Zn}^{2-} are ruled out. Consideration of the positions of the Fermi level, reported to be located at 0.19 eV and above 0.5 eV for low and high resistivity samples, respectively [1], eliminates V_{Te}^0 . If V_{Te} were present in our samples, it would be in its positive state in low resistivity samples and in the neutral state in high resistivity samples. This would result in very different behaviors of the annihilation parameters before (V_{Te}^+ not detected) and after (V_{Te}^0 'visible') annealing. Clearly, this hypothesis contradicts our results.

The amounts of the major contaminants (Na and K) in the source material (0.1–0.5 ppm) are high enough to be detectable by positron techniques, if associated with trapping centers. Na is a more likely candidate to play the role of the small atom discussed above, as its signature has been observed in these samples by photoluminescence [11]. Moreover, it is found as a contaminant by many crystal growers [12]. It is highly mobile and in our case it is reasonable to suppose that it will fill cation vacancies and pair up with V_{Te} . It is logical that V_{Te} instead of V_{Cd} should act as the unfilled vacancy. First of all, group I elements are more likely to fill group II rather than group VI vacancies, due to bond completion considerations. Furthermore, theoretical

analysis predicts similar τ_D/τ_{Bulk} ratios for cation vacancies in CdTe and ZnTe, whereas for V_{Te} it is to be significantly larger in ZnTe compared to CdTe [10]. The slightly larger τ_D/τ_{Bulk} ratio obtained for ZnTe than for CdTe (Fig. 2b) could be a manifestation of this prediction. The proposed defect complex would act as a single donor. To be in agreement with our results it must be in its neutral state. This puts the transition level below at most 0.19 eV (Fig. 3, the Fermi level position for low resistivity samples) above the valence band (or even in the valence band). Such a position of the defect level is quite likely if one considers the trends of vacancy related defects levels in the material system under discussion (Fig. 3).

Following the trapping model, the defect concentration can be determined from the trapping rate, κ (Fig. 2c). For CZT ($0 \leq x \leq 0.25$) we obtain a value of 0.3 ns^{-1} for both sample series. Using a trapping coefficient of $\sim 5 \times 10^{14} \text{ s}^{-1}$ we estimate the complex concentration to be around $2 \times 10^{16} \text{ cm}^{-3}$ for both the low and high resistivity cases. A distinct difference in κ , however, is observed between the low and high resistivity ZnTe samples. As a result of annealing, the concentration of the detected defects in ZnTe is reduced by 50% from $\sim 4 \times 10^{16} \text{ cm}^{-3}$ to $\sim 2 \times 10^{16} \text{ cm}^{-3}$.

Our results have shown no difference in the size (Fig. 2a and b) and concentration (Fig. 2c) of the monovacancies between low and high resistivity CdTe and CZT samples. The detected complex was unaffected by the performed temperature treatment. In ZnTe, however, annealing did reduce the concentration of the detected defect, but it is still present with a concentration of $\sim 10^{16} \text{ cm}^{-3}$. The reduction factor is at least two orders of magnitude too small to explain the reduction of the hole concentration upon annealing (Table 1). This is direct evidence that during annealing the detected defect complex does not take part in the process of increasing the resistivity, and is not connected to p-type conductivity.

2.2. Influence of growth conditions

Table 2 summarizes the results of our study on CZT ($x = 0.05$) grown under different conditions. As was the case in previous samples, low temperature measurements showed no temperature dependence from 15 K up to room temperature, indicating that we are still dealing with a neutral defect. It can be noticed that all of the positron annihilation parameters are in excellent agreement for samples grown from stoichiometric conditions. On this basis, we extend the above discussion and conclusions to undoped stoichiometrically grown CZT material.

The parameters obtained for Cd-rich grown CZT show that growth conditions significantly influence the

Table 2
Comparison of positron lifetime results for CZT ($x = 0.05$) grown under various conditions and/or methods

Growth conditions		Growth method	τ_{Avg} (ps)	τ_{Bulk} (ps)	τ_{D} (ps)	$\tau_{\text{D}}/\tau_{\text{Bulk}}$	κ (ns ⁻¹)	C (cm ⁻³)
Stoichiometric	Undoped	PVT	290 ± 2	285 ± 2	353 ± 16	1.24	0.31 ± 0.14	~2 × 10 ¹⁶
Stoichiometric	Undoped	PVT	290 ± 1	285 ± 1	354 ± 17	1.24	0.33 ± 0.11	~2 × 10 ¹⁶
Stoichiometric	Undoped	Bridgman	291 ± 1	286 ± 1	354 ± 12	1.24	0.26 ± 0.08	~2 × 10 ¹⁶
Cd-rich	Undoped	Bridgman	289 ± 1	284 ± 1	326 ± 8	1.15	0.56 ± 0.13	~4 × 10 ¹⁶
Cd-rich	[In] = 2 × 10 ¹⁴ cm ⁻³	Bridgman	288 ± 1	283 ± 1	330 ± 15	1.17	0.54 ± 0.19	~4 × 10 ¹⁶

end product. The $\tau_{\text{D}}/\tau_{\text{Bulk}}$ ratio clearly indicates that τ_{D} is related to a monovacancy. The value of τ_{D} is distinctively shorter than in the stoichiometric growth case, indicating that a defect of smaller open volume is dominant. It is generally accepted that Cd-rich growth does not produce V_{Cd} in significant concentrations. Rather, it will induce the presence of grown-in V_{Te} . It is reasonable that the open volume of V_{Te} is detected as a part of a neutral impurity complex. This picture is further supported by the observation that the obtained $\tau_{\text{D}}/\tau_{\text{Bulk}}$ ratio agrees more so with the theoretical predictions for V_{Te} rather than V_{cation} . The increase in κ , which reflects an increase in the defect concentration compared to stoichiometric growth, is also consistent with this picture, as more V_{Te} result from Cd-rich growth than from stoichiometric growth.

3. Conclusions

Electrically neutral defects were found in undoped, p-type CdTe, CZT, and ZnTe. Their general characteristics are independent of the Zn content. Isolated native monovacancies can be ruled out and a $(\text{Na}_{(\text{Cd}, \text{Zn})}-V_{\text{Te}})^0$ complex is proposed in concentrations of around 10¹⁶ cm⁻³, with a transition energy level below 0.19 eV above the valence band. The complex has been shown not to be connected to the p-type conductivity and is not affected by annealing under cation overpressure in CdTe and CZT ($x \leq 0.25$), but in ZnTe its concentration is reduced by a factor of two upon annealing.

Both stoichiometric and Cd-rich growth conditions result in grown-in neutral impurity- V_{Te} defect complexes. Cd-rich growth results in smaller open volumes with increased defect concentration as compared to stoichiometric growth.

Acknowledgements

This work was supported by the Natural Sciences and Engineering Research Council of Canada (NSERC). We wish to thank Dr. M. Sochynskyi for the samples grown under Cd-rich conditions.

References

- [1] A. Mycielski, et al., *Proc. SPIE* 3724 (1999) 10.
- [2] R. Krause-Rehberg, H.S. Leipner, *Positron Annihilation in Semiconductors*, Springer, Berlin, 1999.
- [3] G. Tessaro, P. Mascher, *Mater. Sci. Forum* 258–263 (1997) 1335.
- [4] R.N. West, *Adv. Phys.* 22 (1973) 66.
- [5] R. Pareja, R.M. de la Cruz, *Phys. Stat. Sol. B* 178 (1993) K23.
- [6] C. Corbel, et al., *Mat. Sci. Eng. B* 16 (1993) 134.
- [7] G. Tessaro, P. Mascher, *J. Cryst. Growth* 197 (1999) 581.
- [8] S. Brunner, Ph.D. Thesis, Technischen Universität Graz, 2000.
- [9] M.J. Puska, et al., *Phys. Rev. B* 39 (1989) 7666.
- [10] F. Plazaola, et al., *J. Phys.: Condens. Matter* 6 (1994) 8809.
- [11] B.K. Meyer, W. Stadler, *J. Cryst. Growth* 161 (1996) 119.
- [12] C. Szeles, private communication, 2000.



ELSEVIER

Physica B 308 310 (2001) 928–931

PHYSICA B

www.elsevier.com/locate/physb

Influence of the molecular spin–orbit interaction on the orbital triplet levels 4T_1 and 4T_2 of Mn^{2+} in ZnS

R. Parrot^{a,*}, D. Boulanger^b

^a *Institut Universitaire de Formation des Maîtres et Faculté de Technologie de la Guyane, Université des Antilles Guyane, BP 792, 97337 Cayenne Cedex, Guyane Française, French Guiana*

^b *Université de Paris-Sud, Laboratoire d'Informatique, Maîtrise de Sciences Physiques, Bâtiment 479, F-91405 Orsay Cedex, France*

Abstract

An extended cluster model is used to calculate the first-order spin–orbit (SO) interaction for levels 4T_1 (G, P and F) and 4T_2 (G, D and F) of Mn^{2+} in ZnS. The first-order SO interaction is analyzed by using the molecular SO interaction which involves the SO coupling constants of the electrons of the cation and of the ligands. The most striking effect of the molecular SO interaction is obtained for the fluorescent level 4T_1 (G). For this level, it is shown that, with respect to the results of the crystal-field (CF) model, the first-order SO interaction is roughly reduced by an order of magnitude. For the level 4T_1 (P), it is shown that the first-order SO interaction increases with respect to the results of the CF model, but strongly depends on the mixing parameters of the states 4T_1 . For levels 4T_1 (F) and 4T_2 (G, D and F), it is shown that the first-order SO interaction is reduced by a factor of 0.5–0.7 with respect to the results of the CF model. © 2001 Elsevier Science B.V. All rights reserved.

Keywords: II–VI compounds; Impurities; Optical energy levels; Iron group ions

1. Introduction

The fine structure of the optical energy levels of d^5 ions, as Mn^{2+} and Fe^{3+} , has been studied in numerous II–VI and III–V compounds [1–13]. For example, the energy levels of Fe^{3+} have been studied in ZnS [1], ZnO [2], GaAs [3,4], GaN [5], and InP [6]. The fluorescent level and the levels at higher energy of Mn^{2+} have been studied in cubic and axial ZnS [7,8], in ZnSe [9–11], ZnTe [12], and also in GaP [13].

The fine structure of the fluorescent level 4T_1 (G) of Mn^{2+} in cubic symmetry as in cubic ZnS, ZnSe and GaP has long been interpreted by considering a strong Jahn–Teller (JT) reduction (corresponding to a Huang–Rhys factor S of approximately 2) of the spin–orbit (SO) interaction as given by the CF-model [14–16]. First, this model failed to account for the fine structure of the levels 4T_2 (G) of Mn^{2+} in ZnS and in ZnSe [17,18].

Second, the previous interpretation of the fine structure of the fluorescent level 4T_1 (G) of Mn^{2+} in cubic ZnS has recently been questioned [19,20]. Very surprisingly, a careful analysis of the fine structure lines led us to consider that the first-order SO interaction should be very strongly reduced with respect to that given by the CF-model.

The aim of this paper is to compare the molecular SO interaction for the orbital triplet levels 4T_1 (P), 4T_1 (F), and 4T_2 (G), 4T_2 (D), 4T_2 (F) of Mn^{2+} in ZnS to the SO interaction restricted to electrons d of the configuration d^5 following the CF-model of Sugano et al. [21].

2. Molecular orbitals and molecular spin–orbit interaction in orbital triplet states

In the proposed molecular model for the tetrahedral MnS_4 cluster, the mono-electronic molecular orbitals $4t_2$ and $2e$ of the half-filled shell are written in terms of the mono-electronic orbitals of the electrons $3d$ and $4p$ of the cation, and in terms of the orbitals σ_s , σ_p , and πp

*Corresponding author. Tel.: +594-29-62-00; fax: +594-29-62-10.

E-mail address: robert.parrot@libertysurf.fr (R. Parrot).

of the ligands as:

$$|t_2\gamma\rangle = a^d|dt_2\gamma\rangle + a^p|pt_2\gamma\rangle + a^{s^s}|st_2\gamma\rangle \\ + a^{\sigma p}|\sigma pt_2\gamma\rangle + a^{\pi p}|\pi pt_2\gamma\rangle,$$

where $\gamma = \xi, \eta$ or ζ refers to the components of the molecular monoelectronic level $4t_2$, and

$$|e\gamma'\rangle = b^d|de\gamma'\rangle + b^{\pi p}|\pi pe\gamma'\rangle,$$

where $\gamma' = \theta$ or ε refers to the components of the molecular monoelectronic level $2e$.

The first-order SO interaction is calculated by using the molecular SO interaction H_{SOM} defined by Misetich and Buch [22]:

$$H_{\text{SOM}} = \sum_q \sum_i \tau_u^i s_q^i,$$

where τ_u^i is the molecular angular momentum of electron i and where s_q^i are the complex components of the spin operators. $u = x$ or y if $q = \pm 1$ and $u = z$ if $q = 0$.

The relevant matrix elements $\zeta_{et_2} = (i/2)\langle e|\tau_z|t_2\zeta\rangle$ and $\zeta_{t_2t_2} = -i\langle t_2\zeta|\tau_z|t_2\eta\rangle$ are given in terms of the mixing coefficients of the monoelectronic wave functions and of the SO constants of the metal and of the ligands by

$$\zeta_{et_2} = a^d b^d \zeta_M + [1/(2\sqrt{3})]b^{\pi p}(a^{\pi p} + a^{\sigma p}\sqrt{2})\zeta_L$$

and

$$\zeta_{t_2t_2} = (a^d a^d - a^p a^p)\zeta_M + a^{\pi p}(a^{\sigma p}\sqrt{2} - a^{\pi p}/2)\zeta_L.$$

3. First-order molecular so interaction for levels ${}^4T_1(\text{G, P, F})$ and ${}^4T_2(\text{G, D, F})$ of Mn^{2+} in ZnS

For the calculation of the molecular orbitals, the interatomic distance Mn–S of 4.56 a.u. is chosen to be slightly greater than the interatomic distance Zn–S of 4.41 a.u. to account for a slightly greater covalent radius of Mn than of Zn. The effective charge of manganese is $Q_{\text{Mn}} = 0.973$, the effective charge of the lattice is $Q_{\text{lat}} = +0.80$ and $Dq = -420 \text{ cm}^{-1}$.

The calculated monoelectronic wave functions are:

$$|4t_2\gamma\rangle = 0.898|dt_2\gamma\rangle - 0.132|pt_2\gamma\rangle - 0.120|st_2\gamma\rangle \\ + 0.464|\sigma pt_2\gamma\rangle - 0.364|\pi pt_2\gamma\rangle$$

and

$$|2e\gamma'\rangle = 0.863|de\gamma'\rangle - 0.611|\pi pe\gamma'\rangle.$$

It can be noted that the monoelectronic wave functions $|4t_2\gamma\rangle$ are strongly coupled to the wave functions $|dt_2\gamma\rangle$, $|\sigma pt_2\gamma\rangle$, and $|\pi pt_2\gamma\rangle$, and that the coupling to the wave functions $|pt_2\gamma\rangle$ and $|st_2\gamma\rangle$ is relatively small. The wave functions $|2e\gamma'\rangle$ are strongly coupled to the wave functions $|de\gamma'\rangle$ and $|\pi pe\gamma'\rangle$. These values for the coupling coefficients of the

monoelectronic wave functions are in agreement with those obtained in covalent models for Mn in tetrahedral molecules [23,24].

The SO coupling constants of the electrons 3d of the cation and 3p of the ligands, are obtained by interpolating the SO coupling constants given by Blume and Watson [25] for various ionization states of the atoms. Explicitly (all values are in cm^{-1}) we get: $\zeta_{\text{Mn}} = 286 + 47(Q_{\text{Mn}} - 1)$ and $\zeta_{\text{L}}(\text{S}) = 298 + 65(Q_{\text{L}} + 1)$. From the effective charges given above, we get: $\zeta_{\text{Mn}} = 285 \text{ cm}^{-1}$ and $\zeta_{\text{L}} = 308 \text{ cm}^{-1}$ for the electrons p of sulfur.

It is now possible to compare the matrix elements ζ_{et_2} and $\zeta_{t_2t_2}$ as given by the covalent and the CF-model. For ζ_{et_2} , the contribution of the term in ζ_{M} is of 220 cm^{-1} in the covalent model while it is of 300 cm^{-1} for the CF-model. (In the CF-model, we have $\zeta_{t_2t_2} = \zeta_{et_2} = \zeta_{\text{M}}$, with $\zeta_{\text{M}} = \zeta_{3d} = 300 \text{ cm}^{-1}$). In the covalent model, the contribution of the term in ζ_{L} , due to two terms of opposite signs, is of 15 cm^{-1} only, so that the contribution of the ligands is almost negligible. Finally, with respect to the CF-model, the strong reduction of ζ_{et_2} is primarily due to the mixing of the orbitals d of the cation with the orbitals of the ligands.

For $\zeta_{t_2t_2}$, the contribution of the terms in ζ_{M} and ζ_{L} are of 224.8 and -94 cm^{-1} respectively. For the term in ζ_{M} , the contribution involving the orbitals p is very small, so that the contributions of the cation to $\zeta_{t_2t_2}$ and ζ_{et_2} are almost identical. For the term in ζ_{L} , the contributions of the ligands πp and σp are both negative so that their overall contribution is relatively large.

Then, the orbital triplet states $|{}^4T_1\rangle$ and $|{}^4T_2\rangle$ are built from the configurations $4t_3^2e$, $4t_3^2e^2$, and $4t_3^2e^3$, by diagonalizing the matrix of Sugano et al. [21]. The mixing parameters for the states $|{}^4T_1\rangle$ and $|{}^4T_2\rangle$ are given for two sets of values for the Racah parameters B, C, and from the cubic field coefficient Dq . For the first set, we have: $B = 730 \text{ cm}^{-1}$, $C = 2880 \text{ cm}^{-1}$, and $Dq = -420 \text{ cm}^{-1}$ [26]. For the second set, we have: $B = 630 \text{ cm}^{-1}$, $C = 3040 \text{ cm}^{-1}$, and $Dq = -540 \text{ cm}^{-1}$ [27]. The results are summarized in Table 1. This table shows that for the states $|{}^4T_1\rangle$, some mixing parameters differ at most by roughly 10–15% depending on the chosen set of parameters. For the states $|{}^4T_2\rangle$, it can be noted that the mixing parameters for the state $|{}^4T_2(\text{G})\rangle$ are of opposite sign and that some mixing coefficients differ by roughly 10–20%.

The first-order SO interaction for the orbital triplet levels can be described by the equivalent operator $\chi_1 \mathbf{l} \cdot \mathbf{S}$ with $l = 1$ and $S = 3/2$. By using the mixing parameters for the triplet states $|{}^4T_1\rangle$ and $|{}^4T_2\rangle$, we obtain χ_1 in terms of a linear combination $\alpha\zeta_{t_2t_2} + \beta\zeta_{et_2}$ of the matrix elements $\zeta_{t_2t_2}$ and ζ_{et_2} . The values for α and β are given for the six levels considered and for the two sets of parameters in Table 1. The values for χ_1 as given by the proposed molecular model and by the CF-model are given in Table 2 for the six studied levels.

Table 1

Values for the coefficients α , β defined in Section 3 and wave functions for the states 4T_1 and 4T_2 of Mn in ZnS. The wave functions are linear combinations of the form: $a_1 4t_{3/2}^2 e^2 + a_2 4t_{3/2}^2 e^2 + a_3 4t_{3/2}^2 e^3$. The values are given for two sets of parameters B , C , and Dq . Set 1: $B = 730 \text{ cm}^{-1}$, $C = 2880 \text{ cm}^{-1}$, and $Dq = -420$. Set 2: $B = 630 \text{ cm}^{-1}$, $C = 3040 \text{ cm}^{-1}$, and $Dq = -540 \text{ cm}^{-1}$. The energies are in cm^{-1} .

Level	B, C, Dq	a_1	a_2	a_3	α	β
${}^4T_1(\text{G})$	Set 1	-0.2393	-0.1501	0.9593	0.1438	-0.0848
	Set 2	-0.2183	-0.1320	0.9669	0.1479	-0.0737
${}^4T_1(\text{P})$	Set 1	0.8659	-0.4799	0.1409	-0.7300	0.9842
	Set 2	0.8315	-0.5439	0.1134	-0.6785	1.1045
${}^4T_1(\text{F})$	Set 1	0.4392	0.8644	0.2448	-0.1330	-0.4752
	Set 2	0.5109	0.8287	0.2285	-0.2048	-0.6621
${}^4T_2(\text{G})$	Set 1	0.3684	0.6620	-0.6527	0.2902	-0.9219
	Set 2	-0.3455	-0.5690	0.7462	0.4375	-1.1171
${}^4T_2(\text{D})$	Set 1	-0.2566	0.7472	0.6131	0.3100	1.3046
	Set 2	-0.1726	0.8202	0.5455	0.2678	1.4982
${}^4T_2(\text{F})$	Set 1	0.8935	-0.0584	0.4452	-0.6002	-0.3828
	Set 2	0.9224	-0.0597	0.3816	-0.7053	-0.3811

Table 2

First-order spin-orbit interaction for the levels ${}^4T_1(\text{G})$, ${}^4T_1(\text{P})$, ${}^4T_1(\text{F})$, and ${}^4T_2(\text{G})$, ${}^4T_2(\text{D})$, ${}^4T_2(\text{F})$. The values for χ_1 are obtained from the CF-model and from the molecular model (M-model). The two sets of values, as given in Table 1, for B , C , and Dq have been used. For the CF-model, the calculations have been performed by taking: $\zeta(t_2, t_2) = \zeta(e, t_2) = 300 \text{ cm}^{-1}$. For the M-model, we have used: $\zeta(t_2, t_2) = 131 \text{ cm}^{-1}$ and $\zeta(e, t_2) = 205 \text{ cm}^{-1}$. The matrix elements $\zeta(t_2, t_2)$ and $\zeta(e, t_2)$ are defined in Section 2

4T_1	B, C, Dq	$\chi_1({}^4\text{G})$	$\chi_1({}^4\text{P})$	$\chi_1({}^4\text{F})$
CF-model	Set 1	17.70	12.70	-30.40
	Set 2	22.24	21.30	-43.54
M-model	Set 1	1.42	17.71	-19.13
	Set 2	4.22	22.94	-27.17
4T_2	B, C, Dq	$\chi_1({}^4\text{G})$	$\chi_1({}^4\text{D})$	$\chi_1({}^4\text{F})$
CF-model	Set 1	-31.58	80.73	-49.14
	Set 2	-34.00	88.30	-54.30
M-model	Set 1	-25.17	51.33	-26.16
	Set 2	-28.63	57.02	-28.39

Table 2 shows that for the levels 4T_1 , $\chi_1({}^4T_1\text{G})$ is very strongly reduced with respect to the value $\chi_{1\text{CF}}$ of 17.7 cm^{-1} as deduced from the CF-model (by taking $\zeta_{3d} = 300 \text{ cm}^{-1}$), this is due to the fact that χ_1 depends on two terms having approximately the same magnitude and opposite signs. For $\chi_1({}^4T_1\text{P})$, the values given by the molecular model for the set 1 are much greater than those given by the CF-model, while for the set 2, the values are almost identical. It can be noted that for $\chi_1({}^4T_1\text{P})$, the values given by the CF-model strongly depend on the set of parameters B , C , and Dq . For $\chi_1({}^4T_1\text{F})$, the values given by the covalent model are two-thirds of the values of the CF-model.

For the levels 4T_2 , all values of χ_1 as given by the molecular model are reduced with respect to the values of the CF-model. For example, for the set 1, the

reduction factors are of 16–20% for $\chi_1({}^4T_2\text{G})$, 35–36% for $\chi_1({}^4T_2\text{D})$, and 47–48% for $\chi_1({}^4T_2\text{F})$.

4. Conclusion

By analyzing in detail the molecular model for the SO interaction, it has been shown that the first-order molecular SO interaction described by the term $\chi_1 \mathbf{L} \cdot \mathbf{S}$ can be decomposed into three contributions. The first one is due to the mixing of the mono-electronic wave functions, the second depends on the SO coupling constants of the relevant electrons of the cation and of the ligands, and the last is due to the mixing coefficients of the orbital triplet states. It has been

shown that for the studied orbital triplet levels of Mn^{2+} in ZnS, all contributions are of importance.

References

- [1] A. Hoffmann, R. Heitz, I. Broser, *Phys. Rev. B* 41 (1990) 5806.
- [2] R. Heitz, A. Hoffmann, I. Broser, *Phys. Rev. B* 45 (1992) 8977.
- [3] K. Pressel, G. Bohnert, G. Rückert, A. Dörnen, K. Thonke, *J. Appl. Phys.* 71 (1992) 5703.
- [4] K. Pressel, G. Ruckert, A. Dornen, K. Thonke, *Phys. Rev. B* 46 (1992) 13171.
- [5] R. Heitz, P. Thurian, I. Loa, L. Eckey, A. Hoffmann, I. Broser, K. Pressel, B.K. Meyer, E.N. Mokhov, *Appl. Phys. Letter* 67 (1995) 2822.
- [6] K. Pressel, G. Bohnert, A. Dörnen, B. Kaufmann, J. Denzel, K. Thonke, *Phys. Rev. B* 47 (1993) 9411.
- [7] W. Busse, H.E. Gumlich, A. Geoffroy, R. Parrot, *Phys. Stat. Sol. B* 93 (1979) 531.
- [8] W. Busse, H.E. Gumlich, W. Knack, J. Schulze, *J. Phys. Soc. Japan* 49 (1980) 581.
- [9] H.E. Gumlich, private communication.
- [10] J. Leslie, J.W. Allen, *Phys. Stat. Sol. A* 65 (1981) 545.
- [11] S.G. Ayling, J.W. Allen, *J. Phys. C* 20 (1987) 4251.
- [12] W. Gebhardt, private communication.
- [13] A.T. Vink, G.G.P. Van Gorkom, *J. Lumin.* 5 (1972) 379.
- [14] P. Koidl, *Phys. Stat. Sol.* 74 (1976) 477.
- [15] R. Parrot, C. Naud, C. Porte, D. Fournier, A.C. Boccara, J.C. Rivoal, *Phys. Rev. B* 17 (3) (1978) 1057.
- [16] G. Hofman, F.G. Anderson, J. Weber, *Phys. Rev. B* 43 (2) (1991) 9711.
- [17] R. Parrot, C. Naud, F. Gendron, *Phys. Rev. B* 13 (9) (1976) 3748.
- [18] R. Parrot, D. Boulanger, *Phys. Stat. Sol. B* 207 (1998) 113.
- [19] R. Parrot, D. Boulanger, M.N. Diarra, U.W. Pohl, B. Litzenburger, H.E. Gumlich, *Phys. Rev. B* 54 (1996) 1662.
- [20] R. Parrot, D. Boulanger, M.N. Diarra, U.W. Pohl, B. Litzenburger, H.E. Gumlich, *Phys. Rev. B* 58 (1998) 12567.
- [21] S. Sugano, Y. Tanabe, H. Kamimura, in: *Multiplets of Transition Metal Ions in Crystals*, Academic, New York, 1970.
- [22] A.A. Missetich, T. Buch, *J. Chem. Phys.* 42 (1964) 2524.
- [23] L.D. Kandel, M.C.G. Passegi, T. Buch, *J. Phys. Chem. Solids* 30 (1968) 321.
- [24] T. Buch, A. Gelineau, *Phys. Rev. B* 4 (1971) 1444.
- [25] M. Blume, R.E. Watson, *Proc. Roy. Soc. London Ser. A* 271 (1963) 565.
- [26] R. Parrot, C. Blanchard, *Phys. Rev. B* 6 (1972) 3992.
- [27] T. Kushida, Y. Tanaka, Y. Oka, *J. Phys. Soc. (Japan)* 37 (1974) 1341.



ELSEVIER

Physica B 308–310 (2001) 932–934

PHYSICA B

www.elsevier.com/locate/physb

High temperature electrical conductivity of undoped ZnS

K. Lott^{a,*}, L. Türn^a, O. Volobujeva^a, M. Leskelä^b^aDepartment of Chemistry, Institute of Basic and Applied Chemistry, Tallinn Technical University, Ehitajate tee 5, 19086 Tallinn, Estonia^bDepartment of Chemistry, University of Helsinki, FIN-00014, P.O. Box 55, AI Virtasenaukio I, Helsinki, Finland

Abstract

High temperature defect equilibrium (HTDE) in ZnS was analysed to study the conditions of making p-type material. High temperature electrical conductivity (HTEC) under defined component vapour pressure was investigated in undoped ZnS in the temperature range from 600 °C to 1140 °C. HTEC measurements were carried out using a two-zone resistance furnace and a vacuum sealed quartz ampoule with four sealed tungsten or graphite electrodes. All ZnS HTEC isotherms can be divided into three regions. The high zinc vapour pressure (p_{Zn}) and the high sulphur vapour pressure (p_{S_2}) regions are characterized by dominant native donors. In the ZnS HTDE model, antistructure disorder is dominating at high p_{S_2} values, similar to CdS and CdTe HTDE models. Changes occur at low p_{Zn} or at low p_{S_2} values. The increase of HTEC at low p_{Zn} or at low p_{S_2} values is explained by the existence of the p-type area in this region. This p-type area appears in the total range of temperature investigated. © 2001 Elsevier Science B.V. All rights reserved.

Keywords: Zinc sulphide; Electrical conductivity; Defects

1. Introduction

The physical properties of ZnS depend on the properties of point defects. The concentration of native and impurity defects in turn depends on the conditions of preparation and the presence of dopants. Although the room-temperature properties are of interest, the initial defect structure is formed usually at much higher temperatures during crystal growth or annealing, when the high temperature defect equilibrium (HTDE) is established. Our study within high temperature electrical conductivity (HTEC) in undoped and in doped ZnS has been in progress for several years [1–3]. Our earlier work [1] on HTEC in the additive coloration region of ZnS did not concern the phase transition (PT) region. HTEC measurements in ZnS are complicated because of the multiphase origin of ZnS. We found that adequate measurements for determination of HTEC isotherms and isobars without PT confusion can be performed at

temperatures over 1070 °C. At lower temperatures, the effects of PT on HTEC must be taken into account [2]. On the basis of HTEC measurements under zinc vapour pressure (p_{Zn}) we could not explain the HTEC isotherm behaviour at low p_{Zn} values [3]. In the present work, the results of HTEC isotherm and isobar measurements are performed both under p_{Zn} as under sulphur vapour pressure (p_{S_2}) and at large ZnS crystal temperature range.

2. Experimental procedure

HTEC isotherms and isobars were measured in undoped ZnS single crystals, grown by the Bridgman vertical method. The concentration of residual impurities was no more than 10^{16} cm^{-3} . HTEC measurements were carried out using a two-zone resistance furnace and a vacuum sealed two-zone quartz ampoule with four sealed tungsten or graphite electrodes. The HTEC σ was measured as a function of sample temperature T and the partial pressures p_{Zn} or p_{S_2} . The component vapour

*Corresponding author. Tel.: +372-055-697-882; fax: +372-620-2020.

E-mail address: klott@edu.ttu.ee (K. Lott).

pressure (p_{comp}) (p_{Zn} or p_{S_2}) was maintained by controlling the temperature of the reservoir of zinc or sulphur. In all cases, the ampoule was placed in a quartz furnace tube, which was evacuated to 10^{-2} Pa or fulfilled by inert gases. The HTEC experiments within ZnS led us to a power dependence of electron concentration n , on p_{comp} and temperature T as $n \sim p_{\text{comp}}^{\alpha} \exp(-\Delta E/kT)$. Our attempts to measure Hall effect in ZnS at high temperatures were not very successful because of low free carrier mobility values. The sign of Hall coefficient indicates that the conductivity is n-type. The $T^{-3/2}$ dependence of mobility [4] is taken into account by the factor $T^{+3/2}$, so that the conductivity $\sigma T^{+3/2}$ is proportional to the free carrier concentration.

3. Results and discussion

3.1. HTEC isotherms of undoped ZnS

HTEC isotherms of undoped ZnS, measured under p_{Zn} and under p_{S_2} are shown in Figs. 1 and 2. The plots in Fig. 1 can be divided into two regions. If the dependence of the HTEC σ on p_{comp} in Fig. 1 is expressed as $\sigma \sim p_{\text{comp}}^{\alpha}$, then at high p_{Zn} , $\alpha > 0$ and at low p_{Zn} side $\alpha < 0$. The $\alpha = 0$ values shift systematically towards higher p_{Zn} values with increasing the temperature of the crystal. At congruent sublimation, component vapour pressures upon ZnS in equilibrium are calculated from $K_{\text{ZnS}} = p_{\text{Zn}} p_{\text{S}_2}^{1/2}$ values [5]. Unexpected results were obtained in HTEC measurements under sulphur pressures. The absolute value of HTEC in the p_{S_2} region is more than one order of magnitude higher than in the p_{Zn} region. The slopes α in Fig. 2 are not constant in a large range of p_{comp} and varied between 0.1

and 0.4 under high p_{S_2} (p_{S_2} values in Fig. 2 are translated into p_{Zn} values through K_{ZnS} values). It is characteristic that at low p_{S_2} the sign of α is reversed. Between the two conductivity minimums in Figs. 1 and 2, there exists an area of increased conductivity. This region may be characterized as the p-type or bipolar conductivity area. No Hall voltage was measured in this region because of low mobility of holes. Similarly, increasing role of holes at low p_{S_2} and at low p_{Cd} has been observed in CdS [6].

3.2. HTEC isobars of undoped ZnS

HTDE isobars measured under p_{Zn} and under p_{S_2} are shown in Figs. 3 and 4. The step-like changes, caused by PT below 1070°C [2], are eliminated by using only

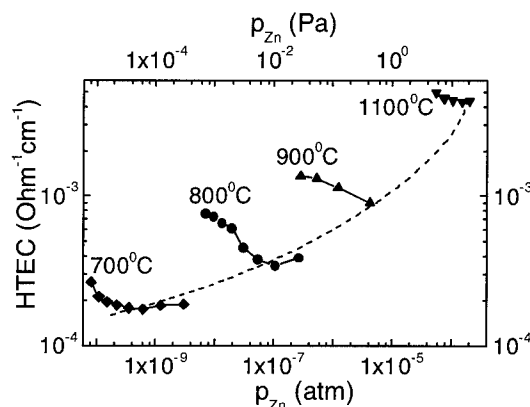


Fig. 2. HTEC isotherms of undoped ZnS, measured at the p_{S_2} side. p_{S_2} is expressed by p_{Zn} using K_{ZnS} [5]. The dashed line connects minimum values of the conductivity.

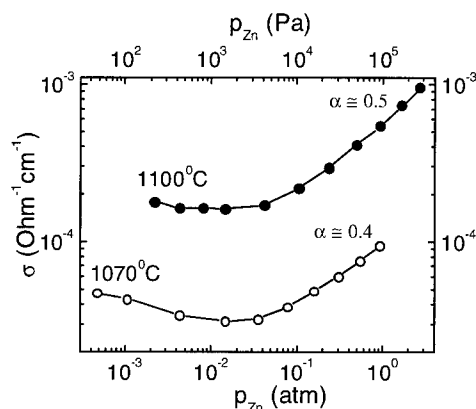


Fig. 1. HTEC isotherms of undoped ZnS, measured at the p_{Zn} side and at temperatures over the PT temperature. Under Zn saturated conditions, the α values are: $\alpha \approx 0.5$ at 1100°C and $\alpha \approx 0.4$ at 1070°C .

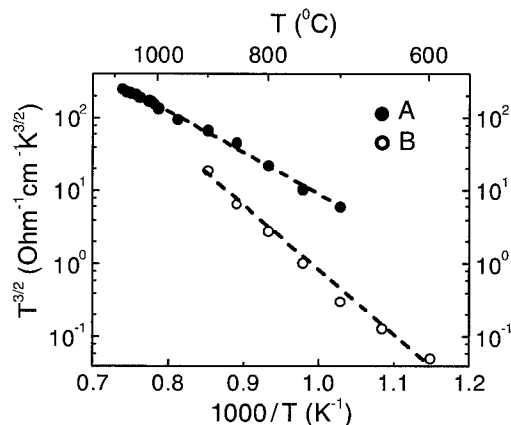


Fig. 3. HTEC isobars of undoped ZnS, measured at the p_{S_2} side. The HTEC isobar activation energies at different p_{comp} : (A) $p_{\text{S}_2} = 1.1$ atm, $\Delta E = 1.1$ eV; (B) $p_{\text{S}_2} = 0.00026$ atm, $\Delta E = 1.8$ eV.

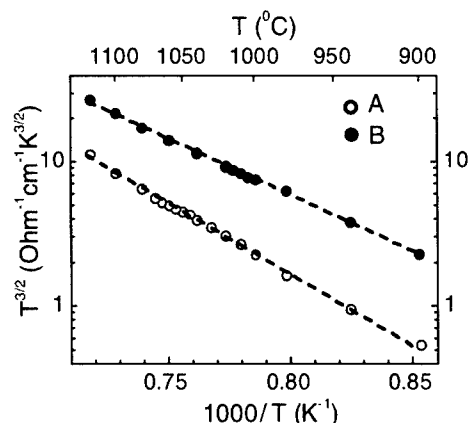


Fig. 4. HTEC isobars of undoped ZnS, measured at the p_{Zn} side: (A) $p_{Zn} = 0.015$ atm, $\Delta E = 1.9$ eV; (B) $p_{Zn} = 0.48$ atm, $\Delta E = 1.6$ eV.

cooling down or heating up isobar curves. The existence of different activation energies for HTEC isobars in Figs. 3 and 4 at different p_{Zn} and p_{S_2} values is characteristic. This indicates that the compensating defects in these regions are different.

3.3. The preliminary HTDE model

We cannot propose any simple HTDE model to calculate Brouwer's approximation [7]. HTEC isotherm slopes α at different temperatures and HTEC isobar activation energies ΔE at different p_{comp} are different which still leaves many possibilities open for the exact defect model. For analysis, we used the method for solving the system of quasi-chemical reactions without approximation [8]. Here we represent some highlights of our preliminary model. For temperature values above the PT temperature and under zinc saturated conditions, sulphur vacancies are the dominant native donor defects and in frozen-in crystals F -centre phenomenon appears [9]. It means that Schottky disorder dominates in hexagonal phase and Frenkel disorder dominates in cubic phase. Our earlier experiments [10] have shown that the total excess of zinc in additively coloured ZnS, determined by atomic absorption photometry, appears to be significantly larger than the concentration of EPR-detected F -centres or the concentration of HTEC measured free carrier concentration. If so, then in the region of high p_{Zn} , the large deviation from stoichiometry must arise at first from the presence of high concentration of neutral vacancies and interstitials compared with the free carrier concentration. The second reason may be related to the adsorption of the excess component on crystal surfaces and interblock boundaries [10]. The appearance of zero slope ($\alpha = 0$) on HTEC isotherms can be explained by a two carrier conduction mechanism involving electrons and holes.

The inversion of sign of α at low p_{Zn} values means the increasing role of free carriers in the electrical compensation of defects. Between these two $\alpha = 0$ values, the p-type region may be formed. In this region no F -centre phenomenon can be found in frozen-in crystals. As in the case of CdS [6], the double inversion of sign of α requires introduction of a specific model. Antistructural disorder involves the occurrence of sulphur at the zinc lattice (S_{Zn}). It must be expected to be a donor. Electrically it must be compensated by zinc vacancies. Tellurium antisite as compensating donor has also been introduced in CdTe defect model [11]. The species S_{Zn} is expected to disappear with increasing p_{Zn} because the energies of formation for antisite defects and defect pairs in ZnS are higher than for vacancies and interstitials [12,13].

4. Conclusions

HTEC was studied in undoped ZnS. It has been found, that at high p_{Zn} and at high p_{S_2} native donors cause the increase of HTEC with increasing of component vapour pressure. The increase of free carrier concentration at low p_{Zn} or at low p_{S_2} is caused by an increasing role of the concentration of holes. In this region p-type HTEC can be found.

Acknowledgements

The authors would like to thank the Estonian Science Foundation for financial support.

References

- [1] K.P. Lott, J. Varvas, Phys. Stat. Sol. A 15 (1973) K51.
- [2] K. Lott, T. Nirk, J. Crystal Growth 197 (1999) 485.
- [3] K. Lott, M. Raukas, A. Vishnjakov, A. Grebennik, J. Crystal Growth 197 (1999) 489.
- [4] H.E. Ruda, B. Lai, J. Appl. Phys. 68 (1990) 1714.
- [5] K.C. Mills, Thermodynamic Data for Inorganic Sulfides, Selenides and Tellurides, Butterworth, London, 1974, p. 687.
- [6] H.R. Vydyanath, F.A. Kröger, J. Phys. Chem. Solids 36 (1975) 509.
- [7] F.A. Kröger, The Chemistry of Imperfect Crystals, North-Holland, Amsterdam, 1974.
- [8] K. Lott, L. Törn, J. Crystal Growth 197 (1999) 493.
- [9] K.P. Lott, Phys. Stat. Sol. A 9 (1972) K43.
- [10] K. Lott, A. Grebennik, A. Dontsova, M. Raukas, A. Vishnjakov, Proc. Estonian Acad. Sci. Chem. 44 (1995) 114.
- [11] M.A. Berding, Phys. Rev. B 60 (1999) 8943.
- [12] J.A. Van Vechten, J. Electrochem. Soc. 122 (1975) 419.
- [13] F.A. Kröger, Ann. Rev. Mater. Sci. 7 (1977) 449.



ELSEVIER

Physica B 308–310 (2001) 935–938

PHYSICA B

www.elsevier.com/locate/physb

Mechanism of laser damage of transparent semiconductors

V.A. Gnatyuk*

Center for Sustainable Development and Ecological Research at the Inter-Regional Academy of Personnel Management,
Frometivs'ka St. 2, 03039 Kyiv, Ukraine

Abstract

Damage of transparent semiconductors and dielectrics under the action of high-intensity laser radiation fluxes is mainly attributed to absorptive inclusions, which being heated up to the melting threshold, result in thermal stresses due to the occurrence of microcracks and pores in materials. In this connection a local spherical area molten by laser radiation and then solidifying in a transparent solid in conditions of external cooling is considered and the temperature fields in the solidified region are calculated. The temperature fields and temporary stress dependences on thickness of a solidified region at different speeds of a solidified front are graphically analyzed. The conditions of occurrence of caverns in irradiated crystals are discussed. The present results can be used in the analysis of the damage processes of optical components of power laser devices, in particular made from ZnSe semiconductors. © 2001 Elsevier Science B.V. All rights reserved.

Keywords: Stress simulation; Temperature field; Laser irradiation; ZnSe crystals

1. Introduction

Interacting with transparent semiconductors high-intensity laser radiation fluxes usually result in local heating of inhomogeneities in the bulk up to the melting point of the material [1]. This has been attributed to the presence of light-absorptive macroinclusions and microinclusions with dimension of the order of wavelength in the crystals. In the last case these inhomogeneities are heated in a recombination mechanism [2]. It was shown [3] that there is also an own mechanism of nucleation of an elementary defect related to accumulating light energy in a thermal fluctuation of density (tensile strain) resulting in the formation of a stable germinal crack. Nevertheless, in all cases laser irradiation of transparent materials with an intensity close to a melting threshold results in heating, melting and subsequent solidifying of local areas in the bulk of a solid. In particular, it is related to short laser pulses of nano- and femtosecond duration [4]. Fast crystallization of a laser-melted area in a crystal forms elastically deformed regions that can

cause the occurrence of microcracks and caverns in materials. It was shown that the irradiation of highly pure, specially undoped, ZnSe single crystals with nanosecond ruby laser pulses can result in both tensile and compressive strain [5,6] as well as in increase of optical absorption in the transparency range of the semiconductor [7]. In the present paper the model of a local spherical area molten by laser radiation and then solidifying in a transparent solid in conditions of external cooling is considered according to the approach reported in Ref. [8]. The stresses and temperature fields in the local solidified region of the bulk of a transparent solid are determined.

2. Definition of the state of solidifying sphere

2.1. The strained state of elastic solid sphere with radial temperature distribution

We consider a hollow sphere with spherically symmetrical distribution of temperature $T(r)$. R is the external radius of a sphere, r_0 is the internal radius. The state of an elastically deformed solid is featured by the strain

*Tel.: +38-44-264-5796; fax: +38-44-264-9511.

E-mail address: gnatyuk@mailcity.com (V.A. Gnatyuk).

vector U , strain tensor U_{ik} and stress tensor σ_{ik} [9]. The equilibrium equation for a deformed solid is

$$\frac{\partial \sigma_{ik}}{\partial x_k} = 0, \quad i, k = 1, 2, 3. \quad (1)$$

The relation between strain tensor and stress tensor, which characterizes an elastic medium, is expressed by the Hook law

$$\sigma_{ik} = 2\mu U_{ik} + \left(K - \frac{2}{3}\mu\right) U_{jj} \delta_{ik} - 3K\alpha(T - T_0)\delta_{ik}, \quad (2)$$

where T_0 is the equilibrium temperature. The last item of this expression represents the stresses which are due to a temperature variation of a body. Here α is the linear expansion coefficient, μ is the shear modulus and K is the compression modulus for an elastic body. These values are regarded as constants. Solving Eqs. (1) and (2) in the spatial polar coordinates (r, φ, θ) and using boundary conditions that both the external and internal sphere surfaces are stressless $\sigma_{rr}|_{r=r_0} = 0$, $\sigma_{rr}|_{r=R} = 0$, the radial and circular components of the stress tensor can be obtained in a view:

$$\sigma_{rr}(r) = \frac{2\mu 9K}{3K + 4\mu} \times \left[\frac{r^3 - r_0^3}{R^3 - r_0^3} \frac{2}{r^3} \int_{r_0}^R \alpha T(r) r^2 dr - \frac{2}{r^3} \int_{r_0}^r \alpha T(r) r^2 dr \right], \quad (3)$$

$$\sigma_{\varphi\varphi}(r) = \sigma_{\theta\theta}(r) = \frac{2\mu 9K}{3K + 4\mu} \left[\frac{2r^3 + r_0^3}{R^3 - r_0^3} \frac{1}{r^3} \times \int_{r_0}^R \alpha T(r) r^2 dr - \frac{1}{r^3} \int_{r_0}^r \alpha T(r) r^2 dr - \alpha T(r) \right]. \quad (4)$$

2.2. The temperature distribution in solidifying sphere

In a solidifying sphere the temperature field $T(r)$ is related with motion of a solidified front. In order to define the temperature dependence $T(r)$ for Eqs. (3) and (4) it is necessary to consider the problem of temperature distribution in a body with varying boundary, the so-called Stephan problem [10]. The condition on the phase boundary is

$$\frac{Q}{c} \frac{\partial \eta(t)}{\partial t} \Big|_{r=\eta(t)} = \frac{\partial T}{\partial t} \Big|_{r=\eta(t)},$$

where Q is the crystallization heat, c is the heat capacity, $\eta(t)$ is the radius of the phase boundary which moves under the law

$$\eta(t) = \sqrt{4wa(t_* - t)}, \quad (5)$$

where w is the dimensionless parameter characterizing the intensity of a heat rejection and thus determining the speed of motion of the phase boundary, $a = \chi/C_v$ is the thermal diffusivity, χ is the thermal conductivity, C_v is the heat capacity at constant volume, t is the time and t_*

is the time during which the crystallization is finished. The initial condition for the solidification boundary is $\eta(0) = 1$ and the second boundary condition requires stationary temperature at a solidified front

$$T(r, t)|_{r=\eta(t)} = T_*,$$

where T_* is the crystallization temperature. Solving the thermal conduction equation [10] for a centrally symmetric temperature field in spatial polar frame while taking into account the initial and boundary conditions above, one can compute the temperature field in a solidifying sphere under external cooling:

$$T(r, t) = \frac{Q}{c} e^{-w} w^{3/2} \int_{(w(r^2)/\eta^2(t))}^w e^x x^{-3/2} dx + T_*, \quad (6)$$

2.3. Definition of temporary stresses in solidifying sphere

We consider a melted sphere with radius $R = 1$. The internal surface of a sphere is a solidified front. The crystallization process is started at $t = 0$ and for $t \geq 0$ a position of the crystallization boundary $r = \eta(t)$ is defined by Eq. (5) and the temperature distribution in the solidified region $T(r, t)$ is expressed by Eq. (6). It is guessed that the speed of material elements is small compared to that of a solidified front. In the solidified region the equilibrium equations, Eq. (1), and the Hook law, Eq. (2) are valid. The thickness of the solid region varies during solidification. Thus it is necessary to determine stresses in a body with a variable boundary. It was shown [8] that the description of such problems was convenient to make using variables characterizing an instantaneous state of a solid. Such variables are a vector field of speeds and tensor field of speeds of deformations. Therefore, in order to characterize an instantaneous state of a solid, Eqs. (1) and (2) differentiated with respect to time are used. These expressions are valid for an ideal liquid using the shear modulus $\mu = 0$. \tilde{K} is the compression modulus for a liquid and the pressure p of a melt instead of stresses σ_{ik} is supposed. In this case the change rate of pressure is used as an instantaneous variable.

The joint change of state of both a strained liquid and solid is esteemed. Therefore the conjugation conditions at the boundary between a melt and solid are used. The density at the crystallization boundary undergoes a jump. The conjugation, which is a consequence of the mass conservation law, reflects this fact:

$$\rho \left(v - \frac{d\eta(t)}{dt} \right) \Big|_{r=\eta(t)} = \tilde{\rho} \left(\tilde{v} - \frac{d\eta(t)}{dt} \right) \Big|_{r=\eta(t)}, \quad (7)$$

where ρ , $\tilde{\rho}$ are the densities and v , \tilde{v} are the strain speeds of a solid and melt, respectively. Usually at solidification of a melt there is a shrinkage which is due to the fact that the density of a solid is more than the density of a melt ($\tilde{\rho}/\rho > 1$); therefore, the liquid appears comprehensively

tensile ($p(t)|_{t \neq 0} < 0$). In the process of moving a solidified front the tension of a liquid increased. At some value of tension (at the moment of $t = t_c$) the collapse in a liquid occurs with forming a gap and therefore a cavern in a solid. Thus, the pressure inside a sphere drops to the zero point.

On the basis of the discussed model and using the initial, boundary and conjugation conditions, the expressions for the temperature dependences and temporary stresses dependences on thickness of a solidified region at different speeds of a solidified front w (or intensity of a heat rejection) were obtained. Inasmuch as the obtained analytical expressions were very cumbersome, it was possible to expediently analyze them graphically in dimensionless variables, using computer calculation (Figs. 1–4). The dimensionless variables were defined using the radius of a melted sphere $R = 1$ and by dividing the obtained expression on the combination of dimension constants characterizing the material [8]. The ZnSe semiconductor constants were used [11].

3. Analysis of theoretical results

The motion of a solidified front (i.e. an increase in thickness of a solidified region) is represented as a decrease in r in the figures. The two cases of the heat rejection intensity ($w_1 = 0.01$ and $w_2 = 0.02$) are considered. Fig. 1 demonstrates that the temperature field is dependent on the thickness of solidified layer. On moving a solidified front, the temperature on the external surface of a sphere is lowered in the course of time because of the heat to be retracted through a more

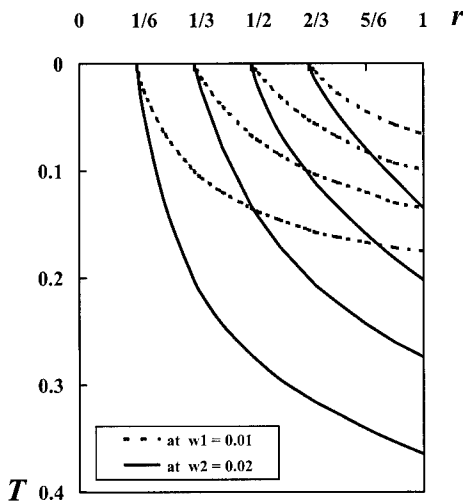


Fig. 1. Temperature distributions $T(r)$ in a solidifying sphere at different thicknesses r of solidified region and at different heat rejection intensities w (solidified front speed).

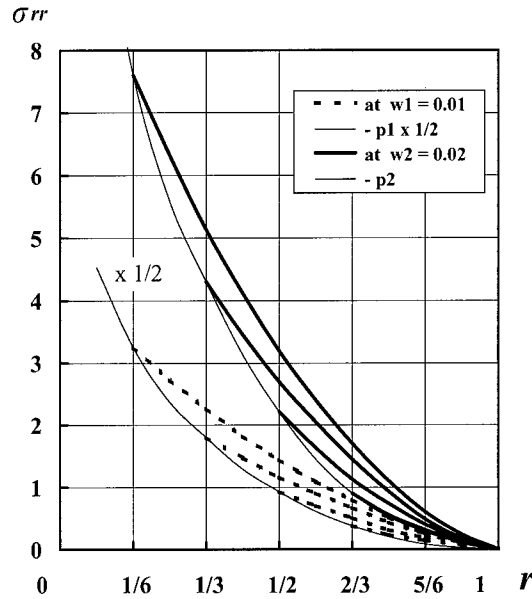


Fig. 2. Radial stresses $\sigma_{rr}(r)$ in a solidifying sphere before forming a cavern at different thicknesses r of solidified region and at different heat rejection intensities w (solidified front speed). Envelopes (thin curves) represent a module of the pressure p of a melt.

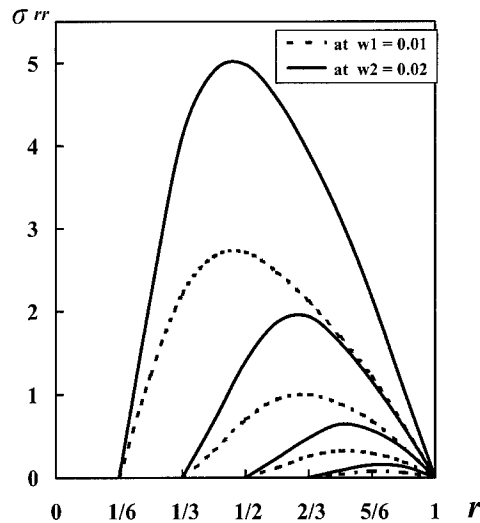


Fig. 3. Radial stresses $\sigma_{rr}(r)$ in a solidifying sphere after forming a cavern at different thicknesses r of solidified region and at different heat rejection intensities w (solidified front speed).

and more thick layer of a rising solid. When the gap in a liquid was not derived yet, the radial stresses have the greatest values on a solidification boundary and numerically are equal to the pressure of a melt (envelopes, i.e. thin curves p_1 and p_2 in Fig. 2) which

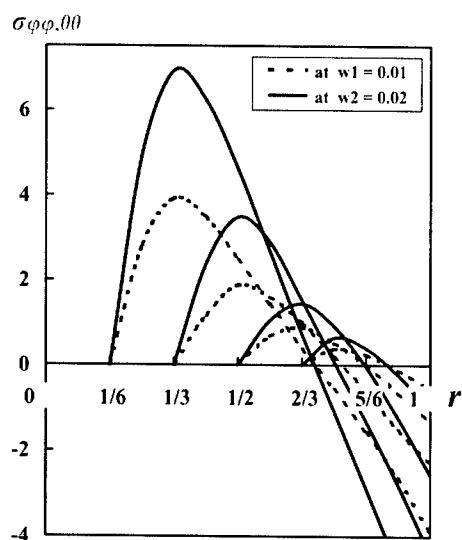


Fig. 4. Circular stresses $\sigma_{\phi\phi, \theta\theta}(r)$ in a solidifying sphere after forming a cavern at different thicknesses of solidified region r and at different heat rejection intensities w (solidified front speed).

sharply increases with moving a solidified front. After formation of a cavern the maximum of radial stresses is shifted to a solidification boundary on moving a solidified front (i.e. toward smaller r in Fig. 3). The circular stresses have negative values at large radius (Fig. 4) that is an evidence of the formation of tensile strained areas in a solid. The difference in the quantitative nature of the stresses is due to the dependence of the temperature on w in a solidifying body. A rise of w results in an increase in the heat rejection intensity (Fig. 1). The intensive cooling of a body (i.e. an increase in w) results in an increase of the stresses. The stresses also increase on raising the thickness of a crystallized region (Figs. 2–4).

The formation of elastically deformed regions could be the reason for the modification of the photoconductivity spectra of ZnSe crystals [5,6] under irradiation with nanosecond ruby laser pulses. In particular, a shift of the maximum and the red edge of the spectrum toward lower energies can be attributed to the formation of deformed regions with residual stresses (tensile strains) in irradiated crystals. The formation of these regions with a smaller bandgap in irradiated samples conformed with the positive pressure coefficient of the change of the bandgap $dE_g/dp = 6 \times 10^{-9} \text{ eV Pa}^{-1}$ for ZnSe [11]. The formation of caverns in local solidified areas of crystals after power laser irradiation (in particular at absorptive inclusions) could cause a rise of the optical absorption in the transparency range of the semiconductor [7].

References

- [1] D.W. Fradin, *Laser Focus* 10 (1974) 39.
- [2] N.N. Grigor'ev, N.A. Kudykina, *Ukr. Phys. J.* 32 (1987) 1460.
- [3] S.N. Gzurkov, V.A. Petrov, A.E. Chmel', *Izv. Akad. Nauk SSSR. Ser. Fiz.* 49 (1985) 745.
- [4] B.G. Gorshkov, *Tr. FIAN* 137 (1982) 81.
- [5] V.A. Gnatyuk, *Phys. Status Solidi A* 175 (1999) 437.
- [6] V.A. Gnatyuk, *Semicond. Sci. Technol.* 15 (2000) 523.
- [7] V.A. Gnatyuk, A. Baidullaeva, A.I. Vlasenko, P.E. Mozol', *Inst. Phys. Conf. Ser.* 160 (1997) 421.
- [8] T.S. Chebanova, *Inzg. J. Mekhan. Tverdogo Tela* 3 (1968) 63.
- [9] L.D. Landau, E.M. Lifshits, *Theory of Elasticity*, Nauka, Moscow, 1965.
- [10] L.I. Rubinshtein, *The Stephan Problem*, Zvaigzne, Riga, 1967.
- [11] L.A. Bovina, M.S. Brodin, M.Ya. Valakh, et al., in: A.N. Georgobiani, M.K. Sheinkman (Eds.), *Physics of A₂B₆ Compounds*, Nauka, Moscow, 1986.



ELSEVIER

Physica B 308–310 (2001) 939–941

PHYSICA B

www.elsevier.com/locate/physb

Stability of chlorine-based complex defects in group II–VI semiconductors

V. Valdna*

Tallinn Technical University, Ehitajate tee 5, 19086 Tallinn, Estonia

Abstract

The influence of variable thermal treatments and cooling rate upon the defect structure and luminescence properties of ZnSe phosphors doped with different dopants has been investigated. It has been found that chlorine-doped and vacuum-annealed ZnSe phosphor samples exhibit an increase of the photoluminescence intensity during the storage at room temperature whereas acceptor codopant copper decreases the instability of samples. The observed unstability of samples has been supposed to be caused by the dissociation of isoelectronic complexes $V_{Zn}2Cl_{Se}$ that gives rise to the concentration of active luminescence centres Cl_{Se} and $V_{Zn}Cl_{Se}$. © 2001 Elsevier Science B.V. All rights reserved.

PACS: 71.55.G; 78.55.C

Keywords: II–VI compounds; ZnSe; Complex defects; Stability

1. Introduction

Group II–VI semiconductor compounds are extensively used as luminescence materials, starting materials for radiation detectors from the far infrared to gamma radiation, solar energy converters, acoustoelectric and optical devices. Chlorine is the most commonly used dopant in II–VI materials as halide fluxes $CdCl_2$ and $ZnCl_2$ are often used for the recrystallization of II–VI powders and films. Substitutional chlorine at the chalcogen site is a single donor. Chlorine forms different complexes with the host intrinsic defects. A-centre, chlorine complex with metal vacancy is an acceptor. A complex that consists of two chlorine atoms and metal vacancy is a neutral defect.

CdTe is the most investigated narrow-gap II–VI compound. Single Cl_{Te} is a shallow donor in CdTe with a binding energy of $E_d = 14$ meV [1]. The A-centre, an acceptor complex $V_{Cd}Cl_{Te}$ with a binding energy of $E_a = 120$ meV, has been identified in CdTe by Meyer

et al. [1]. A-centre is a stable complex [2] that enables to receive as low as $1 \Omega cm$ p-type resistivity in CdTe thin films [4]. $V_{Cd}2Cl_{Te}$ is an isoelectronic complex [4] that causes a high resistivity up to $10^9 \Omega cm$ of chlorine-saturated CdTe [5]. Acceptor levels at 45 meV [6] and 80 meV [7], and a donor level at 60 meV [8] have also been ascribed to this complex. Vacuum annealing of Cl-doped CdTe generates $V_{Te}-V_{Cd}$ pairs that cause a 1.22 eV PL peak and unstable photoconductivity [9].

Wide-gap ZnS and ZnS-based solid solutions are the most efficient and widely used host materials for electroluminescent displays [10]. Compared with group III–V semiconductors, II–VI compounds have been much less studied [11]. ZnSe has long been used as an efficient red electroluminescent phosphor [12], in the last few years it has also been used as a material for the blue and blue–green laser diodes [13], and for the X-ray conversion screens, due to a high radiation stability of ZnSe [14]. A-centre locates in ZnSe band gap at $E_V + 0.35$ eV [15]. Information about other complexes and host intrinsic defects in ZnSe is scarce. A double-charge deep acceptor locates at $E_C - 2.2$ eV [16]. A deep donor V_{Se} has been positioned at $E_V + 1.4$ eV [17], zinc interstitial at donor level $E_C - 0.9$ eV [18].

*Corresponding author. Tel.: +372-620-3366; fax: +372-620-2020.

E-mail address: vellov@hot.ee (V. Valdna).

2. Experimental

For the phosphor samples, starting materials of 6N purity, and ZnCl_2 flux and chemicals for doping of 4–5N purity were used. Mixed with 4wt% ZnCl_2 flux, ZnSe powders were recrystallized isothermally in the evacuated quartz ampoules for 1 h at 1100°C , then cooled down to room temperature together within the tube furnace at a rate of about 1.2 K min^{-1} . For part of the samples 0.02–0.04 at% Ag or 0.05 at% Cu codopants were used. ZnCl_2 flux residue was removed from the recrystallized samples by the vacuum annealing at 470°C . Thereafter samples were vacuum annealed for 30 min at 850°C , then quenched or slowly cooled to room temperature.

3. Results

The integral intensities of phosphor samples measured under X-ray excitation after the thermal treatment and after 9 days storage at room temperature are summarized in Table 1. Samples doped only with chlorine exhibit the lowest conversion efficiency whereas acceptor codopant, especially copper, increases the efficiency, in part, due to a better spectral matching of copper-doped samples to a silicon detector. After 9 days storage at room temperature, all samples showed an increased conversion efficiency. Samples doped only with chlorine have the highest instability, especially at Cl-saturated sample. Copper codopant significantly decreases the rate of instability. PL measurements of the independent samples fabricated from the same phosphors confirm these results.

Fig. 1 shows PL spectrum of chlorine-saturated ZnSe after a thermal treatment with slow cooling to room temperature (curve 1), and after 2 weeks storage at 300 K (curve 2). The PL band peak at 2.02 eV belongs to a known self-activated (SA) emission band [16], caused

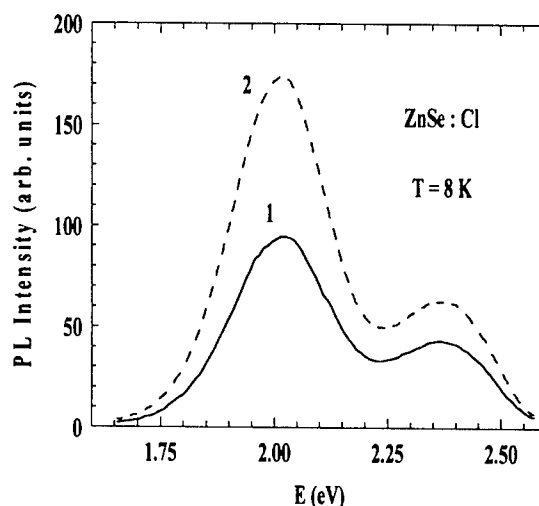


Fig. 1. (1) PL spectrum of ZnSe:Cl , slowly cooled to 300 K. (2) Sample 1, after 2 weeks storage at 300 K.

by charge transitions between the A-centre and donor levels as Cl_{Se} , Zn_i and others. A less intense peak at about 2.37 eV has been ascribed to the host intrinsic defects and bound excitons [19]. Vacuum annealing of chlorine-doped II–VI compounds generates chalcogen and metal vacancies [3,9].

A high cooling rate suppresses the 2.37 eV PL band, as it is seen in Fig. 2. Storage at 300 K causes less changes in the shape of this spectrum, yet a shift to a lower energy side is detected.

Fig. 3 depicts the PL spectra of chlorine- and silver-doped ZnSe . The slowly cooled sample has an intense donor–acceptor pair peak at 2.25 eV, formed by Cl_{Se} and Ag_{Zn} . SA and 2.37 eV bands can be also detected (curve 1). As at a ZnSe:Cl sample, fast cooling rate suppresses the 2.37 eV band, but promotes the SA band (curve 2). Storage at 300 K increases the intensity of this

Table 1
Stability versus thermal treatment of ZnSe -based phosphors^a

No.	Phosphor composition	Thermal treatment	U_F (mV)	U_{F1} (mV)	ΔU (%)
1	ZnSe:Cl	Flux residue removed	9.9	14.3	49.5
		Slowly cooled	21.9	25.8	17.7
		Quenched	22.1	26.4	19.5
2	ZnSe:Cl:Ag	Flux residue removed	19.3	22	14.2
		Slowly cooled	23.4	26.1	11.7
		Quenched	25.7	28.4	10.6
3	ZnSe:Cl:Ag:Cu	Flux residue removed	46.6	50.8	9.1
		Slowly cooled	47.9	50.5	5.4
		Quenched	46.5	51.2	10.1

^a U_F is the photovoltage of photodiode S1336-8BK with the scintillator cap; U_{F1} was measured after 9 days storage of phosphors at 300 K.

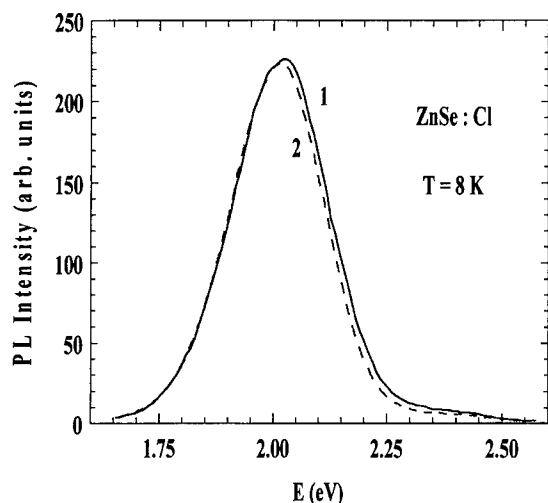


Fig. 2. (1) PL spectrum of ZnSe:Cl, vacuum annealed for 30 min at 850°C, quenched to 300 K. (2) Sample 1, after 2 weeks storage at 300 K.

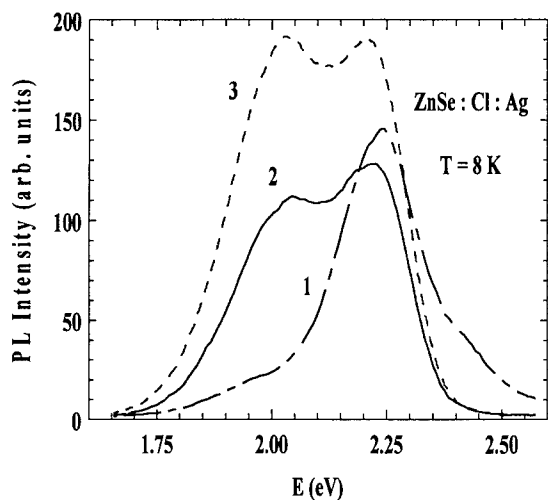


Fig. 3. (1) PL spectrum of ZnSe:Cl:Ag, slowly cooled to 300 K. (2) Sample 1, vacuum annealed 30 min at 850°C, quenched to 300 K. (3) Sample 2, after 2 weeks storage at 300 K.

spectrum also, further increasing the SA part of the broad band (curve 3).

Summarizing the results of this study one can suppose that some chlorine-based complex can cause an increase in the brightness of ZnSe samples stored at room temperature. A neutral complex $V_{Zn}2Cl_{Se}$ is a suitable candidate. We suppose that, supported by the lattice relaxation, part of these complexes can dissociate to the charged defects single Cl_{Se} and $V_{Zn}Cl_{Se}$. Supposedly, this mechanism causes divergent results of different authors [6,7,8]. It is possible that the shallow acceptor levels in II–VI tellurides unidentified so far can be

caused by chlorine complexes with interstitial tellurium [9].

4. Conclusions

It has been found that chlorine-doped and vacuum-annealed ZnSe phosphor samples exhibit an increase of the PL intensity during the storage at room temperature whereas acceptor codopant copper decreases the instability of samples. The observed instability of the PL intensity of samples at room temperature can be explained by post-annealing changes in the defect population. We suppose that part of the isoelectronic complexes $V_{Zn}2Cl_{Se}$ of chlorine-saturated ZnSe can dissociate at room temperature to give rise to the concentration of active luminescence centres Cl_{Se} and $V_{Zn}Cl_{Se}$.

Acknowledgements

The financial support by the Bruker AXS, Inc., and Estonian Science Foundation (Grant No. 4301) is gratefully acknowledged.

References

- [1] B.K. Meyer, et al., *J. Crystal Growth* 117 (1992) 656.
- [2] B.M. Basol, *Proceedings of the 21st IEEE PV Specialists Conference, Kissimmee, 1990*, p. 588.
- [3] V. Valdna, in: J.H. Werner, H.P. Strunk, H.W. Schock (eds.), *Polycrystalline Semiconductors V—Bulk Materials, Thin Films, and Devices, Solid State Phenomena*, Scitech Publ., Uetikon am See, Switzerland, 1999, p. 309.
- [4] O. Ka et al., *J. Appl. Phys.* 68 (1990) 3386.
- [5] V. Valdna, in: M.O. Manasreh, B.J.H. Stadler, I. Ferguson, Yong-Hang Zhang, (Eds.), *Materials Research Society Symposium Proceeding, Vol. 607, Infrared Applications of Semiconductors III*, Warrendale, Pennsylvania, 2000, p. 241.
- [6] Hwa-Yuh Shin, et al., *J. Crystal Growth* 186 (1998) 354.
- [7] M. Laasch, et al., *J. Crystal Growth* 146 (1995) 125.
- [8] M. Fiederle, et al., *J. Crystal Growth* 138 (1994) 529.
- [9] V. Valdna, *Phys. Scripta T* 69 (1997) 315.
- [10] S. Shionoya, *Mater. Forum* 15 (1991) 132.
- [11] H. Luo, et al., *Semicond. Sci. Technol.* 10 (1995) 1041.
- [12] W.G. Gelling, et al., *Philips Res. Rep.* 16 (1961) 371.
- [13] B.C. Cavenett, et al., *Mater. Sci. Forum* 182–184 (1995) 5.
- [14] V.D. Ryzhikov, et al., *Nucl. Tracks Radiat. Meas.* 21 (1993) 53.
- [15] G.F. Neumark, *Mater. Sci. Eng. R* 21 (1997) 1.
- [16] J.W. Allen, *Semicond. Sci. Technol.* 10 (1995) 1049.
- [17] S. Pöykkö, et al., *Mater. Sci. Eng. B* 43 (1997) 1.
- [18] G.D. Watkins, *J. Crystal Growth* 159 (1996) 338.
- [19] S. Kishida, et al., *Phys. Stat. Sol. A* 106 (1988) 283.



ELSEVIER

Physica B 308–310 (2001) 942–944

PHYSICA B

www.elsevier.com/locate/physb

Excitation mechanism of blue anti-Stokes and 2.4 μm infrared emission in ZnSe:Cr

V.Yu. Ivanov^{a,*}, A.A. Shagov^b, A. Szczerbakow^a, M. Godlewski^a

^a*Institute of Physics, Polish Academy of Sciences, Al. Lotników 32/46, 02-668 Warsaw, Poland*

^b*Solar Laser Systems, Minsk, Byelorussia*

Abstract

We report the observation and analyze the mechanism of efficient blue anti-Stokes emission in ZnSe:Cr. This emission and the intra-shell transition of chromium Cr^{2+} at 2.4 μm are induced by $2+ \rightarrow 1+$ ionization transition of chromium ions in ZnSe:Cr. The efficiency of the anti-Stokes photoluminescence anticorrelates with the efficiency of the infrared emission. The latter emission dominates at increased temperatures. We conclude that the photoionization excitation mechanism can be applied for optical pumping of 2.4 μm laser action in ZnSe:Cr. © 2001 Elsevier Science B.V. All rights reserved.

Keywords: ZnSe; Chromium ion; Anti-Stokes emission; Infrared emission

1. Introduction

We reported recently observation of efficient energy up-conversion in chromium doped ZnSe [1]. Based on the results of electron spin resonance (ESR) investigations, we concluded that the anti-Stokes luminescence (ASL) in ZnSe:Cr is accompanying photoionization excitation of chromium ions. In this work, we discuss an inter-link between the ionization transition of Cr ions and the 2.4 μm infrared emission, due to $^5\text{E} \rightarrow ^5\text{T}_2$ emission of Cr^{2+} . The laser action was achieved for the latter photoluminescence (PL) in chromium doped wide bandgap II–VI materials [2–7]. The Cr^{2+} PL at about 2.4 μm , due to $^5\text{E} \rightarrow ^5\text{T}_2$ intra-shell transition, has a relative large PL line width of about 0.5 μm giving possibility of tuning in relatively large spectral range.

2. Experimental

ZnSe samples studied were bulk crystals grown from the melt by the Bridgman–Stockbarger (BS) technique

or from the vapor phase by Markov–Davydov (MD) technique. The first type crystals were purified by zone melting with following treatment in the zinc melt. We also studied some reference ZnSe epilayers obtained by simple deposition from the vapor phase or by atomic layer epitaxy in the gas flow version. Bulk BS crystals were grown from a chromium doped melt, with resulting chromium concentration, determined from the mass spectral analysis of the crystals, varying between 10^{16} and $5 \times 10^{19} \text{ cm}^{-3}$, i.e., both lightly and heavily doped samples were studied. Vapor phase MD crystals and ZnSe epilayers were doped with chromium by diffusion at 800°C temperature during 70–240 h treatment, with Cr metal deposited on the surface by magnetron sputtering. Cr concentration in these samples varied from $5 \times 10^{18} \text{ cm}^{-3}$ to $8 \times 10^{19} \text{ cm}^{-3}$.

A conventional PL set-up was used with samples mounted in a variable temperature cryostat. PL spectra were dispersed with Ebert–Fasti monochromator and detected with CCD camera (for visible and NIR region detection) or InAs photovoltaic detector (1–3.5 μm). The latter detector, assembled with digital oscilloscope was used for the PL kinetics measurements in the infrared. Visible light PL kinetics was measured with PMT in time-correlated photon counting mode. For cw excitation UV and visible lines of argon ion laser

*Corresponding author. Tel.: +48-22-843-6861; fax: +48-22-843-0926.

E-mail address: ivanov@ifpan.edu.pl (V.Yu. Ivanov).

(Innova-400) together with dye-laser (with tuning range of 1.65–2.25 eV) and He–Cd laser (2.807 eV) were used. Excitation intensity was varied with a motorized attenuator in the range of 10^{17} – 10^{24} photon/cm²s. The ESR experiments were performed with Bruker 300 X-band spectrometer equipped with a continuous He gas-flow Oxford Instruments cryostat. Photo-excitation of the samples mounted in a microwave cavity was done either with laser sources used in the PL study or with a high-pressure mercury lamp and set of interference filters.

3. Results and discussion

In Fig. 1 we present the PL spectra observed under 2.41 and 2.807 eV excitation for the relatively heavily chromium doped sample (4.2×10^{18} cm⁻³) and at high excitation density of 10^{19} photons/cm²s. A very bright blue color donor acceptor pair (DAP) emission is observed under 2.41 eV excitation with a weak red DAP PL (not shown). The blue PL is excited by photons of lower energy, thus, it is identified as the ASL [1]. It should be mentioned, that neither excitonic transitions (donor (DBE) and acceptor (ABE) bound exciton) nor free-to-bound (FB) transition, which dominate at the above band gap excitation conditions, are observed under 2.41 eV excitation. This indicates efficient trapping of free carriers by ionized Cr centers. In addition to the visible light PL, two infrared intra-shell emissions of Cr²⁺, the 2.4 μ m PL due to $^5E \rightarrow ^5T_2$ transition and the 0.95 μ m PL (see Fig. 2), are observed upon 2.41 eV excitation. The latter PL was tentatively attributed to $^3T_1 \rightarrow ^5T_2$ emission of Cr²⁺ [8].

We measured temperature and excitation density dependences of anti-Stokes and infrared emissions and their excitation spectra. The PL excitation and photo-ESR data (Fig. 3) prove that the $2+ \rightarrow 1+$ ionization transition of chromium impurity excites the ASL and

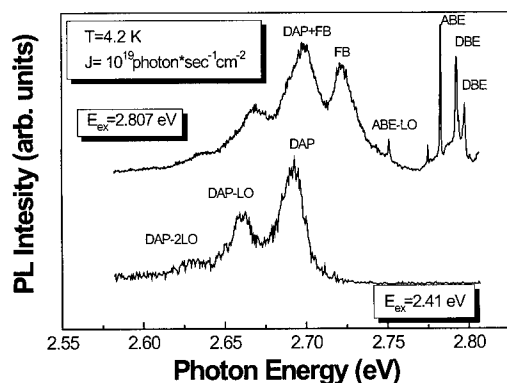


Fig. 1. Low temperature photoluminescence spectrum of ZnSe:Cr under above band gap excitation and the ASL excitation.

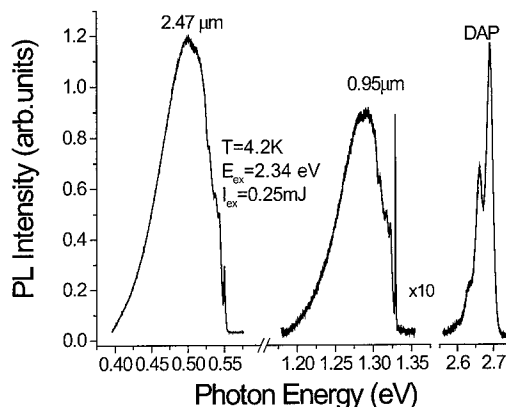


Fig. 2. Chromium-related infrared PL emissions and the ASL emission observed in ZnSe:Cr under the photoionization excitation.

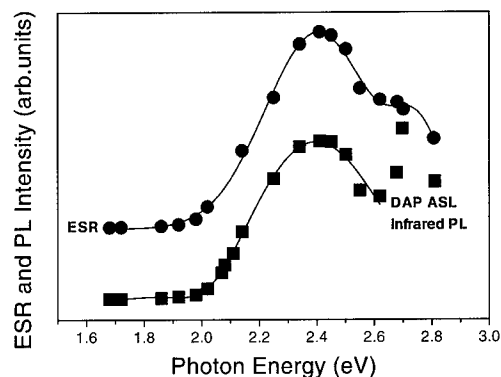


Fig. 3. Comparison of the PL excitation spectra of the ASL and infrared PLs with the Cr¹⁺ photo-excitation band determined in the ESR study.

the Cr²⁺ intra-shell PL. The important question is, if the ASL and the 2.4 μ m PL emissions do not compete as possible channels of energy relaxation. As explained previously, the ASL is excited due to two complementary ionization transitions of chromium ions [1]. Free carriers, photo-created in conduction and valence bands of ZnSe, participate in DAP PL responsible for the blue ASL emission.

For a two-quanta excitation mechanism, one could expect a quadratic dependence on the light intensity. In fact we observed the quadratic dependence of the ASL on excitation density for a two-photon excitation process, studied by us for undoped ZnSe samples. In the latter case a quantum efficiency of the ASL is fairly low, and is below 10^{-5} . The highly efficient ASL process observed by us in ZnSe:Cr (2×10^{-3} upon green color optical pumping and at helium temperature) shows, in a large range of excitation densities, a linear dependence of the ASL on excitation intensity. This, as results from

our photo-ESR studies, is a consequence of a metastable population of photo-excited Cr^{1+} centers, which is observed at low temperatures. Free holes, created in the valence band under chromium $2+ \rightarrow 1+$ ionization, are efficiently trapped by shallow acceptor centers being active in the ASL process. The second photon that is absorbed by photo-generated Cr^{1+} state induces a complementary ionization transition to the conduction band. Thus, both the types of free carriers are photo-generated and can participate in the ASL.

The efficiency of the ASL emission is reduced at increased temperatures, since required retrapping of photo-generated free carriers by shallow donor and acceptor centers active in the ASL becomes temperature deactivated. This is, why the deactivation of the ASL is characterized by deactivation energies of about 110–120 meV (Fig. 4) related to the thermal ionization of shallow acceptors.

The detrimental sensitivity of the ASL to the increase in the temperature turned out to be profitable for the second process studied by us. With decreasing efficiency of the ASL process, the intra-shell emission of Cr^{2+} is more efficient (Fig. 4). The photo-generated holes are at higher temperatures more efficiently retrapped by ionized chromium centers. As a consequence, Cr^{1+} state, an intermediate state in a two-quanta excitation transition, is no longer metastably occupied and a linear dependence on a light density is not observed for both the ASL and the intra-shell excitation processes.

High efficiency of the intra-shell PL means, that hole retrapping by ionized Cr^{1+} centers proceeds via the excited ^5E (and also $^3\text{T}_1$) state of Cr^{2+} impurity and that the process is very efficient at increased temperatures. Moreover, our photo-ESR studies indicate, that such a process occurs also under injection of free carriers. Our ESR studies demonstrate, that the generation of free carriers leads to efficient carrier trapping by Cr ions, by the so-called bypassing mechanism [9]. For example, we observed very efficient Cr^{1+} photo-quenching under

neutralization transition of deep acceptors, and very efficient photo-generation (see Fig. 3) for excitation, when deep acceptors are ionized, i.e., at the conditions when free electrons are created. This means, that the Cr^{2+} centers can compete in electron trapping with shallow donor centers active in visible emission of ZnSe, whereas Cr^{1+} centers in trapping of free holes from the valence band. Thus, we can avoid limitation of optical pumping and obtain efficient 2.4–2.5 μm infrared emission under injection of free electrons and holes.

4. Conclusions

2.4 μm PL of Cr^{2+} is efficient at room temperature and can be either optically pumped upon Cr ionization transitions or it can be excited by injection of free carriers. The former process can be important both for the optical pumping of this PL by easily available and very efficient light sources in green color. The latter process may be important in light emitting devices working under carrier injection conditions.

Acknowledgements

We are indebted to A.A. Davydov for providing vapor grown ZnSe crystals. This work was partly supported by grant no. 5 P03B 007 20 of KBN for the years 2001–2003.

References

- [1] V.Yu. Ivanov, Yu.G. Semenov, M. Surma, M. Godlewski, Phys. Rev. B 54 (1996) 4696.
- [2] L.D. DeLoach, R.H. Page, G.D. Wilke, S.A. Payne, W.F. Krupke, IEEE J. Quant. Electron. 32 (1996) 885.
- [3] R.H. Page, K.I. Schaffers, L.D. DeLoach, C.D. Wilke, F.D. Patel, J.B. Tassano, S.A. Payn, W.F. Krupke, K.T. Chen, A. Burger, IEEE J. Quant. Electron. 33 (1997) 609.
- [4] U. Hommerich, X. Wu, V.R. Davis, S.B. Triverdi, K. Grasza, R.J. Chen, S. Kutcher, Opt. Lett. 22 (1997) 1180.
- [5] J.T. Seo, U. Hommerich, S.B. Triverdi, R.J. Chen, S. Kutcher, Opt. Commun. 153 (1998) 267.
- [6] A.V. Podlipensky, V.G. Shcherbitsky, N.V. Kuleshov, V.P. Mikhailov, V.I. Levchenko, V.N. Yakimovich, L.I. Postnova, V.I. Konstantinov, Opt. Commun. 167 (1999) 129.
- [7] J.T. Seo, U. Hommerich, H. Zong, S.B. Triverdi, S.W. Kutcher, C.C. Wang, R.J. Chen, Phys. Status Solidi A 175 (1999) R3.
- [8] M.U. Lehr, B. Litzenburger, J. Kreissl, U.W. Pohl, H.R. Selbert, H.-J. Schulz, A. Klimakow, L. Worschech, J. Phys.: Condens. Mater 9 (1997) 753.
- [9] M. Surma, M. Godlewski, T.P. Surkova, Phys. Rev. B 50 (1994) 8319.

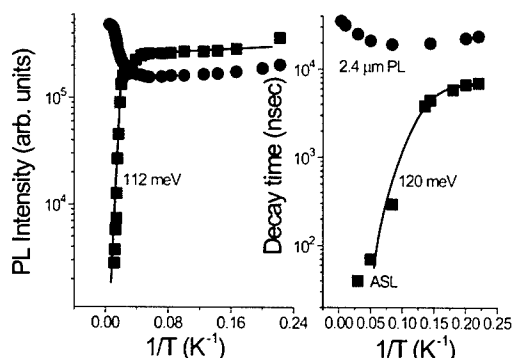


Fig. 4. Temperature dependences of the PL intensity (left) and the PL decay time (right) of the DAP ASL and of the 2.4 μm PL in ZnSe:Cr.



ELSEVIER

Physica B 308–310 (2001) 945–948

PHYSICA B

www.elsevier.com/locate/physb

Donor–acceptor pair transitions in ZnO substrate material

K. Thonke*, Th. Gruber, N. Teofilov, R. Schönfelder, A. Waag, R. Sauer

Universität Ulm, Abteilung Halbleiterphysik, Albert-Einstein-Allee 45, D-89069 Ulm, Germany

Abstract

We investigate the state-of-the-art ZnO substrate material grown by seeded chemical vapour transport. The low-temperature photoluminescence (PL) spectra are dominated by very sharp bound exciton lines, which are followed by two-electron satellite transitions. This identifies the major bound exciton lines as donor related and allows us to derive a binding energy of ≈ 40 meV for the very similar donors observed here. From a donor–acceptor pair transition at ≈ 3.22 eV and its associated band-acceptor line emerging at sample temperatures above 40 K, we calculate the acceptor binding energy as ≈ 195 meV. Hall data confirm these findings. © 2001 Elsevier Science B.V. All rights reserved.

Keywords: ZnO; Two-electron satellite; Donor–acceptor pair transition; PL

1. Introduction

The semiconductor ZnO with its direct band gap of ≈ 3.5 eV is a possible candidate for optoelectronics in the UV and blue spectral ranges. It was initially investigated nearly 40 years ago [1,2] and the wurtzite type band structure was also analysed. ZnO is typically n-type, and light-emitting diodes could only be prepared with metal–semiconductor contacts [3]. The nature of the dominant native donor is still under debate: experimental and theoretical works provide arguments for either interstitial zinc or oxygen vacancies [4].

Attempts to implement p-type doping failed for a long time. Recently, reports on successful p-type doping of ZnO were published [5], and theoretical work also predicted that co-doping should allow to produce shallow acceptors [6,7].

The low-temperature photoluminescence (PL) spectrum of ZnO has been investigated in many aspects in the previous work. Around 30 sharp donor- and acceptor-bound exciton lines were reported in the narrow energy range from 3.348 to 3.372 eV close to the free X_A and X_B exciton–polariton (for a tabulation,

see [8]), and quite a few have been analysed in Zeeman measurements. Nevertheless, the chemical origin of the underlying dopant atoms remained unclear. Also, the ionisation energy of the dominant donor as determined from temperature dependent Hall or conductivity measurements shows a spread from 20 to 130 meV [8].

2. Experimental and results

The ZnO substrates have been obtained from Eagle Picher (USA). They were grown by a seeded chemical vapour transport (SCVT) technique. Hall measurements between 45 and 360 K have been performed using a van der Pauw geometry and a standard DC measurement set-up. Ti/Au contacts have been fabricated by a simple evaporation technique. Typical carrier concentrations at room temperature of $(1\text{--}2) \times 10^{17} \text{ cm}^{-3}$ have been obtained. At 45 K, the carrier concentration is in the $8 \times 10^{14} \text{ cm}^{-3}$ range. We simulated the experimental $n(T)$ curve using Fermi statistics and solving the charge neutrality equation numerically under the assumption of partial compensation. We obtain a donor concentration of $1.7 \times 10^{17} \text{ cm}^{-3}$, a donor activation energy of 35 ± 5 meV, and a concentration of compensating acceptors of $2 \times 10^{15} \text{ cm}^{-3}$. The carrier mobility changes from a value of $(100\text{--}200) \text{ cm}^2 \text{ V}^{-1} \text{ s}^{-1}$ at room temperature to $\approx 800 \text{ cm}^2 \text{ V}^{-1} \text{ s}^{-1}$ at 45 K.

*Corresponding author. Tel.: +49-731-502-6131; fax: +49-731-502-6108.

E-mail address: klaus.thonke@physik.uni-ulm.de (K. Thonke).

In high resolution X-ray diffraction (HRXRD) ω - and $\theta/2\theta$ -scans on several substrates, we observe in several cases asymmetric contributions to the main peak within Bragg angles of $\approx 0.1^\circ$, which are $\approx 1\frac{1}{2}$ orders of magnitude less intense. This hints at the existence of polycrystals in the substrate, which are slightly tilted relative to the main c -axis.

For the optical characterisation, we recorded reflection spectra at 4.2 K in order to get information on the fundamental excitonic band gaps. From a fit to the very pronounced resonances due to the A and B exciton-polariton ($n = 1, 2$) states observable in a $(\mathbf{E} \perp \mathbf{k} \parallel \mathbf{c})$ configuration, we determine for the excitonic band gaps $E_{X,A} = (3374 \pm 1) \text{ meV}$, $E_{X,B} = (3380 \pm 1) \text{ meV}$, and for the exciton binding energies $E_{BX,A} = 64 \text{ meV}$ and $E_{BX,B} = 53 \text{ meV}$. This results in an energy for the fundamental A band gap of $E_{g,A} = 3.438 \text{ eV}$ (literature value: 3.441 eV [8]).

The low-temperature PL spectra are dominated by several close lying bound excitons in the range from 3.3595 to 3.364 eV (see Fig. 1, inset). According to the literature [8], the most intense line at 3.3628 meV is commonly assigned to a donor-bound exciton (“ I_d ”), whereas the slightly weaker line at 3.3597 eV is closer to the location of the acceptor-bound exciton “ I_a ”. All these lines are replicated at 29.9 meV lower energy in the region labelled “TES” (=two-electron satellite). A “TES” related to a donor-bound exciton (D^0, X) occurs in the spectrum, if in the bound exciton recombination

process the neutral donor (i.e. the final state of the recombination process) is excited from the $1s$ ground state to an excited state like $2s$, $2p$, etc. In Fig. 2, the (logarithmic) PL spectrum of the BEs is shifted by 29.9 meV and compared to the TES part. Apart from a line broadening, the TES spectrum mirrors the principal bound exciton spectrum. This strongly suggests that not only the upper BE line is a donor bound exciton, but even the lower energy lines around 3.360 eV are donor- (and not acceptor-) related. (This does not apply for the next weaker line at 3.3566 eV.) Zeeman measurements confirm this conclusion [9]. Obviously, we are concerned with several, but very similar donors in the ZnO substrate material. From the spacing of the TES lines from the (D^0, X) lines, we directly obtain the energy splitting $1s \leftrightarrow (2s/p)$ of the lowest donor states: For the dominant donor in the present sample this splitting is $(29.9 \pm 0.2) \text{ meV}$. Assuming that the effective-mass theory gives a good description of these donors and neglecting central cell corrections, the ionisation energy for these donors should be $4/3 \times 29.9 \text{ meV} = 39.9 \text{ meV}$. The origin of the similarly structured, but weaker hump at $\approx 3.320 \text{ eV}$, shifted by 11.4 meV relative to the TES, is presently not clear. Transitions $1s \rightarrow 3(s/p)$ to the next higher excited states would require an energy of $\approx (1 - \frac{1}{9}) \times E_D = 35.5 \text{ meV}$, i.e. they would be shifted by further 5.6 meV relative to the $1s \rightarrow 2(s/p)$ transition described above. Possibly, the band at $\approx 3.320 \text{ eV}$ is also a TES due to a second donor with a higher binding of

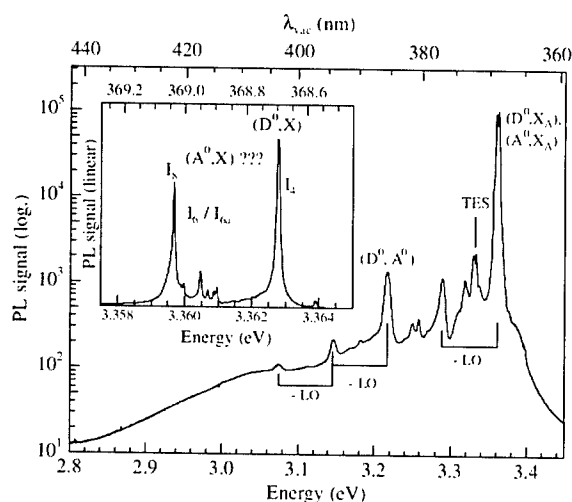


Fig. 1. PL overview spectrum of ZnO substrate material recorded at 4.2 K. The bound exciton lines at $\approx 3.36 \text{ eV}$ are followed by a two-electron replica (“TES”) 30 meV low in energy. At 3.220 eV, the donor-acceptor pair transition (D^0, A^0) is observed. All lines are repeated as LO phonon replicas. Inset: high resolution PL spectrum of the bound exciton region (resolution = $50 \mu\text{eV}$).

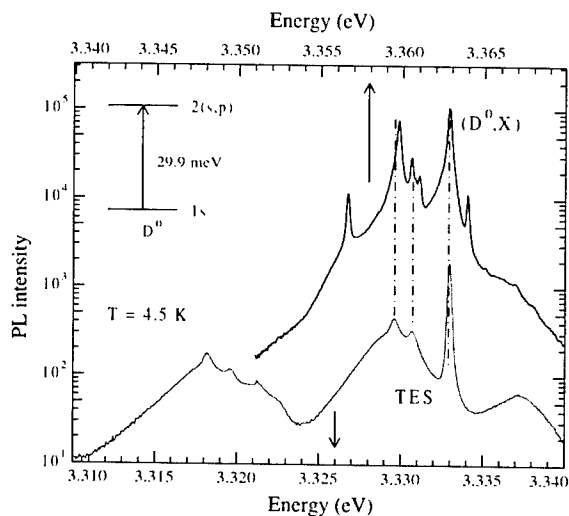


Fig. 2. Details of the BE (upper trace, top energy scale) and the TES regions (lower trace, bottom energy scale) in PL in comparison. The major features of the BE pattern can be rediscovered in the TES spectrum, and similarly repeated in the next peak, which is 11.4 meV low in energy. Note that the top energy axis is shifted by 29.9 meV relative to the bottom energy axis. Inset: The excitation of the D^0 final state taking place in the recombination process, which results in the “TES” line.

$4/3 \times (29.9 + 11.4) \text{ meV} = 55 \text{ meV}$. Independent evidence that the major BE lines are *donor*-related comes from the relative weak coupling to LO phonons for all these transitions: The LO replicas are roughly two orders of magnitude less intense than the BE lines. This is similar to the case of GaN and II–VI semiconductors, where (D^0, X) lines commonly couple only weakly with the optical phonons, while the (A^0, X) lines show much more intense replicas.

After having found a reliable value for the binding energy of the dominant native donors present in the ZnO substrate, we can take a closer look at the donor–acceptor pair transition (D^0, A^0) . This is observed at 3.220 eV in the PL spectrum (Fig. 3). For low sample temperatures, this line is much broader than the BE lines. It is followed by a series of LO replicas, which are relatively intense (hinting at the participation of an acceptor in this transition). With the increasing sample temperature, its intensity drops, and an adjacent line at 3.236 eV on the high energy side increases and gains intensity. This temperature dependence is typical of donor–acceptor pair transitions (D^0, A^0) turning into free electron–acceptor transitions (e, A^0) , when the

donors are thermally ionised. If the average density of the dominant impurity is known from Hall measurements, then the donor binding energy E_D can be calculated from the energy difference of the peak position of the (D^0, A^0) and (e, A^0) lines (see, e.g. [10]):

$$E_D = [E(e, A^0) - k_B T/2] - [E(D^0, A^0) - \alpha N_D^{1/3}]. \quad (1)$$

Here, $N_D^{1/3}$ represents the average distance of the donors, and α is a material dependent constant [8]

$$\alpha = \sqrt[3]{\frac{4\pi}{3}} \frac{e^2}{4\pi\epsilon_0\epsilon} = 2.7 \times 10^{-8} \text{ eV cm} \quad (2)$$

for $\epsilon(\text{ZnO}) = 8.6$.

This constant is needed to calculate the average Coulomb energy between D^0 and A^0 after the recombination process. Using the data determined for our substrates, we calculate a value of $E_D \approx 28 \text{ meV}$. This value is less reliable than the one determined from the $\text{TES} \leftrightarrow (D^0, X)$ energy spacing, but is—within the expected accuracy—compatible with the latter one and the Hall data. With the knowledge of E_D and N_D , we proceed in calculating the acceptor energy from the absolute spacing of the (D^0, A^0) line from the band gap:

$$E_A = [E_{\text{gap}} - E_D] - [E(D^0, A^0) - \alpha N_D^{1/3}]. \quad (3)$$

If we use the value of $E_{\text{gap}} = 3.438 \text{ eV}$ determined from our reflection data, then we get an ionisation energy $E_A = (195 \pm 10) \text{ meV}$ for the unintentional acceptor present in the ZnO substrate. The chemical nature of this relatively shallow acceptor remains presently unclear. Recent first-principle calculations predict for the Zn vacancy a much higher ionisation energy of $\approx 0.8 \text{ eV}$, which seems to rule out V_{Zn} as the acceptor in our ZnO substrates. A good candidate for the acceptor might be substitutional nitrogen on O sites, for which a binding energy of $\approx 200 \text{ meV}$ was calculated [11]. The chemical analysis of the substrate material indeed indicates as the most abundant impurity nitrogen with a content of $\approx 2 \text{ ppm}$ [12]. The donors with 30 meV binding energy might be possibly due to the interstitial hydrogen [4].

3. Conclusions

We investigate the principal PL features in ZnO substrate material and identify the major bound exciton recombination lines as donor-related. From the two-electron-transitions observed for these (D^0, X) lines, we obtain an exact value for the energy difference between the donor $1s$ and $2(s,p)$ ground states, and thus a very reliable estimate for the donor ionisation energy $E_D = 40 \text{ meV}$. The donor–acceptor pair transition at 3.220 eV allows to determine the binding energy of the acceptor involved as $E_A \approx 195 \text{ meV}$. The chemical

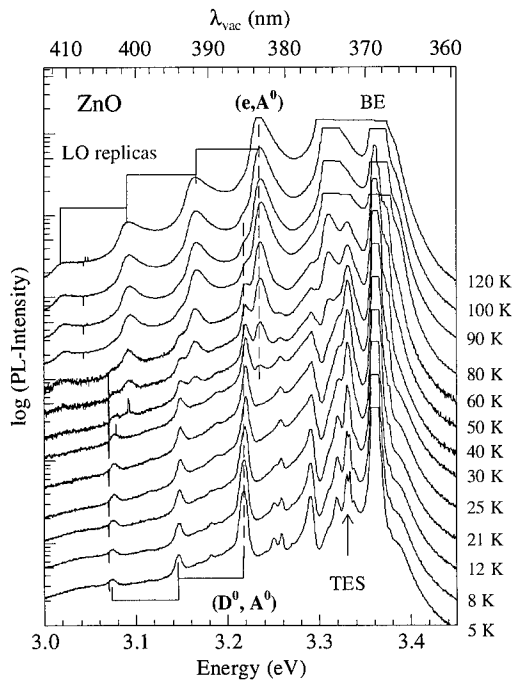


Fig. 3. Series of PL spectra of ZnO substrate material recorded at different temperatures. The plots are vertically shifted, each for a better visibility. Between 30 and 100 K the donor–acceptor pair transition at 3.220 eV decreases, and the adjacent band–acceptor transition at 3.236 eV increases. (The strong BE lines are saturated due to the long exposure time of the CCD camera.)

species responsible for the acceptor might be nitrogen, whereas the donor could be hydrogen.

Acknowledgements

We thank N. Kerwien and M. Haupt for assistance in the experiments.

References

- [1] J.L. Birman, *Phys. Rev. Lett.* 2 (1959) 157.
- [2] D.G. Thomas, *J. Phys. Chem. Solids* 15 (1960) 86.
- [3] T. Minami, S. Takata, M. Yamanishi, T. Kawamura, *Jpn. J. Appl. Phys.* 18 (1979) 1617.
- [4] A.F. Kohan, G. Ceder, D. Morgan, C.G. Van de Walle, *Phys. Rev. B* 61 (2000) 15019, and references therein.
- [5] Y.R. Ryu, S. Zhu, D.C. Look, J.M. Wrobel, H.M. Jeong, H.W. White, *J. Cryst. Growth* 216 (2000) 330.
- [6] T. Yamamoto, H. Katayama-Yoshida, *Jpn. J. Appl. Phys.* 38 (1999) L166.
- [7] T. Yamamoto, H. Katayama-Yoshida, *J. Cryst. Growth* 214/215 (2000) 552.
- [8] Landolt/Börnstein, in: U. Rössler (Ed.), *Numerical Data and Functional Relationships in Science and Technology—New Series III*, Vol. 41B, Springer, Berlin, 1999, p. 85ff. and references therein.
- [9] K. Thonke, et al., to be published.
- [10] M. Körbl, K. Kornitzer, M. Mayer, M. Kamp, K. Thonke, R. Sauer, *Proceedings of the 24th International Conference on the Physics of Semiconductors*, Jerusalem, 1998, World Scientific, Singapore, 1999, article No. 1439.
- [11] C. van de Walle, private communication.
- [12] Eagle Picher, private communication.



ELSEVIER

Physica B 308–310 (2001) 949–953

PHYSICA B

www.elsevier.com/locate/physb

Optical properties and surface morphology of Li-doped ZnO thin films deposited on different substrates by DC magnetron sputtering method

Galal A. Mohamed, El-Maghraby Mohamed*, A. Abu El-Fadl

Physics Department, Faculty of Science, Assiut University, Assiut 71516, Egypt

Abstract

Thin films of zinc oxide doped with $\text{Zn}_{1-x}\text{Li}_x\text{O}$ with $x = 0.2$ ($\text{ZnO}:\text{Li}$), have been prepared on sapphire, MgO and quartz substrates by DC magnetron sputtering method at 5 mTorr. The substrate temperatures were fixed to about 573 K. We have measured the transmission and reflection spectra and determined the absorption coefficient, optical band-gap ($E_{\text{gd}}^{\text{opt}}$), the high frequency dielectric constant ϵ'_{∞} and the carrier concentration N for the as-prepared films at room temperature. The films show direct allowed optical transitions with $E_{\text{gd}}^{\text{opt}}$ values of 3.38, 3.43 and 3.29 eV for films deposited on sapphire, MgO and quartz substrates, respectively. The dependence of the obtained results on the substrate type are discussed. © 2001 Elsevier Science B.V. All rights reserved.

Keywords: ZnO:Li films; DC sputtering; Band gap; Optical properties

1. Introduction

Among different oxides, ZnO thin films (undoped and doped) have in recent years been rediscovered as a subject of considerable research interest due to their very unique physical properties (piezoelectricity, conductivity, magnetic and optical) and a wide range of possible device applications. Special care is directed to optical and magnetic memory devices, laser systems, blue light diodes, solar cells (transparent conducting electrodes), displays, ultrasonic transducers and sensors [1–3]. Since ZnO has the hexagonal structure (Wurtzite type) with four-fold tetrahedral coordination [4] and lies in the border between ionic and covalent semiconductors (II–VI), it is both suitable and important for fabrication of a high-quality oriented or epitaxial thin film which shows typical n-type piezoelectric semiconductor character. This is besides the fact that ZnO-based semiconductors can cover the same wavelength as GaN with an excitonic band energy much larger than that of GaN with large

direct band-gap (3.1–3.32 eV). Hence, ZnO-based thin films are increasingly being used as potential materials for highly coherent light generation and in optical devices in the blue to UV wavelength region.

In order to develop ZnO films with high quality for devices with good performance, it is necessary to clarify the role and effect of so many additives, different conditions of growth and substrate types. This will result in different microstructures being suitable for different applications. Now, it is well established that doping ZnO with Al ions decreases its resistivity while doping with Li ions increases its resistivity [5–8] and induces a ferroelectric phase suitable for optical memory devices [5,9–10].

The study of optical constants with their variation with frequency enables to make correlation with the band structures derived by other methods.

In this research, ZnO:Li thin films have been prepared on sapphire, quartz and MgO substrates at ~573 K by DC magnetron sputtering method. Our goal is to investigate growth and microstructure of ZnO:Li thin films. Another goal is to measure the absorption, reflectance and determine the optical band-gap ($E_{\text{gd}}^{\text{opt}}$), the high frequency dielectric constant ϵ'_{∞} and the carrier

*Corresponding author. Fax: +20-88-342708.

E-mail address: maghrabym@yahoo.com (El-Maghraby Mohamed).

concentration N for the as-prepared films at room temperature and discuss its dependence on the type of substrate.

2. Experimental

Using DC magnetron sputtering method, we prepared ZnO:Li thin films deposited on sapphire MgO and quartz substrates. The sputtering target was a mixture of Li powder and Zn powder, with atomic ratio of Zn/Li (80/20), pressed on a copper saucer with diameter of 100 mm. Li powder was mixed in 20% excess in order to compensate the loss of Li during deposition. It is necessary to continue sputtering for over 40 h to make the target surface Li-rich and the film composition was saturated to the value nearly equal to the target composition. The deposition time for this experiment is fixed to be about 3 h long. When the film samples were deposited, presputtering was carried out for 5 min before opening the shutter which covered the substrate. The discharge was a mixture of Ar and O₂ with the ratio 70:30 and its pressure was about 5 mTorr. The voltage was fixed to 310 V and the current was about 110 mA. The substrate temperature was fixed at 573 K. After deposition, the samples were immediately cooled to room temperature. The identification of the crystalline structure and surface morphology were performed by X-ray diffraction analysis (XRD) (Philips Type: 1710) using Cu K_α radiation ($\lambda = 1.5418 \text{ \AA}$) and scanning electron microscope (SEM Jeol type: JSM-5400 LV).

The optical transmittance and reflectance of ZnO:Li films were recorded using Shimadzu UV-VIS 2101 PC dual beam spectrometer in the wavelength range from 190 to 900 nm. The measurements were carried out at room temperature with surrounding medium of dried air.

3. Results and discussion

Typical XRD measurements of the as-deposited films are shown in Fig. 1(a). It is clear that the type of substrate plays an important role in the crystallinity of the ZnO:Li films. The films deposited onto quartz substrates showed a large peak at $2\theta \cong 34^\circ$, which was attributed to (002) ZnO. This indicates that the deposited film has a good orientation along the c -axis. For films deposited on MgO and Sapphire substrates, c -axis ordering is degraded as shown in Fig. 1(a) but they still give the Wurtzite hexagonal structure. SEM images revealed smooth surface morphology without cracks and hillocks, see Fig. 1(b). The grain distribution is uniform but dense microstructure is relevant in films deposited onto quartz substrate.

The optical transmission and reflection spectra are given in Figs. 2 and 3 in the wavelength from 300 to

800 nm. The observed high transmittivity of these films suggests that ZnO:Li films have good transparency, especially above 700 nm wavelength.

The total absorption coefficient was calculated using the relation [11]

$$\alpha = \frac{1}{d} \ln \left[\frac{(1-R)^2}{2T} + \left\{ \frac{(1-R)^4}{4T^2} - R^2 \right\}^{0.5} \right], \quad (1)$$

where d is the thickness, R is the reflectance and T is the transmittance.

Generally, the equation (written here in a simplified form) used to determine the band-gap nature and the value of E_g (the gap energy) is [12]

$$(\alpha h\nu) = A(h\nu - E')^n. \quad (2)$$

Here, A is a constant that depends on the transition, $h\nu$ is the photon energy and E' the transition energy ($E_{\text{gd}}^{\text{opt}}$ for direct transitions, $E_{\text{gd}}^{\text{opt}} \pm E_p$ for indirect transitions [13], i.e. E_p being the energy of the associated phonon) and the value of the exponent n depends on the nature of the optical transition type ($n = \frac{1}{2}, \frac{1}{3}, 2, \frac{2}{3}$ for allowed and forbidden indirect transitions, and for allowed and forbidden direct ones, respectively). An analysis of the absorption spectrum of Fig. 2 shows that the absorption coefficient can be reasonably well fitted by Eq. (2) with $n = \frac{1}{2}$. This means that (ZnO:Li) films deposited on sapphire, MgO and quartz substrates have an allowed direct interband transition which corresponds to the fundamental absorption edge of these films.

Fig. 4 shows the plot of $(\alpha h\nu)^2$ versus photon energy near the absorption edge of ZnO:Li. Values of the optical energy gap for films deposited on sapphire, MgO or quartz substrates are obtained by extrapolating the linear regions to $(\alpha h\nu)^2 = 0$. Values of the room temperature optical energy gap $E_{\text{gd}}^{\text{opt}}$ and the constant A are listed in Table 1. It is clear that the obtained values of $E_{\text{gd}}^{\text{opt}}$ depend on the substrate type. Also, the admixture of ZnO with Li ions generally increases the value of $E_{\text{gd}}^{\text{opt}}$ over that of pure ZnO films. We can say that Li doping converts the shallow donor Zn sublevels to deep sublevels below the conduction band. This coincides with the results of Sbrveglieri et al. [14]. They conclude that Li ions lead to the formation of two deep-level donors in ZnO thin films which are, respectively, 0.38 and 0.81 eV below the conduction band, while the undoped films show two levels at 0.16 and 0.48 eV. In the case of the quartz substrate, the value of $E_{\text{gd}}^{\text{opt}}$ is near to that of pure ZnO films which may be attributed to the very good c -axis orientation in this case (see Fig. 1 (a)).

For a better understanding of the physical properties of ZnO:Li films, it is interesting to study some optical constants used to describe the optical properties, e.g. the high-frequency dielectric constant ϵ'_ω and the relative carrier concentration N/m^* .

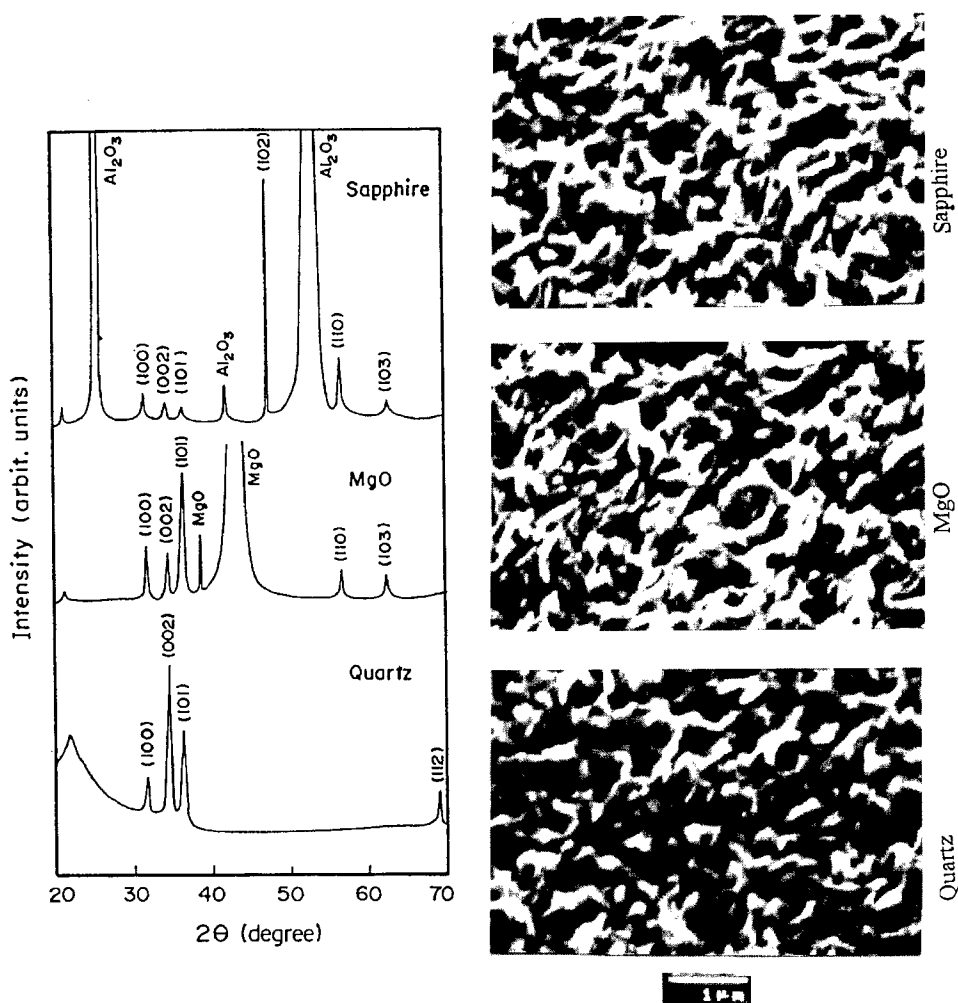


Fig. 1. (a) X-ray diffraction patterns and (b) SEM images of the as-prepared ZnO:Li films deposited on sapphire, MgO and quartz substrates at 573 K.

Table 1
Optical constants for as-prepared ZnO:Li films deposited on sapphire, MgO and quartz substrates

Physical quantity	Films deposited on sapphire substrates	Films deposited on MgO substrates	Films deposited on quartz substrates
Direct allowed energy gap $E_{\text{gd}}^{\text{opt}}$ (eV)	3.384 ± 0.05	3.425 ± 0.05	3.285 ± 0.05
The constant ($A \times 10^{12}$)	2.45	3.61	3.93
High-frequency dielectric constant (ϵ'_{∞})	8.33 ± 0.05	9.06 ± 0.05	4.13 ± 0.05
N/m^* (10^{21} cm^{-3})	8.07 ± 0.05	8.65 ± 0.05	3.39 ± 0.05

Accordingly [15], the real component of relative permittivity (ϵ') and the square of the wavelength (λ^2) are related by

$$\epsilon' = n^2 = (1 + \sqrt{R}/(1 - \sqrt{R}))^2,$$

$$= \epsilon' - e^2/\pi c^2 N/m^* \lambda^2, \quad (3)$$

where n is the refractive index, e is the electronic charge and c the velocity of light.

From this equation, the high-frequency component of the relative permittivity (ϵ'_{∞}) and the ratio of the carrier

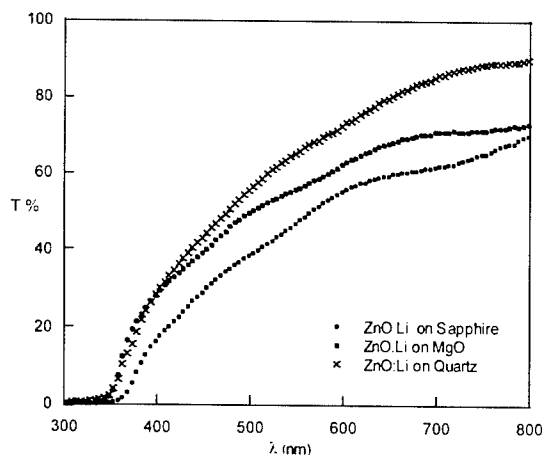


Fig. 2. Spectral distribution of the optical transmittance for the as-prepared ZnO:Li films deposited on sapphire, MgO and quartz substrates at 573 K.

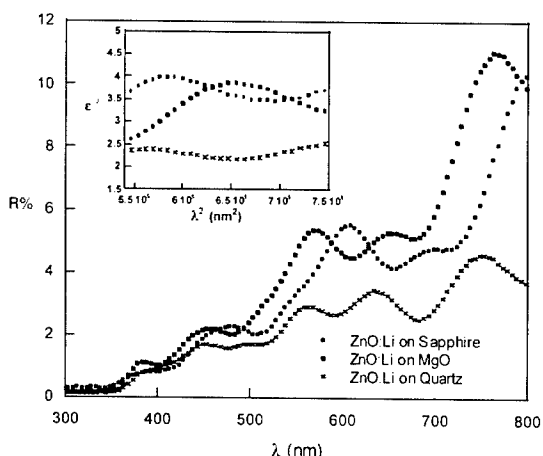


Fig. 3. Spectral distribution of the optical reflectance for the as-prepared ZnO:Li films deposited on sapphire, MgO and quartz substrates at 573 K. The inset is the real dielectric permittivity (ϵ') versus λ^2 .

concentration to the effective mass N/m^* could be determined.

The inset of Fig. 3 shows the relation between relative permittivity (ϵ') and λ^2 for (ZnO:Li) films deposited on sapphire, MgO and quartz substrates. It can be noticed that relative permittivity decreases exponentially with increasing λ^2 . To obtain the high-frequency dielectric constant, Eq. (4) was applied on the linear parts of these curves. The values of ϵ' , and N/m^* are given in Table 1.

In general, it can be concluded that both the the high-frequency dielectric constant and the ratio N/m^* are related to the internal microstructure, as can be emphasized by considering the results in Table 1 together

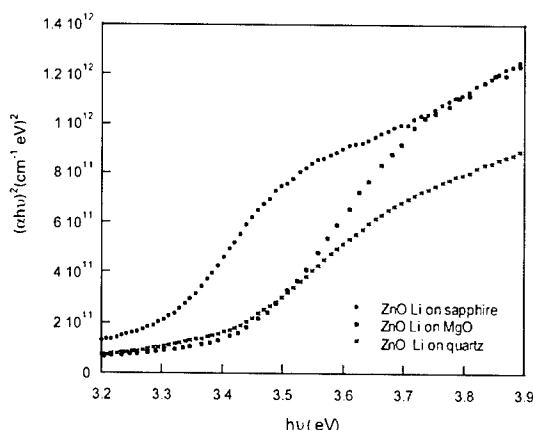


Fig. 4. Relation between $(\alpha h\nu)^2$ and photon energy ($h\nu$) for the as-prepared ZnO:Li films deposited on sapphire, MgO and quartz substrates at 573 K.

with those in Fig. 3, most of the changes in the N/m^* ratio are regarded as corresponding to the change in N .

4. Summary

Zn_{1-x}Li_xO films with $x = 0.2$ onto sapphire, MgO and quartz substrates are prepared by DC sputtering method at about 573 K. The films are highly c -axis-oriented, normal to the surface with high transmittance in the case of quartz substrate, while non-uniform orientation with reduced transmittance is obtained for both sapphire and MgO substrates. The films show direct allowed optical transitions with $E_{\text{gd}}^{\text{opt}}$ values of 3.38, 3.43 and 3.29 eV for films deposited on sapphire, MgO and quartz substrates, respectively. Values of ϵ' , and N/m^* are dependent on the substrate kind. It is important to study the effect of temperature on the optical properties of ZnO:Li thin films. These films are good to examine the ferroelectric phase transition at 613 K by optical measurements at high temperatures above ambient, this is now under study. In this case, the present samples will be very suitable for applications in optical memory devices.

Acknowledgements

We do thank Prof. T. Yamazaki of Toyama university, Japan, for the facilities provided during the preparation of the specimens.

References

- [1] F.S. Hickernell, IEEE Trans. MTT 17 (1969) 957.

- [2] C. Campbell, *Surface Acoustic Wave Devices and Their Signal Processing Applications*, San Diego, Academic Press, 1989.
- [3] T. Shiozaki, M. Ooishi, S. Ohmishi, A. Kawabata, *Proceedings of the First Meeting on Ferroelectric Materials and Their Applications*, Kyoto, 1977, p. 43.
- [4] H.D. Megaw, *Crystal Structures, A Working Approach*, W.B. Saunders Company, Philadelphia, 1973, p. 88.
- [5] E.D. Kolb, R.A. Laudise, *J. Am. Ceram. Soc.* 49 (1966) 302.
- [6] S. Takada, *J. Appl. Phys.* 73 (10) (1993) 4739.
- [7] F.S. Mahmood, R.D. Gould, *Thin Solid Films* 253 (1994) 529.
- [8] K. Tominaga, M. Kataoka, T. Ueda, M. Chong, Y. Shintani, I. Mori, *Thin Solid Films* 9 (1994) 253.
- [9] Z.C. Jin, I. Hamberg, C.G. Granqvist, *J. Appl. Phys.* 64 (1988) 5117.
- [10] M. Joseph, H. Tabata, T. Kawai, *Appl. Phys. Lett.* 74 (19) (1999) 2534.
- [11] Pankove, J.I., *Optical Processes in Semiconductors*, Dover, New York, 1971, p. 103.
- [12] T.S. Moss, *Semiconductor Opto-electronics*, Butterworths, London, 1973, p. 48 (Chapter 3).
- [13] I. Watanabe, T. Okumura, *Jpn. J. Appl. Phys.* 25 (1986) 1851.
- [14] G. Sberveglieri, S. Groppelli, P. Nelli, F. Quaranta, A. Valentini, L. Valentini, *Sensors Actuators B* 7 (1992) 747.
- [15] M. Di Giulio, D. Manano, R. Rella, P. Siciliano, A. Tepore, *Solar Energy Mater.* 15 (1987) 209.



ELSEVIER

Physica B 308–310 (2001) 954–957

PHYSICA B

www.elsevier.com/locate/physb

Metastable defect characterization in $\text{Cd}_{0.9}\text{Mn}_{0.1}\text{Te}:\text{In}$

E. Placzek-Popko^{a,*}, P. Becla^b^a*Institute of Physics, Wrocław University of Technology, Wybrzeże Wyspiańskiego 27, 50 370 Wrocław, Poland*^b*Department of Materials Science and Engineering, Massachusetts Institute of Technology, Cambridge, USA*

Abstract

In indium doped $\text{Cd}_{0.9}\text{Mn}_{0.1}\text{Te}$, the presence of metastable defects has been detected by observation of persistent photoeffects. By DLTS measurements several deep levels have been found and one of them exhibited thermally activated capture cross section, indicating on its metastable character. Photocapacitance measurements performed at liquid nitrogen temperature yield optical threshold energy for the deep-shallow transition equal to around 0.75 eV. This value is 0.63 eV higher than the thermal activation energy. The large difference between these two energies has confirmed strong interaction of related defect with surrounding lattice. © 2001 Elsevier Science B.V. All rights reserved.

PACS: 73.30

Keywords: Deep levels; Metastability; CdTe

1. Introduction

It has been well established that persistent photoeffects observed in many III–V and II–VI semiconducting compounds are due to the presence of metastable defects in the materials, the so-called DX centers. For $\text{Cd}_{1-x}\text{Mn}_x\text{Te}:\text{In}$ persistent photconductivity has been reported for manganese content $x > 7\%$ [1]. These photoeffects were also observed by us in indium doped $\text{Cd}_{0.9}\text{Mn}_{0.1}\text{Te}$ [2] and $\text{Cd}_{0.8}\text{Mn}_{0.2}\text{Te}$ [3]. In the former case the persistent photoeffects were observed after exposure of the samples to illumination at temperatures as high as 150 K. approximately. Illumination from a halogen lamp at 77 K increased the conductivity of the material by about two orders of magnitude and such high conductivity persisted for a very long time after turning off the light [2]. The existence of metastable defects in this material has been further confirmed by the results of thermally stimulated capacitance studies. Identification of the levels responsible for the persistent photoeffects has been reported in Ref. [2]: DLTS studies,

carried out within the 77–360 K temperature range, revealed five distinct traps. One of the traps, labeled as E1, of binding energy equal to 0.12 eV, had a high concentration and its capture cross section was found to be thermally activated. It has been assumed therefore that trap E1 is related to DX center in the studied $\text{Cd}_{0.9}\text{Mn}_{0.1}\text{Te}:\text{In}$ and this trap is responsible for the persistent photoeffects observed in the material.

Direct evidence for DX center presence in the material would be large Stokes shift, i.e. the difference between optical threshold and thermal activation energy of the deep level associated to the center. The aim of present paper was to determine the photoionization threshold energy corresponding to the metastable defect in order to evaluate the Stokes shift. For this purpose, photocapacitance measurements have been performed and the results have been given in this paper.

2. Experiment

Experiments were performed on the as-grown samples of indium doped $\text{Cd}_{0.9}\text{Mn}_{0.1}\text{Te}$ processed by the Bridgman method. Prior to the measurements, the samples were annealed in cadmium atmosphere to reduce the

*Corresponding author. Tel.: +48-71-320-2642; fax: +48-71-328-3696.

E-mail address: popko@if.pwr.wroc.pl (E. Placzek-Popko).

level of compensation in the material due to cadmium vacancies. Slices of the material were prepared by mechanical polishing followed by chemical etching in 2% Br_2 in methanol solution to remove the remaining surface layer. In order to perform capacitance and DLTS measurements, Schottky barriers were prepared by evaporation of gold 1 mm^2 layer on the front side of the samples in the vacuum of 10^{-6} Torr. Ohmic contacts were produced by soldering indium onto the fresh backside surface. Capacitance–voltage measurements yielded the room temperature donor concentration equal to $2 \times 10^{16}\text{ cm}^{-3}$.

The photocapacitance measurements were carried out after exposing the samples, at 77 K, to monochromatic light. Photons of energy within 0.6–1.5 eV range were used. As a light source a tungsten lamp was applied. The monochromatic light beam coming out of the monochromator was focused with the help of a fiber optic onto the sample, mounted in the sample holder immersed into liquid nitrogen. It should be pointed out that photocapacitance measurements are used as a technique complementary to DLTS. The DLTS system (DLS-82E) used by us allows determination of deep levels of energies within 0.1–0.9 eV interval. The photocapacitance measurements provide us with missing higher energy levels.

3. Results and discussion

The photocapacitance transient measurements comprise of the measurements of change in a capacitance of a diode due to photoemission of carriers from metastably occupied deep levels. Initially the diode is cooled down to 77 K at zero voltage bias, so that the deep levels are neutral (here in the case of an n-type sample, occupied by electrons). At this temperature reverse bias is superimposed and after a few minutes, when capacitance reaches its quasi-equilibrium value, the light is switched on and the diode is illuminated with monochromatic light. For a metal–n-type semiconductor, electrons photoemitted from the metastably occupied levels to conduction band are immediately swept out of the depletion region of a diode, revealing increase in the net positive charge of the region and increase in capacitance of a diode. The capacitance transients are then recorded for several minutes by a computer. Since in the case of studied material photoionization was persistent at 77 K, the sample had to be warmed up to the temperature at which persistent photoeffects were no more observed prior to measurement for each wavelength.

It was found that the optical threshold for the light induced capacitance change was equal to 0.67 eV. Exemplary capacitance transients taken at 77 K for three different wavelengths, 1.65 (0.75 eV), 1.35 (0.92 eV)

and $1\text{ }\mu\text{m}$ (1.24 eV) are given in Fig. 1. It was found that only the capacitance transients related to photons of energy lower than 0.83 eV could be well fitted with a single exponential. Photons of higher energies resulted in photocapacitance transients composed of two exponentials: “fast” component of time constant of the order of seconds and “slow” components of the order of tenths or hundreds of seconds, already existing for lower photon energies. The first component dominated capacitance transients for short time period after onset of illumination, whereas the slow was predominant for the longer time periods. Above statements are better documented in Fig. 2, in which parts of the transients presented in Fig. 1, corresponding to the capacitance under illumination, are given in a semi-logarithmic plot. In Fig. 2, capacitance change due to illumination, $\Delta C = C(t) - C(0)$, has been normalized to its steady state value $\Delta C_{ss} = C(\infty) - C(0)$ at each wavelength. The value ΔC_{ss} was determined from the least square fit of capacitance

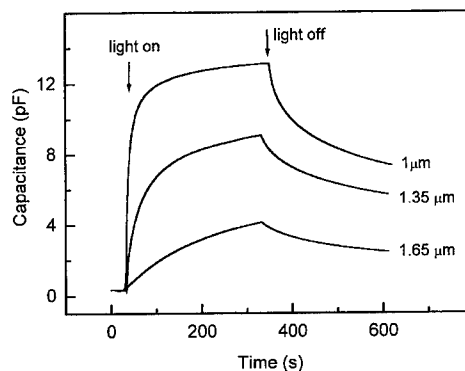


Fig. 1. Exemplary capacitance transients for indium doped $\text{Cd}_{0.9}\text{Mn}_{0.1}\text{Te}$ taken at 77 K for three different wavelengths, 1.65 (0.75 eV), 1.35 (0.92 eV) and $1\text{ }\mu\text{m}$ (1.24 eV).

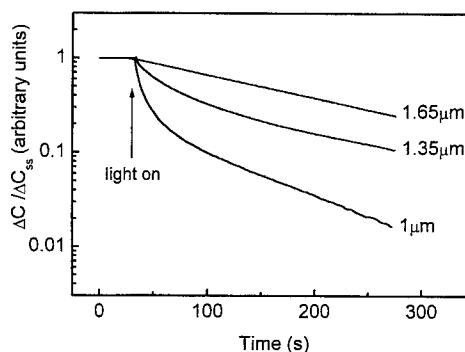


Fig. 2. The parts of the transients presented in Fig. 1, correspond to the capacitance under illumination. The capacitance change due to illumination, $\Delta C = C(t) - C(0)$, has been normalized to its steady state value $\Delta C_{ss} = C(\infty) - C(0)$ at each wavelength.

transients by a single exponential, or sum of exponentials, if necessary.

The results of photocapacitance measurements run within 0.6–1.5 eV photon spectral range are given in Fig. 3. In the figure, the dependence of steady state capacitance ΔC_{ss} on photon energy is shown. The spectrum increases monotonically for photons of energy higher than 0.67 eV. Several steps can be distinguished in the spectrum. In Fig. 3 the steps have been marked by arrows and corresponding threshold energies have been given. The steps are followed by a plateau (or increase), excluding the 1.3 eV threshold, followed by a decrease in capacitance. In order to explain the results, let us remind that $\Delta C_{ss}(h\nu)$ is proportional to the sum of contributions from different levels, located within energy interval extending up to $h\nu$. Each level introduces a step in the spectrum, near its threshold energy. The height of a step is related to the trap concentration N_T [4]:

$$\Delta C_{ss} \propto N_T \frac{e_{no}}{e_{no} + e_{po}}, \quad (1)$$

where e_{no} and e_{po} are electron and hole optical emission rates, and it has been assumed that thermal emission processes can be neglected at 77 K. If the process of photoemission of electrons dominates over the photoemission of holes, then ΔC_{ss} is directly related to N_T . Comparing results presented in Fig. 3 with Eq. (1) we may assume that for all measured capacitance transients excluding those connected with the 1.3 eV threshold, photoemission of electrons prevails over hole photoemission in spite of the fact that the higher energy levels are close to the valence band. According to Eq. (1) it means that for all measured capacitance transients besides the 1.3 eV threshold, photoemission of electrons prevailed over hole photoemission in spite of the fact that the higher energy levels are close to the valence band. This fact has been confirmed by MCTS measure-

ments. It was found, that only one hole trap is present, located 0.16 eV from the valence band top, which makes 1.34 eV distance from the bottom of conduction band, approximately equal to 1.3 eV threshold.

Assuming therefore, that in the case of 0.67, 0.75 and 1.05 eV thresholds, $\Delta C_{ss} \propto N_T$, we may conclude that the concentration of the trap related to the second threshold is predominant, and the contributions from the third and fourth levels can be neglected. We also noted that the decay of all the transients for energy higher than the second threshold was much faster than for the transients related to the first or second thresholds (cf. Fig. 1). Moreover, we also found that turning off the light for energies higher than 0.9 eV revealed immediate capacitance fall off to the level it reached for this energy. The same was observed for the transients induced by photons higher than the first threshold and lower than the second, after turning off the light capacitance relaxed to the value it had for 0.65 eV. Thus, we may assume that the first two thresholds are related to the photoemission from some metastable defects. Bearing this in mind, it becomes clear that the two exponentials, “fast” and “slow”, fitting well experimentally determined capacitance transients, are connected with photoionization of 0.67 and 0.75 eV deep levels related to the metastable defects.

Comparing this result with the previously mentioned suggestion based on DLTS studies, that level *E1* is related to a metastable defect, we come to the conclusion that one of the two thresholds 0.67 and 0.75 eV has to be related to optical transition from the level *E1*. As it was mentioned in introduction, level *E1* is related to some metastable defect of very high concentration. Of the two, 0.67 and 0.75 eV transitions, the latter is referred to as transition from a deep level of very high concentration. Therefore, it seems that we may attribute the 0.75 eV threshold to the optical transition and 0.12 eV energy to thermal transition from the same deep level, *E1*, yielding 0.63 eV Stokes shift. Such a high value of Stokes shift means large lattice relaxation for the defect, which is in accordance with the model of LLR proposed for DX centers in II–VI compounds [5]. Thus, obtained results confirm suggestion that the level *E1* is related to DX center in $\text{Cd}_{0.9}\text{Mn}_{0.1}\text{Te}:\text{In}$.

4. Conclusions

DLTS studies revealed the presence of a deep level, labeled as *E1*, attributed to metastable defect in $\text{Cd}_{0.9}\text{Mn}_{0.1}\text{Te}:\text{In}$, of binding energy equal to 0.12 eV. The photocapacitance measurements yield photoionization thresholds at energies equal to 0.67, 0.75, 1.05 and 1.3 eV. All of them, besides the last one are related to electron photoemission. The 0.75 eV threshold is related to metastable defects of a very high concentration. It has

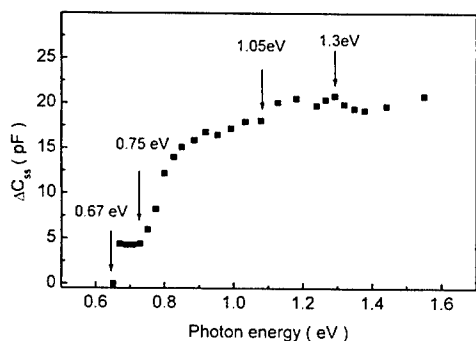


Fig. 3. Photocapacitance spectrum, i.e. the dependence of steady state capacitance ΔC_{ss} on photon energy. The value ΔC_{ss} was determined from the least square fit of capacitance transients by a single exponential, or sum of exponentials, if necessary.

been therefore attributed to the optical transition from the level $E1$. The difference between the optical and thermal transitions for the level $E1$ yields large Stokes shift, equal to 0.63 eV. Thus, it may be assumed that this level is related to DX center.

References

- [1] I. Terry, I. Penny, S. von Molnar, P. Becla, *Solid State Comm.* 84 (1992) 235.
- [2] J. Szatkowski, E. Placzek-Popko, K. Sierański, J. Fiałkowski, J.M. Wróbel, P. Becla, *Physica B* 273–274 (1999) 879.
- [3] J. Szatkowski, E. Placzek-Popko, K. Sierański, J. Fiałkowski, J.M. Wróbel, P. Becla, *Physica B* 292 (2000) 114.
- [4] P. Blood, J.W. Orton, *The Electrical Characterization of Semiconductors: Majority Carriers and Electron States*, Academic Press, New York, 1992 (Chapter 13).
- [5] C.H. Park, D.J. Chadi, *Phys. Rev. B* 52 (1995) 11884.



ELSEVIER

Physica B 308–310 (2001) 958–962

PHYSICA B

www.elsevier.com/locate/physb

Vacancies in CdTe: experiment and theory

S. Lany*, V. Ostheimer, H. Wolf, Th. Wichert

Technische Physik, Universität des Saarlandes, 66041 Saarbrücken, Germany

Abstract

Ab initio calculations in the framework of density functional theory are employed to complement experimental PAC and EPR data on vacancies in CdTe. The Te vacancy is found to be a negative-U centre with a large lattice relaxation in the neutral and the doubly charged state. The electronic state introduced by V_{Te} lies below the valence band maximum for V_{Te}^0 and shifts to above the conduction band minimum for V_{Te}^{+1} . An experimentally observed electric field gradient is interpreted in terms of acceptor compensation by V_{Te}^{+1} . Experimental data available for the Cd vacancy are discussed in the context of the calculated electric field gradients. A Jahn–Teller effect for V_{Cd} is not confirmed. © 2001 Elsevier Science B.V. All rights reserved.

PACS: 61.72.Vv; 71.55.Gs; 76.80.+y

Keywords: Vacancies; CdTe; EFG; DFT

1. Introduction

Besides intentionally introduced dopants and residual impurity atoms, intrinsic defects, e.g. vacancies and interstitials, can strongly influence the optical and electrical properties of semiconductors and consequently have been a subject of intense research [1,2]. Except for the positron annihilation spectroscopy (PAS), most locally sensitive methods investigate vacancies indirectly via the hyperfine interaction (HFI) at neighbouring nuclei. In order to determine vacancy-related HFI parameters, methods such as Mössbauer spectroscopy, electron paramagnetic resonance (EPR), electron nuclear double resonance (ENDOR) and perturbed angular correlation spectroscopy (PAC) have been used. The correct experimental identification and characterisation of vacancies, however, is more difficult compared to the investigation of impurity atoms, which can be introduced into the semiconductor crystal by a controlled doping process, e.g. by ion implantation.

As a theoretical instrument being generally helpful to characterise dopants in semiconductors as well as

intrinsic defects (e.g. Ref. [3]), the density functional theory (DFT) formalism is used in order to compensate for the particular difficulty to investigate vacancies. The DFT calculations yield defect-related information that is difficult to access by experiment such as about the electronic structure and structural relaxations. Additionally, the identification of a particular defect is supported by the calculation of defect-related parameters, such as the electric field gradient (EFG), which is used experimentally as a “fingerprint” of the studied defect.

In the present work, the EFG tensor—characterised by the largest component V_{zz} and the asymmetry parameter η —is measured by PAC (for details, see e.g. Ref. [4]), using the radioactive probe nuclides ^{111}In and ^{111}Ag . In II–VI semiconductors, the $^{111}\text{In}_{Cd}$ donor and the $^{111}\text{Ag}_{Cd}$ acceptor form donor–acceptor (D–A) pairs with dopants, residual impurities or intrinsic defects, and in either case the EFG is determined at the $I = 5/2$ excited state of the daughter isotope ^{111}Cd [4]. It is emphasised that in CdTe, the daughter isotope ^{111}Cd is a host atom and consequently the measured EFG characterises the isolated defect. The absolute number of radioactive probe atoms needed for PAC measurements is 10^{11} – 10^{12} , and the resulting concentrations are generally low enough (10^{15} cm^{-3} and less) that the

*Corresponding author. Tel.: +49-681-302-2702; fax: +49-681-302-4315.

E-mail address: lany@tech-phys.uni-sb.de (S. Lany).

electrical properties of the semiconductor crystals are not changed significantly.

The DFT calculations are performed using the linearised augmented plane wave (LAPW) method implemented in the WIEN97 [5] program package. The general treatment of an impurity in a semiconductor for EFG calculation within this method is described in Ref. [6]. In addition to the 32-atom supercell in BCC structure with T_d symmetry used in that work, a 32-atom cell with C_{3v} symmetry is used in the present case of the cadmium vacancy. In the LAPW method, the basis set consists of plane waves augmented by a spherical harmonics expansion within the so-called “muffin-tin” spheres around the atomic positions. In general, the wave functions are described by the plane wave basis at a vacancy site, but the use of an “empty sphere” allows an angular momentum decomposition of the vacancy-related states for analysis purposes. Magnetic hyperfine fields are not calculated in the present work.

2. The tellurium vacancy

From simple valence arguments, the tellurium vacancy V_{Te} accounts for a double donor, having an occupied a_1 level (s-like) and an unoccupied t_2 level (p-like) in the neutral state. Thus, no Jahn–Teller effect and no symmetry lowering from T_d symmetry is expected. A paramagnetic centre observed by EPR [7] and ENDOR [8] has been interpreted as V_{Te}^+ , but this assignment was questioned in Ref. [9], where calculations with the linear muffin-tin orbital method in the atomic sphere approximation (LMTO-ASA) yielded HFI constants incompatible with the experimental results. Furthermore, the ENDOR data require that the electron spin is localised at the vacancy site to about 96%, which is rather implausible for a vacancy and strongly differs from the theoretical localisation of 20% of the electron spin within the ASA sphere.

Using a 32-atom cell with all neighbouring atoms of the tellurium vacancy fixed at ideal lattice positions, i.e. suppressing the relaxation, we find the a_1 level (Kohn–Sham eigenvalue) within the gap for all three charge states V_{Te}^0 , V_{Te}^+ and V_{Te}^{++} , occupied by two, one and zero electrons, respectively. The localisation of 10% of the electron (a_1 level) within the LAPW muffin-tin sphere for V_{Te}^+ compares well with the 20% for the LMTO-ASA sphere, taking into account the different volumes of the respective spheres. From the positions of the a_1 level for the three charge states with respect to the valence band maximum (VBM), the transition energies $E(+ + / +) = E_{VBM} + 0.76$ eV and $E(+ / 0) = E_{VBM} + 1.22$ eV are inferred, which are in good agreement with the electron removal energies of 0.67 and 1.27 eV, reported in Ref. [9].

Taking into account the relaxation of nearest neighbour (NN) Cd atoms, which was not possible in the LMTO calculations from Ref. [9], has drastic implications. With exception of V_{Te}^+ , strong relaxation occurs resulting in a shift of the energetic position of the a_1 level and a significant lowering of the total energy (see Table 1). In Fig. 1a, the total electronic density of states (DOS) is shown for the relaxed configurations of the three charge states (note that for the unrelaxed configuration of all three charge states, the DOS resembles the DOS shown for V_{Te}^+ , except from the occupation number). In Fig. 1b, the a_1 level and the t_2 level are identified by the respective s and p character within the muffin-tin sphere at the vacancy site. Only for V_{Te}^+ , the a_1 level is still positioned within the band gap after relaxation. While for V_{Te}^0 , the strong inward relaxation of the NN-Cd atoms leads to a shift of the a_1 level to below the VBM, this level is shifted to above the conduction band minimum (CBM) during the outward relaxation in the $2+$ state. The $2+$ state of V_{Te} is comparable with the $3+$ state of the arsenic vacancy in GaAs, which also has an empty a_1 level and was calculated in Ref. [10]. There, the observed outward relaxation of the NN-Ga atoms was interpreted by the authors in terms of a rehybridisation towards sp^2 bonding. A similar argument holds in the present case for V_{Te}^{++} , where the NN-Cd atoms move about 60% of their way towards a planar sp^2 bonding configuration with the NNN-Te atoms. In the neutral state of V_{Te} , the a_1 orbital is *fully occupied* and there is a pronounced p_z-like contribution within the NN-Cd spheres (the local z-axis directs towards the vacancy). Consequently, the sp^3 configuration is retained from the point of view of an NN-Cd atom, causing the strong inward relaxation of the NN-Cd shell. After relaxation, the a_1 level is located 0.5 eV below the VBM (cf. Fig. 1b, left-hand side). In the singly charged state V_{Te}^+ , where the a_1 level is *half occupied*, the counteracting mechanisms described for V_{Te}^0 and V_{Te}^{++} approximately cancel each other, leading to only little relaxation and energy gain (cf. Table 1).

The transition energy between two charge states measures the Fermi level E_F for which the formation

Table 1

Relaxation Δd_{NN} of the NN-Cd atoms about V_{Te} (in per cent of the bond length 2.81 Å of CdTe, a negative sign is indicating an inward relaxation), along with the relaxation energy ΔE_r , which is the energy lowering due to relaxation, and the calculated electric field gradient V_{zz} at a NN-Cd site ($\eta = 0$ due to symmetry)

	Δd_{NN} (%)	ΔE_r (eV)	V_{zz} (10^{21} V/m ²)
V_{Te}^0	−22	0.98	+2.0
V_{Te}^+	−2	0.05	+16.2
V_{Te}^{++}	+20	0.69	+24.6

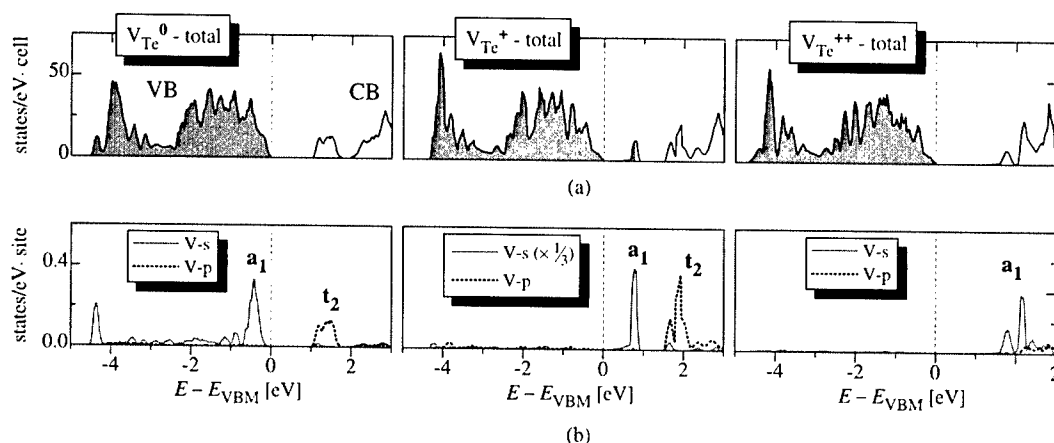


Fig. 1. (a) Total DOS for V_{Te}^0 , V_{Te}^+ , V_{Te}^{++} . Occupied states are shaded. (b) Local DOS at the vacancy site decomposed into s and p contributions. For V_{Te}^+ , the half filled a_1 level in the band gap is very narrow, therefore the s contribution needs a different scaling ($\times 1/3$) to be displayed.

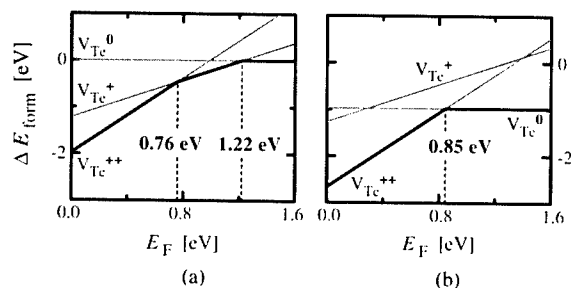


Fig. 2. Relative formation energies for the different charge states of V_{Te} as a function of E_F . (a) Relaxation suppressed. (b) Including relaxation. The left and the right margin of each plot corresponds to the VBM and the CBM, respectively; $\Delta E_{\text{form}} = 0$ corresponds to the unrelaxed configuration of V_{Te}^0 .

energy E_{form} of both states is equal (the formation energy of charged defects depends on E_F). Accordingly, the relative formation energy ΔE_{form} with respect to V_{Te}^0 is plotted in Fig. 2a in the case of suppressed relaxation. Due to the relaxation, however, the formation energies are lowered by the respective relaxation energies ΔE_r (Fig. 2b). In fact, the large relaxation energies for V_{Te}^0 and V_{Te}^+ (cf. Table 1) result in a negative-U behaviour with a transition energy of $E(+/-0) = E_{\text{VBM}} + 0.85 \text{ eV}$ between V_{Te}^+ and V_{Te}^0 , and the paramagnetic state V_{Te}^+ is never the most stable state, independent of the Fermi energy. Consequently, it should not be observed in an EPR experiment. Therefore, the rejection of the EPR identification of V_{Te} in Ref. [9] is confirmed. The fact that for the calculations of the HFI constants in Ref. [9] relaxation was neglected, does not harm, because in the paramagnetic $1+$ state the relaxation is quite small (cf. Table 1).

It is pointed out that the tellurium vacancy exhibits a rather extreme Franck–Condon effect, and thermal and optical excitation energies are no longer comparable. An optical excitation does not seem possible at all, because in the stable states V_{Te}^0 and V_{Te}^{++} , the a_1 level is “hidden” in the valence band and in the conduction band, respectively. According to our LAPW calculations, the negative-U effect for the Te vacancy is very strongly pronounced, so that this property should not be affected by errors that may arise from the local density approximation and the estimation of the transition energies via the level positions. The negative-U behaviour accompanied by large lattice relaxation seems to be a rather general feature of anion vacancies in II–VI semiconductors; it has been found also for V_{Se} in ZnSe [11], while the extreme shift of the a_1 level into the valence band (neutral state) and into the conduction band ($2+$ state) was not reported there.

In order to investigate the interaction between Ag and Cu dopants, 2 nm copper were evaporated onto a CdTe crystal implanted with ^{111}Ag ions. After subsequent annealing at 500 K, PAC measurements yield an EFG of $V_{zz} = \pm 22.8(9) \times 10^{21} \text{ V/m}^2$ with $\eta = 0.0(3)$ ($T_M = 295 \text{ K}$). This value, which is unusually high for an EFG measured at the ^{111}Cd nucleus in CdTe, is close to the calculated EFG at an NN-Cd site for V_{Te}^+ , $V_{zz} = +24.6 \cdot 10^{21} \text{ V/m}^2$ with $\eta = 0$ (see Table 1). Based on the EFG calculations for interstitial Ag in CdTe, it is not expected that the interaction of ^{111}Ag with Cu atoms, e.g. the formation of $^{111}\text{Ag}_{\text{Cd}}\text{—Cu}_i$ pairs, would result in the observation of such a strong EFG. Therefore, the observed EFG is interpreted with the formation of close $^{111}\text{Ag}_{\text{Cd}}\text{—}V_{\text{Te}}^+$ pairs and shows the capability of the Te vacancy to compensate group I acceptors.

3. The cadmium vacancy

After the D–A pair formation of ^{111}In donors with the double acceptor V_{Cd} , the PAC probe is a NNN-atom with respect to the defect causing the EFG. Three distinct EFG have been reported in literature for the $^{111}\text{Cd}-V_{\text{Cd}}$ pair: One, labelled EFG1 in the following (values are given in Table 2), is observed after annealing ^{111}In -doped CdTe under tellurium vapour pressure [12,13]. A set of two EFG, EFG2 and EFG3, is observed simultaneously in crystals doped additionally with stable In to a level higher than 10^{18} cm^{-3} [14]. Similar EFG have been reported for ternary $\text{Hg}_{0.05}\text{Cd}_{0.95}\text{Te}$ compounds [15]. The stronger EFG, EFG2 and EFG3, which are observed when a background donor doping level is present, have been discussed in Refs. [14] and [15] in terms of a different charge state of V_{Cd} and the possibility that two In donors (one stable In atom and one ^{111}In isotope) bind to the double acceptor V_{Cd} . The LAPW calculations, using a 32-atom supercell in T_d symmetry containing a Cd vacancy, yield an atomic relaxation ($\Delta d_{\text{NN}} \approx -13\%$) which is less pronounced than in the case of V_{Te} and essentially independent of the charge state. In Table 2, the experimentally observed EFG are compared with the EFG calculated for the NNN-Cd site: Assigning EFG1, EFG2, and EFG3 to the neutral, singly, and doubly charged Cd vacancy, respectively, yields a relatively good agreement between experimental and theoretical data. It is noted, however, that in the 32-atom supercell, only three of the four Te neighbours to the Cd probe are contained within the supercell and a larger cell should be used. First calculations with a 64-atom supercell are currently running, indicating changes in the calculated EFG that are not very large, but significant. Therefore, the assignment of EFG1, EFG2, and EFG3 to the three charge states of V_{Cd} is only tentative at present, and the possibility that two In atoms bind to V_{Cd} cannot be excluded.

In the simple orbital model, the neutral cadmium vacancy has a fully occupied a_1 level and a t_2 level, which is partly occupied by four electrons. In principle, V_{Cd}^0 and the paramagnetic state V_{Cd}^- can be subject to a Jahn–Teller effect due to the partial occupation of the t_2

level. In this case, the t_2 orbital (p-like) would split into an occupied e level (p_{xy} -like) and an unoccupied (V_{Cd}^0) or half occupied (V_{Cd}^-) upper a_1 level (p_z -like), accompanied by a symmetry lowering from T_d to C_{3v} ; i.e. one NN-Te atom would relax stronger towards the vacancy site than the others (cf. Ref. [16], where V_{Zn} in ZnSe is discussed). An EPR signal, presenting trigonal symmetry, has been interpreted as resulting from V_{Cd}^- in a Jahn–Teller distorted configuration with the hole localised at one Te neighbour [17]. In order to investigate the Jahn–Teller effect theoretically, calculations with a 32-atom supercell in C_{3v} symmetry were performed. The interesting result is that the calculated forces on the NN-Te atoms tend to restore deviations from T_d symmetry for both the neutral and the singly charged state. Even for a strong trigonal distortion, no single, unoccupied band (the upper a_1 level, containing the holes localised at one Te neighbour) would separate from the valence band in the case of V_{Cd}^0 , as expected in the presence of a Jahn–Teller effect. Rather the holes occupy valence band like states and are moderately localised at the NN-Te shell (6% within each muffin-tin sphere of the NN-Te atoms). Thus, the DFT calculations clearly disagree with the assumption of a Jahn–Teller effect. It is further noted that in case of a Jahn–Teller distortion, the NNN-Cd atoms are no longer equivalent, and a set of three EFG instead of a single one should be observed for both the neutral and the singly charged state of V_{Cd} . This behaviour is not reflected by the PAC experiments. The discrepancies regarding the Jahn–Teller effect and the different possible interpretations of the experimentally observed EFG show that the cadmium vacancy still deserves further investigation.

4. Summary and outlook

DFT calculations of the tellurium vacancy in CdTe give access to the complex behaviour of this defect regarding the lattice relaxation and the electron structure which both change drastically with the charge state. Thus, a negative-U behaviour of V_{Te} is predicted and the paramagnetic V_{Te}^+ state should not be stable. Additionally, the acceptor compensation by doubly charged Te vacancies is discussed on the basis of the calculated EFG and experimental PAC data. As for the cadmium vacancy, the presence of a Jahn–Teller distortion is not confirmed. First calculations using a 32-atom supercell with symmetrical relaxation around the Cd vacancy yield a reasonable agreement with experimentally determined EFG, but due to the fact that the site of the probe atom is the next nearest neighbour to the vacancy, the use of a larger supercell is indicated. Calculations with a 64-atom supercell are expected to

Table 2

Experimental and theoretical values for the EFG caused by the Cd vacancy at the NNN-Cd site. V_{zz} values are given in units of 10^{21} V/m^2 . The experimental error of V_{zz} and η is lower than $0.1 \times 10^{21}\text{ V/m}^2$ and 0.05, respectively

	Experiment ($T_M = 295\text{ K}$)			theory		
	EFG1	EFG2	EFG3	V_{Cd}^0	V_{Cd}^-	V_{Cd}^{--}
V_{zz}	± 3.0	± 5.1	± 5.6	−3.0	−4.1	−5.0
η	0.17	0.12	0.20	0.01	0.14	0.24

improve the detailed interpretation of the experimental data.

Acknowledgements

The financial support of the Bundesministerium für Bildung und Forschung (BMBF) under Contract No. 03WI4SAA is gratefully acknowledged.

References

- [1] M. Stavola (Ed.), Identification of defects in semiconductors. Semiconductors and Semimetals, vols. 51A and 51B, Academic Press, San Diego, 1999, and references therein.
- [2] G.F. Neumark, Mater. Sci. Eng. R21 (1997) 1, and references therein.
- [3] C.G. Van de Walle, D.B. Laks, G.F. Neumark, S.T. Pantelides, Phys. Rev. B 47 (1993) 9425.
- [4] Th. Wichert, in: M. Stavola (Ed.), Identification of Defects in Semiconductors. Semiconductors and Semimetals, vol. 51B, Academic Press, San Diego, 1999, pp. 297.
- [5] P. Blaha, K. Schwarz, J. Luitz, WIEN97, A Full Potential Linearized Augmented Plane Wave Package for Calculating Crystal Properties, Karlheinz Schwarz, Techn. Universität Wien, Austria, 1999, ISBN 3-9501031-0-4.
- [6] S. Lany, P. Blaha, J. Hamann, V. Ostheimer, H. Wolf, Th. Wichert, Phys. Rev. B 62 (2000) R2259.
- [7] B.K. Meyer, P. Omling, E. Weigel, G. Müller-Vogt, Phys. Rev. B 46 (1992) 15135.
- [8] D.M. Hofmann, B.K. Meyer, T. Pawlik, P. Altheld, J.-M. Spaeth, Mat. Sci. Forum 143–147 (1994) 417.
- [9] M. Illgner, H. Overhof, Phys. Rev. B 54 (1996) 2505.
- [10] J.E. Northrup, S.B. Zhang, Phys. Rev. B 50 (1994) R4962.
- [11] A. Garcia, J.E. Northrup, Phys. Rev. Lett. 74 (1995) 1131.
- [12] R. Kalish, M. Deicher, G. Schatz, J. Appl. Phys. 53 (1982) 4793.
- [13] Th. Wichert, T. Krings, H. Wolf, Physica B 185 (1993) 297.
- [14] T. Filz, J. Hamann, R. Müller, V. Ostheimer, H. Wolf, Th. Wichert, J. Cryst. Growth 159 (1996) 68.
- [15] J.C. Austin, Wm.C. Hughes, B.K. Patnaik, R. Triboulet, M.L. Swanson, J. Appl. Phys. 86 (1999) 3576.
- [16] G.D. Watkins, J. Cryst. Growth 159 (1996) 338, and references therein.
- [17] P. Emanuelsson, P. Omling, B.K. Meyer, M. Wienecke, M. Schenk, Phys. Rev. B 47 (1993) 15578.



ELSEVIER

Physica B 308–310 (2001) 963–966

PHYSICA B

www.elsevier.com/locate/physb

The strange diffusivity of Ag atoms in CdTe

H. Wolf^{a,*}, M. Deicher^a, V. Ostheimer^a, A. Rodriguez Schachtrup^b,
N.A. Stolwijk^b, Th. Wichert^a, ISOLDE Collaboration^c

^a *Technische Physik, Universität des Saarlandes, D-66041 Saarbrücken, Germany*

^b *Institut für Materialphysik, Universität Münster, D-48149 Münster, Germany*

^c *CERN-EP, CH 1211 Geneva 23, Switzerland*

Abstract

The diffusion of Ag atoms in CdTe was investigated using the radiotracer ¹¹¹Ag, which was introduced by implantation with an energy of 60 or 80 keV. The measured diffusion profiles are explained by assuming the existence of a repulsive interaction between Ag and residual Cu atoms causing a drift of the Ag atoms towards the centre of the crystal, which supposes the diffusion in a concentration gradient. This effect vanishes if the Ag concentration is increased and becomes more pronounced if the crystals are simultaneously co-doped with Cu. © 2001 Elsevier Science B.V. All rights reserved.

Keywords: Ag; Cu; Diffusion; CdTe

1. Introduction

The electrical and optical properties of semiconductors are essentially determined by the presence of impurities and defects. In addition, for the construction and thermal stability of devices, dynamic properties of dopant atoms are important. In CdTe, the group I elements represent potential acceptor atoms if they are incorporated substitutionally on Cd sites. The hole concentration achieved upon doping of CdTe with Ag atoms, however, is limited to about 10^{16} cm^{-3} , although much higher concentrations of Ag are realised [1]. The formation of compensating defect complexes strongly depends on the concentration and the mobility of the participating defects. For Ag atoms in CdTe, the mobility is known to be very high, the experimental data describing the diffusion of Ag in CdTe in the literature are difficult to compare [2–5].

2. Experimental details

¹¹¹Ag atoms were implanted into CdTe single crystals using either the mass separator at the university Bonn or the isotope separator ISOLDE at CERN. The energy and dose used for implantation of the different samples are listed in Table 1. In order to investigate the influence of a higher Ag concentration, a 30 nm thick layer of stable Ag was deposited onto a CdTe crystal and the ¹¹¹Ag atoms were implanted into this layer. In addition, the influence of Cu on the diffusion of Ag was investigated. For this purpose, a 20 nm thick Cu layer was deposited onto the side implanted with ¹¹¹Ag (sample #5) before annealing of the crystal. In each case, the diffusion of the CdTe crystals (6 mm diameter and 500 μm thick) was performed in an evacuated quartz ampoule for 30 min.

The CdTe crystals were mechanically polished and the mass loss was determined by weighing the crystal after each step of polishing. The thicknesses of the abraded layers ranged between 2 and 20 μm . The number of ¹¹¹Ag atoms within each layer was determined by measuring the intensity of the 342 keV γ -line of the radioactive decay of ¹¹¹Ag with a Germanium well-detector.

*Corresponding author. Tel.: +49-681-302-2038; fax: +49-681-302-4315.

E-mail address: h.wolf@tech-phys.uni-sb.de (H. Wolf).

Table 1

Preparation conditions of the CdTe crystals used for the diffusion experiments. The diffusion times were always 30 min

Sample	Ag layer	Energy (keV)	Dose (cm ⁻²)	Ag diffusion (K)	Cu diffusion
#1	—	80	10 ¹⁰	550	—
#2	—	60	10 ¹²	550	—
#3	—	60	10 ¹²	800	—
#4	30 nm	60	10 ¹²	800	—
#5	—	80	10 ¹⁰	550	550 K

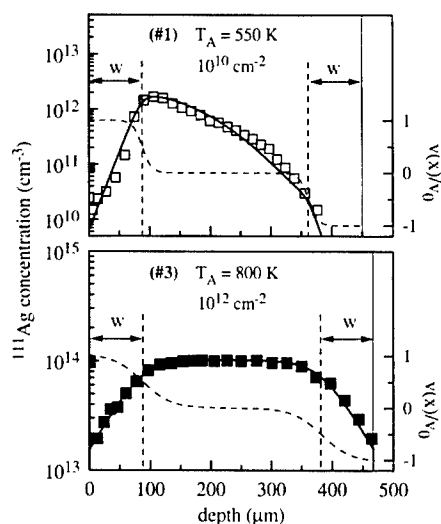


Fig. 1. ¹¹¹Ag profiles measured after annealing at 550 K (top) and 800 K (bottom). The dashed lines correspond to the right axes and show the drift velocity (Eq. (2)) used for fitting the diffusion profiles. The vertical solid line marks the back of the CdTe crystal and the vertical dashed lines indicate the range of different drift velocities described by the parameter w in Eq. (2).

3. Results

Fig. 1 (top panel) shows the diffusion profile of sample #1 after implantation of 10^{10} Ag cm⁻² with an energy of 80 keV and diffusion at 550 K. The measured concentration profile exhibits a depletion layer with a thickness of about 80 μm starting directly at the crystal surface. This region is followed by an asymmetric peak of the Ag concentration at a depth of about 110 μm. Under slightly changed conditions this experiment, which exhibited a peak concentration of only 2×10^{12} Ag cm⁻³, was repeated with a higher Ag concentration: A second crystal (sample #2) was implanted with a dose 100 times higher and with a slightly lower energy of 60 keV. The data in Fig. 2, presented at an enlarged

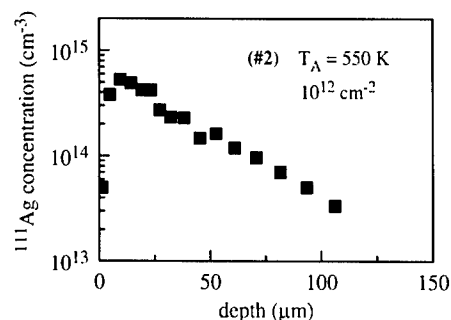


Fig. 2. ¹¹¹Ag profile measured after annealing at 550 K, but in contrast to Fig. 1 (top), a 100 times higher dose of ¹¹¹Ag was implanted. Note the enlarged depth scale.

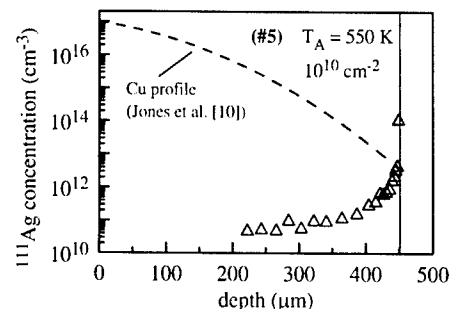


Fig. 3. ¹¹¹Ag profile measured after diffusing of Cu at 550 K. The dashed line shows the Cu profile, expected on the basis of data published by Jones et al. The vertical solid line marks the back of the crystal.

depth scale, still show the depletion zone below the surface, which in this case extends over 10 μm. If the diffusion temperature is increased from 550 to 800 K (sample #3), the data in Fig. 1 (bottom panel) show that the profile becomes symmetric over the entire crystal. The ¹¹¹Ag concentration in the central region of this crystal is almost constant at a value of 10^{14} cm⁻³ and decreases by one order of magnitude within a layer of about 100 μm towards both surfaces. It should be noted that a sample treated at the same temperature of 800 K but containing a significantly higher Ag concentration (sample #4 in Table 1), shows a profile that is nearly homogeneous at a concentration level of 5×10^{18} cm⁻³ over the entire crystal.

A drastic effect is visible if, in addition, Cu is evaporated onto the ¹¹¹Ag implanted surface before diffusion annealing at 550 K (sample #5). The data in Fig. 3 show that in this crystal the ¹¹¹Ag atoms are nearly completely moved to the back (i.e. to the non implanted side) of the crystal. This observation can be explained by assuming a repulsive interaction between the Cu and Ag atoms which causes a diffusion of the Ag

atoms to the other surface of the crystal. By comparing these data with the corresponding results at 550 K shown in Figs. 1 and 2, it could be stated that in Fig. 3 the depletion layer is extended over almost the whole crystal.

4. Discussion

The depletion layers of the ^{111}Ag profiles, visible in Figs. 1 and 2, cannot be explained by out-diffusion of ^{111}Ag during the cooling down process: There was neither a significant loss of the ^{111}Ag activity of the crystals nor a strong enrichment of ^{111}Ag atoms on the surface detectable after annealing of the crystals. In order to explain the depletion layer below the surface the existence of a repulsive effect for the Ag atoms is proposed, as is most drastically reflected by the data in Fig. 3. Motivated by the observed strong influence of the presence of Cu on the Ag diffusion profile, the reason for the repulsive effects in Figs. 1 and 2 can be assigned to the presence of extrinsic or intrinsic defects in the depleted layers of these crystals, probably to Cu. Considering the data in Fig. 1, a quantitative description of the measured ^{111}Ag profiles can be found semi-empirically by assuming a depth dependent drift velocity $v(x)$ of the Ag atoms. The corresponding drift-diffusion equations describing the Ag concentration c can be expressed by

$$j = -D\partial_x c + v(x)c \quad \text{and} \quad \partial_x j = -\partial_t c, \quad (1)$$

where j denotes the flux of Ag atoms through a plane parallel to the surface per time unit and D is the diffusion coefficient for Ag in CdTe. The symmetric Ag profile of sample #3 visible in Fig. 1 (bottom panel) seems to indicate the state of thermal equilibrium at the diffusion temperature of 800 K. The shape within the layer of 100 μm below each surface is determined by the balance between the inward directed drift velocity and the diffusion in a concentration gradient. In order to fit the boundary condition of a symmetric profile in thermal equilibrium, the velocity profile has to be an asymmetric function with respect to the centre of the crystal with thickness L . For fitting the data of samples #1 and #3 the drift velocity $v(x)$ was parameterised by the function

$$v(x) = -v_0\alpha[\tanh(s(x-w)) + \tanh(s(x-L+w))] \quad (2a)$$

with

$$1/\alpha = \tanh(sw) + \tanh(s(L-w)), \quad (2b)$$

which is plotted as a dashed curve in both panels of Fig. 1. This function has the values $+v_0$ and $-v_0$ in the regions of width w neighbouring the two surfaces, is nearly zero in between, and the parameter s controls the

transient between the different regions. Using this function, Eq. (1) was solved numerically. The ^{111}Ag concentration at $t = 0$ is determined by the approximately Gaussian implantation profile of about 20 nm width close to $x = 0$, and the boundary conditions are defined by a vanishing flux ($j = 0$) of ^{111}Ag atoms at both surfaces of the crystal. The diffusion data of samples #1 and #3 were fitted by variation of the parameters D , v_0 , s , and w . The resulting fits (solid lines in Fig. 1) account in a satisfactory way for both diffusion profiles measured at 550 and 800 K. In case of sample #1, the diffusion coefficient D and the drift velocity v_0 are determined to be $D = 3 \times 10^{-8} \text{ cm}^2/\text{s}$ and $v_0 = 0.2 \mu\text{m}/\text{s}$, whereas in case of sample #3 only the ratio $D/v_0 = 45 \mu\text{m}$ can be extracted, which is larger by a factor of 3 than in sample #1. Extrapolating to 550 K the diffusion coefficients for Ag in CdTe, which were determined by Wartlick et al. [3] in the range between 320 and 350 K ($D = D_0 \exp(-0.22 \text{ eV}/kT)$ with $D_0 = 6.5 \times 10^{-6} \text{ cm}^2/\text{s}$) a value of $6.3 \times 10^{-8} \text{ cm}^2/\text{s}$ is obtained, which is in good agreement with the value determined for D in sample #1. The different values of the quotient D/v_0 for samples #1 and #3 are plausible because of the different diffusion temperatures.

This quantitative description of the experimental data in Fig. 1, however, gives no information about the origin of the repulsive interaction acting on the Ag atoms since the used function $v(x)$ is not derived from a physical model. The cause of this interaction may be qualitatively explained by a repulsive interaction between Cu and Ag atoms, best seen in Fig. 3. Cu atoms seem to be present in almost all CdTe crystals as a residual contamination, indicated e.g. by the Cu^0X bond exciton frequently observed in PL investigations [6,7]. Thus, a connection between the repulsive interaction exerted on the Ag atoms and the Cu contamination in samples #1, #2, and #3, which were not intentionally doped with Cu, seems to be possible. The reduction of the depletion layer in Fig. 2 (sample #2) and the invisibility of this interaction in sample #4 is explained by the increasing Ag/Cu ratio in these samples, yielding Ag concentrations that significantly exceed the concentration of the residual Cu contamination. In contrast to the data in Fig. 1, the ^{111}Ag profile of sample #2 shown in Fig. 2 could not satisfactorily be fitted using the simple function of Eq. (2) for describing the drift velocity $v(x)$. This may reflect the physical nature of the repulsive interaction, which is expected to depend on the gradient of the Cu concentration and the concentration of Ag.

Finally, the ^{111}Ag diffusion data of sample #5 shown in Fig. 3 will be considered. The diffusion of Cu in CdTe was investigated e.g. by Woodbury and Aven, Panchuk et al., and Jones et al. [8–10]. Jones et al. used an evaporated Cu layer as diffusion source, similar to the conditions for Cu diffusion chosen in the present experiments, and they detected a slow and a fast

diffusing component of Cu. The diffusion coefficient D and the solubility c_s of the fast component are reported to be nearly independent on temperature in the range 450–600 K and are determined to be $D = 3.3 \times 10^{-8} \text{ cm}^2/\text{s}$ and $c_s = 10^{17} \text{ cm}^{-3}$, respectively. On the basis of the data presented by Jones et al., the Cu profile was calculated assuming an infinite Cu source and plotted in Fig. 3 (dashed line). A comparison with the Ag data shows that the Cu concentration obviously exceeds the Ag concentration over the entire crystal, except for a thin layer at the back of the crystal where most of the Ag atoms are accumulated. The nearly complete diffusion of the ^{111}Ag atoms to the back of the crystal, therefore, seems obviously to be caused by the repulsive interaction between Cu and Ag. It should be remarked that the diffusion of Cu and Ag in CdTe observed here might show up some similarities with the interaction of p-type dopants, i.e. of Zn and Cd, in InP reported by Tuck et al. [11]. In that experiment, the presence of Cd was found to increase the diffusion depth of Zn but, contrary to the present data, the presence of the diffusing Zn greatly increased the rate of out-diffusion of Cd from the semiconductor.

5. Conclusion

The presented data on the diffusion of Ag in CdTe are interpreted in the framework of a repulsive interaction between the diffusing Ag and Cu atoms. In crystals that were not intentionally doped with Cu, the residual concentration of Cu causes a drift of the Ag atoms towards the centre of the crystal which superposes the diffusion in the presence of a concentration gradient. The visibility of this interaction vanishes with increasing Ag concentration. Upon intentional co-diffusion of CdTe with Cu, however, the observed effect becomes more pronounced indicating that the presence of Cu atoms seems to be responsible for the observed repulsion of the Ag atoms. Within a semi-empirical model, quantitatively describing the diffusion data at 550 and 800 K (Fig. 1), the diffusion coefficient of Ag in CdTe

corresponding to a temperature of 550 K was determined. This value is in good agreement with extrapolated data of the temperature dependent diffusion coefficient published by Wartlick et al. [3]. Although the measured ^{111}Ag profiles can be understood qualitatively, on the basis of the present data a microscopic interpretation about the nature of the long range repulsive interaction between Cu and Ag cannot be given yet.

Acknowledgements

The financial support by the DFG under contract Wi715/-1 and the BMBF under contract W15SAA is gratefully acknowledged.

References

- [1] J.P. Chamonal, E. Molva, J.L. Pautrat, *Solid State Commun.* 43 (1982) 801.
- [2] M.A. Kovalets, N.I. Kuchman, E.S. Nikonyuk, I.P. Chiokan, M.M. Shvydka, *Fiz. Khim. Obrab. Mater.* 21 (1987) 125.
- [3] B.O. Wartlick, J.F. Barbot, C. Blanchard, *Philos. Mag. B* 75 (1997) 639.
- [4] I. Lyubomirski, V. Lyakhovitskaya, R. Triboulet, D. Cahen, *J. Electron. Mater.* 26 (1997) 97.
- [5] I. Lyubomirski, M.K. Rabinal, C. Cahen, *J. Appl. Phys.* 81 (1997) 6684.
- [6] B. Monemar, E. Molva, L.S. Dang, *Phys. Rev. B* 33 (1986) 1134.
- [7] J. Hamann, A. Burchard, M. Deicher, T. Filz, V. Ostheimer, F. Strasser, H. Wolf, *ISOLDE Collaboration*, Th. Wichert, *Physica B* 273–274 (1999) 870.
- [8] H.H. Woodbury, M. Aven, *J. Appl. Phys.* 39 (1968) 5485.
- [9] O.E. Panchuk, V.I. Grystiv, D.P. Belotskii, *Inorg. Mater.* 11 (1988) 788.
- [10] E.D. Jones, N.M. Stewart, J.B. Mullin, *J. Crystal Growth* 117 (1992) 244.
- [11] B. Tuck, F.R. Shepherd, G. Kelly, A. Margittai, *Semi-cond. Sci. Technol.* 15 (2000) 254.



ELSEVIER

Physica B 308–310 (2001) 967–970

PHYSICA B

www.elsevier.com/locate/physb

Investigation of lattice defects by means of their drift under electric field

N.E. Korsunskaya^a, I.V. Markevich^a, L.V. Borkovska^{a,*}, L.Yu. Khomenkova^a,
M.K. Sheinkman^a, O. Yastrubchak^b

^a *Institute of Semiconductor Physics, National Academy of Sciences, 45 Prospect Nauky, 03028 Kyiv, Ukraine*

^b *Institute of Physics, Polish Academy of Sciences, 02-668 Warsaw, Al. Lotnikow 32/46, Poland*

Abstract

Copper and silver related local centres in CdS crystals were investigated by means of technique based on drift of defects in external electric field. The impurities were first introduced in crystals and then extracted from them under electric field 100–300 V/cm at 600–750 K. Acceptors Cu_{Cd} and Ag_{Cd} responsible for emission bands 1000 and 610 nm correspondingly were found to be the only local centres created after impurity incorporation. Local centres related to interstitials Cu_i and Ag_i were not revealed. Different photo-enhanced defect reactions were observed in the crystals before and after impurity incorporation. A transformation of the type of reaction as a result of impurity incorporation took place. © 2001 Elsevier Science B.V. All rights reserved.

Keywords: Defects; Electrodiffusion

1. Introduction

One of the important problems in semiconductor studies is the identification of defects related to certain local centres. In such investigations a method based on defect drift in electric field can be quite useful. When defects under consideration are charged and mobile enough, application of external electric field at a fit temperature gives possibility to make a desirable redistribution of these defects along the sample. So, drifting defects can be extracted from any region of the sample and then incorporated in it again. Comparison of electrical and optical characteristics of this region before and after such procedures allows identification of local centres related to the defects. Earlier we used this technique for investigation of mobile shallow donors in undoped and Li-doped CdS crystals [1]. Electron traps related to Cd and Li interstitials were found and participation of these defects in a number of photo-

enhanced defect reactions was established [1,2]. In the present work, Cu- and Ag- related centres in CdS crystals have been investigated.

2. Experimental procedure

Nominally undoped high-resistivity ($\rho > 10^8 \Omega \text{cm}$) bulk CdS crystals were used. The crystals have bright yellow colour. Samples were rectangular parallelepipeds of typical dimensions $5 \times 3 \times 1 \text{ mm}^3$ cut from large boules. The impurity was introduced from electrode containing Cu or Ag, the other electrode being pure In. The sample was heated to $T_d = 600\text{--}750 \text{ K}$ and then electric field $E_d = 100\text{--}300 \text{ V/cm}$ was applied to it during time interval Δt_d so that electrode with the impurity was the anode [3]. Doped region had reddish-brown (in the case of Cu) or bright brown (in the case of Ag) colour. A sharp boundary was observed between doped and undoped regions (Fig. 1(a) and (b)). When the sample was heated to T_d again and electric field of opposite direction was applied to it, extraction of the impurity from the sample took place and the crystal

*Corresponding author. Fax: +380-44-265-83-44.

E-mail address: bork@lumin.semicond.kiev.ua
(L.V. Borkovska).

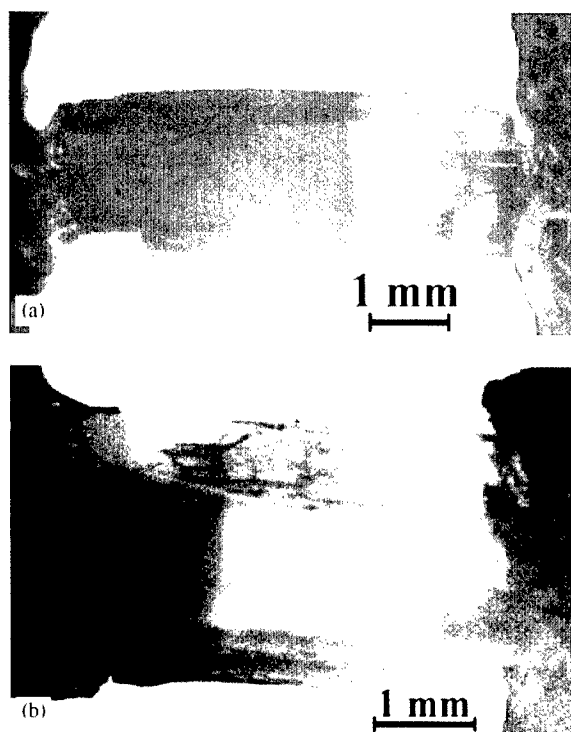


Fig. 1. (a) CdS crystals under visible light at 300 K after incorporation of: (a) Ag ($T_d = 700$ K, $E_d = 250$ V/cm², $\Delta t_d = 80$ min); (b) Cu ($T_d = 650$ K, $E_d = 100$ V/cm², $\Delta t_d = 30$ min).

acquired the initial bright yellow colour. If both electrodes were pure indium, no change of crystal colour was observed after electric field application.

Transmission, photoluminescence (PL), photocurrent (PC) and thermally stimulated current (TSC) spectra of the same sample region were measured in 77–300 K temperature range before and after impurity incorporation and then after its extraction.

3. Results

Transmission spectra measurements showed that after Ag and Cu incorporation a transparency of crystals decreased and absorption edge shifted to the long wavelength side (Fig. 2(a) and (b)).

In PL spectra of initial crystals edge green emission at $\lambda = 515$ nm dominated (Fig. 3(a) and (b)). Doping with Ag or Cu resulted in this emission quenching, while strong orange band at $\lambda = 610$ nm appeared due to Ag introduction (Fig. 3(a)), or infrared (IR) band at $\lambda = 1000$ nm became much more intensive due to Cu introduction (Fig. 3(b)). At the same time, intensity of red band at $\lambda = 715$ nm that, as a rule, was also present in initial crystal PL spectra, remained factually unchanged after doping. In some initial crystals strong self-

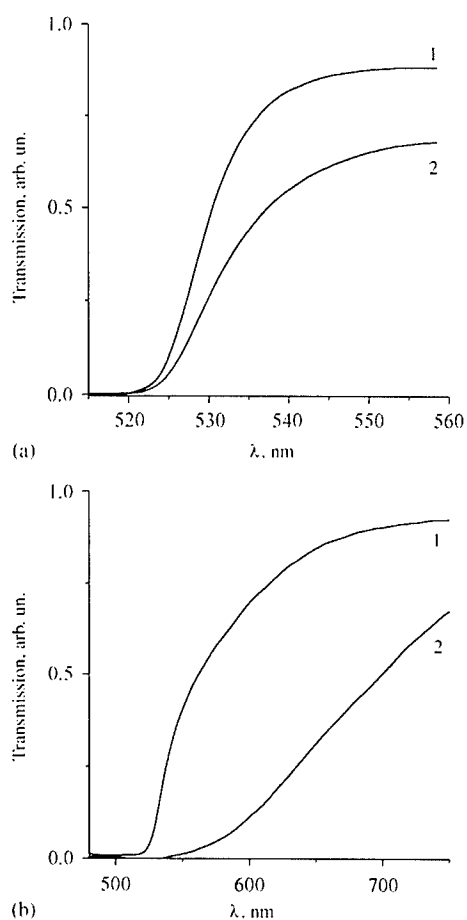


Fig. 2. Transmission spectra of CdS crystals at $T = 300$ K before (1) and after (2) incorporation of Ag (a) and Cu (b).

activated orange PL band at $\lambda = 590$ nm in addition to green and red ones was observed. When both electrodes supplied to the crystal were indium, no essential changes in PL spectra took place after sample treatment by electric field (Fig. 3(c)).

The incorporation of Ag and Cu was accompanied with the increase of crystal photosensitivity in the whole wavelength range, the most effect being observed in the extrinsic region at $\lambda \sim 600$ nm and $\lambda \sim 700$ nm correspondingly (Fig. 4(a) and (b)). Different photo-enhanced defect reactions (PEDR) were found to occur in crystals before and after impurity incorporation. In undoped crystals "sensitizing" PEDR [4] took place: when the crystal was cooled from 450 to 300 K in dark its photosensitivity was smaller than after cooling under visible light illumination (Fig. 4(a) and (b), curves 1, 2). After doping with Cu or Ag "degradation" PEDR [2] was observed: photosensitivity decreased due to visible light illumination (Fig. 4(a) and (b), curves 3, 4). In Cu-

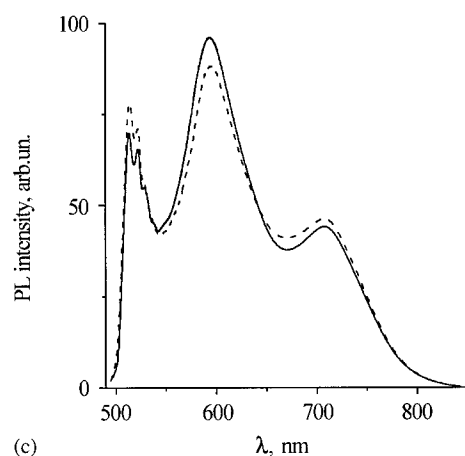
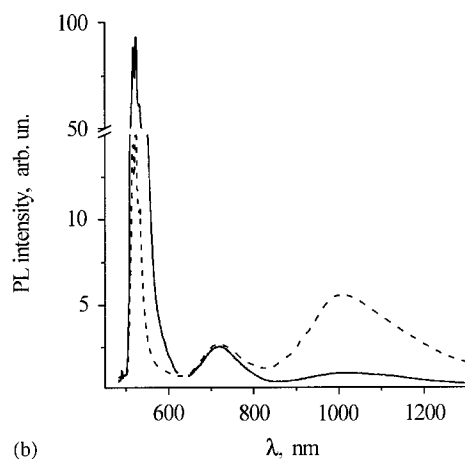
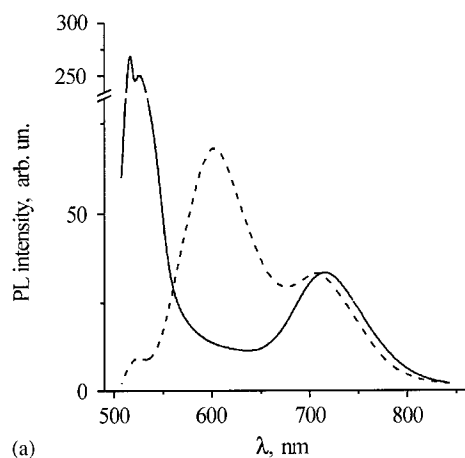


Fig. 3. Photoluminescence spectra of CdS crystals at 77 K before (solid lines) and after (dashed lines) treatment under electric field, the anode containing: (a) Ag, (b) Cu and (c) no impurity.

doped sample regions photosensitivity degradation under illumination was already conspicuous at 300 K, while in Ag-doped ones this effect became noticeable only at $T > 350$ K.

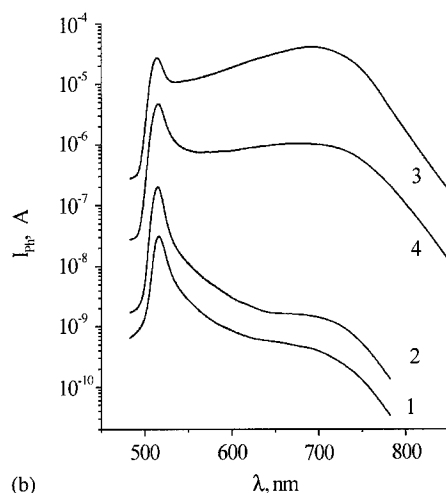
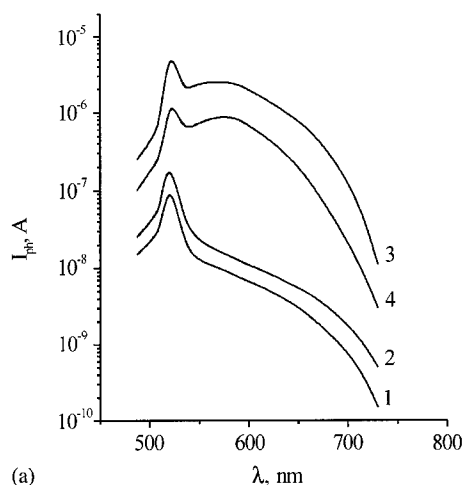


Fig. 4. Photocurrent spectra of CdS crystals at 300 K before (1,2) and after (3,4) incorporation of (a) Ag, (b) Cu. Cooling from 420 to 300 K in dark (1,3) and under intrinsic light illumination (2,4).

After impurity extraction, initial transmission, PL and PC spectra were restored and sensitizing PEDR was again observed.

In TSC spectra of investigated crystals some peaks, in general different in different samples, were present (Fig. 5). After doping the increase of TSC current was observed in the whole temperature range due to the increase of photosensitivity. However, any peak did not appear after impurity incorporation or disappear after its extraction.

4. Discussion

In CdS, copper and silver can create defects of two types: site atoms Cu_{Cd} , Ag_{Cd} and interstitials Cu_i , Ag_i that act as single charged acceptors and donors, correspondingly [5]. The IR band at $\lambda = 1000$ nm and

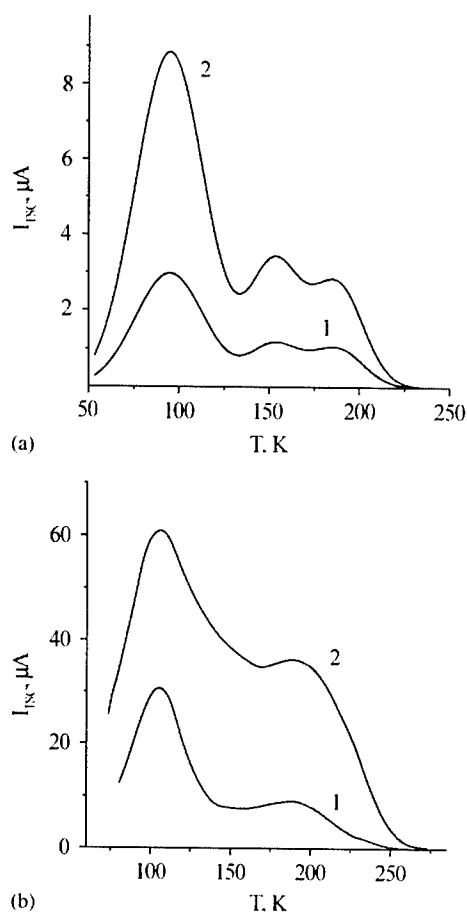


Fig. 5. TSC spectra of CdS crystals before (1) and after (2) incorporation of (a) Ag. (b) Cu.

orange band at $\lambda = 610$ nm, that rose in PL spectra of investigated crystals after doping and quenched after impurity extraction, are probably due to Cu_{Cd} and Ag_{Cd} centres, correspondingly. In fact, these bands were proved to result from recombination of free electrons on acceptor centres [6]. At the same time, in CdS doped with Cu and Ag by usual techniques a strong red emission at $\lambda = 710\text{--}720$ nm is generally also observed and ascribed to Cu- or Ag- related centres [5–8]. This band, however, is often present in nominally undoped crystals [5,6] and, as our investigations showed, Cu and Ag transfer under electric field does not influence on its intensity. Therefore we suppose, that this band is due to native defects. Perhaps, the presence of Cu and Ag enables the creation of such defects. The fact that intensities of self-activated green $\lambda = 515$ nm, orange $\lambda = 590$ nm and red $\lambda = 715$ nm emission bands do not change after action of electric field is the evidence that defects responsible for these emission bands do not drift in electric field at $T \leq 650$ K.

The direction of Cu and Ag drift from the anode to the cathode indicates that these impurities diffuse interstitially as donors Cu_i^+ , Ag_i^+ [3]. Hence, the latter are present in the crystal during doping process. In high-resistivity crystals these donors must manifest themselves as electron traps [6]. The analysis of obtained TSC data showed, however, that any electron trap did not appear after Cu or Ag incorporation. This fact means that equilibrium in reactions $\text{Cu}_i + \text{V}_{\text{Cd}} = \text{Cu}_{\text{Cd}}$, $\text{Ag}_i + \text{V}_{\text{Cd}} = \text{Ag}_{\text{Cd}}$ is essentially shift to the right side. The similar situation takes place in Ge and Si, where copper ions also diffuse as donors Cu_i^+ , but in doped material only acceptors Cu_{Ge} have been revealed [9].

“Sensitizing” and “degradation” defect reactions observed in investigated crystals are known to be characteristic for nominally undoped bulk CdS crystals [4,6] and Cu-doped CdS ones [2,6] correspondingly. In both reactions mobile native donors Cd_i had been shown to participate [4,6]. PEDR in CdS:Ag crystals was observed for the first time. One can suppose, however, that mechanisms of PEDR’s in CdS:Cu and CdS:Ag crystals are similar. Transformation of “sensitizing” PEDR into “degradation” one after impurity incorporation leads to the conclusion that like Cu also Ag atoms participate in the “degradation” process. The fact that in CdS:Ag crystals degradation PEDR occurs at higher temperatures than in CdS:Cu ones can be due to lower mobility of Ag in CdS lattice [5].

Acknowledgements

This work has been financially supported by National Academy of Sciences of Ukraine, and one of authors (L.V.B.) was supported by Grant of the President of Ukraine for young scientists.

References

- [1] N.E. Korsunskaya, I.V. Markevich, T.V. Torchinskaya, M.K. Sheinkman, J. Phys. C 13 (1980) 1275.
- [2] N.E. Korsunskaya, I.V. Markevich, E.P. Shulga, J. Phys. Chem. Sol. 53 (1992) 469.
- [3] B.L. Timan, Yu.A. Zagoruiko, Fiz. Tverd. Tela 21 (1979) 2849.
- [4] L.V. Borkovskaya, B.R. Dzhumaev, B. Embergenov, N.E. Korsunskaya, I.V. Markevich, Ukr. Phys. Zhurn. 43 (1998) 1295.
- [5] Physics and chemistry of II–VI compounds, in: M. Aven, J.S. Prener (Eds.), North-Holland, Amsterdam, 1967, p. 624.
- [6] M.K. Sheinkman, N.E. Korsunskaya, in: A.N. Georgobiani, M.K. Sheinkman (Eds.), Physika soedinenii A2B6, Nauka, Moskva, 1986, pp. 109–142.
- [7] H.H. Woodbury, J. Appl. Phys. 36 (1965) 2287.
- [8] T. Lukaszewich, Phys. Stat. Sol. (A) 73 (1982) 611.
- [9] B.J. Boltaks, Diffuziya v poluprovodnikah, Fizmatgiz, Moskva, 1961, 462pp.



ELSEVIER

Physica B 308–310 (2001) 971–975

PHYSICA B

www.elsevier.com/locate/physb

Laser shock wave stimulated defects in p-CdTe crystals

A. Baidullaeva*, A.I. Vlasenko, A.V. Lomovtsev, P.E. Mozol'

Institute of Semiconductor Physics, National Academy of Sciences of Ukraine, 45, Prospect Nauki, 03028 Kiev-28, Ukraine

Abstract

The changes in the physical properties of high-resistance p-CdTe crystals both during and after the passage of a laser shock wave (SW) were investigated. It was shown that the electrical conductivity of the p-CdTe increases when the SW passes through the crystals and decreases after its passage. The changes in the aforementioned characteristics during the SW passage are defined by the generation of nonequilibrium carriers from deep centers. It is observed that the number of dislocations increases as the power density of the laser radiation increases. This increase is correlated with the decrease in the residual conductivity of the samples. The changes in the residual conductivity are due to the formation of stable defects and their subsequent interaction with defects, existing in the initial crystal. © 2001 Elsevier Science B.V. All rights reserved.

Keywords: Defects; Laser shock wave; Cadmium telluride

1. Introduction

The irradiation of the p-CdTe crystals by ruby laser nanosecond pulses with power density below the damage threshold leads to a change in their electrical, photoelectric and optical properties. These changes occur both in the near-surface region of the material and at a depth of $\sim 5 \mu\text{m}$ which is much more than the light absorption depth (10^{-5}cm^{-1}) [1–3]. These changes are caused by the formation of intrinsic lattice defects due to the lattice “heat-up”, the generation of thermal elastic stresses, and the action of acoustic and shock waves in the course of irradiation of the crystal. Hypothetically, the energy of the laser pulse is transferred to the lattice via the generation, thermalization, and subsequent recombination of the electron-hole pairs. Even a small increase of temperature (up to 200°C) in the irradiation zone in a short time (10^{-8}s) results in a thermal shock. In this case, thermoelastic stresses $\sim 20\text{--}30 \text{ kbar}$, sufficient for breaking weaker

chemical bonds, arise in the lattice. A strong vibration excitation of the centers, located at the surface, could result in the detachment and evaporation of the atoms or different impurities in the semiconductors. The diffusion of impurities and defects into the volume of the crystal was also observed [4,5]. It is expected that a similar mechanism is observed in the case of the CdTe. However, it should be noted that the shock wave (SW) acts jointly with the photoeffect, thermoelastic deformation, and thermal heating.

It is of interest to identify the role of the SW in defect formation in CdTe separately from the above-indicated effects which accompany the laser radiation.

In this paper, we report the specific results of the SW action on the electrical properties and dislocation structures of the p-CdTe crystals.

2. Experimental procedure and results

The above-mentioned properties of the p-CdTe were investigated both during and after the SW passage through the crystal. Nondestructive SW was generated by Q-switched ruby laser pulses of $2 \times 10^{-8} \text{s}$ duration. The intensity of the laser pulses was varied in the range

*Corresponding author. Tel.: +380-44-265-18-75; fax: +380-44-265-83-42.

E-mail address: baidulla@class.semicond.kiev.ua (A. Baidullaeva).

10^7 – 10^9 W cm $^{-2}$ by means of neutrally gray light filters. The technique of sample preparation and its irradiation is similar to the technique described in Refs. [4,5]. The SW pressure was calculated by the formula given in Ref. [6].

The concentration dependence of the nonequilibrium charge carriers (NCC) on the SW pressure is shown in Fig. 1. At low SW pressures the concentration of the NCC exponentially increases, achieving saturation at a SW pressure higher than 3 kbar. In addition, an increase in conductivity of the CdTe was observed when the crystals were irradiated with ruby laser pulses, and then the conductivity returned to its initial magnitude. The kinetics of the conductivity change ($\Delta\sigma/\sigma_0$) of p-CdTe under the action of the SW is shown in the inset in Fig. 1. The relaxation time of the conductivity change under different SW pressures has two components. These are a fast component, which occurs exponentially with relaxation time constant $\tau_1 = 1.56 \times 10^{-4}$ s, and a slow component during which (over time $\tau_2 = 3$ –4 min) the conductivity decreases by several factors and then stabilizes. The residual conductivity of the crystal drops below the initial σ_0 value. The amplitude of the residual conductivity change versus the SW pressure is shown in Fig. 2. At first, the residual conductivity decreases and then saturates.

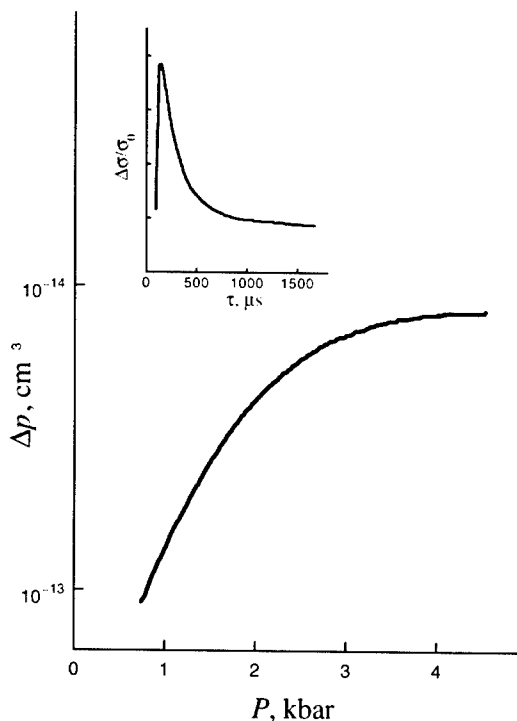


Fig. 1. The dependence of the NCC concentration in the p-CdTe crystal on the SW pressure. Inset: relaxation time of the NCC in a p-CdTe crystal at the SW passage.

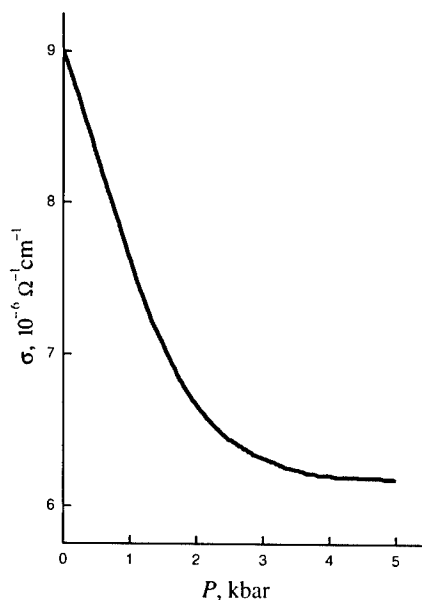


Fig. 2. The dependence of the residual conductivity (σ) in p-CdTe on SW pressure.

The photocurrent of the initial crystals depends weakly on temperature in the 100–300 K range. At the limit of this range, the photocurrent becomes thermally activated and the dependence I_{ph} versus $1/T$ follows the Arrhenius law with activation energy $E_i = 0.8$ – 0.9 eV (Fig. 3, curve 1). Quenching of the photocurrent with activation energy $E_{vt} = 0.13$ eV is observed in the low-temperature region after the SW passage with $P < 2$ kbar. The thermal activation region of the photocurrent remains unchanged above room temperature, and the photocurrent decreases almost by an order of magnitude (Fig. 3, curve 2). The appearance of the temperature range of the photocurrent quenching subsequent to the SW passage with $P < 2$ kbar can be related to the formation of shallow-level centers with the activation energy of ~ 0.13 eV. At low temperatures and at low excitation levels in the region of the fundamental light absorption, a strong optical charge redistribution between r-centers ($E_r = 0.9$ eV) and shallow acceptors ($E_{vt} = 0.13$ eV) proceeds in the CdTe crystals. Namely, photoholes are trapped by the shallow levels, and the hole population of the r-centers is decreased, i.e. quasi-dark formation of the center population by minority carriers with a concentration of N_r^0 takes place [7,8]. Consequently, the N_r^0 rise causes a decrease in τ ($\tau \sim 1/N_r^0$) and in the photocurrent. The photocurrent decreases further by an order of magnitude after repeated SW passage with $P > 2$ kbar. In this case, the temperature dependence form is retained, excluding the region of the temperature quenching of photocurrents, which disappears.

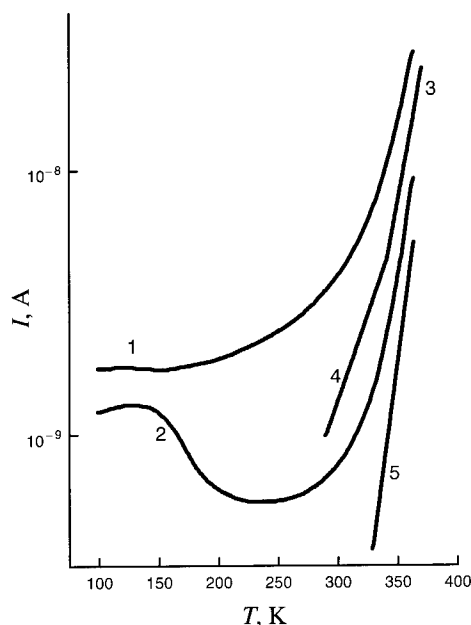


Fig. 3. The temperature dependences of (1,2) photocurrent and (3–5) dark current in p-CdTe (1,3) up to and (2,4,5) after the SW passage.

A region with activation energy $E_1 = 0.6$ eV in the temperature dependence of the dark current of the p-CdTe crystal is observed (Fig. 3, curve 3). The dark current remains unchanged after the SW passage with $P < 2$ kbar. However, an additional region with $E_2 = 0.14$ eV appears (Fig. 3, curve 4). The dark current decreases with further increase of the SW pressure, and activation energies E_1 and E_2 disappear in the temperature dependence of the dark current. However, the level with energy $E_3 = 0.8$ eV corresponding to the deep r-centers is observed (Fig. 3, curve 5). It indicates that after the SW passage with $P > 2$ kbar, charge carriers are generated from deeper levels in comparison with the initial crystal. The level $E_2 = 0.14$ eV in the CdTe crystals corresponds to the energy position of acceptors, the cadmium vacancy [9], and $E_1 = 0.6$ eV corresponds to the double-charged cadmium vacancy [10].

The dislocation densities of the initial crystals were equal to 10^2 cm^{-2} . For the laser radiation power densities used, the SW did not lead to the appearance of visible damage at the entrance and exit surface of the crystals. However, after selective etching, the number of dislocation etch pits increased and its total amount increased with increasing radiation power density or number of pulses (Fig. 4). We note that the threshold laser irradiation power density for which dislocation multiplication is observed corresponds to the threshold of the SW formation.

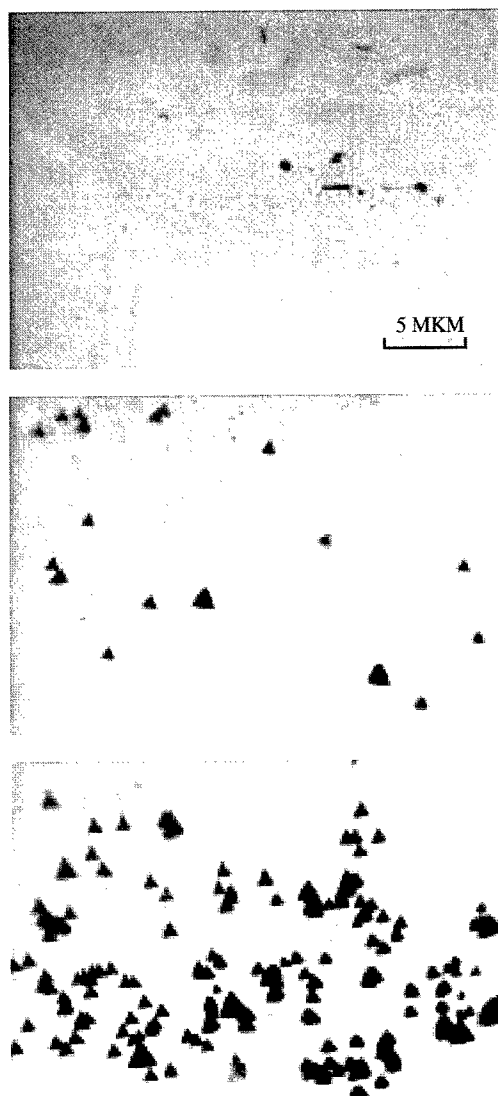


Fig. 4. The distribution of the dislocation etch pits on the (111) surface of p-CdTe: 1—initial sample and 2,3—after the SW passage.

3. Discussion

Increase of the concentration of the NCC of the p-CdTe single crystals, irradiated with nanosecond laser radiation pulses, is possible when additional carriers are generated as a result of the penetration of the thermal wave and laser SW.

The penetration depth of the thermal wave, which is formed under the irradiation of the samples, was $\sim 1.5 \mu\text{m}$, much less than the foil thickness. For this reason, changes in the concentration of the NCC in crystals cannot result from heating. The ionization energy of the defects decreases because of a decrease

of the band-gap energy (E_g) under the SW action. Estimation shows that the E_g change is equal to ~ 0.01 eV in the investigated range of the SW pressure, whereas the conductivity increases by a factor of 2–2.5. This indicates that the concentration of the NCC released from the traps is comparable to the equilibrium concentration. However, the slight change in E_g cannot bring about ionization of all the traps. In relation to the aforementioned, the increase of the NCC concentration at low (below 2 kbar) pressures can be explained by their generation from deep-level point defects (traps). The saturation of the NCC with the increase of the SW pressure above 3 kbar can be explained by accumulation of the residual defects generated by the SW [4].

The mechanism for the formation of the SW under the action of laser pulses is described in Ref. [4]. A thin layer of metal vapor and weakly ionized plasma forms at the interface when the surface of the foil is irradiated. It drives a wave of mechanical compression in front of itself at expansion into the volume. The SW can be considered as a directed flux of phonons which are scattered by the lattice irregularities. Here, the center of scattering acquires a momentum which is sufficient to form defects. These defects, in addition, can be ionized since the lattice, compressed by the SW, is close to the limit of stability.

Let us discuss the experimental results after the SW passage through the crystals. Since the metal vacancies (acceptors) manifest themselves in the equilibrium conductivity of a p-CdTe crystal, we can suppose that the decrease in the equilibrium conductivity after the SW passage with $P > 2$ kbar is related to a changing concentration of acceptor centers in the crystals. Let us consider the behavior of the acceptor centers after repeated SW passage. The Frenkel pairs, isolated vacancies, and interstitial atoms are formed in the crystal under SW action. They can interact with impurity atoms and form stable defect complexes [11]. At repeated SW passage, these steady defects accumulate from pulse to pulse, in a manner that is similar to high-energy radiation influence on a semiconductor [12]. It is possible that a cadmium vacancy forms during the first SW passage, verified by the appearance of the level with $E_2 = 0.14$ eV (Fig. 3, curve 4). The cadmium vacancies are transferred to the dislocations at the second SW passage with $P > 2$ kbar. The vacancy formation energy decreases because of the repeated SW passage through the crystal. For this reason, the large amount of excess vacancies formed brings about the additional distortion of the material [13]. In turn, this distortion can bring about concentration fluxes causing the phenomenon of “uphill” diffusion. Elastically strained layers formed in this case dramatically enhance vacancy diffusion in a bulk material. The enhanced diffusion can be related with: the crowdion mechanism of displacement of the lattice site atoms,

diffusion to sinks, diffusion along the dislocations with the enhanced diffusivity, or drift in the gradient of elastic strains, i.e. “uphill” diffusion [13]. The migration rate of atoms within the local volumes during “uphill” diffusion can be several orders of magnitude higher than the average mobility level of the atoms in crystals at a given temperature. As a result, the vacancies are localized in the compressed regions (formed by both the vacancies themselves and the SW) and form clusters. Depending on the number of vacancies, clusters take the form of a sphere or disk of monatomic thickness, i.e. a dislocation loop. We observe the formation of this dislocation loop in our experiment (Fig. 4). The appearance of the band $\lambda_{\max} = 840$ nm in photoluminescence spectra connected to it was observed previously [5]. In many works of other authors, this dislocation-related band is associated with the point centers of recombination, which include cadmium vacancy [14]. The experimentally observed decrease of conductivity after the SW passage may be explained by an increase of the dislocation density [5].

4. Conclusion

Thus, the action of a laser SW on the p-CdTe single crystals at room temperature leads to the change in its conductivity and dislocation structures. The conductivity of the crystals is increased at the moment of the SW passage, and is decreased afterwards. The increase in conductivity could be explained by the generation of the NCC from deep-level point defects (traps) under the SW action. The increase in the dislocation density, i.e. decrease of the acceptors that determine the value of the conductivity could be an explanation of the conductivity decrease after the SW passage. It has been assumed that the mechanism of dislocation formation is the creation of a large amount of excess vacancies and its formation of clusters under a laser SW action.

References

- [1] V.N. Babentsov, A. Baidullaeva, A.I. Vlasenko, S.I. Gorban, B.K. Dauletmuratov, P.E. Mozol', *Semiconductors* 27 (1993) 894.
- [2] V.N. Babentsov, A. Baidullaeva, A.I. Vlasenko, S.I. Gorban, P.E. Mozol', *Poverkhnost* 12 (1988) 144.
- [3] A. Baidullaeva, B.M. Bulakh, B.K. Dauletmuratov, B.D. Djumaev, N.E. Korsunskaya, P.E. Mozol', G. Garyagdiev, *Semiconductors* 26 (1992) 450.
- [4] V.A. Yanushkevich, A.V. Polyaninov, E.G. Prutskaya, G.A. Poliganov, *Izv. Acad. Nauk SSSR. Ser. Phys.* 5 (1986) 1146.
- [5] A. Baidullaeva, A.I. Vlasenko, Yu.V. Vlasenko, B.K. Dauletmuratov, P.E. Mozol', *Semiconductors* 30 (1996) 756.

- [6] L.I. Ivanov, Yu.N. Nikifrov, V.A. Yanushkevich, *Zh. Eksp. Teor. Fiz.* 67 (1974) 147.
- [7] R. Bube, in: *Photoconductivity of Solids*, Wiley, New York, 1960.
- [8] R. Bube, in: *Photoconductivity of Solids*, Nauka, Moscow, 1962.
- [9] N.V. Agrinskaya, E.N. Arkad'eva, O.A. Matveev, Yu.V. Rud', *Sov. Phys. Semicond.* 2 (1968) 776.
- [10] A.A. Sokolova, V.S. Vavilov, A.F. Plotnikov, V.A. Chaplin, *Sov. Phys. Semicond.* 3 (1969) 612.
- [11] G.G. Bondarenko, L.I. Ivanov, V.A. Yanushkevich, *Fiz. Khim. Obrabotka Mater.* 4 (1973) 147.
- [12] A.I. Vlasenko, V.V. Gorbunov, A.V. Lyubchenko, E.A. Sal'kov, *Ukr. Fiz. Zh.* 29 (1984) 423.
- [13] V.B. Brik, *Diffusion and Phase Transformations in Metals and Alloys*, Naukova Dumka, Kiev, 1985.
- [14] I.M. Figueroa, F.S. Sinensio, J.G. Mendoza-Alvares, *J. Appl. Phys.* 60 (1986) 452.



ELSEVIER

Physica B 308 310 (2001) 976 979

PHYSICA B

www.elsevier.com/locate/physb

Magnetic resonance studies of ZnO

W.E. Carlos^{a,*}, E.R. Glaser^a, D.C. Look^b^aNaval Research Laboratory, Code 6862, Washington, DC 20375, USA^bWright State University, Dayton, OH 45435, USA

Abstract

We have used EPR and ODMR to study state-of-the-art bulk ZnO single crystals. Most of the samples are n-type; however, under certain conditions (e-irradiated or annealed), we observe a center due to residual nitrogen ($g = 1.9953$, $g_{\perp} = 1.9633$ and $A_{\text{iso}} = 1.225$ mT, $A_{\text{aniso}} = 0.864$ mT). The N center is a nitrogen p-orbital along the c -axis, very similar to P or As in ZnSe, which have a Jahn-Teller distorted, deep state, seen in EPR. The intensity of the N center is strongly anisotropic, as would be expected for shallow heavy-hole acceptors with $m_J = \pm \frac{3}{2}$ in which the magnetic dipole transition is forbidden for $\mathbf{B} \parallel c$ and becomes allowed away from that orientation due to mixing with $m_J = \pm \frac{1}{2}$ states. The EPR spectra for the n-type samples are dominated by delocalized donors ($g = 1.9570$ and $g_{\perp} = 1.9551$). In one sample, the donor appears to be localized. These crystals also exhibit a broad PL band at 2.5 eV. ODMR on the 2.5 eV "green" PL band reveals an $S = 1$ triplet center (not seen in EPR) with spin-Hamiltonian parameters of $D = 0.763$ GHz, $g = 1.9710$, and $g_{\perp} = 2.0224$. ODMR of shallow donors is also observed as a luminescence-decreasing feature on the 2.5 eV green emission band. Published by Elsevier Science B.V.

PACS: 71.55.6s; 76.30.Lh; 76.70.Hb

Keywords: ZnO; Magnetic resonance; Acceptors; Donors; Triplet state

1. Introduction

There has been renewed interest in ZnO both as a potential substrate for nitride epitaxy and as an active electro-optical material for near-UV applications in its own right [1,2]. It has the obvious advantage over GaN of being readily grown as bulk crystals. The primary impediment to its development is the lack of a p-type dopant. The crystals are invariably n-type due to an as-yet unidentified donor and while there have been some reports of p-type doping [3,4], they are still somewhat sporadic and not well understood. One potential acceptor is nitrogen and in this work, we use electron paramagnetic resonance (EPR) to examine residual, isolated nitrogen in high-quality bulk crystals and find that it is Jahn-Teller-distorted. We also examine the residual donor line and find no hint of hyperfine splitting, suggesting that an intrinsic defect rather than

an impurity may be responsible. Finally, we use optically detected magnetic resonance (ODMR) and observe an $S = 1$ triplet state and discuss its possible origin. The EPR measurements were all performed in a Bruker 9.5 GHz spectrometer, typically at 4.2 K. The ODMR experiments were performed on the 2.5 eV green photoluminescence (PL) at 24 GHz and 1.6 K using the 351 nm line of an Ar⁺ laser for excitation.

2. Nitrogen

In two samples (one annealed at 850°C and a second e-irradiated), we observe a three-line spectrum due to nitrogen (the only 100% abundant $I = 1$ nucleus), illustrated in Fig. 1 for several rotations about the $(1\bar{1}\bar{2}0)$ axis. In addition to the set of three relatively strong lines, there are several weaker lines, which we shall not discuss further in this paper. These three lines have nearly axial symmetry (rotation about the c -axis does little to either their splitting or their central position) and equal integrated intensities. The EPR parameters are (assuming axial symmetry which fits

*Corresponding author. Tel.: +1-202-404-4573; fax: +1-202-767-0546.

E-mail address: carlos@bloch.nrl.navy.mil (W.E. Carlos).

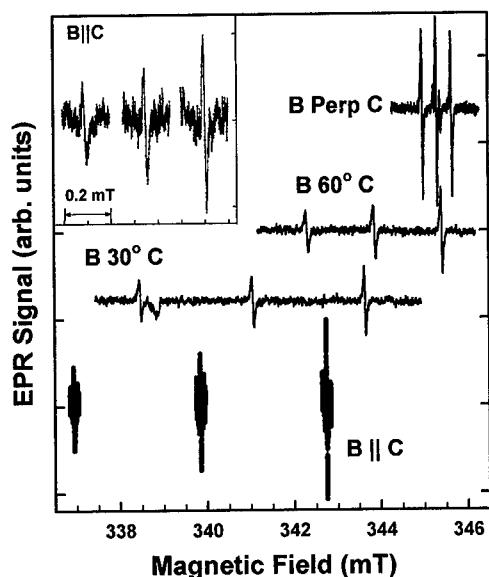


Fig. 1. The EPR signal of the N center at selected orientations. The lineshapes of the signal for $B \parallel c$ are shown in the inset.

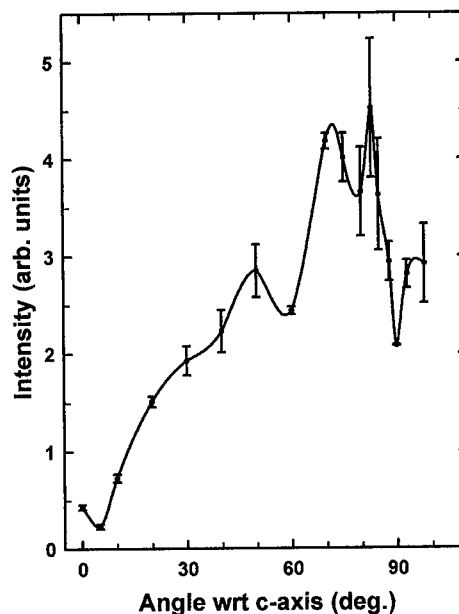


Fig. 2. The integrated intensity of the N center as a function of orientation. The error bars give the range of intensities for the three lines.

very well) $g_{\perp} = 1.9633$ and $g_{\parallel} = 1.9953$ and $A_{\text{iso}} = 1.225$ mT and $A_{\text{aniso}} = 0.864$ mT. The large anisotropy in the hyperfine interaction suggests a p-orbital and an atomic orbital analysis yields a center that is 96% p and 4% s and 45% localized on the N atom. This is very similar to the deep state of As or P in ZnSe [5]—a p-orbital on the impurity atom which is Jahn-Teller-distorted, along the c -axis away from the substitutional site. A qualitative physical argument for the behavior of group V acceptors substituting for S or Se in other II–VI compounds has been given by Chadi [6]. He argued that the acceptor atom must have significantly higher ionization energy than the host anion to avoid a deep Jahn-Teller distorted state. Hence, N does not have a deep state in ZnSe, while As and P do. Extending this argument to ZnO:N, the ionization energies of N and O are similar, suggesting that it may be deep, consistent with our observations. Of course, As and P have even smaller ionization energies [7] and one would expect a deep state for them as well. Recent calculations by Yamamoto and Katayama-Yoshida have also indicated that isolated N forms a deep state [8].

The biggest puzzle with these lines is the variation of intensity with orientation. In Fig. 2, we see that the integrated intensity of all the three lines vary by an order of magnitude with angle (also noticeable in Fig. 1). However, all the three have very similar intensities. (The departure around 85° is an artifact due to one of the weaker resonances mentioned above overlapping with the low field line.) This is more typical of a heavy hole ($m_J = \pm \frac{3}{2}$) in which the EPR transition is forbidden for

$B \parallel c$ but becomes allowed away from that orientation due to mixing with the $m_J = \pm \frac{1}{2}$ states [9].

Note that the linewidth of the high field line is always smaller than that of the low field line. We argue that some of the linewidth is due to inhomogeneities in the g shift and hyperfine interaction. Consider the following argument. A site that is a little more (less) p-like will have a larger (smaller) g shift and a smaller (larger) hyperfine splitting. This will tend to increase the width of the $m_1 = -1$ (low field) line and decrease the width of the $m_1 = +1$ (high field). The central $m_1 = 0$ line is, of course, not affected by a distribution in A but only by a distribution in g values. Near 0° or 90° , we have minimums or maximums in the g shift and the hyperfine parameter A , hence, small variations in the character of the wave function are less important and linewidths become equal to each other. Note that near $B \parallel c$, the spectra are extremely sharp, as seen in the inset to Fig. 1. The g value is near 2 here and so, since the g shift is small, there is virtually no inhomogeneous broadening due to variations in g .

3. Donor resonance

Most of the samples show a strong donor line with an axial g tensor ($g_{\parallel} = 1.9570$ and $g_{\perp} = 1.9551$). The line is Lorentzian, not easily saturated, and approximately 200 μT wide, narrowing with increasing temperature to ~ 20 μT at 20 K. An isolated donor should have a long

relaxation time and is easily saturated—Ga or In in ZnO are easily saturated (at microwave powers of $\sim 1 \mu\text{W}$ vs. 1 mW used for these resonances) [10]. This indicates that the electron is not isolated at a single site but rather in an impurity band, possibly physically hopping from one site to another. This would average out any hyperfine interaction and make identification difficult. The integrated intensity gives $\sim 10^{16}$ spins/cc. This result is somewhat surprising—in general, we observe impurity banding at higher concentrations, i.e., when Bohr orbitals start to overlap. For example, Si:P has two hyperfine split lines for concentrations up to the mid- 10^{17} range [11].

In the samples that show the nitrogen center (either after annealing or after e-irradiation), we do observe what appears to be an isolated donor. The donor line in this sample is badly saturated (i.e., probably due to isolated centers). The upper lineshape in Fig. 3, obtained using rapid passage conditions with low modulation frequencies, has an even sharper width ($\sim 100 \mu\text{T}$) than the delocalized donors more commonly seen. The line shows no splitting and has a significantly different g tensor. ($g = 1.9555$ and $g_{\perp} = 1.9540$) The difference in the g shift is about 3% compared to that of about 7% between isolated donors and impurity band electrons in Si [11].

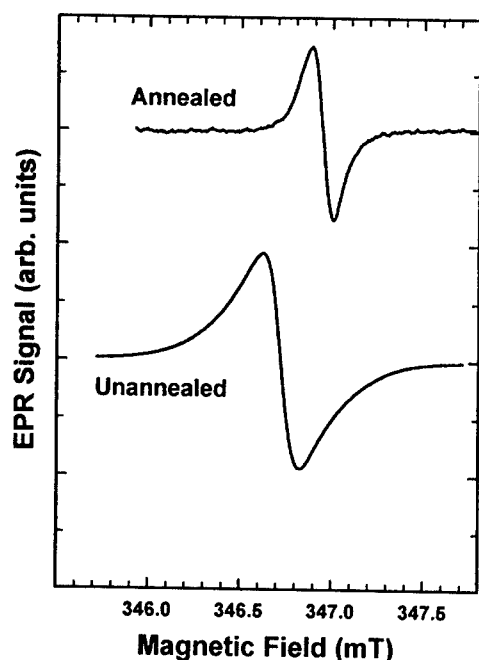


Fig. 3. The EPR signals for the donor line with $\mathbf{B} \parallel \mathbf{c}$ for an unannealed sample and a sample annealed at 850°C . As mentioned in the text, the spectrum for the annealed sample was taken using rapid passage techniques.

There are two classes of ideas for the residual donor: intrinsic defects and impurities. We have not been able to resolve any hyperfine structure due to the 4% abundant ^{67}Zn isotope ($I = 5/2$) which might give us some indication that we are looking at a Zn-interstitial or O-vacancy based center. (The isolated O_V has been observed in e-irradiated material and is thought to be deep.) In either case, hyperfine satellites would be weak ($\sim 1\%$ of the central line). The second class of ideas are impurities, such as hydrogen, as Van de Walle has suggested [12], or a simple impurity such as Ga. All these involve 100% abundant $I \neq 0$ nuclei, which would give a hyperfine splitting. A simple substitutional donor would certainly give observable hyperfine splitting or broadening. However, Van de Walle's calculations indicate that the hydrogen atom would sit in a bond-centered site and muon spin rotation (μSR) studies on other semiconductors do indicate that such a site would have a much smaller central hyperfine interaction. Recent μSR experiments on ZnO powder do indicate a small hyperfine interaction [13] which would not be resolved by ordinary EPR. Electron nuclear double resonance experiments could resolve hyperfine interactions (estimated to be on the order of 100 kHz) and reveal any anisotropy which would be expected for a bond-centered site. It, therefore, remains to be determined whether the dominant residual donor is H (or another impurity) or a lattice defect.

4. ODMR of triplet center

In these samples, there is a broad green PL band centered about 2.5 eV , very similar to that which has been previously observed from ZnO powders and platelets [14]. Several models have been proposed for this emission, including a Frenkel pair transition for a Zn_i to a V_Zn , an electronic transition between an O vacancy and a free hole or an internal transition of Cu_Zn^{2+} . To better understand this emission, we have performed ODMR on this band [15]. The spectra at various orientations are shown in Fig. 4 for an unannealed n-type sample. (Similar spectra were observed for annealed and lightly e-irradiated samples.) In addition to the shallow donor (and the N center in the annealed sample), we observe an $S = 1$ triplet center with resonance parameters of $D = 0.763 \text{ GHz}$, $g = 1.9710$ and $g_{\perp} = 2.0224$. This center is not observed in our EPR measurements. We have performed modulation frequency and excitation power studies, but do not resolve any additional pairs of exchange split lines, as are observed, for example, in ZnSe [16]. This seems to argue for a defect with a more unique electron-hole separation such as an impurity or a simple lattice defect.

As mentioned above, we also observe the shallow donor resonance as a PL-decreasing signal in the

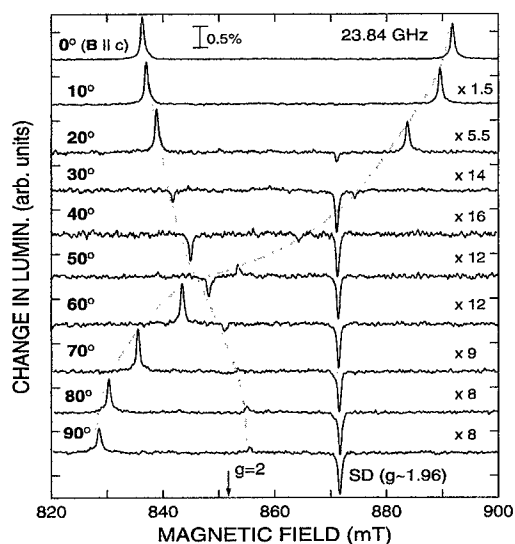


Fig. 4. The ODMR spectrum of the unannealed sample as a function of angle. The dashed line traces the orientation dependence of the triplet center.

ODMR. This suggests a competition for the donor electrons in the optical processes. For example, the donors can trap e–h pairs (“donor-bound excitonic recombination”) and also provide carriers (“spin-dependent electron transfer”) that help to form the $S = 1$ triplet center.

5. Summary

We have discussed three centers in state-of-the-art bulk ZnO single crystals: one due to isolated residual nitrogen, another due to residual donors and the last due to an $S = 1$ triplet center which is only observed using ODMR and is currently unidentified.

Acknowledgements

Work was supported by the Office of Naval Research and the Air Force Office of Scientific Research. Samples were provided by Gene Cantwell of Eagle-Picher.

References

- [1] D.C. Look, *Mater. Sci. Eng. B* 80 (2001) 383.
- [2] Yefan Chen, Darren Bagnall, Takafumi Yao, *Mater. Sci. Eng. B* 75 (2000) 190.
- [3] Kazunori Minegishi, Yasushi Koiwai, Yukinobu Kikuchi, Koji Yano, Masanobu Kasuga, Azuma Simizu, *Jpn. J. Appl. Phys.* 36 (1997) L1453.
- [4] Mathew Joseph, Hitoshi Tabata, Tomoji Kawai, *Jpn. J. Appl. Phys.* 38 (1999) L1205.
- [5] R.K. Watts, W.C. Holton, M. de Wit, *Phys. Rev. B* 3 (1971) 404.
- [6] D.J. Chadi, *Appl. Phys. Lett.* 59 (1991) 3589.
- [7] C.E. Moore, *Atomic Energy Levels*, Vol. I, Washington, DC, US Government Printing Office, 1971, p. XL.
- [8] Yetsya Yamamoto, Hiroshi Katayama-Yoshida, *Jpn. J. Appl. Phys.* 38 (1999) L166.
- [9] G.E. Pake, T.L. Estle, *The Physical Principles of Electron Paramagnetic Resonance*, Benjamin, Reading, MA, 1973, Chapter 5.
- [10] C. Gonzalez, D. Block, R.T. Cox, A. Hervé, *J. Crystal Growth* 59 (1982) 357.
- [11] G. Feher, *Phys. Rev.* 114 (1959) 1219.
- [12] C.G. Van de Walle, *Phys. Rev. Lett.* 85 (2000) 1012.
- [13] S.F.J. Cox, E.A. Davis, S.P. Cottrell, P.J.C. King, J.S. Lord, J.M. Gil, H.V. Alberto, R.C. Vilao, J.P. Duarte, N.A. Campos, A. Weidinger, R.L. Lichti, S.J.C. Irvine, *Phys. Rev. Lett.* 86 (2001) 2601.
- [14] M.S. Tamanachalam, et al., *J. Electron. Mater.* 24 (1995) 413.
- [15] W.E. Carlos, E.R. Glaser, T.A. Kennedy, D.C. Look, *Bull. Am. Phys. Soc.* 46 (2001) 807.
- [16] F.C. Rong, W.A. Barry, J.F. Donegan, G.D. Watkins, *Phys. Rev. B* 54 (1996) 7779.



ELSEVIER

Physica B 308–310 (2001) 980–984

PHYSICA B

www.elsevier.com/locate/physb

Defect identification by means of electric field gradient calculation

S. Lany^{a,*}, V. Ostheimer^a, H. Wolf^a, Th. Wichert^a, ISOLDE Collaboration^b

^a *Technische Physik, Universität des Saarlandes, D-66041 Saarbrücken, Germany*

^b *CERN-EP, CH-1211 Genève 23, Switzerland*

Abstract

The electric field gradients (EFG) caused by group V acceptors, group Ib acceptors and the cadmium vacancy in CdTe are calculated using the linearised augmented plane wave method and compared to the corresponding experimental values. Experimentally, the EFG are determined by the perturbed $\gamma\gamma$ -angular correlation spectroscopy with the radioactive probe isotopes ^{111}In and ^{77}Br . Besides the chemical nature, information about the charge state and the lattice relaxation associated with each defect is obtained. © 2001 Elsevier Science B.V. All rights reserved.

PACS: 61.72.Vv; 71.20.Nr; 76.80.+y

Keywords: Electric field gradients; Perturbed $\gamma\gamma$ -angular correlation; Density functional theory; II–VI semiconductors

1. Introduction

Defects in semiconductors induce characteristic electric field gradients (EFG) at neighbouring lattice sites. The EFG is measured via its interaction with the nuclear electric quadrupole moment of a suitable probe atom by different experimental techniques, such as perturbed $\gamma\gamma$ -angular correlation (PAC), Mössbauer spectroscopy, nuclear quadrupole resonance or electron nuclear double resonance. Defect-related EFG have been successfully used as ‘fingerprints’ of the respective defects in the past, because they are very sensitive to an anisotropic charge distribution about the probe nucleus, caused, for example, by a neighbouring defect [1,2]. However, the EFG by itself does not tell much about its microscopic origin so that due to the lack of appropriate theories for predicting the EFG of a distinct defect, lots of defects, though experimentally well characterised via their EFG, have remained unidentified.

The EFG discussed in this paper, are experimentally determined by PAC spectroscopy, using the radioactive PAC probe atoms ^{111}In and ^{77}Br . The investigation of defects in semiconductors using PAC spectroscopy is described in detail in Ref. [2]. In the II–VI semiconductor CdTe, both ^{111}In and ^{77}Br are donor atoms, which can form close donor–acceptor (D–A) pairs with stable acceptors, driven by the Coulomb attraction of ionised donors and acceptors. The actual PAC measurement takes place after the radioactive decay of the parent probes ^{111}In and ^{77}Br at the $I = 5/2$ excited state of the daughter isotopes ^{111}Cd and ^{77}Se , respectively, and yields the quadrupole coupling constant v_Q , related to the EFG by $v_Q = |eQV_{zz}/h|$, along with the asymmetry parameter $\eta = (V_{xx} - V_{yy})/V_{zz}$ ($|V_{xx}| \leq |V_{yy}| \leq |V_{zz}|$). The component V_{zz} is calculated from v_Q using the quadrupole moments $Q = 0.83 \text{ b}$ for ^{111}Cd [3] and 0.76 b for ^{77}Se ($I = 5/2$) [4]. It is noted that the daughter isotope ^{111}Cd of the PAC probe ^{111}In is a host atom in CdTe, and the EFG characterises the isolated defect originally trapped at the ^{111}In donor. In the case of ^{77}Br , the daughter isotope ^{77}Se is isoelectronic to the Te host and consequently, the EFG characterises the defect pair, consisting of a stable acceptor and the isoelectronic ^{77}Se

*Corresponding author. Tel.: +49-681-302-2702; fax: +49-681-302-4315.

E-mail address: lany@tech-phys.uni-sb.de (S. Lany).

isotope. Exemplified for the group V acceptor N and the group Ib acceptor Ag, the local defect structure after the radioactive decay of the employed PAC probes is sketched in Fig. 1.

By the detection of the fraction of probe nuclei, which are exposed to the characteristic EFG of a distinct defect, the presence of this defect is immediately proven and, at the same time, thermodynamic parameters of the involved defects, such as binding and migration energies, can be determined. If fluctuation rates become comparable to the spin precession frequencies induced by the EFG, electronic as well as geometrical changes of the complex formed with the (daughter) probe can be observed (cf. [2]). Since this kind of information is useful only if the observed EFG is assigned to the correct defect model, the reliable EFG calculation is an appreciated complement to the PAC spectroscopy.

For more than a decade, calculations based on the density functional theory (DFT) formalism have been used for determining, theoretically, the properties of defects in semiconductors (e.g. [5]), but calculations yielding also the EFG caused by impurities, came up only recently [6,7]. In the present work, the linearised augmented plane wave (LAPW) code WIEN97 [8] is employed for EFG calculation. Exchange and correlation effects are treated in the generalised gradient approximation as described in Ref. [9], being a development based on the local density approximation (LDA). The general treatment of a defect in a semiconductor host lattice within this method is performed according to Ref. [7], where a BCC supercell with a 32 atom basis and the tetrahedral symmetry of the T_d point group was used. Here, we are also dealing with cases in which two impurity atoms are introduced into the supercell and consequently, the symmetry is lowered to C_{3v} .

2. Donor–acceptor pairs with ^{111}In in CdTe

For the D–A pairing of ^{111}In donors with group V acceptors in CdTe, the experimental EFG obtained by

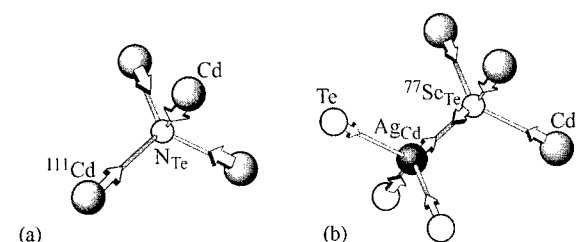


Fig. 1. Local defect structure after the radioactive decay of the parent PAC probe: (a) N acceptor trapped at a ^{111}In donor which decays to ^{111}Cd (tetrahedral symmetry); (b) Ag acceptor trapped at a ^{77}Br donor which decays to ^{77}Se (trigonal symmetry). Arrows indicate structural relaxation.

Table 1

Experimental EFG, calculated EFG, and calculated relaxation of the NN-Cd shell for the group V acceptors in CdTe^a

Acceptor	Experiment [10]	Theory [7]	
	V_{zz} [10^{21}V/m^2]	V_{zz} [10^{21}V/m^2]	Relaxation [%]
N_{Te}^-	$\pm 13.95(5)$	-13.7	21.7
P_{Te}^-	$\pm 10.56(9)$	-11.2	11.0
As_{Te}^-	$\pm 9.27(5)$	-9.5	8.3
Sb_{Te}^-	$\pm 7.62(5)$	-8.1	3.3

^aThe EFG refer to the NN-Cd site and to the ionised acceptor (e.g. N_{Te}^-). The experimental EFG obtained with the ^{111}In PAC probe is axially symmetric ($\eta = 0$), in all cases, as expected for the tetrahedral symmetry of the defect. Relaxation values are given in percent of the NN distance in CdTe (2.81 Å) and refer to the atomic movement indicated by the arrows in Fig. 1a.

PAC is compared to the calculated EFG in Table 1 [10,7]. Here, the use of T_d symmetry in the calculation implies $\eta = 0$. The LAPW calculations yield excellent agreement of the EFG at a nearest neighbour (NN) Cd site with the experimental data in the case of the ionised group V acceptors [7]. Structural relaxation (cf. Fig. 1a) is found to be crucial for an accurate EFG calculation: The relaxation of the NN-Cd atoms towards the group V acceptor by 1% of the undisturbed Cd–Te bondlength increases the calculated EFG by about 10^{21}V/m^2 , i.e. by about 10%. Regarding the strong relaxation of more than 20% for the N acceptor (cf. Table 1), it is clear that without taking into account the relaxation, a calculated EFG is meaningless. The high accuracy of the calculated EFG gives also evidence of the accuracy of the calculated lattice relaxation in the context of the high sensitivity of the EFG to the local structure. The occurrence of a second EFG, experimentally observed after As and additional Li doping, is interpreted in terms of the neutral As acceptor As^0 [7]. The agreement with the calculated value for As^0 shows that the calculation of EFG for non-ionised acceptor states can be reliable even for the rather small cell size of 32 atoms, where the spatial expansion of the bound hole exceeds the size of the supercell. Thus, in cases where the EFG depends significantly on the charge state of the defect, the EFG calculation can be used to determine the actual charge state observed in an experiment.

3. Donor–acceptor pairs with ^{77}Br in CdTe

The implantation of the radioactive ^{77}Br isotopes into CdTe crystals was performed at the ISOLDE mass separator at CERN (Geneva, CH). The experimental results obtained for the D–A pairs of ^{77}Br donors with stable group Ib elements are briefly summarised in

Table 2
Experimental and calculated EFG for group Ib acceptors and V_{Cd}^a

Acceptor	Experiment	Theory
	V_{zz} [10^{21} V/m ²]	V_{zz} [10^{21} V/m ²]
Cu _{Cd}	$\pm 5.3(2)$	-3.6
Ag _{Cd}	$\pm 6.7(2)$	-6.7
Au _{Cd}	$\pm 2.6(3)$	-1.1
V_{Cd}^2	$\pm 10.2(2)$	-10.8

^aThe EFG refer to the NN-Se_{Te} site and to the ionised state of the defect. The experimental EFG obtained with the ⁷⁷Br PAC probe is axially symmetric ($\eta = 0$) in all cases.

Table 2. A more detailed discussion of the experiments is given in Ref. [11]. Due to the relatively weak EFG for the Au acceptor, the corresponding experimental data are difficult to interpret in a unique way. The assumption that the ⁷⁷Se probes are located in a disturbed lattice environment, would also be consistent with the PAC spectra observed after Au doping. Thus, the value for the Au acceptor given in Table 2 is obtained by assuming an axially symmetric EFG tensor, as it is measured for the Cu and Ag acceptors. Attributed to the ⁷⁷Se_{Te}-Au_{Cd} configuration, the EFG is unexpectedly small for an NN pair if it is compared to the EFG for the Cu and Ag acceptors or, for example, with the EFG for the group V acceptors (Table 1). It has rather a strength that is typical for cases where the probe and the trapped defect form more distant next nearest neighbour (NNN) pairs [2]. Thus, based solely on experimental observations, the interpretation of the PAC data obtained with the ⁷⁷Br probe is particularly difficult regarding Au-doped CdTe crystals, and support from theoretical tools is highly appreciated.

After implantation of ⁷⁷Br into undoped CdTe samples, an EFG, characterised by $\nu_Q = 188(4)$ MHz, $\eta = 0.0(1)$ is observed [11]. Based on the annealing behaviour under Cd vapour pressure, this EFG is interpreted with the formation of bromine A centres, i.e. close pairs of ⁷⁷Br donors with the acceptor-like cadmium vacancy. The theoretical determination of EFG is particularly interesting in the case of intrinsic defects, such as the present example of V_{Cd} in CdTe, because here, the defect identification is generally more difficult than in the previous examples where the ⁷⁷Br donors form D-A pairs with deliberately introduced dopants.

As mentioned above, the calculation of the EFG at a Se_{Te} site in CdTe, induced by a neighbouring group Ib acceptor, requires that two impurity atoms are introduced into the supercell used for the LAPW calculation, leading to a C_{3v} symmetry. Compared to the T_d symmetry, the calculation becomes more demanding: First, less symmetry operations can be exploited in order

to reduce the computational effort. Second, there are more degrees of freedom for structural relaxation (cf. Fig. 1b) so that finding the equilibrium positions of the atoms in the supercell becomes a lengthy task. Including relaxation of all atoms in the supercell, the calculated EFG for the ionised group Ib acceptors, i.e. Cu_{Cd}⁻, Ag_{Cd}⁻ and Au_{Cd}⁻, and for the ionised cadmium vacancy V_{Cd}^{2-} are compared to the experimental data in Table 2. Here, the use of C_{3v} symmetry in the calculation implies $\eta = 0$. The detailed results for the relaxation of the ⁷⁷Se probe, the group Ib acceptor, and the neighbouring atoms—i.e. all atomic positions shown in Fig. 1b—are listed separately in Table 3. For the Ag acceptor and the cadmium vacancy, the EFG calculation reaches the high degree of agreement as in the case of the group V acceptors. For the Cu and Au acceptors, the calculated EFG differ from the experimental values by about 1.5×10^{21} V/m², but are still close enough to confirm the proposed defect model, i.e. ⁷⁷Se_{Te}-Cu_{Cd} and ⁷⁷Se_{Te}-Au_{Cd} complexes. (Note that absolute differences between calculated and experimental EFG should be regarded rather than relative ones, because V_{zz} can assume negative and positive values including zero.) In particular, the unusually low magnitude of the EFG caused by the Au acceptor at an NN site, is clearly reproduced. For the neutral state of the group Ib acceptors, the EFG is calculated to be more positive by up to 2.5×10^{21} V/m², yielding less agreement with the experimental data. Consequently, the measured EFG are attributed to the ionised state, in accordance with the observation for the group V acceptors [7]. In contrast, the calculated EFG for the neutral and the singly charged Cd vacancy do not differ much from the value for V_{Cd}^{2-} (-9.6×10^{21} and -9.1×10^{21} V/m² for V_{Cd}^0 and V_{Cd}^+), so that the EFG calculation supports the identification of V_{Cd} , but the assignment of the measured EFG to a specific charge state cannot be made definitively. It is noted, that the trigonal symmetry used for the calculation of the Se_{Te}- V_{Cd} defect complex in principle allows the Jahn-Teller relaxation which is expected for V_{Cd}^0 and V_{Cd}^+ . However, the LAPW calculations give no indication for a Jahn-Teller effect. The properties of both the anion and cation vacancy in CdTe are discussed in detail in a parallel paper [12].

Table 3
Calculated relaxation of the local environment about the group Ib acceptors and V_{Cd} . Values are given in percent of the NN distance in CdTe (2.81 Å) and refer to the relaxations indicated by the arrows along the Te-Ag-Se-Cd chain in Fig. 1b.

	Te	Acceptor	Se	Cd
Cu _{Cd} Se _{Te}	8.7	4.9	7.6	8.0
Ag _{Cd} Se _{Te}	3.2	5.4	0.6	6.0
Au _{Cd} Se _{Te}	3.9	4.6	1.4	6.2
V_{Cd} Se _{Te}	13.4	—	8.6	9.3

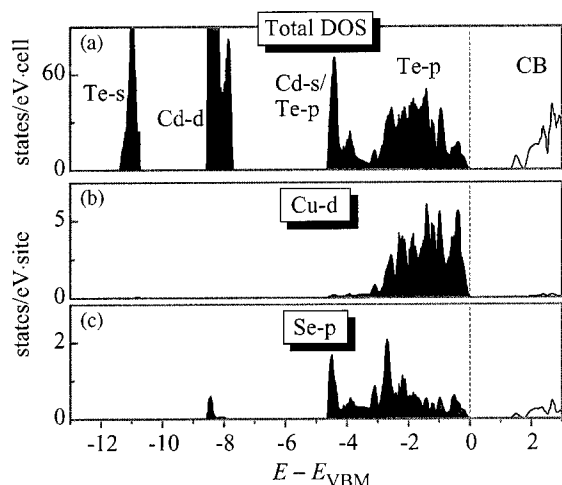


Fig. 2. (a) Total DOS for a CdTe 32 atom supercell containing a $\text{Se}_{\text{Te}}\text{-Cu}_{\text{Cd}}$ pair. The dominant characters of the wavefunctions are indicated; (b) site-projected DOS for Cu_{Cd} , d ($l=2$) contribution; (c) site-projected DOS for Se_{Te} , p ($l=1$) contribution.

Though very useful for the interpretation of the experimental data, the EFG calculations yield somewhat lesser agreement with experiment for the group Ib acceptors, compared to the group V acceptors. This is probably a consequence of the LDA used in DFT calculations, which does not exactly describe the outer d electrons of the group Ib elements. In Fig. 2a, the calculated electronic density of states (DOS) for a supercell containing a $\text{Se}_{\text{Te}}\text{-Cu}_{\text{Cd}}$ pair is shown, and the predominant character of the wavefunctions in the different sections of the spectrum is indicated. In IIb–VI compounds, the outer cation d electrons (e.g. the Cd- $4d$ electrons in CdTe) interact with the anion p states making up the upper part of the valence band [13]. The d states of the group Ib elements in CdTe are more loosely bound than the Cd- d states and lie in an energy region which coincides with the energetic position of the Se- p states. This is clearly visible in Figs. 2b and c, where the site-projected and angular-momentum-decomposed DOS is plotted for Cu- d and Se- p states. The smaller energy separation between the Cu- d and the Se- p states compared to the Cd- d and the Te- p states leads to a stronger interaction, where the Se- p_z orbital (directed towards Cu_{Cd}) is affected rather than the Se- p_x and Se- p_y orbitals due to symmetry. It is well known that the LDA underestimates the binding energy of the cation d electrons (e.g. [13]) and a similar effect can be expected for the outer d electrons of the group Ib acceptors. This means, however, that the coupling between the Se- p states and, e.g. the Cu- d states is not estimated exactly and an error can be introduced in the calculated EFG, because of the anisotropic influence of the Cu- d

electrons from the point of view of the Se atom. This argument holds for all the three group Ib acceptors, so that the exact agreement with the experimental value for the Ag acceptor seems to be rather fortuitous. In general, it should be emphasised that the EFG calculations have proven to be very helpful for defect identification even in the case of the group Ib acceptors in CdTe, which is a rather difficult case for EFG calculations based on the DFT-LDA formalism due to the energetically high-lying d orbitals.

4. Summary and outlook

LAPW calculations are presented for isolated group V acceptors and for defect complexes consisting of a group Ib acceptor and a Se neighbour in the II–VI semiconductor CdTe. The theoretically determined EFG are used to support the identification of defects. In particular for the Au acceptor, where the experimental situation is ambiguous, a clear interpretation is achieved only by support of the EFG calculation. Furthermore, the assignment of an experimentally observed EFG to the Cd vacancy is confirmed by means of the LAPW calculations. Future work will focus on cases, where the PAC probe and the investigated defect are next nearest neighbours, on self-compensation mechanisms such as DX and AX centre formation, and on defects in other II–VI semiconductors than CdTe, such as ZnSe.

In general, it has been shown that by comparing the experimentally and theoretically determined, defect-related EFG, information about the chemical nature, the charge state, and the lattice relaxation associated with each defect is obtained. This is more important as for more than 50 defect complexes, studied in different semiconductors, experimental EFG are available.

Acknowledgements

The financial support of the Bundesministerium für Bildung und Forschung (BMBF) under Contract No. 03WI4SAA is gratefully acknowledged.

References

- [1] G. Langouche (Ed.), *Hyperfine Interaction of Defects in Semiconductors*, Amsterdam, 1992.
- [2] Th. Wichert, in: Stavola (Ed.), *Identification of Defects in Semiconductors, Semiconductors and Semimetals*, Vol. 51B, Academic Press, San Diego, 1999 and references therein.
- [3] P. Herzog, K. Freitag, M. Rauschenbach, H. Walitzki, Z. Phys. A 294 (1980) 13.

- [4] P. Blaha, P. Dufek, K. Schwarz, H. Haas, *Hyperfine Interactions* 97/98 (1996) 3.
- [5] C.G. Van de Walle, P.J.H. Denteneer, Y. Bar-Yam, S.T. Pantelides, *Phys. Rev. B* 39 (1989) 10791.
- [6] A. Settels, T. Korhonen, N. Papanikolaou, R. Zeller, P.H. Dederichs, *Phys. Rev. Lett.* 83 (1999) 4369.
- [7] S. Lany, P. Blaha, J. Hamann, V. Ostheimer, H. Wolf, Th. Wichert, *Phys. Rev. B* 62 (2000) R2259.
- [8] P. Blaha, K. Schwarz, J. Luitz, WIEN97, A Full Potential Linearized Augmented Plane Wave Package for Calculating Crystal Properties, Karlheinz Schwarz, Technical Universität Wien, Austria, 1999, ISBN 3-9501031-0-4.
- [9] J.P. Perdew, S. Burke, M. Ernzerhof, *Phys. Rev. Lett.* 77 (1996) 3865.
- [10] V. Ostheimer, A. Jost, T. Filz, St. Lauer, H. Wolf, Th. Wichert, *Appl. Phys. Lett.* 69 (1996) 2840.
- [11] V. Ostheimer, S. Lany, H. Wolf, Th. Wichert, to be published.
- [12] S. Lany, V. Ostheimer, H. Wolf, Th. Wichert, in these Proceedings (ICDS), *Physica B* 308-310 (2001).
- [13] S.-H. Wei, A. Zunger, *Phys. Rev. B* 37 (1988) 8958.



ELSEVIER

Physica B 308–310 (2001) 985–988

PHYSICA B

www.elsevier.com/locate/physb

Photoluminescence studies in ZnO samples

C. Boemare^{a,*}, T. Monteiro^a, M.J. Soares^a, J.G. Guilherme^b, E. Alves^b

^a Departamento de Física, Universidade de Aveiro, 3800 Aveiro, Portugal

^b Instituto Tecnológico e Nuclear, Sacavém, Portugal

Abstract

The similarities between ZnO and GaN samples reveal that the semiconductor oxide is a potential material as a promising material for optoelectronic devices. In this work, we study by spectroscopic and RBS techniques the characteristics of bulk ZnO. A comparison between the energy separation of the several groups of near band edge photoluminescence emission bands and the energy separation between the free exciton resonances observed in reflectivity is made. We report on the luminescence dependence from temperature and the variation of the relative intensities of the lines. From the data, an assignment of recombination centers is discussed. © 2001 Elsevier Science B.V. All rights reserved.

Keywords: PL; TRPL; RBS; ZnO

1. Introduction

Due to its wide-gap of 3.37 eV at room temperature and its strong exciton binding energy of 60 meV the binary ZnO have many potential applications in short-wavelength light-emitting devices. Recent development in growth techniques has enabled the growth of ZnO epilayers on a wide variety of substrate, even with large lattice mismatch [1,2]. For this reason, there has been a renewed interest in ZnO. The studies of ZnO epilayers has its base on knowledge of the bulk crystal properties, i.e., the band gap evolution with temperature, the binding energies, the transitions of the un-doped crystal including shallow and deep emission levels.

In this paper, we study the photoluminescence and reflectivity of bulk ZnO as a function of temperature. The near band edge is studied in terms of energy separation to the free excitons evolution with temperature. The assignment of the emission centers is made, comparing between excited states, rotator states or binding with the different excitons. Parameters are

obtained for the gap evolution in temperature using three models.

2. Experimental details

PL measurements were carried out with a 325 nm CW He–Cd laser and the excitation power density was typically $<0.6 \text{ W cm}^{-2}$. A 325 nm band pass filter was used to attenuate lines other than the 325 nm laser line and a low pass sharp cut off filter was used to stop the laser light. PL was measured at temperatures between 14 and 300 K using a closed cycle helium cryostat. The luminescence was dispersed by a Spex 1704 monochromator (1 m, 1200/mm) and detected by a cooled Hamamatsu R928 photomultiplier.

The samples were excited with incident light parallel to the *c*-axis of the crystal, i.e. with the electric field perpendicular to *c*. The emitted light was collected in two configuration, at an angle of 0° from excitation, i.e. $E \perp c$, and at 90° , i.e. \perp or \parallel to *c*-axis.

3. Results and discussion

The near band edge photoluminescence recorded at 15 K in the 0° configuration, electric field *E* of the

*Corresponding author. Departamento de Física, Universidade de Aveiro, 3810-193 Aveiro, Portugal. Tel.: +351-34-370-276; fax: +351-34-24965.

E-mail address: clauda@fis.ua.pt (C. Boemare).

emitted light perpendicular to the c -axis, exhibits 14 lines (Fig. 1). The emissions of A free exciton are presents; emission of the B and C band is not observed. The same spectrum was obtained in the 90° configuration. In that configuration the use of a polarizer, in any orientation (\perp or \parallel to c -axis), makes the photoluminescence of the near band edge to collapse, indicating the unexpected non-polarization of the emitted light [3]. Either the intensity of the free excitons relatively to the donor-bound exciton group or the relative intensity of the several bound excitons does not significantly change.

In fact, from group theoretic arguments and the direct product of the group representations of the band symmetries [4] (Γ_7 for the conduction band, Γ_9 for the first valence band, A, Γ_7 for the second and third valence bands, B and C) we obtain the following intrinsic excitons ground states symmetries:

$$\Gamma_7 \times \Gamma_9 \rightarrow \Gamma_5 + \Gamma_6,$$

$$\Gamma_7 \times \Gamma_7 \rightarrow \Gamma_5 + \Gamma_1 + \Gamma_2.$$

In ZnO the donor bound excitons have been attributed to defect-pairs that have the properties of neutral donors [5]. Due to the preferentially incorporation of the defects in a certain crystallographic orientation local strains oriented in the direction of the pair will result, and the electric vector will orient in the strain direction inducing polarization effects. Similarly, free excitons would be expected to show polarization effect since Γ_5 and Γ_1 are allowed transitions with $E \perp c$ and $E \parallel c$, respectively, and Γ_6 and Γ_2 are unallowed. In fact, the Γ_6 and Γ_5 lines are observed in all polarization and this is likely due to the finite momentum of the photon.

Fig. 2 shows the random and $\langle 0001 \rangle$ aligned RBS spectra of the wurtzite ZnO sample. The minimum yield (ratio between the random and aligned spectra) along this direction is 4%, which is an indication of the excellent crystalline quality of the single crystals. More-

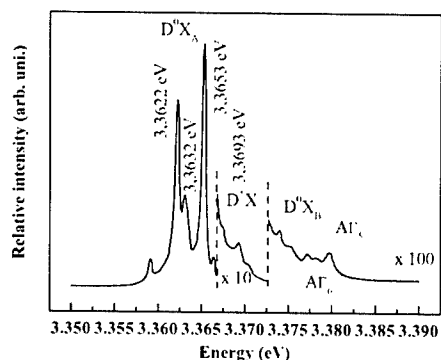


Fig. 1. PL at 15 K in the 0° configuration. The assignments of the lines are indicated by arrows.

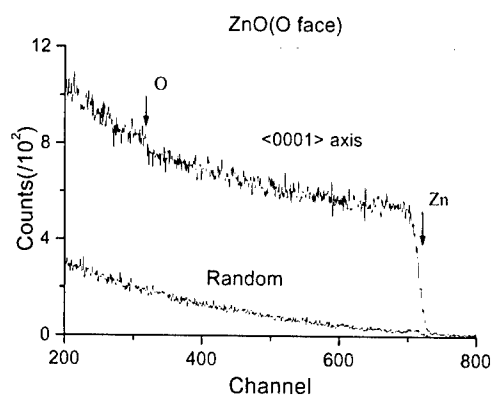


Fig. 2. RBS spectra along the $\langle 0001 \rangle$ axis and in a random direction. The crystals terminate on an oxygen plane.

over the smooth dechanneling rate over all the probed thickness (about $3 \mu\text{m}$ for the $3 \text{ MeV } ^4\text{He}^+$) reveals a nearly defect free crystal over the entire depth also confirmed by the presence of free excitons.

At low temperature the spectrum is dominated by two donor-bound excitons at 3.3653 and 3.3622 eV. As the temperature rises above 50 K, (Figs. 3 and 4), most of the donor lines disappear and above 70 K only the donor lines that were located at 3.3653 and 3.3704 eV at 15 K remain. The line located at 3.3704 eV at 15 K, the A and B free excitons relative intensities increase (Fig. 3). We separate the bound exciton in three groups. The low-energy group is generally accepted to be neutral donor bound excitons, defect pairs or ordinary bound excitons. The second and the third sets of lines on the high-energy side of the neutral donor bound excitons (Fig. 1), between 3.3668 and 3.3725 eV, has been attributed to excited states of these complexes or excited rotator states [5].

Several models were proposed for the rotator states [6–9]: in a model the hole is excited to rotate around the fixed donor, in another one the exciton rather than the hole is rotating. Using the energy separation given by [5] one could identify some of the lines between the neutral donor bound excitons and the free A excitons as rotator states of the dominant neutral bound excitons. But the increase of the relative intensity of the 3.3693 line with temperature rather suggest an exciton bound to ionized defect, here a ionized donor. Furthermore taking into account the energy separation between the A and B exciton $\sim 12 \text{ meV}$, we can attribute these transitions to the same neutral donors now bound to B excitons (Table 1).

In reflectivity both the ground- and excited-states of the A and B free excitons are observed (Fig. 5). The excited states rapidly became unresolved with increasing temperature, whereas the A and B grown-states remain up to 200 K and room temperature, respectively. At low

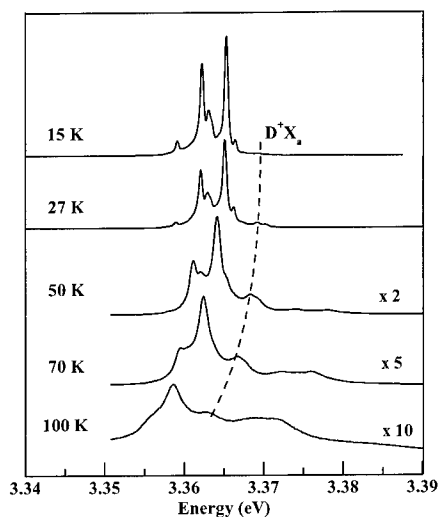


Fig. 3. Evolution of near band PL as a function of temperature. The dashed lines indicate the position of the ionized donor bound exciton.

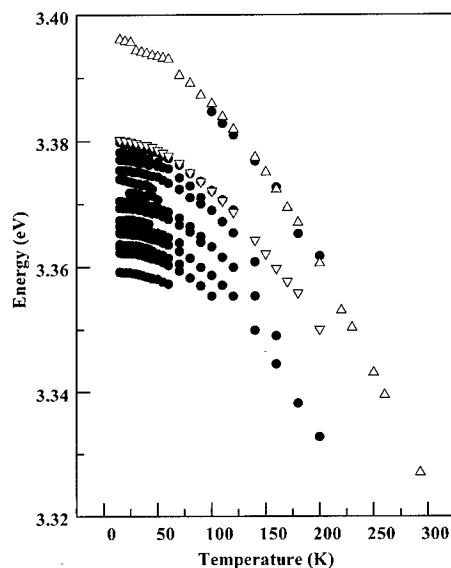


Fig. 4. Temperature evolution of near band edge transition with temperature. (●) data from PL, (▽) data from reflectivity.

temperature in the reflectivity spectra a resonance is visible near the minimum of the B exciton. This is attributed to a resonance with $E \parallel c$, in fact that the angle of reflectivity is not exactly 0 and when increasing the angle its amplitude increases. This feature rapidly became unresolved but can lead to a wrong measurement of the oscillation energy of the B exciton at low temperature. In Fig. 4 the open triangles are the

Table 1

Energy of the neutral donor bound to a A exciton, corresponding rotator state and the same neutral donor bound to a B exciton

D^0X_A (eV)	Rotator states (eV)	D^0X_A (eV)
3.3592	3.3693 (Γ_6), 3.3707 (Γ_5)	3.3707
3.3622	3.3741 (Γ_5)	3.3741
3.3632	—	3.3754
3.3653	3.3754	3.3772

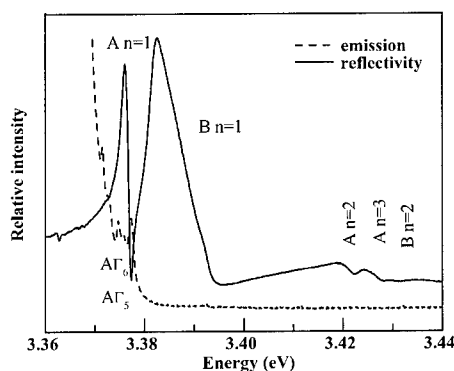


Fig. 5. Reflection and emission spectra in the intrinsic region, at 15 K.

positions of the A and B excitons obtain from reflectivity assuming the inflection point of the resonance as the energy of transition. For the A transition there is no ambiguity, since the splitting longitudinal-transversal is small (~ 1 meV), but this is not the case for the B exciton (~ 12 meV). In fact looking at the temperature evolution, the energy separation between the A and B excitons seems to decrease, from 14.9 meV at 15 K to 11.5 meV at 200 K. The energy separation between A and B exciton is due to the spin-orbit splitting which is not temperature dependent. The energy shift of the lines is due to the gap shrinkage effect in semiconductors that is caused by the cumulative effects of thermal lattice expansion and electron-phonon interaction. The decrease of the A-B splitting could have been attributed to a variation of the exciton binding energies but a weak temperature dependence for the effective Rydberg, R , is expected due the dependence of the exciton binding energy on the reduced effective mass μ and the static dielectric constant ϵ . For II-VI semiconductors the reduction of $R \propto \mu/\epsilon^2$ between 2 K and room temperature is expected to be inferior to 2 meV and be similar for both excitons [10]. At low temperature the binding energies obtained from Eq. (1) give 59.9 meV and 57.0 for the A and B excitons, respectively indicating similar effective masses and in

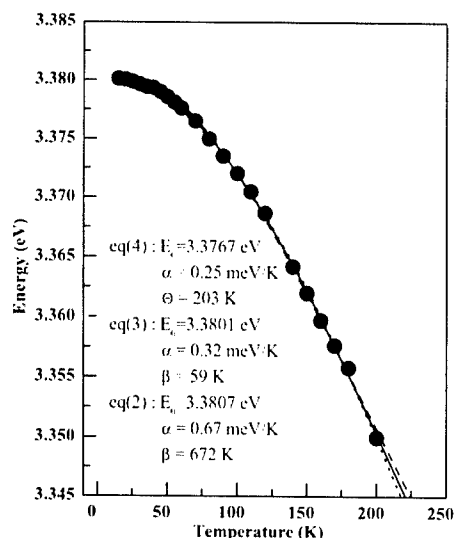


Fig. 6. Evolution of the energy position of the A exciton as function of temperature (●) data, (–) the fittings using the Eqs. (2)–(4).

good agreement with the literature [4]:

$$R = \frac{4}{3} [E_{2s} - E_{1s}]. \quad (1)$$

We performed numerical analyses of the energy position of the A exciton as function of temperature using three models. The Varshni' formula has shown limitations and various attempts have been made to improve the fitting. A modification of Varshni' equation [11] has been given [12] for the band gap temperature dependence:

$$E(T) = E(0) - \frac{\alpha T^2}{\beta + T}. \quad (2)$$

$$E(T) = E(0) - \frac{\alpha T^4}{(\beta + T)^3}. \quad (3)$$

In Ref. [13] the authors suggest a semi-empirical expression equivalent to the Bose–Einstein model proposed by Ref. [14] that provides us with good fitting and an estimative of the Debye temperature. Eq. (4) gives the best fitting to the data (Fig. 6), with a Debye temperature of $\Theta_D = 3/2\Theta = 305$ K, where Θ is the effective phonon temperature. The different values of the

parameters are given in the inset:

$$E(T) = E(0) - \frac{\alpha\Theta}{\exp(\Theta/T) - 1}. \quad (4)$$

4. Conclusion

We have shown the presence 14 transitions in the near band edge in ZnO at 15 K. These transitions are interpreted as transitions of: free excitons from the top valence band, ionized-donor bound exciton and neutral-donor bound either to the first and second top valence bands. We have determined the temperature dependence of the A exciton peak position in these high-quality ZnO crystals and obtained a value of the Debye temperature in good agreement the literature. The high quality of the samples studied is also demonstrated by the RBS measurements.

References

- [1] Y.F. Chen, D.M. Bagnall, Z. Zhu, T. Sekiuchi, K.T. Park, K. Hiraga, T. Yao, S. Koyama, M.Y. Shen, T. Goto, J. Crystal Growth 181 (1997) 165.
- [2] Y.F. Chen, D.M. Bagnall, H.J. Ko, K.T. Park, Z. Zhu, T. Yao, J. Appl. Phys. 84 (1998) 3912.
- [3] D.W. Langer, R.N. Euwena, K. Era, T. Koda, Phys. Rev. B 2 (1970) 4005.
- [4] D.C. Reynolds, D.C. Look, B. Jogai, C.W. Litton, G. Cantwell, W.C. Harsch, Phys. Rev. B 60 (1999) 2340.
- [5] D.C. Reynolds, D.C. Look, B. Jogai, C.W. Litton, T.C. Collins, W.C. Harsch, G. Cantwell, Phys. Rev. B 57 (1998) 12151.
- [6] C. Benoit la Guillaume, P. Lavallard, Phys. Stat. Sol. B 10 (1975) K143.
- [7] W. Ruhle, W. Klingenstein, Phys. Rev. B 18 (1977) 7011.
- [8] D.C. Herbert, J. Phys. C 10 (1977) 3327.
- [9] J. Rorison, D.C. Herbert, P.J. Dean, M.S. Skolnick, J. Phys. C 17 (1984) 6453.
- [10] R. Pässler, F. Blaschta, E. Griedl, K. Papagelis, B. Haserer, T. Reisinger, S. Ves, W. Gebhardt, Phys. Stat. Sol. B 204 (1997) 685.
- [11] Y.P. Varshni, Physica (Utrecht) 34 (1967) 149.
- [12] M. Fernandez, P. Prete, N. Lovergine, A.M. Mancini, R. Cingolani, L. Vasanelli, M.R. Perrone, Phys. Rev. B 55 (1997) 7660.
- [13] R. Pässler, E. riebl, H. Riepl, G. Lautner, S. Bauer, H. Preis, W. Gebhardt, J. Appl. Phys. 86 (1999) 4403.
- [14] L. Viña, Logothetidis, M. Cardona, Phys. Rev. B 30 (1984) 1979.



ELSEVIER

Physica B 308–310 (2001) 989–992

PHYSICA B

www.elsevier.com/locate/physb

Defect reactions of implanted Li in ZnSe observed by β -NMR

F. Kroll^a, B. Ittermann^{a,*}, M. Füllgrabe^a, F. Mai^a, K. Marbach^a, D. Peters^a,
W. Geithner^b, S. Kappertz^b, M. Keim^b, S. Kloos^b, S. Wilbert^b, R. Neugart^b,
P. Lievens^c, U. Georg^d, ISOLDE Collaboration^d

^a Fachbereich Physik und Zentrum für Materialwissenschaften der, Philipps-Universität Marburg, D-35032 Marburg, Germany

^b Institut für Physik, Universität Mainz, D-55099 Mainz, Germany

^c Departement Natuurkunde, Katholieke Universiteit Leuven, B-3001 Leuven, Belgium

^d CERN, PPE Division, CH-1211 Geneva 23, Switzerland

Abstract

Using β -radiation detected nuclear magnetic resonance (β -NMR), we investigated the microscopic behavior of implanted ^8Li in nominally undoped ZnSe crystals. From the temperature-dependent amplitudes of high-resolution NMR spectra we conclude a gradual interstitial-to-substitutional site change between 200 and 350 K. This is in accordance with earlier emission channeling results. We argue that this conversion proceeds via $\text{Li}_i^+ + V_{\text{Zn}}^{2-} \rightarrow \text{Li}_{\text{Zn}}^-$ and involves implantation related Zn vacancies. © 2001 Elsevier Science B.V. All rights reserved.

PACS: 61.72.Vv; 66.30.Jt; 76.60.-k

Keywords: ZnSe; Li; Acceptor doping; Implantation; β -NMR

1. Introduction

Li at substitutional Zn sites (Li_{Zn}) in ZnSe is a well-behaved shallow acceptor [1] at low dopant concentrations. The maximum achievable hole concentration is limited, however, to $p \approx 2 \times 10^{17} \text{ cm}^{-3}$ [2]. In order to explore the underlying “self-compensation” mechanism microscopically we applied β -radiation detected nuclear magnetic resonance (β -NMR) on implanted ^8Li probe nuclei. One advantage of this nuclear technique is a sensitivity high enough to work with negligible concentrations of probe atoms. This way we can “study dopants in undoped semiconductors”.

The final goal of our experiments is to see, whether Li compensation is tied to a low lying Fermi level, or if signs of an inherent instability of Li_{Zn} in ZnSe can be

detected already in intrinsic material. Here we report our first results in nominally undoped ZnSe in the limited temperature range of 150–380 K. An extension of this study to higher temperatures is currently underway. The investigation of pre-doped samples is intended for the future.

Microscopic information on the behavior of ^8Li in ZnSe is already available from Hofsäss and coworkers [3,4]. These authors employed the emission-channeling (EC) technique [5] to investigate the lattice sites of implanted ^8Li nuclei in the temperature regime of $T = 150$ –550 K. Their main results can be summarized as follows: (i) For $T \leq 200$ K Li is incorporated predominantly ($\geq 60\%$) at tetrahedral interstitial sites (T sites). (ii) A site change from interstitial Li_i to substitutional Li_s occurs at $T \approx 230$ K; the sublattice for Li_s was not determined. (iii) The fraction of Li atoms converting to substitutional sites (S sites) is affected by the implantation dose. The substitutional fraction increases if the total fluence of ^8Li exceeds $\sim 5 \times 10^{11} \text{ cm}^{-2}$. This suggests the involvement of implantation related vacancies in this site change. (iv) An

*Corresponding author. Tel.: +49-6421-282-2459; fax: +49-6421-282-6535.

E-mail address: bernd.ittermann@physik.uni-marburg.de (B. Ittermann).

unidentified “random fraction” $f_r \geq 30\%$ is observed at all temperatures.

2. Experimental

The general principles of implantation- β -NMR have been described at various instances [6], here we applied the special variant of collinear laser polarization. The on-line separator ISOLDE at CERN provides a 60-keV beam of radioactive ^8Li ions ($\tau_\beta = 1.21$ s, nuclear spin $I = 2$). The beam is neutralized in a Na vapor cell and optically pumped by a collinear laser beam. The resulting electronic polarization is transferred in flight to the nucleus before the atoms reach the sample, which is mounted in a transverse NMR field B_0 . The implanted ^8Li -probe nuclei can be depolarized by resonant radio frequency (RF) irradiation. The lifetime-averaged polarization is detected via the left/right asymmetry of the emitted β -radiation. More experimental details can be found in Ref. [7].

For an effective sample diameter (beam spot) of ~ 4 mm the implantation flux was $1.7 \times 10^6 \text{ cm}^{-2} \text{ s}^{-1}$. This corresponds to 2.5×10^5 probe nuclei simultaneously in the sample or an equilibrium concentration of $4 \times 10^{10} \text{ cm}^{-3}$ (the implantation profile simulated with the Monte-Carlo code TRIM [8,9] has a width of about 500 nm with a broad maximum at a depth of $d \approx 300$ nm). Up to 6×10^{10} probe nuclei are implanted during a whole run of a few days (not necessarily in the same sample). This is still well below those values where implantation-dose effects were observed in the EC experiments [4].

We used several nominally undoped bulk crystals ($\rho > 10^8 \Omega \text{ cm}$) from commercial sources. The size was typically $10 \times 10 \times 2 \text{ mm}^3$ with (100) or (110) planes as implantation surfaces. All samples used in this study were capped with a ~ 25 -nm layer of amorphous Si_3N_4 to prevent surface decomposition.

3. Measurements and results

A typical β -NMR spectrum of ^8Li in ZnSe, measured at $T = 172$ K, is shown in Fig. 1. The line is centered at the Larmor frequency, the corresponding Li atoms occupy lattice sites with full T_d symmetry. This finding is consistent with the EC result of Li at T sites at this temperature. The spectrum was recorded under saturating RF conditions. The line shape is a pure Lorentzian, its width is determined by the applied RF power. About 80% of the initial polarization is destroyed in the resonance, reflecting the corresponding fraction of Li at cubic lattice sites. The difference to 100% is probably caused by ^8Li stopped in the amorphous Si_3N_4 capping

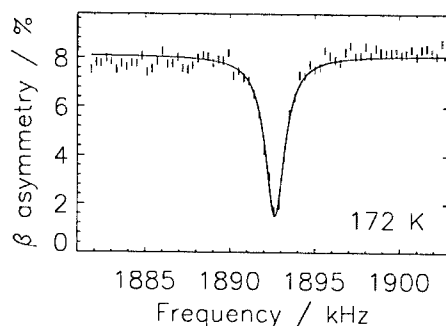


Fig. 1. β -NMR spectrum of ^8Li in ZnSe. $T = 172$ K. $B_0 = 3$ kG, $\langle 110 \rangle \parallel B_0$. The resonance was recorded with a saturating RF intensity of $B_{1,\text{rot}} = 1.0$ G and occurs at the Larmor frequency. The solid line is a Lorentzian fit.

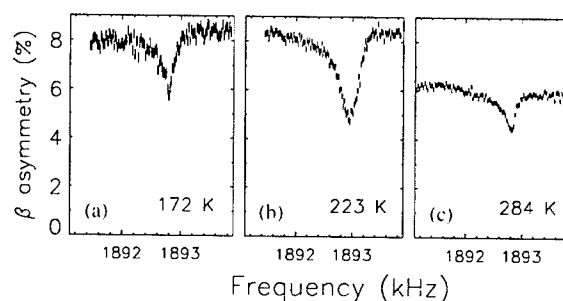


Fig. 2. Larmor resonances recorded at a reduced RF intensity of $B_{1,\text{rot}} = 25$ mG. $B_0 = 3$ kG, $\langle 110 \rangle \parallel B_0$. (a): $T = 172$ K. (b): $T = 223$ K. (c): $T = 284$ K.

layer: in earlier experiments with uncapped samples we observed an almost complete depolarization.

The saturation of this type of resonances was almost independent of temperature in the investigated range. The situation changes, however, if the RF intensity is reduced. The spectra of Fig. 2 were recorded with $B_{1,\text{rot}} = 25$ mG; the corresponding power broadening is only 31 Hz (FWHM), in this case. The observed line shapes are no longer Lorentzians, now, but reflect an inhomogeneous distribution of local magnetic fields.

One reason for this is the random distribution of host nuclei with non-vanishing magnetic moments. This contribution can be estimated by the well-known Van Vleck formula [10]. For our case of $\langle 110 \rangle \parallel B_0$, we obtain second moments M_2 of 119–145 Hz for the ^8Li resonance, depending on which of the four cubic sites is considered. Assuming a Gaussian line shape (admittedly questionable for a dilute spin system like ZnSe) this means FWHM's of 281–343 Hz. These numbers are only estimates of the real situation, however, since the local lattice relaxation around the Li impurity, the influence of impurity induced electric field gradients, or

the contributions of indirect interactions (“pseudo exchange”) are not known. For the moment it may be sufficient to say that the experimental linewidths of Fig. 2 are of the order of the Van Vleck estimates.

The asymmetric line shape of all three spectra of Fig. 2 is currently not understood. An instrumental effect is unlikely but cannot be excluded for certain. Our following conclusions should not be affected by this question, however.

Another prominent feature of Fig. 2 is the reduced baseline polarization of the spectrum measured at $T = 284$ K. This is caused by spin-lattice relaxation and indicates dynamical processes involving *substitutional* Li. This finding is rather surprising at such a low temperature but we have to postpone its discussion to a future publication. The baseline reduction was also observed in a short β -NMR report on recoil implanted ^8Li in ZnSe by Miyake et al. [11]. These authors discussed a substitutional-to-interstitial site change around $T = 300$ K. Our own (see below) as well as the EC results [3,4] clearly contradict such an interpretation.

The physically most important point of Fig. 2 is the temperature dependence of the signal intensity. Amplitudes and widths of a series of low RF resonances are plotted vs temperature in Fig. 3. The amplitudes have a marked maximum at $T \approx 210$ K while the variation of the linewidths with temperature is less pronounced.

The integrated area of an inhomogeneous spectrum reflects in many cases the number of contributing entities. If we integrate the 223-K spectrum of Fig. 2(c), however, and normalize it properly taking the given RF conditions into account, we obtain a corresponding probe fraction of several hundred percent. We also know from Fig. 1 and other saturated resonances (not shown) that the total fraction of Larmor resonant ^8Li nuclei is $\approx 80\%$ for all temperatures in the investigated regime, which appears to contradict Fig. 2. The solution of this puzzle is diffusion. If probe nuclei move in a

spatially inhomogeneous environment they sense a different local field, hence a different resonance frequency, after each jump: physical diffusion causes “spectral diffusion”. An individual probe spin can be depolarized at several different frequencies, therefore. The other way around, we can depolarize more than the initially present number of probe nuclei by just irradiating a fixed frequency and waiting for new spins to become resonant. The physical consequence of this somewhat technical effect is a correlation between signal enhancement and diffusion. What Fig. 3 actually shows us is a peak of the average probe *mobility* at around 210 K.

In a given configuration, the jump frequency of a mobile atomic species is expected to increase exponentially with temperature. We, in contrast, observe a slowly decreasing mobility for $T > 200$ K. This is the signature of a gradual transition from a mobile to an immobile configuration, i.e., a change from interstitial to substitutional lattice sites. At low temperatures we have only diffusing Li_i but between 200 and ~ 350 K the site conversion occurs.

Qualitatively, these results are in perfect agreement with the EC data of Refs. [3,4]. Only concerning the end temperature of the conversion process we have a minor discrepancy. In the EC experiments conversion is completed at $T \approx 275$ K while in our data the Li_i survive up to higher temperatures. The most probable explanation for this difference is the lower implantation fluence in our case. This means a lower concentration of implantation related vacancies, which are obviously needed to promote the site change.

The nature of the S site, Li_{Zn} or Li_{Se} , cannot be read directly from the β -NMR spectra. There are strong arguments, however, in favor of Li_{Zn} . A hypothetical Li at a Se site had to adopt a $\text{Li}_{\text{Se}}^{5-}$ charge state, in order to fill its electronic shell. Such an extreme assumption can certainly be discarded. In any less negative state, however, the defect had a partially filled p shell, hence should undergo a Jahn–Teller distortion to remove its orbital degeneracy, and have no longer T_d symmetry [12]. The narrow Larmor resonance of Fig. 2(c) shows clearly that this is not the case. In the same manner, we can argue that Li_{Zn} has to be in the negative charge state as has to be expected for a shallow acceptor.

Another reason to exclude the Li_{Se} hypothesis is the $T \rightarrow S$ conversion process. We have seen already, that vacancies are involved in this reaction according to $\text{Li}_i + V \rightarrow \text{Li}_s$. Li_i should be positively charged [13] (from our own data Li_i^- and Li_i^+ were both possible, only the paramagnetic neutral state is ruled out). The vacancies in ZnSe are double acceptors (V_{Zn}) or double donors (V_{Se}) [12], in intrinsic ZnSe we had V_{Zn}^{2-} and V_{Se}^{2+} . Therefore, simple Coulomb repulsion prevents a reaction $\text{Li}_i^+ + V_{\text{Se}}^{2+} \rightarrow \text{Li}_{\text{Se}}^{3-}$.

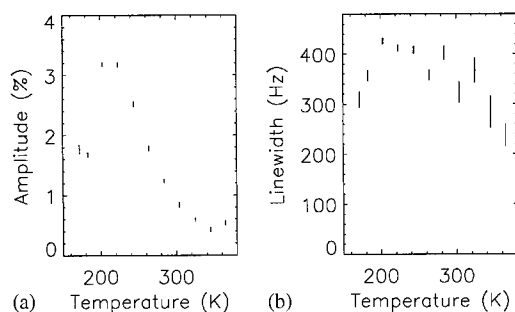


Fig. 3. Temperature dependence of (a) amplitudes and (b) widths (FWHM) of a series of β -NMR resonances. Measuring conditions like in Fig. 2. The parameters were obtained by Gaussian fits to the original spectra.

Acknowledgements

We are grateful to H. Ackermann and H.-J. Stöckmann for continuous support and discussions, to D. Forkel-Wirth, A. Burchard, and M. Dietrich for their assistance at ISOLDE, and to A. Sacher, Marburg, for the capping of our samples. This work was sponsored by the BMBF under contract AC5-MAR.

References

- [1] J.L. Merz, K. Nassau, J.W. Shiever, *Phys. Rev. B* 8 (1973) 1444.
- [2] M.A. Haase, H. Cheng, J.M. DePuydt, J.E. Potts, *J. Appl. Phys.* 67 (1990) 448.
- [3] S.G. Jahn, U. Wahl, M. Restle, H. Quintel, H. Hofsäss, M. Wienecke, I. Trojahn, ISOLDE Collaboration, *Mater. Sci. Forum* 196–201 (1996) 315.
- [4] K. Bharuth-Ram, M. Restle, H. Hofsäss, C. Ronning, U. Wahl, *Physica B* 273–274 (1999) 875.
- [5] U. Wahl, *Phys. Rep.* 280 (1997) 145.
- [6] B. Ittermann, G. Welker, F. Kroll, F. Mai, K. Marbach, D. Peters, *Phys. Rev. B* 59 (1999) 2700.
- [7] B. Ittermann, M. Füllgrabe, M. Heemeier, F. Kroll, F. Mai, K. Marbach, P. Meier, D. Peters, G. Welker, W. Geithner, S. Kappertz, S. Wilbert, R. Neugart, P. Lievens, U. Georg, M. Keim, ISOLDE-Collaboration, *Hyperfine Interactions* 129 (2000) 423.
- [8] J.P. Biersack, L.G. Haggmark, *Nucl. Instr. and Meth.* 174 (1980) 257.
- [9] J.F. Ziegler, J.P. Biersack, U. Littmark, *The Stopping and Range of Ions in Solids*, Pergamon, New York, 1985.
- [10] J.H. Van Vleck, *Phys. Rev.* 74 (1948) 1168.
- [11] T. Miyake, M. Tanigaki, T. Izumikawa, T. Yamaguchi, K. Sato, K. Minamisono, T. Ohtsubo, S. Fukuda, M. Fukuda, K. Matsuta, Y. Nojiri, T. Minamisono, *Hyperfine Interactions C1* (1996) 230.
- [12] G.D. Watkins, in: W. Schröter (Ed.), *Electronic Structure and Properties of Semiconductors*, Materials Science and Technology, Vol. 4, VCH, Weinheim, 1991, p. 105.
- [13] C.G. Van de Walle, D.B. Laks, G.F. Neumark, S.T. Pantelides, *Phys. Rev. B* 47 (1993) 9425.



ELSEVIER

Physica B 308–310 (2001) 993–998

PHYSICA B

www.elsevier.com/locate/physb

Control of the electric and magnetic properties of ZnO films

H. Tabata*, M. Saeki, S.L. Guo, J.H. Choi, T. Kawai

ISIR-Sanken, Osaka University, 8-1 Mihogaoka, Ibaraki, Osaka 567-0047, Japan

Abstract

We have demonstrated a possibility of the growth of p-type ZnO films by a pulsed laser deposition technique combined with a plasma gas source. The p-type ZnO film has been fabricated by passing N₂O gas through an ECR or RF plasma source. N₂O gas is effective in preventing “O” vacancies from occurring and introducing “N” as an acceptor, at the same time. Two-step growth, with a thin ZnO template layer formed at high temperature, is quite effective to realize a well-crystallized growth at low temperature. This non-equilibrium film formation process enables us to produce other new ZnO films which show ferromagnetic properties which means that a transparent magnet is realized with this technique. These various types of ZnO films will open the door for practical applications in various oxide electronic devices. © 2001 Elsevier Science B.V. All rights reserved.

PACS: 72.80.Ey; 73.50.-h; 73.61.Ga; 51.60 + q

Keywords: ZnO; Laser MBE; Thin films transistor

1. Introduction

Zinc oxide (ZnO) is one of the promising materials which is well matched for human being and environment and it is expected to apply across various fields due to its potential applications [1–7]. The problem of p-type doping of ZnO can arise for various reasons such as, the acceptors level may be sufficiently deep such that there are low thermal excitations in the valence band, low solubility of the dopant or inducing self-compensating processes on doping. Recently, a theoretical idea has been proposed, the so-called codoping approach (simultaneous doping of donor and acceptor), to realize the p-type electrical conduction in ZnO. In our experiments, the non-equilibrium process is essential. To do that, we have produced the ZnO films under the condition of excited N and O atmosphere. The active N is formed by passing N₂O gas through an RF plasma source. Furthermore, the two-step growth, with a thin ZnO template layer formed at high temperature, is quite effective to realize a well-crystallized growth at low

temperature. By this technique, transition metals such as Co and V have been substituted into the ZnO films by more than 15%. Eventually, ferromagnetic properties can be observed at room temperature in these highly doped ZnO films. The above-observed new type of ZnO films will open the door for practical applications in various oxide electronic devices.

1.1. Non-equilibrium process

The naturally occurring ZnO has an n-type conductivity which can be enhanced by doping with Al, Ga, etc. The problem of p-type doping in ZnO can arise for various reasons such as, the location of the acceptor level may be sufficiently deep such that there is low thermal excitations in the valence band, low solubility of the dopant or inducing self-compensating processes on doping. Recently, Yamamoto and Katayama-Yoshida [8] have proposed that by adopting a codoping approach (simultaneous doping of donor and acceptor) one can realize the p-type electrical conduction in ZnO. The proposed choice of donors are Al, Ga or In with N as the acceptor. We tried to adopt this method for obtaining p-type ZnO. Thermodynamically, Ga₂O₃

*Corresponding author. Tel.: +81-6-6879-8446; fax: +81-6-6875-2440.

E-mail address: tabata@sanken.osaka-u.ac.jp (H. Tabata).

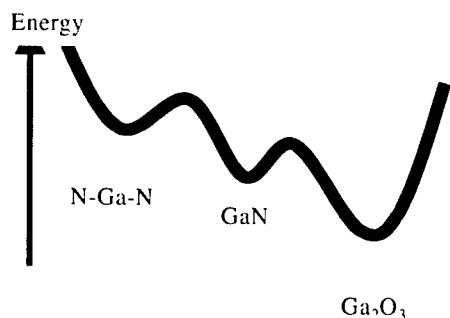


Fig. 1. Energy diagram for Ga_2O_3 , GaN and N-Ga-N.

and GaN are stable phases. To introduce N and Ga at the same time in the ZnO lattice, N-Ga-N binding state must be frizzed. Therefore, the non-equilibrium process is an essential approach (Fig. 1).

2. Experimental

The ZnO films are formed by a pulsed laser deposition technique. The details of the experimental facility are reported elsewhere [9,10]. The films are produced in a vacuum chamber having a base pressure of 1×10^{-8} mbar. An ArF excimer laser is operated at 1 Hz at a fluence of about 0.5 J/cm^2 and the typical deposition rate is about 10 Å/min . During the deposition, the substrates (ZnO single crystals and sapphire single crystals) are kept at $280\text{--}400^\circ\text{C}$ and the required N atmosphere is maintained by passing N_2O with or without plasma source.

The crystal orientation is examined by X-ray diffraction (XRD) and pole figure measurements, using Cu K_α radiation (Rigaku). The electrical resistivity, carrier concentration and mobility are measured using a four-point probe van der Pauw method. The optical transmission through the film is measured using a Vis-UV spectrometer. The major conduction type (either p- or n-type) is confirmed by the measurement of Hall, Seebeck coefficients as well as by electrochemical measurements. X-ray photoelectron spectroscopic (XPS) measurements are carried out by using a VG Scientific ESCALAB 220I-XL spectrometer with monochromatized Al K_α radiation source.

3. Results and discussion

3.1. Electrical properties

3.1.1. Conducting properties

Initially, experiments were conducted on pure (undoped) ZnO with N_2O gas, with and without the use of

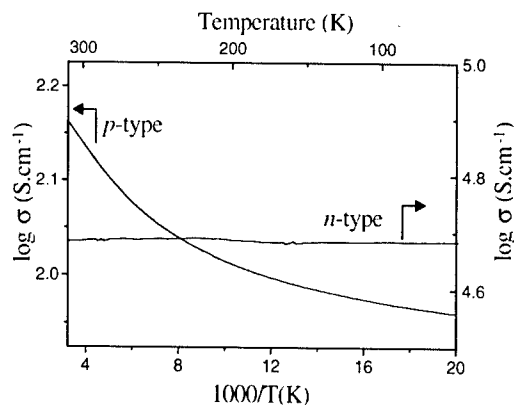


Fig. 2. Temperature versus conductivities of p- and n-type ZnO films.

plasma source. When the plasma source is off (i.e. N_2O is introduced into the vacuum chamber without any pre-ionization), at a pressure of 1×10^{-3} mbar, the obtained film showed a low resistance of $4 \times 10^{-2} \Omega \text{ cm}$ and is clear n-type with properties close to that of a natural n-type ZnO thin film. On increasing the pressure to 3 mbar, the resistivity of the film increased to $1 \times 10^3 \Omega \text{ cm}$ (carrier concentration is $2 \times 10^{14} \text{ cm}^{-3}$). Both Hall and Seebeck coefficient measurements did not clearly indicate the type of carrier—the Hall measurements sometimes showed p-type with very low signal-to-noise ratio, while the Seebeck voltage was almost zero. But with plasma source on, at a pressure of 1×10^{-3} mbar, the maximum operating pressure with our plasma source, the resistivity increased to $1 \times 10^5 \Omega \text{ cm}$ with a corresponding carrier concentration of $2 \times 10^{10} \text{ cm}^{-3}$ and showed a clear p-type behavior by both Hall and Seebeck measurements.

Fig. 2 shows the temperature-dependent electrical conductivity for lowest resistance p-type and n-type films obtained by the codoping method. The p-type film shows a typical semiconductor behavior with an estimated activation energy of $\approx 13 \text{ meV}$ in the high temperature region, whereas, the n-type sample shows a degenerate semiconductor behavior. This type of metallic-like n-type transparent conducting oxide can substitute the expansive commercially used indium-tin-oxide (ITO) films in various applications.

3.1.2. Chemical bonding state [7]

Figs. 3(a) and (b) show the XPS results with and without Ga in the ZnO films which are formed in the N_2O atmosphere through plasma source. Without Ga, the N1s peak occurs close to the position which is observed with neutral N (406 eV, Fig. 3(b)). In the Ga-doped case, on the other hand, the N1s peak is located at around 396–398 eV, which corresponds to the Ga-N

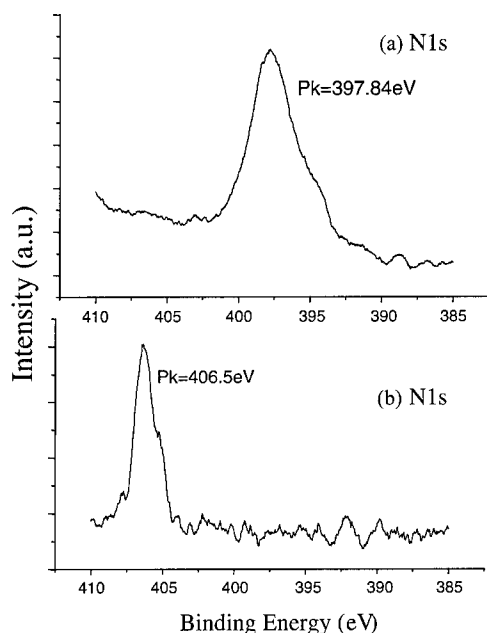


Fig. 3. XPS N1s spectrum of ZnO films formed with and without Ga dopant.

type of bonding [11]. Furthermore, the N1s peak is a build-up peak (Fig. 4). One is well matched for the N peak of GaN (N is nearest neighbor) and the other for second nearest neighbor Ga–N. It is quite evident that an N–Ga–N bond occurs in the ZnO films.

From these observed peak areas and the corresponding sensitivity factors, the approximate relative intensity ratio of Ga : N is obtained as 1 : 6. It is reported [12] that such a relative intensity ratio, by XPS, for GaN film (1Ga:1N) is about 1:3.2. This suggests that in the codoped film, the N:Ga ratio is 2:1. This is one of the basic requirements for observing p-type activity in ZnO by the codoping process as predicted by theoretical calculations.

3.1.3. Structural characterization

Fig. 4(a) shows a typical X-ray diffraction pattern obtained for an N–Ga codoped ZnO film on sapphire (1120) substrate at 400°C. N doping is carried out under N₂O at a pressure of 1×10^{-3} mbar with ECR and using the target containing Ga of 0.1 wt%. Sapphire with its plane of orientation is expected to give minimum lattice mismatch for the ZnO. We could obtain epitaxial growth as confirmed by the Φ scan for the (101) planes of ZnO film as shown in Fig. 4(b). The Φ scan obtained for the (104) planes of the substrate is also shown in Fig. 4(c).

As indicated above, the presence of a well-defined columnar structure and a possible defect structure (due

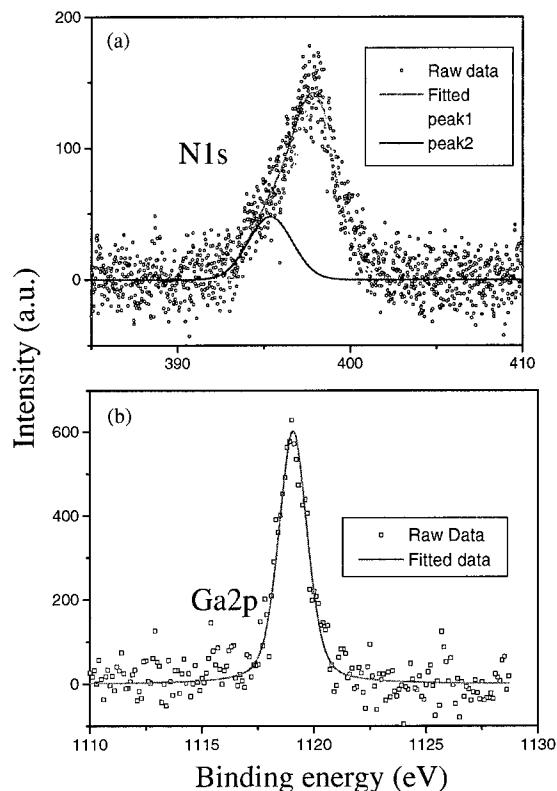


Fig. 4. XPS spectra of N1s and Ga2p in the ZnO films.

to doping processes) can act as scattering centers for the carriers, resulting in low mobility for most of the films. Also, the mobility obtained for the codoped p-type films are much lower than those obtained for the n-type films. However, the mobility of the p-type films on the sapphire substrate is higher than that of the p-type films on glass; this may be attributed to the difference in grain size—on sapphire the average size is ≈ 500 nm, whereas on glass it is ≈ 100 nm, as measured by atomic force microscopy.

3.2. Optical properties

3.2.1. Two-step growth [13]

3.2.1.1. Effect of the high temperature buffer layer.

From the thermodynamic point of view, Ga₂O₃ is the most stable phase when we mix “O”, “N” and “Ga” at the same time. The second stable phase is GaN. If we want to obtain the N–Ga–N complex, low temperature formation is very important. But the ZnO film, formed at a low temperature of 400°C, for example, shows a weak free exciton peak and strong one of deficiency in the PL spectrum. Of course, if it is formed at high temperatures above 600°C, a clear free exciton peak [14–16] is observed at 3.3 eV and the O-vacancy peak

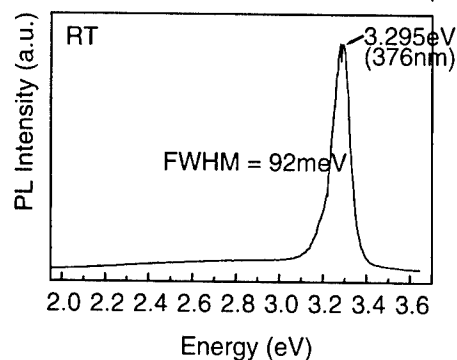


Fig. 5. PL spectrum measured at RT of ZnO film formed at 300 °C.

(around 2.2–2.4 eV) decreases dramatically. There is a dilemma. The higher temperature formation is better for the crystal growth. The low temperature, on the other hand, is better for non-equilibrium growth. The cross point is located at around 550–600 °C. But here, we have the proposed tricky idea: two-step growth. At first, the thin ZnO film (5–10 nm) is deposited at high temperatures of around 600–700 °C. Then, the second ZnO layer (> 200 nm) is successively formed at a low temperature (< 400 °C) on the first template layer. This two-step growth, with a high temperature template layer, is quite effective in improving the crystallinity of the film at a low substrate temperature as low as 300 °C. The PL spectrum changes dramatically as shown in Fig. 5. It shows quality similar to that formed at high temperatures of 600–700 °C.

3.2.2. Optical behavior

Fig. 6 shows a typical visible-UV transmission spectra obtained for films having 5 wt% Ga in ZnO, codoped with N from N₂O (p-type, S.No. 11 of table III) and N₂ with plasma at a pressure of 1×10^{-3} mbar. The transmittance in the visible region is about 90% and this value is almost the same as that reported for the only Ga doped n-type ZnO and higher than the recently reported [17] p-type CuAlO₂. The slight absorption at 550–600 nm could be due to an interference effect. In Fig. 6, the blue shift of the absorption edge for the n-type film is due to high carrier concentration in accordance with the Burstein–Moss shift.

3.2.3. Electro-luminescence [18]

The electrical and photoluminescence properties of the p(or I)-ZnO layer produced on the ZnO single crystal seems to provide another possibility to explain

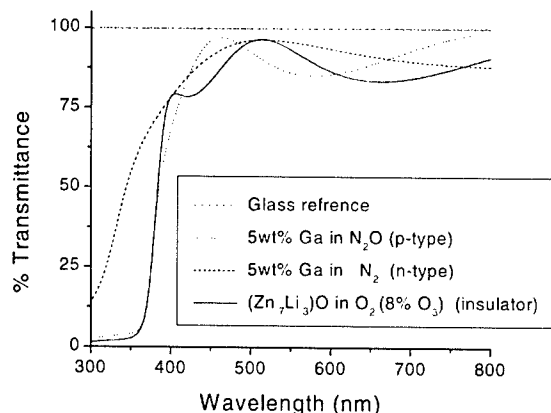


Fig. 6. Optical transmission spectra for: (a) 5 wt% of Ga codoped in ZnO under N₂O atmosphere {p-type}; (b) 5 wt% of Ga codoped in ZnO under N₂.

the light-emitting mechanism with the structure of metal/insulator/semiconductor (MIS) LEDs.

Fig. 7(a) shows the EL spectra of the ZnO homo-structural LED operating under a forward bias voltage with injection currents of 40, 80 and 120 mA, respectively, at room temperature. For comparison and emission analysis, the photoluminescence (PL) spectra excited from the surface of a p(or I)-ZnO layer grown on an Al₂O₃ (1120) substrate and an n-ZnO wafer irradiated by a 325 nm He–Cd laser at 77 K and room temperature (RT) are shown in Figs. 3(b) and (c). The current injection emission was generated when a forward biasing voltage of around 5–10 V was applied to the ZnO LED at room temperature. The light emission increases in the region of 300–900 nm when the injection current is increased from 40 mA to 80 and 120 mA.

Compared with those of the PL spectra in Figs. 7(b) and (c), there are abrupt emission increases in the region of 600–800 nm with the increase of injection current. A broad emission in the region of 370–380 nm is also slightly excited in the EL spectra, which corresponds to the free-exciton band. These broad PL peaks were repeatedly observed in the single nitrogen doped ZnO film. Since the isolated nitrogen dopant is unstable in the ZnO film, the oxygen vacancy is generated to reduce the film energy. In the cases of undoped ZnO and codoped ZnO [7], they show a clear and sharp free-exciton peak at around 380 nm. Similar broad and weak emissions are also observed in the PL spectra of Figs. 7(b) and (c), and occur due to defects such as oxygen vacancies and imperfection of crystallinity due to the low temperature formation (< 390 °C) [19]. The broad EL band emission in the region of 400–1000 nm is most likely due to defect states in the LED structure.

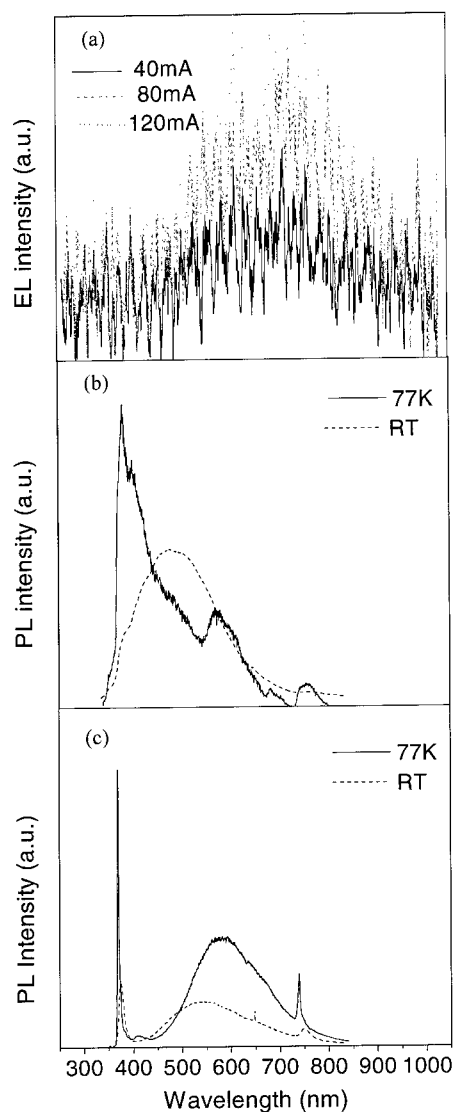


Fig. 7. (a) EL spectra of a ZnO homostructural LED operated at 5–10 V with injection currents of and 40, 80, 120 mA, respectively, at room temperature, (b) PL spectra of an n-ZnO single crystal wafer excited at 77 K and RT, and (c) PL spectra of a ZnO/Al₂O₃ film excited at 77 K and RT.

3.3. Magnetic properties

3.3.1. Cobalt (Co) doped-ZnO [20]

3d-transition metal doped ZnO films (n-type Zn_{1-x}M_xO ($x = 0.05 - 0.25$); M = Co, Mn, Cr, Ni) are formed on sapphire substrates using a PLD technique, and their magnetic and electric properties have been examined. The Co-doped ZnO films showed the maximum solubility limit. Some of the Co-doped ZnO films exhibit ferromagnetic behaviors with the Curie temperature higher than room temperature. The magnetic

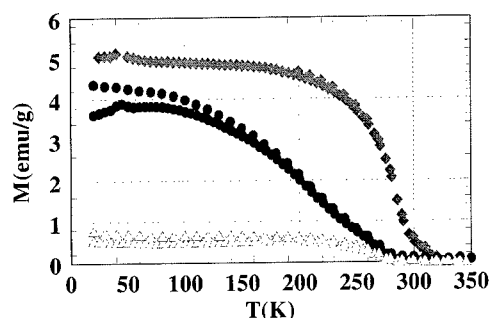


Fig. 8. Magnetization versus temperature curves measured in the field of 0.1 T. Zn_{1-x}Co_xO films ($x = 0.05$ (Δ), 0.15 (\blacklozenge), 0.25 (\bullet)).

properties of Co-doped ZnO films depend on the concentration of Co ions and carriers.

The temperature dependence of magnetization for the Zn_{1-x}Co_xO films ($x = 0.05 - 0.25$) is shown in Fig. 8. A magnetic field of 0.1 T was applied parallel to the surface of the substrate. In the case of the Zn_{0.95}Co_{0.05}O and Zn_{0.75}Co_{0.25}O samples, the abrupt increase of magnetization, which corresponds to the T_C , appeared at 280 K. The $M-H$ curve (field dependence of magnetization) of Zn_{0.95}Co_{0.05}O films measured at 6 K showed a hysteresis shape with the coercive field (H_C) of 50 Oe. The saturation magnetization (M_S) of the film is estimated to be $1.8 \mu_B/\text{Co-site}$ from the $M-H$ curve. These $M-T$ and $M-H$ curves indicate that these films showed ferromagnetic features. The Zn_{0.85}Co_{0.15}O film also showed ferromagnetic behaviors. The T_C appeared at around 300 K, which is 20 K higher than that of Zn_{0.95}Co_{0.05}O film and the M_S is estimated to be $2 \mu_B/\text{Co-site}$ from the $M-H$ curve, which is $0.2 \mu_B$ higher than that of the Zn_{0.95}Co_{0.05}O film. (Fig. 8).

In the Zn_{1-x}Co_xO, only a few films showed ferromagnetic features, while the others showed spin glass-like behaviors. The reproducibility of the method was poor (less than 10%). We should adjust the conditions to make ferromagnetic films with high reproducibility in the near future.

We also produced Cr-, Ni-, or Mn-doped ZnO films and performed magnetic measurements. These films did not show ferromagnetic behaviors. However, we need to perform further experiments to determine their magnetic and electric properties.

3.3.2. Vanadium (V)-doped ZnO

Vanadium-doped ZnO films (n-type Zn_{1-x}V_xO ($x = 0.05 - 0.15$)) were formed on sapphire substrates using a pulsed laser deposition (PLD) technique, and their magnetic and electric properties were examined. Some of the V-doped ZnO films exhibited ferromagnetic behavior with a Curie temperature higher than 350 K. The magnetic properties of V-doped ZnO films were

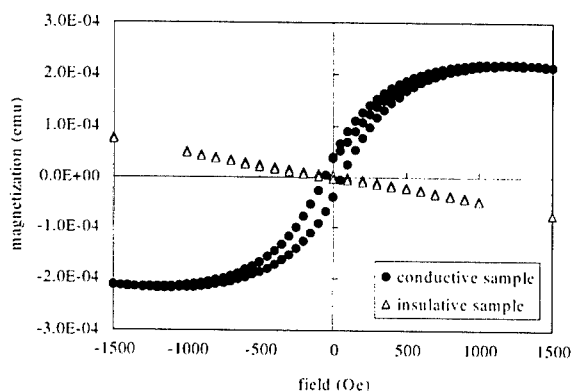


Fig. 9. Hysteresis curves measured at 300 K of $\text{Zn}_{0.85}\text{V}_{0.15}\text{O}$ films (conductive sample (●), insulative sample (△)).

found to depend on the concentration of V ions and carriers. The results of optical transmission spectra indicated that they are transparent ferromagnets at room temperature. The M – H curve (field dependence of magnetization) of $\text{Zn}_{0.85}\text{V}_{0.15}\text{O}$ films measured at 300 K showed a hysteresis loop with the coercive field (H_C) of 200 Oe (Fig. 9(a)). The saturation magnetization (M_S) of the film is estimated to be $0.5 \mu_B/\text{V-site}$ from the M – H curve at 300 K. These M – T and M – H curves indicate that the films showed ferromagnetic features. The V concentration dependence of the M – H curve also showed a hysteresis shape. The $\text{Zn}_{0.90}\text{V}_{0.10}\text{O}$ and $\text{Zn}_{0.95}\text{V}_{0.05}\text{O}$ films also showed ferromagnetic behaviors. The M_S value of each film depends on the vanadium concentration from 5% to 15%. This indicates that ferromagnetism is more stable as the concentration of vanadium increases.

3.4. Conclusions

In summary, high resistivity p-type ZnO thin films have been obtained by doping with active N alone. This p-type conductivity is very much enhanced in terms of conductivity and carrier concentration by adopting a codoping method, using N as acceptor and Ga as donor dopants. The N doping is effective only with N_2O through an RF plasma source, but not with N_2 gas, and ZnO-based LED is also fabricated. EL property is observed. Furthermore, a room temperature ferromagnet has been developed for the first time in the ZnO films. To realize the local minimum phases, a non-equilibrium process is essential. Low temperature growth is one of the key techniques. The two-step growth, using a high temperature buffer layer, is a

powerful technique to obtain the well-crystallized ZnO films at a low temperature.

Acknowledgements

We would like to thank Prof. K. Yoshida (Osaka University) and Prof. T. Yamamoto (Kochi Technical College) for their theoretical suggestion, Dr. E. Rokuta and Prof. H. Kobayashi (Osaka university) for XPS measurements.

References

- [1] M. Kawasaki, et al., *Mater. Sci. Eng. B* 56 (1998) 239.
- [2] H. Hiramatsu, K. Imaeda, H. Horio, M. Nawata, *J. Vac. Sci. Technol. A* 16 (1998) 669.
- [3] K. Minegishi, et al., *Jpn. J. Appl. Phys.* 36 (1997) L1453.
- [4] M. Joseph, H. Tabata, T. Kawai, *Appl. Phys. Lett.* 74 (1999) 2534.
- [5] J.J. Lander, *J. Phys. Chem. Solids* 15 (1960) 324.
- [6] Y. Sato, S. Sato, *Thin Solid Films* 281–282 (1996) 445.
- [7] M. Joseph, H. Tabata, T. Kawai, *Jpn. J. Appl. Phys.* 38 (1999) L1205.
- [8] T. Yamamoto, H.K. Yoshida, *Jpn. J. Appl. Phys.* 38 (1999) L166.
- [9] S. Hayamizu, H. Tabata, H. Tanaka, T. Kawai, *J. Appl. Phys.* 80 (1996) 787.
- [10] H. Tabata, T. Kawai, *Thin Solid Films* 225 (1993) 275.
- [11] M. Dinescu, P. Verardi, C. Boulmer-Leborgne, C. Geradi, L. Mirengi, V. Sandu, *Appl. Surf. Sci.* 127–129 (1998) 559.
- [12] J.K. Kim, J.L. Lee, J.W. Lee, Y.J. Park, T. Kim, *J. Vac. Sci. Technol. B* 17 (1999) 497.
- [13] M. Joseph, H. Saeki, H. Tabata, T. Kawai, *Physica B* 302–303 (2001) 140.
- [14] Yefan Chen, D.M. Bagnall, Hang-jun Koh, Ki-tae Park, Kenji Hiraga, Ziqiang Zhu, Takafumi Yao, *J. Appl. Phys.* 84 (1998) 3912.
- [15] Sunglae Cho, Jing Ma, Yunki Kim, Yi Sun, George K.L. Wong, John B. Ketterson, *Appl. Phys. Lett.* 75 (1999) 2762.
- [16] Sunglae Cho, Jing Ma, Yunki Kim, Yi Sun, George K. L. Wong, John B. Ketterson, *Appl. Phys. Lett.* 75 (1999) 2762.
- [17] Yefan Chen, Hang-ju Ko, Soon-ku Hong, Takashi Sekiuchi, Takafumi Yao, Yusaburo Segawa, *J. Vac. Sci. Technol. B* 18 (2000) 1514.
- [18] S.L. Guo, H. Tabata, T. Kawai, *Jpn. J. Appl. Phys.* 40 (2001) L177.
- [19] T. Aoki, Y. Hatanaka, *Appl. Phys. Lett.* 76 (2000) 3257.
- [20] K. Ueda, H. Tabata, T. Kawai, *Appl. Phys. Lett.* 79 (2001) 988.



ELSEVIER

Physica B 308–310 (2001) 999–1002

PHYSICA B

www.elsevier.com/locate/physb

Modulation of deep level structures in SiO₂ upon nitrogen incorporation

Sukmin Jeong¹, Atsushi Oshiyama**Institute of Physics, University of Tsukuba, 1-1-1 Tennodai, Tsukuba 305-8571, Japan*

Abstract

We present first-principles total-energy calculations that provide energetics, charge states and electronic structures for various bond configurations around N in SiO₂ with and without hydrogen. It is found that the carrier traps are effectively removed near the energy gap upon coexistence of H and N. Effects of spin polarization around the defects are clarified. © 2001 Elsevier Science B.V. All rights reserved.

PACS: 61.72.Gi; 61.72.Bb; 71.55.Ht; 85.40.-e

Keywords: Density functional theory; SiO₂; Carrier trap; Nitridation

1. Introduction

Leakage current across the ultrathin gate dielectrics is one of the major problems in miniaturization of metal-oxide-semiconductor devices. Generation of carrier traps is considered to be a principal cause for the leakage current in oxide films [1,2]. In the conventional oxides, O vacancies [3,4] and H bridges at the O vacancies [5] are proposed to be such carrier trap centers. The Si oxide films with N incorporation are now believed to be a candidate to replace the conventional Si oxides because they show better performances than the conventional oxides [6–13]. It is thus important to identify the carrier traps and their variances upon N incorporation in the Si oxynitride films.

We here explore a variety of bond configurations around N in SiO₂ using a first-principle total-energy method. We map out the energetics, charge states and electronic structures for the total-energy-optimized atomic configurations. We have found that N incor-

poration does not guarantee the improvement in electrical reliabilities of the Si oxynitride films, but that the *coexistence* of N and H is crucial for better electrical properties.

The density-functional theory (DFT) is used within the generalized-gradient approximation (GGA) [14]. The inclusion of spin degree of freedom is important in the structures without H. The nuclear potentials are simulated by ultrasoft pseudopotentials for O and N [15] and norm-conserving pseudopotentials for Si and H [16]. The cutoff energy of the plane-wave basis is 25 Ry. The super cell with 54 atomic sites possesses a triclinic symmetry and a special k point is used for integration in the Brillouin zone [4]. Geometries are optimized for all atoms until the remaining force on each atom is less than 5 mRy/Å.

2. Atomic structures

The bond configurations around the N atom in SiO₂ are not well identified. We thus consider possible atomic configurations containing N atoms in the network of α -quartz (Fig. 1): In the S₂ structure, an N atom substitutes for an O atom and then is bonded to two Si atoms (twofold N); in the S₃ structure, the central Si

*Corresponding author. Fax: +81-298-53-4492.

E-mail address: oshiyama@cm.ph.tsukuba.ac.jp (A. Oshiyama).

¹Present address: National Creative Research Initiative Center for Superfunctional Materials, Pohang University of Science and Technology, South Korea.

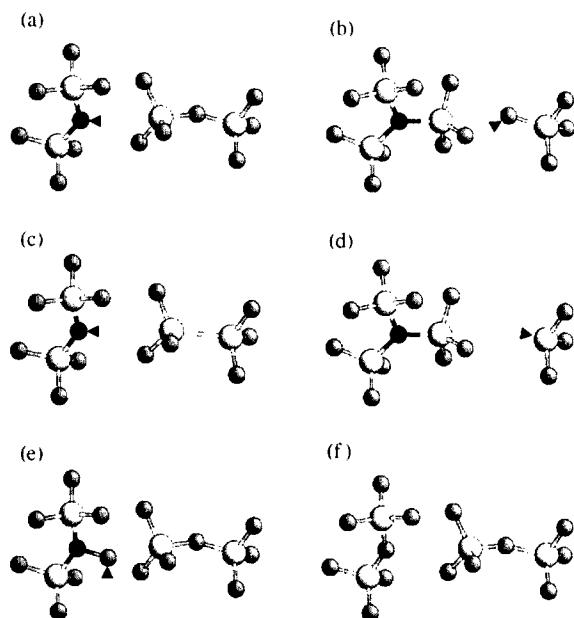


Fig. 1. Structural models for N incorporation in α -quartz: (a) S_2 , (b) S_3 , (c) V_2 , (d) V_3 , (e) S_{2O} , and (f) α -quartz as a reference. Lightly grayed, darkly grayed, and black balls indicate Si, O, and N atoms, respectively. The arrow heads in panels (a)–(e) indicate the atoms that are bonded to an H atom in the corresponding H-terminated structures, labeled as S_{2H} , S_{3H} , V_{2H} , V_{3H} , and S_{2OH} , respectively.

moves leftward to form a threefold N atom, sacrificing the bond with its right O atom; the V_2 structure is the same as the S_2 structure except for the Si–Si dimer formation due to an O vacancy; in the V_3 structure, the threefold N is formed, by breaking the Si–Si dimer bond of the V_2 structure; in the S_{2O} structure, an O atom is added to the S_2 structure and an N–O bond is formed.

We then investigate the stability of the N-incorporated structures with respect to the SiO_2 matrix. We consider the reaction, $\text{NO} + X \rightarrow z\text{O}_2 + Y$, where X represents SiO_2 (perfect α -quartz crystal) or V_O (the α -quartz with an O vacancy). Y represents S_2 , S_3 , or S_{2O} when $X = \text{SiO}_2$, and V_2 or V_3 when $X = V_O$. The coefficient z is 1, except for $z = \frac{1}{2}$ when $Y = S_{2O}$. We choose the NO molecule since it is now widely used in oxynitridation of Si or is produced by dissociation of N_2O that is also another widely used reaction gas [17]. All the reactions are endothermic with reaction energies of 3.3, 4.4, 3.2, 2.8, and 2.1 eV for $Y = S_2$, S_3 , V_2 , V_3 , and S_{2O} ,² respectively, assuming both the reactant (NO) and product (O_2) gas molecules stay in the oxide film. The calculated reaction energies are consistent with most

experiments reporting only a few atomic percent of N concentration in Si oxynitrides. After the reactions, relative stability of the five structures is assessed by comparing the formation energies as a function of the oxygen chemical potential μ_O . For a wide range of physically relevant μ_O , the formation energy of S_{2O} is higher than those of the other four structures by more than 3 eV.

Chemically active dangling bonds (DBs) are likely in the five structures (arrow heads in Fig. 1). Hence, we further consider the H-terminated counterparts of the five structures, labeled as S_{2H} , S_{3H} , V_{2H} , V_{3H} , and S_{2OH} , respectively. The H termination would take place readily, since H is ubiquitous and diffuses very fast in SiO_2 with a barrier of 0.22 eV [18]. In this way, the present models include local arrangements experimentally observed: The most dominant $\text{N} \equiv \text{Si}_3$ species (in S_3 , V_3 , S_{3H} , and V_{3H}) and the minor species such as $\text{N} = \text{Si}_2$ (in S_2 and V_2) [9,11,12], $\text{O} - \text{N} = \text{Si}_2$ (in S_{2O}) [9–11], $\text{H} - \text{N} = \text{Si}_2$ (in S_{2H} and V_{2H}) [13], and $\text{HO} - \text{N} = \text{Si}_2$ (in S_{2OH}).

3. Thermodynamic levels

The stability among different charge states in their equilibria is obtained by comparing $\Omega(Q, \mu) \equiv E(Q) + Q\mu$, where $E(Q)$ is the total energy of the charge state Q , and μ is the electron chemical potential, i.e., the Fermi level in the energy gap. Figs. 2(a) and (b) show $\Omega(Q, \mu)$ for the N-incorporated structures as a function of μ for the doubly positive ($++$; $Q = 2$), positive ($+$; $Q = 1$), neutral (0 ; $Q = 0$), and negative ($-$; $Q = -1$) charge states. The μ value, $\mu_{th}(Q/Q + 1)$, at which $\Omega(Q, \mu) = \Omega(Q + 1, \mu)$, determines the relative stability of the Q and $(Q + 1)$ charge states. The μ_{th} values are also called thermodynamic levels [5]. The thermodynamic levels in Fig. 2 are aligned with respect to band edges, by matching the theoretical and experimental thermodynamic level related to the interstitial H in SiO_2 , located at 0.2 eV above the Si midgap (the energy reference hereafter), and by using the valence-band offset of 4.3 eV between SiO_2 and Si (refer to Ref. [5] for details).

The thermodynamic level defined above is not a single-electron level obtained by the Kohn–Sham equation. The Kohn–Sham (KS) level near μ_{th} , however, provides chemical understanding of changes in charge states since the charge-state changes are processes of carrier capture or emission through some electron state in the gap.

We begin with the V_2 structure since an O vacancy is proposed to be responsible for the leakage current in SiO_2 . The KS levels are originated from the lone-pair-like (LPL) and dangling-bond-like (DBL) states of N and from the Si–Si dimer bond. The LPL state of N with the minority spin, located at -2.4 eV, can capture an

²In evaluating the reaction energies for the structures, we consider their stablest charge states when the Fermi energy is at the Si midgap ($\mu = 0$ in Fig. 2).

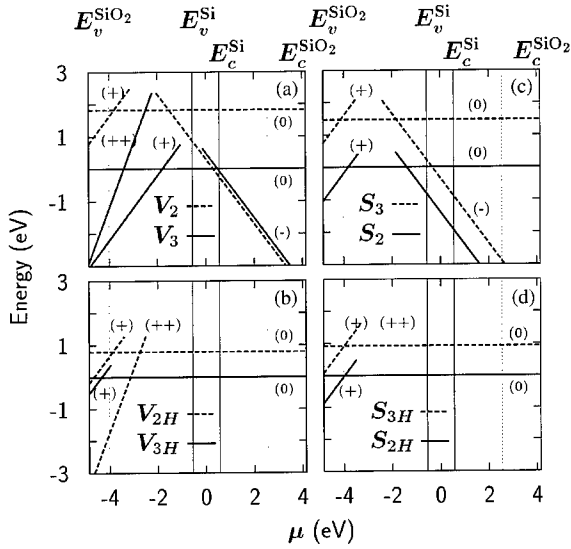


Fig. 2. Relative formation energies $\Omega(Q, \mu)$ of the N-incorporated structures as a function of the electron chemical potential μ in the energy gap of α -quartz: The energies for the doubly positive ($++$), positive ($+$), neutral (0), and negative ($-$) charge states are shown. Both ends of μ in each panel are the experimental valence band maximum (VBM) and conduction band minimum (CBM) of α -quartz ($E_v^{\text{SiO}_2}$ and $E_c^{\text{SiO}_2}$), respectively. The VBM and CBM of bulk Si (E_v^{Si} and E_c^{Si}) are represented by vertical lines. The density-functional VBM and CBM of α -quartz are shown as a reference by vertical dotted lines near both ends of μ .

electron under electron injection since it is empty in the neutral state. The filled DBL state of N with the minority spin, located at -3.1 eV, can release an electron and then plays the role of a hole trap. The Si-Si dimer states of both spins are below the above two states. For the doubly positive charge state, the V_2 structure transforms to the V_3 structure with breaking of the Si-Si bond. This bistability is also observed for an O vacancy in SiO_2 [3,4].

The V_3 structure has different features in the KS levels from the V_2 structure. Instead of disappearance of the DB states of the N atom, the DB states of the right Si atom emerge at -1.7 eV for the majority spin and at 0.7 eV for the minority spin. The LP states of the N atom still remain in the SiO_2 energy gap. Thus the DB of the right Si atom can capture both an electron and a hole, depending on the position of the Fermi energy. The positively charged structure, in this case, is spin-unpolarized unlike the V_2 and S_2 structures.

Table 1 shows the charge-state dependent spin magnitude S for each geometry. The spin magnitude varies depending on the number of electrons accommodated in the corresponding electron states. It is noteworthy that high spin states ($S = 1$) are realized

Table 1

Calculated spin magnitudes S for possible charge states Q (see also Fig. 2) of each N-incorporated geometry. The calculated total-energy gain ΔE due to the spin polarization is also shown

Geometry	Q	S	ΔE (eV)
S_2	$+$	1	0.8
	0	1/2	0.4
	$-$	0	
S_3	$+$	1	0.5
	0	1/2	0.4
	$-$	0	
V_2	$+$	1	0.6
	0	1/2	0.4
	$-$	0	
V_3	$++$	1/2	0.2
	$+$	0	
	0	1/2	0.6
	$-$	0	

around defects in SiO_2 where non-magnetic elements alone exist. The total energy gain ΔE upon the spin polarization is also shown in Table 1 for each charge state. The energy gain is about a half eV. It is thus expected that the experiments such as EPR are capable of observing the high spin states in SiO_2 .

4. Coexistence of N and H

Figs. 2(a) and (b) clearly show that the N-incorporated structures induce the gap states that play roles of charge traps. The occupancy of the charge trap states is sensitive to the position of the Fermi energy that changes according to the external bias voltage across the oxide films. At the zero bias, corresponding roughly to $\mu = 0$, the negative charge states are the most stable except for V_3 . Within relatively small magnitudes of bias (0.2 – 1.8 V), the atomic structures change their charge states from negative to neutral. Larger biases then induce the charged states from neutral to positive. This manifests that the N incorporation in Si oxides itself is inadequate to erase carrier traps and then improve electrical reliabilities of the gate dielectrics.

The N-incorporated structures become much stabilized by capturing an H atom at the sites depicted in Fig. 1. The H-terminated structures have lower energies by 2.8 – 4.1 eV than the corresponding H-free structures (see footnote 2) plus H^+ in SiO_2 (see footnote 2).³ As shown in Figs. 2(c) and (d), the H termination gives rise to remarkable changes in electronic structures and consequently in structural stabilities. All the DB states

³ For H in SiO_2 , the positive charge state has the lowest energy at $\mu = 0$ (see Ref. [19]).

disappear from the energy gap because of formation of strong bonds with H. As a result, we have only the gap states from the LP of N in S_{2H} , S_{3H} and V_{3H} and from the Si–Si dimer bond and the LP of N in V_{2H} . These remaining gap states are in the SiO_2 energy gap. However, they are practically inactive for a wide range of applied voltage due to their sufficiently deep positions in the energy gap [see Figs. 2(c) and (d)]. Further, since all the gap states are already occupied, electrons are unable to be trapped for the whole range of the Fermi energy. Therefore, in the H-terminated structures, S_{2H} , S_{3H} and V_{3H} , the carrier traps are effectively removed from the practical range of the Fermi-level position. This is in agreement with a recent voltage shift measurement for the gate dielectrics grown on the N-implanted Si substrate [8].

The $N \equiv Si_3$ unit, observed as the most dominant species in Si oxynitride, is found to be effective in reducing the charge traps, only if it is *terminated* by H (V_{3H} and S_{3H}). The $H-N = Si_2$ unit is also effective. The existence of N–O bonds, on the contrary, is not desirable for suppression of charge trapping: We have found that the anti-bonding states of LPs of the N and O atoms in the S_{2O} structure become hole traps that are still active for a bias as small as 2.7 V, even after H termination. Of course, it is impossible that the present models cover all the possible bond configurations around N, especially near the SiO_2/Si interface. But we argue that the calculated results are directly extended to other structures and that the charging characters can be predicted based on the generic features of the present model structures.

H termination (without N incorporation), although generally effective in removing the gap states of DBs from the energy gap, does not automatically guarantee suppression of charge trapping. A recent DFT calculation

has shown that the H-complexed O vacancy, where two Si atoms that were bonded to the removed O atom (O vacancy) are terminated by two H atoms, is susceptible to hole injection, through formation of an H_2 molecule [20]. Based on the present DFT calculations as well as this result, we argue that the improvement in electrical reliabilities of Si oxynitrides originates from the *coexistence* of N and H, neither from the presence of N alone nor from the presence of H alone.

References

- [1] P. Olivo, T.N. Nguyen, B. Ricco, IEEE Trans. Electron Devices 35 (1988) 2259.
- [2] E. Rosenbaum, L.F. Register, IEEE Trans. Electron Devices 44 (1997) 317.
- [3] M. Boero, et al., Phys. Rev. Lett. 78 (1997) 887.
- [4] A. Oshiyama, Jpn. J. Appl. Phys. 37 (1998) L232.
- [5] P.B. Blöchl, J.H. Stathis, Phys. Rev. Lett. 83 (1999) 372.
- [6] H. Fukuda, T. Arakawa, S. Ohno, Electron. Lett. 26 (1990) 1505.
- [7] H. Hwang, et al., Appl. Phys. Lett. 57 (1990) 1010.
- [8] D. Misra, Appl. Phys. Lett. 75 (1999) 2283.
- [9] R.I. Hegde, et al., Appl. Phys. Lett. 66 (1995) 2882.
- [10] M. Bhat, et al., Appl. Phys. Lett. 64 (1994) 2116.
- [11] E.C. Carr, et al., Appl. Phys. Lett. 63 (1993) 54.
- [12] H. Ono, et al., Appl. Phys. Lett. 74 (1999) 203.
- [13] J.L. Bischoff, et al., Surf. Sci. 251/252 (1991) 170.
- [14] J.P. Perdew, K. Burkde, Y. Wang, Phys. Rev. B 54 (1996) 16533.
- [15] D. Vanderbilt, Phys. Rev. B 41 (1990) 7892.
- [16] N. Troullier, J.L. Martins, Phys. Rev. B 43 (1991) 1993.
- [17] P.J. Tobin, et al., J. Appl. Phys. 75 (1994) 1811.
- [18] B. Tuttle, Phys. Rev. B 61 (2000) 4417.
- [19] A. Yokozawa, Y. Miyamoto, Phys. Rev. B 55 (1997) 13783.
- [20] A. Yokozawa, Y. Miyamoto, Appl. Phys. Lett. 73 (1998) 1122.



ELSEVIER

Physica B 308–310 (2001) 1003–1006

PHYSICA B

www.elsevier.com/locate/physb

Non-linear 2-mm waveband EPR spectroscopy of spin/charge excitations in organic semiconductors

V.I. Krinichnyi*

Institute of Problems of Chemical Physics, 16 Institutski Prospect, Chernogolovka, MD, 142432 Russia

Abstract

This report summarizes the basic aspects of an investigation at 2-mm waveband EPR of magnetic, relaxation and dynamics parameters of various low-dimensional solid-state organic semiconductors with mobile paramagnetic impurities. At high-registration frequency, all components of the g -tensor of such paramagnetic centers are determined. Relaxation and diffusion rates of paramagnetic impurities with different mobilities are determined by the method of steady-state saturation of spin packets. © 2001 Elsevier Science B.V. All rights reserved.

Keywords: EPR; Organic semiconductors; Relaxation; Dynamics

1. Introduction

The recent years are characterized by a great attention to the synthesis and investigation of new electronic low-dimensional systems, organic polymer and fullerene semiconductors [1]. This happened since the investigation of these systems has generated entirely new scientific conceptions and a potential for its perspective application in molecular electronics.

Normally, these systems contain paramagnetic centers (PC) localized or/and delocalized along molecules, therefore EPR spectroscopy is a powerful method for investigation of different properties of organic semiconductors. However, at the usually used centimeter wavebands EPR, the signals of organic free radicals are registered in a narrow magnetic field range that leads to the overlapping of the lines of complex spectrum or spectra of different radicals with similar g -factors [1]. It was shown earlier [2], that transition to 2-mm waveband EPR and use of saturation methods enable the profound investigation of the structure, dynamics, other specific characteristics of paramagnetic impurities and their local environment, and charge transfer processes in different solid-state systems.

This report is devoted to the potentialities of non-linear 2-mm waveband EPR spectroscopy in the investigation of relaxation and dynamics properties of PC in various organic low-dimensional semiconductors, e.g. polyaniline, $(-\text{C}_6\text{H}_4-\text{NH}-)_x$ (PANI) slightly doped with sulfuric acid and in triphenylamine fullerene complex $(\text{C}_{60}^-\text{TPA}^+)$ irradiated by light with $\lambda > 400$ nm.

2. Polyaniline

Nearly symmetric Lorentzian signals are observed in the 3-cm EPR spectrum of the polyaniline slightly doped with sulfuric acid (Fig. 1a). At 2-mm waveband EPR, this sample demonstrates a more informative spectrum (Fig. 1b). Computer simulation of these EPR spectra showed that at least two types of PC are stabilized in the polymer semiconductor, namely localized polarons R_1 with $g_{xx} = 2.00535$, $g_{yy} = 2.00415$, $g_{zz} = 2.00238$, $A_{xx} = A_{yy} = 0.33$ mT, and $A_{zz} = 2.3$ mT, and polarons R_2 with $g_{\text{eff}} = 2.00395$ moving along polymer chains with a minimum rate $v_{1D}^0 \geq (g_{xx} - g_e)\mu_B B_0 / 2\pi\hbar \cong 5.7 \times 10^7 \text{ s}^{-1}$.

In both the dispersion components, the bell-like signals are detected due to an adiabatically fast passage of the inhomogeneously broadened line (Figs. 1c and d). This effect was not detected earlier at lower magnetic

*Tel.: +7-95-524-5035; fax: +7-96-524-9676.

E-mail address: kivi@cat.icp.ac.ru (V.I. Krinichnyi).

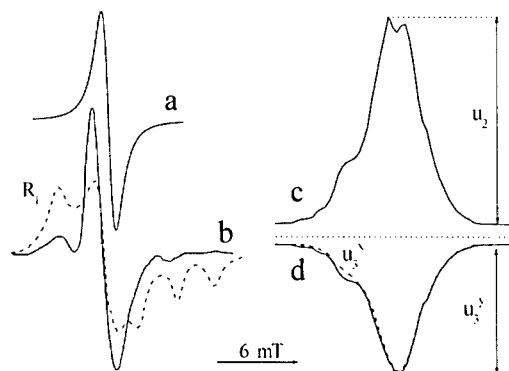


Fig. 1. In phase (a–c) and $\pi/2$ -out-of-phase (d) absorption (a,b) and dispersion (c,d) spectra of polyaniline base detected at 3-cm (a) and 2-mm (b–d) wavebands EPR. Dotted lines show shown calculated PC R_1 and dispersion component u_3 registered at low temperature. The dispersion components u_2 and u_3 are shown.

fields. Indeed, the probability of interaction of the spin packets $P \propto \exp(-\hbar\omega_c/kT)$ decreases strongly at 2-mm waveband EPR such that the spin-packets become non-interacting and are saturated at lower RF power. This type of components is a result of rapid passage of PC as the conditions of the spin packets saturation $\gamma_c B_1 \sqrt{T_1 T_2} > 1$ and adiabatic passage of resonance $dB/dt = B_m \omega < \gamma_c^2 B_1^2$ hold (here T_1 and T_2 is, respectively, the spin–lattice and spin–spin relaxation time, dB/dt is the rate of passage of resonance, B_m and ω_m are the amplitude and angular frequency of magnetic field modulation, respectively, and B_1 is the magnetic component of the polarizing RF field. In this case, the dispersion signal consists of one linear and two non-linear terms [3]:

$$U = u_1 \sin(\omega_m t) + u_2 \sin(\omega_m t - \pi) + u_3 \sin(\omega_m t - \pi/2). \quad (1)$$

The dispersion signal of PANI is determined mainly by the two later terms of Eq. (1), so that both the relaxation times can be calculated from the u_2 and u_3 terms of Eq. (1) as was described earlier [4].

The relaxation times calculated from the dispersion spectra of PC in PANI sample are shown in Fig. 2 as a function of temperature.

The amplitude and shape of the components of the dispersion signal depend not only on the intensity of spin exchange and the rate of electronic relaxation, but also on the relatively slow macromolecular reorientations or torsional librations in the polymer semiconductor. Such motions are usually studied by the saturation transfer EPR spectroscopy (ST-EPR) [5]. Fig. 1 shows that the shape of the u_3 component changes with temperature. It is a typical manifestation of intensification of superslow anisotropic librations of

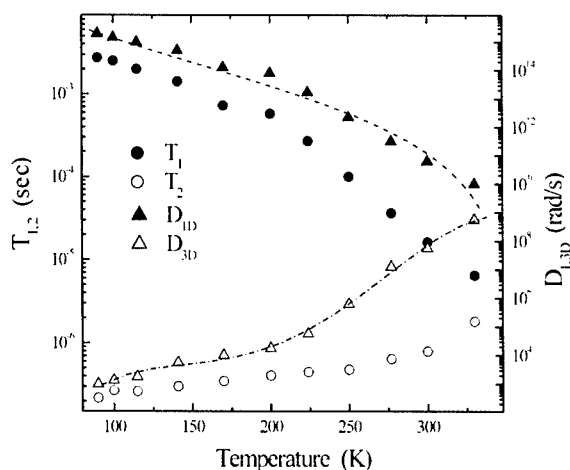


Fig. 2. The temperature dependences of the effective relaxation times, the 1D and 3D translative diffusion coefficients of PC in polyaniline slightly doped with sulfuric acid. The dependences $D_{1D}(T) \propto \ln^4(10^{25} T^{-9.8})$ and $D_{3D}(T) \propto k_1 T \exp(-0.025 eV/kT) + k_2 T \exp(-0.048 eV/kT)$ are shown by a dashed and dash-dotted lines, respectively.

macromolecules with localized R_1 radicals near the main X -axis. The correlation time of such PC motions in PANI was determined from the equation $\tau_c^v = \tau_c^0 (u_3^v/u_3^i)^{-4.8}$ to be $2.7 \times 10^{-7} \exp(0.045 eV/kT)$. The calculated activation energies of macromolecular librations correspond to the energies of optical phonons and are close to the value obtained for poly(tetrathiafulvalene) and poly(bis-alkylthioacetylene) [2].

The experimental data obtained can be explained by the modulation of electron relaxation by 1D diffusion of mobile polarons along the polymer chains and by their 3D hopping between the chains with the diffusion coefficients D_{1D} and D_{3D} , respectively. Such spin motions induce an additional magnetic field at the sites of other PC. This leads to the increase of effective relaxation rates of the spin ensemble [6]

$$T_1^{-1} = \langle \omega^2 \rangle [2J_1(\omega_c) + 8J_2(2\omega_c)], \quad (2a)$$

$$T_2^{-1} = \langle \omega^2 \rangle [3J(0) + 5J_1(\omega_c) + 2J_2(2\omega_c)], \quad (2b)$$

where $\langle \omega^2 \rangle$ is the second momentum of the line, and $J(\omega_c) = (D_{1D}\omega_c)^{-1/2}$ at $D_{3D} \leq \omega_c \leq D_{1D}$ and $J(\omega_c) = (D_{1D}D_{3D})^{-1/2}$ at $\omega_c \leq D_{3D}$ are the spectral density functions at the spin precession frequency ω_c .

1D spin dynamics in PANI can be interpreted in the framework of the Kivelson–Heeger model [7] of isoenergetic electron transfer between the polymer chain involving optical phonons. According to this model, polarons should diffuse along the chain with a diffusion coefficient of

$$D_{1D}(T) \propto D_{1D}^0 \ln^4[k_1 T^{-n-1}], \quad (3)$$

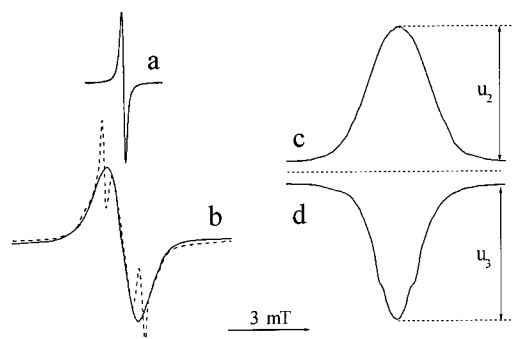


Fig. 3. In phase (a–c) and $\pi/2$ -out-of-phase (d) absorption (a,b) and dispersion (c,d) spectra of $C_{60}TPA^+$ complex detected at 3-cm (a) and 2-mm (b–d) wavebands EPR. The first derivative of quadrature dispersion signal (insert d) is shown by a dashed line (insert b). The dispersion components u_2 and u_3 are shown.

where k_1 is constant and $n \approx 10$. Fig. 2 shows that this function $k_1 = 10^{25} K^{9.8}$ and $n = 8.8$ fit well with the experimental data.

As in case of inorganic semiconductors, 3D spin dynamics in PANI can be explained by activated hopping through a barrier E_a , $D_{3D}(T) \propto T \exp(-E_a/kT)$. It is seen from Fig. 2, that spins and charges hop between polymer chains with $E_a = 0.025$ eV at $T \leq 200$ K and with $E_a = 0.048$ eV at higher temperatures. The latter value lies near the energy of lattice phonons determined above. This leads to a conclusion of modulation of interchain spin/charge transfer by macromolecular motion.

3. Fullerene complex

PC in $C_{60}TPA^+$ demonstrate a single spectrum with $g = 2.0023$ and linewidth of 0.15 and 1.18 mT at 3-cm and 2-mm wavebands EPR, respectively (Fig. 3). At 2-mm waveband, the EPR linewidth decreases down to 1.08 mT for the temperature decreasing down to 100 K. The spin susceptibility follows the Curie law for 100–250 K and it decreases sharply at higher temperatures (Fig. 4).

As in the case of PANI, in both dispersion components, the bell-like signal are detected due to an adiabatically fast passage of the inhomogeneously broadened line (Figs. 3c and d), so that the relaxation times of the sample can be determined from its dispersion components as well.

The temperature dependencies of the effective relaxation times of PC in $C_{60}TPA^+$ are present in Fig. 4. The figure shows that $T_1(T)$ and $T_2(T)$ functions differ on those of some metals and compounds of lower dimension. The break in the curves could be attributed to the structural conformation transition in the system at

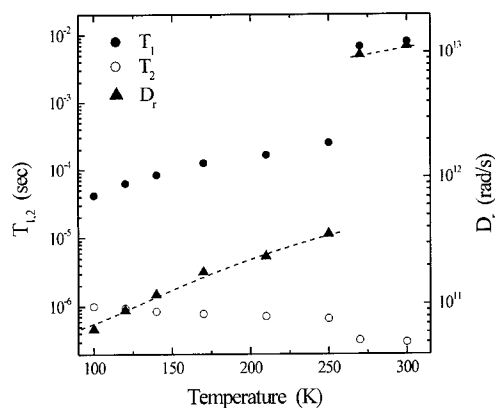


Fig. 4. The temperature dependences of the effective relaxation times, the rotational diffusion coefficient and relative susceptibility of PC in $C_{60}TPA^+$ complex. The dependence $D_r = D_r^0 + k_1 T \exp(-0.027/kT)$ is shown by dashed line.

$T_c \approx 250$ K. The T_c value is closer to that of phase transition in C_{60} single crystal. It is accompanied with the librative reorientation of preferable axis of some C_{60} molecules by 22° and the change of the crystal unit volume.

The temperature dependence of the D_r value calculated for $C_{60}TPA^+$ from Eq. (2) with $J(\omega_c) = 2D_r/(D_r^2 + \omega_c^2)$ is also shown in Fig. 4. The figure shows that the spin rotation frequency increases monotonically with the temperature increase from 100 K up to $T_c \approx 250$ K and then increases sharply up to $\sim 10^{13} s^{-1}$ at 300 K. As in the case of single crystal C_{60} , such a drop is probably caused by the phase transition accompanied by the change of the sample unit size. This process decreases the energy barrier of the molecular rotation that leads to an increase of the motion rate in the complex. The D_r value was determined to be $D_r = D_r^0 \exp(-0.024/kT)$ at $T \leq T_c$. $D_r^0 = 1.2 \times 10^{12} rad s^{-1}$ corresponds to an upper frequency limit for optical phonons in solids. The activation energy E_a is near to the phonon energy of C_{60} single crystal, 0.025 eV [8]; however, it is less than that of C_{60} rotation, 0.052 eV determined by X-ray structure analysis [9]. Such a discrepancy can be explained by the larger size of elemental unit of $C_{60}TPA^+$ complex that should lead to a decrease in the rotational barrier for PC.

The first derivative of $\pi/2$ -out-of-phase component of the dispersion signal shown in Fig. 3d is presented by a dotted line in Fig. 3b. The comparison of this spectrum with the normal absorption one (Fig. 3b) shows that, two PC, R_1 and R_2 with ratio 80:1 and equal g -factors but with different relaxation and dynamics parameters are stabilized in the complex. The singlet attributed to radical R_1 has $\Delta B_{PP} = 1.08$ mT, whereas PC R_2 demonstrates a doublet with $\Delta B_{PP} = 0.19$ mT splitted by $D = 1.37$ mT (Fig. 3b). The shape of the latter

spectrum should be attributed to triplet pairs stabilized in the sample. The distance r_{12} between PC in this triplet can be calculated in the framework of an interaction of two point-like dipoles, $D = 1.5\gamma_c\hbar r_{12}^{-3}$ to be 1.22 nm. This value is lesser than the distances between C_{60}^- anions (1.8334 nm) and that between C_{60}^- anion and TPA^+ cation (1.5394 nm), however, but exceeds another anion–cation distance (0.9953 nm) obtained for the complex by X-ray spectroscopy. This discrepancy can be explained by a more planar conformation of cation in triplet pairs.

As Fig. 3 shows, the spectrum of PC R_2 is manifested only in $\pi/2$ -out-of-phase dispersion signal. This means that the effective relaxation and consequently the rotation rate of this center exceeds at least by order of the value for R_1 . Indeed, the evaluation of D_r from Eq. (2) with $\langle\omega^2\rangle = 1/30\gamma_c^2 D^2$ for the triplet radical pair [10] gives $D_r \sim 10^{15} s^{-1}$ at room temperature that is higher than that estimated for R_1 radical with higher linewidth.

4. Conclusions

Two types of PC with different relaxation and dynamics parameters are stabilized at doped PANI and $C_{60}^-TPA^+$ complex irradiated by visible light. C_{60} molecules rotate actively at low temperatures and the rate of motion increases sharply at phase transition. This is accompanied by a change in the electron relaxation and in the paramagnetic susceptibility of the system. The change in the conformation of the cation complex also leads to a considerable increase in the rotation frequency.

The data obtained show the evident advantages of non-linear 2-mm waveband EPR spectroscopy in the investigation of different organic semiconductors of low dimensionality. The method allows to analyze completely and correctly the magnetic and relaxation parameters of PC of different mobilities in order to obtain fine peculiarities of molecular and spin dynamics in these and other systems.

Acknowledgements

This study was supported in part by the Russian Foundation for Basic Researches, Grant No. 01-03-33255.

References

- [1] H.S. Nalwa (Ed.), *Handbook of Organic Conductive Molecules and Polymers*, Wiley, Chichester, 1997.
- [2] V.I. Krinichnyi, *Synth. Met.* 108 (2000) 173.
- [3] P.R. Gullis, *J. Magn. Reson.* 21 (1976) 397.
- [4] A.E. Pelekh, et al., *Vysokomol. Soedin. A* 33 (1991) 1731.
- [5] J.S. Hyde, L.R. Dalton, in: L.J. Berliner (Ed.), *Spin Labeling. Theory and Application*, Academic Press, New York, 1979 (Chapter 1).
- [6] A. Abragam, *The Principles of Nuclear Magnetism*, Clarendon Press, Oxford, 1961.
- [7] S. Kivelson, *Phys. Rev. B* 25 (1982) 3798.
- [8] R.L. Cappelletti, et al., *Phys. Rev. Lett.* 66 (1991) 3261.
- [9] P.C. Chow, et al., *Phys. Rev. Lett.* 69 (1992) 2943.
- [10] G.L. Closs, et al., *J. Phys. Chem.* 96 (1992) 5228.



ELSEVIER

Physica B 308–310 (2001) 1007–1010

PHYSICA B

www.elsevier.com/locate/physb

Effects of codoping using Na and O on Cu–S divacancy in p-type CuInS₂

Tetsuya Yamamoto^{a,*}, Takayuki Watanabe^b, Yoshihiro Hamashoji^a

^a *Department of Electronic and Photonic Systems Engineering, Kochi University of Technology, 185 Miyanokuchi, Tosayamada-cho, Kami-gun, Kochi 782-8502, Japan*

^b *Central Technology Laboratory, Asahikasei Corporation, 2-1 Samejima, Fuji, Shizuoka 416-8501, Japan*

Abstract

We investigated the effects of the incorporation of Na and O into p-type Cu-deficient CuInS₂. Codoping of Na and O leads to the formation of a complex containing Na_{Cu} and O_S, where they occupy nearest-neighbor sites, causing the annihilation of the deep level in the band gap due to the n-type Cu–S divacancy. © 2001 Elsevier Science B.V. All rights reserved.

PACS: 61.72.Bb; 61.72.–y; 61.72.Ji

Keywords: Divacancies; Na; O; CuInS₂

1. Introduction

The ternary semiconductor CuInS₂ with a chalcopyrite structure is a promising material for high-efficiency solar cells because its band gap of 1.5 eV matches the solar spectrum well. We have demonstrated that Na incorporation into p-type Cu-deficient CuInS₂ thin films is essential for fabricating high-efficiency CuInS₂-based solar cells without employing the KCN process [1–4]. The achieved efficiencies are 10.6% and 11.2% for CuInS₂ and Cu(In,Ga)S₂ solar cells, respectively [4]. We have reported that the Na incorporation annihilates the donor states generated in Na-free CuInS₂ films and, consequently, significantly enhances the electric conductivity of the film [3]. The calculated results using an *ab initio* electronic-band-structure calculation method suggests that the Na atoms move easily toward the Cu-vacancy (V_{Cu}) sites near the surface, where the material becomes more Cu deficient [5,6]. Moreover, we calculated the enthalpies of migration via V_{Cu} of Cu and Na

atoms in Cu-deficient CuInS₂ to be 1.12 and 0.42 eV, respectively [7]. There have been various investigations on defect structures for CuInS₂. It was reported that an acceptor level with 70–105 meV corresponds to V_{Cu} [8–11] and the three donor levels with 35–55, 70–72, and 140–200 meV correspond to sulfur vacancy (V_S) [8–10], interstitial In (In_i) or In at Cu sites (In_{Cu}) [10], and In_{Cu} [9,10,12], respectively. For p-type Cu-deficient CuInS₂ thin films fabricated by us, from the PL measurement, we find a deep donor level with 270 meV. This decreases the conductivity of the thin films, as discussed below.

The purpose of this work is to propose a model regarding the defect structure of Cu-deficient CuInS₂ by a codoping method using Na and oxygen (O) atoms, giving the origin of the defect which behaves as the p-type killer.

2. Methodology

The preparation process of CuInS₂ thin films is given elsewhere [13]. Low-temperature PL was performed using an Ar gas laser with a wavelength of 514.5 nm as the excitation source. PL spectra were obtained for the samples cooled to 9 K inside an optical cryostat. PL

*Corresponding author. Tel.: +81-887-57-2112; fax: +81-887-57-2120.

E-mail address: yamateko@ele.kochi-tech.ac.jp (T. Yamamoto).

signals were processed by means of a liquid-nitrogen-cooled Ge detector and a lock-in amplifier. For excitation intensity dependence measurements, different kinds of optical neutral-density (ND) filters were used to vary the intensity by setting them in the optical path. The SIMS analysis was performed with Cs primary ions to investigate the distribution of Na and O in the films. The measurement area was $100 \times 140 \mu\text{m}^2$. We monitored the $^{149}\text{NaCs}$ ion for positive ion detection and the ^{18}O ion for negative ion detection since the distribution of the ^{16}O overlaps that of the double-charged ion of ^{32}S . Details concerning the preparation for SIMS measurements are given elsewhere [13].

The results of our band-structure calculations for CuInS_2 doped with Na, V_{Cu} or oxygen atoms at S sites (O_S) are based on the local-density treatment of electronic exchange and correlation [14–16] and on the augmented-spherical-wave (ASW) [17] formalism. Further details are given elsewhere [5,7,13].

3. Results and discussion

First, we show the PL spectra for CuInS_2 films codoped with Na and O and without them in Fig. 1. We found four peaks at 1.52, 1.44, 1.40 and 1.20 eV. The most significant difference in the PL spectra between codoped and undoped CuInS_2 films is the intensity of the peak at 1.20 eV. This emission, related to a deep defect level, could be reduced in intensity by the incorporation of both Na and O. In order to investigate

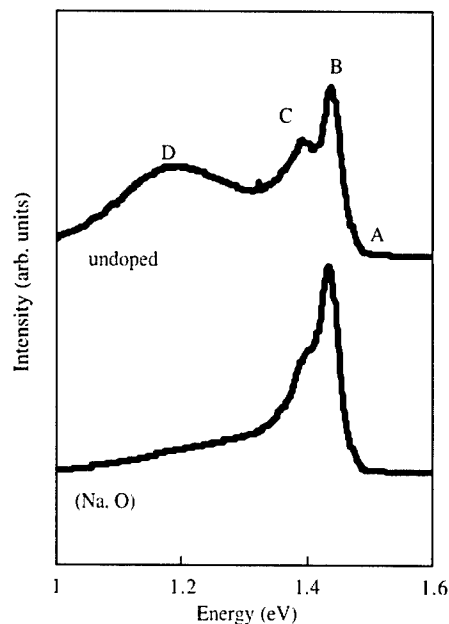


Fig. 1. PL spectra for Na-free and Na-added CuInS_2 thin films.

the origin of the emission peaks, the dependence of the emission peak on both the excitation power and temperature was measured for the Na-free CuInS_2 film as a standard reference.

From the measurement of the dependence of the emission peak energies (E_p) for peaks B, C and D on the excitation power (P), as shown in Fig. 2, we find that the three emission peaks shift towards high energies with increasing excitation intensity. We interpret that all the shifts in terms of the excitation can be considered to be the characteristic criteria of donor–acceptor (DA) pair transitions. For peaks B and C, the increase of E_p with increasing excitation power can be explained for the ratio of only a few meV, ΔE_p to ΔP , on the basis of a decrease of the mean value of the distance between the acceptor and donor atoms at higher excitation levels [18]. On the other hand, for peak D, Fig. 2(c) indicates another mechanism which causes larger values ($> 10 \text{ meV}$) of the ratio. The mechanism may be band perturbation due to high concentrations of defects [19].

For Cu-deficient CuInS_2 , we focus on the idea that a Cu-vacancy (V_{Cu}) is considered to be a dominant defect as acceptor. Hence there are three different donor

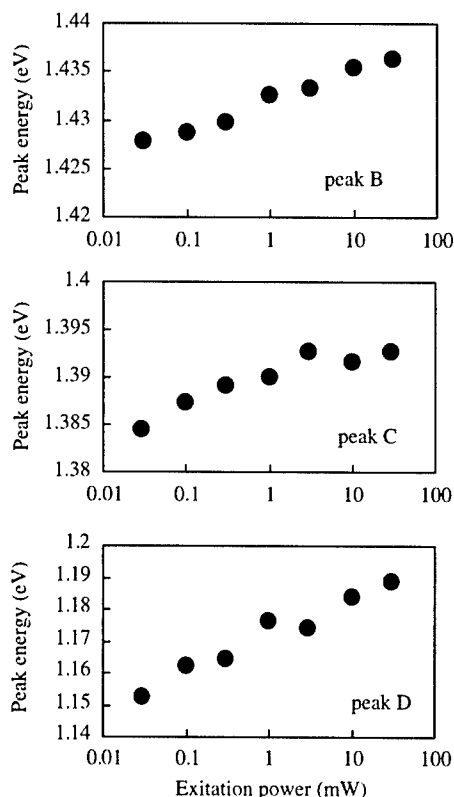


Fig. 2. The dependence of the emission peaks (peaks B–D) on excitation intensity at 9 K for Cu-deficient CuInS_2 undoped film.

defects, such as V_S , indium interstitial (In_i) and In at Cu sites (In_{Cu}), in the $CuInS_2$ films. It was reported that the origins of emissions at 1.447 and 1.41 eV were the DA transitions between a sulfur vacancy (V_S) and V_{Cu} , and that between indium interstitial (In_i) and V_{Cu} , respectively [20]. Our measurements of PL concerning both peaks B and C are in good agreement with those of the above report. Here, we can deduce that the 30 meV level corresponds to V_S , whereas V_{Cu} generates an 80 meV level, based on the measurement of the PL intensity as a function of temperature [13].

We note the origin of the near-edge emission peak at 1.52 eV. The possible recombination origins include both the donor-to-valence-band and the conduction-band-to-acceptor transitions. Two groups reported identifying the origin to be a donor-to-valence-band emission [11,20]. In this work, we have little information concerning the nature of the defects.

With regard to the emission peak at 1.20 eV for undoped $CuInS_2$, which changes significantly in this work, to our knowledge, there has been as yet no investigation. For Cu-deficient $CuInS_2$, the copper and sulfur vacancies are the most probable defects. We predict that the single intrinsic defect levels of $CuInS_2$ will be relatively shallow from the band-structure calculations [21]. Thus, we discuss the possibility of the occurrence of the complex defects including V_S and V_{Cu} . In Table 1, we summarize the difference in the calculated lattice energy (Madelung energy), ΔE_M , between undoped and doped $CuInS_2$. Table 1 shows that as the number of V_{Cu} increases, the Madelung energy increases. This gives rise to a shift in S 3p levels towards higher energy, resulting in the instability of S in the vicinity of the V_{Cu} site [22]. This suggests that the formation of n-type divacancies (V_{Cu-S}), which include V_{Cu} and vacancies of sulfur close to the V_{Cu} site (V_{Cu-S}) will be more favorable with increasing V_{Cu} concentration. Actually, for $CuInSe_2$ with a narrower band gap of 1.04 eV, Kimura et al. suggest that the origin of the deep donor level with 220 meV is the V_{Cu-Se} divacancy [23]. On the other hand, from Table 1, we find that the incorporation of Na, which occupies Cu-vacancy sites, causes a decrease in the Madelung energy. From the analysis of the S 3p levels in the vicinity of the sites of Na for Na-incorporated $CuInS_2$, we find that the Na incorporation stabilizes the S atoms close to the Na

sites. This gives us a solution for the problem concerning the formation of the Cu–S divacancies; a codoping using Na and other elements that strongly correlates with Na atoms. From the band-structure calculations under the condition of minimum total energy, we find that the formation of the complex of Na_{Cu} and O_S that occupy nearest-neighbor sites is energetically favorable. We note that the formation of the complex of Na and O plays an important role in the decrease of the concentrations of the n-type V_{Cu-S} divacancy. Moreover, as shown in Table 1, there is a decrease in the Madelung energy of $CuInS_2:(Na_{Cu} \text{ and } O_S)$ compared with that of undoped $CuInS_2$.

We carried out SIMS after removing secondary phase $NaInS_2$ [2,3,24] by HCl treatment, in order to investigate the distribution of Na and O codoped in the $CuInS_2$ crystal. Considering the above findings based on the calculated results, it is of interest to study the SIMS data shown in Fig. 3, which shows SIMS depth profiles of Na and O after removing the $NaInS_2$ phase. We confirmed that the Na concentration near the film surface was reduced by removing the $NaInS_2$ phase. Even after etching $NaInS_2$, we established high concentration of Na of the order of 10^{19} – 10^{20} cm^{-3} , as determined by SIMS. Note that the shape of the O profile closely resembles that of the Na profile. This indicates that the Na atoms strongly correlate with the O atoms within $CuInS_2$. The SIMS profile shows that both Na and O are incorporated in almost equal amounts. Based on the above results and discussion, we propose a model of the defect structure which includes the complex of Na_{Cu} and O_S which occupy the nearest-neighbor sites for $CuInS_2:(-Na, O)$. That is, the Na–O complex annihilates n-type V_{Cu-S} divacancies existing in the Na-free films.

4. Conclusion

The following conclusions are derived from the experimental and theoretical results and discussion.

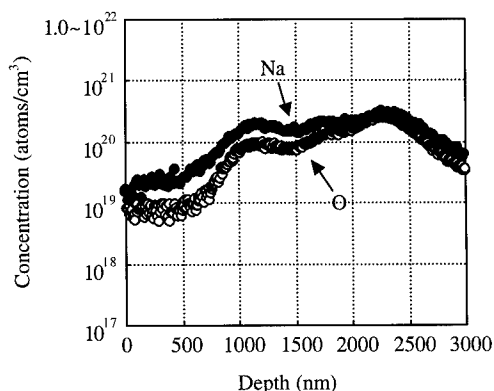


Fig. 3. SIMS depth profiles for $CuInS_2:(Na, O)$ film after removing $NaInS_2$.

Table 1
Calculated difference in the Madelung energy, ΔE_{Mad} , between undoped and doped $CuInS_2$ crystals

Defects	$2V_{Cu}$	V_{Cu}	$Na_{Cu}V_{Cu}$	$2Na_{Cu}$	$Na_{Cu}O_S^a$
ΔE_{Mad}	+11.22	+5.82	+2.81	−9.82	−10.55

^aComplex of Na and O which occupy nearest-neighbor sites.

We succeeded in controlling n-type defects, particularly the defects causing deep levels, by the incorporation of both Na and O species into p-type CuInS₂ thin films. We propose a model of the defect structure for CuInS₂ codoped with Na and O. That is, Na_{Cu} and O_S form a complex in which they occupy nearest-neighbor sites. That annihilates the deep level due to the n-type V_{Cu} s divacancy.

Acknowledgements

The authors are grateful to Dr. Sadao Ibe and Mr. Yasuhiro Ueshima, General Managers of Asahikasei Corporation, who provided encouragement during the course of this study. One of the authors, T.Y., thanks Dr. Jürgen Sticht for his technical support. In this study, we used the ESOCS code of accelrys.

References

- [1] T. Watanabe, M. Matsui, *Jpn. J. Appl. Phys.* 35 (1996) 1681.
- [2] T. Watanabe, H. Nakazawa, M. Matsui, H. Ohbo, T. Nakada, *Solar Energy Mater. Solar Cells* 49 (1997) 357.
- [3] T. Watanabe, H. Nakazawa, M. Matsui, *Jpn. J. Appl. Phys.* 37 (1998) L1370.
- [4] T. Watanabe, M. Matsui, *Jpn. J. Appl. Phys.* 38 (1999) L1379.
- [5] T. Yamamoto, *Jpn. J. Appl. Phys.* 37 (1998) L1478.
- [6] T. Yamamoto, K. Fukuzaki, S. Kohiki, *Appl. Surf. Sci.* 159–160 (2000) 345.
- [7] T. Yamamoto, T. Watanabe, *Jpn. J. Appl. Phys.* 39 (Suppl. 39-1) (2000) 257.
- [8] N. Lahlou, G. Masse, *J. Appl. Phys.* 52 (1981) 978.
- [9] H.Y. Ueng, H.L. Hwang, *J. Phys. Chem. Solids* 51 (1990) 11.
- [10] P. Lange, H. Neff, M.L. Fearheiley, K.J. Bachmann, *J. Electron. Mater.* 14 (1985) 667.
- [11] J.J.M. Binsma, L.J. Giling, J. Bloem, *J. Lumin.* 27 (1982) 35.
- [12] M.P. Vecchi, J. Ramos, *J. Appl. Phys.* 52 (1981) 2958.
- [13] T. Watanabe, T. Yamamoto, *Jpn. J. Appl. Phys.* 39 (2000) L1280.
- [14] W. Kohn, L.J. Sham, *Phys. Rev.* 140 (1965) A1133.
- [15] L. Hedin, B.I. Lundquist, *J. Phys. C* 4 (1971) 3107.
- [16] U. von Barth, L. Hedin, *J. Phys. C* 5 (1972) 1629.
- [17] A.R. Williams, J. Kübler, C.D. Gelatt, *Phys. Rev. B* 19 (1979) 6094.
- [18] E. Zacks, A. Halperin, *Phys. Rev. B* 6 (1972) 72.
- [19] J.I. Pankove, *Optical Processes in Semiconductors*, Dover, New York, 1975.
- [20] H.Y. Ueng, H.L. Hwang, *J. Phys. Chem. Solids* 50 (1989) 1297.
- [21] T. Yamamoto, H. Katayama-Yoshida, *Inst. Phys. Conf. Ser.* 152 (1998) 37.
- [22] T. Yamamoto, H. Katayama-Yoshida, *Jpn. J. Appl. Phys.* 34 (1995) L1584.
- [23] R. Kimura, T. Mouri, T. Nakada, S. Niki, Y. Lacroix, T. Matsuzawa, K. Takahashi, A. Kunioka, *Jpn. J. Appl. Phys.* 38 (1999) L289.
- [24] K. Fukuzaki, S. Kohiki, S. Matsushima, M. Oku, T. Hideshima, T. Watanabe, S. Takahashi, H. Shimooka, *J. Mater. Chem.* 10 (2000) 779.



ELSEVIER

Physica B 308–310 (2001) 1011–1014

PHYSICA B

www.elsevier.com/locate/physb

Coordination defects in chalcogenide amorphous semiconductors studied by positron annihilation lifetime

O.I. Shpotyuk^{a,b,*}, J. Filipecki^b, M. Hyla^b, A.P. Kovalskiy^a, R.Ya. Golovchak^a

^a Lviv Scientific Research Institute of Materials of SRC “Carat”, 202, Stryjska Str., Lviv, UA-79031 Ukraine

^b Physics Institute of Pedagogical University of Czestochowa, 13/15, al. Armii Krajowej, Czestochowa, PL-42201 Poland

Abstract

Defect formation processes in chalcogenide vitreous semiconductors of the ternary As–Ge–S system, induced by the ⁶⁰Co γ-irradiation with 2.82 MGy absorbed dose, are studied using positron lifetime measurements. The obtained results are explained at the level of both short- and medium-range ordering in the framework of coordination topological defects model modified with free-volume microvoids formation. © 2001 Elsevier Science B.V. All rights reserved.

Keywords: Positrons; Semiconductors; Chalcogenides; Glasses

1. Introduction

Positron annihilation method is a powerful instrument for the experimental study of solids at different levels of their structural hierarchy [1]. It is characterized by a high sensitivity to local changes associated with point and linear defects, impurities and inhomogeneities, crystallites and phase incorporates, microvoids and atomic clusters.

The application of this method for disordered solids, such as chalcogenide vitreous semiconductors (ChVS), gives very important and sometimes exclusive information on their structural features as well as on microstructural transformations, induced by different kinds of high-energetic ionizing irradiation. The coordination topological defects (CTD) model for these radiation-induced effects in the binary ChVS was created [2,3] in the framework of well-known D⁺–D[−] point charged defects concept developed by Mott et al. [4]. As a rule, only data of vibrational spectroscopy methods (such as

the Raman, IR Fourier spectroscopy) were obtained on the basis of the above model.

The aim of the present investigations is to obtain additional data on the CTD in the ternary As–Ge–S ChVS of stoichiometric As₂S₃–GeS₂ and non-stoichiometric As₂S₃–Ge₂S₃ cross-sections using positron annihilation lifetime technique.

2. Experimental

The investigated bulk samples of ternary stoichiometric (As₂S₃)_y(GeS₂)_{1−y} ($y=0.1–0.6$) and non-stoichiometric (As₂S₃)_x(Ge₂S₃)_{1−x} ($x=0.2–0.4$) systems were prepared by a well-known melt quenching method described previously elsewhere [5].

The prepared ChVS samples were irradiated by γ-quanta with an accumulated dose of 2.82 MGy and a dose power of 20 Gy/s in the normal conditions of stationary radiation field, created in the closed cylindrical cavity owing to concentrically established ⁶⁰Co ($E = 1.25$ MeV) sources.

The measurements of positron annihilation lifetimes were carried out using an ORTEC spectrometer with the FWHM (full-width at half-maximum) resolution of

*Corresponding author. Lviv Scientific Research Institute of Materials of SRC “Carat”, 202, Stryjska Str., Lviv, UA-79031 Ukraine. Tel.: +380-322-63-83-03; fax: +380-322-63-22-28.

E-mail address: shpotyuk@novas.lviv.ua (O.I. Shpotyuk).

0.270 ns. The ^{22}Na isotope with 0.74 MBq activity was used as a positron source placed between two identical samples, forming a “sandwich” system. The positron lifetimes were calculated from the LT computer program [6] using a single exponential function as well as a sum of two weighted exponential functions fittings.

3. Results and discussion

The positron lifetime characteristics of the investigated ChVS samples before and after γ -irradiation are presented in Table 1. Let us try to explain these results taking into account the previously obtained experimental data of other authors [7–10].

There are two principally different approaches to the interpretation of the positron lifetime measurements in the ChVS.

The first one, developed by Kobrin and Shantarovich with co-workers in the 1980s [7–9] on the basis of the CTD concept, prefers the positron annihilation processes in the ChVS at the negatively charged “dangling” bonds. It was assumed on the basis of numerous experimental data for the various ChVS systems (however, without strong theoretical calculations) that the main types of these CTD were characterized by the following lifetimes—0.32 ns (S_1^-), 0.37 ns (As_2^-) and 0.42 ns (Ge_3^-). The upper index in the CTD signature indicates the charged electrical state, and the lower one,

the number of neighbouring atoms. The experimentally observed positron annihilation lifetime components were treated as a superposition of various combinations of these lifetimes with each other, as well as lifetimes of positron annihilation on non-localized free electrons (0.2 ns) or microcrystalline inclusions (0.5 ns). Thus, only topological changes at the short-range ordering level were taken into account in this consideration. However, in this way it is difficult to explain the positron annihilation lifetimes less than 0.32 ns, because the free-electron concentration is typically too low in the ChVS [11].

The second approach is based on the theoretical lifetime calculations for the positrons trapped by the so-called open volume defects (vacancies and vacancy clusters) in crystalline As_2Se_3 . It was carried out by Jensen et al. at the beginning of the 1990 in order to explain the experimentally observed results on positron lifetime measurements in glassy As_2Se_3 [10]. It was stated that not intrinsic negatively charged CTD, but only microvoids of $25\text{--}100 \text{ \AA}^3$ volume in the form of As- (0.262 ns) and Se-monovacancies (0.274 ns), As–Se divacancy (0.316 ns) and As–Se₃ quadruple vacancy (0.368 ns) were responsible for the positron trapping. The lowest value of the positron lifetime (0.240 ns) was attributed to non-trapped positron annihilation in defect-free bulk crystalline As_2Se_3 . Apart from this, the experimental evidences for the CTD formation processes in the ChVS

Table 1

Positron lifetime characteristics for boundary compositions of the investigated stoichiometric $(\text{As}_2\text{S}_3)_x(\text{GeS}_2)_{1-x}$ and non-stoichiometric $(\text{As}_2\text{S}_3)_x(\text{Ge}_2\text{S}_3)_{1-x}$ ChVS systems before and after γ -irradiation with 2.82 MGy dose

Glass composition	Before γ -irradiation (ns)	After γ -irradiation with 2.82 MGy dose	
		Experimental values (ns)	Mean lifetime (ns)
$y = 0.6$	$\tau_1 = 0.3638 \pm 0.0002$	$\tau_1 = 0.277 \pm 0.002$; $I_1 = 0.67 \pm 0.01$; $\tau_2 = 0.386 \pm 0.003$; $I_2 = 0.33 \pm 0.01$	$\tau = 0.313 \pm 0.003$
$y = 0.1$	$\tau_1 = 0.3644 \pm 0.0004$	$\tau_1 = 0.282 \pm 0.009$; $I_1 = 0.53 \pm 0.05$; $\tau_2 = 0.397 \pm 0.010$; $I_2 = 0.47 \pm 0.05$	$\tau = 0.336 \pm 0.010$
$x = 0.4$	$\tau_1 = 0.3396 \pm 0.0003$	$\tau_1 = 0.275 \pm 0.010$; $I_1 = 0.55 \pm 0.06$; $\tau_2 = 0.392 \pm 0.013$; $I_2 = 0.45 \pm 0.06$	$\tau = 0.328 \pm 0.013$
$x = 0.2$	$\tau_1 = 0.239 \pm 0.006$; $I_1 = 0.43 \pm 0.02$; $\tau_2 = 0.385 \pm 0.005$; $I_2 = 0.57 \pm 0.02$	$\tau_1 = 0.243 \pm 0.017$; $I_1 = 0.33 \pm 0.05$; $\tau_2 = 0.387 \pm 0.009$; $I_2 = 0.67 \pm 0.05$	$\tau = 0.339 \pm 0.017$

are quite convincing [2,3,15] and, consequently, they cannot be rejected fully without any serious arguments.

So none of these approaches can be accepted entirely to explain the experimental results of the positron annihilation measurements in the ChVS.

We believe that positron trapping in the ChVS occurs on microvoids, but their association with the CTD must be taken into account too.

A part of the microvoids have a fluctuating nature and can be frozen technologically at melt quenching [12–15]. Their volumes in the ChVS are typically as high as $15\text{--}30\text{ \AA}^3$, which is less than the volumes of discrete atomic vacancies introduced in Ref. [10]. This value of $15\text{--}30\text{ \AA}^3$ can be reduced even to $5\text{--}10\text{ \AA}^3$ by accepting that fluctuation microvoids are probably connected with boundary shifts of bridge chalcogen atoms [15]. These native microvoids of atomic and sub-atomic sizes lead to a lower compactness of glassy-type atomic network in comparison with the crystalline structures. It means that these native free-volume microvoids can be the traps for positrons with characteristic lifetimes less than $0.25\text{--}0.30\text{ ns}$ (due to the dependence of the positron lifetimes on open volumes presented in Ref. [10]).

But the other part of the microvoids can be created in the ChVS structure by external influences as a result of atomic transformations at the medium-range ordering level in the nearest vicinity of the negatively charged CTD (CTD-based microvoids). This process is shown schematically in Fig. 1 in the example of (S_1^-, As_4^+) CTD formation in amorphous As_2S_3 , caused by photoexposure [16]. It is clear that the appearance of an additional As–As covalent chemical bond instead of the destructed As–S one at the positively charged As_4^+ defect leads to the local densification of the atomic package, while near the negatively charged S_1^- CTD the atomic network is distorted with free-volume microvoid formation (which is crosshatched in Fig. 1).

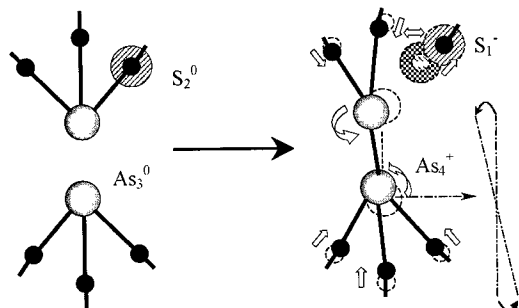


Fig. 1. A topological scheme illustrating the process of additional free-volume formation in the vicinity of the negatively charged S_1^- coordination defect.

It is difficult to quantitatively estimate the real volume of the created CTD-based microvoids for different kinds of the negatively charged CTD, but their appearance in the vicinity of the negatively charged CTD provides the effective positron trapping with characteristic lifetimes given by Kobrin and Shantarovich with co-workers [7–9].

The positron annihilation lifetime measurements show that before the γ -irradiation, all the ChVS samples of the stoichiometric system (the experimental data for two of them with maximal content of As_2S_3 and GeS_2 are presented in Table 1) are characterized by one mean positron lifetime of $\sim 0.36\text{ ns}$.

The fulfilled computer treatment of the obtained results shows the existence of two lifetime components after γ -irradiation: short- and long-lived ones. The first one ($\tau_1 \sim 0.28\text{ ns}$) seems to be responsible for positron annihilation on the native free-volume microvoids and S_1^- CTD with an associated free volume. The second lifetime ($\tau_2 \sim 0.39\text{ ns}$) is attributed to the superposition of lifetimes for positrons trapped on Ge_3^- and As_2^- CTD (with associated microvoids). According to the ratio of these short- and long-lived components (see Table 1), it can be concluded that the S_1^- CTD are dominant in the As_2S_3 -enriched ChVS compositions. On the contrary, the role of the Ge_3^- CTD becomes more essential with GeS_2 content in the investigated stoichiometric ChVS.

The results of the positron annihilation measurements for two-boundary non-stoichiometric ChVS compositions are also presented in Table 1. It is established that the As-enriched non-irradiated glasses are characterized by a lone mean lifetime of positrons ($\sim 0.34\text{ ns}$), while two lifetime components (with average lifetime $\tau = 0.322\text{ ns}$) appear with high Ge content in the $(As_2S_3)_{0.2}(Ge_2S_3)_{0.8}$ sample. The short-lived component ($\tau_1 \sim 0.24\text{ ns}$) can be explained similarly as in the case of the irradiated stoichiometric ChVS. The same interpretation is proper for a long-lived component of $\tau_2 \sim 0.39\text{ ns}$. We treat the latter by positron annihilation on the trapping sites of the Ge_3^- and As_2^- CTD. Such a separation of short- and long-lived components is observed only in the Ge-enriched non-stoichiometric ChVS. It is well known that these samples have a very small atomic compactness [11] and, finally, a high level of structural defectiveness. So, we conclude that a large concentration of the electrically charged CTD with extremely great amount of associated CTD-based microvoids initially exist as positron traps in these glasses.

The structure of the non-stoichiometric ChVS (similar to stoichiometric ones) becomes more defective after the γ -irradiation. As a result, two positron lifetime components with the above attributions to traps on the negatively charged CTD (with associated microvoids) and native free-volume microvoids appear. It is clear that the role of long-lived positron trapping is enhanced

with Ge content in the investigated ChVS owing to the Ge_3^- CTD ($\tau \sim 0.42$ ns) in good accordance with the previously studied concentration dependence of radiation-induced optical effects in this system [5].

4. Conclusions

The obtained results on the positron annihilation lifetime measurements in the ternary As–Ge–S ChVS of stoichiometric As_2S_3 – GeS_2 and non-stoichiometric As_2S_3 – Ge_2S_3 cross-sections prove the essential role of the CTD formation processes in the observed radiation-induced effects. The developed modified model of the CTD formation associated with free-volume microvoids at the levels of both short- and medium-range ordering describes well the compositional features of these effects.

References

- [1] H.J. Ache, *Angew. Chem. Int. Ed.* 11 (1972) 179.
- [2] V.O. Balitska, O.I. Shpotyuk, *J. Non-Cryst. Solids* 227–230 (1998) 723.
- [3] O.I. Shpotyuk, *Phys. Stat. Sol. A* 145 (1) (1994) 69.
- [4] N.F. Mott, E.A. Davis, R.A. Street, *Phil. Mag.* 32 (1975) 961.
- [5] O.I. Shpotyuk, A.P. Kovalskiy, E. Skordeva, E. Vateva, D. Arsova, R.Ya. Golovchak, M.M. Vakiv, *Physica B: Condens. Matter* 271 (1999) 242.
- [6] J. Kansy, *Nucl. Instr. and Meth. A* 374 (1996) 235.
- [7] B.V. Kobrin, V.P. Shantarovich, *Phys. Stat. Sol. A* 83 (1984) 159.
- [8] B.V. Kobrin, V.P. Shantarovich, T.I. Kim, M.D. Michajlov, Z.U. Borisova, *J. Non-Cryst. Solids* 89 (1987) 263.
- [9] B.V. Kobrin, R.M. Kupriyanova, V.S. Minaev, E.P. Prokopiev, V.P. Shantarovich, *Phys. Stat. Sol. A* 73 (1982) 321.
- [10] K.O. Jensen, Ph.S. Salmon, I.T. Penfold, P.G. Coleman, *J. Non-Cryst. Solids* 170 (1994) 57.
- [11] A. Feltz, *Amorphous and Vitreous Inorganic Solids*, Mir, Moscow, 1986.
- [12] A.V. Kolobov, H. Oyanagi, K. Tanaka, Ke. Tanaka, *J. Non-Cryst. Solids* 198–200 (1996) 709.
- [13] R. Zallen, in: *Physics of Amorphous Solids*, Wiley, New York, 1983.
- [14] D.S. Sanditov, G.M. Bartenev, *Physical properties of disordered structures (molecular-kinetic and thermodynamic processes in inorganic glasses and polymers)*, Nauka, Novosibirsk, 1982.
- [15] A.A. Kikineshi, *Quantum Electron. (Kiev)* 37 (1989) 31.
- [16] O.I. Shpotyuk, *Phys. Stat. Sol. B* 183 (1994) 365.



ELSEVIER

Physica B 308–310 (2001) 1015–1019

PHYSICA B

www.elsevier.com/locate/physb

Energy levels of native defects in zinc germanium diphosphide

W. Gehlhoff^{a,*}, R.N. Pereira^{a,1}, D. Azamat^a, A. Hoffmann^a, N. Dietz^b

^a *Institute for Solid State Physics, Technical University Berlin, Sekr. PN5-2, Hardenbergstr. 36, D-10623 Berlin, Germany*

^b *Department of Physics & Astronomy, Georgia State University, Atlanta GA 30303, USA*

Abstract

Electron paramagnetic resonance (EPR) and photo-EPR investigations of as-grown, post-growth annealed and electron irradiated zinc germanium diphosphide (ZnGeP_2) crystals allowed the determination of native acceptor- and donor-related defect levels in the ZnGeP_2 bandgap. From the photoinduced generation of the V_{Zn}^- EPR spectrum for electron-irradiated samples with the Fermi-level above the recharging level it is inferred that the $V_{\text{Zn}}^{-/-}$ acceptor state is located at 1.02 ± 0.03 eV below the conduction band. Observation of the recharging process in as-grown and post-growth annealed samples yields the localization of the Ge anti-site donor level $\text{Ge}_{\text{Zn}}^{+/++}$ at $E_{\text{opt}} = E_{\text{V}} + 1.70 \pm 0.03$ eV. Moreover, photoinduced processes involving the quenching and generation of the V_{Zn}^- and V_{P}^0 EPR spectra, respectively, are observed with an energy of $E_{\text{opt}} = 0.64 \pm 0.03$ eV. A model that can explain the complementary changes of the V_{Zn}^- and V_{P}^0 EPR intensities is briefly discussed. © 2001 Elsevier Science B.V. All rights reserved.

Keywords: ZnGeP_2 ; Photo-EPR; Native defects; Energy levels

1. Introduction

Zinc germanium diphosphide (ZnGeP_2) is one of the most technologically important materials among the ternary II–IV–V₂ compounds due to its promising applications for non-linear optical devices such as tunable mid-infrared optical parametric oscillator (OPO) laser systems. However, up to now the performances of such OPOs are affected by a broad absorption band extending from the fundamental edge near 625 nm up to 2.5 μm , which overlaps with the desirable OPO pump wavelengths. This unwanted absorption with a pronounced plateau near 1 μm is mainly attributed to the photoionization of a deep acceptor center associated with the negatively charged state of the zinc vacancy (V_{Zn}^-) [1]. A large reduction of this unwanted absorption could be obtained by high-energy electron irradiation of the crystals. Electron

paramagnetic resonance (EPR) and photo-EPR investigations of as-grown, electron-irradiated and annealed ZnGeP_2 samples have shown strong differences in the V_{Zn}^- -related EPR signal intensity, which are mainly caused by a meta-stable recharging of the V_{Zn}^- centers owing to the preparation induced shift of the Fermi-level [2]. Photoinduced EPR studies of such highly compensated bulk ZnGeP_2 crystals have identified two donor centers, that have been attributed to the neutral P vacancy (V_{P}^0) [3] and the singly charged Ge_{Zn} anti-site (Ge_{Zn}^+) [4] centers, respectively. No clear defect assignments have been made for the usually broad photoluminescence bands in the range from 1.2 to 1.6 eV. However, a correlation with the concentration of the phosphorus vacancies was observed [5] and some parts of the broad infrared emission exhibit features of classical donor–acceptor recombination in dependence of the excitation density and time-decay character [2,6]. An assignment of the three identified native defects described above to energy levels in the ZnGeP_2 bandgap determined by electrical measurements [7] does not exist to date. In the present article, we report for the first time the wavelength dependence of the photoinduced changes in the EPR signal intensities associated with the acceptor

*Corresponding author. Fax: +49-30-314-22569.

E-mail address: gehlhoff@sol.physik.tu-berlin.de (W. Gehlhoff).

¹Leave from the Department of Physics, University of Aveiro, 3810 Aveiro, Portugal.

center V_{Zn}^- as well as the donors V_P^0 and Ge_{Zn}^+ in $ZnGeP_2$.

2. Experimental details

The $ZnGeP_2$ bulk crystals used in this work were grown by the gradient freezing Bridgman method. For the EPR studies, small samples with dimension $1 \times 1 \times 5 \text{ mm}^3$ were cut along the main crystallographic directions from as-grown, post-growth annealed and electron-irradiated samples. The EPR and photo-EPR measurements were performed at the Q-band ($\nu \approx 34 \text{ GHz}$) in the temperature region 4–50 K using a Bruker ESP 300E spectrometer. The samples could be irradiated with monochromatic light via a 0.4 mm optical fiber in the rod inserted into the helium cryostat, which had the sample mounted on the other end. Light from a 100 W Xenon or Halogen lamp was dispersed by a grating monochromator and coupled, after passing additional glass filters, into another 0.4 mm optical fiber at the end of which the spectral dependence of the photon flux was measured. When illuminating the samples, the two fibers were connected.

3. Experimental results and discussion

In the dark, both the as-grown and annealed $ZnGeP_2$ samples studied exhibit only the strong EPR spectrum described in Ref. [8], which has been identified as the single negatively charged zinc vacancy (V_{Zn}^-) by ENDOR measurements [9,10]. $ZnGeP_2$ has a tetragonal chalcopyrite crystal structure where the c direction is denoted as $[001]$ and the two equivalent a directions are labeled $[100]$ and $[010]$. The line positions of the electron spin transitions are given by the linear Zeeman interaction for $S = 1/2$ and the principal g -values $g_1 = 2.002$, $g_2 = 2.021$ and $g_3 = 2.074$ in the main directions $[011]$, $[\bar{1}00]$, $[0\bar{1}1]$, respectively [3]. In the tetragonal crystal structure, there are four crystallographic equivalent center orientations. Every electron spin transition is split into a triplet with the intensity ratio 1:2:1 by the hyperfine interaction with two equivalent phosphorus nuclei ($I = 1/2$, 100% abundant) varying from 3.5 to 5.5 mT in magnitude. For an arbitrary direction of the magnetic field, an overlapping of the triplets belonging to the four center orientations is observed in the X-band, but a complete resolution of the hyperfine interaction of the different center positions can be obtained at least for some directions in the Q-band owing to the 3.5 times higher Zeeman splitting. Fig. 1(a)–(c) show typical Q-band EPR spectra for the negative charged zinc vacancy (V_{Zn}^-), together with the photoinduced spectra

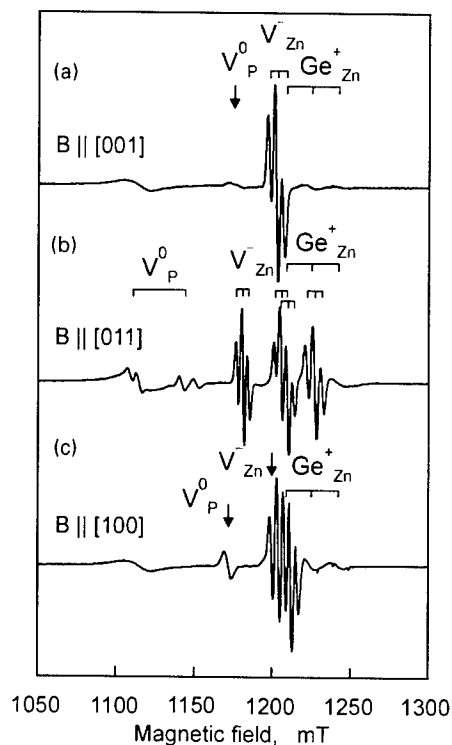


Fig. 1. EPR and photoinduced EPR spectra of the negatively charged zinc vacancy (V_{Zn}^-), the neutral donor (V_P^0), and the anti-site center Ge_{Zn}^+ in as-grown and annealed $ZnGeP_2$ in the Q-band (34.2 GHz) at 15 K with the magnetic field B parallel to the directions (a) $[001]$, (b) $[011]$ and (c) $[100]$. (By a small misorientation of the sample the degeneracy of the inner V_{Zn}^- lines and of the V_P^0 lines is removed, see Fig. 1(b)).

related to the neutral phosphorus vacancy (V_P^0) and the anti-site center Ge_{Zn}^+ for the three directions of the external magnetic field B parallel to $[001]$, $[011]$ and $[100]$. The illumination of as-grown and annealed samples with monochromatic light changes the EPR signal intensity of the V_{Zn}^- centers and generates only the EPR spectrum of the neutral donor V_P^0 for photon energies from 0.6 to 1.5 eV. For photon energies between about 1.55 and 2.5 eV, the spectrum of the anti-site center Ge_{Zn}^+ is produced and a photoinduced enhancement of EPR signal intensities both of the V_{Zn}^- and neutral donor V_P^0 centers is observed. By avoiding saturation effects by corresponding choice of temperature and microwave power, we have determined the dependence of the EPR signal intensity on the photoexcitation energy normalized for a constant photon flux for the three centers (Fig. 2). The presentation establishes that the observed photoinduced quenching of the V_{Zn}^- signal in the low-energy region (0.6–1.5 eV) is always stronger than the photoinduced generation of the V_P^0 signal. For the higher energy

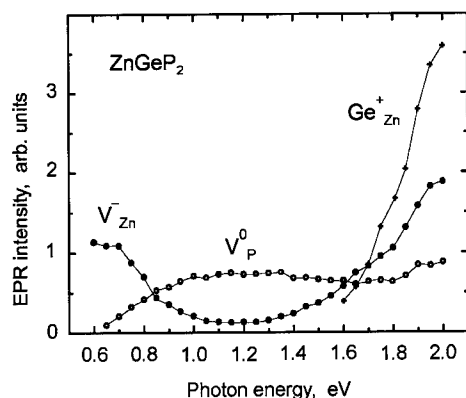


Fig. 2. Spectral dependence of the photoinduced changes of the EPR signal intensities at 15K. The points (\bullet , \circ , $+$) represent the experimental values for the negatively charged zinc vacancy (V_{Zn}^-), the neutral donor (V_P^0) and the anti-site center Ge_{Zn}^+ , respectively. The corresponding lines are provided as a guide to the eye.

region (1.55–2.5 eV), the increase of the Ge_{Zn}^+ signal is always stronger than the sum of the increase of the intensities from the V_{Zn}^- and V_P^0 signals. Since all three centers are systems with spin $S = 1/2$ and both the anisotropy and differences between the g -values are small, the changes of the signal intensity are directly proportional to the number of recharged centers.

In order to monitor further the kinetics and the wavelength dependence of this photoinduced effect in detail, we fixed the external magnetic field \mathbf{B} at the position of maximum intensity of the first derivative of one of the non-overlapping EPR lines belonging to each one of the three centers and monitored the time dependence of the EPR signal intensity (I_{EPR}) upon an illumination sequence of increasing photon energies. As an example, the photoinduced changes of the intensity of the V_{Zn}^- EPR signal are shown for different photoexcitation energies $h\nu$ in Fig. 3. By fitting the time dependence of I_{EPR} by exponential decay functions, we have estimated the saturation value ΔI_{EPR} of the difference between the photoinduced EPR signal intensity and I_{EPR} measured prior to illumination for the different photoexcitations. The Ge_{Zn}^+ related spectral dependence of ΔI_{EPR} normalized to a constant photon flux is presented in Fig. 4(b). In this energy region (1.55–2.5 eV) identical spectral dependencies are observed for the V_{Zn}^- , Ge_{Zn}^+ and V_P^0 -related EPR spectra. This pointed to the fact that the photoionization process responsible for the enhancement of the EPR signals occurs on the same localized states in the $ZnGeP_2$ gap to the conduction (valence) band. In the low-energy region (0.6–1.5 eV) the same spectral dependence for the decrease of the V_{Zn}^- and the generation of the V_P^0 signal is observed. In the context of all the

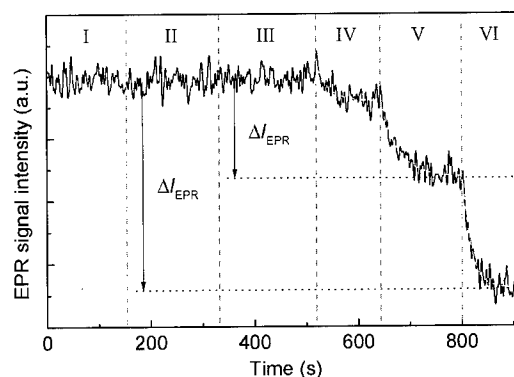


Fig. 3. Time dependence of the EPR signal intensity I_{EPR} of the negatively charged zinc vacancy (V_{Zn}^-) at $T = 15$ K for different excitation photon energies $h\nu$ (eV) = 0.52 (I), 0.57 (II), 0.6 (III), 0.65 (IV), 0.70 (V), 0.75 (VI). The solid lines are experimental data and dashed curves are exponential fits. The horizontal lines represent the saturation values obtained from the fits. The vertical bars give the ΔI_{EPR} values used for the determination of the optical cross sections.

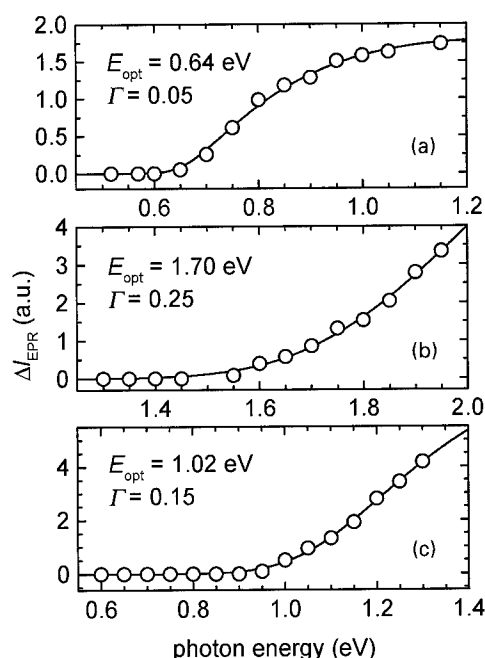


Fig. 4. Dependence of the enhancement of the EPR signal (ΔI_{EPR} as defined in Fig. 3) vs. the photon energy for (a) the V_P^0 center, (b) for the Ge_{Zn}^+ center, (c) photoinduced generation of the V_{Zn}^- EPR signal in an electron irradiated sample. The circles are experimental values and the solid lines are fits to the data by the extended Lucovsky formula, Eq. (1).

observed photoinduced recharging processes, it is unlikely that this process involved the valence band. Therefore, we infer that an electron from the V_{Zn}^- center is directly transferred to the positively charged

phosphorus vacancy (V_P^0), leaving behind the V_{Zn} center in the non-paramagnetic state V_{Zn}^0 .

The ionization energy E_{opt} of a defect involved in such PT is determined by the spectral dependence of the optical cross section, which must be determined from the photo-EPR data. The different methods for the determination of the optical cross section are discussed in Ref. [11]. How the relation between the ΔI_{EPR} values and the optical cross section can be obtained within the framework of the saturation value method is described in detail in Ref. [12]. This method has the advantage that different initial starting populations of the center under study prior to each subsequent photoexcitation can be considered. The $\Delta I_{EPR}(v)$ dependence of the optical cross section for a given PT is described by a system of kinetic equations that includes all excitation, recombination and captures processes in the sample. However, specific shifts of the Fermi-level in the initial samples can be very helpful in verifying the different dominant processes, and restricting the latter to only a few. Also, the complexity can be reduced using the fact that the light intensity I and the optical cross section σ always appear together in the form of $\alpha = I \times \sigma$ in the kinetic equations that describe the photoionization process. Using only values from the linear regime $\Delta I_{EPR}(v) \sim \alpha$ and assuming that only one dominant photoionization process is responsible for the decrease or enhancement of the studied EPR signal, we see that $\Delta I_{EPR}(v)$ is directly proportional to the corresponding optical cross section [12]. Fitting the spectral dependence $\sigma(v)$ of the considered photoexcitation by the modified Lucovsky formula extended to account for the electron-phonon interaction [11]

$$\sigma(v) \propto \int_{-\beta}^{\alpha} dz e^{-z^2} \frac{(hv - E_{opt} + \Gamma z)^{3/2}}{(hv + \Gamma z)^3} \left(1 + \frac{\Gamma z}{hv}\right)^{-1}, \quad (1)$$

where Γ describes the effect of broadening on the PT absorption band with the temperature, the ionization energy E_{opt} can be determined, see Fig. 4. For the recharging of the V_{Zn}^- , Ge_{Zn}^+ and V_P^0 centers we determine $E_{opt} = 1.70 \pm 0.03$ eV and for the decrease of the V_{Zn}^- and generation of the V_P^0 signal $E_{opt} = 0.64 \pm 0.03$ eV.

In agreement with [2], for samples irradiated with high-energy (2 MeV) electrons neither the V_{Zn} EPR signal nor the V_P^0 signal could be detected before optical excitation, if the samples are cooled down in the dark and infrared irradiation by black body emission from the resonator walls is avoided. However, illumination with infrared light simultaneously generates the V_{Zn}^- and the Ge_{Zn}^+ -related EPR signals. While, whether in the dark nor upon illumination the signal from the V_P^0 could be detected, a new center [13] could be observed with increasing signal intensity upon irradiation. The photo-induced generation of the V_{Zn}^- signal was recorded

for different excitation wavelengths. The determined spectral dependence ΔI_{EPR} normalized to a constant photon flux is presented in Fig. 4c. From the fitting procedure described above the photoionization energy $E_{opt} = 1.02 \pm 0.03$ eV is obtained. The observed process is interpreted as direct electron excitation from the doubly negative charged zinc vacancy (V_{Zn}^{2-}) to the conduction band, connected with a partial capture of the photoinduced electrons by the Ge_{Zn} centers recharging these to the paramagnetic state Ge_{Zn}^+ .

4. Conclusions

The present photo-EPR study reveals three photo-induced recharging levels connected with native defects in the bandgap of $ZnGeP_2$. The zinc vacancy acceptor level V_{Zn}^{2-} is established at $E_{opt} = E_C - 1.02 \pm 0.03$ eV and the Ge anti-site donor level Ge_{Zn}^{++} at $E_{opt} = E_V + 1.70 \pm 0.03$ eV. The excitation energy 0.64 ± 0.03 eV connected with the photoinduced decrease and increase of the EPR signals from the V_{Zn}^- and V_P^0 , respectively, seems to be caused by a direct recharging of weakly associated defects $V_{Zn}^-V_P^+$ to $V_{Zn}^0V_P^-$, which can be realized only for Fermi levels below the V_{Zn}^{2-} level at $E_C - 1.02 \pm 0.03$ eV. Above this level position a new center could be detected.

Acknowledgements

This work was partially supported by the BMBF under grant 05 KK 1KTA/4, which is gratefully acknowledged. RNP acknowledges the financial support from FCT under contract PRAXIS XXI/BD/18405/98, which made a longer stay in the Federal Republic of Germany possible.

References

- [1] S.D. Setzler, P.G. Schunemann, T.M. Pollak, M.C. Ohmer, J.T. Goldstein, F.K. Hopkins, K.T. Stevens, L.E. Halliburton, N.C. Giles, J. Appl. Phys. 86 (1999) 6677.
- [2] A. Hoffmann, H. Born, A. Naeser, W. Gehlhoff, J. Maffetone, D. Perlov, W. Rudermann, I. Zwieback, N. Dietz, K.J. Bachmann, Mater. Res. Soc. Proc. 607 (2000) 373.
- [3] N.C. Giles, L.E. Halliburton, P.G. Schunemann, T.M. Pollak, Appl. Phys. Lett. 66 (1995) 1758.
- [4] S.D. Setzler, N.C. Giles, L.E. Halliburton, P.G. Schunemann, T.M. Pollak, Appl. Phys. Lett. 74 (1999) 1218.
- [5] M. Moldovan, K.T. Stevens, L.E. Halliburton, P.G. Schunemann, T.M. Pollak, S.D. Setzler, N.C. Giles, Mater. Res. Soc. Symp. Proc. 607 (2000) 445.

- [6] N. Dietz, W. Busse, H.E. Gumlich, W. Ruderman, I. Tsveybak, G. Wood, K.J. Bachmann, *Mater. Res. Soc. Symp. Proc.* 450 (1997) 333.
- [7] A. Sodeika, Z. Silevicius, Z. Januskevicius, A. Sakalas, *Phys. Stat. Sol. A* 69 (1982) 491.
- [8] M.H. Rakovsky, W.K. Kuhn, W.J. Lauderdale, L.E. Halliburton, G.J. Edwards, M.P. Sripsick, P.G. Schunemann, T.M. Pollack, M.C. Ohmer, F.K. Hopkins, *Appl. Phys. Lett.* 64 (1994) 1615.
- [9] L.E. Halliburton, G.J. Edwards, M.P. Sripsick, M.H. Rakovsky, P.G. Schunemann, T.M. Pollak, *Appl. Phys. Lett.* 66 (1995) 2670.
- [10] K.T. Stevens, S.D. Setzler, L.E. Halliburton, N.C. Fernelius, P.G. Schunemann, T.M. Pollak, *Mater. Res. Soc. Symp. Proc.* 484 (1998) 549.
- [11] M. Godlewski, *Phys. Stat. Sol. A* 90 (1985) 11.
- [12] R.N. Pereira, W. Gehlhoff, N.A. Sobolev, A.J. Neves, D. Bimberg, *J. Phys.: Condens. Matter* 13 (2001), in press.
- [13] D. Azamat, W. Gehlhoff, R.N. Pereira, to be published.



ELSEVIER

Physica B 308–310 (2001) 1020–1022

PHYSICA B

www.elsevier.com/locate/physb

NMR investigation of $\text{CdF}_2:\text{Ga}$

D. Hilger^a, S.A. Kazanskii^b, A.I. Ryskin^b, W.W. Warren Jr.^{a,*}

^aDepartment of Physics, Oregon State University, Weniger Hall 301, Corvallis, OR 97331-6507, USA

^bS.S. Vavilov State Optical Institute, St. Petersburg, Russia

Abstract

^{113}Cd nuclear spin-lattice relaxation measurements have been carried out over the temperature range 200–500 K on semiconducting crystals of $\text{CdF}_2:\text{Ga}$ and co-doped $\text{CdF}_2:\text{Ga,Y}$. The relaxation rates $1/T_1$ in both crystals are found to be enhanced by two to three orders of magnitude relative to undoped CdF_2 . We attribute this enhanced relaxation to the effects of thermally excited conduction electrons. The rates in the Y co-doped crystal are systematically about a factor of two higher than are found in CdF_2 . Analysis of the temperature dependence yields a value $\Delta E = 141 \pm 10$ meV for both $\text{CdF}_2:\text{Ga}$ and $\text{CdF}_2:\text{Ga,Y}$. This result is unexpected in light of the value $\Delta E = 185 \pm 10$ meV found previously for $\text{CdF}_2:\text{In}$, and the expectation that the binding energies of the DX-like ground state of the trivalent impurity should lie deeper for $\text{CdF}_2:\text{Ga}$. © 2001 Elsevier Science B.V. All rights reserved.

Keywords: NMR; Bistability; DX-centers; Ionic semiconductors

1. Introduction

Cadmium fluoride can be prepared as a wide-bandgap ($E_{\text{gap}} = 7.8$ eV) ionic semiconductor in which the trivalent transition metals and rare-earth elements (Sc, Y, La) act as conventional shallow donors [1,2]. Gallium and indium, in contrast, form bistable centers, which exhibit a variety of persistent photoinduced effects such as photorefractivity, photoconductivity, and photomagnetism [3–5]. Because of the relatively high temperatures for metastability of photo-induced changes in these materials, approaching 200 K for $\text{CdF}_2:\text{Ga}$, they are of interest for a variety of applications, including optical data storage.

The ineffective doping, bistability and metastability of $\text{CdF}_2:\text{M}$ ($\text{M} = \text{In, Ga}$) have been proposed to reflect ‘negative U, DX behavior’ [6–11]. In the deep ground state of the impurity, the active dopants undergo disproportionation to form $\text{M}^{1+}-\text{M}^{3+}$ pairs. The doubly occupied (M^{1+}) impurities are stabilized by a local lattice relaxation that compensates the extra coulomb repulsion energy. Calculations of Park and

Chadi [12] suggest that this can be accomplished by movement of the (M^{1+}) ion from a substitutional (Cd) site toward a nearby interstitial. Because of the vibronic barrier associated with the lattice distortion, optically excited shallow donor states are metastable at sufficiently low temperatures.

At temperatures well above the range of metastability, conduction electrons are thermally excited from the deep states. The excitation statistics are those of the three-level system consisting of the ground states, thermally generated, shallow donors, and the conduction band states [13]. The number of conduction electrons at a given temperature depends on both the binding energy of the deep state (0.25 eV for In and 0.7 eV for Ga [12], and the binding energy (~ 0.1 eV) of the shallow donor [14]. The temperature dependence of the carrier concentration should reflect both these binding energies.

In our previous nuclear magnetic resonance studies [15,16] of $\text{CdF}_2:\text{In}$, we found that the ^{113}Cd spin-lattice relaxation rate reflects the concentration of conduction electrons. Nuclei are relaxed by the fluctuating magnetic hyperfine fields of carriers and the temperature dependence of the relaxation rate can be related to that of the conduction electron density. The $\text{CdF}_2:\text{In}$ results are in good agreement with independent determinations of the carrier concentration in these materials. In the present

*Corresponding author. Tel.: +1-541-737-4631; fax: +1-541-737-1683.

E-mail address: wwarren@physics.orst.edu (W.W. Warren Jr.).

work, we report first results for the ^{113}Cd spin-lattice relaxation in crystals of $\text{CdF}_2:\text{Ga}$ and $\text{CdF}_2:\text{Ga,Y}$. Co-doping with Y is known to increase the numbers of active dopants [17].

2. Experimental methods

The samples used in these experiments were converted to semiconductors by a high temperature anneal in a reducing atmosphere of cadmium vapor. The details are reported elsewhere (see, for example, Ref. [16]). This process removes many of the self-compensating fluorine interstitials, but it has been shown that their removal is not complete [18]. The concentration of active bistable impurities is therefore less than the total chemical concentration of the dopants. For $\text{CdF}_2:\text{Ga}$ crystals studied in these experiments, the concentration of active gallium was estimated to be approximately $0.7 \times 10^{18} \text{ Ga/cm}^3$ [19].

The NMR measurements were carried out using a Chemagnetics/Varian CMX-360 spectrometer in a magnetic field of 8 T. Sample temperatures were varied using a temperature-regulated gas-flow system. The spin-lattice relaxation times were determined from the rate of recovery of the equilibrium nuclear magnetization after an initial inverting radio-frequency pulse. The recovery curves were fit to a single exponential function characterized by a time-constant T_1 , the spin-lattice relaxation time.

3. Experimental results

The theory of nuclear spin-lattice relaxation by carriers in a semiconductor yields the following expression for the relaxation rate [20]:

$$\frac{1}{T_1} = \frac{16\pi}{9} n(T) |\Psi(\text{Cd})|^4 \gamma_e^2 \gamma_{113}^2 \left(\frac{m^3 k T}{2\pi} \right)^{1/2}, \quad (1)$$

where $n(T)$ is the temperature-dependent carrier density, $|\Psi(\text{Cd})|^2$ is the conduction electron probability density at the Cd nucleus, and γ_e and γ_{113} are, respectively, the electron and nuclear gyromagnetic ratios. Eq. (1) predicts $1/(T_1 T^{1/2}) \propto n(T)$.

In Fig. 1 we present an Arrhenius plot of the ^{113}Cd spin lattice relaxation data plotted in the form $1/(T_1 T^{1/2})$ versus inverse T . Data are presented for co-doped $\text{CdF}_2:\text{Ga,Y}$ and $\text{CdF}_2:\text{Ga}$ together with our previous results for $\text{CdF}_2:\text{In}$ [15,16]. The temperature dependence of $1/(T_1 T^{1/2})$ in each case can be characterized by an activation energy ΔE where $\Delta E = 185 \pm 10 \text{ meV}$ for $\text{CdF}_2:\text{In}$ and, within the experimental uncertainty, the $\text{CdF}_2:\text{Ga,Y}$ and the

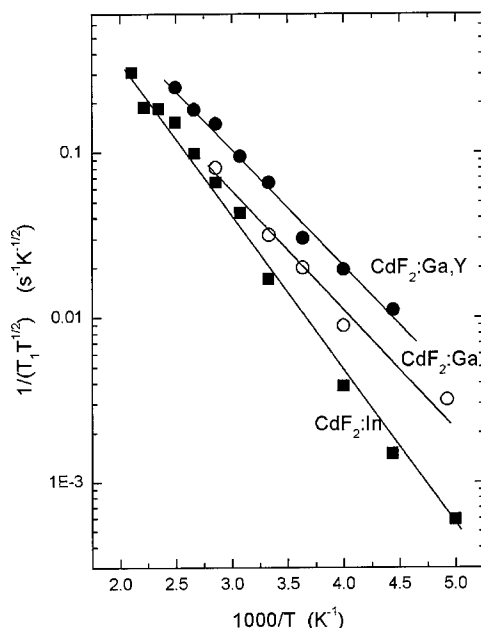


Fig. 1. Arrhenius plot of $1/(T_1 T^{1/2})$ for ^{113}Cd in $\text{CdF}_2:\text{In}$ (solid squares), $\text{CdF}_2:\text{Ga}$ (open circles), and $\text{CdF}_2:\text{Ga,Y}$ (solid circles).

$\text{CdF}_2:\text{Ga}$ crystals exhibit the same value, $\Delta E = 141 \pm 10 \text{ meV}$.

4. Discussion

Previous work [15,16] has shown that the temperature dependence of $1/(T_1 T^{1/2})$ is essentially the same as that of the conduction electron concentration in $\text{CdF}_2:\text{In}$. As noted above, the activation energy of $1/(T_1 T^{1/2})$ is not reflective of single excitation energy. Rather, it represents the combined effects of the binding energies of the deep states ($E_{\text{bind}}^{\text{d}} = 250 \text{ meV}$ [12,13]) and the shallow donor states ($E_{\text{bind}}^{\text{s}} = 100 \text{ meV}$ [14]). A statistical analysis [13] indicates that the conduction electron concentration increases with temperature with an average value $\Delta E = 195 \text{ meV}$. This agrees well with the observed variation of $1/(T_1 T^{1/2})$, a result that is completely consistent with our expectation that the ^{113}Cd spin-lattice relaxation is governed by interactions with conduction electrons as expressed by Eq. (1).

Measurements [16] of the ^{19}F spin-lattice relaxation rates in $\text{CdF}_2:\text{In}$ provide further support for the DX model and the above binding energies in this system. ^{19}F spin-lattice relaxation is dominated by interactions with paramagnetic shallow donor states, rather than conduction electrons. The observed temperature dependence of $1/T_1$ for ^{19}F ($\Delta E = 70 \pm 10 \text{ meV}$) is in good agreement

with the model prediction [13] ($\Delta E = 74$ meV) for the concentration of shallow donors.

Previous work suggests that the deep state in $\text{CdF}_2\text{:Ga}$ is more strongly bound than in $\text{CdF}_2\text{:In}$. Park and Chadi's calculation gives $E_{\text{bind}}^{\text{d}} = 700$ meV for the binding energy of this state. Since the binding energy of the shallow donor is expected to approximately 100 meV in both $\text{CdF}_2\text{:In}$ and $\text{CdF}_2\text{:Ga}$, we might expect to find a larger value of ΔE for $\text{CdF}_2\text{:Ga}$. It is clear from the data in Fig. 1 that this is not the case.

The ^{113}Cd spin-lattice relaxation data in $\text{CdF}_2\text{:Ga}$ imply that the deep states do not play a role in the statistics of the carriers found in the bulk of the material. The conduction electrons appear to be thermally excited from shallower states than previously believed. At the present time, we do not know the identity of these states. Further studies, including ^{19}F relaxation rate measurements, are planned in hopes of resolving the energetics of the $\text{CdF}_2\text{:Ga}$ system.

Acknowledgements

The research reported in this paper was supported, in part, by the US National Science Foundation, grant DMR-0071898 and by the US Civilian Research and Development Foundation, grant RPI-2096.

References

- [1] J.D. Kingslay, J.S. Prener, *Phys. Rev. Lett.* 8 (1962) 315.
- [2] P.F. Weller, *Inorg. Chem.* 4 (1965) 1545.
- [3] F. Trautweller, F. Moser, R.P. Khoshla, *J. Phys. Chem. Solids* 29 (1968) 1869.
- [4] I. Kunze, W. Ulrizi, *Phys. Stat. Solidi (b)* 55 (1973) 567.
- [5] J.E. Dmochowski, W. Jantsch, D. Dobosz, J.M. Langer, *Acta Phys. Polonica A* 73 (1988) 247.
- [6] A.S. Shcheulin, A.I. Ryskin, K. Swiatek, J.M. Langer, *Phys. Lett. A* 222 (1996) 107.
- [7] S.A. Kazanskii, A.I. Ryskin, V.V. Romanov, *Appl. Phys. Lett.* 70 (1997) 1272.
- [8] S.A. Kazanskii, A.I. Ryskin, V.V. Romanov, *Phys. Solid State* 39 (1997) 1067.
- [9] A.I. Ryskin, P.P. Fedorov, *Phys. Solid State* 39 (1997) 943.
- [10] D.E. Onopko, A.I. Ryskin, *Phys. Rev. B* 61 (2000) 12952.
- [11] A.I. Ryskin, A.S. Shcheulin, D.E. Onopko, *Phys. Rev. Lett.* 80 (1998) 2949.
- [12] C.H. Park, D.J. Chadi, *Phys. Rev. Lett.* 82 (1999) 113.
- [13] A.S. Shcheulin, A.K. Kupchikov, A.E. Angervaks, D.E. Onopko, A.I. Ryskin, A.I. Ritus, A.V. Pronin, A.A. Volkov, P. Lunkenheimer, A. Loidl, *Phys. Rev. B* 63 (2001) 205207.
- [14] J.M. Langer, T. Langer, G.L. Pearson, B. Krukowska-Fulda, U. Piekara, *Phys. Stat. Solidi (b)* 66 (1974) 537.
- [15] M. Shroyer, J.K. Furdyna, A.I. Ryskin, W.W. Warren Jr., *Physica B* 273–274 (1999) 852.
- [16] M. Shroyer, A.I. Ryskin, W.W. Warren Jr., unpublished.
- [17] R.A. Linke, A.S. Shcheulin, A.I. Ryskin, I.I. Buchinskaya, P.P. Fedorov, B.P. Sobolev, *Appl. Phys. B (Lasers and Optics)* 72 (2001) 677.
- [18] S.A. Kazanskii, D.S. Rumyantsev, A.I. Ryskin, *Phys. Rev. B*, in press.
- [19] A.I. Ryskin, A.S. Shcheulin, E.V. Miloglyadov, R.A. Linke, I. Redmond, I.I. Buchinskaya, P.P. Fedorov, B.P. Sobolev, *J. Appl. Phys.* 83 (1998) 2215.
- [20] A. Abragam, *Principles of Nuclear Magnetism*, Oxford, London, 1996.



ELSEVIER

Physica B 308–310 (2001) 1023–1026

PHYSICA B

www.elsevier.com/locate/physb

Scattering of charge carriers in semiconductors: models and their criteria

V.V. Mikhnovich Jr.*

Ioffe Physicotechnical Institute, Russian Academy of Sciences, 194021 St. Petersburg, Russia

Abstract

Calculations of mobility of charge carriers in semiconductors are based on some theoretical approaches and models widely used for a long time. In the present work, three main approaches to this problem, the Born approximation as well as the approximation of isolated scattering centers and potential scattering are considered to deduce the criteria of their validity in an analytical form convenient for practical purposes. A comparison between the calculated and experimental data has shown that the adequate theoretical description is rather sensitive to a slight violation of the criterion of isolated scattering centers, in contrast to other approximations with lesser sensitivity to their breaking. © 2001 Elsevier Science B.V. All rights reserved.

Keywords: Mobility of charge carriers; Scattering of charge carriers

1. Introduction

The theory of scattering of charge carriers due to lattice vibrations and impurity centers in semiconductors has been developed in great detail, so the Hall and drift mobility of charge carriers in practically important materials can be calculated in wide regions of impurity concentrations and temperature; see for instance Refs. [1–3]. However, in many handbooks, a variety of empirical formulae for mobility calculations is still in use [4,5], since in the presence of several scattering mechanisms theoretical consideration of the resultant mobility of charge carriers becomes rather complicated. Up to now, a thorough analysis of the validity limits of the theoretical approaches and models adopted are lacking.

The purpose of the present work is to derive the validity limits for the main approaches in an analytical form.

2. Theoretical aspects of the problem

In general, several principal scattering mechanisms are usually taken into consideration when calculating the mobility of charge carriers in semiconductors: (i) scattering by acoustic phonons, (ii) scattering by optical phonons, (iii) scattering by charged centers, and (iv) scattering by neutral centers.

Let us first discuss a simple case of silicon. Then, we will show how a more complicated case of semiconductor compounds like n-GaN can be treated, too.

2.1. Silicon

It is well known that the scattering of charge carriers by acoustic-mode lattice vibrations is dominant over that by optical phonons at temperatures T

$$T \ll \hbar\omega_{\text{opt}}/k_B. \quad (1)$$

Here, k_B and \hbar are the Boltzmann and Planck constants, respectively; ω_{opt} is the frequency of optical phonons ($\hbar\omega_{\text{opt}} = 0.063$ eV [6]). In the subsequent discussion, the temperature interval of interest runs from cryogenic temperatures up to room temperature, so based on

*Fax: +7-95-552-07-03.

E-mail address: cleanair@cityline.ru (V.V. Mikhnovich Jr.).

condition (1) one can neglect the contribution of optical phonons to the scattering of charge carriers.

The next approximation used in calculations requires that the condition

$$l_{\text{eff}} \gg r_0 \quad (2)$$

is also satisfied, the so-called potential scattering. Here, $l_{\text{eff}} = [l_0^{-1} + l_{\text{ph}}^{-1}]^{-1}$, l_0 and l_{ph} are the free paths of charge carriers relative to the scattering by neutral centers and acoustic phonons, respectively; r_0 is the effective radius of potential scattering by a charged center. Under condition (2), all the scattering mechanisms mentioned above can be treated independently. Owing to this, the resultant momentum relaxation time τ of charge carriers is given by

$$\tau^{-1} = \tau_i^{-1} + \tau_0^{-1} + \tau_{\text{ph}}^{-1},$$

where τ_i , τ_0 , and τ_{ph} are the relaxation times relative to scattering by ionized centers, neutral centers, and acoustic phonons, respectively. The fulfillment of condition (2) allows the introduction of the cross-section of charge carrier scattering by ionized centers for calculations of τ .

Another important approximation in mobility calculations is the scattering by isolated charged and neutral centers. The concentrations of relevant centers must be not too high, so that the conditions

$$\tau_i \gg \tau_c, \quad \tau_0 \gg \tau_c, \quad (3)$$

were satisfied. Here τ_c is the time of collision of a charge carrier with a charged center and it is about $\hbar/k_B T$ [2].

The expressions for the drift and Hall mobilities have the form:

$$\mu_d = \frac{e}{m^*} \langle \tau \rangle, \quad \mu_H = \frac{e}{m^*} \frac{\langle \tau^2 \rangle}{\langle \tau \rangle}$$

for a parabolic band.

The energy-dependent relaxation times for the scattering by acoustic phonons τ_{ph} and neutral centers τ_0 can be given in the following form [6]:

$$\tau_{\text{ph}} = \frac{9\rho v_0^2 \hbar^4 E^{-1/2}}{4\sqrt{2} E_1^2 m^{*3/2} (k_B T)}, \quad \tau_0 = \frac{m^{*2} e^2}{20 \epsilon_0 \hbar^3 N_0}.$$

Here ρ is the crystal density, v_0 is the averaged velocity of sound, E_1 is the deformation potential, ϵ_0 is the crystal permittivity, m^* is the effective mass of charge carriers, e is the electron charge, and N_0 is the concentration of neutral centers.

For the description of scattering by charged centers, the Born approximation is widely used. In this approach, one takes into account only the charge carriers whose energy E is greater than the effective Bohr energy E_{Bohr} ($E_{\text{Bohr}} \approx 0.01$ eV) [2], i.e.

$$E \gg E_{\text{Bohr}} \quad \text{for} \quad kr_0 \gg 1, \quad (4)$$

where k is the wave number. Under such conditions $\tau_i(E)$ can be given by the Brooks–Herring expression:

$$\tau_i(E) = \sqrt{2m^* \epsilon_0^2} E^{3/2} / Z^2 e^4 \pi N_i \Phi(y), \quad (5)$$

where Ze is the charge of ionized centers; N_i is the concentration of charged centers:

$$\Phi(y) = \ln(1+y) - y/(1+y) \quad \text{and} \quad y = (2kr_0)^2.$$

It can be demonstrated that conditions (1)–(4) which are, in fact, the criteria for validity of the approximations can be given in the form convenient for practical purposes:

$$N_0 \ll 0.3 \times 10^{20} \left(\frac{m^*}{m_0} \right)^2 \left(\frac{T}{T_0} \right),$$

$$N_i \ll \frac{1.4 \times 10^{19}}{\ln [0.46 \times 10^{20} (T/T_0)^2 (m^*/m_0) (1/n)]} \times \left(\frac{m^*}{m_0} \right)^{1/2} \left(\frac{T}{T_0} \right)^{5/2},$$

$$n^{1/2} \gg 0.8 \times 10^9 \left(\frac{T}{T_0} \right)^{3/2} \left(\frac{m^*}{m_0} \right)^2 \times \left\{ 1 + 1.5 \times 10^{-19} N_0 \left(\frac{m_0}{m^*} \right)^{7/2} \left(\frac{T_0}{T} \right)^{3/2} \right\},$$

$$n^{1/2} \ll 0.3 \times 10^{10} \left(\frac{T}{T_0} \right) \left(\frac{m^*}{m_0} \right)^{1/2},$$

$$50 \text{ K} \ll T \ll 730 \text{ K}, \quad (6)$$

where n is the concentration of charge carriers in the conduction or valence band, m_0 is the free electron mass, and $T_0 = 300$ K.

Criteria (6) are deduced taking $\rho = 2.3$ g/cm³ [7], $v_0 = 6 \times 10^5$ cm/s [7], $\epsilon_0 = 11.8$ [7], $E_1 = 10$ eV, $m^* = 0.26m_0$ and $0.38m_0$ for electrons and holes, respectively [2], and $Z = 1$ for group-III and V impurities.

2.2. Gallium nitride

In this case, to the scattering mechanisms given above one should also add the piezoelectric-potential scattering of charge carriers by acoustic phonons as well as the scattering by optical phonons, deformation and polar ones. The energy-dependent relaxation times for the piezoelectric potential scattering, τ_{pe} , and the scattering by polar optical phonons, τ_{pol} , are determined by the following equations [6]:

$$\tau_{\text{pe}} = \frac{2\sqrt{2}\pi\hbar^2\epsilon_0 E^{1/2}}{(\text{Pe})^2 m^{*1/2} (k_B T)},$$

$$\tau_{\text{pol}} = \frac{1}{2\alpha\omega_{\text{opt}}} \exp\left(\frac{\hbar\omega_{\text{opt}}}{k_B T}\right) \quad \text{for} \quad T \ll \hbar\omega_{\text{opt}}/k_B.$$

Here, P^2 is the piezoelectric coupling coefficient and α is the Fröhlich constant; other symbols have their usual meaning given in Section 2.1. P^2 and α can be expressed in terms of other crystal constants:

$$P^2 = \frac{E_p^2}{\chi \rho v_0^2}, \quad \alpha = \frac{e^2}{\hbar \chi} \left(\frac{m^*}{2 \hbar \omega_{\text{opt}}} \right)^{1/2},$$

$$\chi^{-1} = \varepsilon_{\infty}^{-1} - \varepsilon_0^{-1},$$

where E_p is the piezoelectric constant and ε_{∞} is the high frequency permittivity. In a way similar to that used for silicon, the criteria for validity of the approximation applied can be written in the form:

$$n^{1/2} \gg 0.7 \times 10^9 \left(\frac{T}{T_0} \right)^{3/2} \left(\frac{m^*}{m_0} \right)^2 \times \left\{ 1 + 1.3 \times 10^{-19} N_0 \left(\frac{m_0}{m^*} \right)^{7/2} \left(\frac{T_0}{T} \right)^{3/2} + 28.5 \left(\frac{m_0}{m^*} \right) \left(\frac{T_0}{T} \right)^{3/2} \exp \left(-\frac{\hbar \omega_{\text{opt}}}{k_B T} \right) \right\},$$

$$50 \text{ K} \ll T \ll 1065 \text{ K}. \quad (7)$$

The criteria (7) are identical to the criteria (6).

Criteria (7) are deduced taking $\rho = 6.1 \text{ g/cm}^3$ [5], $v_0 = 4.33 \times 10^5 \text{ cm/s}$ [5], $\varepsilon_0 = 10$ [8], $\hbar \omega_{\text{opt}} = 0.092 \text{ eV}$ [5], $E_p = 0.56 \times 10^{-4} \text{ C/cm}^2$ [5], $\varepsilon_{\infty} = 5.5$ [8], $P^2 = 1.8 \times 10^{-3}$, $\alpha = 0.87 (m^*/m_0)^{1/2}$ and $Z = 1$. The effective mass of electrons in n-GaN is taken $m^* = 0.22 m_0$. The deformation potential E_1 is assumed to be close to 10 eV ; cf. $E_1 = 7.8$ [5] and 9.2 eV [9].

3. Comparison between calculated and experimental data

As an illustration, in Fig. 1a comparison between the experimental and calculated mobilities of electrons in a sample of Si doped with As is given. The experimental data on the electron concentration and mobility were taken from Ref. [10]. The concentration of ionized impurity centers is equal to $N_i(T) = 2N_A + n(T)$ where N_A is the total concentration of compensating acceptors. As is seen from Fig. 1, there is a satisfactory agreement between the calculated and experimental curves of $\mu_H(T)$. It is interesting to note that the criteria for the validity of the Born approximation are not met throughout the entire temperature range; see Eqs. (6)_{4,5}. It means that the Born approximation appears to be valid beyond the strict limits given by these equations. However, analysis of the calculated mobilities of charged carriers in n-Si and p-Si over a wide range of concentrations of ionized centers showed that even a slight violation of the criteria expressed by Eqs. (6)_{1,2}, associated with the approxima-

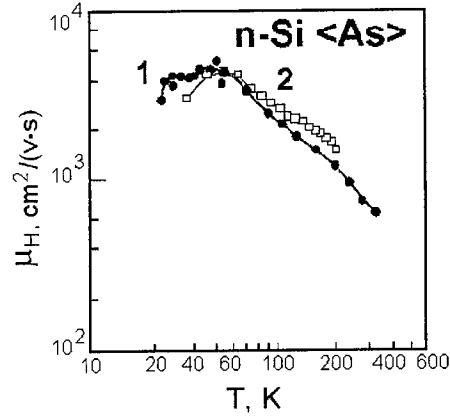


Fig. 1. The electron Hall mobility in n-Si as a function of temperature for $N_A = 5 \times 10^{15} \text{ cm}^{-3}$. 1—experimental curve; 2—calculated curve.

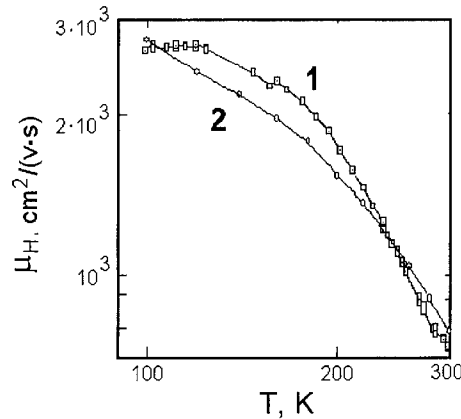


Fig. 2. The electron Hall mobility in n-GaN as a function of temperature. 1—experimental curve [11]; 2—calculated curve.

tion of isolated charged centers, results in misfitting calculated and experimental curves. At concentrations of ionized centers in Si lower than 10^{14} cm^{-3} the criterion for the validity of potential scattering is broken; see Eq. (6)₃. However, at such low concentrations of scattering centers the mobility of charge carriers is mainly determined by the scattering due to acoustic phonons.

Similar conclusions can be drawn from calculations of the electron mobility in n-GaN; see Fig. 2. It can be shown that at $N_i \geq 10^{17} \text{ cm}^{-3}$ the criterion given by Eq. (7) is broken and the approximation of isolated charged centers is not valid any longer. As a consequence, the calculated mobility $\mu_H(T)$ does not fit the experimental one.

4. Conclusions

In the present work, the main approximations used in the calculations of mobility of charge carriers in Si and GaN have been analyzed. The criteria for validity of the approximations of potential scattering by isolated ionized centers as well as Born approximation are given in an analytical form which is convenient for practical purposes. It has been shown that mobility calculations are sensitive even to a slight violation of the approximation of isolated charged centers. In contrast, the Born approximation appears to be valid beyond the strict limits of its validity.

Acknowledgements

I would like to thank V.V. Emtsev for setting up the objective and for many stimulating discussions.

References

- [1] F. Blatt, in: *Physics of Electron Conduction in Solid States*, Mir, Moscow, 1971.
- [2] V.L. Bonch-Bruyevich, S.G. Kalashnikov, in: *Physics of Semiconductors*, Nauka, Moscow, 1977.
- [3] A.I. Anselm, in: *Introduction into the Semiconductors Theory*, Nauka, Moscow, 1978.
- [4] N.M. Tugov, in: *Semiconductor Devices*, Energoatomizdat, Moscow, 1990.
- [5] J.D. Albrecht, et al., *J. Appl. Phys.* 83 (1998) 4777.
- [6] B.M. Askerov, in: *Electronic Phenomena of Transport in Semiconductors*, Nauka, Moscow, 1985.
- [7] I.K. Kikoin, in: *Tables of Physical Values*, Atomizdat, Moscow, 1976.
- [8] A.S. Barker, et al., *Phys. Rev. B* 7 (1973) 7430.
- [9] D.S. Look, et al., *J. Appl. Phys. Lett.* 70 (1997) 3377.
- [10] I.S. Grigoriev, E.M. Meilikhov (Eds.), *Physical Values. Handbook*, Energoatomizdat, Moscow, 1991.
- [11] V.V. Emtsev, et al., *Semicond. Sci. Technol.* 15 (2000) 73.



ELSEVIER

Physica B 308–310 (2001) 1027–1030

PHYSICA B

www.elsevier.com/locate/physb

Mg–H and Be–H complexes in c-BN

N.M.C. Pinho^{a,b,1,*}, V.B. Torres^b, R. Jones^a, S. Öberg^c, P.R. Briddon^d^a School of Physics, The University of Exeter, Exeter EX4 4QL, UK^b Department of Physics, University of Aveiro, Campus Santiago, 3810 Aveiro, Portugal^c Department of Mathematics, Luleå University of Technology, S-97187 Luleå, Sweden^d Department of Physics, The University of Newcastle upon Tyne, Newcastle upon Tyne NE1 7RU, UK

Abstract

Ab initio calculations on hydrogen complexes with Mg and Be impurities in c-BN are reported. We find that both impurities are acceptors and bind H to form passive defects. However, their structures are different. For Be–H, the H atom lies at a puckered bond centre configuration similar to C–H in GaAs, while in Mg–H the H atom lies at an anti-bonding site to an N neighbour of the impurity. The hydrogen related vibrational modes of the two complexes are also reported. © 2001 Elsevier Science B.V. All rights reserved.

Keywords: BN; Hydrogen; Magnesium; Beryllium

1. Introduction

Boron nitride's gap of 6.4 eV makes it the largest band gap in the nitride family. Although it has a very large gap it still shares many common properties with AlN and GaN. It has extreme hardness, high melting point, high thermal conductivity, low dielectric constant and is chemically inert. The zincblende phase is stable under high temperature and high pressure and is easily doped with Be and Mg [1,2]. The relative ease of doping has made p–n junction diodes possible. The most efficient dopants used are beryllium and silicon for p- and n-types. The ionisation energies of Be and Si have been given as 0.23 and 0.24 eV [2]. However, the Be (–/0) level varies with temperature, pressure and concentration. Values of 0.24, 0.31 and 0.35 eV at 7.7 GPa and 2100°C for Be concentrations of 2900, 4500 and 1700 ppm, respectively, have been reported [3].

Hydrogen is a common contaminant in almost all growth techniques, due to its presence in the majority of growth conditions, its high solubility and diffusibility. The existing hydrogen in as-grown material can form passive complexes with defects already present. It also can “tie off” dangling bonds on grain boundaries or dislocations. An example of this was the successful p-doping of GaN achieved with Mg. It is necessary to anneal the material grown by VPE, in order to eliminate hydrogen which forms passive complexes with Mg. Considering these aspects, we may expect hydrogen to passivate dopants in BN as it does in many other semiconductors [4–6].

In Si and GaAs, hydrogen lies at a bond centre near the acceptor [7]. However, in GaN, hydrogen lies at an anti-bonding site to a nitrogen neighbour of Be, which raises a question about the preferred site for H in BN. Park and Chadi [8] demonstrated, using a first-principles LDA method in a 32 atom super-cell, that Be lies at a B site in c-BN and is an acceptor. A full-potential linear augmented plane-wave study [9] showed an outward displacement of 3% for the nitrogen neighbours. It also showed the existence of a (–/0) level to be at $E_v + 0.4$ eV. Nevertheless, theoretical studies on the properties of hydrogen in BN are scarce. An ab initio

*Corresponding author. School of Physics, The University of Exeter, Stocker Road, Exeter EX4 4QL, UK. Fax: +44-1392-264111.

E-mail address: pinho@excc.ac.uk (N.M.C. Pinho).

¹ Financially supported by Fundação para a Ciência e a Tecnologia.

Hartree–Fock study concluded that neutral hydrogen prefers a bond-centred position in c-BN [10], while a local density-tight-binding method [11] found H^0 to be located on the centre of a rhombus formed by two neighbouring B–N bonds.

In view of these contradictory results, we have investigated the location of H in c-BN doped with Be and Mg.

2. Method

All results achieved in this paper have been found using a first-principle density functional method employing Gaussian orbitals (AIMPRO). Details of the method have been given previously [12,13]. 64 atom super-cells were used, together with a 2^3 Monkhorst–Pack Brillouin sampling scheme [14]. The Fourier expansion of the charge density was performed with energy cut-offs up to 100 Ry. Both the cut-off energy and the sampling scheme were checked to guaranty convergence of structure and total energy. Local vibrational modes (LVM) of defects were evaluated from the energy second derivatives between the neighbouring atoms of the defect. A Musgrave–Pople interatomic potential describing the bulk was first derived by fitting to a set of energy double derivatives for c-BN. These potentials could then be used to evaluate the entries to the dynamical matrix for host atoms surrounding a defect.

3. Results

The calculations of basic material properties such as lattice parameter, bulk modulus and its pressure derivative for c-BN, are presented in Table 1. These were found by using a fit to the Birch–Murnaghan equation of state [15]. The error in the calculated lattice parameter is about 1%. The second derivatives of the energy, with respect to atomic positions, were used to find a Musgrave–Pople interatomic potential between B and N [17]. This potential gave an optic phonon frequency at Γ of 1350 cm^{-1} , close to the experimental value of 1305 cm^{-1} [18]. However, the short range potential does not lead to a splitting of the LO and TO modes. Experimentally, the LO mode is at 1066 cm^{-1} .

Table 1
Lattice constant, a_0 , bulk modulus, B , and its first pressure derivative, B'

	a_0 (Å)	B (GPa)	B'
Calc.	3.584	396	3.84
Exper. [16]	3.616	369–400	4.0

Table 2

Musgrave–Pople potential for BN, $\text{eV}/\text{\AA}^2$, $r_0 = 1.5503\text{ \AA}$

Atom	k_r	k_θ	$k_{r\theta}$	k_{rr}	$k_{\theta\theta}$
B	16.161572	−0.315638	−0.319521	4.708087	−3.244078
N	16.161572	0.833029	−1.131736	6.081233	−3.776663

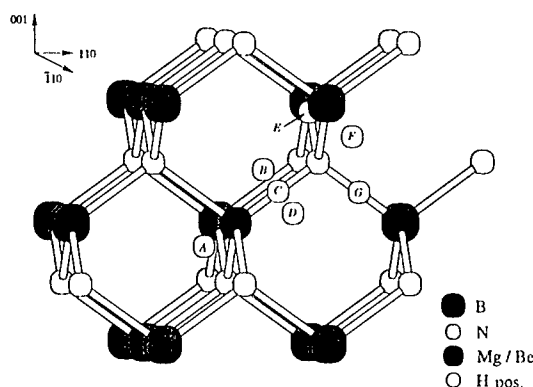


Fig. 1. Configurations investigated for a hydrogen atom passivating Be and Mg in c-BN.

The second derivatives of the energy between these inner 8 atoms of a 64 atom cell were evaluated and fitted to the derivatives of a Musgrave–Pople potential where the potential for atom i is

$$V_i = 1/4 \sum_j k_r^{(i)} (\Delta r_{ij})^2 + r_0^2/2 \sum_{j>k} k_\theta^{(i)} (\Delta \theta_{jik})^2 \\ + r_0 \sum_{k>j} k_{r\theta}^{(i)} (\Delta r_{ij} + \Delta r_{ik}) \Delta \theta_{jik} + \sum_{k>j} k_{rr}^{(i)} \Delta r_{ij} \Delta r_{ik} \\ + r_0^2 \sum_{l>k>j} k_{\theta\theta}^{(i)} \Delta \theta_{jik} \Delta \theta_{kil}.$$

Here, Δr_{ij} and $\Delta \theta_{jik}$ represent the variations in the length of the i – j bond and angle, between the i – j and i – k bond, respectively. Only the nearest neighbours are considered for the sum. Table 2 gives the coefficients $k_r^{(i)}$, $k_\theta^{(i)}$, $k_{r\theta}^{(i)}$, $k_{rr}^{(i)}$ and $k_{\theta\theta}^{(i)}$.

The introduction of either Be or Mg at the boron site leads to an outward breathing displacement of 4.7% and 14.1%, respectively, in the N nearest neighbours. These values become 4.9% and 14.9% for the negatively charged complexes. We then studied the structure and vibrational modes of the Be–H and Mg–H complexes. Seven possible sites (Fig. 1) for H were investigated to ascertain the most stable defect. These include the bond centre (C), an anti-bonding site to the impurity or host atom (A, F), puckered bond centre sites (B, D), a site between two N neighbours (E) and a remote bond centre site (G). The relative energies for the fully relaxed Be–H and Mg–H defects are listed in Table 3. For Be–H, the

Table 3
Relative energies (eV) for the seven hydrogen sites investigated and shown in Fig. 2

H sites	Mg–H	Be–H
A	2.008	1.326
B	0.230	0
C	0.368	0.167
D	\Rightarrow C	0.154
E	\Rightarrow F	\Rightarrow B
F	0	0.512
G	\Rightarrow D \Rightarrow C	\Rightarrow D

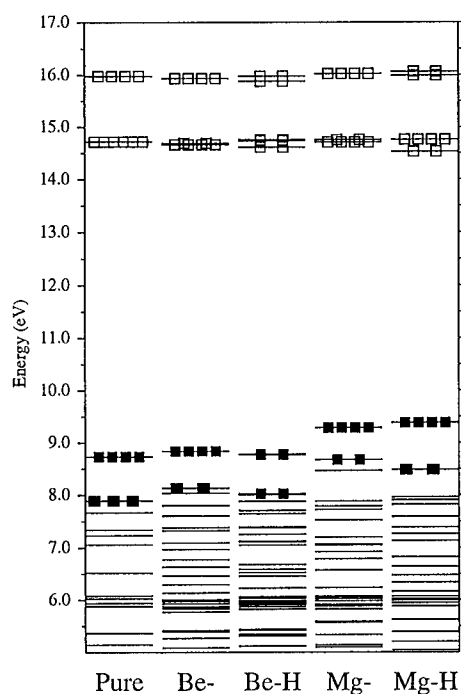
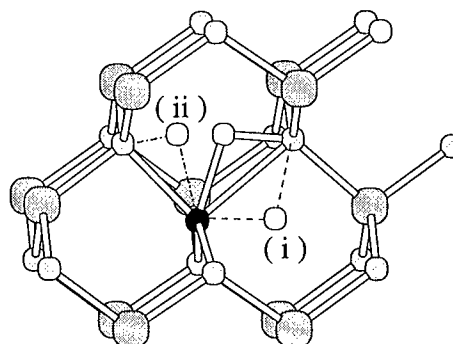


Fig. 2. Kohn-Sham levels for BN, Be^- , Mg^- , Be–H, Mg–H defects.

lowest energy configuration corresponds to the puckered bond centre B, shown in Figs. 1 and 3, and is similar to a configuration found previously for hydrogen [10]. H is bonded to Be and an N neighbour, with a Be–N–H angle of 44° . The N–H, Be–H bond lengths are 1.07 and 1.45 Å, respectively. The Be–N bond is increased by 17% relative to that in the Be acceptor. The binding energy of H to Be was estimated to be 1.45 eV from the difference in energies of the dissociated and bound centres evaluated in the same super-cell.

Reorientation barriers were also calculated. The most straightforward reorientation (i) comes from rotating the hydrogen atom 120° around the (1 1 1) Be–N bond to which the hydrogen is attached. This barrier is only



Be–N–H

Fig. 3. Reorientations for the Be–N–H complex.

0.2 eV. The other reorientation path (ii) consists of the movement of the hydrogen atom, maintaining its C_{1h} plane, to an equivalent position. The barrier for this is also coincidentally 0.2 eV. These two processes are exemplified in Fig. 3.

The energies for the Mg–H complexes are also listed in Table 3. The stable configuration corresponds to an N anti-bonding site labelled F in Fig. 1. This is exactly the same structure found in GaN. The N–H and Mg–N bond lengths are, respectively, 1.01 and 1.79 Å. The binding energy of 1.48 eV H with Mg was found as described above for Be.

Fig. 2 shows the Kohn-Sham energy levels for BN, Be_B^- , Mg_B^- , Be–H and the Mg–H defects in the 64 atom cell corresponding to $\mathbf{k} = (0.25, 0.25, 0.25)$. It is clear that Be and Mg are acceptors and that the hydrogenated centres are passive.

The calculated H-related vibrational modes are given in Table 4. The stretch mode lies at 3315 cm^{-1} and is similar to the corresponding Mg–H defects in c- and w-GaN [19–21]. We also find a resonant E wag mode near the top of the one phonon maxima. This mode is IR-active and in principle might be observed.

4. Conclusions

The calculations made show that substitutional Be and Mg are acceptors in cubic BN and are passivated by hydrogen. The position of H is different in the two defects. In Be–H, the H atom lies at a puckered bond centre while in the Mg–H case it lies at the anti-bonding site to an N neighbour. This difference is undoubtedly due to the different sizes of the impurities. This configuration and its stretch local mode are similar to the corresponding complex in GaN. The awkward positioning of the hydrogen atom in the Be–H case, together with its low reorientation barrier, may prove to be as interesting as the oxygen interstitial in silicon. The

Table 4

H-related vibrational modes, cm^{-1} , for Mg–H and Be–H defects

	Mode	^{14}N				^{15}N			
		$^{10}\text{B-H}$	$^{11}\text{B-H}$	$^{10}\text{B-D}$	$^{11}\text{B-D}$	$^{10}\text{B-H}$	$^{11}\text{B-H}$	$^{10}\text{B-D}$	$^{11}\text{B-D}$
Mg–N–H	A_1	3316	3316	2418	2417	3309	3309	2408	2408
	E	1219	1195	1076	1040	1218	1193	1073	1038
Be–N–H	A'	2537	2537	1873	1873	2537	2537	1873	1873
	A'	1958	1957	1466	1465	1958	1957	1465	1464
	A''	1223	1218	1196	1195	1214	1207	1181	1180

low relative energies for some configurations and the application of stress or strain on the crystal may lead to different conclusions relative to the equilibrium structure. Caution and further investigations are still necessary for the full understanding of these phenomena.

References

- [1] R.H. Wentorf Jr., J. Chem. Phys. 36 (1962) 1990.
- [2] O. Mishima, J. Tanaka, S. Yamaoka, O. Fukunaga, Science 238 (1987) 181.
- [3] T. Taniguchi, J. Tanaka, O. Mishima, T. Ohsawa, S. Yamaoka, Appl. Phys. Lett. 62 (1993) 576.
- [4] C.T. Sah, J.Y.-C. Sun, J.J. Tzou, Appl. Phys. Lett. 43 (1983) 204.
- [5] T.C.T. Sah, J.Y.-C. Sun, J.J. Tzou, Appl. Phys. Lett. 43 (1983) 965.
- [6] J.I. Pankove, D.E. Carlson, J.E. Berkeyheiser, R.O. Wance, Phys. Rev. Lett. 51 (1983) 2224.
- [7] N.M. Johnson, C. Herring, D.J. Chadi, Phys. Rev. Lett. 56 (1986) 769.
- [8] C.H. Park, D.J. Chadi, Phys. Rev. B 55 (1997) 12,995.
- [9] J.L.P. Castineira, J.R. Leite, J.L.F. da Silva, L.M.R. Scolfaro, J.L.A. Alves, H.W.L. Alves, Phys. Stat. Sol. B 210 (1998) 401.
- [10] S.K. Estreicher, C.H. Chu, D.S. Marynick, Phys. Rev. B 40 (1989) 5739.
- [11] J. Widany, M. Sterberg, Th. Frauenheim, Solid State Commun. 102 (1997) 451.
- [12] P.R. Briddon, R. Jones, Phys. Stat. Sol. B 217 (2000) 131.
- [13] J. Coutinho, R. Jones, S. Öberg, P.R. Briddon, Phys. Rev. B 62 (2000) 10824.
- [14] H.J. Monkhorst, J.D. Pack, Phys. Rev. B 13 (1976) 5188.
- [15] F. Birch, J. Geophys. Res. 57 (1952) 227.
- [16] W.R.L. Lambrecht, B. Segall, General remarks and notations on the band structure of pure Group III nitrides, in: J.H. Edgar (Ed.), Properties of Group III Nitrides, Institution of Electrical Engineers, 1994, p. 125.
- [17] M.J.P. Musgrave, J.A. Pople, Proc. R. Soc. London, Ser. A 268 (1962) 474.
- [18] J.A. Sanjurjo, E. Lpez-Cruz, P. Vogl, M. Cardona, Phys. Rev. B 83 (1983) 4579.
- [19] A. Bosin, V. Fiorentini, D. Vanderbilt, Mater. Res. Soc. Symp. Proc. 395 (1997) 503.
- [20] J. Neugebauer, C.G. Van de Walle, Phys. Rev. Lett. 75 (1995) 4452.
- [21] V.J.B. Torres, S. Öberg, R. Jones, MRS Internet J. Nitride Sem. Res. 2 (1997) 35.



ELSEVIER

Physica B 308–310 (2001) 1031–1034

PHYSICA B

www.elsevier.com/locate/physb

Influence of substitution of P by As on exciton and biexciton states in $\text{Zn}(\text{P}_{1-x}\text{As}_x)_2$ crystals

O.A. Yeshchenko*, M.M. Biliy, Z.Z. Yanchuk

Physics Faculty, Kyiv Taras Shevchenko University, 6 Akademik Glushkov prosp., 03127 Kyiv, Ukraine

Abstract

Low-temperature (1.8 K) excitonic absorption, reflection and photoluminescence spectra of mixed $\text{Zn}(\text{P}_{1-x}\text{As}_x)_2$ crystals have been studied at $x = 0.01, 0.02, 0.03$ and 0.05 . Energy gap and rydbergs of excitonic B, C and A-series decrease monotonically with the increase of x . Spectral half-widths of absorption $n = 1$ lines of B and A-series increase monotonically with the increase of x due to fluctuations of crystal potential. Emission lines of excitonic molecules have been observed in photoluminescence spectra of $\text{Zn}(\text{P}_{1-x}\text{As}_x)_2$ crystals. Binding energy of molecule increases with the increase of x due to the decrease of the electron-hole mass ratio. © 2001 Elsevier Science B.V. All rights reserved.

Keywords: Optical spectroscopy; Substitution of atoms; Energy gap variation; Exciton and biexciton binding energy variation

1. Introduction

$\beta\text{-ZnP}_2$ (further ZnP_2) and ZnAs_2 crystals are direct-gap semiconductors, which are characterized by the same symmetry group C_{2h}^5 . Besides symmetry of lattice, the similarity of ZnP_2 and ZnAs_2 exists in the structure of energy bands and exciton states as well. Namely, three excitonic series are observed in the absorption spectra of these crystals: dipole allowed C-series at $\mathbf{E} \parallel \mathbf{Z}(\mathbf{c})$ (C-exciton), forbidden B-series at $\mathbf{E} \perp \mathbf{Z}(\mathbf{c})$ (B-exciton) and partially allowed A-series at $\mathbf{E} \parallel \mathbf{X}$ (A-exciton) polarizations (see e.g. Refs. [1,2] for ZnP_2 and Refs. [3,4] for ZnAs_2). In the photoluminescence (PL) spectra of these crystals at $\mathbf{E} \parallel \mathbf{Z}(\mathbf{c})$ polarization, a series of lines caused by the radiative transitions from the ground $n = 1$ and excited $n = 2, 3$ states of allowed S-paraexciton (C-series) is observed (see e.g. Ref. [2] for $\beta\text{-ZnP}_2$ and Ref. [4] for ZnAs_2). Besides this emission series, the so-called B-line is observed in the PL spectra of ZnP_2 at $\mathbf{E} \perp \mathbf{Z}(\mathbf{c})$. The B-line occurs to the radiative transitions from the ground state of forbidden S-orthoexciton and corresponds to B_1 -line of absorption B-series.

In ZnP_2 crystals excitonic molecule (EM or biexciton) with rather high binding energy $E_{\text{bex}}^b = 6.7 \text{ meV} = 0.15 E_{\text{ex}}^b$ exists, where E_{ex}^b is the binding energy of the lowest-energy B-exciton. In ZnP_2 EMs manifest themselves in PL spectra due to two-electron and two-photon radiative transitions from the ground state of the molecule [5]. The experimental evidences of existence of the EMs in ZnAs_2 are absent at present, though by theoretical estimations they would have binding energy $\approx 1.6 \text{ meV}$.

In present work we study the mixed crystals (solid solutions) of isovalent substitution $\text{Zn}(\text{P}_{1-x}\text{As}_x)_2$, which, to our knowledge, were not studied earlier. In present work the low-temperature (1.8 K) optical spectra of $\text{Zn}(\text{P}_{1-x}\text{As}_x)_2$ crystals have been studied at small levels of substitution of P by As: $x \leq 0.05$. Experimental dependences of parameters of excitons and EMs on x were obtained.

2. Exciton spectra of $\text{Zn}(\text{P}_{1-x}\text{As}_x)_2$ crystals

Absorption, reflection and luminescence spectra of $\text{Zn}(\text{P}_{1-x}\text{As}_x)_2$ crystals at $x = 0.01, 0.02, 0.03$ and 0.05 and pure ZnP_2 ($x = 0$) are presented in Figs. 1–3. The $\text{Zn}(\text{P}_{1-x}\text{As}_x)_2$ crystals are direct-gap semiconductors as

*Corresponding author. Tel.: +380-44-266-4587; fax: +380-44-266-4036.

E-mail address: yes@mail.univ.kiev.ua (O.A. Yeshchenko).

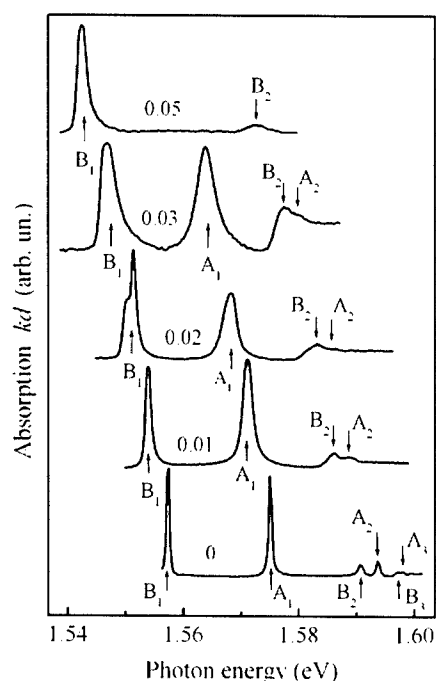


Fig. 1. Absorption spectra of $\text{Zn}(\text{P}_{1-x}\text{As}_x)_2$ crystals at temperature 1.8 K. Observation conditions: $\mathbf{q} \perp (110)$, $\mathbf{E} \perp \mathbf{Z}(\mathbf{c})$ —for crystals with $x = 0, 0.01, 0.02$ and 0.03 ; $\mathbf{q} \perp (100)$, $\mathbf{E} \perp \mathbf{Z}(\mathbf{c})$ —for crystals with $x = 0.05$.

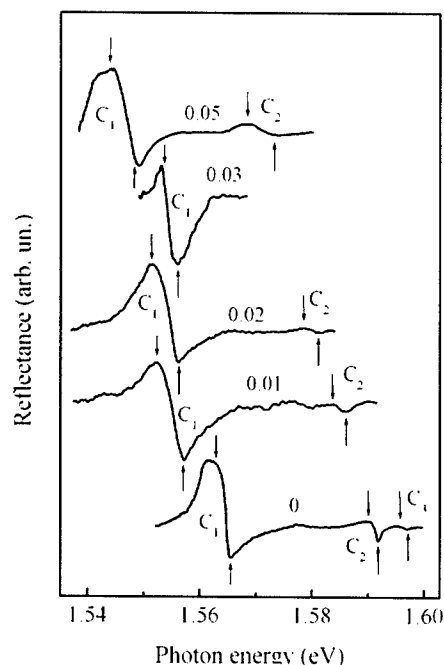


Fig. 2. Reflection spectra of $\text{Zn}(\text{P}_{1-x}\text{As}_x)_2$ crystals at temperature 1.8 K. Observation conditions: $\mathbf{q} \perp (100)$, $\mathbf{E} \parallel \mathbf{Z}(\mathbf{c})$.

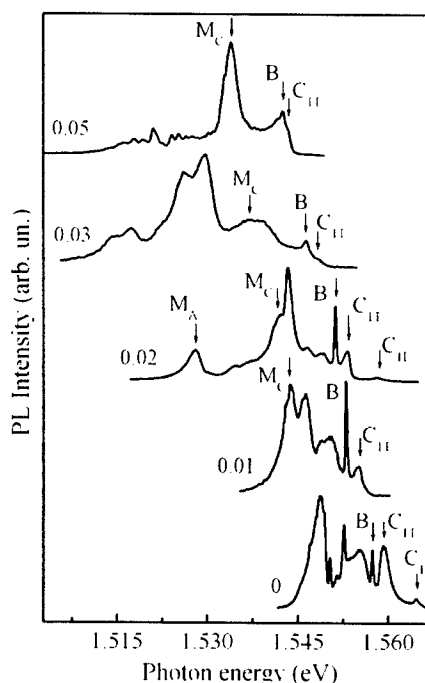


Fig. 3. Photoluminescence spectra of $\text{Zn}(\text{P}_{1-x}\text{As}_x)_2$ crystals at temperature 1.8 K.

well as ZnP_2 . One can see from the figures that in the mixed crystals the same excitonic C, B and A-series are observed, as in pure ZnP_2 . Let's note, that in contrast to ZnP_2 crystals, where in optical spectra the lines up to $n = 7$ for B-series and to $n = 4$ for A and C-series are observed, in spectra of $\text{Zn}(\text{P}_{1-x}\text{As}_x)_2$ crystals of various thickness excitonic lines only with $n = 1, 2$ are observed. Probably, this fact is a result of "blurring" of band edges, which takes place owing to fluctuations of crystal potential and respective fluctuations of energy gap, caused by the statistical distribution of As atoms at P lattice sites. With the increase of concentration x the spectral lines shift to the low-energy side, a behaviour that is caused by decrease of energy gap (see Table 1). This shift could be expected, taking into account the fact, that in ZnAs_2 the energy gap is 0.55 eV smaller than in ZnP_2 . But besides the trivial decrease of E_g at increase of x , there is also decrease of the of excitonic series rydbergs (see Table 1). Values of E_g and rydbergs were obtained by fitting of excitonic series by simple hydrogenlike dependence: $E(n) = E_g - R_Y/n^2$.

Dependences of the half-widths of absorption $n = 1$ lines of B and A-series were also studied (see Table 1). It is seen, that half-widths of B_1 and A_1 -lines increase monotonously with the increase of x . It is known that the increase of the half-width of exciton lines is the result of fluctuations of crystal potential and respective

Table 1
Dependences of the energy gap, exciton and biexciton parameters of $\text{Zn}(\text{P}_{1-x}\text{As}_x)_2$ crystals on x

x	E_g (eV)	ΔE_g (%)	Ry_B (meV)	Ry_C (meV)	Ry_A (meV)	W_{B_1} (meV)	D_{B_1} (meV)	W_{A_1} (meV)	D_{A_1} (meV)	E_{bex}^b (meV)	$E_{\text{bex}}^b/E_{\text{ex}}^b$	$m_c(x)/m_c(0)$ (calculated)	$m_h(x)/m_h(0)$ (calculated)
0	1.6026	0	44.0	39.6	26.5	0.83	0	1.02	0	6.7	0.15	1	1
0.01	1.5957	1.3	41.7	37.7	24.8	1.01	0.18	1.84	0.82	6.8	0.16	0.94	1.09
0.02	1.5913	2.1	39.5	36.2	22.8	1.12	0.29	2.33	1.31	6.9	0.17	0.89	1.18
0.03	1.5865	2.9	39.2	—	22.8	—	—	—	—	7.1	0.18	0.87	1.41
0.05	1.5801	4.1	37.4	33.2	—	1.61	0.78	—	—	7.8	0.21	0.82	1.93

fluctuations of E_g . The theory of the influence of fluctuations of composition x on half-width of exciton absorption lines was developed in Ref. [6], where two extreme cases were considered. If the effective size of the crystal potential fluctuation $R_D = \hbar/(2MD)^{1/2}$, where M is the total mass of exciton and $D(x) = W(x) - W(0)$ ($W(x)$ is the half-width of exciton line), is much larger than exciton Bohr radius $R_D \gg a_{\text{ex}}$ then

$$D(x) = 0.08 \frac{\alpha^4 M^3 x^2 (1-x)^2}{\hbar^6 N^2}, \quad (1)$$

where $\alpha = dE_g/dx$, N is the concentration of sites of lattice, where the substituting atoms can "sit". If $R_D \ll a_{\text{ex}}$ then

$$D(x) = 0.5\alpha \left(\frac{x(1-x)}{Na_{\text{ex}}^3} \right)^{1/2}. \quad (2)$$

The experimental dependences $D(x)$ of absorption B_1 and A_1 -lines in $\text{Zn}(\text{P}_{1-x}\text{As}_x)_2$ crystals were fitted by functions (1) and (2). The experimental points are badly fitted both by an expression (1) and (2). Let us estimate the effective size of the crystal potential fluctuation R_D for different x in $\text{Zn}(\text{P}_{1-x}\text{As}_x)_2$ crystals. Estimations give: $R_D = 82 \text{ \AA}$ at $x = 0.01$, $R_D = 62 \text{ \AA}$ at $x = 0.02$ and $R_D = 30 \text{ \AA}$ at $x = 0.05$. In ZnP_2 the exciton Bohr radius is $a_{\text{ex}} = 15 \text{ \AA}$ (for B and C-excitons). Thus, for $\text{Zn}(\text{P}_{1-x}\text{As}_x)_2$: $R_D \sim a_{\text{ex}}$, i.e. both conditions $R_D \gg a_{\text{ex}}$ and $R_D \ll a_{\text{ex}}$ are not fulfilled. So, in studied crystals the intermediate case takes place which is, nevertheless, more close to (1) as $R_D > a_{\text{ex}}$. Therefore, since the intermediate case takes place, we tried to fit the experimental dependences by the function: $D(x) = (1-c)D_1(x) + cD_2(x)$, which is the superposition of functions $D_1(x)$ of type (1) and $D_2(x)$ of type (2), c is the weighting factor. We have obtained that the superposition function fits the experimental points very well. The fitting of dependences of the half-widths of absorption $n = 1$ lines of B and A-series on x gives: $c_B = 0.05$, $c_A = 0.32$. The fact, that c_A is considerably larger than c_B , indicates that for A_1 -line the function $D_2(x)$ of type (2) makes a considerably larger contribution, than for B_1 -line. It could be expected since the A-exciton has a considerably smaller binding energy than the B-exciton, and correspondingly larger Bohr radius. Thus,

B-exciton is closer to the case 1 ($R_D \gg a_{\text{ex}}$) than A-exciton.

3. Excitonic molecules in $\text{Zn}(\text{P}_{1-x}\text{As}_x)_2$ crystals

In PL spectra of mixed $\text{Zn}(\text{P}_{1-x}\text{As}_x)_2$ crystals, as well as in ZnP_2 crystals, there are M_C and M_A lines (Fig. 3). These lines are due to radiative transitions from the ground state of EM to the ground state of the C-exciton (M_C -line) and ground state of A-exciton (M_A -line). EMs are rather well investigated in pure ZnP_2 . As well as in pure ZnP_2 , the M-lines demonstrate a square-law character of the dependence of their intensity on excitation intensity, which confirms their biexcitonic nature. The binding energy of EM can be determined from PL spectrum as: $E_{\text{bex}}^b = 2E_{\text{ex}} - E_{C1} - \hbar\omega_{M_C}$, where E_{ex} is the energy of lowest B-exciton ground state (B_1 -line), E_{C1} is the energy of the ground state of allowed C-exciton, and $\hbar\omega_{M_C}$ is the energy of a photon of M_C -line. Contrary to rydbergs of excitonic series the binding energy of EM increases with the increase of x both by absolute value and in relation to the binding energy of the lowest B-exciton. The behaviour of E_{bex}^b with the increase of x can be explained as follows. As known (e.g. from Ref. [7]), the ratio $E_{\text{bex}}^b/E_{\text{ex}}^b$ is a function of the ratio of electron and hole masses $\sigma = m_e/m_h$, and with the decrease of σ the ratio of binding energies of EM and exciton increases. At substitution of atoms of one type by atoms of another type the variation of parameters of energy band structure occurs, in particular the variation of masses of carriers. Since the dielectric constant has close values in ZnP_2 and ZnAs_2 crystals, ϵ should not vary considerably in mixed crystals. Therefore, the decrease of exciton rydbergs with the increase of x is an evidence of the decrease of reduced effective mass of carriers μ . The reduced mass at small σ is $\mu \approx m_e$. Since in ZnP_2 crystals the ratio of electron and hole masses is rather small ($\sigma = 0.06$), the decrease of $\mu(x)$ reflects the decrease of $m_e(x)$. The dependence $m_h(x)$ can be estimated in such a way. Knowing the ratio of the reduced masses $\mu(x)/\mu(0) = Ry(x)/Ry(0)$ and the ratio $\sigma(x)/\sigma(0)$ (it can be obtained from the experimental dependence $[E_{\text{bex}}^b/E_{\text{ex}}^b](x)$), one can calculate the ratios

$m_e(x)/m_e(0)$ and $m_h(x)/m_h(0)$ (see Table 1). With the increase of x the electron mass decreases, and the hole mass increases. Thus, the increase of m_h occurs even faster than the decrease of m_e . This behaviour reflects the fact that in ZnP_2 conduction band originate mainly from Zn ions and valence band—from P ions [8]. Therefore, substitution of P atoms by As atoms should first of all have an influence on parameters of a valence band, in particular on hole mass. The simultaneous decrease of m_e and increase of m_h result in appreciable decrease of their ratio, and therefore in the respective increase of binding energy of EM.

References

- [1] I.S. Gorban, M.M. Biliy, I.M. Dmitruk, O.A. Yeshchenko, *Phys. Stat. Sol. (B)* 207 (1998) 171.
- [2] I.S. Gorban, M.M. Biliy, V.A. Borbat, V.O. Gubanov, I.M. Dmitruk, Z.Z. Yanchuk, *Dopov. Akad. Nauk. Ukr. RSR Ser. A* 4 (1988) 48.
- [3] M.M. Biliy, I.S. Gorban, I.M. Dmitruk, O.A. Yeshchenko, Z.Z. Yanchuk, *Ukr. Fiz. Zh.* 44 (1999) 863.
- [4] V.A. Morozova, V.S. Vavilov, S.F. Marenkin, O.G. Koshelev, M.V. Chukichev, *Fiz. Tverd. Tela* 40 (1998) 877.
- [5] I.S. Gorban, I.M. Dmitruk, O.A. Yeshchenko, *Solid State Commun.* 98 (1996) 941.
- [6] N.N. Ablyazov, M.E. Raikh, A.L. Efros, *Fiz. Tverd. Tela* 25 (1983) 353.
- [7] O. Akimoto, E. Hanamura, *J. Phys. Soc. Japan* 33 (1972) 1537.
- [8] E.P. Domashevskaya, V.A. Terekhov, Ya.I. Ugay, V.I. Nefedov, N.P. Sergushin, G.N. Dolenko, *Fiz. Tverd. Tela* 19 (1977) 3610.



ELSEVIER

Physica B 308–310 (2001) 1035–1037

PHYSICA B

www.elsevier.com/locate/physb

DX center gratings in real-time holography

S.A. Kazanskii^a, A.I. Ryskin^{a,*}, A.S. Scheulin^a, R.A. Linke^b, A.E. Angervaks^a^a*S.I. Vavilov State Optical Institute, 12 Birghevaya Line, St. Petersburg 199034, Russia*^b*NEC Research Institute, Inc. 4 Independence Way, Princeton, NJ 08540, USA*

Abstract

CdF₂ crystals doped with Ga or In are the most promising representative of new class of holographic materials, in which a photo-induced change in the density of bistable (DX center) states in a semiconductor crystal produces a local change of its refractive index. Mechanism of holographic gratings decay is considered. Analysis of the decay kinetics shows opportunities of CdF₂:Ga, CdF₂:In as materials of real-time holography with response times in the range of seconds to 1 ms in CdF₂:Ga or to 100 ns or less in CdF₂:In. © 2001 Elsevier Science B.V. All rights reserved.

Keywords: Holographic grating; Diffraction efficiency; Barrier

1. Introduction

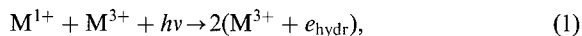
Recently, a new class of holographic materials was proposed, in which a photo-induced change in the density of bistable (DX center) states in a semiconductor crystal produces a local change of its refractive index. (see Ref. [1] and references therein). The excited (“shallow” donor) state of the DX center has a metastable nature being separated from the ground (“deep”) state by a potential barrier due to a strong lattice relaxation in the latter state. Therefore, photo-induced gratings in such crystals are principally dynamic ones. Here, we consider two most promising representatives of this class of materials, CdF₂:Ga and CdF₂:In, having the highest barrier ~1 eV among crystals of this class and very low barrier ~0.1 eV, respectively [2].

Conversion of doped CdF₂ into semiconducting state is realized through an annealing of as grown crystals in reduction atmosphere of Cd vapor (a process called additive coloration), upon which procedure electrons introduced into the crystal locate at the donor levels or in the conduction band.

Together with donor ions, semiconducting CdF₂ crystals contain interstitial fluorine ions, F⁻, which play a function of acceptors in these ionic crystals; they

effectively decrease the concentration of donors, i.e. partly compensate them [3].

At sufficiently low *T*, below 200 K for CdF₂:Ga and 40 K for CdF₂:In, all electrons are associated with M ions (M = Ga, In), in pairs, forming the deep M centers (M¹⁺) [2]. The photo-induced conversion of bistable M centers from the ground state into the metastable donor state (M³⁺ + *e*_{hydr}, where *e*_{hydr} denotes an electron localized at the hydrogenic orbital), in accordance with the reaction



results in a noticeable change of the refractive index of the crystal, δn . This change creates the opportunity of writing phase holograms in the spectral gap between the photo-ionization absorption bands of the deep and shallow centers; these bands are located in the ultraviolet–visible (UV–VIS) and infrared (IR) ranges of the spectrum, respectively (Fig. 1). The refractive index change results from the transition of tightly bound electrons of the deep centers into the loosely bound hydrogenic or free state. Accordingly, δn is proportional to the shallow donor concentration, N_{sh}^0 [4].

2. Samples, details of experiment, and discussion of results

Techniques of growing the crystals and their conversion into a semiconducting state is described elsewhere [4,5].

*Corresponding author. Fax: +7-812-328-3720.

E-mail address: alex@ryskin.spb.su (A.I. Ryskin).

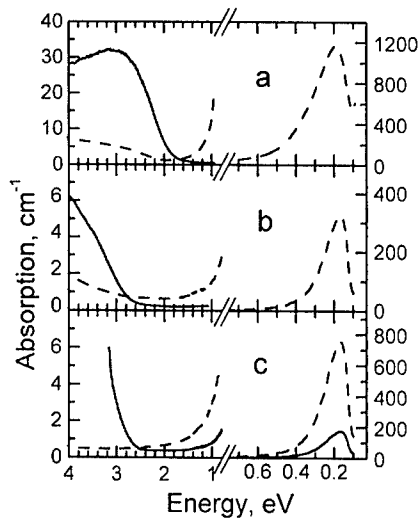
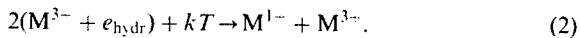


Fig. 1. Absorption spectra of (a) CdF₂:In, (b) CdF₂:Ga, and (c) CdF₂:Ga,Y crystals cooled in the dark (solid line) and after UV-VIS illumination (dashed line) at temperature (a) 5 and (b, c) 77 K.

Along with singly doped CdF₂:Ga, crystals of CdF₂:Ga co-doped with Y were also studied. Co-doping increases the concentration of the optically active Ga and, simultaneously, significantly improves the optical quality of the crystal [5]. Fig. 1 shows the spectra of additively colored CdF₂:Ga, CdF₂:Ga,Y, at $T = 77$ K and CdF₂:In crystals at $T = 5$ K as cooled in the dark and after a strong illumination in the UV-VIS band.

The concentration of electrically and optically active impurity, N_M , in CdF₂:Ga, CdF₂:Ga,Y, and CdF₂:In crystals under investigation was 0.7×10^{18} , 1.7×10^{18} , and $2.7 \times 10^{18} \text{ cm}^{-3}$, respectively.

At $T > 200$ K for CdF₂:Ga and $T > 40$ K for CdF₂:In, the written hologram decays due to conversion of the photo-induced shallow centers in the antinodes of the grating into the deep centers:



This reaction includes the thermal release of an electron from the shallow donor center into the conduction band, its transport in the conduction band, and its capture by another shallow center with the subsequent formation of a deep center. The last stage also requires thermal activation due to the large lattice relaxation accompanying the deep center formation.

The rate equation, which describes the change with time of the shallow donor center concentration and includes the processes of thermal destruction (Eq. (2)) and formation as well as photo-induced formation

(Eq. (1)) of these centers, may be written as

$$\begin{aligned} dN_{\text{sh}}^0/dt = & -[c - (b/4)](N_{\text{sh}}^0)^2 - (b/2)N_M N_{\text{sh}}^0 \\ & + (b/4)(N_M^2 - N_F^2) + I\mu\sigma N_d^-. \end{aligned} \quad (3)$$

Here, c and b are kinetics constants of the shallow center thermal destruction and creation, respectively. N_d^- and N_F are concentration of the deep M centers and interstitial fluorine ions, respectively. I is the light intensity, and σ is the cross-section of photon absorption by the deep centers. Eq. (3) allows one to find, for finite T , the shallow center concentration in the dark ($I = 0$) or under illumination of the crystal, and the transient patterns.

Without specifying the details of the multi-stage processes of thermal destruction of the shallow (Eq. (2)) and deep centers, one may propose that these processes have a thermally activated nature, i.e. they are characterized by activation energies, $E_{\text{bar}}^{\text{sh}}$, $E_{\text{bar}}^{\text{d}}$:

$$c(T) = v_1 \exp(-E_{\text{bar}}^{\text{sh}}/kT),$$

$$b(T) = v_2 \exp(-E_{\text{bar}}^{\text{d}}/kT), \quad (4)$$

where v_1 , v_2 are frequency factors. $E_{\text{bar}}^{\text{sh}}$ and $E_{\text{bar}}^{\text{d}}$ may be considered as effective heights of the barriers separating the shallow state from the deep state and vice versa.

This pattern of the shallow center decay has the following appearance:

$$N_{\text{sh}}^0(t) = n_2 + (n_2 - n_1)/\{\exp[(t + t_0)/\tau] - 1\}. \quad (5)$$

Here, t_0 is an integration constant, $\tau = 1/[(c - b/4) \times (n_2 - n_1)]$ is a parameter which describes the rate of decay, and n_1 , n_2 are roots of the right-hand side of Eq. (3) (see Ref. [5]). The n_2 root is equal to the equilibrium concentration of the shallow donor centers in the dark. It is shown in Ref. [2] that at $N_{\text{sh}}^0 \ll N_M$ $b \ll c$, i.e.

$$\tau \cong 1/[c(n_2 - n_1)]. \quad (6)$$

Analysis of decay curves using Eq. (5) allows one to find the parameters n_2 , $(n_2 - n_1)$, and τ . Under the assumption that $N_F < N_M$ τ can be expressed as follows:

$$\tau \cong 1/(N_M \sqrt{cb}). \quad (7)$$

It is evident from Eq. (7) that an Arrhenius plot for τ allows one to find the quantity $\frac{1}{2}(E_{\text{bar}}^{\text{sh}} + E_{\text{bar}}^{\text{d}})$. Eq. (6) has a smaller temperature range of applicability as compared with Eq. (7). A criterion for its use is a weak dependence of n_2 on T , indicating a low rate of thermal decay of the deep center.

Thus, the shallow center decay is described by the hyperbolic cotangent type dependence of Eq. (5). This dependence converts to a simple exponential for $(t + t_0) \gg \tau$, and this inequality is satisfied either at the final stages of the decay (large t), or at higher temperatures (large n_2 , i.e. small τ).

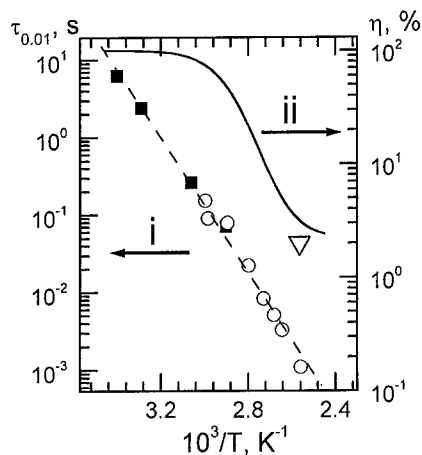


Fig. 2. Temperature dependence of (i) decay time of photo-induced IR absorption ($\lambda = 1.3 \mu m$, black squares) and holographic gratings written in $CdF_2:Ga,Y$ (square root of DE, open circles); the dashed line is the result of a calculation using Eq. (5) and (ii) initial DE of the hologram; the solid line shows the calculation (see [6]), the open triangle shows the experimental value.

Two techniques were used for the experimental study of the decay problem: (i) measurement of the photo-induced IR absorption, which is a direct measure of N_{sh}^0 , and (ii) measurement of the diffraction efficiency (DE), η , of gratings written in the crystal; the square root of this quantity is proportional to N_{sh}^0 for moderate values of $\eta \leq 0.7$ [4,5].

For absorption measurements, the crystals were mounted in a variable temperature cryostat and its transmissivity at $\lambda = 1.3$ or $1.5 \mu m$ was measured as a function of time following a saturating exposure. For DE measurements, gratings were written into the sample using two interfering beams (argon laser, $\lambda = 476$ nm for $CdF_2:Ga$, $CdF_2:Ga,Y$ and ruby laser, $\lambda = 693$ nm for $CdF_2:In$) and the DE was determined versus time by comparing the strengths of the transmitted and diffracted beams using as a probe an attenuated 476 nm beam ($CdF_2:Ga$, $CdF_2:Ga,Y$) or beam of helium–neon laser, $\lambda = 632.8$ nm ($CdF_2:In$). Figs. 2 and 3 show temperature dependencies of decay time corresponding to decrease of DE down to 0.01 of the initial value and of initial DE of holograms written in $CdF_2:Ga,Y$ and $CdF_2:In$. Decay patterns are described finely by Eq. (5). Analysis of these patterns with use of Eqs. (5)–(7) allows one to find the barrier height on the side of the shallow and deep centers as follows: $CdF_2:Ga$ — $E_{bar}^{sh} = 0.95$ eV, $E_{bar}^d = 0.73$ eV; $CdF_2:In$ — $E_{bar}^{sh} = 0.14$ eV, $E_{bar}^d = 0.25$ eV. Therefore, (i) the shallow-to-deep center conversion (Eq. (2)) proceeds with an overcoming of very high barrier for $CdF_2:Ga$ and low barrier for $CdF_2:In$ and (ii) for both Ga and In an activation energy of the deep-to-shallow center conversion practically coincides with a binding energy of the deep center, which is 0.70 eV for $CdF_2:Ga$ and

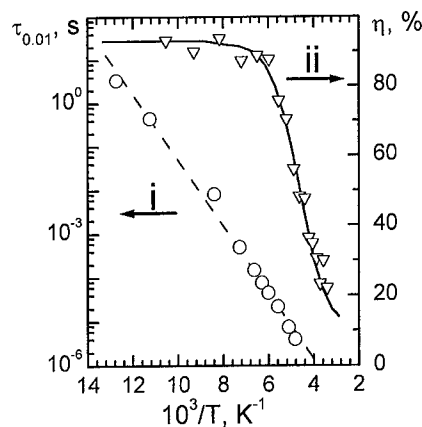


Fig. 3. Temperature dependence of (i) decay time of holographic gratings written in $CdF_2:In$ (square root of DE, open circles); the dashed line is the result of a calculation using Eq. (5) and (ii) initial DE of the hologram; the open triangles are experimental values, the solid line shows a trend.

0.25 eV for $CdF_2:In$ [6]. The latter statement means that after thermal ionization of the deep center, reconstruction of the ionized center into the shallow center proceeds spontaneously.

3. Conclusions

The metastable nature of the photo-induced state of the Ga and In centers in CdF_2 crystals allows the application of these crystals as materials for real-time holography over a wide range of response times of seconds to 100 ns or less, with temperature as the controlling parameter.

Acknowledgements

This work was supported by CRDF under the grant RP1-2096 and RFFI under the Grant # 99-02-17871.

References

- [1] R.A. Linke, I. Redmond, T. Thio, D.J. Chadi, J. Appl. Phys. 83 (1998) 661.
- [2] A.S. Shcheulin, A.I. Ryskin, K. Swiatek, J.M. Langer, Phys. Lett. A 222 (1996) 107.
- [3] S.A. Kazanskii, D.S. Rumyantsev, A.I. Ryskin, unpublished.
- [4] A.I. Ryskin, A.S. Shcheulin, E.V. Miloglyadov, R.A. Linke, I. Redmond, I.I. Buchinskaya, P.P. Fedorov, B.P. Sobolev, J. Appl. Phys. 83 (1998) 2215.
- [5] R.A. Linke, A.S. Shcheulin, A.I. Ryskin, I.I. Buchinskaya, P.P. Fedorov, B.P. Sobolev, Appl. Phys. (Lasers and Optics) B 72 (2001) 677.
- [6] C.H. Park, D.J. Chadi, Phys. Rev. Lett. 82 (1999) 113.



ELSEVIER

Physica B 308–310 (2001) 1038–1041

PHYSICA B

www.elsevier.com/locate/physb

Dielectric response of semiconducting and photochromic CdF_2 on microwaves

S.A. Kazanskii*, D.S. Romyantsev, A.I. Ryskin

S.I. Vavilov State Optical Institute, 12 Birghevaya Line, St-Petersburg 199034, Russia

Abstract

CdF_2 is the only highly ionic dielectric crystal, which can be converted into n-type semiconductor via doping with column-III elements and annealing in the reduction atmosphere. Among donor impurities, Ga and In dopants form DX centers with the shallow metastable state and ground strongly localized state, making these crystals photochromic. We studied the dielectric permittivity, $\epsilon = \epsilon_1 - i\epsilon_2$, of $\text{CdF}_2:\text{Ga}$, $\text{CdF}_2:\text{In}$, and also non-photochromic $\text{CdF}_2:\text{Y}$ in the microwave range ($\lambda \approx 8\text{ mm}$) at low temperatures (T) down to 1.8 K in the darkness and after illumination by the ultraviolet-visible light. Illumination of $\text{CdF}_2:\text{Ga}$ and $\text{CdF}_2:\text{In}$ results in increase of both the dielectric constant, ϵ_1 , by $\Delta\epsilon_1 = (0.5-1.4)$ and the dielectric loss factor, ϵ_2 , by about an order of magnitude. At $T = 1.8\text{ K}$ the low-field dielectric loss factor in these crystals and also in $\text{CdF}_2:\text{Y}$, $\epsilon_2 = 0.1-0.3$, may be decreased by an order of magnitude with increase of the microwave field power; however, ϵ_2 ceases to depend on the field at $T > 4\text{ K}$. These features are explained on the basis of Tanaka theory of resonant saturated absorption of ionized donor pairs, modified here to cover also far infrared range of spectrum. The study shows, that maximum available concentration of neutral donors in CdF_2 could never exceed $\sim 10^{19}\text{ cm}^{-3}$ and the compensation degree be less than 0.5 at any doping level because of the existence of impurity clusters. These clusters store an “excessive” impurity and are “inexhaustible” sources of interstitial F^- ions. © 2001 Elsevier Science B.V. All rights reserved.

Keywords: Semiconductors; Permittivity; Conductivity; Photochromy

1. Introduction

CdF_2 is the fluorite-type crystal that can be converted into a semiconducting state via doping with column-III elements of the periodic table and subsequent annealing in reducing atmosphere [1,2]. During the coloration process interstitial fluorine ions F^- , which are charge compensators of the surplus $+1$ charge of the dopants, diffuse out of the volume of the crystal to the surface. An opposite current of electrons into its volume maintains charge neutrality of the crystal. These electrons localize in the conduction band or at hydrogenic donor orbitals centered on the dopant. The donor state in CdF_2 has a binding energy of $\sim 100\text{ meV}$, and it is responsible for infrared (IR) photo-ionization absorption band

($\lambda_{\text{max}} \approx 7\text{ }\mu\text{m}$), which stretches into the visible range of the spectrum [3,4]. The room-temperature electronic conductivity of additively colored CdF_2 crystals reaches $10\text{ }\Omega^{-1}\text{ cm}^{-1}$. However, the maximum available concentration of free electrons does not exceed $\sim 10^{19}\text{ cm}^{-3}$ [1–3].

Among donor impurities in CdF_2 , Ga and In play a special part since these dopants form bistable centers in the reduced (semiconducting) crystals. Along with the “shallow” hydrogenic state, they also have a “deep”, strongly localized two-electron state characterized by large lattice relaxation [5]. Such large lattice relaxation is typical for two-electron metastable centers (DX-centers) in conventional semiconductors; it is responsible for the energy barrier separating the deep state from the metastable substitutional (shallow donor) state. The barrier height is $\sim 1\text{ eV}$ for Ga and less than 0.1 eV for In [6].

*Corresponding author. Fax: +7-812-328-3720.

E-mail address: kazanski@sk7936.spb.edu (S.A. Kazanskii).

Table 1
Dielectric permittivity of semiconducting CdF₂ crystals studied with $\lambda \approx 8$ mm low-field microwaves at $T = 1.8$ K

Sample	Total electron concentration, N_e (cm ⁻³)	ϵ_1 in the dark	$\Delta\epsilon_1$ after illumination	ϵ_2	
				In the dark	After illumination
CdF ₂ :Ga	7×10^{17}	7.6 ± 0.1	0.5 ± 0.1	0.01 ± 0.005	0.1 ± 0.05
CdF ₂ :In	3×10^{18}	—	1.4 ± 0.4	0.02 ± 0.01	0.1 ± 0.05
CdF ₂ :Y	2×10^{18}	—	—	0.3 ± 0.1	

When cooled in the dark, the reduced CdF₂:Ga and CdF₂:In crystals are semi-insulating since electrons introduced in the crystals during the coloration are predominantly localized at the deep M¹⁺ centers (M=Ga, In). Illumination of the crystals in the ultra-violet-visible (UV-VIS) photo-ionization absorption band of deep centers results in release of the electron into the conduction band with its subsequent capture by an ionized (“empty”) center with formation of a neutral (shallow) donor. An ionized deep center also spontaneously converts into the shallow state. As a result of this “photo-decoloration process”, the UV-VIS band disappears and, instead, an IR band arises in the absorption spectrum of the crystals.

In this work we study the low-temperature complex permittivity of semiconducting CdF₂:Ga, CdF₂:In, and CdF₂:Y crystals in the microwave range ($\lambda \approx 8$ mm) and discuss an important role of the ionized donor pairs in formation of the dielectric response of these crystals in the microwave and far IR (FIR) ranges.

2. Samples, experimental technique, and results of measurements

Microwave measurements of the real, ϵ_1 , and imaginary, ϵ_2 , parts of the dielectric permittivity of CdF₂:In, CdF₂:Ga, and CdF₂:Y crystals over the frequency range of 34.0–37.5 GHz at temperatures 1.8–100 K were made with cylindrical samples of diameter 2.0–2.5 mm set in a cylindrical reflex resonator operating in TE₀₁₁ mode. The cavity perturbation technique used in the experiments is based on measurements of both the loaded quality factor and the frequency shift of the cavity occurring when a sample is inserted into the resonator.

Measurements were made both in the dark and after illumination of the samples with the UV-VIS light. Microwave dielectric properties of CdF₂:Y are independent of its illumination. In contrast, substantial increase of complex permittivity was detected during the process of illumination of photochromic CdF₂:Ga and CdF₂:In crystals. The dielectric permittivity of the samples under consideration at low microwave fields

and the extreme changes observed after illumination at $T = 1.8$ K are shown in Table 1.

At $T = 1.8$ K, a saturation of the dielectric losses with an increase in microwave power was observed for all semiconducting samples studied. The measured value of ϵ_2 could be decreased by about an order of magnitude with an increase of the input microwave power from the minimum level. Experimental $\epsilon_2(T)$ dependences for CdF₂:Ga are shown in Fig. 1.

3. Discussion of results

We assume that all observed phenomena are due to resonant absorption of the nearest pairs of neutral and ionized donors that are called the “ionized donor pairs” [7].

Provided that the nearest-neighbors donors are identical, the single electron of the ionized donor pair has an equal probability to be found at each of these donor centers. The situation is analogous to that for the molecular H₂⁺ ion. The doubly degenerate ground state of such a system splits to lower bonding and excited anti-bonding states separated by an energy interval W depending on the distance r_0 between the donors of the pair. The transitions between these two states are observed in the microwave and FIR absorption experiments. Based on the approach of Tanaka et al. [7], we propose [8] simple analytical expressions for the microwave and FIR absorption coefficient for the intermediate-compensation case over the frequency range in which the donor-pair theory is applicable.

Photo-decolored CdF₂:Ga and CdF₂:In crystals as well as CdF₂:Y may be considered as ordinary n-type semiconductors with donors partly compensated by the interstitial F⁻ ions. The experimental values of ϵ_2 in low microwave fields at $T = 1.8$ K (see Table 1), agree by an order of magnitude with this quantity calculated under condition of moderate compensation degree $0.1 \leq K \leq 0.9$ and reasonable assumptions of the concentration of the interstitial F⁻ ions in these crystals: $N_F \leq 2 \times 10^{19}$ cm⁻³. It follows then that the total concentration N_D of donors in CdF₂:Y, which is equal to the concentration of “isolated” Y³⁺ ions in CdF₂

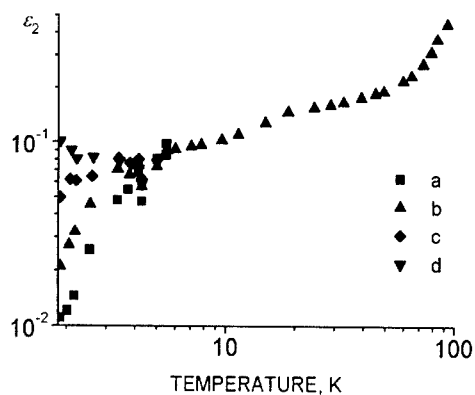


Fig. 1. $\epsilon_2(T)$ -dependence for $\text{CdF}_2:\text{Ga}$ after its illumination, measured with 36 GHz microwaves. Attenuation of the input microwave power: (a) 0 dB, (b) 7 dB, (c) 15 dB, and (d) 25 dB.

lattice, is at least five times less than total concentration of this impurity in the crystal ($(1-3) \times 10^{20} \text{ cm}^{-3}$), that is more than 80% of Y^{3+} ions are bound into clusters. Similar reasoning shows that more than 70% of In and 30% of Ga ions are bound into clusters and do not participate in microwave and FIR resonant absorption. By analogy with Ca, Sr, and Ba fluorides one may assume for CdF_2 a limiting concentration of $\sim 10^{20} \text{ cm}^{-3}$ of RE and Y ions which can be introduced into CdF_2 as statistically distributed substitution centers. The “redundant” impurities, whose solubility in CdF_2 reaches 10 mol% and above, form impurity-fluorine clusters which are readily observed in the optical spectra of RE ions in all the fluoride-type crystals [9–11].

Further limit on K value was found by studying $\text{CdF}_2:\text{Ga}$ and $\text{CdF}_2:\text{In}$ crystals during their deep-to-shallow center conversion. The experimentally found monotonic increase of the dielectric loss factor and the dielectric constant under illumination of the photochromic crystals testify clearly to the fact that $K \geq 0.5$ in the photo-decolored crystals.

Eisenberger et al. [12] observed a FIR absorption band ($10\text{--}150 \text{ cm}^{-1}$) in semiconducting CdF_2 . Our calculations of FIR absorption for the degree of compensation $0.5 \leq K \leq 0.9$ (see Fig. 2(c–e)) agree well with their experimental spectra [12], both by shape of the band and values of absorption coefficient.

It is necessary to define a source of the appreciable increase of the real part of permittivity, $\Delta\epsilon_1$, after illumination of the photochromic $\text{CdF}_2:\text{Ga}$ and $\text{CdF}_2:\text{In}$ crystals (see Table 1). Using the Kramers–Kronig relations, it is possible to show, that the photoinduced buildup of their FIR absorption bands ($10\text{--}150 \text{ cm}^{-1}$) due to ionized donor pairs could result in $\Delta\epsilon_1(\omega \rightarrow 0) \sim 2$ (for $N_c \sim 10^{18} \text{ cm}^{-3}$ and $K = 0.5$) in agreement with the experimental data.

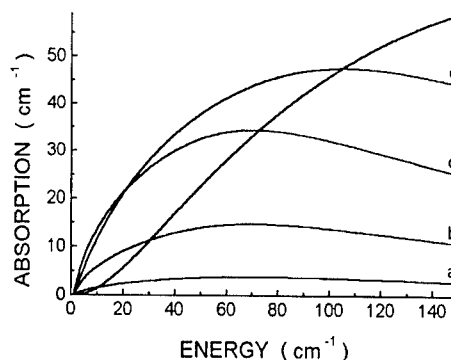


Fig. 2. Calculated in the modified Tanaka et al. approach. FIR absorption spectra of CdF_2 with concentration of neutral donors, $7 \times 10^{17} \text{ cm}^{-3}$, with Bohr radius, $a = 7 \text{ \AA}$ [4] and the degree of compensation: (a) $K = 0.1$, (b) $K = 0.3$, (c) $K = 0.5$, (d) $K = 0.7$, and (e) $K = 0.9$.

4. Conclusions

The occurrence of microwave and FIR broadband absorption, saturation of the microwave absorption in high electromagnetic fields, and significant increase of dielectric constant observed in semiconducting CdF_2 crystals are due to co-existence of neutral and charged donors, which form ionized donor pairs. The change of dielectric response upon illumination of photochromic $\text{CdF}_2:\text{Ga}$ and $\text{CdF}_2:\text{In}$ crystals at low temperature is caused by the photo-induced growth in concentration of donor electrons, and, consequently, the growth in concentration of donor pairs. The obtained limits on the degree of compensation $0.5 \leq K \leq 0.9$ for typical semiconducting CdF_2 are in good agreement with the results of the EPR study of Eisenberger and Pershan [13].

The results of this study show that with additive coloration of CdF_2 doped with column-III elements, total chemical reduction of the impurity and, consequently, total removal of interstitial F^- ions from the crystal lattice, is unachievable. It testifies to the presence of impurity-fluorine clusters [9–11] in the doped CdF_2 , which might supply the crystal with F ions during the process of chemical reduction of the impurity. A substantial part of the donor impurity is certainly collected in clusters, which makes it impossible to obtain a semiconducting CdF_2 crystal with the compensation degree less than 0.5 and with concentration, N_c , of free or weakly bound electrons exceeding $\sim 10^{19} \text{ cm}^{-3}$.

Acknowledgements

The research was supported by CRDF, grant RP1-2096.

References

- [1] P.F. Weller, *Inorg. Chem.* 4 (1966) 1545.
- [2] P.F. Weller, *Inorg. Chem.* 5 (1966) 739.
- [3] F. Moser, D. Matz, S. Lyu, *Phys. Rev.* 182 (1969) 808.
- [4] J.M. Langer, *Rev. Solid State Sci.* 4 (1990) 297.
- [5] C.H. Park, D.J. Chadi, *Phys. Rev. Lett.* 82 (1999) 113.
- [6] A.S. Shcheulin, A.I. Ryskin, K. Swiatek, J.M. Langer, *Phys. Lett. A* 222 (1996) 107.
- [7] S. Tanaka, M. Kobayashi, E. Hanamura, K. Uchinokura, *Phys. Rev.* 134 (1964) A256.
- [8] S.A. Kazanskii, D.S. Rumyantsev, A.I. Ryskin, unpublished.
- [9] S.A. Kazanskii, *Zh. Eksp. Teor. Fiz.* 83 (1985) 1258.
- [10] S.A. Kazanskii, *Sov. Phys. JETP* 62 (1985) 727.
- [11] Sun-II Mho, J.C. Wright, *J. Chem. Phys.* 81 (1984) 1421.
- [12] P. Eisenberger, P.S. Pershan, D.R. Bosomworth, *Phys. Rev.* 188 (1969) 1197.
- [13] P. Eisenberger, P.S. Pershan, *Phys. Rev.* 167 (1968) 292.



ELSEVIER

Physica B 308–310 (2001) 1042–1045

PHYSICA B

www.elsevier.com/locate/physb

Stacking faults and excitons in AgI

S. Mochizuki*

Department of Physics, College of Humanities and Sciences, Nihon University, 3-25-40 Sakurajosui, Setagaya-ku, Tokyo 156-8550, Japan

Abstract

AgI powder is gradually evaporated in vacuum onto a substrate whose temperature is higher than the superionic transition point T_C . During the evaporation, the optical absorption spectrum of the film is measured as a function of time-elapsed after the beginning of evaporation. By increasing the time (i.e., with increasing film thickness), the shifts of the absorption edge and exciton energy are observed, which are due to exciton or carrier confinement effects in the averaged structure of α -AgI. Information as to the electronic structure of the averaged structure is deduced from analyzing the observed spectra. After stopping evaporation, the film is gradually cooled down to 131 K. Through the cooling process, the absorption spectrum is also measured as a function of temperature. New exciton absorption bands (H_1 , H_2 and H_3) appear, together with the $Z_{1,2}$ and Z_3 excitons in the γ -AgI. The H_1 , H_2 and H_3 excitons are assigned to a metastable disordered polytype structure of β -AgI, in the light of the X-ray diffraction data. © 2001 Elsevier Science B.V. All rights reserved.

Keywords: Polytypism; Averaged structures; Excitons; Superionic conductor

1. Introduction

Silver iodide AgI is well known as a solid electrolyte and has three phases designated as α , β and γ at normal pressure in the order of decreasing temperature with the following properties [1]. At superionic transition point T_C (419 K), the superionic conductor α -phase transforms into semiconductor β -phase (wurtzite lattice). The α -phase has a body-centered cubic arrangement of I^- ion with highly mobile Ag^+ ions randomly distributed through the equivalent interstices, which has been known as the averaged structure. Extensive attention has been paid to the mechanisms of the superionic motion and to the electron–phonon interactions in the averaged structure for many years [2,3]. However, an in situ optical study on the electron states of α -AgI is limited in number and many basic problems remain to be solved. Moreover, the interest in AgI-based superionic conducting glasses and AgI:metal oxide composites has significantly grown and extreme conductivity enhancement has been observed at room temperature [4]. For this reason, also, it is necessary to clarify the

electronic and ionic structures of α -AgI. At 408 K, the β -phase transforms mostly into the second semiconductor γ -phase (zinc blende lattice) with a small amount of the β -phase [5]. However, at temperatures lower than T_C , the effects of stacking faults and metastable structures need to be pointed out [6]. It is said that, if annealed and aged, the structures may convert into the wurtzite lattice. Therefore, in order to clarify the details of such a transition between the wurtzite and zinc blende structures, any measurement must be carried out in situ. The exciton absorption spectrum of AgI is very sensitive to such a crystal modification and local structural change [7,8]. While high-temperature α -AgI is cooled down to low temperature, it is useful to measure spectral transition in the exciton absorption.

2. Experimental

Vacuum evaporation experiments are carried out under a base pressure of 10^{-4} Pa. Optically flat-plates of silica glass, sapphire (R-cut) and MgO (100) are used as substrates. The surface temperature of the substrate is monitored with an alumel–chromel thermocouple. A platinum crucible containing nominally pure AgI

*Tel.: +81-3-5317-9733; fax: +81-3-5317-9771.

E-mail address: motizuki@physics.chs.nihon-u.ac.jp (S. Mochizuki).

powder was gradually heated indirectly in an alumina crucible on which a tungsten-wire heater was wound. The thickness of AgI film on the substrate increases with time. During film deposition, the substrate temperature was maintained above T_C . The optical density spectrum of the film was measured as a function of the time t_d elapsed after the beginning of the evaporation with an optical multichannel analyzer system. The experimental procedure is almost the same as the experiments for microcrystals, except for introducing noble gas stream, which has been already reported [9]. After stopping the evaporation, the film is gradually cooled down to 131 K. Through the cooling process, the absorption spectrum of the film was also measured as a function of temperature.

3. Results and discussion

3.1. Optical absorption of α -AgI film

Fig. 1 shows the time evolution of the optical density spectrum of α -AgI. The substrate temperature is 453 K. Although one time-resolved spectrum consists of successive sixty-four spectra in this figure, only eight spectra are selected and presented in order to show clearly the time evolution. The time t_d is indicated in the plots. The final thickness of the film was about 300 nm. At the initial stage of the evaporation, a kink and an absorption edge appear at about 2.8 eV and at about 2.6 eV, respectively. With the progressing evaporation, the absorptions increase and the kink and the edge shift to lower energies, together with the growth of an absorption tail below 2.5 eV. In order to observe the

detail, as shown in Fig. 2, we compared the spectrum measured at $t_d = 48.88$ s (curve A) with that measured at $t_d = 123.63$ s (curve B), by scaling the curve A, so that the optical density at 3 eV coincides with that of curve B. The curve C obtained by such scaling coincides with the curve B not only at the energy region between 3 and 4 eV, but also at the lowest photon energy (1.549 eV). The result shows that, with progressing evaporation, namely, the increasing film thickness, the steepness of the optical density curve in the neighborhood of the absorption edge decreases and the absorption-edge shifts from 2.57 eV to a lower energy 2.52 eV. The red shift nature observed arises from a decrease in the quantum confinement of carriers or excitons in α -AgI film. We investigated the absorption tail below 2.5 eV by replacing the silica glass substrate with a MgO (100) plate and a R-cut sapphire plate, and changing the evaporation speed. The results can be summarized as follows:

- (1) With the increasing evaporation speed, the fabricated films become somewhat cloudy.
- (2) Films on the MgO- and sapphire single-crystal substrates do not show a prominent tail below 2.5 eV.

Therefore, the absorption tail observed below 2.5 eV is closely connected with surface roughness, and with crystalline defects at the film/substrate interface.

3.2. Optical absorption of AgI film below T_C

After stopping the evaporation, the specimen was gradually cooled to 131 K with an average cooling rate

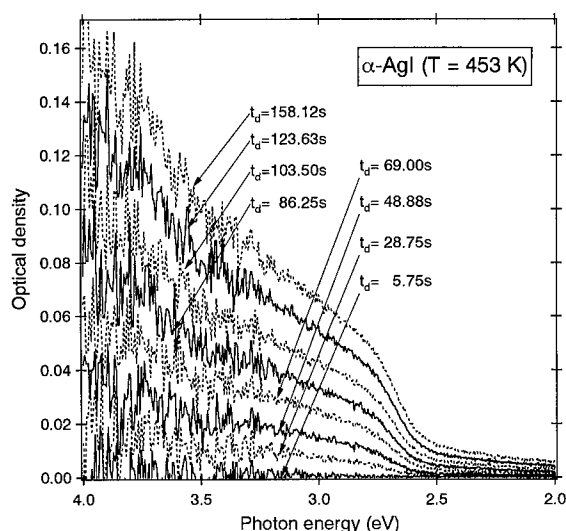


Fig. 1. Time evolution of the optical density spectrum of α -AgI film on a silica glass at 453 K during vacuum evaporation.

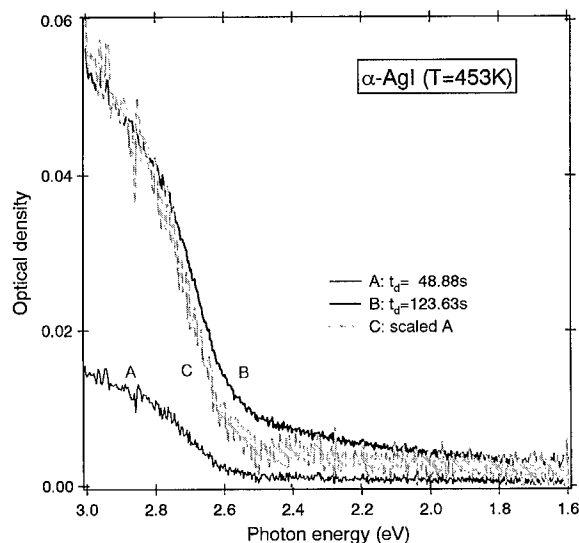


Fig. 2. Comparison of the optical density spectra of AgI film between the early and middle stages of the vacuum evaporation.

of 0.03 K/s. During the cooling process, the optical density spectrum was measured as a function of temperature, at temperature intervals of 5 K. Only the four spectra are presented in order to show clearly the temperature dependence. The result is shown in Fig. 3. During cooling from 453 to 398 K, the optical density spectrum is almost independent of temperature. Urbach rule does not hold in α -AgI. This indicates that the contribution from the electron–phonon interaction characteristic of the α -phase counterbalances that from the temperature-shift of the band gap energy due to thermal contraction of α -AgI. No remarkable spectral change was observed near T_C . This is due to the hysteresis of the superionic conduction transition [8]. At 393 K, several weak exciton absorption peaks and a shoulder appear faintly at 2.934, 2.975 (shoulder), 3.058, 3.110, 3.766 and 3.977 eV. On further cooling, these absorption peaks become prominent. In order to show the detailed spectral structure, the spectrum measured at 131 K is shown, together with that measured at 453 K, in Fig. 4. The X-ray diffraction (XRD) pattern of the AgI film was measured at room temperature. The XRD result shows a considerable amount of γ -AgI and the broadening of the (h0l) diffraction lines of β -AgI. The broadening arises from the stacking disorder in β -AgI hexagonal stacking sequence (ababab...), as pointed out by Lee et al. [10]. Taking into account the X-ray diffraction data, as indicated in the figure, the peaks, the absorption peaks and the shoulder observed at 2.934, 2.975 (shoulder) and 3.766 eV are assigned to the Z_1 -, Z_2 - and Z_3 -exciton absorptions of γ -AgI [7,8], while the peaks observed at 3.058, 3.110 and 3.977 eV are assigned to the H_1 -, H_2 - and H_3 -exciton absorptions of some

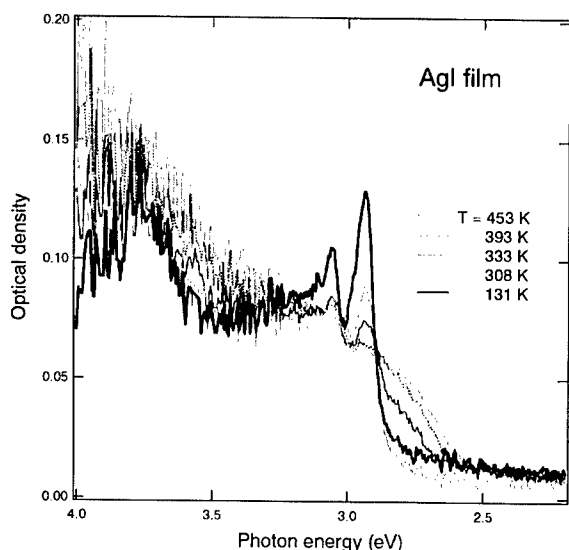


Fig. 3. Optical density spectra of AgI film on a silica glass at different temperatures during cooling process.

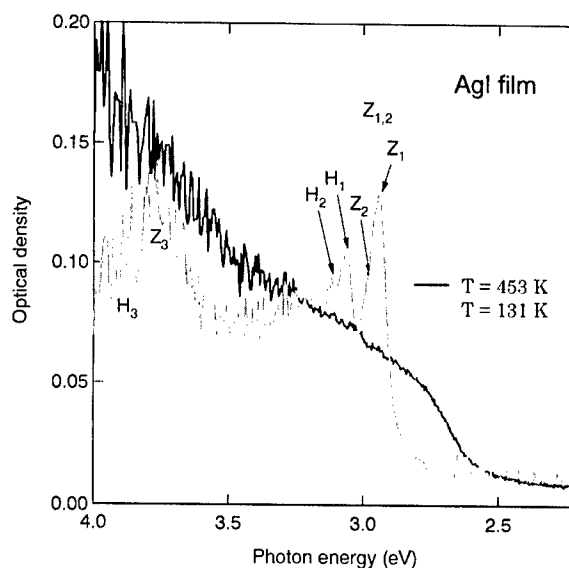


Fig. 4. Optical density spectra of AgI film at 131 and 453 K.

stacking-disorder-induced polytype structure of AgI. Quite a similar exciton absorption due to the polytype structure was found in CuI film evaporated onto a room-temperature substrate [7].

3.3. Miscellaneous

In Fig. 5, the absorption intensity peak energy and photoluminescence intensity peak energy of AgI film at 9 K are plotted as a function of the substrate temperature during vacuum evaporation. The observed absorption and photoluminescence (PL) peaks are due to the $Z_{1,2}$ exciton. The PL intensity peak appears several tens of meV lower than the absorption one, which indicates the existence of shallow exciton traps due to electron–phonon interactions or defects. With the increasing substrate temperature above about 450 K, the redshift becomes prominent. Silica glass substrate, which has an extremely small thermal expansion coefficient, gives a larger shift than that of sapphire. The results are qualitatively explained by the asymmetric stress at the interface coming from thermal shrinking with different thermal expansion coefficients between AgI and substrate material. The stress affects the electronic structure of AgI and induces an additional shift of the $Z_{1,2}$ exciton energy. This thermal stress may be one of the candidates for the cause of polytype structure formation. Our experiments show that the H_1 , H_2 and H_3 absorptions are not observed in thick AgI films which were produced by the vacuum evaporation with a small evaporation rate. Thinner sample tends to be influenced by the thermal stress and, therefore, the H_1 , H_2 and H_3 absorptions become more prominent. In addition to this stress effect, the effect of the deviation from

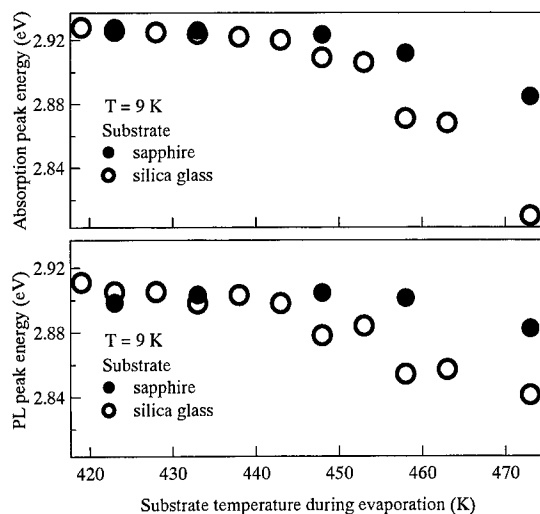


Fig. 5. Substrate temperature dependence of the absorption intensity peak and PL intensity peak energies at 9 K for the silica glass and sapphire substrates.

stoichiometry, $\text{Ag}_x\text{I}_{1-x}$, should also be considered at a high temperature for further discussion.

Effect of the stacking disorder observed in film specimens appears frequently even in the absorption spectra of nanocrystal specimens. Nanocrystals both on a substrate [11] and in a matrix [12] show faint absorption bands between 3.0 and 3.2 eV, which are in the H_1 - and H_2 exciton energy region. This indicates that AgI nanocrystals contain a stacking disorder induced by some reconstruction of surface atoms and

by the stress at the nanocrystal/matrix interface similar to CuI nanocrystals [13].

Acknowledgements

This work is supported by Interdisciplinary General Joint Research Grant for Nihon University and by Project Research Grant from The Institute of Information Sciences, College of Humanities and Sciences, Nihon University. This work is also partially supported by a Grant-in-Aid for Scientific Research from the Ministry of Education, Science, Sports, Culture and Technology, Japan.

References

- [1] G. Burley, *Amer. Min.* 48 (1963) 1266.
- [2] G. Eckold, K. Funke, J. Klaus, R.E. Lechner, *J. Phys. Chem. Solids* 37 (1976) 1097.
- [3] A. Rakitin, M. Kobayashi, *Phys. Rev. B* 53 (1996) 3088.
- [4] St. Adams, J. Maier, *Sol. Stat. Ionics* 105 (1998) 67.
- [5] R. Bloch, H. Moller, *Z. Phys. Chem.* A125 (1931) 245.
- [6] P.R. Prager, *Acta. Cryst.* A30 (1974) 369.
- [7] M. Cardona, *Phys. Rev.* 129 (1963) 69.
- [8] S. Mochizuki, Y. Ohta, *J. Lumin.* 87–89 (2000) 299.
- [9] S. Mochizuki, *J. Lumin.* 70 (1996) 60.
- [10] J.-S. Lee, S. Adams, J. Maier, *J. Phys. Chem. Solids* 61 (2000) 1607.
- [11] S. Mochizuki, K. Umezawa, *Phys. Lett. A* 228 (1997) 111.
- [12] G. Mshvelidse, et al., *Phys. Stat. Sol. (b)* 207 (1998) 369.
- [13] A. Tanji, I. Akai, K. Kojima, T. Karasawa, T. Komatsu, *J. Lumin.* 87–89 (2000) 516.



ELSEVIER

Physica B 308–310 (2001) 1046–1049

PHYSICA B

www.elsevier.com/locate/physb

Valence-change- and defect-induced white luminescence of Eu_2O_3

S. Mochizuki^{a,*}, Y. Suzuki^a, T. Nakanishi^a, K. Ishi^b^a *Department of Physics, College of Humanities and Sciences, Nihon University, 3-25-40 Sakurajosui, Setagaya-ku, Tokyo 156-8550, Japan*^b *Institute of Multidisciplinary Research for Advanced Materials, Tohoku University, Sendai 980-8577, Japan*

Abstract

Under irradiating with a CW UV laser light ($\lambda = 325\text{ nm}$) at room temperature in vacuum and oxygen gas atmosphere, the film, microcrystals and powder compacts of Eu_2O_3 exhibit a reversible photoluminescence (PL) spectral change between a red sharp-line structure and a white broad one. After stopping the UV irradiation, the ability of the white PL lasts for more than several months at room temperature under room light, in spite of changes of atmosphere. The reversible phenomena to be observed are interpreted as the results of both the valence-number change of europium ions ($\text{Eu}^{3+} \rightarrow \text{Eu}^{2+}$) and the oxygen vacancy formation. © 2001 Elsevier Science B.V. All rights reserved.

Keywords: Defect structures; Valence change; White-light emission

1. Introduction

Eu_2O_3 is stable in air and has five phases designated by X, H, A, B and C at atmospheric pressure in order of decreasing temperature as follows [1]. At about 2553 K, the X phase transforms into the H phase which transforms to the A phase at 2413 K. At 2313 K, the A phase (hexagonal structure: space group D_{3d}) transforms into the B phase (monoclinic structure: space group C_{2h}). In the A phase, the europium atoms are seven-coordinate with four oxygen atoms closer than the other three, while, in the B phase, the europium atoms are six- and seven-coordinate. At about 1373 K, the B phase transforms into the C phase (cubic structure: space group T_h) in which the europium atoms are six-coordinate. At room temperature, the present authors have recently observed the reversible UV-laser-light-induced spectral transitions between the red- and white-luminescence states in Eu_2O_3 -powder compacts and —films produced by the radio-frequency sputtering

method [2,3]. The interest in photoluminescent materials showing such photo-induced reversible spectral change at room temperature has significantly grown, because a combination of the reversible phenomenon and the near-field optical microscope [4] is very promising when applied to high-density optical storage with nanometer resolution. It is also the hope that we can find white PL material, which is useful for the wide-band tunable-laser medium. Very recently, we have also observed the similar photoinduced spectral transition in Eu_2O_3 films produced by the pulsed laser ablation method in vacuum and Eu_2O_3 microcrystal films produced by the laser ablation in low-pressure oxygen gas atmosphere.

In this paper, an overview of our results obtained in the past three years will be given, together with a phenomenal model of the photoinduced spectral transition.

2. Experimental

All specimens were made from Eu_2O_3 powder of 99.98% purity. Powder compact specimens were prepared by pressing the Eu_2O_3 powder under a pressure of 0.2 GPa for 1 h at room temperature. They were then

*Corresponding author. Tel.: +81-3-5317-9733; fax: +81-3-5317-9771.

E-mail address: motizuki@physics.chs.nihon-u.ac.jp (S. Mochizuki).

sintered at 1273 K in air for 24 h. First types of Eu_2O_3 films were grown on a silica glass substrate by the radio-frequency sputtering (RFS) method. They are named RFS films. Second-type of Eu_2O_3 films were grown on a silica glass substrate by the pulsed laser ablation (PLA) method in vacuum of 1.33×10^{-4} Pa. They are named PLA-films. Eu_2O_3 microcrystal-accumulated films were grown on a silica glass substrate by the PLA method in oxygen gas of the pressure lower than 100 Pa. They are named PLA-MC film. They are characterized by the X-ray diffraction (XRD) method and the scanning electron microscopy (SEM). Irradiations were carried out with a CW He–Cd laser line ($\lambda = 325$ nm) with power densities between 31438 and 840000 W/m^2 . The same He–Cd laser line excites luminescence. Emitted light is dispersed and detected using a grating spectrograph equipped with a multichannel photodetection system.

3. Results and discussion

The XRD analysis of the produced specimens indicates that the powder compact, RFS film, PLA film, and PLA-MC film are respectively, the C phase, the H phase [1], a mixture of predominantly C phase with a little B phase, and a mixture of predominantly B phase with a little C phase of Eu_2O_3 . The specimens were also examined by the SEM. The powder compacts consist of randomly oriented and connected rectangular-parallelepiped grains, as shown in Fig. 1(a). The RFS-films and the PLA ones have smooth surfaces and are optically transparent. The PLA-MC films consist of a lot of small particles whose sizes is approximately several hundred nanometers and little aggregates whose sizes can be several thousand nanometers, as shown in Fig. 1(b).

Figs. 2–5 show the photoinduced spectral changes at room temperature of the Eu_2O_3 -powder compact,

Eu_2O_3 -RFS film, Eu_2O_3 -PLA film and Eu_2O_3 -PLA-MC film, respectively. In the measurements of the powder compact, the RFS films, the PLA films and the PLA-MC films, their relative sensitivities of the detections are 1, 8, 170 and 34, respectively. Experiments were carried out in alphabetical order: (a) \rightarrow (b) \rightarrow (c). Irradiation time t_{ir} under a given atmosphere and the kind of

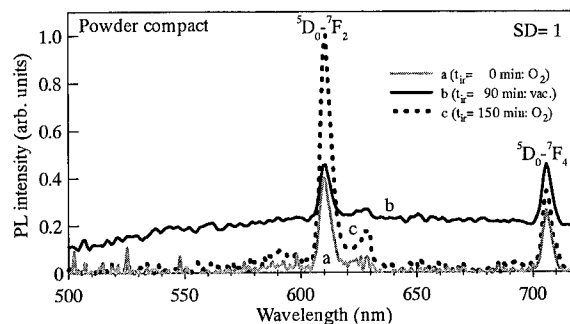


Fig. 2. Reversible spectral change of Eu_2O_3 powder compact.

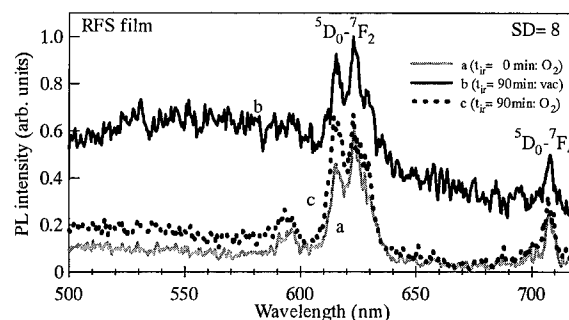


Fig. 3. Reversible spectral change of Eu_2O_3 film produced by the RF-sputtering method.

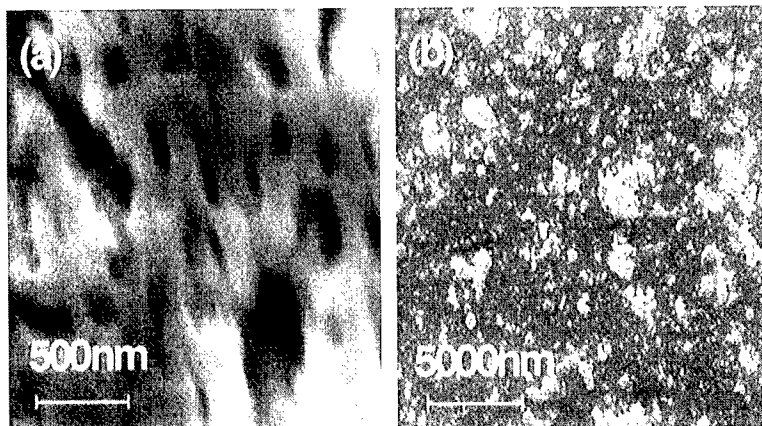


Fig. 1. SEM photographs of the Eu_2O_3 -powder compact (a) and Eu_2O_3 -PLA-microcrystal film (b).

atmosphere are indicated in each plot, together with the relative sensitivity of the detection, SD. First, these as-produced Eu_2O_3 specimens are irradiated with a 325 nm laser line at room temperature under oxygen atmosphere of a pressure 1.01×10^5 Pa. Under 325 nm excitation, these specimens show the red sharp $^5\text{D}_0 \rightarrow ^7\text{F}_J$ ($J = 0, 1, 2, 3, 4$) emissions [5,6]. Depending on the crystal structure of the specimens, the detailed spectral structure of the $^5\text{D}_0 \rightarrow ^7\text{F}_2$ emission differs each other [7,8]. Next, the specimen chamber is evacuated to 1.33×10^{-4} Pa. Under 325 nm irradiation in this vacuum, quite similar photoinduced spectral changes were observed in all the specimens. Namely, with increasing t_{ir} , the $^5\text{D}_0 \rightarrow ^7\text{F}_J$ ($J = 0, 1, 2, 3, 4$) emission intensity of Eu^{3+} ions becomes weak, while a very broad emission band appears and spreads all over the visible light region. The wavelength of the intensity peak of the white PL band observed in all the specimens is between 540 and 620 nm. Especially, the relative intensity decreases of the $^5\text{D}_0 \rightarrow ^7\text{F}_2$ emission of the powder compact, RFS film, PLA film and PLA-MC film are 75.3%, 15.6%, 34.5% and 15.4%, respectively. The intensity decrease indicates the decrease of number of Eu^{3+} ion, which is

due to photoreduction ($\text{Eu}^{3+} \rightarrow \text{Eu}^{2+}$). At this stage, the bright white PL can be seen with the naked eye. The whitening speed of the PLA film specimen was the highest among all specimens. In addition, the wavelength of their intensity maximum of the white PL band is specimen-dependent. The spectral structures to be observed in the $^5\text{D}_0 \rightarrow ^7\text{F}_2$ emission in the RFS film, PLA film and PLA-MC film, incidentally, differ from that for the powder compact specimen (C-phase Eu_2O_3) in which each Eu^{3+} ion is surrounded by six oxygen ions. Seven-coordinate Eu^{3+} ions account for the spectral difference [2,3,7,8].

Oxygen gas is again introduced into the chamber. The change from white PL emission to red emission can be seen with the naked eye. It is found through many successive experiments that the spectral changes as shown in these figures are reversible. Similar experiments were carried out by changing the wavelength of the irradiating laser light. For example, a CW He–Cd laser ($\lambda = 442$ nm), a CW Ar^+ laser ($\lambda = 528.7, 514.5, 501.7, 496.5, 488.0, 476.5, 472.2, 465.8$, and 457.9 nm), and a pulsed Nd^{3+} :YAG laser ($\lambda = 266, 354.7, 532$, and 1064 nm) were used. No spectral change was observed with these lasers, which indicates that the CW UV laser light of the wavelength 325 nm is required to induce the spectral change. The speed of the spectral change is accelerated by increasing the power density of the activating light. The change to the white PL emission can also be observed at low temperatures down to 7 K, which indicates that the phenomenon does not arise from a phonon-assisted process and that it is a purely electronic mechanism. In spite of the changing atmosphere (for example, O_2 gas and air exposures), the white PL state lasts for more than several months at room temperature after the removal of the laser light under room light, and the red PL state re-appears only by irradiating with the same UV laser light under O_2 gas atmosphere of a pressure 1.01×10^5 Pa.

Finally, we turn to the observed photoinduced spectral change between the red- and white PL. Noting the result that the 325 nm photons are essential to induce the spectral change. The 325 nm irradiation in vacuum produces both valence change ($\text{Eu}^{3+} \rightarrow \text{Eu}^{2+}$) and oxygen vacancies. They then induce local structural relaxation (distortion) around photoexcited ions to form a metastable state. A simplified scheme is drawn in Fig. 6, omitting the detailed structure of the 4f electronic states of Eu^{3+} ions. The $^7\text{F}_0$, MS and X represent the ground state of Eu^{3+} ions, the metastable state, and one of some 4f excited energy level of Eu^{3+} ions or charge-transfer state, respectively. The coordinate Q expresses some local structural change due to both the valence number change of Eu^{3+} ions and the oxygen vacancy formation. The potential barrier of the height ΔE separates the metastable state from the ground state. In oxidizing atmosphere, the 325 nm radiation produces

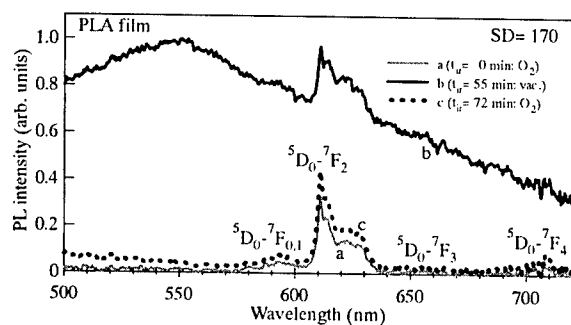


Fig. 4. Reversible spectral change of Eu_2O_3 film produced by the laser ablation method in vacuum.

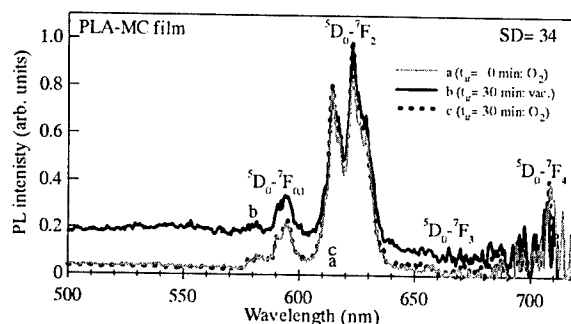


Fig. 5. Reversible spectral change of Eu_2O_3 microcrystal film by the laser ablation method in low-pressure oxygen gas atmosphere.

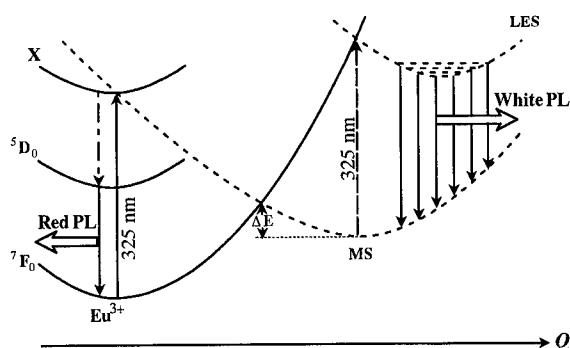


Fig. 6. Schematic energy diagram of the photoinduced reversible spectral change of Eu_2O_3 .

the localized excitation of Eu^{3+} ions and the deexcitation of the photoexcited Eu^{3+} ions provides the red luminescence due to the $^5\text{D}_0 \rightarrow ^7\text{F}_J$ transitions, via the nonradiative transitions (NR) to the $^5\text{L}_6$, $^5\text{D}_J$ ($J = 3, 2, 1, 0$) states. When the photoexcitation is carried out in vacuum, the excited state is relaxed through both a radiative recombination and the local structural relaxation to the metastable state. The 325 nm excitation of the metastable state induces both the backward transition and the transition to the localized electronic state (LES) originating from the Eu^{2+} and oxygen vacancy formations. Since the photoproduced metastable state is extremely stable even at room temperature in oxygen, air and vacuum atmospheres after stopping 325 nm irradiation as described above, the potential barrier separating the ground state ($^7\text{F}_0$) from the MS must be high enough to suppress the thermal-forward and -backward transitions between the $^7\text{F}_0$ state and MS. The LES is a luminescence center strongly coupled with lattice vibrations and, therefore, gives a broadband luminescence as observed. Our PL-excitation spectra measurements on all the specimens show that the laser wavelength 325 nm corresponds the lower-energy

edge of the charge-transfer (CT) absorption band ($\text{Eu}^{3+} + \text{O}^{2-} \rightarrow \text{Eu}^{2+} + \text{O}^{1-}$) and the transition energy to higher excited states of Eu^{3+} ions; for example, $^7\text{F}_0 \rightarrow ^5\text{L}_J$ transitions. Therefore, the CT and $^5\text{L}_J$ states are candidates for the origin of the X state. However, the observed spectral change is thought to be a surface phenomenon. The detailed surface electronic structure should be clarified for further discussion.

Acknowledgements

This work is supported by Interdisciplinary General Joint Research Grant for Nihon University, and by Project Research Grant from The Institute of Information Sciences, College of Humanities and Sciences, Nihon University. This work is also partially supported by a Grant-in-Aid for Scientific Research from the Ministry of Education, Science, Sports, Culture and Technology, Japan.

References

- [1] K.A. Gschneid Jr., L.R. Eyring, in: Handbook on the Physics and Chemistry on Rare Earths, Vol. 3, North-Holland, Amsterdam, 1979.
- [2] S. Mochizuki, T. Nakanishi, Y. Suzuki, K. Ishi, Book of Abstracts, International Chemical Congress of Pacific Basin Societies, Part 2, Honolulu, Hawaii, 2000.
- [3] S. Mochizuki, T. Nakanishi, Y. Suzuki, K. Ishi, Meeting Abstr. Phys. Soc. Jpn, Part 4, 55 (2) (2000) 627.
- [4] E. Bezig, J.K. Trautman, Science 257 (1992) 189.
- [5] G.H. Dieke, Spectra and Energy Levels of Rare Earth Ions in Crystal, Interscience, New York, 1968.
- [6] H.M. Crosswhite, H.W. Moos (Eds.), Optical Properties of Ions in Crystals, Interscience, New York, 1967, p. vi.
- [7] J. Dexpert-Ghys, M. Faucher, P. Caro, Phys. Rev. B 23 (1981) 607.
- [8] G. Wakefield, H.A. Keron, P.J. Dobson, J.L. Hutchison, J. Colloid Interface Sci. 215 (1999) 179.



ELSEVIER

Physica B 308–310 (2001) 1050–1053

PHYSICA B

www.elsevier.com/locate/physb

Defects in heteroepitaxial $\text{CeO}_2/\text{YSZ}/\text{Si}(001)$ films by precise X-ray rocking curve distribution fitness

Chun-Hua Chen*, Naoki Wakiya, Atsushi Saiki, Takanori Kiguchi,
Kazuo Shinozaki, Nobuyasu Mizutani

*Department of Metallurgy and Ceramics Science, Tokyo Institute of Technology, 2-12-1 O-okayama, Meguro-ku,
Tokyo 152-8552, Japan*

Abstract

In this paper, the theory of dislocation density and curvature measurements from X-ray rocking curves is extended to the case of double oxide heteroepitaxial $\text{CeO}_2(001)/\text{YSZ}(001)/\text{Si}(001)$ films mainly by high-resolution X-ray diffraction. According to this theory, we have successfully resolved the rocking curves of CeO_2 and YSZ by two simple components. Thus, the dislocation density and radius of curvature of each layer can be calculated from the distribution of the square of measured FWHM versus $1/\sin^2\theta$. The results show that the YSZ layer has a higher dislocation density and a lower radius of curvature than CeO_2 . The high-resolution transmission electron microscopy (TEM) image of CeO_2/YSZ interface cross-section shows a high dislocation density along the interface with an average interval ~ 3.9 nm. © 2001 Elsevier Science B.V. All rights reserved.

Keywords: Dislocation density; Rocking curve; YSZ; CeO_2

1. Introduction

In recent years, the Yttria-stabilized ZrO_2 (YSZ) and double CeO_2/YSZ epitaxial films on $\text{Si}(001)$ substrates have attracted much attention due to their applications such as the buffer layers in electronic devices [1] and in high Tc superconductors [2,3]. The adding of a YSZ buffer layer between CeO_2 and $\text{Si}(001)$ is necessary to obtain the $\text{CeO}_2(001)/\text{YSZ}(001)/\text{Si}(001)$ epitaxial growth layer [4]. However, the lattice mismatches at interfaces, CeO_2/YSZ and YSZ/Si , (lattice constants of bulk CeO_2 is 0.541 nm, bulk YSZ is 0.514 nm and Si is 0.543 nm), are over 5.0% and will lead to an increase of lattice distortion, random strain and dislocation density as clarified in our previous work [5]. The measurement of dislocation density in heteroepitaxial semiconductor layers is important for the development of microwave

transistors and the integration of devices in dissimilar semiconductors. The X-ray rocking curves provide non-destructive measurements of dislocation densities with accuracy equal to crystallographic etches or TEM. Hordon and Averbach have described the theory of full-width at half-maximum (FWHM) of rocking curves and determined the dislocation densities of metal single crystals of copper and aluminum [6]. On the basis of this theory, Qadri and Dinan calculated the dislocation densities of alloy epitaxial $\text{ZnCdTe}/\text{InSb}$ films and which showed good agreement with TEM observation [7]. Ayers extended the calculation technique in $\text{GaAs}/\text{Si}(001)$ single semiconductor layers by the measurement of several rocking curves from different diffraction planes [8].

In this paper, the aforementioned theory is extended to the case of oxide heteroepitaxial film, $\text{CeO}_2/\text{YSZ}/\text{Si}(001)$, for the estimation of dislocation density and radius of curvature. The calculated result by high-resolution XRD is also compared with the observation of high-resolution TEM.

*Corresponding author. Fax: +81-3-5734-3369.

E-mail address: chenco@sim.ceram.titech.ac.jp
(C.-H. Chen).

2. Experimental

Single YSZ (8 mol% Y_2O_3) and double CeO_2/YSZ layers were prepared by pulsed laser deposition (PLD) with a KrF (248 nm) excimer laser at 1073 K in 5.5×10^{-4} Torr on Si(001) substrates which were RCA cleaned [9] and dilute HF ($\text{HF}:\text{H}_2\text{O}=1:10$) treated. The experimental procedure is described in detail in Ref. [10]. The thickness of the CeO_2 layer was kept at about 78 nm (± 2 nm) and that of the YSZ layer was varied from 20 to 145 nm. Due to the measurement of the precise thickness being quite difficult, we used several techniques for comparison including energy dispersive spectroscopy, a surface profile detector and the glazing X-ray reflectivity measurement and which showed good agreement with each other [11]. The rocking curves from (002), (113), (004), (224), (115), (006), (335) and (226) diffraction planes of CeO_2 and YSZ were performed on the Philips Extended X'Pert Material Research Diffractometer (MRD) employing a graded parabolic X-ray mirror and a four-Ge(220)-single-crystals monochromator in the incident beam. The mirror and monochromator produce a parallel beam with an angular divergence less than 0.005° for Cu K_α ($\lambda = 0.1541$ nm). The settings of the generator were 45 kV and 40 mA with a Cu anode.

3. Results and discussion

According to the theory of X-ray rocking curve that was described by Hordon and Averbach, if β_m is the measured FWHM of the rocking curve of a diffraction plane, then

$$\beta_m^2 = \beta_0^2 + \beta_d^2 + \beta_z^2 + \beta_e^2 + \beta_L^2 + \beta_r^2, \quad (1)$$

where β_0 and β_d are the intrinsic FWHMs for the layer and the analyzing crystals; β_z , β_e , β_L and β_r are the components due to lattice tilting, local strain, crystal size and uniform lattice bending, respectively. The intrinsic β_0 and β_d are usually less than 0.003° [12], thus we can ignore these two parameters here. Then the equation can be re-written as below:

$$\beta_m^2 = K_z + K_e \tan^2 \theta + K_L \frac{\lambda^2}{\sin^2 2\theta} + \frac{K_r}{\sin^2 \theta}, \quad (2)$$

where θ is the Bragg angle, λ is X-ray wavelength and K 's are constants independent of θ and λ [13,14].

According to the definition, all the coefficients, K_z , K_e , K_L and K_r , are positive constants. In order to find a simple relation between the measured FWHM and each K coefficient, β_m^2 was plotted with various functions of the Bragg angle θ , i.e. β_m^2 versus $\tan^2 \theta$, $1/\sin^2 2\theta$ and $1/\sin^2 \theta$. However, we can only find a linear relation in the plot of β_m^2 versus $1/\sin^2 \theta$, which has a reliable

positive slope (K_r) and an intercept (K_z) with β_m^2 axis as defined before. This suggests that within those four K coefficients, K_e and K_L can be ignored in this film system, and thus we have to set both K_e and K_L to zero to obtain a simple linear relation for the estimation of dislocation density and radius of curvature.

Fig. 1 shows the square of measured FWHM, β_m^2 , of CeO_2 and YSZ rocking curves from various diffraction planes, which exhibits a linear relation with $1/\sin^2 \theta$. The K_z and K_r that are obtained from various slopes and intercepts of different samples can be used to calculate the dislocation density and radius of curvature by Eqs. (3) and (4) as below:

$$K_z = 2\pi \ln 2 \times |\vec{b}|^2 D, \quad (3)$$

$$K_r = \frac{w^2}{r^2}, \quad (4)$$

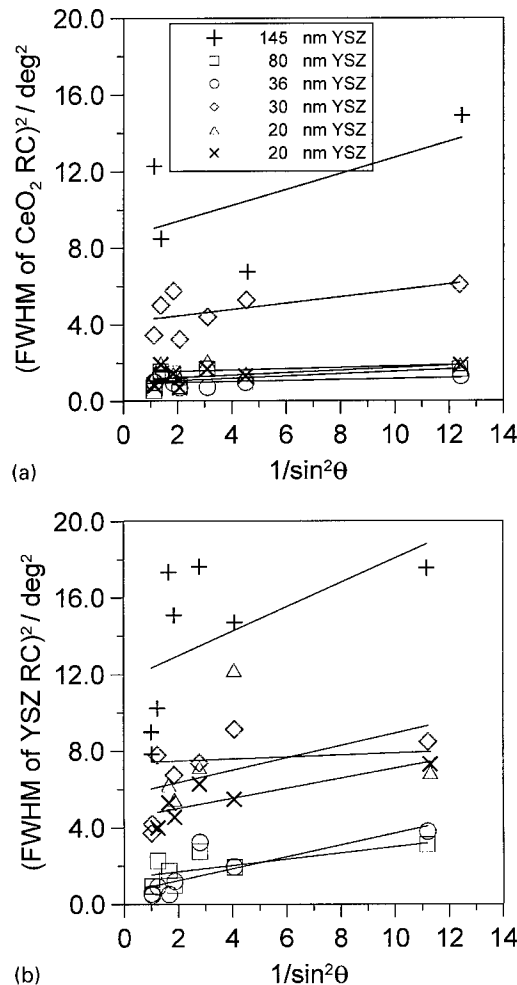


Fig. 1. Squares of measured FWHMs of (a) CeO_2 and (b) YSZ rocking curves versus $1/\sin^2 \theta$.

where b is the burger vector, D is the dislocation density, w is the X-ray beam width and r is the radius of curvature. According to the high-resolution TEM observation, the burger vector of misfit dislocation is $1/2a [1\ 1\ 0]$ in both YSZ and CeO_2 where the values are 0.363 and 0.383 nm for YSZ ($a = 0.514$ nm) and CeO_2 ($a = 0.541$ nm), respectively.

Fig. 2 shows the relationship of dislocation density between YSZ and CeO_2 that is calculated from Fig. 1. The results show that the dislocation density of YSZ (3.3×10^{10} – $6.2 \times 10^{11} \text{ cm}^{-2}$) is a function of that of CeO_2 (4.4×10^{10} – $4.1 \times 10^{11} \text{ cm}^{-2}$). The dislocation density of CeO_2 is always lower than that of YSZ in each sample (all points locate below the broken line). This phenomenon might be caused by the YSZ layer having two interfaces, CeO_2/YSZ and YSZ/Si , containing higher misfit dislocation density. Besides, the dislocation density of YSZ decreases as its thickness increases with a well-fitting function (not shown here), which can be used to estimate the dislocation density of different thicknesses. From this distribution, we can understand the central part of the YSZ layer contains fewer dislocations than its top and bottom interfaces. In our expectation, the dislocation density of CeO_2 should be a constant as its constant thickness (~ 80 nm). However, the dislocation density of CeO_2 changes with that of YSZ indicating that any change in CeO_2 arises from the bottom YSZ layer conditions.

Fig. 3 shows a lattice image of CeO_2/YSZ interface section ($[001] \times [110]$) of 30 nm thick YSZ by high-resolution TEM. After being treated with a fast Fourier transformation, the misfit dislocations around the interface can be seen clearly. The average interval between each misfit dislocation is about 3.9 nm. Here we recall the calculation results from Fig. 2, which is a

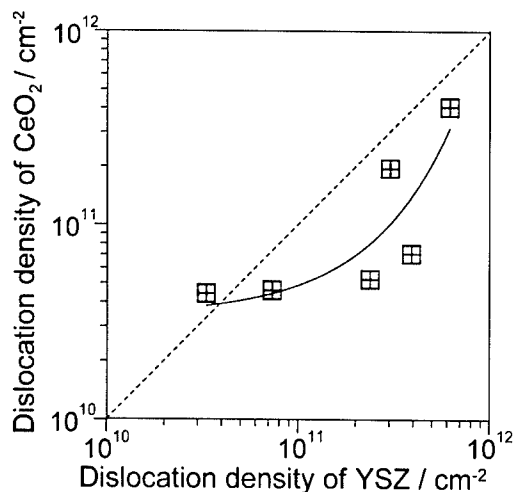


Fig. 2. Dislocation density of CeO_2 is a function of that of YSZ.

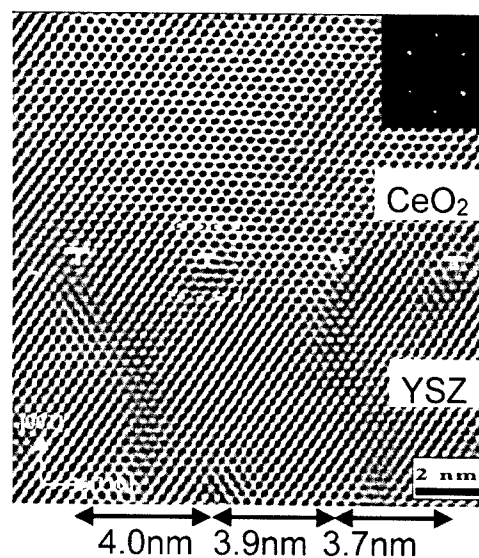


Fig. 3. Cross-sectional high-resolution TEM lattice image of CeO_2/YSZ interface.

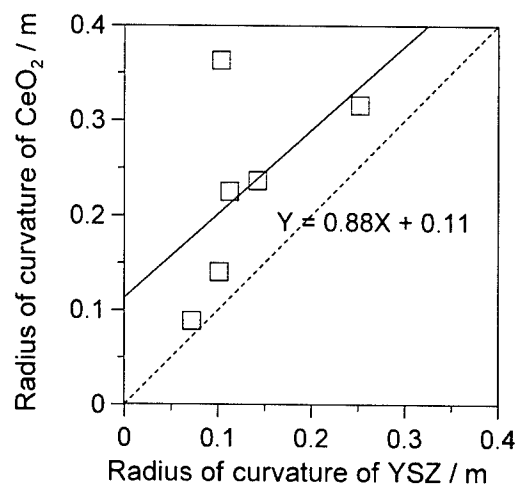


Fig. 4. Radius of curvature of CeO_2 is a function of that of YSZ.

two-dimension dislocation density with a unit cm^{-2} . The one-dimension dislocation density can be estimated by the square root of the previous calculation result, that is, 0.018 – 0.079 nm^{-1} for YSZ and 0.021 – 0.064 nm^{-1} for CeO_2 . Thus, the average interval between misfit dislocation is 56 – 12 nm for YSZ and 48 – 16 nm for CeO_2 . The much higher interval than the observation of high-resolution TEM comes from the result that high-resolution XRD is an average value in any direction rather than just along the interface.

Fig. 4 shows the relationship of radius of curvature between YSZ and CeO_2 that is calculated from Fig. 1.

The radius of curvature of YSZ (0.07–0.25 m) that is caused by uniform lattice bending is much smaller than that of CeO₂ (0.09–0.36 m). The radius of curvature of bare Si(001) substrate has been measured by high-resolution XRD and shows almost no bending (~ 300 m). Therefore, the relatively huge curvatures of YSZ and CeO₂ were not caused by bent substrate. Here, we consider the thermal expansion coefficients of CeO₂, YSZ and Si. Since the thermal expansion coefficient of CeO₂ ($13.5 \times 10^{-6} \text{ K}^{-1}$ at 1100 K) is much larger than that of YSZ ($10.9 \times 10^{-6} \text{ K}^{-1}$ at 1100 K) and Si ($4.5 \times 10^{-6} \text{ K}^{-1}$ at 1100 K), the CeO₂ and YSZ layers undergo tensile stress when the specimen is cooled from deposition temperature, 1073 K, and down to room temperature, 298 K. From the calculation of dislocation density as described in Fig. 2, YSZ always has a much higher dislocation density than CeO₂ for various YSZ thicknesses. In other words, the YSZ layers might contain more mosaic domains than CeO₂ because the domain boundary consists of dislocations. As these small mosaic domains are under tensile stress caused by the difference of thermal expansion between each layer, this will lead to a rocking curve broadening effect almost similar to the curvature broadening.

4. Conclusions

In this paper, we have successfully used the X-ray rocking curve theory to clarify the double oxide heteroepitaxial CeO₂/YSZ/Si(001) films. The YSZ has a higher dislocation density and lower radius of curvature than CeO₂, which is mainly caused by the

larger lattice and thermal mismatches between CeO₂ and YSZ, and YSZ and Si substrate. From the high-resolution TEM observation, the CeO₂/YSZ interface is relaxed by introducing a large amount of misfit dislocations with an average interval ~ 3.9 nm.

References

- [1] C. Pellet, C. Schwebel, P. Hest, *Thin Solid Films* 175 (1989) 23.
- [2] R. Aguiar, F. Sanchez, D. Peiro, C. Ferrater, M. Varela, *Physica C* 235–240 (1994) 647.
- [3] L. Mechin, J.C. Villegier, G. Rolland, F. Laugier, *Physica C* 269 (1996) 124.
- [4] C.A. Copetti, H. Soltner, J. Schubert, W. Zander, O. Hollricher, Ch. Buchal, H. Schulz, N. Tellmann, N. Klein, *Appl. Phys. Lett.* 63 (1993) 1429.
- [5] C.H. Chen, A. Saiki, N. Wakiya, K. Shinozaki, N. Mizutani, *J. Crystal Growth* 219 (2000) 253.
- [6] M.J. Hordon, B.L. Averbach, *Acta Metall.* 9 (1961) 237.
- [7] .Qadri Syed B, J.H. Dinan, *Appl. Phys. Lett.* 47 (1985) 1066.
- [8] J.E. Ayers, *J. Crystal Growth* 135 (1994) 71.
- [9] W.A. Kern, D.A. Poutinen, *RCA Rev.* 31 (1970) 187.
- [10] N. Wakiya, T. Yamada, K. Shinozaki, N. Mizutani, *Thin Solid Films* 371 (2000) 211.
- [11] C.H. Chen, N. Wakiya, A. Saiki, K. Shinozaki, N. Mizutani, *Key Eng. Mater.* 181–182 (2000) 121.
- [12] W.J. Bartels, *Philips Tech. Rev.* 41 (1983) 183.
- [13] B.E. Warren, Theory presented in the Course, X-ray and Crystal Physics, Massachusetts Institute of Technology, 1957.
- [14] W.F. Flanagan, Sc.D. Dissertation, Massachusetts Institute of Technology, 1959.



ELSEVIER

Physica B 308–310 (2001) 1054–1056

PHYSICA B

www.elsevier.com/locate/physb

Influence of semiconductor film structural imperfection on the physicochemical interaction rate in As_2S_3 –Cu system

M.V. Sopinsky*

Institute of Semiconductor Physics, National Academy of Sciences, 45, Prospect Nauky, 03028 Kyiv, Ukraine

Abstract

Physicochemical interactions in amorphous As_2S_3 –copper thin-film systems were studied by the methods of resistometry, ellipsometry, microscopy and by chemical dissolution. It was shown that the considerable variation of chemical process activity observed in these systems is caused by an essential dependence of the physicochemical interaction rate on chalcogenide film stoichiometry and the imperfection of its structure. Application of our thermochemical model for a probability estimation of quasi-molecular reactions of copper and oxygen with polymerised and non-polymerised fragments in arsenic trisulphide film makes it possible to give a qualitative description of the dark interaction mechanism. © 2001 Elsevier Science B.V. All rights reserved.

Keywords: Chalcogenide glassy semiconductors; Physicochemical interactions

1. Introduction

Thin-film systems based on chalcogenide glassy semiconductors (CGS) and some metals (Ag, Cu) [1] have many unique properties. For example, they can be successfully applied in submicron lithography and are very promising in nanolithography as inorganic resists [2,3].

CGS–Me systems, generally, are thermodynamically non-equilibrium ones: there are physicochemical processes which cause their ageing. Besides, the examination of physicochemical interactions (PCI) of CGS and metal films is an important topic of research by itself. We have recently demonstrated that these effects can be applied to the creation of blazed holographic diffraction gratings [4].

2. Experimental

Samples of sandwich-like thin-film CGS–Cu systems were prepared by deposition onto glass substrate

vapours produced by the subsequent thermal vacuum evaporation of the copper load and that of crashed powdered glassy As_2S_3 from tantalum boats at a residual pressure, P , of 5×10^{-3} Pa.

The most universal physical property describing mass transport during solid-state reactions in such systems is the metal layer expenditure, Δh_{Cu} . It was observed by electrical resistance measurements [5].

Multiangle ellipsometrical measurements (LEF-3M ellipsometer, $\lambda = 632.8$ nm) of As_2S_3 –Cu samples and As_2S_3 and Cu control films, were analysed using the Fortran-program which enabled us to distinguish between various ellipsometrical models [6,7].

3. Results and discussion

Thickness changes of the copper film on As_2S_3 –Cu samples prepared in the same vacuum cycle began simultaneously with the start of the chalcogenide film deposition on it and continued after completion of the deposition at the same rate (Fig. 1(2)). During the deposition of As_2S_3 on Cu film covered by the Cu_xS layer, V_c was proportional to the deposition rate, and drops sharply when the deposition is completed

*Fax: +380-44-265-83-42.

E-mail address: sopinsk@class.semicond.kiev.ua (M.V. Sopinsky).

(Fig. 1(3)). As opposed to Cu_xS layers, the Cu_2O ones formed by the exposure of the copper film to free air have barrier properties (Fig. 2).

The As_2S_3 –Cu sample ageing rate depends also on the conditions of the preparation of the As_2S_3 film. During the sample storage in vacuum, the PCI takes place most intensely when the CGS film is obtained by evaporation of primary glassy As_2S_3 . The PCI rate in vacuum slows down by more than one order of magnitude in systems obtained with the evaporation of multiply used As_2S_3 load. The films obtained by evaporating the previously used As_2S_3 shots have a refraction index that is several per cent higher than the films obtained from the fresh load.

The stability of As_2S_3 –Cu systems depends also on the storage conditions: in vacuum or in air. The character of atmospheric influence significantly depends on the conditions of CGS film production.

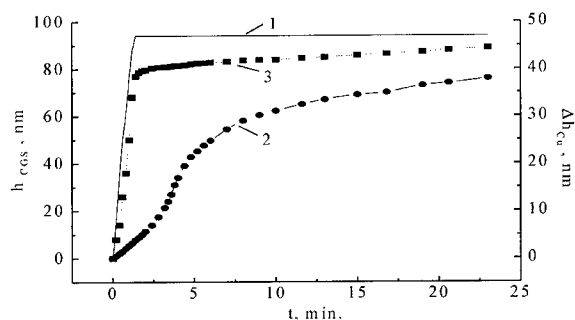


Fig. 1. Time dependence of the As_2S_3 film thickness being deposited (1) and the thickness change of the copper film being stored in vacuum chamber (2, 3).

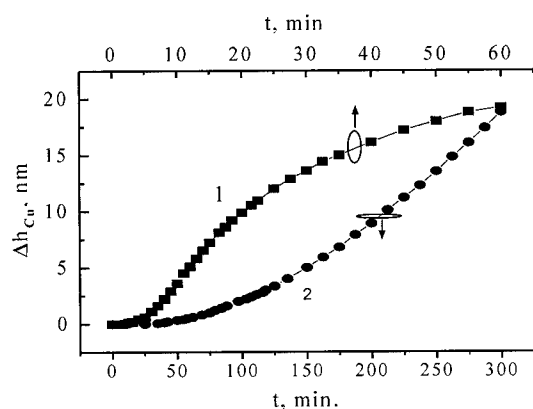


Fig. 2. Copper film thickness change depending on the duration of the As_2S_3 –Cu systems storage in vacuum ($h_{\text{As}_2\text{S}_3} = 150$ nm). Intermediate Cu_2O layer. $h_{\text{Cu}_2\text{O}} = 4$ (1) and 7 (2) nm.

In systems with films obtained from fresh shots, the PCI is slower in air than in vacuum (Fig. 3(1) and (2)). On the contrary, in systems in which CGS films are obtained from earlier used material, the PCI rate in air is higher (Fig. 4). In the sample taken from vacuum right after the deposition, the V_e in air is higher than that in vacuum and is practically stationary (Fig. 4(1)). Longer storage of the sample in vacuum (before placing it in air) gradually causes the occurrence of the low V_e initial period (Fig. 4(3)).

The systems under ellipsometrical investigation were well modelled as multilayer structures with sharp layer interfaces. That is, the thickness distribution of the dissolved copper is almost rectangular in shape. It confirms the reactionary nature of the interaction. In

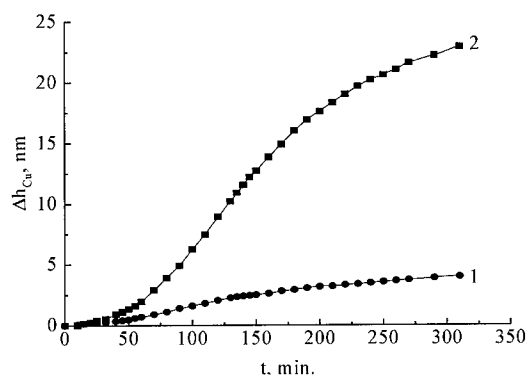


Fig. 3. Change of the Cu film thickness in the As_2S_3 –Cu system being stored in air (1) and in vacuum (2). $h_{\text{As}_2\text{S}_3} = 180$ nm, $h_{\text{Cu}_2\text{O}} = 5.5$ nm.

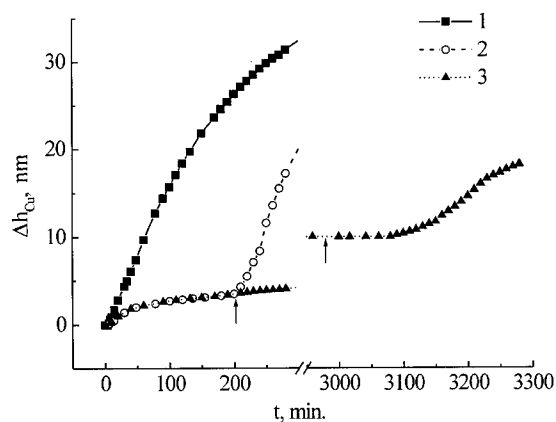


Fig. 4. Time dependence of copper film thickness change for a As_2S_3 – Cu_2O –Cu system over the vacuum-and air-keeping. The As_2S_3 film has been obtained by the evaporation of load used earlier in four evaporations. (1) Keeping in air, (2, 3) keeping in vacuum (up to the time indicated by \uparrow) and in air (after the time indicated by \uparrow) ($h_{\text{As}_2\text{S}_3} = 106$ nm, $h_{\text{Cu}_2\text{O}} = 5$ nm).

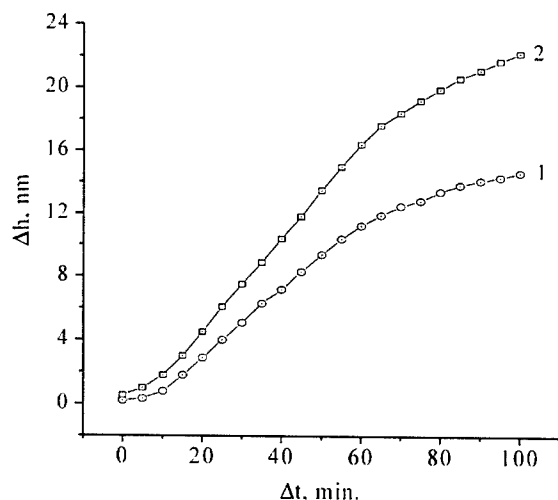


Fig. 5. Thickness change of non-doped (1) and copper-doped (2) parts of CGS film during the storage of the As_2S_3 - Cu_2O - Cu system in air. The CGS film parameters are the same as in Fig. 4.

Fig. 5 the details of ellipsometrical investigations on the acceleration of PCI in air are represented.

The explanation of the observed substantial difference between chemical process rates can be based on heats of formation of copper, and arsenic sulphides and oxides.

For arsenic trisulphide and cupric sulphides the following is true (Table 1):

$$|\Delta H_f(\text{As}_2\text{S}_3)| < |\Delta H_f(\text{Cu}_2\text{S})|, \quad (1)$$

$$|\Delta H_f(\text{As}_2\text{S}_3)| < |\Delta H_f(\text{Cu}_{2-\delta}\text{S})|. \quad (2)$$

From (1) and (2) it follows that if copper and arsenic trisulphide are in contact, fast exothermic exchange reactions should take place, producing the Cu_2S and $\text{Cu}_{2-\delta}\text{S}$ compounds. An interaction rate is determined by the enthalpy and the entropy of the reactions and by the kinetic factors.

It is known [11,12] that the violation of the stoichiometrical composition and structure of As_2S_3 being precipitated due to change of fragmentary composition of vapour phase causes changes of the optical properties of the arsenic trisulphide films. Multiple evaporation of glassy As_2S_3 causes changes in its vapour phase composition—from more volatile sulphur-enriched fractions at the first evaporation of shots to sulphur-deficient fractions when shots are taken through several evaporation cycles. Since (Table 1)

$$\Delta H_f(\text{As}_2\text{S}_5) < |\Delta H_f(\text{As}_2\text{S}_3)| < |\Delta H_f(\text{As}_2\text{S}_2)|, \quad (3)$$

one should expect an intensification of the interaction between the copper and the sulphur-enriched films obtained during the first evaporation of the arsenic trisulphide load. This has been confirmed experimentally.

Table 1

Relative heats of formation (in kcal/mole \times number of chalcogen or oxygen atoms per formula unit) for arsenic, and copper sulphides and arsenic, copper and sulphur oxides

Compounds	$ \Delta H_f $ ([8–10])
As_2S_2	15.95
As_2S_3	13.3
As_2S_5	7.0
$\text{Cu}_2\text{S} \dots \text{Cu}_{1-\delta}\text{S}$	19.6...17.2
$\text{S}_2\text{O} \dots \text{S}_2\text{O}_7$	−0.098...36.8
Cu_2O , CuO	41.4, 38.7
$\text{As}_2\text{O}_3 \dots \text{As}_2\text{O}_5$	43.9...53.0

The effect of the atmospheric influence can also be explained in a non-contradictory manner in terms of the thermochemical approach. The analysis of data in the table shows that the exothermic effect of the 3-, 4-, 5-valence arsenic atoms reaction with oxygen is greater than the oxygen–copper and oxygen–sulphur reactions. This exothermic effect is also greater than that of the reaction of arsenic or copper atoms with sulphur. This enables us to assume that the overall PCI rate in air increases specifically due to the interaction of atmospheric oxygen with arsenic atoms. The acceleration of the PCI interaction processes should be especially noticeable in samples without excess sulphur, such as thin-film samples without surplus of sulphur, in agreement with the experimental results.

References

- [1] M.T. Kostyshin, E.V. Mikhailovskaya, P.F. Romanenko, *Sov. Phys.—Solid State* 8 (1966) 451.
- [2] A.V. Stronski, *Microelectronic Interconnections and Assembly*, NATO ASI Series 3, High Technology, Vol. 54, 1996, p. 263.
- [3] I.Z. Indutnyi, et al., *Photostimulated Interactions in Metal-Semiconductor Structures*, Naukova Dumka, Kiev, 1992 (in Russian).
- [4] M.V. Sopinskyy, et al., *J. Optoelectron. Adv. Mater.* 3(2) (2001) 383–388.
- [5] N.V. Sopinskii, I.Z. Indutnyi, M.Yu. Gusev, *Zh. Nauchn. Prikl. Fotograf.* 41 (1) (1996) 32 (in Russian).
- [6] N.V. Sopinskii, *Optoelectronics, instrumentation and data processing*, *Avtometriya* (1) (1997) 95.
- [7] N.V. Sopinskii, *Russ. Microelectron.* 30 (1) (2001) 35.
- [8] A.V. Novoselova, V.B. Lazareo (Eds.), *Physicochemical Properties of Semiconductor Substances*, Nauka, Moscow, 1979.
- [9] O.P. Zefirov (Ed.), *Thermodynamical Properties of Inorganic Substances*, Atomizdat, Moscow, 1965.
- [10] G.V. Samsonov (Ed.), *Physicochemical Properties of Oxides*, Metallurgiya, Moscow, 1978.
- [11] K. White, B. Kumar, A.K. Rai, *Thin Solid Films* 161 (1988) 139.
- [12] I.M. Pecherichin, I.I. Kryzhanovskii, M.D. Mikhailov, *Fiz. Chim. Stekla* 24 (6) (1998) 721 (in Russian).



ELSEVIER

Physica B 308–310 (2001) 1057–1060

PHYSICA B

www.elsevier.com/locate/physb

Native defects and rare-earth impurities interaction in IV–VI crystals

D. Zayachuk^{a,*}, Ye. Polyhach^a, E. Slynko^b, O. Khandozhko^b,
V. Kempnyk^c, D. Baltrunas^d

^a Lviv Polytechnic National University, Semicond. Electronics Department, 12 vul. Bandery, 290646 Lviv, Ukraine

^b Institute of Material Science NASU, Chernivtsy, Ukraine

^c Institute of Materials, Lviv, Ukraine

^d Institute of Physics, Vilnius, Lithuania

Abstract

Both EPR spectra of Gd impurity and ^{119}Sn Mössbauer spectra in $\text{Pb}_{1-x}\text{Sn}_x\text{Te}$ grown from the melt by Bridgman method and doped with Gd impurity during the growth process were investigated. It was ascertained that EPR spectra behavior depended on rare-earth impurity concentration, doping method and matrix composition. It was shown that there were some correlations between Gd EPR spectra behavior and ^{119}Sn Mössbauer spectra parameters in doping crystals under investigation. The results obtained are treated on the basis of the model “Gd impurity–Te-vacancy” complexes, whose creation is caused by the interaction between point defects in the matrix and Gd impurity ions during growth process. © 2001 Elsevier Science B.V. All rights reserved.

Keywords: EPR; Mössbauer effect; Native defects; Gadolinium

1. Introduction

Investigations of rare-earth element (REE) impurities behavior in semiconductors and their influence on physical properties as well as extension of their practical applications are of great scientific interest at the moment [1–4]. Due to the “cleaning effect” caused by REE and their electronic configuration being different from other impurities as well as the presence of unfilled 4f-electron shells, it could be possible to improve operating parameters of doped semiconducting materials and to create semiconductors with new physical properties for fiber-optics communication and spintronics.

This work keeps on methodical investigation of Gd impurity behavior in lead and tin telluride crystals [4–6]. Its main aim is to provide a model of Gd^{3+} charge state creation in materials under the investigations suggested in the preceding work [6] with new arguments. According to this model Gd^{3+} ion exists as a component part of

“Gd impurity–Te-vacancy” complex and arises out of interaction with Te vacancy. This conclusion was drawn during the investigations of $\text{PbTe}:\text{Gd}$ crystal, where Gd was added as a hyperstoichiometric dopant. Present work is an extension of this case, in which Gd was added as a metal component substituting dopant, during the growth from the melt of both $\text{Pb}_{1-x}\text{Gd}_x\text{Te}$ and $\text{Pb}_{1-x-y}\text{Sn}_y\text{Gd}_y\text{Te}$ solid solutions. It was assumed that if Te vacancy really takes a dominant part in Gd^{3+} charge state creation, then it should be indicated in Gd EPR spectra depending on doping method and metal sublattice composition of $\text{Pb}_{1-x}\text{Sn}_x\text{Te}$, because these factors are directly connected with Te vacancies concentration. Obtained investigation results are presented below.

2. Samples and experiments

Single crystals of PbTe and its solid solutions with SnTe , grown from the melt by Bridgman method and doped with Gd, during the growth process, have been

*Corresponding author.

E-mail address: zayachuk@polynet.lviv.ua (D. Zayachuk).

investigated by means of EPR and ^{119}Sn Mössbauer spectroscopy. Gd impurity was added into the crystals as a stoichiometric lead substituting component according to the following chemical formula $\text{Pb}_{1-x-y}\text{Sn}_x\text{Gd}_y\text{Te}$. Gd is a donor impurity in the investigated crystals and its segregation coefficient strongly depends on impurity concentration in the melt [5]. There exists a possibility to create a growth $n \rightarrow p$ transition by taking Gd in a right y amount within every grown crystal and thus obtaining both n - and p -type samples for further investigations. This factor is of great importance due to the main aim of investigation because a type of crystal conductivity in Pb and Sn tellurides is conditioned by the dominant type of point defects in it. If the Te vacancies concentration predominates over the metal vacancies, then the crystal possesses n -type conductivity, otherwise the crystal possesses p -type conductivity [7]. So, initial Gd concentration was taken equal to $y = 0.005$ for all solid solution compositions investigated, $x = 0; 0.05$ and 0.2 .

EPR spectra and ^{119}Sn Mössbauer spectra were studied according to techniques described in Refs. [4,6]. Mössbauer investigations were carried out only at room temperature, and EPR experiments at both room and liquid nitrogen temperatures. Real Gd concentration in crystals was determined by means of electron microprobe analysis with "Camebax" analyzer.

3. Results obtained

Experimental EPR data presented for systems under investigation together with other previously obtained results [6] have demonstrated the following. Main factors which influence the behavior of EPR spectra are impurity concentration, doping method and chemical composition of the matrix around the impurity ion, whereas Pb and Sn are the elements from the same group, and there is a continuous series of their telluride solid solutions crystallizing into NaCl-type cubic lattice. Furthermore, all these factors are interlocked. This means, for example, that the presence of Gd being present in sufficient concentration in the crystal may or maynot be revealed by EPR measurements depends on the composition and conductivity type of $\text{Pb}_{1-x}\text{Sn}_x\text{Te}$ matrix whether a Gd may or maynot be revealed by EPR measurements in materials with the same type of conductivity and composition depends on the way in which it was added—as a hyperstoichiometric dopant or as a metal component substituting stoichiometric one.

With respect to the main task of experiments, EPR spectra of n - and p -type samples made from ingot regions situated close to $n \rightarrow p$ transition were of greatest interest. These samples differed slightly from each other in their Gd concentration, but differed fundamentally in type and concentration of dominant vacancies in them,

which define the type of conductivity and free carrier concentration in crystals under investigation. Type conductivity inversion of the ingot was observed at different real Gd concentrations $N_{\text{pn}}(\text{Gd})$ depending on melt composition. $N_{\text{pn}}(\text{Gd})$ was changed from $\sim 1 \times 10^{19} \text{ cm}^{-3}$ for $\text{Pb}_{1-x}\text{Sn}_x\text{Te}$ crystal surrounded for $x = 0$ up to $\sim 1 \times 10^{20} \text{ cm}^{-3}$ for nominal composition $x = 0.2$. Main experimental results obtained can be summarized as follows:

- (I) EPR has always been detected in doped n -type crystals for any composition of crystal matrix for x region investigated.
- (II) EPR has been detected or not in doped p -type crystals depends on both crystal composition and doping method.
- (III) EPR has never been detected in doped p -type crystals for nominal composition $x = 0.2$ of $\text{Pb}_{1-x}\text{Sn}_x\text{Gd}_y\text{Te}$ and in p - $\text{PbTe}:\text{Gd}$ doped with Gd as a hyperstoichiometric impurity.
- (IV) Seven fine structure lines corresponding in general terms to Gd^{3+} ion in cubic symmetry local surrounding have been detected only in Sn-free samples of both p - and n - $\text{Pb}_{1-x}\text{Gd}_y\text{Te}$ crystals with Gd concentration less than $1 \times 10^{20} \text{ cm}^{-3}$ in them, Fig. 1.

Fine structure of the EPR spectra was certainly not observed in Sn-containing crystals despite the fact that these samples had perfect crystal structure and were single crystals (minimum amount of Sn was $x \sim 0.02$ in samples made from ingot with nominal composition $x = 0.05$ due to segregation effects). It is for $[001]$ orientation of magnetic field B corresponding to maximum spectrum spread for $\text{Pb}_{1-x}\text{Gd}_y\text{Te}$ that one spectrum line broadened in a greater or lesser degree depending on the real Gd concentration was always registered in n -type $\text{Pb}_{1-x-y}\text{Sn}_x\text{Gd}_y\text{Te}$ crystals. Position of this line was almost the same as for the central fine

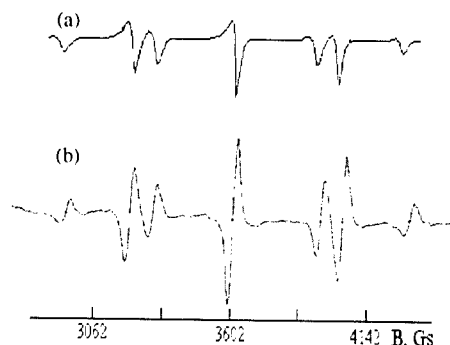


Fig. 1. EPR spectra of $\text{Pb}_{1-x}\text{Gd}_y\text{Te}$ crystals at room temperature: (a) p -type conductivity, $N_{\text{Gd}} = 7.3 \times 10^{18} \text{ cm}^{-3}$ and (b) n -type conductivity, $N_{\text{Gd}} = 2.2 \times 10^{19} \text{ cm}^{-3}$.

structure line of the $\text{Pb}_{1-x}\text{Gd}_x\text{Te}$ EPR spectrum. EPR spectra as a one week intensity line were registered in p-type ingot region close to the grown n→p transition for crystals with $x = 0.05$ only at mainly liquid nitrogen temperature, and were not registered at all in crystals with nominal composition $x = 0.2$, despite a rather high Gd concentration— $\sim(7-8) \times 10^{19} \text{ cm}^{-3}$ —in that ingot region. It should be mentioned here that EPR spectra was registered at both room and liquid nitrogen temperatures in n-PbTe:Gd crystals with Gd concentration that cannot be registered by electron microprobe analysis— $N(\text{Gd}) \ll 10^{18} \text{ cm}^{-3}$.

4. Discussion

We believe that the presented results of the experimental investigations of $\text{Pb}_{1-x-y}\text{Sn}_x\text{Gd}_y\text{Te}$ solid solution EPR spectra give the seal to our model about the origin of the Gd^{3+} charge state in doped lead telluride crystals described above. According to this model, Gd^{3+} ion arises out of Coulomb interaction between Gd^{2+} ion and positive charge point defect (Te vacancy), whereupon Te vacancy captures $5d^1$ electron of Gd^{2+} and makes it a Gd^{3+} .

Due to the constitution diagram specificity [7], tin percentage increase in $\text{Pb}_{1-x}\text{Sn}_x\text{Te}$ leads to a tellurium content increase in the crystals grown, and to a corresponding probability decrease of Te vacancy creation as a result of this. Using Gd as a doping impurity during growth from the melt also decreases total Te vacancy concentration in ingots. This was confirmed by recent Mössbauer investigations of SnTe:Gd crystals [4]. However, this tendency not only belongs to SnTe, but also for solid solutions of SnTe basis and even for not rich SnTe ones. It is clearly shown on the Mössbauer spectra of n- and p-type crystals grown from the gadolinium doped melts for $x = 0.07$, Fig. 2.

Line width Γ of Mössbauer spectrum is defined by local surrounding symmetry of Mössbauer ion and it increases when this symmetry decreases. Γ is always smaller in p-type samples for the same composition in crystals under investigation. As was shown in [4], such a behavior of Γ corresponds to Te vacancy concentration, which is much lower in p-type crystals. Electrostatic field of these vacancies deforms the local cubic symmetry of ^{119}Sn surrounding the crystals.

Taking into consideration the facts mentioned just above as well as the fact that homogeneity region in $\text{Pb}_{1-x}\text{Sn}_x\text{Te}$ for $x \geq 0.2$ never crosses stoichiometric line and fully corresponds to Te-rich compositions [7], there is every reason to believe that Te vacancy concentration in p-type region of $\text{Pb}_{1-x-y}\text{Sn}_x\text{Gd}_y\text{Te}$ ingot grown from the melt for $x \approx 0.2$ should be very low. According to the model presented this should make Gd^{3+} states

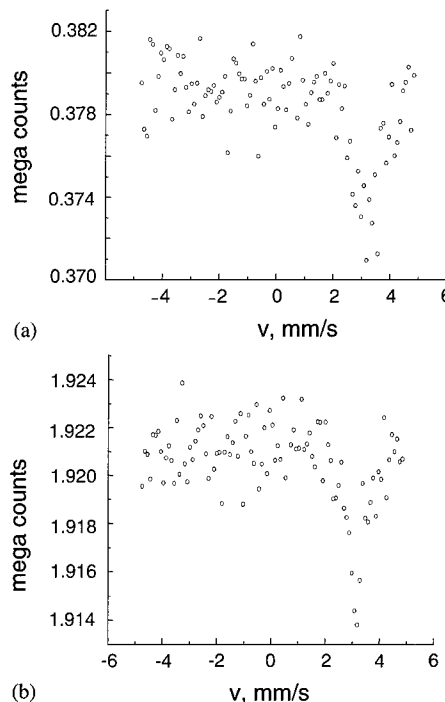


Fig. 2. ^{119}Sn Mössbauer spectra both the n- (a) and p-type conductivity (b) $\text{Pb}_{0.93}\text{Sn}_{0.07}\text{Te}$ crystals doped with gadolinium. Mössbauer spectra parameters: a — $\delta = 3.55 \text{ mm/s}$, $\Gamma = 0.90 \text{ mm/s}$, $S = 0.037 \text{ arb. units}$; and b — $\delta = 3.55 \text{ mm/s}$, $\Gamma = 0.80 \text{ mm/s}$, $S = 0.038 \text{ arb. units}$.

creation very unlikely. This is confirmed by the absence of EPR signal in those crystals despite a rather high— $\sim 7 \times 10^{19} \text{ cm}^{-3}$ —Gd concentration in them. In doped n-type crystals, Te vacancy becomes a dominant point defect. That is why p→n transition from p- to n-type region in doped ingot must be accompanied by a strong increase of V_{Te} concentration. Intensive EPR signal being detected in n-region after transition despite very small increase of Gd concentration, indicates that just Te vacancies are the reason for EPR sensitive state of Gd ion— Gd^{3+} state.

Both the appearance of the EPR spectra in p- $\text{Pb}_{1-x-y}\text{Sn}_x\text{Gd}_y\text{Te}$ crystals for $x = 0.05$ and their rather high intensity for $x = 0$ mean that the difference in degree of order between metal sublattice and chalcogen sublattice becomes lower, while x reduces from 0.2 to 0, so V_{Te} concentration becomes sufficient despite V_{Me} domination. It coincides well with the fact that vacancies in points of the SnTe metal sublattice are generated more easily than in PbTe, because relaxation around the free point gives a larger energy effect [8]. Comparing the absence of the EPR spectra in p-PbTe:Gd crystals and their presence in p- $\text{Pb}_{1-y}\text{Gd}_y\text{Te}$, a conclusion can be drawn that Gd decreases average vacancy concentration in IV–VI crystals more effectively, while it is added as a

hyperstoichiometric dopant into the melt rather than as a metal component substituting dopant. Also it is natural that in that case metal components dominate due to growth conditions making it more difficult to obtain p-type crystals with a dominant Te component in them.

Finally, we would like to pay attention to the following. Besides the correlation described above between EPR data for Gd ions and ^{119}Sn Mössbauer spectroscopy data, experimental results correlate in one important aspect as well. V_{TC} Coulomb field deforms not only cubic symmetry of ^{119}Sn ion local surrounding, which is indicated by line width Γ increasing in Mössbauer spectra, but also deforms, cubic symmetry of Gd ion local surrounding, and that deformation is actually observed in EPR spectra. Fine structure lines positioned in the Gd^{3+} EPR spectra of $\text{Pb}_{1-x}\text{Gd}_x\text{Te}$ is never symmetric, and line intensity ratios never match the binomial 16:12:15:7—a theoretical ratio for paramagnetic ion in the crystal field of cubic symmetry [9]. However, these questions are matter of special investigation.

5. Conclusions

The presented results of experimental investigations of the $\text{Pb}_{1-x}\text{Gd}_x\text{Te}$ single crystals give the seal to the

model according to which gadolinium ions interact with native point defects of crystal lattice during the growth process. One of the results of that interaction is Gd^{3+} charge center creation as a component part of the “Gd impurity–Te vacancy” complex.

References

- [1] H.H. Gao, A. Krier, V.V. Sherstnev, *Semicond. Sci. Technol.* 14 (1999) 441.
- [2] T. Maruyama, H. Sasaki, S. Morishima, K. Akimoto, *Phys. Stat. Sol. (B)* 216 (1999) 629.
- [3] P.H. Haumesser, R. Gaumi, B. Vianal, E. Antic-Fidancev, D. Vivien, *J. Phys.: Condens. Matter* 13 (2001) 5427.
- [4] D.M. Zayachuk, Ye.O. Polyhach, V.I. Mikityuk, D. Baltrunas, *Phys. Stat. Sol. (B)* 225 (2001) 311.
- [5] D.M. Zayachuk, E.L. Matulenien, V.I. Mikityuk, *J. Cryst. Growth* 121 (1992) 235.
- [6] D.M. Zayachuk, V.I. Kempnyk, W. Bednarsky, S. Waplak, *J. Magn. Magn. Mater.* 191 (1999) 207.
- [7] G. Nimtz, B. Schlicht, in: *Narrow-gap Semiconductors: Narrow Gap Lead Salts*, Springer, Berlin, 1985, pp. 1–117.
- [8] Yu.G. Sidorov, I.V. Sabinina, *J. Phys. Chem.* 59 (1985) 2717.
- [9] A. Abragam, B. Bleaney, *Electron Paramagnetic Resonance of Transition Ions*, Dover Publications, New York, 1970.



ELSEVIER

Physica B 308–310 (2001) 1061–1064

PHYSICA B

www.elsevier.com/locate/physb

Quantum chemical modeling of chlorine-doped defects in a-Se

A.S. Zyubin, O.A. Kondakova*, S.A. Dembovsky

Institute of General and Inorganic Chemistry RAS, Leninsky pr. 31, 119991 Moscow, Russia

Abstract

The structure and stability of chlorine-doped defects in amorphous Se were investigated by means of quantum chemical modeling in the frame of cluster approach at B3LYP level. It was found that formation of isolated charged defects (valence alternative pair) is energetically unfavorable. The most stable are terminal positions of Cl atoms at the Se chains (Cl–(Se–)_n). The interaction of Cl-containing fragments of such chains with Se chains or rings so as with hypervalent configurations (HVC) with over-coordinated Se atoms leads to formation of new Cl-doped defects with over-coordinated Se and Cl atoms. Similar configurations are able to activate bonds switching in process of network rearrangement and transformation of HVC to usual network fragments. The destruction of HVC should reduce the concentration of traps for charge carriers. © 2001 Elsevier Science B.V. All rights reserved.

PACS: 31.15.A

Keywords: a-Se; Structure; Defects; Quantum chemical modeling

1. Introduction

In accordance to Refs. [1–3], the introducing of small amount of Cl impurity (~1%) leads to drastic change of viscosity and the electrical characteristics of a-Se, in spite of the preceding proposal about a negligible influence such small additions at the properties of non-crystalline semiconductors. The acute drop of resistance up to 10⁹ Ωcm in a chlorine-doped selenium is accompanied by lowering of conductivity activation energy on 0.26 eV in comparison with non-doped a-Se. The similar results were obtained in the investigations of chlorine-doped liquid selenium [4].

The mechanism of such influence is still unclear. The main previous hypothesis is based on the model of charged centers D⁺, D[−] [5,6]. It is proposed that Cl atoms terminate already existing dangling bonds (D) or instill into Se–Se bonds destroying them with formation of Cl–(Se–)_n chains. In such cases, the Cl atoms are unable to form free charge carriers. In accordance with another variant Cl atom occupies the interstitial position attracting one electron from the lone pair of Se atom and forming C₂⁺ and Cl[−] centers with arising of volume

charge. Such interstitial Cl[−] atoms believed to be the main donor centers [3–5]. At the same time aside from C₂⁺ centers the chlorine atoms can form the other kinds of electron traps in a-Se [7,8]. The halogenated a-Se has a p-type of conductivity the same as the undoped selenium.

The introducing of Cl impurity into a-Se leads to formation of two additional bands (335 and 960 cm^{−1}) in the IR spectrum [9]. The first one is interpreted reliable enough as a vibration of Se–Cl terminal bond. The origin of the second band is still unclear.

The aim of this work is to consider the possible variants of Cl implantation into a-Se network, to investigate the structure and stability of charged and neutral Cl-containing defects, to estimate the participation of such defects in transformation of a-Se network and in destruction of HVC such as VAP-d and C₄⁰ described in the previous papers [10,11].

2. Calculation details

The calculations of the model systems were carried out in the frame of cluster model with (–Se–)_n chains as the main fragments of a-Se network, with termination of the boundary bonds by the H atoms. As a rule the active

*Corresponding author. Fax: +7-095-954-1279.

E-mail address: olgakond@hotmail.ru (O.A. Kondakova).

regions of model clusters were surrounded by two Se–Se links; in this case the influence of boundary atoms onto active region is weak. The geometry optimization was made at B3LYP approach [12] (density functional method). The influence of core electrons was modeled by LANL2 pseudopotential [13] with the appropriate split-valence basis set with the addition of polarizing d-AO. The relative energies of the optimized configurations were refined at the MP2 level (second order of the perturbation theory at the Moller–Plesset scheme). The calculations were made with GAUSSIAN-94 package [14]. The transition states were localized by QST2 method [14].

3. Results

The basic elements of a-Se network are the $(\text{--Se})_n$ chains. The interaction of Cl_2 molecules with such units leads to the more short new chains $\text{Cl}(\text{--Se})_m$ with Cl atoms at the terminal positions. The charge transfer to Cl atom is not very essential $\sim 0.17e$. The appropriate energy lowering calculated at B3LYP level is $\sim 0.82\text{ eV}$. The energies of $(\text{--Se})_n$ and $\text{Cl}(\text{--Se})_m$ chains were taken as zero for determination of relative stabilities of various Cl-containing defects.

The charged defects (valence alternative pare, VAP) were calculated with localization at Cl-containing defects both negative and positive charges. The Cl^+ center is able to form two bonds, and the appropriate configurations 1A and 1B (Fig. 1) were considered with three-coordinated negative center $\text{Se}(3,-)$ (1D, Fig. 1) [11,12] as counterpart (the notation $A(k,-)$ or $A(k,+)$ corresponds to charged defects, k is coordination number of atom A). The relative energies of such pairs are significantly higher than for initial chains (Table 1). The attempts to form interstitial Cl^- center in configuration similar to 1B leads to configuration 1C with single-coordinated Cl and three-coordinated Se atoms, similar to $\text{Se}(3,-)$ center [11,12], but with $\text{Cl}(\text{--Se})_m$ chain instead $(\text{--Se})_n$ one. The relative energy of such defect with positive $\text{Se}(3,+)$ counterpart (1D, Fig. 1) is high as well (Table 1). So, Cl-containing VAPs in Cl-doped a-Se have too high relative energies, similarly to pure a-Se. Additionally, we tried to check the possibility of interstitial location of neutral Cl atom, placing it near the middle of $(\text{--Se})_n$ chain. In this case, the nearest to Cl Se–Se bond was broken with formation of new $\text{Cl}(\text{--Se})_m$ chain and Se chain fragment with dangling bond. The formation of Cl^- center with redistributed positive charge at nearest Se atoms was not found.

The neutral Cl-containing defects is possible to form by interaction of Cl–Se terminal bond from $\text{Cl}(\text{--Se})_m$ chain with fragments of usual Se chain or HVC-defects in a-Se such as VAD-d or C_4^0 (Fig. 2). The rapprochement of Cl–Se bond and polar $>\text{Se}=\text{Se}$ fragment of

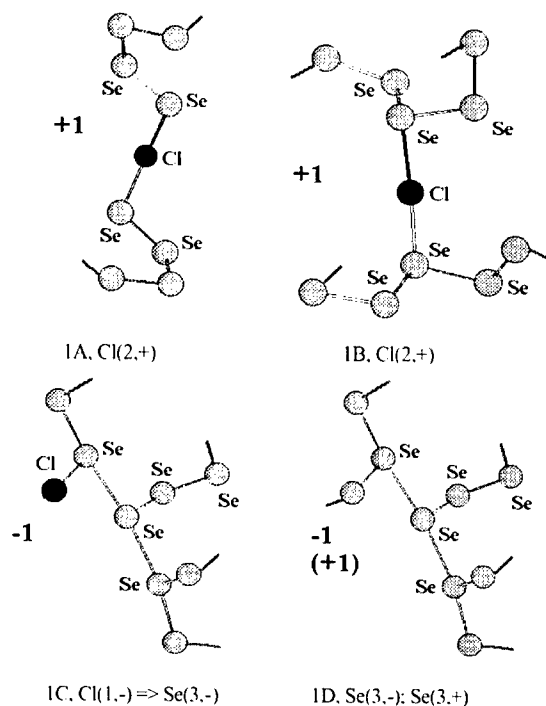


Fig. 1. Schematic representation of the charged Cl-containing defects.

VAP-d leads to formation of 3A transition state, passing to 3C structure. The barrier height for such transformation is not high ($\sim 0.5\text{ eV}$ at B3LYP level), and relative energies for the both configurations are lower than Se–Se bond energy (Table 1). The implantation of the Cl–Se fragment into 'weak' bond of C_4^0 HVC produces 3B TS (Fig. 3), which is transformed into the same 3C structure and usual Se chain. In this case, the barrier is slightly higher, nevertheless it is lower than 1 eV (Table 1). The 3C configuration is similar to C_4^0 HVC of a-Se, but with Cl atom instead of $\text{--Se}(\text{--Se})_k$ half-chain. It is possible to transform this Cl-containing HVC into new local minimum with just the same relative energy (Fig. 3, 3D), by reducing of approximately linear Cl–Se–Se angle to $\sim 60^\circ$. The barrier value for such transformation is small, ~ 0.3 and $\sim 0.4\text{ eV}$ at B3LYP and MP2 levels. The central fragment of this configuration has bi-pyramidal shape with similar Cl–Se and Se–Se bonds (Fig. 3). The 3D structure is ready to split into $\text{Cl}(\text{--Se})_m$ and usual Se chains by three different ways, passing through the barriers $\sim 0.44\text{ eV}$ (Table 1). This opportunity is able to change the direction of Se–Se chain. The relative energy of the appropriate TS is not very high (Table 1), and it is possible to form the 3D configurations directly from $\text{Cl}(\text{--Se})_m$ and usual Se chains. Such configuration is able to reduce the activation energy of bonds switching and network transformation in Cl-doped a-Se. The bonds switching with participating of

Table 1

Relative energies (eV) for different configurations of Cl-doped a-Se defects. Zero of energy corresponds to $(-\text{Se})_n$ and $\text{Cl}(-\text{Se})_n$ chains. The notations $A(k, +)$, $A(k, -)$ correspond to charged defects with k is coordination number of atom A. LM—local minimum, TS—transition state; the value in parenthesis corresponds to barrier height

Config.	Cl_2 and $(-\text{Se})_n$ chain	SeCl_4 and $(-\text{Se})_n$ chain	1A and 1D $\text{Cl}(2, +)$, $\text{Se}(3, -)$	1B and 1D $\text{Cl}(2, +)$, $\text{Se}(3, -)$	1C and 1D $\text{Cl}(1, -)$, $\text{Se}(3, +)$
B3LYP	0.82	0.36	5.7	5.0	4.1
Config.	3C, LM	3D, LM	3A, TS	3B, TS	TS 3D \rightleftharpoons chains
B3LYP	0.63	0.65	1.42 (0.50)	1.95 (0.79)	1.09 (0.44)
MP2	0.47	0.69	1.56 (0.53)	—	1.20 (0.51)

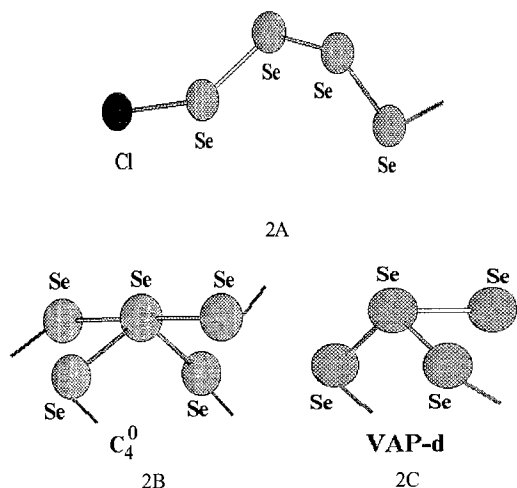


Fig. 2. The representation of $\text{Cl}(-\text{Se})_n$ chain and appropriate HVC.

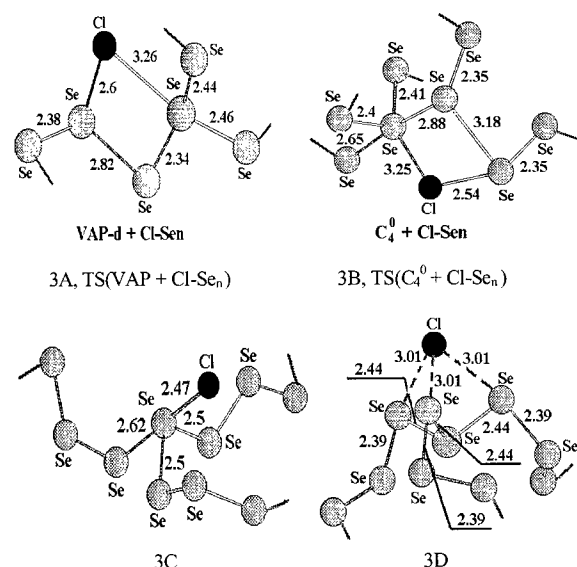


Fig. 3. The transition configurations for the interaction of $\text{Cl}(-\text{Se})_n$ chain and HVC (3A, 3B), metastable Cl-containing HVC (3C, 3D).

pure Se chains is related with potential barrier ~ 1.7 eV at the B3LYP level.

4. Conclusions

According to the obtained results the most energy favorable positions of chlorine atoms in the a-Se network are at the end of Se chains. In this case, Cl atoms terminate the Se–Se dangling bonds. The charged defects are very unstable and their concentration should be low. The interaction of terminal Cl–Se bonds with Se chains and with hypervalent configurations presented in a-Se creates neutral Cl-containing defects participating in bonds switching and destruction of HVC. Similar mechanisms are able to lower the activation energy of network transformation and to reduce concentration of HVC which are traps of charge carriers in a-Se.

Acknowledgements

This work was supported by Russian Foundation of Basic Research, Grant No 00-03-32646.

References

- [1] G.B. Abdullaev, S.I. Mekhtieva, D.Sh. Abdinov, G.M. Aliev, Phys. Stat. Sol. 11 (1965) 891.
- [2] V.A. Twaddell, W.C. Lacourse, J.D. Mackenzie, J. Non-Cryst. Sol. 8–10 (1972) 831.
- [3] M.C. Assuncao, J. Non-Cryst. Sol. 136 (1991) 81.
- [4] M. Yao, S. Hosokawa, H. Endo, J. Non-Cryst. Sol. 59 & 60 (1983) 1083.
- [5] N.F. Mott, E.A. Davis, Electronic Processes in Non-Crystalline Materials, Clarendon Press, Oxford, 1979.
- [6] B.L. Gelmont, B.T. Kolomiets, K.D. Tsendin, Phys. Stat. Sol. A 91 (1985) 319.
- [7] Y. Takasaki, E. Mauryama, T. Uda, T. Hirai, J. Non-Cryst. Sol. 59 and 60 (1983) 949.
- [8] M. Abkowitz, F. Jansen, J. Non-Cryst. Sol. 59 & 60 (1983) 953.
- [9] M.C. Assuncao, Infrared Phys. 31 (1991) 587.

- [10] S.A. Dembovsky, A.S. Zyubin, F.V. Grigor'ev, Gl. Phys. Chem. 26 (2000) 333.
- [11] A.S. Zyubin, F.V. Grigor'ev, S.A. Dembovsky, Russ. J. Neorg. Chem. 46 (2001) 1245.
- [12] A.D. Becke, J. Chem. Phys. 98 (1993) 5648.
- [13] M.W. Schmidt, K.K. Baldrige, J.A. Boatz, et al., J. Comput. Chem. 14 (1993) 1347.
- [14] J. Frisch, A. Frisch, J.B. Foresman, GAUSSIAN 94 (Revision D.1 and higher), Gaussian Inc., Pittsburg PA, 1995.



ELSEVIER

Physica B 308–310 (2001) 1065–1068

PHYSICA B

www.elsevier.com/locate/physb

Photoluminescence of vacuum-deposited CuGaS₂ thin films

J.R. Botha^{a,b,*}, M.S. Branch^b, A.G. Chowles^c, A.W.R. Leitch^b, J. Weber^a^a *Inst. für Tieftemperaturphysik, Dresden University of Technology, D-01062 Dresden, Germany*^b *Department of Physics, University of Port Elizabeth, PO Box 1600, Port Elizabeth 6000, South Africa*^c *Department of Physics, VISTA University, Private Bag X316, Port Elizabeth 6000, South Africa*

Abstract

The photoluminescence (PL) properties of vacuum-deposited CuGaS₂, produced by the co-evaporation of elemental sources, is reported for the first time. Free excitonic PL is observed up to room temperature. The green PL dominating at ~2.4 eV for slightly Ga-rich material, and at ~2.3 eV for slightly Cu-rich material, involves shallow donor–acceptor pair recombination. It appears that the same shallow donor with binding energy ~53 meV is involved in the recombination process. The dominant acceptor in Cu-rich material is obtained at ~210 meV above the valence band, while a shallower acceptor dominates in Ga-rich material. Possible origins of these defects are proposed. © 2001 Elsevier Science B.V. All rights reserved.

Keywords: CuGaS₂; Vacuum deposition; Photoluminescence

1. Introduction

CuGaS₂ is a member of the I–III–VI₂ chalcopyrite semiconductor family, with a direct band gap energy of 2.53 eV at 0 K [1]. It is epitaxially compatible with III–V substrates such as GaAs and GaP and can be grown at moderate temperatures [2]. To date, n-type material has not been realized. Despite its attractiveness for optoelectronic applications, there is presently only an elementary understanding of the influence of intrinsic defects on the radiative processes in the material. This is true for most of the chalcopyrite semiconductors, a possible exception being CuInSe₂, for which a coherent picture is beginning to emerge [3]. For CuGaS₂ the poor understanding at present arises mainly from a lack of experimental data, and from the fact that the composition of the material investigated is often unknown. Furthermore, the formation energies for intrinsic defects have not been determined. In order to gain more clarity on the defect chemistry in CuGaS₂, it is essential to study the dependence of the optical and electrical properties on stoichiometry. The required control over

this parameter is best obtained during epitaxial growth. In the present work, epitaxial growth was achieved by co-evaporation of elemental sources onto heated GaAs substrates. Preliminary results on the photoluminescence (PL) of slightly Cu-rich and Ga-rich material is discussed. This is the first demonstration of PL from layers produced by this method.

2. Experimental details

Thin films of CuGaS₂ were produced in vacuum (background pressure $\cong 10^{-5}$ Torr) by the co-evaporation of the three elemental sources onto GaAs(100) substrates, heated to 600°C. The Cu, Ga and S sources (99.999% purity or better) were kept at ~1150°C, 850°C and 80°C, respectively. X-ray diffraction on the layers always revealed the diffraction peaks expected for the chalcopyrite phase and indicated that the layers were preferentially orientated either with the *c*-axis or the *a*-axis perpendicular to the substrate. Layer thicknesses varied between 0.4 µm and 0.8 µm. The composition of the layers was determined from energy dispersive X-ray spectroscopy. The surfaces of Ga-rich layers had a slight grainy texture, while layers deposited under Cu-rich

*Corresponding author. Tel.: +351-463-5170; fax: +351-463-7060.

E-mail address: botha@physik.tu-dresden.de (J.R. Botha).

conditions became increasingly covered in crystallites containing only Cu and S in the atomic ratio of approximately 1:1. PL spectra were obtained using an Ar⁺-laser (458 nm) or a Kr⁺-laser (413 nm) for excitation. The luminescence was dispersed by a 1 m monochromator (calibrated with the 632.8 nm line of a HeNe laser) and detected using a GaAs photomultiplier.

3. Results and discussion

In Fig. 1 the 4.2 K PL spectra obtained for layers with different compositions are compared. The S-content varied between 46 and 49 at%. For slightly Cu-rich material, the spectra are dominated by lines between 539.0 nm (2.300 eV) and ~560.0 nm. For slightly Ga-rich material, the dominant line is at 517.0 nm (2.398 eV). Smaller Cu/Ga-ratios (≤ 1) lead to a quenching of the near-band edge PL in favor of broad bands involving deeper lying states. For layers #1 to #4, weak luminescence is also observed between 495 and 505 nm. In this paper, the PL measured for layers #1 and #4 (subsequently referred to as Cu-rich and Ga-rich) in the range 490 nm to 560 nm, will be discussed. It will only be mentioned that the PL observed above 600 nm for some layers, appears to be typical for S-poor material: the broad band seen for layer #3 (but almost absent for layer #2) has been suggested by Massé [4] to involve S-vacancies, since it disappeared when chemical vapor transport (CVT) grown single crystals were annealed in a S atmosphere.

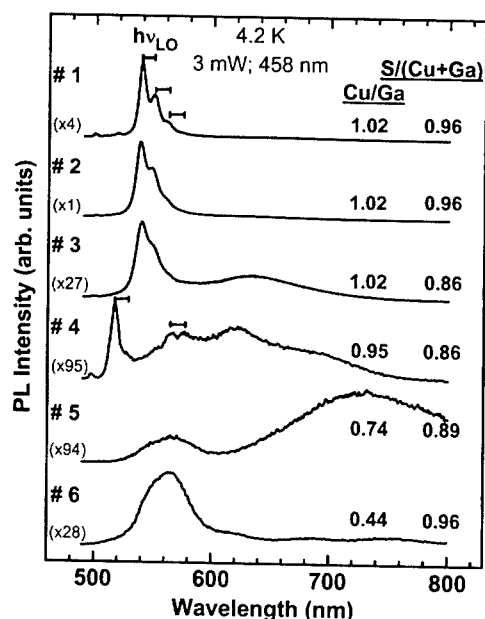


Fig. 1. Typical PL spectra measured at 4.2 K for vacuum-deposited CuGaS₂ with different compositions.

The PL measured for slightly Cu- and Ga-rich material in the range 490–505 nm, is compared in Fig. 2. For the Cu-rich layer, five lines are distinguished at ~495.5 nm (2.502 eV), 497.3 nm (2.493 eV), 498.9 nm (2.485 eV), 500.5 nm (2.477 eV) and 503.1 nm (2.464 eV). Also indicated are the reported range for the recombination of free excitons (FX) in single crystals [1,5] and the calculated positions for donor-bound (D^0, X) and acceptor-bound (A^0, X) exciton recombination, using binding energies for effective mass donors and acceptors of 48 meV and 127 meV, respectively. Effective masses for electrons and holes of $0.26m_0$ and $0.69m_0$, respectively [6] and a dielectric constant $\epsilon_0 = 8.6$ [5] were used, while the binding energies of the bound excitons were estimated from Atzmüller et al. [7]. The peaks measured at ~495.5 nm and 497.3 nm are attributed to FX and (D^0, X) recombination, respectively. The donor involved in the latter transition is probably the same defect giving rise to the line at 500.5 nm (i.e. 53 meV below E_g), the position of which correlates very well with the calculated position (499.5 nm; 2.482 eV) for a transition between a neutral effective mass donor and the valence band (D^0, h). The line at 498.9 nm does not involve an effective mass acceptor, but is attributed to an exciton bound to a deeper acceptor, as discussed below. The line at 503.1 nm is of unknown origin.

The PL for Ga-rich material is broader with a maximum at ~496.7 nm (2.496 eV) and a shoulder at ~498.5 nm (2.487 eV). The latter is of extrinsic origin (i.e. involves defects/impurities) and disappeared above 120 K, while the former line persisted up to 290 K. The energy shift measured for the 496.7 nm line relative to its position at 1.9 K is plotted in Fig. 3 (circles) versus temperature, and compared with the reported change of the A-exciton position obtained from photoreflectance measurements on CVT-grown single crystals [2]. From the identical shifts observed, it is concluded that the line is due to FX recombination.

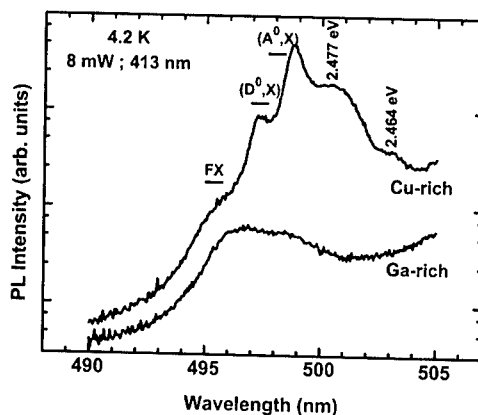


Fig. 2. Comparison of low temperature PL for slightly Cu-rich and Ga-rich material in the excitonic spectral range.

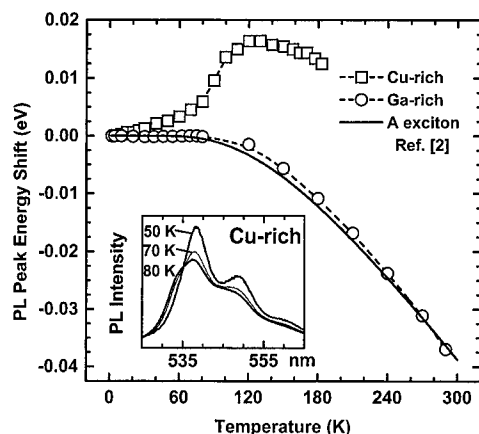


Fig. 3. Temperature dependence for the positions of the PL lines at ~ 496.7 nm in Ga-rich, and at 539.0 nm in Cu-rich material. The dotted lines are guides to the eye.

The strong green PL from slightly Cu-rich material (layer #1-Fig. 1) is attributed to donor-acceptor (D^0, A^0) pair transitions, which interact with lattice phonons. Typically, up to four lines are observed. The intensities are Poisson distributed, and the energy spacing is ~ 45 meV, which correlates with the highest energy $\Gamma(\text{LO})$ phonon modes (43.1, 48 and 49.5 meV [8]). The energy shift of the zero phonon line relative to 3.8 K, is also shown in Fig. 3 (squares). Between 60 K and 120 K the line “blue-shifts” by ~ 14 meV. At the same time, a shoulder was seen to develop on its high-energy side (inset Fig. 3) at ~ 534.0 nm (2.322 eV). These results are consistent with the evolution of a free-to-bound type of transition from the pair emission, where the deeper center involved has a binding energy of ~ 210 meV. In the same temperature range, the integrated PL intensity for the series of lines was thermally quenched with an activation energy of 53 ± 9 meV, which is ascribed to the ionization of the shallower center. The participation of a shallow center is also deduced from the dependence of the zero phonon line energy $h\nu_m$ on laser power (P). This is plotted in Fig. 4 (squares). The solid line is a best-fit using the expression [9]:

$$P = D \frac{(h\nu_m - h\nu_{\text{inf}})^3}{h\nu_B + h\nu_{\text{inf}} - 2h\nu_m} \exp\left(-\frac{2(h\nu_B - h\nu_{\text{inf}})}{h\nu_m - h\nu_{\text{inf}}}\right). \quad (1)$$

Here, D is a proportionality constant, $h\nu_{\text{inf}}$ is the peak position for infinite pair separation, and $h\nu_B - h\nu_{\text{inf}}$ yields the binding energy of the shallower species. The fit yields a binding energy for the shallower defect of 32 ± 4 meV (the error excludes the errors in the data). A comparison of this value and the 53 meV thermal activation for the quenching of the PL, with the position of the line at 2.477 eV, strongly suggests

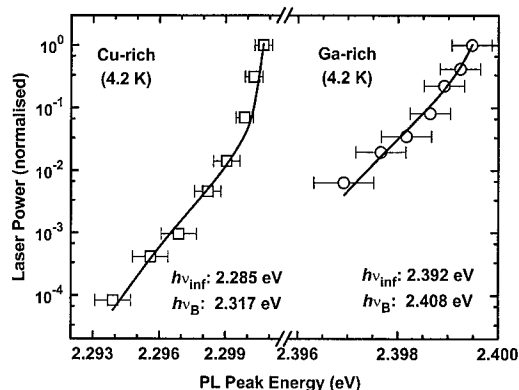


Fig. 4. Laser power induced shift at 4.2 K for the PL lines at 517.0 nm in Ga-rich and at 539.0 nm in Cu-rich material. The solid lines are least-squares-fits to Eq. (1).

that the shallower level is an effective mass-like donor with binding energy of 53 meV, and that the level at ~ 210 meV from the band edge is due to an acceptor. This acceptor is probably also the center binding the exciton, giving rise to the line at 498.9 nm in Fig. 2.

The green PL at 517.0 nm (phonon replica at 527.0 nm) dominating for slightly Ga-rich material, also appears to be (D^0, A^0) in nature. Between 30 and 80 K this line was quenched with an activation energy of 45 ± 5 meV. The shift of the zero phonon line with laser power (Fig. 4, circles) is again typical for pair emission involving an effective mass-like center. A binding energy for the shallower center of 16 ± 4 meV was extracted from the fit to Eq. (1) (solid line), which will contain a large uncertainty due to the limited range of laser power studied.

In summary, it is tempting to assume from the above, that the same shallow level is involved in the green PL dominating for both Cu- and Ga-rich layers. The most likely candidate is the donor at ~ 53 meV below the conduction band edge, deduced from the PL for the slightly Cu-rich layer. Since both layers are S-deficient, this donor is possibly the S-vacancy. A change in the Cu/Ga-ratio then seems to change the dominant acceptor forming in the material, with the acceptor level in Cu-rich material being ~ 210 meV above the valence band. A possible candidate for this acceptor, is the Cu_{Ga} -antisite. The binding energy of the deeper center involved in the pair luminescence for the Ga-rich layer, has not been determined here. However, the green PL at ~ 2.40 eV is typical for Ga-rich and S-deficient single crystals [10]. Bellabarba et al. [5] deduced from absorption measurements that the dominant acceptor in such material is 89 meV

above the valence band and ascribed it to the Cu-vacancy (V_{Cu}). It should also be noted that Zhang et al. [3] recently calculated that for n-type CuInSe_2 (i.e. Se-poor material), the Cu_{In} -antisite has the lowest formation energy in Cu-rich material, while the V_{Cu} has the lowest formation energy in In-rich material. If the same order holds for the corresponding defects in CuGaS_2 , it would fit in excellently with the above assignments. However, in the absence of calculated defect formation energies for CuGaS_2 , any defect assignment remains speculative.

Acknowledgements

J.R. Botha appreciates the financial support from the Alexander von Humboldt Stiftung and the South African National Research Foundation.

References

- [1] J.L. Shay, J.H. Wernick, Ternary Chalcopyrite Semiconductors, Pergamon, Oxford, 1975.
- [2] S. Shirakata, S. Chichibu, *J. Appl. Phys.* 87 (2000) 3793.
- [3] S.B. Zhang, S.-H. Wie, A. Zunger, H. Katayama-Yoshida, *Phys. Rev. B* 57 (1998) 9642.
- [4] G. Massé, *J. Appl. Phys.* 58 (1985) 930.
- [5] C. Bellabarba, J. González, C. Rincón, *Phys. Rev. B* 53 (1996) 7792.
- [6] S. Shirakata, K. Saiki, S. Isomura, *J. Appl. Phys.* 68 (1990) 291.
- [7] H. Atzmüller, F. Fröschl, U. Schröder, *Phys. Rev. B* 19 (1979) 3118.
- [8] J. González, E. Moya, J.C. Chervin, *Phys. Rev. B* 54 (1996) 4707.
- [9] E. Zacks, A. Halperin, *Phys. Rev. B* 6 (1972) 3072.
- [10] H. Miyake, M. Hata, Y. Hamamura, K. Sugiyama, *J. Cryst. Growth* 144 (1994) 236.



ELSEVIER

Physica B 308–310 (2001) 1069–1073

PHYSICA B

www.elsevier.com/locate/physb

Hall effect and surface characterization of Cu_2S and CuS films deposited by RF reactive sputtering

Y.B. He^{a,*}, A. Polity^a, I. Österreicher^a, D. Pfisterer^a, R. Gregor^a,
B.K. Meyer^a, M. Hardt^b

^a I. Physikalisches Institut, Justus-Liebig-Universität Giessen, Heinrich-Buff-Ring 16, D-35392 Giessen, Germany

^b Zentrale Biotechnische Betriebseinheit, Leihgesterner Weg 217, Justus-Liebig-Universität Giessen, D-35392 Giessen, Germany

Abstract

Cu_xS is one of the most prevalent minor phases co-existing in CuInS_2 films. In order to understand its influence on CuInS_2 , we first focus our study on the binary compound Cu_xS . Cu_2S and CuS films were deposited on float glass substrates using a reactive RF sputter process with optimized sputter parameters, such as power, temperature of the substrate, and the gas flow of the H_2S . X-ray diffraction spectra showed that the Cu_2S films have (002) preferential orientation, and both compounds have a hexagonal structure. The surface morphology and the composition of the layers were analyzed by atomic force microscopy and Rutherford back-scattering spectroscopy, respectively. X-ray photoelectron spectroscopy and ultraviolet photoelectron spectroscopy were used to characterize the layer surfaces, as well as the surface composition. Hall-effect measurements were carried out to determine the electrical properties of the films. © 2001 Elsevier Science B.V. All rights reserved.

PACS: 68.55.-a; 73.61.-r; 79.60.Bm

Keywords: Cu_xS ; Thin films; RF sputtering; Hall-effect measurement

1. Introduction

With a direct band gap of 1.55 eV and a high absorption coefficient of more than 10^4 cm^{-1} , CuInS_2 (CIS) has been regarded as a promising absorber for thin film solar cell applications [1]. So far, solar cells based on the CIS have achieved an energy total area conversion efficiency of 11.4% [2]. Cu_xS is one of the most prevalent minor phases co-existing in the CIS films independent from the production techniques and plays an important role both on the structural and electrical properties of the CIS. On the other hand, the Cu_xS ($x = 1-2$) thin films themselves are of interest due to numerous technological applications such as in applications of solar cells [3], in photothermal conversion of solar energy as solar

absorber coatings [4], and as selective radiation filters in architectural windows [5], as well as in electroconductive coatings deposited on organic polymers [6]. So it is important and interesting to study Cu_xS films from both points of view.

Up to date, several methods have been used to produce CIS and Cu_xS films [1,7]. The sputtering technique has the potential for industrial applications due to its advantages of simple and flexible control of the film stoichiometry over a large scale at relatively low cost. The initial goal of this work is to deposit CIS films by radio frequency (RF) reactive sputtering in one step. Prior to this, Cu_xS films have been prepared by the same process for comparison.

2. Experimental

Cu_xS films were prepared on bare float glass substrates by a reactive sputtering process. High-purity

*Corresponding author. Tel.: +49-641-99-33137; fax: +49-641-99-33119.

E-mail address: yunbin.he@physik.uni-giessen.de (Y.B. He).

(99.999%) argon was used to provide the plasma at a base pressure of 10^{-6} Torr, and H_2S (purity: 98.0%) was injected as reactive gas during the sputtering. A metallic 99.999% Cu circular plate with a diameter of 10.16 cm was used as the sputter target. The RF power was in the range between 50 and 300 W ($0.62\text{--}3.70\text{ W cm}^{-2}$), while the H_2S flow was varied from 2.0 to 10 sccm. The substrate temperature was changed from room temperature to 500°C . Typically the film thickness was in the range between 50 and 600 nm mainly depending on the sputtering power and time.

The structure of the layers was studied by X-ray Diffraction (XRD) using a Siemens D5000 diffractometer with $\text{Cu K}\alpha$ ($\lambda = 1.5418\text{ \AA}$) radiation. The surface morphology of the layers was studied by atomic force microscopy (AFM). Photoemission (XPS, UPS) experiments were performed using a VG ESCA system at a photon energy of 1253.6 eV ($\text{Mg K}\alpha$ radiation). The sample surface was sputtered with 4 kV Ar ions. The electrical properties, such as the carrier concentration, Hall mobility, and specific resistivity of the films were characterized by Hall-effect measurements in the temperature range between 77 and 400 K.

3. Results and discussion

3.1. X-ray diffraction

Fig. 1 shows the XRD spectra of $\theta\text{--}2\theta$ mode of three samples, and the standard JCPDS patterns of Cu, Cu_2S and CuS for comparison. It is clearly seen that pure Cu co-exists in the film when the H_2S flow is too low (Fig. 1a). The pure Cu_2S films with hexagonal structure can be obtained when the H_2S flow is sufficient, i.e. in the range of 5.0–9.0 sccm. These films have highly (002) preferential orientation (Fig. 1b), since only reflections from the (002), (004), and (006) planes are detected by the XRD. The full-width at half-maximum (FWHM) of the (004) diffraction peak is about 0.24° , which means the crystallinity of the films is very good. In our experiments, the main parameter for controlling the Cu/S ratio of the films is the H_2S flow, as well as the sputter power. By increasing the H_2S flow and decreasing the sputter power at the same time, pure CuS films with hexagonal structure were deposited (see Fig. 1c). These films are randomly distributed polycrystalline films.

3.2. Atomic force microscopy and scanning electron microscopy

The Cu cones segregation on the surface of the samples sputtered with insufficient H_2S flow can be directly observed by scanning electron microscopy

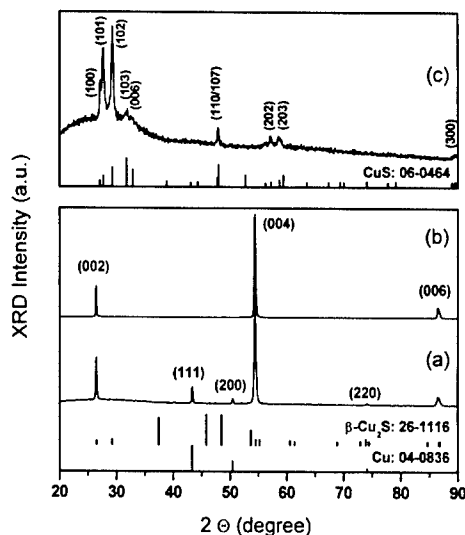


Fig. 1. The XRD spectra of samples sputtered under different conditions. Sample (a) was sputtered at 500°C with a sputter power of 200 W and H_2S flow of 3.5 sccm; sample (b) was sputtered at room temperature with a sputter power of 200 W and H_2S flow of 8.0 sccm; and sample (c) was sputtered at 200°C with a sputter power of 50 W and H_2S flow of 10.05 sccm.

(SEM) as shown in Fig. 2a. This confirms the XRD measurement on the same sample (Fig. 1a). Both pure Cu_2S and CuS films have very good crystallinity, which is not only indicated by the XRD measurements, but also directly supported by the AFM images of the surface of the samples (see Fig. 2b–e). While the Cu_2S film has an average grain size of about 200 nm, the CuS films show relatively smaller grains of around 80 nm, which is mainly due to the relatively lower sputter power. Compared with the CuS films, the Cu_2S films show more uniform and well-grown columnar grains on the surface.

3.3. XPS and UPS characterization

For surface characterization, XPS and UPS studies of Cu_xS samples with varying x values were carried out. The spectra were obtained from films cleaned by a short Ar^+ ion etching prior to the measurement to remove the surface contaminants. Two different samples were chosen for comparison: a CuS film with a Cu/S ratio of 1:1 and another with a Cu/S ratio of 3:2. These stoichiometry values were calculated by quantitative analysis of the XPS-spectra (Fig. 3a and b).

The UPS spectra of these two films are shown in Fig. 3c. The most striking difference is a shift of curve A (stoichiometric CuS) towards lower binding energies.

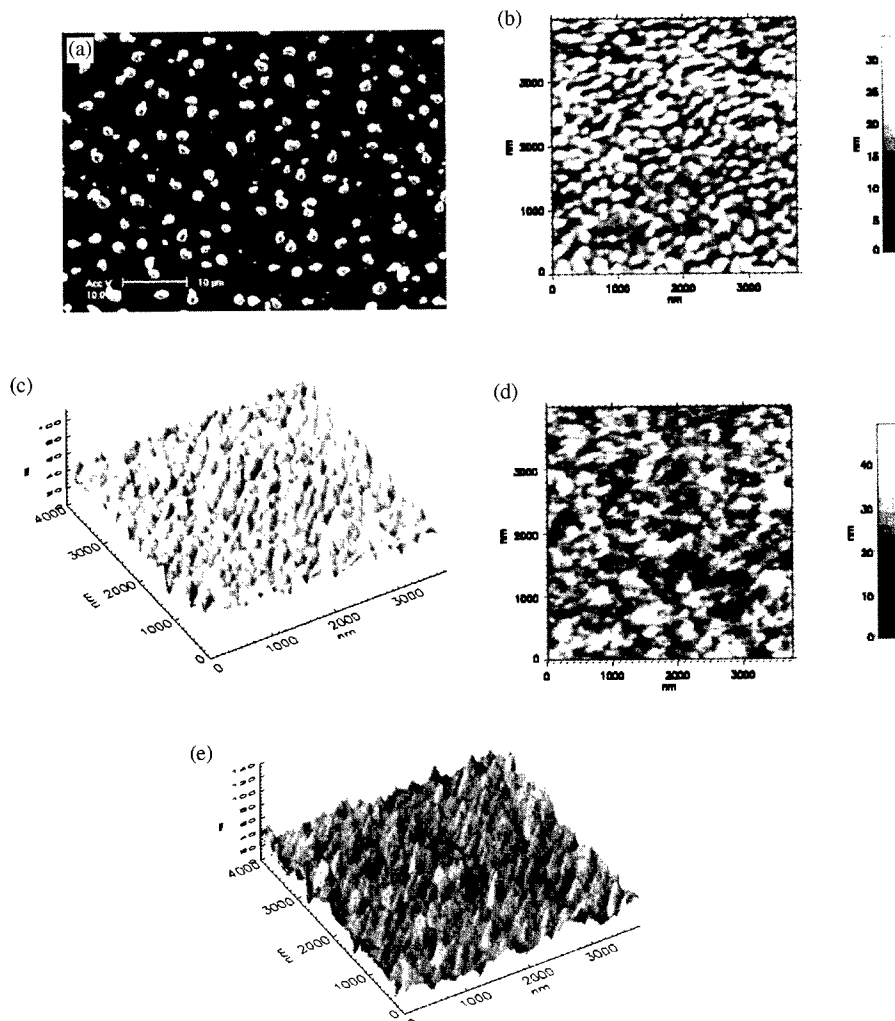


Fig. 2. The SEM and AFM images of the surface of different samples. (a) The SEM image of Cu cones on the surface of sample (a) of Fig. 1; (b) two-dimensional and (c) three-dimensional AFM images of sample (b) of Fig. 1; (d) two-dimensional and (e) three-dimensional AFM images of sample (c) of Fig. 1.

The valence band maximum reaches the Fermi energy at 0 eV, indicating the metallic properties of the film. Curve B (Cu-rich sample) is clearly recognizable as semiconducting due to its gap of 0.5 eV between the valence band maximum and the Fermi energy. The XPS spectra (Fig. 3a and b) show the same shift switching from the metallic to the semiconducting state.

3.4. Hall-effect measurements

Hall-effect measurements were carried out to study the electrical properties of the Cu_2S and CuS films. The carrier (hole) concentrations, Hall mobilities, and specific resistivities of the Cu_2S films range from

1×10^{18} to $3 \times 10^{19} \text{ cm}^{-3}$, 10 to $4 \text{ cm}^2 \text{ V}^{-1} \text{ s}^{-1}$, and 0.8 to $0.04 \Omega \text{ cm}$, respectively, within the temperature interval from 90 to 400 K. At room temperature, the values are $1.0 \times 10^{19} \text{ cm}^{-3}$, $6 \text{ cm}^2 \text{ V}^{-1} \text{ s}^{-1}$, and $0.1 \Omega \text{ cm}$, respectively, which is in agreement with the results of Ref. [8]. In principle, the hole concentration p is dependent on the temperature by

$$p \propto \exp[-\Delta E_A/kT], \quad (1)$$

where ΔE_A is the activation energy of the acceptor, k is the Boltzmann constant, and T is the temperature. A semi-log plot of the hole concentration versus the reciprocal temperature for a typical Cu_2S film is

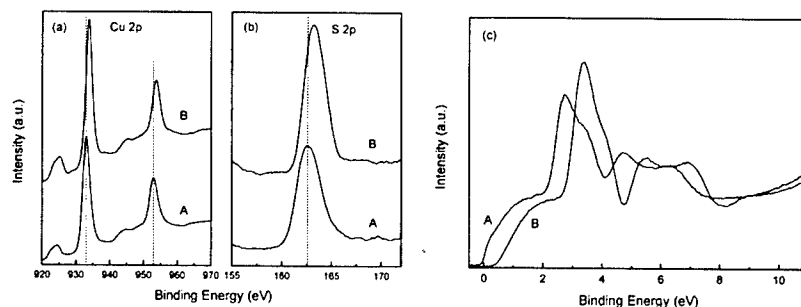


Fig. 3. The XPS spectra of Cu 2p (a) and S 2p (b) peaks, and the UPS spectra (c) of two films: A: CuS and B: Cu₃S₂.

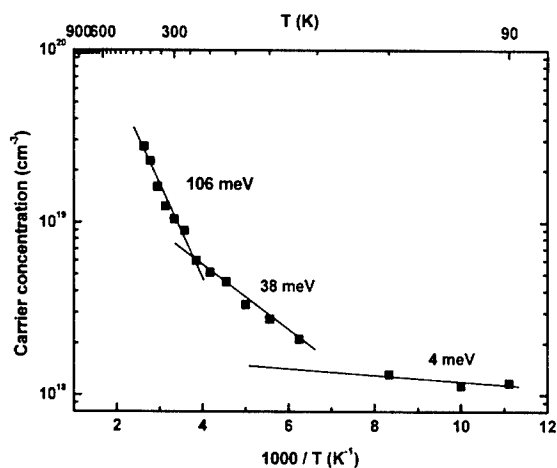


Fig. 4. The temperature dependence of the hole concentration of the Cu₃S films.

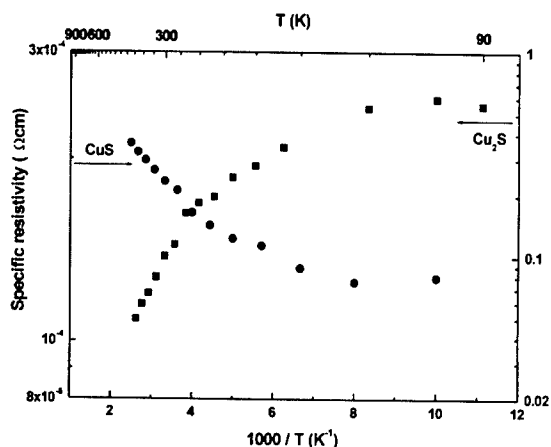


Fig. 5. The temperature dependence of the specific resistivity of the CuS films and Cu₃S films.

presented in Fig. 4. Three activation energies can be estimated as 106 ± 5 , 38 ± 2 , and 4 meV, respectively. The first two are in line with the results given by Ref. [8], and may be related to intrinsic acceptors i.e. the Cu vacancies. The small activation energy observed at low temperatures indicates hopping transport.

Compared with Cu₃S, CuS has a much higher carrier concentration (hole) of around 10^{22} cm^{-3} , which results in a remarkably lower resistivity of about $10^{-4} \Omega \text{ cm}$. The resistivity increases with temperature slightly and almost linearly (see Fig. 5), which is the typical characteristic of the metallic phase, in good agreement with the XPS and UPS results. The CuS film has a lower Hall mobility than the Cu₃S in the range of $1\text{--}4 \text{ cm}^2 \text{ V}^{-1} \text{ s}^{-1}$ mainly due to the higher carrier concentration.

4. Conclusion

Cu₂S and CuS films with good crystallinity have been deposited on bare float glass substrates by RF reactive sputtering. Both films have hexagonal crystal structures at RT as studied by the XRD. Typically Cu₂S films are highly (002) oriented with the FWHM of the (004) peak of about 0.24° . There are Cu precipitate cones coexisting in the Cu₂S films when the H₂S flow during sputtering is not high enough. Two activation energies related to the intrinsic defects in the Cu₂S films have been found by Hall-effect measurements. The CuS is in the metallic phase at RT, and has a relatively high carrier concentration around 10^{22} cm^{-3} , a much lower resistivity of about $10^{-4} \Omega \text{ cm}$, and a slightly lower Hall mobility of about $3 \text{ cm}^2 \text{ V}^{-1} \text{ s}^{-1}$ compared with the semi-conducting phase Cu₂S.

References

- [1] Y.B. He, A. Polity, H.R. Alves, I. Österreicher, W. Kriegseis, D. Pfisterer, B.K. Meyer, M. Hardt, Presented

- at E-MRS 2001, Strasbourg, June 5–8, E-MRS 2001 Spring Meeting, Book of Abstracts, 2001, p. 12; Thin Solid Films, in preparation.
- [2] K. Siemer, J. Klaer, I. Luck, J. Bruns, R. Klenk, D. Bräunig, *Sol. Energy Mater. Sol. Cells* 67 (2001) 159.
- [3] L.D. Partain, R.A. Schneider, L.F. Donaghey, P.S. Mcleod, *J. Appl. Phys.* 57 (1985) 5056.
- [4] P.K. Nair, M.T.S. Nair, *J. Phys. D* 24 (1991) 83.
- [5] M.T.S. Nair, P.K. Nair, *J. Phys. D* 24 (1991) 450.
- [6] T. Yamamoto, K. Tanaka, E. Kubota, K. Osakada, *Chem. Mater.* 5 (1993) 1352.
- [7] C. Nascu, I. Pop, V. Ionescu, E. Indrea, I. Bratu, *Mater. Lett.* 32 (1997) 73–77.
- [8] John Y. Leong, Jick H. Yee, *Appl. Phys. Lett.* 35 (1979) 601.



ELSEVIER

Physica B 308–310 (2001) 1074–1077

PHYSICA B

www.elsevier.com/locate/physb

Characterization of RF reactively sputtered Cu–In–S thin films

Y.B. He*, A. Polity, R. Gregor, D. Pfisterer, I. Österreicher, D. Hasselkamp, B.K. Meyer

I. Physikalisches Institut, Justus-Liebig-Universität Giessen, Heinrich-Buff-Ring 16, D-35392 Giessen, Germany

Abstract

The ternary compound semiconductor CuInS_2 has attracted much attention owing to its potential applications in photovoltaic devices. We deposit CuInS_2 films on float glass substrates by a reactive radio frequency sputter process using a Cu–In inlay target and H_2S gas in one step. The morphology of the films was studied by Atomic Force Microscopy. X-ray Diffraction was used to check the crystal structure of the films. The composition of the layers was determined by Rutherford Back-scattering Spectroscopy and Energy-Dispersive X-ray Analysis. The electrical properties of the layers, i.e. the carrier concentration, Hall mobility, and specific resistivity and their dependencies on temperature were investigated by Hall effect measurements. © 2001 Elsevier Science B.V. All rights reserved.

Keywords: CuInS_2 ; Thin films; Photovoltaic; Defects

1. Introduction

Recently the ternary compound semiconductor CuInS_2 (CIS) has attracted much attention due to its potential applications in photovoltaic devices. Solar cells based on CIS with a total area efficiency of 11.4% have been demonstrated using a rapid thermal process [1]. Usually, Cu-rich films are grown for efficient solar cells, which leads to the formation of a CuS secondary phase on the film surfaces. This phase is subsequently removed by chemical etching with potassium cyanide (KCN). From In-rich films, on the other hand, in which CuIn_3S_8 or In_2S_3 secondary phases co-exist, it was not possible to produce efficient solar cell devices [2,3].

We try to prepare CIS films by a radio frequency (RF) reactive sputter process, using a Cu–In inlay target with H_2S as reactive gas in one step. The crystallinity of the as-sputtered films is studied by X-ray diffraction (XRD) measurements, which indicate that the films are highly (112) oriented CIS films. The composition characterization of the films by both Rutherford back-scattering

spectroscopy (RBS) and energy-dispersive X-ray analysis (EDX) reveals that the films are extremely Cu-rich, i.e. the Cu to In ratio strongly deviates from 1. To resolve the contradiction between XRD and composition results, only the Cu–S binary compound has been sputtered in the same equipment using a pure Cu target and H_2S gas. XRD shows that the sputtered Cu_xS films are also highly oriented, and their XRD peaks are very close to that of as-sputtered “CIS” films. This indicates that the main phases of our “CIS” films are CuS and Cu_2S , which clarifies the problem mentioned above.

2. Experimental

Cu–In–S films were prepared on bare float glass substrates by a reactive sputter process with a conventional RF (13.56 MHz) sputter setup. High purity (99.999%) argon was used to provide the plasma at a base pressure of 10^{-6} Torr, and H_2S (purity: 98.0%) was introduced as reactive gas during the sputtering. A Cu metal disk inlaid by In with the area ratio Cu/In about 1 and diameter of 10.16 cm was used as sputter target. The RF sputter power was in the range between 100 and 500 W ($1.23\text{--}6.15 \text{ W cm}^{-2}$), while the H_2S flow was varied from 3 to 10 sccm. The substrate temperature

*Corresponding author. Tel.: +49-641-99-33137; fax: +49-641-99-33119.

E-mail address: yunbin.he@physik.uni-giessen.de (Y.B. He).

was changed from room temperature to 400°C. Typically the as-sputtered film thickness was in the range from 175 to 1000 nm within a sputter time between 5 and 30 min.

The structures of the layers were studied by XRD using a Siemens D5000 diffractometer with Cu K_{α} ($\lambda = 1.5418 \text{ \AA}$) radiation. Atomic force microscopy (AFM) was used to observe the surface morphology of the layers. The composition of the layers was analyzed by EDX (SiLi-detector with an ultrathin window (UTW) installed in a Philips XL20 SEM equipment) and RBS, respectively. The electrical properties of the films in the range between 77 and 400 K were characterized by Hall effect measurements.

3. Results and discussion

Fig. 1 shows the AFM images on the surface of a typical film, which was sputtered for 15 min at 200°C with a sputter power of 300 W and a H_2S flow of 8.0 sccm. The surface is smooth with the root mean square (RMS) roughness of 4.05 nm, which is derived by AFM, consisting of uniformly sized and densely packed grains. The columnar-shaped and well-grown grains are distributed with an obviously preferential orientation as shown in Fig. 1a and b, which is also revealed by XRD measurements (see below).

A typical XRD spectrum of sputtered film is shown in Fig. 2a. There are only three diffraction peaks appearing at 2θ of 27.80°, 54.40°, and 57.40°, which seem to correspond to the (1 1 2), (1 1 6), and (2 2 4) peaks of CIS, respectively, as compared with the standard CIS pattern: Joint Committee on Powder Diffraction Standards (JCPDS) file 27-0159. It seems that the film is a nearly stoichiometric CIS film with a (1 1 2) preferential orientation in accordance with AFM measurements described above. However, the composition analysis as examined by RBS shows a surprising result—the film is extremely Cu-rich, and there is only very little In content in the film with Cu 49%, In 4%, S 47%, respectively (see Fig. 3a). To be sure, EDX measurements (Fig. 3b) have been carried out from the cross section of the same sample. A comparable result with RBS has been obtained: Cu 50%, In 8%, S 42%, respectively, which means that the In content is too low throughout the whole layer, not only in the surface region, but also in the bulk material. Usually, for Cu-rich CIS films deposited by other techniques, there is only In deficiency on the surface due to secondary phases such as CuS and Cu_2S segregations [2]. However, our sputtered films are completely non-stoichiometric CIS with a low In content throughout the whole layer in a way contradicting with the XRD measurements.

In order to clarify the problem, Cu–S binary compound films were sputtered with identical para-

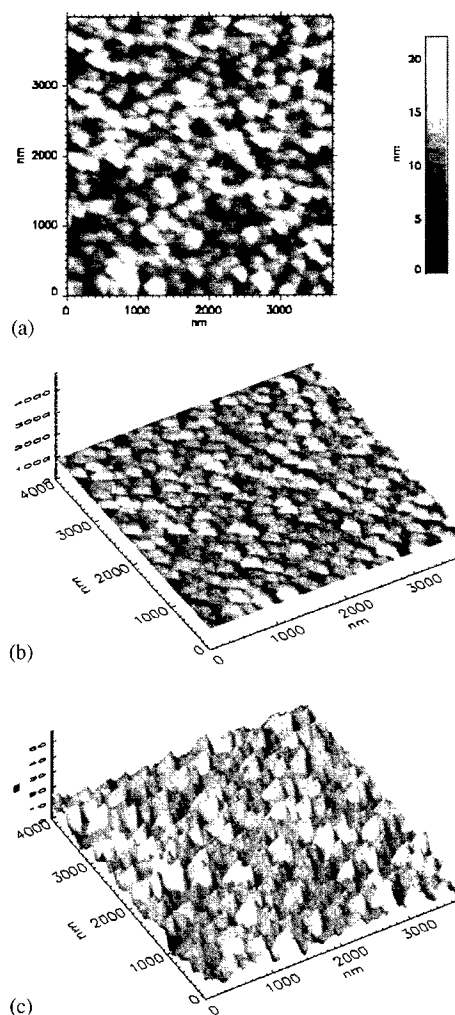


Fig. 1. AFM images on the surface of a typical as-sputtered film. (a) Top view (two-dimensional). (b) Three-dimensional image with the same Z scale as X, Y. (c) Three-dimensional image with the Z scale from 0 to 60 nm.

meters for comparison. As can be seen in Fig. 2b the as-sputtered Cu_2S film is completely oriented with (0 0 2) plane parallel to the substrate, and its (0 0 2), (0 0 4) diffraction peaks overlap exactly with two peaks of “CIS” around 26.45° and 54.40°, which means the formerly identified “CIS” (1 1 6) peak actually originates mainly from Cu_2S (0 0 4). Similarly, comparing the XRD of the “CIS” film with that of CuS, one can clearly see that the formerly identified “CIS” (1 1 2) and (2 2 4) peaks are mainly from CuS (1 0 1) and (2 0 2) peaks, respectively. Now, our puzzle about the conflict between XRD and composition measurements has been clarified. The sputtered “CIS” films consist of three phases: CuS, Cu_2S , and $CuInS_2$, and the In to Cu ratio strongly deviates from 1. Although in Ref. [4] it is reported that

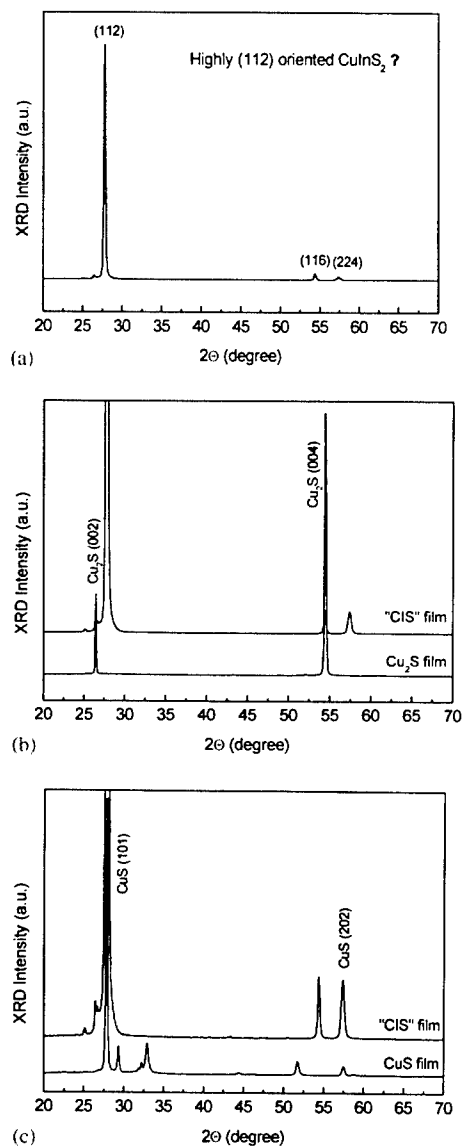


Fig. 2. (a) Typical XRD spectra of an as-sputtered "CIS" film; (b) Comparison of XRD spectra of sputtered a "CIS" film and a Cu_2S film; (c) Comparison of XRD spectra of sputtered a "CIS" film and a CuS film.

stoichiometric CIS films can be produced by a DC reactive sputtering process using a fan-shaped Cu and In metal target with CS_2 introduced as reactive gas, according to our experiments, it is hardly possible to deposit stoichiometric CIS films by a reactive sputtering process using a Cu–In inlay metallic target with a H_2S gas flow. We noticed that there is a black-colored top layer covering the surface of the In inlay after the target has been sputtered for several ten times. We speculate it is an In–S compound due to the reaction of the metallic In with the H_2S gas during sputtering. This top layer on

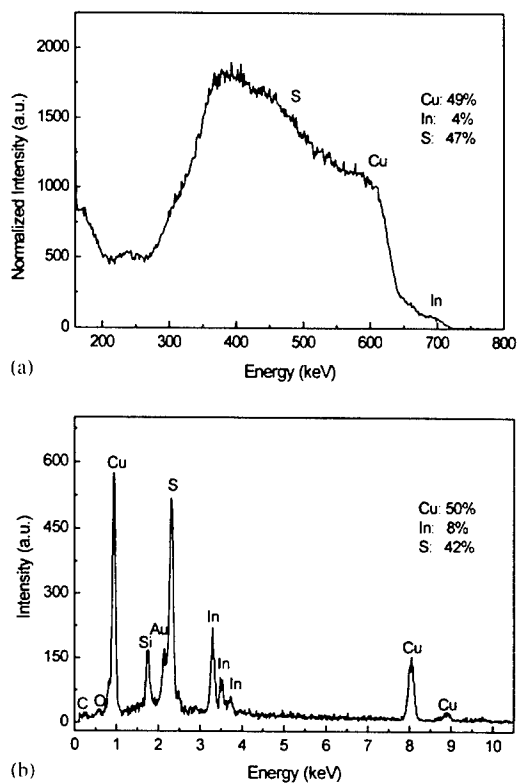


Fig. 3. Composition characterization of a typical film by (a) RBS and (b) EDX.

the In inlay reduces the sputter rate of In, and results in a considerably lower In/Cu ratio in the sputtered films. So the In/Cu ratio in the sputtered films not only depends on its area ratio in the target, but is also influenced by the H_2S flow amount and period. Therefore, the content of Cu and In in the layers may strongly and in a delicate way deviate from its original ratio in the target. By using a Cu–In alloy target instead of the inlay target the problem described above has been overcome, and nearly stoichiometric CIS films have been deposited by the same sputtering process [5].

Characterization of the electrical properties of the films were done by Hall effect measurements. In general, the carrier concentration, Hall mobility and specific resistivity of the sputtered Cu-rich "CIS" films are in the range between 3.55×10^{17} to $1.58 \times 10^{19} \text{ cm}^{-3}$, 4.15 to $1.15 \text{ cm}^2 \text{ V}^{-1} \text{ s}^{-1}$, and 4.24 to $0.35 \Omega \text{ cm}$, respectively, for temperatures between 77 and 350 K. Compared with stoichiometric CIS single crystals and thin films, the Cu-rich "CIS" films have hole concentrations 2–3 orders of magnitude higher [6,7]. This is partly due to CuS and Cu_2S phases co-existing in the films. It is known that CuS is metallic at room temperature (RT) with a hole concentration of about 10^{22} cm^{-3} . Cu_2S is a semiconductor but can have also relatively high hole

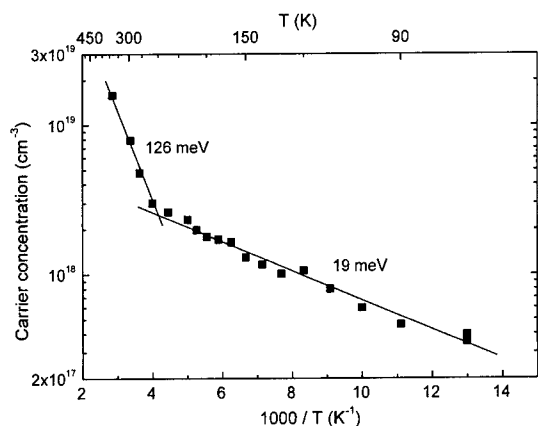


Fig. 4. The temperature dependence of carrier concentration of a sputtered Cu-rich "CIS" film.

concentrations around 10^{19} cm^{-3} at RT [8,9]. By a linear fit to the carrier concentration dependence on temperature (Fig. 4), two thermal activation energies of 126 ± 4 and $19 \pm 2 \text{ meV}$ can be deduced.

4. Summary and conclusions

Cu rich Cu–In–S films with good crystallinity were deposited on float glass substrates by a RF reactive sputter process using a Cu–In inlay target with H_2S as reactive gas in one step. The In/Cu ratio in the sputtered films is much less than 1 although its ratio is nearly 1 in the target. It not only depends on the different sputter yield of In and Cu, but is also influenced by an additional layer covered on the surface of the In inlay due to the reaction of H_2S and In inlay during sputtering. The sputtered film consists of CuS, Cu_2S , and CuInS_2 phases, which results in a strong deficiency

of In in the layer. It is not always reliable to characterize the composition by XRD only. The combination with other kinds of methods for composition examination is necessary, especially when the film is highly oriented and only very few diffraction peaks show up in the XRD spectrum. The hole concentrations of the as-sputtered Cu-rich "CIS" films range between 3.55×10^{17} and $1.58 \times 10^{19} \text{ cm}^{-3}$, for temperatures between 77 and 350 K. The carrier concentration can be tuned from 10^{19} to 10^{17} cm^{-3} by using a Cu–In alloy target as shown in Ref. [5]. From the sputtering process there is still enough freedom to produce CIS films appropriate for solar cells.

References

- [1] K. Siemer, J. Klaer, I. Luck, J. Bruns, R. Klenk, D. Bräunig, *Sol. Energy Mater. Sol. Cells* 67 (2001) 159.
- [2] T. Watanabe, M. Matsui, *Jpn. J. Appl. Phys.* 35 (1996) 1681.
- [3] F.O. Aduridija, J. Song, S.D. Kim, S.K. Kim, K.H. Yoon, *Jpn. J. Appl. Phys.* 37 (1998) 4248.
- [4] S. Kobayashi, D.Y. Yu, M.M. Sarinanto, Y. Kobayashi, F. Kaneko, T. Kawakami, *Jpn. J. Appl. Phys.* 34 (1995) L513–L515.
- [5] Y.B. He, A. Polity, H.R. Alves, I. Österreicher, W. Kriegseis, D. Pfisterer, B.K. Meyer, M. Hardt, presented at E-MRS 2001, Strasbourg, 5–8 June 2001, *Thin Solid Films*, to be published.
- [6] B. Tell, J.L. Shay, H.M. Kasper, *J. Appl. Phys.* 43 (1972) 2469.
- [7] L.L. Kazmerski, M.S. Ayyagari, G.A. Sanborn, *J. Appl. Phys.* 46 (1975) 4865.
- [8] Y.B. He, A. Polity, I. Österreicher, D. Pfisterer, R. Gregor, B.K. Meyer, M. Hardt, ICDS 21, 16–20 July 2001, Giessen, Germany, submitted.
- [9] J.Y. Leong, J.H. Yee, *Appl. Phys. Lett.* 35 (1979) 601.



ELSEVIER

Physica B 308–310 (2001) 1078–1080

PHYSICA B

www.elsevier.com/locate/physb

EDMR of MEH-PPV LEDs

G.B. Silva^a, L.F. Santos^b, R.M. Faria^b, C.F.O. Graeff^{a,*}^a *Dep. de Física e Matemática, FFCLRP-USP, Av. Bandeirantes 3900, 14040-901 Ribeirão Preto, Brazil*^b *IFSC-USP, CP 369, 13560-970 São Carlos, Brazil*

Abstract

In this work, electrically detected magnetic resonance (EDMR) at X-band is used to study the electronic properties of poly(2-methoxy-5-(2'-etil-hexiloxy)-1,4-phenylene vinylene) (MEH-PPV) light-emitting diodes (LEDs). The EDMR signal from MEH-PPV LEDs is found to be composed of two lines, a Lorentzian with peak-to-peak linewidth of 5 G, and a Gaussian with peak-to-peak linewidth of 24 G. The g -factor of both the components is about 2.002. The EDMR signal amplitude is typically 10^{-5} , and only observed at forward bias, for $V > 10$ V. The signal is a quenching, and is assigned to the spin-dependent fusion of two like-charged polarons to spinless bipolarons. The Lorentzian component is attributed to positive polarons fusion, and the Gaussian to negative polarons. The EDMR signal is found to depend on the process of carrier injection, polaron mobility, temperature and indirectly on bipolarons. © 2001 Elsevier Science B.V. All rights reserved.

Keywords: MEH-PPV; LED; Magnetic resonance

1. Introduction

One of the most promising polymers is PPV and its derivatives, showing good processibility and efficiency in optoelectronic devices [1]. Among the various techniques of investigation, electron spin resonance (ESR) has been used intensively [2], since it enables one to directly “see” the polaron, a paramagnetic charge carrier species, which plays a major role in the physics of conjugated polymers. On the contrary, electrically detected magnetic resonance (EDMR), which has provided insight into various transport and recombination processes in a wide array of semiconductors, has not been used frequently [3]. In an EDMR experiment, microwave-induced changes in the conductivity are measured as the sample is subjected to a swept DC magnetic field.

2. Experimental details

The poly(2-methoxy-5-(2'-etil-hexiloxy)-1,4-phenylene vinylene) (MEH-PPV) were obtained through standard procedures [4]. The LED was made using ITO-coated glass as the positive electrode. Over the ITO, a film of MEH-PPV was spin coated using chloroform as solvent. Thermally evaporated Al was used as the negative electrode. Typical MEH-PPV film thickness was around 360 nm. EDMR measurements were done using a modified, computer interfaced Varian E-4 X-Band spectrometer in the temperature range of 145–300 K. In order to avoid degradation induced by O₂ or H₂O, the sample was maintained under a nitrogen flux. The spin-dependent changes of conductivity were measured by modulating the static magnetic field (H_0) and using lock-in detection of the resonant current changes.

The results discussed are obtaining from the investigation of about 7 diodes. An intrinsic problem found in the investigation of these devices was the poor reproducibility of the device itself. For example, the active layer thickness varied from sample to sample; these variations were reflected in the device operation characteristics, in special the luminescence efficiency, and the $I \times V$ curves.

*Corresponding author. Tel.: +55-16-602-3763; fax: +55-16-633-99-49.

E-mail address: cgraeff@dfm.ffclrp.usp.br (C.F.O. Graeff).

The devices investigated were not encapsulated, and even though we have avoided exposing the diode to air and/or light, which are known to be responsible for the device degradation [5], the operation lifetime was hardly longer than 100 h. We have tried to work as close as possible to the room temperature, in an attempt to make sure that the transport/recombination/injection process that we observe are those that are important for the commercial use of these devices.

3. Results and discussion

Fig. 1 shows the typical EDMR spectra from different MEH-PPV light emitting diodes. The signal could only be observed in forward bias. From a phase analysis dependence on modulation frequency, it is found to be a quenching signal, or in other words, the conductivity of the device decreases in resonance. The LEDs spectra in Fig. 1 have different emission efficiencies, decreasing from (a) to (c). Notice, however, that the $I \times V$ characteristics of these samples are quite comparable. For the conditions shown, $V \approx 18$ V and $T \approx 200$ K, the current was around 2×10^{-4} A. In fact, the LED whose spectra are shown in Fig. 1(c) had an electroluminescence that could not be seen by naked eyes. The spectra in general can be simulated by the composition of two lines, a Lorentzian and a Gaussian. The g -factor of both lines varies from sample to sample between 2.001 and 2.003. The origin of the variation in g -factor is not well known; however, the values are closer to those of commonly found for positive or negative polarons in conjugated conductive polymers [3]. The Lorentzian line has a peak-to-peak linewidth of 5.0 ± 0.5 G, while the Gaussian line has $\Delta H_{pp} = 24 \pm 1$ G. Care was taken so that the signals were not saturated. In the worst

situation, saturation started at about 20 mW. As can be seen in Fig. 1, the relative intensities of both Gaussian and Lorentzian lines are dependent on the light emitting efficiency; the bad emitter has the highest Lorentzian/Gaussian line amplitude ratio. In fact, for the sample just mentioned the Gaussian component is hardly observable.

In the samples, where the Gaussian component had a significant amplitude, it was observed that apart from the in-phase signal, there was also a signal in quadrature. By the adequate change in phase settings, in fact, the Gaussian component could be isolated. This phenomenon has been well described by Dersch et al. [6] in a-Si:H. It happens when the EDMR components obtained from process have different response times. Thus, the fact that we do observe such an effect is an indication that the Gaussian and Lorentzian lines come from different spin dependent transport processes in the diode. In some diodes it was possible to observe not just an EDMR signal but also the conventional ESR signal. The ESR lineshape in all cases could be well fitted using the parameters of the Lorentzian line found in the EDMR spectra.

In Fig. 2, the EDMR signal ($\Delta\sigma/\sigma$) is plotted against the bias voltage as filled symbols, for two different samples. In the same plot, the signal-to-noise (S/N) ratio as a function of bias voltage is plotted for one of the samples as open circles. Notice that the two samples present more or less the same behavior. However, the absolute value of the EDMR signal is different by a factor of 2–3. We have observed that for the same diode, normally near the end of its operation lifetime, the EDMR signal could decrease by as much as a factor of 10 in exactly the same experimental conditions. For both diodes, 10 V is just when the diode starts to emit light. As can be seen for $V < 17$ V, the signal increases, remains

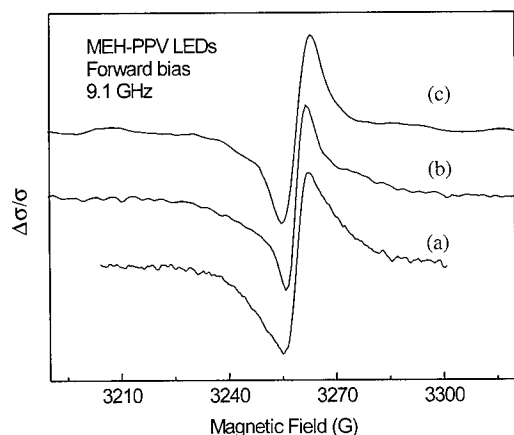


Fig. 1. Typical EDMR signal for different MEH-PPV LEDs. From (a) to (c) the light emission efficiency decreases.

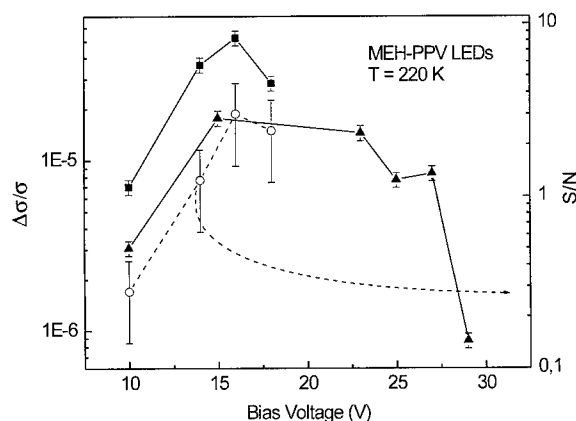


Fig. 2. EDMR signal amplitude (filled triangles) and signal-to-noise ratio (open circles) as a function of bias voltage, for different LEDs.

constant up to $V < 27$ V, and then drops. The variations are small, of the order of a factor 10 maximum. This complex behavior is not understood in detail at present. However one important point to note is that for these devices, the luminescence is not homogeneous for the whole sample, it is in fact concentrated in certain 'hot' spots. We are assuming that the initial increase of $\Delta\sigma/\sigma$ is basically derived from an increase in the number or size of the 'hot' spots. As the current injection increases these hot spots stabilize, and so does the EDMR signal amplitude. For very high injection, a significant local temperature increase cannot be ruled out, increases in temperature are followed by a decrease in $\Delta\sigma/\sigma$. Note that the S/N ratio does follow a similar behavior, and gives further support to the simple picture just described. The consequence of having both a decrease in signal amplitude and S/N ratio, turned the detection at lower voltages (or current injection) nearly impossible.

The temperature dependence of the EDMR signal depends on the emitting efficiency of the diode. For diodes that have both Gaussian and Lorentzian lines the temperature dependence for $T < 220$ K is rather weak, with a drop when the T reaches room temperature. The diode with an EDMR signal identified as 'pure' Lorentzian, has no such change in behavior and can be simulated by $\Delta\sigma/\sigma \propto T^{-2.2}$. This temperature behavior is not understood in detail at present.

EDMR has already been used for the characterization of similar diode structures based on PPV, summarized in Ref. [3]. However, quite different results have been found on ITO/PPV/Ca structures. For example, the EDMR signal amplitude was found to be as strong as 10^{-3} , and temperature independent for $20\text{ K} < T < 296\text{ K}$. The origin of such differences between the present and previous studies is not understood.

EDMR only probes paramagnetic states involved in the conduction process. As a consequence bipolarons which have $S = 0$ for example, are not observed directly by EDMR (or ESR). The two components observed by EDMR are assigned to polaron-polaron fusion, which results in a bipolaron [3]. The Lorentzian line is observed in ESR as well as in the EDMR and for ESR assigned to positive polarons. As mentioned earlier, the diodes with the worst light emission efficiency were those whose Lorentzian line amplitude was dominant. One possible explanation for the bad EL efficiency is an unbalanced carrier injection, in our case a poor negative polaron injection. Thus a surplus of positive carriers exists inside the bad emitting diode, which correlates with a higher Lorentzian line amplitude. Thus we attentively assign the Lorentzian line to $p^+ + p^+ \rightarrow bp^{++}$, while the Gaussian line is attributed to $p^- + p^- \rightarrow bp^{--}$. The differences in linewidth are probably derived from the differences in mobility. One could expect that the more mobile p^+ has a lineshape

that is motionally narrowed. In this simple explanation, the difference in mobility can also explain the quadrature signal. However, at this point more evidence is needed to further attest this proposition. Note that the fact that the amplitude of the EDMR signal varies from sample to sample as well as for the same diode, is an indication that non-spin dependent transport paths are present in this diode. As discussed elsewhere [7], the effect of having non-spin dependent transport paths (bipolarons) parallel to spin dependent ones, is an overall decrease in $\Delta\sigma/\sigma$.

4. Conclusions

EDMR has been used to study the transport/recombination/injection of light emitting diodes based on MEH-PPV. The EDMR signal was found to be composed of two lines a g -factor around 2.002. The first line can be fitted by a Lorentzian with a $\Delta H_{pp} = 5.0 \pm 0.5$ G. The second line is a Gaussian with $\Delta H_{pp} = 24 \pm 1$ G. The relative amplitude of those components was found to be dependent on light emission efficiency of the diode. The Lorentzian is dominant for bad emitters. It is proposed attentively that the Lorentzian line is related to the fusion of positive polarons, which creates a positive bipolaron, while the Gaussian line comes from the same process however for negative polarons. It is found that EDMR in ITO/MEH-PPV/Al LEDs can qualitatively provide information about carrier injection, polaron mobilities as well as indirectly indicate the presence of bipolarons.

Acknowledgements

This work was supported by FAPESP, CNPq and CAPES.

References

- [1] W. Brütting, S. Berleb, A.G. Mückl, *Org. Electron.* 2 (2001) 1.
- [2] S. Kuroda, T. Ohnishi, T. Nogushi, *Phys. Rev. Lett.* 72 (1994) 286.
- [3] J. Shinar, in: H.S. Nalwa (Ed.), *Handbook of Organic Conductive Molecules and Polymers*, Vol. 3, Wiley, New York, 1997, pp. 319–366.
- [4] F. Wudl, G. Srdanov, US Patent No. 5, 189, 136, 1993.
- [5] B.H. Cumpston, K.F. Jensen, *Trends Polym. Sci.* 4 & 5 (1996) 151.
- [6] H. Dersch, L. Schweitzer, J. Stuke, *Phys. Rev. B* 28 (1983) 4678.
- [7] C.F.O. Graeff, C.A. Brunello, *J. Non-Crystal Solids* 273 (2000) 289.



ELSEVIER

Physica B 308–310 (2001) 1081–1085

PHYSICA B

www.elsevier.com/locate/physb

The role of structural properties and defects for the performance of Cu-chalcopyrite-based thin-film solar cells

Hans Werner Schock*, Uwe Rau

Institut für Physikalische Elektronik, Universität Stuttgart, Pfaffenwaldring 47, D-70569 Stuttgart, Germany

Abstract

Polycrystalline thin-films of the multinary chalcopyrite semiconductor $\text{Cu}(\text{In,Ga})\text{Se}_2$ are very well suited for highly efficient thin film solar cells. The material exhibits an astonishingly broad range of compositions in which good electronic properties are maintained. This article analyses some important aspects of the defect physics and defect chemistry of this semiconductor and compares recent models for the surface of polycrystalline $\text{Cu}(\text{In,Ga})\text{Se}_2$ and their consequences for the formation of the $\text{ZnO}/\text{CdS}/\text{Cu}(\text{In,Ga})\text{Se}_2$ heterojunction. © 2001 Elsevier Science B.V. All rights reserved.

PACS: 68.35.Fx; 68.55.-a; 72.20.Jv; 72.40.+w

Keywords: Multinary compound semiconductors; Photovoltaics; Defect formation; $\text{Cu}(\text{In,Ga})\text{Se}_2$; Bulk and surface defects

1. Introduction

The Cu-chalcopyrite CuInSe_2 and its alloys $\text{Cu}(\text{In,Ga})(\text{Se,S})_2$ provide the absorber material for the to date most efficient thin-film solar cells. A high power conversion efficiency of close to 19% obtained with an alloy $\text{Cu}(\text{In,Ga})\text{Se}_2$ (with a $\text{Ga}/(\text{Ga} + \text{In})$ -ratio ≈ 0.2) [1] yet challenges the conventional wafer-based polycrystalline silicon solar cell technology. The usage of the complete $\text{Cu}(\text{In}_{1-x}\text{Ga}_x)(\text{Se}_{1-y}\text{S}_y)_2$ alloy system is interesting when aiming towards high open circuit voltage solar cells as the band gap energy E_g of CuInSe_2 increases upon alloying with Ga and/or S [2]. Besides the technologically advantageous features including the outstanding radiation hardness of CuInSe_2 and its alloys [3,4], the Cu-chalcopyrites attract also considerable scientific interest because of their unusual defect physics: e.g., the ability to form electronically inactive defect complexes [5] explains the large structural tolerance of these materials to anion-cation off-stoichiometry.

High-efficiency $\text{Cu}(\text{In,Ga})\text{Se}_2$ solar cells are produced either by co-evaporation of the elements onto a heated Mo-coated glass substrate or by selenization of the stacked elemental layers. The use of glass substrates restricts the temperature for the film growth to below 600°C , the melting point of glass. The photovoltaically active polycrystalline p-type $\text{Cu}(\text{In,Ga})\text{Se}_2$ absorber has a typical thickness of $1.5\text{--}2\text{ }\mu\text{m}$ and a grain size in the μm range. The device is completed by chemical bath deposition of a 50 nm thin CdS buffer layer and by sputtering of an n-type ZnO front electrode (for recent reviews on device technology and characterization, see [6,7]). It is the relative ease of manufacturing and the large process window for producing efficient absorber layers what makes $\text{Cu}(\text{In,Ga})\text{Se}_2$ a very promising candidate for large-scale production of efficient and cost-effective photovoltaic devices. Prerequisites for an efficient thin-film photovoltaic absorber materials are: (i) The possibility to grow single-phase material of good crystalline quality, i.e., in a multinary compound there should be some tolerance to stoichiometry deviations. (ii) Growth of the material in a substrate configuration implies that during the growth process an ohmic contact with the metal on the glass must be formed which should also have favourable recombination properties for the minority carriers. In addition, this interface plays an

*Corresponding author. Tel.: +49-711-685-7180; fax: +49-711-685-7206.

E-mail address: schock@ipe.uni-stuttgart.de (H.W. Schock).

important role as the seed for the growth of the polycrystalline film. (iii) The absorber film should be thick enough to absorb all sunlight with a photon-energy above the semiconductor's band gap and, in same time, the minority carrier diffusion length should be large enough to enable collection of all photogenerated charge carriers. (iv) Intergrain defects should be few and/or electronically inactive, unless the grain size does not exceed the film thickness by at least one order of magnitude (what is not the case in Cu(In,Ga)Se_2 thin films). (v) The grains should contain a low concentration of electronically active (intra grain) defects. (vi) After growth of the absorber film, the film surface should enable the formation of a heterointerface with a favourable band offset between the absorber and the heterojunction partner in order not to affect the photovoltaic properties.

Twenty years of research were necessary to develop solutions which, after all, almost perfectly meet the requirements (i)–(vi) outlined above. However, most of the achievements accumulated during those years were initiated rather by intuition than by knowledge-based technological design. Only now, we begin to achieve a more detailed understanding of the basic physics working behind the scene. We now recognize that, in many respects, we were just lucky to find the needle, and begin to realize how large the haystack is. Fig. 1 depicts the complete layer sequence of the $\text{ZnO/CdS/Cu(In,Ga)Se}_2\text{-Mo}$ heterostructure. All three interfaces between the four functional layers of the device exhibit interface reactions, e.g. the formation of MoSe_2 at the Mo back contact. Most of the 13 chemical elements tend to interdiffuse between the layers. For example Na from the glass plays an active role during film growth. Nevertheless, it appears that it is just the complexity of the defect physics of Cu(In,Ga)Se_2 which is the reason for the outstanding performance, stability, and radiation hardness of this material. In the following we tempt to outline some of the physics that allows Cu(In,Ga)Se_2 to meet the requirements (i)–(vi) and to perform so well as a photovoltaic material.

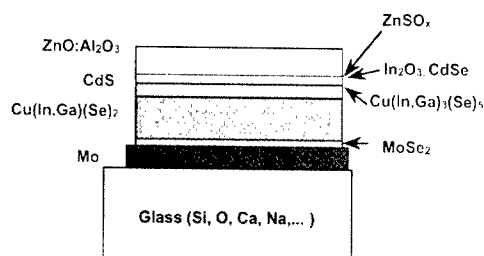


Fig. 1. Schematic representation of the layers and interfaces in a $\text{ZnO/CdS/Cu(In,Ga)Se}_2$ solar cell.

2. Off-stoichiometry, secondary phases, and intrinsic defects

In contrast, to the binary compounds where small deviations from stoichiometry cause drastic changes of the electronic properties, the ternary compounds, in particular CuInSe_2 , are much more tolerant. Note that the Cu content of device-quality CuInSe_2 or Cu(In,Ga)Se_2 absorbers varies typically between 22 and 24 at% Cu. Thus, these films are markedly Cu-poor but maintain excellent semiconducting properties. In terms of point defects, a non-stoichiometry of 1% would correspond to a defect concentration of roughly 10^{21} cm^{-3} . This is by about five orders of magnitude more than the acceptable density of recombination centres in a photovoltaic absorber material and still four orders of magnitude higher than the maximum net doping concentration of some 10^{17} cm^{-3} that is useful for the photovoltaic active part of a solar cell. Even if we allow a degree of compensation of 99%, the respective densities of donors and acceptors would be only in the 10^{19} cm^{-3} range. Thus, as illustrated in Fig. 2, the virtual number of defects related to off-stoichiometry has to be brought down to reasonable quantities which are compatible with the good electronic quality that is required to build a photovoltaic device.

There are basically two ways to reconcile stoichiometry deviations with good electronic properties: either the non-stoichiometry is accommodated in a secondary phase that is not harmful to the photovoltaic performance, or the off-stoichiometry related defects are electronically inactive. Most probably CuInSe_2 realizes both possibilities. The two point defects which are related to an overall Cu-poor composition are the Cu-vacancy V_{Cu} (a shallow acceptor) and the In–Cu antisite In_{Cu} (a deep double donor). According to first-principle calculations [5], these two defects form a defect complex $(2V_{\text{Cu}}, \text{In}_{\text{Cu}})$ which is electronically neutral and has no transitions within the energy gap of CuInSe_2 , thus being electronically inactive as could be. Interestingly, ordered

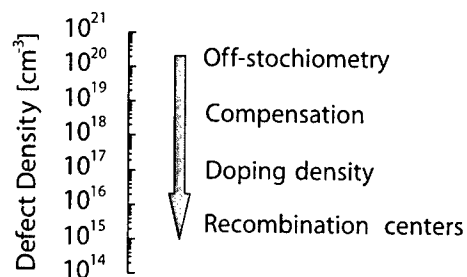


Fig. 2. Virtual number of defects related to off-stoichiometry. This number has to be brought down to reasonable quantities which are compatible with the good electronic quality that is required in a photovoltaic device.

arrays of this complex can be thought as the building stones of a series of Cu–In–Se compounds like CuIn_3Se_5 , CuIn_5Se_8 [8], i.e., the secondary phases that delimit the single-phase region of CuInSe_2 (α -phase) towards the Cu-poor side [9].

The existence range of the α -phase on the quasi-binary tie line Cu_2Se – In_2Se_3 of the phase diagram is from about 24.5–24 at% Cu, thus even not involving the proper stoichiometric composition with 25 at% Cu [9]. The Cu content of device-quality absorbers is between 22 and 24 at% Cu. This lies within the single phase region of the α -phase only at the growth temperature of 500–550°C. But at room temperature, the equilibrium phase diagram [9] predicts a two-phase $\alpha + \beta$ region for Cu contents below 24%. The situation with respect to secondary phase segregations is a bit different in thin films compared to single crystals which are used to determine a phase diagram. First, in these films about 20–30% of the In is replaced by Ga and, second, these films grow on Na-containing glass and, consequently, contain around 0.1 at% Na that diffuses out of the glass during deposition. Both, the incorporation of Ga and Na, inhibit the formation of secondary phases in the bulk of the thin film [10].

However, the surface of these films exhibits the 1-3-5 composition of the $\text{Cu(In,Ga)}_3\text{Se}_5$ defect phase [11], i.e., the surface is always more Cu-poor than the bulk of the material. Most likely, the Cu-poor surface of these thin-films is not the consequence of the segregation of a secondary bulk phase but rather is resulting from the accumulation of Cu-deficiency related defects and defect complexes [10]. The precise properties of this surface defect layer are not yet known. However, it is of some importance (and discussed later in the present paper) that the band gap at the surface of the Cu(In,Ga)Se_2 thin films is somewhat larger than the band gap in the bulk of the material [11].

On the Cu-rich side of the single-phase region of the phase diagram, Cu_2Se segregates as a secondary phase. In thin films Cu_2Se can be easily removed by etching the sample in KCN leaving behind a CuInSe_2 or Cu(In,Ga)Se_2 film with the proper stoichiometry. It is one of the puzzles of that material that films prepared in such a way exhibit good electronic quality (judged, e.g., from photoluminescence experiments [12–14]), whereas solar cells made from material that is grown in such a way are far less efficient than those with a slightly a Cu-deficient absorber.

3. Electronically active defects in Cu(In,Ga)Se_2 thin films

Up to here, we got a rough idea of how the material comes along with non-stoichiometry and meets requirement (i) of our list. In the following, we approach the topic from the experimental point of view, i.e., we

concentrate first on electronically active defects that are found in photovoltaic grade, i.e. slightly In-rich, polycrystalline Cu(In,Ga)Se_2 . The charge density in the space charge region of any photovoltaic device must not exceed a level of 10^{17} – 10^{18} cm^{-3} , because otherwise tunneling enhanced recombination would significantly decrease the open circuit voltage of the solar cell [15]. In fact, in Cu-chalcopyrite semiconductors this limit appears rather to be close to few times 10^{17} cm^{-3} [16]. High-efficiency Cu(In,Ga)Se_2 absorber material has a net charge density of around or few times 10^{16} cm^{-3} [17]. The shallow acceptor level V_{Cu} (around 30 meV above the valence band) is assumed to be the main dopant in this material [5].

The best experimental access to deeper defects in Cu(In,Ga)Se_2 provides admittance spectroscopy (AS) and Deep Level Transient Spectroscopy (DLTS) [18–20]. Fig. 3 displays a defect spectrum as obtained from (AS) by the method of Walter et al. [19] together with the band diagram of a $\text{ZnO/CdS/Cu(In,Ga)Se}_2$ -heterostructure. The spectrum exhibits two distinct peaks N1 and N2, at energies of ~ 100 and ~ 300 meV, respectively. While peak N1 corresponds to donor-like defects at the surface of the Cu(In,Ga)Se_2 absorber [20], peak N2 is an acceptor either in the volume or at the grain boundaries of the Cu(In,Ga)Se_2 absorber [19,20].

The importance of defect N_2 is given by the fact that its concentration is related to the open circuit voltage V_{OC} of the device. Detailed investigations of $\text{Cu(In}_{1-x}\text{Ga}_x\text{)(S}_y\text{Se}_{1-y})_2$ heterojunctions unveil that recombination via defect N_2 determines V_{OC} of solar cells made from absorbers in a composition range covering the $\text{Ga}/(\text{In} + \text{Ga})$ ratio $0 \leq x \leq 1$ [21] as well as the $\text{S}/(\text{S} + \text{Se})$ ratio $0 \leq y \leq 0.4$ [22]. Fig. 4 illustrates the correlation between the maximum defect densities with the open circuit voltage loss $E_g/q - V_{\text{oc}}$ which is a convenient measure to compare V_{oc} of solar cells with different bandgap energies of the absorber. Regardless

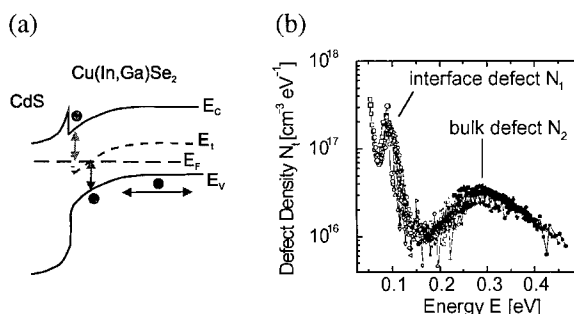


Fig. 3. Defect spectrum as obtained from admittance spectroscopy together with the band diagram of a $\text{ZnO/CdS/Cu(In,Ga)Se}_2$ -heterostructure. The spectrum exhibits two distinct peaks N1 and N2, at energies of ~ 100 and ~ 300 meV, respectively.

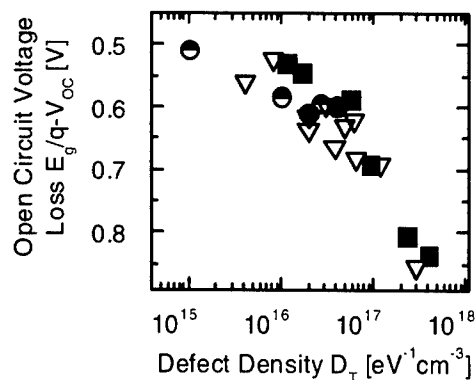


Fig. 4. Band diagrams of the surface of (a) In rich and (b) Cu rich Cu(In,Ga)Se₂. The surface is either more In or more Cu rich compared to the bulk and thus determines the position of the Fermi level.

of the origin of the defects, a clear correlation of defect densities with the loss in open circuit is found. Differences in the absorber quality resulting from preparation of films under different conditions like lower substrate temperature or different growth methods [21], the degradation of the absorbers by damp heat treatments [23], or the defect generation by irradiation with high-energy particles [3,4] can be subsumed in the same correlation of the defect densities and the open circuit voltage loss.

After all, it appears well established that recombination in all devices that are based on Cu(In,Ga)(Se)₂ alloys is determined by defects in the volume of the absorbers, as long as these absorbers are prepared with a slightly Cu-poor final composition. At the moment it is difficult to judge whether these defects are located in the grain volume or at the grain boundaries of the polycrystalline material. A rough estimate from available solar cell output parameters, however, puts a limit of $S_{\text{gb}} < 10^4$ cm/s to the recombination velocity S_{gb} for minority carriers at the grain boundaries [6,7]. Thus, grain boundaries in Cu(In,Ga)Se₂ exhibit only a weak electronic activity. This is considered to be a result from extrinsic passivation of the grain boundaries by oxygen [24,25]. This passivation is either explicitly performed by post-deposition air annealing or implicitly achieved by Na-catalyzed oxygenation of the grain boundaries during absorber growth [26].

4. Interface properties and surface defect layers

In a well-tailored solar cell the thickness of the absorber layer should not exceed the diffusion length of the minority carriers. Therefore, the recombination properties at both contacts to the active layer, at the charge-separating hetero-contact as well as at the ohmic back contact, should be favourable. Analysis of current

collection by Electron Beam Induced Currents (EBIC) indicate a good collection efficiency for *electrons* which are generated *close to the back contact* [27]. An explanation for these findings is provided by the fact that during absorber deposition a MoSe₂ film forms at the Mo surface [28,29]. MoSe₂ is a layered semiconductor with p-type conduction, a band gap of 1.3 eV and weak van-der-Waals bonding along the *c*-axis. The *c*-axis is found either in parallel or perpendicularly to the interface, depending on the initial growth condition of the film [28]. Therefore, the method of film growth has some impact on adhesion and electronic properties of this interface. Due to the larger band gap of the MoSe₂ compared to that of standard Cu(In,Ga)Se₂ films this semiconductor layer provides a back-surface field for photogenerated electrons and at the same time provides a low resistive contact for the holes.

The electronic properties of the front surface of photovoltaic-grade (Cu-poor) Cu(In,Ga)Se₂ result from the properties of the surface defect layer discussed in Section 2. The detailed band diagram of the heterojunction close to the metallurgical CdS/Cu(In,Ga)Se₂ is still under debate (for discussion, see e.g. [30–32]). In spite of the various models that exist for the surface of Cu-poor Cu(In,Ga)Se₂, two important features have to be considered as a matter of fact. (i) In the completed device the surface of the Cu(In,Ga)Se₂ absorber is inverted. The electronic transition (N1 in Fig. 3) due to interface donors has an activation energy of around 100 meV as measured by AS and DLTS [20]. This activation energy just corresponds to the distance ΔE_F between the conduction band of the Cu(In,Ga)Se₂ absorber and the Fermi energy E_F at the heterointerface. The barrier Φ_b^p that hinders holes from the absorber material to recombine at the heterointerface [16,33] is given by $\Phi_b^p = E_g - \Delta E_F$. Thus, a small ΔE_F is necessary to avoid interface recombination. (ii) A widening of the band gap energy towards the Cu-poor surface [11] further increases Φ_b^p as indicated in Fig. 5. In turn, all

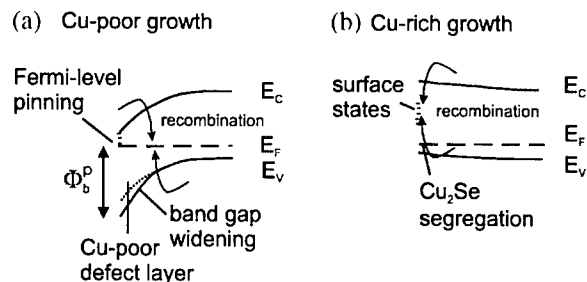


Fig. 5. Correlation of defect densities with the open circuit voltage loss. Regardless of the origin of the defect a clear correlation with the loss in open circuit is found. The different symbols represent different fabrication processes and alloy compositions (open triangles), ageing procedures (circles) and irradiations (solid squares).

devices which are prepared from Cu-chalcopyrite material that has been grown Cu-rich even after removal of the Cu_2Se secondary phase (or CuS in case of Cu-rich grown CuInS_2) are dominated by interface recombination [33,34]. Therefore, we postulate that the properties of the surface defect layers of Cu-poor grown material guarantee the Fermi level pinning close to the conduction band and the band gap widening at the absorber surface as illustrated in Fig. 5. Thus, the advantage of Cu-poor Cu(In,Ga)Se_2 absorber films is essentially given by their favourable surface properties and the ease to form heterojunctions with low losses.

5. Conclusions

The favourable photovoltaic properties of Cu(In,Ga)Se_2 and the wide process tolerance for thin film deposition arise from the ability of the multinary material to form defect complexes which are electrically neutral and fit into the structure of the material as elements of defect phases. These defect phases exhibit a similar structure as compared to the chalcopyrite crystal. The front surface of photovoltaic grade material is characterised by a defect layer with a CuIn_3Se_5 composition. This layer minimises recombination losses at the interface of the photovoltaic heterojunction. As a consequence, the open circuit voltage is determined by the bulk properties of the material, i.e. the defect densities in the bulk of the absorber layer.

Acknowledgements

The author would like to thank all the colleagues at the IPE, especially J.H. Werner, for continuous discussions and support. We also thank our colleagues from the Weizman Institute, Rehovot, from ENCSP, Paris, and the University Warsaw for fruitful discussions.

References

- [1] M. Contreras, B. Egaas, K. Ramanathan, J. Hiltner, A. Swartzlander, F. Hasoon, R. Noufi, *Prog. Photovolt. Res. Appl.* 7 (1999) 311.
- [2] J.L. Shay, J.H. Wernick, *Ternary Chalcopyrite semiconductors: Growth, Electronic Properties, and Applications*, Pergamon Press, Oxford, 1975.
- [3] A. Jasenek, U. Rau, T. Hahn, G. Hanna, M. Schmidt, M. Hartmann, H.W. Schock, J.H. Werner, B. Schattat, S. Kraft, K.-H. Schmid, W. Bolse, *Appl. Phys. A* 70 (2000) 677.
- [4] A. Jasenek, U. Rau, *J. Appl. Phys.* 90 (2001) 650.
- [5] S.B. Zhang, S.H. Wei, A. Zunger, H. Katayama-Yoshida, *Phys. Rev. B* 57 (1998) 9642.
- [6] U. Rau, H.W. Schock, Cu(In,Ga)Se_2 Solar Cells, in: M. Archer, R.H. Hill (Eds.), *Clean Energy from the Sun*, Imperial College Press, London, 1999.
- [7] U. Rau, H.W. Schock, *Appl. Phys. A* 69 (1999) 131.
- [8] S.B. Zhang, S.H. Wei, A. Zunger, *Phys. Rev. Lett.* 78 (1997) 4059.
- [9] T. Haalboom, T. Gödecke, F. Ernst, M. Rühle, R. Herberholz, H.W. Schock, C. Beilharz, K.W. Benz, *Inst. Phys. Conf. Ser.* 152E (1998) 249.
- [10] R. Herberholz, U. Rau, H.W. Schock, T. Haalboom, T. Gödecke, F. Ernst, C. Beilharz, K.W. Benz, D. Cahen, *Eur. Phys. J. AP* 6 (1999) 131.
- [11] D. Schmid, M. Ruckh, F. Grunwald, H.W. Schock, *J. Appl. Phys.* 73 (1993) 2902.
- [12] S. Zott, K. Leo, M. Ruckh, H.W. Schock, *J. Appl. Phys.* 82 (1997) 356.
- [13] Mt. Wagner, I. Dirnstorfer, D.M. Hofmann, M.D. Lampert, F. Karg, B.K. Meyer, *Phys. Stat. Sol. (a)* 167 (1998) 131.
- [14] I. Dirnstorfer, Mt. Wagner, D.M. Hoffmann, M.D. Lampert, F. Karg, B.K. Meyer, *Phys. Stat. Sol. (a)* 168 (1998) 163.
- [15] U. Rau, *Appl. Phys. Lett.* 74 (1999) 111.
- [16] U. Rau, A. Jasenek, H.W. Schock, F. Engelhardt, Th. Meyer, *Thin Solid Films* 161–162 (2000) 299.
- [17] R. Herberholz, *Inst. Phys. Conf. Ser.* 152E (1998) 733.
- [18] M. Schmitt, U. Rau, J. Parisi, in: W. Freiesleben, W. Palz, H.A. Ossenbrink, P. Helm (Eds.), *Proceedings of the 13th Europ. Photovolt. Solar Energy Conference*, Stephens, Bedford, 1995, pp. 1969–1972.
- [19] T. Walter, R. Herberholz, C. Müller, H.W. Schock, *J. Appl. Phys.* 80 (1996) 4411.
- [20] R. Herberholz, M. Igalson, H.W. Schock, *J. Appl. Phys.* 83 (1998) 318.
- [21] G. Hanna, A. Jasenek, U. Rau, H.W. Schock, *Thin Solid Films* 387 (2001) 71.
- [22] U. Rau, M. Schmidt, A. Jasenek, G. Hanna, H.W. Schock, *Solar Energy Mater. Solar Cells* 67 (2001) 137.
- [23] M. Schmidt, D. Braunger, R. Schäffler, H.W. Schock, U. Rau, *Thin Solid Films* 361–362 (2000) 283.
- [24] D. Cahen, R. Noufi, *Appl. Phys. Lett.* 54 (1989) 558.
- [25] D. Cahen, R. Noufi, *Solar Cells* 30 (1991) 53.
- [26] L. Kronik, D. Cahen, H.W. Schock, *Adv. Mater.* 10 (1998) 31.
- [27] P.E. Russell, O. Jamjoun, R.K. Ahrenkiel, L.L. Kazmerski, R.A. Mickelsen, W.S. Chen, *Appl. Phys. Lett.* 40 (1982) 995.
- [28] T. Wada, N. Kohara, T. Negami, M. Nishitani, *Jpn. J. Appl. Phys.* 35 (1996) 1253.
- [29] R. Takei, H. Tanino, S. Chichibu, H. Nakanishi, *J. Appl. Phys.* 79 (1996) 2793.
- [30] R. Scheer, *Jpn. J. Appl. Phys.* 39 (Suppl. 39-1) (2000) 389.
- [31] R. Scheer, *Trends Vacuum Sci. Technol.* 2 (1997) 77.
- [32] U. Rau, *Jpn. J. Appl. Phys.* 39 (Suppl. 39-1) (2000) 389.
- [33] R. Klenk, *Thin Solid Films* 387 (2001) 135.
- [34] V. Nadenau, U. Rau, A. Jasenek, H.W. Schock, *J. Appl. Phys.* 87 (2000) 584.



ELSEVIER

Physica B 308–310 (2001) 1086–1089

PHYSICA B

www.elsevier.com/locate/physb

Positive and negative magnetoresistance in the system silver–selenium

Gesa Beck, Jürgen Janek*

Physikalisch-Chemisches Institut, Justus-Liebig-Universität Gießen, Heinrich-Buff-Ring 58, D-35392 Gießen, Germany

Abstract

The (transversal) magnetoresistance (MR) effect of bulk $\text{Ag}_{2+\delta}\text{Se}$ ($\delta = 0; 5 \times 10^{-4}; 0.33$) in its low-temperature α -phase has been measured at temperatures $-100^\circ\text{C} < T < 50^\circ\text{C}$ in magnetic fields up to $B = 8$ T. A stoichiometric sample with well-controlled metal excess was prepared by growth from the elements and subsequent electrochemical treatment. The MR effect of this sample is relatively small and positive. Silver-rich material exposes both relatively large positive and negative effects, depending on the metal content. © 2001 Elsevier Science B.V. All rights reserved.

PACS: 72.20.My; 77.84.Bw; 61.50.Nw

Keywords: Magnetoresistance; Silver selenide; Nonstoichiometry

1. Introduction

In an early work, Junod [1] determined the magnetoresistance effect of stoichiometric Ag_2Se as approximately 1% at 20°C and at a magnetic field of 1 T. Recently, an unusually large positive MR effect was observed by Xu et al. in bulk material of the nonmagnetic silver-rich silver chalcogenides $\text{Ag}_{2+\delta}\text{Se}$ and $\text{Ag}_{2+\delta}\text{Te}$ [2]. Samples with compositions between “ $\text{Ag}_{2.01}$ ” and “ $\text{Ag}_{2.33}\text{Se}$ ” have been studied, and MR effects up to 120% were observed at room temperature and magnetic fields of 5.5 T. The magnetic field dependence shows no evidence of saturation up to a magnetic field of 5.5 T and is linear down to 10 mT.

Ogorelec et al. also studied $\text{Ag}_{2+\delta}\text{Se}$ in order to optimise the MR effect [3] but were not able to reproduce the large MR effect observed originally by Xu et al. They suggest the Hall mobility of the charge carriers to be the important parameter which has to be optimised. Further experimental studies deal with large magnetoresistance in bulk material and thin films of $\text{Ag}_{2+\delta}\text{Te}$ [4–6].

Motivated by these experimental observations, Abrikosov [7,8] advanced a theoretical explanation for this unusual MR effect. His model grounds on the assumption of material being inhomogeneous on an atomic scale, i.e. he assumes the presence of small metal clusters of excess silver. In addition, the model requires a material which can be regarded as a gapless semiconductor with a linear energy spectrum. For such hypothetic material Abrikosov obtains a positive MR effect with linear dependence on the magnetic field. Since the quantum condition in this model persists to very low fields and high temperatures Abrikosov suggests to call this effect *quantum magnetoresistance*.

In the present study, we investigate the MR effect of two heterogeneous samples obtained from the melt and a stoichiometric sample which is much better characterised with respect to its chemical composition. In the following, we firstly describe the sample preparation, report on the MR effect and discuss our results in the context of the concentration of metal in Ag_2Se and available theories on MR effects.

The phase diagram of the system Ag–Se is well studied between 75°C and 190°C [9]. A phase transformation from the high-temperature phase ($\beta\text{-Ag}_{2+\delta}\text{Se}$) to the low-temperature phase ($\alpha\text{-Ag}_{2+\delta}\text{Se}$) occurs at $T = 133^\circ\text{C}$. Due to the significant density changes during

*Corresponding author. Fax: +49-641-99-34509.

E-mail address: juergen.janek@phys.chemie.uni-giessen.de (J. Janek).

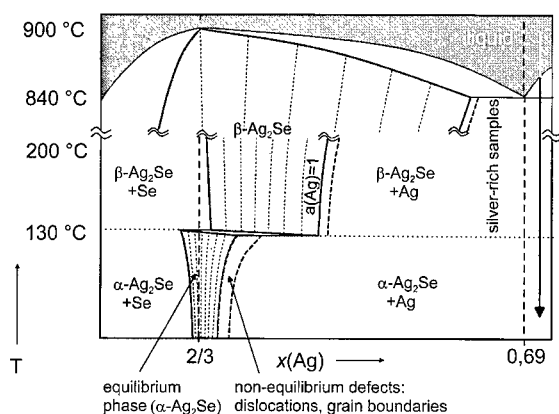


Fig. 1. Schematic phase diagram of the system silver-selenium.

the transformation, dislocations and grain boundaries are created in the α -phase and lead to a material with a high concentration of nonequilibrium defects. Since all practical applications of the MR effect work at room temperature, the α - $\text{Ag}_{2+\delta}\text{Se}$ phase is of primary interest. This phase exists only in a very small range of homogeneity which becomes even narrower with decreasing temperature, as indicated schematically in Fig. 1.

2. Experimental

For the preparation of heterogeneous silver-rich samples, we melted together silver and selenium in the required mass ratio in evacuated silica ampoules. The ampoules were heated for 24 h at 960 °C in a furnace and then cooled down to room temperature. Rectangular specimens were cut from the resulting material. Parts of this material were polished for SEM figures. Other parts of the product were ground and characterised by powder X-ray-diffraction.

Homogeneous silver selenide was grown in a capillary by one-dimensional growth from the elements at $T = 240^\circ\text{C}$. On one side of the capillary, a rod of silver metal was placed. On the other side, selenium was filled into the capillary and melted. Silver reacted with the selenium and a β -silver selenide crystal grew into the capillary with a growth rate of approximately 10 mm/day. By cooling slowly down to temperatures below 133 °C always the α -phase is produced. At 100 °C the crystal was then equilibrated with bulk silver metal for several weeks. This long equilibration period is necessary since the chemical diffusion coefficient of silver in the α -phase is relatively low compared to the β -phase. Furthermore, dislocations which were created during the phase transformation healed out at least partially. Nevertheless, the product remains polycrystalline with coarse grains and with a silver activity of $a_{\text{Ag}} = 1$ at

100 °C. By coulometric titration—a standard technique in solid state electrochemistry [10]—we finally prepared the exactly stoichiometric product $\text{Ag}_{2.000000}\text{Se}$, $\Delta\delta < 10^{-6}$ from this material.

All samples were contacted with platinum wires and the transversal magnetoresistance was measured in fields up to $B = 8$ T using a four probe dc technique.

3. Experimental results

X-ray-diffraction of the silver-rich “ $\text{Ag}_{2.33}\text{Se}$ ” proves that the material is primarily orthorhombic α - Ag_2Se [11]. However, silver metal precipitates are also identified by the (hkl) reflection at $2\theta = 38.1^\circ$.

The “ $\text{Ag}_{2.0005}\text{Se}$ ” and the “ $\text{Ag}_{2.33}\text{Se}$ ” specimens are polycrystalline and contain precipitates of silver metal in the micron scale (see inset in Figs. 3 and 4). The distribution of the precipitates in “ $\text{Ag}_{2.33}\text{Se}$ ” appear to be quite regular, exhibiting typical morphologies of eutectic systems produced from the melt. The size of the precipitates depends on the cooling rate. In “ $\text{Ag}_{2.33}\text{Se}$ ” large dendrite-like precipitates of silver (with dimensions in the 100 micron scale) are formed in regions with reduced cooling rate. Over large areas, small silver particles of approximately 1 μm diameter form chains with almost regular structure. Frequently, small areas with silver particles being arranged almost lattice-like are found. In “ $\text{Ag}_{2.0005}\text{Se}$ ”, we find only few silver precipitates (inset Fig. 3). The smallest silver particles we found here have a diameter of approximately 0.2 μm . Summarizing, all material produced by melting and subsequent solidification is heterogeneous and shows silver precipitates. HSEM studies did not show silver precipitates with diameters less than 0.1 μm .

We obtained different results for the magnetoresistance effect. The MR effect of stoichiometric silver selenide is small and positive. It shows a quadratic field dependence and there is no saturation up to fields of

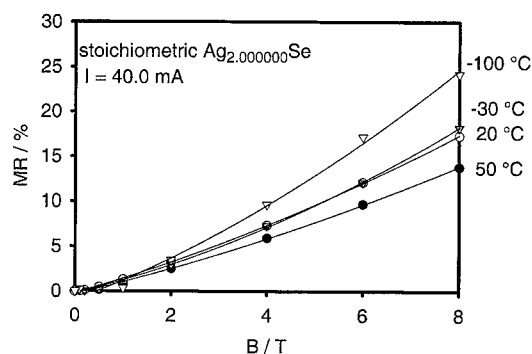


Fig. 2. MR effect of stoichiometric $\text{Ag}_{2.000000}\text{Se}$ measured at different temperatures.

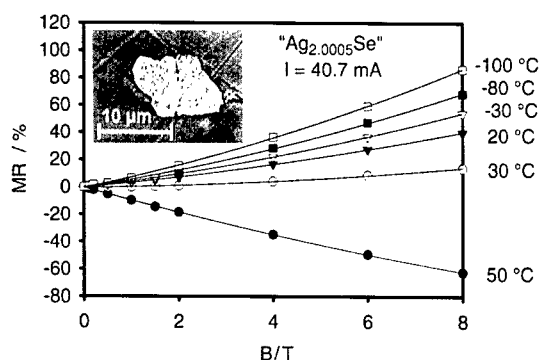


Fig. 3. MR effect in Ag–Se samples with the mean composition “Ag_{2.0005}Se” measured at different temperatures. Inset: SEM micrograph taken from this sample.

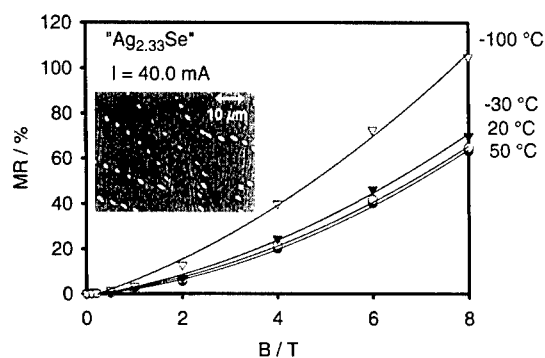


Fig. 4. MR effect in Ag–Se samples with the mean composition “Ag_{2.33}Se” measured at different temperatures. Inset: SEM micrograph taken from this sample.

$B = 8$ T (Fig. 2). “Ag_{2.0005}Se” shows a negative MR effect at 50 °C. With decreasing temperatures, the MR effect becomes more and more positive (Fig. 3). This positive effect is almost linear in its field dependence. For Ag–Se samples with the mean composition “Ag_{2.33}Se”, we find a positive effect which decreases with increasing temperatures. The field dependence is almost quadratic but is better described by an additional linear term (Fig. 4).

4. Discussion

Our data from the coulometric titration of silver selenide show that α -Ag_{2+ δ} Se with a metal excess δ higher than 2×10^{-4} will necessarily be a two-phase mixture of silver and α -silver selenide at 20 °C [11]. Thus, our samples with $\delta = 5 \times 10^{-4}$ and 0.33 are definitely heterogeneous and contain small silver precipitates. Increasing or decreasing the silver excess (silver activity)

within the phase field of α -silver selenide increases or decreases the concentration of electrons or electron holes, respectively. Measurements of the electronic conduction confirm this [12,13]. For the sake of the argument, we assume that any metal excess directly leads to a corresponding increase of the carrier density, i.e. we assume complete dissociation of the metal dopant, irrespective of whether we consider homogeneous or heterogeneous samples.

The classical theory of ordinary magnetoresistance (OMR) in semiconductors yields a positive and quadratic field dependence [14] of the MR effect $\Delta\rho/\rho$ when the product of the Cyclotron frequency ω_c and the relaxation time τ is small compared with 1 (small magnetic fields B) or for stoichiometric semiconductors, where the concentration of electrons n equal to that of holes p .

$$\frac{\Delta\rho}{\rho} \propto B^2, \quad \omega_c \cdot \tau \ll 1,$$

$$\frac{\Delta\rho}{\rho} \propto \text{const}, \quad \omega_c \cdot \tau \gg 1, \quad n \neq p.$$

For nonstoichiometric samples, the OMR effect always reaches saturation at sufficiently large magnetic fields. In the simple case of a non-degenerate semiconductor with a parabolic band structure and electron relaxation by phonon scattering, we can predict the OMR effect for our samples inserting appropriate mobilities and the density of electrons and holes [11].

For stoichiometric silver selenide and for “Ag_{2.33}Se” we indeed measure a square field dependence. The MR effect of the stoichiometric sample shows ordinary magnetoresistance simply caused by the Lorentz force on the charge carriers in the magnetic field. An increased silver excess should lead to an even smaller positive MR effect. Obviously this is in contradiction to the experimental findings—the MR effect of “Ag_{2.33}Se” is much larger than that of the stoichiometric sample.

In the heterogeneous samples, the chemical potential of silver always equals the standard potential of silver. This might have an effect on the band structure of the system. We also observe silver precipitates (see inset in Fig. 4). Thus, we believe that it is unreasonable to describe the MR effect of this material by a simple OMR model.

The “Ag_{2.0005}Se” sample shows a linear MR effect at a low temperatures and a negative effect at 50 °C. Such change of the MR effect has not been reported yet and requires further investigation.

Both the GMR effect in film structures [15,16] and the CMR effect [17] are negative effects. The GMR effect also exists in granular systems [18]. In all these cases, a necessary condition for the occurrence of negative effects are permanent magnetic structures. Yet there is no

doubt that silver selenide and silver metal are diamagnetic, and thus, both the GMR and CMR effect do not explain the present results on $\text{Ag}^{2+}\delta\text{Se}$.

Other types of negative MR effects have been proposed and measured in disordered systems [19–21]. But normally these MR effects appear only at very low temperatures (of a few Kelvin). In the current state of investigation, we believe that a metal excess is indeed necessary for the occurrence of the observed unusual MR behavior. Currently, we investigate whether precipitates in the nano-scale regime might be the origin of this effect. In this case, the linear contribution could be explained by the quantum magnetoresistance model of Abrikosov [7].

Finally, we assume that the measured effects of “ $\text{Ag}_{2.33}\text{Se}$ ” are a superposition of a saturating negative and a linear positive effect. Further, our own measurements in [11] confirm this.

Acknowledgements

We thank Prof. Paul Heitjans and Dr. Silvio Indris (University of Hannover) for their experimental support. We thank Dr. Carsten Korte for assistance in the HSEM measurements. Financial support by the FCI (Fonds der Chemischen Industrie) is gratefully acknowledged.

References

- [1] P. Junod, *Helv. Phys. Acta* 32 (1959) 567.
- [2] R. Xu, et al., *Nature* 390 (1997) 57.
- [3] Z. Ogorelec, et al., *Europhys. Lett.* 46 (1) (1999) 56.
- [4] I.S. Chuprakov, K.H. Dahmen, *Appl. Phys. Lett.* 72 (17) (1998) 2165.
- [5] B.Q. Linag, et al., *Phys. Rev. B* 61 (5) (2000) 3239.
- [6] H.S. Schnyders, M.-L. Saboungi, T.F. Rosenbaum, *Appl. Phys. Lett.* 76 (13) (2000) 1710.
- [7] A.A. Abrikosov, *Phys. Rev. B* 58 (5) (1998) 2788.
- [8] A.A. Abrikosov, *Europhys. Lett.* 49 (6) (2000) 789.
- [9] U.V. Oehsen, H. Schmalzried, *Ber. Bunsenges. Phys. Chem.* 85 (1981) 7.
- [10] C. Wagner, *J. Chem. Phys.* 21 (1953) 1816.
- [11] G.A. Wieggers, *Am. Mineral.* 56 (1971) 1882.
- [12] G. Beck, J. Janek, submitted (2001).
- [13] G. Bonneau, A. Lichanot, S. Gromb, *J. Phys. Chem. Solids* 39 (1978) 299.
- [14] N. Valverde, *Z. Phys. Chem.* 70 (1970) 128.
- [15] A.I. Anselm, In: *Einführung in die Halbleitertheorie*, cp. VIII, Akademie-Verlag, Berlin, 1962.
- [16] P. Grünberg, R. Schreiber, Y. Pang, *Phys. Rev. Lett.* 57 (19) (1986) 2442.
- [17] M.N. Baibich, et al., *Phys. Rev. Lett.* 61 (21) (1988) 2472.
- [18] K. Chandra, et al., *Appl. Phys. Lett.* 62 (7) (1993) 780.
- [19] A.E. Berkowitz, et al., *Phys. Rev. Lett.* 68 (25) (1992) 3745.
- [20] X. Wang, S.C. Ma, X.C. Xie, *Europhys. Lett.* 45 (3) (1999) 368.
- [21] G. Bergmann, *Phys. Rep.* 107 (1) (1994) 1.



ELSEVIER

Physica B 308–310 (2001) 1090–1096

PHYSICA B

www.elsevier.com/locate/physb

Benefits of microscopy with super resolution

C. Kisielowski^{a,*}, E. Principe^b, B. Freitag^c, D. Hubert^c

^a National Center for Electron Microscopy, Ernest Orlando Lawrence Berkeley National Laboratory, Berkeley, CA 94720, USA

^b Applied Materials, 3050 Bowers Avenue, Santa Clara, CA 95054, USA

^c FEI Company, Achtseweg Noord 5, P.O. Box 218, 5600 MD Eindhoven, The Netherlands

Abstract

Transmission electron microscopy developed from an imaging tool into a quantitative electron beam characterization tool that locally accesses structure, chemistry, and bonding in materials with sub-Angstrom resolution. Experiments utilize coherently and incoherently scattered electrons. In this contribution, the interface between gallium nitride and sapphire as well as thin silicon gate oxides are studied to understand underlying physical processes and the strength of the different microscopy techniques. An investigation of the GaN/sapphire interface benefits largely from the application of phase contrast microscopy that makes it possible to visualize dislocation core structures and single columns of oxygen and nitrogen at a closest spacing of 85 pm. In contrast, it is adequate to investigate Si/SiO_xN_y/poly-Si interfaces with incoherently scattered electrons and electron spectroscopy because amorphous and poly-crystalline materials are involved. Here, it is demonstrated that the SiO_xN_y/poly-Si interface is rougher than the Si/SiO_x interface, that desirable nitrogen diffusion gradients can be introduced into the gate oxide, and that a nitridation coupled with annealing increases its physical width while reducing the equivalent electrical oxide thickness to values approaching 1.2 nm. Therefore, an amorphous SiN_xO_y gate dielectric seems to be a suitable substitute for traditional gate oxides to further increase device speed by reducing dimensions in Si technology. © 2001 Elsevier Science B.V. All rights reserved.

Keywords: Transmission electron microscopy; Gallium nitride; Gate oxides; Dislocations

1. Background

Recent progress in high resolution transmission electron microscopy (HRTEM) allows investigating crystalline materials by phase contrast microscopy with a resolution close to the 80 pm information limit of a 300 kV field emission microscope [1–4]. A reconstruction of the electron exit wave from a focal series of lattice images converts the recorded information into interpretable resolution [5,6]. It was reported before that Z-contrast microscopy achieved sub-Angstrom resolution [7].

From a materials point of view, a resolution enhancement in electron microscopy is required to achieve truly mono atomic resolution in most materials systems. A typical point resolution around 0.2 nm does commonly not suffice. Fig. 1 depicts this situation by

plotting the band gap energy of different ceramics and semiconductors versus their inter-atomic spacing. It is seen that the resolution of single atomic columns in ceramic-like materials is barely possible. In practice, their separation often requires a better point resolution because lattice imaging along zone axes of crystals nearly always shortens the inter-atomic spacing by the involved projection into the image plane. For example, the resolution of dumbbell images along the commonly recorded [110] zone axis of silicon, cubic gallium nitride, and diamond require a point resolution of 0.136, 0.113, and 0.089 nm, respectively.

Moreover, band gap energies tend to increase with shorter inter-atomic distances. From the slope of the trend line in Fig. 1 one finds that a reduction by 1 pm typically changes energies by 50 meV. It is for such reasons that electron microscopy strives for the development of equipment that will allow for sub-Angstrom resolution [3,4,7], will pinpoint the position of atomic columns to within 1 pm [12,13], and will enable

*Corresponding author. Fax: +1-510-486-5888.

E-mail address: cfkisielowski@lbl.gov (C. Kisielowski).

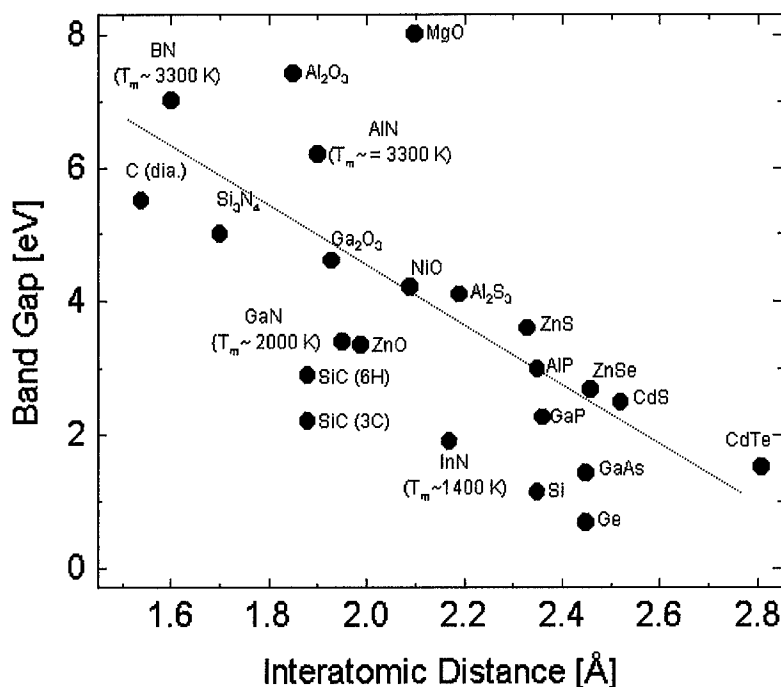


Fig. 1. Band gap energy versus inter-atomic distances in selected semiconductors and ceramics. The slope of the trend line relates 1 pm of distance to 50 meV of energy change.

spectroscopic investigations of single atomic columns with an energy resolution of about 50 meV [8–11].

In the present contribution we investigate interfaces with current state-of-the-art equipment. A CM300 FEG/UT HRTEM with an information limit of 80 pm and a Tecnai F20/ST HRTEM/STEM (scanning transmission electron microscope) with a beam diameter of 0.19 nm, 500 meV of energy resolution, and Z-contrast capability are employed. This allows for a comparison of phase with Z-contrast imaging. Gate oxides in silicon and the interface between GaN and sapphire are examined. Both examples are of substantial technological importance [14,15]. Details of sample preparation procedures are published elsewhere [3].

2. Gate oxides

Fig. 2 depicts images of the amorphous SiO₂ gate dielectric of roughly 2 nm thickness that was deposited on silicon and capped with a poly-silicon layer. Gate oxides of this thickness will be relevant for a 0.1 μm technology that must be standard technology in a few years if Moore's law applies. Excellent film uniformity has to be achieved across wafers and TEM is the primary tool to relate the physical gate oxide thickness to process parameters and to calibrate metrology tools.

We depict three types of images in Fig. 2. Fig. 2a is a usual lattice image which is an interferogram of diffracted beams [16]. As a result the image pattern of the silicon and the poly-silicon changes rapidly with the focus setting of the objective lens that also acts as a filter for spatial frequencies. This produces the speckle contrast of the amorphous material. In addition, there is substantial delocalization of information at interfaces that is visible as a periodic contrast variation in the amorphous layer close to the silicon substrate. It results from the utilization of a field emission electron source [16]. Fig. 2b is a reconstructed phase image of the electron exit wave from a focal series of lattice images [3,5,6]. Delocalization effects are removed during the reconstruction process. Poly-crystalline grains are visible even if they are not imaged along low indexed zone axes because of the 80 pm information limit of the instrument. In thin samples (< 10 nm) the image depicts the 1 s state of the electron wave channeling along atomic columns [17] that are entirely resolved. They appear as bright spots in the phase image. The defocus dependence of the pattern is eliminated. Local phase changes can be analyzed quantitatively since they oscillate with sample thickness. Their oscillation periodicity is given by [17]

$$D_{1s} = \alpha[d^2/Z + 0.276B], \quad (1)$$

where α is a constant, d is the distance between successive atoms, Z is the atomic number and B is the

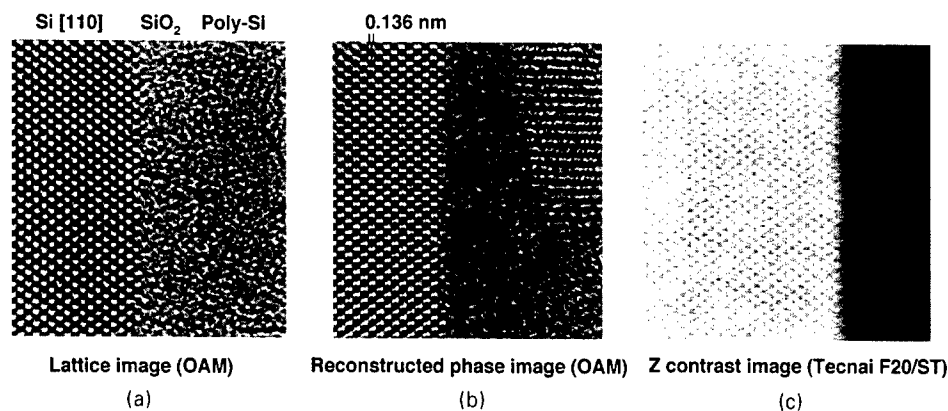


Fig. 2. Gate oxides in silicon. Images were recorded by different techniques. (a) A traditional lattice image recorded with NCEM's One Angstrom Microscope (OAM) that is a specially equipped Philips CM300. (b) Reconstructed electron exit wave from a focus series of twenty lattice images of the OAM. The phase of the electron exit wave is shown. (c) Scanning transmission electron microscopy (STEM) was utilized to produce a Z-contrast image. A Tecnai F20 super twin microscope was used.

Debye Waller factor. Eq. (1) was recently utilized to demonstrate that the phase change at single gold atoms can be detected with a signal to noise ratio of better than 2 [18]. Thus, unlike a lattice image, the phase image of the electron exit wave depicts directly the projection of the layered structure into an image plane. The magnitude of the phase change can be quantified through a simple dependence on sample thickness and chemical composition. However, the speckle contrast of the amorphous SiO₂ remains because the reconstruction process operates over the finite range of spatial frequencies that is determined by the objective lens [5,6]. Finally, Fig. 2c depicts a Z-contrast image. Similarly to the phase images, a Z-contrast image also depicts the 1s state of electrons trapped on atomic columns. However, incoherently scattered electrons are used to build up the picture [19]. Currently, sub-Angstrom resolution is achievable by Z-contrast microscopy at 300 kV [7]. However, the 0.136 nm separation of the dumbbell structure in silicon can already be resolved at 200 kV [20,21]. In comparison with phase contrast images, Z-contrast images lack of speckle contrast in amorphous regions. Its absence eases a quantitative evaluation of intensity profiles to measure the gate oxide thickness and interfacial roughness [22].

Table 1 summarizes results of gate oxide thickness measurements from Z-contrast images and from the phase contrast images. Intensities were evaluated in Z-contrast images and the presence of a pattern from crystalline material was used to locate the position of interfaces in phase contrast images. Two samples were investigated: a control sample (A) and a second sample (B) where nitrogen was diffused into the gate oxide layer. From a comparison of gate oxide thickness in sample A and B one finds that a broadening of the amorphous region occurs as a result of nitrogen incorporation. Moreover, we find that the poly-Si/SiO₂ interface is

rougher by a factor of 2 than the Si/SiO₂ one. Finally, phase contrast images consistently provide a smaller gate oxide thickness than measurements obtained from Z-contrast images. Both procedures reproduce gate oxide thickness data within 0.1–0.2 nm.

We recorded electron energy loss spectra (EELS) by stepping the focused (0.19 nm) electron across the interfaces with 0.1 nm per step. At each step, a full spectrum including the Si L_{2,3}, N K, and O K edges was recorded. Post experiment, we processed the several thousand spectra to produce chemical maps or profiles as shown in Fig. 3. Oxygen, nitrogen and silicon profiles are depicted and the thickness values of the gate oxide as determined from the Z-contrast—and phase contrast images are overlaid. The profiles reveal that O and N gradients are present in the gate oxide. Nitrogen concentrations peak at the poly-Si/SiO_xN_y interface and decrease linearly towards the Si/SiO_x interface. It is not surprising to find that the width determination of the gate dielectric from the Z-contrast images coincides with its chemical width as measured by EELS since the intensities in a Z-contrast image depend on sample thickness and on chemistry.

In summary, we produced a direct comparison between lattice images, electron exit waves, and Z-contrast images of gate oxides. In silicon [110] a resolution of 136 pm suffices to separate individual atomic columns at 300 kV by coherently scattered electrons in combination with exit wave reconstruction and by incoherently scattered electrons. Even the current information limit of leading edge 200 kV equipment allows for a resolution of this dumbbell structure. Both techniques provide pictures of the 1s state of electrons trapped at atomic columns and the signal strength depends on local sample thickness and chemical composition. Differences stem from a larger signal to noise ratio in phase contrast images compared with

Table 1
Quantitative evaluation of gate oxide thickness and interfacial roughness from Z-contrast and phase contrast images^a

Sample	Thickness (nm) Z-contrast	Thickness (nm) phase contrast	Roughness (nm) Si/SiO ₂	Roughness (nm) Poly Si/SiO ₂
A	1.92	1.76	0.06	0.10
B	2.65	2.14	0.08	0.25
B	2.50	2.06	0.06	0.14
B	2.61	2.00	0.07	—

^aSample A: control sample. Sample B: nitrogen containing gate oxide. Roughness measurements were made from Z-contrast images.

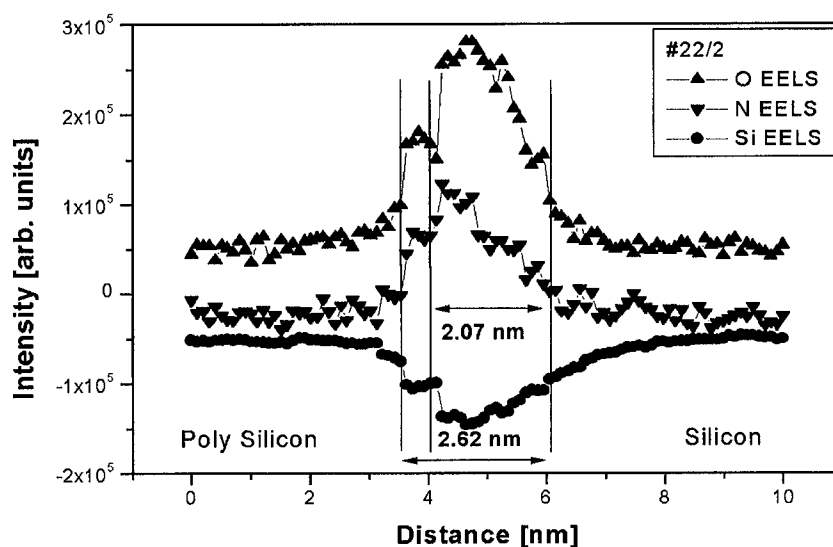


Fig. 3. More than 1000 Electron Energy Loss Spectra were recorded with an electron beam focused to 0.19 nm small spot that was repetitively scanned across the gate oxide (Tecnai F20). An automated data analysis produces the depicted profiles of nitrogen, silicon and oxygen in minutes. A 2.07 nm wide dielectric was measured from image patterns in phase contrast images. An analysis of the local intensity of Z-contrast images reveals a 2 nm wide gate oxide.

Z-contrast images. However, in the presence of amorphous material, the limited bandwidth of transmitted spatial frequencies in phase contrast microscopy generates a speckle contrast in amorphous—and partly in poly-crystalline material. Its absence in Z-contrast images eases a quantitative evaluation of interfacial roughness and the dielectric layer width. A nitridation of the gate oxide increases its dielectric constant and the layer width. Both effects are beneficial for devices because they appear electrically “thinner” but are physically thicker. The equivalent electrical thickness approaches 1.2 nm in this case. Therefore, it is feasible to further increase the switching speed of devices while avoiding tunnel currents. A control of nitrogen diffusion gradients is crucial in this process and electron spectroscopy can provide this information on a scale of 0.1–0.2 nm. From a comparison of phase contrast images, Z-contrast images, and electron spectroscopy we find that O and N diffused into the adjacent crystalline materials.

3. Growth of GaN on sapphire

It is evident from Fig. 1 that an investigation of silicon is not extremely demanding in terms of resolution. In case of GaN or sapphire (Al₂O₃), however, the situation changes for two reasons: the inter-atomic distances are smaller and the light elements O and N are involved with low electron scattering power. It is for these reasons that these materials could not be investigated on a truly atomic scale.

Commonly, lattice images of GaN are recorded along a [1 1 2 0] zone axis as shown in Fig. 4a because it is this projection that allows at least for a separation of the Ga atoms. Even more restricting is the presence of a huge defect density at the interface between GaN and sapphire that is generated to partly accommodate 14% of lattice mismatch [23]. Fig. 4b shows the same region in [1 1 0 0] projection. This experiment benefits from two factors: First, we resolved the GaN lattice in [1 1 0 0] projection, which requires 0.15 nm of resolution.

Second, the $[1\bar{1}00]$ projection eliminates the stacking fault contrast that usually obscures lattice images recorded in $[1\bar{1}\bar{2}0]$ projection. Thus, image interpretation is drastically simplified by simply having a choice of recording lattice images along different zone axes and yet resolving a lattice.

From a focal series of lattice images it is then possible to reconstruct the electron exit wave shown in Fig. 5a. Again, the reconstructed phase image is directly interpretable: a bright spot in the exit wave picture marks the position of atomic columns, its intensity depends on chemical composition and the spacing of atoms along the column (Eq. (1)). It is seen that all atom columns at the interface and in the sapphire are resolvable with a smallest projected aluminum–oxygen spacing of 85 pm in the sapphire. Consequently, it is now possible to detect single columns of oxygen atoms at a sub-Angstrom spacing because of the excellent signal to noise ratio of the phase contrast image and the improved resolution.

An additional advantage of phase contrast imaging comes from the precision as to which lattice parameters can be measured [12]. Fig. 5b summarizes lattice parameter measurements in plane of the interface and normal (out of plane) to it. It is seen that the in plane

lattice parameter does not vary more than 1 pm except for a surprisingly 0.8–1 nm narrow interfacial region. Even the out of plane lattice parameter is reduced by only 10 pm which correspond to a displacement of only 4%. One would estimate an out of plane lattice parameter variation of roughly 30% for fully strained pseudomorphic growth with a lattice mismatch of 14%. Closer inspection of the narrow interfacial region reveals the presence of a misfit dislocation network. One of the misfit dislocations is depicted in Fig. 6. It is seen that its core structure is entirely resolved. The dislocation is of edge character and a row of oxygen or nitrogen atoms terminates the inserted extra half plane. It is not possible to discriminate between nitrogen and oxygen atoms because of their similar Z of 7 and 8, respectively. The misfit dislocation spacing along the interface is regular. From Fig. 5a we find that they are standing off the interface by 0.5–1 nm and that six GaN (1120) planes of 0.1595 nm spacing match seven sapphire (3300) planes spaced by 0.1374 nm. Here we used literature values for lattice parameters. Resultantly, one calculates that 0.957 nm in GaN match 0.962 nm in sapphire along the interface which leaves a residual strain of less than 1%. Such values agree reasonably well with the

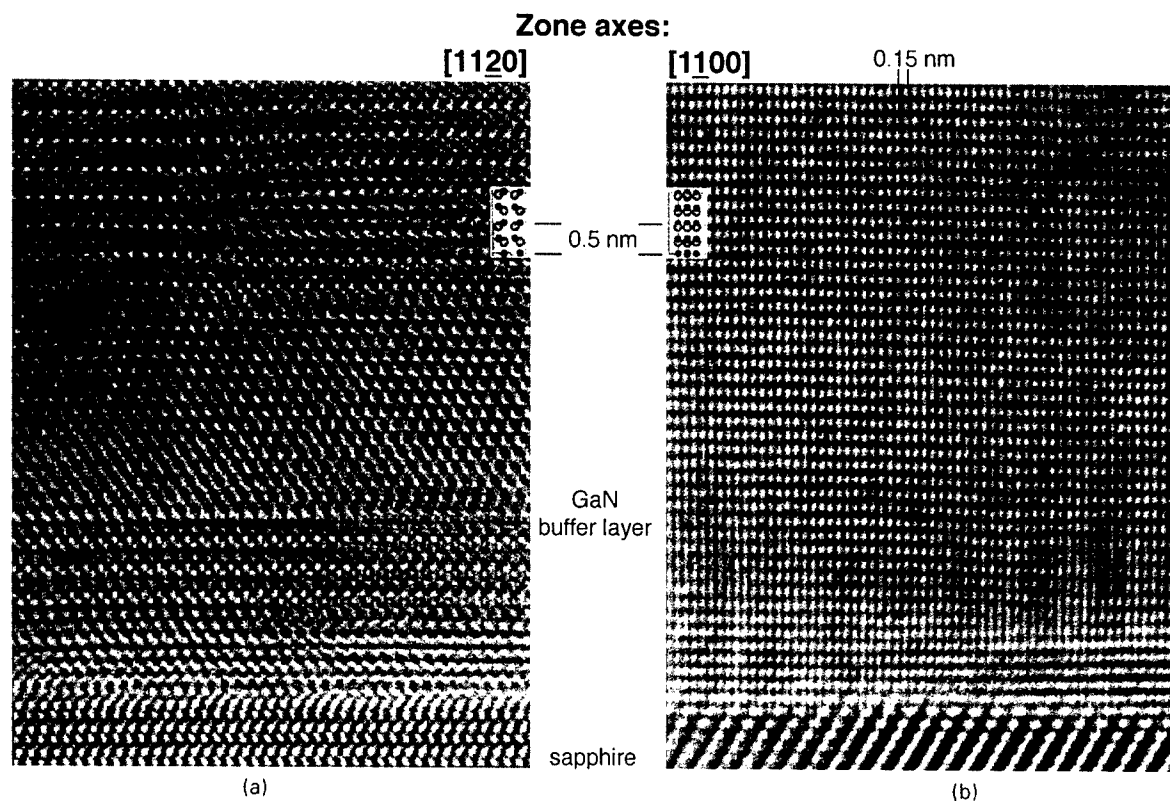


Fig. 4. Lattice images of GaN along two different zone axes a and b . An information limit of 80 pm of the OAM allows for a choice of suitable zone axes. Here, they are chosen such that the contrast of stacking faults is eliminated in b . Insets show the unit cells of hexagonal GaN projected along the two different zones.

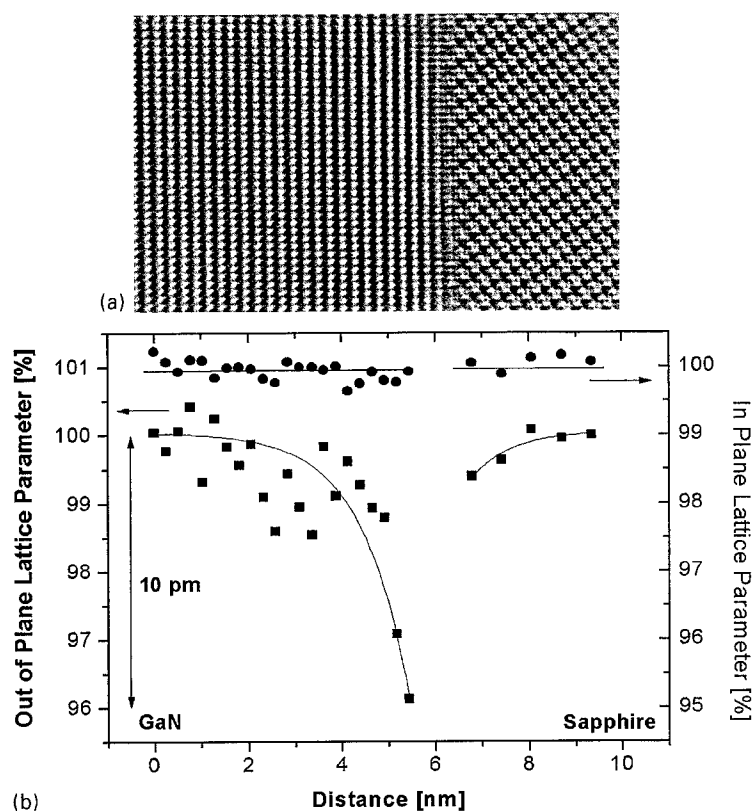


Fig. 5. Top (a) Phase of the electron exit wave reconstructed from 20 lattice images. (b) Measurement of lattice parameters across the field of view. Values in plane of the interface and normal to it (out of plane) are averaged in columns across the picture.

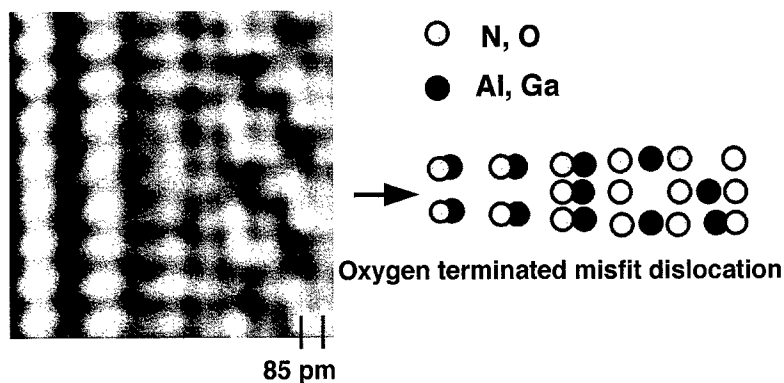


Fig. 6. Core structure of an oxygen terminated misfit dislocation at the interface between GaN and sapphire. The model (right) was obtained from pinpointing atomic columns in the phase image.

measured 5% of the out of plane lattice parameter change considering that GaN growth can be largely non-stoichiometric [23].

In summary, we applied phase contrast microscopy to investigate the interface between sapphire and GaN with sub-Angstrom resolution. The investigation benefits from the gained ability to choose from different zone axes that comes with the improvement of resolution and

the large sensitivity of phase contrast microscopy that enables scientists to detect light elements even if they are closely spaced to heavier next neighbors. Dislocation core structures are now resolvable. In this particular case we find that the complicated process to initiate growth of GaN on sapphire [23] is linked to the fabrication of a misfit dislocation network that accommodates most of the initial lattice mismatch of 14%. The dislocated area

is confined to a 0.8–1 nm narrow interfacial region. Residual displacements are about 5% and they vanish over several nanometers as the distance from the interface increases in the thin TEM foils.

4. Conclusions

Investigations of GaN on sapphire and of the silicon gate oxides are performed to analyze two technologically important materials with state-of-the-art transmission electron microscopy. Phase contrast microscopy, Z-contrast microscopy, and electron spectroscopy are employed. In the case of silicon gate oxides a moderate resolution of 136 pm suffices to resolve the structure which is achievable with all techniques these days. The presence of the amorphous gate dielectric, however, favors applications of Z-contrast microscopy because of frequency limitations that come with the application of phase contrast microscopy and produces a speckle contrast in the amorphous layer. It complicates a quantitative image analyses. The application of electron spectroscopy is desirable in any case. Here we demonstrate that industry seeks to increase switching times in Si based devices by increasing the dielectric constant of the gate oxide with the addition of nitrogen. Its diffusion can be controlled such that the N concentration peaks at the poly-Si side but is negligibly small on the SiO₂/Si side of the gate oxide. In addition a nitridation of the gate oxide increases its width which reduces the risk of undesirable tunnel currents as the dimensions of the devices shrink. In case of GaN on Sapphire, only phase contrast microscopy with sub-Angstrom resolution allows to resolve all atomic columns at this interface for the first time. Even dislocation core structures are now accessible. With such tools it is now possible to systematically study the initiation of thin film growth on ceramic materials and semiconductors with short bond length on a truly atomic level. Overall the investigation demonstrates that newly emerging TEM techniques can be chosen such that they provide a best solution for a particular problem in materials sciences.

Acknowledgements

The project is sponsored by the Director, Office of Science, Office of Basic Energy Sciences, of the US

Department of Energy under Contract No. DE-AC03-76SF00098.

References

- [1] C. Kisielowski, E.C. Nelson, C. Song, R. Kilaas, A. Thust, *Micros. Microanal.* 6 (2000) 16.
- [2] M.A. O'Keefe, *Micros. Microanal.* 6 (2000) 1192.
- [3] C. Kisielowski, C.J.D. Hetherington, Y.C. Wang, R. Kilaas, M.A. O'Keefe, A. Thust, *Ultramicroscopy* (2001), in press.
- [4] M.A. O'Keefe, C.J.D. Hetherington, Y.C. Wang, E.C. Nelson, J.H. Turner, C. Kisielowski, J.-O. Malm, R. Mueller, J. Ringnald, M. Pam, A. Thust, *Ultramicroscopy* (2001), in press.
- [5] W.M.J. Coene, A. Thust, M. Op de Beeck, D. Van Dyck, *Ultramicroscopy* 64 (1996) 109.
- [6] A. Thust, W.M.J. Coene, M. Op de Beeck, D. Van Dyck, *Ultramicroscopy* 64 (1996) 211.
- [7] P.D. Nellist, S.J. Pennycook, *Phys. Rev. Lett.* 81 (1998) 4156.
- [8] G. Duscher, M. Kim, N.D. Browning, S.T. Pantelides, S.J. Pennycook, *Micros. Microanal.* 6 (2000) 114.
- [9] O.L. Krivanek, N. Dellby, A.R. Lupini, *Ultramicroscopy* 78 (1999) 1.
- [10] P.E. Betson, *Ultramicroscopy* 78 (1999) 33.
- [11] P.C. Tiemeijer, *Ultramicroscopy* 78 (1999) 53.
- [12] C. Kisielowski, O. Schmidt, J. Yang, *Mater. Res. Soc. Symp.* 482 (1998) 369.
- [13] C.L. Jia, A. Thust, *Phys. Rev. Lett.* 82 (1999) 5052.
- [14] S. Johnson (Ed.), *Strategies in Light 2001*, Strategies Unlimited, San Francisco, 2001.
- [15] D.A. Muller, T. Sorsch, S. Moccio, F.H. Baumann, K. Evans-Lutterodt, G. Timp, *Nature (London)* 399 (1999) 758.
- [16] D.B. Williams, C.B. Carter, *Transmission Electron Microscopy*, Plenum Press, New York, 1996.
- [17] D. van Dyck, J.H. Chen, *Solid State Commun.* 109 (1999) 501.
- [18] C. Kisielowski, J.M. Plitzko, S. Lartigue, T. Radetic, U. Dahmen, *Micros. Microanal.* 7 (2001) 246.
- [19] S.J. Pennycook, B. Rafferty, P.D. Nellist, *Micros. Microanal.* 6 (2000) 106.
- [20] N.D. Browning, *Ultramicroscopy* 78 (1999) 125.
- [21] E. Boyle, J. Ringnald, M.A.J. van der Stam, T.F. Fliervoet, E. van Cappellen, *Micros. Microanal.* 7 (2001) 232.
- [22] D. Hubert, 2001, unpublished.
- [23] C. Kisielowski, in: J.I. Pankove, T.D. Moustakas (Eds.), *Semiconductors and Semimetals*, 57, Academic Press, New York, 1999, p. 257.



ELSEVIER

Physica B 308–310 (2001) 1097–1099

PHYSICA B

www.elsevier.com/locate/physb

Role of metal impurities in the growth of chains of crystalline-silicon nanospheres

H. Kohno^{a,*}, T. Iwasaki^a, Y. Mita^b, M. Kobayashi^b, S. Endo^c, S. Takeda^a

^a Graduate School of Science, Physics Department, Osaka University, 1-16 Machikaneyama, Toyonaka, Osaka 5600043, Japan

^b Graduate School of Engineering Science, Osaka University, Toyonaka, Osaka, Japan

^c Research Center for Materials Science at Extreme Conditions, Osaka University Toyonaka, Osaka, Japan

Abstract

We reported a novel silicon nanostructure, a chain of crystalline-silicon nanospheres: crystalline-silicon nanospheres are covered with and connected by silicon oxide at a nearly equal spacing forming a chain-like nanostructure. We have found that additional metal impurities such as lead can promote a periodic instability in the vapor–liquid–solid growth of silicon nanowires resulting in the chain formation. By controlling the metal impurities, we have successfully grown dense chains and also measured their phonon structures. Through the analysis of Raman spectra, we have found that the phonons were confined in the silicon nanospheres. © 2001 Elsevier Science B.V. All rights reserved.

Keywords: Silicon; Nanostructure; Impurities; Self-organization

1. Introduction

In the self-organized formation of nanostructured materials, impurities and defects which are involved in the growth process often affect yield, morphology and properties of fabricated materials. Sometimes, impurities and defects obstruct and at other times they enhance the self-organized formation. For instance, it is well known that the formation of porous silicon [1], namely anodization of silicon, is dopant sensitive. In the case of carbon nanotube [2], its growth is governed by metal catalysts and also sensitive to the additional impurities such as sulfur. Therefore, the understanding of the role of impurities and defects is indispensable for controlling the self-organized formation. Of course, the role of impurities and defects is closely related to the growth mechanism; therefore, the understanding will also give useful information on the growth mechanism.

Recently, we found a novel silicon nanostructure, a chain of crystalline-silicon nanospheres [3]. The chain of

crystalline-silicon nanospheres is a self-organized semiconductor–insulator nanostructure: crystalline-silicon nanospheres are covered with and connected by amorphous silicon oxide at a nearly equal spacing forming a chain-like structure. The chains are grown via an extension of the well-known vapor–liquid–solid (VLS) mechanism from gold catalysts. We found that the chain growth is strongly affected by additional metal impurities such as lead [4]. In this paper, we discuss the structure, growth mechanism, role of metal impurities in the chain growth, and properties.

2. Growth and structure

Phosphorous-doped silicon (100) was used as a substrate and gold of about 10 nm thick was deposited on each substrate via vacuum evaporation. In order to add metal impurities such as lead to gold catalyst, each sample was sealed in a silica glass ampoule with a small piece of metal in a vacuum of 10^{-5} Torr and heated at a specific temperature for 30 min. Then, only the sample was sealed in a new ampoule in a vacuum of 10^{-5} Torr and heated at 1230°C. Transmission electron microscopy (TEM) observations were performed using a

*Corresponding author. Tel.: +81-6-6850-5752; fax: +81-6-6850-5764.

E-mail address: kohno@tem.phys.wani.osaka-u.ac.jp (H. Kohno).

200 kV-TEM, JEOL JEM-2010. Energy-filtered TEM images were obtained using a Gatan Image Filter with a charge coupled device (CCD) detector equipped in a 300 kV-TEM, JEOL JEM-3000F instrument at Osaka National Research Institute.

By using gold/lead catalysts, numerous chains were grown on the silicon substrate as shown in Fig. 1(a). The chains have a wire-like one-dimensional structure; however, their diameters are periodically modulated. In fact, there is a silicon nanocrystallite in the core of each knot. Some crystalline-silicon nanospheres are defective and have a twin structure as shown in Fig. 1(b). The necks which connect nanospheres and the surface layers of silicon nanospheres are amorphous silicon oxide.

When lead was not added to the gold catalyst, the chain growth became unstable and many silicon nanowires were grown as by-products of the chains. In Fig. 2, we show the yield of the chain growth against the temperature at which lead was added. Clearly, the chain growth is promoted by additional lead.

3. Growth mechanism and role of metal impurities

As shown in Fig. 1(a), there is a gold particle at the end of a chain. This is a strong evidence that the chains are grown via the VLS process. The growth mechanism of the chains of crystalline-silicon nanospheres was speculated by authors as follows: (i) the diameter of a silicon nanowire changes periodically due to a periodic instability in the wetting property of a molten catalyst at the tip of the wire; (ii) the wire was oxidized completely at the necks and incompletely at the knots leaving a silicon nanosphere in the core of each knot.

The periodic instability in the wetting property is explained by the following feedback mechanism [5,6]. If the diameter of a wire changes, then the curvature of the molten catalyst changes. As a consequence, the amount of vapor silicon taken in the catalyst at the vapor–liquid interface changes due to the Gibbs–Thomson effect. If the mole fraction of silicon in the molten catalyst changes, then the roughness of the liquid–solid interface changes due to the effect of the kinetic roughening resulting in the change in the wetting property of the molten catalyst and the diameter of the wire. Taking the above feedback mechanism into account, we performed computer simulations of the chain growth and found that the periodic instability was induced by the feedback mechanism [6] with adequate parameters such as temperature, size of molten catalyst and balance of interface tensions. Considering the fact that the periodic instability was sensitive to the parameters in our simulations, we speculate that the metal impurities such as lead affect the balance of interface tensions and promote the periodic instability. When we added copper

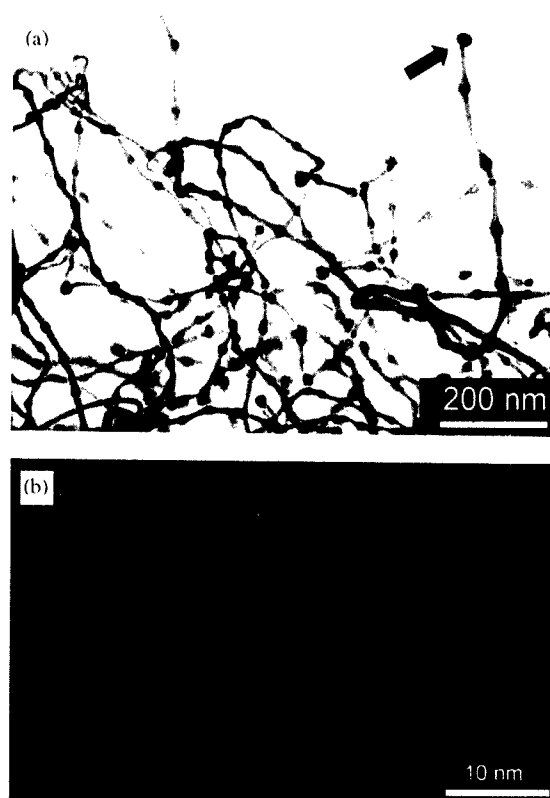


Fig. 1. (a) TEM image of the chains of crystalline-silicon nanospheres. A tip of a chain is indicated by an arrow. (b) High resolution TEM image of a chain showing a twin boundary.

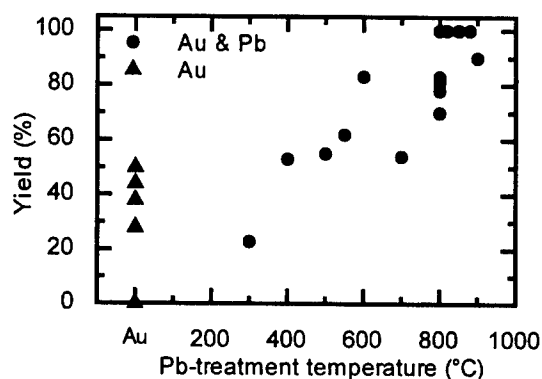


Fig. 2. Yield of the chain growth as a function of the lead-treatment temperature (closed circles). Closed triangles correspond to the yields without lead treatment.

instead of lead, many silicon nanowires were grown instead of the chains. It is likely that copper also changes the balance of interface tensions, but it suppresses the periodic instability.

TEM observations also support our growth model indicating that the surface oxidation plays an essential

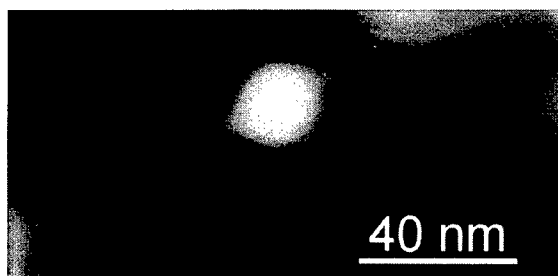


Fig. 3. Energy-filtered TEM image of a chain of crystalline-silicon nanospheres showing tails of a silicon nanocrystallite.

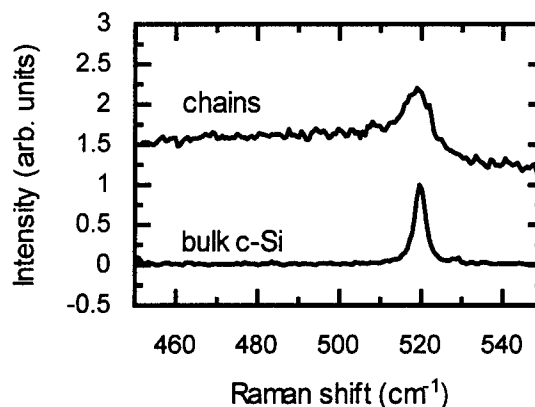


Fig. 4. Raman scattering spectra of chains of crystalline-silicon nanospheres and bulk crystalline-silicon.

role in the chain growth. In Fig. 3, we show an energy-filtered TEM image of chains, where the electrons which lost their energy by exciting silicon bulk plasmon (16–17 eV) were used to form the image [7]. Accordingly, the silicon nanocrystallites in the chain can be seen clearly. As is shown, tails of silicon which extend into the core of wires were observed. This image clearly proves that the silicon nanocrystallites were formed as a consequence of the surface oxidation of diameter-modulated silicon nanowires.

4. Raman scattering measurements

In order to reveal microscopic features of the chains, we performed Raman scattering measurements. The Raman scattering spectra were obtained at room temperature using a Jobin-Yvon T64000 spectrometer with an LN₂-cooled CCD detector. The spectrum resolution was 0.6 cm⁻¹. The 514.5 nm line of an Ar ion laser was used for excitation and the excitation light was focused to a spot of 6 μm in diameter with a power density of about 70 mW/cm². We confirmed that the thermal effect on Raman spectra due to laser heating was negligible. In order to avoid background scattering from a substrate, chains were grown on a molybdenum substrate. A chain sample with silicon nanospheres of 5 ± 1 nm in diameter and oxide layers of 2.7 ± 0.3 nm thickness was examined. In Fig. 4, we show a Raman spectrum of the chain sample with that of bulk crystalline-silicon. The FWHM of the one-phonon Raman line of the chain sample was measured to be 11 cm⁻¹, while that of bulk crystalline-silicon was 3 cm⁻¹ including the instrument broadening. In addition, the line shape of the Raman line of the chain sample was asymmetric. These features can be attributed to the effect of phonon confinement in the silicon nanospheres.

5. Conclusion

We have grown dense chains of crystalline-silicon nanospheres by controlling metal impurities in the growth process. Growth mechanism of the chains was revealed by computer simulations and TEM observations. By adding lead to gold catalysts, the yield of chain growth was remarkably increased. It appears that lead promotes periodic instability in the wetting property of the molten catalysts at the tips of growing chains. We also performed Raman scattering measurements of the chains and found that phonons were confined in the silicon nanospheres in the chains.

Acknowledgements

The authors are indebted to Dr. K. Tanaka at Osaka National Research Institute for help with energy-filtered TEM imaging. One of the authors (H.K.) acknowledges the financial support from the Kazato Research Foundation.

References

- [1] L.T. Canham, *Appl. Phys. Lett.* 57 (1990) 1046.
- [2] S. Iijima, *Nature* 354 (1991) 56.
- [3] H. Kohno, S. Takeda, *Appl. Phys. Lett.* 73 (1998) 3144.
- [4] H. Kohno, T. Iwasaki, S. Takeda, *Solid State Commun.* 116 (2000) 591.
- [5] E.I. Givargizov, *J. Crystal Growth* 20 (1973) 217.
- [6] H. Kohno, S. Takeda, *J. Crystal Growth* 216 (2000) 185.
- [7] H. Kohno, S. Takeda, K. Tanaka, *J. Electron Microsc.* 49 (2000) 275.



ELSEVIER

Physica B 308–310 (2001) 1100–1103

PHYSICA B

www.elsevier.com/locate/physb

An electron spin resonance study of $\text{Si}_{1-x}\text{Ge}_x$ alloy nanocrystals embedded in SiO_2 matrices—effects of P doping

Kimiaki Toshiakiyo^a, Masakazu Tokunaga^a, Shinji Takeoka^a, Minoru Fujii^{b,*},
Shinji Hayashi^{a,b}

^a Graduate School of Science and Technology, Kobe University, Rokkodai, Nada, Kobe 657-8501, Japan

^b Department of Electrical and Electronics Engineering, Faculty of Engineering, Kobe University, Rokkodai, Nada, Kobe 657-8501, Japan

Abstract

The effects of P doping on defects in $\text{Si}_{1-x}\text{Ge}_x$ alloy nanocrystals (nc- $\text{Si}_{1-x}\text{Ge}_x$) embedded in SiO_2 thin films were studied by electron spin resonance (ESR) and photoluminescence (PL) spectroscopy. P doping resulted in a drastic decrease in the ESR signals, which are assigned to the Si and Ge dangling bonds at the interfaces between nc- $\text{Si}_{1-x}\text{Ge}_x$ and matrices (Si and Ge P_b centers). It was found that, with increasing P concentration, the signal from Ge P_b centers is first quenched, and then the quenching of the signal from Si P_b centers starts. The quenching of the ESR signals was accompanied by a drastic enhancement of PL intensity. © 2001 Elsevier Science B.V. All rights reserved.

PACS: 78.55.-m; 78.67.-n; 76.30.-v

Keywords: Dangling bond; Alloy nanocrystals; P doping; Photoluminescence

Si nanocrystals (nc-Si) show efficient luminescence in near-infrared to visible regions due to the quantum confinement effects [1–3]. However, even for nc-Si several nanometers in diameter, the indirect band gap nature of bulk Si crystal is highly preserved [4]. This results in a long luminescence lifetime (small optical transition oscillator strength). This long lifetime is one of the obstacles to realizing Si-based light-emitting devices. $\text{Si}_{1-x}\text{Ge}_x$ alloy formation is expected to offer a way for enhancing the optical transition oscillator strength. In fact, the shortening of the radiative lifetime with increasing Ge concentration has been demonstrated for $\text{Si}_{1-x}\text{Ge}_x$ alloy nanocrystals (nc- $\text{Si}_{1-x}\text{Ge}_x$) in SiO_2 matrices [5,6] and porous $\text{Si}_{1-x}\text{Ge}_x$ [7]. However, the formation of nc- $\text{Si}_{1-x}\text{Ge}_x$ is often accompanied by the degradation of band-edge photoluminescence (PL) efficiency [5].

In our previous work, we studied the electron spin resonance (ESR) and PL properties of nc- $\text{Si}_{1-x}\text{Ge}_x$ in SiO_2 [8]. It was found that the ESR spectrum is a

superposition of signals from Si and Ge dangling bonds at the interfaces between nc- $\text{Si}_{1-x}\text{Ge}_x$ and SiO_2 matrices (Si and Ge P_b centers). As the Ge concentration increased, the signal from the Ge P_b centers increased, while that from the Si P_b centers was nearly independent of Ge concentration. The increase in the number of Ge P_b centers was accompanied by strong quenching of the PL. The observed correlation between the two measurements suggests that the Ge P_b centers act as efficient non-radiative recombination centers for photogenerated carriers, resulting in the quenching of the band-edge PL.

Proper surface passivation is essential in obtaining efficient luminescence. Surface passivation controls the luminescence intensity through the elimination of the P_b centers. The passivation of Si P_b centers by hydrogen and oxygen has been reported to be effective in improving luminescence efficiency [9,10]. Recently, we demonstrated that Si P_b centers can effectively be passivated by P doping [11–13]. It was shown that, as the P concentration increases, the intensity of the band-edge PL increases drastically, while Si P_b centers-related PL decreases. These results suggest that the density of the P_b centers decreases by P doping, leading to the

*Corresponding author. Tel./fax: +81-78-803-1072.

E-mail address: fujii@ceedpt.kobe-u.ac.jp (M. Fujii).

improvement in the band-edge PL efficiency. For nc-Si_{1-x}Ge_x, the passivation of Ge P_b centers by similar approaches might be possible. In this work, we prepared nc-Si_{1-x}Ge_x as small as 4 nm in diameter embedded in phosphosilicate glass (PSG) thin films with different P concentrations and studied the ESR and PL properties.

P-doped Si_{1-x}Ge_x alloy nanocrystals were prepared by co-sputtering of Si, Ge, SiO₂, and PSG [5,6]. After the deposition, films were annealed in an N₂ gas atmosphere for 30 min at 1100°C to grow nc-Si_{1-x}Ge_x in PSG matrices. P and Ge concentrations were determined by electron probe microanalysis and Raman spectroscopy [5], respectively. P concentration was varied from 0 (without P doping) to about 1.0 mol%. Ge concentration (*x*) was fixed at 0.3. Experimental details are found in our previous papers [5,6,8].

Figs. 1(a) and (b) show PL spectra of nc-Si_{0.9}Ge_{0.1} (sample A) and nc-Si_{0.7}Ge_{0.3} (sample B) with various P concentrations, respectively. PL peaks are observed around 1.4 and 0.9 eV. The 1.4 eV PL peak corresponds to the band-edge PL. The 0.9 eV peak is generally assigned to the recombination of photoexcited carriers via Si P_b centers [11,12,14]. The integrated intensities of the band-edge PL and the 0.9 eV PL are shown in Fig. 2 as a function of P concentration. With increasing P concentration, the intensities of the band-edge PL for both the samples first increase and then decrease. The PL intensity of sample A is improved by a factor of 3, while that of sample B by a factor of 14. The maximum PL intensities are almost the same for both series of samples and are also almost the same as the maximum PL intensity of P-doped pure nc-Si [11,12]. In Fig. 2, for sample A, the intensity of the 0.9 eV PL decreases monotonically, while for sample B that takes a maximum at 0.6 mol%.

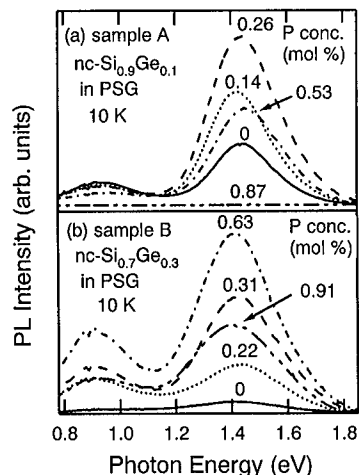


Fig. 1. Photoluminescence from nc-Si_{1-x}Ge_x with (a) *x* = 0.1 and (b) *x* = 0.3 dispersed in PSG thin films at 10 K.

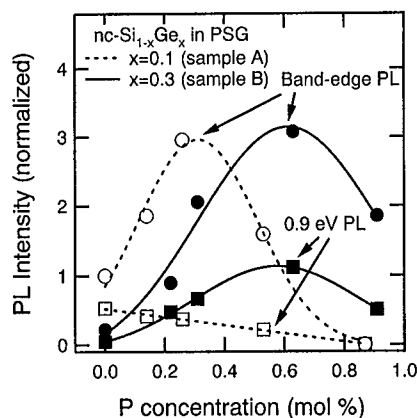


Fig. 2. Intensities of the band-edge PL and Si-P_b-center-related PL at 10 K as a function of P concentration. Vertical axis represents the PL intensity with respect to the band-edge PL intensity of nc-Si_{0.9}Ge_{0.1} in SiO₂ (without P doping).

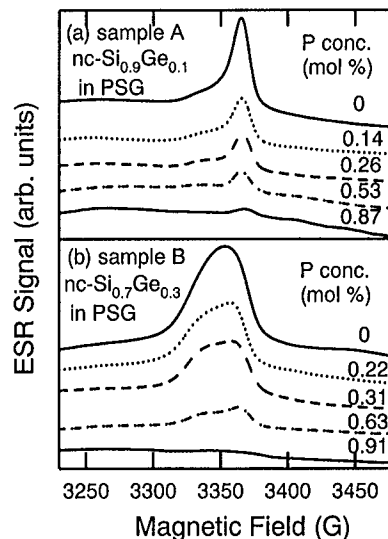


Fig. 3. Integrated ESR spectra of nc-Si_{1-x}Ge_x dispersed in PSG thin films at room temperature.

Figs. 3(a) and (b) show the integrated ESR spectra of samples A and B with various P concentrations, respectively. For the samples without P doping, asymmetric ESR signals are observed; the *g*-value and the line width are 2.0058 and 10.7 G for sample A, and 2.0103 and 36.6 G for sample B. These signals can be assigned to a superposition of signals from Si and Ge P_b centers [8]. As the P concentration increases, the intensity of the ESR signals decreases. Fig. 4 shows the integrated intensities of the ESR signals for Si and Ge P_b centers as a function of P concentration. The intensities are obtained by deconvoluting the ESR spectrum into two Lorentzian functions. In the sample A, intensities of Si and Ge P_b centers decrease at almost the same rate with

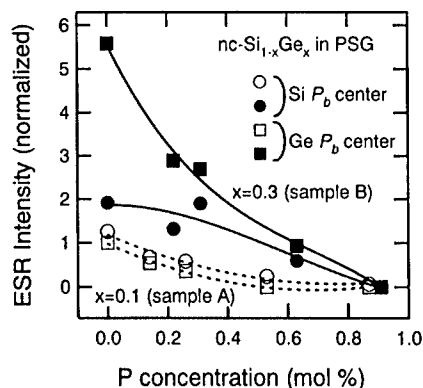


Fig. 4. Integrated intensities of ESR signals from Si and Ge P_b centers as a function of P concentration. Vertical axis represents the ESR intensity with respect to the intensity of Ge P_b centers in $nc-Si_{0.9}Ge_{0.1}$ in SiO_2 (without P doping).

increasing P concentration, indicating that the number of Si and Ge P_b centers decreases monotonically by P doping. On the other hand, in the sample B, Si and Ge P_b centers exhibit different P concentration dependence; the intensity of the signal from Ge P_b centers decreases rapidly with increasing P concentration, while that from Si P_b centers is almost constant at low P concentration range and then decreases gradually with further increasing P concentration.

The present P concentration dependences of PL and ESR properties can consistently be explained by the following model. From a point of view of PL properties, $nc-Si_{1-x}Ge_x$ embedded in SiO_2 matrices can be classified into four categories. One is $nc-Si$ without non-radiative recombination centers, which show the band-edge PL around 1.4 eV. The second kind of nanocrystals are those having at least one Si P_b center. These nanocrystals do not show the band-edge PL but show only the 0.9 eV PL at low temperatures. The third and last kind of nanocrystals are those having at least one Ge P_b centers and both the Si and Ge P_b centers, respectively. In these nanocrystals, photoexcited carriers are thought to be preferentially trapped at Ge P_b centers and recombine non-radiatively even at low temperatures [8]. The present samples are the ensemble of these four kinds of nanocrystals. With increasing Ge concentration, the number of nanocrystals not emitting light increases, resulting in the quenching of both the band-edge PL and Si- P_b -center-related PL. This Ge concentration dependence of the PL and ESR intensities can clearly be seen in Figs. 2 and 4.

Fig. 4 demonstrates that not only Si P_b centers but also Ge P_b centers are passivated by P doping. The passivation is considered to be made electrically, i.e., electrons supplied by P doping are trapped at P_b centers and inactivate the centers. The quenching of the ESR signals from Ge P_b centers is much faster than that from

Si P_b centers. This result indicates that, if both Si and Ge P_b centers exist in one $nc-Si_{1-x}Ge_x$, electrons supplied by P doping are preferentially captured by Ge P_b centers. After completing the passivation of Ge P_b centers, the passivation of Si P_b centers starts.

Preferential passivation of Ge P_b centers increases the number of nanocrystals which do not have electrically active Ge P_b centers. As a result, in $nc-Si_{0.7}Ge_{0.3}$, the intensities of both the band-edge PL and Si- P_b -center-related PL are enhanced by P doping, i.e., Si P_b centers remain active even if the P concentration is relatively high. On the other hand, in $nc-Si_{0.9}Ge_{0.1}$, the number of nanocrystals having Ge P_b centers is small. Therefore, the passivation of Si P_b centers starts at low P concentration, resulting in the quenching of Si- P_b -center-related PL at low P concentration region.

At high P concentration, after completing the passivation of both Si and Ge P_b centers, electrically active P atoms supply free electrons in $nc-Si_{1-x}Ge_x$. Although not shown in this article, in the range where PL intensity decreases, optical absorption due to the intravalley transition of electrons generated by P doping in the conduction band, i.e., free-electron absorption in $nc-Si_{1-x}Ge_x$ is observed. This is the direct evidence that free electrons are generated in $nc-Si_{1-x}Ge_x$. The generation of free electrons and the resultant three-body Auger recombination of electron-hole pairs is considered to be responsible for the observed PL quenching.

In conclusion, the effects of P doping on defects in $nc-Si_{1-x}Ge_x$ in SiO_2 thin films were studied. It was found that doped P atoms can play some different roles, depending on the condition of surface termination. If P atoms are doped in $nc-Si_{1-x}Ge_x$ with Si and Ge P_b centers, electrons supplied by P doping are preferentially captured by Ge P_b centers and inactivate the centers. After completing the passivation of Ge P_b centers, the passivation of Si P_b centers starts. This results in the improvement in the PL efficiency.

The authors are grateful to Kazutomi Shigeeda for his valuable assistance in this work. This work is funded by a Grant-in-Aid for Scientific Research from the Ministry of Education, Science, Sports and Culture, Japan, and a Grant for Research for the Future Program from the Japan Society for the Promotion of Science (JSPS-RFTF-98P-0123). One of the authors (K.T.) is supported by a Research Fellowships of the Japan Society for the Promotion of Science for Young Scientists.

References

- [1] M. Fujii, S. Hayashi, K. Yamamoto, in: S.G. Pandalai (Ed.), Recent Research Development in Applied Physics, Vol. 1, Transworld Research Network, Trivandrum, 1998, p. 193.

- [2] S. Takeoka, M. Fujii, S. Hayashi, *Phys. Rev. B* 62 (2000) 16820.
- [3] G. Polisski, H. Heckler, D. Kovalev, M. Schwartzkopff, F. Koch, *Appl. Phys. Lett.* 73 (1998) 1107.
- [4] D. Kovalev, H. Heckler, M. Ben-Chorin, G. Polisski, M. Schwartzkopff, F. Koch, *Phys. Rev. Lett.* 81 (1998) 2803.
- [5] S. Takeoka, K. Toshiaki, M. Fujii, S. Hayashi, K. Yamamoto, *Phys. Rev. B* 61 (2000) 15988.
- [6] M. Fujii, D. Kovalev, J. Diener, F. Koch, S. Takeoka, S. Hayashi, *J. Appl. Phys.* 88 (2000) 5772.
- [7] M. Schoisswohl, J.L. Cantin, M. Chamarro, H.J. von Bardeleben, *Phys. Rev. B* 52 (1995) 11,898.
- [8] K. Toshiaki, M. Tokunaga, S. Takeoka, M. Fujii, S. Hayashi, *J. Appl. Phys.* 89 (2001) 4917.
- [9] S.P. Withrow, C.W. White, A. Meldrum, J.D. Budai, D.M. Hembree Jr., J.C. Barbour, *J. Appl. Phys.* 86 (1999) 396.
- [10] A.A. Seraphin, S.-T. Ngiam, K.D. Kolenbrander, *J. Appl. Phys.* 80 (1996) 6429.
- [11] M. Fujii, A. Mimura, S. Hayashi, K. Yamamoto, *J. Appl. Phys.* 75 (1999) 184.
- [12] M. Fujii, A. Mimura, S. Hayashi, K. Yamamoto, C. Urakawa, H. Ohta, *J. Appl. Phys.* 87 (2000) 1855.
- [13] A. Mimura, M. Fujii, S. Hayashi, D. Kovalev, F. Koch, *Phys. Rev. B* 62 (2000) 12625.
- [14] B.K. Meyer, D.M. Hofmann, W. Stadler, V. Petrova-Koch, F. Koch, *Appl. Phys. Lett.* 63 (1993) 2120.



ELSEVIER

Physica B 308–310 (2001) 1104–1107

PHYSICA B

www.elsevier.com/locate/physb

Single impurity centers embedded in self-assembled silicon microcavities

N.T. Bagraev*, A.D. Bouravleuv, L.E. Klyachkin, A.M. Malyarenko

A.F. Ioffe Physico-Technical Institute, Russian Academy of Sciences, 26 Polytechnicheskaya ul, St. Petersburg 194021, Russia

Abstract

We present the findings of high efficient light absorption in self-assembled quantum wells (SQW) embedded in silicon microcavities that exhibit a distributed feedback identified by the FIR transmission spectra. The photo and electroluminescence from SQW is found to be enhanced in the range of the Rabi splitting. The intraband hole transitions are shown to give rise to a fast energy transfer into the d-shell transitions of the center incorporated into the microcavity which is caused by the strong sp-d mixing in the built-in electric field and revealed by the intracenter emission. © 2001 Elsevier Science B.V. All rights reserved.

Keywords: Single centers; Microcavity; Scanning tunneling microscopy

1. Introduction

Dopant diffusion in silicon is known to be amenable to control by means of adjusting the fluxes of self-interstitials and vacancies emerging from the mono-crystalline surface [1]. The diffusion of boron has been found to be enhanced along the $\langle 111 \rangle$ axis in the Si(100) wafer covered by the thin oxide overlayer, whereas the presence of thick oxide overlayer on the Si(100) wafer raises the boron diffusion along the $\langle 100 \rangle$ axis [2]. These indications point out the crystallographic orientation of the excess fluxes of self-interstitials and vacancies that seem to involve dopants in the diffusion process and to be split into space-independent parts generated by the oxidized working side. The goal of the present work, which studied the absorption and emission from self-assembled quantum wells (SQW) inside the ultra-shallow boron diffusion profile, is to exhibit silicon microdefects induced by the excess fluxes of self-interstitials that form the microcavities embedded in SQW.

2. Methods

The short-time boron diffusion was carried out from the gas phase into 350 mm thick n-type monocrystalline Si(100)-wafers with resistivities $20 \Omega \text{ cm}$. The wafers were previously oxidized at 1150°C in dry oxygen containing CCl_4 vapors. Short-time impurity doping was done under fine surface injection of both self-interstitials and vacancies into windows which were cut in the oxide after preparing a mask and performing the subsequent photolithography. Additional replenishment with dry oxygen into the gas phase during the diffusion process provides the generation of excess fluxes of intrinsic point defects from the working side. The variable parameters of the diffusion experiment were the oxide overlayer thickness, the diffusion temperature and the Cl levels in the gas phase during the diffusion process. Diffusion profiles were studied using the four-point probe, SIMS, cyclotron resonance (CR), infrared Fourier spectroscopy and scanning tunneling microscopy (STM) techniques.

3. Results

Using SIMS and four-point probe technique under layer-by-layer etching, the analysis of the structures

*Corresponding author. Tel.: +7-812-247-9311; fax: +7-812-247-1017.

E-mail address: impurity.dipole@pop.ioffe.rssi.ru (N.T. Bagraev).

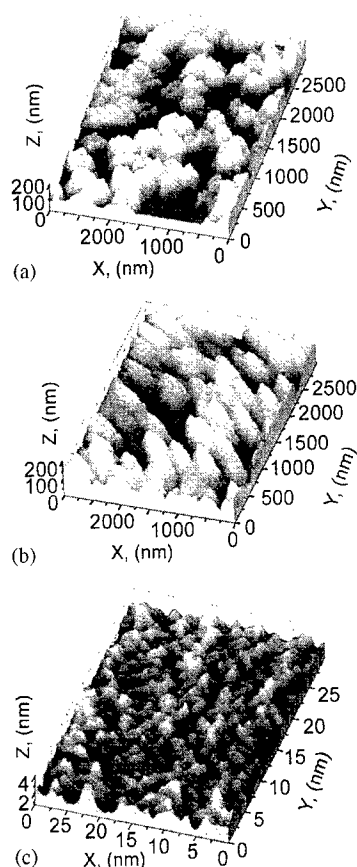


Fig. 1. STM images of the ultra-shallow boron diffusion profiles prepared at diffusion temperature of 800°C (a and b) and 900°C (c) into the Si(100) wafer covered previously by thick (a), thin (b) and medium (c) oxide overlayer. $X \parallel [001]$, $Y \parallel [010]$, $Z \parallel [100]$.

obtained shows that the ultra-shallow boron profiles consist of SQW divided by heavily doped δ -barriers. The SQW characteristics have been identified by the CR angular dependencies and current–voltage (CV) diagrams and brought about the deflection of the bias voltage from the normal to the $p^+ - n$ junction plane.

Space-independent excess fluxes of intrinsic defects that cause the formation of SQW appear to be transformed also into microdefects which can be revealed by the STM technique as the deformed potential fluctuations (DPF) near the Si–SiO₂ interface and the surface of the ultra-shallow diffusion profile. The DPF effect induced by the microdefects of the self-interstitials type that are displayed as light poles in Fig. 1 is demonstrated to be brought about by the previous oxidation and to be enhanced by subsequent boron diffusion. The STM technique allowed to define crystallographic orientation of DPF obtained by using

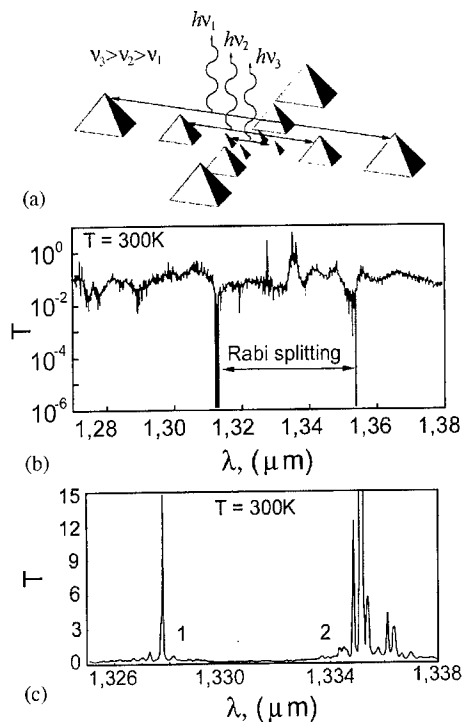


Fig. 2. The model of self-assembled microcavity systems (a) prepared on the Si(100) wafer and revealed by spectral dependence of the light transmission coefficient (b) that demonstrates at $T = 300$ K the enhancement of the photoluminescence (c) from self-assembled quantum well (1) and single residual transition metal center (2).

thick (Fig. 1a) and thin (Fig. 1b) oxide overlayer that corresponds, respectively, to the $\langle 100 \rangle$ and $\langle 111 \rangle$ axis and visualizes practically the orientation of excess fluxes of self-interstitials as a function of the oxide overlayer thickness. The analysis of the STM image of the ultra-shallow boron profile prepared under parity conditions between diffusion mechanisms (Fig. 1c) enables one to hazard a conjecture that the dimension of the microdefect observed is consistent with the parameters expected from the tetrahedral model of the Si₆₀ cluster [3]. Thus, the DPF effect gives rise to the formation of self-assembled quantum antidots with dimensions that are equalized as the diffusion temperature increases. Besides, the interplay between the dimensions of these antidots and their distribution inside the ultra-shallow diffusion profile prepared on the Si(100) wafer is found to be evidence of the fractal mechanism that causes the formation of the microcavities embedded into the SQW system (Fig. 2a).

These silicon microcavities are revealed by the spectral dependencies of the transmission coefficient that exhibits a distributed feedback identified by the Rabi splitting [4]

(Fig. 2b and c). The photoluminescence from the SQW embedded in microcavity is found to be created in spectral range of the Rabi splitting (Fig. 2c). Besides, the strong coupled d-electron states of a residual transition metal center with the s-p electronic states of the host SQW are also revealed by the intracenter emission that seems to exhibit the transitions induced by the Stark effect caused by the built-in electric field of the quantum-size p^+-n junction (Fig. 2c). The quenching and regeneration of the SQW luminescence demonstrated by the angular dependencies of the transmission spectra appears to be defined by the orientation of the self-assembled quantum well along the Si(100) p^+-n junction plane (Fig. 3). The angular dependent positions of the intracenter emission lines that seem to be due to the strong sp-d mixing allow one to propose the excitation of the EPR transitions in the micron range

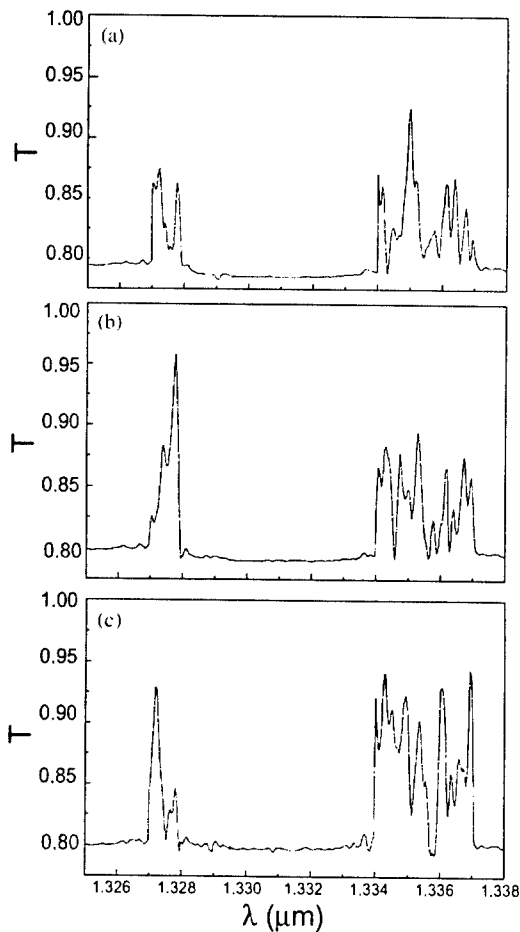


Fig. 3. The transmission spectra measured at different angles between the normal to the Si(100) surface and the light beam, α , that causes the intraband and intracenter emission from the p-type SQW embedded in the silicon microcavity. $T = 300$ K. (a) $\alpha = 0^\circ$, (b) $\alpha = 20^\circ$, (c) $\alpha = 30^\circ$.

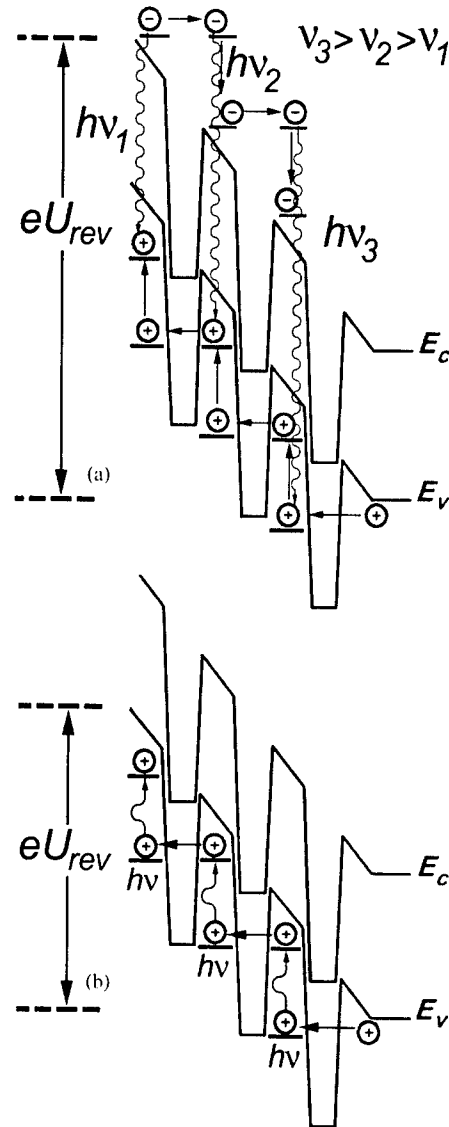


Fig. 4. The energy band diagrams of the ultra-shallow p^+-n silicon junction that consists of quantum wells divided by heavily doped δ -barriers, which exhibit the cascade visible emission under injection of both electrons and holes (a) and the infrared emission under injection of only holes (b).

under strong coupling of the light beam to the microcavity embedded in the SQW series (Fig. 3), the model of which is in progress.

Finally, the resonant tunneling through strongly coupled quantum well series that is accompanied by the cascade emission under injection of both electrons and holes (Fig. 4a) or only holes (Fig. 4b) is able to be a basis of high efficient visible (Fig. 5a) and infrared (Fig. 5b) electroluminescence.

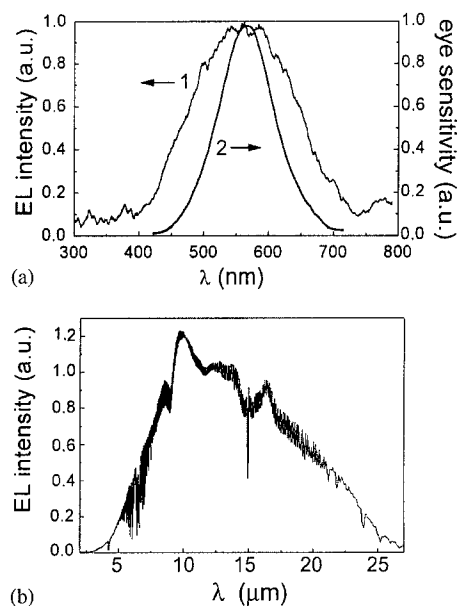


Fig. 5. The electroluminescence spectra caused by the visible (a) and infrared (b) emission from p-type SQW series embedded in the silicon microcavity, $T = 300$ K. (a) The external quantum efficiency of the white light emission (1) is equal to 0.5%, $I_{\text{rev}} = 25$ mA, $U_{\text{rev}} = 40$ V, which is in a good agreement with the spectral eye sensitivity (2). (b) The external quantum efficiency of the infrared light emission is equal to 7%, $I_{\text{rev}} = 30$ mA.

4. Summary

The microdefects that are formed by self-interstitials inside p^+-n junctions in the diffusion process of boron into the Si(100) wafer have been demonstrated to promote the realization of the silicon microcavities embedded in SQW. The luminescence from silicon quantum wells has been found to be enhanced in the range of the Rabi splitting. The intraband hole transitions have been shown to give rise to a fast energy transfer into the d-shell transitions of the center incorporated into the microcavity, which is revealed by the intracenter emission.

References

- [1] N.A. Stolwijk, et al., Def. Diffus. Forum 59 (1988) 79.
- [2] N.T. Bagraev, et al., Def. Diffus. Forum 143–147 (1997) 1003.
- [3] Bao-xing Li, et al., Phys. Rev. B 61 (2000) 1685.
- [4] R. Houdre, et al., Phys. Rev. B 49 (1994) 16761.



ELSEVIER

Physica B 308–310 (2001) 1108–1112

PHYSICA B

www.elsevier.com/locate/physb

Defect related photoluminescence in Si wires

T. Torchynska^{a,*}, J. Aguilar-Hernandez^a, A.I. Diaz Cano^a, G. Contreras-Puente^a,
F.G. Becerril Espinoza^a, Yu.V. Vorobiev^b, Y. Goldstein^c, A. Many^c,
J. Jedrzejewski^c, B.M. Bulakh^d, L.V. Scherbina^d

^a Instituto Politécnico Nacional, U.P.A.L.M., 07738, Mexico D.F., Mexico

^b CINVESTAV—IPN, Unidad Queretaro, Mexico

^c Racah Institute of Physics, Hebrew University of Jerusalem, Jerusalem 91904, Israel

^d Institute of Semiconductor Physics, National Academy of Sciences, Kiev 252028, Ukraine

Abstract

Photoluminescence spectra and their dependence on the temperature have been used to study the peculiarities of the red photoluminescence in low-dimensional Si structures, such as porous silicon and silicon oxide films with an admixture of silicon. It has been shown that red photoluminescence band of Si wires is complex and can be decomposed into two elementary bands. Practically the same positions of photoluminescence bands are observed in silicon oxide films. Comparative investigation of photoluminescence temperature dependence in Si wires and silicon oxide indicates that oxide defect related mechanisms for photoluminescence bands are involved. The photoluminescence excitation mechanisms in both objects are discussed as well. © 2001 Elsevier Science B.V. All rights reserved.

Keywords: Si wires; Porous silicon; Photoluminescence; Silicon oxide

1. Introduction

The room temperature visible photoluminescence (PL) of Si wire structures, such as porous silicon (PSi) and silicon nanoparticles in silicon oxide, has attracted much attention due to the high PL efficiency and its potential applications in Si-based optoelectronics. Since the work of Canham in 1990 [1], many studies of PSi have been carried out [2]. The visible PL can be explained either as related to size distribution of quantum confined nanocrystals [1] or/and as a result of the emission of different types of radiative centres on Si-wire surface [3]: polysilan complexes [4], siloxene molecules [5], water molecules with impurities [6], defects in silicon oxide [7] and suboxide [8]. The possibility of the emission of excitons at the Si/SiO₂ interface has been suggested as well [9]. Surprisingly little attention has been paid to the peculiarities of the luminescence spectrum itself, which is of fundamental

importance. Furthermore, it was proposed earlier [1], that only in porous silicon with a high level of porosity (70–80%) one could expect intensive photoluminescence. But there are many examples of high PL intensity in PSi with very low porosity, like 10% [10] or 22% [11]. Thus, the origin of the visible luminescence from PSi still needs to be clarified.

The investigations of photoluminescence of silicon oxide films with an admixture of silicon are not numerous [12–16]. The main aim of such studies was to determine the photoluminescence mechanism of Si-wire structures. As far as we know, the temperature dependence of the photoluminescence in these structures has not been reported so far.

This paper presents a spectral characterization of the PSi photoluminescence emphasizing its dependence on temperature (*T*) and technological conditions. The photoluminescence of silicon oxide films with an admixture of the silicon has also been investigated. In these films, it was possible to change the content of Si in the oxide from suboxide up to dioxide. Models of two luminescence transitions

*Corresponding author.

E-mail address: ttorch@esfm.ipn.mx (T. Torchynska).

and corresponding excitation and recombination mechanisms are discussed.

2. Experimental results

The PSi samples were prepared from p-type, B-doped, (100) oriented silicon wafers of $1.0\ \Omega\text{cm}$ resistivity. The porous layers were obtained by electrochemical etching in a solution of $\text{HF}:\text{H}_2\text{O}:\text{C}_2\text{H}_5\text{OH}$ (1:1:2). Groups of samples prepared at an etching duration of $t_a = 10$ min and several values of the etching current densities ($I_a = 5, 10, 15, 20, 50$ and $75\ \text{mA/cm}^2$) were investigated.

The co-sputtered films were prepared by sputtering from two electrodes, one with a silicon target and the other with a quartz target on a long (15 cm) quartz substrate. In this manner, variation of the Si content in the film is obtained. The films were subsequently annealed at 1100°C in an inert atmosphere in order to make them photoluminescent. The continuous change of the Si–SiO_x composition could be observed by the change of the film colour from brown at the Si-rich end to transparency at the Si-poor end. The brown colour indicates the formation of a suboxide, while the transparent end is mostly dioxide.

PL spectra have been measured by excitation of the PSi with an Ar⁺ laser tuned at a wavelength of $5145\ \text{\AA}$. The PL signals were dispersed with a Model 1403 Spectrometer. PL was studied in a temperature range of 10–300 K.

2.1. PL spectrum dependences on anodization condition and temperature

Fig. 1 shows PL spectra for PSi samples obtained at different technological conditions. For PSi prepared at low current density ($5\text{--}20\ \text{mA/cm}^2$, Fig. 1a) the PL band, peaked at $h\nu_m = 1.70\text{--}1.73\ \text{eV}$ (for different samples used), with full width at half maximum (FWHM) equal to $300\text{--}320\ \text{meV}$, dominates at 300 K. For all investigated samples this band has essentially a symmetric Gaussian's shape. While for PSi samples prepared at high current densities ($30\text{--}75\ \text{mA/cm}^2$, Fig. 1b) the PL band that dominates at 300 K, is centred at $1.9\text{--}2.1\ \text{eV}$. This high-energy PL band ($h\nu_m = 1.90\text{--}2.10\ \text{eV}$) has a symmetric Gaussian's shape as well, but their FWHMs monotonically increases from 340 up to $390\ \text{meV}$ with increasing PL peak energy. Thus, it is possible in a controlled way to prepare samples with definite PL elementary bands.

The PL spectra variations with temperature for low porosity (10–20%) PSi samples prepared at $I_a = 5\ \text{mA/cm}^2$ are presented in Fig. 1a. At 300 K only the PL band, with a maximum at $1.73\ \text{eV}$ and FWHM of $300\text{--}320\ \text{meV}$, is observed. The spectrum shape, in the T range of $300\text{--}8.5\ \text{K}$, changes with T decrease. This is

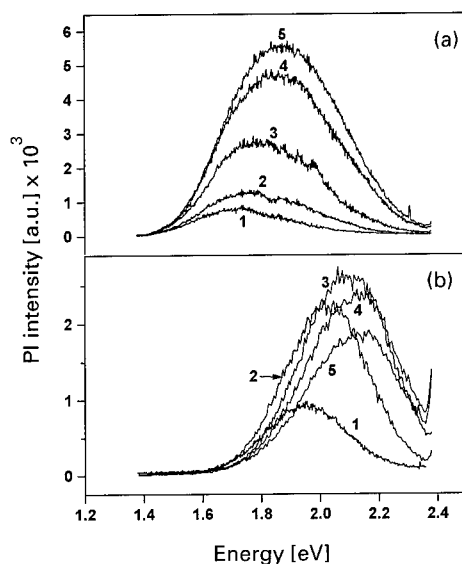


Fig. 1. (a) PL spectra of PSi sample prepared at $I_a = 5\ \text{mA/cm}^2$ and $t_a = 10$ min and measured at the T : 300 (1), 250 (2), 150 (3), 50 (4) and 8.5 K (5). (b) PL spectra of PSi sample prepared at $I_a = 75\ \text{mA/cm}^2$, $t_a = 10$ min and measured at the same temperatures, as for (a).

mainly due to the increase of the high-energy part of the PL band. At the same time, the peak shifts to $1.85\ \text{eV}$ and the FWHM increases up to $450\ \text{meV}$. As can be seen, the low-energy sides of the PL bands at these temperatures change, but not much in comparison with the high-energy sides (Fig. 1a). It is clear that a new PL band appears mainly at the high-energy side of the spectrum when the T decreases (Fig. 1a). Thus, the PL band of PSi at low temperature has a complex nature and can be represented, as the sum of two elementary bands: the original band with a peak at $1.73\ \text{eV}$ and a new one with a peak at $1.95\ \text{eV}$. This new PL band has, in general, a maximum at $1.90\text{--}2.10\ \text{eV}$ (in different samples) and a FWHM, which increases from $340\ \text{meV}$ up to $390\ \text{meV}$ with increase in peak energy. The peak intensity of the first band also risen somewhat with T decreasing (Fig. 2a, curve 1). The second band intensity, on the other hand, monotonically increases noticeable with T decreasing (Fig. 2a, curve 2). The important conclusion to be drawn from the data presented is that the low-energy and high-energy PL bands have different T dependencies (Fig. 2). This indicates the presence of two different radiative mechanisms in this PSi.

In high porosity (70–80%) PSi prepared at high current the PL band, peaked at $1.95\ \text{eV}$, with FWHM of $360\ \text{meV}$ dominates at 300 K. With T decrease in the temperature range of $300\text{--}150\ \text{K}$, the spectrum shape changes, mainly due to the increase of the high-energy part of the PL band as well. The peak maximum shifts to $2.10\ \text{eV}$ and the FWHM increases to $400\ \text{meV}$ (Fig. 1b).

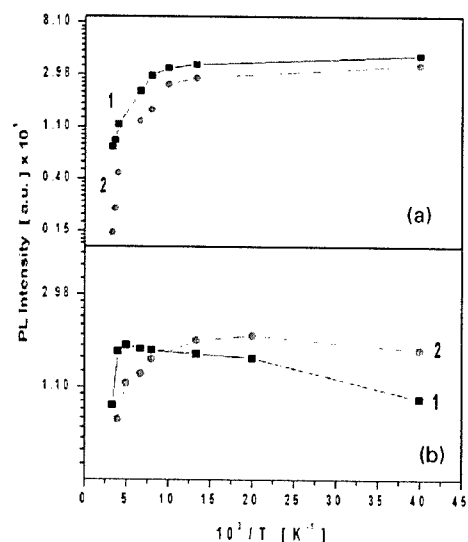


Fig. 2. Variation of PL band intensities with the T increase for PS prepared at $I_a = 5$ (a) and 75 (b) mA/cm^2 and $t_a = 10$ min for PL bands peaked at 1.73 eV (1a), 1.95 (2a), 1.90 eV (1b) and 2.13 eV (2b).

As can be seen, the low-energy sides of the PL bands at these T change only little compared to the high-energy sides (Fig. 1b). There appears also a new PL band when the T decreases (Fig. 1b). The PL band of this PSi at low temperature can be decomposed into two PL bands: the original band at 1.90 eV and a new one at 2.15 eV. The peak intensities of both PL bands increase with T decreasing in the 150 – 300 K range (Figs. 1b and 2b). The intensities of both PL bands decrease with T in the 8.5 – 150 K range (Fig. 2b).

2.2. PL studies of co-sputtered Si-SiO_x films

It was assumed [19–21] that the difference in spectral positions of the PSi luminescent bands might be connected with the different composition of silicon oxide on Si wire surface, where corresponding radiative defects are localized. In this case comparative PL investigation of Si-SiO_x films and PSi can, apparently, confirm such assumption. In Raman scattering spectra of the Si-SiO_x films, the Raman line at 520 cm^{-1} , corresponding to Si-Si vibrations in crystalline Si, has not been registered. This suggests that in these films there are no crystalline Si nanoparticles present. Thus, the different colours of the amorphous oxide films are connected with the change in its composition from suboxide (brown colour) to dioxide (transparent film).

Fig. 3 presents the PL spectra of these films. Two PL bands, peaked at 1.6 – 1.7 eV and at 2.1 – 2.2 eV with an FWHM equal to 320 and 400 meV, respectively, were measured. With increase of the oxygen content in Si-SiO_x film the peak positions of both bands shift towards

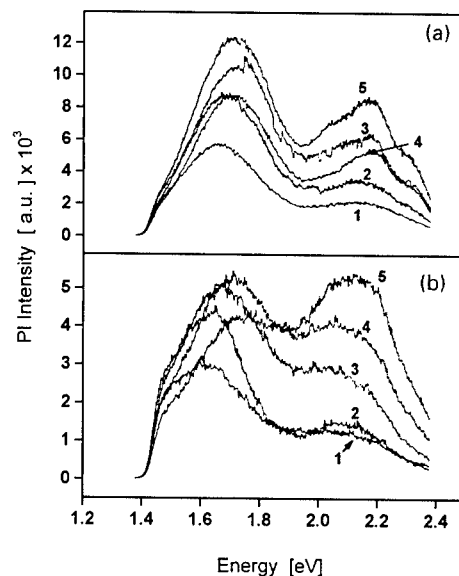


Fig. 3. (a) PL spectra of Si-SiO_x thin films, measured for transparent (dioxide) part at the T : 300 (1), 200 (2), 100 (3), 50 (4) and 10 K (5). (b) PL spectra of Si-SiO_x thin films, measured for brown (suboxide) part at the T : 300 (1), 200 (2), 100 (3), 50 (4) and 10 K (5).

the high-energy side of the spectrum (Fig. 3a). The intensities of PL bands in the dioxide side were highest than in the suboxide side. The FWHMs of the PL bands in the silicon oxide are practically the same as in PSi. The peak positions of both PL bands exhibit a blue shift of 100 meV with decreasing temperature from 300 to 10 K, just the same way as for PSi PL bands. The process of effective thermal quenching with T -increase for PL bands in silicon oxide starts at about 100 – 150 K, similarly as for the PL bands in PSi (Figs. 2 and 4).

It is necessary to emphasize the difference in T -dependences for the PL band at 1.6 – 1.7 eV for Si suboxide and dioxide (Fig. 4b). As one follows from Figs. 3 and 4, the intensity of this PL band in the suboxide decreases when the T decreases from 50 to 10 K. At the same time the intensity of this PL band in silicon dioxide monotonically increases when the T decreases to 10 K.

3. Discussion

The investigation of the PL temperature dependence provides a valuable tool to study the recombination and excitation mechanisms for photo-excited carriers and as a result to study the semiconductor band edges, excitons, impurities and defect level positions. The increase of the PL intensity with T decreasing, usually, reflects an enhancement of exciton recombination or

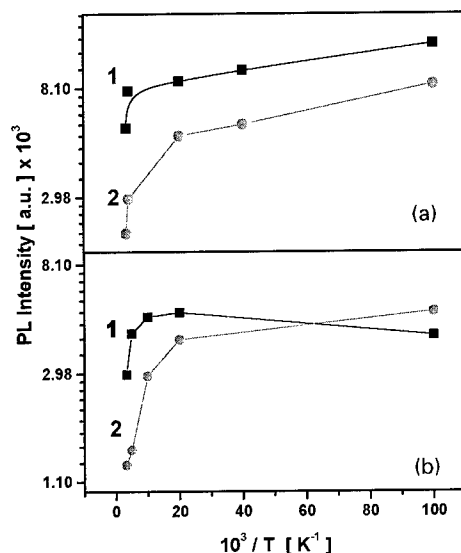


Fig. 4. Variation of PL band intensities with the T increase for transparent (a) and brown (b) Si-SiO_x thin films for PL bands peaked at 1.73 eV (1a), 1.95 eV (2a), 1.90 eV (1b) and 2.13 eV (2b).

defect related recombination in the T ranges lower than the temperature of a thermal quenching process start. The drop of the PL intensity at low T has been usually attributed to the decrease of phonon participation in the recombination process, due to the decrease of the available number of phonons.

Let us discuss, first of all, the T dependence for the PL bands in silicon oxide. As can be seen from Fig. 4a the intensities of both PL bands monotonically increase with T decreasing. Due to the very high value of the energy gap in silicon dioxide (>8 eV) the two investigated PL bands peaked at 1.6–1.7 and 2.1–2.2 eV should be connected with two different types of defects. Their temperature behaviour is the evidence of the enhancement of defect related PL in the T range below thermal quenching. All PL spectra measurements have been made with excitation by an Ar laser (2.41 eV). Such excitation of the PL band in silicon dioxide films should be connected with interdefect optical transitions. Note that the peak positions of PL bands shift towards the high-energy with the change of the composition of silicon oxide from suboxide to dioxide.

The T dependence of the high energy PL band peaked at 2.1–2.2 eV in silicon suboxide is the same as in silicon dioxide (Fig. 4a and b). The T dependence for the PL band centred at 1.6–1.7 eV, however, is different in the low T -ranges for the suboxide film (Fig. 4). The decrease of the intensity with T decreasing in the 10–50 K range for this PL band indicates a phonon-assisted mechanism of excitation. In the case of silicon suboxide, it could be assumed that the excitation light of Ar laser with an energy of 2.41 eV excites the electrons from the valence

into the conduction band due to phonon assisted optical transition in indirect band gap suboxide material. In the second stage, the photo carriers are trapped by defect-related radiative centre, responsible for the 1.6–1.7 eV PL band. Thus, we can conclude that two types of excitation mechanisms are possible for the 1.6–1.7 eV PL band in silicon oxide: interdefect electronic transition in dioxide and trapping of the free carriers by the radiative centres in suboxide.

The radiative defects in silicon oxide films have been investigated very intensively [17–21]. Based on the joint investigation of PL, absorption, as well as electron paramagnetic resonance spectra, the PL band peaked at 1.9 eV is attributed to non-bridge oxygen hole centre (NBOHC) [17–19]. It was also shown, that this band could shift in the 1.7–2.0 eV spectral range depending on the additional OH group content in the silicon oxide. The latter connects with two, and possibly three different configuration forms for NBOHC centres [19]. It was discovered that 2.41 eV Ar laser directly excites NBOHC defects due to intercentre optical transition [19]. Another type of defect known in silicon oxide is the defect responsible for the 2.4–2.7 eV PL band [20]. The latter defect is attributed to oxygen vacancy in silicon oxide crystal lattice.

In PL spectra of the investigated PSi we observed two PL bands with Gaussian's shape centred at 1.70–1.90 eV and 1.90–2.15 eV. Our previous conclusion [8,20,21] that these elementary PL bands in PSi are connected with the defects in silicon oxide at the Si/SiO_x interface is confirmed independently by PL investigation of the Si-SiO_x films. The spectral positions of the PL bands in Si-SiO_x films are similar to that in PSi, and this is a convincing evidence towards the proposed model (Figs. 1 and 4). Some small difference in the peak position of PSi PL bands can be associated with PSi surface chemistry. Moreover, both PL bands in PSi and in sputtered Si-SiO_x films start their effective thermal quenching process at the same temperature interval (100–150 K).

For PL bands peaked at 1.7–1.9 eV and 1.9–2.15 eV in PSi there may exist two mechanism of PL excitation, like in Si-SiO_x films (Fig. 2a and b). For low porosity PSi the PL intensity monotonically increases with T -decreasing in the 10–50 K range, like in silicon dioxide. The decrease of the PL intensity with T -increasing can correspond to a typical excitonic behaviour, proposed in quantum confined PL model. But the excitonic model cannot explain the drop of the PL intensity, when the T approaches 10 K. Really, for high porosity silicon (70–80%), prepared at high current density with big Si/SiO_x interface area, the PL intensity of both bands decreases with T -decreasing in the 10–50 K range, like in silicon suboxide (Fig. 2b). In this case such behaviour could be attributed to the absorption of excitation light in Si wires followed by radiative recombination of the carriers

via defects at the Si/SiO_x interface [3,21–23]. The excitation transition in indirect band gap material (Si) should be phonon assisted.

Finally, we can conclude that the same types of defect related radiative centres are responsible for PL in the Si–SiO_x films and in PSi. These radiative defects are located at the Si/SiO_x interface or in SiO_x layer on Si wire surface. Two types of PL excitation mechanisms are possible in investigated structures: interdefect and fundamental band-to-band optical transitions. The first mechanism dominates in silicon dioxide layers, while the second one dominates in silicon suboxide and in the Si crystallites of PSi.

Acknowledgements

This work was partially supported by CONACYT (Project 33427-U) and CGPI—IPN Mexico, Ministry of Science of Israel, as well as Ministry of Sciences and Education of Ukraine.

References

- [1] L.T. Canham, *Appl. Phys. Lett.* 57 (1990) 1046.
- [2] A.G. Cullis, L.T. Canham, P.D.J. Calcott, *J. Appl. Phys.* 82 (1997) 909.
- [3] Y. Kanemitsu, T. Matsumoto, T. Futagi, *Jpn. J. Appl. Phys.* 32 (1993) 411.
- [4] J.M. Lavine, S.P. Sawan, Y.T. Shieh, A.J. Bellezza, *Appl. Phys. Lett.* 62 (1993) 1099.
- [5] H.D. Fuchs, M. Stutzmann, M.S. Brandt, M. Rosenbauer, J. Weber, A. Breischwerdt, P. Deak, M. Cardona, *Phys. Rev. B* 48 (1993) 8172.
- [6] T.V. Torchynska, N.E. Korsunskaya, L.Yu. Khomenkova, *J. Phys. Chem. Solids* 61 (2000) 937.
- [7] S.M. Prokes, O.J. Glembocki, V.M. Berdudez, R. Kaplan, *Phys. Rev. B* 45 (1992) 13788.
- [8] T.V. Torchynska, N.E. Korsunskaya, L.Yu. Khomenkova, B.R. Dzhumaev, S.M. Prokes, *Microelectron. Eng.* 51–52 (2000) 485.
- [9] Y. Kanemitsu, T. Ogawa, K. Shiraishi, K. Takeda, *Phys. Rev. B* 48 (1993) 4883.
- [10] J.M. Macaulay, F.M. Ross, P.C. Seaton, S.K. Spitz, *Proc. Mat. Res. Soc. Symp.* 256 (1992) 47.
- [11] L.E. Friedersdorf, P.C. Seaton, S.M. Prokes, O.J. Glembocki, *Appl. Phys. Lett.* 60 (1992) 2285.
- [12] Wei Wu, X.F. Huang, L.J. Chen, J.B. Xu, X. Gao, W. Li, *J. Vac. Sci. Technol.* 17(1) (1999) 159.
- [13] J. Zhao, D.S. Mao, Z.X. Lin, X.Z. Ding, B.Y. Jiang, Y.H. Yu, *Appl. Phys. Lett.* 74 (1999) 1403.
- [14] K.S. Min, K.V. Shcheglov, C.M. Yang, H.A. Atwater, *Appl. Phys. Lett.* 69 (1996) 2033.
- [15] P. Mutti, G. Ghislotti, S. Bertoni, L. Bonoldi, G.F. Cerofolini, *Appl. Phys. Lett.* 66 (1995) 851.
- [16] T. Shimizu, K. Fujita, S. Nakao, K. Saitoh, T. Fujita, N. Itoh, *J. Appl. Phys.* 75 (1994) 7779.
- [17] S.M. Prokes, W.E. Carlos, S. Veprek, Ch. Ossadnik, *Phys. Rev. B* 58 (1998) 15632.
- [18] K. Nagasawa, Y. Hoshi, Y. Ohki, K. Yahagi, *Jap. J. Appl. Phys.* 25 (1986) 464.
- [19] S. Munekuni, T. Yamanaka, Y. Ohki, K. Nagasawa, Y. Hama, *J. Appl. Phys.* 68 (1990) 1212.
- [20] T. Suzuki, T. Sakai, L. Zhang, Y. Nishiyama, *Appl. Phys. Lett.* 66 (1995) 215.
- [21] T.V. Torchynska, J. Palacios Gomez, G.P. Polupan, F.G. Becerril Espinoza, H.A. Flores Gonzalez, L.V. Scherbina, *J. Electron Spectrosc. Relat. Phenom.* 114–116 (2001) 235.
- [22] T.V. Torchynska, N.E. Korsunskaya, L.Yu. Khomenkova, B.R. Dzhumaev, S.M. Prokes, *Thin Solid Films* 381/1 (2001) 88.
- [23] T.V. Torchynska, J. Palacios Gomez, G.P. Polupan, F.G. Becerril Espinoza, A. Garcia Borquez, N.E. Korsunskaya, L.Yu. Khomenkova, *Appl. Surf. Sci.* 167 (2000) 197.



ELSEVIER

Physica B 308–310 (2001) 1113–1116

PHYSICA B

www.elsevier.com/locate/physb

The influence of Coulomb effects on the electron emission and capture in InGaAs/GaAs self-assembled quantum dots

M.M. Sobolev*, V.M. Lantratov

A.F. Ioffe Physical Technical Institute, 26 Polytechnicheskaya ul., RAS, 194021 St. Petersburg, Russia

Abstract

The influence of built-in electrostatic potential of interface dipole on barrier energies for the emission and capture of electrons by InGaAs/GaAs quantum dots (QDs) has been found. It was shown that the formation of the interface dipole from carriers localized in QDs and ionized deep level defects depended on isochronous annealing under bias-on-bias-off cooling conditions. The dependence of the height of the capture barrier on the filling pulse duration, related to a manifestation of the Coulomb blockade effects on the capture of electrons into the ground and excited states of the dots, has also been revealed. © 2001 Elsevier Science B.V. All rights reserved.

Keywords: GaAs; Quantum dot; Defects; Heterostructures; Interaction

1. Introduction

The quantum dots (QDs) fabricated by self-organization during strained layer heteroepitaxy have found a wide application as injection laser [1] and they also promise new applications like the memory devices [2]. However, essential improvement of the performances of the QD lasers as well as design and understanding of an operation of memory devices are not well realized. These may be due to, among other factors, the availability of barrier energies for the emission and capture of carriers by QDs. A measurement technique of the temperature-dependent transient capacitance signal of a p–n diode due to filling and emptying of the deep level trap has been used with considerable success for the determination of barrier energies for the emission and capture of carriers by deep level defects and QD [3–4]. Recently, deep level transient spectroscopy (DLTS) was used to determine the capture barriers for carriers in InAs self-assembled QDs embedded in GaAs [4]. These authors showed the existence of these capture barriers, which in their opinion may be due to the built-in strain in self-organized system giving rise to the appearance of the

apexes in the interface InAs/GaAs. In our previous works [3], we reported on the formation of dipoles due to Coulomb interaction between carriers localized in In(GaAs)/GaAs QDs and ionized deep level defects arranged in the nearest neighborhoods with QDs. It is shown that built-in electrostatic potential due to these dipoles reduced barrier energies for the electron emission from the QDs [3]. The dipole formation depended on the temperature of isochronous annealing and bias-on-bias-off cooling conditions ($U_{ra} < 0$, $U_{ra} = 0$). It is of interest to also study the capture barrier energy dependence on annealing conditions by DLTS method.

2. Results and discussion

The structures under investigation were grown by metal organic chemical vapor deposition (MOCVD). The growth temperature was 480°C. After deposition on n^+ -GaAs substrate of 0.5- μm -thick GaAs buffer undoped layer ($n = 3 \times 10^{15} \text{ cm}^{-3}$), QD layer of InGaAs was deposited. Then growth was interrupted and a thin 50-Å-thick layer of GaAs was deposited over the QD layer, the temperature was raised to 600°C and in situ annealing was performed for 10 min. Thereafter, 0.5- μm -thick n-GaAs undoped layer and the top layer

*Corresponding author. Fax: +7-812-247-1017.

E-mail address: m.sobolev@pop.ioffe.rssi.ru
(M.M. Sobolev).

0.3- μm -thick p-GaAs were grown. DLTS investigations were carried out using a BIO-RAD DL4600 spectrometer. Prior to each DLTS measurement the sample was subjected to isochronous annealing for 1 min at 450 K under one of two conditions: (i) reverse bias $U_{\text{ra}} < 0$, (ii) zero bias $U_{\text{ra}} = 0$. After this a sample was cooled down to 80 K. The thermal activation energy E_{a} associated with the carrier emission from traps and their capture cross section σ_{n} were determined with standard DLTS measurement by changing the rate window from Arrhenius plots. The DLTS spectra measured at various conditions of isochronous annealing ($U_{\text{ra}} = 0$ and $U_{\text{ra}} < 0$) were characterized by the presence of three peaks (Fig. 1). Nothing unusual was observed in the behavior of the ED3 peak ($E_{\text{a}} = 667 \text{ meV}$, $\sigma_{\text{p}} = 7.4 \times 10^{-14} \text{ cm}^2$) that obviously belongs to the well-known defect GaAs: E4 ($V_{\text{As}} - \text{As}_{\text{Ga}}$) [5]. It was arranged in the nearest neighborhoods with QDs. The position of the ED1 (ED1#) and ED2 (ED2#) peaks in the DLTS spectra depended on conditions of isochronous annealing. The ED2 (ED2#) peaks are related, respectively, to the ground electron states of the QDs [4]. The parameters of the states corresponding to ED1 and ED2 peaks determined after previous annealing under $U_{\text{ra}} < 0$ were:

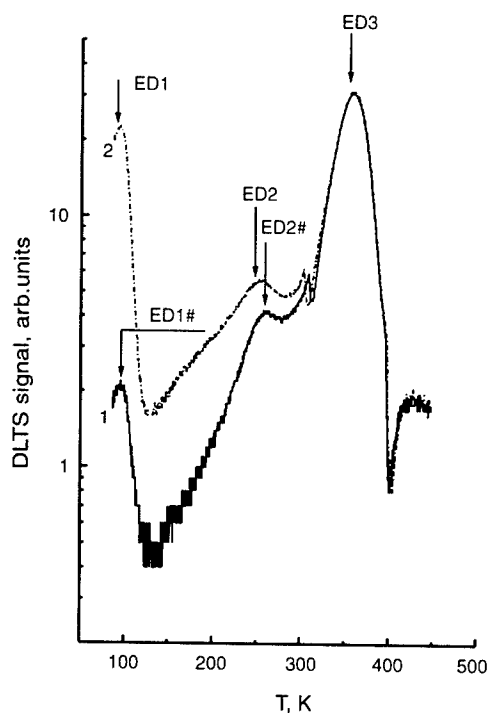
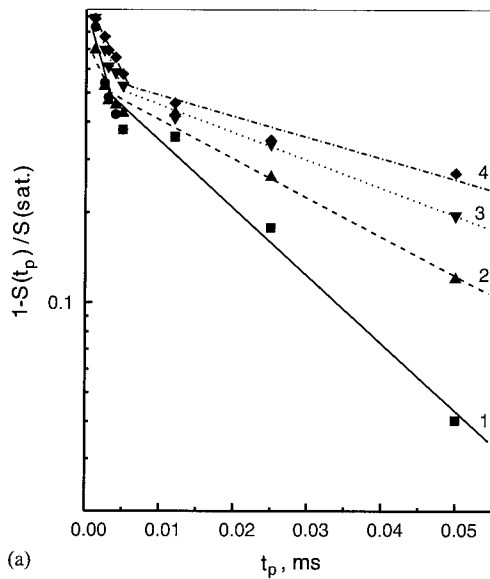
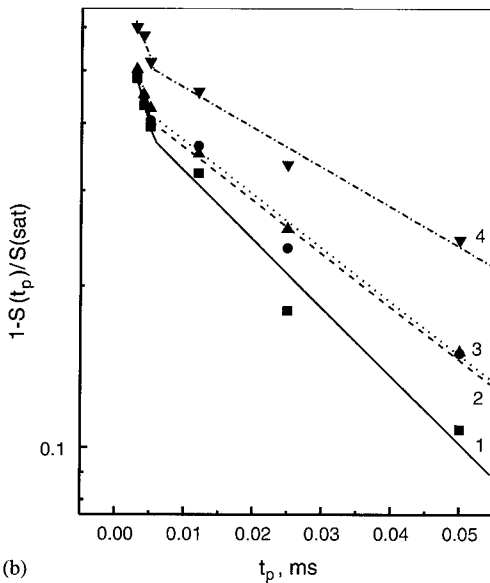


Fig. 1. DLTS spectra of the p-n heterostructure with InGaAs/GaAs QDs measurement under reverse bias $U_{\text{r}} = 0.5 \text{ V}$ and filling pulse bias $U_{\text{p}} = 0$ after previous isochronous annealing at $T_{\text{a}} = 450 \text{ K}$ and cooling down to 80 K under: (1) $U_{\text{ra}} = 0$ and (2) $U_{\text{ra}} < 0$.

$E_{\text{a}} = 122 \text{ meV}$, $\sigma_{\text{n}} = 2.3 \times 10^{-15} \text{ cm}^2$ and $E_{\text{a}} = 347 \text{ meV}$, $\sigma_{\text{n}} = 4.5 \times 10^{-16} \text{ cm}^2$. The annealing under $U_{\text{ra}} = 0$ resulted in the shift of position of the ED1 and ED2 peaks toward higher temperatures, which we denoted as ED1# and ED2#. The parameters of the states corresponding to these peaks were: $E_{\text{a}} = 156 \text{ meV}$, $\sigma_{\text{p}} = 1.8 \times 10^{-13} \text{ cm}^2$ and $E_{\text{a}} = 369 \text{ meV}$ and $\sigma_{\text{p}} = 7.2 \times 10^{-16} \text{ cm}^2$. We observed large DLTS peak height variations of ED1 (ED1#) and ED2 (ED2#) with change of rate windows that indicates a large temperature dependence of the electron capture cross section and this is related with a filling factor. The procedure of defining the capture parameters (σ and E_{a} are thermal capture and activation energy of the cross section) involves measurements of the variation in the heights of the DLTS signal peak ($S(t_{\text{p}})$) versus the time duration of the filling pulse (t_{p}). [4]: $S(t_{\text{p}}) = S_{\text{sat}}[1 - \exp(-(\sigma v_{\text{th}} n) t_{\text{p}})]$, where S_{sat} is the DLTS peak height when the QDs are filled with carrier, v_{th} is the mean thermal velocity of carrier, n is the free electron carrier. The experimental curves of this dependence for ED2 and ED2# peaks (Fig. 2a and b) showed the presence of two exponential portions: fast ($t_{\text{p}} = (1-5) \mu\text{s}$) and slow ($t_{\text{p}} = (5-100) \mu\text{s}$). A dependence temperature of the σ was defined with variation of the rate window for a fixed pulse duration. The activation energy was determined by the following expression: $\sigma = \sigma_{\text{x}} \exp(E_{\text{a}}/k_{\text{B}}T)$, where σ_{x} is a constant independent of temperature, and k_{B} is the Boltzmann constant. From Arrhenius plot (Fig. 3), we deduced E_{a} and σ_{x} . For fast portions of the curves of $S(t_{\text{p}})/S_{\text{sat}} \propto t_{\text{p}}$, measured after previous annealing of the sample under $U_{\text{ra}} < 0$, they were equal to $E_{\text{a}} = 27 \text{ meV}$, $\sigma_{\text{x}} = 1.7 \times 10^{-16} \text{ cm}^2$, whereas the slow portions were $E_{\text{a}} = 77 \text{ meV}$, $\sigma_{\text{x}} = 4.4 \times 10^{-16} \text{ cm}^2$. The values determined for $U_{\text{ra}} = 0$ were, respectively: $E_{\text{a}}^* = 48 \text{ meV}$, $\sigma_{\text{x}} = 6.7 \times 10^{-16} \text{ cm}^2$ and $E_{\text{a}}^* = 104 \text{ meV}$, $\sigma_{\text{x}} = 2.5 \times 10^{-15} \text{ cm}^2$. The difference in two capture energies determined at annealing under $U_{\text{ra}} = 0$ and $U_{\text{ra}} < 0$ were, respectively, $\Delta E_{\text{a}} = E_{\text{a}}^* - E_{\text{a}} = 21 \text{ meV}$ for the fast portion and $\Delta E_{\text{a}} = E_{\text{a}}^* - E_{\text{a}} = 27 \text{ meV}$ for the slow portion. The difference in the two emission energies determined at annealing under $U_{\text{ra}} = 0$ and $U_{\text{ra}} < 0$ was $\Delta E_{\text{a}} = \text{ED2\#} - \text{ED2} = 22 \text{ meV}$. A close inspection of these data shows that the change of the annealing condition from $U_{\text{ra}} < 0$ to $U_{\text{ra}} = 0$ caused an increase in the thermal emission energy and capture barrier alike on some equal values (21–27 meV) with all t_{p} while the differences in capture barrier with fast and slow electron captures under annealing $U_{\text{ra}} < 0$ to $U_{\text{ra}} = 0$ were close and equal: $\Delta E_{\text{a}} = E_{\text{a}} - E_{\text{a}}^* = 56 \text{ meV}$ and $\Delta E_{\text{a}} = E_{\text{a}}^* - E_{\text{a}} = 61 \text{ meV}$. These results show that the mechanism responsible for the observed decrease of the barrier energies for the capture of electrons by QDs under changes of the annealing condition from $U_{\text{ra}} < 0$ to $U_{\text{ra}} = 0$ is common to both portions. Under



(a)



(b)

Fig. 2. Normalized DLTS signal amplitudes as a function of the filling pulse duration under isochronous annealing at (a) $U_{ra}=0$ and at various temperatures (K): (1) 252.7, (2) 241.6, (3) 238.7, and (4) 222.7; (b) $U_{ra}<0$ and at various temperatures (K): (1) 256.6, (2) 245.7, (3) 242.0, and (4) 227.0.

annealing at $U_{ra}<0$, the formation of dipoles from carriers localized in QDs and ionized deep level defects is taking place. The built-in electrostatic potential due to these dipoles reduced barrier energies for the emission and capture of electrons by the QDs. Its value remains equal to $E_{of} \approx 27$ meV at $t_p < 5 \mu\text{s}$. The presence of the capture barrier in this case may be related to Coulomb blockade effect, which arises if a second electron is

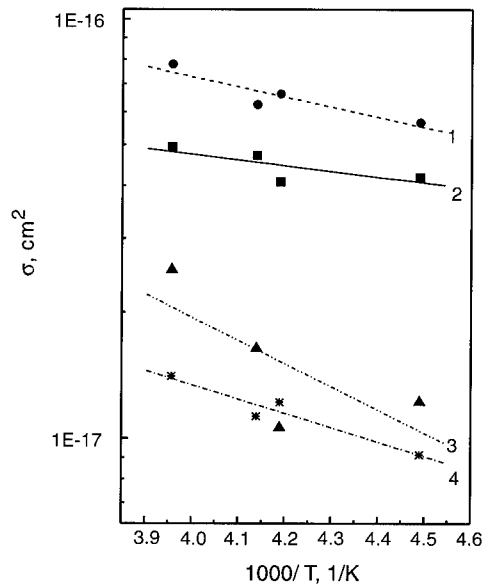


Fig. 3. Variation of the capture cross section versus the inverse of the temperature determined at $U_{ra}=0$ (1,3) and $U_{ra}<0$ (2,4): (1,2) for filling pulse duration $t_p = (1-5) \mu\text{s}$ and (3,4) for filling pulse duration $t_p > 5 \mu\text{s}$.

added into the ground states of the dots. We evaluated the Coulomb charging energy $E_c = e^2/2C$ (C is the self-capacitance of the QD) which for InGaAs QDs diameter of $d \approx 13$ nm embedded in GaAs is $E_c \approx 27$ meV. At $t_p > 5 \mu\text{s}$, we observed that height barrier energy which does not depend on annealing condition increase twice. This may be linked to the placement of a third electron into the first excited state of the dots which, for surmounting Coulomb blockade of two electrons, has to have charging energy $E_c \approx 54$ meV. Under annealing at $U_{ra}=0$, the formation of dipoles is not taking place. The magnitude of the band offset is defined by the formation conditions of the heterointerface during structure growth.

The behavior of the ED1 (ED1#) peaks dependence on the annealing condition was similar (Fig. 1) and is also related to the formatting of the electrostatic dipoles. Moreover, for ED1 (ED1#) peaks curves of $(1-S \times (t_p)/S_{sat}) \propto t_p$ showed the presence of only one exponential portion in the range of $t_p = (1-5) \mu\text{s}$. The activation energy E_a for them is less than for ED2 (ED2#) peaks. These results indicate that ED1 (ED1#) peaks cannot be related to excited states of the dots, they are most likely to result in the emission from the quantum states of the wetting layer.

Thus, we have investigated the processes of the electron emission and capture by the quantum dots in p-n InGaAs/GaAs heterostructures after an isochronous annealing under bias-on-bias-off cooling

conditions and the duration of the filling pulse by the DLTS. These investigations have shown that under annealing at $U_{\text{ra}} < 0$ the formation of dipoles from carriers localized in quantum dots and ionized deep level defects occurs. The built-in electrostatic potential due to these dipoles reduced barrier energies for the emission and capture of electrons by the quantum dots while under annealing at $U_{\text{ra}} = 0$, there is no formation of dipoles. The amount of the band offset is defined by the formation conditions of the heterointerface during the crystal growth. Dependence of the height of the capture barrier on the duration of the filling pulse has also been found, which is explained in terms of manifestation of the Coulomb blockade effects in the sense of the capture of electrons into the ground and excited states of the dot.

Acknowledgements

This work was financially supported by the Russian foundation for Basic Research, by the Program “Physics

of Solid Nanostructures”, by SCOPES 2000-2003, Grant No. 7SUPJ062392.00/1

References

- [1] D. Bimberg, et al., *Quantum Dot Heterostructures*, Wiley, Chichester, 1998.
- [2] G. Yusa, et al., *Appl. Phys. Lett.* 70 (1997) 345.
- [3] M.M. Sobolev, et al., *Semiconductors*, 34 (2000) 195.
- [4] H.L. Wang, et al., *Phys. Rev. B* 61 (2000) 5530.
- [5] D. Pons, et al., *J. Appl. Phys.* 51 (1980) 2038.



ELSEVIER

Physica B 308–310 (2001) 1117–1120

PHYSICA B

www.elsevier.com/locate/physb

Electronic transport through N quantum dots under DC bias

W.Z. Shangguan*, T.C. Au Yeung, Y.B. Yu

Photonics Lab. 1, School of Electrical and Electronics Engineering, Nanyang Technological University, Singapore 639798

Abstract

This work deals with the electronic transport in a system of an arbitrary number of quantum dots connected in series by tunnel coupling. We calculate the “lesser” and retarded Green’s functions based on the nonequilibrium Green’s function formalism developed by Jauho et al. [Phys. Rev. B 50 (1994) 5528] for a one-dimensional N dot array, where N is an arbitrary positive integer, and we derive an analytical formula for the current under DC bias voltage. The retarded self-energy defined for any individual dot in the array is found to be made up of left and right components and to be of the staircase type, terminating at the two electron reservoirs. For simplicity of numerical computation, we take the 3-dot case for demonstration. The density of states of the 3-dot system is studied by plotting the differential conductance against the Fermi level of the left lead. © 2001 Elsevier Science B.V. All rights reserved.

Keywords: Quantum transport; Quantum dot array; Nonequilibrium Green’s function; Equation of motion method

In the last decade, a great deal of work has been done on the transport [1–5] and capacitance spectroscopy [6] of a single quantum dot system to probe its discrete spectrum. It was a significant discovery that the on-site Coulomb interaction leads to important Coulomb-blockade conductance oscillations [7–12] and a Kondo peak in the conductance [13,14].

However, research interest has extended in recent few years to systems of multiple quantum dots [15–18]. For example, electron pumping was studied in a double dot with interdot capacitance [16]; the Kondo effect in a double dot with on-site Coulomb interactions was studied based on the slave-boson mean-field theory [17,18]; and the DC current of a double dot without on-site Coulomb interactions was derived by Kawamura and Aono [19]. In this paper, we study a system of multiple quantum dots connected in series by tunnel coupling. Our formalism is based on the nonequilibrium Green’s function proposed by Jauho et al. [20]. The on-site Coulomb interaction can be ignored when the dot size is relatively large. We calculate the “lesser” and retarded Green’s functions for the N dots connected in

series, where N can be any positive integer, and then derive an analytical formula for the current under a DC bias voltage. For simplicity of numerical computation, we take the 3-dot case for demonstration. We study the density of states of the 3-dot system by plotting the differential conductance against the Fermi level of the left lead.

Consider a system of N quantum dots connected in series by tunnel coupling. The Hamiltonian H is given by

$$H = \sum_{k,\alpha} \varepsilon_{k\alpha} c_{k\alpha}^\dagger c_{k\alpha} + \sum_{i=1}^N \varepsilon_i^0 d_i^\dagger d_i + V_L (c_{kL}^\dagger d_1 + \text{h.c.}) + V_R (c_{kR}^\dagger d_N + \text{h.c.}) + \sum_{i=1}^{N-1} V_{i,i+1} (d_i^\dagger d_{i+1} + \text{h.c.}), \quad (1)$$

where $c_{k\alpha}^\dagger$ ($c_{k\alpha}$) are electron creation (annihilation) operators in reservoir $\alpha = L$ (left), R (right), d_i^\dagger (d_i) are electron creation (annihilation) operators in the i th quantum dot, V_L (V_R) is the tunneling coupling between the 1st (N th) dot and the left- (right-) reservoir, and $V_{i,i+1}$ ($= V_{i+1,i}$) is the tunneling coupling between the i th and $(i+1)$ th dot. The electron spin index is suppressed.

*Corresponding author. Fax: +65-7904161.

E-mail address: p146859457@ntu.edu.sg (W.Z. Shangguan).

By making use of the formalism of nonequilibrium Green's function [20], the left-current J_L flowing from the left lead into the dot array is given by

$$J_L = \frac{2ie}{h} \int \frac{d\varepsilon}{2\pi} \Gamma_L^L(\frac{\varepsilon}{h}) \left[G_{11}^<(\frac{\varepsilon}{h}) + f_L(\varepsilon) \left(G_{11}^r(\frac{\varepsilon}{h}) - G_{11}^a(\frac{\varepsilon}{h}) \right) \right], \quad (2)$$

where the factor 2 takes into account the electron spin $\pm \frac{1}{2}$, and $\Gamma_L^L(\varepsilon/h) = 2\pi V_L^2 \rho_L(\varepsilon)$ is the coupling of the 1st dot to the left-reservoir ($\rho_L(\varepsilon)$ is the density of states of electrons in the left reservoir). We have a similar definition for $\Gamma^R(\varepsilon/h)$ for the right reservoir. The "lesser" and retarded Green's functions are defined by

$$G_{ij}^<(t) = i \langle d_j^\dagger(0) d_i(t) \rangle, \quad (3)$$

$$G_{ij}^r(t) = -i \theta(t) \langle \{ d_i(t), d_j^\dagger(0) \} \rangle \quad (i, j = 1, 2, \dots, N). \quad (4)$$

By the method of equations of motion [21] and Keldysh's contour integration [22], we obtain the following equations for the Green's functions:

$$G_{11}^r = g_{11}^r + g_{11}^r \Sigma_1^r G_{11}^r + g_{11}^r V_{12} G_{21}^r + g_{11}^r V_{12} G_{21}^r, \quad (5)$$

$$G_{i1}^r = V_{i-1,i} g_{ii}^r G_{i-1,1}^r + V_{i-1,i} g_{ii}^r G_{i-1,1}^r + V_{i,i+1} g_{ii}^r G_{i+1,1}^r + V_{i,i+1} g_{ii}^r G_{i+1,1}^r \quad (i = 2, 3, \dots, N-1), \quad (6)$$

$$G_{11}^r(\omega) = \frac{1}{\omega - \varepsilon_1^0 - \Sigma_1^r(\omega) - \frac{V_{12}^2}{\omega - \varepsilon_2^0 - \frac{V_{23}^2}{\omega - \varepsilon_3^0 - \frac{V_{34}^2}{\omega - \varepsilon_4^0 - \dots - \frac{V_{N-2,N-1}^2}{\omega - \varepsilon_{N-1}^0 - \frac{V_{N-1,N}^2}{\omega - \varepsilon_N^0 - \Sigma_2^r(\omega)}}}}}} \quad (16)$$

$$G_{N1}^r = g_{NN}^r \Sigma_2^r G_{N1}^r + V_{N-1,N} (g_{NN}^r + g_{NN}^r) G_{N-1,1}^r \quad (7)$$

and

$$G_{11}^< = g_{11}^r \Sigma_1^r G_{11}^< + g_{11}^r \Sigma_1^a G_{11}^< + g_{11}^r \Sigma_1^r G_{11}^a + V_{12} (g_{11}^r + 2g_{11}^r) G_{21}^< - V_{12} g_{11}^r G_{21}^a, \quad (8)$$

$$G_{i1}^< = V_{i-1,i} (g_{ii}^r + 2g_{ii}^r) G_{i-1,1}^< - V_{i-1,i} g_{ii}^r G_{i-1,1}^a + V_{i,i+1} (g_{ii}^r + 2g_{ii}^r) G_{i+1,1}^< - V_{i,i+1} g_{ii}^r G_{i+1,1}^a, \quad (9)$$

$$G_{N1}^< = g_{NN}^r \Sigma_2^r G_{N1}^< + g_{NN}^r \Sigma_2^a G_{N1}^< + g_{NN}^r \Sigma_2^r G_{N1}^a + V_{N-1,N} (g_{NN}^r + 2g_{NN}^r) G_{N-1,1}^< - V_{N-1,N} g_{NN}^r G_{N-1,1}^a \quad (10)$$

where $(i = 2, 3, \dots, N-1)$ and the free-particle Green's functions are defined by:

$$g_{ij}^<(t, t') = -i \langle T(d_i(t) d_j^\dagger(t')) \rangle, \quad (11)$$

$$g_{ij}^<(t, t') = i \langle d_j^\dagger(t') d_i(t) \rangle, \quad (12)$$

$$g_{ij}^r(t, t') = -i \theta(t - t') \langle \{ d_i(t), d_j^\dagger(t') \} \rangle, \quad (i, j = 1, 2, \dots, N). \quad (13)$$

Also,

$$\Sigma_1^{r,a,<}(t, t') = V_L^2 \sum_k g_{kL}^{r,a,<}(t, t'), \quad (14)$$

$$\Sigma_2^{r,a,<}(t, t') = V_R^2 \sum_k g_{kR}^{r,a,<}(t, t') \quad (15)$$

are self-energies associated with the tunneling between the left-reservoir and the 1st dot, and that between the right reservoir and the N th dot, respectively. The Green's function $g_{kL}^{r,a,<}(t, t')$ and $g_{kR}^{r,a,<}(t, t')$ correspond to free electrons in the left and right reservoir, respectively.

Solving the Eqs. (5)–(7) for $G_{11}^r(\omega)$, we obtain

The result presented by the above equation has an obvious physical interpretation. The retarded self-energy of the first quantum dot in the one-dimensional dot array is composed of two parts: the "left retarded self-energy" $\bar{\Sigma}_{11}^r(\omega)$ which is simply $\Sigma_1^r(\omega)$ defined in Eq. (14) and can be re-written as $\bar{\Sigma}_{11}^r(\omega) = \sum_k V_L^2 / (g_{kL}^r)^{-1}$, and the "right retarded self-energy" which is of form $\bar{\Sigma}_{11}^r = 1 / [(g_{22}^r)^{-1} - \bar{\Sigma}_{22}^r]$, where $(g_{22}^r)^{-1}$ and $\bar{\Sigma}_{22}^r$ are the unperturbed Green's function and the "right retarded self-energy" of dot 2, respectively. As the second dot is connected to the third dot to its right, the "right retarded self-energy" of dot 2 is modified by $\bar{\Sigma}_{22}^r = 1 / [(g_{33}^r)^{-1} - \bar{\Sigma}_{33}^r]$ (here $\bar{\Sigma}_{33}^r$ is the right retarded self-energy of dot 3) instead of $1 / [(g_{33}^r)^{-1}]$, ..., ending up

with the right electron reservoir at $\Sigma_2^r(\omega) = \sum_k V_{Rk}^2 / (g_{kR}^r)^{-1}$. This structure of the retarded Green's function is applicable to all quantum dots in the dot array.

Similarly, solving the Eqs. (8)–(10) for $G_{11}^<(\omega)$, we obtain

$$G_{11}^<(\omega) = \Sigma_1^<(\omega) |G_{11}^r(\omega)|^2 + V_{12}^2 V_{23}^2 \cdots V_{N-1,N}^2 |G_{11}^r(\omega)|^2 \times |G_{22}^0(\omega)|^2 \cdots |G_{NN}^0(\omega)|^2 \Sigma_2^<(\omega), \quad (17)$$

where the Green's functions $G_{ii}^0(\omega)$ are defined by

$$G_{ii}^0(\omega) = \frac{1}{\omega - \varepsilon_i^0 - V_{i,i+1}^2 G_{i+1,i+1}^0(\omega)}, \quad (i = 2, 3, \dots, N-1), \quad (18)$$

$$G_{NN}^0(\omega) = \frac{1}{\omega - \varepsilon_N^0 - \Sigma_2^r(\omega)}. \quad (19)$$

Finally, we arrive at the following current formula by substituting Eqs. (16) and (17) into (2)

$$J_L = \frac{2e}{h} \int d\varepsilon (f_L(\varepsilon) - f_R(\varepsilon)) T(\varepsilon) \quad (20)$$

where $f_\alpha(\varepsilon)$ is the Fermi function in lead α , and $T(\varepsilon)$ which has the physical interpretation of transmission probability, reads

$$T(\varepsilon) = \Gamma^L \left(\frac{\varepsilon}{h} \right) \Gamma^R \left(\frac{\varepsilon}{h} \right) \cdot V_{12}^2 V_{23}^2 \cdots V_{N-1,N}^2 \left| G_{NN}^0 \left(\frac{\varepsilon}{h} \right) \right|^2 \times \left| G_{N-1,N-1}^0 \left(\frac{\varepsilon}{h} \right) \right|^2 \cdots \left| G_{22}^0 \left(\frac{\varepsilon}{h} \right) \right|^2 \left| G_{11}^r \left(\frac{\varepsilon}{h} \right) \right|^2. \quad (21)$$

We remark that when $N = 1$, our formula of J_L in Eq. (20) is identical to that by Jauho et al. for a single quantum dot with proportionate coupling to leads under a time-independent bias [12]. When $N = 2$ (i.e., a double dot), we reproduce the results derived by Kawamura and Aono [11] for a double dot under DC voltage.

Formula (20) is of the Landauer-Büttiker type, as expected. But the transmission probability $T(\varepsilon)$ is tedious to calculate for a large number of dots (i.e., large N). In principle when $i > 2$ the Green's functions $G_{ii}^0(\omega)$ are obtained by recursion using Eqs. (18) and (19). We will consider the wide-band limit in which $\Sigma_{1,2}^r(\omega) = -(i/2)\Gamma^{L,R}$ where the couplings Γ^L and Γ^R are constants. Since $T(\varepsilon)$ reflects the density of states for the system of N dots, we can use the plot of differential conductance to probe the density of states. To demonstrate the analytical results obtained here we take the case of 3 dots for numerical computation of the differential conductance. We assume that the left and right couplings are identical ($\Gamma^L = \Gamma^R = \Gamma$). All the energies are expressed in units of Γ . We set $\varepsilon_1^0 = \varepsilon_2^0 = \varepsilon_3^0 = \varepsilon_0 = -10$, $1/kT = 100$, and $V_{12} = V_{23} = V = 0.1, 2.0, 5.0$. The right Fermi level μ_R is set to zero.

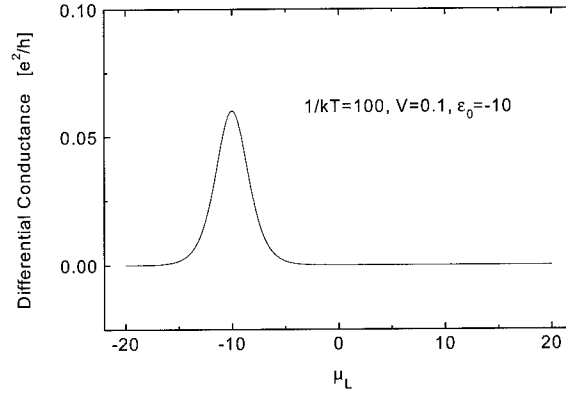


Fig. 1. The plot of differential conductance against the left Fermi level μ_L , with $1/kT = 100$, $V = 0.1$ and $\varepsilon_0 = -10$. All energies are expressed in units of Γ .

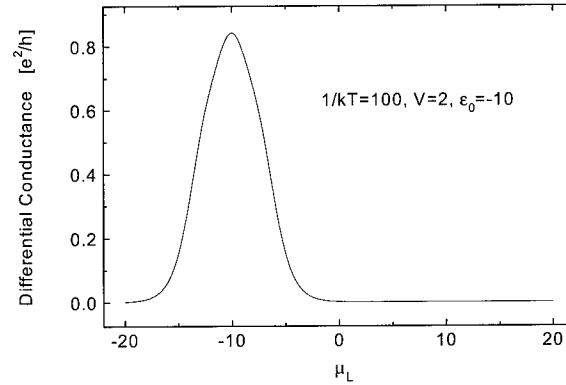


Fig. 2. The plot of differential conductance against the left Fermi level μ_L , with $1/kT = 100$, $V = 2$ and $\varepsilon_0 = -10$. All energies are expressed in units of Γ .

In Figs. 1–3, we plot the differential conductance against the left Fermi level μ_L . When $V = 0.1$ (Fig. 1), there is only one peak at $\mu_L = -10$ in the density of states. We expect this because small V_c means most electrons supplied by the left reservoir to dot 1 turn back before they go forward to the other 2 dots. Thus the electrons see only a single quantum dot in this case. The energy level that they belong to is simply $\varepsilon_1^0 = -10$. Clearly, the single peak in the density of states is due to the coupling of the dot system to the electron reservoirs. We consider $V = 2$ in Fig. 2. There is also one single peak in the density of states. We conclude that V_c should be set at larger values in order to display multiple peaks in the density of states.

In Fig. 3, we set $V = 5$ and there are 3 peaks in the plot of the differential conductance. For large V the electrons oscillate frequently among the 3 dots before

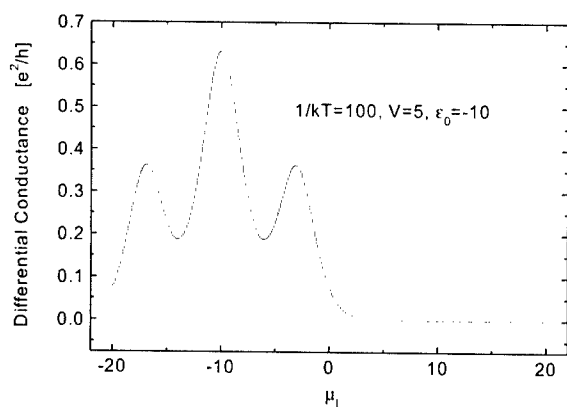


Fig. 3. The plot of differential conductance against the left Fermi level μ_L , with $1/kT = 100$, $V = 5$ and $\epsilon_0 = -10$. All energies are expressed in units of Γ .

they tunnel into the reservoirs. The energy levels of the electrons should be identical to those of an isolated three dot. That is, there should be 3 peaks in the density of states. The couplings Γ^L and Γ^R broaden the 3 peaks.

We then conclude that these are three energy levels in a three dot system for sufficiently large tunneling coupling V . In principle, our current formula (20) can handle any number of dots. We expect that there are N peaks in the density of states for a N dot system.

In summary, by making use of the equation of motion method and Keldysh Green's function technique, we have developed a calculation method for the one-dimensional quantum dot array with arbitrary dots. The retarded Green's function of every dot in the array is found to have a staircase structure, ending at two

electron reservoirs. A general formula for calculating the conductance of the dot array is derived, and the case of a 3 dots is numerically studied.

References

- [1] M.A. Reed, et al., Phys. Rev. Lett. 60 (1998) 535.
- [2] C.G. Smith, et al., J. Phys. C 21 (1988) L 893.
- [3] P.L. McEuen, et al., Phys. Rev. Lett. 66 (1991) 1926.
- [4] E.B. Foxman, et al., Phys. Rev. B 50 (1994) 14193.
- [5] A.T. Johnson, et al., Phys. Rev. Lett. 69 (1992) 1592.
- [6] R. Ashoori, et al., Phys. Rev. Lett. 68 (1992) 3088.
- [7] C.J. Gorter, Physica 17 (1951) 777.
- [8] R.I. Shekter, Sov. Phys. JETP 36 (1973) 747.
- [9] I.O. Kulik, R.I. Shekter, Sov. Phys. JETP 41 (1975) 308.
- [10] L.I. Glazman, R.I. Shekter, J. Phys.: Condens. Matter 1 (1989) 5811.
- [11] M. Amman, K. Mullen, E. Ben-Jacob, J. Appl. Phys. 65 (1989) 339.
- [12] C.W.J. Beenakker, Phys. Rev. B 44 (1991) 1646.
- [13] L.I. Glazman, M.E. Raikh, JETP Lett. 47 (1988) 452.
- [14] T.K. Ng, P.A. Lee, Phys. Rev. Lett. 61 (1988) 1768.
- [15] H. Chen, et al., Phys. Rev. B 55 (1997) 1578.
- [16] C.A. Stafford, Ned S. Wingreen, Phys. Rev. Lett. 76 (1996) 1916.
- [17] T. Aono, et al., J. Phys. Soc. Japan 67 (1998) 1860.
- [18] A. Georges, Yigal Meir, Phys. Rev. Lett. 82 (1999) 3508.
- [19] Kiyoshi Kawamura, Tomosuke Aono, Jpn. J. Appl. Phys. 36 (1997) 3951.
- [20] A.-P. Jauho, Ned S. Wingreen, Y. Meir, Phys. Rev. B 50 (1994) 5528.
- [21] C. Lacroix, J. Phys. F: Metal. Phys. 11 (1981) 2389.
- [22] H. Haug, A.-P. Jauho, Quantum Kinetics in Transport and Optics of Semiconductors, Springer, Berlin, 1996.



ELSEVIER

Physica B 308–310 (2001) 1121–1124

PHYSICA B

www.elsevier.com/locate/physb

Excitation of Tm^{3+} by the energy transfer from Si nanocrystals

Kei Watanabe^a, Hiroyuki Tamaoka^a, Minoru Fujii^{b,*}, Kazuyuki Moriwaki^{a,b},
Shinji Hayashi^{a,b}

^aGraduate School of Science and Technology, Kobe University, Rokkodai, Nada, Kobe 657-8501, Japan

^bDepartment of Electrical and Electronics Engineering, Faculty of Engineering, Kobe University, Rokkodai, Nada, Kobe 657-8501, Japan

Abstract

Photoluminescence (PL) properties of SiO_2 films containing Si nanocrystals (nc-Si) and Tm^{3+} were studied. The average size of nc-Si was changed over wide range in order to tune the exciton energy of nc-Si to the energy separations between the discrete electronic states of Tm^{3+} . At room temperature, the samples exhibited broad PL peaks located at an energy region between 1.35 and 1.6 eV corresponding to the recombination of the excitons in nc-Si, and sharp peaks at 1.57 and 0.69 eV corresponding to the intra-4f shell transition of Tm^{3+} . The intensity of the Tm^{3+} related PL showed a strong dependence on the size of nc-Si. This result implies that only nc-Si which are smaller than a threshold size can efficiently excite Tm^{3+} . At low temperatures, the spectral shape of nc-Si PL was strongly modified by doping Tm. From the analysis of the modified spectral shape, the spectroscopic evidence of the resonant energy transfer from nc-Si to Tm^{3+} was obtained. © 2001 Elsevier Science B.V. All rights reserved.

PACS: 76.30.Kg; 78.55.-m; 61.46.+w

Keywords: Tm; Si; Nanocrystals; Energy transfer

Tm-doped glasses have been investigated as materials for near-infrared light sources and amplifiers. The laser action has been realized at around 0.85 eV (1.46 μm) and 0.69–0.62 eV (1.8–2.0 μm). These lasers and amplifiers have been demonstrated by a Tm-doped fiber [1,2]. However, enough gain has not yet been achieved for practical use. To realize the lasers and amplifiers, it is necessary to excite Tm^{3+} more efficiently. Recently, Si nanocrystals (nc-Si) have been attracting a lot of interest, because Si nanocrystals act as an efficient sensitizer for several rare-earth ions and are believed to yield efficient excitation of Tm^{3+} .

In our previous work, we demonstrated that the photoluminescence (PL) intensity of the intra-4f shell transition of Er^{3+} and Yb^{3+} became stronger by more than 2 orders magnitude by doping nc-Si [3–5]. The excitation of Er^{3+} (Yb^{3+}) is made by transferring the recombination energy of photo-generated excitons in nc-Si. In Er/nc-Si systems, the excitation mechanism of

Er^{3+} has been studied in detail [3,4,6,7] and the direct spectroscopic evidence of the energy transfer has been obtained. Furthermore, energy transfer rates are experimentally determined as a function of nc-Si size. It has been demonstrated that the smaller the size of nc-Si, the larger the energy transfer rate [8]. In contrast to the Er/nc-Si systems, in systems containing other rare-earth ions, detailed mechanism of the interaction with nc-Si has not been well understood, although the enhancement of the intra-4f shell PL is demonstrated.

Tm^{3+} have discrete and complex electronic states. The first ($^3\text{H}_4$), second ($^3\text{H}_5$), third ($^3\text{F}_4$) excited states exist around 0.7, 1.0, 1.6 eV from the ground state ($^3\text{H}_6$), respectively. Furthermore, the band gap of nc-Si continuously changes from bulk band gap to higher energies on decreasing the size of nc-Si [9]. This change in the band gap is due to the zero-dimensional quantum size effects. Therefore, the interactions between the intra-4f shell electrons in Tm^{3+} and nc-Si should depend on the size of nc-Si. For this reason, it is essential to investigate PL in a wide spectral range and to widely change the size of nc-Si. However, the size dependence in

*Corresponding author.

E-mail address: fujii@eedept.kobe-u.ac.jp (M. Fujii).

a wide spectral range has not yet been investigated. Although strong interactions between nc-Si and Tm^{3+} have been demonstrated, the spectroscopic evidence of the energy transfer from nc-Si to Tm^{3+} has not been obtained.

In this work, we studied PL properties of SiO_2 thin films containing nc-Si and Tm^{3+} in the wide spectral range from 0.45 to 1.90 eV. We will show a correlation between the intensities of the nc-Si related peak and Tm^{3+} related peaks as a function of the size of nc-Si and temperature. The mechanisms of the interaction between nc-Si and Tm^{3+} are discussed.

SiO_2 films containing nc-Si and Tm were prepared by a method similar to that used to prepare films containing nc-Si and Er [3,4]. Small pieces of Si chips and Tm oxide pellets were placed on a SiO_2 sputtering target and they were simultaneously sputtered in Ar gas atmosphere. After the deposition, in order to grow nc-Si, samples were annealed in N_2 gas for 30 min at temperatures higher than 1100 °C. In this work, the average size of nc-Si (d_{Si}) was changed from 2.7 to 3.5 nm and Tm concentration was fixed at 1.41 at%. PL spectra were measured using a single grating monochromator. In the spectral range between 0.45 and 0.80 eV, liquid nitrogen cooled InSb photodiode (Hamamatsu) was used as a detector, and in the spectral range between 0.80 and 1.90 eV, liquid nitrogen cooled Ge detector (North Coast) was used. The excitation source was 514.5 nm line of an Ar-ion laser. For all the spectra, the spectral response of the detection system was corrected by the reference spectrum of a standard tungsten lamp.

Fig. 1 shows the PL spectra at room temperature for the samples containing nc-Si with different size. Tm concentration is fixed at 1.41 at%. The energy position of the first ($^3\text{H}_4$), second ($^3\text{H}_5$), and third ($^3\text{F}_4$) excited states measured from the ground state ($^3\text{H}_6$) are shown on the top of the figure. We can see two peaks. The high-energy broad peak is due to the recombination of excitons confined in nc-Si (nc-Si PL) [3,4,9]. The low-energy one is due to the $^3\text{H}_4$ to $^3\text{H}_6$ transition of Tm^{3+} (Tm^{3+} PL) [1,2]. The spectra are normalized at the maximum intensity of nc-Si PL. As the size of nc-Si decreases from 3.5 to 2.7 nm, the peak energy of nc-Si PL is shifted toward higher energy. For the sample with the average nc-Si size of 2.7 and 3.1 nm, a weak peak can be observed at 1.58 eV. This peak corresponds to the $^3\text{F}_4$ to $^3\text{H}_6$ transition of Tm^{3+} .

Fig. 2 shows the intensity ratio of Tm^{3+} (0.68 eV peak) and nc-Si PL peaks ($I_{\text{Tm}}/I_{\text{Si}}$) as a function of the peak energy of nc-Si PL. The inset shows the energy diagram of the intra-4f shell of Tm^{3+} . The energy position of the third ($^3\text{F}_4$) excited state measured from the ground state ($^3\text{H}_6$) is shown in the figure. $I_{\text{Tm}}/I_{\text{Si}}$ depends strongly on the peak energy of nc-Si PL. On increasing the peak energy of nc-Si PL, the intensity of Tm^{3+} PL peak increases. In particular, the intensity

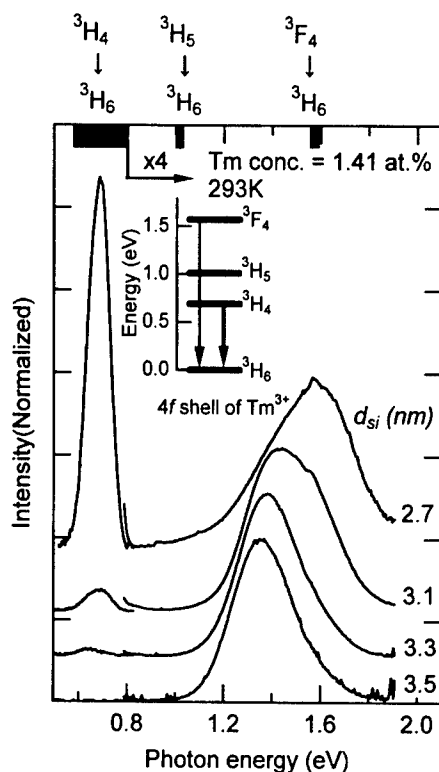


Fig. 1. PL spectra at room temperature as a function of the size of nc-Si in diameter. Tm concentration was fixed at 1.41 at%. The energy position of the first ($^3\text{H}_4$), second ($^3\text{H}_5$), and third ($^3\text{F}_4$) excited states measured from the ground state ($^3\text{H}_6$) are shown.

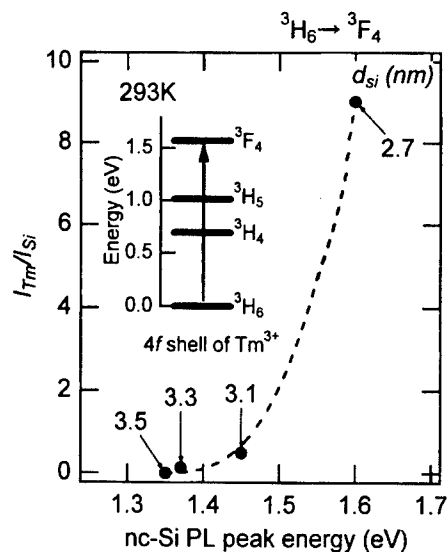


Fig. 2. Intensity ratio of the Tm related and nc-Si related peaks ($I_{\text{Tm}}/I_{\text{Si}}$) as a function of the peak energy of nc-Si PL. The line is drawn to guide the eye.

increase drastically as the nc-Si PL peak approaches 1.6 eV. It should be noted that the intensity of Tm^{3+} for the sample of size 2.7 nm is more than 10 times stronger than that of the sample of size 3.1 nm before normalization of the spectra of Fig. 1.

When nc-Si peak energy is relatively low, i.e., the size of nc-Si is relatively large, the intensity of Tm^{3+} peak is very weak. In this case, the first and the second excited states can be excited. However, the energy transfer efficiency is considered to be low, because the energy mismatches between the recombination energy of the excitons and the first (second) excited state is relatively large. At first approximation, the energy transfer efficiency depends on the energy mismatches. With increasing nc-Si peak energy, the number of the nc-Si with the recombination energy larger than the energy separation between the ground state and the third excited state increases. Therefore, not only the first and the second excited states but also the third excited state can be excited. The steep incline in Fig. 2 suggests that the excitons in nc-Si with the recombination energy of around 1.6 eV mainly interact with the intra-4f shell of Tm^{3+} . Since the energy mismatch of the recombination energy of exciton and the third excited state becomes smaller with increasing nc-Si PL peak energy, the energy transfer efficiency become higher.

Fig. 3 shows PL spectra of the sample with 2.7 nm diameter at various temperatures. The intensity of the spectra above 0.8 eV are expanded by a factor of 10. On decreasing the temperature, the spectral shape changes gradually. First, below 150 K, a new broad peak appears at around 1.0 eV. This peak is considered to be due to the recombination of excitons trapped at P_b centers at the interfaces between nc-Si and SiO_2 matrices [10]. Secondly, a very weak peak appears at around 0.84 eV as indicated by arrows. Thirdly, the 1.58 eV peak becomes more pronounced. The 0.84 and 1.57 eV peaks correspond to the intra-4f shell transitions of Tm^{3+} ($^3\text{F}_4$ to $^3\text{H}_4$, $^3\text{F}_4$ to $^3\text{H}_6$). Fourthly, the 0.69 eV peak is slightly shifted toward lower energy (0.69–0.67 eV) and becomes sharper. Finally, the spectral shape of nc-Si PL is strongly modified. At room temperature, the spectral shape is Gaussian-like. At around 100 K, the lower-energy side of the spectrum is strongly suppressed. At 5 K, both sides of the 1.57 eV peak are suppressed. It should be noted here that without Tm-doping, the spectra shape is almost independent of the temperature.

The energy range of the modification is close to the energy separation between third excited state ($^3\text{F}_4$) and the ground state ($^3\text{H}_6$). The excitation energy of nc-Si is transferred to Tm^{3+} before the radiative recombination of excitons occurs in nc-Si. To our knowledge, this is the first direct evidence of the energy transfer from nc-Si to Tm^{3+} . If the energy transfer is made resonantly (without emitting phonons) or by emitting phonons, the suppression should appear only at the high-energy side of the

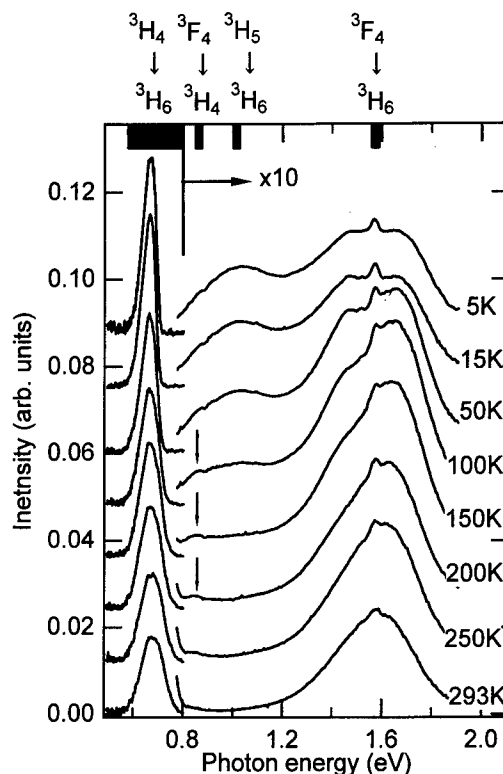


Fig. 3. PL spectra of the sample with Tm concentration = 1.41 at% at various temperatures. The intensities of the spectra above 0.8 eV are expanded by a factor of 10.

1.57 eV peak. However, the spectra are strongly suppressed not only at the high-energy side of the 1.57 eV peak of Tm^{3+} but also at the lower-energy side. This result can be explained by taking the indirect band-gap nature into consideration. As reported previously, the indirect-gap nature of bulk Si crystal is preserved in nc-Si even if the size is a few nanometers in diameter, i.e., radiative recombination of excitons in nc-Si requires the emission of momentum conserving phonons at Δ minima [11]. Since the TO phonon energy at Δ minima is about 57 meV, nc-Si whose exciton recombination energy exactly coincides with the energy of the third excited state of Tm^{3+} (1.57 eV) shows PL at around 1.57 eV–57 meV, if resonant energy transfer does not occur. If the resonant energy transfer occurs, the recombination energy of excitons is preferentially transferred to Tm^{3+} , resulting in the decrease of the intensity of PL at the lower-energy side. Therefore, the appearance of the spectral suppression at the low-energy side of the 1.57 eV peak is the spectroscopic evidence of the resonant energy transfer from nc-Si to Tm^{3+} .

In conclusion, we studied PL properties of SiO_2 films containing nc-Si and Tm^{3+} as a function of the size of nc-Si. The 1.57, 0.84 and 0.69 eV peaks which corre-

spend to the intra-4f shell transition of Tm^{3+} were observed. The intensity of Tm^{3+} PL at 0.69 eV depended strongly on the size of nc-Si. As the PL energy of nc-Si approached the energy difference between the third excited state and the ground state of Tm^{3+} (1.58 eV), the intensity of Tm^{3+} PL increased drastically. This result indicates that nc-Si interacts mainly with the third excited state of Tm^{3+} , and the exciton energy of nc-Si should be larger than this energy to efficiently excite Tm^{3+} . We also showed that PL spectra were strongly modified at low temperature. From the observed PL dip structures, we demonstrated that the suppression at the lower-energy side of the 1.57 eV peak is spectroscopic evidence of the resonant excitation of the third excited state of Tm^{3+} .

Acknowledgements

The authors are grateful to Mr. Keisuke Nakjima for his valuable assistance in this work. This work was

supported by a Grant-in-Aid for Science Research from the Ministry of Education, Science and Culture, Japan, and a Grant for Research for the Future Program from the Japan Society for the Promotion of Science (JSPS-RFTF-98P-0120). One of the authors (K.W.) would like to thank the Japan Society for the Promotion of Science for financial support.

References

- [1] P.J. Suni, et al., *SPIE* 1171 (1989) 234.
- [2] D.C. Hanna, et al., *Opt. Commun.* 1990 (283).
- [3] M. Fujii, et al., *Appl. Phys. Lett.* 71 (1997) 1198.
- [4] M. Fujii, et al., *J. Appl. Phys.* 84 (1998) 4525.
- [5] M. Fujii, et al., *Appl. Phys. Lett.* 73 (1998) 3108.
- [6] G. Franzó, et al., *Appl. Phys. A* 69 (1999) 3.
- [7] P.G. Kik, et al., *J. Appl. Phys.* 88 (2000) 1992.
- [8] K. Watanabe, et al., *J. Appl. Phys.* 90 (2001).
- [9] S. Takeoka, et al., *Phys. Rev. B* 62 (2000) 16 820.
- [10] S. Gardelis, et al., *J. Appl. Phys.* 76 (1994) 5327.
- [11] D. Kovalev, et al., *Phys. Stat. Sol. B* 215 (1999) 871.



ELSEVIER

Physica B 308–310 (2001) 1125–1128

PHYSICA B

www.elsevier.com/locate/physb

Formation energy of vacancy in silicon determined by a new quenching method

N. Fukata^{a,*}, A. Kasuya^b, M. Suezawa^a

^a Institute for Materials Research, Tohoku University, Sendai 980-8577, Japan

^b Center for Interdisciplinary Research, Tohoku University, Sendai 980-8578, Japan

Abstract

By applying a new quenching method, we determined the formation energy of vacancies (V) in high-purity silicon. Specimens were sealed in quartz capsules together with H₂ gas and heated at high temperatures for 1 h followed by quenching in water. By this method, V are quenched in the form of complexes with hydrogen and the formation energy of V can be determined from the quenching temperature dependence of the intensity of the optical absorption peak due to the complexes. The formation energy of V in high-purity silicon was determined to be about 4.0 eV. This value is in good agreement with results of recent theoretical calculations. © 2001 Elsevier Science B.V. All rights reserved.

Keywords: Vacancies; Hydrogen; Optical absorption; Silicon

1. Introduction

It is increasingly important to clarify the properties of vacancies (V) existing at high temperatures in silicon. Secondary defects [1] such as voids and swirls which are formed during crystal growth by agglomerations of V are known to have harmful effects on device performance. To understand the agglomeration process and to prevent it, it is necessary to know the properties of V. From a basic-research point of view, determination of the V formation energy has been a critical issue since the 1960s. Theoretical estimation has been performed every time a new calculation technique has been developed [2]. Until now, two kinds of in situ methods, i.e., positron lifetime measurement and measurements of length and lattice parameter, have been applied to the study of point defects in silicon at high temperature. The results obtained by the former method, however, have been contradictory [3–5]. On the other hand, in the latter measurements [6], V formation energy in silicon was not

determined since the temperature dependence of the net concentration of native defects (V–I) was not simple. Consequently, the V formation energy in silicon has not been established experimentally.

To study point defects in thermal equilibrium in silicon, we applied a quenching method instead of the above-mentioned in situ methods. The quenching method itself is very useful and successful in the case of metals. It is, however, difficult to apply it to silicon since the migration energy of V in silicon is very small (<0.45 eV) [7,8] and V easily rises to the specimen surface or forms complexes. To quench isolated V, the quenching speed should be much faster than 10⁵ K/s, which is too high to prevent specimen breakage. To overcome this difficulty, we applied a new quenching method. In this method, quenching is performed in H₂ gas and therefore V are quenched as H–V complexes which are detected by optical absorption due to the localized vibrational mode of H included in the complexes [9–11].

In this paper, we report a new approach for determination of the V formation energy in high-purity silicon. The value determined by applying the new quenching method is in good agreement with the results of recent theoretical estimations.

*Corresponding author. Fax: +81-22-215-2041.

E-mail address: fukata@imr.tohoku.ac.jp (N. Fukata).

2. Experimental

A high-purity silicon (n-type, $[P] = 4 \times 10^{12} \text{ cm}^{-3}$) crystal was used for this study. The specimens were sealed in quartz capsules together with H_2 gas and heated at 1200–1390°C for 1 h, followed by quenching in water. Optical absorption measurements were performed at 4.6 K by a Fourier transform infrared spectrometer with a resolution of 0.25 cm^{-1} . The specimen thickness was about 12.5 mm. Isochronal annealing was carried out for 30 min at various temperatures in the range of 100–650°C.

3. Results and discussion

Representative optical absorption peaks observed after quenching are shown in Fig. 1. When specimens were quenched from 1300°C, optical absorption peaks due to H_2 [12] and H_2^+ [13] were observed at about 3618.6 (abbreviated 3619 hereafter) cm^{-1} and 1838.7 & 2062.1 cm^{-1} , respectively. When quenched from 1390°C, five peaks were observed at about 2131.5 (2132), 2191.8 (2192), 2202.7 (2203), 2220.8 (2221) and 2222.9 (2223) cm^{-1} , in addition to the above-mentioned peaks. The peak intensity due to H_2^+ absorption was much smaller than that due to H_2 absorption. The 2223 cm^{-1} peak has been assigned to the Si-H stretching mode of V saturated with four H atoms (VH_4) [14–16]. From this, it is definitely confirmed that V are quenched in the form of H–V complexes. In our experimental conditions, almost all V are quenched in the form of H–V complexes before the pair annihilation of V and self-interstitials (I) due to the following reasons: (1) the concentration of H ($\sim 10^{16} \text{ cm}^{-3}$) is much higher than

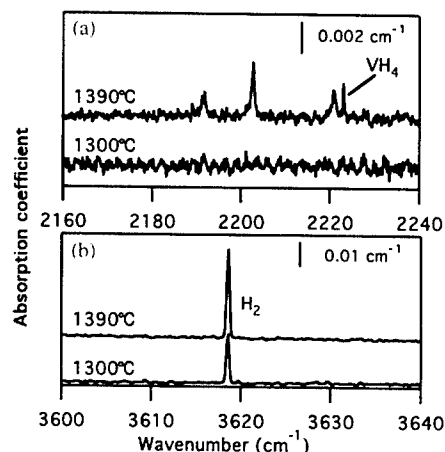


Fig. 1. (a,b) Optical absorption peaks observed in high-purity silicon heated at 1300°C and 1390°C for 1 h in an H_2 gas followed by quenching in water. The resolution was 0.25 cm^{-1} .

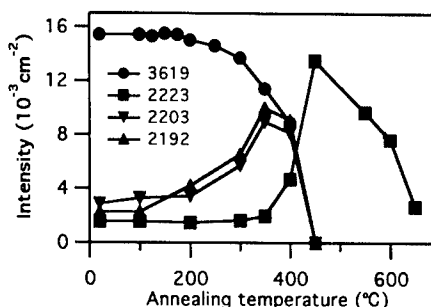


Fig. 2. The isochronal annealing temperature dependence of the integrated intensities of the 2192, 2203, 2223, and 3619 cm^{-1} peaks. The specimen was quenched from 1390°C.

those ($\sim 10^{14} \text{ cm}^{-3}$) of V and I, (2) the reaction between H and V is very fast and (3) the thermal stability of the complexes is also high.

Fig. 2 shows the isochronal annealing behaviors of various peaks. The 2223 cm^{-1} peak intensity increases with the decrease of the 2192, 2203, and 3619 cm^{-1} peak intensities at above 350°C. This shows that the 2192 and 2203 cm^{-1} complexes (termed the wavenumber complexes which are responsible for the optical absorption at the wavenumber) are transformed to the 2223 cm^{-1} complex by the reaction with H_2 . Incidentally, at temperatures between 100°C and 350°C, the 2192 and 2203 cm^{-1} peak intensities increase and the 3619 cm^{-1} peak intensity decreases. These results suggest the existence of “hidden” V–H complexes which could not be detected and furthermore suggest that these hidden complexes are transformed to the 2192 and 2203 cm^{-1} peaks. Based on the annealing behaviors of the 2192 and 2203 cm^{-1} peaks, our previous result regarding the quenching temperature dependence [10] and the result of Qi et al. [17], we have assigned the 2192 and 2203 cm^{-1} peaks to a VH_3 complex with different vibrational modes [11]. As for these peaks, another model has been proposed [18], namely, a V_2H_6 complex. This was proposed in a study of H-implantation. Contrary to H-implantation, local concentrations of V in quenched specimens seem to be very low. Hence, the probability of V_2H_6 complex formation is very small.

We interpret the annealing temperature dependence of the 2192, 2203, 3619, and 2223 cm^{-1} peaks by the following explanation assuming the hidden complexes to be VH and/or VH_2 . Indeed, we have been able to observe an optical absorption peak due to one of the hidden complexes, the VH_2 complex, in quenched silicon doped with carbon and H, where V concentration was higher than that in high-purity silicon [10]. The increase of the intensities of the 2192 and 2203 cm^{-1} peaks at temperatures between 100°C and 350°C is due to the formation of the VH_3 complex by reactions between a VH complex and an H_2 or a VH_2 complex and an H

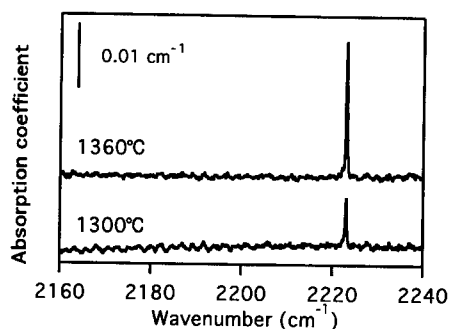


Fig. 3. The quenching temperature dependence of the 2223 cm^{-1} peak observed in specimens heated at 1300°C and 1360°C for 1 h in an H_2 gas followed by quenching in water and subsequent annealing at 450°C for 0.5 h in argon gas.

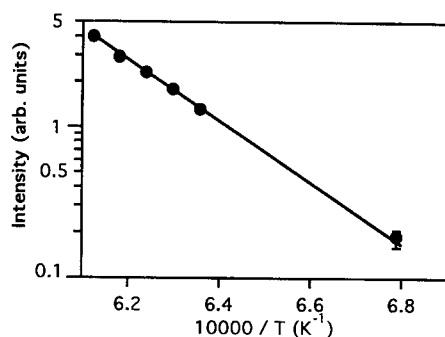


Fig. 4. The quenching temperature dependence of the integrated intensities of the 2223 cm^{-1} peak.

which is dissociated from an H_2 and an H_2^* . The decrease of the 2192 and 2203 cm^{-1} peaks intensities and the increase of the 2223 cm^{-1} peak intensity above 350°C are due to the formation of the VH_4 complex by a reaction between the VH_3 complex and an H_2 or the VH_3 complex and an H. In case of the former reaction, the diffusing H_2 divides into two H atoms when it reacts with the VH_3 complex and one H atom is released after the formation of the VH_4 complex, in the same way as the passivation of B by H_2 ($\text{B} + \text{H}_2 \rightarrow \text{BH} + \text{H}$). The released H atom again reacts with another VH_3 complex (the latter reaction). As already described, the 2221 cm^{-1} peak was also observed. The annealing behavior of this peak shows that the 2221 cm^{-1} complex is also transformed into the VH_4 complex. As for the 2132 cm^{-1} peak, there have been two reports that this peak is due to a defect including interstitial oxygen [17,19]. This peak disappeared after annealing at 450°C .

As shown in Fig. 2, almost all H–V complexes are transformed into only one complex, the VH_4 complex, by annealing at 450°C . Hence, it is considered that the V concentration is proportional to the peak intensity of the VH_4 complex. From this, it is possible to determine the

V formation energy of silicon without determining the V concentrations. Based on this, we annealed specimens quenched from various temperatures at 450°C and then determined the relative concentrations of V from the 2223 cm^{-1} peak intensities. As shown in Fig. 3, the 2223 cm^{-1} peak is sufficiently strong to determine the relative concentrations of the VH_4 complex and, consequently, the formation energy of V. From the Arrhenius plot of Fig. 4, the formation energy of V is determined to be about 4.0 eV . This value is in good agreement with recent theoretical estimations ($3\text{--}4.5\text{ eV}$) [2], confirming the usefulness of our new quenching method.

4. Conclusions

The formation energy of V in high-purity silicon was determined to be about 4.0 eV with our new quenching method. This value is in good agreement with recent theoretical values. This method opens up a new way to determine the formation energy of V in various silicon crystals. Application of this method to Czochralski-grown silicon is highly expected to clarify the void formation mechanism and to lead to new ways of reducing the void density.

Acknowledgements

This work was partly supported by the JSPS Research for the Future Program under the project “Ultimate Characterization Technique of SOI Wafers for Nano-scale LSI Devices” and a Grant-in-Aid for Scientific Research on Priority Areas A of ‘New Protium Function’ from the Ministry of Education, Science, Sports and Culture, Japan.

References

- [1] H.R. Huff, W. Bergholz, K. Sumino (Eds.), *Semicond. Silicon 1994*, Electrochemical Society, Pennington, NJ, 1994.
- [2] M.M. De Souza, E.M. Sankara Narayanan, *Defect Diffusion Forum* 153–155 (1998) 69.
- [3] S. Dannefaer, P. Mascher, D. Kerr, *Phys. Rev. Lett.* 56 (1986) 2195.
- [4] R. Würschum, W. Bauer, K. Maier, A. Seeger, H.E. Schaefer, *J. Phys. Condens. Matter* 1 (1989) SA33.
- [5] J. Throwe, T.C. Leung, B. Nielsen, H. Huomo, K.G. Lynn, *Phys. Rev. B* 40 (1989) 12037.
- [6] Y. Okada, *Phys. Rev. B* 41 (1990) 10741.
- [7] G.D. Watkins, in: F.A. Huntley (Ed.), *Lattice Defects in Semiconductors*, Inst. Phys. Conf. Ser., vol. 23, London, 1975, p. 1.

- [8] G.D. Watkins, J.R. Troxell, A.P. Chatterjee, in: J.H. Albany (Ed.), *Defects and Radiation Effects in Semiconductors*, Inst. Phys. Conf. Ser., Vol. 46, London, 1979, p. 16.
- [9] M. Suezawa, *Jpn. J. Appl. Phys.* 37 (1998) L259.
- [10] N. Fukata, M. Suezawa, *Physica B* 273–274 (1999) 247.
- [11] N. Fukata, M. Suezawa, *J. Appl. Phys.* 87 (2000) 8361.
- [12] R.E. Pritchard, M.J. Aswin, J.H. Tucker, R.C. Newman, *Phys. Rev. B* 57 (1998) 15048.
- [13] B. Bech Nielsen, L. Hoffmann, M. Budde, R. Jones, J. Goss, S. Öberg, *Mater. Sci. Forum* 196–201 (1995) 933.
- [14] B. Bech Nielsen, L. Hoffmann, M. Budde, *Mater. Sci. Eng. B* 36 (1996) 259.
- [15] M. Suezawa, *Jpn. J. Appl. Phys.* 38 (1999) L608.
- [16] B. Bech Nielsen, J. Olajos, H.G. Grimmeiss, *Phys. Rev. B* 39 (1989) 3330.
- [17] M.W. Qi, G.R. Bai, T.S. Shi, L.M. Xie, *Mater. Lett.* 3 (1985) 467.
- [18] M. Budde, B. Bech Nielsen, J.C. Keay, L.C. Feldman, *Physica B* 273–274 (1999) 208.
- [19] B. Pajot, B. Clerjaud, Z.-J. Xu, *Phys. Rev. B* 59 (1999) 7500.



ELSEVIER

Physica B 308–310 (2001) 1129–1132

PHYSICA B

www.elsevier.com/locate/physb

Configuration interaction applied to resonant states in semiconductors and semiconductor nanostructures

I.N. Yassievich^{a,*}, A. Blom^b, A.A. Prokofiev^a, M.A. Odnoblyudov^b, K.-A. Chao^b

^a A.7. Ioffe Physico-Technical Institute of RAS, Politechnicheskaya 26, 194021 St. Petersburg, Russia

^b Division of Solid State Theory, Lund University, S-223 62 Lund, Sweden

Abstract

A new method for calculating the parameters of resonant states as well as the probability of resonant scattering, capture and emission is developed. It is based on the configuration interaction method, which has been first introduced by Fano in the problem of autoionization of He. The method has been applied to resonant states induced by (i) defects in the barrier of GaAs/GaAlAs quantum well structure and (ii) acceptors in Ge under external stress. © 2001 Elsevier Science B.V. All rights reserved.

Keywords: Resonant states; Quantum well heterostructures; Defects in barriers; Strained germanium

0. Introduction

Resonant states have been studied very well in atomic physics. Semiconductors are other systems where resonant states play a significant role in physical processes. Such states appear, for example, in zero-gap semiconductors doped by shallow acceptors. The system of a special interest is uniaxially strained germanium where the generation of THz radiation has been achieved [1,2].

Here, we suggest a new method for calculating the parameters of resonant states and the probability of resonant scattering, capture and emission of carriers. The approach is based on the configuration interaction method, which was first introduced by Fano [3] in the problem of autoionization of He. The main idea is to choose two different Hamiltonians for the initial approximation: one for continuum states and the other for localized states. Then, wave functions are con-

structed in terms of scattering theory following to Dirac [4]. In a result, the energy shift and the width of resonant level as well as amplitude of resonant elastic scattering and capture probability by resonant states is calculated. The method is applied to resonant states induced (i) by impurities in the barrier of quantum wells and (ii) by shallow acceptors in Ge under stress.

1. Resonant states induced by localized states in barriers of QW

We will demonstrate the general idea by applying it to a system consisting of a quantum well (QW) and one impurity in the barrier. The full Hamiltonian is given by

$$\hat{H} = -\frac{\hbar^2}{2m}\Delta + V(z) + V_d(\mathbf{r} - \mathbf{r}_0), \quad (1.1)$$

where $V(z)$ is the QW potential and V_d is the defect potential (see Fig. 1).

As an initial approximation for the wave function of the localized state induced by the impurity we use the solution of the equation

$$\left[-\frac{\hbar^2}{2m}\Delta + V_d(\mathbf{r} - \mathbf{r}_0) \right] \varphi(\mathbf{r} - \mathbf{r}_0) = E_0 \varphi(\mathbf{r} - \mathbf{r}_0). \quad (1.2)$$

*Corresponding author. Tel.: +7-812-247-9974; fax: +7-812-247-1017.

E-mail address: irina.yassievich@pop.ioffe.rssi.ru (I.N. Yassievich).

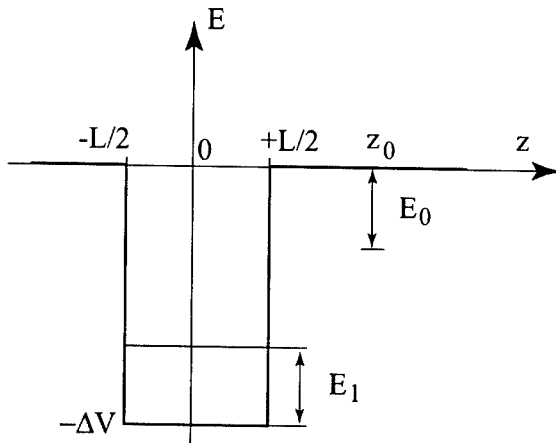


Fig. 1. A schematic of quantum well with introduced impurity level; E_0 is the binding energy of an impurity in the first approximation. E_1 is the space quantization energy.

The initial wave functions of continuum states $\psi_{\mathbf{k}}(\mathbf{r})$ satisfy the following equation:

$$\left[-\frac{\hbar^2}{2m}\Delta + V(z)\right]\psi_{\mathbf{k}}(\mathbf{r}) = E_{\mathbf{k}}\psi_{\mathbf{k}}(\mathbf{r}). \quad (1.3)$$

We are considering QW with one energy level only, so that

$$E_{\mathbf{k}} = -\Delta V + E_1 + \varepsilon_{\mathbf{k}}, \quad (1.4)$$

where ΔV is band offset at the QW boundary (see Fig. 1), E_1 is the space quantization level and $\varepsilon_{\mathbf{k}} = \hbar^2 k^2/2m$ is the kinetic energy of 2D motion. So we can write for $\psi_{\mathbf{k}}(\mathbf{r})$

$$\psi_{\mathbf{k}}(\mathbf{r}) = \frac{1}{\sqrt{S}} \phi(z) \exp(i\mathbf{k}\rho), \quad (1.5)$$

where S is a normalizing square.

Now we consider the problem of scattering of the in-plane moving carrier by the impurity in the barrier. Following Dirac [4], we construct the wave function in terms of a scattering theory in the following form:

$$\Psi_{\mathbf{k}}(\mathbf{r}) = \psi_{\mathbf{k}}(\mathbf{r}) + a_{\mathbf{k}} \phi(\mathbf{r} - \mathbf{r}_0) + \sum_{\mathbf{k}'} \frac{t_{\mathbf{k}\mathbf{k}'}}{\varepsilon_{\mathbf{k}} - \varepsilon_{\mathbf{k}'} + i\gamma} \psi_{\mathbf{k}'}(\mathbf{r}), \quad \gamma \rightarrow +0. \quad (1.6)$$

As long as the presence of one impurity does not perturb the continuum spectrum significantly, $\Psi_{\mathbf{k}}(\mathbf{r})$ corresponds to the energy $E_{\mathbf{k}}$. Solving the Schrodinger equation with the full Hamiltonian (1.1) for $\Psi_{\mathbf{k}}(\mathbf{r})$, we get

$$a_{\mathbf{k}} = \frac{1}{\sqrt{S}} \frac{V_{\mathbf{k}}}{E_{\mathbf{k}} - (E_0 + \Delta E) + i\Gamma/2}, \quad (1.7)$$

$$t_{\mathbf{k}\mathbf{k}'} = \frac{1}{S} \frac{V_{\mathbf{k}} Z_{\mathbf{k}'}^*}{E_{\mathbf{k}} - (E_0 + \Delta E) + i\Gamma/2}, \quad (1.8)$$

The energy shift ΔE and the width $\Gamma/2$ of the resonant level are given by

$$\Delta E = \delta - \frac{1}{(2\pi)^2} \int d^2 k' Z_{\mathbf{k}'}^* W_{\mathbf{k}'} + \frac{1}{(2\pi)^2} P \int d^2 k' \frac{Z_{\mathbf{k}'}^* V_{\mathbf{k}'}}{E_{\mathbf{k}} - E_{\mathbf{k}'}} \quad (1.9)$$

$$\frac{\Gamma}{2} = \frac{1}{4\pi} \int d^2 k' Z_{\mathbf{k}'}^* V_{\mathbf{k}'} \delta(E_{\mathbf{k}} - E_{\mathbf{k}'}) \quad (1.10)$$

Here the matrix elements

$$V_{\mathbf{k}} = \sqrt{S} \langle \phi | V_d | \psi_{\mathbf{k}} \rangle, \quad W_{\mathbf{k}} = \sqrt{S} \langle \phi | \psi_{\mathbf{k}} \rangle,$$

$$\delta = \langle \phi | V(z) | \phi \rangle, \quad Z_{\mathbf{k}} = \sqrt{S} \langle \phi | V(z) | \psi_{\mathbf{k}} \rangle,$$

$$V_{\mathbf{k}\mathbf{k}'} = S \langle \psi_{\mathbf{k}} | V_d | \psi_{\mathbf{k}'} \rangle. \quad (1.11)$$

are introduced. In solution (1.9–1.10) we have taken into account resonant scattering only, neglecting the impurity potential scattering.

The probability of resonant elastic scattering $W_{\mathbf{k}\mathbf{k}'}$ of 2D carriers and the capture probability $W_{\mathbf{k}r}$ are given by

$$W_{\mathbf{k}\mathbf{k}'} = \frac{2\pi}{\hbar} |t_{\mathbf{k}\mathbf{k}'}|^2 \delta(\varepsilon_{\mathbf{k}} - \varepsilon_{\mathbf{k}'}) = \frac{2\pi}{\hbar} \frac{1}{S^2} \frac{|V_{\mathbf{k}}|^2 |Z_{\mathbf{k}'}|^2}{(E_{\mathbf{k}} - E_0 - \Delta E)^2 + \Gamma^2/4} \delta(\varepsilon_{\mathbf{k}} - \varepsilon_{\mathbf{k}'}), \quad (1.12)$$

$$W_{\mathbf{k}r} = |a_{\mathbf{k}}|^2 = \frac{1}{S} \frac{|V_{\mathbf{k}}|^2}{(E_{\mathbf{k}} - E_0 - \Delta E)^2 + \Gamma^2/4}, \quad (1.13)$$

respectively. Both probabilities contain the same resonant denominator.

The resonant scattering should be introduced into the kinetic equation when one solves the problem of the 2D carriers distribution function under an electric field applied in the plane of the quantum well. This scattering affects significantly the distribution function $f_{\mathbf{k}}$ of hot carriers [5]. The population f_r of impurities in the barrier is connected with the distribution function $f_{\mathbf{k}}$ by relation [6]

$$f_r = \sum_{\mathbf{k}} W_{\mathbf{k}r} f_{\mathbf{k}}. \quad (1.14)$$

The position of resonance E_r can be found from the condition $E_r = E_0 + \Delta E(E_{\mathbf{k}} = E_r)$, where ΔE is determined by Eq. (1.9). The resonant width Γ is defined by Eq. (1.10) at $E_{\mathbf{k}} = E_r$.

We will apply the above-described approach to calculate the energy level position and the width of resonant states induced by deep donor centers which appear in the barrier region of $\text{Al}_{0.3}\text{Ga}_{0.7}\text{As}/\text{GaAs}/\text{Al}_{0.3}\text{Ga}_{0.7}\text{As}$ heterostructure doped with Si. These centers were extensively studied experimentally [7] because they heavily affect a performance of heterostructure based electronic and optoelectronic devices.

In doped $\text{Al}_x\text{Ga}_{1-x}\text{As}$ with Al content x larger than 0.27, more than a half of Si donor centers produce deep levels with binding energy $E_c \sim 155$ meV measured from the bottom of the Γ -valley [7]. The results of calculations of E_r and Γ as a function of the distance between defect and QW boundary are presented in Fig. 2 for different QW widths. We have used the band offset $\Delta V = 232$ meV, and effective masses 0.067 and 0.092 in QW and barrier regions, respectively.

2. Resonant acceptor states in uniaxially strained germanium

Germanium has a fourfold degenerate top of the valence band. When strained, it is split into two doubly degenerate states. The ground state of an acceptor shows the same behavior under uniaxial stress. At some critical value of the stress—when the splitting is larger than the acceptor binding energy—one of the split levels is shifted into the continuous spectrum of the other

valence subband and becomes resonant. An effective optical transitions between resonant and localized states of the same impurities can take place. If the electric field is strong enough, an electric impurity breakdown occurs and practically all localized impurity states become depopulated. Now, the capture and emission processes lead to an effective population of resonant states. This may cause an intracenter population inversion that is the basis for THz generation [1,2].

Resonant acceptor states were considered in [6] by using the Dirac approach. It requires choosing an initial approximation Hamiltonian which should give localized states overlapping with the continuous spectrum. The approach in [6] applies for large stresses and for small quasimomenta but it fails for the region of the continuous spectrum where resonant states are present.

Using our new approach, we consider the ground resonant state induced by shallow acceptors in uniaxially strained p-Ge. As the initial approximation for localized states we choose the eigenfunctions of diagonal part of the Luttinger Hamiltonian with Coulomb

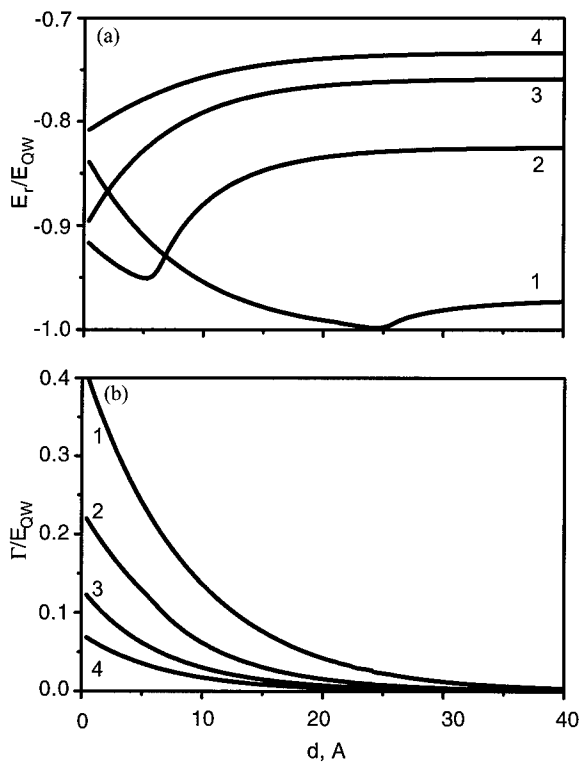


Fig. 2. The resonant position (a) and the resonant width (b) normalized by the energies of the first space quantization level as a function of the distance d between impurity and QW for the case of deep donor in $\text{Al}_{0.3}\text{Ga}_{0.7}\text{As}/\text{GaAs}/\text{Al}_{0.3}\text{Ga}_{0.7}\text{As}$ heterostructure. (1) $L = 5$ nm, $E_{QW} = 157.7$ meV; (2) $L = 7.5$ nm, $E_{QW} = 185.6$ meV; (3) $L = 10$ nm, $E_{QW} = 201.8$ meV; (4) $L = 12.5$ nm, $E_{QW} = 208.8$ meV.

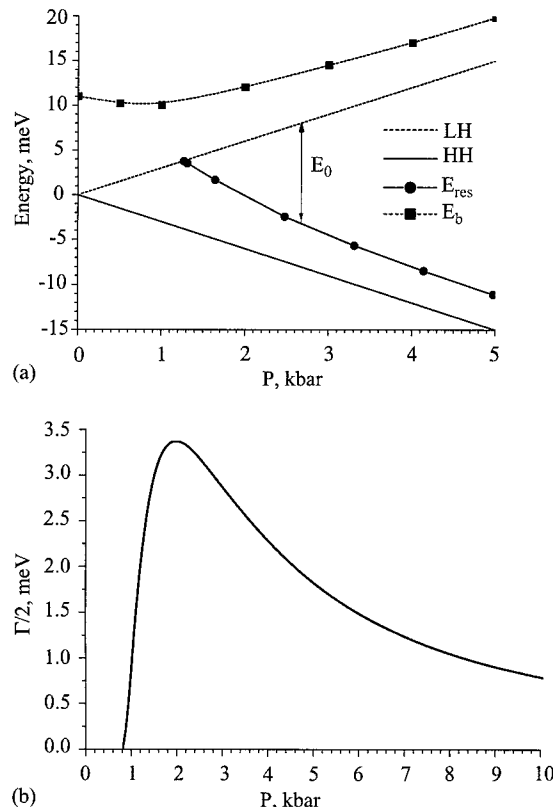


Fig. 3. The position (a) and width (b) of resonant state as a function of uniaxial stress applied to Ge in [001] direction. E_{res} is resonance position and E_b is ground localized state.

potential taken into account. For continuum states we use wave functions $\psi_{\mathbf{k}}^{\pm 1/2}(\mathbf{r})$ of free holes in cylindrical approximation for the Luttinger Hamiltonian. Following the procedure from the first section we are looking for wave functions in the form:

$$\begin{aligned} \Psi_{\mathbf{k}}^{\pm 1/2} = & \psi_{\mathbf{k}}^{\pm 1/2} + a_{\mathbf{k}}^{\pm 1/2, -3/2} \varphi^{-3/2}(\mathbf{r}) \\ & + a_{\mathbf{k}}^{\pm 1/2, -3/2} \varphi^{-3/2}(\mathbf{r}) + \sum_{\mathbf{k}'} \frac{t_{\mathbf{k}\mathbf{k}'}^{\pm 1/2, -1/2}}{\varepsilon_{\mathbf{k}} - \varepsilon_{\mathbf{k}'} + i\gamma} \psi_{\mathbf{k}'}^{\pm 1/2}(\mathbf{r}) \\ & + \sum_{\mathbf{k}'} \frac{t_{\mathbf{k}\mathbf{k}'}^{\pm 1/2, -1/2}}{\varepsilon_{\mathbf{k}} - \varepsilon_{\mathbf{k}'} + i\gamma} \psi_{\mathbf{k}'}^{\mp 1/2}(\mathbf{r}) \end{aligned} \quad (1.15)$$

The capture probability of holes with momentum projection $+1/2$, $W_{\mathbf{k}\mathbf{r}}$ and the probability of elastic resonant scattering $W_{\mathbf{k}\mathbf{k}'}$ are defined now by

$$W_{\mathbf{k}\mathbf{r}} = \left| a_{\mathbf{k}}^{-1/2, -3/2} \right|^2 + \left| a_{\mathbf{k}}^{+1/2, -3/2} \right|^2, \quad (1.16)$$

$$W_{\mathbf{k}\mathbf{k}'} = \frac{2\pi}{\hbar} \left(\left| t_{\mathbf{k}\mathbf{k}'}^{+1/2, -1/2} \right|^2 + \left| t_{\mathbf{k}\mathbf{k}'}^{-1/2, -1/2} \right|^2 \right) \delta(\varepsilon_{\mathbf{k}} - \varepsilon_{\mathbf{k}'}). \quad (1.17)$$

The expressions for the case of momentum projection $-1/2$ are similar.

The results of calculations of the resonant level shift and level width as function of stress applied along $[001]$ direction are given in Fig. 3.

3. Conclusion

The approach for calculation of resonant state energy and lifetime as well as probabilities of resonant capture

and elastic scattering are suggested and applied to resonant states induced by deep donors in the barrier of $\text{Al}_{0.3}\text{Ga}_{0.7}\text{As}/\text{GaAs}/\text{Al}_{0.3}\text{Ga}_{0.7}\text{As}$ QW heterostructure as well as by shallow acceptors in Ge under stress.

Acknowledgements

This work has been partially supported by the RFBR (grants 01-02-16265, 00-15-96768, 00-02-17429, 01-02-02011), The Swedish Foundation for International Cooperation in Research and Higher Education (contract 99/527 (00)) and NorFA Grant.

References

- [1] I.V. Altukhov, E.G. Chirkova, M.S. Kagan, K.A. Korolev, V.P. Sinis, M.A. Odnoblyudov, I.N. Yassievich, JETPh. 88 (1999) 51.
- [2] Yu.P. Gousev, I.V. Altukhov, K.A. Korolev, V.P. Sinis, M.S. Kagan, E.E. Haller, M.A. Odnoblyudov, I.N. Yassievich, K.-A. Chao, Appl. Phys. Lett. 75 (1999) 757.
- [3] U. Fano, Phys. Rev. 124 (1961) 1866.
- [4] P.A.M. Dirac, Principles of Quantum Mechanics, 4th Edition, Clarendon Press, Oxford, 1981.
- [5] A.A. Prokofiev, M.A. Odnoblyudov, I.N. Yassievich, Semicond. 35 (2001) 586.
- [6] M.A. Odnoblyudov, I.N. Yassievich, V.M. Chistyakov, K.-A. Chao, Phys. Rev. B 62 (2000) 2486.
- [7] E.F. Schubert, K. Ploog, Phys. Rev. B 30 (1984) 7021.



ELSEVIER

Physica B 308–310 (2001) 1133–1136

PHYSICA B

www.elsevier.com/locate/physb

Defect diagnostics in multicrystalline silicon using scanning techniques

I. Tarasov^a, S. Ostapenko^{a,*}, W. Seifert^b, M. Kittler^b, J.P. Kaleis^c

^aCenter for Microelectronics Research, University of South Florida, 4202 E Fowler Avenue, Tampa, FL 33620, USA

^bIHP, Frankfurt, Oder, Germany

^cASE Americas, Billerica, MA, USA

Abstract

During crystal growing, many dislocations are created in the multicrystalline silicon (mc-Si) material. Presence of these dislocations significantly changes the electrical properties of mc-Si wafer. We report here on photoluminescence (PL) and electron beam induced current (EBIC) mapping of recombination centers in low recombination regions limiting a performance of the mc-Si solar cells. By comparing PL mapping with the distribution of dislocations, we present experimental evidence that the 0.8 eV band corresponds to electrically active dislocation networks. At low temperature, a characteristic quartet of the dislocation D-lines was observed. One of these dislocation lines (D1) can be tracked as temperature increased and linked to the “defect” band. We also found using temperature dependent EBIC correlated with PL mapping that intense defect band luminescence originates from dislocation with low level of impurity contamination. © 2001 Elsevier Science B.V. All rights reserved.

Keywords: Silicon; Dislocations; Photoluminescence; Lifetime; EBIC

1. Introduction

Vigorous growth in the photovoltaic market over the past decade has been predominantly driven by advances in crystalline silicon technology. Multicrystalline silicon (mc-Si), which can be produced by ribbon or block-casting techniques, can meet both a low-cost production and a high efficiency requirement for solar cells. Since mc-Si wafers are inhomogeneous, this motivated development of mapping techniques to track recombination activity of defects across entire wafer and solar cell. We report here on photoluminescence (PL) and electron beam induced current (EBIC) mapping of recombination centers in high recombination regions of mc-Si wafers. These regions limit solar cell performance, and their monitoring, characterization, and reduction is a primary goal in the search for approaches to achieve high cell conversion efficiencies. We present experimen-

tal evidence that high recombination regions are characterized by an intense “defect” PL band, associated with contaminated dislocations, which are electrically active at room temperature.

2. Samples and methods

Materials used in this study were boron doped mc-Si wafers grown by Edge-defined Film-fed Growth (EFG) technique. The photoluminescence mapping and PL spectra were analyzed using SPEX-500 M grating spectrometer coupled to a liquid nitrogen cooled Ge detector. The PL signal was processed using a conventional lock-in technique. The PL spectra were corrected to the spectral response of the optical setup. A 800 nm AlGaAs laser diode operating in a pulse mode with a peak power up to 140 mW was used. Photoluminescence mapping at room temperature was performed by placing a mc-Si wafer on a computer controlled *X-Z* moving stage. Spatial resolution in PL maps was limited by the diameter of the laser spot, which was approximately

*Corresponding author. Tel.: +1-813-974-2031; fax: +1-813-974-3610.

E-mail address: ostapenk@eng.usf.edu (S. Ostapenko).

0.5 mm. Temperature study was carried out between 4.2 and 300 K in the variable temperature liquid helium cryostat.

3. Experimental results

Inhomogeneity in electronic properties of mc-Si wafers gives rise to distinct high and low lifetime regions. In the regions with low recombination activity and high value of the lifetime, the PL spectrum at room temperature consists of the band-to-band line with maximum at 1.09 eV. This line is caused by the phonon-assisted recombination of bound and non-bound free electrons and free holes [1]. On the contrary, regions with enhanced recombination activity and reduced minority carrier lifetime exhibit also an intensive “defect” PL band with the maximum at about 0.8 eV (Fig. 1, spectrum 1). The defect band maximum varies between 0.76 and 0.8 eV from point to point on the same wafer. Recombination properties of the 0.8 eV band were described previously [2].

The intensity of the defect band is highly inhomogeneous across the wafer. In Fig. 2, we present room temperature PL maps of band-to-band intensity (a) and defect band intensity (b). The dark areas on PL maps correspond to the low PL intensity while the light areas represent the high PL intensity. We observe a distinctive reverse correlation of two maps, i.e. regions with high

band-to-band PL show negligible defect luminescence, and opposite, strong defect band is observed in regions with reduced band-to-band peak.

We reported previously [2,3] that the topography of band-to-band PL distribution correlates with distribution of minority carrier lifetime across the wafer. Fig. 3(b) shows both band-to-band PL and diffusion length line scans. We statistically proved using mapping technique that the band-to-band PL positively correlates with minority carrier lifetime.

To assess a possible origin of the defect band luminescence, we performed measurements of PL spectra at low temperature. Three PL spectra at different temperatures measured at the same spot on an EFG wafer are compared in Fig. 1. At room temperature, the defect band is centered at 0.77 eV. As temperature is lowered, the defect peak shifts to higher energy corresponding to the temperature dependence of Si band gap. At 77 K, rich spectral features are now observed at energies below 1.05 eV. Two bands appear at 0.95 and 1.00 eV. At lower energies, the PL spectrum shows the defect maximum at 0.80 eV with a barely resolved additional band as a shoulder. This band was identified with defect maximum at room temperature. At 4.2 K (Fig. 1, spectrum 3), the band-to-band emission is replaced with exciton lines dominated by the TO-phonon replica of the boron bound exciton at 1.093 eV. Along with the increasing intensity between 77 and 4.2 K, the PL bands below 1.05 eV are now much narrower (~ 10 meV) and exhibit additional sub-bands. The only exception is the 0.8 eV band, which retains a large half-width of ~ 60 meV down to 4.2 K.

We performed a numerical deconvolution of the 77 K PL spectrum in the range of 0.72–1.05 eV, and found that the entire spectrum can be satisfactory fit by four Gaussian peaks, D1'–D4' [2]. A set of four similar PL lines, known as D1–D4, with very close energies to those seen here, was previously observed and studied in detail in plastically deformed Cz and float-zone Si single crystals [4]. These bands are attributed to dislocations. The range of dislocation density, measured in low lifetime regions of our mc-Si wafers, ($1\text{--}8 \times 10^6 \text{ cm}^{-2}$) is in the lower end of the range of dislocation densities reported for the plastically deformed Si exhibiting the dislocation D-lines.

To check further an assumption on dislocation origin of the defect band, we compared the band-to-band and defect band PL distributions in EFG wafer with recombination activity distribution measured on the same wafer by EBIC (Fig. 2). It should be pointed that PL mapping and EBIC mapping have different spatial resolutions. The black areas on EBIC maps are related to the region with high recombination activity of dislocations. In this correlation EBIC/PL study, it became clear that the regions of low band-to-band and high defect PL are caused by dislocations.

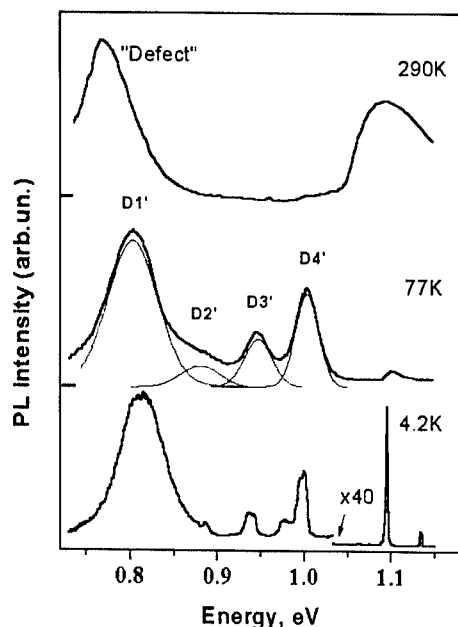


Fig. 1. PL spectra of an EFG wafer at different temperatures. The spectrum at 77 K is deconvoluted numerically to resolve four individual D1'–D4' Gaussian peaks.

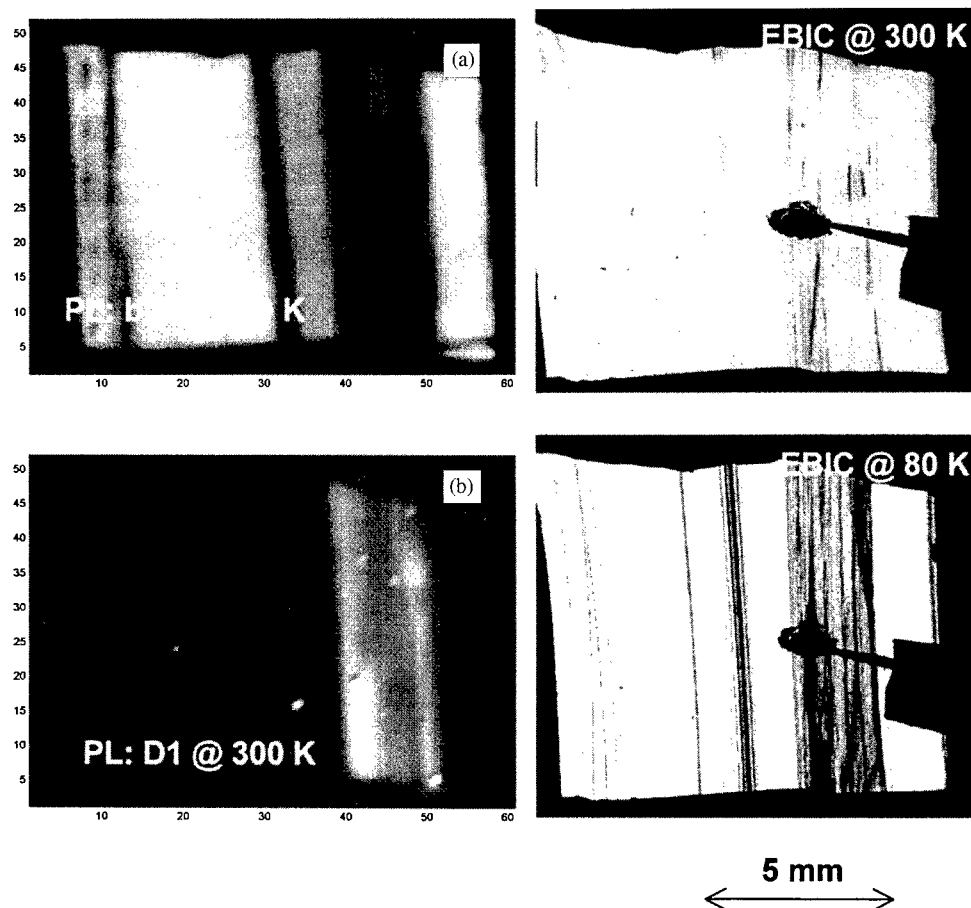


Fig. 2. Room temperature band-to-band (a), defect band (b) PL maps (on the left) and high resolution EBIC maps at room temperature and 80 K (on the right) in EFG wafer.

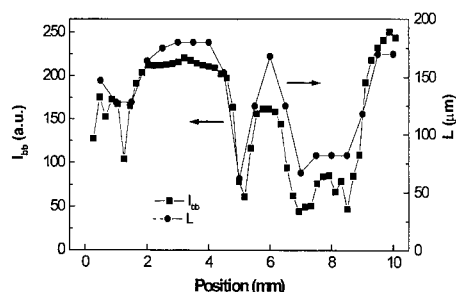


Fig. 3. Line scans of the defect concentration [1] expressed as the ratio of defect PL to band-to-band PL (1) and dislocation density (2) in an as-grown EFG wafer. A vertical arrow indicates the region with a high dislocation density and low defect concentration.

We conclude that the defect PL is associated with dislocations with moderate degree of impurity contamination. In fact, recombination activity of dislocations strongly depends on both the metal impurity contam-

ination and temperature. According to the model proposed in Ref. [5], a moderate contamination level is exhibited as reduction of EBIC contrast at high temperature compared to 77 K EBIC contrast. This is exactly a case of 0.8 eV PL band defects, as illustrated in Fig. 2. If the contamination level is too low ("clear" dislocation) or too high (dislocation decorated by metal silicate precipitates) the defect PL band luminescence is vanished. However, a relatively low contamination level of dislocations, in the order of 10 impurity atoms per micron of the dislocation length produces distinguishable defect band luminescence.

This study demonstrates a utility of the spectroscopic PL mapping to monitor electrically active dislocations at various contamination levels of precipitated defects.

Acknowledgements

This work was supported in part by NREL subcontract ACQ-9-29639-03.

References

- [1] V. Alex, S. Finkbeiner, J. Weber, J. Appl. Phys. 79 (1996) 6943.
- [2] S. Ostapenko, I. Tarasov, J.P. Kalejs, C. Haessler, E.-U. Reisner, Semicond. Sci. Technol. 15 (2000) 840.
- [3] I. Tarasov, et al., Physica B 273–274 (1999) 549.
- [4] R. Sauer, et al., Appl. Phys. A 36 (1985) 1.
- [5] V. Kveder, M. Kittler, W. Schröter, Phys. Rev. B 63 (2001) 115208.



ELSEVIER

Physica B 308–310 (2001) 1137–1140

PHYSICA B

www.elsevier.com/locate/physb

Resonance ultrasonic diagnostics of defects in full-size silicon wafers

A. Belyaev, S. Ostapenko*

Center for Microelectronics Research, University of South Florida, 4202 E Fowler Avenue, Tampa, FL 33620, USA

Abstract

A resonance acoustic effect was observed recently in full-size 200 mm Cz-Si wafers and applied to characterize as-grown and process-induced defects. Ultrasonic vibrations can be excited into wafers using an external ultrasonic transducer and their amplitude is recorded using a scanning air-coupled acoustic probe operated in a non-contact mode. By sweeping driving frequency, f , of the transducer, we observed an amplification of a specific acoustic mode referred to as 'whistle'. In this paper, we performed theoretical modeling of the whistle which allowed in attributing this mode to resonant flexural vibrations in a thin circular plate. We calculated normal frequencies of the flexural vibrations of a circular plate of radius ρ in the case of the free edge. The model gives an excellent fit to experimental data with regard to whistle spatial distribution. The results of calculation allow the evaluation of resonance acoustic effect in wafers of different geometries employed in the industry. © 2001 Elsevier Science B.V. All rights reserved.

Keywords: Cz-Si; Ultrasonic; Vibrations

1. Introduction

The elastic stress in Cz-Si wafers and thin films can be caused by point defects and their complexes. For instance, thermal oxide on Cz-Si creates a residual stress of a few hundreds of MPa in the films due to a difference in thermal expansion of the substrate and oxide, which can be detrimental for gate-oxide integrity and reliability of CMOS devices. Residual elastic stress can also be harmful to silicon substrates, especially, with scaling of wafer diameter up to 300 mm. On the other hand, the stress can be a driving force to various types of defect reactions, such as precipitation of residual impurities deteriorating the electronic quality of material. Therefore, a problem of non-contact and non-destructive monitoring of residual stress/strain in as-grown, oxidized and epitaxial (Cz-Si) wafers is a current issue for microelectronics. Resonance acoustic diagnostics

was developed and employed recently to characterize internal stress in full-size 200 mm Cz-Si wafers [1]. We report here the theoretical analysis of the resonance acoustic effect and compare calculation results with experimental data.

2. Experiment

Ultrasonic vibrations were generated into single-side polished Cz-Si wafers of 200 mm diameter using circular resonance piezoelectric transducer pressed by vacuum against the backside of the wafer [1]. These vibrations are propagated in the wafer beyond the transducer and form standing waves at specific frequencies. The amplitude of the standing wave is measured using an air-coupled acoustic probe. Fig. 1 demonstrates a frequency curve of the acoustic oscillations of Cz-Si wafer measured at probe location of 1 mm above the wafer front surface. By tuning driving frequency, f , of the transducer, we observed amplification of a specific acoustic mode referred to as 'whistle'. By changing the ac driving voltage we

*Corresponding author. Tel.: +1-813-974-2031; fax: +1-813-974-3610.

E-mail address: ostapenk@eng.usf.edu (S. Ostapenko).

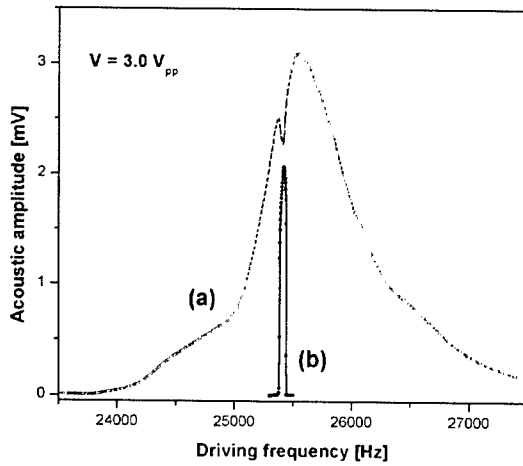


Fig. 1. Frequency scans of the transducer (a) and the whistle mode (b). The later is recorded with lock-in tuned to the half of driving frequency.

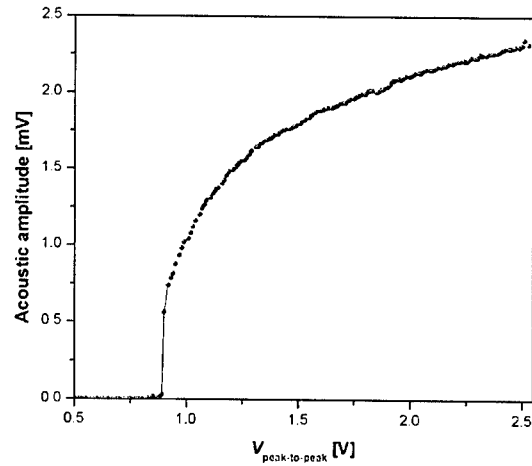


Fig. 2. Amplitude dependence of the whistle mode versus the voltage applied to transducer.

measured an amplitude scan of the acoustic signal. The amplitude scan shows a clear threshold as illustrated in Fig. 2, which is dependent on wafer history [2]. The characteristics of the whistle allow the attribution of this mode to resonance flexural vibrations in a thin circular plate.

3. Modeling

We consider flexural vibrations in a thin circular plate with thickness h and radius ρ ($h \ll \rho$), which is a good model of a full-size 200 mm Cz-Si wafer. The equation for flexural vibrations can be represented as follows:

$$(\nabla^2 \nabla^2 - \beta^4)u = 0, \quad (1)$$

where ∇^2 is the Laplace operator applied to u , and $\beta^4 = \omega^2 \rho^4 h \xi / D$ is a dimensionless variable which depends on vibration frequency (ω), thickness and diameter of the wafer and flexural rigidity $D = Eh^2/12(1 - \nu^2)$, where E and ν , here, are Young's modulus and Poisson coefficient, respectively, and ξ is a density of material [3]. For flexural vibrations, we look for the solutions of the Eq. (1) in the form

$$U(\rho, \varphi) = u(\rho)e^{in\varphi}, \quad (2)$$

where u is a normal displacement of a plate from equilibrium and ρ and φ are radial and polar coordinates with respect to the wafer center. Using the method of the separation of variables, one can obtain the general solution of Eq. (1) in the form

$$u(\rho, \varphi) = [aJ_n(\beta\rho) + bI_n(\beta\rho)] \begin{cases} \sin n\varphi \\ \cos n\varphi \end{cases}, \quad (3)$$

where J_n are Bessel functions and I_n are modified Bessel functions of the order n , respectively. Zero value of elastic stress components at the wafer edge ($\rho = 1$) leads to the free-edge boundary conditions

$$\begin{aligned} \left[\frac{2(\lambda + \mu)}{\lambda + 2\mu} \frac{\partial}{\partial \rho} \nabla^2 u + \frac{\partial^3 u}{\partial \rho \partial \varphi^2} - \frac{\partial^2 u}{\partial \varphi^2} \right] \bigg|_{\rho=1} &= 0, \\ \left(\frac{\lambda}{\lambda + 2\mu} \nabla^2 u + \frac{\partial^2 u}{\partial \rho^2} \right) \bigg|_{\rho=1} &= 0, \end{aligned} \quad (4)$$

where λ and μ are Lamé's constants. All the above, allow the calculation of the deformation pattern of thin silicon plate, which performs flexural vibrations. Figs. 3a and b show a correlation between experimental and calculated maps of the acoustic energy, which is proportional to the square of the acoustic displacement.

In the experiment with (100) oriented 200 mm Cz-Si wafers we observe high order flexural vibrations with $n = 20$ (Fig. 3a). This number is a consequence of four-fold symmetry of the (100) crystal plane, which permits $n = 4m$ ($m = 1, 2, 3, \dots$) values of the index n . Note that ρ is multiplied by a scale factor of 100, in order to raise it over to the experimental wafer's size. There is a clear similarity between the experimental and theoretical maps, especially at wafer periphery. One should mention that the additional maxima in the internal part of the experimental acoustic map are probably caused by a superposition of the major Bessel function of $n = 20$ with lower order solutions of Eq. (1), such as $n = 12, 16$, etc. satisfying $n = 4m$ criterion. What is more important is that, according to our calculations, the lower order solutions shift the maximum of the radial distribution toward the wafer center, as illustrated by arrows in Fig. 4a.

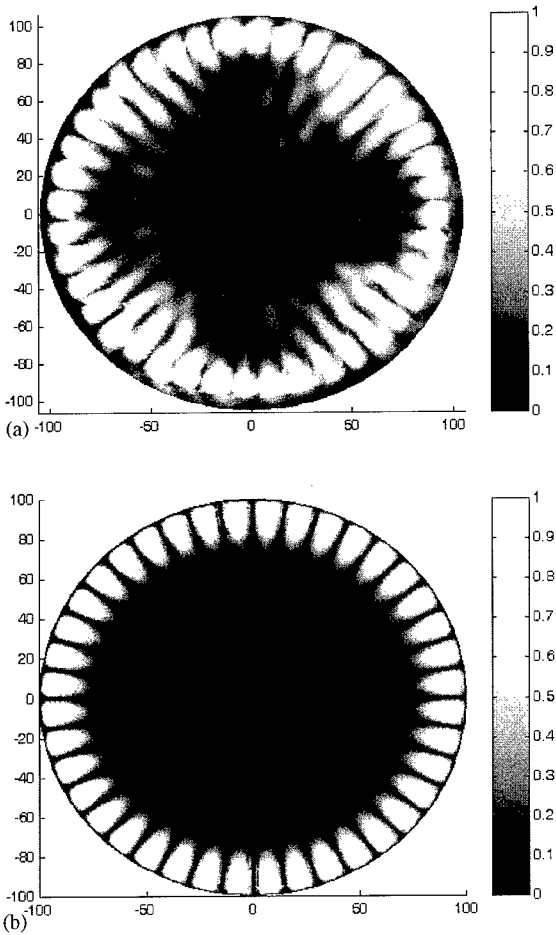


Fig. 3. (a)—acoustical map of the ‘whistle’ measured on 200 mm Cz-Si wafer at $\omega = 12.7$ kHz, $V = 2.8$ Vpp. (b)—theoretical map of the high-order flexural vibrations of thin elastic plate with $n = 20$.

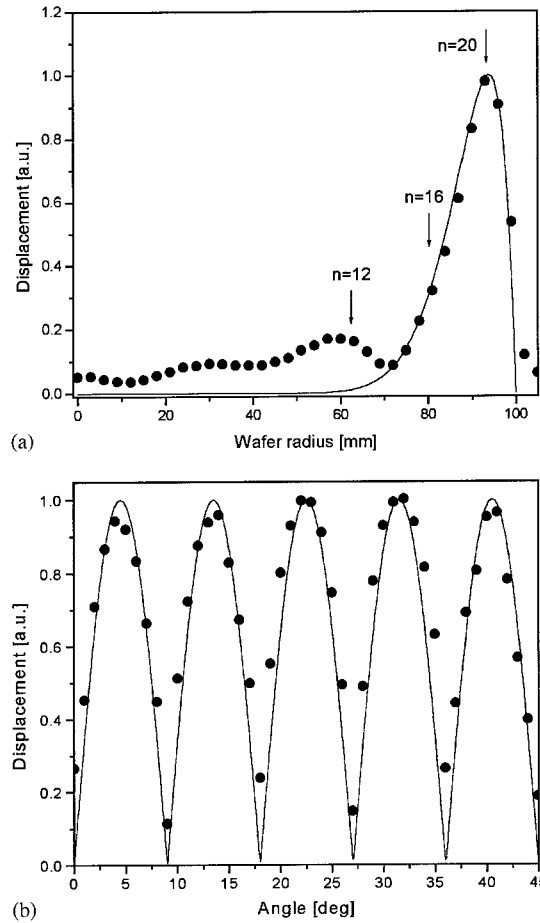


Fig. 4. Experimental distribution of the acoustic power (points) and theoretical fit (solid line) for (a) radial and (b) angular dependencies. Arrows on the radial scan indicate the positions of resonance flexural modes of different orders.

By separating variables in Eq. (1), we fit experimental data for radial and angular part individually. An illustrative example is presented in Figs. 4a and b. The angular curve fits the data with $\sin^2 \varphi$ function. The radial curve shows a very good fit for the main maximum located at the wafer periphery. We notice that the experimental radial distribution of the flexural vibrations (Fig. 4a), shows additional lower index Bessel modes ($n = 12$) as we discussed earlier. Substituting (3) into (4) one can obtain the system of linear equations for coefficients a and b .

$$\begin{pmatrix} -\beta^3 J'_n(\beta) + (1-\nu)n^2[J_n(\beta) - \beta J'_n(\beta)] & \beta^3 I'_n(\beta) + (1-\nu)n^2[I_n(\beta) - \beta I'_n(\beta)] \\ -\beta^2 J_n(\beta) + (1-\nu)[n^2 J_n(\beta) - \beta J'_n(\beta)] & \beta^2 I_n(\beta) + (1-\nu)[n^2 I_n(\beta) - \beta I'_n(\beta)] \end{pmatrix} \times \begin{pmatrix} a \\ b \end{pmatrix} = \begin{pmatrix} 0 \\ 0 \end{pmatrix}. \quad (5)$$

The frequency equation can be expressed by the condition that the determinant of the system

vanishes. The normal (resonance) frequencies of flexural vibrations can be calculated using the equation [3]

$$\omega_{nm} = \frac{\beta_{nm}^2 h}{\rho^2} \sqrt{\frac{\mu}{6(1-\nu)\xi}}. \quad (6)$$

Fig. 5 illustrates the three sets of normal frequencies versus an order of Bessel's function for wafer diameters 150, 200, and 300 mm, which are mainly used in microelectronics. The dashed line indicates the resonant frequency observed in our experiment

with 200 mm Cz-Si wafers. It shows that in the case of 200 mm diameter, one should expect flexural

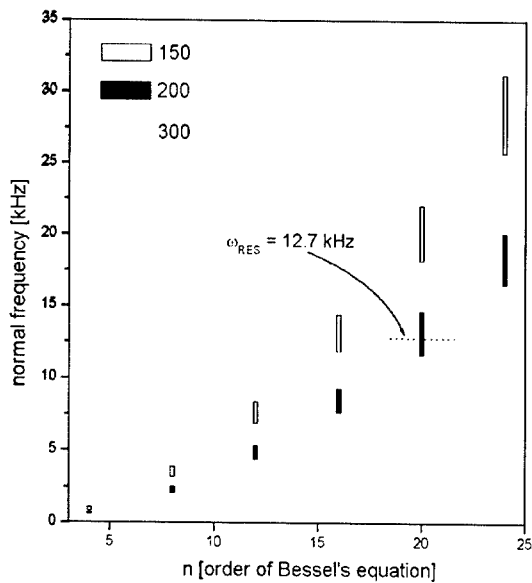


Fig. 5. Normal frequencies of the high-order flexural vibrations in silicon wafers of three diameters. The bars represent the effect on the frequencies the anisotropy of elastic modulus in silicon in $\langle 100 \rangle$, $\langle 111 \rangle$ and $\langle 110 \rangle$.

vibrations at the wafer periphery with $n = 20$. The bars at each Bessel mode n represent anisotropy of the elastic modulus in Si single crystals along $\langle 100 \rangle$, $\langle 110 \rangle$ and $\langle 111 \rangle$ crystallographic directions. The results of this modeling allow the prediction of a resonance acoustic effect in wafers of different geometry, crystallography, and other chemical origin employed by the electronic industry (GaAs, InP).

References

- [1] S. Ostapenko, I. Tarasov, Appl. Phys. Lett. 76 (2000) 2217.
- [2] A. Belyaev, V. Kochelap, I. Tarasov, S. Ostapenko, Characterization and Metrology for ULSI Technology, International Conference, 2000, pp. 207–211.
- [3] K.C. Le, Vibrations of Shells and Rods, Springer, Berlin, 1999, pp. 89–95.



ELSEVIER

Physica B 308–310 (2001) 1141–1144

PHYSICA B

www.elsevier.com/locate/physb

A new approach to analysis of mosaic structure peculiarities of gallium nitride epilayers

A.G. Kolmakov^a, V.V. Emtsev^b, W.V. Lundin^b, V.V. Ratnikov^b,
N.M. Shmidt^{b,*}, A.N. Titkov^b, A.S. Usikov^b

^a *Institute of Metallurgy, Moscow 117911, Russia*

^b *Ioffe Physico-Technical Institute, 26 Polytekhnicheskaya Str. 26, St. Petersburg 19401, Russia*

Abstract

The successful results of multifractal analysis application to a quantitative description of mosaic structure peculiarities, which are typical for GaN epitaxial layer with hexagonal modification grown on (0001) sapphire substrates, have been obtained. A linear dependence of mobility on the multifractal parameters of surface topology of the mosaic structure (the self-organization degree and the disruption of the local symmetry) has been observed in GaN layers. © 2001 Elsevier Science B.V. All rights reserved.

Keywords: Multifractal analysis; Mosaic structure; GaN

1. Introduction

A mosaic structure is typical for GaN epitaxial layers of the hexagonal modification. However, the data on the influence of mosaic structure peculiarities on electric characteristics of the layers and device structures are insufficient. In most publications, the peculiarities are analysed at a local level (from transmission microscopy), at an integral level (from X-ray diffraction), or at a qualitative level using atomic-force microscopy (AFM). The results obtained by these techniques are unlikely to reveal important peculiarities of the mosaic structure completely. Perhaps, due to this fact, a correlation between structural properties and electrical characteristics of III-nitrides was not established.

It has been well known that self-organization of the non-equilibrium defect system in the form of a mosaic structure occupies the highest stage of the rank scale for defect classification in solids. Similar objects, in particular, with the mosaic structure, have been studied well

in metallurgy. It was demonstrated that investigations of the surface topology of the objects with the complicated structure followed by the multifractal analysis (MFA) treatment allow the properties of the complex objects to be characterized quantitatively as a whole [1–4]. These properties are the disruption of both general and local symmetry, and the self-organization degree [1,2].

From these facts, the following aims have been formulated in the present paper: (1) To clarify a role of the mosaic structure in forming the characteristics of both the GaN layers and of the devices based on these layers; and (2) along with conventional experimental techniques, to apply the MFA and to clarify the correlation of the multifractal characteristics with electrical properties of the GaN layers, in particular, with the mobility of charge carriers.

2. Experiment

GaN epitaxial layers of the hexagonal modification with a specular surface, which were grown by metal-organic chemical vapour deposition on (0001) sapphire substrates at a pressure of 200 mbar, were investigated.

*Corresponding author. Tel.: +7-812-247-9193; fax: +7-812-247-1017.

E-mail address: natalia.shmidt@pop.ioffe.rssi.ru (N.M. Shmidt).

Table 1
Characteristics of the GaN epitaxial layers

	Group					
	I	II	III	IV	V	VI
<i>X-ray data</i>						
Domain twist angle	20	6'	18'	20'	25'	20'
Average domain size (nm)	2000	480	500	800	800	500
<i>AFM data</i>						
Surface domain size (nm)	500–1500	200–300	200–500	200–500	300–1500	300–500
Roughness (nm)	2.0	0.4	0.5	0.6	1.0	0.8
Electron mobility at room temperature ($\text{cm}^2 \text{V}^{-1} \text{s}^{-1}$)	55	600	400	30	25	260
Renyi dimension (D_q)	1.62	1.49	1.55	1.63	1.64	1.57

The 3–4 μm thick layers were of n-type conductivity with a carrier concentration of $(1\text{--}2) \times 10^{17} \text{cm}^{-3}$ [5].

Six groups of layers were chosen with different mobilities and with different volume structure properties obtained from the X-ray diffraction [6]. All layers except Group II had the dislocation density of about 10^{10}cm^{-2} . It was one order of magnitude less in II Group layers. The characteristics of these groups are presented in Table 1.

The AFM data allowed both the roughness and the average lateral size of surface domains to be estimated. The AFM data were treated using the MFA. It can ascribe to the structure the quantitative parameters, characterizing the structure as a whole, in addition to the conventional methods of description. In particular, an original technique has been developed by a number of researchers, which involves multifractal parameterization of plane structures on the basis of a new informational-theoretical interpretation of multifractal formalism [1,4] and which allows the degree of order index (the disruption of the local symmetry) of the structures, and the Renyi dimension (the degree of self-organization) to be introduced and to be computed.

Contrary to the conventional fractal analysis, which uses only one level of self-similarity and only one distribution function of a digit ensemble density for the entire system, MFA uses several levels of self-similarity and several distribution functions for large boxes of the system. It allows the distribution functions to be compared both between them and with the whole system. The procedure allows the degree of disruption to be determined quantitatively for local and general symmetry as well as the order degree of a complex system as a whole. Therefore, a more detailed information on the complex system peculiarities can be obtained using MFA.

The procedure of image processing consists of several stages: From the AFM data, the approximated images of the surface are patterned.

Then the binary matrix is obtained assigning “0” and “1” to light and dark points, respectively. In our case, the matrix dimensions are 280×280 units. After that, the matrix is divided into larger boxes consisting of $l_k \times l_k$ elementary units. In our case the maximum l_k is 100. For every rougher partition a characteristic measure P_i was calculated ($P_i = M_i / \sum_i M_i$, where M_i is the sum of the units in the i th larger box, $\sum_i M_i$ is the overall sum of units over the whole rougher partition, and $i = 1, 2, \dots, N$, where $N = (280/l_k)^2$, i.e. the square of the integer part). The conventional multifractal characteristics were calculated in each digitized image using such a collection of either rougher partitions, i.e. the so-called $f(x)$ spectra and the Renyi dimensions $D_q = \tau(q)/(q-1)$ were calculated [2]. D_q carries the information on the thermodynamic conditions of the structure formation. Moreover, it is indicative of both the growth condition non-equilibrium degree and the system self-organization level. It should be noticed that D_q is usable as a means of identification of material structures, which are poorly or not recognized by traditional methods. The dependence of the generalized correlation function $\chi(q)$ on the size l_k of larger boxes: $\chi(q) = \sum_i (P_i)^q \propto (l_k)^{\tau(q)}$, were calculated by a double logarithmic least squares approximation.

Such a technique enables a quantitative evaluation of the uniformity (by the quantity denoted as f_q) and degree of the order index (by the quantity denoted as $\Delta_q = D_1 - D_q$) of the structures investigated. The larger the Δ_q , the more ordered is the structure. The computations are performed using the MFRDrom program developed by Vstovsky [3]. In our case, the maximum value of q was 100 and a number of the canonical multifractal spectra was 38.

3. Results and discussion

The results of our previous AFM and EFM investigations on the structural and electrical properties of GaN

epitaxial layers showed that a random charge distribution was associated with the mosaic structure [7]. The distribution decreased mobility and resulted in unconventional carrier transfer mechanism similar to that observed in low-dimensional structures. The introduction of silicon with the concentration less than 10^{18} cm^{-3} eliminated the charge influence. The greatest impact was observed for the II Group layers (see Table 1). The charge transfer was determined by a classic mechanism [7] in these structures.

Two groups of layers could be separated. Group I and Group II are characterized by strong and weak effects of the mosaic structure on the charge transfer, respectively. The Schottky barriers were formed on the surface of both groups of the layers in one process. For this purpose, the Ni/Au contact of 2 mm diameter was deposited in high vacuum. Ti/Al layers were used as the ohmic contact. As the result, the Schottky barrier height was lower than 0.4 V for Group I, while the leakage current of Group I (Fig. 1, curve 1) was several orders of magnitude higher than that of Group II. The Schottky barrier height of Group II was 0.7–0.8 V, which was closer to the work function difference.

The photoconductivity investigations demonstrated that the persistent photoconductivity was lacking in Group II, while it was high in Group I not only at low temperatures, but at room temperature as well [8].

These results demonstrated at a qualitative level that the mosaic structure peculiarities played an important role in the electrical properties of the layer and device parameters. In this connection, a quantitative characterization of the mosaic structure is required to investigate the influence of its peculiarities on the electrical properties of the layers.

However, the traditional characterization techniques do not allow the peculiarities of the mosaic structure to

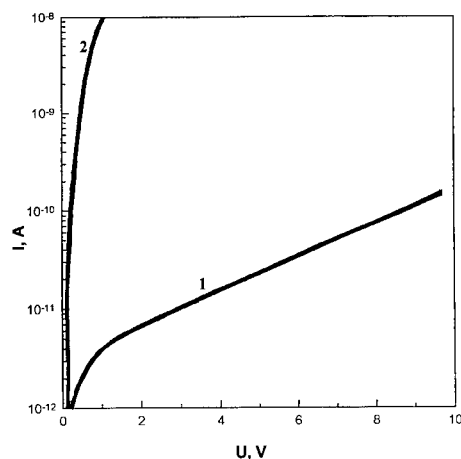


Fig. 1. Current–voltage characteristics of the Schottky barrier photodetectors based on GaN at reverse bias for (1) well and (2) poorly organized mosaic structure.

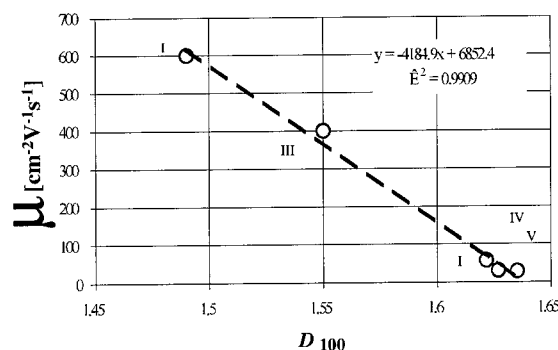


Fig. 2. Correlation between the Renyi dimensions (or the self-organization degree) and the mobility for the GaN epitaxial layers.

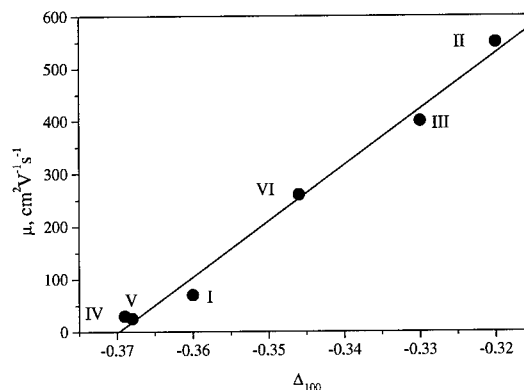


Fig. 3. Correlation of the degree of order index Δ_{100} and mobility μ at room temperature for GaN epitaxial layers.

be described in detail. For instance, the average domain size along with the basic axes is evaluated with X-ray diffraction analysis. Diagnostics of GaN surface topology using AFM gives only qualitative characteristics of the mosaic structure.

Only in Groups I and II with a high difference both in mobility and in average domain size of the mosaic structure, the correlation with the surface structure peculiarities was observed. In Groups III–VI, no direct association of the surface peculiarities with the electrical and volume structure properties was found.

In this connection, an effort was made to describe the mosaic structure peculiarities applying MFA of the AFM data for all non layers. A direct correlation between mobility and multifractal parameters was established (Figs. 2 and 3). The layers of Groups II, III, and VI possessed similar concentrations of carriers and silicon, but differed both in self-organization degree and in the disruption degree of local symmetry for the mosaic structure. From a temperature dependence of the mobility in these layers, it followed that scattering on

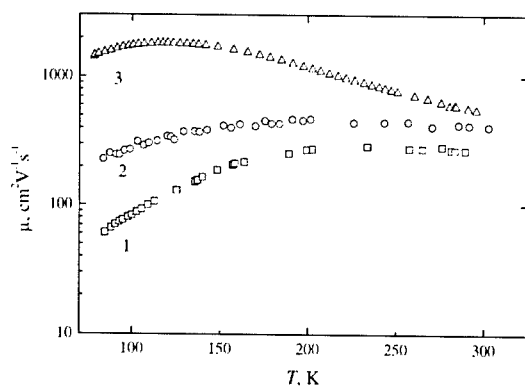


Fig. 4. Temperature dependence of mobility for Si-doped GaN layers with different Δ_{100} : (1) Group VI; (2) Group III; and (3) Group II.

charge centres made a different contribution at low temperatures (Fig. 4). The linear dependence of μ versus D_{100} and Δ_{100} is reasonable, because the carrier transport mechanism is unconventional (for most of the layers, the temperature dependence of conductivity corresponds to materials with localized charge defects or to low-dimensional structures) [7]. The mechanism depends on the probability of the current channel formation. Therefore, the layers with a higher self-organization level of the mosaic structure (i.e. with a small value of D_{100}) have higher mobility.

4. Conclusion

The important role of the mosaic structure peculiarities on the electrical properties of the layers and the device parameters was demonstrated.

New quantitative data: the self-organization degree (D_{100}) and the disruption of local symmetry (Δ_{100}) of mosaic structure have been obtained for GaN epitaxial layers of the hexagonal modification using the MFA of the surface structure.

The direct correlation between mobility of carriers in GaN epitaxial layers and D_{100} and Δ_{100} parameters of the mosaic structure is observed.

The MFA is a new approach to improve the properties of III-nitride layers.

Acknowledgements

The authors would like to thank the Organizing Committee of the 21st International Conference on Defects in Semiconductors for the support, in allowing to attend at the Conference.

References

- [1] A.G. Kolmakov, et al., Surf. Coat. Technol. 72 (1995) 43.
- [2] A.G. Kolmakov, G.V. Vstovsky, Mater. Sci. Technol. 15 (1999) 705.
- [3] G.V. Vstovsky, Found. Phys. 27 (1997) 1413.
- [4] G.V. Vstovsky, I.J. Bunin, J. Adv. Mater. 1 (1994) 230.
- [5] W.V. Lundin, et al., Proceedings of the Eighth European Workshop Metalorganic Vapor Phase Epitaxy and Related Growth Techniques, Prague, 1999, p. 53.
- [6] R.N. Kyutt, et al., Phys. Solid State 41 (1999) 25.
- [7] N.M. Schmidt, et al., Phys. Stat. Sol. B 216 (1999) 581.
- [8] N.M. Schmidt, et al., Proc. SPIE 4340 (2000) 92.



ELSEVIER

Physica B 308–310 (2001) 1145–1149

PHYSICA B

www.elsevier.com/locate/physb

The strain field around a single point defect in semiconductors spatially resolved by electric field modulation scanning tunneling spectro-microscopy

Akira Hida*, Yutaka Mera, Koji Maeda

Department of Applied Physics, School of Engineering, The University of Tokyo, Hongo, Bunkyo-ku, Tokyo 113-8656, Japan

Abstract

We have developed a novel instrumentation that allows us to image with a nano-scale resolution the strain field localized around single point defects in semiconducting crystals. The instrument that coupled the electric field modulation spectroscopy with the scanning tunneling microscopy was applied to point defects in low-temperature-grown GaAs (LT-GaAs) epi-films. The strain field image constructed by the present method exhibited features consistent with other experimental results. © 2001 Elsevier Science B.V. All rights reserved.

Keywords: Strain field; Energy gap; GaAs; Scanning tunneling microscopy

The strain field around a defect not only generally determines the elastic interaction between the defect and other defects/impurities but also can affect the electronic properties of the crystal. Particularly in semiconductors, the defect strain field modifies the local electronic band structure inducing significant effects on physical properties such as transport and confinement of carriers. Also, since the knowledge of the strain field provides insights to the atomic structure of the defect, the study of the strain field around defects is of fundamental importance in the research of defects.

So far, the most conventional techniques that allow us to investigate the strain fields around defects are those based on diffraction of quantum beams such as X-rays and electrons. If we want to *image* the strain field in real space, the transmission electron microscopy (TEM) has the highest spatial resolution. However, the TEM is not capable of imaging the strain field around point defects since the strain field damps quickly within a short distance from the defects. Hence, the development of new methodologies has been desired.

In semiconducting crystals, the elastic strain causes a change in the electronic band structures. The electric

field modulation spectroscopy (EFMS) is a variation of the modulation spectroscopy (see, for example, Ref. [1]) the power of which has been demonstrated in accurate measurements of electronic band structures in semiconductors. The principle of EFMS is based on the fact that the application of an electric field to a solid induces an oscillatory change in the optical absorption coefficient depending on the photon energy (the Frantz–Keldysh effect [2]), as illustrated in Fig. 1(a). The EFMS is superior to other techniques in that it can yield spectra with sharp fine structures, even in measurements at room temperature, each representing singularities in optical transitions such as the absorption edge (schematically illustrated in Fig. 1(b)). The high energy resolution of EFMS is thus advantageous for detecting small changes in the electronic band structures caused by the strain fields due to the point defects. The signal detected in the conventional EFMS is usually a change in the reflectivity of a monochromatized probe light illuminated on a surface of a macroscopic sample whose optical absorption coefficient is modulated by an electric field applied to the sample by some means. Although, the lateral spatial resolution may be achieved by reducing the beam size of the probe light [3], it cannot exceed the diffraction limit and also is practically limited by the signal-to-noise (S/N) ratio inherent in the

*Corresponding author. Fax: +81-3-5841-8888.

E-mail address: hida@exp.t.u-tokyo.ac.jp (A. Hida).

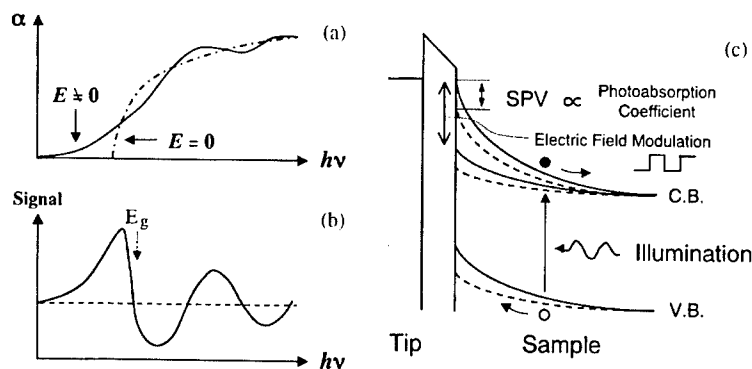


Fig. 1. (a) An oscillatory change in the optical absorption coefficient α depending on the electric field E applied to the crystal (Frantz-Keldysh effect). (b) A schematic energy-derivative spectrum obtained by electric field modulation spectroscopy. The bandgap energy is indicated by E_g . (c) The tunneling current in STM changes with the surface photo-voltage that is modulated by a chopped light with a magnitude responding to the modulated optical absorption coefficient of the material.

detection of the small change in the reflecting light intensity.

Recently, we have developed a new instrumentation that couples scanning tunneling microscopy (STM) [4] with the EFMS (STM-EFMS) that allows us to image the electronic band structures with a nanometer-scale resolution [5,6]. In the present study, we applied the STM-EFMS to low-temperature-grown GaAs (LT-GaAs) epi-films for imaging the local strain field around single point defects in the crystal.

Since the details of the STM-EFMS have been given in a previous paper [5], we only describe the brief outline. When a semiconducting sample is illuminated with a light whose energy exceeds the bandgap of the crystal, a surface photo-voltage (SPV) is induced if the surface band is bent to some extent [9,10] (see Fig. 1(c)). In an STM, the surface band bending may be induced locally by the bias voltage applied between the sample and the tip (tip-induced band bending) [7,8]. The magnitude of the SPV, that induces a change in the tunneling current, is determined by the number of photo-carriers generated by the light illumination or by the optical absorption coefficient of the sample in the photon energy range above the bandgap (superband-gap). Using another superbandgap light that is chopped, we can modulate the SPV and hence the electric field at the surface. Thus, instead of the light reflectivity in the conventional EFMS [2], we could measure the amplitude of the modulated-tunneling current as the EFMS signal. The use of the STM tunneling current, together with the localized tip-induced band bending, renders the extremely high spatial resolution.

The experimental setup is illustrated in Fig. 2. A sample placed on an ultrahigh vacuum (UHV) STM stage (UNISOKU, a custom model) was illuminated with two different light sources: One was a chopped laser light for electric field modulation and another was a

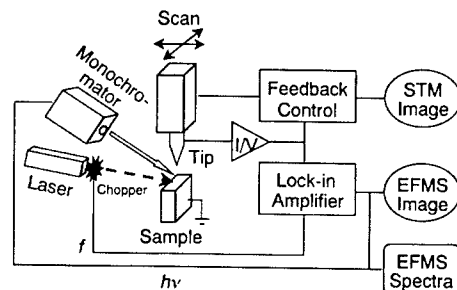


Fig. 2. A schematic diagram of the experimental setup. The sample placed on a UHV-STM stage is illuminated with two different light sources: One is a chopped laser beam ($h\nu = 1.52\text{ eV}$) for electric field modulation and another is a continuous light from a monochromator for spectroscopic measurements. The modulated signal of the tunneling current is detected by a lock-in amplifier tuned at the chopping frequency to obtain an energy-derivative EFMS spectrum at a specific position of the sample and an EFMS image at the bandgap energy reflecting the spatial variation of the bandgap energy in the sample.

continuous light from a monochromator for spectroscopic measurements. The chopping frequency was chosen to be higher than 1 kHz so that the current modulation was not damped by the STM current feedback control. The amplitude of the tunneling current (ΔI signal) was detected by a lock-in amplifier tuned at the chopping frequency as a function of the tip position \vec{r} , the photon energy $h\nu$ of the continuous light and the sample bias voltage V_s . EFMS spectra at given tip positions \vec{r}_0 were obtained by measuring the $\Delta I(\vec{r}_0, h\nu, V_s)$ signal with a fixed bias V_s as a function of the photon energy $h\nu$. Two-dimensional maps of ΔI signal (EFMS images) were acquired by scanning the tip

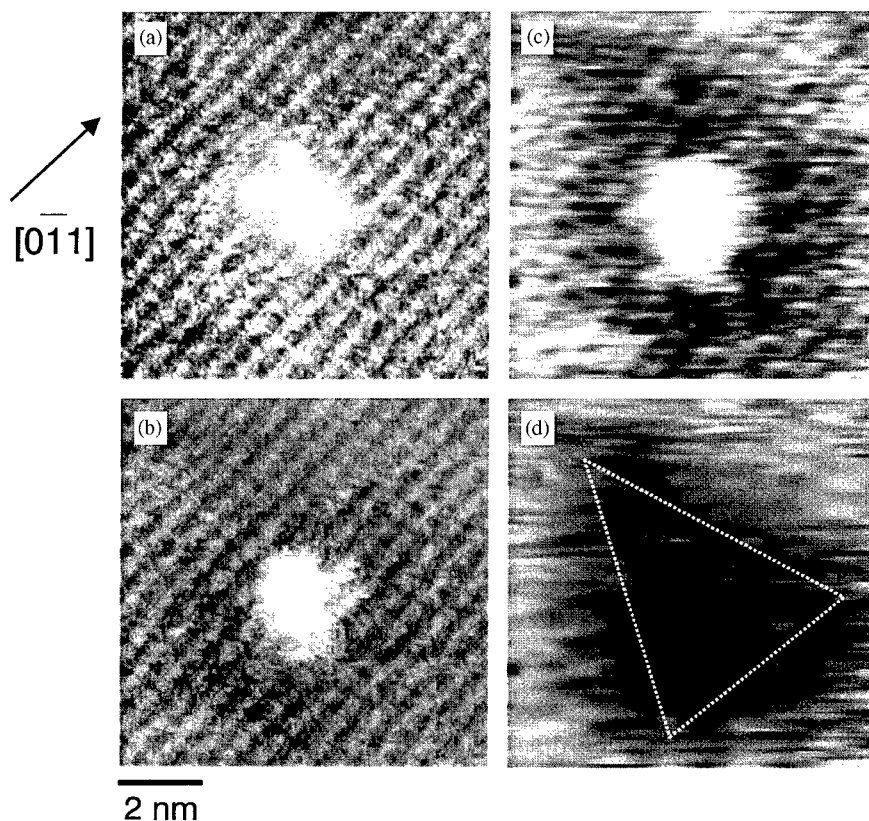


Fig. 3. (a) An occupied state and (b) an unoccupied state STM images of a typical point defect, assigned to an isolated As antisite defect, in an LT-GaAs epi-film. The images were taken at $V_s = -2.1$ V and $V_s = +2.3$ V, respectively. (c) An original EFMS image and (d) the strain field image obtained for the same defect after the corrections described in the text. The dark contrast around the defect in the strain field image represents a compressive strain. The strain field is triangular in shape, consistent with the T_d symmetry of the isolated antisite As.

at a given photon energy and a given bias voltage. Since the ΔI signal changes abruptly across the bandgap energy, if we fix $h\nu$ at a value close to the bandgap of the sample, the positional variation of the bandgap energy can be approximately visualized by the EFMS image. STM images in the constant-current mode were also recorded to compare the EFMS images with the topographic features.

The sample we used was an undoped LT-GaAs film of 200 nm thickness grown at 250°C on a Si-doped n-type GaAs (001) substrate ($n \sim 10^{18} \text{ cm}^{-3}$) in a VG-SEMI-CON VG80H molecular beam epitaxy (MBE) system. X-ray diffraction measurements indicated that the LT-GaAs epi-layer expanded normal to the surface by 0.20%. The cross-sectional (110) surfaces of the epi-film prepared by cleaving in the UHV-STM chamber (the base pressure $< 2 \times 10^{-8}$ Pa) were examined with Pt-Ir tips at room temperature. Normally, the samples were biased at +2.3 V with respect to the tip in order to induce an upward band bending in the GaAs (110) cleavage surface that is otherwise free of band bending

due to the absence of surface states and therefore no SPV is expected to arise [11]. The mean demand tunneling current (I_t) was set at 100 pA.

Fig. 3(a) shows an STM image of a typical point defect in LT-GaAs epi-layers observed at a negative sample bias ($V_s = -2.1$ V). The characteristic contrast is in agreement with that reported previously [12] as an isolated arsenic antisite defect (As_{Ga}) embedded in a few layers of GaAs (110) surface. Figs. 3(b) and (c) show an STM image of the same defect as recorded above with a positive sample bias ($V_s = +2.3$ V) and an EFMS image simultaneously acquired at $h\nu = 1.40$ eV which corresponds to the mean bandgap energy of the LT-GaAs epi-film at room temperature. In the EFMS image, the defect is surrounded by a dark contrast, whereas no such contrast is seen in the normal STM image, which indicates that the dark contrast is not of topographic origin.

Precisely speaking, the current modulation may be caused by mechanisms other than that considered above. This is demonstrated by Fig. 4 that shows a set

of EFMS spectra obtained at the same position of a sample with different sample biases. While the characteristic EFMS spectrum is observed at a sample bias of $V_s = +3.0$ V, no spectral features are seen at $V_s = +1.8$ V. The substantial reduction of the spectral variation in the ΔI signal at the lower bias voltage can be understood if one considers that decreasing the bias voltage reduces the surface band bending and hence the magnitude of the SPV necessary for electric field modulation. We should note, however, that even if the spectroscopic signal dwindles at $V_s = +1.8$ V, some magnitude of the modulated signal still remains, giving the constant background level denoted with G in Fig. 4. Generally, the chopped laser illumination could induce the thermal expansion of the STM tip that also would cause a modulation in the tunneling current. Although the modulation of the tip-sample distance due to the thermal expansion of the tip could be reduced by increasing the chopping frequency, it could not be removed completely at 1 kHz. Therefore, the residual background level obtained at $V_s = +1.8$ V is

$$\frac{\Delta I(\vec{r}, h\nu = 1.42 \text{ eV}, V_s = +2.5 \text{ V}) - \Delta I(\vec{r}, h\nu = 1.55 \text{ eV}, V_s = +1.8 \text{ V})}{\Delta I(\vec{r}, h\nu = 1.55 \text{ eV}, V_s = +2.5 \text{ V}) - \Delta I(\vec{r}, h\nu = 1.55 \text{ eV}, V_s = +1.8 \text{ V})}$$

considered to originate in the thermal expansion effect. Another factor that should influence the ΔI signal is the magnitude of the SPV itself that may vary spatially as reported by Hamers et al. [8,9]. The spectroscopic component of the ΔI signal in our work should be proportional to the magnitude of the SPV caused by the laser light chopped for electric field modulation. The magnitude of the SPV can be evaluated by the difference between the background

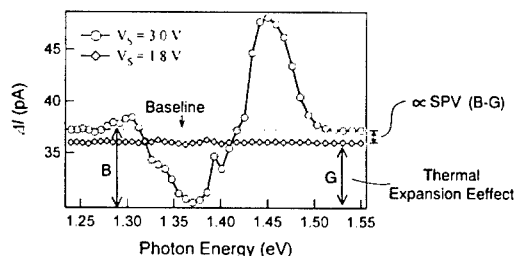


Fig. 4. A set of EFMS spectra obtained at the same position of a GaAs sample with different sample biases. The characteristic EFMS spectrum is observed at a sample bias of $V_s = +3.0$ V, whereas no spectral features are obtained at $V_s = +1.8$ V. The background level denoted by G is considered to be due to the illumination-induced thermal expansion of the tip. The difference between the background and the baseline of the EFMS spectrum is considered to represent the SPV due to the laser light chopped for electric field modulation.

level (G) and the baseline level (B in Fig. 4) of the spectrum.

Therefore, in order to obtain the image that represents with fidelity the spatial variation of the bandgap energy and hence the strain field, we have to remove the contributions of the above origins from the EFMS image. The correction procedures to remove the thermal expansion effect and the possible variation of SPV are as follows: After measuring the EFMS image or the spatial variation of $\Delta I(\vec{r}, h\nu = 1.42 \text{ eV}, V_s = +2.3 \text{ V})$, we measure the spatial variations of the intensity of $\Delta I(\vec{r}, h\nu = 1.55 \text{ eV}, V_s = +2.3 \text{ V})$ and $\Delta I(\vec{r}, h\nu = 1.55 \text{ eV}, V_s = +1.8 \text{ V})$ in the same area. Since the photon energy of $h\nu = 1.55 \text{ eV}$ is remote from the bandgap energy, $\Delta I(\vec{r}, h\nu = 1.55 \text{ eV}, V_s = +2.3 \text{ V})$ and $\Delta I(\vec{r}, h\nu = 1.55 \text{ eV}, V_s = +1.8 \text{ V})$ represent the spatial variations of the baseline level and of the background level, respectively. As the spatial variation of SPV is given by $\Delta I(\vec{r}, h\nu = 1.55 \text{ eV}, V_s = +2.3 \text{ V}) - \Delta I(\vec{r}, h\nu = 1.55 \text{ eV}, V_s = +1.8 \text{ V})$, the spatial map of the energy gap or the strain field that we want is obtained by calculating

Fig. 3(d) shows the strain field image obtained following the above procedures. The contrasts in the image should represent the variation of the bandgap energy. The dark contrasts indicate that the bandgap energy is larger than the surrounding, which means that the crystal near the defect is compressed elastically. This fact is quite consistent with the macroscopic expansive strain in the epi-films detected by the X-ray diffraction measurements. The dark contrast due to the strain field has a triangular shape with the mirror symmetry axis along the $[011]$ direction, consistent with the symmetry of the defect contrast shown in the STM image (Fig. 3(a)). The mirror symmetry is also consistent with the T_d symmetry of the isolated As_{Ga} that is usually assumed.

Acknowledgements

This work has been supported by Grant-in-Aid from the MEXT of Japan and Asahi Glass Foundation.

References

- [1] M. Cardona, *Modulation Spectroscopy*, Academic Press, New York, 1969.
- [2] D.E. Aspnes, *Phys. Rev.* 141 (1966) 554.
- [3] T. Kanata, et al., *Phys. Rev. B* 41 (1990) 2936.
- [4] G. Binnig, et al., *Helv. Phys. Acta.* 55 (1982) 726.

- [5] A. Hida, et al., Appl. Phys. Lett. 78 (2001) 3029.
- [6] A. Hida, et al., Solid State Phenom. 78–79 (2001) 419.
- [7] M. Weimer, et al., Phys. Rev. B 39 (1989) 5572.
- [8] M. McEllistrem, et al., Phys. Rev. Lett. 70 (1993) 2471.
- [9] R.J. Hamers, et al., J. Vac. Sci. Technol. A 8 (1990) 3524.
- [10] D.G. Chahill, et al., J. Vac. Sci. Technol. B 9 (1991) 564k.
- [11] R.M. Feenstra, et al., J. Vac. Sci. Technol. B 5 (1987) 923.
- [12] R.M. Feenstra, et al., Phys. Rev. Lett. 71 (1993) 1176.



ELSEVIER

Physica B 308–310 (2001) 1150–1152

PHYSICA B

www.elsevier.com/locate/physb

Thermo-mechanical stability of wide-bandgap semiconductors: high temperature hardness of SiC, AlN, GaN, ZnO and ZnSe

I. Yonenaga*

Institute for Materials Research, Tohoku University, Katahira 2-1-1, Aoba-ku, Sendai 980-8577, Japan

Abstract

The hardness of single crystals α -SiC, AlN, GaN, ZnO and ZnSe at elevated temperatures was measured by the Vickers indentation method in the temperature range 20–1400°C. The hardness of SiC, AlN, GaN, ZnO and ZnSe is about 25, 18, 11, 5 and 1 GPa, respectively, at room temperature. SiC, AlN and GaN show a decrease in hardness, originating in the beginning of macroscopic dislocation motion and plastic deformation, only at temperature 1200°C. A high thermo-mechanical stability for SiC, GaN and AlN is deduced. © 2001 Elsevier Science B.V. All rights reserved.

Keywords: Wide bandgap semiconductors; Hardness; Thermo-mechanical stability

1. Introduction

Silicon carbide (SiC), aluminum nitride (AlN), gallium nitride (GaN), zinc oxide (ZnO) and zinc selenide (ZnSe) appear promising as wide-bandgap semiconductors for application as high power/high-frequency devices, blue- and ultraviolet light-emitting-devices/photo detectors and chemically stable substrates for epitaxial growth of various materials. Additionally, these materials are supposed to be thermo-mechanically stable and available at elevated temperatures except ZnSe. However, up to now, extremely little is known about the mechanical properties of these materials on microhardness only at room temperature. Information on the mechanical strength of materials at elevated temperatures is essential as a basis in order to control the dislocation generation and plastic deformation during crystal growth and device processing, and in utilizing the potential optical and electronic properties of the materials. The difficulty of the preparation of bulk crystals, especially GaN and AlN, is a limiting factor in obtaining this information. Recently thick films of GaN and AlN have been successfully grown by using a

hydride vapor phase epitaxy (HVPE) technique [1,2]. These crystals can be regarded as bulk materials. The author's group has reported the hardness, which is a material parameter indicating resistance to plastic deformation, in the bulk single crystals GaN and AlN at elevated temperatures [3–5].

This paper reports the hardness of the wide-bandgap semiconductors SiC, GaN, AlN, ZnO and ZnSe at elevated temperatures in comparison with those of other materials Si, GaAs, GaP and α -sapphire.

2. Experiments

The hardness of single crystals α -SiC, GaN, AlN, ZnO and ZnSe of 0.5 mm thickness at elevated temperatures was measured by the Vickers indentation method in the temperature range 20–1400°C. Here, GaN and AlN single crystals were prepared from high-quality thick film grown on substrates by the HVPE technique, the details of which were described elsewhere [1,2].

Hardness measurements on the crystals were carried out by the conventional Vickers indentation method using a pyramidal diamond indenter. The applied indentation load P was 0.5–5 N. The dwell time was 30 s for every temperature tested in the range from room temperature (RT) to 1400°C.

*Tel.: +81-22-215-2042; fax: +81-22-215-2041.

E-mail address: yonenaga@imr.edu (I. Yonenaga).

3. Results and discussion

At room temperature, the indentations formed on the basal plane surfaces of the GaN and AlN crystals sometimes exhibited fracture characteristics for brittle materials with radial cracks propagating from the impression corners under an applied load of more than 2 N.

Hardness H_V was estimated from the load P and diagonal lengths $2a$, measured by optical microscopy, of the impression using the following relation:

$$H_V = P/(2a^2). \quad (1)$$

The fracture toughness K_C was also determined from the radial crack length c :

$$K_C = \xi(E/H_V)^{1/2}(P/c^3)^{1/2}, \quad (2)$$

where E is Young's modulus and ξ is a calibration constant ($=0.016$) for brittle materials.

The hardness is almost comparable for the (0001)/(111) and (0001)/(111) polar surfaces of the crystals with the hcp/cubic-based structure at all temperatures investigated. At RT, the hardness of GaN is 10.8 GPa, about twice and ten times the value of GaAs and ZnSe, respectively, which is similar to 12 and 12.3 GPa given by Drory et al. [6] and Hong et al. [7], respectively. The hardness of AlN at RT is 17.7 GPa. The fracture toughness of GaN is measured to be 1.1 MPa m^{1/2} using Eq. (2) with $E = 295$ GPa [8]. The fracture toughness of AlN is 0.4 MPa m^{1/2} using $E \approx 308$ GPa [9]. Table 1 summarizes the hardness and fracture toughness of various materials at RT [3–5,10–13]. As is evident in the table, AlN is harder than GaN and softer than SiC and α -Al₂O₃ [13]. ZnO is much softer than such materials. The result suggests that the hardness of semiconductors seems to be related to the bonding distance [15], dependent on the group of semiconductors, the elemental and IV–IV, III–V, and II–VI compound.

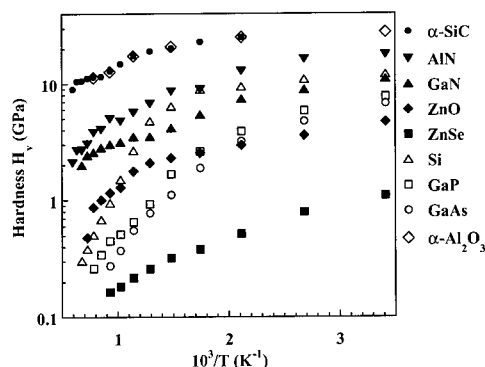


Fig. 1. Vickers hardness of bulk single-crystals α -SiC, AlN, GaN, ZnO and ZnSe plotted against reciprocal temperature, with an applied load of 0.5 N and dwell time of 30 s, together with those of Si, GaP, GaAs and α -Al₂O₃. The hardness of α -Al₂O₃ obtained with an applied load of 2 N and dwell time of 15 s is superimposed [13].

Fig. 1 shows the hardness H_V of SiC, GaN, AlN, ZnO and ZnSe, obtained with an applied load of 0.5 N and dwell time of 30 s, plotted against reciprocal temperature together with the values for Si, GaP, GaAs and α -Al₂O₃.

In the whole temperature range investigated, the hardness of SiC, GaN, AlN and ZnO exhibits a gradual decrease from RT to around 600°C, then something resembling a plateau in the range to around 1000°C, and subsequently a steep decrease. This temperature-dependent tendency is common in semiconductors and sapphire, which have the hcp-based structure, although the temperature range and hardness magnitudes of SiC or α -Al₂O₃ are higher than that of AlN and GaN. The plateau may appear in relation to the operation of different slip systems in the crystal structure. It is found that in the whole temperature range investigated, the hardness magnitudes of ZnO are smaller than those of SiC, AlN and GaN.

Table 1

Vickers hardness and fracture toughness for α -SiC, GaN, AlN and other materials at room temperature or 300°C [3–5,10–13] with an applied load 0.5 N and dwell time 30 s together with bonding distance [14]

Material	Hardness (GPa)	Fracture toughness (MPa m ^{1/2})	Bonding distance (Å)
α -SiC (0001)	22.9 ^a	3.3 (Ref. [10])	1.88
GaN (0001)	10.2 (Ref. [3])	1.1 (Ref. [4])	1.96
AlN (0001)	17.7 (Ref. [5])	0.4 (Ref. [5])	1.92
ZnO (0001)	4.7		1.80
ZnSe (111)	1.1	0.9 (Ref. [10])	2.45
Si (111)	12.0	0.7 (Ref. [10])	2.35
GaP (111)	7.73	0.65 (Ref. [12])	2.36
GaAs (111)	6.8	0.4 (Ref. [11])	2.45
α -Al ₂ O ₃ (0001)	28 ^b (Ref. [13])	2.5 (Ref. [10])	1.92

^a At 300°C.

^b With an applied load 2 N and dwell time 15 s [12].

At low temperature regions, the hardness of GaN and AlN is comparable to, or a little lower than, that of Si, though the hardness of Si may be affected by the phase transformation that occurs at a pressure of about 11.3 GPa beneath the indenter. It is surprising that up to about 1100°C, GaN and AlN maintain their hardness and are harder than Si. Indeed, Si and GaAs exhibit a steep decrease in hardness from 500°C and 200°C, respectively, with an increase in the temperature, which indicates the beginning of macroscopic dislocation motion and plastic deformation. The present results indicate that this macroscopic dislocation motion and plastic deformation of SiC, GaN and AlN may start at around 1100°C. Over the whole temperature range investigated, ZnSe is known to be most unstable thermo-mechanically in the materials.

From the results it is found that SiC, GaN and AlN are of higher thermo-mechanical stability against deformation during device processing at elevated temperatures as compared with Si, GaP, GaAs, ZnSe and possibly other III–V and II–VI compounds with the sphalerite structure. A more complete physical study of hardness in order to derive the dynamic properties of dislocations is still lacking in the absence of sufficient theory and is a task in the future. However, we assume that the present data provide a useful indication of material strength at elevated temperatures. Further work should be required to determine the dislocation mobility, especially, in GaN and AlN bulk crystals under a defined stress distribution.

4. Summary

The Vickers hardness for wide-bandgap semiconductors α -SiC, AlN, GaN, ZnO and ZnSe of 0.5 mm thickness was compared in the temperature range 20–1400°C. The hardness of SiC, AlN, GaN, ZnO and ZnSe is about 25, 18, 11, 5 and 1 GPa, respectively, at room temperature. SiC, AlN and GaN show a decrease in hardness, originating in the beginning of macroscopic dislocation motion and plastic deformation, only at temperature 1200°C. The results imply that these crystals have a smaller susceptibility to deformation during device processing at high temperatures as compared with ZnO, Si, GaP, GaAs and ZnSe.

Acknowledgements

The author is grateful to Professor P. Pirouz of Casewestern Reserve University for supplying the SiC crystals, to Drs. A. Nikolaev, and Y. Melnik of Ioffe Institute and Crystal Growth Research Center, to Dr. V. Dmitriev of TDI, Inc., USA for the AlN crystals, to Dr. A. Usui of NEC corporation for the GaN crystals and to Mr. Y. Kato of Stanley Electric Co., Ltd. for the ZnSe crystals.

References

- [1] A. Usui, H. Sunakawa, A. Sakai, A.A. Yamaguchi, *Jpn. J. Appl. Phys.* 36 (1997) L899.
- [2] A. Nikolaev, I. Nikitina, A. Zubrilov, M. Mynbaeva, Y. Melnik, V. Dmitriev, *Mater. Res. Soc. Symp. Proc.* 595 (2000) W651.
- [3] I. Yonenaga, T. Hoshi, A. Usui, *Jpn. J. Appl. Phys.* 39 (2000) L200.
- [4] I. Yonenaga, T. Hoshi, A. Usui, *J. Phys.: Condens. Mater.* 12 (2001) 10319.
- [5] I. Yonenaga, A. Nikolaev, Y. Melnik, V. Dmitriev, *Jpn. J. Appl. Phys.* 40 (2001) L426.
- [6] M.D. Drory, J.W. Ager III, T. Suski, I. Grzegory, S. Porowski, *Appl. Phys. Lett.* 69 (1996) 4044.
- [7] M.H. Hong, P. Pirouz, P.M. Tavernier, D.R. Clarke, *Mater. Res. Soc. Symp. Proc.* 622 (2000) T618.
- [8] R. Nowak, M. Pessa, M. Suganuma, M. Leszczynski, I. Grzegory, S. Porowski, F. Yoshida, *Appl. Phys. Lett.* 75 (1999) 2070.
- [9] D. Gerich, S.L. Dole, G.A. Slack, *J. Phys. Chem. Solids* 47 (1986) 437.
- [10] I.J. McColm, *Ceramic Hardness*, Plenum Press, New York, 1990.
- [11] G. Michot, A. George, A. Chabli-Brenac, E. Molva, *Ser. Metall.* 22 (1988) 1043.
- [12] K. Hayashi, M. Ashizuka, R.C. Bradt, H. Hirano, *Mater. Lett.* 1 (1982) 116.
- [13] B.Ya. Farber, S.Y. Yoon, K.P.D. Lagerlöf, A.H. Heuer, *Phys. Stat. Sol. (a)* 137 (1993) 485.
- [14] J.C. Phillips, *Bonds and Bands in Semiconductors*, Academic Press, New York, 1973.
- [15] A. Sher A. A.-B. Chen, W.E. Spicer, *Appl. Phys. Lett.* 46 (1985) 54.



ELSEVIER

Physica B 308–310 (2001) 1153–1156

PHYSICA B

www.elsevier.com/locate/physb

Capacitance X-ray absorption fine structure measurement using scanning probe

A new method for local structure analysis of surface defects

Masashi Ishii*

JASRI (Japan Synchrotron Radiation Research Institute), SPring-8, Mikaduki, Sayo-gun, Hyogo 679-5198, Japan

Abstract

A capacitance X-ray absorption fine structure (XAFS) method using a scanning probe is developed for the selective analysis of surface defects in selected local regions. Since capacitance is sensitive to localized electrons in defects, capacitance change owing to X-ray absorption will provide site-selective XAFS spectra of the defects. The capacitance detection by the scanning probe under an X-ray beam gives XAFS spectra dependent on the surface state. An electron transition model, in which the surface density of states is taken into account, reproduces the spectral shape differences between the normal surface and defect surface. © 2001 Elsevier Science B.V. All rights reserved.

Keywords: Surface defects; Site-selectivity; Capacitance XAFS; Scanning probe

1. Introduction

The progress in electronics technology over the last several decades has mainly been based on the integration of semiconductor devices. Various efforts have been made toward forming superior microstructures, with the present result being \sim nm order devices by the recent semiconductor fabrication techniques. In these small structures, the atomic coordination of the defects in the electrically active regions determines the device performance. This fact indicates the need for methods to structurally analyze defects in selected \sim nm regions; One of the ultimate objectives of the defect analysis is defect structure mapping on semiconductor surfaces.

In recent years, we proposed a capacitance X-ray absorption fine structure (XAFS) method that obtains absorption spectra by the X-ray photon energy dependence of the capacitance [1,2]. Since the capacitance is sensitive to localized electrons in defects, the photoionization of the defects owing to X-ray inner-shell absorption changes the capacitance, resulting in site-selective X-ray absorption spectra of the defects.

Generally speaking, the XAFS denotes spectral signal oscillations over the energy range of \sim 1 keV from the inner-shell absorption edge, and its Fourier transformation provides structural information, such as the bond length with a neighboring atom and the coordination number of a specific atom selected by the X-ray photon energy [3]. Moreover, the density of unoccupied states above the Fermi energy can also be estimated from the near edge absorption spectrum [4]. Therefore, the capacitance XAFS method can provide a microscopic local structure and the electronic states of only the defects, owing to its site-selectivity.

In this paper, a capacitance XAFS method using a scanning probe is developed with the aim of achieving the defect structure mapping on the semiconductor surface. By capacitance detection in selected local areas, XAFS spectra correlated with surface states can be observed.

2. Experimental details

Fig. 1 schematically shows the experimental apparatus developed in this study. A mechanically sharpened Ta with a purity of 99.95% is used as the scanning probe. A point contact of the Ta tip with a sample

*Tel.: +81-791-58-0832; fax: +81-791-58-0830.
E-mail address: ishiim@spring8.or.jp (M. Ishii).

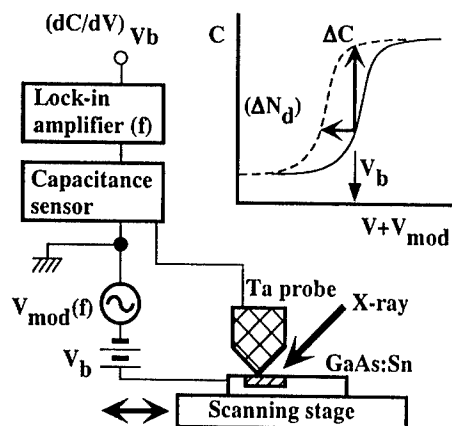


Fig. 1. Experimental setup in this study.

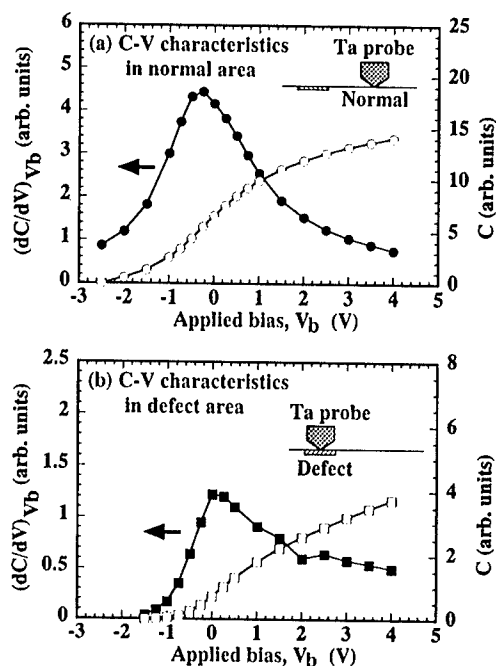
semiconductor surface makes a metal-oxide-semiconductor (MOS) diode structure owing to the native oxide on the semiconductor surface. The MOS diode structure has the capacitance-bias voltage (C - V) characteristics schematically shown by the solid line in the inset of Fig. 1. The X-ray irradiated into this MOS diode induces the photoionization of the surface defects, and the release of localized electrons increases free carriers by ΔN_d . The ΔN_d slightly shifts the C - V characteristics horizontally along the voltage axis as shown by the dashed line, resulting in capacitance changes of ΔC at the specific bias voltage of V_b . In our system, the capacitance of the MOS diode, C , is measured by a capacitance sensor for a videodisc [5]. For the sensitive detection of ΔC , a lock-in amplification technique with V_b modulation is used; the capacitance XAFS signal is observed by derivative of C at V_b (dC/dV) $_{V_b}$, rather than the absolute C . The V_b modulation amplitude, V_{mod} , and modulation frequency, f , are fixed at 500 mV and 131 Hz, respectively.

The sample used in this study is Sn-doped (100) oriented GaAs (GaAs:Sn). The Sn density is $1 \times 10^{17}/\text{cm}^3$. A part of the sample surface is scratched to introduce the surface defects owing to crystal disorder. The sample is mounted on a scanning stage. The substrate temperature is kept at room temperature. Synchrotron radiation (SR) is used as the X-ray source for the XAFS measurements. The beamline for our SR experiments is the BL10XU High Brilliance XAFS station [6] at SPring-8, located in Hyogo Prefecture, Japan.

3. Results and discussions

3.1. Electrical properties of the sample

Fig. 2 shows local C - V characteristics obtained by the Ta probe in (a) a normal (as prepared) surface area and

Fig. 2. C - V characteristics of (a) normal and (b) defect areas.

(b) a defect surface area. The solid circles in (a) indicate the $(dC/dV)_{V_b}$ signal in the normal area. The $(dC/dV)_{V_b}$ has almost symmetrical characteristics with the maximum intensity at $V_b \sim 0$ V. The ordinary C - V characteristics derived from the integration of $(dC/dV)_{V_b}$ are also plotted in this figure by the open circles. As shown in this figure, C - V characteristics with the capacitance saturations at high and low V_b values can be obtained. The characteristics intrinsic to the MOS capacitor indicate the local formation of the MOS diode structure by the Ta point contact.

In contrast, the $(dC/dV)_{V_b}$ signal in the defect area denotes asymmetric characteristics (solid squares in (b)), and the signal intensity is smaller than that in the normal area. Because of these properties, the C - V characteristics have a gentle curve and a small C at a high V_b (open squares). This property of the defect area is consistent with the general fact that electron localized at the surface defects terminate the electric field in the MOS capacitor, resulting in a C reduction.

3.2. Capacitance XAFS measurements using scanning probe

In order to correlate the electric properties shown in Fig. 2 with the X-ray absorption spectrum of the defects, capacitance XAFS measurements using this Ta probe are performed. Fig. 3 shows the capacitance XAFS spectra of (a) the normal area and (b) defect surface

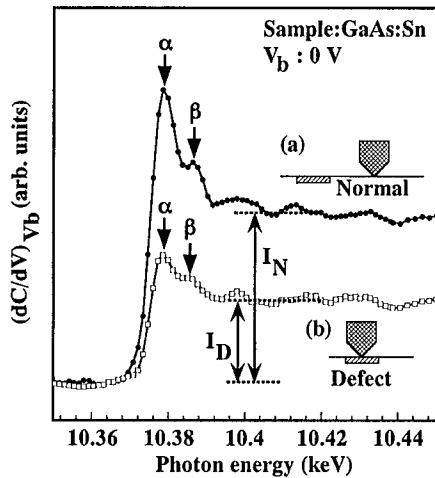


Fig. 3. Capacitance XAFS spectra of (a) normal and (b) defect areas.

area. In this experiment, V_b was fixed at 0 V. As shown in this figure, the edge jumps at the Ga K-edge (10.375 keV), the resonant absorption peaks denoted by α and β , and the following XAFS oscillations in the high energy region can clearly be observed. From a comparison between (a) and (b), we recognized that the spectrum shape depends on the surface state. According to the concept of the capacitance XAFS method, the spectrum differences in (1) the edge jumps and (2) the resonant peaks can be explained as follows.

(1) The actual edge jump minus the resonant peaks for the normal surface (I_N) is higher than that for the defect surface (I_D). As described in Fig. 1, the capacitance XAFS signal is obtained by the photoionization of the defects. Assuming that the photoionization produces almost the same ΔN_d for both areas, it is easily predictable from the inset of Fig. 1 that the gentle $C-V$ characteristics curve yields a small ΔC . In fact, the defect surface has a gentle $C-V$ characteristics curve as shown in Fig. 2, indicating that $I_D < I_N$ in Fig. 3 is consistent with this photoionization model in the capacitance XAFS method.

(2) The resonant peaks of α and β for the normal surface are more intense and sharper than those for the defect surface. Fig. 4 indicates the band diagram of the photoionization process in the capacitance XAFS measurement. Under X-ray irradiation, localized electrons are relaxed into core-holes formed by the inner-shell excitation of the defects. The excitation and following relaxation are identical to a de-localization of the electrons by ΔN_d , resulting in ΔC . In the normal surface area, since the dangling bonds on the GaAs:Sn surface are relatively uniform, the surface density of states (SDOS) is condensed in a narrow energy range as illustrated in Fig. 4(a). The de-localization of the

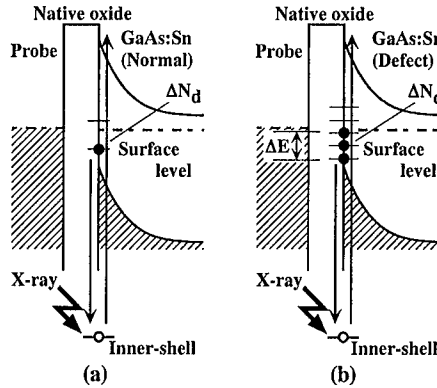


Fig. 4. Band diagrams of (a) normal and (b) defect areas.

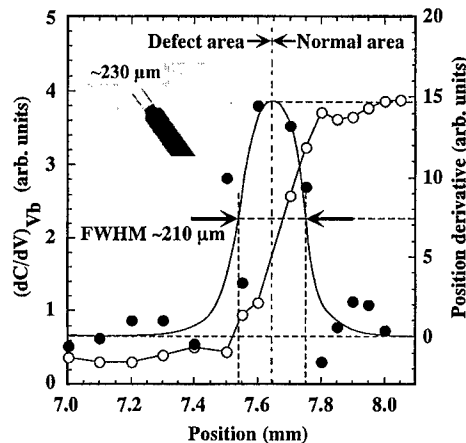


Fig. 5. Comparison between spatial resolution and probe size.

electrons from the condensed level is resonantly induced at the specific photon energy, resulting in the intense and sharp absorption peak. On the other hand, the defect area with various atomic coordinations forms a broad SDOS as shown in Fig. 4(b). In this situation, since the electrons are dispersively trapped in the energy range of ΔE , the resonant absorption becomes broader.

3.3. Spatial resolution

To discuss the spatial resolution of this method, $(dC/dV)_{V_b}$ during a one-dimensional scan is plotted by the open circles in Fig. 5. At this boundary of a defect area and a normal area, the variation of $(dC/dV)_{V_b}$ can be observed. The position derivative of $(dC/dV)_{V_b}$ is also indicated by the solid circles in this figure. From the full-width at half-maximum (FWHM) of the derivative, the spatial resolution can be estimated as $\sim 210 \mu\text{m}$. On the other hand, the diameter of the Ta probe is $\sim 230 \mu\text{m}$ as shown in the inset of this figure. This Ta diameter

comparable to the FWHM indicates that the spatial resolution of this method is limited by the probe size at this time.

4. Summary

A capacitance XAFS method using a scanning probe is proposed for defect structure mapping on a semiconductor surface. Since capacitance is sensitive to localized electrons in defects, the photon energy dependence of the capacitance provides site-selective XAFS spectra of the defects. The capacitance XAFS spectra dependent on the surface states are successfully obtained by using the Ta scanning probe. Since the electrons on the defect surface are dispersively trapped over a wide energy range, the resonant peak at the X-ray

absorption edge becomes broader. We showed that a spatial resolution of $\sim 210\text{ }\mu\text{m}$ is limited by the scanning probe diameter.

References

- [1] M. Ishii, Y. Yoshino, K. Takarabe, O. Shimomura, *Appl. Phys. Lett.* 74 (1999) 2672.
- [2] M. Ishii, Y. Yoshino, K. Takarabe, O. Shimomura, *J. Appl. Phys.* 88 (2000) 3962.
- [3] F.W. Lytle, D.E. Sayers, E.A. Stern, *Phys. Rev. B* 11 (1975) 4825.
- [4] M. Morinaga, N. Yukawa, H. Adachi, T. Mura, *J. Phys. F* 17 (1987) 2147.
- [5] R.C. Palmer, E.J. Denlinger, H. Kawamoto, *RCA Rev.* 43 (1982) 194.
- [6] H. Oyanagi, et al., *J. Synchrotr. Rad.* 7 (2000) 89.



ELSEVIER

Physica B 308–310 (2001) 1157–1160

PHYSICA B

www.elsevier.com/locate/physb

Positron lifetime beam for defect studies in thin epitaxial semiconductor structures

A. Laakso*, K. Saarinen, P. Hautojärvi

Laboratory of Physics, Helsinki University of Technology, P.O. Box 1100, 02015 HUT, Finland

Abstract

Positron annihilation spectroscopies are methods for direct identification of vacancy-type defects by measuring positron lifetime and Doppler broadening of annihilation radiation and providing information about open volume, concentration and atoms surrounding the defect. Both these techniques are easily applied to bulk samples. Only the Doppler broadening spectroscopy can be employed in thin epitaxial samples by utilizing low-energy positron beams. Here we describe the positron lifetime beam which will provide us with a method to measure lifetime in thin semiconductor layers. © 2001 Elsevier Science B.V. All rights reserved.

Keywords: Positron spectroscopy; Vacancies; Instrumentation; Epilayers

1. Introduction

Positron spectroscopy is a method for direct identification of vacancy defects [1]. It is based on monitoring the 511 keV annihilation radiation emitted when thermalized positrons annihilate in solids with electrons. Positrons get trapped at neutral and negative vacancies because of the missing positive charge of the ion cores. At vacancies, the positron lifetime increases and positron–electron momentum distribution narrows due to reduced electron density.

The spectroscopy gives information on vacancies at concentrations 10^{15} – 10^{19} cm⁻³. Positron lifetime is a direct measure of the open volume of a defect. The Doppler broadening of the 511 keV radiation gives the momentum distribution of annihilating electrons $\rho_v(p)$. The core electron momentum distribution can be used to identify the sublattice and impurity surroundings of a vacancy. In addition, under varying temperature and illumination, the positron spectroscopy can yield information on charge states, optical transitions and thermal stabilities of vacancy defects.

The lifetime and Doppler broadening are easily applied to bulk samples. Thin epitaxial semiconductor layers can also be studied by Doppler broadening spectroscopy using a positron beam. However, positron lifetime spectroscopy, which is essential for obtaining the open volume of the defect, has been mainly limited to bulk samples although some lifetime beams have been constructed [3,4]. The purpose of this work is to describe the need for a pulsed positron lifetime beam designed for the semiconductor studies. In Section 2, we discuss the conventional positron techniques. Section 3 describes the principle of the lifetime beam and Section 4 concludes this work.

2. Methods and background

In conventional positron lifetime spectroscopy (see Fig. 1), positron lifetime is defined as a time difference of gamma emitted in β^+ decay and the gamma emitted when electron–positron pair annihilates. The positron lifetime spectrum is composed of exponential decay components with intensities I_i and lifetimes τ_i as $\sum_i I_i e^{-t/\tau_i}$. The different exponential components are associated to annihilations at different positron states

*Corresponding author. Tel: +358-9-451-5801; fax: +358-9-451-3116.

E-mail address: antti.laakso@hut.fi (A. Laakso).

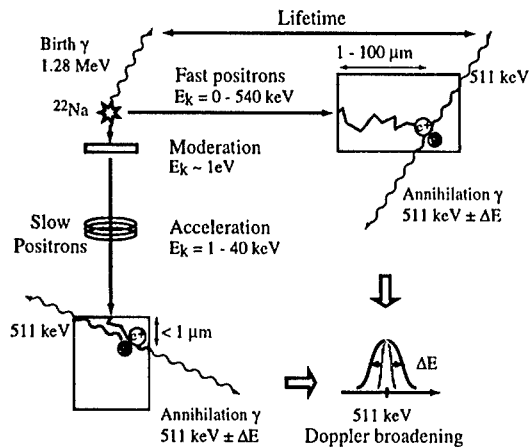


Fig. 1. The principle of positron experiment. Sources and measurable quantities.

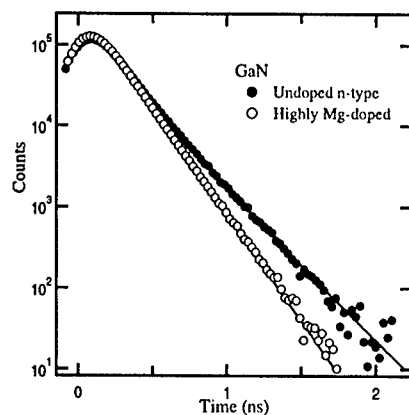


Fig. 2. Positron lifetime spectra from two different GaN bulk samples. In the highly Mg-doped sample (white circles) only one lifetime component 165 ps is present. In an undoped n-type sample a longer lifetime component of 235 ps is present due to vacancies [2].

(bulk vs. vacancy). This spectrum can be relatively easily decomposed and the individual lifetimes and their intensities can be extracted.

As an example in Fig. 2, two different lifetime spectra from undoped and highly Mg-doped GaN bulk samples are shown. In the highly Mg-doped sample only one lifetime component, 165 ± 1 ps can be observed. However, in an undoped sample a second lifetime component is present with a time of 235 ± 5 ps. This second component is due to Ga vacancies existing as native defects in n-type GaN. The intensity of the second component provides an estimate of vacancy concentration (10^{17} cm^{-3} in this case).

The average lifetime τ_{av} is defined as the center of mass of the lifetime spectrum,

$$\tau_{av} = (1 - \eta_V)\tau_B + \eta_V\tau_V = \text{C.M.}, \quad (1)$$

where η_V is the fraction of the positrons annihilating in the vacancies and τ_B is the bulk lifetime. It should be noted that τ_{av} is a statistically accurate parameter and changes below 1 ps can be measured.

In Doppler broadening experiments, the momentum distribution of the annihilating electrons is recorded by measuring the Doppler shift ΔE of the annihilation radiation with Ge-detector. The momentum distribution $\rho(p)$ can be characterized by integrated *S*- and *W*-parameters shown in Fig. 3. The measured momentum distribution $\rho(p)$ is composed of the superimposed distributions from annihilations in vacancies $\rho_V(p)$ and in bulk $\rho_B(p)$ as shown in Eq. (2).

$$\rho(p) = (1 - \eta_V)\rho_B(p) + \eta_V\rho_V(p). \quad (2)$$

Very often this cannot be decomposed on its own. However, the decomposition is possible, if the annihilation fraction η_V and the bulk momentum distribution $\rho_B(p)$, determined by measuring a defect-free reference sample, is known.

In practice, the identification of the vacancies is based on measuring both τ_V and $\rho_V(p)$. τ_V is obtained from the decomposition of the lifetime spectra and it can be used to determine $\rho_V(p)$ (Eqs. (1) and (2)). This means that lifetime is normally needed for identification of vacancies. Furthermore, positron lifetime spectroscopy is approximately ten times more sensitive to defects than Doppler broadening spectroscopy.

The fast positrons emitted directly from ^{22}Na source have continuous energy range from 0 up to 540 keV and

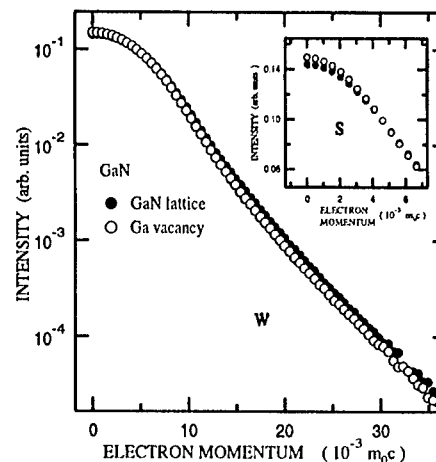


Fig. 3. Area normalized momentum distribution of annihilating electrons measured in Doppler broadening experiment. The *S*- and *W*-parameters, which are commonly used to describe the line shape, are defined as integrals over the shaded areas.

a wide implantation profile ranging up to 100 μm . In the conventional lifetime experiment bulk samples with dimensions of 5 mm \times 5 mm and thicknesses $> 100 \mu\text{m}$ are thus needed.

Slow positrons are obtained from ^{22}Na source by thermalizing the fast positrons in a moderator crystal (e.g. single crystalline W foil). The thermal positrons emitted from the surface of the moderator (energies less than 1 eV) are accelerated in an electric field up to 100 keV in order to study layers with thicknesses of 0–5 μm .

Both lifetime and Doppler broadening measurements can be done routinely with fast positrons. On the other hand, slow positron beam experiments are mainly limited to Doppler measurements. This is because the time information of the positron's entrance to the sample is lost in the beam formation. However, a low-energy pulsed positron beam enables the lifetime measurements in thin layers.

3. Positron lifetime beam

A successful method for positron lifetime measurements in thin layers is a pulsed positron beam [3,4]. In this system, the continuous slow positron beam is converted to very short pulses with a well-defined time structure.

In the following, we will describe the pulsed positron lifetime beam presently under construction in the Helsinki University of Technology [5]. Our beam has been designed especially for studies of defects in semiconductors. Unlike in the other existing systems [3,4], in our beam the sample is at ground potential to simplify its manipulation and temperature control. In addition, the sample can be illuminated to study the optical properties of the defects. Also, the beam energy is variable between 3 and 30 keV which enables the measurements of layers with thicknesses of 0–2 μm .

The principle of pulse generation is shown in Fig. 4. The positrons from a ^{22}Na source are thermalized in a W-foil moderator. Thereafter they are magnetically guided and further accelerated to a velocity selector, which separates the remaining fast positrons from the slow ones. This is done by solenoids and coils arranged perpendicular to each other. In the first pulsing stage, the prebuncher, two sinusoidal voltages (33 and 66 MHz) are used to periodically accelerate and decelerate positrons in two gaps between the middle electrode and the end electrodes. The electrodes are also biased so that positrons are accelerated with constant potentials across the prebuncher.

The prebuncher is followed by a drift tube where the energy-modulated beam compresses to pulses. After the drift tube, the first acceleration stage feeds positrons to the chopper, which is used to cut out the background

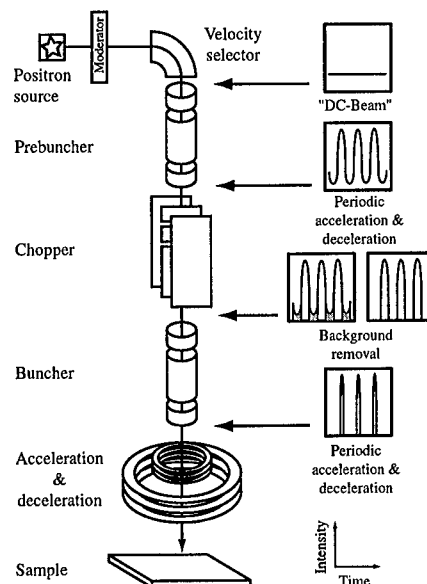


Fig. 4. The pulsed positron lifetime beam. Short pulses are used to measure positron lifetime in thin layers.

between the pulses. This is done with three electrodes; the upper and the lower ones are grounded and the middle one is in an oscillating voltage with a frequency of 16.7 MHz. This voltage creates an electric field perpendicular to the beam, which increases the transversal velocity and the Larmor radius and makes positrons hit the walls of the chopper slit. By carefully adjusting the phase of the chopper voltage it is possible to cut out the background between pulses and pass the pulses through unmodified.

The main buncher is a resonating cavity with a frequency of 167 MHz. The two narrow spaces between the body of the cavity and the center electrode act as an acceleration–deceleration gaps. In this stage, the pulses are squeezed to a final width of 100 ps.

The pulses from the buncher are further accelerated by a constant voltage and slowed down to final energy in an adjustable decelerator before hitting the grounded sample. This kind of two-stage accelerator–decelerator structure is beneficial as it reduces the variation of the flight time through the acceleration stage with varying acceleration energies. It also helps to reduce the effects of the backscattered positrons in the lifetime spectrum. These positrons are accelerated away from the sample surface and they annihilate in the walls of the large chamber two or three nanoseconds after the arrival of the main pulse.

The pulse generation is controlled by electronics, which also provides the necessary timing signal corresponding to the time when positrons enter the sample. The timing signal for the positron annihilation is

measured by a BaF₂ scintillation detector placed behind the sample. The positron lifetime is obtained as a difference of these signals.

4. Conclusions

Positron annihilation spectroscopy can be used to identify vacancy-type defects in bulk semiconductor crystals and epitaxial layers. The identification of both vacancies and their surrounding atoms can be conventionally done only for bulk samples which can be measured with both lifetime and Doppler broadening spectroscopy. The pulsed positron beam described here will provide us with a method to measure positron lifetime in thin semiconductor layers. This enables direct

identification of the open volume of the defect in the layer, more straightforward determination of vacancy concentrations, and improved sensitivity compared with Doppler measurements.

References

- [1] K. Saarinen, et al., in: M. Stavola (Ed.), Identification of defects in semiconductors, Academic Press, New York, 1998, p. 209.
- [2] K. Saarinen, et al., Appl. Phys. Lett. 75 (16) (1999) 2441.
- [3] D. Schodlbauer, et al., Nucl. Instrum. Methods B 34 (1988) 258.
- [4] R. Suzuki, et al., Jpn. J. Appl. Phys. 30 (1991) L352.
- [5] K. Fallström, et al., Appl. Surf. Sci. 149 (1999) 44.



ELSEVIER

Physica B 308–310 (2001) 1161–1164

PHYSICA B

www.elsevier.com/locate/physb

Measurement of diffusion lengths in quaternary semiconducting thin layers by spectrum imaging

T. Walther*

Institut für Anorganische Chemie, Universität Bonn, Römerstrasse 164, D-53117 Bonn, Germany

Abstract

A method is described to detect and measure diffusion in complex layer systems. The technique of spectrum imaging is a combination of electron energy-loss spectroscopy and imaging in a transmission electron microscope with imaging energy filter. It allows to extract chemical profiles with a spatial resolution of about 1 nm at a compositional sensitivity better than 1 at% for most elements. This has been applied to multilayers of quaternary semiconductors, where simple electron microscopy based imaging techniques cannot distinguish between the diffusion of different atomic species. The diffusivities of sulphur in ZnMgSSe/ZnSe quantum well laser structures and of magnesium and manganese across interfaces in CdMnTe/CdTe/CdMgTe quantum wells have been determined. © 2001 Elsevier Science B.V. All rights reserved.

PACS: 68.35.Fx; 68.37.Lp; 68.65.Fg; 81.05.Dz

Keywords: Diffusion lengths; Zn(Mg,S)Se; Cd(Mg,Mn)Te; Energy filtering TEM

1. Introduction

The (opto)electronic properties of quantum well structures depend strongly on the width and the chemical composition of the thin layers used for carrier confinement, as well as on the quality of interfaces between these and the barrier layers [1]. One of the biggest problems of devices made of such layers is thermal degradation due to diffusion and the generation of extended lattice defects. Latter can be investigated by transmission electron microscopy (TEM). High-resolution TEM has been used to study the abruptness of interfaces at near atomic resolution [2–4], but the accuracy is limited by Fresnel effects [5] and the need to determine precisely the imaging conditions that establish the relationship between image contrast and chemical composition [3,4,6]. Higher chemical sensitivity and reliability can be obtained from electron energy-loss spectroscopy (EELS) [7]. Here, the technique of

spectrum imaging, as first described in Ref. [8], is applied quantitatively to thin layers.

2. Experimental

The experiments have been performed with a Philips CM300UT TEM equipped with a Gatan imaging filter. Spectrum imaging exploits the fact that the dispersion of a magnetic sector field is only in one direction, perpendicular to the electron beam and the magnetic field. With an imaging filter and a two-dimensional detector, spatial resolution can be retained in the direction without dispersion so that line profiles across planar faults or interfaces can be recorded. A spectrum image consists of a series of EEL spectra taken simultaneously across the structure. Line-by-line EEL spectra can then be extracted. The interfaces must be accurately aligned relative to the spectrometer in order to avoid spatial blurring. Details of the procedure are given in Ref. [9].

The Zn(Mg,S)Se samples were grown by metal organic vapour phase epitaxy on GaAs (001) substrates at 330°C [10]. The Cd(Mg,Mn)Te samples studied were

*Corresponding author. Fax: +49-228-73-4-205.

E-mail address: walther@sg4.elmi.uni-bonn.de (T. Walther).

grown by molecular beam epitaxy on GaAs (001) at 280°C via a thick CdTe/CdMnTe buffer layer [11].

TEM cross-sectional samples were prepared by standard methods. Ar⁺ ion milling was employed at low angles of 8° and voltages of only 3 kV until perforation, and the holder was cooled which prevents sample damage known from ion irradiated II/VI compounds [12].

3. Results

Fig. 1a depicts a typical spectrum image recorded in 20 s with an energy offset of 2.4 keV of a 10 nm ZnMgSSe/5 nm ZnSe multiple quantum well laser

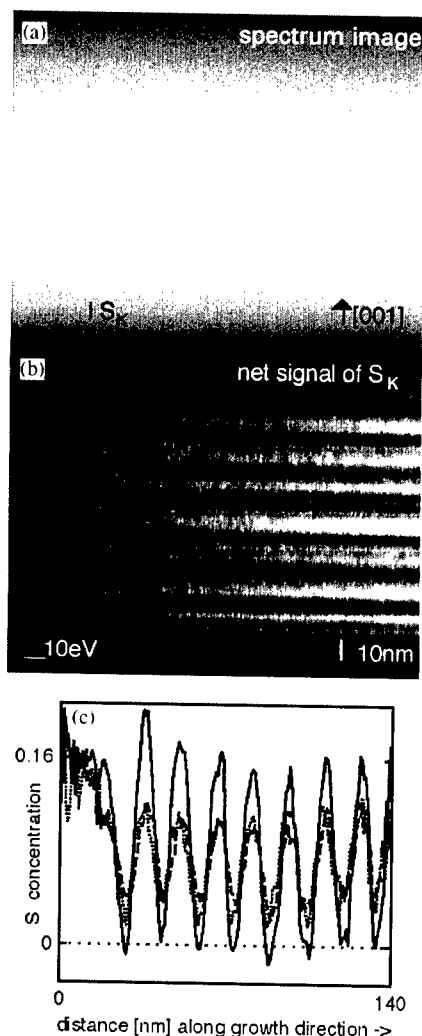


Fig. 1. Spectrum image (a), net signal after background subtraction (b) and calculated sulphur profiles (c) for the as-grown specimen (solid line), an annealed (dotted), and an annealed and irradiated specimen (dashed).

structure. After fitting an inverse power law background in front of the S_K edge at 2472 eV and subtracting it off, the S_K edge is well discernible (Fig. 1b). Twenty spectrum images were thus recorded to improve the signal-to-noise ratio, and this was repeated for each of the three specimens analysed (the as-grown, an annealed, and an annealed and irradiated structure). The net S_K intensity was then integrated over 40 eV from the edge onset. Scaling the sulphur profiles in the ZnMgSSe barrier layers far away from the thin quantum wells to the nominal composition of 16 at% S, the concentration profiles of the different samples are directly comparable (Fig. 1c). The sulphur profiles are approximately Gaussian which allows a straightforward solution of Fick's law of diffusion. From the decrease of the amplitudes of the profile during the anneal (30 min at 277°C) the diffusivity of sulphur in this system has been calculated as $D = 6 \times 10^{-22} \text{ m}^2 \text{ s}^{-1}$. The sulphur concentration measured as $(2.2 \pm 0.6) \text{ at\%}$ in the CdTe quantum wells after anneal was later confirmed independently by modelling the observed blue shift of the emission lines with temperature [13,14].

Fig. 2a shows a $\langle 100 \rangle$ lattice image and Fig. 2b the corresponding averaged intensity profile of the thinnest CdTe quantum well embedded between CdMnTe (left) and CdMgTe (right). Thickness and defocus have been chosen so that the CdTe exhibits strong $\{022\}$ fringes

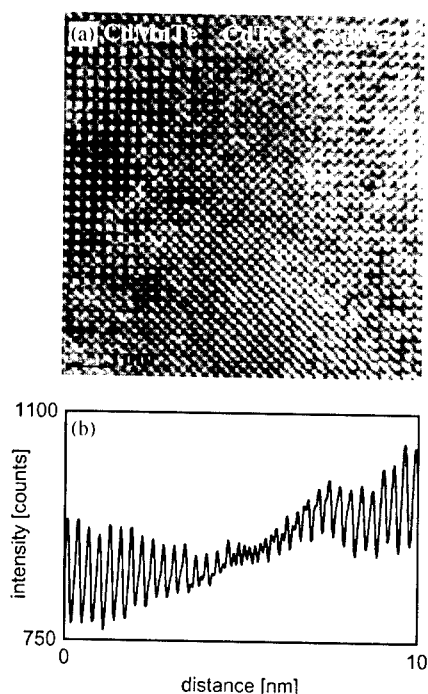


Fig. 2. Lattice image of an as-grown Cd(Mn,Mg)Te quantum well (a) and intensity profile (b), indicating about 3 monolayers transition widths.

while the ternary compounds show dominantly {002} lattice fringes, of opposite contrast. Both interfaces are visible as transition regions about 1 nm wide. Analyses of the other quantum wells gave similar results, with average interface widths of (2.7 ± 1.3) (002) monolayers for the as-grown structures.

Figs. 3a and b depict accumulated spectrum images taken of the as-deposited Cd(Mn,Mg)Te structure with different offsets. Figs. 3c and d show the corresponding net maps after background subtraction before the Mn_L and the Mg_K edges, respectively. The Te_M edge, just in front of the Mn_L edge, makes a background fit to Fig. 3a difficult; the best result was obtained by fitting a reference spectrum of pure CdTe to the wide peak of the Te_M edge. Profiles of the net maps were obtained by integrating over stripes 50 eV wide and are displayed for

all elements in Fig. 3e. The total exposure times for the elemental spectrum images were 5 s for Cd_M, 10 s for Te_M, 20 s for Mn_L and 200 s for the Mg_K edge, to yield comparable count rates. As the count rate, I , of an element (index i) is proportional to its concentration c , the exposure time t , and the ionisation cross-section s , the concentration can be calculated as

$$c_i = \frac{I_i/t_i s_i}{\sum_j I_j/t_j s_j} \quad (1)$$

It is known that the tabulated Hartree–Slater cross-sections used here [15] are accurate for the Mg_K and the Mn_L edge [16] but over-estimate the cross-sections of the delayed Cd_M edge [17]. Hence, the concentration of both Cd and Te will be underestimated and the calculated Mn and Mg concentrations in Fig. 3f will be somewhat too high. However, when the same procedure with the same integration windows is applied to the sample annealed for 15 s at 510°C, then the same systematic error will apply. From the ratios of the maximum concentrations before (c^{T0}) and after (c^{T1}) the anneal, the diffusion length, l , can be calculated from

$$\left(\frac{c^{T0}}{c^{T1}}\right)^2 = \frac{\sigma^2}{\sigma^2 + l^2}, \quad (2)$$

where σ describes the standard deviation of the as-deposited profile and can be approximated by the full interface width divided by 2.35 for a Gaussian [18]. From Figs. 3f and 4, the peak concentrations yield diffusion lengths of $l_{\text{Mn}} = 0.53$ nm for Mn and $l_{\text{Mg}} = 0.68$ nm for Mg. These can be converted into diffusivities, D , from the relationship $l = (2Dt)^{0.5}$ where $t = 15$ s is the annealing time. The results are $D_{\text{Mn}} = 9.2 \times 10^{-21} \text{ m}^2 \text{ s}^{-1}$ and $D_{\text{Mg}} = 1.6 \times 10^{-20} \text{ m}^2 \text{ s}^{-1}$, i.e. Mg is diffusing faster in this system than Mn, which is in accord with previous Zeeman studies [11].

Acknowledgements

Thanks are due to H. Kalisch, Aachen University of Technology, and J.A. Gaj, Warsaw University, for providing the epitaxial layer samples used in this study.

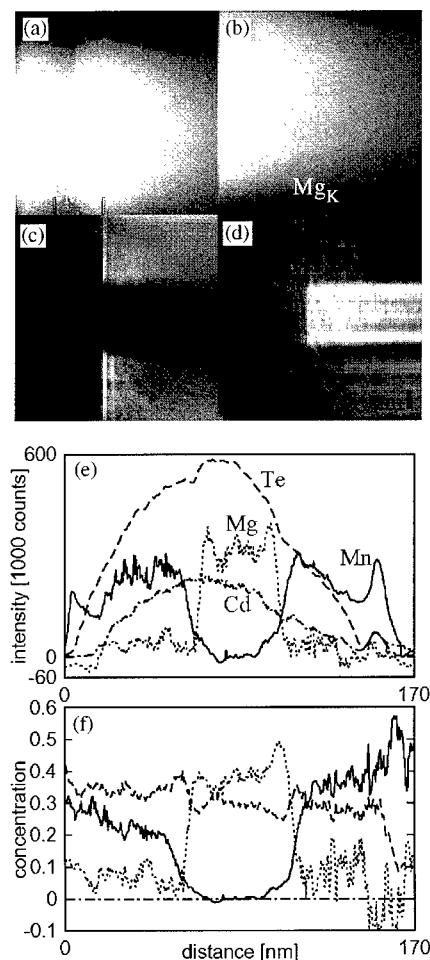


Fig. 3. Spectrum images with 500 eV (a) and 1200 eV (b) offset and background subtracted net maps of the Mn (c) and the Mg (d) signals. From the intensity line scans in (e) concentration profiles (f) can be calculated using Eq. (1). All data are from the as-grown Cd(Mn,Mg)Te.

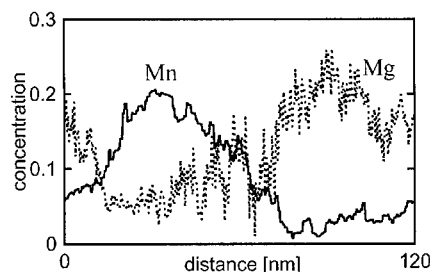


Fig. 4. Concentration profiles of the Cd(Mn,Mg)Te specimen annealed at 510°C for 15 s.

References

- [1] M.J. Kelly, *Low-Dimensional Semiconductors*, Clarendon Press, Oxford, 1995.
- [2] C.J.D. Hetherington, et al., *Mater. Res. Soc. Symp. Proc.* 37 (1985) 41.
- [3] A. Ourmazd, et al., *Phys. Rev. Lett.* 62 (1989) 933.
- [4] T. Walther, D. Gerthsen, *Appl. Phys. A* 57 (1993) 393.
- [5] F.M. Ross, W.M. Stobbs, *Philos. Mag. A* 63 (1991) 37.
- [6] T. Walther, C.J. Humphreys, *Inst. Phys. Conf. Ser.* 147 (1995) 103.
- [7] R.F. Egerton, *Electron Energy-Loss Spectroscopy in the Electron Microscope*, 2nd Edition, Plenum Press, New York, 1996.
- [8] L. Reimer, et al., *Microsc. Microanal. Microstruct.* 3 (1992) 141.
- [9] T. Walther, W. Mader, *Inst. Phys. Conf. Ser.* 164 (1999) 121.
- [10] H. Kalisch, et al., *J. Electron. Mater.* 26 (1997) 1256.
- [11] S. Mackowski, et al., *J. Crystal Growth* 184/185 (1998) 966.
- [12] A.G. Cullis, N.G. Chew, J.L. Hutchison, *Ultramicroscopy* 17 (1985) 203.
- [13] T. Walther, et al., *Phys. Stat. Sol. A* 180 (2000) 351.
- [14] I.P. Marko, et al., *Phys. Stat. Sol. A* 185 (2001) 301.
- [15] P. Rez, *Ultramicroscopy* 9 (1982) 283.
- [16] P. Schorch, H. Kohl, A.L. Weickenmeier, *Optik* 99 (1995) 141.
- [17] J. Auerhammer, P. Rez, F. Hofer, *Ultramicroscopy* 30 (1989) 365.
- [18] T. Walther, C.J. Humphreys, D.J. Robbins, *Defect Diff. Forum* 143 (1997) 1135.



ELSEVIER

Physica B 308–310 (2001) 1165–1168

PHYSICA B

www.elsevier.com/locate/physb

Trapped carrier electroluminescence (TraCE)—A novel method for correlating electrical and optical measurements

F.H.C. Carlsson*, L. Storasta, J.P. Bergman, E. Janzén

Department of Physics and Measurement Technology, Linköping University, SE-581 83 Linköping, Sweden

Abstract

SiC is a semiconductor with very good material properties for high power, high frequency and high temperature applications. During device fabrication irradiation with particles is often used, e.g., ion-implantation, which creates intrinsic defects. The most persistent defect in SiC is D_1 that appears after irradiation and subsequent high temperature annealing. A direct method called Trapped Carrier Electroluminescence (TraCE) for correlating minority carrier traps with luminescence measurements is presented. A semi-transparent Schottky diode under reverse bias is illuminated with a laser pulse of above band gap light to create minority carriers that are captured to traps in the space charge region. Majority carriers are introduced when the reverse bias is removed and the space charge region is reduced. The majority carriers recombine with the trapped minority carriers and the emitted light from the recombination is detected. TraCE has been used to study and correlate the D_1 bound exciton luminescence from intrinsic defects in SiC with an electrically observed hole trap HS1. © 2001 Elsevier Science B.V. All rights reserved.

Keywords: SiC; Defects; TraCE; D_1

1. Introduction

SiC is a semiconductor with very good material properties for high power, high frequency and high temperature applications. For device fabrication ion-implantation is used to create selectively doped regions. The ion-implantation will also produce a high amount of intrinsic defects. The most important of these is the so called D_1 defect [1] which is observed as a bound exciton recombination at low temperatures. The D_1 is observed strongly in photoluminescence (PL) or electroluminescence (EL) after irradiation and subsequent high temperature annealing, it can also be seen in as-grown material. It is persistent even after annealing above 1800°C. The D_1 exciton has previously been shown to be bound to an isoelectronic center and to act as a pseudo-donor [2], i.e., a tightly bound hole with a loosely bound electron. The spectrum and energy levels for the D_1 can be seen in Fig. 1. It has also recently been shown that the

D_1 correlates with a hole trap HS1, as seen in minority carrier transient spectroscopy (MCTS) [3]. Electrical or optical methods are commonly used to characterize defects. They can provide different bits of useful information. It is, however, often difficult to draw any conclusions about a common origin for electrically and optically measured defects. Most attempts to do so are based on annealing behavior in a limited temperature range and are prone to errors. In this work we present a direct method called Trapped Carrier Electroluminescence (TraCE) for correlating electrically observed minority carrier traps with luminescence measurements.

2. Experimental

The sample used was a 4H-SiC epitaxial layer grown by hot wall CVD on a standard Cree substrate irradiated with neutrons and subsequently annealed. The n-type doping was $2 \times 10^{15} \text{ cm}^{-3}$ according to capacitance-voltage measurement. A semi-transparent Ni-Schottky contact was evaporated on top and silver

*Corresponding author. Fax: +46-13-142337.

E-mail address: freca@ifm.liu.se (F.H.C. Carlsson).

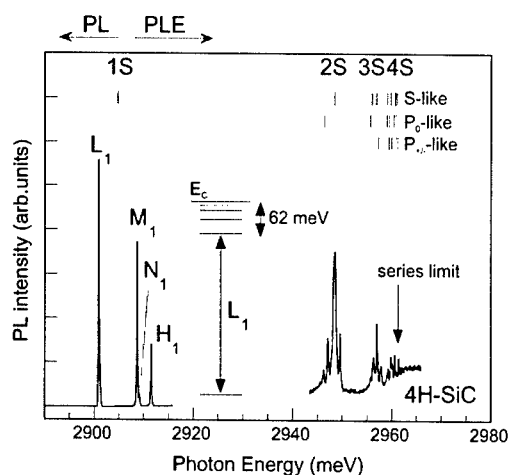


Fig. 1. PL and PLE spectra at 2 K of the D₁-BE in 4H-SiC. In the case of PLE the PL was monitored at the L₁ no-phonon line. The pseudo-donor nature of the D₁-BE is seen in the energy diagram.

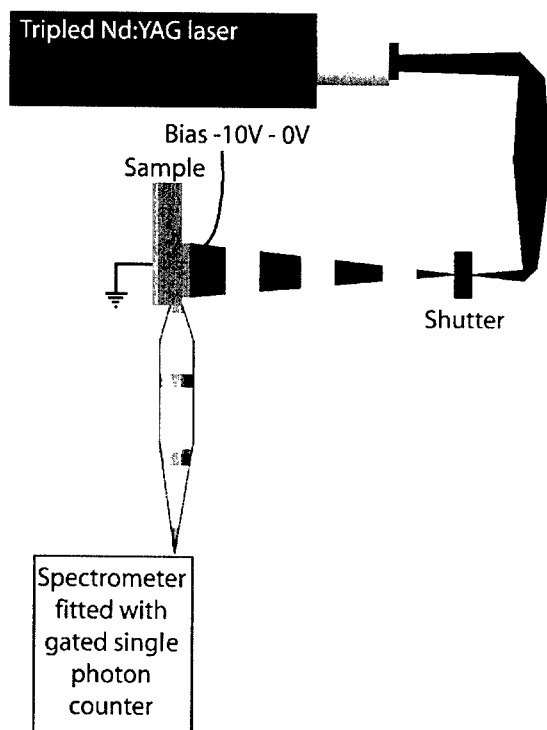


Fig. 2. The experimental setup for TraCE measurements.

paste was used as back contact. The experimental setup can be seen in Fig. 2, where the sample was mounted in a nitrogen cooled Oxford cryostat to control the temperature between 130 and 160 K. The emission was detected with a photomultiplier tube in single photon counting

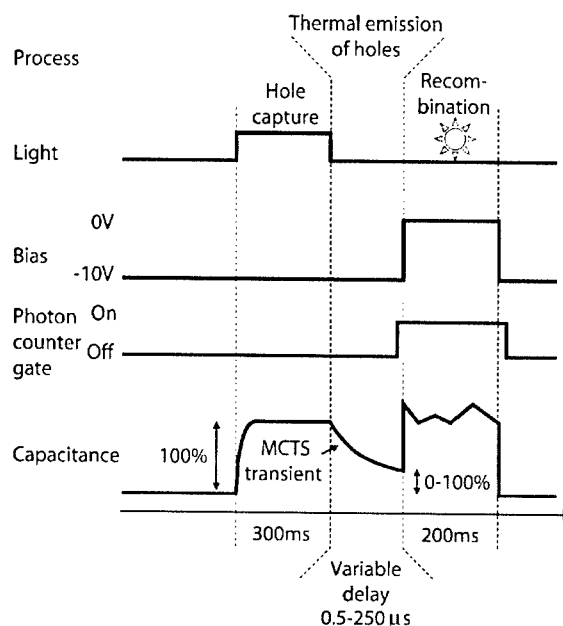


Fig. 3. The pulse sequence that creates the TraCE luminescence.

mode fitted to a 0.46 m spectrometer. For spectral measurements a 1200 l/mm grating with 1.0 mm slits were used and for transient measurements a 300 l/mm and 2.0 mm slits were used. The 1200 l/mm grating and 1.0 mm slits gives a resolution of 12 Å. A bias of -10 V on the Schottky contact was used and it was illuminated with a 300 ms laser pulse, controlled by a mechanical shutter, of above band gap light through the contact to create minority carriers that are captured to the traps in the space charge region. The capacitance was monitored with an oscilloscope to make sure that all the traps were filled with minority carriers. Given enough time and high enough temperature these trapped carriers will thermally be emitted to the band. In a standard MCTS measurement only the capacitance change due to the emitted carriers is observed. In the TraCE measurement a delay is introduced varying between 0.5 and 250 ms after the light pulse where the reverse bias is removed for 200 μs and majority carriers are introduced into the space charge region. The pulses and their individual changes can be seen in Fig. 3. The pulse sequence has a repetition frequency of 1.4 Hz. The majority carriers can then recombine with the remaining trapped minority carriers and create luminescence (see Fig. 4) that was detected through the edge of the sample. A gated photon counter was used to only count photons that were emitted during the emission due to trapped minority carriers. The spectral composition of the luminescence will be similar to that of PL or EL from the defect the minority carrier was trapped at. Experiments have been

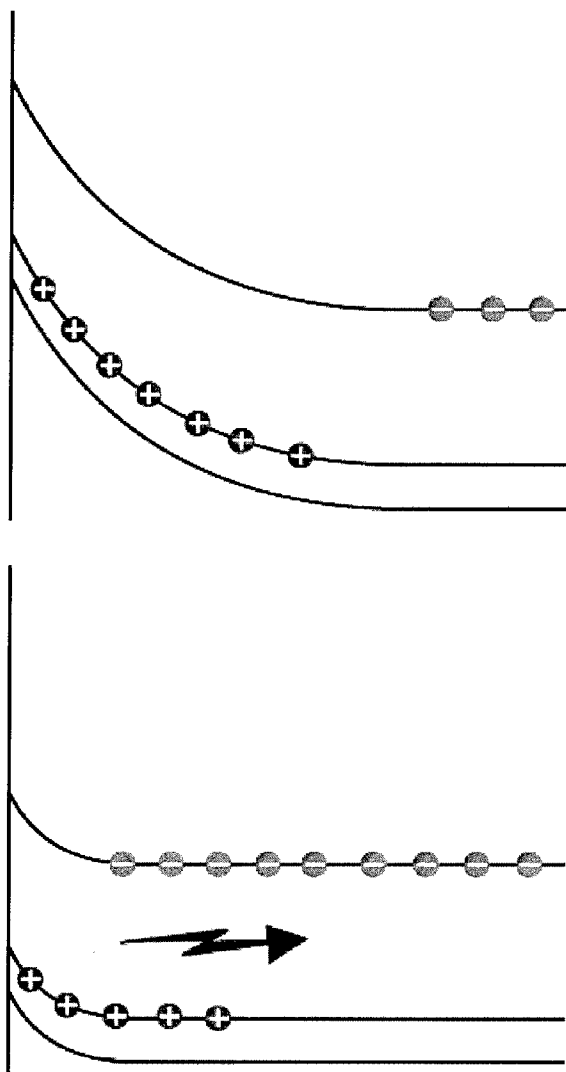


Fig. 4. The band diagram and carriers in the sample: (a) With reverse bias after the light pulse, (b) when the reverse bias is removed and recombination giving an emission occurs.

carried out to make sure that the recorded luminescence was the result of trapped minority carriers recombining with the later introduced majority carriers and not by PL or EL. The varied delay will make it possible to compare TraCE intensities with the capacitance transient in MCTS measurements if the recombination process is fast compared to the thermal emission. The capacitance shows that all the trapped minority carriers are removed after the 200 μ s bias removal.

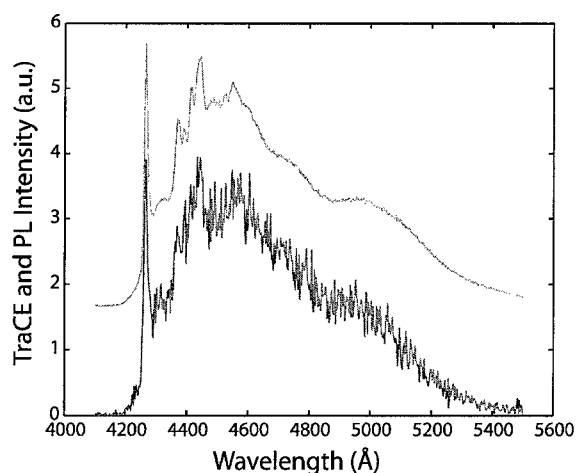


Fig. 5. The emission spectra obtained using TraCE (lower line) and PL (upper line) correspondingly, the PL spectrum is shifted upwards for clarity.

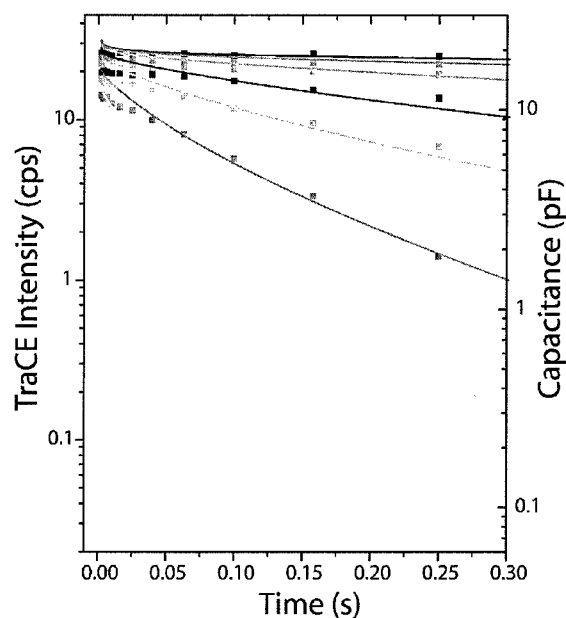


Fig. 6. The TraCE (squares) and MCTS (solid lines) transients for temperatures between 130 and 160 K.

3. Results

In PL and EL D_1 is dominating the spectrum for this sample. In MCTS a high concentration of HSI is seen. The spectrum (see Fig. 5) recorded from the TraCE measurements is identical with that for PL or EL for the same temperatures. Luminescence is only observed from

the sample when the reverse bias is removed. The intensity using the TraCE technique is however much weaker compared to PL or EL due to the low repetition frequency 1.4 Hz of the carrier injection. This gives an effective emission time close to 10^{-5} , with a corresponding intensity reduction. The transients detected by TraCE when the delay of the forward voltage pulse was varied agrees very well with the transients from MCTS for HS1 for the whole temperature range, as can be seen in Fig. 6, proving that the optical and electrical signal originates from the same defect. TraCE has been used to study and correlate the D_1 bound exciton luminescence from intrinsic defects in SiC with an electrically observed hole trap HS1. This correlation is consistent with the proposed model of the defect as a pseudo-donor [2], i.e., a hole is first tightly bound to a neutral defect and an electron is then captured by the coulomb attraction and becomes loosely bound.

4. Discussion

TraCE can correlate electrical measurements by MCTS with optical measurements such as EL and PL.

The luminescence intensities from TraCE are very low, since the luminescence time is only 10^{-5} of the total time, and great care must be taken to avoid any stray light or other sources of noise. The technique has so far only been applied to the D_1 (HS1) defect but can also be used for other minority carrier traps to correlate any luminescence emission with the corresponding electrically observed defect. The direct correlation between electrical and optical measurements avoids mistakes that can be made from other correlation attempts.

References

- [1] T. Egilsson, J.P. Bergman, I.G. Ivanov, A. Henry, E. Janzén, *Phys. Rev. B* 59 (1999) 1956.
- [2] L. Storasta, F.H.C. Carlsson, S.G. Sridhara, J.P. Bergman, A. Henry, T. Egilsson, A. Hallén, E. Janzén, *Appl. Phys. Lett.* 78 (2001) 46.
- [3] R. Brunwin, B. Hamilton, P. Jordan, A.R. Peaker, *Electron. Lett.* 15 (1979) 349.



ELSEVIER

Physica B 308–310 (2001) 1169–1172

PHYSICA B

www.elsevier.com/locate/physb

Defects related to DRAM leakage current studied by electrically detected magnetic resonance

T. Umeda^{a,*}, Y. Mochizuki^a, K. Okonogi^b, K. Hamada^b

^a *Silicon Systems Research Laboratories, NEC Corporation, 34 Miyukigaoka, Tsukuba 305-8501, Japan*

^b *Elpida Memory Incorporation, Sagami-hara 229-1198, Japan*

Abstract

The defects responsible for the charge leak of dynamic random access memory (DRAM) memory cells were revealed by a novel type of electrically detected magnetic resonance measurements. The detection sensitivity was greatly improved by using reverse-biased p–n junctions, which enabled us to specify the defect structure. Two types of defects were identified as the origin of the leakage currents; the spin-1 Si dangling-bond (DB) pair in divacancy-oxygen complexes ($V_2 + O$ and $V_2 + O_2$) or Si DBs of a different kind from the well-known Si DB center ($g = 2.0055$). It is notable that such defects remain in the device structure in spite of their low thermal stability in Si bulk. © 2001 Elsevier Science B.V. All rights reserved.

Keywords: DRAM; Leakage current; Defect; EDMR

1. Introduction

In the present and future Si ultralarge scale integrated circuits (ULSIs), process-induced point defects become increasingly crucial, due to downsizing of the device regions as well as complicated processing steps. At present, microscopic information on defects in ULSIs is quite limited. One major reason is that the amount of the defects is far below the detection limit of electron paramagnetic resonance (EPR). Alternatively, electrically detected magnetic resonance (EDMR) technique was developed (for a review see Ref. [1]) and a successful detection of residual defects in Si planar p–n junctions was demonstrated [2]. Since this technique monitors the magnetic resonance of defects via resonant changes in the device current, it is applicable to small sample volumes of ULSIs; moreover, only defects present along the current path and thus related to the device performance can be selectively detected. These advantages make it possible to approach a very few but important defects in actual ULSIs.

We present an EDMR study on the nude $n^+ - p$ junctions of the dynamic random access memory (DRAM) cells. This type of memory device is one of the most sensitive ULSIs to the influence of residual defects. For DRAMs, leakage currents in reverse-biased p–n junctions (junction leakage current, JLC) have to be suppressed in order to keep the capacitor charges as long as possible. The defects in the $n^+ - p$ junctions, however, act as an efficient source of additional JLC. We thus study the defects responsible for the JLC of DRAM cells. In order to directly correlate the defects with the JLC, the key issue is to measure EDMR under a reverse bias, which was very occasionally reported in previous literatures [3]. We carefully examined the reverse-bias characteristic of EDMR and eventually found that the detection under reverse bias is quite possible and even surprisingly sensitive to defects. Based on such EDMR experiments, we discuss the microscopic structures of point defects that cause the JLC.

2. EDMR measurements on reverse-biased p–n junctions

Fig. 1 shows the basic structure of the chip examined. This sample mimics the DRAM cells fabricated by the

*Corresponding author. Tel.: +81-298-50-1548; fax: +81-298-56-6138.

E-mail address: t-umeda@da.jp.nec.com (T. Umeda).

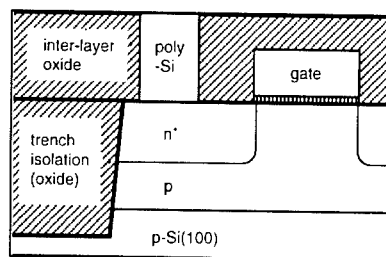


Fig. 1. Sample structure. The p- and n-type regions were produced by the implantation of B and P in a p-type (100) Si wafer.

0.3- μm rule ULSI process. Each cell has an n^+ -p junction with an adjacent switching metal-oxide-semiconductor-FET gate. The leakage current of the n^+ -p junction is used for EDMR. Our EDMR setup is based on a modified X-band EPR spectrometer [2]. The measurement temperature was carefully determined as follows. At low temperatures, the device current (I) decreases due to freeze out of carriers, while a low noise level of the resonant change (ΔI) is achieved due to reduction of the current noise. To gain the highest signal-to-noise ratio and keep the normal current-voltage characteristics, the measurement temperature was set at 230 K. No illumination was done to prevent the generation of photo-excited carriers.

It has been believed that the JLC under reverse bias is unfavorable for EDMR because of the too low current level. However, we found that the reverse JLC becomes extremely sensitive to the defects when high reverse voltages are applied to the junction (Fig. 2). The rate of the resonant current change ($\Delta I/I$) steeply increases over 100 ppm above 5 V. This $\Delta I/I$ value is much higher than observed under forward biases (30 ppm, independent of the forward bias). The reason why such an enhancement occurred will be simply because the reverse JLC was dominated by the defect-induced leakage currents. In contrast, p-n junctions under forward bias or photo illumination generate only a small fraction of recombination currents related to the defects as compared to the diffusion current. Thus, EDMR under a reverse bias has potential as a powerful technique to raise the defect detection sensitivity.

The location of defects can be known by changing the gate bias. Fig. 3(a) and (a') schematically show a role of the gate bias. When the gate is negatively biased with respect to the p-type substrate, the channel region becomes p-type. Further applying a high negative bias, the p-type layer, and thus depletion layer, expands into the near-surface n-type region (a'). The defects in the newly formed depletion region can cause the JLC and EDMR. Actually, both of the JLC (I) and the resonant change (ΔI) are found to increase exponentially with the gate bias [Fig. 3(b)]. This indicates that the defects are

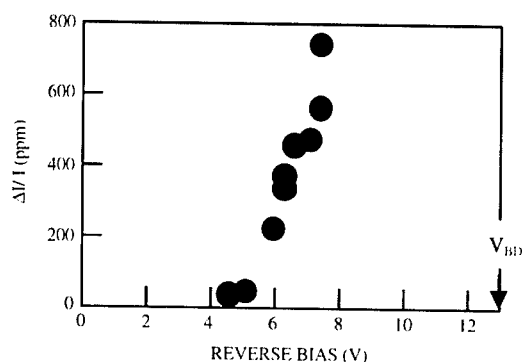


Fig. 2. Reverse bias dependence of the resonant change in a total current ($\Delta I/I$). The magnitude of $\Delta I/I$ is shown in the peak-to-peak intensity of a first-derivative signal. The gate voltage was set to be -3.2 V. V_{BD} represents the breakdown voltage.

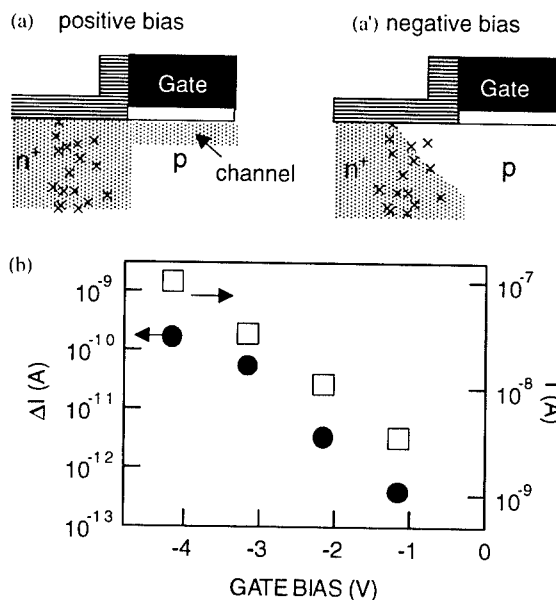


Fig. 3. (a)---(a') Schematic views of the gate-induced expansion of the depletion region. Crosses represent the defects. (b) Gate-bias dependence of ΔI (solid circles) and I (open squares), measured at a reverse bias of 7.3 V.

located in the n-type side of the junction. Also, there is a good correlation between the JLC and ΔI .

3. Identification of defects

A typical EDMR spectrum for the JLC is shown in Fig. 4(a). The spectrum consists of two parts: one main broad resonance at g (g value) = 2.0055 and weak multi lines at the both sides. The main broad signal resembles to those from the well-known Si dangling bond (DB)

observed in amorphous Si [4] and also in Si crystals damaged by implantation [5], radiation [6,7], or mechanical stress [8]. Their isotropic and single-peak features are thought to indicate that the Si DBs are randomly oriented and isolated from each other. However, the same picture of the DBs cannot be applied to the present case, because the n^+ -p junction of our sample is fully composed of crystalline Si lattice. A similar DB signal has been observed in the other type of planar Si p-n junctions which are also composed of crystalline Si lattice [2]. In Ref. [2], the DB signal was so weak that detailed spectroscopic features could not be resolved. On the other hand, very-low-noise spectra we obtained [Fig. 4(b)] reveals that the present DB signal really has anisotropy. As seen in the figure, when the external magnetic field (**B**) is aligned to the [100] direction, the peak moves toward lower magnetic field and becomes slightly sharp. This anisotropy evidences that the Si DBs are not randomly oriented in our samples. We consider that the observed anisotropy is related to the crystalline matrix of the relevant Si DBs, which will be studied in detail elsewhere.

The weak multi-lines seen in Fig. 4(a) seem to be a new EDMR signal. We tentatively call it signal A, hereafter. In contrast to the main DB signal, the signal A showed a strong **B** dependence. Fig. 5(a) shows its angular dependence with respect to a magnetic field rotation in the (0 $\bar{1}$ 1) plane. One notable character of this pattern is that the ratio between the splitting widths at **B**||[100] and **B**||[110] is just 1:2. This strongly suggests that the signal splitting originates from the fine (electron spin–electron spin) interaction which is nearly

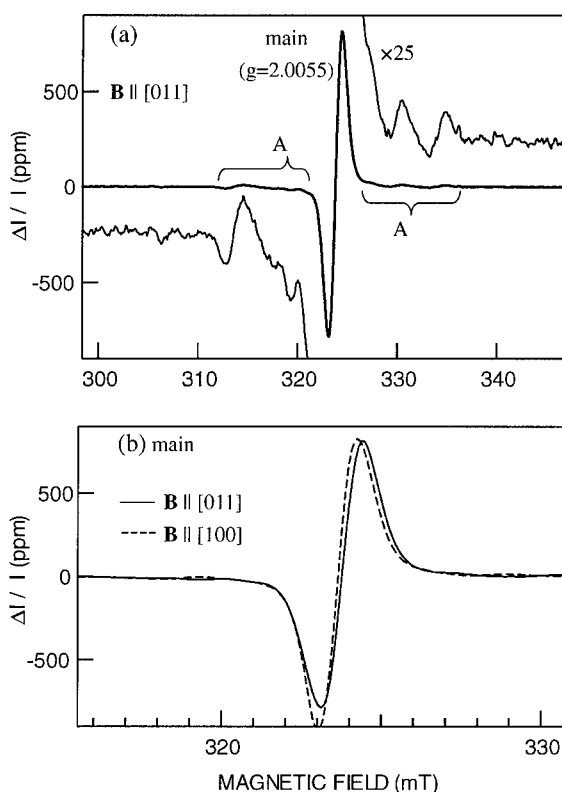


Fig. 4. (a) EDMR spectra for the JLC of the DRAM cells, and (b) the main signal. The magnitude of the JLC was 100 nA at reverse and gate voltages of 7.3 V and -4.2 V, respectively. The spectra in (a) and (b) were measured using the magnetic field modulation of 0.9 and 0.4 mT, respectively.

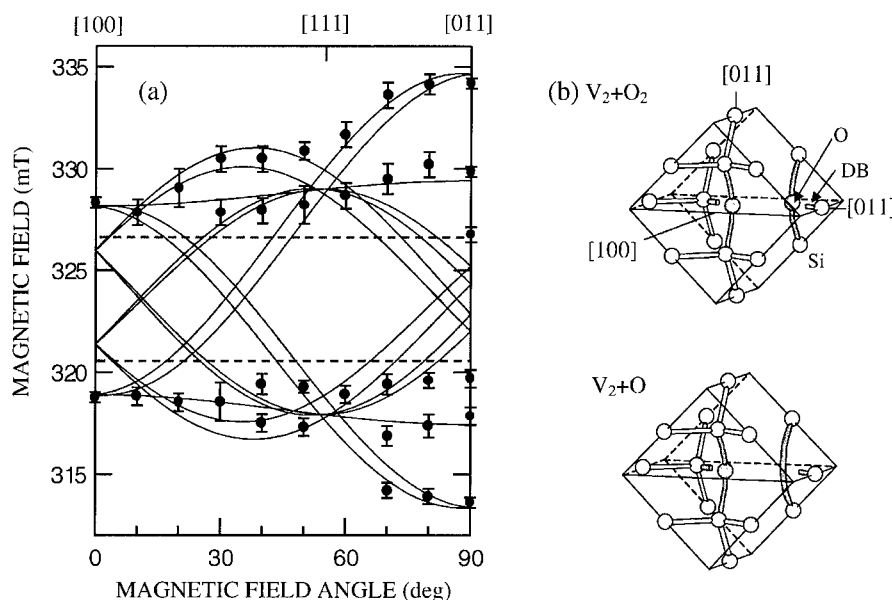


Fig. 5. (a) Angular dependence of the signal A. In the gray area, this signal is not clearly resolved due to the overlapped main signal. (b) The microscopic origins of the signal A.

axial symmetric around the $[011]$ direction. Previously, similar fine interactions were reported for a series of the spin-1 vacancy-oxygen complexes in radiation damaged Si [9–12]. Such complexes retain a pair of Si DBs, which generate the fine interaction. The solid lines in Fig. 5(a) are calculated by adopting the same defect system known for the divacancy plus one oxygen ($V_2 + O$, the A14 center) [10] or that plus two oxygen atoms ($V_2 + O_2$, the P2 center) [9]. The best fit between the calculation and experimental data was obtained with averaged EPR parameters of the two centers. Therefore, we conclude that the signal A originates from a combination of the P2 and A14. The microscopic origins of this signal are given like Fig. 5(b). The oxygen incorporation possibly occurs during the dopant implantation through surface oxides and/or the thermal oxidation process.

Since our chips never received radiation damages or other intentional damages, it is reasonable to consider that the present defects are created by the dopant (phosphorous) implantation. This assignment is also supported by the fact that they are present in the n^+ -type region, which was formed by the ion implantation. After the implantation, our chips were subjected to annealing at a temperature of higher than 800°C . This is much higher than the anneal-out temperature for $V_2 + O$ and $V_2 + O_2$ ($<400^\circ\text{C}$) observed in radiation damaged Si [9]. Also the DB signal ($g = 2.0055$) usually disappears when implantation damaged Si wafers are annealed at the relevant temperature range [5]. Therefore, our observation indicates that the thermal annihilation of the defects is suppressed in the device structures. The device regions are usually surrounded by the substrate surface and isolation structures. These may inhibit the annihilation of the defects.

For the Si DB pairs in $V_2 + O$ and $V_2 + O_2$, it is reasonable to treat their DBs individually, because of the large separation between the DBs [9]. Also the DB center of $g = 2.0055$ can be regarded as a single-DB system [2–4]. Thus, we discuss the EDMR mechanism using a simple system, which consists of one carrier and one unpaired electron (an electrically neutral Si DB) in reverse-biased junctions. This system allows only one primary spin-dependent process in which the DB captures a valence-band electron in p-type Si. On the other hand, the carrier generation via the DB (electron emission to the conduction band of n-type Si) is not a spin-dependent process [13]. Therefore, the appearance of the EDMR signals is supposedly a consequence of the electron tunneling from p-type Si to the DB's levels. Such a tunneling probability naturally increases with the reverse voltage. Besides, the relatively high reverse voltage is necessary to extend the depletion region into

the n^+ -region where the DBs are present. We speculate that the drastic signal increase at high reverse voltages is attributed to these factors.

The actual reverse bias for keeping the capacitor charges is typically 1 or 2 V, which is lower than used for EDMR measurements. At such low voltages, the electron tunneling discussed above is largely suppressed. However, the carrier generation via the DB's levels can effectively contribute to the JLC. Therefore, in order to suppress the defect-induced JLC, it is necessary to remove the DBs from the n^+ -region. This will be achieved by optimizing the ion-implantation process and the subsequent annealing.

4. Summary

We have found implantation-induced point defects in the n^+ -p junctions of DRAM cells by means of a novel EDMR technique. The EDMR results clearly showed that such defects are responsible for the JLC in the reverse-biased junctions. The defect structures were assigned to be Si DBs or the spin-1 Si DB pairs of the divacancy-oxygen complexes ($V_2 + O$ and $V_2 + O_2$). We pointed out that the thermal annihilation of the defects is suppressed in the device structure than in the bulk, which indicates a significance of probing actual device regions.

References

- [1] S. Greulich-Weber, *Mater. Sci. Forum.* 143–147 (1994) 1337.
- [2] T. Wimbauer, K. Ito, Y. Mochizuki, M. Horikawa, T. Kitano, M.S. Brandt, M. Stutzman, *Appl. Phys. Lett.* 76 (2000) 2280.
- [3] F.C. Rong, E.H. Poindexter, M. Harmatz, W.R. Buchwald, G.J. Gerardi, *Solid State Commun.* 76 (1990) 1083.
- [4] T. Umeda, S. Yamasaki, J. Isoya, K. Tanaka, *Phys. Rev. B* 59 (1999) 4849.
- [5] K.L. Brower, W. Beezhold, *J. Appl. Phys.* 43 (1972) 3499.
- [6] M.A. Jupina, P.M. Lenahan, *IEEE Trans. Nucl. Sci.* 36 (1989) 1800.
- [7] D. Vuillaume, D. Deresmes, D. Stievenard, *Appl. Phys. Lett.* 64 (1994) 1690.
- [8] D. Haneman, *Jpn. J. Appl. Phys. (Suppl. 2)* (1974) 371.
- [9] Y.-H. Lee, J.W. Corbett, *Phys. Rev. B* 13 (1976) 2653.
- [10] E.G. Sieverts, J.W. Corbett, *Solid State Commun.* 43 (1982) 41.
- [11] K.L. Brower, *Phys. Rev. B* 4 (1971) 1968.
- [12] W. Jung, G.S. Newell, *Phys. Rev.* 132 (1963) 648.
- [13] F.C. Rong, W.R. Buchwald, E.H. Poindexter, W.L. Warren, D.J. Keeble, *Solid-State Electron.* 34 (1991) 835.



ELSEVIER

Physica B 308–310 (2001) 1173–1176

PHYSICA B

www.elsevier.com/locate/physb

Process-induced defects in nitrogen doped Czochralski silicon in diode processes

J. Lu, D. Yang*, J. Yang, D. Tian, Y. Shen, X. Ma, L. Li, D. Que

State Key Laboratory of Silicon Materials, Zhejiang University, Hangzhou 310027, People's Republic of China

Abstract

The process-induced defects in nitrogen doped CZ silicon (NCZ-Si) are investigated during diode processes. It was found that in the phosphorous predeposition (1230°C for 2 h), stacking faults and dislocations were formed in NCZ-Si, but in the common CZ silicon (ACZ-Si) only dislocations were observed. In boron diffusion process (1260°C for 30 h), the interstitial oxygen (O_i) concentration in NCZ-Si specimens fell to the corresponding solubility and all supersaturated O_i was precipitated. On the contrary, only slight oxygen precipitates were generated in ACZ-Si wafers. Correlated to oxygen precipitates, more dislocations were produced in the high resistance active region in NCZ-Si specimens in comparison with ACZ-Si. It is concluded that nitrogen enhances oxygen precipitation during diode processes. In phosphorous predeposition process, these oxygen precipitates in NCZ-Si resulted in not only dislocations, but also stacking faults. © 2001 Elsevier Science B.V. All rights reserved.

Keywords: Defects; Nitrogen; Diode process; Silicon

1. Introduction

In recent years, nitrogen behavior in single crystal silicon has been intensively studied. In general, nitrogen is used as a protective gas or a carrier gas in manufacture processes of very large scale integration (VLSI) circuits. It is well known that nitrogen in silicon can suppress microdefects [1,2], and lock dislocations to increase wafer mechanical strength [3–5]. It is also reported that nitrogen in silicon can enhance oxygen precipitation [6–8]. Elevated temperature treatment and high concentration doping are two features of the power diode process. In the early studies of oxygen precipitation in NCZ silicon [6–8], the annealing temperatures were all no higher than 1150°C; whereas in the power diode process, the processing temperature is over 1250°C. Usually at those elevated temperatures, grown-in oxygen precipitate nuclei are dissolved and the nucleation rate for new oxygen precipitates is very

slow. Therefore, it is expected that little interstitial oxygen can be precipitated during the diode processes. Furthermore, high concentration phosphorous diffusion during power diode processes generates supersaturated self-interstitial silicon that will impede oxygen precipitation [9–10]. However, up to now, there are few reports about the influence of nitrogen on oxygen precipitation during diode process.

Related to oxygen precipitates, extended defects can be generated in silicon. The difference between the volume of oxygen precipitates and silicon lattices causes strain field near the precipitates, which can then act as heterogeneous nuclei for stacking faults while supersaturated silicon interstitials exist [11]. Meanwhile, oxygen precipitates can also punch out dislocation loops to release the strain energy. This process usually takes place during annealing at medium temperatures or during cooling down processes following high temperature treatment [12]. It was also reported that nitrogen can increase the mechanical strength of silicon wafers by locking dislocations [3–5,13]. Thus, it is interesting to investigate whether and how nitrogen affects process-induced defects during the power diode processes.

*Corresponding author. Tel.: +86-571-8795-1667; fax: +86-571-8795-2322.

E-mail address: mseyang@ dial.zju.edu.cn (D. Yang).

In this paper, the influence of nitrogen on oxygen precipitation and the related defects during power diode processes has been investigated by means of FTIR measurement and optical microscopy technique. It was found that nitrogen enhanced oxygen precipitates, induced stacking faults in the active region in diodes and generated more dislocations during cooling process. Finally, the effect of nitrogen on dislocations caused by thermal stresses is also demonstrated.

2. Experiment

In nitrogen and argon atmosphere respectively, n-type $\langle 111 \rangle$ oriented NCZ and ACZ silicon ingots with the same phosphorous doping level were grown. The specimens marked N0, N1, N2 and N3 were cut from the different positions of the NCZ silicon ingot from seed end to tail end. The specimens marked A0, A1, A2 and A3 were cut from the ACZ silicon at the same positions as those of the NCZ specimens. The wafers with the resistivity of 20–40 Ωcm were about 300 μm in thickness. At first the specimens were annealed at 650°C for 30 min to annihilate thermal donors. And then the wafers were used to fabricate diodes.

The main diode fabrication processes were as follows: phosphorous pre-deposition at 1230°C for 2 h, boron main-diffusion at 1260°C for 30 h and nickel metallization at 650°C for 60 min. After phosphorous pre-deposition and boron diffusion process, the wafers were respectively cleaved off and etched in Sirtl etchant to delineate dislocations and stacking faults by optical microscopy.

The wafers with the thickness of 2 mm were cut from the same positions as those used in diodes fabrication. Those wafers were used to follow diode processes and to monitor the interstitial oxygen concentration in the diode processes. The interstitial oxygen concentration and oxygen precipitates were characterized by FTIR at room temperature according to the absorption lines at 1107 and 1224 cm^{-1} , respectively. The calibration factor of $3.14 \times 10^{17} \text{ cm}^{-2}$ was used for calculating interstitial oxygen concentration.

3. Results and discussion

3.1. Oxygen precipitates and dislocations in NCZ silicon

Fig. 1 shows the interstitial oxygen concentration in ACZ and NCZ silicon before and after diode processing. It demonstrates that in NCZ silicon, the interstitial oxygen concentration fell to the corresponding solubility concentration in the diode process, and all supersaturated interstitial oxygen was precipitated. For the ACZ silicon, only in the A0 specimen with high

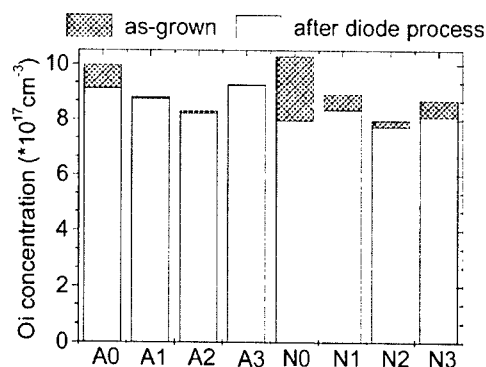


Fig. 1. Interstitial oxygen concentration in silicon wafers before and after diode processes.

oxygen concentration, the interstitial oxygen precipitated slightly. In the A1, A2 and A3 specimens, the interstitial oxygen concentrations have not changed in the diode processes.

In the experiments of Sun [6] and Aihara [7], typical high-low-high annealing as intrinsic gettering sequence and ramp-up annealing were used. They pointed out the enhanced nucleation effect of nitrogen on oxygen precipitation. In the experiment of Yang [8], where one and two step annealing methods were used to investigate the effect of nitrogen on oxygen precipitation, it was found that nitrogen in silicon can enhance oxygen precipitation at lower temperature ($< 750^\circ\text{C}$). In their experiments, the heat treatment temperature was not higher than 1150°C. In our experiments, the phosphorous pre-deposition and boron diffusion were carried out at 1230°C and 1260°C, respectively. It is found that, even in the elevated temperature treatments of diode processes in NCZ silicon, some oxygen precipitates were generated (Fig. 1).

The starting temperature and ramping up rate of the first step annealing during high temperature processes, which determine how many grown-in oxide nuclei can survive and continue to grow in subsequent high temperature treatments, are essential for oxygen precipitation. To avoid oxygen precipitate nuclei to be dissolved in ramping up processes, the ramping up rate must be low enough to guarantee that grown-in oxygen precipitate nuclei grow up and their radius are larger than the critical radius at high temperatures. The ramping up rate is usually chosen at 1–1.5°C/min [7,14]. In the phosphorous pre-deposition process of our experiments, the starting temperature (600°C) was lower and the ramping up rate (2°C/min) was a little higher. Therefore, in ACZ-Si the higher ramping up rate made no precipitated nuclei survive, and the nucleation rate at high temperatures was very slow, so that little oxygen precipitates could be generated in diode processes. During the phosphorous pre-deposition process

supersaturated self-interstitial silicon were produced [9], which also resulted in the dissolution of the grown-in nuclei and oxygen atoms were not easy to precipitate. As for the A0 specimen which was cut from the seed end and had higher oxygen concentration, it has undergone longer heat treatments during crystal growth, and more grown-in oxygen precipitates were formed. In the ramping up process of the diodes a few of grown-in nuclei would not be dissolved so that the smaller amount of interstitial oxygen atoms could precipitate in subsequent high-temperature treatments.

For all of the specimens from NCZ-Si, interstitial oxygen concentration decreased and oxygen precipitates were produced. There are three possible reasons. The first is that due to the enhancement of nitrogen a larger number of oxygen precipitates as nuclei during crystal growth were produced. In the diode processes some grown-in oxygen precipitates survived and oxygen precipitates could be formed. This reason is almost the same as that for the A0 specimen. The second is that although grown-in oxygen precipitates were dissolved in the diode processes, nitrogen as heterogeneous site could enhance oxygen precipitation even at higher temperatures, so that oxygen precipitates were generated. The third is that due to the effect of nitrogen, the grown-in oxygen precipitates nuclei with higher density were more stable and did not dissolve in the diode processes.

3.2. Stacking faults generated in NCZ silicon

After phosphorous pre-deposition process, the wafers were cleaved and were etched in Sirtl etchant for 5 min. The photos are shown in Fig. 2. It can be found that in NCZ specimens not only dislocations, but also stacking faults were generated, while in ACZ-Si wafers, no stacking faults were generated.

On the one hand, oxygen precipitates can induce formation of dislocations or stacking faults which is dependent of the annealing temperature and the structure of oxygen precipitates. If nitrogen was doped into crystal, the structure of oxygen precipitates could be changed [9], and both of stacking faults and dislocations might be generated. On the other hand, it is known that supersaturated self-interstitials are generated during phosphorous diffusion [10]. Normally, stacking fault embryos will be formed at strain centers in the bulk and at the surface [11]. Oxygen precipitates can also act as these strain centers. In the NCZ specimens, more oxygen precipitate nuclei survived as the nucleation centers of stacking faults after the phosphorous pre-deposition.

After boron diffusion process, the wafers were cleaved and were etched in Sirtl etchant for 5 min. The photos are shown in Fig. 3. It can be seen that in NCZ specimens the stacking faults disappeared. Considering the elevated temperature (1260°C) and the prolonged treatment time (30 h), the supersaturation of self-

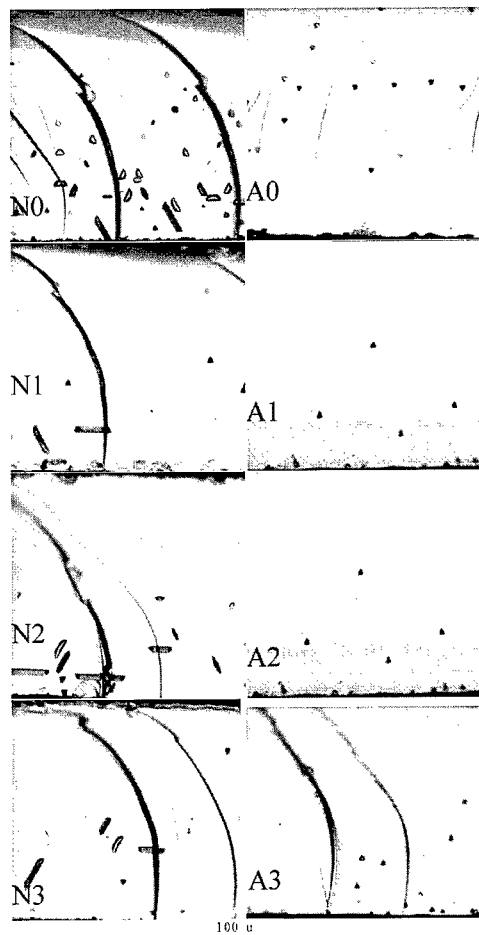


Fig. 2. Optical microscopic photos of ACZ and NCZ specimens cleaved and etched in Sirtl etchant for 5 min, after phosphorous pre-deposition process.

interstitials cannot be sustained in this process because of surface recombination, so the stacking faults will shrink and disappear.

3.3. Dislocations in NCZ silicon

From the photos shown in Fig. 3, it has been found that higher density dislocations were formed in the high resistance active region in the NCZ-Si specimens in comparison with the ACZ specimens, especially in the specimens with high initial oxygen concentration. Furthermore, the more oxygen precipitated, the more dislocations were generated. It can be deduced that those defects were oxygen precipitates related dislocation loops, but not misfit dislocations induced by high concentration diffusion [15]. In prolonged diffusion process, ripening process took place and larger precipitates grew up at the expense of smaller ones' dissolution. As a result, the residual oxygen precipitates

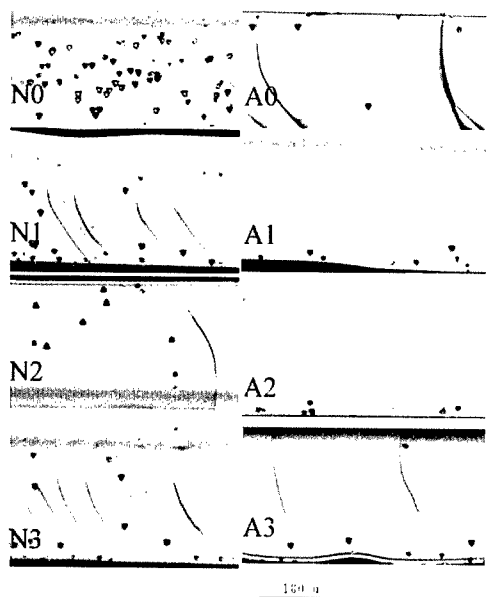


Fig. 3. Optical microscopic photos of ACZ and NCZ specimens cleaved and etched in Sirtl etchant for 5 min. after boron diffusion process.

with lower density grew up to large dimensions and could punch out dislocation loops to release the strain energy. This process usually takes place during cooling down process following high temperature treatment because of the big expansion coefficient difference between oxygen precipitates and silicon bulk [12].

4. Conclusion

In this paper, the behavior of oxygen precipitation and related defects in NCZ and ACZ silicon was investigated. It was found during the diode processes: (1) nitrogen in silicon can enhance oxygen precipitation; (2) in phosphorous pre-deposition process, not only dislocations, but also stacking faults were generated in NCZ specimens, while in ACZ-Si wafers only dislocations were generated. The stacking faults in NCZ silicon

disappeared in the subsequent boron diffusion process; (3) associated with oxygen precipitates, more dislocations were formed in NCZ silicon, especially in high oxygen concentration specimens.

Acknowledgements

The authors would like to thank the Natural Science Foundation of China for the financial supports (No. 59976035 and 50032010).

References

- [1] K. Nakai, Y. Inoue, H. Yokota, A. Ikari, J. Takahashi, *J. Appl. Phys.* 89 (2001) 4301.
- [2] Takao Abe, Hirofumi Harada, Jun-ichi Chikawa, in: S. Mahajan, J.W. Corbett, *Defects in Semiconductor II*, MRS, Boston, MA, 1983, p. 1.
- [3] T. Abe, K. Kikuchi, S. Shirai, S. Muraoka, in: H.R. Huff, R.J. Kriegler, Y. Takeishi, *Semiconductor Silicon 1981*, Electrochemical Society, Pennington, NJ, 1981, p. 54.
- [4] K. Sumino, I. Yonenaga, M. Imai, T. Abe, *J. Appl. Phys.* 54 (1983) 5016.
- [5] D. Li, D. Yang, D. Que, *Physica B* 273–274 (1999) 553.
- [6] Q. Sun, K.H. Yao, H.C. Gatos, *J. Appl. Phys.* 71 (1992) 3760.
- [7] K. Aihara, H. Takeno, Y. Hayamizu, M. Tamatsuka, T. Masui, *J. Appl. Phys.* 88 (2000) 3705.
- [8] D. Yang, Y. Ma, R. Fan, J. Zhang, L. Li, D. Que, *Physica B* 273–274 (1999) 308.
- [9] L. Li, D. Yang, *Microelectron. Eng.* 56 (2001) 205.
- [10] A. Armigliato, M. Servidori, S. Solmi, I. Vecchi, *J. Appl. Phys.* 48 (1977) 1806.
- [11] S.M. Hu, *J. Appl. Phys.* 45 (1974) 1567.
- [12] T.Y. Tan, W.J. Taylor, in: F. Shimura (Ed.), *Oxygen in Silicon, Semiconductors and Semimetals*, Academic, San Diego, 1994, p. 139.
- [13] H. Lu, D. Yang, L. li, Z. Ye, D. Que, *Phys. Stat. Sol. A* 169 (1998) 19.
- [14] G. Kissinger, D. Graf, U. Lambert, H. Richter, *J. Electrochem. Soc.* 144 (1997) 144.
- [15] S. Pressin, *J. Appl. Phys.* 32 (1961) 187.



ELSEVIER

Physica B 308–310 (2001) 1177–1180

PHYSICA B

www.elsevier.com/locate/physb

n-Channel conductance spectroscopy of deep defects in low temperature grown GaAs

C. Steen*, P. Kiesel, S. Tautz, S. Krämer, S. Soubatch,
S. Malzer, G.H. Döhler

Institute for Technical Physics I, University of Erlangen, Erwin-Rommel Str. 1, 91058 Erlangen, Germany

Abstract

We report on a new technique to characterize the deep defects in low temperature grown GaAs (LT-GaAs), based on a thin LT-GaAs layer embedded in the intrinsic zone of a pin diode. At this structure we have performed steady state and time dependent measurements of the n-channel conductance. Thus we deduce information about the activation energy and the capture time constant of the deep defects. © 2001 Elsevier Science B.V. All rights reserved.

Keywords: LT-GaAs; Electron emission rate; As_{Ga} -antisite defect

1. Introduction

GaAs, grown by molecular beam epitaxy (MBE) at low substrate temperatures (190–300°C) has unique electrical and optical properties which drastically differ from those of standard GaAs. Low temperature GaAs (LT-GaAs) has a very short lifetime of photogenerated carriers and close-to-intrinsic conductivity (after annealing) [1–3]. These properties are caused by a high excess of arsenic atoms, which are incorporated into the regular crystalline GaAs lattice as Ga sites (As_{Ga} -antisite defect). This leads to a point defect concentration of the order of 10^{20} cm^{-3} in as-grown material. The As_{Ga} -antisite defects are partially compensated by relatively shallow acceptors [4]. The concentration of As_{Ga} -antisite defects is reduced by thermal annealing at temperatures $> 400^\circ\text{C}$. The annealing process is associated with the formation of As-precipitates [5]. The attractive properties of the material persist in the annealed material. Currently it is not clear, how far the As_{Ga} -antisite defects or the clusters are responsible for the unusual properties of LT-GaAs.

Most investigations of LT-GaAs have been performed on “bulk” material (i.e. layers of about $1 \mu\text{m}$ thickness).

In LT-GaAs samples annealed at temperatures less than 600°C the penetration depth of space charge fields at the contacts is of the order of less than 10 nm, due to the high defect density. So standard methods like capacitance vs. voltage (CV) measurements or deep level transient spectroscopy (DLTS) are not suitable to study the deep defects in this material.

To overcome this drawback we have fabricated pin diodes with a thin layer of LT-GaAs (8 nm e.g.) in the i-layer [6]. In this case the sheet density of deep centers $n_{\text{T}}^{(2)} = N_{\text{T}} d^{\text{LT}}$ becomes so small that possibly all of them can be depleted under reverse bias. Here N_{T} is the concentration of deep defects and d^{LT} the thickness of the LT-GaAs layer. We have performed steady state and transient n-channel conductance measurements at different temperatures. From these investigations we can deduce the charge density $\rho_{\text{LT}}^{(2)}$, the activation energy ΔE and the electron capture cross section of the deep defects in the LT-GaAs layer.

2. Sample design

Here we report on two different pin diodes. A schematic band diagram of the double-hetero p–i–n diode, sample A is shown in Fig. 1. In sample B the $\text{i-Al}_{0.15}\text{Ga}_{0.85}\text{As}$ layer is replaced by an i-GaAs layer and

*Corresponding author. Fax: +49-9131-8527293.

E-mail address: steen@physik.uni-erlangen.de (C. Steen).

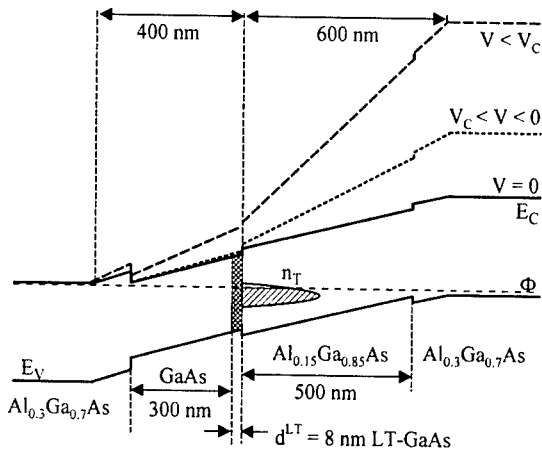


Fig. 1. Schematic band diagram of sample A for different voltages $V=0$, $V < V_C$ and $V > V_C$. For voltages $V \neq 0$ only the conduction band is depicted.

vice versa. The thickness of the $\text{Al}_{0.15}\text{Ga}_{0.85}\text{As}$ is 200 nm whereas the GaAs layer is 400 nm thick. During sample growth the LT-GaAs layer has been annealed in situ at 540°C. Thus, it exhibits both, a high density of As_{Ga} -antisite defects as well as small arsenic precipitates with an average diameter of 3–4 nm and a density of $1.5 \times 10^{17} \text{ cm}^{-3}$. In order to enable a precise evaluation of the effects related to the LT-layer reference samples were grown with the same layer structure except for a GaAs layer grown at 540°C instead of the LT-layer.

In this contribution we present measurements of the n-channel conductance G_{nn} . According to Poisson's equation the sheet carrier density $n^{(2)}$ and, hence, also the conductance of the n-layer, G_{nn} , is linearly related to the electric field F_1 on the left side of the LT-GaAs layer. This n-layer is moderately doped (10^{17} cm^{-3}) and sufficiently thin so that it is possible to detect minor changes of F_1 . According to Poisson's equation also the difference between F_1 and the field F_r on the right side of the LT-GaAs layer depends on the sheet charge density $\rho_{\text{LT}}^{(2)}$ stored in the LT-GaAs layer. Thus from the observed changes of G_{nn} as a function of reverse bias $\rho_{\text{LT}}^{(2)}$ can be deduced [6].

We have investigated both the steady state n-channel conductance as a function of reverse bias and as a function of time under a sudden bias change. Comparing the steady state n-channel conductance curves of the LT-samples and the reference samples we can determine the maximum sheet charge density in the LT-GaAs layer, $\rho_{\text{LT,max}}^{(2)}$. Measurements of the n-channel conductance as a function of time under a sudden change of bias, taken at different temperatures, provide information about the activation energy of the deep defects and their electron capture cross section.

3. Measurement of the steady state n-channel conductance

In Fig. 2 results of steady state measurements on the LT-GaAs and the reference samples are shown. In the reference diodes the n-channel conductance G_{nn} decreases with increasing reverse bias as expected due to the linear decrease of the width of the n-conducting channel. In LT-sample A, however, G_{nn} is almost constant up to a characteristic voltage V_C of about -9 V. For higher reverse bias the n-channel conductance decreases in the same way as in the reference diode.

In sample B the n-channel conductance is almost constant only up to a much lower voltage V_C of about -2 V. Up to around -10 V the slope of the curve is smaller than in the reference diode. For higher voltages the slope of the curve is the same as in the reference sample.

We interpret this behavior in the following way. The Fermi level of the traps Φ_T is pinned to the quasi Fermi level Φ_n of the top n-layer if we apply a reverse bias U_{pn} smaller than the voltage V_C . So the electric field F_1 on the left side of the LT-GaAs layer remains almost constant for these voltages, whereas the electric field on the right side is increasing. The activation energy for electrons in sample B is larger than in sample A due to the Al content on the left side of the LT-GaAs layer. Correspondingly, the activation energy for holes in sample B is smaller than in sample A. Thus, in sample B less defects have to be charged than in sample A, until the hole emission rate becomes comparable to the electron emission rate. So if the hole emission rate becomes comparable to the electron emission rate the Fermi level Φ_T is no longer pinned to Φ_n and F_1 increases in the same way as in the reference sample. The sheet charge density caused by singly charged deep donors and acceptors $\rho_{\text{LT}}^{(2)} = (n_{\text{D}}^{(2)} - n_{\text{A}}^{(2)})d^{\text{LT}}$ or charged As-precipitates can be determined from the increasing electric field kink, as mentioned above, using Poisson's equation $\Delta F = F_1 - F_r = \rho_{\text{LT}}^{(2)} / \epsilon_0 \epsilon_{\text{GaAs}}$.

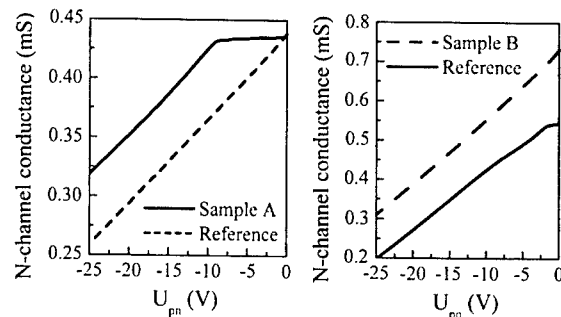


Fig. 2. The n-channel conductance versus applied reverse bias voltage for the reference and the sample A on the left side. The right graph shows the curves for the sample B.

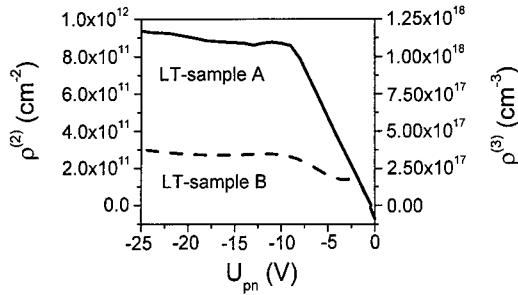


Fig. 3. The charge density in the LT-layer from sample A and B as calculated from the conductance measurements.

By comparison of curves obtained from the LT-GaAs samples and reference samples one can directly deduce the sheet charge density, depicted in Fig. 3. First we discuss the charge carrier density of sample A. The charge carrier density increases from $\rho_{\text{LT}}^{(2)} = -0.5 \times 10^{11} \text{ cm}^{-2}$ at zero bias to a value of $\rho_{\text{LT}}^{(2)} = 0.9 \times 10^{12} \text{ cm}^{-2}$ at a reverse bias of $V_C = -9 \text{ V}$. This charge carrier density screens the field F_1 on the left side of the LT-GaAs layer and so the n-layer conductance does not change up to V_C . For higher voltages the sheet charge carrier density remains practically constant. This corresponds to a density $\rho^{(3)} = \rho_{\text{LT}}^{(2)} / d^{\text{LT}} = 1.15 \times 10^{18} \text{ cm}^{-3}$. At reverse bias exceeding -9 V the field F_1 increases at about the same rate as for the reference sample (see also Fig. 2), indicating that there are no more electrons in deep traps.

The charge carrier density of sample B increases from $\rho_{\text{LT}}^{(2)} = -0.7 \times 10^{11} \text{ cm}^{-2}$ at zero bias (estimated from the equilibrium band picture for $U_{\text{pn}} = 0$) to a value of $\rho_{\text{LT}}^{(2)} = 0.15 \times 10^{12} \text{ cm}^{-2}$ at a reverse bias of $V_C = -2 \text{ V}$. From -2 up to -10 V the charge carrier density increases again to a value of $\rho^{(2)} = 0.3 \times 10^{12} \text{ cm}^{-2}$. For higher voltages the sheet charge carrier density does not change.

4. Measurement of the n-channel conductance under sudden bias change

In thermal equilibrium the electron emission rate of the deep traps, $N_{\text{T,em}}^0$ is equal to the electron capture rate, $N_{\text{T,capt}}^0$. Assuming a sharp trap level we have

$$N_{\text{T,em}}^0(t) = w_{\text{C} \rightarrow \text{T}} \exp\left(\frac{\Delta E}{k_B T}\right) N_{\text{T}}^0(t) N_{\text{C}}(T). \quad (1)$$

Here ΔE is the activation energy for electron emission and N_{T}^0 the number of neutral defects. The microscopic capturing probability $w_{\text{C} \rightarrow \text{T}}$ is related to the electron capture cross section Σ_{C} by $w_{\text{C} \rightarrow \text{T}} N_{\text{C}}(T) = v(T) \Sigma_{\text{C}} N_{\text{C}}(T)$, where $v(T)$ is the thermal velocity of the electrons and $N_{\text{C}}(T)$ the effective conduction band

density of states. The electron capture rate is given by

$$N_{\text{T,cap}}^0(t) = v(T) \Sigma_{\text{C}} N_{\text{C}}(T) \exp\left(\frac{E_{\text{C}}(x_{\text{LT}}) - \Phi_{\text{n}}}{k_B T}\right) N_{\text{T}}^+(t), \quad (2)$$

where N_{T}^+ stands for the concentration of ionized traps, $E_{\text{C}}(x_{\text{LT}})$ for the energy of the conduction band at the position of the LT-GaAs layer x_{LT} , and Φ_{n} for the quasi Fermi level in the n-layer.

In the following we confine ourselves to sample A. In Fig. 4 the n-channel conductance as a function of time is depicted. During the first 10 ms zero bias is applied to fill the defect states with electrons. This time is sufficiently long to reach the equilibrium value $\rho^{(2)} = -0.5 \times 10^{11} \text{ cm}^{-2}$ and the n-channel conductance reaches its equilibrium value as well. After that a reverse voltage U_{pn} is switched on with a time constant less than 1 ms, which is much shorter than the time constant for electron escape processes. The charge $\rho_{\text{LT}}^{(2)}(t)$ and therefore also the kink in the electric field at the LT-GaAs layer cannot change instantly. Therefore, we observe a discontinuous decrease of G_{nn} . Now $\rho_{\text{LT}}^{(2)}$ increases, according to Eq. (1), whereas the contributions due to Eq. (2) are negligible for short times. Shortly before G_{nn} reaches the steady state value corresponding to the applied reverse voltage U_{pn} the conductance change is slowed down rather abruptly, because $E_{\text{C}}(x_{\text{LT}}) - \Phi_{\text{n}}$ approaches the equilibrium value and the electron capture rate becomes relevant again. This will occur soon at a low reverse bias and later at higher U_{pn} as shown in Fig. 4a.

Note that the time constant of the exponential behavior is the same for all curves. Also, the transients occur only in the LT-GaAs sample. In the reference sample no changes are observable so we can be sure that the transients are associated with the LT-GaAs material.

To determine the activation energy we have measured the transients for a bias change of -8 V at different temperatures. Fig. 4b shows some typical transients for a reverse bias of $U_{\text{pn}} = -8 \text{ V}$ at different temperatures

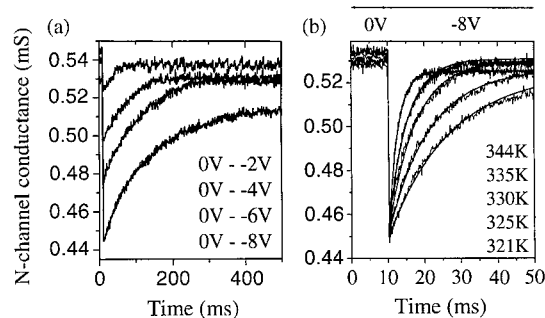


Fig. 4. The n-channel conductance under an abrupt bias change versus time for different reverse bias at room temperature (a) and for different temperatures (b).

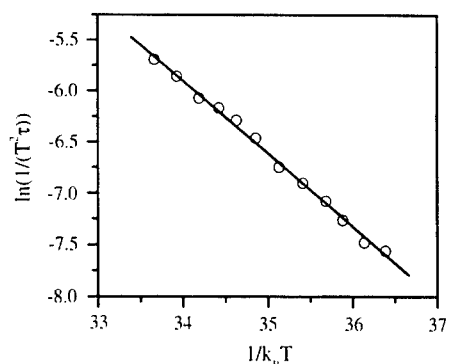


Fig. 5. The Arrhenius plot for the time constants.

with the corresponding exponential fits. The analysis of the exponential part provides the characteristic time constants. In Fig. 5 the Arrhenius plot of the time constants is depicted. Under the assumption of a T^2 dependence of the prefactor we deduce an activation energy $E_T = (710 \pm 60)$ meV and an electron capture time constant $\tau_{\text{cap}} \approx 1/N_T W_C \tau_T \approx 2 \times 10^{-13} \pm 1$ s.

This activation energy close to midgap, and the time constants favor the interpretation that we observe the effects of As_{Ga} -antisite defects and not of the As-precipitates. Also the density of clusters ($1.5 \times 10^{17} \text{ cm}^{-3}$) is hardly compatible with the large value of space charge in the LT-GaAs layer ($1.15 \times 10^{18} \text{ cm}^{-3}$).

5. Conclusions

The investigation of the n-channel conductance of a pin diode with an embedded LT-GaAs layer is a versatile technique to characterize the deep defects in LT-GaAs. We have deduced a concentration of deep traps $N_T = 1.15 \times 10^{18} \text{ cm}^{-3}$, with an activation energy $E_T = (710 \pm 60)$ meV. In particular we point out that the electron capturing time constant of $\tau_{\text{cap}} = 2 \times 10^{13} \pm 1$ s agrees well with the value obtained from optical fs-pulse experiments. Further studies will be devoted to samples with modified design. The results obtained from sample B, e.g., indicate that also hole emission can be studied in samples with suitable design.

References

- [1] M.R. Melloch, et al., Crit. Rev. Solid State Mater. Sci. 21 (1996) 189.
- [2] P. Kordös, et al., Appl. Phys. Lett. 67 (1995) 983.
- [3] S. Gupta, et al., IEEE J. Quantum Electron. 28 (1992) 2464.
- [4] D.C. Look, J. Appl. Phys. 70 (1991) 3148.
- [5] Z. Liliental-Weber, et al., Appl. Phys. Lett. 66 (1995) 2086.
- [6] K.-F.-G. Pfeiffer, et al., Appl. Phys. Lett. 77 (2000) 2349.



ELSEVIER

Physica B 308–310 (2001) 1181–1184

PHYSICA B

www.elsevier.com/locate/physb

Deep-level transient spectroscopy analysis of proton-irradiated n^+/p InGaP solar cells

N. Dharmarasu^{a,*}, M. Yamaguchi^a, A. Khan^a, T. Takamoto^b, T. Ohshima^c,
H. Itoh^c, M. Imaizumi^d, S. Matsuda^d

^a Semiconductor Laboratory, Toyota Technological Institute, 2-12-1 Hisakata, Tempaku, Nagoya 468-8511, Japan

^b Japan Energy Corporation, 3-17-35 Niizo-Minami, Toda, Saitama 335-8502, Japan

^c Japan Atomic Energy Research Institute, 1233 Watanuki, Takasaki, Gunma 370-1292, Japan

^d National Space Development Agency of Japan, 2-1-1 Sengen, Tsukuba, Ibaraki 305-8505, Japan

Abstract

Defects in p-InGaP produced by low-energy protons have been investigated by deep-level transient spectroscopy (DLTS). A new majority-carrier (hole) trap HP1 has been observed in low-energy proton-irradiated p-InGaP at 0.90 ± 0.05 eV above the valance band for the first time. The HP1 introduction rate for 100-keV proton-irradiated p-InGaP is 1500 cm^{-1} , which is 6 times higher than that (260 cm^{-1}) for the 380-keV proton-irradiated one. Isochronal annealing is found to annihilate the proton-induced HP1 defect above 300°C that is higher than the annealing stage (100°C) for 1-MeV electron-induced H2 center in p-InGaP. The carrier removal rates are found to be 61433 and 8640 cm^{-1} for 100 and 380-keV proton irradiation, respectively. Proton energy-dependent effects include decrease in both the carrier removal rate and in the defect introduction rate with increase in proton energy by creating HP1 trap.

© 2001 Elsevier Science B.V. All rights reserved.

Keywords: InGaP; Radiation; Deep level defects

1. Introduction

Studies of radiation effect in $\text{In}_{0.5}\text{Ga}_{0.5}\text{P}$ materials have become vital as a high-efficiency solar cell for space application [1–3]. Recently, 1-MeV electrons and 3-MeV protons irradiation effects in InGaP have been reported by the authors and others in Refs. [4–6]. Radiation-induced defects and the carrier removal effects are the important investigations to evaluate the performance of solar cells for their use in space, however, no reports were available on the aspects of the carrier removal effect and the nature of defects in p-InGaP by low-energy proton irradiation. Proton-induced displacement damage generally increases with decreasing particle energy [7]. Therefore, the contribution of low energy (<1 MeV) protons to the total degradation of solar cells

in a space environment containing protons with energies ranging from a fraction of keV to hundreds of MeV could be quite significant. In this paper, we present the investigation on the low-energy proton-induced deep level defects in n^+/p InGaP solar cells.

2. Experimental procedure

$\text{In}_{0.5}\text{Ga}_{0.5}\text{P}$ layers were grown on Zn-doped GaAs substrates with orientation of 5° off (1 0 0) towards [0 1 1] direction by the metallorganic chemical vapor deposition (MOCVD) method. For deep-level transient spectroscopy (DLTS) measurement, n^+/p junction with junction depth of $0.05 \mu\text{m}$ and area of $9 \mu\text{m}^2$ diodes were fabricated with base carrier concentration of $6.6 \times 10^{16} \text{ cm}^{-3}$. Samples were irradiated with 100 and 380 keV protons for the fluences of 1×10^{10} – $5 \times 10^{12} \text{ cm}^{-2}$ at room temperature using a 400 kV ion

*Corresponding author. Tel.: +81-52-809-1877; fax: +81-52-809-1879.

E-mail address: dharm@toyota-ti.ac.jp (N. Dharmarasu).

implanter. These diodes were characterized with DLTS and capacitance–voltage (C – V) measurements to find out the generations of defect levels and changes in the carrier concentration, respectively. Isochronal annealing has been carried out on the irradiated diodes for 30 min under inert atmosphere. The projected range calculated by stopping and range of ions in matter (SRIM [8]) for 100 and 380 keV protons into InGaP are 0.6 and 3.0 μm , respectively.

3. Results and discussion

3.1. Deep-level defect

DLTS spectra of the pre-irradiated and proton-irradiated p-InGaP layer are shown in Fig. 1. It was recorded with reverse bias 2 V and filling pulse width 1 ms and diodes scanned for the temperature range from 70 to 500 K. In the pre-irradiated p-InGaP, only two minority-carrier (electron) peaks E1 and E2 were observed below room temperature. Arrhenius plots used for the calculation of emission energy of the observed traps are shown in Fig. 2. Also, the native minority-carrier traps E1 and E2 appeared at $E_c = 0.20$ and 0.36 eV below the conduction band, with concentrations of 2.3×10^{15} and $5 \times 10^{14} \text{ cm}^{-3}$, respectively, and

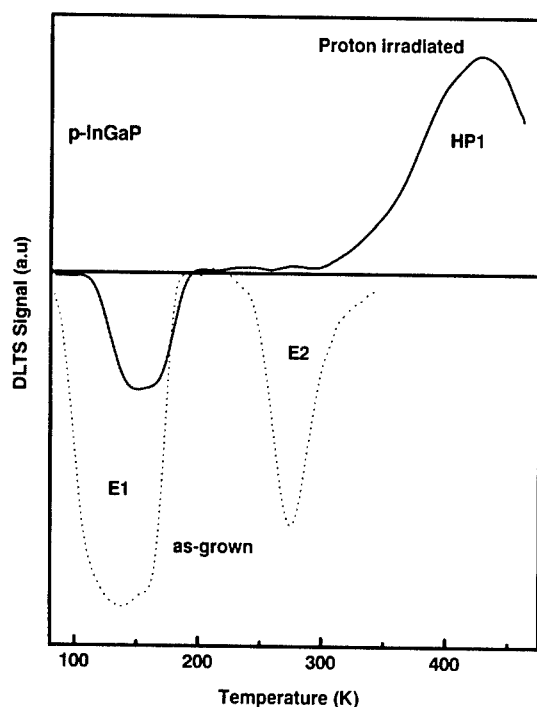


Fig. 1. DLTS spectra of pre-irradiated and 100-keV proton ($5 \times 10^{11} \text{ cm}^{-2}$)-irradiated p-InGaP layer.

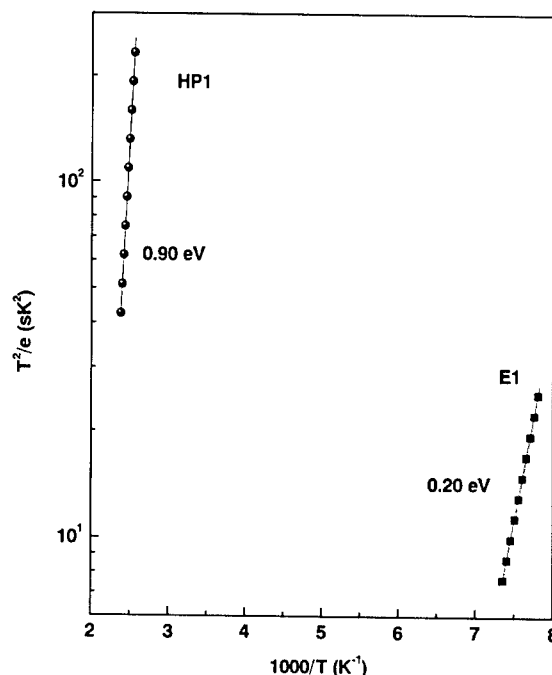


Fig. 2. Arrhenius plots used to calculate the activation energies for emission processes from traps E1 and HP1. E2 did not change with emission rate.

there were no majority-carrier peaks. The trap E1 that appeared during both majority and minority-carrier scans is attributed to the DX center [4]. The peak E2 could not be accurately evaluated, as it did not change with emission rate but its energy was in the range of 0.36 eV. A detailed characteristic of the native traps E1 and E2 are discussed by the authors in Ref. [4].

On the low-energy proton-irradiated p-InGaP, a new majority-carrier (hole) trap labeled HP1 has been observed in p-InGaP at $0.90 \pm 0.05 \text{ eV}$ above the valance band for the first time. The HP1 majority-carrier trap appears at $E_v + 0.90 \text{ eV}$ for both 100 and 380 keV proton-irradiated p-InGaP, which means that the same kind of defect is produced for two different energies of proton irradiation. Majority-carrier traps in 1-MeV electron and 3-MeV proton-irradiated p-InGaP have been reported by the authors in Ref. [4] and others in Refs. [5,6]. In all these reports, the traps appear at relatively lower temperature compared to the present low-energy proton-induced hole trap. All this betokens that the defects induced by low-energy protons are of a different kind than that of the high-energy proton and electron-induced defects in p-InGaP.

Fig. 3 shows the HP1 trap concentration as a function of proton fluence and thermal annealing temperature. HP1 trap concentration increases with increasing proton fluences. The amplitude of HP1 peak provides the concentration N_T and thus the introduction rate $I_i =$

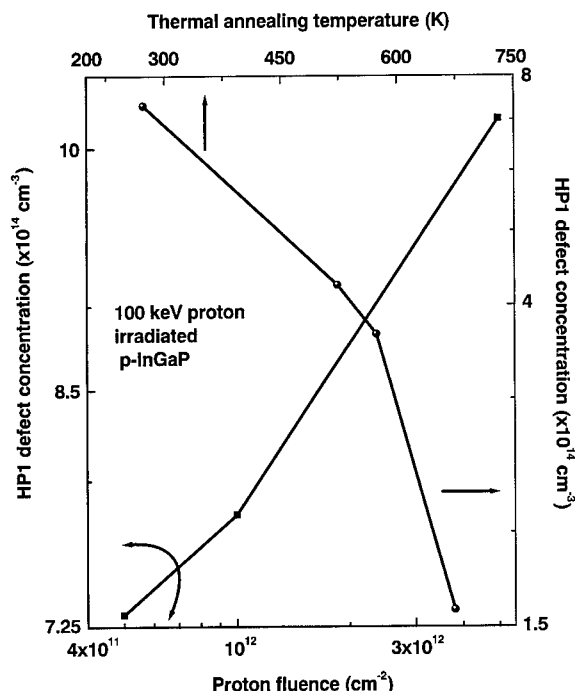


Fig. 3. HP1 trap concentration observed by DLTS as a function of proton fluence and thermal annealing temperature.

N_T/ϕ , where ϕ is the proton fluence. The calculated HP1 defect introduction rate for 100 keV proton-irradiated p-InGaP is 1500 cm^{-1} , which is 6 times higher than that (260 cm^{-1}) for the 380 keV proton-irradiated sample. However, the introduction rate decreases with increasing proton fluences.

To identify the origin of HP1 defect, thermal annealing experiments were carried out on the irradiated diodes. Upon isochronal annealing, it is found that the proton-induced defect HP1 is annihilated and the minority-carrier trap E1 increases with increasing annealing temperature (Fig. 4). The concentration of HP1 begins to decrease for the annealing temperature above 300°C for 30 min (Fig. 3), whose annealing stage is higher than that (100°C) of the 1-MeV electron-induced H2 center in p-InGaP [4]. The high temperature annealing indicates that the HP1 defect may be due to phosphorus-related vacancy complexes. Other possible defects such as In- or Ga-related vacancies are expected to anneal out at room temperature because of their lower migration energy. It has been reported that phosphorus vacancy (V_P) related interface trap is distributed in the energy range of 0.5–0.9 eV below the conduction band in InGaP and the V_P -related defects are expected to offer both acceptor and donor levels [9]. Therefore, HP1 defect is most likely to arise from the phosphorus vacancy-related complex, as the energy matches with trap levels reported in Ref. [9]. However,

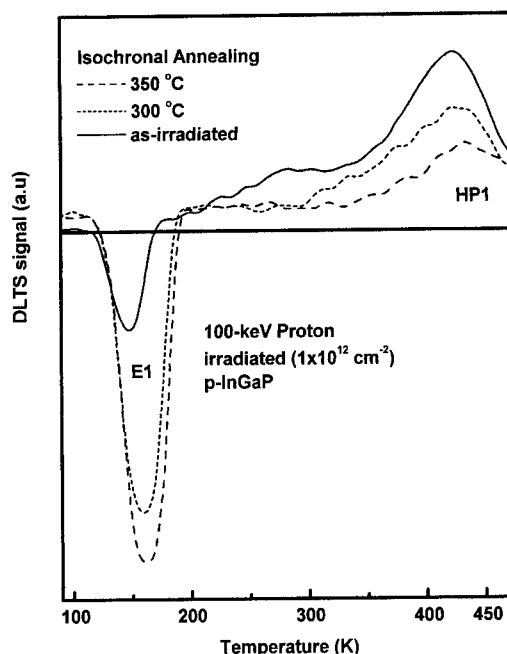


Fig. 4. Isochronal annealed DLTS spectra of the 100 keV proton-irradiated p-InGaP layer for the fluence of $5 \times 10^{12} \text{ cm}^{-2}$.

further work is underway to elucidate the properties and the exact origin of the HP1 defect.

3.2. Carrier removal rate

To find out the HP1 defect influence on the carrier concentration of the proton-irradiated p-InGaP, capacitance–voltage (C – V) measurements were carried out. The change in carrier concentration measured by C – V at room temperature, as a function of proton fluence is shown in Fig. 5. It is seen that there is a remarkable decrease in carrier concentration of p-InGaP base layer as a function of proton fluences for 100 and 380-keV protons. The carrier removal rate R_C is determined by fitting the curve to Eq. (1):

$$p_\phi = p_0 \exp\left(\frac{-R_C \phi}{p_0}\right), \quad (1)$$

where p_0 is the initial carrier concentration, p_ϕ is the carrier concentration as a function of proton fluences, ϕ is the proton fluence and R_C is the carrier removal rate. The carrier removal rates for 100 and 380-keV protons were 61433 and 8640 cm^{-1} , respectively. These are very high rates compared to the carrier removal rate of 0.93 cm^{-1} for 1-MeV electron-irradiated p-InGaP [4]. Carrier removal rate also depends on proton energy and it is observed to increase with decreasing proton energy. The carrier removal rate is 7 times higher for 100-keV

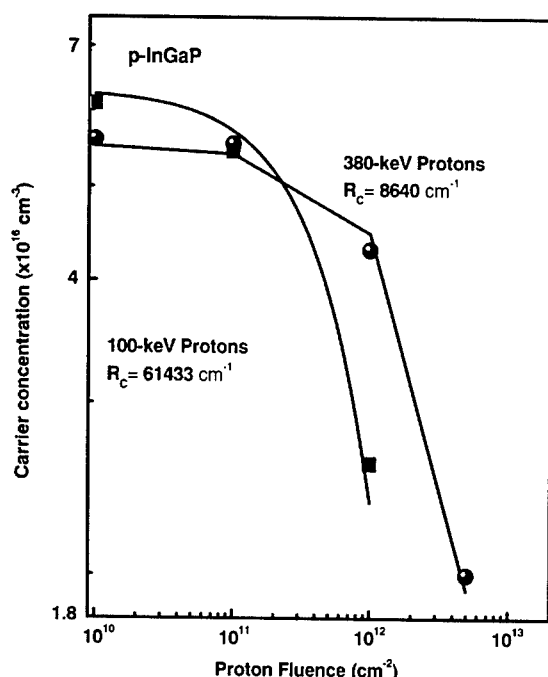


Fig. 5. Analytical and experimental changes in carrier concentrations of 100 and 380-keV proton-irradiated p-InGaP layer, as a function of proton fluence.

protons compared to 380-keV protons, while the HP1 defect introduction rate for 100-keV protons is 6 times higher than that for 380-keV protons. However, it is difficult to explain larger carrier removal rates (61433 and 8640 cm^{-1}) for 100 and 380-keV protons by creating only HP1 defect with lower defect-introduction rates (1500 and 260 cm^{-1}) for 100 and 380-keV protons. Further study is necessary to delineate other centers in p-InGaP. As a result of the decrease in the carrier concentration by creating deep-level defects such as HP1 defect in the p-InGaP layer with proton irradiation, a significant increase in the series resistance of the InGaP cell is induced. Therefore, an increase in the series resistance of the InGaP cell is thought to be one of the causes for the decreases in solar cell properties.

4. Conclusions

In conclusion, deep-level defects in proton-irradiated p-InGaP have been characterized by DLTS. For the first

time, low-energy proton-induced new majority-carrier (hole) trap HP1 in p-InGaP has been observed at $0.90 \pm 0.05\text{ eV}$ above the valance band. The introduction rates and possible origin of HP1 defect have been reported. Isochronal annealing has been found to annihilate the proton-induced HP1 defect above 300°C that is higher compared to the annealing stage for 1-MeV electron-induced H2 center in p-InGaP. Carrier removal rates have also been found to be 61433 and 8640 cm^{-1} for 100 and 380-keV proton-irradiated p-InGaP, respectively. Proton energy-dependent effects include decrease in both the carrier removal rate and the defect introduction rate with increase in proton energy by creating HP1 trap.

Acknowledgements

This work was partially supported by the Ministry of Education Culture, Sports, Science and Technology as a Private University High-Technology Research Center program and by the New Energy and Industrial Technology Development Organization as a part of the New Sunshine Program under the Ministry of Economy, Trade and Industry, Japan.

References

- [1] M. Yamaguchi, T. Okuda, S.J. Taylor, T. Takamoto, *Appl. Phys. Lett.* 70 (1997) 1566.
- [2] M. Yamaguchi, T. Okuda, S.J. Taylor, *Appl. Phys. Lett.* 70 (1997) 2180.
- [3] R.J. Walters, M.A. Xapsos, H.L. Cotal, S.R. Messenger, G.P. Summers, P.R. Sharps, M.L. Timmons, *Solid. State Electron.* 42 (1998) 1747.
- [4] A. Khan, M. Yamaguchi, J.C. Bourgoin, K. Ando, T. Takamoto, *J. Appl. Phys.* 89 (2001) 4263.
- [5] M.A. Zaidi, M. Zazui, J.C. Bourgoin, *J. Appl. Phys.* 73 (1993) 7229.
- [6] J.R. Dekker, A. Tukiainen, R. Jaakkola, K. Väkeväinen, J. Lammasniemi, M. Pessa, *Appl. Phys. Lett.* 73 (1998) 3559.
- [7] G.P. Summers, S.R. Messenger, E.A. Burke, M.A. Xapsos, R.J. Walters, *Appl. Phys. Lett.* 71 (1997) 832.
- [8] J.F. Ziegler, J.P. Biersack, U. Littmark, Pergamon Press, New York, 1985.
- [9] S.D. Kwon, H.K. Kwon, B-D. Choe, *J. Appl. Phys.* 78 (1995) 2482.



ELSEVIER

Physica B 308–310 (2001) 1185–1188

PHYSICA B

www.elsevier.com/locate/physb

Induced lattice defects in InGaAsP laser diodes by high-temperature gamma ray irradiation

H. Ohyama^{a,*}, T. Hirao^b, E. Simoen^c, C. Claeys^{c,d}, S. Onoda^e,
Y. Takami^f, H. Itoh^b

^a Department of Electronic Engineering, Kumamoto National College of Technology, 2659-2 Suya Nishigoshi Kumamoto, 861-1102 Japan

^b Takasaki JAERI, 1233 Watanuki Takasaki Gunma, 370-1292 Japan

^c IMEC, Kapeldreef 75, B-3001 Leuven, Belgium

^d K U Leuven, ESAT-INSYS, Kard. Mercierlaan 95, B-3001 Leuven, Belgium

^e Tokai University, 1117 Kitakaname, Hiratsuka, Kanagawa 259-1292, Japan

^f Rikkyo University, 2-5-1 Nagasaka, Yokosuka, Kanagawa, 240-0101 Japan

Abstract

Results of a study are presented on the degradation of InGaAsP laser diodes by high-temperature γ -ray and electron irradiation. It is shown that the optical power decreases after irradiation. One hole trap is observed in the $\text{In}_{0.76}\text{Ga}_{0.24}\text{As}_{0.55}\text{P}_{0.45}$ multi-quantum well active region after room-temperature γ - or e^- -irradiation. The deep levels are thought to be associated with the Ga-vacancy. The decrease of the optical power is ascribed to the carrier removal and to the mobility reduction by carrier scattering, through the induced lattice defects. The change of device performance and the introduction rate of lattice defects decrease with increasing irradiation temperature. The optical power after a 200°C irradiation is nearly identical as before, for the fluence range studied. © 2001 Elsevier Science B.V. All rights reserved.

Keywords: InGaAsP laser diode; Radiation damage; Induced deep levels

The $\text{In}_{1-x}\text{Ga}_x\text{As}_y\text{P}_{1-y}/\text{InP}$ semiconductor system has attained much interest for optoelectronic devices in the 0.95–1.65 μm wavelength region. Such detectors are good candidates for use in the telecommunication system of a spacecraft. Therefore, it is worthwhile to investigate the operation of such photodevices in a radiation environment. Some results on the radiation damage of laser diodes by proton and neutron irradiation have been reported before e.g. Refs. [1,2].

In the present paper, results are presented of an extensive study on the degradation of InGaAsP laser diodes by γ -ray and 2 MeV electron irradiation. The data are compared with previous neutron irradiation results [2]. In addition, the impact of the irradiation temperature is investigated, to assess the device behaviour in extreme space conditions (100°C and 200°C).

1.3 μm InGaAsP double channel planar buried hetero-structure (BH) laser diodes with an $\text{In}_{0.76}\text{Ga}_{0.24}\text{As}_{0.55}\text{P}_{0.45}$ multi-quantum well (MQW) active region were used in this study. The thickness of the MQW active region fabricated by MOVPE is 0.22 μm . Diodes were fabricated by a two-step LPE process. Pairs of 7 μm -wide and 3 μm -deep channels were formed by chemical etching to make a stripe mesa on a double heterostructure wafer which consisted of an n-InP buffer layer, an undoped InGaAsP active layer and a p-InP cladding layer on a (001) n-InP substrate. CrAu/TiPtAu and AuGeAuNi/TiAu were evaporated for anode and cathode contacts, respectively. Fig. 1 shows the schematic structure of the used InGaAsP laser diodes. More detailed on the diode process are described in previous paper [2].

Diodes were irradiated by an 8150.1 TBq ^{60}Co source at Takasaki JAERI. The fluence of the γ -ray was 1×10^7 rad (Si). Packaged diodes were also irradiated

*Corresponding author. Tel./fax: +81-96-242-6079.

E-mail address: ohyama@ec.knct.ac.jp (H. Ohyama).

with 2-MeV electrons to a fluence of $1 \times 10^{15} \text{ e/cm}^2$ produced by the Dynamitron at Takasaki JAERI. The sample temperature was fixed at 20°C, 100°C or 200°C and was controlled by a panel heater, mounted in a chamber with a Ti window of 50 μm thickness.

Before and after irradiation, the current/voltage (I/V) and capacitance/voltage (C/V) characteristics of the diodes were measured at room temperature. The optical power (P_L) as a function of forward current (I_F) was also characterised at 300 K. Fig. 2 shows the typical P_L/I_F characteristics before irradiation. As shown in this figure, the threshold current (I_{th}) before irradiation is around 9.4 mA. The induced deep levels in the $\text{In}_{0.76}\text{Ga}_{0.24}\text{As}_{0.55}\text{P}_{0.45}$ MQW active region were studied using the deep level transient spectroscopy (DLTS) method in the temperature range between 77 and 300 K. The emission rate window used in the measurements ranged from 1.18 to 26.51 ms. The applied filling pulse

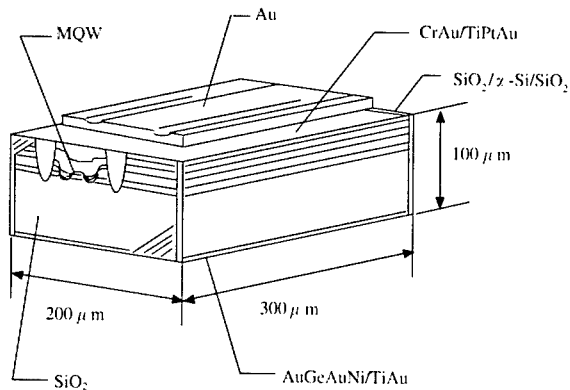


Fig. 1. Cross-sectional view of the InGaAsP laser diodes.

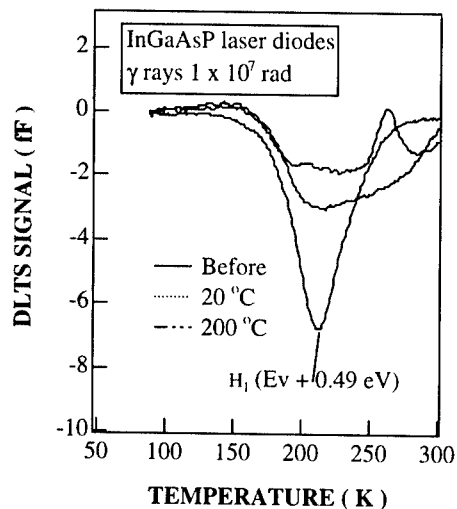


Fig. 2. DLTS spectra of InGaAsP laser diodes for γ -ray irradiations at different device temperatures.

ranged from -1 to 0 V , allowing to observe electron capture levels, and from -1 to 0.8 V to observe hole capture levels as well.

Fig. 2 shows the typical DLTS spectra for hole traps in the $\text{In}_{0.76}\text{Ga}_{0.24}\text{As}_{0.55}\text{P}_{0.45}$ MQW active region of InGaAsP laser diodes before and after a γ -ray irradiation, at different device temperatures. One hole trap with near mid gap energy level (H_1 ($E_v + 0.49 \text{ eV}$)) is observed after γ -ray irradiation at 20°C, while two hole capture levels are induced by a 1-MeV neutron irradiation [2]. The deep level in Fig. 2 is thought to be associated with the Ga-vacancy. After a 200°C irradiation, the levels are not observed, within the measurement resolution. The decrease of the optical power is ascribed to the induced lattice defects in the $\text{In}_{0.76}\text{Ga}_{0.24}\text{As}_{0.55}\text{P}_{0.45}$ MQW active region. The change of the device performance and the introduction rate of the lattice defects decrease with increasing irradiation temperature. This correlates with the behavior of the hole trap, suggesting it to be mainly responsible for the degradation of the optical power as mentioned below.

Both the reverse and forward current increase after irradiation. As shown in Fig. 3, the optical power decreases after a 1-MeV fast neutron irradiation at room temperature, while the threshold current increases [2]. The reason for the positive shift of the threshold current is mainly related to the decrease of the electron density due to the formation of radiation-induced lattice defects in the $\text{In}_{0.76}\text{Ga}_{0.24}\text{As}_{0.55}\text{P}_{0.45}$ MQW active region. The capacitance also decreases after irradiation. Two hole capture traps H_1 ($E_v + 0.25 \text{ eV}$) and H_2 ($E_v + 0.49 \text{ eV}$) are observed after a $1 \times 10^{16} \text{ n/cm}^2$ irradiation. These deep levels are thought to be associated with a Ga vacancy. The decrease of optical

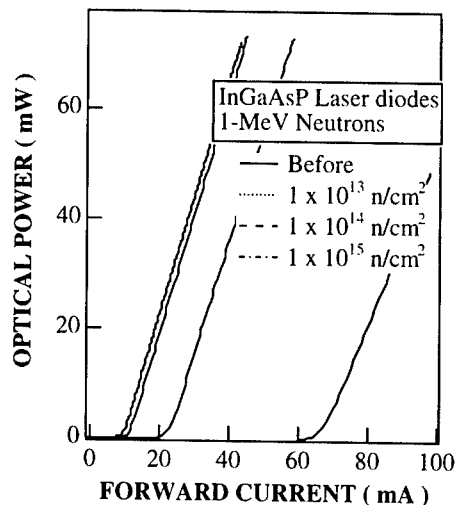


Fig. 3. Influence of 1-MeV neutron irradiation at room temperature on P_L/I_F characteristics.

power is related to the induced lattice defects in the $\text{In}_{0.76}\text{Ga}_{0.24}\text{As}_{0.55}\text{P}_{0.45}$ MQW active region, causing a reduction of the non-radiative recombination lifetime and of the mobility due to carrier scattering [2].

Figs. 4(a) and (b) shows the typical P_L/I_F characteristics for different irradiation temperatures and corresponding with γ -ray and 2-MeV electron exposures, respectively.

One can calculate the damage coefficient of P_L at $I_F = 20$ mA for different radiation sources at room temperature irradiation, defined by the following equation [3].

$$P_L(\phi) = P_L(0) + K_{PL} \phi, \quad (1)$$

where $P_L(\phi)$ and $P_L(0)$ are the P_L after and before irradiation, respectively, ϕ is the fluence.

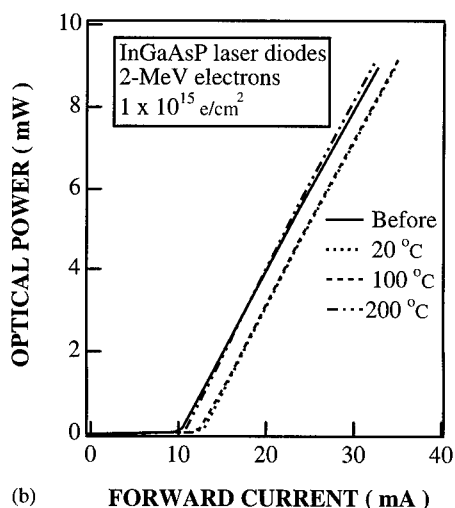
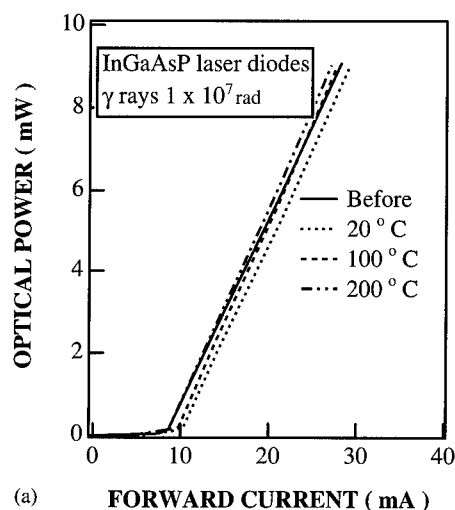


Fig. 4. P_L/I_F characteristics for different irradiation temperatures for γ -ray (a) and 2-MeV electron (b) irradiated InGaAsP laser diodes.

The equivalent 1-MeV electron fluence for 1 rad γ -rays is $1.08 \times 10^7 \text{ e/cm}^2$ [4]. K_{PL} for neutron, electron and gamma (equivalent 1-MeV electrons) irradiation is calculated to be $-3.4 \times 10^{-13} \text{ n}^{-1} \text{ mW cm}^2$, $-6.4 \times 10^{-15} \text{ e}^{-1} \text{ mW cm}^2$ and $-8.3 \times 10^{-16} \text{ e}^{-1} \text{ mW cm}^2$, respectively. The K value for neutrons is about three orders of magnitude larger than the one for electrons. The non-ionizing energy loss (NIEL) of GaAs for 1-MeV neutron and 1-MeV electron irradiation is calculated to be 0.8×10^{-3} and $1.8 \times 10^{-6} \text{ MeV cm}^2 \text{ g}^{-1}$, respectively. Based on this consideration, the radiation source dependence of the performance degradation is attributed to the difference of mass of the incident particle and the possibility of nuclear collision for the formation of lattice defects [5].

Fig. 5 shows the normalized P_L at $I_F = 20$ mA as a function of irradiation temperature for γ -rays and 2-MeV electrons. The optical power after a 200°C irradiation is nearly identical as before. The same tendency was observed for the I/V characteristics. Consequently, during high-temperature exposure, thermal annealing of the radiation damage takes place at the same time, reducing the device degradation.

In conclusion, the optical power decreases after irradiation, while the threshold current increases. One hole capture trap with near mid gap energy level is observed γ or electron after irradiation. The deep level is thought to be associated with the Ga vacancy. The degradation of the diode performance for neutron irradiation is about three orders of magnitude larger than for electron irradiation. The radiation source dependence of the performance degradation is attributed to the difference of mass of the incident particle and the possibility of nuclear collision for the formation of

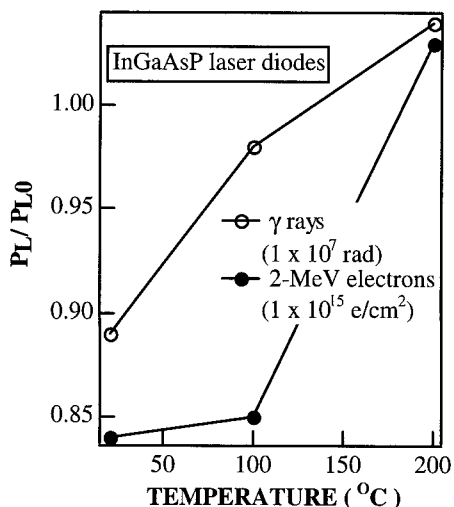


Fig. 5. Normalized P_L at $I_F = 20$ mA as a function of irradiation temperature for γ -rays and 2-MeV electrons.

lattice defects. The decrease of the optical power becomes smaller for higher device temperatures. The optical power after a 200°C irradiation is nearly identical as before, in the fluence/dose range studied.

Acknowledgements

Part of this work was supported by Grant-in-Aid for Scientific Research (No. 11695065 and 116507727) from the Japanese Ministry of Education for Science, by Sagawa foundation for promotion of frontier science and by Inter-University Laboratory for the Joint Use of JAERI Facilities. Mr. H. Takizawa of Takasaki JAERI

is thanked for his cooperation on the irradiation experiments.

References

- [1] B.D. Evans, et al., *IEEE Trans. Nucl. Sci.* 40 (1993) 1645.
- [2] H. Ohyama, et al., *Thin Solid Films* 364 (2000) 259.
- [3] H. Ohyama, et al., *IEEE Trans. Nucl. Sci.* 45 (1998) 2861.
- [4] G.P. Summers, et al., *IEEE Trans. Nucl. Sci.* 40 (1993) 1372.
- [5] H. Ohyama, et al., *IEEE Trans. Nucl. Sci.* 47 (2000) 2546.



ELSEVIER

Physica B 308–310 (2001) 1189–1192

PHYSICA B

www.elsevier.com/locate/physb

Defect characterization by DLTS of AlGa_xN UV Schottky photodetectors

M.J. Legodi*, S.S. Hullavarad, S.A. Goodman, M. Hayes, F.D. Auret

Department of Physics, University of Pretoria, Pretoria 0002, South Africa

Abstract

Deep traps are studied in MBE grown n-Al_xGa_{1-x}N Schottky photodiodes using deep level transient spectroscopy (DLTS). These daylight blind UV photodetectors have cut-off wavelengths of 300 and 250 nm, for $x = 0.12$ and 0.41 , respectively. Other investigations of deep centers are those by Gotz et al. who studied MOCVD Al_{0.12}Ga_{0.88}N (Appl. Phys. Lett. 69 (1996) 2379); and by Polyakov et al. who looked at p-AlGa_xN using an AlGa_xN/GaN heterojunction LED p-i-n structure (Solid State Electron. 43 (1999) 1929). Our photodiodes were MBE grown with carrier density $(5-9) \times 10^{17} \text{ cm}^{-3}$. We detect two levels, EOA2 and EOA1 in each photodetector, below 320 K, independent of the Al mole fraction, x . For Al_xGa_{1-x}N with $x = 0.41$, EOA2 has a DLTS signature ($E_C - 0.567 \text{ eV}$; $1.1 \times 10^{-14} \text{ cm}^2$) while the signature for the second defect, EOA1, is ($E_C - 0.274 \text{ eV}$; $3.1 \times 10^{-13} \text{ cm}^2$). From a comparison with as-grown defects in MBE grown n-GaN, it would appear, based on DLTS signatures that EOA1 is the same as E_1 ($E_C - 0.234 \text{ eV}$) observed by Wang et al. (Appl. Phys. Lett. 72 (1998) 1211) and EOA2 is the 0.61 eV level reported by Gotz et al. (Appl. Phys. Lett. 69 (1996) 2379). Furthermore, proton irradiation introduces an additional electron trap, EpR1, at 0.187 eV . We also determine that He-ions remove carriers in AlGa_xN, at a rate of $23\,770 \text{ cm}^{-1}$, eighty times higher than in GaN. © 2001 Elsevier Science B.V. All rights reserved.

Keywords: Aluminium gallium nitride; Defects; UV photodetectors

The III-Nitrides with bandgap energy 2–6.2 eV, are fast becoming the materials of choice for optoelectronic applications in the blue to ultra violet (UV) region. In particular, recent successes [1] with very low cut-off wavelength ($\sim 230 \text{ nm}$) Al_xGa_{1-x}N-based, visible-blind UV photodetectors, can open up new avenues for space applications. Potential applications include highly sensitive missile plume detectors, flame detectors, ozone monitoring and secure space communications. The materials system is also known for its insensitivity to environmental factors: e.g. corrosion and temperature. Temperature extremes $\pm 200^\circ\text{C}$ and particle irradiation from a few eV to MeVs are characteristic of the outer space environment.

We know from Silicon, GaAs and GaN how defects influence device performance. This knowledge is essen-

tial for predicting device failure and/or engineering desired properties in devices. From the limited investigations into deep levels in Al_xGa_{1-x}N photodetectors, we know that defects are responsible for the UV/visible contrast, the noise equivalent power (NEP) and the device response speed [2,3]. For example, GaN-based photodetectors grown with a GaN or AlN nucleation layer have sharper cut-off wavelengths and an enhanced UV/visible rejection than those grown directly on sapphire substrates. However, the device structure also influences device properties. For example, whereas photoconductors have a slow response of the order of milliseconds, Schottky photodetectors have typically fast response times of the order of nanoseconds.

Gotz et al. [4] detected a prominent deep level at 0.61 eV below the conduction band of MOCVD Al_xGa_{1-x}N ($x = 0.12$). They believed it to be the same as the 0.58 eV deep level in as-grown GaN. To our best knowledge, there are no DLTS reports on “as grown” or particle irradiation induced deep levels in MBE

*Corresponding author. Tel.: +27-12-420-4413; fax: +27-12-362-5288.

E-mail address: mlegodi@postino.up.ac.za (M.J. Legodi).

$\text{Al}_x\text{Ga}_{1-x}\text{N}$ Schottky photodetectors. In this study we observed that: the presence of as-grown defects, EOA1 and EOA2 in MBE $\text{Al}_x\text{Ga}_{1-x}\text{N}$ is independent of the Al mole fraction; EOA2 is similar to the level reported by Gotz et al. [4] in MOCVD AlGaIn ; and, EOA1 is similar to a level at $E_C - 0.234\text{ eV}$ that we detect in MBE GaIn . We also characterized a proton irradiation induced level, EpR1. We also performed dose dependency experiments and determined the carrier removal rate of 1.8 MeV He-ions, which is about 80 times greater than for GaIn similarly irradiated.

The photodetector diodes used were metal/ $\text{Al}_x\text{Ga}_{1-x}\text{N}$ Schottky-type structures with cut-off wavelengths of 250 and 300 nm, corresponding to Al mole fraction $x = 0.41$ and 0.12. The photodetectors were grown on sapphire substrates with a thin low temperature AlN nucleation layer. A 1000 nm thick n^+ - $\text{Al}_x\text{Ga}_{1-x}\text{N}$ Si-doped region was deposited in between the AlN nucleation layer and the 500 nm n - $\text{Al}_x\text{Ga}_{1-x}\text{N}$ Si-doped active layers. The free carrier concentration in the active layers were determined by conventional capacitance–voltage (C – V) measurements to be in the range $(5\text{--}9) \times 10^{17}\text{ cm}^{-3}$. A 10 nm semi-transparent Au Schottky contact facilitated the gathering of light by the diodes while a recessed alloyed Ti/Al contact on the n^+ layer acted as the ohmic.

A van de Graaff accelerator was used for both 1.8 MeV protons and 1.8 MeV He-ion irradiations. During the particle irradiation, the sample temperature did not rise above a few degrees from room temperature. A lock-in-amplifier (LIA) based DLTS [5,6] system with a closed-cycle liquid-Helium cooled cryostat capable of spanning the 20–350 K range was employed for defect characterization. The DLTS defect “signatures” which consist of the energy position, E_T , of the defect in the bandgap together with the defect’s majority carrier capture cross section, σ_n , were extracted from Arrhenius plots of e/T^2 vs. $1/T$, where e is the defect’s emission rate at a temperature T .

The photodetectors we used had responsivities $\sim 0.01\text{ A/W}$ and we typically measured room temperature currents of $\sim 10^{-8}\text{ A}$ with the diode at 1 V reverse bias. DLTS spectra of the diodes before particle irradiation show the presence of two “as grown” peaks, labeled EOA1 and EOA2 as depicted in Fig. 1. For the $\text{Al}_x\text{Ga}_{1-x}\text{N}$ photodetectors we looked at, i.e. with cut-off wavelengths of 300 nm ($x = 0.41$) and 250 nm ($x = 0.12$), EOA2 was always the most prominent defect. However, for $x = 0.41$ the FWHM for EOA1 and EOA2 are broader than for the same defect set in $\text{Al}_x\text{Ga}_{1-x}\text{N}$ with $x = 0.12$. We also find that EOA1 and EOA2 are uniformly distributed (in the area probed by DLTS) as shown by the inset in Fig 1. The depth profile in the inset was obtained using the fixed bias variable pulse mode of DLTS and the formalisms of Zohta [7]. We recorded the DLTS spectra of Fig 1 at a quiescent

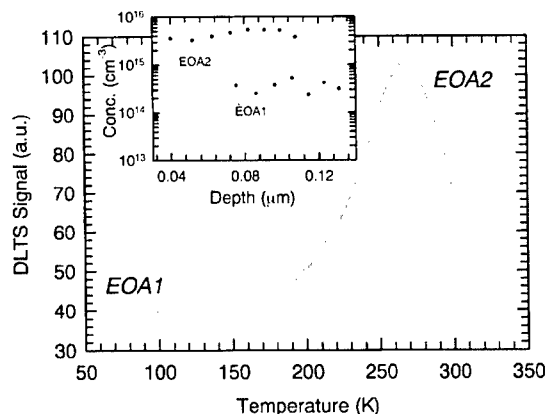


Fig. 1. DLTS spectra of the Schottky diodes before particle irradiation showing the presence of EOA1 and EOA2. The spectrum was recorded with the sample at a quiescent reverse bias of 0.5 V and filling pulse of 0.6 V at a LIA of 22 Hz. The inset is the DLTS depth profile of EOA1 and EOA2 recorded using the fixed bias variable pulse mode of DLTS.

reverse bias of 0.5 V and a pulse amplitude of 0.6 V, a pulse width of 0.2 ms at an LIA frequency of 22 Hz.

Using the LIA-based DLTS between 20 and 320 K, we have determined the defect signatures of the as-grown defects as: ($E_C - 0.567\text{ eV}$; $1.1 \times 10^{-14}\text{ cm}^2$) and ($E_C - 0.274\text{ eV}$; $3.1 \times 10^{-13}\text{ cm}^2$) for EOA2 and EOA1, respectively, for $x = 0.41$; and, $E_C - 0.537\text{ eV}$; $7.2 \times 10^{-14}\text{ cm}^2$ and $E_C - 0.159\text{ eV}$; $1.1 \times 10^{-16}\text{ cm}^2$ for EOA2 and EOA1, respectively, for $x = 0.12$. The prominent defect EOA2 is similar to the 0.61 eV defect detected in $\text{Al}_x\text{Ga}_{1-x}\text{N}$ $x = 0.12$ by Gotz et al. [4]. The differences in the measured values could be accounted for by alloy broadening. Another possibility is the enhancement of the defects’ emission rates by the electric field due to high doping levels. From a comparison with an as-grown defect we detected at 0.262 eV, with a capture cross section of $8.6 \times 10^{-13}\text{ cm}^2$ in MBE grown n - GaIn , it would appear, based on DLTS signatures that EOA1 is the same as E_1 ($E_C - 0.234\text{ eV}$) observed by Wang et al. [8]. Table 1 summarizes DLTS data for the deep levels detected in the $\text{Al}_x\text{Ga}_{1-x}\text{N}$ UV Schottky photodetectors.

From TRIM95 simulations, the projected range of 1.8 MeV protons is greater than the 3.6 μm for 1.8 MeV He-ions, which in turn lies outside the active region of our diodes. After irradiation with 1.8 MeV He-ions, the resulting spectra is no different from the one shown in Fig. 1. However, after proton irradiation, we detected a small peak, EpR1, on the lower temperature side of EOA1. EpR1 was detected using a pulse width of 500 μs and a much higher LIA frequency of 1200 Hz. Fig. 2 is an Arrhenius plot of e/T^2 vs. $1/T$, where e is each defect’s emission rate at a temperature T . Since we do

Table 1

A summary of DLTS data for the deep levels detected in $\text{Al}_x\text{Ga}_{1-x}\text{N}$ the UV Schottky photodetectors

Growth	$E_C - E_T$ (eV); σ_n	Details	Structure	Ref.
MOVPE	$4 \pm 1 \times 10^{16} \text{ cm}^{-3}$ DLN2 dominant $0.61 \pm 0.02 \text{ eV}$; $5 \times 10^{-15} \text{ cm}^2$ and E field dep. \Rightarrow deep donor level $4.2 \times 10^{16} \text{ cm}^{-3}$ OLN ₁ 0.77 eV O-DLTS (Thought to be DLN2) $\sim 10^{14} \text{ cm}^{-3}$ DNL ₁ (not characterized) $4.1 \times 10^{16} \text{ cm}^{-3}$ OLN ₂ 0.83 eV O-DLTS $1.9 \times 10^{16} \text{ cm}^{-3}$ OLN ₃ 1.01 eV O-DLTS	$N_D = 3 \times 10^{17} \text{ cm}^{-3}$ $\text{Al}_{0.12}\text{Ga}_{0.88}\text{N}/\text{SiC}$	$n\text{-AlGaN}/n^+\text{-AlGaN}/\text{SiC}$	W. Gotz et al. [8]
MBE (SVTA)	EOA1 0.274 eV; $3.1 \times 10^{-13} \text{ cm}^2$ DLTS EOA2 0.567 eV; $1.1 \times 10^{-14} \text{ cm}^2$ DLTS	$N_D \sim 10^{17} \text{ cm}^{-3}$ $\text{Al}_{0.12}\text{Ga}_{0.88}\text{N}/\text{Al}_2\text{O}_3$	$n^+\text{-AlGaN}/n^+\text{-AlGaN}/\text{Al}_2\text{O}_3$	This study
300 nm cut-off MBE	0.258 eV; $3.4 \times 10^{-15} \text{ cm}^2$ DLTS 0.262 eV; $8.6 \times 10^{-13} \text{ cm}^2$ DLTS (comparable to EOA1 in SVTA AlGaN)	$N_D \sim 10^{17} \text{ cm}^{-3}$ $N_D \sim 10^{17} \text{ cm}^{-3}$	$n\text{-GaN}/\text{Al}_2\text{O}_3$ $n^+\text{-AlGaN}/n^+\text{-AlGaN}/\text{Al}_2\text{O}_3$	This study This study
MBE (SVTA) 300 nm He-ion and H^+ irrad	As per second row, plus Epr1: 0.187; $8.8 \times 10^{-16} \text{ cm}^2$ DLTS			

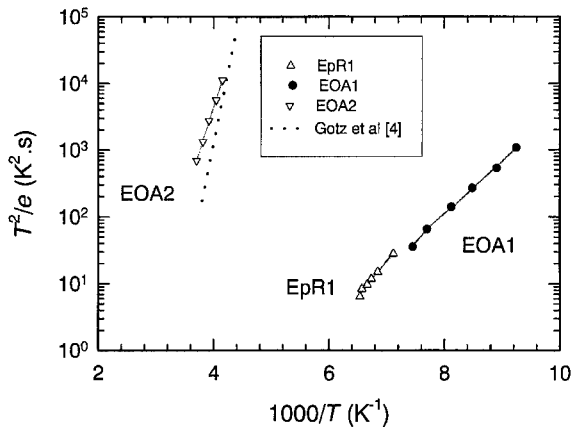


Fig. 2. Arrhenius plots of the emission rates of EOA1 and EOA2. The plot also shows EpR1, which is introduced after 1.8 MeV proton irradiation of the Schottky photodetectors. The plots were constructed from e/T^2 vs. $1/T$, where e is the emission rate at a peak temperature T .

not readily see EpR1 after He-ion irradiation, its presence was confirmed by TSCAP measurements. EpR1's signature was determined as 0.187 eV, $8.8 \times 10^{-16} \text{ cm}^2$.

Fig. 3 shows the current–voltage (I – V) characteristics of a diode before and after it was irradiated with $5.5 \times 10^{12} \text{ He-ion cm}^{-2}$. The leakage current deteriorates

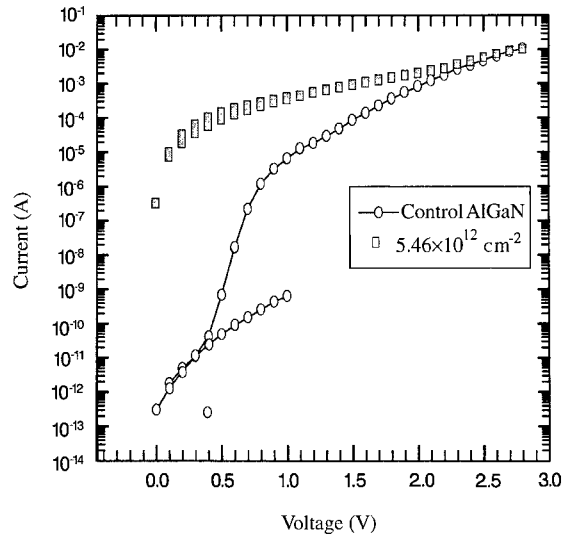


Fig. 3. I – V plots of the Schottky photodetector before and after irradiation with $5.5 \times 10^{12} \text{ He-ions cm}^{-2}$. The leakage current deteriorates from $\sim 10^{-8}$ to $\sim 10^{-3} \text{ A}$ after this dose. After particle irradiation, the I – V curve has a Generation–Recombination component pointing to deep levels.

from $\sim 10^{-8}$ to $\sim 10^{-3} \text{ A}$ after irradiation. After particle irradiation, the I – V curve has a Generation–Recombination component pointing to the presence of deep levels.

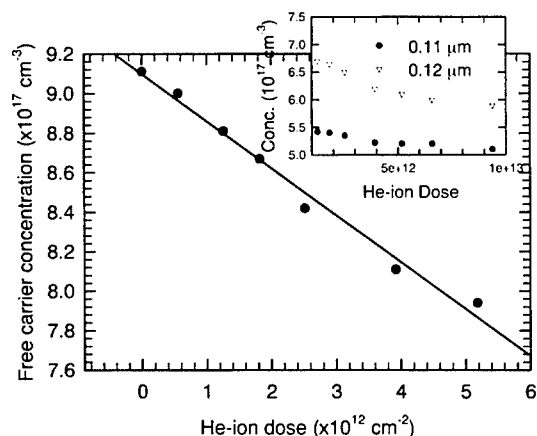


Fig. 4. Removal of carriers near the surface of the photo-detector by He-ions is fairly uniform in the $\text{Al}_x\text{Ga}_{1-x}\text{N}$. He-ion doses between 1.4×10^{11} and $5.2 \times 10^{12} \text{ cm}^{-2}$ were used. The inset shows the carrier removal by 1.8 MeV He-ions at various doses. A carrier removal rate, $\eta = 23\,770 \text{ cm}^{-1}$ was extracted from the slope.

In order to determine the rate, η , at which free carriers are being removed by the He-ions, we irradiated samples from dose 1.4×10^{11} to $5.2 \times 10^{12} \text{ cm}^{-2}$. Fig 4 shows that the He-ion dose removes carriers fairly uniformly in the $\text{Al}_x\text{Ga}_{1-x}\text{N}$ diodes, and the inset, which shows the variation with He-ion dose of the free carrier concentration, is used to determine the carrier removal rate, η . Using the equation $\eta = \Delta N_d / D$, where ΔN_d is the change in free carrier concentration resulting from dose D , we calculated that 1.8 MeV He-ions remove carriers at a rate of $23\,770 \text{ cm}^{-1}$. This value of η is about eighty times greater than for a similarly irradiated GaN.

In conclusion, we have characterized two as-grown defects, EOA1 and EOA2 and a proton irradiation induced defect EpR1 in $\text{Al}_x\text{Ga}_{1-x}\text{N}$ Schottky photo-detectors. The DLTS signatures for EOA1 is 0.274 eV, $3.1 \times 10^{-13} \text{ cm}^{-2}$, and for EOA2 it is 0.58 eV, $1.1 \times 10^{-14} \text{ cm}^{-2}$. The signature for EpR1 is 0.187 eV, $8.8 \times 10^{-16} \text{ cm}^{-2}$. We believe EOA2 is the 0.61 eV level in MOCVD AlGaIn (12% Al), and that EOA1 is the E_i defect in GaN. Furthermore we determined that AlGaIn is radiation “softer” than GaN.

Acknowledgements

The South African National Research Foundation (NRF) is greatly acknowledged for financial support.

References

- [1] D. Walker, V. Kumer, K. Mi, P. Sandvik, P. Kung, X.H. Zhang, M. Razeghi, *Appl. Phys. Lett.* 76 (2000) 403.
- [2] F. Omnes, N. Marenko, B. Beaumont, P. de Mierry, E. Monroy, F. Calle, E. Munoz, *J. Appl. Phys.* 86 (1999) 5286.
- [3] P.P. Chow, J.J. Klaassen, J.M. VanHove, A. Wowchak, C. Polley, D. King, *SPIE Optoelectron*, Vol. 3948 (January 2000), pp. 295–303.
- [4] W. Gotz, N.M. Johnson, M.D. Brensner, R. Davis, *Appl. Phys. Lett.* 69 (1996) 2379.
- [5] D.V. Lang, *J. Appl. Phys.* 45 (1974) 3014, 3023.
- [6] D.V. Lang, in: P. Braulich (Ed.), *Thermally Stimulated Relaxation of Solids*, Springer, Berlin, 1979, pp. 93–133.
- [7] Y. Zohta, J. Watanabe, *J. Appl. Phys.* 53 (1982) 1809.
- [8] C.D. Wang, L.S. Yu, S.S. Lau, E.T. Yu, W. Kim, A.E. Botchkarev, H. Morcroc, *Appl. Phys. Lett.* 72 (1998) 1211.



ELSEVIER

Physica B 308–310 (2001) 1193–1196

PHYSICA B

www.elsevier.com/locate/physb

Anomalous temperature dependence of electroluminescence intensity in InGaN single quantum well diodes

A. Hori, D. Yasunaga, A. Satake, K. Fujiwara*

Kyushu Institute of Technology, Tobata, Kitakyushu 804-8550, Japan

Abstract

Temperature dependence of electroluminescence (EL) spectral intensity of the super-bright green InGaN single quantum well (SQW) light emitting diodes (LEDs), fabricated by Nichia Chemical Industry Ltd., has been studied over a wide temperature range ($T = 15\text{--}300\text{ K}$) and as a function of injection current level. It is found that, when T is decreased slightly to 140 K, the EL intensity efficiently increases probably due to reduced non-radiative recombination processes and/or increased carrier capture by the localized radiative recombination centers. However, by decreasing T , further, down to 15 K, it drastically decreases due to the reduced carrier capture and population, accompanying the disappearance of injection current dependent line shape changes (blue-shift) caused by band filling of the localized recombination centers. These results indicate that the efficient carrier capture by SQW is crucial to enhance the radiative recombination of injected carriers in the presence of the high dislocation density. © 2001 Elsevier Science B.V. All rights reserved.

Keywords: Wide band gap semiconductors; Electroluminescence; Recombination

1. Introduction

Super-bright green and blue light emitting diodes (LEDs) using group III-nitride semiconductor quantum structures have been manufactured successfully [1–3]. Such a quantum well LED shows very bright emission characteristics in spite of the existence of high density misfit dislocations, and the origins of the high quantum efficiency have been receiving much attention [4–8]. Previously, quantum confinement effects on the InGaN alloy well and efficient carrier capturing by the localized radiative recombination centers in the quantum-dot-like states [4–7] have been claimed to be important for origins of the high recombination efficiency. In this paper, the temperature dependence of electroluminescence (EL) spectral intensity of the green InGaN single quantum well (SQW) LEDs with a high recombination quantum efficiency, fabricated by Nichia Chemical Industry Ltd. [2], has been studied over a wide

temperature range and as a function of injection current level. In contrast to a commonly expected trend of reduced non-radiative recombination with decreasing lattice temperature, an anomalous temperature dependence of the EL intensity has been observed at lower temperatures below 100 K. A careful analysis of the detailed EL spectral line shape as a function of injection current reveals that the efficient carrier capture by SQW is crucial to enhance the radiative recombination when the dislocation density is very high ($10^{10}/\text{cm}^2$).

2. Experimental

EL spectral characteristics of the super-bright green InGaN SQW-LED sample, fabricated by Nichia Chemical Industry Ltd. [2], have been studied as a function of lattice temperature. The nominal InGaN well width is 3 nm and the claimed In concentration in the SQW layer is 0.45 [2]. The InGaN SQW layer is confined by p- $\text{Al}_{0.2}\text{Ga}_{0.8}\text{N}$ and n-GaN barrier layers. The detailed diode heterostructure was described previously [1,2].

*Corresponding author. Fax: +81-93-884-3221.

E-mail address: fujiwara@ele.kyutech.ac.jp (K. Fujiwara).

The SQW-LED sample was mounted on a Cu cold stage of a temperature-variable closed-cycle He cryostat to vary the sample temperature over a wide range ($T = 15\text{--}300\text{ K}$). EL spectra were measured by a conventional lock-in technique, employing a GaAs photomultiplier, as a function of current injection level up to 10 mA. In order to get information about the absorption spectra, photocurrent (PC) spectra were also measured using a combination of a halogen lamp and a monochromator for illumination and a DC electrometer for current detection.

3. Results and discussion

EL and PC spectra of the green SQW-LED have been measured between 15 and 300 K. Fig. 1 shows the typical EL (solid curves) and PC (dotted curves) spectra normalized by the respective peaks at 260 and 15 K. The injection current level for EL is 10 mA and the reverse bias voltage for PC is -0.5 V . At 260 K, the green SQW-LED shows an emission band centered around 2.3 eV (540 nm) at the current level of 10 mA with multiple fine structures due to Fabry–Perot fringes. The emission peak shows a blue-shift with increasing injection current (from 0.1 to 10 mA) and is red-shifted from the broad absorption peak located around 3.0 eV (410 nm) as confirmed by the PC spectrum, indicating strong

localization of the injected carriers within the SQW region [4,7]. The peaked nature of the transition that is rather enhanced at 15 K directly indicates the excitonic origin of the absorption transition in the SQW layer, although the line width is very large (170–300 meV) due to inhomogeneous broadening of the confinement potentials. At 15 K, the emission peak energy is also observed at 2.3 eV in Fig. 1 which does not show any significant shifts from the one at 260 K. In Fig. 1 (at 15 K), an absorption peak is observed at 3.45 eV due to the A and B excitonic transitions of the GaN barrier layer [9]. It shows a blue-shift with decreasing temperature, following the temperature dependence of the band gap energy [10,11]. In addition, a weak emission around 3.1 eV is observed at 15 K in Fig. 1. We attribute the emission band to the GaN layer, although the exact origin of the Stokes shift is not clear at present.

The EL spectral intensity from the green SQW layer varies significantly with changing sample temperature. The temperature dependence of the EL spectra is plotted in Fig. 2 at a fixed value of the injection current (10 mA). When T is slightly decreased from 300 to 140 K, the EL spectral intensity efficiently increases. This enhancement of the radiative recombination efficiency at 140–220 K is similar to those usually expected for the reduced non-radiative recombination at lower T in many cases of the GaAs based LEDs. However, by decreasing T down to 15 K furthermore, a drastic reduction of the EL intensity is observed. That is, it is found that the EL efficiency at lower T is quite low. This is in strong contrast to the

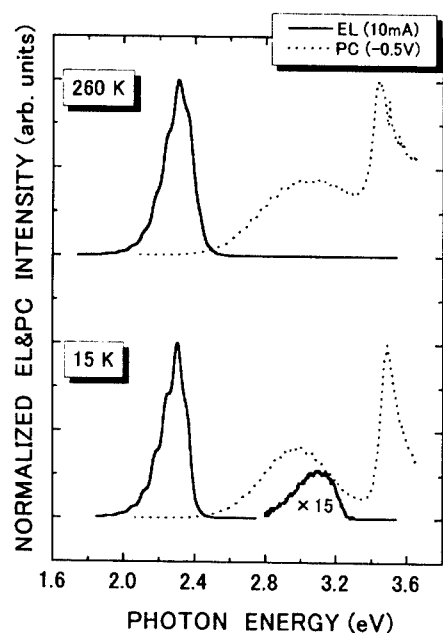


Fig. 1. EL (solid curves) and PC (dotted curves) spectra of the green SQW-LED at 260 and 15 K. For EL spectra the injection current level is fixed at 10 mA, while for PC spectra the reverse bias voltage is -0.5 V .

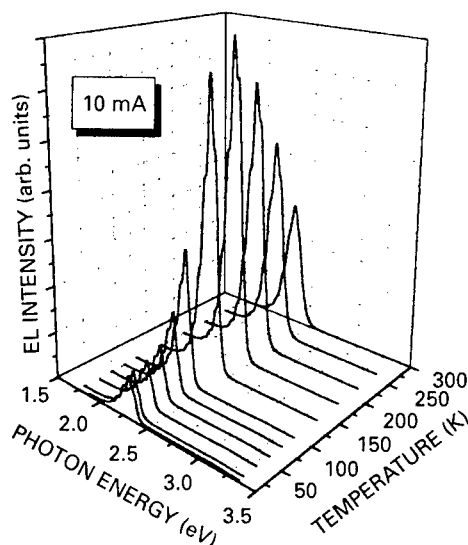


Fig. 2. Three-dimensional plot of EL spectra of the green SQW-LED as a function of lattice temperature at a fixed value of injection level of 10 mA.

usual cases of GaAs based LEDs where significantly reduced non-radiative recombination processes are expected at lower T . This reduction of the EL efficiency at lower T is also seen at other injection currents between 0.5 and 10 mA. In Fig. 3, the spectrally integrated EL intensity is shown as a function of current and temperature to illustrate three-dimensional light-output versus current and temperature characteristics. The EL intensity versus injection current characteristics at intermediate to low temperature regimes are quite astonishing, since the EL intensity shows saturation phenomena at lower output levels above 1 mA. At higher injection currents, say 10 mA, the EL intensity is very low at 15 K. This phenomenon observed at 15 K is obviously not because of the heating effects and reflects the particular recombination characteristics of the InGaN SQW heterostructures by current injection. We note that this trend is even stronger at 15 K than at 120 K.

In order to investigate the causes of the reduced EL efficiency at lower T , the detailed EL spectral line shape has been studied as a function of injection current. The results at 260, 140 and 20 K are shown in Fig. 4. At 140–300 K where the EL efficiency is very high, the spectral line shape changes drastically with increasing current, when the injection level is increased by two orders of magnitude. That is, the EL intensity significantly increases at higher energy sides with the current level due to the band filling of the localized recombination centers [6]. This result indicates that the injected carriers (electrons and holes) are efficiently captured by SQW at those temperatures and more carriers captured by the SQW layer are filling the localized states at higher energies when the current is

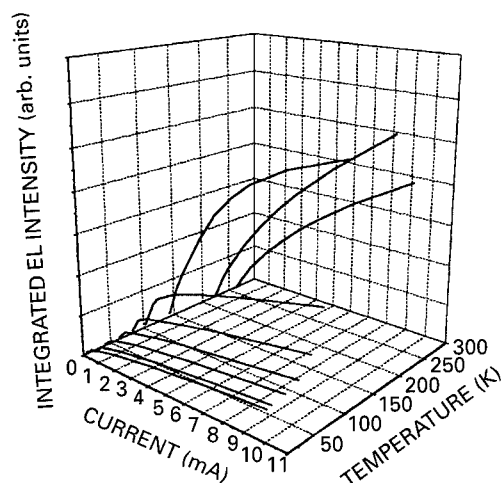


Fig. 3. Three-dimensional plot of integrated EL intensity of the green SQW-LED as a function of injection current and lattice temperature.

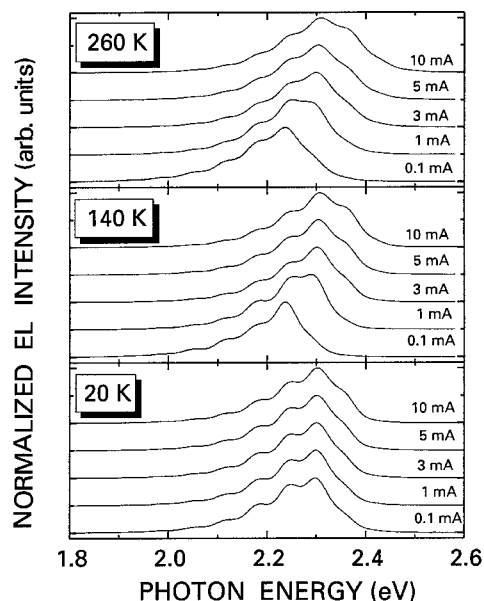


Fig. 4. EL line shape variations of the green SQW-LED as a function of injection current at 260, 140 and 20 K.

increased. On the other hand, it is clear in Fig. 4 that the line shape does not change with the current at 20 K where the EL efficiency is quite low. Absence of the band-filling effects at lower T suggests that carriers are not effectively captured by SQW at lower T , but are transferred to non-radiative recombination centers within the barrier layers. The carrier overflow to the barrier layers is consistent with the appearance of the GaN emission at 3.1 eV, which is observed only at lower T (see Fig. 1). These results indicate that the efficient carrier capture by SQW is crucial to enhance the radiative recombination when the dislocation density is very high ($10^{10}/\text{cm}^3$).

4. Conclusion

Temperature dependence of EL spectral intensity of the super-bright green InGaN SQW-LED has been studied. We find that, when the temperature is decreased down to 15 K, the EL intensity drastically changes due to decreased carrier capture by the localized radiative recombination centers. The injection current dependent line shape changes (blue-shift) caused by band-filling effects of the localized recombination centers allows us to evaluate the population at the localized states at various temperatures. The reduced carrier population due to the carrier overflow to the barriers at lower temperatures conversely indicates that the efficient carrier capture is crucial to enhance the radiative recombination of injected carriers in the presence of the high dislocation density.

Acknowledgements

The authors would like to thank Nichia Chemical Industry Ltd., especially S. Nakamura (at present at the University of California at Santa Barbara) for providing the chip samples used for the present experiments and also K. Satoh and K. Kawashima for their experimental assistance.

References

- [1] S. Nakamura, G. Fasol, *The Blue Laser Diode*, Springer, Berlin, Heidelberg, 1997.
- [2] S. Nakamura, et al., *Jpn. J. Appl. Phys.* 34 (1995) L1332.
- [3] I. Akasaki, *Ret. Soc. Symp. Proc.* 482 (1997) 3.
- [4] S. Chichibu, T. Azuhata, T. Sota, S. Nakamura, *Appl. Phys. Lett.* 69 (1996) 4188.
- [5] Y. Narukawa, et al., *Phys. Rev. B* 55 (1997) R1938.
- [6] T. Mukai, K. Takekawa, S. Nakamura, *Jpn. J. Appl. Phys.* 37 (Part 2) (1998) L839.
- [7] K.P. O'Donnell, et al., *Phys. Rev. Lett.* 82 (1999) 237.
- [8] T. Mukai, M. Yamada, S. Nakamura, *Jpn. J. Appl. Phys.* 38 (1999) 3976.
- [9] J.F. Muth, et al., *Appl. Phys. Lett.* 71 (1997) 2572.
- [10] J.I. Pankove, S. Bloom, G. Harbeke, *RCA Review* 36 (1975) 163.
- [11] J.-L. Reverchen, et al., *J. Appl. Phys.* 88 (2000) 5138.



ELSEVIER

Physica B 308–310 (2001) 1197–1200

PHYSICA B

www.elsevier.com/locate/physb

Production and properties of p–n junctions in reactively sputtered ZnO

S. Tüzemen^{a,b}, Gang Xiong^a, John Wilkinson^a, Brian Mischuck^a, K.B. Ucer^a,
R.T. Williams^{a,*}

^a Department of Physics, Wake Forest University, Winston-Salem, NC 27109, USA

^b Department of Physics, Atatürk University, 25240 Erzurum, Turkey

Abstract

In order to develop electroluminescent and laser devices based on the ultraviolet exciton emission of ZnO, it will be important to fabricate good p–n junctions. As-grown ZnO is normally n-type because of intrinsic donor defects such as oxygen vacancies and zinc interstitials, or unintended hydrogen. Making p-type ZnO has been more difficult, possibly due to self-compensation by easily formed donor defects. In this work, we demonstrate that reactively sputtered, annealed ZnO films can be changed from n-type to moderate p-type by adjusting the oxygen/argon ratio in the sputtering plasma. We report the properties of p–n homojunctions fabricated in this way, and characterize transport in the films by the Hall measurements. Ohmic contacts were formed by deposition of Au/Al films. Our finding of p-type conductivity in apparently intrinsic ZnO formed by reactive sputtering is not inconsistent with calculated defect formation enthalpies if account is taken of the higher chemical potential of the dissociated oxygen reservoir represented by the sputter plasma, compared to the molecular oxygen reservoir assumed in the calculation of formation enthalpies. If hydrogen turns out to be the main compensating donor, the role of oxygen pressure in controlling incorporation of background hydrogen during sputtering may also be implicated. © 2001 Elsevier Science B.V. All rights reserved.

Keywords: ZnO; p–n junction; Ohmic contact

1. Introduction

ZnO with n-type conductivity can readily be produced as intrinsic (undoped) material if grown in zinc-rich conditions, or by extrinsic doping with group-III elements such as Al. Intrinsic ZnO is thought to be n-type primarily because of donor defects such as zinc interstitials (Zn_i) and oxygen vacancies (V_O) [1,2]. It has been suggested that hydrogen in ZnO is also a donor [3]. It is difficult to grow p-type ZnO, although recent studies have reported p-type conductivity achieved by growth in the presence of excited N_2O [4,5] or by co-doping N with H [6] or Ga [4].

Zhang et al. [1] discussed the asymmetry of n- vs. p-type doping in the framework of defect formation

enthalpies calculated on the assumption of growth of ZnO in equilibrium with zinc metal and molecular O_2 . The conclusion of their literature survey was that intrinsic p-type ZnO has not been demonstrated [1]. Butkhuzi et al. reported in 1992 that heat-treating ZnO in atomic oxygen produced p-type conduction [7], but aside from that report, it seems that up to now there has not been another demonstration of p-type conductivity in ZnO undoped by foreign atoms.

In the present paper, we demonstrate that ZnO deposited by reactive sputtering of a Zn target in O_2/Ar atmosphere produces n-type ZnO at low O_2/Ar ratios and moderately p-type ZnO at higher O_2/Ar ratios. The I – V curves of p–n homojunctions formed from these films exhibit rectification characteristics, and the Hall effect measurements verify p- and n-carrier type and concentration. Photoluminescence measurements have been measured on the same materials and will be reported elsewhere.

*Corresponding author. Fax: +1-336-758-6142.

E-mail address: williams@wfu.edu (R.T. Williams).

2. Experiment

ZnO films were deposited by reactive sputtering from a Zn metal target (99.99%) in O_2/Ar atmosphere using a DC planar magnetron source (US Gun II) in a turbomolecular pumped stainless steel chamber. The substrate was heated during deposition, typically to $350^\circ C$. The substrate used in this work was (100) silicon, based on the observation of Fu et al. [8] that efficient near-band-edge cathodoluminescence could be obtained from sputtered and air-annealed ZnO on Si(100) substrates but not on Si(111). Substrate dependence of sputtered ZnO film properties will be investigated in future work.

The p–n junctions were formed by deposition of two sequential layers under oxygen-poor and oxygen-rich conditions. At a total O_2/Ar sputtering pressure of 3×10^{-2} Torr, a fractional composition of 50% oxygen produced n-type ZnO and 83% oxygen produced p-type ZnO, as two examples. The sputtering power was 20 W and a typical sputtering time of 30 min produced films about 5 μm thick, measured by SEM on a freshly cleaved edge. The deposition rate depends on the fraction of Ar in the O_2/Ar mix at constant pressure. A mask was used during the second layer deposition to expose contact areas on the lower layer. We have found that annealing in vacuum ($\sim 10^{-6}$ Torr) at $750^\circ C$ for 30 min gives good band-edge photoluminescence as well as lowering resistivity, and this annealing treatment was employed for the films studied here. Ohmic contacts were formed by depositing Al and Au. The I – V characteristics of an Au/Al contact on both p- and n-type ZnO are shown in Fig. 1.

3. Results and discussion

X-ray diffraction shows a strong peak at 34.5° (2θ) consistent with c -axis oriented wurtzite ZnO. As shown

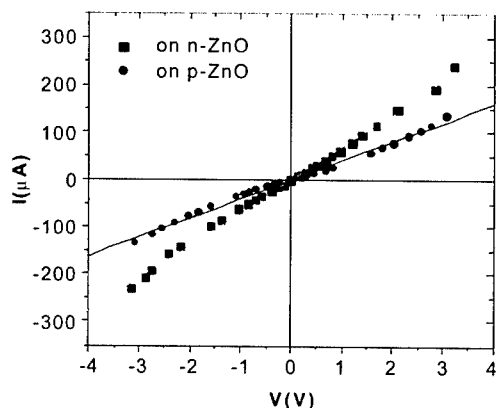


Fig. 1. I – V curves for Au/Al ohmic contacts on n- and p-type ZnO.

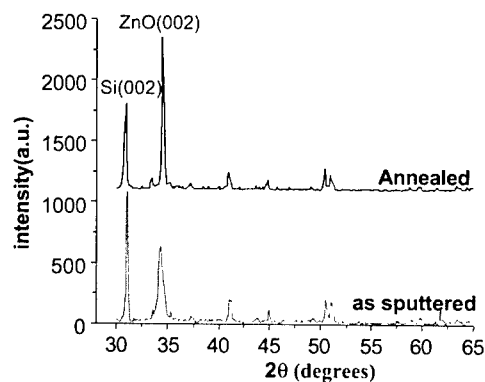


Fig. 2. X-ray rocking curves (2θ degrees) for a ZnO film after sputter deposition at $350^\circ C$ (bottom) and after vacuum annealing at $750^\circ C$ (top).

in Fig. 2 for a film sputtered at $350^\circ C$, annealing in vacuum at $750^\circ C$ sharpens the diffraction peaks significantly. Atomic force microscopy¹ shows crystallite sizes in the 40–65 nm range before annealing, and 80–200 nm after annealing.

The I – V curves for homojunctions of n-type ZnO on p-type ZnO films prepared by controlling oxygen partial pressure during sputtering, as described above, are shown in Fig. 3. Part (a) corresponds to a junction which was not annealed after sputtering, and part (b) corresponds to an annealed junction. Rectification is clearly displayed in both cases. The current conduction (as well as forward and reverse leakage) are significantly greater for the annealed junction in this example. The turn-on voltage is about 1 V, rather than being near the band gap energy of 3.3 eV as we expect in the ideal case. Our diode has low carrier concentrations in both p and n sections, which reduces the expected turn-on voltage somewhat. In this context it is worth comparing the I – V curves measured by other workers for ZnO homojunctions [9] and heterojunctions [10] which were demonstrated to be light-emitting diodes. The turn-on voltage was about 1 V in the homojunction LED [9] and variously 1 and 3 V in two different samples of ZnO heterojunction LEDs [10]. The low turn-on voltage remains a puzzle, but it seems to occur commonly in ZnO junctions qualified by electroluminescence as good p–n junctions.

The Hall effect measurements yielded the approximate parameters summarized in Table 1 for selected films of annealed p- and n-type ZnO. The n-type film represented in the table was optimized for band-gap photoluminescence yield relative to the green

¹ AFM images were taken by Xiaodong Cui at Arizona State University.

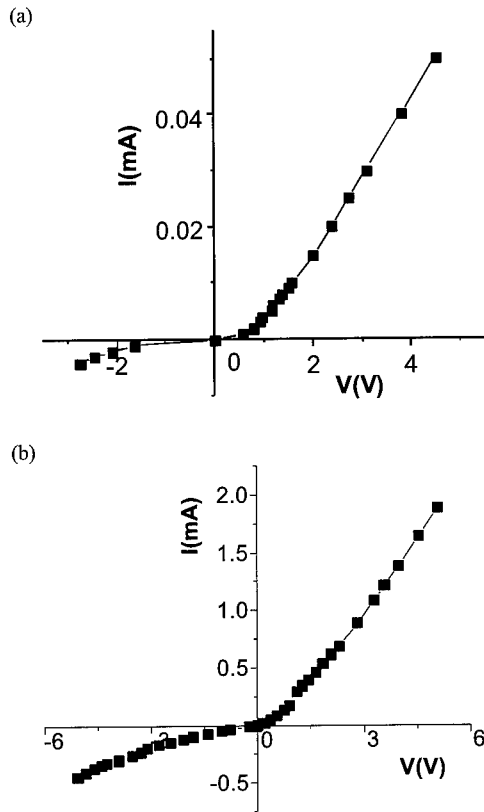


Fig. 3. I - V curves for p-n homojunctions formed by depositing n-type ZnO on p-type ZnO: (a) without annealing, and (b) another junction after annealing.

luminescence attributed to oxygen vacancies and has low conductivity. In the p-type film, we found a hole concentration of about $5 \times 10^{15} \text{ cm}^{-3}$.

The ability to form p-n homojunctions, as illustrated in both Fig. 3 and the Hall effect data in Table 1, show that moderate p-type conductivity has been achieved in ZnO films reactively sputtered in oxygen-rich conditions but not intentionally doped with impurities. This appears to be the second published report of p-type conductivity in intrinsic ZnO exposed to atomic oxygen during preparation. The first was the 1992 work of

Butkhuzi et al. [7], who heat-treated ZnO after growth, in a beam of atomic oxygen. The present study is the first to achieve p-type ZnO by reactive sputtering and vacuum annealing. Since the discussion of intrinsic defect formation enthalpies in Ref. [1] stated that intrinsic p-type ZnO cannot be produced by thermal equilibrium growth processes, it is of interest to examine the present results in light of the works on defect formation enthalpies in ZnO [1,2], and especially the very recent theoretical considerations of nitrogen doping on the same basis [11,12].

It is important to note that a molecular oxygen reservoir is assumed for the calculation, whereas an atomic or ionic oxygen reservoir characterizes the post-treatment of Butkhuzi et al. [7] and the reactive sputtering environment in which the present films were grown. The difference is important because presenting the oxygen reservoir with the O_2 molecular bond already broken (bond energy 5.17 eV [13]) raises its chemical potential by half the O_2 bond energy per atom. It is correspondingly easier to insert oxygen from such a reservoir into the growing crystal to make the acceptor defect V_{Zn} , and harder to remove oxygen to the reservoir forming the donors Zn_i and V_{O} .

The basic equation given in Ref. [1] for formation enthalpy of a structural defect α of charge q is

$$\Delta H^{(q,\alpha)} = \Delta E^{(q,\alpha)} + n_a \mu_a + q E_F, \quad (1)$$

where $\Delta E^{(q,\alpha)}$ contains the calculated total energy of a unit cell including the host material with defect α in charge state q minus the total energy of a unit cell of the host only, and n_a is the number of atoms being removed during the defect formation from the host crystal to the atomic reservoir. The sign of n_a is negative if atoms are moved from the reservoir to the host crystal. The chemical potential of the reservoir is μ_a , assumed in Ref. [1] to correspond to molecular oxygen. E_F is the Fermi energy. Employing the notation of Ref. [1], the formation enthalpies of the intrinsic donor and acceptor defects V_{O} and O_i can be written, respectively, as

$$\Delta H^{(2+, \text{V}_{\text{O}})} = \Delta E^{(2+, \text{V}_{\text{O}})} + \mu_{\text{O}} + 2e E_F, \quad (2)$$

$$\Delta H^{(2-, \text{O}_i)} = \Delta E^{(2-, \text{O}_i)} - \mu_{\text{O}} - 2e E_F. \quad (3)$$

Table 1

Resistivity, mobility, and carrier concentration derived from the Hall effect and resistivity measurements on n- and p-type intrinsic ZnO, before and after annealing at 750°C

	n-type ZnO		p-type ZnO	
	Not annealed	Annealed	Not annealed	Annealed
Resistivity ($\Omega \text{ cm}$)	$> 10^4$	100	200	30
Mobility (cm^2/Vs)	N/A	20	30	130
Concentration (cm^{-3})	N/A	6×10^{15}	5×10^{15}	5×10^{15}

Thus raising the chemical potential of the oxygen, such as by electronic excitation to a dissociated state, will raise the formation enthalpy of the donor V_O and lower the dissociation enthalpy of the acceptor O_i . A similar role of electron cyclotron resonance (ECR) dissociation of nitrogen or N_2O gas in doping ZnO with nitrogen was discussed recently by Yan et al. [11,12].

The suggestion by Van de Walle [3] that hydrogen should be an important shallow donor in ZnO has been supported by very recent experiments reported in these proceedings, particularly experiments on spin rotation of muonium in ZnO [14–16] and optically detected ENDOR in ZnO [17]. Increasing the oxygen pressure relative to a fixed background of H_2 or H_2O in the sputtering chamber may have a dilution effect to suppress hydrogen incorporation in the growing film, in agreement with the trend we report, and in addition to the effect on intrinsic defects already discussed.

Acknowledgements

Research was supported by NSF DMR-9732023 and NATO SfP-973686. S. Tüzemen acknowledges support as a Fulbright Scholar while at Wake Forest University. The authors thank Z. Fu for samples and suggestions, and N.A.W. Holzwarth, Yonas Abraham, E. Glaser, and M. Brozel for helpful discussions.

References

- [1] S.B. Zhang, S.-H. Wei, Alex Zunger, *Phys. Rev. B* 63 (2001) 075205.
- [2] A.F. Kohan, G. Ceder, D. Morgan, Chris G. Van de Walle, *Phys. Rev. B* 61 (2000) 15019.
- [3] Chris G. Van de Walle, *Phys. Rev. Lett.* 85 (2000) 1012.
- [4] M. Joseph, H. Tabata, T. Kawai, *Jpn. J. Appl. Phys.* 38 (1999) L1205.
- [5] X. Guo, H. Tabata, T. Kawai, *J. Crystal Growth* 223 (2001) 135.
- [6] K. Minegishi, Y. Koiwai, Y. Kikuchi, K. Yano, M. Kasuga, A. Shimizu, *Jpn. J. Appl. Phys.* 36 (1997) L1453.
- [7] T.V. Butkhuzi, A.V. Bureyev, A.N. Georgobiani, N.P. Kekelidze, T.G. Khulordava, *J. Crystal Growth* 117 (1992) 366.
- [8] Z. Fu, C. Guo, B. Lin, G. Liao, *Chin. Phys. Lett.* 15 (1998) 457.
- [9] T. Aoki, Y. Hatanaka, D.C. Look, *Appl. Phys. Lett.* 76 (2000) 3257.
- [10] H. Ohta, M. Orita, M. Hirano, H. Hosono, *J. Appl. Phys.* 89 (2001) 5720.
- [11] Y. Yan, S.B. Zhang, S.T. Pantelides, *Phys. Rev. Lett.* 86 (2001) 5723.
- [12] Y. Yan, S.B. Zhang, S.J. Pennycook, S.T. Pantelides, to be published.
- [13] J.A. Kerr, In: *CRC Handbook of Chemistry, Physics* 1999–2000, 81st edition, CRC Press, Boca Raton, FL, USA, 2000.
- [14] S.F.J. Cox, J.S. Lord, P.J.C. King, S.P. Cottrell, E.A. Davis, J.M. Gild, H.V. Alberto, R.C. Vila, J. Pirotto Duarte, Avres de Campos, A. Weidinger, R.L. Lichti, S.J.C. Irvine, in these Proceedings, *Physica B* 308–310 (2001).
- [15] S.F.J. Cox, E.A. Davis, S.P. Cottrell, P.J.C. King, J.S. Lord, J.M. Gil, H.V. Alberto, R.C. Vilao, J. Pirotto Duarte, N. Ayres de Campos, A. Weidinger, R.L. Lichti, S.J.C. Irvine, *Phys. Rev. Lett.* 86 (2001) 2601.
- [16] K. Shimomura, K. Nishiyama, R. Kadono, in these Proceedings, *Physica B* 308–310 (2001).
- [17] F. Leiter, H. Zhou, F. Henecker, A. Hofstaetter, D.M. Hoffmann, B.K. Meyer, S. Orlinskii, J. Schmidt, in these Proceedings, *Physica B* 308–310 (2001).



ELSEVIER

Physica B 308–310 (2001) 1201–1204

PHYSICA B

www.elsevier.com/locate/physb

Defects in scintillators based on ZnS–ZnSe solid solutions

O.A. Christich^a, E.I. Gorohova^a, S.B. Mikhlin^{b,*}, P.A. Rodnyi^b, A.S. Potapov^b^a *S.I. Vavilov State Optical Institute, St. Petersburg, Russian Federation*^b *Experimental Physics Department, Saint Petersburg State Technical University, Politechnicheskay 29, 195251, St. Petersburg, Russia*

Abstract

We describe luminescent (spectral and kinetic) properties of $\text{ZnS}_x\text{Se}_{1-x}$ ($x = 0.5-1.0$) solid solutions doped with different impurities (Ag, Cu as activators, Al as co-activator), and prepared large transparent polycrystalline blocks (with the diameter up to 100 mm, and the thickness up to 5 mm). The light yields of all the studied samples were compared with that of CsI:Ti and varied from sample to sample. These variations depend on impurity concentrations, native defect concentrations and presence of a hexagonal (wurtzite) phase. The best results (120% yield of that CsI:Ti) were obtained for the solid solution with $x = 0.5$ doped with Cu (Al). This sample also exhibits the shortest decay time constant, about 25 ns. A detailed comparison of defect properties of our solid solutions with the known data for similar crystalline systems has been carried out. © 2001 Elsevier Science B.V. All rights reserved.

Keywords: $\text{ZnS}_x\text{Se}_{1-x}$; Native defects; Optical properties

1. Introduction

Applications of A^2B^6 compounds for scintillating detectors of ionized radiation [1–3] are determined by a high conversion efficiency, a short decay time and wide possibilities for spectra (emitting and detector's) adjustment. Using A^2B^6 compounds we can join in one block scintillator and photodiode. In this work we present the results of solid solutions $\text{ZnS}_x\text{Se}_{1-x}$ ($x = 0.5-1.0$) investigation. By varying x (S content) we can shift the maximum in an emission spectrum and fit it to the spectrum of receiver's sensitivity. Solid solutions give us more opportunities to counteract undesirable native defect appearance.

2. Sample preparations

Samples were grown by physical vapor deposition (PVD) in a closed reactor placed in a two-zone vertical furnace. At the bottom of a high temperature zone a capsule with re-crystallizing powder compounds (pre-

viously synthesized at 1000°C ZnS–ZnSe mixture) was placed, and at the top of a low temperature zone (the temperature in that zone, the deposition temperature, is pointed in Table 1) the seed was placed. Doping with Cu, Al, and Ag was carried out at the synthesis stage. We added different solvents (BaCl_2 , CsCl, NaCl) at this stage in order to speed up the synthesis. Solvent concentrations were reduced at every stage of the process. For example, in an initial mixture Na contamination was 0.8%, after synthesis 0.15%, and in a solid solution after PVD was less than 0.01%. The Al contamination in samples after PVD was about 0.01%. In this work we deal with 50 mm diameter samples with 5 mm thickness. The crystallizer gives us an opportunity to grow samples with the diameter up to 100 mm and the thickness up to 10 mm. After the growth samples were cut and polished. The transmittance for most samples (with 1 mm thickness) was not less than 50%.

X-ray diffraction investigations of different phases contamination show that for $x < 0.57$ there is only one cubic modification in samples, for $0.6 < x < 1$ there is only one hexagonal modification, and for $0.57 < x < 0.6$ there are both modifications in the samples. The dependence of the unit cell volume on x is shown in Fig. 1. As one can see in the sample with $x = 0$ (pure

*Corresponding author. Tel./fax: +7-812-552-7574.

E-mail address: mikhlin@tuexph.stu.neva.ru (S.B. Mikhlin).

Table 1
Sample characteristics^a

Sample	x	T deposition (K)	Dopant	Solvent
1	1(H)	1200	Cu (7×10^{-3} wt%)	BaCl ₂ (Ba—0.14 wt%)
2	1(H)	1300	Cu (7×10^{-3} wt%)	BaCl ₂ (Ba—0.14 wt%)
3	1(H)	1300	Cu (7×10^{-3} wt%)	BaCl ₂ (Ba—0.48 wt%)
4	0.5(C)	1200	Cu (5×10^{-3} wt%), Al	BaCl ₂ (Ba—0.14 wt%)
5	0.5(C)	1200	Cu (5×10^{-3} wt%), Al	CsCl
6	0.8(H)	1200	Cu (5×10^{-3} wt%), Al	NaCl
7	0.5(C)	1200	Cu (1×10^{-2} wt%), Al	NaCl
8	0.5(C)	1100	Ag (5×10^{-3} wt%), Al	NaCl
9	0.5(C)	1100	Ag (5×10^{-2} wt%), Al	NaCl

^aH—hexagonal, C—cubic phase.

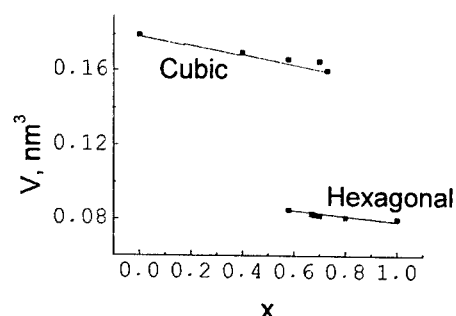


Fig. 1. The unit cell volume dependence on sulfur contamination x in $\text{ZnS}_x\text{Se}_{1-x}$ solid solutions.

ZnSe) unit cell parameter is equal to 0.565 nm—almost the same as for single-crystal (0.5668 nm). The density of this sample corresponds to the calculated density, 5.42 g/cm³. Sample characteristics are summarized in Table 1.

3. Experimental details

Luminescence spectra were measured at constant X-ray excitation (45 keV) in a 100–500 K temperature range with the monochromator MDR-2, and the photo-multiplier tube FEU-83. Kinetic measurements were carried out with the pulse X-ray source (1 ns X-ray pulse duration) described earlier [4] in a 100–500 K temperature range. Thermo-luminescence measurements were carried out after an X-ray irradiation at 100 K and subsequent heating (in the same cryostat) at 0.5 K/s rate. Relative light yields (compared to that of CsI:Ti) were measured by two different methods: (1) at a continuous excitation, and (2) at a pulse excitation (using photon counting). In the latter case an average excitation level was three orders less.

4. Results and discussion

Main properties of the investigated samples are arranged and displayed in Table 2. At the second column we indicate peak positions and in brackets line relative intensities for 300 K. The third column with light yields is divided into two columns: (a) yields at continuous excitation, and (b) at pulse excitations. At the fourth column we indicate decay constants for an initial part of decay curves. The last column contains TSL results. In spite of the equal conditions at TSL measurements (sample dimension and the excitation level) we cannot properly compare trap concentrations for different samples because of entirely different sample light yields. Let us comment on all the results: (1) a very strong dependence of luminescent properties on the deposition temperature—samples #1 and #2; (2) bad reproducibility with a solvent variation—samples #2 and #3; (3) a strong dependence of kinetic properties on used solvents—samples #4 and #5. The Cu-related band (518 nm—#1, 534 nm—#2, 528 nm—#3) in our samples is well known [5]. The shift (0.3 eV for x varying from 1 to 0.5) of this band with λ_m 528 nm (#3, $x = 1$), 556 nm (#6, $x = 0.8$), and 601, 604 nm (#4 and #7, $x = 0.5$) correlates with E_g variation (0.4 eV for x varying from 1 to 0.5). The difference of light yield at different excitations (a, b columns of Table 2) is connected with different traps and non-emission centers contamination. Only sample #2 shows a large light yield drop at continuous excitation, and a giant trap contamination. To clear up this effect we need heat treatment investigations, because the preparing conditions for samples #1–3 were similar. Peak positions in Ag-doped samples with $x = 0.5$ coincide with those for ZnSe:Ag single crystal [6]. This fact can be explained by following an impurity center level after a band (valence or conducting) edge, or by the different natures of the center in solid solutions. Decay curves of all samples (except #1–4 with BaCl₂ solvent) have an initial exponential part, and a hyperbolic decay at 50 μs gate. Cu-doped samples show the first order kinetic, and the Ag-doped samples the second

Table 2
Main properties of the investigated samples

Sample	λ_m (nm)	Light yield		τ (μ s)	TSL	
		<i>a</i>	<i>b</i>		T_m (K)	<i>I</i> (a.u.)
1	0	0.38	0.27	9.2	155	53
	518 (1.0)				245	3.5
	608 (0.12)				295	5.8
					463	93
2	534	0.49	0.06	15	180	6000
3	459 (1.0)	0.62	1.56	4.5	115	22
	528 (0.86)				135	23
					215	2.1
4	604	0.21	0.38	2.5	240	74
5	580	0.42	1.18	0.025	115	20
					245	7.0
6	556	0.06	0.28	0.20	<100	>1
					190	0.20
7	601	0.08	0.04	2.0	<100	>1.2
					240	0.44
8	555	0.07	0.12	0.086	115	
	1.4					
					135	1.1
					190	0.75
9	550	0.07	0.05	0.27	245	1.27

order kinetic. Shallow traps in samples #5 and #8 are different: in Cu-doped sample we have only the 115 K trap (by TSL measurements), and in Ag-doped we have 115 and 135 K traps. So, the difference in kinetic (first and second orders) can be explained by two different means: (1) a recombination cross section σ_r of an Ag-related center is much lesser than that of Cu-related center (115 and 135 K traps have similar cross sections σ_r); or (2) the 135 K trap has a cross section much higher than σ_r of an Ag-related center.

Samples doped with Ag do not show a good performance, the light yields for them are too low.

For some samples with a high light yield we measured temperature dependencies of luminescence intensities for different peaks. The intensities usually drop with increasing temperature. For sample #5 such dependence is shown in Fig. 2. One can observe the spectrum transformation with temperature: the Gaussian shape at 300 K, and the second peak appearing at 100 K with $\lambda_m = 525$ nm, and the half-width two times less—42 nm in comparison with 83 nm at 300 K (the first line at 100 K has a 75 nm half-width). The drop of integral band intensity (the inset in Fig. 2) in a temperature range 130–150 K is connected with 525 nm line disappearance. Decay curves for sample #5 measured at

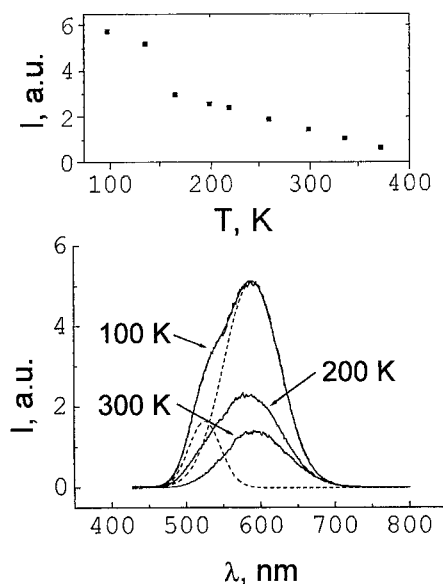


Fig. 2. The temperature dependence of the Cu-related X-ray excited emission spectrum in $\text{ZnS}_{0.5}\text{Se}_{0.5}:\text{Cu}, \text{Al}$ (sample #5). At 100 K the spectrum was fitted with two gaussian curves (dashed lines) also shown. Inset—the temperature dependence of the integral emission band intensity.

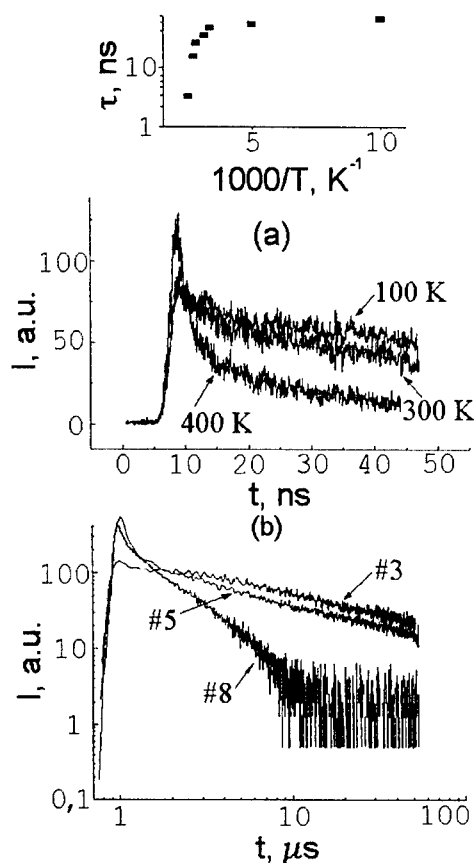


Fig. 3. Decay curves of different samples: measurements at 50 ns gate for sample #5 at different temperatures (a); and at 50 μ s gate for samples # 3,5,8 (b).

different temperatures are shown in Fig. 3. The decay time temperature dependence is shown in the inset of Fig. 3. An activation energy defined from the dependence (similar analysis for a linear case in Ref. [7]) $E_i = (0.26 \pm 0.06)$ eV correlates well with the trap energy corresponding to the 245 K TSL peak (Fig. 4) $E_t = (0.26 \pm 0.03)$ eV. The last value was defined by analyzing the glow peak initial exponential part.

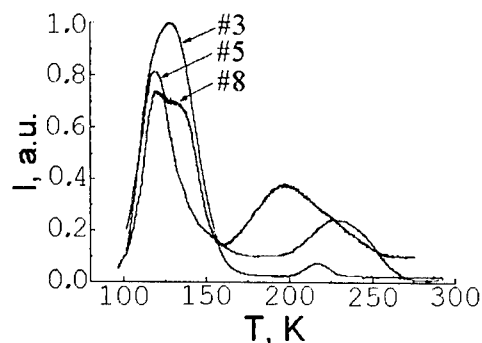


Fig. 4. Thermo-stimulated luminescence curves of different samples.

5. Conclusions

Large transparent samples doped with Cu and prepared by the described technology with CsCl solvent show good scintillating properties for $x = 1-0.5$. However the reproducibility is not satisfactory. It depends, maybe, on the difference in post-growth conditions (differences in cooling rates, etc.), so we need thermal treatment experiments.

References

- [1] L.V. Atroschenko, et al., Scintillator Crystals and Detectors, Naukova Dumka, Kyiv, 1998, p. 312 (in Russian).
- [2] P. Schotanus P. Dorenbos, V.D. Ryzhikov, IEEE Trans. Nucl. Sci. 39 (1992) 546.
- [3] A.A. Avdeyenko, et al., LUMDETR' 2000, 2000, p. 43.
- [4] P.A. Rodnyi, et al., Instrum. Exp. Tech. 43 (2000) 125.
- [5] D. Cuire, et al., in: M. Aven, J.S. Prener (Eds.), Physics and Chemistry of II–VI Compounds, North-Holland, Amsterdam, 1967, p. 624B253.
- [6] G.N. Ivanova, et al., J. Lumin. 82 (1999) 277.
- [7] A. Lempicki, et al., J. Lumin. 81 (1999) 13.



ELSEVIER

Physica B 308–310 (2001) 1205–1208

PHYSICA B

www.elsevier.com/locate/physb

Interface defects in integrated hybrid semiconductors by wafer bonding

P. Kopperschmidt*, St. Senz, R. Scholz

Max-Planck-Institute of Microstructure Physics, Weinberg 2, D-06120 Halle, Germany

Abstract

The integration of materials by wafer bonding offers novel device fabrication for applications in micromechanics, microelectronics, and optoelectronics. Two mirror-polished surfaces are brought into intimate contact by adhesive forces regardless of their crystallography, crystalline orientation and lattice mismatch. Followed by a thermal treatment at several hundred degrees centigrade, the interface energy of the material combination is increased to energies of covalent interatomic bonds. Attempts to break the bond lead to fracturing of the materials. In particular, thermomechanic stress in dissimilar material combinations may result in bending, gliding and cracking of the bonded wafers during annealing. The bonding interface of various hybrid semiconductor materials was studied by transmission electron microscopy. Occasionally, microscopic imperfections at the bonding interface were found in Si/Si, Si/GaAs, GaAs/GaAs, GaAs/Al₂O₃, GaAs/InP and moreover Al₂O₃/Al₂O₃ bonded wafer pairs. The imperfections were identified as voids, negative crystals, and oxide-containing precipitates ranging from 5 to 20 nm in diameter. Microscopic defects at the bonding interface in integrated bulk materials do not affect the mechanical and electrical properties of the device very much. However, in bonding of thin films the defects or precipitates may thread through the thin film, if the diameter of the precipitate surpasses the thickness of the film. These pinholes-containing thin films have a high leakage current, low electrical breakthrough and crystallographic disorder. Epitaxy of material on a pinholes containing, disordered surface results on deposition of bicrystalline grains. In between the grains tilt grain boundaries were observed raising from the bonding interface. Bonding related defects at the interface can be avoided by alternative bonding techniques like UHV wafer bonding and low temperature wafer bonding. © 2001 Elsevier Science B.V. All rights reserved.

PACS: 82.30.Rs; 61.72.Qq; 68.35.Fx

Keywords: Semiconductor wafer bonding; Interface defects; TEM micrographs

1. Introduction

The wafer bonding technique has been established in research and development in terms of integrating various materials [1]. Two mirror-polished wafers are brought into intimate surface contact at room temperature and adhere by van der Waals forces. To receive high bonding strength, the wafer pair must be annealed at elevated temperatures. Two major problems arise for

conventional wafer bonding including a high-temperature annealing step. During heating of wafer pairs containing different materials, thermomechanical stress is introduced into the material leading to bending in analogy to bi-metals. If the stress is sufficiently high, either the two wafers separate by breaking the bonds at the interface or one wafer will fracture [2]. The second problem of the high-temperature procedure arises from the occurrence of voids, crystalline grains and precipitates at the bonding interface. These imperfections are revealed in many materials combinations, e.g. silicon/silicon, GaAs/silicon, GaAs/GaAs, Al₂O₃/GaAs, Al₂O₃/Al₂O₃ and GaAs/InP [3–7].

*Corresponding author. Fax: +49-345-5511223.

E-mail address: kopper@mpi-halle.de (P. Kopperschmidt).

If two bulk materials are joined together, microscopic interface defects may not have a disturbing effect on the mechanical and electrical properties of the device, if the density of the cavities is small. In thin films, however, where the size of the interface defect surpasses the thickness of the thin layer, the surface is decorated with trenches and pinholes and the associated device structure may have preventable properties [2]. In electronic applications these pinholes will lead to high leakage currents and a low electrical breakthrough across the interface. Incidentally, a twist in between a thin pinhole-containing crystalline layer and a single crystalline substrate has some interesting morphological features, as a template for bi-crystalline structures or selected area growing films.

By cross sectional and plan-view transmission electron microscopy (TEM) bonding interfaces of various materials combination are inspected and briefly discussed in the following.

2. Silicon/silicon bonding interfaces

In Czochralski grown silicon (CZ-Si) oxygen is incorporated in silicon with a concentration close to the solubility at the silicon melting point [8]. Oxide precipitates are formed at sufficient temperatures by diffusion processes. Large precipitates grow at the expense of smaller precipitates to reduce the surface energies. Grain boundaries often reduce the velocity of the diffusion and are therefore attractive nucleation centers for precipitates and void formations. In Fig. 1 a high-resolution TEM cross section is presented at the twist-grain boundary between two (001) bulk CZ-Si wafers after Ref [4]. The wafers are bonded hydrophobically with an intentional misorientation of 12° . Similar results were observed in thin silicon layer bonded to silicon substrates by Chen et al. They identified the defects as SiC containing precipitates [3].

3. GaAs/GaAs bonding interfaces

In GaAs/GaAs wafer bonding at 580°C in hydrogen atmospheres two types of interface defects were found. A representative TEM cross section is given in Fig. 2. In addition to amorphous precipitates, well-ordered grains of not-identified crystalline phases were observed at the bonding interface. These grains may be probably formed at elevated temperatures by lowering the surface energy at the boundary between two bonded surfaces with twist and miscut. In thin GaAs films with thickness of a few nm bonded to GaAs substrates, interface defects or cavities occasionally thread through the thin layer [7,9]. The decorated surface of the substrate may play an important role in the strain relaxation during lattice



Fig. 1. High-resolution TEM cross-section at the bonding interface of two slightly twisted (001) silicon wafers. The SiO_2 containing precipitate consists of two tilted pyramids (after Ref. [4]).

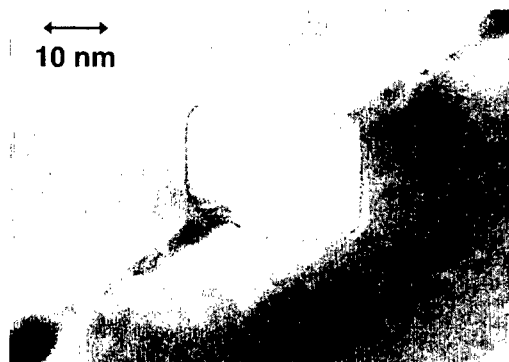


Fig. 2. Crystalline grain at the GaAs/GaAs bonding interface revealed by cross sectional TEM inspection. The crystallographic planes of the grain boundaries are close to [111]. Due to a small surface miscut of the (001) GaAs wafers, the grain is not exactly square-shaped.

mismatched heteroepitaxy on the so-called 'compliant substrates'. Fig. 3 shows a TEM micrograph pointing out the interface of a twist bonded thin GaAs film bonded to GaAs substrate with a cavity defect. While removing the sacrificial layer AlAs, the interface cavities partly open to the surface of the transferred film. Patriarche et al., recently reported on GaAs/GaAs bonding interfaces containing a high density of a regular network of unbonded cavities [9]. Since their thin GaAs layer has a thickness of 20 nm, the cavities do not thread through the thin layer.

4. Si/GaAs bonding interfaces

Since the thermal expansion coefficient of GaAs is nearly twice that of Si, thermomechanical stress cannot

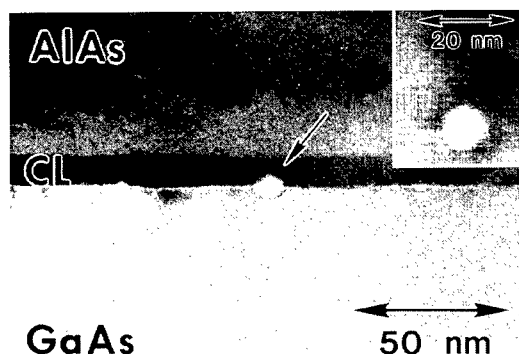


Fig. 3. Cross sectional (large picture) and plan-view (small picture) TEM micrograph of a defect at the interface of a thin GaAs layer bonded to a GaAs substrate. The GaAs thin film is denoted with CL. After removing the sacrificial AlAs layer, the GaAs layer is transferred to the GaAs substrate. If the size of the defect surpasses the thickness of the thin layer, pinholes or trenches are introduced into the thin layer after transfer.

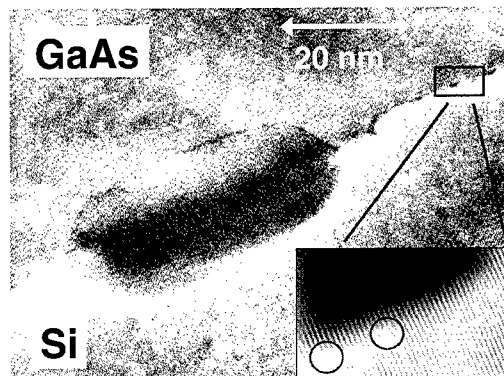


Fig. 4. Defect in Si/GaAs wafer bonding revealed by cross sectional TEM investigation. A Fourier-filtered image shows the bonding interface in detail. Due to the lattice misfit of 4.1%, extra (100) Si lattice planes are introduced (marked by rings).

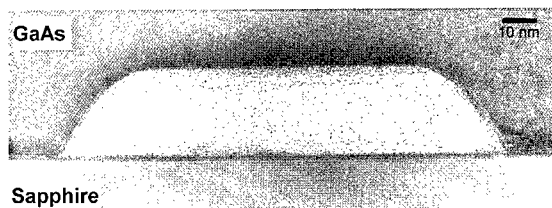


Fig. 5. Interface defect in GaAs/Al₂O₃ wafer bonding. The high-resolution TEM cross section shows the [111] and [100] oriented boundaries of the precipitate within the GaAs wafer. The precipitate is filled with Ga-rich and As-rich compounds.

be suppressed in GaAs/Si wafer bonding followed by an annealing procedure at elevated temperatures. Instead of using silicon wafers, 3 in silicon-on-sapphire (SOS) wafers with 500 nm of epitaxial silicon were bonded to GaAs. Due to the low thermal mismatch between GaAs and sapphire, the thermally induced mechanical stress is insignificant over a wide temperature range [6]. The bonding of SOS/GaAs was performed under arsenic pressure at 800°C for several hours. A high-resolution TEM cross section is presented in Fig. 4. Extra Si lattice planes are introduced at the GaAs/Si bonding interface to balance the lattice mismatch of 4.1%. Precipitates at the GaAs/Si interface, which contain mostly amorphous material, are occasionally observed with diameters ranging from 5 to 20 nm.

5. GaAs/Al₂O₃ bonding interfaces

Precipitates were also found at the bonding interfaces of GaAs and Al₂O₃ (see Fig. 5). The wafers were bonded as received after flushing in hydrogen atmosphere at a few hundred degrees centigrade. Further annealing at 500°C for several hours was necessary in hydrogen to maximize the bonding energies. Precipitates at GaAs/Al₂O₃ interfaces are settled in the GaAs. Since diffusion velocities in Al₂O₃ are rather low at the applied temperature, the defects contain mostly gallium-rich and arsenic-rich precipitates [10]. A closer look at the interface by plan-view TEM investigation reveals unbonded channel-like regions with strong bending contours. These channels can be responsible for the growth of precipitates by providing the mass transport to the interface.

6. Al₂O₃/Al₂O₃ bonding interfaces

Annealing temperatures near 1200°C are required to increase the interface energy of r-cut Al₂O₃/Al₂O₃ bonded wafer pairs to the binding energy of covalent bonds. At these high temperatures, a change of the interface morphology to form low energetic grain boundaries is evident. Wafers with small miscut show atomic steps or terraces at the surface. These steps are moveable during high temperature annealing. In bonded wafers with small surface miscut voids or negative crystals are achieved at the interface. The arrangement of well-ordered voids is shown in the plan-view TEM in Fig. 6. The density of the voids, which is in the range of 10⁸ cm⁻², can be reduced by increasing the annealing time. The ripening of the voids continues at the gain of size.

Conclusively, bonding related defects and imperfections at the interface were observed in many integrated materials. At elevated temperatures, the diffusion length increases for impurities and interstitials within the considered material. Grain boundaries, interfaces or dislocations, however, reduce the diffusion length and

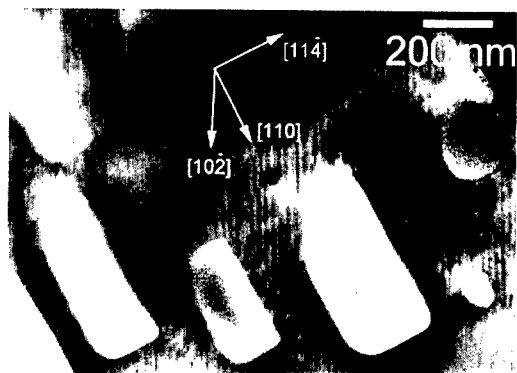


Fig. 6. Voids formation at the $\text{Al}_2\text{O}_3/\text{Al}_2\text{O}_3$ bonding interface revealed by plan-view TEM. During further annealing at 1200°C the density of voids is reduced while the diameters increase. The driving force for changing the surface morphology is to lower the surface energy of bonded wafers with rotational misorientation and surface miscut.

are attractive nucleation centers for the generation of voids, precipitates and novel crystalline phases. The bonding interface of two wafers is due to the material contrast, due to a miscut of the wafers and due to rotational misorientation between the two wafers.

Avoiding high temperatures in dissimilar materials integration, e.g. by low-temperature bonding techniques, is required to prevent the defect formation at the bonding interfaces.

Acknowledgements

Dr. N.D. Zakharov and Dr. G. Kästner are kindly acknowledged for the TEM micrographs and discussions.

References

- [1] Q.-Y. Tong, U. Gösele, *Semiconductor Wafer Bonding*, Wiley, New York, 1999.
- [2] P. Kopperschmidt, et al., *Appl. Phys. Lett.* 70 (1997) 2972.
- [3] C. Chen, et al., *Philos. Mag. A* 80 (2000) 881.
- [4] E. Schroer, et al., *Appl. Phys. Lett.* 70 (1997) 327.
- [5] G. Patriarche, et al., *J. Appl. Phys.* 82 (1997) 4892.
- [6] P. Kopperschmidt, et al., *Appl. Phys. A* 64A (1997) 533.
- [7] P. Kopperschmidt, et al., *Appl. Phys. Lett.* 74 (1999) 374.
- [8] A. Borghesi, et al., *J. Appl. Phys.* 77 (1995) 4169.
- [9] G. Patriarche, et al., *Appl. Surf. Sci.* 164 (2000) 15.
- [10] P. Kopperschmidt, et al., *Proceedings of the 23rd ICPS*, World Scientific, Singapore, 1997, p. 967.



ELSEVIER

Physica B 308–310 (2001) 1209–1212

PHYSICA B

www.elsevier.com/locate/physb

Effect of proton irradiation on the characteristics of GaAs Schottky barrier diodes

R.R. Sumathi^{a,*}, M. Udhayasankar^a, J. Kumar^a, P. Magudapathy^b, K.G.M. Nair^b

^a Crystal Growth Centre, Anna University, Chennai 600 025, India

^b Materials Science Division, IGCAR, Kalpakkam 603 102, India

Abstract

Proton irradiation (80 keV) effect on the electrical properties of Au/n-GaAs Schottky barrier diodes (SBDs), fabricated on an epitaxially grown undoped n-GaAs has been studied for a range of particle fluences from 1×10^{13} to 1×10^{15} particles/cm². Current–voltage (I – V), capacitance–voltage (C – V) and deep level transient spectroscopy (DLTS) measurements have been carried out to study the change in characteristics of the devices and the defects introduction due to implantations, respectively. Reverse leakage current (I_R) of the device is the most sensitive parameter to the incident proton irradiation. The I_R was increased (1.0×10^{-9} to 7.95×10^{-5} A) upon irradiation and it strongly depends on the particle fluence. Annealing of irradiated diodes shows reduction in the I_R and particularly, enhancement in barrier heights of the diodes. A change of effective free carrier concentration in the material has been observed from the C – V measurements for the irradiated diodes when compared to the unirradiated diode. From DLTS measurements, it was found that the low energy proton irradiation of the SBDs increases the concentration of EL2 defects and the concentration was estimated to be 6.42×10^{14} cm⁻³. © 2001 Elsevier Science B.V. All rights reserved.

Keywords: Gallium arsenide; Schottky barrier diode; Proton irradiation; DLTS

1. Introduction

Ion implantation is mainly used to obtain inter device electrical isolation [1]. With the implant isolation technique, free carriers are compensated by either irradiation-induced damages or chemically related deep levels. Significant improvements in the electrical isolation of devices in closely spaced gallium arsenide (GaAs) integrated circuit (IC) have been achieved with low energy proton implantation [2]. Further, proton-induced damages reduce the carrier lifetime in GaAs and very short switching times can also be achieved. Another aspect is that proton environment in space, particularly at low altitudes in trapped radiation belts and during solar events, can have a detrimental effect on semiconductor components and other materials used in spacecraft [3]. In view of this and also

the potential applications of proton irradiation in GaAs, it is of interest to know the proton irradiation induced defects and also to study their effects on the properties of device components like Schottky barrier diodes.

In contrast to electron irradiation, which introduces mainly point defects, implantation with particles such as protons, α -particles may introduce additional defects and various deep levels. Radiation damage produces many defect levels within the depletion layer of the GaAs SBDs [4]. Deep traps of majority carriers can cause variation of field effect transistor (FET) device parameters [5] and can affect the electron mobility at high electric fields [6]. In this paper, we also present the results of DLTS measurements on the low energy proton-irradiated SBDs.

2. Experimental details

Undoped n-type (carrier concentration = 4.4×10^{15} cm⁻³) GaAs epilayers of thickness 4 μ m,

*Corresponding author. I. Physics Institute, Justus-Liebig-University, Giessen, Germany. Fax: +49-641-9933109/119.

E-mail address: radhakrishnan.sumathi@physik.uni-giessen.de (R.R. Sumathi).

grown on semi-insulating (SI) GaAs substrate by metal organic vapour phase epitaxy (MOVPE) technique were used. Samples were cleaned well and chemically etched (wet) in order to remove the presence of native oxides on the surface. Ohmic contacts were realised by evaporating Au:Ge (88:12) alloy under a vacuum of 2×10^{-6} mbar and then annealing the samples at 723 K under the high pure argon atmosphere for 5 min. Schottky contacts were formed (planar structure) by evaporating gold dots of area $7.85 \times 10^{-3} \text{ cm}^2$ and of thickness 1500 Å using electron beam evaporation system. The fabricated SBDs were characterised through I - V and C - V measurements carried out under dark condition, at room temperature.

The SBDs were irradiated by 80 keV protons at room temperature for various particle fluences (or ion doses) of 1×10^{13} , 1×10^{14} and $1 \times 10^{15} \text{ p/cm}^2$ using a 150 KV accelerator under a vacuum of 10^{-6} mbar. The irradiation energy was chosen in such a way that the irradiation-induced defects have been introduced at the metal-semiconductor (M - S) junction and/or within the depletion layer of the Au/GaAs Schottky junction. Penetration depth of 80 keV proton particles in Au/n-GaAs structure has been calculated to be 4580 Å (with straggling, $\Delta R_p = \pm 1270 \text{ Å}$) using TRIM [7] theoretical calculations. The estimated depletion width for a background doping level of 10^{15} cm^{-3} for GaAs is around 5000 Å at zero bias. The irradiated SBDs were annealed at different temperatures (373, 473, 573 and 673 K) for 10 min and they were characterised using I - V and C - V measurements before and after annealing. DLTS measurements have been performed on the as-grown as well as proton-irradiated samples in the temperature range 77–400 K, with -0.2 V reverse bias, 10 ms pulse width.

3. Results and discussions

I - V characteristics of the unirradiated SBDs and the diodes annealed at different temperatures are shown in Fig. 1. The quality of the control SBDs (unannealed, unirradiated) are good with nearly ideal behaviour and low leakage current (about $1 \times 10^{-9} \text{ A}$) as seen from Fig. 1. Barrier height (ϕ_b) and ideality factor (n) of the control diodes fabricated on low free carrier density ($4.4 \times 10^{15} \text{ cm}^{-3}$) samples are 0.79 eV and 1.08, respectively. No significant change in the I - V characteristics of the control diodes has been observed up to the annealing temperature of 573 K. But samples further annealed to 673 K were found to be highly leaky ($I_R \approx 10^{-5} \text{ A}$). It was known that about 623 K, gold starts to in-diffuse into GaAs material. Hence, the high leakage current may be attributed to the metal inter-diffusion at the junction and the M - S interface becomes non-abrupt.

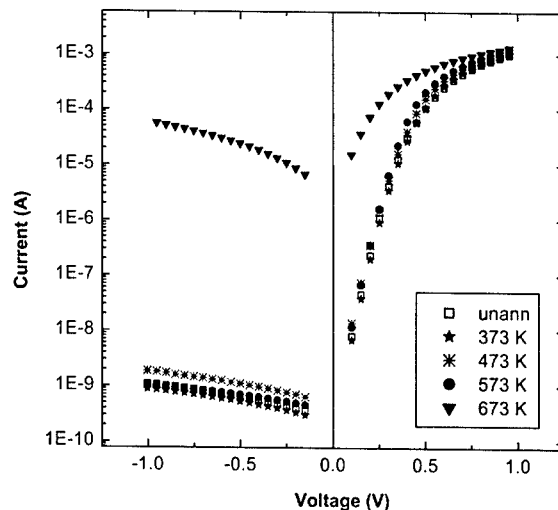


Fig. 1. I - V characteristics of unirradiated (control) Au/n-GaAs SBDs annealed at different temperatures for 10 min.

3.1. Characteristics of irradiated diodes

For proton-irradiated Au/n-GaAs SBDs, the reverse leakage current was observed to be most sensitive parameter to the incident irradiation. Further, the change in $I_R(\Delta I_R)$ was found to increase with increasing particle fluence (Fig. 2). The change in I_R can be attributed to the irradiation-induced defects at the interface and/or nearby regions. Implantation of semiconductors with ion beams introduces electrically active defects which can behave either as traps or as recombination centres in the material, depending on their capture cross section for electrons and holes [8]. The defects that act as recombination centres introduce generation-recombination currents in rectifying devices. Thus the irradiation-induced recombination centres are responsible for the increase in the reverse leakage current. But such changes due to these defects depends on to an extent determined by their concentration. The linear dependence of change in I_R with fluence is in accordance with the increase of concentration of defects, which increases as the incident particle fluence is increased. Moreover, it has been observed that the barrier height decreases and the ideality factor of the diode increases as a function of ion fluence. This fluence dependency is probably connected with the shift (or movement) of Fermi level pinning position at the GaAs surface, since irradiation-induced defects also creates various interface states. Similar behaviour and particle fluence dependency of the ideality factor and apparent barrier height on the neutron bombardment [9] and on helium ion bombardment [10] has been reported. The increase of ideality factor is indicating an increase of

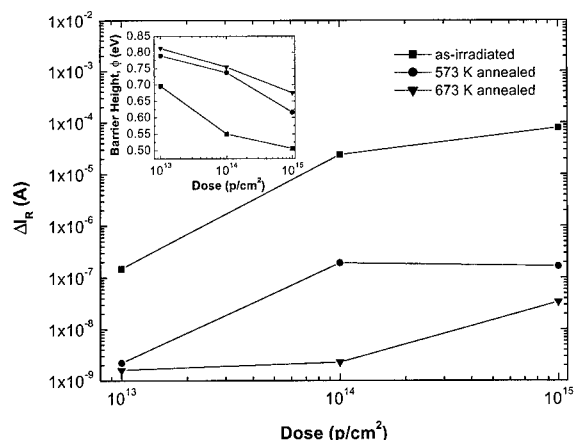


Fig. 2. Change of reverse leakage current and barrier height (inset) with dose, for as-irradiated and irradiated-annealed SBDs.

defect density at the interface with increasing ion dose. For higher fluence of 1×10^{15} p/cm², the I - V curve exhibits almost ohmic behaviour and the current flow mechanism is mainly due to tunnelling.

Damage produced by light ions like protons may usually be unstable and tend to anneal or form complex clusters at higher temperatures. The irradiated diodes have been subjected to thermal treatment to investigate the effect of annealing. Annealing of the irradiated diodes decreases the reverse leakage current as shown in Fig. 2 and the reduction in the reverse leakage current exhibits a strong dependence on the annealing temperature. This is due to annihilation of irradiation-induced defects upon thermal annealing. The reverse leakage current for the 673 K annealed irradiated diodes was slightly higher than that of the unirradiated diode (control diode). This shows that the defects that were produced are not completely annealed out. The annealing of irradiated diode also decreases the ideality factor and increases the apparent barrier height. An enhancement in barrier height (0.812 eV) has been observed for 673 K annealed, irradiated (1×10^{13} p/cm²) SBDs as against the control diode (0.789 eV). Interestingly, it was found that the light ion irradiation and subsequent annealing improves the properties of SBDs, especially the barrier height (inset of Fig. 2).

From C - V measurements, it was observed that the capacitance decreases for irradiated diodes and has weak dependence on the applied bias. This may be due to reduction of effective doping level at the GaAs surface. Implantation can introduce traps that reduce the free carrier density of the semiconductor. A decrease in the capacitance was also attributed to the change in dielectric constant at the interface [11].

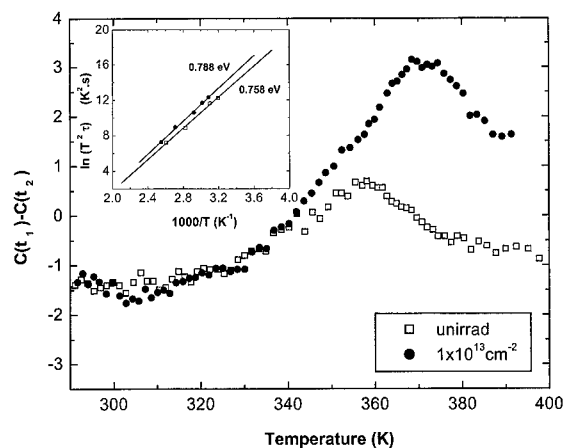


Fig. 3. DLTS spectra and Arrhenius plot (inset) of the unirradiated and as-irradiated (dose = 1×10^{13} p/cm²) samples.

3.2. Deep level transient spectroscopy analysis

DLTS spectra for control and 1×10^{13} p/cm² proton irradiated samples are shown in Fig. 3. For the as-grown samples, a trap level corresponds to deep level defect EL2 was observed. From Arrhenius plot (inset of Fig. 3), the activation energy and the concentration of the trap level was found to be 0.758 eV and 1.1×10^{14} cm⁻³, respectively. The electron trap level, EL2, is assigned to native arsenic antisite (As_{Ga}) defect with activation energy values of 0.76–0.80 eV [12–14]. Upon low energy proton irradiation, the trap level concentration was found to be increased (6.42×10^{14} cm⁻³) with activation energy of 0.788 eV. It may be noted that there is a shift of nearly 15 K (~ 30 meV) in the peak temperature for this defect signature. This may be because at higher defect concentrations their interactions intensified, changing the electrical properties of EL2 defect, thereby changing the thermal activation energy which results such peak shift [15]. Also, due to irradiation, possibility of conversion of the EL2 defect into some other complex defects with the energy close to that of EL2 cannot be excluded.

4. Conclusions

Low energy proton irradiation effect on the electrical properties of Au/n-GaAs SBDs, fabricated on MOVPE grown undoped n-GaAs epilayer has been analysed. I - V measurements show that there is an increase in the reverse leakage current with increase of incident particle fluence. Also, the ideality factor increases and the barrier height decreases as a function of fluence. Annealing of the irradiated diodes improves the diode's properties.

Further, an enhancement of barrier height as compared to the unirradiated diode has been obtained for annealed (673 K), 1×10^{13} p/cm² irradiated SBDs. From these studies it seems that the increase of reverse leakage current depends on the irradiation induced defects (particle fluence). Moreover, the removal of defects and the recovery strongly depend upon annealing temperature and the concentration of defects introduced, respectively. A change in the effective free carrier density in the material has been observed from the *C–V* measurements. DLTS measurements of the irradiated diodes show an increase in the concentration of the deep level defects.

Acknowledgements

One of the authors (R.R. Sumathi) acknowledges the Council of Scientific and Industrial Research (CSIR), Government of India for the award of Senior Research Fellowship (SRF). Authors thank the Department of Science and Technology (DST), for having sanctioned a project to establish the DLTS system. Useful discussions with Dr. V. Pandian is also acknowledged.

References

- [1] A.P. Knights, S. Ruffel, P.J. Simpson, *J. Appl. Phys.* 87 (2000) 663.
- [2] Donald C. D'Avanzo, *IEEE Trans. Electron Dev.* ED-29 (1982) 1051.
- [3] W. Hajdas, L. Adams, B. Nickson, A. Zehnder, *Nucl. Instr. and Meth. B* 113 (1996) 54.
- [4] Paul D. Taylor, D.V. Morgan, *Solid State Electron.* 19 (1976) 481.
- [5] Y.M. Houn, G.L. Pearson, *J. Appl. Phys.* 49 (1978) 3348.
- [6] J.C. Dymant, J.C. North, L.A. D'Asaro, *J. Appl. Phys.* 44 (1973) 2269.
- [7] J.F. Ziegler, J.P. Biersack, U. Littmark, in: *The Stopping Range of Ions in Solids*, Pergamon Press, New York, 1985.
- [8] F.D. Auret, S.A. Goodman, R.M. Erasmus, W.E. Mayer, G. Myburg, *Nucl. Instr. and Meth. B* 106 (1996) 323.
- [9] Zs.J. Horvath, E. Gombia, D. Pal, R. Mosca, G. Capannese, L. Doza, Vo Van Tuyen, in: V. Kumar, S.K. Agarwal (Eds.), *Proceedings of the Tenth International Workshop on the Physics of Semiconductor Devices*, India, 1999, p. 230.
- [10] M.J. Legodi, F.D. Auret, S.A. Goodman, J.B. Malherbe, *Nucl. Instr. and Meth. B* 148 (1999) 441.
- [11] P. Zukowski, J. Partyka, P. Wegierek, *Phys. Stat. Sol. A* 159 (1997) 509.
- [12] A. Jorio, C. Carlone, M. Parenteau, C. Aktik, *J. Appl. Phys.* 80 (1996) 1364.
- [13] M. Noack, K.W. Kehr, H. Wenzl, *J. Crystal Growth* 178 (1997) 438.
- [14] J. Lagowski, M. Kaminska, J.M. Parsey, H.C. Gatos, M. Lichtensteiger, *Appl. Phys. Lett.* 41 (1982) 1078.
- [15] P.N. Brunkov, V.S. Kalinovskiy, V.G. Nikitin, M.M. Sobolev, *Semicond. Sci. Technol.* 7 (1992) 1237.



ELSEVIER

Physica B 308–310 (2001) 1213–1216

PHYSICA B

www.elsevier.com/locate/physb

Studies on the application of CVD diamonds as active detectors of ionising radiation

B. Marczevska^{a,*}, T. Nowak^a, P. Olko^a, M. Nesladek^b, M.P.R. Waligórski^{a,c}

^a *Institute of Nuclear Physics (INP), Health Physics Laboratory, ul. Radzikowskiego 152, PL-31-342 Kraków, Poland*

^b *Institute for Materials Research at the Limburg University, Diepenbeek, Belgium*

^c *Centre of Oncology, Kraków, Poland*

Abstract

Due to its tissue-equivalence, radiation hardness, resistivity to chemicals and thermal stability, diamond is becoming an interesting material for developing dosimeters of ionising radiation. Several types of CVD diamonds grown at the Institute for Materials Research at the Limburg University, Belgium, were used to construct detectors working in ionisation chamber mode, applicable in medical physics. CVD diamonds with substrate removed, cut into $3\text{ mm} \times 3\text{ mm} \times 0.8\text{ mm}$ pieces and with deposited Au contacts, exposed in an external field of 320 kVp X-rays demonstrated sensitivity which varied from 50 to 630 nC/Gy, and a sublinear response with dose rate. A pencil-shaped holder was developed and used for testing the diamond detectors. The main deficiency of the system so far are extended periods required to reach signal saturation and recovery after irradiation. We expect this deficiency to be overcome by improving the quality of CVD diamonds. © 2001 Elsevier Science B.V. All rights reserved.

Keywords: CVD diamonds; Detectors; Ionising radiation

1. Introduction

Detectors based on natural diamond crystals have been developed to measure relative dose distributions in high energy photon and electron beams used in cancer radiotherapy [1]. The most important features which make diamond detectors attractive for medical applications are their tissue equivalence, their small sensitive volume (of a few mm^3) allowing good spatial resolution to be achieved, and the relative lack of dependence of their response on beam energy, dose rate and ambient temperature. A major advantage of a diamond detector in comparison with a gas-filled ionisation chamber is in its small size and high sensitivity, due to the high solid state/gas density ratio (about 3×10^3) and to the lower energy required to produce ion pairs [2]. At present, diamond detectors for dosimetry in radiotherapy beams are produced only by the group of Khrunov at Dubna

(Russia) and offered commercially by PTW Freiburg. The main problem with diamond detectors is to find suitable gems to be used as detecting material. Detector-grade natural diamonds are extremely rare, which limits the availability of such dosimeters.

The development of the chemical vapour deposition (CVD) technique for growing artificial diamonds brought about an effort to produce a CVD diamond-based dosimeter. The CVD technique allows one to control the crystal-growing process in order to obtain materials with well-defined properties. An ideal detector should consist of a single diamond crystal. All substitution impurities of diamond act as trapping centres for free carriers and consequently reduce its radiosensitivity [3]. Polycrystalline CVD diamonds usually consist of columnar grains, which are smaller on the substrate side and increase in size with film thickness [4]. The presence of grain boundaries and of intra-grain defects limits the lifetime of the carriers, giving rise to a high density of localised energy levels in the diamond band gaps. This results in different mechanisms of electrical transport. Han and Wagner [5] showed that the presence of grain

*Corresponding author. Fax: +48-12-6375441.

E-mail address: barbara.marczevska@ifj.edu.pl
(B. Marczevska).

boundaries degraded the detection properties of a CVD diamond by a factor of two or three, as carriers are then more likely to drift across grain boundaries and become trapped or scattered. In spite of the presence of a network of grain boundaries, CVD diamonds could operate as detectors of ionising radiation. The Sheffield group published several papers [6,7] summarising their work on the development and application of CVD diamonds as dosimeters in radiotherapy beams.

Within this work, five batches of CVD diamonds grown at the Institute for Materials Research at Limburg University, Belgium, were used to construct detectors working in ionisation chamber mode. The aim of these studies was to test the CVD diamond detectors in different radiation fields. The construction of the detector holder was optimised in order to eliminate the spurious signal interfering with that from the diamond detector.

2. Materials

Five different batches of CVD diamonds were grown at the Institute for Materials Research at Limburg University, Belgium. The thickness of the CVD diamonds varied between 500 and 800 μm and the grain size, determined by means of scanned electron microscopy (SEM) at the Institute of Metal Cutting in Kraków, varied between 50 and 150 μm . The diamond plates used to produce detectors were typically of an area between 4 and 9 mm^2 .

Contact preparation and detector irradiation was performed at the Institute of Nuclear Physics (INP) in Kraków. The as-received CVD diamond samples were annealed for 30 min at 400°C. Samples were cleaned in

hot chromic acid to eliminate any graphite or non-diamond material from the diamond surface, and then rinsed with de-ionised water and dried. Electrical contacts were prepared on opposite sides of the diamond samples. The side of the diamond which had been in contact with the Si substrate during growth, was flat, and the other featured a polycrystalline structure. On the polycrystalline side, the central contact was surrounded by a guard ring. Au or Cr/Au contacts of thickness of about 500 Å were deposited by evaporating metal in a 10^{-5} Torr vacuum chamber. The Cr/Au contacts were annealed at 400°C for 10 min. Finally, a gold wire, 0.1 mm in diameter, was glued to each side of the detector. The CVD diamond detectors were mounted (i) on small isolating plates with electrical contacts (PCBs), (ii) in a 10 cm \times 10 cm \times 5 cm steel box acting as a Faraday cup and (iii) in a specially developed, pencil-shaped holder.

The CVD diamond detectors were irradiated by ^{90}Sr , 5.3 MeV α -particles of fluence about $7 \times 10^6/\text{cm}^2$ from an ^{241}Am source, and by a Philips X-ray tube. The dose rate varied from 19.6 mGy/min at 100 kV (tube current: 1 mA) to 13.32 Gy/min at the 320 kV (tube current: 12 mA). The current and charge generated in the diamond detector were measured by an UNIDOS (PTW Freiburg) electrometer. The bias voltage of the detector could be increased only in 50 V steps. A Markus ionisation chamber was used to monitor the dose rate during X-ray irradiation.

3. Results and discussion

In our first tests, all detectors with their gold contacts were mounted on a small PCBs free-in-air and tested in

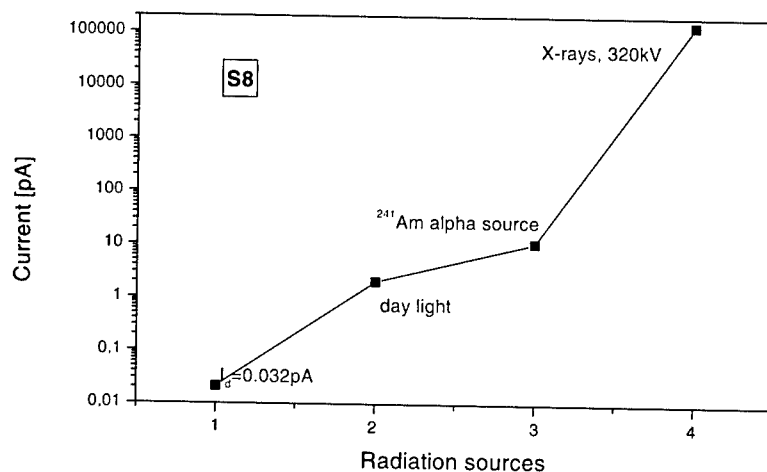


Fig. 1. Response of the S8 detector after irradiation with different sources. I_d means the value of the dark current of the detector S8 before irradiation.

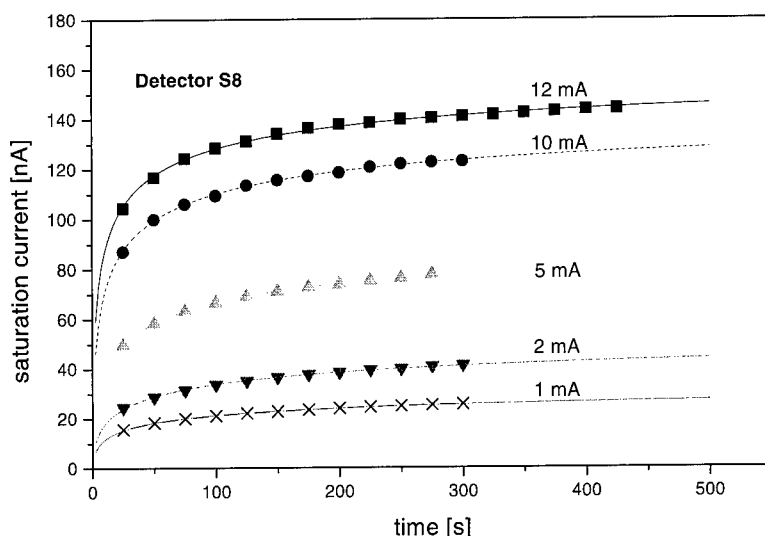


Fig. 2. Saturation of the response of the S8 detector after different dose rates, in a 320 kV X-ray beam.

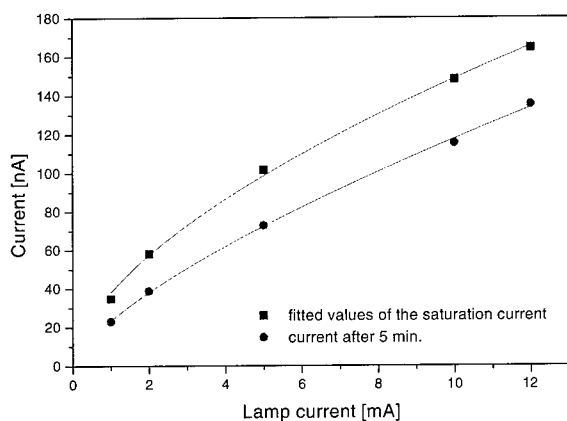


Fig. 3. Best fitted value of saturated current value (squares) and of measured current value (circles) in the S8-type active diamond detector, versus tube current, in a 320 kV X-ray field. Values observed 5 min after turning the X-ray field on were taken as the measured value of current.

the ^{90}Sr field (dose rate: 20 mGy/s). At a 50 V bias voltage detectors showed a dark current of about 10^{-12} A, and a current of a few pA when placed in the ^{90}Sr field. Under these conditions, such a small signal could not be measured in a reproducible and stable manner. Therefore the PCBs-mounted detector was placed inside a grounded metal box acting as a Faraday cup to eliminate distortions caused by external electric fields. Fig. 1 demonstrates the response of one of the detectors (symbol S8) to different radiation fields. The dark current I_d of the S8 detector encapsulated in the

Faraday cup was about 0.032 pA. The detector exposed to day-light showed a current of the 2–3 pA, of about 10 pA under ^{241}Am irradiation and of 140 nA in the 320 kV X-ray beam.

Detectors built from all batches of detectors available to us were tested in the X-ray beam at different dose rates. The response of our CVD detectors varied from 50 to 630 nC/Gy. The signal of the detector is here the total signal, with the signal of the Faraday cup with PCBs plate and electrodes, but without the diamond, subtracted. This spurious signal originated from ions induced by X-rays in air, collected on the electrodes. In Fig. 2 the response of the S8-batch diamond detector, which showed the highest response, is presented as a function of dose rate. The signal of the S8 detector reaches saturation after a period of over 300 s. For all detectors tested, of thickness 0.5 or 0.8 mm, the time required for the signal to saturate was about 5–8 min. After switching the X-ray beam off, the dark current, initially about 2–5 pA, decreased to about 1 pA within 10 h. The initial dark current of virgin (not irradiated) diamond detector ranged between 0.020 and 0.050 pA.

The response of the S8 detector as a function of X-ray dose rate is presented in Fig. 3. Linear response with dose-rate is an absolute requirement for any dosimetric application. On the other hand, the relation between diamond current and the dose rate D provides information on the character of diamond conductivity σ which shows a power dependence with dose-rate, $\sigma \sim D^d$ [7]. The dependence of the S8 detector current versus time since irradiation began, t , was fitted with the function $f(t) = abt^{1/2}/(1 + bt^{1/2})$ (extended Langmuir function) where a (saturation current) and b are free parameters

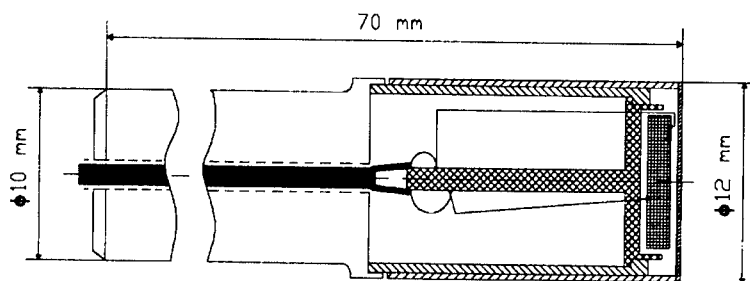


Fig. 4. Construction of the CVD diamond detector holder. The diameter ϕ of the holder is 12 mm and its length is 70 mm.

(Fig. 2). The saturation current a was determined at each dose rate and plotted against the current of the X-ray tube (Fig. 3). The relation between the saturation current and the dose rate was found to be sublinear ($\Delta = 0.59 \pm 0.02$). It has been reported [7] that Δ approaches 1 for some diamond batches and at higher applied voltages. Linearity of response with dose rate is a crucial parameter if medical applications of CVD detectors are to be considered. More work is planned in this area, with new batches of diamonds placed in much smaller holders than those used presently.

Due to the high level of spurious signal encountered during measurements with the Faraday cup, we developed a pencil-shaped holder, to better separate the electrodes of the diamond detector and to minimise other side-effects. This brass holder was designed for the PMMA structure to fit snugly, keeping electrodes well isolated and eliminating as much as possible air gaps inside the detector (Fig. 4). The dark current of the holder and its background signal in the X-ray beam (with no diamond) was too low to be measured with the UNIDOS electrometer. This type of holder can easily be made waterproof, enabling detectors to be placed in a water phantom. Several detectors with Au and Cr/Au contacts were installed in the holder and tested in the X-ray beam. The response of these detectors was similar to that presented in Fig. 2, but no spurious current had to be subtracted.

4. Conclusions

Several batches of CVD diamonds produced at the Limburger University were tested as possible active detectors for the dosimetry of radiotherapy beams. In an

external field of 320 kVp X-rays, pieces of CVD diamonds with deposited Au contacts demonstrated sufficient sensitivity, varying from 50 to 630 nC/Gy, but, unfortunately, also a sublinear response with dose rate. Another major disadvantage of these detectors is in the extended time periods required to achieve signal saturation and recovery. A pencil-shaped holder was developed and used for testing the diamond detectors. More work is planned with new batches of diamonds and with improved detector encapsulation.

Acknowledgements

This work was partially supported by the Research Grant No 8 T11E 019 18 from the Polish State Committee for Scientific Research and by Program Polonium 2001.

References

- [1] V.S. Khrunov, S.S. Martynov, S.M. Vatnitsky, I.A. Ermakov, A.M. Chervjakov, D.L. Karlin, V.I. Fominych, Yu.V. Tarbeye, *Radiat. Prot. Dosim.* 33 (1990) 155.
- [2] B. Planskoy, *Phys. Med. Biol.* 25 (1980) 519.
- [3] E.A. Burgemeister, W. Schouten, *Radiat. Prot. Dosim.* 6 (1984) 145.
- [4] A. Mainwood, *Semicond. Sci. Technol.* 15 (9) (2000) 55.
- [5] S. Han, R.S. Wagner, *Appl. Phys. Lett.* 68 (1996) 3016.
- [6] C.M. Buttar, R. Airey, J. Conway, G. Hill, S. Ramkumar, G. Scarsbrook, R.S. Sussman, S. Walker, A. Whitehead, *Diamond Relat. Mater.* 9 (2000) 965.
- [7] S. Ramkumar, C.M. Buttar, J. Conway, A.J. Whitehead, R.S. Sussman, G. Hill, S. Walker, *Nucl. Instr. and Meth. A* 460 (2001) 401.



ELSEVIER

Physica B 308–310 (2001) 1217–1221

PHYSICA B

www.elsevier.com/locate/physb

Radiation defects in STI silicon diodes and their effects on device performance

K. Hayama^{a,*}, H. Ohyama^a, E. Simoen^b, C. Claeys^{b,c}, A. Poyai^{b,c}, T. Miura^a,
K. Kobayashi^d

^a *Department of the Information and Communication Engineering, Kumamoto National College of Technology, 2659-2, Nishigoshi-cho, Kikuchigun Kumamoto 861-11, Japan*

^b *IMEC, Kapeldreef 75, B-3001 Leuven, Belgium*

^c *KU Leuven, ESAT-INSYS, Kard. Mercierlaan 94, B-3001 Leuven, Belgium*

^d *NEC IC Microcomputer Systems, Ltd., Mashiki Kumamoto, Japan*

Abstract

Results are presented of a deep level transient spectroscopy (DLTS) investigation of the radiation induced lattice defects in shallow trench isolation (STI) silicon diodes by 20 MeV proton and 2 MeV electron irradiation. The correlation between the deep levels and the post-rad device performance will be studied, together with the recovery behavior by isochronal thermal annealing. It will be demonstrated that the reverse and forward current increase after irradiation, which is caused by a decrease of the generation and recombination lifetime, respectively. Two electron capture levels were observed in meander diodes after 10^{14} p cm⁻² proton irradiation. The degraded device performance recovers by isochronal thermal annealing and correlates well with the annealing of the radiation-induced electron traps. During the annealing, the electron traps transform in other more stable defect centers. © 2001 Elsevier Science B.V. All rights reserved.

Keywords: Shallow trench isolation diodes; Irradiation; Induced deep levels; Degradation

1. Introduction

For sub 0.25 μ m CMOS shallow trench isolation (STI) is the only viable scheme for achieving the required packing density and speed performance, by decreasing the parasitic capacitance of the isolation region, enduring the device isolation, and moderating the lithography process margin. It is also considered that the STI is inherently hardened in a radiation-rich environment because of the used process scheme whereby the thickness of the isolation oxide is significantly reduced. Although some reports on the radiation performance of STI structures recently became available [1,2], no systematic studies outlining the relations between

radiation induced lattice defect and the degradation of the electrical performance are available. In this paper, the induced lattice defects and device performance degradation of STI diodes irradiated by 20 MeV protons and 2 MeV electrons were investigated. Moreover, isochronal thermal annealing is performed to study the recovery behavior of the electrical properties of the irradiated diodes.

2. Experimental

The process flow of the STI diodes was based on IMEC's standard 0.18 μ m CMOS technology. The STI process module consists of (1) a dry etching of trenches in the Si substrate, (2) oxidation of the trench sidewalls, (3) filling step with a TEOX oxide, and (4) chemical-mechanical polishing for planarization. A combination

*Corresponding author. Tel.: +81-96-242-2121; fax: +81-96-242-4190.

E-mail address: hayama@tc.knct.ac.jp (K. Hayama).

of a deep (200 keV, $1.2 \times 10^{13} \text{ cm}^{-2}$) and a shallow (55 keV, $1.5 \times 10^{15} \text{ cm}^{-2}$) boron ion implantation and subsequent dopant activation anneal at 850°C for 10 min is used to form a retrograde p-well. The studied n^+ p diodes are fabricated by a shallow As implantation (70 keV, $4.0 \times 10^{15} \text{ cm}^{-2}$) followed by a thermal anneal at 1100°C for 10 s, resulting in a junction depth of about 0.1 μm . The back-end of the process consists of a Co/Ti silicidation, a TEOS IMD layer and an Al-Si-Cu metallization. In order to examine the leakage currents resulting from the bulk and peripheral depletion region, different square (SQ1, SQ2) and meander (ME1) diodes have been characterized. The diodes were irradiated at room temperature by 20 MeV protons and 2 MeV electrons at the Takasaki JAERI in Japan. The current/voltage (I/V) characteristics were recorded before and after irradiation. The radiation induced lattice defects were investigated by deep level transient spectroscopy (DLTS) using a bipolar rectangular weighting function [3]. To study the recovery behavior of the irradiated STI diodes, 30 min isochronal thermal anneals were carried out at temperatures up to 300°C.

3. Results and discussion

The current/voltage (I/V) characteristics of a 20 MeV proton irradiated square and meander STI diodes are represented in Fig. 1. Both the reverse and forward current increase by irradiation, which is caused by a decrease of the generation and recombination lifetime.

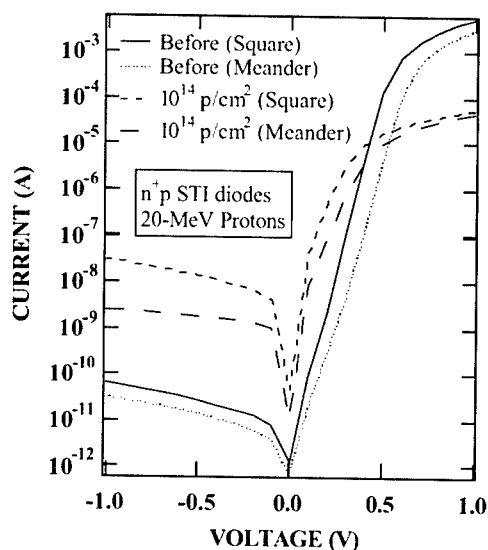


Fig. 1. I/V characteristics of a 20 MeV proton irradiated STI SQ1 and ME1 diode, respectively.

The forward current is, however, lower after irradiation for a forward voltage larger than 0.4 V, which is due to a radiation-induced increase of the p-well resistivity. It is also observed that the increase in current of square diodes is larger than that of meander diodes. This result points to the different influence of irradiation on the bulk and peripheral leakage current, which dominate in square and meander diodes, respectively. The meander diode was more degraded by electron irradiation compared to proton irradiation.

Fig. 2 shows the recovery behavior of the I/V characteristics for STI diodes irradiated with 2 MeV electrons. The device performance was significantly restored by the isochronal thermal annealing.

The degradation of the electrical performance results from the induced lattice defects in the STI diode. The corresponding DLTS spectra have been reported in a recent study [4,5]. Fig. 3(a) and (b) show the DLTS spectra of 20 MeV proton and 2 MeV electron irradiated STI diodes, respectively. In the case of proton irradiation, two electron capture levels E_{14pM1} ($E_c - 0.21 \text{ eV}$) and E_{14M2} have been observed in a meander diode, while only the E_{14pS1} ($E_c - 0.24 \text{ eV}$) level was found in the large area square diode. It was concluded, that E_{14pS1} and E_{14pM1} are most likely associated with the B_i-O_i level [6], while E_{14pM2} is related to radiation-induced SiO_2/Si interface states at the STI sidewalls [5]. In the case of electron irradiation, the E_{15eS1} and E_{15eM1} levels were observed in square and meander diodes, respectively. The E_{15eM1} level might be related to STI interface state. The E_{15eS1} level is thought to be originating from the induced lattice defects in the p-well region.

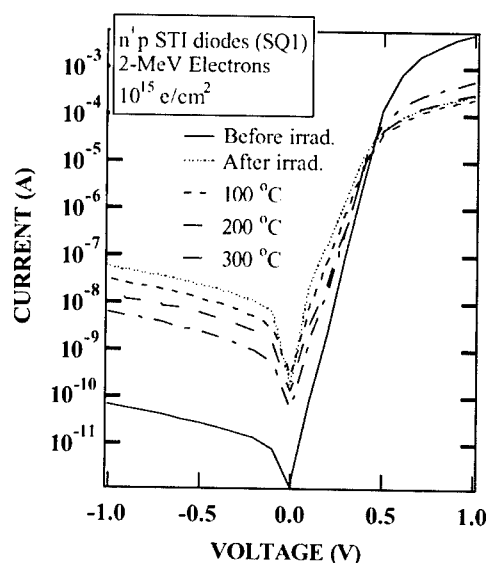


Fig. 2. Recovery of the I/V characteristics for a 2 MeV electron irradiated STI diode (SQ1).

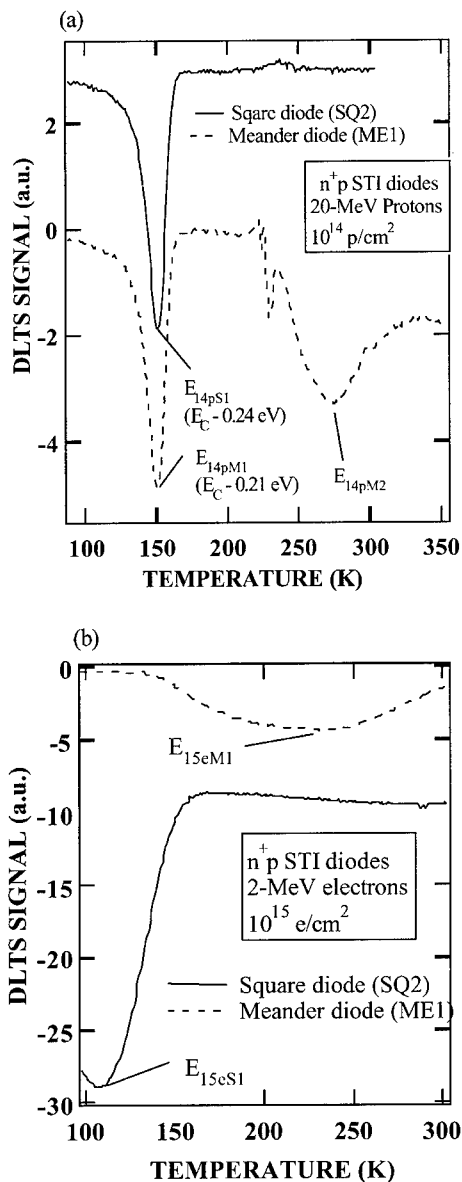


Fig. 3. DLTS spectra at $\tau_{\max} = 7.6$ ms for electron traps in 20 MeV proton (a) and 2 MeV electron (b) irradiated STI diodes (SQ2 and ME1).

Fig. 4 illustrates the impact of an isochronal anneal on the DLTS spectra of a 2 MeV electron irradiated meander diode. As shown in this figure, the E_{15eM1} peak decreases by thermal annealing and disappears after a 200°C annealing.

Fig. 5 shows the electron traps at different τ_{\max} in a 20 MeV proton irradiated STI diode (ME1), after 250°C annealing. The shape of the DLTS spectrum changes significantly with the rate window $1/\tau_{\max}$. The E_{14pM1}

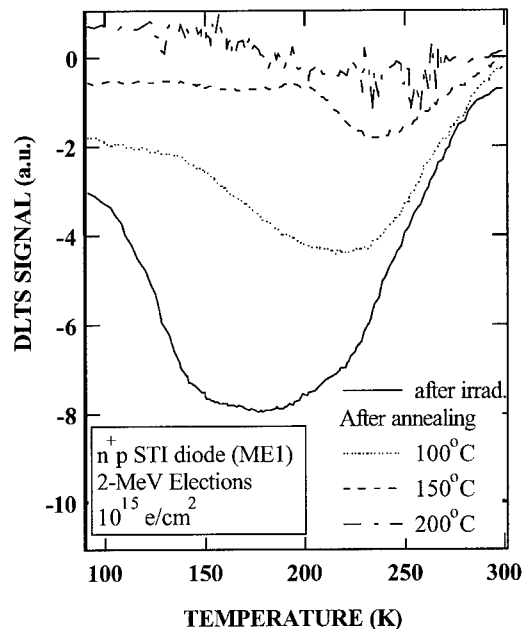


Fig. 4. Recovery behavior of the DLTS spectrum for the electron traps in a 2 MeV electron irradiated STI diode (ME1).

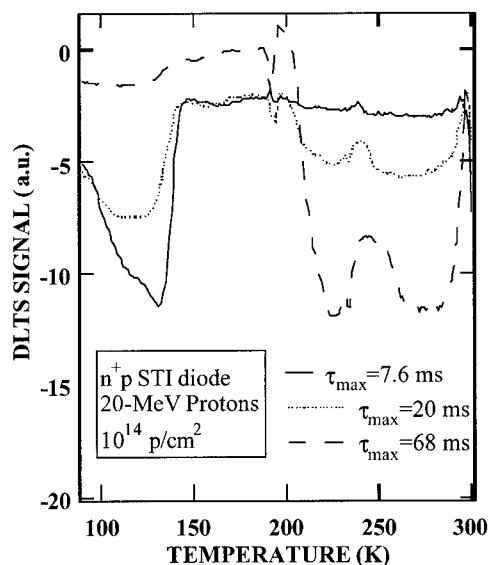


Fig. 5. DLTS spectra at different τ_{\max} for electron traps in a 20 MeV proton irradiated STI diode (ME1) after 250°C 30 min thermal annealing.

peak transformed from a single level peak to a double peaked feature for a higher rate window, while the E_{14pM2} amplitude reduces markedly. It is believed that the E_{14pM1} B_i-O_i level decomposes into the B_i-O_i and

Table 1

Activation energy of recovery of the electron capture levels (E_{AL}) and the reverse current (E_{AI}) of diodes, subjected to 20 MeV protons and 2 MeV electrons

Radiation sources	E_{AL} (eV)	E_{AI} (eV)	
		Square diode	Meander diode
20 MeV protons	E_{14pM1} : —	0.26	0.17
	E_{14pM2} : 0.1	0.26	0.17
2 MeV electrons	E_{15eM1} : 0.11	0.12	0.12

Table 2

Total defect density (N_T), defect introduction rate (η) and damage coefficients for the reverse current of square (K_{SQ}) and meander (K_{ME}) diodes, irradiated by different radiation particles

Radiation sources	N_T (cm ⁻³)	η (cm ⁻¹)	K_{SQ} (A cm ² /particle)	K_{ME} (A cm ² /particle)
20 MeV Protons	2.3×10^{14}	2.3	3.1×10^{-22}	2.5×10^{-23}
2 MeV Electrons	1.5×10^{14}	0.15	5.7×10^{-25}	1.6×10^{-24}

the A center upon annealing at 250°C. A similar transformation was found for the E_{14pS1} level in a SQ diode. The E_{14pM2} interface state peak in Fig. 5 clearly splits up into two new peaks at $\tau_{max} = 68$ ms, while for higher rate windows, its amplitude becomes marginal.

The defect densities of the electron capture levels decrease and the reverse current recovers by thermal annealing. The activation energies of the recovery behavior corresponding with each electron trap (E_{AL}) and with the reverse current for square and meander diodes (E_{AI}) were calculated; the results of this calculation are shown in Table 1. E_{AL} for E_{14pM2} and E_{15eM1} are nearly the same, which is not surprising since they are both thought to be associated with SiO₂/Si interface states. E_{AI} for the electron-irradiated diode was nearly the same as E_{AL} for E_{15eM1} . This demonstrates that the degradation of the reverse current for electron irradiated square and meander diodes is mainly caused by the peripheral damage at the STI sidewalls. In case of proton irradiation, the larger value of E_{AI} for square diodes indicates that the recovery of electrical characteristics is more dependent on the recovery of the radiation-induced lattice defects than on the peripheral damage at the STI edges. On the contrary, the rather small value of E_{AI} for meander diodes indicates the recovery of the I/V curves is caused by the annealing of the peripheral damage.

The total defect density (N_T) of the irradiated meander diodes and the defect introduction rate ($\eta = N_T/\text{fluence}$) have been calculated for the different experimental conditions, as summarized in Table 2. The damage coefficients of the reverse current for square

(K_{SQ}) and meander (K_{ME}) diodes are also indicated in the table. In case of square diodes, the K_{SQ} for proton irradiation was three orders of magnitude larger than for electron irradiation. It has been shown that the higher radiation-induced defect density is related to the difference of particle mass and the possibility of nuclear collision [5]. K_{ME} for protons was about one order of magnitude larger than for electrons. Interestingly, the ratio of K_{ME} for protons and electrons agrees with the ratio of η for protons and electrons. It should be remarked, however, that N_T for the meander diode is not really a physical quantity, as it sums the bulk and interface traps, without making any distinction. Furthermore, the electron traps are minority carrier traps in this case, rendering a quantitative analysis rather difficult. Therefore, N_T should be considered here as an empirical parameter, which shows a good agreement with the respective damage coefficients.

4. Conclusions

The main conclusions from this work are that the device degradation observed after 2 MeV electron, 20 MeV proton irradiation or subsequent isochronal annealing scales well with the observed radiation-induced electron traps. In case of the meander diodes, the degradation is governed by interface traps created at the STI sidewalls. For square diodes, bulk traps in the p-well (B_iO_i or the A center) dominate the device performance after proton irradiation, while both

interface and bulk traps contribute for electron irradiated SQ1 diodes.

References

- [1] F.T. Brady, J.D. Maimon, M.J. Hurt, IEEE Trans. Nucl. Sci. 46 (1999) 1836.
- [2] G. Niu, et al., IEEE Trans. Nucl. Sci. 46 (1999) 1841.
- [3] Y. Tokuda, M. Hayashi, A. Usami, J. Phys. D: Appl. Phys. 14 (1981) 895.
- [4] K. Kobayashi, et al., Solid State Phenom. 78–79 (2001) 357.
- [5] H. Ohyama, et al., Proceedings of E-MRS 2001 Spring Meeting, Strasbourg, France, June 2001, B/P2.14.
- [6] Khan, et al., J. Appl. Phys. 87 (2000) 8389.



ELSEVIER

Physica B 308–310 (2001) 1222–1225

PHYSICA B

www.elsevier.com/locate/physb

Fabrication of periodic nanohole multilayer structure on silicon surface toward photonic crystal

Y. Ohno*, N. Ozaki, S. Takeda

Department of Physics, Graduate School of Science, Osaka University, 1-16, Machikane-yama, Toyonaka, Osaka 560-0043, Japan

Abstract

We have studied a porous structure on silicon surfaces that is introduced by electron irradiation. The structure consists of nanometer-sized holes arranged on silicon surfaces. Investigating the size and the distribution of surface nanoholes in a temperature range from about 4 K to about 600 K, we have estimated the porosity on a surface with nanoholes. We have fabricated a periodic dielectric multilayer structure on a silicon surface by introducing nanoholes periodically in one direction: alternating layers with different dielectric constants (the dielectric contrast of about 1.08), spaced by a distance of 100 nm. We can form periodic dielectric layers at arbitrary locations on surfaces by scanning an electron beam, changing the periodicity and the dielectric constant by varying irradiation condition. © 2001 Elsevier Science B.V. All rights reserved.

Keywords: Silicon; Surface nanohole; Photonic crystal; Transmission electron microscopy

1. Introduction

The modification of surface structure involving point defects has attracted attention because of its potential application in future nanotechnology as well as its novel physics in nonequilibrium states. Even though growth kinetics at the atomistic level on surfaces has been revealed by means of scanning tunneling microscopy (STM) and other experimental techniques, growth kinetics on surface structures involving a number of atoms has not been fully described yet.

In the present paper, we have investigated a porous structure that is introduced on a silicon surface by electron irradiation, namely, surface nanoholes [1]. An array of nanoholes is uniformly nucleated and gradually grown on an electron irradiated surface. The spatial distribution of nanoholes is varied by an irradiation condition such as irradiation temperature. Analyzing the experimental data, the formation mechanism of nano-

holes has been described in terms of the reaction of point defects [1,2].

The size of nanoholes is much smaller than the wavelength of visible light. However, the dielectric constant of the silicon surface with nanoholes is definable from a macroscopic point of view. The dielectric constant of silicon surface with nanohole is, on average, lower than that of flat silicon surface. We have fabricated a periodic dielectric multilayer structure by introducing nanoholes periodically in one direction. Such a periodic multilayer structure is expected to act as a photonic crystal and is potentially useful for optical devices such as waveguides and reflection mirrors.

2. Experiments

Specimens were nondoped Czochralski Si {001} wafers. Disks of 3 mm diameter were cut from the wafers. The surface of a disk was dimpled until the center of the disk was sufficiently thin for TEM observation. The thickness of each disk (about 100 nm) was estimated by convergent beam electron diffraction technique. Some disks were irradiated

*Corresponding author. Tel.: +81-6-6850-5753; fax: +81-6-6850-5764.

E-mail address: ohno@tem.phys.wani.osaka-u.ac.jp (Y. Ohno).

in an ultrahigh vacuum (UHV) TEM (1.8×10^{-7} Pa), and the rest were irradiated in a conventional TEM (1.8×10^{-5} Pa).

3. Results

3.1. Formation of surface nanoholes

Fig. 1 shows the formation process of nanoholes observed by TEM. The formation mechanism of nanoholes [1] is schematically shown in Fig. 2. As the primary event of the formation of nanoholes, single surface vacancies are introduced on an electron exit surface due to sputtering of atoms on the surface (Fig. 2(a)), by irradiation of high-energy (above 40 keV) electrons [2]. The introduced surface vacancies agglomerate on the surface via their diffusion under prolonged electron irradiation (Fig. 2(b)). Indeed, the formation of shallow nanoholes on an electron exit surface is confirmed at the early stage when only a few topmost surface layers are removed by electron irradiation [3]. The excavating follows due to an unisotropic diffusion of surface vacancies on the walls of nanoholes against the ongoing direction of electrons (Fig. 2(c)). The excavation rates for nanoholes on the $\{001\}$ surface is estimated to be 1.3×10^{-23} nm/($e\text{ cm}^{-2}$) [2].

Nanoholes are formed in a wide temperature range (from about 4 K to 610 K), and the average diameter and the planar density of nanoholes vary with temperature [2].

3.2. The porosity of surface with nanoholes

The volume of a nanohole is estimated to be the opening area of the nanohole multiplied by its depth. The porosity of a surface with nanoholes increases as the nanoholes are excavated. The porosity has a maximum value when all nanoholes penetrate the disk. In this case, the porosity is estimated as the ratio between the sum of the opening areas of all nanoholes and the irradiated area.

Fig. 3(a) indicates that the maximum porosity is independent of incident electron energy. The maximum porosity is also independent of electron flux (not shown). We have found that the maximum porosity increases monotonously with increasing irradiation temperature (Fig. 3(b)).

3.3. Fabrication of nanohole periodic multilayer structure

By scanning a focused electron beam (the probe size of about 50 nm) on a silicon disk, we have fabricated a periodic multilayer structure consisting of crystalline silicon and nanoholes (Fig. 4(a)). Fig. 4(b) shows a schematic view of the structure: repeats of the alterna-

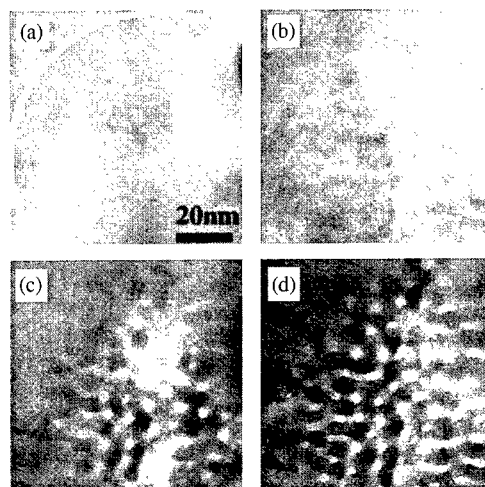


Fig. 1. Nucleation and growth of silicon surface nanoholes. Electron doses are 0.0 , 0.4×10^{24} , 0.8×10^{24} , and $1.2 \times 10^{24} e\text{ cm}^{-2}$ in (a), (b), (c), and (d), respectively [300 K, UHV]. The circle in (a) indicates the irradiated area.

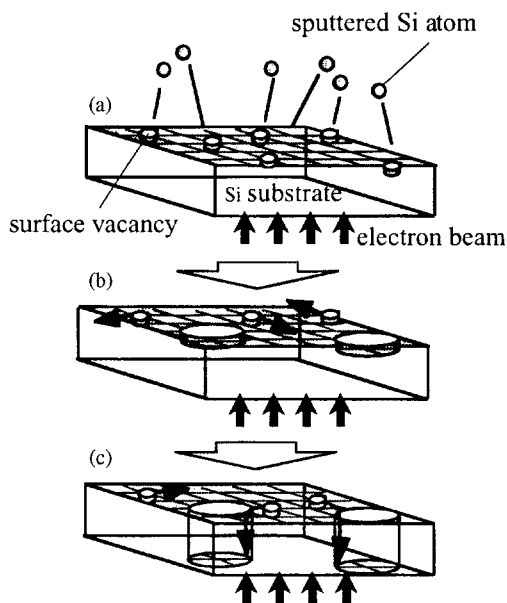


Fig. 2. The formation mechanism of surface nanoholes.

tion of the $(50\text{ nm}) \times (1.6\text{ }\mu\text{m}) \times (100\text{ nm})$ crystalline silicon layer and the $(50\text{ nm}) \times (1.6\text{ }\mu\text{m}) \times (100\text{ nm})$ nanohole layer. The nanohole layers received an electron dose of about $7.2 \times 10^{24} e\text{ cm}^{-2}$, and the depths of the nanoholes are estimated to be about 95 nm. The nanoholes almost penetrate the disk. With the data in Fig. 3, we have estimated the porosity of the nanohole layers to be about 8%.

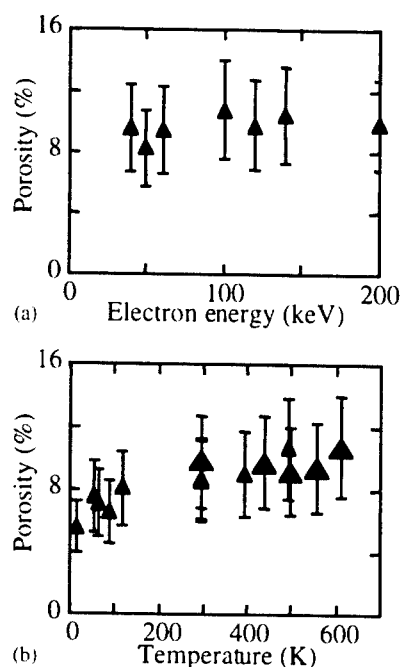


Fig. 3. The maximum porosities of the silicon surface with nanoholes as a function of (a) incident electron energy [300 K] and (b) irradiation temperature. [small triangles: UHV, large triangles: 1.8×10^{-5} Pa].

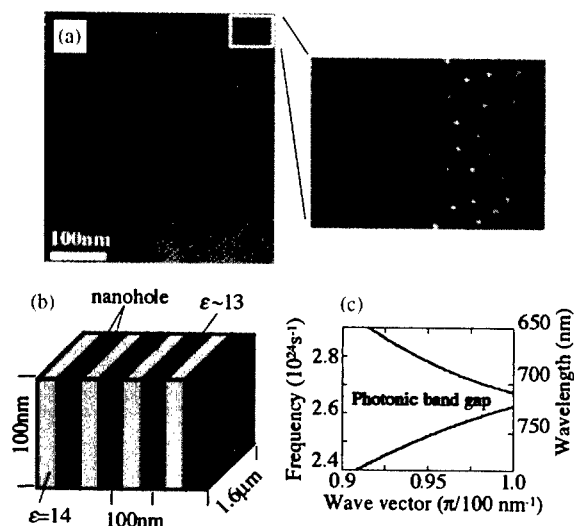


Fig. 4. (a) A TEM image of a periodic nanohole/crystalline silicon multilayer structure. (b) A schematic view of the multilayer structure shown in (a). (c) The calculated photonic band structure.

The dielectric constant of the nanohole layers can be estimated for averaging the dielectric properties of air (in nanoholes) and crystalline silicon. For instance, the dielectric constant at the wavelength of 700 nm is

estimated to be 13, at which wavelength the dielectric constant for crystalline silicon is 14 [4] (the dielectric contrast is about 1.08).

4. Discussion

We discuss the photonic band structure for the periodic multilayer structure shown in Fig. 4(a). Even though it has finite (13) periods of crystalline silicon/nanohole layers, we consider the structure as consisting of the infinite repeats of crystalline silicon/nanohole layers. Fig. 4(c) shows the calculated (for the calculation, we apply the theorem by Joannopoulos et al. [5]) photonic band structure for the infinite multilayer structure. In the calculation, the direction of the wave vector is normal to the layers. A frequency gap in which no mode can exist regardless of wave vectors (photonic band gap) exists: the center frequency of $2.65 \times 10^{14} \text{ s}^{-1}$ (about 710 nm in wavelength) and the width of $8 \times 10^{22} \text{ s}^{-1}$. Both the center frequency and the width of photonic band gap increase on increasing the dielectric contrast. Since the porosity in nanohole layers depends on irradiation temperature and electron dose, the photonic band gap of nanohole periodic multilayer structure can be controlled by varying the irradiation condition. The gap is also controlled by changing the periodicity of the multilayer.

We have measured the reflectance of the periodic multilayer structure shown in Fig. 4(a), and no distinct evidence for photonic band gap is observed at the present moment. Further works, including the theoretical consideration for the effect of finite periods of multilayer on the photonic band gap, are necessitous to understand the optical properties of nanoholes.

Some photonic crystals based on porous silicon are fabricated by an electrochemical etching technique and their optical properties are examined [6,7] (for a recent review see Ref. [8]). We have first attempted to fabricate, to our knowledge, a silicon-based photonic crystal on a surface on which the dielectric is periodic parallel to the surface. We have also expected that nanoholes themselves, an array of small holes on surfaces, exhibit the novel optical properties, since the dielectric response is basically due to electrons of which properties are affected in confined systems.

5. Conclusion

We have shown a potential application of nanoholes to photonic crystal. Nanoholes are also expected to exhibit novel optical properties due to the quantum confinement effect.

Acknowledgements

This work was partially supported by the Ministry of Education, Science, Sports and Culture, Grant-in-Aid for Scientific Research (A) (2) No. 10305006, 1998–2000. We thank M.J. Caldas for her comments and discussions.

References

- [1] S. Takeda, K. Koto, S. Iijima, T. Ichihashi, *Phys. Rev. Lett.* 79 (1997) 2994.
- [2] Y. Ohno, S. Takeda, T. Ichihashi, S. Iijima, to be submitted.
- [3] N. Ozaki, Y. Ohno, M. Tanbara, D. Hamada, J. Yamasaki, S. Takeda, *Surf. Sci.* 493 (2001) 547.
- [4] J. Leng, J. Opsal, H. Chu, M. Senko, D.E. Aspnes, *J. Vac. Sci. Technol. A* 16 (1998) 1654.
- [5] J.D. Joannopoulos, R.D. Meade, J.N. Winn, *Photonic Crystals*, Princeton University Press, Princeton, NJ, 1995, pp. 38.
- [6] G. Vincent, *Appl. Phys. Lett.* 64 (1994) 2367.
- [7] S. Frohnhof, M.G. Berger, *Adv. Mater.* 6 (1994) 963.
- [8] W. Theiss, *Surf. Sci. Rep.* 29 (1997) 91.



ELSEVIER

Physica B 308–310 (2001) 1226–1229

PHYSICA B

www.elsevier.com/locate/physb

Impact of lattice defects on the performance degradation of Si photodiodes by high-temperature gamma and electron irradiation

H. Ohyama^{a,*}, T. Hirao^b, E. Simoen^c, C. Claeys^{c,d}, S. Onoda^e,
Y. Takami^f, H. Itoh^b

^a Department of Electronic Engineering, Kumamoto National College of Technology, 2659-2 Suya Nishigoshi, Kumamoto 861-1102, Japan

^b Takasaki JAERI, 1233 Watanuki Takasaki Gunma 370-1292, Japan

^c IMEC, Kapeldreef 75, B-3001 Leuven, Belgium

^d K U Leuven, E.E. Depart., Kasteelplein 10, B-3001 Leuven, Belgium

^e Tokai University, 1117 Kitakaname, Hiratsuka, Kanagawa 259-1292, Japan

^f Rikkyo University, 2-5-1 Nagasaka, Yokosuka, Kanagawa, 240-0101, Japan

Abstract

Results of a detailed study of the effects of high-temperature γ -ray and electron irradiation on the performance degradation of Si pin photodiodes are presented. The macroscopic device performance will be correlated with the radiation-induced defects, observed by DLTS. After irradiation, two majority electron capture levels with ($E_c - 0.22$ eV) and ($E_c - 0.40$ eV) were induced in the n-Si substrate, while one minority hole capture level with ($E_v + 0.37$ eV) was found. It was found that the dark current increases after irradiation, while the photo current decreases. Additionally, the degradation of the device performance and the introduction rate of the lattice defects decrease with increasing irradiation temperature. At 200 °C irradiation, the reduction of the photocurrent is only 10% of the starting value. This result suggests that the creation and recovery of the radiation damage proceeds simultaneously at high temperatures. © 2001 Elsevier Science B.V. All rights reserved.

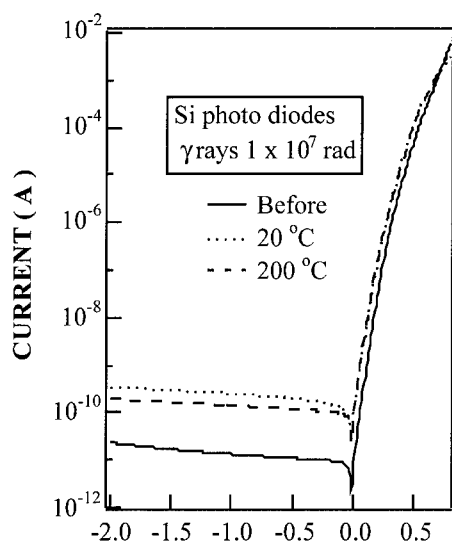
Keywords: Si photodiode; Radiation damage; High-temperature irradiation; γ -irradiation; Electron irradiation; Induced deep levels

For several reasons, interest in high-temperature electronics develops fast. If these components are to be used in a radiation environment, knowledge about the degradation under high-temperature irradiation conditions is highly desirable, as it is difficult to predict from device simulation only. For the same reason, the space community has also developed interest in electronics for extreme environments, ranging from low to high temperatures and for extreme radiation doses. In satellite systems devices can be exposed to irradiation for extended time periods at elevated temperatures. Military specifications also require devices to function over a temperature range of -55 – 125 °C.

Some studies on the physical properties of defects in high-temperature electron-irradiated Si substrates have been reported [1,2]. The effect of the X-ray irradiation temperature on the MOS transistor behaviour has also been investigated [3]. However, not so much is known about the radiation response of microelectronic devices and circuits at high temperatures. There is still some uncertainty about the possible relationship between the induced lattice defects and the performance degradation. In this paper, results are presented of a detailed study of the effects of high-temperature γ -ray and electron irradiation on the device performance of silicon pin photodiodes. The macroscopic device performance will be correlated with the radiation-induced defects, observed by DLTS.

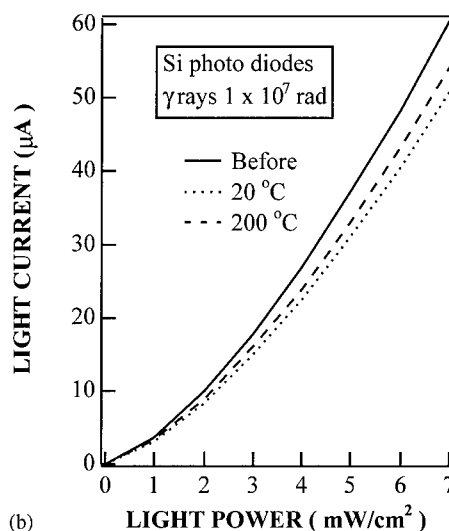
Si photodiodes were fabricated on floating-zone (FZ) n-type (111) Si substrates doped by phosphorus to a

*Corresponding author. Tel./fax: +81-96-242-6079.
E-mail address: ohyama@cc.knct.ac.jp (H. Ohyama).



(a)

VOLTAGE (V)



(b)

LIGHT POWER (mW/cm²)

Fig. 1. I/V (a) and I_L (b) characteristics after γ -ray irradiation at different high temperatures.

resistivity of 2–4 k Ω cm. The p-type region was boron doped. A SiN_x layer of 100 nm thickness formed by chemical vapor deposition was used as passivation and anti-reflection film. Al with 1.5 μ m thickness was evaporated and alloyed to the p contact. After dicing in chips of 1.5 \times 1.5 mm² size, the diodes were encapsulated in TO-18 packages with kovar glass windows of 0.3 mm thickness.

Diodes were irradiated by a 8150.1 TBq ⁶⁰Co source at the Takasaki JAERI. The total dose of the γ -rays was 1 \times 10⁷ rad(Si). Packaged diodes were also irradiated with 2 MeV electrons to a fluence of 1 \times 10¹⁵ ecm⁻² produced by the Dynamitron at Takasaki JAERI. The

sample temperature was fixed at 20°C, 100°C or 200°C and was controlled by a panel heater, mounted in a chamber for γ -ray irradiation. For electron exposures, irradiations at 30°C, 100°C or 200°C were also performed through a 50 μ m thick Ti window.

Before and after irradiation, the current/voltage (I/V) characteristics of the diodes were measured at room temperature to examine the change of the dark current (I_D) by the irradiation. The photocurrent (I_L), measured at room temperature, was also recorded as a function of the white light power (P_L). The deep levels in the Si photodiodes were studied by DLTS in the temperature range between 77 and 300 K. The emission rate window ranged from 1.18 to 26.51 ms and the filling pulse was -2 to 0 V to observe electron capture levels in the n-Si substrate, while it was -2 to 0.5 V to detect possible hole capture levels.

Fig. 1a and b show the typical result of I/V and I_L characteristics for γ -ray irradiation at different high temperatures, respectively. From these figures it can be found that after irradiation the dark current increases, while the photo current decreases. The degradation of the device performance decreases with increasing irradiation temperature as shown in Fig. 2. For a γ -ray irradiation at 200°C, the reduction of the photocurrent is only 10% of the starting value. The same tendency was observed for 2 MeV electron irradiated Si photodiodes. Fig. 3 shows typical I/V characteristics of Si photodiodes after 2 MeV electron irradiation at different temperatures.

To compare the degradation for different radiation sources, one can calculate the damage coefficient (K) of the dark and the photo current by the following

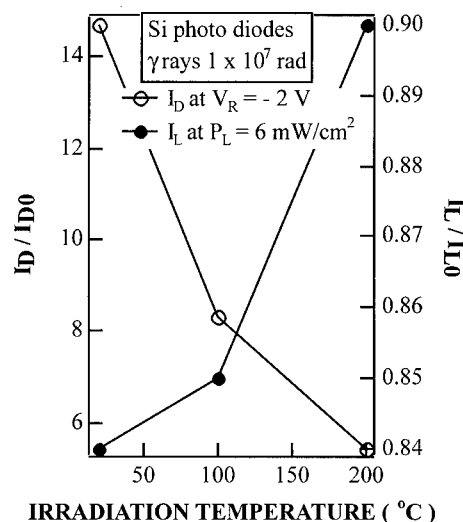


Fig. 2. Normalized dark and photo current as a function of the γ -ray irradiation temperature.

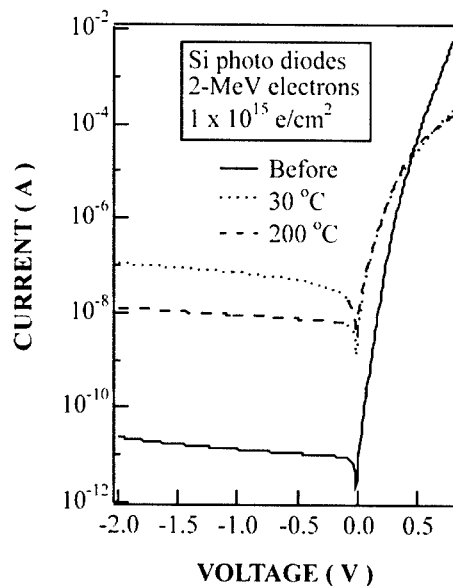


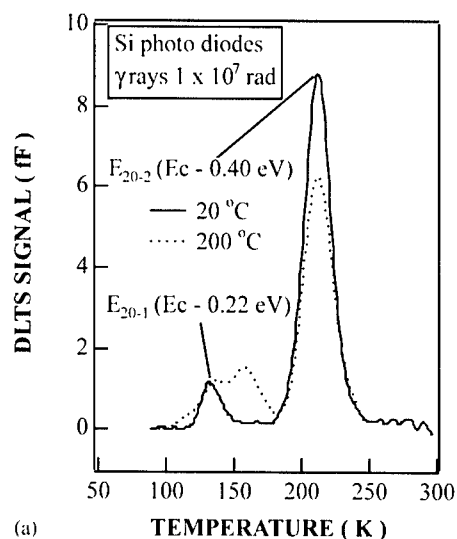
Fig. 3. I/V characteristics of 2 MeV electron irradiated Si photodiodes for different irradiation temperatures.

equation.

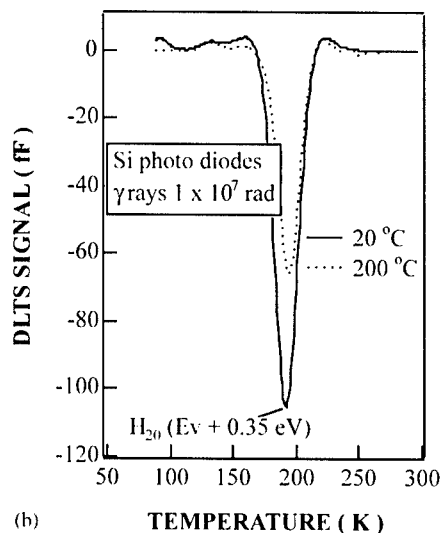
$$K = \partial I_{D,L} / \partial \Phi, \quad (1)$$

where Φ is the fluence. The γ -ray exposure to 10 Mrad (Si) is approximately equivalent to $1 \times 10^{14} \text{ ecm}^{-2}$ at 1 MeV energy [4]. Table 1 shows the K values of the γ -ray and the 2 MeV electron irradiation. From this table, a contrasting behaviour is derived for K_D and K_L . This could point to a different origin of the degradation, i.e., bulk versus surface damage. In the first case, radiation-induced defects will affect the bulk generation/recombination lifetime, while in the second case, the creation of interface traps can increase the surface generation/recombination velocity. Therefore, a study of the microscopic damage is necessary for a better understanding of the device degradation.

Fig. 4a and b show typical DLTS spectra for electron and hole capture levels in γ -ray irradiated Si photodiodes, respectively. After irradiation, two majority electron capture levels with ($E_c - 0.22 \text{ eV}$) and ($E_c - 0.40 \text{ eV}$) were induced in the n-Si substrate, while one minority hole capture level with ($E_v + 0.37 \text{ eV}$) was found. Their concentration is smaller for increasing irradiation temperature. In addition, it is well known that the E-center disappears around 150°C [5], which could partly explain the reduction of the $E_c - 0.40 \text{ eV}$ peak. In principle, it is expected that the $E_c - 0.22$ and $E_c - 0.40 \text{ eV}$ peaks are associated with the di-vacancy. However, the 0.3 eV activation energy is quite low to correspond to the single acceptor state. In addition, the corresponding peak is much higher than the double acceptor at $E_c - 0.22 \text{ eV}$. Apparently, some other



(a)



(b)

Fig. 4. DLTS signal of electron (a) and hole (b) capture levels of γ -ray irradiated Si photodiodes.

unknown level contributes to the electron trap at around 200 K. The hole capture levels are related to a carbon related complex (presumably C_F-O_i). For an irradiation at 150°C , an additional unknown electron capture level is observed around 170 K. The same deep levels are induced for 2 MeV electron irradiated diodes, however, with one order higher introduction rate.

In agreement with the device performance, the introduction rate of the deep levels decreases with increasing irradiation temperature. For a 200°C irradiation temperature, the induced capture levels amount to 60% of the concentrations found after room temperature irradiation. This result suggests that the creation and recovery of the radiation damage proceeds

Table 1
Damage coefficient for γ -ray and 2 MeV electron irradiation

	K_D ($\text{e}^{-1} \text{A cm}^2$)	K_L ($\text{e}^{-1} \text{A cm}^2$)
γ -Rays (equivalent 1 MeV electrons)	3.2×10^{-24}	-7.8×10^{-14}
2 MeV electrons	1.1×10^{-22}	-1.6×10^{-14}

simultaneously at high temperatures. It is also shown that the hole capture levels are mainly responsible for the performance degradation.

In conclusion, after irradiation, two majority electron capture levels with ($E_c - 0.22 \text{ eV}$) and ($E_c - 0.40 \text{ eV}$) were induced in the n-Si substrate, while one minority hole capture level with ($E_v + 0.37 \text{ eV}$) was found. The degradation of the device performance and the introduction rate of the lattice defect decrease with increasing irradiation temperature. This result suggests that the

creation and recovery of the radiation damage proceeds simultaneously at high temperatures.

Part of this work was supported by the Giant-in-Aid for Scientific Research (No. 11695065 and 116507727) from the Japanese Ministry of Education for Science, by the Sagawa foundation for promotion of frontier science and by the Inter-University Laboratory for the Joint Use of JAERI Facilities. Mr. H. Takizawa of Takasaki JAERI is thanked for his cooperation during the irradiation experiments.

References

- [1] P. Hazdra, et al. Nucl. Instr. and Meth. B55 (1991) 637.
- [2] J.G. Xu, et al. Phys. Rev. B 38 (1988) 3395.
- [3] M.R. Shaneyfelt, et al., IEEE Trans. Nucl. Sci. 45 (1996) 1372.
- [4] G.P. Summers, et al. IEEE Trans. Nucl. Sci. 40 (1993) 1372.
- [5] L.C. Kimmerling, IEEE Trans. Nucl. Sci. 23 (1976) 1497.



ELSEVIER

Physica B 308–310 (2001) 1230–1236

PHYSICA B

www.elsevier.com/locate/physb

List of Contributors

- Abdullin, Kh.A. 178
Abe, H. 652
Abe, K. 652
Åberg, D. 776
Abrosimov, N. 550, 558
Abrosimov, N.V. 535
Ackermann, H. 236, 248
Adamczewska, J. 820
Aguilar-Hernandez, J. 1108
Alberto, H.V. 920
Alexandrova, S. 485
Ali, A. 816
Alt, H.Ch. 877
Alves, E. 22, 42, 374, 985
Alves, H. 38
Alves, H.R. 89
Amano, H. 38
Ambacher, O. 69
Amekura, H. 265
Ammerlaan, C.A.J. 350, 361, 387, 408
Andersen, O. 139, 513
Andersson, T.G. 93
Andreev, B. 558
Andreev, B.A. 340, 350, 361
Angervaks, A.E. 1035
Antonelli, A. 470
Antonova, I.V. 317
Aradi, B. 722
Artacho, E. 329
Arutyunov, N.Yu. 110
As, D.J. 34, 126
Asche, M. 788
Assali, L.V.C. 489, 726
Attenberger, W. 81
Au Yeung, T.C. 1117
Auret, F.D. 776, 1189
Avalos, V. 569
Azamat, D. 1015
Bagraev, N.T. 365, 1104
Baidullaeva, A. 971
Baierle, R.J. 329
Bailey, B.A. 920
Bak-Misiuk, J. 313, 317, 820
Bakarov, A.K. 784
Baldovino, S. 69
Baltrunas, D. 1057
Baranov, P.G. 680
Baranowski, J.M. 102, 117
Barbosa, K.O. 726
Barcz, A. 317
Barthe, M.-F. 668
Bauer-Kugelman, W. 668
Beaumont, B. 85
Beck, G. 1086
Becla, P. 954
Beling, C.D. 710, 718
Belyaev, A. 1137
Benamara, M. 854
Berejinskij, L.I. 268
Bergman, J.P. 675, 1165
Bharuth-Ram, K. 418
Bilger, G. 431
Biliy, M.M. 1031
Bimberg, D. 589, 816
Bissiri, M. 850
Blom, A. 1129
Blumenau, A.T. 577
Bockowski, M. 117
Bockstedte, M. 656
Boemare, C. 22, 42, 985
Böhm, M. 38
Bonapasta, A.A. 846
Bonar, J.M. 525
Bondarenko, V. 792
Borkovska, L.V. 967
Börner, F. 442, 812
Botha, J.R. 866, 1065
Bouanani-Rahbi, R. 117
Boulanger, D. 928
Bouravleuv, A.D. 365, 1104
Bozdog, C. 62
Bracht, H. 734, 831, 854
Bradley, I.V. 337, 884
Braga, G.C. 51
Braga, G.C.B. 691
Branch, M.S. 1065
Brandt, M.S. 69, 593
Bratus, V.Ya. 621, 637
Briddon, P.R. 8, 139, 197, 290, 305, 454, 577, 604, 1027
Britton, D.T. 668
Budzulyak, S.I. 325
Bulakh, B.M. 1108
Buyanova, I.A. 106
Caldas, M.J. 329
Cano, A.I.D. 1108
Capaz, R.B. 329
Capizzi, M. 850
Carlos, L.D. 22
Carlos, W.E. 51, 691, 976
Carlsson, F.H.C. 675, 1165
Cerqueira, M.F. 374
Cerva, H. 13
Chang, K.J. 143, 912
Chang, Y.L. 888
Chao, K.-A. 1129
Chen, C.-H. 1050
Chen, R. 612
Chen, W.M. 106
Chen, X.D. 710, 718
Chen, Z.Q. 652
Chiquito, A.J. 843
Choi, J.H. 993
Chow, K.H. 862
Chowles, A.G. 1065
Choyke, W.J. 687
Christen, J. 89
Christich, O.A. 1201
Cich, M.J. 98, 808
Citrin, P.H. 369
Claeys, C. 294, 477, 1185, 1217, 1226
Clauws, P. 294, 477, 517
Clerjaud, B. 117, 253
Coffa, S. 477
Contreras-Puente, G. 1108
Coomer, B.J. 454
Corbel, C. 668

- Côte, D. 117
 Cottrell, S.P. 920
 Coutinho, J. 8, 290, 305
 Cowern, N.E.B. 525
 Cox, S.F.J. 73, 862, 920

 de Campos, N.A. 920
 Dadgar, A. 816
 Dannefaer, S. 569
 Davidov, V.Yu. 110
 Davidson, B.R. 780, 858
 Davies, G. 298, 581
 Davis, E.A. 73, 862, 920
 Davydov, D.V. 641
 Davydov, V.Yu. 58, 181
 De Gryse, O. 294
 Deák, P. 722
 Deenapanray, P.N.K. 190, 776
 Deicher, M. 963
 Dembo, A.T. 598
 Dembo, K.A. 598
 Dembovsky, S.A. 1061
 Desgardin, P. 668
 Devaty, R.P. 687
 Dharmarasu, N. 1181
 Dietrich, M. 418, 542
 Dietz, N. 1015
 Dobaczewski, L. 134, 139, 513
 Döhler, G.H. 1177
 Domagala, J.Z. 820
 Dotsenko, Yu.P. 325
 Dowsett, M.G. 525
 Dravin, V.A. 573
 Duarte, J.P. 920

 Eberl, K. 831
 Eberlein, T.A.G. 454
 Egger, W. 442
 Egorov, A.Yu. 877
 Egorov, S. 558
 Einfeldt, S. 38
 El-Fadl, A.A. 949
 Emtsev Jr., V.V. 350
 Emtsev, V.V. 58, 110, 181, 313, 529, 1141
 Endo, S. 1097
 Engelhardt, M. 13
 Engler, N. 742
 Ermakov, V.M. 325
 Eryu, O. 652
 Espinoza, F.G.B. 1108
 Estreicher, S.K. 1, 147, 202, 510
 Evans, A.G.R. 525
 Evans-Freeman, J.H. 513, 554
 Ewels, C.P. 493

 Fahrner, W.R. 181, 185
 Fall, C.J. 577
 Fanciulli, M. 418
 Fang, Z.-Q. 706
 Faria, R.M. 1078
 Fazzio, A. 470
 Fedders, P.A. 1, 202, 510
 Feick, H. 98
 Feklisova, O. 159, 210, 213
 Ferreira, J.A. 374
 Ferrer, J. 147
 Figielski, T. 757
 Filipecki, J. 1011
 Fischer, M. 850
 Forcales, M. 337
 Forchel, A. 850
 Fortunato, W. 772, 843
 Frank, T. 633, 660
 Frank, W. 431, 542
 Frauenheim, T. 577
 Frauenheim, Th. 497, 645
 Freitag, B. 1090
 Freitas Jr., J.A. 51, 691
 Frova, A. 850
 Fujii, M. 1100, 1121
 Fujiwara, K. 765, 1193
 Fujiwara, Y. 796, 891
 Fukata, N. 197, 216, 220, 276, 321, 438, 474, 539, 1125
 Fukuda, K. 240
 Füllgrabe, M. 236, 248, 989
 Fung, S. 710, 718

 Gad, M.A. 554
 Gali, A. 722
 Galzerani, J.C. 772, 843
 Gaspari, V. 850
 Gebauer, J. 442, 792, 808, 812
 Geddo, M. 850
 Gehlhoff, W. 365, 589, 1015
 Geithner, W. 989
 Georg, U. 989
 Gerlach, J.W. 81
 Gerstmann, U. 497, 561, 625
 Gharaibeh, M. 510
 Giangregorio, M.M. 374
 Giannozzi, P. 846
 Gibart, P. 85
 Gil, J.M. 920
 Gilinsky, A.M. 784
 Gippius, A.A. 573
 Gislason, H.P. 130, 804
 Glaser, E.R. 51, 691, 976
 Glukhanyuk, V. 34
 Gnatyuk, V.A. 935

 Godlewski, M. 102, 942
 Goennenwein, S.T.B. 69
 Goldstein, Y. 1108
 Goldys, E.M. 102, 106
 Golovchak, R.Ya. 1011
 Gong, M. 710, 718
 Goodman, S.A. 1189
 Gorelkinskii, Yu.V. 178
 Gorohova, E.I. 1201
 Goss, J.P. 454, 604
 Goss, J.P.G. 577
 Graeff, C.F.O. 1078
 Graf, T. 593
 Grau, P. 446
 Gregie, J.M. 18, 26, 30
 Gregor, R. 1069, 1074
 Gregorkiewicz, T. 337, 340, 348, 357, 414, 884
 Greulich-Weber, S. 253, 625, 649
 Grillot, P.N. 888
 Grimmeiss, H.G. 558
 Gruber, Th. 945
 Gründig-Wendrock, B. 745
 Grzegory, I. 47, 51, 77, 117
 Gösele, U. 742
 Gudjonsson, G.I. 804
 Gudmundsson, J.T. 804
 Guilherme, J.G. 985
 Gulyaev, D.V. 784
 Gunnlaugsson, H.P. 418
 Guo, S.L. 993

 Haidar Khan, S. 816
 Hajdusianek, A. 769
 Hajnal, Z. 645
 Hallberg, T. 284, 290
 Hallén, A. 664
 Haller, E.E. 58, 521, 831, 854
 Halova, E. 485
 Hamada, K. 1169
 Hamann, D.R. 369
 Hamashoji, Y. 1007
 Han, B. 18
 Harada, H. 244
 Hardt, M. 1069
 Harima, H. 378, 391
 Harris, J.S. 870
 Hashimoto, M. 378
 Hasselkamp, D. 1074
 Hässlein, H. 529
 Hattendorf, J. 535
 Hautojärvi, P. 1157
 Hawkins, I.D. 513
 Hayama, K. 1217
 Hayashi, S. 1100, 1121

- Hayes, M. 1189
 He, Y.B. 1069, 1074
 Heemeier, M. 248
 Heggie, M.I. 493
 Heissenstein, H. 702
 Helbig, R. 702
 Hempel, A. 668
 Henecker, F. 908
 Henkel, T. 710, 718
 Henry, L. 668
 Henry, R.L. 51
 Herfort, J. 823
 Hermansson, J. 197, 284
 Heuken, M. 89
 Hida, A. 738, 1145
 Hierlemann, M. 13
 Hilger, D. 1020
 Hirao, T. 1185, 1226
 Hishita, S. 163, 171
 Hitti, B. 73, 862
 Hobgood, H.McD. 671
 Hoffmann, A. 1015
 Hofmann, D.M. 38, 89, 908
 Hofstaetter, A. 38, 908
 Hommel, D. 38
 Hori, A. 1193
 Hori, F. 224, 261
 Hoshikawa, K. 261
 Hourahine, B. 139, 197
 Huang, J.-W. 888
 Huang, L. 206
 Huang, Y. 710
 Hubert, D. 1090
 Hübers, H.-W. 232
 Hullavarad, S.S. 1189
 Hutchison, M.T. 598
 Huy, P.T. 408
 Hyla, M. 1011

 Iakoubovskii, K. 585, 598
 Iida, S. 916
 Ikari, T. 427
 Imaizumi, M. 1181
 Inoue, K. 891
 Inoue, N. 244, 502
 Irmscher, K. 730
 Ishi, K. 1046
 Ishida, Y. 684
 Ishii, M. 1153
 Ishioka, K. 163, 171
 Ishiyama, T. 240
 Isogai, Y. 796
 ISOLDE Collaboration 418, 431, 963, 980, 989
 Itoh, H. 629, 633, 652, 1181, 1226
 Itoh, K.M. 521
 Ittermann, B. 236, 248, 989
 Ivanov, V.Yu. 942
 Iwagami, Y. 240
 Iwasaki, T. 1097

 Jagadish, C. 776
 Jäger, Ch. 895
 Jäger, W. 895
 Janek, J. 1086
 Jantsch, W. 34, 344, 354, 558
 Janzén, E. 675, 722, 1165
 Jasinski, J. 874
 Jedrzejewski, J. 1108
 Jelezko, F. 608
 Jenny, J.R. 671
 Jeong, S. 999
 Jiang, F. 122
 Jin, Y.-G. 912
 Jinno, S. 796
 Job, R. 181, 185
 Johansen, A. 769
 Johnston, K. 565
 Jones, R. 8, 139, 197, 290, 305, 454, 577, 604, 1027
 Jones, R.L. 698
 Junquera, J. 147
 Jurisch, M. 745, 835
 Justo, J.F. 470, 489

 Kagadei, V.A. 827
 Kalabukhova, E.N. 698
 Kaleis, J.P. 1133
 Kamiura, Y. 240
 Kamon, Y. 391
 Kappertz, S. 989
 Kasuya, A. 276, 1125
 Katayama-Yoshida, H. 378, 391, 904
 Kato, J. 521
 Kawai, T. 993
 Kawasuso, A. 629, 633, 660
 Kazanskii, S.A. 1020, 1035, 1038
 Keim, M. 989
 Kempnyk, V. 1057
 Kerr, D. 569
 Khan, A. 1181
 Khandozhko, O. 1057
 Khirunenko, L. 550
 Khirunenko, L.I. 301, 458
 Khmel'nitsky, R.A. 573
 Khomchenko, V.S. 268
 Khomenkova, L.Yu. 967
 Khomich, A.V. 573
 Khorunzhii, I.A. 185
 Kiesel, P. 749, 1177
 Kiguchi, T. 1050
 Kilin, S.Ya. 608
 Kim, H. 93
 Kim, Y.-S. 143, 912
 Kimerling, L.C. 228
 King, P.J.C. 546, 920
 Kishimoto, N. 265
 Kishimoto, S. 916
 Kisielowski, C. 1090
 Kitagawa, H. 427
 Kitagawa, I. 424
 Kitajima, M. 163, 171
 Kittler, M. 1133
 Klettke, O. 687
 Kleverman, M. 197, 284
 Kliemann, R. 442
 Klik, M.A.J. 348, 414, 884
 Klochikhin, A.A. 58
 Kloos, S. 989
 Klyachkin, L.E. 365, 1104
 Klyuev, Yu.A. 598
 Knack, S. 213, 404
 Kobayashi, K. 1217
 Kobayashi, M. 1097
 Kobayashi, N. 710, 718
 Kobitski, A.Yu. 761
 Kocher, G. 344, 558
 Kögel, G. 442, 668
 Kögler, R. 442
 Köhler, U. 126
 Kohno, H. 1097
 Koide, T. 796
 Koizumi, A. 891
 Koizumi, S. 593
 Koleske, D.D. 51
 Kolmakov, A.G. 1141
 Kolomoets, V.V. 325
 Komarov, B.A. 284
 Kondakova, O.A. 1061
 Kono, K. 265
 Kononov, V.V. 671
 Kon'kov, O. 382
 Kopperschmidt, P. 1205
 Korbutowicz, R. 114
 Kordes, M.E. 695
 Korotkov, R.Y. 18, 26, 30
 Korshunov, F.P. 181
 Korsunska, N.E. 967
 Koschnick, F.K. 85
 Kovalskiy, A.P. 1011
 Kozanecki, A. 34, 354
 Kozlovski, V.V. 641
 Kozlovskii, V.V. 58

- Kozłowski, J. 114
 Krambrock, K. 749, 753
 Krasil'nik, Z.F. 340, 361
 Krause-Rehberg, R. 442, 629, 633, 660, 792, 812
 Krüger, T. 155
 Kriegseis, W. 89
 Krinichnyi, V.I. 1003
 Krispin, P. 870
 Kristianpoller, N. 612
 Krämer, S. 1177
 Kroll, F. 236, 248, 989
 Kryzhkov, D.I. 361
 Kühnel, G. 800
 Kumar, J. 1209
 Kuritsyn, D. 354
 Kuznetsov, A.Yu. 664
 Kuznetsov, V.P. 361
- Laakso, A. 1157
 Lalancette, M. 462
 Langhanki, B. 253
 Lantratov, V.M. 1113
 Lany, S. 958, 980
 Larionova, T.P. 181
 Larsen, A.N. 477
 Laube, M. 734
 Lavrov, E.V. 151, 206
 Lay, M. 776
 Lebedev, A.A. 641
 Lebedev, O. 294
 Lee, E.-C. 912
 Lee, K.Y. 51
 Legodi, M.J. 1189
 Lei, H. 446
 Leigh, R.S. 858
 Leipner, H.S. 446, 742, 792
 Leitch, A.W.R. 193, 866, 1065
 Leite, J.R. 772
 Leiter, F. 908
 Lemke, H. 404
 Leskelä, M. 932
 Leszczynski, M. 51, 102
 Li, D. 450
 Li, L. 1173
 Li, Q. 710
 Lichti, R.L. 73, 862, 920
 Lievens, P. 989
 Liliental-Weber, Z. 854, 874
 Lindström, J.L. 197, 284, 290, 305, 458
 Lingner, Th. 625, 649
 Linke, R.A. 1035
 Lischka, K. 34
- Litvinov, V.V. 290
 Litwin-Staszewska, E. 47, 117
 Liu, C. 42
 Lomovtsev, A.V. 971
 Londos, C.A. 313
 Look, D.C. 77, 706, 976
 Lopes, J.C. 616
 Lord, J.S. 920
 Lorenz, D. 446
 Lorenz, K. 22
 Losurdo, M. 374
 Lott, K. 932
 Lu, J. 1173
 Lübbers, M. 126
 Lukin, S.N. 698
 Lundin, W.V. 1141
 Luysberg, M. 808, 823
 Lysenko, V. 382
- Ma, X. 1173
 Machado, V.V.M. 726
 Maeda, K. 738, 1145
 Magnusson, B. 675
 Magudapathy, P. 1209
 Mai, F. 248, 989
 Mainwood, A. 565, 581
 Majid, A. 816
 Makarenko, L.F. 465
 Makeeva, I.N. 621
 Makosa, A. 757
 Malyarenko, A.M. 365, 1104
 Malzer, S. 1177
 Many, A. 1108
 Marbach, K. 248, 989
 Marczevska, B. 1213
 Markevich, I.V. 967
 Markevich, V.P. 197, 253, 284, 290, 305, 513
 Martsinovich, N. 493
 Martyniuk, M. 924
 Maruizumi, T. 424
 Mascher, P. 924
 Matics, S. 431
 Matsuda, S. 1181
 Mattausch, A. 656
 McAfee, J.L. 202
 McCluskey, M.D. 780
 Mchedlidze, T. 321, 400, 421, 474
 Medvedeva, I.F. 513
 Meguro, T. 257
 Meier, P. 248
 Meister, D. 89
 Mell, H. 248
 Mera, Y. 738, 1145
 Meyer, B.K. 38, 89, 908, 1069, 1074
- Meyer, J.D. 877
 Mezdrogina, M.M. 365
 Michael, K. 85
 Michel, J. 228
 Mikayama, T. 244
 Mikhailin, A.V. 110
 Mikhnovich Jr., V.V. 1023
 Mikhlin, S.B. 881, 1201
 Mimkes, J. 126
 Miriametro, A. 850
 Mischuck, B. 1197
 Misiuk, A. 313, 317, 820
 Mita, Y. 1097
 Mitchel, W.C. 698, 706
 Miura, T. 1217
 Mizokawa, Y. 502
 Mizuta, M. 122
 Mizutani, N. 1050
 Mochizuki, S. 1042, 1046
 Mochizuki, Y. 1169
 Mohamed, E. 949
 Mohamed, G.A. 949
 Mokhov, E.N. 680
 Molnar, R.J. 51
 Mondelaers, W. 517
 Monemar, B. 102
 Monge, J.L. 637
 Monteiro, T. 22, 42, 985
 Moore, W.J. 691
 Moreno, M. 823
 Morgado, E. 174
 Mori, T. 163, 171
 Moriwaki, K. 1121
 Morooka, M. 280
 Morozova, E.N. 361
 Morris, R. 525
 Mozol', P.E. 971
 Mudryi, A.V. 181
 Mukashev, B.N. 167, 178
 Müller, M. 529
 Müller, St.G. 671
 Murakami, K. 163, 171
 Murin, L.I. 197, 284, 290, 305, 458, 513
- Nair, K.G.M. 1209
 Nakagawa, S.T. 272
 Nakanishi, A. 216
 Nakanishi, T. 1046
 Nakashima, K. 652
 Nakashima, S. 684
 Nakatake, Y. 684
 Naletov, A.M. 598
 Naud, C. 117, 253
 Nazaré, M.H. 616

- Nazarov, A. 382
 Nebel, C.E. 593
 Nesladek, M. 1213
 Neugart, R. 989
 Neves, A.J. 589, 616
 Newman, R.C. 197, 780, 858
 Nicols, S.P. 854
 Nielsen, B.B. 122, 134, 206
 Nielsen, K.B. 134, 139
 Niklas, J.-R. 800
 Niklas, J.R. 745
 Niu, F. 26
 Nizovtsev, A.P. 608
 Nonaka, M. 539
 Norseng, M.S. 831
 Northrup, P.A. 369
 Nowak, T. 1213

 Öberg, S. 8, 139, 197, 290, 305, 454, 1027
 Odnoblyudov, M.A. 1129
 Oganessian, G. 181
 Oganessian, G.A. 58, 350
 Ohkubo, I. 244
 Ohmura, Y. 257
 Ohno, Y. 1222
 Ohshima, T. 652, 1181
 Ohtsuka, K. 163
 Ohyama, H. 1185, 1217, 1226
 Okonogi, K. 1169
 Okulov, S.M. 621
 Okumura, H. 684
 Olko, P. 1213
 Onoda, S. 1185, 1226
 Ordejón, P. 1, 147, 202
 Orlinskii, S.B. 680
 Orlova, E.E. 232
 Oshima, R. 224, 261
 Oshiyama, A. 999
 Ostapenko, S. 714, 1133, 1137
 Österreich, I. 1069, 1074
 Ostheimer, V. 958, 963, 980
 Otsuka, K. 171
 Overhof, H. 497, 561, 625
 Ozaki, N. 1222

 Pakula, K. 102, 117
 Palmethofer, L. 344
 Pankratov, O. 656
 Parakhonsky, A.L. 396
 Park, S.S. 51
 Park, Y. 98
 Parrot, R. 928
 Paszkiewicz, R. 114
 Patuk, A.I. 181

 Pavlov, S.G. 232
 Peaker, A.R. 139, 513
 Penchina, C.M. 581
 Pensl, G. 361, 633, 660, 687, 734
 Pereira, R.N. 589, 1015
 Perjeru, F. 695
 Peters, D. 236, 248, 989
 Petrenko, T.L. 621, 637
 Petrenko, T.T. 621, 637
 Petters, K. 629, 792
 Pfisterer, D. 1069, 1074
 Phillips, M.R. 106
 Piccirillo, C. 581
 Pierreux, D. 481
 Pinho, N. 454
 Pinho, N.M.C. 1027
 Pintilie, I. 730
 Pintilie, L. 730
 Pinto, P. 374
 Piotrkowski, R. 47
 Placzek-Popko, E. 769, 954
 Ploog, K.H. 765, 823, 870
 Poirier, R. 462
 Polimeni, A. 850
 Polity, A. 1069, 1074
 Poloskin, D.S. 58, 350
 Polyhach, Ye. 1057
 Pölzl, M. 13
 Pomezov, Yu. 550
 Pomezov, Yu.V. 301, 458
 Porowski, S. 51
 Potapov, A.S. 1201
 Potsidou, M. 313
 Poyai, A. 1217
 Pozina, G. 102
 Pöpping, J. 895
 Preobrazhenskii, V.V. 820
 Principe, E. 1090
 Privitera, V. 477
 Prokofiev, A.A. 1129
 Pruneda, J.M. 147, 202
 Prystawko, P. 102
 Przybylinska, H. 344
 Przybylińska, H. 34, 340, 354
 Pu, A. 569
 Pusep, Yu.A. 772, 843

 Que, D. 450, 1173

 Raineri, V. 317
 Räisänen, J. 542
 Ranalli, F. 850
 Ratajczak, J. 317
 Ratnikov, V.V. 1141
 Rau, U. 1081

 Rauls, E. 497, 625, 645
 Rauschenbach, B. 81
 Reddy, A.J. 228
 Redmann, F. 442, 629, 660, 812
 Reinhardt, M. 850
 Reshanov, S.A. 687
 Riechert, H. 877
 Riemann, H. 232, 404
 Riemann, T. 89
 Rodnyi, P.A. 1201
 Rogulis, U. 66, 85
 Romanov, V.V. 365
 Romas, L.M. 827
 Roorda, S. 462
 Rummeli, M.H. 232
 Rüschemschmidt, K. 734
 Rummyantsev, D.S. 1038
 Ryskin, A.I. 1020, 1035, 1038

 Sá Ferreira, R.A. 22
 Saarinen, K. 77, 664, 1157
 Sadowski, H. 702
 Saeki, M. 993
 Safonov, A.N. 298
 Saiki, A. 1050
 Saito, K. 438
 Saito, M. 220
 Sakamoto, N. 257
 Sangster, M.J.L. 858
 Santos, L.F. 1078
 Sarbey, O.G. 788
 Satake, A. 1193
 Sato, K. 904
 Sato, Y. 434
 Sauer, R. 945
 Savkina, N.S. 641
 Sax, A.F. 155
 Saxler, A. 698, 706
 Scarle, S. 493
 Schachtrup, A.R. 963
 Scherbina, L.V. 1108
 Scheulin, A.S. 1035
 Schiettekatte, F. 462
 Schmidt, J. 680
 Schock, H.W. 1081
 Scholz, R. 1205
 Scholz, R.F. 742
 Schönfelder, R. 945
 Schröder, W. 535, 550
 Schulz, D. 730
 Schweizer, S. 66
 Seghier, D. 130
 Seifert, W. 1133
 Senz, St. 1205
 Shagov, A.A. 942

- Shakin, I.A. 181
 Shamirzaev, T.S. 761
 Shanabrook, B.V. 691
 Shangguan, W.Z. 1117
 Shastin, V.N. 232
 Sheinkman, M.K. 967
 Shen, Y. 1173
 Shinozaki, K. 1050
 Shinozuka, Y. 506
 Shiryaev, A.A. 598
 Shishkin, Y. 687
 Shmagin, V.B. 361
 Schmidt, N.M. 58, 1141
 Shpotyuk, O.I. 1011
 Shtel'makh, K.F. 881
 Shui, Q. 450
 Siegel, W. 800
 Sielemann, R. 418, 529
 Sienz, S. 81
 Silva, G.B. 1078
 Simoen, E. 294, 477, 1185, 1217, 1226
 Sjue, S.K.L. 73, 862, 920
 Skorupa, W. 442
 Skvortsov, A.P. 365
 Slotte, J. 664
 Slynko, E. 1057
 Soares, M.J. 22, 42, 985
 Sobolev, M.M. 1113
 Sobolev, N.A. 333, 350, 589
 Södervall, U. 895
 Soerensen, C. 769
 Søgård, S. 134
 Sokolov, S.S. 772
 Soltanovich, O.A. 827
 Son, N.T. 722
 Sopinsky, M.V. 268, 1054
 Sosnin, M. 550
 Sosnin, M.G. 301, 458
 Soubatch, S. 1177
 Spaeth, J.-M. 66, 85, 253, 649, 749, 753
 Spaeth, J.M. 625
 Specht, P. 98, 808, 812
 Sperr, P. 660, 668
 Spruytte, S.G. 870
 Sridhara, S. 675
 Staab, T.E.M. 645
 Stadler, L. 529
 Stavola, M. 122
 Steen, C. 749, 1177
 Steinegger, T. 800
 Steinegger, Th. 745
 Stepikhova, M. 344
 Stepikhova, M.V. 374
 Stesmans, A. 481, 585
 Stockman, S.A. 888
 Stöckmann, H.-J. 236, 248
 Stolwijk, N.A. 734, 895, 963
 Storasta, L. 675, 1165
 Strel'chuk, A.M. 641
 Strohm, A. 431, 542
 Stutzmann, M. 69, 593
 Suezawa, M. 197, 216, 220, 224, 276, 321, 400, 421, 434, 438, 474, 1125
 Suleimanov, Yu.M. 714
 Sumathi, R.R. 1209
 Suski, T. 47, 51, 77, 117
 Suzuki, M. 257
 Suzuki, Y. 1046
 Svavarsson, H.G. 804
 Svensson, B.G. 284, 776
 Szatkowski, J. 769
 Szczerbakow, A. 942
 Szekeres, A. 485
 Tabata, H. 993
 Takada, Y. 224
 Takahashi, M. 257
 Takahashi, T. 434
 Takami, Y. 1226
 Takamoto, T. 1181
 Takeda, S. 1097, 1222
 Takeda, Y. 796, 891
 Takeoka, S. 1100
 Talkahashi, T. 684
 Tamano, T. 224, 261
 Tamaoka, H. 1121
 Tan, H.H. 776
 Tanahashi, K. 502
 Tanaka, S. 427
 Taniguchi, R. 224, 261
 Tanoue, H. 710, 718
 Tarasov, I. 1133
 Tautz, S. 1177
 Teofilov, N. 945
 Terukov, E. 382
 Thenikl, T. 13
 Thieß, H. 248
 Thonke, K. 945
 Tian, D. 1173
 Tietz, C. 608
 Titkov, A.N. 1141
 Tkach, I. 749, 753
 Tlaczala, M. 114
 Tokmoldin, S.Zh. 167
 Tokunaga, M. 1100
 Torchynska, T. 1108
 Toropov, A.I. 784
 Torres, V.B. 1027
 Toshikiyo, K. 1100
 Tóth, A.L. 757
 Triftshäuser, W. 442, 660, 668
 Tröster, Th. 85
 Tsvetkov, V.F. 671
 Tu, C.W. 106
 Törn, L. 932
 Tüzemen, S. 1197
 Twigg, M.E. 51
 Ucer, K.B. 1197
 Udhayasankar, M. 1209
 Uedono, A. 652
 Ulrici, W. 823, 835
 Ulyashin, A.G. 181, 185
 Umeda, T. 1169
 Umehara, N. 163, 171
 Uppal, S. 525
 Usikov, A.S. 58, 1141
 Uskova, E.A. 361
 Usui, A. 122
 von Bardeleben, H.J. 621
 von Högersthal, G.B.H. 850
 Valdna, V. 939
 Van de Walle, C.G. 899
 Van Landuyt, J. 294
 Vanhellemont, J. 294
 Vanmeerbeek, P. 517
 Veit, P. 89
 Vekshin, V.A. 58
 Venger, E.F. 325
 Vianden, R. 22
 Vilão, R.C. 920
 Vinh, N.Q. 340, 357, 414
 Vlasenko, A.I. 971
 Vlasenko, L.S. 62
 Volobujeva, O. 932
 Vorobiev, Yu.V. 1108
 Voss, T. 431, 542
 Vovk, Ja. 382
 Waag, A. 945
 Wagener, M.C. 866
 Wagner, H.P. 761
 Wagner, J. 858
 Wakiya, N. 1050
 Waligórski, M.P.R. 1213
 Walther, T. 1161
 Walukiewicz, W. 874
 Wang, G. 450
 Warren Jr., W.W. 1020
 Washburn, J. 874

- Wasik, D. 117
Watanabe, K. 1121
Watanabe, N. 891
Watanabe, T. 1007
Watkins, G.D. 62
Weber, E.R. 98, 808, 812
Weber, J. 151, 159, 206, 210, 213, 404, 1065
Wei, S.-H. 839
Weidinger, A. 920
Weidner, M. 633, 660
Weinstein, M.G. 122
Weiss, D. 612
Wells, J.-P.R. 337, 884
Werner, P. 742
Wessels, B.W. 18, 26, 30
Weyer, G. 418
Wichert, Th. 958, 963, 980
Wickenden, A.E. 51
Wiedemann, B. 877
Wierzchowski, W. 317
Wieteska, K. 317
Wilbert, S. 989
Wilkinson, J. 1197
Williams, R.T. 1197
Willoughby, A.F.W. 525
Wolf, H. 958, 963, 980
Woodin, R.L. 695
Wosiński, T. 757
Wrachtrup, J. 608
Wu, L. 193
Xin, H.P. 106
Xiong, G. 1197
Xu, S.J. 710
Yakimov, E.B. 210, 213, 396, 827
Yamada-Kaneta, H. 220, 309
Yamaguchi, M. 1181
Yamamoto, T. 916, 1007
Yamanaka, Y. 244
Yamashita, Y. 240
Yanase, A. 378, 391
Yanchuk, Z.Z. 1031
Yang, D. 396, 450, 1173
Yang, J. 450, 1173
Yarykin, N. 159, 210, 213
Yassievich, I.N. 357, 1129
Yastrubchak, O. 757, 967
Yasunaga, D. 1193
Yeshchenko, O.A. 1031
Yonenaga, I. 539, 546, 1150
Yoshikawa, M. 652
Yu, K.M. 874
Yu, Y.B. 1117
Zabrodsii, A. 558
Zafar Iqbal, M. 816
Zafar, N. 816
Zaharchenko, I. 714
Zahn, D.R.T. 761
Zasuha, V.A. 301
Zayachuk, D. 1057
Zeckzer, A. 446
Zeisel, R. 69
Zeitz, W.-D. 535
Zhang, S.B. 839
Zhang, W. 89
Zhao, R. 98, 808, 812
Zhou, H. 908
Zhukavin, R.Kh. 232
Zhuravlev, K.K. 780
Zhuravlev, K.S. 761, 784, 820
Zikovsky, J. 462
Zistl, Ch. 529
Zvanut, M.E. 671
Zychowitz, G. 800
Zyubin, A.S. 1061



ELSEVIER

Physica B 308–310 (2001) 1237–1241

PHYSICA B

www.elsevier.com/locate/physb

Subject Index

- α -irradiation 769
 β -NMR 236, 248, 535, 989
 γ -irradiation 1226
 μ c-Si:H 248
- a-Se 1061
AA12 454
Ab initio calculation 378
Ab initio methods 726
Ab initio theory 454
Absorption 30, 585
Absorption bands 197
Acceptor diffusion 888
Acceptor doping 989
Acceptor segregation 888
Acceptors 126, 117, 220, 976
AFM 98
Ag 963
Agglomeration 272
AlGaAs 769
AlGaAs alloys 772, 843
AlGaN 130
AlGaN/GaN 93
Alloy fluctuations 558
Alloy nanocrystals 1100
AlN 69, 73
Aluminium gallium nitride 1189
Aluminum 722
Amorphous hydrogenated silicon 382
Amorphous Si:H 155
Amorphous silicon 174
Anion vacancies 908
Annealed InP:C 858
Annealing 47, 171, 462, 569, 598, 629
Annihilation 110
Anti-Stokes emission 942
Antisite 625
Arsenic 866
Arsenic antisite 812
As antisite defect 738
As self-diffusion 742
As_{Ga}-antisite defect 1177
- As_{Ga}-related defect 749
¹⁹⁵Au-diffusion in amorphous Si₃N₄ and Si₄N₃ 431
Averaged structures 1042
- Band gap 949
Barrier 1035
Be doping 808
Beryllium 710, 718, 1027
Beryllium inclusion 820
Bistability 159, 1020
Blue-Ag emission 916
BN 1027
Boron 236, 248, 257, 525, 581, 722
Boron diffusion 734
Boron implantation 535
Bulk 4H-SiC 706
Bulk and surface defects 1081
- (C–C) precipitates in InP:C 858
Cadmium telluride 971
Cadmium zinc telluride 924
Calorimetry 462
Capacitance XAFS 1153
Capture kinetics 757
Carbon 126, 197, 305, 823
Carbon vacancy 621, 637, 671
Carbon-carbon pair 513
Carrier trap 999
Cd(Mg,Mn)Te 1161
CdS 920
CdTe 954, 958, 963
CeO₂ 1050
Chalcogenide glassy semiconductors 1054
Chalcogenides 1011
Chromium ion 942
Co-implantation 652
Codoping 916
Coherent capture 506
Compensated semiconductor 521
Compensating donors 38
Compensation 912
- Complex defects 939
Computer simulation 493
Concentration profile of Au in Si 280
Conductivity 130, 881, 1038
Configuration interaction 497
Copper 404, 800
Counterdoping 888
Cr 434
Crystal growth 539
Crystalline silicon 163
Cu 963
Cu diffusion 792
Cu impurity 391
Cu(InGa)Se₂ 1081
Cu-wire bonding 391
CuGaS₂ 1065
CuInS₂ 1007, 1074
Cu_xS 1069
CVD diamonds 585, 1213
Cz-Si 1137
Czochralski-grown silicon 261
Czochralski-silicon 546
- Dangling bond 228, 1100
DC sputtering 949
Deep donors 558
Deep level defects 718, 1181
Deep level transient spectroscopy 193, 477, 529
Deep levels 134, 382, 589, 757, 769, 954
Deep-level transient spectroscopy 776
Defect distribution 102
Defect formation 1081
Defect mobility 73
Defect passivation 761
Defect reactions 404, 506
Defect states 325, 714
Defect structures 1046
Defects 102, 110, 130, 190, 193, 265, 333, 408, 481, 675, 684, 695, 710, 745, 776, 846, 924, 932, 967,

- 971, 1061, 1074, 1113, 1165, 1169, 1173, 1189
 Defects in barriers 1129
 Deformation 446
 Degradation 1217
 Density functional theory 369, 980, 999
 Denuded zone 185
 Detectors 1213
 Deuterium 474, 835
 Device 13
 DFT 958
 DFT calculations 535, 637
 D_1 1165
 Diamond 561, 565, 569, 573, 577, 581, 593, 598, 604, 612, 616
 Diffraction efficiency 1035
 Diffusion 213, 236, 391, 418, 525, 645, 800, 963
 Diffusion coefficients 391
 Diffusion lengths 1161
 D_{II} center 656
 Dilation 604
 Diode process 1173
 Dislocation density 1050
 Dislocation sources 446
 Dislocations 13, 470, 489, 493, 577, 757, 1090, 1133
 Disturbance 301
 Divacancies 462, 550, 1007
 DLTS 190, 240, 633, 641, 660, 687, 695, 706, 730, 816, 1209
 Donor–acceptor pair transition 945
 Donors 276, 976
 Dopant boron 261
 Doping 126, 248, 257, 593, 839, 899
 Double heterostructures 891
 Double-exchange mechanism 904
 DRAM 1169
 DX-centers 69, 788, 1020
 Dynamics 1003
 Dy–Er center 796
 Dysprosium 796

 EBIC 1133
 EDMR 593, 1169
 EELS 577
 EFG 958
 EL2 738, 753
 Electric field gradients 980
 Electrical conductivity 932
 Electrically active centers 361
 Electrodiffusion 967
 Electroluminescence 268, 344, 1193

 Electron emission rate 1177
 Electron irradiation 216, 224, 261, 276, 284, 1226
 Electron paramagnetic resonance 625, 649
 Electronic noise 69
 Embedding calculations 155
 ENDOR 753
 Energy filtering TEM 1161
 Energy gap 1145
 Energy gap variation 1031
 Energy levels 465, 1015
 Energy transfer 1121
 Enhanced diffusion 178
 Enhanced site-exchange rate 427
 Epilayers 1157
 EPR 66, 408, 434, 589, 621, 671, 680, 691, 730, 753, 1003, 1057
 Equation of motion method 1117
 Equilibrium concentration 502
 Er-doped Si 369
 Erbium 34, 337, 348, 354, 357, 374, 382, 387, 891
 Erbium luminescence 344
 Erbium-related centers 365, 687
 Er–O complex 378
 ESR 321, 400, 421, 481, 881
 EXAFS 369
 Excitation mechanisms 354
 Exciton and biexciton binding energy variation 1031
 Excitons 765, 1042
 Extended defects 106, 470, 489

 Fe 400, 421
 Fermi level 163
 Ferromagnetism 904
 First-principles calculation 424
 Flow-modulation growth 89
 Fluctuating potential 804
 Free electron laser 337, 884
 Frenkel pair 224
 FTIR 877

 Ga interstitial 62
 Ga self-interstitial 854
 Ga vacancy 62, 77, 812
 GaAs 738, 742, 745, 753, 776, 792, 796, 800, 804, 816, 827, 835, 862, 1113, 1145
 GaAs quantum well 765
 GaAs:Be 820
 Gadolinium 1057
 Gallium antimonide 854
 Gallium arsenide 202, 1209

 Gallium arsenide isotope structure 831
 Gallium nitride 30, 34, 58, 1090
 Gallium phosphide 895
 Gallium self-diffusion 831
 GaN 18, 22, 38, 42, 47, 51, 62, 66, 73, 77, 85, 89, 102, 114, 117, 122, 126, 369, 1141
 GaN polytypes 81
 GANP 106
 GaN_xAs_{1-x} 874
 GaP 862
 GaSb 862
 Gate oxides 1090
 ^{71}Ge self-diffusion 542
 Germanium 8, 290, 517, 525, 550
 Germanium defects 529
 Germanium–silicon alloys 539
 Gettering 442
 Glasses 1011
 Gold diffusion 396
 Gold state in silicon 280
 Graphitisation 573
 Group-III nitrides 69
 GS-MBE 98

 4H–SiC 633, 671
 6H silicon carbide 687
 6H–SiC 633, 710, 730
 6H–silicon carbide 718
 Hall-effect measurement 1069
 Hardness 1150
 Helium 181
 Heterostructures 1113
 High hydrostatic pressure 820
 High-pressure anneals 313
 High-temperature irradiation 1226
 Hole and electron traps 870
 Holographic grating 1035
 Homoepitaxial 51
 Hot electrons 788
 HPHT diamond 589
 HVPE 51
 Hydrogen 1, 73, 117, 122, 134, 143, 147, 151, 159, 167, 178, 181, 185, 190, 193, 197, 202, 206, 210, 213, 216, 220, 253, 321, 404, 434, 438, 474, 546, 722, 780, 827, 835, 850, 899, 920, 1027, 1125
 Hydrogen mobility 862
 Hydrogen molecule 163, 171
 Hydrogenated amorphous silicon 257
 Hydrogen–carbon pair 139
 Hydrostatic pressure 317

- Hyperfine interactions 497, 561
 Hyperfine parameters 637

 III–V semiconductors 846
 II–VI compounds 928, 939
 II–VI semiconductors 980
 Implantation 22, 42, 122, 181, 248, 350, 664, 710, 718, 874, 989
 Impurities 502, 784, 928, 1097
 Impurity absorption 521
 Impurity and defect levels 47
 Impurity complexes 197
 Impurity diffusion in Si 280
 Impurity distribution 521
 Impurity solubility 839
 Impurity subband 881
 Impurity-free disordering 776
 Impurity-defect complexes 839
 Indium nitride 58
 Induced deep levels 1185, 1217, 1226
 Infrared 780
 Infrared absorption 244, 309, 581
 Infrared emission 942
 Infrared spectroscopy 294, 539
 InGaAsN 98, 877
 InGaAsP laser diode 1185
 InGaN 102
 InGaP 1181
 InP 884
 InP: C Raman scattering 858
 InP: Mn 881
 InSbBi 866
 Instability 506
 Instrumentation 1157
 Interaction 1113
 Interface defects 765, 1205
 Interface traps 485
 Interstitial-type diffusion mechanisms 431
 Interstitials 265, 454, 645
 Intra-4f shell transition 796
 Intrinsic and extrinsic defects 706
 Intrinsic defect 621, 671
 Intrinsic-related defect centers 633
 $\text{In}_x\text{Ga}_{1-x}\text{As}_{1-y}\text{N}_y$ 850
 Ion beam assisted deposition 81
 Ion beam induced defects 81
 Ion implantation 236, 333, 462, 525, 573
 Ionic semiconductors 1020
 Ionising radiation 1213
 IR 691
 Iron 418
 Iron group ions 928

 Irradiation 58, 77, 313, 458, 517, 1217
 Irradiation effects 612
 Isochronal annealing 190
 Isoelectronic impurities 850
 Isovalent impurity 301

 Kick-out mechanism 734
 Kick-out model 854

 Laplace DLTS 139, 513
 Laplace MCTS 554
 Laser diode 98
 Laser irradiation 935
 Laser MBE 993
 Laser shock wave 971
 Lateral correlation length 114
 Leakage current 1169
 LED 1078
 Li 989
 Lifetime 1133
 Lift-off 749
 Light-emitting structures 333
 Line shape 220
 Line widths 298
 Local vibrational modes 147, 780, 823
 Localization 772, 843
 LSDA 497, 561
 LT-GaAs 749, 812, 823, 1177
 LTPL 687, 702
 Luminescence 106, 354, 365, 598
 LVM 656

 M3/M4 defects 827
 Macrostructure 268
 Magnesium 1027
 Magnetic circular dichroism of the absorption 649
 Magnetic resonance 51, 253, 976, 1078
 Magnetoresistance 1086
 Manganese 30
 MBE 93
 MBE-grown Ga(As,N) 870
 MCDA 812
 MCDA-EPR 749
 Mechanical strength 450
 MEH-PPV 1078
 Metal impurity 424
 Metalorganic chemical-vapor-deposition-grown 130
 Metastability 827, 954
 Mg-acceptor 38

 Microcavities 26, 1104
 Microstructure 268, 874
 Microvoids 155
 Migration barrier 391
 Minority carrier lifetime 228
 Mn doping 18
 Mobility of charge carriers 1023
 MOCVD 816
 Molecular beam epitaxy 823
 Molecular dynamics 1, 202, 272, 510
 Molecular orbital 244
 Monte Carlo simulation 493
 Morphology 89
 Mosaic structure 1141
 Mössbauer effect 1057
 Mössbauer spectroscopy 418
 Multi-vacancy 171
 Multifractal analysis 1141
 Multinary compound semiconductors 1081
 Muonium 73, 546, 862, 920

 n-type silicon 477
 Na 1007
 Nanoclusters 178
 Nanocrystalline silicon 374
 Nanocrystals 1121
 Nanoindentation 446
 Nanostructure 1097
 Native defects 899, 1015, 1057, 1201
 Native point defects 808
 Neutrons 702
 Nickel 427, 589, 616
 Nitridation 999
 Nitrides 110
 Nitrogen 244, 396, 450, 877, 912, 1173
 Nitrogen levels 706
 NMR 881, 1020
 Non-stoichiometric GaAs 808
 Nonequilibrium Green's function 1117
 Nonstoichiometry 1086
 NRA 877
 NTD 702

 O-doped GaN 26
 ODEPR 62, 85
 Ohmic contact 1197
 Optical absorption 276, 438, 1125
 Optical energy levels 928
 Optical properties 616, 850, 949, 1201

- Optical spectroscopy 1031
 Optically detected magnetic resonance 608, 908
 Order–disorder phase transition 431
 Organic semiconductors 1003
 Organometallic vapor phase epitaxy 891
 Oxidation 329
 Oxide charges 485
 Oxygen 8, 117, 134, 216, 265, 284, 290, 298, 301, 305, 309, 321, 539, 891, 1007
 Oxygen accumulation 317
 Oxygen adsorption 329
 Oxygen dimer 517
 Oxygen impurities 309
 Oxygen isotopes 458
 Oxygen precipitation 294
- P6 454
 P doping 47, 1100
 PAS 633
 Passivation 228, 722
 Permittivity 1038
 Perturbed angular correlation 529
 Perturbed $\gamma\gamma$ -angular correlation 980
 Phonon kick 506
 Phonons 581
 Phosphorus 593
 Photo EPR 698, 1015
 Photochromy 1038
 Photoconductivity 174, 585
 Photoinduced effects 174
 Photoluminescence 18, 26, 34, 51, 181, 337, 340, 357, 414, 477, 698, 710, 761, 765, 784, 884, 1065, 1100, 1108, 1133
 Photonic crystal 1222
 Photovoltaics 1074, 1081
 Physicochemical interactions 1054
 PICTS 745, 800
 PL 22, 42, 945, 985
 Plasma treatment 761
 Plasmons 772, 843
 Platelets 143, 151, 167
 Platinum 438
 Platinum–hydrogen complex 240
 p–n junction 1197
 Point defects 220, 489, 656
 Polytypism 1042
 Porous silicon 1108
 Positron 110, 1011
 Positron annihilation 77, 442, 569, 629, 652, 660, 664, 792
 Positron annihilation spectroscopy 924
 Positron lifetime 261
 Positron spectroscopy 1157
 Post-growth treatment 870
 Precipitates 344
 Precipitation 427
 Pressure 780
 Pressure and temperature dependence 85
 Pressure-induced negative effective U 424
 Proton implantation 668
 Proton irradiation 477, 641, 1209
 Pseudo-Jahn–Teller interaction 391
- Quantum chemical modeling 1061
 Quantum dot 1113
 Quantum dot array 1117
 Quantum optics 608
 Quantum transport 1117
 Quantum well heterostructures 1129
 Quantum wells 554, 788
- $R_p/2$ 442
 Radiation 1181
 Radiation annealing 272
 Radiation damage 1185, 1226
 Radiation defects 159, 210, 305, 465, 612, 629
 Radiation-induced defects 485
 Radiotracer technique 431, 542
 Raman scattering 151, 206, 684, 866
 Rare-earth doped Si 333
 Rare-earth impurity 378
 Rare-earth ions 340, 350
 RBS 22, 985
 RBS/C 42
 Recombination 174, 1193
 Recombination afterglow 66
 Relaxation 1003
 Resonant states 1129
 RF sputtering 1069
 Rocking curve 1050
- Scanning probe 1153
 Scanning tunneling microscopy 738, 1104, 1145
 Scattering of charge carriers 1023
 Schottky barrier diode 1209
 SDR 321
- Segregation 470
 Self-assembled silicon quantum wells 365
 Self-implantation 442
 Self-interstitials 1, 224, 284, 396, 458, 510, 604, 895
 Self-organization 1097
 Semi-insulating 691
 Semi-insulating SiC 698
 Semiconductor heterostructures 757
 Semiconductor wafer bonding 1205
 Semiconductors 1011, 1038
 Shallow acceptor passivation 213
 Shallow donors 920
 Shallow impurity 232
 Shallow thermal donors 253
 Shallow trench isolation diodes 1217
 Si photodiode 1226
 Si self-interstitial 734
 Si wires 1108
 Si-doping 804
 Si/SiO₂ interface 481
 Si_{1-x}Ge_x 550
 Si:Au 280
 Si:Er/Si structures 361
 Si:H 317
 Si:He 317
 SiC 561, 629, 637, 641, 645, 660, 675, 680, 684, 695, 702, 722, 1165
 SiGe 554
 Silicon 1, 8, 134, 139, 143, 147, 151, 159, 167, 178, 181, 185, 193, 197, 202, 206, 210, 213, 216, 220, 224, 232, 236, 240, 244, 253, 265, 276, 284, 290, 294, 298, 301, 305, 309, 313, 321, 348, 350, 357, 378, 387, 391, 396, 400, 404, 408, 414, 418, 421, 427, 434, 438, 442, 450, 458, 462, 465, 474, 493, 510, 513, 577, 1097, 1121, 1125, 1133, 1173, 1222
 Silicon carbide 621, 625, 649, 652, 656, 668, 691, 714, 726, 734
 Silicon monoxide 268
 Silicon oxide 354, 1108
 Silicon surfaces 329
 Silicon–germanium 546
 Silicon–germanium crystals 535
 Silver 414
 Silver selenide 1086
 SIMS 93
 Si–Ge 558
 Si–Ge epi-layers 542

- Single centers 1104
Single defect 608
Si–H 171
SiO₂ 999
Site-selectivity 1153
Site-switching 804
Slow positron annihilation 668
Small-angle scattering 598
Spectroscopic ellipsometry 374
Spectroscopy 387
Spin resonance 593
Spin-orbit 616
Sputtering 257
Stability 565, 939
Stacking faults 675, 684
Staebler–Wronski effect 155
Stimulated emission 232
Strain 106, 481
Strain field 1145
Strained germanium 1129
Stress 13, 502
Stress simulation 935
Stress tensor 604
Stress-induced splitting 240
Structural defects 89
Structure 1061
Sub-band-gap excitation 348
Sublimation MBE 361
Substitution of atoms 1031
Sulfur diffusion 742
Superionic conductor 1042
Superlattice 784
Surface defects 228, 1153
Surface nanohole 1222

Tantalum 730
TEM 294, 792, 874
TEM micrographs 1205
Temperature field 935

Theoretical methods 846
Thermal donors 8, 185, 290, 350, 517
Thermal SiO₂ 485
Thermal stability 808
Thermo-mechanical stability 1150
Thermodonor 325
Thin films 1069, 1074
Thin films transistor 993
THz 232
Tin-vacancy 477
Titanium 714
Tm 1121
TraCE 1165
Transition from interstitialcy to vacancy mechanism 542
Transition metals 30, 565, 714, 726, 816, 904
Transition-metal impurity 391
Transition-metal–hydrogen complexes 408
Transmission electron microscopy 13, 446, 1090, 1222
Transport process 788
Triplet state 976
TRPL 985
Tungsten 730
Two-electron satellite 945

Ultrasonic 1137
Uniaxial pressure 325
Uniaxial stress 139
UV photodetectors 1189

Vacancies 167, 206, 224, 321, 400, 421, 474, 497, 502, 569, 585, 625, 645, 649, 660, 664, 680, 895, 958, 1125, 1157

Vacancy clusters 792
Vacancy defects 668
Vacancy-type defects 652
Vacancy–phosphorus pair 513
Vacuum deposition 1065
Valence change 1046
Valence force 244
Vibrational modes 122, 290, 835
Vibrations 1137

White-light emission 1046
Wide bandgap semiconductors 1150, 1193

X-irradiation 66
X-ray 820
X-ray diffraction 114
XRD pole figures 81

Yellow luminescence intensity 85
YSZ 1050
Ytterbium 884

Zeeman effect 340
Zinc diffusion 831, 854, 895
Zinc selenide 387
Zinc sulphide 932
Zinc-induced interdiffusion 831
Zn(Mg,S)Se 1161
ZnGeP₂ 1015
ZnO 899, 904, 908, 912, 920, 945, 976, 985, 993, 1197
ZnO:Li films 949
ZnS 916
ZnSe 939, 942, 989
ZnSe crystals 935
ZnS_xSe_{1-x} 1201

PHYSICA B

INSTRUCTIONS TO AUTHORS

Submission of papers

Manuscripts (one original + two copies) should be sent to one of the following regular editors:

Prof. Dr. F.R. de Boer, Amsterdam
Prof. L. Degiorgi, Zürich
Dr. Z. Fisk, Tallahassee, FL
Dr. R. Jochemsen, Leiden
(Addresses: see p. 2 of cover)

Original material: Submission of a manuscript implies that it is not being simultaneously considered for publication elsewhere and that the authors have obtained the necessary authority for publication.

Types of contributions

Original research papers and letters to the editor are welcomed. Both should contain an Abstract (of up to 200 words) and a Conclusions section, which, particularly in the case of theoretical papers, translates the results into terms readily accessible to most readers.

Manuscript preparation

All manuscripts should be written in proper English. The paper copies of the text should be prepared with double line spacing and wide margins, on numbered sheets.

Structure: Please adhere to the following order of presentation: Article title, Author(s), Affiliation(s), Abstract, PACS codes and keywords, Main text, Acknowledgements, Appendices, References, Figure captions, Tables.

Corresponding author: The name, complete postal address, telephone and fax numbers and the E-mail address of the corresponding author should be given on the first page of the manuscript.

PACS codes / Keywords: Please supply one to four classification codes (PACS and/or MSC) and up to six keywords of your own choice that describe the content of your article in more detail.

References: References to other work should be consecutively numbered in the text using square brackets and listed by number in the Reference list.

Illustrations

Illustrations should also be submitted in triplicate: one master set and two sets of copies. The *line drawings* in the master set should be original laser printer or plotter output or drawn black india ink, with careful lettering, large enough (3–5 mm) to

remain legible after reduction for printing. The *photographs* should be originals, with somewhat more contrast than is required in the printed version. They should be unmounted unless part of a composite figure. Any scale markers should be inserted on the photograph itself, not drawn below it.

Colour plates: Figures may be published in colour, if this is judged essential by the editor. The publisher and the author will each bear part of the extra costs involved. Further information is available from the publisher.

After acceptance

Notification: You will be notified by the Editor of the journal of the acceptance of your article.

Copyright transfer: In the course of the production process you will be asked to transfer the copyright of the article to the publisher. This transfer will ensure the widest possible dissemination of information.

Electronic manuscripts

The publisher welcomes the receipt of an electronic version of your accepted manuscript. If there is not already a copy of this (on diskette) with the journal editor at the time the manuscript is being refereed, you are invited to send a file with the text of the accepted manuscript directly to the Publisher on diskette (allowed formats 3.5" or 5.25" MS-DOS, or 3.5" Macintosh) to the address given below. Please note that no deviations from the version accepted by the Editor of the journal are permissible without the prior and explicit approval of the Editor. Such changes should be clearly indicated on an accompanying printout of the file.

Author benefits

No page charges: Publishing in Physica B is free of charge.

Free offprints: The corresponding author will receive 25 offprints free of charge. An offprint order form will be supplied by the publisher for ordering any additional paid offprints.

Discount: Contributors to Elsevier Science journals are entitled to a 30% discount on all Elsevier Science books.

For specific enquiries on the preparation of electronic artwork, consult <http://www.elsevier.com/locate/authorartwork/>

Other enquiries

For enquiries relating to the status of accepted articles through our Online Article Status Information System (OASIS), author Frequently Asked Questions and any other enquiries relating to Elsevier Science, please consult <http://www.elsevier.com/locate/authors/>

Contact details for questions arising after acceptance of an article, especially those relating to proofs, are provided when an article is accepted for publication.



North-Holland, an imprint of Elsevier Science